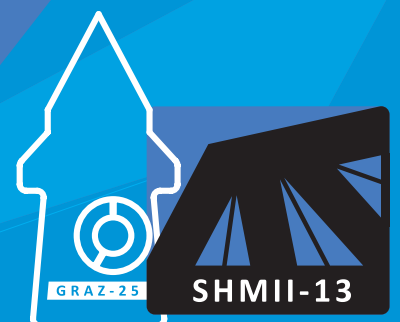




# 13<sup>th</sup> International Conference on Structural Health Monitoring of Intelligent Infrastructure SHMII-13

September 1-5, 2025 | Graz, Austria  
Organized by Graz University of Technology

Edited by:  
Prof. Dr. Werner Lienhart  
Prof. Dr. Markus Krüger





# Imprint

Editors	Lienhart Werner and Markus Krüger
Cover layout & pictures	IGMS - Institute of Engineering Geodesy and Measurement Systems, Graz University of Technology, Austria

2025 Verlag der Technischen Universität Graz  
[www.tugraz-verlag.at](http://www.tugraz-verlag.at)

ISBN 978-3-99161-057-1  
DOI 10.3217/978-3-99161-057-1



This work is licensed under the Creative Commons Attribution 4.0 International (CC BY 4.0) license.  
<https://creativecommons.org/licenses/by/4.0/deed.en>

This CC license does not apply to the cover, third party material (attributed to other sources) and content noted otherwise.

Dear colleagues,

It is with great respect and appreciation that we present the proceedings of the 13th International Conference on Structural Health Monitoring of Intelligent Infrastructure (SHMII-13), organized under the auspices of the Society for Civil Structural Health Monitoring (SCSHM, formerly ISHMII). This conference served as a dynamic forum for scientists, engineers, industry leaders, researchers, public sector experts, infrastructure owners, and representatives of technical associations from around the world to engage in meaningful exchange and collaboration.

Hosted by Graz University of Technology in Austria, the five-day event brought together a vibrant international community to share recent advances in the field of structural health monitoring (SHM). More than 200 contributions were presented across over 30 sessions, highlighting cutting-edge developments in smart sensing technologies, sensor networks, data processing and management, diagnostics and prognostics, and life-cycle performance evaluation. The scope of discussions spanned a wide range of civil infrastructure, including bridges, dams, tunnels, retaining walls, road and rail networks, high-rise buildings, and more.

These proceedings contain the extended abstracts and full papers presented at the conference. We sincerely thank all authors for their valuable contributions and the scientific committee for their commitment to a thorough and thoughtful double-review process.

We also extend our heartfelt gratitude to everyone who contributed to the successful organization of SHMII-13. This includes the local organizing team, student volunteers, technical staff, supporting institutions, and sponsors, whose dedication, professionalism, and hard work were essential to making this event a success. Their behind-the-scenes efforts ensured a smooth and enriching experience for all participants.

We hope these proceedings will serve as a lasting resource and inspiration for future research, innovation, and international collaboration in the field of SHM.

With kind regards,



Werner Lienhart & Markus Krüger

Chairs of the SHMII-13 Conference

# Table of Contents

<b>Keynotes</b>	<b>1</b>
Digitalizing Infrastructure: Advancing Structural Health Monitoring for Smarter Asset Management	2
SHM for bridges – the work flow	3
Bridge in service structural monitoring: the SCSHM benchmark	4
Distributed fiber optic sensing in civil structural health monitoring at the next level – Realization of a comprehensive sensing network along the Brenner Base Tunnel	5
Distributed fiber optic sensing in civil structural health monitoring at the next level – Realization of a comprehensive sensing network along the Brenner Base Tunnel	6
Stevenson Creek Experimental Dam Monitoring Centenary: Overview and Perspectives of Strain Sensing and Strain-Based Monitoring of Civil Structures	10
The Power of Optical and SAR Imaging for Remote Monitoring of Land and Infrastructure	11
<b>Session 1: Field Applications of SHM to extend the Lifespan of Railway Bridges</b>	<b>12</b>
Monitoring of fatigue crack propagation by means of distributed fiber optic sensing	13
Updating prediction of fatigue reliability index of railway bridges using structural monitoring data and updated load histories	23
Monitoring of wind induced vibration on a tied-arch railway bridge	31
Acoustic emission monitoring of fatigue cracks for railway steel bridge inspection	36
<b>Session 2: Geophysical Monitoring of Infrastructure</b>	<b>42</b>
Rail track subsurface imaging from train vibrations recorded at dark fiber networks	43
Monitoring of Concrete Infrastructure with Active Ultrasound Coda Wave Interferometry	45
Finite element mesh construction for seismic analysis using drone imagery	52
A review of methods and challenges for monitoring of differential settlement in railway transition zones	57
<b>Session 3: SHM in the frame of a Digital Twin in Civil Engineering</b>	<b>67</b>
Advanced Structural Health Monitoring and Predictive Maintenance of the Parchi Viaduct Using Distributed Fiber Optic Sensors and Digital Twin Technology	68
A digital twin based integrated sustainability and quality assurance concept for subway constructions	78
Evolving reliability-based condition indicators for structural health monitoring into a digital twin of a cable-stayed bridge	80
<b>Session 4: Structural Health Monitoring of Intelligent Civil Infrastructure using Fibre Optic Sensing</b>	<b>91</b>
Advancements in Distributed Fiber-Optic Sensing: Comparing Brillouin and Rayleigh Technologies for Geotechnical and Structural Monitoring	92
Hybrid monitoring systems: synergising distributed fibre optic sensing with spot measurements	99
Water distribution pipeline anomaly detection using distributed acoustic sensing (DAS)	108
Integrating Distributed Acoustic Sensing for Damage Detection in Old Pre-Stressed Concrete Girders: Preliminary Experimental Results	118
Structural performance monitoring for concrete girder bridges with distributed fiber optic sensors	124
AI-Driven Smart-Liner System with DFOS for Digital Twin-Based Real-Time Monitoring of Oil and Gas Infrastructure	132
Middle range, rapid strain sensing based on PNC-OFDR and its application to bridge monitoring	140



Advanced Structural Monitoring and Predictive Maintenance for Railway Bridges Using Distributed Fiber-Optic Sensors	144
Structural health monitoring in underground mining using fiber-optic sensing and 3D laser scanning for digital twin development	151
Fibradike sensor: validation through full-scale field testing	160
Identification and quantification of concrete cracks using various distributed fiber optic sensing techniques	167
DFOS-Based Monitoring of Prestressed Concrete Bridge Girders	170
Proposed approach for direct rail state monitoring with distributed acoustic sensing DAS	178
Monitoring Timber Structures with Fiber Optic Sensors: State of the Art and Application to a Timber Beam	188
Pi-bracket fatigue sensor for crack detection monitoring near stiffeners in bridge girders	194
<b>Session 5: Implementing Structural Monitoring in Daily Practice: Challenges and Solutions</b>	<b>202</b>
Monitoring of civil engineering structures - current and future use cases	203
A Structural Health Monitoring Framework For Intelligent and Sustainable Infrastructure: A Conceptual Perspective	209
Best Practices for Data Acquisition System Design: Practical Wisdom for Engineers and Practitioners	217
From Insight to Action: Deploying SHM for a suspension bridge	223
Use of Monitoring for Highway Bridges on Federal Highways in Germany – Current Status and Future Development	230
Study on the suitable sensor locations for tilt monitoring of power transmission tower	237
On potentials and challenges of physics-informed structural health monitoring for civil engineering structures	245
Retrofitting load measurement devices on existing anchored structures	252
Reliability Assessment of Structural Health Monitoring Systems using Model – Assisted Probability of Detection and Bayesian Model Updating	259
Advanced Monitoring Systems for Infrastructures: Integrating 6D Sensors and Low-Cost High-Precision GNSS	267
<b>Session 6: Engineering Applications of Artificial Intelligence for SHM</b>	<b>276</b>
Structural damage detection, localization, and quantification for high-rise buildings under earthquake excitations based on machine learning and sub-structuring approach	277
Machine Learning-Based Data Interpretation and Visualization for Tunnel Monitoring: A Case Study of Changshui Airport Tunnel	284
Developing physics-informed neural networks for structural parameters identification of beam with moving loads	295
Structural Health Monitoring of a suspended steel infrastructure: A statistical approach	304
Is it possible that AI can help us detect all damage in structural assets? A discussion on the scope of applicability of DL methods for diagnosis of the construction asset's technical condition	311
<b>Session 7: Computer Vision-based SHM</b>	<b>314</b>
Perspectives on vision-based bridge vibrational monitoring by drones	315
Universal unsupervised image segmentation model of multi-type component and damage for vision-based autonomous UAV inspection of bridges	322
Large-Scale Structural Anomaly Detection During Seismic Events Using Optical Flow and Transfer Learning from Video Data	329
Development of a Wireless Stereo Vision System for 3D Displacement Online Long-Term Monitoring of Tall Structures	332
Overview and Challenges of Computer Vision-Based Visual Inspection for the Assessment of Bridge Defects	336
Integrating Mixed Reality Technology, Deep Learning and Domain Knowledge for bridge inspection	345
3D projection of AI-derived concrete cracks on a Hydro Dam outlet tower	355



Computer vision-based recognition of random traffic flow for live load performance analysis of existing bridges	357
A novel approach to bridge repair using photogrammetry and additive manufacturing	359
Machine Vision-Based Super-Resolution Reconstruction for High-Precision Displacement Monitoring of Hydraulic Structures	363

## **Session 8: Advanced Geospatial and Engineering Surveying Solutions for Infrastructure Health Monitoring** **373**

Monitoring Slow and Dynamic Deformations of High-Rise Buildings Using Low-Cost GNSS Receivers	374
Potential of profile laser scanning (PLS) for the application in load tests	383
Advanced Infrastructure Health Monitoring with Multi-Sensor Systems and Geospatial Technologies	391
LiDAR for vibration monitoring of infrastructure: stretching limits by spatio-temporal time domain frequency analysis	399
Application of LiDAR technology in geodetic monitoring of reclaimed landfills	403

## **Session 9: International SHM Standards and Guidelines** **410**

Global Perspectives on Structural Monitoring in Civil Engineering	411
Structural health monitoring guidelines for road bridges in Germany	420
Structural Health Monitoring in the Italian Guidelines for Bridges	428
ANYTWIN - Characterization and standardization of monitoring data	431
Inspection as a basis for structural health monitoring	441

## **Session 10: Advanced Filtering in Structural Dynamics** **449**

Dynamic Monitoring using Hidden Markov Regression Model for Predicting Remaining Useful Life	450
Identification of Damping Coefficients of Multi-degree of Freedom System	457
Integrated Motion Measurement – a Tool for Structural Health Monitoring?	463
Solving structural dynamics with uncertainty quantification via evidential neural operators	473
Nonparametric identification of structural nonlinear behavior based on extended Kalman particle filter and Chebyshev polynomial model	479

## **Session 11: Fibre Optic Sensing in Field Applications** **487**

Insights into Rail Track Buckling from Distributed Fibre Optic Sensing Data	488
Distributed Acoustic Sensing for Civil and Geotechnical Infrastructure Monitoring Applications	496
DFOS solutions covering full monitoring needs of an enlarged concrete deck viaduct	501
Experimental study on two tunnel micro-leakage monitoring methods based on distributed fiber optic sensing technology	508

## **Session 12: Point Cloud Data Applications to evaluate Structural Conditions and Performances** **514**

A PC based FE model as an innovative learning tool in structural mechanics	515
RTK-Enabled UAV for Structural Health Monitoring Without GCPs	518
Advanced and Efficient Monorail Facility Inspections Using Optical Measurement Technologies, Including Laser and Imaging	520
Application Method of SfM/MVS Technique Combined with Point Cloud Data for Inspection of Steel Bridges	529
Re-meshing Method for Finite Element Model Updating based on Extracting Structural Anomalous Information from Point Cloud Data	538
Synthetic environment for close-range photogrammetry-based surface friction assessment of road infrastructures	540
Developing a Deep Learning-Based Method to Segment Bridge Members by using 2D Cross Sectional Point Clouds	550
A 3D Virtual Assembly Method for Cable-Stayed Bridge Closure Using Laser Scanning	558



Short- and long-term monitoring of bridges using terrestrial laser scanning data	562
--	-----

### **Session 13: Non-destructive Test Methods used for Inspection and Damage Assessment of Concrete Structures** **568**

External Magnetization based Elasto-Magnetic Sensing Technique for Tension Monitoring of Aged PSC Structures	569
Development of SFCW Radar System for Concrete Structure Inspection	571
A Novel System Identification-Based Method for Rebar Radius Estimation in Radar SAR-Based Non-Destructive Testing	577
Non-contact non-destructive monitoring of concrete structures using pulsed Laser and microphones	581

### **Session 14: Smart Sensing and Artificial Intelligence for Advanced Civil Infrastructure Monitoring and Management** **588**

AI-Powered vehicle classification for scalable infrastructure monitoring	589
Structural condition monitoring through information transferring with dimensional expansion	595
Unsupervised Anomaly Detection for Structural Health Monitoring: A Vibration-Based Approach Using Isolation Forest	597
Deep generative models to mitigate data scarcity in bridge structural health monitoring	604
Smart adaptive triggering strategy for edge intelligence enabled energy-efficient sensing	609

### **Session 15: Fibre Optic Sensing for Damage Detection at Bridge Structures** **617**

Post-tensioned wire breaks detection method using distributed acoustic sensing in bridges & viaducts	618
Detection of steel fractures in existing prestressed bridges with DFOS	628
Distributed fiber optic sensing of bridges with stress corrosion cracking	631
Lifetime elongation of existing prestressed bridges with a lack of structural integrity using DFOS	641
Concrete signature in long-term Distributed Fiber Optic Strain Sensing: Challenges and opportunities for Structural Health Monitoring	644

### **Session 16: Smart Integrated Sensors and Wireless Sensors (IoT)** **651**

Integrated Sensor Technology for Basalt-Reinforced Segmental Lining Elements	652
Wind Input and Acceleration & Displacement Outputs Monitoring System for High-Guyed Masts in ROSEHIPS Project	661
Wireless Multisensor Monitoring of Engineering Structures	664
Practical approach to calibrating wireless sensors for use in structural health monitoring in an outdoor environment	672
eNodes: GNSS Time-Synchronised Wireless Acceleration Measurement Nodes capable of operating indoors	682

### **Session 17: Smart Sensing Enhanced Resilient Civil Infrastructures** **685**

Study on the Propagation Law of Magnetic Induction Signals for Wireless Communication in Underground Structures	686
Smart Pavement Subsurface Monitoring with Distributed Embedded Passive RF Sensor Network	690
A Wireless Passive RFID Patch Antenna Strain Sensor	693
25-year Field Monitoring of the Tsing Ma Suspension Bridge in Hong Kong	697

### **Session 18: FBG and DFOS Applications for Infrastructure and Environmental Monitoring** **699**

Towards Accurate Road Health Monitoring: A Damage Detection System Using FBG Sensors	700
Etched fiber bragg grating sensor-based groundwater salinity monitoring for seawater intrusion	709
Geo-hazard DFOS Monitoring and its Applications	713
Structural Behaviors of Prestressed Double-T Slab under Loadings with Seasonal Effects	718
Vibration Analysis of Ship Hulls using Fiber Bragg Grating	722





<b>Session 19: Risk Assessment and Monitoring of Civil Structures</b>	<b>729</b>
Structural monitoring of Zeeland Bridge - improved structural identification by combining a modular model updating framework with a mobile measurement setup during load tests	730
Scotiabank Saddledome Roof Monitoring Program	737
Long-term monitoring and data processing of a continuous prestressed concrete bridge	745
Smart Structural Health Monitoring with Acoustic Emission	755
The Collapse of the Carola Bridge – Forensic Engineering and Palliative Monitoring	762
<b>Session 20: Wind-Loaded Structures and Monitoring under Environmental Conditions</b>	<b>768</b>
Understanding the Dynamic Behavior of Large Sign Structures Under Wind Loading	769
6-Component Operational Modal Analysis of wind turbines for damage detection	772
Estimation of Wind Turbine Foundation Settlement and Error Modeling Using High-Resolution Dual-Orbit Satellite Data	776
Distributed fibre optic sensing of decommissioned wind turbine blades under bending	786
Prediction of urban wind speed during tropical cyclones using a novel deep learning-based spatiotemporal model	792
<b>Session 21: Intelligent Sensing and Safety Assessment of Bridge Cluster Service Performance</b>	<b>799</b>
Graph network representation and intelligent evaluation for service performance of bridge clusters	800
Lightweight vision fundamental model-based structural surface crack segmentation using model distillation	803
Spatial-Temporal Graph Model for Environmental Temperature and Traffic Flow Prediction of City Regions	811
Ultimate flexural strength analysis of serving concrete main girders considering bridge deck pavement	817
<b>Session 22: Structural Health Monitoring of Transport Infrastructures using Drive-by Monitoring</b>	<b>822</b>
Data-Driven Monitoring Solutions for Concrete Structures: Long-Term Insights with CorroDec2G Sensors	823
Numerical dataset for benchmarking of drive-by bridge monitoring methods	831
Indirect footbridge damage classification using explainable deep learning: A field-testing study	834
Drive-by bridge modal identification under multi-source excitations	839
Field test on tunnel indirect damage identification from moving train response	842
<b>Session 23: Population Based Structural Health Monitoring (PBSHM)</b>	<b>848</b>
A methodology for data collection and aggregation in population-based structural health monitoring ecosystems	849
Towards a plug and play population-based structural health monitoring aggregation pipeline design for resource constrained systems	856
Advancing PEAR: Development of a Bridge Benchmark Datasets for PBSHM Research	864
A Transfer Learning approach for damage identification in operational viaducts	873
The future of conservation: Citizen Science models for the Photomonitoring of cultural heritage	882
Correlation of natural frequencies of bridges that are under similar environmental conditions	891
A Novel AI-Wavelet Based Framework for Benchmark Data Analysis in Structural Health Monitoring	898
<b>Session 24: Advancements in Vibration-Based Bridge Health Monitoring</b>	<b>905</b>
Preliminary results from a field application of dynamic monitoring on three spans of a railway bridge	906
A damage screening method of the concrete slab focusing on correlation of mode shapes	914
Feasibility of micro-motion from SAR imagery for vibration-based SHM	920
Setting an optimal threshold for novelty detection in data-driven Structural Health Monitoring	928
A Comprehensive Approach for Vision-Based Dynamic Monitoring of Structures and Infrastructure	936
Model Updating and Damage Detection for Bridge Integrity Management	944



On a data compression technique for acceleration signals from a railway bridge	951
--	-----

## **Session 25: Materials-Based Monitoring and Structural Health Assessment 960**

Intelligent Imaging: Transforming Concrete Health Assessment with AI	961
Monitoring of Non-Linearities in Fatigue Degradation of Metallic Materials Using Techniques beyond Stress and Strain	971
Towards structural health monitoring of clay-printed structures	979
Icelandic turf houses: A one-year monitoring overview	987
Gas permeability under varying laboratory conditions	995
Detailed material testing of adobe structures to complete a comprehensive SHM approach that includes laser scanning and ambient vibration studies	1000
Redundant Monitoring Strategies for Structural and Geohazard Assessment Using Wireless Tiltmeters and LiDAR on Linked Highway Bridges in Colombia	1008

## **Session 26: Bridge Model Calibration and Validation Using Structural Health Monitoring Data 1016**

Optimizing Bridge Recalculation: Uncertainty in SHM-Based Recalculation of Prestressed Concrete Bridges	1017
Hangar Stressing on the 6th Street Viaduct Replacement, Los Angeles, CA	1026
SHM Application in Development of New Live Load Distribution Factors for Timber Bridges	1032
Full-Scale Bridge Testing: Lessons from the Demolition of the Steinavötn Bridge	1041
Advancing high-fidelity Digital Twin Technology for Structural Health Monitoring	1049
Advancing High Fidelity Finite Element Model Updating Using Cooperative Game Theory: A Novel Framework for Structural Optimization	1057
Efficacy of decoupling techniques to extract the static strain response from the dynamic response of a bridge under a moving vehicle using low pass filter	1064
Laboratory Testing of Old Bridge Girders: Preliminary Results	1073
Investigation of the causes of the unusual gap between the bridge and abutment using long-term monitoring	1077
Monitoring the dynamic sensitivity of the Solkan footbridge to user-induced excitation	1083

## **Session 27: Monitoring applications using InSAR 1088**

InSAR as a Component of Geotechnical Monitoring During Subway Construction in Prague	1089
Utilizing PSDefoPAT™ to analyze surface deformation of embankment dams	1094
Exploring InSAR Capabilities for Bridge structural health monitoring using TerraSAR-X and Sentinel-1 Data	1101
Satellite-based InSAR for monitoring and safeguarding high-voltage power pylons amid the energy transition	1108
Remote Sensing for Stability Assessment of River Bridges: Case Study of the Red River Bridge in Winnipeg, Canada	1112
Potential of InSAR for Structural Health Monitoring of Flood Protection Systems	1120
ISABEL (Integrated SATellite and ground-based monitoring for Bridge HHealth Lifetime assessment)	1130
SGAM – Smart Geotechnical Asset Management: Enhancing predictive maintenance with data-driven insights and Earth Observation technologies	1140

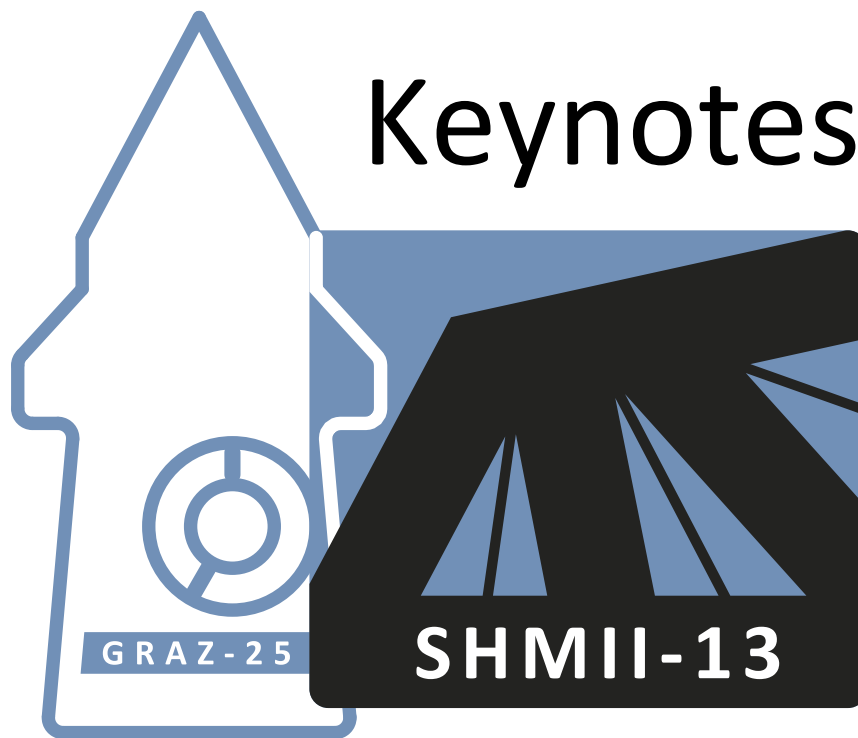
## **Session 28: Smart Embedded Sensors and Non-destructive Test Methods for Quality Control 1143**

An EMI-based approach for Structural Health Monitoring of a Space Reinforced Concrete Frame Structure	1144
Tactile Pressure Sensors to analyse Anchor Wall Behaviour in mid-scale Experiments	1151
Long term monitoring of the Balladelaan bridge using Smart Aggregates	1158
Structural Health Monitoring of Composite Plate using Piezoelectric Transducer	1165



<b>Session 29: Hazard, Disaster and Damage Detection for Infrastructure</b>	<b>1168</b>
Study on Methods for Identifying and Evaluating Damage to Cross-Sea Bridges Subjected to Ship Collisions	1169
An automatic system for the rapid post-earthquake safety assessment of bridges	1176
Bridge superstructure vibrational analysis as means to detect scour in a medium span bridge	1183
2D sonar techniques for monitoring the canal bed morphology of entrances to navigation locks	1189
<b>Session 30: SHM of Tendons and Pipelines</b>	<b>1199</b>
On-Line Health Monitoring of Underground Pipelines by Source Localization of Leak Damages	1200
Effects of grout-strand interface modelling on the degradation of external grouted post-tensioning tendons	1203
Autonomous peak-picking procedure for tension force estimation in cables and external post-tensioning tendons	1210
Field monitoring and mitigation for high-mode vortex-induced vibrations of cables in cable-stayed bridges	1218
Field Application of TFC-based Electromagnetic Sensors for Monitoring Cross-sectional Loss in Tendons of Bridges	1225
<b>Session 31: System-level SHM and Emerging Technologies</b>	<b>1230</b>
Exploration of edge computing for monitoring a four-story building frame model	1231
On the use of 6C seismic station for bending-to-shear and torsional building response assessment	1239
Integration of Seismic Interferometry and System Identification Techniques for Real-Time Structural Health Monitoring: Automated Detection of Shear-Wave Velocity Changes Using Skyscraper Data for Validation	1241
Experimental assessment of GNSS-smartphone performance in monitoring dynamic motion	1247
Identification of Structural Dynamic Loads- From Physical Methods to Physics Informed Deep Learning Paradigm	1255
<b>Session 32: The SCSHM Benchmark bridge: first studies and results</b>	<b>1258</b>
Multi-purpose bridge strain data fusion for BWIM and structural monitoring	1259
Vehicle Speed estimation using convoluted reciprocity for bridge structural monitoring	1261
Physics-Informed Surrogate Modeling of the SCSHM Benchmark	1267
Vibrational analysis of the benchmark data set	1270
<b>Session 33: SHM of Tall and Historic Buildings</b>	<b>1275</b>
Study of Semi-Rigid Joints Effect on Global Stiffness of Space Steel Structure Based on Monitoring Data	1276
Sustaining vertical giants: Autonomous monitoring solutions for the construction and lifecycle of tall buildings	1282
Multi-scale digital twin for a high-rise structure combining ANN and monitoring data	1286
Assessment method for torsional performance of high-rise buildings based on period ratio	1294
<b>Session 34: Implementation and Digitalization in SHM</b>	<b>1301</b>
Digitalization of existing measurement equipment as a valid basis for monitoring and structural behaviour	1302
Increasing the value of bridge SHM data by leveraging network-level open data	1308
A comprehensive workflow for digitizing and determining condition indicators for bridge and building construction	1318
Principles and Case Study of IMSGeo: Automatic Displacement Monitoring System for Construction Sites	1326





# **Digitalizing Infrastructure:**

## **Advancing Structural Health Monitoring for Smarter Asset Management**

Sylvia Keßler<sup>1</sup>

<sup>1</sup>Helmut Schmidt University/University of the Federal Armed Forces, Hamburg, Germany  
email: sylvia.kessler@hsu-hh.de

### **ABSTRACT:**

Our transportation infrastructure faces increasing demands, driven by larger and heavier trucks that place growing stress on bridges with ever-higher frequency. At the same time, much of this infrastructure is aging, with many structures having reached or exceeded their intended service lives and operating near their capacity limits. Addressing these challenges requires innovative tools and approaches to monitor, evaluate, and maintain infrastructure assets effectively.

Structural Health Monitoring (SHM) offers a transformative solution by enabling continuous, sensor-based condition assessment. SHM systems can track changes in structural behavior, detect damages, and provide valuable data for condition evaluation and prediction. However, to fully realize the potential of SHM, the integration of sensor data into a seamless digital process chain—built on Building Information Modeling (BIM)—is essential. This linkage ensures that data is not only collected but also analyzed and utilized in a way that is directly connected to the structure's digital twin.

Within the DTEC-SHM project, we equipped two bridges with over 400 sensors to enable comprehensive monitoring. These included conventional sensors for measuring accelerations, inclinations, and temperatures, as well as weather stations for capturing environmental conditions. Additionally, innovative sensors were deployed for durability monitoring and axle load measurement through Bridge Weigh-In-Motion (B-WIM) technology. To complement the sensor network, a detailed finite element (FE) model was developed and calibrated using monitoring data and load testing results, enabling a deeper understanding of the bridges' structural behavior.

Now, we focus on advancing SHM applications by developing a predictive maintenance management system based on Key Performance Indicators (KPIs). This will allow for proactive and efficient maintenance planning. Furthermore, the digital twin of bridges will be refined and tested to enhance its integration with SHM systems. In addition, by prioritizing the preservation of infrastructure over new construction, the project promotes significantly more sustainable practices in infrastructure management.

For asset owners, SHM provides critical insights into the health of their structures, enabling informed decision-making to prioritize repairs, optimize maintenance schedules, and allocate resources efficiently. By leveraging SHM and digital twin technologies, asset owners can transition from reactive to predictive maintenance, enhance safety, and ensure the long-term sustainability of infrastructure. This keynote will explore these innovations, emphasizing what asset owners need to harness the full potential of SHM in addressing today's infrastructure challenges. In addition, the keynote provides an overview about the datasets collected through the DTEC-SHM project, which we are committed to sharing with the broader research and engineering community to foster collaboration and innovation.



## SHM for bridges – the work flow

Christian Sodeikat <sup>1</sup>

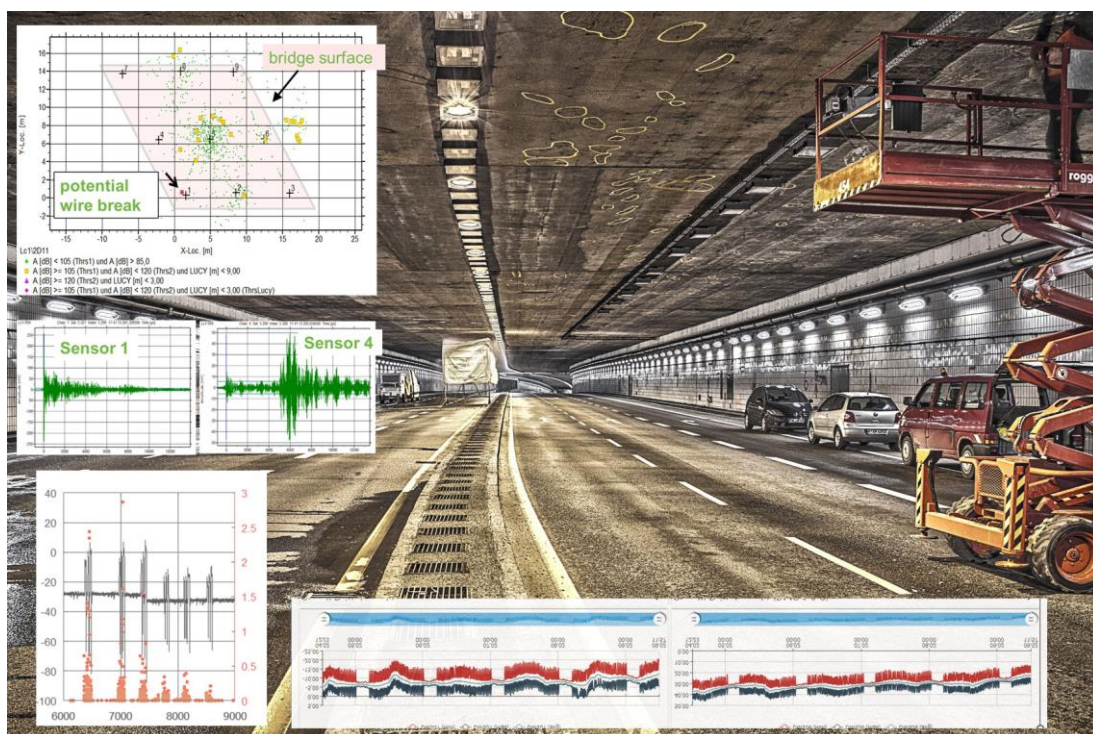
<sup>1</sup> Ingenieurbüro Schiessl Gehlen Sodeikat GmbH, Munich, Germany  
email: sodeikat@ib-schiessl.de

### ABSTRACT:

Numerous bridges in Germany and worldwide are subject to high stress from increased heavy traffic and their advanced age. Due to advanced damage and unfavourable construction methods, many bridges can no longer be repaired at a reasonable cost and must be replaced with new structures. However, to maintain traffic flow, they often need to remain in operation for years and be monitored in real-time for deterioration to ensure safe continued use. Complex measurement systems are now available for this purpose, capable of detecting various structural conditions, such as strain, or events, such as acoustic emissions from wire breaks of the prestressed reinforcement.

The planning of a monitoring system should proceed in a stage manner. The first step involves identifying the structural weaknesses and potential damage mechanisms of the structure, such as wire breaks, crack formation of the cross-section or reinforcement corrosion etc. Based on this, the structural responses resulting from the damage mechanisms are determined. In the final planning step, the measurement systems suitable for measuring the structural responses are selected.

This keynote presents the workflow for planning a monitoring system and provides examples of the implementation, visualization and evaluation of various measurement systems and measurement data in a common monitoring system.





## Bridge in service structural monitoring: the SCSHM benchmark

Maria Pina Limongelli<sup>1</sup>

<sup>1</sup> Politecnico di Milano, Italy

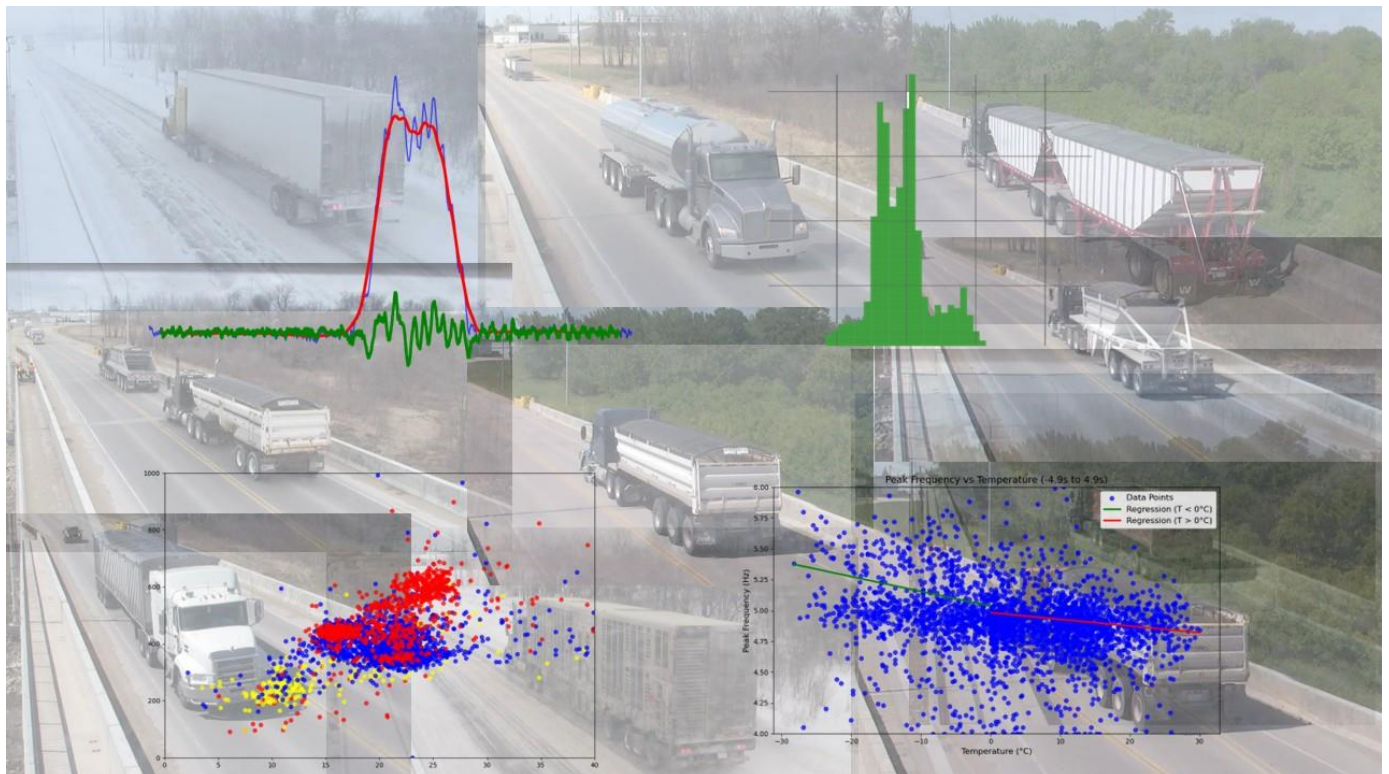
email: mariagiuseppina.limongelli@polimi.it

### ABSTRACT:

In 2023, the Data-Enhanced Infrastructures Management Committee of the Society of Civil Structural Health Monitoring (SCSHM) launched a benchmark study on in-service structural monitoring of bridges. A comprehensive dataset, developed in collaboration with the University of Manitoba, was made available to the engineering community to promote the validation and comparison of methods for structural performance evaluation.

The benchmark structure is a span of a multi-supported bridge with a total length of 291 meters. A monitoring system was installed on the structure and operated for approximately nine months. The instrumentation included strain gauges and thermocouples to record strain measurements and air/structure temperatures beneath the deck.

This presentation outlines the details of the structure, the objectives of the study, the dataset shared with the engineering community, and reports some initial applications that leverage the dataset to validate in-service monitoring approaches.



## Distributed fiber optic sensing in civil structural health monitoring at the next level – Realization of a comprehensive sensing network along the Brenner Base Tunnel

Christoph Monsberger <sup>1</sup>

<sup>1</sup>ACI Monitoring GmbH, Merangasse 73/3, 8010 Graz, Austria, Europe

### ABSTRACT:

The Brenner Base Tunnel (BBT) is one of the key civil infrastructure projects currently under construction world-wide and will be the longest underground railway connection globally with a total length of about 64 km once completed. Its service lifetime of 200 years implies essential requirements on the tunnel design, with focus on reducing risks and enabling optimized maintenance works based on appropriate monitoring. The tunnel owner BBT SE has therefore initiated an enhanced distributed fiber optic sensing (DFOS) network inside concrete tunnel lining segments for structural monitoring without human access. This contribution introduces the designed DFOS network, consisting of more than 35 km sensing cable along numerous tunnel cross-sections, spread over more than 30 km tunnel drive and two different construction lots.



# Distributed fiber optic sensing in civil structural health monitoring at the next level – Realization of a comprehensive sensing network along the Brenner Base Tunnel

Christoph M. Monsberger<sup>1</sup>, [ORCID No 0000-0003-0937-014X], Fabian Buchmayer<sup>1</sup>, [ORCID No 0009-0009-1722-0740],  
Madeleine Winkler<sup>1</sup>, Tobias Cordes<sup>2</sup>, [ORCID No 0000-0001-6765-2044]

<sup>1</sup> ACI Monitoring GmbH, Merangasse 73/3, 8010 Graz, Austria, Europe

<sup>2</sup> Brenner Base Tunnel BBT SE, Amraser Str. 8, 6020 Innsbruck, Austria, Europe

email: christoph.monsberger@aci-monitoring.at, fabian.buchmayer@aci-monitoring.at, madeleine.winkler@aci-monitoring.at,  
tobias.cordes@bbt-se.com

**ABSTRACT:** The Brenner Base Tunnel (BBT) is one of the key infrastructure projects currently under construction and will be one of the longest underground railway connection with a total length of approximately 64 km once completed. Its service life of 200 years implies essential requirements on the tunnel design. One important focus is to increase the availability of the tunnel, e.g. by enabling optimized maintenance work based on appropriate monitoring. The tunnel owner BBT SE has therefore initiated an enhanced Distributed Fiber Optic Sensing (DFOS) network inside the segmental lining for structural health monitoring without human access. The technology has significantly evolved in recent years to monitor large scale infrastructure, especially for in-situ tunnel monitoring as the distributed sensing feature can provide a complete picture of the strain distribution without blind spots. This contribution introduces the designed DFOS network, consisting of more than 35 km sensing cable along numerous tunnel cross-sections, spread over more than 30 km tunnel drive and two different construction lots. The monitoring data is autonomously evaluated and transferred to the online dashboard in real time. Analysis of the strain distribution provides fundamental information about the actual loading state of the segmental lining. The results together with experiences gained from practical implementations demonstrate the technology's high potential for innovative civil structural health monitoring.

**KEY WORDS:** Distributed fiber optic sensing; segmental tunnel lining; structural integrity monitoring; deformation behavior; strain distribution

## 1 PROJECT CHARACTERISTICS AND MONITORING OBJECTIVES

The Brenner Base Tunnel (BBT), a flat rail link with high transport capacity, will connect the Tulfes portal (near Innsbruck, Austria) with the Franzensfeste portal (Italy) over a total length of approximately 64 km in the near future. The cross-alpine rail link is a key project of the 9,121 km long TEN-T Scan-Med (Scandinavian-Mediterranean) corridor and cuts the alpine crest in the base, with high overburdens of up to 1,720 m. It consists of two single-track railroad tunnels with a diameter of 8.1 m, spaced 70 m apart and accompanied by a continuous exploratory tunnel running 12 m below in-between (Figure 1). The exploratory tunnel improves the geological forecast for the rail tunnels, which are partially being advanced by tunnel boring machines afterwards.

Availability plays a decisive role for key infrastructures such as long cross-alpine rail tunnels. The tunnel design includes increased partial safety factors and concrete cover to reach a 200-year service life. Maintenance should be possible without interruption of the operation as far as technically feasible. Tunnel equipment has therefore been shifted to accessible areas or high-maintenance installation areas became accessible by horizontal shafts from the accompanying exploration tunnel.

In addition, the BBT-SE has incorporated an enhanced strategy for structural health monitoring (SHM) during construction and operation using Distributed Fiber Optic Sensing (DFOS). The technology is beneficial compared to conventional techniques as the fiber optic sensing cable can be directly embedded inside the structure to enable distributed strain (and temperature) assessment along hundreds of sensing points. The measurement results can be well compared to

traditionally used vibrating wire sensors [1], but also allow an overall assessment of the strain and temperature without blind spots. The sensing unit itself may be placed even kilometers away from the measurement location, even outside of the tunnel and monitoring is possible without any interference with construction works or later operation. The sensor's durability and insensitivity against electromagnetic interferences are essential with respect to the use in rail operation.

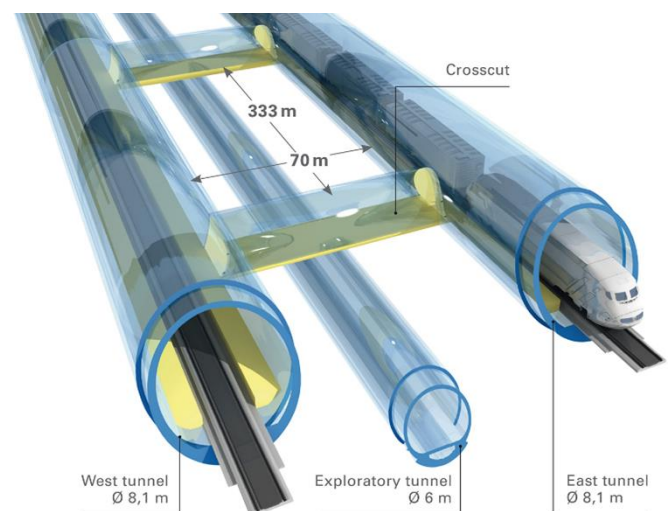


Figure 1. Schematic representation of the typical tunnel cross-sections at Brenner Base Tunnel project (based on [2])



The DFOS implementation at the BBT focusses on structural health monitoring of the segmental lining, with the aim of optimizing maintenance works by monitoring during operation [3].

Machine-driven tunnel structures within the BBT are constructed efficiently as single shells. Various monitoring approaches have been initiated during construction including chord length measurements, geodetic displacement readings of discrete targets using total stations, laser scanning and fiber optic sensors in defined cross-sections. While the first three are used for accompanying the construction process. The DFOS measurement ring is installed only at structural cross sections of interest like the intersection of rail tunnel and cross-passage as well as in fault zones. The deep-lying machine-driven tunnel and the high stiffness of the segmental lining require a load monitoring with high accuracy. The DFOS strain sensing feature is deployed to analyze the loading condition at dedicated locations inside the segmental lining. Hence, decisions can be made based on these results by choosing the appropriate pre-designed supporting measure for the openings of the cross passages. Additionally, supporting measures like secondary linings are placed according to the load bearing capacity of the existing lining.

The DFOS approach is therefore designed to pursue three primary monitoring objectives:

- 1) **Construction phase monitoring:** Verification of segmental ring openings and cross-passage advancements.
- 2) **Load-bearing assessment:** Ensuring compliance with structural safety requirements.
- 3) **Operational Structural Health Monitoring:** Enabling long-term monitoring without interrupting rail operations.

## 2 DFOS DESIGN AND MONITORING NETWORK

The instrumentation of concrete tunnel lining segments can be performed outside of the tunnel apart from excavation. This procedure is advantageous in terms of installation as the sensing cables can be reliably attached without time-consuming and cost-intensive inferences with the excavation works, which have not to be interrupted due to the sensor installation.

For more information about the implemented DFOS sensing cables for strain and temperature monitoring as well as the sensor installation inside the individual tunnel lining segments, reference is given to [4].

Inside the tunnel, the fiber optic monitoring segments are built as a normal ring without restrictions after the excavation has been performed. Once the ring is set, the connection boxes for each segment can be opened and the individual segments can be connected to establish a continuous monitoring loop. Supply cables are used to connect the fiber optic sensing cables inside the ring to the reading unit, which is placed in a measurement equipment box approx. 150 m to 200 m behind the monitoring cross-section (see Figure 2). This location is advantageous as the space along the TBM's back-up system is limited and the reading unit shall be as accessible as possible during monitoring for potential maintenance. The equipment

box itself is waterproof and does not only contain the reading unit, but also an uninterruptible power supply and an industrial PC with stable internet connection for reliable data transfer. The fiber optic installation works can be usually performed in about 90 to 120 minutes once the ring is constructed. Monitoring is started immediately after the installation, with the monitored segmental lining ring inside the shield, before the TBM continues its further excavation work.

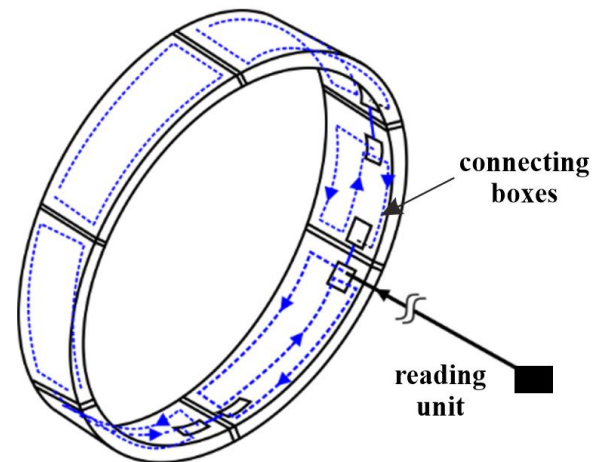


Figure 2. Schematic representation of tunnel installation (based on [5])

The DFOS system's long-term performance and its suitability must be well considered within the network design to provide reliable monitoring over decades. Each individual monitoring cross-section is therefore not only linked to their equipment box behind the TBM, but also connected to a continuous network, which allows monitoring of numerous cross-sections using only one reading unit per tube (Figure 3, top). The so-called active monitoring zone during construction can therefore include up to 7 cross-sections in the actual configuration, excluding additional cross-sections in geological interference zones, where the reading unit is placed in the central equipment box. After the excavation works are completed, the overall system will be adapted for operational monitoring. The DFOS equipment boxes and corresponding connecting cables will be re-located to the maintenance cross-passages (cf. Figure 3, bottom), from where measurements can be performed without interruption during rail operation by accessing from the exploratory tunnel.

## 3 DFOS DESIGN AND MONITORING NETWORK

The installed fiber optic sensing network has been interrogated using the fTB 5020 from fibris Terre Systems GmbH (Germany). Based on the Brillouin Optical Frequency Domain Analysis (BOFDA) technique, this sensing unit enables distributed measurements up to 25 kilometers within several minutes per monitoring channel, a standard spatial resolution of 0.5 m and a strain repeatability of about 2–10  $\mu\text{m/m}$  depending on the sensing fiber [6]. The interrogation unit is placed inside the DFOS equipment boxes, where the raw data is collected and transferred to external databases via FTP gateway.

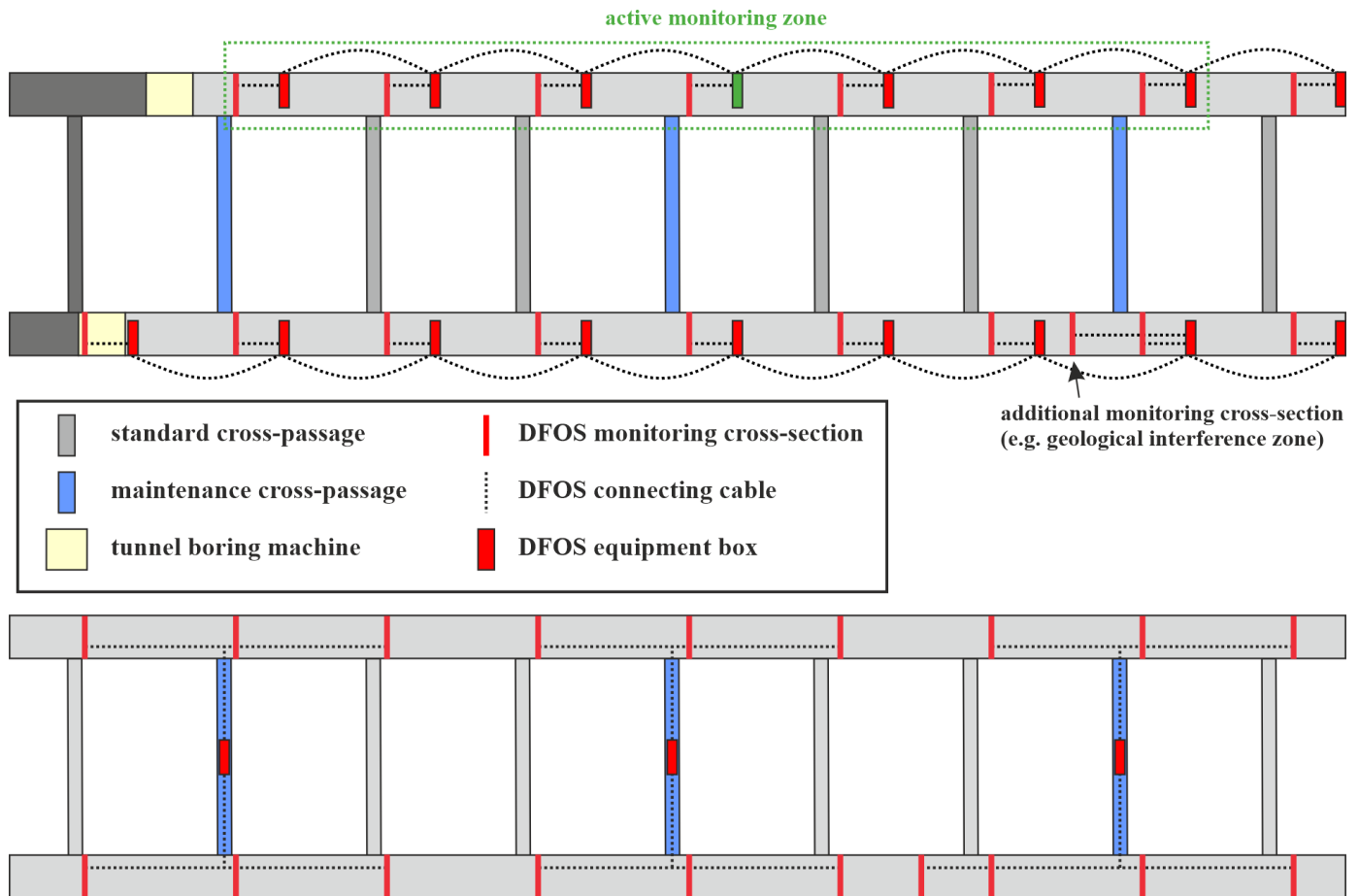


Figure 3. Schematic representation of overall monitoring setup during construction (top) and operation (bottom) [4]

The quality of the conversion from the raw measurement quantity (cf. Brillouin frequency shift) to strain (and temperature) depends on reliability of the sensor characteristics curve, usually not specified by manufacturers in detail. Using standard coefficients might however results in errors of up to several percent, cf. [7] or [8]. Therefore, each sensing cable production batch was calibrated at the unique calibration facilities at Graz University of Technology [9] to derive individual coefficients for cables installed at BBT.

Each DFOS monitoring ring delivers high-resolution strain measurements at three circumferential locations within each tunnel segment (beginning, middle and end), enabling the assessment of its circumferential total strain distribution at different locations within one monitoring ring. In addition to structural related strains, the recorded information along the individual layers includes also creepage, shrinkage and temperature-related strains. Furthermore, stress profiles are calculated from the derived strain profiles at the inner and outer layer based on the experimentally determined stress-strain behavior of the concrete [10]. This enables the integration of the circumferential normal force and bending moment distribution, which are finally compared to the internal forces of the segmental lining design to assess the rock loading conditions.

The monitoring workflow was validated by comparative DFOS measurements from loading tests of real-scale segmental

loading tests [11]. These experimental studies, performed under well-documented loading conditions, depict high correlation between calculated internal forces derived from DFOS measurements and analytical models utilizing traditional load cell data.

#### 4 CONCLUSIONS

The integration of DFOS technology at the BBT demonstrates that distributed fiber optic sensors have significantly developed within recent years and have reached the next level for civil structural health monitoring. Their capability to monitor fully distributed strain and temperature profiles with high measurement repeatability and resolution in real-time, without disrupting tunnel operation, qualify them as an ideal solution for long-term monitoring of relative deformations.

Known practical limitations can be overcome by suitable monitoring design and appropriate installation techniques, which also represent the DFOS technology path from fundamental research into innovative practice. It should be however highlighted that the quality of the monitoring approach is essentially related to its design and installation. It is therefore strongly recommended to include the monitoring design as early as possible into the project planning process, to use suitable, high-quality fiber optic components (i.e. interrogation unit and sensing cable) and to fit the sensor



installation to the construction process and reduce any interruption on-site to a minimum.

The tunnel construction lots at the BBT project were already being tendered with enhanced fiber optic monitoring solutions, aiming to provide an overall assessment of the structural behavior. This especially beneficial with respect to long-term monitoring since arising changes in the structural performance can be detected at an early stage to plan and design predictive maintenance works in due time during the operational lifetime. The DFOS system is designed to provide measurements without any interference with the regular railway operation from the maintenance cross-passages, which can be accessed from the exploratory tunnel. This fact combined with the fiber optic's insensitivity against electromagnetic interferences are essential for reliable sensing over decades.

## DISCLAIMER

This contribution is submitted as an **extended abstract** for the 13th International Conference on Structural Health Monitoring of Intelligent Infrastructure and presents an enhanced project review of the DFOS monitoring system realized at the Brenner Base Tunnel. Figures, texts and contents are therefore already partly or fully published elsewhere.

## ACKNOWLEDGMENTS

We would like to acknowledge the collaborative efforts of all involved project partners, all construction companies, and all engineers on-site.

## AUTHOR CONTRIBUTIONS

**ACI Monitoring GmbH:** Distributed fiber optic sensing system design and execution:

**Brenner Basistunnel BBT-SE:** Structural health monitoring concept

## REFERENCES

- [1] B. Moritz, R. Heissenberger, T. Schachinger and W. Lienhart, Long-term monitoring of railway tunnels, *Geomechanics and Tunneling* 14(1), 35-46, 10.1002/geot.202000049, 2021.
- [2] BBT SE, Europäische Dimension, <https://www.bbt-se.com/tunnel/europaeische-dimension/> (Accessed: May 24, 2025), 2025.
- [3] T. Cordes, K. Mair am Tinkof, C. Crapp and N. Radončić, Geomechanical loading of the segmental linings of the Brenner Base Tunnel, *Geomechanics and Tunneling* 17(1), 52-63, 10.1002/geot.202300053, 2024.
- [4] C. M. Monsberger, F. Buchmayer, M. Winkler and T. Cordes, Implementation of an enhanced fiber optic sensing network for structural integrity monitoring at the Brenner Base Tunnel, *Procedia Structural Integrity* 64, 1665-1672, 10.1016/j.prostr.2024.09.171, 2024.
- [5] W. Lienhart and R. Galler, Tübbingelement mit Dehnungsmessung, Patent AT516158 (B1), 53 p., 2016.
- [6] fibrisTerre Systems GmbH, fTB 5020, Fiber-optic sensing system for distributed strain and temperature monitoring, [https://www.fibristerre.de/file\\_download/15/fTB+5020+-+Product+Brochure.pdf](https://www.fibristerre.de/file_download/15/fTB+5020+-+Product+Brochure.pdf) (Accessed: May 24, 2025), 2019.
- [7] F. Moser, W. Lienhart, H. Woschitz, and H. Schuller, Long-term monitoring of reinforced earth structures using distributed fiber optic sensing, *Journal of Civil Structural Health Monitoring* 6(3), 321-327, 10.1007/s13349-016-0172-9, 2016.
- [8] C. Monsberger, H. Woschitz, W. Lienhart, V. Račanský and M. Hayden, Performance assessment of geotechnical structural elements using distributed fiber optic sensing, *SPIE Smart Structures and NDE*, Portland, USA, 10168Z, 10.1117/12.2256711, 2017.
- [9] H. Woschitz, F. Klug and W. Lienhart, Design and Calibration of a Fiber-Optic Monitoring System for the Determination of Segment Joint

Movements Inside a Hydro Power Dam, *Journal of Lightwave Technology* 33(12), 2652-2657, 10.1109/JLT.2014.2370102, 2015.

- [10] L. Walter, Evaluation of distributed fibre-optic strain measurements using the example of the BBT, Master's thesis, University of Innsbruck, Austria, 2024.
- [11] P. Gehwolf, Tragverhalten von Tübbing im maschinellen Tunnelbau - Experimentelle und numerische Analyse, PhD thesis, Montanuniversität Leoben, Austria, 10.34901/mul.pub.2023.67, 2018.

# Stevenson Creek Experimental Dam Monitoring Centenary: Overview and Perspectives of Strain Sensing and Strain-Based Monitoring of Civil Structures

Branco Glisic<sup>1</sup>

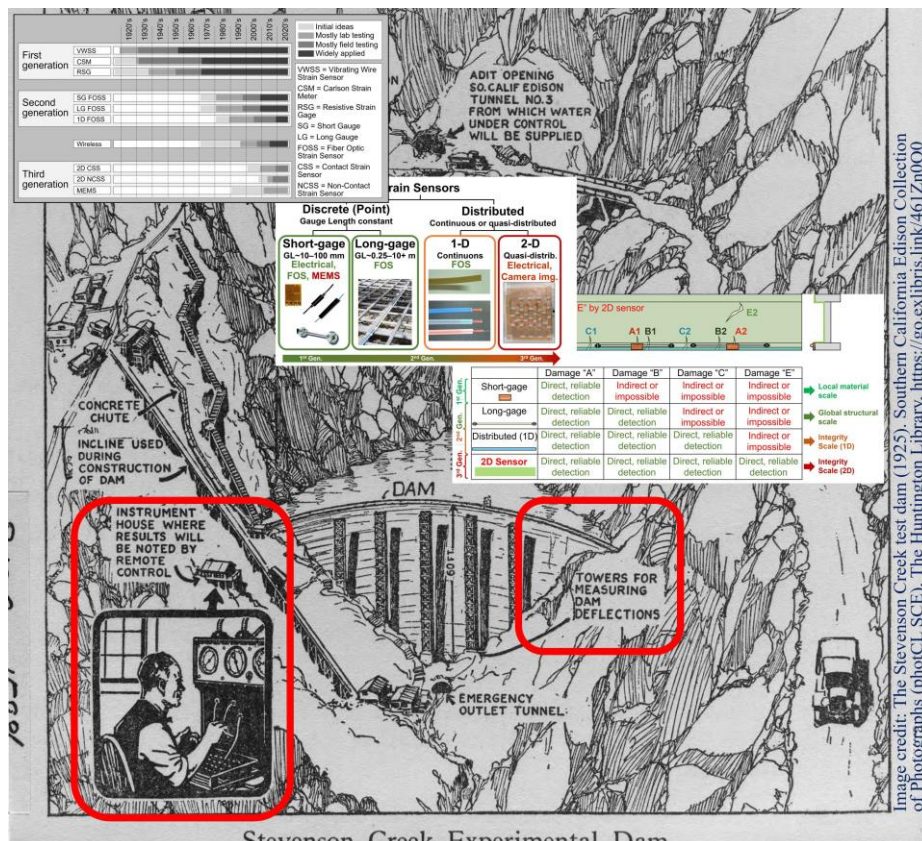
<sup>1</sup> Princeton University, Department of Civil and Environmental Engineering, USA  
email: bglisic@princeton.edu

## ABSTRACT:

The year 2025 marks the centenary of Stevenson Creek Experimental Dam tests. While the sensors were used in monitoring real civil structures under the test loading since the 19th century, these early sensors measured external changes in the structures, mostly deflections, and relied on direct human access to sensors to read the measurements. To the best of the author's knowledge, the first practical sensor to measure internal changes in civil structures with indirect remote reading capability was strain sensor, and the first such sensor was based on vibrating wire (VW) principle, invented in Germany in 1919.

The Stevenson Creek Experimental Dam Project motivated American scientists to develop, in 1924, a resistive strain sensor consisting of a stack of carbon discs. Several such sensors were embedded in the dam, and the scientists performed reading of the sensors remotely, using wired connections. This 100-year anniversary represents the moment for reflection on advancements in the development of strain sensors for applications in civil structures, and the impact that strain-based monitoring has in the field of structural health monitoring.

The aim of this presentation is to summarize the progress in strain sensing technologies over the last hundred years, overview the techniques for detection of unusual structural behaviors that various strain sensor types enabled, and present perspectives on the future developments related to strain-based monitoring.



# The Power of Optical and SAR Imaging for Remote Monitoring of Land and Infrastructure

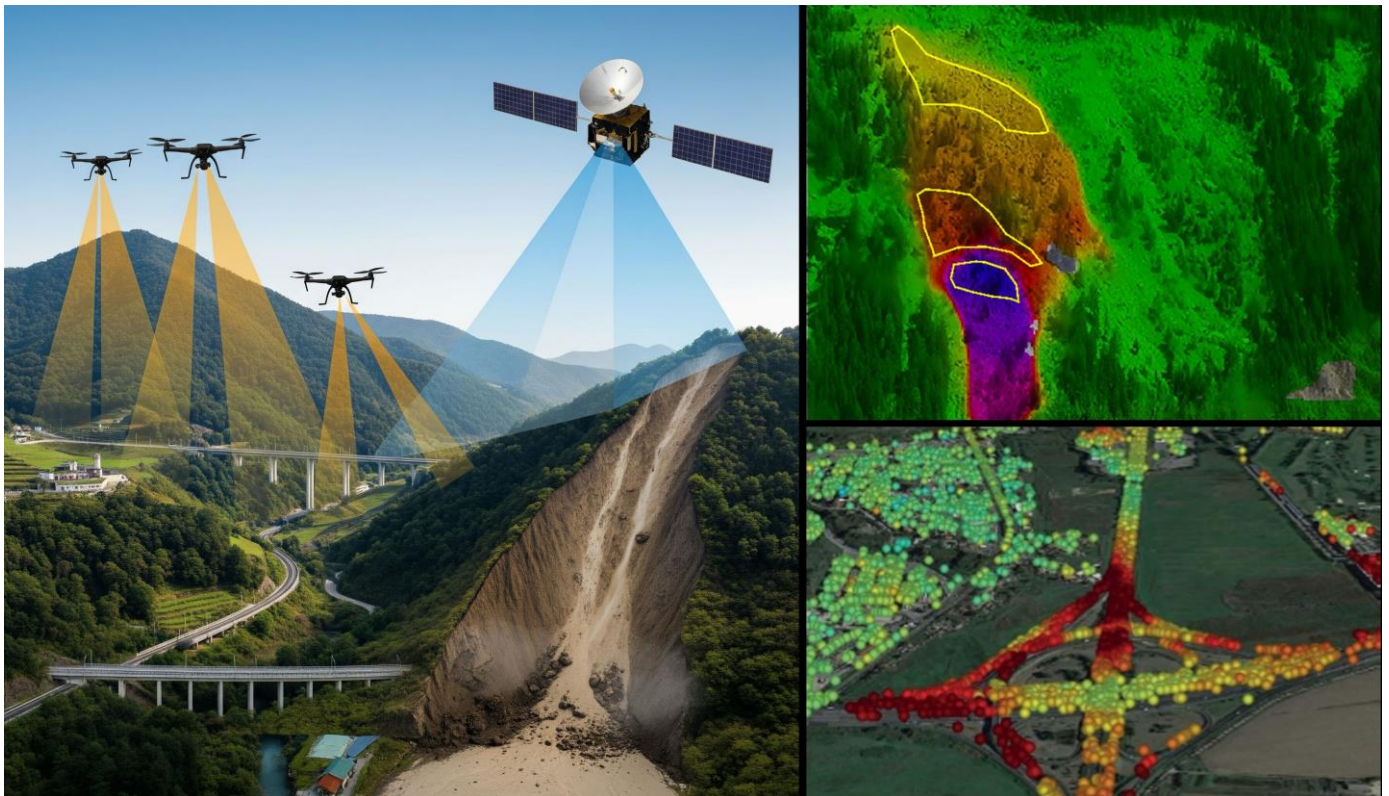
Paolo Mazzanti<sup>1</sup>

<sup>1</sup> Sapienza Università di Roma, Dipartimento di Scienze della Terra, Rome, Italy  
email: [paolo.mazzanti@uniroma1.it](mailto:paolo.mazzanti@uniroma1.it)

## ABSTRACT:

The growing availability of high-resolution multi-frequency imagery from satellite, aerial, and ground-based platforms is revolutionizing the monitoring of geohazards, land deformation, and the structural health of critical infrastructure.

State-of-the-art image processing techniques—including Synthetic Aperture Radar Interferometry (InSAR), Digital Image Correlation (DIC), Speckle Tracking, Change Detection, and Structure-from-Motion (SfM) photogrammetry—enable the extraction of surface displacements and structural changes with unprecedented spatial density, precision, and temporal resolution. These fully remote and non-invasive methodologies support the systematic observation of large-scale areas, offering significant benefits for continuous and pervasive monitoring. Their integration into operational workflows enhances the ability to assess risks, improve infrastructure resilience, and inform data-driven decision-making processes in both natural and built environments.







# Field Applications of SHM to extend the Lifespan of Railway Bridges

# Monitoring of fatigue crack propagation by means of distributed fiber optic sensing

Petr Dohnalík<sup>1</sup>, Stefan Lachinger<sup>1</sup>, Maciej Kwapisz<sup>1</sup>, Alois Vorwagner<sup>1</sup>

<sup>1</sup> Transportation Infrastructure Technologies, Austrian Institute of Technology,  
Giefinggasse 4, 1210 Vienna, Austria

email: Petr.Dohnalik@ait.ac.at, Stefan.Lachinger@ait.ac.at, Maciej.Kwapisz@ait.ac.at, Alois.Vorwagner@ait.ac.at

**ABSTRACT:** Distributed Fiber Optic Sensing (DFOS) is an innovative technique for Structural Health Monitoring (SHM). Taking advantage of the fact that DFOS can conveniently measure mechanical strain continuously along an optical fiber, it is increasingly used in monitoring of concrete bridges and tunnels. However, DFOS still needs research in new application areas, such as monitoring of steel bridges. In the present study, DFOS is used to investigate the potential to monitor fatigue crack initiation and propagation by experiments. In a full-scale test, a steel railway bridge was dynamically excited into resonance, generating fatigue-effective vibration amplitudes. The fiber was glued to the flange of the main beam in several loops to cover a larger area for crack detection. The measured strain signal was compared with results obtained from Finite Element Method (FEM) simulations supported by data acquired from conventional strain gauges and extensometers. The strain measurement with DFOS showed excellent agreement with the simulated strain. In this context, additional information about crack initiation, propagation, opening and length can be obtained indirectly from the DFOS measurement. However, when the crack is crossing the fiber, nonlinear effects come into play. To consider the nonlinear effects, a hysteresis model taking steel-fiber interaction into account was applied. The results of the study are presented and the applicability and potential of DFOS for fatigue crack monitoring in railway bridges is discussed.

**KEYWORDS:** Distributed Fiber Optic Sensing; Structural Health Monitoring; Crack propagation; Steel railway bridge; Finite Element Method; Dynamic excitation.

## 1 INTRODUCTION

Structural health monitoring of fatigue cracks in steel bridges aims to detect and evaluate cracks as early as possible before they can cause serious consequences. The current well-established method for detecting and monitoring fatigue cracks is visual inspection, which does not necessarily imply crack detection due to its inherent limitations [1]. Conventional extensometers, vibrating wire sensors, or strain gauges are well suited for monitoring only a small area of a component. This is suitable for monitoring of known cracks, but not for detecting new cracks [2].

To overcome the drawbacks of these methods, various sensors and monitoring techniques have been proposed. For example, a soft elastomeric capacitor that monitors a particular area of interest [3], coating sensors that use the change in potential difference [4], or the strain-based method employs fiber optic sensors [5].

When it comes to crack monitoring along bridges, the ability to simultaneously measure strain along a fiber, is the main advantage of the DFOS technique over other sensors that utilize different measurement principles [2].

The measurement principle of distributed fiber optic sensing is based on the backscattering of light sent through an optical fiber. Changes in temperature and mechanical strain lead to changes in the characteristics of the backscattered light, which are evaluated by reflectometer [1], [2], [6]. Rayleigh, Raman, and Brillouin scattering are commonly studied and mentioned in the scientific literature as types of scattering, where Rayleigh type achieves much higher spatial resolution and it is preferred for crack monitoring and micro-damage detection [1].

Spatial resolution is one of the most important factors in DFOS measurement. It can be thought of as the fiber being divided into small virtual gauges. The distance between the two closest gauges is also known as the “gauge pitch” (the term “gauge pitch” is used interchangeably in the literature). In this study, the finest available spatial resolution of 0.65 mm can be used with up to 20 m long fibers [7]. The spatial resolution decreases with increasing fiber length or sampling frequency. Small gauge pitches should be preferred in regions with large strain gradients, such as around cracks [1]. However, if the strains or strain gradients are too high and exceed the technical capabilities of the interrogator, the measurement software will replace unreliable values with not a number (NaN) value, also known as dropouts. Dropouts can also occur in the area of small bending radius, poor terminations, at the fiber splices, or due to high frequency effects during vibration [1].

The DFOS technique has found application in broad range of industries. One example can be taken from the structural health monitoring of a prestressed concrete highway bridge in Austria [8]. The authors took advantage of this DFOS technique to monitor mechanical strains and temperatures of approximately 2×30 m long bridge sections during the construction process. Within the observed time period, several cracks resulting from concrete shrinkage were detected. DFOS also allowed to observe the cracks closing while prestressing.

To the best knowledge of the authors, it is identified that the investigation of the crack propagation in a steel bridge under cyclic loading by means of DFOS remains unexplored. The present contribution wants to explore this possible new application and wishes to close this knowledge gap.

## 2 MATERIALS AND METHOS

The bridge investigated in this study was a steel railroad bridge built in 1953 and decommissioned in 2022. The single-span girder bridge with a length of 21.5 m and a width of about 2.2 m (after cutting the sidewalks) was transported as a whole, with crossties and rails, to the test site of the Austrian Federal Railways (ÖBB) in St. Pölten, see Figure 1, where it was subjected to an experimental campaign.



Figure 1: Pinkabach Bridge without sidewalks at the ÖBB test site.

### 2.1 Loading and investigated areas of the Pinkabach Bridge

Six concrete blocks, each weighing 11 tons, were placed on top of the rails to ensure that the minimum and maximum peaks of the imposed harmonic loading were always in tension. Harmonic excitation near to the bridge's natural frequency was applied using a large hydraulic exciter, the Mobile Seismic Simulator (MoSeS), provided by Austrian Institute of Technology (AIT). The amplitude of the imposed harmonic loading was intended to be on the same level as the maximum amplitude of a passing train.

Two critical areas (details) of the bridge were considered in this investigation. These were located on the lower right and left flanges near the transverse plane of symmetry of the bridge, see Figure 2. The right and left locations of interest are further referred to as Q3R and Q3L, respectively.

In order to initiate a fatigue crack at these locations, a notch was made on each side by an angle cutter near the gusset plates of the girders, which were used to attach the transverse and diagonal struts inside the bridge. At the Q3R location, the notch was 150 mm away from the symmetry plane; at the Q3L location, the notch was 360 mm from the transverse symmetry plane. Both notches were about 30 mm long and 3 mm wide.

### 2.2 Conventional measurement techniques

The experimental methods relevant to this study consisted of conventional strain gauge and extensometer measurements, positioned as shown in Figure 3. The latter allowed the measurement of crack openings, while the strain gauges provided information on the strain response of the structure due to the harmonic excitation. The strain oscillations were recalculated to stresses and the cyclic stress levels were evaluated using the rainflow counting algorithm. These results served as: i) an input for fracture mechanics calculations and ii) comparative values for the innovative DFOS application.

The strain gauges for ferritic steel 1-LY41-6/120 (HBK GmbH, Germany) were attached to the underside of the flanges directly below their webs, 800 mm from the transverse plane of symmetry, see DMS positions in Figure 2. Two extensometers K-WA-U020W (HBK GmbH, Germany) were installed at the tips of the notches on the left and right sides of the bridge. It should be noted that the mounting points of the extensometers were 40 mm away from the notch tip (80 mm from each mounting point), as indicated by the two crosses in Figure 3.

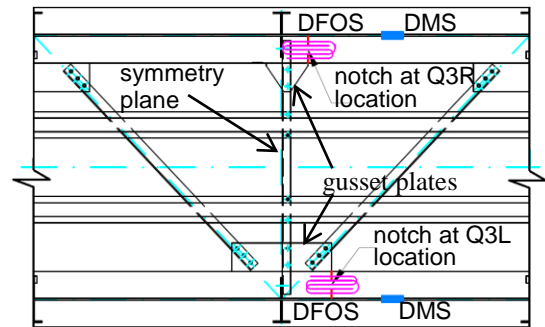


Figure 2: Top view of the central area of the Pinkabach Bridge plan showing the arrangement of the strain gauges, DMS (marked by blue rectangles), and DFOS fibers (pink loops) near the gusset plates.

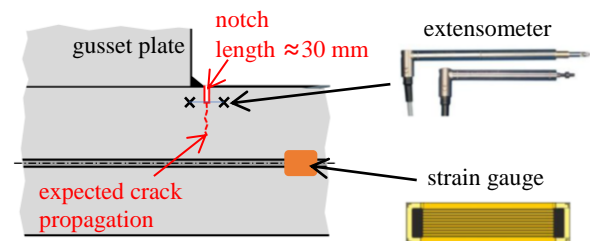


Figure 3: Detailed scheme of the conventional measurement instruments installed near the center of the girder. Source: TU Graz, Hottinger Brüel & Kjaer GmbH.

### 2.3 DFOS measurement technique

Two polyimide optic fibers (Polytec GmbH, Germany) were glued (Loctite EA 3430, Henkel AG, Germany) at the Q3R and Q3L locations in front of the cut notches where crack initiation and propagation were expected. The fibers were laid in multiple loops on the underlying flange and are referred to as fiber sections 1 to 5, numbered ascending from the flange edge. Due to the minimum allowable bend radius of the fiber, the order of the acquired signal by ODISI 6000 interrogator (Luna Innovations Inc., USA), differs from the section numbering and corresponds to the winding of the loops that as illustrated in Figure 4. An example of the received signal from the five sections and their numbering is shown in Figure 5.

### 2.4 Linear FEM modeling of the DFOS measurements

The arrangement of the notched flange with a crack and an optical fiber was represented as a finite element method (FEM) model. The Ansys Mechanical Solver (Ansys Inc., USA) was used together with APDL coding to perform linear elastic calculations. In order to facilitate the manipulation and parameterization of the model and to speed up the calculations, a 2D FEM model was used to carry out the main numerical



simulations. Since the Q3R and Q3L locations are at very similar positions with respect to the length of the bridge, the 2D FEM model with the same geometry was used for both Q3R and Q3L locations.

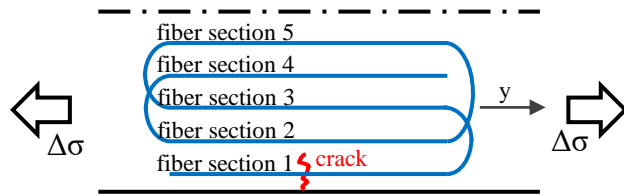


Figure 4: Schematic representation of the half-flange with the fiber winding layout in relation to the fiber section numbering.

The dash-dotted and the continuous lines represent the web and the edge of the flange, respectively. The arrows indicate the uniaxial tensile stress state.

One of the most important parameters investigated in this study is the crack width, also referred to as the crack opening. Because the crack opens in the longitudinal direction of the flange ( $y$ -direction as shown in Figure 4), the contribution of the web to the girder stiffness was investigated as it is expected to have the most influence affecting the results of the 2D FEM model. In this context, the crack openings of the 2D model were compared with the 3D FEM model of the main longitudinal girder of the Pinkabach Bridge. The motivation was to investigate the effect of the absence of the web and the upper (compressed) flange on the stiffness of the 2D FEM model. This is described in more detail in Section 2.7.

### 2.5 Linear 2D FEM model of cracked flange and DFOS optical fibers

The geometry of the flange was modeled as a rectangle 400 mm wide, corresponding to the width of the flange, and 600 mm long, which is long enough to have a uniform stress state at its ends. The shape of the notch does not affect the calculated crack widths. Therefore, it was not accounted for in the present study and only the material discontinuity was considered, i.e., the nodes on the axis of symmetry located at the position of the crack were allowed to move freely. The fibers were modeled as beams with a thickness of 0.5642 mm at each position, taken from [2].

The flange mesh was generated with 8-node quadrilateral PLANE183 elements using plane stresses with a thickness

option [9] corresponding to the flange thickness. A mapped mesh with an element size of 5 mm and 1 mm in the longitudinal and transverse directions, respectively, was applied to the flange. The optical fibers were meshed using a three-node BEAM189 element with quadratic shape functions [9]. The length of the beam elements was 5 mm, and the position of the nodes coincided with the nodes of the flange. COMBIN14 elements [9] were used as spring elements connecting the coincident nodes of the flange and optical fibers and representing the glue between these two components. The COMBIN14 elements were used for nodes that were more than 5 mm away from the axis of symmetry.

The boundary conditions for the optical fibers were as follows: the nodes of the fibers lying on the axis of symmetry were constrained in their longitudinal displacement as well as in their total rotation. On the other side of the flange, the last nodes of the beam elements were coupled in all directions to their corresponding elements of the flange. The nodes of the flange that were on the axis of symmetry were constrained in the longitudinal direction, where there was also a fixed material on the other side. There was no constraint for the nodes in the cracked area, i.e. the crack length is controlled by the constraining the displacements of the nodes in the  $y$ -direction. One node on the symmetry axis, located in the center of the flange, was also constrained in transverse direction. The tensile load was applied in the form of pressure on the shorter edge opposite to the axis of symmetry. The geometry, mesh and boundary conditions are shown in Figure 6.

The material properties of the components were linear elastic. For the steel flange, standard elastic properties were used with a modulus of elasticity of 210 GPa and a Poisson's ratio of 0.3. The glass fiber was assigned a modulus of elasticity of 30 MPa and a Poisson's ratio of 0.3 [2]. The elastic modulus of the glue was initially unknown and it was subject of the investigation. After the investigation, a modulus of elasticity of 900 kPa was assumed.

### 2.6 Linear 3D FEM model of the main girder

The 3D FEM model simulates a crack in the flange of one of the main girders of the Pinkabach Bridge. The girder length, web height, web thickness, flange thickness, flange width of the girder amount to 21500 mm, 1875 mm, 14 mm, 30 mm, 400 mm, respectively.

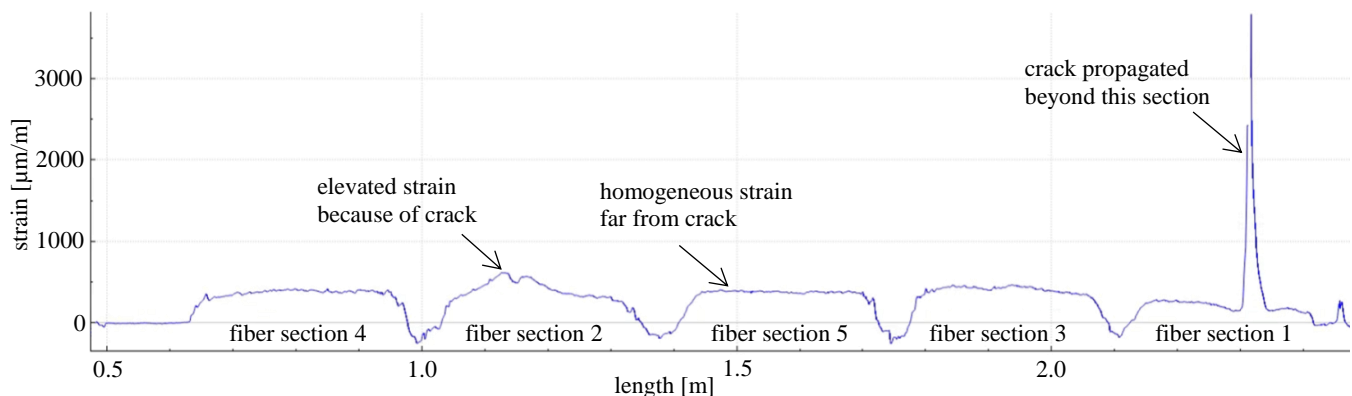


Figure 5: An example of the acquired strain signal along the fiber at a specific time instance. The plateaus of the received signal correspond to the straight fiber sections shown in Figure 4.

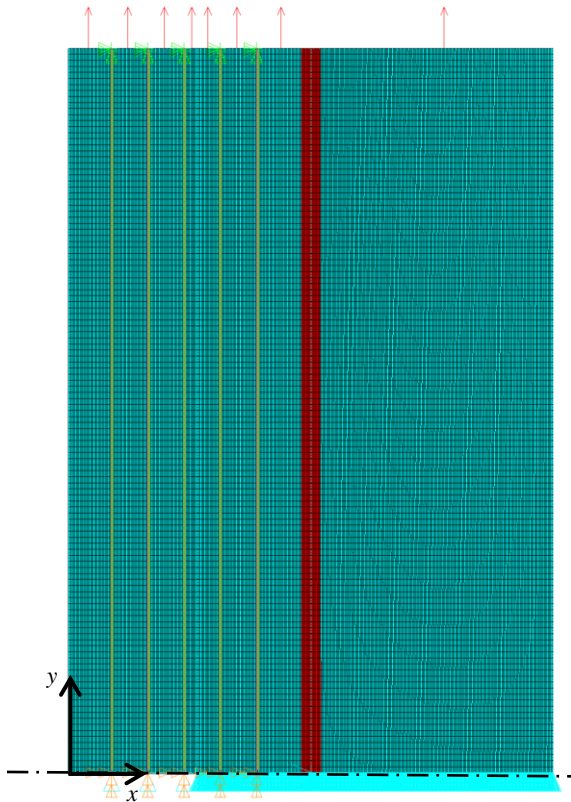


Figure 6: The 2D FEM model of the cracked flange. The dashed line corresponds to the transverse axis of symmetry; the blue rectangles represent finite elements; the red rectangles mark the area of higher web stiffness; the yellow vertical lines mark the optical fibers. The blue rectangles on the symmetry axis indicate the boundary condition for the displacement. The orange rectangles applied to each fiber ending on the axis of symmetry are rotational constraints, while the green triangles correspond to coupled nodes between the fiber and the flange. Red arrows indicate the direction of the applied stress.

The flanges as well as the web were meshed by SHELL281 elements with quadratic base functions [9]. Around the notch, the mesh was finer than in the rest of the girder and its properties are the same in terms of element type and element size. Outside of the fine area, a coarse mesh was used. As for the web, elements with a length of 697 mm and a width of 127 mm were used. For the coarse part of the flange, the elements were 697 mm long and 200 mm wide. Mapped mesh with quadrilaterals was used on most of the girder geometry, as shown in Figure 7.

The boundary condition of the 3D FEM model was analogous to a simple supported girder, corresponding to suppression of longitudinal, and vertical displacements of the nodes at the short edge of the lower flange (with crack) on one side and the suppression of vertical displacements along the edge of the other side, see Figure 7. In addition, one node in the middle of the edge of the bottom flange at the end is constrained in transverse direction.

The loading of the numerical 3D FEM model was carried out by a single point force in the middle of the upper flange. The elastic material properties of all parts used in the 3D FEM model were the same as in the 2D model.

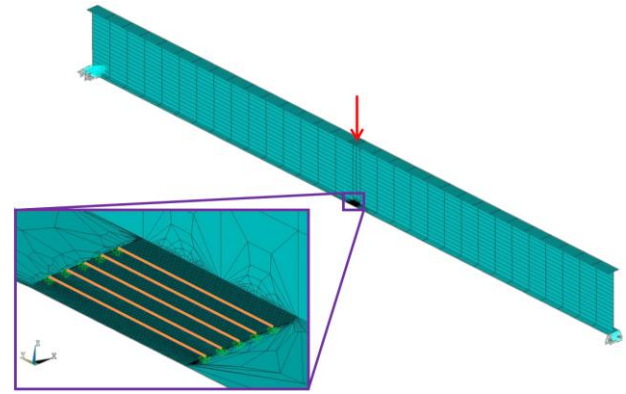


Figure 7: The 3D FEM model of the Pinkabach Bridge main girder with cracked flange and DFOS fibers. The displacement boundary condition, and the point load are marked by blue triangles and red arrow, respectively. The detail of the fine-mesh area with crack and DFOS fibers (yellow lines) is shown in the lower left.

## 2.7 Comparison of the linear 2D and 3D FEM models: web stiffening factor

The crack openings of the 2D FEM model were compared with those of the 3D model in order to investigate the influence of the absence of the web in the 2D model. This absence was manifested by a higher crack opening of the 2D model, indicating a lower stiffness of the 2D model. As a remedy, a strip of higher stiffness than the surrounding steel was inserted to the 2D FEM model. This strip is 14 mm wide and is located in the middle of the flange, geometrically corresponding to the footprint of the web, see the red area in Figure 6. The modulus of elasticity of the strip was expressed as a multiplication factor to the surrounding steel with a modulus of elasticity of 210 GPa. Depending on the crack length, higher elastic moduli were assigned to the strip in order to match the crack openings of the 3D and 2D models. The multiple of the higher steel elastic modulus of the strip is referred to as the web stiffening factor in this document.

The procedure for finding the web stiffening factor was as follows:

- Find the single point load of the 3D model (red arrow in Figure 7) that yields the same stress of 50 MPa in the homogeneous stress field in the vicinity of the notch (with crack length = 0) of the 2D and 3D models.
- After harmonizing the homogeneous stress fields in the vicinity of the notch and finding the point load of the 3D model, the distance between the two corner nodes at the very end of the notch was measured. This "notch opening" was compared to the 3D and 2D models.
- The strip stiffness of the 2D model (red area in Figure 6), which caused the same "notch opening" in the 2D and 3D models, was expressed as a multiple of the steel stiffness of 210 GPa. In this way, the web stiffening factor was obtained.
- The crack length behind the notch tip was increased by a certain increment, and the step iii) was repeated.

The web stiffening factors were obtained for crack lengths from 0 mm up to 160 mm by means of repeating steps iii) and iv). The increments for crack lengths from 0 mm to 140 mm were 20 mm, and for crack lengths from 140 mm to 160 mm

were 10 mm. The web stiffening factors as a function of crack length are plotted in Figure 8.

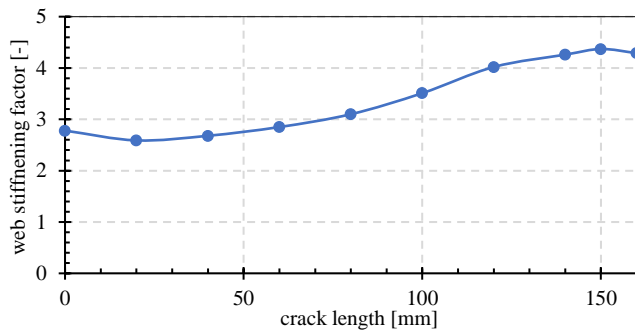


Figure 8: Web stiffening factors as a function of the crack length. Web stiffening factors are the multiples of the flange steel elastic modulus assigned to the strip in the 2D model.

### 2.8 Modeling the glue between the flange and optic fibers

The glue bonds the DFOS optical fiber with the underlying steel flange, see Figure 9 a). In the linear FEM models, this bond was modeled by linear springs characterized by their stiffness, see Figure 9 b). The springs connect coincident nodes of the flange and the fiber. The springs were active in the y-direction, the longitudinal axis of the flange. In the FEM models, the first spring was located 5 mm away from the symmetry axis. The next springs connected the flange and fibers from this point to the end of the fiber where the flange and fiber nodes were coupled, see Figure 6.

The stiffness of the glue was investigated based on experience from previous work [2] and the current DFOS measurement. Softer springs (i.e., softer glue) produced flatter strain peaks when the crack was close to the fiber. Increasing the stiffness caused the calculated strain response curve to become narrower, see Figure 9 c). The calculated strain response from the 2D model was compared to the measured DFOS signal. A glue stiffness of 900 kPa gave satisfactory agreement between the calculated and measured strain shapes and was used in further calculations.

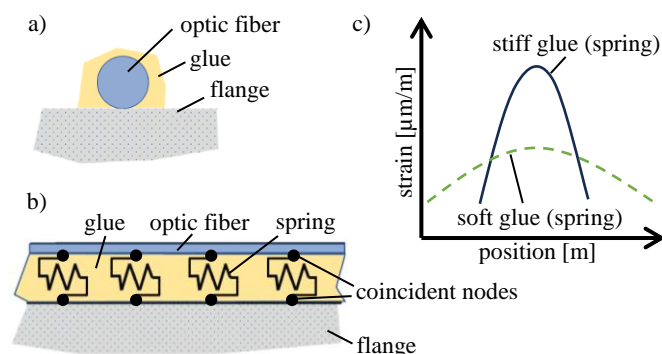


Figure 9: Detailed sketch of a) cross-section of the bond between fiber, glue, and the flange, b) glue being represented as linear springs connected to coincident nodes (zero glue thickness). c) strain response corresponding to soft glue (dashed curve) and hard glue (orange curve).

### 2.9 Nonlinear hysteresis model for determining crack width

The linear FEM model, simulating the strain distribution from the glass fiber to the underlying object, is able to reproduce the

measured values up to the crack formation. However, as it will be shown in the result section, once the crack reaches the fiber, there is no longer sufficient agreement and the strain from the linear FEM model deviates more and more from the measured values as the crack increases in size. This is due to nonlinearities in the fiber and the glue that occur at very high strains and can no longer be represented by the linear model.

Although this phenomenon is known from earlier studies, as explained in [2], the physical background has not yet been clarified in detail. The most likely explanation is a permanent mutual displacement between fiber and base material in the glue layer (sliding), which occurs after exceeding the mutual friction, or plastic deformation of the optical fiber. A mechanical model based on this hypothesis had already been developed by the AIT research group and proved to be very effective. It allowed the strain behavior to be simulated with a high degree of accuracy under various loading and unloading scenarios and crack widths of up to 2.8 mm.

An overall model of the optical fiber structure and the glue was adopted from [2], with the parameters being slightly adjusted to the actual fiber used. This model makes it possible to calculate the interaction of these elements and also to calculate non-measurable strain signal during high-frequency excitation with large crack widths (high amplitudes) using FE methods. The hysteresis model consists of a combination of linear and nonlinear spring and beam elements. The fiber structure, including the connecting elements, is shown in Figure 10 a) and b). The glue (3) is modeled as a linear spring, while the coating (2) and the fiber (1) are defined as 1D beam elements. The crucial connection between the fiber and the coating is modeled by nonlinear springs (4). This is an elasto-plastic spring element whose force  $F$  increases linearly with the deformation  $V$  and the stiffness  $k_{int}$  up to the limit force  $F_S$ . After the limit force  $F_S$  is exceeded, slippage  $V_{SL}$  occurs as a permanent displacement of the fiber optic cable (1) relative to the coating (2), see Figure 10 c).

The model was implemented in the FE program Ansys, whereby, in contrast to the linear model, only a 20 cm long section around the crack and only one fiber at a time is considered separately. The aim of this investigation is to interpret the measurement signal and to draw conclusions about the crack width. During the interpretation, it can be determined whether the crack is currently closing or opening or whether a larger crack has occurred previously. It is not necessary to apply the nonlinear model to recalculate the crack width if a complete, continuous measurement signal is available, as the crack width can be calculated by integrating the signal over the fiber length. Since it is known that transient or permanent dropouts can occur at higher amplitudes and higher excitation frequencies, this step is important to significantly increase the accuracy of the crack width determination.

In the present case of the linear model described in Section 2.8, a fiber without a coating was used, which theoretically results in differences to the model shown in Figure 10, as the comparison with the simplified model in Figure 9 shows. However, since comparable nonlinear effects occurred in the measurement data despite the absence of the fiber coating, the model described in [2] was also applied here and showed good results.



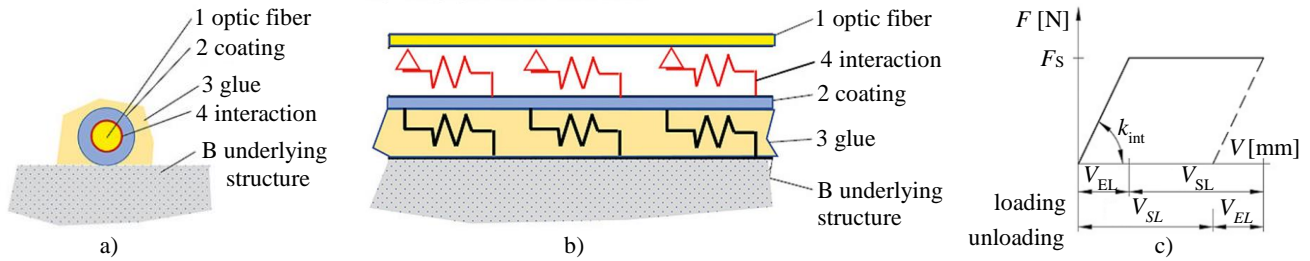


Figure 10: Schematic drawing of a) cross section and b) side view of the nonlinear model used to estimate the crack width; c) the material model prescribed to the springs where slippage is initiated when the force  $F$  exceeds the limit force  $F_s$ .

This is also due to the fact that the model parameters were not determined individually, but were found empirically from the measurement data by model fitting as an overall model. These determined characteristic values in Table 1 thus do not represent any physical material parameters, but the overall structure including the glue. These characteristic values determined in this way are not transferable to other fiber applications, even with the same fiber, without slight adjustment.

Table 1: Input parameters for the nonlinear FE analysis.

element size	glue (spring)	coating (beam)	interaction (spring)	glass fiber (beam)
2 mm	$K = 10^6 \text{ N/m}^2$	$A = 10^{-4} \text{ m}^2$ $E = 30 \text{ MPa}$	$K = 7 \cdot 10^6 \text{ N/m}^2$ $F_s = 0.35 \text{ N/m}$	$A = 10^{-5} \text{ m}^2$ $E = 30 \text{ MPa}$

### 3 RESULTS

#### 3.1 Crack width vs. crack length under unit load

One of the main results of this study is the relationship between crack width and crack length. Since the problem is modeled with linear elasticity, it is reasonable to do this for a unit load. The calculations were carried out using the 2D model.

The crack widths were obtained for the following locations: at the notch tip ( $x = 30 \text{ mm}$ ), at the fiber locations, at the location of the crack tip, and the notch tip ( $x = 30 \text{ mm}$ ), but 40 mm above the axis of transverse symmetry of the 2D model ( $y = 40 \text{ mm}$ ). This location corresponds to the extensometer mounting points. The crack widths were determined for crack lengths from 0 mm to 160 mm with 5 mm increments. For each calculation, the appropriate web stiffening factor was taken into account. The results are shown in Figure 11. It is noteworthy, that the extensometer reading is non-zero even for zero crack length, which is caused by the elasticity of the steel between the extensometer mounting points.

#### 3.2 Comparison of crack growth and fracture mechanics

As part of the test evaluation, a fracture mechanics analysis of the fatigue tests on the Pinkabach Bridge was carried out by the scientific partner, the Institute of Steel Structures of the Technical University Graz (TU Graz), which also included the evolution of the crack length over the number of cycles for the two locations Q3L and Q3R shown in Figure 12. This fracture mechanics analysis is compared to the crack width vs. crack length relationship derived from the 2D FEM model in the previous Section 3.1, shown in Figure 11.

In order to perform this comparison, the number of cycles was determined at each measurement time instance. At this particular measurement time instance, the crack length was

determined using Figure 11 and the extensometer reading. This crack length and number of load cycles were entered into the fracture mechanics diagrams in Figure 12.

Comparison with the fracture mechanics analysis "best fit" (green curve) shows reasonable agreement, although it is not perfect. The numerical results tend to be slightly higher than the fracture mechanics results for short crack lengths. For long crack lengths, however, the numerical results are slightly lower than the fracture mechanics results. There are uncertainties in both, the fracture mechanics analysis and the numerical analysis, and it is expected that there will be differences. For example, a complete 3D model of the main girder including the gusset plates, and the influence of the bracing would allow a more accurate analysis. However, the method is considered to be adequate for estimating the crack length for practical construction purposes based on simple extensometer readings.

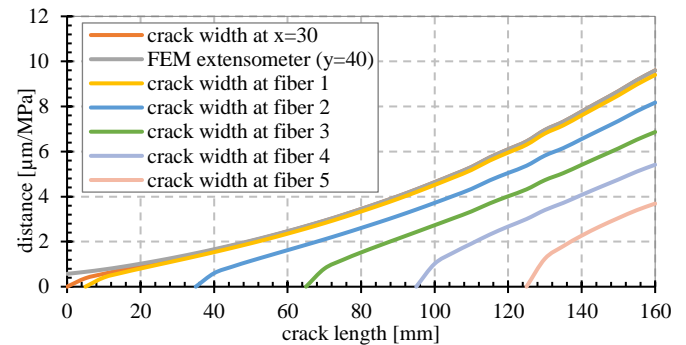


Figure 11: Crack width as a function of crack length; FEM extensometer corresponds to the displacement reading at the location of the extensometer attachment, i.e.: at the notch tip ( $x = 30 \text{ mm}$  from the flange edge) and  $y = 40 \text{ mm}$  above the axis of transverse symmetry of the 2D model.

#### 3.3 Comparison of the linear 2D FEM model with the DFOS measurement at the Q3R and Q3L locations

The strains calculated by the 2D FEM model, to which the conventional experiments provided input, are compared in side-by-side plots with the DFOS strain signal at multiple time instances throughout the experimental campaign. The results from the 2D FEM model at a time instance were obtained in 3 steps. First, the loading stress was determined as the difference between the minimum and maximum amplitude readings from respective strain gauge at the corresponding time instance, multiplied by the modulus of elasticity of 210 GPa. Second, the crack length was extracted from Figure 11 (FEM extensometer), by knowing the displacement reading of the extensometer divided by the loading stress derived from the

strain gauge reading for the corresponding time instance. Third, the applied stress and crack length were used as input for the FEM simulations.

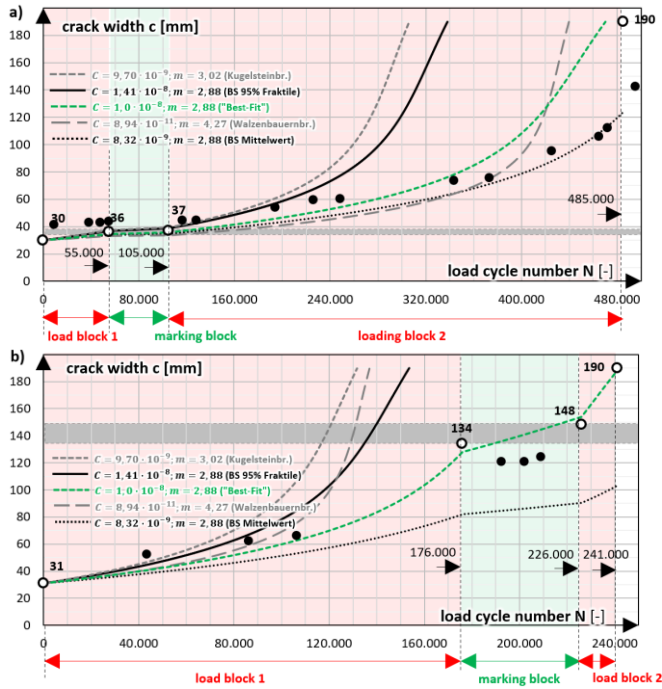


Figure 12: Fatigue calculations provided by TU Graz showing the crack length as a function of the number of load cycles for the two locations: a) Q3R and b) Q3L; the solid black circles show the results derived from the linear elastic FEM model; the monotonically rising curves correspond to different fatigue models. Credit: TU Graz.

The measured DFOS signal used for comparison with the numerical simulations was obtained by subtracting the minimum DFOS signal (red graph in Figure 13) from the consecutive maximum DFOS (green graph in Figure 13) signal for the corresponding time in order to account for the mean strain value (blue graph in Figure 13). In this way, the difference between the numerical and measured signals is “tared”, and they can be directly compared. The elevated strain values reminiscent of plateaus in this blue graph correspond to individual fiber sections. The order of the fiber sections is the same as shown in the Figure 4 and Figure 5.

An example of a typical comparison of the measured and simulated strain signals at fiber section 5 is shown in Figure 14, where the signals are almost identical. It was observed that when the fiber is far away from the crack tip, the measured and simulated signals are in good agreement.

The measured DFOS signal indicates that the cracks were already present near the fiber section 1 already on the first day of measurements at both Q3R and Q3L locations. At this time, it can be seen that the simulated and measured signal amplitudes do not match each other, see Figure 15. This suggests that a nonlinear effect is at play, which may be caused by the interaction between the optic fiber, coating, glue, and the flange due to excessive strain loading. This effect is even more pronounced as the crack propagates further behind the fiber, resulting in an “inversion” of the signal and an increasing number of dropouts, as shown in Figure 16.

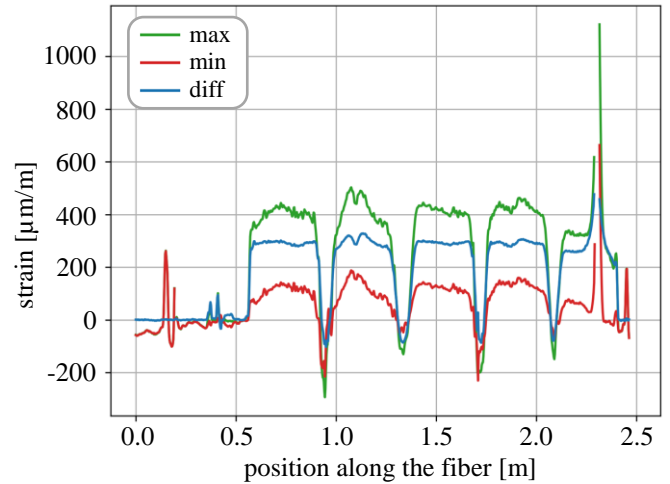


Figure 13: Subtraction of the minimum (red) and maximum (green) DFOS signal from May 9, 2023, at 10:52 to obtain the mean (blue), which was compared to the output from the numerical simulations; Q3R location.

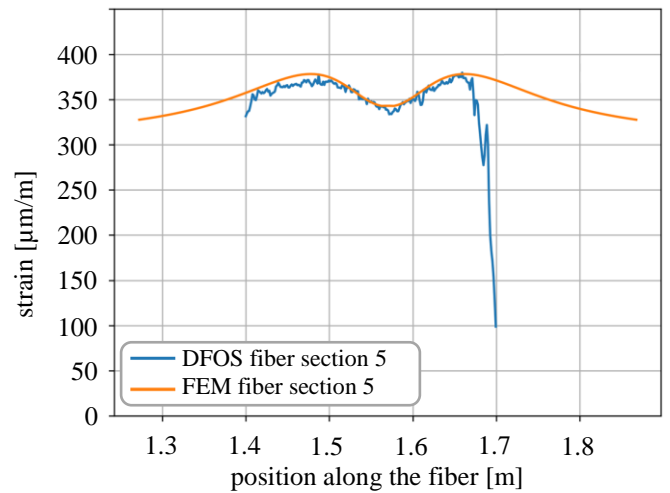


Figure 14: Comparison of the strain signal at fiber section 5 from the linear FEM simulation and the DFOS measurements taken on the sixth measurement day at the Q3R location.

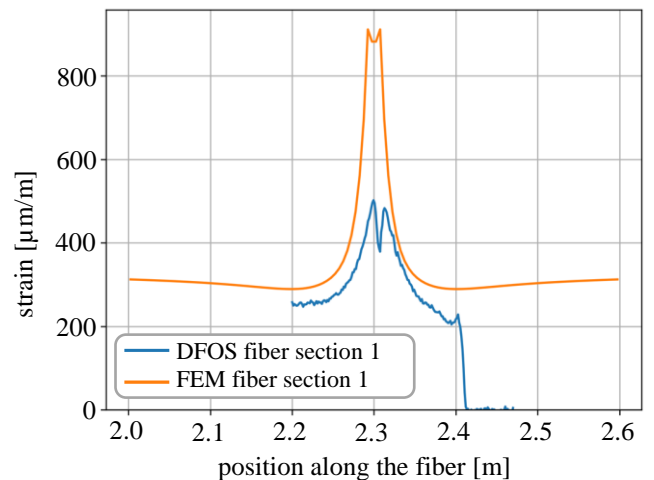


Figure 15: The crack tip near fiber section 1 causing nonlinear effect resulting in smaller strain peaks, first day of measurement at Q3R location.



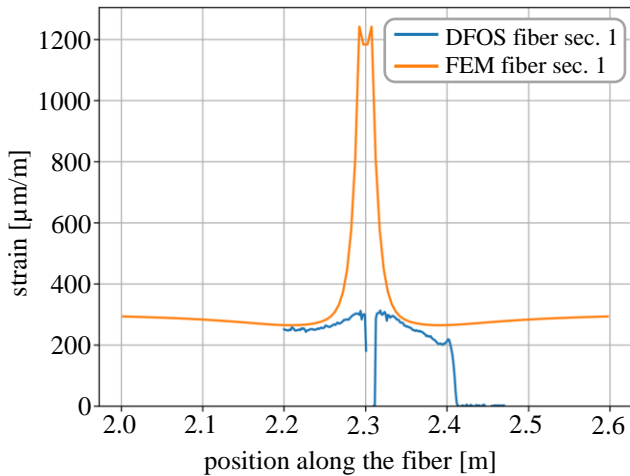


Figure 16: An “inversion” of the measured DFOS signal showing dropouts due to the wide crack opening inducing excessive strain. Third day of measurements at the Q3R location of fiber section 1.

### 3.4 Crack widths determined by the nonlinear model

The crack widths for the Q3L and Q3R locations were determined using the nonlinear FE hysteresis model. The following paragraphs describe the procedure at the Q3L location for fiber section 1. Here, two points in time were selected where the crack had already grown considerably, both on May 12, 2023, one at about 06:45 and one at about 10:30.

The best results were obtained in the earliest measurement because the crack widths were still not very large. The times of the maximum (load), minimum (unload) and constant load (resting state) of a cycle is considered in each loading case. At 06:41, the cyclic loading was stopped for a short time, which led to a brief complete reappearance of the DFOS strain signal. At this point, the permanent crack under constant load became very well measurable. The corresponding signal is shown in purple continuous line in Figure 17. The unloading curve (gray continuous line) is also clearly visible and shows only a few interruptions. It can be seen here that the measured values in the crack area are even slightly negative, while the areas where the load is applied remain virtually unchanged. This can be well modeled by means of the hysteresis model. It should be noted that as the crack width increases, so does the number of dropouts in the data. The loading curve (red) is only partially visible and must be reconstructed to determine the underlying area corresponding to the crack width. This is done by the accompanying FE analysis, which is shown in the Figure 17 as a dash-dotted line in the respective colors. Since the parameters of the FE model were optimized once for all processes, each recalculation only searches for the crack width that best matches the measurement data.

The crack widths,  $w$ , in Figure 17, indicate the crack opening at each loading phase. If  $w_{max}$  is given, it means that at an earlier point in time a larger crack caused a change in the fiber. This can be beneficial if there was no measurement at that point in time or if the signal was too disturbed to measure. In this case, the amplitudes of the crack widths are compared and validated with the results of the displacement sensors in combination with the relationship between crack length and width in Figure 11 derived from the linear 2D FEM model.

They result from the differences in crack width during loading (red) and unloading (gray) and thus correspond to the change in crack width during harmonic loading. The crack width at rest (purple) should be exactly between the two values for a symmetrical load amplitude. This also makes it possible to calculate the static crack opening without harmonic excitation. The crack opening under constant load at the fiber section 1 after crack crossing is therefore 0.205 mm and the amplitude of the crack opening under cyclic loading is 0.22 mm.

The same procedure was carried out for the later measurement at 10:28, see Figure 18, whereby the crack is considerably more developed. In this case, no DFOS strain signal could be measured in the loading phase. The strain data for unloading and constant load phases was very fragmented, but could be reconstructed by numerical simulation. The resemblance to the existing data is not as good as in the previous example, which indicates that there are more extensive nonlinearities that cannot be simulated by the model that is used. Therefore, it is expected that the evaluation of the crack widths will be less accurate in this case. Despite the absence of a loading phase, the crack width could be estimated from the difference between the unloading and the constant loading phases.

- 2023-05-12 06:46,  $w = 0.32$  mm
- 2023-05-12 06:46,  $w = 0.1$  mm,  $w_{max} = 0.32$  mm
- 2023-05-12 06:41,  $w = 0.205$  mm,  $w_{max} = 0.32$  mm

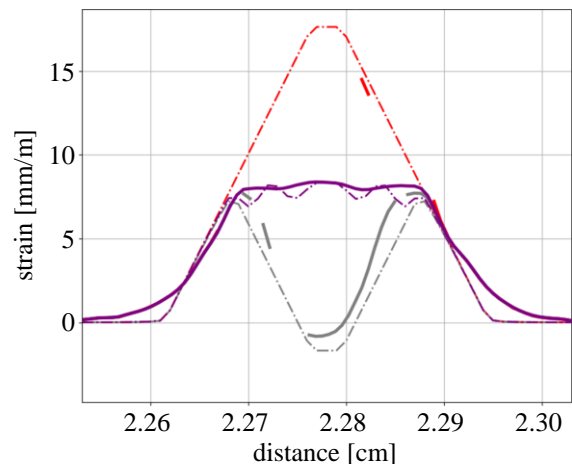


Figure 17: Matched strain signals of DFOS (“continuous lines”) and the nonlinear FEM model (dash-dotted lines) for fiber section 1; measurement location Q3L; loading curves are red, unloading in gray, and constant load in purple.

## 4 DISCUSSION

### 4.1 Influence of gage pitch on dropouts

Three gage pitches (0.65 mm, 1.3 mm, and 2.6 mm) were used during the DFOS experimental campaign in order to investigate their suitability for monitoring of crack propagation under harmonic loading. Although it is recommended to use the shortest gage pitches for regions with high strain gradients [1], in this case the signal acquired with the 0.65 mm gage pitch contained the most dropouts and noise. The larger the crack opening, the more pronounced this effect was. Therefore, it was not suitable for further processing and the two longer gage pitches were preferred for evaluation as the acquired signal

contained fewer dropouts, with 2.6 mm gage pitch having the fewest.

It is recognized that the situation can be remedied by using optical fibers with higher sensitivity. In [1], the authors monitored cracks in a concrete beam using four different optical fibers and gage pitch of 0.65 mm. The results emphasized the need for careful selection of optical fibers that are better suited for measuring high gradients, if case that the crack location and crack opening are to be reliably quantified.

— 2023-05-12 10:28,  $w = 0.05$  mm,  $w_{max} = 0.4$  mm  
— 2023-05-12 10:28,  $w = 0.33$  mm,  $w_{max} = 0.4$  mm

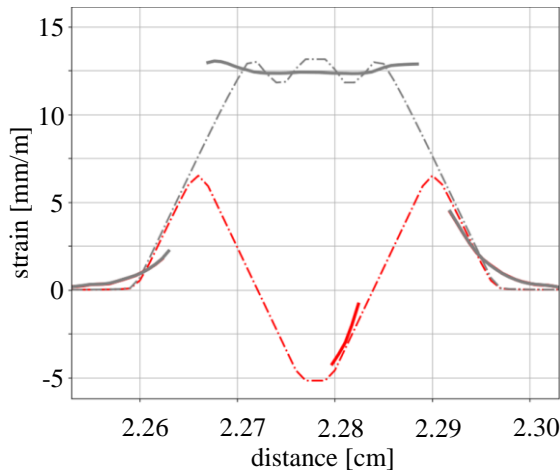


Figure 18: Matched strain signal of DFOS (“continuous lines”) and the nonlinear FEM model (dash-dotted line) for fiber section 1; measurement location Q3L at 10:28; unloading curves are red, constant loading in gray.

#### 4.2 Fiber layout – loop length and minimum fiber radius

In order to maintain the minimum fiber radius that can cause additional signal dropouts the optic fiber was laid in the following order of fiber section 1, 3, 5, 2, and 4. The lower the number, the closer the fiber section is to the flange edge and the notch. Although the length of the straight part of each fiber section was sufficient to capture the uniaxial stress state, it would be preferable to make these straight sections even longer, so there are no sudden signal drops as it can be seen, for example, on the right hand side of the blue line in Figure 14.

#### 4.3 Limitation of the linear FEM models

Although the handling of the 2D FEM model was significantly easier than the full-scale 3D FEM model of the main girder, significant amount of was required to correctly create the 2D FEM model. As a side effect, the contribution of the web to the stiffness of the flange in the presence of a crack was investigated. Interestingly, the web stiffening factor as a function of crack length is not monotonic. For crack lengths from 0 to 20 mm (and in the presence of the notch), the web stiffening effect slightly decreases, but from 20 mm to 150 mm, the web contributes to the overall stiffness by a factor 2.5 to 4.5, respectively.

It would be also of interest to investigate, how incorporating more construction details, e.g. constraining lateral movement of the main girder, modeling the gusset plates, or using

displacement loading, would manifest itself on the web stiffening factor as well as on the overall results. However, it is anticipated that these effects are rather small and would not significantly change the results.

#### 4.4 Validation and limitation of the nonlinear model

This study shows that the nonlinear hysteresis model is able to reproduce the measured DFOS strain signal for smaller crack widths where the interaction between the optical fiber and the flange is governed by nonlinear behavior. However, for larger crack widths, it remains subject to certain inaccuracy. The deviations increase with crack growth, indicating additional nonlinearities not represented in the model. It is therefore important to consider the expected crack widths of interest when selecting fibers. A thicker coating would smear the strain peaks around cracks over the longer part of the fiber core, resulting in lower peak values and thus preventing highly nonlinear effects from occurring.

The resulting crack widths for the two locations, the considered time instances, and the optical fibers were compiled and validated. The validation was done by comparing the crack width and crack length relationship developed from the extensometers and the linear FEM model in Figure 11 in Section 3.2. The results are summarized in Table 2 for measurement location Q3L and fiber sections 1 to 4.

For the considered time instances and the location Q3L, almost complete measured values are only available for the measurement time around 06:30. Therefore, the first validation was carried out at location Q3L for May 12, 2023, at 06:28, see third and sixth row in Table 2. The maximum deviations for this time instance are only 0.03 mm. This result is consistent with the previous findings on the accuracy of crack width measurements using DFOS in [2]. The comparison at 10:28 for the same location and measurement day shows significantly larger deviations of up to 0.09 mm.

Table 2: Comparison of the crack widths from the linear and nonlinear FEM models at Q3L location on May 12, 2023

		linear model + extensometer [mm]			
date	time (UTC)	fiber sec. 1	fiber sec. 2	fiber sec. 3	fiber sec. 4
12.05.2023	06:28	0.19	0.15	0.12	0.05
12.05.2023	10:28	0.35	0.30	0.24	0.17
		nonlinear model + DFOS [mm]			
12.05.2023	06:28	0.22	0.15	0.12	0.08
12.05.2023	10:28	0.35	0.21	0.21	0.11

#### 4.5 Practical applicability of the crack monitoring using DFOS

The DFOS measurement technique could be implemented in real-world scenarios analogous to the current study. The fiber can be placed in different shapes around critical details of new or existing bridges if the minimum bending radius requirement is met. Since the unit cost of a basic optical fiber is relatively low, two or more parallel fibers can be used to measure a quantity to increase redundancy in case of fiber damage.

If the structure is exposed to different temperatures, temperature compensation is required. In this case, it is recommended to install a fiber for temperature measurement next to the fiber for strain measurement. The temperature sensing fiber should be able to move freely so that it is not

affected by mechanical strain and can provide reliable temperature values.

One of the challenges is the risk of fiber damage during installation in the busy and harsh conditions of a construction site. To mitigate this risk, it is recommended to use a specialized company to install the fibers.

A notable practical example of the use of DFOS is on a concrete highway bridge near Aurachkirche, Austria, documented in [8]. In this pilot project, approximately 60 m of the Aurach Bridge is monitored in two 30 m long sections using 2.6 mm gage pitch. In each section, temperatures and strains were measured in the top and bottom slabs. During the observation period, several cracks were detected as a result of concrete shrinkage. The DFOS measurements also allowed to observe the crack closure due to prestressing. By integrating the area under the obtained strain signal, the crack widths were estimated, which were in line with the expectation for a prestressed concrete bridge. It was concluded that DFOS can be used to monitor important milestones in the construction process, including the development of cracks.

Another practical example is the recent installation of DFOS technology during the replacement of a railway bridge in Eschenau, Upper Austria. In this project, optical fibers will monitor temperature and strain throughout the construction process and future service life, enabling the detection of potential crack development. These examples demonstrate the growing adoption of DFOS in structural health monitoring projects and highlight the suitability of this technique for integration into routine bridge maintenance.

## 5 CONCLUSIONS

Based on the current study, the following conclusions are drawn: The FEM simulations fed with strain gauge and extensometer data can provide good qualitative and quantitative agreement with the measured DFOS strain signal. The simulated strain signal from the linear elastic FEM model agrees well with the measured DFOS strain signal in cases where linear elasticity governs the interaction between the optical fiber and the underlying steel flange. Once the crack is close enough to the fiber, the nonlinear effect comes into play and the nonlinear model must be used to reproduce the measured DFOS strain signal. In these cases, the nonlinear model can also be used to estimate the crack opening, see Section 2.9.

With increasing crack opening, the high strain in the optical fiber causes signal dropouts. This is usually the case when the crack has propagated well beyond the fiber.

The crack propagation can be clearly seen in the cyclic loading test using DFOS. First, the nonlinear effects come into play, which can be accompanied by some dropouts. Then, in the next phase, the peak of the measured strain signal changes to a trough so that it is "inverted" with respect to the previous state, see Figure 16.

The further away the fiber section is from the crack tip, the better the agreement between the measured and simulated strain signals was obtained. Typically, the best agreement between simulated and measured strain was observed for fiber section 5.

The DFOS have proven to be very good at determining steel strain up to crack initiation, crack detection, and crack widths

up to 0.2 mm. Beyond that, the measured strain signal become more incomplete and the signal reconstruction is subject to increasing inaccuracy. This is exacerbated by dynamic excitation, which disturbs the strain signal. If large crack widths are still of interest, it is advisable to use coated fibers for such measurements, which reduces the peak strains. If the information on whether and where a crack has occurred is sufficient, simple and inexpensive commercially available fibers, such as those used in the Pinkabach Bridge tests, can provide adequate information. When more precise evaluations were required, it became apparent that the fiber had to be selected precisely according to the expected crack widths. Overall, the DFOS technique was found to be suitable for crack detection and crack propagation monitoring.

## ACKNOWLEDGMENTS

The work presented here was carried out as part of the FFG COMET research project 'Railways for Future: Resilient Digital Railway Systems to enhance performance' (in short: Rail4Future) 882504, which was led by the Austrian Federal Railways ÖBB-Infrastruktur AG. The authors would also like to thank Alfred Lechner and Stefan Wittmann for their support with the measurements and the partners involved in the project for their excellent cooperation.

## REFERENCES

- [1] M. Herbers, B. Richter, und S. Marx, „Rayleigh-based crack monitoring with distributed fiber optic sensors: experimental study on the interaction of spatial resolution and sensor type“, *Journal of Civil Structural Health Monitoring*, S. 1–25, Dez. 2024, doi: 10.1007/s13349-024-00896-5.
- [2] A. Vorwagner, M. Kwapisz, W. Lienhart, M. Winkler, C. Monsberger, und D. Prammer, „Verteilte Rissbreitenmessung im Betonbau mittels faseroptischer Sensorik – Neue Anwendung von verteilten faseroptischen Messsystemen“, *Beton- und Stahlbetonbau*, Bd. 116, Nr. 10, S. 727–740, 2021, doi: <https://doi.org/10.1002/best.202100060>.
- [3] S. A. Taher u. a., „Structural Health Monitoring of Fatigue Cracks for Steel Bridges with Wireless Large-Area Strain Sensors“, *Sensors*, Bd. 22, Nr. 14, Art. Nr. 14, Jan. 2022, doi: 10.3390/s22145076.
- [4] W. Xu, C. Cui, C. Luo, und Q. Zhang, „Fatigue crack monitoring of steel bridge with coating sensor based on potential difference method“, *Construction and Building Materials*, Bd. 350, S. 128868, Okt. 2022, doi: 10.1016/j.conbuildmat.2022.128868.
- [5] A. Mufti, D. Thomson, D. Inaudi, H. Vogel, und D. McMahon, „Crack detection of steel girders using Brillouin optical time domain analysis“, *Journal of Civil Structural Health Monitoring*, Bd. 1, Dez. 2011, doi: 10.1007/s13349-011-0006-8.
- [6] K. Kishida, T. L. Aung, und R. Lin, „Monitoring a Railway Bridge with Distributed Fiber Optic Sensing Using Specially Installed Fibers“, *Sensors*, Bd. 25, Nr. 1, Art. Nr. 1, Jan. 2025, doi: 10.3390/s25010098.
- [7] „Luna ODISI 6000 Optical Distributed Sensor Interrogator“, Zugegriffen: 4. April 2025. [Online]. Verfügbar unter: <https://lunainc.com/product/odisi-6000-series>
- [8] V. Boros, A. Vorwagner, D. Prammer, und W. Lienhart, „Application of Embedded Distributed Fiber Optic Sensors on a Highway Bridge as a Support for Bridge Inspections“, Sep. 2024.
- [9] Ansys® *Mechanical APDL*, Release 17.0, Help System, Element Reference, Ansys Inc., 2015.



# Updating prediction of fatigue reliability index of railway bridges using structural monitoring data and updated load histories

Marian Ralbovsky<sup>1</sup>, ORCID 0000-0001-9323-4508, Stefan Lachinger<sup>1</sup>, ORCID 0009-0005-6705-6118

<sup>1</sup>Center for Transport Technologies, Austrian Institute of Technology GmbH, Giefinggasse 4, 1210 Wien, Austria  
email: marian.ralbovsky@ait.ac.at, stefan.lachinger@ait.ac.at

**ABSTRACT:** The assessment of fatigue consumption and the remaining lifetime of structural components is affected by considerable uncertainties on the side of the traffic loads, fatigue resistance and structural response. The purpose of the presented work was to develop methods for dealing with these uncertainties, as well as methods for improving the accuracy of assessment with the use of additional data.

Within the research project Assets4Rail, a structural monitoring system was installed on a railway bridge located on a local track in Austria. The system consisted of strain sensors, acceleration sensors and inclinometers. It was used to measure the bridge response during train passages with known axle loads in course of a test with controlled conditions. This data was used to calibrate the structural model and develop probabilistic methods for fatigue assessment. Influence lines at fatigue-critical locations were evaluated from measured bridge strain response including their uncertainty. Further uncertainties considered in the assessment include the load histories and the fatigue resistance.

The results showed the largest contribution by evaluation of model uncertainties from monitoring data. The effect of model updating was also considerable, but less significant. Further increase of estimation accuracy is achieved using section-specific traffic data. Whereas wayside monitoring data represent the reference scenario, the use of traffic management data provides a usable alternative.

**KEY WORDS:** fatigue; probabilistic; reliability; monitoring; updating.

## 1 INTRODUCTION

Railway bridges are often designed in steel. Their high ratio of traffic load to dead load as well as the high train axle forces makes them prone to fatigue issues. Many structures or components are reaching their planned lifetime. A survey conducted by the European project Sustainable Bridges, revealed that 75% of steel railway bridges are over 50 years old and almost 35% of them are over 100 years old [1]. Although fatigue damage is not among the leading causes of bridge collapses [2], it plays a role in maintenance of railway infrastructure. To optimize the investment planning for railway bridge maintenance and replacement, it is therefore advantageous to perform more accurate assessment of their expected remaining fatigue lifetime.

Several techniques to this end have already been developed and tested. The application of monitoring techniques to capture the real structural behavior has been implemented in many variants, usually evaluating the stress spectra from strain data acquired at fatigue-critical locations and consequent application of the Miner's rule to determine the damage accumulation [3]. The use of monitoring data leads often to lower stress ranges compared to results predicted by numerical models due to their inherent simplifications and their aspiration to ensure sufficient structural safety. Thus, SHM-based evaluations tend to predict a more extended fatigue lifetime. However, some application cases [4] show that it is not to be generalized as a rule.

Through a combination of monitoring data with calibrated FE-models, stress spectra can be evaluated also at unmeasured locations. This technique of virtual sensing has been validated

[5], [6] to obtain nominal stresses at railway bridges equipped with strain and acceleration sensors. The modelling can be further extended using the multiscale approach to also evaluate the local stresses – for example using a 3-scale concept encompassing the global scale, the structural member scale and the local scale [7].

Besides monitoring the structural response, the estimation of overpassing axle-load histories is the next important parameter in the fatigue accumulation assessment. While the train mixes defined in the Eurocode are suitable for design of new bridges, for the assessment of existing structures it is more expedient to use axle-load histories specific to the respective track location. The actual axle loads can be acquired for example using wayside monitoring systems applied on rails. However, the application of such systems is relatively new, so they provide data on the current state of traffic loading and axle-load histories prior to their installation remain unmeasured. During bridge lifetime, the axle-load histories may have changed significantly. Reconstruction of historic traffic loads provides a possible solution, as shown in a study for Norwegian railway bridges [8]. In here, it was identified that modern freight trains introduced after 1985 increased the fatigue damage accumulation rate significantly. Based on axle-load measurements in Dutch railway network, new fatigue load models for bridge assessment were proposed [9]. One of the load models addresses the period before 1970 and is based on limited available data and expert judgement. In another study [10], a simple approach was proposed, which considers development of total rail traffic volumes on national level, but neglects changes in train composition over time.

The evaluation of remaining fatigue lifetime is typically based on S-N curves as the definition of material resistance to fatigue loads. This approach features a fair amount of conservatism [11], which is understandable considering the significant variance of fatigue test results and the requirements of structural reliability, and it is necessary in semi-probabilistic assessment. However, the uncertainties can be modeled using a full-probabilistic approach by formulating the fatigue resistance as a random variable and evaluating probabilities of its exceedance. This type of evaluation results in estimating the reliability index and its development as the fatigue damage accumulates over time [12].

This work, which was done within the Shift2Rail project Assets4Rail [13], combines several abovementioned aspects, with the aim to highlight the joined effect of several methods. Three areas of more accurate fatigue assessment are addressed here: monitoring of structural response, track-specific axle-load histories, and probabilistic modelling of fatigue resistance. Moreover, the issue of track-specific axle-load histories is handled in different cases of data availability.

## 2 STRUCTURAL MONITORING AND MODEL CALIBRATION

### 2.1 Bridge description

The bridge is a semi-through type truss steel bridge (U-frame), which was constructed in the 1990's (Figure 1). It is a single span of 41.67 m length, which consists of 10 segments of equal length. The top chord has a rectangular cross-section, while the bottom chord is U-shaped. The diagonals have I-shaped cross section, except for the outer diagonals with rectangular cross-section. The truss members are constructed from welded steel plates and the truss members connect to each other with bolted plates.

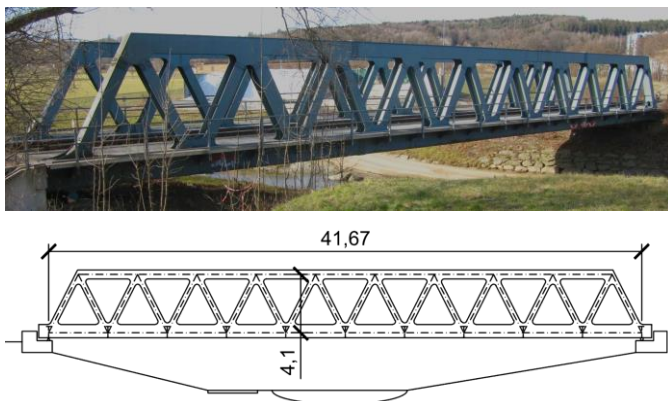


Figure 1. Side view of the bridge.

The bridge carries a single unballasted railway track. The rails are placed on top of wooden sleepers carried by longitudinal beams, which are rigidly connected to transverse beams (Figure 2). The transverse beams connect to bottom chord of the truss. The connections are again executed using bolted plates. The bridge deck has two layers of diagonal bracing, stiffening the longitudinal beams under the sleepers, as well as bottom chords of the truss.



Figure 2. Structure of the bridge deck.

The bridge is located on a side track in Austrian railway network and experiences very low traffic volumes. This facilitated performing various tests and measurements on this bridge. For purposes of this study, a traffic constitution was assumed with properties that correspond to a main railway line, thus simulating high traffic volumes.

### 2.2 Measurement system

The bridge was equipped with 31 optical strain gauges. The sensor locations concentrated around truss-member connections between truss segments 4 and 5 (Figure 3), as well as connection between longitudinal and transverse beams at segment 8 and the transverse beam to truss chord connection (Figure 4). Since the fatigue evaluation was indented to be based on nominal stresses, the purpose of this monitoring system was to capture nominal stresses in structural members, which explains positioning the sensors at a little distance from the connection nodes and not directly on the fatigue hot spots.

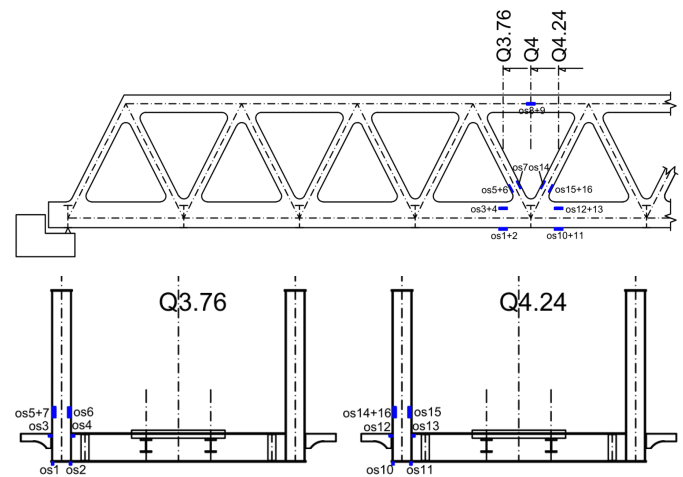


Figure 3. Locations of fibre-optic strain sensors on truss members.

The sensors were located on several points of the same cross-section to increase accuracy of the measurement and also to capture secondary effects like transverse bending or warping of cross-sections. Additionally, acceleration sensors were placed on several locations across the bridge, as well as inclinometers and temperature sensors. However, they are not relevant for the purposes of the work presented here, therefore they will not be described here.



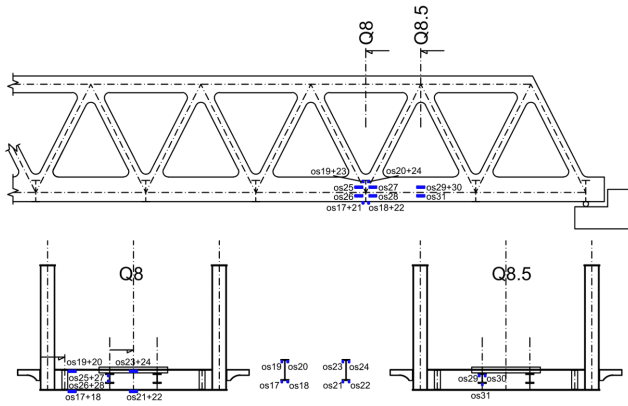


Table 1. Comparison of measured eigenfrequencies with predictions of the initial numerical model.

Parameter	Measured	FE-Model
$f_1$ , vertical bending	5.40 Hz	5.48 Hz
$f_2$ , upper chord 1 wave	9.99 Hz	10.22 Hz
$f_3$ , upper chord 1.5 waves	12.19 Hz	13.04 Hz

### 2.3 Model calibration

The numerical analysis was done using a shell model, which was constructed, meshed and calculated using FOSS (Free and Open Source Software) products. In particular the Pre- and Post-Processing platform SALOME [14] was used for the geometrical construction and meshing of the model, while the FEM-Solver CalculiX [15] was used for solving the meshed model. The model optimization of the FE-model was conducted using self-made algorithms in the Python programming language, utilizing optimization routines of the SciPy (Scientific Python) package.

The symmetry of the structure as well as the loading was used to reduce the model size and work with only half of the bridge and respective symmetry conditions (Figure 7, top). As the analysis will be done on the level of nominal stresses, a detailed modelling of the bolted connections was not necessary; the connections were modeled as rigidly connected plates (Figure 7, bottom).

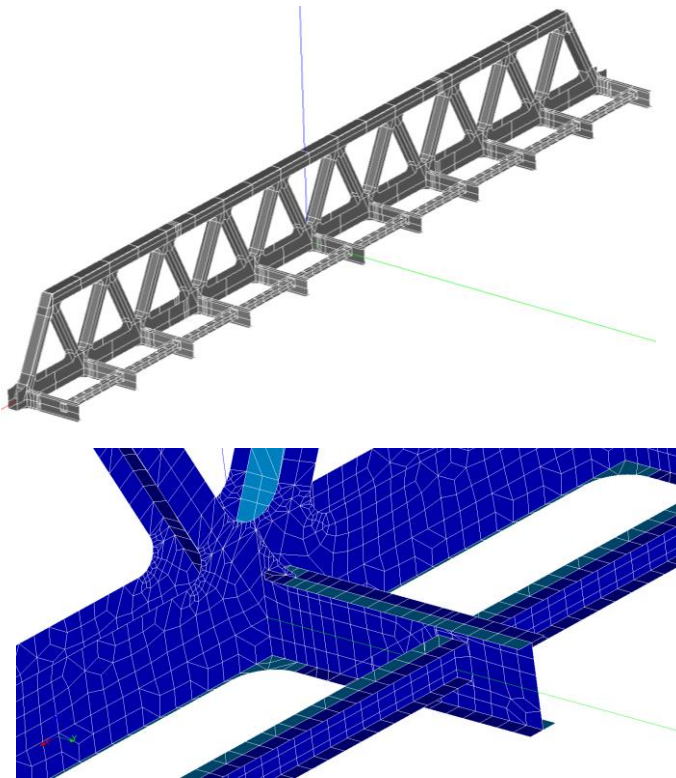


Figure 7. Geometry of the FE-model (top) and a detail of its mesh (bottom).

Using modal analysis of the bridge structure, several eigenfrequencies and mode shapes were calculated; the first two of which are displayed in Figure 8.

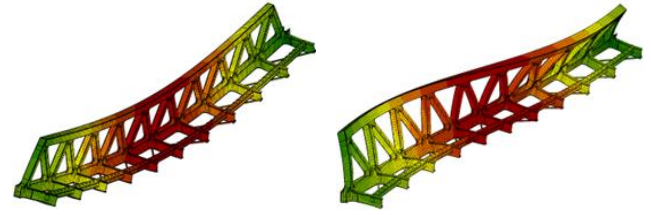


Figure 8. Mode shapes of the FE-model:  $f_1=5.48$  Hz (left) and  $f_2=10.22$  Hz (right).

The model calibration was performed in three steps: 1. using measured strain responses during train passages, 2. using measured eigenfrequencies and mode shapes, 3. using both sets of measured data together. The updating was done twice, using two different objective functions: the squared differences approach (Eq.1) and the Gauss error function approach (Eq.2).

$$J_{sq} = \sum_{i=1}^m \left( \frac{z_n(i) - z_e(i)}{\sigma_e(i)} \right)^2 \quad (1)$$

$$J_{erf} = \sum_{i=1}^m \operatorname{erf} \left( w \cdot \frac{|z_n(i) - z_e(i)|}{\sigma_e(i) \sqrt{2}} \right) \quad (2)$$

The structural parameters that were subjected to updating are listed in Table 2. They comprise of relevant parameters affecting the global stiffness, stiffness of connections, as well as distribution of structural masses.

Table 2. Values of updating parameters.

Parameter	Initial value	Updated with $J_{sq}$	Updated with $J_{erf}$
Young's modulus [GPa]	210	220.5	205.8
Steel density [kg/m <sup>3</sup> ]	7850	8282	8282
Coef. for cross-girder connection stiffness	1	1.5	1.31
Coef. for main truss connection stiffness	1	1.5	0.683
Translation rail spring [MN/m]	0	0	0
Rotational bearing spring [MNm/m]	0	1000	0
Coef. for sidewalk mass	1	1.1	0.9
Cover plate mass coef.	1	1.1	0.9
Thickness of stiffener at cross-girder connection [mm]	17.5	20.2	19.2

The two updating algorithms suggested different solutions for the updating parameters. While the squared differences approach favored increase of both stiffness (global and connections) and masses, the updating approach of Gauss error function suggested in comparison lower connection stiffness and non-structural masses. The agreement of the updated parameters with their real values could not be checked due to significant effort that would be required for such testing. This would be also the usual case in any other real applications.

The updated models were subsequently used in evaluation of fatigue damage evaluation at selected fatigue-critical details. Five critical details were identified in total. The first three of them are displayed in Figure 9. Most critical was detail nr.3, which covers fatigue failure in the lateral direction in the stiffener plate at the toe weld. The upper fillet weld produced a



detail category of 36 N/mm<sup>2</sup> for a root crack at the weld, which ranked it as most fatigue-critical spot on the structure.

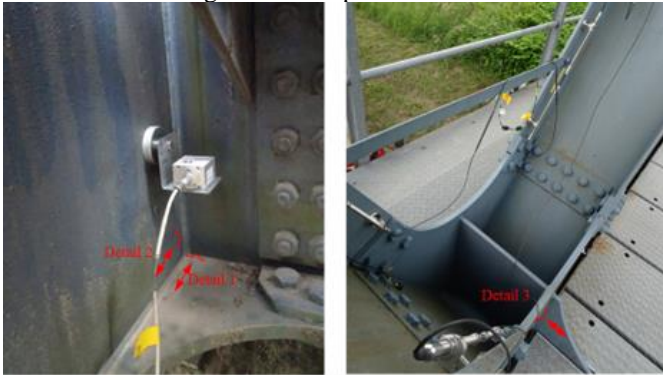


Figure 9. Three fatigue-critical details at the connection of cross-girder to bottom chord of the truss.

The differences in updated structural parameters resulted in influence lines of strain at fatigue-critical location as presented in Figure 10.

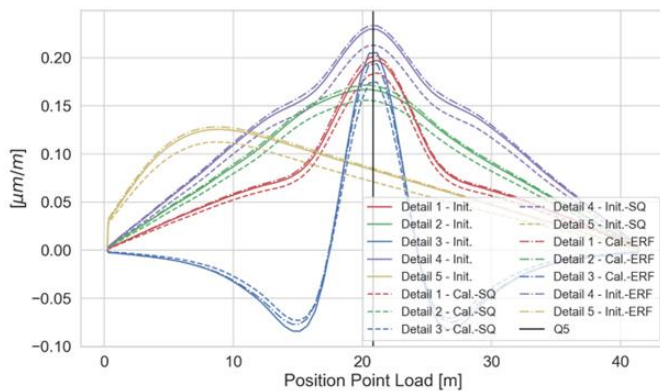


Figure 10. Influence lines of strain at five fatigue-critical details before updating (solid lines), after updating with... (dashed lines) and after updating with ... (dash-dotted lines).

### 3 TRAFFIC LOADS

To highlight the difference of traffic load assumptions in different cases of data availability, three cases were considered:

- No track-specific data available
- Traffic management data available for given section
- Wayside monitoring data available for given section

The first case represents the usual situation used in design of new bridges, where the train mix according to Eurocode is used. In the second case, the traffic management data provide basic information about train traffic specific to the track section. This information includes total train length, total train weight (estimated from wagon specifications), number of wagons and type of locomotive, and is listed for all train passages in a given time period. The third case represents the most accurate information: data from a wayside monitoring system, which provide axle forces and axle spacings of all train passages in a given time period.

Since the availability of wayside monitoring data is generally limited, it is expedient to have a methodology that can use traffic management data to generate track-specific estimation of traffic loads. Such a methodology was developed within the Assets4Rail project. Detailed description of the methodology

can be found in [16]; in this paper only a brief outline can be presented.

The procedure evaluates basic properties of trains from train management data and groups similar trains into clusters. For freight trains, the chosen basic properties were: unit mass of wagons [t/m], unit mass of locomotive(s) [t/m], and the number of carriages. Clustering algorithms were used to create train groups from available data, and then evaluate statistical properties of each group created. Figure 11 shows an example of evaluated train groups, represented by individual boxes. The placing and dimension of the displayed boxes correspond to the range  $\langle \pi - \sigma; \mu + \sigma \rangle$  of the three parameters annotated on the respective axes. The number in center of each box indicated the cluster size, i.e. number of train passages that were grouped in the respective cluster.

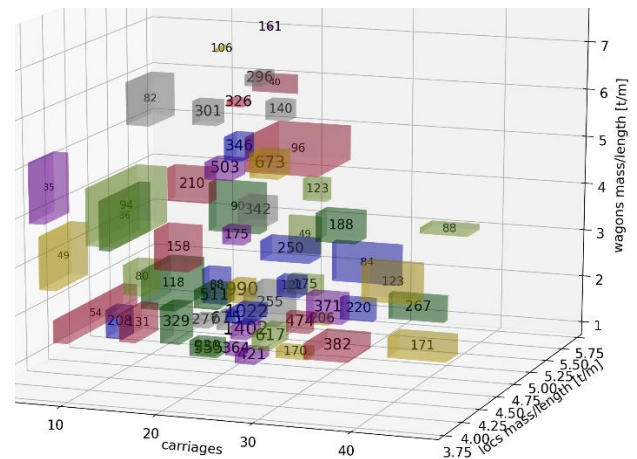


Figure 11. Clustered train management data of freight trains.

In the next step, a representative axle sequence was generated for each cluster. A database of wagon properties and a train model generation algorithm developed within the Assets4Rail project was used to this end. This algorithm requires deterministic values of basic train properties (number of carriages, etc.) as input: one set of values for each cluster. From the statistical evaluation of train data within each cluster, different quantiles can be chosen to represent each cluster. In order to compare the differences, the quantiles of 25%, 50%, 75% and 95% were used in further evaluations.

Schemes of generated axle sequences for 10 selected clusters of freight trains is partly shown in Figure 12; they consist of a sequence of arrows, height of which is proportional to the axle force magnitude. Loading situation of individual wagons (empty / full) is considered.

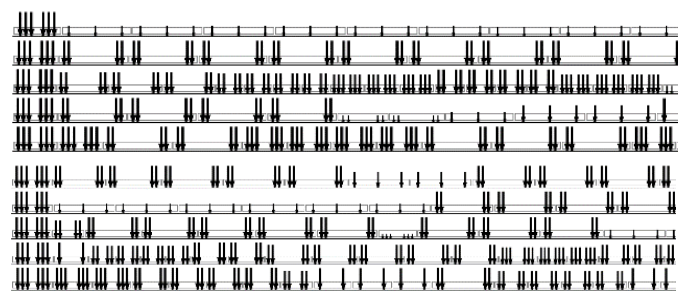


Figure 12. Partial schemes of freight train axle-sequences generated for selected train clusters.

In each train scheme, a locomotive with 6 axles is visible on the left side; the axle-force arrows display a force of 220 kN. The empty wagons can be recognized by the very small axle-forces shown at the wheel positions, which correspond to forces of less than 100 kN. The wagons feature different lengths (15 – 25 m) and axle configurations, which were chosen from catalogues of existing wagon stock.

Comparison of the track-specific train properties with the fatigue load model of the Eurocode showed some differences presented in Figure 13. The unit mass of the trains was considerably lower compared to the Eurocode standard traffic mix, while the number of axles was slightly higher in the freight trains. The shown results refer to one of the locations within Austrian railway network that was analyzed.

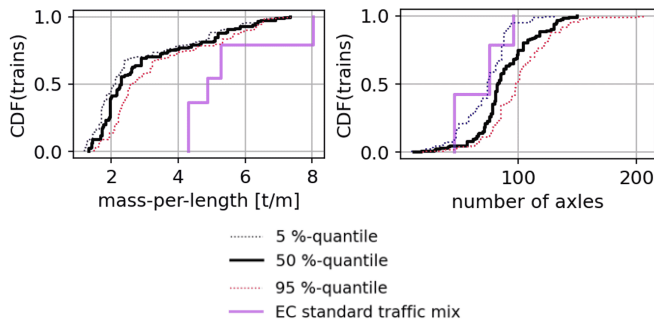


Figure 13. Cumulative Density Functions of the unit train mass (left) and number of axles (right) for trains generated from train management data compared to Eurocode.

In order to compare the differences between different axle-load sequences, their effect on the fatigue damage accumulation on different systems was analyzed. For this purpose, the midspan bending moment in simply-supported single-span bridges was used, simulating fatigue critical details governed by longitudinal stresses at such location. The span length was varied between 4 and 60 m. Eight traffic load mixes were analyzed: three Eurocode traffic mixes (light, standard, heavy), four traffic mixes generated the train management data using 25%, 50%, 75%, 95% quantiles of basic train properties for each cluster (TRGEN: \_q25, \_q50, \_q75, \_q95), and finally axle-sequences as measured by a wayside monitoring system. The fatigue damage accumulation evaluated using the wayside monitoring data was used as reference ( $d_{ref}$ ), since it represents the most accurate result. To eliminate the influence of total traffic volume, all traffic mixes were normalized the total traffic volume of 25 Mt/year. Figure 14 shows a comparison of the evaluated fatigue damages in relation to the reference (wayside monitoring data).

This comparison shows that the Eurocode standard traffic mix produced a fatigue damage that exceeds the reference by 50% - 160%, depending on the span length. The dependance of this exceedance on the span length could be caused by the way the Eurocode models were calibrated, and may vary for bridges with different static systems.

Using the train management data, this conservatism would be reduced to 35% - 105% exceedance.

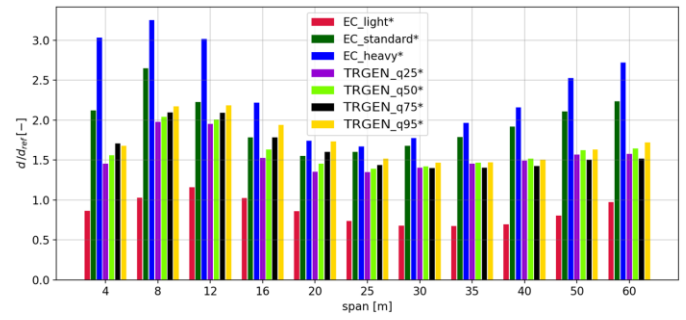


Figure 14. Fatigue damage accumulation evaluated for different normalized traffic mixes relative to  $d_{ref}$ .

#### 4 FATIGUE RELIABILITY EVALUATION

A full-probabilistic approach was chosen to evaluate the reliability index of fatigue damage occurrence. This included probabilistic modelling of structural properties, traffic load actions, as well as the fatigue resistance. The distributions of many of the probabilistic variables were adopted based on the recommendations of the probabilistic model code [17]. The limit state function was defined according Eq. 3, where  $D_{cr}$  is the accumulated fatigue damage at the failure (defined as a probabilistic variable) and  $D_{year}$  is the fatigue damage accumulation within one year (also a probabilistic variable).

$$G(t) = D_{cr} - D_{year} \cdot t \quad (3)$$

The failure probability and the reliability index are then evaluated using Eq. 4 and 5, respectively.

$$P_f(t) = P[T \leq t] = P[G(t) < 0] \quad (4)$$

$$\beta = -\Phi^{-1}(P_f) \quad (5)$$

Figure 15 shows  $D_{year}$  for the detail Nr. 3, compared between different models. The blue curve represents the case without using any monitoring data (no prior information) and results into the highest estimates of damage accumulation. If the model uncertainty can be estimated from the monitoring data, it can substantially reduce the total uncertainties. In here, the model uncertainty was determined from the uncertainty of influence lines evaluated from the measurements with the test train and the resulting distribution of damage accumulation (the orange curve) shows a significant reduction as result. The influence lines still correspond to the initial model, i.e. without updating.

After the model updating, the evaluated damage accumulation shows further reduction, as it can be observed from the green curve obtained using updating with the squared differences approach (Eq.1), and red curve obtained using updating with the Gauss error function approach (Eq.2).

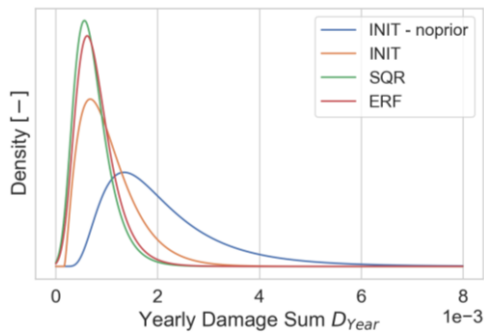


Figure 15. Distribution of the yearly fatigue damage accumulation on detail 3 using different numerical models.

The Figure 16 shows the reliability index evaluated at different points in time, comparing the same evaluation cases as in Figure 15: blue curve – without monitoring, orange curve – model uncertainty from monitoring but no updating, green and red curves – with additional model-updating step. The minimum required value of the reliability index is specified to be in range 1.5 – 3.8, depending on the accessibility of the detail and other factors. This range is displayed as a grey area. The failure probabilities related to reliability indices of  $\beta=1.5$  and  $\beta=3.8$  are  $P_f=0.067$  and  $P_f=7.23 \cdot 10^{-5}$ , respectively.

Whereas without monitoring data, the reliability index would reach after 100 years the value of  $\beta=2.1$  ( $P_f=0.018$ ), the inclusion of monitoring data combined with model updating could increase the reliability index value up to  $\beta=4.35$  ( $P_f=6.8 \cdot 10^{-6}$ ) in this particular case.

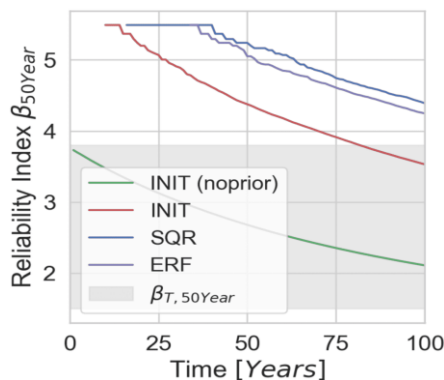


Figure 16. Development of the reliability index for detail 3 over time: comparison of different models.

## 5 CONCLUSIONS

The presented work summarizes the uncertainty parameters affecting fatigue damage evaluations and shows a way of dealing with them in a full-probabilistic analysis. The traffic loads can be updated using section-specific data, preferably wayside monitoring data that provide measured axle-load sequences. Alternatively, train management data can also be used to derive alternative, section-specific axle-sequences for fatigue evaluations. Since they rely on less accurate data regarding train masses compared to wayside monitoring, they tend to provide more conservative results. The use of train management data could be regarded as intermediate step between wayside monitoring (which is the reference) and the use of Eurocode fatigue load models.

Probabilistic fatigue evaluations have shown that updating of the uncertainty of influence lines using monitoring data contributed significantly to improving the result accuracy, as compared to the case with no prior information, in which model uncertainties according to recommendations of the probabilistic model code were used.

The updating of the numerical model provided a further increase of estimated reliability indices, at a cost of significant computational effort required to perform the model updating.

The results presented in this use case cannot be generalized. The increase of reliability index due to more accurate models of traffic loads and the numerical model of the bridge depend on many factors that are specific to the respective track section, the bridge structure and the monitoring system applied.

The purpose of this work was rather to present an approach that encompasses dealing with uncertainties on the side of traffic loads as well as of the structural response, and joins them together with probabilistic definition of fatigue resistance in a full-probabilistic evaluation of the fatigue reliability index.

The application of the presented methods could be recommended especially for cases where larger discrepancies between the original fatigue assessment assumptions and the reality are suspected. This may apply to bridges on track sections with much lower (or much higher) portion of freight traffic, or sections where freight trains operate with a significant number of empty wagons. Further, bridges with larger modelling uncertainties may profit from the use of monitoring data, for example short bridges (due to uncertain track interaction) or bridges that were calculated using models with significant simplifications, especially simplifications of member connections.

## ACKNOWLEDGMENTS

This work was done within the scope of the Shift2Rail project Assets4Rail (Grant agreement no: 826250) funded by the European Commission.

## REFERENCES

- [1] A. Dinas, Th.N. Nikolaidis, C.C. Baniotopoulos: Sustainable Restoration Criteria for a Historical Steel Railway Bridge, *Procedia Environmental Sciences* vol. 38, p. 578-585, 2017.
- [2] G. Zhang, Y. Liu, J. Liu, S. Lan, J. Yang: Causes and statistical characteristics of bridge failures: A review, *Journal of. Traffic and Transportation Engineering (engl. ed.)* vol. 9, p. 388-406, 2022.
- [3] X.W. Ye, Y.Q. Ni, K.Y. Wong, J.M. Ko: Statistical analysis of stress spectra for fatigue life assessment of steel bridges with structural health monitoring data, *Engineering Structures* vol. 45, p. 166-176, 2012.
- [4] J. Leandera, A. Andersson, R. Karoumi: Monitoring and enhanced fatigue evaluation of a steel railway bridge, *Engineering Structures* vol. 32, p.854-863, 2010.
- [5] S.E. Azam, M.M. Didyk, D. Linzell, A. Rageh: Experimental validation and numerical investigation of virtual strain sensing methods for steel railway bridges, *Journal of Sound and Vibration* vol. 537, 117207, 2022.
- [6] K. Maes, G. Lombaert: Validation of virtual sensing for the reconstruction of stresses in a railway bridge using field data of the KW51 bridge, *Mechanical Systems and Signal Processing* vol. 190, 110142, 2023.
- [7] R. Teixeira, C.S. Horas, A.M.P. De Jesus, R. Calçada, T.N. Bittencourt: Innovative hierarchical fatigue analysis of critical riveted railway bridges: A case study, *Engineering Structures* vol. 317, 118629, 2024.
- [8] G.T. Frøseth, A. Rönquist: Load model of historic traffic for fatigue life estimation of Norwegian railway bridges, *Engineering Structures* vol. 200, 109626, 2019.



- [9] S. Verdenius, S. Hengeveld, J. Maljaars: New fatigue load models for assessing railway bridges in Europe, *Engineering Structures* vol. 284, 115914, 2023.
- [10] M. Ralbovsky, A. Vorwagner, S. Lachinger: History of rail traffic volumes in the evaluation of fatigue consumption in steel bridges, 5<sup>th</sup> International Conference on Railway Technology, Montpellier, France, 22.-25.8.2022
- [11] C.S. Horas, J.N. Silva, J.A.F.O. Correia, A.M.P. De Jesus: Fatigue damage assessment on aging riveted metallic railway bridges: A literature review, *Structures* vol.58, 105664, 2023.
- [12] Y.H. Su, X.W. Ye, Y. Ding: ESS-based probabilistic fatigue life assessment of steel bridges: Methodology, numerical simulation and application, *Engineering Structures* vol. 253, 113802, 2022.
- [13] S. Lachinger, M. Ralbovsky, A. Anžlin, M. Kosič: project Assets4Rail - H2020 Shift2Rail ERJU grant 826250 - Deliverable D3.4: Fatigue consumption and remaining lifetime of structural components, 2022.
- [14] SALOME, 2019 v 9.4. [Online]. Available: [www.salome-platform.org](http://www.salome-platform.org)
- [15] G. Dhondt: Calculix v 2.16. [Online]. Available: [www.calculix.de](http://www.calculix.de)
- [16] A. Anžlin, M. Ralbovsky, D. Hekič, J. Kalin, M. Kreslin: project Assets4Rail - H2020 Shift2Rail ERJU grant 826250 - Deliverable D3.2: Section-specific fatigue load models: method and application, 2021.
- [17] Joint Comitee on Structural Safety, JCSS Probabilistic Model Code; Parts I - IV, JCSS, 2001-2015

## Monitoring of wind induced vibration on a tied-arch railway bridge.

Pablo Castillo Ruano<sup>1</sup>, Cesar Martínez<sup>1</sup>, Sonja Dallinger<sup>2</sup>

<sup>1</sup>RED Bernard GmbH, Erns-Melchior-Gasse 24, 1020 Vienna, Austria

<sup>2</sup>ÖBB-Infrastruktur AG, Fachbereich Bautechnik Brückenbau und konstruktiver Ingenieurbau, Lassallestraße 5, 1020 Vienna, Austria

email: pablo.castillo@bernard-gruppe.com, cesar.martinez@bernard-gruppe.com, asonja.dallinger@oebb.at

**ABSTRACT:** The ÖBB Rheinbrücke, situated in the vicinity of Lustenau, represents a novel approach to steel-concrete composite arch structure engineering, boasting a span of 102 meters. The primary supporting structure is a tied-arch comprising 12 round steel hangers, each with a diameter of 100 mm, situated on either side of the bridge. The maximum length of the hangers is 18.9 meters. In arch bridges of this type with steel hangers, wind-induced vibrations in the hangers can result in high-frequency, high-amplitude fluctuations in stress levels, particularly in the hangers and their connections. This can be problematic from the perspective of fatigue, particularly given that the hanger connections often have notch-sensitive details. Following the completion of the bridge, comprehensive monitoring was conducted in accordance with the original plan. This was done with the objective of acquiring data regarding the vibrations experienced by the hangers and the subsequent damage to the material. This data was then used to determine whether vibration-reducing measures were necessary. During the course of monitoring and subsequent evaluation, it was observed that wind-induced vibrations in the hangers could result in the occurrence of fatigue-relevant stress ranges. This article serves to emphasise the importance of structural health monitoring in confirming the efficacy of vibration reduction measures, which have the potential to extend the service life of railway bridges.

**KEY WORDS:** monitoring; wind-induced vibrations; fatigue.

### 1 INTRODUCTION

Railway bridges, integral to transportation networks, are subjected to diverse and dynamic loading conditions, necessitating diligent monitoring and maintenance strategies to guarantee their continued safety and operational efficiency. Specifically, the application of SHM to railway bridges enables the early detection of potential damage or deterioration, thereby averting catastrophic failures and extending the lifespan of these critical infrastructures. The implementation of SHM systems typically involves the deployment of various sensors, data acquisition systems, and communication networks to continuously monitor key structural parameters such as strain, displacement, acceleration, and temperature [1]. By analyzing the data acquired from these sensors, engineers can identify anomalies or deviations from baseline behavior, which may indicate the presence of damage or deterioration [2]. The integration of advanced data analytics, significantly augments the capabilities of SHM systems, enabling the detection of nuanced changes in structural behavior that might elude traditional inspection methodologies. These analytical techniques can discern patterns and trends in the data, thereby providing valuable insights into the underlying mechanisms driving structural degradation. [3]. In light of these considerations, this paper delves into the practical application of SHM in assisting the decision to apply correction measurements, with a particular focus on the ÖBB Rheinbrücke near Lustenau. the ÖBB Rheinbrücke is single-track and electrified. It is a total of 276.5 m long and 7.95 m wide and consists of a 102 m wide tied arch bridge over the Rhine as well as four trough bridges over the western foreland and two trough bridges over the eastern foreland (Figure 1).



Figure 1. ÖBB Rheinbrücke

The entire bridge has a continuous ballast bed. The tied arch bridge has two parabolic arches made of reinforced concrete, which are clamped in steel sleeves on the end cross girders. The bridge structure has twelve round steel hangers with a diameter of 100 mm on each side of the bridge. The maximum hanger length is 18.9 m. The connection of the hanger trapeziums to the connecting plate and the connecting plate to the upper flange of the longitudinal beam are designed as welded seams (Figure 2).

Wind-induced vibrations in these hangers can lead to high-frequency, high-amplitude stress fluctuations, particularly in the hangers and their connections, posing a significant fatigue risk. The susceptibility to fatigue is exacerbated by the presence of notch-sensitive details in the hanger connections, rendering them vulnerable to crack initiation and propagation under cyclic loading conditions [4]. Great attention was already paid to this issue during the planning phase of the bridge built in 2011. However, in order to gain experience of the phenomenon of hanger vibrations for this and future bridges, the hangers

were initially designed without vibration-reducing measures. nevertheless, precautions were taken for the later installation of measures to reduce vibrations.

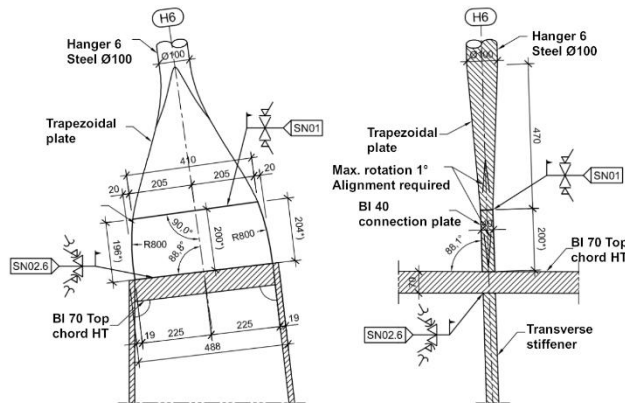


Figure 2. Detail of the hanger connection

Two wind related physical phenomena, vortex-induced transverse vibrations and rain-wind-induced vibrations, can appear during the structure's service life. Those characteristics of those phenomena are briefly described below.

- **Vortex-Induced Vibrations:** These vibrations are caused by vortices detaching alternately from each side of the hanger. The frequency of this oscillating force is related to the Strouhal number, approximately 0.2 for cylinders. According to [5], the critical wind speed for the respective mode shape is calculated using equation (1)

$$v_{crit,i} = \frac{f_i D}{St} \quad (1)$$

Where  $D$  is the hanger diameter,  $f_i$  is the natural frequency of the respective mode shape and  $St$  is the Strouhal number.

- **Rain-Wind-Induced Vibrations:** These vibrations occur during simultaneous rain and wind events. They are characterized by low frequency and high amplitude, potentially leading to high stress amplitudes. According to [5], [6] the critical wind speed for this type of excitation can be calculated using equation (2).

$$v_{crit,i} = 73.5 \cdot D \cdot f_0 \cdot \left(\frac{f_i}{f_0}\right)^{0.6} \quad (2)$$

where  $D$  is the hanger diameter,  $f_0$  is the reference frequency and  $f_i$  the natural frequency for the respective mode shape

Empirical studies [7],[8],[9] indicate these vibrations are most likely in light to moderate rain and wind speeds between 4 and 20 m/s.

## 2 MONITORING SYSTEM AND DATA EVALUATION

After the construction of the bridge, an extensive measurement program was started as planned. The monitoring system deployed on the ÖBB Rheinbrücke comprised an array of sensors strategically positioned to capture the dynamic response of the hangers. In the preliminary stage of the program, two cables of varying lengths were subjected to monitoring. H6, the longest cable on the bridge, measures 19 meters, while H4 measures 14 meters. The most critical

element in terms of fatigue failure was used as the reference point for calculating the stresses. In the present case of the Rheinbrücke, they are the connections between the connecting plates of the hanger and the upper flange of the longitudinal girder (Figure. 2) which present a notch type of 45 N/mm(2) ([10], Table 8.5, Design Detail 1). Strain gauges were affixed to these hanger connection plates to measure stress variations, while accelerometers were installed to capture vibrational frequencies and amplitudes on the hangers. In addition, temperature sensors were integrated into the system to account for thermal effects on the structural behavior of the bridge. The acquired data was transmitted in real-time to a central data acquisition system, where it underwent processing, analysis, and storage. Table 1 and Figure 3 show the number and location of the installed sensors.

Table 1. Sensors at the Rheinbrücke

	Ref.in Figure 3	Number of Sensors
Acceleration	AS	8
Displacement	Weg	2
Temperature (Component)	TEMP	4
Linear strain gauges	DMS-L	35
Rosette strain gauges	DMS-R	10
Wind speed		1
Wind direction		1
Rain intensity		1
Air temperature		1

In order to keep the amount of data reasonably limited, the strain values are recorded in a triggered manner; the recordings are started at accelerations greater than  $0.4 \text{ m/s}^2$  at the hangers. The weather data and temperature, on the other hand, are recorded continuously.

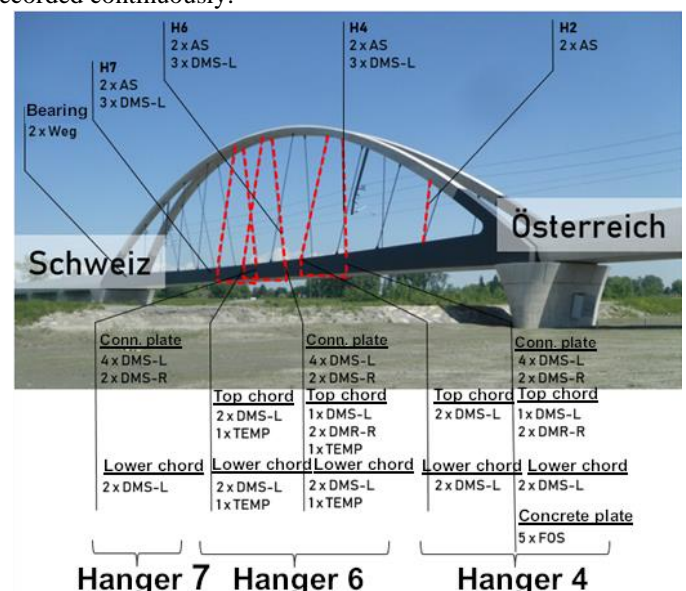


Figure 3. Position of the installed sensors

During the almost ten-year monitoring period (April 2013 to the end of 2022) on the Rhine bridge, numerous events with vortex-induced transverse vibrations and rain-wind-induced

vibrations were recorded. To evaluate the recorded data, the critical wind speeds were calculated using formula (1) for vortex-induced vibration and formula (2) for rain-wind-induced vibration. The calculated speeds were useful for the analysis and classification of the different events.

To assess the effects of the wind induced vibrations on the fatigue resistance of the structure, the cut-off limit for the fatigue strength was calculated according to [10], resulting in a value of 15.8 N/mm<sup>2</sup>. This implies that every stress range above this limit is relevant for the fatigue resistance, and must be considered for the damage accumulation. The process of damage accumulation is an important aspect of fatigue analysis as it is used to predict the remaining service life of a component or structure. The Palmgren-Miner rule [11,12] has been used to calculate the amount of damage produced by a given loading history by summing the damage caused by each loading cycle.

The following sections describe one event of each type, providing a better insight into the effects of these events on the structure.

### 2.1 Vortex induced vibrations

Table 2 shows the calculated frequencies for the monitored hangers.

Table 2. Natural frequencies

Hanger Mode Shape	H4 f[Hz]	H6 f[Hz]
1	4.0	3.5
2	8.7	7.4
3	14.5	11.9

The measurements carried out show that the critical wind speed calculated for the 3rd natural frequency wind speed  $v_{crit,3} = 6$  m/s caused the hanger H6 to oscillate over longer periods of time with stress oscillation amplitudes above the fatigue strength threshold value, as the stress history plot in figure 4 shows. During the duration of the event, the condition for vortex-induced vibration excitation was fulfilled by a constant wind speed around the calculated critical speed for a long period of time (over two hours in this event).

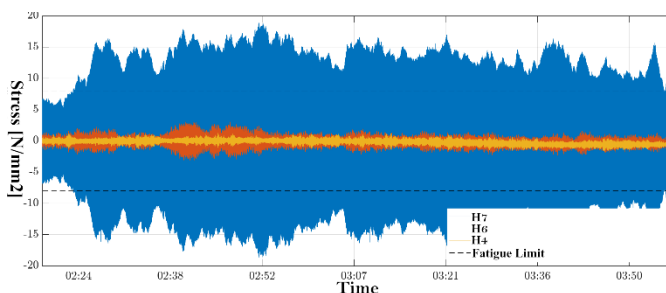


Figure 4. Stresses caused by a vortex-induced vibration event

Figure 4 shows that the stresses measured on cable H6 are much higher than those measured on cable H4. The stresses on cable H4 are irrelevant for fatigue damage. Figure 5 clearly shows that the measured frequencies are close to the calculated third natural frequency. This indicates that higher natural modes than the first must be considered when evaluating fatigue damage.

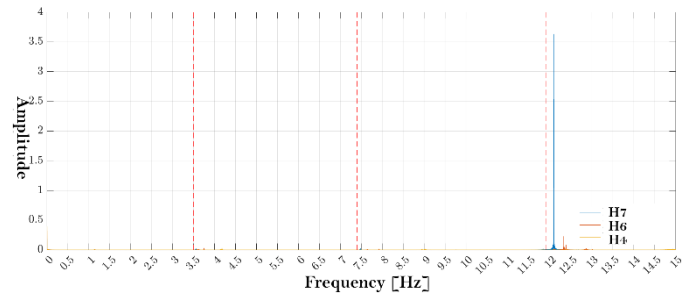


Figure 5. Frequency of the vortex-induced vibration

### 2.2 Rain-wind induced vibration

To detect and characterize event of this type, a criterion based on the calculated critical speed (table 2) for the first natural frequency and the presence of persistent precipitation has been applied. A typical stress history for this type of events is presented in figure 6.

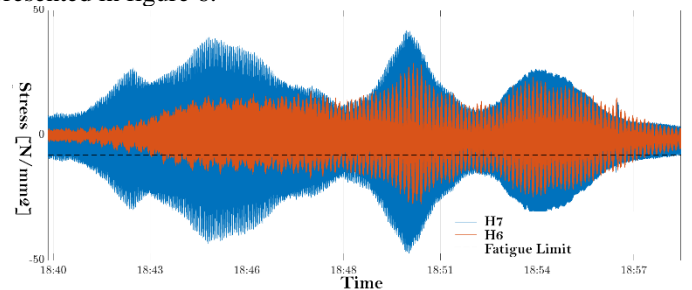


Figure 6. Stress history over a rain-wind induced vibration event

During the duration of this event, the wind speed was only occasionally in the range of the calculated critical wind speed  $v_{crit,1} = 15.7$  m/s, the damaging vibrations nevertheless occurred for a longer period of time. It should be also noted that it rained unusually heavily (over 50 mm/h) shortly before the build-up. Generally, from the recorded rain-wind-induced events, it can be inferred that the stress range of hanger H6 is significantly higher than in events in which vibrations are caused solely by vortex-excited transverse vibrations.

## 3 FATIGUE DAMAGE AND LIFE CYCLE

During the entire bridge monitoring period, regular calculations of the remaining service life of the critical weld seam between the connecting plate and the top chord of the longitudinal girder were carried out on the basis of the Palmgren-Miner rule. In order to be able to make a statement as to whether the observed stresses could become a problem for the hanger connections over the years, the stress range collective recorded during the measurement period was extrapolated to a service life of 100 years in this work. For this purpose, it is assumed that exactly the same stresses occur during the extrapolation period as during the period in which the monitoring was carried out. Under this assumption, the collective stress range measured can simply be multiplied by a corresponding factor and thus a forecast for the theoretical service life can be created using the Palmgren-Miner hypothesis. No distinction was made between individual vibration types in these forecasts; all vibration sources such as



rain-wind-induced vibrations and vortex-induced transverse vibrations, as well as train passages, are therefore included here. The data are added together to obtain a statistically sound statement about the remaining service life of the monitored hangers. It should be noted at this point that only heavy freight trains can cause stress oscillation amplitudes relevant to fatigue, and that these do not significantly reduce the remaining service life, due to their low frequency. The history of the theoretical residual service life is shown in Table 3

Table 3. Progress of theoretical service life (years)

Hanger	Marz 2018	July 2019	June 2020	June 2021	June 2022	Nov. 2022
H4	465	269	394	475	573	626
H6	42	40	21	18	22	23
H7	207	360	265	353	461	518

The remaining service life forecasts show that the influence of wind induced vibrations, on the hanger H6 is remarkable, while the influence on the shorter hanger (H4) plays a subordinate role with regard to the planned service life.

#### 4 VIBRATION-REDUCING MEASURES

Following the results of the monitoring campaign, it was decided to install a system to reduce the effects of vibration on the Rheinbrücke. Interconnecting adjacent cables using cross-ties is a method that has been experimentally tested on numerous suspension bridges [13], which simply and effectively mitigates the effects of wind-induced vibrations. In addition, this vibration reducing measure was already proposed during the planning phase in case of need. It consists of connecting the bridge hangers with small-diameter cables. In this way, the vibration energy is distributed over several hangers with different natural frequencies. In this manner, unexcited hangers act as dampers [13,14].

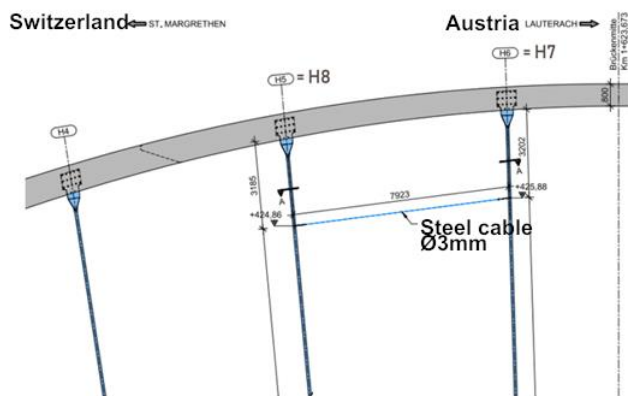


Figure 7. Vibration reducing cable

In May 2017 such measure was implemented by installing a 3 mm cable connecting hanger H7 and hanger H8 (Figure 7). After installation, H7, which has the same length as H6, was also monitored to evaluate the effectiveness of the procedure. As can be seen in figures 3 and 4, the amplitude of the measured stresses is significant reduced when compared with those in

hanger H6. Using this method, it is possible to improve the issue of fatigue damage in the structure, as can be seen from the calculation of the theoretical service life in Table 3. In the summer of 2021, the measure was installed on the remaining bridge cables. The data presented in Table 3 unequivocally reveals a trend change in the theoretical service life of cable H6 since the installation of the connecting cable. This finding is confirmed by calculations for the subsequent years, thereby underscoring the beneficial effect of this measure.

#### 5 CONCLUSION

This article presents the effects of vortex-excited transverse vibrations and rain-wind-induced vibrations on the ÖBB Rheinbrücke near Lustenau. Data collected during a long and extensive monitoring campaign on the bridge were used for this purpose.

The following conclusions can be drawn from the analyzed data:

- Wind-induced events cause fatigue-relevant stresses that are dependent on the weather conditions
- The effects of vortex-induced and rain-wind-induced events on the fatigue strength are much more pronounced for the hangers with greater length.
- The damaging effect of such events can be effectively reduced by installing cables joining adjacent hangers. The theoretical service life increases progressively, which confirms the positive effect of the measure against fatigue failure.

These findings underscore the critical importance of considering wind-induced vibrations in the design and maintenance of arch bridges, especially those with slender steel hangers. The implementation of a structural health monitoring system proved invaluable in detecting and quantifying these vibrations, allowing for timely intervention and mitigation strategies. The SHM system enabled the detection of wind-induced vibrations in the hangers, which could have led to fatigue damage and premature failure, thus contributing to the mitigation of potential risks.

#### REFERENCES

- [1] Wu, T., Tang, L., Shao, S., Zhang, X., Liu, Y., & Zhou, Z. Cost-effective, vision-based multi-target tracking approach for structural health monitoring. *Measurement Science and Technology*, 32(12), 125116. <https://doi.org/10.1088/1361-6501/ac2551> (2021).
- [2] Chen, L., Zhu, C., Wu, Z., Yuan, X., & Moreu, F. Measuring Total Transverse Reference-free Displacements of Railroad Bridges using 2 Degrees of Freedom (2DOF): Experimental Validation. *arXiv (Cornell University)*. <https://doi.org/10.48550/arxiv.2110.08701> (2021).
- [3] Spuler, T., Moor, G., & Majumdar, S. Assessment of the condition and performance of long span bridges using automated monitoring systems – optimising inspection and maintenance efforts. Report, 101, 1. <https://doi.org/10.2749/222137813815776331> (2013).
- [4] Castillo Ruano, P.; Dallinger, S.; Bruschetini-Ambro, Z.; Bartl, T. Windinduzierte Schwingungen an den Hängern der ÖBB-Rheinbrücke. *Stahlbau* 94, H. 3, S. 131–141. <https://doi.org/10.1002/stab.202400036> (2025)
- [5] DIN EN 1993-2/NA:2014-10 National Annex - Steel bridges. Berlin: Beuth. Edition October 2014. (2014)
- [6] BASt Leitfadens zum Anhang NA.F Bemessung von Hängern an Stabbogenbrücken der DIN EN 1993-2/NA:2014-10. Bergisch Gladbach: Bundesanstalt für Straßenwesen. Ausgabe Februar 2018 (2018)

- [7] Zuo, D.; Jones, N. P.; Main, J. A. Field observation of vortex- and rain-wind-induced stay-cable vibrations in a three-dimensional environment. *Journal of Wind Engineering and Industrial Aerodynamics* 96, pp. 1124–1133. <https://doi.org/10.1016/j.jweia.2007.06.046> (2008)
- [8] Matsumoto, M.; Shiraishi, N.; Shirato, H. Rain-wind induced vibration of cables of cable-stayed bridges. *Journal of wind engineering and industrial aerodynamics* 43, pp. 2011–2022 (1992)
- [9] Phelan, R. S.; Sarkar, P. P.; Mehta, K. C. Full-Scale Measurements to Investigate Rain-Wind Induced Cable-Stay Vibration and Its Mitigation. *Journal of Bridge Engineering* 11, pp. 293–304. [https://doi.org/10.1061/\(ASCE\)1084-0702\(2006\)11:3\(293\)](https://doi.org/10.1061/(ASCE)1084-0702(2006)11:3(293)) (2006)
- [10] ÖNORM B 1993-1-9 Eurocode 3: Bemessung und Konstruktion von Stahlbauten – Teil 1-9: Ermüdung – Nationale Festlegungen zu ÖNORM EN 1993-1-9, nationale Erläuterungen und nationale Ergänzungen. Wien: Austrian Standards. (1993)
- [11] Palmgren, A. G. Die Lebensdauer von Kugellagern. *Zeitschrift des Vereines Deutscher Ingenieure (ZVDI)* 14, S. 339–341 (1924)
- [12] Miner, M. Cumulative damage in fatigue. *J. Appl. Mech.*, vol. Vol. 12, pp. A159–A164, (1945)
- [13] Geier, R. Systemidentifikation seilgestützter Tragwerke: die dynamische Strukturantwort von Schrägseilen. Technische Universität Wien (2004)
- [14] Geißler, K., Mager, M. Die Problematik der winderregten Schwingungen an Brückenhängern in Theorie und Praxis. *Berichte aus dem Konstruktiven Ingenieurbau* 6. (2010)

# Acoustic emission monitoring of fatigue cracks for railway steel bridge inspection

Prokofyev, M.<sup>1</sup>, Marihart, H.<sup>1</sup>, Lackner, G.<sup>1</sup>

<sup>1</sup>TÜV AUSTRIA GMBH, Deutschstraße 10, 1230 Vienna, Austria

email: mikhail.prokofyev@tuv.at, heribert.marhart@tuv.at, gerald.lackner@tuv.at

**ABSTRACT:** Railway steel bridges are often affected by material fatigue, i.e. crack formation and crack growth at areas of high stress concentrations under millions of load cycles due to the traffic load. To support the continued safe operation of these structures a flexible and robust system solution for structural health monitoring is needed. It provides the responsible bridge inspector with useful information regarding the current condition and the future development of the monitored area. This offers the infrastructure operator an opportunity for optimised planning of inspection intervals and maintenance measures and helps to extend the service life of these structures. For this purpose, the RISE system was developed by TÜV AUSTRIA in close cooperation with the Austrian Federal Railways ÖBB. The RISE system monitors fatigue cracks and/or highly stressed areas using acoustic emission (AE). The system records the AE response from the monitored area while the material is stressed by the usual day-to-day railway operations. The analysis of the change of this material response over the monitoring period is used to predict the future development of the crack. In this paper the application of the RISE system for bridge inspection is presented for steel bridges in the railway network of ÖBB. The system solution is presented as a whole, from the installation on-site until the evaluation of the monitoring data and the obtained results supporting the responsible bridge inspectors.

**KEY WORDS:** SHMII-13; acoustic emission, fatigue cracks, steel bridges.

## 1 INTRODUCTION

Steel bridges are often affected by fatigue cracks due to cyclical loading caused by trains passing over them. Bridges at the end of their service life inevitably develop such cracks. The ÖBB team takes care of the maintenance of the bridges in its railway network and thus ensures the safety of the day-to-day train traffic. ÖBB employees inspect the bridges at regular intervals and assess their condition.

ÖBB was looking for a way to find a tool for these bridge inspectors to give them a way to monitor fatigue cracks and detect cracks at locations where cracks are suspected. In addition, this tool should be able to predict the future development of the condition of the monitored component when cracks already present, to help with a more precise planning for inspections intervals and repair measures. As part of the Rail4Future program co-financed by the Austrian Research Promotion Agency, the monitoring of cracks using acoustic emission (AE) was selected as the method. TÜV AUSTRIA and ÖBB have been cooperating for years in the implementation of acoustic emission as a monitoring tool for railway steel bridges. As part of this cooperation, a stand-alone solution, RISE (**R**emote **I**nspection **S**ystem **E**dge), has been developed. A monitoring solution for the detection and monitoring of fatigue cracks on railway steel bridges.

RISE offers monitoring as a service for railway infrastructure operators, from setting up the monitoring, recording the data to generating the report. In addition, a prediction on the future development of the crack is also provided.

This method is known as the failure forecast method (FFM). A method that is utilizing the near constant measurement data

stream from the device to predict the time until the maximum utilization of the monitored component is reached.

The RISE device was developed with the focus point to be a reliable and easy to install acoustic emission monitoring system. RISE is specifically designed for monitoring due to its compact design, low power consumption and simple installation.

## 2 OVERVIEW OF MONITORING SYSTEM

### 2.1 Technical overview

RISE by TÜV AUSTRIA is an acoustic emission system designed for detection and continuous monitoring of fatigue cracks. RISE consists of a hardware component, the RISE-Core, which is installed on site and a server infrastructure for data evaluation and monitoring result presentation on an online dashboard. The data from the RISE-Core is sent to this data platform via a mobile network and an encrypted connection. The data stream is processed on the server. The results are displayed on a graphical online interface, the RISE dashboard, where they are accessible by the customer.

The RISE-Core is installed at the position where a crack is suspected, or an already existing crack needs to be monitored. The system has four acoustic emission channels. The connected piezoelectric sensors detect the mechanical waves generated by the growth of cracks inside the material. Acoustic emission occurs when the defects in the material are excited by a load. The propagation of the defect is accompanied by the release of energy in form of an elastic wave. Acoustic emission is therefore a passive non-destructive method. In the case of railway steel bridges, the load needed for activation of cracks is the passage of trains over the bridge from the usual daily

traffic. Monitoring with the system therefore provides information about the acoustic emission material response to the currently operational load.

The preprocessing of the signals in the form of extraction of basic acoustic emission parameters takes place on site. The system is designed so that the power can be provided via a small off-grid solar system. A mobile network connection is required to outsource the needed computing power to a server. It is possible to use several RISE-Cores on one bridge. For every monitoring position one RISE system is required.

## 2.2 Theory of operation

Every time a train passes over the steel bridge, the material is stressed. This can cause fatigue crack growth to occur at locations with high stress concentrations due to periodic overloading of the material. The crack growth is accompanied by a stress reconfiguration and a sudden release of energy in form of elastic waves in the material. The mechanical waves propagate in the material and can be converted into an electrical signal utilizing the piezoelectric sensors. This signal is digitalized and the acoustic emission parameters that are relevant for further evaluation are extracted from it. The system therefore is recording the AE material response to the operational load.

As first processing of data on the server, located events are calculated. This method deals with combining the signal information from the whole sensor array and not an individual sensor only and providing the information about the point of origin of the mechanical wave. To indicate an acoustic emission event as a located event, several sensors must be excited by the mechanical wave and the strength of the electrical signal generated by the piezoelectrical element must exceed a specified threshold (in mV). In addition, the time difference on arrival at the different sensors must not exceed a certain specified value (1st-Hit Discrimination Time). This time value is related to the distance between the sensors and the time it takes for the mechanical wave to travel this distance at a defined speed of sound. The calculation of the wave's point of origin is calculated from the time differences of the individual signals, the speed of sound and the position of the sensors. The detection of the events relevant for further evaluation is carried out by 3 measuring sensors, which surround the crack or the monitored area in a triangular configuration.

So-called guard sensors are used to ensure that no noise from outside the monitored area interferes with the measurement. These are placed around the measuring array consisting of the three measuring sensors. Incoming waves that are first detected by one of the four guard sensors are not used to calculate the material response, as the system recognizes that the mechanical wave originated outside the monitored area of interest.

RISE provides a statement about the further development of the crack after a given measurement time. This method is known as the failure forecast method. The information helps the infrastructure operator to plan the inspection intervals and repair measures for ageing bridges. The method is based on rate-based structural health monitoring and requires near-continuous measuring data [1].

Many load-controlled processes, such as fatigue crack growth, show positive feedback. Crack growth accelerates as the degree of degradation progresses. The closer the system

gets to the point where it has exhausted its capacity to withstand the load, the higher the rate at which the degradation progresses.

This point in time is therefore the time when the maximum utilization of the monitored component is reached. The advantage of this method is that it is not the crack growth per se that is monitored, e.g. the crack length, but the change in a measured value that is symptomatic for the degradation (see Figure 1).

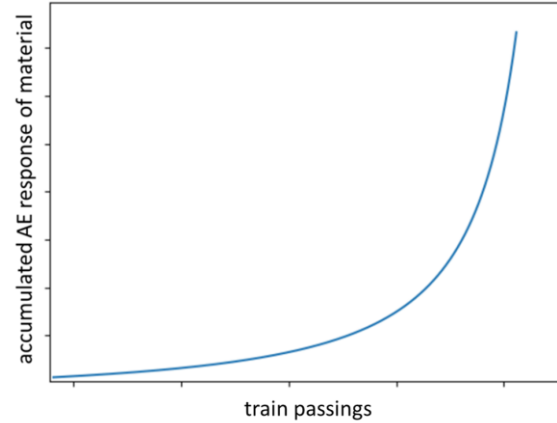


Figure 1 Illustration of the acoustic emission material response with the progression of a fatigue crack growth due to the cyclic loading of trains passing over the bridge.

In the case of acoustic emission monitoring, this value can be the energy of the acoustic emission signals, localized events, or hits detected from the monitored area.

Crack growth generates a mechanical wave that propagates through the material by releasing elastic energy stored in the crack tip. These mechanical waves can be converted into an electrical signal using piezoelectric sensors, which is then digitized and made available for further evaluation. The advantage of FFM over conventional methods for assessing degradation is that it does not require any detailed information about material properties and crack geometry. Only the material response to the operational conditions over time provides the data required to make a statement about future development.

Fukuzono [2] and Voight [3][4] were able to show in their works that there is a correlation for many degradation processes that can be expressed in Equation 1:

$$\frac{d^2\Omega}{dt^2} = A \left( \frac{d\Omega}{dt} \right)^\alpha \quad (1)$$

$\Omega$  is the measured variable associated with the degradation. In the case of monitoring fatigue cracks on steel bridges, the variable is the accumulated acoustic emission response of the material (see Figure 1). The two constants  $A$  and  $\alpha$  are empirical parameters that are dependent on the process under consideration. The equation can be integrated in the range from  $t$  to time  $t_f$  (time of maximum utilization of the component) with  $\alpha > 1$  (Equation 2):

$$\left( 1 / \frac{d\Omega}{dt} \right)^{\alpha-1} \approx (\alpha - 1) A (t_f - t) \quad (2)$$

The equation can be further simplified for the case that  $\alpha \approx 2$ , which is the case for fatigue crack growth [1]. This can be



verified from the measurement data by plotting the logarithm of the first and second time derivatives of  $\Omega$  and finding  $\alpha$  from the calculated slope.

So obtained equation shows a linear correlation (Equation 3).

$$\frac{1}{\Omega} \approx A(t_f - t) \quad (3)$$

As the rate of change of the material response is very high at the point in time at which the maximum material utilization of the monitored component is reached, a statement can be made from the monitoring data about this point in time. For this purpose, the inverse rate of the material response is plotted against time. The calculated linear regression line intersects the time axis at the point where the inverse rate of change of the material response approaches zero (see Figure 2).

Based on the remaining time until the maximum utilisation of the component is reached, a traffic light rating system is set up and the operator is given a recommendation on how to proceed. If the time until maximum utilisation is reached is longer than the time window of a regular periodic inspection, further monitoring is only necessary within the designated time (green area). If the time interval is shorter than the time window of a periodic inspection, a permanent monitoring is recommended (yellow area). If the time to maximum utilisation of the component is very short, not only a further inspection is required, but also safety measures are appropriate (red area).

The failure forecast method is shown to be tolerant for random variable amplitude loading that is statistically stationary as it is the case for train passages that have a variety of train mass [7]. A significant change in the exploitation of the bridge would require a new monitoring of the material response due to drastically changed traffic loads.

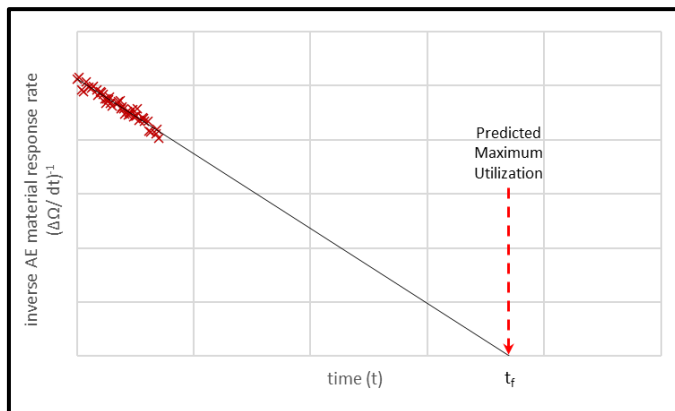


Figure 2 Illustration of application of the failure forecast method on continuous monitoring data. The linear regression line is intersecting the time axis at the time point of maximum utilization of useful life of the monitored component.

### 3 FIELD APPLICATIONS

#### 3.1 Bridge with fatigue cracks in the area of the transverse stiffener to the main girder web plate

During the regular inspection of this bridge, cracks were discovered in the area of the main girder web plates. In the first on-site analysis, these cracks could be identified as fatigue

cracks [5]. The cracks were limited to the connection detail of the transverse stiffeners welded to the main girder web plate.



Figure 3 Monitored position with the suspected crack at the welded connection of the transverse stiffener to the main girder web plate

A concept of measures was developed to carry out an objective assessment of the cracks on the main girder based on calculations and measurements and to make a statement about the future development. In the subsequent measurements, TÜV AUSTRIA was called in to help assess reinforcement measures by means of acoustic emission measurements at the crack positions [5]. Around 14% of the 140 identical elements were affected by the cracks. During this initial AE measurements, also at some reference points with no reinforcement installed, a new crack indication was detected. It was decided to do a further AE-monitoring using the RISE system at this position of interest (see Figure 3) and to assess the possible future development of the crack. The aim was to test the RISE as a tool for detecting cracks in the early stages and to use the measurement results of the monitoring to predict the future development of the cracks.

The measuring equipment required for the monitoring was installed while the bridge was in operation, so the train traffic was not affected. The piezoelectric sensors (VS150-RSC from Vallen, peak frequency at 150 kHz, integrated preamplifier with gain of 34 dB) were installed as shown in Figure 5. Three sensors were installed near the crack position. These sensors record the mechanical waves coming from the crack. To improve the coupling of the sensors to the surface, they were mounted with a coupling agent. In addition, the paint layer was removed off at the sensor positions. The sensors were attached to the surface using magnet holders. The connection to the sensors was made via BNC-cables (1.5 m). The RISE-Core measuring system was also attached near the measuring position using a magnetic holder. Four guard sensors were installed around the measurement position to shield the measurement setup from interfering noise from sources other than the crack position. These were positioned to suit the installation location in such a way that possible interference signals were first detected by the guard sensors and thus filtered in the signal processing. As a 230V connection was available near the bridge, the measuring system was connected to this. This was the only cable that had to be laid out to the measuring position.

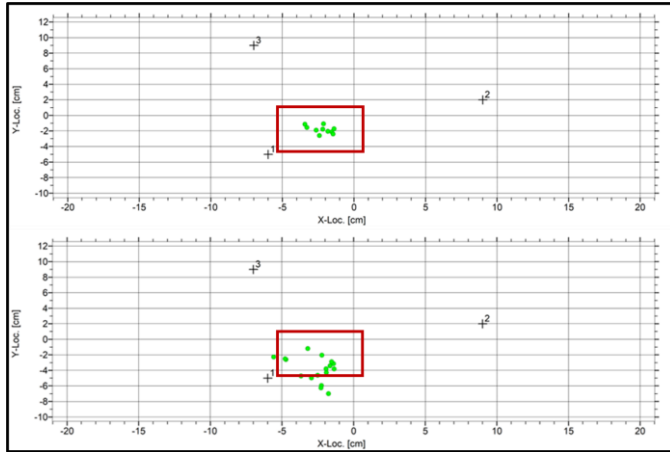


Figure 4 Top - Location map of events from pencil lead breaks at the position of the suspect crack. Bottom – Location map of events acquired after one train passage over the bridge in the position of the crack indication localized with pencil lead break test.

The functionality of the installation of the measuring device (RISE-Core) and the sensors for condition monitoring could be checked using user friendly installation software known as "Client Setup Mode". This software solution offers a supporting function for checking the functionality of the measuring chain, coupling verification of the sensors and localization in accordance with the EN 17391:2022-06 standard. Verification is carried out using a pencil lead break (0.5mm/ 2H, in accordance with ASTM E976). A simple and reproducible event with energy in the order of magnitude of crack growth events. To check the function and the correctness of the set parameters, pencil lead breaks were carried out in the area of the suspected crack (Figure 4).



Figure 5 AE sensor arrangement at the monitored position with suspected crack. Sensor 2, not in the picture, is positioned behind the connection detail in the distance of 12 cm from the suspected crack.

This area is also where the crack growth events are to be expected. The Figure 4 shows in the bottom map the localized events after a train passing over the bridge. The entire

installation and inspection of the measurement setup can be carried out by a trained technician within one hour. The measurement period was 6 months.

During this time, the passages of the individual trains and the resulting AE material response were recorded.

### 3.2 Monitoring at five representative points on a riveted steel bridge

This case involves a riveted steel bridge built in 1936, which was found to be in good condition during a visual inspection by the ÖBB bridge inspectors. The bridge was to be given a new corrosion protection. As this is a cost-intensive maintenance measure for the infrastructure operator, the ÖBB wanted to help with additional useful information to support the final evaluation of the condition of the bridge through the responsible bridge inspectors.

With the help of the bridge inspectors, five neuralgic areas on the bridge were selected. These points were selected from the experience of the technicians responsible for the inspection as the components most affected by cracks and can thus be used to assess the general condition of the bridge. This field example deals with the measurement of the first selected area, a transverse stiffener in the area of the fixed bearing of the bridge. This case is an example for monitoring of a hot spot. A larger area is monitored than in the case of already known cracks. Here too, the 3 measuring sensors (see Figure 6) detect the incoming mechanical waves in a triangular arrangement, which are triggered in the material by the load of the trains crossing over the bridge.

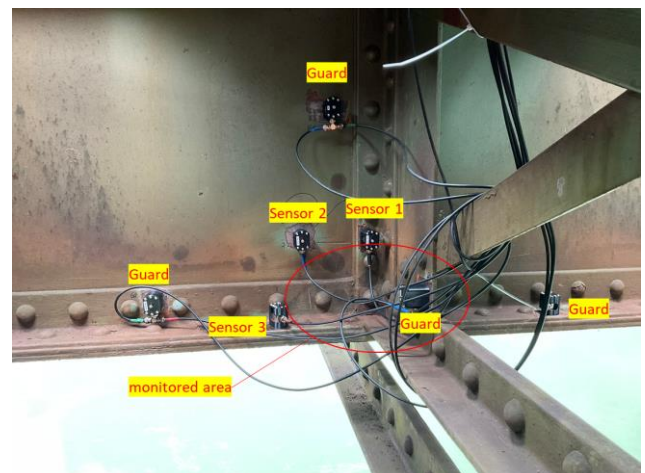


Figure 6 AE sensor arrangement at the monitored position for hot spot monitoring at the area of the riveted connection element of the transvers stiffener to the main girder.

The material response is evaluated for crack growth and provides information about the condition of the material in the monitored area. As commercially available magnetic sensor mounts are too large for the distance between the individual rivets, in-house developed sensor mounts are used for the riveted bridges. In addition, 4 guard sensors were applied around the triangular configuration of the measuring sensors in order to exclude spurious noise outside the measuring arrangement.



Figure 7 Modular PV-solution for RISE.

As there was no power supply on site at this bridge, a modular PV system was installed (see Figure 7) to supply the RISE device with power.

RISE requires less than 10 W of power when all sensor channels are fully utilized. The entire equipment could be transported to the site by three men.

#### 4 RESULTS

The material response was recorded by the RISE system during the monitoring process. The results of the cumulative plot of the AE material response can be seen in the Figure 8. At first glance, different trends in the material response can be recognised in the progression of the individual curves. The curve with the most pronounced progressive course is the Pinkabach bridge. A bridge that was completely dismantled in a single piece by ÖBB and equipped in the workshop with a shaker. It was subjected to a fatigue test [41]. As part of the Rail4Future project, TÜV AUSTRIA, in cooperation with ÖBB, carried out an acoustic emission measurement on the main girder bottom flange during the fatigue test, where an artificial crack was introduced and the AE material response during fatigue crack growth was observed.

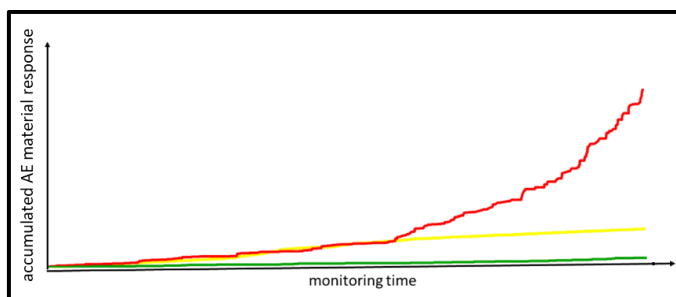


Figure 8 Comparison of AE material response of the different bridges. Monitoring time is normalized. Red: fatigue test on the Pinkabach bridge with artificial introduced crack. Yellow: monitoring of a bridge at crack position. Green: representative hot spot on a bridge with no known crack indications.

The crack had grown after its initiation at the notch near to the edge of the bottom flange in transversal direction almost till to the web plate at the centre of the girder.

The material response shows a progressive growth, which is a well-known trend in the acoustic emission for sever degradation. In comparison to the Pinkabach bridge, both the trends of the crack affected bridge and the riveted bridge show a linear progression. The slope of the cumulative AE response is significantly more pronounced on the crack affected bridge where crack monitoring was performed than on the riveted bridge.

The application of the FFM like in the Figure 9 delivered the prediction of time of maximum utilization of the monitored components for the two bridges. In the case of the crack monitoring, for example, it was possible to conclude that further monitoring should be carried out at the next scheduled inspection interval. The riveted bridge showed that the remaining time until maximum utilisation of the first monitored position is so far in the future that a new investment in a new corrosion protection will be reasonable, when the other positions will show a similar result. Other positions on this bridge are still being monitored in order to make a general statement about the overall condition of the bridge. The results are made available to the customer on an online dashboard using a traffic light system. This allows the customer to track the status of their monitored bridges and components.

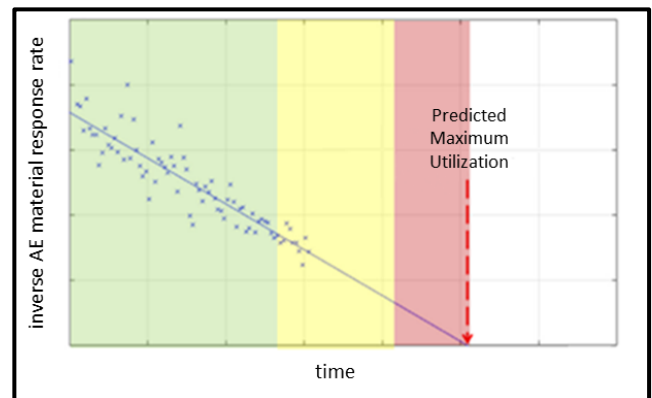


Figure 9 Failure forecast method applied on the monitoring data. Areas for the traffic light result grading system are marked.

#### 5 SUMMERY

The system solution RISE by TÜV AUSTRIA was presented as an acoustic emission monitoring tool for railway steel bridges. The acoustic emission monitoring system is able to detect and monitor cracks. Based on the failure forecast method, a statement can be made about the condition of the monitored component and after several months of measurement a further prognosis when the maximum utilization of the component is reached.

Two field examples were used to demonstrate how RISE could support the ÖBB bridge inspectors. A field case for identification of a suspected crack at the monitored component of interest was shown. After the detection of the crack a forecast for remaining time, until the maximum utilization time of the component, was done. In the second case a hot spot monitoring



was shown. Where the component was monitored to make sure that it was in good condition and no crack activity was present.

The system helps the infrastructure operators and bridge inspectors to plan maintenance intervals, repairs and new reinvestments measures for ageing bridges. This saves the infrastructure operator costs and reduces the man-hours required for monitoring. The examples showed that the system can be installed easily and in a short time. The monitoring does not require any major interventions and the installation can often be carried out while the bridge is in operation. The results and recommendations for the customer can be made available via an online dashboard using an easy-to-understand traffic light system.

In addition to the numerous monitoring projects already carried out on railway steel bridges, further bridge monitoring projects are planned with the help of which RISE can be established as an indispensable tool in bridge inspection and a helpful addition to the classic periodic inspections.

## REFERENCES

- [1] Corcoran, J. (2017). Rate-based structural health monitoring using permanently installed sensors, *Proc. R. Soc. A*, vol. 473.
- [2] Fukuzono, Teruki. "A new method for predicting the failure time of slope." *Proceedings, 4th Int'l. Conference and Field Workshop on Landslides*. 1985.
- [3] Voight B. 1988 A method for prediction of volcanic eruptions. *Nature* 332, 125–130.
- [4] Voight B. 1989 A relation to describe rate-dependent material failure. *Science* 243, 200–203.
- [5] Unterweger, Derler. „Walzenbauernbrücke – Quersteifenanschlussdetail: Entwicklung von drei Verstärkungsvarianten und Betriebsmessungen zu deren Effizienz sowie Anwendbarkeit bei anderen Brücken“. Institut für Stahlbau / TU Graz, Project report, March 2022.
- [6] Lackner, G., Marhart, H., & Prokofyev, M. (2024). Monitoring of a fatigue test on a full-size railway steel bridge with acoustic emission. 36th Conference of the European Working Group on Acoustic Emission, 18-20 September 2024, Potsdam, Germany. *e-Journal of Nondestructive Testing* Vol. 29(10).
- [7] Michael Siu Hey Leung, Joseph Corcoran, Peter Cawley, Michael D. Todd (2019). Evaluating the use of rate-based monitoring for improved fatigue remnant life predictions, *International Journal of Fatigue*, Volume 120, 162-174.





## Session 2

# Geophysical Monitoring of Infrastructure

# Rail track subsurface imaging from train vibrations recorded at dark fiber networks

Michael Behm<sup>1</sup>, Michael Brauner<sup>2</sup>

<sup>1</sup>GEODATA ZT GmbH, Hans-Kudlich-Straße 28, 8700 Leoben, Austria

<sup>2</sup>ÖBB-Infrastruktur AG, Lassallestraße 5, 1020 Wien, Austria

email: michael.behm@geodata.com, michael.brauner@oebb.at

**ABSTRACT:** We demonstrate the practical feasibility of assessing geotechnical parameters of rail infrastructure based on ‘dark fiber’ distributed acoustic sensing (DAS) recordings using trains as sources. A workflow to image the shallow (3 m – 20 m depth) subsurface in terms of shear wave velocity has been established. The shear wave velocity distribution is obtained from inversion of seismic surface waves excited by the trains and recorded on the fiber optic cables, and is used as a proxy for the geotechnical strength (e.g., shear modulus). Our results allow for the interpretation of potential geologic hazards and other features relevant for assessing the geotechnical integrity of rail infrastructure. This approach does not require dedicated field measurements or interruption of the train schedule, and therefore represents a cost-effective and robust method for different application scenarios.

**KEY WORDS:** DAS, hazard, infrastructure, rail, near-surface geophysics

## 1 INTRODUCTION

Shallow geologic hazards such as washouts, karstification, liquefaction, or mass movements pose risks to rail infrastructure and operations. Additionally, the stability of artificial rail embankments may be affected by poor consolidation or external influences such as extreme weather events or neo-tectonic activity. While the conventional near-surface geophysical toolbox provides a range of suitable investigation methodologies, their application to rail networks is challenged by the train operation schedule and the potentially large spatial extent.

In recent years, Distributed Acoustic Sensing (DAS) performed on existing fiberoptic cable infrastructure (‘dark fiber’) has become a widely used approach for seismic subsurface imaging and monitoring (Li et al, 2022). As many rail tracks are equipped with fiber optics for telecommunication purposes, and trains are sources of abundant seismic energy, the method is potentially well suited for seismic subsurface imaging below rail tracks (Hernandez et al., 2023; Fuchs et al, 2018).

We present a case study from Austria (Europe), where DAS registrations of commuter trains along a 6.5 km long rail track section were used to image the shallow subsurface. A workflow comprising data selection, seismic interferometry, and advanced MASW (multi-channel analyses of surface waves) techniques resulted in almost continuous coverage of the shear wave velocity ( $V_s$ ) in the depth interval ~3 m - ~20 m. The results were validated against conventional MASW data and existing geologic/geotechnical information.

## 2 METHOD

DAS measurements provide strain or strain rate variations along a fiberoptic cable with potentially high resolution and accuracy. Dynamic strain variations are an expression of dynamic medium deformations, and therefore DAS data can be considered as first-order proxies to seismic wavefields. Seismic processing techniques can be used to model and characterize the subsurface in terms of shear wave velocity ( $V_s$ ) distribution which is indicative of geotechnical properties (e.g., shear modulus). Our workflow starts with geometrical calibration of the DAS recordings and selection of recording periods which

include trains. In a next step, the seismic interferometry method (e.g., Wapenaar et al., 2010, and references therein) is applied to reconstruct surface Rayleigh waves propagating in-between individual DAS channels and is used to synthesize virtual shot gathers for each channel. Those shot gathers are subjected to a proprietary MASW workflow (Xia et al., 1999) with emphasis on improving the S/N (signal-to-noise) ratio and taking advantage of the dense spatial sampling capabilities of DAS (Guan et al., 2024). The final output is a continuous 2D-model of the shear wave velocity distribution  $V_s$  below the rail tracks.

## 3 DATA, PROCESSING, AND RESULTS

The used fiber optic cable is installed in a hard-plastic protective tubing which runs inside a large concrete duct, therefore poor ground coupling is to be expected. Several loops and partial re-routing of the cable required careful geometrical calibration. A Febus A1 interrogator (Febus, 2025) was used for the measurement. Aiming for compromise between resolution and S/N ratio, the gauge length and channel spacing were chosen as 2 m and 0.8 m, respectively, such that finally 8,751 channels were recorded along the 6.5 km long section. The total recording length cumulates to ~7 h, during which time 29 commuter trains were registered with a temporal sampling rate of 2 ms, resulting in a data volume of ca. 370 GB. The trains are short (3 – 6 carriages) and operate with low speed (~70 km/h). From the continuous recordings, we only use short time windows around the train arrivals which contribute to ca. 5% of the entire data set.

The MASW workflow aims at deriving  $V_s$ -depth profiles at a nominal spacing of 5 m which are interpolated into continuous 2D models (Fig 1). The average frequency range for the retrieved surface waves is ~7 Hz - ~16 Hz. Due to partially insufficient fiber-ground coupling and re-routing, 70% of the section could be imaged continuously (Fig. 1). The resulting  $V_s$ -models were verified against conventional active source MASW profiles, geological and borehole information, and CPT logs. Overall, those different methods support the results obtained from the seismic imaging workflow.

The results allow for the interpretation of weakened embankment zones and shallow potential geologic hazards. A suspected small-scale mass movement is indicated by

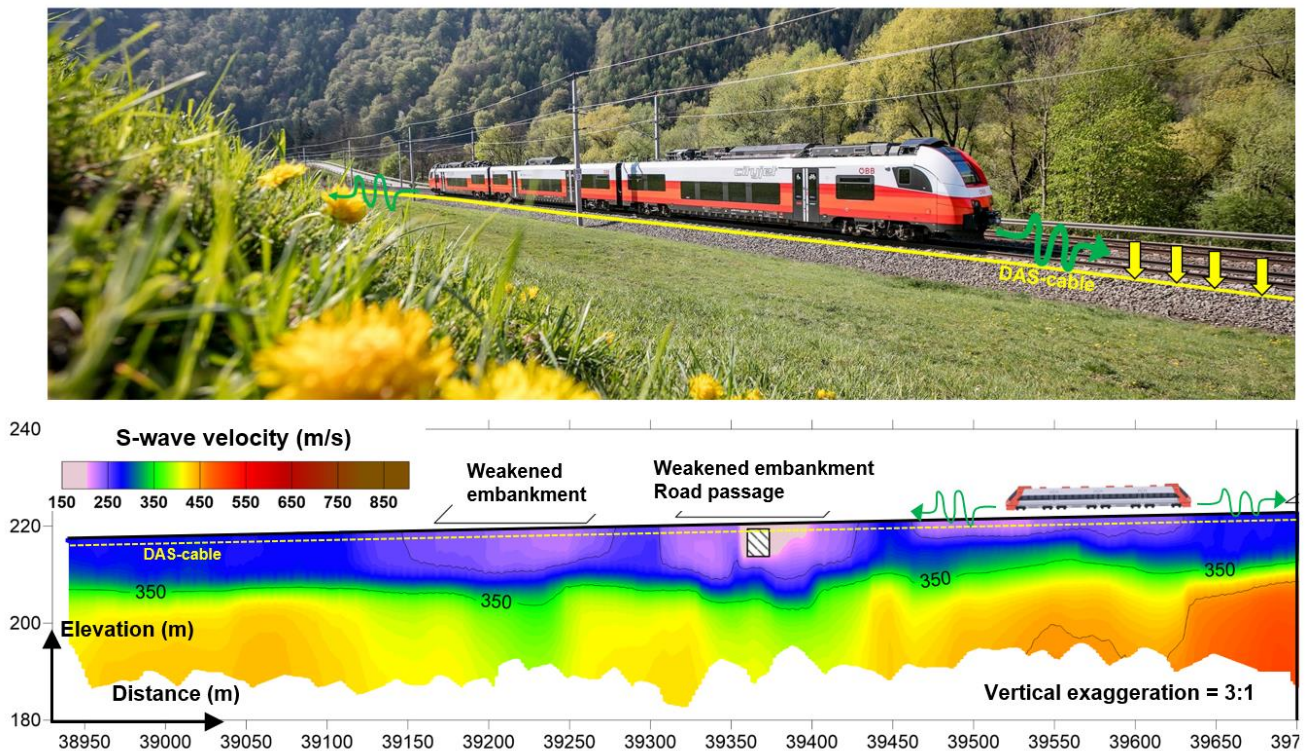


Figure 1: Concept and result of the seismic processing workflow applied to DAS-data. Passing trains excite seismic surface waves (green wiggles), which are recorded at existing fiberoptic telecommunication cables (yellow line). The recorded seismic waves are inverted for the shear-wave (S-wave) velocity structure below the fiberoptic cable. Zones of low S-wave velocity (pale/purple colors) are interpreted for reduced shear strength and thus reduced geotechnical integrity (e.g., weakened embankments). Velocity variations at larger depths are indicative of lithological inhomogeneities.

significantly decreased velocities, and a known large-scale fault zone with the potential for neo-tectonic reactivation correlates with low velocities at larger depths.

#### 4 CONCLUSIONS

We have developed an efficient and robust workflow for imaging potential geologic hazards along rail tracks from seismic waves excited by trains and recorded on existing fiber infrastructure. This approach does not require dedicated field measurements or interruption of the train schedule. It can be used for large-scale mapping of entire rail networks as well as for time-lapse monitoring of selected and potentially hazardous sections. The methodology might also be applied to roads using vehicle noise as seismic sources.

#### ACKNOWLEDGMENTS

We thank Martin Litzenberger from the Austrian Institute of Technology (AIT) for supporting the DAS-measurement.

#### REFERENCES

Febus, 2025: Febus A1 data sheet. Accessed through <https://www.febus-optics.com/en/page/a1>, August 2025

Fuchs, F., G. Bokelmann, and AlpArray Working Group, 2018, Equidistant Spectral Lines in Train Vibrations, *Seismological Research Letters*, **89**, 56-66

Guan, J., Cheng, F., Xia, J., Mi, B., Sun, H., and Ajo-Franklin, J.B., 2024, Multigrid Spatially Constrained Dispersion Curve Inversion for Distributed Acoustic Sensing (DAS), *IEEE Transactions on Geoscience and Remote Sensing*, **62**, 1-17

Hernandez, E.O., P. Hölscher, P. Doornenbal, C. Mas, J. van't Schip, and A. van Uiter, 2023, Characterization of Shallow Ground in Railway Embankments Using Surface Waves Measured by Dark Fiber Optics Sensors: A Case Study, *Sensors*, **23**, 9397

Li, Y., M. Karrenbach, and J.B. Ajo-Franklin (Eds.), 2022, *Distributed Acoustic Sensing in Geophysics*, AGU Geophysical Monograph Series 268, Wiley

Wapenaar K., Draganov D., Snieder R., Campman X., and Verdel A., 2010, Tutorial on seismic interferometry: Part 1 – Basic principles and applications, *Geophysics* **75**, 75A195–75A209.

Xia, J., Miller, R.D., and Park, C.B., 1999, Estimation of near-surface shear-wave velocity by inversion of Rayleigh waves, *Geophysics*, **64**(3), 691–700



# Monitoring of Concrete Infrastructure with Active Ultrasound Coda Wave Interferometry

Niklas Eppe<sup>1</sup>, [0000-0001-8697-6378](https://orcid.org/0000-0001-8697-6378), Camila Sanchez Trujillo<sup>1</sup>, [0009-0009-1041-7655](https://orcid.org/0009-0009-1041-7655), Daniel Fontoura Barroso<sup>2</sup>, [0000-0003-2936-1523](https://orcid.org/0000-0003-2936-1523), Julia Hau<sup>1</sup>, Ernst Niederleithinger<sup>1</sup>, [0000-0002-2501-2249](https://orcid.org/0000-0002-2501-2249)

<sup>1</sup>Bundesanstalt für Materialforschung und -prüfung (BAM), Unter den Eichen 87, 12205 Berlin, Germany  
email: niklas.eppe@bam.de, camila-andrea.sanchez-trujillo@bam.de, daniel.barroso@bam.de,  
julia.hau@bam.de, ernst.niederleithinger@bam.de

**ABSTRACT:** Coda Wave Interferometry has been used in Geophysics to detect weak changes in scattering media. Past research in Structural Health Monitoring has shown that this methodology can be applied to concrete structures to detect material changes by calculation of relative velocity changes. Successive measurements with embedded ultrasonic transducers provide a repeatable signal for reliable long-term monitoring of concrete. To research the application in real-world structures, we have embedded ultrasonic transducers in a bridge in Ulm and a Metro station in Munich, Germany. This study gives an overview of the monitoring of these two structures. The results show the potential and challenges of the method. Data evaluation can be largely automated to gain insights into material changes and other influences on the structure, such as traffic-induced load and temperature variations. The experiments demonstrate the ease of installation, longevity of the sensor installation, and sensitivity of the measurement technique, but highlight problems with the application, especially if electromagnetic noise affects data quality. As no confirmed substantial damage was recorded during the monitoring period on both structures, we evaluate load tests to investigate the effect of static load on the structures and the coda monitoring results. The experiments show that the influence of load can be detected, even if the temperature influence is not removed from the data. This indicates that online damage detection with coda monitoring is possible, but further research on damage detection in real-world structures has to be conducted to confirm laboratory findings.

**KEY WORDS:** Active Ultrasound Measurements, Coda Wave Monitoring, Embedded Transducers

## 1 INTRODUCTION

Coda Waves – multiply scattered late-arriving seismic waves – have been studied in seismology for decades. Beginning with Keiiti Aki's work in 1969 [1], where he developed a method to determine the seismic moment of earthquakes from coda waves the analysis of these waves has since evolved as a valuable tool for understanding subsurface properties. In *Coda Wave Interferometry* (CWI), the medium acts as an interferometer, combining the scattered waves originating at a source at the receiver [2]. This enables the detection of small velocity variations in a material volume with a limited number of sources and receivers. These changes are often not detected by analyzing the direct wave. Applications of CWI include the detection of stress, temperature, and damage-related material alterations across multiple scales.

The heterogeneous composition of concrete allows the application of CWI in infrastructure as most structures are composed of concrete. Planès and Larose [3] have summarized the applications of CWI in concrete, including sensitivity to thermal fluctuations and stress-induced changes via the acoustic-elastic effect. Their following work has also shown the potential of localizing change with a sensor network [4], highlighting the potential of CWI for monitoring changes in large concrete structures. Their sensitivity-kernel-based approach leverages the spatial sensitivity of coda wave measurements, which allows analysis of different volumes of material with a limited number of measurements and sensors.

These advancements and the necessity of constant coupling for long-term monitoring have initiated the design of special

embedded piezoelectric transducers [5]. To further investigate the potential of concrete damage assessment by coda waves on the micro and macro scale, a DFG funded research group (FOR 2825) has combined modelling, simulations, laboratory experiments, and applications of CWI in large structures [6] using these transducers.

This publication intends to give an overview of two monitored structures, the applied technology, and key findings with their implications for future wider application of CWI-Monitoring to ensure early damage detection in infrastructure and support authorities and infrastructure owners in the process of long-term maintenance and infrastructure planning. The monitoring of large structures poses unique challenges as influences of temperature, traffic-induced load, and other external factors are detected with CWI. These factors must be taken into account to isolate indicators of material degradation. In this context, we will present results from monitoring a road bridge in the city of Ulm and a subway station in Munich. At both structures, retrofitted transducers have been used to monitor material degradation and environmental influences for several years. Therefore, they are representative specimens for analyzing the potential of CWI monitoring.

## 2 METHODOLOGY

### 2.1 Active Ultrasonic Measurements and Coda Wave Interferometry

For active CWI measurements in concrete, ultrasonic waveforms are consecutively recorded as time series  $u_1(t)$  and  $u_2(t)$ . When a pulse is emitted at the source, elastic waves travel through the medium and are scattered at inhomogeneities (e.g.



grains) or reflected at boundaries (e.g. concrete-air boundary). Therefore, when recording several milliseconds of signal after emission of the pulse, a waveform consisting of the direct wave travelling between source and receiver and later arriving scattered and reflected coda waves is recorded (for a sample waveform, see section 2.4, Figure 3). Changes in the medium (e.g. cracks) change the wave propagation and therefore the recorded waveforms. To detect such waveform changes, the basic measure for signal comparison is the *correlation coefficient* ( $-1 \leq CC \leq 1$ ), calculating a measure of signal similarity on a time window  $[t1, t2]$ . A decrease of CC indicates a change in wave propagation but is not linked to a specific physical property of the material.

Changes in the material affecting the bulk or shear modulus, directly influence the propagation velocity of P- and S-waves respectively. Therefore, CWI evaluates velocity changes, by analyzing phase shifts in the signals. The standard method for this analysis is the stretching technique [7], where the first signal is time-stretched to align with the second. The following equation describes the calculation of a velocity change using the stretching technique [3]:

$$\begin{aligned} & \operatorname{argmax}(CC(\varepsilon)) \\ &= \frac{\int_{t_1}^{t_2} u_1[t(1 + \varepsilon)]u_2[t]dt}{\sqrt{\int_{t_1}^{t_2} u_1^2[t(1 + \varepsilon)]dt \int_{t_1}^{t_2} u_2^2[t]dt}} \end{aligned} \quad (1a)$$

$$\varepsilon = -\frac{dv}{v} \quad (1b)$$

By varying the stretching factor  $\varepsilon$ , the correlation coefficient in equation (1a) is maximized. The maximizing stretching factor corresponds to the relative velocity change (equation 1b) between the recording of  $u_1$  and  $u_2$ . To analyze spatially localized changes, CC and  $\varepsilon$  can be evaluated on different time windows  $[t1, t2]$ , which corresponds to different sensitivities described by sensitivity kernels (see [8]).

For CWI in monitoring a reference needs to be chosen to determine the baseline. After choosing the baseline, all material changes altering wave propagation in a structure can be tracked by repeated ultrasonic recordings given source and receiver position and coupling do not change. In practice, several different approaches for choosing the reference exist, depending on the magnitude of change and the minimum threshold of CC that allows a reliable analysis of velocity change. If the medium is influenced by non-permanent environmental changes, the reference can be kept fixed, (fixed-reference technique), making a comparison to the baseline timestamp straightforward. Other methods change the reference constantly, e.g. the stepwise reference method [9] or a rolling reference method [10]. The velocity change can be referenced to the baseline as well, but the correlation coefficient is not referenced to the baseline anymore. The rolling reference method is especially advantageous in practical monitoring scenarios, as the reference lag can be adjusted based on external influences such as temperature or known stress variations, thereby improving the robustness of the velocity change estimation over time.

## 2.2 Sensors and Sensor Installation

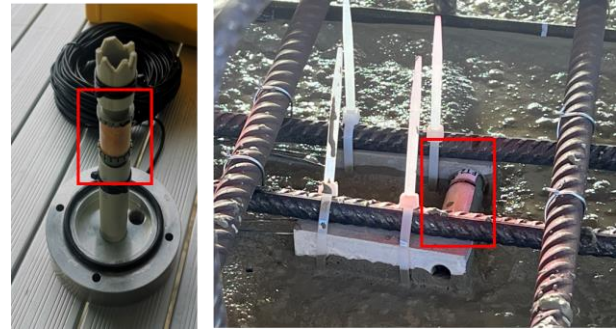


Figure 1. ACS S0807 (red square) prepared for retrofit with a grouting cap, prepared for the desired installation depth (left) and attached to the rebar before concreting (right).

For long-term monitoring of real structures, it is essential to ensure constant coupling. Therefore, cylindrical piezoelectric P-wave transducers (type: S0807, dimensions: length 72mm, diameter 20mm) described in [5] and developed in cooperation with Acoustic Control Systems (ACS) are designed to be embedded in concrete, either attached to the reinforcement before concreting or retrofitted in an existing structure (Figure 1). In retrofit applications, the structure is evaluated with Ground Penetrating Radar (GPR) before drilling to avoid damage to rebars and tendons. The sensors are then placed within the borehole and regouted using reusable grouting caps.

These transducers can function both as sources and receivers, converting electrical signals into mechanical vibrations (elastic waves) and vice versa. In a sensor network, a typical configuration involves a source transducer emitting waves with one or several transducers acting as receivers (pitch-catch configuration). These roles can be interchanged, so source transducers can become receivers. With a bandwidth between 50 and 100 kHz, the transducers combine the possibility of analyzing direct waves for a large transducer distance with the high-frequency scattering properties required for CWI. Therefore, they are well suited for long-term structural health monitoring of concrete structures.

## 2.3 Measurement Devices

For monitoring with CWI, a custom measurement device was developed, as described in [11]. The device (Figure 2) is based on a Raspberry Pi and is capable of measuring one sensor combination every 5-10 seconds. The core component, the Raspberry Pi serves as the control unit, addressing the measurement PCBs, data storage, and transmission.

The system includes a power and pulse board that can send a 300Vpp double rectangular pulse to up to 75 multiplexed channels. The signal is then digitized and saved on the Raspberry Pi. The modular design of the measurement board allows the addition of temperature and humidity sensors to track environmental parameters.

The measurement device has shown that it can produce good data quality compared to a commercial system based on a NI-DAQ Mx and Keithley Multiplexer as described in [12]. The major advantage of the commercial system is the measurement

repetition rate. Therefore, it is used in experiments where fast dynamic changes in the medium require quick data collection.

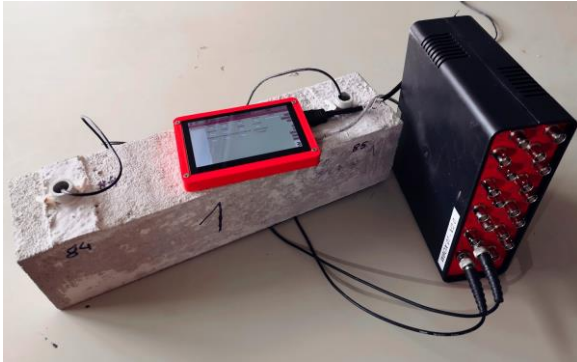


Figure 2. W-Box, custom made CWI Measurement device based on a Raspberry Pi.

#### 2.4 Ultrasonic Measurements – Direct Wave and Coda

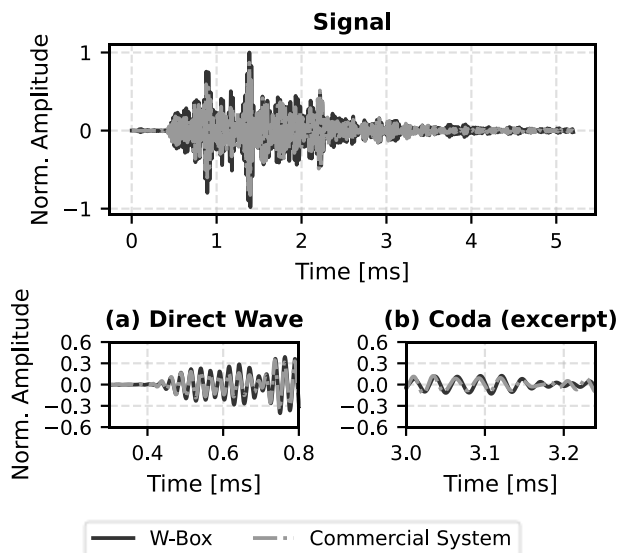


Figure 3. Two ultrasonic signals were recorded at a bridge in Ulm, Germany comparing the commercial US data acquisition device and the self-made W-Box. (a) The direct wave and (b) an excerpt of the coda.

Figure 3 shows two signals recorded with the W-box and the commercial data acquisition system in November 2021 and December 2021. In the direct wave (a), small amplitude differences are visible, primarily due to the different resolutions of the systems (14-bit vs. 16-bit). Despite this, the waveforms align closely. This supports the use of the slower W-box for long-term monitoring, supplemented by the faster commercial system when higher temporal resolution is required.

Figure 3 (b) shows an excerpt of the coda. A small shift can be detect, caused by temperature variations. During the time between the two displayed measurements, the temperature at the bridge decreased by approximately 3.5 degrees. This shows the sensitivity of the coda. The influence of temperature on the ultrasonic velocity measured by CWI has been researched, e.g. in [13] and quantified at around 0.03-0.06 percent per Kelvin,

which varies depending on the investigated structure. The onset of coda waves is a gradual transition. Even after the first arrival in figure 3, high energy reflections are recorded until 1.5 ms. Nevertheless, at this time the recordings do already include scattered coda waves. Therefore, the evaluation window for CWI has to be chosen individually for every source receiver pair after analysis of the wave recording.

### 3 MONITORED STRUCTURES

In the past years, we have instrumented two structures with the embedded ultrasonic transducers and recorded data with the W-Box. The recorded signals are directly uploaded to a database, where the signals can be analyzed (e.g. CC analysis) or requested for further evaluation through a MySQL API in Python.

#### 3.1 Gänstorbrücke Ulm

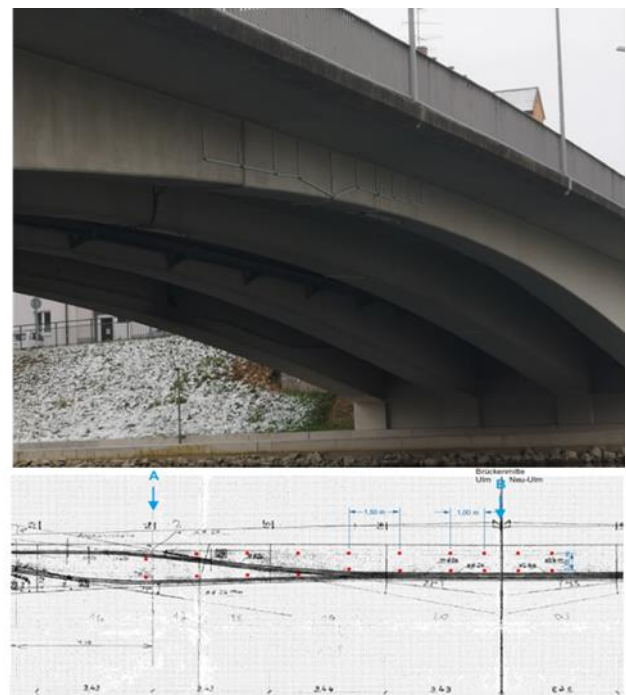


Figure 4. Sensor installation at 'Gänstorbrücke', Ulm. 20 sensors are installed in an array in the centre of the bridge (marked with red dots).

In 2020, 24 Ultrasonic transducers were embedded in the 'Gänstorbrücke' bridge in Ulm to monitor damage to the structure under constant traffic between the cities of Ulm and Neu-Ulm, Germany. The sensors were installed in the abutment and the center of the bridge (Figure 4). The bridge, designed by Ulrich Finsterwalder, is a 96m prestressed concrete structure, composed of two parallel partial structures with two slabs per partial structure. Of the 24 sensors, 20 were installed in the centre of the bridge in a single slab. Prior to the installation of the CWI monitoring system, the bridge was instrumented with a commercial monitoring system including acoustic emission, strain sensors, and temperature sensors in 2018 [14], after significant damage was detected to ensure safe operation until demolition and reconstruction in 2025.

To further evaluate CWI monitoring capabilities, in 2021, a static load experiment was conducted using a 15t and a 32t

truck to evaluate the behaviour of the bridge under a substantial load and the influence on coda waves. The monitoring system remained operational from 2020 until February of 2025 to test the longevity of the sensors as well as the signal quality. Over the five years of monitoring, no additional permanent damage was recorded on the bridge by the commercial monitoring system, confirming the stability of the bridge and the reliability of the monitoring systems.

### 3.2 Metro Station Scheidplatz Munich

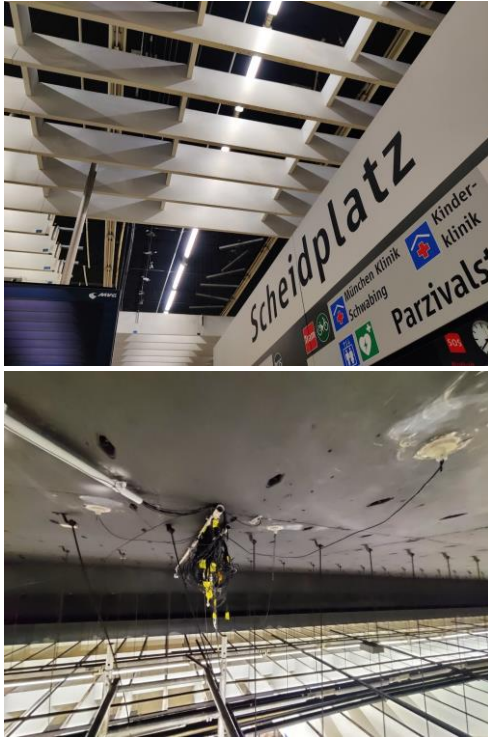


Figure 5. Sensor installation at ‘Scheidplatz’, Munich.

The ‘Scheidplatz’ metro station in Munich, Germany opened in 1972, just before the Munich 1974 Summer Olympics. On the surface of the metro construction, several tramways and bus stops are located. As a result, the ceiling structure is subject to constantly varying loads due to public transport activity. To monitor the crack behaviour and load variations caused by passing and stopping tramways, 15 sensors were embedded in the ceiling in 2022 (Figure 5).

The brittle outer layer of the ceiling made overhead regrouting difficult. As a result, two sensors have bad coupling to the structure, leading to reduced signal quality. Nevertheless, they are still operational. Therefore, surface inspection is advised before retrofitting sensors, to devise the suitable regrouting technique. Besides the monitoring aspect, the installation was a pilot run for the W-Box and the installation procedure in an environment with significant electromagnetic noise.

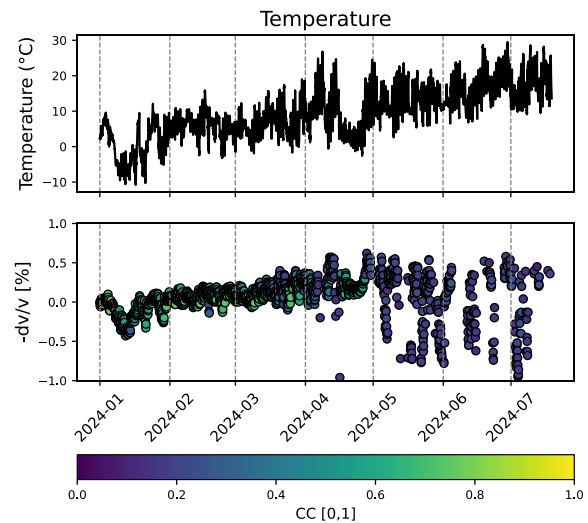


Figure 6. Temperature (top) and CWI velocity change at Gänstorbrücke for the first half of 2024. The color of the scatters represents the correlation coefficient.

## 4 MONITORING RESULTS

### 4.1 Gänstorbrücke Ulm

Since its installation in 2020, the monitoring system has remained operational with only a few periods of downtime caused by instrument failures and network problems. Neither the coda monitoring system nor the commercial acoustic emission monitoring system recorded significant new damage during this period. This shows that the measures taken to preserve the bridge until reconstruction were sufficient.

The data quality throughout the entire monitoring period is consistently good. A minimal number of measurements were influenced by electromagnetic noise, which can be eliminated by frequency analysis. Without any new damage in the monitored area, we cannot make conclusions about the ability to distinguish damage from environmental influences in a real-world monitoring setup, however.

Nevertheless, the dataset provides valuable insights to assess the requirements for a real-world monitoring setup. Especially temperature changes cause strong signal decorrelation. Figure 6 shows the temperature and the relative velocity change of a representative transducer pair for the first half of 2024. During this time the temperature ranges from  $-10^{\circ}\text{C}$  to nearly  $30^{\circ}\text{C}$ . The velocity change was calculated on the first three milliseconds of the signal, thus investigating both, the direct wave and the coda, using the fixed reference method. Figure 6 shows a clear correlation of temperature and velocity change, particularly visible in the trough in January 2024. The relation between temperature and velocity change is linear, as shown in [15]. For ‘Gänstorbrücke’ we estimate a change of  $-0.025$  percent per Kelvin.



The color scale in Figure 6 indicates the correlation coefficient. When CC remains high, the results of the fixed reference CWI can be interpreted reliably. This is only valid for small temperature variations ( $\pm 10^\circ\text{C}$ ). In summer, the correlation coefficient decreases significantly, causing outliers and jumps in the results, which cannot be physically interpreted due to the strong decorrelation.

To improve the robustness for a long-term analysis, one could shift to the stepwise or rolling reference CWI. However, preliminary analyses of the ‘Gänstorbrücke’ dataset have shown that this does not significantly improve the interpretation of the long-term trends. Furthermore, these methods require more computational power and time. Given the focus on detecting short-term permanent change (i.e. damage) we propose to analyse the data in short rolling time windows while tracking the temperature to define a corridor of expected velocity change induced by temperature. To this purpose, a linear regression model is trained using temperature measurements and corresponding calculated velocity changes. This model allows the prediction of temperature induced ‘normal’ velocity changes. Based on the root mean square error (RMSE) of this model, a corridor can be defined indicating the velocity change attributed to temperature change with a certainty of 95%. This corridor can serve as a threshold for outlier detection and enable the automatic detection of no temperature induced changes.

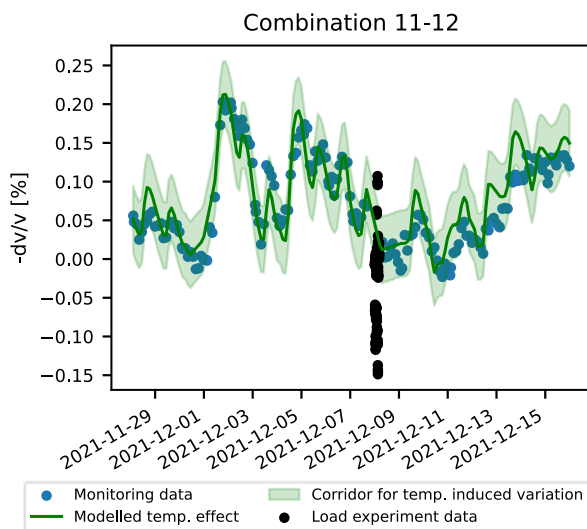


Figure 7. CWI velocity change in December of 2021. The temperature effect on the velocity change is modeled and a corridor of expected temperature induced velocity change is calculated. The data from the load experiment is highlighted in black.

Figure 7 shows this method for a three-week period in December of 2021, the time of the static load test. As the load test represents the largest known mechanical disturbance to the structure during the monitoring period, it serves as the best representation of damage-induced changes. A detailed analysis of the load test can be found in [15]. One can see that the linear model of temperature-induced velocity change fits well for the analyzed period. Using the fixed reference approach, CC

remains above 0.65 throughout the analysed subset. The temperature changes in these weeks were below  $\pm 10^\circ\text{C}$ . The permanent monitoring data is represented with blue scatters and the load test data is highlighted using black scatters.

One can see in Figure 7, that the velocity change induced by load is of the same magnitude as the change induced by temperature. Nevertheless, as the temperature model gives a corridor of expected change, the outliers can be detected. Combination 11-12 is a sensor combination with a minimum distance to the nearest loading point of 10 meters. Importantly, as during the load test, the bridge was not loaded all the time, the datapoints at unloaded measurements are within the temperature corridor. For sensor combinations located closer to the load application points, stronger deviations were observed (see [15]).

With the results of the load experiments, we show that for permanent monitoring a windowed approach can be beneficial for damage detection. Although no new damage was detected, the results show the capabilities of monitoring using CWI and embedded sensors. Key conclusions of this long-term experiment are:

- Data quality remains consistent with embedded transducers, although temperature variations have a big influence on the signals.
- The fixed reference method cannot be applied over long periods, even if no damage has been recorded.
- The load-induced perturbations can be detected within the temperature trend, even if they are of similar magnitude.
- A short window, fixed reference approach enables fast automated data analysis, and potentially allows for edge computing on site, while allowing for the detection of perturbations in the temperature trend.

#### 4.2 Metro Station Scheidplatz Munich

Since the sensor installation in 2022, signals have been continuously recorded at 10-minute intervals at ‘Scheidplatz’. This cycle reveals results indicating general increasing and decreasing trends in relative velocity change, which are attributed to temperature variations inside the concrete ceiling.

From February 24th to March 13th, 2023, the measurement frequency was increased to one measurement per minute to determine whether it was possible to study the structural behaviour following a transient load. In this case, the transient load was induced by tramways stopping directly above the sensor array. The total load of these tramways varies depending on the vehicle type, ranging from 560 kN to 722 kN, distributed over three or four axles. The results of March 18<sup>th</sup> are displayed in Figure 8.

During this period, the overall change in  $dv/v$  was approximately 0.20%, primarily attributed to temperature variations. Additionally, multiple frequent relative velocity drops of approximately 0.02% were observed, which generally recovered to their original values within 10 to 15 minutes.



These relative velocity drops were caused by the transient loads exerted by the passing tramways. Tramway operations conclude at approximately 1:15 AM; however, some relative velocity drops were detected even after this time. This is likely due to tramways passing through the station without stopping as they transit to the depot.

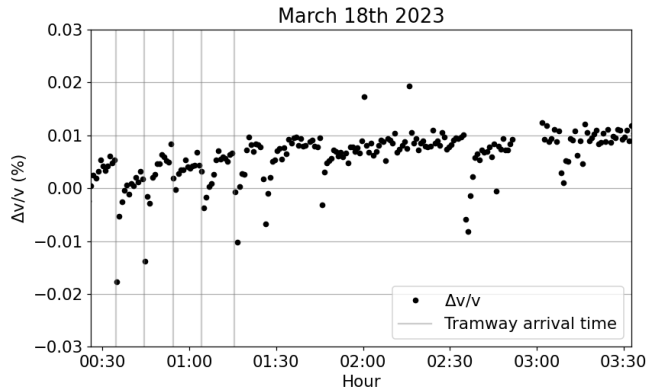


Figure 8. Relative velocity change. Velocity drops visible after the tramway stops above the sensor array.

This confirms that both stopping and passing tramways induce velocity drops in the structure. Previous experiments with CWI in 4-point bending tests [16, 17] have shown that velocity changes are predominantly negative. While we expect an increase in velocity in the pressure zone due to an increase in bulk modulus, the tension zone is dominant, especially in cracked specimens, causing a velocity drop with increasing load. As the installed structure is already cracked, the opening of cracks with load contributes to the velocity decrease. The observed velocity drops are reminiscent of the time-dependent nature of rock healing [18], and similar applications to assessing damage in concrete materials through slow dynamics [19]. To examine potential long-term variations in the relaxation processes of the structure, high-temporal-resolution measurements were repeated a year and a half later. This test was conducted from October 18th to November 7th, 2024, this time, the signal quality was significantly degraded. Additionally, we conducted controlled experiments by positioning a tramway stationary above the sensor array and regulating the passage of tramways to analyse their impact on the recorded signals.

Upon reviewing the data, it was evident that, starting in September 2024, electromagnetic noise levels had abruptly increased. This increase did not coincide with maintenance work on the electrical network, making the source of the noise not identifiable. Since then, data quality has deteriorated considerably, as illustrated in Figure 9, to the point where the recovery curves can no longer be extracted as in previous periods.

Various low-quality data rejection strategies were implemented based on waveform characteristics such as amplitude, duration, and signal-to-noise ratio (SNR). However, while these strategies were successful in filtering out the low-quality data, the remaining usable waveforms were insufficient for a detailed

slow dynamics analysis. Alternative approaches involving frequency filtering were explored, but in this case, the frequency bandwidths of the ultrasonic signals and the electromagnetic noise overlapped, rendering this method ineffective. The measurement device was inspected, confirming that it was not the source of the recorded noise. While poor sensor coupling or cable damage has not yet been ruled out, further investigation is necessary to determine the exact cause of the signal degradation. To prevent similar interference in future implementations of this method, it is recommended to monitor and mitigate potential sources of electromagnetic noise, such as maintenance work on nearby electrical networks, and to establish shielding or filtering techniques that preserve signal integrity.

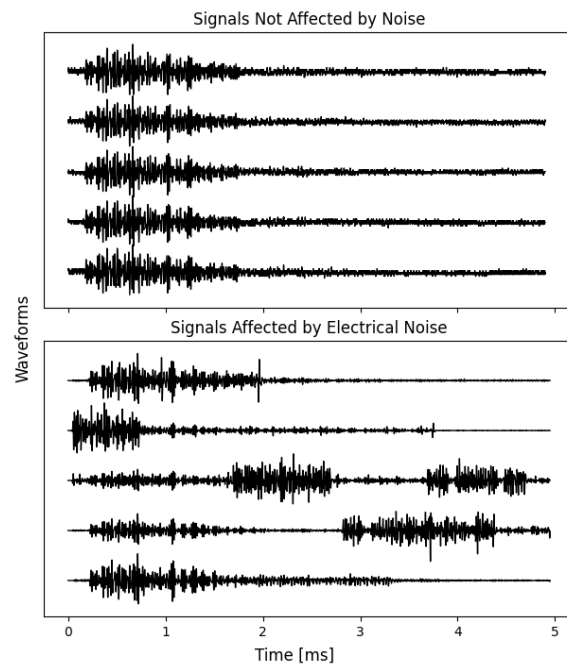


Figure 9. Representative pre-processed waveforms with good quality (Top) and low quality likely due to electrical noise (Bottom).

## 5 CONCLUSION AND OUTLOOK

The presented CWI monitoring experiments show the potential and challenges of application in real world structures.

**Installation:** Embedding sensors either in existing structures or previously to casting the concrete is an easy way to ensure coupling and longevity.

**Data quality:** The measurement devices and cables must be tailored to the monitoring situation. In high electromagnetic noise locations like metro stations, data quality can suffer. An increased measurement repetition rate, or on-site rejection of ‘bad’ measurements can improve the data quality, but better shielding of cables and the measurement device can avoid data quality problems and ensure a seamless dataset.

**Data evaluation:** Temperature influences the data evaluation strategy. The influence depends on the individual structure and the location of the monitoring system. If long-term monitoring is the goal of the installation, temperature must be monitored. To display long-term trends, advanced methods like the stepwise method must be applied, but its benefits have to be evaluated individually. If the data is only evaluated on shorter time windows, the fixed reference method suffices, and corridors can be defined allowing automated outlier detection. This accelerates the calculation of results, enabling data analysis on-site, with online and automated monitoring results.

**Detection of changes not induced by temperature:** The target of CWI monitoring is the detection of irreversible change. Previous research has shown that CWI analysis can detect e.g. cracking [16] or alkali silica reaction [20], and can potentially monitor all material altering damage processes in concrete. In this study, we have shown the influence of traffic and load, which must be accounted for to distinguish between reversible changes and material degradation. Combining traffic/load monitoring with CWI could improve damage detection reliability. Furthermore, the analysis of recovery curves after repeated loading, as explored in the ‘Scheidplatz’ experiment, suggests the potential for damage state assessment. This aspect requires further controlled laboratory research.

The presented experiments and the datasets offer a strong foundation for further research. In February of 2025, shortly before the decommissioning of the ‘Gänstorbrücke’, a tendon was deliberately cut, and the effects of its destruction were monitored closely with CWI. This dataset provides the opportunity to further determine the detection and localization capabilities of CWI in real-world structures. Additionally, monitoring continues at ‘Scheidplatz’, where further experiments targeting damage assessment under repeated controlled loading can be conducted once electromagnetic noise issues are resolved. The continuous monitoring gives the opportunity to confirm laboratory experiments showing the potential of damage detection using CWI [4, 16, 20].

## ACKNOWLEDGMENTS

The Authors would like to thank the cities of Ulm and Neu-Ulm for their support in monitoring the ‘Gänstorbrücke’, as well as the Stadtwerke München, for giving us access and support in monitoring the ‘Scheidplatz’ subway station.

## FUNDING

The authors would like to thank the DFG for funding DFG FOR 2825 CoDA and the German Federal Highway and Transport Research Institute (BASt) for funding the instrumentation of the ‘Gänstorbrücke’ (Project 89.0345/2022).

## REFERENCES

- [1] K. Aki, "Analysis of the seismic coda of local earthquakes as scattered waves," *Journal of geophysical research*, vol. 74, no. 2, pp. 615-631, 1969.

- [2] R. Snieder, A. Grêt, H. Douma, and J. Scales, "Coda wave interferometry for estimating nonlinear behavior in seismic velocity," *Science*, vol. 295, no. 5563, pp. 2253-2255, 2002.
- [3] T. Planès and E. Larose, "A review of ultrasonic Coda Wave Interferometry in concrete," *Cement and Concrete Research*, vol. 53, pp. 248-255, 2013.
- [4] Y. Zhang, T. Planès, E. Larose, A. Obermann, C. Rospars, and G. Moreau, "Diffuse ultrasonic monitoring of stress and damage development on a 15-ton concrete beam," *J Acoust Soc Am*, vol. 139, no. 4, p. 1691, Apr 2016.
- [5] E. Niederleithinger, J. Wolf, F. Mielentz, H. Wiggenshauser, and S. Pirskawetz, "Embedded ultrasonic transducers for active and passive concrete monitoring," *Sensors (Basel)*, vol. 15, no. 5, pp. 9756-72, Apr 27 2015.
- [6] D. F. CoDA. "Publications of DFG Research Unit CoDA." <https://www.mae.ed.tum.de/en/coda/publications/> (accessed 27.03, 2025).
- [7] C. Sens-Schönfelder and U. Wegler, "Passive image interferometry and seasonal variations of seismic velocities at Merapi Volcano, Indonesia," *Geophysical Research Letters*, vol. 33, no. 21, 2006.
- [8] T. Planès, E. Larose, V. Rossetto, and L. Margerin, "LOCADIFF: Locating a weak change with diffuse ultrasound," in *AIP conference proceedings*, 2013, vol. 1511, no. 1: American Institute of Physics, pp. 405-411.
- [9] E. Niederleithinger, X. Wang, M. Herbrand, and M. Muller, "Processing Ultrasonic Data by Coda Wave Interferometry to Monitor Load Tests of Concrete Beams," *Sensors (Basel)*, vol. 18, no. 6, p. 1971, Jun 19 2018.
- [10] R. Zötz-Wilson, T. Boerrigter, and A. Barnhoorn, "Coda-wave monitoring of continuously evolving material properties and the precursory detection of yielding," *J Acoust Soc Am*, vol. 145, no. 2, p. 1060, Feb 2019.
- [11] D. Fontoura Barroso, N. Eppe, and E. Niederleithinger, "A portable low-cost ultrasound measurement device for concrete monitoring," *Inventions*, vol. 6, no. 2, p. 36, 2021.
- [12] X. Wang, E. Niederleithinger, and I. Hindersmann, "The installation of embedded ultrasonic transducers inside a bridge to monitor temperature and load influence using coda wave interferometry technique," *Structural Health Monitoring*, vol. 21, no. 3, pp. 913-927, 2021.
- [13] E. Niederleithinger and C. Wunderlich, "Influence of small temperature variations on the ultrasonic velocity in concrete," in *AIP Conference Proceedings*, 2013, vol. 1511, no. 1: American Institute of Physics, pp. 390-397.
- [14] A. Müller *et al.*, "Die Gänstorbrücke in Ulm–Untersuchung, Probelastung und Brückenmonitoring," *Beton-und Stahlbetonbau*, vol. 115, no. 3, pp. 164-178, 2020.
- [15] N. Eppe, C. A. Sanchez-Trujillo, and E. Niederleithinger, "Ultrasonic monitoring of large-scale structures-input to engineering assessment," in *Life-Cycle of Structures and Infrastructure Systems*: CRC Press, 2023, pp. 1805-1812.
- [16] F. Clauß, N. Eppe, M. A. Ahrens, E. Niederleithinger, and P. Mark, "Comparison of experimentally determined two-dimensional strain fields and mapped ultrasonic data processed by coda wave interferometry," *Sensors*, vol. 20, no. 14, p. 4023, 2020.
- [17] F. Clauß, M. A. Ahrens, and P. Mark, "Thermo-mechanical experiments on reinforced concrete beams: Assessing thermal, mechanical, and mixed impacts on fiber optic measurements," *Structural Concrete*, vol. 23, no. 6, pp. 3521-3537, 2022.
- [18] R. Snieder, C. Sens-Schönfelder, and R. Wu, "The time dependence of rock healing as a universal relaxation process, a tutorial," *Geophysical Journal International*, vol. 208, no. 1, pp. 1-9, 2017.
- [19] É. Larose, N. Tremblay, C. Payan, V. Garnier, and V. Rossetto, "Ultrasonic slow dynamics to probe concrete aging and damage," in *AIP Conference Proceedings*, 2013, vol. 1511, no. 1: American Institute of Physics, pp. 1317-1324.
- [20] S. Mehdinia, K. S. T. Chopperla, A. Hafiz, T. Schumacher, and J. H. Ideker, "Ultrasonic Coda Wave Monitoring of Alkali-Silica Reactivity in Concrete Laboratory Prisms," *Materials Evaluation*, vol. 80, no. 10, pp. 40-51, 2022.

# Finite element mesh construction for seismic analysis using drone imagery

Evan T. Delaney<sup>1</sup>, Patrick Marty<sup>1</sup>, Lars Gebraad<sup>2</sup>, Andrea Zunino<sup>1</sup>, Andreas Fichtner<sup>1</sup>

<sup>1</sup>Institute of Geophysics, Department of Earth and Planetary Sciences, ETH Zurich, Sonneggstrasse 5, 8092 Zurich, Switzerland

<sup>2</sup>Mondaic AG, c/o Impact Hub Zurich, Sihlquai 131, 8005 Zurich, Switzerland

email: delaney@student.ethz.ch, patrick.marty@eaps.ethz.ch, lars.gebraad@mondaic.com, andrea.zunino@eaps.ethz.ch, andreas.fichtner@eaps.ethz.ch

**ABSTRACT:** Computational meshes serving as input to wave simulations are often crafted manually and bear a significant cost to construct. The aim of this work is to minimize that overhead and apply it to structures lacking models and meshes, particularly in earthquake-prone regions, to image and monitor their structural health in response to ground movement. To address this challenge, we have developed a workflow to facilitate the creation of 3D finite element meshes, starting with 2D photos acquired by an inexpensive consumer-level unmanned aerial system (i.e., a drone). After photo acquisition, the process proceeds by utilizing computer graphics and vision software to transform these photos into a 3D surface composed of triangles. Surface meshes are generally sufficient products for other workflows that likewise create 3D assets via reconstruction methods (e.g., for topographic mapping, archiving, and entertainment). However, to simulate waves through complex structures with high fidelity, we employ a spectral element wave solver, which requires a 3D volume composed of hexahedra. The steps from a 3D triangular surface to a 3D hexahedral volume include enclosing the surface, conditioning, and remeshing it with appropriate element geometry. We apply a first version of this workflow to the Contra (Verzasca) dam in Switzerland, from which we discuss key stages, challenges, and learnings in developing the pipeline – showcasing elastic wave simulation through the constructed mesh.

**KEY WORDS:** Photogrammetry; UAS; UAV; Gridding; Meshing; Numerical modelling; Geophysics; Seismology.

## 1 INTRODUCTION

Seismological research focused on understanding the behavior of complex media and structures to ground motion requires the use of computational meshes, which permit the physical world to be discretized in order to numerically solve the wave equation. These meshes must be constructed in a way that not only honors structural topography and field parameters, but also maintains efficiency, preserves the physics, and upholds numerical stability requirements dictated by grid size, frequency, and velocity parameters [1,2]. When no compatible computational mesh or model exists for the object or area of interest, a mesh must then be constructed from scratch. This is an arduous task for geoscientists, being a bottleneck for those wishing to focus their attention on imaging the Earth and likewise on deriving insights from the non-destructive testing of engineering structures and their responses to earthquakes.

A proposed solution to this challenge is a workflow that incorporates the use of unmanned aerial vehicles (i.e., UAVs, unmanned aerial systems (UASs), or drones) along with computer vision and graphics software to process the imagery and generate meshes for wave propagation and seismic research problems. Significant advances in hardware (e.g., digital cameras, GPS, drone portability, etc.) have opened the door to more flexibly capture thousands of images without resorting to expensive equipment, non-trivial calibration methods, and the use of priors (e.g., camera settings, motion, etc.) [3-6]. This lower barrier to entry has furthermore been complemented by improvements in key computer vision algorithms (namely, Structure-from-Motion and Multi-View Stereo) which now make it practical to reconstruct 3D surface models from these thousands of images using a high-end laptop or modest workstation [7].

We develop a first iteration of this workflow and apply it to the Contra dam located in the Verzasca valley in southern Switzerland, whose results we present. This structure and its surroundings have no known mesh, making it an ideal candidate to qualify whether it is possible to generate a useable mesh with minimal effort via these off-the-shelf and improved technologies.

## 2 WORKFLOW AND RESULTS

### 2.1 Methodology

The workflow to generate a computational-ready mesh for input into a spectral element wave solver, as applied to the Contra dam, is as follows:

- 1) identifying the object or area of interest
- 2) survey design
- 3) photo acquisition
- 4) color calibration
- 5) surface model generation
- 6) surface model enclosing
- 7) conditioning and layer additions
- 8) hexahedral remeshing
- 9) populating field parameters

We now proceed in the following paragraphs to describe these steps in further detail.

#### 2.1.1.a Identifying the object or area of interest

The Contra dam is selected as a test candidate, given the fact that it lies within a seismically active region and lacks a mesh for itself and its surrounding environment. Located near the city of Locarno, it is embedded in somewhat steep mountain flanks with outcropping metamorphic synfolds [8,9]. At the time of acquisition, the dam was undergoing maintenance with the



reservoir (Lago di Vogorno) drained to allow for an acquisition of not only the dam, but also the lakebed topography leading into the dam. The field site is presented in Figure 1.

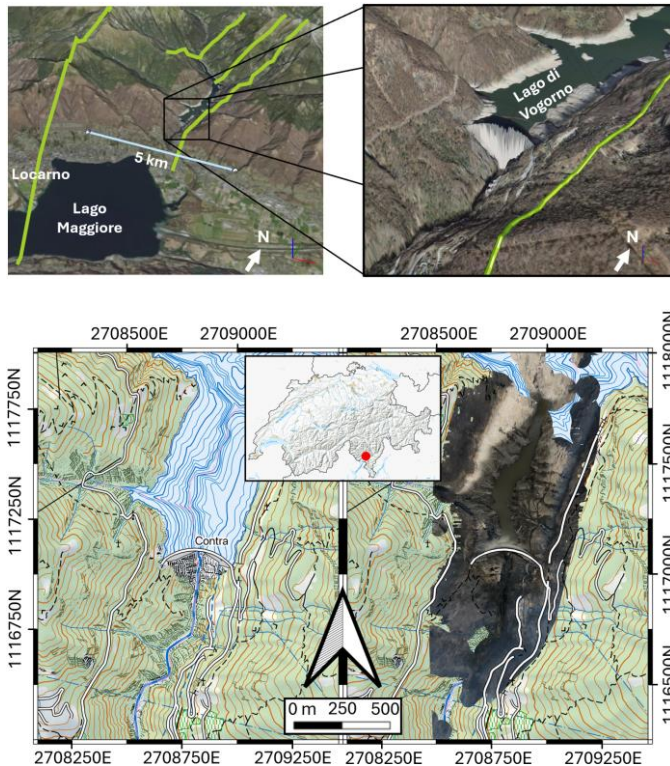


Figure 1. (top left) Location of the Contra dam zoomed out and in respect to the city of Locarno to its southwest. The light teal line represents 5 km. Lime lines are mapped faults. (top right) A zoomed view of the area, as taken from swisstopo, with the dam near the center and the reservoir Lago di Vogorno behind. The lime polyline to the right of the dam is the edge of a mapped fault. (bottom left) A terrain map of the field site. (bottom right) A reconstructed orthophoto overlay revealing the drained lakebed.

#### 2.1.1.b Survey design

Data are collected with significant overlap among the photos such that common features could be identified. We achieve this by flying at different heights and by also adjusting the camera's angle. For the drone, we choose the DJI Mavic Air 2, retailing for under 1000 USD. With a field-of-view of 84° and given a fixed  $f/2.8$  aperture with equivalent focal length of 24mm, this brand of drone gives us the flexibility to acquire photos from seven meters or greater to achieve a reasonable depth of field, which is vital in the later step of identifying common features among the fore-, mid-, and backgrounds. In terms of acquisition paths, we opt for circular and linear hyperlapse defaults as found within the drone's support software. We do not use ground control points or calibration tables.

We additionally plan and coordinate with the dam operators and Locarno air traffic control prior to and during acquisition.

#### 2.1.1.c Photo acquisition

During a period of three hours, we pilot a Mavic Air 2 drone and use its camera to acquire 1143 images at 12 MP (4000 x 3000 MP). We select a shutter speed of 1/640 s and a 100 ISO

setting due to sunny conditions. A subset of the acquired photos is given in Figure 2.



Figure 2. Various photos of the dam and lakebed as taken from a drone.

#### 2.1.1.d Color calibration

Having acquired the photos on a sunny day over a few hours, we observe inconsistent lighting (Figure 2). As this may hinder mesh reconstruction [10], we apply basic post-photo processing to correct for various degrees of whiteness, brightness, and moving shadows.

#### 2.1.1.e Surface model generation

Multiple photogrammetry software options (WebODM, Meshroom, RealityCapture, and Metashape) are evaluated in terms of their speed, accuracy, ease-of-use, functionality, and of particular concern, ability to reconstruct 3D surface meshes with minimal topological issues (e.g., holes). RealityCapture (RC) and Metashape perform the best, with RC having the added benefit of being free. However, RC only runs on Windows and requires an Nvidia CUDA GPU. But due to clever memory management, RC does not require significant amounts of RAM. Metashape can run on Linux, Mac, and Windows, with RAM demands scaling with number of 2D photos. We move forward with a 3D surface mesh created in Metashape on a 16-core CPU/40-core GPU M3 Max MacBook Pro laptop with 64 GB of unified memory shared between the CPU and GPU. The photogrammetry process of importing photos, to feature matching, to image alignment, to the eventual mesh generation, decimation, and smoothing requires less than thirty minutes to complete.

#### 2.1.1.f Surface model enclosing

To perform 3D wave simulations using the spectral element method, we require a volumetric mesh and not a surface mesh. Our workflow uses a specific implementation of the spectral element method called Salvus [11], which requires a mesh either composed of hexahedra if solving 3D wave solutions or quadrilaterals for 2D problems. The reason for this is to exploit a fundamental benefit of using spectral element methods for wave propagation modelling: 2D quads or 3D hexes result in a diagonal mass matrix and thus trivialize inverting the mass matrix [11-13]. Given the 3D nature of our dam, we take the 3D triangular surface mesh from 2.1.1.e and extrude the mesh outwards and downward before sealing the base, thus creating



a watertight 3D surface mesh. This is accomplished using Blender, a free and open-source 3D computer graphics software package [14].

#### 2.1.1.g Conditioning and layer additions

Before converting the 3D enclosed surface mesh of triangles into a 3D volumetric mesh of hexes, we further correct for any additional topology issues using Blender's 3D sculpting tools and then remesh the surface into quads. Any unhandled spikes or non-physical geometries may result in bad elements (with small or negative Jacobians – i.e., squished elements) which would render subsequent wave simulations infeasible. And the reason for converting from triangles to quads is that the next step more robustly remeshes when given a quad surface. Once satisfied with the mesh, we add a water layer on top.

#### 2.1.1.h Hexahedral remeshing

The surface mesh is then transformed into a volumetric hexahedral mesh using Cubit, a meshing software tool developed to create tetrahedral and hexahedral meshes for finite element analysis and fluid dynamics [15]. To preserve the topography of the dam and the surface, we choose an element size of approximately 2.5 m x 2.5 m x 2.5 m. Based on results at this stage, an iterative process takes place by returning to 2.1.1.d to further improve the quality of this mesh. We accomplish this by conditioning the surface mesh in a manner that prevents Cubit from outputting volumetric meshes containing elements with a small Jacobian, as these elements are unphysical or dimensioned smaller than desired. A smaller element size dictates a decrease in timestep, which adversely increases simulation time and memory requirements. Results from steps 2.1.1.e to 2.1.1.h are presented in Figure 3.

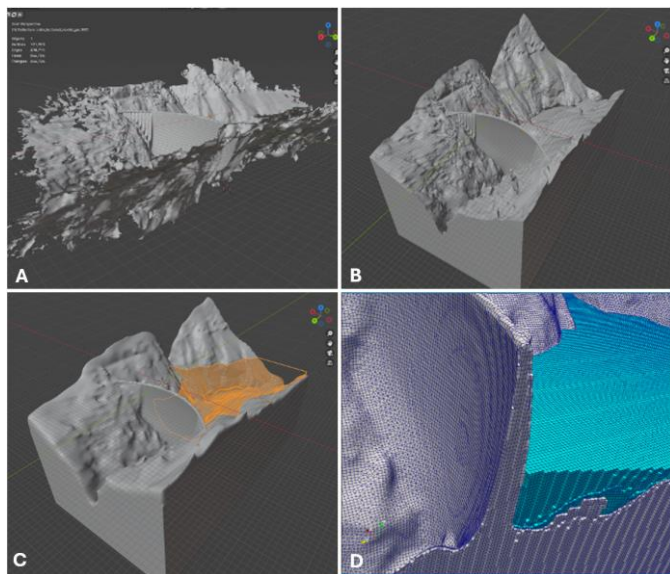


Figure 3. (A) displays the 3D surface mesh output as described in section 2.1.1e; (B) is the result of enclosing that surface mesh as detailed in section 2.1.1f; (C) shows a despiked and smoother version of (B) with the inclusion of a water layer in orange as noted in section 2.1.1.g; and (D) is an arbitrary slice through the hexahedral mesh, with bedrock and dam in gray and the water layer in blue as discussed in section 2.1.1h.

#### 2.1.1.i Population field and simulation parameters

To qualify the mesh, we must populate it with elastic field parameters. We use a homogeneous compressional velocity of 4800 m/s, shear velocity of 2800 m/s, and density of 2710 kg/m<sup>3</sup> for the basement bedrock and dam. The water layer is given a sonic velocity of 1500 m/s and density of 1000 kg/m<sup>3</sup>.

#### 2.2 Simulation

The prepared mesh can now be used as input to the wave solver. For illustrative purposes, we initiate a 130 Hz Ricker spherical explosive point source (i.e., the curl of displacement is zero in an elastic homogeneous model). Dirichlet boundary conditions are assigned to the water-air, dam-air, and basement-air interfaces, and absorbing boundaries are placed on the other outer faces. Snapshots in both 2D and 3D are showcased in Figure 4. The mesh thus succeeds in allowing a solution to the wave equation, thus validating the workflow for this use case.

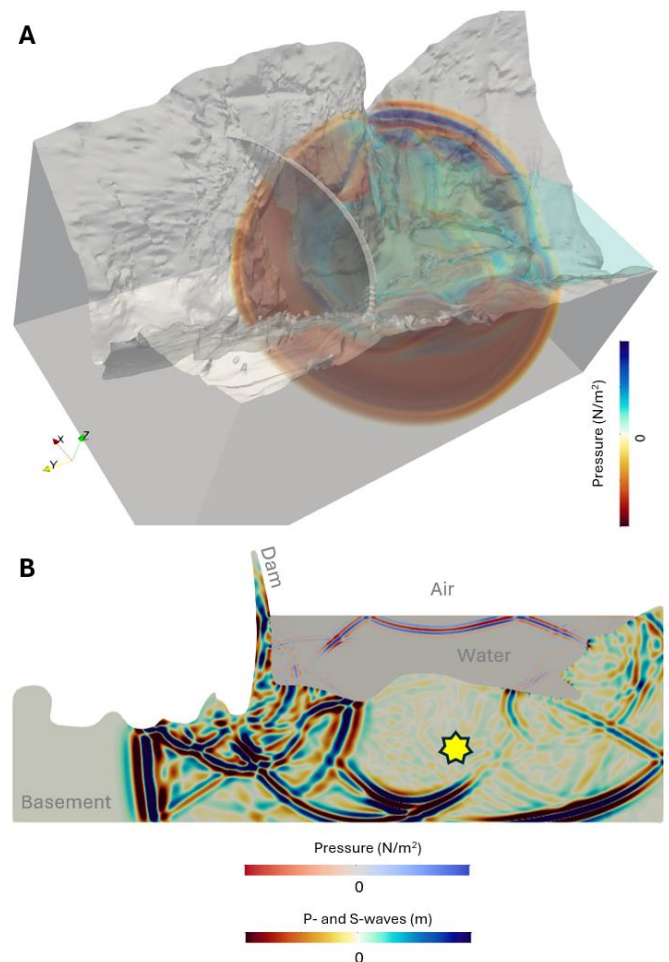


Figure 4. (A) shows a snapshot of an acoustic wavefield successfully propagating through the 3D mesh created from a drone photo acquisition. (B) is a slice through that 3D model at a later timestep to showcase various wave modes propagating through different media and structures in the model due to a point source activated at an earlier time at the location given by the yellow star. Waves within the water column are measured in pressure, whereas within the basement and dam they are given in terms of compressional and shear wave particle displacement.

### 3 DISCUSSION

#### 3.1 Alternative acquisition methods and inputs

Though the workflow emphasizes the use of drones to acquire photos as input, this is not a requirement. In fact, a LiDAR system, a phone camera, and other capture methods and tools could be employed – each with its own trade-offs [7]. We also consider the use of satellite imagery to construct a usable mesh. Unfortunately, it does not yield the necessary 3D detail or resolution to faithfully recover the dam and surrounding topography – which are paramount in ground motion studies [11,16,17]. Furthermore, satellite imagery is unable to capture complex 3D surface structures such as the dam's overhang. Figure 5 compares surface meshes created from various satellite sources to that generated from drone imagery.

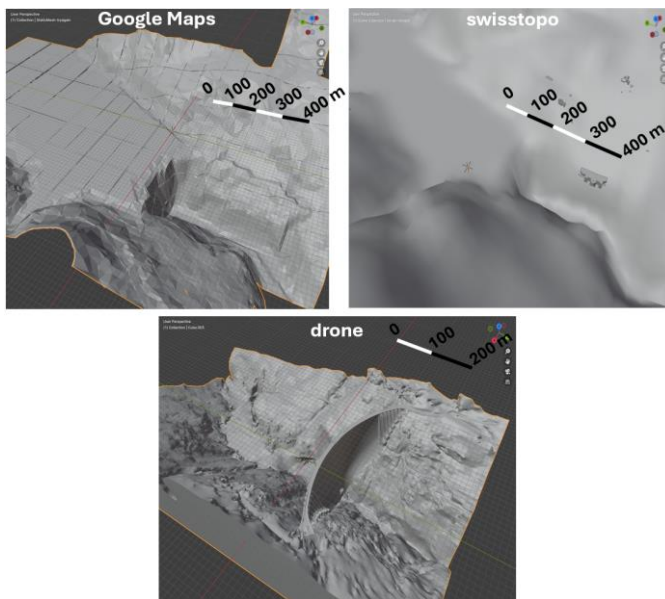


Figure 5. A comparison of different surface meshes created using satellite imagery input from Google Maps and swisstopo to that generated from drone imagery. There is added serendipity in having acquired the drone footage during dam maintenance. Meshes are displayed in perspective view.

#### 3.2 Seismic hazard and risk analysis

We now have a beneficial workflow that substantially reduces the burden of constructing meshes. This leaves us with ample time to prioritize our focus on other problems within seismology. One of these problems includes quantifying ground shaking and its impacts on the environment.

As an example, we may now compute ground acceleration in our model and hypothetically venture to assess the risk of structural failure. For this demonstration, we simulate two different rupture sites at the dam and note the acceleration values that the dam and the bedrock (basement) may experience, as given in Figure 6. Analyzing the wavefields further would allow one to compute peak ground acceleration (PGA) values as input to probabilistic hazard and risk calculations [18]. As can be observed, ground motion values are amplified and dampened by many factors, including the topography, orientation of the rupture mechanism, and the presence of air or water at an interface.

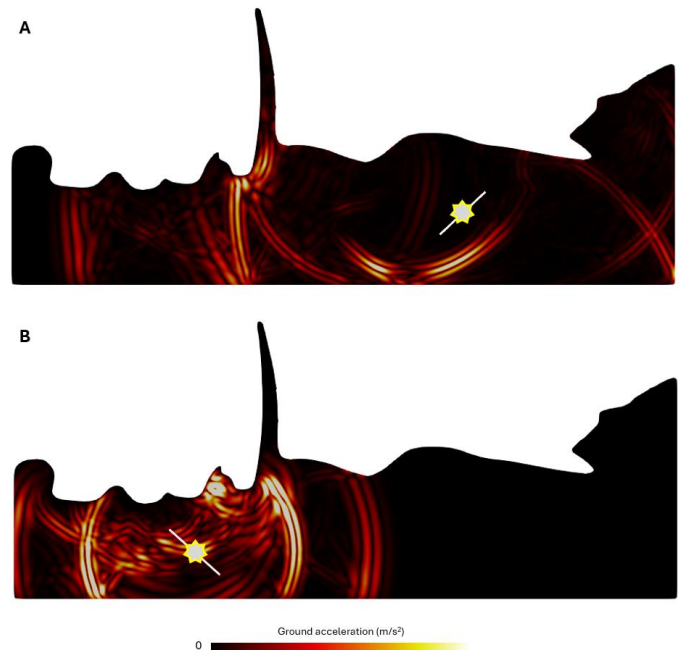


Figure 6. Magnitude of ground acceleration from two different sources, with snapshots taken near peak acceleration within the dam region for each scenario. Earthquake rupture location is indicated with a star, along with its orientation. The source at (A) is located farther from the dam and is underneath a water layer with smoother topography. (B)'s source lies closer to the dam below an air interface with rougher topography.

### 4 CONCLUSION

We provide a workflow outlining how images acquired from drones can be leveraged to create hexahedral meshes that may serve as input to wave simulations, successfully applying it to the Contra dam in Switzerland. The workflow has many steps, all of which may be readily accomplished by performing minor tweaks to off-the-shelf technologies. For situations where no computational mesh exists, acquiring the photos may take no more than a day or two – and in our case three hours. Given proficiency with the tools in the workflow, the simulation-ready mesh may be created in under a week, which marks a substantial improvement to the process of manually creating these meshes over the course of months. Nevertheless, some manual work is still required to make the mesh physics-ready – though this may be greatly reduced by spending more time upfront with the survey design to ensure the object of interest is properly photographed. Selecting photogrammetry software tools which are more robust to poorer acquisitions may further aid the process.

The way forward includes further workflow automation and determining how to more adaptively discretize the mesh such that we use fewer elements. Ideally, we envisage employing this methodology on structures lacking computer models, including historical structures in earthquake-prone regions. Up to this point, we have described a forward modelling process in response to a source. Naturally, using ambient or active vibrations to then invert for 3D elastic field parameters and possibly detect time-lapse changes at intermediate scales within such structures would be among the next steps to investigate.

## ACKNOWLEDGMENTS

The authors wish to thank ETH Zurich for its support.

## REFERENCES

- [1] Courant, R., K. Friedrichs, and H. Lewy. "On the partial difference equations of mathematical physics." *IBM journal of Research and Development* 11, no. 2 (1967): 215-234.
- [2] Igel, H. *Computational seismology: a practical introduction*. Oxford University Press, 2017.
- [3] Szeliski, R. *Computer vision: algorithms and applications*. Springer Nature, 2022.
- [4] Förstner, W., and B.P. Wrobel. *Photogrammetric computer vision*. Vol. 6. Switzerland: Springer International Publishing, 2016.
- [5] Hartley, R. *Multiple view geometry in computer vision*. Vol. 665. Cambridge university press, 2003.
- [6] Custers, B. "Drones here, there and everywhere introduction and overview." *The future of drone use: Opportunities and threats from ethical and legal perspectives* (2016): 3-20.
- [7] Kovanič, L., B. Topitzer, P. Peťovský, P. Blišťan, M.B. Gergeľová, and M. Blišťanová. "Review of photogrammetric and lidar applications of UAV." *Applied Sciences* 13, no. 11 (2023): 6732.
- [8] Spicher, A., and E. Wenk. "Erläuterungen zu Geologischer Atlas der Schweiz, 1: 25'000, Blatt 1313, Bellinzona." *Schweiz. Geol. Komm* (1981): Atlasblatt 66.
- [9] Pfeifer, H.-R., H. Kobe, A. Colombi, D. Pozzorini, A. Steck, and Y. Gouffon. "Blatt 1312 Locarno.-Geol. Atlas Schweiz 1: 25'000, Erläuterungen 159." *Geologischer Atlas der Schweiz 1: 25'000* (2018).
- [10] Lowe, D.G. "Object recognition from local scale-invariant features." In *Proceedings of the seventh IEEE international conference on computer vision*, vol. 2, pp. 1150-1157. Ieee, 1999.
- [11] Afanasiev, M., C. Boehm, M.v. Driel, L. Krischer, M. Rietmann, D.A. May, M.G. Knepley, and A. Fichtner. "Modular and flexible spectral-element waveform modelling in two and three dimensions." *Geophysical Journal International* 216, no. 3 (2019): 1675-1692.
- [12] Liu, Y., J. Teng, T. Xu, and J. Badal. "Higher-order triangular spectral element method with optimized cubature points for seismic wavefield modeling." *Journal of Computational Physics* 336 (2017): 458-480.
- [13] Ferroni, A., P.F. Antonietti, I. Mazziere, and A. Quarteroni. "Dispersion-dissipation analysis of 3-D continuous and discontinuous spectral element methods for the elastodynamics equation." *Geophysical Journal International* 211, no. 3 (2017): 1554-1574.
- [14] Blender Development Team. (2023). Blender (Version 4.0.2) [Computer software]. <https://www.blender.org>
- [15] Coreform Cubit (Version 2024.8) [Computer software]. Orem, UT: Coreform LLC. Retrieved from <http://coreform.com>
- [16] Anggraeni, D. "Modelling the impact of topography on seismic amplification at regional scale." Master's thesis, University of Twente, 2010.
- [17] Castellazzi, G., A.M. D'Altri, S.d. Miranda, F. Ubertini, G. Bitelli, A. Lambertini, I. Selvaggi, and A. Tralli. "A mesh generation method for historical monumental buildings: an innovative approach." In *Proceedings of the VII european congress on computational methods in applied sciences and engineering (ECCOMAS Congress 2016), Crete Island*. 2016.
- [18] Baker, J., B. Bradley, and P. Stafford. *Seismic hazard and risk analysis*. Cambridge University Press, 2021.



## A review of methods and challenges for monitoring of differential settlement in railway transition zones

Kourosh Nasrollahi<sup>1</sup>, 0000-0002-9696-8467, Jens C.O. Nielsen<sup>1</sup>, 0000-0002-7271-4913, Jelke Dijkstra<sup>2</sup>, 0000-0003-3792-0727

<sup>1</sup>Department of Mechanics and Maritime Sciences, Division of Dynamics/CHARMEC, Chalmers University of Technology, SE-412 96 Gothenburg, Sweden

<sup>2</sup> Department of Architecture and Civil Engineering, Chalmers University of Technology, SE-412 96 Gothenburg, Sweden

email: kourosh.nasrollahi@chalmers.se, jens.nielsen@chalmers.se, jelke.dijkstra@chalmers.se

**ABSTRACT:** Differential settlement in ballasted railway tracks, particularly in transition zones between two track forms, poses a critical challenge for railway infrastructure. Such settlement, often exacerbated by a stiffness gradient due to changes in track superstructure and substructure, typically causes a local dip in the longitudinal track level a few metres from the transition, leading to higher dynamic traffic loading and reduced passenger comfort. Regular monitoring of transition zones is essential for safe operations and cost-effective maintenance. This paper reviews methods for monitoring differential settlement in railway tracks. To measure the properties and loading of the superstructure, potential methods include fibre Bragg grating (FBG) sensors, point receptance measurements, track geometry (and track stiffness) recording cars, and wheel load impact detectors (WILD). Characterisation of the subgrade can be carried out via a multichannel analysis of surface waves (MASW), dynamic cone penetration tests (CPT), interferometric synthetic aperture radar (InSAR), frost sticks for temperature monitoring, and total stations. Lessons learned from an in-situ measurement involving an extensive FBG-based system deployed in northern Sweden to monitor a transition zone in harsh weather conditions are presented. Integrating a combination of monitoring methods with a simulation model to verify and support the accurate prediction of differential settlement is a useful approach to addressing challenges associated with track stiffness gradients and guiding the improvement of transition zone designs.

**KEY WORDS:** Differential settlement, railway transition zone, condition monitoring, fibre Bragg grating sensors

### 1 INTRODUCTION

In transition zones between two different railway track forms, there is a discontinuity in the track structure, resulting in a gradient in track stiffness. Examples include transitions between different superstructures, such as slab track to ballasted track, and/or between different substructures, such as an embankment to a bridge or tunnel structure. Differences in the cyclic loading and supporting substructure on either side of the transition may lead to differential settlement of the ballasted track and an irregularity in longitudinal rail level soon after construction due to densification of ballast and consolidation of the subgrade layers. This results in an amplification of dynamic traffic loading along the transition, contributing to the degradation process of the foundation and further deterioration of the vertical track geometry. Historically, the design of transition zones has aimed to minimise the difference in track stiffness between the ballasted track on the embankment and the engineering structure [1–4].

Some researchers argue that the main causes of track deterioration in transition zones are the non-uniform stiffness and damping between different layers of subgrade materials, which are impacted by variations in moisture and other geotechnical factors [5,6]. In a field test conducted in Sweden [7], it was observed that the displacement of sleeper ends varied significantly from one sleeper to the next due to differences in support conditions. This highlights the importance of ballast and subgrade conditions in a railway network.

Various transition zone designs have been implemented to mitigate variations in loading and support conditions. Many of these solutions aim to achieve a gradual and smoother variation in track stiffness from one track form to another. Some approaches are designed to enhance the support of the subgrade, such as transition wedges and approach slabs, while others focus on the superstructure, including the

implementation of track components such as wider sleepers, auxiliary rails, and elastic pads (including conventional rail pads with varying stiffness along the transition zone and/or under sleeper pads). A review of transition zone designs can be found in [5,6]. In parallel, advancements in real-time data acquisition, computational techniques, and the emergence of 'big data' approaches have enhanced the analysis and modelling of railway degradation, facilitating more comprehensive and precise evaluations [8].

Increasing frequency of traffic, higher axle loads and train speeds result in quicker deterioration of the infrastructure. Infrastructure managers need up-to-date information on both the current condition (diagnosis) and the expected future state (prognosis) of their assets to effectively plan maintenance and renewal efforts. Structural health monitoring (SHM) has emerged as a valuable tool for railway systems, enabling efficient asset management by providing real-time feedback on the condition of various components. By facilitating early damage detection, SHM enhances structural reliability and reduces life cycle costs. Condition-based maintenance means that system operators schedule maintenance based on the actual condition of the system and the anticipated deterioration rate. To achieve this, operators need to employ a monitoring strategy for recording the condition of their assets. The collected data can serve to develop or create regulations, such as acceptable condition thresholds [6], which are used to determine if maintenance should be performed.

### 2 LITERATURE REVIEW

Emerging sensing techniques, along with innovations in sensors and data analytics, present exciting opportunities in geotechnical, structural, and railway engineering to enhance the understanding of infrastructure performance during both construction and operation. A monitoring system could, and



perhaps should, be integrated into the construction package to facilitate long-term, proactive operational monitoring, thereby contributing to quality control, maintenance, resilience against hazards, and reuse. Such a system should include techniques capable of capturing a wide range of data, ranging from low sampling rate parameters such as temperature, humidity, moisture, settlement, and inclination to high sampling rate data including acceleration, noise, rotation, wind velocity, and more.

In railway engineering, monitoring techniques can be categorised into trackside monitoring of both geotechnical and structural elements, onboard monitoring, and inspection. Trackside monitoring involves the use of instrumentation in or adjacent to the track to monitor the track, vehicles passing by, or the interactions between them [9]. For the track, this includes observing the status of various track layers, their geometry, and how they evolve over time [10]. Examples include assessing the condition of ballast and subgrade using methods such as ground-penetrating radar (GPR) [11] and cone penetration tests (CPT) [12]. GPR uses electromagnetic waves to scan and map subsurface features within the railway industry, offering geospatial data on subsurface conditions [13]. To evaluate the stiffness and stratification of the layered substructure at a test site, a multi-channel analysis of surface waves (MASW) can be used [14]. Furthermore, fibre optic sensors can be embedded in the track bed to monitor settlement and detect early signs of degradation and potential landslides in the embankment [15,16]. Research has also been conducted on technologies capable of accurately monitoring the average settlement of railway lines over extensive areas using synthetic aperture radar (SAR) and interferometric SAR (InSAR) techniques [17].

On the other hand, onboard track monitoring and inspection are generally carried out using in-service vehicles, as their regular passing over longer sections of track allows for efficient monitoring of track status. Onboard component monitoring is carried out by instrumentation on vehicles, evaluating their condition over time. Dedicated vehicles are equipped with advanced equipment that enables in-depth inspections, which are vital for railway safety. However, these vehicles require special scheduling and trained personnel, limiting their usage [18]. Measurement units on these vehicles use technologies such as laser imaging, image processing, GPR, ultrasonic sensors, vibration sensors, high-precision accelerometers, and electromagnetic sensors.

Several in situ investigations utilising trackside monitoring have been conducted to assess the dynamic behaviour of railway track using instruments such as accelerometers, strain gauges, and displacement transducers. In [19], results were presented from an extensive monitoring campaign of transition zones (embankment to culvert) in the Netherlands. Vertical displacement at various depths of ballast and subgrade, axle load, and average track stiffness were measured using geophones, uniaxial accelerometers (within the ballast), triaxial accelerometers (within the soil below the track), strain gauges, and a high-speed camera. It was concluded that voided sleepers in the transition zone, due to long-term differential track settlement, were the main sources of large track displacements that caused increased impact loading and accelerated track degradation. Zuada Coelho et al. [12] used CPT and borehole data to consider stochastic variations in support conditions on

a network scale in the Netherlands when predicting track settlement using a two-dimensional model.

In [20], a track deflection and stiffness survey was carried out using micro-electro-mechanical-systems (MEMS) accelerometers. About 80 of these devices were placed on successive sleeper ends, primarily on the field side of the track, and then moved along the site during consecutive night-time possessions. This was done in two batches of 200 sleepers with an overlap of 50 sleepers, and measurements were repeated three months apart [21]. Additionally, a webcam mounted on a telescope was positioned at 6 m from the track to reduce the influence of ground vibration. It captured an image of the target, which was mounted on the sleeper for the measurement of peak-to-peak displacement. A key limitation of this method was that the video recording system could monitor the displacement of only one or two sleepers at a time.

Optical fibre sensors offer significant advantages over conventional and other smart sensors due to their high sensitivity, small size, and potential for short- and long-distance measurement. For example, Wang et al. [22] attached two FBG sensors on the rail web as a bi-directional device to measure longitudinal force in a high-speed railway line. Temperature compensation via calibration tests was conducted. Wheeler et al. [23,24] measured rail strains using Rayleigh backscattered, distributed optical fibre sensors. Their field test instrumentation included a 7.5 m long section of rail with nylon-coated single-mode fibres installed on the rail web at 20 mm and 155 mm from the bottom of the rail. The measured rail strains were used to determine shear forces, which, together with the known static wheel loads, were employed as part of the calibration to determine the rail seat loads for 14 consecutive sleepers as the train traversed the instrumented track. These data were then combined with measurements of dynamic rail displacement captured through high-speed imaging using digital image correlation (DIC) to process the rail seat load–deflection relationships for each sleeper.

On-board monitoring techniques have been investigated in research and used in infrastructure management [25]. This leads to better maintenance planning and reduces the delay between decision-making and the execution of maintenance actions. For example, in Finland, ballast degradation due to traffic and freeze-thaw cycles, leading to further particle breakage, settlement, or heaving, has been investigated using track geometry recording cars [26]. In Sweden, vertical track geometry degradation between 1999 and 2016 has been studied using regular monitoring by track geometry recording cars [27,28]. Furthermore, in Switzerland, an on-board monitoring policy is considered in infrastructure maintenance planning [29], and similarly in Australia [30].

This paper presents a review of methods and challenges associated with monitoring of differential settlement in railway transition zones. Specifically, it discusses the results and lessons learned from an extensive measurement campaign conducted under harsh conditions on a heavy haul line in northern Sweden. These measurements included both short-term dynamic and long-term static responses of the transition zone in different sleeper bays, using an FBG-based sensor setup and complementary measurements.

### 3 MONITORING AND MEASUREMENT METHODS

Monitoring in a railway transition zone may involve numerous sensor types and measurement techniques, such as seismic, electrical, electromagnetic, and resistivity methods in geophysics. Brief descriptions and definitions of some of these are presented below. In Section 4, the practical use of many of these techniques will be discussed with reference to the challenges encountered during an extensive field test recently carried out in a transition zone on Malmaban in northern Sweden.

#### 3.1 MASW

The Multi-channel Analysis of Surface Waves (MASW) method is a cost-effective and non-destructive geophysical technique used to evaluate subsurface conditions (and to determine the location of bedrock) by analysing the propagation of surface waves, particularly the dispersion of Rayleigh waves. It provides shear wave velocity profiles down to a depth of up to 20 m, which are used to obtain small-strain stiffness and damping properties of the soil [31].

In this specific field test, an excitation source, such as a sledgehammer, weight drop, or specialised loading device, generates surface waves. An array of geophones, typically ranging from 12 to 48, is placed in a straight line on the ground at regular intervals. These geophones detect and record the waveform and arrival time of the seismic waves. The Rayleigh waves exhibit dispersion, meaning their velocity changes with frequency due to variations in subsurface material properties. Lower-frequency waves penetrate deeper into the ground, while higher-frequency waves provide information about shallower layers [31]. Typically, earth models are formulated using CPT data to distinguish the number of soil layers and provide a reasonable estimation of soil density. Consequently, shear wave velocity is fitted to the data at smaller strains.

#### 3.2 CPT

The Cone Penetration Test (CPT) is a geotechnical investigation technique to provide a detailed soil profile by assessing the mechanical cone resistance of different layers of subgrade soils. The cone resistance is directly linked to the strength of the soils, and empirical relations are established to identify the soil type [32]. The data obtained from a CPT aids in designing track foundations, evaluating ballast and sub-ballast layers, and identifying soft soil layers that could lead to settlement or instability [32]. However, the density of data per square kilometre in railway infrastructure is generally relatively low due to the high cost of these boreholes [12].

The test is conducted by jacking or driving a steel cone into the ground at a controlled rate while continuously measuring cone resistance. Two primary types of CPT are used: Static Cone Penetration Testing (SCPT) and Dynamic Cone Penetration Testing (DCPT). In SCPT, the cone is jacked into the soil at 1 – 2 m intervals at a constant rate using a hydraulic system. This method records key parameters such as (1) cone resistance, which indicates soil strength, (2) sleeve friction, which helps to determine soil type, and (3) (excess) pore water pressure, which provides insights into soil drainage and consolidation behaviour. SCPT is frequently used in railway infrastructure to investigate embankment stability.

In DCPT, a steel cone is driven into the ground using a standardised weight dropped from a specified height. The number of weight drops required to penetrate a specific depth is recorded, providing an estimate of soil resistance and compaction quality. DCPT is widely utilised in ballast and subgrade assessment, as well as rapid evaluations of soil stability [32]. The data from CPT or MASW tests can be used to estimate dynamic subsoil stiffness and damping along the track using analytical approaches, such as the cone method from [33] and the analytical formulae in [34].

#### 3.3 GPR

Ground-Penetrating Radar (GPR) is a non-destructive electromagnetic geophysical technique used to investigate and analyse subsurface structures. These systems can be mounted on track geometry recording cars, enabling continuous data collection at operational train speeds. This allows infrastructure managers to efficiently assess large sections of the track network and make data-driven decisions for maintenance planning. GPR operates by emitting electromagnetic waves (EM) into the ground and measuring their reflections using a receiving antenna to identify issues such as ballast fouling, moisture intrusion, and subsurface voids, as these can be linked to changes in electrical impedance [13]. GPR functions within a finite frequency range where the velocity and attenuation of the EM wave are independent of frequency (typically 1 MHz – 1 GHz) [13].

The receiving antenna captures the reflected signals, and the system measures the time delay and amplitude of these reflections. This data is then processed and visualised in radargrams, in the form of black-and-white, or coloured, waves and patterns, each corresponding to the radar signals reflected by different underground materials. These radargrams enable engineers to analyse subsurface conditions, detect hidden defects, and determine the thickness of different layers. The frequency of the radar waves plays a critical role in determining both the resolution and depth of penetration. High-frequency waves, typically above 1 GHz, provide detailed images but can only penetrate shallow depths, making them ideal for inspecting ballast conditions. Lower-frequency waves, in the range of 100 – 500 MHz, penetrate deeper but offer lower resolution, making them more suitable for analysing subgrade and deeper structural layers. Water-saturated or clay-rich soils tend to absorb radar waves, limiting penetration, while dry, coarse materials like gravel or sand allow for better wave transmission [13].

#### 3.4 InSAR

Interferometric Synthetic Aperture Radar (InSAR) is a remote sensing technique that uses satellite-based radar imagery to measure ground surface deformation with millimetre-level precision. By analysing the phase differences between radar signals captured at different times, InSAR provides detailed information about land subsidence, uplift, and ground movement [32,35]. The precision of this technique is of the order of 3 – 5 mm.

#### 3.5 FREE AND FORCED VIBRATION

Point receptance analysis in railways is a testing technique used to assess the dynamic properties of track by measuring its response to applied forces. A sledgehammer with a steel tip, or

a falling weight of 8 kg, has been used in free vibration tests to generate an excitation impulse on the rail [36]. In a forced vibration test, a hydraulic actuator generates linear frequency sweeps with constant load amplitudes to stimulate various natural frequencies of a structure, such as a bridge [37]. The resulting accelerations are recorded using accelerometers or laser Doppler vibrometers at different positions, and the data is processed to compute Frequency Response Functions (FRFs). Measured FRFs can then be compared with corresponding calculated FRFs from a simulation model to identify the stiffness and damping of different parts of the structure [38].

### 3.6 PERMANENT DISPLACEMENT, SETTLEMENT

Various tools and instruments are available for measuring and monitoring settlement in track layers. These include the Multi-Depth Deflectometer (MDD), which is embedded in the track bed, uniaxial and triaxial accelerometers [39], settlement plates paired with total stations, vibrating wire-based measurement systems, liquid level sensors, inclinometers, Linear Variable Differential Transformers (LVDTs), Global Navigation Satellite Systems (GNSS), and FBG sensors.

The MDD is specifically designed to assess the mechanical response and deformation of soil layers. It is widely used at railway track sites to evaluate soil stiffness and condition. Primarily, the MDD serves as a reliable tool for accurately measuring the permanent deformation of different pavement layers. Additionally, it facilitates the calculation of the effective elastic moduli of multilayered pavement structures based on the collected data [40].

The LVDT is a displacement sensor used to detect linear movements in both the short and long term. It is commonly applied in railway infrastructure to monitor the displacement of components, such as sleepers, rails, bridges, and slabs [15].

A total station is an advanced electronic and optical instrument designed for precise measurement of angles, distances, and coordinates. In railway applications, it plays a crucial role in ensuring accurate track alignment, calculating gradients, and maintaining track conditions by detecting deviations and elevation changes [15].

The GNSS utilises satellite signals to determine the position of objects on Earth. It operates through a network of orbiting satellites that transmit signals to ground receivers, which process the timing and strength of these signals to compute position, altitude, and velocity. In railway systems, GNSS is used for continuous real-time monitoring of track settlement, enabling a better understanding of foundation changes at different stages and enhancing railway safety [41,42].

### 3.7 BALLAST INSPECTION

Ballast degradation occurs when fine materials or fouling agents accumulate in the spaces between ballast particles. This fouling can result from ballast fragmentation, contamination from external elements, or the infiltration of fines from the subgrade soil. Over time, as ballast continues to age, it becomes increasingly affected by fouling and degradation due to particle breakage and surface wear. These processes contribute to inadequate drainage, excessive settlement, track misalignment, and diminished lateral stability, all of which negatively impact railway track performance. In severe cases, excessive ballast degradation can lead to operational disruptions and safety risks [43]. Assessing ballast conditions typically involves visual

inspections, manual measurements, and field sampling, which is often followed by sieve analysis. Additionally, automated methods such as the Ballast Scanning Vehicle (BSV) have been introduced to enhance evaluation processes. The BSV is capable of capturing field ballast images, video footage, and 3D height maps from both plan and depth profile perspectives, enabling a thorough assessment of ballast conditions [44].

### 3.8 WILD

Wheel flats and other forms of wheel out-of-roundness can be detected through acoustic or visual inspections, or by measuring vertical wheel–rail contact forces using wheel impact load detectors (WILDs). These detectors help operators monitor force levels, enabling proactive maintenance to prevent excessive wheel out-of-roundness. Commercial WILD systems use various types of sensors, including strain gauge circuits, fibre optic technology for measurements of rail bending, and load cells for rail seat loads [45].

### 3.9 FROST DEPTH

Extreme weather conditions in northern European countries may lead to recurrent issues with freeze-thaw cycles and seasonal variations in track geometry. Frost depth can be measured using frost sticks [15].

### 3.10 TRACK GEOMETRY AND TRACK STIFFNESS RECORDING CAR

Track geometry recording cars are specialised rail vehicles equipped with advanced measurement systems such as laser profilometers, accelerometers, and ultrasonic sensors. Track geometry is evaluated based on band-pass filtered indicators, such as longitudinal level, horizontal alignment, cant, curvature, gauge, and twist. These indicators are assessed based on the specific wavelength intervals defined in EN13848-5, see Table 1 [46].

Table 1. Wavelength ranges according to EN 13848–5[46].

Longitudinal level	Wave type	Wavelength range (m)
D <sub>0</sub>	Short wave	1 – 3
D <sub>1</sub>	Mid wave	3 – 25
D <sub>2</sub>	Long wave	25 – 70

### 3.11 POINT MEASUREMENTS

Strain gauges (traditional or FBG-based), accelerometers, and contact pressure cells [39] are widely used in railway measurements to monitor track and vehicle dynamics, ensuring safety and performance. Strain gauges are installed on rails, sleepers, and train components to assess strain, stress, load distribution, and deformation under varying operational conditions.

## 4 CASE STUDY: THE GRANSJÖ TEST SITE

In 2022–2023, an extensive field measurement campaign was carried out in a transition zone at *Gransjö*, north of Boden, on the Swedish heavy haul line *Malmbanan* [15]. The transition zone was between a conventional ballasted track on embankment and a Moulded Modular Multi-Blocks (3MB) slab track. An FBG-based long-term monitoring arrangement, with a high temporal resolution, was used for both short-term and long-term condition monitoring of the operational railway track in the harsh conditions of northern Sweden. The test set-



up was limited to measuring the response in four selected sleeper bays.



Figure 1. An overview of the test site including a transition zone between ballasted track and 3MB slab track at Gransjö, north of Boden, Sweden.

#### 4.1 TEST SITE

Traffic on the line is dominated by iron ore freight trains with axle loads up to 32 tonnes, operating from the mines in Kiruna and Malmberget to the ports in Narvik and Luleå. The speed of the loaded heavy haul trains is 60 km/h. The line is also used by passenger trains at maximum speed 135 km/h and by other freight trains. The annual traffic load is of the order of 14 MGT (mega gross tonnes).

The track design includes 60 kg/m rails, rail fastenings with 10 mm rubber rail pads, and concrete sleepers designed for axle loads of 35 tonnes at a sleeper distance of 0.6 m. The 3MB track at Gransjö was constructed in September 11 – 15, 2022, as part of the Horizon 2020 Shift2Rail EU project In2Track3. [15]. It was decommissioned in August 2023, see Figure 1.

#### 4.2 GEOTECHNICAL SURVEY

Prior to the construction of the 3MB track, geotechnical tests in the form of CPT and MASW were conducted to determine the stiffness and stratification of the layered substructure. The results indicated that the subgrade at the site consists almost exclusively of moraine, mixed with large blocks of rock, with a maximum depth of 5 m to bedrock [47]. The embankment height varies between 2 and 2.5 m. Due to years of maintenance involving tamping and re-ballasting of the track, the thickness of the ballast layer (nominally 30 cm) has increased to 80 cm. This necessitated additional excavation depth to remove the ballast layer (and large blocks) during the construction of the 3MB slab system.

In the MASW survey [47], the dispersion of Rayleigh waves on the ground surface, acquired using vertical geophones, was used for the interpretation of small strain shear stiffness. See Figure 2 for an example of measured distribution of wave speed in a cross-section of the subgrade at the test site.

Track geometry was measured using a track geometry recording car. For reference, in another study conducted on Malmaban, track geometry car recordings from 1999 to 2016 were analysed to investigate rates of vertical track geometry degradation. This analysis indicated some correlation between track stiffness gradient and differential settlement, providing insights into how variations in substructure stiffness can lead to local track irregularities. As expected, it was concluded that the

settlement rate along Malmaban varies significantly depending on the local conditions and properties of the subgrade. For a poorly supported section of the track, the standard deviation of the longitudinal level (1 – 25 m), evaluated over a 50 m track segment, increases by approximately 1 mm per annum [27,28].

Track stiffness at rail level, measured using the same track geometry recording car before and after construction of the 3MB track, is presented in Figure 3. A large gradient in stiffness is observed at either end of the 48 m slab track. The mean value of the track stiffness is particularly low for the slab track due to the softer elastic pads and the poor compaction of the backfill material after the excavation carried out during construction.

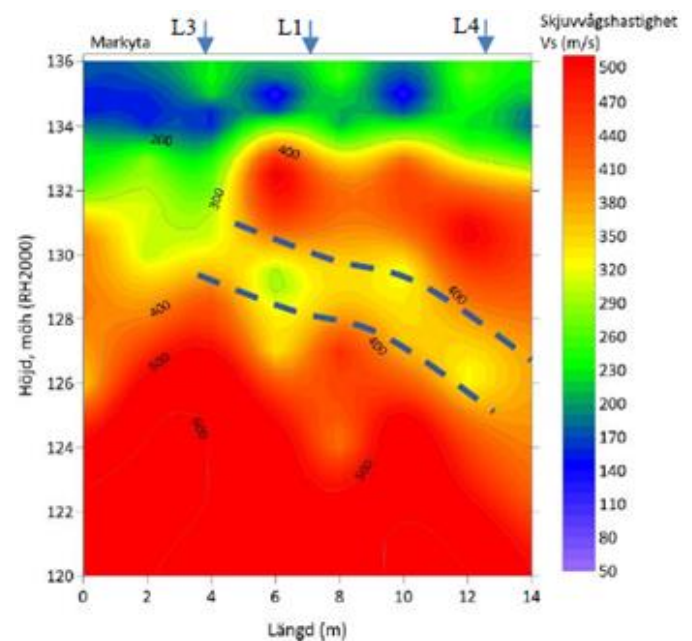


Figure 2. An example of measured shear wave speed distribution of layered soil at the test site [47].

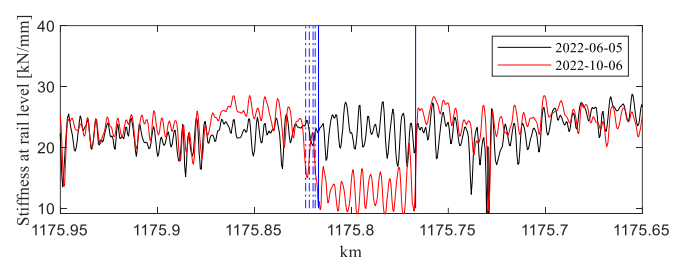


Figure 3. Track stiffness at rail level for ballasted track on embankment, two transition zones, and 48 m of slab track at Gransjö, measured by a track geometry recording car before and after construction. Blue vertical solid lines indicate the positions of two transitions (slab ends). Blue vertical dashed-dotted lines show the positions of instrumented sleepers 3, 5, 8, and 11, numbered from the slab.

#### 4.3 FROST DEPTH AND INSAR

The extreme weather conditions at the test site, with temperatures down to  $-40^{\circ}\text{C}$  during the winter and relatively warm summers, result in recurrent issues associated with freeze-thaw cycles and seasonal variations in track geometry.



The Swedish Transport Administration monitors frost depth using frost sticks, which record the temperature in the subgrade at various levels down to a depth of a few metres, thereby generating a temperature profile. The variation in frost depth over a period of eight months, recorded at a station near the test site, is shown in Figure 4. It is observed that prior to the end of October 2022, the ground was not frozen at all. By mid-December 2022, the ground had commenced freezing gradually down to a depth of 2 m. From mid-December 2022 until the beginning of May 2023 more than 2 m of the ground remained frozen.

Frost penetrating to a certain depth may induce the expansion of the subgrade, resulting in ground uplift. This phenomenon, known as frost heave, poses a significant issue on Malmbanan. To evaluate the average settlement at the test site, InSAR data was used, providing the average settlement over a specified surface area at various times. It was found that the average settlement at a track point near the test site is about 1 – 2 mm per year [31], see Figure 5.

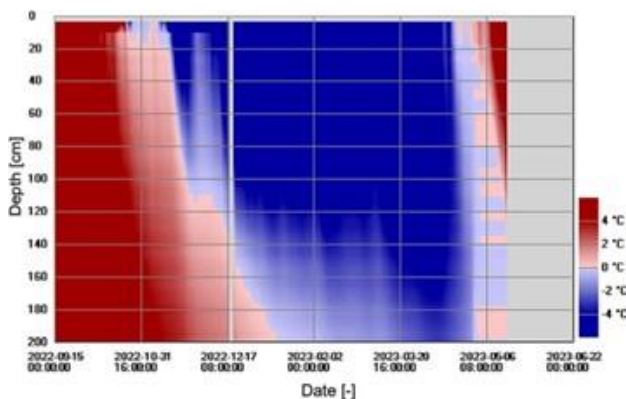


Figure 4. Temperature profile of subgrade down to 2 m depth at a measurement station near the test site [15].

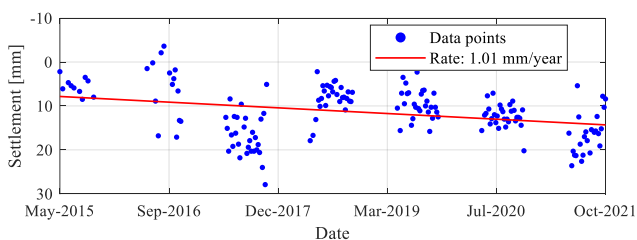


Figure 5. An example of InSAR long-term settlement measurements at a track point near the Gransjö site, covering the period from 2015 to 2021 [48]. Positive settlement numbers indicate downward permanent displacement.

#### 4.4 TRAFFIC LOAD

Information regarding traffic loading is crucial for evaluating railway infrastructure. In this campaign, data from a nearby wheel impact load detector was used to assess the range of mean wheel–rail contact forces for a specific train passage traversing the test site [15].

Additionally, to evaluate the influence of the stiffness gradient and to detect potential voids beneath sleepers, the wheel–rail contact force was measured within the transition zone. Temporary electrical strain gauges were used to measure the contact forces in sleeper bays 3, 5, and 8 from the transition. A Wheatstone bridge comprising two waterproof strain gauges,

each with a sensing area of 6 mm × 2.2 mm, was glued to the neutral axis of the rail within a specified span between two adjacent sleepers, oriented at  $\pm 45^\circ$  relative to the horizontal and vertical coordinate axes, see Figure 6. Shear deformations of the rail web were measured on two occasions, with a six-month interval.

It was concluded that the wheel–rail contact force in sleeper bay 3 was higher than in sleeper bays 5 and 8. The higher load could be attributed to vehicle dynamics when traversing the transition between two track forms with a stiffness gradient and potentially voided sleepers on the ballasted side. Consequently, the greater settlement of sleeper 3 could be a result of the higher loading. Additionally, it was observed that the wheels were generating forces, on average, about 5 kN higher in May 2023 than in October 2022 due to the evolving irregularities in the longitudinal level along the transition. The magnitude of forces derived from WILD data for the same train was consistent with the measured wheel–rail contact forces.



Figure 6. Full Wheatstone bridge mounted on the neutral axis of the rail web

#### 4.5 TRACK FORM DYNAMICS

Vertical point and cross receptances (frequency response functions) of both track forms were measured by exciting the rail using an instrumented impact hammer and recording the track response with accelerometers. The rail was excited either above a rail seat or at the centre of a sleeper bay. Apart from the hammer excitation, the track was in unloaded conditions. Accelerations were measured at locations sufficiently far from the transition to mitigate any boundary effects resulting from the change in track form.

For the ballasted track, see Figure 7, three resonance peaks can be observed in the measured receptance at 30, 290, and 950 Hz. The first peak corresponds to a vertical in-phase vibration of the rail and sleepers, characterised by high damping due to the propagation of waves in the ballast and subgrade. The second peak corresponds to an out-of-phase motion between the rail and sleepers, influenced by the flexibility of the rail pads. The third peak represents the pinned-pinned resonance mode, which is a vertical bending mode with a wavelength twice the sleeper span.

#### 4.6 SHORT-TERM TRACK RESPONSE

The instrumentation setup included sensors for measuring axial rail strains to assess rail bending moment and rail seat load, vertical sleeper displacement, and vertical acceleration at the sleeper ends. The setup consisted of four clusters placed in sections between two sleepers in sleeper bays 3, 5, 8, and 11, numbered from the transition. Each FBG-based cluster consisted of one accelerometer, one displacement transducer, and one strain array with four strain gauges. In total, 30 FBG sensors were installed. Aluminium covers and cable conduits

were added to protect the sensors and cables from mechanical damage and harsh weather conditions.

The interrogator was housed in a heated cabinet to maintain operational temperatures (0 – 60 °C) and positioned near a power source and data connection. Additional site equipment included a field computer, hard drive, junction box, temperature sensors, thermostat, fan, 4G antenna for backup, and a network switch. The interrogator continuously recorded sensors data at a 2 kHz sampling rate, distributing data via a network socket to a computer. A custom LabVIEW-based program, FemtoGateway, processed and stored the data locally before synchronising it with a server at Chalmers.

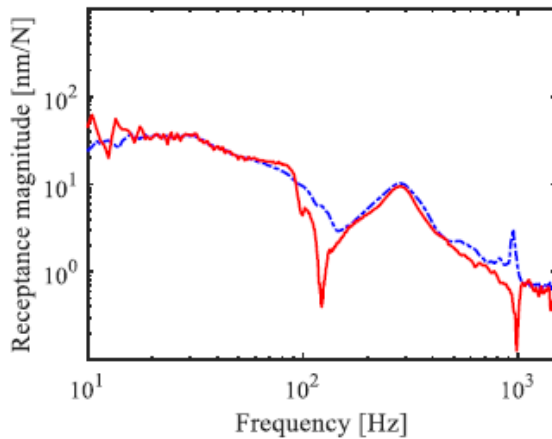


Figure 7. Magnitudes of measured rail receptances for the ballasted track. Vertical hammer excitation on the rail at midspan. Response measured on the rail at midspan (point receptance shown using a blue line) or on the rail at railseat (cross receptance shown using a red line).



Figure 8. Overview of the four clusters (C1 – C4), and strain sensor numbering for each cluster.



Figure 9. Detail of an instrumented sleeper equipped with a vertical base plate, an L-shaped mechanism, one accelerometer and one displacement transducer.

Axial rail strains were measured using strain gauges at the positions indicated in Figure 8. Based on the measured strains and assuming Euler-Bernoulli beam theory, examples of the evaluated time histories of rail bending moment above sleepers 5 and 11 for part of a loaded iron ore train are shown in Figure 10. Each peak corresponds to a passing axle. It is observed that the rail bending moment above sleeper 11 is higher than that above sleeper 5, indicating that sleeper 11 has softer support conditions. This was confirmed by comparing the corresponding measured sleeper displacements.

Based on the elongation of the displacement transducer, the vertical displacement of the sleeper was measured relative to a fixed anchor embedded deep into the ground (fixed reference), as indicated in Figure 9. Additionally, vertical accelerations were measured using six FBG-based accelerometers. Five of these were placed at the sleeper ends (3, 5, 8, 11, and 31), while one was positioned on the first block on the slab track side.

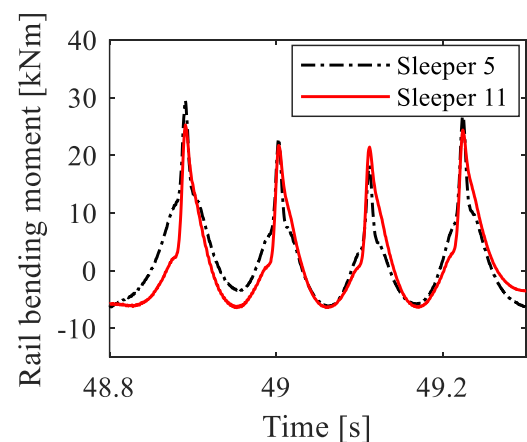


Figure 10. Rail bending moment above sleepers 5 and 11 along the transition.

#### 4.7 LONG-TERM TRACK SETTLEMENT

Permanent displacements of the track structure were determined by extracting the at-rest positions of the instrumented sleepers from intervals between train passages. The resulting long-term track settlements for sleepers 5 and 11, evaluated over a period of about 11 months, including one winter, are shown in Figure 10. It is observed that the initial settlement rate immediately after the installation of the slab track and transition zone was very high, but it slowed down after a few weeks of traffic. For sleeper 11, there was a reversal in the permanent displacement during the winter due to frost heave.

To verify the trend in measured permanent sleeper displacements, a sleeper level survey was conducted using a Trimble SX12 self-levelling, automatic-scanning total station with an active prism. The survey was carried out on six occasions over a period of ten months. Overall, the long-term sleeper displacement data aligned well with the total station survey results for the ballasted track until the end of December. Subsequently, the relative measurement from the FBG system, which was referenced to a ground anchor, indicated less upward movement of sleeper 5 due to frost heave compared to the total station survey results. This discrepancy may be due to the short (2 m) length of the anchor that did not extend below the frozen ground layers, see Figure 4. To obtain a fixed

reference, longer anchors extending beneath the frozen layers would have been necessary. For sleeper 11, the total station survey results were consistent with the relative track displacement measurements since the anchor length exceeded 4 m.

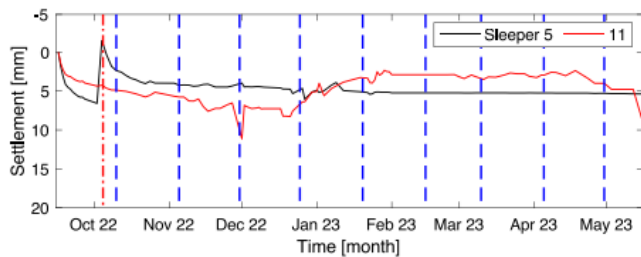


Figure 11. Evolution of permanent sleeper displacement (settlement) over time for sleepers 5 and 11. Sleeper 5 was tamped after 20 days of operation.

The Swedish Transport Administration utilises frost sticks to monitor frost depth. These instruments are capable of measuring temperature profiles to a depth of a few metres. Based on these measurements it was concluded that the ground remained unfrozen until late October, at which point it gradually froze to a depth of 2 m by mid-December. This depth was exceeded until early May 2023, cf. Figure 4. As air temperatures declined below  $-10^{\circ}\text{C}$  and frost depth exceeded 2 m, sleeper settlement at positions 5 and 11 ceased and initiated a reverse process. This indicated that frost heave was the probable cause of this uplift.

## 5 CONCLUSIONS AND LESSONS LEARNED

In this paper, various methods for measurement and monitoring of differential settlement in railway infrastructure have been reviewed. The case study presented, conducted in a transition zone between ballasted track and a short demonstrator section of 3MB slab track at Gransjö on Malmbanan, aimed to integrate existing data, such as geotechnical surveys and InSAR measurements, with observations from an extensive FBG-based instrumentation system that captured both short-term dynamic track responses and long-term static settlements (permanent displacements) of selected sleepers.

Given the sensor requirements, harsh weather conditions at the test site on Malmbanan, operational railway track with heavy haul train traffic, and budget constraints, FBG sensors were selected. This system reduced the installation time, which was critical due to the narrow installation window during the construction of the 3MB slab track. Another benefit was the simplified routing of optical cables, allowing the interrogator to be placed in a heated cabinet to maintain operational temperatures ( $0 - 60^{\circ}\text{C}$ ), as well as to be near the available power source and data connection provided by the track owner.

FBG-based sensors have a higher initial cost than traditional sensors but offer superior performance, including multiplexing capabilities, reduced installation complexity, and greater durability in harsh environments. Their high sensitivity and immunity to electromagnetic interference enhance reliability, making them a more efficient and sustainable choice for advanced monitoring applications despite the higher upfront investment.

The measured data have been used for a long-term assessment of the transition zone and the new slab track design, as well as for the calibration of track models for further simulation studies [38]. It was concluded that most implemented sensors performed reliably. The FBG-based strain gauges enabled the setup to successfully detect the type of vehicle, train speed, and the number of axles in each train. The spatial and temporal resolution of the observed rail curvature distribution were found to be sufficient for analysing rail bending moments.

A considerable variation in measured displacements between the selected adjacent sleepers in the transition zone was observed. These displacements depend on the initial and evolving support conditions of each sleeper and their distance from the transition. For example, sleeper number 3, located near the transition, became voided shortly after installation, while sleeper 8 appeared to be supported by a very stiff foundation, leading to minimal settlement. Good agreement was observed between the displacement data from the FBG sensors and the total station survey.

Unfortunately, the conditions and available time window during the construction of the transition zone and slab track at Gransjö were far from optimal. The excavated volume of ballast and subgrade was replaced with insufficiently compacted backfill material before the construction of the slab, leading to significant settlement of the slab track soon after installation. Due to the excessive settlement of the slab track, the fasteners on the slab side had to be adjusted to their desired height by sliding shims after 20 days of operation. At the same time, the first six sleepers on the ballasted side were tamped to restore the longitudinal level. Still, the substantial settlement of the slab track continued, albeit at a lower rate. This had a significant effect on the support conditions also for the sleepers near the transition, particularly indicated by the measured short-term displacements and settlement of sleeper 3.

The signal-to-noise ratio of the acceleration data was too low because the delivered accelerometers were designed to measure higher acceleration levels than anticipated, preventing the use of the acceleration data for reconstructing sleeper displacements [49]. This issue could not be resolved, as the sensors were deployed in clusters, and replacing them in the field was not feasible. To address this issue, it is recommended to implement more rigorous quality control tests prior to installation.

Furthermore, based on Euler-Bernoulli beam theory and the measured difference in rail bending moment across the width of the rail pad [23], the plan to evaluate time histories of rail seat loads failed due to inconsistent data from different strain gauges.

The test site was distant from the university, leading to high travel costs in the event that anomalies needed to be addressed during the measurement period. For example, the displacement sensors and anchor arrangements needed adjustments on a few occasions due to the unexpectedly high levels of settlement. The measurements were conducted during winter, with heavy snowfall and low temperatures, which further complicated access to the sensors and made the process more challenging.

Nevertheless, it is argued that the combination of the described FBG-based test set-up (improved with accelerometers with higher signal-to-noise ratio and more



consistent strain data) with existing geotechnical and traffic load data is a powerful approach that can be employed by infrastructure managers to justify, test, and evaluate transition zones and new track designs across their network.

This study has focused on the heavy haul track on Malmaban in northern Sweden, but insights discussed here are relevant to railways operating in other climates. Accurate monitoring of differential settlement in railway infrastructure is a common challenge worldwide, regardless of the type of loading and climate. It is argued that elements of the setup used here will assist infrastructure managers across the network in justifying, testing, and assessing new track designs.

## ACKNOWLEDGEMENTS

The current study is part of the ongoing activities in CHARMEC – Chalmers Railway Mechanics ([www.chalmers.se/charmec](http://www.chalmers.se/charmec)). Parts of the study have been funded from the European Union's Horizon 2020 research and innovation programme in the In2Track3 project under grant agreement 101012456, and the Europe's Rail Flagship Project IAM4RAIL – Holistic under grant agreement 101101966.

## REFERENCES

- [1] Nasrollahi K., Nielsen J.C.O., Aggestam E., Dijkstra J., Ekh M. Prediction of long-term differential track settlement in a transition zone using an iterative approach. *Engineering Structures* 2023; 283:115830.
- [2] Ramos A., Gomes Correia A., Nasrollahi K., Nielsen J.C.O., Calçada R. Machine learning models for predicting permanent deformation in railway tracks. *Transportation Geotechnics*, 2024; 47, 101289.
- [3] Coelho B., Hölscher P., Priest J., Powrie W., Barends F. An assessment of transition zone performance. *Proceedings of the Institution of Mechanical Engineers, Part F: Journal of Rail and Rapid Transit* 2011;225:129–39.
- [4] Nasrollahi, K., Differential railway track settlement in a transition zone: Field measurements and numerical simulations. Thesis for the degree of Licentiate/Department of Mechanics and Maritime Sciences 2023; 2023: 07.
- [5] Indraratna B., Babar Sajjad M., Ngo T., Gomes Correia A., Kelly R. Improved performance of ballasted tracks at transition zones: A review of experimental and modelling approaches. *Transportation Geotechnics* 2019; 21:100260.
- [6] Nasrollahi K., Nielsen J.C.O. Influence of sleeper base area and spacing on long-term differential settlement in a railway track transition zone. *Proceedings of the Sixth International Conference on Railway Technology: Research, Development and Maintenance* 2024; 7:1–
- [7] Oscarsson J. Dynamic train–track interaction: Variability attributable to scatter in the track properties. *Vehicle System Dynamics* 2002; 37:59–79. <https://doi.org/10.1076/vesd.37.1.59.3538>.
- [8] Rempelos, G., Ognibene, G., Le Pen, L., Blainey, S., Preston, J., & Powrie, W. Railway track deterioration models: A review of the state of the art. *Transportation Geotechnics*, 2024;101377.
- [9] Kouroussis G., Caucheteur C., Kinet D., Alexandrou G., Verlinden O., Moeyaert V. Review of trackside monitoring solutions: From strain gages to optical fibre sensors. *Sensors* 2015; 15:20115–39.
- [10] Rahman M.A., Taheri H., Dababneh F., Karganroudi S.S., Arhamnamazi S. A review of distributed acoustic sensing applications for railroad condition monitoring. *Mechanical Systems and Signal Processing* 2024; 208:110983.
- [11] De Chiara F., Fontul S., Fortunato E. GPR laboratory tests for railways materials dielectric properties assessment. *Remote Sensing* 2014; 6:9712–28.
- [12] Zuada Coelho B., Varandas J.N., Hijma M.P., Zoeteman A. Towards network assessment of permanent railway track deformation. *Transportation Geotechnics* 2021; 29.
- [13] Annan, A.P. GPR – History, trends, and future developments. *Subsurface Sensing Technologies and Applications*, 2002; 3(4), 253-270.
- [14] Le Ngai N., Pramumijoyo S., Satyarno I., Brotopuspito K.S., Kiyono J., Hartantyo E. Multi-channel analysis of surface wave method for geotechnical site characterization in Yogyakarta, Indonesia. *E3S Web of Conferences* 2019; 76:1–5.
- [15] Nasrollahi K., Dijkstra J., Nielsen J.C.O. Towards real-time condition monitoring of a transition zone in a railway structure using fibre Bragg grating sensors. *Transportation Geotechnics* 2024; 44:101166.
- [16] Allil R.C.S.B., Lima L.A.C., Allil A.S., Werneck M.M. FBG-based inclinometer for landslide monitoring in Tailings dams. *IEEE Sensors Journal* 2021; 21:16670–80.
- [17] Wang H., Markine V., and Liu X. Experimental analysis of railway track settlement in transition zones. *Proceedings of the Institution of Mechanical Engineers, Part F: Journal of Rail and Rapid Transit* 232.6, 2018; 1774-1789.
- [18] Berggren E.G. Railway track stiffness – Dynamic measurements and evaluation for efficient maintenance. PhD Thesis, KTH, Stockholm, Sweden 2009.
- [19] Coelho B., Priest J., Hölscher P., Powrie W. Monitoring of transition zones in railways. *Railway Engineering-2009* 2009:1–9.
- [20] Milne D., Harkness J., Le Pen L., Powrie W. The influence of variation in track level and support system stiffness over longer lengths of track for track performance and vehicle track interaction. *Vehicle System Dynamics* 2021; 59:245–68.
- [21] Milne D., Le Pen L., Watson G., Thompson D., Powrie W., Hayward M., et al. Proving MEMS technologies for smarter railway infrastructure. *Procedia Engineering* 2016; 143:1077–84.
- [22] Wang P., Xie K., Shao L., Yan L., Xu J., Chen R. Longitudinal force measurement in continuous welded rail with bi-directional FBG strain sensors. *Smart Materials and Structures* 2015; 25.
- [23] Wheeler L.N., Take W.A., Hoult N.A., Le H. Use of fiber optic sensing to measure distributed rail strains

- and determine rail seat forces under a moving train. *Canadian Geotechnical Journal* 2019; 56:1–13.
- [24] Wheeler L.N., Pannese E., Hoult N.A., Take W.A., Le H. Measurement of distributed dynamic rail strains using a Rayleigh backscatter-based fiber optic sensor: Lab and field evaluation. *Transportation Geotechnics* 2018; 14:70–80.
- [25] Stoura C.D., Dertimanis V.K., Hoelzl C., Kossmann C., Cigada A., Chatzi E.N. A model-based Bayesian inference approach for on-board monitoring of rail roughness profiles: Application on field measurement data of the Swiss Federal Railways network. *Structural Control and Health Monitoring* 2023; 2023.
- [26] Sauni M., Luomala H., Kolisoja P., Vaismaa K. Framework for implementing track deterioration analytics into railway asset management. *Built Environment Project and Asset Management* 2022; 12:871–86.
- [27] Berggren E.G., Nissen A., Paulsson B.S. Track deflection and stiffness measurements from a track recording car. *Proceedings of the Institution of Mechanical Engineers, Part F: Journal of Rail and Rapid Transit* 2014; 228:570–80.
- [28] Nielsen J.C.O., Berggren E.G., Hammar A., Jansson F., Bolmsvik R. Degradation of railway track geometry – Correlation between track stiffness gradient and differential settlement. *Proceedings of the Institution of Mechanical Engineers, Part F: Journal of Rail and Rapid Transit* 2020; 234:108–19.
- [29] Yan T.H., Hoelzl C., Corman F., Dertimanis V., Chatzi E. Integration of on-board monitoring data into infrastructure management for effective decision-making in railway maintenance. *Railway Engineering Science* 2025.
- [30] Bernal E., Spiryagin M., Cole C. Onboard condition monitoring sensors, systems and techniques for freight railway vehicles: A review. *IEEE Sensors Journal* 2019; 19:4–24.
- [31] Park C.B., Miller R.D., Xia J. Multichannel analysis of surface waves. *Geophysics* 1999; 64:800–8. <https://doi.org/10.1190/1.1444590>.
- [32] Robertson, P.K. Soil classification using the cone penetration test. *Canadian Geotechnical Journal*, 1990; 27(1), 151–158.
- [33] Wolf J.P., Deeks A.J. *Foundation vibration analysis: A strength-of-materials approach*. Elsevier 2004; 42:218.
- [34] Gazetas G. *Foundation vibrations*. *Foundation Engineering Handbook* 1991:553–93.
- [35] Palmqvist C.-W., Ochsner M., Jamali S., Hashemi H., Åmerbilly, K., Nilfouroushan F., et al. Satellite monitoring of railways using Interferometric Synthetic Aperture Radar (InSAR). 2021:0–53.
- [36] Theyssen J.S., Aggestam E., Zhu S., Nielsen J.C.O., Pieringer A., Kropp W., et al. Calibration and validation of the dynamic response of two slab track models using data from a full-scale test rig. *Engineering Structures* 2021; 234:111980.
- [37] Tehrani S.A.H., Zanganeh A., Andersson A., Battini J.M. Simplified soil–structure interaction modelling techniques for the dynamic assessment of end shield bridges. *Engineering Structures* 2024; 319:118803.
- [38] Nasrollahi K., Ramos A., Nielsen J.C.O., Dijkstra J., Ekh M. Benchmark of calibrated 2D and 3D track models for simulation of differential settlement in a transition zone using field measurement data. *Engineering Structures* 2024; 316:118555.
- [39] Milosevic M.D.G., Pålsson B.A., Nissen A., Nielsen J.C.O., Johansson H. Condition monitoring of railway crossing geometry via measured and simulated track responses. *Sensors* 2022; 22.
- [40] Xue W., Flintsch G.W., Diefenderfer B.K. Measuring pavement permanent deformation in accelerated pavement testing. *Transportation Research Record* 2020; 2674:340–8.
- [41] Bahati P.A., Le V.D., Lim Y. A multi-depth deflectometer/global navigation satellite system method for measuring concrete slab track deformation. *Applied Sciences* 2024; 14.
- [42] Dai W., Huang D., Cai C. Multipath mitigation via component analysis methods for GPS dynamic deformation monitoring. *GPS Solutions* 2014; 18:417–28.
- [43] Indraratna B., Salim W. Modelling of particle breakage of coarse aggregates incorporating strength and dilatancy. *Proceedings of the Institution of Civil Engineers: Geotechnical Engineering* 2002; 155:243–52.
- [44] Luo J., Ding K., Huang H., Hart J.M., Qamhia I.I.A., Tutumluer E., et al. Toward automated field ballast condition evaluation: Development of a ballast scanning vehicle. *Transportation Research Record* 2024; 2678:24–36.
- [45] Mattsson K., Nielsen J.C.O., Fehrlund L., Maglio M., Vernersson T. On wayside detector measurement of wheel-rail impact loads induced by wheel flats - Data analysis, alarm levels and regulations. *Proceedings of the Sixth International Conference on Railway Technology: Research, Development and Maintenance* 2024; 7:1–14.
- [46] *Railway Applications – Track – Track Geometry Quality – Part 5: Geometric Quality Levels – Plain Line (UNE-EN 13848-5:2009+A1)*. Spanish Association for Standardization (AENOR), 2011; pp. 8–16.
- [47] Trafikverket. Trafikverket. Markteknisk undersökningsrapport, Geoteknik och Miljögeoteknik, Gransjö, Boden, (Survey of ground conditions, in Swedish), Sweden, Report number: TRV2014/165 445; 2014.
- [48] Swedish National Space Agency, "InSAR Monitoring Platform," Available: <https://insar.rymdstyrelsen.se/>. [Accessed: 06-03-2025].
- [49] Milosevic M.D.G., Pålsson A., Nissen A., Nielsen J.C.O., Johansson H. Reconstruction of sleeper displacements from measured accelerations for model-based condition monitoring of railway crossing panels. *Mechanical Systems and Signal Processing* 2023; 192: 110225.



# SHM in the frame of a Digital Twin in Civil Engineering



# Advanced Structural Health Monitoring and Predictive Maintenance of the Parchi Viaduct Using Distributed Fiber Optic Sensors and Digital Twin Technology

Nils Weissenbach<sup>1</sup>, Massimo Penasa<sup>1</sup>

<sup>1</sup>CAEmate s.r.l., via Alessandria 15, Bolzano, 39100, Italy  
email: massimo.penasa@caemate.com, nils.weissenbach@caemate.com

**ABSTRACT:** Aging infrastructure poses significant challenges in ensuring safety, reliability, and long-term serviceability. The Parchi Viaduct, a 3-km multi-span structure on Milan's A51 Eastern Ring Road, experienced critical degradation in its Gerber saddles, necessitating temporary closure for safety assessments. In response, Milano Serravalle Milano Tangenziali S.p.A. and CAEmate S.R.L. deployed an advanced Structural Health Monitoring (SHM) system, integrating distributed fiber optic sensing (DOFS) and a physics-informed digital twin (PINN) to enable real-time load-bearing capacity evaluation and predictive maintenance. This paper presents the implementation of the WeStatiX SHM platform, utilizing DOFS to capture strain, temperature, and vibration data while dynamically updating a finite element model (FEM) through inverse analysis and multi-objective optimization. By continuously refining modal parameters such as natural frequencies, mode shapes, and damping ratios, the system enables early detection of structural anomalies and degradation trends.

The validated digital twin successfully predicted real-world structural behavior, confirming residual load-bearing capacity despite saddle deterioration and supporting the safe reopening of the viaduct under real-time monitoring per Italian NTC standards. Load test results and FEM simulations demonstrated excellent agreement, with taller piers exhibiting ~20% greater deflection, emphasizing pier height's impact on load distribution and deformation patterns. These findings enhance predictive maintenance planning, improve stress redistribution modeling, and contribute to prolonging the structural lifespan of aging infrastructure assets.

**KEY WORDS:** Structural Health Monitoring (SHM); Digital Twin; Distributed Fiber Optic Sensors (DOFS); Finite Element Modeling (FEM); Predictive Maintenance; Artificial Intelligence (AI); Operational Modal Analysis (OMA); Physics-Informed Neural Networks (PINN); Machine learning (ML)

## 1 INTRODUCTION

The Milano Serravalle Milano Tangenziali S.p.A. manages a motorway network with over 400 bridges and viaducts, requiring regular structural assessment to comply with national safety regulations. Increasing traffic loads, environmental exposure, and material aging necessitated the implementation of an advanced Structural Health Monitoring (SHM) system for real-time diagnostics and predictive maintenance.

Following the Ponti Guidelines, the SHM deployment prioritizes viaducts with high traffic volumes, complex configurations, or significant material degradation. The strategy captures structural responses under traffic-induced loading, providing quantitative safety assessments. The network includes various bridge types, many built in the 1960s and expanded in the 1990s, making SHM essential for early damage detection, optimized maintenance, and long-term serviceability.

This paper presents the Milano Serravalle SHM initiative, detailing sensor deployment, real-time data processing, and AI-driven digital twin modeling for viaduct safety assessment and predictive maintenance.



Figure 1. Sensors installed under the deck of viaducts over piazza Maggi.

## 2 SYSTEM ARCHITECTURE

### 2.1 Structural Health Monitoring Framework

The SHM system deployed on the Milano Serravalle motorway network provides real-time structural diagnostics by continuously measuring key mechanical and dynamic parameters. It integrates threshold-based evaluation with a data-driven digital twin, ensuring a comprehensive and adaptive approach to infrastructure monitoring.

### 2.2 Threshold-Based Evaluation Approach

Conventional SHM relies on predefined safety thresholds derived from design standards, material properties, and historical data to detect deviations from expected behavior. While effective for early anomaly detection, this method is limited by uncertainties in aging structures, undocumented modifications, and hidden defects such as microcracks and corrosion. To address these gaps, advanced sensor-driven modeling techniques complement threshold-based assessments.

### 2.3 Model-Driven Digital Twin Approach

To overcome static threshold limitations, the SHM system employs a model-driven digital twin that continuously refines structural models using real-time sensor data. A finite element model (FEM) serves as the foundation, integrating as-built documentation, material properties, and initial boundary conditions. However, continuous refinement is essential to align the model with actual structural behavior.

Real-time sensor data from distributed fiber optic sensors (DOFS), MEMS-based accelerometers, and inclinometers is processed in the SHM cloud platform, where inverse modeling techniques, including physics-informed neural networks (PINNs), adjust structural parameters dynamically. This

feedback loop enhances damage detection, predictive maintenance, and risk assessment.

Modal and frequency analysis further refine the model by tracking changes in natural frequencies, mode shapes, and damping ratios, key indicators of stiffness loss, fatigue, or settlement issues. This enables early intervention and cost-effective maintenance planning.

#### 2.4 Multi-Sensor Data Acquisition System

The SHM system relies on a multi-sensor network to capture the structure's response under various conditions. Triaxial MEMS accelerometers facilitate Operational Modal Analysis (OMA) for detecting stiffness reductions. Inclinometers and displacement transducers measure rotations and deflections at critical structural interfaces, identifying foundation movements and misalignment.

DOFS technology provides continuous strain, temperature, and stress distribution data, crucial for detecting localized stress

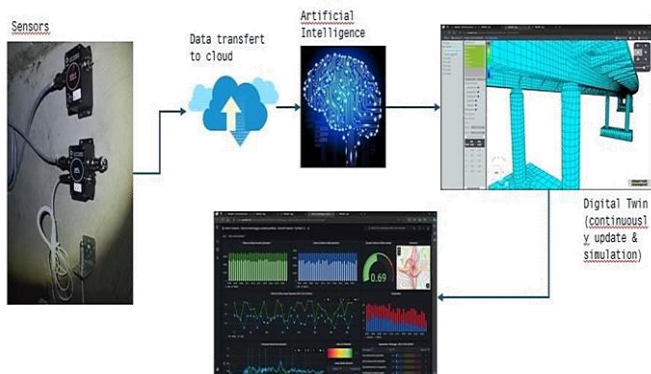


Figure 2. Logical scheme of the system architecture implemented by Milano Serravalle.

concentrations and thermal expansion effects contributing to material fatigue.

All sensor data is synchronized via satellite-linked data acquisition units (UCLs) and transmitted through fiber optic networks to the SHM cloud platform, ensuring precise temporal alignment for real-time analysis.

### 3 DISCRETE SENSORS

The structural health monitoring (SHM) system deployed across the Milano Serravalle motorway network incorporates a comprehensive array of discrete sensors, each carefully selected to measure critical structural and environmental parameters. The placement and configuration of these sensors were strategically determined based on the structural scheme, constraint conditions, and anticipated mechanical behavior of each viaduct. This systematic deployment ensures that all relevant dynamic, thermal, and displacement-related phenomena are captured with high accuracy and precision.

#### 3.1 Sensor Types and Technical Specifications

A range of high-precision sensors was employed to monitor key structural response parameters, including vibrations, rotations, displacements, and temperature variations. The primary sensor types used in the monitoring network include:

- **Triaxial MEMS-Based Accelerometers:** These sensors are used for capturing dynamic structural response by

measuring accelerations in three orthogonal directions. The accelerometers deployed in this system have a measurement range of  $\pm 2$  g, with a frequency response spanning from 0 Hz to 500 Hz and a spectral noise level of  $\pm 22.5 \mu\text{g}/\sqrt{\text{Hz}}$ , ensuring high-resolution vibration monitoring. Their role is particularly critical for Operational Modal Analysis (OMA), which enables real-time identification of stiffness variations and localized damage detection.

- **Biaxial MEMS Inclinometers:** The inclinometers are installed to measure angular rotations at key structural joints and supports. These sensors feature a measurement range of  $\pm 15^\circ$  with an angular resolution of  $0.001^\circ$ , enabling precise detection of structural tilting, pier settlements, and deformation trends over time.
- **Potentiometric Displacement Transducers:** To monitor relative displacements between structural components, potentiometric displacement transducers were installed at expansion joints and pier connections. These devices have a measurement range of 0–150 mm, with a precision of 0.05 mm, allowing for accurate tracking of longitudinal and transverse displacement variations.
- **High-Sensitivity Thermometers:** Thermal effects play a significant role in structural deformation and stress redistribution, particularly in reinforced and prestressed concrete structures. Thermometers were deployed across critical structural sections, enabling the continuous monitoring of temperature variations. This data is essential for compensating thermal expansion effects in stress analysis and predicting long-term material fatigue due to cyclic temperature fluctuations.

#### 3.2 Sensor Placement Strategy

The placement of sensors was carefully optimized to ensure maximum coverage of structural behavior while minimizing redundancy. In general, accelerometers and inclinometers were mounted along the lateral edges of the bridge decks, with installations concentrated at on-axis sections and quarter-span positions. These locations were selected to provide a detailed characterization of modal behavior, resonance effects, and dynamic loading conditions.

To capture pier behavior and bridge support movements, inclinometers and displacement transducers were positioned at the tops of piers and at expansion joints, where rotational deformations and relative displacements are most pronounced. This setup allows for early detection of differential settlements, support degradation, and abnormal structural movements that could indicate potential failure mechanisms.

Thermometers were distributed across key structural regions, including deck intrados, piers, and expansion joints, ensuring comprehensive thermal profiling. This placement allows for accurate correlation of temperature-induced stresses with real-time displacement and strain measurements.

#### 3.3 Data Acquisition and Synchronization

All sensors were hardwired to a high-speed data transmission network, ensuring continuous and reliable data flow to the central processing platform. The monitoring system employs a satellite-synchronized local control unit (UCL), which manages data acquisition, synchronization, and pre-processing before transmitting the information to the SHM cloud platform.

The optical fiber transmission BUS provides a secure and interference-free data link, enabling real-time sensor readings to be collected, processed, and stored in a structured database. The synchronized nature of this setup ensures that all measurements are precisely time-aligned, allowing for accurate modal and frequency analysis of the structures.

Once collected, the sensor data is integrated with the digital twin platform, where it undergoes automated noise filtering, anomaly detection, and inverse modeling-based calibration. This process allows engineers to rapidly detect deviations from expected structural behavior and implement predictive maintenance strategies.

### 3.4 Role of Discrete Sensors in the Digital Twin Model

The real-time measurements from discrete sensors serve as the foundation for updating and refining the digital twin model. By continuously integrating modal data from accelerometers, rotational data from inclinometers, and displacement readings from transducers, the FEM-based digital twin can iteratively adjust its parameters to match actual structural behavior.

The long-term tracking of temperature variations and displacement trends further enhances the predictive capabilities of the model, allowing for proactive intervention before critical failure conditions arise. As a result, the combination of discrete sensor data and AI-driven model updating enables a high-fidelity representation of viaduct performance, significantly improving the reliability of maintenance planning and infrastructure resilience.



Figure 3. Discrete sensors used: displacement transducers (top), biaxial inclinometer (bottom left), triaxial accelerometer and biaxial inclinometer (bottom right).

## 4 THE “VIADOTTO DEI PARCHI” AND THE DISTRIBUTED FIBER OPTIC SENSORS (DOFS)

### 4.1 Structural Characteristics of the Viadotto dei Parchi

The Viadotto dei Parchi is a critical viaduct on Milan’s A51 Eastern Ring Road. Originally designed by engineer Silvano Zorzi in 1970, the structure features a continuous deck plate integrated with the piers, forming spans of 24 meters. Its design includes a zero-moment point positioned 7 meters from the pier axis, materialized through a Gerber-type saddle system that ensures efficient load redistribution and structural continuity.

The viaduct consists of two parallel structures, each supporting a separate motorway carriageway, with a center-to-center distance of approximately 29 to 30 meters. Extending nearly 3,000 meters in total length, it is one of the longest and most strategically significant bridges within the Milan motorway network.

### 4.2 Structural Expansion and Modification

In 1992, the viaduct underwent a major expansion to accommodate increased traffic demand, adding a third lane to the Eastern Ring Road. The available space between the two existing viaducts allowed for the construction of two additional structures, effectively increasing capacity while maintaining overall structural integrity. However, this intervention introduced engineering challenges, including increased dynamic loads, differential settlements, and stress redistribution between the old and new structures.

Due to the viaduct’s scale and the number of spans, an advanced monitoring system was required to assess its real-time structural performance, particularly in response to dynamic traffic loading, thermal variations, and long-term material degradation. This necessity led to the deployment of a Distributed Fiber Optic Sensor (DOFS) network, providing high-resolution continuous monitoring across the entire structure.



Figure 4. “Viadotto dei Parchi” after the widening in the early 1990s.

### 4.3 Advantages of Distributed Fiber Optic Sensors Over Discrete Fiber Sensors

The DOFS system implemented on the Viadotto dei Parchi represents a significant advancement over traditional discrete fiber optic sensors, such as Fiber Bragg Gratings (FBG). FBG sensors operate through spectroscopic techniques that measure strain at discrete points along the fiber. While useful in localized assessments, they present several limitations, including restricted spatial resolution, installation complexity, and fragility.

FBG sensors are typically deployed in limited chains, resulting in spatial gaps in the monitoring data and reduced effectiveness in capturing localized stress concentrations or progressive deformation. Their fabrication process modifies the fiber optic core, making them prone to breakage, and installation requires precise alignment with specialized equipment, increasing deployment costs and long-term maintenance efforts.



DOFS technology overcomes these limitations by using a continuous optical fiber embedded into the structure with mortar or adhesive compounds. This approach enables uninterrupted, high-resolution measurements of strain, temperature, and mechanical deformation along the entire monitored length. The method ensures superior durability, simplified installation, and greater resistance to environmental degradation, making it a more reliable solution for long-term structural health monitoring.

#### 4.4 Measurement Principles and Data Acquisition in DOFS Systems

DOFS measurements rely on light scattering phenomena that occur within the optical fiber when subjected to external loads. The Brillouin Scattering Effect, a nonlinear optical phenomenon, forms the foundation of the measurement system. By analyzing the Brillouin frequency shift, the system determines absolute strain and temperature variations with high precision.

The system achieves a strain resolution in the micro-epsilon range, allowing the detection of extremely subtle structural deformations. The spatial resolution is adjustable, ranging from a few meters to a few centimeters, depending on the interrogation time and system configuration. Temperature effects are automatically compensated through a dual-wavelength technique, ensuring that strain measurements remain unaffected by thermal fluctuations. A secondary optical fiber within the same system provides independent temperature readings, allowing precise differentiation between temperature-induced expansion and load-induced deformation.

In addition to static strain and temperature measurements, DOFS systems capture real-time structural vibrations, enabling the identification of natural frequencies, mode shapes, and transient dynamic events. Unlike traditional accelerometers, which have bandwidth limitations, DOFS technology measures broad-spectrum vibrational activity with unmatched sensitivity, further enhancing the accuracy of structural assessments.

#### 4.5 Deployment of DOFS on the Viadotto dei Parchi

The DOFS network was installed to maximize monitoring effectiveness across critical structural components. Optical fibers were embedded along both the intrados and extrados of the deck, covering longitudinal stress paths to ensure comprehensive strain tracking. Their positioning was optimized based on FEM simulations, allowing accurate assessment of curvature, bending moments, and stress redistribution.

By integrating DOFS with the digital twin model, the monitoring system provides real-time structural assessments. This integration enables the early detection of microcracking and stress concentrations before they evolve into critical failures. Additionally, long-term deformations associated with creep, shrinkage, and fatigue effects can be tracked, ensuring that maintenance strategies are data-driven and proactive. The continuous monitoring and validation of FEM predictions ensure that theoretical models remain aligned with real structural behavior.

The sensors used in this project were developed as a patented technology by a spin-off company of the Polytechnic of Milan, further enhancing the resolution, reliability, and predictive

capabilities of SHM methodologies employed on the Viadotto dei Parchi.

#### 4.6 Impact of DOFS-Based Monitoring on Structural Management

The implementation of DOFS-based SHM on the Viadotto dei Parchi has significantly improved structural assessment methodologies. The ability to obtain continuous, high-resolution strain and temperature data across the entire viaduct allows for more effective maintenance planning and risk mitigation.

Real-time monitoring enables early detection of evolving structural anomalies, allowing timely intervention before critical damage occurs. By tracking long-term performance trends, engineers can optimize reinforcement and retrofitting strategies, extending the viaduct's service life while reducing maintenance costs. Furthermore, the integration of DOFS technology with digital twin modeling minimizes reliance on costly manual inspections, enhancing efficiency in infrastructure management while ensuring compliance with safety regulations.

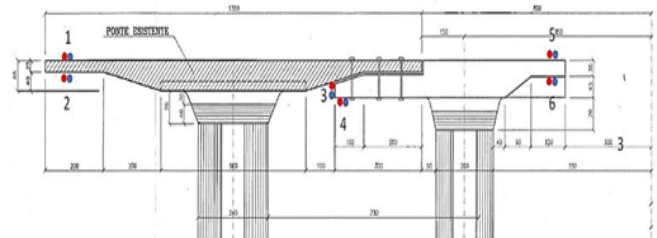


Figure 5. Cross section of DOFS fiber arrangement.

#### 4.7 DOFS Findings

The Viadotto dei Parchi serves as a pioneering case study in the application of distributed fiber optic sensing for SHM. The successful deployment of DOFS technology has demonstrated its superiority over traditional discrete sensor networks, providing unmatched measurement resolution, real-time diagnostics, and enhanced predictive maintenance capabilities. The combination of DOFS with AI-enhanced digital twin modeling establishes a comprehensive framework for long-term structural health assessment. By continuously integrating high-fidelity monitoring data into predictive maintenance strategies, this approach sets a new benchmark for SHM in large-scale civil infrastructure applications. Future implementations of similar systems across other critical viaducts will further refine predictive models and improve infrastructure resilience.

## 5 FINITE ELEMENT MODELING AND DIGITAL TWIN TECHNOLOGY

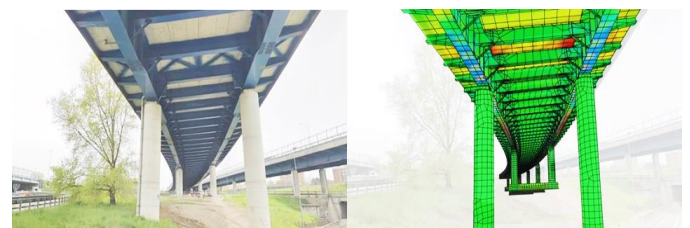


Figure 6. Comparison between real structure and Digital Twin.

### 5.1 The Role of Digital Twins in Structural Health Monitoring

The integration of digital twin technology within the Milano Serravalle motorway network represents a paradigm shift in structural health monitoring (SHM), enabling a continuous, bidirectional exchange of information between the physical structure and its virtual counterpart. These simulation-based digital twins leverage high-fidelity finite element models (FEMs) to replicate the mechanical, thermal, and dynamic behavior of infrastructure assets, allowing engineers to conduct real-time diagnostics, predictive maintenance, and performance optimization.

The development of digital twins follows a phased modeling approach, in which each structural component is incrementally integrated into the model, mirroring the actual construction sequence of the viaduct. This approach ensures that time-dependent effects, such as viscosity (creep), concrete shrinkage, and load redistribution, are accurately accounted for. By incorporating historical construction data, including post-tensioning phases and material aging effects, the digital twin provides a high-fidelity representation of the viaduct's evolving mechanical properties over its operational lifespan.

The thermomechanical behavior of the structure is also explicitly modeled, allowing for the simulation of temperature-induced stresses, expansion effects, and seasonal thermal cycles. This is particularly relevant for large-scale viaducts, where differential thermal expansion between spans can lead to progressive degradation and altered load paths over time.

### 5.2 Finite Element Model Development for the Parchi Viaduct

A comprehensive FEM was developed for the Parchi Viaduct, following standard structural simulation methodologies used in the design and assessment of large-scale infrastructure assets. The model accurately represents the structural geometry, material properties, and support conditions of the viaduct, ensuring that its simulated response aligns with real-world structural behavior.

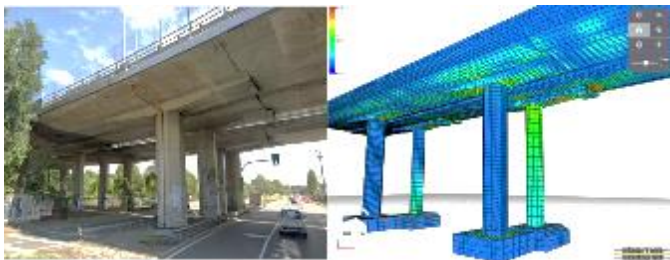


Figure 7. Parchi Viaduct and its Digital Twin (side view).

The deck, piers, and foundations were modeled using 20-node brick finite elements with quadratic shape functions, which provide a high degree of accuracy in stress and strain calculations. The DYWIDAG bars and post-tensioning tendons were modeled as axially loaded structural elements, ensuring a realistic representation of prestress-induced force distributions.

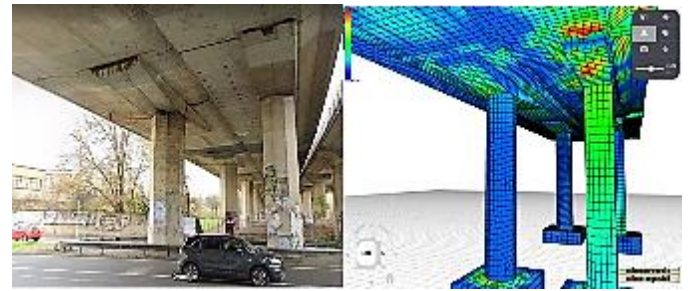


Figure 8. Parchi Viaduct and its Digital Twin (bottom view).

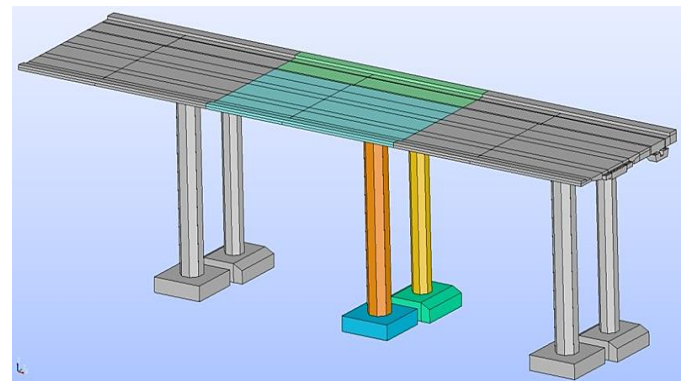
Given the variable pier heights of the viaduct, multiple models were generated to account for differential stiffness effects associated with varying substructure configurations. The selected pier heights of 7.5 m, 12.5 m, and 17.5 m reflect the actual structural conditions encountered during field inspections. These variations were included in the FEM to ensure accurate modeling of load redistribution effects and differential settlements.

### 5.3 Interaction Between Spans and Load Redistribution Effects

One of the key challenges in modeling the Parchi Viaduct was accurately simulating the interaction between successive spans. The viaduct's Gerber saddle system introduces complex load redistribution mechanisms, requiring nonlinear contact elements to properly model stiffness discontinuities and stress transfer zones.

The interaction between successive spans was simulated using contact elements with linear elastic behavior, which were constrained to react only in compression. This approach captures the realistic load transfer behavior between deck segments, allowing for accurate assessment of bending moments and shear forces (Figure 9).

The original deck structure incorporated a system of longitudinal



and transverse post-tensioning bars, while the widened deck sections utilized 12 additional longitudinal cables, each containing 19 strands of 0.6-inch steel tendons. The interaction between these newly introduced elements and the existing structural components was modeled using tensioned beam-type elements, accurately representing the anchoring effects and prestress redistribution mechanisms (Figure 10).

Figure 9. Model of three adjacent spans of the Parchi Viaduct.



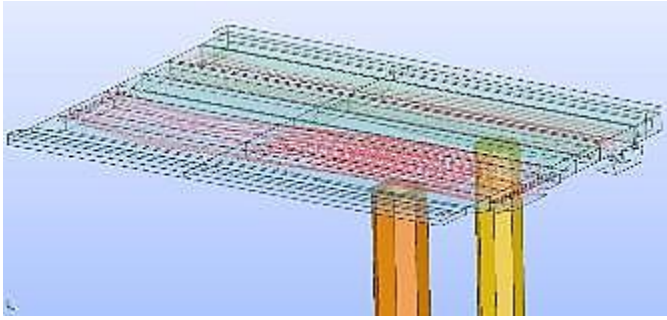


Figure 10. Modelling of the bars and longitudinal tendons within the original and widened deck.

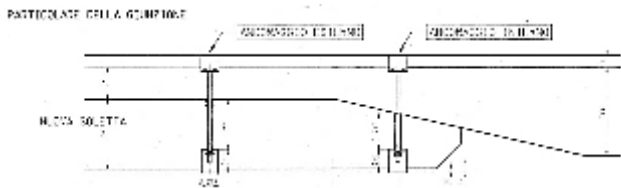


Figure 11. Anchor detail used in the joint area.

#### 5.4 Calibration of the Digital Twin Using SHM Data

To ensure that the finite element model remains an accurate representation of the actual viaduct, the WeStatiX SHM platform employs AI-driven inverse modeling techniques for continuous model updating. The calibration process follows a multi-step approach:

- 1) Initial FEM Validation
  - The FEM is initially validated against historical design calculations and load test results from the viaduct's original construction phase.
- 2) Integration of Real-Time SHM Data
  - Sensor data from DOFS, MEMS accelerometers, and displacement transducers is used to update strain fields, displacement trends, and modal parameters in the model.
- 3) Iterative Model Refinement via AI Optimization
  - A multi-objective optimization framework iteratively refines material properties, boundary conditions, and stiffness coefficients, ensuring alignment with measured structural response data.
  - Physics-informed neural networks (PINNs) are employed to enhance the accuracy of model predictions, particularly in identifying early-stage stiffness degradation.
- 4) Utilization Factor Computation and Structural Safety Assessment
  - The stress state of individual structural components is computed through numerical integration of the finite element stress field.
  - The exploitation coefficient of materials (concrete, reinforcement bars, prestressing cables) is evaluated to ensure compliance with design safety margins and regulatory requirements (Figure 9).

#### 5.5 Structural Joint Modeling and Connection Reinforcement

The integration of widened structural segments introduced new connection challenges, requiring specialized modeling techniques to assess joint behavior and stress redistribution. In the transition zones between the original deck and the expanded deck, beam-type elements were used to model anchor

connections, ensuring that the prestress force transfer was accurately simulated (Figure 12).

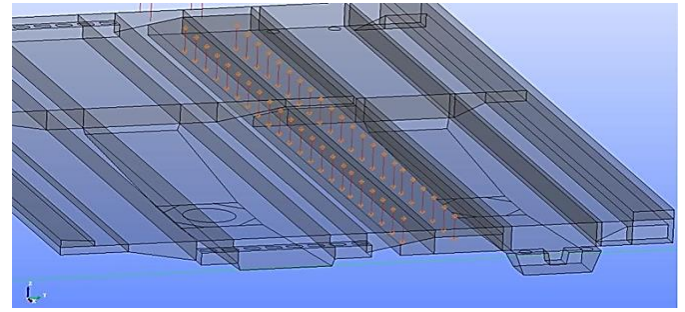


Figure 12. Modelling of the anchors used in the joint area.

Additionally, the joints were analyzed under both static and dynamic loading conditions, allowing for detailed assessment of fatigue-induced stress cycles. By incorporating nonlinear contact constraints, the model was able to replicate realistic load transfer mechanisms, ensuring that joint regions remained within safe stress limits under operational loads.

#### 5.6 Structural Monitoring and Digital Twin Utilization for Predictive Maintenance

The calibrated digital twin model serves as a decision-support tool for predictive maintenance, enabling engineers to:

- Simulate various loading conditions and forecast long-term degradation trends.
- Identify structural weaknesses by detecting deviations in modal properties.
- Optimize maintenance schedules by predicting the remaining fatigue life of critical components.
- Ensure regulatory compliance by continuously monitoring stress utilization factors.

By integrating real-time SHM data with FEM simulations, the digital twin enables a data-driven approach to infrastructure management, reducing reliance on reactive maintenance strategies and minimizing the risk of unexpected structural failures.

### 6 POST-PROCESSING OF MEASUREMENTS AND DIGITAL TWIN CALIBRATION

#### 6.1 Dynamic Adaptation of the Digital Twin to Measured Data

A fundamental feature of the digital twin framework employed in the Milano Serravalle motorway network is its ability to dynamically update its properties based on the real-time behavior of the structure. Unlike static numerical models, which rely solely on design assumptions and material properties, the digital twin is designed to minimize discrepancies between theoretical simulations and measured structural response data. This ensures that the computed stress states, deformation patterns, and modal properties of the viaducts reflect their actual in-service conditions rather than idealized design scenarios.

The primary objective of the digital twin calibration process is to ensure that the numerical model accurately represents the structure's response across its entire load history. By continuously refining key structural parameters, the system enhances predictive accuracy and enables early detection of damage mechanisms. Through an automated and iterative



inverse analysis (back-analysis) framework, the digital twin minimizes deviations between sensor-acquired data and finite element simulations, allowing for high-fidelity structural assessments.

### 6.2 Inverse Analysis and Model Calibration Techniques

The real-time calibration of the digital twin is achieved using advanced inverse modeling techniques, which allow for the automated identification and refinement of uncertain structural parameters. The WeStatiX SHM platform implements an iterative multi-objective optimization framework, leveraging surrogate models trained on thousands of numerical simulations to efficiently estimate unknown properties.

The parameters subject to calibration include both linear and nonlinear material characteristics, whose variation over time may indicate the onset of damage or degradation. Some key parameters continuously updated in the digital twin include:

- Elastic and nonlinear material properties (stiffness variations due to progressive damage).
- Time-dependent effects such as creep, shrinkage, and corrosion-related stiffness reductions.
- Boundary conditions and joint behavior changes caused by foundation settlements or bearing degradation.
- Temperature-dependent stress redistributions due to seasonal thermal cycles.

Through inverse analysis, these parameters are iteratively adjusted until the numerical model converges with real-world sensor measurements, ensuring that structural assessments remain highly accurate and reliable (Figure 13)

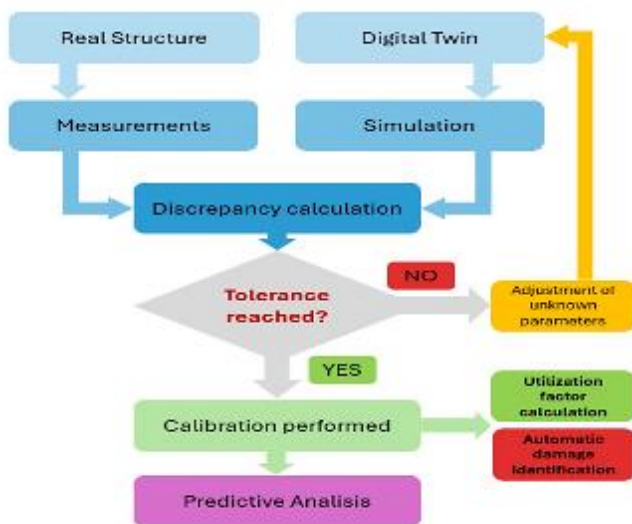


Figure 13. Calibration through inverse analysis.

### 6.3 Operational Modal Analysis (OMA) for Dynamic Parameter Identification

A key component of digital twin calibration is the identification of the structure's dynamic properties through Operational Modal Analysis (OMA). Unlike traditional modal testing, which requires artificial excitation sources such as shakers or impact hammers, OMA leverages the ambient vibrations naturally

present in the structure, such as those induced by wind, traffic loads, and micro-seismic activity.

By processing acceleration data from MEMS-based sensors placed along the viaduct deck and piers, the system is able to accurately determine the structure's modal frequencies, mode shapes, and damping ratios (Figure 14). This enables continuous tracking of structural stiffness variations, which are critical for detecting:

- Local reductions in stiffness caused by fatigue, cracking, or reinforcement deterioration.
- Progressive changes in modal parameters indicative of structural aging.
- Sudden shifts in dynamic response due to damage events such as bearing failures or impact loads.

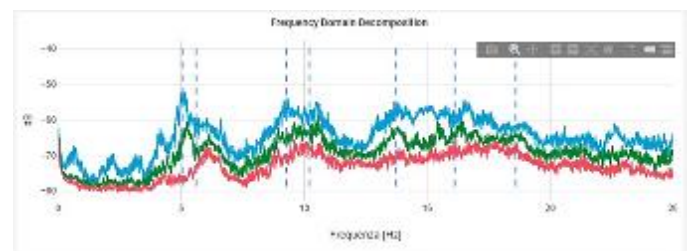


Figure 14. Inverse analysis calibration.

The digital twin is continuously updated to minimize discrepancies between FEM-based modal predictions and OMA-extracted parameters, ensuring real-time identification of structural changes. This approach allows for the detection of subtle stiffness reductions before they become critical, enabling early intervention strategies.

### 6.4 Distinguishing Thermal, Transient, and Permanent Deformation Components

One of the key challenges in long-term structural monitoring is the ability to differentiate between transient deformations (due to environmental conditions) and permanent structural changes (indicative of damage evolution). The WeStatiX SHM platform employs an automated algorithmic framework to process rotation, displacement, and strain data, allowing it to reconstruct the full deformation state of the viaduct. The system applies multi-stage filtering and correlation techniques to distinguish between:

- Thermal deformations, caused by seasonal and diurnal temperature fluctuations.
- Transient load-induced deformations, resulting from traffic loads and dynamic excitation.
- Permanent deformation trends, which may indicate creep effects, prestress losses, or progressive material fatigue.

Unlike traditional calibration approaches that simply enforce measurement-matching, the WeStatiX SHM methodology does not impose measured data onto the numerical model directly. Instead, it utilizes a cause-and-effect framework, ensuring that the structural behavior is characterized over time, across its entire operational lifespan.

### 6.5 Multi-Timescale Calibration Strategies

To provide a comprehensive assessment of structural performance, the digital twin employs two interrelated

calibration procedures, tailored to identify different categories of structural changes:

#### 1) Long-Term Calibration

This process is designed to track slow-evolving structural characteristics, such as material degradation, creep progression, and corrosion effects.

Using longitudinal datasets spanning months to years, the calibration process refines the governing material laws, ensuring that the digital twin reflects the actual deterioration mechanisms influencing the structure (Figure 15).

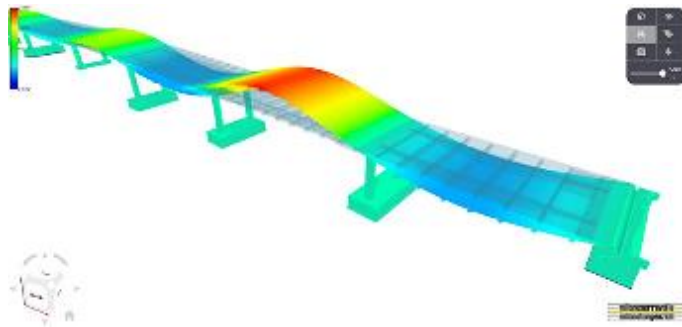


Figure 15. Modal shape identification.

#### 2) Short-Term Calibration

This process is focused on detecting rapid changes in structural behavior, such as those caused by thermal fluctuations, sudden damage events, or traffic-induced loading variations.

It enables precise assessment of thermomechanical material properties, as well as the quantification of elastic and plastic deformations caused by transient loads.

Both calibration processes work in tandem, allowing the system to accurately separate transient anomalies from permanent structural changes while ensuring that the digital twin remains an accurate and reliable decision-support tool.

### 6.6 Digital Twin Utilization for Predictive Maintenance and Decision Support

The continuously calibrated digital twin provides a quantitative basis for structural decision-making, allowing engineers to:

- Predict the remaining service life of critical components based on degradation trends.
- Assess real-time stress utilization factors to ensure that safety margins are maintained.
- Optimize maintenance schedules based on accurate forecasts of fatigue life and prestress losses.
- Trigger automated damage alerts, allowing for targeted inspections and cost-effective interventions.
- Through automated calibration, inverse modeling, and real-time FEM updating, the digital twin enables a fully predictive maintenance approach, shifting away from traditional schedule-based inspections toward data-driven infrastructure management.

The post-processing and calibration methodologies implemented in the WeStatix SHM platform represent a state-of-the-art approach to real-time structural assessment. By leveraging inverse analysis, OMA-based modal tracking, and AI-driven

optimization techniques, the system ensures that the digital twin remains dynamically synchronized with real-world structural behavior.

This multi-layered calibration framework provides a powerful tool for early damage detection, predictive maintenance, and infrastructure resilience assessment, setting a new benchmark for SHM in large-scale civil infrastructure applications.

## 7 VALIDATION RESULTS AND PREDICTIVE ANALYSIS

### 7.1 Load Testing and Digital Twin Validation

To ensure the accuracy and reliability of the digital twin model, validation was conducted by simulating controlled load tests, comparing the numerical results with real-world structural behavior observed during field testing. For the Parchi Viaduct, these load tests took place in May 2021, during which multiple spans of the viaduct were subjected to static loading using a maximum of six fully loaded trucks, each weighing approximately 30–32 tons. The arrangement of the vehicles on the deck, as illustrated in Figure 16, was designed to produce representative loading conditions for evaluating the structural response.

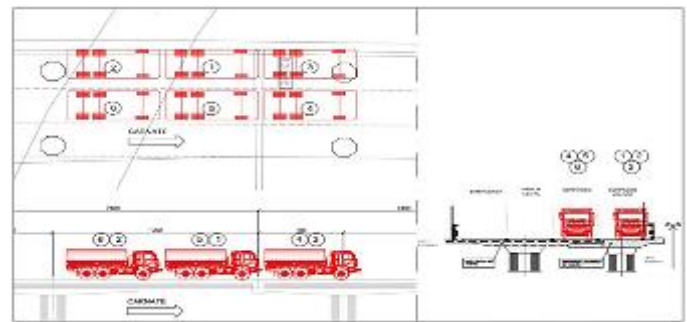


Figure 16. Truck loading configuration.

During the tests, topographic survey methods were used to measure deck displacements and assess deformation trends under loading conditions. The digital twin model, previously described, was utilized to numerically simulate the load tests, integrating precise vehicle positions, tire contact pressures, and asphalt-layer load distribution effects in accordance with regulatory standards. These elements were accurately modeled to ensure a realistic representation of stress propagation through the bridge deck and substructure (Figures 17, 18, 19).

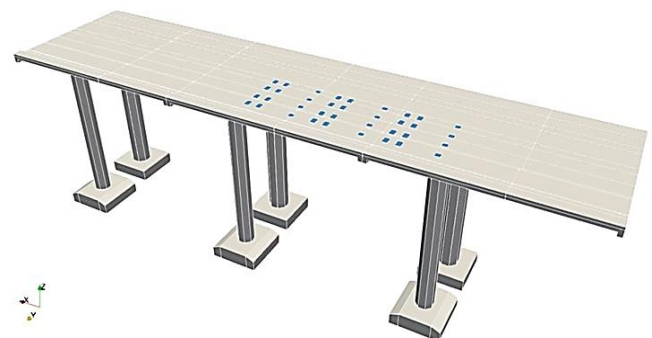


Figure 17. Parchi Digital Twin load configuration (side view).

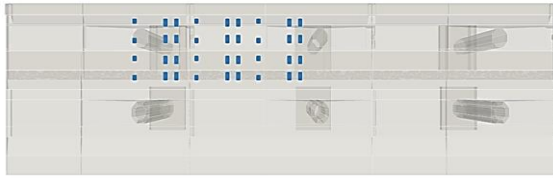


Figure 18. Parchi Digital Twin load configuration (top view).

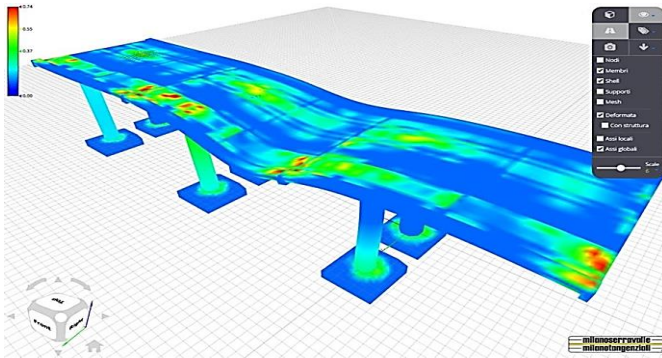


Figure 19. Utilization factor visualization of Parchi Twin.

## 7.2 Pier Height Influence on Structural Response

The simulation model was further refined by incorporating variations in pier heights, introducing additional pier elevations of 15 m and 9 m, corresponding to different spans of the viaduct. The results demonstrated a significant correlation between pier height and deflection response, with taller piers exhibiting approximately 20% greater maximum deflection under the same applied loads (Figure 20). This effect highlights the importance of accounting for pier stiffness variations in structural assessment and maintenance planning, as local stiffness differences can influence global load redistribution patterns.

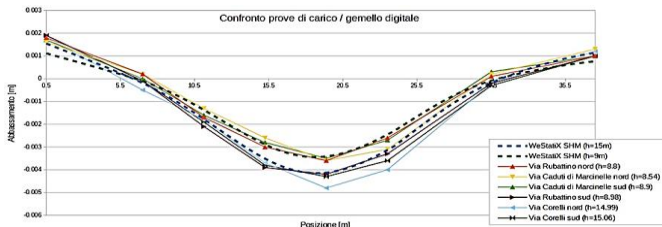


Figure 20. Pier height load test correlation of Parchi Twin.

Comparisons between measured displacements from the load tests and simulated results from the digital twin showed excellent agreement, with negligible discrepancies in both maximum deflection values and the overall deformation trends (Figure 20). These results confirm the high fidelity of the digital twin model and its ability to accurately capture real-world structural behavior under operational conditions.

## 7.3 Distributed Fiber Optic Sensor Data Analysis

In addition to traditional displacement monitoring, the distributed fiber optic sensing (DOFS) system installed on the Parchi Viaduct provided continuous real-time strain measurements, enabling both dynamic characterization and modal parameter identification for each individual span. The DOFS system measures strain rate values, defined as the derivative of strain over time.

This data is automatically processed by the SHM platform to extract modal characteristics, including natural frequencies and damping ratios (Figure 21).

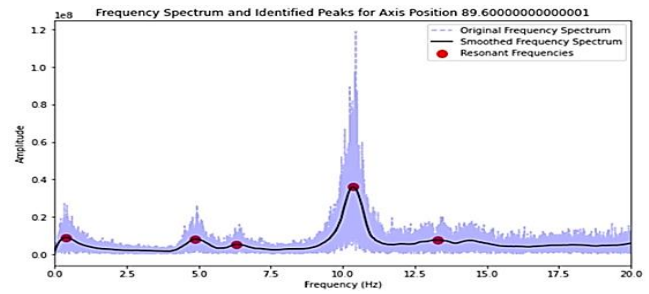


Figure 21. Natural frequency identification.

Continuous strain measurements allow for full-field reconstruction of structural deformation.

Any anomalous strain distributions or unexpected deformation patterns are automatically flagged, triggering maintenance alerts before failure conditions develop.

For other viaducts within the highway network, similar modal parameter identification and deformation reconstructions were performed using accelerometer and inclinometer data, combined with temperature compensation models. An example of this modal analysis workflow is shown in Figure 22, where deformation trends were reconstructed based on correlated inclinometrics and temperature data.

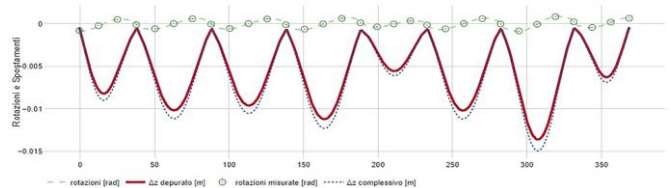


Figure 22. Deformation reconstruction using inclinometric data.

## 7.4 Interactive Visualization and Digital Twin Integration

One of the key features of the WeStatix SHM platform is the integration of digital twins within an interactive geospatial interface, providing real-time access to structural health data for all monitored viaducts in the motorway network. Through an interactive map interface, engineers can:

- Select specific viaducts and bridge structures to access real-time monitoring data.
- Perform virtual inspections through 3D visualization of the digital twin model.
- Review sensor data trends, including modal parameters, stress distributions, and temperature variations (Figure 23).

This user-friendly visualization system ensures that structural assessment personnel can efficiently analyze infrastructure health indicators, facilitating rapid response to emerging issues while streamlining the decision-making process for maintenance planning.



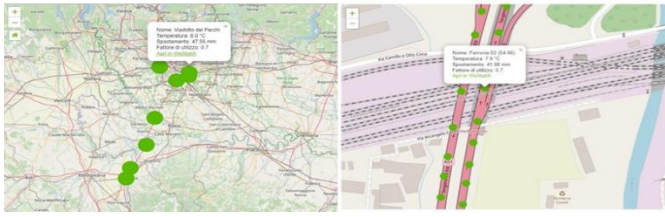


Figure 23. Interactive map.

### 7.5 AI-Based Predictive Maintenance and Self-Learning Algorithms

A distinguishing feature of the WeStatiX SHM platform is its advanced predictive analysis capabilities, which leverage physics-informed artificial intelligence to anticipate future structural behavior based on:

- Historical SHM data trends
- Machine learning-trained degradation models
- Structural simulations under progressive load scenarios

By continuously assimilating real-world monitoring data, the digital twin functions as a self-learning system, progressively improving its predictive accuracy (Figure 24). This automated learning process enhances the platform's ability to:

- Predict structural degradation trends and forecast the remaining service life of individual bridge components.
- Simulate long-term performance under variable load conditions, identifying potential failure scenarios before they occur.
- Optimize maintenance scheduling, ensuring that interventions are proactively planned based on data-driven insights rather than reactive repairs.



Figure 24. Monitoring and prediction dashboard.

The WeStatiX SHM system integrates a suite of real-time dashboards, enabling infrastructure managers to analyze monitoring data and numerical simulation outputs simultaneously. These dashboards display key structural health indicators, including:

- Current stress states and utilization factors
- Real-time displacement and deformation trends
- Predicted deterioration pathways based on historical load conditions

By integrating AI-driven forecasting with SHM diagnostics, the platform provides unprecedented decision-making capabilities, supporting a predictive maintenance strategy that optimizes

resource allocation, minimizes intervention costs, and ensures long-term infrastructure resilience.

## 8 CONCLUSIONS

The AI-enhanced digital twin framework implemented for the Pavia Viaduct has demonstrated the effectiveness of real-time SHM in large-scale infrastructure monitoring. By integrating DOFS, OMA, and PINN-based inverse modeling, the WeStatiX SHM platform accurately captures structural behavior, detects damage progression, and optimizes predictive maintenance.

Load test comparisons validated the high accuracy of the digital twin, with minimal discrepancies in displacement predictions. The observed 20% increase in deflection for taller piers underscores the need to incorporate pier height variations in FEM-based assessments. Real-time monitoring has provided crucial insights into stress redistribution, long-term deformation, and material degradation, enabling early anomaly detection.

Beyond reactive damage identification, self-learning AI algorithms support long-term deterioration forecasting and data-driven maintenance planning. Interactive visualization tools further enhance usability, enabling real-time virtual inspections and safety assessments.

This study establishes a scalable SHM methodology for infrastructure asset management, lifecycle extension, and cost-effective maintenance. Future work will refine AI-driven anomaly detection, expand digital twin applications, and integrate multi-hazard risk assessments, advancing proactive structural assessment and predictive maintenance strategies.

## REFERENCES

- [1] Linee Guida per la Classificazione del Rischio, la valutazione della sicurezza ed il monitoraggio dei ponti esistenti, Allegate al parere del Consiglio Superiore dei LL.PP. n. 54/2022
- [2] M. Martinelli, M. Ferrario, SYNOPTIC FIBER OPTIC SENSOR", Patent
- [3] M. Martinelli, The dynamical behaviors of a single-mode optical fiber strain-gage IEEE Journal of Quantum Electronics, QE 18, 666, (1982)
- [4] C. Liguori, M. Martinelli, Integral phase modulation properties of a single mode optical fiber subjected to controlled vibrations, Applied Optics, 20, 4319, (1981)
- [5] NTC 2018 – Testo aggiornato delle norme tecniche per le costruzioni (NTC2018), di cui alla legge 5 novembre 1971, n. 1086, alla legge 2 febbraio 1974, n. 64, al decreto del Presidente della Repubblica 6 giugno 2001, n. 380, ed al decreto-legge 28 maggio 2004, n. 136, convertito, con modificazioni, dalla legge 27 luglio 2004, n. 186.
- [6] Circolare NTC 2018 – CIRCOLARE 21 gennaio 2019, n. 7 C.S.LL.PP. Istruzioni per l'applicazione dell'«Aggiornamento delle "Norme tecniche per le costruzioni"» di cui al decreto ministeriale 17 gennaio 2018.
- [7] ANSFISA Istruzioni Operative per l'applicazione delle Linee guida per la classificazione e gestione del rischio, la valutazione della sicurezza ed il monitoraggio dei ponti esistenti.
- [8] WeStatiX SHM – westatix.com – Piattaforma per monitoraggio e manutenzione predittiva delle infrastrutture.

# A digital twin based integrated sustainability and quality assurance concept for subway constructions

Christian U. Grosse<sup>1+2, 0000-0002-7956-0558</sup>, Otto Wurzer<sup>1</sup>

<sup>1</sup>WTM Engineers GmbH Munich, Rablstr. 26, 81669 München, Germany

<sup>2</sup>Chair of Non-Destructive Testing, Center for Building Materials, TUM School of Engineering and Design,  
Technical University of Munich, Lichtenbergstr. 2, 85748 Garching bei München, Germany  
email: c.grosse@wtm-m.de

**ABSTRACT:** In regard to subway structures, non-destructive testing and structural health monitoring techniques are beneficial for construction and operation, which require an integrated quality control and sustainability concept. Such an integrated concept is presented, focusing on two main tasks. Inspection during construction will lead to a better quality of the components and structures. Proper data can be integrated into a building information model (BIM). The conceptual design should, however, anticipate later impacts and possible deteriorations at critical parts. The building information model could then be continued (updated) in the form of structural health monitoring (SHM) to make (visual) maintenance of subway structures more efficient, resulting in fewer disruptions (fewer closures, less downtime) and lower costs. It can also contain sensors at non-visible or non-assessable locations. Recording impacts on the structure (e.g. loads, vibrations, chlorides) enables a digital model as a so-called digital twin and the calculation of the remaining service life. Such a concept is presented for a new subway station in Munich.

**KEY WORDS:** Digital model; BIM; Subway station; Monitoring.

## 1 MOTIVATION

In order to minimize the carbon footprint of constructions over their life cycle, it is necessary to maximize their service life. In addition, operational disruptions or breakdowns must be kept to a minimum in terms of number and duration to avoid "switching effects" to private transport. Up to now, quality control during construction has mainly been carried out visually. Conformity with the approved and released execution documents is examined, representative random samples of the building materials to be installed are taken, and compatibility with subsequent components and equipment elements is checked. However, as soon as a component or construction section has been concreted, quality control is essentially only carried out on the surfaces (e.g. gravel pockets, cracks, etc.).

During the operation of the construction, inspection of infrastructure in Germany is carried out based on the German standard DIN 1076, establishing an inspection cycle of 6 years for so-called "major structural inspections" (German: Hauptprüfung). So-called "minor inspections" (German: Nebenprüfung) with a reduced scope must be carried out every adjacent 3<sup>rd</sup> year.

## 2 STRATEGY FOR NOVEL QUALITY INSURANCE

### 2.1 New constructions

A customized selection and combination of BIM (Building Information Modelling), non-destructive testing (NDT) inspection techniques, and monitoring procedures can improve quality assurance during the construction phase and make condition monitoring and maintenance easier and more competent during operation. The first step would be categorizing all structural components with regard to their importance for stability, traffic safety, and durability. This can be done based on a Building Information Modeling (BIM)

approach. The BIM model can be the basis for a digital model (sometimes referred to as a *Digital Twin*) containing physical or chemical material parameters for each structural component. To derive the resistivities of the materials, the monitoring of exogenous impacts can lead to a better understanding of material degradation. Proper monitoring techniques have the capability to measure such impacts as well as physicochemical conditions of the material in near real-time to update the digital model. Such a model is often called *Digital Shadow*, which always represents the actual state of the construction.

### 2.2 Existing structures

Such implementations are most efficient if they are implemented during the construction of the structure. However, there is also considerable potential for such a monitoring approach to increase resilience, durability, and, therefore, sustainability of existing structures from the perspective of retrofitting during operation. Such techniques can be combined with conventional visual inspection during certain intervals (as mentioned above), but can contribute information from the interior of the structures and from structural parts that are inaccessible.



Figure 1. BIM model of a new subway station.

## 3 COMBINED APPROACH

To exemplify the above-given strategy, a novel monitoring concept is illustrated for a new subway station to be built (see

a BIM model in Fig. 1). Assuming that the station has a total length of 400 m, such an underground structure is typically built in the so-called “cut-and-cover” technique (“Deckelbauweise” or “Schlitzwand-Deckel”, see the example in Fig. 2). The outer walls are first inserted into the ground as diaphragm walls. The reinforced concrete cover is then produced in a shallow cover construction pit. Under the protection of the already constructed diaphragm walls and the tunnel cover, the ground is excavated up to the lower edge of the floor slab. The floor slab, the inner shell, the mezzanine floors, and the platforms are then constructed from bottom to top using solid construction methods. This construction process considerably limits the traffic restrictions caused by the construction work as well as the dirt and noise emissions. The subway station significantly impacts the groundwater, which is why all external components must be designed as watertight concrete structures and complex culvert structures are required.

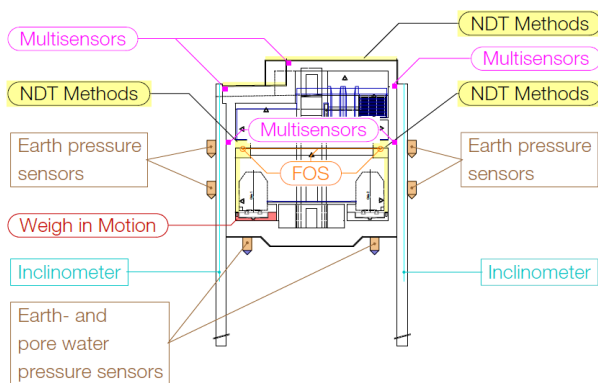


Figure 2. Cross-section of the BIM model in Fig. 1 of the subway station.

Fig. 2 provides, in addition, some elements of an integrated quality control concept, which is divided into measures for quality assurance during the construction phase and for structural maintenance during operation. Non-destructive testing methods such as endoscopy, ultrasound, radar, electromagnetic induction, etc., are primarily used. These are mainly operated right after the production of concrete components that are important, for example, in terms of structural design or for the tightness of the building. This is intended to rule out damage that is not visible on the surface, such as cavities, etc. Continuous monitoring methods such as fiber optic measuring methods are used in the construction phase, for example, for concrete parts with architecturally high-quality surface design to control the development of hydration heat and thus the early forced stresses in order to control the post-treatment and thus limit the formation of cracks.

Sensor systems and monitoring methods are also very important for repetitive structural testing and for structural maintenance during operation. For this reason, a new subway station can be equipped with a series of measuring devices for continuous monitoring of the structure: Earth pressure and pore water pressure sensors to record the load conditions, inclinometers to measure the structural deformations, multi-sensors, particularly in the area of component or structural joints, to detect the penetration of moisture and possible corrosion activity [1] (Fig. 3), fibre optic measuring systems to observe the stress conditions and possible load redistributions

in the load-bearing components [2] and, last but not least, so-called “weigh in motion” systems for vibration measurements in the track bed. For more information on sensing systems for structural health monitoring it is to be referred to the literature [3].

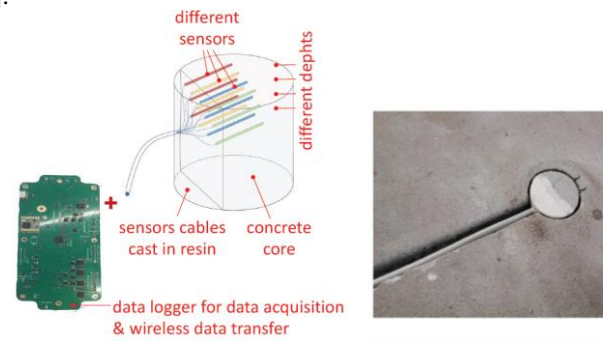


Figure 3. Multi-sensor system for corrosion monitoring [1] including different sensor modalities (left) and embedded into a concrete structure via a borehole (right).

#### 4 CONCLUSIONS

Quality assurance for subway stations, as presented here, essentially consists of a combination of a digital model with modern measurement methods. This makes it possible to improve the quality achievable during the construction of the structure and to maintain the structure's condition at a high-quality level for a long time during operation. The structure's service life can be significantly extended, and the probability of occurrence and extent of operational disruptions minimized, as was shown earlier for wind turbines [4].

It is certainly true that the development of a digital twin and the installation and operation of inspection and continuous monitoring procedures are associated with costs. However, these costs are very low in relation to the structure's life cycle and the considerable monetary and environmental benefits associated with extending the service life.

#### ACKNOWLEDGMENTS

The authors recognize the support from several companies providing information on sensors and measurement equipment, including Duramon, Switzerland, namely Dr. Seguí Femenias. The help of all WTM Engineers Munich team members, including Helmut Heiserer, Benedikt Maier, Taha Mohiuddin, Andrea Paci and Stefanie Setzer, is gratefully acknowledged by the authors.

#### REFERENCES

- [1] Angst UM, Seguí Femenias Y, Moro F. *The role of durability monitoring in taking infrastructure maintenance to the level of industry 4.0*. ce/papers 6(5): 2509-7075. <https://doi.org/10.1002/cepa.2066>. 2023.
- [2] Sieńko R, Zych M, Bednarski Ł, Howiacki T *Strain and crack analysis within concrete members using distributed fibre optic sensors*. Struc. Health Mon. 18(5-6):1510-1526. <https://doi.org/10.1177/1475921718804466> 2019.
- [3] DGZfP Merkblatt B09 (Guideline). *Dauerüberwachung von Ingenieurbauwerken*. UA Dauerüberwachung im Fachausschuss ZfP im Bauwesen der DGZfP, Berlin, 103 p. (in German, to be translated). 2022. Grosse CU. *Monitoring and Inspection Techniques Supporting a Digital Twin Concept in Civil Engineering*. In E. Ganjian (Ed.), Proc. 5<sup>th</sup> Int. Conf. on Sustainable Constr. Mat. & Techn. (SCMT5). ISBN: 978-1077905702. pp 4-18. 2019.



# Evolving reliability-based condition indicators for structural health monitoring into a digital twin of a cable-stayed bridge

Martin Herbrand<sup>1</sup>, ORCID 0000-0003-2513-2686, Marc Wenner<sup>2</sup>, Alex Lazoglu<sup>3</sup>, Christof Ullerich<sup>4</sup>, Gerhard Zehetmaier<sup>1</sup>, Steffen Marx<sup>2</sup>

<sup>1</sup>WTM Engineers GmbH, Johannissbollwerk 6-8, 20459 Hamburg, Germany

<sup>2</sup>MKP GmbH, Zum Hospitalgraben 2, 99425 Weimar, Germany

<sup>3</sup>DB InfraGO AG, Zum Güterbahnhof 9, 99085 Erfurt, Germany

<sup>4</sup>Hamburg Port Authority AöR, Neuer Wandrahm 4, 20457 Hamburg

email: m.herbrand@wtm-hh.de, marc.wenner@marxkrontal.com, alex.lazoglu@al-ing.com,  
christof.ullerich@hpa.hamburg.de, g.zehetmaier@wtm-hh.de, steffen.marx1@tu-dresden.de

**ABSTRACT:** In Germany, the bad condition of many older bridges and changes in the code provisions often result in deficits after assessment and recalculation. In case the necessary structural safety is not provided, structural health monitoring can be employed to gain knowledge about the time variant actions, the progression of structural damage and the overall condition of structures. To allow for effective use of the usually dense monitoring raw data, the derivation of condition indicators is key, since they indicate a need for action for the owners and the engineers. At the same time, real-time data as well as comprehensive condition indicators are key elements for creating a Digital Twin of a structure, as a Digital Twin requires a bidirectional flow of data, which affects the physical entity of the twin. In this paper, a method for deriving condition indicators from monitoring data is described which was developed for a large cable-stayed bridge, the Köhlbrand Bridge in Hamburg, Germany. The method allows for the calculation of a reliability index as a time variant condition indicator based on dynamic monitoring data, which is then implemented into a Digital Twin of the structure.

**KEY WORDS:** SHM, reliability, condition indicators, condition monitoring, digital twin, bridges.

## 1 INTRODUCTION

Due to the poor condition of many older bridges and changes in the regulations, there are often deficits in the recalculation of existing bridges according to the German recalculation guidelines (NRR) [1]. If the required structural safety cannot be verified using standardized load models and modified resistance models in accordance with the various NRR standards, structural measurements can be carried out for a limited period or as continuous structural health monitoring (SHM) to gain knowledge about actions that vary over time. This makes it possible, for example, to derive object-specific traffic load models by using complex algorithms and models to infer the traffic volume and traffic composition based on structural measurements [2]-[4]. In the case of time variant physical state variables, an approach can be to reduce these to extreme values in defined time intervals and describing the frequency of their occurrence using approximation functions [5],[6]. These approximation functions allow for a prediction of which extreme values of the state variable will occur in the future [7] and what reliability against structural failure will result from this [8]. It is important here that sufficiently long measurement periods are available for such an investigation [9] and that the long-term stability of the measurement system is guaranteed for the measurement period [10].

The general aim of SHM is to assess the condition or performance of the structure. The key to this is the derivation of condition indicators for the structure which can relate, for example, to the state of preservation, safety or maintenance [11] and indicate to operators and engineers any need for action. Key figures relating to structural safety can be determined using a component-based or system-based approach [12]. In the simplest case, for example, a physical state variable of an individual component is compared with a corresponding threshold value to determine a degree of

utilization. However, since these utilization rates are based on different actions, materials and failure modes with different variability, a utilization rate does not allow any conclusions to be drawn about the existing risk and, strictly speaking, only enables a binary assessment of the risk (exceedance or no exceedance). In this article, a procedure is therefore explained and implemented using the example of the Köhlbrand Bridge in Hamburg, which allows a reliability index to be derived from the dynamic monitoring ring data as a time-varying condition indicator in relation to a buckling monitoring. As part of the smartBRIDGE Hamburg project, the condition indicator was integrated into a digital twin of the structure, which contains a total of over 40 different condition indicators.



Figure 1. Köhlbrand Bridge Hamburg (source: HPA-archive Martin Elsen).

Since the buckling verification in this example is to be classified as a decisive structural check, this safety index does not refer to the system reliability but is determined for the

critical components of the structure. The structure and the problem are explained in more detail in the following chapter.

## 2 PROBLEM DESCRIPTION AND MEASUREMENT MEASURES

### 2.1 Problem Description

As one of Hamburg's most important traffic arteries, the Köhlbrand Bridge has been crossing the Köhlbrand between the Elbe island of Wilhelmsburg and Waltersdorf since 1974. The middle section, the river bridge, is a two-legged cable-stayed bridge with individual spans of 97.5 m, 325 m and 97.5 m (Fig. 1). The superstructure is designed as a single-cell steel box girder with an orthotropic deck [13].

In the course of a recalculation of the current bridge carried out in 2016 in accordance with levels 1 and 3 of the German recalculation guideline [1], the verification against buckling of the web and base plates in the pylon area for the required target load level (i. e. LM1 according to the German bridge code DIN-FB 101) could not be provided [14],[15]. The buckling verifications were carried out using the so-called reduced stress method in accordance with the German code for steel bridges DIN-FB 103 [16]. Due to the normal force distribution in the stiffening girder, the pylon area represents the decisive area for the buckling checks, with the checks being exceeded by up to 30 %. As part of level 3 of the recalculation guideline [17], cable force measurements were carried out to determine the stresses from permanent actions, which resulted in slightly lower longitudinal compressive stresses. However, the buckling check could not be provided here either using the reduced stress method. The degrees of utilization resulting from the calculation according to level 3 are shown in Fig. 2.

The iterative verification using the method of effective widths according to DIN FB 103 [16] Chapter III-4 also led to an intolerable exceedance. As a result, a distance requirement

of 50 m for trucks was added to the existing truck overtaking ban as a compensatory measure in accordance with the 1st amendment to the recalculation guideline [17] in order to reduce the traffic loads on the outer lanes and to be able to apply the reduced BK60 load model in accordance with the older traffic load code DIN 1072 (1967) [18]. However, this measure leads to considerable disturbance of regional and national traffic in Hamburg.

To be able to lift the distance requirement in the medium term, early monitoring measures were commissioned by the Hamburg Port Authority AöR (HPA) as part of the smartBRIDGE Hamburg project [19], the piloting of a digital twin of the Köhlbrand Bridge. These include strain measurements in the web and floor plates in the area at risk of buckling, as well as acceleration measurements on some of the harp cables to assess the risk of buckling. To assess the risk of buckling, the long-term buckling monitoring data from a 12-month period from July 2019 to June 2020 was evaluated as a first step. The data evaluation has recently been extended to December 2024. The aim of the monitoring is to determine whether there is a risk of buckling for the superstructure in the current load situation with the distance requirement and whether there are sufficient load-bearing reserves to lift the distance requirement. Probabilistic evaluation concepts of different levels of complexity were developed for this purpose. In the following, a simplified evaluation concept for the detection of buckling risk is described and applied to the long-term data of the buckling monitoring to derive a suitable condition indicator for assessing the risk of buckling.

### 2.2 SHM Measures

As the buckling of the web and floor plates could not be verified analytically, even with the aid of cable force measurements, MKP GmbH and WTM Engineers GmbH developed a measurement concept for a continuous structural monitoring. Variable actions in the superstructure were to be recorded via strain measurements on the superstructure and converted into acting stresses. In addition to the strain measurements, sensors for measuring the temperature of the structure, meteorological data (air temperature, radiation, humidity, wind direction and wind speed) and accelerations on the superstructure were provided. In conjunction with a Weigh-in-motion system installed on the structure, the additional sensors record the external effects on the bridge structure almost completely and should, for example, make it possible to assign the measured stress components in the web and floor plates to the different traffic load components. In addition, acceleration sensors (y- and z-axis) were permanently installed on 22 harp cables, which corresponds to a quarter of all cables on the current bridge. These sensors enable, among other things, the continuous determination of the cable forces,

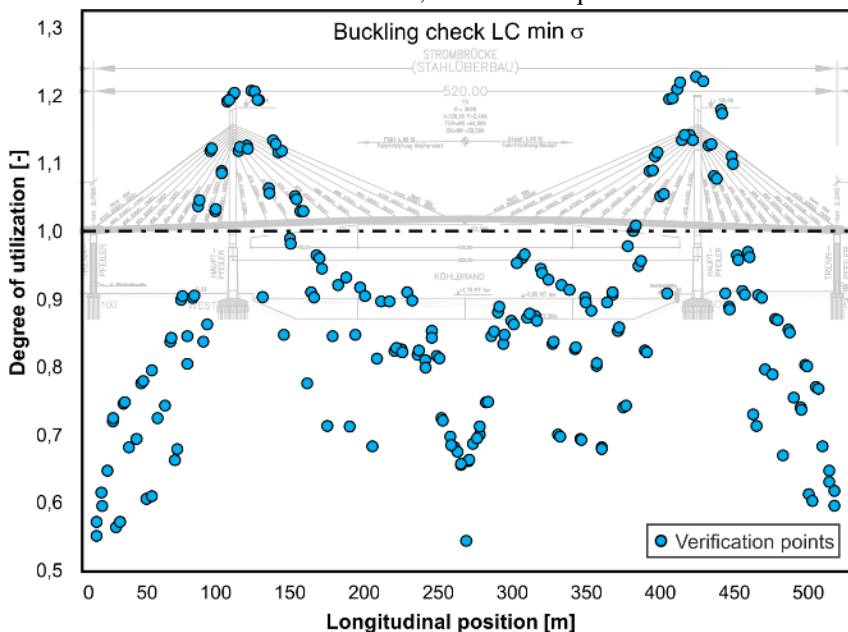


Figure 2. Utilization of buckling verification after recalculation level 3 (taken from [15])

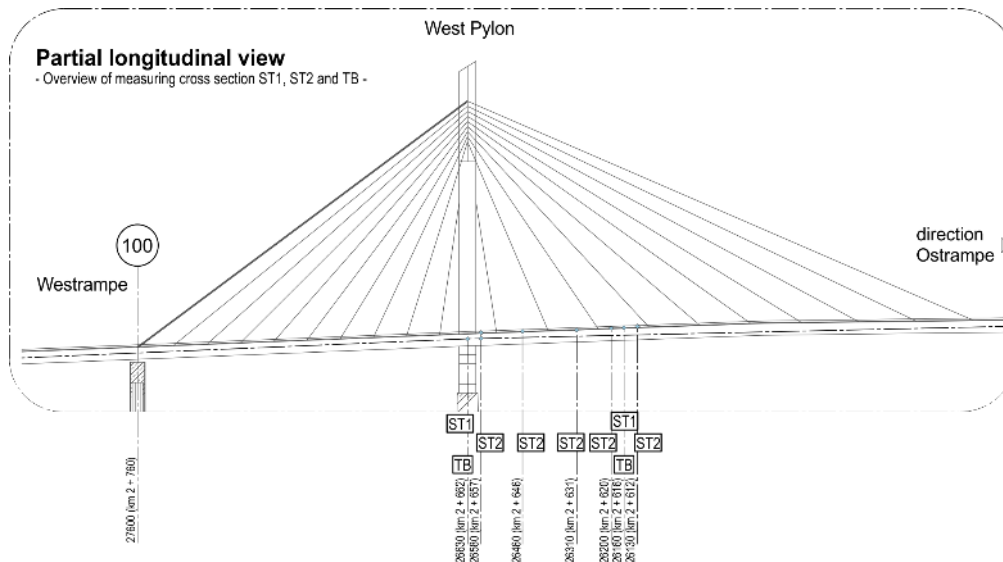


Figure 3. Position of the measuring cross-sections in longitudinal direction  
(source: MKP GmbH)

on which the stresses due to dead load of the superstructure depend on to a large extent.

The strain measurements were carried out in a total of seven measurement cross-sections along the longitudinal axis of the current bridge (Fig. 3).

A distinction is made between two types of measuring cross-section: Measuring cross-section ST1 (Fig. 4a) comprises nine Y-rosette strain gauges (arrangement of the measuring elements  $0^\circ/45^\circ/90^\circ$ ) on the web, bottom and top plates, through which three independent directions of strain are recorded to determine the main stress states. Measuring cross-section ST2 (Fig. 4b) is a reduced measuring cross-section and comprises four T-rosette type sensors in the corners of the box girder. These record two directions of strain (arrangement of the measuring grids  $0^\circ/90^\circ$ ) to accurately determine the strain

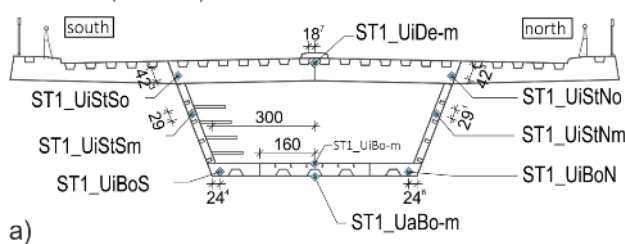
distribution in the horizontal and vertical directions, considering transverse strain influences, but without the possibility of determining the main stress directions. The details of the strain sensor arrangement of the ST1 and ST2 measuring cross-sections are shown in Figures 4c and 4d. The strain sensors of the monitoring system measure at a frequency of 100 Hz, whereby the minimum (min), maximum (max) and average values (avg) of the strains and stresses of 5-minute intervals are stored and evaluated.

The sensor system is very extensive with a total of 94 strain sensors in the superstructure, 44 acceleration

sensors on the cables, nine acceleration sensors on the superstructure, 20 temperature sensors and eight additional meteorological sensors. The scope of the measurements can also be explained by the continued use of the measuring system as part of the smartBRIDGE Hamburg project [19], in which additional condition indicators were developed and monitored. In addition, the aim was to check whether the Finite Element (FE) hybrid model of the structure provides accurate strain states under a defined load, which requires an accurate measurement of the strain distribution over the entire cross-section height.

**Sensor arrangement in the measuring cross-section ST1**

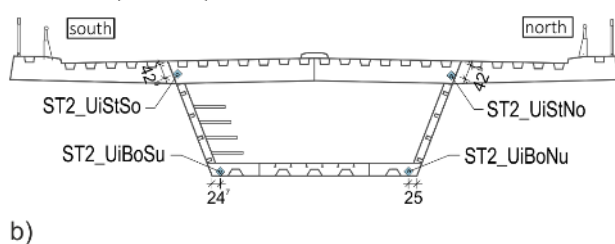
Axis: 26630 (km 2 +662)



### Detail 01: ST1

**Sensor arrangement in the measuring cross-section ST2**

Axis: 26580 (km 2+ 657)



b)

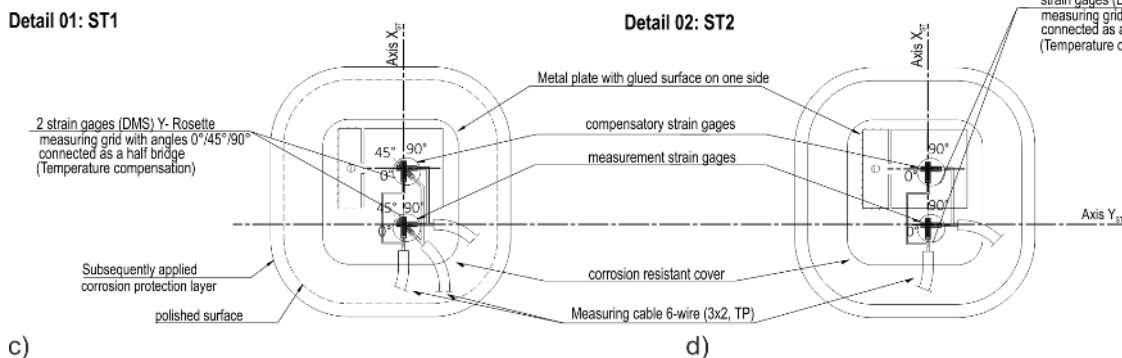


Figure 4. Measuring cross-sections and arrangement of the strain sensors (Source: MKP GmbH)



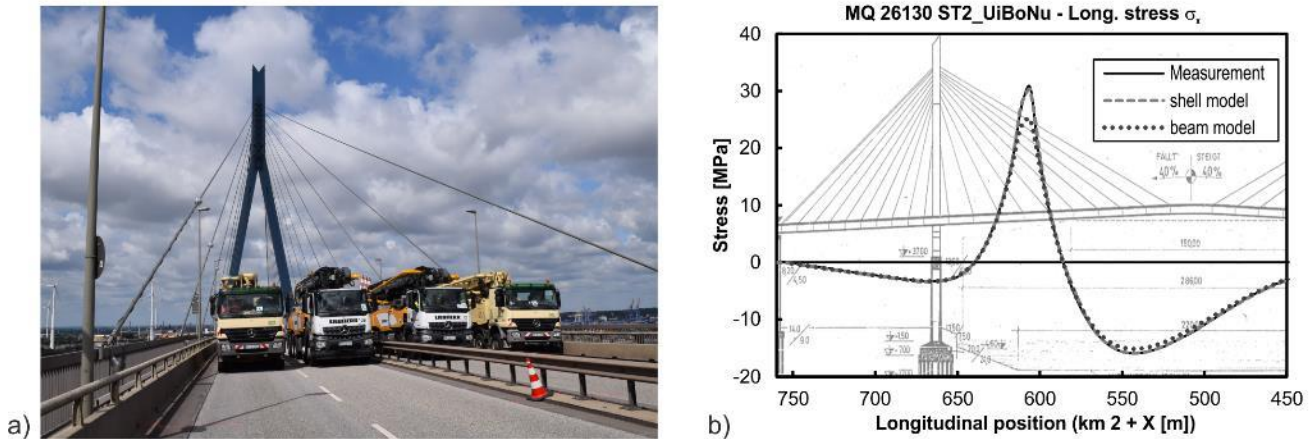


Figure 5. a) Load test on the structure; b) Comparison of measured and calculated longitudinal stresses (source: WTM Engineers)

### 2.3 Load Tests

Defined load tests and model calibrations are required to verify the plausibility of the stress values measured on the structure and to be able to relate them to the stress values calculated using normative load models. For this reason, the sensor system installed in June 2019 was tested as part of extensive load tests during a full closure of the structure in July 2019. The structure was driven over with four concrete pump vehicles with a total weight of around 180 tons in different formations (Fig. 5a). In addition, measurements were carried out on cables under ambient and harmonic excitation with installed and removed dampers to determine the damping parameters. The evaluation of the load tests generally showed very good agreement between the measured longitudinal stresses and the stresses of the FE models [20]. The influence line of a real crossing and the influence line of an FE beam and shell model are compared as an example in Fig. 5b. The FE shell model shows almost complete agreement with the measured longitudinal stresses, while the beam model slightly underestimates the stresses. This is to be expected as longitudinal stress concentrates in the corner areas of the box girder, an effect which is not captured by a beam model. The functionality and accuracy of the monitoring system could thus be confirmed by the field test and the FE model.

## 3 EVALUATION METHODOLOGY

### 3.1 Semi-probabilistic evaluation concept

The developed concept for the monitoring-based buckling analysis is shown in Fig. 6. The concept is focused on the metrological determination of the acting stresses, whereby the resistance side of the buckling analysis is not directly included in the consideration (Section 3.2). The following two methods are available as examples for determining the design stresses from variable effects: Direct measurement of the steel stresses in the buckling field (method (a)) and indirect measurement by determining the external actions (method (b)).

Direct measurement according to method (a) requires strain measurement on the cross-section using strain gages at the relevant points. The existing stresses from dead loads can be

determined by cable force measurements or taken from the recalculation. The extreme values of stresses from a relatively short measurement period (e.g. one year) can be converted into design values of the acting stresses by a statistical evaluation of the variable stresses. On the resistance side, the permissible stresses according to DIN FB 103 [16] are applied. The target values for reliability can be taken from EC0 [21].

In the indirect measurement according to method (b), the main effects on the current bridge are recorded and characteristic values for the respective actions are derived. These can in turn be applied to the structural FE model to determine the characteristic stresses in the buckling areas. The design value of the compressive stress can then be determined conventionally using the design partial safety factors and combination coefficients of German bridge codes. Alternatively, the combination coefficients can be derived individually based on the data from the long-term monitoring.

In this article, the design stresses are determined based on method (a), as this method does not require a distinction between different types of action, but only a distribution function for the measured extreme values is derived.

### 3.2 Determination of target reliability

The total design resistance stresses in the ultimate limit state (ULS) are determined in accordance with the recalculation of the bridge [14],[15] based on the concept of reduced stresses in accordance with DIN-FB 103. The design resistance of the variable compressive stresses in the longitudinal direction  $\sigma_{Q,Rd}$  results from the difference of the total design resistance according to DIN FB 103  $\sigma_{Rd,DIN-FB}$  minus the design value of the permanent actions  $\sigma_{g,Ed}$ . For the area of the base plate, the design resistance of the variable compressive stresses results according to Eq. (1).

$$\sigma_{Q,Rd} = \sigma_{Rd,DIN-FB} - \sigma_{g,Ed} = -113 \text{ N/mm}^2 \quad (1)$$

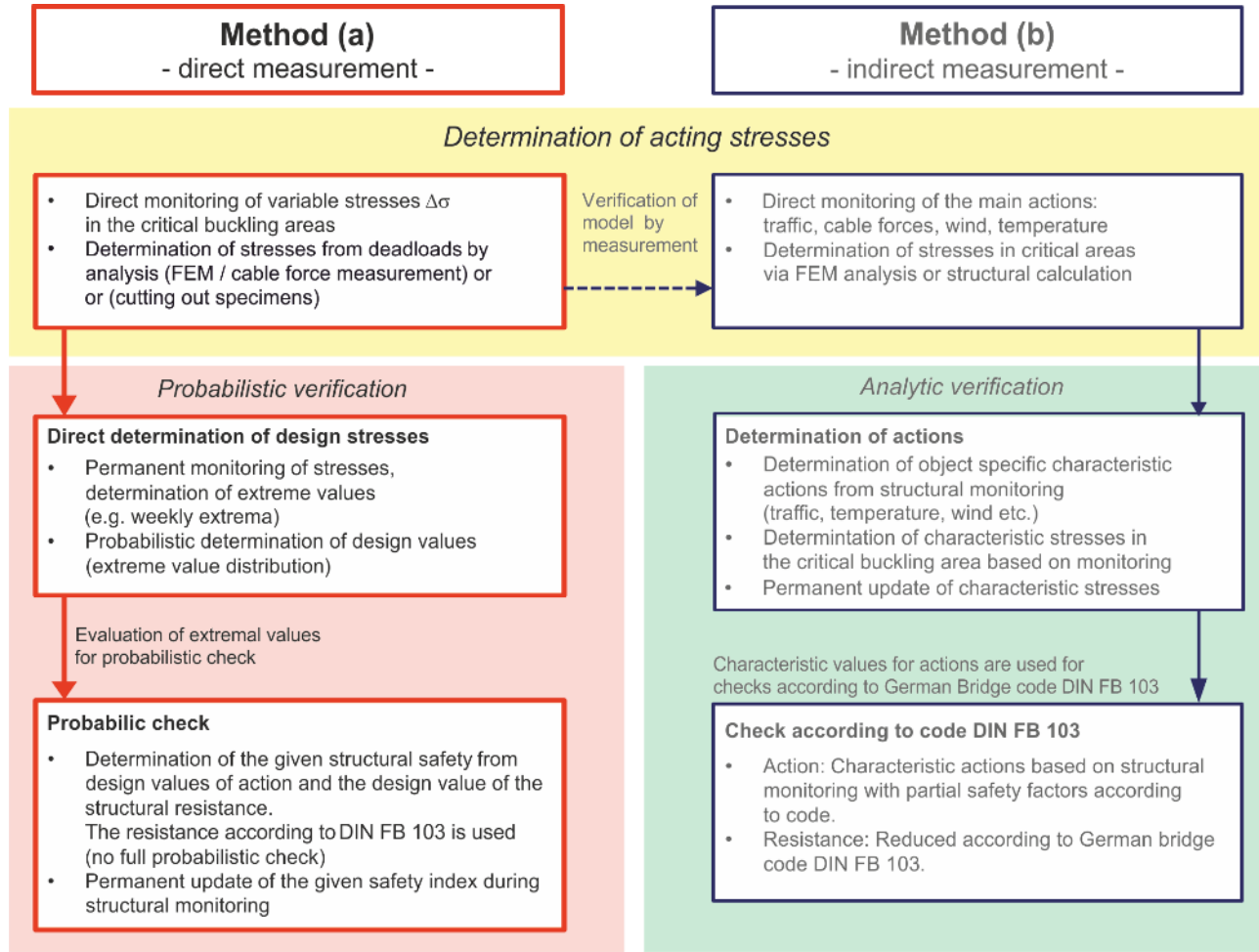


Figure 6. Concept for compensating for safety deficits through SHM (source: WTM Engineers)

For the area of the web plates, the design resistance of the variable compressive stresses at the point of intersection with the base plate are given by Eq. (2).

$$\sigma_{Q,Rd} = \sigma_{Rd,DIN-FB} - \sigma_{g,Ed} = -123 \text{ N/mm}^2 \quad (2)$$

Since the resistance side is not considered further when determining the design values of the action or when calculating the existing reliability, the target value of the reliability index for the actions  $E_d$  is determined with  $\beta_E = \alpha_E \cdot \beta$  (EC0 [21], Eq. C.6a), with  $\alpha_E = -0.7$  and  $\beta = 3.8$  according to EC0, Table C.2 [21].

For the case of normally distributed basic variables of the actions, Eq. (3) applies to the determination of the measurement value  $E_d$ .

$$E_d = m_E + \alpha_E \cdot \beta \cdot \sigma_E \quad (3)$$

Here,  $m_E$  is the mean value of the actions with the standard deviation  $\sigma_E$ . The target value of the reliability index  $\beta$  thus refers to both permanent and variable loads. However, the evaluation concept presented here is based on the stresses from dead loads determined in the recalculation and only the design value of the variable stress is determined probabilistically from monitoring data. For this purpose, it should first be checked under which boundary conditions a separate consideration of

permanent and variable actions is on the safe side. Permanent and variable loads can be divided on the safe side according to Eq. (4).

$$E_{g,d} + E_{Q,d} = m_g + m_Q + \alpha_E \beta \sqrt{\sigma_g^2 + \sigma_Q^2} < m_g + m_Q + \alpha_E \cdot \beta (\sigma_g + \sigma_Q) \quad (4)$$

Due to the fact that the permanent actions are determined with  $E_{g,d} = \gamma_g \cdot m_g$  and  $\gamma_g = 1.35$ , Eq. (4) can be transformed into Eq. (5).

$$E_{Q,d} < m_g \left[ \alpha_E \cdot \beta \cdot \frac{\sigma_g}{m_g} + 1,0 - \gamma_g \right] + [m_Q + \alpha_E \cdot \beta \cdot \sigma_Q] < m_Q + \alpha_E \cdot \beta \cdot \sigma_Q \quad (5)$$

The estimate at the end of Eq. (5) is valid for the conditions  $V_g = \sigma_g/m_g < 0.132$ ,  $\gamma_g = 1.35$  and  $\beta_E = \alpha_E \cdot \beta = 2.66$ . In the event that the aforementioned boundary conditions apply, the design value of the variable actions  $E_{Q,d}$  can therefore be determined on the safe side with the target safety index  $\beta_E = \alpha_E \cdot \beta$ . These are generally complied with for normal bridge structures, as the coefficient of variation  $V_g$  for dead loads should be well below 10 %. As a cable-stayed bridge is a structure with a complex interaction between cable forces and stiffening girders, further investigations were carried out as part of the buckling monitoring to determine the variability of the self-weight stresses using Monte Carlo simulations. The previous consideration still only applies to the case of normally

distributed variables, whereas the measured minimum values of the stresses are to be described here by an extreme value distribution of type I (Gumbel-distribution). However, as this provides values that are on the safe side compared to a normal distribution, the design value of the variable actions  $E_{Q,d}$  with the target safety index  $\beta_E = \alpha_E \cdot \beta$  is determined on the basis of an extreme value distribution in the simplified procedure presented here.

### 3.3 Determining the rated values from measurement data

To determine the parameters of the extreme value distribution, the selected reference period must be chosen in such a way that the structure experiences a load series that recurs as evenly as possible during this period. In the case of an hourly evaluation, strong stress differences arise between day and night hours, as well as in the case of a daily evaluation between working days and weekends. This results in unfavorable standard deviations of the extreme values. A comparatively uniform exposure is obtained if a weekly evaluation is selected as the reference period [4],[22].

For a continuous monitoring period of one year, 52 weekly extreme values are available for determining the parameters of the distribution function. The standard deviation  $\sigma_x$  and the mean value  $m_x$  can be estimated from the available weekly extreme values, e.g. using the method of moments or the maximum likelihood method. The density and distribution function of the extreme value distribution type I (Gumbel distribution) for minimal values are given in Eqs. (6) and (7) [23].

Density function for minimum values:

$$f(x) = a \cdot \exp[a(x - u) - \exp[a(x - u)]] \quad (6)$$

Distribution function for minimum values:

$$F(x) = 1 - \exp[-\exp[a(x - u)]] \quad (7)$$

Using eqs. (8), (9) the parameters  $a$  and  $u$  of the distribution function can be determined.

$$a = \frac{\pi}{\sigma_x \cdot \sqrt{6}} \quad (8)$$

$$u = m_x + \frac{0,577216}{a} \quad (9)$$

A special characteristic of the extreme value distribution type I is that the standard deviation of the distribution function does not change when the reference period is altered. Accordingly, the extreme value distribution for a selected reference period results from the shift of the extreme value distribution along the horizontal axis by converting the expected values (Fig. 7). The initial reference period of one week can thus be adapted to the corresponding target period for the measurement.

The reference period can be converted by calculating the corresponding fractile value. The associated exceedance

probability  $q$  is calculated for maximum values according to Eq. (10) [24].

$$q = 1 - \frac{1}{n_a \cdot a} \quad (10)$$

where

$n_a$  values per year depending on the reference period of the extreme values (here  $n_a = 52$ )

$a$  Return period or assessment period in years

Next, Eq. (10) must be adjusted for minimum values according to Eq. (11):

$$q = \frac{1}{n_a \cdot a} \quad (11)$$

The calculation of fractile values of an extreme value distribution type I is carried out for minimum values according to Eq. (12).

$$F^{-1}(x) = u + \frac{1}{a} \ln(-\ln[1 - q]) \quad (12)$$

where

$q$  undercut probability

The characteristic value of the effect  $E_k$  for a reference period of 50 years is obtained as a 2% fractile value of the expected value of the annual extreme value distribution (with  $q = 1/(1 \cdot 50) = 0.02$ ) or as a 0.038% fractile value of the expected value of the weekly extreme value distribution (with  $q = 1/(52 \cdot 50) = 3.8 \cdot 10^{-4}$ ). The reference period for which the characteristic value of the action is to be determined cannot be clearly determined. While according to EC1 [25] the characteristic values for some types of action refer to a reference period of 50 years (e.g. wind or temperature), a return period of 1000 years is specified for the LM1 load model according to EC1-2. In [26] examples are given according to which reference periods between 50 and 1000 years were applied for characteristic traffic loads. Since no normative partial safety factor for variable loads is applied in the present evaluation, the choice of the reference period is of secondary importance, since the target value of the reliability for different reference periods according to EC0 [21], Eq. C.3 is to be

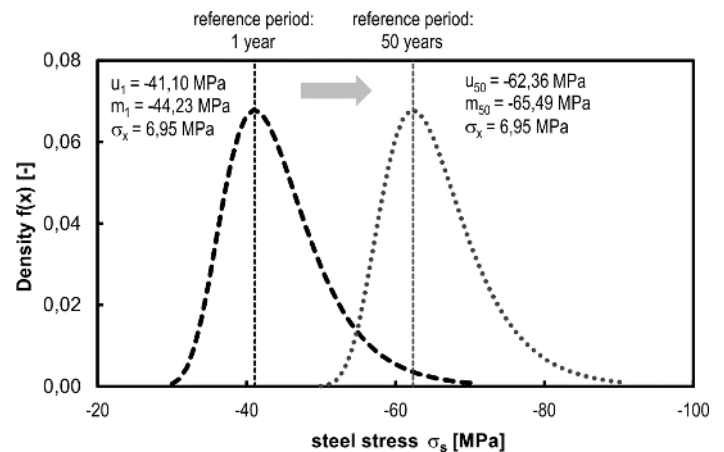


Figure 7. Exemplary conversion of the extreme value distributions for two reference periods (source: WTM Engineers)



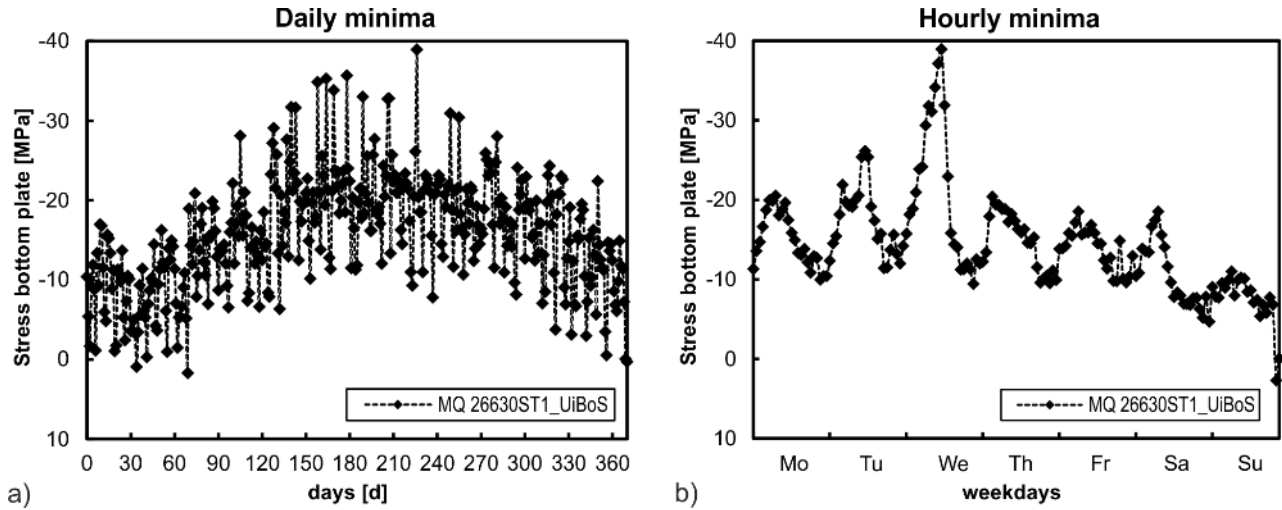


Figure 8. a) Daily minima of the measurement period; b) Hourly minima of a week in February 2020 (source: WTM Engineers)

converted in such a way that the same design values result for all reference periods.

It is important to note here that the weighting factors specified in the standards  $\alpha_R = 0.8$  and  $\alpha_E = -0.7$  only apply to a reference period of 50 years and may therefore only be applied to the value  $\beta_{50}$  (see also DIN 1055-100 [27], Eq. B.7).

The  $\beta_{50}$  index can be converted to other reference periods by applying the weighting factors for maximum values according to Eq. (13) (corresponding to EC0, Eq. C.3).

$$\Phi(\beta_n) = [\Phi(\beta_1)]^n = [\Phi(\beta_{50})]^{n/50} \quad (13)$$

Here,  $\Phi(\beta)$  is the cumulative distribution function of the standardized normal distribution. Eq. (14) applies for minimum values with  $\beta < 0$ .

$$\begin{aligned} \Phi(\beta_n) &= 1 - [1 - \Phi(\beta_1)]^n \\ &= 1 - [1 - \Phi(\beta_{50})]^{n/50} \end{aligned} \quad (14)$$

To determine the design value of the action  $E_d$ , the fractile value of the action associated with the reference period  $n$  must be determined with the undercut probability  $q = \Phi(\beta_{E,n})$  based on the characteristic value  $E_k$  determined according to Eq. (12).

The safety index for actions  $\beta_{E,50}$  is 2.66 for a reference period of 50 years, which corresponds to an undercut probability of  $q = \Phi(-2.66) = 0.4\%$ .

#### 4 VERIFICATION OF BUCKLING RISK

##### 4.1 Evaluation of long-term data

The statistical evaluation of the variable stresses from the long-term monitoring is only shown here for the critical base plate of the measurement cross-section 26630 in the pylon area (see Fig. 3). The daily minima measured on the south side of the base plate during the measurement period are shown in Fig. 8a. The seasonal influence of the compressive stresses, which increase towards winter, can be clearly seen. The diurnal influences of temperature and traffic can also be seen in the hourly minima of a February week shown in Fig. 8b.

Figures 9a and 9b show the weekly minima of two measuring points each in the base plate and in the web in measuring cross-section 26630 over the measuring period. In addition to a greater variance, the measured values of the base plate on the

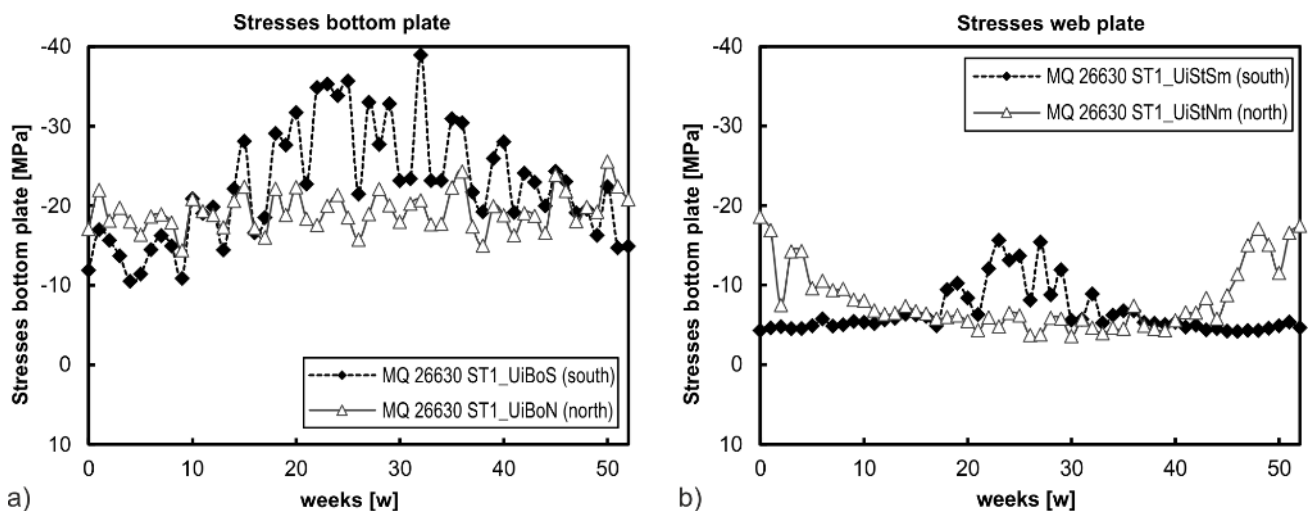


Figure 9. Weekly minima of the measuring points a) 26330 ST1\_UiBoS (south side); b) 26330 ST1\_UiBoN (north side) (source: WTM Engineers)

south side (Fig. 9a) show a clear influence of the seasonal temperature profile compared to the same measuring point on the north side. Analyses of the different types of actions have shown that influences from direct sunlight are much more pronounced at this measuring point, which explains the stronger basic variance. In addition, there likely is a local temperature-related constraint that does not exist in this form on the north side. Similar effects are visible for the evaluation of the web stresses, whereby these are due to the influence of direct solar radiation (Fig. 9b). A more detailed investigation was carried out, which, however, is not the subject of this paper.

The distribution of the weekly extreme values of the two measuring points in the relevant measuring cross-section 26630 is shown in Fig. 10. The parameters of the extreme value distribution (type I)  $m_x$  (expected value) and  $\sigma_x$  (standard deviation) as well as the minimum compressive stress  $\sigma_{s,min}$  recorded at the measuring point during the measuring period are each shown in the diagram. It can be seen that the Gumbel distribution represents a very good approximation of the actual distribution of the weekly extreme values at the measuring points investigated.

However, it is also clear that the distribution functions differ significantly with regard to the standard deviations. The critical stresses occur at the measuring point MQ 26630 ST1\_UiBoS (Fig. 10a)) on the south side of the superstructure. The parameters of the distribution functions determined for the individual measuring points are the basis for the design stresses determined in the following.

#### 4.2 Determination of the design values

Based on the weekly extreme values recorded during the measurement period and presented in the previous section, the design values of the action were determined with an extreme value distribution of type I according to the calculation steps explained in Section 3. Table 1 summarizes the target reliabilities  $\beta_t$  and  $\beta_{E,t}$ , the weighting factors  $\alpha_E$ , characteristic values of the actions  $E_k$  and the design values  $E_d$  for different

reference periods. The partial safety factors  $\gamma_Q$  result from the ratio of the design value  $E_d$  to the characteristic action  $E_k$ .

Table 1. Comparison of target reliability and characteristic expected values for different reference periods

Reference period t	1 year	50 years	100 years	200 years	1000 years
Target reliability $\beta_t$	4,68	3,80	3,62	3,44	2,98
Target reliability $\beta_{E,t}$	-3,78	-2,66	-2,42	-2,16	-1,44
Weighting factor $\alpha_E = \beta_{E,t} / \beta_t$	-0,81	-0,70	-0,67	-0,63	-0,48
Expected value $E_{k,t} = u(t)$ [MPa]	-41,27	-63,18	-67,05	-70,92	-79,91
Design value $E_d$	-94,2				
Partial safety factor $\gamma_Q = E_d/E_k$	2,28	1,49	1,40	1,33	1,18

The calculation of the design value of the stress is carried out below as an example for a reference period of 200 years. The parameters  $a$  and the model value  $u$  result in

$$a = \pi / (7.182 \cdot \sqrt{6}) = 0.179$$

and

$$u = 22.47 + 0.577216 / 0.179 = 19.25 \text{ MPa}$$

for the weekly extreme value distribution (initial values cf. Fig. 10a). The fractile value for determining the characteristic value  $E_k$  for a reference period of 200 years is

$$q = 1 / (52 \cdot 200) = 9.615 \text{E-}5.$$

The characteristic expected value is therefore

$$E_{k,200} = 19.25 + 1 / 0.179 \cdot \text{LN}[\text{LN}(1 - 9.615 \text{E-}5)] = 70.92 \text{ MPa}.$$

The fractile value of the target reliability for the ULS for a reference period of 200 years is

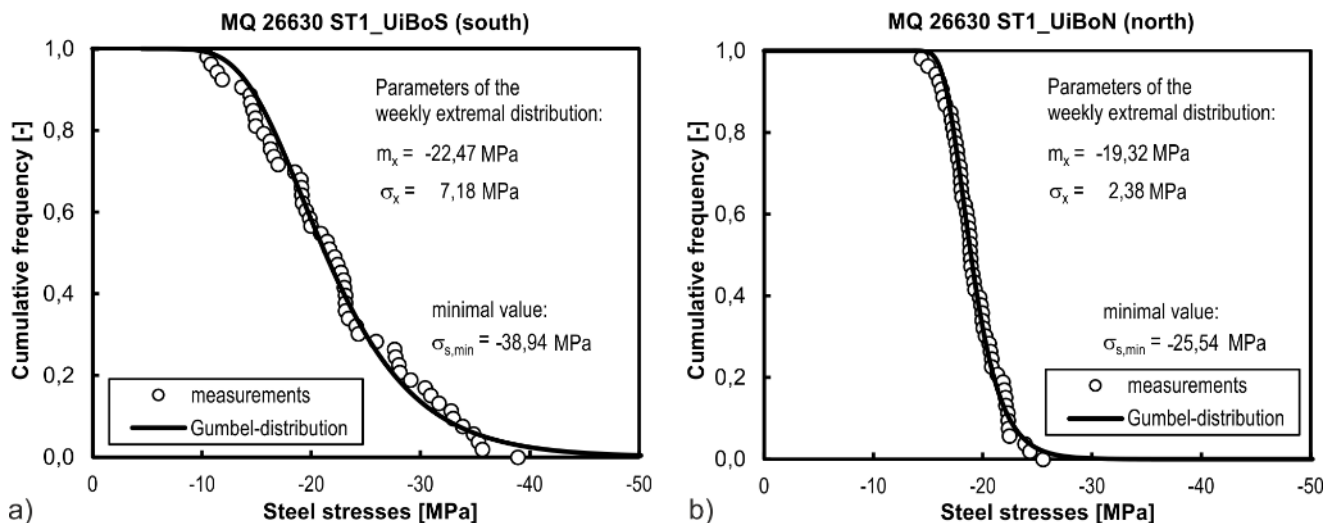


Figure 10. Distribution of the weekly extreme values in the base plate of measurement cross-section 26630 for a) the south side; b) the north side (source: WTM Engineers)

$$P_f = \Phi(\beta_{E,200}) = 1 - [1 - \Phi(-0.7 \cdot 3.8)]^{200/50} = 1.539E-2$$

(here the reliability index for a reference period of 50 years is the starting point). This corresponds to a safety index of

$$\beta_{E,200} = \Phi^{-1}(1.539E-2) = -2.16.$$

The design value thus results in

$$E_d = -70.92 + 1 - 0.179 \cdot \text{LN}[\text{LN}(1 - 1.539E-2)] = 94.2 \text{ MPa}.$$

Based on this evaluation, it can be determined that the safety against buckling can also be provided for the safety level applicable to new structures with a significant safety margin. The ratio of permissible compressive stress to design compressive stress ( $\eta = \sigma_{Q,Rd} / \sigma_{Q,Ed}$ ) is  $\eta = 113/94.2 = 1.20$ .

#### 4.3 Additional stress due to lifting of the distance requirement

The calculations to date reflect the state of traffic under the distance requirement in force during the measurement period. However, one aim of the permanent monitoring was to lift the current distance requirement in the event that sufficient safety reserves arise with regard to the buckling proof. One question to be clarified is the extent to which the stresses are likely to increase as a result of the removal of the distance requirement. According to Table A1-3 of the NRR [17], the traffic compensation measures of a truck overtaking ban and a truck distance requirement of 50 m correspond to a reduction of the target load level from LM1 to BK60.

In simplified terms, the load can increase from load model BK60 to LM1 if the spacing requirement is lifted. A comparison of the UDL loads distributed over a large area of the load models BK60 and LM1 results in a potential increase of  $q_{LM1}/q_{BK60} = 1.18$  if the traffic mix is largely maintained when the distance requirement is lifted.

According to the recalculation of the Köhlbrand Bridge [15], the share of traffic loads in the variable loads is approx. 50 %. This means that an increase in the traffic load by 18 % results in an increase in the variable loads by a total of around 9 %. Even if the distance requirement is lifted, the buckling check is not expected to fall below the safety requirements for new structures. In any case, permanent monitoring would be continued if the distance requirement is lifted in order to be able to assess the actual effects on buckling safety.

#### 4.4 Dynamic monitoring of reliability

To enable dynamic monitoring of reliability as a condition indicator, the existing safety index can be calculated for a reference period of 50 years to assess the buckling safety with

$$\begin{aligned} \beta_{E,50,prov} &= \Phi^{-1}(F(\sigma_{Q,Rd})) \\ &= \Phi^{-1}(1 - \exp[-\exp(0.179 \cdot (-113 + 63,18))]) = -3.64 \\ (\text{with } \sigma_{Q,Rd} &= 113 \text{ MPa}). \end{aligned}$$

In continuous long-term monitoring, the existing safety index  $\beta_{E,50,prov}$  can be updated weekly in this way. This is shown as an example in Fig. 11. From the 25th week of long-term

monitoring, the database for calculating the existing reliability  $\beta_{E,50,prov}$  is expanded and updated by one value every week. In this way,  $\beta_{E,50,prov}$  approaches the final value of -3.64 after one year of monitoring. If the distance requirement is lifted, the effects on buckling safety can be assessed immediately after a few weeks using this diagram. The advantage of this reliability-based parameter is that it reflects the cumulative load history and exceptional load events can be directly classified here. In addition, lower reliability requirements can be defined as threshold values for existing structures with a short remaining service life. The advantage of this parameter is also that, unlike a degree of utilization, its threshold values are independent of the kind of verification to be performed (and therefore do not have to be scaled) and the procedure shown here is therefore transferable to other types of verification.

#### 4.5 Integration into the digital twin of the Köhlbrand Bridge

The condition indicator described above was used as part of a higher-level project to develop a digital twin of the Köhlbrand Bridge [19] and integrated directly into the system. The system is based on a BIM model of the current bridge and the ramp structures and combines the available information from structure books, the German digital structures database (SIB), information from structure diagnostics and the structure monitoring within one system. Instead of operating separate data silos, all available key information on the condition of the structure is combined in one system. A major advantage is that it is much easier to recognize correlations between different sources of information. For example, information on structural damage is displayed directly in the 3D model (Fig. 12).

The taxonomy of the BIM model is based on the component groups according to the German taxonomy code ASB-ING. For the “Strombrücke” substructure of the Köhlbrand Bridge, a condition indicator was developed for each component group, which summarizes all available information on the component group into a condition group. A procedure was developed to combine the condition scores from the structural inspections with the information from structural monitoring to form a condition score [28]. Fig. 13a shows the condition indicator “superstructure” (steel box girder). The overall condition of the

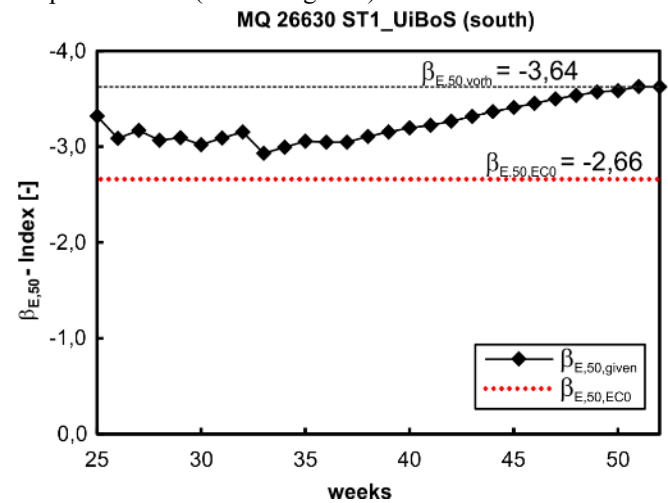


Figure 11. Dynamic development of existing reliability from long-term monitoring (source: WTM Engineers)





Figure 12. Visualization of structural damage information  
(source: MKP GmbH)

superstructure results from the PCI (Partial Condition Indicator) of the structural inspection and the PCI of the measurement-based calculations. With the PCIs “buckling safety” and “fatigue safety of transverse frame”, the CI includes the monitoring of two potential damage scenarios that were classified as critical for the structure based on sensitivity analyses.

The buckling safety is assessed by the previously described probabilistic evaluation of the strains measured at the areas at risk of buckling (Fig. 13b). The calculation of the existing safety index for buckling failure on the basis of structural measurements is explained in Section 4. The reliability index (here  $\beta_E$ -index, related to the action side) is permanently determined from the existing measurement data, which in turn is converted into a condition rating as explained in [28],[29]. In the visualization, the changes in the condition scores are shown in order to illustrate the effect of the damage scenario under consideration on the overall structure. In addition, a time diagram with the development of the reliability index over time

is shown to illustrate the development of the condition over time and, if necessary, for an initial plausibility check.

## 5 SUMMARY AND OUTLOOK

In this paper, long-term buckling monitoring data from a twelve-month period from July 2019 to June 2020 was evaluated to derive a reliability-based condition indicator for assessing the risk of buckling of the Köhlbrand Bridge superstructure. The aim was to use probabilistic methods to determine whether there is a risk of buckling for the superstructure in the current load situation with a distance requirement in place and whether there are sufficient load reserves to lift the distance requirement.

The statistical evaluation of the weekly extreme values showed that the critical stress values occur on the south side in the pylon area of the superstructure. As expected, the distribution of the measured values could be approximated very well by a type I extreme value distribution. Based on the distribution function, the design values of the variable actions were determined and compared with the structural resistances. This data was used to derive a time-variable reliability index as a condition indicator, which places exceptional load events in the context of the load history and whose threshold values can be defined independently of the verification to be performed. In this example, there were sufficient reserves to lift the distance requirement. Continuous monitoring will nevertheless be continued, also in order to be able to assess the actual effects on safety against buckling if the distance requirement is lifted. In a further step, the condition indicator described in this article was implemented with other condition indicators as part of the smartBRIDGE Hamburg project in a digital twin of the Köhlbrand Bridge. By combining and aggregating all available information on the condition of the structure into a condition score, operators and structural engineers can immediately identify any need for action on the structure.

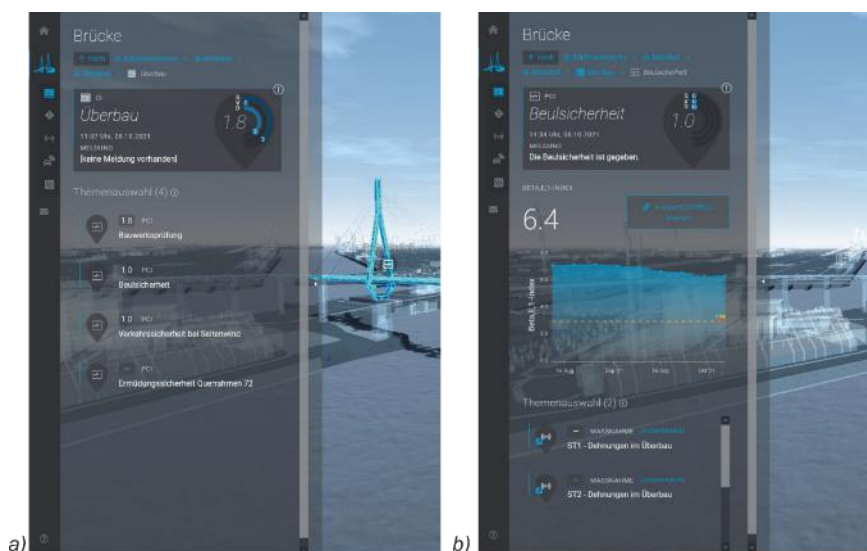


Figure 13. Visualizations in the Condition Control smartBRIDGE Hamburg of the a) CI “Superstructure” of the Köhlbrand Bridge with the associated PCIs; b) Detailed view of the PCI “Buckling safety” (source: MKP GmbH)

## REFERENCES

- [1] BMVBS (2011) Richtlinie zur Nachrechnung von Straßenbrücken im Bestand (Nachrechnungsrichtlinie). Ausgabe 05/2011
- [2] Böning S. (2013) Entwicklung einer geschlossenen Vorgehensweise zur Ermittlung von Beanspruchungen von Brückenbauwerken infolge Straßenverkehr. Dissertation Bauhaus Universität Weimar, Düren: Shaker Verlag
- [3] Nowak, M.; Fischer, O. (2017) Objektspezifische Verkehrslastansätze für Straßenbrücken in: Beton- und Stahlbetonbau 112, H. 12, S. 804–814
- [4] Geißler, K.; Steffens, N.; Stein, R. (2019) Grundlagen der sicherheitsäquivalenten Bewertung von Brücken mit Bauwerksmonitoring in: Stahlbau 88, H. 4, S. 338–353
- [5] Frangopol, D. M.; Strauss, A.; Kim, S. (2008) Use of monitoring extreme data for the performance prediction of structures: General approach in: Engineering Structures 30, S. 3644–3653
- [6] Strauss, A.; Frangopol, D. M.; Kim, S. (2008) Use of monitoring extreme data for the performance prediction of structures: Bayesian Updating in: Engineering Structures 30, S. 3654–3666
- [7] Liu, M.; Frangopol, D. M.; Kim, S. (2009) Bridge Safety Evaluation Based on Monitored Live Load Effects in: Journal of Bridge Engineering 14, S. 257–269
- [8] Frangopol, D. M.; Strauss, A.; Kim, S. (2008) Bridge Reliability Assessment Based on Monitoring in: Journal of Bridge Engineering 13, S. 258–270
- [9] Treacy, M. A.; Brühwiler, E.; Caprani, C. C. (2013) Monitoring of traffic action local effects in highway bridge deck slabs and the influence of measurement duration on extreme value estimates in: Structure and Infrastructure Engineering 10, Iss. 12, S. 1555–1572
- [10] Anderegg, P.; Brönnimann, R.; Meier, U. (2018) Referenzmessdaten beim Langzeitmonitoring von Infrastrukturen in: Bautechnik 95, H. 7, S. 494–498
- [11] Frangopol, D. M.; Saydam, D. (2014) Structural Performance Indicators for Bridges in: Bridge Engineering Handbook, 2nd Edition, S. 185–205, CRC Press
- [12] Ang, A. H.-S.; Tang, W. H. (1984) Probability Concepts in Engineering Planning and Design - Volume II. Singapore: John Wiley & Sons
- [13] Boué, P.; Höhne, K.-J. (1975) Der Stromüberbau der Köhlbrandbrücke in: Stahlbau 44, H. 6, S. 161–174 & H. 7, S. 203–211
- [14] LAP AG (2015) Köhlbrandbrücke Strombrücke (Los 1) - Nachrechnung Statische Berechnung (Stufe 1). Leonhardt, Andrä und Partner VBI AG, 25. Juni 2015
- [15] LAP AG (2016) Köhlbrandbrücke Strombrücke (Los) - Nachrechnung Stufe 3 Statische Berechnung. Leonhardt, Andrä und Partner VBI AG, 30. Juni 2016
- [16] DIN-Fachbericht 103 (2009) Stahlbrücken. Ausgabe 03/2009
- [17] BMVI (2015) Richtlinie zur Nachrechnung von Straßenbrücken im Bestand (Nachrechnungsrichtlinie) - 1. Ergänzung. Ausgabe 04/2015
- [18] DIN 1072 (1967) Straßen- und Wegbrücken, Lastannahmen. Ausgabe 11/1967
- [19] Grabe, M.; Ullerich, C.; Wenner, M.; Herbrand, M. (2020) smartBridge Hamburg – prototypische Pilotierung eines digitalen Zwillings in: Bautechnik 97, H. 2, S. 118–125
- [20] Matz, F. (2020) Messtechnisch gestützte Überwachung von Brückentragwerken am Beispiel der Hamburger Köhlbrandbrücke. Diplomarbeit, TU Dresden
- [21] DIN EN 1990 (2010) Grundlagen der Tragwerksplanung Ausgabe 12/2010 + A1:08/2012, Berlin: Beuth Verlag
- [22] Steffens, N.; Degenhardt, K.; K. Geißler, K. (2019) Modifiziertes Ziellastniveau bei Straßenbrücken durch Bauwerksmonitoring in: Schriftenreihe Konstruktiver Ingenieurbau Dresden, Heft 48 2019
- [23] Spaethe, G. (1992) Die Sicherheit tragender Baukonstruktionen. 2. Auflage, Wien: Springer-Verlag
- [24] Steffens, N. (2019) Sicherheitsäquivalente Bewertung von Brücken durch Bauwerksmonitoring. Dissertation TU Berlin, Düren: Shaker Verlag
- [25] DIN EN 1991-2 Einwirkungen auf Tragwerke – Verkehrslasten auf Brücken Ausgabe 12/2010, Berlin: Beuth Verlag
- [26] Freundt, U.; Vogt, R.; Böning, S.; Michael, D. (2014) Einsatz von Monitoringsystemen zur Bewertung des Schädigungszustands von Brückenbauwerken. Forschungsbericht, BASt Heft B 106
- [27] DIN 1055-100 (2001) Einwirkungen auf Tragwerke - Teil 100: Grundlagen der Tragwerksplanung, Sicherheitskonzept und Bemessungsregeln. Ausgabe 03/2001, Berlin: Beuth Verlag
- [28] Herbrand, M. et al.: Aggregation von Zustandsindikatoren aus Inspektions- und Monitoringdaten im Brückenbau in: Bautechnik 99, H. 2, S. 95–103
- [29] Herbrand, M. et al.: Beurteilung der Bauwerkszuverlässigkeit durch Bauwerksmonitoring in: Bautechnik 98, H. 2, S. 93–104



# Structural Health Monitoring of Intelligent Civil Infrastructure using Fibre Optic Sensing



# Advancements in Distributed Fiber-Optic Sensing: Comparing Brillouin and Rayleigh Technologies for Geotechnical and Structural Monitoring

Nöther, N.<sup>1</sup>, Facchini M.<sup>1</sup>, <https://orcid.org/0000-0002-7511-0357>, Aguilar-López J. P.<sup>2</sup>, <https://orcid.org/0000-0003-2930-5812>

<sup>1</sup>fibrisTerre Systems GmbH, Torellstr. 7, 10243 Berlin, Germany

<sup>2</sup>Faculty of Civil Engineering and Geosciences, Delft University of Technology, Stevinweg 1,  
2628 CN Delft, The Netherlands

email: nils.noether@fibristerre.de, massimo.facchini@fibristerre.de, j.p.aguilarlopez@tudelft.nl

**ABSTRACT:** We report on recent developments in distributed fiber-optic strain and temperature sensing (DTSS) technologies. In recent years, both Brillouin- and Rayleigh-based fiber-optic sensing systems have found an increasing number of applications measuring static and dynamic displacement and deformation events in geotechnical and structural health monitoring. The focus of this contribution is on Brillouin-based DTSS systems, for which we present recent advancements in spatial resolution and signal-to-noise ratio under harsh real-world conditions. The state-of-the-art Brillouin DTSS technology is considered also in relation to Rayleigh-based technologies like c-OFDR and DAS systems that also play an increasing role in geotechnical and structural monitoring, in order to illuminate the technology-specific strengths and challenges within the DFOS family. Recent insights from industrial projects and research activities in embankment monitoring are presented.

**KEY WORDS:** Distributed Fiber Optic Sensing, Structural Health Monitoring, geotechnical monitoring, Brillouin DTSS, BOFDA, embankment monitoring, crack detection

## 1 INTRODUCTION

Fiber-optic sensing is applied in many different domains of structural and geotechnical surveillance. Among the various technologies available, Brillouin-based Distributed Temperature and Strain Sensing (DTSS) offers particular advantages in that it addresses the analysis of physical parameters with measurement performance that meets engineering requirements particularly well. These performances, in particular the spatial resolution, accuracy and measurement range, integration time, long-term reliability continue to evolve thanks to a continuous development effort from the scientific and industrial community. The type of optical sensing fibers and deployed sensors in general, as well as the installation procedures and the management techniques for sophisticated measurement data sets must also be continuously adapted to the demanding needs of continuously more complex projects and the new technological possibilities that become available.

In this study, an overview of the most widely used distributed fibre-optic sensing technologies is presented, with a comparison of these technologies according to their key advantages.

In particular, we demonstrate the latest developments achieved by the Brillouin Optical Frequency Domain Analysis (BOFDA) technology, in terms of enhanced spatial resolution and deployability on various types of sensing fibers.

These performances make it possible to achieve measurement results with previously unattained quality and flexibility. This is demonstrated by the application of crack detection on dike covers presented in this article.

## 2 DISTRIBUTED FIBER OPTIC SENSING TECHNIQUES FOR STRUCTURAL AND GEOTECHNICAL MONITORING

Monitoring of buildings, transport infrastructure and the geotechnical and hydrogeological natural environment using distributed fiber optic sensors is becoming widespread.

The availability of a range of complementary measurement techniques on the market to suit the specific requirements of diverse applications and environments has enabled DFOS to be used on a large scale and for a variety of different Structural Health Monitoring (SHM) and geotechnical monitoring projects [1]. Even more importantly, a new generation of interdisciplinary engineers is arising and tackling large-scale and complex DFOS-based projects mastering dedicated instrument and sensors integration procedures as well as data management models complying with the spatially distributed nature of the DFOS, also deploying artificial intelligence and digital twins [2].

Complementary DFOS measurement techniques can be applied alternatively or jointly in structural monitoring campaigns [3, 4]. Different sensing technologies have advantages and disadvantages in terms of sensitivity to specific physical quantities, spatial distribution, temporal response, stability, field applicability, and financial cost.

The most relevant DFOS technique of interest for structural and geotechnical monitoring are shortly presented here after.

### 2.1 High-spatial resolution coherent Optical Frequency Domain Reflectometry (c-OFDR)

In the case of structures of limited dimensions (typically smaller than 100 m), monitoring with coherent Optical Frequency Domain Reflectometry (c-OFDR) [5, 6] is often the preferred choice.

The c-OFDR technology measures the distributed profile of the intensity of Rayleigh backscattering. This backscattering profile constitutes a unique fingerprint of the microscopic distribution of the scattering centers along the optical fiber, and is assumed to be stable over time – with limitations due to ageing, water intrusion, radioactive impact, etc. With its sub-centimeter spatial resolution and microstrain accuracy over tens of meters, c-OFDR is well suited for precise monitoring in SHM applications, achieving high acquisition rates (up to few hundreds of Hz for small objects under test), allowing for dynamic measurements. Commercial instruments are, on the other hand, limited in monitoring large structures and for long-term measurement campaigns. Even if rectification of the decorrelation of measurements in the long-term have been demonstrated in post-processing of acquired data [7, 8], the technique is mostly deployed in laboratory environments or for short, discrete measurement campaigns.

For the structural and geotechnical monitoring of larger objects, long spatial range DFOS techniques such as Distributed Temperature and Strain Sensing (DTSS) based on Brillouin analysis, and Distributed Acoustic Sensing (DAS) based on the dynamic analysis of Rayleigh scattering are widely preferred.

## 2.2 Dynamic measurements by Distributed Acoustic Sensing (DAS)

Distributed acoustic sensing (DAS), also referred to as phase sensitive optical time-domain reflectometry ( $\Phi$ -OTDR), is a fiber optic sensing technology also relying on Rayleigh backscattering and is sensitive to strain and temperature perturbations in the fiber [9, 10]. By injecting pulses of coherent laser light into an optical fiber, an optical phase change is recorded, resulting from the backscattered light between two sections of fiber. DAS broadband capability at frequencies of several kHz and its high sensitivity in the picostrain range makes it ideally to be deployed in application fields such as geophysics (seismology, oil and gas, geothermal energy), electricity distribution, and perimeter monitoring. On the other hand, its inadequate performance to detect strain changes at low frequencies implies that its deployment is rare in long-term quasi-static geotechnical applications, where changes occur in time scales ranging from seconds (e.g. by pile loading tests) to years (e.g. for monitoring tunnel convergence, subsidence in transport infrastructure, landslides). One of the rare deployment examples of low-frequency DAS to characterize the movement of slow-moving shallow landslides is recurrently cited in literature [11].

On the other hand, DAS finds possible deployment opportunities in SHM, for example for monitoring the dynamic response of built structures such as bridges [4]. Namely the combination of DAS with long-term stable DFOS techniques, such as Distributed Temperature and Strain Sensing (DTSS) based on Brillouin Optical Time/Frequency Domain Analysis (BOTDA / BOFDA), comes with several advantages. Both the Brillouin and Rayleigh backscatter are sensitive to strain and temperature changes, but complementary spectral information can be gained. DAS is mainly sensitive to strain changes caused by acoustic signals or vibration along the fiber with acquisition rates up to several kHz. This allows insights on the vibration behavior of the bridge. Brillouin sensing, in contrast, offers

highly stable and reliable measuring of long-term evolutions of strain and temperature.

## 2.3 Long-term stable DTSS by Brillouin Optical Time/Frequency Domain Analysis (BOTDA / BOFDA)

Brillouin scattering allows for measurement of the absolute material density state of an optical fiber, thereby providing strain and temperature profiles over more than 50 km, with a spatial resolution down to 50 cm. These performance figures make distributed Brillouin sensing highly suitable for monitoring large structures [12, 13, 14].

The basic principle of all distributed sensing principles based on Brillouin scattering is to spatially resolve the nonlinear Brillouin interaction along an optical fiber in order to retrieve the locally characteristic Brillouin frequency shift, which in turn is (over most of the strain and temperature ranges that are relevant for geotechnical monitoring) linearly connected with the fiber's density. The Brillouin frequency shift can be retrieved from the Brillouin backscattering in a reflectometric set-up, which requires access to only one end of the sensing fiber; such configurations are denoted by the letter "R" in the common acronyms (BOTDR/BOFDR). The signal quality of distributed Brillouin sensing can be highly improved by analyzing the resonance frequency between two counterpropagating optical signals injected from both ends of the sensing fiber. Such configurations bear the letter "A" at the end of the specifying acronyms (BOTDA/BOFDA). Whether the spatially resolved profile of the Brillouin frequency shift is recorded in the time domain or the frequency domain, is denoted by the letters "T" and "F" (BOTDA/R, BOFDA/R).

Due to its primarily measured material parameter being the intrinsic density of the optical fiber, the BOTDA/BOFDA technology is specifically long-term stable and free from the requirement of on-site sensor calibration both at the initial baseline measurements and during long-term operation. With the calibration parameters known for the fiber-optic sensing cables in use (to be acquired from one-time laboratory tests), the Brillouin frequency shift from each measurement iteration can be converted into absolute values for temperature and strain, with no drift being caused by aging, fatigue, or changes in the optical properties of the cables and connectors. Therefore, the technique is especially suitable for geotechnical and structural monitoring over a time horizon even of many years.

For reliable and stable measurements, the behavior of the bonding between the fiber-optic strain sensing cable and the surrounding structure under test must be considered. This is a key point when defining the integration procedures of the sensors in the host structure. On concrete structure the sensor can be embedded with high during the construction process, e.g. close to reinforcement elements (re-bars, pre-stained tendons), or applied on surface by retrofitting (by continuous gluing or using discrete fixation anchors). In the case of geotechnical monitoring this can be optimized, for example by burring the sensing cables in compacted soil or more efficiently in combination of smart geocomposites [15].

Often it is necessary to compensate the effect of temperature on the strain measurement (since Brillouin, as well as Rayleigh sensing show strain-temperature cross-sensitiveness). In order

to separate strain and temperature, the use of dedicated (loose-tube) fiber-optic temperature sensing cables, in which the fiber is mechanically decoupled, in parallel to a tight-buffered strain sensing cable is often the preferred monitoring configuration.

#### 2.4 Cracks, voids, debonding detection by Distributed Temperature Sensing (DTS)

Distributed Temperature Sensing (DTS) using Raman (and also Brillouin and Rayleigh) scattering is widely used in geotechnical and structural monitoring. It ensures accurate deformation measurements by compensating for thermal effects, tracks exothermic reactions in concrete curing, and detects fluid seepage in dams, pipelines, and tailings storage [16]. It has also been shown how DTS can be effectively applied to detect the presence of subsurface defects (voids) in concrete-filled structures [17]. The DTS methodology combined with heat conduction modeling, and inverse analysis has been applied to measure the geometry of foundation piles and to calculate their bearing capacity [18]. Recent studies demonstrate how Brillouin-based DTS can be used for non-intrusive detection of desiccation cracks in dikes. This application is discussed in a later section of this work.

#### 2.5 Key takeaways

- DTS & Brillouin-based DTSS offer the best long-term stability, making them ideal for infrastructure monitoring over decades.
- DAS is highly reliable for dynamic applications, such as seismic, traffic monitoring, vibrational mode analysis.
- c-OFDR provides high precision, but is more sensitive to environmental factors over time.

### 3 PERFORMANCE PARAMETERS AND PRACTICAL IMPLICATIONS OF BOFDA MEASUREMENTS

Specifically for the Brillouin Optical Frequency Domain Analysis (BOFDA), the technology on which the focus of this work lies, we would like to go into deeper detail on two performance aspects for practical distributed measurements in optical fibers.

#### 3.1 Performing DFOS measurements in multi-mode optical fibers using Brillouin sensing system:

It is commonly accepted that for each of the different DFOS technologies, the respective optimum fiber type shall be used in order to gain optimum performance. In Raman DTS systems, these will be multi-mode optical fibers due to their ability to handle high optical power levels (even though dedicated single-mode Raman DTS systems exist, minimizing modal dispersion to achieve higher distance ranges). In contrast, for Brillouin DTSS, literature clearly states that the use of single-mode optical fibers is mandatory. The reason here is that, in multi-mode optical fibers, the excitation of the Brillouin interaction needs to be achieved for each optical mode separately, which makes the backscattering intensity (or the Brillouin gain) highly sensitive to the arbitrary modal distribution of the involved optical signals [19]. While earlier works had shown that a strict limitation to exciting the fundamental mode only

when injecting the optical signals into the fiber under test [20], such an approach has not found its way into practice, with the consequence of a clear directive to practical users of Brillouin DTSS to exclusively use single-mode optical fibers as sensors.

However, in many real-world application scenarios, the user might not have the choice of the fiber type – be it due to previously installed fiber-optic cables that comprise multi-mode fibers for whatever reason, or due to imperfect project design or any other cause. Therefore, Brillouin DTSS measurements in multi-mode fibers have been frequently reported, and the results show that they are indeed suitable for quantitatively meaningful strain and temperature sensing. One of such application scenarios is reported in a later section of this work.

In general, the design variety of multi-mode optical fibers contains specifications on the core diameter (typically 50  $\mu\text{m}$  and 62.5  $\mu\text{m}$ ), and the refractive index profile between core and cladding being a gradient or a step-function profile.

On order to give a generic orientation for Brillouin DTSS performance in a common-type multi-mode optical fiber, we present laboratory measurements from a step-index 50/125  $\mu\text{m}$  (core/cladding diameters) step-indexed optical fiber of 445 m length. The measurements are performed using a BOFDA system on an optical fiber loop with the multi-mode optical fiber under test connected in series with a standard single-mode optical fiber (ITU-T G.652) of 120 m length for reference.

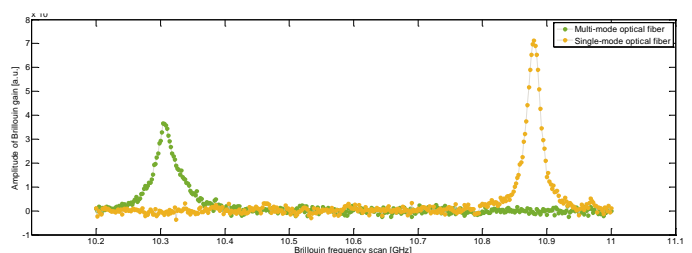


Figure 1. Brillouin gain spectra from one BOFDA measurement on a multi-mode and a single-mode optical fiber

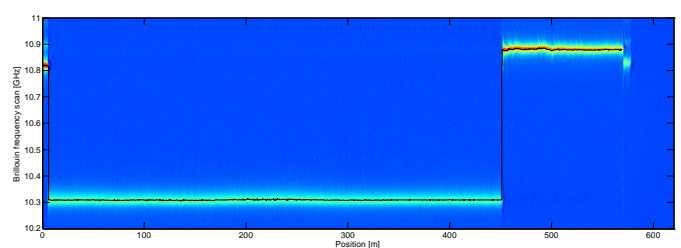


Figure 2. Full BOFDA measurement result: Intensity of Brillouin interaction (color map); local Brillouin frequency shift (black trace)

The measurement results (figures 1, 2) show that the characteristics of Brillouin sensing for a specific fiber type, specifically the characteristic parameters of the Brillouin gain spectrum, indeed differ between the multi-mode optical fiber under test and the reference single-mode fiber:

1. Brillouin frequency shift: While single-mode fibers have a characteristic Brillouin frequency shift (at room temperature and under strain-free conditions) at values between 10.6 GHz and 10.9 GHz, the multi-mode fiber shows a considerably



lower Brillouin frequency shift at 10.31 GHz. This is a quantitative difference, but does not at all compromise the performance of Brillouin sensing, because the observed frequency lies well within the scan range of commercial interrogator units.

2. Brillouin linewidth: The full width at half its maximum of the Lorentzian-shaped Brillouin gain spectrum is observed as 36 MHz for the multi-mode fiber and 25 MHz for the single-mode fiber. Again, this is merely a quantitative characterization and does not imply a significant degradation of the measurement quality.

3. Brillouin gain: The amplitude of the Brillouin gain spectrum of the multi-mode fiber is observed to be 3 dB (half intensity) below the reference single-mode fiber. The direct consequence of this discrepancy is a loss of 3 dB in signal-to-noise ratio between the two fiber types, confirming that single-mode optical fibers are better suited for distributed Brillouin sensing. However, considering the very clear implication of single-mode fibers being the obligatory choice, this 3 dB difference is considerably small. All in all it can be stated that multi-mode optical fibers can in fact be used for distributed Brillouin sensing.

### 3.2 The spatial resolution of BOTDA and BOFDA systems

The spatial resolution is one of the central performance figures of any DFOS system. In general, the following definition has been widely accepted throughout the industry [21]:

*The spatial resolution is specified for a fiber by the minimum distance between two step transitions of the fiber's strain / temperature condition. It is directly related to the pulse length of the measuring instrument.*

For general time-domain DFOS systems, the relation between the pulse length  $\Delta t_p$  and the spatial resolution  $\delta z$  is

$$\delta z = \frac{1}{2} \frac{c_0}{n} \Delta t_p$$

with  $c_0$  being the vacuum light speed and  $n$  the group refractive index of the optical fiber. A rectangular pulse of 10 ns length thus allows a spatial resolution of 1 m.

When considering incoherent frequency-domain systems, such as BOFDA, the pulse length is not directly determinable because no physical pulses are used. In BOFDA, a series of sinusoidally modulated signals is injected into the optical fiber as the pump light; the received signal (the Stokes wave, upon which the sinusoidal modulation is transferred) is analyzed by gain and phase, which – over the full series of different modulation frequencies – results in the complex transfer function, that, eventually, can be converted into the pulse response (and thereby the equivalent time-domain signal of a BOTDA system) by means of an inverse Fourier transform. Whereas in a time-domain system, the spatial resolution is directly related to the pulse width, in a frequency-domain system it is related to the width of the virtual pulse after the inverse Fourier transform, and therefore, in its origin,

determined by the bandwidth (or range of the frequency scan) of the sinusoidal intensity modulation.

The equivalent relation found in literature implies that a bandwidth of 100 MHz results in a spatial resolution of 1 m. We hereby state that this appears to be not consistent with the theory behind nor with experimental results. The key to this discrepancy between commonly accepted literature and everyday observation is that these literature sources neglect the complex nature of the retrieved transfer function. The true assumption there is that the number of scanned frequencies of the transfer function within the given bandwidth equals the number of points along the equivalent time axis for the relation 100 MHz bandwidth  $\Leftrightarrow$  1 m spatial resolution.

However, every frequency point of the complex transfer function comprises two values in the complex domain (gain and phase, or real and imaginary part, respectively). Conservation of information energy results in the fact that this doubles the number of points along the time axis (and thus the equivalent spatial axis), and results in a spatial resolution twice as narrow as the above cited literature implies. The relation for incoherent frequency-domain systems, specifically BOFDA, becomes

$$\delta z = \frac{1}{4} \frac{c_0}{n} \frac{1}{\Delta f_m}$$

in which  $\Delta f_m$  is the bandwidth of the sinusoidal intensity modulation.

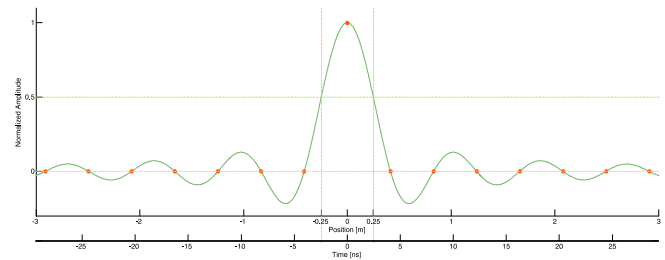


Figure 3. Virtual pulse in the time / spatial domain from a BOFDA acquisition scan

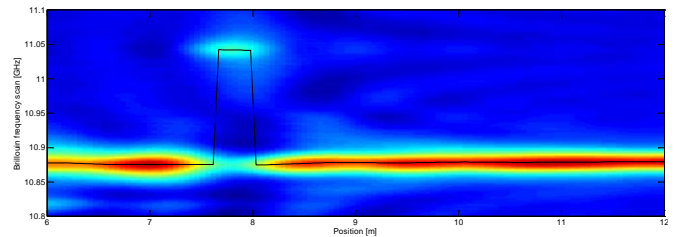


Figure 4. Discrete strain event of 0.5 m along an optical fiber, measurement result from BOFDA ( $\Delta f_m = 101.76$  MHz)

For future developments, this means that a native spatial resolution (virtual pulse width) of 0.25 m is achievable by increasing the bandwidth of the intensity modulation to 200 MHz, which is subject to current research by the authors.

#### 4 APPLICATION CASE: UNINTRUSIVE CRACK DETECTION ON DIKE COVERS BASED ON DTS

In the Netherlands, levees also referred to as ‘dikes’ are built from locally obtained materials like sand, clay, and peat, with peat and clay as the most common and abundant materials. They are used as they are the least permeable and most cohesive, thus most mechanically stable and erosion resistant. The outer portions of dikes tend to be made of grass covered hard clay, while the inner portions may be made of sand or peat for easier drainage and flexibility. Nonetheless, these materials respond differently to prolonged drought conditions. Under prolonged periods of dry weather, clay and peat dominated soils tend to develop desiccation cracks in the outer parts and thus the evaporating of moisture tends to increase their dimensions in time. Peat for example, is also a very organic and porous soil which shrinks massively during drought periods which also causes mechanical fracturing of the outer covers of dikes. These processes can seriously compromise the dike’s ability during a sudden storm as faster infiltration will saturate the dike core faster which in combination with a high-water level may result in a slope stability failure and consequently an eventual dike breach.

Currently, the detection of desiccation cracks over dikes involves is done mostly by visual inspection and only prior and during drought periods which normally occur during the spring and summer [22]. These inspections, often result in subjective conclusions and their spatial density and frequency are significantly low with respect to their natural occurrence [22]. Some attempts have been made to increase efficiency in their detection by developing artificial intelligence methods which combine visual inspection and satellite data in machine learning algorithms to analyze dike sections susceptible to cracking and predict them based on exogenous variables [23]. Such methods are useful, but they still depend on extensive human-supplied datasets, which can be inaccurate and relatively small.

For the present study, the main hypothesis is that a DTS fiber-optic (FO) cable-based sensor can be used to differentiate ‘healthy’ dike cover area from a similar area with desiccation cracks, without requiring the sensing cable to be buried in the ground. It is expected that the thermal response along the FO cable must differ significantly among the two types of surfaces given that the thermal emission and absorption will be highly influenced by the difference in thermal capacity and thermal conductivity. FO cables have been already widely used in geohydrological research [7] such as temperature monitoring for abnormal seepage water flow detection and soil moisture content measurement [26, 27]. It is important to note that by making the system as less intrusive as possible, the collected thermal signal is highly influenced by a larger number of external environmental heat sources such as solar radiation (absorption and reflection) wind thermal advection, convection and dispersion, grass moisture content, evapotranspiration, ground heat flux cycle and cable material emissivity among the most important. All these processes and their influence in the thermal response recorded by the sensor have been studied in detail via finite element model and can be found in [24].

To test the main hypothesis, setup under real scale and representative environmental conditions was built at ‘Flood Proof Holland’; a Dutch real scale dike and flood defense testing facility operated by Delft University of Technology among other local governmental and private partners.

The setup consisted in the installation of a multi sensor thermal monitoring system over a pre-existing desiccation peat-based crack found on one of the lab dikes. The cracked area thermal emission was monitored during a period of 20 days and 20 nights with a frequency of 15 minutes. The crack was monitored simultaneously with a Thermal Forward-looking infrared Remote sensor Camara (TRC), a conventional pc webcam and a DTS based FO sensor (See Figure 5).

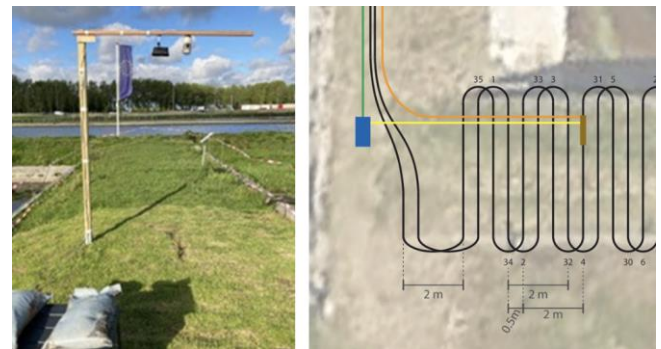


Figure 5. Dike Crack Monitoring setup at FPH, The Netherlands.

The TRC recorded 16-bit (uint16) thermal images of the crack throughout the measurement period (See figure 6). Each image had a thermal resolution of  $256 \times 320$  thermal pixels and an intensity range spanning from 0 to  $2^{16}-1$ . Its calibration was performed using the recorded air temperature in the climatological Rotterdam Airport from the KNMI (Royal Dutch Metrological Institute), located approximately 5 km from FPH.

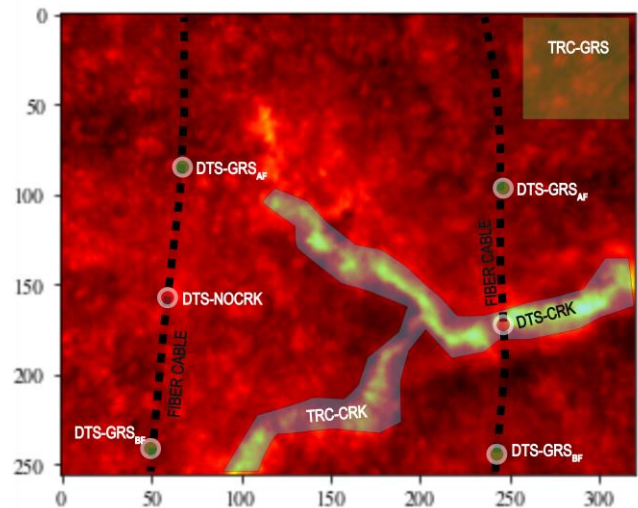


Figure 6. Thermal image of crack with chosen TRC areas for pixel averaging and point DTS fiber cable measurement locations for time series retrieval.

The TRC was mounted just on top of the crack at an elevation of 2.6 m. This made possible to cover an approximate area of 2 m by 1.80 m wide. Over the same surface, the FO multimode

cable was laid and anchored to the ground in linear transects orthogonally directed with respect to the main axis of the crack. The DTS system consisted on a BOFDA interrogator manufactured by fibrisTerre Systems GmbH type fTB 2505 [28] and a fiber-optic cable of 3 mm of external diameter (including Kevlar isolation, armoring and polystyrene jacket) with a multi-mode optical fiber as the sensing elements.

Each transect was approximately 4.5 m in length spaced every 0.5 m as shown in Figure 1. The first part of the study consisted in analyzing and post-processing time series extracted only from the TRC images by choosing representative areas inside them and averaging their temperature values per area from the thermal pixels. The time series are presented in Figure 7. Each area represented different elements (see Figure 2) to be analyzed such as a bare grass covered area (TRC-GRS), a cracked area (TRC-CRK) and the environmental air temperature (KNMI).

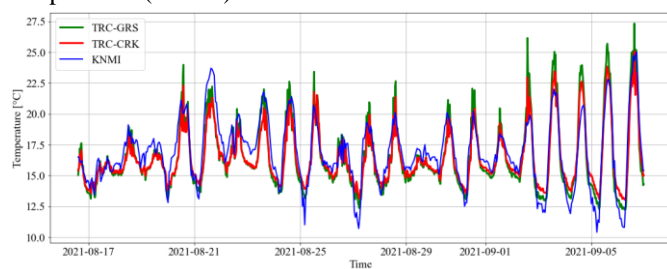


Figure 7. Time series generated from averaging thermal pixel on each image at different locations.

From Figure 7, it can already be observed that there is almost no delay among the three different time series given the chosen recording frequency (15 minutes). However, in terms of amplitude of the signal it can be observed that the TRC-GRS is greater most of the time with respect to the TRC-CRK which implies that the cracked areas have less capacity of storing the heat and may also release the stored one in a faster way, especially for the hotter days at the end of the monitored period. In addition, it can also be observed that both type of dike surfaces is always warmer when comparing them to the nocturnal environmental temperature during the last days which also can be explained by the stored heat during the day. So, from this preliminary analysis, it was concluded that the best way to characterize the thermal response of each of the surfaces while reflecting both emission and storage of heat, was by estimating the maximum daily amplitude on each of the surfaces. To validate this, the time series analysis of specific points over the grass before and after the crack (See figure 6) and the temperature in the segment of FO exactly over the crack were analyzed as well.

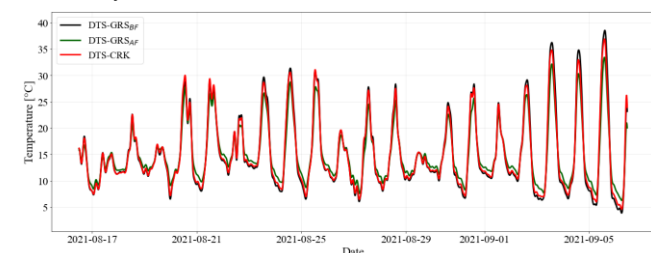


Figure 8. Thermal image of cracks with chosen areas for pixel averaging and DTS fiber cable approximate locations for time series retrieval.

It is important to note that the cable's exposure to the environment affects its temperature readings. The estimated temperature from the TRC-GRS will differ from the DTS-GRS due to the thermal properties and emissivity of the cable jacket material, which absorbs and releases heat at a different rate compared to the grass surface. This is why in the Figure 4, it can be observed that the amplitude values is greater for the cable in cracked zones which contradicts what was observed with the TRC in Figure 7. This is due to the effect of the very different thermal properties of the cable with respect to the grass and crack cover when directly exposed to the solar radiation and environment moisture. Nonetheless while inverse, the relation holds trough out the whole-time span of the experiment which means that it can still be used for crack detection despite of presenting the opposite thermal behavior of the actual soil medium.

Now based on these conclusions, a way of reflecting the difference in thermal properties at each location (cracked and healthy), is proposed based on the estimation of the maximum daily amplitude value ( $A_{max}$ ) from each thermal signal withdrawn from the DTS. To do that, we propose to plot the cracked and non-cracked  $A_{max}$  ratio between DTS and KNMI versus the same  $A_{max}$  from KNMI as shown in Figure 9.

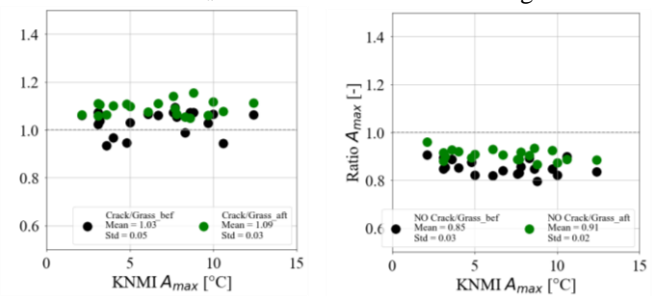


Figure 9. Amplitude ratios of DTS over KNMI plotted against maximum daily amplitude from KNMI. Left plot corresponds from cable over crack. Right plot comes from cable where no crack is present (see Figure 6).

From this last figure, the results indicate that indeed, in locations where a crack is present, the ratio of heat amplitude at a point with a crack compared to a point without one is typically greater than 1 due to the influence of the thermal properties of the cable. In contrast, at locations where no crack exists at the midpoint, this ratio is consistently less than 1. This suggests that areas with cracks tend to release heat more quickly and cool to lower temperatures at night compared to areas where the grass remains unfractured. We have also confirmed these findings through a finite element model study. Based on all the observations reported earlier, this study concludes that a DTS FO based sensor can be used to effectively detect cracks using daily cycle measurements taken at three points along a cable sensor. This conclusion relies on the physical principle that the recorded internal temperature of the cable tends to be higher in cracked surfaces during daytime and colder during nighttime with respect to the cable reading over grass. This behavior is inverse to the one observed by monitoring the temperature with TRC which reflect the actual thermal emission from the grassed surface without any interference.



## 5 CONCLUSIONS

This study highlights the effectiveness and evolving capabilities of distributed fiber-optic sensing technologies for structural and geotechnical monitoring. Among these, Brillouin-based systems, particularly BOFDA, demonstrate specifically long-term measurement stability, making them well-suited for complex infrastructure applications. The successful use of DTS for non-intrusive crack detection on dike covers further underlines the potential of fiber-optic sensors in surface-level diagnostics without the need for invasive installation. By leveraging the thermal response differences across varied surface conditions, DTS proves to be a powerful tool for environmental and structural assessments. The findings presented herein lend further support to the ongoing integration of DFOS in contemporary monitoring strategies, a process that is set to be further accelerated by the ongoing advancement of sensing technologies (instrumental performance, sensors quality), integration procedures, and complex data interpretation methodologies.

## REFERENCES

- [1] Shi, B., Zhang, D., Zhu, H. *et al.* DFOS Applications to Geo-Engineering Monitoring. *Photonic Sens* 11, 158–186 (2021)
- [2] M. Penasa, B. Helminger, E. Helminger, T. Fierz, Cloud-based 3D digital twin and fiber optic instrumentation of a pre-stressed concrete bridge for the continuous evaluation and monitoring of its structural condition, 11th International Symposium on Field Monitoring in Geomechanics (ISFMG2022), 2022
- [3] N. Nöther, A. Künzel, F. Vogdt, Surface-applied distributed fiber-optic monitoring for crack detection in concrete structures: Technology overview and application challenges, 5th International Conference on Smart Monitoring, Assessment and Rehabilitation of Civil Structures, August 2019 in Potsdam, Germany, *e-Journal of Nondestructive Testing* Vol. 25(1). <https://www.ndt.net/?id=24945>
- [4] L. Strasser, W. Lienhart, M. Winkler, Static and dynamic bridge monitoring with distributed fiber optic sensing, In *Structural Health Monitoring 2023: Designing SHM for Sustainability, Maintainability, and Reliability: Proceedings of the 14th International Workshop on Structural Health Monitoring* (pp. 1745 - 1752) <https://doi.org/10.12783/shm2023/36932>
- [5] M. Froggatt, J. Moore, High-spatial-resolution distributed strain measurement in optical fiber with Rayleigh scatter. *Applied Optics*, 37(10), 1735-1740 (1998)
- [6] Palmieri, L.; Schenato, L.; Santiagiustina, M.; Galtarossa, A. Rayleigh-Based Distributed Optical Fiber Sensing. *Sensors* 2022, 22, 6811. <https://doi.org/10.3390/s22186811>
- [7] L. Schenato, M. Cappelletti, D. Orsuti, A. Galtarossa, M. Santiagiustina, S. Cola, L. Palmieri, Enabling long-term distributed OFDR monitoring by exploiting the persistency of the Rayleigh signature, *Procedia Structural Integrity*, Volume 64, 2024, Pages 1636-1641, ISSN 2452-3216, <https://doi.org/10.1016/j.prostr.2024.09.419>
- [8] S. Heinze, A. T. Echtermeyer, A running reference analysis method to greatly improve optical backscatter reflectometry strain data from the inside of hardening and shrinking materials, *Appl. Sci.* 2018, 8, 1137; doi:10.3390/app8071137
- [9] R. Juškaitis, A.M. Mamedov, V.T. Potapov, S.V. Shatalin, Interferometry with Rayleigh backscattering in a single-mode optical fiber. *Opt. Lett.* 1994, 19, 225–227
- [10] A. Masoudi and T. P. Newson. High spatial resolution distributed optical fiber dynamic strain sensor with enhanced frequency and strain resolution. *Optics Letters*, 42(2):290, 2017
- [11] S.M., Ouellet, J. Dettmer, M.J. Lato *et al.*, Previously hidden landslide processes revealed using distributed acoustic sensing with nanostrain-rate sensitivity. *Nat Commun* 15, 6239 (2024), <https://doi.org/10.1038/s41467-024-50604-6>
- [12] M. Iten, F. Ravet, M. Niklès, M. Facchini, T. Hertig, D. Hauswirth and A. M. Puzrin, Soil-embedded fiber optic strain sensors for detection of differential soil displacements. 4th International Conference on Structural Health Monitoring on Intelligent Infrastructure (SHMII-4), 2009
- [13] M. F. Bado, J. R. Casas, A Review of Recent Distributed Optical Fiber Sensors Applications for Civil Engineering Structural Health Monitoring. *Sensors* 2021, 21(5), 1818; <https://doi.org/10.3390/s21051818>
- [14] A. Minardo, L. Zeni, A. Coscetta, E. Catalano, G. Zeni, E. Damiano, M. De Cristofaro, L. Olivares, Distributed Optical Fiber Sensor Applications in Geotechnical Monitoring. *Sensors* 2021, 21, 7514. <https://doi.org/10.3390/s21227514>
- [15] Facchini, M., Nöther, N., & Neff, L. (2024). Distributed Fiber Optic Smart Geosynthetics for Geotechnical Applications in Transportation. *Procedia Structural Integrity*, 64, 1597-1604.
- [16] Schenato, L.. A review of distributed fibre optic sensors for geohydrological applications. *Applied Sciences*, 7(9), 896 -2017.
- [17] Gong, S., Feng, X. & Zhang, G. A thermal-driven method based on Brillouin fiber-optic sensors for the quantitative identification of subsurface cavities in concrete-filled steel tube structures. *J Civil Struct Health Monit* 11, 521–536 (2021). <https://doi.org/10.1007/s13349-020-00464-7>
- [18] Höttges A, Rabaiotti C, Züger R and Hauswirth D, Methodology for geometry assessment of self-drilling micropiles using distributed fibre opticsensors. *Proceedings of the Institution of Civil Engineers – Geotechnical Engineering*, (2024), <https://doi.org/10.1680/jgeen.23.00113>
- [19] Minardo, A, Bernini, R, and Zeni, L, Experimental and numerical study on stimulated Brillouin scattering in a graded-index multimode fiber, *Opt. Express* 22, 17480-17489 (2014)
- [20] Lenke, P. and Nöther, N, Stimulated Brillouin scattering in graded index multimode optical fiber by excitation of the fundamental mode only. *Proc SPIE*. 6582. 20-. 10.1117/12.722954. (2007).
- [21] COST Action 299 “FIDES” Optical Fibres for New Challenges Facing the Information Society - “Guideline for Use of Fibre Optic Sensors” (2006)
- [22] Klerk, W. J., Kanning, W., Kok, M., Bronsveld, J., & Wolfert, A. R. M. - Accuracy of visual inspection of flood defences. *Structure and Infrastructure Engineering*, 19(8),1076-1090, 2023.
- [23] Chotkan, S., van der Meij, R., Klerk, W. J., Vardon, P. J., & Aguilar-López, J. P. A data-driven method for identifying drought-induced crack-prone levees based on decision trees. *Sustainability*, 14(11), 6820, 2022.
- [24] Roos, S – Crack Detection for Dikes using DTS – MSc thesis, <https://resolver.tudelft.nl/uuid:61999eab-1630-43b2-9b49-b2691d630e4e>, TU Delft open Repository, 2022.
- [25] Schenato, L.. A review of distributed fibre optic sensors for geohydrological applications. *Applied Sciences*, 7(9), 896 -2017.
- [26] Lagos, M., Serna, J. L., Muñoz, J. F., & Suárez, F. Challenges in determining soil moisture and evaporation fluxes using distributed temperature sensing methods. *Journal of Environmental Management*, 261, 110232, 2020.
- [27] Sun, M. Y., Shi, B., Zhang, D., Liu, J., Guo, J. Y., Wei, G. Q., & Cheng, W. Study on calibration model of soil water content based on actively heated fiber-optic FBG method in the in-situ test. *Measurement*, 165, 108176, 2020.
- [28] User’s Manual Fiber-optic sensing system for distributed strain and temperature monitoring (fibristerre fTB series, fTB 121, fTB 2505, fTB 5020). [https://www.fibristerre.de/file\\_download/15/fTB+5020+-+Product+Brochure.pdf](https://www.fibristerre.de/file_download/15/fTB+5020+-+Product+Brochure.pdf), 2022.

## Hybrid monitoring systems: synergising distributed fibre optic sensing with spot measurements

Rafał Sienko<sup>1</sup>, 0000-0002-2751-7558, Tomasz Howiacki<sup>1,3</sup>, 0000-0002-6833-7203, Łukasz Bednarski<sup>2</sup>, 0000-0002-5404-9921,  
Katarzyna Zuziak<sup>3</sup>, 0000-0002-3577-399X

<sup>1</sup>Faculty of Civil Engineering, Cracow University of Technology, Warszawska 24, 31-155, Kraków, Poland

<sup>2</sup>Faculty of Mechanical Engineering and Robotics, AGH University of Science and Technology in Krakow,  
Mickiewicza 30, 30-059, Kraków, Poland

<sup>3</sup>SHM System / Nerve-Sensors, Libertów ul. Jana Pawła II 82A, 30-444 Kraków, Poland  
email: rafal.sienko@pk.edu.pl, th@nerve-sensors.com, lukaszbednarski@agh.edu.pl, kz@nerve-sensors.com

**ABSTRACT:** The diagnosis and maintenance of both new and ageing infrastructure are among the main challenges facing the civil engineering and geotechnical industries today. The effectiveness of monitoring systems depends on several factors, including the choice of measurement techniques. Conventional point-based methods (e.g., vibrating wire sensors, electrical strain gauges, or accelerometers) are inherently limited by their locality, as they cannot directly capture what occurs between discrete measurement points. In contrast, distributed fibre optic sensing (DFOS) introduces new capabilities for structural condition assessment by enabling continuous measurement of various physical quantities along the entire length of the sensor. This eliminates the risk of missing localized extreme events or damages, such as cracks, leakages, or stress concentrations. However, the widespread adoption of DFOS is hindered by the high costs of optical interrogators, which often restrict its use to periodic measurements rather than fully automated monitoring. A practical solution to this challenge is the synergistic combination of point-based and distributed technologies within hybrid monitoring systems. Such systems leverage the strengths of both approaches, offering a more comprehensive understanding of structural behavior. This paper explores the concept of hybrid systems, illustrating their potential and real-world applications through selected case studies.

**KEY WORDS:** hybrid system, DFOS, distributed sensing, optical sensors, bridges.

### 1 INTRODUCTION

Diagnostics and maintenance in an appropriate technical condition of existing, ageing infrastructure (including bridges, tunnels, pipelines and other safety-critical facilities) is one of the key challenges currently faced by both Polish and global civil engineering. Today, experts conducting periodic inspections have significantly broader responsibilities than in the past [1], along with an increased scope of accountability for the decisions they make. Therefore, the decision-making process [2] related to the operational safety of structures, particularly those with large spans [3] or unconventional structural solutions, should be supported by objective, effective, and cost-efficient diagnostic methods. As a result, integrated structural health monitoring (SHM) systems [4] are increasingly being used, enabling the measurement of selected physical and mechanical parameters of structures during their normal operation.

Beyond the growing awareness within the engineering community, the development of monitoring systems is also, unfortunately, driven by the recurring occurrence of structural failures and collapses [5][6]. These incidents often stem from errors made during the design, construction, and maintenance of bridge structures. From a statistical standpoint, it is impossible to completely eliminate such errors. However, it is essential to take measures aimed at minimising the risk of structural failures. SHM systems contribute to this objective by providing early warnings of potential hazards, detecting trends that enable forecasting of structural behaviour over time, and supplying objective data for the calibration of theoretical and numerical models.

The effectiveness of monitoring systems, however, depends on numerous factors, including the choice of measurement

techniques, data acquisition methods, installation quality, selection of measurement locations, accuracy of applied data processing algorithms, thermal compensation, and the adopted diagnostic procedures. Developing an effective system requires interdisciplinary knowledge that often extends beyond the expertise of civil engineers and even mechanical specialists. Another challenge is the wide range of measurement techniques available on the market, each with its own advantages and limitations. There is no universal solution. Monitoring systems should therefore be designed individually, tailored to the specific characteristics and operational conditions of a given structure.

Analysing the rapidly evolving market for structural diagnostics and monitoring, certain trends shaping the general approach to monitoring systems design can be observed. One of the most promising directions is the development of hybrid monitoring systems, which aim to synergistically combine selected measurement techniques to optimise the information obtained about the structural safety while simultaneously reducing overall system costs. The following sections of this article explain the concept of hybrid systems and present their operational principles using the selected case studies, with the main focus on bridge structures.

### 2 SPOT MEASUREMENTS CONTINUOUS IN TIME

The fundamental requirement for implementing an early warning system is to carry out measurements automatically and continuously over time. The vast majority of such systems are built using spot sensors, installed at selected locations within the structure – Fig. 1.

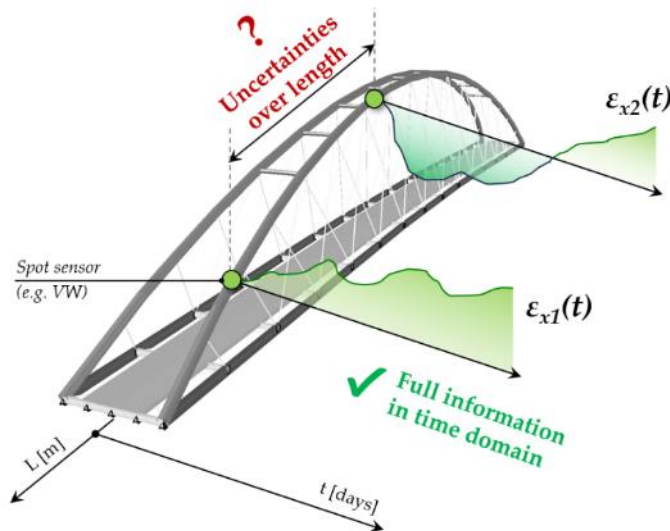


Figure 1. The scheme of the monitoring based on automatic spot sensors, performing continuous measurements over time at selected locations of the structure.

Thanks to their long-term stability, high accuracy, and resistance to environmental conditions, vibrating wire gauges [7] have found widespread use in such systems. The most commonly measured physical quantities are strains [8], based on which local stress in the monitored material can be estimated. Nowadays, all vibrating wire gauges are equipped with integrated thermistors, allowing for appropriate corrections to the measured strain values due to temperature changes over time, as well as enabling an assessment of the global structural performance due to the thermal loading [9]. This approach allows for the analysis of time-dependent phenomena, including trend identification, forecasting the behaviour of the structure, and identifying potential threats that become apparent in changes in locally measured parameters.

Depending on the design of the vibrating wire gauge, in addition to strains, it is possible to measure other physical quantities such as stress, displacements, rotations or forces. Other spot measurement technologies are also used, such as piezoelectric accelerometers for vibration monitoring, MEMS inclinometers for measuring rotations, inductive sensors, and many others. A typical scheme of a spot-based monitoring system for a bridge structure is shown in Figure 2.

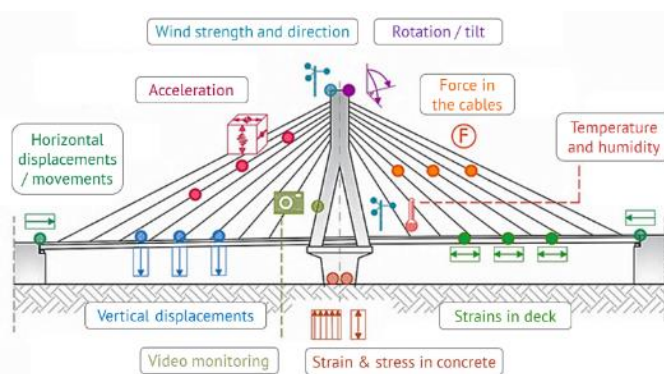


Figure 2. A typical monitoring system for a bridge structure designed with spot gauges.

The gauges are connected to local dataloggers that send measurement data to a remote server, where further analysis and interpretation are carried out. The cost of such loggers is typically negligible in the context of the entire investment. However, despite the many advantages of this approach, it also has several limitations. First, measurements are only taken at selected spots. Aside from the need to choose optimal measurement locations, which is often not a trivial task, there is a lack of information during operation about what is happening with the structure between the measurement points. In other words, this system does not allow for the direct detection of local threats, such as cracks, damage, or stress concentrations. Furthermore, the unit cost of a single gauge is relatively high due to the justified necessity of using high-quality sensors. Another issue is often the need to install long and complex cable routes, as each sensor must be connected to the logger using dedicated signal cables.

### 3 DISTRIBUTED FIBRE OPTIC SENSING (MEASUREMENTS CONTINUOUS OVER LENGTH)

Distributed fibre optic sensing (DFOS) [10] features a number of advantages such as high accuracy, measurement stability over time, and immunity to electromagnetic interference. However, its primary characteristic and advantage, distinguishing it from traditional discrete methods, is the ability to perform measurements of strain, temperature, displacement, and vibration not only at selected points of the structure but along its entire length (Fig. 3), ranging from a few centimetres to several hundred kilometres. Therefore, the analysis of the structure's performance can be carried out not only in the time domain  $\epsilon(t)$  but also in the length domain  $\epsilon(l)$ , providing entirely new insights and diagnostic possibilities.

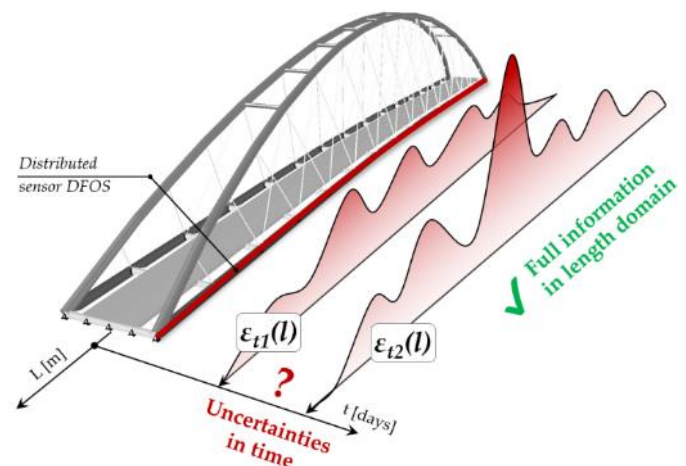


Figure 3. The scheme of the monitoring based on fibre optic sensors (DFOS), performing continuous measurements along the entire length of the structure.

Thanks to the use of linear sensors, there is no need to select optimal locations for measurement locations, the number of which is often limited by budget constraints. DFOS sensors are installed along the entire length of the monitored elements or entire structures [11], such as bridges [12][13], roads [14], tunnels [15], railways [16][17], collectors and pipelines [18], or linear concrete elements like girders [19]. A significant



consequence of performing geometrically continuous measurements is the ability to directly detect local damage or threats, such as concrete cracking [20][21], local stress concentrations, sinkholes, leaks, and others. As a result, the effectiveness of the measurement system in early risk identification is very high – there is no possibility of missing extreme values of the measured physical quantities. This is one of the main reasons for the dynamic growth and development of DFOS technology in construction and civil engineering, which translates into a noticeable increase in its practical applications. Figure 4 shows selected examples of implementations within Polish bridges only [22, 23, 24, 25, 26, 27]. The full list of bridges and various types of structures is much longer.

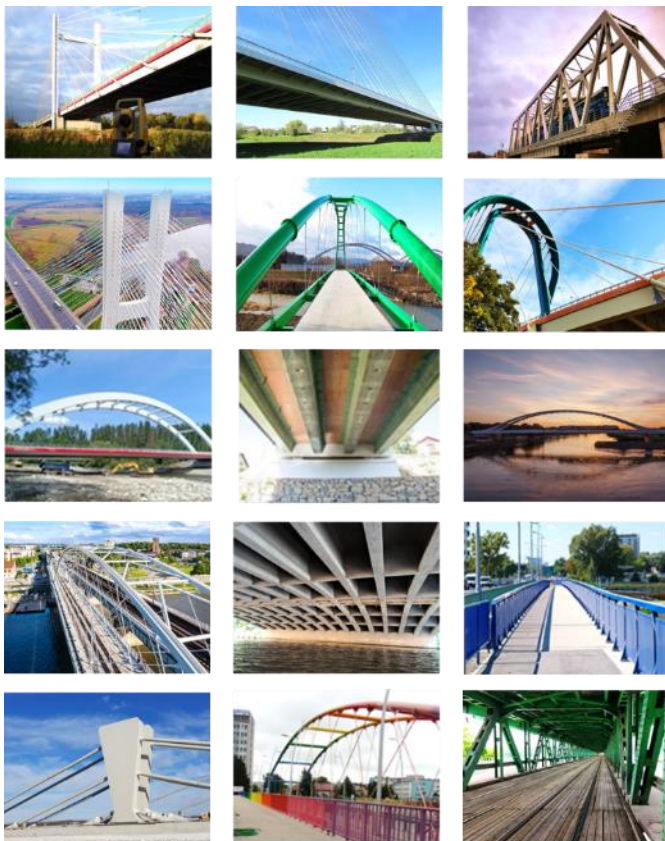


Figure 4. Example bridge structures in Poland equipped with distributed fibre optic sensing DFOS systems.

It is worth emphasising that depending on the type of chosen interrogator (optical datalogger), sensors, and installation approaches, the DFOS technique allows for the measurement of various physical quantities. The most commonly measured parameters include mechanical-thermal strains [28], but also shape changes (displacements) [29][30] and vibrations. Interestingly, there is the possibility of connecting the same sensors to different optical interrogators for simultaneous measurements of various quantities, such as strain and temperature. It should also be noted that, although the DFOS technique can represent a breakthrough in monitoring and diagnosing structures, there is no one universal solution for optimal sensor and interrogator properties. In other words, a wide range of optical fibres, cables, and sensors is available

on the market [31][32][33], each characterised by its own advantages and limitations. When selecting a specific sensor, attention should be given to aspects such as:

- size and shape of the cross-section (round, rectangular),
- internal construction (layered, monolithic),
- core material parameters such as elasticity modulus or maximum elongation,
- type of outer surface (smooth, ribbed, with a braid),
- mechanical, chemical, and environmental resistance,
- minimum bending radius.

It is important to emphasise that both the parameters of the interrogators and sensors should be selected individually based on the needs of a given project. For example, in the case of embedding sensors in concrete, round cross-sections and an external braid to improve adhesion are preferred. On the other hand, for gluing to flat surfaces, a flat rectangular cross-section without a braid is better. Sensors are a key component of the entire system. Once integrated into the monitored structure, they should provide reliable information about its performance throughout the entire service life. In telecommunications applications, optical fibres are used with various protective coatings, as well as layered cables, where the fibre is protected by additional protective layers. However, these layers usually do not adequately transmit strain to the sensing fibre inside the cable, creating the risk of data misinterpretation [20]. Therefore, in engineering applications, sensors designed as composite elements with fibres fully integrated with the single-material core during production are more often applied. Fig. 5 shows the family of various monolithic sensors. The EpsilonSensor has a low modulus of elasticity (3 GPa), making it particularly sensitive to detecting cracks in concrete. The EpsilonRebar, with a modulus of 50 GPa, can, in addition to its sensing function, also serve as reinforcement with parameters similar to typical GFRP (glass fibre reinforced polymer) bars. The EpsilonFlat is suitable for bonding to the surface of structures, while the EpsilonGraph is ideal for projects where rapidly changing temperature is a key parameter.



Figure 5. Typical monolithic sensors for mechanical-thermal strains [courtesy of SHM System / Nerve-Sensors].

There is no doubt that a well-designed DFOS system can provide unique information, allowing reliable inferences about the technical condition of a structure. However, a key limitation of this technology in practice, slowing down its widespread

adoption, is the high cost of optical interrogators. Therefore, a common practice is to use a single device for periodic readings from sensors installed on multiple structures. Of course, the cost efficiency of the system will also depend on the scale of the investment and the responsibility (failure consequences) of the monitored structure.

While DFOS measurements are most commonly performed periodically today, it is worth noting the rapid development of optical equipment. In recent years, new devices have appeared on the market, and existing ones have been improved in terms of selected parameters, such as spatial resolution or maximum measurement range. The high cost is partly due to the patents in place, which, in some cases, will expire in a few to several years. Therefore, it is expected that the cost of such devices will decrease in the future, while their diagnostic capabilities will increase. Creating intelligent infrastructure today, equipped with relatively not expensive DFOS sensors, will not only allow precise periodic measurements but also prepare for the use of future, yet unknown capabilities.

It is also worth noting that DFOS sensors are, at the same time, signal cables (transmitting information from thousands of measurement points directly to the interrogator). In spot measurements, a signal cable must be routed (and secured) from each sensor to the local datalogger, which in many cases can be problematic. This applies especially to structures such as bridges, large-scale buildings (halls and stadiums), and linear infrastructure such as pipelines, collectors, or railways. A comparison in cross-section volume of 20 typical signal cables with a single optical fibre is shown in Figure 6.

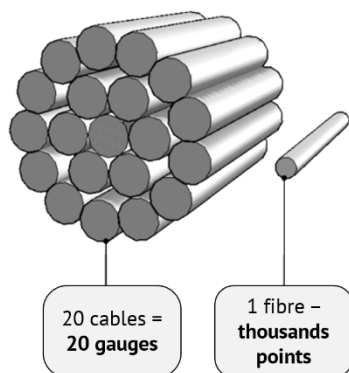


Figure 6. Comparison of 20 typical signal cables with a single optical fibre, capable of handling tens of thousands of measurement points.

#### 4 HYBRID SYSTEMS

To summarise the above considerations, it should be stated that the primary limitation of classical spot techniques is their locality, while the limitation of DFOS methods is their periodicity (resulting from economic, rather than technical, factors). Therefore, a natural consequence of attempting to solve this problem is the synergistic combination of spot technology with geometrically continuous sensing through the design of a hybrid system – Figure 7. In this approach, automatic spot measurements (continuous in time) are supported by periodic DFOS measurements (continuous in length) to optimise the obtained information, while maintaining

economic feasibility. Hybrid systems have the following advantages:

- low cost of distributed fibre optic sensors,
- possibility of limiting the number of relatively expensive spot gauges and cabling,
- no need to purchase expensive DFOS interrogators,
- ability to install distributed sensors during the construction phase, with measurements taken at later times (a “time-delayed investment”),
- increased system reliability through comparative analysis of data from at least two independent measurement techniques,
- direct detection of local damage, cracks, or stress concentrations (using DFOS sensors),
- possibility of analysing and identifying long-term trends in the operation of the structure (forecasting with spot gauges).

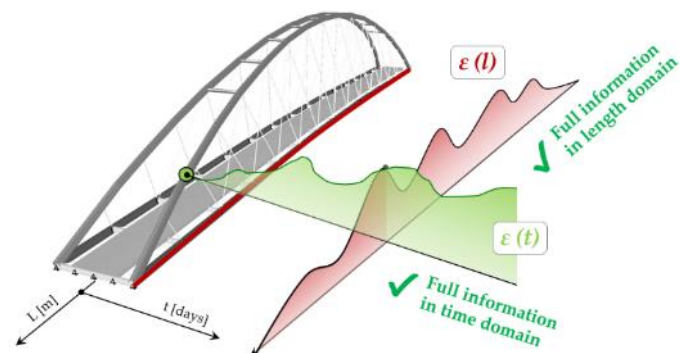


Figure 7. Concept of a hybrid system providing information about the technical condition of the structure both as a function of time and as a function of length.

Hybrid systems are not just a theoretical concept, but an increasingly common solution used in practice. According to the authors, it is one of the main directions that the structural health monitoring market will follow in the coming years. The further part of this article discusses the examples of the use of a hybrid approach for the diagnostics of one of the polish bridge and gas pipeline.

#### 5 EXAMPLE APPLICATION – THE CONCRETE BRIDGE IN NOWE MIĘSTO LUBAWSKIE

The analysed system concerns the road bridge over the Wel River, which is the longest and most technologically complex structure on the Polish national road DK15. This five-span bridge, with a total length exceeding 267 m, was built as part of the bypass around the city “Nowe Miasto Lubawskie”. The load-bearing structure of the bridge is a prestressed concrete box girder (Figure 8) with a structural height of 3.5 m. The installation of the box girder system using longitudinal launching technology was divided into 9 segments, each of which was cast in two stages. Due to certain concerns regarding the durability of the structure, it was decided to equip the existing bridge with a hybrid monitoring system, consisting of: 1) distributed fibre optic sensors for strain measurements and crack detection, and 2) automatic vibrating wire gauges for strain and temperature measurements continuous in time.





Figure 8. General view of the analysed bridge from the outside (top) and inside of the prestressed box (bottom).

Distributed strain sensors (EpsilonSensors) with an external braid were installed in four measurement lines (A, B, C, D) along the entire length of the bridge, achieving a total of 1040 meters of sensing path. Assuming a spatial resolution of the interrogator used at 5 mm, this results in a total of 208,000 measurement locations within a single session. Installing such a large number of spot gauges with cabling would be impossible both technically and economically. The sensors were installed inside the prestressed box in near-to-surface grooves using a dedicated mortar. Additionally, 4 sections were installed on the side wall of the box along the prestressing cables, with a total length of 44 m, by gluing the sensors without external braid directly to the surface (Figure 9).



Figure 9. Installation of the EpsilonSensors with braid in near-to-surface grooves (top) and without braid directly on the concrete surface (bottom).

For the automatic measurements, spot strain gauges in the form of vibrating wire transducers were chosen, installed in 3 cross-sections, with 4 gauges in each section. This resulted in a total of 12 measurement locations, additionally equipped with reference thermistors – Figure 10.

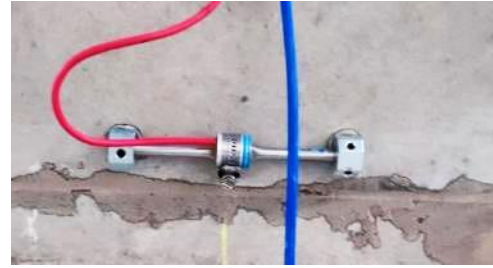


Figure 10. Example view of vibrating wire strain gauge (Geokon 4000) during installation.

The location of all the sensors (both spot gauges and distibued EpsilonSensors) within the hybrid system in question is shown in Figure 10.

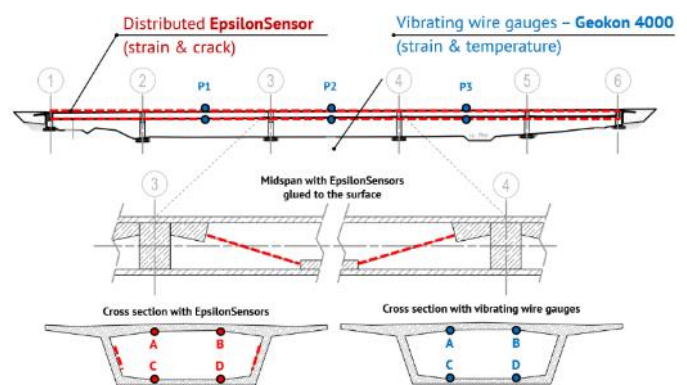


Figure 11. Location of distributed sensors (red) and vibrating wire gauges (blue) within the considered hybrid system.

An example of the strain and temperature plot as a function of time for a selected spot gauge is presented in Figure 12. The period under consideration is the first year of system operation, from July 2023 to July 2024. The obtained results indicate a complete dependency of strain on temperature changes on an annual basis, without any visible alarming trends. The graph shows three vertical blue lines marking the moments of periodic DFOS measurement sessions (S00, S01, and S02). The S00 session was the reference state (zero reading) for both independent techniques to enable their direct comparison.

On the other hand, the profile of the measured strains along the entire length of the central span (60 m) obtained during the periodic, but distributed measurements is presented in Figure 13. The DFOS-based strains profiles exhibit a smooth course, without distinct local extremes characteristic of cracking. Based on the measurements, no open cracks were found along the entire length of the bridge, which is a crucial piece of information for assessing the durability of the analysed structure. Local fluctuations are related to the typical behaviour of concrete as a heterogeneous material. During the first measurement session (S01), a temperature drop of approximately 30°C was recorded in reference to zero reading, which caused the bridge length to decrease due to thermal contraction (negative strain values). Measurements in session S02 were taken under similar thermal conditions to session S00, so the measured strain profile is close to the zero axis.



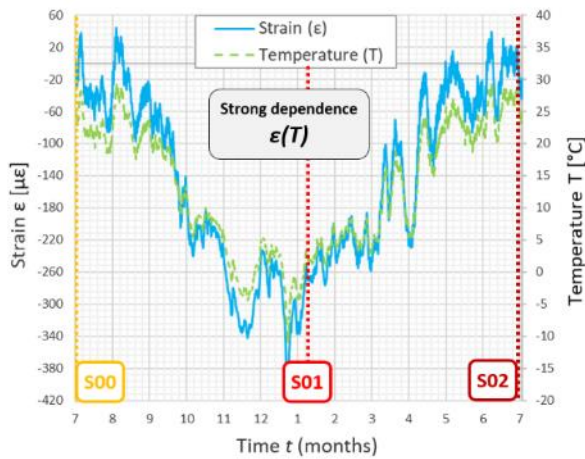


Figure 12. Example strain changes versus temperature changes over time at selected location.

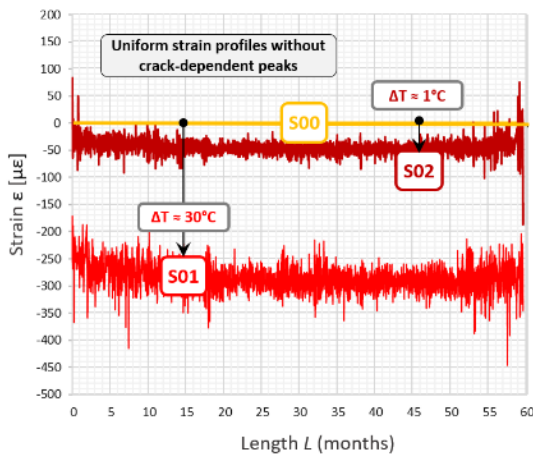


Figure 13. Example strain distribution along the central span in subsequent measurement sessions.

The data from the first year of system operation indicate the normal behaviour of the bridge (in accordance with theoretical predictions) under varying thermal conditions. No hazardous trends were identified through continuous measurements, nor were any local damages detected by distributed sensing.

## 6 EXAMPLE APPLICATION - PIPELINE

The second example concerns the high-pressure pipeline monitored with a hybrid approach. The general concept of the system is visualised in Figure 14. The installation included 12 vibrating wire strain transducers (Geokon 4150) arranged within four cross-sections (Figure 15). On the other hand, the entire 180 m long segment of the pipeline was equipped with distributed strain sensors (EpsilonRebas) and distributed shape sensors (3DSensors).

There were two types of installation approaches. The first one (and more challenging) included the gluing the strain sensors directly to the pipeline surface (Figure 16). On the other hand, both strain and displacements sensors were embedded in surrounding ground (Figure 17), which is relatively simple procedure. The goal of that was to analyse the quality and possible correlation of the data obtained with these two methods and thus to optimise the future installations.

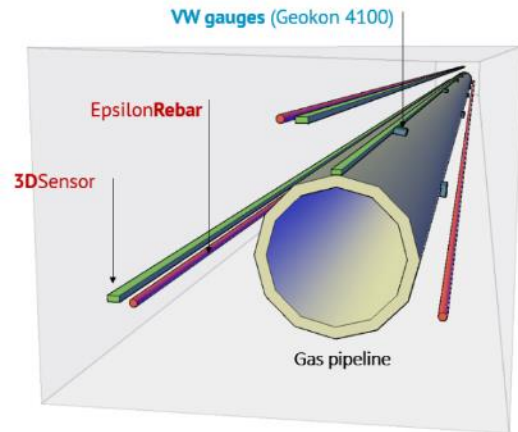


Figure 14. Visualisation of the hybrid monitoring system for the analysed gas pipeline segment



Figure 15. Vibrating wire gauges and their initial check during installation on the pipeline section.



Figure 16. Distributed strain sensors (EpsilonRebars) during the installation (just before gluing) directly on the pipeline.



Figure 17. Distributed displacement sensors (3DSensors) during the installation within the surrounding ground.

Figure 18 shows the analysed segment of the pipeline equipped with all the sensors in the final installation stage, right before backfilling the entire section with soil.



Figure 18. The view of the monitored section during final stage of installation (just before its backfilling with the soil).

The example data provided by the system in the first year of its operation are discussed hereafter. Figure 19 shows the relationship between strain and thermal changes measured by one of the spot gauges at a selected location. As with the previously presented bridge, the data indicate the normal, cyclic behaviour of the pipeline with no alarming trends. There is a full correlation between these two quantities, indicating that other potentially hazardous mechanical actions (e.g. mass movements, settlements, or sinkholes) are not present.

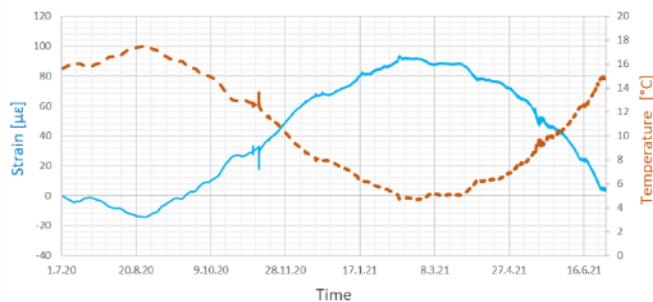


Figure 19. Example strain changes versus temperature changes over time at selected location.

Despite the importance of the above findings, it is not possible to determine the extreme strain (and stress) values or directly answer the question regarding the pipeline's state between measurement locations based on spot gauges. Since no significant deformations were identified throughout the entire year of operation, the results from the pressure test conducted before the pipeline was put into service were selected to demonstrate the capabilities of distributed measurements.

Figure 20 presents the influence of spiral welds, resulting in local distortions in strain profiles. These welds cause both tensile and compressive strains. In the theoretical analysis of a continuous pipeline section under the pressure test, only tensile strains are expected. A similar effect, but much stronger, was observed at the pipeline bends, as shown in Figure 21. Such effects are not always considered in engineering analysis during the design stage, nor are they detectable by conventional spot techniques. This is why the DFOS approach enhances the understanding of the structural performance of pipelines,

enabling better (safer) designs in future applications, as well as effective monitoring for optimised maintenance.

The last, but not least, example of DFOS data shows strain distributions at the beginning of the analysed section (Figure 22). Based on this, it is possible to estimate the length of the transition zone along which the friction between the pipeline and surrounding ground is mobilised. After this length, the mean strains in the pipeline section oscillate around zero due to full constraint.

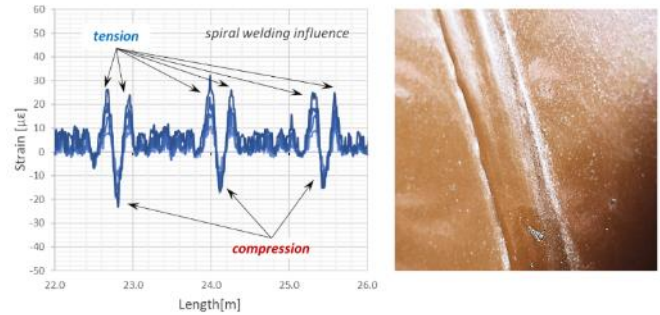


Figure 20. Distributed strain sensing results: the local influence of spiral weld along the length

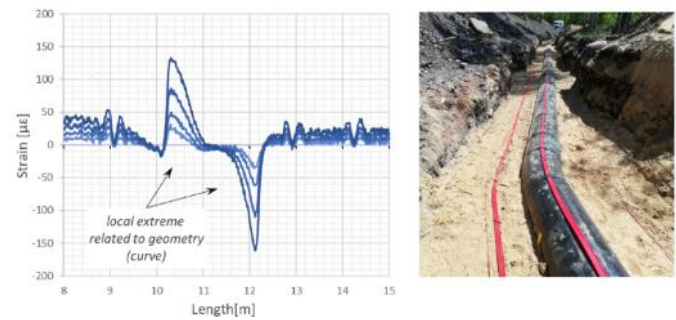


Figure 21. Distributed strain sensing results: the local influence of the turn (curve) along the length

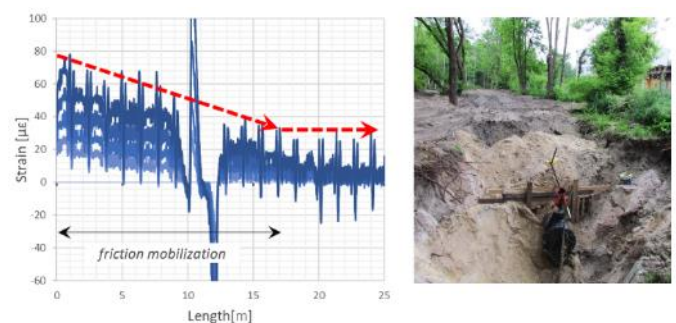


Figure 22. Distributed strain sensing results: the estimation of friction mobilisation at the beginning of the section

An important feature and, at the same time, an advantage of DFOS technology is its capability to measure various physical quantities using exactly the same sensors connected to different optical interrogators. In the present project, EpsilonRebars provided mechanical strain data, as shown above, but also enabled distributed temperature sensing (DTS) with a Raman-based interrogator. Example temperature profiles measured over three consecutive months along the entire length of the



monitored pipeline section are presented in Figure 23, alongside results from reference spot thermistors. The data comparison shows very good agreement, demonstrating the required accuracy of DFOS technology in practical field applications.

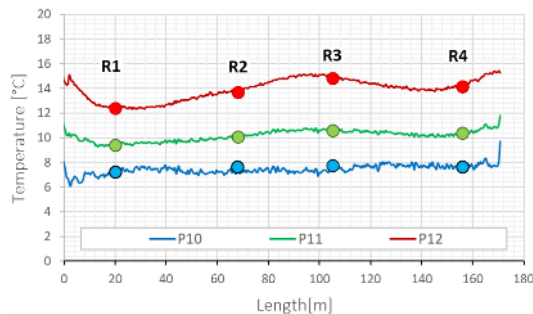


Figure 23. Example temperature distributions along the pipeline in three subsequent months versus results from reference spot thermistors (R1, R2, R3 and R4).

The temperature can be averaged over the entire length and presented in the time domain to observe changes on an annual basis and identify possible trends. Such data are presented in Figure 24 for three EpsilonRebars glued directly to the pipeline surface. The colours in the last three months correspond to the colours in the temperature distributions in Figure 24.

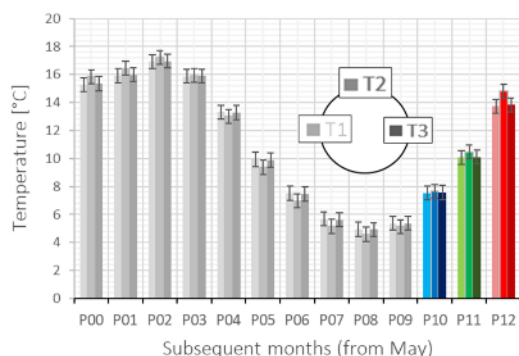


Figure 24. Mean temperature values from three EpsilonRebars in subsequent months over the entire year.

## 7 SUMMARY

The article discusses the concept and an example implementation of a hybrid monitoring system on a bridge and a gas pipeline. Thanks to the adopted approach, it was possible to obtain extensive information about the technical condition of these structures while maintaining economic feasibility.

In the first year of the systems' operation, the full correlation between strain and temperature over time was identified using automatic spot measurements. No concerning trends in the structures' performance (e.g., a monotonic increase in strains unrelated to temperature changes) were observed.

Meanwhile, periodic, geometrically continuous DFOS measurements enabled a detailed analysis in the length domain. In the case of the prestressed bridge structure, they confirmed that it remained in an uncracked state along its entire length - crucial information for assessing technical condition and structural safety. For the pipeline, DFOS provided deep

insights into the local influence of welds and geometrical bends on strain distribution, an aspect that could not be captured by other spot sensing technologies.

The technical effectiveness and economic benefits of hybrid monitoring systems, along with lessons learned from previous applications, suggest that this approach will be increasingly adopted in the structural health monitoring market in the near future, particularly within safety-critical infrastructure.

## ACKNOWLEDGMENTS

The research on monolithic sensors design was funded by European Funds through the National Centre for Research and Development under the Intelligent Development Operational Program 2014–2020, as part of the following projects:

- “Innovative Fibre Optic Sensor for Measuring Strain and Temperature” (POIR.01.01.01-00-1154/19),
- “Development of the new fibre optic sensor allowing for the determination of the vertical and horizontal displacements of the studied objects at the distances of up to 120 km” (POIR. 01.01.01-00-0550/15)

These projects were implemented by SHM System (Kraków, Poland, [www.shmsystem.pl](http://www.shmsystem.pl) (accessed on 10 March 2025), [www.nerve-sensors.com](http://www.nerve-sensors.com) (accessed on 10 March 2025)).

## REFERENCES

- [1] W. Radmoski, "Utrzymanie i diagnostyka mostów w aspekcie działalności rzeczoznawcy budowlanego," *Nowoczesne Budownictwo Inżynieryjne*, wrzesień-październik 2016.
- [2] M. H. Faber, *Statistics and Probability Theory in Pursuit of Engineering Decision Support*, Springer, 2012, ISBN 978-94-007-4055-6.
- [3] Y. L. Xu and Y. Xia, *Structural Health Monitoring of Long-Span Suspension Bridges*, Spon Press, 2012, ISBN 978-1138075634.
- [4] D. Balageas, C. P. Fritzen, and A. Güemes, *Structural Health Monitoring*, Wiley-ISTE, 2006, ISBN 978-1-905-20901-9.
- [5] C. Pellegrino, "Management of road bridge networks in Italy by means of integrated SHM systems," in *SMAR 2024 - 7th International Conference on Smart Monitoring, Assessment and Rehabilitation of Civil Structures*, Salerno, Italy, 4-6 września 2024.
- [6] G. Zhang, Y. Liu, J. Liu, S. Lan, and J. Yang, "Causes and statistical characteristics of bridge failures: A review," *Journal of Traffic and Transportation Engineering (English Edition)*, vol. 9, pp. 388–406, 2022. <https://doi.org/10.1016/j.jtte.2021.12.003>.
- [7] E. Dibiagio, "A case study of vibrating-wire sensors that have vibrated continuously for 27 years," in *Field Measurements in Geomechanics*, 2003, pp. 445–458. <https://doi.org/10.1201/9781439833483.ch59>.
- [8] Ł. Bednarski and R. Sieńko, "Pomiary odkształceń konstrukcji czujnikami strunowymi," *Inżynieria i Budownictwo*, nr 11, 2013.
- [9] Ł. Bednarski, R. Sieńko, and T. Howiacki, "Analysis of post-tensioned girders structural behaviour using continuous temperature and strain monitoring," *IOP Conf. Ser.: Earth Environ. Sci.*, vol. 92, p. 012003, 2017. <https://doi.org/10.1088/1755-1315/92/1/012003>.
- [10] A. Güemes, A. Fernández-López, and B. Soller, "Optical Fiber Distributed Sensing - Physical Principles and Applications," *Structural Health Monitoring*, vol. 9, pp. 233–245, 2010. <https://doi.org/10.1177/1475921710365263>.
- [11] H.-H. Zhu, W. Liu, T. Wang, J.-W. Su, and B. Shi, "Distributed Acoustic Sensing for Monitoring Linear Infrastructures: Current Status and Trends," *Sensors*, vol. 22, no. 19, p. 7550, 2022. <https://doi.org/10.3390/s22197550>.
- [12] T. Howiacki, R. Sieńko, Ł. Bednarski, and K. Zuziak, "Structural monitoring of concrete, steel, and composite bridges in Poland with distributed fibre optic sensors," *Structure and Infrastructure Engineering*, pp. 1–17, 2023. <https://doi.org/10.1080/15732479.2023.2230558>.
- [13] T. Siwowski, M. Rajchel, T. Howiacki, R. Sieńko, and Ł. Bednarski, "Distributed fibre optic sensors in FRP composite bridge monitoring: Validation through proof load tests," *Engineering Structures*, vol. 246, p. 113057, 2021. <https://doi.org/10.1016/j.engstruct.2021.113057>.
- [14] R. Sieńko, Ł. Bednarski, T. Howiacki, and K. Zuziak, "Composite and Monolithic DFOS Sensors for Load Tests and Long-Term Structural



- Monitoring of Road Infrastructure," in European Workshop on Structural Health Monitoring (EWSHM 2022), Springer, Cham, 2022. [https://doi.org/10.1007/978-3-031-07254-3\\_60](https://doi.org/10.1007/978-3-031-07254-3_60).
- [15] R. Sieńko, Ł. Bednarski, T. Howiacki, K. Zuziak, and Ch. Monsberger, "Monitorowanie tunelu i jego otoczenia z wykorzystaniem strunowej i światłowodowej techniki pomiarowej DFOS," *Drogownictwo - Road Engineering*, vol. 7, 2022, ISSN 0012-6357.
- [16] I. Vidovic and S. Marschnig, "Optical Fibres for Condition Monitoring of Railway Infrastructure - Encouraging Data Source or Errant Effort?" *Applied Sciences*, vol. 10, no. 17, p. 6016, 2020. <https://doi.org/10.3390/app10176016>.
- [17] Ł. Bednarski, T. Howiacki, R. Sieńko, and K. Zuziak, "Distributed Fibre Optic Sensors (DFOS) in Measurements of Rail Strain and Displacements," in SMAR 2024 - 7th International Conference on Smart Monitoring, Assessment and Rehabilitation of Civil Structures, Salerno, Italy, 4-6.09.2024.
- [18] B. Bednarz, P. Popielski, R. Sieńko, T. Howiacki, and Ł. Bednarski, "Distributed Fibre Optic Sensing (DFOS) for Deformation Assessment of Composite Collectors and Pipelines," *Sensors*, vol. 21, p. 5904, 2021. <http://doi.org/10.3390/s21175904>.
- [19] B. Piątek, T. Howiacki, M. Kulpa, T. Siwowski, R. Sieńko, and Ł. Bednarski, "Strain, crack, stress and shape diagnostics of new and existing post-tensioned structures through distributed fibre optic sensors," *Measurement*, vol. 113480, 2023. <http://doi.org/10.1016/j.measurement.2023.113480>.
- [20] T. Howiacki, R. Sieńko, Ł. Bednarski, and K. Zuziak, "Crack Shape Coefficient: Comparison between Different DFOS Tools Embedded for Crack Monitoring in Concrete," *Sensors*, vol. 23, p. 566, 2023. <http://doi.org/10.3390/s23020566>.
- [21] T. Howiacki, "Analysis of cracks in concrete structures with the use of distributed optical fibre measurements," Ph.D. dissertation, Faculty of Civil Engineering, Cracow University of Technology, Poland, 2022.
- [22] T. Siwowski, R. Sieńko, Ł. Bednarski, M. Rajchel, and T. Howiacki, "Światłowodowe pomiary odkształceń elementów mostów kompozytowych na przykładzie wybranych badań," in *Wrocławskie Dni Mostowe. MOSTY. Przemiany w projektowaniu i technologiach budowy*, Wrocław, Poland, Nov. 2017.
- [23] R. Sieńko, Ł. Bednarski, and T. Howiacki, "Pomiary deformacji mostu podwieszonego z wykorzystaniem światłowodowych czujników geometrycznie ciągłych DFOS," in *Wrocławskie Dni Mostowe. Mosty hybrydowe*, Wrocław, Poland, Nov. 2018.
- [24] R. Sieńko, Ł. Bednarski, and T. Howiacki, "Smart Composite Rebars Based on DFOS Technology as Nervous System of Hybrid Footbridge Deck: A Case Study," in *European Workshop on Structural Health Monitoring. Special Collection of 2020 Papers, Volume 2*, Springer, 2021, pp. 340-350. ISBN: 978-3-030-64908-1.
- [25] J. Biliszczuk, T. Howiacki, and K. Zuziak, "Heightened sensitivities: fibre optic sensing-based insight into crack-width changes on Polish link," *Bridge Design & Engineering*, vol. 109, 2022.
- [26] R. Sieńko, Ł. Bednarski, and T. Howiacki, "University bridge in Bydgoszcz: Distributed fibre optic measurements (DFOS) of steel anchorages during their renovation," in *30th International Conference on Structural Failures, Międzyzdroje, Poland, 2022*.
- [27] R. Sieńko, Ł. Bednarski, T. Howiacki, K. Makowska, K. Topolewicz, and M. Topolewicz, "Wykorzystanie Czujników Światłowodowych DFOS w Czasie Obciążeń Próbných Mostów," in *Wrocławskie Dni Mostowe OBIEKTY KOLEJOWE*, Wrocław, Poland, Nov. 2023.
- [28] K. Kishida, Y. Yamauchi, and A. Guzik, "Study of optical fibers strain-temperature sensitivities using hybrid Brillouin-Rayleigh system," *Photonic Sensors*, vol. 4, pp. 1-11, 2013. <http://doi.org/10.1007/s13320-013-0136-1>.
- [29] Ł. Bednarski, R. Sieńko, M. Grygierek, and T. Howiacki, "New Distributed Fibre Optic 3DSensor with Thermal Self-Compensation System: Design, Research and Field Proof Application Inside Geotechnical Structure," *Sensors*, vol. 21, p. 5089, 2021. <http://doi.org/10.3390/s21155089>.
- [30] M. Amanzadeh, S. M. Aminossadati, M. S. Kizil, and A. D. Rakić, "Recent developments in fibre optic shape sensing," *Measurement*, vol. 128, pp. 119-137, 2018. <http://doi.org/10.1016/j.measurement.2018.06.034>.
- [31] F. Bastianini, R. Di Sante, F. Falcetelli, D. Marini, and G. Bolognini, "Optical Fiber Sensing Cables for Brillouin-Based Distributed Measurements," *Sensors*, vol. 19, p. 5172, 2019. <http://doi.org/10.3390/s19235172>.
- [32] M. S. Bado and J. R. Casas, "A Review of Recent Distributed Optical Fiber Sensors Applications for Civil Engineering Structural Health Monitoring," *Sensors*, vol. 21, p. 1818, 2021. <http://doi.org/10.3390/s21051818>.
- [33] Ł. Bednarski, R. Sieńko, T. Howiacki, and K. Zuziak, "The Smart Nervous System for Cracked Concrete Structures: Theory, Design, Research, and Field Proof of Monolithic DFOS-Based Sensors," *Sensors*, vol. 22, p. 8713, 2022. <http://doi.org/10.3390/s22228713>.

## Water distribution pipeline anomaly detection using distributed acoustic sensing (DAS)

Maksymilian Jasiak<sup>1</sup>, Shih-Hung Chiu<sup>1</sup>, Jaewon Saw<sup>1</sup>, Peter Hubbard<sup>2</sup>, David Katzev<sup>3</sup>, Kenichi Soga<sup>1</sup>

<sup>1</sup>Department of Civil and Environmental Engineering, University of California, Berkeley, USA

<sup>2</sup>FiberSense, USA

<sup>3</sup>East Bay Municipal Utility District, USA

email: jasiak@berkeley.edu, shchiu@berkeley.edu, jaewon.saw@berkeley.edu,  
peter.hubbard@fibersense.com, david.katzev@ebmud.com, soga@berkeley.edu

**ABSTRACT:** Leak detection for water pipelines, and anomaly detection more broadly, is vital to ensuring reliable access to drinking water. Monitoring transmission and distribution pipelines supports proactive fault detection to reduce water loss amid deteriorating infrastructure and depleting water resources. Distributed acoustic sensing (DAS) in the form of phase-sensitive optical time-domain reflectometry ( $\phi$ -OTDR) can quantify vibrations and sound along fiber optic cables over long distances with high spatial resolution and frequency. In this study, DAS was deployed on a new fiber optic cable-instrumented pipeline to investigate DAS sensitivity to pipe water leakage noise. A reproducible workflow for system deployment and signal processing aimed at pipe water leak detection in field conditions is presented. The influence of fiber optic cable type (tight-buffered vs. loose tube) and installation condition (pipe-mounted vs. trench-lain) on DAS sensitivity was assessed during pipe water filling and simulated leakage. Findings demonstrate relatively high sensitivity to water leak noise detection when DAS is deployed on fiber optic cables near the pipeline. This informs best practices for data-driven pipeline monitoring by presenting a reproducible procedure to operationalize water pipeline leak detection using DAS.

**KEY WORDS:** Water pipeline leak detection; Distributed fiber optic sensing (DFOS); Distributed acoustic sensing (DAS).

### 1 INTRODUCTION

Water leak detection on transmission and distribution pipeline networks is critical to reduce water loss. Growing challenges, such as deteriorating infrastructure and depleting water resources, highlight the need for resilient water infrastructure to ensure reliable access to drinking water. Proactive monitoring plays an important role in helping track down unaccounted non-revenue water losses across geographically distributed pipeline systems. Monitoring also helps water supply agencies effectively predict life expectancy and plan maintenance and rehabilitation of lifeline pipelines. Furthermore, water infrastructure monitoring in low-resource environments is vital for resilient asset management in vulnerable communities.

Conventional methods for pipeline water leak detection are often limited in their balance of scale or spatial resolution. Satellite sensing with synthetic aperture radar (SAR) as well as unmanned aerial vehicle (UAV) sensing with multi-spectral or thermal imaging can detect elevated levels of underground soil moisture caused by leaking water. These offer regional-scale monitoring, but at relatively low spatial resolution. Various pipe-mounted or in-pipe point sensors can detect leakage-related water pressure drops or acoustic emissions, but their scale and spatial resolution is dependent on sensor density (which scales poorly due to high installation and maintenance costs). Ground penetrating radar (GPR) to detect subsurface moisture and listening sticks to listen for water leakage noise can offer pipe segment scale and spatial resolution, but their large-scale deployment is constrained by slow manual labor. In short, conventional methods balance between scale and spatial resolution due to technical constraints. As a result, they typically need to be deployed in parallel to attempt comprehensive monitoring of entire pipeline networks.

However, regional-scale sensing with meter-level spatial resolution is in fact achievable with Distributed Fiber Optic Sensing (DFOS). This family of technologies is at the forefront of large-scale infrastructure performance monitoring of strain, temperature, vibrations, and sound along fiber optic cables over long distances at a high spatial resolution with high measurement frequencies [1]. Distributed acoustic sensing (DAS) in the form of phase-sensitive optical time-domain reflectometry ( $\phi$ -OTDR) has proven uniquely suitable for vibration and sound monitoring of linear civil infrastructure such as offshore wind turbines [2][3], roadways [4], boreholes [5], and pipelines [6][7]. Furthermore, DAS has proven an effective tool even in noisy acoustic environments [8].

Previous work has investigated ground movement-induced pipeline deformation, a common cause of pipe water leakage, in both laboratory and field conditions using Distributed Strain and Temperature Sensing (DSTS) [9][10][11]. This study builds on this work to develop robust methods to directly investigate pipe water leakage by characterizing the distributed acoustic signal of typical and atypical pipeline activities. DAS was deployed on a new 120 m (394 ft) segment of 15.3 cm (6-inch) Earthquake Resistant Ductile Iron Pipe (ERDIP) in a residential neighborhood within the Hayward Fault Zone in Berkeley, California. This new pipeline replaced the old existing pipe which had previously experienced multiple main breaks and major leakage events.

Operationalizing DAS involves implementing an interpretable and reproducible workflow for system deployment and signal processing. Data gathering should be grounded in domain knowledge encompassing real world conditions and decisions and adaptable to past, present, and future data. Data processing should support: 1) predictable outputs withstanding scrutiny from reality checks; 2) computationally efficient use of data storage and processing resources; 3) stability under perturbations in input data and data

gathering and processing judgement calls [12]. In this context, this study presents a reproducible workflow for DAS system deployment and signal processing aimed at pipe water leak detection in field conditions.

## 2 DAS METHOD

Distributed Fiber Optic Sensing (DFOS) quantifies backscattered light in optical fibers to quantify strain, temperature, or vibrations and sound. DFOS involves a sensing device (optical interrogator) connected to one end of a long linear sensor (fiber optic cable). The interrogator sends pulses of light through the optical fiber core of the cable. As these light pulses travel through the core, they interact with imperfections in the silica glass material and are backscattered. Light is backscattered in three typical mechanisms: Raman, Brillouin, and Rayleigh scattering. These mechanisms are sensitive to changes in temperature, strain, or vibrations/sound along the fiber. Rayleigh backscattered light is detected by the interrogator and processed with optical interferometry for distributed acoustic sensing (DAS) [1]. Specifically, phase-sensitive optical time-domain reflectometry ( $\phi$ -OTDR) uses the phase change  $\Delta\phi$  of coherent Rayleigh backscattering to quantify vibrations and sound as dynamic strain  $\varepsilon$  given a known operational wavelength  $\lambda$ , fiber refractive index  $n$ , gauge length  $G$ , and photoelastic scaling factor  $\xi$  [8].

$$\varepsilon = \frac{\lambda}{4\pi n G \xi} \Delta\phi \quad (1)$$

### 2.1 System selection

A DAS system includes a sensing device (optical interrogator) and sensor (fiber optic cable). Optical interrogator hardware and data acquisition parameter selection must ensure adequate sensing range, sampling frequency, spatial resolution, and sampling interval to capture the signal of interest. The sensing range must be sufficiently long to capture measurements along the entire sensing fiber. Sampling frequency should ensure sufficient temporal resolution to capture signals of interest at frequencies below the Nyquist frequency. For context, the Nyquist frequency is the highest frequency that can be accurately measured in a discrete signal and is typically defined as half the sampling frequency. In short, sampling frequency should be greater than double the expected frequency of the signal of interest. Spatial resolution (gauge length) [13] and sampling interval (gauge pitch or channel spacing) [14] depend on optoelectronic hardware component capabilities. In short, spatial resolution and sampling interval should be sufficiently low to capture localized signals along the fiber. Generally, data acquisition parameters are limited by hardware limitations and data processing constraints.

In this study, data acquisition parameters were set to a sampling frequency up to 100 kHz, a minimum spatial resolution of 2 m, and a minimum sampling interval of 1 m for 690 m total sensing fiber length using an OptaSense ODH4 DAS interrogator unit. Note, the 100 kHz raw ping rate was decimated down to 25 kHz during data acquisition and down to 5 kHz during data processing for reasons explained later.

Fiber optic cable selection must ensure proper protection of the optical fiber core and adequate coupling between the core and the external environment. Protecting the optical fiber core from moisture, chemicals and physical damage in the external

environment is necessary to ensure fiber survival. This protection is achieved through various layers separating the central core from the outer cable jacket. Two typical protection designs are tight-buffered (Figure 1) and loose-tube (Figure 2). Tight-buffered cables tightly envelop the optical fiber with a plastic buffer to protect from moisture, steel reinforcement wires to protect from physical damage, and a plastic outer jacket to serve as a fluid barrier. Loose-tube cables loosely suspend the optical fiber with gel-filled tube to protect from excessive tension or bending, surrounded by aramid yarn and a plastic outer jacket to protect from fluid moisture.

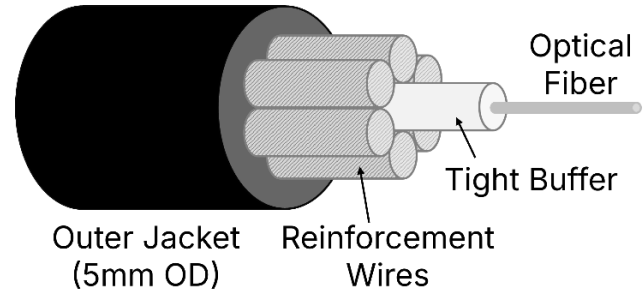


Figure 1. Tight-buffered fiber optic cable

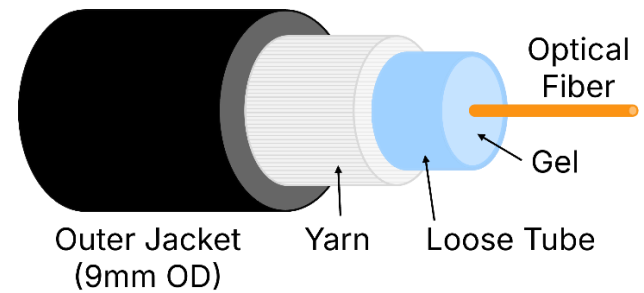


Figure 2. Loose-tube fiber optic cable

In terms of DFOS performance, the tight layer boundaries of tight-buffered cables provide a high degree of strain transfer from the outside environment to the fiber optical core. This enables high acoustic signal transmission from outside the cable to the fiber core. On the other hand, the gel-suspension layer boundary in loose-tube cables results in a significantly lower degree of strain transfer from the outside environment to the fiber optical core. This results in lower acoustic signal sensitivity from outside the cable to the fiber core.

In terms of durability and long-term environmental longevity, tight-buffered cables are more rugged and flexible during handling and installation but less resistant to extreme environmental conditions. On the other hand, loose-tube cables are more fragile during installation, but more resistant to hard environments with significant moisture and temperature changes. As a result, tight-buffered cables are typically used for DFOS applications or short-distance telecommunications, while loose-tube cables are used for long-distance telecommunications. Accordingly, tight-buffered cables are often more expensive due to lower niche demand, while loose-tube cables are more affordable given the high demand during mass deployment in global telecommunications networks.

In this study, tight-buffered cables and loose-tube fiber optic cables were both used to compare their DAS sensitivity to



pipeline water leakage noise. Tight-buffered cables were sourced from NZ Sensing (NZS-DSS-C02). Loose-tube cables were sourced from Belden (FSSC002N0).

## 2.2 System deployment

DAS system sensitivity is influenced by the ability of the signal of interest to reach the fiber optic cable. The closer the cable sensor is to the signal source, the better the dynamic strain transfer-related acoustic signal transmission between the cable outer jacket and the fiber core, the better the DAS sensitivity.

If it is possible to install fiber optic cables designated for DAS directly on the monitored structure, they should be positioned as close as possible to the expected signal source location. Structure-mounted (or even structure-embedded) fiber optic cables intuitively offer the best DAS sensitivity. Installing both tight-buffered and loose-tube fiber optic cables supports DSTS (tight-buffered cables with high strain transfer for strain sensing vs. loose-tube cables with low strain transfer for temperature sensing). In the case of DAS, installing both enables a robust comparison between the two. However, deploying structure-mounted fiber optic cables has financial and logistical challenges due to the material and labor cost associated with custom installations.

Instead, existing buried fiber optic cables can be used. Conveniently, these existing cables are widespread under city streets in urban areas with fiber optic internet and telecommunications networks. This provides a cost-effective opportunity to deploy DAS on “dark” (currently unused) fibers in these existing cables without having to install new cables. However, deploying dark fiber DAS on existing telecommunications cables has two significant challenges: 1) existing cables may not be close to the monitored structure and 2) existing cables typically have a loose-tube (either gel-filled or air-filled) internal structure. This results in typically lower dark fiber DAS sensitivity using these types of existing cables.

In short, structure-mounted fiber optic cables offer superior DAS sensitivity but require resources to deploy, while existing buried fiber optic cables offer a convenient low-cost sensor but have lower DAS sensitivity. Using dark (unused) telecom fibers offer unique opportunities for widespread urban DAS activity monitoring. However, quantifying dark fiber DAS sensitivity to pipe water leakage remains a technical challenge.

In this study, both characteristic cable configurations were simulated to investigate their influence on DAS sensitivity to pipeline water leakage noise. Four sensing cable type and location configurations were deployed: 1) pipe-mounted tight-buffered; 2) pipe-mounted loose-tube; 3) trench-lain loose-tube; 4) trench-lain tight-buffered (Figure 3). Pipe-mounted cables were epoxied along the top of the pipe directly to the external pipe wall (Figure 4). A generic field-grade epoxy (toughened methacrylate adhesive system) was used to securely attach the fiber optic cables to the outer surface of the top of the pipe. Cables were aligned and epoxied straight along each approximately 6 m (20 ft) pipe segment. A small loop of slack cable was left at each joint between pipe segments to accommodate the discontinuity in the pipeline surface. Overall, the pipe-mounted cable installation process had a productivity of about 30 minutes per pipe segment. This time was primarily spent on placing and smoothing out the epoxy along the cables.

Trench-lain cables were aligned parallel to the pipeline and laid out on the bottom of the excavated pipe trench (Figure 5).

This process was relatively fast and did not require any specialized tools. Reasonable effort was taken to ensure the cables were aligned straight along the pipeline with an approximately 5 cm offset from the side of the pipe.

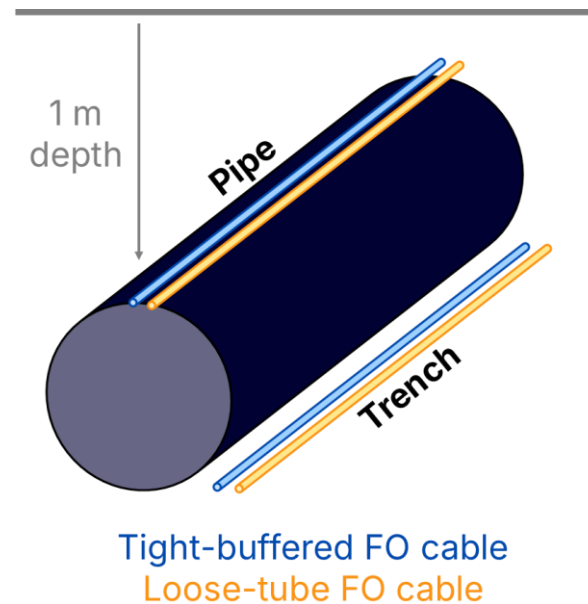


Figure 3. Fiber optic-instrumented pipeline

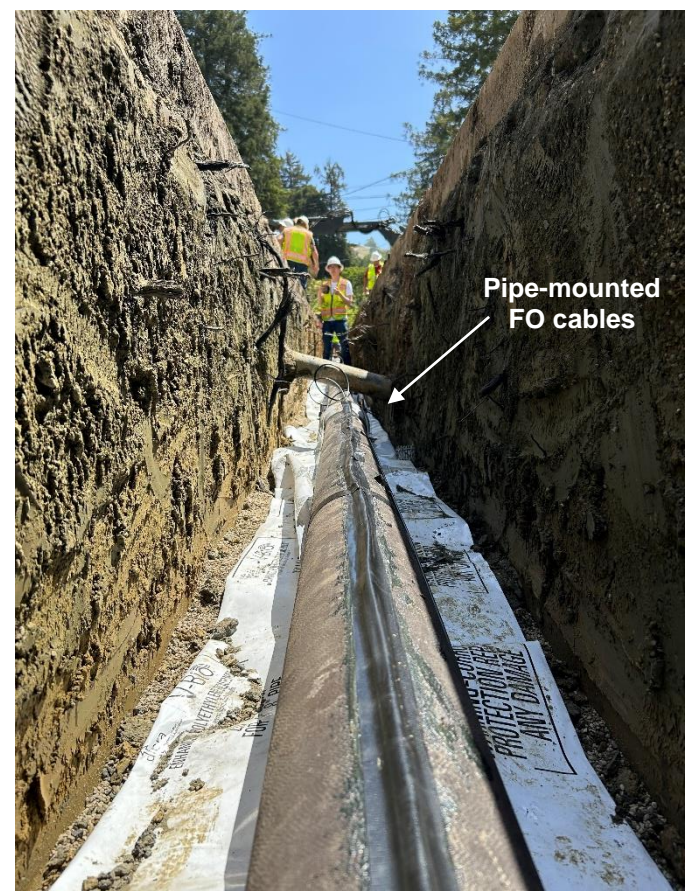


Figure 4. Pipe-mounted fiber optic cable installation

Regarding fiber protection, no additional protection measures were taken. This was to simulate a simple direct-



burial fiber cable installation process. After fiber optic cables were epoxied to the pipeline and lain in the trench, the entire trench was backfilled with coarse sand. The backfill material (Class I backfill) is a typical crushed stone manufactured aggregate used in pipeline construction in the region. The trench backfill material was poured into the trench and was not compacted. A final thin layer of pavement subbase layer of coarse aggregate was placed on top of the trench backfill. This pavement subbase was compacted at the ground surface.



Figure 5. Trench-lain fiber optic cable installation

These four combinations were compared to investigate the influence of fiber-environment coupling conditions. Pipe-mounted cables were expected to exhibit higher DAS sensitivity to signals originating from the pipeline than trench-lain cables. Tight-buffered cables were expected to exhibit lower noise levels with a higher signal-to-noise (SNR) ratio than loose-tube cables with higher noise and lower SNR.

DAS measurements were performed during pipeline commissioning in which this 120-meter pipeline section was connected to the wider water distribution pipeline network. After the two ends of this pipeline was physically connected to the network with valves, the commissioning process involved 1) filling the empty pipe with water and 2) high flow flushing water through the pipe to flush out random debris.

During both tasks, a valve was opened at the downhill end of the pipe to allow water from the pressurized network to flow into the pipe, and a second valve at the uphill end of the pipe was open to air pressure. This water then flowed up into the pipe and filled the pipe with a velocity of approximately 0.7 m/s (2.3 ft/s). This filling process took approximately 180 seconds to fill 120 m of pipe. This meant that once the water level inside the pipeline reached the uphill valve, water would flow out to the ground surface. In the case of the second task, the high flow flushing process resulted in water violently

erupting into the air (Figure 6). These conditions uniquely resembled a violent pipeline break and high flow pipe water leakage. This presented an opportunity to quantify DAS signal characteristics during simulated pipe water leakage.



Figure 6. Simulated leakage at uphill end pipe valve

### 2.3 Signal processing

Analysis of  $\phi$ -OTDR DAS data started with downsampling the raw measured phase shift data to reduce dataset size while preserving key signal characteristics. The 100 kHz interrogator ping rate was decimated down to 25 kHz during data acquisition and down to 5 kHz during data processing to reduce computational costs and facilitate data handling. Data acquisition decimation was performed by a proprietary OptaSense algorithm inside the ODH4 operating software. Data processing decimation was performed by filtering (order 8 Chebyshev type I zero-phase anti-aliasing digital filter) and downsampling the signal. This effective sampling rate of 5 kHz with a Nyquist frequency of 2.5 kHz was sufficiently high to capture the relatively acoustic signal of pipeline water flow.

Next, phase change  $\Delta\phi$  was related to dynamic strain  $\varepsilon$  as presented earlier (Equation 1). Next, frequency band extraction (FBE) was used to inspect the acoustic signal energy content at a specific frequency band appropriate for pipe water leakage noise. Given the dynamic strain spatial timeseries  $x_{ch}(t)$  across time  $t$  for each channel location  $ch$ , each timeseries is divided into time frames and windowed with a periodic Hann window applied to each frame  $w(t)$ , and detrended by subtracting the mean value within the time frame  $\mu_{ch}$ .

$$\tilde{x}_{ch}(t) = (x_{ch}(t) - \mu_{ch}) \cdot w(t) \quad (2)$$

Detrending helps remove low-frequency signal drift, while windowing helps reduce spectral leakage in the signal [12][15]. A Fast Fourier Transform (FFT) is then then applied to the detrended and windowed signal.

$$X_{ch}(f) = FFT(\tilde{x}_{ch}(t)) \quad (3)$$

Next, the power spectrum for each channel is estimated on the FFT and scaled based on the FFT size  $N_{FFT} = 256$ , sampling frequency  $f_s$ , and energy correction factor  $C_w = \sqrt{8/3}$  for Hann window coherency gain.

$$P_{ch}(f) = \frac{2}{N_{FFT} \cdot f_s} \cdot |X_{ch}(f)|^2 \cdot C_w \quad (4)$$

Afterwards, the frequency band extracted (FBE) power for each channel is extracted by averaging the power across the number of frequency bins  $N_f$  within the target frequency band from  $f_{min}$  to  $f_{max}$ .

$$FBE_{ch} = \frac{1}{N_f} \sum_{f_{min}}^{f_{max}} P_{ch}(f) \quad (5)$$

Finally, the mean FBE power in the frequency band is expressed on a logarithmic scale as decibels (dB).

$$FBE_{ch}^{dB} = 10 \log_{10} FBE_{ch} \quad (6)$$

Given the initial input strain spatial time series in units of microstrain  $\mu\epsilon$ , the units of FBE power are  $dB(\mu\epsilon^2/Hz)$ . The FBE power spatiotemporal trend was visualized along the entire fiber length using a waterfall plot format of space (y axis) vs. time (x axis) vs. FBE power (pixel color). This full fiber signal encompassed multiple pipe-sensing strands on the pipe or in the trench separated by intermediate fiber sections which were spliced together at pull boxes at either end of the pipeline. By inspection, the start/end points of each relevant sensing strand were indexed, and the dataset was partitioned by strand. FBE power was compared between the four combinations of cable type and installation location to assess acoustic signal quality and identify channels with signals of interest.

These signals of interest were then evaluated using channel-specific spectrograms and magnitude spectra. Spectrograms visualize signal power spectral density (PSD) across frequencies and time. The spectrogram is computed using the short-time Fourier transform (STFT) with a Hann window  $N_{window} = 2048$ , overlap of 50%, and FFT size  $N_{FFT} = 1024$ .

$$S(t, f) = STFT(\tilde{x}_{ch}(t)) \quad (7)$$

PSD is then computed on the STFT across frequency and time and reported as decibels (dB/Hz).

$$PSD(t, f) = 10 \log_{10}(|S(t, f)|^2) \quad (8)$$

The magnitude spectrum visualizes signal magnitude  $M$  at various frequencies. The magnitude spectrum in decibels (dB) is computed on the FFT across the total signal frequency range.

$$M = 20 \log_{10}|X_{ch}(f)| \quad (9)$$

To compare different characteristic signals of interest, signal-to-noise (SNR) ratio was computed using root-mean-square amplitude of the signal  $A_{signal}$  and “noise” (absence of signal of interest)  $A_{noise}$  strain timeseries using the expressed as decibels (dB).

$$SNR = 20 \log_{10} \left( \frac{A_{signal}}{A_{noise}} \right) \quad (10)$$

### 3 DAS RESULTS

DAS measurements were performed continuously during a 1-hour pipeline commissioning procedure to capture acoustic signals during three characteristic processes (Figure 7):

- 1) water flow as the pipe is filled with water
- 2) pressure transient-related resonance vibrations
- 3) simulated leakage

First, time-domain signals during both characteristic processes were explored by visualizing FBE power across time and space. Waterfall plots of FBE power were created using DAS measurements from all signal channels along the 120-meter pipeline. Furthermore, to facilitate comparing DAS sensitivity between the four cable deployment configurations, signals from each were plotted in four stacked subplots.

Second, frequency-domain signals were investigated at the simulated leakage location at the uphill end valve. DAS measurements from channel 120 (location 120 meters) were selected for this purpose. Acoustic signal frequency content over time was explored with spectrograms. Signal baselines were assessed with time-independent magnitude spectra and quantified with signal-to-noise (SNR) ratio to compare between the four sensing cable configurations. Note, SNR was computed using the same strain amplitude signals used to compute the magnitude spectrum of the “signal” and “noise” spectrum. In full transparency, SNR was computed for the full pipe signal relative to the empty pipe noise (water flow detection), resonance signal relative to the no resonance noise (pressure transient detection), leaking pipe signal relative to the full pipe noise (leakage detection).

Ultimately, the objective of this proof-of-concept experimental setup was to explore DAS signals from fiber optic cables along a water distribution pipe in the context of local installation methods and environmental conditions.

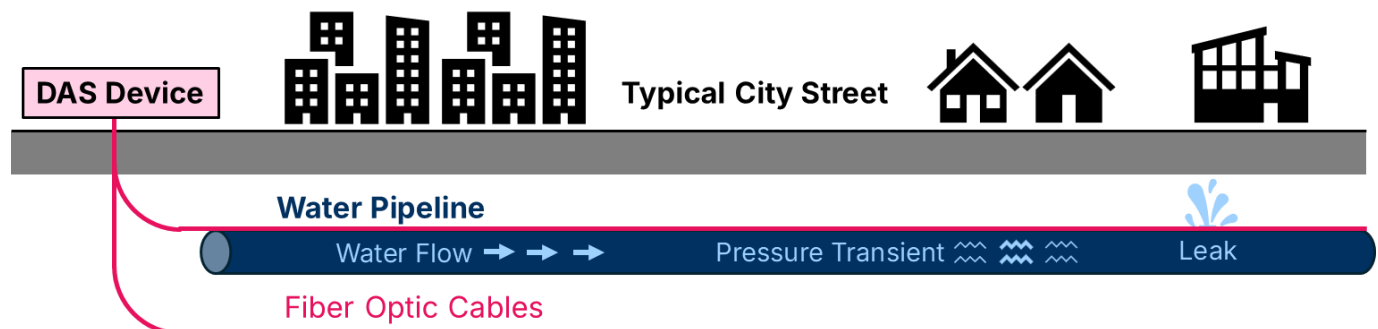


Figure 7. DAS for water pipeline monitoring



### 3.1 Water flow detection

DAS sensitivity to water flow inside the pipe during water filling was investigated. Water flowed into the empty pipe from the downhill end valve. The uphill end valve was open to air pressure. This resulted in a rising water level inside the inclined pipe (Figure 8). As the water level advanced up pipe, water flow and sloshing emitted vibrations and sound. This characteristic acoustic signal was detected and tracked across time along the pipeline. The spatiotemporal trend of 10 to 100 Hz frequency band extracted (FBE) reveals the advancing water level from the downhill end (location 0 m) to the uphill end (location approx. 120 m) (Figure 9). Signal visibility is best on tight-buffered cable on pipe, and progressively worse for other sensing configurations.

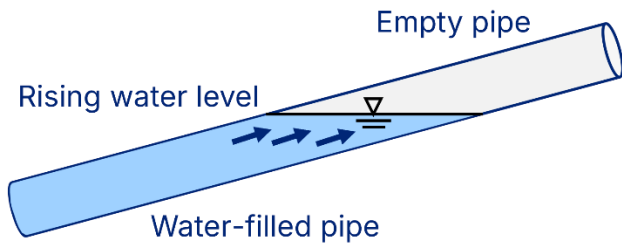


Figure 8. Pipe water flow condition

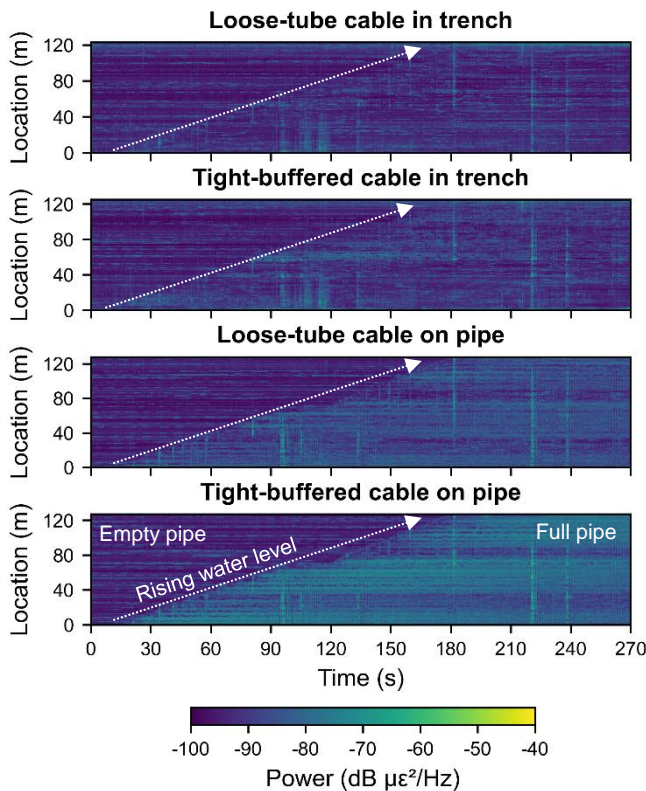


Figure 9. 10 to 100 Hz FBE power during pipe water filling

Spectrograms of frequency-domain signals at the uphill pipe end (location 120 m) reveal a characteristic jump in PSD at 0 to 400 Hz frequencies as the water level passes (Figure 10). This PSD signal is similarly visible on all sensing configurations. Differences in magnitude spectra before and after water level arrival highlight the relatively high SNR between the empty pipe noise floor and the water-filled pipe signal on all sensing configurations (Figure 11).

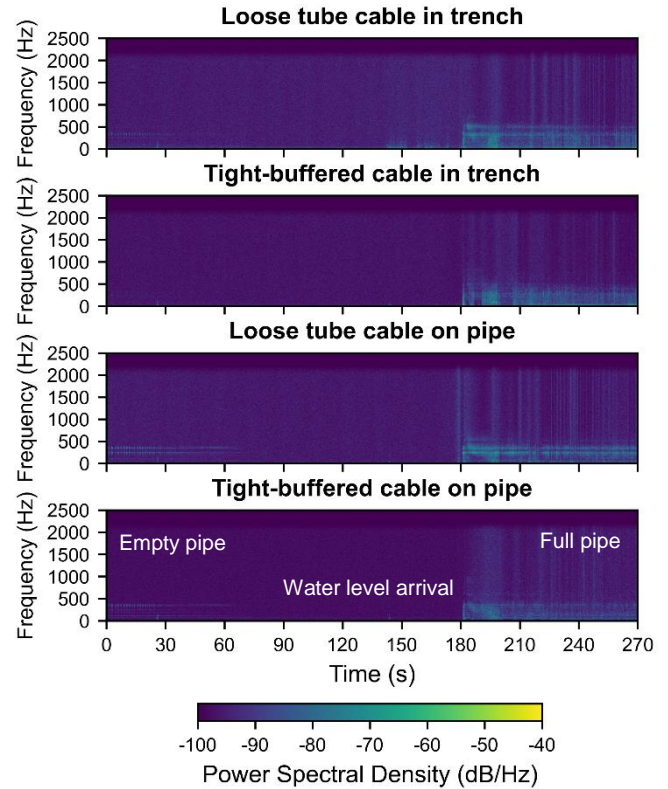


Figure 10. Spectrogram during passing water level

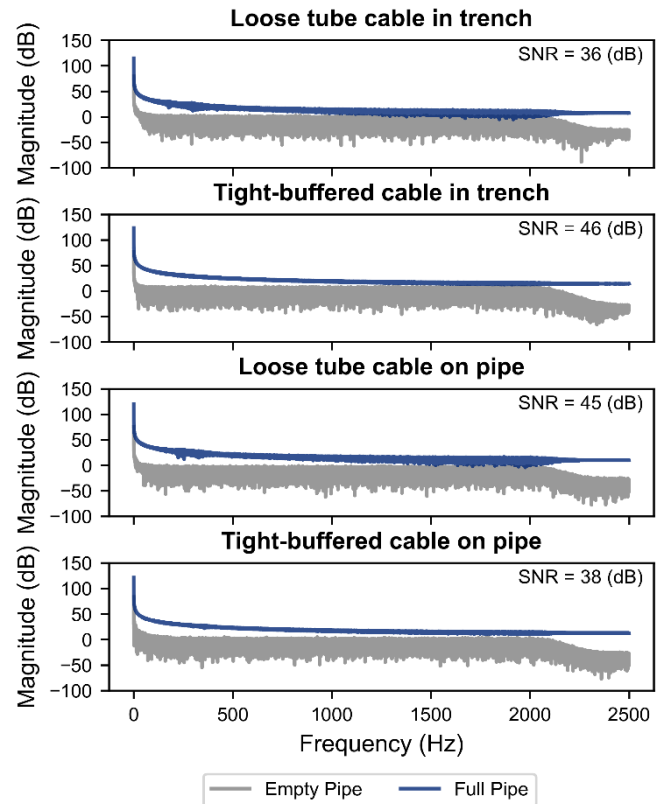


Figure 11. Magnitude spectra during passing water level

In short, DAS detected pipe water flow on all four sensing cable configurations. FBE Power signal is most visible on tight-buffered cable on pipe. Nonetheless, frequency-domain signal was relatively similar on all four sensing cable configurations.

### 3.2 Pressure transient detection

DAS sensitivity to pipe water pressure transients was assessed. After the pipe was filled and the simulated leakage experiment was finished, the final steps of the pipeline commissioning procedure were performed. During this time, a water pressure transient was detected (Figure 12). FBE power from 2 to 20 Hz reveals a 10 second period of elevated acoustic signal along the entire pipeline (Figure 13). The resonant acoustic signal grows, stabilizes, and then disappears. It is most visible on the tight-buffered cable on the pipe, with progressively lower visibility on the other cable configurations.

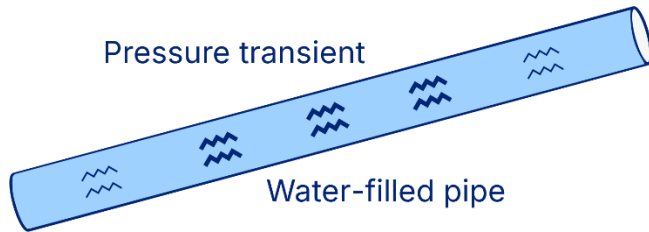


Figure 12. Pipe water pressure transient condition

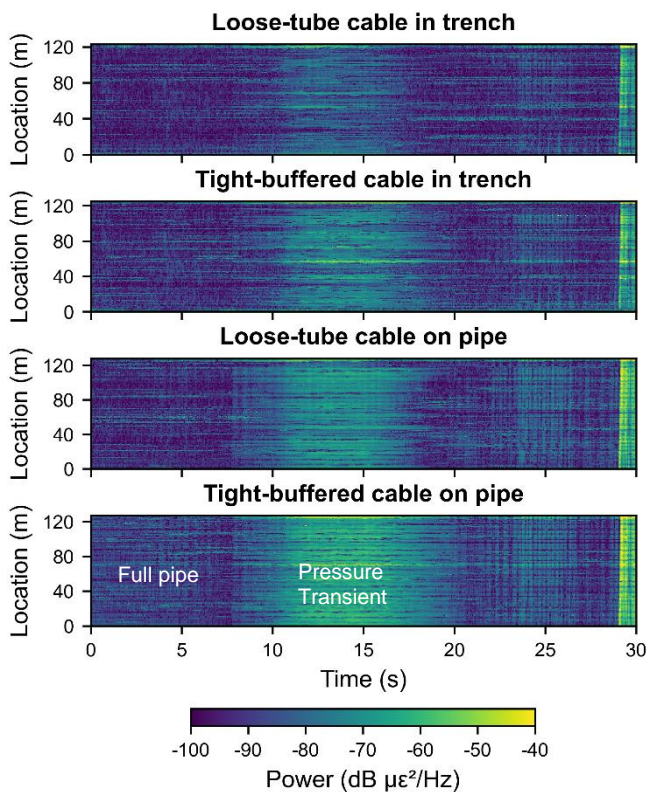


Figure 13. 2 to 20 Hz FBE power during pressure transient

Spectrograms at the uphill pipe end (location 120 m) reveal elevated PSD at low 0 to 20 Hz frequencies (Figure 14). PSD levels at higher frequencies remain relatively low and do not display a matching trend between the different sensing cables configurations. However, magnitude spectra reveal a much clearer difference between signals during the resonant pressure transient and the signal before without acoustic resonance (Figure 15). Both tight-buffered cables and the loose-tube cable on the pipe exhibited less noisy magnitude spectra and a higher SNR than the loose-tube cable in the trench.

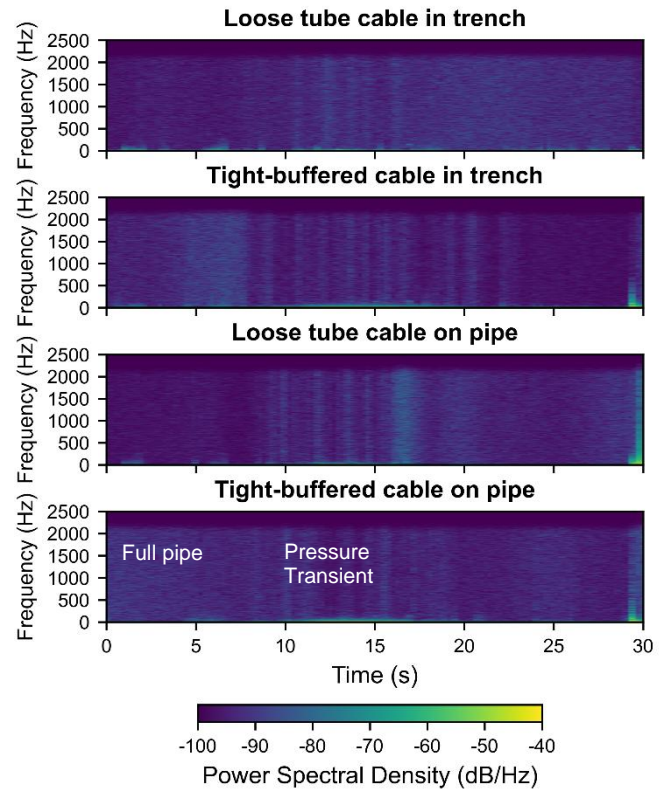


Figure 14. Spectrogram during pressure transient

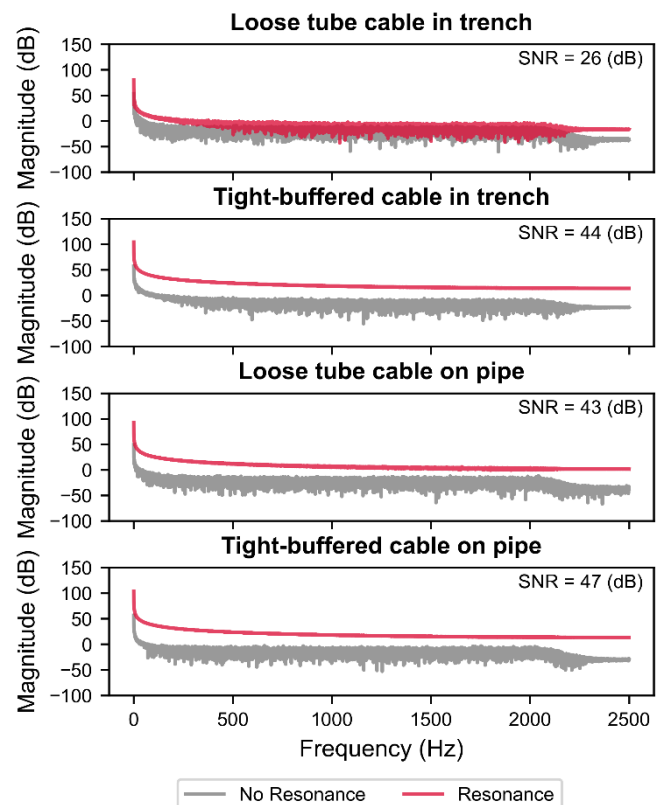


Figure 15. Magnitude spectra during pressure transient

In short, DAS detected a pipe water pressure transient on all four sensing configurations, albeit with lower SNR on loose-tube cable in the trench.



### 3.3 Leakage detection

DAS sensitivity to pipe water leakage noise was evaluated. After the pipe was filled with water, water inflow increased by further opening the downhill end valve. This ensured water would escape from the open valve at the uphill pipe end to simulate high-flow leakage (Figure 16). Simulated leakage was maintained for 6 to 7 minutes until the downhill valve was closed. Water rushing through and exiting the pipe generated vibrations and sound. FBE power from 10 to 100 Hz highlights the start and end of the heavy water flow along the entire pipeline (Figure 17). FBE power was similarly visible on all four sensing configurations. As expected, the maximum acoustic signal was measured at the simulated leakage location.

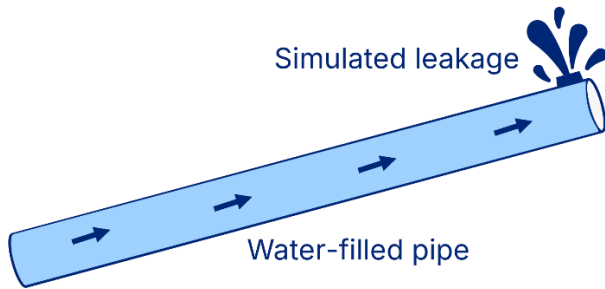


Figure 16. Pipe water leakage condition

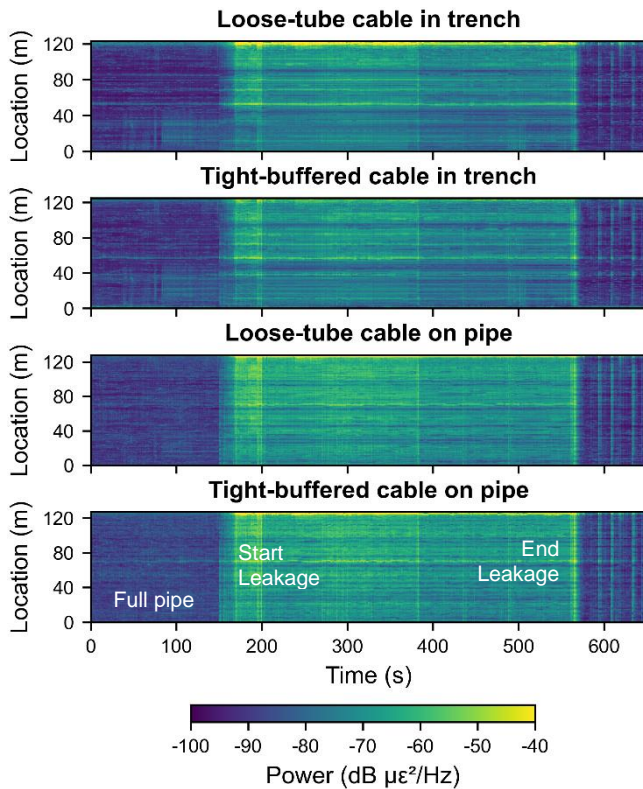


Figure 17. 10 to 100 Hz FBE power during simulated leakage

Spectrograms of frequency-domain signals at the simulated leakage location (location 120 m) display a striking jump in PSD at 0 to 400 Hz, and elevated PSD at 400 to 1000 Hz during simulated leakage (Figure 18) on all sensing cable configurations. Differences in magnitude spectra for signals from the full pipe and leaking pipe suggest a reasonably high SNR between the leaking pipe signal against the full pipe baseline (Figure 19).

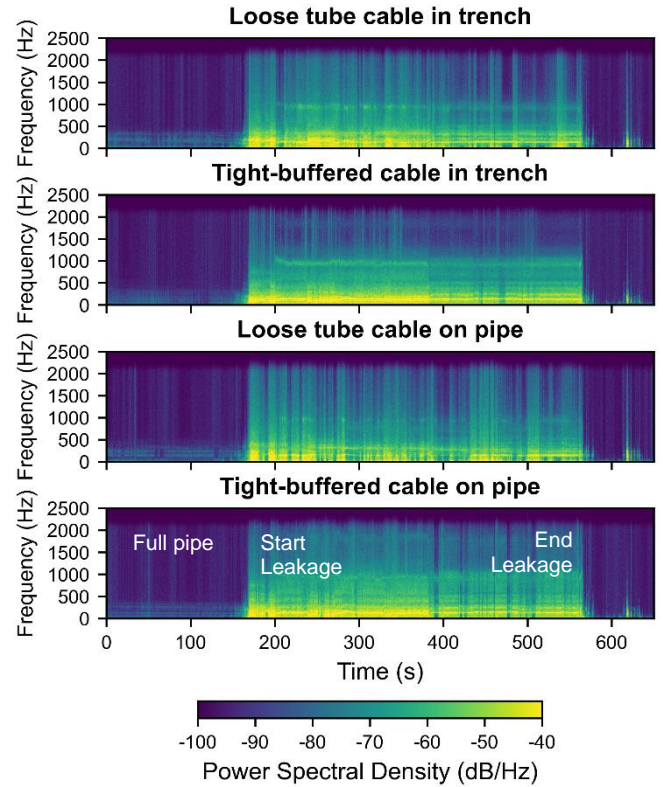


Figure 18. Spectrogram of channel at simulated leak

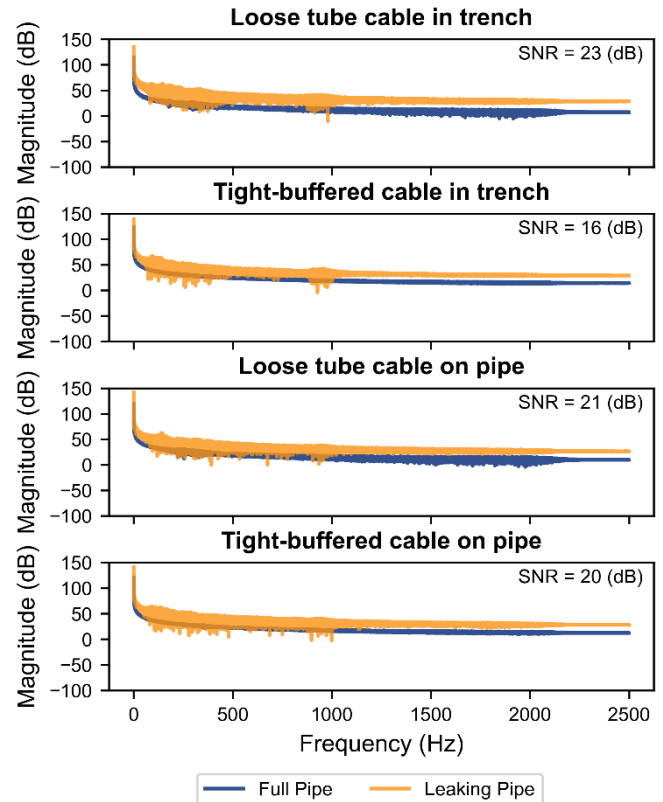


Figure 19. Magnitude spectra of channel at simulated leak

In short, DAS detected pipe water leakage on all four sensing configurations, with similar sensitivity on all four sensing cable configurations.



To summarize, each of the three pipe signal states: 1) pipe water flow, 2) pressure transient-induced resonance, and 3) simulated leakage exhibited unique DAS data characteristics in terms of FBE power, spectrogram power spectral density, and magnitude spectrum trends.

Pipe-mounted cables exhibited a higher degree of FBE power sensitivity than trench-lain cables. Tight-buffered cables generally exhibited a higher degree of FBE power sensitivity than loose-tube cables. At the channel near the simulated leakage location, all sensing configurations exhibited relatively high frequency-domain signal visibility. Notably, trench-lain fibers turned out more sensitive than expected. Their high signal sensitivity was possible because they were located very close to the pipeline. This suggests that trench-lain fiber optic cables can offer sufficient DAS sensitivity to detect pipeline signals if the cables are located close to the pipeline.

#### 4 DISCUSSION

Deploying DAS for water pipeline leakage monitoring presents a trade-off between DAS signal sensitivity and fiber optic cable deployment feasibility and cost (Figure 20).

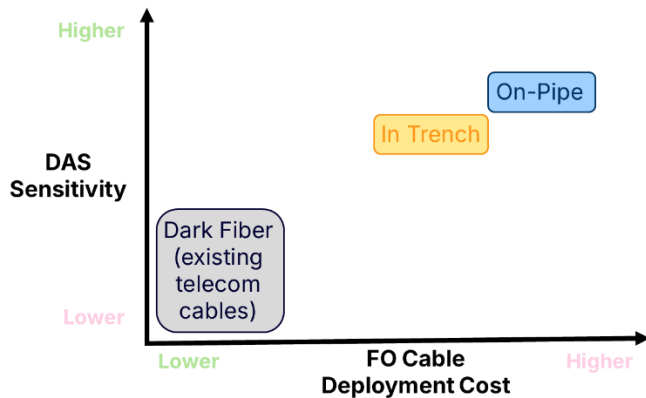


Figure 20. Qualitative comparison of DAS sensitivity to pipeline signals vs. fiber optic cable deployment cost

Mounting fiber optic sensing cables directly to the pipe offers superior DAS sensitivity. This is because pipeline acoustic signals can transmit directly to the fiber. However, this approach requires significant manual labor and installation logistics coordination. In short, it is a high-cost high reward approach appropriate for high resource deployment conditions such as new installations or retrofits for lifeline pipelines.

On the other hand, laying fiber optic sensing cables in the trench along the pipeline offers relatively lower DAS sensitivity. This is because pipeline acoustic signals need to travel through the trench backfill soil to reach the fiber. However, this approach requires less manual labor and is faster than attaching cables to the pipe. With reasonable DAS sensitivity, this medium cost approach may be a more feasible alternative for low resource deployment conditions. Nonetheless, both methods require resources and coordination to deploy sensing cables during pipeline construction excavations. They are therefore only usable if a DAS deployment is planned before pipeline construction activities.

Long term monitoring and maintenance are also a challenge. Although sensing cables typically have a long lifespan, when deployed in a pipeline alignment, they may be accidentally

damaged during pipeline maintenance operations. Installing DAS interrogators in the field may be cost prohibitive given the need for power supply, climate control, and theft-prevention. From a scaling perspective, deploying sensing cables inside the pipeline alignment as done in this study can be difficult. Accordingly, it works best for critical pipelines with committed stakeholders in a supportive regulatory environment.

Alternatively, dark fiber DAS using existing buried telecommunications fiber optic cables is incredibly convenient with zero physical deployment installation and negligible maintenance costs. In this approach, a DAS interrogator is safely connected to an existing telecommunications cable network that runs from a datacenter through the pipeline network of interest. From a scaling perspective, a standardized dark fiber DAS method for detecting water pipeline leakage would offer a truly low cost and large-scale solution. However, this approach typically has lower DAS sensitivity given that existing cables may be far away from the monitored pipeline and may have poor acoustic signal coupling with subsurface soil. Therefore, further research is needed to better understand and improve dark fiber DAS sensitivity to pipe water leakage.

#### 5 CONCLUSIONS

This study presents a reproducible workflow for DAS system deployment and signal processing for water pipeline leak detection in field conditions. The experimental configuration involved fiber optic sensing cables deployed directly in the pipeline alignment during construction. Both tight-buffered and loose-tube cables were installed on the pipe and in the trench. All four sensing cable configurations exhibited relatively high DAS sensitivity (high SNR) to pipeline acoustic signals during pipe water filling and simulated leakage. These results approximate a potential upper-bound for DAS sensitivity to water pipeline leak detection for each of the sensing cable configurations.

In contrast to other past work which simulated pipeline leakage in fully controlled laboratory conditions, this study consciously pursued the complete opposite approach to embrace the potentially high levels of uncertainty associated with deploying fiber optic cables and DAS in the field. In this context, we acknowledge this study is limited to a single location with a single pipeline and a single simulated leakage signal source. The presented optimistic results of high SNR for all sensing cable configurations near the simulated leakage may be due to supportive experimental conditions. Intuitively, all four deployed sensing cables were on or very close to the pipe, so they detected pipeline acoustic signals reasonably well. Had the sensing cables been further away, their DAS sensitivity to pipeline signals would likely have been reduced.

Further work will investigate DAS sensitivity for water pipeline leakage detection with sensing cable configurations where fiber-optic cables are further away from the pipeline of interest. This will help demonstrate the workflow is applicable to dark fiber conditions where DAS is deployed on existing buried telecommunications cables which may be not close to the monitored pipeline. Furthermore, additional testing in locations with different subsurface conditions (soil type, temperature, moisture), with various pipe materials and leakage mechanisms is needed to develop a comprehensive dataset of pipe water leakage noise signals. This will support a robust and

adaptable workflow for dark fiber DAS to operationalize water pipeline leakage detection. This standardization effort can be scaled up with engagement from public agency stakeholders and regulators to ultimately transform the state of practice for water pipeline monitoring.

To summarize the main contributions of this work:

1. Developed reproducible framework for DAS system deployment and signal processing for water distribution pipeline monitoring.
2. Characterized influence of fiber optic cable type (tight-buffered vs. loose-tube) and installation location (on pipe vs. along pipe in trench) on DAS sensitivity to pipeline acoustic signals.
3. Explored time-domain and frequency-domain content of acoustic signals relevant to pipeline anomaly and leakage detection.

## ACKNOWLEDGMENTS

The authors gratefully acknowledge the support of Dr. Yaobin Yang, Dr. Chien-Chih Wang, and James Xu (University of California, Berkeley), the East Bay Municipal Utility District (EBMUD), and the Berkeley Center for Smart Infrastructure (CSI).

## REFERENCES

- [1] Soga, K., & Luo, L. (2018). Distributed fiber optics sensors for civil engineering infrastructure sensing. *Journal of Structural Integrity and Maintenance*, 3(1), 1–21. <https://doi.org/10.1080/24705314.2018.1426138>
- [2] Hubbard, P. G., Xu, J., Zhang, S., DeJong, M., Luo, L., Soga, K., Papa, C., Zulberti, C., Malara, D., Fugazzotto, F., Garcia Lopez, F., & Minto, C. (2021). Dynamic structural health monitoring of a model wind turbine tower using distributed acoustic sensing (DAS). *Journal of Civil Structural Health Monitoring*, 11(3), 833–849. <https://doi.org/10.1007/s13349-021-00483-y>
- [3] Xu, J. T., Luo, L., Saw, J., Wang, C.-C., Sinha, S. K., Wolfe, R., Soga, K., Wu, Y., & DeJong, M. (2024). Structural health monitoring of offshore wind turbines using distributed acoustic sensing (DAS). *Journal of Civil Structural Health Monitoring*. <https://doi.org/10.1007/s13349-024-00883-w>
- [4] Hubbard, P. G., Ou, R., Xu, T., Luo, L., Nonaka, H., Karrenbach, M., & Soga, K. (2022). Road deformation monitoring and event detection using asphalt-embedded distributed acoustic sensing (DAS). *Structural Control and Health Monitoring*, 29(11). <https://doi.org/10.1002/stc.3067>
- [5] Saw, J., Zhu, X., Luo, L., Correa, J., Soga, K., & Ajo-Franklin, J. (2025). Distributed Fiber Optic Sensing for in-well hydraulic fracture monitoring. *Geoenergy Science and Engineering*, 250, 213792. <https://doi.org/10.1016/j.geoen.2025.213792>
- [6] Gemeinhardt, H., & Sharma, J. (2024). Machine-Learning-Assisted Leak Detection Using Distributed Temperature and Acoustic Sensors. *IEEE Sensors Journal*, 24(2), 1520–1531. *IEEE Sensors Journal*. <https://doi.org/10.1109/JSEN.2023.3337284>
- [7] Muggleton, J. M., Hunt, R., Rustighi, E., Lees, G., & Pearce, A. (2020). Gas pipeline leak noise measurements using optical fibre distributed acoustic sensing. *Journal of Natural Gas Science and Engineering*, 78, 103293. <https://doi.org/10.1016/j.jngse.2020.103293>
- [8] Saw, J., Luo, L., Chu, K., Ryan, J., Soga, K., & Wu, Y. (2025). Distributed Acoustic Sensing for Whale Vocalization Monitoring: A Vertical Deployment Field Test. *Seismological Research Letters*. <https://doi.org/10.1785/0220240389>
- [9] Araica, K. (Moita), Cicala, G., McLeod, M. P., Soga, K., Jasiak, M., Hubbard, P., Wang, C.-C., Yang, Y., Luo, L., Yeskoo, A., & Chiu, S.-H. (2024). Design and Installation of Distributed Fiber Optic Sensing Technology to Monitor HDPE Pipelines at an Earthquake Fault Crossing. *Pipelines 2024*, 561–571. <https://doi.org/10.1061/9780784485569.060>
- [10] Chiu, S.-H., Jasiak, M., Dong, C., Banushi, G., Soga, K., Riemer, M., Katzev, D., Wham, B., Berger, B., Mason, J., & O'Rourke, T. (2025). Design of Distributed Fiber Optic Sensing Monitoring System for Earthquake-Resistant Ductile Iron Pipelines Crossing Seismic Fault. 567–575. <https://doi.org/10.1061/9780784485996.055>
- [11] Chiu, S.-H., Zhang, Q., Soga, K., Takhirov, S., Cha, W., Katzev, D., & Mason, J. (2024). Performance Evaluation of Earthquake Resistant Ductile Iron Pipe Joints Using Combined Experimental and Numerical Method. 261–271. <https://doi.org/10.1061/9780784485583.028>
- [12] Yu, B., & Barter, R. L. (2024). *Veridical data science: The practice of responsible data analysis and decision making*. MIT Press. <https://vdsbook.com/>
- [13] Lu, B., Pan, Z., Wang, Z., Zheng, H., Ye, Q., Qu, R., & Cai, H. (2017). High spatial resolution phase-sensitive optical time domain reflectometer with a frequency-swept pulse. *Optics Letters*, 42(3), 391–394. <https://doi.org/10.1364/OL.42.000391>
- [14] Eickhoff, W., & Ulrich, R. (1981). Optical frequency domain reflectometry in single-mode fiber. <https://doi.org/10.1063/1.92872>  
Oppenheim, A. V., Buck, J. R., & Schaffer, R. W. (1999). *Discrete-time signal processing* (2nd ed.). Prentice Hall. <https://books.google.com/books?id=cR3CQgAACAAJ>
- [15] Saw, J. (2025). *Listening with Light: Distributed Acoustic Sensing for Event Detection, Characterization, and Classification* (Doctoral dissertation). University of California, Berkeley.

# Integrating Distributed Acoustic Sensing for Damage Detection in Old Pre-Stressed Concrete Girders: Preliminary Experimental Results

Lisa Strasser<sup>1</sup>, Werner Lienhart<sup>1</sup>, Thomas Moser<sup>1</sup>, Andrej Anžlin<sup>2</sup>, Mirko Kosič<sup>2</sup>, Maja Kreslin<sup>2</sup>, Doron Hekič<sup>2</sup>

<sup>1</sup>Institute of Engineering Geodesy and Measurement Systems, Faculty of Mathematics, Physics and Geodesy, Graz University of Technology, Steyrergasse 30, 8010 Graz, Austria

<sup>2</sup>Slovenian National Building and Civil Engineering Institute, Dimičeva ulica 12, 1000 Ljubljana, Slovenia  
email: [lisa.strasser@tugraz.at](mailto:lisa.strasser@tugraz.at)

**ABSTRACT:** In this study, we investigate the load-bearing capacity of pre-stressed concrete girders under various damage levels. We employed Distributed Acoustic Sensing (DAS) technology to monitor and quantify changes in the girder response as damage levels were incrementally introduced. This approach enabled the real-time measurement of dynamic behavior over the entire length of the girder, allowing for a detailed characterization of damage-induced structural changes. To complement the DAS-based approach, we also applied classical acceleration-based damage detection techniques. By integrating these methods, we aimed to cross-validate the results and provide a more comprehensive understanding of damage progression and its impact on structural performance.

The experimental campaign, conducted in Ljubljana, ZAG, involved full-scale testing of pre-stressed concrete girders subjected to controlled damage scenarios. This setup ensured a realistic assessment of the girders' residual capacity and failure mechanisms. The paper presents preliminary results from this experimental study, emphasizing the capability of DAS measurements to detect and characterize damage, while also comparing its performance against traditional methods. By combining advanced sensing technologies with established techniques, this research highlights the potential of DAS as a transformative tool in structural health monitoring.

**KEY WORDS:** Distributed Acoustic Sensing; Distributed Fiber Optic Sensing; Structural Health Monitoring; Frequency Analysis; Load Test; Infrastructure Monitoring; Bridge Monitoring.

## 1 INTRODUCTION

Structural Health Monitoring (SHM) of civil structures is gaining more and more significance in the recent years, especially in the case of bridges, since many of them are coming to the end of their design life time or even have to be replaced earlier due to increased loads on the structure. Current incidents such as the collapse of the Carola Bridge in Dresden, Germany draw international attention to the importance of infrastructure monitoring.

In order to gain more knowledge on the structural response due to increasing loads and damages, laboratory load tests on a bridge girder were carried out. The bridge girder stems from a bridge partly collapsed due to flooding in summer 2024. More detailed information about the tested bridge beam and the test procedure can be derived from [1]. The aim of the controlled load tests was to determine the structural behavior and perform measurements at all damage states in order to get a better understanding for condition assessment. This can be done using different measurement techniques, which can be broadly categorized in point-wise and distributed sensors. Suitable point-wise sensors are e.g. accelerometers, but also static or dynamic Robotic Total Station (RTS) measurements [2][3] can deliver valuable results. The drawback of these point-wise techniques is that they require several sensors in order to monitor the structure, and all of them need to be mounted in appropriate positions to obtain meaningful results. Distributed Fiber Optic Sensing (DFOS) functions as a distributed sensor, where one fiber can precisely sense information along its entire

length. Different DFOS techniques can provide insights on the frequency behavior of the structure, but also on the bending due to the applied force. Furthermore, cracks appearing in the structure can be detected. The fiber can be glued on the structure, but also embedded directly inside the structure if it is newly constructed. The application of DFOS for bridge monitoring is currently becoming of more interest [4].

All of the mentioned measurement techniques were applied at the conducted laboratory tests. However, this paper focuses on the results and comparison of Distributed Acoustic Sensing (DAS) and accelerometers.

## 2 BRIDGE MONITORING WITH DFOS

The general principle of DFOS is light coupled into a glass fiber, which gets scattered at natural impurities at every point inside the fiber. A part of the light gets backscattered to the interrogation unit, where different information, especially temperature ( $T$ ), strain ( $\epsilon$ ) or strain rates ( $\epsilon/t$ ), can be derived depending on the measured backscatter effect (see Figure 1). As the light propagates through the fiber, information is sensed along the entire length of the fiber, which can amount up to several tens of kilometers. Significant advantages of DFOS are immunity to electromagnetic interferences and only the small and lightweight fiber being needed on-site, a passive element which requires no power supply.

Since this paper focuses on Distributed Acoustic Sensing (DAS) only, the following paragraph will describe the working principle in more detail.



Pulsed light is coupled into the fiber with high frequency, whereby the maximum sampling frequency  $f_{max}$  is dependent on the fiber length  $L$  by

$$f_{max} = \frac{c}{2nL} \quad (1)$$

in order to avoid overlapping pulses in the fiber.

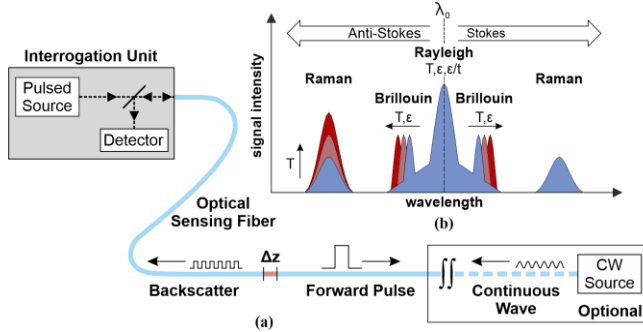


Figure 1. (a) Schematic representation of the operating principle of distributed fiber optic sensing techniques and (b) different backscatter effects, based on [5].

DAS interrogation units only detect and measure Rayleigh backscatter, which has the highest intensity [6]. Rayleigh backscatter is affected by strain and temperature changes, which in turn cause differences in the optical path length. The optical path length is determined from the differential phase between two scatter points [7]. Since the measurand is the optical phase change within a certain distance (the gauge length), the output consists of relative measurements describing the behavior of strain within a certain period of time, resulting in strain rate measurements. The gauge length is typically on the order of several meters and defines the spatial resolution of the measurement. Compared to other DFOS techniques, DAS provides lower spatial resolution, but much higher temporal resolution reaching up to several kHz, making it suitable for dynamic measurements.

The seamless high frequency measurements can provide valuable information about the structural integrity of a bridge by deploying only one fiber to the structure. By numerically integrating the derived strain rate measurements to strain, additional information about the strain distribution along the structure can be gained.

### 3 LOAD TESTS

#### 3.1 Setup

The structure under test is a prestressed girder with a deck plate and has a length of about 10 m. It was placed in the laboratory of the Slovenian National Building and Civil Engineering Institute (ZAG) underneath a hydraulic actuator able to apply vertical load. More information about the placement of the girder on the testing facility can be found in [1]. Several sensors were mounted on the structure. The location of the sensors discussed in this paper can be seen in Figure 2, but also other sensors such as tilt sensors, RTS and camera have been used.

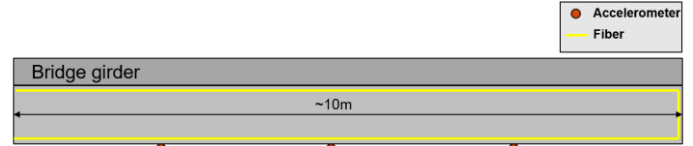


Figure 2. Schematic representation of tested structure with mounted sensors.

As also shown in Figure 3, the fiber was mounted on the upper and lower part of the girder along its entire length. A second fiber was glued in order to be able to perform simultaneous measurements with different DFOS techniques, which are not subject of this present paper. For the DAS measurements, the inner fiber was used.

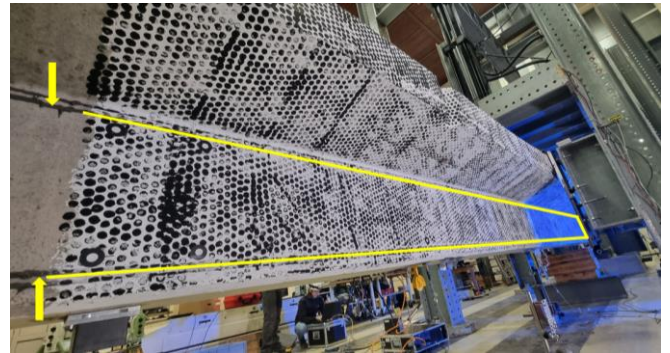


Figure 3. Glued fibers on the bridge girder placed in the laboratory.

The measurement settings for DAS and accelerometers were as stated in Table 1.

Table 1. Measurement settings.

	DAS	Accelerometers
Sampling frequency	5000 Hz	200 Hz
Measurement channels	25	3
Measurand	$\mu\text{m}/\text{m}/\text{s}$	$\text{m}/\text{s}^2$

#### 3.2 Test procedure

The test procedure consisted of 10 load phases with 2 cycles each, increasing the maximum load with every phase. For the first three phases, the applied load was increased stepwise with a waiting time of 2 minutes after every load increment, while for the latter phases a constant linear load increase was applied. The loading speed was 1 kN/s, and the same procedure was applied for both loading and unloading. The load cycles are shown in Figure 4. Note that the pause between the load phases 3 and 4 is not shown correctly in the plot, since there was an overnight pause in between.

In between the phases, ambient vibration tests were performed. These aimed to stimulate the girder in a way so the eigenfrequencies could be detected. The stimulation was performed by a human jumping on the girder in order to induce an impulse. After phase 5, shaker tests were performed by placing a vertical shaker on the beam, stimulating it with different singular frequencies as well as with a frequency sweep.

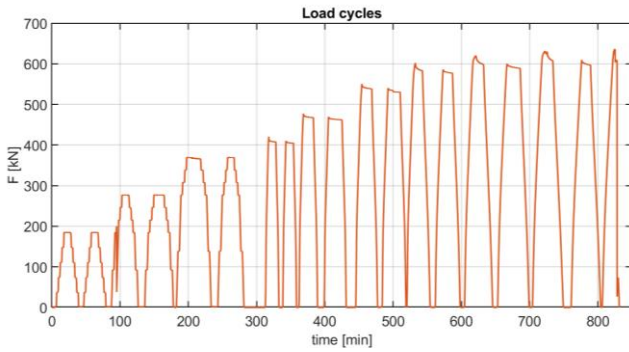


Figure 4. Performed load cycles.

### 3.3 Eigenfrequencies

The eigenfrequencies can be determined from the ambient vibration tests and provide significant information about the structural integrity, since a change in the eigenfrequency indicates structural damage. Figure 5 shows the ambient vertical vibration of the girder after phase 2, measured with the accelerometers at 3 discrete positions on the beam bottom.

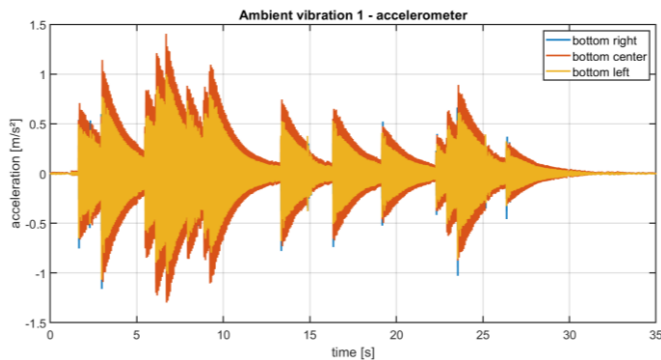


Figure 5. Accelerometer measurements of ambient vibration, 3 positions on the bottom.

DAS measurements can be obtained along the entire fiber. The occurring strain rates caused by the excitation of the girder can be seen in Figure 6, whereby the y-axis shows the distance along the fiber, and the x-axis depicts the change over time.

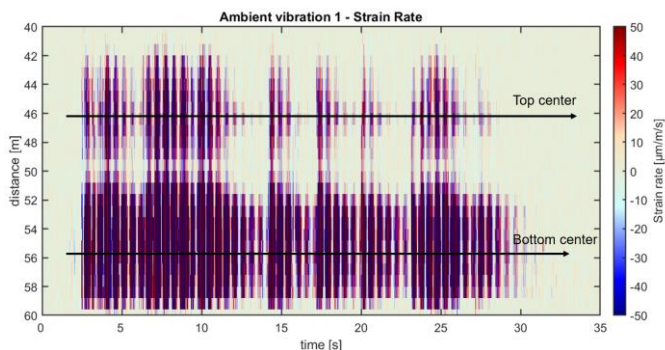


Figure 6. DAS waterfall plot of ambient vibration.

From the DAS waterfall plot, a location on the fiber close to the accelerometer can be selected. For comparison, a location at the bottom center and also in the upper center was chosen. Note

that the spatial resolution of the DAS amounts to 0.8 m. When compared with the accelerometers, it is noticeable that the measurements look very comparable with the single impacts being clearly differentiable in both (Figure 7). For better comparison, the DAS measurements have been down sampled to the same sampling frequency as the accelerometers (200 Hz). What stands out in the DAS measurement is the significant difference between the upper and lower part of the beam, with the lower section showing considerably more movement than the upper section. This indicates a high vertical position of the neutral axis. As the measured vibrations on the upper and lower fiber are in phase (see Figure 8.), the neutral axis must be located above the upper fiber.

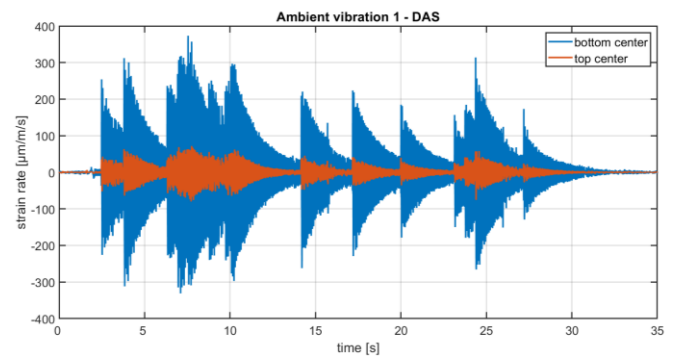


Figure 7. DAS measurements of ambient vibration, top and bottom center.

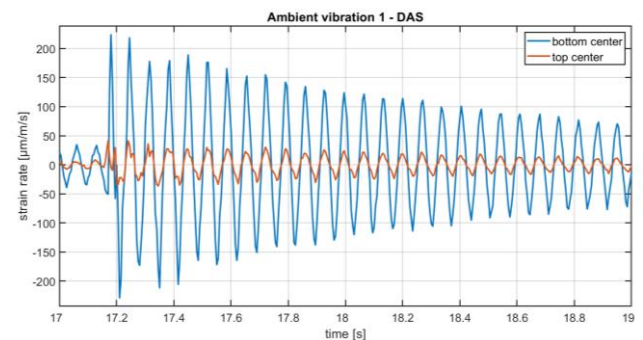


Figure 8. Measurements of upper and lower fiber are in phase for measurement of ambient vibration.

In order to determine the eigenfrequencies appearing through the excitation, a Short Time Fourier Transform (STFT) with a window length of 4 s was computed both for the accelerometers and DAS measurements. For the accelerometer mounted at the bottom center of the girder, the resulting amplitudes of each window are shown in Figure 9. The appearing main frequency amounts to 14.75 Hz. The same procedure was applied to the DAS measurements. Again, a bottom center position on the fiber, as well as a top center position were chosen for comparison. For both positions, the same eigenfrequency of 14.75 Hz was observed (Figure 10), which is in agreement with the accelerometer measurements shown in Figure 9.

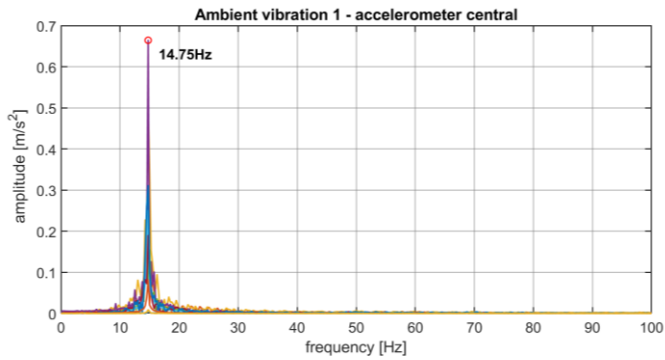


Figure 9. Eigenfrequency of the beam after loading phase 2, bottom center accelerometer.

However, the measured amplitudes at the bottom and top part vary significantly, with the bottom part responding about 5 times stronger than the top part (note the different scaling in Figure 10). This again implies a high vertical position of the zero line of the beam.

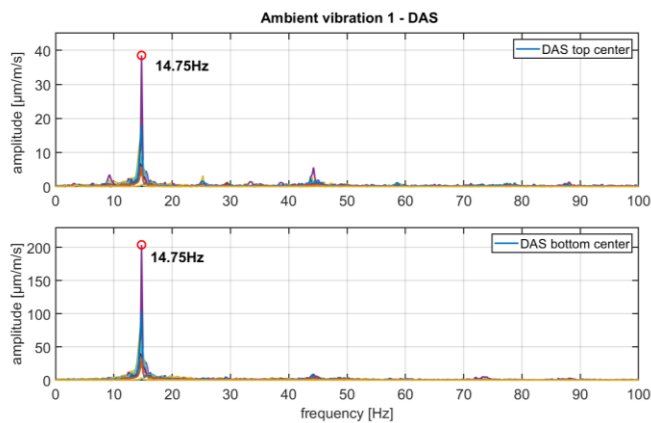


Figure 10. Eigenfrequency of the beam after loading phase 2, bottom and top center measured with DAS.

One of the main advantages of Distributed Fiber Optic Sensing is the seamless measurement along the entire fiber. The frequency and amplitude can be obtained at any point and give a more complete picture of the overall structural behavior. Therefore, a frequency analysis was carried out for every point along the fiber. The eigenfrequency of 14.75 Hz remained constant along the entire girder, but the amplitude varies strongly as it can be seen in Figure 11.

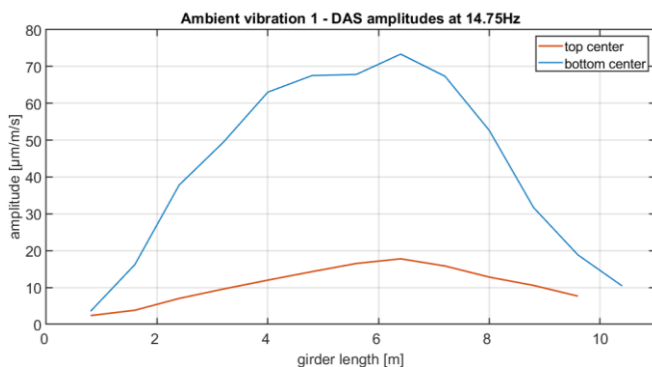


Figure 11. Amplitude curve for eigenfrequency of 14.75 Hz along the top and bottom part of the beam.

Note that the different dimension of the amplitudes compared to Figure 10 stems from the FFT being computed over the entire event, instead of 4 s windows. Again, it can be observed that the bottom part of the beam shows stronger reaction, and also the middle part of the beam shows increasing amplitudes for both the upper and lower side.

The eigenfrequencies have been determined for every ambient vibration event, which was carried out after each load phase. With increasing damage, the measured eigenfrequencies decrease significantly. The first cracks appeared in load phase 2. Table 2 shows the results for both DAS and accelerometers, which are in complete agreement for every measurement. Note that due to the window size of 4 s, the frequency resolution only amounts 0.25 Hz.

Table 2. Comparison of eigenfrequencies for DAS and accelerometers, ambient vibration at different damage states.

Impulse Excitation	After load phase	$f_{Acc.}$ [Hz]	$f_{DAS}$ [Hz]
1	Phase 2	14.75	14.75
2	Phase 3	14.25	14.25
3	Phase 4	14.25	14.25
4	Phase 6	13.75	13.75
5	Phase 7	12.50	12.50
6	Phase 8	10.50	10.50
7	Phase 9	10.00	10.00

### 3.4 Shaker Tests

In addition to the ambient vibration tests, experiments with a shaker were carried out. The shaker weighs approx. 100 kg and can oscillate vertically. Different singular frequencies and amplitudes can be set, and also frequency or amplitude sweeps can be performed. The shaker was placed as close to the middle of the girder as possible (Figure 12).



Figure 12. Placement of the vertical shaker on the girder.

First, a frequency sweep from 2-100 Hz was carried out. After that, the shaker was operated with different constant frequencies but increasing amplitude. An overview of the test procedure is shown in Figure 13. The different amplitude sweeps can be clearly seen in the DAS raw data. A STFT shows in more detail the appearing frequencies and amplitudes. The frequency sweep ( $t=100-350$  s) is visible well, with higher amplitudes appearing when the shaker frequency matches the eigenfrequency. Also, the second harmonics can be detected.



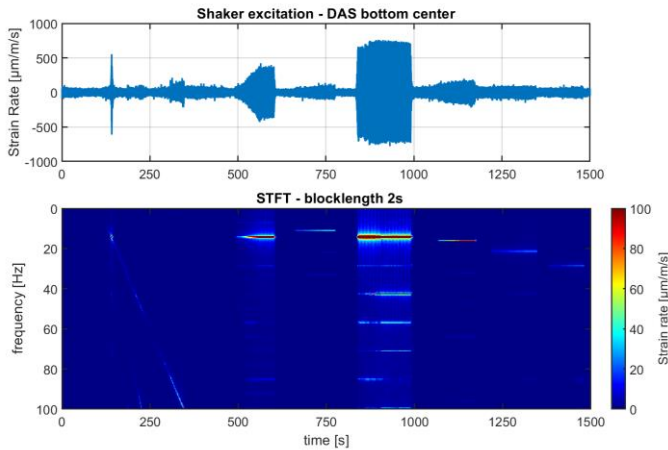


Figure 13. Overview shaker tests - raw data and STFT.

After that, the STFT with a window size of 2 seconds clearly shows the amplitude sweeps ( $t=500-1500$  s) at different constant frequencies. A strong structural response can be detected when the input frequency amounts to the eigenfrequency or the latter is a harmonic of the stimulating frequency. This can be seen in the first ( $t=500-600$  s) and third ( $t=840-1000$  s) sweep, where the input frequency is 7.1 Hz and 14.2 Hz. Furthermore, a detailed look is taken at the excitation close to the eigenfrequency. Note that the eigenfrequency already decreased to 14.25 Hz, since the shaker tests were carried out after phase 5 (compare Table 2).

Taking a closer look at sweep 3, where the girder was stimulated with the eigenfrequency, also the harmonics can clearly be detected. This can be seen at the bottom position as well as at the upper position (Figure 14). The most dominant is the third harmonic at 42.6 Hz.

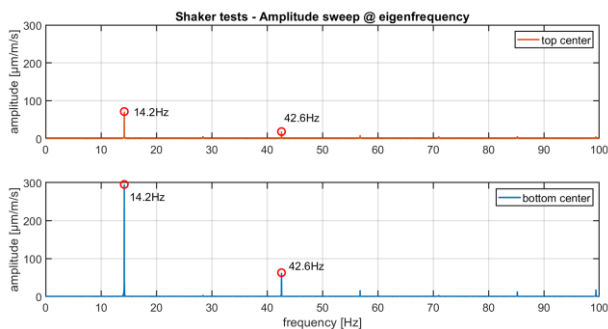


Figure 14. FFT at top and bottom center position.

### 3.5 Load Capacity

In addition to a frequency analysis, DFOS measurements can also serve to determine the applied strain on the structure. Typically, static DFOS measurements such as Optical Frequency Domain Reflectometry (OFDR) or Brillouin backscattering are used to measure absolute strain. These systems usually provide a better spatial resolution, but a poor sampling rate, if at all capable of performing dynamic measurements.

By numerically integrating the measured strain rates over time, the appearing strain can be calculated from the DAS

measurements. For this purpose, a known starting value (initial strain) is needed. In case of the load tests, this was accomplished by starting the measurement before any load is applied, thereby minimizing the induced integration error. However, this is based on the assumption that the fiber does not experience any permanent strain from the previous load cycles. Figure 15 shows a waterfall plot of the appearing strain along the entire fiber. The load increments can be seen as progressively increasing elongation of the fiber over time, as well as a clear difference between the upper and lower part of the beam.

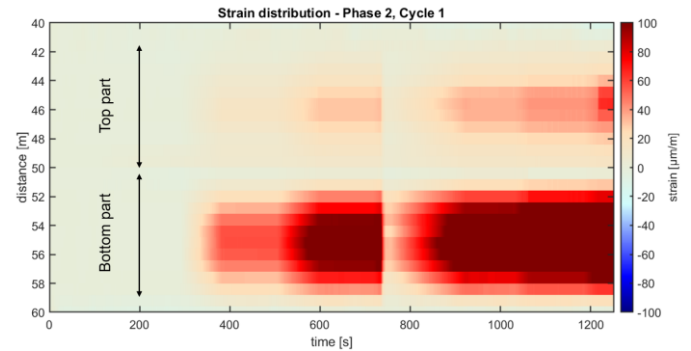


Figure 15. Waterfall plot of induced strain along the fiber, load phase 2.

Taking a closer look at the top and bottom center position of the girder, the load increments and pause time in between are visible (Figure 16), as well as the significant difference in strain between the upper and lower part. Note that the outlier in the load strain profile ( $t=750-900$  s) derives from a failure of the hydraulic actuator.

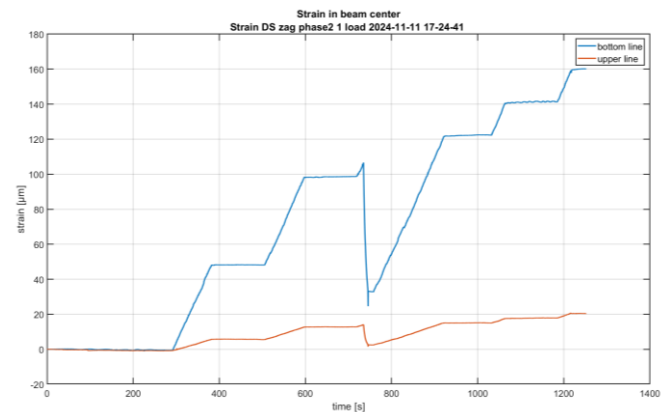


Figure 16. Increasing strain at top and bottom center, phase 2.

Figure 17 shows the strain distribution along the fiber for load phase 4, cycle 2. At this phase, there was no load incrementation followed by a waiting period, but a linear increase of the load until the maximum load. The applied load is approximately one third higher than in phase 2 (see Figure 4), which results in significantly higher strain. Figure 17 shows the loading as well as the unloading of the element.

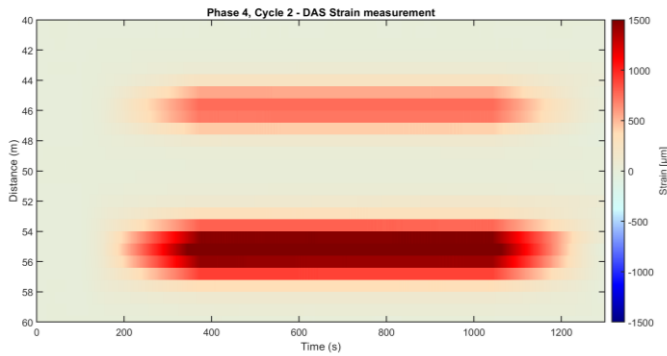


Figure 17. Waterfall plot of strain distribution, phase 4, cycle 2.

Of particular interest is the strain distribution, which appears very concentrated in the center of the girder, where the force is applied (Figure 18, right).

Also, a more detailed look can be taken at the strain distribution on the bottom and top center of the girder (Figure 18, left). The lower part experiences significantly higher strain, amounting more than twice as much as the upper part. It should also be noted that with increasing force the ratio of the measured strain between the lower and upper part increases, which implies an upwards moving neutral axis with increasing load.

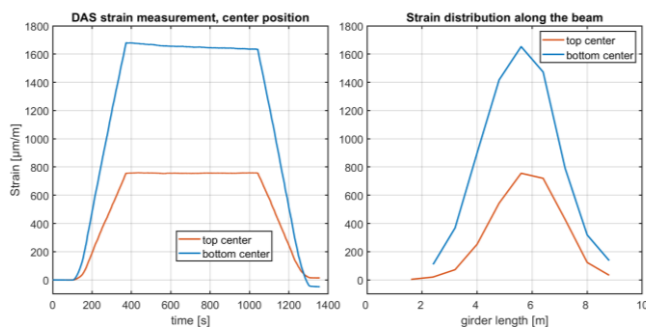


Figure 18. Load phase 4. Left: Measured strain at top and bottom center. Right: Strain distribution along the fiber at maximum load.

#### 4 SUMMARY AND CONCLUSION

The loading tests have shown that Distributed Fiber Optic Sensing is a suitable measurement technique to determine the structural integrity of girders or bridges. While delivering comparable results to other sensing techniques, it can provide significant advantages compared to pointwise sensors. A frequency analysis can be performed seamlessly along the entire fiber, whereby the high sampling rates can determine any changes in the eigenfrequencies. In addition to the high frequency strain rate measurements, the occurring strain at the structure can also be determined. The obtained results can provide valuable insights about the damage state of the structure. All this information can be sensed with only one fiber mounted to the structure, whereby after the initial installation no further direct interaction with the structure is necessary.

Further work will include a deeper look on detecting the tearing of tension cables, as well as a more detailed look on damage assessment using mode shapes.

#### ACKNOWLEDGMENTS

We want to acknowledge the collaboration with the Slovenian National Building and Civil Engineering Institute (ZAG), which carried out the load tests at their laboratory and gave us the opportunity to install our sensors and carry out the measurements.

#### REFERENCES

- [1] M. Kreslin, M. Kosič, A. Šajna, A. Anžlin, D. Hekič, V. Požonec and P. Triller, Laboratory Testing of Old Bridge Girders: Preliminary Results, *SHMII-13 Proceedings*, Graz, Austria, September 2025.
- [2] P. Psimoulis and C. Stiros, Measuring Deflections of a Short-Span Railway Bridge Using a Robotic Total Station, *Journal of Bridge Engineering*, 18(2): 182-18, 2013.
- [3] C. Schönberger, W. Lienhart and T. Moser, Dynamic monitoring of civil infrastructures with geodetic sensors, in *Proceedings 5th Joint International Symposium on Deformation Monitoring JISDM*, pp. 537-543, 2022.
- [4] M. Morgese, C. Wang, T. Taylor and F. Ansari, Distributed Operational Modal Analysis of Multispan Bridges, *Journal of Bridge Engineering*, 30(5), 2025.
- [5] C. Monsberger and W. Lienhart, Distributed Fiber Optic Shape Sensing of Concrete Structures, *Sensors* 2021, 21, 6098, 2021.
- [6] A. H. Hartog, *An Introduction to Distributed Optical Fibre Sensors*. CRC Press, Taylor & Francis Group, 2017.
- [7] Febus Optics SAS, Technical User Guide Febus A1-R, Version 9, Pau, France, 2023.

# Structural performance monitoring for concrete girder bridges with distributed fiber optic sensors

Francesco Fabbriatore<sup>1</sup>, ORCID (0009-0003-2198-6868), Numa Bertola<sup>2</sup>, ORCID (0000-0002-4151-3123)

<sup>1</sup> Department of Engineering, Faculty of Science, Technology and Medicine, University of Luxembourg, Maison du Nombre 6, Avenue de la Fonte, L-4364 Esch-Sur-Alzette, Luxembourg.  
 email: francesco.fabbriatore@uni.lu, numa.bertola@unil.lu

**ABSTRACT:** The alarming frequency of bridge collapses in recent years underscores the critical need for advanced monitoring strategies tailored to existing infrastructure. Many concrete bridges, built decades ago, now face increasing traffic demands and environmental stressors that threaten their structural integrity.

This study investigates the use of distributed fiber optic sensors (DFOSs) with high spatial resolution (independent strain measurements every 2.6 mm) during static load tests to assess the structural performance of concrete girder bridges. The goal is to gain a deeper understanding of their condition using data-driven approaches. The fiber optic technology provides detailed strain profile information that gives insights into global bridge behavior, such as stress distributions, support conditions and static responses. It also allows the detection of cracks along the fiber path and other localized effects that may remain undetected without a calibrated numerical model.

This method of structural performance monitoring is applied to a prestressed concrete bridge in Switzerland. Static load tests have been performed on a full-scale bridge in Switzerland and the resulting distributed strain datasets allow the accurate understanding of bridge behavior, including deflection extrapolation and crack detection. The results underline the potential of DFOS to develop novel data-driven solutions for extending the service life of structures.

**KEY WORDS:** Distributed fiber optic sensors, Structural identification, Structural performance monitoring, Structural health monitoring, Load testing, Concrete bridge.

## 1 INTRODUCTION

Across the globe, bridge networks are experiencing a rapid deterioration amid rising traffic demands and environmental effects, posing significant challenges to infrastructure safety and management. Budgetary constraints and the potential socioeconomic disruptions from closures or failures, such as the catastrophic collapse of the Morandi Bridge in Genoa [Calvi et al., 2019], highlight the critical need for accurate structural safety assessments to optimize resource allocation and ensure public safety.

Traditional engineering approaches, created for the design of new structures, are not adapted to existing bridges, where material degradation and unforeseen modifications obscure true conditions. Compounding this issue, visual inspections suffer from subjectivity and an inability to detect hidden flaws, driving the need for more reliable, data-driven solutions [1]. To address these shortcomings, researchers have developed advanced monitoring methodologies that harness field measurements to either pinpoint damage or deepen understanding of structural behavior [2]. Structural performance monitoring (SPM), in particular, seeks to uncover hidden reserves of load-bearing capacity by leveraging precise measurements from real-world conditions [3]. The effectiveness of such frameworks hinges on the choice of monitoring technology. Since the 1950s, strain gauges have been a cornerstone of structural assessment, valued for their affordability and durability [4]. However, their discrete spatial sampling limits their ability to capture the full spectrum of a bridge response, especially in aging concrete structures prone to localized deterioration.

The introduction of fiber optic sensors (FOS) has marked a pivotal advancement, enabling distributed strain monitoring over extended distances with high spatial resolution [5]. More recently, distributed fiber optic sensors (DFOS) have pushed this boundary further, achieving gauge pitches as fine as 1.3–2.6 mm through breakthroughs in optical technology. This development, depicted in Figure 1, facilitates precise detection of local strain anomalies, such as impacts of concrete cracks, by analyzing time- and frequency-domain signals, far exceeding the capabilities of traditional sensors [6].

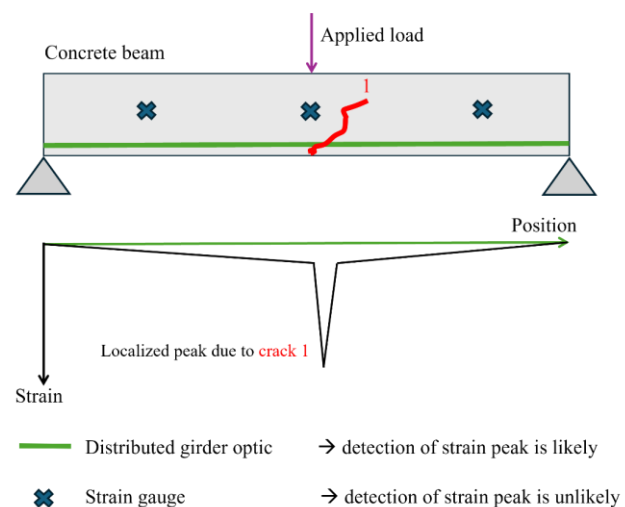


Figure 1. Comparison between distributed fiber optic sensors and conventional strain gauge for concrete-structure monitoring.



Despite these advances, notable gaps remain in the literature. Most research focuses on long-term structural health monitoring (SHM) to track trends over time [7], while the potential of DFOS for SPM, evaluating immediate responses under specific loads, remains largely untapped.

This study explores the transformative potential of DFOS in concrete bridge monitoring, with a focus on the role of signal processing in unlocking comprehensive structural understanding. Using datasets collected during static load tests on a full-scale prestressed concrete bridge, the approach demonstrates how DFOS-derived strain profiles provide a dual lens, detecting local effects like cracks and elucidating global responses like girder interactions and boundary effects. The primary objective of this study is to show the result of application a novel SPM methodology that integrates DFOS technology with static load testing to provide detailed evaluations of both local and global structural behaviors [8].

This approach is applied to an existing prestressed concrete bridge, Ferpècle bridge in Switzerland. This methodology illustrates the substantial benefits of DFOS and signal processing in providing a holistic understanding in enhancing safety, optimizing maintenance strategies, and extending the service life of critical infrastructure.

## 2 BRIDGE BEHAVIOURS IDENTIFICATION – 6 STEPS METHODOLOGY

Evaluating the structural integrity of existing bridges, especially those with complex geometries, demands detailed knowledge of their characteristics and construction history, yet such information is frequently incomplete or absent for older structures. This section outlines a new methodology [8] that utilizes static load test data to generate new insights, enhancing the accuracy of structural assessments. The methodology, illustrated in Figure 2, centers on SPM of girder bridges using DFOS.

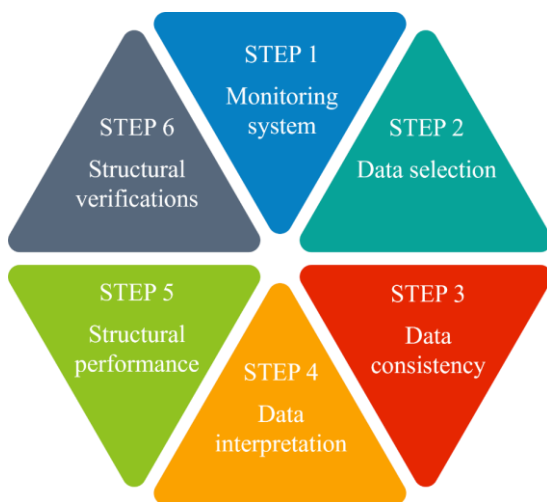


Figure 2. Overview of the methodology for the examination of existing girder concrete bridges with DFOS.

Step 1 involves selecting monitoring systems and load test configurations to acquire informative datasets. Multiple DFOS, coupled with a high-resolution data acquisition system, capture strain responses with fine spatial detail during controlled static load tests. Supplementary sensors, such as linear variable

differential transformers (LVDTs), may be incorporated to augment data richness. Step 2 entails analyzing and refining the collected data. At each measurement point, the most probable value is extracted and anomalies are filtered to ensure only reliable, representative data proceed to analysis. In Step 3, the consistency of strain data is validated against expected values derived from the bridge structural properties and the load test configurations. Step 4 examines the strain distribution to determine the bridge's static behavior, revealing global structural patterns and localized effects, such as concrete cracks (via strain peaks) and the impact of secondary elements on main girder deformations.

Step 5 extrapolates stress distributions among girders, support conditions, and bridge deflection from the strain data, yielding refined insights into structural behavior for improved assessments. Step 6 addresses structural safety through standard verifications, though these lie beyond this study's scope; further details are available in [9]. This model-free approach systematically converts raw data into actionable knowledge, facilitating a comprehensive understanding of three-dimensional bridge behavior.

## 3 STRUCTURAL PERFORMANCE MONITORING WITH DISTRIBUTED FIBER OPTIC SENSORS

### 3.1 Bridge presentation

Located in Les Haudères in the Swiss Alps (canton of Wallis) at an altitude of 1450 meters, the Ferpècle Bridge is a prestressed reinforced concrete structure erected in 1958. Designed with a single 35-meter span, the bridge originally consisted of two girders, each 1.5 meters high, arranged in a slender TT cross-section and is one of the first prestressed bridges in the country (Figure 3). In 2023, a structural intervention expanded the deck width from 5.3 meters to 7.9 meters using ultra-high-performance fiber-reinforced cementitious composite (UHPFRC). This intervention employed a cantilevered UHPFRC slab with varying thickness, rigidly linking the superstructure to the abutments and converting the bridge into a semi-integral static system (Figure 4) [9].

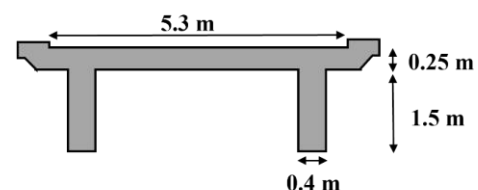


Figure 3. Photograph and cross-section scheme before intervention.

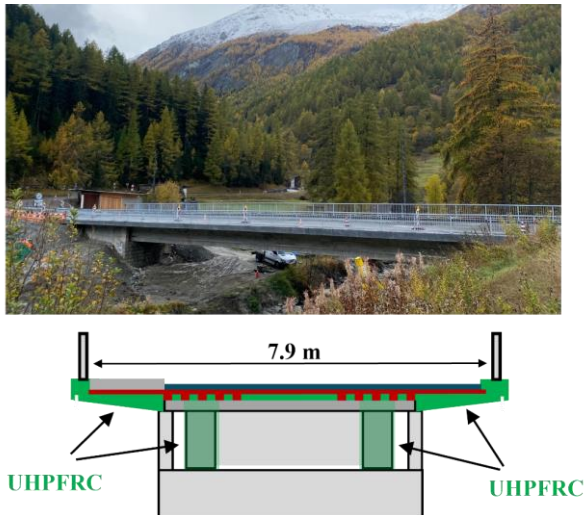


Figure 4. Photograph and cross section scheme after intervention.

This structural modification, accomplished by establishing a monolithic connection between the superstructure and abutments, redistributes bending moments, removes expansion joints and increases support capacity. As a result, the bridge benefits from significantly enhanced rigidity, bending capacity, and shear strength, while the low permeability of UHPFRC improves its long-term durability.

Materially, the bridge was initially built with C30/37 concrete, now reassessed as C40/50 to account for strength increases over time [10]. The reinforcing steel has a characteristic tensile yield stress of  $f_{yk}=345$  MPa, and the prestressed bars feature a strength of  $f_{pd}=840$  MPa. The UHPFRC, categorized as type UB, meets Swiss standards with a tensile strength of  $f_{Utd}=6.9$  MPa [11].

### 3.2 Distributed fiber optic monitoring campaign

Comprehensive monitoring campaigns were conducted in 2023 and 2024, following the intervention on the Ferpècle Bridge to evaluate its structural behavior and mechanical properties. During the deck widening from 5.3 to 7.9 meters, scaffolding facilitated the installation of distributed fiber optic sensors (DFOS) along the full 35-meter span of both prestressed concrete girders. Grooves 6 mm deep were cut into the external web of each girder, 0.5 meters from the girder bottom. DFOS cables (SMARTeC-DiTeSt SMARTProfile Sensor [12]) were affixed with glue and protected by aluminum plates to shield against environmental exposure, as illustrated in Figure 5. This figure also depicts the fiber optic positioning process and a schematization of the SMARTeC sensor, which incorporates two fibers for detecting temperature variations and two for measuring strain, both monolithic sensors with standard acrylate coating, further shielded by UHPFRC cantilevers. The installation presented challenges, requiring a scaffolding to groove the concrete and the careful gluing of fiber optic cables to avoid sensor slip. Uniform glue distribution was critical to ensure consistent response in the concrete-glue-coating-sensor system. The upstream girder is designated Channel 1 (CH1) and the downstream girder Channel 2 (CH2). Strain data were recorded using a LUNA ODiSI 6100 system [13] at a 2.6 mm resolution, yielding approximately 12,000 data points per

girder, at a 5 Hz sampling rate. Five static load tests were performed using one or two three-axle trucks, each weighing 26.4 tons (axle loads: 8.9 tons, 10.4 tons, 7.1 tons; transverse axle spacing: 2.0 meters). These configurations, detailed in Figure 4, included single-truck midspan loading (LT1 and LT2), dual-truck side-by-side placement at midspan (LT5) and longitudinal alignment along one girder (LT1 and LT2) to maximize the effects in one-quarter span.

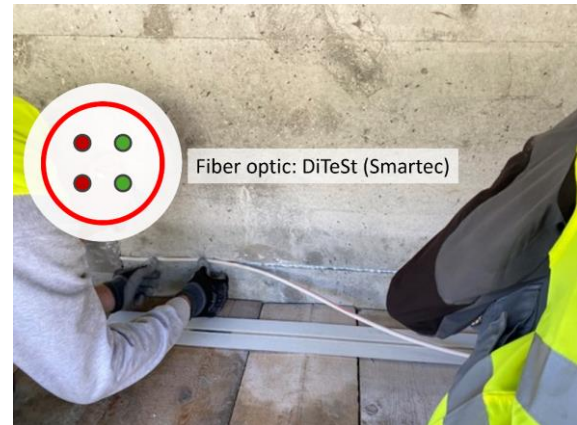


Figure 5: SMARTeC fiber optic installation

Six linear variable differential transformers (LVDTs) were installed vertically beneath the girders at midspan, near abutments and quarter-span positions, recording deflection at 10 Hz to complement DFOS datasets.

A similar monitoring campaign was conducted in 2024, differing only in the repositioning of the two LVDTs from near the abutments to the transverse beam at quarter-span locations and an increase in truck load to approximately 28 tons.

For both campaigns, temperature compensation was deemed unnecessary due to the short data collection period (approximately 30 minutes) and cloudy sky conditions. These conditions did not result in temperature changes significant enough to alter the structural response compared to the calibration baseline. This assumption is validated by the strain and LVDT signals in the time domain, as shown in Figure 9, where signals start at zero when no truck is on the bridge and return to zero after the truck leaves, indicating no effects necessitating temperature compensation.

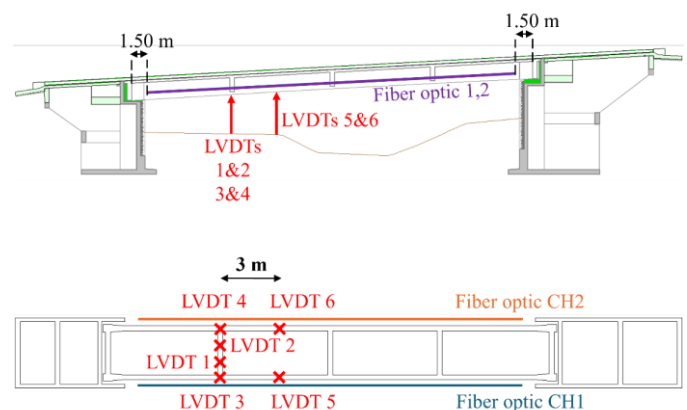


Figure 6. Sensor configuration. (Up) Elevation view; (Down) Plan view.





Figure 7. Sensor configuration. (Up) Cross section in one quarter-span for the load configuration LT3; (Down) Photo of the bridge with sensor locations.

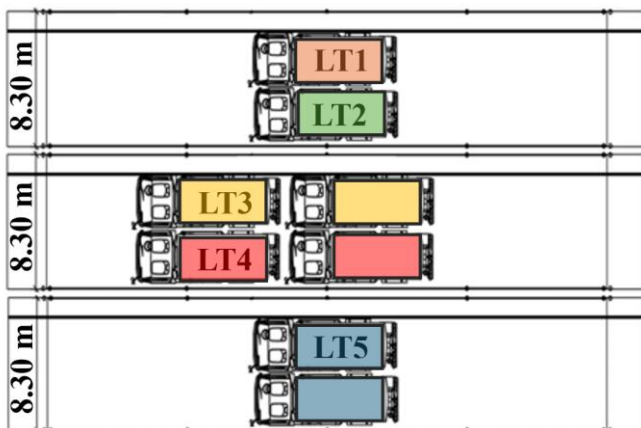


Figure 8. Static load tests with either one truck (LT1 and LT2) or two trucks (LT3, LT4 and LT5).

Each test produced two strain vectors per girder ( $N \times T$  dimensions, where  $N \approx 12,000$  points and  $T$  denotes time steps), totaling ten vectors across the campaign. LVDTs yielded six deflection vectors per test ( $1 \times T$  dimensions), totaling 30 vectors.

### 3.3 Application of the methodology for LT3

The methodology of Section 2 is applied considering the strain measurements by the DFOS for CH2 during LT3 from the monitoring campaign of 2024.

As a first step, the raw DFOS and LVDT data are processed to extract reliable structural response measurements. Consistent strain and deflection values are determined by averaging measurements taken while the trucks remain stationary (Figure 9), filtering out anomalies. For CH2, the most probable strain value at a midspan DFOS point is  $20 \mu\epsilon$  while for LVDT4 (one quarter span of CH2), the deflection is 2.32 mm. Post-selection, DFOS datasets are reduced from  $N \times T$  to  $N \times 1$  vectors ( $N \approx 12,000$ ), and LVDT datasets from  $1 \times T$  to  $1 \times 1$ , streamlining subsequent analysis. Figure 10 illustrates the reconstructed signal for LT3 in CH2.

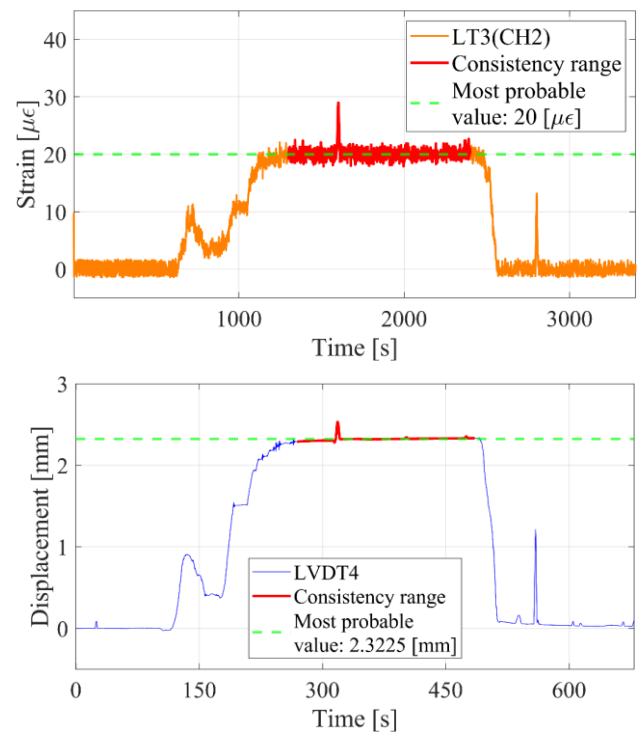


Figure 9. Signal selection. (Up) Strain value at a specific DFOS measurement of CH2 under LT3; (Down) Deflection value for LVDT4 under LT3.

The reliability of LT3 strain data is validated by confirming their consistency with expected structural behavior. The strain distribution for LT3, as shown in Figure 10, aligns fully with the load configuration and the fixed-fixed static scheme. Strain data exhibit negative values near the abutments, positive values at midspan, and zero values near the transverse beams at the one-quarter and three-quarter span positions, following the expected bending-moment diagram. Notably, the strain on the left side of the diagram is higher at the one-quarter span than at



the three-quarter span, which is entirely consistent since the load is applied at the one-quarter span.

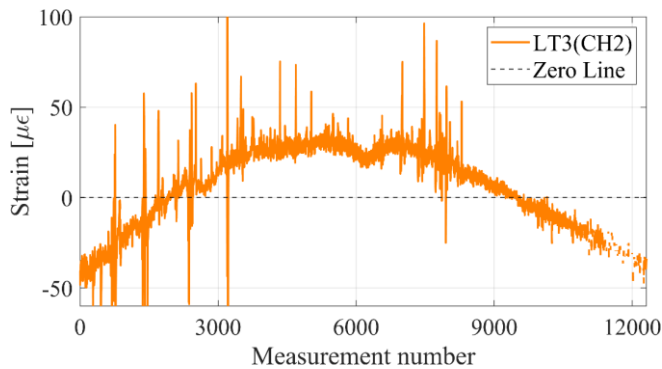


Figure 10. Reconstructed strain signal with the selected value at every DFOS measurement location of CH2 under LT3.

Beyond the noise range (approximately  $\pm 5 \mu\epsilon$ ), strain peaks are observed on the left side and near midspan on the right side, represented by red dots in Figure 11.

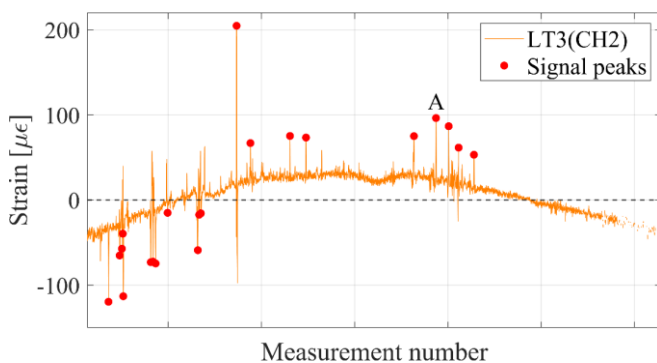


Figure 11. Peaks characterization for LT3 data in CH2.

These peaks are localized using the prominence technique [14], which identifies significant strain values by measuring how much they stand out from their surroundings. The strain peaks are detected in the negative strain zone when the strain is negative (at the initial and end sides of the bridge) and in the positive strain zone when the strain is positive (at the middle of the bridge), reflecting the expected strain distribution. This method ensures that only relevant peaks, corresponding to structural responses rather than noise, are detected. Furthermore, as depicted in Figure 12, these peaks persist throughout the monitoring period when the truck is stationary, confirming their consistency rather than indicating transient anomalies. They likely indicate concrete cracks or stress concentrations, which, for this case study, cannot be confirmed through visual inspection or unmanned aerial vehicle (UAV) photogrammetry due to the protective steel plates covering the fiber optic locations. Since the available data do not allow differentiation between cracks and stress concentrations, all strain peaks are conservatively treated as cracks. The relative crack opening (positive strain) and relative crack closing (negative strain) are evaluated by integrating the strain over the effective influence length of the crack.

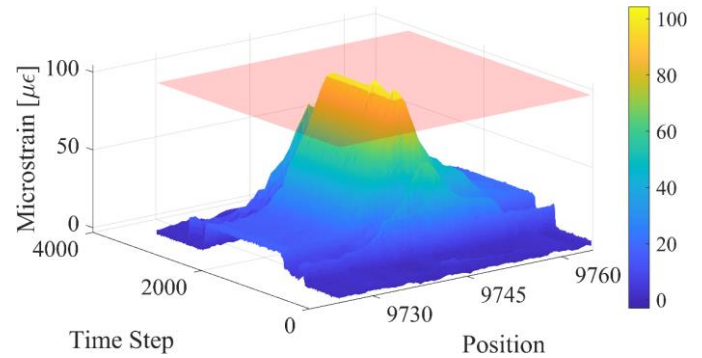


Figure 12. Consistency of DFOS measurements at peak A location in time.

Figure 13 presents histograms of relative crack opening and closing, clearly showing that the magnitudes are very low and do not pose structural concerns. The term ‘relative’ is used because the DFOS signal captures only the strain induced by the load test, not pre-existing crack widths. The width of pre-existing cracks and the causes of these strain peaks will be investigated in future monitoring campaigns. Additionally, some data are absent on the right side of the signal, but given the high spatial resolution (2.6 mm gauge pitch), the dataset remains sufficiently consistent for analysis.

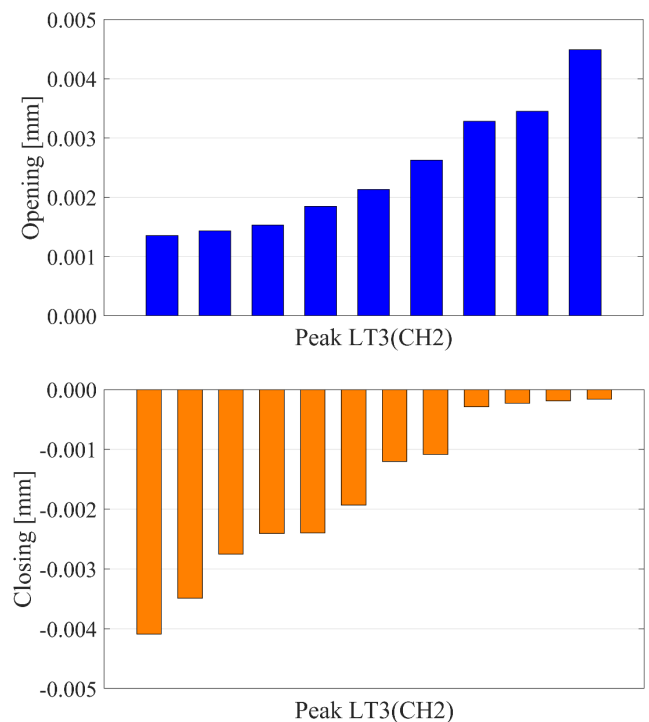


Figure 13: Crack width variation for LT3 in CH2. (Up) Relative crack opening; (Down) Relative crack closing.

The analysis of DFOS data highlights the localized impacts on strain distribution at the interfaces between the main girders and secondary beams, significantly shaped by the specific load configurations applied. The strain distribution across CH1 and CH2 displays distinct localized effects near the crossbeam edges. The LT3 load configuration induces a noticeable strain

reduction near the junctions with secondary beams, as evident in Figure 14.

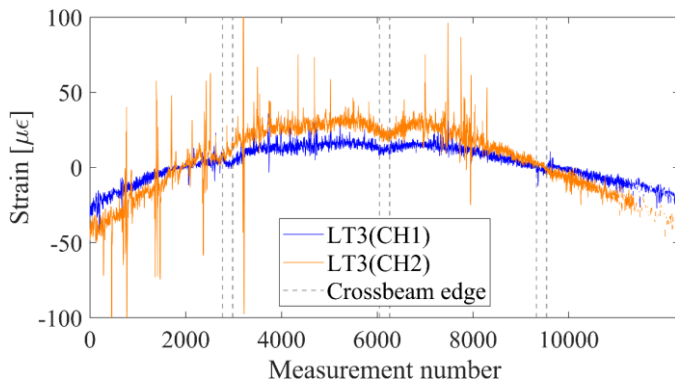


Figure 14. Strain measurements along the main girders for LT3 data of 2024.

This phenomenon stems from the transverse positioning of the axial load and the three-dimensional interactions between the main girders and secondary beams.

At this stage, the structural performance can be assessed using three key parameters:

- transverse load distribution between the main girder, quantifying the traffic load carried by each girder;
- boundary conditions;
- deflection of the main girders.

The transverse load distribution is evaluated by analyzing the strain ratio from DFOS datasets for the two main girders. This approach captures the influence of structural characteristics and load configurations while ensuring robustness by minimizing the impact of localized anomalies through reliance on spatially continuous strain data.

To illustrate the effectiveness of DFOS measurements, five monitoring scenarios are examined, each using different methods to calculate load distribution coefficients derived from sensor data:

- Scenario 1 uses strain data from the DFOS, focusing on the ratio between CH1 and CH2 measurements;
- Scenario 2 employs values calculated from equilibrium equations based on classical beam theory (De Saint-Venant), typically used in bridge assessments without monitoring data;
- Scenario 3 relies on discrete strain measurements at midspan, simulating a conventional strain gauge at that location;
- Scenario 4 combines discrete strain measurements at midspan and quarter-span strain data;
- Scenario 5 integrates discrete strain measurements at midspan and near-support measurements.

Results for load distribution coefficients ( $\epsilon_{CH2}/\epsilon_{CH1}$ ) for LT3 are presented in Figure 15. The strain ratios using DFOS display a near-Gaussian distribution. For Scenario 1, the strain ratio is thus taken as the mean value of this distribution. When calculated using only discrete measurements (Scenarios 3 to 5), the results are substantially affected by local phenomena linked to boundary effects and strain variability at critical sections. Moreover, employing classical pre-design approaches based on equilibrium equations (Scenario 2), the strain ratio obtained

differs significantly from the measured DFOS strain ratio, indicating that load distribution between girders is more balanced than suggested by conservative design assumptions.

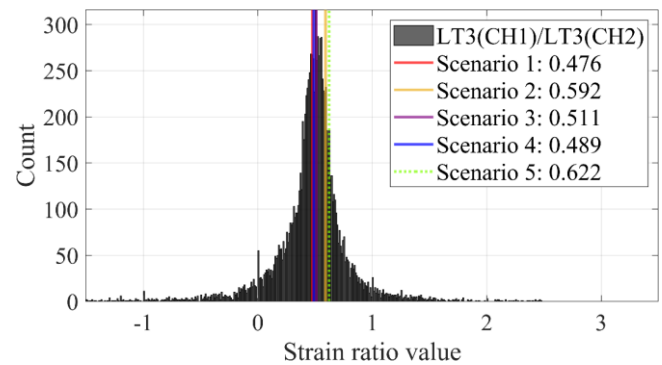


Figure 15. Transversal load distribution evaluation.

These scenarios result in inaccurate bending moment evaluations, as shown in Figure 16, potentially overestimating or underestimating safety.

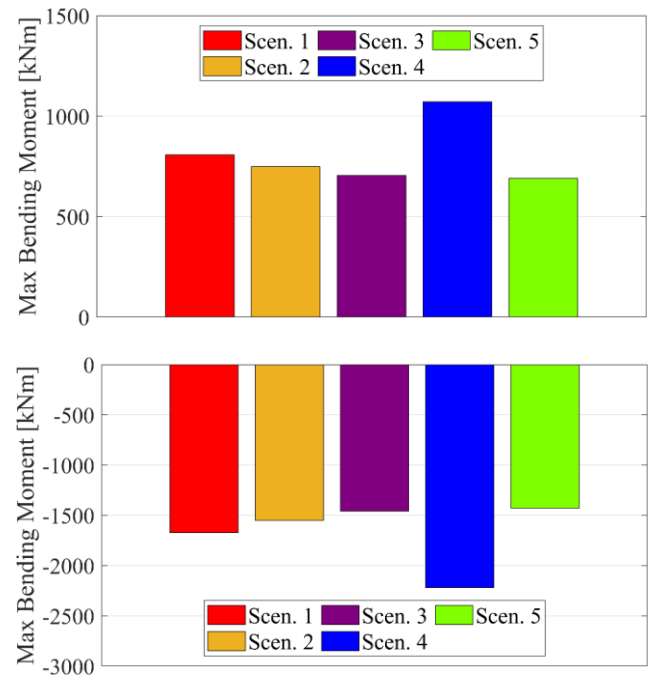


Figure 16. Bending moment comparison. (Up) Maximum bending moment in CH2; (Down) Minimum bending moment in CH2.

Once the load distribution is established, the characterization of boundary conditions becomes essential. These are evaluated by comparing DFOS strain profiles with theoretical distributions for simply supported and fixed-fixed configurations (Figure 17). From the graph, the theoretical fixed-fixed model closely aligns with the observed data (negative strains at supports, positive at midspan), confirming the post-intervention static scheme. Minor discrepancies, due to uncertainties in elastic modulus ( $E$ ), stiffnesses of abutments, and load distribution coefficients, do not compromise this conclusion, confirming the structural modification's effectiveness.

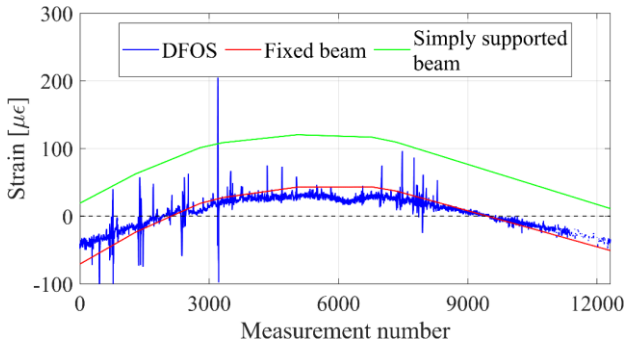


Figure 17. Boundary-condition valuation in CH2 under LT3.

Subsequently, bridge deflection is derived from DFOS datasets via double integration of the strain profile, following the methodology outlined in [8]. This process relies on load distribution data, boundary conditions, and structural rigidity. Since the latter cannot be directly measured from DFOS datasets, it is approximated between 33 GPa (C30/37) and 42 GPa (C80/95). Simulations with different rigidity values enable defining an envelope of possible bridge deflections, with the best fit, calibrated across all five load tests, determined by aligning rigidity with LVDT measurements, as shown in Figure 18.

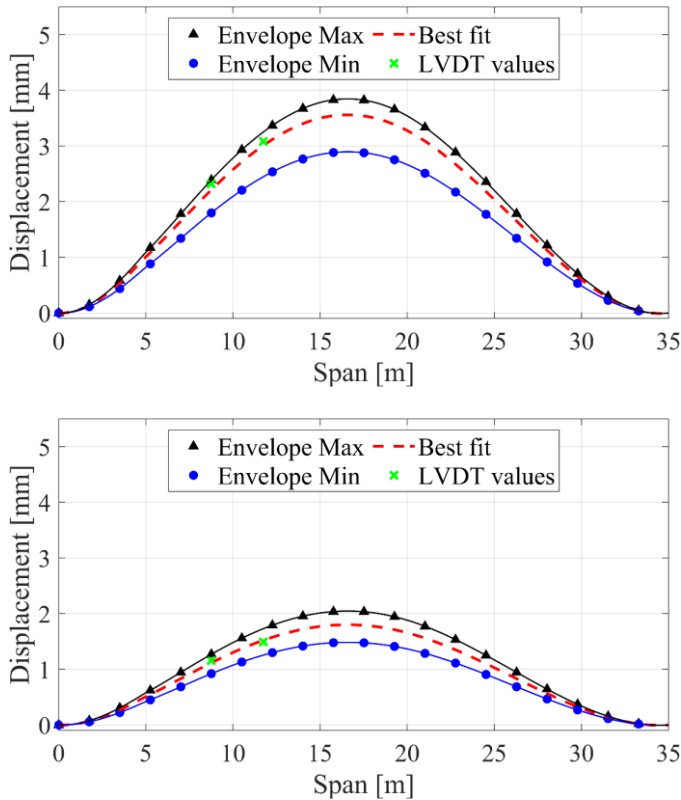


Figure 18. Comparison DFOS displacement predictions vs LVDT measurements under LT3. (Up) Comparison in CH2; (Down) Comparison in CH1.

The mean discrepancy between best-fit predictions and LVDT measurements, considering all load tests (LT1 to LT5) for both

channels (CH1 and CH2), is 0.065 mm. This compares favorably to the 0.101 mm mean absolute difference reported in [8] using 2023 datasets, possibly due to greater uncertainty in LVDT positioning in 2023 compared to 2024. The small differences between these predictions demonstrate that DFOS-based deflection estimates can closely match actual measurements when rigidity is calibrated.

Furthermore, the impact of discrete strain measurements and conservative pre-design assumptions on displacement prediction is evaluated. Table 1 presents the maximum, minimum and mean absolute relative displacement differences between DFOS and LVDT measurements for Scenarios 1 to 5. The maximum difference increases significantly from Scenario 1 (0.162 mm) to others: 405% (0.818 mm) in Scenario 2, 253% (0.571 mm) in Scenario 3, 1909% (3.252 mm) in Scenario 4, and 264% (0.590 mm) in Scenario 5. The minimum difference varies slightly, from 0.00018 mm in Scenario 4 to 0.020 mm in Scenario 3. The mean difference rises by 362% (0.299 mm) in Scenario 2, 267% (0.238 mm) in Scenario 3, 1141% (0.803 mm) in Scenario 4, and 183% (0.183 mm) in Scenario 5 relative to Scenario 1 (0.065 mm).

Table 1. Maximum, minimum, and mean absolute relative displacement values between DFOS and LVDT measurements for Scenarios 1 to 5.

	Max discrepancy [mm]	Min discrepancy [mm]	Mean discrepancy [mm]
Scenario 1	0.162	0.013	0.065
Scenario 2	0.818	0.002	0.299
Scenario 3	0.571	0.020	0.238
Scenario 4	3.252	0.0018	0.803
Scenario 5	0.590	0.005	0.183

These findings indicate that Scenarios 2 to 5 yield mean displacement estimation errors ranging from 0.2 mm to 0.8 mm, whereas Scenario 1 has a mean error around 0.065 mm, establishing it as a reliable tool for displacement monitoring. It demonstrates that load-distribution estimations using only discrete strain measurement may be inaccurate and lead to significant discrepancies in the expected bridge deflection.

#### 4 CONCLUSIONS

This study investigates the DFOS-based methodology from [8], originally developed for 2023 datasets, to analyze the 2024 Ferpècle Bridge datasets. By evaluating strain data across both channels under various static load configurations, the approach demonstrates its ability to capture local phenomena (e.g., cracks, secondary beam effects) and global responses (e.g., boundary conditions, load distribution, displacement estimates) with exceptional accuracy and precision. Compared to traditional discrete strain sensors, DFOS offers significant advantages, yielding the following insights:

- **High-resolution monitoring.** DFOS enables spatially continuous strain measurements with millimeter-scale precision, accurately determining load distribution coefficients, bending moment diagrams, and displacement estimates with ~0.1 mm accuracy, surpassing the capabilities of discrete sensors.



- **Longitudinal (1D) crack detection.** The methodology reliably identifies cracks and stress concentrations but faces challenges in classification due to limited data on pre-existing micro-crack distributions (sometimes difficult to detect due to their size and locations) and its linear sensing configuration, which restricts bi-dimensional (2D) strain mapping.
- **Consistency across years.** The 2024 results align closely with 2023 findings, confirming the methodology's reliability, high accuracy, and precision, while indicating no significant structural changes in the bridge.
- **Future directions.** Further research should investigate temperature effects under ambient daily and seasonal loads, integrate visual inspection or UAV photogrammetry alongside 2D strain mapping to enable proper crack characterization and develop a calibrated finite element model (FEM) to support long-term SHM.

This high-resolution DFOS methodology provides detailed insights into structural behavior, enabling precise safety assessments and informed decision-making for sustainable bridge maintenance and management.

## ACKNOWLEDGMENTS

The authors are thankful to the Structural Engineering Platform (GIS) from École Polytechnique Fédérale de Lausanne (EPFL) and Prof. Eugen Brühwiler for supporting the data collection process. The authors are also thankful to the DMTE – Service de la mobilité from the Wallis Canton for supporting the monitoring campaign.

## REFERENCES

- [1] N. Bertola and E. Brühwiler, 'Risk-based methodology to assess bridge condition based on visual inspection', *Structure and Infrastructure Engineering*, vol. 19, no. 4, pp. 575-588, 2021. DOI: [10.1080/15732479.2021.1959621](https://doi.org/10.1080/15732479.2021.1959621).
- [2] N. Bertola et al., 'A global framework for data-informed bridge examination', *Structure and Infrastructure Engineering*, pp. 1–20, 2024. DOI: [10.1080/15732479.2024.2337088](https://doi.org/10.1080/15732479.2024.2337088).
- [3] M. Q. Feng et al., 'Baseline Models for Bridge Performance Monitoring', *Journal of Engineering Mechanics*, vol. 130, no. 5, pp. 562–569, 2004. DOI: [10.1061/\(ASCE\)0733-9399\(2004\)130:5\(562\)](https://doi.org/10.1061/(ASCE)0733-9399(2004)130:5(562)).
- [4] B. Glisic, 'Concise historic overview of strain sensors used in the monitoring of civil structures: The first one hundred years', *Sensors*, vol. 22, no. 6, pp. 2397, 2022. DOI: [10.3390/s22062397](https://doi.org/10.3390/s22062397).
- [5] H.-N. Li et al., 'Recent applications of fiber optic sensors to health monitoring in civil engineering', *Engineering Structures*, vol. 26, no. 11, pp. 1647–1657, 2004. DOI: [10.1016/j.engstruct.2004.05.018](https://doi.org/10.1016/j.engstruct.2004.05.018).
- [6] F. I. H. Sakiyama et al., 'Structural health monitoring of concrete structures using fibre-optic-based sensors: a review', *Magazine of Concrete Research*, vol. 73, no. 4, pp. 174–194, 2021. DOI: [10.1680/jmacr.19.00185](https://doi.org/10.1680/jmacr.19.00185).
- [7] L. Zhang et al., 'Over 25-year monitoring of the Tsing Ma suspension bridge in Hong Kong', *J Civil Struct Health Monit*, vol. 15, pp. 263–283, 2024. DOI: [10.1007/s13349-024-00842-5](https://doi.org/10.1007/s13349-024-00842-5).
- [8] F. Fabbriatore and N. Bertola, 'Methodology for concrete girder bridge performance monitoring through distributed fiber optic sensors', *Structural Health Monitoring*, under review, 2025.
- [9] N. Bertola and E. Brühwiler, 'Transforming The Static System of Prestressed Concrete Bridges Using UHPFRC', *Journal of Bridge Engineering*, vol. 30, no. 7, 2025. DOI: [10.1061/JBENF2.BEENG-7234](https://doi.org/10.1061/JBENF2.BEENG-7234).
- [10] 'SIA 269 - Existing structures', 2011.
- [11] 'SIA 2052 - Béton fibré ultra-performant (BFUP) - Matériaux, dimensionnement et exécution', 2016.
- [12] SMARTProfile II, Smartec, 2017. <https://smartec.ch/en/product/smartprofile-ii/>
- [13] 'ODiSI 6100 User's Guide', 2020. <https://lunainc.com/sites/default/files/assets/files/resource-library/ODiSI%206100%20User%20Guide.pdf>
- [14] B. Richter et al., 'Crack monitoring on concrete structures with distributed fiber optic sensors—Toward automated data evaluation and assessment', *Structural Concrete*, vol. 25, no. 2, pp. 1465-1480, 2023. DOI: [10.1002/suco.202300100](https://doi.org/10.1002/suco.202300100).

# AI-driven Smart-Liner System with DFOS for Digital Twin-Based Real-Time Monitoring of Oil and Gas Infrastructure

Junyi Duan<sup>1</sup>, Xingyu Wang<sup>2</sup>, Huaixiao Yan<sup>1</sup>, Sike Wang<sup>1</sup>, Ying Huang<sup>2</sup>, Chengcheng Tao<sup>1\*</sup>

<sup>1</sup>School of Construction Management Technology, Purdue University, West Lafayette, Indiana 47907, USA

<sup>2</sup>Department of Civil, Construction, and Environmental Engineering, North Dakota State University, Fargo, North Dakota 58102, USA

Email: duan102@purdue.edu, xingyu.wang@ndsu.edu, yan486@purdue.edu, wang6711@purdue.edu, ying.huang@ndsu.edu, tao133@purdue.edu

**ABSTRACT:** This study presents an innovative AI-powered smart-liner system designed to enhance the safety and efficiency of oil and gas transportation and storage infrastructure. By integrating polymer composite liners with distributed fiber optic sensors (DFOS), the system enables continuous monitoring of mechanical deformations and damage formation, providing real-time insights into the infrastructure's condition throughout its lifespan. Finite element analysis (FEA) is employed to simulate the mechanical responses of the smart-liner-protected specimen over time. Machine learning (ML) algorithms are applied to analyze images generated from collected DFOS data, enabling the identification and assessment of risk variations across different locations and time steps. This approach demonstrates the high accuracy and effectiveness of ML in automatically detecting deformations and crack formation under buckling loading conditions. The methods enable comprehensive structural health monitoring, allowing for precise localization, visualization, and quantification of mechanical changes and damage within the infrastructure. With the above approaches, the smart-liner system facilitates continuous data collection across the entire protected surface, supporting the development of a dynamic digital twin model that evolves alongside the infrastructure. The findings provide critical insights for the oil and gas industry, offering an advanced and efficient solution for monitoring and mitigating risks associated with transportation and storage infrastructure.

**KEY WORDS:** Distributed fiber optic sensors; Structural health monitoring; Finite element analysis; Machine learning.

## 1 INTRODUCTION

As the traditionally most energy-consuming industry in the United States [1], the oil and gas industry relies on an extensive network of pipelines, storage tanks, and processing facilities to transport and store hydrocarbons. The infrastructure network is crucial for maintaining the stability and efficiency of the energy supply chain, ensuring that the country can meet its growing energy demands and support rapid economic growth. However, pipeline infrastructure is subjected to various mechanical, environmental, and operational stresses that can lead to material degradation, structural deformations, and eventual failures. Such failures pose significant risks, including environmental pollution, financial losses, and safety hazards for personnel and surrounding communities. A notable example of oil and gas infrastructure failure is the Deepwater Horizon oil spill in the Gulf of Mexico, which occurred in 2010. This disaster is one of the largest and most devastating oil spills in history. The primary cause was the failure of the cement and shoe track barriers, allowing the uncontrolled surge of high-pressure hydrocarbons to escape from the wellbore, travel up the riser, and ignite the oil spillage [2]. Additionally, the San Bruno pipeline explosion occurred in the same year due to the fracture in the welded seam, resulting in the eight deaths [3]. These catastrophic events show significant needs for protecting and monitoring the health conditions of the oil and gas infrastructure.

Ensuring the mechanical resilience of infrastructure is crucial. One way to protect the oil and gas infrastructure is by implementing a polymer composite liner, which is made of fiber fabric and polymer composite. It serves as an additional protective layer, protecting metallic pipelines and storage tanks

from mechanical stress, corrosion, and environmental degradation [4], [5]. Polymer composite liners provide significant advantages, including high strength-to-weight ratios, corrosion resistance, and enhanced durability [6]. The liners are engineered to withstand extreme environmental conditions, making them ideal for high-risk applications such as oil and gas transportation and storage. However, despite these benefits, the liner-protected infrastructure still faces structural challenges. One critical issue is mechanical deformation, which can occur due to factors such as thermal expansion, pressure fluctuations, external impacts, and ground movement. Over time, these deformations may lead to localized buckle or collapse, ultimately compromising the structural integrity [7]. Traditional monitoring techniques, such as periodic visual inspections and ultrasonic testing, are often insufficient in detecting infrastructure early-stage damage, as many deformations occur beneath the surface or in hard-to-reach areas. Additionally, the liner is always installed on the interior surface of infrastructure, making the inspection and maintenance even more difficult. To address these limitations, a practical and efficient structural health monitoring (SHM) system is necessary to ensure prolonged service of liner-protected oil and gas infrastructure.

Distributed fiber optic sensor (DFOS) is widely used in monitoring structural health, for its ability of continuous measurement along the fiber length [8]. DFOS operates by transmitting light pulses through optical fibers and analyzing the backscattered signals to measure strain and temperature along the fiber length. This capability is particularly important for large-scale infrastructure, where traditional sensors are impractical or insufficient. Besides, DFOS has advantages in

small size, lightweight, water resistance, and suitable for harsh working environments such as extreme weather conditions and seismic-prone regions, making it applicable and reliable in the oil and gas industry [9]–[11]. Zhang et al. [12] attached DFOS on the exterior surface of the pipeline to monitor its compressive and tensile strain distribution. Inaudi and Glisic [13] monitored the conditions of gas pipelines with DFOS for two years. The measured strain and temperature results showed high accuracy. The installation method of both DFOS and liner involves attaching them to the interior surface of the target object. Therefore, the integration of DFOS and polymer composite liner is worth exploring, as it has the potential for simultaneous structural protection and real-time SHM. The DFOS-embedded liner system becomes “smart”, which facilitates continuously track of strain variations, and provides early warnings before critical failure occurs. For example, with the continuous measurement and sensitivity properties of DFOS, it is widely applied to detect cracks in concrete structures [14]. Thus, it also has the potential to detect cracks in liners for the development of a comprehensive SHM for oil and gas infrastructure. This integration marks a significant advancement in SHM, enabling a proactive approach to oil and gas infrastructure maintenance.

With the development of smart sensor and AI technology, digital twin becomes an emerging technology in civil and infrastructure applications. DFOS is a critical component in a digital twin model, for its capacity of collecting and updating real-time data [15]. Digital twin model acts as a dynamic, real-time, virtual representation of physical structures. It continuously evolves based on data and simulators for real-time monitoring purpose [16]. Although DFOS provides real-time strain monitoring data, the digital twin model has limitations in presenting the structural shape, for example, the deformation information. To address this issue, finite element analysis (FEA) is an alternative solution, for its capacity in simulating structural mechanical responses efficiently. As the infrastructure is monitored using DFOS, real-time strain data can be correlated to FEA simulation results to find the corresponding deformation information, which supports the development of the digital twin model. The correlation approach requires a high-efficiency method to satisfy the requirement of real-time monitoring purpose. Hence, the AI-driven machine learning (ML) based method is proposed to automatically identify the most accurately correlated pairs. Then the structural deformation is reconstructed and provided to establish an efficient, real-time digital twin model in a rapid response time. Additionally, minor damages are found in the polymer composite liners of oil and gas pipelines [17]. The early detection and maintenance are vital for structural safety. By integrating DFOS with FEA and AI-driven correlation methods, an efficient and real-time digital twin model can be developed to enhance structural health monitoring. This approach not only improves real-time visualization of structural behavior but also facilitates early damage detection, ultimately contributing to the safety and longevity of critical oil and gas infrastructure.

In this paper, we develop a smart-liner system with DFOS to protect and real-time monitor the strain responses of oil and gas infrastructure. FEA and AI-driven approaches are paired with the smart sensor data to identify the digital twin-based real-time

SHM function. Section 2 introduces the experimental design, including the materials used to prepare the test sample and experimental instrumentation. Section 3 provides the method of DFOS strain field generation and interpolation function for damage identification and localization. Furthermore, the steps for the digital twin model establishment are introduced, including developing the finite element model for experimental validation and conducting AI-driven strain field correlation between DFOS and FEA results. Section 4 presents the strain field comparison results. Meanwhile, the minor damages in the test sample are identified and localized. Afterward, the best correlated strain fields are fed back to FEA for the development of the digital twin model. This study aims to investigate the feasibility of a smart-liner system with DFOS in real-time structural health monitoring of oil and gas infrastructure, and the accuracy of the digital twin model in representing the structural information. By inducing the buckling load, the study has the potential to provide valuable insights into damage identification, localization, and prevention, contributing to the enhanced safety and reliability of oil and gas infrastructure.

## 2 EXPERIMENTAL DESIGN

### 2.1 Materials

The materials prepared to develop the smart-liner protected metallic substrate, including metallic substrate, polymer composite liner, DFOS, and adhesive layer. A 152.4 mm × 304.8 mm (W × L) steel plate is used as a substrate, which represents the metallic pipes and vessels that store and transport oil and gas. A commercial Starline® 2000 polymer composite liner made of woven fabric and polyurethane/polyethylene coating serves as a protective layer for the metallic substrate. The installation of DFOS is a critical step in sample preparation. One Luna high-definition DFOS is first firmly attached to the surface of the liner with a thin coating of 3M DP460 epoxy adhesive. After the adhesive is consolidated, the DFOS-installed liner is then securely attached to a metallic substrate through a 1 mm thick epoxy resin adhesive layer, which simulates the liner rehabilitation for oil and gas pipelines. The prepared sample is placed at room temperature for 24 hours to ensure it is fully cured. The installation of DFOS does not require specialized tools or expert personnel, making it suitable for practical field applications where ease of deployment is essential.

The schematic of a smart-liner protected metallic substrate sample is shown in Figure 1. The sample contains three layers: polymer composite liner, adhesive layer, and metallic substrate. The DFOS is embedded into the interface between the liner and adhesive layer. The thicknesses of each layer from top to bottom are 1.94 mm, 1 mm, and 0.81 mm, respectively. The DFOS, though delicate and easily fractured, is flexible which allows for embedding in a semi-circular style for turning installation direction. It is equipped with a thin, sensitive optic fiber inside, and protected by a multi-layer coating. The DFOS used in this study relies on Rayleigh scattering of light. When a laser pulse travels through the fiber, a small portion of the light is scattered in all directions due to its natural inhomogeneities [18]. External loads, such as mechanical stress, thermal expansion, or vibrations, induce strain in the fiber, causing measurable changes in the backscattered Rayleigh signal. By analyzing these changes, the system can detect variations in



strain along the length of the fiber. We install a 5 m fiber length long DFOS, covering the strain measurement area in a zig-zag pattern.

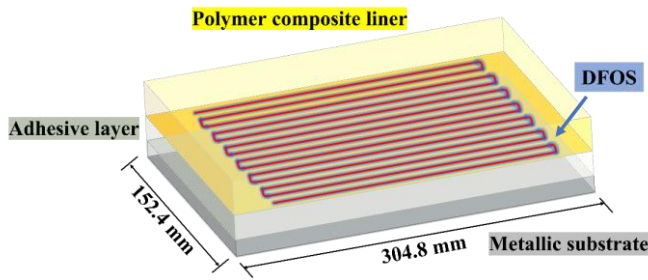


Figure 1. Schematic of a smart-liner protected metallic substrate.

## 2.2 Experimental instrumentation

To introduce the buckling damage on the smart-liner protected metallic substrate, it is placed in an MTS Criterion® Electromechanical Test Systems, which has a force capacity up to 600 kN. As shown in Figure 2, the sample is clamped on the two edges along the longitudinal direction and subjected to an eccentric buckling load, simulating real-world complex structural deformation. The two clamped sections have same dimension with 25.4 mm × 30 mm (W × L). The loading machine is controlled by a constant displacement rate of 0.2 mm/min, with a total vertical displacement of 5 mm. Luna optical distributed sensor interrogator (ODiSI) 6100 is used for strain data collection from DFOS. When backscattered light interferes with the reference signal in the interrogator, it generates an interference pattern containing phase and amplitude information, which correlates with strain variations along the fiber. By applying a fast Fourier transform, the system extracts high-resolution, spatially continuous strain data. This processed data is used to generate a high-resolution strain profile along the fiber length, providing a real-time, visually accessible strain plot on the ODiSI control platform.

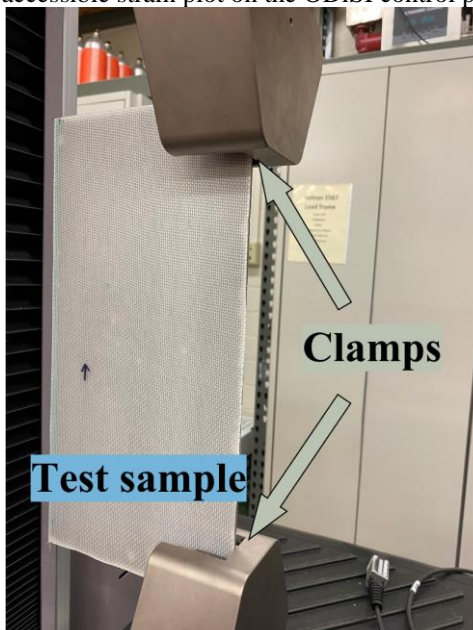


Figure 2. The smart-liner protected metallic substrate sample clamped in loading machine.

## 3 RESEARCH METHODOLOGY

### 3.1 DFOS strain field generation

The measurement performance of DFOS is highly reliant on its settings, including measurement rate and gauge pitch. If the measurement rate is too high, the generated strain data not only occupies excessive storage and computational resources but also contains unnecessary noise. Previous DFOS applications in engineering practices used measurement rates ranging from 5 to 50 Hz [19]–[21]. In this study, the measurement rate is set to 10 Hz to balance the measurement accuracy and efficiency. Gauge pitch, also called spatial resolution, refers to the distance between each measurement point along the optic fiber. The measurement area in our case is relatively small, as shown in Figure 2. A large gauge pitch, for example, 5.2 mm [22], is inapplicable. Since this is a laboratory experiment conducted with a short DFOS length, the highest available spatial resolution of 0.65 mm is selected to achieve a dense strain measurement [23].

The illustration of the smart-liner system with DFOS is shown in Figure 3. The DFOS is attached to the polymer composite liner surface in a zig-zag pattern, forming 14 distinct measurement lines with a uniform spacing of 10 mm. L1 represents the first line, and L14 is the last line close to the clamped edge, which is subjected to the largest buckling deformation. The blue stars represent the measurement point along the fiber. As discussed earlier, the distance between two contiguous measurement points equals the gauge pitch of 0.65 mm. DFOS covers an area of 130 mm × 200 mm, for strain monitoring purpose.

The generation of the DFOS strain field contains the conversion of the one-dimensional strain data to the two-dimensional strain field, through the X-Y coordinate system, as shown in Figure 3. For example, to map the strain data point on L1 into the strain field, the Y-coordinate is fixed along the line, and the X-coordinate is uniformly increasing at the rate of gauge pitch. In this approach, the DFOS strain field is generated, enabling visualization representation of strain distribution for smart-liner system.

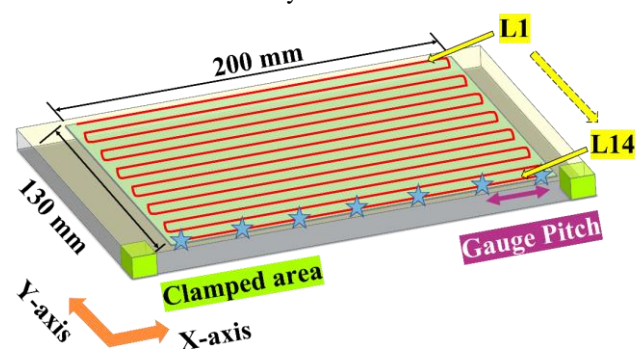


Figure 3. Schematic illustration of the smart-liner system with DFOS.

### 3.2 Damage identification and localization

To promote the application of DFOS for real-time monitoring of large oil and gas infrastructures, automated damage identification and localization are essential. When the DFOS

passes through a crack, a significant increase in strain rate is always detected, making it applicable to identify the presence and location of cracks [24]. To achieve the identification, obtaining strain values on a finer grid is the prerequisite. Bilinear interpolation and triangle-based interpolation are two widely employed planar interpolation algorithms for estimating unknown data based on known data in two-dimensional plane [25]. This study applies bilinear interpolation to estimate the strain on a finer grid, because DFOS has a fixed gauge pitch, the collected strain is uniformly distributed. Bilinear interpolation is a method that uses repeated linear interpolation to interpolate functions of two variables, which typically used on regular grids. Equation (1) illustrates how this method estimates the value for a target point using four neighboring lattice points.

$$f(x, y) \approx w_{11}f(Q_{11}) + w_{12}f(Q_{12}) + w_{21}f(Q_{21}) + w_{22}f(Q_{22}) \quad (1)$$

where  $(x_1, y_1)$ ,  $(x_2, y_2)$ ,  $(x_1, y_2)$ ,  $(x_2, y_1)$  are the coordinates of the four neighboring lattice points  $Q_{11}$ ,  $Q_{12}$ ,  $Q_{21}$ ,  $Q_{22}$ . The weights  $w$  are listed as follows:

$$\begin{aligned} w_{11} &= \frac{(x_2 - x)(y_2 - y)}{(x_2 - x_1)(y_2 - y_1)} \\ w_{12} &= \frac{(x_2 - x)(y - y_1)}{(x_2 - x_1)(y_2 - y_1)} \\ w_{21} &= \frac{(x - x_1)(y_2 - y)}{(x_2 - x_1)(y_2 - y_1)} \\ w_{22} &= \frac{(x - x_1)(y - y_1)}{(x_2 - x_1)(y_2 - y_1)} \end{aligned}$$

The gradient calculation formula, shown in Equation (2), represents the slope limit as the distance between two neighboring lattice points  $d$  approaches zero. A denser grid provides a gradient closer to the true value but increases computational costs. Based on a convergency study, we determine to interpolate strain value on  $0.1 \text{ mm} \times 0.1 \text{ mm}$  grid, as further reducing the grid size has little impact on the gradient.

$$\text{gradient} = \lim_{d \rightarrow 0} \frac{f(x + d) - f(x)}{d} \quad (2)$$

### 3.3 Establishment of digital twin model

This study aims to develop a smart-liner system with DFOS to enable digital twin-based real-time monitoring of oil and gas infrastructure. Once the smart-liner system with DFOS collects the real-time, accurate strain results, we establish a digital twin model for virtual and real-time representation. To build the virtual model, we create a three-dimensional finite element model to replicate the experimental testing on smart-liner protected metallic substrate. Section 3.3.1 presents the detailed design, including geometry, interfacial contact, and mesh information, to construct the finite element model to simulate the smart-liner protected metallic substrate under the eccentric buckling load. Section 3.3.2 shows the AI-driven method to correlate the DFOS-measured strain field and FEA-predicted strain field. This method facilitates deformation reconstruction and the digital twin model establishment to visualize buckling deformed smart-liner system in the real-time.

#### 3.3.1 Finite element model design

FEA is carried out to simulate the smart-liner protected metallic substrate under the buckling load, correlate strain results with the experimental study, and generate deformation information to establish the digital twin model. FEA is a powerful computational tool that enables accurate prediction of structural behavior under various loading conditions, which is widely applied in the oil and gas transportation and storage infrastructure [26]. By simulating experimental scenarios, it reduces the need for costly physical samples, saving both time and resources. Abaqus/CAE 2024 is employed to generate and analyze the finite element model in this study. The finite element model has same geometry and material settings as the test sample with three layers: metallic layer, the adhesive layer, and liner layer. To generate the mesh for this thin and multi-layer object, the widely-used C3D8R (8-node linear brick element with reduced integration) element is not the best choice. Instead, we select the C3D8S (8-node linear brick element with improved surface stress visualization) element for discretization, because of its advantage in estimating surface strain [27]. The mesh size of this model is 2.5 mm uniformly. The material properties of each layer are presented in Table 1. The metallic substrate is made of high-ductility steel and simulated using a bilinear model with strain hardening. The adhesive layer and polymer composite line have significantly lower stiffness compared to the metallic substrate. Thus, elastic models are applied in the analysis.

Table 1. Material properties in finite element model.

Layer	Material property
Metallic substrate	Young's modulus = 210 GPa
	Poisson's ratio = 0.3
	Yield strength = 500 MPa
	Ultimate strength = 635 MPa
Adhesive layer	Ultimate strain = 0.2
	Young's modulus = 1 GPa
Polymer composite liner	Poisson's ratio = 0.3
	Young's modulus = 400 MPa
	Poisson's ratio = 0.4

Figure 4 exhibits the finite element model of the smart-liner protected metallic substrate. The bottom edge areas are constrained to move and rotate, identical to the bottom clamped area in the experiment. The top edge is also constrained to rotation but allowed for a vertical displacement of 5 mm, accurately replicating the experimental buckling load setup. The interfacial contact between two interfaces is simplified as tied, given the careful curing procedures, to simulate a perfectly bonded condition.

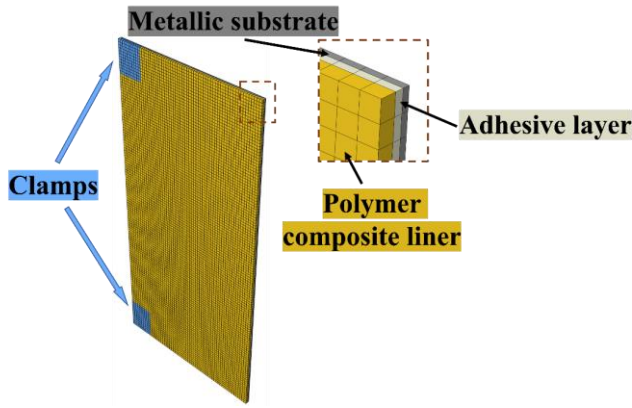


Figure 4. Finite element model of smart-liner protected metallic substrate.

Performing a buckling analysis in Abaqus involves two steps: linear eigenvalue analysis, and nonlinear Riks analysis. The linear eigenvalue analysis is the first step, which estimates the critical buckling load and corresponding mode shape. This method assumes small deformations and linear material behavior, making it computationally efficient. While this method is useful for obtaining a quick estimate of the buckling load, it does not account for geometric imperfections, material nonlinearities, or post-buckling behavior, which may lead to inaccurate predictions. Therefore, we also conduct nonlinear Riks analysis that accounts for geometric and material nonlinearities, as well as initial imperfections. The geometric and material nonlinearities are enabled by changing the setting and inputting material nonlinear properties. The first three mode shapes from linear eigenvalue analysis serve as the initial imperfections. The magnitudes of the first, second, and third buckling mode shapes are set as 1.00%, 0.50%, and 0.25% of the plate thickness, respectively [28]. The predicted strain distribution is compared with the DFOS strain field result for validation purpose, and then correlated with the DFOS strain field to generate corresponding deformation distribution to establish the digital twin model.

### 3.3.2 AI-driven strain field correlation

It is common for the strain data from experiments and simulations to exhibit slight differences, because of the discreteness of the experiment. To fill this gap, this research implements a strain field correlation method based on the convolution neural network (CNN) to find the most similar pair between DFOS and FEA results. Figure 5 illustrates the basic process of strain field correlation. The inputs are strain field images generated from DFOS and FEA, from which CNN can be used to extract the abstract features. Then, the cosine similarity between the extracted features of the DFOS and FEA data is compared. Through iterating over the entire FEA database, the best matching pair is found. In order to enhance the feature-extracting capability of CNN, the pre-trained ResNet18 model is used to process the input images. ResNet is a classic CNN that has shown extraordinary feature extraction ability in engineering fields [29], [30]. We employ ResNet18, one of the smallest models of ResNet, to process images, and its output feature maps are flattened to a one-dimensional vector for comparison. The best matching pair will be fed back

into FEA for deformation generation and digital twin model establishment.

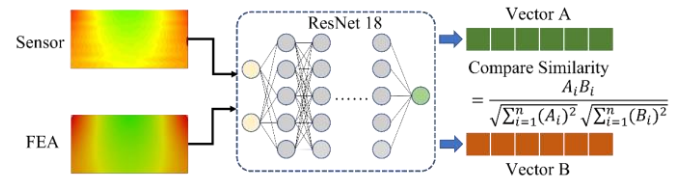


Figure 5. The workflow of strain field correlation.

## 4 RESULTS AND DISCUSSION

### 4.1 Strain field comparison between experiment and FEA

The one-dimensional DFOS data collected on the interface between the adhesive layer and polymer composite liner is converted to a two-dimensional strain field for visualization and comparison, following the methodology introduced in Section 3.3.2. The strain results with the increasing vertical displacement levels are shown in Figure 6. The positive strain in the middle of the right edge is represented in yellow, indicating the tensile strain. The negative strain at the corners of the right edges is represented in dark blue showing the compressive strain. The strain fields show an approximately symmetric pattern with respect to the central transverse line. As the test sample is subjected to an eccentric load and clamped at the corners of the left edges symmetrically, resulting in a symmetric strain distribution. The slight asymmetry can be attributed to the instrumental limitations such as the minor drifts.

Additionally, the strain distribution contours on the interface between the adhesive layer and liner are obtained from FEA results, as shown in Figure 6. To facilitate the comparison, the strain fields from DFOS and FEA are extracted at the same displacement level and share the same colormap. Due to the advantage of numerical analysis is free of external disturbances, the comparison results show that FEA has a symmetric strain distribution, which is highly similar to the results from DFOS. For further validation, we apply pixel-based comparison to quantify the similarity between DFOS and FEA results, by using the parameters including structural similarity index measure (SSIM) and mean absolute percentage error (MAPE). Table 2 presents the strain field comparison results. The SSIM results for the three cases are approximately around 0.9, indicating the results from DFOS and FEA have high similarities. MAPE results provide the relative error percentage between DFOS and FEA results, which demonstrate that the difference is less than 0.60%. Overall, the strain comparison demonstrates that the FEA results have good agreement with the DFOS results, validating the accuracy of the finite element model. Building on this, FEA can help DFOS expand the capacity from strain monitoring to mechanical performance monitoring, reconstruct the structural deformation, and facilitate the establishment of the digital twin model.



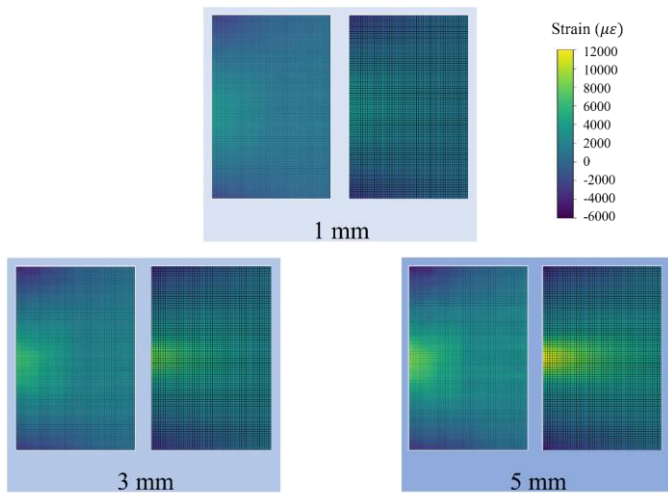


Figure 6. Strain distribution fields with increasing vertical displacements collected from DFOS (left), and FEA (right).

Table 2. Strain field comparison results.

Displacement level	SSIM	MAPE
1 mm	0.91	0.56%
3 mm	0.91	0.22%
5 mm	0.89	0.60%

#### 4.2 Identification and localization of potential damages in adhesive layer

The identification of potential damages is important, as they often correspond to the areas where failure initiates. The damages on the adhesive layer are hard to detect visually so a non-destructive monitoring method is necessary. As introduced in Section 3.2, the DFOS strain rate has a significant increase when it passes a crack. By converting the location of the strain rate surge into two-dimensional coordinates, we can localize the damage in the structure, which enables real-time structural damage monitoring. After processing the strain data from DFOS using interpolation and gradient calculation, we can visualize the region where the strain rate increases rapidly. Figure 7 shows the plot of strain gradient distribution. We set the strain gradient limit of damage as 200, any region with a strain gradient greater than 200 is highlighted in red circles. The results show that damages commonly occur close to the edge, near the highest strain region. It is also observed that, although the strain field distribution has a symmetric pattern, the potential damage has not. Therefore, the identification and localization of damage becomes more significant, as they are unpredictable. This method leverages the continuous measurement capacity of DFOS, enabling the detection and mapping of the potential damage. It enhances the efficiency of real-time structural damage monitoring, can be employed to identify potential damages in liner-rehabilitated oil and gas infrastructure, and extends the structural service life.

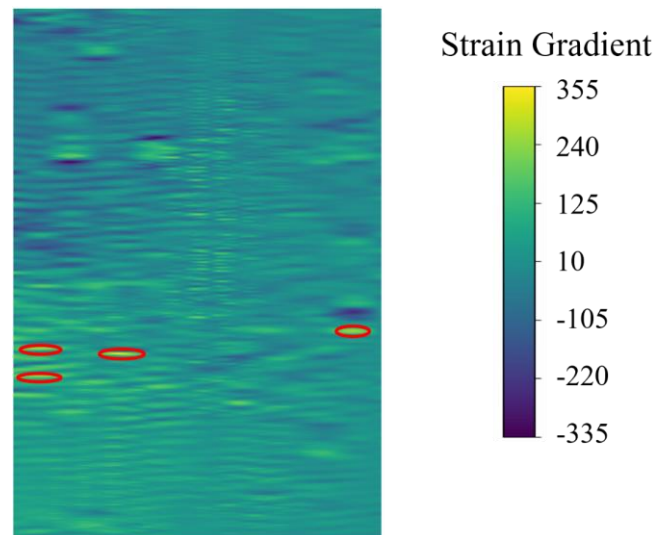


Figure 7. The location of potential damages in adhesive layer.

#### 4.3 Strain correlation and digital-twin model establishment of buckled liner-protected metallic substrate

Although DFOS and FEA results demonstrated a good agreement, the strain field correlation is required for an accurate representation of deformation reconstruction. In terms of the strain field correlation methods as introduced in Section 3.3.2, the DFOS strain fields at 1 mm, 3 mm, and 5 mm displacement levels are inputted into the AI-driven strain correlation model and set as ground truth. FEA strain fields are organized as a database, which includes all FEA strain fields at every 0.01 mm displacement. By extracting the features from DFOS strain fields and iteratively comparing the cosine similarities of the FEA strain field database, the most similar pairs are found. Table 3 shows the strain correlation results. We compare the corresponding displacements of the correlated strain field pairs. It can be seen that the correlation results have some differences, but the difference is not significant, remaining within an acceptable millimeter-level range for practical applications in the oil and gas industry.

Based on strain correlation results, we reconstruct the deformation and establish the digital twin model of the buckled liner-protected metallic substrate, as illustrated in Figure 8. The digital twin model presents the key deformation characteristics and provides a predictive framework for real-time monitoring. The comparison and correlation between the experimental and numerical strain fields verify the effectiveness of the digital twin model. The digital twin framework enables continuous tracking of deformation states, which is crucial for real-time SHM, enabling dynamic, real-time, virtual representation of the liner-protected metallic substrate. This study highlights the potential of a smart-liner system with DFOS in combination with a digital twin model for structural integrity assessment. The findings support the feasibility of using digital twin models for predictive maintenance and damage prevention in oil and gas infrastructure. Although the implementation of the digital twin model faces challenges, such as high initial investment and potential incompatibility, experimental investigation demonstrates its capability for real-time monitoring of liner-protected substrate conditions, with the potential to prevent even greater financial losses resulting from pipe failure. Additionally, the installation of CIPP liners is a mature and

widely adopted practice. The integration method developed in this study also confirms the durability of DFOS under buckling conditions. Therefore, the implementation of the smart-liner system is both feasible and promising for practical applications.

Table 3. Strain field correlation results.

Displacement level	Correlated displacement	Difference
1 mm	0.81 mm	-0.19 mm
3 mm	3.38 mm	+0.38 mm
5 mm	4.75 mm	-0.25 mm

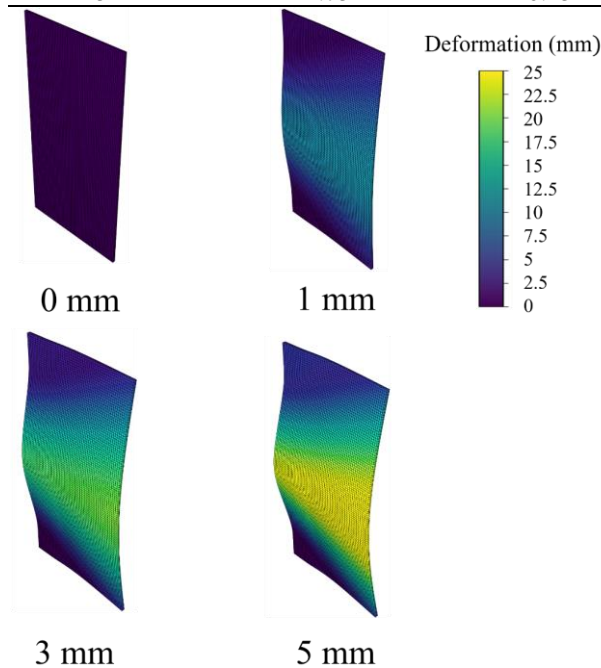


Figure 8. Digital twin model of buckled liner-protected metallic substrate with increasing deformation.

## 5 CONCLUSION

In this paper, we establish a digital twin-based real-time monitoring system for oil and gas infrastructure by integrating smart sensor technology, finite element analysis, and deep learning algorithms. Through the embedment of the distributed fiber optic sensor into the polymer composite liner, this study validates the feasibility and accuracy of the smart-liner system in real-time monitoring of the strain fields, without compensating the protective capability of the liner. Enhanced by finite element analysis, the smart-liner system achieves the capability from strain monitoring to structural mechanical performance monitoring. Further improved with a deep learning-based approach, the digital-twin model is generated for visualization of a three-dimensional smart-liner protected substrate with accurate deformation representation. In addition to the external visualization, some flaws inside of the structure, such as cracks, are detected through the smart-liner system, showing the robust health monitoring capabilities. Several summarized conclusions are listed as follows:

- The durability of DFOS under large deformation is promising. Under an extreme buckling scenario, as shown in this study, the DFOS can constantly

provide accurate and continuous data, and facilitate strain field monitoring for oil and gas infrastructure.

- The finite element analysis results are of high accuracy, with a lowest SSIM of 0.89, and highest MAPE of 0.60% compared to experimental results. This validates the reliability of developed finite element model in predicting structural behavior, supporting its use in generating digital twin model.
- The smart-liner system has the capacity to identify and localize minor cracks in the adhesive layer with high efficiency, realizing early maintenance and rehabilitation.
- The AI-driven strain correlation analysis establishes a foundation for developing the digital twin model. This model provides a real-time, three-dimensional representation of the structural physical conditions, enabling accurate structural health monitoring for oil and gas infrastructure.

In summary, this study proposes a framework for establishing the digital twin model for real-time structural health monitoring of oil and gas infrastructure. This study has limitations in assessing the proposed framework on the smart-liner protected metallic substrate. Scaling this study to large and complex oil and gas transportation and storage infrastructure networks introduces challenges such as data management, sensor deployment, and integration with existing large-scale infrastructure. With the advancement of high-performance computing technologies, data analytics is becoming increasingly capable of handling the vast amount of information generated by distributed sensing systems. Distributed sensing technologies have already been applied in large-scale structures such as bridges, railways, and pipelines [31], [32], demonstrating their feasibility and robustness in extensive monitoring applications. Furthermore, the widespread application of polymer composite liners in the oil and gas industry supports the practical applicability of scaling up the developed smart-liner system for structural health monitoring across extensive networks of pipelines and storage facilities. Future work will be expanded to the long-term durability test, aiming to investigate the long-term performance of smart-liner system and digital-twin models.

## ACKNOWLEDGMENTS

The authors express their gratitude to the funding provided to support this study from USDOT PHMSA through Grant Number 693JK32250009CAAP, an Early-Career Research Fellowship from the Gulf Research Program of the National Academies of Sciences, Engineering, and Medicine through Grant Number SCON-10000955, and the American Chemical Society Petroleum Research Fund through Grant Number PRF # 67005-DNI9. The findings and opinions expressed in this article are those of the authors only and do not necessarily reflect the views of the sponsors.

## REFERENCES

- [1] M. C. Guilford et al., 'A new long term assessment of energy return on investment (EROI) for US oil and gas discovery and production', *Sustainability*, vol. 3, no. 10, pp. 1866–1887, 2011.
- [2] M. Bly, *Deepwater Horizon accident investigation report*. Diane Publishing, 2011.

- [3] R. M. Peekema, 'Causes of Natural Gas Pipeline Explosive Ruptures', *J. Pipeline Syst. Eng. Pract.*, vol. 4, no. 1, pp. 74–80, 2013.
- [4] L. C. Hollaway, 'Using fibre-reinforced polymer (FRP) composites to rehabilitate differing types of metallic infrastructure', in *Rehabilitation of Metallic Civil Infrastructure Using Fiber Reinforced Polymer (FRP) Composites*, Elsevier, 2014, pp. 323–372.
- [5] V. Motaharnejad et al., 'Enhancement of adhesion between the polymeric liner and the metallic connector of high-pressure hydrogen storage tank', *Int. J. Mater. Form.*, vol. 14, no. 2, pp. 249–260, 2021.
- [6] M. A. Karim et al., 'An assessment of the processing parameters and application of fibre-reinforced polymers (FRPs) in the petroleum and natural gas industries: A review', *Results Eng.*, vol. 18, p. 101091, 2023.
- [7] B. Harrison et al., 'Measurement of lined pipe liner imperfections and the effect on wrinkling and collapse under bending', in *International Conference on Offshore Mechanics and Arctic Engineering*, 2016, vol. 49965, p. V005T04A036.
- [8] T. Howiacki et al., 'Crack shape coefficient: comparison between different DFOS tools embedded for crack monitoring in concrete', *Sensors*, vol. 23, no. 2, p. 566, 2023.
- [9] I. Ashry et al., 'A review of distributed fiber-optic sensing in the oil and gas industry', *J. Light. Technol.*, vol. 40, no. 5, pp. 1407–1431, 2022.
- [10] M. C. L. Quinn et al., 'Distributed Fiber Optic Sensing in Cold Regions', in *Geo-Congress 2024*, Vancouver, British Columbia, Canada, 2024, pp. 536–544.
- [11] B. Glisic and Y. Yao, 'Fiber optic method for health assessment of pipelines subjected to earthquake-induced ground movement', *Struct. Health Monit.*, vol. 11, no. 6, pp. 696–711, 2012.
- [12] S. Zhang et al., 'Pipeline deformation monitoring using distributed fiber optical sensor', *Measurement*, vol. 133, pp. 208–213, 2019.
- [13] D. Inaudi and B. Glisic, 'Long-range pipeline monitoring by distributed fiber optic sensing', 2010.
- [14] M. Herbers et al., 'Crack monitoring on concrete structures: Comparison of various distributed fiber optic sensors with digital image correlation method', *Struct. Concr.*, vol. 24, no. 5, pp. 6123–6140, 2023.
- [15] M. F. Bado et al., 'Digital twin for civil engineering systems: An exploratory review for distributed sensing updating', *Sensors*, vol. 22, no. 9, p. 3168, 2022.
- [16] A. Rasheed et al., 'Digital twin: Values, challenges and enablers from a modeling perspective', *IEEE Access*, vol. 8, pp. 21980–22012, 2020.
- [17] H. U. Khalid et al., 'Permeation Damage of Polymer Liner in Oil and Gas Pipelines: A Review', *Polymers*, vol. 12, no. 10, p. 2307, 2020.
- [18] K. Sharma et al., 'A System Design Perspective for Measurement of Parameters Using Different Scatterings Associated with Fibre Optic Sensors', in *Proceedings of Third International Conference on Communication, Computing and Electronics Systems*, vol. 844, Singapore: Springer Singapore, 2022, pp. 793–813.
- [19] L. Meng et al., 'A research on low modulus distributed fiber optical sensor for pavement material strain monitoring', *Sensors*, vol. 17, no. 10, p. 2386, 2017.
- [20] C. G. Berrocal et al., 'Crack monitoring in reinforced concrete beams by distributed optical fiber sensors', *Struct. Infrastruct. Eng.*, vol. 17, no. 1, pp. 124–139, 2021.
- [21] L. Fan et al., 'Feasibility of distributed fiber optic sensor for corrosion monitoring of steel bars in reinforced concrete', *Sensors*, vol. 18, no. 11, p. 3722, 2018.
- [22] Y. Tang et al., 'Structural and sensing performance of RC beams strengthened with prestressed near-surface mounted self-sensing basalt FRP bar', *Compos. Struct.*, vol. 259, p. 113474, 2021.
- [23] M. Herbers et al., 'Rayleigh-based crack monitoring with distributed fiber optic sensors: experimental study on the interaction of spatial resolution and sensor type', *J. Civ. Struct. Health Monit.*, 2024.
- [24] X. Tan and Y. Bao, 'Measuring crack width using a distributed fiber optic sensor based on optical frequency domain reflectometry', *Measurement*, vol. 172, p. 108945, 2021.
- [25] I. Amidror, 'Scattered data interpolation methods for electronic imaging systems: a survey', *J. Electron. Imaging*, vol. 11, no. 2, pp. 157–176, 2002.
- [26] P. Jukes et al., 'The latest developments in the design and simulation of deepwater subsea oil and gas pipelines using FEA', in *ISOPE International Deep-Ocean Technology Symposium*, 2009, p. ISOPE-D.
- [27] C. Colombo et al., 'Numerical investigation of wire-clamp contact for a drawing machine', *Procedia Struct. Integr.*, vol. 24, pp. 225–232, 2019.
- [28] E. L. Liu and M. A. Wadee, 'Mode interaction in perfect and imperfect thin-walled I-section struts susceptible to global buckling about the strong axis', *Thin-Walled Struct.*, vol. 106, pp. 228–243, 2016.
- [29] T. S. Prajwal and I. A. K., 'A Comparative Study Of RESNET-Pretrained Models For Computer Vision', in *Proceedings of the 2023 Fifteenth International Conference on Contemporary Computing*, Noida India, 2023, pp. 419–425.
- [30] W. Xu et al., 'ResNet and its application to medical image processing: Research progress and challenges', *Comput. Methods Programs Biomed.*, vol. 240, p. 107660, 2023.
- [31] J. Xu et al., 'Full scale strain monitoring of a suspension bridge using high performance distributed fiber optic sensors', *Meas. Sci. Technol.*, vol. 27, no. 12, p. 124017, 2016.
- [32] K. Soga and L. Luo, 'Distributed fiber optics sensors for civil engineering infrastructure sensing', *J. Struct. Integr. Maint.*, vol. 3, no. 1, pp. 1–21, 2018.



# Middle range, rapid strain sensing based on PNC-OFDR and its application to bridge monitoring

Yuichi Yoshimura<sup>1</sup>, Kotaro Fujiwara<sup>1</sup>, Yohei Taira<sup>1</sup>, Michio Imai<sup>1</sup>, Chao Zhang<sup>2</sup>, Fumihiko Ito<sup>3</sup>

<sup>1</sup> Kajima Technical Research Institute, 2-19-1 Tobitakyu, Chofu-shi, Tokyo, Japan

<sup>2</sup>Kogakuin University of Technology & Engineering, 2665-1 Nakano-machi, Hachioji-shi, Tokyo, Japan

<sup>3</sup>Shimane University, 1060 Nishikawatsu-cho, Matsue-shi, Shimane, Japan

email: yoshyuic@kajima.com, fujiwkot@kajima.com, ytaira@kajima.com,  
michio@kajima.com, chao@cc.kogakuin.ac.jp, ito@ecs.shimane-u.ac.jp

**ABSTRACT:** Distributed fiber optic sensing is a suitable method for long-term, wide-area monitoring of civil engineering structures such as the ground, tunnels, dams, and bridges. In recent years, distributed strain sensing technologies such as distributed acoustic sensing (DAS) and optical frequency domain reflectometry (OFDR), which can realize real-time monitoring, have made remarkable progress. In particular, OFDR, which performs strain sensing with high spatial resolution, can quantitatively evaluate the strain distribution of civil engineering structures with an accuracy comparable to conventional strain gauges. This method has been limited in its application to structural health monitoring due to its short measurement range. However, by extending the sensing distance, it is evolving into a practical technology for on-site testing. This paper introduces middle-range, rapid strain sensing based on Phase-noise-compensated OFDR (PNC-OFDR) and its application to bridge monitoring. Optical fiber sensors were installed on bridge girders, and the change in strain distribution when the moving load was applied by vehicles was measured using the PNC-OFDR sensing system.

**KEY WORDS:** PNC-OFDR; bridge monitoring; strain; dynamic strain.

## 1 INTRODUCTION

Distributed optical fiber sensing, in which an optical fiber is installed as a sensor on a target object to measure strain and temperature distribution, is actively applied for long-term, wide-range monitoring of civil engineering structures such as the ground, tunnels, dams, and bridges. For example, ground anchors embedded with optical fiber sensors are installed on on-site slopes, and landslide monitoring is performed by the tension measurement using optical fiber sensors [1]. This monitoring has been carried out over several years, and the measurement data acquired over a certain period are compared quantitatively. The long-term feasibility of the distributed strain sensing using Rayleigh backscattered light spectrum, which is a high-precision measurement technique, was reported. In addition, seafloor fiber optic cables and terrestrial fiber networks (dark fiber) over tens of kilometers are used as sensing fiber to monitor seismic activity [2] and traffic flow [3].

In terms of sensing technology, with the advent of wavelength tunable coherent OTDR [4] and DAS based on phase-OTDR [5] that detect Rayleigh backscattered light with high intensity, high-precision strain sensing on the order of  $1\mu\epsilon$  and real-time monitoring over the entire length can be performed at the construction site [6]. Currently, distributed fiber optical sensing is utilized to evaluate construction quality and manage safety in the construction field. Strain and temperature distribution data are converted into physical quantities such as displacement and tension force, and construction management based on the sensing data is carried out. For a detailed analysis of the data, it is important to verify that the strain measured by the distributed fiber optical sensing matches the value indicated by a conventional electrical strain gauge. In regard to bridge monitoring, bridge structure shows a variety of responses, from

slowly changing static strain to dynamic strain caused by traffic loads. However, few methods can evaluate strain distribution statically and dynamically with a gauge length of a few centimeters, similar to that of a strain gauge. A comparison table of DFOS spatial resolution and sample rate is shown in Figure 1. Brillouin-based sensing technology BOTDR and Rayleigh-based sensing technology TW-COTDR, which have been widely used for structural health monitoring, have a spatial resolution of about 1m or 10cm and are suitable for static sensing. Phase OTDR, one type of DAS, is utilized as a dynamic sensing method to capture vibration distributions with a spatial resolution of several meters. OFDR is both a static and dynamic sensing method [7, 8, 9] with spatial resolution close to that of a strain gauge. Despite its excellent sensing performance, OFDR has been restricted to applications in structural health monitoring due to the sensing distance limited by the temporal coherence of a laser source. Since the sensing

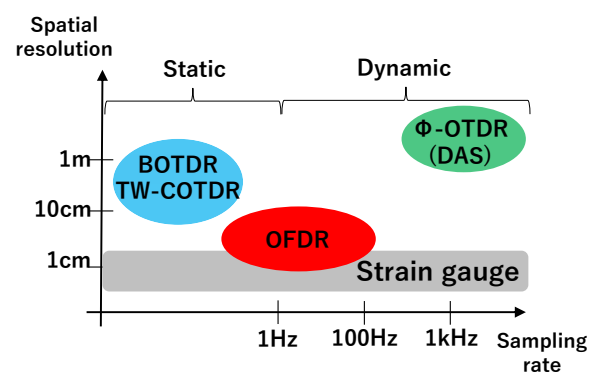


Figure 1. Performance comparison of distributed strain sensing technology.

distance is generally less than 100 m, OFDR has been widely used for laboratory use in civil engineering. On the other hand, in the field of telecommunications, a PNC (phase noise compensation) algorithm for demodulating the coherence of a laser source has already been verified, and PNC-OFDR, which implements the PNC algorithm in OFDR, has succeeded in measuring with a spatial resolution of 5 cm over a distance of 40 km [10]. However, this PNC-OFDR has not been confirmed for strain and temperature measurements performed in structural health monitoring. The authors expected that PNC-OFDR would be a practical strain sensing technology for on-site structural health monitoring and developed a distributed strain analyzer based on PNC-OFDR (Figure 2). This paper describes an overview of the PNC-OFDR based strain measurement system and reports its application to static and dynamic strain measurements on an actual bridge.



Figure 2. PNC-OFDR based distributed strain analyzer and a laptop PC for data processing.

## 2 PNC-OFDR BASED STRAIN SENSING SYSTEM

### 2.1 Rapid sensing with a fast wavelength-swept laser source

OFDR, known as a high-precision strain measurement method, incorporates a wavelength-tunable laser source with excellent coherence. Most of these tunable laser sources sweep the output wavelength slowly by motor drive and are used for the static strain analyzer that samples data over several seconds. Recently, Anritsu released a new high-speed wavelength swept light Source [11]. This laser realizes both high-speed wavelength-sweeping using a MEMS (Micro-Electro-Mechanical System) scanning mirror and high coherence, contributing to middle-range fiber sensing. Especially, sweep repetition frequency, which corresponds to the time interval in strain sensing, reaches 150 Hz. According to the Nyquist theorem, the maximum observable frequency is 75 Hz, making it possible to measure dynamic strain caused by traffic vibrations. Besides, another feature of this system is the short data acquisition time. Acquisition time per one shot is 2 msec. This property is similar to taking photographs that are resistant to subject blur using a high-speed camera and is believed to be suitable for stable static and vibration (dynamic strain) monitoring of infrastructure structures that are subjected to live loads. Figure 3 shows about data sampling when measuring static and dynamic strain with this system. The laser wavelength is swept periodically with a 15 nm width, and dynamic sensing can be performed by arbitrarily setting the time interval in synchronization with the sweep period. It is also possible to perform long-term static strain sensing, such as creep monitoring.

### 2.2 Extending the sensing distance by the PNC algorithm

In distributed strain sensing using Rayleigh scattered light, reference and measurement data are obtained, and the relative strain variation is output. Strain is calculated from the spectral correlation to each segment, corresponding to the distributed fiber optic sensor gauge. Figure 4 shows a schematic diagram of OFDR-based distributed strain sensing. The data for the entire length of the optical fiber is converted into spectral data

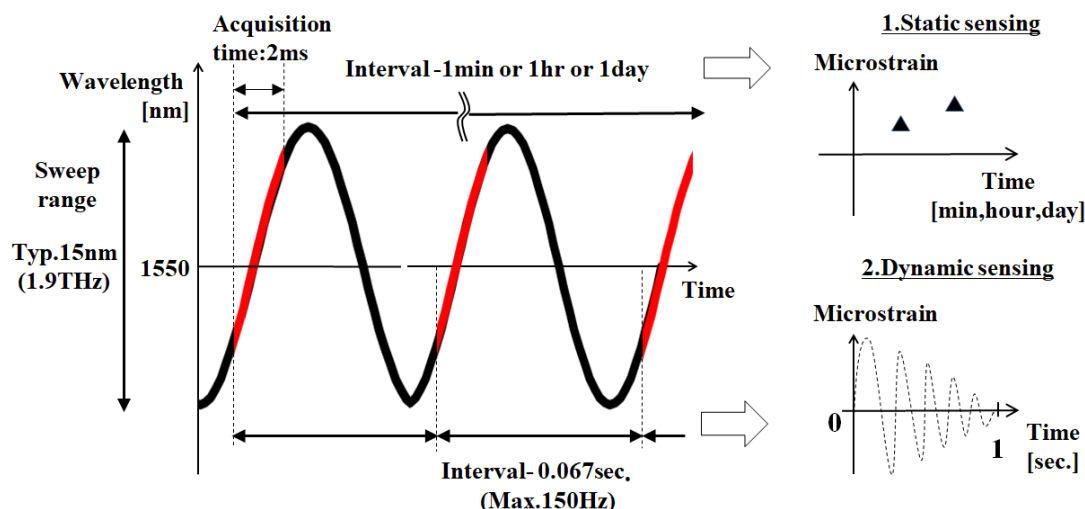


Figure 3. Static and dynamic strain sensing using with a fast wavelength-swept laser source.

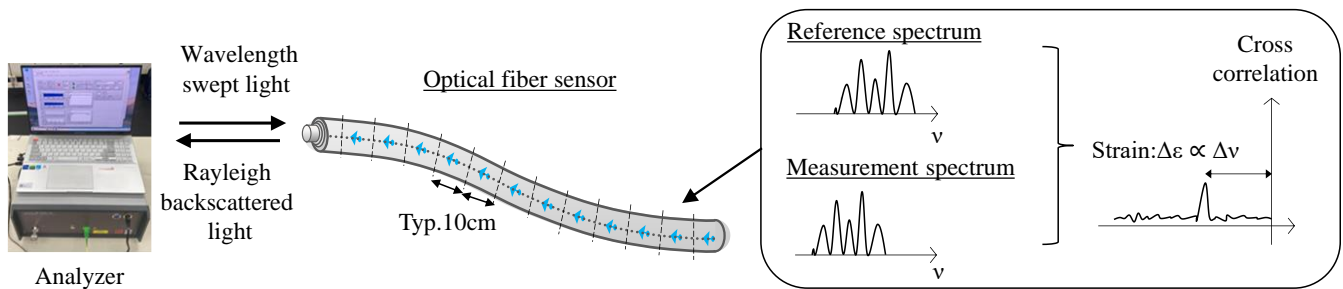


Figure 4. Schematic diagram of OFDR-based distributed strain sensing.

for each gauge, and strain is calculated by multiplying the strain coefficient by the spectral shift frequency that shows the cross-correlation peak. Since this measurement method utilizes the repeatability of the spectrum, it is particularly important to perform a linear wavelength sweep to reproduce the spectrum. To achieve high spectral correlation, wavelength sweep correction is performed, which resamples the raw data based on clock timing with a constant wavelength interval. While this wavelength sweep correction works well up to the coherence length of the source, further correction algorithms are required to go beyond the distance limit of the source. The analyzer implements a PNC algorithm to extend the sensing distance to 1,000 m [12], over 70 times the coherence length of the swept laser. Table.1 shows the measurement specifications of the PNC-OFDR based strain sensing system.

Table.1 Specifications of PNC-OFDR based strain sensing system.

Sensing distance [m]	1000
Acquisition time [ms/shot]	2
Max. sampling rate [Hz]	150
Strain resolution [ $\mu\epsilon$ ]	1
Spatial resolution [cm]	0.5~10

### 3 APPLICATION TO BRIDGE MONITORING

By applying this sensing technology to bridge monitoring, it is expected to capture the distribution of static strain changes used to evaluate seasonal variations, as well as the dynamic strain response subject to moving vehicles. In addition to identifying stress variations that indicate structural strength and the location of damage, it may be possible to obtain information useful for the maintenance and management of civil engineering structures, such as estimating traffic loads. In this study, we report the results of measuring the strain distribution when vehicles are stopped and passing through an existing bridge with optical fiber sensors installed on the bottom of the bridge girder. The applicability of PNC-OFDR sensing system to bridge maintenance was verified.

#### 3.1 Bridge monitoring methods

These tests were conducted on the prestressed concrete bridge of the Atami Beach Line (Figure5.). Figure 6. shows the layout of the optical fiber sensors and strain gauges installed on the bottom of the girder. 0.9 mm tight-buffered single-mode fiber

was used as the optical fiber sensor, and it was firmly bonded with epoxy glue to the concrete surface on the bottom of the girder closest to the mountain side.

First, a load test was conducted in which a vehicle was placed at the center of the bridge span to measure the static strain. Three vehicles with different weights were used for quantitative static strain evaluation. Then, as a dynamic load test, a 20-ton truck runs at a speed of 60 km/h on the road close to the mountain side. The strain distribution was output with a sampling interval of 5 cm and a spatial resolution of 10 cm. In the dynamic loading test, the sampling rate was set to 5 Hz.

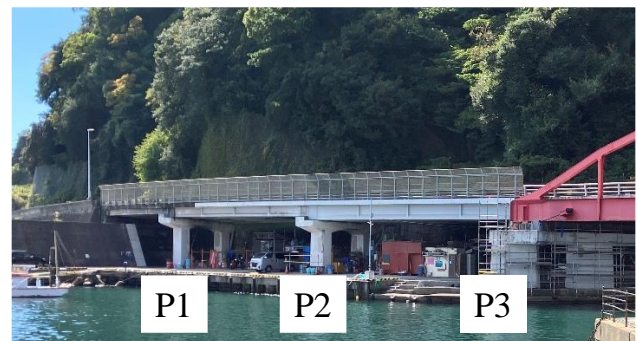


Figure 5. PC bridge of the Atami Beach Line (Testing site).

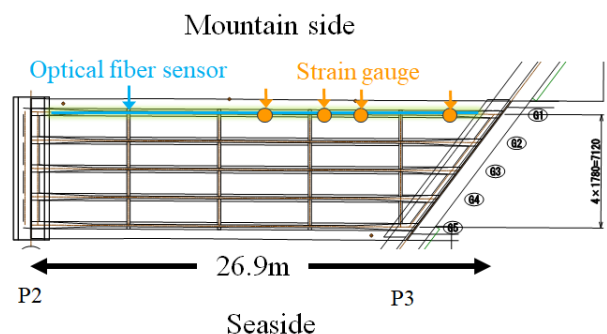


Figure 6. Location of the strain gauges and installed fiber sensors during the load test.



### 3.2 Results

Figure 7 shows the strain distribution on the bottom of the girder when cars were placed at the center position between P2 and P3. The results of the strain gauges measured at the same time were also plotted. The downward direction on a vertical axis represents tensile strain value. Tensile strain due to deflection at the bottom of the girder can be seen. The strain increases in proportion to the vehicle weight, and the strain gauge and DFOS values match well. The relationship between the strain at the center of the span and the vehicle weight is shown in Figure 8. This linear correlation indicates the elastic response of the bridge girder. These results suggest that DFOS could be used to detect overloaded vehicles that cause damage to road bridges.

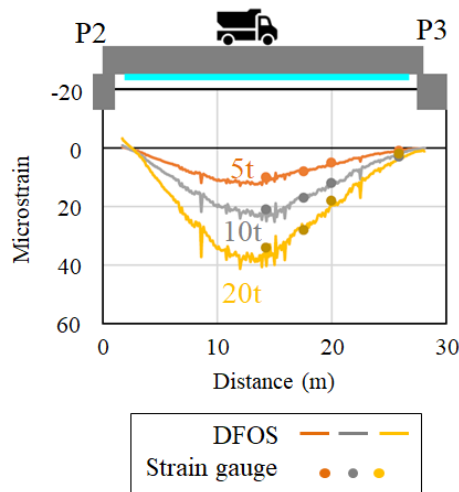


Figure 7. Strain distribution in static loading tests.

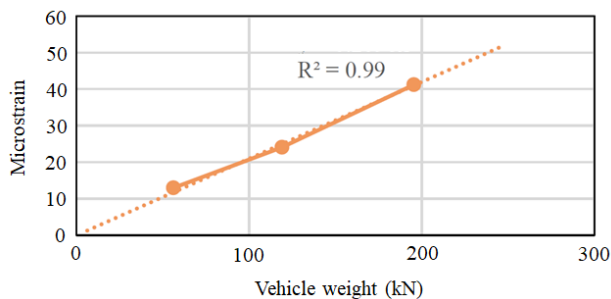


Figure 8. Relationship between strain at the center of span and vehicle weight.

Figure 9. shows the dynamic strain distribution when a 20-ton truck was running as a dynamic loading test. The strain distribution according to the vehicle position can be confirmed. At a speed of 60 km/h, it takes about 1.6 seconds to pass through the 26.9 m span. Strain distribution changes over a period of 1.6 seconds, and the dynamic strain caused by the vehicle movement is accurately captured by the PNC-OFDR based strain sensing system. Strain values at the center of the span observed in the static and dynamic loading tests were nearly equal, suggesting the possibility of dynamic weight monitoring such as the bridge weigh in motion.

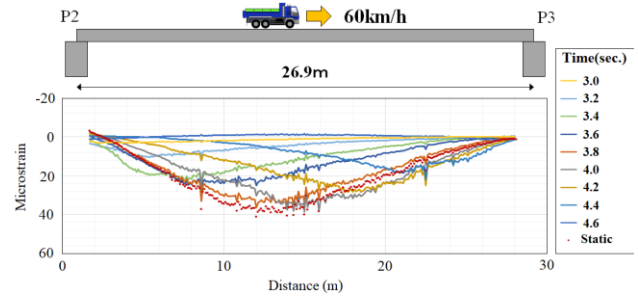


Figure 9. Dynamic strain distribution during vehicle movement with 5Hz sampling.

### 4 CONCLUSION

We investigated a PNC-OFDR based strain sensing system equipped with a high-speed wavelength-swept laser source and its application to bridge monitoring. This system can obtain static and dynamic strain distribution with the same accuracy as a strain gauge. Currently, the sensing distance of this system has been extended to 1000m.

We will continue to develop PNC-OFDR so that it will become a sensing technology necessary for quantitative evaluation of civil engineering structures, such as bridges.

### REFERENCES

- [1] L. Schenato, M. Cappelletti, D. Orsuti, A. Galtarossa, M. Santagiustina, S. Cola, L. Palmieri, "Long-term persistence of Rayleigh signature of optical fibers in harsh environment," *J. Lightwave Technol.*, vol.42, no.18, 6254-6261, 2024.
- [2] A. Sladen, D. Rivet, J. Ampuero, L. Barros, Y. Hello, G. Calbris, P. Lamere, "Distributed sensing of earthquakes and ocean-solid Earth interactions on seafloor telecom cables," *Nat. Comm.*, 10, 5777, 2019.
- [3] G. Wellbrock, T. Xia, M. Huang, Y. Chen, M. Salemi, Y. Huang, P. Ji, E. Ip, T. Wang, "First field trial of sensing vehicle speed, density, and road conditions by using fiber carrying high speed data," *optical fiber communication conference (OFC.) paper Th4C.7*, 2019.
- [4] Y. Koyamada, M. Imahama, K. Kubota, K. Hogari, "Fiber-optic distributed strain and temperature sensing with very high measurand resolution over long range using coherent OTDR," *J. Lightwave Technol.* 27, 1142-1146, 2009.
- [5] Wang, Z. Zhang, L. Wang, S. Xue, N. Peng, F. Fan, M. Sun, W. Qian, X. Rao, J. Rao, Y., "Coherent  $\Phi$ -OTDR based on I/Q demodulation and homodyne detection," *Opt. Express* 24, 853-858, 2016.
- [6] K. Kishida, M. Imai, J. Kawabata, A. Guzik, "Distributed optical fiber sensors for monitoring of civil engineering structures," *Sensors*, 22(12), 4368, 2023.
- [7] Froggatt, M., and Moore, J., "High-spatial-resolution distributed strain measurement in optical fiber with Rayleigh scatter," *Appl. Opt.*, 37, 1735-1740, 1998.
- [8] D. Zhou, L. Chen, X. Bao., "Distributed dynamic strain measurement using optical frequency-domain reflectometry," *Appl. Opt.*, 35(24), 6735-6739, 1996.
- [9] P. Hubbard, J. Xu, S. Zhang, M. Dejong, L. Luo, K. Soga, C. Papa, C. Zulberti, D. Malara, F. Fugazzotto, F. Lopez, and C. Minto, "Dynamic structural health monitoring of a model wind turbine tower using distributed acoustic sensing (DAS)," *J. Civ. Struct. Health Monit.*, Vol. 11, pp. 833-849, 2021.
- [10] X. Fan, Y. Koshikiya, and F. Ito, "Centimeter-level spatial resolution over 40 km realized by bandwidth-division phase-noise-compensated OFDR," *Opt. Exp.*, Vol. 19, No. 20, pp. 19122-19128, 2011.
- [11] K. Nakamura, M. Koshihara, T. Saitoh, K. Kawakita, "High-Coherence Wavelength Swept Light Source," *Anritsu Technical Review.*, 25, 38, 2017.
- [12] D. Tanimura, D. Miyake, C. Zhang, F. Ito, Y. Yoshimura, H. Aoshika, and M. Imai, "Long range, wide bandwidth, and rapid optical frequency domain reflectometry employing concatenative referencing method," *OFS-27. Paper W4.10* 30 2022.

# Advanced Structural Monitoring and Predictive Maintenance for Railway Bridges Using Distributed Fiber-Optic Sensors

Felipe Muñoz<sup>1,2</sup>, Iván Eguidazu<sup>3</sup>, Julio Rodríguez<sup>3</sup>, Diego Gaston-Beraza<sup>1</sup>, Fernando Basarte<sup>1</sup>, Javier Urricelqui<sup>1</sup>, José María Pérez Casas<sup>3</sup>, Marco Jimenez-Rodriguez<sup>1</sup>

<sup>1</sup> Uptech Sensing, Pol. Ind. Mutilva Baja, 31192 Mutilva Baja, Navarra, Spain

<sup>2</sup> Universidad Técnica Federico Santa María, Valparaíso, Chile

<sup>3</sup> SENER Mobility c\ Severo Ochoa 4, Tres Cantos. Madrid.

Email: felipe.munoz@uptech-sensing.com

**ABSTRACT:** This submission presents a structural monitoring solution for railway bridges and viaducts that leverages distributed fibre optic sensors (distributed temperature and strain sensing, DTSS, and distributed acoustic sensing, DAS) to capture both long-term static trends and dynamic behaviour under train loads. The long-term monitoring uses hourly DTSS strain measurements, accounting for day/night and seasonal variations, while the dynamic monitoring system records real-time strain and vibration data during train passages. By integrating these measurements with structural calculation services, the system can detect anomalies (e.g., stiffness changes, potential cracking) and inform predictive maintenance. Lastly, the results are displayed via a digital twin, providing an intuitive, web-based platform for analysing historical data and forecasting future conditions.

**KEY WORDS:** Distributed acoustic sensors, Distributed temperature and strain sensors, Structural health monitoring, Railway bridges.

## 1 INTRODUCTION

The increasing demand for reliable and efficient monitoring of critical infrastructure has driven the development and deployment of advanced sensing technologies. Among these, distributed fibre optic sensing (DFOS) has emerged as a powerful tool, offering continuous, real-time measurements over long distances with high spatial resolution [1]. Distributed temperature sensing systems (DTSS) and distributed acoustic sensing (DAS) have demonstrated significant potential in a wide range of civil engineering applications [2], [3], [4]. State-of-the-art implementations of DFOS include structural and crack monitoring, geotechnical engineering (such as landslide detection and tunnelling construction and integrity monitoring), the surveillance of buried infrastructure, and transportation infrastructure monitoring (including railways and bridges) [2]. Within this broad landscape, DAS and DTSS have been successfully applied to railway bridge monitoring, enabling early detection of structural degradation, train-induced vibrations, temperature variations, and other anomalies that could compromise safety or performance [5], [6], [7]. These implementations establish DFOS as a multi-scale monitoring solution capable of addressing both immediate safety concerns (through real-time anomaly detection) and long-term preservation needs (via historical trend analysis), while overcoming traditional limitations of discrete sensor systems through its distributed, high-resolution measurement capabilities.

In this paper, we present the results obtained from monitoring a 471-meter-long concrete viaduct used by high-speed trains. The system integrates three main units: a sensing unit, a computing unit, and an information analysis unit. The sensing unit consists of two distributed fibre optic sensors that simultaneously monitor the structure by interrogating optical fibres embedded along the structure. These sensors include a distributed acoustic sensor (DAS) and a distributed strain and temperature sensor (DTSS). The computing unit processes the

measurements acquired by these sensors to calculate various structural parameters under both static and dynamic conditions. Static structural parameters are derived from measurements obtained when the viaduct is at rest, while dynamic structural parameters are obtained from measurements obtained during and after a train passage. The following static parameters are calculated: vertical displacement of the deck and displacement of the piers. Also, the calculated dynamic parameters include deck dynamic properties, vertical acceleration of the deck, bending rotation of the deck, fatigue caused at longitudinal and transverse reinforcement of the deck, and dynamic displacement of the piers. The analysis unit analyses the results to determine whether the obtained structural parameters fall within a normal range or exhibit any anomalies compared to historical data and theoretical modelling.

The structural monitoring system provides operators with two key functionalities based on temporal scope: (1) current state assessment, enabling remote evaluation of real-time structural health through comprehensive indicators and immediate risk alerts, which reduces inspection needs and optimizes maintenance responses; and (2) future state prediction, using advanced analytics to forecast structural evolution and assess capacity for future operational scenarios, thereby improving maintenance planning and infrastructure adaptability. This dual approach transforms traditional reactive maintenance into a proactive, data-driven strategy while enhancing both safety and resource efficiency.

## 2 METHODS

### *Distributed fibre optic sensors*

#### 2.1.1 Distributed Temperature and Strain Sensing (DTSS)

The DTSS system employs Brillouin backscattering in optical fibres to provide continuous, high-resolution measurements of strain and temperature along the entire bridge structure. By analysing spectral shifts in the Brillouin backscattered light, DTSS achieves a spatial resolution of 0.5–1 m with strain accuracy of  $\pm 10 \mu\epsilon$  and temperature precision of  $\pm 0.5^\circ\text{C}$  [8], [9], [10]. In this application, DTSS monitors long-term deformations and detects gradual anomalies such as settlement or bearing degradation. Its absolute strain measurement capability and high spatial resolution make it particularly suited for structural health monitoring. The optical fibre is interrogated by a UTS-FB1000 DTSS system from Uptech Sensing [11]. It is configured with 20 Hz sampling rate, a spatial resolution of 1 m, and a spatial sampling interval of 1 m, covering the full 470 m of the viaduct.

#### 2.1.2 Distributed acoustic sensor (DAS)

The DAS system utilises phase-sensitive optical time-domain reflectometry ( $\phi$ -OTDR) to detect dynamic strain variations along the optical fibre [1], [12]. Sensitive to vibrations up to several kHz, DAS captures high-frequency events including train-induced vibrations, impact loads, and sudden structural changes. In this implementation, DAS provides real-time monitoring of dynamic responses during train crossings, enabling the identification of transient phenomena. The system's dense spatial sampling allows for localised event detection across the entire bridge span. The optical fibre is interrogated by a UTS-AS1000 DAS system from Uptech Sensing [13]. It is configured with 1kHz sampling rate, a pulse width of 50 ns, a gauge length of 5 m and a spatial sampling interval of 5 m.

#### 2.1.3 Limitations and Complementarity

While DTSS excels in static or quasi-static monitoring, its sampling rate (typically  $< 100$  Hz) [14] limits dynamic response characterisation. This limitation can be mitigated by integrating complementary information from DTSS, which provides accurate temperature measurements. By combining data from both sensors, it is possible to decouple temperature effects from true mechanical responses, enhancing the reliability of dynamic strain interpretation. Their integration in this study creates a synergistic monitoring framework: DTSS establishes baseline structural behaviour and detects slow-evolving damage, while DAS identifies transient events and verifies dynamic performance. This dual-sensor approach overcomes individual limitations, providing comprehensive structural assessment across all relevant timescales, from gradual deterioration to instantaneous dynamic loading.

### *Optical fibre cable installation on the structure*

The monitoring system integrates DTSS and DAS interrogators within Span 1 at the viaduct's northbound section. A single optical fibre, epoxy-bonded to the structure, completes two full

round trips (totalling  $\sim 2.5$  km) following a systematic path: starting from the interrogators, it sequentially traverses the upper right (UR), upper left (UL), lower left (LL) and lower right (LR) surfaces. Strategic fibre loops are incorporated at deck cross-sections to capture transverse structural responses, while vertical runs instrument the piers, descending one side and ascending the opposite. This configuration achieves four complete viaduct passes, enabling comprehensive 3D monitoring through: (1) longitudinal strain profiling along all critical surfaces, (2) transverse deformation assessment via deck loops, and (3) pier behaviour characterization. Figures 1 and 2 detail the installation geometry and pier instrumentation respectively.

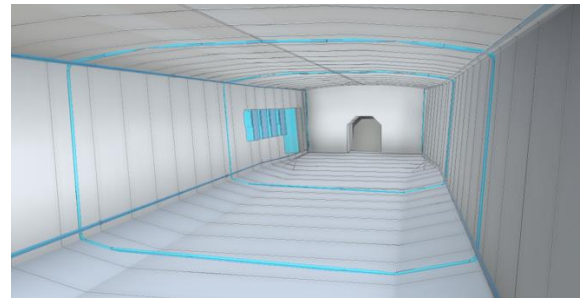


Figure 1: Optical fibre installation on a viaduct deck. Four optical fibre segments (blue lines) are installed, one on each side, as well as on the top and bottom of the deck. Additionally, loops of fibre are placed across the transverse section of the deck.

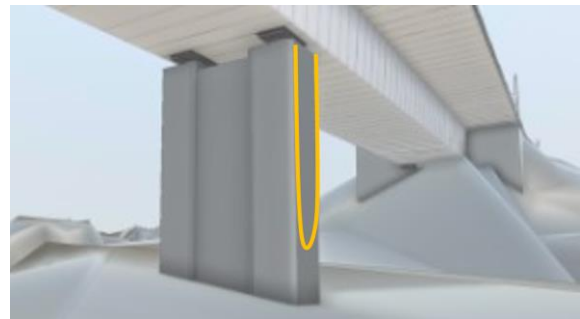


Figure 2: Optical fibre installation on the piers (orange line).

### *Data acquisition and processing architecture*

The monitoring system utilizes both sensors in a coordinated manner to capture complementary structural responses. The DTSS sensor operates in a dual-mode configuration, performing periodic static measurements at fixed intervals to monitor long-term deformations and thermal effects, then automatically switching to dynamic-measurements mode. Simultaneously, the DAS sensor provides continuous, real-time vibration monitoring with millisecond temporal resolution, ensuring comprehensive detection of all dynamic events.

The software architecture employs modular microservices for all computational operations (characterization, alarm detection, and predictive analytics), executed through orchestrated workflows. Local processing units on the viaduct handle real-time structural characterization and immediate



alarm detection, reducing data transmission volumes via 4G VPN by preprocessing sensor outputs. Cloud-based Azure services perform historical data analysis and predictive modelling, supported by: (1) a NoSQL database storing processed results in JSON format, (2) blob storage for raw sensor data archiving, and (3) a web-accessible frontend for operator interaction. Orchestrators in both environments manage service dependencies and execution sequences, ensuring proper data flow between services where outputs become subsequent inputs. This hybrid architecture optimizes bandwidth usage while maintaining complete data traceability for verification and system upgrades throughout the infrastructure's lifecycle. The data handling pipeline scheme is shown on Figure 3.

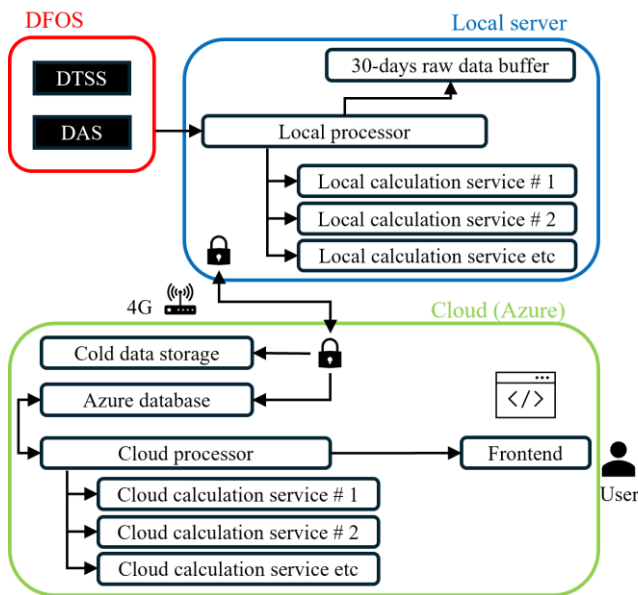


Figure 3: Data handling pipeline.

Given the dual-mode sensing architecture, accurate time synchronization is essential to correlate static (DTSS) and dynamic (DAS) measurements for event-based diagnostics and digital twin integration. Both systems independently generate data streams with embedded timestamps. To align these streams, the local processing unit performs time correlation by matching temporal features, such as strain peaks, slope reversals, or train-induced vibration signatures, across both modalities.

Time references are maintained through a hybrid synchronization approach: GPS-disciplined oscillators provide high-precision absolute timing, while NTP (Network Time Protocol) ensures fallback synchronization across distributed edge nodes and cloud-based analytics. This architecture enables sub-millisecond temporal alignment between DTSS and DAS outputs, ensuring that combined measurements reflect coherent physical events and supporting reliable fusion of static and dynamic data streams in the digital twin environment.

### 3 STRUCTURAL MEASURANTS AT VIADUCTS

#### *Static measurements*

At 30-minute intervals (or at a user-defined sampling rate), the system captures a ‘snapshot’ of the current deformed shape of the monitored deck and piers. Each measurement is checked to ensure displacements remain within predefined thresholds while also detecting: (1) substructure settlements, (2) bearing lockups (in instrumented piers), and (3) excessive deck deformations. This automated process enables real-time structural integrity assessment and early anomaly detection.

#### 3.1.1 Deck’s vertical displacement

The calculation is based on the execution of four fundamental steps: (1) computation of the strains measured at the four corners of the section; (2) fitting of the curvature plane passing through these four points using a least-squares adjustment; (3) application of the generalised Mohr’s theorem in three-dimensional space to determine rotations and deflections at all points [15]; and (4) enforcement of boundary conditions at the initial point to derive displacements and rotations at any location along the deck. This systematic approach ensures accurate structural deformation analysis while accounting for geometric constraints.

Figure 4 shows the viaduct and its spans (grey background scheme) along with the static vertical displacement at all spatial locations for a specific datetime (black line). Also, historical data from 18 months (orange line indicating the historical average, while the shaded area represents the standard deviation) is shown. Analysis of the historical data reveals that each span experiences a distinct vertical displacement.

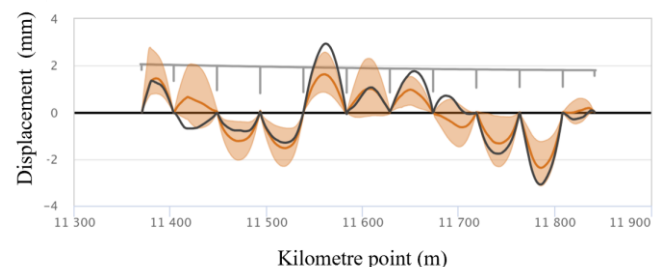


Figure 4: Deck’s static vertical displacement.

#### *Dynamic measurements*

#### 3.2.1 Dynamic properties

This constitutes an essential service as it provides the foundation for detecting structural changes through dynamic behaviour analysis. Using the DAS measurements, the system continuously calculates the viaduct’s dynamic characteristics, specifically determining for each of the first N vibration modes: (1) the natural frequency, (2) the vibrational mode shape (structural deformation pattern), and (3) the damping ratio. Using the Stochastic Subspace Identification-Covariance method (SSI-Cov) reliable operational modal analysis under ambient vibrations is performed [16]. This calculation forms the critical baseline for structural health monitoring by quantifying the bridge’s dynamic fingerprint and enabling subsequent detection of behavioural deviations that may indicate damage or degradation.

### 3.2.1.a Calculation method

The vibration characterization process involves three key stages: (1) The SSI-Cov algorithm computes vibration poles (mode shapes, natural frequencies, and damping ratios) across multiple solution orders, generating both physical and spurious results. (2) A pole stabilization stage filters non-physical poles by eliminating those with inconsistent dynamic properties (e.g., negative damping) or insufficient consensus across solution orders. (3) A final pole clustering stage, using HDBSCAN's density-based algorithm [17], groups duplicate poles from different orders while automatically determining the optimal number of clusters based on modal similarity in multidimensional space.

This robust three-stage process ensures only validated, unique vibration modes are returned, with the clustering step providing additional quality control by rejecting any remaining outliers. Figure 5 and Figure 6 shows the results of stages (1) and (3), respectively, demonstrating the algorithm's capability to distinguish physical vibration modes from computational artifacts. The implemented filtering and clustering successfully identify 20 meaningful vibration modes. Each identified vibration mode is associated to a specific mode shape which enables structural engineers to do a comprehensive analysis of the algorithm result.

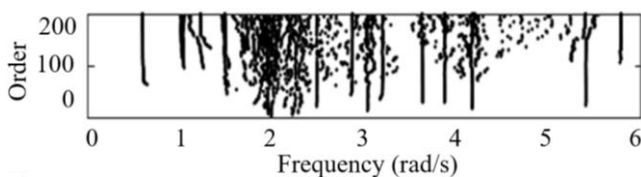


Figure 5: Vibration modes calculation at stage (1), SSI-Cov method result.

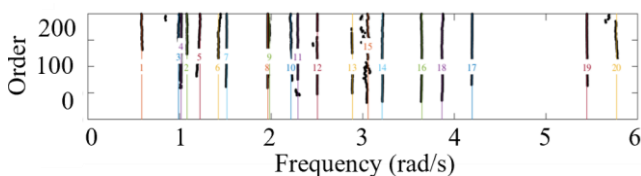


Figure 6: Identified vibration modes at stage (3) after filtering and clustering. Each mode is numbered and represented by a distinct coloured line.

### 3.2.1.b Dynamic behaviour change detection

This service identifies structural degradation by monitoring changes in dynamic characteristics (natural frequencies, damping ratios, and vibration modes) across multiple monitoring events, while accounting for temperature effects measured by DTSS. Using HDBSCAN clustering, it groups historically observed frequencies based on their associated mode shapes rather than simple frequency proximity. For each cluster, the algorithm: (1) quantifies temperature's influence on frequency variations, and (2) compares current frequencies against their temperature-adjusted historical interquartile ranges. When frequencies deviate beyond expected thermal-effect boundaries, the system triggers alarms indicating

potential stiffness reduction (e.g., from cracking). This dual analysis of vibrational patterns and thermal compensation ensures reliable damage detection while preventing false alarms from normal temperature-induced variations.

### 3.2.2 Dynamic vertical displacement and bending rotation

#### 3.2.2.a Calculation method

The dynamic analysis is initiated automatically upon detection of train passage across the structure, employing the same method used for static displacement calculations. The system acquires displacement and rotation data at each timestep, with sampling frequencies ranging from 50 Hz to 1000 Hz depending on whether DTSS or DAS sensors are utilised. For each monitored cross-section, temporal evolution analysis of the deformation data provides dynamic curvatures, dynamic rotations, instantaneous dynamic deflections, velocities (first derivatives), and accelerations (second derivatives). This methodology enables comprehensive characterisation of the structure's dynamic response under live loading conditions, while maintaining consistency with the static analysis framework through shared computational architecture.

#### 3.2.2.b Regulatory compliance and operational limits

These parameters are strictly regulated by railway standards as they critically impact both passenger comfort and operational safety. UIC guidelines establish specific limits for dynamic structural responses, including [18]: (1) maximum permissible passenger-perceived accelerations during bridge crossings, and (2) dynamic deflection thresholds expressed as a percentage of span length - with stricter limits applying to higher train speeds. The standards define "good comfort" levels when dynamic displacements remain below these velocity-dependent thresholds. Additionally, the regulations mandate compliance with complementary safety-related limits governing structural vibrations and deformations, ensuring simultaneous satisfaction of both comfort criteria and essential safety requirements throughout the infrastructure's operational life. These parameters are used together with the historical behaviour of structural parameters to define alarms and behavioural changes.

#### 3.2.2.b.1 Vertical dynamic displacement

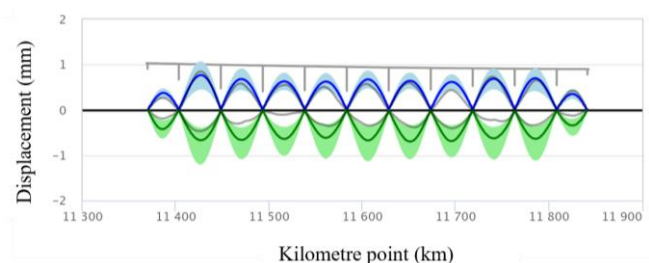


Figure 7: Deck's dynamic vertical displacement.

Figure 7 illustrates the viaduct and its piers (grey background scheme) together with the vertical dynamic displacement of the deck induced by a train passage for all spatial locations of the viaduct (grey line). Additionally, statistical values derived from

18 months of operational data are presented. The blue and green lines indicate the maximum and minimum average displacement values, respectively, while the shaded areas represent the corresponding standard deviations for positive (blue) and negative (green) displacement values. This visualization enables direct comparison between instantaneous structural response and long-term performance trends, facilitating the identification of anomalous behaviour or progressive stiffness degradation. The historical displacement monitoring results demonstrate two key structural behaviours: spans in direct contact with the ground (Spans 1 and 11) exhibit significantly reduced displacement amplitudes (0.2-0.4 mm) due to enhanced restraint from soil-structure interaction, while all spans show consistent asymmetric response with positive displacements (+0.8 mm peak) being approximately 30% smaller than negative displacements (-1.2 mm peak). Also, the results indicate that vertical displacement is maximum at midspans and minimum at the piers, being consistent with expected behaviour for this type of structure.

### 3.2.2.b.2 Vertical dynamic acceleration

Deflection calculation throughout curvature integration allows the derivation of vertical accelerations of the deck, enabling to check safety and comfortability on the train. Figure 8 illustrates the vertical dynamic acceleration of the deck induced by a train passage for all spatial locations of the viaduct (grey line), together with its historical values. The blue and green lines indicate the maximum and minimum average acceleration values, respectively, while the shaded areas represent the corresponding standard deviations for positive (blue) and negative (green) acceleration values. Similar to the previous case, the historical acceleration data reveals consistent spatial trends across the viaduct: Spans 1 and 11, which interface with the ground, exhibit lower peak accelerations compared to intermediate spans. Also, the maximum acceleration occurs at the centre of the spans and minimum at the piers.

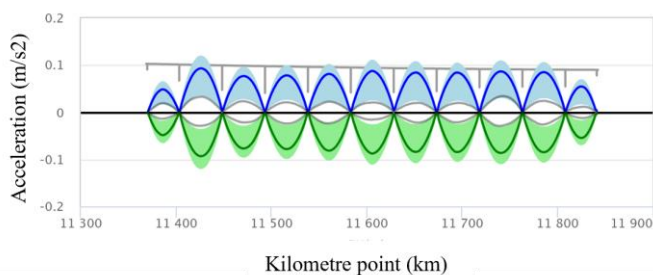


Figure 8: Deck's dynamic vertical acceleration.

### 3.2.2.b.3 Bending rotation

Curvature integration enhances the calculation of the induced rotations of pot bearings. Figure 9 illustrates the bending rotation induced by a train passage for all spatial locations of the viaduct (grey line), together with its historical values. The blue and green lines indicate the maximum and minimum average bending values, respectively, while the shaded areas

represent the corresponding standard deviations for positive (blue) and negative (green) bending values. The historical data analysis reveals distinct rotational pattern along the viaduct, with maximum rotation occurring near the piers and minimum rotation at midspan locations. This behaviour is consistent with expected structural mechanics for simply supported spans.

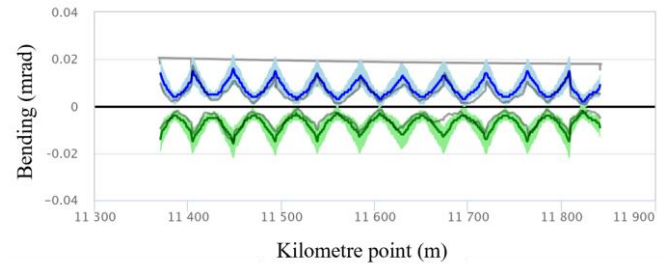


Figure 9: Deck's dynamic bending rotation.

### 3.2.2.b.4 Pier's dynamic displacement

The monitoring system extends its dynamic characterization methodology to instrumented piers, employing an analogous analytical process to that implemented for the deck structure. Figure 10 shows one of the piers (grey background scheme) together with its vertical dynamic displacement after a passing train (black lines), together with its statistical values. The blue and green lines indicate the maximum and minimum average height values, respectively, while the shaded areas represent the corresponding standard deviations for positive (blue) and negative (green) height values. Historical monitoring data reveals a distinct asymmetry in displacement variability, with negative displacements exhibiting greater variance than positive displacements.

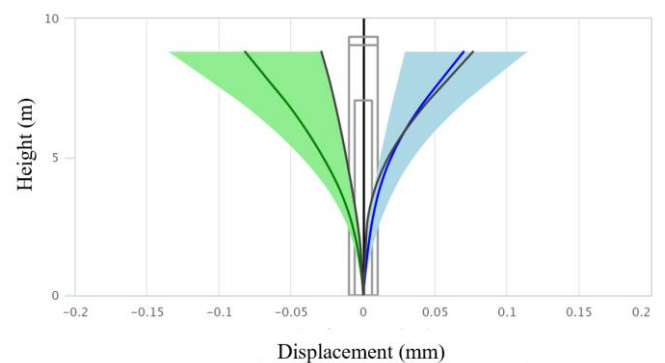


Figure 10: Pier's dynamic displacement.

### 3.2.3 Fatigue check of reinforcement

A major concern in railway bridges is degradation due to material fatigue, especially of steel reinforcement and prestressing [19]. Dynamic measure of the induced strain both along the deck and at specific cross sections allows to compute stress variations and fatigue cycles induced both at longitudinal prestress and transverse reinforcement [20].



### 3.2.3.a Calculation method

Building on the dynamic strains and curvatures obtained from the previous calculation service, this module determines strain distributions across any point of the cross-section. Through extrapolation, it specifically evaluates strain conditions at reinforcement locations (which are typically more eccentric than measurement points). This enables the analysis of stress variations in both longitudinal and transverse reinforcement during each train passage.

### 3.2.3.b Fatigue analysis

This service analyses DTSS-measured stress data from train crossing events to quantify fatigue life consumption. The algorithm: (1) performs rainflow cycle counting to identify stress ranges and mean stresses, (2) optionally converts to equivalent alternating stress (per Eurocode EN 1992-1-1 guidelines for reinforcement/prestressing steel [21]), (3) compares results against material S-N curves to determine allowable cycles, and (4) applies Miner's rule for cumulative damage assessment [22]. Separate analyses are conducted for transverse reinforcement (from transverse fibre loops data) and longitudinal prestressing steel (from longitudinal deck fibres), with material-specific fatigue limits applied in each case.

### 3.2.3.c Results

Figure 11 illustrates the transverse stress distribution in the internal reinforcement (Fi) of the upper slab at section L/4 of Span 1 under different train loading scenarios. The stress profiles are evaluated for both minimum and maximum train load cases. The colour legend distinguishes the results: Min Fi is represented in green, Max Fi in gray, the average minimum stress in red, and the average maximum stress in orange. This figure highlights how internal forces respond to varying operational loads, providing insights into the structural performance of the interior reinforcement.

Figure 12 presents the transverse stress distribution in the superior reinforcement (Fs) of the upper slab at the same section under identical loading conditions. The color coding for Fs is as follows: minimum Fs is shown in red, maximum Fs in gray, the average minimum stress in green, and the average maximum stress in blue. By comparing these results with Figure 11, the figure reveals differences in stress behavior between internal and superior reinforcement layers, aiding in the assessment of load distribution and reinforcement efficiency in the slab structure.

Both figures collectively enhance the understanding of stress variations under different train loads, supporting the evaluation of structural integrity and design optimization.

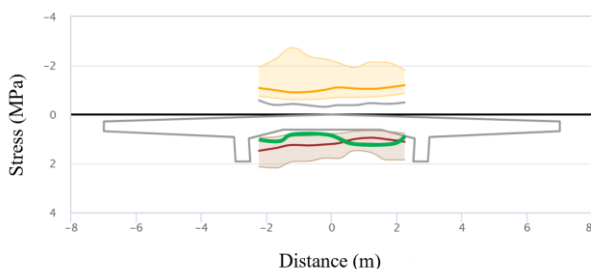


Figure 11: Deck's transverse internal reinforcement.

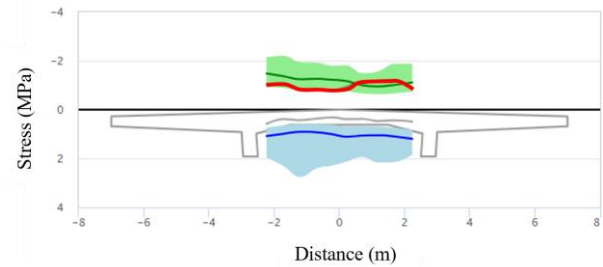


Figure 12: Deck's transverse superior reinforcement.

## 4 CONCLUSION

This study demonstrates the successful implementation of a dual-mode DFOS monitoring system integrating DTSS and DAS technologies for comprehensive railway bridge assessment. The system provides: (1) synchronized static-dynamic measurements (static deformations via DTSS, vibrations up to 1 kHz via DAS), (2) historical trend analysis revealing temperature-compensated structural evolution, and (3) event-based diagnostics (train responses). Results validate the approach's capability to detect stiffness changes, bearing anomalies, and fatigue-critical stress variations. The DTSS-DAS synergy establishes a new paradigm for infrastructure monitoring, combining kilometre-scale coverage with meter-resolution measurements for lifecycle management.

In addressing practical deployment aspects, the survivability of optical fibers in harsh environments, particularly under sustained dynamic loads, was considered. While tight-buffered cables were selected to minimize micro-bending losses, ongoing vibration exposure may still induce attenuation changes. Future deployments could integrate real-time loss monitoring and fiber routing strategies (e.g., loose-tube or armored cable designs) to improve durability.

Although this study focused on a 471-meter concrete viaduct, the proposed dual-mode system is adaptable to a broad range of bridge typologies, including steel truss, cable-stayed, and segmental concrete structures. For longer spans, signal processing techniques (e.g., dynamic range scaling, adaptive windowing) and distributed computing architectures can be extended to preserve performance without compromising spatial or temporal resolution.

Overall, the dual-mode DFOS platform, enhanced by edge computing, time-synchronized sensing, and AI-driven analytics, offers a robust and scalable solution for intelligent bridge monitoring across diverse operational and structural contexts.

## ACKNOWLEDGMENTS

The author would like to acknowledge ADIF for lending the monitored viaduct for this project.

## FUNDING

This work has been partially funded from the following projects: PTQ2021-011958 Torres Quevedo Grant from Ministerio de Ciencia, Innovación y Universidades, Government of Spain, 0011-1408-2023-000026 Doctorados Industriales of 2023 from Government of Navarra and CPP

03/2021 “Soluciones tecnológicas para mantenimiento predictivo de Puentes y Viaductos” from CDTI and ADIF.

## REFERENCES

- [1] A. H. Hartog, *An Introduction to Distributed Optical Fibre Sensors*. CRC Press, 2017. doi: 10.1201/9781315119014.
- [2] M. F. Ghazali *et al.*, “State-of-The-Art application and challenges of optical fibre distributed acoustic sensing in civil engineering,” *Optical Fiber Technology*, vol. 87, Oct. 2024, doi: 10.1016/j.yofte.2024.103911.
- [3] T. Wu, G. Liu, S. Fu, and F. Xing, “Recent progress of fiber-optic sensors for the structural health monitoring of civil infrastructure,” Aug. 02, 2020, *MDPI AG*. doi: 10.3390/s20164517.
- [4] M. F. Bado and J. R. Casas, “A review of recent distributed optical fiber sensors applications for civil engineering structural health monitoring,” Mar. 01, 2021, *MDPI AG*. doi: 10.3390/s21051818.
- [5] L. Cheng, A. Cigada, E. Zappa, M. Gilbert, and Z. Q. Lang, “Dynamic monitoring of a masonry arch rail bridge using a distributed fiber optic sensing system,” *J Civ Struct Health Monit*, vol. 14, no. 4, pp. 1075–1090, Apr. 2024, doi: 10.1007/s13349-024-00774-0.
- [6] K. Kishida, T. L. Aung, and R. Lin, “Monitoring a Railway Bridge with Distributed Fiber Optic Sensing Using Specially Installed Fibers,” *Sensors*, vol. 25, no. 1, Jan. 2025, doi: 10.3390/s25010098.
- [7] H. C. Su, T. H. Hsu, Y. L. Lee, W. K. Hsu, N. T. Yang, and N. H. Chang, “Fiber Monitoring System Applied to Railway Bridge Structures in a Near-Fault Region,” *Applied Sciences (Switzerland)*, vol. 14, no. 17, Sep. 2024, doi: 10.3390/app14177883.
- [8] “BOTDA-Nondestructive Measurement of Single-Mode Optical Fiber Attenuation Characteristics Using Brillouin Interaction: Theory.”
- [9] T. Horiguchi, K. Shimizu, T. Kurashima, M. Tateda, S. Member, and Y. Koyamada, “Development of a Distributed Sensing Technique Using Brillouin Scattering,” 1995.
- [10] M. A. Soto, “Distributed Brillouin Sensing: Time-Domain Techniques,” in *Handbook of Optical Fibers*, G.-D. Peng, Ed., Singapore: Springer Singapore, 2019, pp. 1663–1753. doi: 10.1007/978-981-10-7087-7\_7.
- [11] Uptech Sensing, “UTS-FB1000: High-resolution Distributed Temperature and Strain sensing unit,” <https://uptech-sensing.com/producto-ampliado-uts-fb1000.html>.
- [12] Z. He and Q. Liu, “Optical Fiber Distributed Acoustic Sensors: A Review,” Jun. 15, 2021, *Institute of Electrical and Electronics Engineers Inc.* doi: 10.1109/JLT.2021.3059771.
- [13] Uptech Sensing, “UTS-AS1000: High-resolution Distributed Acoustic Sensing Unit,” <https://uptech-sensing.com/producto-ampliado-uts-as1000.html>.
- [14] Y. Dong, “High-Performance Distributed Brillouin Optical Fiber Sensing,” Mar. 01, 2021, *Springer Verlag*. doi: 10.1007/s13320-021-0616-7.
- [15] S. P. Timoshenko and J. N. Goodier, *Theory of Elasticity*, 3rd ed., vol. 144. New York: McGraw-Hill, 2018. doi: 10.1061/(ASCE)ST.1943-541X.0002064.
- [16] P. Van Overschee and B. De Moor, “Subspace algorithms for the stochastic identification problem,” *Automatica*, vol. 29, no. 3, pp. 649–660, 1993, doi: [https://doi.org/10.1016/0005-1098\(93\)90061-W](https://doi.org/10.1016/0005-1098(93)90061-W).
- [17] C. Malzer and M. Baum, “A Hybrid Approach To Hierarchical Density-based Cluster Selection,” Apr. 2019. doi: 10.48550/arXiv.1911.02282.
- [18] International Union of Railways (UIC), “UIC Code 776-2: Design requirements for rail-bridges based on interaction phenomena between train, track, and bridge,” Jun. 2009.
- [19] European Committee for Standardization, “N 1991-2: Eurocode 1: Actions on structures – Part 2: Traffic loads on bridges,” 2003.
- [20] I. Bayane, A. Mankar, E. Brühwiler, and J. D. Sørensen, “Quantification of traffic and temperature effects on the fatigue safety of a reinforced-concrete bridge deck based on monitoring data,” *Eng Struct*, vol. 196, p. 109357, 2019, doi: <https://doi.org/10.1016/j.engstruct.2019.109357>.
- [21] European Committee for Standardization, “EN 1992-1-1: Eurocode 2: Design of Concrete Structures – Part 1-1: General Rules and Rules for Buildings,” 2004.
- [22] C. Ríos, J. C. Lancha, and M. Á. Vicente, “Fatigue in Structural Concrete According to the New Eurocode 2,” *Hormigón y Acero*, Mar. 2023, doi: 10.33586/hya.2023.3100.

# Structural health monitoring in underground mining using fiber-optic sensing and 3D laser scanning for digital twin development

Michael Dieter Martin<sup>1</sup>, 0009-0003-7881-6456, Nils Nöther<sup>2</sup>, Jens-André Paffenholz<sup>1</sup>, 0000-0003-1222-5568

<sup>1</sup>Clausthal University of Technology, Institute of Geotechnology and Mineral Resources, Geomatics for Underground Systems, Erzstraße 18, 38678 Clausthal-Zellerfeld, Germany

<sup>2</sup>fibrisTerre Systems GmbH, Torellstraße 7, 10243 Berlin, Germany

email: michael.dieter.martin@tu-clausthal.de, nils.noether@fibristerre.de, jens-andre.paffenholz@tu-clausthal.de

**ABSTRACT:** This study aims to evaluate the use of distributed fiber-optic strain and temperature sensing for structural health monitoring in underground mining drifts and chambers including 3D mobile laser scanning. This method seeks to create a digital twin to improve safety and efficiency through better digital planning. Temperature and deformation data from distributed fiber-optic sensing (DFOS) cables will serve as boundary conditions of the combined ventilation and geomechanical models of the drift and chambers. Initially, a 60-meter-long drift will be monitored using fiber-optic cables. Next, deformations of a flexible arch support, induced by hydraulic cylinders, will be observed. A hydraulic cylinder will then apply load orthogonally to the rock. Fiber-optic cables will be inserted and cemented into the rock, along rock bolts, and in boreholes around each bolt to measure deformations from rock bolt pull-out tests. Preliminary examinations identified the best adhesive bonding method for DFOS cables, considering the specific ambient conditions. A 3D point cloud will be used to plan and validate the cable installation. The meshed 3D cloud will serve as the foundation for the combined ventilation and geomechanical models, creating a virtual reality-capable digital twin enhanced with live DFOS measurements.

**KEY WORDS:** fiber-optic sensing, 3D point cloud, digital twin, underground mining

## 1 INTRODUCTION

In the recent years, digital twins have increasingly been investigated within the realms of tunnel construction [1] and mining [2], [3] with promising results. All digital twins must be provided with real data to capture and model reality as closely as possible (e.g. [1], [3], [4]). Depending on the particular use of the digital twin, various types of datasets and sensors are used including 3D laser scanners, environmental data such as temperature and humidity [1] and information on geology and rock deformation [3] to name only a few. Since the beginning of modern fiber-optic development in the 1960s, distributed fiber-optic sensing (DFOS) has found a wide range of applications ranging from infrastructure health monitoring [5], [6], river dikes [7], volcano monitoring [8] and tunnel monitoring as well as underground mine monitoring [9], [10]. In the context of the latter, the DFOS technique enables the detection of small temperature and strain changes and their resulting deformations [9], [10]. In the realm of DFOS based measurement principles, the Brillouin optical frequency domain analysis (BOFDA) technique [11] allows for distributed measurements along several kilometers with a spatial resolution below 1-meter [7] and has been successfully used for structural health monitoring [5], river dike monitoring [7] and tunnel inspection [9].

In this paper, the BOFDA based fiber-optic solution provided by fibrisTerre Systems GmbH (Germany) is used. The mine used for installation of the fiber-optic cables and for

construction of the underground lab is the research and education mine “Forschungs- und Lehrbergwerk (FLB) Reiche Zeche” at TU Bergakademie Freiberg (TUBAF) in Germany. The fiber-optic cables will be installed in a 60 m long drift and additionally in four chambers for experimental setups. Both the main drift and the chambers form part of the FLB mine and are referred to underground lab in the following. The first part of the installation of the fiber-optic cables is scheduled to be completed by September 2025.

The strain and temperature measurements will be used as boundary conditions for geomechanical and ventilation models, which will be coupled including a geometrical and geological model of the underground lab. The creation of an artificial intelligence (AI)-supported coupled model will enable real-time visualization of changes in physical parameters in the coupled geomechanical and ventilation model, which will ultimately lead to development of a digital twin. For a more detailed overview about the individual models see [12]. To our knowledge, fiber-optic sensing data was not yet used for providing temperature and strain measurements as boundary conditions for creating a digital twin in an underground mine. Therefore, the overall aim of the collaborative research project “MODEL coupling in the context of a VIRTUAL underground lab and its development process” (MOVIE) is to develop a digital twin of the underground lab provided with fiber-optic sensing-based temperature and strain data, which will ultimately be visualized using a Meta Quest 3 mixed-reality headset (see Figure 1).



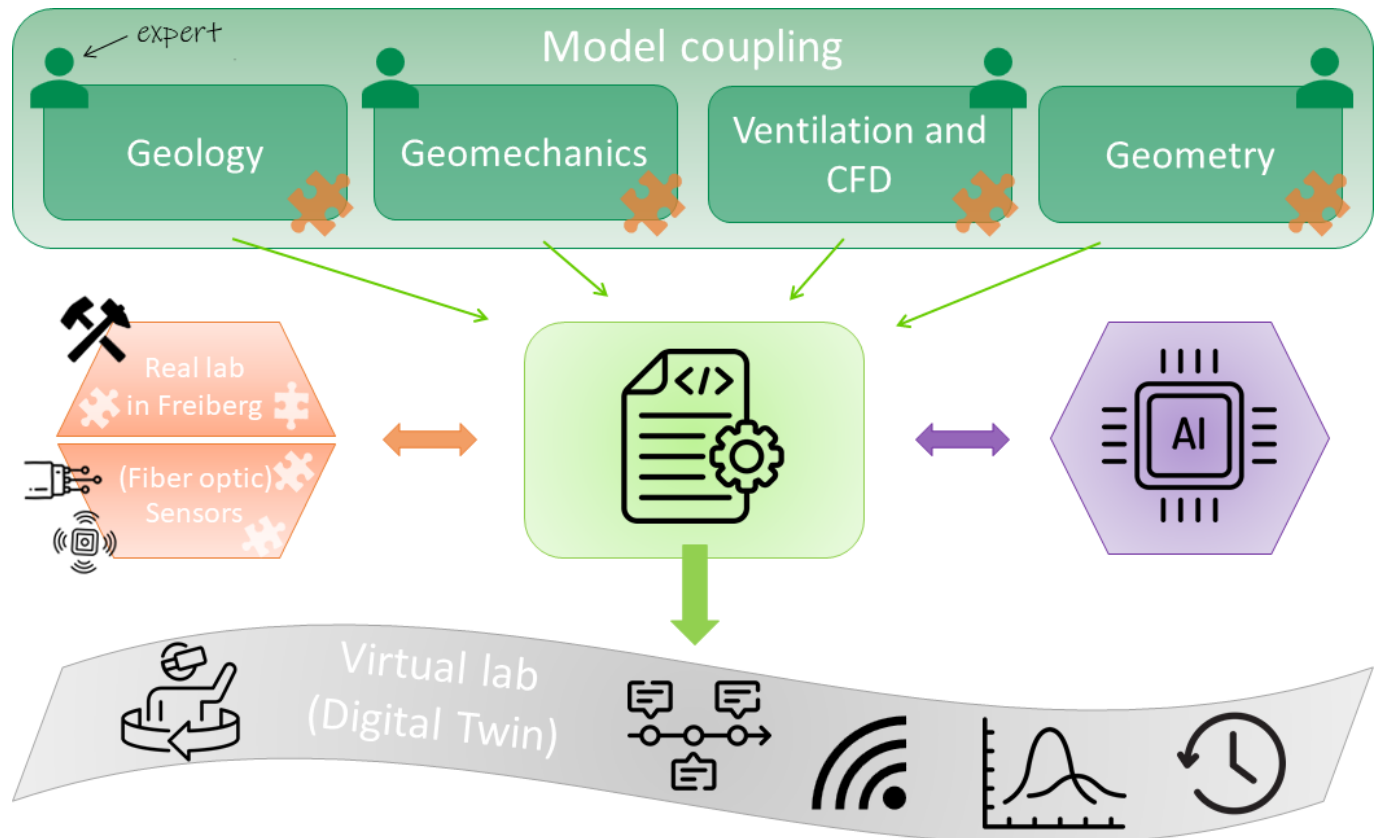


Figure 1 MOVIE project overview. Special emphasis in this paper is on fiber-optic sensing and laser scanning (Geometry).

The MOVIE project includes partners at five different departments at the Clausthal University of Technology (TUC) and one department at the TU Bergakademie Freiberg (TUBAF). Additionally, one external industry partner is included, fibrisTerre Systems GmbH (fibrisTerre). The project is led by the Chair of Geomatics for Underground Systems within the Institute of Geotechnology and Mineral Resources (IGMR) at the TUC. Despite the MOVIE project covering various aspects of geomechanical and ventilation modeling and AI application, this paper focuses on the installation of the fiber-optic cables, supported by a 3D point cloud acquired with a Zoller+Fröhlich (Z+F) FlexScan 22 mobile mapping SLAM platform. Additionally, the meshed surface of the underground lab, i.e., the geometrical model, generated from the 3D point cloud is of concern in this paper.

## 2 MATERIALS AND METHODS

### 2.1 The underground lab

Geologically, the FLB mine consists of ortho- and paragneisses and is veined with silver/lead/zinc mineralization. From the first discovery of silver-rich ores in 1168, active mining was maintained until 1969 with a focus on lead and zinc in the last exploitation stage [13]. Currently, the mine hosts more than 30 national and international collaborative research projects conducted in the underground space. The decision to plan the underground lab here is based on this particular part of the mine being relatively isolated from the other mine workings and experiments. The area of the underground lab can only be accessed via two raises from a lower level, however, only one

of the raises has a mine ladder, while the other access is intended for material transport via winches. This isolated location allows the conditions to be well controlled, particularly in terms of temperature and ventilation. The underground lab (see Figure 5) consists of a 60 m long main drift and four chambers with variable roof heights ranging between 2.75 and 4.9 m.

### 2.2 3D point cloud acquisition and data processing

Two 3D point clouds of the underground lab were acquired in two different field campaigns using a Z+F FlexScan 22 mobile mapping SLAM platform (Figure 2). The first point cloud was acquired in March 2024 containing a total of 368,291,128 points (~9.75 GB in e57-format). The second point cloud was acquired in May 2024 containing a total of 621,441,614 points (~16.5 GB in e57-format). The Z+F FlexScan 22 system incorporates a Z+F IMAGER 5016a laser scanner mounted on a backpack, merging the high spatial resolution of a stationary laser scanner with the versatility of a mobile platform. This technology is based on the simultaneous localization and mapping (SLAM) approach, which enables to create a map of the environment while data capturing [14].

The acquired 3D point clouds were processed using the software Z+F Lasercontrol 10.0.7.1. including loop closure, intensity based filtering and manual cleaning of noisy data points. Additionally, the 3D point clouds were aligned and registered using the open-source software packages CloudCompare 2.13.2. In the next processing stage, the resulting aligned and registered 3D point cloud was meshed based on a Poisson-Surface reconstruction approach using the

open-source software package MeshLab 2023.12 to generate triangular meshes with variable spatial resolutions. The generated mesh, i.e., the geometrical model, serves as the input to the geomechanical and ventilation models created by the project partners at TUC. Additionally, the geometrical model was visualized using the software package LiquidEarth One provided and developed by Terranigma Solutions GmbH. This software package was specifically designed for the visualization of geologic models in virtual reality including the use of a Meta Quest 3 VR headset and serves as the target software for visualization of the digital twin to be developed in the MOVIE project.



Figure 2 Z+F FlexScan22 mobile mapping SLAM platform.

### 2.3 Gluing experiments on fiber-optic cables using epoxy resin glue and injection mortar

The use of the fiber-optic cable type Fibrasens DSS-S and the fiber-optic cable type Solifos BRUsens DFOS B-DTS 2SMF was decided due to their specific design to perform strain and temperature measurements, respectively. Additionally, the cables have an overall good flexibility and proved to be reliable in former projects of fibrisTerre.

Especially for fiber-optic strain measurements, optimal bonding conditions to the object to be measured have to be ensured. Typically, DFOS cables for strain and temperature measurements are installed on pre-existing structures, e.g. in geotextiles [7], along rock bolts [10] or on reinforcement grids [9]. However, in the underground lab, none of these structures are present and installation along, e.g., rock bolts would result in a spatial discretization of the deformation measurement to the span interval between the rock bolts, e.g., [10]. Therefore, gluing experiments using the Fibrasens DSS-S strain cable were conducted on-site in the underground lab and under room temperature conditions in the Geomatics Indoor Lab at the IGMR using hand specimens taken from the underground lab to identify the optimal adhesive bonding method. Based on experiences of fibrisTerre, the epoxy resin glue Sikadur 31+ from Sika and the injection mortar FIS VS Low Speed 300 T from Fischer were tested. The Sikadur 31+ consists of two components that must be mixed in an external container before application. One container of the epoxy glue, containing a total of 1.2 kg, was used for the test. The epoxy glue is a moisture-tolerant adhesive designed to bond a variety of different

materials including concrete, natural stone, ceramics etc. and is used for repairs, joint fillings and crack sealing. According to the manufacturer information [15] the Sikadur 31+ has a compressive strength of ~50 MPa and a tensile strength of ~6 MPa after 3 days curing time at +10°C. The shear strength is reported as ~16 MPa. In contrast, the FIS VS Low Speed 300 T is delivered in a cartridge press containing 490 g of two components that are instantly mixed in the press upon handling. This injection mortar has approved use in water-filled drill holes and is used for fixations in cracked and non-cracked concrete as well as masonry. Due to its preferred use with anchors in drill holes, the strength metrics of the FIS VS Low Speed 300 T depend on the diameter of the anchor/rod used and the composition of the concrete/masonry. Information on bonding strength metrics were taken from the manufacturer homepage [16]. According to manufacturer information, permissible tensile loads are in the order of 0.34 kN up to 3.43 kN and permissible shear loads are in the order of 0.26 kN to 3.28 kN for solid and perforated masonry. In normal concrete, values for permissible tension and shear loads ranging from 3.9 kN up to 121.2 kN are reported depending on the anchor/rod type used. The characteristics of the epoxy resin glue and the injection mortar were estimated to be suitable to securely bond the Fibrasens DSS-S cable with a weight of 9 kg/km to the gneiss host rock.

Handling and application were tested using both a cartridge press and a trowel. The behavior of both the epoxy glue and injection mortar under dry and wet surface conditions was tested. Before gluing a cable to the wall or the specimen, the surface was prepared using a scratch brush to remove loose particles and dust. For temporarily fixing the fiber-optic cable to the rock surface, two fabric tapes were tested. The first was a standard tape for domestic use, and the second was the natural rubber tape “Beton- und Mauerband Premium, 44 mm x 50m” specifically manufactured for use on poorly adhering surfaces such as walls and concrete [17].

### 2.4 The DFOS measurement system

The fiber-optic measurements presented in this paper are based on the DFOS principle, specifically using the BOFDA, which enables spatially resolved strain and temperature measurements along the profile of the fiber. The measurement hardware consists of an interrogation unit (model name: fTB 5020), a fiber-optic switch for channel extension (a total of 12 channels for this project), an industrial PC and an ethernet switch for internet connection (Figure 3). For data analysis, the software fTView will be used and the cloud platform fTScope for data storage (not shown in Figure 3).

The BOFDA measurement enables a range of spatial resolutions for temperature and strain measurements of 0.2 m to 2.5 m depending on the fiber length. The minimum resolvable event is >2 microstrain [ $\mu\epsilon$ ] and >0.1°C for temperature measurements. Total fiber lengths of up to 80 km are possible [18].

The BOFDA technique makes use of the so-called Brillouin frequency shift of the fiber, which in a first instance is dependent on the intrinsic properties of the fiber material itself. However, small changes in the local density also impact the Brillouin frequency shift, which are interpreted in terms of changes in temperature and strain [7].

The conversion from Brillouin frequency shift [GHz] to temperature and strain for each position along the fiber is performed using the following relationships:

$$f_B = f_{B0} + \varepsilon \cdot c_\varepsilon \quad (1)$$

$$f_B = f_{B0} + (T - T_0) \cdot c_T \quad (2)$$

where  $f_B$  is the measured Brillouin frequency shift [GHz],  $T$  is the temperature [°C] and  $\varepsilon$  is the applied strain in microstrain [ $\mu\varepsilon$ ]. The calibration parameters  $f_{B0}$ ,  $c_\varepsilon$  and  $c_T$  are dependent on the specific optical fiber and cable type used (strain or temperature cable).

To test the DFOS measurement configuration, an aluminum frame was installed in the Geomatics Indoor Lab at the IGMR, which will be equipped with clamping jaws and deflection rolls to enable test strain and temperature measurements using both cable types.

## 2.5 Fiber-optic cable installation configuration and experimental setup in the underground lab

On-site in the underground lab, the fiber-optic sensors will be installed along the main drift to obtain longitudinal temperature and strain along the entire drift. These sensors will be installed with the aim of providing continuous measurements throughout the MOVIE project period. In contrast to the strain cable, the temperature cable in the main drift is planned to be installed disconnected from the drift wall using clamps, as measurements of the temperature of the air inside the drift is of interest. The temperatures on the surface of the rock, where the fiber-optic strain sensing cable is installed, are assumed to be overall stable and in equilibrium with air temperatures, with no sudden variations to be expected. The temperature distribution retrieved from the fiber-optic temperature sensing cable will

therefore be suitable to temperature compensate the strain measurements along the drift, where the fiber-optic strain sensing cable is largely running in parallel to the temperature sensing cable. For the strain cable installations that are directed further into the gneiss body, being the rock bolt test installations, the temperature is assumed to be even more stable and constant over the cable length. The temperature impact on these strain measurements will therefore be neglected, and no temperature compensation is assumed to be necessary. To induce measurable deformation in the gneiss that is large enough to be used as boundary conditions for the geomechanical model, three test rigs will be installed in three of the four chambers to perform short-term push and pull experiments. In the first chamber, an arch support will be installed in such a way that a distance from direct contact with the rock is maintained, allowing exertion of pressure on specific points of the support structure. In the second chamber, a hydraulic cylinder will be installed, which enables to transfer a load orthogonally onto the rock.

For both chambers, stress and strain changes will be recorded with fiber-optic cables installed superficially either in the support structure of the arch or directly on the chamber wall surrounding the hydraulic cylinder.

In the third chamber, four separate configurations of 4 m long anchor boreholes surrounded by four 5 m long measurement boreholes are planned, resulting in a total of four anchor boreholes and 20 measurement boreholes to be drilled. The fiber-optic cables will be directly cemented into the rock along the rock bolts. For each of the four configurations separately, the rock bolt cemented in the anchor borehole will be pulled and deformations of the surrounding concrete and rock will be measured in the measurement boreholes along the cemented fiber-optic cables.

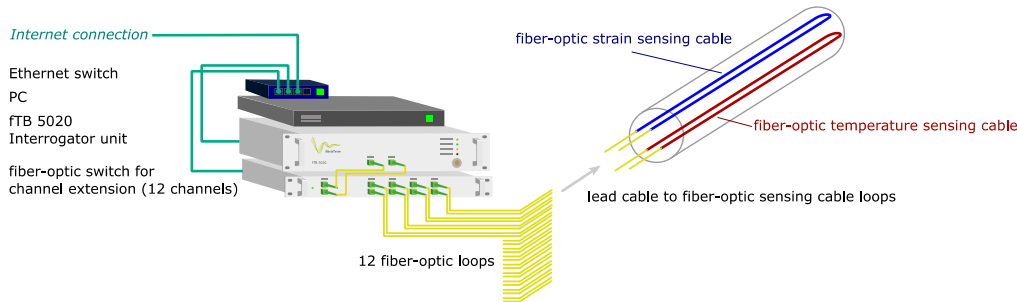


Figure 3 fibrisTerre measurement setup (principle).

Additional numerical simulations were conducted by the Geomechanics department at the TUC based on the rock elasticity modulus, the mechanical properties of the steel and the detection limit of the fibrisTerre interrogation unit of 2  $\mu\varepsilon$  to ensure optimal fiber-optic cable installation planning. The simulation parameters are based on the dimensions of the planned experiments. For the hydraulic cylinder in chamber 2, a steel plate with diameters of 0,30 m was modeled, which was placed on a rock cube 1.5 m in diameter with an assumed elastic modulus of 50 GPa. A maximum pressure of 182 MPa was exerted on the steel plate. The simulation results were used to identify the maximum radius in which a superficial strain change can still be measured if a load is transferred onto the

rock. Results showed a maximum radius of ~52 cm around the steel plate to be maintained for the cable installation (Figure 4). For the rock bolt pull out test in chamber 3, a borehole with a radius of 38 mm and a depth of 4 m was assumed, in which a rod with radius 25 mm and a length of 3975 mm is installed. The scenario was modeled under the assumption of inelastic grout and steel and a rock elasticity modulus of 50 GPa. The simulation results were used to identify the maximum distances between the anchor and measurement boreholes in which a strain change in the measurement borehole is expected to be still measurable. The results showed a maximum distance of ~36.2 cm to be maintained (Figure 4).



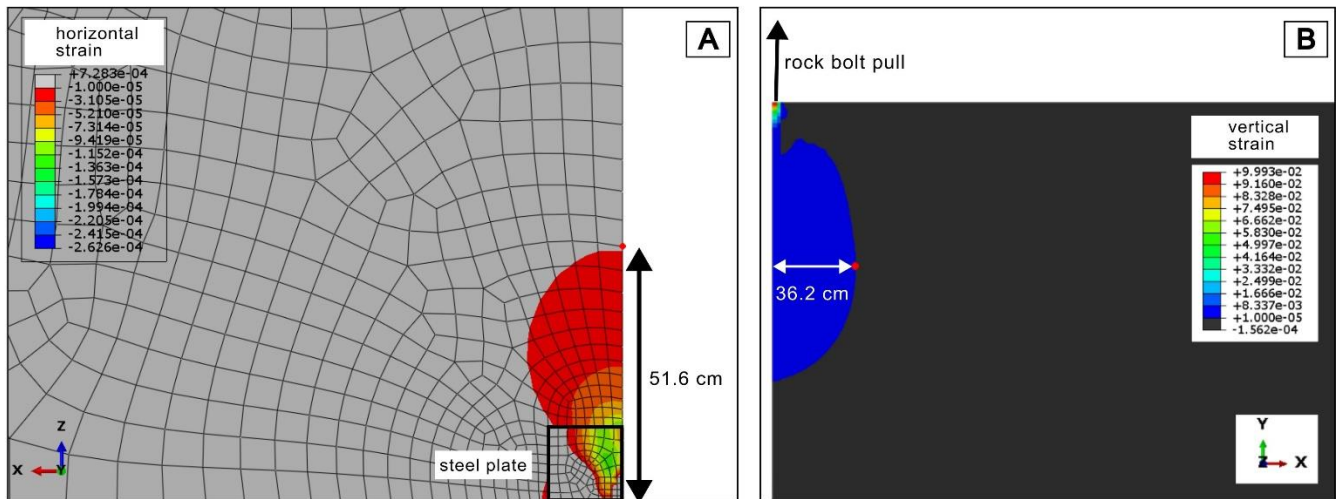


Figure 4 Geomechanical simulation results of (A) plate load test and (B) rock bolt pull out test. A strain cut off value of  $10^{-5}$  was used in both cases. To save computational effort and under the assumption of radial symmetry, only one fourth of the geometry was simulated.

The 3D point cloud acquired in May 2024 was used for fiber-optic cable installation planning for the main drift and the test rigs separately. The Trace Polyline tool available in the software package CloudCompare 2.13.2. was used to draw polylines in the 3D point cloud representing the fiber-optic cables to be installed. To estimate the overall lengths of the cables, the individual polylines were summed up in CloudCompare. Since the 3D point cloud only allows for estimating the lengths of cables installed superficially, the lengths of the cables needed for the rock bolts were added to the calculated superficial installation lengths.

All cables from the main drift installation and the test rigs will be installed in a loop configuration from and towards a fiber-optic cable termination box connected with the fibrisTerre measurement configuration, which both will be installed roughly opposite of chamber 2.

### 3 RESULTS

#### 3.1 Visualization of 3D point cloud and determination of fiber-optic cable positions and their lengths

The 3D point cloud acquired in May 2024 was scanned with an average spatial resolution, i.e., average point distance, of approximately 0.76 mm in roughly 29.5 minutes. Due to computational performance reasons, a subsampled version of the original 3D point cloud with a resolution of ~3.63 mm (22,378,105 points; ~417 MB in .e57-format) was used for planning the installation of the fiber-optic cables, which still captured enough details to ensure realistic positioning of the cables. Figure 5 shows the subsampled 3D point cloud of the underground lab, including its four chambers. Additionally, Figure 5 shows the meshed 3D point cloud visualized in the target software for the digital twin LiquidEarth One. Figure 6 presents views within the 3D point cloud, showing the polylines representing the positions of the fiber-optic cables for the main drift and exemplary for chambers 1 and 2. Based on a high resolution meshed version of chamber 2, a relatively flat

section extending across a large portion of the roof was identified, making it an ideal candidate for the installation of the hydraulic cylinder unit and the cables surrounding the terminating steel plate of the cylinder (see Figure 6C).

Table 1 Estimated lengths [in meters] of the Fibrasens strain cable and Solifos BRUsens temperature cable based on polylines drawn in the 3D point cloud

Position	Experiment setup	Cable type	Length [m]
Main drift	Continuous monitoring	Strain	138
Chamber 1	Arch support structure	Strain	29
Chamber 2	Hydraulic cylinder	Strain	35
Chamber 3	Rock bolt pull out	Strain	387
<b>SUM [m]</b>			<b>589</b>
Main drift	Continuous monitoring	Temperature	<b>138</b>

The lengths of the cables to be installed were determined in the 3D point cloud supported by the results of the geomechanical simulations. The overall length of the Fibrasens strain cable to be installed for the main drift and the test rigs was estimated to be roughly 600 m, while the overall length of the Solifos BRUsens temperature cable was estimated to be roughly 140 m. Table 1 presents the detailed estimated lengths for the strain cable along the main drift and the test rigs separately. Since temperature measurements are only performed along the main drift, the estimated length of the temperature cable is added at the bottom of Table 1.

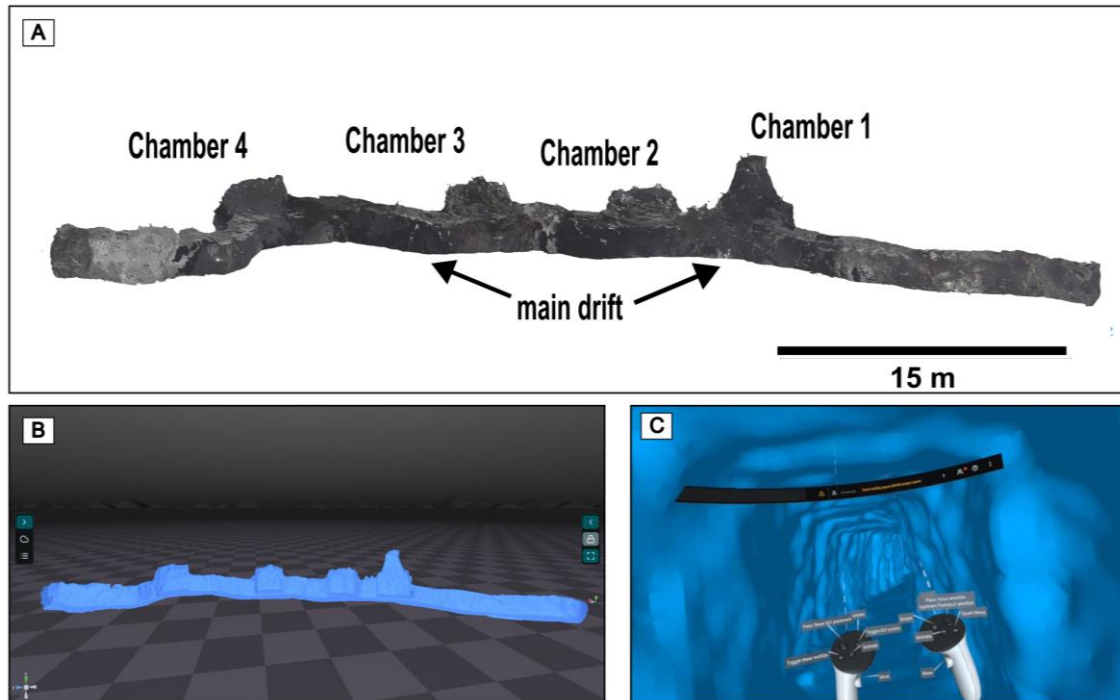


Figure 5 (A) 3D point cloud of underground lab including main drift and four chambers (chambers numbered 1 to 3 are used for installation of the test rigs); (B) Meshed 3D point cloud visualized in software LiquidEarth One developed by Terranigma Solutions GmbH; (C) View inside the underground lab in LiquidEarth One using a Meta Quest 3 VR headset.

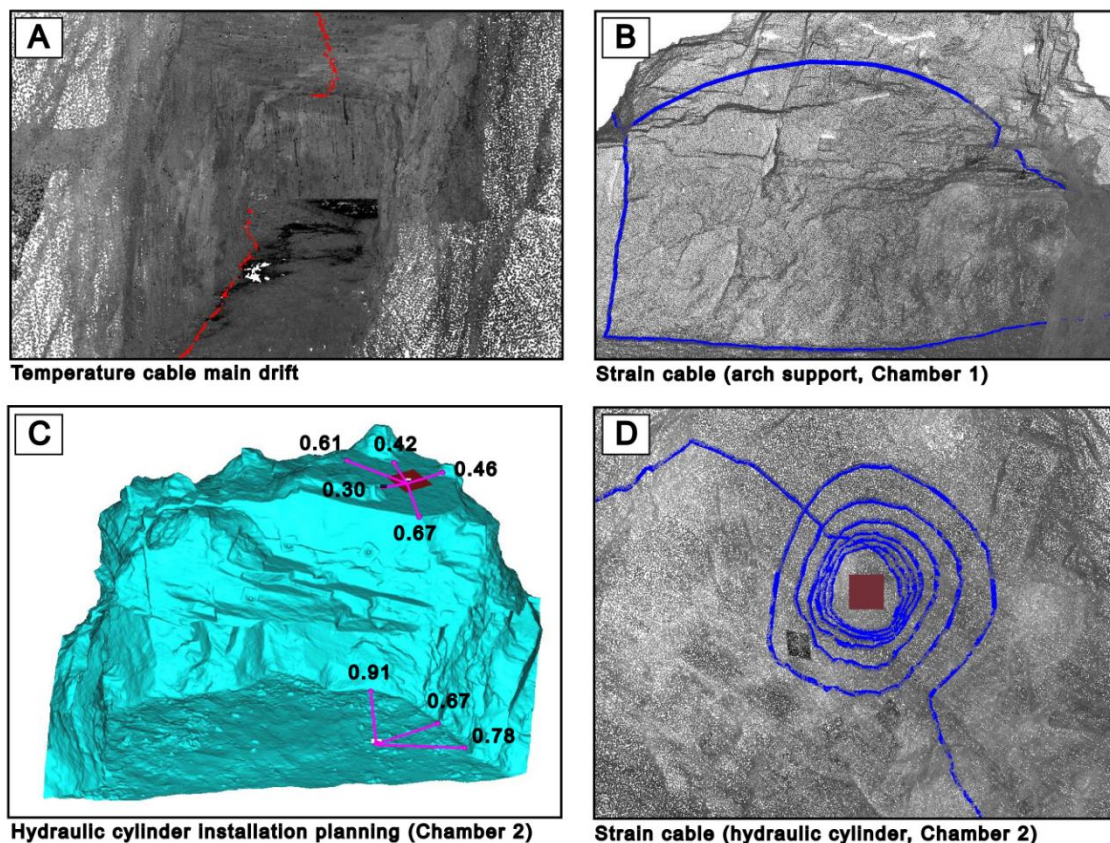


Figure 6: Views in the 3D point cloud (and mesh) showing the positions of the fiber-optic cables to be installed as polylines (A) BRUsens temperature cable in main drift, (B) Fibrasens strain cable in the arch support structure (Chamber 1), (C) Meshed 3D point cloud of Chamber 2 for estimation of distances (in meters) to the walls for installation planning of the hydraulic cylinder.

The terminating steel plate of the hydraulic cylinder is shown as a dark red square on the chamber roof (D) Fibrasens strain cable around the steel plate of the hydraulic cylinder (dark red) in Chamber 2 (view towards the chamber roof)



### 3.2 The gluing experiments

Several gluing tests were conducted to ensure optimal bonding between the Fibrasens strain cable and the drift wall (Figure 7). For temporarily fixing the cable to the rock surface, the tape for domestic-use did not provide sufficient adhesion for both dry and wet surfaces. However, the special wall and concrete tape adhered well to a dry surface. Under room temperature conditions in the Geomatics Indoor Lab at IGMR, the Sikadur 31+ epoxy resin glue achieved its maximum bonding strength one day after application, with no observable differences for wet and dry surfaces. After mixing, the epoxy resin glue remained usable for approximately 60-70 min, but became sticky (and therefore unworkable) after roughly 90 min. Once applied, the cables were securely fixed to a rock specimen in the Geomatics Indoor Lab or on-site on the drift wall and could not be removed by pulling on the cable. In contrast, the FIS VS Low Speed 300 T injection mortar reached maximum bonding strength after just 3.5-5 min. However, on damp surfaces, the cured mortar broke off with slight force. Application of both the glue and the mortar to a vertical wall and overhead was challenging, as a lot of material crumbled or fell off and did not adhere to the rock. The use of a cartridge press and a trowel partially solved this problem and proved to be the most effective method to best apply both the glue and the mortar to the rock.

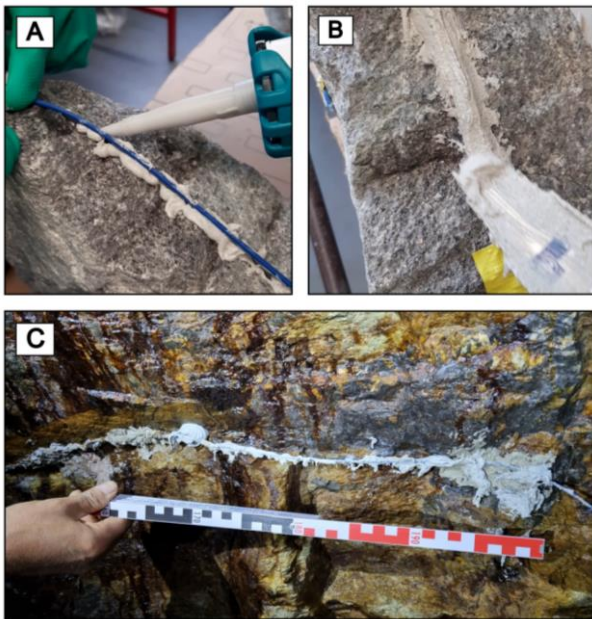


Figure 7 Gluing tests with Fibrasens strain cable on a hand specimen (A) using a cartridge press and (B) a trowel; (C) Fibrasens strain cable glued to drift wall on-site in the underground lab (measuring rod for scale)

## 4 DISCUSSION

### 4.1 3D mobile laser scanning and determination of fiber-optic cable positions/lengths

The Z+F FlexScan22 mobile backpack laser scanner solution proved capable of accurately capturing the complex wall geometry of the underground lab with a very high resolution of approximately 0.76 mm in about 29.5 min

acquisition time. Compared to a classical terrestrial laser scanning system, at least about eight different stationary scanner positions would have been necessary to capture the underground lab, resulting in a much longer data acquisition time. Despite the high data acquisition speed, a shortcoming of the mobile laser scanning system are omnipresent noise pixels in the drift, which requires greater (manual) cleaning efforts compared to data acquired with a stationary terrestrial laser scanner system. In contrast, the registration of independently acquired 3D point clouds is not necessary when using a mobile laser scanner system, which should result in an overall shorter time for data acquisition and processing using the Z+F FlexScan22 solution.

Using this approach made it possible to identify optimal positions for the fiber-optic cables and to estimate their required lengths in the 3D point cloud. Due to the high point density, it is not possible to click every successive point in the 3D point cloud as a vertex point of the polyline. This might lead to some of the distances between individual vertex points being shorter than in reality, since some of the line segments between individual vertex points might not follow the wall roughness, which might result in a slight underestimation of the cable lengths. Conversely, due to uncertainties in the distance measurements themselves stemming from intrinsic device errors and external factors such as dust particles and/or humidity, the points in the 3D point cloud are slightly spread, i.e., not exactly matching with their position on the wall. This might lead to greater roughness in the 3D point cloud compared to the drift wall, which could, in contrast, result in a slight overestimation of the cable lengths. However, for the practical installation of the cables on-site, the estimated positions and cable lengths will act as a guiding principle and do not need to be accurate on a centimeter-scale. Additionally, the practical installation of the cables requires consideration of the maximum allowed bending radii, which are 3.8 cm for the Fibrasens strain cable and 9.6 cm for the Solifos BRUsens temperature cable. Due to the large roughness of the drift walls, the bending radii might be exceeded in some places particularly for the strain cable.

### 4.2 The gluing experiments and fiber-optic cable installation configuration

The Geomatics Indoor Lab and on-site experiments presented in this paper showed that gluing the strain cable to the drift wall is a difficult task, since most of the glue and mortar crumbles or falls off especially when working on a perpendicular wall or overhead. Still, direct installation on the wall is necessary in this project, since there are no pre-existing structures present in the underground lab, which the cable can be installed at and direct installation on the wall allows to make full use of the system's spatial resolution. To overcome this issue, cutting a ~3-25 mm deep and ~4 mm wide slit in the drift wall is planned with the strain cables placed in. After its installation, the slit will be closed with the injection mortar due to its easier handling and the shorter setting time if compared to the epoxy resin glue. Before application of the mortar, the acquisition of another 3D point cloud is planned to document the position of the slit (and therefore the position of the fiber-optic cable).



The overhead installation of the cables might still be challenging, but could be successfully addressed with combined use of the cartridge press and trowel. If needed, “modeling” rough parts using the injection mortar is possible, which will ensure optimum bonding between the strain cables and the drift wall. Cable installation within the arch support structure and installation along the rock bolts for the rock bolt pull out test requires a different setup, which is in the planning phase at the time of writing this paper.

The current fiber-optic cable setup plans the installation of a termination box and the fibrisTerre measurement configuration in the underground laboratory. This results in the shortest possible spanned distances between the termination box and the individual test rigs (see Table 1). The same applies for the temperature and strain cables installed in the main drift for continuous measurements. Still, the planned setup in chamber 3 requires longer cable lengths if compared to the installations in chamber 1 and 2 due to cable installation along the 4 to 5 m long rock bolts. Additionally, each of the four configurations of anchor and measurement boreholes must be connected to the termination box separately, as the cable will most likely be destroyed after performing a pull out test. Besides pure cable installation with the help of a 3D point cloud, meshes were created for visualization purposes and a highly resolved mesh of chamber 2 was used for installation planning of the hydraulic cylinder. The mesh allowed to identify a region most suitable for installation of the terminating steel plate and to precisely determine the distances to the wall to ensure enough space for installation of the cylinder foot.

It is planned to prepare the cables based on the determined lengths in the Geomatics Indoor Lab at IGMR before installing them in the underground lab. This preparatory step might be beneficial, since the very sensitive splicing work should be kept away from the harsh and dark environment of an underground environment.

#### 4.3 Long-term stability of the BOFDA measurement system

Due to its primarily measured material parameter being the intrinsic density of the optical fiber, the BOFDA technology is specifically long-term stable and free from the requirement of on-site sensor calibration both at the initial baseline measurements and during long-term operation. With the above calibration parameters known for the fiber-optic sensing cables in use (to be acquired from one-time lab tests), the Brillouin frequency shift from each measurement iteration can be converted into absolute values for temperature and strain, with no drift being caused by aging, fatigue, or changes in the optical properties of the cables and connectors. Therefore, the technique is especially suitable for the monitoring of the underground structure over a time horizon of many years. More critical, however, will be the long-term behavior of the bonding between the fiber-optic strain sensing cable and the rock and grout structures under test.

#### 4.4 Preparation of data fusion and comparison to El Teniente mine (Chile)

A first attempt at fusing the fiber-optic position data, i.e., the polylines, with the BOFDA strain and temperature

measurements provided promising results via exporting the strain and temperature data from fTView and merging them with the exported fiber-optic position data from CloudCompare using a Python script. When merged, the strain and temperature data can be re-loaded into CloudCompare as scalar fields of the position data and can be visualized. The strain and temperature measurements will serve as the boundary conditions for a coupled geomechanical and ventilation model provided by our project partners. As a first step towards visualization, the meshed version of the acquired 3D point cloud, i.e., the geometrical model, was uploaded and visualized in the target software for our digital twin LiquidEarth One using a Meta Quest 3 VR headset. The final product, i.e., the digital twin, to be visualized in LiquidEarth One and using virtual reality will be a coupled geomechanical and ventilation model provided with measurements from the fiber-optic sensors as boundary conditions and speeded-up with AI to shorten processing times and to enable real-time user interaction. The planned AI based approach is currently developed at TUC and is based on the Equilibrium Neural Operator (EquiNO) for solving steady-state multiscale modeling problems [19]. The expected results of the MOVIE project might be transferable to active mining environments such as e.g. the El Teniente mine in Chile. In this mine, fiber-optic sensors were installed in the ventilation level of a 201 m long test field and measured deformations were interpreted in terms of mining activities conducted in the production level [10]. The results presented in this paper are expected to be transferable to mines in a hard rock setting, such as e.g., the El Teniente mine [cf. [20]]. Additionally, the use of a digital twin, as described in this paper, might simulate the impacts of mining activities in terms of geotechnical parameters and ventilation even before a particular mine is opened, thereby enhancing safety and efficiency. Due to the capability of the BOFDA technology to measure within a range of up to 80 km, the results of this project should also be scalable to large mining areas. However, challenges remain in installing and protecting fiber-optic strain sensing cables when considering the occurrence of (locally constrained) deformations in the macrostrain region, such as e.g., in coal mines [21]. With both metallic and non-metallic fiber-optic sensing cable designs being typically specified for operation up to 1% strain, other strategies than straight gluing and pre-strained anchoring will need to be considered.

Since this is an ongoing research project, future changes to the described configurations and workflows might apply. Nevertheless, the results presented show the great potential of using 3D mobile laser scanning data for installation planning of fiber-optic cables in the underground space.

## CONCLUSION

This paper presents the current state of the work done within the larger collaborative research project MOVIE with the aim of developing a digital twin of a 60 m long underground lab located in the FLB research mine in Freiberg (Germany) including real-time DFOS based temperature and strain measurements and visualization in VR. The installation planning of the fiber-optic cables was supported by SLAM based mobile laser scanning using a Z+F FlexScan 22

platform. The acquired 3D point cloud was successfully used to estimate the lengths of the fiber-optic strain and temperature cables to be installed for both a continuous measurement setup and additional temporary experimental setups. Additionally, a meshed version of the 3D point cloud, i.e., the geometrical model, was visualized in virtual reality using a Meta Quest 3 VR headset. Since no pre-existing structures are present in the underground lab, several gluing tests under dry and wet conditions using the epoxy resin glue Sikadur 31+ from Sika and the injection mortar FIS VS Low Speed 300 T from Fischer were conducted. Overall, the injection mortar outperformed the epoxy resin glue due to its shorter setting time and easier handling and application. Future steps in the project will include installation of the strain cables in a slit cut in the drift wall and subsequent gluing with the injection mortar, which will enable a safe installation of the cables. An additional 3D point cloud will be acquired to document the positions of the cables once installed. The results of the DFOS temperature and strain measurements will be used as boundary conditions for a coupled geomechanical and ventilation model, which is supported with an AI model to enable real-time visualization of changes in physical parameters.

## 5 ACKNOWLEDGMENTS

The project "Modellkopplung im Kontext eines Virtuellen Untertagelabors und dessen Entwicklungsprozess - MOVIE" is part of the research program "GEO:N - Geosciences for Sustainability" on the topic "Digital Geosystems: Virtual Methods and Digital Tools for Geoscientific Applications" funded by the German Federal Ministry of Research, Technology and Space (BMFTR). GEO:N is thus part of the BMFTR program "Research for Sustainable Development (FONA)". For the opportunity to realize this project, the consortium thanks the BMFTR and the project management organization.

[Reference: 03G0921A/ 2024-01 till 2026-12]

## 6 REFERENCES

- [1] Z. Ye *et al.*, "A digital twin approach for tunnel construction safety early warning and management," *Computers in Industry*, vol. 144, p. 103783, Jan. 2023, doi: 10.1016/j.compind.2022.103783.
- [2] H. Gong, D. Su, S. Zeng, and X. Chen, "Advancements in digital twin modeling for underground spaces and lightweight geometric modeling technologies," *Automation in Construction*, vol. 165, p. 105578, Sept. 2024, doi: 10.1016/j.autcon.2024.105578.
- [3] M. Ghahramanieisalou and J. Sattarvand, "Digital Twins and the Mining Industry," in *Technologies in Mining [Working Title]*, IntechOpen, 2024, doi: 10.5772/intechopen.1005162.
- [4] F.-J. Kahlen, S. Flumerfelt, and A. Alves, Eds., *Transdisciplinary Perspectives on Complex Systems: New Findings and Approaches*. Cham: Springer International Publishing, 2017, doi: 10.1007/978-3-319-38756-7.
- [5] K. Krebber *et al.*, "Structural Health Monitoring by Distributed Fiber Optic Sensors Embedded into Technical Textiles," *tm - Technisches Messen*, vol. 79, no. 7–8, pp. 337–347, Aug. 2012, doi: 10.1524/teme.2012.0238.
- [6] J. M. Lopez-Higuera, L. Rodriguez Cobo, A. Quintela Incera, and A. Cobo, "Fiber Optic Sensors in Structural Health Monitoring," *J. Lightwave Technol.*, vol. 29, no. 4, pp. 587–608, Feb. 2011, doi: 10.1109/JLT.2011.2106479.
- [7] N. Nöther, *Distributed fiber sensors in river embankments: advancing and implementing the Brillouin optical frequency domain analysis*. in BAM-Dissertationsreihe, no. 64. Berlin: Bundesanstalt für Materialforschung und -prüfung (BAM), 2010.
- [8] P. Jousset *et al.*, "Fiber optic sensing for volcano monitoring and imaging volcanic processes," May 05, 2024, *Physical Sciences and Mathematics*. doi: 10.31223/X5HM6J.
- [9] F. Buchmayer, C. M. Monsberger, and W. Lienhart, "Advantages of tunnel monitoring using distributed fibre optic sensing," *Journal of Applied Geodesy*, vol. 15, no. 1, pp. 1–12, Jan. 2021, doi: 10.1515/jag-2019-0065.
- [10] H. Naruse *et al.*, "Application of a distributed fibre optic strain sensing system to monitoring changes in the state of an underground mine," *Meas. Sci. Technol.*, vol. 18, no. 10, pp. 3202–3210, Oct. 2007, doi: 10.1088/0957-0233/18/10/S23.
- [11] D. Garcus, T. Gogolla, K. Krebber, and F. Schliep, "Brillouin optical-fiber frequency-domain analysis for distributed temperature and strain measurements," *J. Lightwave Technol.*, vol. 15, no. 4, pp. 654–662, Apr. 1997, doi: 10.1109/50.566687.
- [12] E. Farys *et al.*, "Concept of a Digital Twin for an Underground Laboratory at the Reiche Zeche Mine Utilizing Artificial Intelligence," in *2025 Preprints*, Colorado (USA): Society for Mining, Metallurgy & Exploration (SME), Feb. 2025, pp. 199–208. [Online]. Available: [https://store.smenet.org/23c8kse#=\\_](https://store.smenet.org/23c8kse#=_).
- [13] J. Ostendorf, F. Henjes-Kunst, T. Seifert, and J. Gutzmer, "Age and genesis of polymetallic veins in the Freiberg district, Erzgebirge, Germany: constraints from radiogenic isotopes," *Miner Deposita*, vol. 54, no. 2, pp. 217–236, Feb. 2019, doi: 10.1007/s00126-018-0841-1.
- [14] H. Taheri and Z. C. Xia, "SLAM; definition and evolution," *Engineering Applications of Artificial Intelligence*, vol. 97, p. 104032, Jan. 2021, doi: 10.1016/j.engappai.2020.104032.
- [15] "Sikadur®-31+." Accessed: June 30, 2025. [Online]. Available: <https://industry.sika.com/en/home/renewable-energies/wind-energy/concrete-tower/structural-bonding/sikadur-31.html>
- [16] "fischer Injection mortar FIS VS Plus 300 T." Accessed: June 30, 2025. [Online]. Available: <https://www.fischer-international.com/en/products/chemical-fixings/injection-mortar/injection-mortar-fis-v-plus>
- [17] "Beton- und Mauerband Premium, 44 mm x 50 m Farbe: gelb kaufen Farbe: gelb." Accessed: June 30, 2025. [Online]. Available: <https://www.hygi.de/beton-und-mauerband-premium-44-mm-x-50-m-farbe-gelb-pd-125091>
- [18] fibrisTerre Systems GmbH, "FTB 5020 - Product Brochure." 2019. [Online]. Available: [https://www.fibristerre.de/file\\_download/15/FTB+5020++Product+Brochure.pdf](https://www.fibristerre.de/file_download/15/FTB+5020++Product+Brochure.pdf)
- [19] H. Eivazi, J.-A. Tröger, S. Wittek, S. Hartmann, and A. Rausch, "EquiNO: A Physics-Informed Neural Operator for Multiscale Simulations," Apr. 25, 2025, *arXiv: arXiv:2504.07976*. doi: 10.48550/arXiv.2504.07976.
- [20] J. Cannell, D. R. Cooke, J. L. Walshe, and H. Stein, "Geology, Mineralization, Alteration, and Structural Evolution of the El Teniente Porphyry Cu-Mo Deposit," *Economic Geology*, vol. 100, no. 5, pp. 979–1003, Aug. 2005, doi: 10.2113/gsecongeo.100.5.979.
- [21] H. Gong, M. S. Kizil, Z. Chen, M. Amanzadeh, B. Yang, and S. M. Aminossadati, "Advances in fibre optic based geotechnical monitoring systems for underground excavations," *International Journal of Mining Science and Technology*, vol. 29, no. 2, pp. 229–238, Mar. 2019, doi: 10.1016/j.ijmst.2018.06.007.

## Fibradike sensor: validation through full-scale field testing

A. Höttges<sup>1,2</sup>, 0000-0003-0315-2563, C. Rabaiotti<sup>1</sup>, 0000-0002-6217-5848, A. Rosso<sup>3</sup>

<sup>1</sup>Institute for Building and Environment (IBU), Dept. of Architecture, Building, Landscape and Space (ABLR), Eastern University of Applied Sciences (OST), Oberseestrasse 10, 8640 Rapperswil, Switzerland

<sup>2</sup>Laboratory of Hydraulics, Hydrology and Glaciology (VAW), Dept. of Civil Environmental and Geomatic Engineering (D-BAUG), Swiss Federal Institute of Technology in Zurich (ETHZ), Rämistrasse 101, 8092 Zurich, Switzerland

<sup>3</sup>Interregional Agency for the Po River, Strada Giuseppe Garibaldi 75, 43121 Parma, Italy

email: alessio.hoettges@ost.ch/alessioh@student.ethz.ch, carlo.rabaiotti@ost.ch, alessandro.rosso@agenziapo.it

**ABSTRACT:** Earthen geohydraulic structures, such as dams and river embankments, are vital for water resource management and flood control, especially as climate change and urbanization increase hydrological risks. Internal erosion, often triggered by seepage, remains a major failure mechanism and can cause sudden, catastrophic collapses. Traditional monitoring systems lack the spatial and temporal resolution needed for effective early detection. To address this gap, a novel Distributed Pressure Sensor (DPS) based on distributed fiber optic (DFO) technology has been developed by the University of Applied Sciences of Eastern Switzerland (OST). The DPS offers high spatial resolution and extended range, enabling precise measurement of distributed pore water pressure - key for early detection of internal erosion processes. Following successful laboratory validation, the DPS was deployed in a full-scale test embankment (84 m long, 39 m wide, 4 m high) at the AIPo Research and Technical Centre in Boretto, Italy. Preliminary results show that the DPS accurately captured pore pressure evolution, matching conventional piezometer readings while detecting localized variations and two-dimensional flow effects that point sensors could not resolve. These findings highlight the DPS system's strong potential for improving early warning capabilities in geohydraulic structure monitoring.

**KEY WORDS:** Dike Monitoring, Distributed Pressure Sensor, Distributed Fiber Optic technology.

### 1 INTRODUCTION

River dikes and earthen dams play a crucial role in water management, including energy production and flood risk protection. Following the catastrophic events in northern Italy of May 2023 [1] and the Rhone region of Switzerland in June 2024 [2], the need for enhanced protection and monitoring of such structures has become evident.

The primary failure mechanisms of these structures are overtopping and internal erosion [3]. Among them, internal erosion is often underestimated and typically not clearly detectable after failure [4].

Conventional monitoring systems, which rely mainly on point-based sensors, are limited in both spatial and temporal resolution. As a result, monitoring during flood events often still depends on visual inspections, sometimes involving hundreds of volunteers, which reflects an outdated approach [4].

In last decades, a promising monitoring alternative has emerged: the use of Distributed Fiber Optic (DFO) technology, which enables high-resolution measurements of temperature and deformation along the entire length of the installed sensing cable [5]-[6]. In this context, an innovative development within the DFO sensor family has been proposed by Höttges, et al. [7], who introduced a Distributed Pressure Sensor (DPS). This sensor is capable of measuring pore pressure with high sensitivity and accuracy, over distances of several kilometers. The DPS is designed to monitor seepage anomalies by directly measuring pore pressure within the structure, which can serve as an early indicator of internal erosion processes as pointed out by Fell, et al. [4].

The DPS has already been validated through extensive laboratory testing on model dikes (Höttges, et al. [7]; Höttges, et al. [8]). This paper presents a further step in the validation

process of this novel sensor by reporting preliminary results obtained under full-scale field conditions, using a dedicated full-scale test embankment constructed at the AIPo Research and Technical Centre. The objective is to assess both the installation process and the sensor's performance in a controlled field environment that closely replicates field operating conditions.

### 2 DISTRIBUTED PRESSURE SENSOR - DPS

The sensor was developed within the framework of the FIBRADIKE project [9], whose core objective was the development of a DPS based on DFO technology. The sensor, whose latest design has a diameter of 13 mm, consists of an optical fiber that is wound helically around a cylindrical, compressible central element (Figure 1). When the central element is subjected to hydrostatic pressure, it compresses, causing the helical fiber to deform accordingly. The hydrostatic pressure is then back calculated using a calibration coefficient ( $C_p$ ) that converts the measured radial strain of the fiber into corresponding pressure values. This coefficient is determined by laboratory testing under controlled pressure conditions. According to Höttges, et al. [8] the sensor can reach a sensitivity of 100 Pa and an accuracy of 15 % RD (relative deviation of reading) for a spatial resolution in the order of a few centimeters using the Rayleigh interrogation technique [10]. Additionally, the core of the central element is equipped with two single-mode fibers and two multi-mode fibers, loosely housed in a central tube (see Figure 1), which can be used for Distributed Temperature Sensing (DTS). This configuration enables simultaneous monitoring of pore pressure and temperature, enhancing the sensor's capability for detecting and characterizing seepage-related anomalies. Additionally, the inner part of the central element is filled with aramid yarns (see



Figure 1), which according to Höttes, et al. [8], can provide a tensile strength of up to 20 kN. This feature is particularly useful for installations requiring high tensile strength of the cable, such as pulling or trenching operations.

The sensor was developed and calibrated for pressures up to 200 kPa, specifically designed to operate within the typical pressure range found in river dikes. Although higher pressure ranges are possible, they were not tested in this study. The sensor demonstrates good repeatability and low hysteresis within the tested pressure range [7].

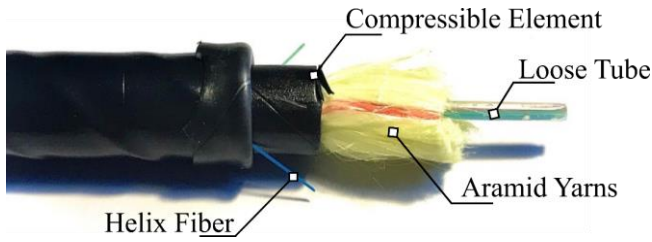


Figure 1. Design of the DPS, adapted from [7].

### 3 FULL-SCALE TEST EMBANKMENT

#### 3.1 Embankment design and construction

The test embankment is constructed at the AIPo Research and Technical Centre situated in the municipality of Boretto - Province of Reggio Emilia (RE - Italy). The test embankment has a length of 84 m, 39 m wide and 4 m high with a slope 1:2 [9], see Figure 2. The embankment is founded on 16 m thick clay layer and 16 m thick medium to coarse sand (aquifer), from which water is pumped to fill the reservoir.

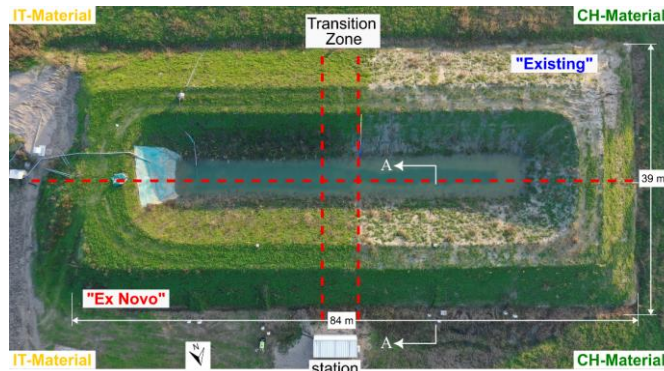


Figure 2. Test embankment with the 4 different sections.

The test embankment was constructed using two different materials: a coarse soil typical of Swiss river dikes and a finer soil characteristic of the river dikes along the Po River plain. These two zones are referred to as Swiss (CH) and Italian (IT) sections, respectively. According to the Unified Soil Classification System (USCS), the IT-Material is classified as sandy clay (CM), while the CH-Material is classified as clayey sand (SC). The granulometric distribution of the two materials is shown in Figure 3. Based on in-situ permeability tests, the permeability  $k_m$  is approximately  $1 \cdot 10^{-5} \text{ m/s}$  for the CH and  $2 \cdot 10^{-7} \text{ m/s}$  for the IT-Material.

Two different sensor installation methods were also implemented, each applied to a different section. The first, referred to as "ex novo", simulates the sensor installation during the construction process. The second, referred to as "existing",

involves the installation of the sensors after the construction of the basin has been completed, using the Horizontal Directional Drilling (HDD) technique [11].

In total, four different zones were constructed, each representing a unique combination of material type and installation method (Figure 2). This paper focuses solely on the installation and results of the "ex novo" section.

The test embankment was constructed using the described two different materials, placed in 30 cm thick compacted layers. Each layer was compacted using a roller compactor (about 6 passes per layer) with the optimal water content determined in the laboratory. The Swiss section was additionally equipped with a gravel filter, designed to prevent toe erosion failure. To prevent localized seepage inhomogeneities, the transition zone between the two materials (Figure 2) was constructed by interlayering both material types.

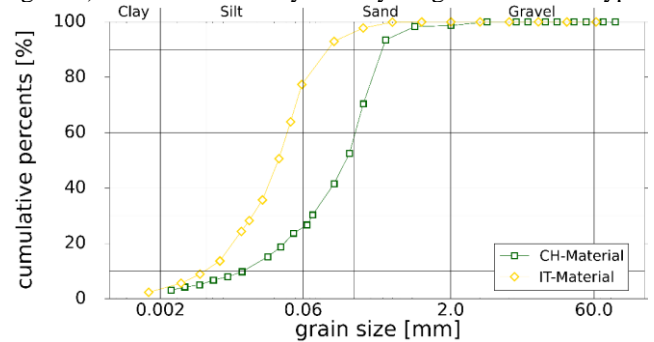


Figure 3. Granulometry of CH-material and IT-material.

#### 3.2 Experimental setup

The DPS sensor was installed in the "ex novo" section during construction, arranged in a mesh pattern at three different elevations ( $z$ ) from the bottom of the basin:  $z = 0.3 \text{ m}$  (Layer 01),  $z = 1.3 \text{ m}$  (Layer 02), and  $z = 2.3 \text{ m}$  (Layer 03). Figure 4 illustrates the DPS cable mesh installed in Layer 01, showing two main orientations: the longitudinal (L) direction (x-axis) and the transversal (T) direction (y-axis). The longitudinal direction is defined as parallel to the assumed river flow, while the transversal direction is parallel to the seepage flow within the dike. The DPS was installed in two different configurations: as a free cable, and within saturable tubes (black rectangles in Figure 4) equipped with porous stones. These tubes are designed to protect the DPS from earth pressure variations and to ensure that only hydrostatic pressure is measured in those sections.

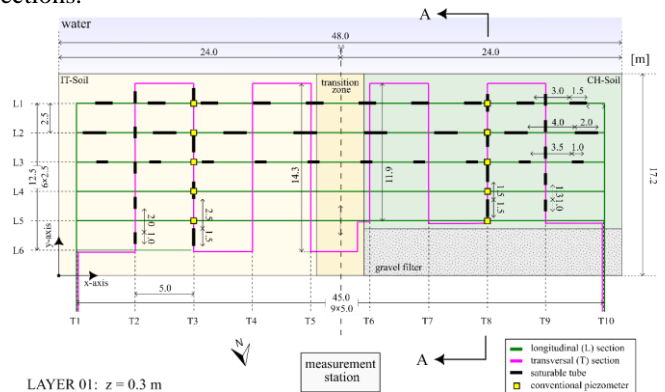


Figure 4. Mesh installation of the DPS in Layer 01 of the "ex novo" section.

To validate the DPS measurements, 10 conventional piezometers were installed in two main cross-sections (T3 and T8) of the “ex novo” section in Layer 01 (indicated by yellow square in Figure 4). The piezometers are of the vibrating wire (VW) type, with a measurement range of 0-170 kPa and an accuracy of  $\pm 0.4\%$  of full scale (FS). Figure 5 shows the installation layout of both the DPS sensors and the piezometers along the A-A cross-section indicated in Figure 2.

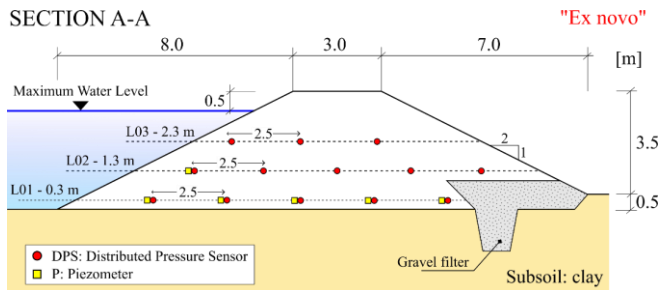


Figure 5. A-A cross section of the installation.

### 3.3 Testing procedure

The water level values recorded during the test are presented in Figure 6. Initially, the water level stood at 1 meter due to rainfall accumulation and was raised to 2.3 meters by pumping groundwater from the aquifer through an existing well (Phase 1: Filling – about 5 h). After reaching the target level, the basin was allowed to drain naturally for approximately one week (Phase 2: Self-Drain – about 165 h). This was followed by a controlled, three-stage emptying process designed to reduce the risk of instability associated with rapid drawdown (Phase 3: Emptying – about 70 h). The water level was monitored using a piezometer installed at the water-side toe of the test embankment.

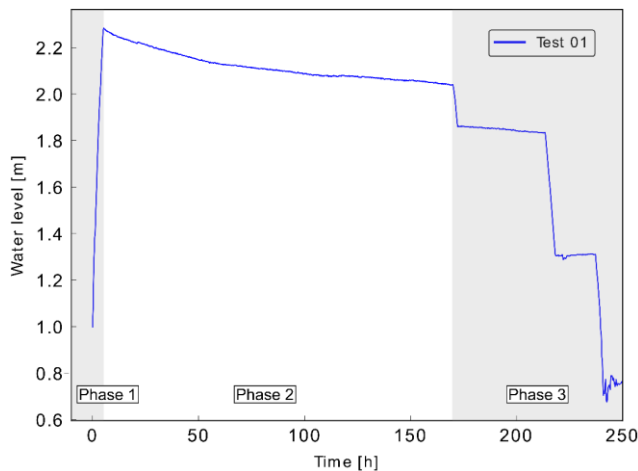


Figure 6. Water level inside the basin during the test.

The data from the DPS helical fiber were collected manually at approximately 30-minute intervals using a commercially available Rayleigh-based Optical Backscatter Reflectometer (OBR 4600, Luna Innovations [12]). Due to the manual acquisition process, measurements were limited to the initial filling Phase 1 and continued for approximately 12 hours of the Phase 2. The core temperature fiber was automatically interrogated using a Raman-based system (AP Sensing, DTS - N45 Series [13]), with an acquisition time of 4 minutes.

Conventional instruments recorded data automatically every 15 minutes. Temperature and piezometer measurements were recorded continuously until the end of the test, when the basin was fully emptied (after approximately 240 hours).

### 3.4 Data processing

The data obtained from the DPS were post-processed using a spatial sampling interval of 10 cm and a spatial resolution of 10 cm, with a reference that was updated after each measurement. This approach reduces noise that would otherwise accumulate if the initial measurement were used as a fixed reference throughout the test. The spectral shift values were then cumulatively summed after each iteration.

Subsequently, artificial peaks were removed using the “peak prominence” method available in Python [14], which identifies local maxima by comparing each value to its neighboring points. Detected peaks were then replaced with the median value of their surrounding neighbors. The resulting data were then smoothed using a Savitzky-Golay filter [15].

The filtered values obtained were then converted to pressure using the pressure coefficient  $C_p$  (described in section 2).

The raw data from the DTS system were not post-processed, as the results provided by the instrument were already corrected through automatic calibration in loop mode. A sampling interval of 1 meter, a spatial resolution of 0.5 meters, and a measurement time of 1 minute were used.

The piezometer data were not corrected, as both barometric and temperature corrections have minimal influence and were therefore neglected.

### 3.5 Preliminary Results

Figure 7 illustrates the pore pressure measured with piezometers in Layer 01 (Figure 4) for the two different materials at four time intervals: at the start of the test, and after 12, 24, and 60 hours (Figure 6). The corresponding water levels, shown in blue, are also reported in Figure 7, for these intervals.

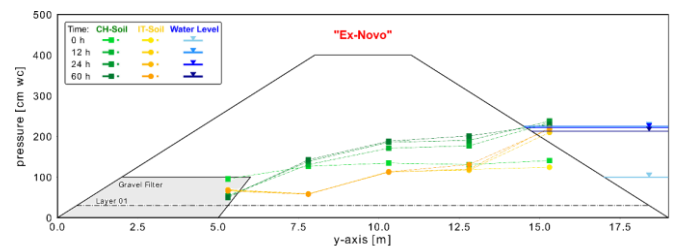


Figure 7. Piezometer measurements for the two soil materials at four time intervals (0h, 12h, 24h and 60 h) in Layer 01.

Figure 8 presents the post-processed pressure variation measurements across all transversal sensor lines from T4 to T9 in Layer 01 (Figure 4) for five different time: 1.6 h, 3.1 h, 4.2 h, and 10.2 h. These results represent the distributed pressure data along the full fiber length (axial cable development), obtained from the DPS system after applying filtering and peak correction techniques, as described in section 3.4. The pressure variation is calculated cumulatively by changing the reference measurement taken from the beginning of the test when the water level in the tank was already 1 m high. The longitudinal segments of the transversal loop are referred to as the “wet

side” (WS) when the segment is on the water-facing side of the embankment, and the “dry side” (DS) when it is on the air-facing side; see Figure 4.

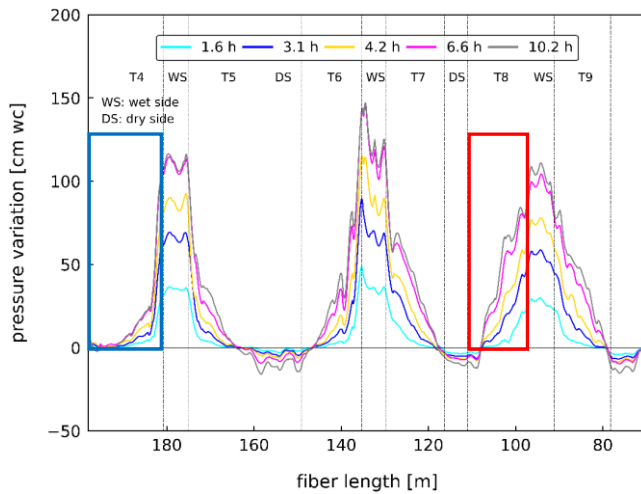


Figure 8. Pressure variation measured during the filling phase using the transversal DPS cables in Layer 01.

It should be noted that the data from lines T2 and T3 exhibited increased noise and irregularities, due to localized issues related to sensor splicer connections during the test. For this reason, these data were excluded from the results analysis.

Figure 9 (a) shows a comparison between the vibrating wire piezometer sensors (VWPS) and the transversal DPS cable measurements at T4 (see Figure 4), while Figure 9 (b) presents the same comparison at location T8. The analysis was conducted at T4, which is also situated within the IT-Material section. Both figures show the results for the same time intervals as shown in Figure 8.

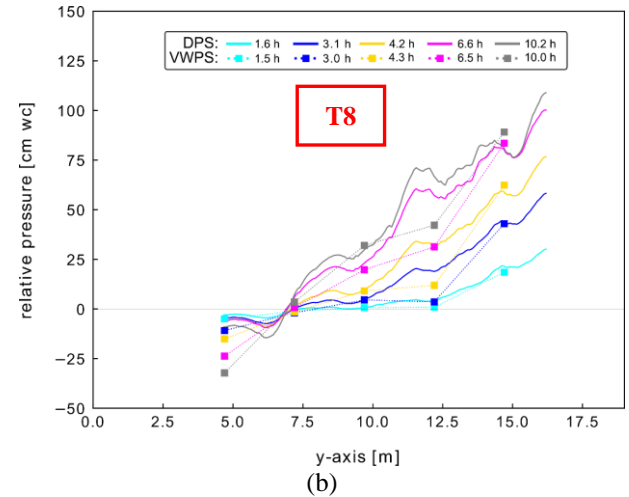
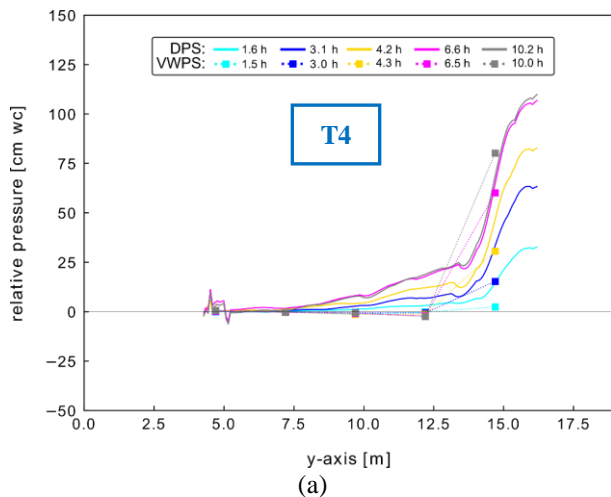
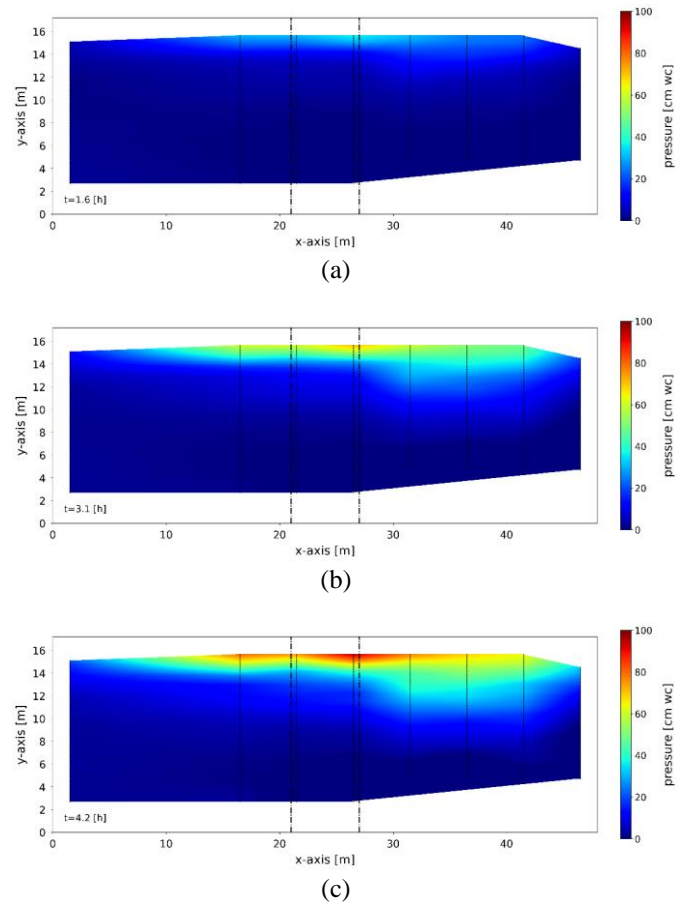


Figure 9. Comparison between the DPS measurements and the vibrating wire piezometer sensors (VWPS) at different time intervals in the transversal direction: (a) T4 and (b) T8.

Figure 10 shows a colormap of Layer 01 based on the transversal DPS measurements presented in Figure 8. The colormap was generated using bicubic interpolation of the transversal DPS data, with additional measurement from T1 and T10, which were obtained from the longitudinal cable L1 (see Figure 4).





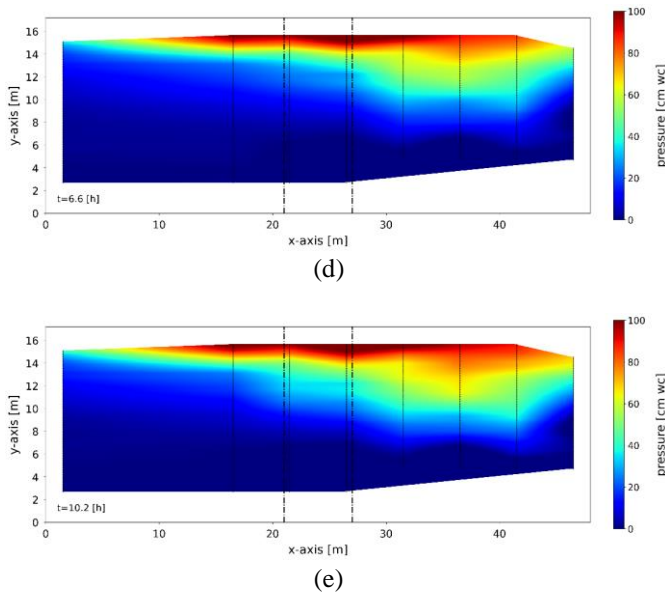


Figure 10. Distributed temperature results for transverse section of Layer 01 at (a) 1.5 h, (b) 3.1 h, (c) 4.2 h, 6.6 h, and (d) 10.2 h after the start of the test.

The absolute temperature distribution obtained by the core temperature fiber of the DPS cable is shown in Figure 11 at four time intervals: 1 hour, 12 hours, 24 hours, and 144 hours after the start of the test. Similar to Figure 10, the data are displayed as colormaps using bicubic interpolation, derived from both the longitudinal and transversal cable sections in Layer 01 (see Figure 4).

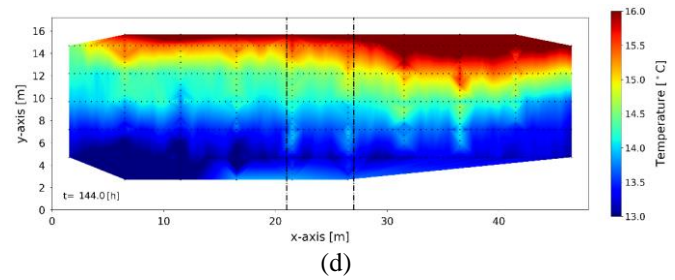
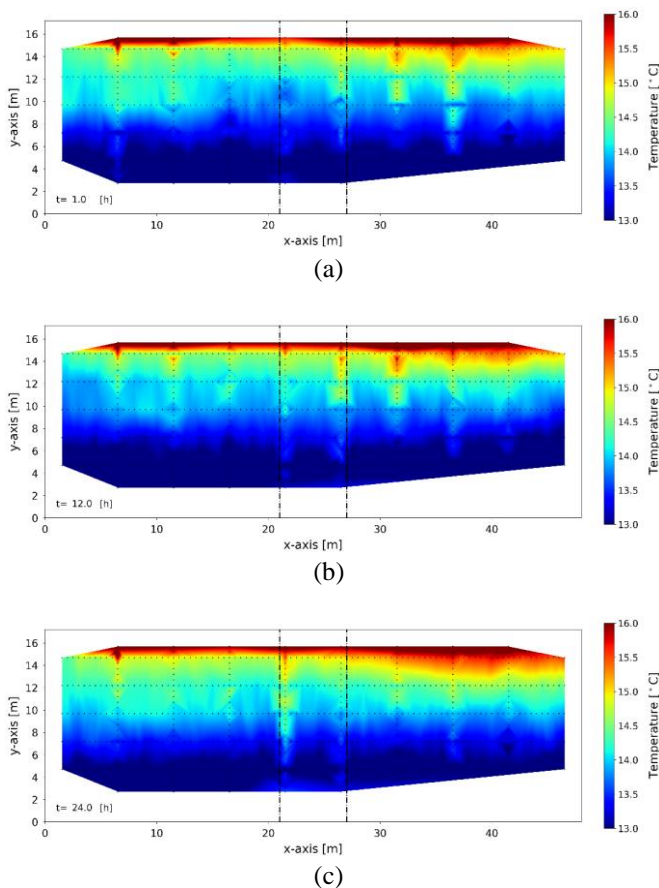


Figure 11. Distributed temperature results for Layer 01 at (a) 1 h, (b) 12 h, (c) 24 h, and (d) 144 h after the start of the test.

#### 4 DISCUSSION

The initial pore pressure measurements (Figure 7) confirmed that the sensors installed in Layer 01 were already below the seepage line prior to the test, consistent with the 1 m water level maintained due to prolonged rainfall.

The Swiss (CH) material, with its coarser granulometry and higher permeability, responded more rapidly to water level changes compared to the IT-Material, which had a finer particle distribution and lower permeability. This contrast is evident in both the vibrating wire piezometer sensor (VWPS) measurements (Figure 7) and the DPS readings (Figure 8 and Figure 9). In particular, the DPS captured a steeper and delayed pressure curve within the IT section, aligning with the expected slower hydraulic response. Additionally, a minor effect from the activation of the drainage filter in the Swiss section is observed, indicated by a slight decrease in pore pressure recorded by the piezometer and the DPS installed at that location.

A good agreement was observed between the VWPSs and the DPS measurements (Figure 9). However, in the central part of the transversal section, the DPS shows slightly higher pore pressure variations compared to the VWPS. When comparing the time intervals, it is evident that the DPS system responds more rapidly than the VWPS particularly during the first interval at 1.5 hours. The DPS captures changes in pore pressure almost instantaneously, whereas the VWPS exhibits a slightly delayed response due to its mechanical components and different response time [16, 17]

The effect of the saturable tube on the DPS cable is particularly noticeable in the CH-Material section, as shown in Figure 9 (b), where a region of constant pore pressure is observed at a distinct location.

Colormap visualization (Figure 10) clearly delineates the transition between the CH and IT materials, demonstrating the DPS's capability to resolve subtle spatial variations in pore pressure distribution. Moreover, the boundaries around sensor lines T1 to T10 exhibit signs of two-dimensional (2D) pore pressure effects within the plane of Layer 01, suggesting more complex flow dynamics in these regions that deviate from the assumed one-dimensional (1D) behavior.

Temperature measurements (Figure 11) remained stable during the first 24 hours. Since the DTS cables were installed below the initial seepage line (see Figure 7), no significant temperature changes were expected during the test period, which is consistent with what was observed. A slight temperature increase was detected only after approximately 144 hours, particularly in the CH section, which is consistent with the higher thermal conductivity expected in coarser soils.

Since the DPS data were collected within the first 17 hours - during which temperature variations were negligible - no temperature correction was applied to the pressure data.

Approximately one year after installation and following the test results presented, some localized disturbances or breaks in the sensor signal were observed. These problems were probably caused by small mammals such as mice or beavers - and were related to the reduced mechanical robustness of the earlier DPS cable design, which was installed in the "ex novo" section and featured a thinner outer protective layer. This vulnerability highlighted a practical limitation in field applications. In response, newer DPS cable designs were developed with an enhanced outer protective layer to improve durability and mitigate such risks, thereby increasing long-term reliability in real-world conditions.

## 5 CONCLUSION AND OUTLOOK

The application of a novel Distributed Pressure Sensor (DPS) system was evaluated through field testing on a full-scale test embankment at the Research and Technical Centre of the Agency for the Po River (AIPo) in Boretto, Italy. Preliminary results, supported by comparisons with traditional piezometer measurements, confirm that the DPS system can be effectively deployed as a distributed pore pressure sensor. In contrast to point-based sensors, the DPS system provides high spatial resolution data, enabling the detection of localized phenomena - such as preferential flow paths or, as observed in the test embankment, changes in permeability due to variations in soil materials or their properties - that may be overlooked by discrete sensors.

DPS systems offer significant advantages over traditional point-based instrumentation, particularly in terms of spatial resolution and potential cost efficiency. Although the initial cost of interrogation units is relatively high, the ability to continuously monitor pore pressure along the full length of the cable reduces the need for multiple point sensors. In terms of coverage efficiency, an approximate ratio of 1:10 can be considered - meaning that for every point sensor replaced, approximately 10 meters of DPS cable can be installed, providing continuous data across that distance. This estimate does not yet account for further cost savings from reduced installation time, simplified cabling, and fewer data loggers or interrogation devices.

Overall, DPS systems show strong potential to provide substantial technical and logistical benefits, especially in large-scale or long-term geotechnical and hydraulic monitoring applications. However, to further validate the long-term reliability of the DPS technology, future work should include extended monitoring campaigns to assess sensor drift, determine optimal calibration intervals, and develop standardized maintenance protocols. Although the DPS technology has not yet been extensively tested, several research projects are planned to explore its deployment in various environmental and structural settings, aiming to broaden its validation across different use cases, such as:

- Application of DPS for detecting and monitoring backward erosion piping within the framework of the LIFE SandBoil project [18];

- Implementation of the DPS system in a real river dike section of the Rhone dike in the Canton of Valais, (Switzerland) [9].
- Large-scale testing of DPS for dynamic wave measurement, expanding upon previous work introduced by Höttinger, et al. [19]

These developments are expected to contribute significantly to the broader adoption of distributed sensing technologies in hydraulic and geotechnical engineering.

## ACKNOWLEDGMENTS

The authors would like to thank the financial supporters of this project: the Swiss Federal Institute for the Environment (FOEN) and the Cantonal Service for Flood Protection of the 3<sup>rd</sup> Rhone.

Special thanks go to the team at the University of Applied Sciences in Rapperswil (OST), particularly Isabel Bohren for designing the test embankment and assisting with sensor installation, and Dr. Antonio Salazar for his help with data analysis and processing.

We are also grateful to the AIPo team - especially Agnese Bassi, Giuseppe Capuano and Luca Crose - for their support during the embankment construction and sensor installation. Thanks to Idrovie Ltd. construction company for their dedication during the work.

The authors also wish to thank SISGEO Ltd. for their support during the installation of the conventional monitoring system, especially Daniel Naterop and Vincenzo Caci.

We further acknowledge the geotechnical group at the University of Bologna, with thanks to Prof. Dr. Guido Gottardi, Dr. Michela Marchi, and Dr. Ilaria Bertolini for their support and expertise during the design of the embankment and the sensor installation. Appreciation is also extended to the geotechnical group at the University of Padova of Prof. Dr. Simonetta Cola, particularly Dr. Nicola Fabbian, for his assistance with the sensor installation and the design of the measuring system.

Finally, sincere thanks to Dr. Massimo Facchini for his assistance during the measurement campaign and his contribution to the design of the DFO measuring system.

## REFERENCES

- [1] L. Cremonini, P. Randi, M. Fazzini, M. Nardino, F. Rossi, and T. Georgiadis, "Causes and Impacts of Flood Events in Emilia-Romagna (Italy) in May 2023," *Land*, vol. 13, no. 11, p. 1800, 2024. [Online]. Available: <https://www.mdpi.com/2073-445X/13/11/1800>.
- [2] D. Zumofen, "Flooding of the Rhone in Switzerland on 29/30 June 2024: Problems, immediate measures and projects,," in *30th Meeting of the European Working Group on Internal Erosion in Embankment Dams, Dikes and Levees and their Foundations*, Bologna, 2024.
- [3] M. Foster, R. Fell, and M. Spannagle, "The statistics of embankment dam failures and accidents," *Canadian Geotechnical Journal*, vol. 37, no. 5, pp. 1000-1024, 2000.
- [4] R. Fell, C. F. Wan, J. Cyganiewicz, and M. Foster, "Time for development of internal erosion and piping in embankment dams," (in English), *Journal of Geotechnical and Geoenvironmental Engineering*, vol. 129, no. 4, pp. 307-314, Apr 2003.
- [5] L. Schenato, "A Review of Distributed Fibre Optic Sensors for Geo-Hydrological Applications," (in English), *Applied Sciences-Basel*, vol. 7, no. 9, Sep 2017.
- [6] N. Fabbian, P. Simonini, F. De Polo, L. Schenato, and S. Cola, "Temperature monitoring in levees for detection of seepage,"

- Bulletin of Engineering Geology and the Environment*, vol. 83, no. 2, pp. 1-12, 2024.
- [7] A. Höttges, C. Rabaiotti, and M. Facchini, "A novel distributed fiber optic hydrostatic pressure sensor for dike safety monitoring," *IEEE Sensors Journal*, vol. 23, no. 23, pp. 28942-28953, 2023, doi: 10.1109/JSEN.2023.3315062.
- [8] A. Höttges, C. Rabaiotti, and M. Facchini, "A ground-breaking Distributed fiber-optic Pressure Sensor for geohydraulic applications," *Procedia Structural Integrity*, vol. 64, pp. 1613-1620, 2024/01/01/ 2024, doi: <https://doi.org/10.1016/j.prostr.2024.09.416>.
- [9] C. Rabaiotti, A. Höttges, M. Facchini, and I. Bohren, "FIBRADIKE, a novel distributed fiber optic monitoring system for dikes and earth dams," in *IOP Conference Series: Earth and Environmental Science*, 2023, vol. 1195, no. 1: IOP Publishing, p. 012004.
- [10] M. Froggatt and J. Moore, "High-spatial-resolution distributed strain measurement in optical fiber with Rayleigh scatter," *Applied optics*, vol. 37, no. 10, pp. 1735-1740, 1998.
- [11] E. N. Allouche, S. T. Ariaratnam, and J. S. Lueke, "Horizontal directional drilling: Profile of an emerging industry," *Journal of Construction Engineering and Management*, vol. 126, no. 1, pp. 68-76, 2000.
- [12] LUNA, "OBR 4600 Data Sheet," ed: Luna Innovations Incorporate, 2025.
- [13] APSensing, "DTS N45-Series Data Sheet," ed: AP Sensing 2025.
- [14] N. Coca-Lopez, "An intuitive approach for spike removal in Raman spectra based on peaks' prominence and width," *Analytica Chimica Acta*, 2024.
- [15] A. Savitzky and M. J. Golay, "Smoothing and differentiation of data by simplified least squares procedures," *Analytical chemistry*, vol. 36, no. 8, pp. 1627-1639, 1964.
- [16] K. Terzaghi, R. B. Peck, and G. Mesri, *Soil mechanics in engineering practice*. John wiley & sons, 1996.
- [17] M. W. Bo and J. Barrett, "Types of instruments," in *Geotechnical Instrumentation and Applications*: Springer, 2023, pp. 31-72.
- [18] L. Tonni, M. Marchi, A. Bassi, and A. Rosso, "A Sand Boil Database for Piping Risk Management in the Po River, Italy," *Water*, vol. 16, no. 10, p. 1384, 2024. [Online]. Available: <https://www.mdpi.com/2073-4441/16/10/1384>.
- [19] A. Höttges, M. Smaadahl, F. M. Evers, R. M. Boes, and C. Rabaiotti, "Dynamic wave measurement with a high spatial resolution distributed fiber optic pressure sensor," *IEEE Sensors Journal*, vol. 24, no. 14, pp. 22387-22396, 2024, doi: 10.1109/JSEN.2024.3401414.



# Identification and quantification of concrete cracks using various distributed fiber optic sensing techniques

Christoph M. Monsberger<sup>1</sup>, [ORCID No 0000-0003-0937-014X], Madeleine Winkler<sup>1</sup>,  
Anna Theresa Kornberger<sup>2</sup>, [ORCID No 0009-0004-9804-3371], Dirk Schlicke<sup>3</sup>, [ORCID No 0000-0003-3543-7459]

<sup>1</sup> ACI Monitoring GmbH, Merangasse 73/3, 8010 Graz, Austria

<sup>2</sup> König und Heunisch Planungsgesellschaft mbH Leipzig, Sebastian-Bach-Straße 4, 04109 Leipzig, Deutschland

<sup>3</sup> Graz University of Technology, Institute of Structural Concrete, Lessingstraße 25, 8010 Graz, Austria

email: christoph.monsberger@aci-monitoring.at, madeleine.winkler@aci-monitoring.at, kornberger@khp-leipzig.de,  
dirk.schlicke@tugraz.at

**ABSTRACT:** Distributed fiber optic sensors (DFOS) are extensively used for concrete crack monitoring in recent years, especially in scientific-related applications and laboratory testing. These mainly focus on Rayleigh scattering due to its high spatial resolution and strain resolution, but with significant limitations in the sensing range. This contribution introduces an enhanced laboratory test series, in which five individual test specimens were equipped with multiple installation setups and tested under well-known conditions. The sensing network was interrogated using four different sensing units based on high-resolution Rayleigh as well as Brillouin scattering. The resulting strain sensing profiles do not only allow an identification of the crack location itself, but also a quantification of the crack width. It can be demonstrated that Brillouin sensors are definitely capable of capturing reliable crack widths over long distances, despite their limitation in the spatial resolution. The outcomes are significantly important in practice as civil infrastructures often require monitoring over several kilometers.

**KEY WORDS:** Distributed fiber optic sensing, crack sensing, concrete structures, structural integrity monitoring, laboratory testing

## 1 MONITORING OBJECTIVES & TEST SETUP

In recent years, the capabilities of distributed fiber optic sensors (DFOS) for monitoring concrete cracks are demonstrated in various scientific-related projects and laboratory testing, which commonly utilize Rayleigh scattering (e.g. [1] or [2]). This sensing technique can provide measurements with high spatial and strain resolution, but with significant restrictions in the sensing range. Brillouin sensing is capable of monitoring large-scale civil infrastructure as they can provide measurements over numerous kilometers, which however results in spatial limitations and therefore impedes the capabilities for strain-based crack monitoring.

This contribution analyzes the suitability of Brillouin interrogators for identifying and quantifying evolving cracks inside concrete. An enhanced laboratory test series including five individual test concrete specimens equipped with multiple installation setups was realized at Graz University of Technology (TU Graz, Laboratory for Structural Engineering). For applying the loading force during testing, one central reinforcement bar (diameter: 18 mm) was embedded in each concrete specimen (total length: 3000mm). Thin steel plates were attached to the formwork and cast into the concrete to weaken the cross-section at defined locations, which ensures a controlled cracking of the structure during loading. The five specimens vary depending on the number of crack locations, ranging from one to five defined cracks.

The testing specimens were equipped with twelve different layers of fiber optic sensing cables per specimen, including tight-buffered optical fibers [3] as well as prefabricated sensing cables from numerous manufacturers [4–6]. The sensors were either glued to the reinforcement, directly embedded inside the specimens in different arrangements or glued to the outer surface using different adhesive after concreting. Each

specimen was tested separately under controlled axial loading, where the rebar was fixed at the bottom and pulled apart at the top side (Figure 1) to initialize the crack opening along the specimen at the predefined locations.



Figure 1. Practical realization of laboratory test setup with one defined crack location.

Loading for all specimens was performed in two steps with 15 kN each up to the initial cracking, which was determined to be around 30 kN. Afterwards, the load was further increased in 10 kN steps up until the ultimate failure of the specimen at around 100 kN and beyond. By applying the mechanical crack initiation steel plates, it could be ensured that primary cracks only open at well defined locations.

The DFOS sensing network was interrogated by Brillouin interrogators from three different manufacturers utilizing the Brillouin Optical Time Domain Analysis (BOTDA) as well as the Brillouin Optical Frequency Domain Analysis (BOFDA) with a spatial resolution of 0.5 m at each load step. To verify the recorded Brillouin strain distributions, reference measurements were acquired using a high-resolution OBR from Luna Innovations Inc. (USA) based on the OFDR (Optical Frequency Domain Reflectometry). The load was kept constant for each load step to ensure identical loading conditions for all interrogators. Multiple distance transducers (DD-1) from HBM GmbH (Germany) were placed at the specimens' surface to measure the true crack width.

## 2 CRACK ANALYSIS & TESTING RESULTS

The aim of the five sample test series is to analyze crack patterns with different spacing and crack widths. The analysis presented in this extended abstract focus on the crack localization and width derivation, which is why only one specimen with one defined crack location is discussed. The resulting strain sensing profiles along a concrete-embedded sensing cable [4] for all different interrogators are depicted in 2. It must be noted that the data represents the raw measurement signal with a physical spatial resolution of 0.5 m, but with different spatial sampling and is not further processed or filtered. The high-resolution OFDR measurements (left) confirm the initial crack opening at the loading step of 30 kN, with a significant peak arising in the middle of the specimen

(position: 1.5 m) over an area of approx. 200 mm. The Brillouin sensing techniques are not capable to visualize the initial cracking with such high resolution due to their spatial limitations, although interrogator B-02 also indicates cracking already at 30 kN. The peak width and magnitude is continuously increasing with each subsequent load step up to the maximum load of 130 kN applied for the actual specimen. Even if the strain peak appears over a larger area, Brillouin interrogators B-02 and B-03 can represent the OFDR technique well for loads higher than 30 kN. The B-01 signal, however, only represents major strain events for the last three load steps.

The strain distribution for Brillouin sensors is usually derived by determining the mean Brillouin frequency for each position along the optical fiber using curve fitting methods (e.g. Lorentzian fitting). In order to optimize the strain sensing results for B-01, comprehensive data reprocessing has been performed by low-pass filtering of the full Brillouin spectrum before curve fitting. The resulting strain profiles depicted in Figure 3 demonstrate that the data can be significantly optimized to reproduce the strain peak due to the developing crack similar to other Brillouin interrogators.

The crack width derivation itself may be performed by numerical integration of the measured strain sensing values over the area of interest, i.e. the strain peak area. The integration length, or rather the start and end point of the crack induced area along the signal, can be practically determined by analyzing the strain gradient at each side of the peak. These points are identified as the locations, at which the strain variation does not exceed a certain threshold within a defined number of subsequent data points. For further information and details on the determination principle reference is given to [7].

The crack widths derived for all DFOS technologies and the reference distance transducer are listed in Table 1. The results of the Brillouin interrogators are in good agreement with those of the high-resolution OFDR, with maximum deviations lower

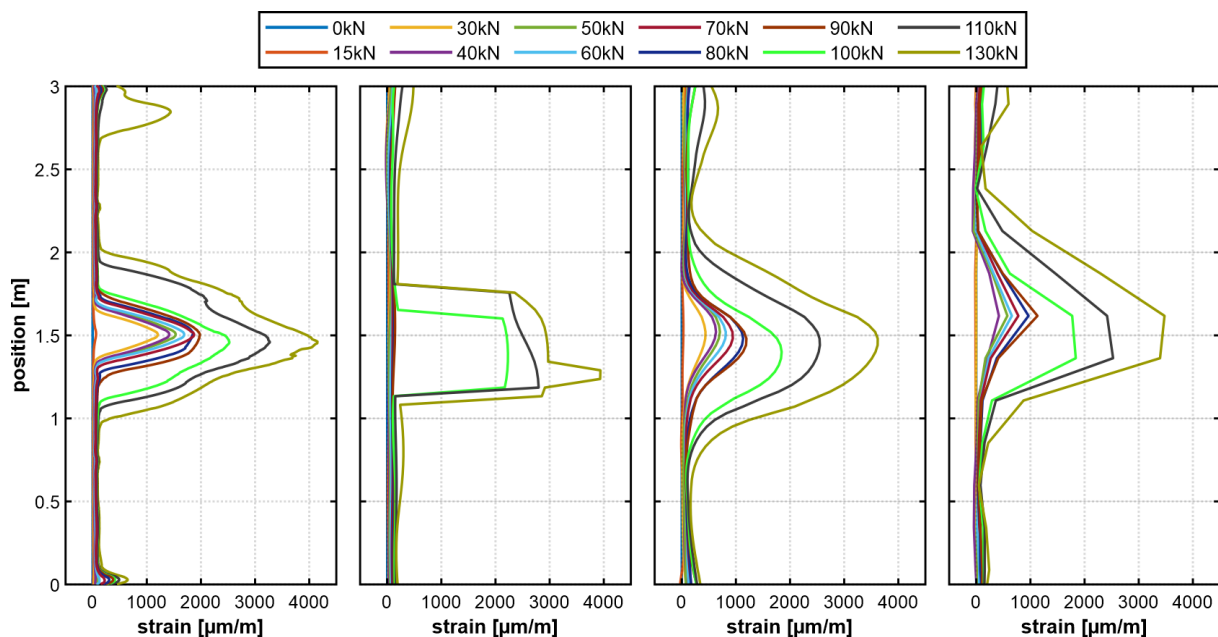


Figure 2. Strain profiles recorded by various DFOS interrogators during load test: Rayleigh OFDR and Brillouin B-01/B-02/B-03 (left to right).

than 0.1 mm at loads of up to 90 kN or rather a width of approx. 0.6 mm. Cracks in reinforced concrete structures are usually controlled under service in a range of 0.2 to 0.4 mm [8], which can be obviously determined for all sensors. The distance transducers mounted on the surface also confirm the absolute accuracy for load steps up to 90 kN. Higher loads indicate minimal local slippage between the sensing cable and the concrete or even the different sensing cable layers at the crack location, which is why the width derivation using numerical strain integration seems to be no longer applicable.

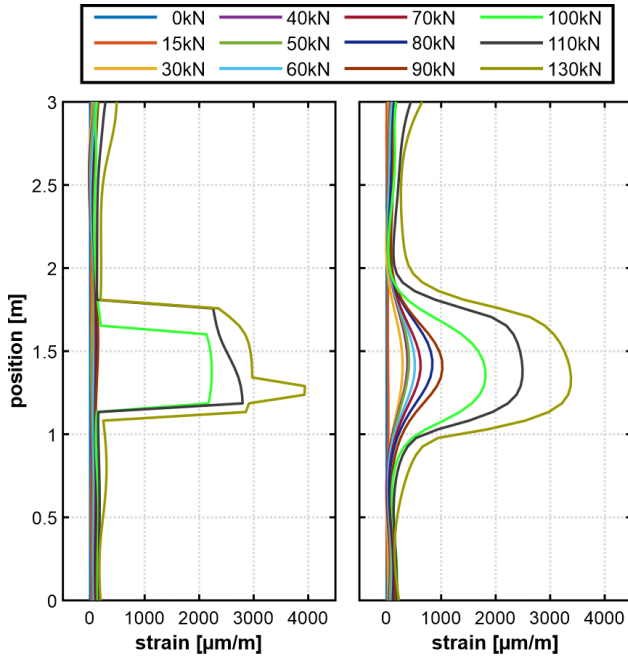


Figure 3. Strain sensing profiles of Brillouin interrogator B-01 before (left) and after spectrum filtering (right).

It must be noted that the quality of the crack width derivation is strongly related to the parameter settings for the integration length. These vary depending on not only the sensing technique but also the installation technique of the optical sensing cable. The dedicated test series is capable of providing an essential lookup table to appropriately perform the integration length determination for different configurations for future monitoring applications.

Table 1. Crack widths derived from various DFOS interrogators and measured by conventional distance transducers at different load levels.

load [kN]	crack width [mm]				
	DD-01	OFDR	B-01	B-02	B-03
15	0.00	0.00	0.05	0.00	0.00
30	0.28	0.22	0.20	0.18	0.00
40	0.38	0.30	0.27	0.25	0.26
50	0.39	0.35	0.30	0.30	0.32
60	0.40	0.41	0.36	0.34	0.37
70	0.46	0.48	0.43	0.40	0.46
80	0.53	0.57	0.55	0.52	0.52
90	0.61	0.66	0.67	0.56	0.60
100	0.72	1.10	1.21	1.08	1.11
110	1.24	1.81	1.88	1.77	1.77
130	1.57	2.68	2.85	2.79	2.87

### 3 CONCLUSIONS & OUTLOOK

This extended abstract discussed the suitability of numerous Brillouin interrogators for localizing concrete cracks and quantifying their corresponding width. An enhanced test series with five individual specimens equipped with multiple DFOS installation setups was realized to investigate crack opening under well-known laboratory conditions. The crack location along the resulting strain profiles could be well captured by all interrogation units and enabled the derivation of crack widths for different load levels using numerical integration. The derived values correspond well with reference measurements from the distance transducer mounted at the surface for all tested Brillouin interrogators, with maximum deviations of approx. 0.1 mm within the usual service range for reinforced concrete structures.

It could also be demonstrated that the original data processing might fade out local deficiencies like cracks in the strain sensing profiles. This limitation may be overcome in this specific case by applying appropriate filtering to the raw Brillouin spectrum data.

The presented research focused on the traditional strain-based data analysis. In addition, initial tests for crack width determination using a feature extractor based on a CNN (Convolutional Neural Network) autoencoder, which was applied to the raw Brillouin spectrum along the sensing network [9]. This artificial intelligence (AI) approach will be further investigated and optimized to provide more comprehensive methods for analyzing concrete cracks along civil infrastructure.

### ACKNOWLEDGMENTS

The laboratory test series and the monitoring program was carried out within the collective research project “AI FORschung” (Nr. 52106504) financed by the Austrian Research Promotion Agency (FFG), which is part of the EUREKA Clusters AI Call 2021.

### REFERENCES

- [1] B. Richter, M. Herbers and S. Marx., Crack monitoring on concrete structures with distributed fiber optic sensors—Toward automated data evaluation and assessment, *Structural Concrete* 25(2), 1465–1480, 10.1002/suco.202300100, 2024.
- [2] A. Vorwagner, M. Kwapisz, W. Lienhart, M. Winkler, C. Monsberger and D. Prammer, Verteilte Rissbreitenmessung im Betonbau mittels faseroptischer Sensorik –Neue Anwendung von verteilten faseroptischen Messsystemen, *Beton- und Stahlbetonbau* 116(10), 727–740, 10.1002/best.202100060, 2021.
- [3] The Light Connection Inc., Data Sheet: Tight Buffer, Rev. 3.0 11/12/2020, 2020.
- [4] SOLIFOS AG, Data Sheet: BRUsens DSS 3.2mm V9 grip 3 50 2 005, 2025.
- [5] SHM Systems Company, Data Sheet: EpsilonSensor, 2025.
- [6] success4u GmbH, FIBRASSENS DSS 2f, Datasheet Fiber Optic Cable DS220801D, 2023.
- [7] A.T. Kornberger, Dehnungsvergleiche von FE basierten Analysen und Faseroptikmessungen an Zugversuchen, Master’s thesis, Graz University of Technology, Graz, Austria, 2024.
- [8] EN 1992-1-1, E Eurocode 2: Design of concrete structures, European Committee for Standardization, 2004.
- [9] C.M. Monsberger, M. Winkler, R. Pavelkin, L.Z. Mondragon, F. van der Sommen, A.T. Kornberger, D. Schlicke, and W. Lienhart, Analyzing concrete cracking along civil infrastructure using distributed fiber optic sensing, 15th International Workshop on Structural Health Monitoring 2025 (IWSHM), Stanford, USA, 2025.



# DFOS-Based Monitoring of Prestressed Concrete Bridge Girders

Kleo Lila<sup>1</sup>, Max Herbers<sup>1</sup>, Bertram Richter<sup>1</sup>, Andrea Agreiter<sup>2</sup>, Maja Kreslin<sup>3</sup>, Petra Triller<sup>3</sup>, Andrej Anžlin<sup>3</sup>, Werner Lienhart<sup>2</sup>, Steffen Marx<sup>1</sup>

<sup>1</sup>Institute of Concrete Structures, TUD Dresden University of Technology,  
01062 Dresden, Germany

<sup>2</sup>Institute of Engineering Geodesy and Measurement Systems, Faculty of Mathematics, Physics and Geodesy, Graz University  
of Technology, Steyrergasse 30, 8010 Graz, Austria

<sup>3</sup>Slovenian National Building and Civil Engineering Institute, Dimičeva ulica 12, SI 1000 Ljubljana, Slovenia  
email: @ [kleo.lila@tu-dresden.de](mailto:kleo.lila@tu-dresden.de), @ [max.herbers@tu-dresden.de](mailto:max.herbers@tu-dresden.de), @ [bertram.richter@tu-dresden.de](mailto:bertram.richter@tu-dresden.de) @  
[andrea.agreiter@tugraz.at](mailto:andrea.agreiter@tugraz.at), @ [andrej.anzlin@zag.si](mailto:andrej.anzlin@zag.si), @ [maja.kreslin@zag.si](mailto:maja.kreslin@zag.si), @ [petra.triller@zag.si](mailto:petra.triller@zag.si) @  
[werner.lienhart@tugraz.at](mailto:werner.lienhart@tugraz.at) @ [steffen.marx1@tu-dresden.de](mailto:steffen.marx1@tu-dresden.de)

**ABSTRACT:** Due to bridges' critical role in transportation networks, the assessment and maintenance of existing bridges have become a priority. Prestressed concrete bridges constitute a significant portion of Europe's transportation network, yet many no longer meet today's technical requirements. This is primarily due to two factors: (i) the unforeseen increase in heavy goods traffic, and (ii) insufficient experience with early reinforced and prestressed concrete construction methods, coupled with inadequate regulations, which resulted in design weaknesses and structural deficiencies. One critical failure mechanism, identified when recalculating existing bridges based on updated guidelines, is insufficient shear load-bearing capacity, which has prompted the premature demolition of numerous bridges. A thorough understanding and rigorous monitoring of shear behavior is essential since neglecting this problem could lead to notable consequences, especially for aging infrastructure. In this paper, a distributed fiber optic sensor (DFOS) based monitoring system, inspired by shear detection concepts, is tested. A decommissioned prestressed concrete bridge girder was equipped with a DFOS grid, allowing for detailed monitoring of crack width, location, and shape. Preliminary test results confirm the successful installation and early detection of cracks, highlighting the system's potential to identify microcrack formation, monitor crack growth, and support maintenance strategies.

**KEYWORDS:** Structural Health Monitoring; Distributed Fiber Optic Sensors; Microcracking; Crack Growths; Load Testing; Prestressed Concrete.

## 1 INTRODUCTION

Concrete serves as the cornerstone of contemporary infrastructure, valued for its adaptability, strength and longevity. Nonetheless, despite its formidable exterior, concrete exhibits inherent material characteristics that, if neglected, may result in structural failures. Among these, shear forces are a critical and complex failure mechanism, due to the brittle behavior. Improper management of shear stresses may lead to abrupt, severe cracking, endangering the service life and safety of infrastructures such as bridges. One of the reasons for this is that these aging bridges were originally designed for lower traffic loads, and this issue is intensified by the absence or insufficient shear reinforcement [1], [2]. Modern codes surpass traditional visual inspections in terms of objectivity, repeatability, and sensitivity, imposing higher safety margins, often revealing structural deficiencies when existing bridges are recalculated for shear strength.

Unlike flexural failures, which can be predicted with relative precision using established theoretical frameworks, shear-related issues lack a universally accepted conceptual model [1]. Ductile failure provides a clear warning signal, such as plastic deformation, while brittle failure occurs suddenly, offering minimal warnings. This distinction is crucial because, under shear forces, concrete exhibits rapid crack development without the gradual yielding seen in flexural failures. With the growing demands on bridge structures due to increasing traffic loads, particularly from heavy goods vehicles, the need for advanced monitoring and assessment techniques are expected

to intensify in the coming years [3]. Current methods for shear monitoring rely mostly on visual inspections, which are labor-intensive, subjective [4], and not effective when surface damages are not present in the structure.

As shear load-bearing behavior remains a challenging aspect of structural evaluation, innovative monitoring technologies such as distributed fiber optic sensors (DFOS) offer promising solutions to ensure the safety, durability, and sustainability of critical infrastructure. To improve the efficiency and precision of crack detection, integrating continuous strain monitoring systems like DFOS can provide real-time, comprehensive data on damage states [4]. DFOS can accurately measure small strain changes during the linear elastic state, an advantage that surpasses traditional visual inspections in terms of objectivity, repeatability, and sensitivity. Although the application of fiber optic sensing in construction is relatively recent, the technology is rapidly evolving and has shown potential in various infrastructure applications [5]–[8]. Low-cost optical fibers that serve as sensors can be retrofitted onto existing structures or embedded into new constructions, providing a convenient approach for distributed structural health monitoring.

Inspired by the shear monitoring concepts [2], [9]–[13], this paper presents an application of a DFOS grid for crack monitoring in a prestressed concrete girder. The aim is to further investigate the potential and to assess the effectiveness of surface-bonded DFOS for microcrack detection, formation, and the sensor placement for short-term monitoring. A two-dimensional DFOS grid was designed and applied to the surface of a prestressed concrete bridge girder, which was

subsequently tested under load. Following a brief state-of-the-art review in Chapter 2, the experimental setup and corresponding results are presented.

## 2 SHEAR BEHAVIOR AND DIAGNOSTICS

### 2.1 *Critical shear behavior*

Concrete bridges, especially those older than 30 years old, were designed under shear-reinforcement rules now known to be insufficient for modern traffic loads, and routinely exhibit calculated shear deficits, which raise significant concerns about their long-term structural performance [14]. The shear failure is governed by diagonal cracking: when inclined tensile stresses (highest near supports) exceed the concrete's tensile strength, a rapid chain of web-shear cracks propagates toward loading areas and supports, often with little warning [15], [16]. When a beam is subjected solely to pure bending, tensile stresses that exceed the concrete's tensile strength will cause vertical cracks to form and extend up to the neutral axis. However, when shear forces are present, they cause the flexural cracks to rotate, resulting in flexural-shear cracks, which are typical in slender reinforced concrete girders subjected to shear. In flanged girders, deep girders, and prestressed ones, the dominant shear failure mode is web-shear cracking. Cracks initiate at the beam's centroid where the principal elastic tensile stress exceeds the concrete strength, and then extend toward both the loading area and the supports [16].

Concrete shear resistance arises from aggregate interlock, dowel action of longitudinal bars, and, in deep members, arch action. Geometry (shear-span/depth ratio) and reinforcement ratios critically govern which mechanism dominates [15]. Moreover, large members display a pronounced size effect, failing more abruptly. Analytical frameworks, such as strut-and-tie models, compression field theory, and critical shear-crack theory, seek to capture these phenomena, but each has limitations when applied to prestressed girders, where axial compression and anchorage stresses further complicate shear behavior [1], [17]. This sudden and complicated failure mode underscores the need for continuous monitoring systems, such as DFOS grids, to detect microcrack initiation and propagation before diagonal crack development.

### 2.2 *Need for shear monitoring*

Following the bridge recalculation and assessment guideline (May 2011), Fischer et al. [18] performed the statical recalculation of 115 bridges' superstructure that required shear reinforcement, and 57% of them exhibited low shear capacity. Notably, it is the case that some of these structures do not display visible shear cracks. This highlights the need to implement a monitoring system that measures the development and long-term performance of these structures, to accurately estimate the remaining service life and ensure the safety of the infrastructure [2], [4], [16]. Critical shear behavior is primarily marked by the development of diagonal cracks, which present challenges in early detection. These cracks, which form at inclined angles relative to the beam's axis and do not align with the reinforcement, are inherently more unpredictable than flexural cracks. The heterogenous nature of concrete, diagonal cracks' orientation, and variable crack width introduce significant uncertainties in early crack detection and crack propagation [19], [20]. Consequently, effective shear

measurement systems are essential for reliable structural analysis and monitoring of shear failures [15].

Currently, shear monitoring predominantly relies on visual inspection of the concrete surfaces [4]. While this approach can reveal surface-level damages, it is labor-intensive and susceptible to human error, potentially leading to missed early signs of deterioration [4].

Developing a robust measurement concept for shear monitoring in real-world bridge applications is a challenging problem. While controlled laboratory conditions allow for predetermined critical sections and failure locations, practical implementations face challenges such as limited sensor measurement range, harsh environmental conditions, and economic constraints. These factors increase the risk of missing critical zones during monitoring. To overcome these challenges, there is a clear need for an innovative, autonomous, and robust measurement system, potentially leveraging advanced techniques like DFOS and digital image correlation (DIC), to accurately reflect the evolving structural state and enhance long-term infrastructure safety [4].

### 2.3 *Distributed fiber optic sensing (DFOS)*

Fiber optic measurement has evolved remarkably over the recent decades. Initially developed for telecommunications [21], its adoption in structural health monitoring (SHM) within the construction industry has surged, particularly for concrete structures [22]. They offer a unique advantage by providing continuous, high-resolution strain data over entire structural elements, an attribute that is very valuable for monitoring complex damage patterns associated with shear failure. Because of the relatively recent application of fiber optics in concrete construction, the field is developing dynamically in both research and industry [23].

Unlike conventional sensors, which provide data at discrete points, DFOS capture the full strain distribution along their length with high resolution, enabling the early detection of microcracks and the tracking of crack initiation, propagation, and width changes [24]. By continuously mapping strain across large areas, DFOS can reveal subtle changes in crack patterns that might otherwise remain undetected.

DFOS can be integrated into new structures during construction or retrofitted onto existing bridges. When embedded, they offer immediate insights into load-bearing behavior, prestressing levels, and deformation characteristics [25], [26]. Whether surface-bonded in retrofit scenarios or embedded during construction, DFOS provide real-time strain data to validate structural models and support continuous, long-term performance monitoring. In retrofit applications, bonding DFOS to the concrete surface also enables the direct identification of strain hotspots for targeted inspections. Advanced techniques even allow the derivation of 2D strain images from 1D strain curves, which can be used to get a direct understanding of the situation and stress/strain-state [27]. Given that diagonal cracking is a defining feature of shear failure, a complex and unpredictable 2D phenomenon, employing DFOS is a highly promising approach for SHM.

Because of their ability to monitor the crack pattern over large areas, several research groups [2], [9]–[13] have investigated the possibility of utilizing DFOS for creating a shear monitor concept. DFOS are arranged in a mesh-like manner and installed on the concrete surface to compute 2D strain

measurement in the critical shear force zone (as shown in Figure 1). A key advantage of DFOS over other measurement techniques, like DIC, is that they do not require a direct line of sight to the shear-affected area, allowing measurements to be carried out regardless of lighting conditions. By contrast, DIC's noise floor and measurement accuracy are highly sensitive to both the spatial resolution of the images and the size of the measurement field.



Figure 1. 2D sensor arrangement for shear monitoring

The skew angle of the cracks must be taken into account to evaluate the crack widths, since the traditional integration approach that is effective for bending cracks perpendicular to the sensor fails for skewed cracks. In [4], [28], the fundamental process of DFOS-based shear force measurement is explained. A method that incorporates the skew angle into the crack width calculation has been proposed and experimentally validated in [28]. The suitability of DFOS to be used for monitoring shear forces has been confirmed by both laboratory and practical applications. In existing structures, DFOS sensors are typically bonded to the concrete, as demonstrated by Rodriguez et al. [12], [27]. Additionally, Poldon et al. [10] successfully installed DFOS on both longitudinal and transverse reinforcement to track the development of shear and flexural cracks in reinforced concrete beams, a method further validated by practical case studies [9], [13].

Although the initial results are promising, they also highlight the need for further testing and research to rigorously validate the DFOS grid concept's reliability, not only in monitoring shear-induced cracking, but also for tracking the development and precise localization of general bending cracks, to fully determine its practical applicability in real bridge monitoring.

### 3 TEST AND MEASUREMENT CONCEPT

#### 3.1 Test specimen and test setup

For this experiment, a prestressed concrete girder from a decommissioned road bridge near Ljubljana, Slovenia, was selected for its representative characteristics and historical modifications. Spanning the Kamniška Bistrica River, the bridge measures 52.60 m in length and 8.2 m in width, with five spans ranging from 9 m to 13 m supported by thin wall intermediate supports (Figure 2). Notably, the bridge underwent widening in 1989 to accommodate pedestrians and cyclists by adding prefabricated prestressed reinforced concrete T-girders and an interconnected reinforced concrete slab. The girders and deck were designed with concrete grades MB40 and MB30, which correspond to Eurocode classes C30/37 and C20/25, respectively, in accordance with EN 206-1 and EN 1992-1-1. Prestressing cables with a strength of 1840/2090 MPa were used, while other types of

reinforcements, including smooth and ribbed rebars as well as mesh reinforcement, ranged from 240 MPa to 500 MPa.

Six girders were extracted from the structure for laboratory bending and shear tests (see Figure 2). To investigate the girder's behavior under a damaged state, it was deliberately damaged before testing by cutting one of three prestressing layers comprising of six tendons, thereby providing an opportunity to monitor the resulting changes in structural behavior using the DFOS grid.

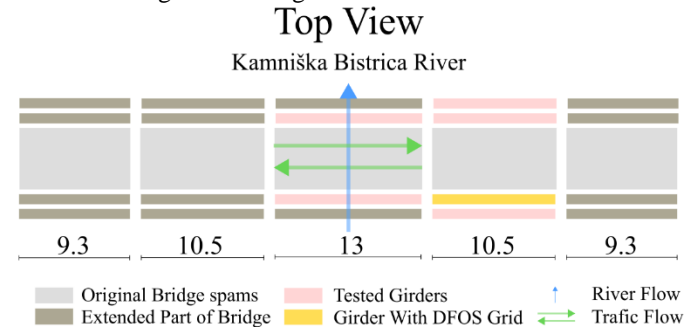


Figure 2. Schematic bridge representation

#### 3.2 Sensor placement and experimental procedure

In the damaged girder, the DFOS grid (as shown in Figure 1) was applied to the web's concrete surface to capture continuous strain data. The DFOS grid consisted of two sensors, with lengths of 12 m and 13 m, respectively. The first sensor (DFOS 1) was arranged in both horizontal and vertical orientations: initially, it was installed horizontally in three parallel layers of 1.6 m segments with a 0.165 m spacing between layers to obtain distinct horizontal strain readings; subsequently, the remaining fiber was configured vertically into 0.33 m segments spaced 0.2 m apart. The second sensor (DFOS 2) was installed diagonally, with each diagonal segment measuring 0.52 m. Additionally, the intersection points of the sensors were aligned as closely as possible, ideally converging at a single point, to enhance data precision and ensure optimal strain transfer. This configuration formed a comprehensive sensing grid capable of capturing crack formation across sensor length, thereby providing a complete strain field of the targeted area. A schematic representation of the sensor layout and test setup is presented in Figure 3.

The fibers employed were single-mode (SM) fibers with a tight buffer made of Hytel and an overall diameter of 900  $\mu\text{m}$ . Measurements were carried out with an Optical Distributed Sensor Interrogator (ODiSI) 6100 series from LUNA Innovations. This technology leverages the principles of Rayleigh scattering and optical frequency domain reflectometry, providing high-resolution local strain data. The ODiSI was operated in full-optimization mode, delivering a spatial resolution of 0.65 mm and a per-channel measurement rate of 3.13 Hz.

Ensuring optimal bonding to the concrete surface is important for accurate strain measurements. Since the girder was prefabricated, it possessed a smooth finish that required only dust and debris removal. The installation process involved initially fixing the sensor pointwise at predetermined intervals with a fast-curing cyanoacrylate adhesive (CYN), followed by the application of a two-component injection mortar along its entire length. This high-viscosity mortar rapidly hardens and is



suitable for bonding sensors on vertical surfaces. At the intersection points, the sensors overlap three times, introducing bending and less reliable results. Figure 3 depicts the DFOS sensor grid configuration and its precise mounting locations on the prestressed concrete girder.

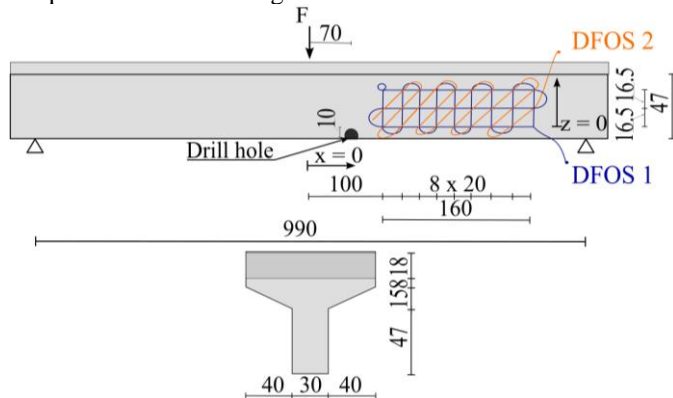


Figure 3. Test setup and cross-section representation (in cm)



Figure 4. Sensor bonding procedure on concrete

After applying the grid, the surface was painted to facilitate DIC measurements. However, the DIC evaluation is beyond the scope of this paper.



Figure 5. DFOS grid covered with DIC speckle pattern

The girder was simply supported on rollers and subjected to three-point bending. The loading test spanned two days and involved cyclic loading and sustained constant load conditions to replicate diverse operational states and observe the crack initiation and propagation phases. In the initial cutting stage, a hole of 10 cm in diameter was drilled to induce damage in the specimen (Figure 6). A full drill-through was performed to cut the bottom layer of tendons, thereby deliberately weakening the girder. This intervention was carried out at a location 70 cm from the loading point, providing a controlled site to monitor the ensuing changes in structural behavior using the DFOS grid.

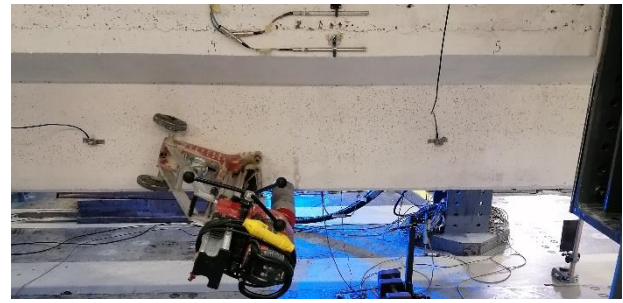


Figure 6. Test initiation with the cutting procedure

## 4 PRELIMINARY RESULTS

### 4.1 Load-displacement behavior

Loading was applied under force control at a rate of 1 kN/s (phases P1 to P3), and then under displacement control at a rate of 0.1 mm/s (phases P4 to P6) with a maximum load of 428 kN. Figure 7 shows the load-displacement behavior, where the vertical displacement was measured with a displacement transducer located in the middle of the girder.

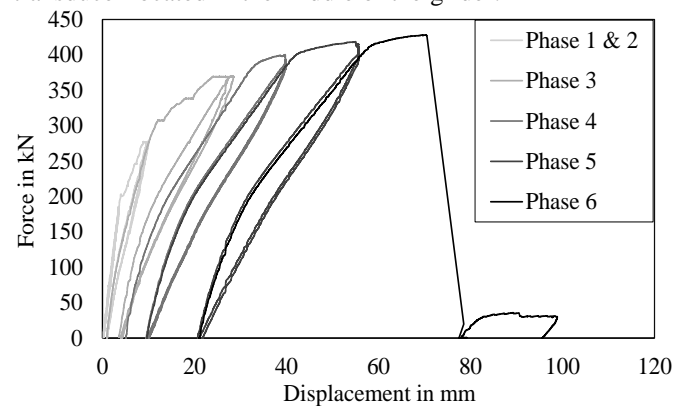


Figure 7. Force-displacement behavior of the girder

The load was gradually increased in six distinct phases, P1–P6, with each phase consisting of two loading–unloading cycles. After the second unloading cycle of each phase, the girder was put to rest for 20 minutes under ambient vibration conditions. Upon completing phase 3 on the first test day, the girder was brought to the phase 3 peak load (369 kN) and maintained at this constant level overnight. On the following day, the load was released (unloading phase) before initiating phase 4, creating three stages between phases 3 and 4: loading, constant force, and unloading.

The graph in Figure 7 illustrates a progressive stiffness reduction and the onset of plastic deformation with increasing load. In the early phases P1–P2, the steep force–displacement slope denotes the girder’s high initial stiffness, with visual crack initiation occurring during the first cycle of phase 2 (P2–C1) in the damaged zone. As loading advances into phases P3–P4, the slope diminishes, reflecting stiffness loss from crack propagation and the commencement of permanent deformations. In the final phases P5–P6, approaching the ultimate capacity of 428 kN, the response becomes distinctly nonlinear, marked by successive crack formation and partial yielding of the reinforcement.

In Figure 8 below, the crack patterns on the face of the girder opposite to where the DFOS grid was installed, overlaid with a

schematic representation of the sensor layout for comparison, are shown. At the peak load of phase 5, multiple cracks are visible, with crack openings marked directly on the concrete surface during the test. In the region corresponding to the DFOS grid, the first signs of cracking appeared as early as loading phase 3, indicating that the sensor network would have detected these strain concentrations in real time.

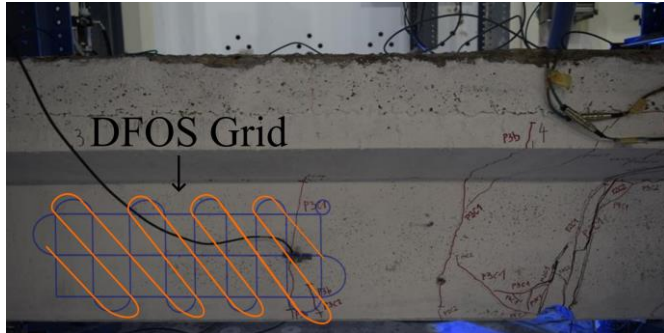


Figure 8. Crack pattern from the other side of the girder at load phase 5 (418 kN)

#### 4.2 Framework and labeling

The data from the DFOS grid was analyzed using the fosanalysis framework (available at <https://github.com/TUD-IMB/fosanalysis/>) developed at TU Dresden, which enables a streamlined workflow from data parsing and preprocessing to crack detection and crack width estimation [24]. This approach yielded excellent agreement between measured and calculated crack widths across different loading stages, indicating the robustness of both the DFOS system and the analysis framework [29].

The preprocessing procedure within the fosanalysis V0.4 framework involves a series of steps designed to enhance the quality and interpretability of the raw strain data obtained from DFOS. Initially, the so-called Strain Reading Anomalies (SRA) are removed using the Global Threshold Method (GTM), where a strain threshold of 300  $\mu\text{m/m}$  is applied to eliminate extreme or unphysical values. Following this, data recorded during phases of constant load are aggregated over time by computing the median value of several consecutive readings, thereby reducing short-term fluctuations and improving stability. Data dropouts, instances where sensor readings are missing or corrupted, are linearly interpolated. To further enhance the signal quality, a sliding mean filter with a window radius of 2 is applied, which smooths the strain profile by averaging adjacent values. A detailed explanation of each method and its implementation is provided in [30].

Figures 9 and 10 plot the peak strains recorded along the DFOS 1 and DFOS 2 sensors at the maximum load of each phase, confirming that a surface-bonded sensor grid, installed without surface grooving, can reliably capture strain evolution under short-term loading. On the horizontal axis of the graphs in figures 9 and 10, sensor lengths are shown; the vertical axis displays strain with maximum peaks of around 3500  $\mu\text{m/m}$  and 4000  $\mu\text{m/m}$ , respectively. High strain peaks started to appear during load phase 3, corresponding well with crack initiation marked with red in Figure 8. During phase 5 of the loading test, the highest strain peaks were recorded. It should be noted that some of the observed strain peaks are associated with sensor turns, and these locations must be carefully accounted for in the

analysis, not to be addressed as crack indicators. The true regions of interest are listed in Table 1 below.

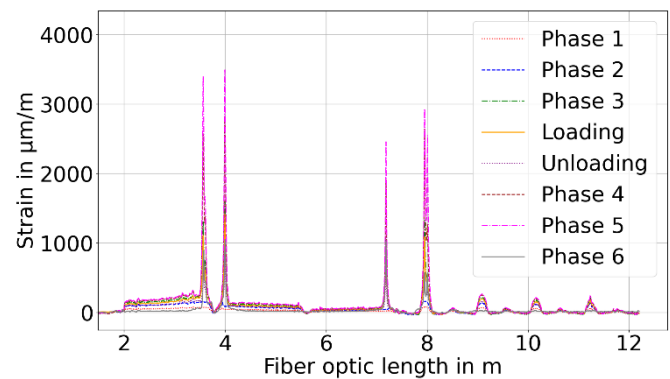


Figure 9. Strain Profile from DFOS 1

An important aspect to be noted is the documentation of the sensor installation, including the exact lengths of sensor segments, starting positions of the grid, and loop configurations. Such detailed records are essential for distinguishing between strain peaks arising from actual structural behavior and those that may result from sensor turns or installation artifacts.

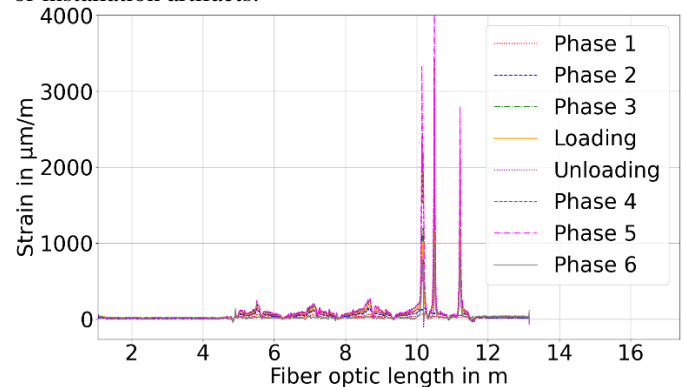


Figure 10. Strain profile from DFOS 2

By defining segments and specifying the length range of strain readings, the analysis was divided into horizontal and vertical components for DFOS 1 and diagonal components for DFOS 2. This allowed for accurate localization of areas of interest and targeted data cuts, thereby improving the reliability of crack detection and width estimation at different loading phases.

#### 4.3 Segment cuts and crack detection

Table 1 summarizes the segment crops analyzed for strain peak identification. For DFOS 1, three horizontal layers: bottom, middle, and top, were identified in the region surrounding the primary flexural crack at approximately 3.6 m, 4.0 m, and 7.0 m along the fiber, as confirmed by the crack pattern in Figure 8. Two vertical segments (segments 1 and 2) in DFOS 1 were also selected, with a prominent strain peak observed near the 8.0 m mark. Strain readings were measured in the sensor length between 5 to 12 m for DFOS 2. Within this range, inclined segments labeled 7, 8, and 9 exhibited significant strain peaks and were therefore selected for detailed analysis.



Table 1. Cropped region summary

Cropped Region	Sensor Length Range (m)
Bottom Crop (DFOS 1)	1.98-3.76
Middle Crop (DFOS 1)	3.86-5.56
Top Crop (DFOS 1)	5.64-7.28
Vertical 1 (DFOS 1)	7.42-7.77
Vertical 2 (DFOS 1)	7.79-8.145
Inclined 7 (DFOS 2)	9.335-9.855
Inclined 8 (DFOS 2)	10.075-10.595
Inclined 9 (DFOS 2)	10.865-11.3

By using DFOS, early-stage strain peaks can be identified, allowing for the detection and measurement of potential crack widths. As shown in Figure 11, during phase 3 of the test, the horizontal parts of the sensor exhibit strain peaks ranging from 80  $\mu\text{m/m}$  (top segment) to 300  $\mu\text{m/m}$  (bottom, vertical and inclined segment). These readings indicate a potential onset of crack formation, providing valuable insights into the early development of damage in the beam and allowing monitoring of the structures in the early stages. In the horizontal and inclined segment plots (a, c), the vertical axis denotes strain, while the horizontal axis indicates the sensors' relative positions. For the vertical segment plot (b), the axes are swapped.

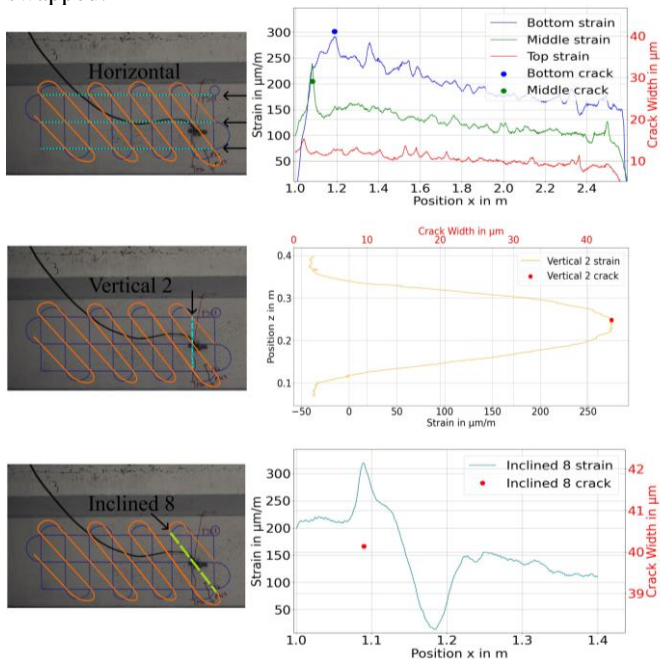


Figure 11. Early-stage DFOS strain profiles indicating incipient crack formation (a) Horizontal, (b) Vertical, and (c) Inclined segments

Building on these early observations, the evolution of strain profiles in three directions of the grid is analyzed. In Figure 12, the measured strain profiles of the horizontal segments of DFOS 1 (top, middle, and bottom) reveal a clear bending response. The readings are shown in temporal order, starting with loading up to phase 3, unloading part, and then loading in phase 5. The top segment exhibits strain peaks up to 2500  $\mu\text{m/m}$ , while the middle and bottom segments reached peaks up to 3500  $\mu\text{m/m}$ . Notably, prominent strain peaks at the

bottom correspond to the initial bending crack detected in Figure 11 (a), which becomes more pronounced as load levels increase and the crack propagates further into the beam cross-section.

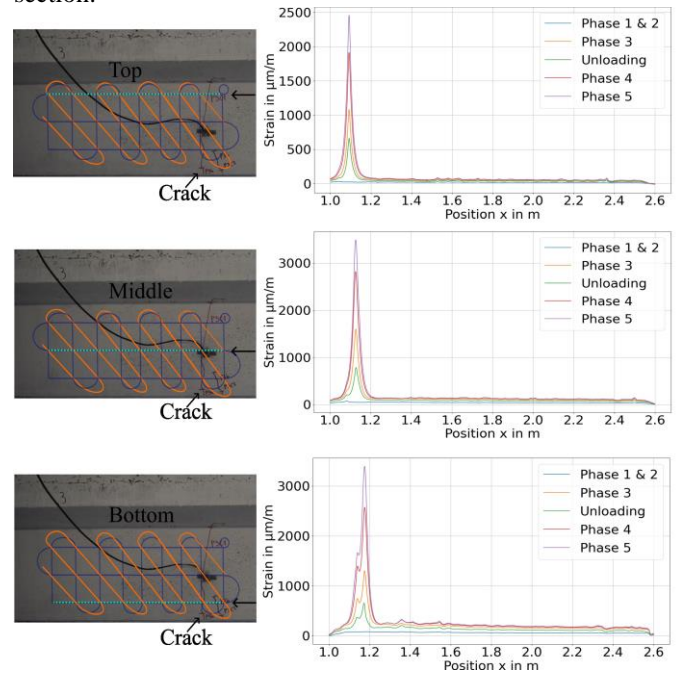


Figure 12 Horizontal strain profiles (a) Top, (b) Middle, and (c) Bottom for DFOS 1

Progressing from the top to the bottom segment, an increase in strain magnitudes can be observed, indicating the development of a crack near the left side of the sensor grid, in the region between 1.2 m to 1.4 m from the origin (check Figure 3). These peaks remain even after the unloading phase, marking a potential crack opening, which is also identified in the corresponding image of the girder. Even after the unloading phase, notable strain remains, indicating the presence of residual crack widths and partial permanent deformation in the beam. These peaks could also be detected by the diagonal and vertical segments, as will be seen in Figures 13 and 14 below.

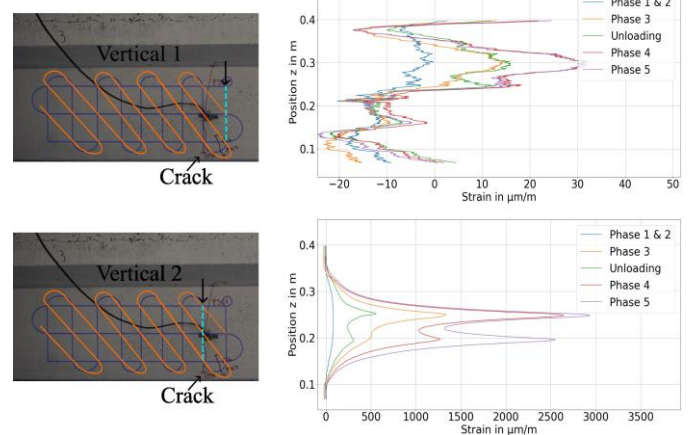


Figure 13. Vertical strain profiles (Vertical 1 and 2) from DFOS 1

The measured vertical strain profiles (Figure 13), under the same load steps, correspond well with the expected structural response of the beam. The vertical axis represents the sensor



location in the  $z$  direction (check Figure 3), while the horizontal axis shows strain in  $\mu\text{m/m}$ . Vertical segment 1, located along the left side of the beam, exhibits strain variations indicative of localized stress redistribution. In these regions, negative strains reflect compression, while positive strains indicate localized tensile effects. The strain readings in this segment, although only in a few  $\mu\text{m/m}$ , can suggest an interaction between bending and shear forces, likely influenced by crack propagation near the sensor grid.

The vertical segment 1 remains within  $\pm 30 \mu\text{m/m}$ , indicating a low-stress or compression zone near the neutral axis. As the load increases, the strain peaks in segment 2 become more noticeable (up to  $2500 \mu\text{m/m}$ ) in the region between 0.2 m to 0.3 m in  $z$  direction. This peak is also an indicator that a crack has been formed in this region, similar to the horizontal readings from the DFOS 1, which detected crack initiation from an early stage (Figure 11) and propagation in both directions.

Figure 14 presents the strain profiles measured along three diagonally oriented segments (labeled inclined 7, 8, and 9, check Table 1) under the same load steps as for DFOS 1. The horizontal axis denotes the relative sensor position in the  $x$  direction (origin at  $x = 0$ ), and the vertical axis shows strain measurement. In these diagonal segments, located within a region of potential crack formation, distinct differences in strain behavior were observed.

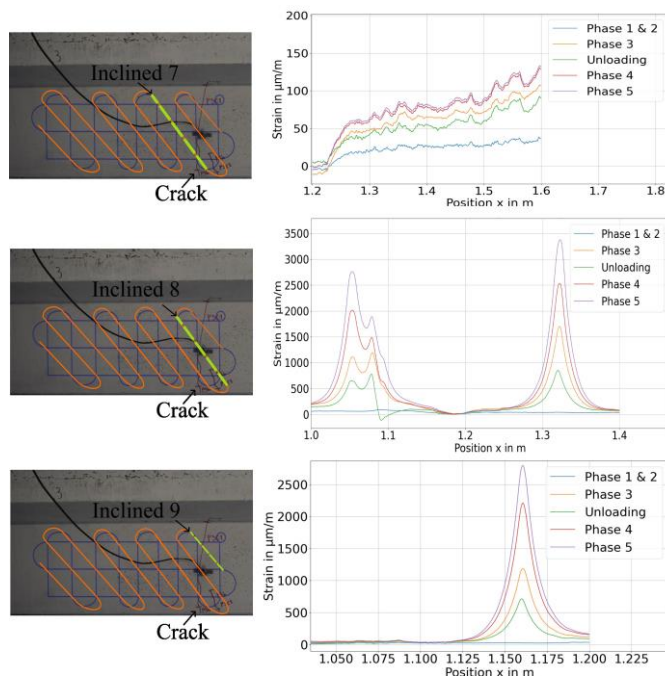


Figure 14 Strain profiles in diagonal segments 7-9 from DFOS  
2

Segment 7 displayed a steady increase in strain with loading but showed no pronounced peaks (up to  $120 \mu\text{m/m}$ ), suggesting that no major crack crossed this particular sensor path. In contrast, segments 8 and 9 exhibited prominent strain peaks under higher loads (between  $2500 \mu\text{m/m}$  to  $3500 \mu\text{m/m}$ ), especially segment 8, where two distinct peaks of  $2700 \mu\text{m/m}$  and  $3400 \mu\text{m/m}$  were observed. This suggests a concentration of cracking or stress in a relatively confined zone. The difference in peak heights for various load steps also

demonstrates how the crack opening widens under load and partially closes upon unloading.

The prominent peaks in each plot correspond to localized cracking, which was successfully detected and quantified by the DFOS grid. Furthermore, strain readings in vertical (vertical 2) and inclined sections (inclined 8) reveal the presence of two distinct strain peaks, which may be attributable to crack branching phenomena.

Despite initial expectations to capture diagonal cracking, such cracks were not observed within the grid region. However, the DFOS grid effectively captured and localized vertical cracks from early stages, confirming its potential as a robust tool for structural health monitoring (SHM). The experimental results indicate that for short-term measurements, good bonding between the optical fiber and the concrete surface can be achieved without the need to mill a groove. However, for long-term monitoring under varying environmental conditions, DFOS installation in grooves is recommended. Notably, as observed in the research [23], DFOS sensors installed without grooves can capture higher strain peaks.

Overall, the DFOS-based monitoring proved effective in capturing the strain behavior of the prestressed bridge beam. The results validate the early detection of cracks, well before they become visible to the human eye, similarly to previous research [24] and provide a detailed understanding of crack evolution under varying load conditions. The observed strain peaks could be partially validated through experimental visualization, as evidenced by the crack pattern visible on the opposite side of the beam. Early registration of cracks, especially shear cracks, can be critical, as the development of small shear cracks in large critical regions can, with increasing load, precipitate a sudden shear collapse of the entire reinforced concrete structure.

## 5 CONCLUSION

The experimental investigation demonstrates that the surface-bonded DFOS grid can be reliably installed without grooving and delivers effective short-term monitoring of prestressed concrete girders. Its high spatial resolution enabled the early detection of microcracks and captured the subsequent growth and spatial pattern of vertical cracks. Strategic sensor placement proved essential for localizing damage zones. These promising results lay the groundwork for advanced structural health monitoring of concrete bridges. Future work at the openLAB Research Bridge in Bautzen, Germany [26], will further validate and refine this DFOS-based monitoring concept.

## ACKNOWLEDGMENTS

The authors gratefully acknowledge the financial support provided by the German Federal Ministry for Digital and Transport (BMDV) through the research project ANYTWIN (Standardizing Monitoring-Based Safety Assessments of Bridges and the Integration into Digital Twins, funding reference: 01F2248B), funded within the mFUND innovation program.

The authors would like to express their gratitude to colleagues from Technische Universität Graz for their assistance during the installation and measurement of the DFOS grid. Special thanks are also due to colleagues at the Slovenian National

Building and Civil Engineering Institute (ZAG) for their expertise in conducting the experimental tests and coordinating critical aspects of the research. The authors acknowledge the financial support from the Slovenian Research and Innovation Agency: Research core funding No. P2-0273 and Infrastructure funding IO-0032.

## REFERENCES

- [1] M. Herbrand, 'Shear strength models for reinforced and prestressed concrete members', RWTH Aachen University, 2017.
- [2] H. Becks et al., 'Monitoring the Fatigue-Induced Strain Evolution of Concrete Bridges using Fiber Optic Sensors', *ce papers*, vol. 6, no. 5, pp. 1119–1126, Sep. 2023.
- [3] M. Herbrand and J. Hegger, *Assessment of the shear capacity of existing bridges – short term solutions*, 2014.
- [4] H. Becks et al., 'Measuring Strain and Crack Evolution in Reinforced Concrete under Monotonic and Fatigue Tension using Fiber Optic Sensors', *Procedia Structural Integrity*, vol. 64, pp. 1279–1286, Jan. 2024.
- [5] W. Lienhart et al., 'Distributed Vibration Monitoring of Bridges with Fiber Optic Sensing Systems', in *Experimental Vibration Analysis for Civil Engineering Structures*, Cham, 2023, pp. 662–671.
- [6] Ł. Bednarski et al., 'New Distributed Fibre Optic 3DSensor with Thermal Self-Compensation System: Design, Research and Field Proof Application Inside Geotechnical Structure', *Sensors*, vol. 21, no. 15, p. 5089, Jul. 2021.
- [7] M. Bertullessi et al., 'Experimental Investigations of Distributed Fiber Optic Sensors for Water Pipeline Monitoring', *Sensors*, vol. 23, no. 13, p. 6205, Jan. 2023.
- [8] C. M. Monsberger et al., 'Large-scale distributed fiber optic sensing network for short and long-term integrity monitoring of tunnel linings', *J Civil Struct Health Monit*, vol. 12, no. 6, pp. 1317–1327, Dec. 2022.
- [9] S. Gehrlein and O. Fischer, 'Großversuche zur Querkrafttragfähigkeit bestehender Spannbetonbrücken an der Saalebrücke Hammelburg', *Beton- und Stahlbetonbau*, vol. 113, no. 10, pp. 696–704, 2018.
- [10] J. J. Poldon et al., 'Distributed Sensing in Large Reinforced Concrete Shear Test'.
- [11] O. Fischer et al., 'Quasikontinuierliche faseroptische Dehnungsmessung zur Rissdetektion in Betonkonstruktionen', *Beton- und Stahlbetonbau*, vol. 114, no. 3, pp. 150–159, 2019.
- [12] G. Rodriguez et al., 'Shear crack pattern identification in concrete elements via distributed optical fibre grid', *Structure and Infrastructure Engineering*, vol. 15, no. 12, pp. 1630–1648, Dec. 2019.
- [13] B. Novák et al., 'Neues Potential im Structural Health Monitoring: Verteilte faseroptische Sensoren für Bestandsbauwerke', in *12. Symposium Experimentelle Untersuchungen von Baukonstruktionen*, 2023.
- [14] J. Hegger 'Assessment of the shear and torsion capacity of existing bridges - extended design approaches', Bremen: Fachverlag NW in der Carl Ed. Schünemann KG, 2020.
- [15] G. Schacht et al., 'Experimentelle Bewertung der Schubtragsicherheit von Stahlbetonbauteilen', *Beton und Stahlbetonbau*, vol. 111, no. 6, pp. 343–354, Jun. 2016.
- [16] P. Valerio, *Realistic shear assessment and novel strengthening of existing concrete bridges*, the University of Bath's research portal, 2009.
- [17] T. Hertle, 'On Mechanical Shear-Models in Reinforced and Prestressed Concrete Constructions'. Universit at der Bundeswehr Munchen, Nov. 2023.
- [18] O. Fischer et al., *Nachrechnung von Betonbrücken - systematische Datenauswertung nachgerechneter Bauwerke*. Bremen: Fachverlag NW, 2016.
- [19] G. Rodriguez et al., 'Shear crack pattern identification in concrete elements via distributed optical fiber grid.'
- [20] T. Wu et al., 'Recent Progress of Fiber-Optic Sensors for the Structural Health Monitoring of Civil Infrastructure', *Sensors*, vol. 20, no. 16, p. 4517, Aug. 2020.
- [21] L. Stiny, *Passive elektronische Bauelemente*, 2019.
- [22] M. F. Bado and J. R. Casas, 'A Review of Recent Distributed Optical Fiber Sensors Applications for Civil Engineering Structural Health Monitoring', *Sensors*, vol. 21, no. 5, p. 1818, Jan. 2021.
- [23] M. Herbers et al., 'Crack monitoring on concrete structures: Comparison of various distributed fiber optic sensors with digital image correlation method', *Structural Concrete*, Jun. 2023.
- [24] B. Richter et al., 'Towards an Automated Crack Monitoring using Distributed Fiber Optic Sensors', *ce papers*, vol. 6, no. 5, pp. 635–643, Sep. 2023.
- [25] B. Richter et al., *Monitoring of a prestressed bridge girder with integrated distributed fiber optic sensors*, vol. 64. 2024, p. 1215.
- [26] M. Herbers et al., 'openLAB – Eine Forschungsbrücke zur Entwicklung eines digitalen Brückenzwillings', *Beton- und Stahlbetonbau*, vol. 119, no. 3, pp. 169–180, 2024.
- [27] G. Rodriguez et al., 'Shear crack width assessment in concrete structures by 2D distributed optical fiber', *Engineering Structures*, vol. 195, pp. 508–523, Sep.
- [28] X. Lu and S. Zhang, 'Investigation of Mixed-Mode Crack Quantification with Distributed Fiber Optic Sensors', *e-Journal of Nondestructive Testing*, vol. 29, Jul. 2024.
- [29] M. Herbers et al., 'Rayleigh-based crack monitoring with distributed fiber optic sensors: experimental study on the interaction of spatial resolution and sensor type', *J Civil Struct Health Monit*, Dec. 2024.
- [30] B. Richter et al., 'Advances in Data Pre-Processing Methods for Distributed Fiber Optic Strain Sensing', Nov.2024.

## Proposed approach for direct rail state monitoring with distributed acoustic sensing DAS

Szymon Długosz<sup>1, 0009-0005-1626-366X</sup>, Tomasz Howiacki<sup>1,2, 0000-0002-6833-7203</sup>, Rafał Sienko<sup>2, 0000-0002-2751-7558</sup>,  
Łukasz Bednarski<sup>3, 0000-0002-5404-9921</sup>

<sup>1</sup>SHM System / Nerve-Sensors, Libertów ul. Jana Pawła II 82A, 30-444 Kraków, Poland

<sup>2</sup>Faculty of Civil Engineering, Cracow University of Technology, Warszawska 24, 31-155, Kraków, Poland

<sup>3</sup>Faculty of Mechanical Engineering and Robotics, AGH University of Science and Technology in Kraków,  
Mickiewicza 30, 30-059, Krakow, Poland

email: sd@shmsystem.pl, th@nerve-sensors.com, rafal.sienko@pk.edu.pl, lukaszb@agh.edu.pl

**ABSTRACT:** Railways are one of the fundamental modes of transportation, dating back centuries. They allow for the movement of people and goods across hundreds and thousands of kilometres. Such a large system relies on precise timing and excellent organization. Any incident or failure can result in losses amounting to millions of euros and cause unacceptable delays. Monitoring the condition of the railway is necessary to ensure safety and system effectiveness, but it is challenging due to the long distances that need to be monitored. Conventional sensors can provide high-quality data, but they do not offer a complete picture of the railway's state, and local defects can be overlooked. A great solution for railway monitoring is DAS. A fibre optic sensor integrated with the structure can be used to obtain information about strain and vibration, with a fine resolution of even down to 1 metre, over tens of kilometres of track. Installing the sensor in the railway substructures can be challenging and exposes the sensor to potential damage. Another approach discussed in the article is to attach the sensor directly to the rail. Long sections of track can be covered with monitoring within a few hours using automated machine, enabling direct measurement of the rail's condition. This paper presents the results of such installation, showing the potential of synergizing monolithic distributed fibre optic sensors with DAS technology to increase the safety and reliability of rail transport.

**KEY WORDS:** rail, railway, DAS, strain-rate, monolithic sensors, dynamic measurement.

### 1 INTRODUCTION

Research presented in the paper is mostly driven by the goal of improvement of safety in railway transport. We live in the times when due to galloping climate changes, sustainable ways of transportation, like railways may be one of the key ways of slowing down the global temperature from increasing [1]. However, there are challenges that have to be overcome to increase sustainability level of rail transport. The development is eagerly promoted due to its considerably lower emission rates than other modes of transportation. However, greenhouse gas emission is not the only environmental threat coming from transport industry. Another factors worth consideration are noise pollution and direct threats to wild animals [1]. Rail tracks run through the whole countries and continents. Their paths all possible zones, cities, wildlands and rural areas. The span between the stations reaches tens of kilometres, which makes it extra-ordinarily difficult to control and limit threats. Additionally, railway structures are prone to experience local damages due to deterioration. During the operation time, railways are exposed to harsh weather conditions, rapid temperature changes, uneven substrate settlement and massive vertical loads of passing trains. Exposition to such conditions may cause change of the track geometry. Damaged tracks may influence not only comfort of the passengers but also their safety. In most extreme case the train may fall of the track. Such an accident may be a huge environmental or urban catastrophe. Fixing is difficult, slows down or even completely blocks other trains and causes large costs and labour consumption [2, 3].

Following risks may be significantly limited or even completely avoided by proper monitoring the railway. Effective solution for such an application is Distributed

Acoustic Sensing (DAS). The DAS technology is subpart of the Distributed Fibre Optic Sensing (DFOS). All the DFOS technologies utilise optical fibre as an array of sensors. Sensing device - optical interrogator - divides the fibre into set of aligned segments. As a result of the measurement, each segment (gauge) is represented as a discrete data point in result array. Value of each data point is a mean value of a measured physical quantity in all the points located in specific gauge [4, 5]. The DAS interrogators divide the fibre into dense set of overlapping channels (gauges) providing full continuity of the measurement along the fibre path. The distributed nature of this sensing technique allows continuous recording with multiscale grid of virtual unit gauges. Virtual placement of the gauges allows free manipulation on their arrangement without necessity of rearranging the setup. All the changes can be introduced by proper tuning of the interrogators [6,7]. Crucial part of system designing is proper placement and installation of the sensor. Industrial practice is to install the sensor in the trackside or to use already installed telecom cables [8, 9]. Installation of the sensors in the ballast layers of the railway may be challenging due to the complexity of the structure, traffic and law regulations. Moreover, such installation method requires placing additional cable duct which disturbs strain transfer mechanism. Another unfavorable phenomenon occurring in soil mechanic is non-elastic behavior of gravel ballast layers. Rocky, non-expansive soils as gravel used for sub-track construction do not transfer tensile forces. In such configuration only vibrations can be measured. More comprehensive solution is to attach the sensors directly to the track. This way system can measure direct strain of the element to give more information about the actual track condition [10]. Nevertheless, DAS interrogators have limited dynamic range.



Strong, high amplitude vibration may lead to saturation effect occurrence. This may lead to the substantial data loss [11]. Correct configuration of interrogator settings and adoption of sensor properties is crucial for proper operation of the measurement system. In this paper, authors propose the solution for direct rail track monitoring, allowing dynamic measurements of high-speed trains, passing with velocity of up to 250km/h, alongside with the long-term static strain measurements. The solution was tested during full-scale field experimental sessions, proving the feasibility and correctness of such an approach.

## 2 DISTRIBUTED ACOUSTIC SENSING PRINCIPLES

### 2.1 Rayleigh backscattering application in DAS

Rayleigh backscattering can be effectively used for precise strain and temperature measurements in both silica and polymer fibres. Two main approaches of Rayleigh phenomenon can be distinguished: Optical Time-Domain Reflectometry (OTDR) and Optical Frequency Domain Reflectometry (OFDR). OTDR-based measurements are usually much faster and can be performed on significantly longer sections of the fibre than OFDR [12]. DAS interrogators operate on OTDR combined with phase control coherency ( $\phi$ -COTDR) in order to deliver high-quality information about the rate of the strain change (strain-rate), along the fibre. Distribution of the reflected light intensity in the fibre for COTDR is random.

Regardless this randomness nature of the signal, it varies harmonically, as shown in Fig. 1. This way, with application of phase control approach, the phase information can be revealed. Whereas the phase angle is directly proportional to the strain change along the fibre axis [13], creating the opportunities for practical applications in civil engineering and geotechnics.

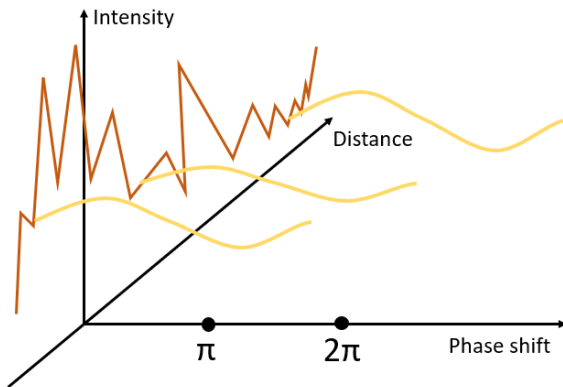


Figure 1. Intensity changes are irregular along distance but harmonic along phase shift axis [13].

### 2.2 Dynamic range of DAS interrogators

Dynamic range of acoustic sensing device (interrogator) is the magnitude of the strain change between two time samples that can be accurately unwrapped. Due to harmonic behavior of the intensity, only certain magnitude of strain change can be measured accurately. Because of that, DAS interrogators differentiate the strain in time domain in order to obtain strain-rate, using the following equation:

$$\frac{\mu\epsilon}{s} = \frac{\partial\mu\epsilon}{\partial t} \quad (1)$$

where  $\frac{\mu\epsilon}{s}$  is strain rate given in microstrains ( $\mu\epsilon$ ) per second and  $\frac{\partial\mu\epsilon}{\partial t}$  is a derivative of strain in time-domain.

Use of strain-rate allows to measure wider range of strain by measuring small changes and then stitching them together, by phase unwrapping in order to obtain whole picture, as shown in Fig. 2 [13].

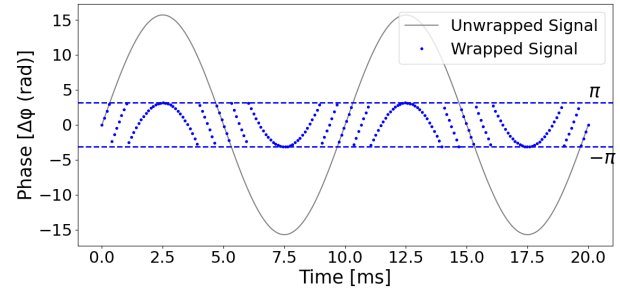


Figure 2. Wrapped and unwrapped differential phase.

As the value of the strain change can be both positive and negative, the dynamic range of any DAS interrogator is limited between  $[-\pi; \pi]$ . Return signal is always within this range, even if the input strain in the time  $dt$  would move outside the limit [14].

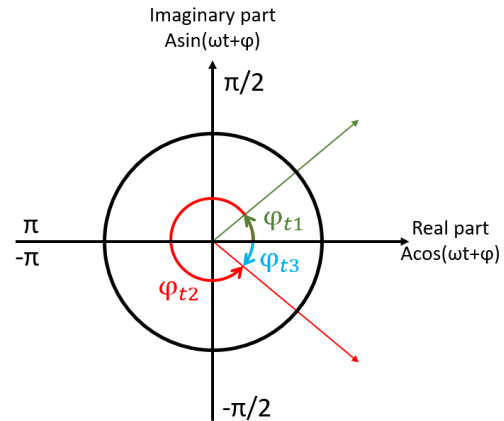


Figure 3. Phase angle change in complex coordinate system.

The phase angle change between the two following samples should not exceed  $|\pi|$ . If so,  $\phi_{t2}$  is non-distinguishable from  $\phi_{t3}$ . The exceeding the limit due to the high vibration amplitude during recording is being called saturation effect. Dynamic range can be improved with higher sampling resolution or shorter gauge length. Due to higher sampling frequency, time distance  $dt$  is shortened, allowing to observe the events of higher dynamics (higher amplitude change in time). Shortening the gauge length limits the part of the fibre from which energy is being acquired (averaged) from.

Exact effect of the gauge length value can be observed in the relation between the angle phase shift and strain [15]:

$$d\phi = \frac{4\pi G \zeta}{\lambda} \epsilon \quad (2)$$

Where  $d\phi$  is a phase angle shift,  $G$  is gauge length,  $\zeta$  is opto-elastic scaling factor,  $\lambda$  is the operational optical wavelength in vacuum and  $\varepsilon$  is the strain. Based on the equation (2), we can conclude that the relation between gauge length and phase angle shift is linearly proportional.

### 3 PROPOSED APPROACH FOR DAS-BASED DIRECT RAIL TRACK STATE MONITORING

#### 3.1 System design

The system in question was deployed on a railway line in south-central Poland to monitor its technical condition and enable the maximum speed of trains to be increased to 250 km/h.

A key objective of the system was to enable multiple fibre optic measurement techniques using a single sensor, making it adaptable to various sensing methods beyond just DAS. This flexibility allows to use other interrogation schemes simultaneously (including for example Brillouin-based strain sensing DSS and Raman-based temperature sensing DTS). In the designed system, it was decided to install two sensors on the side surface of the rail web (Figure 4) in order to add Distributed Displacement Sensing (DSS) functionalities to the system. Knowing the spacing between the sensors, measuring strain distributions over the entire length and assuming relevant boundary conditions, both local curvatures and vertical displacements (shape changes) can be calculated.

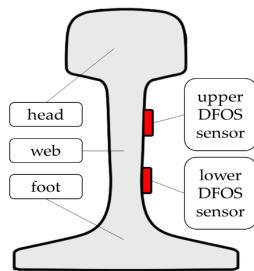


Figure 4. Cross-section of rail with sensors' location.

The sensor integrated into the system is an adjusted version of the EpsilonFlat – the monolithic solution from Nerve-Sensors family. Unlike the standard EpsilonFlat, which utilises two sensing fibres, this modified version employs four fibres, as shown in Figure 5. Table 1 summarises selected mechanical properties of the sensor.

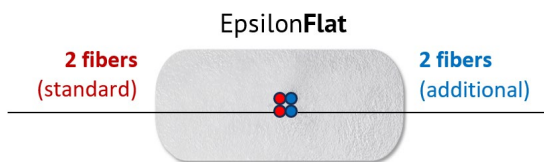


Figure 5. Cross-section of the sensor used in the system.

Table 1. Selected mechanical parameters of the EpsilonFlat

Parameter	Value
Strain range	±4%
Elastic modulus	3 GPa
Bending radius	100 mm

The monolithic core of the sensor, coupled with its flat cross-section, ensures the best possible strain transfer mechanism,

resulting in precise and high-quality readings [16]. Low elastic modulus of the sensor itself combined with the elastic glue causes minimal, negligible influence of the sensor on the mechanical parameters of the rail. This design effectively captures and transmits strains with minimal distortion, guaranteeing the accuracy and reliability required for monitoring the rail's performance over time.

Additional fibres within the sensor cross-section allowed for the world-unique approach in system configuration. This adjustment enhances the sensor's versatility, providing additional configuration possibilities to meet the unique challenges of the project. Sensors were delivered on site in 50 m long sections. Two fibres were spliced together creating one long loop to be measured with long-distance interrogators. However, two additional fibres allow for connection of high-spatial resolution interrogators to scan shorter sections with higher precision, if necessary (Figure 6). It shows, that various measurement devices do not have to compete with each other, but can be used synergistically to expand the diagnostic capabilities of the entire system. While maintaining high-resolution data acquisition capabilities, it is also possible to offer a cost-effective and versatile solution for large-scale monitoring applications.

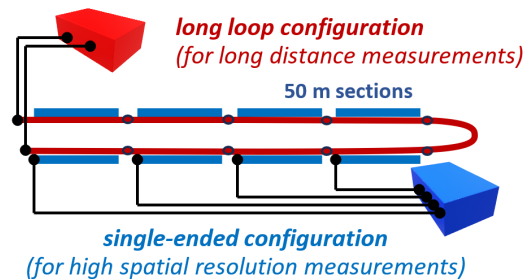


Figure 6. Scheme of the measurement path.

The sensors were arranged in a 2 x 250-metre-long loop, featuring two continuous sensing paths and independent, shorter 50-metre-long sections. Every 50 metres, the sensor paths passed through connection wells, where the necessary connections were made – Figure 7.



Figure 7. Connections between segments of the sensors during installation and the view of the protective well.

This configuration ensured that the system maintained optimal functionality across the entire loop, allowing for continuous monitoring while facilitating easy maintenance and troubleshooting through strategically placed connection points. The segmentation of the fibres into shorter paths also enhanced the flexibility of the system, accommodating long-distance spans without compromising signal integrity or performance.

Chosen arrangement allowed simultaneous acquisition of dynamic and static measurement data.

### 3.2 Sensor installation

The installation of the sensor required initial pre-sanding of the rail's side, aimed at achieving proper grip. The goal was to exfoliate only a thin layer of loose corrosion, ensuring minimal impact on the rail's mechanical parameters. This effect was successfully achieved using a water under pressure, a method that provided the necessary surface preparation without compromising the rail's integrity. The selection of materials for the bonding process was critical to the success of the installation. High durability, a low elastic modulus, excellent corrosion resistance, and strong adhesion were essential to ensure the sensor's secure attachment. To meet these requirements, epoxy-based adhesives were employed for gluing the sensor to the rail. The selection of the glue was preceded by research into various solutions in the laboratory.

To guarantee precision and time effectiveness of the installation, a specialised piece of equipment was designed and developed specifically for this project (Figure 8). The cart system utilises electric motors and pneumatic glue dispensers to ensure an even and consistent application of adhesive. The electric motors power the movement of the carts, enabling precise control over the positioning and alignment during installation.



Figure 8. Semi-automatic rail cart used for sensors' effective installation along the rail.

This technology allows for a highly efficient, repeatable, and controlled gluing process, contributing to the overall success and reliability of the sensor installation. Before the final application within the operate railway line, the solution was tested on an experimental section of the rail (Figure 9) to better understand on-site challenges and minimise the risk of errors. The success of the installation in Poland allowed for the commercialisation of the cart in Germany and UK.



Figure 9. EpsilonFlats after test installation.

The combination of innovative installation technology, high-quality materials, and specially designed sensors resulted in a gluing speed of up to 120 metres per hour. This makes the approach an excellent solution for km-long sections, where conventional manual bonding is very difficult, if not impossible to achieve. In the current project, the total length of 2,200 metres of sensors was installed directly to the rail surface.

### 3.3 Spatial survey

Chosen configuration of the sensing path, despite of multiple benefits, is also connected with some challenges. Complicated layout requires the proper selection of the active sensing segments (excluding loops, patchcords and pigtails) within the whole optical path. DAS-based interrogators usually operate on spatial resolutions of not less than 1 m. In this scale, it is challenging to clearly distinguish the measurement part of the fibre from the connecting part.

The proposed solution to the problem was to use pigtails (connecting cables between the segments) with different fibre properties, causing the clear differences in the Brillouin signal. To make a detailed documentation of the sensing path, the hybrid Rayleigh & Brillouin interrogator Neubrex NBX-7031 (Figure 10) was used with its backscattering-based mode.

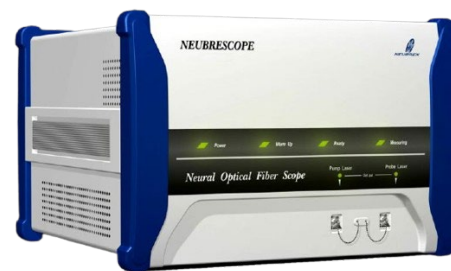


Figure 10. Neubrex NBX-7031 hybrid interrogator.

Brillouin backscattering allows direct fibre parameters identification without necessity of providing reference reading. The Brillouin shift, quantity linearly connected with absolute strain of the fibre [17], allows to clearly distinguish between the measurement sections glued to the rail and free connecting patchcords. – Figure 11.

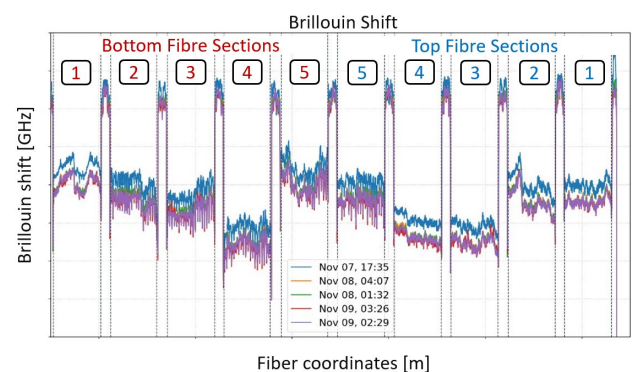


Figure 11. Brillouin Shift measurement results.

Brillouin survey provided very precise information about the exact length of the measurement path components. Proper tuning of the optical device reflection coefficient  $ROI=1.468$



with the coefficient used in DAS interrogator resulted in 1:1 translation of measurement path between the fibres. In the cases where standard methods for spatial surveying may be not efficient enough, shown approach is an ideal solution for self-survey of the sensor.

### 3.4 Used DAS interrogator and measurement settings

Observing a highly dynamic event, such as the high-speed passage of a train, demands both the highest possible sampling frequency and the shortest achievable gauge length. Achieving this balance is crucial for capturing rapid changes in strain distribution along the fibre optic sensor. There are multiple ways to enhance gauge length, both at the sensor and interrogator levels. For example, one approach involves implementing weak Fibre Bragg Gratings (weak-FBGs) along the entire fibre, which can improve spatial resolution and measurement precision. However, this method is often costly and not universally compatible with all interrogator devices, making it less practical for certain applications. Alternatively, gauge length optimisation can be achieved through advanced signal processing techniques and the use of appropriate interrogation technology.

In the project, the Febus A1 DAS interrogator (Figure 12) was deployed – a device that utilises Phase-Sensitive Coherent Optical Time-Domain Reflectometry ( $\phi$ -COTDR) to enhance reading quality. Unlike the classical DAS approach, where the injected light pulse is a simple impulse, the Febus A1 leverages optimised coding and signal processing algorithms to improve sensitivity and spatial resolution. This advanced approach ensures reliable interrogation over fibre optic paths exceeding 100 km, while mitigating the risks of signal fading and significant Signal-to-Noise Ratio (SNR) degradation.



Figure 12. FEBUS A1 interrogator.

A key advantage of  $\phi$ -COTDR in the Febus A1 is its ability to achieve a gauge length as short as 1 metre, a spatial resolution that is typically unattainable with standard interrogators. Conventional DAS systems often struggle to maintain short gauge lengths due to limitations in pulse-based interrogation methods, which can lead to reduced spatial resolution and increased noise. By employing optimized signal processing, the system effectively enhances precision without compromising signal integrity. This feature is particularly valuable for applications requiring highly localised strain and vibration measurements, such as high-speed train monitoring, where detecting rapid structural changes with fine spatial granularity is crucial. This makes the device a perfect choice for railway dynamic monitoring.

For the in-situ testing, it was decided to measure the dynamic passages of the trains using combination of the parameters summarised in the below table.

Table 2. Used DAS acquisition parameters.

Parameter	Value
Gauge length	2 m
Sampling frequency	40 kHz
Channel (gauge) spacing	20 cm

### 3.5 Methodology of the experiment

To evaluate the performance of the monitoring system in a real-world high-speed scenario, an experiment was conducted using a Pendolino ED250 train. The location of the measurement section was a long, mostly straight section of the railway track. During the experiment, multiple train passages were recorded under varying speeds to assess the system's capability in detecting and analysing strain signals associated with different train dynamics. To minimise the influence of temperature fluctuations on the readings and provide maximally stable conditions, all DAS measurements were conducted at night. The railway traffic was suspended for the duration of the experiment, ensuring an undisturbed testing environment. The measurement crew maintained constant communication with train operators to ensure that the train traveled at the predefined speeds. A total of four test runs were performed at velocities of 200, 220, 240, and 250 km/h within a single night. The time interval between consecutive passages was determined by the necessary stopping, reversing, and re-accelerating of the train to the target speed, with a minimum of 45 minutes between the runs. This ensured that the rails had sufficient time to fully stabilise after each passage, preventing residual strain effects from influencing subsequent measurements. As a reference technique, heavy-duty accelerometers with dynamic range of 50 G and frequency range from 5 to 2000 Hz were employed.

## 4 RESULTS AND PROCESSING

### 4.1 Raw data: strain-rates

The raw data recorded by the device is a strain-rate array (Figure 13) at discrete points located in the centers of predefined gauges. Each discrete value represents an average of the rate of strain change along the single gauge length. As the fibre is interrogated as whole, initial processing (or post-processing) has to be introduced in order to cut-out measurement sections from the entire path.

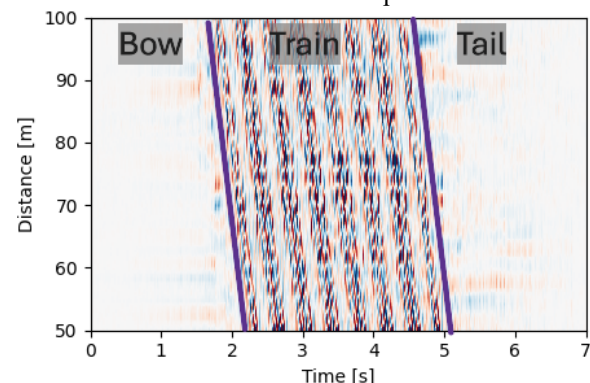


Figure 13. Example strain-rates recorded by the bottom sensor during train passage with 250 km/h speed.

A recorded image provides high-quality insights into dynamic processes existing in the railway structure during high-speed train passage. Three main zones of the signal may be distinguished. In the bow-zone, a para-seismic wave travelling through the rail may be observed. In the main part of the signal – the train-zone – signal is complex. Eight skew lines on the map represents the moments in time where the wheel bogies of the train were in specific locations along the rail. Number of the lines correspond with number of the bogies. Empty spaces between the lines represents the spans of every carriage between the subsequent bogies. Last zone of the signal is a zone of tail waves, the ones lasting in the structure for some time after the train passage [18]. Overall check at the signal allows to assume that used acquisition parameters, combined with dedicated monolithic-core of fibre optic sensors, resulted with non-saturated, high-quality signal, recorded in extraordinary proximity to the strong vibration source.

#### 4.2 Spectral analysis

Distributed Acoustic Sensing can be used as a network of virtual, unit-like channels, each functioning akin to a geophone, measuring strain or displacement at various points along the fibre-optic sensor. The system output can thus be understood as an array of time-series recorded by specific virtual gauges positioned along the fibre, capturing the strain dynamics of the monitored structure. Due to this nature of the signal, any method of classical digital signal processing is valid, allowing for a wide range of analytical techniques to be applied to the DAS data.

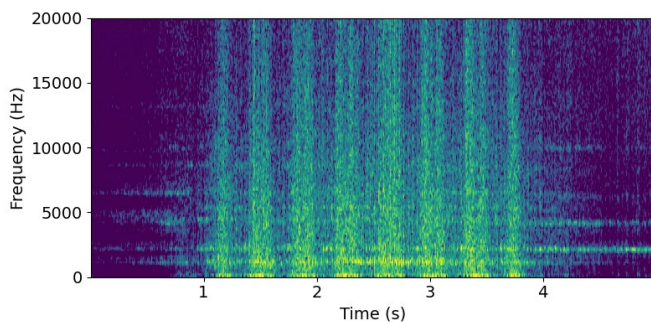


Figure 14. Spectrogram of the single time-series of strain-rate recorded in the middle of measurable section.

The example data presented in Fig. 14 clearly reflects the direct influence of train passage, with distinct frequency components corresponding to the mechanical events. Notably, the spectrogram reveals a predominant contribution from low-frequency waves. This phenomenon is likely linked, inter alia, to a rapid rise in temperature within the rail due to its loading by the passing train, coupled with a relatively slow heat dissipation rate from the rail. The thermal effects associated with the train passage thus become embedded in the strain measurements, manifesting as low-frequency trends.

Given the dynamic nature of the observed event, the authors opted to mitigate the influence of these thermal effects by applying a low-cut Butterworth filter of the third order. The chosen cut-off frequency of 5 Hz serves to effectively attenuate the low-frequency components, which are primarily attributable to temperature-induced strain. This filtering step not only reduces the trend-like behaviour often observed in the

integrated strain signal but also compensates for the confounding effects of temperature variations, enabling a clearer view of the mechanical strain caused by the train passage.

This approach illustrates how DAS measurements supported with proper sensors, can be refined to focus on the relevant mechanical signals, removing the thermal noise that may otherwise obscure the true nature of the event under study. While reference measurements using accelerometers were also employed, it is worth noting that these sensors primarily capture signals from 5 Hz and above, aligning with the chosen filtering approach but playing a less central role in addressing the low-frequency thermal effects observed in the strain data.

Deeper understanding of the signal can be achieved by application of the Frequency Band Energy (FBE) analysis. This approach allows for comparison between energy levels in specific frequency bands. The energy  $E$  of the discrete, finite-time signal, denoted as  $x$  is sum of the signal's absolute value square in proper time  $t$  boundaries (3).

$$E = \int_{t_1}^{t_2} |x(t)|^2 dt \quad (3)$$

Since the total energy remains conserved between the two domains, it is possible to analyse the distribution of the energy across different frequency components by examining the squared magnitudes of the Fourier coefficients. Hence, by summing the squared magnitudes of a specific portion of the Fast Fourier Transform (FFT) coefficients, denoted as  $X$ , one can determine the energy contained within a particular frequency  $f$  band [19] using equation (4).

$$FBE = \sum_{f_{min}}^{f_{max}} |X(f)|^2 \quad (4)$$

From the Distributed Acoustic Sensing (DAS) perspective, such a method provides the capability to monitor the occurrence of different frequencies along the entire fibre length and provide neat visualisation. This ability is particularly valuable for analysing dynamic changes in the recorded signal and distinguishing specific patterns based on their spectral characteristics. By integrating this approach with the Short-Time Fourier Transform (STFT), it becomes possible to not only categorise signals by their frequency components but also track their temporal evolution, offering deeper insight into underlying phenomena.

In the presented research, the authors conducted STFT analysis twice, utilising two distinct window lengths to maximise the level of detail in signal examination. The first calculation employed a longer window, consisting of 8129 samples – chosen as the eightfold multiple of 1024 – which was specifically applied to the first six bands corresponding to the lowest frequencies. This selection was made to enhance frequency resolution in the low-frequency domain, where finer spectral details are often crucial for accurate interpretation. For the remaining higher-frequency bands, a window of 1024 samples was determined to provide optimal results, balancing time and frequency resolution to ensure a comprehensive and precise analysis of the recorded signal.

Presented results of FBE were calculated from the signal after low-cut filtration introduced previously.



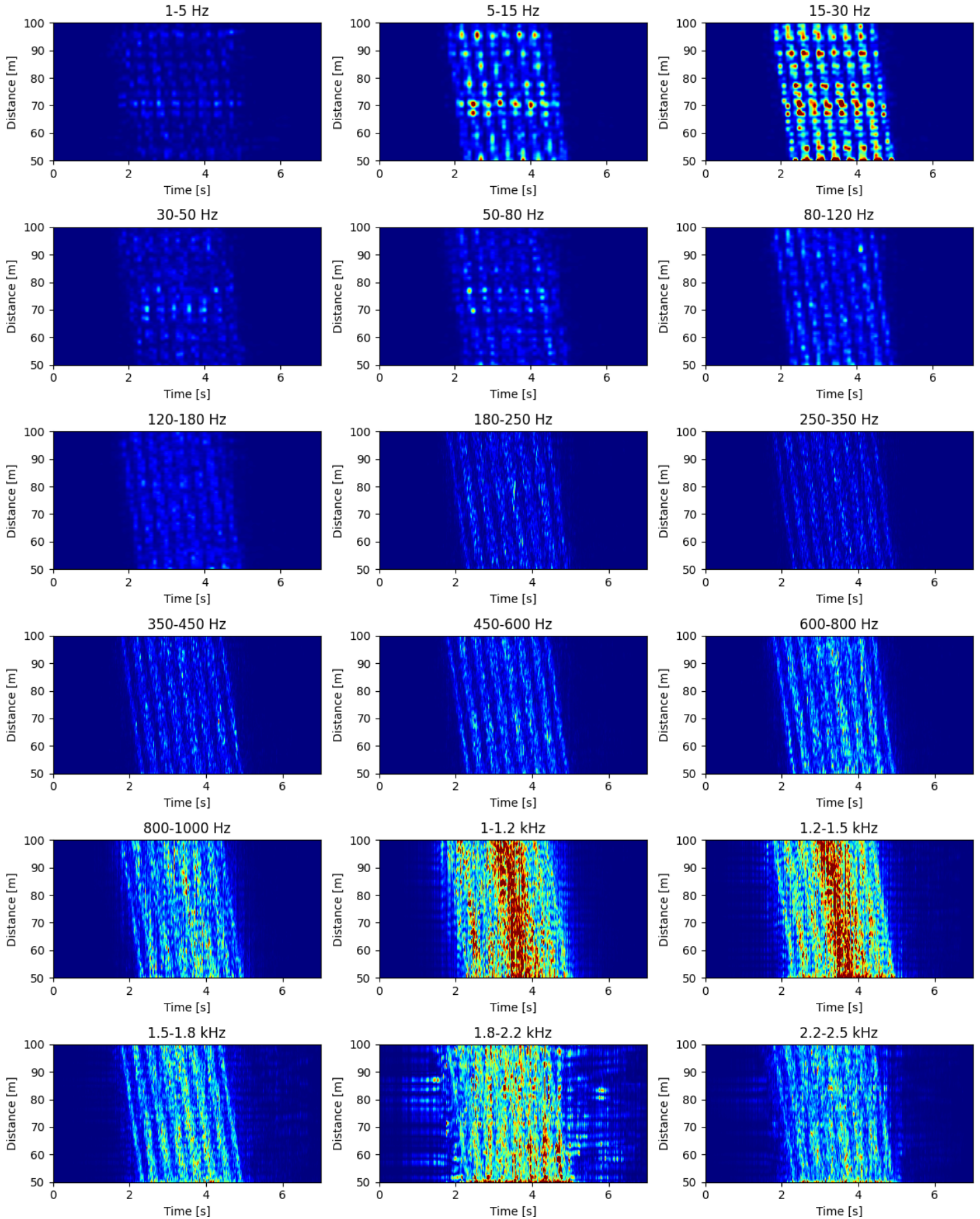


Figure 15. Comparison of energy levels within specific frequency bands.



When a train travels along the track, various phenomena generate acoustic noise in addition to mechanical changes. The primary sources of this noise include the train's machinery, braking system, and, most significantly, the interaction between the wheels and the rail. Most of these acoustic noises are concentrated at frequencies above 500 Hz [20].

However, noise-induced mechanical vibrations consist of low-amplitude waves with high attenuation, meaning they do not significantly affect the mechanical state of the rail. The authors empirically analysed the entire frequency spectrum and determined that the range of  $<0; 2.5>$  kHz is the most relevant, either due to its contribution to overall strain rates or the information it carries. The frequency bands for calculation were selected to maximise information and comparability while ensuring proper coverage within the chosen range. Since energy levels decrease across subsequent bands, the bands were gradually widened to maintain sufficient values for comparison.

The data exhibits a clear pattern, showing that the majority of the signal is concentrated in the low-frequency range, up to 50 Hz. Higher frequencies, up to 600 Hz, contain relatively low energy. A significant portion of the signal consists of acoustic noise. Above 600 Hz, the energy level progressively increases, peaking between 1.1 kHz and 1.5 kHz. In this range, a highly visible noise band appears, particularly around the third and fourth carriages. According to the technical documentation of the Pendolino ED250, this high-noise area corresponds to the placement of traction transformers within the train. These findings highlight the direct relationship between onboard equipment and noise influence on the measurements. Noise-carrying frequency bands in this case are clearly separated from the valuable parts of the signal. With this information, authors decided to apply additional Butterworth low-pass filter of the 3<sup>rd</sup> order, with cut-off frequency of 1 kHz.

Characteristics of the FBE maps allow assumption that wide frequency distribution is connected with wide frequency range of an event rather than with saturation effect occurrence.

#### 4.3 Spectral coherence check

To ensure high-quality measurements, the fibre signal must not be saturated. To verify that clipping due to exceeding the dynamic range does not occur, spectral coherence between collocated channels should be calculated. Authors estimated spectral coherence by the following equation:

$$\gamma^2(f) = \frac{|G_{xy}(f)|^2}{G_{xx}(f)G_{yy}(f)} \quad (5)$$

where  $G_{xy}(f)$  is the cross-spectral power density, and  $G_{xx}(f)$  and  $G_{yy}(f)$  are the spectral power densities of either signal. High coherence ( $\gamma^2 \approx 1$ ) signifies a strong correlation between DAS signals with synchronous recording, while low coherence suggests a weaker correlation or the possible presence of noise caused by signal clipping (saturation) [11].

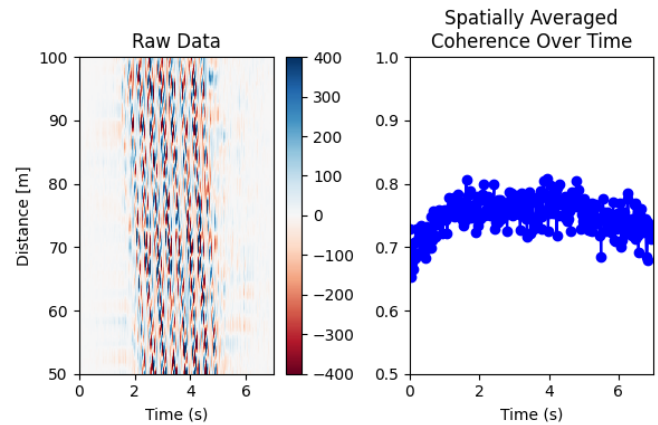


Figure 16. Side by side comparison of the raw strain rate (left) with the calculated signal spectral coherence (right).

Spectral coherence had been calculated between all the following DAS channels with window length of  $10^3$  samples and presented in Fig. 16. Values on the diagram represent spatial mean coherence from each set of windows. Results show high spectral coherence, mostly  $> 0.7$ . High magnitude of spectral coherence between adjacent channels indicates that signal has not been saturated.

#### 4.4 Strain-change and reference check

All DAS interrogators measure the strain change in time. If properly recorded, the strain-rate signal can be integrated over time to reconstruct the train change – a quantity that is more intuitive from engineering perspective and easier interpreted in comparison to direct strain rate signal. Moreover, when considering the Bernoulli hypothesis – which assumes that plane sections remain plane and perpendicular to the neutral axis after deformation – it follows that vertical displacements and longitudinal strains are intrinsically linked.

In the case of steel rails with expected very small displacements ( $< 1.5$  mm), this assumption is especially valid, also due to the high stiffness of the steel and its homogeneity. Consequently, accelerometer measurements, which capture vertical motion, can serve as a reliable reference for strain-based calculations. This interrelation reinforces the validity of using accelerometer data to compare with DAS measurements.

Accelerations  $a$  measured by accelerometers were integrated twice in time  $t$  to obtain vertical displacements in specific points.

$$d(t) = \iint a(t)dt \quad (6)$$

As the quantities to be compared are known to be proportional, but exact coefficient of proportion is unknown, only the tendencies were compared. For that sake, values have been normalised and presented in Figure 17.

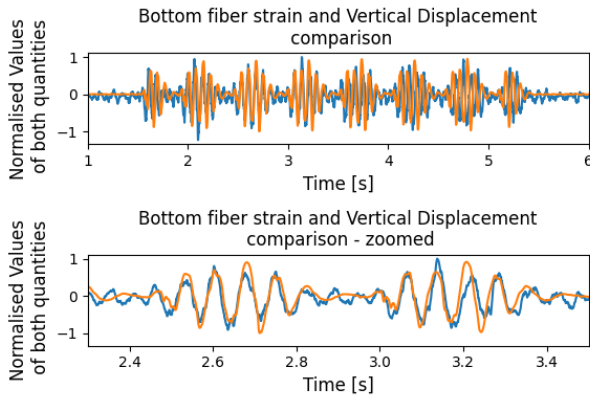


Figure 17. Comparison of DAS-measured strains (blue) with displacements from accelerometers (orange).

The compared data clearly show the expected correlation. Since the sensor is positioned in the bottom zone of the rail, its strain behaviour reflects its location relative to the neutral axis of the rail. In a downward displacement of the rail, the bottom sensors experience positive strain (tension). Conversely, during upward displacement, the same sensors are compressed, resulting in negative strain.

## 5 CONCLUSION

The study briefly discussed in the article demonstrates a robust approach for direct rail state monitoring using Distributed Acoustic Sensing (DAS) and specially designed monolithic sensors. By directly attaching the sensors to the rail surface, the system is capable of simultaneously capturing both dynamic and static strain data over very long distances using various types of interrogators, including those with high spatial resolution. Experimental results from high-speed train passages validate that the measured strain signals align with classical beam theory: fibres located at the bottom of the rail exhibit positive (tensile) strain during downward displacement and negative (compressive) strain during upward displacement. Furthermore, advanced signal processing techniques, including spectral analysis and energy band evaluations, effectively isolated the mechanical strain effects from thermal influences, thereby ensuring reliable data assessment and interpretation. The innovative semi-automatic installation method significantly enhanced deployment speed and consistency, making the solution both scalable and cost-effective. Overall, the proposed DAS-based monitoring system offers a promising tool for real-time railway infrastructure assessment, leading to improved safety, optimised maintenance strategies, and enhanced operational reliability in rail transportation.

## ACKNOWLEDGMENTS

The research on sensor design was funded by European Funds through the National Centre for Research and Development under the Intelligent Development Operational Program 2014–2020, as part of the project “Innovative Fibre Optic Sensor for Measuring Strain and Temperature” (POIR.01.01.01-00-1154/19). This project was implemented by SHM System (Kraków, Poland, [www.shmsystem.pl](http://www.shmsystem.pl) (accessed on 10 March 2025), [www.nerve-sensors.com](http://www.nerve-sensors.com) (accessed on 10 March 2025)).

## REFERENCES

- [1] Milewicz, J., Mokrzan, D., Szymański G.M., Environmental Impact Evaluation as a Key Element in Ensuring Sustainable Development of Rail Transport. Sustainability 2023.
- [2] Vivanco J.R., et. al., Importance of geotechnical diagnosis in railway management, Transportation Engineering 18 2024.
- [3] Fortunato E., et. al. Railway Track Transition Zones: Design, Construction, Monitoring and Numerical Modelling, International Journal of Railway Technology, 2023.
- [4] Kechavarzi C., et al., Distributed Fiber Optic Strain Sensing for Monitoring Civil Infrastructure, ICE Publishing, London, England, 2016.
- [5] Masoud A., Al-Sakkaf A., Bagchi A., Investigation of a Holistic Application of Fibre optic Sensors in structural Health Monitoring (SHM), 11<sup>th</sup> International Conference on Structural Health Monitoring of Intelligent Infrastructure, Montreal, Canada, 2022.
- [6] Bakulin A., et. al, Surface seismic with DAS: An emerging alternative to modern point-sensor acquisition, The Leading Edge, 2020.
- [7] Bakulin A., et. al., Surface seismic with DAS: Looking deep and shallow at the same time, SEG International Exposition and 88<sup>th</sup> annual meeting, 2018.
- [8] Gongbo Z., et. al., Railway Traffic monitoring with trackside fiber-optic cable by distributed acoustic sensing Technology, frontiers, 2022.
- [9] Kishida K., Thein L.A, Lin R., Monitoring a Railway Bridge with Distributed Fiber Optic Sensing Using Specially Installed Fibers
- [10] Milne D., et. al., An analysis of railway track behavior based on distributed optical fibre acoustic sensing, Mechanical Systems and Signal Processing 142, 2020.
- [11] Chen-Ray L., Analysis of Saturation Effects of Distributed Acoustic Sensing and Detection on Signal Clipping for Strong Motions
- [12] Cooperman A., Martinez M., Load monitoring for active control of wind turbines, Renewable and Sustainable Energy Reviews, Volume 41, 2015.
- [13] Shatalin S., et. al., Chapter 2 High Definition Seismic and Microseismic Data Acquisition Using Distributed and Engineered Fiber Optic Acoustic Sensor, Distributed Acoustic Sensing in Geophysics: Methods and Applications, 2021
- [14] Hartog A. H., An introduction to Distributed Optical Fiber Sensors, CRC Press, 2017
- [15] SEAFOM, Measuring Sensor Performance Document- 02 (SEAFOM MSP-02), IOP Publishing SEAFOM Fiber Optic Group, 2018
- [16] Bednarski, Ł., Sieńko, R., Howiacki, T., & Zuziak, K. (2022). The Smart Nervous System for Cracked Concrete Structures: Theory, Design, Research, and Field Proof of Monolithic DFOS-Based Sensors. In *Sensors* (Vol. 22, Issue 22, p. 8713). MDPI AG. <https://doi.org/10.3390/s22228713>
- [17] DeMerchant M. D., Brillouin scattering based strain sensing, Symposium on Smart Structures and Material, Newport Beach, USA, 1999
- [18] Hernandez E. O., Characterization of Shallow Ground in Railway Embankments Using Surface Waves Measured by Dark Fiber Optic Sensors: A Case Study, Sensors, 2023.
- [19] Proakis J. G. and Manolakis D. G., Third Edition Digital Signal Processing Principles, Algorithms, and Applications, USA, 1996.
- [20] Yang X., Yan C., Simulation of Wheel/Rail Noise of High Speed Train Running on the Slab Track, ICCTP 2009.





# Monitoring Timber Structures with Fiber Optics Sensors: State of the Art and Application to a Timber Beam

R. Mansilla-Ruiz<sup>1, 0009-0004-2617-7303</sup>, I. Paya-Zaforteza<sup>1, 0000-0002-3995-8772</sup>, E. García-Castillo<sup>1, 0000-0003-4665-730X</sup>, P.A. Calderón-García<sup>1, 0000-0002-9783-9333</sup>

<sup>1</sup>Instituto Universitario de Investigación de Ciencia y Tecnología del Hormigón (ICITECH), Universitat Politècnica de València, Camino de Vera S/N, 46022 Valencia, Spain

email: romanrui@upv.edu.es, igpaza@cst.upv.es, esgarcas@upv.es, pcaldero@cst.upv.es

**ABSTRACT:** Fiber optic sensors (FOS) offer compelling advantages for Structural Health Monitoring (SHM). However, their application in timber structures remains underexplored. This article reviews the state-of-the-art use of FOS in timber structures and presents an experimental study conducted at the Universitat Politècnica de València. A 3-meter-span timber beam was subjected to a four-point bending test and instrumented with long-gauge strain FOS. The measured strains were used to derive stresses, which were then compared to theoretical values. The results highlight the potential of FOS for accurate stress monitoring in timber elements and contribute valuable insights to the advancement of SHM in sustainable construction.

**KEYWORDS:** Timber structures; Historic structures; Fiber optic sensors; Strain monitoring; Stress.

## 1 INTRODUCTION

The built environment is responsible for approximately 39% of global energy-related CO<sub>2</sub> emissions, of which about 11% arises from embodied emissions—those generated during the production, transportation, and installation of building materials [1]. Shifting towards a Circular Economy model is increasingly recognized as essential to mitigate this impact. Among the strategies, the rehabilitation and reuse of existing structures plays a critical role. Among the different potential construction materials, timber stands out as a sustainable material due to its low carbon footprint, high recyclability, and significant cultural value, especially in heritage buildings (see e.g. Figure 1).



Figure 1. Timber beams at “Estació del Nord”, a train station in Valencia, Spain.

Structural Health Monitoring (SHM) is a key enabler of sustainable rehabilitation strategies. SHM techniques provide continuous insights into the condition of built structures, which helps to optimize maintenance, supports resource-efficient interventions, and extends service life. Within this context, fiber optic sensors (FOS) present compelling advantages over traditional electrical sensors, offering immunity to

electromagnetic interference, high sensitivity, and multiplexing capabilities [2]. Despite growing interest in sustainable rehabilitation methods, the application of FOS in timber structures remains limited and underexplored. Most existing SHM studies have focused on concrete and steel, with relatively few addressing timber. This research seeks to fill that gap by experimentally evaluating the performance of long-gauge FOS in monitoring strain and stress distributions in a timber beam subjected to bending. The main objective is to assess the feasibility and accuracy of using FOS for SHM in timber structures, particularly in heritage or rehabilitated buildings.

The paper is structured as follows: Section 2 briefly reviews the state of the art in fiber optic monitoring of timber structures. Section 3 describes the experimental setup and testing procedure. Section 4 presents the experiment results and Section 5 discusses the performance of FOS in timber. Finally, Section 6 summarizes the main findings and outlines directions for future research.

## 2 REVIEW OF THE CURRENT STATE OF THE ART

Early explorations of fiber optic sensing in timber structures began with Sargent (2009) [3], who used Fabry–Perot interferometric FOS to monitor temperature during the kiln drying of radiata pine boards, confirming the method’s accuracy but also highlighting sensor fragility under extreme conditions. Marsili et al. (2017) [4] applied Fiber Bragg Gratings (FBGs) to both small specimens and historic timber beams (before and after carrying out a strengthening operation), successfully measuring strain and damping, and demonstrating the potential of FBGs for both laboratory and field applications. Expanding on structural monitoring and reinforcement assessment, Li et al. (2018) [5] instrumented Chinese traditional timber structures, including mortise-tenon joints, using FBGs to effectively track beam deflections and column inclinations under load. Further advancing this line of research, Helmer-Smith et al. (2021) [6] tested a scaled timber Warren truss monitored with distributed fiber sensors (DFOS),

successfully capturing strains, and highlighting the capabilities of FOS in truss systems.

More recently, advanced applications have focused on distributed sensing and bond-slip monitoring. Ernewein and Woods (2023) [7] used DFOS to study glued-in steel rods within glulam elements during pull-out tests, capturing detailed strain distributions and bond-slip behavior that surpassed the resolution of traditional strain gauges. Extending DFOS application, Felicita et al. (2024) [8] instrumented timber foundation piles and monitored the stress distribution along their length, validating DFOS accuracy and showcasing its potential for buried timber elements.

### 3 EXPERIMENT DESIGN

#### 3.1 Loading Set-Up

To evaluate the capability of FOS in monitoring the behavior of timber beams under bending, a four-point bending test was conducted, as shown in Figure 2. A sawn timber beam, graded as C18 according to the Spanish code [9], was placed on two hinged supports to simulate a simply supported condition. The dimensions of the steel plates at the supports that were in direct contact with the timber beam were 180x180x40 mm. The load was applied using a hydraulic jack placed at the center of a rectangular steel spreader beam, which transferred the force to two loading points spaced 1 meter apart. Steel plates measuring 85 mm in width and 3 mm in thickness were placed on the top surface of the timber beam at these two points to facilitate uniform load application. The total length of the tested beam was 3400 mm, with a span of 3000 mm. The beam had a depth ( $h$ ) of 202 mm and a width ( $b$ ) of 75 mm.

#### 3.2 Equipment installed

The beam's vertical displacements were recorded using two linear variable differential transducers (LVDTs). Additionally, five long-gauge strain sensors were installed on the beam using brackets screwed into the timber. Table 1 provides the detailed positions of these sensors. The gauge length of the FOS was 500 mm. Figure 3 shows the position of the sensors installed for the test, both LVDTs and FOS. Figure 4 shows a detail of the elements used to distribute the load to the beam, while Figure 5 and Figure 6 provide a detailed view of the long-gauge sensors installed at sections S1 and S2.

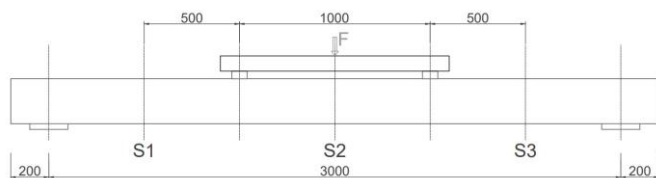


Figure 2. Loading set-up. Position of the monitored cross sections.

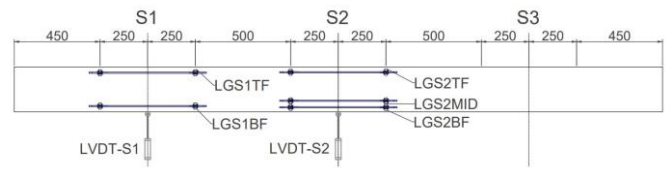


Figure 3. Sensors installed in the tested beam.

Table 1. Specifications for the sensors installed.

Sensor ID	Measuring units	Related section	Position
LVDT-S2	mm	S2	Mid-span
LVDT-S1	mm	S1	1 m from mid-span
LGS2TF	microstrains	S2	27.88 mm from the beam's top face
LGS2BF	microstrains	S2	26.58 mm from the beam's bottom face
LGS2MID	microstrains	S2	57.54 mm from the beam's bottom face
LGS1TF	microstrains	S1	30.48 mm from the beam's top face
LGS1BF	microstrains	S1	30.05 mm from the beam's bottom face



Figure 4. Central segment of the tested beam showing the loading elements.



Figure 5. FOS installed in Section S2.

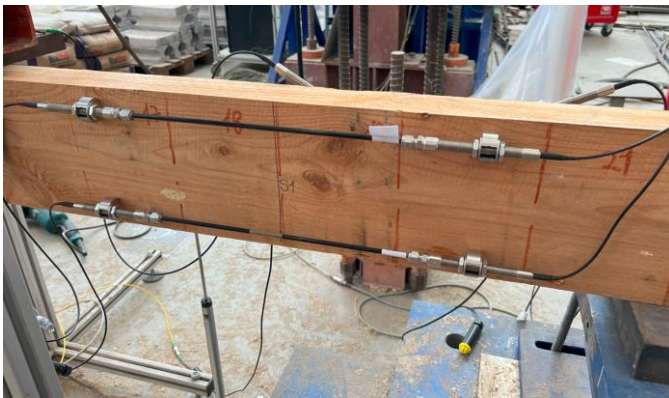


Figure 6. FOS installed in Section S1.

#### 4 RESULTS

This section presents the results obtained from monitoring the timber beam during the bending test. A step-loading protocol was employed, in which the load was incrementally increased to predefined thresholds and then held constant to allow for stabilization. Displacement control was displacement-driven, with a constant loading rate of 0.05 mm/s.

Figure 7 displays the force applied by the hydraulic jack over time, along with the displacements recorded by the LVDTs, plotted on a secondary vertical axis. The curves follow the same trend, showing that the displacements increase proportionally with the applied force. The number of steps in the displacement curves corresponds exactly to the loading steps of the applied force. The maximum recorded force was 11.19 kN, which resulted in LVDT displacements of 7.18 mm at Section S2

(LVDTs2) and 4.99 mm at Section S1 (LVDTs1).

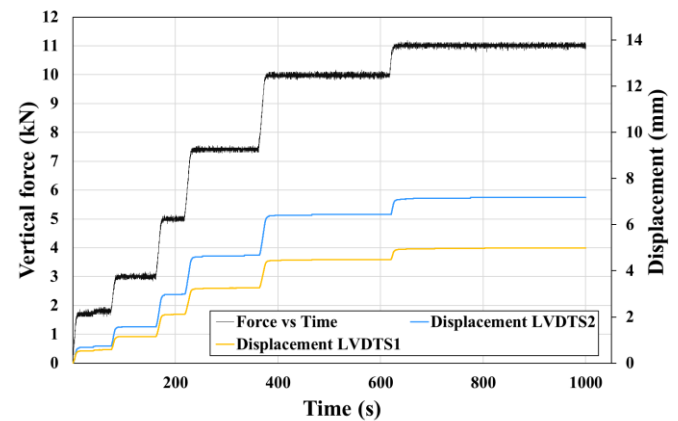


Figure 7. Force and LVDT displacements over time during the bending test.

Figure 8 and Figure 9 display the strain curves recorded by each long-gauge sensor throughout the test. Sensors installed below the geometric centroid of the beam cross section are expected to record tensile strains (negative values), while those positioned above the geometric centroid should register compressive strains (positive values). As expected, sensors LGS1TF and LGS2TF, both located above the geometric centroid, measured compressive strains and sensors LGS1BF, LGS2BF and LGS2MID measured tensile strains.

A comparison of the curves also shows that, as expected, the further a sensor is from the geometric centroid of the cross section, the greater the strain it experiences. Additionally, sensors positioned at the mid-span of the beam experienced higher strain levels than those located at Section S1, which is nearer to the support.

More specifically, the maximum recorded compressive strain at Section S2 was 590  $\mu\epsilon$ , while the maximum tensile strain reached 502  $\mu\epsilon$ . Sensor LGS2MID, located closer to the geometric centroid recorded a maximum strain of 277  $\mu\epsilon$ . LGS2BF recorded a strain 1.81 times greater than that of LGS2MID.

In contrast, the FOS located at Section S1 recorded significantly lower strain values, with a maximum compressive strain of 269  $\mu\epsilon$  and a maximum tensile strain of 155  $\mu\epsilon$ . This notable difference highlights the effect of the bending moment distribution along the beam. Since Section S2 is in the segment of the beam where the bending moment is at its maximum, higher strain values are expected and observed. Conversely, Section S1, being nearer to the supports where the bending moment is lower, experiences lower strain levels.



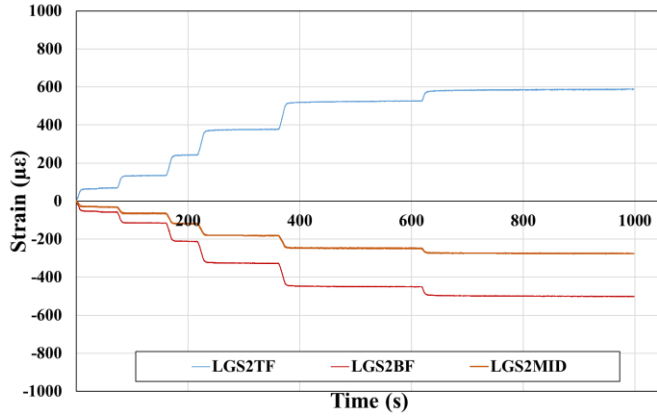


Figure 8. Strain curves for the long-gauge fiber optic sensors installed at S2.

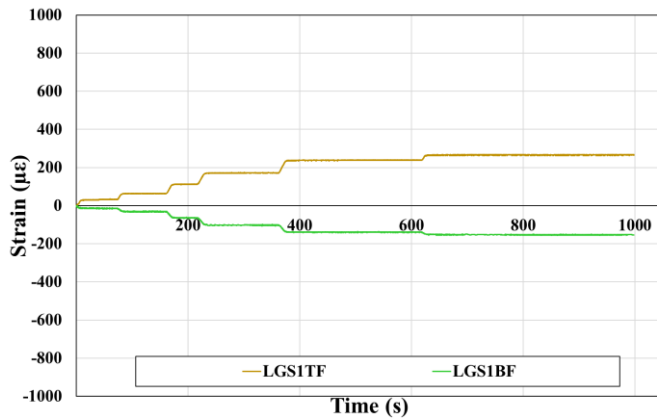


Figure 9. Strain curves for the long-gauge fiber optic sensors installed at S1.

## 5 DISCUSSION

### 5.1 Determination of the modulus of elasticity

To validate the use of fiber optic sensors (FOS) in this test, experimental stress values are compared to their theoretical counterparts.

Theoretical stresses are calculated using Equation 1, while experimental stresses are derived from Equation 2. In both equations,  $\sigma$  represents the tensile or compressive stress (in N/mm<sup>2</sup>). In Equation 1,  $M$  is the bending moment at the cross-section (N·mm),  $I$  is the moment of inertia of the cross-section (mm<sup>4</sup>), and  $y$  is the vertical distance (mm) from the location of the strain measurement to the geometric centroid of the cross-section. In Equation 2,  $\varepsilon$  is the strain measured by the FOS, and  $E_{m,g}$  is the timber modulus of elasticity (in N/mm<sup>2</sup>).

$$\sigma = \frac{M}{I} y \quad (1)$$

$$\sigma = \varepsilon E_{m,g} \quad (2)$$

The modulus of elasticity  $E_{m,g}$  can be obtained either from the Spanish code CTE-DB-SE-M, based on the timber strength

class, or measured experimentally according to UNE-EN 408:2011+A1 [10], using the expression shown in Equation 3:

$$E_{m,g} = \frac{3al^2 - 4a^3}{2bh^3 \left( 2 \frac{w_2 - w_1}{F_2 - F_1} - \frac{6a}{5Gbh} \right)} \quad (3)$$

The parameters in this equation are defined as follows:

- $a$ : the distance from a loading point to the nearest support (1 m in this test),
- $l$ : the span between supports (3 m),
- $b$  and  $h$ : the width and height of the timber beam, respectively (provided in Section 3),
- $F_2$  and  $F_1$ : two load values within a linear portion of the force–displacement curve (with a correlation coefficient  $\geq 0.99$ ),
- $w_2$  and  $w_1$ : the corresponding displacements for forces  $F_2$  and  $F_1$ ,
- $G$ : the transverse modulus of elasticity, taken from the code for class C18, with a value of 560 MPa.

Using the following values:

- $F_2 = 10990$  N,
- $F_1 = 3200$  N,
- $w_2 = 7.14$  mm,
- $w_1 = 1.66$  mm,

the calculated value of  $E_{m,g}$  is 14577 MPa.

### 5.2 Stresses at section S1

Experimental stresses calculated for section S1 were compared to their theoretical values, as shown in Figure 10. The difference between the experimental and theoretical value for LGS1TF accounts for 0.10 MPa, which is negligible. However, the difference for LGS1BF is 1.59 MPa. More specifically, theoretical calculations provided greater values of tension, but lower compression stress than those obtained from the monitored strains. The maximum theoretical stress values are 3.83 MPa (at the location of the top sensor) and 3.85 MPa (at the location of the bottom sensor), which suggest the exact same stress at the tensioned fibers and at the compressed fibers, and it is justified by the 0.31 mm difference at the installation position in relation to their respective extreme face (top face or bottom face of the beam). However, experimental results of maximum stresses for LGS1TF and LGS1BF locations are 3.93 MPa and 2.26 MPa respectively. These values denote a clear dominance of compression over tension along the length where the sensors are installed for section S1.

At this point it is worth noting that the calculations assumed several hypothesis. Stress calculated with Equation 1 assumes that the material is homogeneous and linear elastic. As it is known for timber, this constitutes a simplification, since it is a heterogeneous material, with varying properties in each direction. Local defects, such as the presence of knots, where the density of the timber grain is higher, and some variability in the direction of the timber fibers can also influence the behavior of the beam under loading, leading to differences between the compression and the tension stresses. Minor differences in the installation of the sensors to the beam can also lead to differences in the results, such as the distance from sensor LGS2TF's axis to the top face of the beam, which is 27.88 mm, while for LGS2BF is 23.54 mm. Accuracy during

the installation should be as precise as possible to reduce variability.

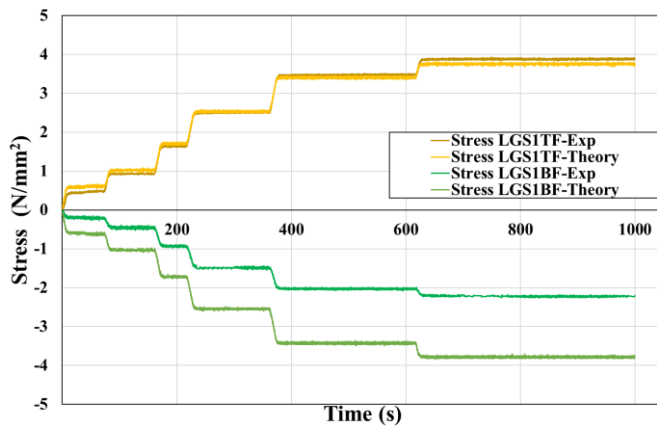


Figure 10. Theoretical stress versus experimental stresses at section S1.

### 5.3 Stresses at section S2

As shown in Figure 11, differences can be observed between the experimental and theoretical stress values for each long-gauge sensor installed at section S2. These differences are more evident when comparing the stress values at the final loading step (Step 6) of the test.

For sensor LGS2TF, located in the compression zone of the beam, the experimental stress at Step 6 is 0.68 MPa higher than the theoretical value, representing an 8% difference. In the tension zone, for sensor LGS2BF, the theoretical stress exceeds the experimental value by 1.07 MPa, resulting in a 12.75% difference. Similarly, for sensor LGS2MID (also in tension), the theoretical stress is 0.66 MPa greater than the experimental, corresponding to a 14.12% difference. These discrepancies highlight the complexity of comparing real-world measurements with simplified analytical predictions, particularly in anisotropic materials such as timber. In addition, comparing sensors LGS2MID and LGS2BF — both located in the tension zone but at different distances from the centroid — further illustrates the consistency of the results. The maximum recorded strain at LGS2MID was  $277 \mu\epsilon$ , while LGS2BF registered  $502 \mu\epsilon$ , yielding an experimental strain ratio of 1.81 as detailed in Section 4. Using Equation 1 and considering the sensors' relative positions and the maximum applied force of 11.19 kN, the corresponding theoretical stresses are 4.61 MPa for LGS2MID and 8.24 MPa for LGS2BF — a ratio of 1.79. This close agreement between theoretical and experimental ratios supports the validity of the strain measurements and suggests a good correlation between sensor position and measured mechanical response.

To provide a more comprehensive comparison, Table 2 presents the absolute values of experimental and theoretical stresses for loading steps 3 and 6, along with the corresponding percentage differences. All long-gauge sensors were installed within the region of constant bending moment, as defined by the four-point bending configuration, ensuring that there is no uncertainty regarding the bending moment acting on the segment of the beam being analyzed.

To ensure the accuracy of theoretical stress calculations, key geometric parameters were precisely measured. The vertical distances ( $y$ ) from each sensor to the beam's geometric centroid

were verified using a digital caliper, and the cross-sectional dimensions of the timber beam were also recorded with high precision. The modulus of elasticity, used to derive experimental stress values from strain measurements, was obtained through an independent experimental procedure following standard guidelines [10]. Therefore, it is not considered a source of significant error in the comparison.

The observed differences are more likely attributed to the natural anisotropy and heterogeneity of timber, including the presence of knots, cracks, grain deviations, or localized density variations. These factors can influence the mechanical response at specific cross-sectional locations and lead to deviations from the idealized behavior predicted by classical bending theory.

Table 2. Comparison of stresses at section S2 for loading steps 3 and 6.

	LGS2TF	LGS2BF	LGS2MID
Experimental stress at step 3 (MPa)	3.52	3.08	1.73
Theoretical stress at step 3 (MPa)	3.61	3.82	2.14
Difference (%)	2.49	19.37	19.15
Experimental stress at step 6 (MPa)	8.54	7.26	4.01
Theoretical stress at step 6 (MPa)	7.78	8.24	4.61
Difference (%)	8.90	11.92	13.99

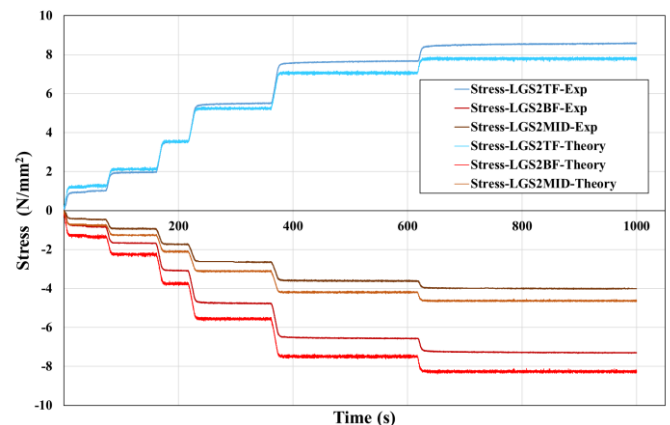


Figure 11. Theoretical stress versus experimental stress at section S2.

## 6 CONCLUSIONS AND FUTURE RESEARCH

This study focused on monitoring key parameters of a classified timber beam subjected to a four-point bending test, enabling a comparison between stresses derived from strain measurements and theoretical values based on classical strength of materials principles. The following conclusions can be drawn:

- Fiber optic sensors (FOS) are effective tools for monitoring the strain behavior of timber structural elements. The results obtained during testing showed strong agreement with the expected behavior under a step-loading protocol. FOS provided high-resolution strain data, from which stress was reliably derived

using appropriate mechanical models and material properties. This capability highlights their value in structural health monitoring (SHM) applications.

- FOS have the potential to detect localized anomalies in material behavior. For example, sensor LGS1TF-Exp exhibited a 58.7% deviation from its theoretically derived stress value, a difference which cannot be overlooked. Possible explanations include the presence of defects—such as knots or abrupt grain deviations—that alter local strain behavior. Installation-related issues may also have contributed to the anomaly.
- Precision in FOS installation is critical. The accuracy of strain measurements is highly dependent on proper sensor alignment, bonding quality, and the technician's skill. Even with optimal procedures, a certain level of uncertainty is inevitable due to the high sensitivity of these sensors (on the order of  $2\ \mu\epsilon$ ), underscoring the importance of meticulous installation and calibration.
- Further research is needed to systematically explore the causes of large deviations between measured and theoretical stress values. The nearly 59% error observed at the location of sensor LG-S1-BF is too large to be attributed solely to timber's natural variability—such as knots, fiber misalignment, or moisture content—though these factors do influence strain-stress correlation. It is therefore likely that some form of installation or operational error occurred. Future work should include defect mapping, and improved sensor validation protocols to try to isolate and quantify these effects.

## ACKNOWLEDGEMENTS

This article is part of the grant PID2021-128152NB-I00 funded by MICIU/AEI/10.13039/501100011033 and by ERDF/EU. The authors also wish to acknowledge the support received through the predoctoral grant PRE2022-103404, funded by MICIU/AEI/10.13039/501100011033 and by FSE+ (European Social Fund Plus). This grant was awarded to the first author to support his doctoral research.

## REFERENCES

- [1] World Green Building Council. Bringing Embodied Carbon Upfront: Coordinated Action for the Building and Construction Sector to Tackle Embodied Carbon. 2019.
- [2] Torres B, Payá-Zaforteza I, Calderón PA, Adam JM. Analysis of the strain transfer in a new FBG sensor for Structural Health Monitoring [Internet]. Vol. 33, Engineering Structures. Elsevier BV; 2011. p. 539–48. Available from: <http://dx.doi.org/10.1016/j.engstruct.2010.11.012>
- [3] Sargent R. Measurement of Board Temperatures during Kiln Drying Using Fiber Optic Sensors [Internet]. Vol. 37, Journal of Testing and Evaluation. ASTM International; 2009. p. 306–9. Available from: <http://dx.doi.org/10.1520/jte101914>
- [4] Marsili R, Rossi G, Speranzini E. Fibre Bragg Gratings for the Monitoring of Wooden Structures [Internet]. Vol. 11, Materials. MDPI AG; 2017. p. 7. Available from: <http://dx.doi.org/10.3390/ma11010007>
- [5] Li NL, Jiang SF, Wu MH, Shen S, Zhang Y. Deformation Monitoring for Chinese Traditional Timber Buildings Using Fiber Bragg Grating Sensors [Internet]. Vol. 18, Sensors. MDPI AG; 2018. p. 1968. Available from: <http://dx.doi.org/10.3390/s18061968>
- [6] Helmer-Smith H, Vlachopoulos N, Dagenais MA, Forbes B. Comparison of multiple monitoring techniques for the testing of a scale model timber Warren truss [Internet]. Valsangkar A, editor. Vol. 6, FACETS. Canadian Science Publishing; 2021. p. 1510–33. Available from: <http://dx.doi.org/10.1139/facets-2021-0001>
- [7] Ernewein B, Woods JE. Distributed fiber optic strain sensing in axially loaded glued-in steel rods in glued-laminated timber [Internet]. Vol. 392, Construction and Building Materials. Elsevier BV; 2023. p. 132020. Available from: <http://dx.doi.org/10.1016/j.conbuildmat.2023.132020>
- [8] Felicita M, Pagella G, Ravenshorst G, Mirra M, van de Kuilen JW. Assessment of in-situ stress distribution and mechanical properties of wooden foundation piles instrumented with distributed fiber optic sensors (DFOS) [Internet]. Vol. 20, Case Studies in Construction Materials. Elsevier BV; 2024. p. e03139. Available from: <http://dx.doi.org/10.1016/j.cscm.2024.e03139>
- [9] Código Técnico de la Edificación. Documento Básico SE-M Seguridad Estructural - Madera. Ministerio de Fomento, España, 2019.
- [10] UNE-EN 408:2011+A1. Timber structures - Structural timber and glued laminated timber - Determination of some physical and mechanical properties. AENOR, 2011+A1



# Pi-bracket fatigue sensor for crack detection monitoring near stiffeners in bridge girders

B. Telehanic<sup>1,3</sup>, A. Mufti<sup>1,3</sup>, D. Thomson<sup>2,3</sup>, B. Bakht<sup>1,3</sup> and E. Murison<sup>4</sup>

<sup>1</sup>Department of Civil Engineering, University of Manitoba, Winnipeg, Canada

<sup>2</sup>Department of Electrical and Computer Engineering, University of Manitoba, Winnipeg, Canada

<sup>3</sup>SIMTReC Centre, University of Manitoba, Winnipeg, Canada

<sup>4</sup>Manitoba Transportation and Infrastructure, Winnipeg, Canada

email: telehanb@myumanitoba.ca, aftab.mufti@umanitoba.ca, douglas.thomson@umanitoba.ca, bbakht@hotmail.com, evangeline.murison@gov.mb.ca

**ABSTRACT:** This study investigates an innovative pi-bracket sensor system integrating distributed fiber optic sensing with Brillouin Optical Time Domain Analysis to detect cracks in bridge girders near stiffeners. The system is designed to overcome challenges in crack detection at these critical locations. Experimental validation was conducted on a 3-meter steel beam featuring a welded stiffener positioned 25mm from a simulated crack. An aluminum pi-bracket served as a mounting device for the fiber optic sensor. Comparative analysis between experimental measurements and finite element simulations demonstrated the system's ability to detect crack openings as small as 0.2mm. Abaqus Finite Element Analysis predicted strain values of 145 $\mu\epsilon$ , while laboratory experiments recorded 129 $\mu\epsilon$ , a discrepancy of approximately 11%. Strain concentrations were localized to the regions where the pi-bracket was in direct contact with the beam. The strong correlation between computational models and empirical data substantiates the efficacy of the proposed sensing system. These findings highlight the system's potential for structural health monitoring of bridge infrastructure, particularly for detecting and quantifying cracks near stiffeners.

**KEY WORDS:** Structural health monitoring; Crack detection; Fiber optic sensing; Brillouin optical time domain analysis.

## 1 INTRODUCTION

Short and medium span bridges are critical components of national transportation networks, significantly contributing to economic activity. As these structures age, they become increasingly vulnerable to structural deficiencies such as reduced load-bearing capacity, accidental damage, material deterioration, fatigue cracking, and foundation problems. Of particular concern is the formation and propagation of cracks in steel bridge girders, which can severely compromise structural integrity [1, 2, 3].

Steel girders, typically constructed from web plates with welded flanges, are fundamental to bridge design, however, they are prone to cracking. These cracks often arise due to cyclic stresses caused by vehicular traffic and environmental factors. Early detection is critical to prevent unexpected service disruptions and mitigate associated economic losses [4, 5].

Advancements in distributed fiber optic sensing (FOS) systems have significantly enhanced the monitoring of bridge structures. However, a critical limitation of this technology is its inability to reliably detect cracks that form near stiffeners, components that are especially susceptible to crack initiation and propagation due to residual stresses, geometric discontinuities from welding, and stress concentrations arising from restricted deformation under repeated loading cycles [8]. Because the FOS is distributed, it is often left unattached in the vicinity of stiffeners, resulting in unmonitored zones extending 5-10 inches on either side of the stiffener, as illustrated in Figure 1. Furthermore, these unattached portions of the FOS lack the support and protection provided by the surrounding structure, rendering them more vulnerable to mechanical damage. These limitations raise concerns regarding the reliability of current monitoring systems in ensuring the structural integrity of steel bridges [1].

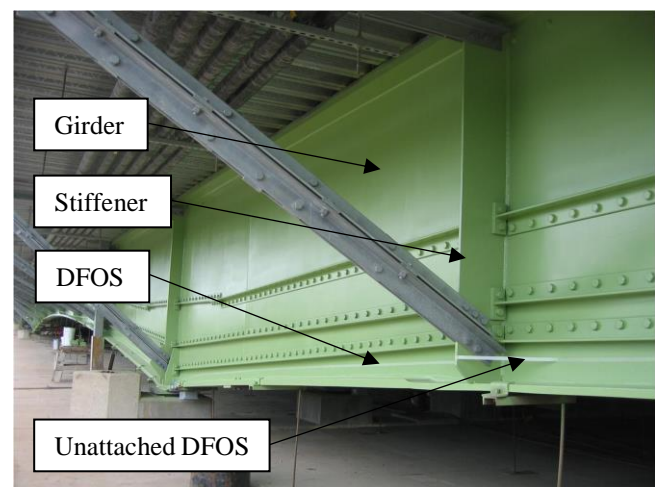


Figure 1. Steel girder with welded stiffener and DFOS in current monitoring system

This study seeks to address these challenges by evaluating a pi-bracket fatigue sensor integrated with FOS technology and Brillouin Optical Time Domain Analysis (BOTDA) for crack detection in steel girders. The pi-bracket serves as protective housing for the FOS, preventing mechanical damage while enabling crack detection near stiffeners. Conventional Structural Health Monitoring (SHM) practices often avoid attaching FOS near stiffeners due to fiber bending constraints, limited space, or risks of mechanical damage during installation.

This research aims to evaluate the pi-bracket sensor system's ability to accurately detect and monitor cracks in critical areas of a simulated bridge girder and compare its performance with

Finite Element Analysis (FEA) predictions. Ultimately, this study aims to advance the development of more reliable SHM systems, promoting enhanced safety, proactive maintenance, and extended service life for bridge structures.

## 2 METHODOLOGY AND EXPERIMENTAL SETUP

### 2.1 FEA Model

A three-dimensional finite element model was developed using ABAQUS to simulate the experimental setup (Figure 2). The model consisted of three main components: the steel girder, aluminum pi-bracket, and steel stiffener, all modeled as deformable planar shell elements with thicknesses corresponding to experimental dimensions (8.9mm for girder web, 15.7mm for girder flanges, and 3.175mm for pi-bracket). Two distinct material properties were incorporated: steel and aluminum. The simulation focused on the linear elastic behavior within the elastic region of the elastic-plastic relationship, defining only Young's modulus and Poisson's ratio for both materials. Aluminum was characterized by a Young's modulus of 69000 MPa and a Poisson's ratio of 0.33, while steel was defined by a Young's modulus of 210000 MPa and a Poisson's ratio of 0.3.

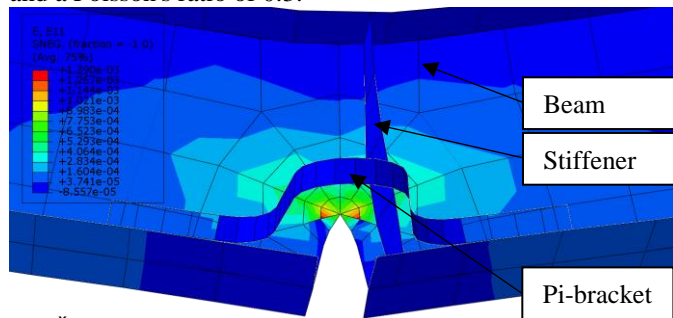


Figure 2. FEA model of the beam with the stiffener crack and pi-bracket.

The connections in the ABAQUS model between the FOS, pi-bracket, and beam were modeled as rigid interfaces using tie constraints. This modeling approach enforces identical displacements and rotations at the interface, effectively simulating a completely rigid bond between the connected components. Although this represents an idealized scenario, it is sufficient for the purposes of this study, which focuses on the ability to detect the initiation of cracks.

Regarding fiber rupture concerns, our detection system targets very small crack openings, significantly below thresholds that would risk fiber damage. Even in the unlikely event of rupture due to extreme crack propagation, the distributed nature of the FOS (with its dense sampling points) would instantly identify the failure location, enabling immediate inspector dispatch for visual assessment. This aligns with the research objective: developing a continuous monitoring system for early crack detection to support timely intervention and maintenance.

To simulate a simply supported 3-meter steel girder, appropriate boundary conditions were applied to each end of the beam. A pinned support at one end restricted U1, U2, U3, UR2, and UR3, while a roller support at the other end allowed axial displacement. The crack was explicitly defined as a stationary geometric discontinuity using a face partition at the

beam's midspan web location, extending 57mm vertically from the bottom edge of the web. The crack was defined as a contour integral, with the crack extension direction specified by selecting q-vectors. The singularity was modeled as a collapsed element side with a single node, with the mid side node parameter set to 0.3 to accurately capture the stress singularity.

The simulation employed displacement-controlled loading (crack opening 0.1mm and 0.2mm), with concentrated forces applied at the midspan of the beam. The applied displacement was defined as the relative movement between two nodes located at the same height as the pi-bracket, on either side of the crack. This approach does not imply that the entire crack opens uniformly by the prescribed amount. Instead, the displacement at the crack tip remains zero, while the maximum opening occurs at the bottom of the web, between the flanges. For example, when a 0.2 mm displacement is specified the actual opening at the crack tip is zero, and the opening at the bottom of the web is larger.

The model was primarily meshed using Quad 4-node shell elements (S4R), with Tri 3-node shell elements (S3) used in areas surrounding the crack. The S4R element is a general-purpose quadrilateral element suitable for large-strain analysis, featuring six degrees of freedom per node with bilinear interpolation.

This FEA model configuration enables accurate simulation of the beam's behavior under specified loading conditions, allowing detailed analysis of stress distributions and deformations, particularly in critical regions surrounding the crack and pi-bracket. The objective was to assess the pi-bracket sensor system's ability to detect strain changes resulting from crack formation, aligning with the study's focus on evaluating sensor performance for SHM applications.

### 2.2 Experimental Setup

The test configuration used a W250x67 (W10x45) structural steel beam in a simply supported arrangement spanning 3 meters to replicate typical in-service conditions (Figure 3). A controlled crack was introduced at midspan through precision machining, extending through the bottom flange and vertically 57 mm into the web from the beam's underside.

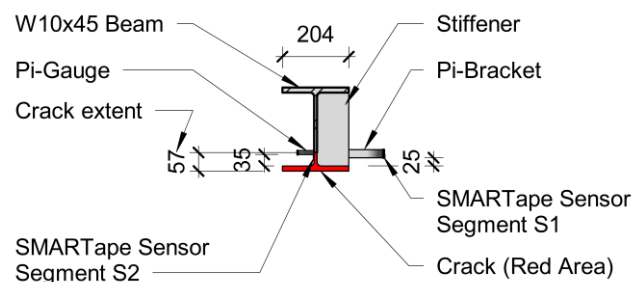


Figure 3. Beam - Section.

To simulate realistic bridge girder geometry, a transverse stiffener was welded to the beam 25 mm from the crack edge on one side. This asymmetric design was chosen to generate asymmetric stress distributions characteristic of operational bridge environments, and to allow a comparative assessment between stiffened and non-stiffened regions.

The pi-bracket assembly was installed at a vertical offset of 35 mm above the bottom flange's upper edge, with its central axis aligned to the stiffener position (Figure 4). This spatial

configuration was optimized to facilitate sensor routing while maintaining proximity to critical stress zones, enhancing detection sensitivity to crack-induced strain fields. The geometry of the stiffener, crack location, and pi-bracket placement were designed to emulate common failure scenarios observed in aging bridge infrastructure.

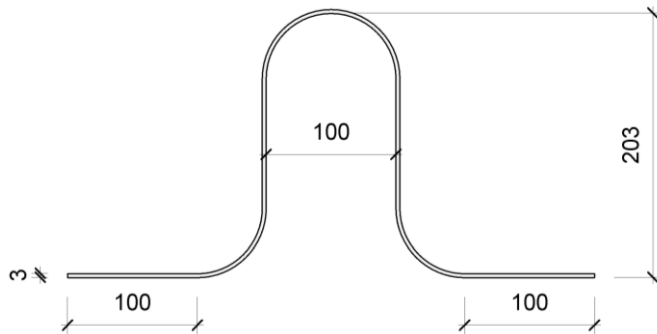


Figure 4. Pi-bracket geometry.

### 2.3 Instrumentation

The primary sensing technology used in this study was the DiTeSt SMARTape II fiber optic sensor, developed by Smartec. This high accuracy distributed strain sensor, comprising a single continuous optical fiber, was adhered to both sides of the beam using epoxy adhesive. On the front face, the sensor was routed over the simulated crack using the Pi-Bracket, which acted as a protective harness (Figure 5a). In contrast, on the rear face, the sensor was directly bonded to the surface of the beam, passing through the crack region (Figure 5b). Fiber continuity was ensured by routing it back at one end of the beam to transition from the front to the rear face.

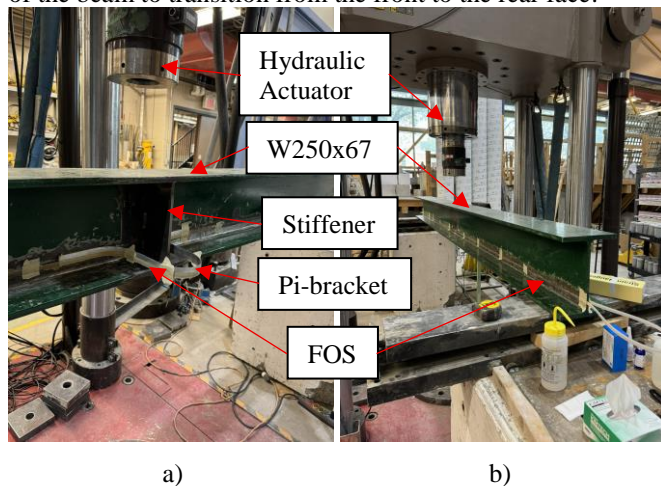


Figure 5. a) SMARTape on the front face; b) SMARTape on the rear face.

The termini of the SMARTape sensor were fusion spliced to extension fiber optic cables and connected to a Data Acquisition (DAQ) system, enabling real-time monitoring and data collection throughout the experiment. Various configurations of the Neubrescope NBX-6050 DAQ system were tested to identify optimal parameters prior to this experiment. The optimal configuration utilized a 5 cm sampling interval and a 10 cm spatial resolution. This system used

BOTDA technology to achieve high-resolution strain distribution measurements along the length of the FOS.

In the context of steel bridges, critical fatigue cracks are typically considered to be those with widths in the range of 0.1 mm to 0.3 mm, as cracks within this interval are generally regarded as significant for early intervention and maintenance [10]. According to the manufacturer's specifications, the DiTest SMARTape II fiber optic sensor can detect cracks as small as 0.2 mm, and we anticipated that the proposed pi-bracket system would achieve comparable performance. It is important to note that the objective of this study is to evaluate the ability of the pi-bracket sensor system to accurately detect and monitor the presence of cracks, rather than to quantify their exact widths. The primary goal is to determine whether the system can detect the initiation of a crack and enable the immediate intervention of an inspector for further evaluation. This approach supports proactive maintenance and timely intervention, which are critical for ensuring the safety and longevity of bridge infrastructure.

### 2.4 Fiber Optic Sensor Calibration

The initial strain measurements lacked sufficient resolution to clearly identify the positions of the beam and pi-bracket along the FOS, as shown in Figure 6.

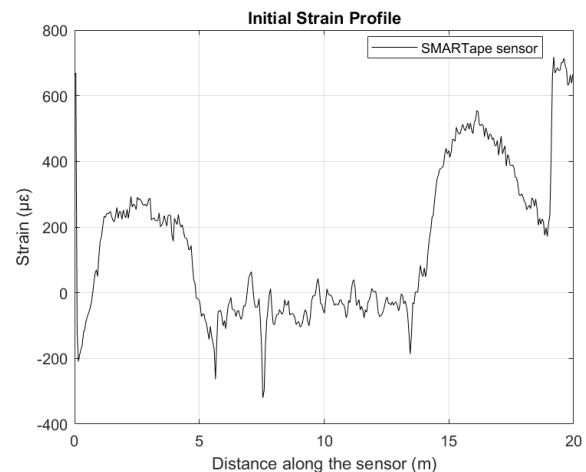


Figure 6. Initial calibration strain profile.

To address this limitation, a thermal localization method was used to enhance spatial resolution and accurately determine key positions. This involved applying localized heat to specific points on the beam, including both ends and the pi-bracket apex. The resulting strain response was recorded and compared to the initial unheated strain profile to isolate the thermal effect.

Thermal localization was employed to precisely determine the positions of the beam faces and the pi-bracket along the FOS strain profile (Figure 7). In the experimental setup, a single, continuous SMARTape sensor was routed from the front to the rear face of the beam, enabling comprehensive strain measurements across the entire structure. By applying thermal localization, the locations of key structural features, such as the front face, back face, and the pi-bracket, were accurately mapped onto the strain profile. Specifically, Sensor S1 corresponded to the portion attached to the front of the beam, spanning from 5.75 meters (A) to 9.35 meters (C) along the sensor length, with the pi-bracket located at 7.55 meters (B). Sensor S2 referred to the segment affixed to the rear of the



beam, extending from 10.25 meters (D) to 13.25 meters (E), with the crack opening situated at 11.75 meters.

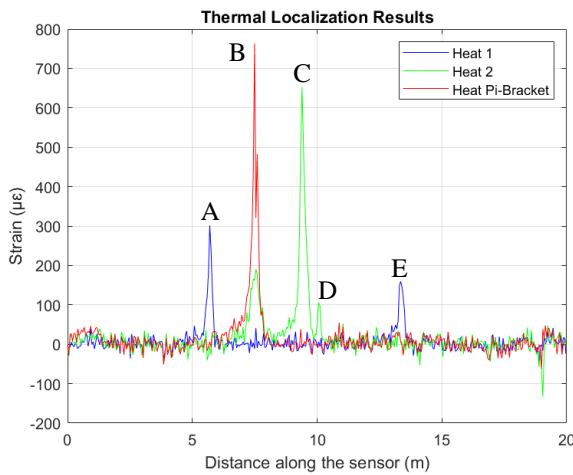


Figure 7. Thermal localization of FOS segments.

Figure 8 provides a comprehensive schematic representation of the entire FOS configuration, illustrating the spatial relationships between the SMARTape II sensor and the pi-bracket.

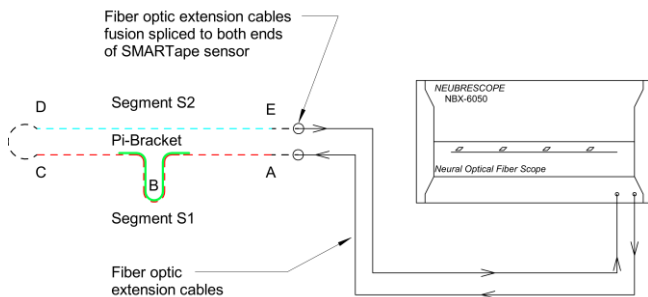


Figure 8. Schematic diagram of fiber optic sensor.

## 2.5 Experimental Procedure

The experimental protocol was designed to rigorously assess the efficacy of the FOS and pi-bracket for crack detection and monitoring. This process involved a sequence of executed stages, beginning with initial configuration and calibration. The experimental apparatus, comprising the beam, pi-bracket with attached FOS and pi-gauge, was interfaced with the DAQ system. The Neubrescope NBX-6050 was adjusted to its optimal parameters, and the FOS was calibrated to ensure measurement accuracy.

According to the manufacturer's specifications, the DiTest SMARTape II fiber optic sensor can detect cracks as small as 0.2 mm [6]. We anticipated that the proposed pi-bracket system would achieve comparable performance. The static load experiment was conducted under controlled laboratory conditions at an ambient temperature of 19.8°C. The crack opening was controlled by a pi-gauge (PI-5-100, Tokyo Sokki Kenkyujo) with a resolution of 0.001 mm and an accuracy within  $\pm 1\%$  according to the manufacturer, which was installed at the same height as the pi-bracket to ensure precise crack width [9]. Strain data from the SMARTape sensor were collected for the no-crack condition (referred to as the “initial

crack”), as well as for crack opening widths of 0.1 mm and 0.2 mm, with baseline readings taken before load application.

A hydraulic actuator applied midspan loading to induce crack opening. The experiment used displacement control, pausing at a 0.1 mm crack width to record load and beam displacement data (Table 1). Strain measurements were taken at this point. The load was then increased to achieve a 0.2 mm crack width, where additional readings were obtained. Multiple measurements were taken and averaged to generate strain profiles for each crack opening width.

## 3 RESULTS AND DISCUSSION

### 3.1 FEA Results

The FEA model developed in Abaqus was used to simulate the experimental setup and to investigate the strain behavior of the pi-bracket sensor system under controlled crack opening conditions. This modeling enabled a detailed examination of strain patterns along the FOS.

Two distinct strain profiles were analyzed, as shown in Figure 9. The first strain profile (blue line in Figure 9) represents a scenario without the pi-bracket, reflecting current SHM practices where a continuous FOS is left unattached near stiffeners, resulting in an unmonitored zone of about 10 cm on each side due to installation constraints. This profile serves as a baseline for comparison, illustrating the strain distribution in the absence of the pi-bracket's influence.

The second profile (red line in Figure 9) incorporates the pi-bracket, capturing strain measurements continuously along the entire beam span, including the areas near stiffeners. The green vertical lines in Figure 9 identify the position of the pi-bracket along the strain profile, providing spatial reference points for interpreting the sensor configuration.

To match the DAQ averaging from the experiment, strain profiles were averaged between two points along the path.

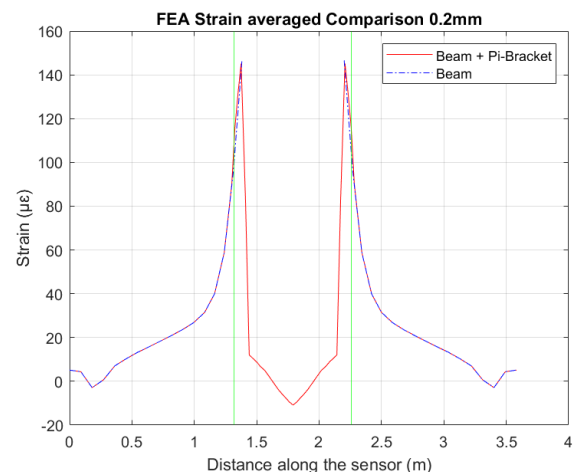


Figure 9. FEA strain profiles for 0.2mm crack: Comparison of Beam with and without Pi-Bracket.

Figure 9 demonstrates that the pi-bracket allows for uninterrupted strain monitoring across the region near the stiffener and crack, effectively eliminating the unmonitored gaps seen in the baseline scenario. Specifically, the region between 1.3 m and 2.2 m along the sensor corresponds to the segment of the FOS routed through the pi-bracket for the second modeled scenario. In contrast, for the first scenario

without the pi-bracket, the strain profile is interrupted to reflect current practice where the FOS is left unattached to the surface near stiffeners and therefore does not register any strain in these regions.

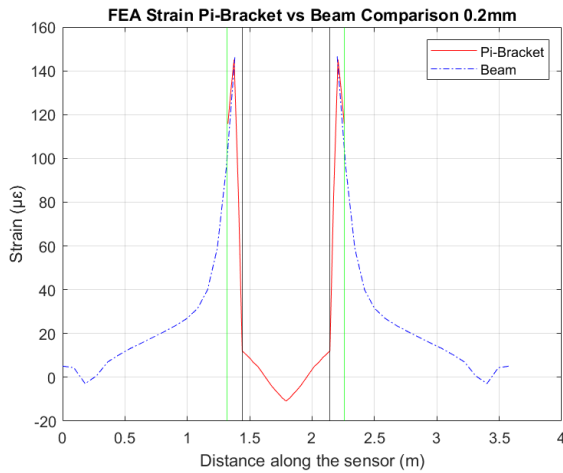


Figure 10. FEA strain profile of Pi-Bracket for 0.2mm crack: Identification of contact and non-contact Pi-Bracket regions.

Figure 10 further isolates the strain response of the pi-bracket section from the overall profile shown in Figure 9, again for a 0.2 mm crack opening. In this figure, black vertical lines indicate the portions of the pi-bracket that are not attached to the beam, while the areas marked by green vertical lines on either side represent the sections of the pi-bracket that are glued to the beam. This distinction is important for interpreting the strain distribution, as the attached and unattached regions of the pi-bracket exhibit different mechanical behaviors due to their interaction with the beam.

For further clarification, Figure 11 provides a schematic of the pi-bracket, highlighting the attached and unattached regions relative to the beam, which aids in interpreting the strain profiles in Figures 9 and 10.

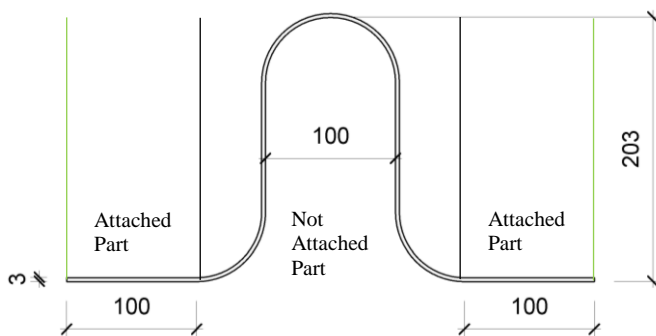


Figure 11. Pi-bracket – part identification

These FEA results demonstrate the effectiveness of the pi-bracket in capturing and distributing strain from the crack region, allowing for continuous monitoring even near critical features such as stiffeners. This provides a valuable reference for comparison with the experimental data.

### 3.2 Experimental Results

The experimental phase of this investigation yielded extensive strain data collected by the SMARTape FOS system. These measurements provide valuable insights into the

performance of the pi-bracket sensor configuration under controlled crack propagation conditions. Figure 12 displays the averaged strain profiles derived from multiple measurements, showing the sensor's response to progressive crack opening widths of 0.1 mm and 0.2 mm, as well as the initial state with no crack for direct comparison before and after crack initiation. The green vertical lines in Figure 12 identify the strain segments S1 and S2: S1 corresponds to the front face of the beam, where the FOS is routed via the pi-bracket, and S2 corresponds to the back face of the beam, where the FOS is attached directly over the crack (since there was no stiffener on this side). This setup, with the stiffener welded to one side only, allows for a direct comparison of the strain profiles between both regions.

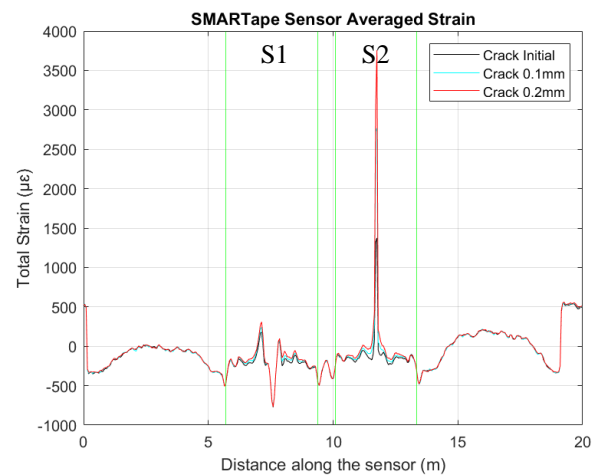


Figure 12. SMARTape averaged strain profiles.

Figure 13 presents the strain profiles obtained by subtracting the initial strain profile (no crack condition) from those measured at 0.1 mm and 0.2 mm crack openings. This approach isolates the strain response resulting specifically from crack widening, eliminating any residual or pre-existing strains within the FOS. The data indicates a significantly higher strain value (2382.1 µε) recorded by the sensor section S2, which was directly bonded over the crack, compared to the maximum strain recorded by sensor section S1, distributed over the pi-bracket (129.1 µε). All the results are summarized in Table1.

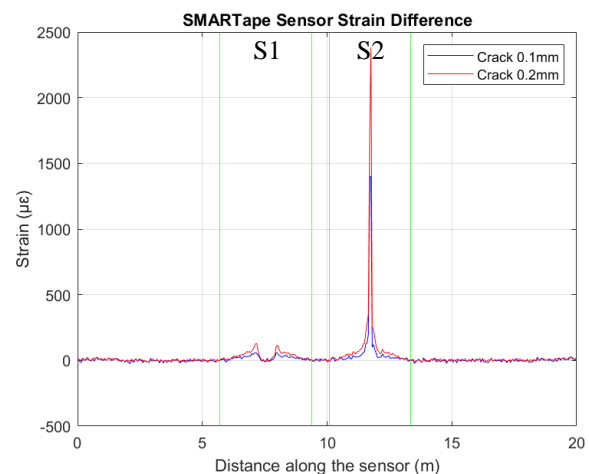


Figure 13. SMARTape strain profiles isolating crack-induced strain.

Table 1. Experiment and FEA Results.

Experiment						FEA Simulation		
Crack width [mm]	Load [kN]	Beam displacement [mm]	S1 Strain max. [ $\mu\epsilon$ ]	Strain Pi-Bracket Crown [ $\mu\epsilon$ ]	S2 Strain max. [ $\mu\epsilon$ ]	Strain Pi-Bracket Crown [ $\mu\epsilon$ ]	Strain Pi-Bracket max. [ $\mu\epsilon$ ]	Strain Beam no bracket max. [ $\mu\epsilon$ ]
0	0	0	0	0	0	0	0	0
0.1	15.9	-1.26	60.6	-8.3	1402.9	-5.4	72.95	73.7
0.2	31.9	-2.38	129.1	-11.04	2383.1	-10.8	145.14	146.6

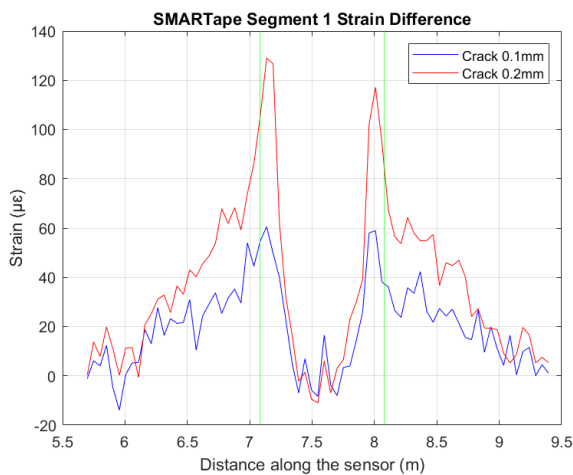


Figure 14. Detailed strain profiles for Section S1.

Figure 14 presents a detailed analysis of the strain profiles for section S1, which includes the pi-bracket at its center. The green vertical lines indicate the position of the pi-bracket along the strain profiles. Although the data exhibits some residual noise, the overall trends in the strain profiles demonstrate the sensor's capacity to detect strain changes induced by crack opening, even when mediated by the pi-bracket. Potential sources of noise include environmental vibrations and temperature fluctuations. The data from S1 provides insights into how the pi-bracket influences strain distribution compared to the direct measurement at the crack location (S2).

### 3.3 Comparison

This section presents a comparative analysis of experimental results obtained from SMARTape sensor measurements and FEA predictions, evaluating the efficacy of the pi-bracket sensor system for crack detection near stiffeners. The comparison focuses on strain measurements at critical locations, specifically the pi-bracket and crack-adjacent regions (Figures 15, 16).

FEA simulations predicted a maximum strain of 145.1  $\mu\epsilon$  in the pi-bracket at the location of direct beam attachment for a 0.2 mm crack opening. Experimentally, the maximum strain recorded by sensor section S1, distributed over the pi-bracket, was 129.1  $\mu\epsilon$  for an equivalent crack opening (Figure 15). Again, the green vertical lines indicate the position of the pi-bracket along the strain profile. This

represents an approximate 11% discrepancy between the FEA prediction and the experimental measurement. The observed level of agreement suggests that the numerical model adequately predicts the strain behavior of the pi-bracket under the applied loading conditions.

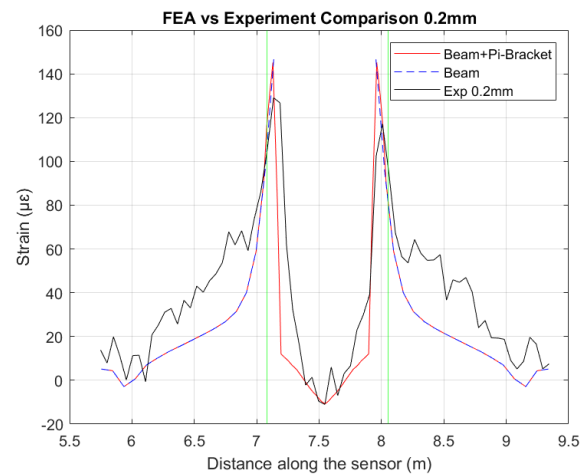


Figure 15. FEA vs Experiment comparison for 0.2mm crack.

Figure 16 presents the same strain results as Figure 15 but focuses exclusively on the strains within the pi-bracket for both the FEA simulations and laboratory experiment at a 0.2 mm crack opening.

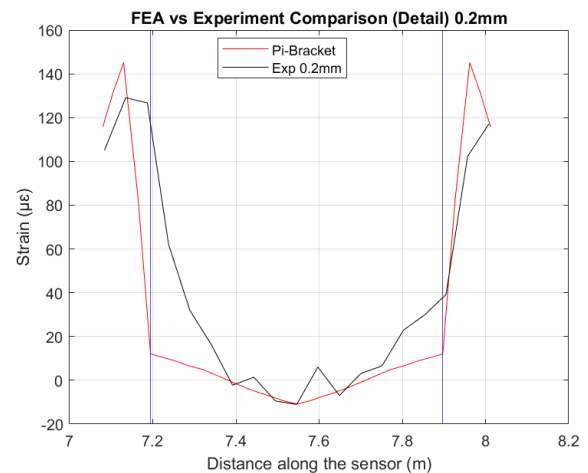


Figure 16. FEA vs Experiment comparison of Pi-Bracket for 0.2mm crack.



Figure 16 illustrates the separation of the unattached central region of the pi-bracket from the beam by blue vertical lines, distinguishing it from the attached areas on either side. The FEA predicted a maximum strain of  $-10.8 \mu\epsilon$  at the crack tip for a 0.2 mm crack opening. Experimentally, the SMARTape sensor section S1 recorded a strain of  $-11.04 \mu\epsilon$  at the pi-bracket crown (Figure 15), demonstrating close agreement with the FEA results.

Although the strain magnitudes at the pi-bracket crown were relatively small compared to those measured directly over the crack ( $2383.1 \mu\epsilon$ ), the SMARTape sensor affixed to the beam-bonded portions of the pi-bracket successfully detected the crack, registering strains of  $129.1 \mu\epsilon$  versus  $145.1 \mu\epsilon$  predicted by FEA. This 11% discrepancy validates the numerical model's capability to simulate the pi-bracket's behavior under crack propagation while highlighting the sensor system's sensitivity.

#### Key Findings:

**Validation of Computational Framework:** The strong correlation between experimental strain measurements ( $129 \mu\epsilon$ ) and FEA predictions ( $145 \mu\epsilon$ ) confirms the reliability of the numerical model in representing the pi-bracket response to crack-induced strain.

**Strain Gradient Localization:** Elevated strain values were predominantly localized at the crack interface, with sensor section S2 (directly over the crack) showing significantly higher strains than section S1 (pi-bracket region). This confirms the influence of geometric discontinuities on strain distribution.

**Detection Validation:** The pi-bracket sensor system demonstrated sufficient sensitivity to detect crack initiation, with strain magnitudes large enough to be readily observed.

**Pi-Bracket Efficacy:** The pi-bracket functions effectively as both a strain-transfer mechanism and a protective interface for the fiber optic sensor, supporting its potential integration into SHM systems.

The observed 11% difference between experimental and simulated strains can be attributed to simplifications in the FEA model, real-world experimental factors such as sensor performance and data acquisition variability, and mesh density limitations imposed by the software version used. Despite these factors, the overall agreement substantiates the pi-bracket sensor system's effectiveness for crack detection in bridge girders.

Despite these discrepancies, the overall agreement between the experimental results and FEA predictions validates the effectiveness of the pi-bracket sensor system for crack detection in bridge girders. The observed 11% discrepancy suggests that simulation captures experimental behavior with reasonable accuracy, as expected.

### 3.4 Advantages of the Pi-bracket Sensor System

The pi-bracket sensor system provides improved accuracy in detecting cracks near stiffeners, which are typically challenging to monitor. It functions as a protective harness, shielding the continuous FOS from mechanical damage, a common issue when sensors are left unattached around stiffeners due to bending limitations. This design enables uninterrupted and direct strain measurements along the entire length of the girder, including critical regions near stiffeners.

By integrating BOTDA technology, the system simplifies data acquisition and demonstrates strong alignment with FEA predictions. This combination offers a reliable and efficient approach for validating computational models and facilitating proactive bridge maintenance strategies.

### 3.5 Real-World Applicability, Limitations, and Capabilities

The findings of this study highlight the potential of the pi-bracket sensor system for practical application in bridge infrastructure, particularly for monitoring high-risk areas near stiffeners. The system is recommended for use in both new bridge construction and retrofitting existing structures to enable targeted monitoring of these critical regions. Its localized measurement capability allows for deployment in areas prone to cracking, while the pi-bracket serves as a protective harness for the FOS.

It should be emphasized, however, that the authors do not recommend the use of this system for monitoring existing cracks. Given the higher cost of FOS compared to conventional methods such as strain gauges, it is not cost-effective for short-term monitoring where the sensor would be installed, the crack repaired at some point, and then the sensor removed or replaced. Instead, this system is best suited for long-term, continuous monitoring, where the FOS is permanently attached to the surface of the girder. This makes it particularly advantageous for bridges that are approaching or have exceeded their intended service life, especially in cases where local authorities lack the financial resources for comprehensive retrofitting or replacement. In such scenarios, the pi-bracket sensor system provides a cost-effective solution for ongoing structural health monitoring, enabling proactive maintenance and extending the operational lifespan of critical infrastructure. Furthermore, the system is well-suited for deployment immediately following crack repair, to monitor the repaired region and prevent recurrence.

It is important to recognize that this system has certain limitations. The installation process can be complex, and environmental factors may influence performance. Additionally, the initial cost of implementation may exceed that of traditional methods, although the long-term benefits could outweigh these expenses. Furthermore, experimental validation was limited to a single beam, necessitating further testing on larger-scale structures to confirm its effectiveness.

Despite these constraints, the pi-bracket sensor system offers several advantages, including accurate crack detection, quantitative strain measurement, remote monitoring capabilities, and integration with FEA models. Its protective design enhances sensor durability and reliability. These attributes make it a valuable tool for improving crack detection in bridges, contributing to enhanced safety, reliability, and longevity of critical infrastructure.

While the initial cost of the pi-bracket FOS system may exceed that of traditional methods, its long-term benefits provide significant value. The system enables continuous, real-time monitoring of strain and crack development, allowing for early detection and timely maintenance interventions that enhance structural safety and reliability. This proactive approach helps extend the service life of

bridges by preventing severe damage and delaying costly retrofits or replacements. Additionally, continuous monitoring reduces the need for frequent manual inspections, lowering maintenance costs and minimizing traffic disruptions. The protective design of the pi-bracket also improves sensor longevity, reducing replacement frequency.

It is essential to emphasize that the primary objective of this study was not to investigate fracture mechanics or crack interaction phenomena but rather to evaluate the pi-bracket sensor system's ability to detect early-stage cracks. This capability facilitates preventative measures against potential structural failures in bridge infrastructure.

Given the limitations of existing inspection protocols [3, 7], which rely heavily on periodic manual assessments, this system offers a continuous real-time monitoring solution. It enables immediate crack detection and automated alert generation, allowing for timely deployment of inspectors for detailed visual examination and initiation of necessary repairs.

To address challenges associated with fatigue loading and environmental variations in real-world conditions, future implementations could incorporate frequent data acquisition (e.g., every five minutes). By subtracting consecutive strain measurements, the system could isolate strain changes attributable solely to crack formation while minimizing the influence of dynamic bridge responses or environmental factors. Further investigation is needed to validate this differential approach under complex loading scenarios. Additionally, research should explore the effects of temperature fluctuations and determine optimal averaging times to enhance accuracy and reliability.

### 3.6 Recommendations for Future Research

Future research should refine the FEA model with higher-resolution meshing to better match experimental results. The pi-bracket system also requires testing under dynamic and fatigue loading, ideally on full-scale bridges, to evaluate durability and real-world performance. Laboratory testing at a constant 19.8°C does not account for temperature variations; therefore, it is recommended to assess temperature effects to distinguish them from crack-induced strains. Additionally, future work should address detection threshold quantification and evaluate false-alarm rates. Developing standardized mounting protocols, including adhesive choice and bracket alignment, will improve field deployment consistency. Finally, cost-benefit analyses comparing system costs to savings from early crack detection are essential to support practical adoption.

## 4 CONCLUSIONS

This study demonstrates the efficacy of the pi-bracket sensor system as a viable method for crack detection near stiffeners in bridge girders, exhibiting reliable detection capabilities for crack opening widths of 0.2 mm. The FOS distributed over the Pi-bracket recorded a strain of 129  $\mu\epsilon$  at a 0.2 mm wide crack opening. Comparative analysis between FEA and laboratory experiments utilizing a FOS provided significant insights into the pi-bracket sensor's performance. The concordance between experimental

results and Abaqus simulations corroborates the system's effectiveness and reliability, illustrating the robustness of both the sensor and the modeling approach employed for design optimization.

The pi-bracket configuration successfully addresses the challenge of monitoring traditionally inaccessible areas near stiffeners, while the integration of BOTDA sensing facilitated reliable distributed measurements along the beam length. These findings indicate that the pi-bracket sensor system presents a promising and practical solution for SHM of bridge infrastructure, particularly in critical regions susceptible to fatigue cracking.

Future research directions may include comparative analysis of girder strain profiles under two loading conditions, first resulting in crack openings of 0.2 mm, versus the same load applied to an uncracked girder. The primary objective would be to isolate and quantify the strain variations attributable solely to crack formation. To achieve this, the strain profile of the uncracked girder to be subtracted from that of the cracked girder under identical loading conditions. This approach effectively eliminates the influence of the applied load, revealing the strain signature specific to the presence and severity of the crack.

## ACKNOWLEDGMENTS

The authors would like to express their sincere gratitude to Research Manitoba for providing the necessary funding to support this project. Additionally, we appreciate the administrative support provided by Charleen Choboter, whose assistance has been invaluable throughout the project's duration and beyond.

## REFERENCES

- [1] Mufti A., Thomson, D., Inaudi, D., Vogel, H. M. & McMahon, D. Crack detection of steel girders using Brillouin optical time domain analysis. *Journal Civil Structural Health Monitoring*. (2011) 1: 61-68. 2011.
- [2] Lydon, M., Taylor, S.E., Robinson, D., Mufti, A. & O'Brien, E. J. Recent developments in bridge weight in motion (B-WIM). *Journal of Civil Structural Health Monitoring* 6, 69-91. 2016.
- [3] Raeisi, F., Mufti, A., and Thomson, D. J. A finite-element model and experimental investigation of the influence of pre-straining of wire on the sensitivity of binary crack sensors. *J. Civil Struct. Health Monit.*, 8(4), 673-687. 2018.
- [4] Mufti, A. A. Structural health monitoring of innovative Canadian civil engineering structures. *Struct. Health Monit.*, 1(1), 89-103. 2002.
- [5] Raeisi, F., Mufti, A., Algohi, B. and Thomson, D. J. Placement of distributed crack sensor on I-shaped steel girders of medium-span bridges, using available field data. *Structural Control Health Monitoring*. 2019 (26). 2019.
- [6] Roctest. DiTeSt SMARTape II Strain Sensor. n.d.
- [7] Ettouney, M. M., and Alampalli, S. *Infrastructure health in civil engineering: Theory and components*. Springer, New York. 2012.
- [8] Russo, F. M., Mertz, D. R., Frank, K. H., and Wilson, K. E. Design and evaluation of steel bridges for fatigue and fracture – Reference manual. Report No. FHWA-NHI-16-016, U.S. Department of Transportation, Federal Highway Administration, National Highway Institute, Washington, DC. 2016.
- [9] Tokyo Sokki Kenkyujo Co., Ltd. Pi Gauge for Crack Width Measurement: PI-5-100, PI-5-200. 2024.
- [10] Federal Highway Administration (FHWA). *Steel Bridge Design Handbook: Design for Fatigue and Fracture*. FHWA-IF-12-052 – Vol. 12, November 2012.



## Session 5

# Implementing Structural Monitoring in Daily Practice: Challenges and Solutions



## Monitoring of civil engineering structures – current and future use cases

Joyal K. George<sup>1</sup>, Kristian von Wangenheim<sup>1</sup>, Felix Kaplan<sup>1</sup>, Ronald Schneider<sup>2</sup>, 0000-0002-6319-9657,  
Iris Hindersmann<sup>3</sup>, 0000-0002-9875-1106

<sup>1</sup>Landesbetrieb Straßenwesen Brandenburg, Lindenallee 51, 15366 Hoppegarten, Germany

<sup>2</sup>Bundesanstalt für Materialforschung und –prüfung (BAM), Unter den Eichen 87, 12205 Berlin, Germany

<sup>3</sup>Bundesanstalt für Straßenwesen (BASt), Brüderstraße 53, 51427 Bergisch Gladbach, Germany

email: JoyalKannampuzha.George@LS.Brandenburg.de, Kristian.vonWangenheim@LS.Brandenburg.de,  
Felix.Kaplan@LS.Brandenburg.de, ronald.schneider@bam.de, Hindersmann@bast.de

**ABSTRACT:** Monitoring represents an effective approach for addressing the diverse challenges associated with the maintenance of civil engineering structures. It contributes to improving both the availability and safety of these structures. By increasing the amount of information available about the structure, monitoring supports better-informed decisions regarding its preservation. Due to the complexity of monitoring applications, specific use cases are outlined. A key advantage of these use cases is that new technologies can be tested within well-defined and limited scopes. The use cases “monitoring of known, localized damage,” “monitoring of known deficits identified through reassessment or resulting from outdated design procedures” and “monitoring aimed at assessing traffic loads and their effects” currently account for the majority of implemented monitoring measures. Their practical implementation is demonstrated through case studies from the Brandenburg State Road Authority. Additional use cases, such as “monitoring to support structural inspections” - for example through the use of imaging techniques - and “monitoring of major structures,” such as large viaducts, are gaining importance, with initial practical examples already present in Europe. Future applications reveal potential for expanded use, particularly in the context of “monitoring to support predictive lifecycle management.” This will become increasingly important in the implementation of digital twins, as announced in the national BIM master plan. Furthermore the concept of a “Birth Certificate” is intended to establish a reference state of the structure prior to commissioning, which can then be used for comparison with future measurements over time. The integration and interaction of these individual use cases pave the way for the implementation of digital twins.

**KEY WORDS:** STRUCTURAL HEALTH MONITORING, USE CASES, BRIDGES, DIGITAL TWIN

### 1 INTRODUCTION

Currently, the maintenance management of civil engineering structures is characterized by a reactive approach, where interventions are only initiated once visible damage has occurred. The introduction of a predictive lifecycle management strategy offers considerable potential to fundamentally improve the reliability, resilience and long-term availability of infrastructure systems.

Today’s civil engineering structures are confronted with a growing set of challenges — including aging infrastructure, significant maintenance backlogs, rising traffic loads, and a shortage of qualified personnel to plan and carry out necessary maintenance activities.

These challenges are contrasted by advancements in the field of digitalization. Examples include planning with Building Information Modeling (BIM), data analysis using artificial intelligence (AI) methods, the implementation of digital twins, and the use of augmented or virtual reality (AR/VR) for periodic condition assessment as part of structural inspections. These technologies -including the use of monitoring systems as highlighted in this article - can contribute significantly to supporting the objectives of structural maintenance. By combining these various methods, a holistic evaluation of digitally available information becomes possible, paving the way for more efficient, proactive, and integrated infrastructure management.

### 2 CURRENT USE OF MONITORING ON FEDERAL HIGHWAYS

This article follows the definition of monitoring provided in the DBV (German Concrete and Construction Technology Association) guideline. According to this definition, monitoring describes the overall process of recording, analyzing, and evaluating structural responses and/or loads using a measurement system over a representative period of time (i.e., temporal development of the measured variable; continuous, periodic, or event-based measurements, either global or local) [1].

Monitoring is currently limited to addressing existing damages and deficits, as shown by a survey conducted by the German Federal Ministry for Digital and Transport (BMDV) among state road authorities and the Federal Highway Company. The survey, conducted in 2020, identified approximately 100 monitoring applications, which primarily involved bridges built between 1960 and 1980. The main reason for implementing monitoring was to capture structural responses, typically using deformation and temperature sensors [2].

There are several reasons why the use of monitoring on bridges along federal highways remains relatively limited. One major factor is the lack of specialized knowledge regarding the implementation of monitoring. This gap can be addressed through the development and application of standardized guidelines such as the DBV leaflet “Monitoring: Planning,

Contracting, and Operation,” the DGZfP (German Society for Non-Destructive Testing) leaflet B 09 “Continuous Monitoring of Structures,” and the pre-published report “Guidelines for Strategic Monitoring of Structures” [1; 3; 4].

Professional training, along with the involvement of engineering firms and specialist consultants for the various aspects of monitoring, can also provide valuable support. Another key barrier is the difficulty in demonstrating the economic benefit of monitoring. The methodology presented in the research project “Economic Analysis of Monitoring Measures” for evaluating the cost-effectiveness and added value of monitoring can help encourage broader adoption [5]. The high complexity of the topic - particularly regarding the planning, implementation, and evaluation of monitoring measures - is another limiting factor. In this regard, the use of defined application cases and the step-by-step introduction of new technologies within clearly defined and manageable scopes can provide effective support.

### 3 USE CASES MONITORING

The implementation of use cases is a strategy to increase the use of monitoring. Use cases can be derived from project objectives and represent processes for achieving those objectives [6]. The advantage of use cases is that the use of new technologies can be tested in defined and limited areas, allowing obstacles to be overcome. The monitoring use cases existing in the federal highway sector are shown in Figure 1.

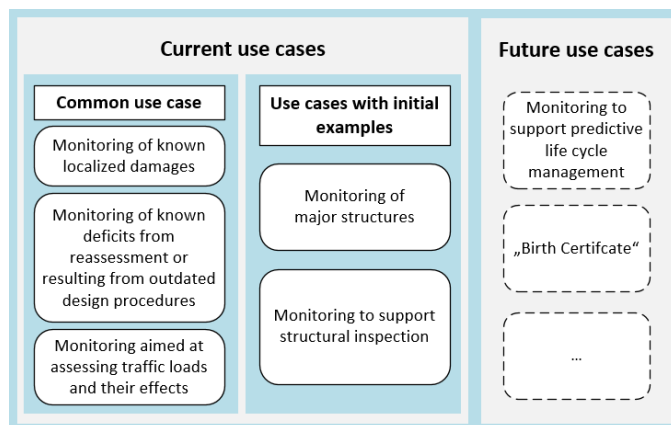


Figure 1. Monitoring use cases.

#### 3.1 Common use cases

The use cases of monitoring of known localized damages, of known deficits from reassessment or resulting from outdated design procedures and using monitoring to determine loads and loads effects representing the most common use cases in Germany. These use cases are employed to address specific questions regarding the civil engineering structures, their condition, and its development over time. Starting from known damages or deficits, a monitoring concept is developed that is tailored to the structure and the specific question at hand.

##### Monitoring of known localized damages:

In this case, a local monitoring system is typically deployed. This local monitoring provides a good opportunity for monitoring the progression of damage. By monitoring the local condition, an estimation of further local developments can be

made. This approach serves to extend the remaining service life and increase safety.



Figure 2. Bridge over the DB AG facilities along the B1 in Brandenburg an der Havel.

This use case is implemented on the bridge over the facilities of the Deutsche Bahn AG (DB AG) along the B1 in Brandenburg a der Havel (Figure 2). The structure was built in 1971 and is a single-span bridge with a span length of 47 meters. Separate, parallel superstructures carry the two traffic lanes. Their cross-sections are nearly identical and consist of two steel box girders and an orthotropic deck plate.

Numerous damages were identified on the structure during the structural inspection. These include, among others, cross-sectional reductions due to corrosion, fatigue cracks in the deck, and an abnormal positioning of the roller bearings. An object-specific damage analysis (OSA) demonstrated that the bearing positions are due to misalignment of the abutments caused by settlement. Geodetic measurements of the abutments showed that this process has not yet stabilized, indicating that further tilting is to be expected. Since the deformation capacity of the roller bearings is already highly stressed, permanent monitoring of the bearing movements is required.



Figure 3. Monitoring system on the bridge bearing.

This monitoring task is realized by installing inductive displacement transducers on each roller bearing (Figure 3) [9]. This allows for the monitoring of the remaining available bearing travel to ensure it is not exceeded. To identify long-

term trends, the measurement data from the temperature monitoring system of the superstructure are also used. Over the years, a nearly linear relationship between bearing movement and temperature has been observed (Figure 4). Changes in the regression relationship between temperature and bearing movement can serve as an indicator of a system change.

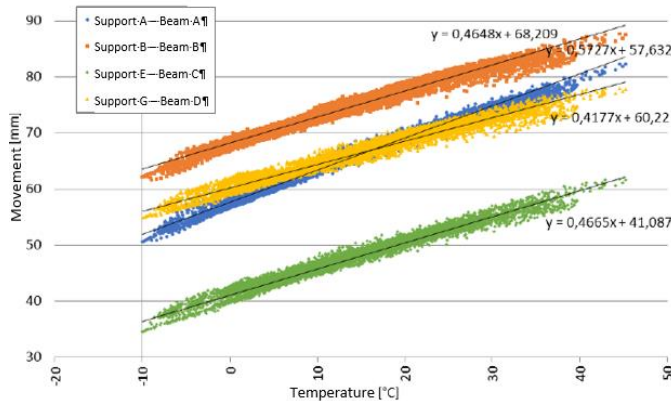


Figure 4. Evaluation of measurement data for one year.

#### Monitoring of known deficits from reassessment or resulting from outdated design procedures:

This use case is relevant when deficits in structures are identified during reassessment or when similar deficits are found in comparable constructions. Often, there are no visible damages yet, and the type or location of potential damage is unknown. Global monitoring enables the monitoring of the deficient structure. Global monitoring is designed to capture and evaluate global parameters of a structure that may indicate damage. A significant change in the global stiffness of the structure is generally required to enable precise system response measurements via global monitoring.

These parameters can be determined from the system response, for example, by measuring acceleration or deformation. The measurements serve to capture changes that develop in the structure over time. Provided the structure behaves in a ductile manner with failure warning signs, the basis for global monitoring of system reactions is that impacts and damages significantly affect the system stiffness, thereby having a direct influence on the load-bearing behavior of the structure. The various methods of global structural monitoring are based on the assumption that damages in the structure can be detected by changes in its global load-bearing behavior. Through measurements of these parameters and subsequent evaluation, conclusions can be drawn about the nature and location of the damage [10; 11].

Alternatively, global monitoring can be designed to detect the cause of the damage. For this, an acoustic emission monitoring system could be used, for example, to detect strand wire fractures in pre-stressed concrete structures [12] or fatigue crack formation in orthotropic deck slabs [13]. With a sufficiently large monitoring system, all areas where the deficit was identified can be monitored. The monitoring system detects and localizes any damage that occurs from the start of the monitoring.

The use of local monitoring can be applied, for example, in the case of fatigue in the coupling joint during recalculation deficits or shear force recalculation deficits, such as in the local

monitoring of shear areas to detect the formation of shear cracks.



Figure 5. Bridge over the Havel along the B96 in Fürstenberg/Havel.

The measure for the bridge over the Havel River along the B96 in Fürstenberg/Havel serves as an example of this use case (Figure 5). The structure was built in 1968 as a single-span pre-stressed concrete slab with a span of approximately 16 meters. Hennigsdorf pre-stressing steel was used, which is now classified as being at risk of stress corrosion cracking. As part of the object-specific investigations to verify the failure warning behavior, samples of the pre-stressing tendons were taken. Broken tendons were already identified during the sample extraction. Laboratory tests confirmed that the tendons did not meet the required fracture elongation or tensile strength. The fracture patterns show significant initial cracks due to stress corrosion cracking.

Due to the importance of the structure for traffic, closure to traffic is only permissible in extreme cases. Therefore, a monitoring system using acoustic emission was installed on-site. The measurement system consists of 12 acoustic emission sensors, each positioned outside the navigation channel of the Havel River. Since its commissioning, a total of 10 tendon fractures have been recorded at the structure by the end of 2022. Each tendon fracture triggered an event-based structural inspection.

#### Monitoring aimed at assessing traffic loads and their effects

The actions on the structure can include direct effects from external loads (e.g. dead loads, traffic loads, wind or snow loads) and indirect effects due to restrained deformations (thermal stresses) caused by climatic influences (temperature) or settlement differences.

Climatic influences such as humidity and temperature can be measured through weather stations. The impact of temperature on the structure is measured using temperature sensors within and on the structure. Determining the temperature plays an important role in compensating for the temperature effect on measurements. In certain use cases (e.g., monitoring of coupling joints), temperature is a significant influencing factor for the assessment. Traffic and the composition of traffic are also of great importance for capturing the relevant effects on bridge structures. The use of Bridge Weigh-in-Motion (B-WIM) systems can, for example, determine the actual current traffic loads [14].





Figure 6. Bridge over the Spree along the L35 in Fürstenwalde/Spree.

In the State Road Agency, a study was conducted to realistically capture object-specific target load levels. Monitoring systems were installed on individual structures to accurately record the respective boundary conditions [15]. One example is the bridge over the Spree River along the L35 in Fürstenwalde/Spree. The Spree crossing consists of a main bridge and a bridge over a side branch of the river (Archen arm) (Figure 6). The main bridge is a pre-stressed arch bridge with a span of 67 meters. The bridge over the Archen arm was constructed as a composite structure with a steel girder deck and concrete deck plate. It has individual spans of 25.5 meters, 28 meters, and 29 meters.

The determination of the target load level is relevant because there is a comparatively high traffic load and congestion due to junctions before and after the structure.



Figure 7. Measuring system on the bearing shelf/seat of the abutment.

To capture the effect, strain gauges were used, and temperature sensors were deployed to compensate for the measurement values' temperature influence. Temperature compensation in this use case is carried out in two steps: first, real-time compensation during measurement using a Wheatstone bridge; second, calibration of the recorded values by determining a baseline load level for a specific time series.

The measurement system was installed on the bearing shelf of the abutment (Measurement system on the bearing shelf/seat of the abutment, Figure 7). The verification of the measurement results was carried out through camera recordings of the ongoing traffic. The measurement took approximately two

years. As a result, it was demonstrated that the target load level BK30/30 can be justified for the structure. The subsequent recalculation revealed deficits in the fatigue performance. However, the available measurement data allows for the derivation of an object-specific fatigue load model to optimize the verification process. This step is still pending.

### 3.2 Use cases with initial practical examples

"Monitoring to support structural inspection" and "Monitoring of major structures" are use cases where initial implementations are present in practice, but further research and support for implementation are still necessary.

#### Monitoring to support the structural inspection:

As part of the structural inspection according to [8], monitoring can be used to provide supplementary information that cannot be obtained through conventional inspections. The use of monitoring is possible at various stages in the structural inspection process. One option is the use of instrumented components to assess the behavior. For example, instrumenting bridge deck expansion joints and measuring performance parameters offers the advantage that these components are repaired based on actual loading. Instrumented components provide information on existing damage to the relevant parts and, if necessary, allow the prediction of future developments [16]. By now this use case is not aligned with DIN 1076 and is currently under discussion in the relevant standardization committees.

An alternative is the use of image-based monitoring, where structural images are automatically captured, and the georeferenced 3D geometry of the structure is subsequently determined. This allows the identification of areas of the structure that should be further examined during the structural inspection.

The image data can also be used for AI-supported analysis to automate the detection of cracks, spalling, or changes [17; 18]. Extracting damage information and locations, such as cracks from the captured image datasets, parallels the system identification methods of sensor-based monitoring [19]. Parts of traditional hands-on inspections can be enhanced and improved through digital tools.

Alternatively, Virtual and Augmented Reality (VR/AR) can also be used in the context of structural inspections. In this case, image-based techniques are also applied, where image data is georeferenced and linked to an existing 3D model.

#### Monitoring of major structures:

Monitoring of major structures refers to structures whose failure would have a large impact on the transportation network. Examples of such structures include major viaducts or river crossings. For these structures, the use of monitoring can be a useful addition to ensuring availability, even when no damage or deficits are currently known. To implement this use case, identification of the relevant structures is necessary. Their significance can stem from traffic-related or structural reasons. Traffic-related reasons include the importance of the structure for network availability or high traffic volumes. Structural reasons arise from the size and location of the structure, considering any limited options for providing short-term replacement. For this use case, global monitoring is relevant. In contrast to the use case "Monitoring with known deficits," no

deficits need to be known in this case. This use case can apply to both new and existing structures.

Monitoring of major structures is more widespread abroad, as demonstrated by the monitoring of the Ponte da Lezíria bridge built in Portugal in 2007 [20]. The bridge was equipped with an extensive monitoring system to measure static and dynamic parameters. This system supports the structural inspections, and the asset owner has continuous access to an assessment of the structure's condition [20].

Similarly, at the bridge in the Digital Test Field Highway, the embedded sensors and the aggregation of the measured data provide the asset owner with continuous access to the current condition of the bridge, allowing for quick and effective decision-making when changes in the condition are detected [21]. The benefits of using preventive monitoring for bridges without existing damage have been demonstrated in [22].

### 3.3 Potential future use cases

The use case "Monitoring to support a Predictive Lifecycle Management" will gain significant importance in the context of implementing Digital Twins, which are announced in the BIM Master Plan [23]. Initial steps and ideas for implementing this use case were outlined in [19].

The potential of monitoring arises from the ability to monitor structures over long periods and detect changes. The potential lies in determining the structural condition and quantifying the reliability of the structure, characterizing the behavior of the structure with the goal of anomaly detection, and securing the remaining service life [19].

Monitoring data can provide information, for example, about damage mechanisms. This information can then serve as the basis for determining performance indicators in combination with other data. This approach aims to reduce uncertainties in the condition assessment and identify appropriate maintenance measures [19].

The use case "Birth Certificate" aims to establish a reference condition of the structure before commissioning, providing a basis for interpreting the impact of later changes and making statements about the expected behavior of the structural and equipment components. This reference condition can be compared with subsequent measurements, thus providing a decision-making foundation for determining the timing of necessary measures, such as permanent monitoring. For clarification the single measurement as mentioned above does not constitute monitoring in the classical sense, which generally implies continuous data acquisition.

The performance of a baseline measurement, including a proof load test, is mandatory in Switzerland, Italy, and France [24–26]. In [17], the performance of a baseline measurement at the Hochmosel Bridge is described. Here, in addition to vibration and strain measurements to determine the behavior of the bridge, imaging techniques were also used, among other things, to determine the 3D geometry.

## 4 INTEGRATION OF USE CASES

The interaction of the individual use cases can be envisioned through the implementation of Digital Twins. A Digital Twin can be understood as a digital representation of the real road infrastructure, which interacts with the real structure, records all properties throughout the entire lifecycle, and generates

information for decision support from the data [27]. Figure 8 provides a schematic representation of a bridge's digital twin, highlighting the various data sources and the role of monitoring within the system.

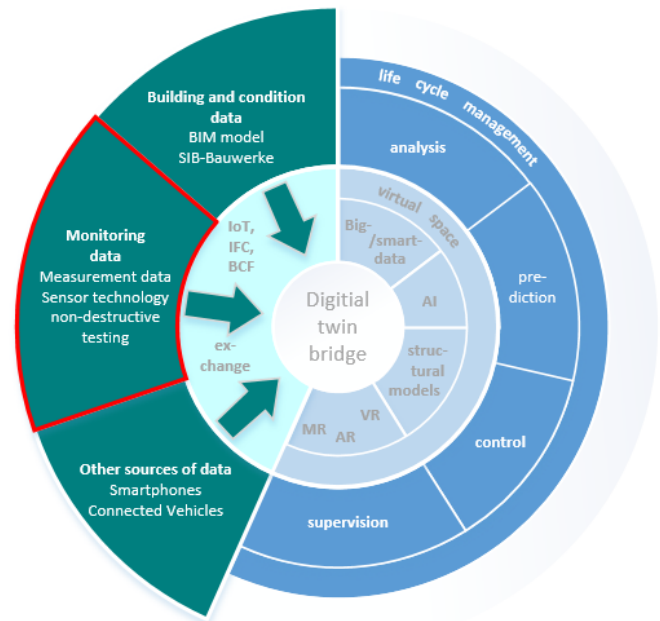


Figure 8. Monitoring as part of the digital twin according to [28].

Monitoring and the information and insights gained from it are essential foundations for the development and use of Digital Twins. The monitoring data provides insight into the current condition of the structure and serves as input data for determining future behavior. Therefore, the use of monitoring is fundamental to the processes of monitoring, analysis, prediction, and control that occur within the Digital Twin.

## 5 CONCLUSION

The use of monitoring on engineering structures of the federal highways is still not widely spread, but it is gaining in importance. Through the use cases, there is the opportunity to demonstrate the potential of monitoring and overcome barriers to its implementation. Currently, monitoring is of great importance in supporting the availability of engineering structures and, in particular, ensuring the remaining service life. A wealth of experience is already being gathered in these use cases today, which can be beneficial in the long term for the introduction of Digital Twins. Initial results, within the framework of Digital Shadows, can already demonstrate the potential on a smaller scale.

The benefits resulting from the application of monitoring measures can be quantified in monetary terms – for example, through savings on inspections, extended service life or early damage detection. In contrast, the benefits of the digital twin cannot yet be expressed in concrete figures, but they can be described qualitatively – such as improved decision-making, increased transparency regarding the structural condition and long-term potential for process optimization.

In conclusion, monitoring and the demonstrated use cases help bridge the gap between the physical structure and its digital representation.

## REFERECNES

- [1] Deutscher Beton- und Bautechnikverein (2018) *Merkblatt: Brückenmonitoring*.
- [2] Hindersmann, I. (2021) Anwendung von Monitoring bei Brücken der Bundesfernstraßen und zukünftige Monitoringstrategien in: Krieger, J. [Hrsg.] Fachkongress Digitale Transformation im Lebenszyklus der Verkehrsinfrastruktur: Tagungshandbuch 2021. Tübingen: Expert Verlag.
- [3] DGZfP (2022) Merkblatt B 09 – Dauerüberwachung von Ingenieurbauwerken.
- [4] Wedel, F. et al. *Leitfaden - Strategischer Einsatz von Monitoring für Ingenieurbauwerke*. Vorabveröffentlichung der Bundesanstalt für Straßen- und Verkehrswesen (BASt)
- [5] Schubert, M. et al. (2020) Wirtschaftlichkeitsuntersuchungen von Monitoringmaßnahmen – Entwicklung eines Konzepts für die Analyse von Nutzen und Kosten. Berichte der Bundesanstalt für Straßenwesen B, Brücken und Ingenieurbau B156.
- [6] Bundesministerium für Verkehr und digitale Infrastruktur (2019) Handreichungen und Leitfäden – Teil 6 – Steckbriefe der wichtigsten BIM-Anwendungsfälle. Arbeitsgemeinschaft BIM4INFRA2020.
- [7] Bundesministerium für Verkehr, Bau und Stadtentwicklung (2007) Richtlinien für die Erhaltung von Ingenieurbauten RI-ERH-ING - Leitfaden Objektbezogene Schadensanalyse (OSA).
- [8] DIN 1076:1999 DIN 1076: Ingenieurbauwerke im Zuge von Straßen und Wegen - Überwachung und Prüfung.
- [9] Jansen, A.; Geißler, K. (2020) Ausreißererkennung zur Strukturüberwachung von Bestandsbrücken durch Bauwerksmonitoring mit vier Signalmerkmalen in: Isecke, B.; Krieger, J. [Hrsg.] TAE Brückenkolloquium: Tagungshandbuch. Tübingen: Expert Verlag.
- [10] Retze, U. (2007) Beispielhafte Untersuchung zum Einsatz von Monitoringmethoden an einer Brücke [Dissertation]. Universität der Bundeswehr.
- [11] Schnellenbach-Held, M.; Karczewski, B.; Kühn, O. (2014) Intelligente Brücke - Machbarkeitsstudie für ein System zur Informationsbereitstellung und ganzheitlichen Bewertung in Echtzeit für Brückenbauwerke. Berichte der Bundesanstalt für Straßenwesen, Brücken und Ingenieurbau B 105.
- [12] Kaplan, F. et al. (2022) *Überwachung der Brücke am Altstädter Bahnhof* in: Bautechnik 99, H. 3, S. 222–230. <https://doi.org/10.1002/bate.202200008>
- [13] Salg, D.; Schmidt, S. (2020) Structural Health Monitoring am Beispiel von zwei Autobahnbrücken in: DGZfP [Hrsg.] Bauwerksdiagnose 2020: Tagungsband.
- [14] Freundt, U. (2014) *Roadtraffic Management System (RTMS)*. Berichte der Bundesanstalt für Straßenwesen B, Brücken und Ingenieurbau B 100.
- [15] Degenhardt, K. et al. (2020) Mehrstufiges Verfahren zur Festlegung des erforderlichen Ziellastniveaus für die Nachrechnung von Straßenbrücken in: Isecke, B.; Krieger, J. [Hrsg.] TAE Brückenkolloquium: Tagungshandbuch. Tübingen: Expert Verlag.
- [16] Haardt, P. et al. (2017) *Die intelligente Brücke im digitalen Testfeld Autobahn* in: Bautechnik 94, H. 7, S. 438–444. <https://doi.org/10.1002/bate.201700035>
- [17] Kühne, J. et al. (2021) *Die Digitalisierung der Zustandsüberwachung von Windenergieanlagen und Brücken im Vergleich* in: Stahlbau 90, H. 2, S. 128–137. <https://doi.org/10.1002/stab.202000093>
- [18] Morgenthal, G.; bim auf (2021) Bauwerksprüfung gemäß DIN 1076 – Unterstützung durch (halb-)automatisierte Bildauswertung durch UAV (Unmanned Aerial Vehicles – Unbemannte Fluggeräte). Berichte der Bundesanstalt für Straßenwesen Brücken- und Ingenieurbau B171.
- [19] Morgenthal, G. et al. (2023) Potenziale von Monitoringdaten in einem Lebenszyklusmanagement für Brücken – unveröffentlichter Bericht zu FE 69.0006. Veröffentlichung in Vorbereitung.
- [20] Sousa, H. et al. (2011) *Design and implementation of a monitoring system applied to a long-span prestressed concrete bridge* in: Structural Concrete 12, Nr. 2, pp. 82–93. <https://doi.org/10.1002/suco.201000014>
- [21] Windmann, S. (2022) *Intelligente Brücke – Reallabor Intelligente Brücke im Digitalen Testfeld Autobahn*. Berichte der Bundesanstalt für Straßenwesen B, Brücken- und Ingenieurbau B178.
- [22] Sousa, H.; Courage, W. (2022) Value of information of a pro-active SHM-based tool supported by advanced FE models and Bayesian statistics towards efficiency in bridge management in: Structure and Infrastructure Engineering 18, H. 4, S. 554–572. <https://doi.org/10.1080/15732479.2021.1978507>
- [23] BMVI (2021) Masterplan BIM Bundesfernstraßen.
- [24] Bundesamt für Straßen (2005) Richtlinie - Projektierung und Ausführung von Kunstbauten der Nationalstrassen.
- [25] Bundesamt für Straßen (2005) Richtlinie Überwachung und Unterhalt der Kunstbauten der Nationalstrassen.
- [26] Transport Research Board (2019) *Primer on Bridge Load Testing* [online]. <https://onlinepubs.trb.org/onlinepubs/circulars/ec257.pdf>.R [Access at: 16th June 2025].
- [27] Bednorz, J. et al. (2021) *BIM - auf dem Weg zum Digitalen Zwilling* in: Straße + Autobahn, H. 11, S. 917–924.
- [28] Nieborowski, S. et al. (2023) *Digitaler Zwilling Brücke im Betrieb – Mögliche Anwendungsfälle* in: Bautechnik 100, H. 2, S. 86–93. <https://doi.org/10.1002/bate.202200089>



# A Structural Health Monitoring Framework For Intelligent and Sustainable Infrastructure: A Conceptual Perspective

Masoud Pedram,<sup>1</sup>, <https://orcid.org/0000-0002-9422-1001>

Su Taylor,<sup>1</sup>, <https://orcid.org/0000-0003-4796-1928>

Gerard Hamill,<sup>1</sup>, <https://orcid.org/0000-0002-8962-5933>

<sup>1</sup> Department of Civil Engineering, School of Natural and Built Environment, Queen's University Belfast,  
BT7 1NN, Northern Ireland, United Kingdom  
email: [m.pedram@qub.ac.uk](mailto:m.pedram@qub.ac.uk), [s.e.taylor@qub.ac.uk](mailto:s.e.taylor@qub.ac.uk), [g.a.hamill@qub.ac.uk](mailto:g.a.hamill@qub.ac.uk)

**ABSTRACT:** This paper presents a vision for next-generation Artificial Intelligence (AI) based structural health monitoring (SHM) systems through the lens of DREAM-SHM: a framework comprising Dynamic, Real-time, Evaluative, Adaptive (AI-based), Modular, Self-diagnostic, Holistic, and Multi-sensory principles. The aim is to enable smart infrastructure that can sense, and evolve corresponding to structural behaviour, material degradation, environmental effects, and changing operational or economic constraints. The paper reviews current SHM technologies, highlighting the strengths and limitations of contact-based sensors, such as accelerometers, strain gauges, fibre optic sensors, and non-contact approaches including vision-based systems, infrared thermography, radar, and ultrasonic techniques. Emphasis is placed on their integration with wireless sensor networks, Internet of Things (IoT) platforms, and Artificial Intelligence (AI) for advanced data fusion, anomaly detection, and predictive analytics. The computational aspects underpinning SHM systems, such as cloud-edge processing, machine learning, and multi-modal sensor data integration, are described to enable timely and informed decision-making. In addition, the paper situates DREAM-SHM within the context of sustainability, demonstrating how adaptive and intelligent SHM systems support the goals of circular economy and net-zero carbon by prolonging asset life, reducing maintenance burdens, and improving environmental responsiveness. This work outlines a pathway toward structurally intelligent and resource-efficient infrastructure.

**KEYWORDS:** Structural Health Monitoring (SHM), Intelligent infrastructure, Sustainable infrastructure, Multi-modal sensing, Contact-based sensing, Non-contact sensing, Internet of Things (IoT).

## 1 INTRODUCTION

The infrastructure of the future should be smart, adaptive, and capable of responding to both operational and environmental challenges in real-time. As urbanisation continues to accelerate and infrastructure ages, ensuring safety, efficiency, and longevity of our built environment has never been more crucial. Traditional methods of structural inspection and maintenance, though important, are often time-consuming, costly, and prone to human error. The Structural Health Monitoring (SHM) paradigm offers an innovative solution to these challenges, enabling continuous, non-destructive assessment of structural integrity and performance [1-3]. SHM aims to detect and diagnose faults early, ensuring that any issues are addressed before they escalate into catastrophic failures. It involves assessing factors such as structural loads, damage status, defect localisation and quantification, growth rate estimation, future performance prediction, and remaining life estimation [1, 4, 5]. In an ideal SHM system, these evaluations are performed in real-time, providing global insights into the health of a structure as it operates [3].

At its core, SHM involves several essential components, including sensing, load identification, damage detection, damage characterisation, and future performance prediction [1, 6]. SHM systems incorporate continuous or periodic sensing and data collection, allowing for the real-time monitoring of structures under various operational and environmental loads. Sensors, whether passive or active [7], are integrated into the structure during manufacturing or retrofitted for ongoing monitoring. These sensors can be classified as contact-based (e.g., accelerometers, strain gauges, fibre optic sensors, Linear

Variable Differential Transformers (LVDT), and thermometers) or non-contact-based (e.g., vision-based systems, infrared thermography, and radar). Both types of sensors capture critical data about the structure's behaviour, environmental conditions, and operational status, transmitting this information to storage systems or cloud-based servers for analysis and decision-making [8, 9].

Contact-based sensors offer high accuracy but often require direct attachment to the structure, periodic maintenance, and replacement, resulting in increased operational costs. Moreover, critical measurement points may be difficult or impossible to access, leading to incomplete or inaccurate data [10, 11]. To address these challenges, non-contact sensors provide an alternative by enabling wide-area and mobile sensing. These sensors operate without requiring direct attachment to structures and are typically positioned at a distance. They capture optical images and videos using technologies such as digital cameras, high-speed cameras, and synthetic aperture radar from satellite sensors. Smartphone-based sensing technologies are also increasingly integrated into SHM systems, expanding their capabilities [9]. By utilising mobile platforms such as unmanned aerial vehicles (UAVs), automobiles, trains, and boats, fly-by, drive-by, tram-by, or sail-by monitoring systems can be deployed, enhancing spatial coverage and reducing data gaps. This more efficient approach enables broader monitoring capabilities across large infrastructure networks, offering a more comprehensive assessment of structural health over time.

As infrastructure becomes more interconnected and intelligent, the need for adaptive, dynamic systems that respond

in real time to changing conditions is greater than ever. This is where DREAM-SHM as a novel Structural Health Monitoring framework offers a transformative solution. By integrating contact-based and non-contact sensors, Internet of Things (IoT) platforms, and Artificial Intelligence (AI), DREAM-SHM enables structures to not only monitor their health but also adapt dynamically to both environmental and operational changes. The system continuously collects data from sensors and uses AI-driven algorithms to analyse this information, allowing the structure to respond in real time to conditions such as temperature fluctuations, humidity, material stress, and even operational demands. By optimising these factors, DREAM-SHM can maintain both the structural integrity of the building and the comfort of its occupants, while also reducing energy consumption and lowering carbon emissions. Moreover, this integration can help address issues such as overcrowding or traffic congestion by adjusting building operations based on real-time data.

This paper explores the concept of DREAM-SHM, detailing how its combination of advanced sensors, IoT networks, and AI technologies unlocks the next generation of intelligent infrastructure. It reviews the different sensor technologies used in SHM, both contact-based and non-contact, and presents a discussion of the computational aspects that enable DREAM-SHM to adapt to changing conditions. This paper explores the potential of these technologies to revolutionise infrastructure monitoring and maintenance, highlighting their ability to optimise not just structural health but also the environment within and around the infrastructure.

## 2 SENSOR TECHNOLOGIES FOR STRUCTURAL HEALTH MONITORING

SHM systems depend on sensor technologies to collect continuous or periodic data from infrastructures under operational and environmental conditions. These sensors are typically classified into contact-based and non-contact types, each with unique advantages and limitations [12]. A thorough understanding of both categories is essential for developing a more adaptive and intelligent SHM framework.

### 2.1 Contact-Based Sensors

Contact-based sensors are physically attached to the structure to capture direct measurements of parameters such as strain, stress, acceleration, displacement, and temperature. These sensors have traditionally formed the backbone of SHM systems, especially in critical and high-risk infrastructure.

#### 2.1.1 Strain Gauges

Strain gauges are widely used to measure strain resulting from applied loads. They are typically bonded to the surface of structural elements and detect minute changes in length as electrical resistance variations. Despite their accuracy, they are susceptible to environmental degradation and require careful installation and protection [13-15].

#### 2.1.2 Accelerometers

Accelerometers are essential in dynamic monitoring, capturing vibrations, modal properties, and transient responses during events such as traffic loading or seismic activity. They can be deployed in arrays across a structure to identify changes

in stiffness or detect anomalies associated with damage [10, 16-18].

#### 2.1.3 Fibre Optic Sensors

Fibre optic sensors, including Fibre Bragg Gratings (FBGs), are capable of long-range, high-resolution measurements of strain and temperature. Their immunity to electromagnetic interference and ability to multiplex multiple sensing points along a single fibre make them highly suitable for harsh environments and large-scale infrastructures [19-21].

#### 2.1.4 Linear Variable Differential Transformers (LVDTs)

LVDTs are used to measure displacement and deformation with high precision. These sensors are commonly applied in laboratory tests and long-term monitoring of joints, cracks, and bearing movements in bridges and buildings [22].

#### 2.1.5 Thermocouples and Thermistors

These sensors measure temperature variations, essential for understanding thermal loading effects on structural behaviour. They are often used in combination with other sensors to decouple environmental influences from structural responses.

#### 2.1.6 Limitations of contact-based sensors

Despite their reliability and accuracy, contact-based sensors have several drawbacks, such as installation and maintenance can be labour-intensive and costly. Sensor failure due to environmental exposure requires frequent inspection and replacement. Coverage is often limited to selected points, leading to sparse spatial resolution [23].

### 2.2 Non-Contact Sensors

Non-contact sensors offer remote sensing capabilities and are particularly valuable for large-scale structures where full-field contact-based monitoring is impractical [24]. These sensors can be deployed on stationary platforms or mobile carriers such as UAVs, vehicles, or boats to conduct “fly-by”, “drive-by”, or “sail-by” inspections.

#### 2.2.1 Vision-Based Methods

Vision-based SHM systems use digital or high-speed cameras to capture visual data from structures [25]. Techniques such as Digital Image Correlation (DIC) [26] and photogrammetry allow for the measurement of displacement, deformation, and surface cracking [27, 28]. These methods are enhanced through artificial intelligence (AI), particularly deep learning algorithms that automate defect detection and characterisation [29].

#### 2.2.2 Infrared Thermography (IRT)

IRT detects subsurface anomalies such as delamination and voids by capturing thermal patterns on a structure's surface. It is non-invasive and efficient for inspecting large areas. However, it is sensitive to environmental conditions and often requires post-processing with deep learning models to reduce false positives [30-38].

#### 2.2.3 Ultrasound-Based Techniques

Air-coupled ultrasound techniques use high-frequency waves to detect micro-cracks and internal flaws. These are particularly useful in metallic and composite materials where internal

defects may not be visible externally. Non-contact ultrasound methods allow remote application, reducing the need for physical access[24].

#### 2.2.4 Radar Vibration-Based Methods

Microwave and millimetre-wave radar systems can remotely monitor structural vibrations and dynamic responses with sub-millimetre accuracy. These non-contact methods are particularly effective for tall, slender, or otherwise inaccessible structures such as towers, bridges, and wind turbines. They offer robust performance in challenging environmental conditions, as they are less affected by lighting, fog, or moderate precipitation compared to optical techniques. Radar-based monitoring enables real-time displacement and modal analysis without requiring physical sensor installation on the structure[24].

#### 2.2.5 Magnetic-Based Techniques

Magnetic-based methods such as Magnetic Flux Leakage (MFL) and magnetostrictive sensors are used to detect stress concentrations, cracks, corrosion, and other anomalies in ferromagnetic materials. These techniques work by measuring disturbances in the magnetic field when it encounters defects or discontinuities within the material. They are particularly valuable for monitoring pipelines, prestressed cables, steel-reinforced concrete, and metallic bridge components, offering a non-destructive means of assessing structural integrity in inaccessible or high-risk environments [24].

#### 2.2.6 Wireless Sensor Networks (WSNs)

WSNs use embedded or surface-mounted sensors that wirelessly transmit structural data to remote data acquisition systems. This reduces installation complexity and allows for scalable deployment across large infrastructures. Integration with energy harvesting solutions enhances their long-term viability [24, 39].

#### 2.2.7 Hybrid and Mobile Monitoring Approaches

Combining multiple non-contact methods or integrating them with mobile platforms (e.g., UAVs or autonomous ground vehicles) provides comprehensive spatial and temporal data. These systems are especially useful for structures with limited accessibility or under high traffic loads [9].

#### 2.2.8 Advantages of Non-Contact Sensors

These sensors enable full-field and remote monitoring, reduce maintenance and installation costs, improve safety for inspectors and increase spatial coverage and flexibility.

#### 2.2.9 Challenges of Non-contact Sensors

Environmental conditions (e.g., lighting, humidity, wind) can affect the accuracy of these sensors. Data processing complexity increases with large-scale visual or radar datasets. These sensors are high dependent on robust algorithms for data interpretation.

### 2.3 Summary and Considerations

The combined application of contact and non-contact sensor technologies can provide complementary insights into structural integrity. While contact sensors offer high accuracy for localised measurements, non-contact sensors excel in wide-

area and remote assessments. The integration of AI and the Internet of Things (IoT) further enhances data acquisition, fusion, and interpretation capabilities [40, 41].

A future-forward SHM system, such as DREAM-SHM, should not only integrate these sensors intelligently but also enable self-reflection and prediction, adapting its sensing strategies based on structural performance, environmental changes, and user demands. This vision sets the stage for the next generation of intelligent, adaptive, and sustainable infrastructures.

## 3 DREAM-SHM: TOWARDS INTELLIGENT, AND ADAPTIVE STRUCTURES

The future of civil infrastructure depends on its capacity to sense, adapt, and evolve, and attributes central to the next generation of intelligent systems. In this context, this paper suggests the DREAM-SHM framework: a novel approach to Structural Health Monitoring that is Dynamic, Real-time, Evaluative, Adaptive (AI-based), Modular, Self-diagnostic, Holistic, and Multi-sensory (Figure 1).

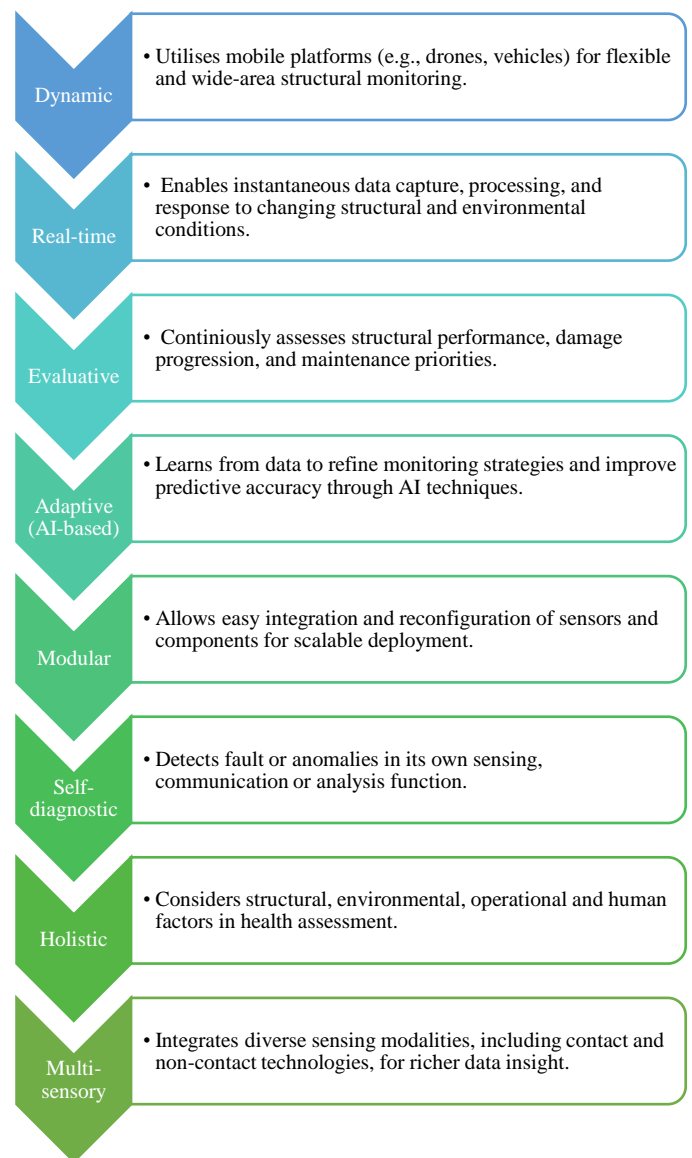


Figure 1. Elements of DREAM-SHM framework



Rather than functioning as static systems for passive data collection, DREAM-SHM envisions infrastructure as active learning, self-reflective, and responsive entities, capable of anticipating change, optimising performance, and supporting lifecycle decisions with unprecedented insight and autonomy. The DREAM-SHM system is inherently computational, relying on advanced data processing, predictive algorithms, machine learning, and cloud computing to support its highly adaptive and intelligent functionality. It operates through a robust digital backbone that enables the processing of vast amounts of real-time data, the prediction of future conditions, the optimisation of structural health, and the dynamic adjustment of environmental parameters.

### 3.1 From Traditional to Dreaming Structures

Conventional SHM systems provide snapshots of structural conditions based on sensor data. In contrast, DREAM-SHM envisions a system that continuously "dreams." That is, it reflects on past data, analyses current performance, and simulates future outcomes. Much like human brain consolidates information during sleep [42, 43], DREAM-SHM uses advanced analytics, AI, and IoT integration [44] to consolidate multisource data and learn structural behaviour patterns over time. This cognitive leap transforms infrastructure into living digital twins, constantly updating their condition, adapting to changes in the environment, and providing valuable feedback to engineers and designers.

### 3.2 Integrating Contact and Non-Contact Sensors with IoT and Data Processing Fusion

In a DREAM-SHM framework, both contact and non-contact sensors are integrated into a broader Internet of Things (IoT) ecosystem. IoT enables sensor networks to communicate, synchronise, and share real-time data through cloud computing or edge processing devices. Contact-based sensors (e.g., strain gauges, accelerometers) provide high-fidelity, localised data critical for detecting internal stress, fatigue, or localised failures, while non-contact sensors (e.g., vision systems, thermography, radar) expand coverage, capture surface conditions, and enable remote inspections.

These sensors generate large, multidimensional datasets that require careful processing and alignment to create a coherent and reliable model of the structure's condition. Advanced data fusion algorithms are applied to integrate multimodal data from multiple sources, resolving discrepancies caused by noise, sensor faults, or varying environmental conditions [39]. Techniques such as Kalman filtering, Bayesian inference, and decision tree models [45] enhance the accuracy of the fused data by accounting for uncertainties and interdependencies across sensor inputs.

IoT platforms facilitate seamless connectivity between sensors, edge devices, data storage, and decision-making systems, enabling real-time alerts, remote diagnostics, distributed data storage, cloud analytics, and cross-sensor data fusion and redundancy to reduce uncertainty. The fusion of contact and non-contact sensor data within this infrastructure supports a comprehensive, context-aware SHM system capable

of interpreting data as part of a broader ecosystem influenced by environmental, operational, and human factors [44].

### 3.3 The Role of AI in Creating Self-Adaptive Structures

AI lies at the core of the DREAM-SHM system, functioning as the central engine that empowers intelligent data interpretation, autonomous decision-making, and adaptive system behaviour. By leveraging machine learning (ML) and deep learning (DL) techniques, the system can extract meaningful patterns, detect anomalies, and respond dynamically to evolving structural and environmental conditions [46].

Deep learning models, particularly Convolutional Neural Networks (CNNs) [12, 46-48], are instrumental in analysing visual inputs from vision-based sensors or thermal imagery from infrared cameras. These networks can automatically classify and detect structural anomalies such as cracks, deformations, corrosion, or delamination, significantly reducing the reliance on manual inspections. This automation increases the speed and accuracy of damage detection while minimising human error.

AI algorithms are trained on historical and real-time sensor data to enable predictive maintenance, allowing the system to forecast when and where damage is likely to occur. In addition to supervised learning, unsupervised learning approaches are used to uncover previously unseen patterns or emerging failure modes, enhancing the system's adaptability and sensitivity over time.

AI also plays a critical role in fusing data from multiple sensor modalities, including thermal, acoustic, visual, and vibration sources. By integrating these diverse inputs, AI improves fault detection accuracy and reduces false positives. Furthermore, AI enables the autonomous operation of robotic inspection platforms, such as UAVs, which can plan flight paths, adjust actions in real time, and focus on areas of concern based on live feedback.

Reinforcement learning techniques further enhance the self-adaptive capabilities of the DREAM-SHM system. Through continuous learning, the system can optimise its monitoring strategies, improving how it prioritises sensor data, allocates resources, and adapts to changing structural and environmental conditions.

### 3.4 Dynamic, Self-Reflective, and Adaptable Systems

The DREAM-SHM system represents a significant evolution in how infrastructure is designed, operated, and maintained. At its core, it enables dynamic, self-reflective, and adaptable behaviour through the seamless integration of cloud computing, the IoT, and AI. By combining real-time sensor data with intelligent analytics, the system continuously monitors, analyses, and responds to both internal structural health and external environmental conditions.

IoT-enabled sensor networks form the backbone of this intelligent infrastructure. These networks connect contact and non-contact sensors, environmental monitoring devices, and

operational systems, allowing continuous data transmission to cloud-based platforms. Cloud computing provides the scalable computational resources needed to handle large volumes of sensor data across wide geographic areas, making it possible for engineers, facility managers, and maintenance teams to access up-to-date structural health reports, plan maintenance, and respond to safety concerns in real time. Edge computing ensures that critical decisions can be made locally and rapidly, particularly when immediate intervention is required. For example, structural anomalies detected by sensors, such as sudden changes in strain or temperature, can trigger instant responses without needing to wait for centralised cloud processing.

This intelligent system also extends to the optimisation of internal environments. By monitoring temperature, humidity, and occupancy levels, DREAM-SHM can automatically adjust heating, ventilation, air conditioning (HVAC), or dehumidification systems. These adjustments not only enhance occupant comfort but also protect structural materials from accelerated degradation, such as corrosion in steel or cracking in concrete, caused by unfavourable environmental conditions.

Moreover, the system adapts to changing operational demands. If a room becomes highly occupied, ventilation can be increased, or air conditioning fine-tuned to maintain air quality and comfort. By learning usage patterns, tracking external weather forecasts, and recognising early signs of material fatigue, AI within the system can anticipate and prepare for future operational needs. This may include adjusting HVAC schedules ahead of temperature drops, deploying shading systems in response to sunlight exposure, or activating safety protocols in anticipation of extreme weather or seismic activity.

Ultimately, DREAM-SHM goes far beyond traditional monitoring. It creates an intelligent feedback loop where data, environment, and structural health are interwoven, enabling buildings and infrastructure to adapt in real time. This not only preserves structural integrity and enhances user wellbeing, but also significantly reduces energy consumption and carbon emissions, contributing to more sustainable and resilient built environments.

### 3.5 *Designing for Longevity Through Predictive Intelligence*

One of the transformative aspects of the DREAM-SHM system is its ability to influence future design practices, material selection, and lifecycle strategies through predictive insight. By collecting and analysing long-term structural health monitoring data, the system enables the refinement of design codes based on actual performance under diverse environmental and loading conditions. This data-driven feedback loop allows engineers to make informed decisions, enhancing structural reliability and efficiency over time.

Machine learning algorithms are central to this predictive capability. Trained on historical and real-time data from contact and non-contact sensors, such as accelerometers, infrared thermography, and ultrasound, the system detects early signs of damage and estimates future deterioration, fatigue, and failure.

Time-series forecasting models, including autoregressive integrated moving averages (ARIMA) and recurrent neural networks (RNNs) [49, 50], leverage trends in sensor data to guide proactive interventions that extend the service life of the structure.

Supervised learning techniques, including decision trees and support vector machines (SVM), classify structural conditions into actionable states, while reinforcement learning enables continuous model improvement as new data is acquired. By integrating predictive models with real-time monitoring, the system enhances structural safety, minimises operational costs, and maintains optimal performance.

This fusion of predictive analytics with adaptive control transforms infrastructure into self-reflective and intelligent systems. DREAM-SHM further supports generative design processes, where artificial intelligence proposes optimised structural forms and materials tailored to specific environmental and operational conditions. Such insight enables the design of modular, reconfigurable structures that can evolve over time in response to predictive indicators. In doing so, DREAM-SHM contributes to a new generation of infrastructure that is sustainable, resilient, and energy-efficient, with a significantly reduced carbon footprint.

### 3.6 *Unlocking the Next Generation of Intelligent Infrastructure*

The implementation of DREAM-SHM signifies a fundamental shift from static to living structures. These infrastructures think through artificial intelligence and predictive modelling, feel through extensive and multimodal sensor networks, communicate through Internet of Things platforms and edge computing, and adapt based on environmental conditions, user demands, and system health. By integrating advanced sensing, communication, and intelligence, future infrastructures will no longer be passive assets, but active participants in their maintenance and evolution.

In doing so, they offer immense societal benefits, including enhanced safety and reliability, reduced maintenance costs and downtime, improved energy efficiency and user comfort, and a deeper understanding of structural behaviour over time. The DREAM-SHM paradigm represents not merely a technological upgrade, but a philosophical reimagining of what infrastructure can be, structures that not only endure but evolve, guided by the very data they produce.

## 4 DREAM-SHM, CIRCULAR ECONOMY AND NET ZERO GOALS

The transition towards smarter infrastructure must be harmonised with global imperatives such as the circular economy and the pursuit of net zero carbon emissions. The DREAM-SHM framework, defined as Dynamic, Reflective, Evaluative, Adaptive, Modular, Self-diagnostic, Holistic, and Multi-sensory naturally aligns with these objectives by enabling more efficient, resilient, and sustainable infrastructure systems throughout their entire lifecycle.

### 4.1 *Enabling Resource Efficiency and Longevity*

One of the primary pillars of the circular economy is resource optimisation through prolonged material use, reusability, and

reduced waste [51]. DREAM-SHM contributes to this by allowing structures to continuously evaluate their health, detect minor degradations before they escalate, and schedule maintenance proactively. Such real-time diagnostics reduce the need for premature demolition or over-conservative replacement strategies. The *modular* and *adaptive* attributes of DREAM-SHM also support retrofitting and component-based upgrades, enabling structures to evolve without complete reconstruction, an essential strategy in circular design.

#### 4.2 Data-Driven Lifecycle Decision-Making

DREAM-SHM's use of AI and IoT technologies facilitates whole-life performance monitoring. This continuous data stream allows engineers, asset managers, and policymakers to make informed decisions that extend beyond first costs, incorporating embodied energy, operational efficiency, and end-of-life recyclability. For example, the system can inform decisions about optimal repair versus reuse, estimate embodied carbon for design alternatives, or determine the feasibility of adaptive reuse of ageing infrastructure.

#### 4.3 Supporting Carbon Emission Reduction

Smart structures equipped with DREAM-SHM do not only monitor their mechanical performance, they also track environmental parameters such as energy use, indoor temperature, humidity, and CO<sub>2</sub> levels. These insights enable buildings and infrastructures to dynamically adjust internal conditions to optimise comfort and reduce energy consumption, especially under varying occupancy patterns or extreme climate conditions. Integration with renewable energy sources and smart energy grids can further reduce reliance on fossil fuels, directly supporting net zero building operations.

Moreover, DREAM-SHM facilitates operational carbon tracking, where the carbon cost of maintenance activities and material replacements can be quantified in real-time. This capability encourages low-carbon interventions, the use of environmentally friendly materials, and the minimisation of transport or logistical carbon footprints.

#### 4.4 Designing for a Regenerative Future

The holistic nature of DREAM-SHM, combined with its dynamic and evaluative features, can help shift the infrastructure sector from a linear to a regenerative model[52]. Rather than just sustaining performance, future structures can be designed to learn, evolve, and regenerate over time. By treating structures almost like living systems, ones that sense, learn, and adapt, DREAM-SHM lays the foundation for self-regulating and self-improving built environments.

This continuous evolution aligns with the vision of net positive design, where buildings not only minimise harm but actively contribute to ecological and social value. For instance, a bridge equipped with DREAM-SHM could dynamically coordinate traffic to reduce congestion-related emissions or monitor its own runoff water quality and feed data back into environmental management systems.

#### 4.5 Digital Twin Synergies

Another key synergy lies in the integration of DREAM-SHM with digital twins[53, 54], creating a real-time, data-enriched virtual model of the structure. These twins can simulate environmental impacts, forecast degradation under climate

stressors, and test low-carbon renovation scenarios before implementation. This predictive capability enhances resilience planning and supports sustainability certification and reporting frameworks.

#### 4.6 Energy Efficiency and Sustainable Power Supply

For DREAM-SHM to be deployed at scale and operate autonomously, it must also be energy-conscious. The system leverages low-power wireless sensor networks (WSNs)[55], which minimise energy usage through efficient communication protocols and duty cycling. Where possible, sensors and edge computing units are powered by renewable sources, including solar panels mounted on structures and wind energy microgenerators integrated into exposed components. Additionally, the framework supports energy harvesting, converting ambient vibrations, thermal gradients, or even electromagnetic noise into small but continuous power sources for embedded sensors. This self-sufficiency allows long-term deployment without frequent battery replacements, reducing both maintenance burdens and electronic waste. By embedding energy-awareness into its architecture, DREAM-SHM aligns itself with net-zero goals not only in terms of what it monitors but how it functions, enabling smarter, cleaner, and more self-reliant infrastructures.

#### 4.7 Example of potential performance of a DREAM-SHM system

To demonstrate the potential of the DREAM-SHM framework, imagine a long-span bridge operating under extreme weather conditions and subject to cyclical loading. During a sudden windstorm, real-time data from accelerometers, fibre optic strain sensors, and vision-based surface monitoring systems are synchronised through the IoT layer and processed at the edge. The AI engine identifies anomalous vibration patterns that signal early-stage fatigue in a critical joint. At the same time, thermal imaging highlights abnormal heat signatures associated with bearing friction. The digital twin continuously simulates the structural state and projects the need for a targeted inspection as conditions stabilise. In response to predictive outputs, the system autonomously modifies traffic flow and delivers a real-time alert to maintenance teams. Concurrently, environmental control systems within nearby infrastructure are adjusted to reduce energy use due to temporary low occupancy. This scenario illustrates how the DREAM-SHM framework functions as an adaptive, multi-sensory, and context-aware system, supporting decision-making under dynamic operational demands.

## 5 CONCLUSION

This paper presents a conceptual perspective for a future SHM system: DREAM-SHM as summarised in Figure 2.



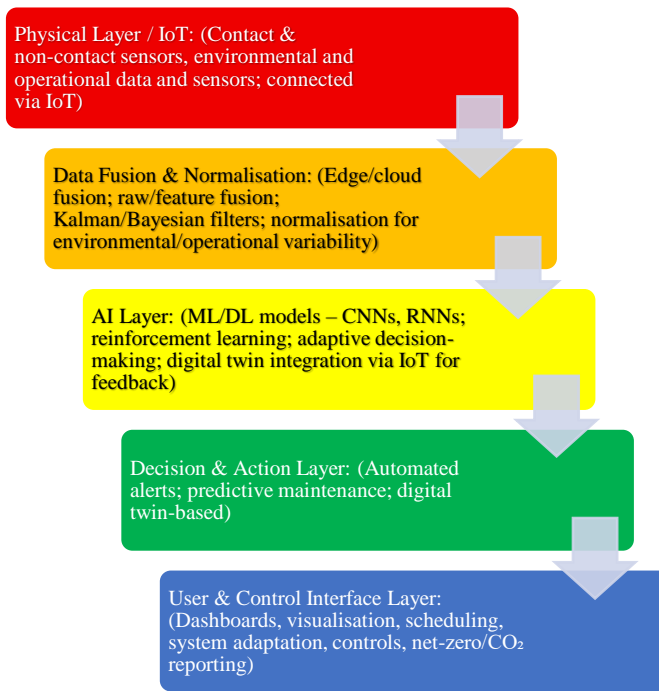


Figure 2. Schematic of the layers of FREAM-SHM framework

This system represents a significant leap forward in structural health monitoring and management. By combining advanced sensor technologies, AI, IoT, and predictive analytics, it provides a comprehensive solution for real-time, adaptive, and sustainable infrastructure management. The computational framework driving the system ensures it can process vast amounts of data, predict future structural performance, and optimise operational conditions dynamically.

While the DREAM-SHM framework offers transformative potential, its implementation at scale presents several challenges primarily rooted in interdisciplinary coordination. Successful deployment requires the integration of diverse expertise across structural engineering, data science, sensor technologies, and artificial intelligence, which demands not only cross-disciplinary collaboration but also specialised training to bridge gaps in knowledge and practice. From an ethical standpoint, careful consideration must be given to the types of human and operational information shared with the system, particularly in contexts involving surveillance, usage patterns, or sensitive infrastructure behaviour. In addition, maintaining cybersecurity and the resilience of communication networks becomes critical, as the framework relies on distributed sensing, edge processing, and cloud-based integration. Despite these challenges, the practical realisation of DREAM-SHM remains promising. The system unlocks the next generation of intelligent infrastructure, where structures are not only monitored but also able to self-adapt and self-maintain. By doing so, DREAM-SHM promotes safety, efficiency, and sustainability in the built environment, while also providing a unifying platform that encourages collaboration between academia and industry. It serves as a compelling motivation for advancing research, developing standards, and forging partnerships that can help turn this vision into reality.

## REFERENCES

- [1] D. Adams, *Health monitoring of structural materials and components: methods with applications*. 2007: John Wiley & Sons.
- [2] Y. Ji, et al., *Real-time in-service structural health monitoring method based on self-sensing of CF/PEEK prepreg in automated fiber placement (AFP) manufactured parts*. Composites Part A: Applied Science and Manufacturing, 2025. **194**.
- [3] C. Surace and C. Surace, *Novel Approaches for Structural Health Monitoring*. 2021, Basel, Switzerland: MDPI - Multidisciplinary Digital Publishing Institute.
- [4] A. Rytter, *Vibrational based inspection of civil engineering structures*. 1993.
- [5] A. Entezami, *Structural health monitoring by time series analysis and statistical distance measures / Alireza Entezami*. 1st 2021. ed. PoliMI SpringerBriefs. 2021, Cham, Switzerland: Springer.
- [6] C.R. Farrar and K. Worden, *An introduction to structural health monitoring*. Philosophical Transactions of the Royal Society A: Mathematical, Physical and Engineering Sciences, 2007. **365**(1851): p. 303-315.
- [7] L. Jerome Peter, S. Arvind, H.L. Kincho, S. Hoon, and R.F. Charles. *Design of a wireless active sensing unit for structural health monitoring*. in *Proc.SPIE*. 2004.
- [8] H. Sarmadi, A. Entezami, K.-V. Yuen, and B. Behkamal, *Review on smartphone sensing technology for structural health monitoring*. Measurement, 2023. **223**: p. 113716.
- [9] T.M. Fayyad, S. Taylor, K. Feng, and F.K.P. Hui, *A scientometric analysis of drone-based structural health monitoring and new technologies*. Advances in Structural Engineering, 2025. **28**(1): p. 122-144.
- [10] M. Pedram, A. Esfandiari, and M.R. Khedmati, *Damage detection by a FE model updating method using power spectral density: Numerical and experimental investigation*. Journal of Sound and Vibration, 2017. **397**: p. 51-76.
- [11] M. Pedram and A. Esfandiari, *Mitigating the Effect of Incomplete Measurement in Sensitivity-Based FE Model Updating by Enhanced Transfer Function*. Iranian Journal of Science and Technology, Transactions of Civil Engineering, 2019. **43**(1): p. 467-486.
- [12] A. Mardanshahi, A. Sreekumar, X. Yang, S.K. Barman, and D. Chronopoulos, *Sensing Techniques for Structural Health Monitoring: A State-of-the-Art Review on Performance Criteria and New-Generation Technologies*. Sensors, 2025. **25**(5).
- [13] M. Pedram, A. Esfandiari, and M.R. Khedmati, *Finite element model updating using strain-based power spectral density for damage detection*. Structural Control and Health Monitoring, 2016. **23**(11): p. 1314-1333.
- [14] A. Esfandiari, *Structural model updating using incomplete transfer function of strain data*. Journal of Sound and Vibration, 2014. **333**(16): p. 3657-3670.
- [15] X.Y. Li, L.X. Wang, S.S. Law, and Z.H. Nie, *Covariance of dynamic strain responses for structural damage detection*. Mechanical Systems and Signal Processing, 2017. **95**: p. 90-105.
- [16] Z. Helalat and A. Esfandiari, *Structural damage detection using a sensitivity-based model updating approach with autocorrelation function data*. Ships and Offshore Structures: p. 1-15.
- [17] A. Esfandiari, F. Bakhtiari-Nejad, A. Rahai, and M. Sanayei, *Structural model updating using frequency response function and quasi-linear sensitivity equation*. Journal of Sound and Vibration, 2009. **326**(3): p. 557-573.
- [18] W.K. Ao, D. Hester, and C. Higgins. *Using approximately synchronised accelerometers to identify mode shapes: A case study*. in *9th International Conference on Structural Health Monitoring of Intelligent Infrastructure: Transferring Research into Practice, SHMII 2019*. 2019. International Society for Structural Health Monitoring of Intelligent ....
- [19] S.K.T. Grattan, S.E. Taylor, T. Sun, P.A.M. Basheer, and K.T.V. Grattan, *Monitoring of Corrosion in Structural Reinforcing Bars: Performance Comparison Using In Situ Fiber-Optic and Electric Wire Strain Gauge Systems*. IEEE Sensors Journal, 2009. **9**(11): p. 1494-1502.
- [20] X. Zhang, L. Long, W. Broere, and X. Bao, *Smart sensing of concrete crack using distributed fiber optics sensors: Current advances and perspectives*. Case Studies in Construction Materials, 2025. **22**.
- [21] R. Soman, et al., *Investigating the effect of orientation of polarization maintaining fiber Bragg grating sensor on its sensitivity to fundamental symmetric and antisymmetric guided wave modes*.

- Measurement: Journal of the International Measurement Confederation, 2025. **252**.
- [22] N.T.C. Nhung, et al., *Development and Application of Linear Variable Differential Transformer (LVDT) Sensors for the Structural Health Monitoring of an Urban Railway Bridge in Vietnam*. Engineering, Technology and Applied Science Research, 2023. **13**(5): p. 11622-11627.
- [23] K. Alkady, A.G. Rasquinha, J.T. Brandl, C.E. Wittich, and C. Detweiler. *Target-Free, Vision-Based System Identification of Civil Structures Using Unmanned Aerial Vehicles*. in *Structural Health Monitoring 2023: Designing SHM for Sustainability, Maintainability, and Reliability - Proceedings of the 14th International Workshop on Structural Health Monitoring*. 2023.
- [24] S.T. Vegas and K. Lafdi, *A literature review of non-contact tools and methods in structural health monitoring*. Eng. Technol. Open Access J., 2021. **4**(1): p. 9-50.
- [25] D. Lydon, et al., *Development and field testing of a vision-based displacement system using a low cost wireless action camera*. Mechanical Systems and Signal Processing, 2019. **121**: p. 343-358.
- [26] W. Dong, X. Wang, G. Zhao, and Q. Mao, *A novel digital image correlation based on a reliable subset strategy for discontinuous displacement measurement*. Optics and Lasers in Engineering, 2025. **191**.
- [27] H. Habenzu, *Development of Structural Assessment Approaches for Bridges using Vision Based Unmanned Aerial Systems*. 2023, Queen's University Belfast.
- [28] H. Habenzu, P. McGetrick, and D. Hester. *Towards automated UAV assisted bridge inspections using photogrammetry and image processing techniques*. in *Civil Engineering Research in Ireland Conference 2020*. 2020.
- [29] F. Shahriyar, et al., *AI-based bridge maintenance management: a comprehensive review*. Artificial Intelligence Review, 2025. **58**(5): p. 135.
- [30] M. Pedram, et al., *Experimental investigation of subsurface defect detection in concretes by infrared thermography and convection heat exchange*. Journal of Civil Structural Health Monitoring, 2022. **12**(6): p. 1355-1373.
- [31] M. Pedram, et al., *Experimental evaluation of heat transition mechanism in concrete with subsurface defects using infrared thermography*. Construction and Building Materials, 2022. **360**: p. 129531.
- [32] M. Pedram, et al., *Objective characterisation of reinforced concrete with progressive corrosion defects through clustering and thresholding of infrared images*. Measurement, 2024. **225**: p. 114017.
- [33] M. Pedram, S. Taylor, G. Hamill, and D. Robinson. *Subsurface defect detection in concrete by active infrared thermography*. in *IABSE Symposium: Challenges for Existing and Oncoming Structures*. 2022. International Association for Bridge and Structural Engineering (IABSE).
- [34] M. Pedram, S. Taylor, G. Hamill, and D. Robinson. *Effect of thermal excitation mechanism on detection of subsurface defects in concrete using infrared thermography*. in *International Conference on Structural Health Monitoring of Intelligent Infrastructure: Transferring Research into Practice, SHMII*. 2022. International Society for Structural Health Monitoring of Intelligent Infrastructure, ISHMII.
- [35] M. Pedram, S. Taylor, D. Robinson, and G. Hamill. *FEA for improved implementation of IRT for monitoring of concrete bridges*. in *Procedia Structural Integrity*. 2024.
- [36] T. Omar and M.L. Nehdi, *Remote sensing of concrete bridge decks using unmanned aerial vehicle infrared thermography*. Automation in Construction, 2017. **83**: p. 360-371.
- [37] G.F. Sirca Jr and H. Adeli, *Infrared thermography for detecting defects in concrete structures*. Journal of Civil Engineering and Management, 2018. **24**(7): p. 508-515.
- [38] M. Jankü, P. Církle, J. Grošek, O. Anton, and J. Stryk, *Comparison of infrared thermography, ground-penetrating radar and ultrasonic pulse echo for detecting delaminations in concrete bridges*. Construction and Building Materials, 2019. **225**: p. 1098-1111.
- [39] F. Zhang, Y. Fu, K. Shen, Y. Zhang, and J. Wang, *Distributed edge intelligence for structural dynamic response estimation using knowledge distillation and data fusion*. Engineering Structures, 2025. **335**: p. 120406.
- [40] M.S. Ram, et al. *Data Fusion Opportunities in IoT and its Impact on Decision- Making Process of Organisations*. in *2022 6th International Conference on Intelligent Computing and Control Systems (ICICCS)*. 2022.
- [41] X. Qin and Y. Gu, *Data fusion in the Internet of Things*. Procedia Engineering, 2011. **15**: p. 3023-3026.
- [42] S. Brodt, M. Inostroza, N. Niethard, and J. Born, *Sleep-A brain-state serving systems memory consolidation*. Neuron, 2023. **111**(7): p. 1050-1075.
- [43] J. Born and I. Wilhelm, *System consolidation of memory during sleep*. Psychological Research, 2012. **76**(2): p. 192-203.
- [44] H. Fu, et al., *AIoT: Artificial Intelligence and the Internet of Things for Monitoring and Prognosis of Systems and Structures*. IEEE Transactions on Instrumentation and Measurement, 2025. **74**: p. 1-32.
- [45] S. Theodoridis, *Machine Learning: A Bayesian and Optimization Perspective, Second Edition*. Machine Learning: A Bayesian and Optimization Perspective, Second Edition. 2020. 1-1131.
- [46] G. Xu and T. Guo, *Advances in AI-powered civil engineering throughout the entire lifecycle*. Advances in Structural Engineering, 2025. **28**(9): p. 1515-1541.
- [47] Y. Fang, C. Li, S. Wu, and M. Yan, *A New Approach to Structural Damage Identification Based on Power Spectral Density and Convolutional Neural Network*. International Journal of Structural Stability and Dynamics, 2025. **25**(7).
- [48] M. Almahakeri, A.J. Al-Mahasneh, M. Abu Mallouh, and B. Jouda, *Deep neural network-based intelligent health monitoring system for oil and gas pipelines*. Applied Soft Computing, 2025. **171**.
- [49] B. Qu, P. Liao, and Y. Huang, *Outlier Detection and Forecasting for Bridge Health Monitoring Based on Time Series Intervention Analysis*. SDHM Structural Durability and Health Monitoring, 2022. **16**(4): p. 323-341.
- [50] Q. Ge, C. Li, and F. Yang, *Research on the Application of Deep Learning Algorithm in the Damage Detection of Steel Structures*. IEEE Access, 2025. **13**: p. 76732-76746.
- [51] A.P.M. Velenturf and P. Purnell, *Principles for a sustainable circular economy*. Sustainable Production and Consumption, 2021. **27**: p. 1437-1457.
- [52] F. Sommesse, et al., *Towards a Regenerative and Climate-Resilient Built Environment: Greening Lessons from European Cities*. Buildings, 2025. **15**(11): p. 1878.
- [53] S. Kaewunruen, C. O'Neill, and P. Sengsri, *Digital twin-driven strategic demolition plan for circular asset management of bridge infrastructures*. Scientific Reports, 2025. **15**(1): p. 10554.
- [54] D. Sahu, et al., *A multi objective optimization framework for smart parking using digital twin pareto front MDP and PSO for smart cities*. Scientific Reports, 2025. **15**(1): p. 7783.
- [55] F. Fanian, M. Kuchaki Rafsanjani, and M. Shokouhifar, *Combined fuzzy-metaheuristic framework for bridge health monitoring using UAV-enabled rechargeable wireless sensor networks*. Applied Soft Computing, 2024. **167**.

# Best Practices for Data Acquisition System Design: Practical Wisdom for Engineers and Practitioners

Tony Simmonds<sup>1</sup>, Brent Randall<sup>2</sup>

<sup>1</sup>AJS Consult USA LLC, Asheville, North Carolina

<sup>2</sup>Campbell Scientific, Inc. 815 West 1800 North, Logan, Utah, USA

email: t.simmonds@re-monitor.com, brandall@campbellsci.com

**ABSTRACT:** As global infrastructure ages and demands on new and existing structures increase, effective monitoring programs are essential for managing risk and public safety. This paper provides a practical guide for practitioners to design and implement structural health monitoring (SHM) systems, leveraging the combined expertise of the authors, who have extensive experience with leading equipment manufacturers.

Building on the 10 Steps of Data Acquisition System Design, the paper outlines best practices for developing robust monitoring systems tailored to bridges, dams, and other critical infrastructure. These steps include defining objectives, selecting appropriate sensors, communications design, data acquisition (DAQ) system design, power system considerations, civil works and mounting structures, installation, and managing data effectively.

A significant focus is placed on sensor and DAQ selection, exploring their critical roles in SHM system performance. The paper covers practical techniques for selecting, installing, maintaining, calibrating, and verifying sensors across traditional analog, frequency, and digital technologies. Examples from large channel count wired systems and distributed wireless monitoring systems are shared to illustrate diverse applications.

This paper aims to deliver actionable insights and practical wisdom, equipping attendees with the tools to overcome real-world challenges and achieve reliable, scalable, and long-lasting SHM implementations.

**KEY WORDS:** Structural Health Monitoring (SHM); Data Acquisition System Design; Sensor Selection; Critical Infrastructure Monitoring; Risk Management; Monitoring System Implementation; Wireless and Wired Monitoring

## 1 INTRODUCTION

Improvements and technological developments in sensors, data acquisition systems, and software in recent years have enabled engineers to implement advanced monitoring solutions on critical Structural Health Monitoring (SHM) projects worldwide. These systems often comprise hundreds or even thousands of sensors, delivering real-time performance data through synchronized acquisition platforms and intuitive visualization tools.

These developments, coupled with a rising demand for timely and reliable data, often exceed the capability of that which can be manually collected or interpreted, and thus necessitates the need for robust automation for real-time monitoring to detect potential hazards in advance.

Today, automated monitoring systems are far more cost-effective, reliable, and user-friendly than ever before, making them feasible not only for large projects with many sensors, for a more comprehensive assessment of structural behavior, but also for smaller-scale projects which, until recently, were rarely considered for, or enjoyed the benefits of automation.

There are also those projects, which started out as being manually read, but later moved to automated systems because of one or all the following: being unable to find enough qualified staff to read all the instruments, being unable to safely access the instruments to read them manually and being unable to obtain reliable data through manual readings.

While automated monitoring systems help reduce the burden on project owners by enabling reliable and timely data collection without interfering with ongoing construction

activities. They also facilitate the early identification of potential issues, allowing for prompt implementation of corrective measures. Moreover, the development of wireless network technologies has made it easier to expand or reconfigure monitoring systems quickly, with minimal disruption to both the existing setup and the construction process. To support this progression from concept to implementation, Figure 1 illustrates a logical sequence of design steps that guide the development of a robust SHM system.

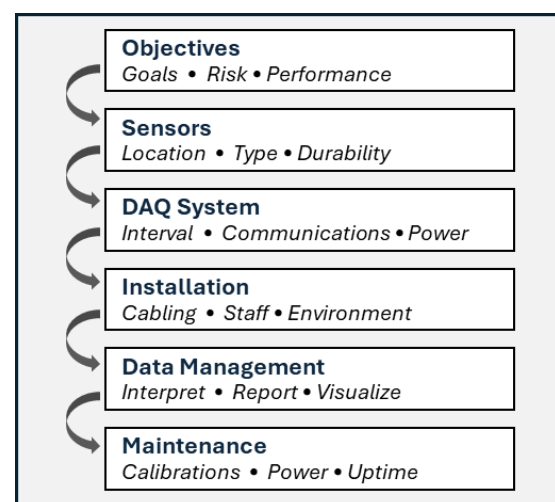


Figure 1: An overview of the SHM design process.



## 2 MONITORING OBJECTIVES

The success of any SHM project, whether automated or manual, hinges on meticulous planning, precise execution, and the development of an action plan (or plans) to address the findings based on the collected data. Peck's Observational Method laid the foundational philosophy for most monitoring programs, which Dunnicliff further enhanced with a detailed, systematic approach.

Essentially, Peck emphasized the importance of defining the geotechnical questions that need to be answered and then selecting the appropriate instruments and their placement to help answer those questions; stating, without a question, there is no need for instrumentation. Dunnicliff expanded on this by underscoring the necessity of defining the purpose of the instrumentation, asserting that it should only be used if there is a valid, defensible reason.

### 2.1 *Define the Appropriate DAS*

Before the Data Acquisition System (DAS) is designed, consideration should be given to the present (and future) scope of the monitoring system, with a bias on starting simple, using systems that are easily scalable as the project needs grow, and only implemented when required, after the initial system is functioning and is well understood.

Other considerations should determine the choice between site vs cloud hosted platforms, subscription vs capital expenditures (CAPEX), the ultimate sensor, DAS, and software suppliers, the maintenance requirements and who will be ultimately responsible for operation of the DAS the over the life of the project. When these decisions have been made, we can then start to look at sensor selection and DAS design in earnest.

### 2.2 *Stakeholders and their Interests*

Structural Health Monitoring (SHM) projects often involve a wide range of stakeholders, each with distinct objectives, responsibilities, and perspectives on data utility. Key stakeholders typically include project owners, engineers, contractors, regulators, insurers, asset operators, and in some cases, the general public. Project owners and developers are primarily motivated by risk reduction, cost control, and regulatory compliance, often seeking early warnings to avoid catastrophic failure and unplanned downtime. Engineers use monitoring data to validate design assumptions, assess structural behavior under real-world conditions, and guide adaptive decision-making during construction or operation. Contractors may rely on SHM data to sequence work safely, protect temporary works, or defend against claims. Regulators and permitting authorities seek assurance that infrastructure meets safety and environmental standards, with SHM providing a traceable, defensible record of performance. Insurers may view monitoring as a tool to reduce liability and claims exposure by demonstrating proactive asset management. Operators and maintenance teams use SHM systems to prioritize interventions, plan maintenance efficiently, and extend the life of the structure. Finally, for high-visibility projects, community stakeholders and the public may demand transparency and accountability—especially when safety is a concern—making clear, visual communication of monitoring data essential. Understanding these varied

motivations is crucial in designing a system that delivers the right data to the right people at the right time.

## 3 SENSORS

Sensors general definition, sensors are devices that detect and respond to physical input from the environment in which they are installed. Inputs may include parameters such as temperature, strain, pressure, deformation and inclination, or other environmental or structural conditions. Sensors then convert their input into signals that can be read by an observer, with a portable readout instrument, or with an electronic system, such as a computer or DAS.

The choice of any sensor is determined, for the most part, by the application and the environment in which they are to be deployed. As they must function satisfactorily, often under very harsh conditions, throughout the life of the project, they should be as simple in concept as is consistent with their function (with respect to accuracy, repeatability and response time).

Additionally, they should be robust and reliable, to be durable under the environmental and operating conditions in which they will be deployed and, ideally, have a satisfactory (well proven) performance history. Moreover, the sensors should provide optimum cost benefit ratios to deliver acceptable performance throughout the life of the project considering the sum of purchase, installation, maintenance and monitoring.

For critical applications, and/or at primary monitoring locations, consideration should be given to adopting back-up instruments, maybe of a different technology to corroborate the measurements provided and/or to substitute in the event of primary sensor failure or damage.

### 3.1 *Sensor Selection*

In keeping with the intent of this paper, with respect to best practices and practical wisdom, it is appropriate, at this point, to remind ourselves of the systematic approach to designing monitoring systems as defined by John Dunnicliff in his renowned book, "Geotechnical Instrumentation for Monitoring Field Performance" published in 1988. In this context he identified 25 important steps to be considered and, wherein, the selection of the sensors comes in at step number 8, after steps addressing; the project conditions, mechanisms which control behavior, the purpose of the instrumentation and the parameters to be measured, the predicted magnitudes of change, the remedial action to be made and the responsibility of the various stakeholders. Readers are encouraged to read more on this subject in Chapter 26 of the aforementioned reference.

When selecting a sensor, several factors need to be considered to ensure it meets the requirements of your application. Following are some key factors:

**Type of Measurement** - The primary consideration is to choose a sensor which can detect the measurand, i.e. the specific physical quantity, object or property to be measured (e.g., temperature, pressure, strain, load etc.).

**Environmental Conditions** - Consider factors such as temperature, humidity, chemicals and electromagnetic interference which can affect the sensor performance. Keep in mind too, not only any limitations of the sensor in adverse environments, but also and associated cabling or conduits.

**Durability and Lifespan** - For harsh or long-term applications, sensor ruggedness and reliability are critical, check with the manufacturer for compatibility and compliance.

**Measurement Range** - Ensure the sensor's measuring range aligns with the physical range of the application to obtain precise readings. While choosing a sensor with a range greater than that which is likely to be measured may be considered safe, be mindful of any corresponding loss in accuracy and resolution.

**Accuracy and Precision** - Ensure the sensor provides the necessary accuracy (how close a measurement is to the true or actual value) and precision (how close repeated measurements are to each other) for your application

**Resolution/Sensitivity** - Understand what the smallest change in measurand is that the sensor can deliver and check to determine that the DAS to which the sensor will be connected can discriminate such changes (see also Measurement Range above)

**Response Time** - As some applications (esp. real-time systems, and where dynamic measurements are required) often need sensors with fast response times, ensure that the selected sensor can satisfy same or, with the appropriate DAS, be readily converted from one taking static measurements to dynamic measurements.

**Excitation and Power Consumption** - Is especially relevant in battery-powered or remote systems, therefore it is necessary to ensure the DAS can deliver the required excitation and, at the same time, not introduce any errors into the measurements.

**Output Type and Signal Conditioning** - Understand whether the sensor outputs analog or digital signals, or communicates via protocols like I2C, SPI, etc. and if the associated DAS requires protection circuits and signal conditioners to minimize electrical noise and errors. (Digital sensors are often preferred over analog sensors as they can reduce errors during data conversion)

**Size and Mounting Constraints** - It is important to understand the physical dimensions and weight of the sensor, and how and where it will be installed. Make sure adequate space is available for installation and that any fixtures required for mounting will not affect sensor operation or performance. Ensure that the physical size or weight of the sensor does not negatively impact the environment being measured.

**Calibration and Maintenance** - Understand any calibration and maintenance requirements required for the sensor to continue to deliver according to its stated accuracy or, where sensor access and recalibration is not possible, opt for sensors with proven long-term stability (See also Section 3.3)

**Price and Availability** - Does the price of the sensor meet the budget and is it readily available for deployment according to the project schedule and/or in the event replacements are needed. Consideration might also be given to the budget for more costly (reliable) sensors for long-term applications where replacement is not possible.

Careful consideration of these factors will help you choose a sensor that is efficient, reliable, and cost-effective for your specific needs.

### 3.2 Sensor Installation

Sensor performance is often only as good as the way in which it was installed. Therefore, it is critical that the correct installation procedures are followed and documented. Of

course, installation methods will vary according to sensor type but adhering to the following guidelines will help deliver reliable performance and accurate data.

#### Plan Installation Procedures (Dunnicliff)

- Prepare written step-by-step procedures well in advance of scheduled installation dates
  - Including a detailed listing of required materials and tools
- Prepare installation record sheets
- Plan staff training
- Coordinate installation plans with the construction contractor
- Plan access needs and any protection of the installed instruments from damage/vandalism
- Prepare installation schedule consistent with the construction schedule.

#### Pre-Installation Tests (Dunnicliff)

- Check the Documentation
  - Check, by comparing with procurement document,
  - That model, dimensions, and materials are correct
  - That quantities received correspond to quantities ordered
- Check the Instruments
  - Check the cable length(s)
  - Check tag numbers on instrument & cable
  - Verify that all components fit together in the correct configuration
  - Check all components for signs of damage in transit
- Check Data Provided by the Manufacturer
  - Examine factory calibration curve & tabulated data, to verify completeness
  - Examine manufacturer's final quality assurance inspection checklist, to verify completeness
- Function Checks
  - Connect to readout & induce change in parameter to be measured
  - Make and remake connectors several times, to verify correct functioning
- Calibration Checks (Note: This is an approximate check only)
  - Check 2 or 3 points if possible
  - Allow sensors to come to thermal equilibrium
  - Check Zero reading
  - Calibrate any Readout Instruments (used during installation and troubleshooting) regularly

### 3.3 Sensor Calibration & Maintenance

Where accuracy, reliability and consistency are required it is particularly important that sensors are calibrated correctly and in accordance with internationally recognized standards.

**Accuracy** - Certain sensors may drift over time and, if not regularly calibrated, can report biased data. Calibration

guarantees that the sensor output is traceable to a known standard or reference which is critical when taking trustworthy measurements for confident decision making. (Where sensors are inaccessible after installation consider using types with proven long-term stability).

**Consistency** – Where different sensors are used in any one project, calibration allows data from each device to be compared over time. For example, two temperature sensors, from the same batch, may read slightly differently unless calibrated.

**Safety and Compliance** – It goes without saying that incorrect readings can lead to safety hazards including loss of reputation, asset and or life. Therefore, it is common practice for regulatory standards to require periodic calibration to maintain certification and indemnity.

**System Performance** – In digital twins, where historical data is integrated with, and relies upon, updates from sensors in DAS to represent near real time status, it is of paramount importance that sensors are properly calibrated as small inaccuracies can propagate and degrade the system's overall performance or decision-making.

**Cost Savings** - Accurately calibrated sensors help prevent inaccurate data from causing false conclusions, resource waste, and or project failures and delays.

Similarly, sensor maintenance is equally important as it contributes to ensuring accuracy, reliability, and longevity, all of which are critical for making informed decisions, maintaining asset quality, complying with safety standards, and avoiding costly downtime or repairs.

## 4 DESIGN - DATA ACQUISITION SYSTEM

A DAS—also referred to as a DAQ, ADAS, or ADAQ—is the electronic backbone of any SHM program. It serves to collect, condition, log, and transmit sensor data from the field to the end user or database. Effective DAS design must align with the sensor types and quantities, sensor placement, measurement timing requirements, communication protocols, and site-specific environmental constraints. Additionally, DAS architecture should anticipate future scalability, integration with other systems, maintenance access, and power availability.

### 4.1 System Architecture & Scalability

DAS architectures for SHM systems typically fall into two categories: **centralized (wired)** and **distributed (wireless)**. In practice, hybrid approaches are often adopted to best suit varying site conditions, sensor layouts, and project phases.

**Centralized (Wired) System** – Often built using a customizable datalogger or modular components, a centralized system offers the flexibility and expandability to read a wide variety of sensors and can often be expanded to be a high channel count or high speed system.

Advantages include:

- Easier serviceability and diagnostics via a single access point
- Superior time synchronization across measurements
- Suited for real-time or safety-critical applications

- Flexibility in supporting advanced measurements and redundancies
- Robust power backup options

Additional considerations or challenges may include:

- Longer sensor cable runs may increase cost
- Higher initial setup time and effort

**Distributed (Wireless) DAS** – These involve smaller, self-contained DAS nodes placed closer to sensor clusters and typically use radio, LoRa, or cellular protocols for data transmission.

Advantages include:

- Reduced cabling complexity
- Modular installation
- Natural electrical isolation (air gap) for surge protection

Additional considerations or challenges may include:

- Requires management of wireless networks and data synchronization
- Battery-powered nodes may limit lifespan or require frequent servicing
- Multiple access points for maintenance

**Scalability** – A good DAS design should accommodate changes in monitoring scope over time. Scalability should include:

- Additional sensor capacity (via modularity or spare channels)
- Upgradeable communications infrastructure
- Data routing to multiple stakeholders or databases
- Power system upgrades (e.g., larger solar arrays, battery banks)
- Lifecycle support—ensure vendors provide long-term maintenance and part availability over the next 1, 5, or 10 years.

### 4.2 System Timing

Time management is central to a reliable monitoring program, understanding the different timing intervals is needed to ensure that the system operates as intended. Pro-Tip: just because you can collect data fast doesn't necessarily mean that you should. Timing considerations may include:

- **Sampling Rate:** Frequency of raw sensor measurements
- **Recording Interval:** Frequency of data logging, which may include statistical reduction (min/max/avg)
- **Transmission Interval:** Frequency of data being sent to the database/user
- **Measurement Synchronization:** How critical it is for measurements from different sensors or systems to be time-aligned. This becomes increasingly important—and potentially more complex—when multiple data acquisition devices are deployed across a site, especially when correlating events across a site.



### 4.3 Data Collection

The frequency of data collection and transmission should align with the decisions that rely on that data. Data must be transmitted—and reviewed—at intervals no longer than the maximum time allowed to respond to undesirable system behavior. For instance, a safety monitoring system may require data transmission every second to enable timely alarms that protect personnel. In contrast, a system used for regulatory reporting might only need to collect data monthly or quarterly, often in conjunction with manual site inspections.

### 4.4 Communications

Communications are typically considered in two layers: onsite communication between sensors, loggers, and gateways; and offsite communication from a device to the cloud, server, or database. Each layer offers various communication methods, but these can generally be categorized into two types—wired and wireless—each with its own set of considerations.

**Wired-Onsite:** Ideal for permanent installations, wired onsite systems offer high reliability and noise immunity but require protected cable routing and can be more costly initially but may have a lower total cost of ownership (lower maintenance). Onsite wired systems may use a combination of copper or fiberoptic cables to address communication distance or electrical noise interference challenges. A wired onsite system is generally built for the specific and exclusive needs of the monitoring system.

**Wireless-Onsite:** Enable fast, modular deployment in difficult locations but require careful planning for power, interference, and network management. Generally built using radios that offer a point-to-point or mesh network communication. Wireless performance and protocols used are based on the selected wireless technology.

**Wired-Offsite:** Wired offsite connections deliver secure, consistent performance but is reliant on existing network infrastructure or it may need to be added. Typically, this taps into an existing ethernet network that is already existing or needs slight improvements to accommodate the needs and connection points of the monitoring system.

**Wireless-Offsite:** Wireless offsite communication provides flexible, trench-free connectivity for remote sites, but it depends on external networks and typically requires a subscription. Most often, this involves using a cellular or satellite network managed by a third-party provider, accessed through a compatible modem and associated service plan.

**Pro Tip:** When considering a communication option, consider seasonal conditions, for example, a radio network installed in the winter/spring may work great but the added vegetation in the summer could significantly impact onsite radio performance or give consideration to winter conditions where deep snow may cover communication antennas.

### 4.5 System Power: Power Budgeting & Backup

The power system is the backbone of any remote data acquisition system and is often a primary point of failure if not properly designed. Power configurations can range from simple, single-use batteries that require periodic replacement to advanced systems incorporating solar panels, charge controllers, and rechargeable batteries—ideal for long-term or high-demand deployments. Self-contained DAS units often

favor compact, non-rechargeable batteries for their simplicity and reliability, while modular or scalable systems typically use rechargeable batteries paired with external charging sources such as solar or AC power. Because total power consumption depends on design decisions—like sensor type and duty cycle, logging hardware, communication method (e.g., radio, cellular, satellite), and data collection frequency—the power system should be specified last. When designing it, account for worst-case scenarios such as reduced battery performance in cold temperatures, limited sunlight during winter months, and extended outages caused by events like snow-covered solar panels.

### 4.6 Installation Considerations

A successful installation requires careful planning and thorough verification of sensor operation, wiring, communication links, and power systems—both in the office and in the field. Equipment should be securely mounted in enclosures designed to withstand environmental challenges. When selecting cabinets or enclosures, consider factors such as humidity, temperature extremes, corrosive environments (e.g., seawater or acidic mine conditions), lightning protection, and the need for secure mounting. A site visit before installation is essential to assess available utilities, site conditions, cable routing, and required structures for a quality setup. As with any project, qualified personnel are crucial to ensure proper handling, installation, and operation verification. Comprehensive documentation is key to a quality installation, outlining system operations, wiring, equipment labeling, and data access. Since deployed equipment often transitions through multiple field staff over time, well-documented and carefully executed installation practices help ensure the system's longevity, beyond the tenure of any individual staff member.

## 5 MAKING SENSE OF THE DATA

The objectives of a monitoring system must be clearly defined at the start of any project. The data produced should directly address the specific questions that need to be answered. The value of any monitoring system's data depends on its interpretability, reliability, and ability to be transformed into actionable insights for key stakeholders.

### 5.1 Data Interpretation

Interpreting sensor data depends on the type of measurement and the reference baseline used for comparison. Measurements with clear reference points—such as water level (relative to elevation) or tilt (relative to gravity)—are easier to understand, and thresholds can easily be established based on design specifications or comparing to other sensors. However, measurements like strain may be more relative and require establishing a baseline at installation or during an initial project event. Regardless of the sensor type, engineers must interpret data within the context of the monitored structure, considering sensor placement, behavioral characteristics, environmental conditions, and long-term performance trends.

### Questionable Data & Anomalies

All monitoring systems will generate data that raises questions at some point. Questionable data may stem from external

factors, such as environmental changes or nearby construction activities, or issues within the measurement system itself, such as sensor interference from electromagnetic noise, damaged cables, or inadequate power supply. Additionally, stakeholders might question data when it contradicts project schedules or crew activities, often to avoid disruptions.

When data is questioned, a useful first step is to ask: "Is what I'm seeing possible, or am I dealing with a faulty measurement?" In cases where the data could impact safety or project costs, the system should incorporate redundant measurements using different technologies to quickly verify whether the reported data reflects actual site conditions. While anomalies may initially appear alarming, they can often become part of the normal dataset as understanding of the system's behavior improves over time. Caution is needed when dismissing outliers as anomalies, as this could result in missing genuine early warnings. If a sensor consistently generates unreliable data, further investigation is necessary to address the root cause.

### 5.2 Reporting & Visualization

Data that cannot be easily understood or communicated effectively will not be used. The key question in determining how to report or visualize data is: who will use this data, and what format will best help them understand it? Technical users, such as engineers and scientists, may prefer raw data, like simple tables, for further analysis. In contrast, data intended for the general public should be presented visually, with clear indicators of what the data represents, where it's installed on the structure, and what thresholds exist and what to do if those thresholds are met. Many SHM projects involve multiple audiences, so data presentation should evolve to meet the needs of different stakeholders throughout the project's lifecycle.

## 6 CONCLUSION

Over the past ten years or so, modern DAS has played a key role in supporting site decisions that enhance the health and safety critical projects, and those working on them, all the while delivering significant time and cost savings during construction and operation and providing input for safer and more cost-effective designs.

Advances in sensor technology, data acquisition systems, and cloud computing have resulted in many monitoring programs involving a greater number of instruments than previously used, all of which collect data at much higher frequencies and generate vast volumes of information.

Thus, it is purported that a well-designed data acquisition system (DAS) will offer several key benefits, especially on projects which involve a large number and variety of sensor types:

**Data Integration Across Sensor Types** - Seamlessly collects and unifies data from diverse sensors (e.g., geotechnical, structural, environmental), enabling holistic analysis and reduces the need for manual aggregation or format conversions.

**Real-Time Monitoring and Alerts** - Enables high-frequency data collection and real-time transmission, which facilitates immediate alerts when thresholds are breached, thereby improving safety and responsiveness.

**Improved Data Quality and Reliability** - Minimizes data loss, signal noise, and errors through appropriate filtering, calibration, and validation, thus ensuring accurate and consistent data across all sensor types.

**Scalability and Flexibility** - Supports the addition of new sensors and or sensor types or locations without re-engineering the entire system and adapts to evolving project needs, whether during construction or long-term monitoring.

**Centralized Data Management** - Consolidates data into a single, accessible platform, reducing fragmentation and enhancing collaboration among engineers, analysts, and decision-makers.

**Efficient Data Processing and Visualization** - Supports automated analysis, dashboards, and trend detection, reducing time spent on manual review and enabling timely insights to inform decision-making.

**Reduced Operational Costs** - Lowers labor costs associated with manual readings and data handling, while minimizing downtime and damage through proactive maintenance.

**Enhanced Regulatory Compliance and Reporting** - Provides traceable, well-documented data logs to meet legal, environmental, or safety standards, and simplifies reporting for stakeholders and authorities.

In closing, the authors wish to remind readers that it still remains appropriate, that no matter how well an instrumentation DAS and monitoring program is designed, it will ever replace the need for site surveys and visual inspections. While monitoring can check specific points continuously, and alert if alarm conditions are exceeded (in a timely manner), site surveys and visual inspections (although less frequent) allow for "macroscopic" observations to be made, that a network of instruments could quite easily miss; be warned.

## REFERENCES

- [1] Dunnycliff, John (1988). "Geotechnical Instrumentation For Monitoring Field Performance" Wiley Interscience
- [2] Randall, Brent (2023). "Fundamentals of Automated Field Instrumentation" Summit 47
- [3] Barrett, Jeff & Simmonds, Tony (2022). "The role of Automated Monitoring Systems: How to avoid being data-rich and information-poor". Proceedings of the 11<sup>th</sup> International Symposium Field Monitoring in Geomechanics

# From Insight to Action: Deploying SHM for a suspension bridge

Heikki Lilja<sup>1</sup>, Atte Mikkonen<sup>2</sup>, Eero Ukkonen<sup>3</sup>

<sup>1</sup>HLC Analytics, Finland; <sup>2</sup>SOFiN Consulting; <sup>3</sup>Savcor Oy

**ABSTRACT:** This paper presents the implementation of a structural health monitoring (SHM) system for a suspension bridge approaching the end of its service life. Constructed in the 1960s with a 220-meter main span, the bridge is the sole vital link to a region hosting key socioeconomic industries. Over time, heavy traffic—with vehicles often exceeding 80 tons—has led to pronounced fatigue issues. Throughout its operational life, extensive repairs—such as the addition of a cantilevered pedestrian lane, modifications to the bearing system, and hanger replacements—have been undertaken. More than a decade of monitoring via over 50 sensors has yielded comprehensive data that both ensures safety and informs maintenance strategies. A sophisticated finite element (FE) model, developed in 2023 and calibrated using real-time data, improved the correlation between simulated and actual performance. Following this, a streamlined near-real-time monitoring framework was established in early 2024 to promptly identify structural anomalies. Designed for adaptability, the SHM system can be implemented on various structures. This study highlights the importance of clear data presentation in enabling informed decisions that optimize infrastructure management and enhance operational safety.

**KEY WORDS:** SHM, suspension bridge, fatigue, data-informed decision making, safety, reliability, FEM, predictive maintenance, sustainability

## 1 BACKGROUND AND MOTIVATION

Ensuring the safety and longevity of aging infrastructure is increasingly challenging as many critical bridges worldwide approach or exceed their intended service life. Traditionally, structural integrity is assessed via periodic inspections—typically every three to six years—which may overlook gradual deterioration. Historically, bridge monitoring data has been analyzed on a case-by-case basis, a fragmented approach that hinders a comprehensive understanding of structural behavior over time. A shift toward a structured and standardized methodology is essential to interpret monitoring results more effectively, optimize sensor placement, reduce instrumentation costs, and fully leverage the rich datasets available. Grounded in big data principles, such an approach can transform stored information into actionable insights.

Constructed in the 1960s, the case bridge is the sole transportation route serving a region with vital socioeconomic industries. Unlike modern bridges, it was designed based on historical traffic load models that did not anticipate today's heavier vehicles and increased traffic density. Heavy trucks, often exceeding 80 tons, regularly traverse the structure, introducing forces well beyond the original design assumptions. Although various repairs have been undertaken over the years, concerns regarding progressive material fatigue and overall structural performance persist.

In response to these challenges, an SHM system was implemented to deliver real-time insights into structural behavior—facilitating early anomaly detection, proactive maintenance, and a reduction in the risk of sudden failures. By integrating continuous monitoring with analytical tools, this system represents a significant advancement in managing aging infrastructure.



Figure 1. The case bridge.

## 2 CHALLENGES IN MAINTAINING AGING BRIDGES

A significant portion of the bridge network was constructed over 50 years ago, using traffic load models that are no longer representative of current conditions. At the time of design, fatigue considerations were not always fully incorporated into design practices, leading to unforeseen long-term issues. Suspension bridges, such as the case bridge, face particularly complex challenges. Increased traffic loads exacerbate non-linear deformations and amplify fatigue effects, contributing to localized failures.

Traditional periodic inspections suffer from significant blind spots. Critical issues such as fatigue cracks and unforeseen deformations can evolve and propagate well between scheduled evaluations, resulting in missed opportunities for early intervention. This limitation underscores the urgent need for continuous, data-driven monitoring to capture dynamic structural behaviors in real time.

While periodic inspections provide valuable assessments, they



often fail to capture detailed long-term behavioral trends. Undetected fatigue cracks, excessive displacement, or gradual load redistribution may develop between inspections, increasing the risk of structural failure. This growing need for a proactive approach has driven the development of Structural Health Monitoring (SHM) systems. By continuously tracking critical parameters, SHM provides timely insights into bridge performance, allowing for early interventions and more informed maintenance decisions.

### 3 KEY STRUCTURAL CHALLENGES AND REPAIRS OF THE CASE BRIDGE

One of the problems detected has been the formation of fatigue cracks in the wind bracings, which has altered the bridge's behavior. In some cases, these changes have been noticeable under traffic loads, with visibly increased vibrations and unexpected movement patterns. However, assessing whether the main load-bearing components have also been affected remains a challenge.

Another significant concern was the corrosion of the hangers, particularly the shorter ones. Due to their positioning, these hangers experienced greater angular movements as the main cable deformed under traffic loads. This fluctuation in stress accelerated wear, leading to localized material deterioration. In 2020, a heavily corroded hanger was removed and subjected to laboratory testing, which provided crucial insights into the remaining safety margins of the hangers. The results confirmed that the less-corroded hangers were still within operational limits.



Figure 2. Corroded hanger



Figure 3. Installation of temporary hanger bars.

Additionally, the ongoing construction of a new cable-stayed bridge to the west of the case bridge has introduced further challenges. The transportation of construction materials over the existing bridge has led to increased loads, while related

activities—such as the drilling of large-diameter steel piles and controlled blasting—have induced minor disturbances. The continuous monitoring system has furnished real-time insights into the bridge's condition, thereby ensuring its safe operation throughout these construction activities.

These challenges illustrate the limitations of relying solely on periodic inspections. Although past repairs addressed specific damage, they did not provide a comprehensive picture of the bridge's evolving condition. This underscores the critical need for continuous monitoring to detect subtle structural changes before they escalate into major failures.

### 4 DESIGN AND IMPLEMENTATION OF SHM SYSTEM

The case bridge is equipped with over 50 sensors, including strain gauges, displacement sensors, accelerometers, as well as temperature and wind sensors. These instruments provide a comprehensive dataset for assessing the bridge's structural behavior under varying conditions. Over its lifespan, additional sensors were installed to monitor specific concerns, such as localized fatigue-prone areas; however, until recently, data analysis was performed sporadically and primarily in response to observed anomalies.

In 2023, the construction of a new bridge adjacent to the case bridge prompted a shift toward a more structured and systematic data analysis framework. The client required assurance that the existing bridge could safely serve its final years of operation while construction was ongoing. Consequently, a daily evaluation system was introduced to track changes in load distribution, deformations, and stress concentrations over time.

This transition from sporadic analysis to continuous monitoring has provided deeper insights into the bridge's behavior, significantly enhancing the ability to detect subtle structural changes before they escalate into critical issues. By integrating real-time sensor data with analytical tools, the monitoring framework has evolved from a reactive assessment method into a proactive instrument for infrastructure management.

### 5 FINITE ELEMENT MODEL CALIBRATION

Before beginning the more detailed structured data analysis phase, a state-of-the-art nonlinear finite element (FE) model of the case bridge was developed. This model was designed to replicate the bridge's actual behavior under modern traffic loads, using sensor data for validation. However, early comparisons between the model and real-world measurements revealed significant discrepancies, indicating that the first iteration did not fully capture the actual structural response.

This phase was crucial in enhancing the understanding of the bridge's performance. Iterative refinements identified previously overlooked structural traits, leading to a more accurate representation of the bridge's behavior. To ensure reliable comparisons, known heavy vehicles with documented

axle weights were used as test loads during operation, allowing for direct validation of the model against real-world conditions.



Figure 4. 3D visualization of the FE model.

For example, calibration provided insights into the behavior of the elastomeric bearings between the deck structure (a concrete slab with longitudinal steel girders) and the main steel truss. The bridge deck was observed to move unpredictably in both longitudinal directions, raising concerns until the behavior was computationally verified and found to be harmless, given the bridge's remaining service life.

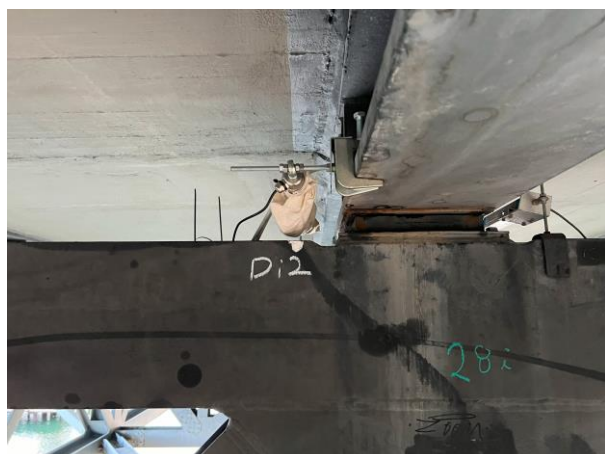


Figure 5 deck structure supported by the steel cross truss by elastomeric bearings.

This movement had not been anticipated; the elastomeric bearings had deteriorated to such an extent that their response was no longer elastic and, therefore, not linear. Instead of behaving elastically, the bearings acted as fixed supports until the friction between the rubber and steel was overcome, causing them to slide. This resulted in residual movement, which initially caused confusion until it was successfully captured in the FE model and understood. A comparison of monitoring results and the FE model (depicting the movement of the concrete slab relative to the cross beam) is shown in Figures 6 and 7.

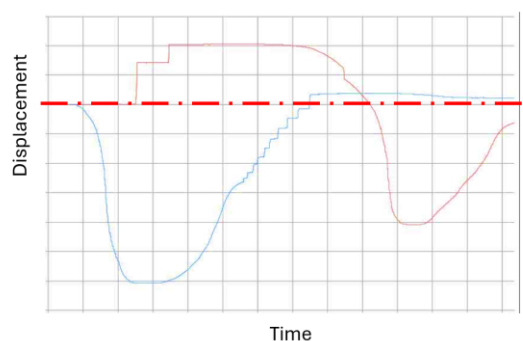


Figure 6. relative displacements while a vehicle crossing the bridge (monitored results). Staggered displacements showed the friction exceeded on the bearing leading to residual displacement at the end.

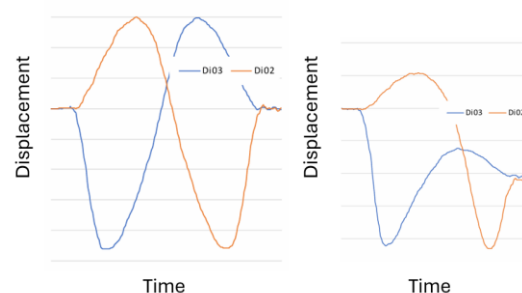


Figure 7. Analysis results of the differential displacement between the deck and the cross truss. Elastic bearings (left) vs nonlinear (sliding) bearings.

Another complex aspect addressed was the behavior of the replaced hanger. The original corroded hanger, consisting of a pair of spiral cables arranged perpendicular to the bridge axis, was replaced with two steel bars. Unlike the cables, the new steel bars run along the bridge axis, allowing for their installation before dismantling the existing hangers. However, this configuration complicates load distribution predictions. Additionally, the longitudinal steel bars are susceptible to bending, particularly when the superstructure sways in the bridge's longitudinal direction. A refined analysis helped define the expected range of stress variations and identify conditions requiring closer monitoring—such as instances when a hanger comes into contact with the edge of its recess.

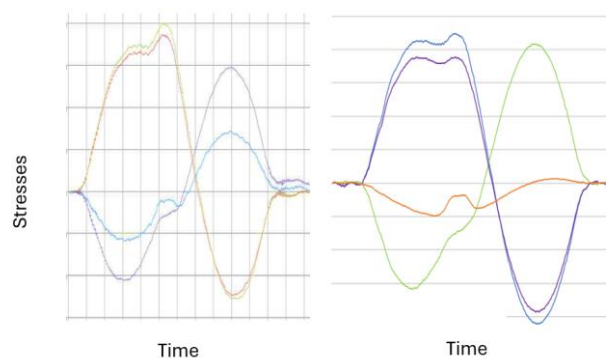


Figure 8 compares the monitoring readings in 4 strain gauges to the FE model under service loads.



Figure 9. Hanger arrangement resulting in bending stresses due the superstructure longitudinal movement,

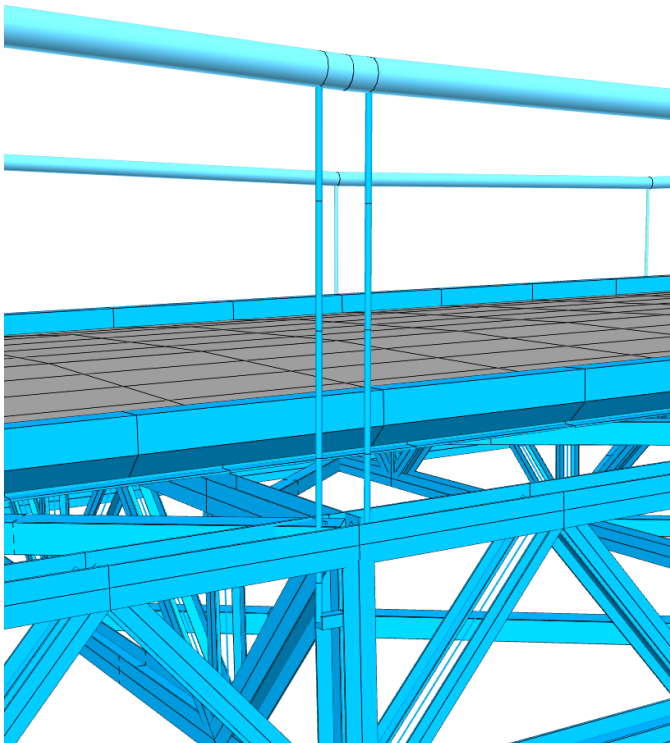


Figure 10. Hanger arrangements in the FE model.

Most of the main elements were easier to model; as an example, Figure 11 shows the typical behavior of main truss stresses and Figure 12 shows the typical behavior of the stresses in cross beam diagonals.

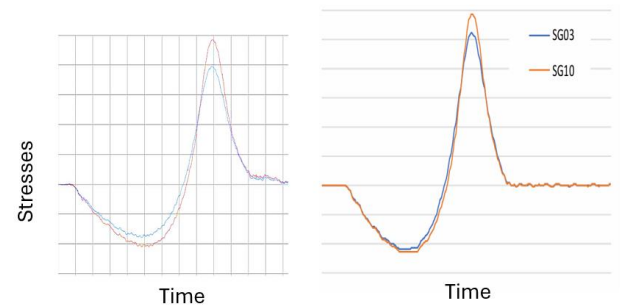


Figure 11. Main truss stresses (measured/modelled).

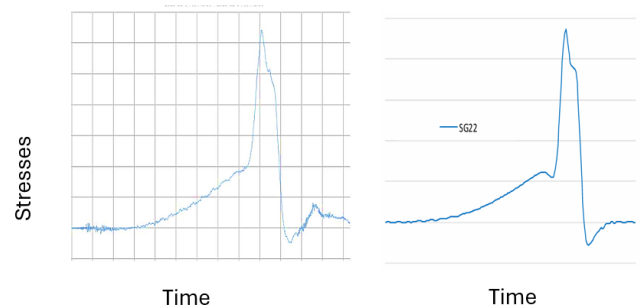


Figure 12. Cross beam diagonal stresses (measured/modelled).

The calibration of the FE model against monitoring results provided assurance that the behavior of the bridge is well understood, enhancing the potential for data-driven decisions.

## 6 REAL-TIME MONITORING FRAMEWORK

To manage the vast amounts of sensor data efficiently, an automated preselection of loading events was introduced. This system relies on a designated "trigger sensor"—in the case bridge, the maximum deflection of the main span. Each day, the ten most severe loading events are identified, ensuring that comparisons are made based on similar traffic conditions.

Once trigger events are selected, a full one-minute dataset is retrieved for all sensors, ensuring that both immediate effects and short-term recovery behaviors are captured. To establish a reference point for long-term monitoring, the first 30 days of operation were designated as the baseline, against which all subsequent readings are compared.

For comparative analysis, stress and displacement fluctuations under traffic loads were selected. These results provide insights into structural response variations and were also utilized for fatigue analysis of critical details.

The real-time monitoring system is accompanied by a standardized dashboard, which presents weekly summaries of key indicators. This allowed the Client to easily track trends



without needing to analyze raw data manually. While the current monitoring system does not yet fully utilize advanced AI tools, its structured approach has already demonstrated reliability, providing trustworthy insights that inform safety decisions.

The work done in the calibration of the FE model offered such detailed insights into the bridge's behavior that it significantly enhanced our interpretation of the monitoring results, enabling us to differentiate between normal operating patterns and potential anomalies.

Figures 13 to 15 illustrate the primary views of the dashboard, which facilitates the detection of both long-term trends and short-term changes in the bridge's behavior. The dashboard is engineered to emulate the analytical interpretations of an experienced structural engineer, significantly reducing the time required for data interpretation while still necessitating periodic expert review—an achievement made possible by advances in AI. Notably, the fatigue view has spurred a spin-off project aimed at developing comprehensive fatigue assessment software applicable to any structure monitored by the system, including preliminary studies on HFMI-treatment in line with the forthcoming second-generation Eurocodes.

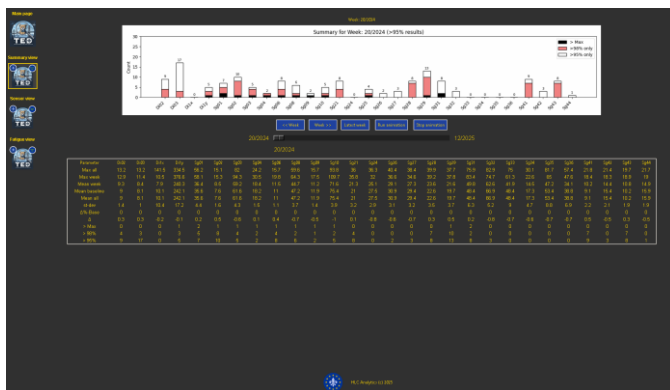


Figure 13. Summary view of the dashboard.

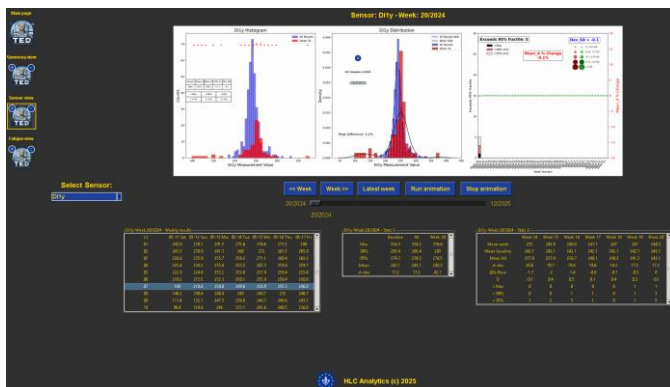


Figure 14. Detailed sensor-view of the dashboard.

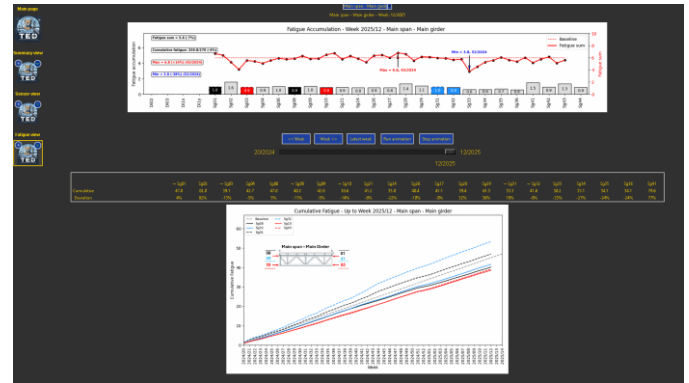


Figure 15. Fatigue-view of the dashboard.

The dashboard will provide clear alarms when anomalies are detected, offering users the ability to explore the data further. Each meaningful event can be visualized as needed, enabling a deeper understanding of the bridge's condition and facilitating informed decision-making.

In addition to these dashboard views, a largely automated weekly report and other analytical insights are provided. The implementation of this system reduces the active expert time required from hundreds of hours to single-digit hours per report. Naturally, any detected changes in behavior can trigger more in-depth studies.

## 7 EXAMPLES OF ABNORMALITIES DETECTED WITH THE INSTALLED SHM-SYSTEM

The new hangers have occasionally exhibited higher stress values, indicating that relative motion is occurring between the hangers and the deck. This behavior is likely driven by temperature-induced movements of the main cables, although displacements from heavy traffic loads are also contributing—especially if the deck does not fully return to its original position after loading. As a result, this relative motion may cause the hanger bars to contact adjacent structural components, leading to elevated strain gauge readings. Since the hanger bars are designed with considerable built-in safety factors, these modest increases (occasionally up to 50%) in sensor readings do not presently signify an immediate structural risk; however, if not adequately addressed through maintenance, they could eventually evolve into more critical issues.

The changes in the behavior are well seen when the fatigue accumulation for the hanger bars is plotted for each week (see Figure 16), from week 47/2024 the Fatigue accumulation increases strongly.

Following the removal of a cover plate (see Figure 17), stress levels temporarily decreased, only for similar patterns to re-emerge a few weeks later. Although the current stress levels are not critically hazardous, the repeated contact between the hanger bars and adjacent structural elements could eventually lead to fretting fatigue cracks. As a precaution, immediate repairs to widen the openings around the bars were

recommended. These stress increases were quickly detected by the dashboard, which employs AI algorithms with accuracy comparable to that of a human expert, ensuring that such anomalies are reliably flagged.

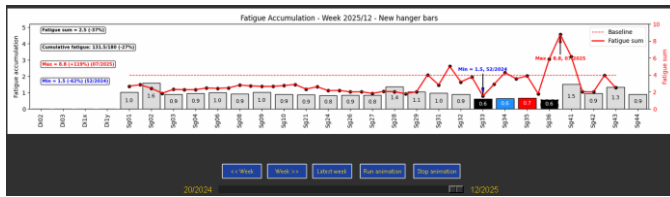


Figure 16. Sudden increase in fatigue accumulation of new hanger bars



Figure 17. Contact of the hanger bar and cover plate

Additionally, significant deflections and stress variations were detected sporadically, often coinciding with instances when heavy vehicles failed to comply with the new restrictions. Camera footage confirmed that two—or sometimes even three—heavy vehicles crossed the bridge simultaneously (see Figure 18). Although the occurrence of multiple heavy vehicles clearly violates the established restrictions, these restrictions remain essential, as frequent violations could have a much more detrimental impact than isolated incidents.



Figure 18. Two heavy vehicles at main span

## 8 BROADER APPLICATIONS OF THE SHM SYSTEM

The development of the SHM dashboard was carried out in close collaboration with the Client responsible for the bridge's safety. Their involvement ensured that the system presented clear, actionable information, making it easier to interpret monitoring data without requiring specialized expertise. As a result, the dashboard became a practical tool for real-time decision-making, rather than just a data visualization platform.

Bridging the gap between large-scale monitoring efforts and local stakeholders is crucial. Often, local communities must place their trust in decisions made at a national or corporate level. By bringing monitoring tools closer to end clients and asset owners—through transparent, standardized, and analytically robust dashboards—we empower them with the insights needed for informed decision-making. This approach not only enhances transparency but also fosters a culture of shared responsibility and improved safety at the local level.

Due to its successful implementation, the system was designed with scalability in mind, allowing it to be applied to other projects with minimal modifications. The fundamental approach—selecting relevant loading events, establishing a baseline, and tracking deviations—can be adapted to any bridge or infrastructure type. In fact, this methodology extends beyond bridge SHM and can be used in any time-series data analysis application where there is a need to detect long-term trends or sudden changes in any monitored metric.

Furthermore, a deep understanding of the bridge's structural behavior enables the optimization of sensor placement. This refined design not only enhances data quality but also reduces the number of sensors required, thereby lowering the overall costs of individual monitoring projects.

Recognizing this potential, developers began shifting focus toward building a next-generation standardized SHM analysis

dashboard. The next iterations will incorporate AI-assisted automated damage detection and advanced pattern recognition, allowing engineers to identify anomalies without needing to manually go through raw data. Importantly, all collected data has been stored in a structured format, ensuring that future enhancements—such as machine learning-based predictive maintenance—can be integrated without requiring a complete system overhaul.

Even in its current form, without full AI-driven analysis, the SHM system has proven reliable and trustworthy, providing the data necessary for the Client to make informed maintenance decisions. As computational power increases, real-time monitoring will continue evolving, allowing asset owners to shift from reactive to fully predictive maintenance strategies, ultimately reducing costs and improving safety across critical infrastructure networks.

## 9 CONCLUSIONS AND FUTURE PERSPECTIVES

Effective infrastructure management relies not just on data collection but on extracting meaningful insights from vast amounts of sensor information. To make data-informed decisions, monitoring systems must filter out irrelevant readings while capturing every critical structural event. In this project, a trigger-based system was implemented to identify the most relevant high-load situations per day, ensuring that engineers could track changes in bridge behavior over time without being overwhelmed by excessive data.

The high-flying promise of adopting a structured and analytical approach in SHM lies in transforming ‘known unknowns’ into ‘known knowns.’ By systematically standardizing data analysis, we can significantly enhance the reliability of our decision-making processes. This increased understanding naturally leads to improved safety, cost reductions, and substantial socioeconomic benefits. Ultimately, a more data-informed framework will pave the way for more predictive and preventative maintenance strategies.

Future iterations of the system will incorporate more trigger-sensors, improving detection accuracy and allowing for a more detailed understanding of how different parts of a structure respond to varying loads. Additionally, with advancements in automated data processing and machine learning, monitoring systems will not just detect anomalies but ultimately also predict future deterioration trends, enabling truly proactive maintenance strategies.

For long-term viability, monitoring frameworks must remain scalable and adaptable, allowing new technologies to be integrated without major system overhauls. Greater emphasis should also be placed on load testing and FE-model calibration, ensuring that monitoring data is interpreted within a robust engineering framework.

As SHM systems become more mainstream and data handling becomes more systematic, there is a significant opportunity for transfer learning. By systematically analyzing results from a diverse range of structural configurations, it will be possible to

enhance the understanding of different structural behaviors. This transfer learning process has the potential to greatly amplify the benefits of SHM in the future, enabling more accurate predictions and more efficient maintenance strategies for a wide variety of infrastructure types.

We are confident that soon, extremely cost-efficient real-time SHM systems will become a standard part of infrastructure management, allowing asset owners to make fully data-driven maintenance decisions. This shift will significantly reduce long-term costs while improving the safety and reliability of critical infrastructure worldwide.

## ACKNOWLEDGMENTS

The financial support was provided by the Centre for Economic Development, Transport and the Environment (ELY Centre), and the data for the analysis was supplied by Savcor Oy.



# Use of Monitoring for Highway Bridges on Federal Highways in Germany – Current Status and Future Development

Iris Hindersmann<sup>1</sup>, 0000-0002-9875-1106

<sup>1</sup>Federal Highway and Transport Research Institute, Brüderstraße 53, 51527 Bergisch Gladbach, Germany  
email: hindersmann@bast.de

**ABSTRACT:** The use of monitoring for bridges on federal highways is currently not widespread. Monitoring is primarily used when damage is already present or when deficits resulting from the recalculation or which occur due to the design. The potential of monitoring to support maintenance towards a predictive lifecycle management approach is not being fully utilized.

As part of the exchange with the structure managers in Germany and a literature search, it has been shown that the challenges lie in the lack of standardization, insufficient expertise, and missing fundamental principles. To address these challenges, various research projects have been planned and carried out. These include the “Documentation on Monitoring of Bridge Structures,” the “Guideline – Strategic Use of Monitoring for Civil Engineering Structures,” the “Birth Certificate for Bridge Structures,” and the project on “Standardized Data Models.”

This article aims to present the challenges and initial solution approaches from these projects. The goal is to illustrate support options for the increased and targeted use of monitoring in bridge structures on Germany’s federal highways. Additionally, the article provides a classification of these challenges within the European context.

**KEY WORDS:** monitoring, road bridge, standardization

## 1 INTRODUCTION

The bridges on federal highways face a variety of challenges. The main causes include the significant increase in traffic, especially in freight transport, the advanced age of the bridges, and a backlog of maintenance measures. Monitoring offers a way to address these challenges. It can be used effectively to ensure availability by detecting, assessing, and tracking safety reserves, changes, and weaknesses, thereby enabling predictions of future behavior. Additionally, monitoring allows for the recording of actual loads and impacts.

The data obtained through monitoring can support and optimize maintenance management, as it enables a more precise assessment of the current condition and better forecasting of condition changes. This, in turn, helps gain valuable time for necessary repair measures or replacement constructions.

However, the full potential of monitoring has not yet been realized. This article discusses the use of monitoring in Germany, as well as challenges in Europe, and particularly Germany. It serves as a foundation for identifying necessary developments and projects that can promote a more extensive and targeted application of monitoring.

## 2 MONITORING – CURRENT STATUS

### 2.1 General

Monitoring refers to the overall process of recording, analyzing, and evaluating structural responses and/or impact factors using a measurement system over a representative

period. This includes tracking the temporal development of the measured variable through continuous, periodic, or event-based measurements, both on a global and local scale [1].

The effective use of monitoring encompasses the entire process, from the “definition of the research question” to the “evaluation.” This process ensures that monitoring contributes to answering open questions related to a structure. [1; 2].

The goal of monitoring is to obtain additional information about the condition of the structure. This information serves as a basis for describing the current state and deriving forecasts for future behavior. The results can then be used to make maintenance decisions on a more informed basis.

### 2.2 Current use of monitoring

A survey conducted by the Federal Ministry of Transport in 2020 revealed that the use of monitoring for bridges on federal highways is limited to existing damage and deficits. The 100 monitoring measures identified in the survey primarily focused on bridges built between 1960 and 1980 and reflected the typical distribution of bridge types on federal highways, with a particular emphasis on prestressed concrete bridges (Figure 1 and Figure 2). The monitoring measures were mostly carried out to capture the structural response using deformation and temperature sensors [3].

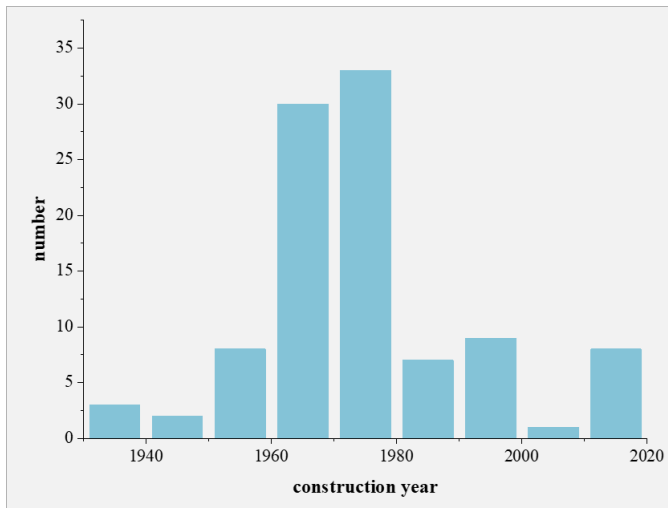


Figure 1: Age of the structures with monitoring

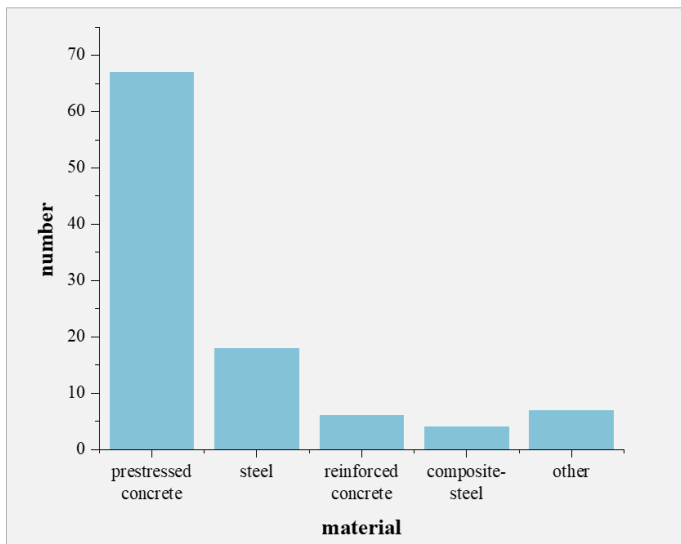


Figure 2: Material of the bridges with monitoring

The potential that monitoring offers to support maintenance decisions through additional information is not being utilized. Decisions are made on a case-by-case basis, relying on the individual knowledge of the structure managers and their supporting teams.

### 2.3 Cost-benefit of monitoring

Compared to other compensatory measures such as traffic restrictions, the use of monitoring is applied significantly less frequently. However, the benefit-cost ratio of using monitoring as a compensatory measure is very high. Monitoring allows for the continued operation of a structure under traffic. Alternative traffic-related compensatory measures would include speed limits, the closure of individual lanes, or even entire bridges. Reference [4] demonstrates that alternatives to monitoring have significant economic impacts. These impacts include, for example, congestion costs and detour costs, which in turn lead to increased environmental pollution and loss of travel time.

Increased use of monitoring can therefore also have positive effects on the economy, the environment, and social aspects.

### 2.4 Use cases of monitoring

To enable a structured analysis of the previous case-by-case decisions regarding monitoring measures, the existing application examples were categorized according to the reasons for implementing monitoring. The goal was to enable a standardized assessment. During the evaluation of the previous monitoring applications, it became evident that a systematic approach can be derived in relation to individual use cases. Use cases are known from the BIM methodology and are derived from the project goals [5].

The following commonly used use cases can be derived: "Monitoring of known locally identified damages," "Monitoring for deficits from recalculations and construction," "Monitoring for determining loads and impacts," and "Construction-related monitoring." (Figure 3) [6; 7].

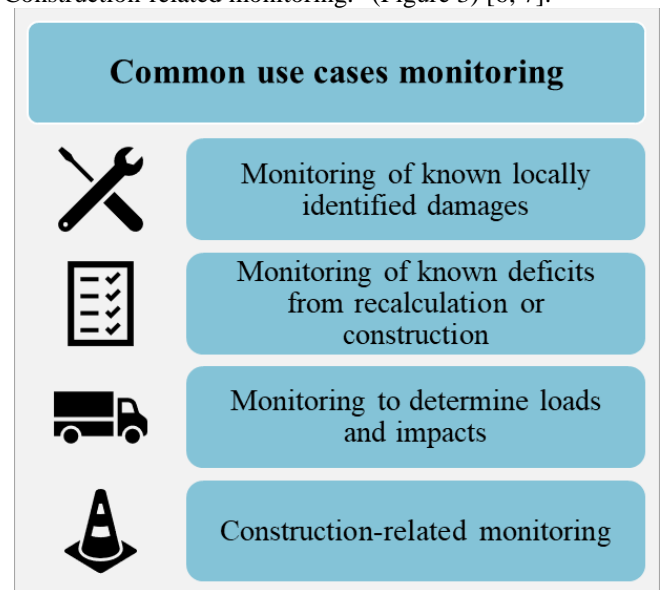


Figure 3: common use cases of monitoring (Modified according to [6])

Monitoring of known locally identified damages is used when structural inspections reveal damages such as corrosion or fatigue cracks. Typically, a local monitoring system is employed to track the progress of damage. The goal is to extend the remaining service life and ensure adequate safety.

Monitoring for known deficits arising from recalculations or due to construction-related factors is used when deficits are identified in a structure or in structures with a similar design. However, visible damage does not necessarily need to be present at this stage. In this case, a global monitoring system can be used to capture the overall structural response, or a local monitoring system can be employed to monitor critical areas. Examples of this use case include structures with stress corrosion cracking or joint connection issues.

Monitoring for determining impacts is used to capture external factors such as traffic loads or climatic conditions. For instance, Bridge-Weigh-in-Motion (B-WIM) systems can be used to determine actual traffic loads. This information is particularly useful in the recalculation of bridges starting from recalculation stage 3 [8].

Monitoring during construction is used to track the performance of structures in real-time while they are being built or if construction work is taking place directly next to the

structure. This type of monitoring allows for immediate identification of issues such as unexpected deformations or material behavior, enabling timely adjustments. It helps ensure that the structure is being constructed according to design specifications and that any potential risks are mitigated early in the process. Examples include monitoring during the construction of new bridges or during major rehabilitation projects.

In addition to the common use cases, it is also possible to derive use cases with initial use examples, such as the monitoring of special structures or future use cases such as the certificate of birth. However, these applications currently play a subordinate role in the maintenance of structures.

### 2.5 Challenges in the use of monitoring

The reasons for the limited use of monitoring on federal highway bridges so far are diverse. Figure 4 provides an overview of the challenges that arise throughout the entire process, from planning to evaluation. The main causes include a lack of standardization, insufficient expertise, and missing fundamental principles [9].

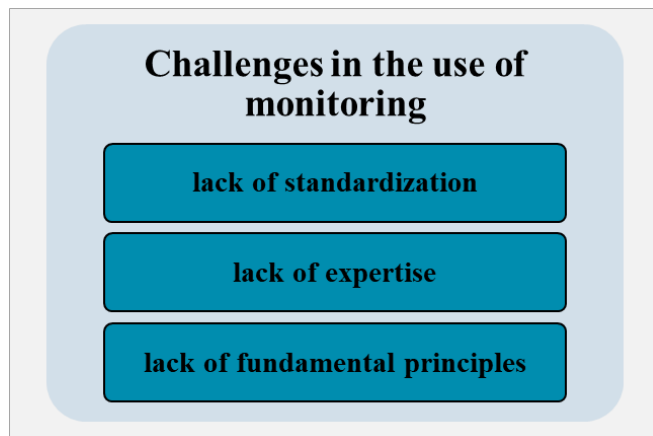


Figure 4: challenges in the use of monitoring

One challenge in the use of monitoring is the lack of standardization. Currently, monitoring is decided on a case-by-case basis, and there are no standardized guidelines for tendering, awarding, evaluating, or selecting a monitoring system. Defining use cases [6], describing individual monitoring methods [10], or outlining processes and stakeholders [1; 2] could help address this issue. In this context, templates for tender documents could, for example, provide valuable support.

Another crucial aspect of the lack of standardization is the absence of an established regulatory process. Currently, the use of monitoring is neither mandated nor recommended in any official guidelines. As a result, a key challenge is demonstrating the economic benefits of monitoring. In cases where damage or deficits are already present, the necessity is usually straightforward to justify, as all alternatives involve compromises in safety or availability. However, if monitoring is to be used proactively as a basis for better maintenance decisions in the future, the cost-effectiveness of the measure must be evaluated. This requirement has led to only sporadic use so far. Approaches from projects such as the “Economic

Feasibility Study of Monitoring” offer valuable solutions but are rarely applied in practice [4]. The establishment of standardized processes is still pending. However, with the revision of DIN 1076, monitoring can be integrated into the structural inspection and maintenance process [11; 12]. This step is crucial for a more widespread and targeted use of monitoring. Additionally, incorporating monitoring aspects into existing guidelines, such as the “Manual for the Awarding and Execution of Freelance Services in Road and Bridge Construction” (Handbuch für die Vergabe und Ausführung von freiberuflichen Leistungen im Straßen- und Brückenbau - HVA F-StB), could further support the standardization process [13].

Another important aspect is the lack of expertise. Monitoring involves a high level of complexity, for example, in preparation of a monitoring plan, selecting the appropriate monitoring concept from various offers, or evaluating the results in terms of their significance for structural maintenance. The acquisition of the necessary expertise is not a standard part of the training for those responsible for infrastructure. Therefore, it is essential to either obtain this knowledge independently or compensate for gaps by involving specialized personnel, such as engineering office. The lack of expertise also results in an absence of confidence in applying monitoring effectively, making it difficult to recognize its benefits for structural maintenance.

In some areas, fundamental principles for the use of monitoring are still missing. This is particularly evident in data management. Efficient data collection, reduction, analysis, and storage, as well as the development of user-friendly solutions for all stakeholders, are crucial. At the same time, data security and ownership must be ensured, especially when granting usage rights to third parties. Additionally, integrating monitoring data with structural models and embedding them into maintenance management systems to derive relevant key performance indicators is another essential step toward the broader and more targeted application of monitoring.

## 3 PROJECTS TO SUPPORT THE TARGETED USE OF MONITORING

### 3.1 General

At present, various fundamental principles for the targeted and standardized use of monitoring are available. The currently existing foundations include:

- DBV Guideline: "Monitoring: Planning, Tendering, and Operation" (DBV-Merkblatt - Monitoring: Planung, Vergabe und Betrieb“) [1]
- DGZfP Guideline B 09: "Continuous Monitoring of Structures" (DGZfP-Merkblatt B 09 „Dauerüberwachung von Bauwerken“) [14]
- Directive SE05: "Detection of Tendon Wire Breaks Using Acoustic Emission Analysis (Richtlinie SE05: Detektion von Spanndrahtbrücken mit Schallemissionsanalyse) [10]

In addition to these guidelines, several projects have been initiated with the goal of promoting the more widespread and targeted use of monitoring, thereby addressing various challenges. The following research projects have been initiated, conducted, or supported by the Federal Highway and Transport



Research Institute (Bundesanstalt für Straßen- und Verkehrswesen BAST):

- Documentation: "Monitoring in Bridge Structures" (Erfahrungssammlung "Monitoring bei Brückenbauwerken") [15]
- Guideline: Strategic Use of Monitoring for Engineering Structures (Leitfaden – Strategischer Einsatz von Monitoring für Ingenieurbauwerke) [2]
- "Birth Certificate" for Bridge Structures (Geburtszertifikat für Brückenbauwerke) [16]
- Documentation on the Application of Innovative Methods in Condition Assessment, with a Focus on Standardized Data Models (Erfahrungssammlung über die Anwendung innovativer Verfahren in der Zustandserfassung insbesondere bzgl. standardisierter Datenmodelle) [17]

The following sections introduce these projects and illustrate how they contribute to developing solutions for existing challenges.

Table 1 consolidates the challenges and current projects of BAST. It assesses the extent to which these projects are suitable for addressing the existing challenges. The results presented in Table 1 are further elaborated in the chapters discussing each individual project.

Table 1: Consolidation of Challenges and Current Projects

challenges	lack of standard-ization	lack of expertise	lack of fundamental principles
documentation of monitoring experience		++	
guidelines to the strategic use of monitoring	+	++	+
birth certificate	+	+	+
standardized data models	+	+	++

### 3.2 Documentation: "Monitoring in Bridge Structures"

In recent years, documentations have been created on several topics commissioned by the BAST. These serve to compile and systematize the experiences gained so far in specific areas [15; 18]. As such, they represent an initial step in preparing a topic for practical application. The documentations have always been structured in an analogous manner, with examples of applications related to bridges being compiled after an initial categorization.

The documentation on monitoring is divided into two main sections: one focuses on the state of the art in monitoring, and the other presents a collection of examples of monitoring measures carried out in Germany [15].

The main section "State of the Art in Monitoring of Structures" defines the monitoring objectives, which primarily focus on capturing various structural responses, such as deformations or crack developments. The measurement techniques applied in practice are assigned to the respective measurement objectives. Additionally, information about the functioning and performance of the measurement technology, as well as the information gained, is provided. Notes on the limitations of monitoring and quality assurance supplement this section.

The second main section contains a collection of examples of selected monitoring measures. The categorization in this part is based on the monitoring objectives developed in the first main section. Building on this, specific monitoring projects and their results are described. The reasons for monitoring, relevant structural features, measurement goals, employed measurement technology, responsibilities in the monitoring process, information gained, and data management are detailed. Additionally, statistical evaluations on tenders, awards, and the responsibilities of the stakeholders in the monitoring process are presented.

The documentation, with its structured and uniform presentation of examples, provides a good entry point into the topic and can contribute to building the necessary expertise in this field.

### 3.3 Guideline: Strategic Use of Monitoring for Engineering Structures

The Guideline - Strategic Use of Monitoring for Engineering Structures was developed based on the requirements of infrastructure managers [2]. The goal of the guideline is to provide a practical guide for the targeted use of monitoring in engineering structures, particularly bridges. The project aims to support infrastructure managers throughout the entire process of planning, implementing, and evaluating monitoring measures.

The research project combined literature reviews, expert interviews, online surveys, and workshops to compile challenges and essential foundations for the strategic use of monitoring. The report defines use cases for monitoring, ranging from monitoring localized damage to the use of digital twins for predictive lifecycle management, and describes the project participants and the process from defining the issue to evaluating the monitoring. Furthermore, the guideline includes practical recommendations for tendering, awarding contracts, contract design, economic analysis, and is supplemented by checklists to support infrastructure managers.

Another key topic is data management; client data requirements were developed to ensure structured storage and analysis of monitoring data.

A key reason for the limited use of monitoring by infrastructure owners is the lack of expertise and standardized procedures. The project can help by providing standards and presenting fundamental principles. Additionally, it plays a significant role in building expertise to address the complexity of the topic. With standardized use cases, a defined process, and potential support services, this project can address these challenges. This also applies to the missing fundamental principles in data management. The development of client data

requirements has made a first step toward creating foundations in this area.

### 3.4 Birth certificate for bridge structures

The research project aims to develop a comprehensive concept for a "birth certificate" for bridge structures and the foundations for a prototype implementation on a real bridge [2]. The birth certificate serves as the basis for condition monitoring and maintenance planning throughout the entire lifecycle of a structure. Central to this concept is the so-called zero measurement, where the initial condition of the structure – immediately after completion and before being opened to traffic – is captured in detail and systematically using various parameters. This reference state will later serve as a basis for comparison to detect, document, and evaluate changes and damages at an early stage.

The concept defines a wide range of parameters: Physical parameters such as material strains, displacements, as well as natural frequencies and modes provide insights into the load-bearing behavior, while chemical aspects such as chloride content, carbonation depth, and moisture content of the concrete offer essential information about durability. Additionally, the geometric properties of the bridge are recorded – for example, through a georeferenced 3D structural model created photogrammetrically or by scanning methods. This model allows precise localization of all recorded parameters and forms the foundation for future deformation analyses and damage-focused condition assessments.

The birth certificate will be created in a standardized, easily accessible form as a PDF document, containing references to all data sets, models, and measurement data, which will then be stored in the SIB-BW infrastructure database. Furthermore, all information related to the birth certificate will be located within the 3D model, and the data will be linked. This will provide a foundation for supporting predictive lifecycle management through Digital Twins. This represents a crucial step toward more sustainable and efficient use of infrastructure resources.

The project constitutes an important effort to lay the groundwork for the targeted use of monitoring. With the birth certificate, a comprehensive overview of the structural behavior before the opening to traffic is provided. This captures a reference state that will serve as the basis for future deviations. As a result, the acceptance of monitoring can be increased, and a valuable contribution to the standardization and development of expertise in this field can be made.

### 3.5 Foundations for data management in structural maintenance

A workshop with infrastructure managers, the necessary foundations for data management in structural maintenance were developed. It became clear that standardized data models and defined interfaces are essential.

As a first step, a project on "Documentation on the Application of Innovative Methods in Condition Assessment, Particularly Regarding Standardized Data Models" was initiated.

The success and utility of innovative methods, such as the use of monitoring, strongly depend on structured and standardized data management. A relevant foundation of data management

consists of data formats and models. The data model here refers to a model of the data to be described and processed in structural maintenance and their relationships with each other. Data models help in structuring, presenting, and understanding data, and serve as a plan for organizing, connecting, and storing the data. For all datasets used and generated in the context of maintenance, including planning and construction, data models and their metadata are required. The goal is to determine structured and standardized data formats, data models, and metadata for the data collected during structural maintenance.

This project aims to establish the missing foundations in the field of data management and standardization.

## 4 IMPLEMENTATION OF MONITORING IN THE EU

The use of monitoring in Europe is not harmonized, as demonstrated by the Horizon 2020 project "IM-SAFE." The main goals of IM-SAFE include the development of new European standards for the monitoring, maintenance, and safety of transport infrastructures. This aims to enable well-founded decisions regarding maintenance needs and optimized maintenance strategies [19].

The following technical and organizational challenges were identified during the project [20]:

- Different national regulations and standards complicate the creation of unified European standards. While some countries focus on preventive maintenance, others prioritize reactive measures after damage has occurred.
- Technological advancements require continuous adaptation, but it is complex to incorporate rapid technological changes into standardization processes. As a result, implementations often lag current technological possibilities.
- Heterogeneous responsibilities and interests between public and private infrastructure operators may exist.
- Standardization of data formats and protocols is necessary to enable interoperable use of collected information.
- The implementation of standardized monitoring and maintenance procedures requires significant investments.

Despite these challenges, there are efforts to achieve greater harmonization in standardization. These include initiatives at the European level, as well as the development of new technical solutions that enable more flexible and efficient adaptation to existing standards.

Other European countries already have regulations for the standardized use of monitoring:

In Austria, the RVS 13.03.01 guideline on the monitoring of bridges and other civil engineering structures allows for special inspections (e.g., monitoring) to assess damage. Monitoring does not replace structural inspections but can be used as an additional objective method. Monitoring objectives could include the measurement-based documentation of structural conditions or the early detection of critical structural conditions [21].

In Switzerland, the guidelines for the monitoring and maintenance of civil engineering structures mandate the use of monitoring within the framework of zero and control measurements [22].

Lombardy, in its newly developed bridge monitoring guidelines, has set the following objectives: increasing safety, efficient maintenance strategies, standardized monitoring, and integrating innovative technologies. To achieve these goals, sensor-based monitoring with various sensor technologies will be used for the continuous collection of key structural parameters. Furthermore, real-time data analysis through the implementation of digital platforms and AI-supported decision-making will be introduced to automate pattern recognition in sensor data for the identification of potential damage. The monitoring will support periodic inspections, and the data will be integrated into existing maintenance strategies. Additionally, the creation of digital twins, including for scenario simulation, is planned. This approach is currently being implemented in nine pilot projects [23].

## 5 CONCLUSION

The use of monitoring in federal highways is currently limited to a few applications. In all cases, it is a case-by-case decision. To promote and target the use of monitoring to support structural maintenance, ways must be found to address the current challenges (lack of standardization, insufficient expertise, and missing fundamental principles). An overview of the challenges and monitoring use in Europe shows that similar challenges exist here as well. Initial solutions, foundations, and new projects are available, but they still need to be implemented on a larger scale.

## REFERENCES

- [1] Deutscher Beton- und Bautechnikverein: Merkblatt: Brückenmonitoring. 2018,
- [2] Wedel, F.; Pitters, S.; Hille, F.; Herrmann, R.; Schneider, R.: Leitfaden – Strategischer Einsatz von Monitoring für Ingenieurbauwerke – *Veröffentlichung in der BAST Schriftreihe in Vorbereitung*. 2024,
- [3] Hindersmann, I.: 2021: Anwendung von Monitoring bei Brücken der Bundesfernstraßen und zukünftige Monitoringstrategien in: Krieger, J. [Hrsg.] *Fachkongress Digitale Transformation im Lebenszyklus der Verkehrsinfrastruktur: Tagungshandbuch 2021*. Tübingen: Expert Verlag,
- [4] Schubert, M.; Faber, M. H.; Betz, W.; Straub, D.; Niemeier, E.; Ziegler, D.; Walther, C.; Majka, M.: Wirtschaftlichkeitsuntersuchungen von Monitoringmaßnahmen – *Entwicklung eines Konzepts für die Analyse von Nutzen und Kosten*. Berichte der Bundesanstalt für Straßenwesen B, Brücken und Ingenieurbau, Berichte der Bundesanstalt für Straßenwesen B, Brücken und Ingenieurbau B156, 2020,
- [5] BMVI Masterplan BIM Bundesfernstraßen [online]2021. [https://bmdv.bund.de/SharedDocs/DE/Anlage/StB/bim-rd-masterplan-bundesfernstrassen.pdf?\\_\\_blob=publicationFile](https://bmdv.bund.de/SharedDocs/DE/Anlage/StB/bim-rd-masterplan-bundesfernstrassen.pdf?__blob=publicationFile) [Zugriff am: 1. Feb. 2024].
- [6] Hindersmann, I.; Müller, M.; Kaplan, F.: Juni 2023: Strategischer Einsatz von Monitoring bei Ingenieurbauwerken mit Anwendungsbeispielen in: Curbach, M. et al. [Hrsg.] *12. Symposium Experimentelle Untersuchungen von Baukonstruktionen: 01. Juni 2023*. Dresden: Institut für Massivbau Technische Universität Dresden,
- [7] Hindersmann, I.; Bednorz, J.; Nieborowski, S.: Monitoring on federal highways bridges: current situation, future opportunities & digital implementation . ce/papers 62023, H. 5 - <https://doi.org/10.1002/cepa.2068>
- [8] BMVBS: Richtlinie für die Nachrechnung von Straßenbrücken im Bestand (Nachrechnungsrichtlinie). 2011,
- [9] Hindersmann, I.; Panzer, R.; Kraus, S.; Windmann, S.; Holst, R.; Nieborowski, S.; Richter, C.; Marzahn, G.: Entwicklung der digitalen Bauwerkserhaltung bei Ingenieurbauwerken der Bundesfernstraßen . Bautechnik 1012024, H. 10 - <https://doi.org/10.1002/bate.202400054>
- [10] DGZfP-SE 05:2024-05 – *Detektion von Spanndrahtbrüchen mit Schallemissionsanalyse*.
- [11] DIN 1076:1999: DIN 1076: Ingenieurbauwerke im Zuge von Straßen und Wegen - Überwachung und Prüfung.
- [12] Marzahn, G.; Anwander, K.; Mertens, M.; Morgenthal, G.; Pinnel, R.: Bauwerksprüfung nach DIN 1076 . Bautechnik 1002023, H. 11 - <https://doi.org/10.1002/bate.202300090>
- [13] BMDV: HVA B-StB Handbuch für die Vergabe und Ausführung von Bauleistungen im Straßen- und Brückenbau. 2023,
- [14] DGZfP: Merkblatt B 09 – *Dauerüberwachung von Ingenieurbauwerken*. 2022,
- [15] Novák, B.; Stein, F.; Farouk, A.; Thomas, L.; Reinhard, J.; Zeller, T.; Koster, G.: Erfahrungssammlung Monitoring für Brückenbauwerke – Dokumentation 2021. 2024,
- [16] Wedel, F.; Stark, Y.; Morgenthal, G.; Rau, S.: FE 89.0352/2023 Geburtszertifikat für Brückenbauwerke - die Nullmessung als Bewertungsgrundlage des Bauwerkszustands im Lebenszyklus – *Projekt in Bearbeitung*. 2024,
- [17] Steinjan, J.; Braun, J.-D.: Erfahrungssammlung über die Anwendung innovativer Verfahren in der Zustandserfassung insbesondere bzgl. standardisierter Datenmodelle – *Projekt FE 15.0702/2022/LRB in Bearbeitung*. 2025,
- [18] Schnellenbach-Held, M.; Welsch, T.; Fickler, S.; Hegger, J.; Reissen, K.: Verstärkungen älterer Beton- und Spannbetonbrücken: Erfahrungssammlung: Dokumentation 2016 – *BAST: FE 15.0570/2012/NRB*. 2016,
- [19] TNO IM-SAFE project [online]17.03.2025. <https://im-safe-project.eu/> [Zugriff am: 17. Mrz. 2025].
- [20] Bigaj-van Vliet, A.; Allaix, D. L.; Köhler, J.; Scibilia, E.: 2022: Standardisation in Monitoring, Safety Assessment and Maintenance of the Transport Infrastructure: Current Status and Future Perspectives in: Pellegrino, C. et al. [Hrsg.] *Proceedings of the 1st Conference of the European Association on Quality*



- Control of Bridges and Structures*. Cham: Springer International Publishing, S. 1152–1162.
- [21] RVS 13.03.01: Qualitätssicherung bauliche Erhaltung  
Überwachung, Kontrolle und Prüfung von Kunstbauten  
– Monitoring von Brücken und anderen  
Ingenieurbauwerken. 01.02.2022,
- [22] Bundesamt für Straßen: Richtlinie Überwachung und  
Unterhalt der Kunstbauten der Nationalstrassen. 2005,
- [23] Limongelli, M. P. et al.: Bridge structural monitoring:  
the Lombardia regional guidelines . Structure and  
Infrastructure Engineering 2020/24, H. 4 -  
<https://doi.org/10.1080/15732479.2022.2107023>

# Study on the suitable sensor locations for tilt monitoring of power transmission tower

T. Kurihara<sup>1</sup>, M. Saeki<sup>2</sup>

<sup>1</sup>Tokyo Electric Power Service Co., Ltd, Tokyo 1350062, Japan

<sup>2</sup>Department of Civil Engineering, Tokyo University of Science, Chiba 2780022, Japan,  
email: T. Kurihara [t.kurihara@tepsco.co.jp](mailto:t.kurihara@tepsco.co.jp), M. Saeki [saeki@rs.tus.ac.jp](mailto:saeki@rs.tus.ac.jp)

**ABSTRACT:** Due to recent extreme weather conditions, there have been many reports of damage to infrastructure. For example, two power transmission towers collapsed due to landslides in 2022. The landslides may not only cause the tower collapse but also cause the base displacement. The base displacement of only a several millimeters can generate secondary stress, resulting in member deformation and insufficient strength of the steel tower members. Therefore, the towers that are at risk of landslides are surveyed once a year to investigate the progress of base displacement. However, the on-site investigation creates other risks, such as delays in detection and accidents during the travel to the site. So, the authors have been developing the tilt monitoring system of the power transmission towers. In the tilt monitoring system, one tilt sensor is installed on each of the four main members of the tower. The progress of base displacement is monitored by checking whether the observed tilt change exceeds a set threshold. In the current system, the threshold value is tentatively set to be 0.05 degrees. This system has already been installed to about one hundred towers in the field. In this study, a full-scale experiment is newly conducted to examine the optimal installation location of the tilt sensors to monitor the base displacement. In this experiment, ten tilt sensors are placed on each of the four main members, and the sensitivities to the base displacement are examined in detail.

**KEY WORDS:** Transmission towers; Base displacement; Remote monitoring; Tilt sensor

## 1 BACKGROUND AND OBJECTIVE

Due to abnormal weather in recent years, there have been many disasters in Japan, such as landslides and river flooding caused by heavy rain. The heavy rains of July 2021 caused a large-scale mudslide on the embankment of Atami City, which is still fresh in our memory. At the time of the disaster, an observation station in Atami City, which was relatively close to the disaster site, recorded an accumulated rainfall of 488mm, the highest rainfall ever recorded in July in the local history [1]. This mudslide disaster led to revisions of fill regulations to ensure safety of fills and effective penalties. In addition, when heavy rainfall and flood warnings are issued, the Japan Meteorological Agency has begun to issue detailed evacuation information, but even so, many lives have still been lost.

Power transmission towers have also been damaged by heavy rains and landslides. Two transmission towers collapsed in 2022 due to landslides caused by heavy rainfall. Although there was no direct loss of life at that time, approximately 120,000 households experienced large-scale power outages. Damage

caused by landslides on transmission towers also includes displacement of tower bases due to landslides in the vicinity of the towers. This base displacement of only a few millimeters can cause secondary stress from the base, resulting in member deformation and insufficient strength. If this base displacement is detected too late and progresses, the member will buckle, requiring large-scale repair work or reconstruction.

The management of towers where landslides are a concern is conducted once a year to check the progress of base displacement by surveying. However, there is a risk of on-site attendance and delay in detection. Therefore, the authors propose tilt monitoring to remove these risks. Figure 1 shows the operational image proposed by the authors. In the proposed method, tilt sensors are installed on the four legs of a transmission tower and single pipe piles driven near the collapsed soil surface, and the measured values are monitored remotely. When an abnormality is detected, an alert is sent out and the risk is assessed by analyzing the observed data.



Figure 1. Operational image diagram

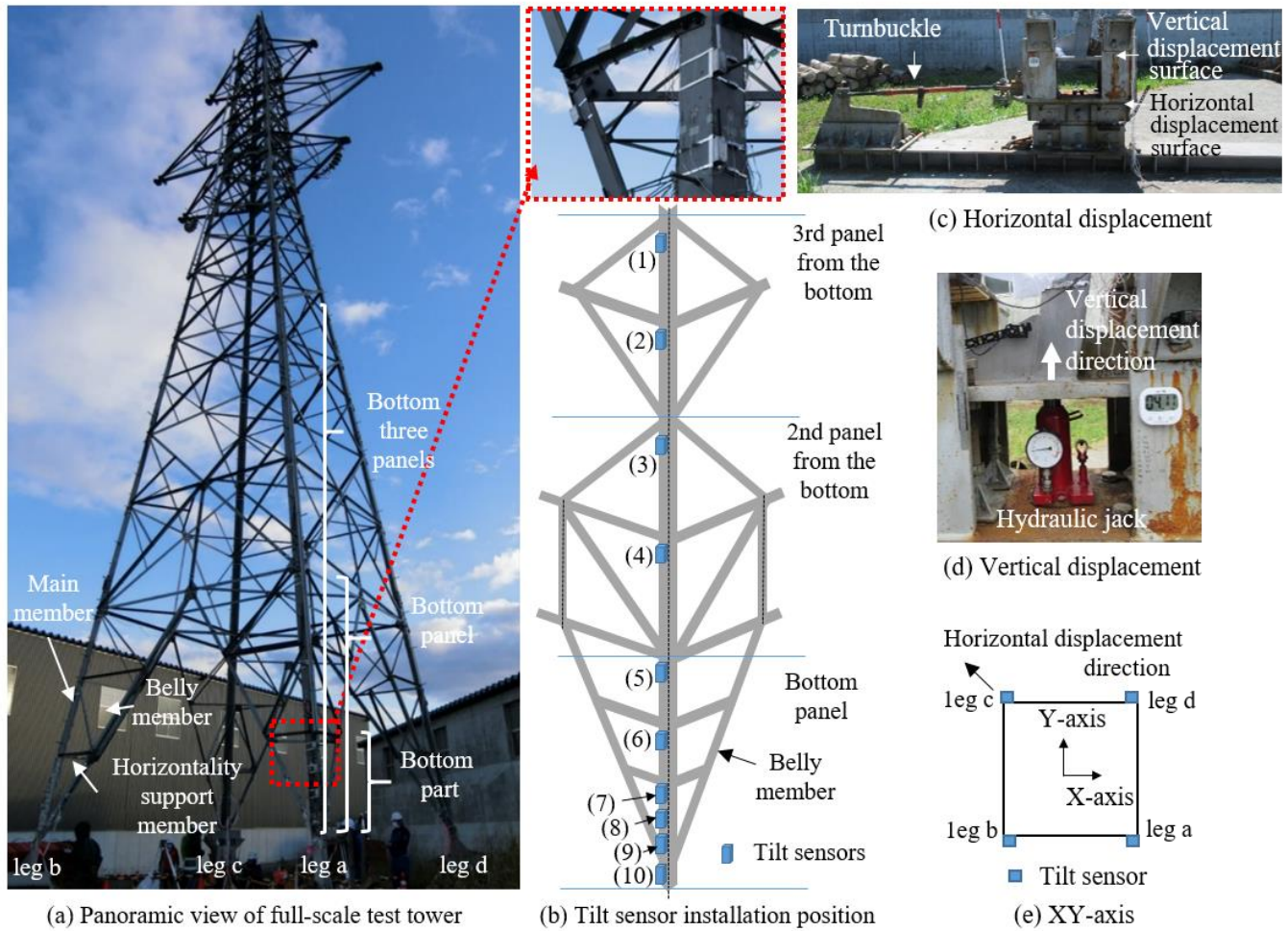


Figure 2. A full-scale test steel tower and test overview

This system is already in use on about 100 transmission towers in the real field. A provisional threshold value of 0.05deg is proposed based on the results of a full-scale test conducted previously. This value of 0.05deg corresponds to the allowable base displacement described in the non-statutory standard JEC-5101-2022 [2]. The allowable base displacement is defined by Equation (1), (2). In the equation,  $V$  is the allowable vertical base displacement,  $B$  is the distance between legs, and  $H$  is the allowable horizontal base displacement.

$$V[\text{mm}] = B[\text{mm}]/1200 \quad (1)$$

$$H[\text{mm}] = B[\text{mm}]/800 \quad (2)$$

Equation (1), (2) is not a legal requirement of the “Ministerial Ordinance Establishing Technical Standards for Electrical Equipment and Interpretation Thereof”. The equations are used as a control standard value for safety purposes [3].

In the test results previously conducted to calculate the above threshold values, the three tilt sensors installed on the same member had different sensitivity to tilt change [4]. This suggests that the sensitivity of tilt change may differ depending on the installation location, even for the same member. In this study, the number of tilt sensors was increased and retested, and the results indicated the best locations for observation.

## 2 PREVIOUS TEST RESULT

### 2.1 Overview of the test tower

The results of the previous test are presented here. Figure 2 (a) shows a full-scale test steel tower. This steel tower is made of L-shaped section steel, with a tower height of 28.20 m, a distance between legs of 6.08 m, and a tower weight of 10.3 tons. Generally, a transmission tower consists of main members, belly members, and support members. The main members and belly members are structural members, and the support members are designed as buckling stiffeners. For convenience of explanation, the legs of the tower are designated as leg a to leg d, as shown in the lower part of the photograph in Figure 2. The coordinate system xyz is set up with the center of the four legs as the origin, the x axis parallel to the ab plane (in the line orthogonal direction), the y axis parallel to the ad plane (in the line direction), and the z axis points upward perpendicular to the ground. Figure 2(b) shows the installation of the tilt sensor on one member, where all four legs are installed in almost the same way. The section from the ground to the connection between the horizontal members and the main member is called the bottom panel, and the section sandwiched between the belly members is called the panel. Since the influence of base displacement is generally



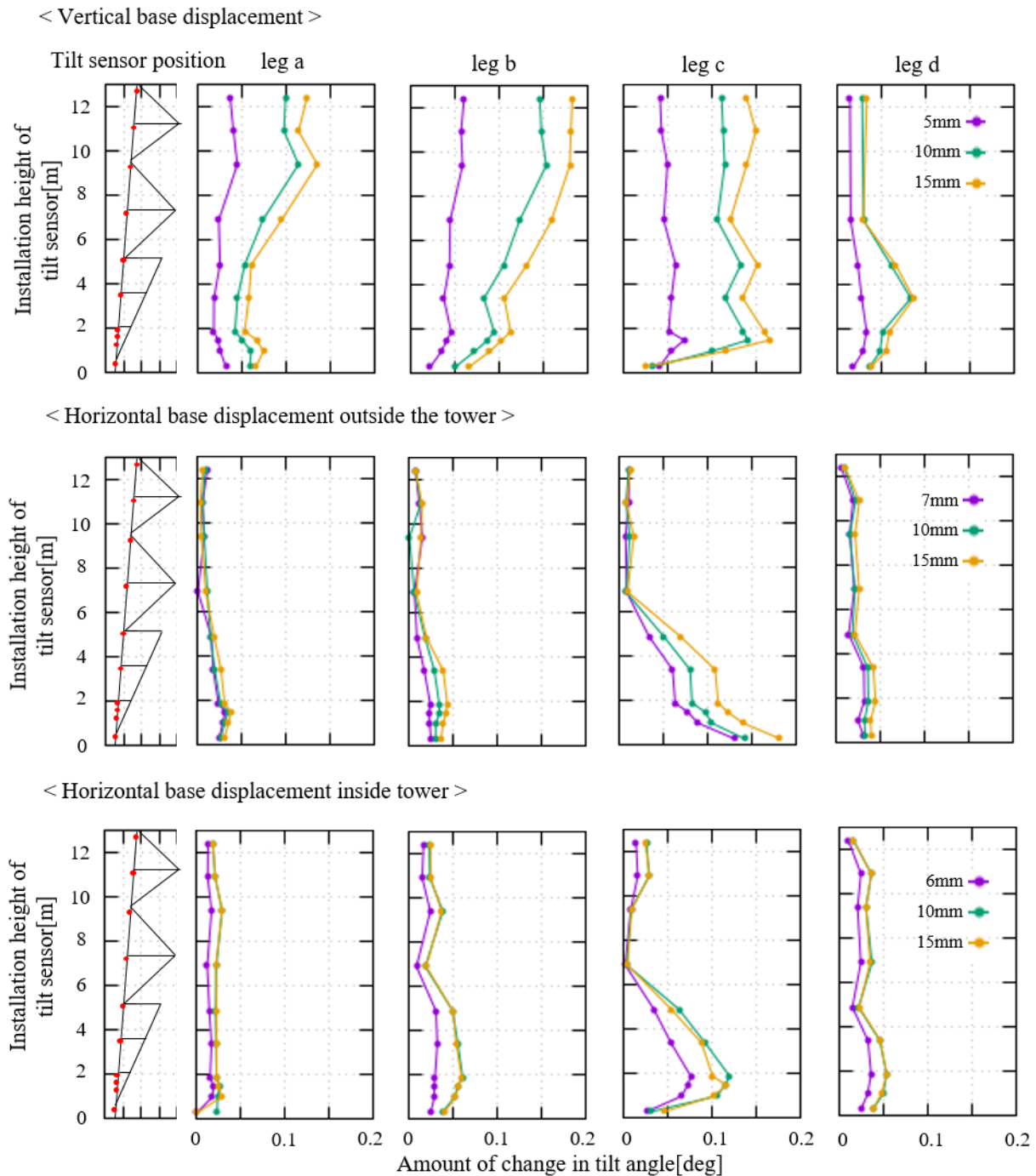


Figure 3. Relationship between tilt change and base displacement

considered to be limited to the third panel from the bottom, ten tilt sensors were installed per main member leg from the bottom to the third panel [5]. Since structural eccentricity due to joints may affect the tilt change at the lowest section, tilt sensors were installed at three locations to check. The tilt sensors near the member intersections could not be installed until a short distance from the intersections, so they were installed 10 cm lower from the intersections. The sensors measured tilt in the x-axis and y-axis directions with a measurement interval of 1 minute and a resolution of 0.0035 deg. The tilt sensor was glued

to the member, and the top and bottom of the sensor were fixed with stainless steel bands.

## 2.2 Forced base displacement method

The three legs except leg c are completely fixed. Only leg c is a movable leg; leg c has vertical upward displacement and horizontal displacement at an angle of 45 degrees to the inside and outside of the tower. Figures 2(c) and 2(d) show how the forced base displacements were given. As shown in Figure 2(c), the fixed point is located approximately 2 m from the movable leg in the outward direction of the tower. A turnbuckle was fixed between that fixed point and the movable leg to provide

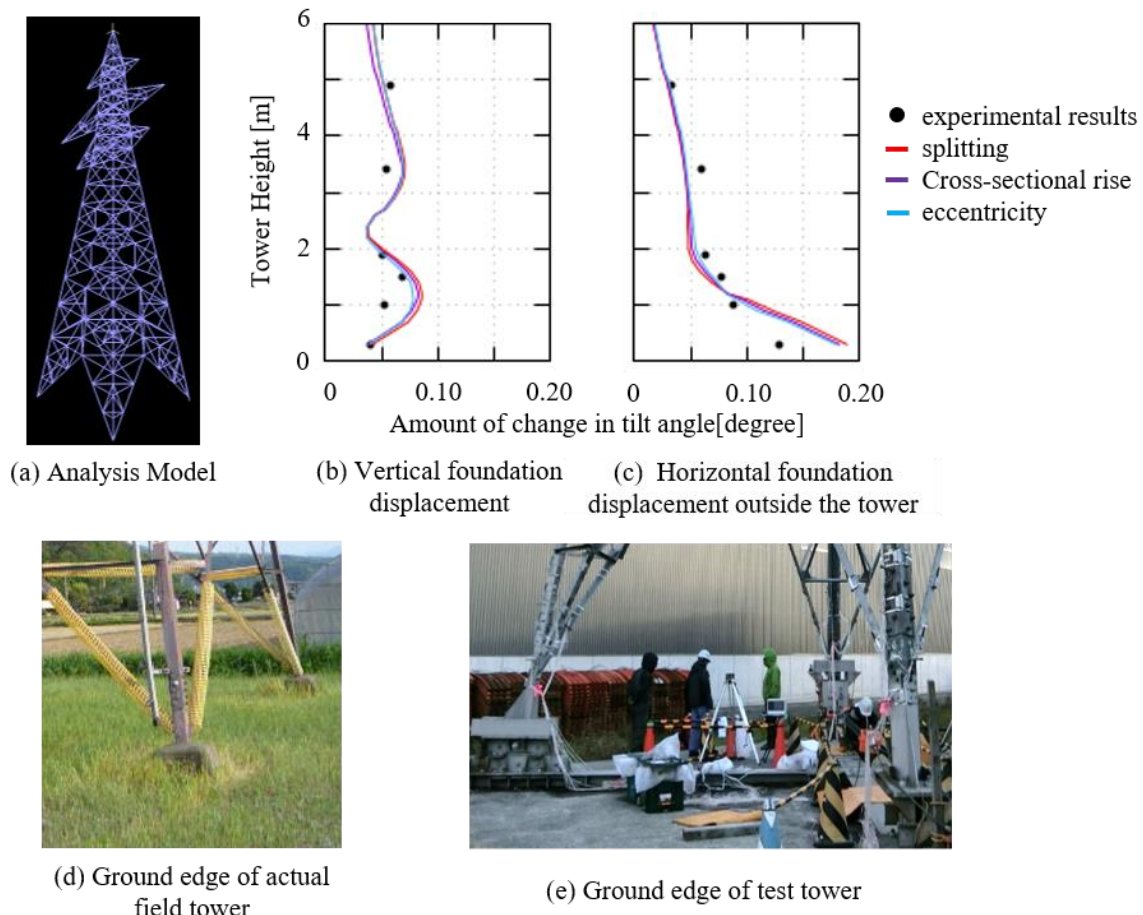


Figure 4. Analysis Model and Results

horizontal base displacement inward and outward. The horizontal displacement surface is not vertically constrained, so when the leg c is displaced horizontally, it may also be displaced vertically. As shown in Figure 2(d), vertical displacement was displaced by hydraulic jacks. The boundary of the legs is housed in a box-like frame that allows vertical movement but does not allow horizontal movement.

The allowable vertical base displacement was 5 mm, and the allowable horizontal base displacement was 7 mm, calculated from the formula for allowable base displacement. Tilt changes at base displacements of 10 and 15 mm were also observed.

### 2.3 Tilt change due to base displacement

The results of the test are shown in Figure 3. The top row of Figure 3 shows the results of vertical displacement, the middle row shows the results of horizontal displacement outside the tower, and the bottom row shows the results of horizontal displacement inside the tower. The vertical axis is the installation height of the tilt sensor, and the horizontal axis is the vector composite change in tilt angle. Unfortunately, leg d was the furthest away from the data logger, so some data was missing due to poor radio communication.

Figure 3 shows that when leg c is displaced vertically upward by 5 → 10 → 15 mm, the overall change in tilt angle at each measurement point becomes larger. Focusing on legs a, b, and c, the amount of change in tilt angle was greater at the top than at the bottom panel. During allowable vertical displacement,

the three sensors installed on the same member at the lowest section differ in tilt change by a maximum of 0.02 deg. Also, leg c shows that the member is bent.

Next, the results for horizontal displacement are shown. As in the case of vertical displacement, the change in tilt angle increases with the increase in base displacement. However, the amount of change for main members other than leg c, which is subjected to forced displacement, is considerably smaller than that of leg c by approximately 30 % or less.

During allowable horizontal displacement, the three sensors installed on the same member of the lowest section show that the tilt change differs by a maximum of 0.04 deg. In particular, a large tilt change can be seen in the movable leg at the time of horizontal displacement outside the tower, even though it is the same component.

## 3 ANALYSIS MODEL AND RESULTS

The change in tilt of the lowest part due to base displacement be confirmed by analysis. The analytical model was created using ADINA (ver. 9.4). The analytical model created is shown in Figure 4 (a). The analytical model was made up of nodes at the member intersections and a beam element between the nodes. The analytical model was subjected to the same forced base displacements as in the test, and the member stresses, displacements of the member nodes, and member tilt were calculated and compared with the test results. The test tower

has only one movable leg (leg c). When the leg c was displaced horizontally, the vertical displacement was fixed and rotations were free as the boundary condition. On the other hand, the boundary conditions were free for vertical displacement and rotation in all directions when the vertical displacement was given to leg c.

The tower used for the full-scale test did not have any electric cables. Therefore, an analytical model without the weight of the wires and tension loads was used in the analysis. Bolt slippage model [6] was considered in the analytical model. The steel tower consists of members joined by bolts. Since there is a bolt clearance of 1.5 to 2.0 mm, the bolts may slip when base displacement occurs. To account for the deflection of the main column members identified in the test results, the main column members were divided into the bottom to the fourth panel of horizontal members. In addition, a model was also created to account for the cross-sectional area of the overlapping joints of the main column members and the eccentricity of the joints of the main column members. Tilt changes were compared in these models.

The above analytical model was used to perform the analysis, and Figure 4 (b), (c) shows a comparison of the analytical and experimental results at the allowable base displacement. The vertical axis is the steel tower height, and the horizontal axis is the vector composite change in tilt angle. Figure 4(b) shows that the eccentric model has the smallest error of 0.001 degrees in the range of 1.5 m to 1.9 m from the lowest point of the analytical model. Figure 4(c) shows the comparison results for the horizontal displacement outside the tower. As with the vertical displacement, the eccentricity model had an error of 0.004 degrees at 1.5 m to 1.9 m from the lowest point. Both vertical and horizontal displacements showed a large change in tilt and sensitivity at the lowest point. This analytical model is a simplification of the actual structure. Therefore, the accuracy of the model should be improved by refining the model in accordance with the actual situation. In this model, it can be said that the experimental data can be almost explained by refining the model up to the joints of the main column members. However, the model was not able to represent changes in tilt near the bottom of the tower. This is due to the shape of the base of the tower. As shown in Figure 4(d), there are areas near the base of a transmission tower in actual operation where only the main member is present. This area is called the bottom main leg. In general, the bottom main leg of a transmission tower in actual operation is about 300 mm. In contrast, the bottom main leg of the test tower was conducted is indicated as 500 mm on the drawing. In addition, the test tower has no concrete base. Therefore, the boundary between the tower and the base is ambiguous, and the length of the bottom main leg is also ambiguous. From the above, the authors believe that the difference in tilt change near the ground is due to the effect of the bottom main leg. In addition, a comparison of the case in which the eccentricity of the main column joints and the cross-sectional characteristics of the main column joints were taken into account showed that the maximum difference in tilt change was only 0.004deg.

## 4 RETEST RESULT

### 4.1 Test overview

The results of previous tests and analyses reveal that the bottom tilt change is highly sensitive to the sensor location. Therefore, a full-scale test was conducted again to investigate the sensitivity of the tilt change of the lowest section. The target tower was the same as in the previous test (Figure 2). In this experiment, 10 tilt sensors were installed on the main member of the legs as shown in Figure 5. Note that all four legs were installed in almost the same manner. However, the measurement interval of the tilt sensors was changed to 20 seconds to obtain more detailed data.

The base displacement was targeted at the allowable base displacement of 5 mm vertically and 7 mm horizontally. As in the previous test, vertical displacement was performed with hydraulic jacks and horizontal displacement was performed with turnbuckles.

### 4.2 Test result

Figure 5 shows the change in tilt of all sensors at the allowable base displacement. The horizontal axis is the tilt change along the x-axis and the vertical axis is the tilt change along the y-axis. From left to right: vertical displacement, horizontal displacement outside the tower, and horizontal displacement inside the tower. Purple dots indicate leg a, green dots indicate leg b, blue dots indicate leg c, and yellow dots indicate leg d. The one square interval in the figure indicates 0.05deg, and the red circle indicates the threshold value. The leg c of Id3 has no data because the sensor has failed. Also, the Id10 of leg c has too large tilt changes (-0.109, 0.144) to display the dots on the figure when the horizontal displacement outside the tower is given. The dots are plotted in the hidden upper left corner of the figure. The findings from Figure 5 are summarized below. The threshold value was exceeded only in the leg c where the base displacement was given.

The leg a has a larger tilt change from the top to the bottom. The leg b has the same tilt change at all points, but there is a twisting movement to the right in the upper to lower tilt change. The leg c subjected to base displacement showed a greater tilt change toward the top. The direction of the tilt change at Id10 was inverted from that of the other sensors. The threshold value was exceeded at any point when the height was 130 cm or more from the ground (Id6 or more). The leg d has the same tilt change at all points, but there is a twisting movement to the left in the upper to lower tilt change.

Except for leg c, the tilt change was very small at all locations. The tilt change was greater toward the lower part of leg c. Tilt change exceeding the threshold was observed below 150 cm from the ground (Id5 or less). Except for leg c, the tilt change was the same at all locations. The amount of tilt change was larger than the horizontal displacement outside the tower and was about the same as the vertical displacement. In leg c, the tilt change was greater toward the bottom. In addition, the tilt change occurred in the opposite direction to the other legs. Tilt changes that exceeded the threshold were observed when the leg was less than 150 cm from the ground (Id5 or less).

From the above, the recommended location for the tilt sensor is in Id 5 and 6. In addition, only the base displacement leg exceeded the threshold when the allowable base displacement was loaded. Therefore, the leg that exceeds the threshold value



may be considered the leg where base displacement occurred. The direction of base displacement is determined by the total tilt change of the four legs.

Vertical displacement: Total tilt change of the 4 legs > Maximum tilt change of 4 legs

should be taken in the installation position when conducting actual monitoring.

It is easy to check the direction of inclination in more detail by checking the difference between ID2 and ID9. Vertical base displacement is larger for ID2 at the top when comparing ID2

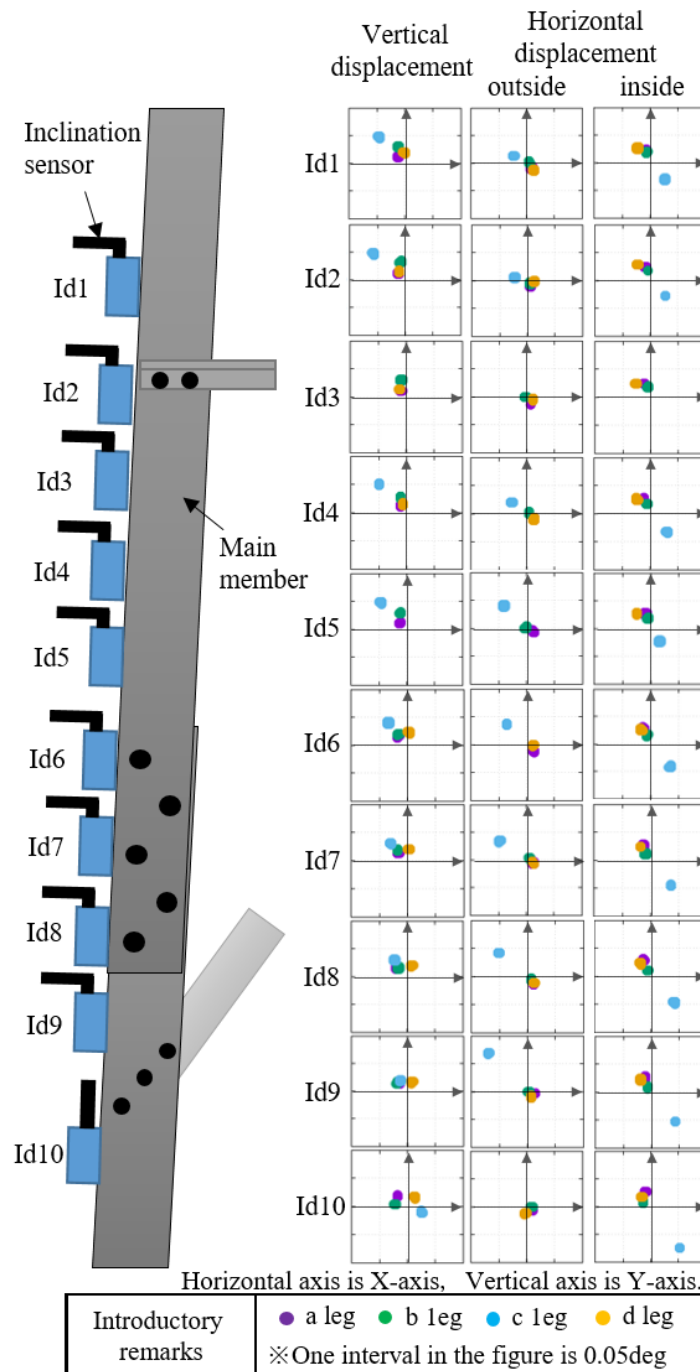


Figure 5. Test result

Horizontal displacement outside: Total tilt change of the 4 legs  $\hat{=}$  Maximum tilt change of 4 legs

Horizontal displacement inside: Total tilt change of 4 legs < Maximum tilt change of 4 legs

This test confirmed that the tilt change varies with base displacement, even for the same member. Therefore, care

and ID9. Horizontal base displacement is larger for ID9 near the ground when comparing ID2 and ID9. Thus, if several sensors can be installed, the direction of base displacement can be easily ascertained.

#### 4.3 Re-comparison with analysis

The results of the analysis presented in Chapter 3 were compared with the results of the present measurement. The

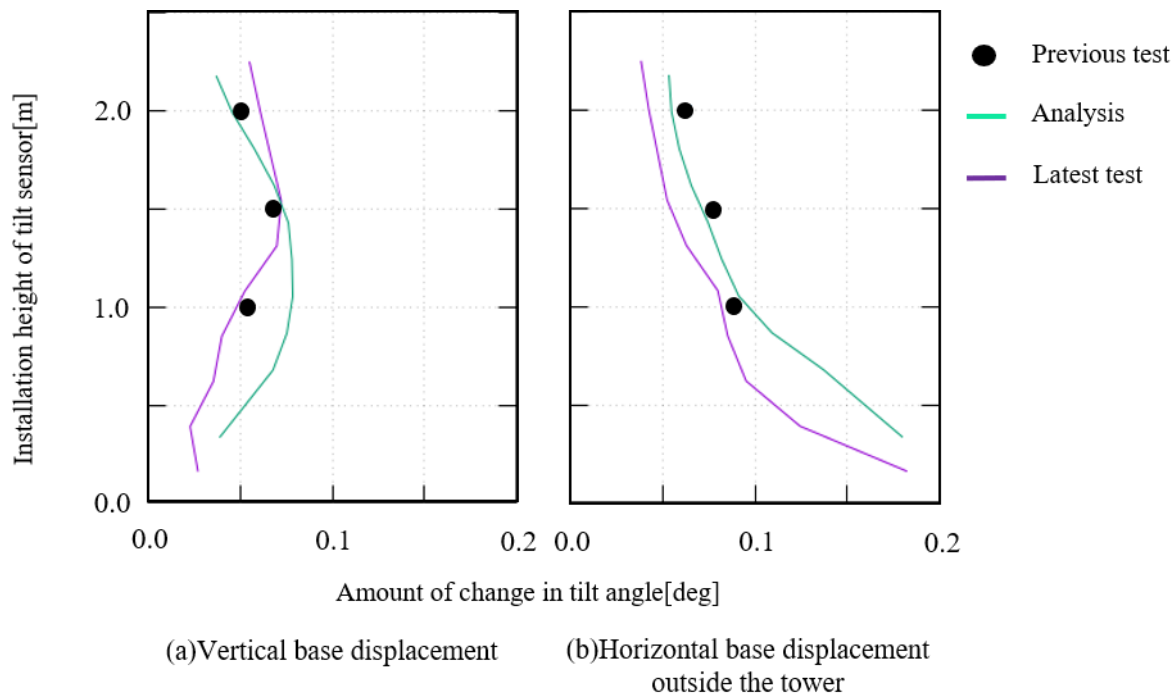


Figure 6. Re-comparison with analysis

results are shown in Figures 6(a) and 6(b). In Figures 6(a) and 6(b), the vertical axis is the steel tower height and the horizontal axis is the tilt change. The tilt change was assumed to be a vector in the line direction and in the direction orthogonal to the line. Figure 6(a) shows the comparison results of vertical base displacement and Figure 6(b) shows the comparison results of horizontal base displacement outside the tower. The black dots are the results of the previous test, the green line is the results of the analysis, and the purple line is the results of the latest test.

Figure 6(a) shows that the trend of tilt change was consistent with the previous test results. However, there was a difference of about 0.01deg at 2.0m. The retest was conducted two years later. Therefore, the authors consider it to be the effect of rust and other factors that were not present last time. Also, the last test was in October and the current test was in May. The difference in temperature may have affected the expansion of the materials. Compared to the analysis results, the overall trend was similar, but the height directions did not match. However, the locations between 1.4 m and 1.6 m were in general agreement with the analysis.

Figure 6(b) shows that the overall tilt change was smaller than the previous result, but the trend of tilt change was consistent. The trend was consistent with the analysis results. The factors contributing to the overall small change in tilt are considered to be the same as for the vertical displacement. From the above, it was found that the trend of tilt change due to base displacement was generally consistent for the 1.4 to 1.6 m point.

## 5 CONCLUSION

As a result of the full-scale test, only the displacement leg had a large tilt change that exceeded the threshold value for vertical displacement. In the horizontal displacement, the tilt changes

also exceeded the threshold value only for the displacement leg. This indicates that base displacement is most likely to occur at the leg with the greatest change in tilt. The recommended location is between 1.4 m and 1.6 m, which was in high agreement with the analytical calculations.

Horizontal displacement and vertical displacement can be determined by comprehensively checking the tilt changes of the four legs. The direction of base displacement can be determined by the sum of the tilt changes of the four legs as follows.

Vertical displacement: Total tilt change of the 4 legs > Maximum tilt change of 4 legs

Horizontal displacement outside: Total tilt change of the 4 legs  $\approx$  Maximum tilt change of 4 legs

Horizontal displacement inside: Total tilt change of 4 legs < Maximum tilt change of 4 legs

If the direction of base displacement is to be determined in more detail, it is desirable to install the sensor near the base in addition to the recommended position of 1.4 m to 1.6 m. The reason for this is that the closer to the ground, the greater change in inclination can be observed due to horizontal displacement, so by checking the difference in inclination from the recommended position, the direction of base displacement can be determined more clearly.

The results of this test showed that by installing tilt sensors on the four legs at the recommended locations, it is possible to determine the leg where base displacement occurred and the direction of base displacement.

## ACKNOWLEDGMENTS

We are very grateful to Hokkai Electric for their cooperation in the experiment.

## REFERENCES

- [1] Erosion Control Society of Japan, Emergency Investigation Report on the Mudslide Disaster that Occurred in Atami City, Shizuoka Prefecture in July 2021 (Preliminary Report), September 21, 2021
- [2] The Institute of Electrical Engineers of Japan, Standard of the Japanese Electrotechnical Committee, Design Standard on Structures for Transmission (JEC-5101-2022), 2023.
- [3] Corporate judicial person Japan electrotechnical standards and codes committee, *The transmission line rule 6001*, 2021
- [4] T. Kurihara, K. Takahashi, T. Aizawa, N. Nakamura and M. Saeki, Experimental study on the threshold and arrangement of inclination sensors for transmission towers management, *Journal of Japan Society of Civil Engineers*, Vol. 79, No. 11, 2023.
- [5] Yamazaki, M., Nakamura, H., Hongo, E. and Kubota, K., Reproduction tests and analyses concerning bolt loosening and drop at brace member joints of the transmission tower, *Journal of structural engineering*, Vol. 61A, pp. 522-531, 2015
- [6] Yamazaki, M., Hongo, E. and Nakamura, H., A practical load bearing analysis method of transmission towers with base displacement considering bolt slip and ensuring consistency with stress measurement values, *Journal of structural engineering*. Vol. 59A, pp. 131-142, 2013



# On potentials and challenges of physics-informed structural health monitoring for civil engineering structures

Matthias Baeßler<sup>1</sup>, Gino Ebell<sup>1</sup>, Ralf Herrmann<sup>1</sup>, Falk Hille<sup>1</sup>, Ronald Schneider<sup>1</sup>

<sup>1</sup>Bundesanstalt für Materialforschung und -prüfung (BAM), Unter den Eichen 87, 12205 Berlin, Germany

email: {matthias.baessler, gino.ebell, ralf.herrmann, falk.hille, ronald.schneider}@bam.de

**ABSTRACT:** Physics-informed structural health monitoring, which integrates realistic physical models of material behavior, structural response, damage mechanisms, and aging processes, offers a promising approach to improve monitoring capabilities and inform operation and maintenance planning. However, the associated technical challenges and model requirements are context-specific and vary widely across applications. To illustrate the relevance and potential of the topic, two application examples are presented. The first focuses on monitoring the modal characteristics of a prestressed road bridge, where strong sensitivity to temperature variations limits the diagnostic capabilities of conventional vibration-based global monitoring. The discussion highlights how environmental influences can obscure structural changes, and emphasizes that purely data-based approaches are inherently limited to detecting anomalies and do not enable comprehensive condition diagnostics. The second example explores a physics-informed monitoring approach for prestressed concrete bridges affected by hydrogen-induced stress corrosion cracking. By combining acoustic emission data with a calibrated acoustic model of the structure, it is possible to detect and localize wire failures. As an outlook, the integration of mechano-electro-chemical models for stress corrosion cracking is discussed, enabling predictive assessments of the strand condition.

**KEY WORDS:** Physics-informed SHM; Diagnostics, Prognostics, Structural Assessment, Structural Integrity Management

## 1 INTRODUCTION

Civil engineering structures are subject to damage, aging and deterioration processes such as fatigue, corrosion, shrinkage, creep, and scour – all of which can affect their safety and serviceability. Additionally, they are exposed to environmental and operational variations. In particular, fluctuating structural temperature distributions caused by changing environmental conditions may alter structural behavior and, in some cases, even impact structural capacity. Moreover, structures may experience rare and extreme events during their service lives – such as storms, floods, fires, explosions, earthquakes, extreme traffic loads or ship impacts – which can also impair safety and serviceability. Some structures may even already exhibit damage, which could progress to a critical state, affecting structural performance.

To effectively manage the structural safety and serviceability of engineering structures, owners and operators require information on loads and their effects, environmental influences, operational conditions, and the structural condition. This information forms the basis for assessing and forecasting structural performance, thereby enabling informed decisions on operation and maintenance.

Structural health monitoring (SHM) – in the sense of monitoring the condition of a structure – is intended to support diagnostics, prognostics, structural assessment, and maintenance planning. Diagnostics involves inferring the current condition or changes in structural characteristics from measurements or observations that are indirectly related to them. In this process, environmental and operational variability must typically be taken into account, as their impact on structural behavior can alter the measured signals, thereby potentially masking the presence of damage.

Ideally, the diagnostic information obtained through SHM is used to predict the future structural condition and to quantitatively assess structural safety and serviceability.

Research in SHM for engineering structures has a long history [1]. While significant progress has been made in the field, in practice, SHM is primarily used to measure loads and their effects, collect structural response data as a basis for calibrating structural models, and monitor known damages locally [2]. SHM-informed diagnostics, prognostics, structural assessment, and maintenance planning for engineering structures remain an evolving field.

This contribution discusses the potential and challenges of integrating physical modelling into SHM to enhance these tasks. At its core, physics-informed SHM couples physical models that describe the processes influencing structural condition and capacity with models of the structural performance, and continuously updates them with inspection and monitoring data from the actual system [3]. Within this framework, physical models are also employed to link measurements and observations to the structural condition and damage states, thereby providing an indirect connection to the processes driving deterioration and structural damage.

The paper is organized as follows: Section 2 provides a more detailed discussion on the motivation for adopting a physics-informed approach in SHM, drawing from our group's long-term monitoring experience of a road bridge in Berlin. Section 3 then explores the potential and challenges of applying physics-informed SHM to extend the lifetime of prestressed concrete bridges subject to stress corrosion cracking. Finally, Section 4 provides concluding remarks.

## 2 THE MOTIVATION BEHIND PHYSICS-INFORMED SHM: THE WESTEND BRIDGE EXPERIENCE

### 2.1 Westend Bridge

Our group's research related to SHM began in 1994 with the continuous monitoring of the Westend Bridge. This example is also used because the bridge is currently being demolished. The 30-year measurement project is likely to be one of the longest in the world. The Westend Bridge in Berlin, which has been carrying heavy traffic for several decades, had suffered a number of damages since its construction. Strengthening work was repeatedly required to ensure adequate load-bearing capacity in the long term. Figure 1 shows the normal operating conditions at the start of the monitoring measure. Figure 2 and Figure 3 are recent photos taken shortly before and during disassembly respectively.



Figure 1. Westend Bridge in service.



Figure 2. Westend Bridge in recent years, featuring implemented safety measures.



Figure 3. Demolition of the Westend Bridge, April 2025.

Among other things, it was found that the coupling joints of the bridge deck had opened. Under the influence of external loads and temperature changes, significant changes in joint width were observed during inspection and finally monitored by measurement. It was found that above a certain temperature, the crack width of the joint increased disproportionately under traffic load.

Westend Bridge is or was a prestressed concrete box girder bridge, commissioned in (1965) with full prestressing. It has 7 spans and a total length of 237m. The cross-sections of the bridge proved to be problematic: The flat three-cell box girder has a tendency to high residual stresses due to temperature, but also a significant influence of the asphalt layer on the structural behavior and a significant influence of the nominally non-structural components (rails and caps) was identified. The effect of temperature variations in the structure has not been considered in the design.

The prestressing tendons are coupled at couplers. Shear reinforcement and concrete cover (chloride ingress) have been shown to be inadequate. In addition, the bridge is subject to heavy traffic. As a result, the bridge has been strengthened several times.

The bridge reacts non-linearly due to temperature changes and high traffic loads. The coupling joint has opened due to traffic loads at high temperatures, resulting in increased fatigue demands on the prestressing tendons. Temperature variations affect the stiffness of the asphalt, change the stress/strain state within the section and lead to longitudinal cracking in the webs and base plate.

From a detailed modelling perspective, the degree of fixation between the columns and the box girder is unknown, as is the degree of fixation between the columns and the foundation.

The management of the structural data is similar to that of a normal existing bridge: Data and information about the bridge is recorded and stored in printed documents and drawings. Minimal or no as-built documentation is available. There is no information on actual physical parameters (e.g. material properties). The lack of physical information in the documentation and the lack of digitization of the data are a major obstacle to the introduction of a SHM system.

### 2.2 SHM Installation and global damage detection

An SHM system has been installed for the purpose of identifying damage or changes in structural characteristics based on data indirectly related to these damage/changes in structural characteristics.

At the beginning, an experimental modal analysis was carried out with a hydraulic shaker from EMPA. The bridge was then equipped with geophones, temperature sensors and local strain gauges in one section for a continuous monitoring.

At the time of initial installation, the aim was to identify structural changes based on a shift in natural frequencies. This initial diagnostic idea quickly proved to be flawed, as the bridge has a strong dependence of its natural vibration behavior on the structural temperatures (Figure 4). Possible approaches to understanding the temperature dependency were subsequently analyzed in a diploma thesis [4]. A major influence for this bridge is attributed to the significant stiffness contribution of the asphalt at low temperatures.

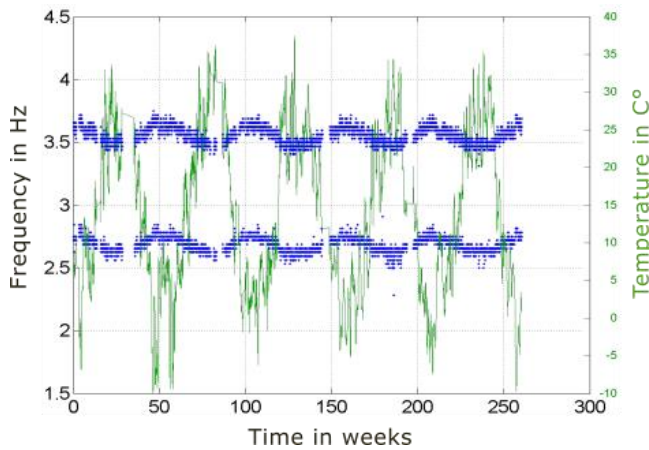


Figure 4. Dependence between natural frequency and temperature (or changes in structural behavior due to temperature effects).

Detection of damage or changes in structural properties has been further explored using signal processing techniques for dynamic data in [5]; This attempt provides a feature that is sensitive to global and significant structural damage/changes in structural properties. The procedure eliminates the effect of temperature-dependent periodic variations by normalizing the vibration data.

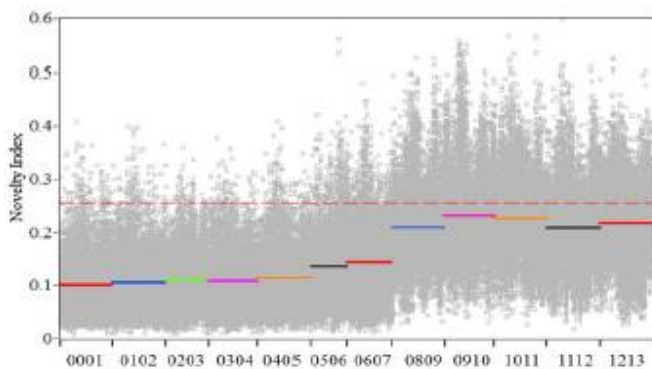


Figure 5. Statistical damage indicator derived with the novelty detection method [5].

In this example, the global damage identification can optimally show that there is a change in the measurement data and possibly in the building response. Such an anomaly would generally be recognizable after a few measurement intervals (e.g. 10-minute intervals), see Figure 5. It would then be possible to start a diagnosis as to whether there is a measurement error or whether a change in the structure is actually the cause of the changes in the measurement signal. As no information about the size and location of the damage can be determined, further damage diagnosis is only possible on site and, depending on the structure, involves considerable effort.

### 2.3 Physical modelling

It is not possible to infer the structural safety and service ability from variations in the natural frequency alone.

The SHM at Westend bridge as previously outlined lacks information on damage location, damage size and damage evolution. One of the most serious problems, however, is that it is not clear whether and to what extent the structural changes represent damage relevant to structural safety.

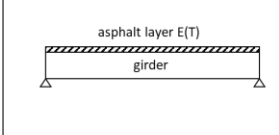
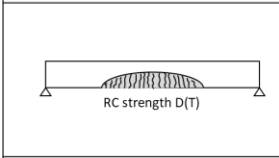
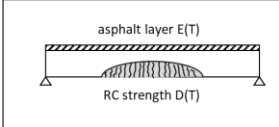
	<b>Asphalt Layer:</b> Strong temperature dependence of asphalt stiffness; contributes to overall structural stiffness, but not to structural load-bearing capacity.
	<b>Concrete – RC and prestressed:</b> Stiffness can vary <ul style="list-style-type: none"> <li>Stiffness depends on temperature and humidity</li> <li>Cracks of coupling joints may open with temperature and effect capacity</li> </ul>
	<b>Combination</b> How can the individual mechanisms be distinguished?

Figure 6. Influence of temperature on structural components.

As shown in Figure 6, a load-bearing contribution of the asphalt layer is not relevant to safety. However, if cracks open in the reinforced concrete under temperature, a temperature load represents real damage to the load-bearing structure. In reality we see a combination of both mechanism which have to be separated in a structural assessment.

In order to enable a more precise analysis, it is usually necessary to switch from a model-free data analysis to a model-based data analysis. Figure 7 shows a general scheme. Identifying a structural model is a necessary step that must be accompanied by an assignment of physical material and component properties.

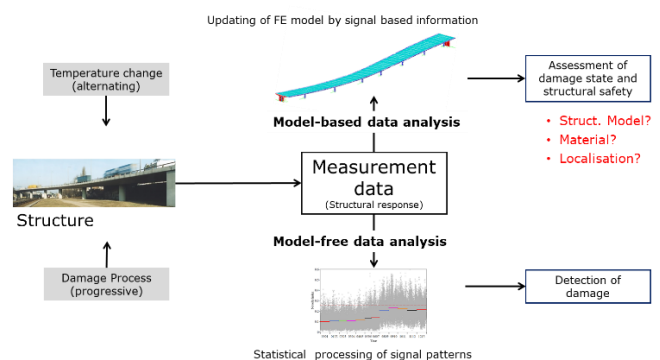


Figure 7. Updating scheme for SHM that accounts for temperature fluctuations, which may mask structural damages.



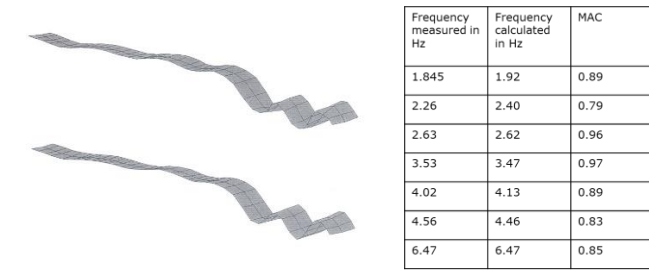


Figure 8. left: Vibration mode identified from measurements (top) vs vibration mode determined via finite element modelling (bottom). right: Identified and numerical natural frequencies

Various detailed FE models were created for the Westend Bridge and adapted to reality by means of experimental modal analyses. The models make a significant contribution to understanding the structural behaviour. The updated model is good, see Figure 8, but unfortunately not very sensitive to severe damage when compared to environmentally induced changes. The general lack of a link between the modal parameters and the (local) strength properties continues to prevent a substantial structural assessment.

#### 2.4 What can be learned from Westend bridge

The key findings from the Westend Bridge monitoring can be summarised as follows:

- Data management: Construction documents are available in paper form. These are primarily planning data (not as built, no material parameters). The data storage is not linked to ongoing digital data management.
- A global damage detection has been successfully implemented. However, the detection of a specific damage or of changes in structural characteristics was not possible. Global damage detection provides incomplete diagnostic information, no information on type, location and size of damage.
- To obtain complete diagnostic information based on SHM data it is necessary couple data with physical models. A physical model should consist of a structural model and its physical parameters describing local strength and deterioration characteristics.
- The Westend Bridge has many weak structural points, but specific hot spots are difficult to identify. What becomes apparent is that a scenario-free monitoring is extremely difficult. A monitoring task becomes easier the more clearly the potential damage scenarios can be described. This is particularly the case when disturbances such as temperature fluctuations mask changes in the structure's condition.  
→ Chapter 3 presents a scenario-orientated approach for a physics-based SHM procedure.

### 3 PHYSICS-INFORMED SHM OF BRIDGES SUBJECT TO STRESS CORROSION CRACKING

Numerous incidents in Germany have shown that concrete bridges containing prestressing steel susceptible to hydrogen-induced stress corrosion cracking experience a characteristic deterioration process [6-8]. Damage typically initiates during

the construction phase due to a mechanical-electrochemical mechanism triggered by aggressive ambient conditions. As the bridge enters its operational phase, and the prestressing ducts are grouted, damage continues to develop due to fatigue crack growth caused by dynamic traffic loads and temperature fluctuations. Over time, this can result in the failure of individual prestressing wires, each of which emits acoustic signals upon breaking. If a critical number of wires fail, the structural integrity of the bridge can be severely compromised, potentially leading to substantial damage or even collapse. In this context, the following section discusses the challenges and potentials of physics-informed SHM to extend the lifetime of bridges identified as vulnerable to this specific deterioration process.

A fundamental prerequisite for SHM-informed, model-based integrity management of bridges is the implementation of a consistent digital data management. Such a system must provide storage and access to all relevant physical information across the design, construction, and operational phases of a bridge's lifetime. It must be able to handle heterogeneous data objects, including design reports, quality control protocols, inspection records, sensor data, and assessment results. Furthermore, the system should support automated workflows that integrate this diverse data with model-based methods to enable accurate diagnosis and prediction of structural condition, as well as assessment of structural safety.

The first step in developing a physics-informed strategy for monitoring and managing the structural integrity of concrete bridges susceptible to stress corrosion cracking is to thoroughly analyze the potential failure modes resulting from the loss of a significant number of prestressing wires. It is crucial to ensure that the bridge possesses sufficient structural redundancy so that the failure of prestressing strands does not lead to sudden, catastrophic collapse. This redundancy is typically provided through reinforcement, which allows for large deformations after strand failure – acting as warning signs before failure and preventing brittle, unannounced collapse. Furthermore, it must be demonstrated that observable indicators accompany significant damage to prestressing strands. Examples of such indicators include horizontal longitudinal cracks in the webs of box girders or beams [6]. The appearance of these signs suggests advanced damage and necessitates immediate action, including bridge closure for detailed assessment, reinforcement measures, or potential decommissioning.

If the previously discussed conditions are fulfilled—in addition to the requirements that the bridge is intact, shows no signs of significant damage to the prestressing tendons, and retains sufficient load-bearing capacity (potentially confirmed through a proof load test)—then a dedicated monitoring strategy can be implemented. In this case, the evolution of stress corrosion cracking, specifically the failure of individual prestressing wires, can be monitored using acoustic emission techniques. Following the detection of a tendon failure event, a detailed visual inspection of the bridge has to be carried out to check for any newly developed visible indicators of advanced damage.

The primary aim of acoustic emission monitoring is to detect failures of prestressing wires in time and space [9, 10]. This identification problem is currently approached by utilizing pure data-based signal processing methods. However, by adopting a

physics-informed strategy—combining physical modeling of the acoustic wave propagation from wire failures with measured data—the accuracy of rupture identification can be significantly improved. In this approach, data and modeling of wire failures are brought together by identifying the model prediction that best explains the measured acoustic signal, either through optimization or Bayesian updating. Research has been initiated at BAM to develop and validate this combined methodology [11].

The first step in a physics-informed approach to diagnosing wire failures from acoustic emission signals is the development of an acoustic reference model that accurately captures the acoustic properties of the structure. This model can be established and refined using data collected during in situ reference tests. A valuable source of such data comes from the sampling of prestressing wires, which emit acoustic signals when cut. These samples, typically taken to check for defect initiation and perform material testing, provide relevant emission characteristics that support model development.

Within a physics-informed approach to SHM, the reference model is a central component of a reference certificate or birth certificate, if created at the beginning of the structure's lifetime, as outlined in the upcoming revision of DIN 1076 [12]. The reference certificate contains all information required to develop and describe the reference model, including the underlying assumptions, the data used for its calibration and validation, as well as calibration and validation results. It is incorporated into the structure's data management system to ensure traceability and long-term use.

The first major application of the calibrated reference model is the optimization of sensor placement for the acoustic emission monitoring system. Sensor locations are selected to maximize the system's ability to perform the intended diagnostic tasks. This can be achieved, for example, through model-based value of information (VoI) analysis [13].

As an outlook, a physical model of the deterioration process can provide a basis for predicting the condition of prestressing tendons. The initiation of stress corrosion cracking during the construction phase may be described using mechano-electro-chemical principles [14], while crack propagation during the operational phase can be modeled through fracture mechanics [15]. Material properties and data on the initiation and evolution of the deterioration process from laboratory tests can be used to calibrate the model. Fatigue demands resulting from traffic loads and temperature variations are incorporated via models of the respective actions and a structural model to simulate the evolution of damage over time. Capturing the stochastic nature of the deterioration process is essential to ensure realistic predictions. By coupling the deterioration model with diagnostic information from acoustic emission monitoring and visual inspection, predictions can be continuously updated. Furthermore, integrating the deterioration model with a structural model allows for assessments of safety and serviceability throughout the structure's extended lifetime [16].

Currently, BAM is developing a physics-informed SHM procedure within the research project ReSKoMB, aimed at enabling the safe extension of the service life of prestressed road bridges suspected to be affected by stress corrosion cracking. The procedure is being developed using the

Baumgarten Bridge near Potsdam as a reference structure (Figure 9).



Figure 9. Baumgarten Bridge near Potsdam.

A key element of the procedure is the collection of prestressing wire samples taken directly from the bridge, providing essential information about the current condition of the wires (Figure 10).



Figure 10. Sampling of prestressing wires from an existing road bridge for material testing (source: LS Brandenburg).



These material samples are subject to various tests, including non-destructive testing to detect defect initiation. Additionally, laboratory experiments are conducted to study the onset of damage through stress corrosion cracking and the subsequent growth of fatigue cracks under cyclic loading (Figure 11).

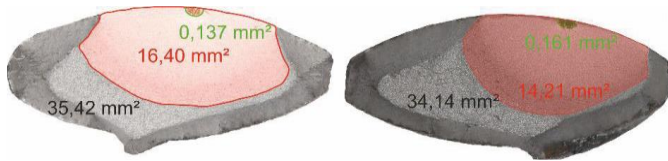


Figure 11. Fracture surfaces of two prestressing wires after a fatigue test. Green: pre-existing defects, red: crack propagation during the fatigue test, light gray: residual fracture surface [6].

A physical model of the damage processes is then developed based on these tests, allowing for predictions of the time to wire failure. To enhance these predictions, object-specific traffic load models are developed for the bridge. As part of this modeling, traffic loads are classified based on vibration measurements, enabling a more accurate representation of the actual loading conditions (Figure 12). This work builds on a project funded by the German Research Foundation within the Priority Programme "Hundred Plus" [17]

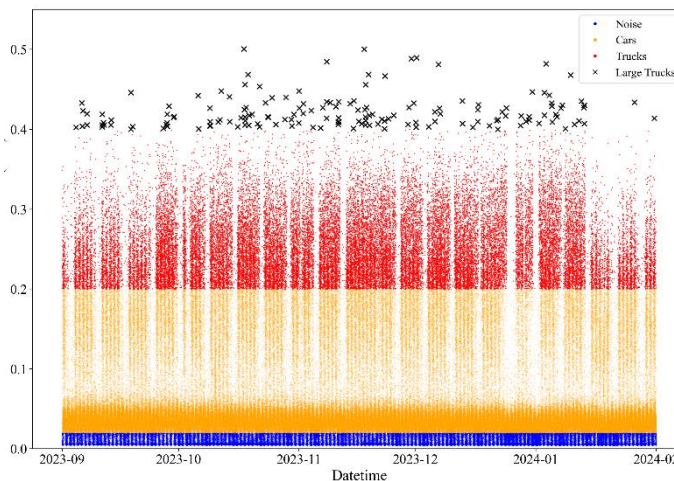


Figure 12. Classification of vehicles crossing a road bridge using machine learning techniques. The classification is based on acceleration signals [17].

Further, diagnostic information from acoustic emission monitoring, enhanced with physical modeling of acoustic wave propagation from wire failures, is used to update the predictions (Figure 13). This work is being performed as part of a parallel project at BAM called SimAS, which focuses on acoustic modeling techniques to improve the diagnosis of wire failures based on acoustic emission data [11].

As an alternative to acoustic emission methods, the project is also exploring the potential to detect wire failures using acceleration signals recorded with MEMS sensors, a method which has been successfully used in a previous project with progressive severing of prestressing wires (Figure 14).

Additional information on visible indicators of critical damage, such as horizontal longitudinal cracks in the bridge webs, is obtained through automated UAS-based inspections

[18], which is triggered by continuous monitoring of prestressing wire failures.

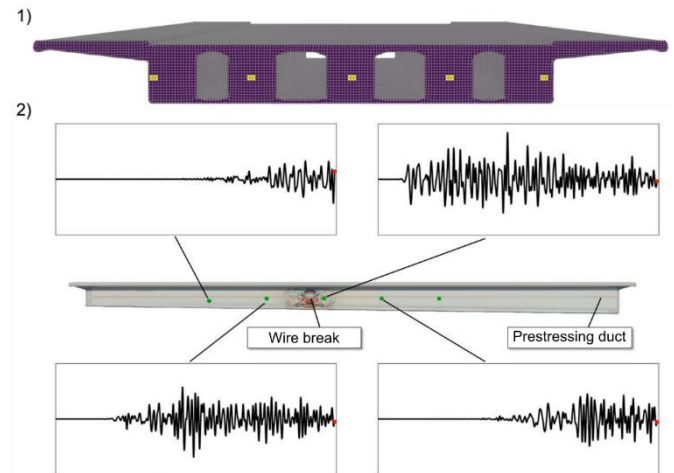


Figure 13. Simulation of acoustic wave propagation from a prestressing wire fracture in a box girder bridge. 1) Numerical mesh. Different material properties for concrete and wires (e.g., sound speed, density, damping) can be assigned to the elements. 2) Side view of the bridge with a simulated wire failure and several point evaluations of the simulated sound emission. [11].

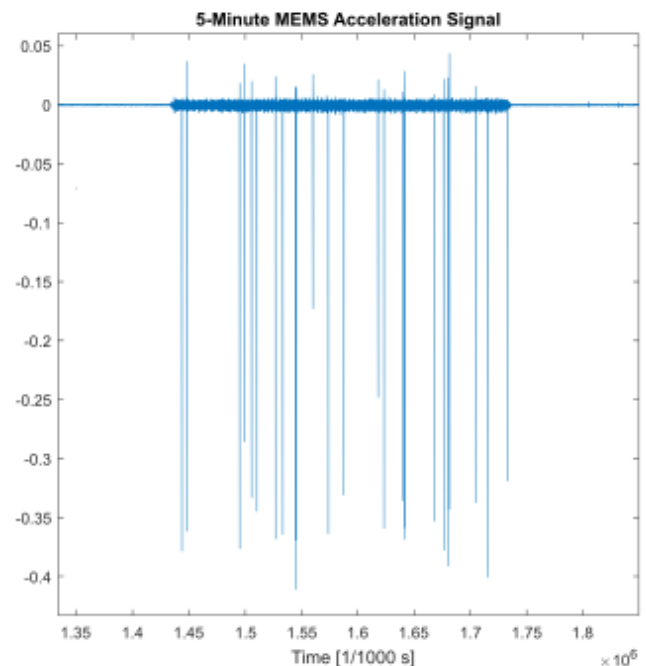


Figure 14. Accelerations measured with MEMS sensors on a bridge during progressive severing of prestressing wires [6].

#### 4 CONCLUDING REMARKS

As outlined in this contribution, physics-informed SHM holds significant potential to enhance diagnostics, prognostics, structural assessment, lifetime evaluation, and planning of operation and maintenance activities. By incorporating physical models into the SHM process, this approach offers a promising way to account for operational and environmental



variations that typically challenge conventional diagnostic methods.

However, the effectiveness of physics-informed SHM ultimately depends on the inherent sensitivity of the monitoring system to damage. These methods cannot compensate for a lack of sensitivity in the underlying measurement technique – rather, they can only leverage and enhance existing capabilities. Thus, careful consideration must be given to the selection and design of monitoring systems.

Implementing physics-informed SHM approaches requires proper digital data management to enable automated and scalable workflows. It is also associated with substantial modeling effort, making it essential to assess the return on investment for each application context.

These challenges and opportunities will be discussed further with the community at the upcoming CSHM-10 workshop in 2026, to be held in Berlin. As a dedicated forum for experts in SHM and non-destructive evaluation (NDE), CSHM-10 will provide an ideal platform to explore how physics-based models and monitoring data can be effectively combined to improve the safety, resilience, and efficiency of civil infrastructure systems.

## ACKNOWLEDGMENTS

Parts of presented work are being carried out within the ReSKoMB project (project no. FE 88.0219/2024/AV14), funded by the German Federal Highway and Transport Research Institute (BAST). Additional support has been provided by the German Research Foundation (DFG) within the Priority Programme "Hundred Plus" (SPP 2388) under project no. 501829185.

## REFERENCES

- [1] C. R. Farrar, N. Dervilis, and K. Worden, "The Past, Present and Future of Structural Health Monitoring: An Overview of Three Ages," *Strain*, vol. 61, no. 1, p. e12495, 2025.
- [2] F. Wedel, S. Pitters, F. Hille, R. Herrmann, and R. Schneider, "Leitfaden – Strategischer Einsatz von Monitoring für Ingenieurbauwerke," Marx Krontal und Partner (MKP) und Bundesanstalt für Materialforschung und -prüfung (BAM), Abschlussbericht zum Forschungsprojekt FE 15.0707/2022/LRB 2024. [Online]. Available: <https://www.bast.de/DE/Publikationen/Fachveroeffentlichungen/Ingenieurbau/Downloads/B-fv-15-0707.html>
- [3] P. Simon, R. Schneider, M. Baeßler, and G. Morgenthal, "A Bayesian Probabilistic Framework for Building Models for Structural Health Monitoring of Structures Subject to Environmental Variability," *Structural Control and Health Monitoring*, vol. 2024, no. 1, p. 4204316, 2024.
- [4] R. Rohrmann, M. Baeßler, S. Said, W. Schmid, and W. Rücker, "Structural causes of temperature affected modal data of civil structures obtained by long time monitoring," presented at the 18. Int. Modal Analysis Conference (IMAC), San Antonio, TX, USA, 2000–02–07, 2000.
- [5] W.-H. Hu, S. Said, R. Rohrmann, W. Rücker, A. Cunha, and A. Rogge, "Vibration-based structural health monitoring of a highway bridge based on continuous dynamic measurements during 14 years," in *Proc. 7th International conference on structural health monitoring of intelligent infrastructure (SHMII-7)*, A. De Stefano, Ed., 2015 2015, pp. 1–12.
- [6] Landesbetrieb Straßenwesen Brandenburg [Hrsg.], "B1 – BrückeAltstädter Bahnhof in Brandenburg an der Havel – Bauwerksuntersuchungen vor dem Rückbau," 2021.
- [7] O. Steinbock, T. Bösche, G. Ebell, F. Kaplan, and G. Marzahn, "Erfahrungen aus dem Rückbau der Brücke am Altstädter Bahnhof in der Stadt Brandenburg – Teil 1: Untersuchung und Erkenntnisse zum Ankündigungverhalten bei großformatigen Spanngliedern mit spannungsrissskorrosionsgefährdetem Spannstahl," *Beton- und Stahlbetonbau*, vol. 117, no. 8, pp. 572–580, 2022, doi: doi.org/10.1002/best.202200051.
- [8] S. Marx *et al.*, "Einsturz der Carolabrücke in Dresden Teil 1," *Beton- und Stahlbetonbau*, doi: 10.1002/best.202500029.
- [9] M. Fiedler *et al.*, "Detektion von Spanndrahtbrüchen mit Schallemissionsanalyse," *Beton- und Stahlbetonbau*, vol. 120, no. 2, pp. 150–164, 2025.
- [10] Richtlinie SE 05, "Detektion von Spanndrahtbrüchen mit Schallemissionsanalyse," Deutsche Gesellschaft für Zerstörungsfreie Prüfung (DGZfP), 2024.
- [11] S. Pirsakewitz, G. Zaripova, N. Brinkmann, L. Gebraad, C. Boehm, and H. Trattig, "Simulation der Schallemissionen von Spanndrahtbrüchen," in *SCHALL 25 – Schallemissionsanalyse und Zustandsüberwachung mit geführten Wellen*, Dresden, Germany, 2025, vol. 4: Deutsche Gesellschaft für Zerstörungsfreie Prüfung (DGZfP), pp. 1–6.
- [12] *Ingenieurbauwerke im Zuge von Straßen und Wegen - Überwachung und Prüfung*, DIN 1076:2024-02 - Entwurf, Berlin, 2024.
- [13] L. Eichner, R. Schneider, and M. Baeßler, "Optimal vibration sensor placement for jacket support structures of offshore wind turbines based on value of information analysis," *Ocean Engineering*, vol. 288, p. 115407, 2023.
- [14] M. Askari, P. Broumand, and M. Javidi, "Numerical modeling of stress corrosion cracking in steel structures with phase field method," *Engineering Failure Analysis*, vol. 158, p. 107921, 2024.
- [15] R. 805, "Traglast bestehender Eisenbahnbrücken," DB Netz AG, 2010.
- [16] D. Straub, R. Schneider, E. Bismut, and H.-J. Kim, "Reliability analysis of deteriorating structural systems," *Structural Safety*, vol. 82, p. 101877, 2020.
- [17] E. K. Ramasetti, R. Herrmann, S. Degener, and M. Baeßler, "Development of generic AI models to predict the movement of vehicles on bridges," (in eng), *SMAR 2024 – 7th International Conference on Smart Monitoring, Assessment and Rehabilitation of Civil Structures*, vol. 64, pp. 557–564, 2024.
- [18] G. Morgenthal *et al.*, "Framework for automated UAS-based structural condition assessment of bridges," *Automation in Construction*, vol. 97, pp. 77–95, 2019.

## Retrofitting load measurement devices on existing anchored structures

Matthias J. Rebhan<sup>1</sup>, 0000-0002-0638-6202, Hans-Peter Daxer<sup>1</sup>, 0009-0006-7216-4348, Markus A. Schuch<sup>2</sup>, Clemens Klass<sup>3</sup>, Florian Scharinger<sup>4</sup>, Michael Reiterer<sup>5</sup>, 0000-0002-5212-9389

<sup>1</sup>Institute of Soil Mechanics, Foundation Engineering and Computational Geotechnics, Faculty of Civil Engineering Sciences, Graz University of Technology, Rechbauerstraße 12, 8010 Graz, Austria

<sup>2</sup>ÖBB Infrastruktur AG, Austria

<sup>3</sup>ASFINAG-Baumanagement GmbH

<sup>4</sup>GDP ZT GmbH

<sup>5</sup>Revosys GmbH

email: rebhan@tugraz.at, daxer@tugraz.at, clemens.klass@asfinag.at, markus.schuch@oebb.at, f.scharinger@gdp.at, michael.reiterer@revosys.at

**ABSTRACT:** Anchored structures are an essential part of infrastructure corridors, as they enable high cuts and the reinforcement of existing structures. As pre-stressed elements, anchors allow for economical construction with low-deformation, making them critical components for ensuring stability. Consequently, comprehensive monitoring is often required alongside inspections, especially when the reliability of the load-bearing elements is in question - e.g., due to creep or corrosion of metallic components. Based on research activities due to the ageing of such structures, several options have been investigated to retrofit load measurement devices to already installed pre-stressed anchors. In addition to different types of coupling methods, this paper presents first results from a trial in which, through the retrofitting of an external thread to strands, a new method for load monitoring is investigated. These methods are particularly useful when information about the current anchor load is lacking, as they provide better insight into the condition of the tension elements and, furthermore, the overall behavior of the structure. The paper shows some approaches already in use and the results of an initial test series, in which the potential of a new approach to amend a load measuring device to an already installed pre-stressed anchor is investigated and validated.

**KEY WORDS:** Anchor testing, Load monitoring, Existing structures, Asset management, Retrofitting.

### 1 ANCHORED STRUCTURES

Due to their ability to transfer large tensile forces into deeper or more competent strata, anchored structures using tension elements are often an economical design option in geotechnical engineering. Grouted anchors [1] & [2]], in particular, can be used to reduce deformations, allowing for more compact and slender geometries. Examples of such structures include newly constructed anchor and pilaster walls (Figure 1), as well as structures that have been subsequently anchored during refurbishment or repair (Figure 2).



Figure 1. Anchored pilaster wall.



Figure 2. Pre-stressed anchors used for the remediation of a cantilever retaining wall.

Over the designed service life of up to 100 years, such technically demanding structures require increased inspection and maintenance. In Austria, the specifications for structure operators are defined in the FSV guidelines [2]. The inspection procedure for anchored structures is identical to that for non-anchored retaining structures. On the one hand, the focus is on the surrounding terrain, drainage system and structural

components, which are typically made of reinforced concrete. On the other hand, anchors undergo a more intensive assessment to determine their state of preservation. Inspections (or checks) are generally carried out every 3 to 6 years and must be performed manually and visually during on-site activities.

In addition, the special inspection of tension elements and anchored structures is described in detail in a separate working paper [5]. The aim of these activities is not only to determine the current condition of the structure, but also to detect changes in the state of preservation or the development of damage patterns on the tendons, in order to assess their impact on safety and reliability.

At the end of such an inspection, and in addition to the assessment, recommendations for necessary measures are provided. Alongside the suggestion to carry out special inspections, this may include advices on implementing monitoring systems for the structure. The aim is, on the one hand, to gain a better understanding of the structure's behaviour, and on the other hand, to integrate these systems into alarm and warning plans - especially for severely damaged structures - in order to enable early response to potential or imminent failure.

## 2 INSPECTION AND DAMAGE IDENTIFICATION ON ANCHORED STRUCTURES AND TENDONS

As a structure ages, the requirements for inspection and maintenance increase in order to ensure an accurate and conclusive assessment of its condition. The regular performance of inspections [6] enables the early detection of defects and thus forms the basis for a long-term, continuously optimized maintenance strategy. The scope of [2] covers all structures in which anchorages [1] have been installed. Therefore, this guideline includes a wide range of applications - from anchored retaining structures (see [5]) to pier footings and anchored bridge abutments, as well as retrofitted anchored structures ([7]). For inspection purposes, a distinction has to be made between the structure itself and the relevant structural components. In this context, the term "structure" also includes the adjacent terrain at the head or base of the structure.

Relevant structural components of anchored structures cannot be completely examined during inspections (i.e. they can only be examined to a limited extent). This is, on the one hand, due to the apparent free length and the bond length (see Figure 3) of a pre-stressed anchor, which are located in the subsoil and thus not accessible. On the other hand, for many structures, the anchor heads were sealed during construction and are therefore not directly visible.

As with other structures, damage or an increase in damage can also be observed over time on anchored structures and the installed tendons. In addition to damage to the structural components (e.g. concrete elements and shells), corrosion damage to the metallic components of pre-stressed anchors is particularly critical. For permanent anchors with a designed service life of up to 100 years, corrosion protection for all components must be ensured. When it comes to tension elements and anchored structures, a general distinction can be made between two types of corrosion.

Oxygen corrosion refers to a chemical process in which iron and steel materials oxidize when they interact with oxygen and an electrolyte (e.g. water). The product of this process is

commonly referred to as rust. This rust layer is generally very porous and, in contrast to other reaction products (e.g. the pyrolysis layer of burned wood), provides little or no protection against the progression of the process. The corrosion can only be halted by removing one of the reaction partners (oxygen or water) or by passivating the surface. In contrast to oxygen corrosion, stress corrosion cracking typically occurs in pre-stressed steel elements under prolonged tension. These stresses can result either from an externally applied load or from internal constraints. Additionally, hydrogen atoms, which may be produced from oxygen corrosion, penetrate the metal lattice. This slight disturbance in the metal's microstructure forms a crack capable of growth under the influence of tensile stresses. These chemical reactions and processes can occur in pre-stressing steels, which are sensitive to such damage. In the case of high-strength steels, commonly used for tendons, the process is referred to as hydrogen-induced stress corrosion cracking. In contrast such a process generally does not produce any significantly recognizable damage pattern during propagation, and can therefore not be clearly identified by the reaction products.

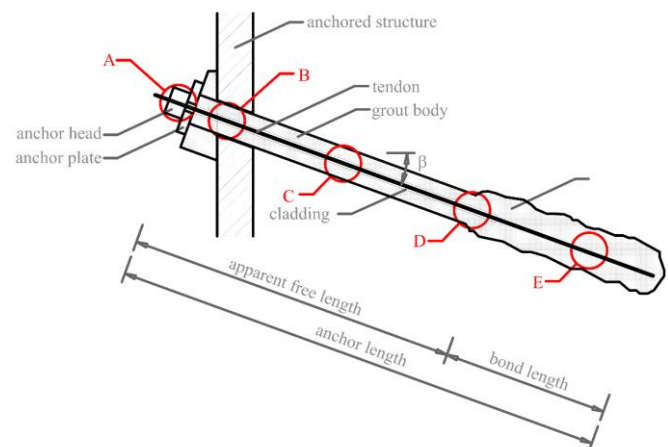


Figure 3. Parts of a pre-stressed anchor.

In the absence of corrosion protection and when environmental conditions are conducive to corrosion, uniform surface corrosion can affect the entire cross-section. This is mainly observed on exposed steel components, strands and bars with insufficient corrosion protection. In contrast to uniform surface corrosion, pitting corrosion occurs at points where the corrosion protection is absent or inadequate in certain areas of the cross-section. This corrosion phenomenon is typically found in improperly manufactured or cracked grout bodies. In chloride-contaminated environments (e.g. de-icing agents), such phenomena are also more likely to occur. This process begins in a relatively small area on the surface and spreads relatively quickly into the interior, significantly reducing the cross-section locally.

As mentioned above, corrosion damage to anchored structures and tendons mainly occurs in unprotected or inadequately protected areas of the structure. Some of these areas are a result of the design itself, while others stem from the manufacturing process or associated weaknesses and deficiencies.





Figure 4. Corroded tension elements of the external parts of strand anchors.

Corrosion damage to insufficiently protected outer surfaces of the anchor (Figure 3 area A) can lead not only to a visual impairment of the anchored structure but also to a loss of load-bearing capacity of individual tendons or even the failure of an entire anchor over time. However, due to the often rather massive design of the anchor head components, some reserves remain. Improperly filled anchor head niches or protective covers often lead to increased corrosion, which can manifest as the release of reaction products or visible rust plumes. As shown in Figure 4, exposed components of the anchor, which are subjected to weathering and environmental conditions, are particularly susceptible to corrosion. Such damage can usually be detected by a visual inspection of the anchor head.

The most critical point is found in the section directly behind the anchor head (Figure 3 area B). Defects in the inner anchor head can occur during construction, but also due to ageing or volatilization of the corrosion protection material. The absence of corrosion protection at the anchor head (see Figure 5) can be considered severe damage to both the tendon and the anchored structure.

In addition to the two types of damage in the anchor head area, corrosion processes can also occur along the entire anchor length. Likewise, ageing effects on the grout material can occur along the entire apparent free length, potentially leading to corrosion of the tension element (Figure 3 area C). Due to the load transfer from the tendon into the underground along the bond length and the associated tensile stresses in the grout body, cracks may develop. These cracks create damaged areas in the corrosion protection (Figure 3 area E), serving as potential sources for corrosion. Especially in the transition zone between the apparent free length and the bond length (Figure 3 area D), cracks occur more frequently due to the strong increase of the stresses in the grout body [8]].



Figure 5. Corroded strands within the anchor head area.

Furthermore, if design documents or long-term monitoring data are available, the inspection of the structure can usually be carried out by trained personnel without major difficulties. However, if no or only limited geological, geotechnical and structural information is available at the time of inspection, a more detailed investigation is required to make a reliable assessment of the structure's condition.

### 3 MONITORING OF ANCHORED STRUCTURES

As already mentioned, it is often necessary to implement appropriate monitoring measures during the maintenance phase of a structure, especially if significant defects are identified. In addition to deformation monitoring, the pre-stressing force is a key parameter for anchored structures. Throughout the service life of an anchor, the anchor load can either be observed with installed monitoring systems, or assessed by performing lock-off-tests. While a monitoring system, such as load cells, offer the possibility to survey the anchor load over a longer period (depending on the monitoring interval), a lock-off-test only determines the load acting on the anchor at the time of testing.

#### 3.1 Anchor Lock-Off-Testing

Regarding the safety assessment of anchors and anchored structures in Austria (e.g. [7] & [9]), the normative rules of EN 1537 [1] are supplemented by the requirements outlined in the RVS guidelines [3] and a Working Paper [4]. To ensure the capability of an anchor or the functionality of a preliminary anchor system design, three different test types - namely, investigation, suitability and acceptance tests - are performed. A lock-off-test solely indicates the load currently applied to an anchor. In general, the anchor load depends on a variety of factors and can be influenced by daily and seasonal fluctuations (e.g. temperature, groundwater), but can also vary due to damage (e.g. corrosion) or creep effects. Taking these factors into account, however, a lock-off test can provide an accurate assessment of the anchor's condition and functional efficiency.

Research (e.g. [10] & [11]) and the results of safety assessments on anchors have shown that anchors, especially the anchor head, are often exposed to de-icing agents and salt, making them highly susceptible to corrosion damage. Such damage is usually not detectable through the results of lock-off tests. Therefore, in addition to a lock-off-test, endoscopic examinations [12] can provide valuable insights into the

condition of an anchor. Especially the visual inspection of the anchor head area can help to detect manufacturing defects or corrosion damage in the anchor head.

Besides – mostly durability related – damages to an anchor (e.g. [10] & [13]), an increasing number of corrosion damages to reinforcement elements (e.g. [11] & [14]) can be observed.

The result of an anchor lock-off test can be seen in Figure 6. This load-deformation-diagram illustrates the compression and slippage of the test setup (green line) alongside with the elastic elongation of the anchor strand. The intersection point, marked by the two equalisation lines in Figure 6, represents the point where the anchor head lifts off the anchor plate (or the structure), which defines the currently applied anchor load.

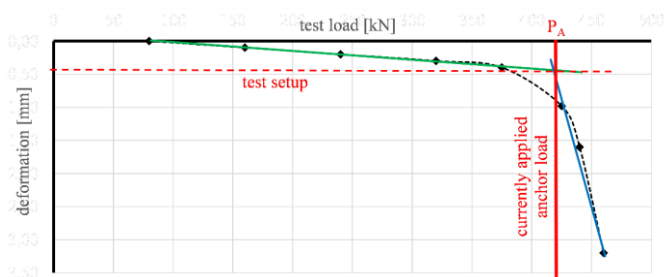


Figure 6. Deformation-load-diagram of an anchor lock-off test.

In comparison to the test loads in a suitability or acceptance test of anchors (e.g. [1], [15] & [17]), the determine of the lock-off load is not described in normative or design regulations. As this load reflects the current state of the anchor and is therefore subject to change over time, making it therefore often necessary to define the lock off load  $P_A$  in advance based on knowledge and experience. The number of strands or the diameter of the bar, for example, can provide information on this and define the limits and boundaries for such tests in combination with a preceding endoscopic surveillance of the anchor head and a stepwise load increase during the testing process.

### 3.2 Anchor load monitoring

By monitoring the anchor forces, any changes (both decreases and increases) in the anchor force and their resulting effects on the structure, or the potential failure of the anchor, should be recorded in a timely manner. This is necessary to comply with the requirement of Eurocode 7 [17], Chapter 8.3, which states that *'the effects of anchor failure must be taken into account'*, even though there are limited specifications in terms of standards and calculation methods (see [18], [19] & [20]) for how this requirement should be addressed.

For this purpose, anchor load measuring devices are used, typically installed during the construction of the structure. In addition to electrical force measuring devices (e.g. eddy current) or traditional systems based on strain gauges, hydraulic measuring devices as shown in Figure 7 are commonly used.

Such measuring devices are usually installed at the anchor head and are equipped with analogue reading devices. However, the accuracy of these readings is often limited, influenced by factors such as viewing angle and accessibility. Additionally, these measuring devices are usually exposed to weathering, ranging from temperature changes, rain and wind to harsh environmental conditions like snow, frost and the effects of de-icing agents used during winter maintenance.



Figure 7. Anchor load plate installed during the construction of the structure.

## 4 RETROFITTING LOAD MEASUREMENT DEVICES ON PRE-STRESSED ANCHORS

If assessing the state of preservation, the results of a lock-off test or the need for more comprehensive information on the behaviour of an anchor require it, digitising existing measuring equipment or installing force measuring devices may become necessary.

The following sections present various approaches for implementing such measures, as well as the key considerations related to planning, execution and data interpretation.

### 4.1 Digitalization of load measurement devices

Force measuring devices installed on structures, such as shown in Figure 7, usually feature only an analogue reading, limiting their ability to provide close-meshed time series or assess temperature-related behaviour of the structure. To address this limitation, the digitalisation and real-time collection of measurement data have therefore been increasingly used for such existing elements.

Although force measuring devices can already be digitised during installation - i.e. during the production of the anchorage - this was often not done, or the technology was not yet available at the time the anchorage was installed. In the following, however, the digitalisation of already installed anchor load plates is briefly discussed - a possibility to add digital data acquisition to almost all installed and still functional devices.

Figure 8 shows an example where an existing anchor load plate with an analogue reading device was upgraded with a



digital data acquisition unit. The exact implementation steps involved are listed in [21]]. In addition to digitising the anchor load measurement, environmental factors such as the outside temperature, humidity and structural temperature at different depths should also be recorded to gain a comprehensive understanding of the structure's behaviour.



Figure 8. Digitization of an already installed anchor load plate.

This type of digitisation process, combined with the installation of both analogue and digital data acquisition systems, can offer significant added value for the structure and inspection personnel. While the analogue reading allows for a fast check of functionality and a direct determination of the anchor force, the digital interface enables the collection of comprehensive time series data on the behaviour of the anchor. An example of this is shown in Figure 9.

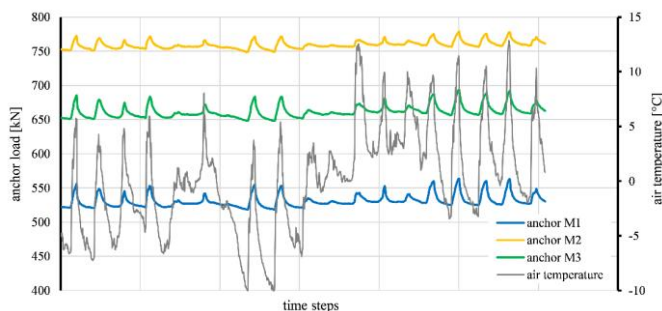


Figure 9. Time series of digitized anchor load cells in relation to temperature.

The diagram shows the recorded anchor loads of three anchors (M1 to M3) alongside the measured air temperature (from -10°C to +13°C) over an observation period not further defined here. A clear correlation between changes in air temperature and the recorded anchor loads can be observed. Furthermore, the anchor load responds almost immediately to changes in temperature, suggesting that these variations are largely attributable to the thermal expansion of the measuring device or the structural elements of the wall.

#### 4.2 Retrofitting load measurement devices on anchor heads

If no load measurement devices are present on a structure, or if additional pre-stressed anchors are to be equipped with such

systems, several retrofitting options are available. If the anchor head offers a thread (either internally in the wedge plate or externally), a force measuring device can be retrofitted relatively easy - enabling a short-circuit setup similar to a lock-off test. Alternatively, the existing tendon overhang can be used for attaching a measurement device. However, this is rarely feasible with existing anchorages in Austria, necessitating the exploration of alternative solutions. Two such approaches are briefly described below.

Figure 10 shows the first retrofitting possibility, which involves attaching an additional press chair to facilitate the subsequent lifting of the anchor head via two threaded rods. This enables the creation of a load short circuit through the installation of a new anchor load plate. However, this design is only possible if suitable contact points are available on the anchor head (e.g. free strand holes, internal threads, bayonet at the wedge plate) that allow the anchor head to be properly engaged. In this particular case, the approach was possible because only two strands were installed in a four-strand wedge plate, leaving two free strand holes. Threads were cut on-site into these unused holes to accommodate the threaded rods.

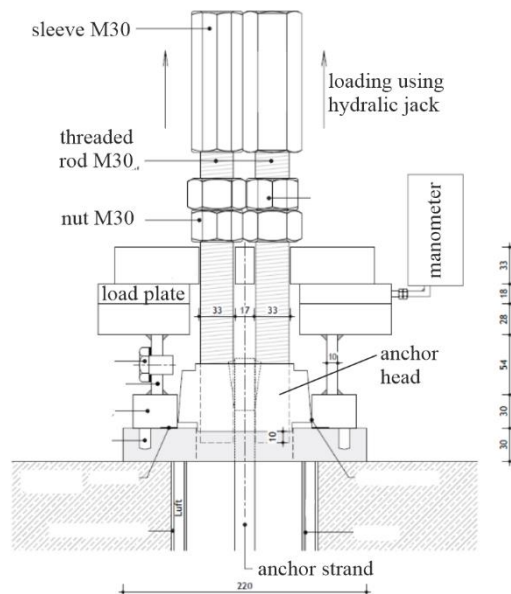


Figure 10. Example of retrofitting an anchor load plate on a partially occupied anchor head.

The figure below shows a special type of anchor known as a wire anchor. Its distinctive feature is that the wires within the drill hole are bundled by a rod attached in the centre. This system, referred to as a PZ anchor [22], allows for relatively straightforward attachment of a new load short circuit and the retrofitting of an anchor load plate, due to the presence of a fine-threaded rod at the anchor head.

Both options share a common factor in that they involve considerable effort. Sufficient expansion paths must be available to enable a load short circuit and the geometric requirements for attaching an anchor load plate must also be met. It should also be noted that such interventions, such as the on-site installation of threads in installed wedge plates, represent a significant impact on the system. This may raise concerns not only regarding liability but also with respect to durability and integrity. Nevertheless, in cases where



significant changes in anchor loads are suspected, the added value of enabling anchor load measurement typically outweighs these concerns and becomes the primary focus of such investigations and considerations.

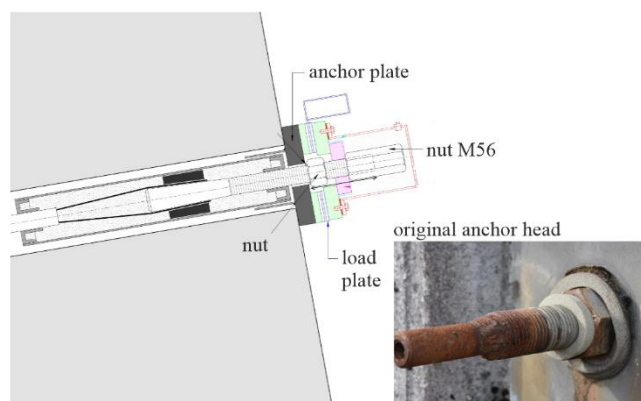


Figure 11. Example of retrofitting an anchor load plate for tensile elements or anchor heads with threaded component.

#### 4.3 Retrofitting load measurement devices on anchor strands

Often, there is insufficient strand overhang, the wedge holes of an anchor head are occupied and other structural components required to create a force-locking connection are unavailable. As a result, the options listed in Chapter 4.2 for retrofitting an anchor load plate to existing pre-stressed anchors may not be feasible. Nevertheless, to accurately assess the behaviour of the structure, it would be beneficial to obtain information about any potential changes in the pre-stressing force.

One possible option is to cut an external thread on the existing strand overhang. From a practical point of view, this section of the tendon is usually 15 - 20 mm long, which may allow a fine thread to be screwed on and subsequently a threaded nut to be fitted. An example for testing purposes is shown in Figure 12 and Figure 13. A fine thread M16x1 (core diameter 14.92 mm) was screwed onto a strand with an outer diameter of 15.6 mm. The manufacturing test demonstrated that even with low pre-stressing forces on the strand and a resulting small wedge bite, the thread could still be successfully installed.

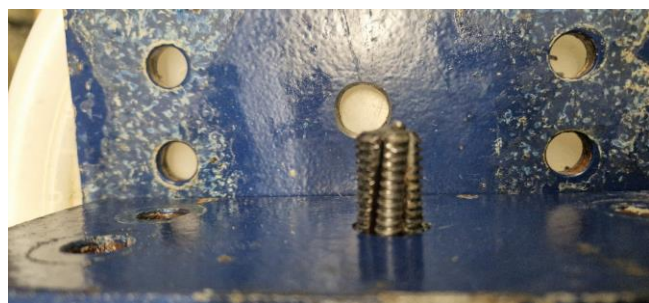


Figure 12. External thread retrofitting to a pre-stressed anchor strand.

The embossed thread on the strand overhang allows for the creation of a force-locking connection between the strand, which would otherwise only be gripped by friction, and other structural elements. An example of this can be seen in Figure

13, where two nuts were screwed onto the embossed thread of the strand to facilitate a tensile test.



Figure 13. External thread used for the application of a threaded nut on an anchor strand.

The result of a series of tests showed that a force-locking connection can be achieved by installing an external thread onto the overhang of already installed anchor strands. Obviously, the amount of load that can be transmitted depends on the length of the thread, the pitch and the condition of the strand. More detailed investigations are currently underway. Nevertheless, this first series revealed the following points:

- It is possible to emboss an external thread onto the overhang of already installed, pre-stressed anchor strands;
- There is no unacceptable mechanical damage to the high-strength steel strands due to cold forming during the cutting process;
- With sufficient strand overhang, it is possible to achieve a force-locking connection;
- An externally applied thread on strands can be used to attach threaded nuts for force input or transmission.

This approach therefore enables the creation of a subsequent force-locking connection with the individual strands of a pre-stressed anchor. This can facilitate the installation of threaded rods to extend the strands, simplifying the execution of lock-off testing or enabling the retrofitting of force measuring devices, as shown in Chapter 4.1 and 4.2.

Furthermore, innovative and new measuring devices, such as the e-Bolt [23]], could also be implemented in anchor technology. This system consists of a nut that, in addition to securing and transmitting loads, also serves as a measuring device. Such systems are already used in various measurement applications, for example to measure the pre-load force of dynamically stressed objects like noise barriers along railways. Beyond retrofitting force measuring devices, this technology could also enable the digitization of anchor force measurement.

## 5 CONCLUSIONS & SUMMARY

There are several methods to assess the condition of anchored structures, particularly the condition of the tension elements. In addition to traditional structural inspections, monitoring data is often used. Typically, geodetic surveys, readings from existing measuring devices and, if necessary, special tests to determine the material properties are used to record any changes regarding the state of preservation of anchors and anchored structures.

Since lock-off testing is associated with higher personnel costs and potential restrictions, such as road closures or other impacts on the availability of infrastructure, it is usually

conducted on a limited number of anchors and at periodic intervals. If such tests are not possible, for example due to the shape and type of anchorage, or if a continuous time series of the currently applied anchor load is required, retrofitting a force measuring device may be an appropriate solution.

One of the most common options is to attach anchor load measurement devices directly to the anchors under consideration. However, this is only possible if such provisions have already been accounted for during the planning stage. These measuring elements can be enhanced with continuous data acquisition by digitising the measuring devices, providing comprehensive information on the behaviour of the structure. In addition to possible seasonal influences such as temperature, monitoring can also be implemented in order to detect damage processes or imminent failure of single elements or the anchored structure itself.

Current investigations and research activities in this area indicate that, in addition to various methods of coupling to the anchor head construction of pre-stressed anchors, it is also possible to retrofit anchor load measurement equipment by subsequently cutting threads onto the strand overhang. This approach allows for the use of a force-locking mechanism to attach measurement devices or to enable additional lock-off testing.

This article has attempted to compile a comprehensive overview of the available options for retrofitting anchor load measurement solutions. Given the decline in the state of preservation of anchored structures and tension elements, along with their frequent use in geotechnical engineering, such retrofitting solutions are expected to receive increasing attention in the future.

## ACKNOWLEDGMENTS

The investigations and developments presented in this article were conducted as part of a series of service and research projects. Among other things, the concept for attaching threads to existing strand protrusions was developed as part of the SaRAS - Safety and Risk of Anchored Structures - research project, which was initiated by VÖBU and funded by the Austrian Research Promotion Agency (FFG).

## REFERENCES

- [1] Austrian Standards Institute. 2015. Ausführungen von Arbeiten im Spezialtiefbau – Verpressanker. No. ÖNORM EN 1537. Vienna.
- [2] Ostermayr H. and Barley T. 2002. Ground Anchors. Chapter 2.5 in Geotechnical Engineering Handbook. 169-215.
- [3] FSV. 2013. *Quality Assurance for Structural Maintenance, Surveillance, Checking and Assessment of Bridges and Tunnel, Anchored Retaining Walls*. No. RVS 13.03.21. Vienna.
- [4] FSV. 2022. *Quality Assurance for Structural Maintenance, Surveillance, Checking and Assessment of Bridges and Tunnel, Methods for special inspections of anchored structures and anchors*. AP33. Vienna.
- [5] Sabatani P.J. and Pass D.G. and Bachus R.C. 1999. Geotechnical Engineering Circular NO. 4 – Ground Anchors and Anchored Systems. FHWA-IF-99-015. Federal Highway Administration - Office of Bridge Technology.
- [6] Hanel J. and Prehan W. 2006. Beurteilung der Standsicherheit und Gebrauchstauglichkeit von dauerhaft rückverankerten Bauwerken. Bautechnik. 83. Heft 10. Ernst & Sohn. p. 688-694.
- [7] Scharinger F. and Stadlbauer J. and Antony C. and Karigl W. 2017. Beurteilung und Instandsetzung von schwer mangelhaften, geankerten Konstruktionen. In 32. Christian Veder Kolloquium – Zugelement in der Geotechnik. Graz University of Technology. Gruppe Geotechnik Graz. p. 57-70.
- [8] Fabris, Carla M. (2020): Numerical Study on Pullout Tests of Ground Anchors Monitored with Fibre Optic Sensors. Dissertation. Technische Universität Graz, Graz. Institut für Bodenmechanik, Grundbau und Numerische Geotechnik.
- [9] Schäfer F. and Timmermann V. and Spang C. 2013. Nachprüfung von Dauerankern nach DIN4125:1990 und EC7-1. Bautechnik 90. Heft 9. Ernst & Sohn. p. 585-592.
- [10] Burtscher S.L. and Rebhan M.J. and Marte R. and Scharinger F. 2017. Neue Methoden zur Korrosionsdetektion an Litzen- und Stabankersystemen, in Dietzel, M., Kieffer, S., Marte, R., Schubert, W. and Schweiger, H.F. (Eds.), Beiträge zum 32. Christian Veder Kolloquium: Zugelemente in der Geotechnik - Anker | Nägel | Zugpfähle. Graz. Graz University of Technology, pp. 71–86.
- [11] Hunkeler F. and Matt P. and von Matt U. and Werner R. 2005. Prestressing tendons, stay cables and ground anchors – Description of the systems and lessons learnt from corrosion damages. Bundesamt für Strassen. Forschungsauftrag AGB2000/470 auf Antrag der Arbeitsgruppe Brückenforschung (AGB). Eidgenössisches Department für Umwelt, Verkehr, Energie und Kommunikation. Wildegg.
- [12] Hung-Jiun Liao. 2018. Ground anchors corrossions – the beginning of the end. MATEC Web of Conferences 195. ICRMCE 2018.
- [13] Ebeling R. M. and Strom R. W. and Hite Jr. J. E. and Haskins R. W. and Evans J. A. 2013. Assessing Corrosion Damage and Corrosion Progression in Multistrand Anchor Systems in Use at Corps Projects. US Army Corps of Engineers Engineering Research and Development Center. ERDC TR-13-3.
- [14] Rebhan M.J. and Vorwagner A. and Kwapisz M. and Marte R. and Tschuchnigg F. and Burtscher S. 2017. Safety assessment of existing retaining structures. Geomechanics and Tunneling 10. No. 5. p. 524-532. Ernst & Sohn. Berlin.
- [15] ÖNORM B 4455, 01.01.1979: ÖNORM B 4455.
- [16] Austrian Standards Institute. 2019. *Geotechnical investigation and testing – Testing of geotechnical structures – Part 5: Testing of grouted anchors*. No. ÖNORM EN ISO 22477-5. Vienna.
- [17] Austrian Standards Institute. 2009. *Eurocode 7: Entwurf, Berechnung und Bemessung in der Geotechnik: Teil 1: Allgemeine Regeln*. No. ÖNORM EN 1997-1. Vienna.
- [18] Daxer H.P. 2020. *The behaviour of anchored structures affected by the failure of ground anchors*. Master's Thesis. Graz University of Technology. Institute of Soil Mechanics, Foundation Engineering and Computational Geotechnics. Graz.
- [19] Spring Singapore. 2010. *Technical reference for deep excavation*. Vol. 93.020 No. TR 26:2010. Spring Singapore. Singapore.
- [20] Zhao W. and Han J.-Y. and Chen Y. and Jia P.-J. and Li S.-G. and Li Y. and Zhao Z. 2018. *A numerical study on the influence of anchorage failure for a deep excavation retained by anchored pile walls*. Advances in Mechanical Engineering. 10(2). pp. 1–17.
- [21] Rebhan et. al. 2024. *Erfassung der Vorspannkraft bei bestehenden geankerten Konstruktionen – Abhebeversuche, Nachrüstung und Digitalisierung von Kraftmessvorrichtungen zu Monitoringzwecken*. Mitteilung des Instituts für Geomechanik und Geotechnik, Technische Universität Braunschweig. Messen in der Geotechnik 2024. 22./23. Februar 2024. Heft Nr. 116.
- [22] Institut für Bautechnik, 1993. *Zulassungsbescheid, Felsanker "Polensky & Zöllner"*, Z-20.1-48.
- [23] <https://www.revosys.at/en/e-bolt-en>

# Reliability Assessment of Structural Health Monitoring Systems using Model – Assisted Probability of Detection and Bayesian Model Updating

Yogi Jaelani<sup>1</sup>, Francesca Marsili<sup>1</sup>, Jan Grashorn<sup>1</sup>, Sven Knoth<sup>2</sup>, Sylvia Keßler<sup>1</sup>

<sup>1</sup>Engineering Materials and Building Preservation, Faculty for Mechanical and Civil Engineering, Helmut Schmidt University/University of the Federal Armed Forces Hamburg, Holstenhofweg 85, 22043 Hamburg, Germany

<sup>2</sup>Department of Mathematic and Statistics, Faculty of Economics and Social Sciences, Helmut Schmidt University/University of the Federal Armed Forces Hamburg, Holstenhofweg 85, 22043 Hamburg, Germany  
email: yogi.jaelani@hsu-hh.de

**ABSTRACT:** Structural health monitoring (SHM) is a key method for assessing the condition of civil infrastructure, detecting and localizing damage through continuous data acquisition. Damage detection methods are divided into physically based approaches, using finite element (FE) models, and data-driven approaches, relying on signal processing. A key challenge in SHM is the lack of data from the damaged state, which complicates the validation of the technique. However, the successful deployment of SHM systems on real civil infrastructure depends mainly on their reliability. For non-destructive testing (NDT) systems, the Probability of Detection (POD) is an accepted approach for quantifying reliability. In contrast to NDT, there is no generally applicable procedure to assess the reliability of SHM systems.

This study addresses this gap by evaluating SHM reliability with POD models and data generated from calibrated FE models. These FE models are calibrated through Bayesian inverse methods. To manage computational challenges, generalized Polynomial Chaos Expansion (gPCE) surrogate models are employed. These methods are tested using vibration-based measurements on a laboratory-scale four-degree-of-freedom (4-DOF) wood frame. The results highlight the use of MAPOD and limitations of the method, emphasizing their potential to enhance SHM reliability and enable smarter infrastructure systems.

**KEY WORDS:** MAPOD; SHM; Bayesian inverse methods; vibration-based measurements.

## 1 INTRODUCTION

Structural Health Monitoring (SHM) is a key method for assessing the condition and integrity of civil infrastructure through continuous or periodic data acquisition. By deploying sensor networks, SHM systems are capable of detecting and localizing damage of structures, thereby enhancing maintenance strategies and extending service life. Damage detection methods in SHM are typically categorized into two major classes: physics-based methods, which utilize for example finite element (FE) models to simulate structural behavior; and data-driven methods, which rely on signal processing, statistical analysis, and machine learning [1].

A major challenge in SHM is the lack of damaged-state data, which complicates the validation and benchmarking of diagnostic techniques. This issue becomes critical when aiming to ensure the operational reliability of SHM systems in real civil infrastructure applications. While Non-Destructive Testing (NDT) technologies benefit from standardized reliability assessment procedures such as the Probability of Detection (POD), the SHM community is still developing a generally applicable methodology for quantifying SHM system reliability.

POD is a metric used to evaluate the performance of Inspection system of NDE. POD quantifies the likelihood that a flaw of a given size will be reliably detected by the inspection system NDE. POD curves have been widely applied in the aerospace and nuclear power industries to ensure structural safety [2–4]. The conventional approach for estimating POD curves as used in the aerospace industry is based on empirical testing as outlined in MIL-HDBK-1823A [2]. This approach requires the generation of a sufficiently large and representative data set covering a range of flaw sizes. Two primary techniques are commonly used: the **Hit/Miss** method and the **â vs. a**

(response vs. flaw size) method. These procedures form the foundation of standardized POD analysis in NDE.

In contrast, the Model-Assisted Probability of Detection (MAPOD) approach integrates physics-based model simulation for estimating POD. MAPOD aims to extend and complement the basic MIL-HDBK methodology by reducing (though not eliminating) the need for physical testing samples.

The application of MAPOD has been investigated in several studies [7–9]. Smith et al. [8] successfully conducted a fully model-assisted POD validation for immersion ultrasonic inspection targeting embedded flat-bottom holes. Their results demonstrated equivalence to those obtained using the conventional MIL-HDBK-1823 approach.

Knopp et al. [7] explored a MAPOD approach for evaluating crack detection in a two-layer airframe structure with countersunk fasteners using Eddy Current Testing (ECT). The study involved 171 fasteners, including 38 with known cracks, with crack lengths ranging from 0.69 mm to 4.29 mm. Physical models were calibrated with experimental data, and 5000 synthetic data points were generated via Monte Carlo simulation for MAPOD estimation. The results showed excellent qualitative agreement between the empirical and simulation-based POD curves, although uncertainties in the input parameters were not explicitly addressed.

By leveraging FE models or numerical simulations, MAPOD can significantly lower the time, cost, and logistical complexity of traditional POD studies [7]. This numerical simulation-based method has great potential in evaluating the reliability of SHM systems, where empirical data is often limited or difficult to obtain.

This study proposes a framework for evaluating the reliability of SHM systems using POD and MAPOD models. The framework is enhanced by simulated data generated from



finite element (FE) models, which are calibrated in the reference/undamaged state using Bayesian inverse methods to capture uncertainties and improve prediction accuracy based on experimental observations. As a result, simulations of parametric variations, such as the initiation and progression of damage, can be conducted with higher accuracy, thereby improving the predictive capability and overall reliability of the SHM system.

To address the computational demands of FE simulations, surrogate models based on generalized Polynomial Chaos Expansion (gPCE) theory are employed.

The calibration of the FE model is performed by applying a Polynomial Chaos Expansion-based Kalman Filter (PCE-KF). This method is validated using a laboratory-scale experiment involving a four-degree-of-freedom (4-DOF) wooden frame subjected to vibration-based measurements. The measurements are performed under both reference and changed states, where the changes are introduced through controlled mass variations.

The results demonstrate the feasibility of applying MAPOD techniques within the SHM context and provide insight into the limitations and practical considerations of this approach. Ultimately, this work contributes to the development of reliable SHM systems for civil infrastructure.

## 2 METHODOLOGY

The overall workflow proposed for the MAPOD construction is illustrated in Figure 1, while a detailed explanation of each component is provided in the subsequent sections.

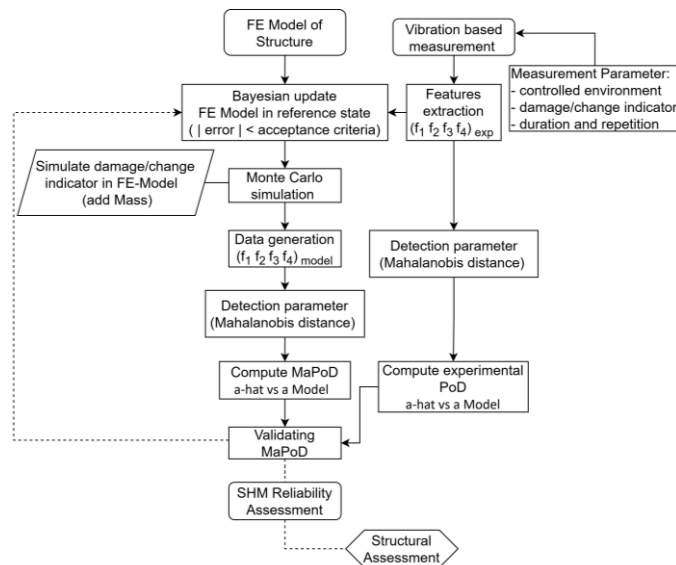


Figure 1. MAPOD model building process

### 2.1 Experimental Setup

A laboratory-scale four-story wooden frame structure is designed to simulate the response of four degrees of freedom system. To achieve this, the column dimensions are carefully adjusted to ensure that the stiffness in one translational direction is significantly greater than in other translational or rotational directions. The column cross-section is 300 mm by 6.4 mm. The total height of the wooden frame is 1000 mm, with a width of 500 mm. Each story has a height of 250 mm. The

beam cross-section is 60 mm by 60 mm. The columns are constructed from laminated wood sheets, while the beams are made of solid wood. The mass of each structural element is determined by weighing the components prior to assembly. The frame is instrumented with triaxial accelerometers to record its vibration response under random excitation induced by a handheld rubber hammer. A data acquisition system from Dewesoft and MMF KS903B100 triaxial accelerometers are used in this experiment. The experimental setup is illustrated in Figure 2, and the structural geometry and mass is summarized in Table 1.

Table 1. Structural geometry and mass

Geometry [mm]		Mass [gr]	
Column cross-section	300x6.4	Column 1	885
		Column 2	915
		Beam 1st Floor	1122
H, Height	1000	Beam 2nd Floor	1060
		Beam 3rd Floor	1046
Beam cross-section	60x60	Beam 4th Floor	1020
L, Length	500	Triaxial Accelerometer	11

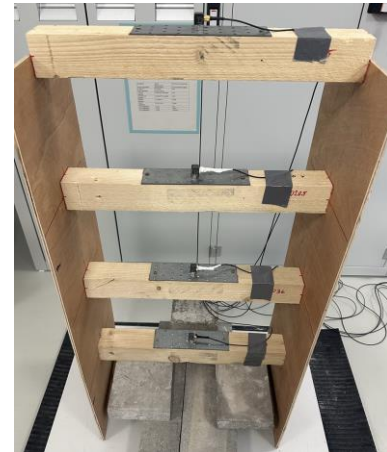


Figure 2. Experimental setup

The measurements are conducted under both reference (undamaged) and changed (damaged) states. The changed state is simulated by incrementally adding mass to the fourth floor of the structure. For each state, vibration responses are recorded for 90 seconds at a sampling rate of 1000Hz, with each test repeated at least 15 times to ensure statistical consistency. The experiments are performed over several days, from March 24<sup>th</sup> to March 29<sup>th</sup> 2025, to ensure sufficient data collection and to capture a broader range of variability even under stable environmental conditions.

All experiments are conducted under constant room temperature ranges and humidity conditions. This experimental setup serves as the basis for validating the MAPOD analysis compared to real physical test data. Details of the measurement set and repetition are provided in Table 2.

Table 2. Measurement set

Measurement Set	Added Mass [gr]	[%] to the Mass of 4 <sup>th</sup> floor	Repetition
Reference	0	0	267
Mass 1	25	2.4 %	69
Mass 2	51	4.9 %	55
Mass 3	75	7.3 %	20
Mass 4	102	9.9 %	70
Mass 5	153	14.8 %	66
Mass 6	204	19.8 %	55
Mass 7	255	24.7 %	15

## 2.2 Finite element model and Bayesian updating

A three-dimensional finite element (FE) model of the four-story wooden frame structure is developed in Ansys to simulate its modal dynamic response. The model geometry reflects the actual dimensions of the physical structure, incorporating column and beam cross-section. Shell elements are used to represent the thin column sections, while beam elements are used to represent beams. The beam-column connections are assumed to be rigid. The boundary conditions simulate fixed line support at the base, consistent with the physical setup.

Material properties are initially assigned based on measured values. The material density is then calculated as the ratio of mass to volume for each element. The elastic modulus is unknown and is treated as random variable in wood properties. In addition to the elastic modulus, the thickness of the columns is also modeled as a random variable, accounting for imperfections in the thickness of the wood elements. The elastic modulus and column thickness are then treated as input random parameters in the Bayesian model updating. Meanwhile the natural frequencies and mode shapes obtained from modal analysis are used as output (observed) parameters for the Bayesian model updating.

## 2.3 Polynomial Chaos Expansion based Kalman Filter

A Bayesian model updating approach is applied to minimize discrepancies between the outputs of the FE model and the experimental measurements. The uncertain parameters, such as elastic modulus and thickness of columns, are treated as random input parameters  $\mathbf{Q} \in \mathbb{R}^{N_n}$  where  $N_n$  is the number of input parameters, modeled as Gaussian independent variables

$$\mathbf{Q} = \mathcal{N}(\boldsymbol{\mu}_Q, \mathbf{C}_Q) \quad (1)$$

where  $\boldsymbol{\mu}_Q \in \mathbb{R}^{N_n}$  is the vector of mean values and  $\mathbf{C}_Q \in \mathbb{R}^{N_n \times N_n}$  is the covariance.

The system random inputs are transformed by a forward model operator  $\mathcal{M}$  into the outputs  $\mathbf{Y} = \mathcal{M}(\mathbf{Q}) \in \mathbb{R}^{N_m}$  where  $N_m$  is the number of measured outputs. The measurement  $\mathbf{Z} \in \mathbb{R}^{N_m}$  is affected by an error  $\mathbf{E} \in \mathbb{R}^{N_m}$ , which follows a normal distribution and combines linearly with the measured output

$$\mathbf{Z} = \mathcal{M}(\mathbf{Q}) + \mathbf{E}, \mathbf{E} = \mathcal{N}(0, \mathbf{C}_E) \quad (2)$$

where  $\mathbf{C}_E \in \mathbb{R}^{N_m \times N_m}$  is error covariance. The scope of the Bayesian updating is to improve the estimation of the random input  $\mathbf{Q}$  given output measurements  $\mathbf{z}$ . An efficient approach to

Bayesian updating consists in applying the linear Bayesian Filter

$$\mathbf{Q}' = \mathbf{Q} + \mathbf{K}(\mathbf{z} - \mathbf{Y}) \quad (3)$$

where  $\mathbf{Q}$  are prior parameter estimates,  $\mathbf{Q}'$  are the posterior,  $\mathbf{z}$  are output measurements,  $\mathbf{Y}$  are measured system outputs and  $\mathbf{K}$  is the Kalman Gain

$$\mathbf{K} = \mathbf{C}_{QY}(\mathbf{C}_Y + \mathbf{C}_E)^{-1} \quad (4)$$

where  $\mathbf{C}_Y$  is the system outputs covariance,  $\mathbf{C}_E$  is the error covariance and  $\mathbf{C}_{QY}$  is the covariance between system inputs and outputs.

The application of the linear Bayesian filter requires to assess the above mentioned covariances. This process is not straightforward in the case of implicit and/or non-linear forward model operators. To speed up the uncertainty propagation process and the application of the linear Bayesian filter, it is possible to represent each random variable in polynomial chaos expansion (PCE) form

$$\begin{aligned} \hat{\mathbf{Q}} &= \sum_{\mathbf{j}} \hat{q}_{\alpha} \boldsymbol{\Phi}_{q,\alpha}, & \hat{\mathbf{Y}} &= \sum_{\mathbf{j}} \hat{y}_{\alpha} \boldsymbol{\Phi}_{y,\alpha}, \\ \hat{\mathbf{E}} &= \sum_{\mathbf{j}} \hat{e}_{\alpha} \boldsymbol{\Phi}_{e,\alpha}, & \hat{\mathbf{Z}} &= \sum_{\mathbf{j}} \hat{z}_{\alpha} \boldsymbol{\Phi}_{z,\alpha} \end{aligned} \quad (5)$$

where  $\hat{q}_{\alpha}$ ,  $\hat{y}_{\alpha}$ ,  $\hat{e}_{\alpha}$ ,  $\hat{z}_{\alpha}$  are coefficients,  $\boldsymbol{\Phi}_{[\cdot],\alpha}$  multi-variate orthogonal polynomials for the quantity  $[\cdot]$ , and  $\mathbf{j}$  represents the set of multi-indices  $\boldsymbol{\alpha}$  truncated to the polynomial order  $p$ . In this case, the linear Bayesian filter takes the following form

$$\hat{\mathbf{Q}}' = \hat{\mathbf{Q}} + \mathbf{K}(\hat{\mathbf{z}} - \hat{\mathbf{Y}}) \quad (6)$$

and the covariances required to calculate the Kalman Gain can be analytically computed by the expansion coefficients. Detailed information about the polynomial chaos expansion based Kalman filter (PCE-KF) can be found in Rosic et al. (2012) and Rosic et al. (2013).

## 2.4 POD estimation and reliability metrics

The POD curve in this study is estimated using the  $\hat{a}$  vs.  $\hat{a}$  approach. The  $\hat{a}$  vs.  $\hat{a}$  model POD is a technique used in NDT to quantify the capability of a detection system based on continuous damage indicators. Unlike hit/miss POD methods, which rely on binary detection outcomes, the  $\hat{a}$  vs.  $\hat{a}$  model POD utilizes a continuous detection metric  $\hat{a}$  that reflects measurable differences in the system's response between undamaged and damaged states. This approach allows for an assessment of detection performance, particularly in systems where subtle changes in dynamic characteristics, such as natural frequencies or mode shapes, are used to infer damage. In vibration-based monitoring, such metrics are often derived from modal parameter shifts or other features sensitive to structural changes.

The  $\hat{a}$  vs.  $\hat{a}$  model involves fitting a linear function to the response feature,  $\hat{a}$ , as a function of the parameter of interest  $\mathbf{a}$ ,

$$\hat{\mathbf{a}} = \beta_0 + \beta_1 \mathbf{a} + \epsilon \quad (7)$$

where  $\beta_0$  and  $\beta_1$  are parameters that are estimated by performing a fit to the data and  $\epsilon$  is a noise term,  $\epsilon \sim \mathcal{N}(0, \sigma^2)$ . The noise term  $\epsilon$  is assumed to follow a normal distribution. The aforementioned parameters  $\beta_0$ ,  $\beta_1$  and  $\sigma$  are estimated in

the usual way by deploying ordinal least squares. We can ignore the more elaborated Tobit regression modeling from MIL-HDBK-1832A [2], because the observed  $\hat{a}$  values (see below) are far away from their natural bounds.

When multiple response features are available, a representative scalar value is needed to consolidate the relevant information into a single damage-sensitive metric. To address this, the Mahalanobis distance (MD) is employed as a fault indication metric. The Mahalanobis distance is a multivariate measure that accounts for correlations between variables, providing a statistically normalized distance of an observation from a reference distribution. For an observation vector  $\mathbf{x}_i$  (e.g., the measured eigenfrequencies of a structure at a specific time or condition), and a reference data set (e.g., the average eigenfrequencies in the undamaged state) characterized by mean vector  $\boldsymbol{\mu}$  and covariance matrix  $\boldsymbol{\Sigma}$ , the Mahalanobis distance is defined as

$$D_M(\mathbf{x}_i) = \sqrt{(\mathbf{x}_i - \boldsymbol{\mu})\boldsymbol{\Sigma}^{-1}(\mathbf{x}_i - \boldsymbol{\mu})} \quad (8)$$

To determine the statistical decision threshold for damage detection, the confidence interval approach based on the Chi-squared distribution is employed. Since the Mahalanobis distance  $D_M$  follows a Chi-squared distribution with degrees of freedom equal to the number of variables  $d$ , the decision threshold is defined as:

$$T = \sqrt{\chi_{1-\alpha, d}^2} \quad (9)$$

Where  $\chi_{1-\alpha, d}^2$  denotes the critical value from the Chi-squared distribution at a confidence level of  $1 - \alpha$ , and  $d$  is the dimensionality of the feature. For example, at a 99.9% confidence level and  $d = 3$ , the threshold is  $\chi_{0.999, 3}^2 = 16.27$ , corresponding to a Mahalanobis distance threshold of  $T = \sqrt{16.27} \approx 4.03$ . This captures the upper 0.1% of the reference distribution and yields a very strict false alarm rate.

The Probability of Detection (POD) as a function of damage size  $a$  is expressed as:

$$POD(a) = \Phi\left(\frac{a - \mu_a}{\sigma_a}\right) \quad (10)$$

Where  $\Phi(\cdot)$  is the cumulative distribution function of the standard normal distribution, and  $\mu_a$  and  $\sigma_a$  are suitable parameters controlling the shape of the POD curve. These parameters are derived from the linear regression model, with  $\mu_a = (T - \beta_0)/\beta_1$  and  $\sigma_a = \sigma/\beta_1$ , where  $\beta_0$ ,  $\beta_1$  and  $\sigma$  are the model parameters. The threshold corresponding to a 90% detection probability,  $a_{90}$  with  $POD(a_{90}) = 0.9$ , is then calculated as  $a_{90} = \mu_a + 1.645 \cdot \sigma_a$ . To account for the uncertainty in this threshold, the value  $a_{90/95}$ , representing the damage size for 90% POD with 95% confidence bounds, is computed using the Delta method referred to MIL-HDBK-1832A [2]. These performance metrics are used to assess and compare the detection capabilities of the SHM system. Following the same methodology, the Probability of Detection (POD) is also calculated using data generated from the calibrated finite element (FE) model.

### 3 ANALYSIS

#### 3.1 Data Analysis/Operational Modal Analysis

The recorded vibration data are analysed using operational modal analysis (OMA) to identify the dynamic parameters of the wooden frame. OMA is chosen because it enables the extraction of modal parameters under ambient or operational conditions without requiring controlled excitation forces. Using Artemis Modal Pro 7.2 software, the OMA is performed, and the natural frequencies ( $f$ ), damping ratios ( $\zeta$ ), and mode shapes of the structure are estimated. Based on the analysis results, four resonance frequencies are identified, corresponding to the four translational modes of the wooden frame. Figure 3 illustrates the identified mode shapes of the wooden structure in the reference state.

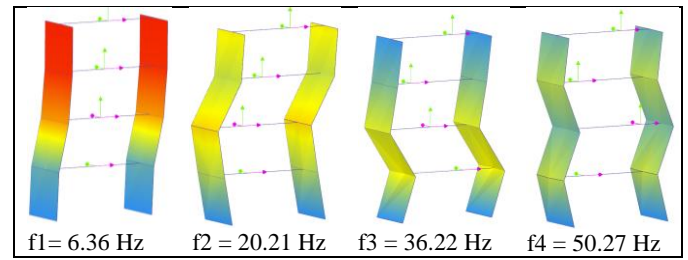


Figure 3. Mode shapes and frequency of wooden frame in reference state

OMA is also performed for all added mass configurations. Modal tracking is carried out to identify the mode similarities between each configuration to the reference state, with the Modal Assurance Criterion (MAC) threshold set to greater than 80%. The tracked resonance frequencies across all data sets are presented in Figure 4.

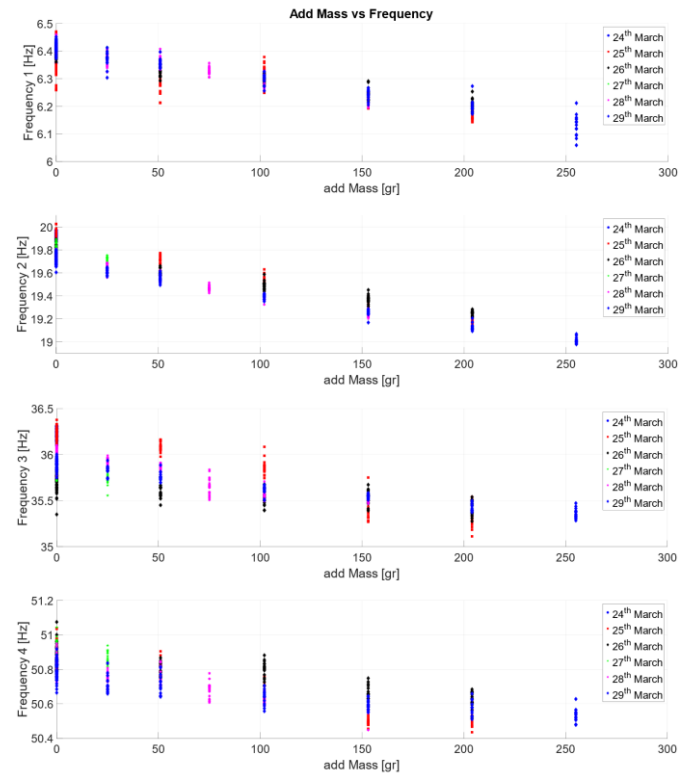


Figure 4. Tracked frequency (MAC > 80%) for the reference state and various added mass configurations



From Figure 4, it can be observed that the addition of mass on the fourth floor affects the dynamic response of the structure, particularly the resonance frequencies. As the added mass increases, the natural frequencies tend to decrease, which is consistent with the theoretical expectation that an increase in mass leads to a reduction in the system's stiffness-to-mass ratio. In addition to the frequency shifts, the damping ratios of the structure were also examined; however, no clear trend was observed in relation to the parameter changes. Furthermore, the first four dominant mode shapes remained largely unchanged, indicating that the modifications had minimal influence on the modal characteristics.

The results of the Operational Modal Analysis in the reference state, as shown in Figure 3, are used as the baseline data for calibrating the FE-model through a Bayesian model updating approach. An overall Operational Modal Analysis, as shown in Figure 4, is used to compute the empirical Probability of detection.

### 3.2 Bayesian model updating

A finite element (FE) model of the structure is developed using Ansys Mechanical, based on the given structural conditions. The FE model is then calibrated through Bayesian updating to estimate random model parameters. In this study, two key parameters are considered: the elastic modulus of the columns and the column thickness, as previously described. The FE-Model in Ansys is illustrated in Figure 5.

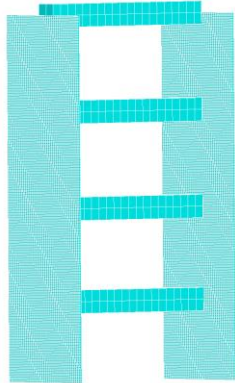


Figure 5. FE-Model in Ansys Mechanical

Initially, the prior distributions of the uncertain model parameters defined by their mean ( $\mu$ ) and standard deviation ( $\sigma$ ) are established based on engineering judgment and available data. The Bayesian model updating is performed using the generalized Polynomial Chaos-based Kalman Filter (gPC-KF) approach. These methods incorporate measurement uncertainties to update the parameter distributions, resulting in posterior distributions ( $\mu'$ ,  $\sigma'$ ) that reflect improved estimates conditioned on the observed vibration data. The summary statistics of both prior and posterior distributions are presented in Table 3 and the resulting posterior approximation distribution is shown in Figure 6.

The results of the Bayesian updating process show a reduction in the standard deviations of the posterior distributions, indicating improved parameter certainty in a model calibration. To assess the accuracy of the updated FE model, its predicted mean resonance frequencies – computed

using the mean values of the parameters from the posterior distributions – are compared against those obtained from Operational Modal Analysis (OMA) in the reference state, as detailed in Section 3.1. The relative difference between the simulated and experimental frequencies observed for the four modes is 0.54%, which is well within the maximum relative error of 0.6% in reference data. This close agreement confirms the reliability of the Bayesian-updated model.

Table 3. Prior and posterior of random parameters

Parameter	Elastic Modulus of Column	Thickness of Column
Prior	4000, 400	6.4, 0.32
Mean value, standard deviation ( $\mu$ , $\sigma$ )	[MPa] $\sigma = 0.1\mu$	[mm] $\sigma = 0.05\mu$
measurement error	0.6 %	
Posterior	3800, 316	6.18, 0.18
Mean value, standard deviation ( $\mu'$ , $\sigma'$ )	[MPa] $\sigma' = 0.083\mu'$	[mm] $\sigma' = 0.29\mu'$
relative difference	0.54 %	
$\epsilon_i = \frac{ f_{i\_FE\ model} - f_{i\_OMA} }{f_{i\_OMA}}$		

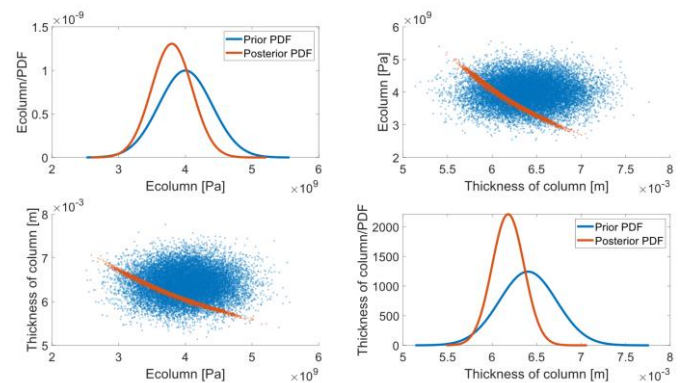


Figure 6. Results from updating with Bayesian model updating approach

Table 4. Comparison of resonance frequencies between the updated finite element (FE) model and experimental measurements from Operational Modal Analysis (OMA)

Mode No.	Frequency FE-Model	Frequency OMA	relative difference [%]	MAC [%]
1	6.39	6.40	0.21	97
2	19.91	19.81	0.53	90
3	36.16	35.97	0.54	90
4	50.81	50.56	0.10	98

Following the successful calibration of the FE model in the reference state, a Monte Carlo simulation is performed to generate modal frequency data for various added mass configurations. Based on the posterior distributions of the elastic modulus and column thickness, combined with discrete

added mass values to simulate different structural states, 120 samples of frequencies are generated for each state. The additional masses varied from 0 to 200 grams in increments of 25 grams. The resulting dataset is then used as the input for computing the Model-Assisted Probability of Detection (MAPOD), providing a statistical basis for assessing the detection performance under varying conditions.

### 3.3 Simulation of Model-Assisted Probability of Detection

This section presents a comparative analysis between the experimental Probability of Detection (POD) and the Model-Assisted POD (MAPOD) derived from the simulations. The comparison aims to validate the simulation framework and assess its capability to replicate detection performance observed in physical experiments. The observed strategy is based on changes in modal frequencies associated with varying levels of added mass, simulating structural changes/damage.

Figure 7 illustrates the comparison of resonance frequencies identified from OMA experimental data measurements and those predicted by the calibrated FE model, demonstrating

good agreement and confirming the effectiveness of the model updating process. Modes 1 and 2 are highly sensitive to the added mass, showing noticeable shifts in frequency. In contrast, Mode 3 exhibits only minor changes, while Mode 4 shows the least response to mass variation. This behavior is to be expected, as higher-order modes typically require more energy to be effectively excited and are thus less influenced by localized changes in structural mass [16,17]. Therefore, only Modes 1, 2, and 3 will be considered for further POD estimation, as they exhibit measurable sensitivity to the added mass and are thus more suitable for damage detection analysis.

To evaluate the consistency between the experimental POD and the MAPOD derived from simulated data, Mahalanobis distances from the 1<sup>st</sup>, 2<sup>nd</sup> and 3<sup>rd</sup> modes are computed and plotted against the corresponding flaw sizes, as shown in Figure 8. Finally, the POD curves are presented in Figure 9, comparing the empirical POD derived from experimental data with the MAPOD computed from the simulation results.

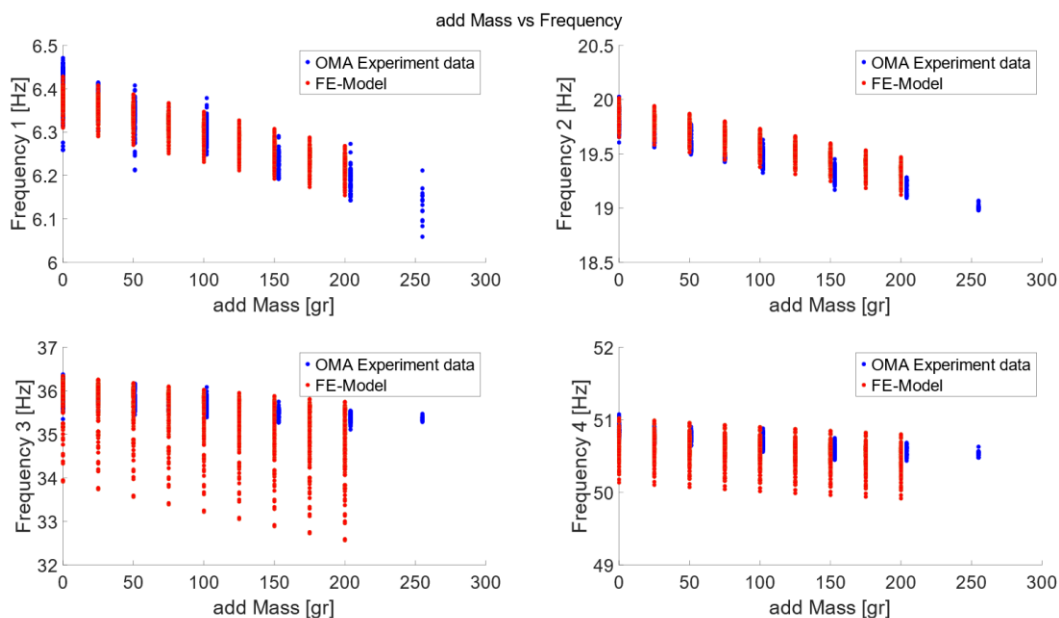


Figure 7. Added Mass-Frequencies comparison from OMA experimental data and FE-Model

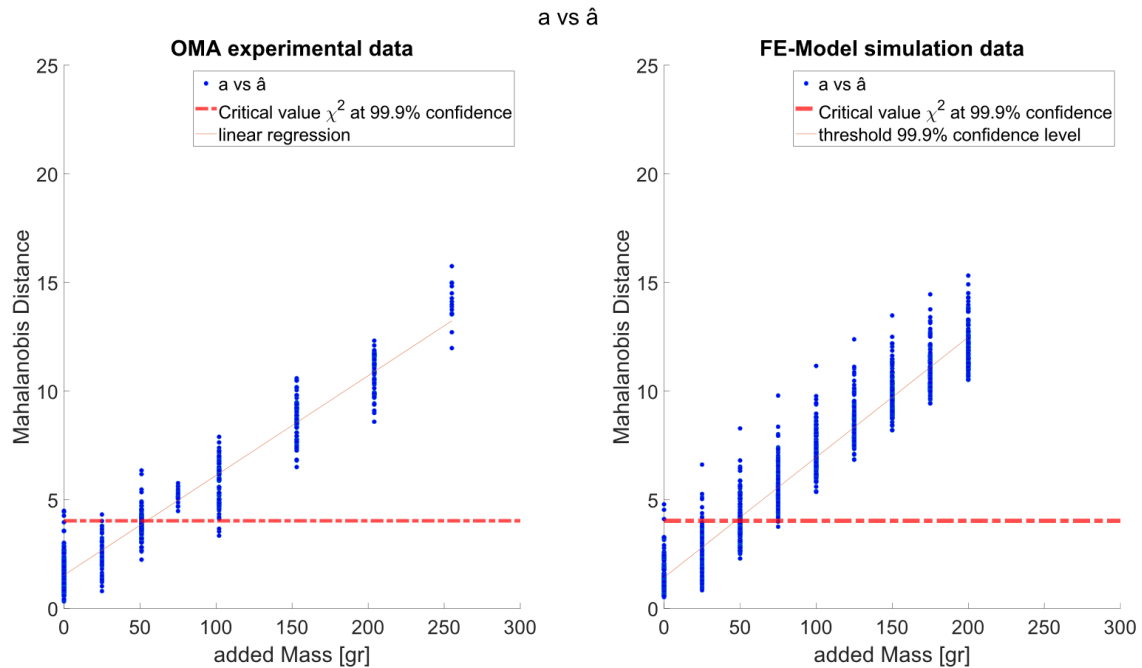
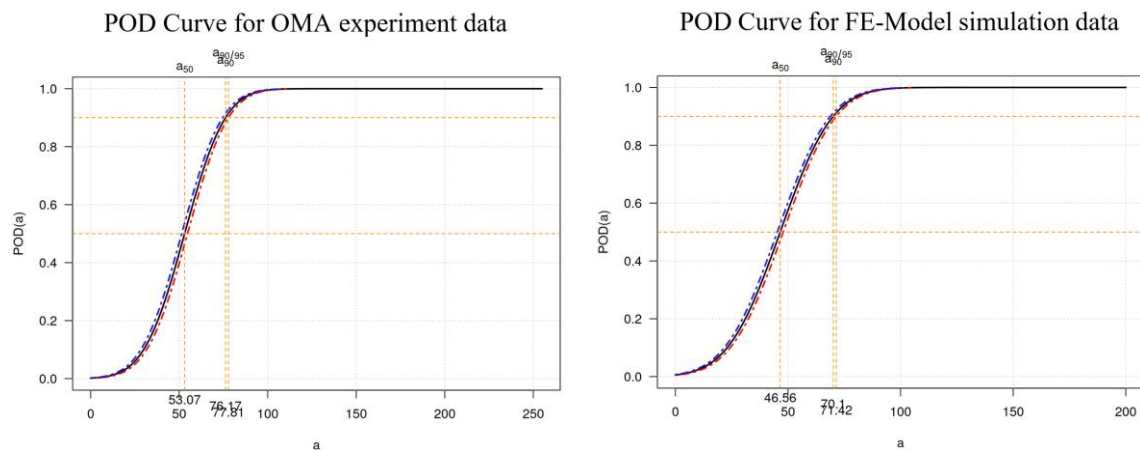

Figure 8.  $a$  vs  $\hat{a}$  for OMA experimental data and FE-Model


Figure 9. POD OMA experimental data and FE-Model simulation data

From Figure 9, the experimentally derived  $a_{90/95}$  value from the POD curve is 77.81 grams, while the simulated MAPOD yields an  $a_{90/95}$  of 71.42 grams, representing a relative difference of 8.2%. This  $a_{90/95}$  value corresponds to 7.0% of the total mass of the fourth floor. These results indicate that the POD derived from the calibrated FE model in the reference state provides sufficient predictions of the structural response to varying added mass conditions on the fourth floor. The alignment between the experimental and simulated POD curves demonstrates that the simulation-based MAPOD can approximate the experimental detection, supporting its application for scalable and cost-effective SHM reliability assessments.

#### 4 CONCLUSION AND OUTLOOK

This study presents a framework for evaluating the reliability of Structural Health Monitoring (SHM) systems using Probability of Detection (POD) and Model-Assisted POD (MAPOD) approaches. A laboratory-scale 4-DOF wooden

frame structure was used as a case study, with varying mass configurations to simulate structural changes. Experimental modal data were collected using Operational Modal Analysis (OMA) and used to calibrate a Finite Element (FE) model through Bayesian updating. The updated FE-Model served as the basis for generating simulated response/modal data through Monte Carlo simulations under various mass configurations, enabling the construction of MAPOD curves.

The comparison between experimental POD and MAPOD simulation data shows the relative difference with less than 10% deviation in key detection metrics such as a  $a_{90/95}$ . The MAPOD approach can effectively supplement physical testing by providing scalable, repeatable reliability assessments with reduced experimental effort.

#### Outlook:

Future research should aim to extend the MAPOD framework by incorporating more complex damage scenarios—such as sequential cracking or cross-sectional area reduction leading to structural stiffness degradation—exploring a wider range of



SHM sensing techniques and expanding the set of observed response features beyond the four considered in this study. Furthermore, integrating environmental and operational variability into the model could further enhance its predictive robustness. Finally, applying this method to real-scale structures will be a crucial step toward broader implementation in practical SHM deployments.

## ACKNOWLEDGMENTS

This research is funded by dtcc.bw -- Digitalization and Technology Research Center of the Bundeswehr. dtcc.bw is funded by the European Union -- NextGenerationEU. We thank all DTEC Project supporters. For future research, both the experimental measurement data and the finite element model developed in this study are available upon request.

## REFERENCES

- [1] C. R. Farrar and K. Worden. "Structural Health Monitoring: A Machine Learning Perspective". Chichester, UK: Wiley, 2012.
- [2] U.S. Department of Defense. "Nondestructive Evaluation System Reliability Assessment, MIL-HDBK-1823A, 2009".
- [3] Y. Deng, X. Liu and L. Udpa, "Magneto-Optic Imaging for Aircraft Skins Inspection: A Probability of Detection Study of Simulated and Experimental Image Data," in *IEEE Transactions on Reliability*, vol. 61, no. 4, pp. 901-908, Dec. 2012, doi: 10.1109/TR.2012.2221613.
- [4] Berens, Alan P. "NDE reliability data analysis." *ASM Handbook*. 17 (1989): 689-701.
- [5] Kabban, Christine & Greenwell, Brandon & Desimio, Martin & Derriso, Mark. (2015). "The probability of detection for structural health monitoring systems: Repeated measures data. *Structural Health Monitoring*". 14. 252-264. 10.1177/1475921714566530
- [6] Meeker, W., Roach, D. & Kessler, Seth. (2019). "Statistical Methods for Probability of Detection in Structural Health Monitoring". 10.12783/shm2019/32095.
- [7] Knopp, J. Aldrin, John Lindgren, E. & Annis, Charles. (2007). "Investigation of a Model-Assisted Approach to Probability of Detection Evaluation (Preprint)". *AIP Conference Proceedings*. 894. 1775-1782. 10.1063/1.2718178.
- [8] Kevin Smith, Bruce Thompson, Bill Meeker, Tim Gray, Lisa Brasche; Model-Assisted Probability of Detection Validation for Immersion Ultrasonic Application. *AIP Conf. Proc.* 21 March 2007; 894 (1): 1816–1822. <https://doi.org/10.1063/1.2718184>
- [9] Calmon, Pierre & Mesnil, Olivier & Miorelli, Roberto & Artusi, Xavier & CHAPUIS, BASTIEN & d'Almeida, Oscar. (2019). "Model Assisted Probability of Detection for Guided Wave Imaging Structural Health Monitoring". 10.12783/shm2019/32190.
- [10] G. E. Box and G. C. Tiao. "Bayesian Inference in Statistical Analysis". New York: Wiley, 1992.
- [11] D. Higdon, J. Gattiker, B. Williams, and M. Rightley. "Combining field data and computer simulations for calibration and prediction". *SIAM Journal on Scientific Computing*, vol. 26, no. 2, pp. 448–466, 2004.
- [12] Vogel, T., & Thöns, S. (2018). "Detection and localization of structural changes using Mahalanobis distance and frequency response functions". *Structural Control and Health Monitoring*, 25(5), e2160. <https://doi.org/10.1002/stc.2160>.
- [13] Bojana V. Rosić, Alexander Litvinenko, Oliver Pajonk, Hermann G. Matthies. (2012) "Sampling-free linear Bayesian update of polynomial chaos representations". *Journal of Computational Physics*, Volume 231, Issue 17, 2012.
- [14] Bojana V. Rosić, Anna Kučerová, Jan Sýkora, Oliver Pajonk, Alexander Litvinenko, Hermann G. Matthies. (2013). "Parameter identification in a probabilistic setting". *Engineering Structures*, Volume 50, 2013.
- [15] F. Marsili, A. Mandler, F. Landi, und S. Kessler. (2023). "Minimum detectable changes based on linear Bayesian filters". *Mechanical Systems and Signal Processing*, Bd. 202, S. 110656, Nov. 2023, doi: 10.1016/j.ymssp.2023.110656.
- [16] Chopra, A.K. (2012). "Dynamics of Structures: Theory and Applications to Earthquake Engineering (4<sup>th</sup> Edition)". Pearson.
- [17] Ewins, D.J. (2000). "Modal Testing: Theory, Practice and Application (2nd ed.)". Research Studies Press.

# Advanced Monitoring Systems for Infrastructures: Integrating 6D Sensors and Low-Cost High-Precision GNSS

Roman Windl<sup>1</sup>, Herbert Weitensfelder<sup>1</sup>, Werner Stempfhuber<sup>2</sup>

<sup>1</sup>SuessCo Sensors GmbH, Rathausplatz 18, A-3130 Herzogenburg (Austria)

<sup>2</sup>Berliner Hochschule für Technik (BHT-Berlin), Luxemburgerstr. 10, D-13353 Berlin (Germany)

email: [roman.windl@suessco.com](mailto:roman.windl@suessco.com), [herbert.weitensfelder@suessco.com](mailto:herbert.weitensfelder@suessco.com), [Werner-Vitus.Stempfhuber@bht-berlin.de](mailto:Werner-Vitus.Stempfhuber@bht-berlin.de)

**ABSTRACT:** Structural Health Monitoring (SHM) is vital for ensuring the safety and longevity of infrastructures, utilizing various sensor-based techniques to detect damage, assess performance, and monitor long-term deterioration. Traditional methods, such as visual inspections, lack precision and are prone to human error, whereas more advanced techniques like vibration-based monitoring, acoustic emission, strain gauges, and GNSS offer real-time damage detection and millimeter-level precision but often require complex planning and high costs. The presented 6D sensor, developed for infrastructure monitoring, accurately measures complex displacements and rotations, offering enhanced precision through a combination of machine learning and mathematical algorithms. When paired with low-cost, high-precision GNSS systems, it provides comprehensive real-time data on both localized and large-scale structural movements, improving insights into infrastructure behavior under various environmental conditions and loads. This paper explores the integration of 6D sensors with GNSS technology, discussing the advantages of real-time monitoring for predictive maintenance and presenting insights from ongoing project results.

**KEY WORDS:** IoT, Sensors, AI, SHM, 6D, GNSS

## 1 INTRODUCTION

Structural Health Monitoring (SHM) is essential for ensuring the safety and longevity of bridges, employing various techniques to detect damage, assess performance, and monitor deterioration over time. Traditional methods, such as visual inspection [1], are widely used due to their simplicity and cost-effectiveness but often lack precision and are prone to human error. More advanced techniques include vibration-based monitoring [2], which identifies global structural changes through dynamic responses, and acoustic emission [3] methods that detect stress waves from internal cracks. Both offer real-time damage detection but vary in sensitivity and applicability.

Strain gauges and fiber optic sensors (FOS) [4]-[6] provide localized measurements of stress and deformation with high accuracy. FOS excels in long-term durability and precision but comes with higher installation costs. Laser scanning and LiDAR [7] are effective in capturing surface deformations and creating detailed 3D models but can be limited by weather conditions. GNSS [8][11] is used in infrastructure structural health monitoring to provide high-precision, real-time measurements of large-scale displacements and deformations, enabling accurate tracking of structural movements over time for enhanced safety and maintenance planning.

Emerging technologies like wireless sensor networks (WSN) [9],[12] enable real-time data collection of multiple physical measurement parameters reduced costs, but allowing data fusion and better remote data interpretation.

## 2 TECHNOLOGY OVERVIEW

### 2.1 Magnetic 6D-Sensor

The continuous monitoring of the structural integrity of transportation infrastructure requires precise and reliable measurement methods.

The 6D sensor from SuessCo is based on a magnetic field sensor array that measures position and rotation relative to a permanent magnet with high accuracy [13]. The system captures movements in all six degrees of freedom (X, Y, Z as well as roll, pitch, and yaw) and achieves a repeatability of  $\pm 50 \mu\text{m}$  in the translational axes and  $\pm 0.1^\circ$  in the rotational axes. This is accomplished through a combination of machine learning and mathematical algorithms that allow precise recalculation of the measured values in real time. The high precision and easy installation make these sensors particularly suitable for monitoring critical infrastructure components such as bridge bearings.

Using an array of magnetic field sensors for position determination offers significant advantages, particularly due to the overdetermined nature of the system, which enhances accuracy and reduces the impact of external influences. With multiple sensors, the system collects redundant data, allowing it to cross-reference measurements and filter out inconsistencies caused by magnetic stray fields, interference from electrical fields (such as those from power lines), and thermal fluctuations. The overdetermined setup enables compensation for temperature-induced changes in the magnetic field, ensuring that the sensors remain accurate even in varying thermal conditions. This redundancy improves robustness, compensates for local anomalies, and results in more precise and stable position determination.

Self-diagnostic feature ensures that the sensor operates reliably by detecting potential faults, calibration drift, or performance degradation in real time. As a result, the system can immediately alert operators to any issues, reducing the risk of inaccurate data or sensor failure.

Therefore, accurate recalculation of the position is performed on a webserver to allow the usage of low performance microprocessors. Transmitting the sensor data is possible via

Wi-Fi or LTE-M allowing worldwide usage. For the 6D sensor also an external antenna is used to increase RF performance. An external battery pack with cable connection allows long time measurements with measurement frequencies down to 15 minutes and sending intervals of 1h. The Battery pack can be placed where they can be reached easily. The sensor itself has dimensions of 170 mm x 100 mm x 45 mm for a 60 mm x 30mm x 20mm measurement range allowing direct installation inside bridge bearings for example. This design features a physically separated sensor array and reference point. Unlike traditional systems, where precise alignment between components is often required, the 6D sensor allows the sensor array and reference magnet to be installed independently of each other. Traditional systems often require meticulous positioning to ensure accurate data collection, which can be labor-intensive and time-consuming. This flexibility is especially beneficial in challenging environments, such as bridges or large infrastructure, where precise alignment may be difficult to achieve. Additionally, a separated system is more adaptable to various structural configurations, improving scalability and reducing the risk of installation errors.

Additionally, a 3D version of this sensor type is available. It has internal antennas and batteries further reducing the footprint by sacrificing the euler angle values.

## 2.2 Low-cost high-precision GNSS

Both commercially available systems and in-house developments have demonstrated reliable measurement performance in various studies [11][12][14]. For comparison, 3D polar measurements from tachymetric monitoring systems were used as a reference. In recent years, a range of GNSS multi-frequency OEM boards with corresponding antennas has become available [15]. Before deploying GNSS technology for automated monitoring, it is crucial to evaluate its performance, particularly its 3D accuracy and long-term stability. Optimal results are generally achieved through the analysis of 24-hour session averages [11][12][14], which can also be evaluated on an hourly basis by incrementally extending the evaluation window. However, this approach introduces latency, which reduces the system's responsiveness.

An alternative method involves RTK-GNSS for direct deformation measurements, with some OEM boards supporting a measurement frequency of up to 100 Hz. Manufacturers have integrated carrier-phase ambiguity resolution algorithms into GNSS boards, and through efficient transmission of RTCM correction data via NTRIP, these receivers can deliver RTK positions in standardized NMEA format. Additionally, affordable antennas are now widely available, and their impact on measurement accuracy has been thoroughly investigated in several studies [8],[10],[15]. On-site data is transferred to a web service where the Wa2 module [15] computes, analyzes, and adjusts each baseline combination. However, this method is not suited for large-scale network extensions due to its inherent limitations.

Further testing with the open-source software RTKLib [16] has shown comparable accuracy, with ambiguity fix rates ranging from 95% to 100%. Using this approach, the GNSS system was implemented and tested in various pilot projects. In one such project, GNSS measurements provided results comparable to those from tachymetric systems. GNSS is particularly effective in tracking absolute deformation trends

over extended periods in outdoor environments, offering greater insights than a four-week total station measurement. This capability enhances safety on construction sites. Although GNSS systems can operate independently of other monitoring systems, their high-power consumption remains a limitation for long-term, battery-powered applications. Addressing this issue is a key focus of future developments.

## 2.3 Installation and mounting

The 6D sensors are mounted directly on or inside the bridge bearings to precisely detect movements and rotations. This type of installation is particularly suitable for monitoring thermally induced displacements caused by temperature changes. The sensors can be configured to detect even the smallest changes in bearing position, which may indicate structural issues.

The 6D sensors are designed to be installed even in hard-to-reach areas, such as bridge bearings or expansion joints. The physical separation between the sensor array and the reference magnet allows flexible installation without requiring precise alignment of components. In many cases, the sensors can be mounted directly in polymer or roller bearings using magnets. However, depending on the complexity of the bearing structure, detailed planning in advance is necessary. For this purpose, creating a digital model of the bearing is recommended to precisely design the mounting structure and ensure optimal sensor placement. This approach minimizes installation errors and allows for perfect integration, especially in bearings with complex geometries.

For monitoring large-scale displacements, particularly of bridge piers and foundations, GNSS systems are used. These systems detect movements in the sub-centimeter range and are especially effective in open, unobstructed environments. When installing GNSS systems, the cable length to the antenna is limited. To bridge longer distances, expensive signal amplifiers are often required. Therefore, it is important to define during the planning phase where the GNSS antenna and the processing unit should be positioned to minimize signal loss.

To simplify the installation of GNSS antennas, we have developed a custom 3D-printed component that allows the antennas to be mounted directly onto standard satellite dish brackets. These mounts are not only stable and widely available but also easy to install, offering a cost-effective solution for most standard applications.

For more complex requirements, it may be beneficial to develop custom mounts specifically tailored to local conditions to ensure the optimal performance of the GNSS systems.

# 3 SENSOR INTEGRATION AND DATA FUSION

## 3.1 Combining 6D-Sensors and GNSS

The combination of using high precision 6D sensors to measure bridge bearings, along with advanced GNSS technology, provides a comprehensive solution for monitoring and quantifying the behavior of bridges under various conditions. The 6D sensors, capable of capturing movements in all six degrees of freedom, three translational (X, Y, Z) and three rotational (pitch, yaw, roll)—offer precise insights into the thermal expansion and contraction of bridge structures. Thermal movements, which occur due to temperature fluctuations, can cause significant structural shifts, particularly in bridge bearings. With the 6D sensors, it becomes possible to



detect and quantify these minute thermal movements, providing engineers with real-time data to assess how the bridge reacts to environmental changes.

In addition to thermal movements, the 6D sensors can also capture the influence of external loads, such as wind pressure or traffic. The dynamic load exerted by vehicles crossing the bridge, combined with the fluctuating forces of wind, can cause stress and movement within the structure. By continuously monitoring these factors, the sensors help assess how well the bridge is handling daily operational stresses. This data is crucial in predicting potential issues and mitigating risks, allowing for proactive maintenance and increased safety.

When paired with a GNSS system, such as a high-precision multi-frequency GNSS module, the monitoring system becomes even more powerful. GNSS technology provides sub-centimeter accuracy in measuring the movement of the bridge's supporting pillars. While the 6D sensors offer detailed data on the local movements at the bearings, the GNSS system can monitor the larger-scale displacements of the bridge's foundations or pillars. This combined approach enables a thorough understanding of whether observed movements are due to thermal expansion of the bridge deck or are indicative of potential structural issues with the bridge's pillars or foundations.

For example, if the sensors detect movement at both the bearings and the pillars, the GNSS system can help differentiate between the natural thermal expansion of the bridge deck and actual shifts in the foundation. This distinction is crucial because movements caused by thermal expansion are usually temporary and reversible, whereas foundation movements could signal more serious issues, such as settlement or structural fatigue.

Moreover, the integrated system can operate continuously, providing real-time data on the structural health of the bridge. Such monitoring is essential for infrastructure located in areas subject to environmental stresses like fluctuating temperatures, high winds, or heavy traffic. By combining these two advanced technologies, engineers gain a better understanding of the bridge's behavior under various conditions, leading to more informed decision-making regarding maintenance schedules and potential reinforcements. In the long run, this can help extend the lifespan of critical infrastructure while ensuring the safety of its users.

This integration of 6D sensor technology with GNSS monitoring is part of a broader trend toward smart infrastructure, where real-time data is leveraged to optimize performance and prevent catastrophic failures. The ability to continuously monitor both short-term factors, such as thermal expansion, and long-term movements of the bridge's pillars offers a level of detail previously unavailable through traditional surveying methods alone. With further developments, especially in reducing power consumption for GNSS systems, the future of bridge monitoring promises even more efficient, reliable, and autonomous systems.

### 3.2 Communication and data transmission

The presented sensors use state-of-the-art encryption to protect the data during transmission. When data is sent from the sensors to the webservice, it is encrypted to prevent any unauthorized access or tampering while it's in transit. Data transmission is provided as an integrated service, eliminating

the need to manage SIM cards, mobile plans, or network connectivity. This streamlined approach allows for effortless deployment and continuous monitoring with minimal technical oversight. The used LTE-M [17] standard is part of the 4G standard leading to nearly global coverage without any additional checks, only 4G coverage needs to be present. LTE-M normally uses lower frequencies with lower data rate leading to more penetration and coverage than 4G. Most countries offer detailed LTE-M coverage maps, allowing users to accurately check reception in advance and ensure reliable connectivity in the deployment area.

Wi-Fi serves as an additional, efficient method for providing internet connectivity to the sensor, particularly in environments where LTE-M coverage may be unavailable, such as tunnels, mine shafts, or lower basement floors. This alternative communication method is advantageous in settings where the penetration of cellular signals is limited due to physical obstructions or underground conditions. By utilizing existing Wi-Fi networks, the sensor can maintain reliable data transmission in these challenging environments.

High data transfer rates, provided by Wi-Fi connections, are particularly beneficial for transmitting large datasets or high-frequency measurement updates in real time. In industrial or remote monitoring applications, utilizing Wi-Fi ensures continuous sensor operation without the reliance on extensive cellular infrastructure. This capability is especially valuable in areas where stable, high-speed communication is critical for maintaining data integrity and operational efficiency.

The use of Wi-Fi [18] in such scenarios is further supported by modern advances in mesh networking and extended-range Wi-Fi technologies, which improve coverage and signal stability even in hard-to-reach areas. For example, industrial-grade Wi-Fi routers and repeaters can be used to strengthen signals and extend network coverage to areas that would otherwise be unreachable by standard Wi-Fi systems. Wi-Fi's adaptability, combined with robust encryption protocols, ensures secure data transmission and minimizes the risk of loss or interference, making it a suitable solution for reliable infrastructure monitoring in challenging environments.

### 3.3 Webservice with dashboards

SuessCo developed and provides a web service as an infrastructure solution providing the ability to collect, process, visualize, and manage data from connected devices, such as sensors. It is commonly used for integrating various sensors and IoT devices, enabling real-time data monitoring and control. Web services support data collection through different protocols like MQTT, CoAP, and HTTP, and can process this data using custom logic for actions and alerts. Target applications are remote monitoring and control of IoT devices in sectors like infrastructure monitoring, smart cities, and agriculture.

While this web service provides robust data processing capabilities, it is also possible to configure it for collecting sensor data without relying on any specific platform's native dashboard or visualization tools. In this case, the sensors would send their data via a web service instead of using a predefined interface, allowing them to manage the data independently. This approach offers more flexibility in terms of integrating with alternative visualization platforms or custom-built solutions. Users can access, analyze, and display data from

their sensors in a more customizable manner, enabling a variety of applications such as advanced data analysis or machine learning.

#### 4 CASE STUDIES

The following chapter presents and analyzes various case studies involving bridges, buildings, and other infrastructure. These projects provide valuable insights into the practical applications of monitoring technologies and the findings related to structural integrity. At the request of the involved clients, the projects have been anonymized to ensure confidentiality.

The values in the following chapter are zeroed by subtracting the initial measurement, allowing for the detection of relative displacements and ensuring comparability.

##### 4.1 Bridge bearings influenced by unintentional manipulation, surface treatment and flood disaster

The first pilot project, which was successfully transitioned into an ongoing monitoring project and has now been running for over four years, involves the monitoring of a steel-element road bridge. Initially, it was unclear whether the end elements at the abutment were impacting, which is why the sensors were first installed there. However, once it was proven that this was not the case, the sensors were subsequently relocated to the bearings of the central pier in the river over the course of the project.



Figure 1. Images of the Monitored Roller Bearing: Left: Condition at installation with corresponding axes; Right: Sensor after maintenance work, displaced and sandblasted

Since July 1, 2022, the sensors have been operating at their new position and have been continuously monitoring the bridge — including during the flood event in 2024, which provided valuable data on structural integrity.

The following section includes both an analysis of the effects of unintended sensor displacement during bridge renovation work (see Figure 4 and Figure 5) and a detailed evaluation of the measurement data collected during the 2024 flood.

The diagram in Figure 2 shows, in the upper part, the sensor's positional displacements along the x-axis (blue), y-axis (green), and z-axis (red). The lower part of the diagram displays the internal temperature of the sensor. The measurements, recorded at 15-minute intervals, are presented here as daily average values.



Figure 2. Measurement data for monitoring a roller bearing: effects of unintended displacements during maintenance work and wildlife damage

As expected, significant fluctuations can be observed along the x-axis due to the thermal expansion of the bridge element. In October 2022, a sharp and abrupt change is visible, which can be attributed to a mechanical shift in the sensor setup (see Figure 1, right). During this period, the sensor was also sandblasted, but this had no relevant impact on the measurement results.

A disruption in sensor data in March 2023 was caused by wildlife damage—specifically, pigeons pecking at the cable. In December 2023, the sensor failed due to a hardware defect, which has already been resolved in the new hardware version of the sensor. Aside from these events, the data shows a very good correlation with the expected thermal expansion and only minor movements along the y- and z-axes.

The diagram in Figure 3 consists of three subplots showing the positional displacements of a sensor along the x-, y-, and z-axes ( $\Delta X_0$ ,  $\Delta Y_0$ ,  $\Delta Z_0$ ) as a function of temperature. The measured data points are displayed as blue violin plots with error bars, illustrating the distribution of values at different temperatures. The number of measurements per temperature interval is indicated along the bottom of the x-axis. A different sensor is used in Figure 3 than in Figure 1 and Figure 2. The Sensor in Figure 3 is mounted on a polymer bearing and summarizes historical data from the year 2021.

**Top subplot ( $\Delta X_0$  position):** Shows a strong linear correlation between temperature and displacement along the x-axis. The linear fit (orange line) has a slope of 0.75 mm/°C, indicating thermal expansion of the monitored bridge element, which also aligns well with the expected values. The data spread is relatively small, indicating consistent thermal expansion.

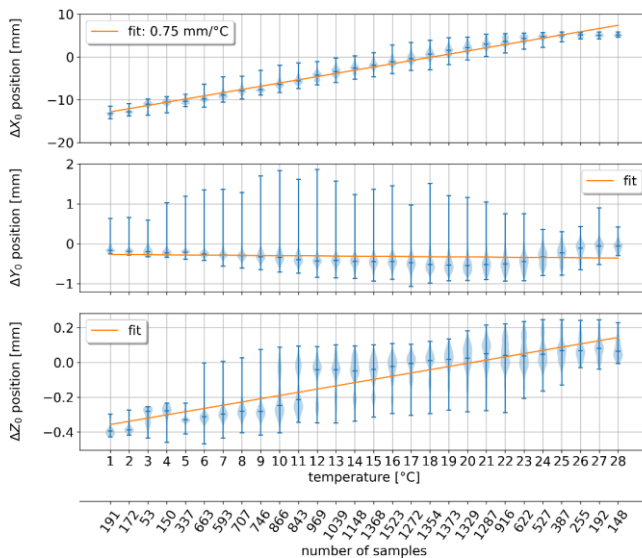


Figure 3. Representation of the Thermal Dependence of Positional Displacement Based on Historical Data.

Middle subplot ( $\Delta y_0$  position): No significant correlation is observed between temperature and displacement along the y-axis. The data shows high scatter, indicating non-systematic influences, possibly due to mechanical impacts or disturbances. The fit is nearly flat, suggesting that no temperature-induced movement is expected along this axis.

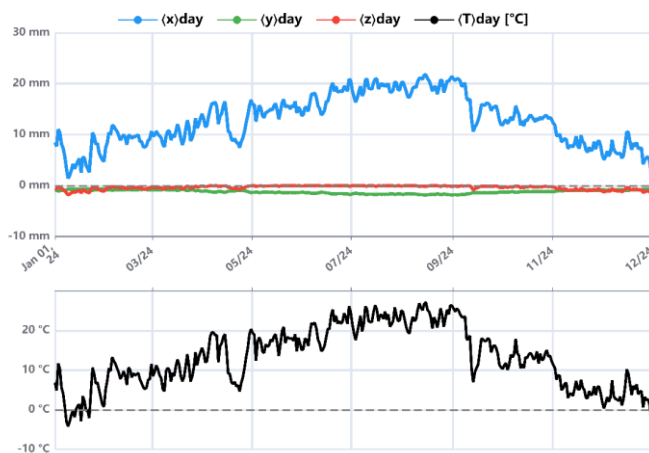


Figure 4. Daily Average Values Independent of the Sensor's Measurement Interval in Figure 1. The data shown is from the year 2024 and includes a flood event in September.

**Bottom subplot ( $\Delta z_0$  position):** A slight correlation between temperature and displacement along the z-axis is evident; however, the effect is much weaker than along the x-axis. The linear fit shows a small but consistent displacement, indicating minimal thermal movement in the vertical direction. The data scatter is moderate, and the amplitude is significantly smaller compared to the other axes, suggesting lesser influences in this direction.

The diagram in Figure 4 illustrates how the bridge responds to seasonal temperature fluctuations and simultaneously shows the impact of exceptional events such as the flood disaster in September 2024. Monitoring data is essential for assessing the

structural integrity of the bridge during such extreme situations. The diagram presents the positional displacements of the sensor along the x-axis (blue), y-axis (green), and z-axis (red) throughout the year. The x-axis shows significant variation, with displacements increasing up to 30 mm, indicating thermal expansion of the monitored bridge element. In contrast, the y- and z-axes show only minimal movement, suggesting that the bridge remains largely stable in those directions.

The lower subplot shows the temperature trend over the course of the year. A clear seasonal pattern is visible, with temperatures falling below 0°C in winter and rising above 20°C in summer.

From September 13 to 20, 2024, the bridge was affected by a flood disaster, yet no significant anomaly is visible in the measurement data. The diagram clearly shows that while the displacements along the x-axis temporarily dropped during the flood event, the behavior was consistent with previous temperature fluctuations. Even after the flood, no significant changes in the measurement values were observed. This indicates that the bridge did not suffer any lasting damage from the flood and that its structural integrity remained intact.

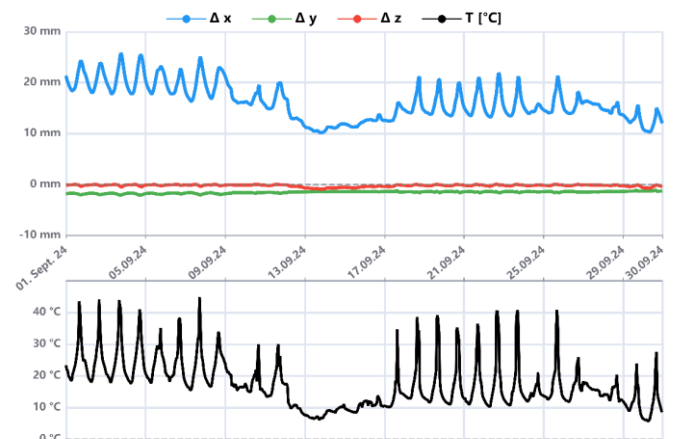


Figure 5. Same Bearing as in Figure 4, but with Detailed Data at 1-Hour Intervals for the Month of September.

This example highlights the importance of continuous monitoring at bridge bearings: On one hand, continuously collected data allows for immediate response to unexpected deviations; on the other hand, it enables the assessment of changes before and after exceptional events such as flooding. This makes it possible to detect potential damage early—during and after such events—and to take targeted action, significantly improving the long-term safety of the infrastructure.

In Figure 5, the data for September is shown at the actual measurement interval of one hour. Even at this higher temporal resolution, no unexpected movements are visible. Even during the flood disaster from September 13 to 20, 2024, the measurements display stable behavior consistent with the typical pattern of thermal expansion. Furthermore, the peak temperature recorded here is significantly higher than the air temperature, as the sensor housing is exposed to direct sunlight.



#### 4.2 Bridge bearing with transverse displacement

In another bridge project, measurements were conducted at multiple points along a curved bridge located on a creeping slope. The results (Figure 6 and Figure 7) showed that individual bearings exhibited consistent but slow displacement along the y-axis—that is, transverse to the roller bearing's intended direction of movement.



Figure 6. A 6D sensor installed on a roller bearing of a railroad bridge

This motion leads to wear on the bearing's retaining plates. It has not yet been conclusively determined whether the bearings reach a point at which they can no longer compensate for the movements, which could result in unanticipated stresses within the bridge structure.



Figure 7. Measurement Results of the Roller Bearing on a Curved Bridge Showing Increased Y-Axis Movement Leading to Wear of the Bearing's Retaining Plates.

Notably, these displacements could not be detected using conventional measurement systems such as total stations or rail surveying; only the wear itself had previously been observed. The precise and multi-axis sensors enabled more detailed detection that was not possible with other methods and thus provided valuable insights into the maintenance strategy.

#### 4.3 Measurement of crack formation on a natural stone railway viaduct

In this project, several sensors were installed on different cracks of a natural stone railway viaduct. The cracks either ran directly through the stones or along the joints between them. The sensors were strategically placed to monitor both types of cracks and to analyze potential differences in deformation behavior.

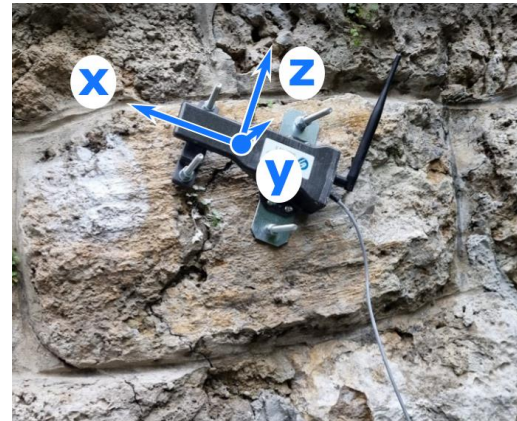


Figure 8. Mounting of the Sensor Above a Crack in the Natural Stone of a Railway Viaduct.

The goal was to monitor the behavior of the cracks: Are they stable, or do they show dependencies on temperature and humidity fluctuations? presents the results from one of these sensors, whose position is shown in Figure 8. In this project, the sensors and reference points could be mounted directly using stone screws or bonded threaded rods, without the need for additional mounting materials. This method enabled a secure and stable attachment directly to the natural stone, allowing for efficient and durable installation.

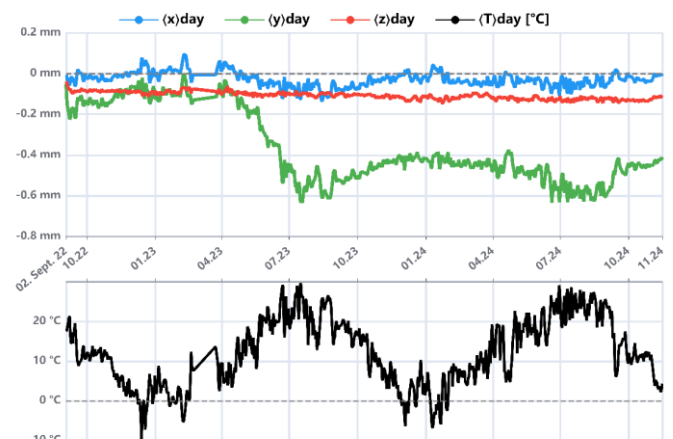


Figure 9. A significant and irreversible change is visible along the y-axis (green). However, the amplitude of this displacement is only about 0.4 mm, indicating a very small but still measurable change.

In Figure 9, only very small changes can be observed overall, as the total amplitude range on the y-axis is just about 1 mm. Nevertheless, a significant and irreversible displacement is evident starting in April 2023. Compared to the measurement

data from the bridge bearings, the values recorded here differ considerably, confirming the thermal stability of the sensor. This crack exhibits the most active movement among all measured points; however, it was determined that most cracks are generally stable. Therefore, it was decided to reduce the measurement interval to one hour in order to maximize battery life. If necessary, the interval can be remotely adjusted again.

#### 4.4 Crack measurement in a building with supplementary GNSS measuring points

As part of the subway construction works in Vienna, the groundwater level had to be lowered, which led to significant cracking in surrounding buildings even before the actual tunneling began. For this project, several 3D and 6D sensors () as well as GNSS measurement points were installed on the exterior walls of the affected buildings. The GNSS system [11],[12] used in this project (Figure 10) was developed in collaboration with Werner Stempfhuber. The 3D and 6D sensors were easily mounted using conventional screws, while the installation of the GNSS brackets on the building facade had to be carried out by specialized personnel.



Figure 10. Left: Mounted GNSS antenna on the exterior wall of the residential building. Right: 6D sensor mounted in a building corner near the GNSS antenna.

By combining these two measurement systems, it was possible to precisely monitor the relationship between the cracks and the surrounding walls, while the absolute GNSS system additionally allowed for the detection of potential subsidence of the entire building or individual sections. This approach increases the significance of the measurements and provides the private property owner with reliable data to demonstrate to the construction client any potential effects of the construction work on their property. At the same time, monitoring enables early warning in the event of sudden significant movements, allowing the developer to intervene in time to prevent further structural damage.

Positive feedback also came from the residents of the building, who now feel somewhat safer due to the continuous monitoring of the visible cracks in the structure.

In Figure 10, the sensor is located inside the building, as indicated by the significantly more stable temperature profile compared to previous case studies. Notably, a jump along the z-axis (red) is visible in September (high amount of rain). Although the initial change in September measured only 0.6 mm over a period of about two weeks, it marked the beginning

of a continuous increase in movement. By February 2025, the sensor recorded a total displacement of up to 2.3 mm. This deviates significantly from the crack's previous behavior and indicates a structural issue.

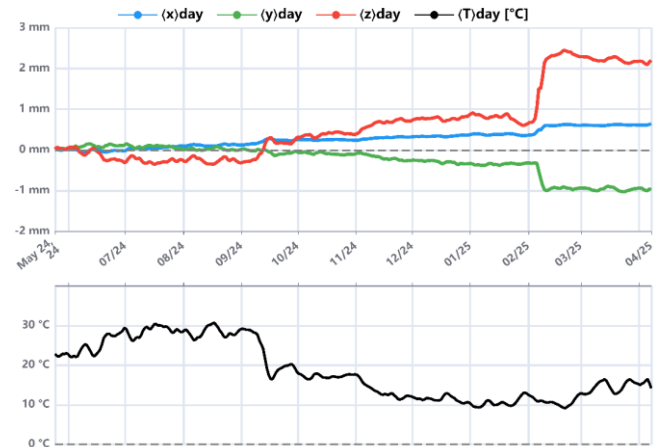


Figure 11. The change in z-axis behavior (red), of the Sensor shown in Figure 10, observed in September 2024, was triggered by heavy rainfall and led to a structural damage event in February 2025.

A different 3D sensor shows even greater displacements (see Figure 12), starting in September 2024 and peaking at up to 10 mm along the x-axis in February 2025. This increased movement is likely due to the sensor's alternative mounting configuration.

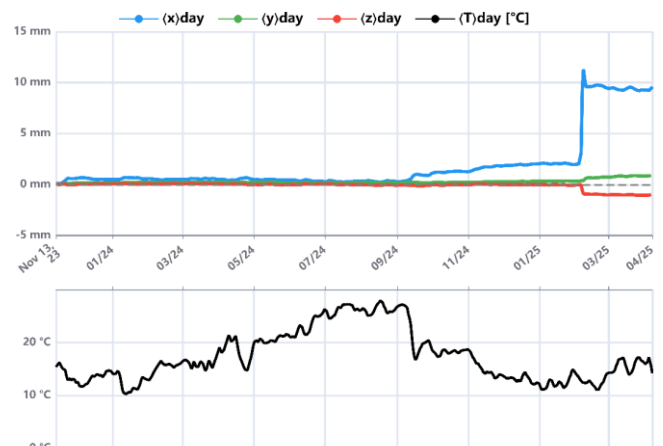


Figure 12. Even higher x-axis peak in February of 2025.

Similar behavior has also been observed in other 3D sensors throughout the building, suggesting that the structural movement is not limited to a single location but affects the entire structure. This indicates a widespread response of the building to external influences, likely requiring a comprehensive structural assessment.

However, these observations were not limited to the 3D sensors inside the building—four GNSS sensors installed at each corner of the structure also exhibited similar behavior. The GNSS points are numbered clockwise, starting from the southeast corner of the building.

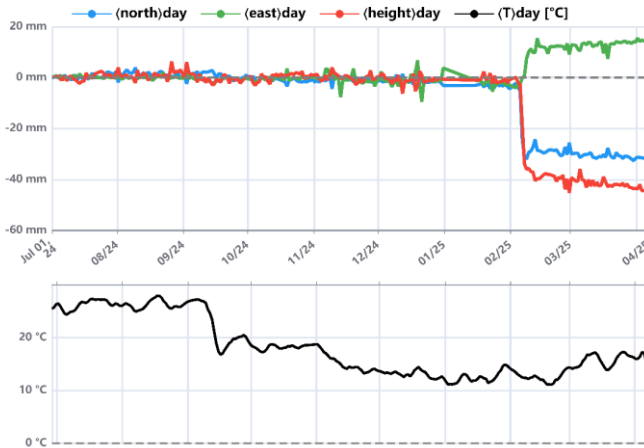


Figure 13. GNSS Point 1 in the south east corner of the building.

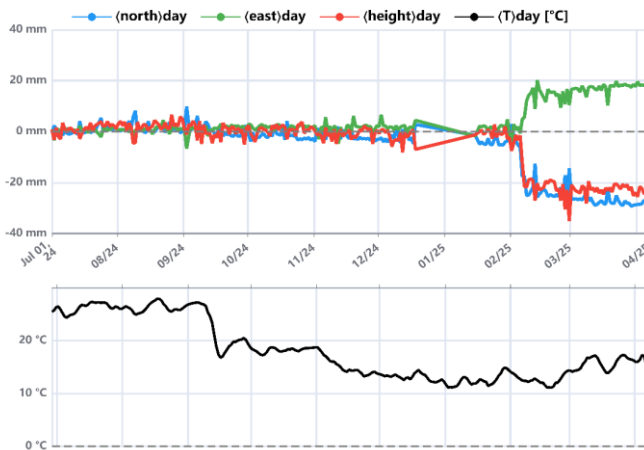


Figure 14. GNSS Point 2 in the south west corner of the building.

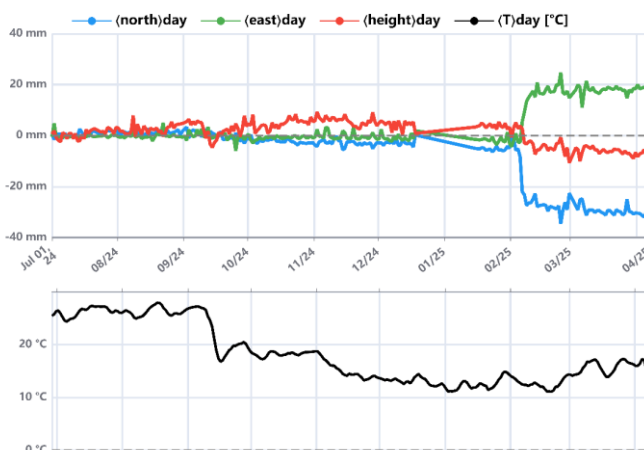


Figure 15. GNSS Point 3 in the north west corner of the building.

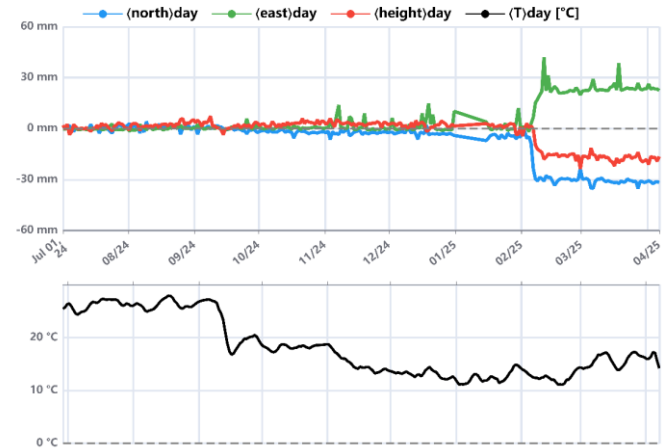


Figure 16. GNSS Point 4 in the north east corner of the building.

For the initial monitoring period (July 2024 to early February 2025), all sensors exhibited only minor fluctuations within a  $\pm 5$  mm range across all axes. This behavior is consistent with expected seasonal thermal expansion and contraction, as confirmed by the relatively stable and slowly varying temperature profile. Unfortunately due to a power fault there is missing data from beginning to mid-January.

However, a significant and abrupt shift in the displacement data was observed across all GNSS sensors starting in early February 2025. This event was not associated with any comparable temperature anomaly and is thus interpreted as a non-thermal structural movement. The magnitude and direction of the displacements varied by sensor location:

**GNSS 1 (Southeast Corner, Figure 13):** Displacements of approximately  $-30$  mm in the north direction and  $-20$  mm in height were recorded, accompanied by an increase of  $+25$  mm in the east direction.

**GNSS 2 (Northeast Corner, Figure 14):** This sensor registered the largest displacements, with  $-40$  mm in the north, and the vertical direction, and  $+20$  mm in the east. The scale of movement suggests significant subsidence and lateral displacement.

**GNSS 3 (Northwest Corner, Figure 15):** Moderate movement was recorded, particularly to the north with  $-30$  mm and east  $+20$  mm directions. But height stays very stable compared to all other sensors.

**GNSS 4 (Southwest Corner, Figure 16):** Displacements at this location were also substantial, with movements of approximately  $-20$  mm in the vertical axis and  $+20$  mm in the east direction.

The synchronized onset and consistent directional trends of the displacements across all sensors strongly suggest a global response of the building structure, likely triggered by high rain period in September of 2024 and leading to a massive structural movement in February 2025. Given the known construction activities related to subway excavation in the vicinity, it is plausible that the observed displacements are a direct consequence of these works.

The GNSS and 3D position data thus provides reliable and high-resolution evidence of structural movement, which is essential for assessing building integrity and potential damage progression. This type of sensor-based monitoring offers a valuable basis for initiating countermeasures, engaging with



responsible parties, and supporting claims for damage compensation.

## 5 CONCLUSIONS

The multi-year investigations clearly demonstrate the advantages of combining 6D sensors with GNSS measurement systems for monitoring the structural integrity of infrastructure and buildings. This integrated approach offers a significantly enhanced perspective on structural motion detection: while 6D sensors enable detailed analysis of local displacements across all degrees of freedom, GNSS systems provide highly accurate measurements of absolute positional changes. The synergy between these two technologies not only increases the informative value of the measurements but also improves the monitoring of structures under variable environmental conditions, such as temperature fluctuations or groundwater drawdowns—factors that present particular challenges in urban settings.

The deployment of these systems in the presented projects has resulted in a robust data foundation, allowing stakeholders to produce well-founded evidence of potential structural impacts caused by construction activities or environmental influences. Continuous data acquisition supports the early detection of damage risks and contributes significantly to the safety and longevity of the monitored structures. Particularly noteworthy is the real-time monitoring capability enabled by the integrated system, which allows for immediate response to unexpected structural movements and thereby minimizes the risk of significant damage.

Looking ahead, the focus will be on further optimizing the energy efficiency of the deployed sensors and expanding the integration of AI-assisted anomaly detection. These developments will further enhance the precision and operational efficiency of monitoring systems while reducing maintenance costs. The insights and experiences gained from the current projects provide a solid basis for future advancements aimed at improving the reliability and sustainability of monitoring solutions in demanding infrastructure environments.

## REFERENCES

- [1] N. J. Bertola and E. Brühwiler, "Risk-based methodology to assess bridge condition based on visual inspection," *Structure and Infrastructure Engineering*, vol. 19, no. 4. Informa UK Limited, pp. 575–588, Aug. 03, 2021. doi: 10.1080/15732479.2021.1959621.
- [2] S. W. Doebling, C. R. Farrar, M. B. Prime, and D. W. Shevitz, "Damage identification and health monitoring of structural and mechanical systems from changes in their vibration characteristics: A literature review," Office of Scientific and Technical Information (OSTI), May 1996. doi: 10.2172/249299.
- [3] L. Golaski, P. Gebiski, and K. Ono, "Diagnostics of reinforced concrete bridges by acoustic emission," *Journal of Acoustic Emission*, vol. 20, 2002.
- [4] C. I. Merzbacher, A. D. Kersey, and E. J. Friebele, "Fiber optic sensors in concrete structures: a review," *Smart Materials and Structures*, vol. 5, no. 2. IOP Publishing, pp. 196–208, Apr. 01, 1996. doi: 10.1088/0964-1726/5/2/008.
- [5] A. Vorwagner et al., "Rissweitenmessung mittels nachträglich angebrachten, verteilten faseroptischen Messsystemen," in *Proc. 11. Symposium experimentelle Untersuchungen von Baukonstruktionen, Schriftenreihe Konstruktiver Ingenieurbau Dresden*, vol. 55, pp. 78–86, 2021.
- [6] A. Vorwagner, M. Kwapisz, W. Lienhart, M. Winkler, C. Monsberger, and D. Prammer, "Verteilte Rissbreitenmessung im Betonbau mittels faseroptischer Sensorik – Neue Anwendung von verteilten faseroptischen Messsystemen," *Beton- und Stahlbetonbau*, vol. 116, no. 10. Wiley, pp. 727–740, Sep. 17, 2021. doi: 10.1002/best.202100060.
- [7] M. Rashidi, M. Mohammadi, S. Sadeghlo Kivi, M. M. Abdolvand, L. Truong-Hong, and B. Samali, "A Decade of Modern Bridge Monitoring Using Terrestrial Laser Scanning: Review and Future Directions," *Remote Sensing*, vol. 12, no. 22. MDPI AG, p. 3796, Nov. 19, 2020. doi: 10.3390/rs12223796.
- [8] J. R. Vazquez-Ontiveros, G. E. Vazquez-Becerra, J. A. Quintana, F. J. Carrion, G. M. Guzman-Acevedo, and J. R. Gaxiola-Camacho, "Implementation of PPP-GNSS measurement technology in the probabilistic SHM of bridge structures," *Measurement*, vol. 173. Elsevier BV, p. 108677, Mar. 2021. doi: 10.1016/j.measurement.2020.108677.
- [9] Y. Xie, S. Zhang, X. Meng, D. T. Nguyen, G. Ye, and H. Li, "An Innovative Sensor Integrated with GNSS and Accelerometer for Bridge Health Monitoring," *Remote Sensing*, vol. 16, no. 4. MDPI AG, p. 607, Feb. 06, 2024. doi: 10.3390/rs16040607.
- [10] J. Glabsch, *Konzeption und Realisierung kosteneffizienter GNSS Monitoring-Systeme für ingenieurgeodätische Überwachungsmessungen*, Dissertation, UniBW, 2017. [Online]. Available: <https://athene-forschung.unibw.de/doc/123564/123564.pdf>
- [11] W. Stempfhuber, "Möglichkeiten und Grenzen von modularen Low-cost-Komponenten für automatisierte Deformationsmessungen," *Allgemeine Vermessungs-Nachrichten (AVN)*, no. 04, 2022.
- [12] R. Windl, E. Windhör, D. Suess, and W. Stempfhuber, "Zuverlässige Bauwerksüberwachung mit Multisensorsystemen," in *22. Internationale Geodätische Woche Oberurgl 2023*, p. 231, VDE Verlag, 2023.
- [13] R. Windl, "Method for measurement of the orientation between two bodies," EP3792587B1, European Patent, 2021.
- [14] L. Zhang, *Qualitätssteigerung von Low-Cost-GPS Zeitreihen für Monitoring Applikationen durch zeitlich-räumliche Korrelationsanalyse*, Dissertation, Universität Stuttgart, Fakultät Luft- und Raumfahrttechnik und Geodäsie, Deutsche Geodätische Kommission, vol. C-776, München, 2016, ISBN 978-3-7696-5188-1.
- [15] L. Wanninger, M. Thiemig, and V. Frevert, "Multi-frequency quadrifilar helix antennas for cm-accurate GNSS positioning," *Journal of Applied Geodesy*, vol. 16, no. 1. Walter de Gruyter GmbH, pp. 25–35, Sep. 15, 2021. doi: 10.1515/jag-2021-0042.
- [16] T. Takasu and A. Yasuda, "Development of the low-cost RTK-GPS receiver with an open source program package RTKLIB," in *Proc. International Symposium on GPS/GNSS, Seogwipo-si, Republic of Korea, International Convention Center Jeju Korea*, 2009, pp. 1–6.
- [17] S. R. Borkar, "Long-term evolution for machines (LTE-M)," *LPWAN Technologies for IoT and M2M Applications*. Elsevier, pp. 145–166, 2020. doi: 10.1016/b978-0-12-818880-4.00007-7.
- [18] F. Montori, R. Contigiani, and L. Bedogni, "Is WiFi suitable for energy efficient IoT deployments? A performance study," *2017 IEEE 3rd International Forum on Research and Technologies for Society and Industry (RTSI)*, vol. 8. IEEE, pp. 1–5, Sep. 2017. doi: 10.1109/rtsi.2017.8065943.
- [19] J. S. Steelman, L. A. Fahnestock, E. T. Filipov, J. M. LaFave, J. F. Hajjar, and D. A. Foutch, "Shear and Friction Response of Nonseismic Laminated Elastomeric Bridge Bearings Subject to Seismic Demands," *Journal of Bridge Engineering*, vol. 18, no. 7. American Society of Civil Engineers (ASCE), pp. 612–623, Jul. 2013. doi: 10.1061/(asce)be.1943-5592.0000406.
- [20] Y. Liu, Z. Qian, L. Chen, and J. Hu, "Investigation on Temperature Effect of Bridge Bearing System during Steel Bridge Deck Pavement Paving," *International Journal of Geomechanics*, vol. 22, no. 5. American Society of Civil Engineers (ASCE), May 2022. doi: 10.1061/(asce)gm.1943-5622.0002361.
- [21] B. M. Noade and T. C. Becker, "Probabilistic Framework for Lifetime Bridge-Bearing Demands," *Journal of Bridge Engineering*, vol. 24, no. 7. American Society of Civil Engineers (ASCE), Jul. 2019. doi: 10.1061/(asce)be.1943-5592.0001430.



# Engineering Applications of Artificial Intelligence for SHM

# Structural damage detection, localization, quantification for high-rise buildings under earthquake excitations based on machine learning and sub-structuring approach

Mohamed H. Abdelbarr<sup>1</sup>, ORCID (0000-0003-4558-7119), Yoshiki IKEDA<sup>2</sup>, Sami F. Masri<sup>3</sup>

<sup>1</sup>Structural Engineering Department, Faculty of Engineering Cairo University, Giza, Egypt

<sup>1</sup>Dar Al-Handasah, Giza, Egypt

<sup>2</sup>Earthquake Disasters Disaster Prevention Research Institute, Kyoto University Gokasyo, Uji, Kyoto, Japan

<sup>3</sup>Civil Engineering Department, University of Southern California, Los Angeles, CA, USA

email: abdelbarr@eng.cu.edu.eg, ikeda.yoshiki.6r@kyoto-u.ac.jp, masri@usc.edu

**ABSTRACT:** This work presents an evaluation of promising sub-structuring and machine learning SHM approaches suitable for high-rise buildings, based on real data from an 18-story steel-moment resisting framing building, tested at an E-Defense facility in Japan. This building is instrumented with a relatively dense set of sensor arrays and is subjected to different excitation levels until full collapse. The main contribution of this study is to demonstrate the practical feasibility of the proposed sub-structuring approach in conjunction with machine learning when relying on different levels of response measurements. The study assesses the accuracy and reliability of the estimates of the dominant modal features of the structure and can subsequently provide a probabilistic measure of confidence in the extent and location of changes/damage if an anomaly is detected, as well as the propagation of damage throughout the structure's life span. Due to the minimal computational resources needed to implement the sub-structuring approach, it is shown to be quite efficient for near-real-time applications where important structures need to be continuously monitored for sustainability as well as resiliency requirements.

**KEY WORDS:** Parametric identification; Nonparametric identification; Damage detection; Structural health monitoring; Condition assessment; High-rise building.

## 1 INTRODUCTION

Structural Health Monitoring (SHM) and condition assessment of high-rise buildings through vibration signature analysis have been extensively studied over time. SHM approaches for damage detection and condition assessment are generally classified into two main categories: local and global methods. Local methods focus on analyzing specific, limited areas of a structure using localized measurements. In contrast, global methods provide a comprehensive understanding of the system's condition by utilizing data from a distributed network of sensors. The selection of an appropriate method depends on several factors, including the problem's scope, the sensor network's configuration, the structural topology, and the level of detail required for the assessment.

Recent advancements in dense sensor networks, capable of collecting extensive data, have enabled the application of advanced data processing algorithms. These algorithms can effectively identify, localize, classify, and quantify changes or damages in civil infrastructure, including high-rise buildings, which are the primary focus of this study.

Prior to utilizing the identified vibrational signature of a structure for health monitoring, it is essential to comprehend the dynamic behavior modeling of high-rise buildings. This modeling is inherently complex due to various factors, including uncertainties in geometrical characteristics, material properties, nonlinear material behavior, foundation modeling, and soil effects. Therefore, integrating experimental and numerical data analysis enhances methods for identifying and localizing damage or changes within structural systems.

Extensive research in damage and change detection, as well as system identification for linear structural systems, has yielded numerous sophisticated global approaches based on vibration data analysis in both the time and frequency domains [13-15]. However, there is a notable lack of studies that leverage the topological features of the target structure to improve the detectability of minor changes. By employing appropriate substructuring techniques, these methods demonstrate superior sensitivity to small variations in the structural characteristics of the system under observation compared to global system identification methods.

In this study, one-third full-scale 18-story high-rise building was developed and instrumented with state-of-the-art instrumentation, installed on each floor and operated by E-Defense in Japan. This detailed testbed facilitated the creation of various data-driven, input-output, reduced-order models based on nonparametric identification approaches presented in [1-6], which have been successfully applied to both analytical and experimental data [7-8]. The approach discussed here does not require prior knowledge of the system characteristics (i.e., linear versus nonlinear) and is applicable to linear, nonlinear nonhysteretic, and hysteretic systems, without restrictions on the type of probing signal used for identification. However, it is limited to structures with chain-like topology, as will be subsequently explained in the study.

Several damage configurations in the building's lateral load-resisting system were investigated using data from base excitation dynamic tests performed on the building. The processes of damage detection, localization, and quantification were conducted by examining the variability in the primary features of the developed reduced-order models. It is important to note that in this study, the identification approaches were applied deterministically. The effects of variability in environmental or operational conditions, as well as uncertainties in modeling, measurement, and data analysis



processes, were not considered in the identified change-sensitive features (i.e., stiffness-like parameters and modal parameters) of the structures.

## 2 FORMULATION CHAIN-ID

Consider a multi-degree-of-freedom (MDOF) system with a chain-like topology, as illustrated in Figure 1. This system comprises  $n$  lumped masses, each with a magnitude  $m_i$ , subjected to base excitation and/or directly applied forces  $F_i$ . The lumped masses are interconnected by linear elements, whose restoring forces are primarily dependent on the relative displacement and velocity between the masses. The equations of motion for this system can be expressed as described by [9].

$$\ddot{x}_n + G^{(n)}(z_n, \dot{z}_n) = \frac{F_n}{m_n} \quad (1a)$$

$$G^{(n)}(z_n, \dot{z}_n) = \frac{F_n}{m_n} - \ddot{x}_n \quad (1b)$$

$$G^{(i)}(z_i, \dot{z}_i) = \frac{F_i}{m_i} - \ddot{x}_i + \frac{m_{i+1}}{m_i} G^{(i+1)}(z_{i+1}, \dot{z}_{i+1}) \quad (1c)$$

for  $i = n-1, n-2, \dots, 1$

where  $G^{(i)}(z_i, \dot{z}_i)$  is the mass-normalized restoring force function of the element connecting  $m_i$  and  $m_{i-1}$ ;  $x_i$  is the absolute acceleration of the mass  $m_i$ ;  $z_i$  the relative displacement between two consecutive masses; and  $\dot{z}_i$  the relative velocity between two consecutive masses. Equation (1) can be rewritten in more compact form as follows:

$$G^{(i)}(z_i, \dot{z}_i) = \sum_{j=i}^n \frac{F_j}{m_j} - \sum_{j=i}^n \bar{m}_{ij} \ddot{x}_j \quad (2)$$

where  $\bar{m}_{ij} = \frac{m_j}{m_i}$  represents the ratio between the lumped masses  $m_j$  and  $m_i$ . This approach assumes that the acceleration time responses  $\ddot{x}_i$  are available from observations, along with the applied forces  $F_i$  and/or the base excitation, as well as the values of the lumped masses  $m_i$ .

In addition, each of the estimated restoring force functions can be converted to a power series of the form

$$G^{(i)}(z_i, \dot{z}_i) = \sum_{q=0}^{q_{\max}} \sum_{r=0}^{r_{\max}} a_{qr}^{(i)} z_i^q \dot{z}_i^r \quad (3)$$

## 3 BUILDING DESCRIPTION AND CONFIGURATION

To evaluate the fundamental characteristics and validate the proposed methodology for earthquake responses and damage assessment in high-rise buildings, the data obtained from the shaking table test conducted at E-Defense in Japan are analyzed. E-Defense, operated by the National Research Institute for Earth Science and Disaster Resilience (NIED), is a 3D full-scale earthquake testing facility featuring the world's largest shaking table. The testbed is an 18-story moment-resisting frame structure, measuring 25.3 meters in height and weighing approximately 4179 kN, scaled down to one-third of a full-scale building [12]. Figure 2 and Figure 3 provide an overview and outline of the test specimen, respectively.

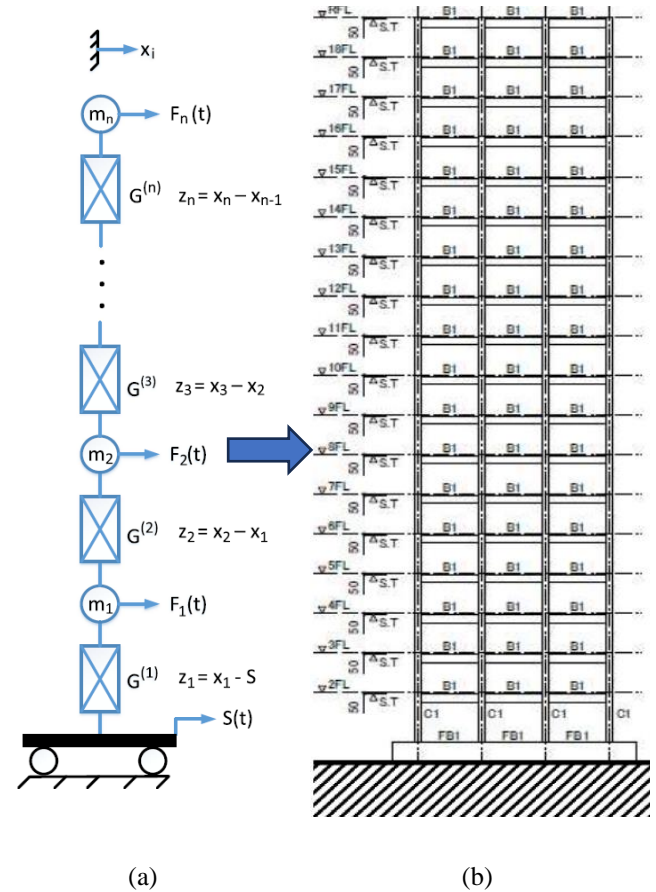


Figure 1. Modeling of the 18-story building used in this study: (a) reduced order representation (mathematical model), and (b) experimental setup.

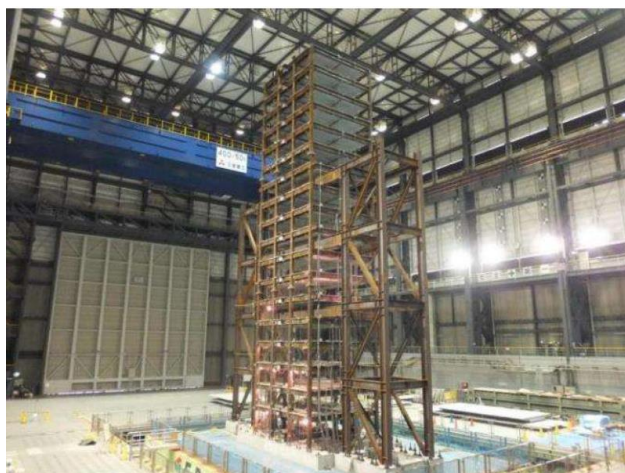


Figure 2. Overview of testbed.

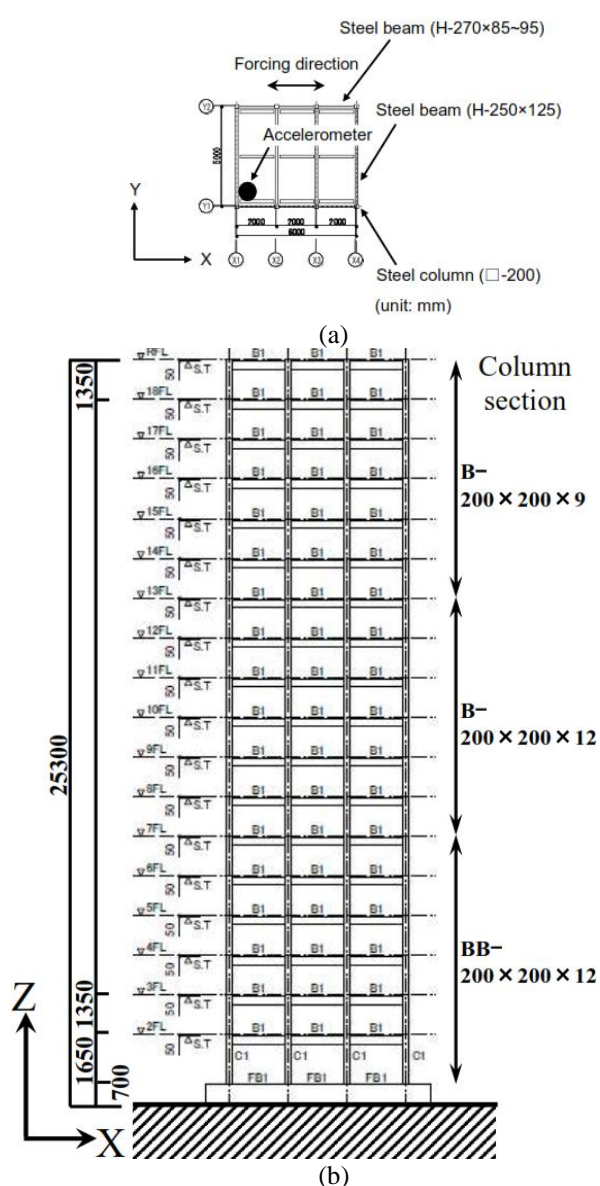


Figure 3. Outline of test specimen (a) floor plan and (b) structural framing elevation.

The floor plan measures 2000 mm by 3 spans in the longitudinal X-direction and 5000 mm by 1 span in the transverse Y-direction. The structure consists of moment-resisting frames with box-shaped steel columns measuring 200 mm by 200 mm, and H-shaped steel beams measuring 270 mm by 85-95 mm in the X-direction and 250 mm by 125 mm in the Y-direction. Servo-type three-axis accelerometers are installed at the corners of the X1 and Y1 bay on each floor of the test building. Measurement records from all floors and roof, totaling 18 accelerometers, are utilized for response estimation and damage evaluation in this study. The sensor signals are sampled at 200 Hz. The test specimen was subjected to a uniaxial excitation in the X-direction, with a first natural period of approximately 1.15 seconds in the X-direction.

The earthquake input motion is an artificially created Tokai, Nankai, and Tonankai consolidated-type earthquake occurring at the Nankai Trough, assumed to be recorded at Tsushima, Aichi Prefecture, Japan (Takahashi et al., 2013). Its peak ground acceleration (PGA) is about 300 cm/s<sup>2</sup>, with a velocity response spectrum value (pSv) of approximately 110 cm/s for periods between 0.8 and 10 seconds, and a duration of about 460 seconds. In the shaking table test, the input motion was scaled down to one-third of the original form to match the scale of the test specimen. The maximum excitation levels are set to various levels and applied to the test specimen multiple times.

Figure 4 shows the acceleration time history of the input motion to the testbed. Figure 5 illustrates the root mean square (RMS) for absolute acceleration, velocity, and displacement time-history for all floors in x- direction for the testbed. Figure 6 shows computed for relative displacement, relative velocity, and restoring force time-history for all floors in x-direction based on Equations 1 and 2.

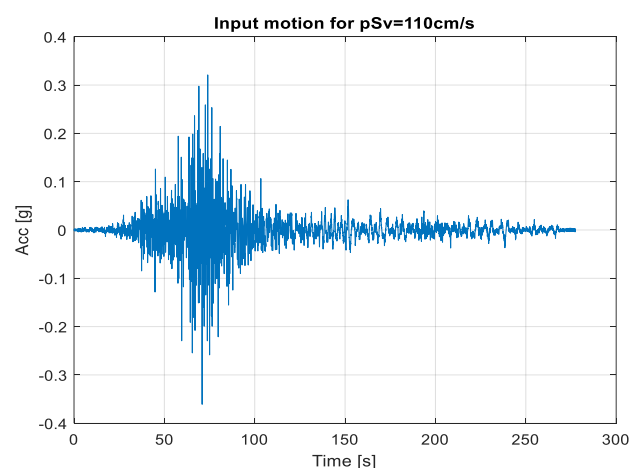


Figure 4. Acceleration time history of input motion for  $pSv=110\text{cm/s}$ .

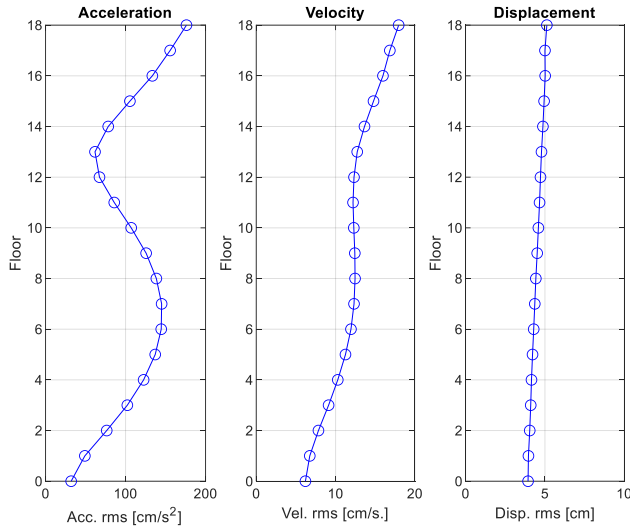


Figure 5. Computed RMS for absolute acceleration, velocity, and displacement time-history for all floors in x-direction.

## 4 DAMAGE IDENTIFICATION

### 4.1 Sample Data Processing

The acceleration responses were acquired from each floor of the testbed at a sampling frequency of 200 Hz. Corresponding velocity and displacement time histories were obtained through digital signal processing and numerical integration. Additionally, it was assumed that the building slabs were rigid; therefore, the available acceleration measurements corresponded to the acceleration response of the structure at each slab's geometric center. It is important to note that the experimental data contains all sources of measured uncertainty as the data was recorded from a real physical structure. To create a set of data, the time-history record for each structural state/configuration was partitioned into 40 ensembles with 20% overlap (i.e., in a sliding window of 30-second duration). Each ensemble includes more than five fundamental periods of the system.

### 4.2 Decomposition Approach

The building structure was utilized to demonstrate the results of implementing the proposed approach detailed in the second section of the paper, aimed at constructing a reduced-order model for the building structure. The decomposition approach for restoring force identification was executed using a third-order polynomial in both normalized variables  $z_i$  and  $\dot{z}_i$  for all floors in the building structure. The selection of a third-order polynomial was intentional to illustrate that the nonparametric identification approach discussed is capable of autonomously detecting whether the system is linear or nonlinear.

Once the relative displacements and velocities were computed, the ChainID identification approach was applied to develop the associated nonparametric representation for each floor in the 18-story building structure by calculating the corresponding restoring force coefficients for each floor in the reference structural configuration. Figure 7 illustrates sample time-history plots for the relative displacement  $z_i$ , relative velocity  $\dot{z}_i$  and measured mass normalized restoring force  $G^{(14)}$  between the 14<sup>th</sup> and 13<sup>th</sup> floors, in the x-directions.

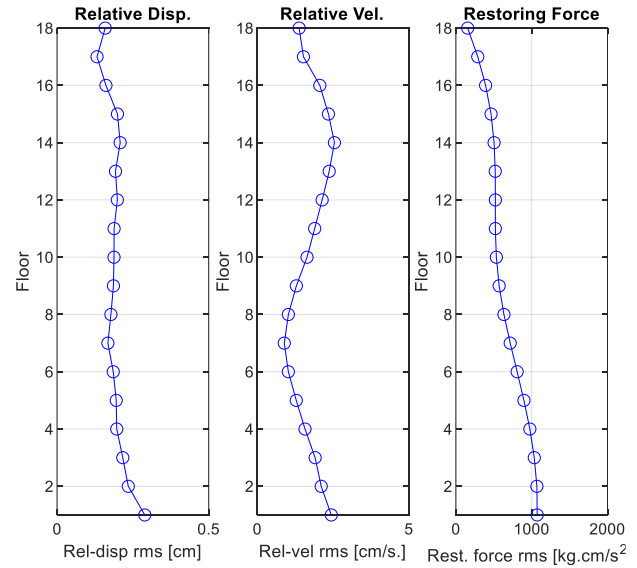


Figure 6. Computed RMS for relative displacement, relative velocity, and restoring force time-history for all floors in x-direction.

The analysis of the identified restoring force coefficients (i.e., power series coefficients  $a_{qr}^{(i)}$  for all building floors indicated that the linear term associated with relative displacements in the nonparametric representation (i.e.,  $a_{10}^{(i)}$ ) had the most significant contribution to the restoring force  $G^{(i)}$ , while the nonlinear terms were negligible. Figure 8 summarizes the identified mean of mass-normalized stiffness-like coefficient ( $a_{10}^{(i)}$ ) for all floors in x-direction.

For brevity, only the identification results computed for the 14<sup>th</sup> floor will be presented and discussed in this section. The power series coefficients  $a_{qr}^{(14)}$  of the nonparametric representation for the 14<sup>th</sup> floor are summarized in Table 1. It is evident that the mass-normalized stiffness-like coefficient  $a_{10}^{(14)}$  was the dominant term in the nonparametric representation.

It can be seen from Table 1 that only the linear terms in the identified model are found to be dominant. However, for the 1<sup>st</sup> floor, nonlinear terms had more contribution due to the presence of plastic hinges at the damaged location, as will be discussed in the upcoming section. It is important to mention that the same control parameters were used to perform the analysis without making any assumptions regarding the presence or absence of nonlinear response features. Figure 9 illustrates the time-history of the measured (experimental data) and reconstructed (after the application of ChainID approach) mass-normalized restoring forces for the 14<sup>th</sup> floor in the reference configuration in the x-direction. The two curves are essentially identical, indicating that the reduced-order model was able to replicate the dominant behavior of the 14<sup>th</sup> floor.



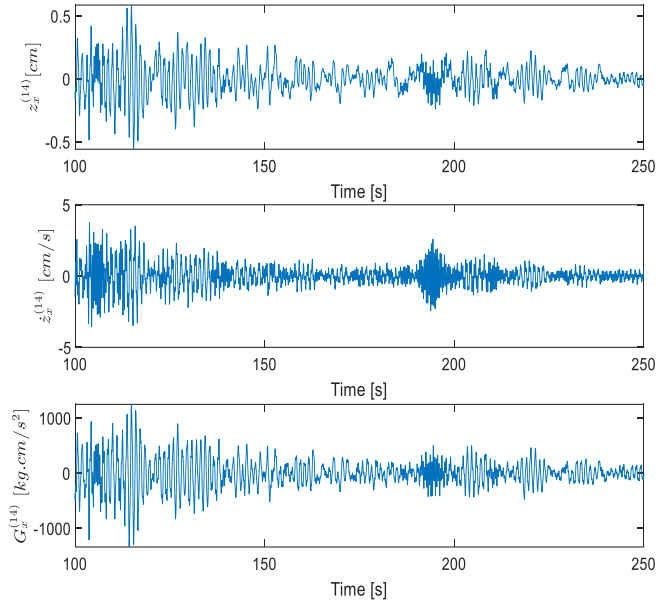


Figure 7. Sample relative displacement  $z_i$  and relative velocity  $\dot{z}_i$  computed between the 14<sup>th</sup> and 13<sup>th</sup> floors. The third row presents the measured restoring force time-history for element  $G^{(14)}$ .

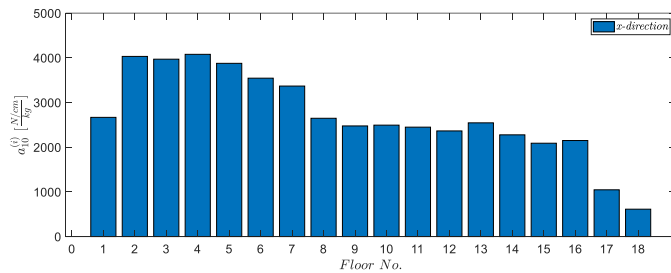


Figure 8. Identified mean of mass-normalized stiffness-like coefficient ( $a_{10}^{(i)}$ ) for all floors in x-direction.

Table 1. Identified mass-normalized restoring force coefficients  $a_{qr}^{(14)}$  for the 14th floor.

q\r	X-direction			
	0	1	2	3
0	0.00	2.10	-0.13	0.00
1	2276	0.90	0.20	0.00
2	12.30	3.20	0.00	0.00
3	78.00	0.00	0.00	0.00

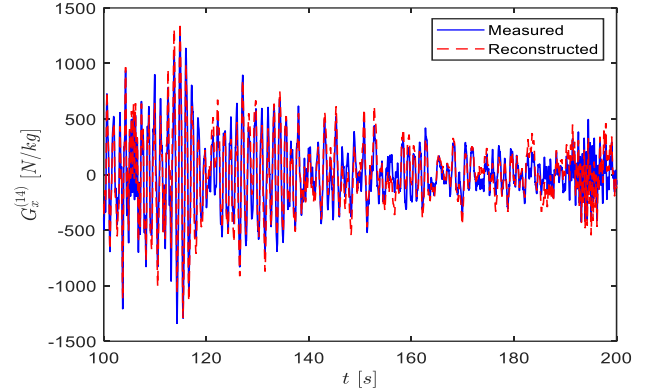


Figure 9. Comparison of measured and estimated restoring forces  $G^{(i)}$  for 14<sup>th</sup> floor in x-direction. Solid lines correspond to measured restoring force time-history; and dotted lines correspond to reconstructed restoring force time-history.

### 4.3 Damage Detection

To visualize the primary dynamic features of the system, the experimental phase plots (blue line) and the reduced-order representation using the ChainID approach (dotted red line) as well as the restoring force surface, are compared for the 14<sup>th</sup> and 1<sup>st</sup> floors, as shown in Figure 10.

It can be seen from Figure 10 (a), the reconstructed reduced-order model successfully captured the dominant linear dynamic characteristics of the 14<sup>th</sup> floor. Similarly, the reconstructed restoring force surface is planar, despite the use of a third-order expansion in both state variables (i.e., relative displacement and relative velocity) to characterize the dynamics of the 14<sup>th</sup> floor. The actual restoring force measurements are plotted as a point cloud, as shown in the second row of Figure 10 (a).

It is important to note that the data set under discussion was obtained from the testbed, where significant damage was observed on the 1<sup>st</sup> floor. This damage was characterized by the formation of plastic hinges at several columns, indicating a localized failure mechanism. The presence of plastic hinges suggests that the columns experienced substantial stress and deformation, leading to a reduction in their load-bearing capacity. This observation is crucial for understanding the structural behavior and integrity of the building under dynamic loading conditions.

The presence of plastic hinges and damage in the columns of the 1<sup>st</sup> floor led to the anticipated nonlinear behavior of the floor. This nonlinear response is indicative of the significant stress and deformation experienced by the columns, restoring forces  $G^{(i)}$  versus relative displacements  $z_i$  for the 1<sup>st</sup> floor and corresponding estimated restoring force surface for the 1<sup>st</sup> floor in the x-direction. In the first row, solid lines correspond to phase plot for the measured restoring force, and dotted lines correspond to reconstructed restoring force. In second row, actual restoring force measurements were plotted as a point cloud, which compromised their structural integrity and load-bearing capacity. The formation of plastic hinges is a critical factor in understanding the overall dynamic performance and failure mechanisms of the building under applied loads.

Figure 10(b) illustrates that the presence of nonlinearity can be visually inspected from the reconstructed restoring force for the 1<sup>st</sup> floor ( $G^{(1)}$ ), compared to the restoring force plot for the 14<sup>th</sup> ( $G^{(14)}$ ) floor under the same excitation. The effects of the nonlinear element in the response of the 1<sup>st</sup> floor are evident in both phase plots of the restoring force when compared to the reference condition, as shown in Figure 10 (b). In the phase plot of restoring force and relative displacement, the change in the restoring force slope indicates a pinching effect in the introduced nonlinearity. This pinching effect is observed on both sides of the restoring force, as the introduced damage is symmetric.

Additionally, a nonlinear effect in the restoring force surface can be seen in the plot of restoring force versus relative displacement and relative velocity, which is a typical signature of damage features. It is important to note that the nonparametric reduced-order representation using the ChainID approach successfully captured the dominant features of the dynamics at the correct location within the modules where the damage elements occurred. This demonstrates the effectiveness of the ChainID approach in accurately identifying and characterizing the nonlinear dynamic behavior resulting from structural damage.

## 5 MODAL IDENTIFICATION USING GLOBAL IDENTIFICATION

In addition to the local identification of the dynamic properties of each floor in the building, the modal identification (i.e., modal parameters) of the building was accomplished using the identified restoring force coefficients, as detailed in [10]. The estimated modal parameters were compared to those directly identified by implementing the natural excitation technique (NExT) in combination with the eigensystem realization algorithm (ERA) [11] a global identification technique.

The estimated values for the modal parameters (i.e., natural frequencies and damping ratios) for the first four mode shapes in x- directions are summarized in Table 2. It is noteworthy that the natural frequencies estimated from the reduced-order models developed in this study closely align with those computed using the NExT/ERA approach. As shown in Table 2, the estimated damping ratios computed using the two different approaches are similar for the first mode shape; however, damping was not identified for the remaining modes. This discrepancy is attributed to the varying contributions of the different modal constituents in characterizing the restoring forces.

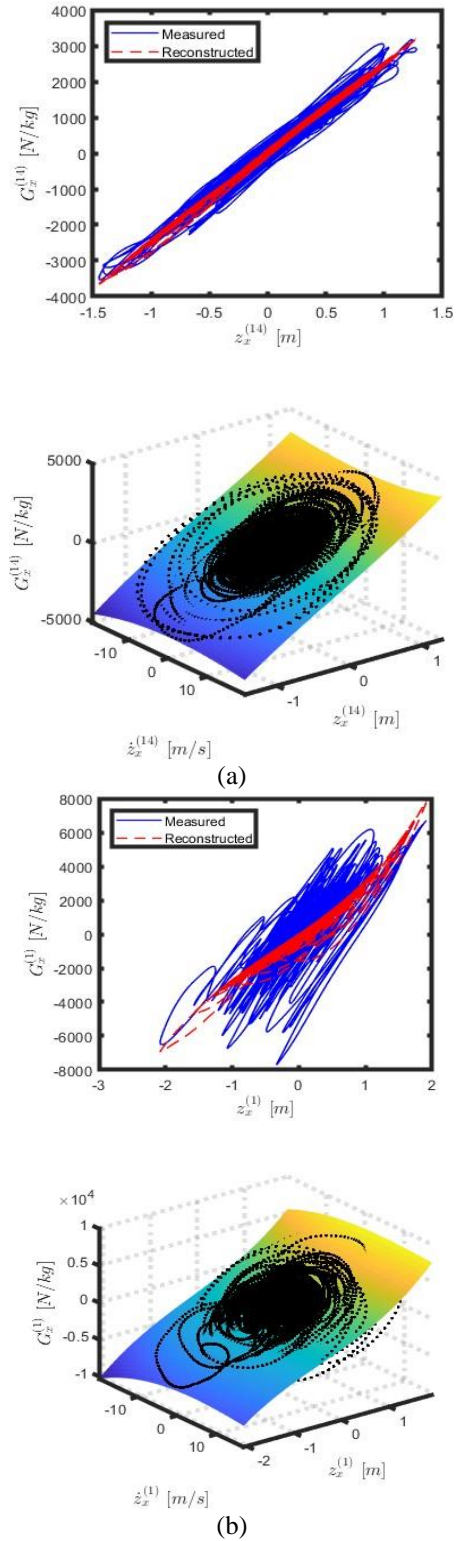


Figure 10. Phase plot of (a) restoring forces  $G^{(i)}$  versus relative displacements  $z_i$  for 14<sup>th</sup> floor and corresponding estimated restoring force surface for 14<sup>th</sup> floor in x-direction; and (b) restoring forces  $G^{(i)}$  versus relative displacements  $z_i$  for the 1<sup>st</sup> floor and corresponding estimated restoring force surface for the 1<sup>st</sup> floor in x-direction. In first row, solid lines correspond to phase plot for measured restoring force, and dotted lines correspond to reconstructed restoring force. In second row, actual restoring force measurements were plotted as a point cloud.

Table 2. Summary of natural frequencies and damping ratios for the first four lateral modes in the x-directions of the 18-story building structure, identified from the reduced-order model developed using ChainID and NExT/ERA approaches.

Mode	Chain ID		NExT/ERA	
	$\omega$ [Hz]	$\zeta$ [%]	$\omega$ [Hz]	$\zeta$ [%]
1 <sup>st</sup> mode	0.38	1.78	0.48	1.75
2 <sup>nd</sup> mode	0.81	-	0.82	0.40
3 <sup>rd</sup> mode	1.19	-	1.16	0.20
4 <sup>th</sup> mode	1.65	-	1.79	1.00

## 6 SUMMARY AND CONCLUSIONS

In this study, a one-third full-scale model of an 18-story high-rise building, developed under the E-Defense project, was constructed and instrumented to investigate the damage on individual floors. Sample results from these damage scenario models were used to evaluate the effectiveness and reliability of employing reduced-order models to detect, locate, and quantify changes or damages in a physical building structure.

Input-output data from the 18-story building under base excitation were used to develop reduced-order models for different floors. Two approaches were implemented: the nonparametric chain-like system identification approach (ChainID), which is the focus of this study, and a global identification approach (NExT/ERA). The results demonstrated that significant changes identified in the reconstructed restoring forces of the reduced-order models built using the ChainID approach could be correlated to the presence and location of the actual physical changes or damages, even in the presence of modeling, measurement, and data processing errors.

The initial findings of this study demonstrate that the structural health monitoring methodology presented is capable of accurately detecting, locating, and quantifying structural changes or damage in monitored systems, provided the necessary data set is available.

The presented work is part of an ongoing effort. Future developments will focus on evaluating the algorithm's sensitivity and effectiveness by analyzing multiple earthquake events with varying magnitudes. This will help assess the approach's capability in detecting, locating, and quantifying different levels of structural damage. Additionally, further studies aim to enhance the model's ability to predict potential structural failures under diverse seismic conditions.

## REFERENCES

- [1] Masri, S. 1978. "Response of a multidegree-of-freedom system to nonstationary random excitation." *ASME J. Appl. Mech.* 45 (3): 649–656. <https://doi.org/10.1115/1.3424376>.
- [2] Masri, S., G. Bekey, H. Sassi, and T. Caughey. 1982. "Non-parametric identification of a class of non-linear multidegree dynamic systems." *Earthquake Eng. Struct. Dyn.* 10 (1): 1–30. <https://doi.org/10.1002/eqe.4290100102>.
- [3] Masri, S., J. Caffrey, T. Caughey, A. Smyth, and A. Chassiakos. 2004. "Identification of the state equation in complex non-linear systems." *Int. J. Non Linear Mech.* 39 (7): 11–27. [https://doi.org/10.1016/S0020-7462\(03\)00109-4](https://doi.org/10.1016/S0020-7462(03)00109-4).
- [4] Masri, S., and T. Caughey. 1979. "A nonparametric identification technique for nonlinear dynamic problems." *Trans. ASME. J. Appl. Mech.* 46 (2):433–447. <https://doi.org/10.1115/1.3424568>.
- [5] Masri, S., R. Miller, A. Saud, and T. Caughey. 1987a. "Identification of nonlinear vibrating structures: Part I. Formulation." *Trans. ASME. J. Appl. Mech.* 54 (4): 918–922. <https://doi.org/10.1115/1.3173139>.
- [6] Masri, S., R. Miller, A. Saud, and T. Caughey. 1987b. "Identification of nonlinear vibrating structures: Part II—Applications." *J. Appl. Mech. Trans. ASME* 54 (4): 923–929. <https://doi.org/10.1115/1.3173140>.
- [7] Hernandez-Garcia, M., S. Masri, R. Ghanem, E. Figueiredo, and C. Farrar.
- [8] 2010. "An experimental investigation of change detection in uncertain chain-like systems." *J. Sound Vib.* 329 (12): 2395–2409. <https://doi.org/10.1016/j.jsv.2009.12.024>.
- [9] Hernandez-Garcia, M. R. 2014. "Analytical and experimental studies in modeling and monitoring of uncertain nonlinear systems using data driven reduced-order models." Ph.D. thesis, Dept. of Civil and Environmental Engineering, Univ. of Southern California.
- [10] Abdelbarr M, Massari A, Kholer M, Masri S 2020. Decomposition approach for damage detection, localization, and quantification for a 52-story building in downtown Los Angeles. *J Eng Mech.* [https://doi.org/10.1061/\(ASCE\)EM.1943-7889.0001809](https://doi.org/10.1061/(ASCE)EM.1943-7889.0001809).
- [11] James, G., T. G. Carne, and J. P. Lauffer. 1995. "The natural excitation technique (NExT) for modal parameter extraction from operating structures." *Modal Anal. Int. J. Anal. Experimental Modal Anal.* 10 (4):260–277.
- [12] Tomohiko Hatada, Yoshiki Ikeda, Hajime Hagiwara, Yoshihiro Nitta, and Akira Nishitani 2018. "Damage Evaluation Method based on Acceleration Measurement on Some Restricted Floors." *Proceedings of the 16th European Conference on Earthquake Engineering.*
- [13] Doebling, S. W., C. R. Farrar, and M. B. Prime. 1998. "A summary review of vibration-based damage identification methods." *Shock Vib. Digest* 30 (2): 91–105.
- [14] Doebling, S. W., C. R. Farrar, M. B. Prime, and D. W. Shevitz. 1996. *Damage identification and health monitoring of structural and mechanical systems from changes in their vibration characteristics: A literature review.* Los Alamos, NM: Los Alamos National Laboratory.
- [15] Farrar, C. R., and K. Worden. 2007. "An introduction to structural health monitoring." *Philosophical Trans. Royal Soc. London A: Math. Phys. Eng. Sci.* 365 (1851): 303–315. <https://doi.org/10.1098/rsta.2006.1928>.



# ‘Machine Learning – Based Data Interpretation and Visualization for Tunnel Monitoring: A Case Study of Changshui Airport Tunnel’

Asif Ahmed Sourov<sup>1</sup>, Yadong Xue<sup>1</sup>, Yongfa Guo<sup>2</sup>, Wenyun Ding<sup>2</sup>, Jinjing Yang<sup>2</sup>

<sup>1</sup>Department of Geotechnical, College of Civil Engineering, Tongji University, 1239 Siping Road, Shanghai – 200092, China

<sup>2</sup>China Railway Eryuan Engineering Group Kunming Survey and Design Research Institute Co., Ltd, Kunming, Yunan, China

Email: asifahmedsourov@icloud.com, yadongxue@tongji.edu.cn, 524965753@qq.com, 592938576@qq.com, 357080499@qq.com

**Abstract:** Specially, when it comes to such risky construction projects as the Changshui Airport Railway Tunnel, the ground settlements surrounding the structure will be observed and evaluated. This case study is a combination of advanced machine learning algorithms, which are augmented with MATLAB to reinterpret, visualize and analyze settlement trends based on real – world tunnel monitoring data. The research starts with some of the time – series data that had been registered in the tunnel (settlement, factors that impact settlement, temperature, etc.). K – means clustering and hierarchical clustering are used to classify the settlement patterns and the clustering result indicates the difference in settlement monitoring points. Finally, we have used the feature importance analysis to explore the most significant factors that affect settlement decisions and to know more about the settlement processes in tunnels. The discussion of the Random Forests, Gradient Boosting and Artificial Neural Networks regression models is provided to predict settlement patterns to enable predictive risk. Heatmaps, time – series graphs and scatter plots are some of the comprehensive visualizations constructed to convey the discovery and help in decision making. The indicators to assess the model performance are  $R^2$ , RMSE, MAE and the findings show how to forecast settlements in the most optimal manner. Besides presenting the utility of machine learning tunnel surveillance, the case study also provides data driven decision making framework in underground engineering projects.

**Keywords:** Tunnel Monitoring, Ground Settlements, Machine Learning, Data Visualization, Changshui Airport Tunnel, Underground Infrastructure

## 1. Introduction

Tunnel monitoring is a highly significant element of safety and life of underground infrastructure, especially in high – stakes projects, like airport tunnels (Bao et al., 2018). The geotechnical and environmental forces that control the settlement behavior of these structures are complex and may undermine the structural integrity of these structures (Muhammed et al., 2019). Monitoring is thus essential in the realization of the impacts and of the excavation works on the surrounding ground and structural stability. The conventional approaches, however, despite their usefulness, are time – consuming and prone to errors because they involve a lot of manual analysis that may need human interpretation (Hua et al., 2021). Monitoring systems generate a lot of data in the course of a tunnel project life cycle because of the technology development (Wang et al., 2020). It is also difficult to analyze such datasets to draw conclusions, identify trends and discover impact factors. Nevertheless, the existing practices fail to capture this information in a manner that would allow proactive maintenance and safety decision – making.

The given Case study examines the application of machine learning approaches that have been adopted in the MATLAB environment to solve the above – mentioned issues. Using the data of Changshui Airport Tunnel Monitoring, it aims to interpret, visualize and analyze settlement behavior using clustering algorithms, feature importance analysis and regression models, thus determining patterns, whether to fill or settle and which factors have a significant impact on ground activity. The introduction of machine learning based systems into the tunnel monitoring process is a paradigm shift, since such methods enable quicker and more precise

analyses due to automation of the extraction of complex datasets (Jin-miao et al., 2022). The results of the study can thus be used to make improved decisions, improve predictive maintenance and support the safety and efficiency of underground structures. The power of this study shows its ability to use the existing computational tools to produce engineering solutions that can have a significant real – life effect.

## 2. Settlement Monitoring and Prediction

Figure 1 is a summary of the settlement monitoring and prediction process, its challenges and developments. Settlement monitoring is an important aspect of safety and life of underground infrastructure in high-risk projects like airport tunnels (Jin-miao et al., 2022). The construction induced behaviors such as boring induced stresses, change in ground water level and geological heterogeneities are some of the causes of ground settlement (Ayasrah et al., 2020). These deformations can be hazardous and in case they are not identified or misinterpreted, they can result in structural instability, which can result in catastrophic failures (Ayasrah et al., 2020). Monitoring of landslides is achieved by surface and subsurface movements which are traditionally monitored by geodetic surveys, inclinometers and extensometers. Figure 1 represents the key areas of monitoring of settlements, including the traditional and contemporary approaches, and the utilization of the advanced instruments like machine learning and visualizations, to analyze large amount of data. It has been increasingly possible to obtain continuous deformation data, as newer forms of instrumentation have been developed well, including automated total stations, satellite-based InSAR (interferometric synthetic aperture radar) and fiber optic sensors, all modern (Karamvasis & Karathanassi, 2020).

Monitoring therefore plays a role beyond detection to mechanisms of settlement (Martins et al., 2020).

### 2.1. Machine Learning in Civil Engineering

Machine learning (ML) is easy to use and understand complex data and predict structural behaviors in civil engineering (Marsella & Scaioni, 2018). Various clustering techniques (E.g.: K-means clustering, hierarchical clustering, etc.) are increasingly being used in settlement monitoring to classify settlement patterns as well as to detect spatially heterogeneous risks (Vadyala et al., 2021). To illustrate, showed that clustering had the potential to significantly increase the ability to distinguish settlement behavior at up to eight monitoring sites and could be applicable in the implementation of sector-specific mitigation measures (Zhou et al., 2020). The most important machine learning techniques of settlement monitoring are clustering and regression models, which allow identifying patterns and predicting trends in ground deformation, as illustrated in Figure 1. All regression models, including RF, GB, and ANN, had better predictive performance and modeled settlement trend than statistical methods (Jin-miao et al., 2022). This type of models is particularly applicable when there are non-linear relationships and high dimensional data as is the case in geotechnical applications. Other related fields where ML can be applied, i.e. SHM and anomaly detection (Mousavi & Beroza, 2022). The former includes clustering methods which have been applied to identify deformation anomalies in bridge structures and regression models are widely applied to predict loads in buildings (Jasmine & Arun, 2021).

### 2.2. Advanced Data Integration and Visualization

The capability to successfully integrate the heterogeneous data, which are position, deformation, temperature and environmental parameters in a single effective mechanism has been one of the most remarkable issues in tunnel monitoring (Zhao et al., 2021). MATLAB, which has a vast array of tools to conduct machine learning and visualization, is a perfect candidate to conduct such workflows (Ma et al., 2021). Settlement dynamics can be shown in time-series plots, and areas with high-risk levels can be shown in heatmaps (Yan et al., 2019). Together with clustering and regression analyses, these visualizations may give a complete image of the behavior of ground and in responsivity.

### 2.3. Research Gap and Addressing

Although the ML techniques have shown promising progress in geotechnical engineering, studies have been mainly focused on specific tasks (Marcher et al., 2020). As far as the authors are aware, few studies have attempted to develop a coherent framework to interpret and visualize settlement data that include clustering, feature importance analysis, and regression modeling (Chen et al., 2022). The literature also shows evidence of the need of domain-specific adaptations in ML algorithms. Or, feature engineering based on site condition, geological and environmental driven feature engineering could be used in settlement prediction models (Fan et al., 2019). These methods, however, offer more access and utility of data, yet there is no standard workflow to those adjustments, and thus, the overall use of these models becomes cumbersome (Merghadi et al., 2020).

We suggested a machine learning pipeline that included clustering, feature importance, regression, and application of that regression with clustering to provide a general analysis framework (as illustrated in Figure 1) to be used in tunnel monitoring.

### 3. Data Preprocessing

Monitoring of settlement is an important process in the safety of high-risk infrastructure projects like tunnels during construction and long-term prevention and remedial maintenance of the infrastructure after construction (Tan et al., 2019). These techniques offer optimal solutions to capture high-resolution spatial-temporal trends but the traditional settlement monitoring methods (geodetic surveys, inclinometers) are time-consuming, subject to human error, and do not capture such trends (Wang et al., 2020). In this section, a step-by-step data-driven framework of the analysis of the settlement behavior in the Changshui Airport Tunnel will be discussed. Figure 2 gives a general description of the proposed framework.

#### 3.1. Data Preprocessing

The pre-processing of data is performed to clean, standardize and prepare the data to be utilized in future machine learning activities. Using MATLAB workspace, we can see that our original data has 13 columns and 10,704 rows. The notable variables are dated Measurement Time, Cumulative Settlement, Relative Settlement, Settlement Rate, Geological Grade, and Distance from Start. The selection of these variables reflects the time and space aspects of the settlement monitoring which constitutes the basis analysis of any type of settlement monitoring.

- Standardization of Time Intervals:** The time interval of data collection is not of regular nature (Time Interval Days) and is recorded in Measurement Time. Time matching functions in MATLAB where timestamps are converted to fixed equidistant time (e.g. 0.5 days, 1 day) to provide uniform time-based monitoring of settlement patterns.
- Missing Values:** Handling Missing Values in Missing Values: Interpolated Settlement Rate and Relative Settlement with the fill missing () function in MATLAB. Linear interpolation maintained the trends of time in the data to avoid bias.
- Normalization of Variables:** Cumulative Settlement, Settlement Rate, and Geological grade were normalized by the min-max scaling by using the normalize () function of MATLAB. This process minimizes the differences between the applications of different systems that improve the performance of the machine learning models.
- Detect and Remove Outliers:** The sensor errors and environmental disturbances that caused the sudden anomalies in the settlement rates were detected by using the Z-scores to detect statistical outliers and examine sudden spikes by plotting time-series data.

### 3.2. Clustering Analysis

Settlement behaviors were used to mine, which was done through clustering analysis. This step exposes spatial settlement patterns and points out areas of intervention. Clustering Techniques:

- a. K-Means Clustering: The variables such as Settlement Rate, Cumulative Settlement, Geological Grade were used as inputs. Elbow Method was used to determine the best number of clusters using within-cluster sum of squares (WCSS). The MATLAB assigned the monitoring points to various clusters using the K – means () function.
- b. Hierarchical Clustering: The results of K-means were confirmed through the hierarchical clustering which provided a hierarchical view of settlement behaviors. The hierarchical relationships between the settlement points were visualized with the help of the linkage () function in MATLAB that produced a dendrogram.
- c. Clustering Results: Cluster 1: Monitoring points outside structural elements (i.e. tunnel border), i.e. the address which was above the maximum settlement value; Cluster 2: intermediate settlement rates -> transitional zones; Cluster 3: Stable regions with thin layers.

### 3.3. Feature Importance Analysis

The feature importance analysis shows the most important factors in the determination of settlement behavior (Oh et al., 2021). This procedure increases the interpretability of the predictive models and follows the geotechnical principles. The following is the outline of feature importance analysis:

- a. Supervised Learning Models: To rank predictor variables Random Forest (RF) and Gradient Boosting (GB) models were applied. Dependent Variables: Settlement Rate, Cumulative Settlement Predictor variables: Geological Grade, Distance from Start, Monitoring Point Elevation and Time Interval Days
- b. Feature Importance Ranking: The RF and GB models provided feature importance scores of all the predictors. The strongest features were: Geological Grade: The main factor that affects settlement, which means the effect of soil properties; Distance from Start: Settlement is not evenly distributed along the length of the tunnel; Time Interval Days: Settlement behavior varied greatly depending on the time of year.

### 3.4. Predictive Modeling

Predictive modeling was also carried out to forecast settlement patterns in order to carry out proactive maintenance. It entailed a split of the data into 80 percent training and 20 percent test and the models were ranked based on their capacity to predict Cumulative Settlement.

- a. Training and Testing: Single supervised machine learning models were trained and tested: Random Forest (RF): It is interpretable and robust; Gradient Boosting (GB): Very accurate iterative model; ANNs: Can capture potential non-linear relationships and required tuning up; The robustness was achieved by cross-validation.

- b. Evaluation Metrics: Models were tested on  $R^2$ :  $R^2$  is a measure that compares the predicted values with the actual values in the training data; RMSE (Root Mean Square Error): How large is the error of the prediction; MAE (Mean Absolute Error): A measure to normalize the error of the prediction.

### 4. Graphical Analysis and Data Interpretation

Some of the visual outputs and the interpretation applied in this section include Feature Importance, Predictive Modeling, and other statistics that are used to monitor and predict on settlements. Dataset Summary: The target variable Cumulative Settlement was initially analyzed statistically and then feature importance analysis was done. The most important statistics are:

Rows in Dataset: 10,704; Missing Values: 841 (preprocessing step); Minimum Settlement Value: 0; Median Vela Value: 14.1412; Settlement Value Max: 2,064.6; Average Settlement Value: 940.1619; Standard Deviation: 1,019.7

Following data cleaning, 9863 rows remained to be used in train and evaluation. Such preprocessing steps were followed to ensure data reliability in the execution of the following model.

#### 4.1. Analysis of Feature Importance

The results are displayed graphically with measures Table 1. Numerical Insights from ANN Feature Importance.. Figure 3 below is a bar chart that indicates the importance of each feature (e.g. Time Interval Days, Distance from Start, Monitoring Point Elevation, Relative Settlement) to the prediction of settlement rates using Random Forest (RF) model. As we observe, Monitoring Point Elevation is the most influential predictor with an importance of 50, which dwarfs the other features. Monitoring Point Elevation remains the most influential predictor in the List of Features in Gradient Boosting with an importance by value of more than 10,000 as in Figure 4. With the permutation-based importance, the ANN indicates that the most important predictor of settlement rates is Monitoring Point Elevation with an importance score of approximately 1,000 as indicated in Figure 5. The importance score of Monitoring Point Elevation is overwhelmingly high (1,028.8246). The architecture of ANN employed in the prediction of settlement in Changshui Airport Tunnel is shown in Figure 6. The model has an input layer that has the four main predictors of interest, which are Time Interval Days, Distance from Start, Monitoring Point Elevation, and Relative Settlement, which cover the effects of time, distance, and elevation on settlement, and the effects of relative settlement.

Random Forest Figure 3 – Monitoring Point Elevation is the most important, and all others (Time Interval Days, Distance from Start, Relative Settlement) are practically 0. Gradient Boosting Figure 4 - The importance score of Monitoring Point Elevation is about 10,000, which again confirms its importance. ANN Figure 5 The permutation-based analysis of ANN shows that Monitoring Point Elevation has an extremely high importance score of 1,028.8246, which is far higher than any other feature. Temporal (Time Interval Days) and spatial (Distance from Start) features were of moderate



importance in all models: Random Forest Figure 3 – Time Interval Days and Distance from Start are rather insignificantly contributing yet still distinguishable compared to Relative Settlement. Gradient boosting Figure 4 in this case, these features have small but distinctly visible impact.

#### 4.2. Analysis of Model Performance Metrics

Figure 7 shows that the random forest (RF) model possesses a good prediction power ( $R^2$  close to 0.90). Similarly, the Root Mean Square Error (RMSE) is also very small, implying that the difference between the actual value and the predicted value is less. Thus, we can say that RF is very efficient when it comes to this dataset. The MAE (Mean Absolute Error) indicates the average absolute error between the predicted and actual values and as it can be seen, it is very low and hence RF can make accurate predictions. In Figure 8, Gradient Boosting (GB) has similar  $R^2$  values ( $\sim 0.90$ ) to RF, which means that it performs well in predicting.

In Figure 9 it reflects the data non-linearities more than RF and GB since the third ANN model has the greatest degree of accuracy in the terms of  $R^2$ . RMSE of ANN is slightly greater than GB but in general ANN is more able to capture the patterns but that can also be a sign of ANN overfitting or high variance in localized predictions. The grouped bar chart Figure 10 in Figure 7, Figure 8, Figure 9 gives a summary of the performances of the model in terms of  $R^2$ , RMSE, and MAE of the RF, GB, and ANN. The three models are remarkable in accuracy ( $R^2$  close to 0.90). However: ANN does get a bit better in  $R^2$ , so it is now the most successful model in the sense of understanding complex interactions. The RMSE of GB is lower than other models, which means that the predictions of GB are better in magnitude, especially in the pleasant regions. These results in Figure 10 showed that the choice of the model depends on the application, ANN is better to work with highly non-linear data, GB is the preferred method to minimize catastrophic errors, and that RF is a universal and interpretable solution.

#### 4.3. Residual Analysis

The residual plot of RF Figure 11 indicates that the residuals are between -60 and +60. The majority of them are clustered at the zero line, which shows that the accuracy of many of the predictions was reasonable, but the dispersion of residuals, particularly at higher values, provides a clue as to how this model performed poorly on some of the cases where the predictions were relatively too distant to the actual value. Figure 12 The range of residuals is -2 to +2 in Gradient Boosting, which is much narrower, showing much higher precision compared to RF. The Figure 13 ANN shows the least range of residuals, -1.2 to +0.2 residuals that are tightly clustered around zero. This means that it is the most accurate in predicting among the models, and it has the fewest errors and excellent generalization abilities. Based on Figure 14 these findings are pointing out that ANN is the most effective in capturing complex relationships in the data and therefore it would emerge as the most accurate model in predicting settlement. Combined Residual Plot - RF, GB and ANN The combined residual plot displays residuals of RF, GB, and ANN. RF has the broadest scope of residuals between -60 and +60, thus performing the worst in the minimization of

prediction error. ANN residuals are the closest to each other, and they are well within the range of -1.2 to +0.2, which is exceptionally precise.

#### 4.4. Settlement Risk Analysis

The Actual Settlement and the RF, GB, and ANN model predictions of spatial settlement risks are shown in Figure 15 below. Actual Settlement (Top Left) The baseline comparison is provided by this heat map because it indicates the settlement values that actually took place. It demonstrates the actual pattern of settlement risk by subterrains as reflected by the data recorded in Figure 15. However, at the higher risk regions at Figure 15, there are minute differences. This means that RF will only capture the overall trend and will not be in a position to follow the minor details, particularly in cases where the values of settlements are extreme. GB Predicted Settlement (Bottom Left) The gradient boosting heat map would see it to be in good fitness to real settlement. ANN Predicted Settlement (Bottom Right): ANN is the most accurate model among RF and GB and it gives the closest resemblance to the actual settlement. All the heatmaps show that ANN gives the most accurate approximation of spatial settlement risks, then Gradient Boosting, and then Random Forest. It also agrees with the results that were obtained previously that ANN is more accurate overall, especially on complex data, GB is moderately accurate; RF is less accurate in extreme cases as indicated in Figure 15.

#### 4.5. Error Distribution Analysis

Figure 16 Error Histogram (RF, GB, ANN) The histograms of RF, GB, and ANN give a detailed statistic of the accuracy errors of the three models. The Errors variance is very broad in RF & a range of approximately -60 ~ +60 is essentially eminent. When the value of minimum is high, it means that the model is not as precise as other models. The GB histogram range is lower, with a range of mostly between -2 and + 2, which means that it minimizes errors and is more stable in performance. The distribution of errors is the most concentrated in ANN and the errors are near -0.01 and +0.01 and this indicates that ANN predicts settlement values more accurately than other networks. Figure 17 Grid density plot of Errors RF, GB and ANN The mixed density plot indicates the variations in the distribution of the various errors of these three models to indicate the difference in performance. This Figure 17 graph therefore reinstates the ability of ANN to generalize complex patterns and to be highly accurate in the predictions.

#### 4.6. Clustering Analysis

The Elbow Method to validate the number of the optimal clusters in the K-Means clustering analysis (Schubert, 2023). The y-axis indicates the within-cluster sum of squares that is an indicator of the compactness of the clusters and the x-axis indicates the number of clusters. Figure 18, The decrease in WCSS as  $k = 1$  to  $k = 2$  means that the variance can be explained by two clusters only to a reasonable extent. WCSS begins to flatten out after  $k=2$ , the returns to adding more clusters are getting small. K mean clustering  $k=2$ , frequencies of prevailing settlement patterns in the data set. X: The following scatter plot presents the outcome of K-Means clustering of the settlement data. The data are shown as color-

coded clusters: red = Cluster 1, green = Cluster 2, blue = Cluster 3. In these two axes, the x-axis (Feature 1) would show something like Time Interval Days and the y-axis (Feature 2) could show Distance from Start. The clusters indicate spatial settlement patterns: Cluster 1 (red): The regions of maximum movement, most probably in the area of structural features or ground disturbance. 4465 points, Cluster 2 (green): The regions of transition with average settlement rates and medium stability. 1341 points, Cluster 3 (blue): Stable areas, where there are few changes in the settlement, corresponding to less vulnerable areas. 4057 points. The Euclidean distances between clusters are plotted on the y-axis and the data points (e.g., monitoring locations) on the x-axis Figure 20. The vertical lines are also branched vertically on the height of the dendrogram where the significant differences are found and this is another evidence that there are three main groups that are identified in the hierarchy. Table 4. Feature Importance of Each Cluster Model.

## 5. Results

A detailed analysis of the Changshui Airport Tunnel based on various state-of-the-art machine learning algorithms-Random Forest (RF), Gradient Boosting (GB), and Artificial Neural Networks (ANN) was conducted to analyze and predict the settlement behaviors. we are presenting the results with performance metrics and feature importance of all the models. Model Performance Metrics Table 2. Model Performance Metrics for Each Model summarizes quantitative performance metrics of each model, presented in Figure 7. Performance Metrics – RF.. These results indicate that ANN model is more accurate in predicting the settlement behavior, which proves its strength and reliability in predicting the settlement behavior more accurately than the other models. Table 3. Feature Importance of Each Model below shows the importance of each feature to the respective models. The importance scores enable us to know the values of features that are most closely associated with model predictions. In addition, the significance scores are also graphically illustrated in Figure 3, Figure 4, Figure 5, which indicates that Feature 3 is dominant in all models, which is a significant environmental or geotechnical factor. The total residuals are presented in Figure 14, which indicates that ANN has predicted very little wrong. The heatmap plots of the actual and predicted settlement were very similar, and this fact proved that the ANN predictions are the closest to the actual ones, and the predictions of GB and RF were the second. This spatial disaggregation plays an important role in the proper depiction of risk distribution. The error distribution in each model is described and shown in Figure 16, which shows the frequency of the prediction errors that have been observed in some ranges. Elbow Method determines the number of clusters as illustrated in Figure 18. In order to get a meaningful segmentation of settlement patterns the elbow plot indicates that the optimal number of clusters is three. The outcome of the clustering can still be visualized, which is K-means clustering of data points in Figure 19 and the dendrogram of hierarchical clustering in Figure 20, which confirm the segmentation results based on hierarchical relationships between individual points of settlement.

## 6. Discussion

The study demonstrates that geotechnical monitoring can be enhanced considerably with the assistance of deep analysis based on ML to process complicated data sets(Ritter & Frauenfelder, 2021). The concentration of monitor location to some clusters that depict characteristics assists in the development of particular place of resident behaviors. In general, Cluster 1 had 4,465 points (marked as RESILIENT / STABLE on the map) and we can use these areas as reference areas, or even a baseline of comparison of how we can improve and others areas came out as Cluster 2, which had 1,341 points and marked as THREATENED on the maps, which are transitional or Undeveloped areas, which need more care and attention with interventions more proactive. These clusters are consistent with the predictive data of machine learning models (ANN, GB, etc.) that showed Monitoring Point Elevation as the most correlated parameter, which confirms that the higher settlement was observed in the sites of well locations that were in Cluster 2. The clustering results give the necessary information and confirmations to help in maintenance planning and resources allocation besides confirming the model predictions.

### 6.1. Analysis of Improved Model Effectiveness, Interpretation and Consequences

The ANN is the solution to risk prediction and mitigation in tunnel scenarios because of its excellent capacity to comprehend complex, non-linear relationships in geotechnical data(Ramezanshirazi et al., 2019). On the other hand, GB and RF were good alternatives, and GB reduced prediction errors by iterative refinement and RF was easy to interpret. The elevation of the monitoring point was also identified as a critical factor in all the models since the feature significance analysis revealed the critical importance of the elevation changes in influencing the tunnel settlements(Apoji et al., 2022). According to this conclusion, the influence of the elevation changes on the stress distribution and the following settlement patterns is considerable, which is consistent with the geotechnical principles (Figure 3, Figure 4, and Figure 5).

Both models possessed some advantages within the context of geotechnical data, Random Forest: It was very robust and provided interpretable results and therefore it can be applied to problems where the impact of a specific feature is of interest. Gradient boosting was very good in minimizing the prediction error and managing the interaction between features. This meant that it was suitable in the modeling of the non-linear dynamics of the settlement data. Artificial Neural Networks: Have proven to be very accurate in handling complex data structure, but they are very demanding in terms of processing power and they need to be fine-tuned to avoid overfitting.

### 6.2. Prospective Research Directions

The proactive management of infrastructure is being embraced by integrating machine learning (ML) in tunnel monitoring(Plevris & Papazafeiropoulos, 2024). Machine learning enhances tunnel safety and life by identifying potential danger zones early enough due to its ability to process and analyze large volumes of data. Nevertheless, the

indictment also points to areas that should be further investigated, to enhance the effectiveness of machine learning in the area of tunnel monitoring: These are the incorporation of real-time data inputs to enable adaptive responses to environmental deviations, and a data-driven dynamic update of predicted models as part of a real-time processing solution (Zhang et al., 2020). Cross-Project Validation: experiments are conducted on a number of tunnel projects to determine the generalizability of the models to standardize ML applications in civil engineering.

## 7. Conclusion

Further use of machine learning methods in this field may assist us in getting nearer to the realization of the role of different parameters in the monitoring of tunnel (as a part of Geotechnical Engineering) and the qualitative side of Geotechnical engineering as perceived through the eyes of a geotechnical engineer. This paper was restricted to the monitoring of tunnel in Changshui and the monitoring system is comprehensive to monitor the deformation patterns of Changshui. Security aspects of Geotechnical Engineering Which are likely to be messages of improved predicting performances and functional profitability of the Geologist economical relevant hazard mapping linked with geological changes (Wu et al., 2021). Therefore, Random Forests, Gradient Boosting Machines, and Artificial Neural Networks have been applied effectively in enhancing the accuracy and reliability of settlement predictions, which is essential to the stability, as well as sustainability, of tunnel infrastructures (Yan et al., 2019). This was the main area/work in the investigation of the possibilities of these models, where, as they have a good understanding of complex and nonlinear data interactions, in the sense of the higher  $R^2$  and lower RMSE and MAE on the Artificial Neural Network, the best results were obtained. These excellent results demonstrate the potential of sophisticated ML models to become a disruptive technology to traditional geotechnical monitoring practices that allow the risk assessment and mitigation plans to go much deeper than ever before. The effective use of these technologies can also be extended to other geotechnical events that are high risk (Wang et al., 2021). Moreover, the use of machine learning methods must be applied to various project scenarios in other studies, which will allow a better idea of whether/what algorithms can be used in different construction conditions in real time.

## 8. Mind Maps, Figures and Tables

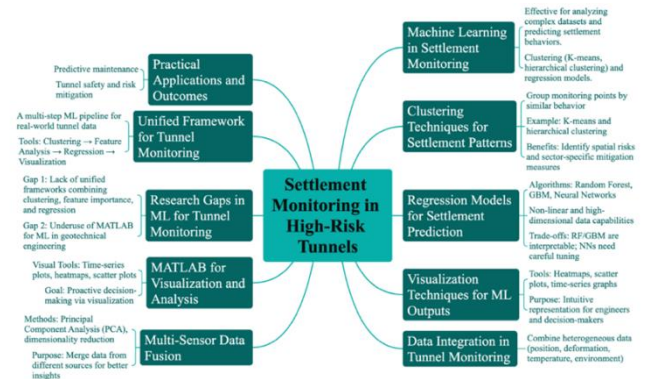


Figure 1. Mind map of settlement monitoring in high-risk tunnels.

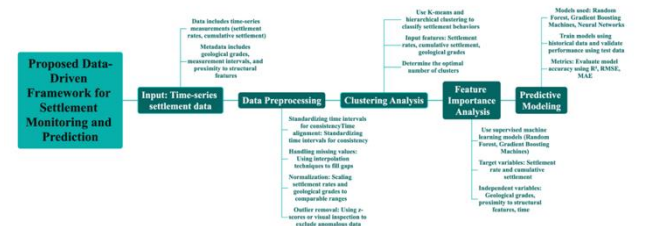


Figure 2. Mind Map of Proposed Data-Driven Framework for Settlement Monitoring and Prediction

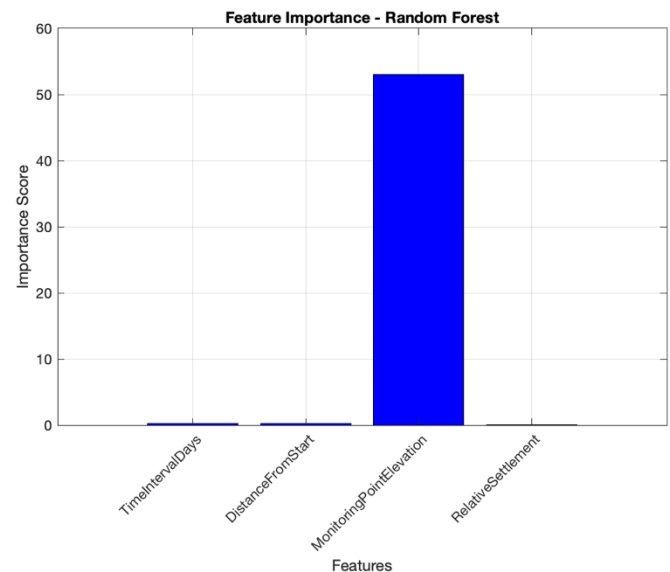


Figure 3. Feature Importance – RF.



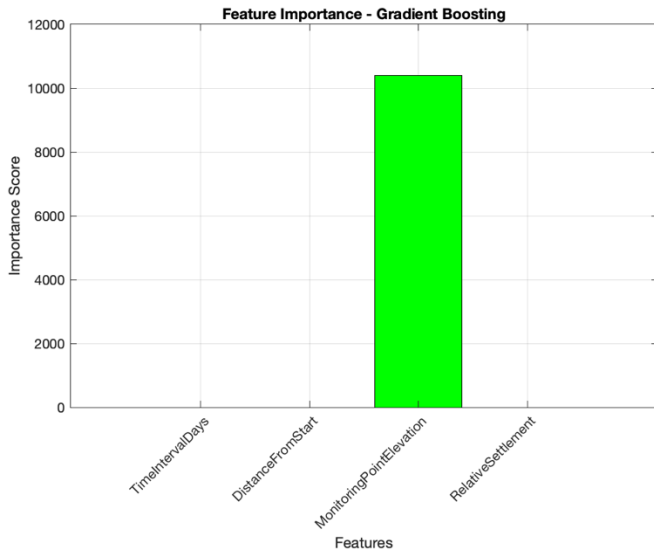


Figure 4. Feature Importance – GB.

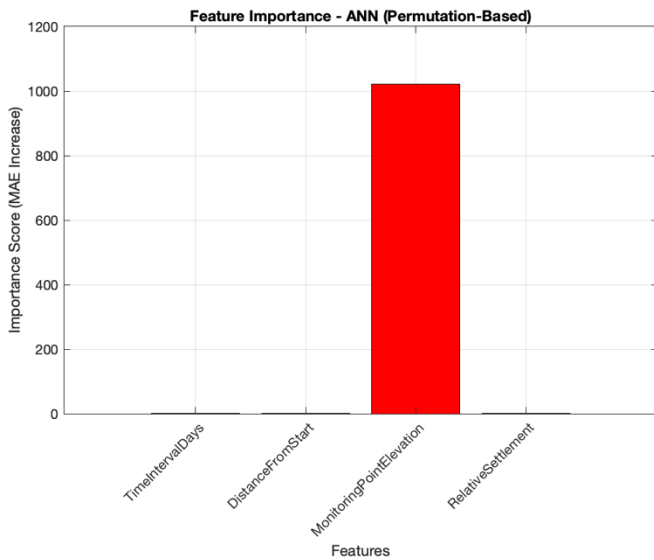


Figure 5. Feature Importance – ANN.

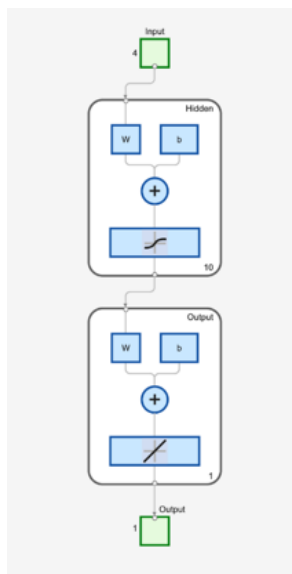


Figure 6. Architecture of ANN.

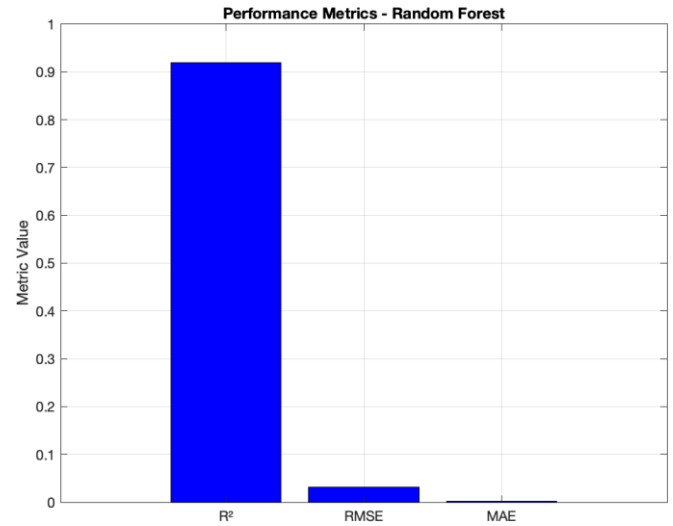


Figure 7. Performance Metrics – RF.

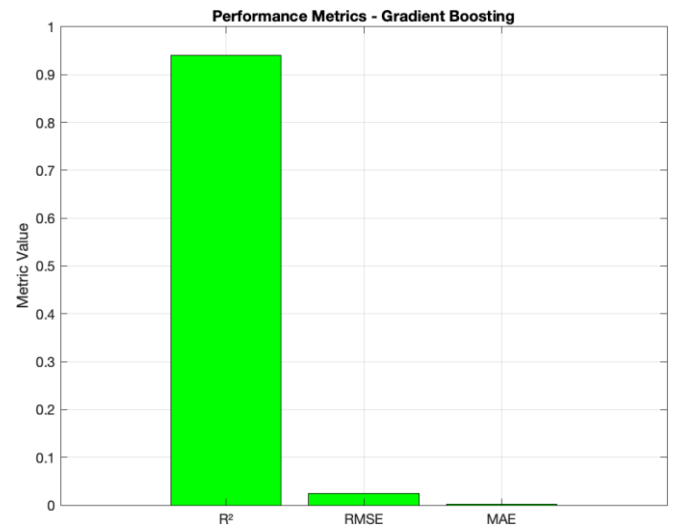


Figure 8. Performance Metrics – GB.

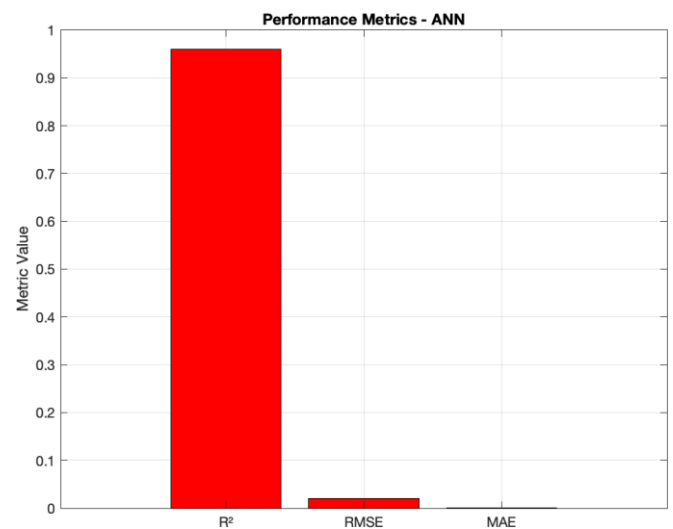


Figure 9. Performance Metrics – ANN.

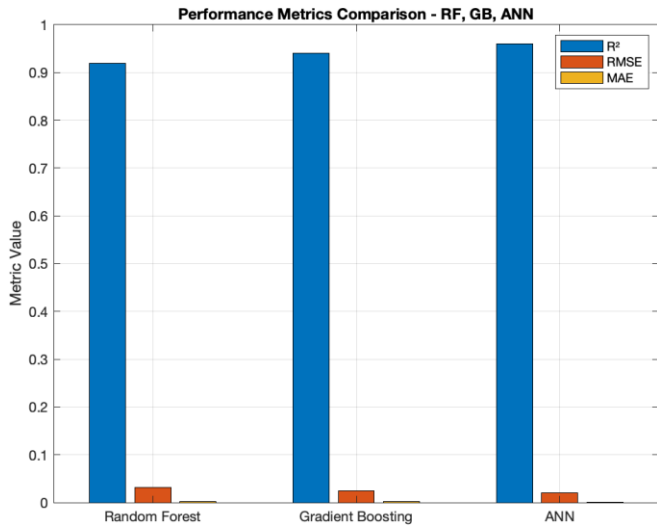


Figure 10. Performance Metrics – RF, GB, ANN.

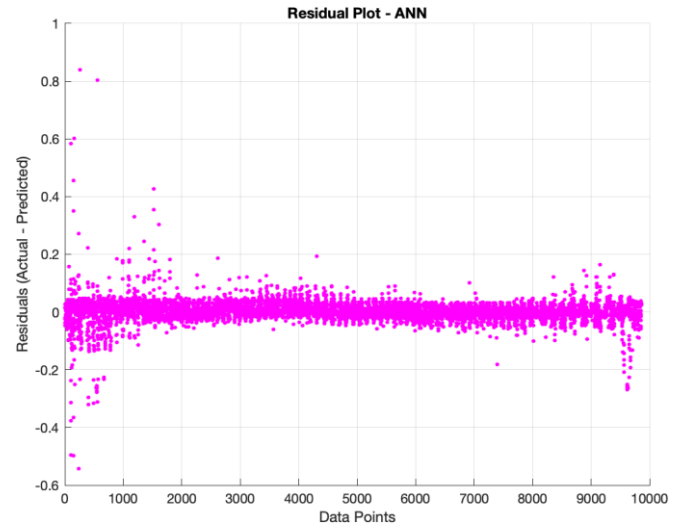


Figure 13. Residual Plot – ANN.

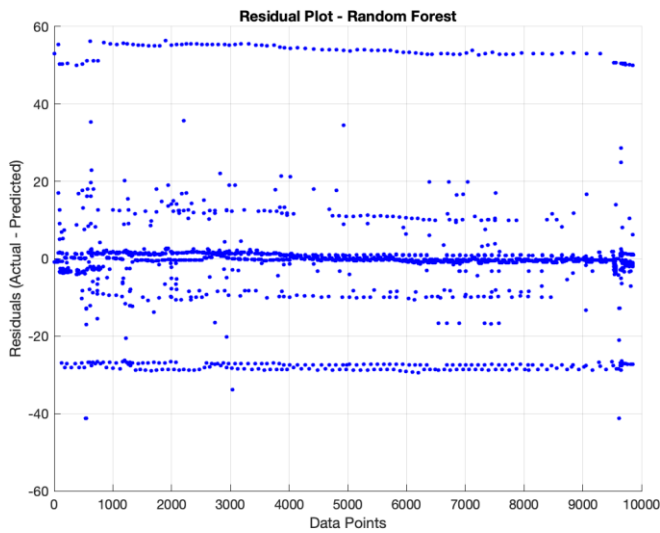


Figure 11. Residual Plot – RF.

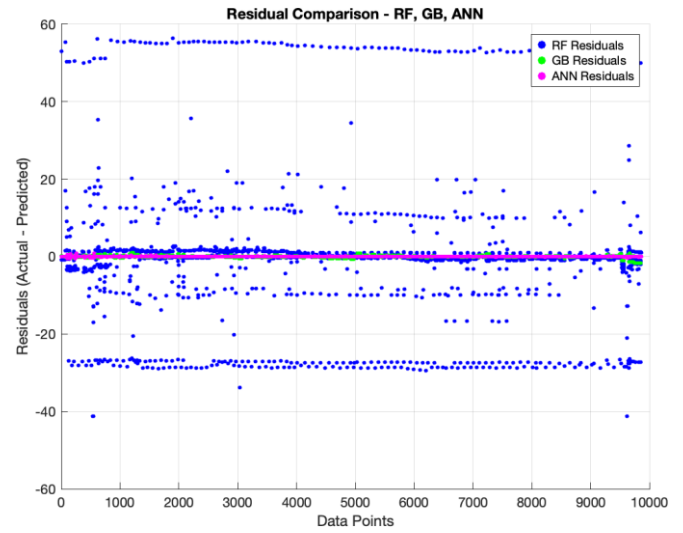


Figure 14. Residual Plot – Rf, GB, ANN.

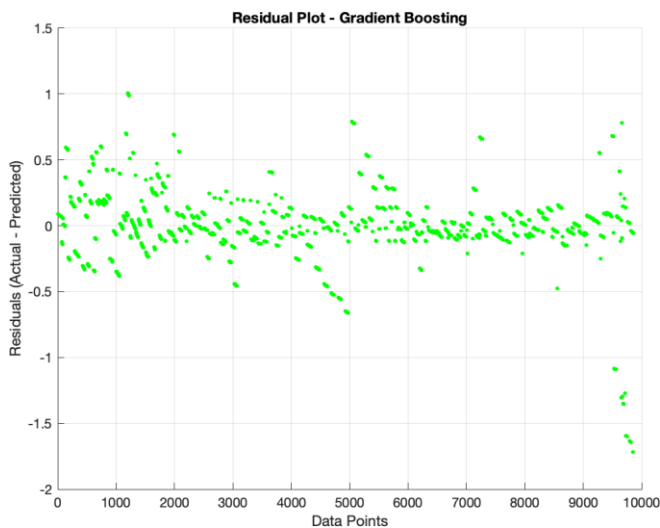


Figure 12. Residual Plot – GB.

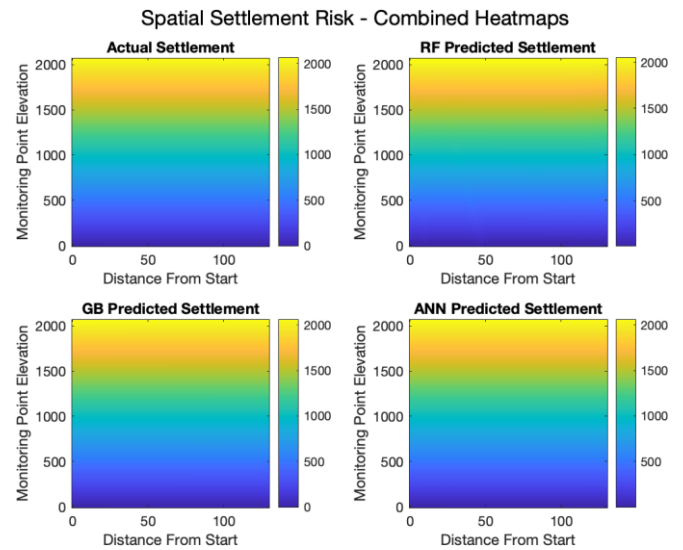


Figure 15. Spatial Settlement Risk – Combined Heatmaps of RF, GB, ANN.

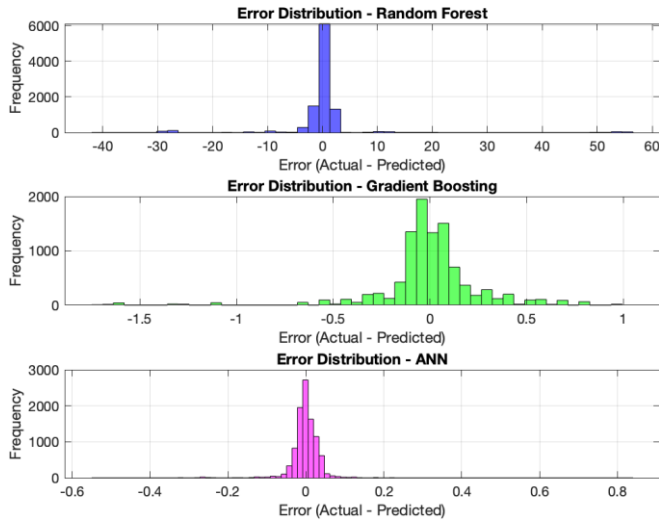


Figure 16. Error (Actual – Predicted) RF, GB, ANN.

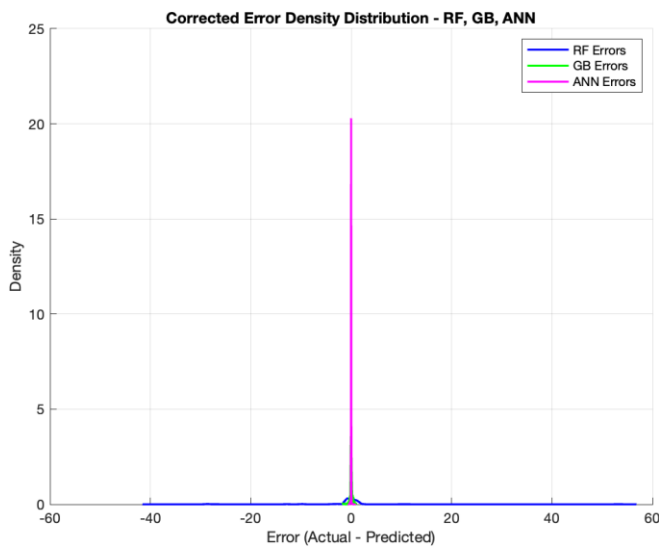


Figure 17. Density Combined Error (Actual – Predicted) RF, GB, ANN.

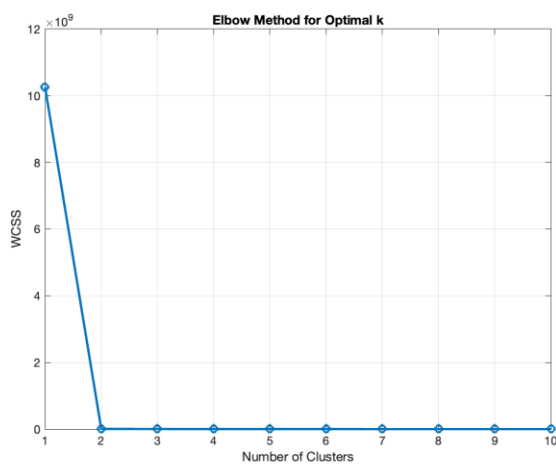


Figure 18. Elbow Method for Optimal  $k$ .

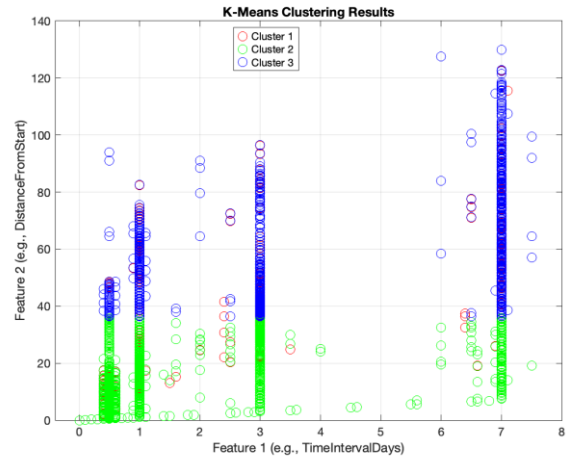


Figure 19. K-Means Clustering Results.

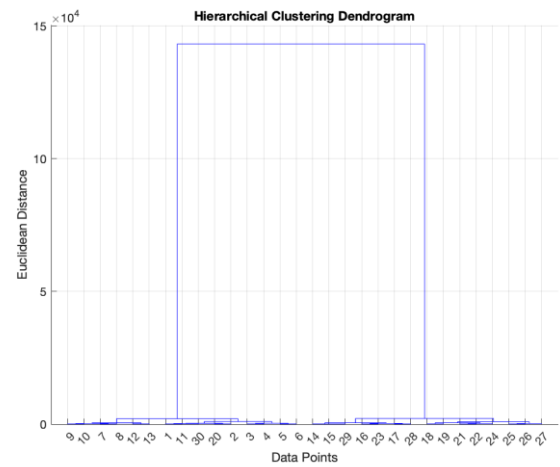


Figure 20. Hierarchical Clustering Dendrogram.

Table 1. Numerical Insights from ANN Feature Importance.

Feature	Permuted MAE	Importance Score	Interpretation
Time Interval Days	0.0038008	0.0016423	Temporal variations moderately affect settlement.
Distance From Start	0.003671	0.0015125	Distance influences settlement slightly
Monitoring Point Elevation	1028.8267	1028.8246	Elevation dominates as the most critical factor
Relative Settlement	0.0021976	0.00003908	Minor impact on model predictions

Table 2. Model Performance Metrics for Each Model

Model	R <sup>2</sup>	MAE	RMSE
RF	0.92	0.002	0.031
GB	0.94	0.0015	0.025



ANN	0.96	0.001	0.02
-----	------	-------	------

Table 3. Feature Importance of Each Model

Feature	RF Importance	GB Importance	ANN Importance
1	0.23432	0	0.0078671
2	0.24303	0	0.004688
3	50.255	10396	987.70
4	0.085561	0	0.00029713

Table 4. Feature Importance of Each Cluster Model

Cluster	Points	Feature 1	Feature 2	Feature 3	Feature 4
Cluster 1	4465	0.0018	0.0249	2.0613	0.0004
Cluster 2	1341	4.6088	60.327	12.856	0.3447
Cluster 3	4057	1.4209	11.926	12.834	0.4621

### Acknowledgement

The financial support of the Key Technology R&D Plan is appreciated (Grant No. 202303AA080003) by the Yunnan Provincial Department of Science and Technology. This grant enabled the research that is the subject of this paper. We would also like to express our gratitude to all the colleagues and technical personnel who participated in the model and implementation of this project in particular to their contribution and efforts.

### References

- [1] Apoji, D., Fujita, Y., & Soga, K. (2022). Soil Classification and Feature Importance of EPBM Data Using Random Forests. *Geo-Congress 2019*, 520. <https://doi.org/10.1061/9780784484029.052>
- [2] Ayasrah, M., Qiu, H., Zhang, X., & Daddow, M. (2020). Prediction of Ground Settlement Induced by Slurry Shield Tunnelling in Granular Soils. *Civil Engineering Journal*, 6(12), 2273. <https://doi.org/10.28991/cej-2020-03091617>
- [3] Bao, Y., Tang, Z., Li, H., & Zhang, Y. (2018). Computer vision and deep learning-based data anomaly detection method for structural health monitoring. *Structural Health Monitoring*, 18(2), 401. <https://doi.org/10.1177/1475921718757405>
- [4] Chen, Q., Yang, Z., Xue, B., Wang, Z., & Xie, D. (2022). Monitoring and Prediction Analysis of Settlement for the Substation on Soft Clay Foundation. *Advances in Civil Engineering*, 2022(1). <https://doi.org/10.1155/2022/1350443>
- [5] Fan, C., Sun, Y., Zhao, Y., Song, M., & Wang, J. (2019). Deep learning-based feature engineering methods for improved building energy prediction. *Applied Energy*, 240, 35. <https://doi.org/10.1016/j.apenergy.2019.02.052>
- [6] Hua, J., Cheng, J., Zhang, J., Zhang, J., Su, Y., & Zheng, Y. (2021). Principle and application of in-situ monitoring system for ground displacement induced by shield tunnelling. *Tunnelling and Underground Space Technology*, 112, 103905. <https://doi.org/10.1016/j.tust.2021.103905>
- [7] Jasmine, P. H., & Arun, S. P. (2021). Machine learning applications in structural engineering - a review [Review of Machine learning applications in structural engineering - a review]. *IOP Conference Series Materials Science and Engineering*, 1114(1), 12012. IOP Publishing. <https://doi.org/10.1088/1757-899x/1114/1/012012>
- [8] Jin-miao, C., Shen, X., & Chen, Q. (2022). Prediction of Maximum Surface Settlements of Bai~Hua Tunnel Section based on Machine Learning. *Journal of Physics Conference Series*, 2185(1), 12042. <https://doi.org/10.1088/1742-6596/2185/1/012042>
- [9] Karamvassilis, K., & Karathanassi, V. (2020). Performance Analysis of Open Source Time Series InSAR Methods for Deformation Monitoring over a Broader Mining Region. *Remote Sensing*, 12(9), 1380. <https://doi.org/10.3390/rs12091380>
- [10] Ma, G., Zhang, S., Li, H., Li, P., & Liu, Y. (2021). A Method of Monitoring the Cross-Section Deformation of Tunnels Using the Strain Data from the Fully Distributed Optical Fibre Sensors. *IOP Conference Series Materials Science and Engineering*, 1203(2), 22125. <https://doi.org/10.1088/1757-899x/1203/2/022125>
- [11] Marcher, T., Erharder, G. H., & Winkler, M. (2020). Machine Learning in tunnelling – Capabilities and challenges. *Geomechanics and Tunnelling*, 13(2), 191. <https://doi.org/10.1002/geot.202000001>
- [12] Marsella, M., & Scaioni, M. (2018). Sensors for Deformation Monitoring of Large Civil Infrastructures. *Sensors*, 18(11), 3941. <https://doi.org/10.3390/s18113941>
- [13] Martins, B. H., Suzuki, M., Yastika, P. E., & Shimizu, N. (2020). Ground Surface Deformation Detection in Complex Landslide Area—Bobonaro, Timor-Leste—Using SBAS DInSAR, UAV Photogrammetry, and Field Observations. *Geosciences*, 10(6), 245. <https://doi.org/10.3390/geosciences10060245>
- [14] Merghadi, A., Yunus, A. P., Dou, J., Whiteley, J., Pham, B. T., Bui, D. T., Avtar, R., & Boumezeur, A. (2020). Machine learning methods for landslide susceptibility studies: A comparative overview of algorithm performance. *Earth-Science Reviews*, 207, 103225. <https://doi.org/10.1016/j.earscirev.2020.103225>
- [15] Mousavi, S. M., & Beroza, G. C. (2022). Machine Learning in Earthquake Seismology. *Annual Review of Earth and Planetary Sciences*, 51(1), 105. <https://doi.org/10.1146/annurev-earth-071822-100323>
- [16] Muhammed, H. H., Zakaria, W. A., & Mahdi, Q. A. (2019). Prediction of Stresses and Settlement for TBM Tunnel Surrounding Soil. *Diyala Journal of Engineering Sciences*, 12(4), 50. <https://doi.org/10.24237/djes.2019.12405>
- [17] Oh, D.-W., Kong, S.-M., Lee, Y.-J., & Park, H. (2021). Prediction of Change Rate of Settlement for Piled Raft Due to Adjacent Tunneling Using Machine Learning.

Applied Sciences, 11(13), 6009.  
<https://doi.org/10.3390/app11136009>

- [18] Plevris, V., & Papazafeiropoulos, G. (2024). AI in Structural Health Monitoring for Infrastructure Maintenance and Safety. *Infrastructures*, 9(12), 225. <https://doi.org/10.3390/infrastructures9120225>
- [19] Ramezanshirazi, M., Sebastiani, D., & Miliziano, S. (2019). Artificial Intelligence to Predict Maximum Surface Settlements Induced by Mechanized Tunnelling. In *Lecture notes in civil engineering* (p. 490). Springer Nature. [https://doi.org/10.1007/978-3-030-21359-6\\_52](https://doi.org/10.1007/978-3-030-21359-6_52)
- [20] Ritter, S., & Frauenfelder, R. (2021). InSAR monitoring data to assess building response to deep excavations. *IOP Conference Series Earth and Environmental Science*, 710(1), 12036. <https://doi.org/10.1088/1755-1315/710/1/012036>
- [21] Schubert, E. (2023). Stop using the elbow criterion for k-means and how to choose the number of clusters instead. *ACM SIGKDD Explorations Newsletter*, 25(1), 36. <https://doi.org/10.1145/3606274.3606278>
- [22] Tan, X., Chen, W., Wang, L., Tan, X., & Yang, J. (2019). Integrated Approach for Structural Stability Evaluation Using Real-Time Monitoring and Statistical Analysis: Underwater Shield Tunnel Case Study. *Journal of Performance of Constructed Facilities*, 34(2). [https://doi.org/10.1061/\(asce\)cf.1943-5509.0001391](https://doi.org/10.1061/(asce)cf.1943-5509.0001391)
- [23] Vadyala, S. R., Betgeri, S. N., Matthews, J. C., & Matthews, E. (2021). A review of physics-based machine learning in civil engineering [Review of A review of physics-based machine learning in civil engineering]. *Results in Engineering*, 13, 100316. Elsevier BV. <https://doi.org/10.1016/j.rineng.2021.100316>
- [24] Wang, J., Tang, S., Heap, M. J., Tang, C., & Tang, L. (2021). An auto-detection network to provide an automated real-time early warning of rock engineering hazards using microseismic monitoring. *International Journal of Rock Mechanics and Mining Sciences*, 140, 104685. <https://doi.org/10.1016/j.ijrmms.2021.104685>
- [25] Wang, L., Xu, S., Qiu, J., Wang, K., Ma, E., Li, C., & Guo, C. (2020). Automatic Monitoring System in Underground Engineering Construction: Review and Prospect. *Advances in Civil Engineering*, 2020(1). <https://doi.org/10.1155/2020/3697253>
- [26] Wu, J., Chen, J., Chen, G., Wu, Z., Yu, Z., Chen, B., Ke, W., & Huang, J. (2021). Development of Data Integration and Sharing for Geotechnical Engineering Information Modeling Based on IFC. *Advances in Civil Engineering*, 2021(1). <https://doi.org/10.1155/2021/8884864>
- [27] Yan, K., Dai, Y., Xu, M., & Mo, Y. (2019). Tunnel Surface Settlement Forecasting with Ensemble Learning. *Sustainability*, 12(1), 232. <https://doi.org/10.3390/su12010232>
- [28] Zhang, P., Chen, R., Tian, D., Wang, Z.-T., & Wu, K. (2020). An AIoT-based system for real-time monitoring of tunnel construction. *Tunnelling and Underground Space Technology*, 109, 103766. <https://doi.org/10.1016/j.tust.2020.103766>
- [29] Zhao, Y., Han, Y., Kou, Y., Li, L., & Du, J.-H. (2021). Three-Dimensional, Real-Time, and Intelligent Data Acquisition of Large Deformation in Deep Tunnels. *Advances in Civil Engineering*, 2021(1). <https://doi.org/10.1155/2021/6671118>
- [30] Zhou, C., Kong, T., Jiang, S., Chen, S., Zhou, Y., & Ding, L. (2020). Quantifying the evolution of settlement risk for surrounding environments in underground construction via complex network analysis. *Tunnelling and Underground Space Technology*, 103, 103490. <https://doi.org/10.1016/j.tust.2020.103490>

# Developing physics-informed neural networks for structural parameters identification of beam with moving loads

Anmar I. F. Al-Adly<sup>1</sup>, [ORCID](#), Prakash Kripakaran<sup>1</sup>, [ORCID](#)

<sup>1</sup>Department of Engineering, Faculty of Environment, Science and Economy, University of Exeter, Stocker Road, Exeter, EX4 4HF, United Kingdom, England

email: aa1224@exeter.ac.uk, P.Kripakaran@exeter.ac.uk

**ABSTRACT:** Physics-Informed Neural Networks (PINNs) seamlessly integrate the predictive capabilities of neural networks with established physical principles. By integrating constraints such as displacement and force boundary conditions alongside governing equations, PINNs can generate digital twins of physical systems and processes. This fusion allows for more accurate modelling and simulation of complex physical phenomena, bridging the gap between data-driven approaches and traditional physics-based methods. Nevertheless, the practical implementation of PINNs remains challenging, primarily due to numerous influential hyperparameters and the complex nature of modelling the governing physics through partial differential equations (PDEs). This challenge becomes especially critical in the context of dynamic loads, where higher-order PDEs encompassing both spatial and temporal domains, alongside relevant structural parameters and generalised (distributed) load's function, must be carefully optimised during the PINNs training process. This study presents a novel application of PINNs model, developed, trained, and validated using real-world bridge monitoring data, for the inverse problem of predicting structural parameters of a girder subjected to moving loads. Two case studies are considered. In the first, PINNs model is utilised to estimate the structural parameters of a bridge girder under varying levels of noise in the data. In the second, the model is trained with actual field monitoring measurements to estimate structural parameters while predicting girder deflection and other internal forces. The findings advance the existing body of knowledge in structural health monitoring (SHM) by demonstrating a practical PINNs-based solution for bridge girders under moving loads.

**KEY WORDS:** PINNs; Inverse problem; Parameter identification; Neural networks (NNs); SHM.

## 1 INTRODUCTION

Bridges are critical components of transportation infrastructure, and ensuring their safety and longevity through structural health monitoring (SHM) is a top priority [1]. Over time, bridges are subjected to environmental deterioration and repetitive traffic loads that can induce damage or stiffness degradation, potentially reducing their service life [2]. A key aspect of SHM is structural parameter identification – determining properties such as stiffness (flexural rigidity) – which enables the assessment of a structure's condition [3].

Recently, physics-informed neural networks (PINNs) have emerged as a promising tool for tackling inverse modelling problems [4], [5]. PINNs are a type of deep learning framework that embeds physical laws—often expressed as partial differential equations (PDEs)—into the neural network's training process. Instead of relying solely on labelled input-output pairs, PINNs are trained to predict outputs that both fit observed data and satisfy governing physics. This is achieved by incorporating physics-based constraints, such as PDE residuals, into the loss function alongside data-fitting terms [6]. For instance, PINNs have been employed to enforce structural dynamics and damping evolution equations while matching measured responses [3].

In the context of inverse problems, the primary objective of PINNs is to estimate unknown parameters within partial PDEs based on observed data. PINNs have been applied to various domains, including fluid dynamics, where they determine density, velocity, and pressure fields for one-dimensional Euler equations from observed density gradient data [7]. Rasht et

al.[8] utilised PINNs for seismic imaging, estimating wave speed from observed data in full waveform inversions. Current advancements have further extended the application of PINNs to SHM, particularly in civil engineering structures such as bridges and beams. For example, in the context of railway bridges, PINNs have been employed for structural analysis and monitoring, addressing challenges such as load distribution modelling, SHM, and failure prediction under dynamic train loads [9]. Moreover, studies have demonstrated the ability of PINNs to predict structural response from sparse sensor data, even in the presence of noise for Kirchhoff–Love plates under static loads [10]. These applications highlight the capability of PINNs to integrate data fidelity with physical consistency, making them particularly suitable for SHM tasks, where field measurements are often limited.

However, a key challenge lies in applying PINNs to identify structural parameters of beams subjected to moving loads using real-world data. This research aims to address this challenge by proposing a novel approach that integrates physics-based modelling with real-world monitoring data to improve the accuracy and reliability of structural parameter identification.

The main contributions of this study are as follows:

- The development, training, and validation of PINNs to solve the problem of a bridge girder subjected to a moving load. In doing so, this work addresses the challenge of incorporating higher-order PDEs spanning both spatial and temporal domains.



- Demonstration of how PINNs can predict structural parameters, alongside other outputs such as deflection and its derivatives.
- A thorough examination of the PINNs' performance and predictive accuracy under varying levels of data noise. By testing the models across a range of signal-to-noise ratios, the study evaluates their robustness, providing insights into their reliability and resilience in practical settings where data imperfections are common.
- An investigation of the PINNs' adaptability and generalisation capabilities when trained on real-world monitored data from a bridge.

This paper is organised as follows: Section 2 introduces the problem definition and outlines the methodology. Section 3 provides discussions on Case Studies 1 and 2, along with their respective results. Section 4 presents the conclusions and recommendations for future research.

## 2 METHODOLOGY

This section considers the architecture of a fully connected feedforward neural network and describes the PINNs setup for inverse problems. Specifically, it includes an explanation of PINNs model hyperparameters and the loss function terms for a bridge girder with a moving load. The analysis includes a detailed discussion on the training of PINNs, as well as the investigated and selected hyperparameters of the neural networks.

### 2.1 Neural networks Architecture

The network consists of hidden layers (H), each formulated to process inputs recursively. For each hidden layer  $h$ , where  $h$  ranges from 1 to H, the output  $f(h)$  is determined by Equation (1):

$$f(h) = \sigma(W(h)f(h-1) + b(h)) \quad (1)$$

Here,  $f(0)$  signifies the initial input to the neural network. The function  $\sigma(\cdot)$  denotes the nonlinear activation function, which is crucial for enabling the network to model complex patterns. The weight matrix  $W(h)$  and the bias vector  $b(h)$  pertain to the  $h$ -th hidden layer respectively [11].

The output of the neural network, denoted as  $u$  (i.e., *beam's deflection*), is derived from the last hidden layer's output through the Equation (2):

$$u = W(H+1)f(H) + b(H+1) \quad (2)$$

In this formulation,  $W(H+1)$  and  $b(H+1)$  represent the weight matrix and bias vector of the output layer, respectively. The entire set of parameters within the network, which includes all the weights and biases for each layer, is collectively denoted by  $\theta$  as listed in Equation (3):

$$\theta = \{W(1), b(1), \dots, W(H), b(H), W(H+1), b(H+1)\} \quad (3)$$

This parameter set  $\theta$  encapsulates all elements necessary for the neural network's function, facilitating a unified approach to training and adjustment during the learning process.

The structure of this neural network combines linear operations and nonlinear activation functions. Utilising

activation functions that are infinitely differentiable, such as hyperbolic functions, the architecture enables the calculation of derivatives of any order for the output relative to the input of the neural network via automatic differentiation [4], [5]. These derivatives are instrumental in incorporating basic physical principles into the loss functions used in PINNs.

### 2.2 Framework of PINNs for inverse problems

PINNs presents an approach for addressing forward and inverse problems in partial differential equations (PDEs) across various systems [4]. A typical inverse problem for a simple beam (girder) subjected to a moving can be described by the following formulation:

1. Governing Equation: The Bernoulli-Euler beam theory [12] is widely used to describe beam behaviour under bending. This theory neglects shear deformation and rotational effects [13], which are typically minor in mostly bending conditions. Previous studies [14], [15] have numerically modelled bridges using this theory, focusing on moving loads that simulate vehicular traffic. Therefore, this paper briefly presents only the essential PDE needed for developing PINNs.

For a linearly elastic beam, the vertical deflection,  $u(x, t)$  along the  $z$ -direction satisfies the PDE shown in Equation (4) [14], [16]:

$$EI \frac{\partial^4 u(x, t)}{\partial x^4} + \mu \frac{\partial^2 u(x, t)}{\partial t^2} = P \delta(x - vt) \quad (4)$$

Where:  $\frac{\partial^4 u(x, t)}{\partial x^4}$  is the beam's curvature under bending,  $EI$  is the flexural rigidity,  $\frac{\partial^2 u(x, t)}{\partial t^2}$  represents beam acceleration due to vibration,  $\mu$  is the constant mass per unit length,  $P$  is the moving load magnitude,  $v$  is the load's constant speed,  $\delta$  is the Dirac delta function modelling the instantaneous position of the moving load.

This paper employs a Gaussian-based approach to approximate the Dirac delta function, leveraging its smoothness and regularity [17]. The approximation is defined by Equation (5):

$$P \delta(x - vt) \approx \frac{1}{\beta \sqrt{\pi}} e^{-\frac{(x-vt)^2}{\beta^2}} \quad \text{as } \beta \rightarrow 0 \quad (5)$$

Where  $\beta$  the regularisation parameter governs the approximation's smoothness and accuracy. The  $vt$  term specifies the vehicle's position as the product of speed and time since it entered the structure.

2. Initial (IC) and Boundary (BC) conditions: The beam is assumed to be at rest initially. This is given in mathematical form in Equations (6) and (7). Equation (6) indicates that vertical deflection  $u(x, t)$  is zero along the whole length of the beam at  $T = 0$ , while Equation (7) indicates the beam is perfectly still, experiencing no vibration, at  $T = 0$  [14], [16].

$$u(x, t) = 0 \text{ for } x \in [0, L], \quad T = 0 \quad (6)$$

$$\frac{\partial u}{\partial t}(x, t) = 0 \text{ for } x \in [0, L], \quad T = 0 \quad (7)$$

For a simple beam supports at its two ends. The beam cannot move vertically but is free to rotate about y-axis at these locations, namely at  $x = 0$  and  $x = L$ . The latter necessitates that the corresponding force quantity - the bending moment, which is directly proportional to the beam curvature and computed as the second derivative of  $u(x, t)$ , must always be zero at  $x = 0$  and  $x = L$ . Equations (8), and (9) mathematically represent these boundary conditions.

$$u(0, t) = 0, \text{ and } u(L, t) = 0, \text{ for } t \in [0, T] \quad (8)$$

$$\frac{\partial^2 u}{\partial x^2}(0, t) = 0, \text{ and } \frac{\partial^2 u}{\partial x^2}(L, t) = 0, \text{ for } t \in [0, T] \quad (9)$$

3. Loss function: In this study, we develop PINNs to predict structural parameters and internal forces—such as deflection and moment—in a bridge girder under a moving load of known magnitude and constant speed. Unlike traditional neural networks, which minimise the mean squared error (MSE) using training data, PINNs incorporate additional loss terms to enforce the governing partial differential equation (PDE), initial conditions, and boundary conditions, ensuring physically consistent predictions [18]. Accordingly, let us assume that  $\gamma$  represents parameters related to the physics of the system—some or all of which may be unknown and must be estimated in inverse problems. To achieve this, PINNs are trained to minimise a composite loss function ( $\mathcal{L}$ ), which can be expressed as in Equation (10).

$$\mathcal{L}(\theta) = \alpha_f \mathcal{L}_f(\theta) + \alpha_i \mathcal{L}_i(\theta) + \alpha_b \mathcal{L}_b(\theta) + \alpha_d \mathcal{L}_d(\theta) \quad (10)$$

Where  $\Theta = \{\theta, \gamma\}$ , with  $\theta$  as neural network parameters defined in Equation (3) and  $\gamma$  as unknown physical parameters to be estimated (EI, flexural rigidity),  $\mathcal{L}_f$  for the PDE,  $\mathcal{L}_i$  for the initial conditions,  $\mathcal{L}_b$  for the boundary conditions, and  $\mathcal{L}_d$  for the measured data. Each term is scaled by a corresponding weight— $\alpha_f$ ,  $\alpha_i$ ,  $\alpha_b$ , and  $\alpha_d$ . With prediction of PINNs,  $u(x, t; \theta)$ , the individual loss terms are expressed by Equations (11-15):

$$\mathcal{L}_f(\theta) = \frac{1}{N_f} \sum_{i=1}^{N_f} \|F[g(x_i, t_i; \theta); \gamma]\|^2 \quad (11)$$

$$g(x_i, t_i; \theta) = EI \frac{\partial^4 u(x_i, t_i; \theta)}{\partial x^4} + \mu \frac{\partial^2 u(x_i, t_i; \theta)}{\partial t^2} - P \delta(x_i - vt_i) \quad (12)$$

$$\mathcal{L}_i(\theta) = \frac{1}{N_i} \sum_{i=1}^{N_i} \left\| u(x_i, t_i; \theta) + \frac{\partial u(x_i, t_i; \theta)}{\partial t} \right\|^2 \quad (13)$$

$$\mathcal{L}_b(\theta) = \frac{1}{N_b} \sum_{i=1}^{N_b} \left\| u(x_i, t_i; \theta) + \frac{\partial^2 u(x_i, t_i; \theta)}{\partial x^2} \right\|^2 \quad (14)$$

$$\mathcal{L}_d(\theta) = \frac{1}{N_d} \sum_{i=1}^{N_d} \|D(x_i, t_i; \theta) - u(x_i, t_i; \theta)\|^2 \quad (15)$$

Where  $N_f, N_i, N_b$ , and  $N_d$  are the number of data points (collocation points) in training datasets:

- PDE residual:  $\{(x_i, t_i) : 0 \leq i \leq N_f, 0 \leq x_i \leq L, 0 \leq t_i \leq T\}$
- Initial condition:  $\{(x_i, 0) : 0 \leq i \leq N_i, 0 \leq x_i \leq L\}$ ,
- Boundary condition:  $\{(0, t_i) \text{ and } (L, t_i) : 0 \leq i \leq 2N_b, 0 \leq t_i \leq T\}$ , and
- Data points:  $\{(x_i, t_i) : 0 \leq i \leq N_d, 0 \leq x_i \leq L, 0 \leq t_i \leq T\}$ , respectively.

The minimiser of  $\mathcal{L}(\theta)$  can be expressed by Equation (16):

$$\theta^* = \arg \min_{\theta} \mathcal{L}(\theta) \quad (16)$$

where  $\Theta^* = \{\theta^*, \gamma^*\}$  with  $\theta^*$  and  $\gamma^*$  being the optimal parameters and the estimated unknown parameters, respectively, and  $\arg \min(\cdot)$  is the arguments of the minimum.

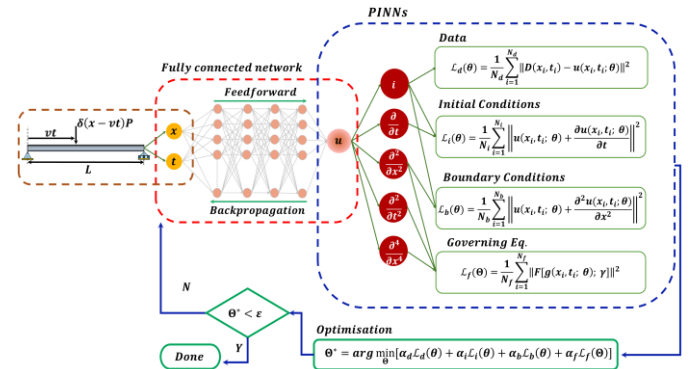


Figure 1. Physics-informed neural networks (PINNs) Schematic for an inverse problem of a beam with moving loads.

### 2.3 Training of PINNs

Figure 1 presents a schematic overview of the PINNs framework configuration. The setup consists of a fully connected feed-forward neural network (NN) that takes spatial and temporal inputs ( $x, t$ ) to predict the solution  $u(x, t)$ —representing the expected deflection at a given location and time on the bridge's girder—and to estimate unknown physical structural parameters ( $\gamma$ ). The training process is guided by the composite loss function defined in Equation (10) and optimised as shown in Equation (16). The training of the PINN is guided by the combined loss function given in Equation (10) and optimised as showed in Equation (16). Training the PINNs involves careful tuning of various hyperparameters, including the number of hidden layers, the number of neurons per layer, the choice of activation functions, the number of collocation points in the training dataset, optimiser configurations, and loss weighting factors.

Table 1 provides a summary of these hyperparameters, detailing their respective ranges and final selected values. The NN architecture, comprising five hidden layers and 64 neurons per layer, was chosen after testing various configurations. The Tanh activation function was selected due to its non-linear characteristics, outperforming others such as ReLU, SiLU, and Sigmoid. The collocation points, set at 2500 for the PDE, 2000

for the boundary conditions, and 1000 for the initial conditions, provide a balance between computational efficiency and the resolution needed to accurately enforce the underlying physics. Adam optimiser was employed for its reliable convergence characteristics, and the learning rate was scheduled to decrease quadratically with epochs, starting from an initial value of  $10^{-2}$ . Additionally, an adaptive loss-weighting strategy was used to balance the various terms, scaling each component relative to the smallest observed loss. Furthermore, the number of training iterations (epochs) was chosen to be 60,000, from a tested range of 10,000–100,000, to achieve robust convergence and accurate results.

The code presented in Table 2 is written in Python [19] and leverages PyTorch [20], a robust deep learning library. The PINNs in this implementation employ the 32-bit single-precision floating-point (FP32) format, which serves as PyTorch's default precision. The training process takes place on a computer system featuring an NVIDIA RTX A4000 GPU and an Intel Core i9-14900K processor.

Table 1. Hyperparameters for PINNs: Tuning ranges and selected values.

Hyperparameter	Range	Chosen Value
No. of Layers	3-9	5
No. of Neurons	32-186	64
Activation function	ReLU, SiLU, Sigmoid, Tanh	Tanh
Collocation points	PDE: 1500-3000	2500
	BC: 1200-2400	2000
	IC: 600-1200	1000
Optimiser	SGD, Adam, L-BFGS-B, Adagrad	Adam
Optimiser Learning rate	Decays quadratically over epochs, based on the following scheduler: $\varphi_0 = 10^{-2}, \varphi_1 = 0.70\varphi_0$ $\varphi_i = \left(1 - \left(\frac{i}{N}\right)^2\right)\varphi_0 + \left(\frac{i}{N}\right)^2\varphi_1, \quad i = 0, \dots, N$ N being the number of epochs.	
loss weighting factors	An adaptive weighting strategy is used [18]: $\alpha_f = \frac{\mathcal{L}_f}{\mathcal{L}_{min}}, \alpha_i = \frac{\mathcal{L}_i}{\mathcal{L}_{min}}, \alpha_b = \frac{\mathcal{L}_b}{\mathcal{L}_{min}}, \alpha_d = \frac{\mathcal{L}_d}{\mathcal{L}_{min}}$ $\mathcal{L}_{min}$ is the minimum among $\mathcal{L}_f, \mathcal{L}_i, \mathcal{L}_b, \mathcal{L}_d$	
Iterations (Epochs)	10,000-100,000	60,000

### 3 CASE STUDIES

The Bascule Bridge in Exeter, as shown in Figure 2, is investigated in this study. The bridge features a 17.28-metre simply supported lifting span, a 6.7-metre-wide carriageway, and a 2-metre-wide footway along the parapet. Its structural configuration includes two longitudinal girders, 17 cross beams, and a composite aluminium deck. This research focuses on the east girder, where sensors measure vertical stiffness. Since the girders are pinned at both ends, each can be approximated as a simply supported beam. The cross beams, bolted to the vertical web stiffeners, primarily transfer shear forces and provide lateral resistance, contributing little to the girders' vertical stiffness. Parameters in Equation (4), outlined in Table 3, are

based on section properties derived from structural drawings supplied by Exeter City Council, Devon, UK, as described in [21].

Table 2. PINNs Pseudo-code for the identification of structural parameters in a beam under moving loads.

#### Algorithm

**Input:** Spatial and temporal collocation points and measured data  $(x_i, t_i)$ .

**Output:** Optimal parameters  $\theta^*$  and estimated unknown parameters  $\gamma^*$ :  $\theta^* = \{\theta^*, \gamma^*\}$ .

#### Initialisation:

- 1: Initialise neural network architecture parameters  $\theta$
- 2: Generate random dataset for  $N_f, N_i$  and  $N_b$
- 3: Prepare the measured data points  $N_d$
- 4: Define the total loss functions:  $\mathcal{L}(\theta) = \alpha_f \mathcal{L}_f(\theta) + \alpha_i \mathcal{L}_i(\theta) + \alpha_b \mathcal{L}_b(\theta) + \alpha_d \mathcal{L}_d(\theta)$
- 5: Initialise the loss weights:  $\alpha_f, \alpha_i, \alpha_b, \alpha_d$
- 6: Initialise the structural parameters  $\gamma$

#### Training:

- 7: Set the optimiser: Adam.
- 8: Set  $N$ : Define the maximum number of training iterations
- 9: **WHILE** converge not reached **DO**
- 9.1: **FOR**  $k = 1$  to  $N$  **DO**
- 9.2: **FOR** each batch of points in  $N_f, N_i, N_b, N_d$  **DO**
- 9.3: Compute loss function:
  - $\mathcal{L}_f(\theta)$ : PDE residual at  $N_f$
  - $\mathcal{L}_i(\theta)$ : Initial condition at  $N_i$
  - $\mathcal{L}_b(\theta)$ : Boundary condition at  $N_b$
  - $\mathcal{L}_d(\theta)$ : Measured data mismatch at  $N_d$
- 9.4: Update loss function weights  $\alpha_f, \alpha_i, \alpha_b, \alpha_d$
- 9.5: **END FOR**
- 9.6: Compute the total loss  $\mathcal{L}(\theta)$
- 9.7: Update parameters  $\theta = \{\theta, \gamma\}$  using Adam optimiser based on the gradient of  $\mathcal{L}(\theta)$
- 9.10: **END FOR**
- 9.11: **END WHILE**
- 10: Save the trained model: Store the optimised parameters  $\theta^* = \{\theta^*, \gamma^*\}$
- 11: Deploy the model: Use the trained PINNs to predict the structural response.

Table 3. Dimensions and properties of the Bascule bridge main girder (symmetrical I-section).

Dimensions	Value	Properties	Value
Length	17.28 m	Elastic Modulus (E1)	205 GPa
Depth	926.60 mm	Moment inertia (I)	$50.40 \times 10^8 \text{ mm}^4$
Flange width	307.70 mm	Mass per unit length ( $\mu$ )	289 kg/m
Flange thickness	32 mm		
Web thickness	19.50 mm		





Figure 2. Bascule bridge, constructed in 1972, carrying the A379 over the Exeter Canal in Devon, England, UK.

### 3.1 Case Study 1

In this case study, PINNs are trained to model the effects of a 37 kN axle load, representing the front axle of a truck. This axle load magnitude corresponds to those used in a controlled loading test previously conducted on the Bascule Bridge, as detailed in [22]. The truck's total load consisted of front axles weighing 67.20 kN and rear axles weighing 89.80 kN each. Axle spacing was 2.00 metres between the first and second axles, 3.10 metres between the second and third, and 1.40 metres between the third and fourth. During the test, the truck crossed the bridge in 3.342 seconds, travelling in the lane closest to the east girder, which was estimated to bear approximately 55% of the total load. For the time configuration, the front axle is estimated to take a total of 2.43 seconds to cross the bridge. This timing reflects the sequence and delay with which each of the four axles engages with the bridge as observed during the field tests. Based on these observations, the first front axle enters the bridge at  $t = 0$ , and the fourth rear axle exits at  $t = 3.342$  seconds. The truck's speed is calculated using the span length of the bridge (17.28 m), the distance between the first and fourth axles (6.50 m), and the total crossing time of 3.342 seconds. This yields a vehicle speed of 7.115 m/s. Using this speed and the known axle spacings, the times at which the first front axle entered and exited the bridge are determined.

### 3.2 Synthetic data under varying signal-to-noise ratios

In this case study, the objective is to estimate the bridge's main girder flexural stiffness (EI), deflection, and its derivatives. This requires generating training data for the PINN model, as described in Section 2. To achieve this, we developed a finite element (FE) model comprising 10 beam elements in ANSYS APDL [23]. The model was solved using a transient analysis with 1,000-time steps, providing the synthetic data needed for training. A total of 100 points were randomly selected across the spatial and temporal domains to represent the deflection solution. However, SHM data often contain noise due to environmental and operational factors, such as temperature fluctuations, variable live loads, and sensor inaccuracies. To reflect these real-world conditions, we introduced white Gaussian noise into the simulated data. Incorporating this noise increases the fidelity of the synthetic data, making it more representative of the challenges encountered in real-world SHM

data analysis. In addition to estimating the girder's stiffness and deflection, another objective of this study was to assess the adaptability and performance of PINNs when trained with and without noise.

Various noise levels are evaluated by considering different signal-to-noise ratios (SNRs). White Gaussian noise is added to the deflection data generated by the finite element (FE) model, as defined by Equation (17):

$$u_{noise} = u + \mathcal{N}(0, \sigma^2) \quad (17)$$

Where  $u$  is the true deflection predicted by the FE model, and  $\mathcal{N}(0, \sigma^2)$  represents white Gaussian noise with a mean of zero and a standard deviation  $\sigma$  determined by the target SNR. The SNR in decibels (dB), is given by Equation (18):

$$SNR(dB) = 10 \log_{10} \left( \frac{\text{Signal Power}}{\text{Noise Power}} \right) \quad (18)$$

In this study, four SNR levels—10, 20, 30, and 40 dB—are considered and are illustrated in Figure 3. A lower SNR, such as 10 dB, indicates significant noise levels, making the prediction task more challenging. In contrast, a higher SNR, like 40 dB, suggests that noise has only a minor effect.

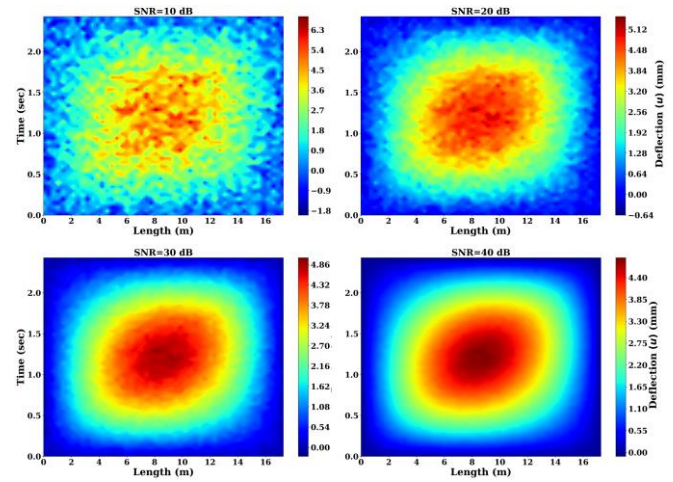


Figure 3. Influence of signal-to-noise ratio (SNR) on deflection data quality.

### 3.3 Results and discussion of Case Study 1

The results presented in Tables 4 and 5 highlight the performance of the PINNs in predicting the flexural rigidity (EI) and internal forces (deflection and moment) of a Bascule bridge girder under various signal-to-noise ratio (SNR) conditions. The analysis assesses prediction accuracy using relative error percentages (Re%) for EI, as well as Root Mean Square Error (RMSE), Coefficient of Variation (CV%), and Normalised Mean Bias (NMB%) metrics for deflection ( $u$ ) and moment ( $M_x$ ) at different time instances. Table 4 indicates that PINNs can provide accurate estimates of EI even in noisy conditions. When using clean data, the relative error is only 0.24%. As noise increases, the error rises slightly, reaching 0.96% at 10dB. However, the PINNs still demonstrate strong robustness, with errors staying below 1% even under the lowest SNR conditions. For higher SNR levels, such as 30dB and 40dB, the errors drop

to 0.34% and 0.29%, respectively. This trend confirms that the PINNs can effectively handle varying noise levels, maintaining a high degree of accuracy in estimating the bridge girder's flexural rigidity.

Table 5 examines deflection and moment predictions at different time instances under varying SNR conditions. As expected, lower SNR values lead to higher RMSE, CV, and NMB percentages, reflecting the impact of noise on prediction accuracy. For instance, at 10dB, deflection RMSE ranges from 0.161 mm to 0.178 mm, and CV percentages are as high as 8.26%. In contrast, under a better condition (30dB and 40dB), these values are significantly reduced, with RMSE as low as 0.036 mm and CV percentages dropping to around 1.45%–2.05%. The moment prediction metrics follow a similar pattern, showing that as SNR improves, RMSE and CV percentages consistently decrease. The results of this case study demonstrate that PINNs can accurately predict both flexural rigidity and internal forces in a bridge girder, showing robustness against noise and the potential for practical application in SHM tasks.

Furthermore, Figure 4 illustrates the ability of the PINN trained with data of 40 dB SNR to accurately predict both the beam's deflection and its internal forces, including moments. The data presented in the figure corresponds to a specific time instance,  $t = 1.22$  seconds. Although this example focuses on a single time point for demonstration purposes, the PINN methodology can similarly generate deflection and its derivatives at any chosen moment.

The results displayed in the figure highlight an agreement between the PINN predictions and the FE results. The PINN accurately reproduces the deflection and moment profiles along the beam, aligning closely with the established FE data. This consistent match provides further validation of the PINN's reliability and effectiveness.

Table 4. PINNs predictions of flexural rigidity (EI) for a Bascule bridge girder across varying SNR.

SNR	EI Actual (N.m <sup>2</sup> )	EI predicted (N.m <sup>2</sup> )	Re%
Clean	1,033,610	1,036,091	0.24
10dB	===	1,043,533	0.96
20dB	===	1,041,879	0.80
30dB	===	1,037,124	0.34
40dB	===	1,036,607	0.29

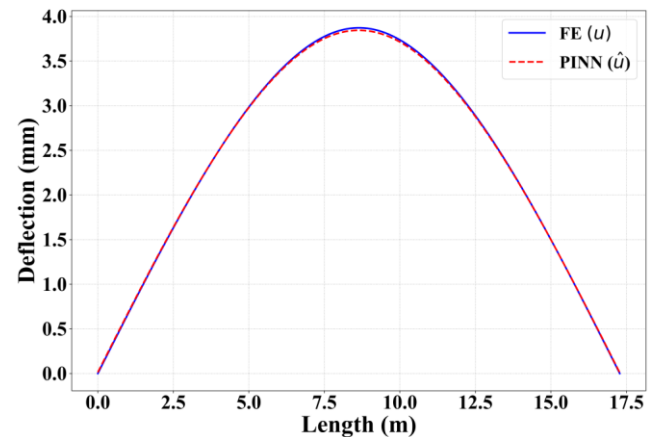
### 3.4 Case Study 2

In this case study, a PINN model is used to predict the flexural rigidity and structural behaviour of a girder, informed by strain measurements from sensors installed on the bridge's main girder during a truck crossing. The objective is twofold: to examine the PINN's ability to represent real-world structural behaviour and to assess how measurement data influences its accuracy and generalisation. Four weldable strain gauges were installed, two on the top flange (S1 and S2) and two on the bottom flange (S3 and S4), to measure bending strains along the girder's longitudinal axis as shown in Figure 5. These sensors, featuring a 5.84 mm active grid length and a resistance of 120  $\Omega$ , were deployed and documented as detailed in [12]. The strain data were collected at 2000 Hz, then baseline-adjusted and smoothed. Figure 6 illustrates the strain time histories

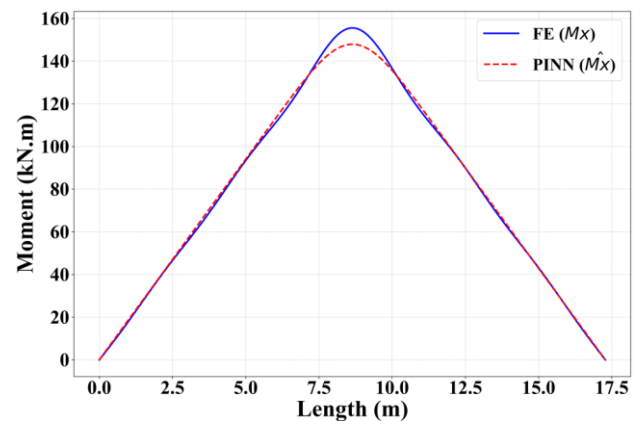
recorded by sensors S1 to S4, confirming that the truck took approximately 3.342 seconds to cross, consistent with Case Study 1.[22].

Table 5. PINNs predictions metric errors of deflection and moment for a Bascule bridge girder across varying SNR and different time instances.

SNR	Time (Sec)	Deflection (u)			Moment (Mx)		
		RMSE (mm)	CV %	NBM %	RMSE (kN.m)	CV %	NBM %
Clean	0.60	0.013	0.62	-0.02	3.06	4.07	-0.89
	1.22	0.017	0.57	-0.27	2.94	2.94	-0.18
	1.82	0.014	0.67	-0.32	3.19	4.30	0.37
10dB	0.60	0.161	7.51	7.52	2.75	3.66	-0.13
	1.22	0.178	5.91	5.90	2.90	2.91	0.56
	1.82	0.175	8.26	8.24	3.09	4.16	0.99
20dB	0.60	0.055	2.56	2.13	3.83	5.10	-2.35
	1.22	0.050	1.67	1.09	3.50	3.51	-1.13
	1.82	0.038	1.81	1.51	3.42	4.62	-1.12
30dB	0.60	0.096	4.49	4.44	3.16	4.21	-1.00
	1.22	0.087	2.91	2.84	3.12	3.12	-0.24
	1.82	0.059	2.80	2.74	3.29	4.44	-0.28
40dB	0.60	0.036	1.67	1.52	2.97	3.96	-0.57
	1.22	0.044	1.45	1.29	2.88	2.89	0.25
	1.82	0.044	2.05	1.98	3.29	4.43	0.81



(a) Beam deflection ( $u$ , mm)



(b) Moment distribution ( $M_x$ , kN.m)

Figure 4: Case Study 1 – comparing PINNs predictions to finite element (FE) results: (a) beam deflection and (b) moment distribution at  $t = 1.22$  seconds.

Unlike Case Study 1, which trained the PINN on a single axle load, this case study models the effect of the entire truck. The truck is represented as four axle loads, spaced at known intervals. The combined load function is approximated as a sum of Dirac delta functions,  $\delta_j$ , which are expressed in Equations (19) and (20). The load ( $P$ ) due to all axles is formulated as:

$$P = \sum_{j=1}^4 p_j \cdot \delta_j(t_j, v, L) \quad (19)$$

Where  $\delta_j(t_j, v, L)$  is defined as:

$$\delta_j(t_j, v, L) = \frac{1}{\beta\sqrt{\pi}} e^{-\frac{(x-v(t-t_j))^2}{\beta^2}} \quad (20)$$

The parameters are:  $L$ , the beam length;  $v$ , the vehicle speed;  $p_j$ , the load for the  $j$ -th axle;  $\beta$ , the regularisation parameter of the Gaussian approximation for  $\delta_j$ ; and  $t_j$ , the time lag for the  $j$ -th axle relative to the first. Incorporating this Dirac delta approximation into the governing PDE yields Equation (21):

$$EI \frac{\partial^4 u(x, t)}{\partial x^4} + \mu \frac{\partial^2 u(x, t)}{\partial t^2} = \sum_{j=1}^4 p_j \cdot \delta_j(t_j, v, L) \quad (21)$$

In addition, the PINN training process includes a data loss term,  $\mathcal{L}_D$  as defined in Equation (15), which quantifies the discrepancy between sensor measurements and the PINN's predicted strains. The strain  $\varepsilon$  is linked to the beam's curvature  $\frac{d^2 u(x, t)}{dx^2}$ , as shown in Equation (22):

$$\varepsilon = -y \frac{d^2 u(x, t)}{dx^2} \quad (22)$$

Here,  $y$  is the distance from the neutral axis. This relationship allows  $\mathcal{L}_D$  to be computed by comparing measured and predicted strains. The formulation of  $\mathcal{L}_D$  is given in Equation (23):

$$\mathcal{L}_D(\theta) = \frac{1}{N_d} \sum_{i=1}^{N_d} \left\| -y \frac{d^2 u(x_i, t_i; \theta)}{dx^2} - \varepsilon(x_i, t_i; \theta) \right\|^2 \quad (23)$$

$\mathcal{L}_D$  is then incorporated into the overall loss function (Equation 10) to guide the PINN's training and improve its alignment with the observed data.

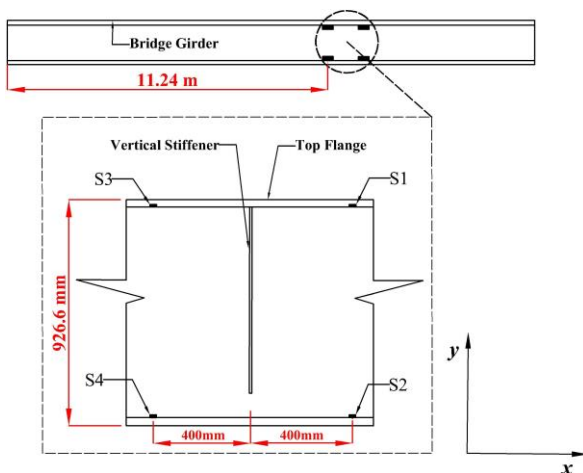


Figure 5. Illustration depicting the positions of weldable strain gauges on the main girder (side view) of a bascule bridge.

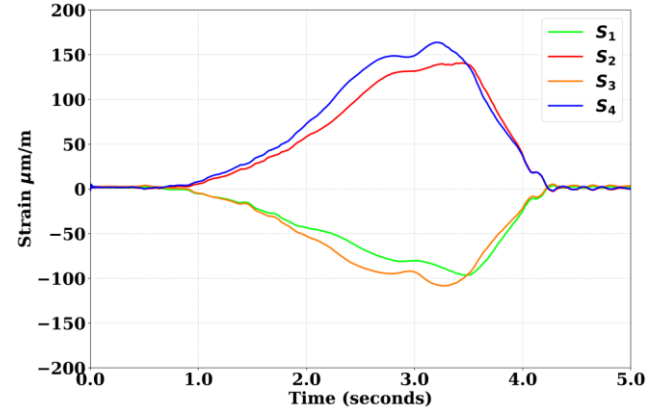


Figure 6. Raw strain measurements from sensors S1 to S4 on the main girder of a bascule bridge as a truck crossed.

### 3.5 Results and discussion of Case Study 2

The results presented in Table 6 highlight the impact of incorporating real-world strain measurements on the accuracy of PINN predictions for the bridge girder's flexural rigidity (EI). When trained without sensor data, the PINN predicted an EI value that deviated from the actual parameter by over 14%, underscoring the limitations of relying solely on physics-informed constraints. In contrast, the inclusion of strain data from only one sensor S2 reduced the relative error to approximately 1.6%, demonstrating a substantial improvement in predictive performance. This outcome suggests that integrating field measurements enables the PINN to capture the structural behaviour more effectively, enhancing its generalisation and reliability. The ability of PINNs to leverage sparse sensor data offers advantages for SHM applications, providing engineers with more precise estimates of key structural parameters. Additionally, Figure 7 demonstrates the predictive efficacy of the PINN trained with measured data. The model was trained utilising strain data from sensor S2, with the sensor's location and strain time profile shown in Figures 5 and 6, respectively. The displayed results indicate the model's prediction at the position of sensor S4. Accordingly, the results underline the potential for PINNs, when combined with real-world data, to serve as robust tools for both assessing current structural performance.

Table 6. PINN predictions of flexural rigidity (EI) for a Bascule bridge girder with and without sensor Data.

Strain data	EI Actual (N.m <sup>2</sup> )	EI predicted (N.m <sup>2</sup> )	Re%
No	1,033,610	1,178,315	14.16
Yes	===	1,050,458	1.63



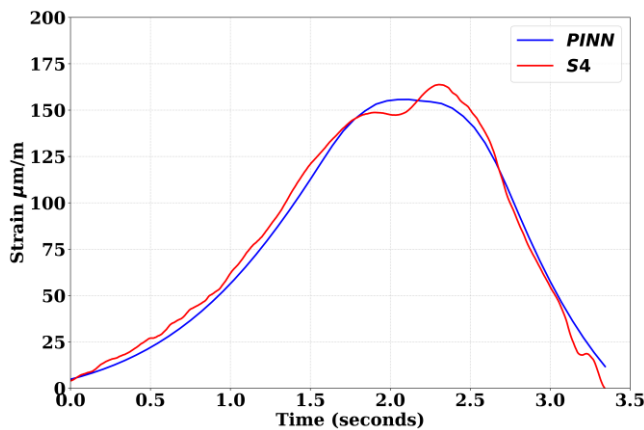


Figure 7. Comparison of strain time history predicted by PINN and measurements from sensor S4.

#### 4 CONCLUSIONS

This study demonstrates the application of a physics-informed neural network (PINN) framework to accurately predict both structural parameters — flexural rigidity (EI) — and structural responses (e.g., deflections and moments) of a bridge girder under a moving load. The investigation is based on two case studies that evaluate the PINN's performance, accuracy, and generalisability, offering valuable insights into its practical application for SHM. In Case Study 1, the PINN was trained under varying levels of synthetic noise to assess its robustness. In Case Study 2, the PINN's ability to integrate real-world strain measurements was explored. Using field measurements, the model achieved significant improvement in prediction accuracy.

The following points summarise the key outcomes from this study:

1. The PINN maintained reasonable accuracy even at low signal-to-noise ratios (SNRs), with predictions becoming increasingly reliable as noise levels decreased. The study revealed that at higher SNRs, the PINN effectively captured the bridge's flexural rigidity, achieving relative errors below 1% and confirming its capacity for precise parameter estimation.
2. In Case Study 2, the PINN trained without sensor data overestimated the girder's flexural rigidity. Incorporating field measurements reduced the relative error from 14% to approximately 1.6%. This demonstrates the value of integrating field data into the PINN framework, enabling more accurate reflection of real-world structural behaviour.
3. The study showed that even a limited number of strain sensors could provide sufficient constraints to enhance the PINN's generalisation and performance, reinforcing its practical utility.
4. The findings show that integrating field measurements not only enhances the accuracy of the flexural rigidity estimation but also allows the model to reflect actual structural behaviour. This demonstrates the PINNs' potential as a practical tool for SHM.

Overall, this research illustrates a novel application of PINNs and contributes to the existing body of knowledge in structural

health monitoring (SHM) by introducing a PINN-based approach for estimating the structural parameters of bridge girders. Future work will focus on extending the use of PINNs to damage detection scenarios and integrating multiple PINNs to model more complex structural systems comprising assemblies of discrete elements.

#### DATA AVAILABILITY

Data will be made available on request.

#### ACKNOWLEDGMENTS

The first author would like to acknowledge the financial support of The Higher Committee for Education Development in Iraq (HCED) scholarship reference D-14-2968.

#### REFERENCES

- [1] E. Figueiredo and J. M. W. Brownjohn, "Three Decades of Statistical Pattern Recognition Paradigm for SHM of Bridges," *Struct Health Monit*, vol. 21, no. 6, pp. 3018–3054, 2022, doi: 10.1177/14759217221075241.
- [2] R. Chacón, J. R. Casas, C. Ramonell, H. Posada, I. Stipanovic, and S. Škarić, "Requirements and Challenges for Infusion of SHM Systems Within Digital Twin Platforms," *Structure and Infrastructure Engineering*, pp. 1–17, 2023, doi: 10.1080/15732479.2023.2225486.
- [3] T. Liu and H. Meidani, "Physics-Informed Neural Networks for System Identification of Structural Systems with a Multiphysics Damping Model," *J Eng Mech*, vol. 149, no. 10, Oct. 2023, doi: 10.1061/jenmdt.emeng-7060.
- [4] M. Raissi, P. Perdikaris, and G. E. Karniadakis, "Physics-Informed Neural Networks: A Deep Learning Framework for Solving Forward and Inverse Problems Involving Nonlinear Partial Differential Equations," *J Comput Phys*, vol. 378, pp. 686–707, 2019, doi: 10.1016/j.jcp.2018.10.045.
- [5] S. Cuomo, V. S. Di Cola, F. Giampaolo, G. Rozza, M. Raissi, and F. Piccialli, "Scientific Machine Learning Through Physics-Informed Neural Networks: Where we are and What's Next," *J Sci Comput*, vol. 92, no. 3, pp. 1–62, 2022, doi: 10.1007/s10915-022-01939-z.
- [6] M. Raissi, P. Perdikaris, and G. E. Karniadakis, "Inferring Solutions of Differential Equations Using Noisy Multi-Fidelity Data," *J Comput Phys*, vol. 335, pp. 736–746, 2017, doi: 10.1016/j.jcp.2017.01.060.
- [7] Z. Mao, A. D. Jagtap, and G. E. Karniadakis, "Physics-Informed Neural Networks for High-Speed Flows," *Comput Methods Appl Mech Eng*, vol. 360, no. 112789, 2020, doi: 10.1016/j.cma.2019.112789.
- [8] M. Rasht-Behesht, C. Huber, K. Shukla, and G. E. Karniadakis, "Physics-Informed Neural Networks (PINNs) for Wave Propagation and Full Waveform Inversions," *J Geophys Res Solid Earth*, vol. 127, no. 5, May 2022, doi: 10.1029/2021JB023120.
- [9] Y. Martinez, L. Rojas, A. Peña, M. Valenzuela, and J. Garcia, "Physics-Informed Neural Networks for the Structural Analysis and Monitoring of Railway Bridges: A Systematic Review," *Mathematics*, vol. 13, no. 10, p. 1571, May 2025, doi: 10.3390/math13101571.
- [10] A. I. F. Al-Adly and P. Kripakaran, "Physics-informed neural networks for structural health monitoring: a case study for Kirchhoff–Love plates," *Data-Centric Engineering*, vol. 5, p. e6, 2024, doi: 10.1017/dce.2024.4.
- [11] I. J. Goodfellow, Y. Bengio, and A. Courville, *Deep Learning*. MIT Press, 2016.
- [12] S. P. Timoshenko, *History of Strength of Materials*. New York: McGraw-Hill, 1953.
- [13] J. M. Gere and S. Timoshenko, *Mechanics of Materials*. in *Mechanics of Materials*. PWS Publishing Company, 1997.
- [14] Ladislav Fryba, *Vibration of Solids and Structure under Moving Loads*, vol. 3rd edition. Thomas Telford (ICE Publishing), 1999.
- [15] John M. Biggs, *Introduction to Structural Dynamics*. New York: McGraw-Hill, 1964.
- [16] L. Meirovitch, *Analytical Methods in Vibrations*. United State of America: The Macmillan Company, 1967.

- [17] S. A. Eftekhar, "A differential quadrature procedure with regularization of the Dirac-delta function for numerical solution of moving load problem," *Latin American Journal of Solids and Structures*, vol. 12, no. 7, pp. 1241–1265, 2015, doi: 10.1590/1679-78251417.
- [18] H. M. Zhang, X. Shao, Z. F. Zhang, and M. Y. He, "E-PINN: extended physics informed neural network for the forward and inverse problems of high-order nonlinear integro-differential equations," *Int J Comput Math*, vol. 101, no. 7, pp. 732–749, 2024, doi: 10.1080/00207160.2024.2374820.
- [19] G. Van Rossum and F. L. Drake, "Python Language Reference, version 3.11," 2022, Python Software Foundation.
- [20] J. Ansel et al., "PyTorch 2: Faster Machine Learning Through Dynamic Python Bytecode Transformation and Graph Compilation," in *Proceedings of the 29th ACM International Conference on Architectural Support for Programming Languages and Operating Systems*, Volume 2, in *ASPLOS '24*. New York, NY, USA: Association for Computing Machinery, 2024, pp. 929–947. doi: 10.1145/3620665.3640366.
- [21] J. Kwad, "Estimating fatigue life of steel bridges using continuous response monitoring: Methodology and applications," Doctor of Philosophy in Engineering, University of Exeter, 2018.
- [22] J. Kwad and P. Kripakaran, "Hybrid approach combining modelling and measurement for fatigue damage estimation of welded connections in bridges," *Structure and Infrastructure Engineering*, vol. 17, no. 1, pp. 20–33, 2021, doi: 10.1080/15732479.2020.1730407.
- [23] Ansys, "ANSYS Workbench, Release number 2023 R1, Help System, Theory Guide, ANSYS, Inc.," 2023, ANSYS, Inc., Canonsburg, USA: Release number 2023 R1.

# Structural Health Monitoring of a suspended steel infrastructure: A statistical approach

Nicola Molon<sup>1</sup>, Filippo Casarin<sup>2</sup>, Alessandro Targa<sup>3</sup>, Renzo Codato<sup>4</sup>, Francesca da Porto<sup>1</sup>

<sup>1</sup> University of Padova, Dept. of Geosciences, Via Gradenigo 6, 35131 Padova, Italy

<sup>2</sup> Expin srl, via Pisacane 34, 35138 Padova, Italy

<sup>3</sup> Alessandro Targa – studio di ingegneria, viale dell'Industria 23/B – 35129 Padova, Italy

<sup>4</sup> Veneta Sanitaria Finanza di Progetto S.p.a., via Paccagnella 11, 30174 Mestre, 30174 - Venezia, Italy

email: nicola.molon@phd.unipd.it, casarin@labexpin.com, alessandro@studiotarga.com, rcodato@vsfp.it, francesca.daporto@unipd.it

**ABSTRACT:** The inspection, maintenance and monitoring of existing infrastructure are critical aspects for ensuring a proper structural performance during their lifespan, also guaranteeing their capacity vs. the ultimate limit state. The use of structural health monitoring systems has become increasingly important for managing infrastructural assets, not only to detect structural damages and degradation phenomena but also to evaluate the performance of structures subjected to retrofit interventions. This is achieved using signal processing techniques that integrate statistical methods and machine learning algorithms within the framework of statistical pattern recognition. The proposed framework introduces a novel statistical analysis framework aimed at characterizing the *normal* behaviour of structures, detecting potential damage development. The method is applied to a suspended steel truss healthcare facility, demonstrating its effectiveness in characterizing its typical structural behaviour, detecting any onset of possible structural decay. While the method is demonstrated on a specific case study, it is designed to be adaptable to a wide range of structural systems. The ultimate objective is to develop a reliable analysis tool for the early detection of damage, thereby enhancing the efficiency of maintenance strategies and ensuring long-term structural safety.

**KEY WORDS:** Structural health monitoring, statistical pattern recognition, damage detection, data analysis.

## 1 INTRODUCTION

Infrastructure systems play a crucial role in modern society, making it essential to ensure their functionality under both normal and extraordinary loading conditions. Maintenance, inspections, and structural monitoring are fundamental for preserving resilience [1]. In recent decades, traditional inspection systems have been increasingly replaced by structural health monitoring (SHM) systems, particularly for structures that are highly exposed to atmospheric actions and external loads, such as bridges and wind turbines [2], but also for historical buildings [3], [4]. SHM has been introduced to support owners and authorities to find optimal life-cycle management solutions and, ultimately, to prevent structural failures. This is achieved through a damage identification strategy, which encompasses the detection, diagnosis, and prognosis of damage [5].

These systems rely on the implementation of a monitoring-based strategy, which includes real-time measurement of structural responses and data analysis to identify anomalies and/or damage at an early stage [6]. In this context, damage is defined as any alteration in the material and/or geometric properties of bridge components that negatively affect the bridge's current or future service performance and safety [5]. Another significant application of SHM systems involves the assessment of retrofit interventions on existing structures. Specifically, SHM can be used to determine the most suitable intervention strategy, evaluate the structural response after the intervention, and monitor the structure's behaviour throughout the different phases of the intervention [7], [8].

This study proposes a robust framework for processing SHM data from existing infrastructure, with the goal of enabling early detection of structural anomalies or damage. The

proposed methodology combines time series modelling using statistical algorithms for the characterization of normal structural behaviour, filtering out environmental influences—such as temperature—and identifying deviations indicative of potential structural issues.

The manuscript is structured as follows: Section 2 describes the case study and presents the initial analyses conducted on the structure; Section 3 introduces the SHM data and provides preliminary evaluations; Section 4 details the proposed data analysis framework and its application to the case study; finally, Section 5 presents the conclusions and outlines directions for future research.

## 2 DESCRIPTION OF THE CASE STUDY

The analysed structure is a suspended steel truss that serves as the roof of a strategic infrastructure located in northern Italy. The building was completed in 2008. This structure is particularly complex because, as illustrated in Figure 1, the truss system supports the upper three floors through steel columns subjected to tensile stresses. The roof is directly connected to continuous concrete walls that extend from the foundations to the roof.

The building, and specifically its roof, underwent a retrofit intervention aimed at enhancing the strength of the connections within the roof structure. Following the retrofit process, the installation of a SHM system was defined with the objective of assessing the effectiveness of the strengthening interventions, monitoring the real time safety conditions of the structure, and supporting infrastructure owners in identifying optimal life-cycle management solutions.



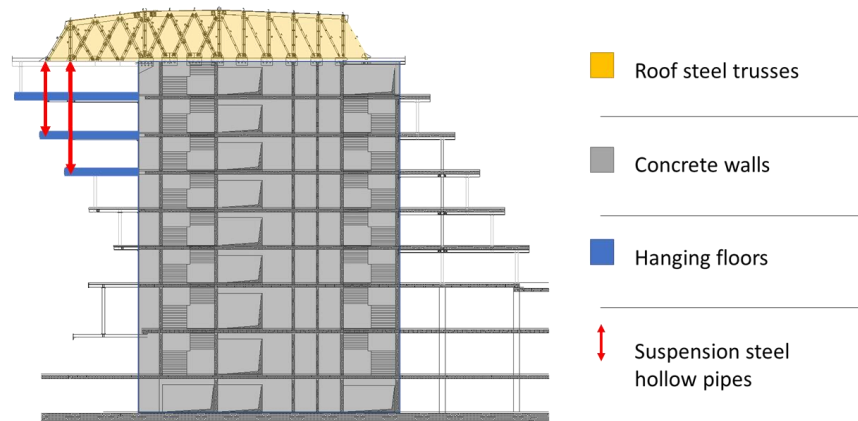


Figure 1. Schematic representation of the structure

### 2.1 Operational modal analysis of the case study

Before the design of the SHM system an operational modal analysis (OMA) was performed with the aim of identify dynamic parameters of the steel truss structure and better understand the complex behaviour of the entire steel structure. This type of analysis is commonly performed on various types of structures like bridges [9], historical buildings [10], and timber structures [11].

The OMA was performed by installing eight piezoelectric monoaxial accelerometers in different positions and configurations on the roof, resulting in a total of 33 measurement locations. The results of the modal identification are presented in Figure 2.

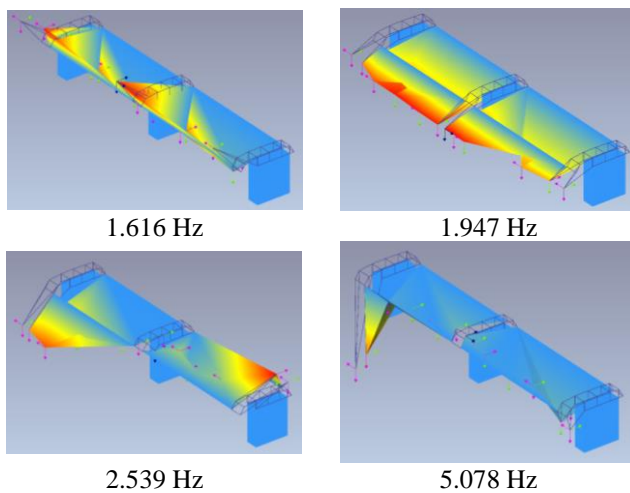


Figure 2. First mode shapes of the structure

These results indicate that the longitudinal and transverse modes exhibit a behaviour involving the overall structure, whereas vertical modes are related to individual truss elements, without demonstrating a global structural response. Table 1 presents the modal frequencies and the corresponding complexity of the mode shapes obtained from the OMA analysis. The analysis was conducted using the frequency domain decomposition method with Artemis Modal Pro software.

Table 1. Principal vibration frequencies

Mode type	Frequency [Hz]	Complexity [%]
1 <sup>st</sup> Longitudinal	1.66	0.899
1 <sup>st</sup> Transversal	1,953	1,741
2 <sup>nd</sup> Transversal	2,539	5,886
1 <sup>st</sup> Vertical	5,078	18,075
2 <sup>nd</sup> Vertical	16.992	6.052
3 <sup>rd</sup> Vertical	17.969	19.657

### 2.2 Description of the monitoring system

The SHM system was installed in 2021 to monitor both static and dynamic parameters, enabling the acquisition of the structure's modal characteristics and the evaluation of stress in the most heavily loaded elements of the truss roof. Additionally, thermocouples and ambient temperature sensors were implemented to assess the environmental conditions of the site, as temperature is one of the primary sources of variability in structural systems [12]. The setup for the analysis of vibration characteristics was based on the results of the OMA analysis reported in section 2.1. In this context, 11 uniaxial piezoelectric accelerometers were installed on the steel truss elements.

Ambient temperature sensors were installed in two different locations to assess variations in ambient temperature and humidity within the roof structure. Additionally, a wind sensor was used to investigate potential interactions between this external load and the structural behaviour of the building.

The data acquisition system selected for the monitoring system is structured around a primary acquisition unit (master), which is connected to the infrastructure's LAN for remote data transmission. This master unit is linked to two subordinate units (slaves) via a backbone running along the extrados of the roof, which, in turn, are connected to both static and dynamic sensors. Figure 3 shows the configuration of the SHM system implemented for the case study.

The evaluation of stresses was conducted through the installation of 24 vibrating wire strain gauges on the truss elements, equipped with an internal temperature sensor, complemented by 4 steel thermocouples to assess the influence of temperature on the steel elements. Both types of sensors were welded onto the steel elements of the roof structure, as shown in the configuration presented in Figure 4. A relevant

number of sensors was installed on the vertical steel elements connecting the lower floors to the roof, as these components are critical to the floor stability.

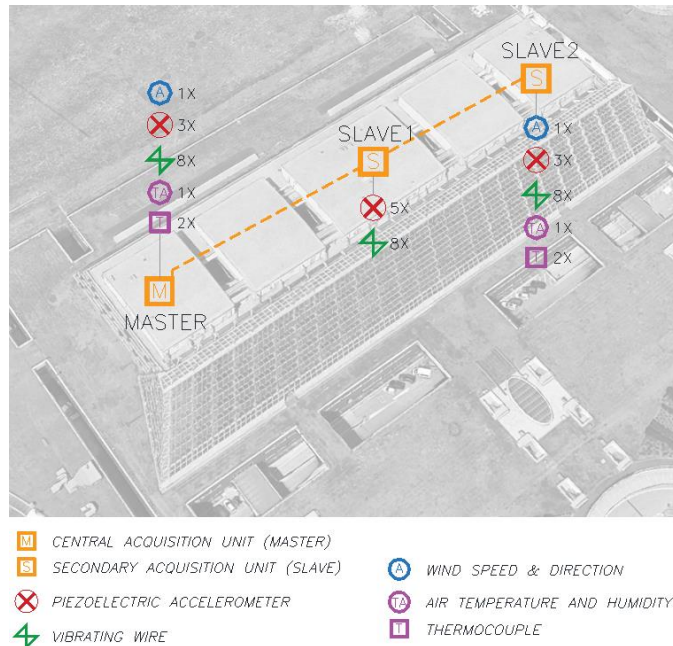


Figure 3. Configuration of the SHM system

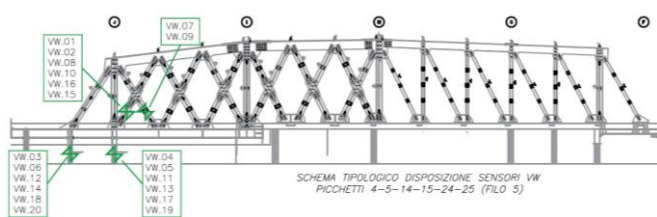


Figure 4. Typological configuration of vibrating wire strain gauges and thermocouple sensors in the truss structure

### 3 ANALYSIS OF THE MONITORED DATA

In this paper, only the data related to the static sensors are presented, with a particular focus on the analysis of strain sensor measurements.

Figure 5 illustrates the strain behaviour over a three-year period for five sensors. In some of that, such as VW.01 and VW.03, strain variations closely follow seasonal temperature fluctuations. Conversely, in other cases, such as VW.02, the strain behaviour appears independent of temperature variations.

This observation is further emphasized by analysing the correlation between strain sensor data and temperature variations. In Figure 6 the strain measurements are plotted against ambient temperature fluctuations to assess the extent to which thermal effects influence structural behaviour. This comparative analysis helps distinguish temperature-dependent responses from other potential factors affecting strain variations.

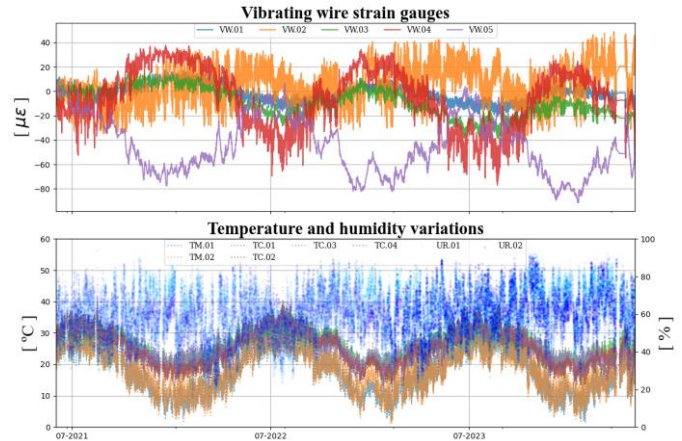


Figure 5. Strain sensors behaviour – block A

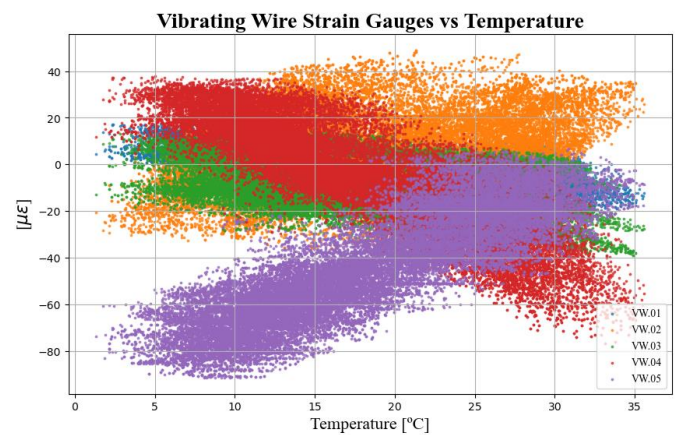


Figure 6. Representation of the strain observation against the temperature value

The behaviour of some sensors exhibits a linear correlation with temperature, whereas others do not show this dependence, as observed in the cases of VW.02 and VW.06. Noticeably, VW.02 appears to be completely uncorrelated with temperature; however, distinct patterns can still be identified. Specifically, its behaviour reflects a horizontal translation of an inclined line along the horizontal axis.

This pattern is influenced by temperature variations occurring during specific periods of the year. When analysing the behaviour of an individual sensor in relation to temperature, with measurements categorized by month (Figure 7), it becomes evident that each period of the year corresponds to a distinct structural state of the element. Furthermore, after one year, the sensor's behaviour tends to return to a state similar to that of the previous year, indicating a recurring annual trend.

After an on-site inspection, it was found that this behaviour was likely caused by friction grip bolted connections which, due to possible loss of preload, converted into standard shear connections. As a result, the structural elements exhibited a different behaviour compared to the expected response of roof elements subjected to daily and seasonal temperature variations. It emerged that some sensors exhibited a typical linear relationship with temperature variations, while others displayed a distinct behaviour characterized by multiple linear trends that were temperature dependent.

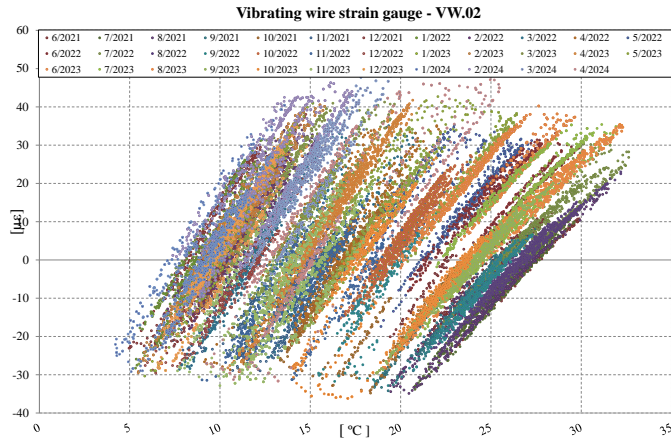


Figure 7. Representation of strain sensor respect to external temperature, divided by period

#### 4 STATISTICAL ANALYSIS OF THE STATIC SENSORS

The adopted methodology consists of several phases. First, a data-cleaning process is performed on the raw data and the entire timeseries was divided in three different groups: train dataset, covering two years, in which the statistical algorithm was trained; validation dataset, spanning in the next ten months, used to define the warning and the alarm boundaries for the control chart; and the test dataset consisting on thirty days, using to validate the entire statistical process. In this phase also an under sampling was performed and the median of each four hours was assumed like the values.

Then, for each sensor, a time series model is estimated to capture the natural variations in the data while accounting for daily and seasonal cycles. By employing this approach, the estimated model effectively represents the expected sensor behaviour under normal operating conditions. Additionally, the model enables the removal of the influence of steel temperature, from the signal.

The developed monitoring system is designed to track real-time prediction errors generated by each estimated model. Specifically, a control chart is implemented for each sensor, based on a statistical control metric and equipped with alert and alarm thresholds. The control chart triggers an alarm when deviations from the expected behaviour are detected. Furthermore, it is designed to differentiate between temporary anomalies and structural anomalies, as specified in the system requirements.

##### 4.1 Statistical model development

The forecasting methodology used in this study is based on the seasonal autoregressive integrated moving average with exogenous variables (SARIMAX) model. This class of autoregressive models is extensively applied in SHM to detect structural anomalies, particularly in time series data analysis for damage identification [5], [13]. By leveraging past observations and incorporating external influencing factors, SARIMAX models effectively characterize the expected behaviour of a system over time [14].

In this application, temperature readings from thermocouples served as exogenous inputs. The autoregressive (AR) components define the present response as a function of previous observations, while the moving average (MA)

components refine predictions by accounting for past errors. To enhance accuracy, the model also integrates seasonal components to capture periodic fluctuations occurring on both daily and annual scales. The generalized formulation of this model is expressed as:

$$\begin{aligned} (1-B)^d(1-B^S)^Dy_t &= \phi_1y_{t-1} + \phi_2y_{t-2} + \dots + \phi_p y_{t-p} \\ &+ \Phi_1y_{t-s} + \Phi_2y_{t-2s} + \dots \\ &+ \Phi_Py_{t-PS} + \theta_1\epsilon_{t-1} + \theta_2\epsilon_{t-2} \\ &+ \dots \theta_q\epsilon_{t-q} + \theta_1\epsilon_{t-s} + \theta_2\epsilon_{t-2s} \\ &+ \dots \theta_Q\epsilon_{t-Qs} + \epsilon_t + \beta X_t \end{aligned} \quad (1)$$

Where:

- B is the lag operator, such that:

$$\begin{aligned} (1-B)y_t &= y_t - y_{t-1} \\ (1-B^S)y_t &= y_t - y_{t-s} \end{aligned} \quad (2)$$

- $\phi_1, \dots, \phi_p$  are the autoregressive parameters.
- $\theta_1, \dots, \theta_q$  are the moving average parameters.
- $\Phi_1, \dots, \Phi_P$  are the seasonal autoregressive parameters.
- $\theta_1, \dots, \theta_Q$  are the seasonal moving average parameters.
- $\epsilon$  represents an error term, assumed to follow a Gaussian distribution.
- $X_t$  represents the temperature recorded by the temperature.

The selection of the model, including the determination of the parameters p, d, q, P, D, Q, as well as the subsequent estimation of model coefficients, was guided by the second-order Akaike information criterion. This criterion was employed to optimize model selection by balancing goodness-of-fit and complexity, ensuring an optimal trade-off between model accuracy and overfitting.

The results of the models for the sensor VW.01 are presented in Figure 8 where the entire time series was reported, and in Figure 9 where only the results for the test dataset is presented. The figures show the relatively low and uncorrelated behaviour of the residuals that's denotes the good behaviour of the algorithm for this type of analysis.

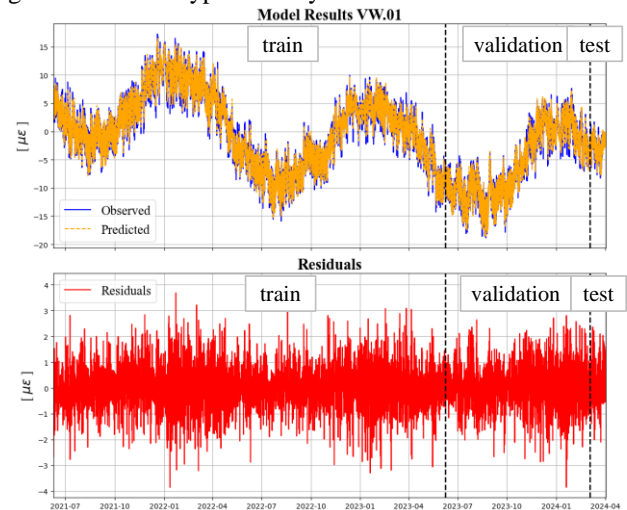


Figure 8. Representation of the results of the SARIMAX model for the entire time series for sensor VW.01



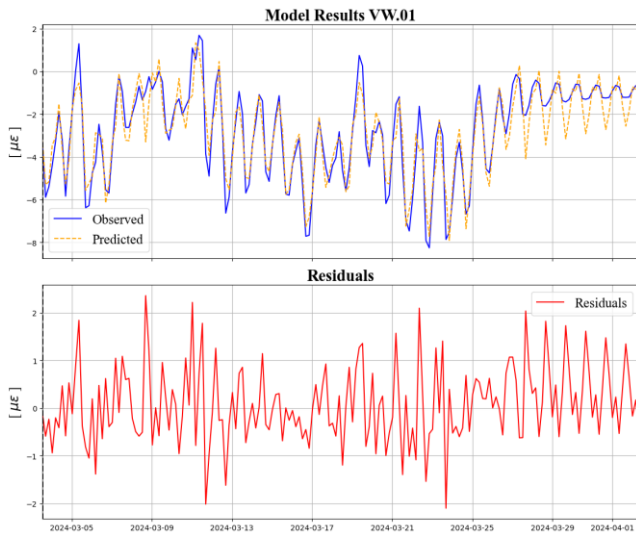


Figure 9. Representation of the SARIMAX model for the test dataset for sensor VW.01

In Table 2, different metrics are presented to compare the model's performance for the analysed sensors. The used metrics include root mean square error (RMSE), mean absolute error (MAE), median absolute error (MedAE), and the coefficient of determination ( $R^2$ ) for the test dataset residuals.

The model's performance demonstrates generally strong predictive capability, with high  $R^2$  values in most cases. A subset of three sensors exhibits optimal performance, characterized by minimal error metrics and an  $R^2$  of 0.99, indicating an excellent model fit. Another group of ten sensors shows good performance, with moderate error values yet maintaining high  $R^2$ , suggesting the model effectively captures underlying patterns. However, five sensors present higher error values, with some displaying lower  $R^2$ , particularly those with RMSE exceeding 2, which may indicate limitations in the model's predictive accuracy for these cases.

Table 2. Residuals metrics values

Sensor	RMSE	MAE	MedAE	$R^2$
VW.01	0.81	0.63	0.52	0.86
VW.02	0.94	0.69	0.55	0.99
VW.03	0.93	0.71	0.56	0.92
VW.04	1.35	0.98	0.73	0.94
VW.05	0.62	0.42	0.25	0.99
VW.06	0.60	0.38	0.25	0.99
VW.07	1.08	0.85	0.70	0.99
VW.08	1.17	0.83	0.61	0.99
VW.09	2.26	1.74	1.36	0.97
VW.10	2.68	1.95	1.41	0.77
VW.11	0.37	0.29	0.23	0.99
VW.12	1.08	0.78	0.51	0.95
VW.13	2.64	1.90	1.47	0.88
VW.14	2.02	1.48	1.08	0.93
VW.15	1.53	1.20	1.01	0.99
VW.16	1.03	0.75	0.61	0.99
VW.17	1.31	0.97	0.68	0.88
VW.18	1.25	0.95	0.74	0.80
VW.19	1.77	1.30	0.81	0.96
VW.20	0.69	0.52	0.40	0.99

## 4.2 Control chart development

For the monitoring phase, an adaptive exponentially weighted moving average (AEWMA) control chart is proposed [15], [16]. This type of control chart integrates exponential smoothing with an adaptive mechanism that allows for a faster response to significant changes. As a result, the control statistic is dynamic and adjusts based on observed variations.

The mathematical formulation of this adaptive statistic is given by:

$$S_i = S_{i-1} + \varphi(x_i - S_{i-1}) \quad (3)$$

Where  $\varphi$  is defined as:

$$\varphi(e) = \begin{cases} e + (1 - \lambda)k & \text{se } e < -k \\ \lambda e & \text{se } -k \leq e \leq k \\ e - (1 - \lambda)k & \text{se } e > k \end{cases} \quad (4)$$

The advantage of this generalization lies in its ability to enable the control statistic to respond more rapidly to abrupt and high-intensity deviations, specifically when  $|e| > k$ . In this case the values used for the analysis are  $\lambda = 0.1$  e  $k = 3$  [15].

By incorporating exponential smoothing, the AEWMA control chart is able to detect anomalies that develop gradually over time. However, its adaptive nature also allows for the identification of sudden, unexpected deviations.

This adaptability will later be leveraged to distinguish transient anomalies, which return to a normalized operational state within a short time frame. In essence, this type of control chart enables differentiation between structural anomalies, which persist over time, and transient anomalies, which resolve naturally after a brief period.

## 4.3 Definition of warning and alert boundaries

To determine the warning and alarm thresholds associated with the control statistic described in the equation (3), a statistical approach is employed based on the concept of mean time to false alarm. Specifically, the average run length ( $ARL_0$ ) represents the expected number of observations that occur before a false alarm is triggered.

The selection of alert thresholds is carried out by specifying a predefined  $ARL_0$  value. Once this value is established, the corresponding threshold can be determined using statistical simulation techniques.

In particular, the thresholds are computed to ensure compliance with the  $ARL_0$  criterion through the bisection method, as discussed in Qiu (2013) [17]. This approach ensures that the alarm system maintains a controlled balance between sensitivity and reliability.

## 4.4 Results of the analysis

In this section the results for the application of the AEWMA control chart for different sensors are shown. Figure 10 reports the results of the AEWMA control chart and the boundaries definition for the test dataset of the sensor VW.01. It shows a good behaviour that has value around zero, even if in the last part the behaviour of the control chart denotes a linear trend that is contained into the defined boundaries elsewhere.



Figure 10. Control chart for VW.01 test dataset

In Table 3 the boundaries for all the vibrating wire sensors are reported. It shows that the value of the boundaries is different one to each other and, clearly, the higher value is related to the timeseries that shows more difficulties for the model to fit the data and determine higher residuals value also in Table 2. But, caused by the limits were defined with the same  $ARL_o$ , we aspect that the resilience of the control chart is the same for all the sensors.

Table 3. Evaluation of the boundaries of each sensor

Sensor	RMSE	MAE	MedAE	R2
VW.01	0.607	1.156	0.607	1.156
VW.02	3.735	8.950	3.735	8.950
VW.03	1.258	2.729	1.258	2.729
VW.04	8.620	10.540	8.620	10.540
VW.05	0.878	6.292	0.878	6.292
VW.06	0.318	1.150	0.318	1.150
VW.07	4.264	5.465	4.264	5.465
VW.08	15.821	35.360	15.821	35.360
VW.09	5.335	7.336	5.335	7.336
VW.10	7.513	20.983	7.513	20.983
VW.11	0.372	0.542	0.372	0.542
VW.12	1.624	3.294	1.624	3.294
VW.13	11.633	16.041	11.633	16.041
VW.14	7.964	9.995	7.964	9.995
VW.15	6.237	8.872	6.237	8.872
VW.16	5.176	9.579	5.176	9.579
VW.17	3.223	7.446	3.223	7.446
VW.18	21.752	37.891	21.752	37.891
VW.19	7.421	10.413	7.421	10.413
VW.20	3.031	6.434	3.031	6.434

#### 4.5 Manual introduction of external perturbations

This paragraph analyses the behaviour of the control chart when different outliers appear in the time series.

In this case, an outlier was manually introduced into the test measurements. The variation was added at observation number 50 in the test dataset, with a value equal to twice the standard deviation of the validation dataset ( $12.0\mu\epsilon$ ). The control chart (Figure 11) shows two consecutive outliers at the point where the anomaly was introduced, indicating an isolated change in sensor behaviour.

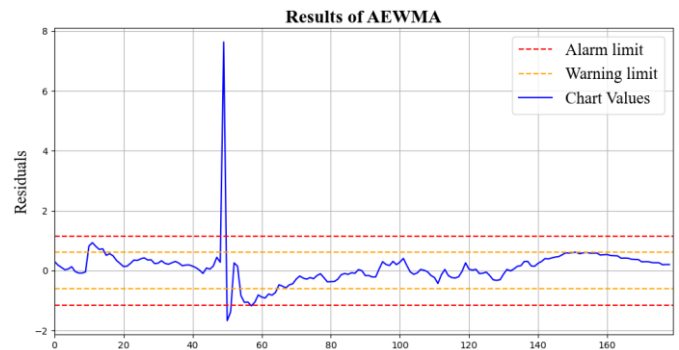


Figure 11. Control chart found with introduction of instant changing of the timeseries

Instead, if a constant shift or a linear trend occurs at the same point in the time series, the variation in the control chart differs from the previous case. In Figure 12 a constant shift equal to twice the standard deviation of the validation dataset was introduced. Notably, in the subsequent observation of the time series, there is no opposite variation in the values.

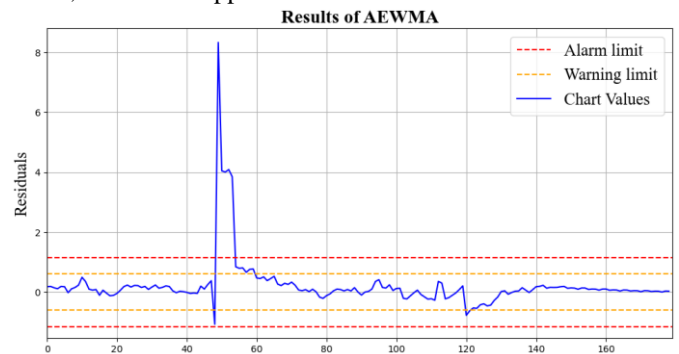


Figure 12. Control chart found with introduction of shift in the observations

This analysis demonstrates how different types of anomalies can be detected using this statistical approach and how variations in the control chart can help distinguish between them. Specifically, it allows for the differentiation between instantaneous sensor variations and constant offsets or linear trends in the time series. These distinctions can differentiate appropriate maintenance strategies for both the structure and the SHM system itself.

Moreover, this type of control, associated with the first data cleaning phase, makes it possible to differentiate issues related to data acquisition—such as corrupted signals—which may result in uncorrelated spikes within the time series. These anomalies can be separated from other types of perturbations, such as constant shifts, linear trends, and correlated spikes, which are more likely to be associated with structural phenomena.

## 5 CONCLUSIONS

This article proposes a statistical approach for continuously evaluating data collected from SHM systems, supporting infrastructure authorities in making informed decisions for the life-cycle assessment of their assets. The proposed framework individually analyses static sensors along with their associated

external variables—in this case, thermocouples—to define the system's normal behaviour.

A SARIMAX model is applied to identify both long-term and short-term patterns in the sensor measurements, assess correlations with external variables, and filter out their effects from the data. Subsequently, the residuals are monitored using an AEWMA control chart, which does not only consider the current residual value but also accounts for deviations from previous residuals. This method further enables the differentiation of various types of anomalies.

The control chart within the proposed framework enables the differentiation of various types of signal perturbations associated with different forms of structural degradation. Additionally, the data cleaning process and the control chart allow for the distinction between these structural anomalies and those arising from data acquisition issues.

For this case study, the framework demonstrated effective performance. The next phase of this research involves extending the framework to groups of sensors, ensuring that potential sensor-specific issues do not trigger unnecessary alarms or warnings for infrastructure authorities, thereby improving the robustness of the monitoring system. In the future, it will also be necessary to apply this type of control to various types of structures to verify and confirm its effectiveness under different conditions and with varying input parameters. This will help assess the system's reliability and adaptability across various structural and environmental scenarios.

## ACKNOWLEDGMENTS

Part of the work presented in this paper includes outcomes derived from a research contract between ADEL srl and the Department of Statistical Sciences at the University of Padova.

## REFERENCES

- [1] M. Pina, L. Mehmet, and Ç. Editors, "Seismic Structural Health Monitoring From Theory to Successful Applications." [Online]. Available: <http://www.springer.com/series/15088>
- [2] E. Figueiredo and E. Cross, "Linear approaches to modelling nonlinearities in long-term monitoring of bridges," *J Civ Struct Health Monit*, vol. 3, no. 3, pp. 187–194, Aug. 2013, doi: 10.1007/s13349-013-0038-3.
- [3] F. Lorenzoni, F. Casarin, M. Caldon, K. Islami, and C. Modena, "Uncertainty quantification in structural health monitoring: applications on cultural heritage buildings," 2014.
- [4] F. Lorenzoni, F. Casarin, C. Modena, M. Caldon, K. Islami, and F. da Porto, "Structural health monitoring of the Roman Arena of Verona, Italy," *J Civ Struct Health Monit*, vol. 3, no. 4, pp. 227–246, Dec. 2013, doi: 10.1007/s13349-013-0065-0.
- [5] E. Figueiredo and J. Brownjohn, "Three decades of statistical pattern recognition paradigm for SHM of bridge," 2022. [Online]. Available: <http://hdl.handle.net/10871/129482>
- [6] C. R. Farrar and K. Worden, "An introduction to structural health monitoring," *Philosophical Transactions of the Royal Society A: Mathematical, Physical and Engineering Sciences*, vol. 365, no. 1851, pp. 303–315, Feb. 2007, doi: 10.1098/rsta.2006.1928.
- [7] A. Pierdicca, F. Clementi, P. Mezzapelle, A. Fortunati, and S. Lenci, "One-year monitoring of a reinforced concrete school building: Evolution of dynamic behaviour during retrofitting works," in *Procedia Engineering*, Elsevier Ltd, 2017, pp. 2238–2243. doi: 10.1016/j.proeng.2017.09.206.
- [8] S. Fan, L. Ren, H. Li, and B. Song, "Real-Time Monitoring and Early Warning Method Utilizing FBG Sensors in the Retrofitting Process of Structures," *Int J Distrib Sens Netw*, vol. 2015, 2015, doi: 10.1155/2015/359549.
- [9] A. Gennaro, A. Caprino, V. Pernechele, F. Lorenzoni, and F. da Porto, "In-situ test and model updating of an RC tied-arch bridge," in *Procedia Structural Integrity*, Elsevier B.V., 2022, pp. 822–829. doi: 10.1016/j.prostr.2023.01.107.
- [10] F. Casarin, N. Molon, and D. Talozzi, "OMA and dynamic SHM of the Urbino Cathedral struck by the 2016 central Italy seismic events," in *Proceedings of the 10th International Operational Modal Analysis Conference (IOMAC 2024)*, IOMAC 2024, 2024.
- [11] M. Salvalaggio, F. Lorenzoni, and M. R. Valluzzi, "Impact of sound-insulated joints in the dynamic behaviour of Cross-Laminated Timber structures," *Journal of Building Engineering*, vol. 91, Aug. 2024, doi: 10.1016/j.jobbe.2024.109525.
- [12] H. Sohn, "Effects of environmental and operational variability on structural health monitoring," *Philosophical Transactions of the Royal Society A: Mathematical, Physical and Engineering Sciences*, vol. 365, no. 1851, pp. 539–560, Feb. 2007, doi: 10.1098/rsta.2006.1935.
- [13] H. Sohn, C. R. Farrar, N. F. Hunter, and K. Worden, "Structural health monitoring using statistical pattern recognition techniques," *Journal of Dynamic Systems, Measurement and Control, Transactions of the ASME*, vol. 123, no. 4, pp. 706–711, 2001, doi: 10.1115/1.1410933.
- [14] Charles. R. Farrar and K. Worden, *Structural health monitoring: a machine learning perspective*. Wiley, 2013.
- [15] G. Capizzi and G. Masarotto, "An Adaptive Exponentially Weighted Moving Average Control Chart," 2003.
- [16] A. Mitra, K. B. Lee, and S. Chakraborti, "An adaptive exponentially weighted moving average-type control chart to monitor the process mean," *Eur J Oper Res*, vol. 279, no. 3, pp. 902–911, Dec. 2019, doi: 10.1016/j.ejor.2019.07.002.
- [17] Qiu Pehiua, "Introduction to Statistical Process Control," 2013. Accessed: Mar. 05, 2025. [Online]. Available: <https://doi.org/10.1201/b15016>



# Is it possible that AI can help us detect all damage in structural assets? A discussion on the scope of applicability of DL methods for diagnosis of the construction assets's technical condition

Karolina Tomaszekiewicz<sup>1</sup>, ORCID 0000-0003-1443-4689, Tomasz Owerko<sup>1</sup>, ORCID 0000-0002-2873-3535

<sup>1</sup>Department of Engineering Surveying and Civil Engineering, AGH University of Krakow, al. A. Mickiewicza 30, 30-059 Krakow, Poland

email: tomaszki@agh.edu.pl, owerko@agh.edu.pl

**ABSTRACT:** The use of computer vision supported by artificial intelligence methods is growing in popularity for solving problems concerning the assessment of building and civil engineering structures. At the same time, SHM-class systems allow for the collection of large amounts of data. Despite the rapid development of machine learning and the increasing number of solutions supporting the process of technical condition diagnosis of objects, the amount of damage that can be detected in images using these algorithms is significantly limited. At the same time, due to the lack of publicly available datasets that can be used to train AI algorithms, the actual support of the civil engineer's work with these algorithms is limited to a few of the most common problems. This paper presents the current applicability of artificial intelligence methods for damage detection of buildings and engineering structures based on images. At the same time, the authors focus on showing the limitations for the development of artificial intelligence algorithms due to the lack of publicly available datasets. The paper identifies a research gap related to the lack of datasets for damage, pointing out the types of damage, types of damaged materials and solution classes not covered in research on the application of deep learning to the diagnosis of the technical condition of buildings and civil engineering structures.

**KEY WORDS:** SHMII-13; Extended Abstract; Deep learning; Dataset; Damage; Technical condition.

## 1 INTRODUCTION

The rapid development of artificial intelligence (AI) algorithms, including deep machine learning (DL), means that these methods are more and more often being used as tools to support the assessment of the technical condition of building and engineering structures. At the same time as SHM-class systems are adopted more widely, they facilitate the gathering of data on structural behavior, suitable for deep machine learning analysis. [1], [2]. The authors understand SHM-class systems as those that collect data about the structure's condition, analyze these data, and provide information when limit values are exceeded. This allows for early response to potential threats (e.g., informing about excessive strain in a structural element, which could lead to a reduction in load capacity) and supports the development of predictive maintenance strategies.

Researchers are implementing deep learning-based solutions for a wide range of data types. Satellite images [3], [4], Ground Penetrating Radar images [5], measurements from inclinometers and strain gauges [1], signals from devices passing over bridge structures [6], XCT images [7], damage images [8], video data [9] are being used.

The assessment of the technical condition of building and engineering structures can be carried out both on a global level (e.g., classification of damaged buildings after disasters [3], detection of ground deformations [4]) as well as with regard to building components (e.g., crack detection in brickwork masonry [8]), down to the level of detecting internal damage within materials (e.g., corrosion of reinforcement bars in concrete elements [7]).

This paper explores the current capabilities of applying deep learning and computer vision techniques to the damage

detection in buildings and engineering structures using image data. For the purposes of this study, the term "image" is defined specifically as a photograph depicting damage, as opposed to general raster data derived through digital processing of alternative data sources - such as structural vibrations transformed into spectrograms with Digital Signal Processing. Moreover, it should be noted that satellite images [3], [4], Ground Penetrating Radar images [5], XCT images [7] are not discussed here. The article particularly highlights limitations in the development of artificial intelligence algorithms due to lack of publicly available datasets. A research gap is discussed regarding the absence of damage datasets, in terms of damage types and types of damaged materials.

Neural network architectures and their associated performance are not the subject of this discussion. However, it should be mentioned that a likely solution to the problem of limited datasets for construction-related data may be the adaptation of architectures dedicated to Embedded Vision Systems.

## 2 OVERVIEW OF SOLUTION. DEVELOPMENT AND AVAILABILITY OF DATASETS

The application of deep learning in the assessment of the technical condition of buildings and engineering structures based on image data involves addressing tasks such as damage classification, detection, and segmentation. Researchers are using deep learning for the classification of damage such as paint deterioration [10], vegetation [10], cracks [10], [11], [12], [13], corrosion [10], [11], [12], spalling [11], [12], efflorescence [11], exposed bars [11], [12]. Object detection is used, among others, for problems such as cracks [14], [15], [16], spalling [14], [15], [17], pop-out [14], exposed rebar [14],

efflorescence [17]. Segmentation helps to solve problems such as cracks [16], [18], corrosion [19], mildew [19], ponding [19], exposed rebar [20], [21], delamination [20], [21], steel fatigue crack [22].

The development of deep learning algorithms is strongly dependent on the availability of data that can be used to train these models. Despite the wide range of damage types for which deep learning-based solutions have been developed, as described above, the number of open datasets (i.e., those available for download without the need to contact the author) remains significantly limited. As demonstrated by the research conducted by the authors of this publication [23], in the case of bridge structures, out of more than 120 identified damage types that may occur, yet open training datasets are available for only 10 of them. The lack of openly accessible datasets is a significant factor constraining the progress of deep learning algorithm development. In the lack of shared data, subsequent researchers are compelled to create new solutions from scratch, rather than refining or building upon existing methods.

Among the various research problems addressed in the field, crack detection - particularly in concrete and asphalt elements - emerges as the one for which the largest number of open datasets is available. Datasets have also been developed for components made of brick and structural steel. However, it is important to emphasize that, from an engineering point of view, the characteristics of cracks - especially their shape and size - differ significantly depending on the material. A considerable number of datasets are also available for issues related to the corrosion of concrete and reinforcing steel.

When categorized by material type, most identified datasets refer to damage in concrete and asphalt structures. In contrast, datasets concerning damage in timber and stone elements remain limited.

It is important to emphasize the existing imbalance between the range of damage types addressed in proposed solutions and the availability of corresponding datasets that have been made publicly accessible by the research community. A notable example is the detection of honeycomb defects, which, although investigated in scientific publications [24], [25]. In both cited cases, the datasets used in the experimental studies were not disclosed, and this specific type of defect is not represented in any existing public datasets. This situation highlights that, at present, the detection of honeycomb-related damage is only possible within individual research groups that maintain proprietary datasets, thereby limiting the broader applicability and scalability of deep learning methods for structural diagnostics.

To enable meaningful progress in this area, particularly regarding the development and refinement of algorithms targeting such defects, the creation and dissemination of open-access datasets is an essential prerequisite. Only then can the research community effectively train and improve deep learning-based diagnostic tools for widespread engineering applications.

For datasets, the following aspects should be noted [23]:

- Some of the open datasets are described in a not very detailed way and do not contain information relevant for the engineers (for example, the damage size).
- Some of the open datasets are shared in unusual locations (e.g., via the author's cloud storage, rather than on

dedicated data sharing websites like Zenodo, GitHub, kaggle, Mendeley Data).

- For many damage types, available open datasets were not identified. As important, there are datasets in which different damage types are labeled as a single damage type class. Re-labeling them, using classes dedicated to specific damage types, could increase the applicability of DL methods for diagnosis of the construction asset's technical condition.
- It should also be taken into account that a large number of datasets for a particular damage type does not mean yet that the problem of damage detection has been solved. Often, the developed solutions allow only to detect damage of a certain size or occurring on a surface with a similar appearance.

An essential aspect of applying deep learning methods for the assessment of a construction asset's technical condition is the manner in which datasets are prepared. Most publicly available datasets contain damage labels that are purely geometric in nature. Based on these annotations, it is possible to localize pixels within an image that correspond to a specific damage type. However, such data is strictly visual and lacks critical contextual information necessary for a comprehensive engineering assessment - such as expert evaluation, georeferencing, the material type of the damaged element, or the date of damage detection.

Consequently, solutions developed using such datasets primarily address visual recognition tasks and enhance the visibility of defects in imagery, but they do not resolve engineering-level diagnostic challenges.

Data should comply with the FAIR principles [26] - that is, they should be Findable, Accessible, Interoperable, and Reusable. The datasets should be hosted in a permanent way on servers and be accessible to train deep learning models at any time, interoperable between different systems and replicable for different construction structures.

The datasets used for training should pass technical validation and have a high level of rawness. They should not be processed before training, in particular, it is not good practice to collect a small amount of data and then augment the data to present this as a dataset. Augmentation - if it is planned to be executed - should be implemented as part of the model training process. In particular, it should be considered that for engineering problem solving, inadequate planning of the data augmentation process can result in the loss of information relevant to structural engineers, such as the direction of damage or its size.

### 3 CONCLUSION

The conducted analysis has demonstrated that algorithms based on deep learning and computer vision are a frequent subject of research. Although the solutions presented by researchers address the detection of a wide range of defects in concrete, steel, brick, and asphalt components, the number of publicly available datasets for training deep neural networks is significantly smaller.

This situation considerably limits the potential for developing deep learning algorithms for the assessment of a construction asset's technical condition. Moreover, the time that researchers must dedicate to creating their own datasets -

due to the lack of publicly available ones - could instead be allocated to improving the robustness or computational efficiency of deep learning algorithms.

However, in order to develop solutions that address engineering-level challenges (e.g., classification of the degree of damage), rather than solely visual tasks (e.g., identifying the damage area through pixel-wise prediction), it is necessary to establish guidelines for dataset creation. These datasets should include not only visual information but also metadata relevant from the perspective of structural and civil engineers.

## REFERENCES

- [1] A. Fernandez-Navamuel, D. Pardo, F. Magalhães, D. Zamora-Sánchez, Á. J. Omella, and D. Garcia-Sanchez, "Deep neural network for damage detection in Infante Dom Henrique bridge using multi-sensor data," *Struct Health Monit*, Jan. 2024
- [2] Y. Li *et al.*, "A new dam structural response estimation paradigm powered by deep learning and transfer learning techniques," *Struct Health Monit*, vol. 21, no. 3, pp. 770–787, May 2022
- [3] I. Alisjahbana, J. Li, B. Strong, and Y. Zhang, "DeepDamageNet: A two-step deep-learning model for multi-disaster building damage segmentation and classification using satellite imagery," May 2024.
- [4] N. Anantrasirichai *et al.*, "Detecting Ground Deformation in the Built Environment Using Sparse Satellite InSAR Data With a Convolutional Neural Network," *IEEE Transactions on Geoscience and Remote Sensing*, vol. 59, no. 4, pp. 2940–2950, Apr. 2021
- [5] J. Wang *et al.*, "Arbitrarily-oriented tunnel lining defects detection from Ground Penetrating Radar images using deep Convolutional Neural networks," *Autom Constr*, vol. 133, p. 104044, Jan. 2022
- [6] Z. Li, Y. Lan, and W. Lin, "Footbridge damage detection using smartphone-recorded responses of micromobility and convolutional neural networks," *Autom Constr*, vol. 166, p. 105587, Oct. 2024
- [7] M. Zhang and W. Wang, "Deep learning-based extraction and quantification of features in XCT images of steel corrosion in concrete," *Case Studies in Construction Materials*, vol. 20, p. e02717, Jul. 2024
- [8] S. Katsigiannis, S. Seyedzadeh, A. Agapiou, and N. Ramzan, "Deep learning for crack detection on masonry façades using limited data and transfer learning," *Journal of Building Engineering*, vol. 76, p. 107105, Oct. 2023
- [9] J. Shu, C. Zhang, X. Chen, and Y. Niu, "Model-informed deep learning strategy with vision measurement for damage identification of truss structures," *Mech Syst Signal Process*, vol. 196, p. 110327, Aug. 2023
- [10] S. Shahrabadi, D. Gonzalez, N. Sousaa, T. Adao, E. Peres, and L. Magalhaes, "Benchmarking Deep Learning models and hyperparameters for Bridge Defects Classification," *Procedia Comput Sci*, vol. 219, pp. 345–353, Jan. 2023
- [11] M. Mundt, S. Majumder, S. Murali, P. Panetsos, and V. Ramesh, "Meta-learning convolutional neural architectures for multi-target concrete defect classification with the concrete defect bridge image dataset," *Proceedings of the IEEE Computer Society Conference on Computer Vision and Pattern Recognition*, vol. 2019-June, pp. 11188–11197, Jun. 2019
- [12] V. Hoskere, Y. Narazaki, T. A. Hoang, and B. F. Spencer, "Vision-based Structural Inspection using Multiscale Deep Convolutional Neural Networks", May 2018
- [13] D. Arya *et al.*, "Deep learning-based road damage detection and classification for multiple countries," *Autom Constr*, vol. 132, p. 103935, Dec. 2021
- [14] C. Zhang, C. C. Chang, M. Jamshidi, and H. Kong, "Bridge Damage Detection using a Single-Stage Detector and Field Inspection Images", Dec. 2018
- [15] P. Kumar, S. Batchu, N. Swamy S., and S. R. Kota, "Real-time concrete damage detection using deep learning for high rise structures," *IEEE Access*, vol. 9, pp. 112312–112331, 2021
- [16] Z. F. Elsharkawy, H. Kasban, and M. Y. Abbass, "Efficient surface crack segmentation for industrial and civil applications based on an enhanced YOLOv8 model," *J Big Data*, vol. 12, no. 1, pp. 1–20, Dec. 2025
- [17] N. Wang, X. Zhao, P. Zhao, Y. Zhang, Z. Zou, and J. Ou, "Automatic damage detection of historic masonry buildings based on mobile deep learning," *Autom Constr*, vol. 103, pp. 53–66, Jul. 2019
- [18] M. Zheng, Z. Lei, and K. Zhang, "Intelligent detection of building cracks based on deep learning," *Image Vis Comput*, vol. 103, p. 103987, Nov. 2020
- [19] F. Jiang, Y. Ding, Y. Song, F. Geng, and Z. Wang, "Automatic pixel-level detection and measurement of corrosion-related damages in dim steel box girders using Fusion-Attention-U-net," *J Civ Struct Health Monit*, vol. 13, no. 1, pp. 199–217, Jan. 2023
- [20] J. J. Rubio *et al.*, "Multi-class structural damage segmentation using fully convolutional networks," *Comput Ind*, vol. 112, p. 103121, Nov. 2019
- [21] W. Deng *et al.*, "Vision based pixel-level bridge structural damage detection using a link ASPP network," *Autom Constr*, vol. 110, p. 102973, Feb. 2020
- [22] X. Wang, Q. Yue, and X. Liu, "SBDNet: A deep learning-based method for the segmentation and quantification of fatigue cracks in steel bridges," *Advanced Engineering Informatics*, vol. 65, p. 103186, May 2025
- [23] K. Tomaszewicz, "Support of selected bridge condition assessment processes using deep learning and integration of assessment results in BIM information models" (in Polish), Doctoral Thesis, AGH University of Krakow, Faculty of Geo-Data Science, Geodesy, and Environmental Engineering, 2025.
- [24] A. Cardellicchio, S. Ruggieri, A. Nettis, V. Renò, and G. Uva, "Physical interpretation of machine learning-based recognition of defects for the risk management of existing bridge heritage," *Eng Fail Anal*, vol. 149, p. 107237, Jul. 2023
- [25] S. Ruggieri, A. Cardellicchio, A. Nettis, V. Renò, and G. Uva, "Using machine learning approaches to perform defect detection of existing bridges," *Procedia Structural Integrity*, vol. 44, pp. 2028–2035, Jan. 2023
- [26] M. Wilkinson, M. Dumontier, I. Aalbersberg *et al.*, "The FAIR Guiding Principles for scientific data management and stewardship", *Sci Data*, vol. 3, p. 160018, Mar. 2016





## Computer Vision-based SHM

# Perspectives on vision-based bridge vibrational monitoring by drones

Tommaso Panigati<sup>1</sup>, 0009-0001-4077-8058, Pier Francesco Giordano<sup>1</sup>, 0000-0003-0396-0253, Daniel Tonelli<sup>2</sup>, 0000-0002-9089-4583, Maria Pina Limongelli<sup>1,3</sup>, 0000-0002-9353-5439, Daniele Zonta<sup>2</sup>, 0000-0002-7591-9519

<sup>1</sup> Politecnico di Milano, Department of Architecture, Built environment and Construction engineering, Piazza Leonardo da Vinci 32, 20133 Milan, Italy

<sup>2</sup> University of Trento, Department of Civil, Environmental and Mechanical Engineering, Via Mesiano 77, 38123 Trento, Italy

<sup>3</sup> Lund University, Faculty of Engineering, John Ericssons väg 1, Lund, Sweden

email: [tommasso.panigati@polimi.it](mailto:tommasso.panigati@polimi.it), [pierfrancesco.giordano@polimi.it](mailto:pierfrancesco.giordano@polimi.it), [daniel.tonelli@unitn.it](mailto:daniel.tonelli@unitn.it), [mariagiuseppina.limongelli@polimi.it](mailto:mariagiuseppina.limongelli@polimi.it), [daniele.zonta@unitn.it](mailto:daniele.zonta@unitn.it)

**ABSTRACT:** Vision-based vibrational monitoring aims to extract the modal parameters of civil structures—such as natural frequencies—from recorded video data for Structural Health Monitoring (SHM) purposes. The use of drones for vision-based vibrational monitoring is particularly promising, as drones can access vantage points for video recording that may otherwise be difficult to reach. However, certain drawbacks exist, including potential limitations in resolution, stability, and environmental sensitivity. This paper explores the capabilities, opportunities, and limitations of using drones for vision-based vibrational monitoring. To evaluate technological limits, a target with controlled displacement is used to test various combinations of target distances, displacement amplitudes, and displacement frequencies. Additionally, factors such as environmental conditions and drone hardware are considered. The study defines the practical limits of this approach, aiming to determine the minimum displacement of a vibrating bridge that can be detected by drones. Case studies from the literature are used as benchmarks to identify the dynamic properties of different types of bridges.

**KEY WORDS:** drones, structural health monitoring, computer vision

## 1. INTRODUCTION

The deterioration of transportation infrastructure and the limited availability of resources have made Structural Health Monitoring (SHM) essential for supporting bridge management. Within the framework of SHM, vibrational monitoring relies on the global dynamic response of a structure—typically extracting modal parameters such as natural frequencies and mode shapes—to identify damage [1]. Traditionally, vibrational monitoring is performed using fixed systems installed on structures. However, the high cost of components and maintenance makes this approach viable only for a limited number of bridges [2]. Therefore, there is a growing demand for affordable, reliable, portable, and reusable SHM instrumentation to reduce monitoring costs. Among emerging sensing technologies, commercial devices such as smartphones, cameras, drones, and robotic sensors present promising applications [3]. For instance, smartphones can gather vibrational measurements with embedded accelerometers [4]. Moreover, advancements in computer vision techniques enable the extraction of displacement and vibrational data from videos recorded by commercial smartphone and drone cameras [5]. While smartphones and fixed cameras need the physical presence of an operator to record videos close to the target point, drones can be controlled remotely and can reach vantage viewpoints without compromising operator safety [6]. Moreover, in addition to vibrational measurements, drones can gather 2D images of multiple bridge components during the same inspecting session. When combined with advanced computer vision and machine learning techniques, these images can enable a fast and efficient system for surface damage and crack detection [7], [8]. However, being flying objects, drones experience in-flight vibrations and unwanted movements (referred as egomotion) that may interfere with their ability to record small structural vibrations of the bridge. As highlighted in [9], there

is still the need to assess the field of applicability of commercial drone technology for bridge dynamic identification. The goal of this study is to evaluate the capabilities and limitations of drone-based vision systems for vibrational monitoring. The final scope is to define the practical limits of their application in identifying the dynamic behavior of bridges. Two stages are involved. Firstly, a literature survey identifies the typical range of frequencies and displacements for bridges with different materials, structural typology and span. Secondly, experimental tests are performed to assess the limits of applicability of vision-based approach using drones. The results of the tests are compared with the displacement and frequency range exhibited by real-scale bridges.

This paper is structured as follows. Section 2 describes the typical range of vibrational displacements and frequencies for different types of bridges. These ranges are then compared in section 3 with drone vision-based system capabilities determined with laboratory tests. Results are critically discussed in section 4 while section 5 presents conclusions. The overall flowchart is shown in Figure 1.

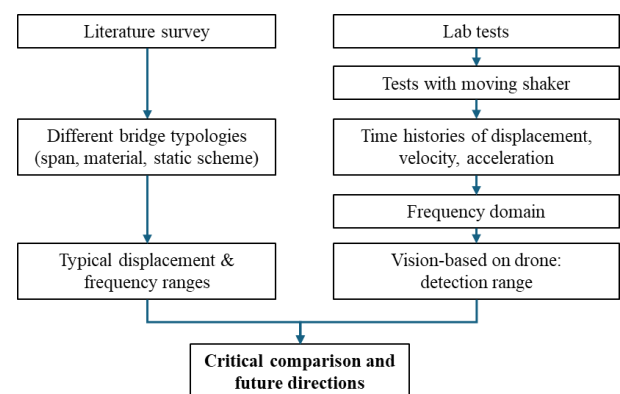


Figure 1: flowchart of the paper.

## 2. LITERATURE SURVEY

This section reviews existing literature to evaluate the typical behavior of bridges in terms of deflections and natural frequencies. This preliminary analysis, combined with the

results presented in Section 3, will support the assessment of the feasibility of a vision-based approach using drones. Table 1 presents displacement and frequencies data for various types of bridges, including pedestrian bridges, masonry bridges, concrete bridges, and cable-stayed bridges. The row of the table are organized in ascending order based on the length of the

Table 1. Vibrational displacements and frequencies of different types of bridges, ordered by main span length.

Reference	Bridge Type and main span [m]	Load type	Static deflection [mm]	Dynamic deflection [mm]	First natural frequency [Hz] and mode type	Second natural frequency [Hz] and mode type	Measurement type
[10]	Masonry Arch Bridge, 7.7	Train (weight of each boogie 34 ton)	< 1	n.a.	n.a.	n.a.	Fibre Bragg Grating cables and Digital Image Correlation
[11]	Concrete bridge, first span 13.7	2-axle truck a 3-axle bus	0.25 (truck) and 0.45 (bus)	< ±0.05	n.a.	n.a.	Fiber Optics and camera
[12]	Steel-concrete bridge, 19	32-ton truck	3	< ±0.04	n.a.	n.a.	LVDT and accelerometers
[13]	Pedestrian bridge, 23	Pedestrians (single jump)	n.a.	± 2	3.86	5.87	Vision-Based on drone
[14]	Steel road bridge, 25	Heavy trucks	6	± 1.5	3	n.a.	Vision-Based fixed
[15]	Pedestrian bridge, 27	Single person jumping	n.a.	± 2	2.98 (bending)	3.70 (torsional)	Vision-Based
[16]	Concrete, 32	Heavy trucks	< 5	±1	3.48	n.a.	Vision-Based
[17]	Continuous steel-concrete bridge, 40+40	40-ton truck	< 41	±1	2.7 (not specified)	4.7 (not specified)	Vision-Based, on drone, corrected with on-camera accelerometers
[18]	Continuous steel bridge, 4x45	30-ton and 40-ton truck	<5	< ±0.5	Between 2 and 3	n.a.	Vision-Based
[19]	PC railway bridge, 50	High-speed train	1.5	< ±0.2	3.19 (symmetric bending)	3.87 (torsional)	Laser velocity displacement transducer (LVDT)
[6]	Suspended pedestrian bridge, 67	Pedestrians (jumping)	n.a.	±15mm	n.a.	0.5	Vision-Based on drone
[20]	Concrete Bridge, 110	8-ton truck	5.65	n.a.	n.a.	n.a.	Vision-Based on drone
[21]	Single tower suspension bridge, 248	Heavy truck	40	n.a.	n.a.	n.a.	Vision-Based
[17]	Cable-stayed railway bridge, 432	High-speed train and freight train	30 (high-speed) and 75 (freight)	<±3	0.336 (vertical bending)	0.764 (vertical bending)	Vision-Based, corrected with on-camera accelerometers, distance 150 m
[22]	Suspended bridge, 1410 (main span)	2x heavy trucks	200	n.a.	n.a.	n.a.	Vision-Based fixed camera

main span. Deflections are divided into static and dynamic: static deflections are caused by the quasi-static presence of the load (for instance a truck when the truck itself is on the bridge), while dynamic deflections are the residual free-vibration amplitudes experienced around the static deflection baseline and once the load is released. This distinction is important because static deflections are typically an order of magnitude larger than dynamic deflections, making them easier to

measure. However, static deflections are not suitable for the dynamic characterization of the bridge (i.e., extraction of natural frequencies). For this purpose, dynamic deflections during the transient period after unloading are typically used. In Table 1, static deflections are presented with a positive sign, meaning they are pointing downwards, while dynamic deflections are reported with the ± sign, referring to their oscillation around the static deflection. It is possible to observe



the significant variation of the displacement range (from  $<1$  mm to  $\approx 200$  mm) for different combinations of span and stiffness. All the deflections are caused by defined forcing loading conditions (for instance a truck or a train). Conversely, vibrations caused by environmental solicitations are generally too small to be detected by a vision-based system [23]. This poses a challenge for dynamic extraction, as the time frame valid for the extraction of modal parameters is just limited within a few seconds after the excitation. Moreover, the loading itself may present some peculiar periodicity that is not related to the bridge, therefore affecting the result with spurious peaks in the spectral content. This is the case of trains passing over a bridge, where the periodicity is given by bogies passing over the sampling point [19], or of people walking over a pedestrian bridge, where walking has specific frequency.

Table 1 also presents the first two identified frequencies, when available. The peaks of the bridge frequency spectrum should be compared with the dominant peaks of the drone egomotion spectrum. If the bridge frequency peak overlaps with the drone egomotion peak, it becomes more difficult to accurately capture the dynamic behavior of the bridge using drones.

From Table 1, it emerges that, when a conventional load such as a heavy truck passes, static deflections are between  $1/20000$  and  $1/5000$  of the bridge span, while dynamic deflections are between  $1/50000$  and  $1/10000$  of the bridge span. These estimates provide a useful reference for the expected vibration amplitudes of a bridge and help define the range of applicability of the vision-based approach using drones presented in Section 3.

### 3. LABORATORY TESTS

The laboratory tests were conducted using a commercial DJI MINI 2 drone, which was directed at a moving target oscillating vertically. Two experimental setups were tested. In the first setup, the moving target was simulated on a screen, representing a concrete-like surface with a sinusoidal displacement time history in the vertical direction, controlled

by user-defined displacement amplitude and frequencies. In the second setup, the target was a physical point subjected to vertical sinusoidal displacement driven by a pre-programmed shaker, see Figure 2. The tests aim to determine under which conditions the input (known) oscillation frequencies can be identified from the resulting time-domain and frequency-domain plots. For the video-target case, displacements ranged from  $\pm 0.25$  mm to  $\pm 10$  mm, with frequencies between 0.5 Hz and 15 Hz. For the physical-target case, displacements ranged from  $\pm 0.5$  mm to  $\pm 2.5$  mm, with frequencies between 1 Hz and 5 Hz. In both cases, the drone, with its camera recording the target, was flown at varying distances between 1.5 m and 10 m. Different video lengths were tested, ranging from 10 to 60 s. Videos were recorded in 4K resolution ( $3840 \times 2160$ ) at 30 frames per second (fps). Tests were conducted both indoors and outdoors, yielding similar results. Under outdoor conditions, the increased drone oscillations caused by gentle wind gusts were compensated for by more accurate positioning provided by the Global Navigation Satellite System (GNSS). In both cases, also a fixed target was tracked for the sake of measuring the drone egomotion.

From the recorded video, a script using Kanade-Lucas-Tomasi tracking [24], [25], was employed to extract the time history of vertical and horizontal displacements. From these displacement data, velocities and acceleration were also computed. Finally, the Fast Fourier Transform (FFT) algorithm was applied to the displacement, velocity, and acceleration data to analyze their frequency content.

Figure 2 presents the results of a test conducted in the second setup. In the test, the drone was flown at a distance of 10 m, recording the vertical oscillation of the target, which had an amplitude of  $\pm 2.5$  mm (total range 5 mm) and a frequency of 3 Hz. In Figure 3, time histories of displacements, velocities and accelerations of a fixed reference target (orange) and the oscillating target (blue) are shown, in both horizontal (X) and vertical (Y) direction. The displacement of the fixed target is exclusively due to drone egomotion. The low-frequency

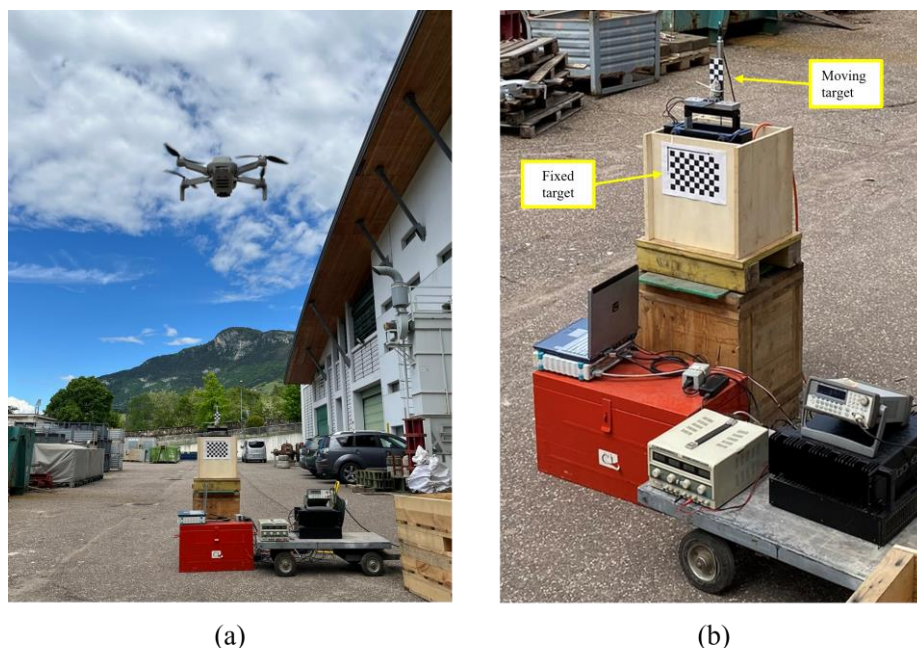


Figure 2. Experimental setup: (a) Drone and targets; (b) Detail of targets.

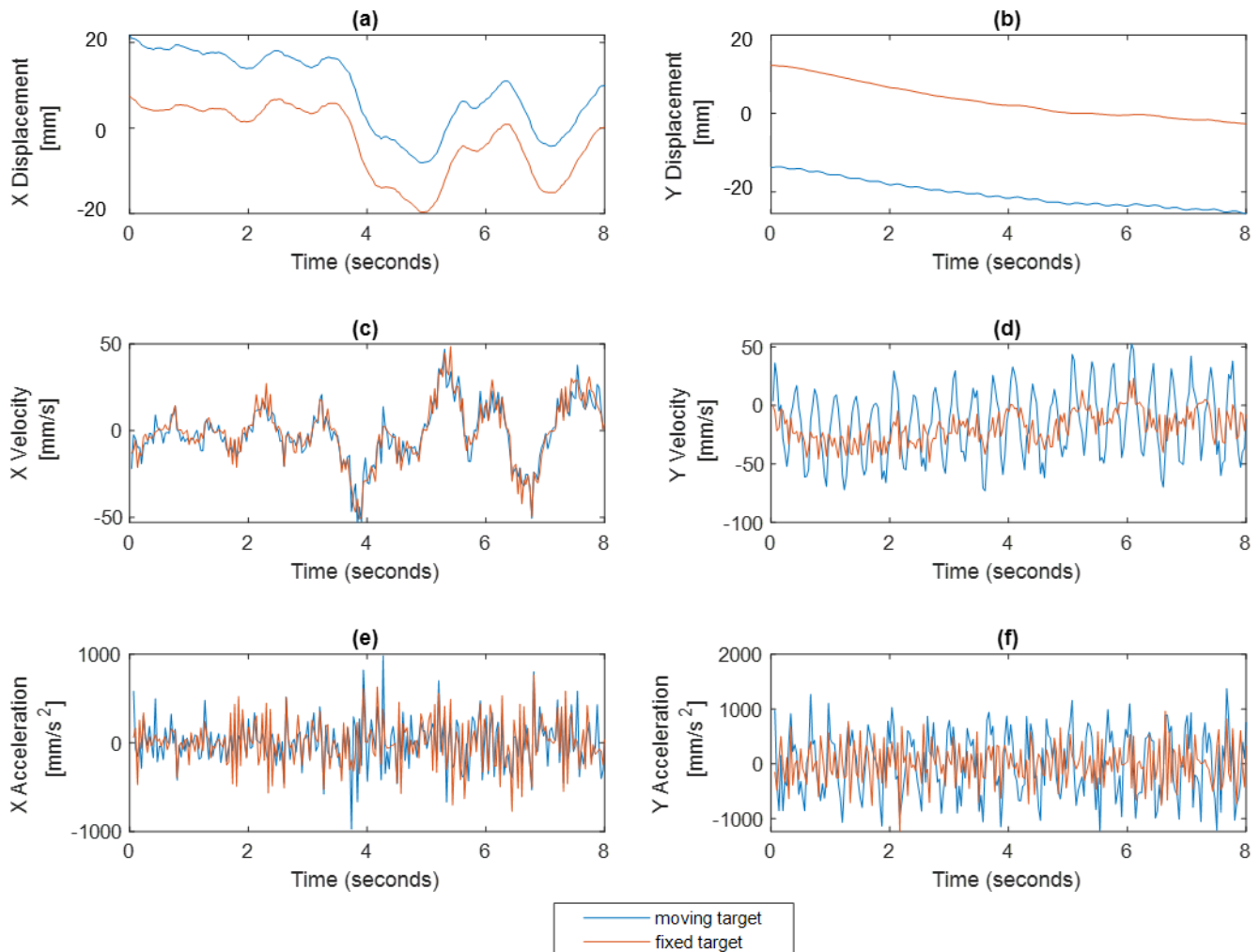


Figure 3. Time histories for a point with 5 mm / 3 Hz oscillation; drone camera at 10 m distance. Time histories of: displacement, (a) x direction and (b) y direction; velocity, (c) x direction and (d) y direction; acceleration, (e) x direction and (f) y direction.

oscillations, especially in the X direction, are due to drone egomotion. Conversely, high frequency vibrations of the moving target are due to the shaker user-defined vibrations. Figure 3 shows spectra of displacement (a), velocity (b) and acceleration (c) in horizontal and vertical direction, for the time histories shown in Figure 2. In Figure 3, a prominent peak in the frequency spectrum of the vertical acceleration and velocity corresponds to the shaker's oscillation frequency.

Results from all the tests provide valuable insights. In particular, some quantities have proven more effective for analyzing the results. Spectra of acceleration and velocity are less sensitive to low-frequency disturbances, resulting in sharp and easily detectable peaks. Conversely, spectra of displacement tend to present less distinct peaks near the

frequency of interest. As the frequency of the input excitation increases, the spectrum of acceleration becomes clearer, while the spectrum of velocity becomes less distinct. As a general rule, if the spectrum of acceleration does not allow for capturing the peak, the spectra of velocity and displacement are unlikely to succeed either. For this reason, the spectrum of acceleration is used as the primary means for identifying the frequency of interest.

The results are summarized in presence of moderate noise, yet low enough to avoid missing real and distinguishable peaks. Results confirm that for the range of frequency above 3 Hz the performance of vision-based tracking is optimal, and sub-millimetric displacements can be captured. On the other hand, at lower frequencies, the drone non-compensated egomotion (which typically falls within the 0–2 Hz range) negatively

affects the results. In this low-frequency range, only displacements with larger amplitudes are detectable if egomotion compensation are applied. Drones with better optics might have a wider range of detectable displacements, while heavier drone might suffer less from egomotion disturbance. Table 2, where the comparison is shown for a distance of 1.5 m, that is a compromise between optical precision and safety distance to avoid collision, using data from both setups. For simplicity, the results have been categorized into two groups: Yes (Y) when the peak in the acceleration spectrum was clearly visible, and No (N) when the identification was uncertain. There are several criteria for peak detection [26]. In this study, the criterion used to distinguish between Yes and No involved calculating the ratio between the peak value and the average signal in the spectrum. If the ratio exceeded 5, the result was marked as Yes; otherwise, it was marked as No. The threshold of 5 was selected because it is high enough to allow clear identification of the peak even in the

captured. On the other hand, at lower frequencies, the drone non-compensated egomotion (which typically falls within the 0–2 Hz range) negatively affects the results. In this low-frequency range, only displacements with larger amplitudes are detectable if egomotion compensation are applied. Drones with better optics might have a wider range of detectable displacements, while heavier drone might suffer less from egomotion disturbance.

Table 2. Range of detectability of frequencies.

		Frequency [Hz]						
		0.5	1	2	3	7	10	13
Displ. [mm]	±0.25	N	N	N	Y	Y	Y	Y
	±0.50	N	N	N	Y	Y	Y	Y
	±0.75	N	N	N	Y	Y	Y	Y
	±1.00	N	N	Y	Y	Y	Y	Y
	±5	N	N	Y	Y	Y	Y	Y
	±10	N	Y	Y	Y	Y	Y	Y

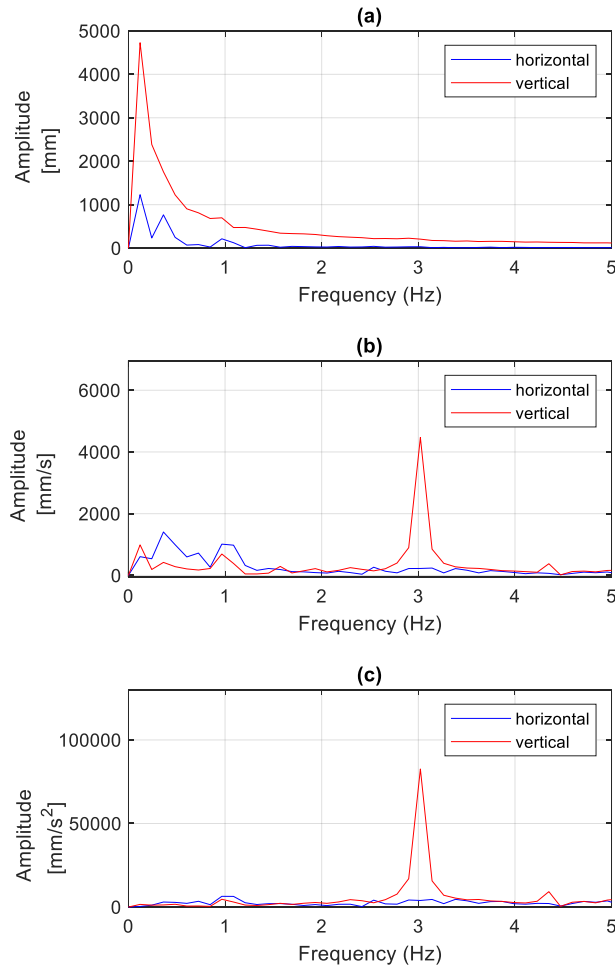


Figure 4. Spectra of (a) displacement, (b) velocity, (c) acceleration, for horizontal (X) and vertical (Y) displacement, calculated using FFT algorithm, for a point with 5 mm / 3 Hz oscillation; drone camera at 10 m distance.

presence of moderate noise, yet low enough to avoid missing real and distinguishable peaks. Results confirm that for the range of frequency above 3 Hz the performance of vision-based tracking is optimal, and sub-millimetric displacements can be

#### 4. CRITICAL DISCUSSION

The results obtained in section 3 can be critically compared with the data presented in section 2. When a heavy load passes over a bridge, the resulting static displacement is typically a few millimeters; once the load is released, the amplitude of free vibrations usually falls below 2–5 mm. In a controlled laboratory test, a low-cost drone demonstrated the ability to detect the dynamic behavior of vertically oscillating targets even for oscillations of less than 1 mm, provided that the free vibration frequency is above 2 Hz — allowing for the decoupling of drone egomotion from target vibrations. Based on these findings, drones might be capable of identifying the first frequency of selected bridges, provided that (i) the bridge is loaded by a heavy vehicle, (ii) the bridge is sufficiently flexible, and (iii) its first natural frequency does not coincide with the dominant frequencies of the drone's egomotion. Given those constraints, bridges that might be suitable for the capability of the existing drone technology are:

- Pedestrian bridges spanning more than 20 m, as those presented in [13], [15];
- Slender mid-span concrete and steel bridges, spanning more than 40 m, as those presented in [16], [17].

Conversely, short-span bridges and arch bridges of all materials are typically too stiff to exhibit significant displacement. Moreover, long-span suspended and cable-stayed bridges typically have low frequency modes that overlap with drone egomotion peaks, hindering vision-based dynamic identification with drones. It must be remarked that results from Table 2 are based on a controlled environment with sinusoidal oscillations; in contrast, the free vibrations of real bridges are less regular and, therefore, more challenging to be captured.

It must also be noted that the experiment was performed using an entry level commercial drone, weighing less than 250 g and costing less than 500€. Using a superior category drone could improve the results for three key reasons: (i) higher quality camera, (ii) reduced oscillations due to increased weight, and (iii) more stable hovering with enhanced gimbal stabilization. A list of suitable drones with their specifications is provided in Table 3. It must be remarked that drone weighting less than 250



grams can be flown with less restrictions in European Union, while heavier drones typically require pilot training.

Table 3. Commercial drone specifications.

Model	Year	Weight (g)	Camera	Obstacle Avoidance	Cost (€)
DJI Mini 2	2020	249	12 MP, 4 K/30 fps	Downward	~450
DJI Mini 4 Pro	2024	249	48 MP, 4 K/60 fps; HDR	Omni-directional	~800
Autel Evo Nano +	2023	249	50 MP, 4 K/30 fps	Forward/Backward	~800
Potensic Dreamer Pro	2022	745	12 MP, 4 K/30 fps	None	~500
DJI Air 3	2023	720	24 MP wide + 5 × tele	Omni-directional	~1,100
DJI Mavic 3 Pro	2022	895	4/3" 20 MP + tele + wide	Omni-directional	~2,100

Results could be improved by applying inertial-based egomotion compensation using data from accelerometers [6] or vision-based egomotion compensation using external reference points, such as background features [27]. However, most commercial drones, including the DJI MINI 2, do not allow access to accelerometric data, making inertial-based egomotion compensation unfeasible.

## 5. CONCLUSIONS

This study presented a comparison between bridge dynamic behavior and capabilities of drone vision-based dynamic monitoring. The literature review assessed the typical dynamic displacement ranges of bridge with varying length, material and static scheme. Laboratory tests validated the usage of vision-based dynamic monitoring on drones for vibrations happening with frequencies above 2 Hz and displacement ranges above 1 mm. These values match with properties of pedestrian bridges and of slender mid-span concrete and steel bridges. Further on-field tests should be conducted to verify the applicability to real cases. Improving egomotion compensation is expected to enhance the accuracy of dynamic identification using drones. The need to perform dynamic monitoring, with the constraint of the presence of a passing vehicle, introduces new challenges, such as the need to perform vibrational monitoring using very short and transient time histories, which falls outside the traditional framework of operational modal analysis.

## ACKNOWLEDGMENTS

This work was supported by PRIN: PROGETTI DI RICERCA DI RILEVANTE INTERESSE NAZIONALE – Bando 2022, under grant number Prot. 2022P44KA8, provided by the Italian Ministry of Education, Universities and Research. This work was financed by European Union - Next Generation EU, Mission 4 Component 1 CUP D53D23003870006.

## REFERENCES

- [1] M. Modesti, C. Gentilini, A. Palermo, E. Reynders, and G. Lombaert, "A two-step procedure for damage detection in beam structures with incomplete mode shapes," *J Civ Struct Health Monit*, 2024, doi: 10.1007/s13349-024-00839-0.
- [2] P. F. Giordano, S. Quqa, and M. P. Limongelli, "The value of monitoring a structural health monitoring system," *Structural Safety*, vol. 100, 2023, doi: 10.1016/j.strusafe.2022.102280.
- [3] S. Sony, S. Laventure, and A. Sadhu, "A literature review of next-generation smart sensing technology in structural health monitoring," *Struct Control Health Monit*, vol. 26, no. 3, 2019, doi: 10.1002/stc.2321.
- [4] E. Figueiredo, I. Moldovan, P. Alves, H. Rebelo, and L. Souza, "Smartphone Application for Structural Health Monitoring of Bridges," *Sensors*, vol. 22, no. 21, 2022, doi: 10.3390/s22218483.
- [5] C. Ferraris, G. Amprimo, and G. Pettiti, "Computer Vision and Image Processing in Structural Health Monitoring: Overview of Recent Applications," *Signals*, vol. 4, no. 3, 2023, doi: 10.3390/signals4030029.
- [6] V. Hoskere, J.-W. Park, H. Yoon, and B. F. Spencer, "Vision-Based Modal Survey of Civil Infrastructure Using Unmanned Aerial Vehicles," *Journal of Structural Engineering (United States)*, vol. 145, no. 7, 2019, doi: 10.1061/(ASCE)ST.1943-541X.0002321.
- [7] S. Feroz and S. A. Dabous, "Uav-based remote sensing applications for bridge condition assessment," *Remote Sens (Basel)*, vol. 13, no. 9, 2021, doi: 10.3390/rs13091809.
- [8] S. Jiang, Y. Cheng, and J. Zhang, "Vision-guided unmanned aerial system for rapid multiple-type damage detection and localization," *Struct Health Monit*, vol. 22, no. 1, pp. 319–337, 2023, doi: 10.1177/14759217221084878.
- [9] T. Panigati *et al.*, "Drone-based bridge inspections: Current practices and future directions," *Autom Constr*, vol. 173, p. 106101, May 2025, doi: 10.1016/J.AUTCON.2025.106101.
- [10] S. Acikgoz, M. J. . DeJong, C. Kechavarzi, and K. Soga, "Dynamic response of a damaged masonry rail viaduct: Measurement and interpretation," *Eng Struct*, vol. 168, 2018, doi: 10.1016/j.engstruct.2018.04.054.
- [11] D. Lydon, M. Lydon, S. Taylor, J. M. Del Rincon, D. Hester, and J. Brownjohn, "Development and field testing of a vision-based displacement system using a low cost wireless action camera," *Mech Syst Signal Process*, vol. 121, 2019, doi: 10.1016/j.ymssp.2018.11.015.
- [12] D. Hester, J. Brownjohn, M. Bocian, and Y. Xu, "Low cost bridge load test: Calculating bridge displacement from acceleration for load assessment calculations," *Eng Struct*, vol. 143, 2017, doi: 10.1016/j.engstruct.2017.04.021.
- [13] Y. Bai, H. Sezen, A. Yilmaz, and R. Qin, "Bridge vibration measurements using different camera placements and techniques of computer vision and deep learning," *Advances in Bridge Engineering*, vol. 4, no. 1, 2023, doi: 10.1186/s43251-023-00105-1.

- [14] Z. Aliansyah, K. Shimasaki, T. Senoo, I. Ishii, and S. Umemoto, "Single-camera-based bridge structural displacement measurement with traffic counting," *Sensors*, vol. 21, no. 13, 2021, doi: 10.3390/s21134517.
- [15] T. Panigati, A. Abbozzo, M. A. Pace, E. Temur, F. Cigan, and R. Kromanis, "Dynamic Identification of Bridges Using Multiple Synchronized Cameras and Computer Vision," *Infrastructures (Basel)*, vol. 10, no. 2, 2025, doi: 10.3390/infrastructures10020037.
- [16] F. Micozzi, M. Morici, A. Zona, and A. Dall'Asta, "Vision-Based Structural Monitoring: Application to a Medium-Span Post-Tensioned Concrete Bridge under Vehicular Traffic," *Infrastructures (Basel)*, vol. 8, no. 10, 2023, doi: 10.3390/infrastructures8100152.
- [17] T. Wu *et al.*, "Accurate structural displacement monitoring by data fusion of a consumer-grade camera and accelerometers," *Eng Struct*, vol. 262, 2022, doi: 10.1016/j.engstruct.2022.114303.
- [18] J. J. Lee and M. Shinozuka, "A vision-based system for remote sensing of bridge displacement," *NDT and E International*, vol. 39, no. 5, 2006, doi: 10.1016/j.ndteint.2005.12.003.
- [19] H. Xia, G. De Roeck, N. Zhang, and J. Maeck, "Experimental analysis of a high-speed railway bridge under Thalys trains," *J Sound Vib*, vol. 268, no. 1, 2003, doi: 10.1016/S0022-460X(03)00202-5.
- [20] S. Ri, J. Ye, N. Toyama, and N. Ogura, "Drone-based displacement measurement of infrastructures utilizing phase information," *Nat Commun*, vol. 15, no. 1, 2024, doi: 10.1038/s41467-023-44649-2.
- [21] Y. Han, G. Wu, and D. Feng, "Vision-based displacement measurement using an unmanned aerial vehicle," *Struct Control Health Monit*, 2022, doi: 10.1002/stc.3025.
- [22] J. M. W. Brownjohn, Y. Xu, and D. Hester, "Vision-based bridge deformation monitoring," *Front Built Environ*, vol. 3, 2017, doi: 10.3389/fbuil.2017.00023.
- [23] K. Luo, X. Kong, J. Zhang, J. Hu, J. Li, and H. Tang, "Computer Vision-Based Bridge Inspection and Monitoring: A Review," *Sensors*, vol. 23, no. 18, 2023, doi: 10.3390/s23187863.
- [24] B. D. Lucas and T. Kanade, "ITERATIVE IMAGE REGISTRATION TECHNIQUE WITH AN APPLICATION TO STEREO VISION.," in *7th joint international conference on Artificial Intelligence*, Vancouver, 1981.
- [25] C. Tomasi, "Detection and Tracking of Point Features," *School of Computer Science, Carnegie Mellon Univ.*, vol. 91, no. April, 1991.
- [26] G. K. Palshikar, "Simple Algorithms for Peak Detection in Time-Series Simple Algorithms for Peak Detection in Time-Series," *Design*, no. July, 2002.
- [27] H. Yoon, J. Shin, and B. F. Spencer, "Structural Displacement Measurement Using an Unmanned Aerial System," *Computer-Aided Civil and Infrastructure Engineering*, vol. 33, no. 3, 2018, doi: 10.1111/mice.12338.

# Universal unsupervised image segmentation model of multi-type component and damage for vision-based autonomous UAV inspection of bridges

Guangshuo YANG<sup>1</sup>, Chuao ZHANG<sup>1</sup>, Yang XU<sup>1,2\*</sup> 0000-0002-8394-9224

<sup>1</sup>School of Civil Engineering, Harbin Institute of Technology, Harbin, 150090, China

<sup>2</sup>Key Lab of Smart Prevention and Mitigation of Civil Engineering Disasters of the Ministry of Industry and Information Technology, Harbin 150090, China

\*Corresponding Author: Dr. Yang XU, [xyce@hit.edu.cn](mailto:xyce@hit.edu.cn)

**ABSTRACT:** Although recent advances have been widely gained in UAV-based visual inspection for bridges, the accuracy and generalization ability of recognition model highly rely on sufficient, complete, and high-quality annotations. Current damage segmentation models are often trained in a fragmented manner based on substantial pixel-level labels for specific structural components and damage types, lacking universality and robustness under real-world open scenarios. This study establishes a universal unsupervised image segmentation model of multi-type component and damage for vision-based autonomous UAV inspection of bridges using a teacher-student network architecture. The inputs are unlabeled image pairs after data augmentation including random clipping, rotation, illumination transformation, and color transformation. The pre-trained backbone of original DINO is adopted as frozen image feature extractor to obtain high-level feature representations, and a CNN-based segmentation head with learnable parameters is designed to generate dense segmentation maps with strong point-wise correlations. A synthetic loss function, comprising a correlation loss and a contrastive loss, is proposed for model training. The proposed method is validated on a unified multi-scale imageset including various structural components and surface damage for cable-supported bridges and concrete bridges. The recognition accuracy, generalization ability, and robustness under complex background are demonstrated.

**KEY WORDS:** UAV Bridge Inspection; Universal Unsupervised Segmentation; Teacher-Student Network; Cross-level Feature Alignment; Contrastive Learning.

## 1 INTRODUCTION

Maintaining safe operation throughout the entire life cycle of bridge structures is crucial. Timely and accurate identification of surface damage (such as cracks, corrosion, etc.) not only provides a basis for scientifically formulating maintenance strategies but also effectively prevents structural performance degradation, significantly reducing major safety risks like collapse and instability. For decades, bridge inspection has primarily relied on manual methods. However, this approach is not only time-consuming and labor-intensive but also susceptible to inspector experience, environmental conditions, and fatigue factors, resulting in issues such as strong subjectivity, low efficiency, and poor consistency, making it difficult to ensure reliability and timeliness in practical applications [1].

In recent years, computer vision technology has demonstrated significant advantages in image-based structural health monitoring and damage identification, providing an efficient and reliable alternative to traditional manual inspection methods. By integrating digital image processing with machine learning algorithms, computer vision enables automated identification and quantitative analysis of structural surface damage. Early research mainly focused on traditional image processing methods like edge detection and threshold segmentation, but their performance heavily relied on manual parameter tuning and showed limited generalization capability for damage features in complex environments. With breakthroughs in deep learning, data-driven methods represented by convolutional neural networks (CNNs) have exhibited outstanding performance in automatic feature extraction and damage pattern recognition, greatly improving

the accuracy and adaptability of structural health monitoring systems. However, these methods still depend on manually designed features as input and face challenges in robustness across complex real-world scenarios and generalization across different damage types [2].

Deep learning achieves end-to-end automatic mapping between images and object annotations through deep neural networks, with CNNs as multi-level feature extractors being the most extensively studied [3-5]. Existing structural damage identification methods are typically developed based on specific datasets covering only limited damage types and application scenarios, resulting in constrained generalization capability for new damage categories or under disaster conditions [6-7]. Moreover, these methods often require large amounts of annotated data to achieve ideal performance, but the nonlinear and sparse nature of structural damage makes high-quality annotated data difficult to obtain in practice [8-9]. Consequently, identification accuracy is easily affected by sample size, class balance, and damage diversity. However, real-world engineering applications demand models that maintain good generalization across diverse scenarios while achieving high-precision identification performance on unannotated data [10-11]. To overcome the limitations of existing methods trained separately on different datasets, it is necessary to develop a universal visual recognition model for structural damage that can accurately identify multiple damage types while maintaining stable performance in complex backgrounds and multi-scale real-world scenarios [12].

In the field of structural health monitoring, unsupervised and self-supervised learning paradigms are gradually becoming key technological pathways to address few-shot damage detection



challenges [13-14]. Currently, although contrastive learning-driven unsupervised semantic segmentation methods have shown potential in general computer vision domains, their adaptation to bridge UAV visual inspection scenarios faces significant bottlenecks: on one hand, there is a need to develop a universal segmentation framework adapted to Transformer architectures; on the other hand, the challenge of pixel-level damage parsing in real-world environments with massive unannotated data must be overcome (although certain few-shot learning algorithms have been proposed [15-17], a proper number of samples with pixel-level annotations should be required in advance). To address these challenges, this study proposes a large vision model for universal structural damage segmentation. The main scientific contributions are summarized as follows:

(1) We propose an unsupervised structural damage segmentation method based on teacher-student network knowledge distillation, using unlabeled augmented image pairs as input. The dual-branch architecture incorporates pre-trained frozen Transformer backbones and fine-tunable CNN segmentation heads.

(2) We design a dual-strategy collaborative mechanism combining cross-level self-supervised correlation learning and cross-network contrastive learning. The former achieves feature alignment through point-to-point correlations between high-level features and dense segmentation maps, while the latter maintains instance similarity and separability through feature vector comparison between teacher-student networks.

(3) We construct a joint optimization objective integrating correlation loss and contrastive loss. The student branch is rapidly updated via gradient descent, while the teacher branch is stably adapted through momentum-based exponential moving average, achieving end-to-end fine-tuning of the segmentation head.

The remainder of this paper is organized as follows. Section 2 introduces the network architecture of the proposed universal unsupervised damage segmentation model. Section 3 describes the investigated imageset of multi-scale multi-type structural components and surface damage. Section 4 presents a series of test results to demonstrate the effectiveness, robustness, and generalization capability of the established model under real-world inspection scenarios with complex background disturbances for cable-supported bridges and concrete bridges. Finally, Section 5 concludes this paper.

## 2 METHODOLOGY

The architecture of the proposed universal structural damage segmentation model is illustrated in Figure 1, employing an unsupervised learning paradigm based on collaborative optimization of teacher-student networks through an end-to-end self-supervised knowledge distillation mechanism for effective feature learning. Distinct from conventional approaches dependent on manual annotations, our framework integrates three fundamental components: a data augmentation module, a Transformer-based frozen feature extraction backbone, and a tunable CNN segmentation head. A specially designed hybrid loss function combining feature-space correlation loss with instance contrastive loss enables the network to autonomously identify essential damage characteristics in unsupervised settings. During deployment,

input images undergo sequential processing through the frozen feature extraction backbone, optimized segmentation head, and semantic clustering-based post-processing module to generate pixel-accurate structural damage segmentation results, with the complete pipeline demonstrating enhanced robustness for practical engineering applications. This integrated approach effectively bridges the gap between unsupervised learning and precise damage identification in complex real-world scenarios while maintaining computational efficiency throughout the segmentation process.

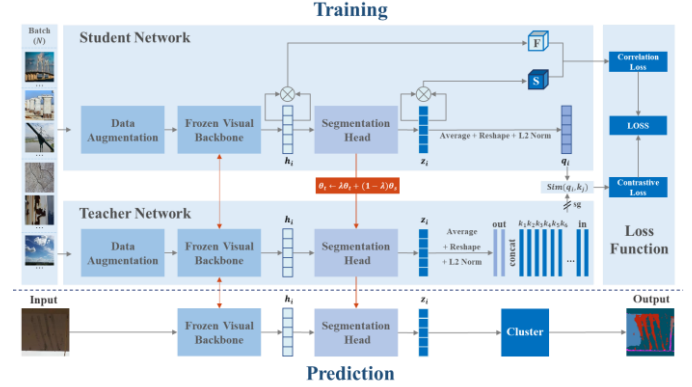


Figure 1. Model architecture for universal unsupervised segmentation of multi-type structural component and damage.

For each individual instance of input image, feature maps with the same dimensions of channel, height, and width are obtained before and after the segmentation head. For each branch of student and teacher networks, spatial points on feature maps before the segmentation head are noted as  $f_{chw}$  and  $g_{ch'w'}$ , while spatial points on feature maps after the segmentation head are noted as  $s_{chw}$  and  $t_{ch'w'}$ , respectively. The feature correspondence  $F_{hwh'w'}$  between  $f_{chw}$  and  $g_{ch'w'}$  and segmentation correspondence  $S_{hwh'w'}$  between  $s_{chw}$  and  $t_{ch'w'}$  are obtained by calculating the point-wise cosine similarity as

$$F_{hwh'w'} = \frac{\sum_{c=1}^C f_{chw} \times g_{ch'w'}}{\|f_{chw}\|_2 \times \|g_{ch'w'}\|_2} \quad (1)$$

$$S_{hwh'w'} = \frac{\sum_{c=1}^C s_{chw} \times t_{ch'w'}}{\|s_{chw}\|_2 \times \|t_{ch'w'}\|_2} \quad (2)$$

For  $N$  input images within an input batch, the feature correspondence tensors and segmentation correspondence tensors could be denoted as  $F_1, \dots, F_N \in \mathcal{R}^{H \times W \times H \times W}$ ;  $S_1, \dots, S_N \in \mathcal{R}^{H \times W \times H \times W}$  with four-dimensional elements of  $F_{hwh'w'}$  and  $S_{hwh'w'}$ .

The dense semantic correlation loss  $L_{corr}$  is calculated based on feature correspondence tensors and segmentation correspondence tensors by

$$F_{hwh'w'}^{SC} = F_{hwh'w'} - \frac{1}{HW} \sum_{h',w'} F_{hwh'w'} \quad (3)$$

$$L_{corr} = -\sum_{h,w,h',w'} (F_{hwh'w'}^{SC} - b) \max(S_{hwh'w'}, 0) \quad (4)$$

where  $F_{hwh'w'}^{SC}$  denotes the feature correspondence tensor after spatial centralization,  $b$  is a hyperparameter to avoid model collapse and ensure a positive correlation loss value for loss descending.

The contrastive loss between the teacher-student networks is defined as

$$L_{cont} = -\sum_{i=1}^N \log \left\{ \frac{\exp[\text{Sim}(q_i, k_+)/\tau]}{\sum_{j=1}^K \exp[\text{Sim}(q_i, k_j)/\tau]} \right\} \quad (5)$$

where Sim denotes the cosine similarity between two vectors,  $q_i$  denotes the  $i$ th query feature vector obtained from the student branch for the  $i$ th image in a batch,  $k_+$  denotes the feature vector obtained from the teacher branch as the positive sample of the corresponding query image,  $N$  denotes the batch size,  $k_j$  denotes the  $j$ th referenced feature vector in the feature dictionary,  $K$  denotes the queue length of the preset feature dictionary,  $\tau$  denotes a temperature hyperparameter to enhance an exponential amplification effect.

The synthetic loss function is defined by a weighted sum of correlation loss and contrastive loss as

$$Loss = \alpha L_{corr} + (1 - \alpha) L_{cont} \quad (6)$$

where  $\alpha$  denotes the weight coefficient of the correlation loss.

Upon completion of training, the system can directly generate predicted segmentation results for new test images using the frozen visual backbone network and optimized segmentation head. As shown in Figure 2, the prediction network incorporates a semantic clustering post-processing module consisting of K-means clustering and fully connected Conditional Random Field (CRF). Based on predefined label-category mapping relationships, the system automatically associates pixel-level annotations with specific categories including structural components, surface damage, and background. For newly added categories, only a single annotated sample is required to update the label mapping table. It should be noted that as standard post-processing modules for unsupervised image segmentation, the specific implementations of K-means clustering, fully connected CRF, and label alignment can be referenced in existing literature. To highlight this study's core contribution - the construction of a large-scale model for universal structural damage segmentation - the relevant implementation details are omitted here for brevity.

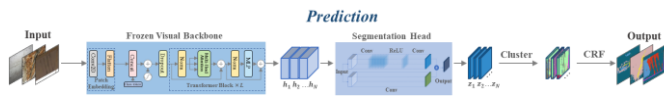


Figure 2. Schematic of prediction network structure with post-processing of semantic clustering.

### 3 IMPLEMENTATION DETAILS

This study addresses the key scientific challenge of unsupervised semantic segmentation for multiple types of structural damage under complex engineering conditions, proposing an integrated analytical framework that combines multi-source environmental interference factors with intrinsic structural features. Specifically, by fusing multi-dimensional key characteristics—including environmental background noise interference, macro-structural morphological features, micro-component texture details, and spatial distribution patterns of cable systems—we developed a dedicated scene model for damage detection in typical bridge structures such as cable-stayed bridges and concrete bridges. As illustrated in

Figure 3, representative damage samples from the two-level structural damage image database constructed in this study are presented.

#### Cable-supported and Concrete Bridges

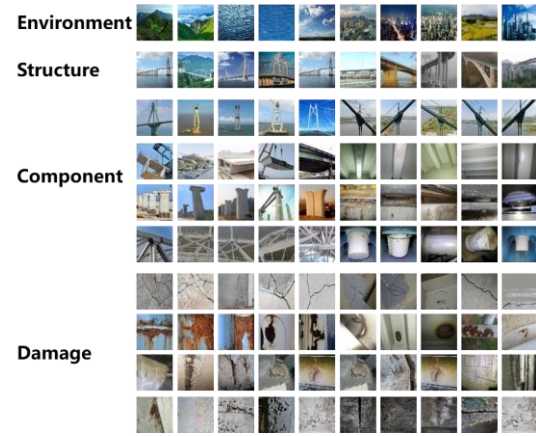


Figure 3. Representative images of hierarchical structural damage with multi-scale information for cable-supported and concrete bridges.

A total of 20K images with varying resolutions were standardized to a uniform resolution of  $1,024 \times 1,024$  pixels. Each resized image was subsequently partitioned into  $224 \times 224$  patches using a sliding window approach with a 100-pixel stride, thereby generating an extensive collection of image patches while circumventing potential feature degradation associated with direct downsampling. From this collection, 128 patches were randomly sampled to constitute the input batches for the proposed methodology.

It must be particularly emphasized that implementing traditional supervised CNN-based semantic segmentation models on such large-scale image patches inevitably encounters multiple computational challenges. Specifically, the exponential growth in computational complexity caused by high-resolution input space, coupled with the enormous manual annotation costs and time resources required for pixel-level labeling, constitutes two fundamental bottlenecks. These core limitations fundamentally undermine the feasibility of traditional supervised learning paradigms in the current application scenario, thereby significantly diminishing their practical value.

Through extensive experimental validation and parameter tuning, this study has ultimately determined the hyperparameter configuration scheme for model training as shown in Table 1. It is particularly important to note that while the current parameter settings may not represent the global optimal solution, empirical research demonstrates that this configuration ensures the large vision model for general structural damage segmentation achieves satisfactory segmentation accuracy, maintains excellent robustness against complex background interference, and exhibits strong generalization capability for new scenarios. Based on this, the primary objective of this research is not to pursue the optimal combination of hyperparameters, but rather to systematically validate through experiments the technical feasibility and practical effectiveness of the proposed large vision model in achieving general structural damage segmentation in real-world detection scenarios.

Table 1. Configurations of key training hyperparameters.

Hyperparameter Variables	Values
Number of images included in each batch	128
Dimension of feature representation after patch embedding	512
Length of query, key, and value vectors in attention mechanism	64
Number of multiple attention heads	8
Number of stacked transformer blocks	6
Dimensions of extracted feature maps by frozen visual backbone	16, 16, 8
Length of query and referenced feature vectors in preset feature dictionary	64
Number of feature queue size	12,800
Positive parameter to avoid model collapse in correlation loss	0.18
Weight coefficient of correlation loss	0.67
Temperature coefficient of contrastive loss	0.07
Learning rate in stochastic gradient descent updating of student network	5e-4
Momentum in exponential moving average updating of teacher network	0.999
Number of training iterations	5,000

To obtain quantitative evaluation metrics for semantic segmentation, a set of test images are pre-labelled with pixel-level annotations, and the following pixel accuracy (PA), mean intersection-over-union (mIoU), and frequency-weighted intersection-over-union (FWIoU) are calculated by

$$PA = \frac{\sum_i p_{ii}}{\sum_i \sum_j p_{ij}} \quad (7)$$

$$mIoU = \frac{1}{N_C + 1} \sum_{i=0}^{N_C} \frac{p_{ii}}{\sum_{j \neq i} p_{ij} + \sum_{j \neq i} p_{ji} - p_{ii}} \quad (8)$$

$$FWIoU = \frac{1}{\sum_{i=0}^{N_C} \sum_{j=0}^{N_C} p_{ij}} \sum_{i=0}^{N_C} \frac{p_{ii} \sum_{j=0}^{N_C} p_{ij}}{\sum_{j \neq i} p_{ij} + \sum_{j \neq i} p_{ji} - p_{ii}} \quad (9)$$

where  $p_{ij}$  denotes the number of pixels in the  $i$ th class (actual category) classified to the  $j$ th class (predicted category), the total number of pixel categories equals  $N_C + 1$ , including 1 for the background and  $N_C$  for the foreground, and  $N_C$  is determined by actual label categories of selected test images.

The proposed large vision model for universal structural damage segmentation is trained and tested under the software environment of PyTorch 1.8 and Python 3.7 on a 48G GPU of NVIDIA RTX A6000, and the average training time with the reported hyperparameter configurations is about 48 hours to obtain a well-trained model.

## 4 RESULTS AND DISCUSSION

Figure 4 shows some representative prediction results on coarse-grained segmentation of main bridge structures: (a) for cable-supported bridges and (b) for concrete bridges. The test PA, mIoU, and FWIoU are 97.17%, 91.47%, 94.64% for cable-support bridges and 92.72%, 82.46%, 86.98% for concrete bridges. The results show that main components of pylon, cable, girder, deck, and pier can be generally identified from entire images of bridge structures.

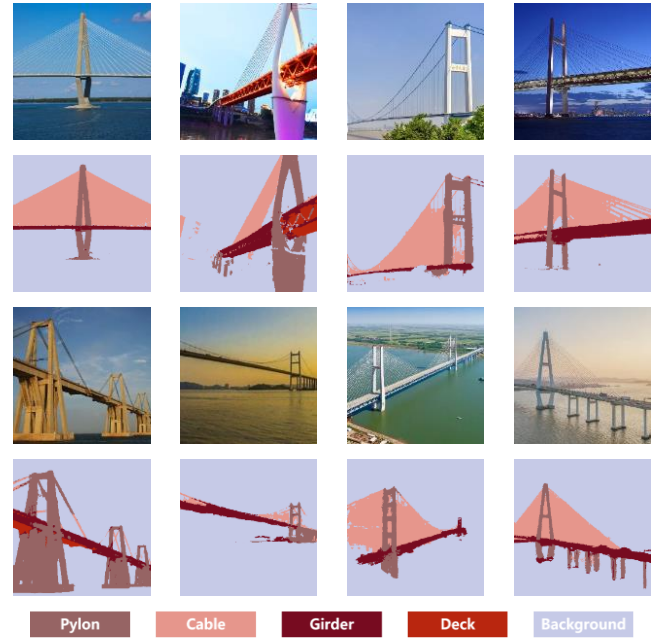


Figure 4. Representative predictions on coarse-grained segmentation of main bridge structures.

Figure 5 shows some typical prediction results of fine-grained damage segmentation on bridges, including concrete cracks, spalling, exposed rebar, seepage, salt damage, rebar fatigue cracks, coating peeling, and corrosion. Table 2 lists the evaluation metrics. The results show that this method can effectively detect various bridge damages from close-range images. Moreover, it can distinguish between combined concrete spalling and rebar exposure, as well as separate severe and slight corrosion areas.





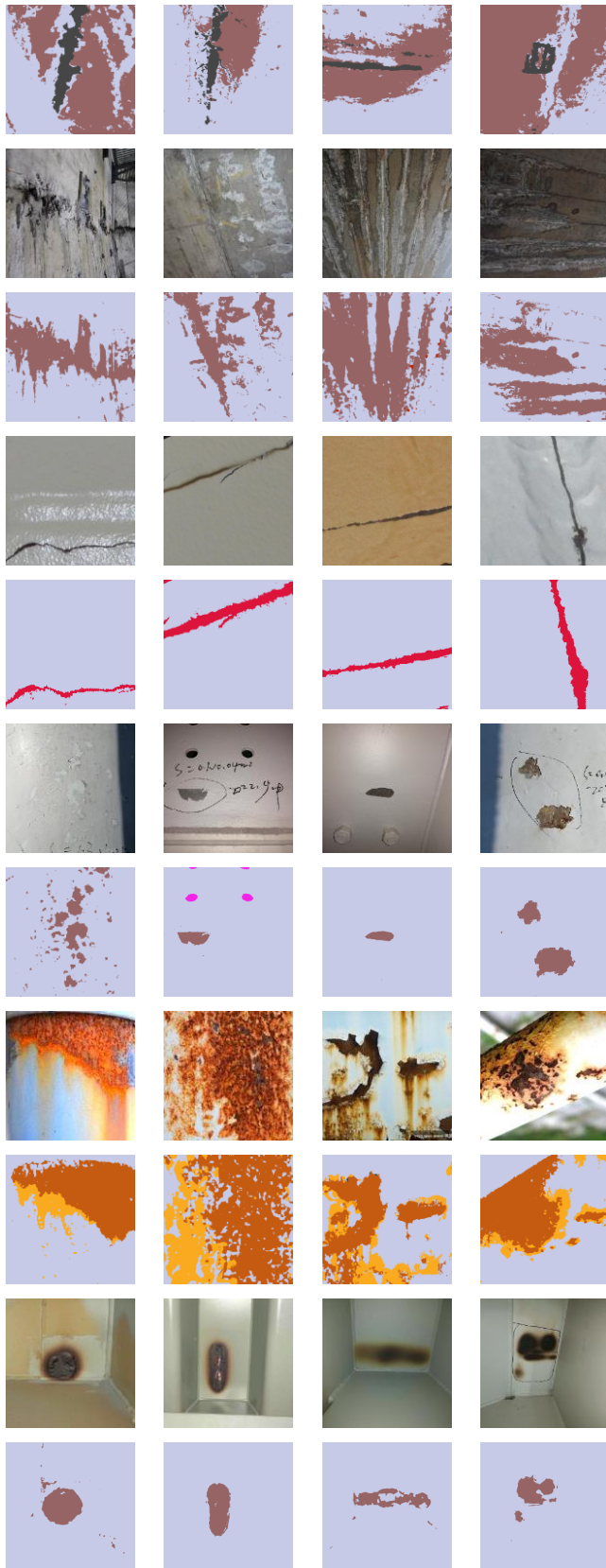
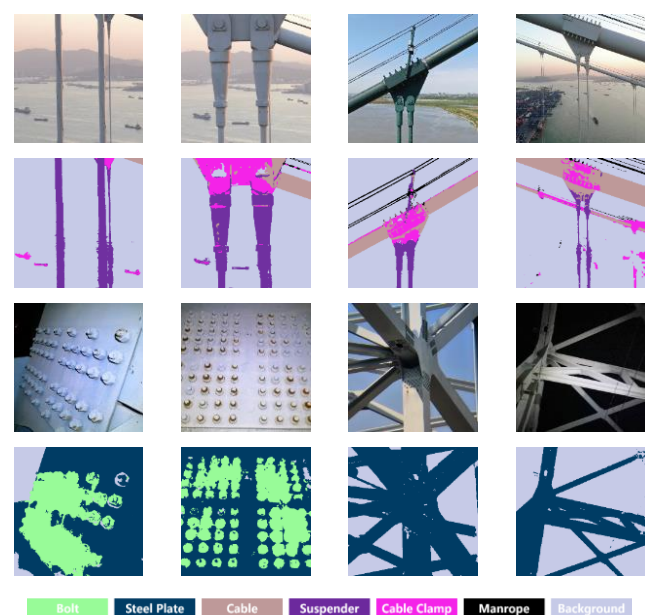


Figure 5. Representative predictions on fine-grained multi-type structural damage for bridges.

Table 2. Evaluation metrics for multi-type structural damage segmentation of bridges.

Bridge structural damage type	PA	mIoU	FWIoU
Concrete crack	96.19%	69.85%	93.35%
Concrete spalling/rebar exposure	98.97%	74.12%	98.30%
Water seepage/salt petering	88.28%	75.15%	79.21%
Steel fatigue crack	96.21%	68.07%	94.69%
Coating spalling/steel corrosion	91.07%	75.39%	84.83%
Fire burning	95.85%	76.22%	93.02%

Figure 6 shows some representative prediction results on new bridge components and ship collision damage, and Table 3 shows the corresponding evaluation metrics. The results suggest that the proposed method have achieved generalization capacity on unseen categories of bridge components and damage apart from the existing structural components and surface damage included in the training imageset. Figure 12(a) shows that despite some misrecognitions of background boats with similar color to cable clamp, key components of cable-suspension bridges such as cable, suspender, cable clamp, and bolts on steel plate can be individually recognized. Figure 12(b) demonstrates that even for a never-appeared emergency of ship collision, the deck scratch, buckling and deformation of steel plate, coating spalling, and handrail failure fragments could be generally identified. It should be noted that some misrecognitions have been observed between the cable plane and distant background and that spurs-like pixels occur along the boundary of damage regions. Possible reasons might attribute to similar material and morphological features with indistinguishable member edges. Geometrical constraints of different component and damage regions would be further considered to address these issues in future study.



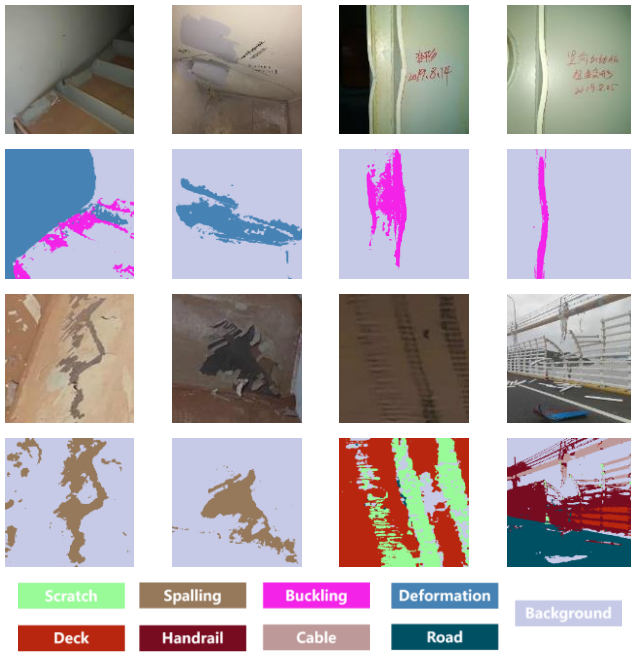


Figure 6. Representative predictions on new bridge components and ship collision damage.

Table 3. Evaluation metrics for segmentation of new bridge components.

New bridge component type	PA	mIoU	FWIoU
Bolt	81.39%	63.88%	70.97%
Steel plate	82.25%	69.24%	70.21%
Cable	96.23%	78.87%	93.84%
Suspender	96.70%	81.51%	94.37%
Cable clamp	95.19%	61.46%	90.96%

Furthermore, the effectiveness and necessity of the proposed method are demonstrated via performance comparisons between the proposed model and SCSEgamba [18], a recently-reported supervised structural damage segmentation model. The model architecture of SCSEgamba is shown in Figure 7. The core architecture incorporates a structure-aware visual state space (SAVSS) module and a multi-scale feature segmentation (MFS) head. The SAVSS captures continuous textures of multi-directional cracks through an innovative structure-aware scanning strategy and dynamically enhances crack features using a lightweight gated bottleneck convolution (GBC). Meanwhile, the MFS integrates multi-scale information to generate refined segmentation maps. Using a unified dataset (containing both concrete cracks and spalling/exposed reinforcement damages), we trained SCSEgamba for 100 epochs using the default training setups and selected the optimal model (with minimal validation loss) for evaluation. Quantitative results demonstrate that our method outperforms SCSEgamba across all three metrics (PA, mIoU, and FWIoU) for both crack and spalling/rebar exposure damage types (see detailed values in Table 4).

Figure 8 presents typical comparative results between the proposed method and SCSEgamba in structural damage

segmentation. The experimental results demonstrate that compared to the blurred boundaries and missed reinforcement detections generated by SCSEgamba, our method can more accurately capture fine crack branches and complex boundary contours of spalling areas. Particularly in the identification tasks of concrete spalling and exposed reinforcement damage, the proposed teacher-student network architecture effectively enhances recognition robustness in weak-texture regions through the synergistic optimization mechanism of feature distillation and contrastive learning. Experimental results indicate that this method can precisely capture edge irregularities in spalling areas while maintaining high sensitivity to exposed reinforcement textures in low-contrast environments, ultimately achieving pixel-level precision in damage segmentation.

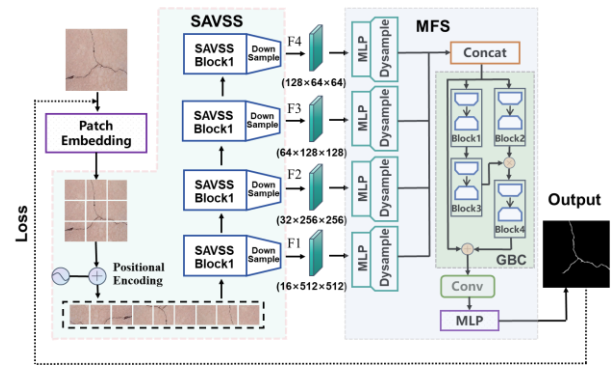


Figure 7. Model architecture of SCSEgamba as comparative validation (reproduced from [18]).

Table 4. Performance comparison with supervised crack segmentation model SCSEgamba on multi-class damage.

Method	Bridge structural damage type	PA	mIoU	FWIoU
SCSEgamba [18]	Concrete crack	96.11%	65.20%	92.77%
Ours	Concrete crack	96.19% (↑)	69.85% (↑)	93.35% (↑)
SCSEgamba [18]	Concrete spalling/rebar exposure	82.38%	60.47%	85.43%
Ours	Concrete spalling/rebar exposure	95.19% (↑)	61.46% (↑)	90.96% (↑)

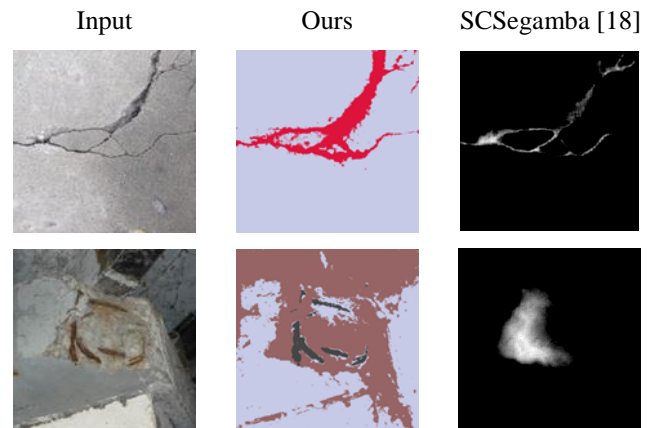


Figure 8. Some representative comparative results of structural damage segmentation between the proposed method and SCSEgamba.

## 5 CONCLUSIONS

This study proposes an unsupervised structural damage semantic segmentation framework based on relational learning and contrastive learning. By constructing a cross-scale feature interaction mechanism and a dynamic negative sample mining strategy, the framework achieves robust recognition and pixel-level localization of multiple types of structural damage in complex engineering scenarios without manual annotation. It effectively addresses the strong dependency of traditional supervised segmentation paradigms on large-scale fine-grained annotated data and the resulting limitations in model generalization. The main research conclusions are as follows:

(1) Based on a teacher-student network knowledge distillation framework, a unified semantic segmentation architecture for multiple types of structural components and surface damages was constructed. Each branch of the teacher-student network contains a pre-trained Transformer visual backbone and a fine-tunable CNN segmentation head.

(2) Using randomly augmented unlabeled image pairs as input, a pre-trained DINO backbone is employed as a frozen feature extractor to generate high-level feature maps. A CNN segmentation head with learnable parameters is designed to produce dense segmentation maps that maintain strong point-wise correlations with the high-level feature maps.

(3) Proposed an inter-layer correlation learning strategy between high-level feature maps from the frozen backbone network and dense segmentation maps from the fine-tuned segmentation head, achieving cross-level feature alignment for different structural components and damage regions within a single image. Developed a contrastive learning module with normalized feature aggregation between teacher-student branches to quantify intra-instance similarity and inter-instance discriminability across different images.

(4) A synthetic loss function comprising a correlation loss and a contrastive loss is designed. The segmentation head is efficiently fine-tuned by fastly optimizing the student network with direct error backpropagation by gradient descent and stably adapting the teacher network with exponential moving average by momentum updating.

(5) This study constructs a multi-scale image dataset encompassing various types of bridge structures and their damage patterns. Through systematic comparative experiments, the proposed model has demonstrated outstanding segmentation accuracy, strong generalization capability, and excellent robustness under complex background interference. The experimental results indicate that the large-scale visual model developed in this study has successfully achieved deep visual understanding of unlabeled bridge component damage images and effectively mastered their unsupervised learning mechanism.

## ACKNOWLEDGMENTS

Financial support for this study was provided by the National Key R&D Program of China [Grant No. 2023YFC3805800], National Natural Science Foundation of China [Grant No. 52192661], Heilongjiang Provincial Natural Science

Foundation [Grant No. LH2022E070], and Fundamental Research Funds for the Central Universities [Grant No. HIT.NSRIF202334].

## REFERENCES

- [1] Xu, Y., Qian, W., Li, N., & Li, H. (2022). Typical advances of artificial intelligence in civil engineering. *Advances in Structural Engineering*, 25(16): 3405-3424.
- [2] Xu, Y., Li, S., Zhang, D., Jin, Y., Zhang, F., Li, N., & Li, H. (2018). Identification framework for cracks on a steel structure surface by a restricted Boltzmann machines algorithm based on consumer-grade camera images. *Structural Control and Health Monitoring*, 25(2), e2075.
- [3] Xu, Y., Wei, S., Bao, Y., & Li, H. (2019). Automatic seismic damage identification of reinforced concrete columns from images by a region-based deep convolutional neural network. *Structural Control and Health Monitoring*, 26(3), e2313.
- [4] Xu, Y., Li, Y., Zheng, X., Zheng, X., & Zhang, Q. (2023). Computer-vision and machine-learning-based seismic damage assessment of reinforced concrete structures. *Buildings*, 13(5), 1258.
- [5] Xu, Y., Bao, Y., Chen, J., Zuo, W., & Li, H. (2019). Surface fatigue crack identification in steel box girder of bridges by a deep fusion convolutional neural network based on consumer-grade camera images. *Structural Health Monitoring*, 18(3), 653-674.
- [6] Xu, Y., Fan, Y., & Li, H. (2023). Lightweight semantic segmentation of complex structural damage recognition for actual bridges. *Structural Health Monitoring*, 22(5), 3250-3269.
- [7] Zhao, J., Hu, F., Qiao, W., Zhai, W., Xu, Y., Bao, Y., & Li, H. (2022). A modified U-Net for crack segmentation by Self-Attention-Self-Adaption neuron and random elastic deformation. *Smart Structures and Systems*, 29(1), 1-16.
- [8] Wang, Y., Jing, X., Xu, Y., Cui, L., Zhang, Q., & Li, H. (2023). Geometry-guided semantic segmentation for post-earthquake buildings using optical remote sensing images. *Earthquake Engineering & Structural Dynamics*, 52(11), 3392-3413.
- [9] Wang, Y., Cui, L., Zhang, C., Chen, W., Xu, Y., & Zhang, Q. (2022). A two-stage seismic damage assessment method for small, dense, and imbalanced buildings in remote sensing images. *Remote Sensing*, 14(4), 1012.
- [10] Cui, L., Jing, X., Wang, Y., Huan, Y., Xu, Y., & Zhang, Q. (2022). Improved swin transformer-based semantic segmentation of postearthquake dense buildings in urban areas using remote sensing images. *IEEE Journal of Selected Topics in Applied Earth Observations and Remote Sensing*, 16, 369-385.
- [11] Wang, Y., Jing, X., Cui, L., Zhang, C., Xu, Y., Yuan, J., & Zhang, Q. (2023). Geometric consistency enhanced deep convolutional encoder-decoder for urban seismic damage assessment by UAV images. *Engineering Structures*, 286, 116132.
- [12] Xu, Y., Qiao, W., Zhao, J., Zhang, Q., & Li, H. (2023). Vision-based multi-level synthetical evaluation of seismic damage for RC structural components: a multi-task learning approach. *Earthquake Engineering and Engineering Vibration*, 22(1), 69-85.
- [13] Xu, Y., Bao, Y., Zhang, Y., & Li, H. (2021). Attribute-based structural damage identification by few-shot meta learning with inter-class knowledge transfer. *Structural Health Monitoring*, 20(4), 1494-1517.
- [14] Xu, Y., Fan, Y., Bao, Y., & Li, H. (2023). Task-aware meta-learning paradigm for universal structural damage segmentation using limited images. *Engineering Structures*, 284, 115917.
- [15] Zhong, J., Fan, Y., Zhao, X., Zhou, Q., & Xu, Y. (2024). Multi-type structural damage image segmentation via dual-stage optimization-based few-shot learning. *Smart Cities*, 7(4), 1888-1906.
- [16] Xu, Y., Fan, Y., Bao, Y., & Li, H. (2024). Few-shot learning for structural health diagnosis of civil infrastructure. *Advanced Engineering Informatics*, 2024, 62, A, 102650.
- [17] Fan, Y., Li, H., Bao, Y., Xu, Y. (2024). Cycle-consistency-constrained few-shot learning framework for universal multi-type structural damage segmentation. *Structural Health Monitoring*.
- [18] Liu, H., Jia, C., Shi, F., Cheng, X., & Chen, S. (2025). SCSegamba: Lightweight Structure-Aware Vision Mamba for Crack Segmentation in Structures. *CVPR 2025*, arXiv:2503.01113.



# Large-Scale Structural Anomaly Detection During Seismic Events Using Optical Flow and Transfer Learning from Video Data

Sifan Wang<sup>1</sup>, 0000-0003-2212-711X, Taisei Saida<sup>2</sup>, 0000-0002-2678-5286, Mayuko Nishio<sup>1</sup>, 0000-0003-1079-2577

<sup>1</sup>Institute of Systems and Information Engineering, University of Tsukuba, 1-1-1 Tennodai, Tsukuba, Ibaraki, Japan

<sup>2</sup>Department of Engineering Mechanics and Energy, University of Tsukuba, 1-1-1 Tennodai, Tsukuba, Ibaraki, Japan  
email: wang.sifan.xs@alumni.tsukuba.ac.jp, s2330199@u.tsukuba.ac.jp, nishio@kz.tsukuba.ac.jp

**ABSTRACT:** Civil structures inevitably experience anomalies and damage, especially during disasters like earthquakes, tsunamis, and hurricanes, causing performance degradation or even collapse. Identifying such anomalies plays an extremely critical role in the maintenance and life extension of civil structures. This study proposes a novel approach based on video data due to its accessibility and rich temporal-spatial information for anomaly detection in large-scale civil structures by integrating transfer learning (TL) techniques with optical flow. Given the low importance of structural Region-of-Uninterest (RoU) like windows and doors, TL with BEIT+UPerNet pre-trained models identifies them. The extended node strength network then leverages video data to focus on structural components and detect disturbances in the nonlinearity vector field. The approach was validated using open video data from E-Defense, capturing two large-scale structural shaking-table tests that featured both pronounced shear cracks and tiny cracks. The detection and quantitative analysis results confirmed the method's effectiveness in detecting structural anomalies and improved computational efficiency by approximately 10%, with a positive correlation observed between this efficiency gain and the proportion of structural RoUs in the video. This study advances anomaly detection in large-scale structures, offering a promising approach to enhancing safety and maintenance practices for critical infrastructure.

**KEY WORDS:** Anomaly detection; Optical flow; Transfer learning; Video data; Node strength network; Shaking-table test

## 1 INTRODUCTION

Engineering structures often sustain damage throughout their service life, deteriorating over time due to various environmental and mechanical factors. Both immediate and prolonged damage contribute to the aging of structures and a subsequent reduction in their service life, highlighting the importance of the structural health monitoring (SHM) process [1].

In recent years, the traditional reliance on manual inspection and scheduled maintenance has evolved with the integration of advanced imaging technologies and machine learning (ML) [2]. For instance, Ji et al. [3] proposed vision-based measurement methods for deformation estimation and cracks identification and demonstrate much higher efficiency and provide more useful information than the traditional measurement techniques. Wu et al. [4] developed an improved algorithm based on YOLOv5s which made mAP@0.5 (mean Average Precision when IoU equal 0.5) values improve by around 10%. Furthermore, Xiong et al. [5] proposed a novel computer vision model based on YOLOv8 for automated concrete bridge crack detection. Structural cracks, as a representative form of anomaly event, can serve as indicators of the deterioration in structural service performance.

The authors previously conducted research on anomaly event detection, focusing on nonlinear occurrences, and validated the efficiency of their proposed methods through a small-scale frame model shaking table test [6]. This method detects nonlinearity in structural vibrations using video data, with feature extraction performed via optical flow techniques. However, a significant challenge persists across the field: the high computational costs associated with the analysis process. Addressing this issue is crucial for advancing SHM technologies and methodologies.

This study introduces a novel method for detecting anomalies due to structural nonlinearity in video data, validated through a

3-D full-scale shaking table test conducted by NIED. The method involves extracting nonlinear disturbances from anomaly events in the velocity vector field estimated by optical flow, constructing an extended node strength network, and applying a morphological opening operation for feature extraction and enhancement. This study presents two key advancements for applying the method to general video data. First, the developed algorithm, which was previously applied only to small-scale experimental models, is now tested on large-scale engineering structures to assess its effectiveness in real-world scenarios. Second, to address the challenge of excessive computational time, we integrate a transfer learning (TL) algorithm to initially identify and filter out the Region-of-Uninterest (RoU), thereby enhancing identification efficiency.

The remainder of this extended abstract is organized as follows: Section 2 presents the framework of the proposed algorithm, while the detailed mathematical formulations are omitted due to the page limit of the extended abstract. Section 3 describes the 3D large-scale shaking table tests, including concrete and wooden building tests, followed by the identification results of TL for structural RoU. It also compares visualization results before and after anomaly events (pronounced shear cracks and tiny cracks) to demonstrate the feasibility of the proposed method. Additionally, a morphological opening operation is introduced to enhance features and denoise visualization results. Computational efficiency, with and without TL, is also compared in Section 4. Finally, conclusions are presented in Section 5.

## 2 METHODOLOGY

The proposed method for detecting structural anomaly events during earthquakes, relying solely on video data, integrates TL with an extended node strength network. Figure 1 illustrates the framework of this method and the flowchart detailing the subsequent steps.

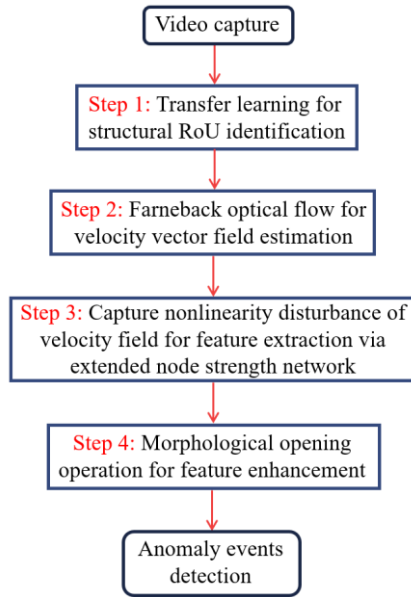


Figure 1. Flowchart of the proposed method

### 2.1 Transfer learning for RoU identification

Recently, Transformer-based models have gained attention for image recognition as alternatives to Convolutional Neural Networks (CNN). Transformers excel at capturing long-distance dependencies, which partly accounts for their superior performance compared to CNN. However, Transformers generally require large amounts of training data. TL addresses this issue by allowing models trained on extensive datasets to perform effectively on specific tasks with smaller datasets. Consequently, BEiT [7], a transformer-based model, was employed, leveraging TL to segment the RoU components. BEiT utilizes the BERT approach [8], a widely used transformer-based model in natural language processing, for image recognition. BEiT treats images as sequences of words and learns to extract features through a masked part-prediction task.

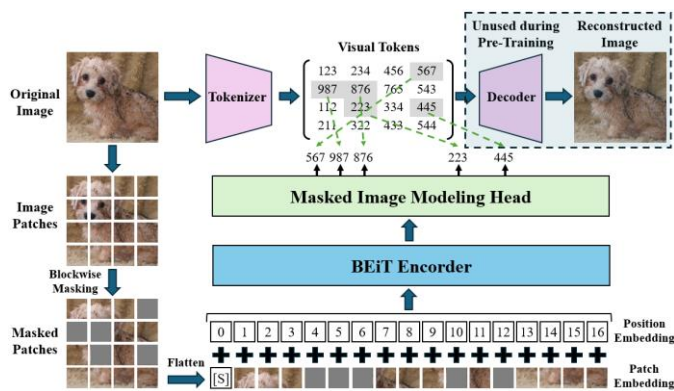


Figure 2. The overview of pre-training BEiT

After pre-training BEiT using Masked Image Modeling (MIM) as shown in Figure 2, the BEiT+UPerNet model, pre-trained for semantic segmentation, was further trained to segment the RoU, specifically targeting windows and doors. An example of RoU recognition for removing the window parts of a building using NIED video data is shown in Figure 3. These images depict the frames before and after RoUs

recognition. In the detected area, pixel values are set to zero, allowing for the removal of these pixels in the subsequent anomaly event detection process. By successfully identifying the structural RoUs, video data that exclusively contains structural component information is utilized, thus improving the computational efficiency of the feature extraction process.



Figure 3. An Example for structural RoUs identification based on TL (a) original frame (b) processed frame

### 2.2 Anomaly events detection by proposed extended node strength network

The anomaly event detection method for video data, as detailed in [6] is summarized here and shown in Figure 4. The method comprises three main steps: (1) estimating the velocity field using Farneback optical flow, (2) extracting anomaly features with the extended node strength network, and (3) enhancing features through a morphological opening operation. This approach allows for the visualization of the timing and location of anomalous events, which result from local disturbances in the vector field caused by nonlinear structural vibrations.

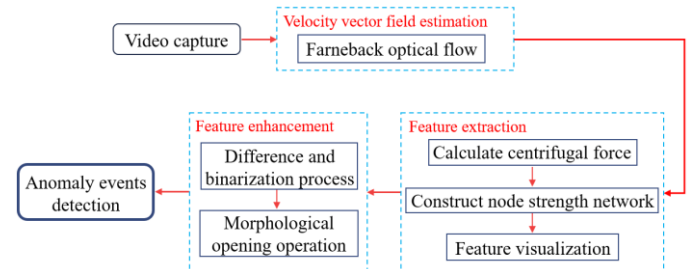


Figure 4. Flowchart of the anomaly events detection method

## 3 ANOMALY EVENT DETECTION FOR 3D SCALED SHAKING TABLE TEST

In this section, the proposed method is validated using two cases from a full-scale shaking table test conducted by the National Research Institute for Earthquake Science and Disaster Resilience (NIED) in Hyogo, Japan. The test included a 1/3 scale model of a six-story Reinforced Concrete (RC) building and a three-story full-scale wooden house. The example frames for the two cases are shown in Figure 5.

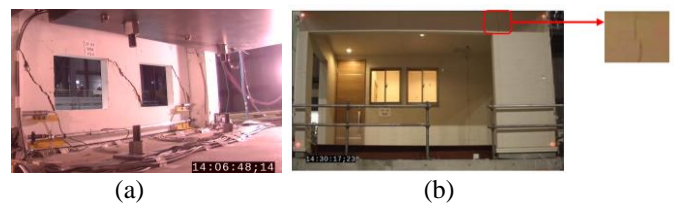


Figure 5. Example frames for (a) RC building (b) wooden house

TL is first applied to identify the RoUs and the results are represented in the black area of Figure 6. Then, Farneback optical flow is employed to estimate the velocity field, the results for the damage frame of the two cases are shown in Figure 6. The length of the arrows represents the instantaneous velocity of the pixel points, while the direction of the arrows indicates the velocity direction. In Figure 6(a), It is observed that the occurrence of shear cracks caused a distinct nonlinear change in velocity within the affected area. However, Figure 6(b) reveals that only short arrows are present in the area of the tiny crack, making it difficult to identify the crack solely by evaluating the velocity field. This limitation is due to the fact that changes in velocity cannot uniquely identify anomalous events, as other regions, such as window edges and areas around wires and bolts, also show velocity variations.

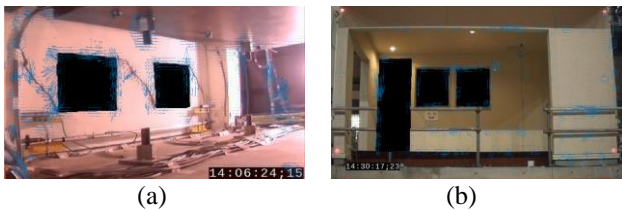


Figure 6. Results of velocity field estimation: (a) RC building (b) wooden house

To represent the anomaly event and enhance its features, an extended node strength network, and a morphological opening operation are utilized. After feature enhancement, as illustrated in Figure 7, nearly all noise areas are effectively removed and only the highlighted area near the crack is retained. The results demonstrate the occurrence of anomalous events and indicate improved detection effectiveness.



Figure 7. Results of anomaly detection: (a) RC building (b) wooden house

#### 4 DISCUSSION FOR COMPUTATIONAL EFFICIENCY

In this study, a key advantage of combining TL is the improvement in computational efficiency. Early identification and removal of RoUs reduce the number of input pixels needed for subsequent node strength network construction. Table 1 compares computational efficiency before and after employing TL for structural RoU identification. Additionally, we expanded our dataset for comparison by incorporating data from the 4-story steel structure shaking-table test mentioned in Figure 3. Table 1 illustrates a positive correlation between improvements in computational efficiency and the proportion of structural RoUs. The selected test cases demonstrate an average efficiency improvement of approximately 10%. In practical applications, analyzing cases with a larger proportion of structural RoUs results in greater efficiency gains.

Table 1. Comparison of computational efficiency after using TL.

Case	Computing time sec/frame		Improve- ment ratio	RoU proportion
	Before	After		
Four-story steel building	64	59	7.81%	8.59%
Six-story RC frame building	159	144	9.43%	9.66%
Three-story wooden house	249	224	10.04%	10.21%

#### 5 CONCLUSIONS

This study proposed a novel anomaly detection algorithm that focused on nonlinearity occurrence by combining deep learning techniques with an optical flow-based extended node strength network. The approach stems from the observation that such events cause nonlinear disturbances in the velocity vector field, which can be estimated from video data. Additionally, structural RoUs, such as doors and windows, are often not the primary focus of structural health monitoring. Pre-identifying these areas before initiating damage detection can significantly enhance the efficiency of the process.

#### ACKNOWLEDGMENTS

This study was supported by the JST SPRING Program (grant number JPMJSP2124) and the JST FOREST Program (grant number JPMJFR205T). The authors also thank to use of the video data on “Archives of E-Defense Shaking table Experimentation Database and Information (ASEBI),” National Research Institute for Earth Science and Disaster Resilience (NIED), Japan.

#### REFERENCES

- [1] Wang S, Nishio M. Review for vision-based structural damage evaluation in disasters focusing on nonlinearity. *Smart Structures and Systems*, 2024, 33: 263.
- [2] Avci O, Abdeljaber O, Kiranyaz S, et al. A review of vibration-based damage detection in civil structures: From traditional methods to Machine Learning and Deep Learning applications. *Mechanical systems and signal processing*, 2021, 147: 107077.
- [3] Ji X, Miao Z, Kromanis R. Vision-based measurements of deformations and cracks for RC structure tests. *Engineering Structures*, 2020, 212: 110508.
- [4] Wu X, Ma T, Zhao Q, et al. Research on YOLOv5s Improved Algorithm for Pavement Crack Detection in Complex Environments. *IEEE Access*, 2024.
- [5] Xiong C, Zayed T, Abdelkader E M. A novel YOLOv8-GAM-Wise-IoU model for automated detection of bridge surface cracks. *Construction and Building Materials*, 2024, 414: 135025.
- [6] Wang S, Nishio M. Anomaly detection in structural dynamic systems via nonlinearity occurrence analysis using video data. *Mechanical Systems and Signal Processing*, 2024, 216: 111506.
- [7] Bao H, Dong L, Piao S, et al. Beit: Bert pre-training of image transformers. *arXiv preprint arXiv:2106.08254*, 2021.
- [8] Vaswani A, Shazeer N, Parmar N, et al. Attention is all you need. *Advances in neural information processing systems*, 2017, 30.



# Development of a Wireless Stereo Vision System for 3D Displacement Online Long-Term Monitoring of Tall Structures

Miaomin Wang, Ki-Young Koo

Vibration Engineering Section, Faculty of Environment, Science and Economy, University of Exeter, Exeter, EX4 4QF, UK

**ABSTRACT:** This paper presents a novel wireless stereo vision system for 3D displacement monitoring of tall structures. The system uses two GNSS wireless camera nodes to capture images of a target and calculate its 2D displacement independently. Each node uploads its data to the cloud, where 3D displacement is reconstructed using a triangulation technique. This system has several advantages over traditional cable-based stereo vision systems for tall structures: 1) The distance between the two camera nodes is not limited, allowing flexible deployment to optimise measurement accuracy for structures of varying heights. 2) It avoids transmitting large volumes of image data between the cameras and the 3D image-processing computer, reducing the need for high network bandwidth. 3) It simplifies the stereo calibration process by eliminating the need for a checkerboard, which is often impractical to be positioned in the field of view of the cameras in tall structure applications. An outdoor test was conducted to validate the system, with the cameras placed about 200 m from the target and 100 m apart. The results showed a measurement accuracy of approximately 1 mm within the horizontal plane.

**KEY WORDS:** Computer Vision, Structural Health Monitoring, Stereo Vision, Wireless Sensor, 3D Displacement Measurement.

## 1 INTRODUCTION

Vision-based systems provide a contactless alternative to traditional sensors. They enable the collection of structural displacement data for structural health monitoring (SHM). As a result, these systems have become popular in the SHM field. The imaging process projects objects in 3D space onto a 2D image plane [1]. Therefore, a single camera can only measure 2D displacement unless special calibration patterns are used.

To measure displacement in 3D, two cameras are combined into a stereo vision system. The depth information of objects is obtained through triangulation. Usually, both cameras are connected to a common controller computer via Ethernet cables. Before measurement, stereo calibration is performed to determine the essential matrix between the images from the two cameras. Next, the controller triggers and synchronizes the two cameras simultaneously to capture images. These images are then transmitted to the controller for processing, including stereo rectification, stereo correspondence, and 3D point reconstruction. Stereo vision systems have been successfully applied to measure the 3D displacement of structures such as wind turbines [2] and bridges [3].

However, measurement accuracy in depth decreases when the measurement distance increases if the distance between the two cameras (the baseline) remains constant. For tall structures, the distance between cameras and structures can be significant. To maintain measurement accuracy in depth, a baseline of potentially hundreds of meters is required. In such cases, conventional cable-based stereo vision systems become impractical.

To address this limitation, cable-free stereo vision systems have been developed. Yang et. al [4] introduced a mobile stereo vision system with an adjustable baseline distance. Images from the cameras are transmitted wirelessly to a controller computer. Sumetheeprasit et. al [5] developed a stereo vision system using two drone-mounted cameras with a variable baseline. However, existing cable-free stereo vision systems mainly target short-term, offline measurements. Long-term online monitoring poses additional challenges, such as ensuring

long-term synchronized image capture, managing the large bandwidth needed for wireless image transmission, and performing real-time stereo image processing. These challenges complicate the long-term online monitoring of tall structures.

This paper presents a novel wireless stereo vision system designed for long-term online monitoring of 3D displacement in tall structures. Figure 1 illustrates the overall workflow of this system:

- 1) The left and right cameras are strategically positioned to target a common point on the structure.

- 2) Stereo calibration is performed by measuring the relative geometrical relationship (the essential matrix) between the two cameras using GPS-RTK. A world coordinate system is established, with the origin located at the center of the left camera. The Z-axis extends from the center of the left camera toward the center of the right camera. The Y-axis points vertically upward, and the X-axis is defined according to the right-hand rule. This approach simplifies coordinate system transformation during 3D reconstruction.

- 3) Both cameras are simultaneously triggered by 10 Hz pulse-per-second (PPS)-based signals to capture synchronized images.

- 4) Reference images from both cameras are selected, and feature points are detected using the deep learning algorithm SuperPoint [6]. These detected points are matched using the LightGlue algorithm [7]. Bounding boxes around these matched point pairs serve as candidates for selecting a tracking target using the zero-normalized cross-correlation (ZNCC) algorithm.

- 5) The cameras capture images every half hour or one hour to document illumination changes throughout the day. The ZNCC scores of candidate targets across these images are calculated, and the bounding box with the highest ZNCC score is selected for long-term tracking.

- 6) Measurement begins, with each camera independently processing its captured images to determine the 2D pixel position of the selected target.

7) The extracted 2D data from each camera is automatically uploaded to Amazon Web Services (AWS) S3 for storage.

8) AWS Lambda computes the 3D displacement using the uploaded 2D data from both cameras.

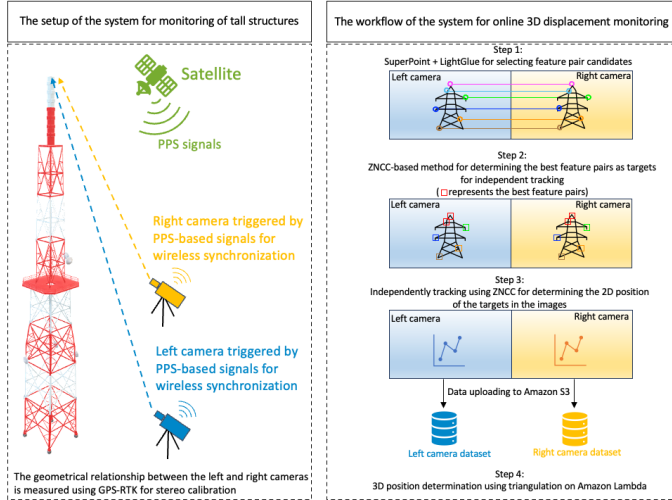


Figure 1. The workflow of the wireless stereo vision system.

## 2 WIRELESS STEREO VISION SYSTEM

### 2.1 Hardware

The wireless stereo vision system consists of left and right camera nodes, each with identical hardware components. Each node includes a SONY IMX296 camera with a lens, two Raspberry Pi 4B computers, a GNSS board, a GNSS antenna, and a 4G module. The camera can be triggered by external signals. To wirelessly trigger both cameras simultaneously, PPS signals are used. Once the first Raspberry Pi receives the PPS signal from satellites, it generates a 10 Hz trigger signal to control the camera's image capture. The PPS signal from the satellites occurs precisely at the start of every second, providing nanosecond-level accuracy. To ensure durability for long-term field operation, the hardware components of each camera node are enclosed in a CCTV camera housing.

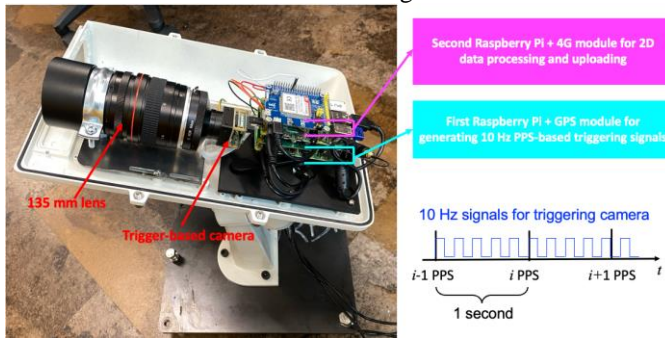


Figure 2. The hardware of the left/right camera.

### 2.2 software

The software workflow for online 3D displacement monitoring is shown in Figure 1 and described in the Introduction. This section explains how 3D displacement is calculated from the 2D data captured by the two cameras.

In the proposed system, unlike conventional stereo vision systems, the left and right cameras are not permanently fixed during manufacturing. Instead, their relative positions can be

adjusted according to different scenarios. Therefore, stereo calibration must be performed before each measurement. Stereo calibration determines the essential matrix, which describes the geometric relationship between the image planes of the two cameras. This essential matrix combines the intrinsic parameters of the two cameras and a fundamental matrix.

Typically, the two cameras are placed far apart, with a large overlapping field of view (FOV), aimed at the top of the monitored structures. In this setup, using a calibration pattern to directly obtain the essential matrix is challenging. As a result, the intrinsic camera matrices and the fundamental matrix are calibrated separately.

The intrinsic matrices of the two cameras,  $K_{left}$  and  $K_{right}$ , can be obtained using Zhang's calibration method [8]. The fundamental matrix is calculated using GPS-RTK, as shown in Figure 3. The calibration process for the fundamental matrix follows these steps:

1) The coordinates of the left and right cameras, as well as the structure's ground level, are measured using GPS-RTK. A world coordinate system is defined with the origin at the center of the left camera. The camera centers are adjusted to point toward the target, and the roll angles are set to zero. The yaw angles of both cameras are then calculated. The left camera is located at  $(0, 0, 0)$ , and the right camera at  $(0, V, S)$ .

2) The target's coordinates in the world coordinate system are determined based on structural drawings. The pitch angles of the cameras are then calculated. The rotation matrix from the left camera's coordinate system to the world coordinate system is:  $R_{left} = R(Yaw_{left}) R(Pitch_{left}) R(Roll_{left})$ , where

$$R(Yaw_{left}) = \begin{bmatrix} \cos(Yaw_{left}) & -\sin(Yaw_{left}) & 0 \\ \sin(Yaw_{left}) & \cos(Yaw_{left}) & 0 \\ 0 & 0 & 1 \end{bmatrix}$$

$$R(Pitch_{left}) = \begin{bmatrix} \cos(Pitch_{left}) & 0 & \sin(Pitch_{left}) \\ 0 & 1 & 0 \\ -\sin(Pitch_{left}) & 0 & \cos(Pitch_{left}) \end{bmatrix}$$

$$R(Roll_{left}) = \begin{bmatrix} 1 & 0 & 0 \\ 0 & \cos(Roll_{left}) & -\sin(Roll_{left}) \\ 0 & \sin(Roll_{left}) & \cos(Roll_{left}) \end{bmatrix}$$

The translation vector from the left camera to the world coordinate system is  $T_{left} = (0, 0, 0)$ . Similarly, the rotation matrix and translation vector for the right camera are:  $R_{right} = R(Yaw_{right}) R(Pitch_{right}) R(Roll_{right})$  and  $T_{right} = (0, V, S)$ .

3) The fundamental matrix  $F$  between the left and right cameras is calculated by  $F = (R_{right} T_{right})^{-1} (R_{left} T_{left})$ . Then the essential matrix  $E$  is obtained as  $E = (K_{right})^T F K_{left}$ .



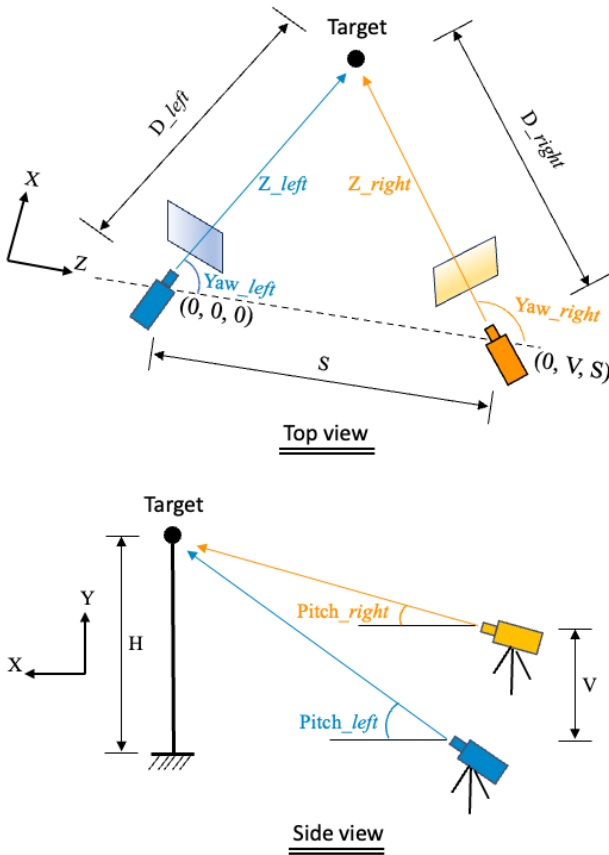
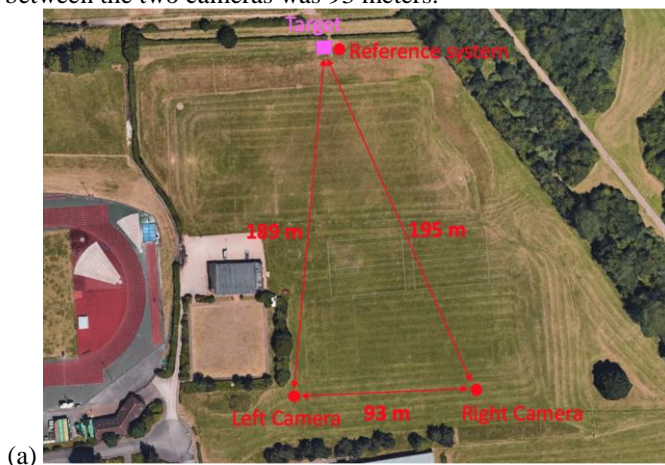


Figure 3. The determination of the foundation matrix.

### 3 VALIDATION TEST

To evaluate the measurement accuracy of the system, an outdoor experiment was conducted. The experimental setup is shown in Figure 4. A vertical cantilever, 2 meters in height, was used as the measurement target. The left and right camera nodes were placed at long distances from the cantilever—189 meters and 195 meters away, respectively. The baseline distance between the two cameras was 93 meters.



(a)



(b)

(c)

Figure 4. The setup of the validation experiment.

The stereo vision system measured the 3D displacement of an artificial target (concentric circles) placed at the top of the cantilever. For reference, the horizontal displacement was also measured using a separate 2D vision-based system. A chessboard target was used for this reference measurement.

The results from the stereo vision system were compared with those from the 2D reference system, as shown in Figure 5. The average root mean square error (RMSE) between the two measurements was 1.02 mm.

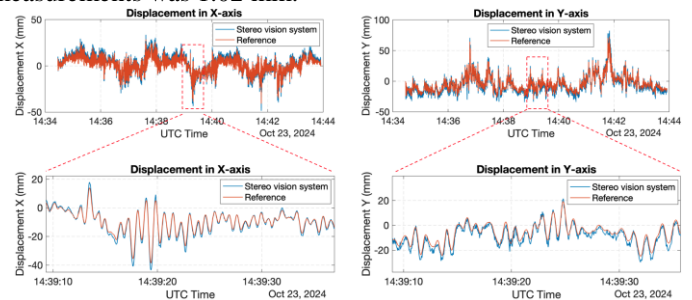


Figure 5. The measurement results of the validation experiment.

### REFERENCES

- [1] M.M. Wang, W.K. Ao, J. Bownjohn, F.Y. Xu, A novel gradient-based matching via voting technique for vision-based structural displacement measurement, *Mech Syst Signal Pr*, 171 (2022).
- [2] W. Feng, Q. Li, W. Du, D. Zhang, Remote 3D displacement sensing for large structures with stereo digital image correlation, *Remote Sensing*, 15 (2023) 1591.
- [3] X.-H. Long, W.-W. Zhan, X.-L. Gui, Research on displacement monitoring method of heavy load bridge structure based on stereo vision, 2020 IEEE



International Conference on Industrial Application of Artificial Intelligence (IAAI), IEEE, 2020, pp. 432-437.

[4] Y. Wang, X. Wang, A mobile stereo vision system with variable baseline distance for three-dimensional coordinate measurement in large FOV, *Measurement*, 175 (2021) 109086.

[5] B. Sumetheeprasit, R. Rosales Martinez, H. Paul, R. Ladig, K. Shimonomura, Variable baseline and flexible configuration stereo vision using two aerial robots, *Sensors*, 23 (2023) 1134.

[6] D. DeTone, T. Malisiewicz, A. Rabinovich, Superpoint: Self-supervised interest point detection and description, *Proceedings of the IEEE conference on computer vision and pattern recognition workshops*, 2018, pp. 224-236.

[7] P. Lindenberger, P.-E. Sarlin, M. Pollefeys, Lightglue: Local feature matching at light speed, *Proceedings of the IEEE/CVF international conference on computer vision*, 2023, pp. 17627-17638.

[8] Z. Zhang, A flexible new technique for camera calibration, *IEEE Transactions on pattern analysis and machine intelligence*, 22 (2000) 1330-1334.

# Overview and Challenges of Computer Vision-Based Visual Inspection for the Assessment of Bridge Defects

R.U. Khan, R. Kromanis

Department of Civil Engineering and Management, Faculty of Engineering Technology, University of Twente,  
Drienerlolaan 5, 7522 NB Enschede, The Netherlands  
Email: r.u.khan@utwente.nl, r.kromanis@utwente.nl

**ABSTRACT:** Visual inspection remains the most fundamental and widely used method for assessing the condition of bridges. This process involves observation of structural surfaces at a close distance to identify visible signs of deterioration such as cracking, spalling, corrosion, and delamination. Traditionally, human inspectors perform visual inspections manually. This labour-intensive process is associated with many limitations, for example, subjectivity to an inspector's interpretation, difficulty accessing structural components, management of large volumes of unstructured data and the lack of consistent historical records. Recent advancements in computer vision and artificial intelligence have enabled considerable progress toward automating visual inspections. However, the full automation of visual inspections in practical, real-world scenarios remains constrained by several challenges: (i) the continued need for human intervention, (ii) the limited availability of high-quality labelled datasets, (iii) the generalizability of existing models, and (vi) the lack of standardized inspection protocols. In this positioning paper, we present an overview of the current state of automated visual inspection for defects identification in bridges. It reviews key open-source datasets of defects and state-of-the-art deep learning models. We give our forward-looking perspective on fully automated defects identification systems that align with standardized visual inspection guidelines.

**KEY WORDS:** Visual Inspection; Defects Identification; Condition Assessment; Automated Bridge Inspection; Computer Vision; Structural Health Monitoring (SHM); SHM at Local level.

## 1 INTRODUCTION

Bridges are critical components of our transportation infrastructure. Rigorous and timely inspections are needed to ensure their long-term performance and operational safety, and to avoid catastrophic failures. In general, bridge inspections are classified as general, principal, and special inspections. Each type of inspection serves a distinct purpose, i.e., from basic visual checks, to more in-depth often involving touching distance examinations, to address specific concerns or unusual events such as accidents (e.g., collisions by heavy loads trucks) or natural disasters (e.g., earthquake, flooding) [1]. Among these, visual inspection is the most employed method, particularly during general and principal inspections. It involves systematic observation of the bridge's surface to detect visible signs of deterioration such as cracking, corrosion, spalling, and delamination. These observable defects serve as initial indicators of potential structural issues and guide/suggest evaluation or maintenance actions.

The traditional visual inspection, while primary for initial defects detection, is inherently labour-intensive and often requires close-proximity access to structural elements, which is frequently unfeasible in hard-to-reach locations [2]. The process is also highly subjective, relying heavily on the individual expertise and judgment of trained inspectors. Research indicates a substantial probability (approximately 50%) of inconsistent classification of concrete defects when different inspectors evaluate the same defects [3]. This poses a significant challenge, as the availability of experienced personnel is steadily declining [4]. Inconsistencies often arise from the disconnect between the on-site surveyor and the off-site expert who interprets and documents findings, leading to a

potential mismatch between observed conditions and reported assessments. Also, inspections typically generate a huge amount of unstructured data, including images and reports. Historical inspection reports are rarely utilized in subsequent evaluations due to inadequate data organization and retrieval systems. This lack of continuity poses a challenge for inspectors to accurately visualize and locate previously identified defects, complicating re-localization of defects and trend analysis over time, which involves monitoring defects progression across inspections, identifying deterioration patterns, and anticipating future degradation or necessary interventions. These challenges collectively highlight the need for integrated, data-driven, and automated visual inspection workflows that improve consistency, traceability, and long-term asset management of bridges.

Recent advancements in computer vision (CV) and artificial intelligence (AI) have matured to a level that enables the enhancement and partial automation of visual bridge inspections [5], [6]. These technologies are promising for digitizing inspection workflows, making them significantly fast, reliable, and repeatable. By using AI-driven image analysis, defects identification, and data management systems, bridge visual inspections can be completely automated and independent of subjectivity. Previous literature reviews [7], [8] on CV and deep learning (DL) based bridge visual inspection, have provided foundational overviews of the field up to 2020. While valuable, these reviews have limitations that necessitate an updated perspective. For instance, [7] comprehensively covers structural health monitoring (SHM) with an emphasis on CV-based defects detection (e.g., cracks, spalling, delamination, rust, and bolt loosening). However, its scope is

restricted to datasets and algorithms available prior to 2020, thereby omitting crucial post-2020 advancements in both novel defect types and state-of-the-art AI-driven techniques. Similarly, [8] offers a broad exploration of DL-based SHM, encompassing CV, unmanned aerial vehicles (UAVs), vibration-based methods, and physics-informed approaches, effectively linking traditional machine learning with modern DL strategies. Nevertheless, it lacks critical discussion on the practicalities of real-world applications of visual inspection, the availability of experimental/test datasets, and open-source implementations, thus highlighting a significant gap in addressing deployment challenges and reliability of automated visual inspection. This collective gap highlights the urgent need for a contemporary position that re-evaluates automated visual inspections considering recent research advances and emerging trends, with a focus on improvements in the enrichment of defects dataset, DL-based defects identification algorithms, and practical deployment strategies.

In this positioning paper, we critically evaluate the current state-of-the-art in available defects datasets and DL-based defects identification algorithms, systematically identify the principal barriers to real-world implementation, and propose a forward-looking perspective on the future development of automated visual inspection of defects for bridges. The rest of the paper is organized as follows: Section 2 describes the dataset utilized for bridge defects detection, including data sources and characteristics. Section 3 details the baseline algorithms and the proposed enhancements for defects recognition. Section 4 provides a perspective on the future overview of automated visual inspection. Finally, Section 5 summarizes the overall position paper and draws conclusions.

## 2 RELEVANT DEFECTS DATASETS

Most highway bridges are reinforced concrete (RC) bridges [9]. While a reliable identification of RC defects is essential, existing datasets are often limited in size and class diversity, raising concerns about their real-world applicability and suitability as benchmarks. Over the past decade, significant progress has been made through datasets enabling binary classification [13, 23, 24, 25], multi-class classification [1, 7, 26], multi-label classification [16], binary semantic segmentation [8, 27], and multi-label semantic segmentation [10, 28, 29]. Each dataset contributes to advancing defects assessment methodologies reviewed in this section.

### 2.1 Binary-class classification

The Cambridge Bridge Inspection Dataset (CDS) [10] combines two primary data sources to enhance defects recognition in RC structures. The first source comprises 21,284 high-resolution images captured from 10 RC highway bridges in Cambridge. The focus is on critical structural elements such as decks, columns, piers, and abutments. Since these bridges are in good condition, the dataset lacks sufficient diversity of defects. To address this limitation, a second set of 22,121 images was incorporated from the U.S. Federal Highway Administration and the Georgia Department of Transportation, enriching the dataset with a variety of examples of defects. All images are categorized into two classes “healthy” and “potentially unhealthy,” providing a foundational binary classification benchmark for structural condition assessment. This hybrid approach ensures broad applicability. SDNET [11]

is also a large-scale binary annotated image dataset designed to train, validate, and benchmark AI-driven crack detection models for concrete structures. Comprising over 56,000 images of cracked and non-cracked surfaces of diverse structural elements such as bridge decks, walls, and pavements. The dataset captures a wide range of crack widths, from 0.06 mm to 25 mm, enhancing its applicability to real-world scenarios. SDNET incorporates various challenging conditions such as shadows, surface roughness, scaling, edges, holes, and background debris, simulating shared challenges encountered in visual inspections. While the dataset covers many structural elements, its initial version suffered from labeling inaccuracies, which may require preprocessing or correction for reliable model training. Despite this limitation, SDNET remains a valuable resource for advancing automated structural defects assessment.

The Image-based Concrete Crack Database (ICCD) [12] is developed using 1,455 high-resolution crack images captured via smartphone from suspension bridge towers and anchor chambers in Dalian, China. To ensure diversity, images were taken at varying distances (0.1 – 1.0 m) and under different lighting conditions (daylight, nighttime, direct sunlight, and shaded surfaces), simulating real-world inspection conditions. These images were then cropped into  $256 \times 256$  px patches and manually labeled into two classes – cracked and uncracked concrete. Through data augmentation, the final dataset was expanded to 60,000 images, significantly enhancing its utility for training robust DL models in automated crack detection. This approach improves generalization and addresses variability in real-world visual inspection scenarios. The Bridge Crack Dataset (BCD) [13] is specifically designed for robust crack detection in bridge inspection scenarios. The original dataset consists of 2,068 images of bridge cracks, which were processed and augmented to generate 6,069 image patches, optimizing them for DL applications. To enhance real-world applicability, the dataset intentionally includes challenging conditions such as bridge shading, water stains, and bright light reflections, common obstacles in field inspections. By incorporating these complexities, BCD serves as a valuable benchmark for developing generalizable and noise-resistant crack classification models, ensuring practical utility in automated visual inspection systems. While these datasets provide valuable benchmarks for binary crack detection, they suffer from critical limitations, for example, CDS [10] lacks natural defects diversity, SDNET [11] has labeling errors, ICCD [12] relies on artificial augmentation, and BCD's [13] small scale and synthetic challenges may not reflect real-world complexity.

### 2.2 Multi-class classification

The Bearing Condition State Classification dataset [14] comprises 947 annotated images of structural bridge bearings. The annotations adhere to the condition state assessment guidelines outlined by the American Association of State Highway and Transportation Officials [21] and the Bridge Inspector's Reference Manual [22]. The dataset categorizes steel corrosion into four distinct condition states: good, fair, poor, and severe. Detailed annotation guidelines, along with explanatory examples, are provided to ensure consistent and accurate condition assessment. The dataset serves as a valuable resource for visual inspection and deterioration assessment of



bridge bearings. The Multi-classifier Dataset (MCDS) [3] consists of 38,408 annotated images capturing various deterioration patterns in concrete structures. Defects are classified into eight distinct categories including spalling, cracks, rust staining, efflorescence, scaling, abrasion/wear, exposed reinforcement, and general defects. This comprehensive taxonomy enables detailed analysis of concrete degradation assessment and supporting visual inspection.

### 2.3 Multi-label classification

Concrete DEfects BRIDGE Image (*CODEBRIM*) dataset [16] is the largest and most realistic multilabel dataset for RC deterioration classification. The dataset categorizes defects into six distinct classes: crack, spalling, exposed reinforcement bar, efflorescence, corrosion, and background. The unbalanced version of *CODEBRIM* consists of 7,729 annotated image patches extracted from 30 bridges, selected to represent diverse deterioration levels, defects sizes, severity, and surface textures. High-resolution images were captured under different weather conditions and using multiple cameras at different scales. To address accessibility challenges, a subset of data was acquired via UAV for defects located at elevated positions. Despite its comprehensiveness, *CODEBRIM* present a key challenge for real-world transferability. The dataset is composed of cropped image patches, where original images are subdivided into rectangular segments based on maximum defects dimensions. This approach may disrupt contextual information, which is critical for holistic defects assessment.

### 2.4 Binary-class semantic segmentation

The *UAV75* dataset [17] comprises 75 images featuring pixel-wise manual annotations for binary semantic segmentation tasks. This dataset provides precise delineation of target features at the pixel level, enabling detailed analysis of structural characteristics. The fixed image dimensions and binary classification scheme facilitate consistent model training and evaluation, while the limited sample size positions this dataset as a specialized benchmark for targeted applications in structural assessment. Kulkarni et al. [18] introduced *CrackSeg9k*, currently the largest and most diverse binary crack segmentation dataset, comprising 9,255 images aggregated from ten preexisting sub-datasets including *Crack500*, *Deepcrack*, *SDNET*, *CrackTree*, *GAPs*, *Volker*, *Rissbilder*, *Noncrack*, *Masonry*, and *Ceramic*. The dataset addresses key limitations in individual source datasets (e.g., noise, distortion) through standardized preprocessing, while maintaining diversity in surface materials (concrete, masonry) and crack morphologies. Despite its focus on binary crack segmentation as shown in Figure 1, the dataset's practical utility depends on recognizing at least nine distinct defect types. Notably, *CrackSeg9k* homogenizes acquisition conditions including camera pose, lighting, and hardware across sub-datasets to minimize confounding variables. This curation enhances its reliability for benchmarking semantic segmentation algorithms in visual inspection for RC defects applications.

### 2.5 Multi-label semantic segmentation

The Structural Defects Dataset (S2DS) [20] is the first multi-class semantic segmentation dataset for RC defects analysis, containing 743 annotated images of RC bridges. It classifies five defect types: cracks, spalling, corrosion, efflorescence, and

vegetation along with control points for georeferencing as shown in Figure 2. While the dataset is pioneering in enabling multi-class segmentation and features high-quality manual annotations by a trained expert, its limited size and diversity raise concerns about real-world applicability. The *dacl10k* dataset [5] represents the first large-scale benchmark for multi-label semantic bridge defects segmentation, featuring 9,920 annotated images sourced from bridge inspections in Germany between 2000 and 2020. Developed to support AI-assisted defects recognition and documentation, the dataset aligns with structural inspection guidelines, focusing on defects that can be legally assessed. It includes 19 classes as shown in Figure 3 categorized into concrete defects, general defects, and objects, capturing complex real-world scenarios where multiple defects often overlap. The *dacl1k* dataset [19] addresses critical limitations in existing RC defects datasets by providing 1,474 uncropped, real-world inspection images with multi-label annotations across five damage classes including Crack, Efflorescence, Spalling, Bars Exposed, Rust, and a No Damage category, derived from diverse sources including authorities and engineering offices. Unlike datasets such as *CODEBRIM* (which uses cropped patches) or *MCDS*, *dacl1k* preserves raw image heterogeneity varying in camera types, poses, lighting, and resolutions to better reflect real inspection challenges. However, while its diversity enhances practical applicability, the dataset's small size (1,474 images) and moderate label count (2,367 total labels) raise concerns about statistical robustness and class balance. Despite the shortcomings, *dacl1k* represents a step toward bridging the gap between controlled research datasets and actual field conditions, though larger-scale, more granular annotations and rigorous benchmarking remain unmet needs for reliable *RC defects* assessment.

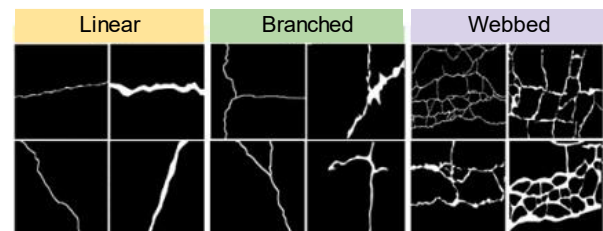


Figure 1. CrackSeg9k's categorization of crack types [18]

## 3 DEFECTS IDENTIFICATION MODELS

Dong et al. study [7] provide a detailed review of computer vision-based structural health monitoring at local level (CV-SHM-LL), outlining various applications and methodological approaches. The work scrutinizes a wide range of models designed for localized analysis, including both patch-based and pixel-based techniques. Additionally, it discusses traditional methods alongside data-driven machine learning approaches. However, it is limited to approximately eight types of structural defects. Cha et al. [8] provides a broad overview of DL-based SHM techniques applied to various infrastructure systems, such as bridges, and different construction materials like concrete and steel. The study extensively reviews the historical development of DL architecture, as illustrated in Figure 4. However, it does not explore deeply into the precise



Figure 2. S2DS Classes and Labels: crack (black), spalling (red), corrosion (orange), efflorescence (blue), vegetation (green), and control point (purple) [20]

application of visual inspection methods for bridges defects identification and their real-world implementation challenges.

Hüthwohl et al. [10] proposed an automated method for detecting intact concrete areas using image segmentation and classification. By applying morphological operations to generate boundary masks, their approach filters out defects-free regions, optimizing inspection efficiency by concentrating analysis on potential damage zones. Dorafshan et al. [11] introduced SDNET dataset and benchmarked performance using AlexNet [23], validating the dataset's utility for algorithm development. Li et al. [12] developed a convolutional neural network (CNN) based crack detection method using an enhanced AlexNet [23], overcoming traditional limitations like noise sensitivity. Their model achieved 99.06% validation accuracy and was deployed as a smartphone app for real-world use. Xu et al. [13] developed an end-to-end CNN-based crack detection model. Achieving 96.37% accuracy without pre-training, it outperformed traditional methods and showed potential as a versatile feature extraction module for other networks.

Hüthwohl et al. [3] developed a three-stage multi-classifier system for concrete defects detection in bridges using fine-tuned deep neural networks trained on multi-source inspection data. Their approach first identifies five defect types along with defects-free areas, then detects exposed reinforcement, and finally recognizes rust staining. The approach achieves 85% average classification accuracy. Mundt et al. [16] developed a meta-learning approach for automated CNN design targeting multi-defects concrete classification. Using their CODEBRIM dataset containing images with overlapping defects, they employed MetaQNN [24] and ENAS [25] reinforcement learning methods to generate optimized architectures. The resulting CNNs achieved higher multi-target accuracy than manually designed models while using fewer parameters, with validation accuracy serving as the reinforcement learning (RL) controller's reward signal. Benz et al. [17] presents CRACKNAUSNET, a transfer learning-based CNN for crack detection in unmanned aircraft system (UAS) imagery,

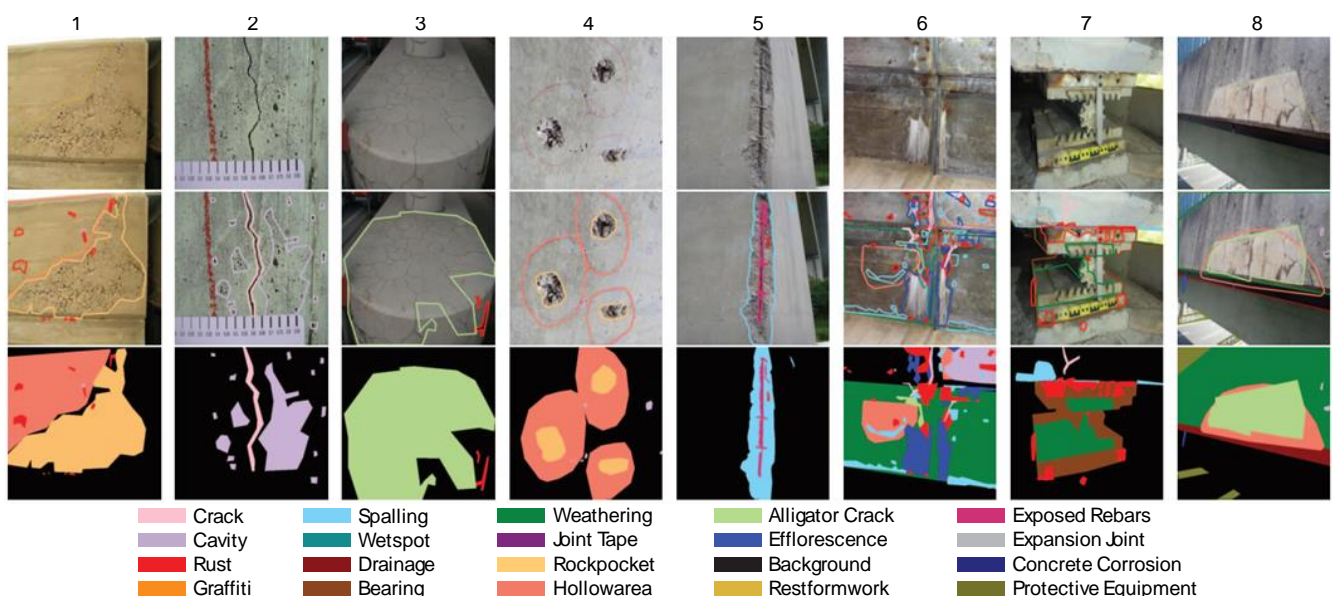


Figure 3. dacl10k dataset and labels [5]. The font size of the caption has been adjusted for clarity.

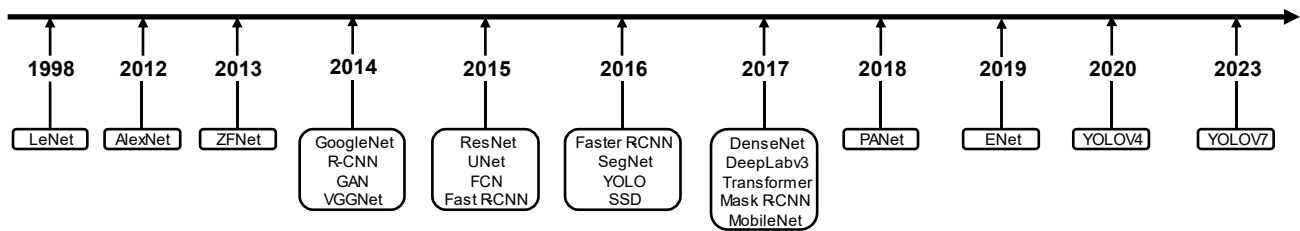


Figure 4. Popular architectures of DL over the years [8]

adapting TerausNet [26] with VGG16's [27] first 16 layers as a pre-trained encoder. The model addresses UAS-specific challenges (low resolution, faint cracks, planking artifacts) using the novel UAV75 dataset, which includes a dedicated class to mitigate planking-induced false positives, where inspection planks were mistakenly identified as defects. While achieving 75% average accuracy on UAV75 outperforming existing approaches, the model's performance declined on external datasets, indicating dataset-dependent effectiveness.

Kulkarni et al. [18] proposed an advanced crack segmentation framework combining YOLOv5 [28] for detection, DINO for unsupervised feature extraction, and FPN-based models [29] for precise segmentation. Their approach utilizes self-supervised transformer attention to enhance CNN performance, overcoming challenges like crack variability and background noise. The method was validated on a newly compiled, meticulously annotated dataset demonstrating improved generalization across diverse crack types and surfaces.

The study [20] proposed a hierarchical multi-scale attention (HMA) model for multi-label semantic segmentation using an HRNet-OCR backbone to oversee objects of varying sizes. The model employs contrastively learned attention maps to dynamically fuse multi-scale features, enhancing pixel-level and contextual representations through transfer learning from Cityscapes. A significant contribution is the line-based tolerant IoU metric designed specifically for crack detection, addressing the shortcomings of conventional area-based metrics (IoU/F1). The evaluation compared CNN-based architectures (DeepLabV3+, FPN with MobileNetV3 / EfficientNet encoders, some with auxiliary losses) and Transformer-based SegFormer (trained with Dice loss). All models used Adam optimization with cosine learning rate scheduling, ImageNet initialization, and 512×512 input resolution over 30 epochs, demonstrating the approach's effectiveness particularly for challenging crack segmentation tasks.

The dacl-challenge [6] aimed to advance automated defects identification in bridges using its large, real-world dataset. It benchmarked CV models as shown in Figure 5 for accurate, detailed detection and classification of bridge defects and components.

a) *Baseline Model:* The dacl-challenge baseline employed SegFormer [30] MiT-b1, pre-trained on ImageNet-1k [23]. This model features a multi-label segmentation head and a compact encoder with 13.1M parameters. For the challenge, SegFormer was trained for 10 epochs on the development set and 30 epochs on the final test set.

- b) *First Place Approach (Sheoran):* The top-performing solution by Sheoran utilized an ensemble of predictions from several models. Initially trained with MMsegmentation, the models were adapted to the segmentation-models-pytorch library for multi-label handling. The training process incorporated diverse augmentations and the RangersLars optimizer. Predictions from six distinct models were aggregated for specific classes, leading to enhanced overall performance.
- c) *Second Place Approach (Bridge Protector):* Bridge Protector's approach involved training the Mask2Former model [31] with an InternImage-H [32] backbone using the MMsegmentation framework. Pre-trained weights from the ADE20K dataset [33] were utilized. To address the multi-label nature of the data, the problem was divided into 19 individual binary segmentation models, one for each class. The outputs of these 19 models were then combined.
- d) *Third Place Approach (Winning Wieners):* Winning Wieners combined a feature pyramid network (FPN) [29] with a multi-axis vision transformer (MaxViT) [34] as the backbone. MaxViT integrates convolutional blocks with the attention mechanism of vision transformers. The xlarge version of MaxViT, pre-trained on ImageNet, was used. The model was trained using a five-fold cross-validation strategy, resulting in an ensemble of five models. Prediction-level threshold optimization was performed for the final ensemble.

Top-performing approaches heavily used transfer learning and adapted existing architectures, potentially limiting exploration of novel structural defects segmentation techniques. Their performance is more sensitive to training configurations than architectural innovation. While ensemble learning improved the results (see Figure 5) their computational cost warrants investigate efficient high-performance strategies. The bar chart presented here shows only the top performance values for defects (objects excluded), compared to the baseline performance. While many deep learning-based approaches for structural defects identification in bridge infrastructure achieve high accuracy using CNNs, transformers, and ensemble methods, their generalizability is often constrained by dataset dependency, high computational demands, and reliance on pre-trained architectures. Future research should prioritize the development of specialized models and training strategies tailored to visual structural assessment, moving beyond generic transfer learning paradigms.

#### 4 FUTURE OVERVIEW OF VISUAL INSPECTION

Over the past decade, different AI and CV-based methodologies have been proposed for the identification of



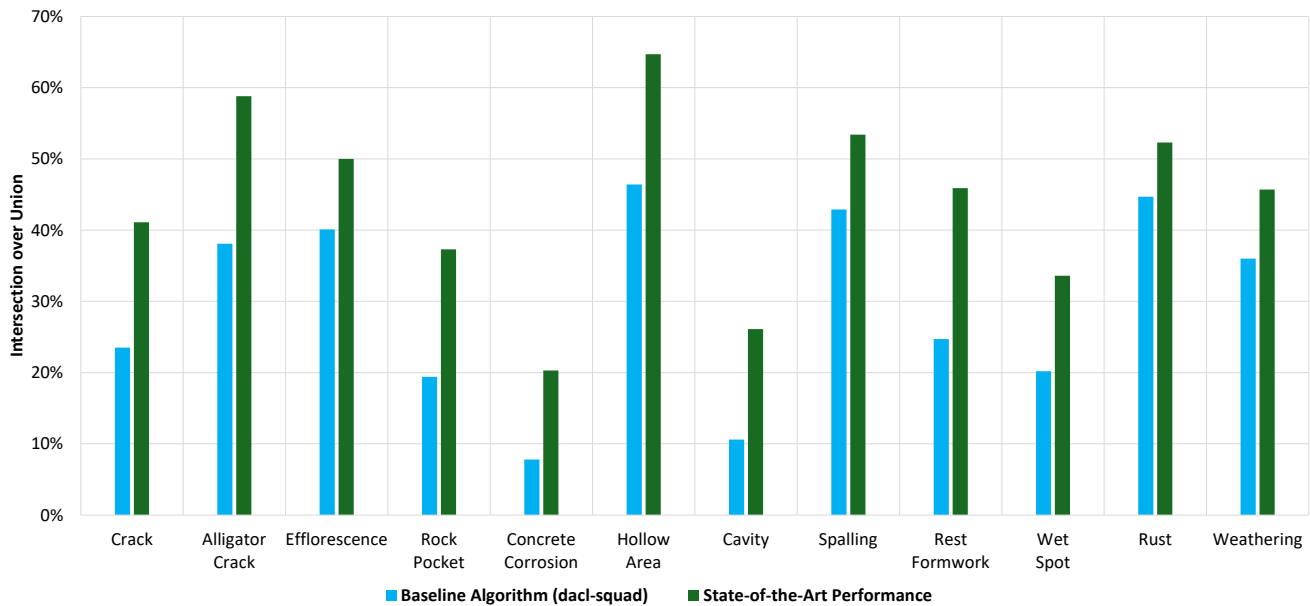


Figure 5. dacl-challenge: state-of-the-art performance achieved vs. baseline algorithm accuracy (% IoU) [6]

local-level defects [7], [8], [36], [37], [38], [39], [40], [41]. However, despite promising results in controlled research settings, many of these solutions have not yet achieved the robustness or scalability approaches for deployment in real-world environments. Most current approaches fall short of industrial standards and remain insufficient for fully automating visual inspections under diverse operational conditions. Thus, while foundational technologies are in place, further developments, validations, and standardizations are necessary to enable their widespread adoption in bridge inspection practices.

Despite all current advancements, the complete automation of visual bridge inspection remains unrealistic at present. This is primarily due to the complexity of standardized inspection protocols such as NEN 2767 in the Netherlands [42], AASHTO in the United States [21], CS 450 in the UK [43], CSA-S6 in Canada [44], AS5100.7 in Australia [45]. These standards define a multi-layered assessment framework, spanning from general structural classification to detailed defects evaluation. For example, NEN 2767 organizes infrastructure assessment across five hierarchical levels. Figure 6 represents inspection levels with an example decomposition for a RC bridge.

- Level-1.** Element Group (i.e., type of bridge such as reinforced concrete) bridge,
- Level-2.** Elements (i.e., main parts of that bridge such as handrail),
- Level-3.** Building Components (i.e., sub-parts of element such as the structural frame of a handrail and protective coating),
- Level-4.** Materials (i.e., material type of each building component (e.g., steel for the structural frame and paint for the protective coating),
- Level-5.** Defects (i.e., defect types of building component, like corrosion and rust in case of steel handrail, color peel off in case of paint coating).

During visual inspection, inspectors primarily interact with bridge at material and defects levels. For each observed defect, the inspector manually assigns three critical parameters including severity, extent, and intensity. These judgments, informed by domain expertise, are used to calculate the condition score for each building component (Level-3), which are then aggregated to yield scores for Elements (Level-2) and the overall condition index for the entire Element Group (Level-1). In the NEN 2767 standard the condition score ranges from 1 (very good) to 6 (very poor). It quantifies the current condition of inspected components of the inspected bridge based on observed defects.

While CV techniques have made substantial progress in defects identification (i.e., detection, localization, and classification of defects such as cracks, corrosion, or spalling), the current state of approaches are not yet capable of reliably performing the significant evaluation required by inspection standards. Specifically, automatic quantification of defects parameters (severity, extent, and intensity), contextual cause analysis, and risk assessment still require manual measurements and expert's (e.g., inspector's) interpretation. As a result, human oversight remains essential, and existing AI-based inspection systems are best viewed as decision-support tools rather than fully autonomous solutions.

To fully understand the current limitations in automating bridge inspections, it is important to examine the fundamental challenges associated with defects identification across multiple levels. In SHM, first Rytter in 1993 [46] and then Worden et al. in 2004 [47] outlined hierarchical levels of damage identification including damage detection, localization, classification, assessment, and prediction. While damage refers to changes in structural properties that adversely affect performance, defects in the visual inspection refer to observable surface-level anomalies. An equivalent framework of object detection as previously highlighted in [48] and now in further extended form, as shown in Figure 7, can be applied to CV-based defects identification. The following levels for

object (or defects, in this case) identification are defined: detection, localization, classification (or segmentation), quantification, and propagation. Currently, most CV-based approaches [6] in bridge inspection have achieved automation up to the classification (or segmentation) level, identifying and labelling regions of interest such as cracks or corrosion patches [7], [8]. However, progressing to quantification is essential to comply with inspection standards, which require precise evaluation of defects parameters (severity, extent and intensity) to calculate the condition score of a component (refer to Figure 6).

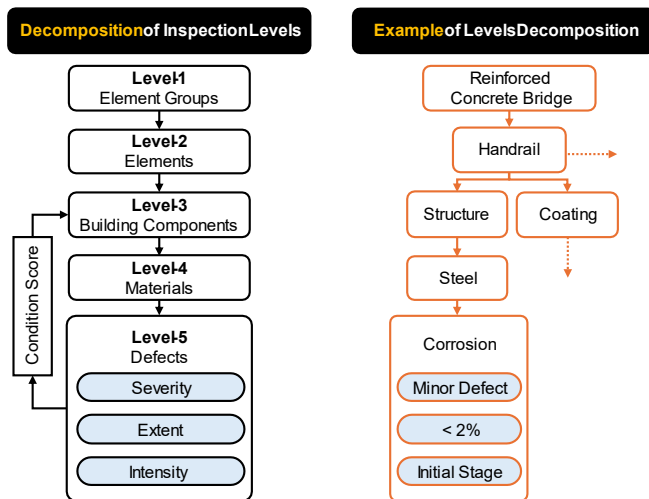


Figure 6. Decomposition and example of levels of inspection process in NEN 2767 standard

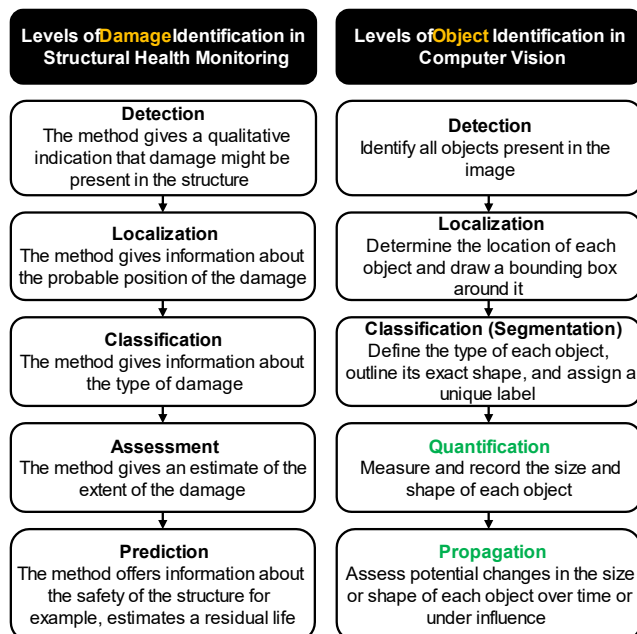


Figure 7. An identification analogy between damage identification [24], [25] and object (or defects in this case) identification

While limited success has been achieved in quantifying specific types of defects (e.g., crack width and length) [49], [50], [51], [52], [53], the methods are not generalized across the

wide spectrum of defects encountered in practice. For instance, NEN standard alone defines approximately 128 distinct defect types relevant to bridge visual inspection, each with distinct characteristics and assessment criteria [42]. This diversity presents a significant challenge for developing universal quantification algorithms. Once automated systems can reliably assign defects-level (Level-5) condition scores as shown in Figure 6, this would enable near-complete automation of the visual inspection process and facilitate systematic and periodic data collection at the local (defects) level.

To address these limitations and pave the way for practical CV-SHM implementation, this paper proposes an automated visual inspection system with a future direction, as conceptually illustrated in Figure 8. The proposed system is envisioned as a continuously evolving ecosystem, driven by progressive enhancements in defects identification capabilities and adherence to established inspection standards, such as the Dutch NEN2767 standard. It is initially trained on a comprehensive dataset synthesized by merging existing state-of-the-art datasets, specifically curated to encompass a diverse range of defect types. A user-friendly application is developed in close collaboration with visual inspection experts to ensure seamless integration with current inspection workflows. Once it achieves a satisfactory level of performance, the system is deployed across various on-site inspection platforms, including mobile devices, tablets, drones, and augmented reality (AR) headsets. In its operational phase, the system functions as a semi-autonomous tool for human inspectors. It provides real-time defects predictions, allowing inspectors to contribute their expertise through manual annotations and comments. All data, including system predictions and human input, are securely stored on a cloud platform, facilitating continuous expert evaluation and ongoing system refinement. Furthermore, the system integrates AR tools to analyze historical defects data, including location and characteristics, to predict future defects propagation over time. This predictive capability empowers initiative-taking maintenance strategies and enhances the long-term sustainability of bridges and other civil infrastructures.

## 5 CONCLUSION

This paper reviews RC defects datasets for bridges and state-of-the-art algorithms and proposes an automated visual inspection system for computer vision-based structural health monitoring at local level (CV-SHM-LL) that integrates deep learning methodologies with standardized inspection protocols and human expertise to advance bridge inspections. Addressing current limitations in data availability, holistic component-level defects evaluation, and deployment feasibility, this study aims to translate theoretical advancements into practical solutions for enhanced SHM. The following conclusions can be drawn from this positioning paper:

- To improve the reliability, robustness, and resilience of the inspection systems, it is necessary to utilize and integrate comprehensive and diverse datasets with unique types of defects, and state-of-the-art prediction models.
- For the inspection system to be useful in real-world scenarios, it must be able to quantify defects by determining their extent, severity, and intensity. This will allow for a step-by-step approach to reach level of quantification as shown in Figure 7.

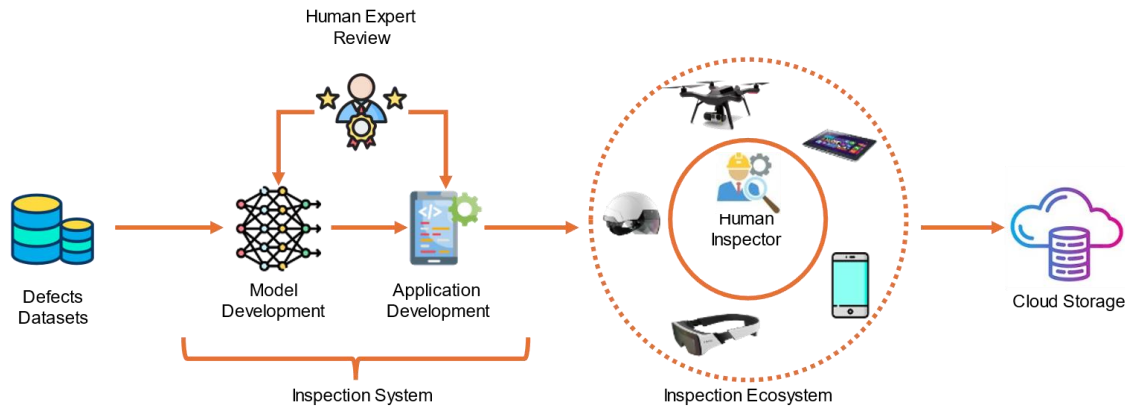


Figure 8. Proposed visual inspection system and future overview of CV-SHM-LL

- Inspection standards must be applied to connect surface-level observations with a deeper understanding of overall structural behaviour. This will bridge the gap to achieving insights into global structural performance.

Future research should focus on the deployment of lightweight neural networks and integration of augmented reality (AR) features on handheld edge devices. This interface should enable the visual overlay of previously identified structural anomalies onto the physical infrastructure. This capability would facilitate targeted inspection efforts and the identification of how defects propagate over time. By leveraging computational models, such an AR-enhanced system should aim to provide inspection personnel with intuitive, real-time data to enable efficient and comprehensive structural evaluations.

## ACKNOWLEDGEMENT

This project has received funding from the European Union's Horizon 2022 research and innovation programme under grant agreement No. 101119554 "BRIDGITISE" (call HORIZON-MSCA-2022-DN-01).

## REFERENCES

- [1] "Bridge Inspector Certification Scheme Scheme Manual National Highway Sector Scheme 31 for the Bridge Inspector Certification Scheme Bridge Inspector Certification Scheme", Accessed: May 06, 2025. [Online]. Available: [www.lantra-awards.co.uk](http://www.lantra-awards.co.uk)
- [2] J. M. W. Brownjohn, "Structural health monitoring of civil infrastructure," *Philosophical Transactions of the Royal Society A: Mathematical, Physical and Engineering Sciences*, vol. 365, no. 1851, pp. 589–622, Feb. 2007, doi: 10.1098/RSTA.2006.1925/ASSET/215B12C1-A04E-4972-A61C-5D4B625F522/ASSETS/GRAPHIC/589FIG13.JPEG.
- [3] P. Hühwohl, R. Lu, and I. Brilakis, "Multi-classifier for reinforced concrete bridge defects," *Autom Constr*, vol. 105, p. 102824, Sep. 2019, doi: 10.1016/J.AUTCON.2019.04.019.
- [4] R. van Gils, "The power of monitoring for life extension of civil engineering structures." Accessed: Jun. 04, 2025. [Online]. Available: [https://www.bouw.nl/en/bridge-construction/the-power-of-monitoring-for-life-extension-of-civil-engineering-structures/?utm\\_source=chatgpt.com](https://www.bouw.nl/en/bridge-construction/the-power-of-monitoring-for-life-extension-of-civil-engineering-structures/?utm_source=chatgpt.com)
- [5] J. Flotzinger, P. J. Rösch, and T. Braml, "dacl10k: Benchmark for Semantic Bridge Damage Segmentation," in *2024 IEEE/CVF Winter Conference on Applications of Computer Vision (WACV)*, 2024, pp. 8611–8620. doi: 10.1109/WACV57701.2024.00843.
- [6] J. Flotzinger *et al.*, "dacl-challenge: Semantic Segmentation during Visual Bridge Inspections," in *2024 IEEE/CVF Winter Conference on Applications of Computer Vision Workshops (WACVW)*, 2024, pp. 716–725. doi: 10.1109/WACVW60836.2024.00084.
- [7] C. Z. Dong and F. N. Catbas, "A review of computer vision-based structural health monitoring at local and global levels," 2021. doi: 10.1177/1475921720935585.
- [8] Y.-J. Cha, R. Ali, J. Lewis, and O. Büyüköztürk, "Deep learning-based structural health monitoring," *Autom Constr*, vol. 161, p. 105328, 2024, doi: <https://doi.org/10.1016/j.autcon.2024.105328>.
- [9] "Renewal of civil infrastructure. Dutch national forecast for replacement and renovation," 2021. [Online]. Available: [www.tno.nl](http://www.tno.nl)
- [10] P. Huethwohl, "Cambridge bridge inspection dataset," 2017.
- [11] S. Dorafshan, R. J. Thomas, and M. Maguire, "SDNET2018: An annotated image dataset for non-contact concrete crack detection using deep convolutional neural networks," *Data Brief*, vol. 21, pp. 1664–1668, 2018, doi: <https://doi.org/10.1016/j.dib.2018.11.015>.
- [12] S. Li and X. Zhao, "Image-Based Concrete Crack Detection Using Convolutional Neural Network and Exhaustive Search Technique," *Advances in Civil Engineering*, vol. 2019, no. 1, p. 6520620, Jan. 2019, doi: 10.1155/2019/6520620.
- [13] H. Xu, X. Su, Y. Wang, H. Cai, K. Cui, and X. Chen, "Automatic Bridge Crack Detection Using a Convolutional Neural Network," *Applied Sciences 2019, Vol. 9, Page 2867*, vol. 9, no. 14, p. 2867, Jul. 2019, doi: 10.3390/APP9142867.
- [14] E. Bianchi and M. Hebdon, "Trained Model for the Classification of Bearing Condition States," Apr. 2021, doi: 10.7294/16628698.v1.
- [15] E. Bianchi and M. Hebdon, "Visual structural inspection datasets," *Autom Constr*, vol. 139, p. 104299, Jul. 2022, doi: 10.1016/J.AUTCON.2022.104299.
- [16] M. Mundt, S. Majumder, S. Murali, P. Panetos, and V. Ramesh, "Meta-learning Convolutional Neural Architectures for Multi-target Concrete Defects Classification with the Concrete Defects BRIDGE Image Dataset," *Proceedings of the IEEE Computer Society Conference on Computer Vision and Pattern Recognition*, vol. 2019-June, pp. 11188–11197, Apr. 2019, doi: 10.1109/CVPR.2019.01145.
- [17] C. Benz, P. Debus, H. K. Ha, and V. Rodehorst, "Crack Segmentation on UAS-based Imagery using Transfer Learning," *International Conference Image and Vision Computing New Zealand*, vol. 2019-December, Dec. 2019, doi: 10.1109/IVCNZ48456.2019.8960998.
- [18] S. Kulkarni, S. Singh, D. Balakrishnan, S. Sharma, S. Devunuri, and S. C. R. Korlapati, "CrackSeg9k: A Collection and Benchmark for Crack Segmentation Datasets and Frameworks," *Lecture Notes in Computer Science (including subseries Lecture Notes in Artificial Intelligence and Lecture Notes in Bioinformatics)*, vol. 13807 LNCS, pp. 179–195, Aug. 2022, doi: 10.1007/978-3-031-25082-8\_12.
- [19] J. Flotzinger, P. J. Rösch, N. Oswald, and T. Braml, "dacl1k: Real-World Bridge Damage Dataset Putting Open-Source Data to the Test," Sep. 2023, Accessed: Apr. 05, 2025. [Online]. Available: <https://arxiv.org/abs/2309.03763v1>
- [20] C. Benz and V. Rodehorst, "Image-Based Detection of Structural Defects Using Hierarchical Multi-scale Attention," *Lecture Notes in Computer Science (including subseries Lecture Notes in Artificial Intelligence and Lecture Notes in Bioinformatics)*, vol. 13485 LNCS, pp. 337–353, 2022, doi: 10.1007/978-3-031-16788-1\_21/TABLES/3.
- [21] "AASHTO Bridge Element Inspection Guide Manual," 2010.
- [22] T. W. Ryan, C. E. Lloyd, M. S. Pichura, D. M. Tarasovich, S. Fitzgerald, and M. B. International, "Bridge Inspector's Reference Manual (BIRM) (2022 NBIS)," Mar. 2023, doi: 10.21949/1503647.



- [23] A. Krizhevsky, I. Sutskever, and G. E. Hinton, "ImageNet Classification with Deep Convolutional Neural Networks", Accessed: Apr. 07, 2025. [Online]. Available: <http://code.google.com/p/cuda-convnet/>
- [24] B. Baker, O. Gupta, N. Naik, and R. Raskar, "Designing Neural Network Architectures using Reinforcement Learning," *5th International Conference on Learning Representations, ICLR 2017 - Conference Track Proceedings*, Nov. 2016, Accessed: Apr. 07, 2025. [Online]. Available: <https://arxiv.org/abs/1611.02167v3>
- [25] H. Pham, M. Y. Guan, B. Zoph, Q. V. Le, and J. Dean, "Efficient Neural Architecture Search via Parameter Sharing," *35th International Conference on Machine Learning, ICML 2018*, vol. 9, pp. 6522–6531, Feb. 2018, Accessed: Apr. 07, 2025. [Online]. Available: <https://arxiv.org/abs/1802.03268v2>
- [26] V. Iglovikov and A. Shvets, "TernausNet: U-Net with VGG11 Encoder Pre-Trained on ImageNet for Image Segmentation," Jan. 2018, Accessed: Apr. 07, 2025. [Online]. Available: <https://arxiv.org/abs/1801.05746v1>
- [27] K. Simonyan and A. Zisserman, "Very Deep Convolutional Networks for Large-Scale Image Recognition," *3rd International Conference on Learning Representations, ICLR 2015 - Conference Track Proceedings*, Sep. 2014, Accessed: Apr. 07, 2025. [Online]. Available: <https://arxiv.org/abs/1409.1556v6>
- [28] G. Jocher *et al.*, "ultralytics/yolov5: v7.0 - YOLOv5 SOTA Realtime Instance Segmentation", doi: 10.5281/ZENODO.7347926.
- [29] T.-Y. Lin, P. Dollár, R. Girshick, K. He, B. Hariharan, and S. Belongie, "Feature Pyramid Networks for Object Detection," Dec. 2016, Accessed: Apr. 07, 2025. [Online]. Available: <https://arxiv.org/abs/1612.03144v2>
- [30] E. Xie, W. Wang, Z. Yu, A. Anandkumar, J. M. Alvarez, and P. Luo, "SegFormer: Simple and Efficient Design for Semantic Segmentation with Transformers," *Adv Neural Inf Process Syst*, vol. 15, pp. 12077–12090, May 2021, Accessed: Apr. 07, 2025. [Online]. Available: <https://arxiv.org/abs/2105.15203v3>
- [31] B. Cheng, I. Misra, A. G. Schwing, A. Kirillov, and R. Girdhar, "Masked-attention Mask Transformer for Universal Image Segmentation," *Proceedings of the IEEE Computer Society Conference on Computer Vision and Pattern Recognition*, vol. 2022-June, pp. 1280–1289, Dec. 2021, doi: 10.1109/CVPR52688.2022.00135.
- [32] W. Wang *et al.*, "InternImage: Exploring Large-Scale Vision Foundation Models with Deformable Convolutions," in *2023 IEEE/CVF Conference on Computer Vision and Pattern Recognition (CVPR)*, Los Alamitos, CA, USA: IEEE Computer Society, Jun. 2023, pp. 14408–14419. doi: 10.1109/CVPR52729.2023.01385.
- [33] W. Xia, Z. Cheng, Y. Yang, and J.-H. Xue, "Cooperative Semantic Segmentation and Image Restoration in Adverse Environmental Conditions," Nov. 2019, Accessed: Apr. 07, 2025. [Online]. Available: <https://arxiv.org/abs/1911.00679v3>
- [34] Z. Tu *et al.*, "MaxViT: Multi-Axis Vision Transformer," *Lecture Notes in Computer Science (including subseries Lecture Notes in Artificial Intelligence and Lecture Notes in Bioinformatics)*, vol. 13684 LNCS, pp. 459–479, Apr. 2022, doi: 10.1007/978-3-031-20053-3\_27.
- [35] A. Howard *et al.*, "Searching for MobileNetV3," *Proceedings of the IEEE International Conference on Computer Vision*, vol. 2019-October, pp. 1314–1324, May 2019, doi: 10.1109/ICCV.2019.00140.
- [36] X. W. Ye, C. Z. Dong, and T. Liu, "A Review of Machine Vision-Based Structural Health Monitoring: Methodologies and Applications," *J Sens*, vol. 2016, no. 1, p. 7103039, Jan. 2016, doi: 10.1155/2016/7103039.
- [37] X. W. Ye, T. Jin, and C. B. Yun, "A review on deep learning-based structural health monitoring of civil infrastructures," *Smart Struct Syst*, vol. 24, no. 5, SI, pp. 567–585, Nov. 2019, doi: 10.12989/sss.2019.24.5.567.
- [38] Q.; Yuan *et al.*, "A Review of Computer Vision-Based Crack Detection Methods in Civil Infrastructure: Progress and Challenges," *Remote Sensing* 2024, Vol. 16, Page 2910, vol. 16, no. 16, p. 2910, Aug. 2024, doi: 10.3390/RS16162910.
- [39] A. Gomez-Cabrera and P. J. Escamilla-Ambrosio, "Review of Machine-Learning Techniques Applied to Structural Health Monitoring Systems for Building and Bridge Structures," *APPLIED SCIENCES-BASEL*, vol. 12, no. 21, Nov. 2022, doi: 10.3390/app122110754.
- [40] M. Azimi, A. D. Eslamlou, and G. Pekcan, "Data-Driven Structural Health Monitoring and Damage Detection through Deep Learning: State-of-the-Art Review," *SENSORS*, vol. 20, no. 10, May 2020, doi: 10.3390/s20102778.
- [41] L. Sun, Z. Shang, Y. Xia, S. Bhowmick, and S. Nagarajaiah, "Review of Bridge Structural Health Monitoring Aided by Big Data and Artificial Intelligence: From Condition Assessment to Damage Detection," *JOURNAL OF STRUCTURAL ENGINEERING*, vol. 146, no. 5, May 2020, doi: 10.1061/(ASCE)ST.1943-541X.0002535.
- [42] "NEN 2767 Part-2 Defects List - 297633".
- [43] "CS 450 - Inspection of highway structures." Accessed: Jun. 01, 2025. [Online]. Available: <https://www.standardsforhighways.co.uk/search/c5c2c3e5-f7f3-4c94-8254-184e41ccd1a0>
- [44] "CSA S6:19, Canadian Highway Bridge Design Code - CSA Group." Accessed: Jun. 01, 2025. [Online]. Available: <https://www.csagroup.org/canadian-highway-bridge-design-code/>
- [45] "AS 5100.7:2017 - Standards Australia." Accessed: Jun. 01, 2025. [Online]. Available: <https://www.standards.org.au/standards-catalogue/standard-details?designation=as-5100-7-2017>
- [46] A. Rytter, "Vibrational Based Inspection of Civil Engineering Structures," 1993. Accessed: Apr. 07, 2025. [Online]. Available: <https://vbn.aau.dk/en/publications/vibrational-based-inspection-of-civil-engineering-structures>
- [47] K. Worden and J. M. Dulieu-Barton, "An Overview of Intelligent Fault Detection in Systems and Structures," *Struct Health Monit*, vol. 3, no. 1, pp. 85–98, 2004, doi: 10.1177/1475921704041866.
- [48] S. Wang, S. A. Zargar, and F. G. Yuan, "Augmented reality for enhanced visual inspection through knowledge-based deep learning," *Struct Health Monit*, vol. 20, no. 1, pp. 426–442, Jan. 2021, doi: 10.1177/1475921720976986;PAGE:STRING:ARTICLE/CHAPTER.
- [49] J. Zhang, S. Qian, and C. Tan, "Automated bridge surface crack detection and segmentation using computer vision-based deep learning model," *Eng Appl Artif Intell*, vol. 115, Oct. 2022, doi: 10.1016/j.engappai.2022.105225.
- [50] G. Xu, Q. Yue, and X. Liu, "Deep learning algorithm for real-time automatic crack detection, segmentation, qualification," *Eng Appl Artif Intell*, vol. 126, Nov. 2023, doi: 10.1016/j.engappai.2023.107085.
- [51] X. Wang, Q. Yue, and X. Liu, "SBDNet: A deep learning-based method for the segmentation and quantification of fatigue cracks in steel bridges," *Advanced Engineering Informatics*, vol. 65, May 2025, doi: 10.1016/j.aei.2025.103186.
- [52] E. Mohammed Abdelkader, O. Moselhi, M. Marzouk, and T. Zayed, "Entropy-Based Automated Method for Detection and Assessment of Spalling Severities in Reinforced Concrete Bridges," *Journal of Performance of Constructed Facilities*, vol. 35, no. 1, Feb. 2021, doi: 10.1061/(asce)jcf.1943-5509.0001544.
- [53] S. Wang, J. Wan, S. Zhang, and Y. Du, "Automatic Detection Method for Concrete Spalling and Exposed Steel Bars in Reinforced Concrete Structures Based on Machine Vision," *Buildings*, vol. 14, no. 6, Jun. 2024, doi: 10.3390/buildings14061580.

# Integrating Mixed Reality Technology, Deep Learning and Domain Knowledge for bridge inspection

Zheyu Liu<sup>1</sup>, Zhen Sun<sup>1</sup>, Patricia Vanova<sup>2</sup>

<sup>1</sup>School of Civil Engineering, Southeast University, Nanjing 211189, China

<sup>2</sup>Center of Research and Innovation in Construction, Faculty of Civil Engineering, Technical University of Kosice, Vysokoskolska 4, Kosice, 042 00, Slovakia

Email: [1318276241@qq.com](mailto:1318276241@qq.com); [sunzhen@seu.edu.cn](mailto:sunzhen@seu.edu.cn); [patricia.vanova@tuke.sk](mailto:patricia.vanova@tuke.sk)

**ABSTRACT:** This study presents an integrated intelligent framework for bridge inspection that synergizes Mixed Reality (MR) technology, deep learning-based object detection, and domain-specific engineering knowledge. Utilizing Microsoft HoloLens 2 as the hardware platform, the system captures real-time 3D bridge surface imagery and deploys the optimized YOLOv11n-ZY model—enhanced with a ZZ convolutional module, YY attention mechanism, and SPPF-LSKA fusion module—to automatically detect and classify multi-category defects including cracks, corrosion, and spalling. Detection results are visualized within an MR interface and dynamically assessed through embedded expert knowledge. Validated on a custom dataset containing 4,176 images of 12 defect types under complex backgrounds, the proposed model achieves 40.3% mAP50 at 60 FPS with only 2.87 million parameters, outperforming existing YOLO variants. Implementation at the case study bridge demonstrates real-time defect localization, 3D model updating, and closed-loop maintenance functionality. The framework advances intelligent infrastructure management by establishing a scalable pipeline for accurate defect assessment and lifecycle-oriented bridge maintenance.

**KEY WORDS:** HoloLens 2; Object detection; YOLOv11; Visualization interface; Intelligent bridge operation and maintenance.

## 1 INTRODUCTION

As a critical component of modern transportation infrastructure, bridges are essential for maintaining socio-economic stability and ensuring public safety [1]. Consequently, their structural safety, stability, and health status are of paramount importance.

At present, traditional inspection methods, while capable of detecting visible defects such as cracks and corrosion, are constrained by inefficiency, heavy dependence on specialized knowledge, and challenges in handling complex environments, limiting their application in modern bridge inspection [2]. However, with the rapid development of computer vision technologies, deep learning-based object detection algorithms (e.g., YOLO, Faster R-CNN) have gradually been introduced into industrial defect detection, achieving significant improvements in efficiency and accuracy.

In the field of bridge defect detection [3], Mixed Reality (MR) technology has also provided novel solutions to traditional inspection approaches. Utilizing devices like HoloLens 2, 3D models can be projected into the real world, enabling engineering personnel to observe bridge surfaces from multiple angles and dimensions, thereby enhancing defect identification accuracy. For instance, certain Chinese bridge institutes have integrated 3D laser scanning with BIM technology to control modeling errors within  $\pm 2\text{mm}$  [4]; however, algorithm robustness in complex environments still requires further improvement.

The integration of emerging technologies such as deep learning, augmented reality (AR), and mixed reality (MR) has rendered bridge defect detection more efficient, precise, and intelligent [5]. At the same time, machine learning approaches have been integrated for defect detection in concrete structures

in the past few years [6]. Nonetheless, adaptability to complex environments and capabilities for lifecycle management still need enhancement to better meet practical operational demands.

This study aims to develop an intelligent bridge defect detection system by integrating multiple technologies. The research focuses on two main objectives.

First, HoloLens 2 is leveraged to develop a mixed reality system that enables 3D visualization, virtual-physical integration, and multi-dimensional defect observation.

Second, the system combines real-time scanning data processed by YOLOv11 with pre-constructed 3D virtual models to create an innovative bridge inspection framework supporting long-term intelligent operation and maintenance.

## 2 UNITY-BASED 3D BRIDGE MODEL AND HOLOLENS 2 DEPLOYMENT

### 2.1 Case Study Bridge Information

This study selects the Wenxi Bridge (Figure 1) in Suijiang New County, Yunnan Province, China, as the exemplar bridge for the visualized intelligent bridge inspection platform. By leveraging the 3D scanning capabilities of HoloLens 2, comprehensive structural information of the bridge was collected. Through comparison with preliminary design drawings, discrepancies between the actual bridge structure and the original plans—caused by on-site construction adjustments or undocumented modifications—were effectively resolved, enabling the successful creation of a 3D model of the Wenxi Bridge in Unity.



Figure 1. Case study bridge - Wenxi Bridge.

The deck width of the case study Bridge is 9 m + 2×1.5 m (pedestrian walkways). The superstructure comprises 9×30 m prestressed concrete simply supported T-beams arranged in three-span continuous units. The substructure includes column piers, U-shaped abutments, and ribbed abutments, with foundation types consisting of spread foundations and pile foundations.

## 2.2 Characteristics of Mixed Reality (MR) Technology and HoloLens 2

Mixed Reality (MR) technology digitizes physical environments and integrates them with virtual objects to create a visualized interactive space where physical and virtual elements coexist. Compared to Virtual Reality (VR) and Augmented Reality (AR), MR not only superimposes virtual entities into real environments but also achieves precise spatial mapping and real-time interaction between virtual objects and physical spaces, forming a spatially consistent mixed reality environment [7].

Microsoft HoloLens 2 (Figure 2), the second-generation MR device released by Microsoft, demonstrates technical advantages in bridge defect detection [8].



Figure 2. HoloLens 2.

## 2.3 Unity Model Deployment on HoloLens 2

The mixed reality (MR) application development for HoloLens 2 is based on the following software and toolkits: Windows 10 SDK, Visual Studio 2023, HoloLens 2 Emulator, Unity 2022.3.53f1c1, Unity Hub, and MRTK 2.8. To ensure efficient development and deployment, the hardware configuration listed in Table 1 was adopted:

Table 1. Computer Hardware Configuration.

CPU	GPU	RAM	Storage	Display
i9-14900HX	RTX 4070	64GB	3TB SSD	2560x1600 / 240Hz / 18-inch

Deployment Workflow is described as follows. "Developer Mode" on both the host computer and HoloLens 2 within the Windows operating system is firstly enabled. And the following procedures are adopted.

### (1) Project Creation:

Create a new project via the Unity Hub integrated development environment and access the Build Settings interface. Select Universal Windows Platform (UWP) and execute the "Switch Platform" operation. This process automatically performs platform compatibility checks and restructures project resource formats through the underlying engine to meet UWP-specific technical requirements.

### (2) MR Toolkit (MRTK) Integration:

Import the Mixed Reality Toolkit using the Mixed Reality Feature Tool (MRFT).

The core principle involves modifying the manifestation configuration file to guide the Unity engine in correctly identifying and loading MRTK modules. Upon returning to the Unity environment, the system automatically initiates dependency detection and resource loading. Compared to traditional methods, MRFT integration effectively avoids dependency conflicts [7], significantly reducing the complexity of managing mixed reality toolchains.

### (3) Unity Project Configuration:

As mixed reality applications fall under the extended reality (XR) domain, activate Unity's built-in XR framework. After configuring the Player module, navigate to the XR Plug-in Management section and install the plugin management component. Enable the "Initialize XR on Startup" parameter and activate "Windows Mixed Reality" to ensure precise hardware-software compatibility, laying the foundation for subsequent MR development.

### (4) Unity Project Export:

Select the target scene file and configure parameters: (1) Set device compatibility to "Any Device" for universal platform support. (2) Select the x64 architecture for optimal runtime efficiency. (3) Optimize auxiliary parameters based on specific development requirements. Initiate the conversion of the Unity project to a Visual Studio solution via the Build button, establishing a standardized framework for application compilation and deployment.



#### (5) Deployment to HoloLens 2 Device:

Open the completed project in Visual Studio 2023 and proceed to the deployment parameter configuration phase. Simultaneously, ensure that the host development environment and the target device are connected to the same wired or wireless local area network (LAN), with sufficient network bandwidth to meet real-time transmission requirements for application image files, thereby guaranteeing the validity of the deployment process.

Within the Visual Studio integrated development environment (IDE), sequentially perform three critical configurations: (1) Program compilation using Debug mode; (2) Selection of the ARM64 instruction set architecture to align

with the target device's hardware specifications; (3) Configuration of remote computer deployment options.

Subsequently, input the target device's network IP address in the debugging parameters module and set the authentication protocol to Universal (Unencrypted) mode. After completing the above parameter configurations, initiate the compile-deploy automation process via the Start Debugging command.

This mechanism synchronously executes the generation of application binary files, their transmission, and device-side loading, establishing a complete end-to-end deployment pipeline. Through the above workflow, the Unity-based 3D model of the case study Bridge was successfully deployed on HoloLens 2, achieving 3D visualization as demonstrated in Figure 3.



Figure 3. 3D Model layout diagram of case study Bridge.

To accurately simulate defect morphologies under real-world conditions and enable interactive analysis of damage data within the HoloLens 2 digital model, high-fidelity defect simulations were integrated into the case study bridge model. Leveraging HoloLens 2's augmented reality system, 3D defect visualization and spatial mapping were implemented [10]. This framework, combined with depth perception and multi-source data fusion algorithms, supports three critical technical requirements: on-site auxiliary defect diagnosis, remote collaborative structural assessment by experts, and dynamic coupling analysis of multidimensional human-machine interaction

### 3 DATASET CONFIGURATION

This work referenced and adapted the data collection standards of the VisDrone2021 [11] dataset, employing methods including web crawling, video frame extraction, and filtering of multiple publicly available bridge defect datasets [12]. Simultaneously, to enhance the model's generalization capability and prevent overfitting, data augmentation techniques—such as random rotation [13], random occlusion, color jittering, Gaussian blur, and noise addition—were applied to the dataset [14], as shown in Figure 4.



Figure 4. Defects on the bridge.

The experimental dataset for this study was ultimately compiled and generated, containing 4,176 images. Label files for the dataset were created using the labeling tool, with a total of 32,201 annotated bounding boxes. These annotations encompass bridge defect information across multiple categories, including exposed reinforcement, spalling, corrosion, water seepage in wet joints, mold growth, and cracks, as illustrated in Figure 5. The dataset aligns with the simulated defect conditions previously generated on the Unity bridge model.



Figure 5. Spalling & Exposed reinforcement.

Distinct from traditional bridge defect datasets that focus on one or several common types of surface-level defects, the self-constructed dataset employed in this study—"Small-Target Detection Dataset for Multi-Category Bridge Defects under Complex Background Interference"—simultaneously incorporates 12 bridge defect types, including those with low occurrence frequencies. To replicate real-world inspection scenarios and simulate the scanning and observational perspectives of inspectors wearing HoloLens 2 for subsequent comparative analysis and digital model superimposition tasks, no image or semantic segmentation [15] is performed on bridge defects in this dataset, preserving full panoramic small-target detection and recognition. Furthermore, unlike conventional small-target datasets, bridge defect images in real-world scenarios exhibit challenges such as blurred backgrounds, high inter-defect similarity, strong deceptive features, and extremely

small defect targets. These characteristics lead to core technical detection challenges, including weak multi-scale target sensitivity, significant complex background interference, insufficient fine-grained feature representation, and high inter-category similarity. Through the aforementioned diverse image augmentation methods, the dataset is further enriched and expanded to enhance robustness. The highly challenging "Small-Target Detection Dataset for Multi-Category Bridge Defects under Complex Background Interference" imposes greater demands on subsequent target detection and recognition tasks.

## 4 YOLOV11 ALGORITHM

### 4.1 YOLOv11 Model Introduction and Advantages

Ultralytics recently released YOLOv11, designed as a detection model achieving state-of-the-art (SOTA) performance across multiple tasks. The architecture of previous models has been optimized, enabling YOLOv11 to attain cutting-edge

performance in diverse tasks (object detection, segmentation, pose estimation). The overall network architecture is illustrated in Figure 6.

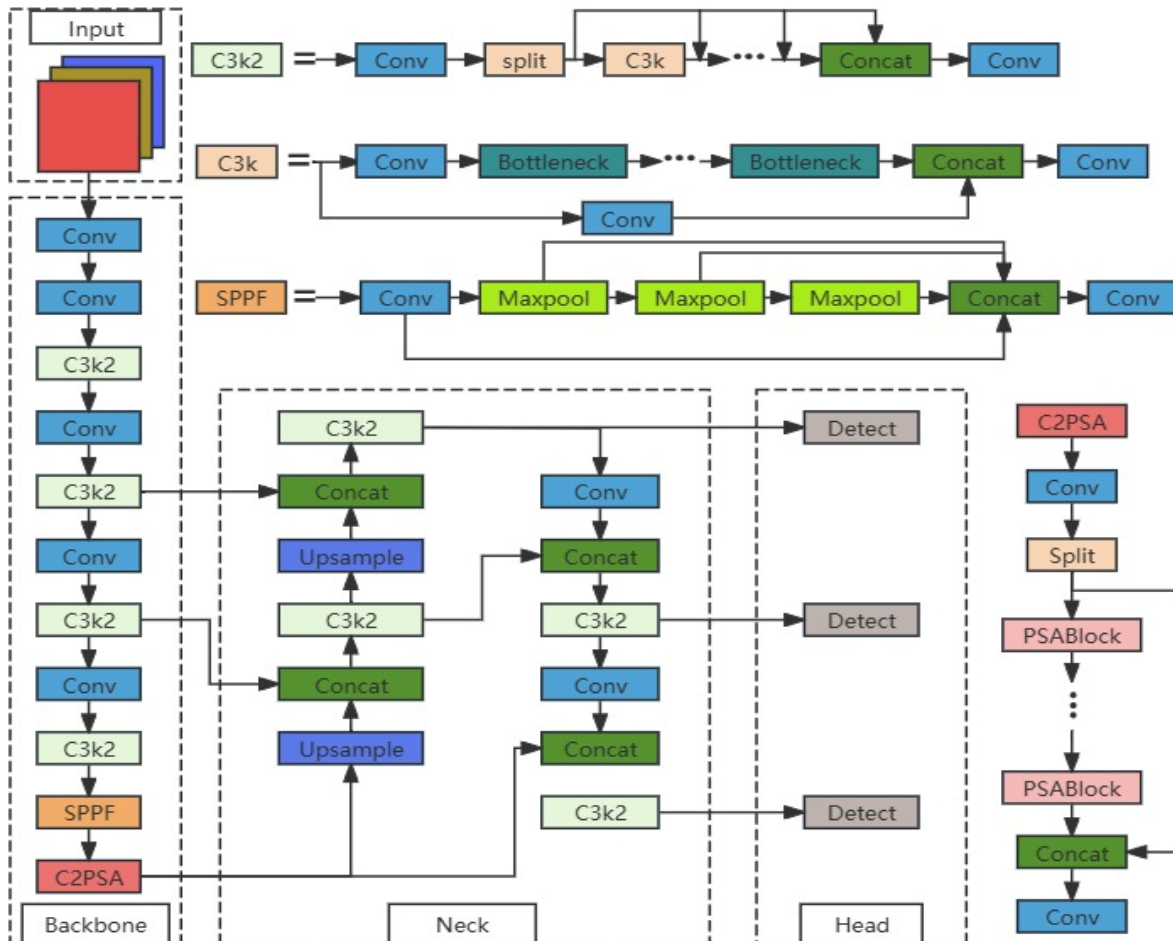


Figure 6. Overall network architecture diagram of YOLOv11.

Compared to YOLOv8, YOLOv11 reduces parameters by 22% on the COCO dataset while achieving higher mean Average Precision (mAP), as shown in Figure 7. Simultaneously, its inference speed is approximately 2% faster

than YOLOv10, reaching 60 frames per second (FPS), making it one of the fastest object detection models and providing enhanced support for real-time applications.



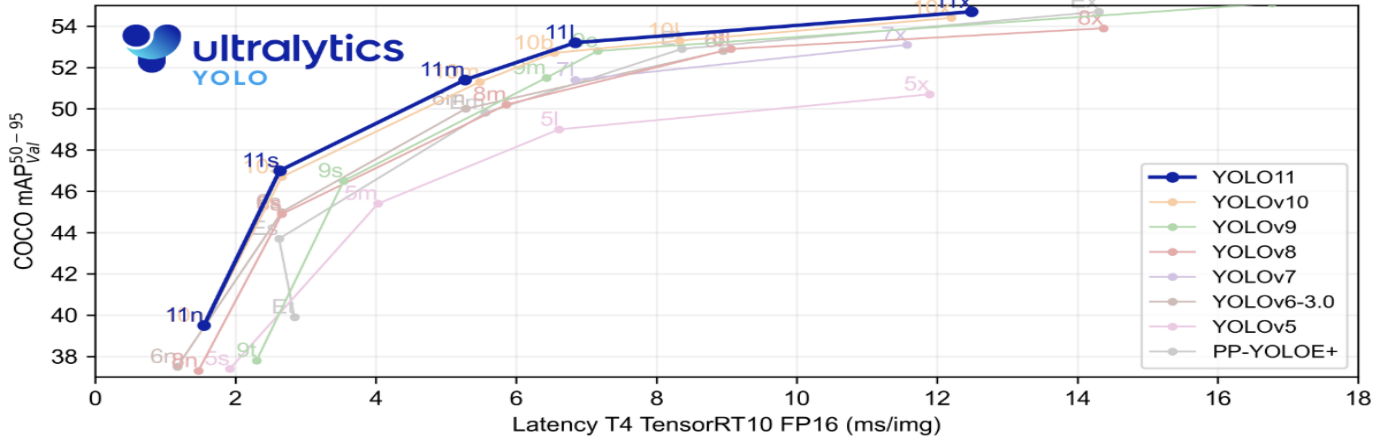


Figure 7. Performance comparison diagram between YOLOv11 and previous versions.

This study innovatively proposes the YOLOv11n-ZY model, an optimized and improved framework based on YOLOv11, to address core technical challenges in bridge defect detection tasks, including weak multi-scale target sensitivity, significant complex background interference, and insufficient fine-grained feature representation.

By deeply integrating the new ZZ convolutional module, new YY attention mechanism module, and SPPF-LSKA fusion module, a collaborative optimization system is constructed. The model adopts a hierarchical feature processing architecture, embedding three innovative modules into the feature extraction layer, attention enhancement layer, and multi-scale fusion layer, respectively, thereby establishing a complete technical chain from microscopic feature analysis to macroscopic semantic correlation. The three modules achieve compatible deep integration through granular allocation of computational resources and functional positioning: The ZZ module focuses on enhancing multi-granularity extraction efficiency of low-level features. The YY module implements domain-adaptive calibration during feature transmission. The SPPF-LSKA module accomplishes complementary fusion of multi-level semantic features. These three components collectively establish a progressive optimization pathway of “feature encoding → attention enhancement → pyramid fusion.”

At the parameter optimization level, the three modules respectively introduce learnable convolutional kernel scale ratios [17], dynamic attention weights [18], and large-kernel decoupled computation mechanisms. Through joint backpropagation, these components synergistically optimize the detection loss function. This hierarchically deployed collaborative paradigm provides a technical solution that combines theoretical innovation and engineering value for intelligent bridge defect detection.

#### 4.2 Simulation Environment

The simulation was conducted on a Windows 11 operating system with 3T memory and an RTX 4070 GPU (64GB VRAM). Python 3.8 was utilized, with the PyTorch framework (Torch 1.12.0 version). The YOLOv11n-ZY model was trained

for 200 epochs with a batch size of 32 and a learning rate of 0.01.

To evaluate the comprehensive performance of the model, this experiment adopts the following quantitative evaluation metrics: parameter count, precision (P), recall (R), mean average precision (mAP), frame rate (FPS), and F1-score. These metrics collectively characterize the model’s robustness across detection accuracy, computational efficiency, and multiple confidence thresholds [16].

The mathematical definitions of precision and recall are given in Equations (1) and (2), where TP (True Positives) denotes the number of correctly detected positive samples, FP (False Positives) represents the number of positive samples incorrectly classified as negative, and FN (False Negatives) indicates the number of undetected positive samples. The F1-score is defined by Equation (3), which is essentially the harmonic mean of precision and recall. In the field of object detection, mAP serves as a core evaluation metric, quantified through the weighted average of precision values across confidence thresholds, with its computational methodology detailed in Equations (4) and (5).

$$P = \frac{TP}{TP+FP} \quad (1)$$

$$R = \frac{TP}{TP+FN} \quad (2)$$

$$F_1 = 2 \cdot \frac{P \cdot R}{P+R} \quad (3)$$

$$AP = \int_0^1 p(r) dr \quad (4)$$

$$mAP = \frac{1}{n} \sum_{i=1}^n AP(i) \times 100\% \quad (5)$$

In the equations, the mAP reflects the balance between the detection precision and recall of the model across all categories (unit: %); mAP50 refers to the mAP value when the IoU is 0.5; AP<sub>i</sub> is the average precision of the *i*-th category; and *n* is the total number of categories.

#### 4.2.1 Comparison Experiments

To further validate the detection performance of the improved YOLOv11n-ZY model proposed in this paper, the algorithm is compared and analyzed with common algorithms in this field, and the results are shown in Table 2.

Table 2. Comparative Experimental Results.

Model	mAP50/%	P/%	R/%	Params/10 <sup>6</sup>
YOLOv5s	33.8	37.0	39.7	7.82
YOLOv8n	33.4	40.5	36.7	3.01
YOLOv8s	35.1	40.7	39.1	11.13
YOLOv11n	34.9	44.6	37.8	2.58
YOLOv11s	36.3	43.0	41.1	9.41
Ours	40.3	49.3	41.1	2.87

According to the experimental results in Table 2, compared to the detection results of previous official Yolo series models (Yolov5s, Yolov8n, Yolov8s), the proposed Yolov11n-ZY algorithm in this study achieves significant improvements in mAP50 by 6.5%, 6.9%, and 5.2%, while reducing parameter sizes by 4.95 MB, 0.14 MB, and 8.26 MB, respectively. Compared to the baseline model YOLOv11n and its series counterpart YOLOv11s, the Yolov11n-ZY algorithm achieves accuracy improvements in mAP50 of 5.4% and 4%, respectively, despite a slight increase in parameter size. In summary, the proposed algorithm outperforms other methods in the accuracy of "multi-category bridge defect small target detection under complex background interference," including mAP50, precision (P), and recall (R), while maintaining real-time performance and achieving an optimal balance in model size.

## 5 VISUALIZATION INTERFACE DESIGN

The visual interactive interface of the proposed detection and recognition system integrates the YOLOv11n-ZY model for bridge defect detection and recognition, featuring multi-modal input source processing capabilities (including static images, video streams, real-time camera capture, and batch file processing). A multi-threaded parallel processing mechanism is adopted to ensure real-time responsiveness of the human-machine interaction interface. Detection results are visualized in real-time through the graphical interface, with dynamic parameter adjustment functions (confidence threshold, IoU threshold) and detection process control interfaces (start, pause, terminate detection, and result storage). The specific visual interface system is shown in Figure 8.

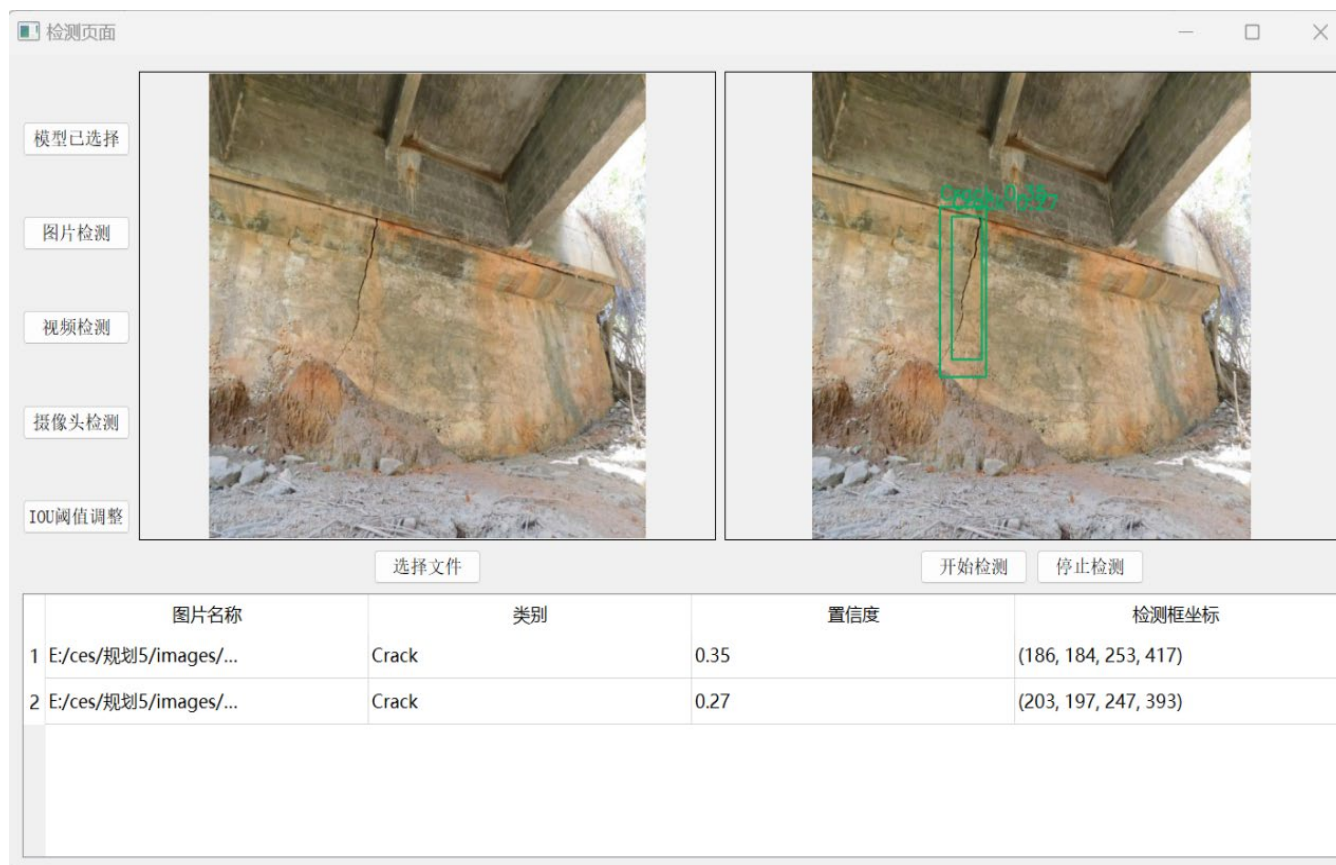


Figure 8. Visualization interface for bridge defect object detection.

In the input source selection unit, specify the camera capture device or local file path; dynamically configure the confidence threshold (Conf) and Intersection over Union threshold (IoU) of the target detection model through slider controls. The background processing thread is automatically initialized upon configuration completion.

The system routes the processing results to the main thread, transmitting bounding box-annotated detection images via

the (*send\_detect\_img*) signal and category statistics via the (*send\_detect\_info*) signal. Finally, the streaming inference approach governs the actual inference loop, as illustrated in Figure 9, which includes: reading input sources (images, videos, camera streams, etc.), preprocessing, executing model inference, processing post-inference results, and transmitting final recognition outcomes to the visualization main interface through signals.



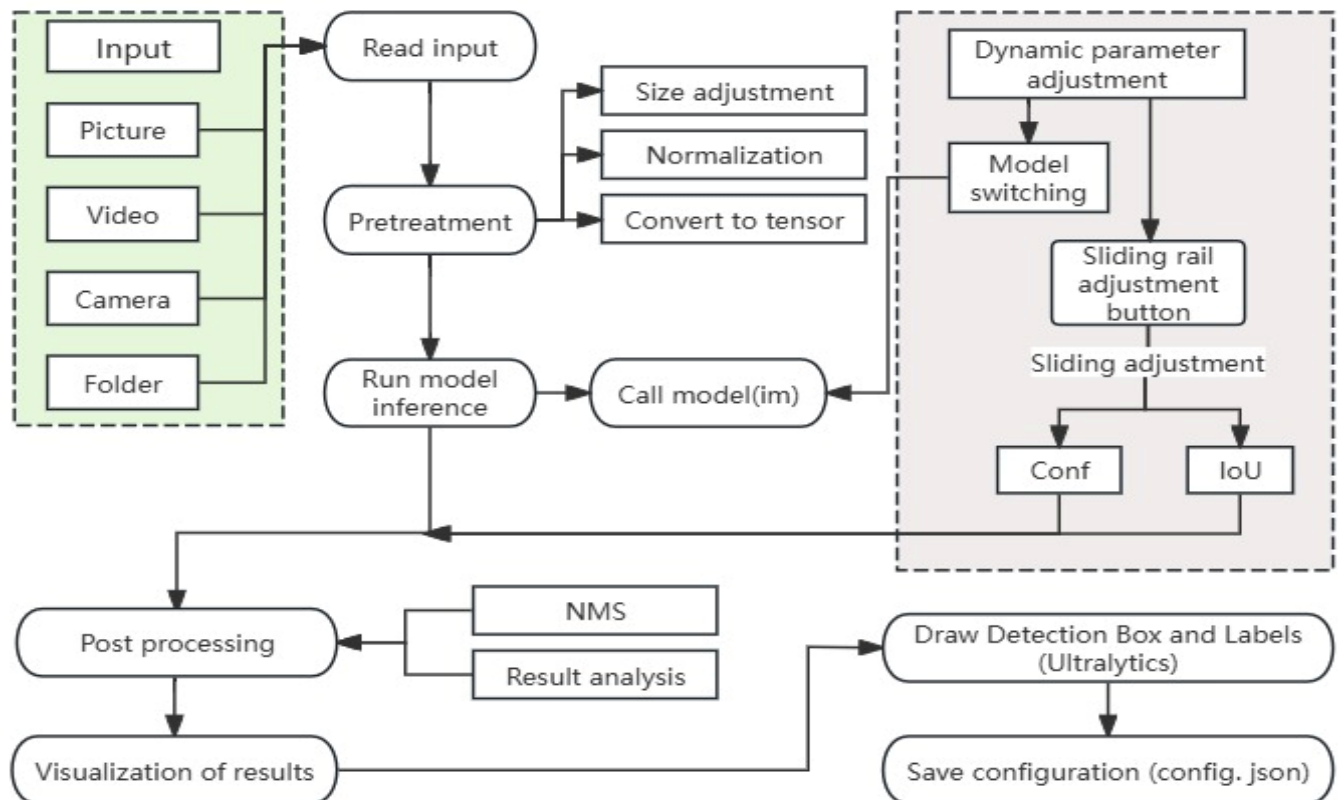


Figure 9. Flowchart of the visualization interface system operation.

## 6 CONCLUSION

Aiming at the bottleneck problems of low efficiency and insufficient accuracy in traditional bridge inspection methods, this paper proposes a "Comprehensive Visual Intelligent Bridge Inspection Platform" that integrates Mixed Reality (MR) technology, deep learning algorithms, and domain-specific bridge engineering knowledge. By leveraging the high-precision spatial perception capabilities of the HoloLens 2 device, the optimized architecture of the YOLOv11n-ZY model, and multimodal human-computer interaction technologies, a bridge defect detection system with real-time inspection, dynamic visualization, and full lifecycle management functions has been successfully established. Experimental results demonstrate that the improved YOLOv11n-ZY model significantly outperforms existing mainstream algorithms in detecting multi-category small-target defects under complex background interference, achieving a detection precision (mAP50 of 40.3%). Simultaneously, the MR technology facilitates closed-loop management of defect localization, remote collaboration, and dynamic 3D model updating. This study not only provides an efficient and reliable technical pathway for intelligent bridge operation and maintenance but also offers theoretical support and practical exemplars for the deep integration of mixed reality and deep learning in infrastructure inspection. Future work will focus on optimizing the lightweight deployment capability of the model, further enhancing the precision of the algorithm, expanding multi-source sensor data fusion mechanisms, and exploring a

digital twin-based predictive system for bridge performance throughout its lifecycle to advance the engineering application and standardized development of intelligent infrastructure inspection technologies.

## ACKNOWLEDGMENTS

This study is supported by 'Data-Driven Intelligent Assessment of Bridge Infrastructure' granted by the Slovak Research and Development Agency under the contract No. SK-CN-23-0037.

## REFERENCES

- [1] Spencer Jr, Billie F., Vedhus Hoskere, and Yasutaka Narazaki. "Advances in computer vision-based civil infrastructure inspection and monitoring." *Engineering* 5.2 (2019): 199-222.
- [2] Feng, D. C., Wang, W. J., Mangalathu, S., & Sun, Z. (2023). Condition Assessment of Highway Bridges Using Textual Data and Natural Language Processing-(NLP-) Based Machine Learning Models. *Structural Control and Health Monitoring*, 2023(1), 9761154.
- [3] Zhang, Yongjian , X. Chen , and W. Yan . "Automated intelligent detection system for bridge damages with Fractal-features-based improved YOLOv7." *Signal, Image and Video Processing* 19.3(2025).
- [4] Hsieh, Chang Cheng , H. M. Chen , and S. K. Wang . "On-site Visual Construction Management System Based on the Integration of SLAM-based AR and BIM on a Handheld Device." *KSCE Journal of Civil Engineering* 27.11(2023):20.
- [5] Malek, Kaveh, Ali Mohammadkhorasani, and Fernando Moreu. "Methodology to integrate augmented reality and pattern recognition for crack detection." *Computer-Aided Civil and Infrastructure Engineering* 38.8 (2023): 1000-1019.

- [6] Sun, Z., Caetano, E., Pereira, S., & Moutinho, C. (2023). Employing histogram of oriented gradient to enhance concrete crack detection performance with classification algorithm and Bayesian optimization. *Engineering Failure Analysis*, 150, 107351.
- [7] Kun, J. , Zhenhai, Z. , Jiale, Y. , & Jianwu, D. . A deep learning-based method for pixel-level crack detection on concrete bridges. *IET Image Processing*.
- [8] Mascarenas, David DL, et al. "Augmented reality for next generation infrastructure inspections." *Structural Health Monitoring 20.4* (2021): 1957-1979.
- [9] Wang, Ying , et al. "Could I Have a Stack Trace to Examine the Dependency Conflict Issue?." *ACM* (2019).
- [10] Sahraie, A. , et al. "Psychophysical and pupillometric study of spatial channels of visual processing in blindsight." *Experimental Brain Research* 143.2(2002):249.
- [11] Zhu, Pengfei , et al. "Vision Meets Drones: A Challenge." *Springer, Cham* (2018).
- [12] Flotzinger, Johannes , P. J. Rsch , and T. Braml . "dacl10k: Benchmark for Semantic Bridge Damage Segmentation." *IEEE* (2023).
- [13] Liu, Yu , et al. "Rotating Target Detection Method of Concrete Bridge Crack Based on YOLO v5." *Applied Sciences* (2076-3417) 13.20(2023).
- [14] LinXinrui, et al. "CCTSDDB dataset enhancement based on a cross-augmentation method for image datasets." *Intelligent Data Analysis* (2024).
- [15] Jin, T. , X. Ye , and Z. X. Li . "Establishment and evaluation of conditional GAN-based image
- [16] Peng, Shifeng , et al. "PS-YOLO: a small object detector based on efficient convolution and multi-scale feature fusion." *Multimedia Systems* 30.5(2024):1-16.
- [17] Wang, Hao , et al. "Multi-scale Location-aware Kernel Representation for Object Detection." *IEEE* (2018).
- [18] Jiang, Zhichao , D. Liu , and L. Cui . "Deep adaptively dynamic edge graph convolution network with attention weight and high-dimension affinity feature graph for rotating machinery fault diagnosis." *IOP Publishing Ltd* (2024).

## 3D projection of AI-derived concrete cracks on a Hydro Dam outlet tower

Ludvig Emgård<sup>1</sup>, SPOTSCALE

<sup>1</sup>Spotscale AB, Storgatan 42, 58223 Linköping, Sweden  
email: ludvig.emgard@spotscale.com

**ABSTRACT:** In a Structural Health Monitoring (SHM) project, a hydro-dam's outlet tower in Northern Sweden required inspection and assessment. This was due to the lack of digital records regarding existing damage and the client's concerns about its progression. The tower's location in a lake made traditional inspection methods like scaffolding or skylifts extremely difficult. The concrete engineering expert hired for the evaluation was uncomfortable with rope access, making data collection an expensive and cumbersome task. The structure is significantly affected by fluctuating water levels in the lake, leading to suspicions of certain types of damage (e.g., freeze-thaw damage, erosion damage).

For this project, a Phase One P3 camera was used to capture thousands of 100-megapixel images from every angle of the tower. Every inch of the concrete surface was covered by at least five different images.

From these images, a 3D reconstruction was created using Spotscale's proprietary software pipeline<sup>1</sup>, which is specifically designed for high-resolution processing. Subsequently, each image was analyzed by Spotscale's machine learning algorithm to detect cracks, spalling, and visible rebar. For every pixel on the 3D model, all images that observed that pixel were analyzed, and this information was used to project the best possible representation of the damage onto the model, creating a 3D texture of the damage.

The results revealed a distinct crack pattern, identified with a 98.7% confidence level when compared to human assessment of the same cracks. This provided the dam owner with a comprehensive understanding of the overall damage and an overview of the most severely affected areas.

**KEY WORDS:** 3D reconstruction; Machine learning; Crack identification; 3D visualization.

### 1 INTRODUCTION

Structural Health Monitoring (SHM) plays a crucial role in ensuring the safety and longevity of infrastructure. In this project, an outlet tower connected to a hydro-dam in Northern Sweden required inspection due to the absence of reliable digital records of past damage, combined with recent concerns about deterioration. The structure, situated in a lake and measuring approximately 30 meters in height, posed significant logistical challenges for traditional inspection techniques such as scaffolding, skylifts, or rope access.



Figure 1. An overview of the tower structure

Given these limitations and the client's need for high-resolution documentation, a remote sensing approach was adopted, enabling comprehensive data collection without direct human contact with the structure.

### 2 DATA

#### CAPTURING

To achieve detailed visual coverage of the entire concrete surface, a PhaseOne P3 camera with an 80 mm lens was mounted on a drone platform. A total of 3,000 ultra-high-resolution images (11664 × 8750 pixels each) were captured in a single day of fieldwork. The drone operated at a consistent distance of approximately 4 meters from the structure, resulting in a ground sampling distance (GSD) of 0.2 mm. This resolution ensured that even fine surface anomalies were detectable.

Every area of the structure was photographed from multiple angles, with at least five images covering each point on the surface, enabling robust 3D reconstruction and redundancy in damage analysis.

High-resolution imaging using the PhaseOne P3 setup involves pre-planned flight paths or starting coordinates for drones or stationary setups for static structures. This ensured complete coverage and minimized data gaps. The image collection for the needed accuracy was performed with a minimum of 80% overlap, with 7-10 meters distance to the object, ensuring that every defect was visible in at least 5 different images from different angles.



### 3 DATA PROCESSING

The captured imagery was processed using Spotscale's proprietary photogrammetry pipeline, optimized for handling high-resolution inputs and generating accurate 3D models. The resulting models are both metrically correct and visually intuitive, making them ideal for expert inspection and annotation.

Following model generation, Spotscale's AI-based damage detection system was applied. This system analyzes all available views of each pixel on the surface to detect features such as cracks, spalling, and exposed rebar. The AI consolidates information from overlapping images to create a high-fidelity texture projection of damage across the entire 3D surface, producing a visual damage map with sub-millimeter precision.

### 4 RESULTS

The final output was a detailed 3D model textured with detected damage patterns. The AI identified a prominent and recurring crack pattern, which was verified with a 98.7% confidence level when benchmarked against expert human assessments. Figure 2 illustrates the resulting damage map, with clearly visible areas of cracking and localized spalling. The damage texture allowed for both global overview and close-up inspection, enabling prioritization of critical zones for further manual investigation or remedial work.

By applying the AI interpretation, concrete experts can predict future decay such as concrete loss from the surface (spallings). The Spotscale software further enables the expert to measure depth on spallings that occurred in a sub-mm accuracy depth representation.

### 5 CONCLUSION

The combination of ultra-high-resolution imaging, advanced photogrammetry, and machine learning provided a complete and reliable overview of the structural condition of the outlet tower. The results were instrumental in helping concrete specialists understand the underlying causes of the damage, including environmental factors such as freeze-thaw cycles and water erosion.

Beyond the immediate inspection, this methodology offers several benefits: it reduces inspection time and cost, minimizes safety risks, and produces a digital baseline for future comparisons. The success of this project demonstrates the value of remote sensing and AI-powered analysis in modern infrastructure monitoring.

The AI algorithms are also able to detect and classify cracks based on predefined criteria, such as width and orientation. Each single crack can be interpreted as a separate object and represented either in projected raster on the geometry or as a 3D polyline along the center line (medial axis) of the crack (not performed on this specific project). To achieve this kind of geometry, the crack pixels are analyzed from several different viewpoints and compared before projected on the mesh. This analysis significantly enhances the robustness of the Spotscale approach. The ability to transform the pixels to 3D polylines (vectors) enables the possibility to

automatically determine medium and max width over the crack length and establish the length in three dimensions.

This innovative approach to non-destructive testing unlocks new possibilities in infrastructure monitoring, making it possible to conduct inspections with greater frequency, precision, and ease. Structures and areas that were previously inaccessible or hazardous to manually inspect—such as the undersides of bridges, confined spaces inside industrial facilities, or elevated constructions—can now be examined in high detail without requiring extensive scaffolding or safety interruptions.

The ability to assess these components without disrupting day-to-day operations or public life significantly broadens the application of this technology. For instance, critical assets like highway bridges, retaining walls, and overpasses can be inspected while traffic continues to flow, eliminating the need for costly detours or shutdowns. Similarly, energy and water utilities can maintain full operational output during inspection processes, reducing the risk of service interruptions and increasing overall efficiency.

With more precise data on structural health, renovation efforts can be optimized both spatially and chronologically. Repairs can be strategically localized and planned based on the most urgent needs, which minimizes waste and maximizes the lifespan of concrete infrastructure. Over time, this data-driven approach contributes to a more sustainable and resilient built environment, where maintenance decisions are grounded in actual structural behavior rather than estimations or reactive measures.



Figure 2. Resulting 3D projected AI interpretation of crack pattern

### ACKNOWLEDGMENTS

Spotscale would like to acknowledge the engineering partners KIWA and SWECO who participated in the project.

### REFERENCES

- [1] [www.spotscale.com](http://www.spotscale.com)

# Computer vision-based recognition of random traffic flow for live load performance analysis of existing bridges

Weilei Yu<sup>1</sup>, 0000-0002-6492-6051, Mayuko Nishio<sup>2</sup>, 0000-0003-1079-2577

<sup>1</sup>Department of Engineering Mechanics and Energy, University of Tsukuba, 1-1-1 Tennodai, Tsukuba, Ibaraki, Japan

<sup>2</sup>Institute of Systems and Information Engineering, University of Tsukuba, 1-1-1 Tennodai, Tsukuba, Ibaraki, Japan  
email: s2336033@u.tsukuba.ac.jp, nishio@kz.tsukuba.ac.jp

**ABSTRACT:** The dynamics and complexity of stochastic traffic flows play a crucial role in the management of infrastructure such as bridges. This study presents a computer vision-based method for random traffic flow identification and load estimation that integrates the YOLOv8 object detection model and the DeepSORT multi-target tracking algorithm. By utilizing high-resolution bridge surveillance video, the method can accurately identify vehicle type, axle count, and traffic flow. A case study conducted on an actual bridge validates the effectiveness of the method. The results show that the accuracy of vehicle identification based on 24-hour video data is more than 93%, the statistical error is less than 10%, and the temporal distribution of traffic flow matches well with the actual situation. This study provides a new technical reference for AI-based bridge traffic management and low cost structural health monitoring solutions.

**KEY WORDS:** Random traffic flow; Computer vision; Bridge monitoring; Object detection; Object tracking; Traffic flow statistical analysis.

## 1 INTRODUCTION

Stochastic traffic flow is one of the key research areas in traffic flow analysis, which is characterized by randomness and uncertainty in dynamic parameters such as vehicle arrival time, spacing, speed and type. In bridges and other critical infrastructures, the characteristics of random traffic flow can lead to irregular spatial and temporal load distributions, which can seriously affect the design safety and operational efficiency of the infrastructure. Stochastic traffic flow is equally crucial to understanding the performance of bridges under dynamic loading.

Studies [1], [2] linked traffic-induced dynamic amplification factors to bridge fatigue life, while [3] emphasized bridge health monitoring under frequent heavy traffic flow. [4], [5] investigated the effect of random traffic flow on bridge dynamics under consideration of pavement roughness and proposed structural maintenance strategies.

Therefore, accurate identification and statistical analysis of stochastic traffic flow is not only the basis for understanding traffic dynamics, but also an important tool for optimizing transportation systems and improving infrastructure performance.

Traditional methods for stochastic traffic flow statistics usually rely on dynamic weighing systems or radar techniques. Although these methods can capture key traffic flow parameters to some extent, they face limitations such as lack of real-time performance, limited accuracy, and high cost. In recent years, with the rapid development of computer vision technology, its application in the field of intelligent transportation has become a focus of research. Deep learning-based target detection and multi-target tracking technologies provide new solutions for real-time traffic flow information acquisition. By analyzing video streaming data, computer vision techniques can efficiently identify and quantify vehicle types, numbers, speeds, and lane distributions, providing the possibility of real-time monitoring of random traffic flows. However, how to improve the robustness of recognition and the accuracy of statistical analysis in complex and changing

environments remains one of the main challenges in current research.

The aim of this study is to develop an integrated approach for recognizing and statistically analyzing random traffic flows using computer vision to address the challenges in traffic flow research. The study integrates YOLOv8 object detection and DeepSORT multi-target tracking techniques to achieve real-time monitoring and accurate characterization of traffic flow in complex dynamic environments. The practical applicability of the method in stochastic traffic flow statistics is verified through a case study.

## 2 COMPUTER VISION-BASED FOR RANDOM TRAFFIC FLOW RECOGNITION

### 2.1 Video data capture settings and processing

High-resolution cameras are deployed on the bridge deck to capture real-time multi-lane traffic data, including vehicle types, counts, speeds, and directions. Data is collected across seasons and traffic conditions to ensure diversity. This non-intrusive method improves accuracy and efficiency over manual monitoring, avoids physical interference, and reduces costs compared to sensor networks.

Video data undergoes preprocessing (frame extraction, resolution normalization, and augmentation) to enhance model robustness. A labeled dataset of 12,000 images, annotated with vehicle types and axle counts, is split into training (75%), validation (15%), and testing (10%) sets for model development and evaluation.

### 2.2 Traffic flow object detection and tracking principle

This study employs an integrated approach combining YOLOv8 for vehicle detection and DeepSORT for multi-object tracking to analyze bridge traffic flows. YOLOv8, the latest iteration of the YOLO series, demonstrates superior speed and accuracy in vehicle detection. The algorithm processes images through a grid-based system ( $S \times S$ ), where each cell predicts bounding box coordinates ( $x, y, w, h$ ) and classification probabilities via convolutional neural networks. Experimental

validation yielded a training loss of 0.9 and F1 score of 0.88, with vehicle detection precision reaching 93% for cars, 85% for buses, and 89% for trucks.

DeepSORT enhances the system's capability by maintaining vehicle trajectory continuity across video frames. The algorithm integrates five key phases: (1) initial detection using YOLOv8 outputs, (2) feature extraction for appearance-based identification, (3) motion prediction via Kalman filtering, (4) data association through the Hungarian algorithm, and (5) state updates for refined tracking. This multi-stage process ensures reliable vehicle tracking in complex traffic scenarios while assigning persistent unique IDs to each vehicle.

### 3 ACTUAL BRIDGE TRAFFIC FLOW IDENTIFICATION AND STATISTICAL RESULTS

This study validates a computer vision-based stochastic traffic flow analysis method through a case study of an urban bridge in eastern China. High-resolution cameras were strategically deployed on the bridge for continuous 24/7 monitoring over two weeks, capturing comprehensive traffic data including vehicle types, counts, speeds, and directions. The collected dataset enables evaluation of the method's performance in complex multi-lane environments, demonstrating its practical applicability for real-world traffic monitoring and analysis.

Using the YOLOv8 and DeepSORT algorithms, all vehicles on the bridge over a 24-hour period were successfully identified and tracked, shown in Figure 1. Vehicles, along with their axle counts, were categorized into seven types: 2-axle passenger cars, 2-axle buses, 3-axle buses, 2-axle trucks, 3-axle trucks, 4-axle trucks, and trucks with more than 4 axles. The recognition accuracy for each vehicle type was as follows: passenger cars 94%, trucks 90%, and buses 89%, with an overall vehicle recognition accuracy exceeding 93%. The model demonstrated robust performance during both peak traffic periods and low-traffic intervals.

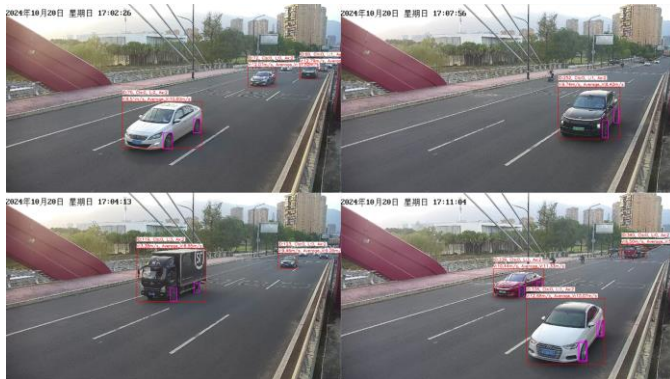


Figure 1. Vehicle identification results

According to the statistics of one-day traffic flow, passenger vehicles accounted for the highest proportion of total traffic flow, which was 6,820 vehicles, accounting for 73.5% of the total traffic flow. In contrast, buses and trucks accounted for a relatively small proportion of 19% and 7.5% respectively, which is about 9.3% error compared with the actual total traffic flow on the bridge based on WIM data, proving its practical value in actual traffic monitoring and analysis.

The results of the statistical analysis of the distribution of traffic flow on the bridge in 24 hours are shown in Figure 2. The 7:00-9:00 and 17:00-19:00 are the peak traffic flow, with more than 400 vehicles passing through every half hour respectively; the off-peak traffic flow is relatively stable. Nighttime traffic is significantly reduced. The proportion of trucks in the nighttime traffic has increased, and buses account for about 20% of the total traffic, which is mainly concentrated in the morning and evening peak hours. The time series analysis of the traffic flow reveals the fluctuation pattern of the traffic flow throughout the day, and the intensive traffic flow period corresponds to the peak commuting hours in the city, which provides intuitive data support for traffic management and bridge maintenance.

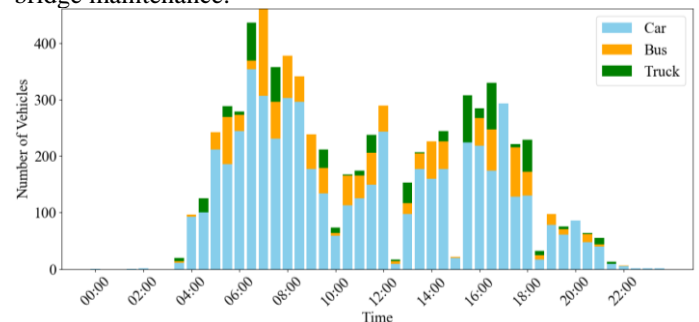


Figure 2. Full-day vehicle distribution

### 4 CONCLUSION

This study combines YOLOv8 and DeepSORT algorithm to propose a computer vision-based method for random traffic flow recognition and analysis of bridges. The method can efficiently and accurately realize real-time monitoring and statistical analysis of traffic flow and provide technical support for structural health monitoring of bridges, with the advantages of low cost and easy deployment. In the future, the performance can be further optimized through efficient deep learning algorithms, multimodal data fusion and edge computing.

### ACKNOWLEDGMENTS

This work was supported by JST SPRING, Grant Number JPMJSP2124.

### REFERENCES

- [1] Li, Z., Cao, Y., Ma, M., & Xiang, Q. (2023). Prediction of ground-borne vibration from random traffic flow and road roughness: Theoretical model and experimental validation. *Engineering Structures*, 285, 116060.
- [2] Maddah, N. (2013). Fatigue life assessment of roadway bridges based on actual traffic loads (No. 5575). EPFL.
- [3] Saviotti, A. (2014). Bridge assessment, management and life cycle analysis. *Modern Applied Science*, 8(3), 167.
- [4] Tang, T. Q., Caccetta, L., Wu, Y. H., Huang, H. J., & Yang, X. B. (2014). A macro model for traffic flow on road networks with varying road conditions. *Journal of Advanced Transportation*, 48(4), 304-317.
- [5] Ho, H., & Nishio, M. (2020). Evaluation of dynamic responses of bridges considering traffic flow and surface roughness. *Engineering structures*, 225, 111256.



# A novel approach to bridge repair using photogrammetry and additive manufacturing

Raguez Taha<sup>1</sup>, Didem Ozevin<sup>1</sup>

<sup>1</sup> Department of Civil, Materials, and Environmental Engineering, University of Illinois Chicago,  
842 W Taylor Street Chicago, IL USA  
email: rtaha2@uic.edu, dozevin@uic.edu

**ABSTRACT:** Traditional inspections of aged steel bridges rely primarily on visual assessment, often depending on qualitative analysis and requiring expert engineering judgement. Additionally, these methods are often labor-intensive, time-consuming, and costly, limiting their feasibility for widespread implementation. Accurate condition assessment, due to corrosion loss, remains a challenging factor in structural inspection, complicating the evaluation of its impact on bridge performance. This paper presents a novel workflow that integrates smartphone-based photogrammetry and metal additive manufacturing (AM) to improve condition assessment and enable data-informed repairs. High-resolution 3D models of a corroded decommissioned steel beam retrieved from a Chicago Transit Authority bridge were generated using a photogrammetry pipeline optimized for image quality and overlap. These models allowed for precise quantification of section loss and the design of custom-fit repair parts. A proof-of-concept repair component was fabricated using metal 3D printing and designed to restore the original geometry of a corroded flange section. While mechanical validation of the repair part is ongoing, this workflow demonstrates the potential for scalable, low-cost integration of digital imaging and AM in bridge maintenance.

**KEY WORDS:** Photogrammetry, Additive manufacturing, Smartphone, Bridge inspection, SHM.

## 1 INTRODUCTION

In the United States, there are more than 617,000 bridges, and 42% of them are at least 50 years old. About 7.5% are in “poor” condition (or structurally deficient) [1]. Although these bridges are classified as being in poor condition, they are not considered unsafe. However, they require significant maintenance and rehabilitation and are at a higher risk of future closures and weight restrictions. Illinois has the third-largest bridge inventory in the U.S., with 2,405 bridges in poor condition, most of which are locally owned. This creates a significant maintenance backlog. To address this issue, the Illinois Department of Transportation has adopted a cost-effective, continuous maintenance strategy to prevent the need for major rehabilitation [2].

These maintenance strategies rely on visual inspection methods, which require expert engineers and are often subjective, depending on the engineer's expertise. While some nondestructive evaluation (NDE) methods are used, more accurate NDE techniques are often very expensive and require trained personnel to collect and process the data. As a result, they are not widely implemented. A major issue that steel bridges face is corrosion, and quantifying corrosion becomes difficult when relying solely on visual inspections. Additionally, the current repair technologies for corrosion loss are not effective in the long run. The most common repair method for corrosion is reinforcing the affected area with built-up shapes on both sides, which are either bolted or welded to the existing structure. While this 'sandwiching' method restores the cross-sectional area, it does not address the underlying corroded plate, which remains exposed. Corrosion damage can continue to grow, leading to earlier repair needs.

The absence of a cost-effective, easy-to-use method for accurately assessing corrosion loss in steel bridges highlights

the need for a more effective approach to documenting and evaluating bridge conditions, as well as for implementing better repair strategies.

This study proposes a practical workflow that integrates smartphone-based photogrammetry and metal additive manufacturing (AM) to enhance the condition assessment and repair of corroded steel bridge components. By utilizing high-resolution 3D reconstructions generated from smartphone-based photogrammetry, this approach enables precise quantification of section loss, improved visualization of deterioration patterns, and more data-driven repair recommendations for aged steel bridges. Additionally, it uses metal additive manufacturing to produce custom repair parts based on the 3D reconstruction models generated from the photogrammetry analysis. By directly translating detailed digital models of the deteriorated sections into precise, tailored components, this approach not only ensures a perfect fit but also improves the overall quality and efficiency of repairs. It reduces material waste by using only the necessary amount of material, minimizes labor by automating the production of repair parts, and shortens repair times by streamlining the manufacturing process. The goal of this proof-of-concept study is to evaluate the feasibility of this workflow as a scalable, low-cost solution that can be incorporated into existing maintenance practices.

## 2 BACKGROUND

### 2.1 *Photogrammetry in structural health monitoring*

Photogrammetry has become a powerful tool in structural health monitoring (SHM), offering a non-contact, high-precision method for assessing and documenting structural conditions. In a study by Valença et.al, photogrammetry was shown to be a reliable alternative to LVDT methods for SHM,

especially in inaccessible environments. They developed a methodology using photogrammetry to generate accurate 3D measurements on long-span beams and pedestrian bridges in Aveiro, Portugal. They were able to achieve an average accuracy in the displacement accuracy of 0.1 mm in steel connection tests, which focused on the 'strong beam/column/weak beam' connection [3].

Recently, Unmanned Ariel Vehicle (UAV) photogrammetry has been utilized to create high precision 3D models for dam monitoring to enhance the damage detection and emergency inspection capabilities [4]. In this study, researchers successfully generated detailed 3D models, achieving a Root Mean Square Error (RMSE) of 3.00 cm and 3.95 cm in the horizontal and vertical directions, respectively, when compared to the Ground Control Points (GCPs) [4].

Backhaus et. al combined UAV photogrammetry and structured light scanning to enhance the structural health monitoring of concrete bridges. UAV data was used for crack detection, while SLS scanning was used to obtain detailed measurements. The study found that UAV could detect cracks as small as 0.05 mm [5].

These studies demonstrate that photogrammetry is a reliable method for SHM, enabling accurate damage detection and 3D reconstruction. Its application has shown to improve the effectiveness of structural assessments which would enhance the safety and maintenance planning in the future.

## 2.2 Additive manufacturing in civil engineering

Additive manufacturing is a process of joining materials layer by layer to create an object from a 3D model (ASTM Standard F2792-12a, 2012). Additive manufacturing enables greater geometric flexibility, allowing for the creation of complex shapes and structures [6-9]. In civil engineering, AM has been utilized in the optimization of connections such as the Nematov façade node [10] and lighting pole nodes [11]. Additionally, it has been utilized in the construction of steel and concrete bridges as well as houses and offices, more notably the MX3D metal pedestrian bridge, Castilla-La Mancha concrete bridge in Madrid, and Winsun houses and offices in Dubai [12-14].

Limited research has been conducted on utilizing AM as a repair technology except most recently in a study by Zhang et al, which investigated the effectiveness of laser additive manufacturing (LAM) for repairing corroded steel bridge beams. This study specifically focused on the mechanical properties and microstructural characteristics of the repaired materials were investigated [15]. The researcher found that the AM repair successfully restored the mechanical properties of the defective specimen.

## 3 METHODOLOGY

This approach can be broken down into three main steps: image capturing, image reconstruction, and repair manufacturing. Further explanation of each of these steps is discussed next.

### 3.1 Image capturing

Capturing high-quality images is the foundation of reliable 3D reconstruction in photogrammetry. Several variables influence the accuracy and resolution of the resulting model. These variables include image resolution, image overlap percentage, and the camera setup. Image resolution depends on

the camera specifications. For example, Agisoft Metashape—used in this study—recommends a minimum resolution of 5 megapixels to achieve suitable model detail. In this study, smartphone cameras were used to demonstrate a low-cost, accessible method for data collection. Another key factor is image overlap, which ensures that surface features are captured from multiple perspectives. A high overlap percentage allows the software to accurately identify and match common points between images. This is critical for generating a consistent and complete point cloud.

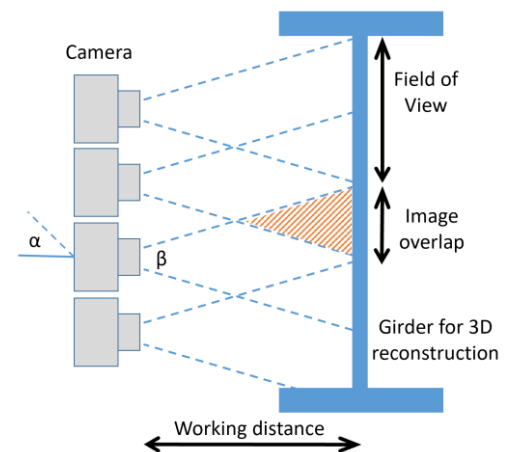


Figure 1. Photogrammetry variables and camera setup.

The overlap ratio is defined using the relationship between the field of view ( $\beta$ ) and the camera rotation angle ( $\alpha$ ), as shown in Equation (1):

$$\text{Overlap ratio (\%)} = \frac{\beta - \alpha}{\beta} \quad (1)$$

In this equation,  $\beta$  represents the camera's field of view, and  $\alpha$  is the angular increment between successive images. A smaller  $\alpha$  (i.e., closer spacing between photos) leads to higher overlap and better reconstruction accuracy.

Camera orientation and distance to the object also influence data quality. For best results, the object should be captured from multiple angles (e.g., top, side, diagonal views), maintaining consistent lighting and focus. Figure 1 illustrates the recommended image acquisition setup and key photogrammetry variables.

### 3.2 Image reconstruction

Once images have been captured, the photogrammetric reconstruction process is carried out using Agisoft Metashape. The first step is to upload and review all images, removing any that are blurry or do not contribute additional information about the object. This pre-processing step helps optimize both processing time and model quality. Next, the alignment step generates a sparse point cloud to estimate the camera positions based on the common features detected across the image set. Following alignment, a dense point cloud is generated using depth maps. Using a higher accuracy setting during this step helps preserve finer details.

After generating the dense cloud, Metashape constructs a 3D mesh that interpolates the point cloud data into a continuous surface. A confidence map is also produced, indicating the software's certainty in reconstructing each part of the model. Areas with low confidence may correspond to regions with poor image coverage or lighting inconsistencies and should be reviewed to assess the need for additional images.

Finally, a texture layer is applied to the model, projecting the original image data onto the 3D surface to create a realistic visual representation. At this point, the model can be exported for further analysis or used to design a custom repair part.

### 3.3 Repair manufacturing

After the 3D model is finalized in Agisoft Metashape, it is exported to Autodesk Fusion for design of the repair component. The goal is to digitally reconstruct the missing or deteriorated geometry based on the scanned surface.

To begin, a solid rectangular block is positioned over the corroded area in Fusion. This block is finely meshed to capture the geometry of the underlying surface with high resolution. The Modify → Intersect tool is then used to trim the repair block to match the corroded profile of the scanned model. The result is a 3D repair component that conforms precisely to the section loss, as illustrated in Figure 2.

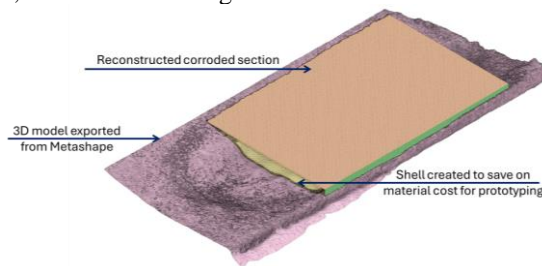


Figure 2. Reconstructed section of 3D model corroded section exported from Autodesk Fusion software.

Once the repair part has been reconstructed, a model is create which can then be sent to an appropriate 3D metal printing system to print the part. After which, this part can be fixed to the corroded section using epoxy and welding. Epoxy will be used to bond the corroded section to the repaired part and fill any gaps that were not captured during the printing process. Welding will be applied around the edge of the part, to ensure the repair part and the existing structure act as one system and it reducing the likelihood of the repair part detaching under flexural loading.

## 4 RESULTS AND DISCUSSION

To evaluate the proposed workflow, a section of the bottom flange from a naturally aged steel beam—retrieved from a decommissioned bridge in Chicago—was selected for reconstruction. This section exhibited visible corrosion, making it a suitable test case for photogrammetry-based defect capture. Various configurations were investigated to determine the optimal case for on-site inspections. The linear configuration, which focuses on a localized section, proved to be the most feasible option given the limitation of the existing structures on site.

This method was applied to a girder measuring approximately 1675 mm (5'-6") in length. The bottom flange of the girder was because visible corrosion was detectable. The initial test used 6 images, and a test used 108 images. This model was also used to create the repair part, as shown in Figure 2. From these two tests, it is evident that the number of images impact the confidence of the Metashape software in accurately reconstructing the features with the given images. As shown in Figure 3, with 6 images, the confidence level in the middle of the section increases as the overlap increases.

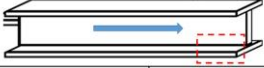
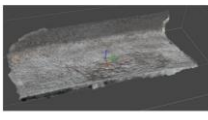
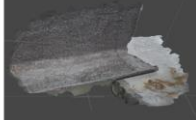
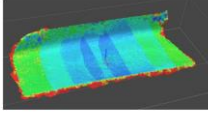
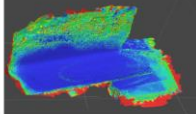
Image capturing configuration		
Number of images	6	108
Metashape reconstruction		
Confidence map		

Figure 3. Reconstruction of bottom flange of aged steel beam using different number of images.

To further validate the workflow, a prototype repair part was fabricated using PLA plastic, based on the 3D model generated from the 108-image dataset. The purpose of this prototype was to assess the feasibility of capturing fine geometric details required for accurate fitment during future metal printing. The PLA part aligned well with the corroded geometry, suggesting that the photogrammetric model is suitable for generating repair components, as illustrated in Figure 4.



Figure 4. Reconstruction of bottom flange of aged steel beam using different number of images.

While this prototype was not intended for mechanical testing, it serves as a low-cost validation of the model-to-manufacture transition. Future work will include metal AM fabrication and mechanical testing to assess structural performance and long-term durability of the printed repair.



## 5 CONCLUSION

This study presented a proof-of-concept workflow that integrates smartphone-based photogrammetry and additive manufacturing (AM) for the inspection and repair of corroded steel bridge components. The results demonstrate that high-resolution 3D models can be generated from smartphone images, even under field-like conditions, and used to design repair components that closely match the original geometry.

Initial tests using a naturally aged steel beam confirmed that image overlap and quantity significantly affect reconstruction quality. A prototype repair part was successfully fabricated in PLA based on the photogrammetry-derived model, supporting the feasibility of transitioning from image capture to repair part fabrication.

While promising, this workflow is still in its early stages. Future efforts will focus on transitioning from proof-of-concept to full-scale implementation. This includes fabricating repair components using metal additive manufacturing processes and performing mechanical tests—such as tensile and flexural loading—to evaluate the structural integrity of the repaired sections. Additional research will assess the scalability of the workflow for larger or more complex bridge components, ensuring it can be applied to diverse geometries and field conditions. The impact of environmental factors on photogrammetric accuracy, such as lighting variability, surface reflectivity, and site accessibility, will also be explored. Finally, a quantitative comparison between this workflow and traditional repair methods will be conducted, evaluating differences in cost, material efficiency, labor requirements, and repair duration to better understand the practical advantages and trade-offs of the proposed approach.

With further development, this approach has the potential to provide a cost-effective, accurate, and scalable tool for condition assessment and customized repair in routine steel bridge maintenance.

## ACKNOWLEDGMENTS

This work was partially supported by the GAANN program for the project EXTending Civil Infrastructure RESiliency for Multihazards and Extreme Events (EXTREME), the Chancellor's Undergraduate Research Award, and the Chicago Transit Authority for the donation of aged steel beams and girders. We would also like to express our sincere thanks to Stephanie Bonilla, Undergraduate Research Assistant, for her contributions to image capturing.

## REFERENCES

- [1] ASCE (2021). "2021 Report Card for America's Infrastructure," Reston, VA: American Society of Civil Engineers. (2021). Available at: <https://infrastructurereportcard.org>.
- [2] ASCE. (2022). "2022 Report Card for Illinois' Infrastructure". Accessed January 10, 2025. Available at: <https://infrastructurereportcard.org/state-item/illinois/>
- [3] Valença, J., Júlio, E., & Araújo, H. (2008, June). Application of photogrammetry to bridge monitoring. In *Structural Faults & Repair, 12th International Conference* (pp. 10-12).
- [4] Zhao, S., Kang, F., Li, J., & Ma, C. (2021). Structural health monitoring and inspection of dams based on UAV photogrammetry with image 3D reconstruction. *Automation in Construction*, 130, 103832.
- [5] Backhaus, J., Lopez, V. D. A., Maboudi, M., Bestmann, U., & Gerke, M. (2024). Combining UAV-based photogrammetry and structured light

- scanning to support the structural health monitoring of concrete structures. *Journal of Nondestructive Testing*, 29(7).
- [6] Berman, B. (2013). 3D printing: the new industrial revolution. *IEEE Engineering Management Review*, 41(4), 72-80.
- [7] Perkins, I., & Skitmore, M. (2015). Three-dimensional printing in the construction industry: A review. *International Journal of Construction Management*, 15(1), 1-9.
- [8] Tay, Y. W. D., Panda, B., Paul, S. C., Noor Mohamed, N. A., Tan, M. J., & Leong, K. F. (2017). 3D printing trends in building and construction industry: a review. *Virtual and physical prototyping*, 12(3), 261-276.
- [9] Gardner, L. (2005). The use of stainless steel in structures. *Progress in Structural Engineering and Materials*, 7(2), 45-55.
- [10] Strauss, H., AG, E. P. P., & Knaack, U. (2015). Additive Manufacturing for Future Facades: The potential of 3D printed parts for the building envelope. *Journal of Facade Design and Engineering*, 3(3-4), 225-235.
- [11] Arup. 3D makeover for hyper-efficient metalwork. Arup News; 2015.[accessed February 23, 2025].
- [12] Parkes, J. (2021, July 19). *MX3D unveils world's first 3D-printed stainless steel bridge in Amsterdam*. Dezeen. <https://www.dezeen.com/2021/07/19/mx3d-3d-printed-bridge-stainless-steel-amsterdam/>
- [13] Institute for Advanced Architecture of Catalonia. (2017). 3D printed bridge. IAAC. <https://iaac.net/project/3d-printed-bridge/>
- [14] World Economic Forum. (2016). Winsun – Demonstrating the viability of 3D printing at construction scale. World Economic Forum.
- [15] Zhang, S., Hou, P., Kang, J., Li, T., Mooraj, S., Ren, Y., ... & Chen, W. (2023). Laser additive manufacturing for infrastructure repair: A case study of a deteriorated steel bridge beam. *Journal of Materials Science & Technology*, 154, 149-158.

# Machine Vision-Based Super-Resolution Reconstruction for High-Precision Displacement Monitoring of Hydraulic Structures

You Yang<sup>1,2</sup>, Bo chen<sup>1,2</sup>, Weiqi Liu<sup>3</sup>, Zekai Ma<sup>1,2</sup>

<sup>1</sup>The National Key Laboratory of Water Disaster Prevention, Hohai University, Nanjing 210098, China;

<sup>2</sup>College of Water Conservancy and Hydropower Engineering, Hohai University, Nanjing 210098, China;

<sup>3</sup>POWERCHINA Chengdu Engineering Corporation Limited, Chendu 610072, China

email: 1638615936@qq.com, chenbo@hhu.edu.cn, sdgmlwq@163.com, 764987173@qq.com

**ABSTRACT:** In response to the issues of high cost, limited monitoring accuracy, and susceptibility to environmental factors in traditional hydraulic structure displacement automation monitoring methods, a non-contact intelligent monitoring method based on machine vision image super-resolution reconstruction is proposed. This method uses artificial targets as markers and combines a high-order image degradation model with a camera to analyze real monitoring scenarios, carry out image data collection, and perform displacement calculation. It innovatively introduces a feature fusion attention mechanism to improve the Real-ESRGAN network and generator, enabling the reconstruction of image contours and fine details to enhance displacement calculation accuracy. Laboratory and field test results show that this method can effectively improve image resolution and clarity, achieving sub-pixel and millimeter-level precise monitoring of hydraulic structure surface displacement. Compared with traditional super-resolution algorithms and target tracking methods, the improved Real-ESRGAN algorithm performs the best, with a coefficient of determination ( $R^2$ ) of up to 0.9975, an average absolute error (MAE) as low as 0.5552, and residual errors controlled within 5mm. The edge contours and details in the images are successfully reconstructed, effectively improving the displacement monitoring accuracy of hydraulic structures based on machine vision.

**KEY WORDS:** Machine vision displacement monitoring; Image super-resolution reconstruction; Real-ESRGAN improvement; Feature fusion attention mechanism; Hydraulic structure safety monitoring.

## 1 INTRODUCTION

As critical infrastructure in water resource management systems, hydraulic engineering projects play a pivotal role in ensuring water security and sustaining watershed economic development. Efficient and stable operation of these structures not only guarantees essential water supply for socio-economic sustainability but also serves as a vital safeguard for regional ecological security [1,2]. In the field of structural health monitoring (SHM), accurate surface displacement measurement forms the basis for safety assessment and early warning systems [3]. However, existing monitoring technologies exhibit notable limitations: traditional displacement measurement methods are not only costly but also susceptible to environmental interference, while demonstrating inadequate responsiveness to sudden structural risks [4-6].

A further complication arises from the multi-physics coupling effects (including hydraulic loads, thermal stresses, and mechanical vibrations) that hydraulic structures endure during service. These complex interactions induce nonlinear deformation behaviors, potentially leading to progressive damage or even catastrophic failure, posing dual threats to both structural integrity and economic viability [7]. Consequently, there is an urgent need to develop intelligent, automated displacement monitoring methods and establish digitalized smart monitoring systems to enhance lifecycle safety management of hydraulic structures.

Current displacement monitoring techniques for hydraulic structures can be broadly categorized into contact-based and non-contact approaches [8]. Contact-based methods, such as strain gauges and fiber-optic sensors, suffer from complex installation and environmental sensitivity, making them unsuitable for long-term monitoring [9, 10].

In the field of non-contact structural monitoring, laser displacement sensors[11][12], machine vision[13][14], total stations[15][16], and Global Navigation Satellite Systems (GNSS) [17][18] have emerged as critical technologies for deformation monitoring of large-scale hydraulic structures such as sluice gates and dams, owing to their non-invasive nature and operational flexibility.

Laser displacement sensors employ optical triangulation principles, utilizing photoelectric receivers including position-sensitive detectors (PSD), charge-coupled devices (CCD), and complementary metal-oxide-semiconductor (CMOS) sensors to achieve high-precision displacement measurements. However, the measurement accuracy of this technology exhibits an inverse correlation with monitoring distance due to the inherent limitations of laser reflection-based triangulation, significantly reducing its suitability for long-range monitoring scenarios. Furthermore, the installation requirements for reflective targets impose additional constraints on deployment flexibility, particularly for vertical displacement monitoring of hydraulic structures[19].

GNSS technology has demonstrated robust capabilities in dynamic displacement monitoring for structural health monitoring (SHM) and seismic engineering applications. Nevertheless, its sampling frequency is constrained by satellite signal update rates, limiting its effectiveness in high-frequency vibration monitoring. Compared to conventional sensors such as accelerometers, GNSS also exhibits inferior measurement accuracy in the vertical direction[20].

Total stations, as multifunctional surveying instruments, integrate high-precision distance measurement, angular measurement, coordinate acquisition, and elevation determination, making them widely applicable in engineering surveying and structural monitoring[15][16][21]. However, in

practical applications for dam displacement monitoring, these instruments face challenges such as unfavorable cost-benefit ratios, line-of-sight obstructions at measurement points, and operational complexity, which hinder their widespread adoption in large-scale engineering projects.

To address these challenges, machine vision-based displacement monitoring enhanced by image super-resolution reconstruction has emerged as a promising solution. By employing deep learning algorithms to recover fine details from low-resolution images, this method overcomes the precision constraints of traditional vision-based measurements while avoiding the range limitations of laser displacement sensors and the environmental dependencies of drone-based remote sensing. Compared to fiber-optic sensing and conventional SHM systems, this approach offers superior flexibility, cost efficiency, and adaptability, providing a novel pathway for high-precision, automated displacement monitoring of hydraulic structures.

Recent advances in computer vision have demonstrated its potential in SHM applications. such as the Harris corner detection method[22], the Lucas-Kanade (LK) optical flow matching algorithm[23], and template matching algorithms[24] are employed. For instance, Yoon et al. [23] combined Harris corner detection with the Lucas-Kanade (LK) optical flow algorithm to achieve high-precision displacement tracking in building structures. Brownjohn et al.[25] deployed a vision-based monitoring system on the Humber Bridge, validating its engineering applicability. Bocian et al. [26] extracted modal parameters of cable-stayed bridges using template matching and sparse LK optical flow, enabling vibration characteristic analysis. Kohut et al.[27] applied digital image correlation (DIC) to measure structural deflection, providing intuitive deformation indicators.

Algorithmic optimizations have further enhanced performance: Wu et al. [28] improved computational efficiency in template matching for real-time monitoring; Molina-Viedma[29] integrated phase-based motion magnification with digital image processing techniques [30] to identify the modal shapes of a cantilever beam, thereby overcoming the limitation of conventional digital image methods in accurately capturing high-frequency structural vibrations. Khuc et al. [22] refined Harris corner extraction with FREAK descriptors for sub-pixel matching accuracy. Guo et al. [31] leveraged projection correction to enhance displacement measurement under seismic conditions.

Despite these advancements, machine vision-based monitoring for hydraulic structures—particularly gates and dams—remains underdeveloped due to complex operational environments and stringent safety requirements. Existing systems still face data acquisition constraints, lacking a mature framework for deformation monitoring.

This study proposes a non-contact intelligent monitoring method integrating machine vision with image super-resolution reconstruction to address the cost, precision, and environmental limitations of conventional techniques. The methodology employs artificial targets as fiducial markers, coupled with high-resolution imaging and higher-order image degradation modeling, to achieve precise displacement data acquisition. At the algorithmic level, we innovatively introduce a feature fusion attention mechanism to enhance the Real-ESRGAN

network, specifically improving its contour detail reconstruction and texture recovery capabilities. This approach is expected to significantly elevate displacement calculation accuracy, offering a cost-effective, intelligent solution for hydraulic structure safety monitoring.

## 2 DEEP LEARNING-BASED SUPER-RESOLUTION METHODS: OPTIMIZATION AND APPLICATION OF GENERATIVE ADVERSARIAL NETWORKS

This study aims to transcend the limitations of conventional image resolution through deep learning techniques, thereby providing higher-precision machine vision measurement solutions for structural displacement monitoring in engineering applications. The following sections will focus on image super-resolution algorithms based on Generative Adversarial Networks (GANs), offering in-depth analysis of their core principles, network architectures, and optimization strategies.

### 2.1 Image Super-Resolution Based on Generative Adversarial Networks

The Super-Resolution Generative Adversarial Network (SRGAN) architecture primarily consists of two core modules engaged in adversarial competition: the Generator and the Discriminator, as illustrated in Figure 1. During model training, low-resolution (LR) images serve as input data to the generator network, which performs nonlinear transformations through deep neural networks to produce high-resolution (HR) images. Subsequently, both the generated super-resolution images and authentic HR images form the input sample space for the discriminator, which evaluates the authenticity probability of input samples through feature extraction and pattern recognition. Within this adversarial training framework, the generator optimizes its parameter space to minimize the distribution divergence between generated and real samples, aiming to produce super-resolution images with high visual fidelity. Concurrently, the discriminator continuously enhances its discriminative capability to maximize identification accuracy of generated samples. This minimax game process achieves dynamic equilibrium that ultimately enables the generator to produce super-resolution reconstruction results perceptually indistinguishable from genuine high-resolution images.

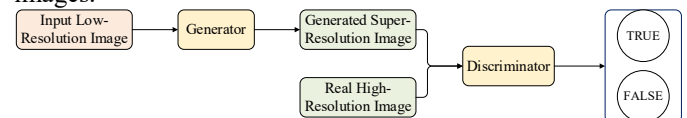


Figure 1. Architectural illustration of the Generative Adversarial Network framework

### 2.2 Image Super-Resolution Based on Generative Adversarial Networks

The Enhanced Super-Resolution Generative Adversarial Network (ESRGAN) represents an advanced generative adversarial network for super-resolution that achieved state-of-the-art performance in the field of image super-resolution at its time of introduction. This method primarily builds upon the aforementioned SRGAN architecture while implementing several key improvements.

To enhance model stability and generalization capability while reducing computational complexity, ESRGAN eliminates all



batch normalization layers from the original SRGAN framework and replaces the basic residual blocks with Residual-in-Residual Dense Blocks (RRDBs). Each RRDB consists of three dense blocks, with each dense block comprising five convolutional layers. The RRDB architecture effectively combines the advantages of dense connections and multi-level residual networks while removing block normalization, thereby reducing computational overhead while simultaneously minimizing artifacts in generated images. ESRGAN further modifies the loss function to produce more realistic super-resolution outputs through two principal innovations: (1) replacing the original feature extractor with a VGG16 network, and (2) introducing a Relativistic average Discriminator (RaD) to substitute the conventional discriminator architecture. The BN-free residual block and Residual-in-Residual Dense Block (RRDB) structure are shown in Figure 2.

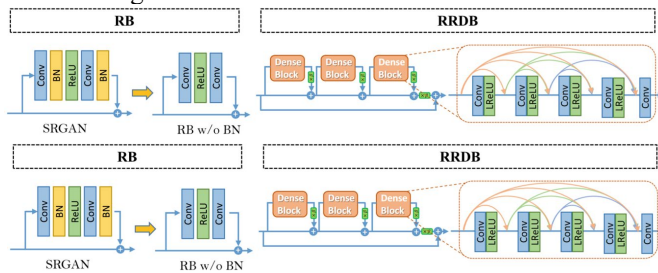


Figure 2. The BN-free residual block and Residual-in-Residual Dense Block (RRDB) structure

### 2.3 High-Order Image Degradation Model

This study innovatively proposes a high-order degradation modeling approach that overcomes the limitations of traditional first-order models, enabling more accurate simulation of complex, multi-stage and multi-factor coupled image degradation processes in real-world scenarios.

Through systematic analysis of interaction relationships among various degradation mechanisms, we extend the conventional first-order model to a more expressive second-order degradation model. This model achieves precise simulation of real degradation processes through the following innovative designs:

Incorporation of temporal characteristics in the degradation process to simulate multi-stage degradation in practical imaging systems;

Establishment of an adaptive coupling mechanism for degradation parameters to reflect nonlinear superposition effects of different degradation factors;

Achievement of optimal balance between computational complexity and model accuracy through a carefully designed second-order approximation scheme.

As illustrated in Figure 3, the constructed second-order degradation model generates low-resolution images that better approximate real-world scenarios through meticulously designed degradation path combinations. Training datasets synthesized based on this model effectively enhance the generalization capability of super-resolution networks under complex degradation conditions. Experimental results confirm that compared to networks trained with traditional degradation models, those trained with the second-order degradation model

demonstrate significant advantages across various real-world test datasets.

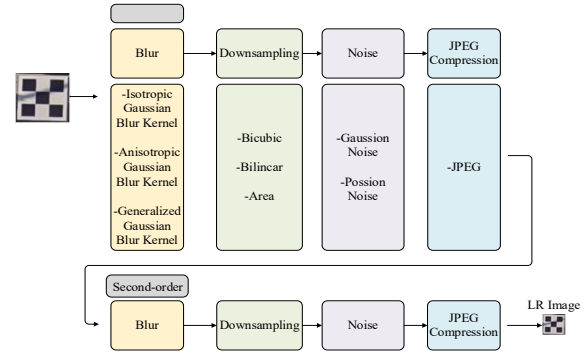


Figure 3. Advanced-order image deterioration model

### 2.4 Generator Architecture

The generator network begins with a primary feature extraction module, which takes the low-resolution (LR) image obtained from the high-order degradation model as input and extracts shallow features using a  $3 \times 3$  convolutional layer. This process is formulated as:

$$F_{primary} = \text{Conv}(I_{LR}) \quad (1)$$

The advanced feature extraction module, located at the core of the generator, serves as a bridge between shallow and deep representations. It extracts multi-level high-level features through stacked fundamental blocks for subsequent reconstruction. Based on the original Real-ESRGAN network, we improve this module by introducing: Coordinate Attention Residual-in-Residual Dense Blocks (CARRDBs), a feature fusion layer and a global spatial attention block.

The CARRDB is an enhanced version of the original RRDB, incorporating a Coordinate Attention (CA) submodule after each Dense Block to refine local feature extraction. All activation functions use Leaky ReLU for faster convergence. The output of each CARRDB is fed into the next residual group for deeper feature extraction while being directly propagated to the feature fusion layer.

The feature fusion layer aggregates all CARRDB outputs through channel-wise concatenation, followed by a  $1 \times 1$  convolution for dimensionality reduction:

$$F_{GF} = H_{GFF}(\text{Concat}(G_1, \dots, G_D)) \quad (2)$$

The first component of this module is an upsampling layer that performs convolutional operations on  $F_{high}$ , followed by pixel shuffling to generate high-resolution feature maps from low-resolution inputs. This process can be mathematically represented as:

$$F_{up} = \text{Shuffle}(\text{Conv}(F_{high})) \quad (3)$$

Where :  $F_{primary}$  denotes the primary output features,  $\text{Conv}(\cdot)$  represents the convolutional operation,  $I_{LR}$  indicates the input low-resolution image,  $F_{GF}$  corresponds to the advanced fused features with output size of,  $H_{GFF}(\cdot)$  stands for the convolutional operation,  $\text{Concat}(\cdot)$  signifies the feature concatenation operation,  $G_i$  refers to the output features of the  $i$ -th CARRDB (Cascaded Residual-in-Residual Dense Block),

$F_{up}$  represents the upsampling output result,  $Shuffle()$  denotes the pixel shuffle operation.

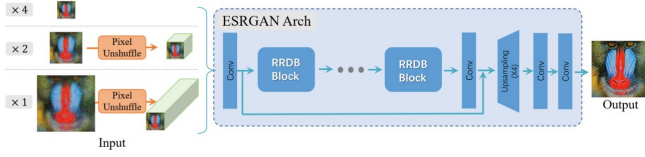


Figure 4. The architectural configuration of the conventional Real-ESRGAN generator

## 2.5 Attention Mechanism

Building upon the Real-ESRGAN framework, this study incorporates two attention mechanisms—Coordinate Attention (CA) and Spatial Attention (SA)—to enhance the network's image reconstruction performance. The implementation details of these attention mechanisms are elaborated below.

The Coordinate Attention (CA) mechanism captures long-range dependencies along two spatial directions while preserving precise positional information. This capability facilitates improved extraction of fine-grained features. Compared to alternative attention mechanisms, CA exhibits advantages such as fewer parameters and easier implementation. A schematic diagram of its structure is presented in Figure 5.

The coordinate attention mechanism is implemented through two distinct computational stages. Initially, channel attention is decomposed into dual one-dimensional feature encodings along the orthogonal X-axis and Y-axis directions, thereby addressing the inherent limitation of conventional spatial pooling methods in preserving precise positional information. For an input feature map of dimensions  $C \times H \times W$ , directional average pooling operations are independently performed along each spatial axis, generating orientation-aware feature representations  $z_c^h(h)$  and  $z_c^w(w)$ , as formally expressed.

Subsequently, the coordinate attention weights are generated through the following procedure: The output features from both directional encodings undergo concatenation, followed by channel dimensionality reduction via a  $1 \times 1$  convolutional layer and nonlinear activation. These operations yield the intermediate feature representation  $m$ , formally expressed as:

$$m = \delta(\text{Conv}[z^h, z^w]) \quad (4)$$

The intermediate feature  $m$  is then partitioned into two separate feature tensors,  $m^h$  and  $m^w$ , which subsequently undergo channel-wise dimensionality expansion via independent  $1 \times 1$  convolutional layers. These expanded features are activated using the Sigmoid function to generate coordinate-level attention weights. This process is formally expressed as:

$$\begin{cases} g^h = \sigma(\text{Conv}_h(m^h)) \\ g^w = \sigma(\text{Conv}_w(m^w)) \end{cases} \quad (5)$$

Where :  $g^h$  and  $g^w$  denote the attention weight maps along the X-axis and Y-axis directions, respectively. By applying these weights to the input features, the calibrated output feature map is obtained as:

$$y_c(i, j) = x_c(i, j) * g_c^h(i) * g_c^w(j) \quad (6)$$

Where :  $x_c(i, j)$  and  $y_c(i, j)$  denote the values at coordinate  $(i, j)$  in channel  $c$  of the input and output feature maps, respectively.

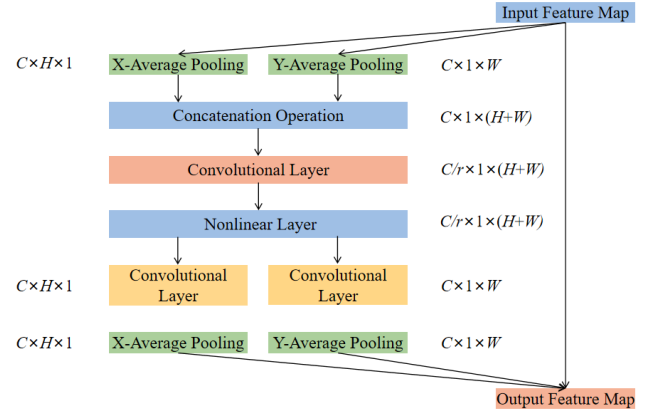


Figure 5. Architectural illustration of the Coordinate Attention module

The spatial attention mechanism captures critical spatial information within feature maps by dynamically weighting different regions of the image based on their relative importance. This enhances the model's ability to focus on semantically significant spatial locations, thereby improving the effectiveness of super-resolution reconstruction. The fundamental architecture of this mechanism is illustrated in Figure 6.

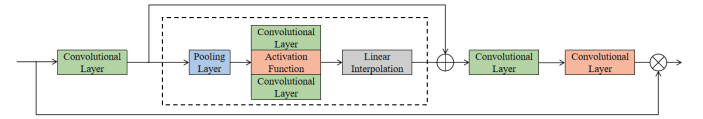


Figure 6. Architectural illustration of the Spatial Attention Module

For the input feature map  $X$ , a  $1 \times 1$  convolutional layer is first applied to perform channel dimensionality reduction, yielding the output feature map  $X'$ , as formally expressed by:

$$X' = \text{Conv}(X) \quad (7)$$

Subsequently, a  $7 \times 7$  max-pooling operation with stride 3 is applied to  $X'$ , followed by two  $3 \times 3$  convolutional layers to extract spatial attention features. To restore the feature map to its original dimensions, bilinear interpolation  $F_{linear}$  is employed for upsampling. The resultant features are then element-wise summed with  $X'$ , yielding the intermediate feature representation  $X_{mid}$ , as mathematically formulated below:

$$X_{mid} = F_{linear} \left( \text{Conv} \left( \text{ReLU} \left( \text{Conv} \left( F_{pool}(X') \right) \right) \right) \right) + X' \quad (8)$$

Finally, a  $1 \times 1$  convolutional layer is employed to restore the channel dimensionality of the output features to match the input feature map, followed by activation via the Sigmoid function  $\sigma$  to generate the final spatial attention weights. These weights are then multiplied element-wise with the input feature map  $X$  to produce the output feature map  $Z$ , as mathematically formulated below:

$$Z = \sigma(F(X_{mid})) \odot X \quad (9)$$

### 2.6 Discriminator Architecture

The high-order degradation model employed in this study exhibits significantly greater complexity than conventional low-order degradation models, inevitably leading to an orders-of-magnitude increase in computational demands. To address the consequent challenges in discriminator design, we propose an innovative U-Net architecture with spectral normalization (SN) to replace traditional VGG-based discriminators (as illustrated in Figure 7). This architectural modification offers two key advantages:

First, the spectral normalization technique effectively constrains the Lipschitz constant of network parameters, ensuring convergence within a predefined parameter space, thereby significantly enhancing training stability. Second, the U-Net's fully convolutional architecture enables pixel-wise discrimination, which maintains global semantic coherence while facilitating refined evaluation of local texture details, ultimately improving the visual realism of generated images. Experimental results demonstrate that the proposed design achieves substantial improvements in modeling fine-grained features without compromising overall image quality.

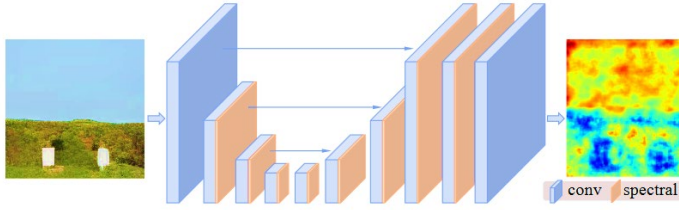


Figure 7. Spectral Normalization-incorporated U-Net Structure

## 3 CASE STUDIES AND ANALYSIS

### 3.1 System Configuration and Dataset Composition

To address the lack of specialized image datasets for hydraulic structure displacement monitoring, this study employs a transfer learning strategy. The model is pretrained on DIV2K, a widely adopted benchmark dataset in computer vision. DIV2K contains 800 high-quality 2K-resolution images (see Figure 8), encompassing diverse texture features and edge structures. This dataset has been proven to exhibit strong generalization performance in image super-resolution tasks, ensuring that the model learns robust generic feature representations before fine-tuning for hydraulic structure-specific scenarios.

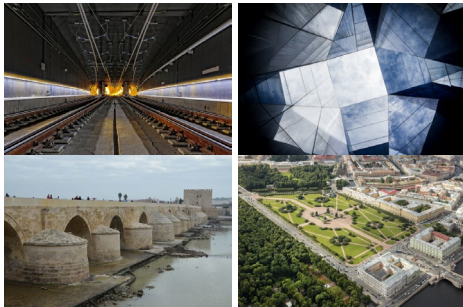


Figure 8. Representative high-resolution images from the DIV2K dataset

The network training strategy of the proposed algorithm is largely consistent with the original Real-ESRGAN model, with minor adjustments made to certain training parameters. In terms of global settings, the HR patch size is set to 256, the batch size to 48, and the Adam optimizer is employed. The network training process consists of two distinct phases. Initially, a Real-ESRNet model is trained using the L1 loss function based on a pre-trained ESRGAN model, with the iteration number set to  $1 \times 10^6$  and the learning rate to  $2 \times 10^{-4}$ . Subsequently, the trained Real-ESRNet model is utilized as the generator initialization for the enhanced Real-ESRGAN, which is further trained with a combination of three loss functions: L1 loss, perceptual loss, and GAN loss. In this phase, the iteration number is set to  $4 \times 10^4$  and the learning rate to  $1 \times 10^{-4}$ .

### 3.2 Image Super-Resolution Reconstruction Quality Evaluation

The proposed algorithm is trained to achieve a  $4 \times$  super-resolution model, meaning it reconstructs input images at four times their original resolution. To evaluate the algorithm's performance, high-resolution (HR) images were first captured using a high-definition camera in several small- and medium-scale hydraulic engineering machine vision displacement monitoring scenarios. These images served as the reference HR images. Artificial targets within the images were cropped and selected as regions of interest (ROIs) for super-resolution reconstruction. The cropped images were then subjected to a high-order degradation process to generate low-resolution (LR) images. Subsequently, the trained model was applied to perform  $4 \times$  upsampling, producing super-resolution (SR) reconstructed images.

To assess the quality of the super-resolved images, two metrics were employed: Peak Signal-to-Noise Ratio (PSNR) and Structural Similarity Index (SSIM). The definitions of these metrics are as follows:

Peak Signal-to-Noise Ratio (PSNR) measures the ratio between the maximum possible signal power and the mean squared error (noise power). A higher PSNR value indicates less distortion and better image quality, with the unit expressed in decibels (dB).

$$PSNR = 10 \lg \frac{F^2}{MSE} \quad (10)$$

Where:  $F$  denotes the maximum grayscale value of the image,  $MSE$  represents the mean squared error of the image.

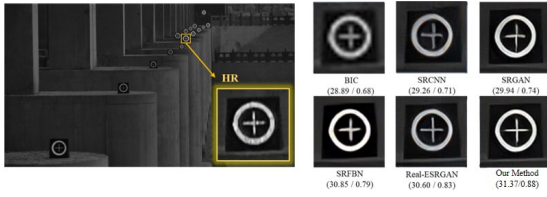
The Structural Similarity Index (SSIM) provides a comprehensive quality assessment by evaluating three key attributes: luminance, contrast, and structural fidelity. The SSIM metric is bounded within the range  $[0, 1]$ , with higher values indicating better preservation of image integrity and lower distortion.

$$SSIM = l(x, y)^\alpha \cdot c(x, y)^\beta \cdot s(x, y)^\gamma \quad (11)$$

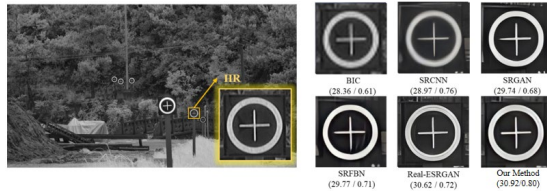
Where:  $l(x, y)$ 、 $c(x, y)$ 、 $s(x, y)$  represent the luminance, contrast, and structural measure functions, respectively;  $\alpha$ 、 $\beta$ 、 $\gamma$  denotes the adjustment parameter.

To validate the superiority of the proposed method, five super-resolution approaches - BIC, SRCNN, SRGAN, SRFBN, and Real-ESRGAN - were applied to the LR images for comparative performance evaluation, with the results illustrated in Figure 9.

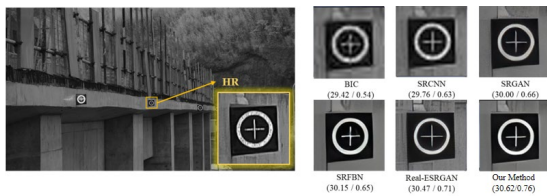




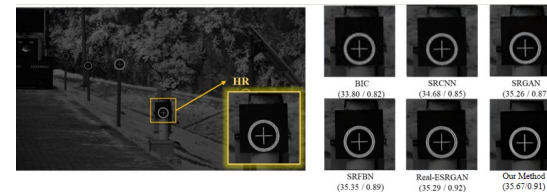
(a) Scenario 1: Machine Vision Surveillance Imagery of a Control Gate



(b) Scenario 2: Machine Vision Surveillance Imagery of a Reservoir



(c) Scenario 3: Machine Vision Monitoring Image of a Ship Lock



(d) Scenario 4: Machine Vision Monitoring Image of a Reservoir

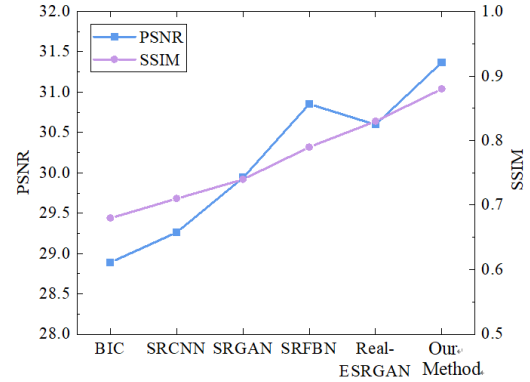
Figure 9. Super-Resolution Reconstruction Results for the Four Scenarios

The figure provides an intuitive comparison of the image reconstruction performance among different super-resolution methods. Among them, the interpolation-based BIC method performs poorly, merely enlarging the original low-resolution image without effectively restoring the texture and edge details of the target in the image. In contrast, several deep learning-based methods yield significantly better results, though with notable variations in performance. While the four other algorithms (excluding the proposed method) can reconstruct the main contours of the image reasonably well, they still fall short in recovering fine textures and edge details.

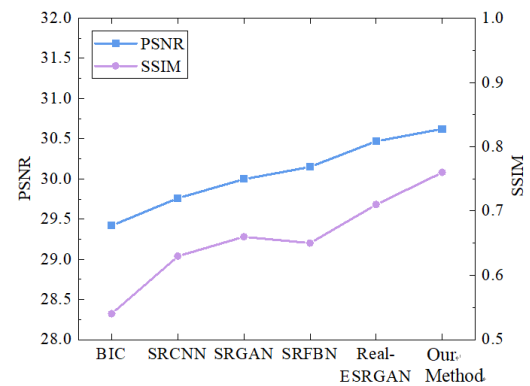
By comparison, the proposed algorithm demonstrates the best performance. When compared to the original high-resolution (HR) image, the super-resolved (SR) image generated by our method achieves a more realistic restoration in terms of both overall visual quality and fine texture details. Moreover, owing to the improvements in feature fusion and attention mechanisms, our approach delivers more refined edge and contour reconstruction.

To further quantify the performance differences, the PSNR and SSIM evaluation curves of images reconstructed by different

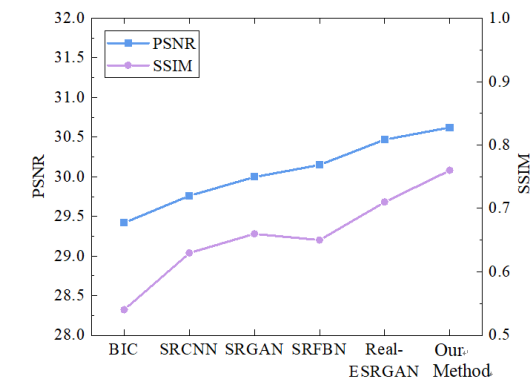
super-resolution algorithms are plotted in Figure 10. The results clearly indicate significant disparities among the algorithms, with the proposed method exhibiting superior performance in both metrics.



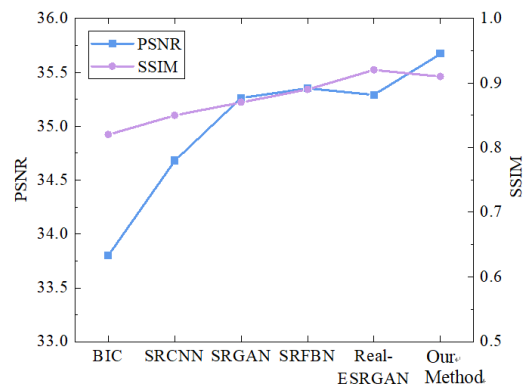
(a) Image Quality Assessment for Scenario 1



(b) Image Quality Assessment for Scenario 2



(c) Image Quality Assessment for Scenario 3



#### (d) Image Quality Assessment for Scenario 4

Figure 10. Quality validation of super-resolution reconstructed images across four distinct scenarios

### 3.3 Verification of Displacement Monitoring Accuracy Improvement

The purpose of image super-resolution reconstruction is to compensate for insufficient resolution from an algorithmic perspective when the hardware capabilities of machine vision cameras are limited or the available image resolution is low, thereby improving displacement monitoring accuracy. Therefore, it is necessary to validate the effectiveness of image super-resolution through machine vision displacement monitoring experiments.

To accurately quantify and analyze the improvement in displacement monitoring accuracy, this study selects an open-source experimental dataset for investigation. In 2018, the University of California, San Diego conducted a series of shake table tests to study the lateral response characteristics of cold-formed steel frame building structures. The related design schemes, test reports, videos, and data were all publicly released. This experiment provides comprehensive video recordings and measured data from various sensors, making it highly suitable for verifying displacement monitoring accuracy in this study.

For this research, a specific shear wall specimen from the test series was selected, and its dynamic test video data under seismic loading were analyzed. The vibration input was scaled from the recorded ground motion of the 1994 Northridge earthquake in Los Angeles, USA, ensuring the specimen remained elastic throughout the test. The experimental setup of the shake table test is illustrated in Figure 11. Specifically: Displacement sensors were installed on the side of the load-transfer beam at the top of the specimen to measure lateral displacements induced by horizontal loading.

A machine vision camera\*\* was positioned directly in front of the specimen to record the entire dynamic testing process. This configuration allows for a comparative evaluation of displacement measurements obtained from traditional sensors and machine vision-based methods, facilitating an assessment of the accuracy enhancement achieved through super-resolution reconstruction.

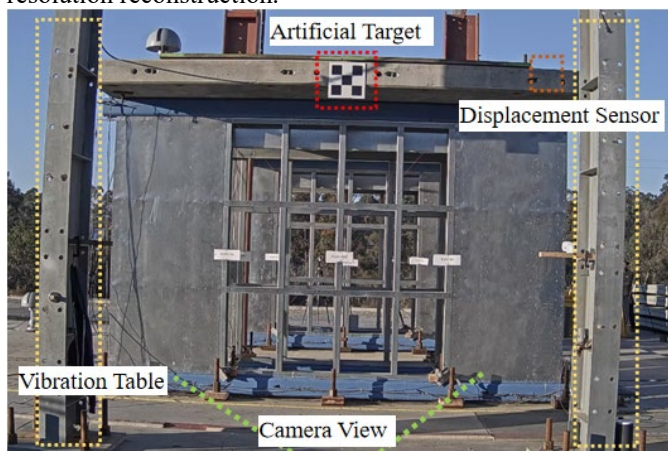


Figure 11. Overview of the Shaking Table Field Test

The checkerboard-pattern artificial target installed on the load-transfer beam at the top of the specimen served as the region of interest (ROI) for machine vision-based displacement monitoring. The specific geometry and dimensions of this target are illustrated in Figure 12. The sensor-measured displacement data recorded during the vibration test are presented in Figure 13.

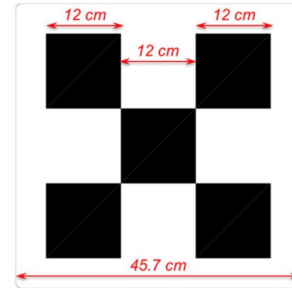
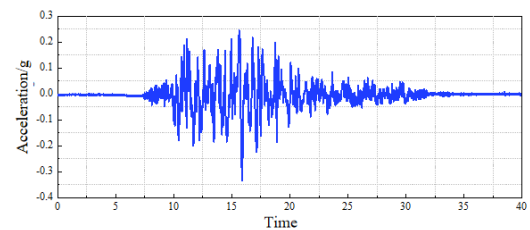
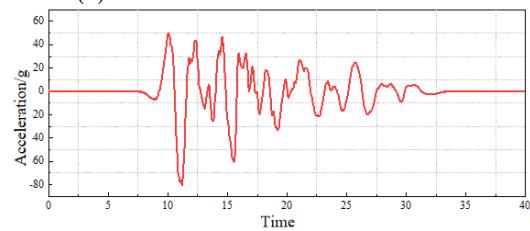


Figure 12. Shape and Dimensions of the Artificial Target



(a) Accelerometer measurement data



(b) Displacement sensor measurements

Figure 13. Experimental sensor data recorded during vibration testing

During the experimental testing process, the images were captured at close range using a high-quality camera, resulting in high-resolution footage that meets the requirements of machine vision-based displacement monitoring under normal conditions. Therefore, the actual captured monitoring images were treated as high-resolution (HR) images, and displacement monitoring was performed on the HR image sequence. The tracking target was a checkerboard-pattern artificial target, and the calculated results are presented in the following figures and tables. The results demonstrate that the machine vision-based displacement monitoring using high-resolution images achieved high accuracy, closely matching the measured displacement values from sensors, thereby validating the effectiveness of the machine vision approach.

To evaluate the accuracy improvement effects of different super-resolution methods, the original HR images (120×120 pixels) of the target region were first degraded according to the higher-order degradation model proposed in this study, generating corresponding low-resolution (LR) images (30×30 pixels) as the baseline LR images for the accuracy enhancement validation experiment (all super-resolution algorithms were

applied to these LR images for enhancement). Subsequently, the bicubic interpolation (BIC) method was employed to perform  $4\times$  upsampling super-resolution reconstruction on the LR images, producing corresponding BIC super-resolution (SR) images ( $120\times120$  pixels) for comparative analysis with other super-resolution algorithms. The entire process is illustrated in Figure 14 below.

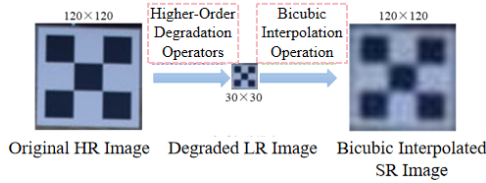


Figure 14. Processing results of artificial target images

For the low-resolution (LR) images, the proposed algorithm in this study was employed to perform super-resolution (SR) reconstruction, and the results were compared with those of other SR methods, as illustrated in the following figure. As shown in Figure 15, the visual differences among the outputs of different methods can be easily observed. Among them, the BIC and SRCNN super-resolution algorithms exhibited the poorest performance, with noticeable blurring visible to the naked eye. The other four algorithms achieved better reconstruction results, but the proposed method outperformed them all, achieving the highest scores in both PSNR and SSIM metrics. When comparing the super-resolved images generated by the proposed method with those obtained from the original Real-ESRGAN (before improvements), it is evident that the proposed method produces images with sharper edges and more detailed textures, demonstrating the effectiveness of the introduced feature fusion and attention mechanism enhancements.

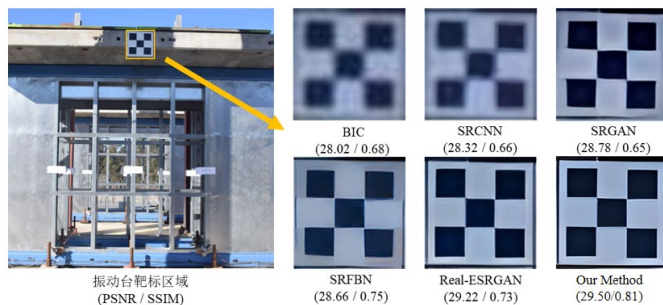


Figure 15. Super-resolution reconstruction results of the target image

To further analyze the quality improvement effects of image super-resolution, corner detection was performed on different types of images using OpenCV's goodFeaturesToTrack detector, followed by cornerSubPix refinement for sub-pixel accuracy. All detection parameters remained consistent throughout the process, and the resulting corner detection outcomes are illustrated in Figure 16. Given the noticeable differences in performance among the algorithms, the superiority of each method can be clearly determined based on the number and positional accuracy of detected corners.

Taking the original high-resolution (HR) image as a reference, a total of 16 inner checkerboard corners and 5 outer corners were detected, with their positions precisely aligned to the edges and intersections of the checkerboard pattern. The

comparison among different super-resolution algorithms revealed significant discrepancies. For instance, BIC and SRCNN exhibited evident corner misalignment and missing detections, failing to fully capture the expected number of corners. In contrast, the proposed method demonstrated the best performance, detecting the same number of corners as the HR image while maintaining accurate positional correspondence, further validating its effectiveness.

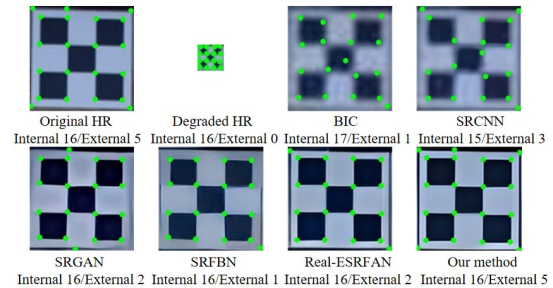


Figure 16. Corner detection results for images reconstructed using different super-resolution methods

Subsequently, target tracking and displacement calculation were performed on the reconstructed image sequences obtained from the aforementioned super-resolution methods, yielding the corresponding displacement time-history curves for each method, as illustrated in Figure 17. The results demonstrate that the low-resolution (LR) images without any processing exhibited degraded tracking performance due to substantial loss of effective information and noise contamination, leading to unsatisfactory displacement monitoring results. Specifically, the displacement curve of the LR images displayed significant fluctuations and drift phenomena, particularly in the intermediate segment with larger vibration amplitudes (as clearly observed in the zoomed-in subplot). The resulting errors substantially exceeded the acceptable threshold, rendering the displacement monitoring results unreliable.

In contrast, the six curves derived from super-resolution-processed images exhibited significantly improved performance, mitigating the accuracy degradation caused by image resolution reduction to varying degrees. Among these, the Bicubic Interpolation (BIC) algorithm demonstrated relatively inferior performance, while the proposed feature-fusion-enhanced Real-ESRGAN algorithm with attention mechanisms achieved the best results. The displacement curve generated by the proposed method closely aligned with both the sensor-measured displacement curve and the vision-based measurement curve obtained from high-resolution (HR) images, outperforming even the original Real-ESRGAN algorithm. This comparative analysis further validates that the proposed model improvements contribute effectively to enhancing displacement monitoring accuracy.

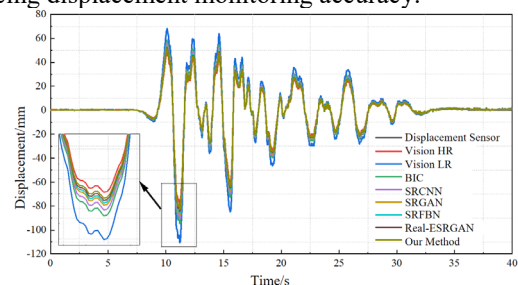




Figure 17. Vibration displacement monitoring results using different super-resolution methods

Finally, four evaluation metrics—Mean Absolute Error (MAE), Mean Absolute Percentage Error (MAPE), Root Mean Square Error (RMSE), and the Coefficient of Determination ( $R^2$ )—were employed for further quantitative assessment. The corresponding residual box plots and evaluation metric radar charts are presented in Table 1 and Figure 18, respectively. The results demonstrate that the proposed method consistently outperformed all other approaches across all evaluation metrics, achieving an  $R^2$  value of 0.9975, which is remarkably close to the monitoring results obtained from the high-resolution (HR) images. Although the proposed method cannot fully compensate for the degradation caused by image downsampling, it significantly mitigates the impact of resolution reduction compared to other methods, exhibiting superior performance.

The residual box plots reveal that the monitoring results based on HR images exhibited the highest accuracy, with residuals fluctuating only within a very narrow range. Considering that this case involves large-amplitude vibration displacement, which inherently introduces error drift in target tracking, the BIC super-resolution algorithm displayed the largest residual fluctuations, while the residuals of other algorithms also exceeded 5 mm. In contrast, the proposed method effectively confined the residuals within 5 mm, demonstrating a substantial improvement in monitoring accuracy over competing approaches.

Table 1 Displacement monitoring accuracy evaluation across different super-resolution methods

Test Category	MAE	MAPE	RMSE	$R^2$
Visual HR	0.101	0.316	0.233	0.999
Visual LR	3.822	0.495	6.697	0.918
BIC	1.954	0.416	3.355	0.972
SRCNN	1.488	0.393	2.522	0.982
SRGAN	1.114	0.373	1.856	0.991
SRFBN	0.928	0.362	1.525	0.993
Real-ESRGAN	0.741	0.351	1.195	0.995
Proposed Method	0.555	0.340	0.870	0.997

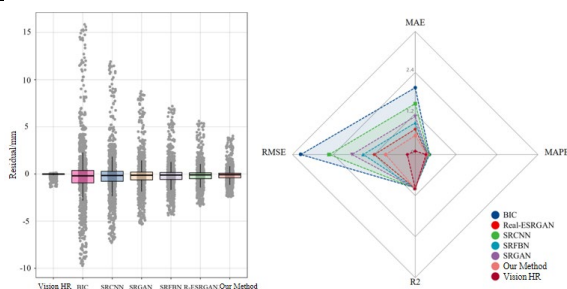


Figure 18. Error evaluation visualization across different super-resolution methods

#### 4 CONCLUSION

Departing from conventional approaches that rely on hardware upgrades (e.g., higher-resolution cameras, precision optical lenses) or subpixel algorithm refinement, this research innovatively explores image super-resolution (SR) reconstruction based on deep learning, proposing a software-algorithm-level solution for breakthrough accuracy enhancement in displacement monitoring. The key research contributions and findings are systematically summarized as follows:

A thorough analysis of image degradation processes and super-resolution reconstruction principles was conducted. An SR reconstruction model was innovatively developed using a generative adversarial network (GAN) architecture. By establishing a multi-factor coupled higher-order degradation model, the study accurately simulates complex imaging processes in real-world engineering environments, significantly improving the algorithm's adaptability to various degraded images.

The study innovatively integrates Coordinate Attention (CA) and Spatial Attention (SA) mechanisms into the Real-ESRGAN framework, constructing a feature fusion attention network. The CA mechanism enables channel-space feature co-optimization, while the SA mechanism enhances the representation of critical regions. Without modifying hardware configurations, this approach significantly improves target feature discriminability, providing a reliable foundation for high-precision displacement monitoring.

The proposed method was rigorously validated through engineering case studies, assessing both image quality metrics and displacement monitoring accuracy. Comparative experiments with five state-of-the-art algorithms demonstrate the superior performance of the proposed method, which effectively restores edge and contour details in reconstructed images. Moreover, the displacement monitoring results derived from the SR-enhanced image sequences exhibit significantly improved accuracy, offering an innovative technical pathway to overcome the precision limitations in machine vision-based monitoring of hydraulic structures.

#### REFERENCES

- [1] Zhao, Y., Wang, H., Ma, H., et al. (2022). Construction concept of China's "Double T" water network economic pattern. *Journal of Hydraulic Engineering*, 53 (11), 1271-1279, 1290.
- [2] Wang, J., Zhao, H., & Ye, Y. (2018). Smart water network engineering: The engine driving China's water governance modernization. *Journal of Hydraulic Engineering*, 49(9), 1148–1157.
- [3] YANG L, SU H, WEN Z. Improved PLS and PSO methods-based back analysis for elastic modulus of dam[J]. *Advances in Engineering Software*, 2019, 131: 205–216.
- [4] Ban, Y., Liu, Y., Wang, N., et al. (2024). A review of measurement methods for the main reflector surface of radio telescope antennas. *Scientia Sinica: Physica, Mechanica & Astronomica*, 54(1), 23–37.
- [5] WANG X, ZHAO Q, XI R, et al. Review of bridge structural health monitoring based on GNSS: from displacement monitoring to dynamic characteristic identification[J]. *IEEE Access*, 2021, 9: 80043–80065.

- [6] Liu, Y. (2023). Research on construction monitoring technology for the swivel bridge of the overpass crossing Yanshi Railway [Master's thesis, North China University of Technology].
- [7] Li, G. (2023). Thoroughly implement the spirit of the 20th CPC National Congress and solidly promote high-quality development of water conservancy in the new stage: Speech at the 2023 National Water Conservancy Work Conference. China Water Power & Electrification, 2023(2), 1–11.
- [8] Liu Z.P., Fu H., Guo X.L., et al. 2017. Integrated dual-frequency radar measurement system for ice-water conditions. Journal of Hydraulic Engineering 48(11): 1341-1347.
- [9] ZHOU Q, LI Q-S, HAN X-L, et al. Improvement of GPS displacement measurement accuracy for high-rise buildings by machine learning[J]. Journal of Building Engineering, 2023, 78: 107581.
- [10] NURKOWSKI J, NOWAKOWSKI A. Inductive sensor for measuring linear displacement and velocity – Version with stationary magnetic core[J]. Measurement, 2023, 222: 113675.
- [11] HAN J, XIONG G, LIU J. Detection and analysis of pavement-section based on laser displacement sensor[J]. Sensors, 2023, 23(15): 6758.
- [12] SUH Y S. Laser sensors for displacement, distance and position[J]. Sensors, 2019, 19(8): 1924.
- [13] LIU T, LEI Y, MAO Y. Computer vision-based structural displacement monitoring and modal identification with subpixel localization refinement[J]. T.-C. Huynh. Advances in Civil Engineering, 2022, 2022: 1–11.
- [14] LUO L, FENG M Q, WU Z Y. Robust vision sensor for multi-point displacement monitoring of bridges in the field[J]. Engineering Structures, 2018, 163: 255–266.
- [15] KARSZNIA K, OSADA E, MUSZYŃSKI Z. Real-time adjustment and spatial data integration algorithms combining total station and GNSS surveys with an earth gravity model[J]. Applied Sciences, 2023, 13(16): 9380.
- [16] ZHOU J, HE L, LUO H. Real-time positioning method for uavs in complex structural health monitoring scenarios[J]. Drones, 2023, 7(3): 212.
- [17] LI X, ZHONG B, LI J, et al. Inversion of GNSS vertical displacements for terrestrial water storage changes using slepian basis functions[J]. Earth and Space Science, 2023, 10(2): e2022EA002608.
- [18] CAO S, LU X, SHEN S. GVINS: tightly coupled gnss–visual–inertial fusion for smooth and consistent state estimation[J]. IEEE Transactions on Robotics, 2022, 38(4): 2004–2021.
- [19] KIM K-H, JUNG H-K. Development of a remote displacement measuring laser system for bridge inspection[J]. Sensors, 2022, 22(5): 1963.
- [20] PAZIEWSKI J, STEPNIAK K, SIERADZKI R, et al. Dynamic displacement monitoring by integrating high-rate GNSS and accelerometer: on the possibility of downsampling GNSS data at reference stations[J]. GPS Solutions, 2023, 27(3): 157.
- [21] FA G, LI K, CAO T. Improving vibration monitoring of structures using theodolites with built-in image sensors[J]. International Journal of Structural Stability and Dynamics, 2023, 23(11): 2350125.
- [22] KHUC T, CATBAS F N. Completely contactless structural health monitoring of real-life structures using cameras and computer vision: structural health monitoring using computer vision[J]. Structural Control and Health Monitoring, 2017, 24(1): e1852.
- [23] YOON H, ELANWAR H, CHOI H, ET al. Target-free approach for vision-based structural system identification using consumer-grade cameras: Target-Free Vision-based structural system identification[J]. Structural Control and Health Monitoring, 2016, 23(12): 1405–1416.
- [24] DONG C Z, YE X W, JIN T. Identification of structural dynamic characteristics based on machine vision technology[J]. Measurement, 2018, 126: 405–416.
- [25] BROWNJOHN J M W, XU Y, HESTER D. Vision-Based bridge deformation monitoring[J]. Frontiers in Built Environment, 2017(3): 23.
- [26] BOCIAN M, NIKITAS N, KALYBEK M. Dynamic performance verification of the Rędziński Bridge using portable camera-based vibration monitoring systems.[J]. Archives of Civil and Mechanical Engineering, 2023(23): 1–19.
- [27] KOHUT P, HOLAK K, MARTOWICZ A, et al. Experimental assessment of rectification algorithm in vision-based deflection measurement system[J]. Nondestructive Testing and Evaluation, 2017, 32(2): 200–226.
- [28] WU T, TANG L, SHAO S, et al. Cost-effective, vision-based multi-target tracking approach for structural health monitoring[J]. Measurement Science and Technology, 2021, 32(12): 125116.
- [29] MOLINA-VIEDMA A J, FELIPE-SESÉ L, LÓPEZ-ALBA E, et al. High frequency mode shapes characterisation using digital image correlation and phase-based motion magnification[J]. Mechanical Systems and Signal Processing, 2018, 102: 245–261.
- [30] Wang J., Huang Y., Deng Y., et al. 2021. Study on fracture characteristics of Yellow River ice based on digital image correlation method. Journal of Hydraulic Engineering 52(9): 1036-1046.
- [31] GUO J, XIANG Y, FUJITA K, et al. Vision-Based Building Seismic Displacement Measurement by Stratification of Projective Rectification Using Lines[J]. Sensors, 2020, 20(20): 5775.



## Advanced Geospatial and Engineering Surveying Solutions for Infrastructure Health Monitoring



# Monitoring Slow and Dynamic Deformations of High-Rise Buildings Using Low-Cost GNSS Receivers

JMO Jayamanne<sup>1</sup>, PA Psimoulis<sup>1</sup>, J Owen<sup>1</sup>, NT Penna<sup>2</sup>, C Xue<sup>1</sup>

<sup>1</sup>Faculty of Engineering, University of Nottingham, Nottingham, UK

<sup>2</sup>School of Engineering, Newcastle University, Newcastle, UK

jaymanne.jayamanne@nottingham.ac.uk

**ABSTRACT:** The structural integrity and safety of high-rise buildings rely heavily on effective deformation monitoring. Global Navigation Satellite System (GNSS) techniques are frequently utilized to monitor these deformations; yet, despite their great accuracy, they possess possible limitations due to high costs. Thus, this research investigates the potential of low-cost GNSS receivers for monitoring deformations in high-rise structures. The study focuses on incorporating low-cost GNSS receivers to capture slow motion movements caused by factors such as solar radiation and temperature fluctuations as well as dynamic movements induced by forces including wind loads and seismic forces. The performance of low-cost GNSS receivers is assessed against high-precision geodetic-grade GNSS receivers through a series of experiments conducted on a high-rise building under both slow-motion and dynamic conditions. The study primarily investigates the U-blox F9P dual-frequency GNSS receiver with Leica AS10, Tallysman TWI, and U-blox patch antennas. Results indicate that low-cost GNSS receivers demonstrate significant potential for capturing accurate and precise deformation measurements. The selection of GNSS antenna is found to significantly influence the overall quality of the GNSS data. However, the results indicate that with proper configuration, these low-cost receivers can be successfully integrated to develop an efficient and sustainable deformation monitoring system for high-rise buildings.

**KEY WORDS:** High-rise buildings; geodetic monitoring; Low-cost GNSS

## 1 INTRODUCTION

Structural Health Monitoring (SHM) is vital for ensuring safety, maintenance, and structural integrity of infrastructure. Structural Health Monitoring (SHM) facilitates continuing observation of structural performance, allowing for early problem detection, hence reducing the likelihood of failure and lowering maintenance costs. The necessity to implement novel SHM systems becomes critical as rapid urban expansion leads to significant structural development across the world [1], [2].

High rise buildings in particular, are exposed to both slow and dynamic deformations which necessitates for specialised monitoring techniques [3]. High-rise structures undergo continuous slow movements due to factors such as solar radiation and dynamic movements due to wind load and seismic activities. The conventional monitoring approaches for high-rise buildings require expensive installation efforts, along with other significant expenses and requirements such as time, physical and human resources [4].

Global Navigation Satellite Systems (GNSS) have emerged as a better option for deformation monitoring in recent decades, owing to advancements in high-quality GNSS receivers and effective processing techniques [5], [6]. GNSS-based monitoring systems now provide a precise system to observe both static and dynamic movements of structures [7], [8]. GNSS acquires multiple satellite signals to determine accurate positional coordinates, thereby facilitating the effective collection of long-term deformations, while simultaneously monitoring real-time dynamic motions. Modern geodetic grade GNSS receivers equipped with dual-frequency capability

mitigate atmospheric errors and improve their accuracy in location measurement [9]. High-rate GNSS receivers provide data acquisition exceeding 10 Hz, hence enabling the observation of sudden structural displacements during events such as earthquakes and wind-related phenomena [10]. GNSS operates more effectively in conjunction with other sensors, such as accelerometers, as it enhances monitoring precision and accuracy. However, the significant high cost of a GNSS monitoring station which will allow mm level positioning, limit their application in deformation monitoring applications [9], [11], [12].

Low-cost GNSS receivers have emerged as a viable alternative for structural monitoring. These receivers, considerably more economical than geodetic-grade alternatives, include dual-frequency functionality that improves positioning precision and reduce atmospheric errors [7], [9], [11]. Recent improvements in low-cost GNSS technology have resulted in the creation of multi-constellation receivers that employ signals from GPS, GLONASS, Galileo, and BeiDou to enhance positional precision and signal accessibility in urban settings [13]. The cost-effectiveness of these receivers, typically priced under £500, renders them a practical option for extensive implementation in structural monitoring applications. This is evidenced by the findings of several researchers who have utilized low-cost receivers for monitoring deformations of bridges and other infrastructure [9], [11], [14].

Experimental validation is essential to evaluate the feasibility of low-cost GNSS receivers for monitoring both slow and dynamic deformations in tall buildings. Prior research has illustrated the effective utilisation of low-cost GNSS for bridge

monitoring, emphasising its capability for monitoring structural displacements. Researchers have employed low-cost GNSS receivers to observe the deformation and oscillation of suspension and cable-stayed bridges, attaining sub-centimeter precision in both static and dynamic assessments. Recent studies indicates that employing suitable data processing methodologies, including Precise Point Positioning (PPP) and Real-Time Kinematic (RTK) corrections, enables low-cost GNSS to yield accurate displacement measurements equivalent to those from high-end geodetic GNSS receivers [7], [9], [11].

Despite considerable advancements in bridge applications, the accuracy of low-cost GNSS in high-rise structural health monitoring remains mostly unexamined. High-rise structures present additional obstacles, including multipath effects, signal obstructions, and dynamic loading conditions, requiring further investigation to evaluate the reliability and accuracy of low-cost GNSS in this context [15], [16]. This study attempts to assess the performance of low-cost dual-frequency GNSS receivers in monitoring the deformations of high-rise buildings and to compare their findings with geodetic grade GNSS receivers and other traditional surveying techniques such as total station-based monitoring.

Thus, the ultimate objective of this study is to assess the feasibility of low-cost GNSS receivers in high-rise structural health monitoring, hence advancing the creation of low-cost and sustainable monitoring solutions. The results will offer significant insights into their precision, accuracy, and limitations supporting further developments in SHM technology.

## 2 SLOW MOVEMENT SIMULATION

This experiment aimed to assess the performance of a low-cost GNSS system during periodic horizontal displacements. The Tallysman TWI low-cost GNSS antenna was evaluated using a low-cost receiver (U-blox F9P) through the experiment.

The Tallysman TWI antenna is engineered to provide precise GNSS performance in low-cost applications. It has a compact, lightweight design and facilitates multi-constellation, dual-frequency signal reception, rendering it appropriate for high-precision positioning. The durable design guarantees reliable signal quality and phase centre stability, crucial for applications necessitating precise and reproducible measurements [17], [18]. The U-blox F9P is a high-performance, low-cost GNSS receiver that facilitates multi-band and multi-constellation tracking, encompassing GPS, GLONASS, Galileo, and BeiDou. Engineered for accurate positioning applications, it provides real-time kinematic (RTK) functionalities. U-blox receivers has been incorporated for several deformation monitoring observations in the recent past [19], [20].

The experimental set up comprised with a movement simulation device which was utilised to simulate 1 cm horizontal (along E-W axis) movements every hour. Dual frequency GNSS data were collected with 1 Hz sampling rate

and the reference data were obtained through a Leica TS30 Robotic Total Station.

The experimental setup is depicted by figure 1.



Figure 1: Left- Tallysman TWI antenna and U-blox F9P receiver, Right: The movement simulation device

Collected data were processed through RTKlib processing software. RTKlib is an open-source software which has been utilised and validated in many GNSS applications and research [7], [9]. The software has been included into the analysis of GNSS data within the context of Structural Health Monitoring, owing to its capacity to assess carrier phase and pseudo range residuals. This enables users to gain a thorough comprehension of the quality of GNSS data and fluctuations in noise [21], [22], [23]. The following GNSS processing parameters were utilised in the post processing of the experimental data.

Parameter	Value
Processing mode	Kinematic (PPK)
Elevation mask	7°
Filter Type	Combined
Ephemeris	Broadcast
Ionospheric Correction	Broadcast
Tropospheric Correction	Saastamoinen

### 2.1 Analysis and Results

This study highlights the horizontal and vertical movements recorded by the Tallysman TWI low-cost GNSS antenna with the U-blox F9P low-cost GNSS receiver against the movements recorded by the Robotic Total Station. In figure 2 and 3 is depicted the horizontal and vertical movement time series of the Tallysman antenna for different satellite combinations as GPS only, GPS and Galileo and GPS, Galileo and Beidou.

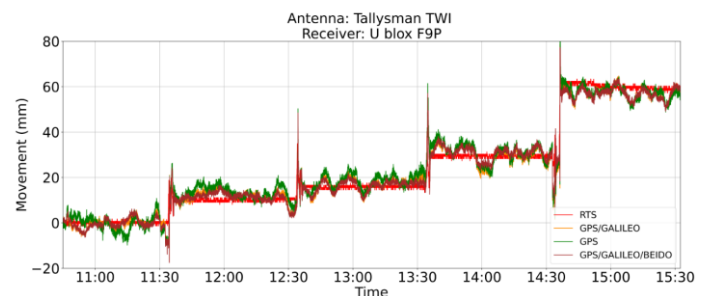


Figure 2: Horizontal (E-W) movement recorded by the Tallysman TWI antenna connected to U-blox F9P low-cost GNSS Receiver for GPS only, GPS/Galileo, GPS/ Galileo and Beidou Satellite combinations.

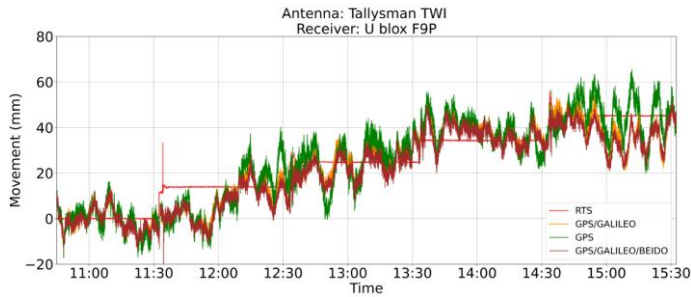


Figure 3: Vertical movement recorded by the Tallysman TWI antenna connected to U-blox F9P low-cost GNSS Receiver for GPS only, GPS/Galileo, GPS/ Galileo and Beidou Satellite combinations.

All satellite combinations follow a similar trend in both Horizontal and vertical movements. The vertical movement observations show a comparatively higher noise levels than the horizontal observations. The following mean errors have been obtained during each movement for the different configurations.

Movement	Error (mm)		
	GPS	GPS/GAL	GPS/GAL BDS
H 01	3.78	2.52	1.87
H 02	0.92	1.09	0.9
H 03	1.86	1.22	0.28
H 04	3.49	2.84	4
Mean	2.51	1.92	1.76
V 01	2.46	3.91	5.92
V 02	3.6	5.66	4.61
V 03	3.81	2.94	4.69
V 04	3.65	11.95 (outlier)	12.06 (outlier)
Mean	3.38	4.17	5.07

For horizontal movements, the results were evident by the mean errors where the combination of GPS, Galileo and Beidou signals showed the best performance for the GNSS setup. This agrees with the findings of other studies where the use of multiple satellite systems increase the number of visible satellites and the satellite geometry thereby minimizing the noise [24], [25].

However, for the vertical observations the use of GPS only provided the best performance compared to the other combinations. This may result from enhanced signal stability, well-defined orbital characteristics, and advanced error modelling of GPS, especially in the vertical dimension. Furthermore, multi-GNSS integration may result in inter-system biases and discrepancies in vertical positioning due to fluctuations in satellite elevation angles, hardware delays, and ionospheric delay modelling among various systems, thereby compromising vertical accuracy if not adequately corrected [26], [27], [28].

A Welch Power Spectral Density (PSD) analysis was conducted to further explain the noise characteristics of the GNSS set up. The Welch technique calculates a signal's power distribution by segmenting the data, applying a window function, and averaging the periodogram. In GNSS data analysis, Welch PSD is especially effective for identifying signal artefacts, multipath effects, or oscillator instabilities, which appear as frequency-specific abnormalities in the spectrum domain. The resultant spectrum discusses the fundamental noise structures, which is essential for enhancing the reliability and precision of satellite-based positioning systems [29], [30].

The Welch PSD of the Tallysman antenna for different satellite combinations as GPS only, GPS and Galileo Only and GPS, Galileo and Beidou for horizontal and vertical movements have been depicted in figures 4 and 5 respectively.

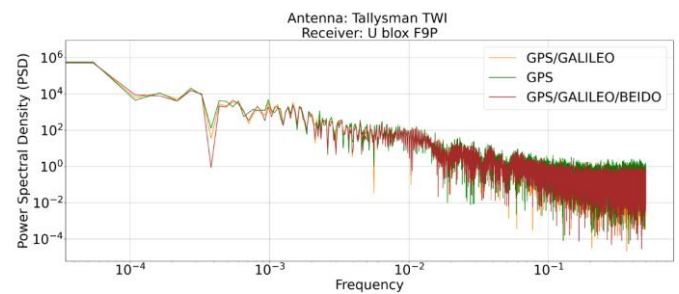


Figure 4: Welch PSD for horizontal (E-W) movement recorded by the Tallysman TWI antenna connected to U-blox F9P low-cost GNSS Receiver for GPS only, GPS/Galileo, GPS/ Galileo and Beidou Satellite combinations.

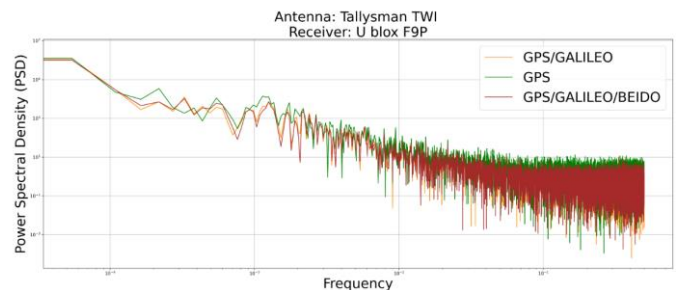


Figure 5: Welch PSD for vertical movement recorded by the Tallysman TWI antenna connected to U-blox F9P low-cost GNSS Receiver for GPS only, GPS/Galileo, GPS/ Galileo and Beidou Satellite combinations.

The PSD results further indicate that the integration of GPS, Galileo, and Beidou satellites will result in the least amount of noise. Thus, a combination of multiple satellite constellations is suggested for optimum results with Tallysman TWI low-cost antenna and the U-blox F9P low-cost GNSS receiver. However, further experimentation is necessary to assess the impact of atmospheric errors and multipath toward the low-cost antennas and further tests will be carried out to test different atmospheric models for a deeper performance and noise analysis.



### 3 DYNAMIC MOVEMENT SIMULATION

A dynamic movement simulation test was conducted to assess the performance of Tallysman Antenna with the U-blox F9P receiver. This test was conducted through controlled vibrations of specific frequency range, incorporating the APS 113 shaker [31]. The APS 113 is a long-stroke, air-bearing electrodynamic shaker designed for the precise calibration and evaluation motion transducers. It delivers a force output of 133 N and a peak-to-peak displacement of 158 mm, operating within a frequency range up to 200 Hz. The air-bearing system ensures minimum friction, hence diminishing noise and distortion. Through the shaker a controlled vibratory platform was introduced to simulate a real-world oscillation [32].

The Tallysman TWI antenna was tested with the U-blox F9P receiver for vibrations at frequencies of 0.1 Hz and 0.25 Hz, produced by an analogue signal generator. The selection of low-frequency simulations aimed to recreate long-range oscillations, which are the primary vibrations of high-rise buildings caused by wind load. Three vibration amplitudes in the E-W direction (i) below 1 cm (ii) around 2-3 cm, and (iii) around 6-7 cm were manually introduced for 10 minutes. The accuracy of the GNSS data were determined through the E-W amplitudes compared against the measurements collected through LeicaTS30 Robotic Total Station. Same observation

and processing parameters as the slow movement simulation test were utilised for this test.



Figure 6: Left- The APS 113 shaker used for the experiment with Tallysman TWI, U-blox Patch and Leica AS10 Geodetic antennas. Right- U-blox F9P receivers connected to the antennas and Raspberry Pi devices to log the data.

#### 3.1 Analysis and Results

Displacement time series were obtained for the three introduced amplitude values. The exact oscillating amplitude cannot be controlled by the APS 113 shaker hence, the amplitudes were manually controlled and the RTS observation was taken as the reference amplitude [33].

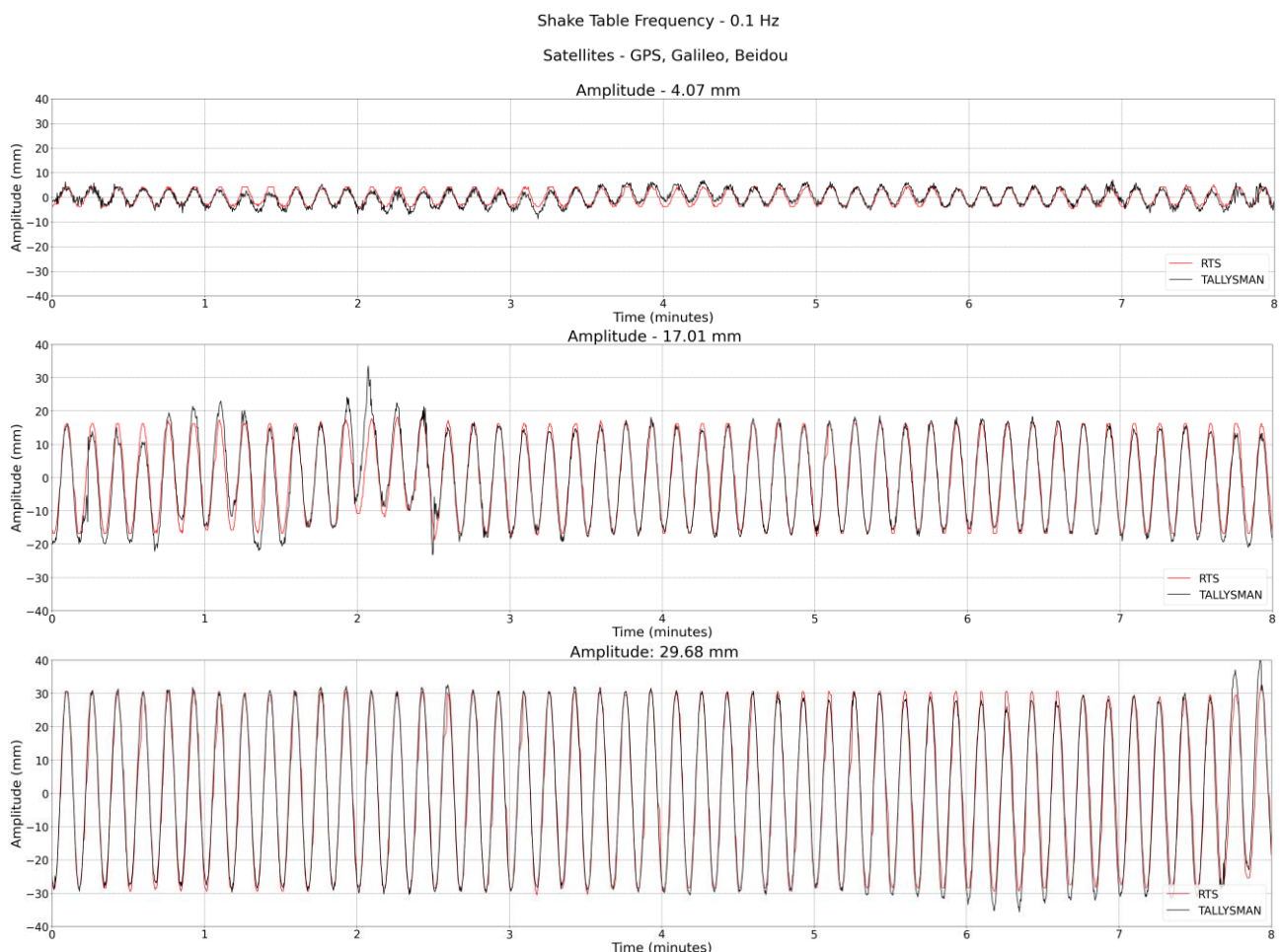


Figure 7: The amplitudes recorded by the Tallysman TWI antenna connected to U-blox F9P low-cost GNSS Receiver for 0.1 Hz shake table oscillation.

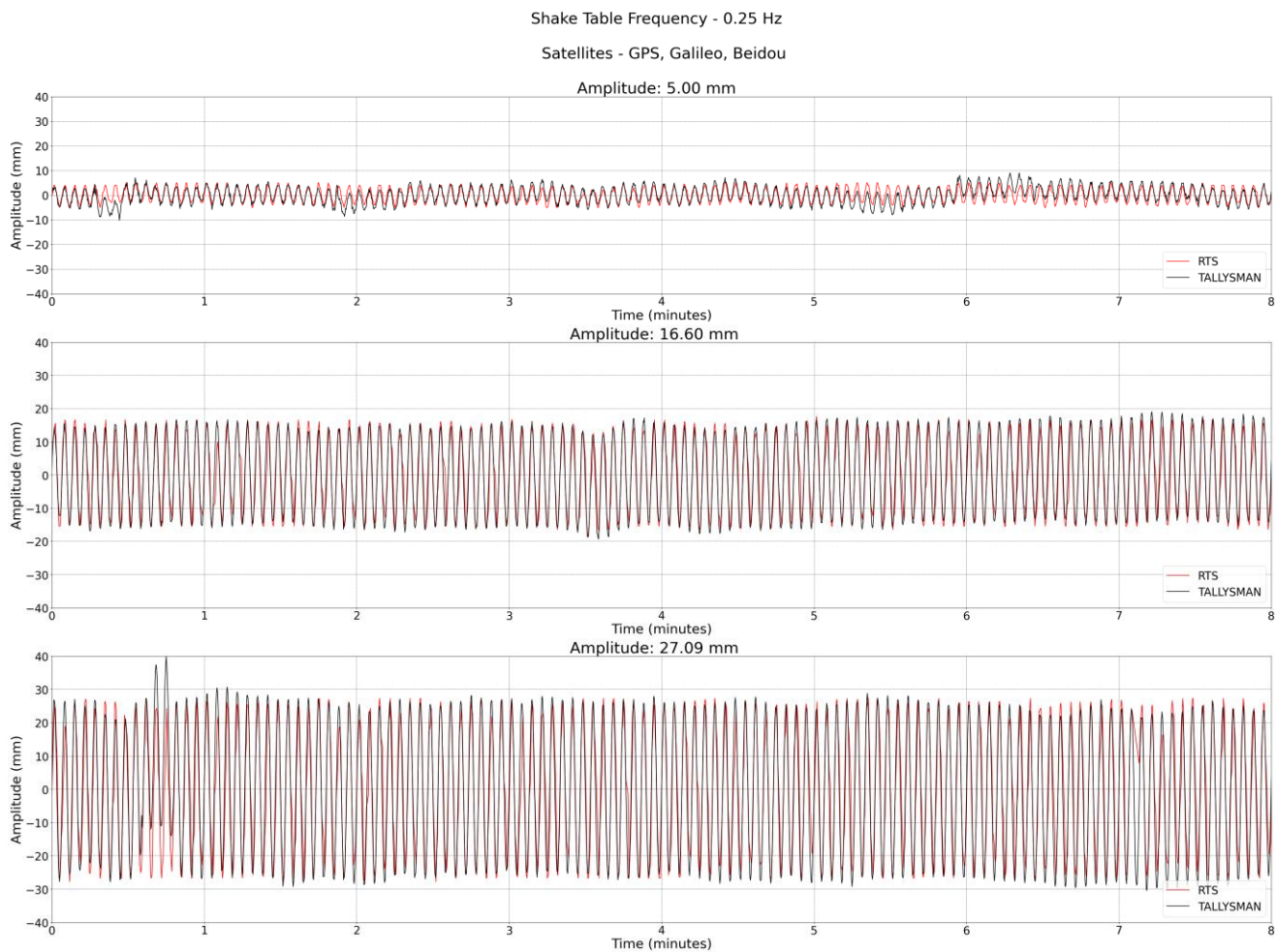


Figure 8: The amplitudes recorded by the Tallysman TWI antenna connected to U-blox F9P low-cost GNSS Receiver for 0.25 Hz shake table oscillation.

Figures 7 and 8 depict the displacement time series at frequencies of 0.1 Hz and 0.25 Hz, respectively. The results indicate that the Tallysman antenna closely replicates the displacement achieved by the RTS. Further, the mean errors of positive and negative peaks were determined to provide further insight into the noise levels. The overall absolute error recorded by the Tallysman antenna with U-blox receiver is 0.6 mm for 0.1 Hz oscillation and 2.5 mm for 0.25 Hz oscillation.

The mean error of each amplitude value can be summarised as follows:

	Amplitude (mm)		Absolute Error (mm)
	RTS (Reference)	Tallysman (Observed)	
0.1 Hz	4.1	3.3	0.8
	17.0	16.4	0.6
	29.7	30.1	0.4
0.25 Hz	5.0	7.8	2.8
	16.6	17.6	1.0
	27.1	30.6	3.5

The mean amplitude values obtained from the Tallysman- U-blox low-cost GNSS configuration validate the feasibility of utilising such systems for monitoring dynamic movements.

#### 4 CASE STUDY

A preliminary case study was performed on a 220-meter-high residential building utilising a low-cost GNSS setup that included a Tallysman antenna and a U-blox F9P receiver. The building, a concrete-steel composite structure, serves as an effective testbed for structural monitoring because of its vulnerability to deformation under environmental pressures.

In high-rise structures, the variations of solar radiations and wind forces are among the most significant factors influencing structural performance [1]. Thermal impacts induce differential expansion between concrete and steel, potentially leading to internal tensions and long-term deformations due to the disparity in thermal expansion coefficients [1], [34]. The impacts are particularly evident in composite systems, where restricted expansion can result in cracking or the accumulation of residual strain over time. Wind-induced lateral loads concurrently create building wobble and oscillations, which compromise structural stability and affect serviceability and

occupant comfort [35], [36], [37]. Comprehending these environmental factors is crucial for the advancement of resilient high-rise structures and facilitates the larger incorporation of low-cost GNSS as an effective instrument for structural health monitoring.

Data for this case study were gathered using an 11-hour, 1 Hz GNSS data collection conducted on the building's rooftop. The reference data were acquired using a full geodetic GNSS configuration consisting of a Leica AS10 antenna and a Leica AS10 receiver. The rover stations were strategically positioned to minimize multipath interference, which is a common challenge in GNSS measurements due to signal reflection from nearby surfaces such as walls, windows, or metallic structures. To mitigate multipath errors, several strategies were implemented during the setup and data collection phases. First, the rooftop was chosen as the primary location to ensure a clear line of sight to the satellites and to minimize the presence of reflective surfaces in the vicinity. The GNSS antennas were mounted on the handrails of the building with sufficient height to reduce signal reflection from the ground.

During the planning stage, satellite geometry and the surrounding environment were carefully analysed using software-based sky plots to select observation periods with optimal satellite visibility and reduced likelihood of low-angle reflections. The rover stations were placed at locations with minimal obstruction and reflective surfaces, avoiding

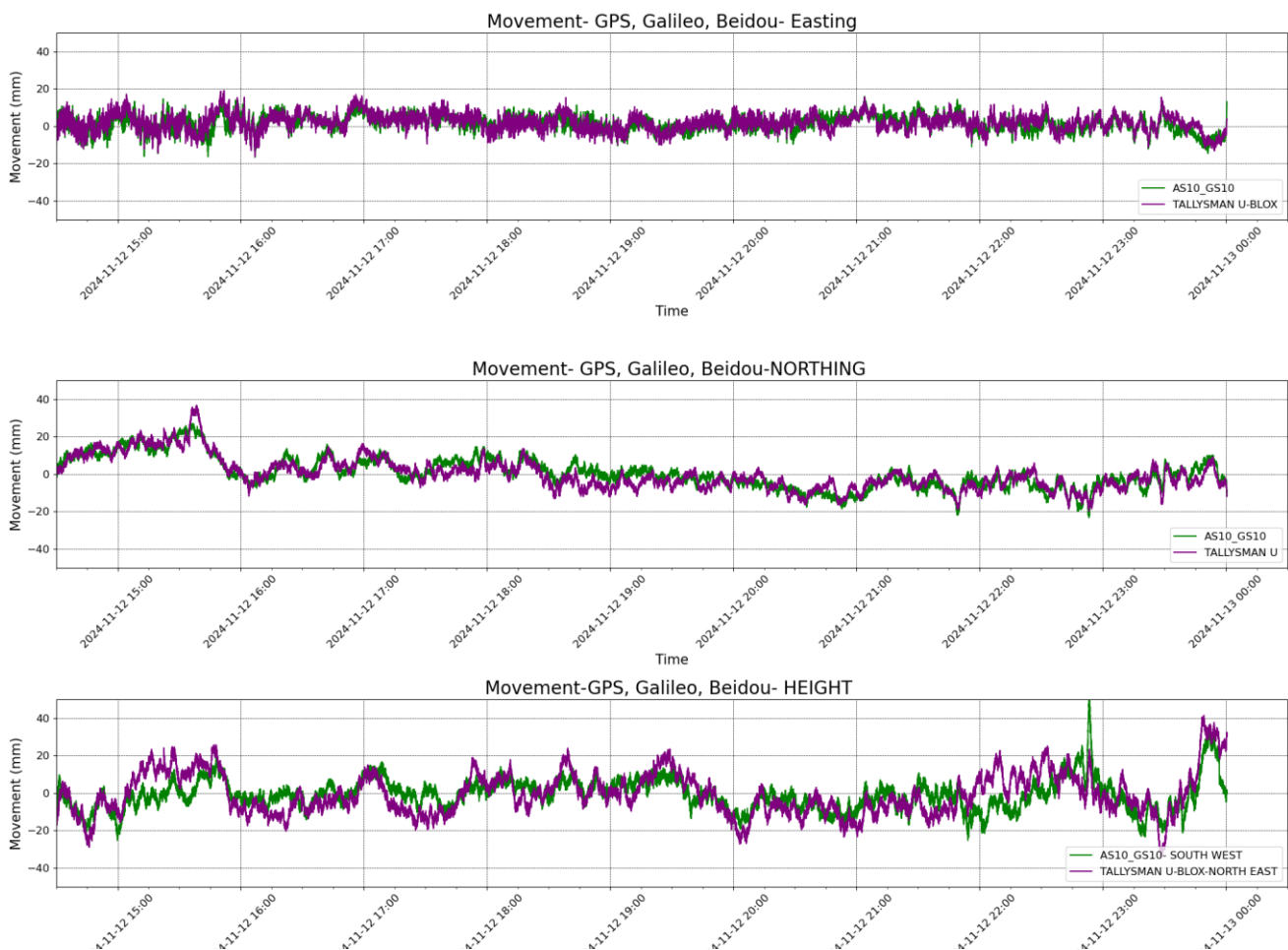
proximity to glass façades or metallic rooftops that could induce strong signal reflections. While these strategies significantly reduced the impact of multipath interference, it should be noted that completely eliminating multipath is unfeasible in real-world settings, particularly in urban or semi-urban environments.



Figure 9: Tallysman TWI antenna connected to the handrail of the building rooftop. Right- U-blox F9P receiver connected to the antenna and Raspberry Pi device to log the data.

#### 4.1 Analysis and Results

The data were post-processed via a short baseline double difference solution through RTKlib software. The Base Station is a continuously operating reference station (CORS) equipped





with a full geodetic setup and a baseline distance of 5.1 km. A time series analysis is conducted for the GPS, Galileo and Beidou satellite constellations to identify the positional variations in Northing, Easting and Height components of the monitoring points. As depicted by the time series in figure 10, the Tallysman antenna combined with the U-blox receiver

For the further understanding of the long-term variations in position, a moving average was calculated for a rolling window of 300s (5 minutes).



Figure 11: Moving average variation of the low-cost system and fully geodetic system.

demonstrates precision comparable to that of a full geodetic configuration. Although a dataset of 10 hours is inadequate for delivering comprehensive information into building movement, it sufficiently illustrates the potential of the low-cost system. This is further demonstrated by the following standard deviation values.

	Standard Deviation (mm)		
	E	N	H
Low-cost	4.50	8.50	11.31
Geodetic	4.23	8.08	7.63
Difference	0.27	0.42	3.68

Based on figure 11, it is evident that the low-cost GNSS setup share the similar trend as the geodetic setup. Adhering to the same trend suggests that the temporal variations and directional changes observable in the positional data of both configurations demonstrate similarly over time—indicating that, despite variation in accuracy, the low-cost setup can capture the same movement patterns and positional dynamics as the high-precision geodetic reference.

However, further testing on high-rise buildings is needed to assess the performance of low-cost GNSS systems over long-term deployments. Short-term tests do not capture the gradual effects of component wear, thermal drift, or mounting stability issues that may reduce accuracy over time. Weather conditions such as heavy rain, snow, or high winds can also impact signal quality by causing attenuation, multipath reflections, or antenna

movement. In addition, variations in the ionosphere and troposphere can introduce delays that low-cost receivers may not correct effectively. Long-term studies under different weather and seasonal conditions are therefore essential to better understand noise levels and reliability, and to guide improvements in system design and calibration.

## 5 CONCLUSION AND FUTURE DIRECTIONS

This paper presented the results of control experiments testing Tallysman TWI low-cost GNSS antenna with U-blox F9P dual frequency low-cost GNSS receiver in slow moving conditions and dynamic motion conditions. It further presented results from an initial case study conducted on a high-rise building testing the low-cost system.

The results indicate that the low-cost system can reach a comparable precision with the geodetic systems and can obtain sub-centimeter accuracy through rigorous observation and processing methods, such as the use of multiple satellite constellations for observations [7], [9]. The horizontal component can reach an accuracy of less than 5mm for both slow motion and dynamic motion conditions which depicts the potential of low-cost systems in achieving a sub-centimeter accuracy. The noise levels in the vertical component are generally higher than that of the horizontal movements, however, they are still less than a couple of centimeters.

The case study on the building further demonstrates the efficiency of low-cost systems, since they exhibit comparable accuracy and precision to full geodetic configurations in practical scenarios when atmospheric and multipath challenges are not completely mitigated. The findings of this work align with the results of other research on the utilisation of low-cost GNSS systems for monitoring deformations in flexible structures, such as tall buildings and bridges [7], [9], [14].

This work is part of an ongoing study evaluating various low-cost technologies under diverse atmospheric and environmental circumstances. Subsequent investigation will involve testing low-cost systems for long-term deformation observations across various environmental conditions and seasons. This will facilitate better understanding of the accuracy and precision of low-cost devices, as well as their suitability for long-term deployment. It will further evaluate the fluctuations in noise under various atmospheric circumstances, so facilitating the identification of methods to mitigate or minimise those errors.

## ACKNOWLEDGMENTS

This research is funded by the EPSRC, UK through the Center for Doctoral Training in Geospatial Systems, with the grant reference EP/S023577/1.

## REFERENCES

[1] Y. D. Hu, R. Hou, Q. Xia, and Y. Xia, 'Temperature-induced displacement of supertall structures: A case study', *Advances in Structural Engineering*, vol. 22, no. 4, pp. 982–996, Mar. 2019, doi: 10.1177/1369433218795288/ASSET/IMAGES/LARGE/10.1177\_1369433218795288-FIG12.JPEG.

[2] J. Z. Su *et al.*, 'Long-term structural performance monitoring system for the Shanghai Tower', *J Civ Struct Health Monit*, vol. 3, no. 1, pp. 49–61, Feb. 2013, doi: 10.1007/S13349-012-0034-Z/FIGURES/16.

[3] M. G. Mustafin, V. A. Valkov, and A. I. Kazantsev, 'Monitoring of Deformation Processes in Buildings and Structures in Metropolises', *Procedia Eng*, vol. 189, pp. 729–736, Jan. 2017, doi: 10.1016/J.PROENG.2017.05.115.

[4] S. Yuan, 'High-Rise Building Deformation Monitoring Based on Remote Wireless Sensor Network', *IEEE Sens J*, vol. 21, no. 22, pp. 25133–25141, Nov. 2021, doi: 10.1109/JSEN.2021.3067378.

[5] C. O. Yigit, A. El-Mowafy, A. Anil Dindar, M. Bezcioglu, and I. Tiryakioğlu, 'Investigating Performance of High-Rate GNSS-PPP and PPP-AR for Structural Health Monitoring: Dynamic Tests on Shake Table', *Journal of Surveying Engineering*, vol. 147, no. 1, p. 05020011, Feb. 2021, doi: 10.1061/(ASCE)SU.1943-5428.0000343/ASSET/8989E20D-C683-42F9-8C4B-89891B85CD09/ASSETS/IMAGES/LARGE/FIGURE16.JPG.

[6] P. Psimoulis, S. Pytharouli, D. Karambalis, and S. Stiros, 'Potential of Global Positioning System (GPS) to measure frequencies of oscillations of engineering structures', *Journal of Sound and Vibration*, vol. 318, no. 3, pp. 606–623, 2008.

[7] C. Xue, P. A. Psimoulis, and X. Meng, 'Feasibility analysis of the performance of low-cost GNSS receivers in monitoring dynamic motion', *Measurement*, vol. 202, p. 111819, Oct. 2022, doi: 10.1016/J.MEASUREMENT.2022.111819.

[8] J. Jayamanne, R. Vandebona, and J. Karalliyadda, 'Optimization of Conventional Land Survey Techniques Using Modern Technology', 2020, Accessed: Mar. 27, 2025. [Online]. Available: <http://ir.kdu.ac.lk/handle/345/3258>

[9] C. Xue, P. Psimoulis, A. Horsfall, Q. Zhang, and X. Meng, 'Assessment of the accuracy of low-cost multi-GNSS receivers in monitoring dynamic response of structures', *Applied Geomatics*, vol. 15, no. 2, pp. 315–326, Jun. 2023, doi: 10.1007/S12518-022-00482-8/FIGURES/16.

[10] J. Yu, X. Meng, B. Yan, B. Xu, Q. Fan, and Y. Xie, 'Global Navigation Satellite System-based positioning technology for structural health monitoring: a review', *Struct Control Health Monit*, vol. 27, no. 1, Jan. 2020, doi: 10.1002/STC.2467.

[11] C. Xue and P. A. Psimoulis, 'Monitoring the dynamic response of a pedestrian bridge by using low-cost GNSS receivers', *Engineering Structures*, vol. 284, p. 115993, 2023, doi: 10.1016/j.engstruct.2023.115993.

[12] S. Oğutcu, S. Alcay, H. Duman, B. Numan Özdemir, and C. Konukseven, 'Static and kinematic PPP-AR performance of low-cost GNSS receiver in monitoring displacements', *Advances in Space Research*, vol. 72, no. 11, pp. 4795–4808, Dec. 2023, doi: 10.1016/J.ASR.2023.09.025.

[13] C. Xue, P. Psimoulis, Q. Zhang, and X. Meng, 'Analysis of the performance of closely spaced low-cost multi-GNSS receivers', *Applied Geomatics*, vol. 13, no. 3, pp. 415–435, 2021, doi: 10.1007/s12518-021-00366-3.

[14] A. Cina and M. Piras, 'Performance of low-cost GNSS receiver for landslides monitoring: test and results', *Geomatics, Natural Hazards and Risk*, vol. 6, no. 5–7, pp. 497–514, Jul. 2015, doi: 10.1080/19475705.2014.889046.

[15] F. Moschas, P. A. Psimoulis, and S. C. Stiros, 'GPS/RTS data fusion to overcome signal deficiencies in certain bridge dynamic monitoring projects', *Smart Structures and Systems*, vol. 12, no. 3–4, pp. 251–269, 2013, doi: 10.12989/ss.2013.12.3\_4.251.

[16] I. Peppas and P. A. Psimoulis, 'Detection of GNSS antenna oscillatory motion and multipath conditions via exploitation of multipath-induced SNR variations', *GPS Solutions*, vol. 27, no. 3, p. 117, 2023, doi: 10.1007/s10291-023-01470-7.

[17] V. Hamza, B. Stopar, T. Ambrožič, G. Turk, and O. Sterle, 'Testing Multi-Frequency Low-Cost GNSS Receivers for Geodetic Monitoring Purposes', *Sensors 2020, Vol. 20, Page 4375*, vol. 20, no. 16, p. 4375, Aug. 2020, doi: 10.3390/S20164375.

[18] M. Khalil, F. Crenna, and G. B. Rossi, 'GNSS Signals for Sea Wave Measurements', *2024 IEEE International Workshop on Metrology for the Sea, MetroSea 2024 - Proceedings*, pp. 329–333, 2024, doi: 10.1109/METROSEA62823.2024.10765644.

[19] D. A. Kogogin, A. V. Sokolov, I. A. Nasyrov, V. O. Dementiev, and R. V. Zagretidinov, 'Signal Receiver for Global Navigation Satellite Systems Based on a U-blox ZED-F9P Module for Ionospheric Research', *Journal of Communications Technology and Electronics*, vol. 68, no. 6, pp. 682–691, Jun. 2023, doi: 10.1134/S1064226923060074/TABLES/2.

[20] R. Hohensinn *et al.*, 'Low-Cost GNSS and Real-Time PPP: Assessing the Precision of the U-blox ZED-F9P for Kinematic Monitoring

- Applications', *Remote Sens (Basel)*, vol. 14, no. 20, p. 5100, Oct. 2022, doi: 10.3390/RS14205100/S1.
- [21] T. Takasu and A. Yasuda, 'Development of the low-cost RTK-GPS receiver with an open source program package RTKLIB'.
- [22] T. Everett, T. Taylor, D. K. Lee, and D. M. Akos, 'Optimizing the Use of RTKLIB for Smartphone-Based GNSS Measurements', *Sensors* 2022, Vol. 22, Page 3825, vol. 22, no. 10, p. 3825, May 2022, doi: 10.3390/S22103825.
- [23] J. Jayamanne, C. Perera, and R. Vandebona, 'Evaluating the applicability of Open Source GNSS Post-Processing Software for Applications of Surveying', 2019.
- [24] S. Caldera, S. Barindelli, F. Sansò, and L. Pardi, 'Monitoring of Structures and Infrastructures by Low-Cost GNSS Receivers', *Applied Sciences* 2022, Vol. 12, Page 12468, vol. 12, no. 23, p. 12468, Dec. 2022, doi: 10.3390/APP122312468.
- [25] L. Poluzzi, L. Tavasci, F. Corsini, M. Barbarella, and S. Gandolfi, 'Low-cost GNSS sensors for monitoring applications', *Applied Geomatics*, vol. 12, no. 1, pp. 35–44, Apr. 2020, doi: 10.1007/S12518-019-00268-5/FIGURES/13.
- [26] N. Quesada-Olmo, M. J. Jimenez-Martinez, and M. Farjas-Abadia, 'Real-time high-rise building monitoring system using global navigation satellite system technology', 2018, doi: 10.1016/j.measurement.2018.03.054.
- [27] S. Caldera, S. Barindelli, F. Sansò, and L. Pardi, 'Monitoring of Structures and Infrastructures by Low-Cost GNSS Receivers', *Applied Sciences* 2022, Vol. 12, Page 12468, vol. 12, no. 23, p. 12468, Dec. 2022, doi: 10.3390/APP122312468.
- [28] T. H. Yi, H. N. Li, and M. Gu, 'Recent research and applications of GPS-based monitoring technology for high-rise structures', *Struct Control Health Monit*, vol. 20, no. 5, pp. 649–670, May 2013, doi: 10.1002/STC.1501.
- [29] X. Jun, C. Xiaozhun, L. Chonghua, and L. Tianxiong, 'Analysis Technique of Signal Bandwidth for GNSS'.
- [30] X. Niu *et al.*, 'Using Allan variance to analyze the error characteristics of GNSS positioning', *GPS Solutions*, vol. 18, no. 2, pp. 231–242, Apr. 2014, doi: 10.1007/S10291-013-0324-X/TABLES/10.
- [31] G. Oku Topal and B. Akpinar, 'High rate GNSS kinematic PPP method performance for monitoring the engineering structures: Shake table tests under different satellite configurations', *Measurement*, vol. 189, p. 110451, Feb. 2022, doi: 10.1016/J.MEASUREMENT.2021.110451.
- [32] V. Patnana and D. C. Rai, 'SEISMIC PERFORMANCE OF PLASTERBOARD SUSPENDED CEILINGS UNDER SHAKING-TABLE GENERATED MOTIONS'.
- [33] P. A. Psimoulis and S. C. Stiros, 'Experimental Assessment of the Accuracy of GPS and RTS for the Determination of the Parameters of Oscillation of Major Structures', *Computer-Aided Civil and Infrastructure Engineering*, vol. 23, no. 5, pp. 389–403, Jul. 2008, doi: 10.1111/J.1467-8667.2008.00547.X.
- [34] P. Breuer, T. Chmielewski, P. Górski, E. Konopka, and L. Tarczyński, 'The Stuttgart TV Tower-displacement of the top caused by the effects of sun and wind', *Eng Struct*, vol. 30, pp. 2771–2781, 2008, doi: 10.1016/j.engstruct.2008.03.008.
- [35] O. & M. Preetam Biswas, Skidmore, *Tall Buildings for Wind*. 2020.
- [36] Q. S. Li, L.-H. Zhi, A. Y. Tuan, C.-S. Kao, S.-C. Su, and C.-F. Wu, 'Dynamic Behavior of Taipei 101 Tower: Field Measurement and Numerical Analysis', *Journal of Structural Engineering*, vol. 137, no. 1, pp. 143–155, Jan. 2011, doi:10.1061/(ASCE)ST.1943-541X.0000264.
- [37] J. Wu, H. Xu, and Q. Zhang, 'Dynamic performance evaluation of Shanghai Tower under winds based on full-scale data', 2019, doi: 10.1002/tal.1611.



# Potential of profile laser scanning (PLS) for the application in load tests

Florian Schill<sup>1</sup>, 0000-0002-7463-9152, Gregor Schacht<sup>2</sup>, Torsten Harke<sup>2</sup>

<sup>1</sup>i3mainz – Institute for Spatial Information and Surveying Technology, University of Applied Sciences Mainz, Lucy-Hillebrand-Straße 2, 55128 Mainz, Germany

<sup>2</sup>Marx Krontal Partner GmbH, Altenzeller Str. 29, 01069 Dresden, Germany

email: florian.schill@hs-mainz.de, gregor.schacht@marxkrontal.com, torsten.harke@marxkrontal.com

**ABSTRACT:** The transport infrastructure is reaching in many cases the end of its effective life cycle. The present condition is attributable to a combination of ageing and progressive deterioration as traffic volumes continue to increase. However, it is possible that even recently constructed bridges may already have significant structural damage. Consequently, the maintenance management of existing bridges is becoming increasingly important. However, there is often a lack of up-to-date information on the actual condition of the structures. This is because measuring infrastructure is merely the final stage of the monitoring process, given that tactile sensors are extremely time-consuming and labour-intensive to use. Additionally, due to these principles, measurements can only be taken at a few selected points. The combination of these limitations offers great potential for the use of non-contact profile laser scanning (PLS) in the context of load testing of bridge structures. The structure is scanned with a high-frequency laser beam without the necessity of entering the structure. The spatially distributed displacement measurements obtained in this manner provide a significantly higher density of spatial information about the structure than was previously feasible. Until now, dynamic investigations have been primarily conducted in the domain of profile scanning. This study primarily focuses on static load tests, where spatial resolution and measurement precision can be further enhanced. Two case studies are presented, illustrating non-contact PLS measurements for load testing: one example is on a 160 m arched railway bridge, and the other example is on a steel-concrete composite motorway bridge. It has been demonstrated that a precision of a few tenths of a millimetre can be attained with a spatial resolution in the centimetre range.

**KEY WORDS:** profile laser scanning (PLS); displacement; bridge monitoring; load testing; SHM; SHMII-13; Full paper

## 1 INTRODUCTION

Against the background of an ageing infrastructure and the clear trend towards faster trains, higher track utilisation and increasing freight traffic on the roads, reports about the poor condition of the transport infrastructure, decaying bridges and the problems of steel or prestressed concrete bridges from the 1960s and 1970s are becoming increasingly frequent. Damage to newer bridge structures is rarely reported [1], as the quality of planning and execution as well as testing and monitoring should generally ensure appropriate quality.

In order to cover the entire spectrum, two completely different structures are considered in the following:

A motorway bridge from the 1960s, which has basically reached the end of its life due to the enormous freight traffic on the Brenner motorway and the expansion to three lanes per direction. And a railway bridge that is only a few years old and has already suffered massive damage due to manufacturing defects.

What both structures have in common is that assessing the condition of existing bridges is becoming an increasing challenge when important decisions have to be made about cost-intensive replacement or renovation measures, especially if these become necessary after just a few years. In this context, precise knowledge of the actual structural behaviour is a valuable tool for condition assessment, which in many cases can lead to an extension of the remaining service life and thus to considerable benefits for bridge owners and society.

The actual structural behaviour is usually determined by experimental investigations, which may include measurements

of accelerations, velocities, strains, inclinations and/or temperatures [2-4]. In addition, displacement measurements based on linear displacement transducers (LVDT) are used to determine relative displacements at abutments [2], between neighbouring superstructures of the same bridge [5] or the width of existing cracks. This type of displacement measurement is possible in principle, as a fixed reference point can be used for the installation of the sensor.

Another important parameter of the structural behaviour would be the absolute vertical displacement of the bridge. This can provide direct information about the actual stiffness of the structure, which in turn can be used in the updating process of the structural model [6, 7].

However, the direct measurement of absolute displacements with classical LVDTs is usually very complex, if not impossible, due to the lack of fixed reference points [4] or because the bridge is simply too high. To close this gap, significant progress has been made in recent years in the field of non-contact displacement measurement. Corresponding sensors enable the measurement of structural displacements without the need to attach sensors to the structure. Suitable technologies for non-contact displacement measurements include terrestrial laser scanning (TLS) [8, 9, 10, 11, 12], laser vibrometer [13, 14], image-based total stations [15], and microwave interferometry [10, 16, 17, 18].

Compared to other non-contact measurement techniques, which only allow measurements at one point, TLS or profile laser scanners (PLS) can also be used to perform spatially distributed measurements. The spatial resolution offers the

advantage that larger areas of the structure can be monitored with only one sensor, allowing a deeper understanding of the structural response in an efficient way.

This study expands the application of PLS by demonstrating its capability for dense, high-precision deformation monitoring on two large-scale bridges under static loading. The novel aspects include the spatial resolution achieved, the scale of the structures examined, and a worst-case precision evaluation strategy, which has not been systematically addressed in previous studies.

Before going into more detail on TLS and in particular its use as a PLS for dynamic and static load tests in section 3, the two investigated bridges are presented in section 2.

## 2 INVESTIGATED BRIDGES AND PERFORMED LOAD TESTS

As mentioned in Section 1, the following section presents load tests on two quite different bridges, which will first be discussed in more detail in this section.

### 2.1 Motorway bridge

The Austrian Brenner motorway is part of the European route E45, which crosses Europe in a north-south direction from northern Finland to southern Italy. The Alpine crossing in Austria is an important part of the route and is also crucial for cross-border freight transport in Europe. The motorway route across the Alps was mainly built in the 1960s, and the bridge under investigation was also built during this period.



Fig. 1: View of the motorway bridge: span 7.

The bridge was originally designed for two lanes in each direction, but a third lane was added in the 1980s due to the increasing amount of traffic. However, the basic load-bearing structure of the bridge has remained essentially unchanged over the years. As an important part of a European transit route, the structure must therefore be carefully monitored.

The structure itself consists of a steel-concrete composite construction and is designed as a 7-span continuous girder, with the outer spans having a length of 70 m and all other spans having a length of 84 m. The total length is therefore 560 m.

Part of this monitoring strategy was a load test, which was carried out in May 2023. One direction of travel on the motorway bridge was temporarily closed in order to place two trucks, each weighing 50 tonnes, on the bridge to create

different load scenarios. In addition, four quasi-static tests were carried out.

The profile laser scanner measurements focussed on the outermost span (span 7) next to the southern bridge abutment, as shown in Figure 1.

In addition to the profile scanner, 3D TLS [19, 20, 21], fibre optic sensors [19, 21, 22], dynamic and static total stations [19, 20, 23], a terrestrial microwave interferometer, modular digital camera total stations [24], GNSS [21] and acceleration sensors [21] were used.

### 2.2 Railway bridge

The railway bridge is a 370 m long double-track railway overpass designed as an arch bridge. The longest span is 165 metres. The track is up to 71 m above the valley floor and is straight in the construction area at a design speed of 300 km/h, see Figure 2.



Fig. 2: View of the railway bridge.

The bridge structure has only been under traffic for a few years and already shows significant construction-related damage. In the course of the structural inspection, structural defects and concrete spalling were initially recognised and appropriate repair measures were planned. During the repair work, it turned out that the gravel pockets and the severe segregation of the structure were not only localised, but affected large areas of several square metres, see Figure 3.



Fig. 3: Damaged area with heavily segregated concrete structure.



The damage is due to segregation and washing out processes during concreting. In order to determine the full extent of the damage, structural diagnostics were carried out on the entire arch bridge. The investigations confirmed the assumptions regarding the poor concrete quality of the arch concrete. The results raised questions about the serviceability and stability of the structure under traffic.

As a mathematical analysis of the damage alone was not conclusive, the owner decided to carry out a load test. The static load test was carried out with five locomotives with a total weight of 550 tonnes in various load positions. In order to be able to determine the deformations under the applied load as simple and reliable as possible, a non-contact PLS was used.

### 3 TERRESTRIAL LASERSCANNING (TLS)

TLS such as the Z+F IMAGER 5016 make it possible to digitise the entire environment in a 360° panorama in the form of a 3D point cloud. During the scanning process, a high-frequency rotating mirror deflects the laser beam and the TLS also rotates around its vertical axis. This sequential recording process produces a high-resolution point cloud of the visible environment, see Figure 4.

The non-contact distance measurement of the Z+F IMAGER 5016 works according to the AMCW method (Amplitude Modulated Continuous Wave). To obtain the absolute distance value, the phase shift between the reflected and emitted signal is used, which is induced by the light path in the intensity-modulated periodic signal. To resolve the phase ambiguities and thus determine the absolute distance, several wavelengths are modulated onto the carrier wave. In addition, the user is provided with the amplitude (intensity), which represents the ratio of emitted to received energy, see grey scales in Figure 4.



Fig. 4: Extract from the 3D point cloud of span 7 of the motorway bridge. Intensity values are shown as grey scales.

In principle, the measurement method is characterised by a very high spatial resolution, but in turn only allows a low

temporal resolution. In addition, the single point precision is in the millimetre range and is therefore not sufficiently accurate for most monitoring applications.

#### 3.1 Profile laser scanning (PLS) dynamic

In contrast, a profile laser scanner (TLS in profile mode, 2D) [8, 10, 25, 26] only uses the high-frequency rotating deflection mirror, but there is no rotation around the standing axis, see diagram in Figure 5 and section of a profile in Figure 6.



Fig. 5: Schematised representation of PLS.

As special properties of the sensor are important for bridge monitoring applications, these are explained in more detail in the following.

##### 3.1.1 Measuring Frequency

The usable measurement frequency for deformation monitoring of bridges with the Z+F IMAGER 5016 in profile mode depends on the rotation speed of the deflection mirror, which is up to 55 Hz. It should be noted that there is a relationship between temporal and spatial profile resolution: at the same laser measurement rate, doubling the measurement frequency halves the spatial resolution.

##### 3.1.2 Measurement Precision

The precision of the measurement depends significantly on the energy reflected back from the structure and thus on its backscattering properties in the corresponding wavelength band, since the phase measurement precision is directly coupled to the signal-to-noise ratio (SNR) of the reflected signal [27].

For the Z+F IMAGER 5016, as is common practice in the TLS field, the manufacturer provides range measurement standard deviations for different surface reflectivities and ranges. These are based on a fixed laser measurement rate of 127 kHz and range from 0.2 mm to just under 10 mm.

However, these accuracy specifications are not very meaningful in practice and only cover a very small range of applications: The specified reflectivity of the structure to be measured is usually not known and can also vary spatially. In addition, the measurement geometry plays a crucial role in the specification of realistic measurement uncertainties; it is partly responsible for the occurrence of predominant forward reflection, i.e. the shallower the angle of incidence, the greater the potential for forward reflection and low SNR. The



measurement geometry is also critical for the derivation of the projected vertical deformations. Furthermore, no reflectors are to be used in the application scenario considered, so an accuracy specification based on a defined reflector is not meaningful.

For TLS in general, the stochastic modelling of the range measurement based on the registered intensities [28,29] is possible and allows a practical (insitu) determination of the range precision. This approach takes into account all effects affecting the measurement process (surface reflectivity, measurement geometry, atmosphere, etc.).

### 3.1.3 Spatial Resolution

With the Z+F IMAGER 5016 the range is part of the raw measurement. The range resolution is 0.1 mm and is defined by the size of the modulated fine scale used in combination with the implemented phase measurement.

The actual spatial resolution of a profile scanner is defined by the rotation speed of the deflection mirror, the laser measurement rate and the divergence angle of the laser beam. The actual spatial resolution is usually lower than the angular resolution specified by the manufacturer for two reasons:

- Depending on the choice of parameters, the laser spots of successive measurements overlap to a greater or lesser extent, which reduces the actual resolution on the surface of the structure.
- The rotational speed causes an additional deformation of the laser footprint in the profile direction (elongation), as a corresponding angular range is always covered during the measurement time. This can be interpreted as a larger "true" divergence angle or as an increasing overlap of successive measurements according to [30, 31].

Another aspect when considering the spatial resolution actually available in practical applications is that the single-point precision of a PLS is usually not sufficient for the requirements of the application scenario [8]. Therefore, in order to achieve the required precision, an averaging of neighbouring measurement points is performed (class formation), which further reduces the spatial resolution of the profile scanning in favour of a qualitatively better derivation of displacements.

Two examples are given below to give an idea of the spatial resolution that can be achieved:

- 20,000 points are measured per profile at a measurement frequency of 55 Hz, which corresponds to a theoretical angular increment of  $0.018^\circ$ . If 75 adjacent points are combined (class formation, see colour coding in Figure 6), the actual available angular increment is reduced to  $1.35^\circ$ , which corresponds to a spatial resolution of 0.24 m at a distance of 10 m.
- If the measurement frequency is reduced to 14 Hz, 80,000 points are measured per profile and a spatial resolution of 0.06 m at a distance of 10 m is achieved.

Depending on the measurement geometry, deformation time series with a precision in the sub-millimetre range can be derived from the spatially distributed time series generated in this way.

Compared to other measurement techniques for monitoring applications, which only allow measurements at a single point, PLS thus also allow a spatially distributed recording of the structural response. The spatial resolution offers the advantage

that larger areas of the structure can be monitored and verified with a single sensor, which enables a deeper understanding of the structural response in a very efficient way.

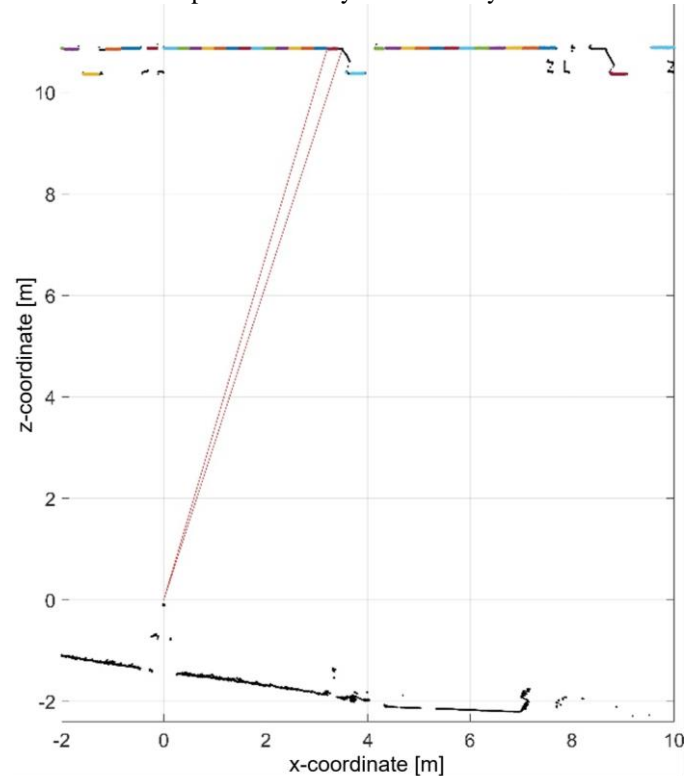


Fig. 6: Extract from profile measurement, with coloured representation of class formation.

### 3.1.4 Projection of displacements

The purpose of using a PLS for deformation monitoring of bridges is to obtain deformations in a defined direction (usually vertical or horizontal). Therefore, the "raw" measurements need to be projected in the desired direction. For projection, it is usually assumed that the vertical displacement of a bridge is dominant, while possible horizontal components are considered negligible. Since the raw measurements of a profile scanner consist of distance and internal angle measurements, the projection of deformations is inherent and possible with high accuracy. The manufacturer specifies an angular accuracy of  $0.004^\circ$  for the Z+F IMAGER 5016. The horizon reference is provided by an internal dynamic compensator which operates in the same accuracy range as the angle encoders. The dynamic compensator also detects and corrects for low frequency movements of the sensor during the measurement.

Up to this point, it has been assumed that there is only vertical displacement of the bridge structure due to an applied load. However, it is possible that there is an additional horizontal displacement component. As the PLS is a 2D sensor, these can be measured directly at suitable locations (vertical areas) if the displacement is in the profile direction.

### 3.2 Profile laser scanning (PLS) static

For use in static load tests, the temporal dimension plays a subordinate role, but in static profile laser scans the precision and spatial resolution can be further increased by additional temporal averaging during the load retention phases.

With a load retention phase of 5 minutes, at least 4,200 profiles are measured. This corresponds to 315,000 individual measurements in the example defined above with 75 points per class and profile that can be used for further derivation of the measured values, which enables a significant increase in precision.

The major challenge in static load tests with profile laser scanners is to keep the external conditions constant so that, for example, no tilting of the tripod occurs, e.g. due to solar radiation or unstable ground. TLS, like almost all non-contact measuring sensors, are sensitive to atmospheric conditions, which in extreme cases, e.g. due to rain or fog, can completely prevent measurement.

#### 4 QUASI-STATIC LOAD TEST

For quasi-static load tests, the speed at which the load (truck or locomotive) passes over the measurement object (bridge) is usually kept low in order to minimise dynamic effects that could falsify the result. This is in favour when using profile scanners, as the overall measurement rate of approximately 55 Hz is not comparable with conventional sensors and the spatial resolution has to be reduced at higher repetition rates.

Accordingly, it makes practical sense in these cases to use the lowest repetition rate of 14 Hz, as this allows up to 80,000 points per profile to be measured and maximises the spatial resolution.

For the two sample bridges, a quasi-static load scenario was only carried out for the motorway bridge, which is why this section focuses on the measurements at the Brenner Pass.

The quasi-static load test was performed with two trucks of 50 tonnes each, which crossed the entire bridge directly one behind the other at a speed of 5 and 30 km/h respectively. The position and speed of the two trucks were monitored using GNSS so that the resulting displacements could be synchronised with the position of the trucks.

The measurements with the PLS took place in span 7, the scanner was located approx. 13 m below the bridge and a main girder was measured. As the bridge is located in a curve, the horizontal measuring range on the main girder was limited to approx. 50 m of the total span length of 70 m due to the curvature of the bridge.

In this case, approx. 75 measuring points are averaged per class, so that ultimately 117 classes, i.e. 117 spatially distributed displacement time series can be derived, whose standard deviations are in a sector around 0.1 mm. The standard deviation tends to increase towards the edge due to the deteriorating geometry.

Figure 7 shows a section of the measurement results for a crossing at 5 km/h. In the upper diagram, a time series approximately in the centre of the field is shown in black. In addition, three coloured markers show the times at which the two trucks are located in the middle of span 5 (blue), in the middle of span 6 (red) and in the middle of span 7 (yellow). The design of the bridge as a continuous girder is evident here, as the measured span (span 7) already reacts to the loads in the other spans and rises or falls accordingly.

This representation as a time series based on just a single analysed class corresponds to the result that an LVDT would provide.

In the lower diagram in Figure 7, the points in time marked in different colours (trucks on span 5, span 6, span 7) are shown in full spatial resolution with 117 classes in the corresponding colour. The PLS enables the evaluation of the bending line for the entire scanned field section at any point in time.

The data gap in the centre of the diagram is caused by a combination of installed sensors (cabling) and a reinforced, heavily bolted area (see Figure 4 in the centre of the main girder).

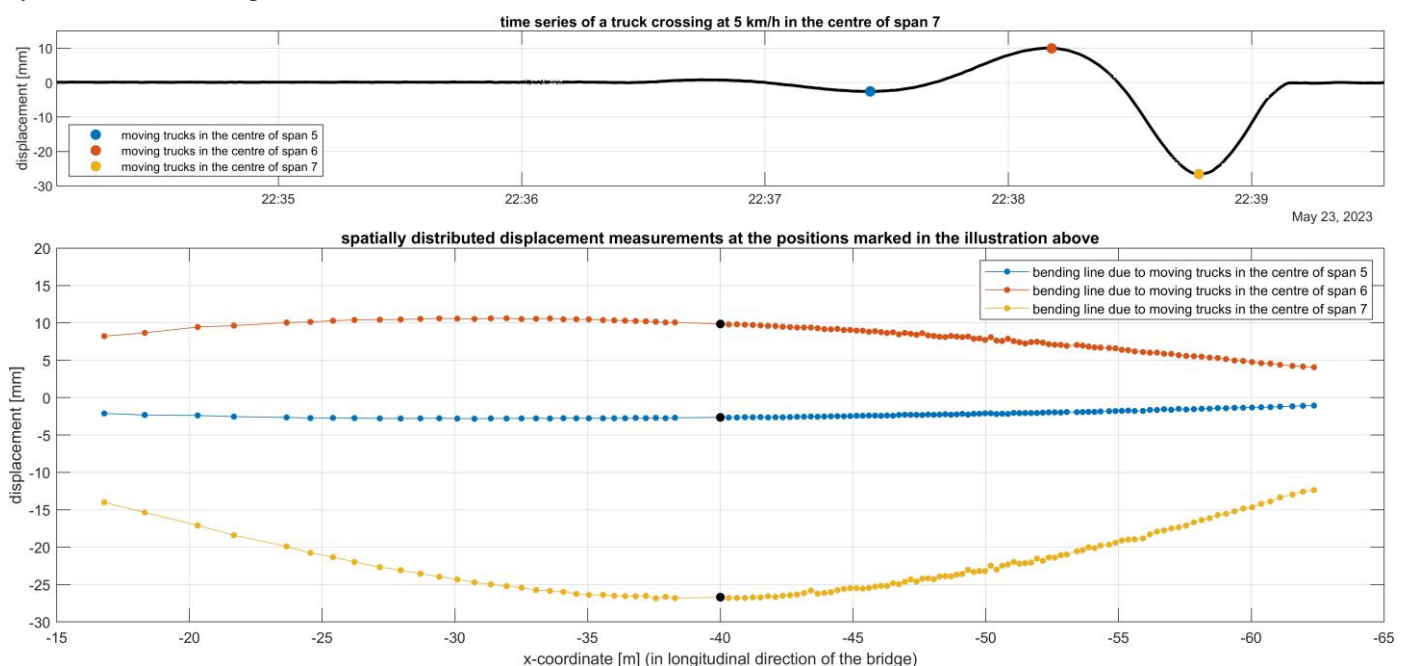


Fig. 7: Exemplary results of the evaluation of a quasi-static load test: In the upper diagram a simple pointwise time-displacement representation can be seen, while the lower diagram shows the potential of profile scanning, as a bending line can be analysed over the entire visible area at any point in time.

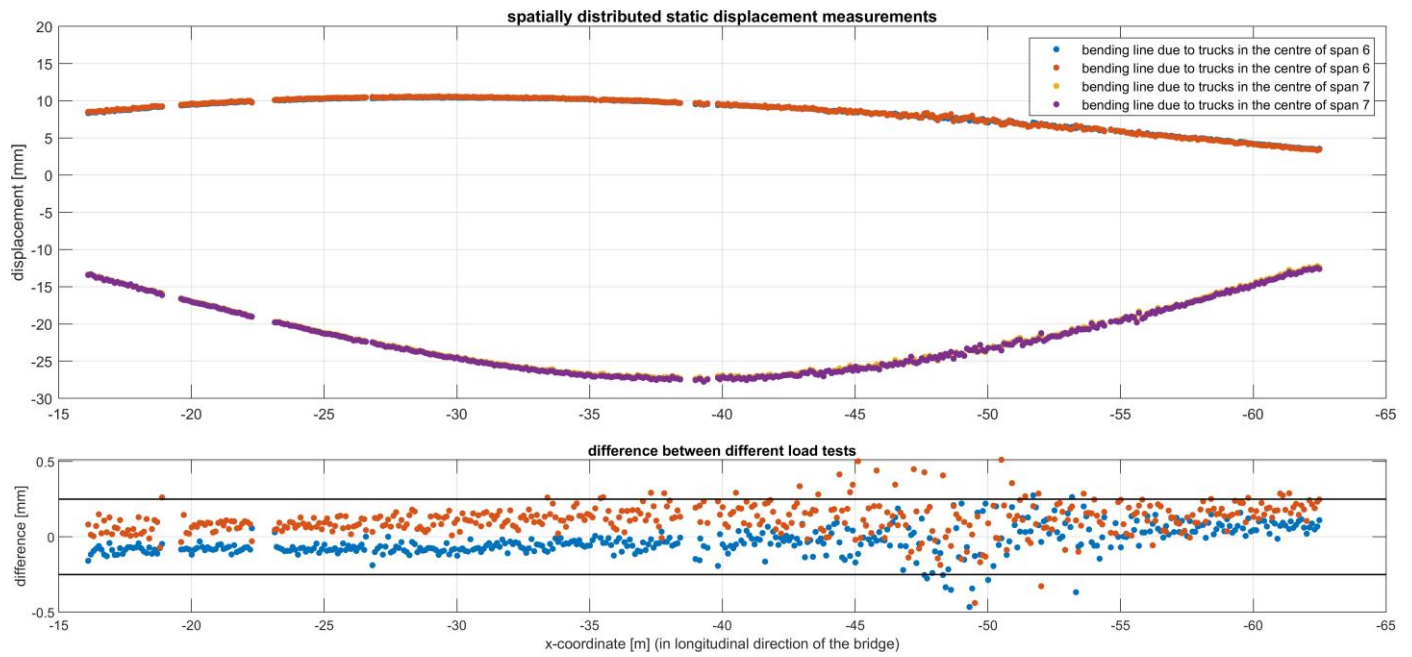


Fig. 8: Results of the evaluation of four static load tests: In the upper diagram, the bending lines of the two load positions are each shown twice. The lower diagram shows the differences between the respective tests and provides an estimate of the achievable precision of the measurements using profile scanning.

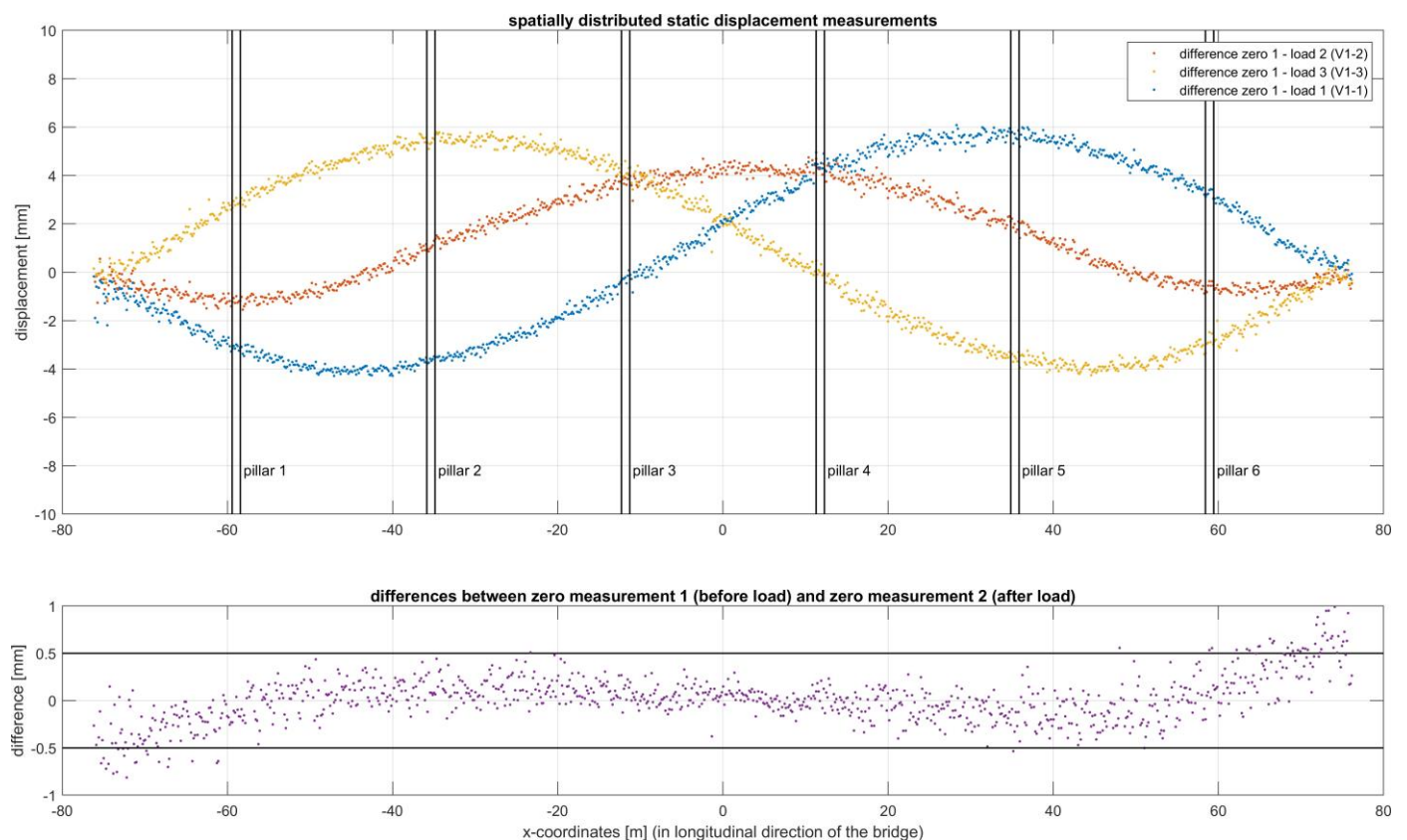


Fig. 9: Results of the evaluation of three static load positions: The upper diagram shows the bending lines induced by the load positions. The lower diagram shows the differences between two independent zero measurements (bridge without load) before and after the actual measurements.



## 5 STATIC LOAD TESTS

A static load test was conducted on both structures: This entailed the deployment of two trucks (with a total weight of approximately 100 tonnes) on the motorway bridge and five locomotives (with a total weight of approximately 550 tonnes) on the railway arch bridge. For each bridge different load configuration were tested and the structural response was measured using static profile laser scanning (PLS).

As outlined in Section 3.2, the enhanced spatial resolution in static profile scanning enables a measurement point spacing of 10 cm across the full scan range in both cases. This enabled the acquisition of over 400 spatially distributed displacement measurements on the motorway bridge and almost 1000 on the railway bridge (see upper diagrams in Figures 8 and 9). Those diagrams illustrate the measured displacements for the various load configurations, which are colour-coded according to the load configuration. As illustrated in Figure 7, analogous data deficiencies have been observed to occur due to external factors such as sensor interference or bolted connections.

In comparison with previous PLS applications, this study introduces a significantly higher density of measurement points on large-scale infrastructure due to the use of static PLS and demonstrates the feasibility of applying PLS as a primary deformation measurement technique during full-scale static load tests.

In order to provide further illustration of the precision potential of static PLS, two novel evaluation strategies were applied: For the motorway bridge (see Figure 8), a comparative analysis of repeated load positions was conducted (see lower diagram). For the railway bridge (see Figure 9), the evaluation is based on two independent zero measurements (see lower diagram). It is important to note that both approaches provide a conservative estimate of measurement precision under realistic test conditions. This is due to the fact that they account for potential systematic effects, such as slight variations in load positioning or residual structural deformations.

Despite the presence of these influencing factors, the deviations between the individual tests for the Brenner motorway remain predominantly below 0.25 mm, with systematic offsets of 0.1 mm and 0.05 mm, respectively, as previously described.

For the measurements at the railway bridge, a vertical precision of 0.5 mm was specified in the area of the piers (-60 m to 60 m) that support the track on the arch. As illustrated in the lower diagram of Figure 9, this order of magnitude could be sustained. The deviations exhibit a slight increase towards the edge, a phenomenon that can be attributed to the substantial dimensions of the structure and the deteriorating measurement geometry towards the edge. Furthermore, a discernible residual systematic remains identifiable in the observed discrepancies, potentially attributable to residual deformation of the bridge arch. Irrespective of the underlying cause, this further distorts the precision estimate, thereby leading to the expectation of even better results.

For the profile scanning and load retention phases, a duration of five minutes was deemed adequate for both bridges. Consequently, a test involving three load retention phases and double zero measurement could be conducted in approximately 30 minutes under optimal conditions. However, it was

necessary to deviate from this ideal procedure for the two static load tests. It was determined that load retention phases of 10 minutes would be implemented on the Brenner motorway, a measure necessitated by the substantial deployment of individual sensors (see Section 2.1).

In the case of the arch bridge, only profile scanning was used and a load retention phase of 5 minutes was planned, although this had to be extended in some cases due to fog passing through.

## 6 CONCLUSION

Compared to conventional sensors, PLS can be used to obtain a large number of spatially distributed measurements with just one sensor, which enables an extremely efficient measurement and also a previously unimaginable understanding of the structural reaction.

Even for the quasi-static load test, it was possible to derive over 100 spatially distributed displacement time series over a range of almost 50 metres. The analysable range of the section was not limited by the sensor, but by the radius of curvature of the bridge.

Implementing static load tests enhances spatial resolution by enabling the temporal averaging of additional measurement data. This assertion is substantiated by the case study of the railway bridge, in which the deformation of the entire 160 metre arch was captured using almost 1,000 measurement points. Despite challenging environmental and structural conditions, sub-millimetre precision of up to 0.5 mm was achieved in the critical areas.

Unlike previous PLS applications, this study uses static PLS as the primary measurement method for full-scale static load tests on large infrastructure. The high density of measurement points, over 400 on the motorway bridge and almost 1,000 on the railway bridge, enabled detailed, spatially resolved deformation analysis for various load configurations. To assess measurement precision under realistic conditions, two innovative evaluation strategies were employed. The first involved repeated load configurations on the motorway bridge and the second involved two independent zero measurements on the railway bridge. Both approaches yielded conservative estimates of precision, which is advantageous when accounting for systematic effects such as variability in load placement and residual deformations.

The findings demonstrate not only the technical feasibility of static PLS in such scenarios but also its robustness under non-ideal conditions, including sensor interference, structural complexity, and environmental influences such as fog. The study demonstrates the potential of static PLS for precise, efficient, and large-scale deformation monitoring in structural testing contexts.

## REFERENCES

- [1] Schacht, G.; Hampel, T.; Curbach, M.: Temporärer Korrosionsschutz von Spanngliedern – Stand des Wissens und Erfahrungsbericht. *Beton- und Stahlbetonbau*, 109, 2014, 8, S. 524-533.
- [2] Ding, Y.L.; Wang, G.X.; Sun, P.; Wu, L.Y.; Yue, Q.: Long-Term Structural Health Monitoring System for a High-Speed Railway Bridge Structure. *The Scientific World Journal*, 2015.
- [3] Reiterer, M.; Firus, A. Dynamische Analyse der Zugüberfahrt bei Eisenbahnbrücken unter Berücksichtigung von nichtlinearen Effekten. *Beton- und Stahlbetonbau*, 2022, 117, S. 90–98.
- [4] Ko, J.M.; Ni, Y.Q. Technology developments in structural health monitoring of large-scale bridges. *Engineering Structures*, 2005, 2, S. 1715–1725.
- [5] Bigelow, H.; Pak, D.; Herrmann, R.; Schneider, S.; Marx, S.; Petraschek, T.; Feldmann, M.; Hoffmeister, B.: Dynamische Messungen an einer Eisenbahnbrücke als Stahlbetonverbundrahmen: Untersuchung der Eisenbahnüberführung über die Salzach bei Schwarzach/St. Veit. *Stahlbau*, 2017, 86, S. 778–788.
- [6] Firus, A.: A Contribution to Moving Force Identification in Bridge Dynamics. Ph.D. Thesis, Technische Universität Darmstadt, Darmstadt, Germany, 2021.
- [7] Firus, A.; Schneider, J.; Berthold, H.: Experimental validation of a moving force identification method for applications in railway bridge dynamics. In: *Bridge Safety, Maintenance, Management, Life-Cycle, Resilience and Sustainability*; CRC, USA, 2022.
- [8] Schill, F.: Überwachung von Tragwerken mit Profilsclannern. Ph.D. Thesis, Technische Universität Darmstadt, Darmstadt, Germany, 2018.
- [9] Schill, F.; Schacht, G.: Berührungslose Überwachung von Brücken mit großer Stützweite. 11. Symposium Experimentelle Untersuchungen von Baukonstruktionen (SEUB), 2021.
- [10] Schill, F.; Michel, C.; Firus, A.: Contactless Deformation Monitoring of Bridges with Spatio-Temporal Resolution: Profile Scanning and Microwave Interferometry. *Sensors*, 2022.
- [11] Medic, T.; Ruttner, P.; Holst, C.; Wieser, A.: Keypoint-based deformation monitoring using a terrestrial laser scanner from a single station: Case study of a bridge pier. In: *Proceedings of the 5th Joint International Symposium on Deformation Monitoring, JISDM2022*, 2022, S. 167–175.
- [12] Rashidi, M.; Mohammadi, M.; Sadeghlo Kivi, S.; Abdolvand, M. M.; Truong-Hong, L.; Samali, B.: A decade of modern bridge monitoring using terrestrial laser scanning: Review and future directions. *Remote Sensing*, 12(22), 2020.
- [13] Firus, A.; Schneider, J.; Becker, M.; Pullamthara, J.J.: Microwave Interferometry Measurements for Railway-Specific Applications. In: *Proceedings of the COMPDYN 2017, 6th ECCOMAS Thematic Conference on Computational Methods in Structural Dynamics and Earthquake Engineering*, Greece, 2017.
- [14] Nassif, H.H.; Gindy, M.; Davis, J.: Comparison of laser Doppler vibrometer with contact sensors for monitoring bridge deflection and vibration. *NDT International*, 2005, S. 213–218.
- [15] Malekjafrican, A.; Martinez, D.; O'Brien, E.J.: The Feasibility of Using Laser Doppler Vibrometer Measurements from a Passing Vehicle for Bridge Damage Detection. *Shock and Vibration*, 2018.
- [16] Zschiesche, K.; Fitzke, M.; Schlüter, M.: Self-Calibration and Crosshair Tracking with Modular Digital Imaging Total Station. *PFG - Journal of Photogrammetry, Remote Sensing and Geoinformation Science*, 2022, S. 543–557.
- [17] Gentile, C.; Bernardini, G.: An interferometric radar for non-contact measurement of deflections on civil engineering structures: Laboratory and full-scale tests. *Structure and Infrastructure Engineering*, 2009, S. 521–534.
- [18] Bernardini, G.; De-Pasquale, G.; Bicci, A.; Mara, A.; Coppi, F.; Ricci, P.; Pieraccini, M.: Microwave interferometer for ambient vibration measurement on civil engineering structures: 1. Principles of the radar technique and laboratory tests. In: *Proceedings of the EVACES '07—Experimental Vibration Analysis for Civil Engineering Structures*, Portugal, 2007.
- [19] Lienhart, W.; Moser, T. & Strasser, L.: Large scale monitoring of a highway bridge with remote sensing and distributed fiber optic techniques during load tests. *e-Journal of Nondestructive Testing*, 2024.
- [20] Moser, T.; Lienhart, W.; Schill, F.: Static and dynamic monitoring of bridges with contactless techniques. In: *Proceedings of the 12th International Conference on Bridge Maintenance, Safety and Management (IABMAS2024)*, Bridge Maintenance, Safety, Management, Digitalization and Sustainability, 2024, S. 332-340.
- [21] Schönberger, C.; Lienhart, W.: Drive-by Structural Monitoring using GNSS measurements at alpine bridges. *e-Journal of Nondestructive Testing*, 2024.
- [22] Strasser, L.; Lienhart, W.; Winkler, M.: Static and dynamic bridge monitoring with distributed fiber optic sensing. In *Proceedings of Structural Health Monitoring 2023: Designing SHM for Sustainability, Maintainability and Reliability*, 2023, S. 1745 – 1752.
- [23] Lienhart, W.; Schill, F.; Moser, T.: Dynamic bridge monitoring with remote sensing techniques. In *Proceedings of Structural Health Monitoring 2023: Designing SHM for Sustainability, Maintainability and Reliability*, 2023, S.184-191.
- [24] Schlüter, M.; Zschiesche, K.: Bewegungsmuster von Brückenbauwerken bei laufendem Verkehr messen und auswerten. *Allgemeine Vermessungs-Nachrichten (avn)*, 2024, S. 9 – 16.
- [25] Schill, F.; Sviridova, A.; Eichhorn, A.: Deformation monitoring of noise barriers with profile laser scanning. In: *Proceedings of the 4th Joint International Symposium on Deformation Monitoring (JISDM)*, Greece, 2019.
- [26] Schill, F.; Eichhorn, A.: Deformation Monitoring of Railway Bridges with a Profile Laser Scanner. *ZfV - Zeitschrift für Geodäsie, Geoinformation und Landmanagement*, 2019, S. 109-118.
- [27] Salido-Monzú, D.; Meca-Meca, F.J.; Martín-Gorostiza, E.; Lázaro-Galilea, J.L.: SNR degradation in undersampled phase measurement systems. *Sensors*, 2016.
- [28] Wujanz, D.; Burger, M.; Mettenleiter, M.; Neitzel, F.: An intensity-based stochastic model for terrestrial laser scanners. *ISPRS Journal of Photogrammetry and Remote Sensing*, 2017.
- [29] Schill, F.; Holst, C.; Wujanz, D.; Hartmann, J.; Paffenholz, J.-A.: Intensity-based stochastic model of terrestrial laser scanners: Methodological workflow, empirical derivation and practical benefit. *ISPRS Open Journal of Photogrammetry and Remote Sensing*, 2025.
- [30] Chaudhry, S.; Salido-Monzú, D.; Wieser, A.: A modeling approach for predicting the resolution capability in terrestrial laser scanning. *Remote Sensing*, 2021.
- [31] Schmitz, B.; Kuhlmann, H.; Holst, C.: Investigating the resolution capability of terrestrial laser scanners and its impact on the effective number of measurements. *ISPRS Journal of Photogrammetry and Remote Sensing*, 2020.

# Advancing Infrastructure Health Monitoring with Multi-Sensor Systems and Geospatial Technologies

Dr. Ernst Geutebrück<sup>1</sup>, Ahmed Elsaid, MSc<sup>1</sup>, Bastian Merten, MSc<sup>1</sup>, Mag. Georg Glueck<sup>2</sup>

<sup>1</sup>Texplor Exploration & Environmental Technology GmbH, Am Bürohochhaus 2-4  
14478 Potsdam-Babelsberg, Germany

<sup>2</sup>Texplor Austria GmbH, Hosnedlgasse 5/1, 1220 Wien, Austria

email: ernst.geutebrueck@texplor.com, ahmed.elsaid@texplor.com, bastian.merten@texplor.com, georg.glueck@texplor.com

**ABSTRACT:** This paper presents an integrated structural health monitoring (SHM) system combining multi-sensor networks with geospatial GNSS technologies to enhance infrastructure resilience. Developed by the authors, the system unites millimeter-accurate TEXTant® GNSS monitoring with MSS® leak detection and environmental parameter sensing, all synchronized via the TEX-Sky Monitoring Cloud. Validation efforts included comparative field testing against International GNSS Service (IGS) standards at GFZ Potsdam, demonstrating millimeter-level positioning precision. Real-world deployments—including the Aquitaine Bridge (France), slope monitoring for mining operations (Germany), tank basin and catch basin monitoring at a chemical facility (Germany), and the first station of the cross-border Asia Minor GNSS Network—confirmed the system's operational robustness. Time-synchronized multi-sensor datasets enable predictive maintenance, early anomaly detection, and asset life extension. The modular and scalable system architecture adapts flexibly to diverse infrastructure contexts. Future integration with machine learning technologies is anticipated to enhance pattern recognition and anomaly detection. This work highlights the role of synchronized, multi-parameter monitoring as a foundation for next-generation infrastructure management and public safety.

**KEY WORDS:** Structural Health Monitoring (SHM), GNSS, Multi-Sensor Systems, Autonomous GNSS Monitoring, TEXTant, TEX-Sky Monitoring Cloud, MSS Leak Monitoring, Big Data Analytics, Predictive Maintenance, Tectonic Monitoring

## 1 INTRODUCTION

The increasing age of global civil infrastructure, combined with escalating environmental stresses and rising usage demands, has highlighted critical vulnerabilities in bridges, tanks, basins, slopes, and other key structures. Traditional inspection practices—largely reliant on manual surveys and infrequent assessments—often fail to detect the early-stage, progressive deformations that precede catastrophic failures. Recent advancements in geospatial positioning, sensor miniaturization, and wireless data technologies offer unprecedented opportunities for real-time, high-precision structural health monitoring (SHM). Among these, Global Navigation Satellite System (GNSS) monitoring, capable of millimeter-level displacement measurements, has emerged as a core technology. When augmented with complementary sensing modalities—such as leakage detection, corrosion monitoring, and environmental parameter tracking—an integrated, multi-sensor SHM network becomes feasible. This paper presents the development, validation, and practical deployment of such an autonomous multi-sensor SHM system, rooted in high-precision GNSS science, geodetic surveying, and real-world engineering applications. Field-tested at critical infrastructure sites—including the Aquitaine Bridge in France, containment structures in the chemical sector in Germany, and a planned tectonic GNSS monitoring network across Asia Minor—the system demonstrates the viability of scalable, time-synchronized, automated infrastructure health management.

The system's foundation lies in two core technologies developed in-house: the TEXTant® GNSS movement monitoring system and the MSS® Leak Monitoring system. Since 2011, the MSS® system has been successfully deployed in landfill and hazardous waste facilities, starting with the first permanent installation at a power plant in Eemshaven, Netherlands. Building upon this experience, the TEXTant® GNSS system introduces fully autonomous, millimeter-accurate displacement monitoring without dependence on local reference networks. Both technologies are unified under the TEX-Sky Monitoring Cloud, a scalable, modular platform enabling synchronized multi-sensor integration, advanced data analysis, and future AI-assisted pattern recognition. The development of this platform addresses urgent needs for resilient, autonomous, and real-time infrastructure monitoring to enhance public safety, optimize maintenance strategies, and support sustainable asset management.

## 2 SCIENTIFIC BACKGROUND AND MOTIVATION

The urgent need for continuous, high-resolution monitoring of civil infrastructure becomes increasingly apparent as traditional inspection methods often fail to detect subtle but critical early-stage deformations. As Ghaffarian et al. (2023) emphasized, aging structures and increased environmental stress demand real-time monitoring solutions. While several commercially available GNSS systems can achieve millimeter-level precision using base-rover configurations, they depend on local reference infrastructure and often require significant setup and must all be post-processed by experts. These constraints render them impractical for fully autonomous real-time PPP monitoring



across multiple or remote sites. Motivated by these challenges, the authors developed a new system architecture aiming to bridge the critical gap between high-precision monitoring and full automation.

As Elsaïd (2025) demonstrated, low-cost, multi-frequency GNSS receivers can achieve comparable accuracy to high-end systems when calibrated and combined with precise point positioning (PPP) software. PPP enables centimeter- to millimeter-level positioning accuracy by combining precise satellite orbits, clock corrections, and advanced error modeling, without reliance on local differential reference stations (Teunissen & Montenbruck, 2017).

Moreover, a significant gap persists: there is a lack of fully autonomous GNSS-based SHM systems capable of delivering millimeter-level real-time accuracy without requiring expert recalculations. Traditional IGS stations, for example, do not recalibrate continuously, and thus their displacement data may not reflect real-time changes critical to detecting early-stage structural degradation. Millimeter accuracy is essential because slight, continuous movements—caused by temperature, dynamic loads, or tectonic effects—can serve as precursors to catastrophic failures such as bridge collapses, landslides, dam breaches or earthquakes. Monitoring vulnerable and aging infrastructure without such precision carries unacceptable risks. The collapse of the Carolabrücke in Dresden, Germany, in September 2024, illustrates the fatal consequences of undetected structural fatigue (City of Dresden, 2024).

Therefore, the TEXTant® GNSS system was conceived with three key objectives: to provide continuous, unmanned, millimeter-accurate monitoring; to automate data processing and alarm generation without human intervention; and to support early hazard detection across a wide range of critical infrastructure types. It operates autonomously 24/7, with real-time or daily processed datasets accessible through the TEX-Sky Monitoring Cloud.

The importance of rapid deployment and flexibility was highlighted when, just one month after the completion of the TEXTant® system's one-year trial phase, a devastating earthquake struck Turkey and Syria in February 2023. Responding immediately, the first TEXTant® GNSS station for tectonic monitoring was donated to the city of Adana, Turkey, and installed in April 2023 atop the City Hall with support from Mayor Zeydan Karalar. The Adana station now delivers daily millimeter-level movement results to the TEX-Sky Monitoring Cloud, marking the first operational node of the Asia Minor GNSS Network project.

Beyond GNSS-based monitoring, integrated multi-sensor networks further expand system resilience. Cawley (2018) highlighted the necessity of linking strain, acoustic, and environmental data streams to enhance the robustness of predictive analytics. Multi-sensor systems like TEXTant®, when combined with leak detection, corrosion monitoring, and environmental sensing, offer unprecedented opportunities for proactive, data-driven maintenance strategies.

### 3 TEXTANT® GNSS TECHNOLOGY: DEVELOPMENT AND VALIDATION

#### 3.1 System Design and Autonomy

The TEXTant® GNSS system was developed by the authors as a modular, autonomous monitoring solution designed to meet the millimeter-accuracy requirements of geodetic infrastructure monitoring. The device architecture includes an energy-efficient processing unit, solar power modules, and the capacity to host up to four GNSS antennas per station. The entire system is configured for fully autonomous operation, from data acquisition to daily processing, and network transmission via secure cloud protocols.

#### 3.2 PPP Algorithm and Accuracy Optimization

Building on the scientific foundation presented, the development of the GNSS-based monitoring solution centers on the integration of autonomous, low-cost multi-frequency receivers configured to operate without dependence on local reference networks. The approach leverages precise point positioning (PPP) as its core processing strategy, supported by algorithms specifically refined for structural health monitoring applications.

In Elsaïd's doctoral research (Elsaïd, 2025), the implementation of improved dynamic modeling within GNSS algorithms was shown to increase both stability and precision in real-world environments. The TEXTant® system developed through this research was subjected to rigorous field testing, including comparative validation with a conventional geodetic reference system. Results revealed a convergence between autonomous GNSS solutions and classical base-rover measurements, confirming the capability for millimeter-accurate displacement tracking over long time periods.

#### 3.3 Field Validation at GFZ Potsdam

A pivotal phase in this validation process was conducted at the IGS station POTS, located at the German Research Centre for Geosciences (GFZ) in Potsdam, Germany. The developed TEXTant® system was connected in parallel to the existing geodetic Javad receiver at the GFZ, sharing the same GNSS antenna. This configuration enabled a direct comparison under identical atmospheric and signal conditions.

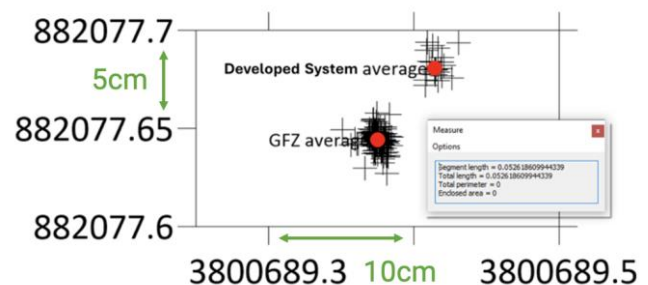


Figure 1. Comparative analysis of the developed TEXTant® GNSS system (23-day dataset) and the GFZ reference system (90-day dataset), demonstrating consistent millimeter-level precision (Elsaïd, 2025).

As detailed in Elsaid's thesis, a 23-day dataset collected from the TEXtant<sup>®</sup> receiver was compared against a 90-day reference dataset from the GFZ system. The comparative analysis yielded exceptional results: horizontal and vertical deviations remained within millimeter thresholds, and no long-term drift or divergence was observed throughout the monitoring period (Elsaid, 2025).

Elsaid emphasized that despite the economical and compact design of the TEXtant<sup>®</sup> device, the results demonstrated its capacity to meet professional-grade geodetic standards. The thesis further highlighted the device's resilience under fluctuating atmospheric conditions and its reliable convergence behavior during daily sessions.

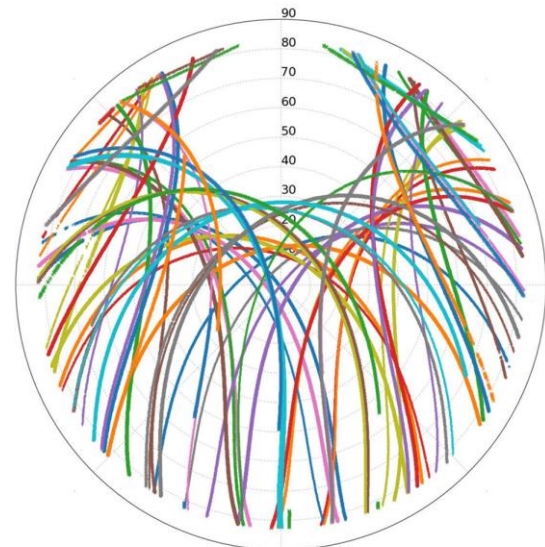


Figure 2. TEXtant<sup>®</sup> GNSS station initiating autonomous operation and data processing upon activation.

### 3.4 Cross-Validation with Bernese and NRCAN

Further scientific credibility was added through collaboration with the Canadian Geodetic Survey (NRCAN), where raw GNSS datasets from TEXtant<sup>®</sup> were submitted to the Natural Resources Canada PPP server for validation. The NRCAN PPP analysis confirmed the integrity and reliability of the device's positioning performance. Additionally, Bernese GNSS Software, a respected academic processing tool developed at the University of Bern, was used for post-processing, yielding comparable accuracy (Elsaid, 2025).

Hardware-level accuracy was validated by comparison with the co-located IGS reference station at GFZ, equipped with a high-grade Javad GNSS receiver. Despite its simplified electronics and energy-saving design, the TEXtant<sup>®</sup> system achieved millimeter-accurate results closely matching the IGS benchmark, demonstrating scientific and operational robustness.



★ G01	★ G09	★ G23	★ G31	★ R07	★ R17
★ G03	★ G10	★ G24	★ G32	★ R08	★ R18
★ G04	★ G12	★ G25	★ R01	★ R09	★ R19
★ G05	★ G14	★ G26	★ R02	★ R12	★ R20
★ G06	★ G15	★ G27	★ R03	★ R13	★ R21
★ G07	★ G17	★ G29	★ R04	★ R14	★ R22
★ G08	★ G18	★ G30	★ R05	★ R15	★ R24

Figure 3. Satellite distribution improvement after antenna calibration and receiver tuning, highlighting enhanced tracking stability and reduced signal loss (Elsaid, 2025).

### 3.5 Deployment and Scalability of the TEXtant<sup>®</sup> System

A critical innovation of the TEXtant<sup>®</sup> development is the deployment of solar-powered, autonomous GNSS stations requiring minimal maintenance. As highlighted by Liu et al. (2016), low-power GNSS configurations enable extensive, scalable monitoring across geographically distributed assets without compromising precision.

TEXtant<sup>®</sup> units operate fully independently, automatically processing data and uploading daily results to the TEX-Sky Monitoring Cloud. Field deployments—including the Aquitaine Bridge and landslide-prone slopes in Germany—validated the system's capability to detect millimeter-level displacement, including thermal expansion effects and gradual settlement trends.

These applications demonstrate the robustness and scalability of the TEXtant<sup>®</sup> concept, enabling broader use in earthquake-prone regions, industrial facilities, and coastal infrastructure. Furthermore, the modular architecture supports integration of supplementary sensors such as accelerometers, leak detectors, and strain gauges, providing a comprehensive and expandable framework for structural health diagnostics.

## 4 THE TEX-SKY MONITORING CLOUD ARCHITECTURE

The TEX-Sky Monitoring Cloud represents the data infrastructure backbone of the multi-sensor SHM platform. Developed to support continuous, time-synchronized acquisition and correlation of high-frequency monitoring data, the cloud-based system functions as a central interface for real-time infrastructure condition analysis. Its architecture enables

integration across multiple sensor nodes and locations, transforming raw data into accessible and actionable insights. Monitoring networks benefit significantly from centralized cloud-based storage and synchronized databases. As noted by Wu et al. (2018), cloud platforms offer scalability and interoperability, two essential features for long-term SHM in complex environments. Within this architecture, each GNSS or auxiliary sensor station independently uploads data via secure protocols, with redundant backups to ensure data integrity. The system maintains strict time-stamping and correlation rules across parameters such as displacement, leakage, temperature, or vibration, thereby enabling consistent multi-variable analysis.

By enabling daily automated reports and long-term pattern visualization, the TEX-Sky Monitoring Cloud supports transition from reactive to preventive maintenance regimes. This shift aligns with Su et al. (2018), who emphasize that cloud-enabled SHM platforms foster predictive analytics through longitudinal data analysis. The TEX-Sky interface provides stakeholders with graphical dashboards, alarm notifications, and exportable analytics, tailored to engineering, operational, or regulatory needs.

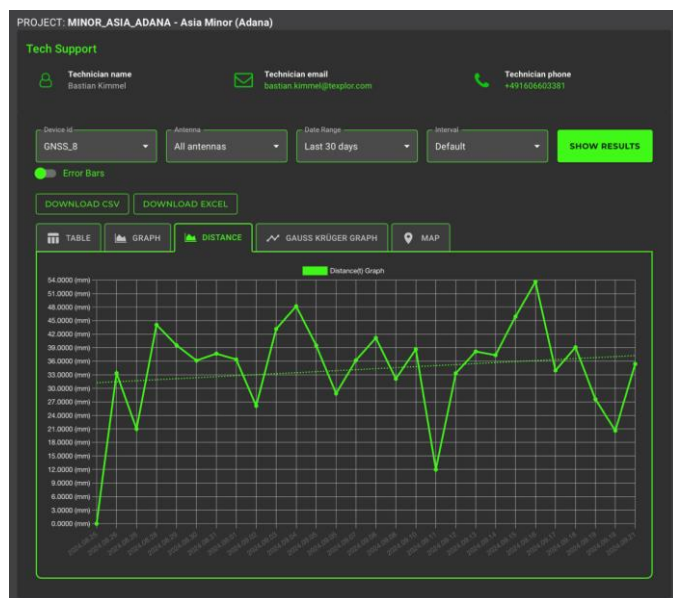


Figure 4. TEX-Sky interface displaying visualized GNSS results, including Gauss-Krüger and UTM coordinates.

The TEX-Sky Monitoring Cloud was developed in-house to support flexible, scalable integration of diverse sensor types. Its modular database structure not only enables real-time SHM across multiple sites but also prepares the platform for future machine learning applications. By continuously expanding the database design, the system already allows seamless transfer of automatically generated monitoring data into AI-based anomaly detection tools, ensuring technological adaptability for evolving SHM needs.

Dang et al. (2022) describe such systems as forming the foundation of Digital Twin implementations, enabling structures to be mirrored in real-time for deeper analysis. While such features remain under development, the system architecture already supports seamless upgrades. Collectively,

the TEX-Sky Monitoring Cloud transforms raw sensor data into centralized knowledge—paving the way for more resilient, data-informed infrastructure management.

## 5 MULTI-SENSOR NETWORK INTEGRATION

An essential component of advanced structural health monitoring (SHM) is the ability to integrate various sensor types into a single, interoperable network architecture. The system developed by the authors merges geospatial GNSS data with time-synchronized readings from multiple environmental and structural sensors, including MSS<sup>®</sup> leak detection, humidity, temperature, corrosion, inclination, and accelerometers. The integrated network ensures comprehensive infrastructure monitoring across dynamic and static parameters.

The two key pillars of this multi-sensor network are the TEXtant<sup>®</sup> GNSS system for precise movement tracking and the MSS<sup>®</sup> Leak Monitoring system for sealing integrity control. Since 2011, the MSS<sup>®</sup> leak monitoring system has been successfully deployed across a wide range of applications and several continents, including hazardous waste landfills, mining operations, and chemical containment basins, starting with its first major deployment at a power plant project in Eemshaven, Netherlands.

The MSS<sup>®</sup> leak detection technology is central to monitoring the integrity of sealed systems, particularly for tank farms and containment basins. Its use of conductive cord networks and automated alerting mechanisms has proven effective in early detection of micro-leaks, contributing to environmental safety and regulatory compliance. As demonstrated in deployments such as the tank basins monitored since 2020, this technology reduces inspection effort while ensuring 24/7 leak monitoring capacity.

The interoperability of all sensor modules relies on the synchronized timing and unified data architecture provided by the TEX-Sky Monitoring Cloud. Each sensor type, regardless of its function or installation context, transmits data tagged with precise timestamps, allowing multi-dimensional correlation and anomaly detection. The TEX-Sky Monitoring Cloud itself was independently developed by the authors to serve as a flexible, modular database architecture. It is designed for the long-term storage, processing, and visualization of synchronized SHM data, and it is continuously updated to remain compatible with machine learning (ML) techniques for anomaly detection and predictive analytics.

Kazmierski et al. (2018) note that modular SHM architectures enhance adaptability, enabling sensor types to be added or removed depending on project-specific risks and requirements. This modularity is especially crucial for retrofitting existing infrastructure, where different physical layouts and constraints may exist.

The integration strategy employed supports preventive and predictive maintenance practices by providing a more holistic view of structural conditions. Furthermore, combined datasets improve diagnostic confidence: for example, identifying correlated patterns between displacement, moisture ingress, and thermal expansion.

With ongoing development, future sensor classes—including gas sensors, advanced corrosion probes, and customized client-



specific sensors—may further extend this multi-sensor network’s diagnostic capacity. By consolidating diverse sensing modalities within a unified, scalable system, the platform demonstrates the technical feasibility and operational benefits of fully integrated SHM for modern infrastructure.

## 6 FIELD DEPLOYMENTS AND CASE STUDIES

This section presents the implementation of the authors’ system in diverse real-world environments to evaluate its performance, scalability, and scientific contribution to structural health monitoring (SHM).

### 6.1 Aquitaine Bridge Monitoring (France)

The Aquitaine Bridge in Bordeaux, completed in 1967, is one of France’s major river crossings and represents a landmark of civil engineering from the postwar period. Given its age and strategic importance, it was selected as an ideal candidate to validate the TEXTant<sup>®</sup> GNSS monitoring system under real-world operational conditions. The bridge’s susceptibility to thermal expansion, structural aging, and dynamic traffic loads provides a comprehensive environment to assess long-term monitoring technologies.



Figure 5. GNSS antenna installation on the 90-meter-high pylon of the Aquitaine Bridge in Bordeaux, France.

Since April 2022, an autonomous TEXTant<sup>®</sup> GNSS station has been continuously operating on one of the 90-meter-high pylons. The system collects millimeter-precise daily displacement data across the X, Y, and Z axes in the ECEF (Earth Center Earth Fixed) coordinate system, processed automatically through precise point positioning (PPP) without the need for local base stations.

The monitoring initiative is carried out in cooperation with Cerema Sud-Ouest. Validation against conventional geodetic measurements confirmed the system’s accuracy. As John Dumoulin, MA (Cerema), reported, the TEXTant<sup>®</sup> system reliably delivers absolute millimeter-accurate displacement values on a daily basis without requiring a fixed reference station (Dumoulin, 2025).

Analysis of the time-synchronized monitoring data has revealed a clear correlation between structural displacement and ambient temperature variations. Specifically, movements

along the X-axis exhibit a direct correlation with temperature, while displacements along the Y-axis are inversely correlated. These findings reflect thermal expansion and contraction effects acting asymmetrically on the bridge structure. The observed patterns provide insight into seasonal deformation behavior and demonstrate the utility of high-resolution GNSS data for capturing structural response under environmental loading.

Future plans include the addition of temperature sensors and strain gauges to further enrich the TEX-Sky Monitoring Cloud database with synchronized multi-parameter datasets.

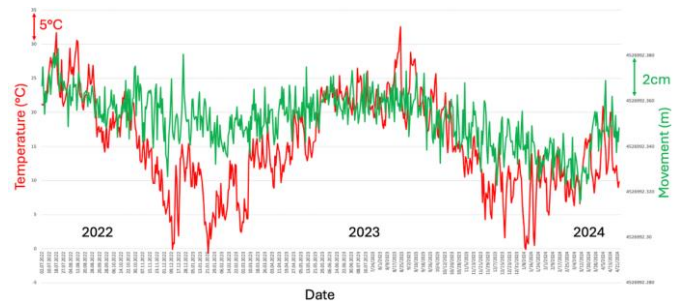


Figure 6. Correlation between X-axis movement (green) and temperature variations (°C, red) from 2022–2024.

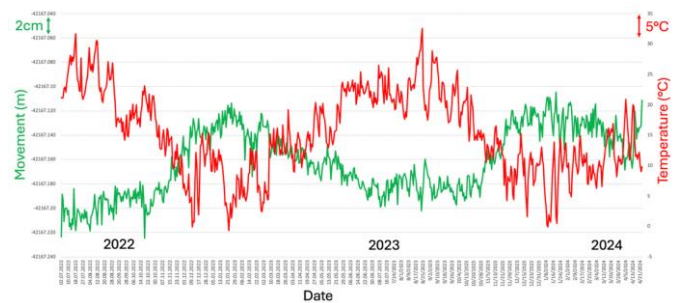


Figure 7. Correlation between Y-axis movement (green) and temperature variations (°C, red) from 2022–2024.

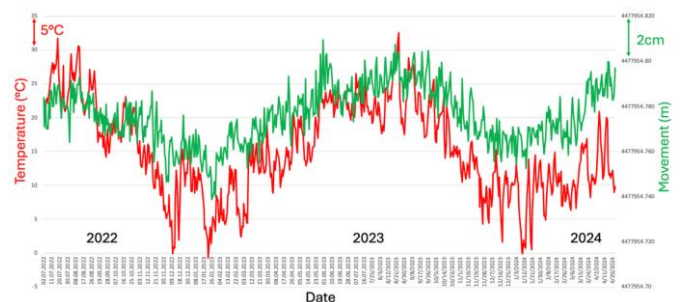


Figure 8. Correlation between Z-axis (height) movement (green) and temperature variations (°C, red) from 2022–2024.

### 6.2 Asia Minor Cross-Border GNSS Network

The Asia Minor GNSS Network was initiated as a donation-based scientific infrastructure project following the devastating

Turkey–Syria earthquakes in February 2023. The project aims to establish a cross-border tectonic monitoring and early warning system in one of the most geodynamically active regions worldwide.

Tectonic complexity in the area is driven by the interaction of the African Plate, Arabian Plate, and Anatolian Block. Near the city of Adana, the northward motion of the Arabian Plate compresses the Anatolian Block, forcing it westward along the East Anatolian Fault. This geodynamic regime results in frequent high-magnitude seismic events, making the region a critical focus for real-time geodetic monitoring initiatives. The first TEXTant<sup>®</sup> GNSS station was successfully installed atop the City Hall in Adana in April 2023, with the support of the local administration. The GNSS station has been operating autonomously since then, delivering daily millimeter-precision displacement data in X-Y-Z axes. It reliably records both the gradual tectonic drift of the Anatolian Block and abrupt height anomalies associated with seismic events exceeding magnitude 5.

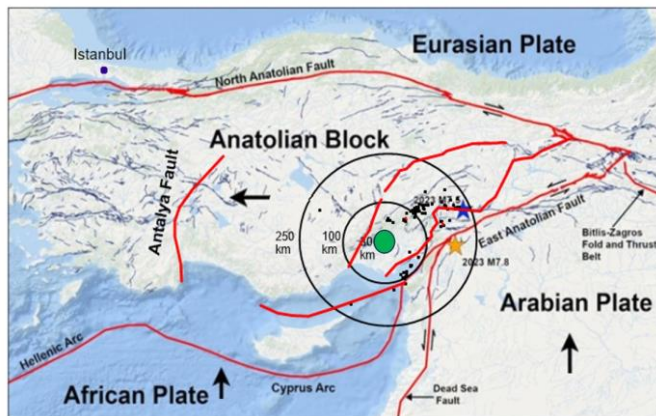


Figure 9. TEXTant<sup>®</sup> GNSS station in Adana (green), recorded earthquakes (black), and earthquakes >5M magnitude (red).

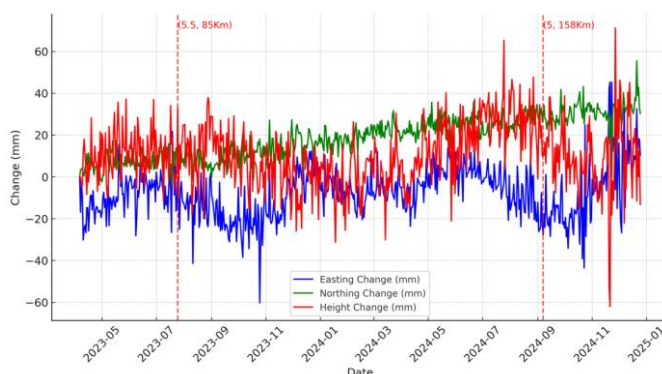


Figure 10. Displacement tracking at the TEXTant<sup>®</sup> GNSS station in Adana: Easting (blue), Northing (green), and Height (red) changes.

In collaboration with the CNRS National Center for Geophysics in Lebanon and the University of Jordan, preparations are underway for the installation of two additional TEXTant<sup>®</sup> GNSS stations. Discussions regarding station

placement are ongoing, and the delivery and commissioning are scheduled for 2025. These installations mark the next steps in expanding the Asia Minor Network.

The broader objective is to establish a cross-border GNSS infrastructure covering six countries—Turkey, Syria, Lebanon, Jordan, Egypt, and Saudi Arabia. All recorded data are automatically processed via PPP algorithms and archived within the TEX-Sky Monitoring Cloud, facilitating scientific collaboration, seismic risk research, and the future development of regional early warning systems.

This initiative represents the first operational cross-border PPP-based GNSS tectonic monitoring network in the Asia Minor region.

### 6.3 Landslide Risk Monitoring (Germany)

In a geologically sensitive mining region in Germany, an autonomous TEXTant<sup>®</sup> GNSS monitoring network was deployed to monitor slope stability. The project area was characterized by historic mining activities, creating a heightened risk of slope destabilization and landslides over time.

Two solar-powered TEXTant<sup>®</sup> GNSS stations, equipped with a total of six antennas, were installed on the potentially unstable slope. These stations operate autonomously and transmit daily displacement results in X, Y, and Z axes to the TEX-Sky Monitoring Cloud, where the time-synchronized datasets are automatically processed and archived.

Previously, the slope was inspected at intervals by land surveyors, with weeks-long delays between measurements and data interpretation. The introduction of daily, continuous GNSS monitoring significantly enhanced the ability to detect subtle deformations at an early stage. Regular automated reports now document absolute movements in local coordinate systems, offering actionable insights into both spatial displacement and temporal trends. These visualized datasets are used to create detailed deformation maps, illustrating where and by how much the terrain is shifting.

This deployment demonstrates how continuous GNSS-based monitoring provides superior resolution, frequency, and responsiveness compared to traditional manual surveying, contributing to improved risk mitigation strategies for landslide-prone areas.



Figure 11. GNSS antenna connected to an autonomous TEXTant<sup>®</sup> station powered by a solar energy system.



#### 6.4 Industrial Multi-Sensor SHM (Germany)

At an industrial site in Germany, a multi-sensor SHM system was implemented to monitor the structural integrity of critical containment infrastructure exposed to heavy operational loads, fluctuating groundwater conditions, and tidal forces from the nearby Elbe River. The aim was to reliably assess structural status, extend service life, and minimize costly manual inspections that disrupt operations.

Since 2020, MSS<sup>®</sup> leak monitoring has been deployed across three containment structures: a storage tank, a concrete catch basin, and a reinforced concrete basin with a liquid liner. In total, 32 leak sensors were installed—eight around the tank, sixteen around the catch basin, and eight within the basin floor—embedded into both new and existing structures. Early-stage leak detection during commissioning enabled targeted repairs, demonstrating the system's preventive maintenance value.



Figure 12. Leak monitoring system with eight sensors embedded around the perimeter of the monitored tank using mounting sleeves.

In 2024, TEXtant<sup>®</sup> GNSS movement monitoring stations were added to the network, providing autonomous daily X-Y-Z displacement data with millimeter precision. This data is essential for detecting differential settlements and deformations linked to seasonal groundwater variations and river-induced soil dynamics.

A corrosion monitoring system, featuring 64 embedded sensors across both original and newly built concrete walls, enables comparative degradation analysis. Additionally, moisture sensors were installed between double-wall structures to monitor water ingress risks via resistance measurements.

All sensor modules are integrated into the TEX-Sky Monitoring Cloud, allowing centralized, time-synchronized data correlation and automated reporting. The system has been approved by TÜV-Nord, supporting regulatory compliance while optimizing inspection intervals. By reducing the need for frequent manual interventions, the multi-sensor SHM deployment contributes to enhanced operational reliability, environmental safety, and lifecycle cost savings.



Figure 13. The monitoring computer sends all multi-sensory results (movement, leakage, corrosion) to the TEX-Sky Monitoring Cloud.

These case studies demonstrate the adaptability, precision, and value of the authors' multi-sensor SHM system in diverse structural contexts, from heritage bridges to critical industrial assets and geohazard zones.

## 7 DISCUSSION: PREDICTIVE MAINTENANCE AND AI OPPORTUNITIES

The integration of time-synchronized data streams from geospatial and structural sensors provides a foundation for advanced data-driven maintenance strategies. As infrastructure systems age and face intensifying environmental pressures, the transition from reactive to predictive maintenance becomes increasingly necessary. Long-term datasets derived from autonomous monitoring technologies enable trend analysis, anomaly detection, and system-wide diagnostics—laying the groundwork for intelligent decision support systems.



A core advantage of synchronized SHM networks lies in their ability to generate longitudinal datasets that capture subtle structural changes over time. As Razali et al. (2020) note, big data analytics applied to sensor data can enhance preventive maintenance by identifying hidden correlations and early-warning indicators. The TEX-Sky Monitoring Cloud facilitates such analyses through automated reporting tools and correlation matrices spanning parameters like displacement, leak detection, inclination, and corrosion.

Furthermore, the platform supports early-stage integration with machine learning frameworks. According to Wu et al. (2018), AI-enhanced SHM platforms can extract latent patterns from high-volume sensor streams, offering insights unattainable through manual evaluation. The cloud's architecture, which time-aligns and stores multi-dimensional data across geographically distributed sites, enables the application of supervised learning algorithms for condition classification and anomaly detection.

The evolution toward data-driven maintenance is also aligned with Digital Twin paradigms. Dang et al. (2022) describe Digital Twins as dynamic virtual replicas of physical infrastructure, continuously updated through real-time sensor inputs. In our framework, the combination of daily GNSS-derived position data and environmental sensor feedback enables a similar mirroring of structural states, especially in applications like slope monitoring and tank basin surveillance. The benefits of such an approach are multifold: improved lifecycle predictions, optimized inspection intervals, targeted intervention planning, and enhanced safety margins. Ultimately, by embedding intelligence into SHM workflows, engineers can ensure that infrastructure resilience evolves in tandem with societal needs and technological capability.

## 8 CONCLUSION AND FUTURE PERSPECTIVES

This paper has presented the development, scientific rationale, and field validation of a modular, autonomous monitoring system that integrates multi-sensor technologies with advanced geospatial GNSS capabilities. Designed to achieve millimeter-level accuracy in displacement, leakage detection, and environmental monitoring, the system represents a fundamental shift toward data-driven, real-time structural health monitoring (SHM).

Central to this approach are two core technologies developed by the authors: the TEXTant<sup>®</sup> GNSS movement monitoring system and the MSS<sup>®</sup> Leak Monitoring technology. Their integration through the TEX-Sky Monitoring Cloud enables scalable, synchronized monitoring across diverse infrastructure types—from heritage bridges and industrial containment systems to tectonic plate boundaries and geotechnically unstable slopes.

Field deployments in France, Germany, and Turkey have demonstrated the system's scientific robustness, operational reliability, and its capacity to support predictive maintenance strategies. The introduction of fully autonomous, daily-updating monitoring solutions fills a critical technological gap, particularly where traditional inspection cycles or manual GNSS data post-processing fall short.

Continuous, unmanned monitoring systems capable of high-precision results offer new opportunities to prevent disasters

such as bridge collapses, dam breaches, and infrastructure failures due to undetected degradation.

Future work will focus on expanding cross-border SHM networks, contributing to the development of international standards for autonomous infrastructure monitoring, and strengthening global collaboration to enhance structural resilience.

## REFERENCES

- [1] Cawley, P. (2018). Structural health monitoring: Closing the gap between research and industrial deployment. *Structural Health Monitoring*, 17(5), 1225–1244.
- [2] City of Dresden. (2024). Teileinsturz der Carolabrücke Dresden – Informationen und Gutachten. Available at: <https://www.dresden.de/de/stadtraum/zentrale-projekte/carolabruecke.php> (Accessed: 22 April 2025).
- [3] Dang, H. V., Tatipamula, M., & Nguyen, H. X. (2022). Toward Digital Twin in Industrial Informatics: A Survey. *IEEE Transactions on Industrial Informatics*, 18(6), 3823–3833.
- [4] Dumoulin, J. (2025). Precise Movement Monitoring at the Aquitaine Bridge in France. *Texplor Group*, 5 April 2025, <https://texplor.com/millimeter-movement-monitoring-textant-gnss-network-aquitaine-bridge/>
- [5] Elsaid, A. (2025). Improving Real-Time Autonomous Algorithm to Multi-Frequency Low-Cost GNSS Receivers for Geodetic Dynamic Monitoring. PhD Thesis, TU Berlin. (PhD thesis not yet completed)
- [6] Ghaffarian, H., Tavakkoli, S. M., Ghasemi, H., & Torabzadeh, H. (2023). A systematic review of structural health monitoring techniques for bridges. *Sensors*, 24(3), 4269.
- [7] Kazmierski, M., Ostrowski, Z., & Tchórzewska-Cieślak, B. (2018). The application of the monitoring system for the diagnostic of water supply pipelines. *Proceedings of ECOpole*, 12(2), 387–394.
- [8] Liu, L., Wang, Y., Li, B., & Liu, W. (2016). Research on automatic GNSS monitoring system and its application in highway slope deformation monitoring. *Proceedings of the 8th International Conference on Environmental Science and Technology*.
- [9] Razali, S. F. M., et al. (2020). Big data analytics for predictive maintenance strategies: Review, challenges, and future research directions. *IOP Conf. Series: Materials Science and Engineering*, 864, 012109.
- [10] Teunissen, P. J. G., & Montenbruck, O. (2017). *Springer Handbook of Global Navigation Satellite Systems*. Springer.
- [11] Wu, Z., et al. (2018). Cloud-based health monitoring system for civil structures using Internet of Things. *Advances in Structural Engineering*, 21(8), 1201–1213.
- [12] Xue, L., Zhang, P., Xu, C., & Chen, X. (2020). Development and evaluation of a multi-GNSS real-time kinematic positioning system for structural health monitoring. *Sensors*, 20(9), 2778.

# LiDAR for vibration monitoring of infrastructure: stretching limits by spatio-temporal time domain frequency analysis

Oliver L. Geißendörfer<sup>1</sup>, [ORCID](#), Christoph Holst<sup>1</sup>, [ORCID](#)

<sup>1</sup>Chair of Engineering Geodesy, TUM School of Engineering and Design  
Technical University of Munich, Arcisstraße 21, 80333 München, Germany  
email: o.geissendoerfer@tum.de, christoph.holst@tum.de

**ABSTRACT:** Structural health monitoring (SHM) is crucial for ensuring the integrity and safety of infrastructure. Traditional vibration analysis techniques rely on sensors such as Inertial Measurement Units (IMU) and Global Navigation Satellite Systems (GNSS), total stations (TS) and fibre-optics (FO), which require a physical attachment to structures in the observation process. However, Light Detection and Ranging (LiDAR) offers a contactless alternative, enabling high-resolution, time-synchronized observations that capture spatially continuous deformation information. This paper presents an innovative framework for SHM that leverages LiDAR-based time-domain frequency analysis to monitor dynamic structural behavior effectively. By integrating spatio-temporal modeling techniques, we establish a robust methodology for detecting oscillations and deformations in infrastructure. Our approach enhances current SHM practices by providing a scalable solution that does not require physical sensor deployment. Thus, this methodology provides information in much higher spatial resolution compared to the aforementioned approaches. The proposed methodology is evaluated by controlled experiments, demonstrating its applicability to real-world SHM scenarios and its potential for continuous, non-invasive structural assessment.

**KEY WORDS:** Structural Health Monitoring; Laser Scanning; B-Splines; Harmonic Oscillation; Point Cloud.

## 1 INTRODUCTION

Structural integrity is a fundamental concern in civil engineering, necessitating continuous monitoring of deformations and vibrations in infrastructure. Bridges, buildings, and other structures are subject to environmental and mechanical forces, including wind, traffic loads, temperature variations, and seismic activity. These forces induce static and dynamic deformations, which must be accurately tracked to prevent structural failures.

Traditionally, SHM relies on point-based sensors such as Global Navigation Satellite System (GNSS) [1, 2], Inertial Measurement Unit (IMU) [3, 4], total stations [5], and fiber-optic (FO) [6, 7] sensors, which provide precise motion data but require physical attachment to structures (Fig. 1). Optical sensors, including cameras [8, 9, 10], Vibrometers [11, 12, 13, 14], and Light Detection and Ranging (LiDAR) [15, 16], offer contactless observations, reducing maintenance effort and enabling long-term deployment. Among these, LiDAR has gained prominence due to its ability to capture high-resolution, time-synchronized spatial data, making it well-suited for SHM applications.

While prior research has explored LiDAR-based monitoring, empirical validation and integration into SHM workflows remain limited. This study addresses these gaps by presenting a comprehensive framework for contactless structural vibration monitoring using LiDAR. Our research focuses on leveraging time-domain frequency analysis to capture oscillatory behavior and quantify structural deformations more effectively.

This paper addresses the following research questions:

- Can LiDAR-based time-domain frequency analysis provide reliable results for SHM applications?

- How does point-wise processing compare to area-wise processing in structural vibration analysis?
- Do observation residuals exhibit systematic patterns that can inform SHM decision-making?

We answer those questions applied to SHM methodologies by integrating 3D point clouds of LiDAR, that improve vibration analysis, uncertainty quantification, and structural condition assessment.

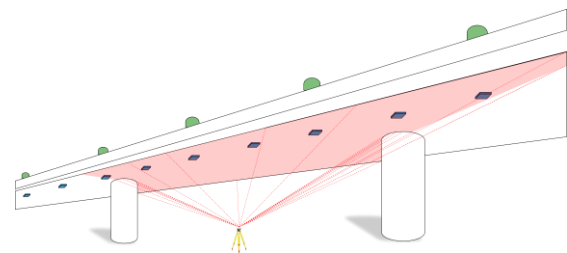


Figure 1. Potential 4D bridge monitoring with GNSS (green), IMU (blue) or LiDAR (red)

## 2 SPATIO-TEMPORAL PROCESSING

LiDAR sensors naturally observe their surroundings with a high point sampling rate of several MHz and a spatial resolution in the mm-level. This observation principle enables to record high frequent 4D (3D + time) deformation signals of structures, as displayed in Figure 1 in comparison to using IMU and GNSS sensors. To use LiDAR point clouds for vibration monitoring, we present within this work an implementation of spatio-temporal connections, which we evaluate experimentally. Therefore, we first introduce into our experimental setup within section 2.1 to show a coarse

overview of the object and used sensor. In section 2.2, we briefly describe our developed methodology to tackle 4D LiDAR data processing. Lastly, we discuss results regarding the outcome and limitations in section 2.3.

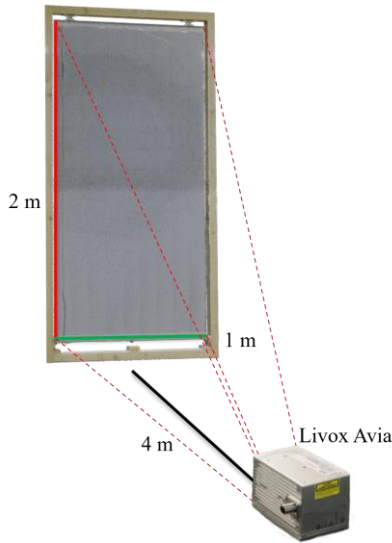


Figure 2. Experimental measurement setup

### 2.1 Experimental Setup

We evaluate our methodology using continuous observations of micro-electro-mechanical system (MEMS) LiDAR sensors to capture the periodic motion of a forced-excited acrylic glass sheet in Figure 2. This sheet is two by one meter and clamped on the upper and lower sides. Since it is also erected vertically, gravity acts asymmetrically on the test construction. Our experimental setup simulates real-world conditions by introducing controlled periodic excitation forces induced by a linear actuator with a frequency of about 0.3 Hz. Furthermore, we test the adaptability of our approach across different configurations and object geometries to assess its scalability. The selected process enables a continuous frequency mode description of a dynamically oscillating object, which ensures accurate spatial approximation and robust frequency estimation, enabling a fully automated analysis using low-cost sensors.

### 2.2 Methodology

Our approach harnesses LiDAR data to exploit its contactless observations and high sampling rate for time domain frequency estimation [17]. However, dimensions are limited to the LiDAR sensors used in respective monitoring settings [16]. To further enhance processing efficiency, we integrate point cloud observations within a time-domain framework directly. This reduces computational complexity by minimizing intermediate processing steps while maintaining spatial and temporal coherence.

In our workflow, we first implement an initial frequency estimation process based on spectral analysis techniques in the time domain, ensuring that dominant oscillation modes are accurately captured. Furthermore, consecutive points and their spatial neighborhoods facilitate establishing temporal and spatio-temporal connections, allowing direct oscillation modeling simultaneously in time and the metric space. By

introducing spatial B-spline modeling, we establish smooth spatial transitions between neighboring observations [16]. Additionally, we connect observations in time by their underlying periodic signal. With both spatial and temporal connections, we formulate spatio-temporal connections

$$w(u, v) = \mu(u, v) + \sum_{i=0}^N a(u, v) \cdot \cos(2\pi f_i t) + b(u, v) \cdot \sin(2\pi f_i t)$$

as a combination of the Fourier Series [18] and functions used in geometric modeling [19]. By employing a sophisticated mathematical model in time  $t$ , we approximate components like an immovable mean surface  $\mu(u, v)$ , amplitude variations, and phase shifts corresponding to frequencies  $f_i$  by Fourier parameters  $a(u, v)$  and  $b(u, v)$  [20]. Except frequencies, all components are described as geometric functions expressed with their first and second principal component  $u, v$  in Figure 3 and the movement in time along the third principal component  $w$ . Figure 4 displays the signal  $w$  along the time axis  $t$  (not sorted for  $u, v$ ) for experimental data of 100 sec: Clearly, the oscillations are visible.

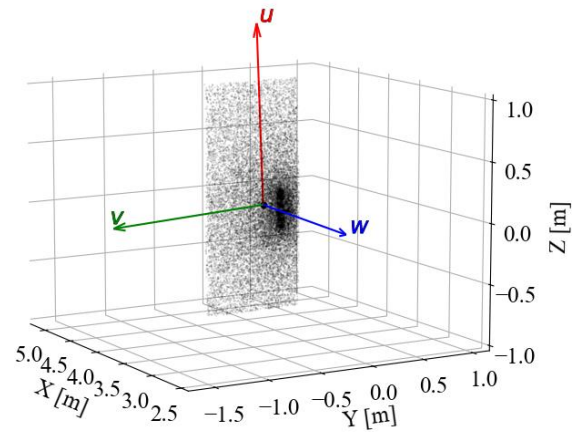


Figure 3. Observation point cloud with its principal components  $u, v, w$ .

We further quantify parameter uncertainty to evaluate the reliability of estimated variables, thereby enabling robust movement and vibration analysis of spatially connected surfaces. Generally, our method simplifies the representation of periodic signals while preserving essential spatial characteristics for interpretation.

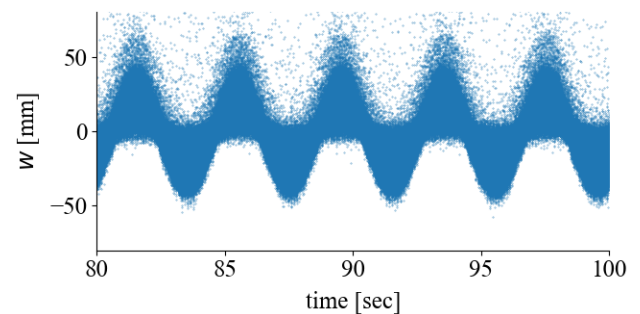


Figure 4. Part of the noisy time series observed along principal component  $w$



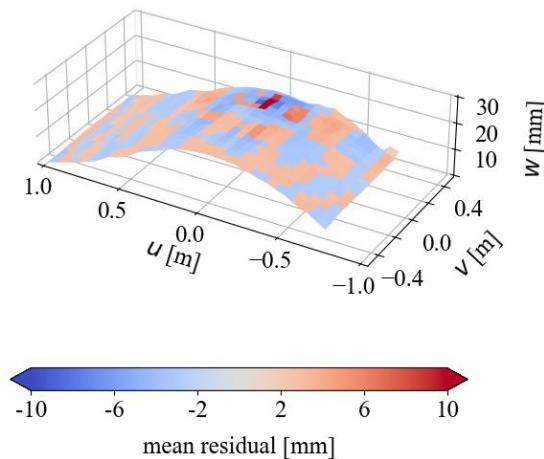


Figure 5. mode shape of the dominant amplitude with overall mean residuals as colors

### 2.3 Results and discussion

Our developed methodology effectively captures and describes enforced motion in both space and time. The integration of LiDAR-based time-domain frequency analysis offers a significant advancement in dynamic object monitoring, reducing reliance on traditional sensor frameworks. Moreover, it automatically combines observations compared to the individual processing of individual sensors e.g. IMU and GNSS.

Thus, we can explore interdependencies between parameters and their impact on results, highlighting the adaptability of our approach across different LiDAR systems. Besides the continuous amplitude shape shown in Figure. 5, we further analyze residuals from estimated parameters to identify systematic patterns that may indicate underlying structural characteristics in Figure 5. Therefore, our results show that continuous processing in the time domain produces higher fidelity reconstructions compared to point-wise approaches like mode description using IMU and GNSS sensors. Additionally, uncertainty propagation studies reveal the high sensitivity of estimated frequencies concerning sensor noise as well as environmental factors at the observation sight [16].

We further investigate the influence of different geometric modeling methods for establishing spatio-temporal relationships. The results indicate that B-spline modeling outperforms polynomial approximations in capturing smooth transitions while maintaining high-frequency response accuracy [16]. This highlights advantages of flexible basis functions in vibration analysis applications.

## 3 CONCLUSION

Our study demonstrates that LiDAR-based time-domain processing enables high-resolution monitoring of dynamic objects, offering advantages over traditional sensor-based methods as contactless observations and processing of the full object. The developed methodology ensures robust frequency estimation, efficient uncertainty quantification, and improved adaptability across different application domains.

Future research will extend our methodology to real-world scenarios such as bridge vibration analysis, integrating additional sensor modalities for enhanced robustness. Herein, we will also evaluate the limits of our approach in more detail.

Further improvements will focus on refining uncertainty quantification and optimizing computational efficiency to facilitate large-scale implementations. Additionally, we aim to investigate the potential for hybrid sensor fusion, combining LiDAR data with conventional methods to enhance the accuracy and robustness of vibration analysis in complex monitoring environments.

## ACKNOWLEDGMENTS

This research was funded by German Research Foundation (DFG) under grant number 536704264, project "Processing models for analyzing the 3D vibration response of structures using terrestrial laser scanners (PROVILAS)"

## REFERENCES

- [1] R. Hohensinn, S. Häberling and A. Geiger, "Dynamic displacements from high-rate GNSS: Error modeling and vibration detection," *Measurement*, vol. 157, 2020.
- [2] C. Schönberger, W. Lienhart and B. Kaden, "Static and dynamic structural monitoring of civil infrastructure objects with GNSS," 2023.
- [3] C. Xiong, H. Lu and J. Zhu, "Operational Modal Analysis of Bridge Structures with Data from GNSS/Accelerometer Measurements," *Sensors*, vol. 17, 2017.
- [4] A. Sabato, C. Niezrecki and G. Fortino, "Wireless MEMS-Based Accelerometer Sensor Boards for Structural Vibration Monitoring: A Review," *IEEE Sensors Journal*, vol. 17, pp. 226-235, 2017.
- [5] A. Wagner, P. Wasmeier, C. Reith and T. Wunderlich, "Bridge Monitoring By Means Of Video-Tacheometer – A Case Study," *avn - Allgemeine Vermessungs-Nachrichten*, vol. 120, pp. 283-292, 2013.
- [6] J. M. Lopez-Higuera, L. Rodriguez Cobo, A. Quintela Incera and A. Cobo, "Fiber Optic Sensors in Structural Health Monitoring," *Journal of Lightwave Technology*, vol. 29, pp. 587-608, 2011.
- [7] W. Lienhart, L. Strasser and V. Dumitru, "Distributed Vibration Monitoring of Bridges with Fiber Optic Sensing Systems," in *International Conference on Experimental Vibration Analysis for Civil Engineering Structures*, 2023.
- [8] J. G. Chen, A. Davis, N. Wadhwa, F. Durand, W. T. Freeman and O. Büyükoztürk, "Video Camera-Based Vibration Measurement for Civil Infrastructure Applications," *Journal of Infrastructure Systems*, vol. 23, p. B4016013, 2017.
- [9] R. D. Sal, L. D. Bo, E. Turco, A. Fusiello, A. Zanarini, R. Rinaldo and P. Gardonio, "Structural vibration measurement with multiple synchronous cameras," *Mechanical Systems and Signal Processing*, vol. 157, p. 107742, 2021.
- [10] K. Luo, X. Kong, J. Li, J. Hu and L. Deng, "Motion magnification for video-based vibration measurement of civil structures: A review," *Mechanical Systems and Signal Processing*, vol. 220, p. 111681, 2024.
- [11] M. Martarelli, G. M. Revel and C. Santolini, "Automated modal analysis by scanning laser vibrometry: Problems and uncertainties associated with the scanning system calibration," *Mechanical Systems and Signal Processing*, vol. 15, pp. 581-601, 2001.
- [12] W. J. Staszewski, B. C. Lee and R. Traynor, "Fatigue crack detection in metallic structures with Lamb waves and 3D laser vibrometry," *Measurement Science and Technology*, vol. 18, p. 727, January 2007.
- [13] D. D. Maio, P. Castellini, M. Martarelli, S. Rothberg, M. S. Allen, W. D. Zhu and D. J. Ewins, "Continuous Scanning Laser Vibrometry: A raison d'être and applications to vibration

- measurements," *Mechanical Systems and Signal Processing*, vol. 156, p. 107573, 2021.
- [14] T. Yu, Q. Tang and S. Vinayaka, "Identifying structural properties of a steel railway bridge for structural health monitoring using laser Doppler vibrometry," *Automation in Construction*, vol. 160, p. 105320, 2024.
- [15] F. Schill and A. Eichhorn, "Deformation Monitoring of Railway Bridges with a Profile Laser Scanner," *ZfV Z. Geodäsie Geoinf. Landmanag.*, vol. 2, p. 109–118, 2019.
- [16] O. L. Geißendörfer and C. Holst, "Combining LiDAR and Time-Domain Frequency Analysis for Enhanced Spatial Understanding of Vibration Responses," *IEEE Open Journal of Instrumentation and Measurement*, vol. 3, pp. 1-14, 2024.
- [17] C. Holst and H. Neuner, "Spatio-temporal models for vibration monitoring of elongated structures using profile laser scans," *Remote Sensing*, vol. 13, 2021.
- [18] J. W. Cooley and J. W. Tukey, "An algorithm for the machine calculation of complex Fourier series," *Mathematics of computation*, vol. 19, p. 297–301, 1965.
- [19] C. Harmening and H. Neuner, "Choosing the Optimal Number of B-spline Control Points (Part 1: Methodology and Approximation of Curves)," *Journal of Applied Geodesy*, vol. 10, p. 139–157, 2016.
- [20] O. Geißendörfer and C. Holst, "Spatio-temporal mode description in LiDAR point clouds," in *6th Joint International Symposium on Deformation Monitoring (JISDM 2025)*, 2025.

# Application of LiDAR technology in geodetic monitoring of reclaimed landfills

Grzegorz Pasternak<sup>1</sup>, 0000-0002-7320-6347, Janina Zaczek-Peplinska<sup>2</sup>, 0000-0003-4875-4250

<sup>1</sup>Institute of Civil Engineering, Warsaw University of Life Sciences—SGGW, Nowoursynowska 159, 02-776 Warsaw, Poland

<sup>2</sup>Faculty of Geodesy and Cartography, Warsaw University of Technology, Pl. Politechniki 1, 00-661 Warsaw, Poland  
email: grzegorz\_pasternak@sggw.edu.pl, janina.peplinska@pw.edu.pl

**ABSTRACT:** Geodetic monitoring of reclaimed landfills is essential in ensuring the geotechnical safety of slopes and for monitoring the process of landfill settlement caused by biological and physico-chemical decomposition of the deposited waste. Insufficient recognition of the size and directions of displacements may lead to severe damage to the landfill body (landslides, sinkholes) and endanger the environment and the life and health of people living near the landfill. Classic geodetic monitoring of such facilities is based on measurements of single control points (benchmarks) located on the landfill body, the displacements of which often do not represent actual changes occurring in the area of the entire facility. The solution to this problem is to use Light Detection and Ranging (LiDAR) technology, which allows surface measurement of the entire studied area, making it possible to obtain a complete image of changes in the geometry of the landfill body. This paper presents a case study of a reclaimed municipal solid waste landfill located in Poland for which monitoring was applied using Terrestrial Laser Scanning (TLS) and Airborne Laser Scanning (ALS) from an Unmanned Aerial Vehicle (UAV). The acquired 3D data made it possible to obtain reliable information on the deformation processes on the landfill's surface and to decide on the direction of development of the post-remediation landfill as a Renewable Energy Sources (RES) station with solar panels and a biogas plant.

**KEY WORDS:** LiDAR; ALS; TLS; Deformation monitoring; Landfill reclamation; UAV.

## 1 INTRODUCTION

Landfilling is still the most popular method of waste disposal in Poland. According to the Central Statistical Office (Główny Urząd Statystyczny - GUS) 2022 data, 259 active landfills in Poland and more than 600 landfills closed and partially or fully reclaimed. The 1999 European Union (EU) Landfill Directive and the EU's overall policy for sustainable waste management imply a gradual reduction in municipal waste sent to landfills. It also imposes technical and environmental requirements that landfills must meet, indirectly leading to the closure and rehabilitation of old, substandard landfills and the creation of new landfills that meet standards [1,2]. There will be a further increase in reclaimed landfills in the coming years. Municipal landfills are usually located near large cities, whose dynamic growth causes landfills to be integrated into the urban fabric over time. Often, in such cases, as compensation for the long-standing negative impacts of the landfill on the immediate neighborhood (unpleasant odor, birds), they are transformed into public facilities with recreational, park, sports, museum, or exhibition functions [3]. It is also common to use these facilities in electricity production (biogas plant, photovoltaic farm, wind farm). An example of such a landfill is the Słabomierz-Krzyżówka landfill site located in Poland, whose future post-remediation development has been earmarked for a photovoltaic farm and where energy is currently being produced from extracted biogas [4].

Geodetic monitoring of deformation is essential in ensuring safety at reclaimed landfills by monitoring the impassibility of critical states defined for slope stability and monitoring the uniformity of settlement of the landfill body. In their design, reclaimed landfills can be compared to earth structures made of anthropogenic materials, supplemented by protective structures

such as seals, drains, or reinforcements. The peculiarity of these structures is due to their large surface area (up to several tens of hectares), large volume (up to several million m<sup>3</sup>), considerable thickness (up to several tens of meters), and long-time operating period (several decades). Due to the high heterogeneity of the stored waste (different mechanical, physico-chemical, and biological-chemical factors), the course of the subsidence process is difficult to predict. Compared to soils, wastes show very high compressibility, making the site's settlement dynamic, especially during reclamation [5-8].

The dynamics of landfill mass settlement are variable over time. The subsidence process can be divided into three phases: immediate settlement, primary settlement, and secondary settlement. Immediate settlement (pseudo-consolidation) is caused by the load from the weight of the landfilled waste and the process of mechanical compaction of the waste, which can reach up to 20% of the initial thickness. Primary settlement is caused by biological and physicochemical decomposition processes (e.g., oxidation, incineration, digestion, leaching) of the deposited waste and by the creep process. The processes associated with biodegradation of waste take place over a long period (several to several years), and the settlement volumes resulting from these processes can reach about 20% of the initial thickness of the deposited waste [5, 9]. Secondary settlement is caused by mechanical creep, can last for several decades, and can amount to a few percent of the initial thickness of landfilled waste. The course of the landfill settlement process is shown in Figure 1.



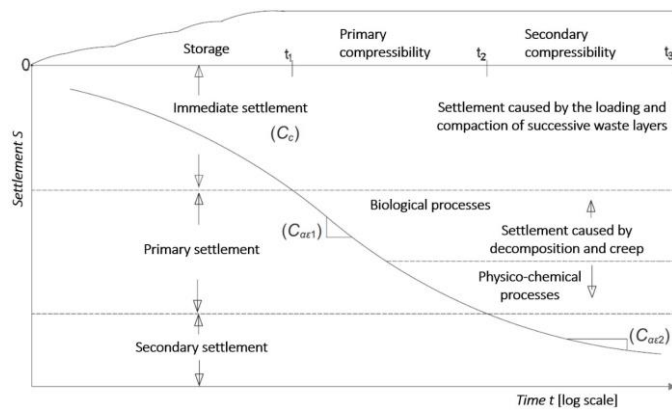


Figure 1. Landfill mass settlement process [8].

The influence of water from precipitation is also a factor in the deformation of the landfill surface. Heavy and torrential rains can lead to soil leaching from the top layer covering and adding weight to the reclaimed landfill. Water infiltration into the landfill can destabilize the slopes and subsequent deformation. Short-term, heavy, and torrential rains are an increasingly frequent phenomenon in a changing climate. The elements of the water balance are shown in Figure 2.

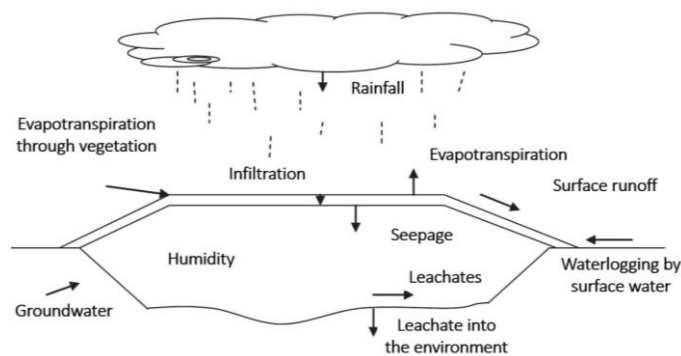


Figure 2. Elements of the landfill water balance [8].

In Poland, the requirement for geodetic monitoring of landfills is set out in the Regulation of the Minister of the Environment of 30 April 2013 on landfills [10]. The Regulation specifies a minimum frequency of landfill surveying every 3 months during the operational and 12 months during the post-operational phases. The monitoring period for landfills is 30 years after closure. The monitoring defined in the regulation consists of controlling the settlement of the landfill's surface by geodetic methods based on measurements of displacements of control points stabilized on the facility's surface and in assessing the stability of slopes determined by geotechnical methods [11]. However, the regulation does not specify the number of monitoring points and their location on the landfill, so the monitored point movements often do not represent the entire landfill area.

Classical geodetic monitoring at landfills is based on the point method - measurements of individual controlled points (points of interest) located on the body of the landfill in various geodetic marks (metal tubes, concrete posts, granite posts). This method makes it possible to accurately determine the movements of the selected points - their size, direction, and speed. It also assumes that the observed points are representative of the phenomenon. A denser network of points

approximates the distribution of displacements more accurately but increases costs and time-consuming measurements. In practice, the determined displacements often do not reflect the actual changes occurring in the object area. Insufficient recognition of the magnitude and directions of these changes may lead to severe damage to the body of the landfill and consequently also endanger the environment and the life and health of people near the landfill [4,12,13].

A solution to this problem may be to use a surface measurement method using Light Detection and Ranging (LiDAR) technology. The surface method involves measuring the entire surface of an object - unstabilized points. This method makes it possible to observe any parts and the whole of the surveyed object. This method is free of the fundamental disadvantage of the point method - the surveyed surface is covered by a much larger number of points (in the LiDAR method, the surveyed surface is covered by millions of points). It is also possible to select observation points that depict the phenomenon depending on its dynamics. However, the disadvantage of this method is that the coordinates of the points are determined with less accuracy than in the point method. In the absence of pre-determined observation conditions and accuracy of results, a good solution is to use a hybrid method, a combination of point and surface methods. Such a strategy allows areas at risk of displacement to be detected and new stabilized points to be established in these areas [7, 13-17].

This paper presents a case study of the Słabomierz-Krzyżówka landfill site in Poland, where LiDAR-based geodetic monitoring was applied. The measurements used an approach using Airborne Laser Scanning from Unmanned Aerial Vehicles (ALS-UAV) and Terrestrial Laser Scanning (TLS). This paper presents the results of the annual monitoring of one of the slopes of the landfill, which was exposed to both deformations caused by the impact of landfill subsidence and surface water run-off caused by damage to the defenses by wild animals (wild boar, deer).

## 2 MATERIALS AND METHODS

This section presents the characteristics of the study area (Section 2.1) and the measurement equipment used (Section 2.2). The proposed methodology for determining slope deformation from TLS and ALS-UAV measurements is also described (Section 2.2).

### 2.1 Study area

The research object is the reclaimed municipal solid waste landfill "Słabomierz-Krzyżówka". The landfill is located ca. 40 km south-west of Warsaw. The landfill was established in 1970 on the site of an old pit after sand and gravel mining. From 1970 to 1992, unsegregated municipal and industrial waste was deposited in the landfill. From 2016 onwards, only construction ballast waste was deposited at the landfill, such as concrete and concrete rubble from demolition and renovation, mixed concrete waste, brick rubble, ceramic materials, non-conforming compost, and soil, soil, and stones. In 2022, the landfill was closed and rehabilitated. A degassing and drainage network and a vertical screen were built to prevent contaminants' escape. The target reclamation of the landfill was set for use as a Renewable Energy Station (RES) with solar panels and a biogas plant. Currently, the landfill site and its

technical facilities cover an area of approximately 14 ha, and the landfill covers an area of approximately 9 ha. The current height of the landfill body is approximately 27 meters measured from its base to the crown of the landfill. There are 15 controlled points (benchmarks) on the site to monitor the settlement of the landfill body. The current appearance of the landfill is shown in Figure 3.



Figure 3. View from the sky of the Słabomierz-Krzyżówka landfill with the study area (marked in red).

The study was carried out on one of the slopes of the landfill, which was exposed to negative external influences and was a representative part of the entire landfill. The study area is marked in red on Figure 3.

## 2.2 Methodology

The monitoring of the study area presented in this article was conducted over a one-year period from March 2023 to March 2024. The representative area of the slope selected in the study covers an area of approximately 2000 m<sup>2</sup>. Due to the vegetation on the landfill, the measurements were carried out in early spring to minimize the influence of the vegetation on the measurement results as much as possible. The survey adopted two approaches: the TLS and ALS-UAV methods. The TLS measurements used a Leica RTC360 scanner, and the ALS-UAV measurements used a LiAir S50 scanner with a Matrice M600 UAV. The LiAir S50 LiDAR system mounted on the platform consists of a scanner, Velodyne's VLP-16, and a Sony A6000 RGB camera. The specification of the instruments used is shown in Figure 4.









Method	TLS	ALS – UAV
Platform		
Features	Leica RTC360 Scanning range: 130 m Distance accuracy: ±2.0 mm (at 100 m) Scanning frequency: 2,000,000 pts/s	Matrice M600 with LiAir S50 Scanning range: 100 m Distance accuracy: ±30.0 mm (at 100 m) Scanning frequency: 300,000 pts/s
Reference targets	 	 DRTK station on reference point
Control targets	 	

Figure 4. Overview of the research measurements.

The measurements were related to reference grid points outside the object's influence area. The resulting point clouds from both methods were oriented in the same coordinate system. Reference matrix coordinates were determined in the PL-2000 coordinate system and PL-EVRF2007-NH height system. For the absolute georeferencing, the TLS scanner stations and reference targets were precisely tied to these external reference points, established through GNSS RTK and angular-linear measurements. The angle-linear network was then aligned using the least squares method. This allowed the TLS data to be transformed into a unified, absolute coordinate system compatible with the ALS-UAV data. For the ALS-UAV method, absolute georeferencing was achieved by integrating D-RTK GNSS corrections with onboard IMU data, UAV positioning sensors during the flight, and reference targets, ensuring precise alignment of the point cloud within the same coordinate system as the TLS data. Two measurement series were carried out (March 2023 and March 2024). A flowchart of the research methodology is shown in Figure 5. The research in flowchart consists of 4 stages: a preliminary study, fieldwork, data processing, and data analysis and results.

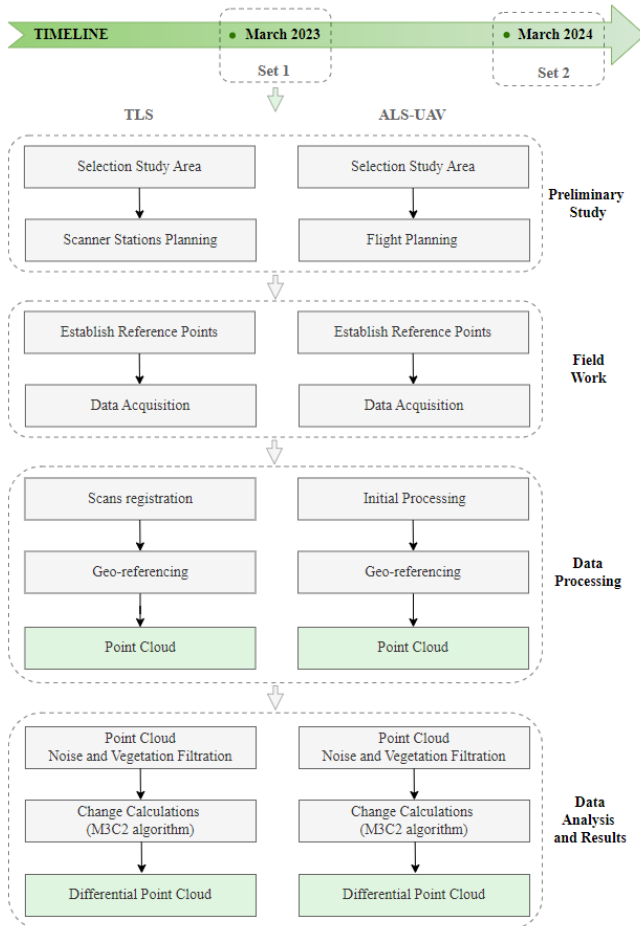


Figure 5. Flowchart of research methodology.

The TLS method first required planning the positions of the scanner stations and reference points (targets on tripods), which were referenced to the reference points (Preliminary study). The positions were planned so that the mutual coverage of scans from successive scanner positions was not less than 50%. It allowed the mutual orientation of the scans to be performed using the cloud-to-cloud (C2C) method. Additionally, overlapping stations were used to strengthen the “connections” between the scans. This strategy allowed mutual orientation of all sites even in the case of a weak “connection” - too few common points between scanner sites. The problem of mutual orientation of the scans is particularly relevant in the case of reclaimed landfills, which are overgrown with lush vegetation. Branches, leaves, and blades of grass moving in the wind can make it difficult to orient the scans using the C2C method. A solution to this problem may be the use of reference spheres. A diagram of the scanner positioning strategy is shown in Figure 6.

The Leica RTC360 scanner used in the survey has a dedicated Leica Cyclone FIELD 360 application, which allows a rough mutual orientation of the scans locally directly in the field. It enables the assessment of whether adjacent scans have the required percentage of mutual coverage and whether there is a need for additional stations. The scans were acquired at a resolution of 3 mm at 10 meters. A total of nine scans were acquired (Field work).

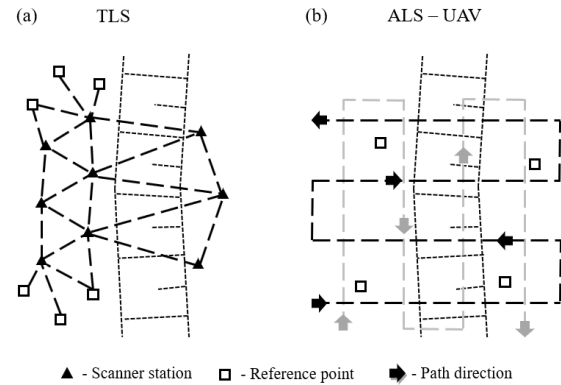


Figure 6. Scheme of measurements by a) TLS and b) ALS – UAV method.

Orientation of the scans was performed using the dedicated Leica Cyclone REGISTER 360 PLUS software (Data processing). The resulting point clouds were de-noised (SOR Filter) and filtered from vegetation (CSF Filter) in Cloud Compare v.2.13.2 [18]. The parameters of the applied filtering were selected empirically (Data analysis and results). The average density of the resulting point cloud was approximately 10,000 pts/m<sup>2</sup>.

(18).

The ALS-UAV method first required planning a flight path (Preliminary study). The flight was performed in two transversely oriented directions (Fig. 6) at an altitude of 50 m. The distance between each flight path was 20 m. During the flight, a D-RTK reference station was used for data reference (Fig. 4). The field-acquired data (Field work) was processed in the dedicated Green Valley LiDAR360 software. The geo-reference of the resulting point cloud was given based on the data from the D-RTK station and the antenna and IMU on board the UAV. As with the TLS data, the resulting point clouds were de-noised and filtered from vegetation in Cloud Compare. The average density of the resulting point cloud was approximately 250 pts/m<sup>2</sup>.

### 3 RESULTS

Based on the obtained point clouds, a differential point cloud was calculated in the Cloud Compare program, representing the deformation of the slope over the annual period for the TLS method (Fig. 7a) and ALS-UAV (Fig. 7b). Differential point cloud was calculated using the Multiscale Model to Model Cloud Comparison (M3C2) algorithm [19,20]. The M3C2 algorithm determines the distance along a local normal vector, estimated from each point's neighborhood. The method considers the surface's local orientation in the distance calculation process. The general principle of the algorithm is based on developing search cylinders along normal vectors to locally average the changes between two point clouds. The parameters in the M3C2 algorithm used were chosen empirically. The best results were obtained with a cylinder size of 25 cm, which was used in the study [19].



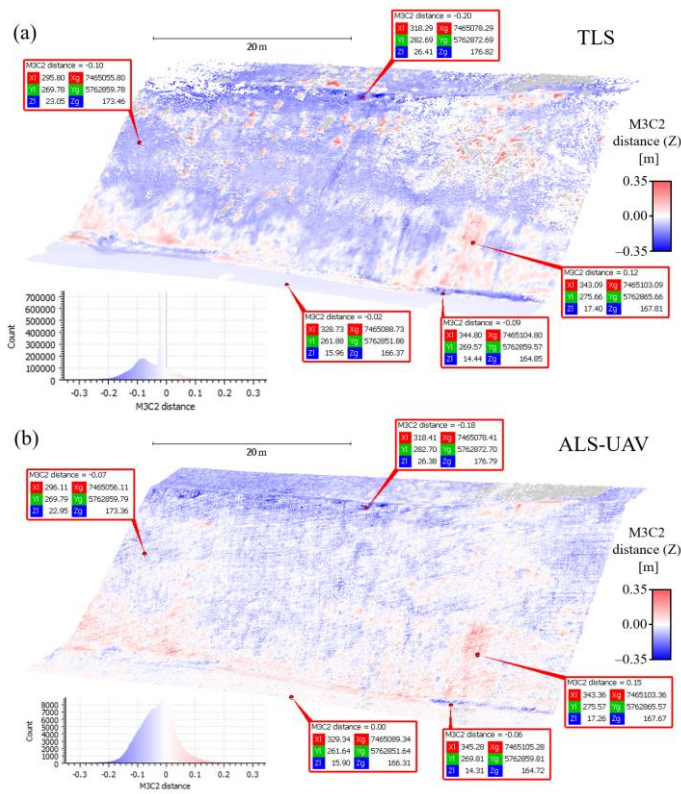


Figure 7. Differential point cloud showing vertical slope displacements from a) TLS and b) ALS-UAV.

Figure 7 shows deformations occurring between March 2023 and March 2024. Figure 7a shows the TLS measurement results, while Figure 7b shows the ALS-UAV measurement results. The blue color shows subsidence, while the red color shows uplift. The absence of changes is marked in white, as indicated in the legend. The range of these values is between -35 and 35 cm. Similar results can be seen in both figures. The most significant subsidence can be seen in the upper and middle parts of the slope, while uplift is noticeable in the lower part of the slope. The values of these changes are approximately -20 cm for the upper part of the slope, approximately -10 cm for the middle part of the slope, and 10 cm for the lower part. This is an expected result and is related to the plastic deformation of the slope caused by the dead weight of the soil and the compaction of waste embedded in the body of the landfill. A diagram of this phenomenon is better shown in Figure 8.

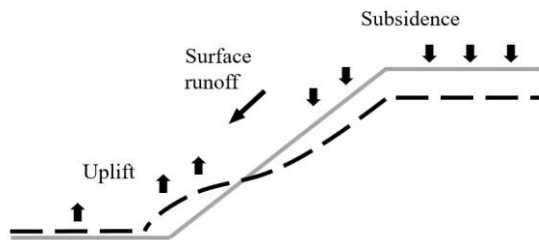


Figure 8. Diagram of the landfill slope deformation process over time.

Figure 8 shows the process of slope deformation over time. Settlement is noticeable in the upper part of the slope, while the slope in the lower part is uplifted by compression of the soil mass. Sometimes, uplift at the foot of the slope may also be caused by the so-called apparent uplift - surface water run-off and deposition of washed-out soil at the foot of the slope. Such a phenomenon can also be observed in Figure 7. At the foot of the slope, between the technical road and the slope, the dark blue longitudinal stripes are a remnant of washed-out soil, which the landfill workers removed as part of maintenance works. The values in this area are approximately -10 cm.

In Figure 7, characteristic features appearing in the two data sets are marked with red references to compare the results. The average difference between the selected points is approximately 3 cm. A differential point cloud was created to compare the two results better, showing the differences between the displacement results of the two methods, TLS and ALS-UAV (Fig. 8).

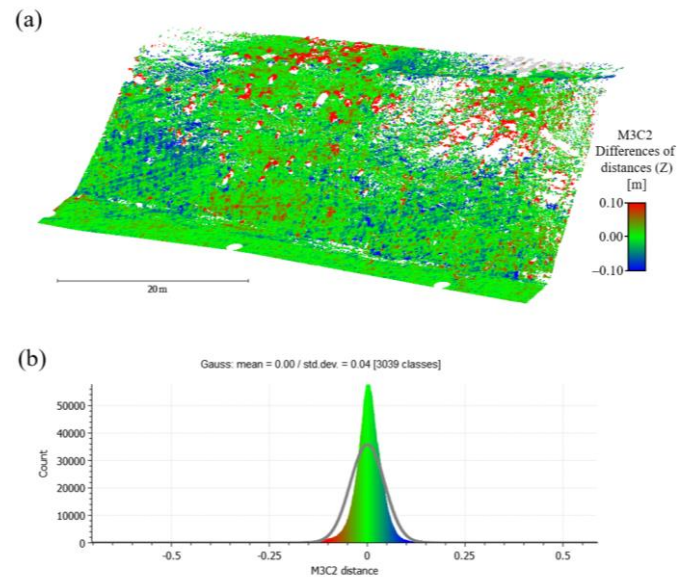


Figure 8. Differential point cloud of displacements from TLS and ALS-UAV (differences of vertical displacements) (a) and histogram of a differential point cloud of displacements (b).

Figure 8 shows the difference between the results of the TLS and ALS-UAV methods (Fig. 8a) and a histogram of the distribution of score values (Fig. 8b). The red and blue colors show significant differences in the results. In contrast, the green color indicates no differences in areas with low or zero values. These values range from -10 to 10 cm. Fig. 8 predominantly shows green points - close to the zero value. This means that the results of both methods were very similar. Possible differences are due to the accuracy of the two measurement methods, the different roughness of the point cloud, the different densities, orientation errors, and the effectiveness of the vegetation filtering. It can be assumed that the TLS method is more accurate than the ALS-UAV method and could be the reference method in the study. However, the TLS method in the application presented here has one key disadvantage - the unfavorable slope scanning angle. The laser scanner beam hits the slope at a vast angle, both in positions below and above the slope, preventing effective vegetation penetration. In contrast to the TLS method, in the ALS-UAV method, the laser beam

strikes almost perpendicular to the scanned area, allowing better vegetation penetration and ground scanning. The most significant differences between the two methods are particularly evident in the central part of the slope, where the ground scanner beam does not reach the ground but only scans the grassroots. This situation can lead to errors in interpreting phenomena occurring in the landfill regarding slope deformation processes.

The histogram in Figure 8b shows the statistical distribution of the differences between the TLS and ALS-UAV methods. The distribution has the character of a normal distribution, with a mean of 0.00 m, showing that there is no systematic shift between the methods. The standard deviation is 0.04 m, which means that most of the differences are within  $\pm 4$  cm, confirming both measurement methods' high consistency and precision.

#### 4 DISCUSSION AND CONCLUSIONS

This paper presents a case study of the Słabomierz-Krzyżówka landfill located in Poland and the results of annual measurements of one of the slopes of the landfill exposed to damaging factors causing its deformation, such as the influence of soil gravity, waste compaction, and surface water run-off. Two measurement methods were adopted in the study: TLS and ALS-UAV.

The results showed that both methods can be effectively used for periodic monitoring of the landfill surface. Similar results were obtained for both methods, demonstrating their effectiveness. Possible differences may be caused by:

- different accuracy of the measurement methods,
- different roughness of the point cloud,
- different density,
- different observation geometry,
- orientation errors,
- or the effectiveness of vegetation filtration.

The TLS method should be assumed to be more accurate than the ALS-UAV method, assuming a suitable measurement methodology. Nevertheless, each method has its advantages and disadvantages. In the case of the TLS method, it was possible to measure with high accuracy and resolution. The disadvantage, however, is the scanner's position, which, in the case of slope scanning, creates an unfavorably wide scanning angle and makes it impossible to scan the ground in the case of high vegetation. The partial solution to this problem can be telescopic tripods, which allow the scanner position to be raised several meters. Changing the scanner's height to a higher one may allow scanning the slope at a better angle but will not solve the problem completely. Another disadvantage is the time-consuming nature of the measurements. In paper [13] the authors compare the acquisition time and processing time of TLS and ALS-UAV measurements. The results show that scanning reclaimed landfills, by the TLS method, is 5 times more time-consuming than by the ALS-UAV method. In the case of large objects, it is necessary to set up additional control points to establish the measurements and maintain adequate accuracy of the results. The overabundance of measurement data can also be a problem. The scanner records two million points per second, which, in the case of measurements at the landfill, translated into the acquisition of approximately 70 million points per measurement site (when using the highest

resolution mode). In the case of the ALS-UAV method, an advantage is the ability to scan a large area of land, which is particularly useful in landfill measurements characterized by a large surface area (up to several tens of hectares). Another advantage is better vegetation penetration and the laser scanner's beam reaching the ground because of almost perpendicular laser beam to the scanned ground. However, the disadvantage of the ALS-UAV method is its lower accuracy than the TLS method. Measurement solutions of this type offer measurement accuracy similar to that of the GPS RTK method. One should also know that using UAVs in air traffic requires appropriate authorizations and competencies. Using this technology is impossible everywhere and under all conditions (direct vicinity of airports, detention centers, and military units).

An important aspect to consider when selecting a measurement method is cost-effectiveness, especially if both methods meet the required accuracy criteria. TLS, while offering higher accuracy, typically incurs higher operational costs due to longer measurement times and the need for specialized equipment and personnel. Conversely, the ALS-UAV method can rapidly cover larger areas, potentially lowering labor and time expenses. However, initial investment in UAV equipment and obtaining necessary flight authorizations can be significant. Compared to traditional surveying methods, both TLS and ALS-UAV provide improved efficiency and richer data, but the overall cost-effectiveness depends mainly on the specific project scale and requirements. Including an economic evaluation alongside technical factors offers a more comprehensive basis for choosing the optimal measurement approach.

The LiDAR monitoring applied allowed for a comprehensive assessment of slope deformation on an annual basis. Comparison of the data between the two measurement series made it possible to identify the general trends of the landfill slope settlement and the local deformations caused by external phenomena, such as surface erosion caused by rainwater.

The use of LiDAR technology - in both the TLS and ALS-UAV methods - significantly increased the efficiency of the measurements compared to the traditional point method. Thanks to the obtained point clouds, it was possible to detect displacements, visualize them spatially, and analyze the direction and intensity of deformation. The ALS-UAV method allowed a larger area to be measured quickly and comprehensively, while TLS provided data with a higher local resolution.

Periodic monitoring using LiDAR can be critical in the decision-making and design process. The ALS-UAV method allows data collection over a large area in a short time with high spatial and temporal resolution. It is also a non-invasive method. The person carrying out the measurement is not exposed to direct contact with factors negatively affecting human health, such as biogases or leachates. On the other hand, the TLS method provides high-accuracy data, allowing detection of even the smallest damage. The best way to monitor reclaimed landfills will be to integrate both methods and use each method's advantages. TLS data can also be a source for referencing or validating ALS-UAV data to improve accuracy.

## REFERENCES

- [1] Główny Urząd Statystyczny [GUS] (2020). Składowiska (P2840). Retrieved from: <https://bdl.stat.gov.pl/bdl/dane/podgrup/tablica> [accessed 07.04.2025].
- [2] Council Directive 1999/31/EC of April 26 1999 on the landfill of waste. OJ L 182/1 of 16.07.1999.
- [3] Koda E, Rybak-Niedziółka K, Winkler J, Černý M, Osiński P, Podlasek A, et al. Space Redevelopment of Old Landfill Located in the Zone between Urban and Protected Areas: Case Study. *Energies*. 2022 Jan;15(1):146.
- [4] Pasternak G, Pasternak K, Koda E, Ogrodnik P. Unmanned Aerial Vehicle Photogrammetry for Monitoring the Geometric Changes of Reclaimed Landfills. *Sensors*. 2024 Jan;24(22):7247.
- [5] Koda E. Stateczność rekultywowanych składowisk odpadów i migracja zanieczyszczeń przy wykorzystaniu metody obserwacyjnej. *Rozprawy Naukowe i Monografie Szkoła Główna Gospodarstwa Wiejskiego w Warszawie* [Internet]. 2011 [cited 2024 Nov 24];(384). Available from: <http://agro.icm.edu.pl/agro/element/bwmeta1.element.agro-80cc3ebf-5289-4222-91fc-989299d8734a>
- [6] Pasternak G. Geodetic monitoring of geotechnical structures displacements: a case study of Radiowo landfill site in Warsaw. *Acta Scientiarum Polonorum Architectura*. 2022;21(2):75–83.
- [7] Eugeniusz Koda, Jarosław Chormański, Grzegorz Pasternak, Piotr Osiński, Jacek Jóźwiak. Drones capabilities and use in post remediated landfill sites development plans. *ISSMGE* [Internet]. 2022 Jul [cited 2024 Aug 15]; Available from: <https://doi.org/10.53243/ICEG2023-200>
- [8] Koda E. Stateczność rekultywowanych składowisk odpadów i migracja zanieczyszczeń przy wykorzystaniu metody obserwacyjnej (Landfill stability under reclamation and pollutant transport using the observational method). 2011.
- [9] Koda E. Stateczność rekultywowanych składowisk odpadów i migracja zanieczyszczeń przy wykorzystaniu metody obserwacyjnej (Landfill stability under reclamation and pollutant transport using the observational method). [cited 2024 Nov 24]; Available from: [https://www.akademia.edu/54690457/Stateczno%C5%9B%C4%87\\_rekultywowanych\\_sk%C5%82adowisk\\_odpad%C3%B3w\\_i\\_migracja\\_zanieczyszcze%C5%84\\_przy\\_wykorzystaniu\\_metody\\_obserwacyjnej\\_Landfill\\_stability\\_under\\_reclamation\\_and\\_pollutant\\_transport\\_using\\_the\\_observational\\_method](https://www.akademia.edu/54690457/Stateczno%C5%9B%C4%87_rekultywowanych_sk%C5%82adowisk_odpad%C3%B3w_i_migracja_zanieczyszcze%C5%84_przy_wykorzystaniu_metody_obserwacyjnej_Landfill_stability_under_reclamation_and_pollutant_transport_using_the_observational_method)
- [10] Rozporządzenie Ministra Środowiska z dnia 30 kwietnia 2013 r. w sprawie składowisk odpadów [Internet]. [cited 2024 Aug 15]. Available from: <https://isap.sejm.gov.pl/isap.nsf/DocDetails.xsp?id=WDU20130000523>
- [11] Rozporządzenie Ministra Środowiska z dnia 9 grudnia 2002 r. w sprawie zakresu, czasu, sposobu oraz warunków prowadzenia monitoringu składowisk odpadów. [Internet]. [cited 2024 Nov 24]. Available from: <https://isap.sejm.gov.pl/isap.nsf/DocDetails.xsp?id=WDU2002201858>
- [12] Geodezyjne metody badania osuwisk | Wydawnictwo AGH [Internet]. [cited 2024 Nov 24]. Available from: <https://www.wydawnictwo.agh.edu.pl/produkt/658-geodezyjne-metody-badania-osuwisk>
- [13] Pasternak G, Zaczek-Peplinska J, Pasternak K, Jóźwiak J, Pasik M, Koda E, et al. Surface Monitoring of an MSW Landfill Based on Linear and Angular Measurements, TLS, and LIDAR UAV. *Sensors*. 2023 Jan;23(4):1847.
- [14] DE WET A. Discovering and Characterizing Abandoned Waste Disposal Sites Using LIDAR and Aerial Photography. *Environmental & Engineering Geoscience*. 2016 May 1;22(2):113–30.
- [15] Stewart JP, Hu J, Kayen RE, Lembo AJ, Collins BD, Davis CA, et al. Use of Airborne and Terrestrial Lidar to Detect Ground Displacement Hazards to Water Systems. *Journal of Surveying Engineering*. 2009 Aug 1;135(3):113–24.
- [16] Baiocchi V, Napoleoni Q, Tesei M, Servodio G, Alicandro M, Costantino D. UAV for monitoring the settlement of a landfill. *European Journal of Remote Sensing*. 2019 Dec 6;52(sup3):41–52.
- [17] Pasternak G, Pasternak K, Koda E, Ogrodnik P. Unmanned Aerial Vehicle Photogrammetry for Monitoring the Geometric Changes of Reclaimed Landfills. *Sensors*. 2024 Jan;24(22):7247.
- [18] Zhang W, Qi J, Wan P, Wang H, Xie D, Wang X, et al. An Easy-to-Use Airborne LiDAR Data Filtering Method Based on Cloth Simulation. *Remote Sensing*. 2016 Jun;8(6):501.
- [19] Lague D, Brodu N, Leroux J. Accurate 3D comparison of complex topography with terrestrial laser scanner: Application to the Rangitikei canyon (N-Z). *ISPRS Journal of Photogrammetry and Remote Sensing*. 2013 Aug;82:10–26.
- [20] DiFrancesco PM, Bonneau D, Hutchinson DJ. The Implications of M3C2 Projection Diameter on 3D Semi-Automated Rockfall Extraction from Sequential Terrestrial Laser Scanning Point Clouds. *Remote Sensing*. 2020 Jan;12(11):1885.





# International SHM Standards and Guidelines

# Global Perspectives on Structural Monitoring in Civil Engineering

Frank A. Lehmann<sup>1</sup>, 0000-0002-0192-7364, Falk Hille<sup>2</sup>, 0000-0002-2697-5370, Branko Glišić<sup>3</sup>, 0000-0002-1852-5310

<sup>1</sup>Materials Testing Institute (MPA), University of Stuttgart, Pfaffenwaldring 2b, 70569 Stuttgart, Germany

<sup>2</sup>Federal Institute for Materials Research and Testing (BAM), Unter den Eichen 87, 12205 Berlin, Germany

<sup>3</sup>Princeton University, E330 Engineering Quadrangle, Princeton, New Jersey 08544, USA

e-mail: frank.lehmann@mpa.uni-stuttgart.de, falk.hille@bam.de, bglicis@princeton.edu

**ABSTRACT:** Structural Monitoring (SM) is crucial in civil engineering for ensuring the safety, functionality, and longevity of civil infrastructure, especially bridges. As its importance grows, SM practices are guided mainly by national standards, leading to fragmented approaches and limited global integration. This paper examines SM guidelines, focusing on contributions from Germany, while exploring the broader international framework.

In Germany, key guidelines such as the DGZfP Merkblatt B09 and others offer structured methods and practice examples for long-term monitoring and performance assessment. Internationally, countries have developed their own SM frameworks. Amongst others, Austria's RVS Richtlinie 13.03.01, France's COFREND Livre Blanc, Canada's ISIS Guidelines, the ACI Report 444.2-21 from the USA, the TRB Circular E-C246 and the CIRIA Guideline from the UK contribute to a global understanding of SM. These guidelines address common technical, theoretical, and economic challenges across regions.

This paper highlights the need for international collaboration, identifying synergies and gaps to promote a unified approach to SM. It offers insights into global standards and how successful strategies can foster innovation and cohesion in SM practices worldwide.

**KEY WORDS:** Structural Monitoring, International Guidelines.

This paper adopts the term structural monitoring (SM) instead of the more commonly used structural health monitoring (SHM), following the definition provided in the Transportation Research Circular E-C246 [1]. While SHM is widely recognized, its interpretation varies across disciplines, leading to ambiguity, particularly regarding the meaning of "health" in an engineering context. By contrast, SM explicitly refers to the automated, technology-driven collection of structural data over time to objectively assess performance, without implying a predefined goal such as "health", thereby broadening its applicability. Adopting this terminology helps ensure clarity and consistency, emphasizing the role of continuous, instrumented monitoring as a valuable complement to conventional structural assessment methods.

## 1 THE IMPORTANCE OF STRUCTURAL MONITORING IN MODERN INFRASTRUCTURE GUIDELINES

The increasing complexity and age of infrastructure necessitate advanced monitoring techniques to detect and address potential issues proactively. SM is a critical practice for ensuring the safety, functionality, and longevity of civil infrastructure, particularly bridges. By continuously assessing structural conditions, SM enables the early detection of potential issues, allowing for timely maintenance and preventing failures. This proactive approach not only enhances public safety but also contributes to the sustainable development of infrastructure by extending its service life.

The evolution of SM has been marked by significant advancements in sensor technology, data acquisition systems, and analytical methods. Modern SM systems employ a variety of sensors to monitor parameters such as strain, vibration, and

temperature, providing comprehensive insights into structural performance. The integration of artificial intelligence and machine learning algorithms further enhances the ability to interpret complex data, facilitating automated damage detection and assessment.

Despite technological advancements, the implementation of SM is often shaped by national standards, resulting in fragmented methodologies and limited global integration. While Germany, for example, has developed comprehensive guidelines like the DGZfP Merkblatt B09 (2022) to standardize monitoring practices, similar guidelines exist in other countries, with many offering largely the same content. This suggests that the diversity in approaches is unnecessary. However, factors such as local or strategic interests, language barriers, lack of networking, economic considerations, varying financial framework conditions (such as budget constraints, funding availability, and investment priorities), the local acceptance of structural monitoring, and some isolated differences in scientific perspectives, though less prominent in practical implementation, continue to prevent a unified, global approach to SM. Additionally, the differing levels of acceptance of relatively new and unestablished methods in civil engineering, such as Structural Monitoring, remain a decisive factor, as some regions embrace innovative techniques while others remain hesitant to adopt them.

To address these challenges, there is a need for increased international collaboration and the development of standardized SM protocols. By harmonizing guidelines and sharing best practices, the global engineering community can enhance the effectiveness of SHM systems, leading to more resilient and sustainable infrastructure worldwide.

## 2 SM GUIDELINES IN GERMANY

In Germany, the significance of SM has been recognized through the development of a robust monitoring framework through a series of comprehensive guidelines, particularly for bridges and other civil engineering structures and aimed at standardizing monitoring practices. Together, these guidelines emphasize a data-driven approach for maintaining usability and availability of infrastructure and generally the preservation of structures.

These guidelines collectively contribute to a structured approach in SM within Germany, promoting uniformity in monitoring practices. The development of such guidelines is crucial, as it offers building owners and operators a framework for implementing effective monitoring systems, thereby enhancing decision-making processes related to construction and maintenance. By establishing clear protocols and methodologies, the guidelines aim to reduce fragmentation in monitoring approaches and promote a unified strategy for ensuring structural integrity.

### 2.1 DGZfP Merkblatt

Notably, the German Society for Non-Destructive Testing (DGZfP) has been instrumental in this endeavor. The publication of the DGZfP Merkblatt B 09 “Dauerüberwachung von Ingenieurbauwerken” [2] provided a cornerstone resource for owners, operators, and planners, detailing established methods for long-term monitoring and performance evaluation of civil engineering structures with a particular focus on concrete and prestressed concrete bridges. The document provides a practical guideline to help stakeholders implement effective monitoring solutions while considering the unique conditions of each structure. It delivers the necessary knowledge for the optimal design, installation, and operation of monitoring systems.

The guideline offers an overview of suitable technical systems and sensors designed for long-term structural monitoring. It differentiates SM from temporary inspection, emphasizing that monitoring does not replace regular structural inspections but serves as a crucial supplement by providing real-time condition assessments and detection of time-varying parameters.

A key focus of the document is the conceptual design of monitoring systems, from preliminary investigations, the definition of measured variables, the decision for or against a monitoring system, basic considerations for safety-relevant monitoring systems, the selection of suitable sensors, definition of measuring points, sensor connection/signal transmission, power supply, control, data verification, data storage, evaluation and alarming to the external communication connection and control of actuators.

It outlines the specific questions that monitoring can help answer. Unlike most other documents, which primarily describe existing sensor technologies and leave it to the reader to determine their applicability to a given monitoring task or rather generally to a question that may be answered with the help of SM, this guideline approaches monitoring from the end user's perspective, making it more accessible. The addressed monitoring tasks range from geometric aspects (strains, displacements, deflections, inclinations) to crack monitoring, force and strain measurements, vibration and shock monitoring,

material moisture, corrosion, prestressing wire breakage detection and the influencing factors of temperature, humidity, traffic loads, etc., which must always be taken into account.

Additionally, the leaflet emphasizes data management, ensuring that collected information is effectively processed and utilized. Like many other referenced documents, it also provides detailed examples of real-world implementations. [3], [4]

### 2.2 DBV Merkblatt

A different focus is set in the DBV Merkblatt “Brückenmonitoring” [5]. Issued by the German Society for Concrete and Construction Technology (DBV), the guideline addresses the monitoring of bridge structures, although it is also applicable to other engineering structures and buildings. It details the services that need to be tendered when implementing a structural monitoring system and highlights the economic considerations involved in such measures. It is less technical than the DGZfP guideline and aims specifically at administrations and engineering offices responsible for preparing tenders, helping them assess whether structural monitoring is a cost-effective option for their specific projects.

The guideline defines relevant actors and comprehensively structures the monitoring process in different phases, beginning with defining the monitoring task, followed by the development of a qualified monitoring concept, implementation planning, installation and operation, data processing, data analysis and concluding with the evaluation of monitoring results. The structured process is supplemented by considerations on quality assurance and information on tendering.

As structural monitoring is not yet a standardized service in civil engineering, the guideline also provides insights into the economic viability of monitoring measures, helping stakeholders evaluate the financial feasibility of these activities in relation to the benefits they bring.

### 2.3 DIN 1076

In the context of this compilation, the new DIN 1076 [6] is the most authoritative document in terms of recognition, dissemination, acceptance and legal validity. However, as a general standardization document, it takes a more global approach and does not provide detailed guidance on planning, tendering, or implementation of monitoring systems. The standard explicitly permits the use of monitoring systems under specific conditions and for certain purposes, recognizing their value in preventive structural preservation.

DIN 1076 highlights two key applications for monitoring in the context of the standard: supplementing regular structural inspections and addressing special situations, such as the end of a structure's service life or ensuring structural and traffic safety. It mandates that monitoring data must provide clear condition assessments that can be incorporated into overall structural evaluations. In safety-critical applications, the standard requires defining warning or threshold values along with clear instructions for responsible personnel.

Each monitoring application must follow a detailed, structure-specific assessment program covering the entire process (based on the DBV Merkblatt). The selected measurement methods must reliably detect the type, extent, and progression of damage or defects.



Overall, the standard takes a very conservative and selective approach to monitoring, limiting its scope to structural testing under DIN 1076. However, it leaves room for effective and beneficial use of monitoring in other defined applications.

In summary, DIN 1076 is very conservative and exclusive with regard to monitoring. Yet, it does not mandate the use of monitoring but defines specific applications where monitoring can be considered "in accordance with DIN 1076". However, the scope and reasons for using SM extend far beyond these applications, which are not covered by the standard but still remain valid and necessary. This flexibility allows for other approaches to use monitoring sensibly, effectively and profitably, which are defined in other documents within this compilation.

#### 2.4 *BASf Leitfaden*

The recent BASf "Leitfaden Strategischer Einsatz von Monitoring für Ingenieurbauwerke" [7] offers strategic recommendations for the use of monitoring in engineering structures. It summarizes the state of the art, limits and potentials for monitoring in Germany, taking particular account of the three documents [2], [5] and [6]. In addition, it explicitly addresses why the possibilities of monitoring have not yet been used to the extent that they could be and how acceptance could be improved.

Data management considerations form a large part of the guideline, as the sustainable storage of monitoring data, easy accessibility and systematic evaluation are central to effective monitoring projects.

#### 2.5 *BASf Erfahrungssammlung*

The complementary BASf "Erfahrungssammlung Monitoring für Brückenbauwerke" [8], compiled by the Federal Highway Research Institute (BASf), provides a comprehensive collection of practical experiences in bridge monitoring, complementing previous documents. It offers insights into the application, capabilities, and limitations of monitoring systems.

In its general section, the document outlines the state-of-the-art in bridge monitoring, reflecting the contents of the DGZfP and DBV Merkblatt. It follows a similar structure to the DGZfP Merkblatt, addressing key aspects from an end-user perspective, such as deformation, inclination, temperature, and crack monitoring, among others. It explains how different measurement techniques align with monitoring objectives and discusses their reliability, limitations, and quality assurance. The second part presents real-world examples, detailing the reasons for monitoring, the methods used, and key findings.

### 3 INTERNATIONAL SM FRAMEWORKS

SM practices have evolved worldwide to address regional infra-structure challenges and priorities. Despite variations in methodologies, national guidelines share common goals of ensuring safety, reliability, and long-term functionality of civil structures. This section explores international SM frameworks, focusing on selected approaches adopted in countries such as Austria, France, the US, Canada, and the UK.

#### 3.1 *Austria*

Austria's RVS guideline RVS 13.03.01 "Monitoring von Brücken und anderen Ingenieurbauwerken" [9] provides a structured framework for the monitoring of bridges and other

civil engineering structures, reflecting the country's commitment to SM. Compared to other referenced documents, it is relatively concise, comprising 32 pages, with a structure comparable to the DGZfP Merkblatt. One notable feature of the guideline is its classification of monitoring into local vs. global and static vs. dynamic approaches, each accompanied by a brief summary outlining the objectives and applicable sensor technologies. While this classification provides a structured perspective, it remains open to debate whether it offers significant practical advantages in the retrievability of information.

A novel aspect that distinguishes the RVS guideline from other standards is its Safety Management Plan (SMP), which defines action sequences, assigns responsibilities, and references pre-established warning and alarm thresholds. The guideline specifies the content of such a plan and introduces a process scheme incorporating a traffic light system (green, orange, red) to represent different alert levels, ranging from normal operation (green) to immediate intervention, such as bridge closure (red).

Additionally, an annex provides an overview of various measurement instruments referenced in the guideline, briefly explaining their principles of operation. A second appendix explores the role of the Internet of Things (IoT) in structural monitoring, emphasizing its relevance for data acquisition and management in modern SHM systems.

#### 3.2 *France*

The COFREND "Le Livre Blanc du SHM" [10] has a different focus and approach than other referenced international SHM guidelines. Rather than detailing the technical implementation of monitoring systems, it addresses overarching challenges associated with SM, including scientific and technological hurdles, regulatory concerns, and intellectual property issues.

This white paper is the result of discussions within COFREND's SM branch to develop a national strategy for SM in France. The document outlines key aspects of the field, such as its historical background, market potential, and major scientific and industrial challenges. It highlights the growing demand for SM in sectors like civil engineering, aerospace, and industrial equipment, where aging infrastructure and safety concerns drive the need for continuous monitoring solutions.

A central theme of the Livre Blanc is the necessity for structuring an SM industry in France. It emphasizes the need for standardized methodologies, interoperable systems, and regulatory frameworks to enable widespread adoption. Additionally, it discusses how digital technologies such as IoT, AI, and digital twins are transforming SM by enabling real-time monitoring and predictive maintenance.

The document also examines international approaches, comparing France's SM landscape with that of the US, Germany, and the UK. By advocating for a coordinated effort among stakeholders, the Livre Blanc aligns with the ambitions of the present paper, which aims to structure international efforts in SM. It reinforces the necessity of global collaboration, regulatory alignment, and knowledge exchange to drive innovation and ensure the reliability of SM systems worldwide.

### 3.3 Italy

The MIT guideline “Linee guida per la classificazione e gestione del rischio, la valutazione della sicurezza ed il monitoraggio dei ponti esistenti” [11], that has been continuously updated since its first publication, presents a discussion on the permanent and continuous monitoring of bridges, outlining the key principles, necessary technologies, and critical applications of SM systems. The chapter on monitoring is framed within a broader context of visual inspections, risk assessment, and safety evaluations, positioning SM as a complementary tool alongside routine inspections, load testing, and numerical degradation analysis. Rather than being an isolated process, continuous monitoring is presented as an integral component of a comprehensive strategy for bridge management, enhancing both preventive maintenance and decision-making processes.

The document carries a strong authoritative tone by advocating for the mandatory use of SM in high-risk scenarios, particularly for aging or strategically important bridges. It emphasizes the importance of long-term surveillance, particularly for large, complex, or high-risk structures, and highlights the operational requirements for implementing effective monitoring strategies.

The text underscores the necessity of carefully designing SM systems to ensure durability, accuracy, and maintainability. It addresses fundamental aspects such as sensor selection, network architecture, power supply, and data processing, with a strong emphasis on integrating SM data into a broader bridge management system. The document also details specific applications of SM, including structural, seismic, geotechnical, hydraulic, and landslide monitoring. For each of these, it describes the most suitable technologies and analytical methods, ranging from dynamic response measurements for structural assessments to advanced remote sensing techniques for landslide detection.

A key argument is that continuous monitoring enables early detection of structural deterioration, environmental hazards, and other risk factors, facilitating data-driven maintenance and decision-making. The discussion particularly stresses the value of integrating SM with real-time communication networks and automated data analysis to provide accurate, actionable insights into bridge behavior over time.

The UNI/TR 11634 guideline “Linee guida per il monitoraggio strutturale” [12], by reference of [13] and [14], establishes a structured approach to SM, emphasizing its role in supporting asset management decisions. It outlines the entire monitoring process, covering system design, implementation, and data analysis. The document provides criteria for developing SM systems and identifies appropriate methodologies for evaluating structural conditions based on different classes and types.

An aspect of the guideline is its focus on data processing methods, which leverage both data-driven and model-based techniques to assess structural integrity. It also defines the essential components of an SM system, detailing the processes for detecting structural damage and material degradation. Furthermore, the report discusses best practices for system installation, maintenance, and data acquisition to ensure effective monitoring and long-term performance.

### 3.4 United States

The ACI PRC-444.2-21 report “Structural Health Monitoring Technologies for Concrete Structures” [15] provides a comprehensive examination of structural monitoring (SM) technologies applicable to concrete structures. Building upon an in-depth discussion of relevant material properties and the unique characteristics of concrete, the report systematically explores available sensor types, their underlying physical principles, and the specific monitoring objectives they serve. Additionally, it outlines the necessary measurement equipment, deployment methodologies, and existing standards and codes of practice.

The report adopts an academic approach, extensively referencing scientific literature, thus enabling readers to deepen their understanding of the subject matter. Rather than presenting information in a condensed form, the document offers a thorough insight into sensor technologies, categorizing them into three main types: structural response sensors, environmental condition and load sensors, and supporting technologies.

Complementing this perspective, the Transportation Research Board’s Circular E-C246 “Structural Monitoring” [1] provides a broader, application-oriented discussion of SM. Unlike the ACI report, which focuses on technical aspects, this document addresses the practical implementation of monitoring systems from the perspective of potential clients rather than monitoring specialists. It highlights synergies between SM and traditional visual inspections, discusses key considerations for deciding when monitoring is warranted, and outlines the expected benefits.

The circular briefly introduces relevant sensor types based on their measured parameters, such as inclination, acoustic emission, and temperature. A notable aspect is the emphasis on a progressive diagnostic approach, wherein monitoring is continuously refined to determine whether more extensive data collection is necessary in a cost-effective manner. This process accounts for multiple factors, including preliminary information gathering, structural criticality, financial constraints, installation feasibility, durability, and data management. Moreover, the document distinguishes itself by addressing the financial return of SM investments, outlining strategies for evaluating cost-effectiveness in advance. A dedicated FAQ section further enhances its practical utility by succinctly answering common questions related to SM implementation.

### 3.5 Canada

Canada’s ISIS “Guidelines for Structural Health Monitoring” [16] represents one of the foundational references on SM included in this compilation. As an early comprehensive guideline outside the academic context, it contextualizes modern SM within the broader framework of various testing methodologies used to assess the in-situ condition and performance of structures under different load scenarios and potential damage conditions. The document systematically categorizes these methodologies based on the frequency and duration of measurements, distinguishing between static field testing, dynamic field testing, periodic monitoring, and continuous monitoring, the latter of which is now commonly referred to as structural monitoring.

Each of these testing approaches is introduced in detail, outlining its specific objectives, practical implementation strategies, and the potential benefits it offers for structural assessment. Moreover, the guideline provides multiple real-world case studies to illustrate the practical application and effectiveness of the described methods in diverse structural contexts.

The appendices of the manual offer additional technical depth, including explanations of the operational principles of selected sensor technologies, an introduction to data acquisition systems, and an overview of various algorithms used for vibration-based damage detection. While the sections on sensor technology and data acquisition have become somewhat outdated due to significant technological advancements since the publication of the manual, they still serve as a valuable foundation for understanding fundamental principles.

### 3.6 United Kingdom

The CIRIA guide “Structural Health Monitoring in Civil Engineering” [17] provides a comprehensive, low-level introduction to SM for various stakeholders, including infrastructure owners, operators, and engineers. The guide begins by defining SM and explaining its role in risk management for civil infrastructure. It highlights how SM can support intervention planning by providing valuable data to enhance safety, reduce costs, and extend the lifespan of assets.

A key focus of the guide is distinguishing between traditional visual inspections, periodic manual assessments, and automated continuous monitoring, emphasizing the advantages of sensor-based SM. The document underscores the importance of data quality, modeling, and redundancy in effective monitoring systems, recognizing data as the “currency” of SM.

The guide discusses the business and technological drivers behind SM adoption, outlining both proactive and reactive applications. It provides guidance on conceptual design and implementation, including sensor selection and system integration. A dedicated chapter addresses data management, storage, security, ownership, and analysis, ensuring the effective use of collected information.

Procurement considerations, risk assessment, and specification requirements are also covered in detail, offering a structured approach for organizations planning to implement SM. Additionally, the guide presents real-world case studies that illustrate the practical applications of SM, detailing the sensors used, data acquisition strategies, and resulting insights.

### 3.7 China

The accessibility of Chinese SM standards to the international community is often hindered by language barriers and differences in normative frameworks. Unlike widely adopted international standards, Chinese regulations and guidelines are primarily available in Mandarin, making it challenging for non-Chinese researchers and practitioners to engage directly with them. However, it is possible to gain indirect insight into the scope of Chinese SM standards by referencing available review documents, such as [18] or [19].

The extent of standardization efforts in China is remarkable, with a vast array of documents addressing various aspects of SM at multiple regulatory levels. These include national standards, which apply nationwide, professional standards that govern specific industry sectors, as well as provincial and

company-level regulations. An often-cited national standard in this context is the GB 50982 technical code [20], that is discussed in detail in [21].

Instead of detailing the full list of normative documents available in China in a reproduction of the aforementioned articles, it is noteworthy to highlight the early adoption and impressive breadth of topics already addressed within their SM standards. These standards begin with foundational aspects, including the definition of basic terms and concepts, and extend to more specific areas such as SM design standards, operational maintenance, and management practices for SM systems. Additionally, there are guidelines governing the construction and acceptance of SM systems, as well as those focused on massive data processing for SM applications. Notably, China's SM standards also include regulations tailored to specific infrastructure types, such as bridges, with comprehensive technical codes and specifications. These bridge-related standards cover critical aspects such as fiber optic monitoring systems, concrete bridge monitoring, threshold levels for intervention, and the selection and placement of sensors.

The breadth and depth of this standardization effort suggest a strong institutional commitment to SM, reflecting the country's large-scale infrastructure development and emphasis on long-term structural safety and reliability.

### 3.8 Others

One relevant document outside national application, of a very general nature, is the FIB Bulletin 109 [22]. One of the chapters is devoted to certain aspects of structural monitoring, in the wider context of structural condition survey (in particular NDT and load testing), condition assessment and sensor placement.

Other specific national standards or guidelines for SM in civil engineering are not prominently documented in the available literature. While [23] references a withdrawn Russian standard [24], comprehensive national frameworks remain scarce. Some ISO standards address related aspects, such as vibration monitoring, but do not specifically focus on structural monitoring as a whole. Instead, much of the existing knowledge is found in scientific literature and technical reports. Notable examples of research results include, amongst others, and without assessing their value above others without further review, the SAMCO report [25], the Sustainable Bridges Report [26], the SMooHS Report [27], or the recent IM-SAFE Reports [28], which provide valuable insights into monitoring methodologies, system design, and long-term structural assessment. However, these documents primarily originate from research initiatives rather than regulatory bodies, highlighting the ongoing need for standardized international guidelines in structural monitoring.

## 4 SYNERGIES AND CHALLENGES

A shared objective in structural monitoring (SM) guidelines is to ensure the safety, reliability, and longevity of civil infrastructure. These guidelines reflect the diverse needs, priorities, and technical capabilities of different countries, addressing common challenges and promoting best practices globally.

### 4.1 Synergies

Despite differences in local infrastructure conditions, economic constraints and environmental factors, there are surprisingly no



significant differences, only variations in focus, in methodologies, performance metrics and monitoring technologies. One reason for this may be that the technical challenges are comparable, which ultimately leads to similar guidelines. This basic agreement helps efforts to develop a unified approach. Therefore, a list of key aspects can be extracted from the different guidelines, which are relevant to be taken into account in a common effort for a harmonized monitoring strategy.

- Definition of terms and notations: While terminology is often similar across guidelines, differences exist. For example, the distinction between SM and structural health monitoring (SHM) varies. A clear definition of terms is crucial to ensure consistency and avoid ambiguity in communication and implementation.
- Promoting the benefits of SM: Guidelines highlight achievable goals, such as enhanced safety and risk reduction, while also acknowledging scientific technological challenges, i.e., what can not be achieved by employing SM. They emphasize early detection and prevention of structural degradation through continuous monitoring, proactive measures to mitigate risks, and data-driven strategies for assessing infrastructure health and performance.
- SM in civil engineering and other industries: Structural monitoring in civil engineering is placed in the broader context of its application in other industries, such as aeronautics, space, mechanical engineering, energy, and automotive sectors. These comparisons provide insights into cross-sector best practices and technological advancements.
- Locally governing codes, standards, and practices: SM guidelines must align with national and international regulatory frameworks, integrating with existing structural assessment methods such as visual inspections, load tests, and non-destructive testing. They also play a role in maintenance planning and intervention strategies.
- Criticality and asset value considerations: The relevance of SM depends on factors such as a structure's criticality, asset value, and degradation state. Guidelines help prioritize monitoring efforts based on risk assessment and long-term economic benefits.
- Monitoring-relevant characteristics of structures and materials: Guidelines address the unique monitoring needs of different structures and materials, considering their physical properties, environmental influences, and long-term durability. The focus is often on bridges, especially those of reinforced and prestressed concrete, most likely because a large proportion of the monitoring systems installed to date have been applied to such structures, and therefore a wealth of experience is available and the need for regulation is particularly great.
- Preliminary research and assessment: Prior investigations are necessary to determine monitoring scope, relevant parameters, priority structures, and measurement locations. NDT techniques play a crucial role in identifying potential vulnerabilities and optimizing monitoring strategies. Based on these investigations, numerical models and simulations play an essential role in the further planning of monitoring systems for complex structures, broadly defined problems and unclear structural behaviour, in order to be able to estimate the sensitivity of SM systems with regard to the desired objectives.
- Cost-benefit analysis of SM implementation: Guidelines provide methodologies for estimating financial benefits, considering cost-effectiveness and the value chain. Decision-makers can evaluate whether implementing SM is justified for specific projects.
- Monitoring process and stakeholder responsibilities: Information is provided on the entire monitoring process, including relevant stakeholders, their responsibilities, the division of tasks, and the coordination required to ensure effective decision-making.
- Procurement and tendering processes: Guidelines outline necessary specifications for tendering SM systems to ensure meaningful, comparable, and complete bids. They also address procurement considerations from a technical and administrative perspective.
- Conceptual design of SM systems: Developing an effective SM system requires extensive considerations, ensuring alignment with project requirements and stakeholder expectations. Guidelines offer insights into designing target-oriented systems tailored to specific infrastructure needs.
- Technical information on sensors and applications: Guidelines detail available sensor technologies, their capabilities, and the types of structural insights they provide. This includes both resistance- and load-related monitoring for comprehensive assessment. There are generally two different approaches: the (technical) contractor's view – what sensors are available and what can be achieved with them, and the (administrative) client's view – what tasks can be accomplished and what sensors are available to do so.
- Supporting technologies: Integration of local and global data transmission, communication systems, and energy supply and harvesting technologies plays a crucial role in ensuring effective SM system functionality.
- Practical implementation considerations: Guidelines address real-world challenges in SM deployment, including installation, maintenance, exchangeability, expandability, remote access and operational reliability, ensuring that systems function as intended over time.
- Ensuring data quality and management: Strategies for maintaining consistent data quality, handling short- and long-term storage, and ensuring accessibility and visualization are essential components of SM guidelines.
- Extracting meaningful insights for decision-making: Automated data analysis methods, i.e. how to (automatically) extract relevant knowledge about the monitored structure at the relevant time (preferably in real time) from the data for decision making, often referred to as “intelligence” in this context, i.e. feature extraction instead of mere data collection. This enables the detection, characterization, prognosis and risk assessment of degradation and damage and thus proactive maintenance. Some recent guidelines include artificial intelligence as a keyword.
- Alarm processes and safety considerations: Guidelines provide ways of establishing alarm chains, escalation

procedures and personnel responsibilities to ensure an effective response to critical structural conditions, particularly in safety-related applications. They provide information on the special features of safety-related monitoring systems, in which considerations such as availability, redundancy, verifiability, etc. play an extremely important role compared to other monitoring systems.

- Integration with broader digital systems: SM results can seamlessly integrate with building information modeling (BIM), digital twins, risk management systems, and structural databases to enhance decision-making and lifecycle management.
- Qualification of monitoring personnel: Training and certification requirements for personnel involved in SM are essential to maintain high-quality data collection, interpretation, and response measures. It should be noted that there are hardly any standardized qualification paths that can be queried or specified.
- Best practices and case studies: Guidelines often include a compilation of real-world monitoring projects, that showcase successful implementations and lessons learned to guide future applications in diverse environments. The technical and scientific depth of planning, execution, data analysis and results achieved in the examples vary widely.

Harmonization of regulatory practices requires a balance between regional needs and global best practice, while ensuring that local priorities are not undermined. Encouraging international collaboration and knowledge sharing can help create adaptable, yet standardized, SM guidelines that meet different infrastructure requirements.

#### 4.2 Challenges

The integration of SM practices on a global scale faces numerous challenges. While SM has proven effective in improving infrastructure safety, functionality, and longevity, achieving a cohesive international framework requires overcoming these obstacles through harmonization, technological accessibility, and policy alignment.

- Data Standardization and Interoperability: A major obstacle to global SM integration is the lack of standardized data formats and protocols. Different monitoring systems employ proprietary technologies, leading to inconsistencies in sensor calibration, data interpretation, and reporting formats. These discrepancies create challenges in comparing and integrating monitoring results. Establishing universal standards for data acquisition, processing, and analysis is essential for facilitating collaboration, ensuring data consistency, and improving the reliability of infrastructure assessments. Industry-wide cooperation and policy-driven initiatives can help create a unified data-sharing ecosystem.
- Economic and resource constraints: Reservations about the long-term economic viability of monitoring systems play an important role, as the costs of designing, implementing and operating a monitoring system on a (presumably) intact structure must be weighed against the future, currently fictitious and elusive, savings of a preventive maintenance strategy using structural monitoring. Expenses related to implementing and maintaining SM

systems is a significant barrier, particularly in regions with constrained infrastructure budgets. To mitigate these challenges, cost-effective solutions and scalable monitoring strategies must be developed. Encouraging public-private partnerships and leveraging emerging technologies such as energy-efficient sensors and cloud-based data storage can also help improve affordability and accessibility.

- Qualification of SM personnel: The effectiveness of SM depends on the expertise of personnel involved in data collection, analysis, and interpretation. However, specific training standards – if available at all – vary across regions, leading to inconsistencies in monitoring quality. Establishing global certification programs, standardized training curricula, and skill development initiatives can help ensure that SM personnel possess the necessary expertise to operate and maintain monitoring systems effectively.
- Communication barriers: A fundamental and very essential hurdle are the communication challenges that hinder international cooperation in SM implementation. Even within Europe, the exchange of information on directives is limited because guidelines they are written in national languages and are not available in English. At the international level, language barriers make it much more difficult to exchange information, as it is often not even possible to search for specific national regulations because the necessary keywords are unknown in the relevant language. Although this challenge is lessened by the digital possibilities of translation, it remains, as availability is still limited to individuals. An effort to provide English translations of relevant documents would be desirable. However, multilingual resources are by far the better option, as English is not the "world language" for everyone.
- Cultural barriers: The general openness to new technologies varies from region to region. The construction industry itself stands out as a particularly conservative industry, most likely because the financial investment values are very high and therefore the willingness to innovate is limited. Cultural differences and varying perspectives on risk management, maintenance priorities, and the perceived benefits of SM lead to inconsistencies in adoption and execution strategies. Differences in administrative procedures and organizational structures add to complexity. Effective collaboration requires fostering a culture of cooperation.
- Intellectual property rights and industrial espionage concerns: Fears regarding intellectual property rights and industrial espionage pose challenges in international SM collaboration. Companies and institutions may be reluctant to share proprietary monitoring technologies or data due to concerns over competition and data misuse. Establishing clear legal frameworks and international agreements on IP protection, data ownership, and ethical data sharing can help alleviate these concerns while promoting cooperative advancements in SM technologies.
- Data privacy and security concerns: Sharing sensitive infrastructure data across borders requires stringent cybersecurity measures and clear agreements on data

ownership and accessibility. Unauthorized access to monitoring data can pose security risks, including cyber threats and infrastructure vulnerabilities. Establishing robust rules for data protection, encryption technologies, and regulatory agreements is crucial for ensuring secure and ethical data exchange between stakeholders.

- The importance of a well-developed SM concept: A properly developed SM strategy is crucial for ensuring that monitoring efforts align with infrastructure needs and long-term maintenance goals. Without a clear conceptual framework, SM implementations lack focus and efficiency, leading to reservations in the implementation in other projects and thus the widespread use of SM.
- Availability of guidelines and standards: The accessibility of SM guidelines and standards significantly impacts their adoption and awareness. Documents that are not open-access or are only available in print form limit their distribution. Promoting open-access policies and digital dissemination can improve the reach and influence of SM best practices, fostering wider implementation and international collaboration.

Addressing these challenges calls for coordinated international efforts. By overcoming these barriers, the global engineering community can unlock the full potential of SM, ensuring safer, more resilient infrastructure for future generations.

To address these gaps, increased international collaboration is essential. It is most viable to appreciate the efforts that have been made by others and then embrace and integrate them in a joint effort, at least referencing and appreciating best practice.

Establishing common protocols, such as data exchange standards and unified terminology, can enhance the interoperability of SM systems. This alignment will not only improve the safety and performance of infrastructure but also pave the way for sustainable development and resilient infrastructure worldwide.

## 5 CONCLUSION: TOWARDS A UNIFIED GLOBAL APPROACH TO SM

The globalization of SM practices is essential for tackling shared challenges such as aging infrastructure, climate change, and rapid urbanization. While national guidelines serve as critical frameworks for monitoring and maintaining structures, international collaboration presents an opportunity to harmonize practices, facilitate knowledge exchange, and leverage technological advancements across borders.

SM has become a fundamental tool in ensuring the safety, reliability, and longevity of civil infrastructure. However, as infrastructure systems grow increasingly complex and interconnected, a unified global approach to SM is more crucial than ever. By fostering cooperation and standardization, nations can maximize the potential of SM technologies, creating a safer, more resilient, and better-integrated global infrastructure network.

Achieving global cohesion in SM requires a concerted effort to address existing disparities and align diverse methodologies. This endeavor can build upon the wealth of detailed and well-established guidelines outlined in this paper. The missing piece is a comprehensive synthesis that bridges regional differences

and integrates best practices into a cohesive framework, fostering interoperability and broader applicability.

Looking ahead, the convergence of SM with emerging technologies holds immense potential for transforming infrastructure management and preservation. The adoption of digital twins, for instance, could enable real-time monitoring, predictive maintenance, and advanced scenario modeling. Additionally, advancements in machine learning and artificial intelligence promise to revolutionize data analysis, providing deeper insights into structural behavior and enhancing decision-making processes.

As infrastructure networks become more complex and the demand for resilient systems continues to rise, SM will play an increasingly pivotal role in the global engineering landscape. The path forward lies in collaboration – sharing expertise, aligning methodologies, and driving innovation together. By embracing these principles, the global engineering community can solidify SM as a cornerstone of modern infrastructure management, ensuring a safer, more sustainable, and future-proof built environment for all.

## REFERENCES

- [1] TRC E-C246. Structural Monitoring. Transportation Research Board (TRB), Washington, District of Columbia, 2019.
- [2] DGZfP Merkblatt B 09. Dauerüberwachung von Ingenieurbauwerken. Deutsche Gesellschaft für Zerstörungsfreie Prüfung (DGZfP), Berlin, 2022.
- [3] F. Lehmann, M. Schreiner and S. Laumann: The new DGZfP Guideline Monitoring of Civil Engineering Structures. *Otto-Graf-Journal* 20, pp. 161-166, 2021.
- [4] F. Lehmann and F. Hille: Dauerüberwachung von Ingenieurbauwerken – Das neue Merkblatt B 09 der DGZfP. *Beton- und Stahlbetonbau* 118(4), pp. 275-280, 2023. <https://doi.org/10.1002/best.202200122>
- [5] DBV Merkblatt Brückenmonitoring – Planung, Ausschreibung und Umsetzung. Deutscher Beton- und Bautechnik-Verein e.V. (DBV), Berlin, 2018.
- [6] E DIN 1076:2024-02. Ingenieurbauwerke im Zuge von Straßen und Wegen – Überwachung und Prüfung. DIN Deutsches Institut für Normung e.V., Beuth Verlag, Berlin, 2024.
- [7] BASt Leitfaden – Strategischer Einsatz von Monitoring für Ingenieurbauwerke. Bundesanstalt für Straßenwesen (BASt), Bergisch Gladbach, 2024.
- [8] BASt-Bericht B 197. Erfahrungssammlung Monitoring bei Brückenbauwerken – Dokumentation 2021. Bundesanstalt für Straßenwesen (BASt), Bergisch Gladbach, 2024.
- [9] RVS Merkblatt 13.03.01. Monitoring von Brücken und anderen Ingenieurbauwerken. Österreichische Forschungsgesellschaft Straße – Schiene – Verkehr (FSV), Wien, 2022.
- [10] COFREND. Le livre blanc du SHM. Confédération Française des Essais Non Destructifs (COFREND), Paris, 2022.
- [11] MIT 54/2022. Linee guida per la classificazione e gestione del rischio, la valutazione della sicurezza ed il monitoraggio dei ponti esistenti. Ministero delle Infrastrutture e dei Trasporti. Allegate al parere del Consiglio Superiore dei Lavori Pubblici n.54/2022, espresso in modalità “agile” a distanza dall’Assemblea Generale in data 10.06.2022, 2022.
- [12] UNI/TR 11634. Linee guida per il monitoraggio strutturale. Ente Nazionale Italiano di Unificazione (UNI), 2016.
- [13] M.P. Limongelli. Standardization of structural performance monitoring: existing documents and open questions. IABSE Symposium Report, Prague, pp.1285-1291, 2022. <https://doi.org/10.2749/prague.2022.1285>
- [14] D.L. Allaix, A.B. van Vliet, B. Cerar. Review of the current state of standardisation on monitoring, data-informed safety assessment and decision-making regarding maintenance of the transport infrastructure. IABSE Symposium Report, Prague, pp. 1309-1313, 2022. <https://doi.org/10.2749/prague.2022.1309>
- [15] ACI PRC-444.2-21. Structural Health Monitoring Technologies for Concrete Structures – Report. American Concrete Institute (ACI), Committee 444, Farmington Hills, Michigan, 2021.



- [16] ISIS Design Manual No. 2. Guidelines for Structural Health Monitoring. The Canadian Network of Centres of Excellence on Intelligent Sensing for Innovative Structures (ISIS Canada), Winnipeg, Manitoba, 2001.
- [17] CIRIA C788. Structural health monitoring in civil engineering. Construction Industry Research and Information Association (CIRIA), London, 2020.
- [18] G.-D. Zhou, T.-H. Yi, W.-J. Li, J.-W. Zhong and G.-H. Zhang. Standardization construction and development trend of bridge health monitoring systems in China. *Advances in Bridge Engineering* 1, 13, 2020. <https://doi.org/10.1186/s43251-020-00016-5>
- [19] G. Wang and J. Ke. Literature Review on the Structural Health Monitoring (SHM) of Sustainable Civil Infrastructure: An Analysis of Influencing Factors in the Implementation. *Buildings*, 14, 402 (2024). <https://doi.org/10.3390/buildings14020402>
- [20] GB 50982-2014. Technical Code for Monitoring of Building and Bridge Structures. Housing and Urban-Rural Development of PRC China. China National Standards, 2014.
- [21] Y. Yang, Q.S. Li and B.W. Yan. Specifications and applications of the technical code for monitoring of building and bridge structures in China. *Advances in Mechanical Engineering* 9(1), pp. 1–10, 2017. <https://doi.org/10.1177/1687814016684272>
- [22] S. Keßler, M.P. Limongelli and A. Eftychia (Eds.). Existing concrete structures life management, testing and structural health monitoring. State-of-the-art report. *Fédération internationale du béton (fib), Bulletin* 109, 2023. <https://doi.org/10.35789/fib.BULL.0109>
- [23] A.E. Del Grosso. Structural Health Monitoring Standards. IABSE Symposium Report, pp. 2991-2998, 2014. <https://doi.org/10.2749/222137814814069804>
- [24] GOST R 53778-2010. Building and Structures – Technical Inspections and Monitoring Regulations. National Standard of the Russian Federation, 2010.
- [25] F08b Guideline for Structural Health Monitoring. SAMCO Final Report, 2006. [http://www.samco.org/network/download\\_area/mon\\_guide.pdf](http://www.samco.org/network/download_area/mon_guide.pdf) (14.02.2025)
- [26] Assessment for Future Traffic Demands and Longer Lives. Sustainable Bridges Final Report, 2007. [https://cordis.europa.eu/docs/results/1/1653/121979191-6\\_en.pdf](https://cordis.europa.eu/docs/results/1/1653/121979191-6_en.pdf) (14.02.2025)
- [27] Smart Monitoring of Historic Structures. SMooHS Final Report, 2011. [https://www.irbnet.de/daten/kbf/kbf\\_e\\_F\\_2823.pdf](https://www.irbnet.de/daten/kbf/kbf_e_F_2823.pdf) (14.02.2025)
- [28] Harmonised Transport Infrastructure Monitoring in Europe for Optimal Maintenance and Safety. IM-SAFE, 2023. <https://doi.org/10.3030/958171>, <https://im-safe-project.eu/> (14.02.2025)

# Structural health monitoring guidelines for bridges in Germany

Falk Hille<sup>1</sup>, 0000-0002-2697-5370, Frederik Wedel<sup>2</sup>, Frank A. Lehmann<sup>3</sup>, 0000-0002-0192-7364, Stephan Pirskawetz<sup>1</sup>, 0000-0003-0626-5002

<sup>1</sup>Bundesanstalt für Materialforschung und -prüfung (BAM), Unter den Eichen 87, 12205 Berlin, Germany

<sup>2</sup>Marx Krontal Partner MKP GmbH, Werftstraße 17, 30163 Hannover, Germany

<sup>3</sup>Materials Testing Institute (MPA), University of Stuttgart, Pfaffenwaldring 2b, 70569 Stuttgart, Germany

e-mail: falk.hille@bam.de, frederik.wedel@marxkrontal.com, frank.lehmann@mpa.uni-stuttgart.de,  
stephan.pirskawetz@bam.de

**ABSTRACT:** With the advancement of digitalization and related technological developments, Structural Health Monitoring (SHM) has become a useful and increasingly widespread tool to assist in the maintenance management of bridges and other engineering structures. The process of implementing monitoring requires expertise in many fields such as civil engineering, bridge operation and maintenance, monitoring technology, and data analysis. In recent years, monitoring has moved from method and technology development to standard practice. However, the implementation of monitoring as a standardized process can be an obstacle, especially for bridge operators, due to a lack of practical experience combined with the various expertise required. This can affect several areas, such as determining the cost-effectiveness of a monitoring measure, proper tendering and contracting, quality control, analysis and evaluation of measurement data, and last but not least, data management. In order to support the introduction of monitoring technologies into the practice of infrastructure operators, several guidelines have been developed in Germany in recent years by different interest groups, each with a different focus and essentially complementing each other. This paper aims to provide an overview of four different recently published guidelines and to highlight their strengths and advantages.

**KEY WORDS:** Structural Health Monitoring; Guidelines.

## 1 INTRODUCTION

Germany's road and railway infrastructure faces several challenges, including a significant increase in traffic and a high average age of bridge structures. Bridge maintenance management is currently based on standardized inspections, which largely assess the condition of the structure visually and manually. At the same time, the development of procedures and technical requirements for Structural Health Monitoring (hereinafter referred to as "monitoring" for short) has by now progressed to the point where it is one of the most widely used tools for determining the structural condition of bridges and, if necessary, predicting developments. However, at present the use of monitoring is largely limited to event-related (reactive) actions while a great potential lies in the future support of predictive maintenance.

Surveys conducted among federal and state road authorities found that the use of monitoring is limited to existing damage and deficiencies [1]. According to the survey, barriers include a lack of knowledge about the applications and benefits of monitoring, the procurement process of monitoring services as well as the handling of data storage.

Due to the wide variety of construction methods and building materials, monitoring might vary greatly in its conception and implementation, depending on the specific object. Furthermore, there can be different approaches to the same objectives in terms of the parameters to be monitored, each with its own advantages and disadvantages. Therefore, there is no single approach that can be universally applied to the setup of monitoring systems for civil engineering structures. A recent challenge specific to Germany is that the current version of the German standard for bridge inspections DIN 1076 [2] does not include monitoring as part of the inspection process. This has led to a regulatory gap, as bridge authorities have not yet

established a systematic monitoring process. This will change in the near future with the introduction of a current revision of DIN 1076. The next version will include monitoring as a standard inspection routine [3].

The discrepancy between state-of-the-art monitoring methods and technology, on one hand, and the challenges associated with their implementation by bridge owners and operators, on the other, has become more apparent in recent years. One primary method to address this challenge is the implementation of guidelines that can provide direction and regulate the utilization of procedures to some extent. Several institutions have expressed a need for such guidelines, and they have taken steps to promote and facilitate their publication.

The German Concrete and Construction Technology Association (Deutscher Beton- und Bautechnik-Verein e.V. DBV) played a pioneering role in developing and publishing the "DBV-Guideline Bridge Monitoring - Design, Tender, and Implementation" (DBV-Merkblatt Brückenmonitoring - Planung, Ausschreibung und Umsetzung) in 2018 [4]. The document meticulously delineates a range of monitoring applications and, most notably, methodically analyzes and structures the bridge monitoring process into multiple steps. Concurrently, the players involved in the process were assigned to the individual steps. Those involved in the practical application found this structuring to be very helpful. Additionally, the guideline briefly addressed tendering and economic considerations.

As an extension of the support provided by guidelines, the German Society for Non-Destructive Testing (Deutsche Gesellschaft für Zerstörungsfreie Prüfung e.V. DGZfP) has published the "Guideline B09 Structural Monitoring" (Merkblatt B 09 Dauerüberwachung von Ingenieurbauwerken) [5]. The guideline is a comprehensive document that provides

a detailed overview of the conception of monitoring systems. It also includes a compilation of possible technical systems and sensors, depending on the specific tasks at hand. Additionally, aspects of data processing and data management are addressed. Operators of the structures are further supported by a compendium of best practice examples.

Despite the existence of published guidelines, the practical application of monitoring specifically for road bridges did not gain widespread traction. In response, the German Federal Highway Research Institute (Bundesanstalt für Straßen- und Verkehrswesen BAST) initiated a research project in 2023. The objective of the project was to produce a brochure-type guide that would provide practical application instructions for monitoring road bridge structures. As a brochure cannot be expected to address every potential issue or question that may arise in the context of a monitoring application in great detail, the compendium-type final project report, "Guideline - Strategic application of monitoring for engineering structures" (Leitfaden – Strategischer Einsatz von Monitoring bei Brückenbauwerken), was pre-published in 2024 [6]. This report encompasses both technical aspects and addresses economic feasibility, tendering, and contracting of monitoring services. It includes a collection of typical monitoring applications on road bridges, organized by use cases, describing their common usage and benefits, supplemented by model examples. Currently, the monitoring system operator generally holds the measurement data, with no principal data transfer to the client. As monitoring applications become more widespread, standardizing procedures and establishing data management systems becomes crucial. The road administration is responsible for storing processed measurement data in a machine-readable format to enable future evaluations. The project developed foundations for designing suitable data management systems and explored how user agreements for data description and transfer can be incorporated into contracts.

The final guideline in this series differs slightly from the previous guidelines. The primary focus of this guideline is the monitoring of prestressed wire breaks in prestressed concrete structures using the method of acoustic emission analysis, as opposed to the broader field of engineering structure monitoring. The DGZfP guideline "SE 05 - Detection of tendon wire breaks with acoustic emission" (Richtlinie SE 05 – Detektion von Spannstahlbrüchen mit Schallemissionsanalyse) aims to standardize the application of acoustic emission (AE) analysis for detecting prestressing wire breaks and to outline the method's capabilities and limitations [7]. It provides detailed instructions for planning, tendering, installation, operation, and evaluation of an AE monitoring system. The guideline also offers recommendations on technical and personnel requirements and quality standards to ensure a high-quality information system. Its scope includes bridge and engineering structures with bonded prestressing wires, though the described methods could also apply to unbonded post-tensioning systems.

The contribution presents a compilation of the four different guidelines developed and published in recent years in Germany. These guidelines aim to structure and regulate the conception and implementation of monitoring applications to support the introduction of monitoring into the practice of managing bridge and other engineering structures. In addition

to the guidelines presented here, several other documents have been published recently to assist those involved in the management of bridges and other engineering structures. For instance, these documents may include reports on a particular subject, such as corrosion monitoring of reinforced concrete structures [8], or documents that compile reports of applied monitoring activities in civil engineering, such as [9].

## 2 DBV-GUIDELINE BRIDGE MONITORING

The German Society for Concrete and Construction Technology (DBV) was the first to address the issue of harmonization approaches to planning and implementation of monitoring measures for engineering structures. In 2018, the DBV published the guideline "Bridge Monitoring - Design, Tender and Implementation" [4]. The guideline was developed by a consortium of bridge operators, monitoring providers, and representatives of the scientific community. This consortium was formed to consider the perspectives of all parties involved in the realization of monitoring projects.

### 2.1 Motivation and objectives

The primary objectives behind developing this guideline were twofold: first, to catalog potential use cases of structural health monitoring throughout the life cycle of engineering structures, and second, to describe the monitoring process in detail, including all its phases, in conjunction with clearly defining responsibilities. The guideline was developed to serve as a practical resource for the planning and execution of monitoring activities. While the guideline is centered on bridge monitoring, its principles can be applied to a variety of engineering structures and buildings.

### 2.2 Content of the guideline

The guideline underscores the importance of various monitoring applications across a structure's life cycle. However, the text also describes monitoring applications in the pre-construction, construction, and demolition phases. The list of use cases is not exhaustive, but it provides an overview of monitoring's potential.

The implementation of bridge monitoring entails more than just installing sensors on a structure and recording the measured values. To successfully receive the requested structural information based on monitoring, it must be understood as a comprehensive process, from the definition of the task to the extraction of the qualified answer. The success of a monitoring project hinges on a structured process with clearly defined phases and service profiles for all involved parties. The guideline suggests a systematic monitoring process comprising the following six sequential phases:

- Defining the monitoring objective and assessing its feasibility.
- Developing a monitoring concept.
- Detailed design of the monitoring system.
- Implementation, including installation, operation, and data acquisition.
- Data processing and evaluation.
- Assessment, where results are interpreted using supplementary analyses.

Stakeholders involved in monitoring projects have specific roles and responsibilities. While tasks are clearly assigned,



depending on project size and complexity, a limited number of experts may fulfill multiple roles. In complex projects, there may be a need for different specialists, particularly when advanced measurement techniques are required.

Quality assurance is critical at every stage of the monitoring process to ensure consistent, high-caliber standards. Internal quality control is always required, while external proofs may be necessary for critical projects. The guideline recommends a structured procedure for each of the three main subjects in terms of quality assurance: the monitoring concept, data integrity, and the key feature assessment.

Additionally, the process of tendering monitoring services is complex due to the specialized nature of SHM. A well-structured approach ensures coordinated data flow among stakeholders, leading to consistent quality. As defining monitoring services precisely in tenders can be challenging, functional descriptions focusing on objectives and expected outcomes can serve as an alternative. However, achieving comparable offers and execution quality remains a key challenge. The guideline delineates various approaches, contingent upon the complexity of the monitoring project.

Finally, the cost-effectiveness of monitoring must be assessed before any action is taken. Monitoring provides valuable information that can extend a structure's service life, reduce the need for costly upgrades, and improve risk management. Monitoring is essential for preventing unnecessary restrictions or interventions. It helps optimize infrastructure maintenance and safety. The guideline covers the net present value method and the downtime costs accounting method, and it includes examples that illustrate the economic benefits of monitoring measures. Additionally, the text presents a method for evaluating the risk associated with the uncertainty of the monitoring results.

### 2.3 Guideline summary

The proposed DBV-guideline "Bridge Monitoring - Design, Tender and Implementation" aims to catalog structural health monitoring use cases and describes the monitoring process with defined responsibilities. The process is structured in six phases, from defining objectives to result assessment. The guideline emphasizes quality assurance, addresses the complexities of tendering monitoring services, and discusses the cost-effectiveness of monitoring. While the primary focus is on bridge monitoring, the principles can be applied to other engineering structures as well. The guideline is intended to serve as a practical resource for the planning and implementation of monitoring actions, taking into account the perspectives of bridge operators and monitoring providers.

## 3 DGZFP-GUIDELINE B 09 STRUCTURAL MONITORING

### 3.1 Motivation and objectives

The DGZfP has developed the "Guideline B 09 Structural Monitoring" to assist owners, operators, and those responsible for structural maintenance, as well as qualified planners tasked with designing monitoring systems [5].

Guideline B 09 is a clear complement to the DBV guideline Bridge Monitoring. As the previous section explains, it focuses on the description of monitoring applications, the monitoring process, and economic considerations. The DGZfP B 09

guideline clearly states the objective: to provide readers with easy access to monitoring systems and to illustrate the conditions and limits under which monitoring specific structural parameters can serve as a useful supplement or alternative to manual structural inspections. It provides a solid foundation for a realistic assessment of the financial and time requirements from the initial idea to the evaluation of the results of structural monitoring.

The guideline provides detailed descriptions of the aspects to consider when designing continuous monitoring systems and examines tasks that can realistically be addressed by structural monitoring. It also discusses critical issues for data management and quality assurance. The document emphasizes practical relevance. The explanations of monitoring tasks are formulated from the perspective of typical structural engineering questions rather than from the perspective of sensor technology. The authors of the guideline made a point of including a catalogue of practical examples. This collection includes monitoring applications from various structures (bridges, wind converters, etc.), different building materials (steel, concrete, etc.), and different monitoring objectives (damage monitoring, load monitoring, etc.).

Given the increasing presence of providers of hardware and monitoring services in the marketplace, it is becoming increasingly important to have a common understanding of the factors that need to be considered during the various phases of structural monitoring. It is therefore imperative to ensure that monitoring systems reliably meet customer requirements for specific tasks and to avoid unrealistic expectations of potential results. According to the authors of the new DGZfP Guideline B 09 Structural Monitoring, this document makes a significant contribution to achieving this goal.

### 3.2 Content of the guideline

The guideline covers all essential technical steps that must be considered during the design and implementation of a monitoring project according to the current state of knowledge. The focus is on large-scale monitoring systems, i.e., sensor networks with multiple sensors at different locations, with special consideration of applications to reinforced and prestressed concrete bridge structures. The substantive chapters of the guideline are presented below.

**Conception of Continuous Monitoring Systems:** This chapter provides comprehensive guidance on the technical design of continuous monitoring systems. The necessary steps are described in detail along the measurement chain: The structure consists of the following: sensor connection, base station, and peripherals. The text starts by clearly explaining the preliminary investigations of existing structures. These investigations determine potential weak points, existing damage, and probable damage mechanisms. The text also describes the determination of measurement parameters. Next, we will critically assess whether monitoring is appropriate in each case. If the decision is positive, suitable sensors must be selected and suitable measurement locations determined. These locations must take into account the aspects described in the guideline.

The signals collected at measurement points are transmitted to a base station or central computer via cable or wirelessly, depending on the sensor type and system layout. The data converges at the base station, where it is processed, verified,

and stored. The text explains different data acquisition modes (time-controlled, event-based) and considers event detection, data volume, and energy consumption. Remote transmission components enable continuous monitoring, alarming, and data backup. Actuators trigger events like switching traffic lights. Data evaluation is automated and based on specific standards. Challenges in larger projects include ensuring reliable communication and appropriate measurement intervals.

**Monitoring Tasks:** This central chapter of the guideline deals with various typical construction issues that are fundamentally accessible to monitoring in civil engineering structures. For each monitoring task, only established methods and sensors are the topics of discussion. The selection and description of monitoring tasks is based on the practical experience and scientific expertise of the committee members. The authors of the guideline were aware that each structure is unique and that each type of sensor and sensor behavior is different. Generalizations are difficult to make, but they are necessary for a foundational document such as this guideline. Monitoring systems must be tailored to the task at hand. Therefore, it is essential to involve a monitoring expert in the design, planning, and implementation of monitoring projects.

The guideline covers the following monitoring tasks:

- Geometric quantities: Strain, displacement, deflection, tilt, cracks.
- Static and dynamic quantities: Force, Stress, Prestressing Force, Vibration, Shock.
- Material Properties: Material moisture, reinforcement corrosion, prestressing wire break detection.
- Environmental influences: Temperature, humidity, other environmental conditions, traffic characterization.

To improve comparability and readability, each monitoring task in this chapter is divided into four identical sections:

- Purpose.
- Sensors and Instrumentation.
- Data Analysis.
- Application and Limitations.

**Data Management:** The primary task of any monitoring system is straightforward: to collect data from the operation of the monitored structure. This data must be stored and analyzed automatically. It must be visualized, uniquely assigned, and accessible, while ensuring data security. As the scope of the measure increases, data management plays a decisive role. The guideline devotes a separate chapter to this topic, describing in detail the aspects of data management that must be considered for optimal use of monitoring data.

**Quality Assurance of Measurement Systems:** To ensure the highest quality monitoring results, which is critical for safety-related tasks, it is essential to consider several key aspects, outlined in this chapter. This chapter addresses topics such as personnel qualifications, quality assurance during design and tendering, installation planning, actual installation, and ensuring quality assurance during operation and data preparation and evaluation.

**Practical Examples:** The guideline concludes with a number of practical examples. We have thoroughly documented both large lighthouse projects and the monitoring of the "broad mass" on bridges, where a significant portion of the currently installed continuous monitoring systems are located. Each project is summarized on about three pages. The summaries

include a description of the structure, the task, the monitoring system installed, and the results.

### 3.3 Guideline summary

The new DGZfP Guideline B 09 Structural Monitoring is one of the most comprehensive publications in the guideline series to date. It comprehensively covers the entire technical process, from the decision for or against monitoring to the practical implementation of extensive instrumentation, focusing on the technical components of monitoring systems. A key feature is a catalog of practical examples that illustrate monitoring applications for different structures, materials, and objectives. The guideline's clear purpose is to provide a common understanding of essential considerations to ensure that systems meet client needs while avoiding unrealistic expectations, given the increasing availability of monitoring services.

## 4 BAST GUIDELINE FOR THE STRATEGIC APPLICATION OF MONITORING OF ROAD BRIDGES

### 4.1 Motivation and objectives

A 2020 survey of experts from federal and state road authorities conducted by the German Federal Highway Research Institute (BAST) [1] revealed that the use of monitoring is limited to existing damages and deficiencies, despite the publication of the DBV guideline. The survey identified three key barriers: a lack of knowledge about the applications and benefits of monitoring, the procurement process for monitoring services, and the handling of data storage. The use of monitoring will be actively promoted within the structure's maintenance committee groups. Operators of road bridges must be supported by best practice examples, training, and standardized procedures for the use of monitoring. The German standard governing road bridge inspections is currently being revised, and the next version will include monitoring as a standard inspection routine [3].

In response, BAST initiated a research project to produce a brochure-type guide for the practical application of monitoring road bridge structures. A booklet cannot cover all the issues and questions that may arise in the context of a monitoring application. An additional compendium-type report was published to address these issues and questions. This report must address technical issues and specifically cover the assessment of economic viability of monitoring, the tender and award process for installation and operation of monitoring systems, and the considerations for drafting contracts. The report is available for pre-publication on the BAST website [6].

### 4.2 Content of the guideline

The content of the guideline is based on the best possible applicability to the use of monitoring within the road bridge maintenance process.

**Monitoring use cases:** The various possible uses of monitoring are summarized in the following section in the form of monitoring use cases. The project-specific use cases are derived from the project objectives and represent processes that contribute to achieving the defined goals.

Several use cases have already been identified in [1], which are already frequently used in practice or have potential for future application. At present, monitoring is mostly limited to reactive measures, such as monitoring known damage or

deficits from recalculation or construction. However, the great potential of monitoring also lies in supporting predictive maintenance.

The use cases are structured in the form of fact sheets. This clear and plausible presentation of the comprehensive ways in which monitoring can be used to reduce barriers is essential. Each use case is thoroughly described, including the initial task, the implementation, and the benefits. Concrete examples are used to illustrate the application in practice.

The following list summarizes the various use cases, described in the guideline [10]:

- Known localized damages.
- Known deficits from recalculation or construction.
- Determination of effects.
- Support for regular inspection procedure.
- Accompaniment for major buildings.
- Maintenance and reinforcement measures.
- Load tests.
- Predictive life cycle management.
- Birth certificate.
- Measures during the construction period.
- Protection of buildings during neighboring construction work.

#### Monitoring Process and its Actors:

As described in the section on the DBV guideline, structural monitoring is a multi-stage process from the description of the objectives to the assessment of the monitoring results. The operating authority of the structure must implement a system that divides the task into phases and assigns actors responsible for processing each phase. The tasks of the phases can be tendered separately or combined. The phases are defined similarly to [4].

Economic feasibility studies: Bridge owners and operators must determine the benefit-cost ratio of any monitoring system before implementation. To evaluate this ratio, it is necessary to estimate the expected costs associated with the future use of a road bridge with and without monitoring. This is a complex task. The expected costs depend on future developments in the condition and performance of the bridge, the quality of the monitoring system and data processing, possible monitoring results, future decisions related to these monitoring results (i.e., decisions on actions such as traffic restrictions, inspection, maintenance, bridge replacement, etc.), the direct and indirect costs associated with these actions, and the costs of installing, operating, and maintaining a monitoring system. The difference between the expected cost of operating a bridge without and with monitoring is the value of monitoring provided by a monitoring system. If this metric is positive, the cost of a surveillance system is justified by its benefits. The guideline draws on literature and the expertise of the German road authorities. It highlights the similarities and differences between existing procedures for assessing the economic feasibility of maintenance measures and analyses for evaluating the benefit-cost ratio of monitoring systems. It also provides clear, practical advice on how to assess this ratio and discusses situations where such analyses are less relevant [11].

Procurement process: As previously outlined, one of the most challenging areas for bridge agencies in implementing monitoring into their daily operations is the management of tendering, awarding, and contracting activities. This is due to

the novelty of monitoring as a technique for determining bridge safety measures. The following aspects are the main areas of concern:

- What are the required services to be tendered and provided?
- Who are the players and which specifications and expertise potential bidders must provide?
- What are appropriate award criteria?
- What constraints need to be considered when drafting the contract?
- How should liability claims be regulated and formulated?

The guideline authors' experience with bridge monitoring bridges provides a solid foundation for the proposed procedure. Tendering is a viable option. Parts of the overall service can be tendered separately, depending on the requirements. There are also different types of tenders, depending on whether specific service points or the entire service is functionally tendered. The right choice is influenced by several factors. In addition to price, these include quality assurance criteria such as the qualifications of the bidders. This is especially crucial because vendors sometimes make exaggerated promises. When drafting contracts, it is essential to address specific issues that differ from a standard bridge inspection. It is essential to know how to deal with a temporary outage of parts the measurement equipment, e.g., due to vandalism. Minimum response times must be defined. Rules must be established for very long measurements to account for the additional costs of aging measurement equipment that may need replacing. Liability issues must also be addressed. The guideline provides clear recommendations for choosing the right type and scope of tender. The guideline also provides clear recommendations for negotiating contracts.

Further, the brochure includes checklists for the topics discussed above. These include tendering and awarding, as well as contract design and liability.

Measurement technology: Instrumentation combines all the technical components of a monitoring system. This includes not only the actual sensors, but also components for signal transmission, data processing, and storage. A classical monitoring system is made up of sensors, sensor connection components, data acquisition systems, and a measurement computer to which other external components can be connected. The guideline lists and presents the various aspects that influence the selection of measurement technology to assist in the best practice application of monitoring in bridge condition assessment. The selection of measurement technology is based on the monitoring concept, which considers all aspects of the technical implementation of a monitoring task in the monitoring system. In addition to the monitoring objective, this includes the type and size of the structure to be monitored, requirements for long-term stability or, if necessary, interchangeability, and economic criteria. It is essential that the selection of the sensor technology be based on clearly defined requirements. These requirements include the measuring range, measuring accuracy, sensitivity, measuring resolution, and sampling frequency. Finally, it is essential to consider potential technical and environmental influences.

The guideline clearly describes the different technical components of conventional monitoring systems. Additionally, new types of IoT (Internet of Things) monitoring systems,



typically organized in sensor network structures, are briefly discussed. The relationship between the measurement task and the measurement technology is presented to assist road bridge authorities. The previous section clearly outlined the most well-known and commonly used sensors. The sensors mentioned have clear applications, measurement, and target variables. The measurement principle is presented, and if necessary, comments on advantages and disadvantages or special notes on application limitations are given.

**Data Management:** Although managing monitoring data is challenging for road authorities, it is valuable for future inspections and new methods. Data management is covered in national and international literature. The focus is on solving data management challenges as a governmental task to preserve information for the long term. Only one third of the monitoring data is stored at road agencies due to difficulties in structuring and sharing data between private companies and public agencies. This means that data management recommendations are needed. Currently, specialized structural measurement service providers (SSMSPs) handle most of the data. Some advanced road authorities also act as SSMSPs.

Both SSMSPs and road authorities are responsible for storing monitoring data. SSMSPs are responsible for collecting and analyzing data, while road authorities are responsible for receiving, archiving, and sharing it. The requirements for road authorities were collected in user stories to help prioritize data management needs. These user stories are visualized as a user story map, which will help road authorities prioritize their requirements when evaluating data management software. The discussion revealed that road authorities must address SHM data governance and sovereignty but currently lack structured processes for receiving, archiving, and sharing SHM data, including quality control. To address this issue, two business processes were developed to facilitate the receipt of structured data.

The first process begins with an inspection request and involves creating an employer's data requirement (EDR) document that specifies data formats, metadata, and delivery cycles. After the road authority approves the EDR, the SSMSP delivers the data as agreed. Then, the road authority verifies the data delivery and makes it available in asset management systems.

The second process describes how stakeholders who oversee structural assessments use monitoring data. If the SSMSP performs the assessment, they must ensure the data is reusable and well-documented. This process includes negotiating a usage agreement and providing access to the data for automated and manual workflows.

Long-term data preservation should be independent of proprietary software to enable broad accessibility and new business opportunities.

#### 4.3 Guideline summary

The guideline was developed due to a lack of awareness regarding which structural use cases should be monitored to provide information or improve bridge integrity, and which measurement technology is appropriate. Most importantly, there is a lack of a standardized monitoring process, as well as an unknown set of parties involved in the process. Additionally, there is a lack of knowledge on how to determine the economic feasibility of monitoring and how to tender and award

monitoring services. Data management is another area of concern. The guide suggests approaches here and describes important boundary conditions that need to be considered.

The final document offers solutions to all these issues. In addition to the detailed guideline report, the most important statements are summarized and published in a short, concise brochure. Throughout the guideline development process, consultations and discussions were held with the target audience of state and federal road agencies. These consultations are seen as a necessary basis for successfully introducing and accepting the guideline. [10, 11].

## 5 DGZFP GUIDELINE FOR DETECTION OF WIRE BREAKS BY ACOUSTIC EMISSION ANALYSIS

### 5.1 Motivation and objectives

Prestressed concrete construction began in Germany in the 1950s. It was characterized by experimental approaches and diverse prestressing systems, although the relevant codes were slow to develop. The key was recognizing the need for high tensile strength in prestressing steel to maintain effectiveness despite creep and shrinkage. While tempering and alloying improved the strength of prestressing steels, it also increased their susceptibility to stress corrosion cracking (SCC). This issue affected steels from the 1950s to the 1970s, and in East Germany until the 1990s [12]. SCC can cause brittle fractures in prestressing steel that are observed during construction and are attributed to the storage, installation, and pre-grouting periods. Damage can also occur after prolonged use in well-built structures. Evaluating these structures is challenging due to the difficulty of inspecting internal tendons and detecting wire breaks. Some structures lack sufficient reinforcement to ensure safe load transfer when prestressing steel fails, which can lead to sudden failure. Many structures with vulnerable prestressing steel are still in use today, and significant damage continues to be observed.

The challenge lies in the limited accessibility of tendons embedded within concrete. In recent years, acoustic emission (AE) monitoring has become a key method for detecting prestressing wire breaks in Germany. AE was originally used to test high-safety industrial equipment, and its potential for construction was recognized in the 1990s. AE monitoring was first applied to suspension and cable-stayed bridges, followed by prestressed concrete bridges. AE offers continuous, comprehensive monitoring, enabling immediate detection and localization of damage. Through automated analysis, it provides reliable data on wire breaks, making it indispensable for owners. Affected structures can continue operating safely, which allows for better planning and resource management.

Ensuring safe and reliable bridge operation is critical. Regular inspections according to DIN 1076 are an important tool for this. Shorter inspection cycles are recommended for bridges with SCC-prone prestressing steel. Continuous monitoring methods, such as AE can detect wire breaks permanently and allow for the dynamic evaluation and adjustment of inspection intervals. AE monitoring significantly contributes to safe bridge operation by transitioning from a scientific method to a standardized procedure. In this context, the guideline SE 05 "Detection of prestressing wire breaks with acoustic emission" [7] establishes a framework for procurement and quality-assured operation.

The SE 05 guideline aims to standardize the application of AE monitoring for detecting prestressing wire breaks as well as outline the method's capabilities and limitations. The guideline provides detailed instructions for planning, tendering, installing, operating, and evaluating an AE monitoring system. The guideline also offers recommendations on technical and personnel requirements as well as quality standards to ensure an effective information system. The guideline's scope includes bridges and other engineering structures with bonded prestressing wires, though the described methods could also apply to unbonded tensioning systems.

### 5.2 Content of the guideline

The guideline is structured to help interested readers first understand the methodology and a proposed practical approach to applying AE monitoring for lifetime detection of wire breaks. After an introduction to the guideline, important terms, definitions, and abbreviations are presented.

**Methodology:** AE detects damage by capturing the elastic energy released as shock waves, which can be detected by surface sensors. This guideline explains this principle as it applies to monitoring prestressing wire breaks and provides basic implementation instructions. AE analysis requires high sampling rates and complex data analysis. Recommendations include the type of sensor, the frequency range, and pre-amplification. Piezoelectric sensors with a resonant frequency of 20-80 kHz are typically used to ensure sensitivity and minimize interference from low-frequency noise. Optimal sensor placement is critical for accurate detection and localization. Sensors should be strategically distributed based on the structure's geometry, material properties, and expected signal attenuation. The maximum allowable distance between sensors depends on factors such as signal strength, noise level, and the structure's damping characteristics.

The effectiveness of AE monitoring depends on distinguishing signals from background noise. Additionally, AE only detects active damage and not preexisting wire breaks. Complementary methods, such as non-destructive testing or invasive inspections, are required to establish baseline conditions at the start of monitoring.

**Implementation and service description:** After identifying the need for continuous monitoring, the system requirements must be defined and the procurement process initiated. Because each bridge has unique characteristics, such as structural geometry (e.g., box girder or T-beam), material properties (e.g., concrete type), and environmental factors (e.g., traffic load), each bridge requires a customized monitoring design. The guideline provides detailed instructions for acoustic analysis, sensor layout, and performance specifications.

**Qualification of provider:** As no official certifications exist, personnel and operational qualifications for AE monitoring can only currently be demonstrated by reference projects and experience. Design, installation, and operation must be performed by qualified personnel. Detailed recommendations for qualification verification are provided.

**Data analysis and reporting process:** This section outlines the steps from data collection to action. Automated analysis identifies potential wire breaks that require verification using additional methods or by engineers. Confirmed breaks are then used for structural evaluation. The discussion covers essential information for documenting candidate wire breaks.

**Appendices:** The appendices offer supplementary technical information, including recommendations for supervising wire removal via acoustic emission, methods for determining background noise levels and signal attenuation, and calculations for maximum allowable sensor distances based on structural geometry and material properties.

### 5.3 Guideline summary

This guideline introduces acoustic emission (AE) analysis as a tool for continuously monitoring prestressing wire breaks in concrete bridges. AE technology can detect and locate wire breaks in real time, offering critical information about the structural health of bridges. Therefore, it offers a unique opportunity to assess and manage structures at risk of stress corrosion cracking. AE is the only method that can directly detect wire breaks and requires specialized knowledge. This method applies to bonded prestressing systems but not to unbonded tensioning systems. However, it cannot detect wire breaks that occurred prior to the start of monitoring.

The increased interest and use of AE systems has led to better regulation of procedures and requirements, as recognized by the DGZfP committee. This resulted in the SE 05 guideline. This guideline, developed by multiple parties, represents accepted technical standards and provides detailed instructions for the procurement and quality assurance of AE systems during installation and operation.

## 6 CONCLUSIONS AND OUTLOOK

### 6.1 Conclusions

The reviewed German guidelines - DBV Bridge Monitoring, DGZfP B09 Structural Monitoring, BASt Strategic Application of Monitoring, and DGZfP SE 05 Detection of Wire Breaks Acoustic Emission Monitoring - collectively provide a structured framework for conceiving, implementing, and managing SHM in bridges and other engineering structures. The guidelines address different aspects, ranging from process structuring and economic assessment to technical system selection and quality assurance, and offer complementary strengths.

Despite these advances, the practical implementation of SHM is limited and is often restricted to event-driven responses rather than proactive and predictive maintenance. Key barriers include a lack of practitioner experience, challenges in procurement and tendering, and unresolved issues in data management and ownership. While the guidelines have helped clarify roles, standardize processes, and provide examples of best practices, they also reveal gaps, particularly the absence of a unified, one-size-fits-all approach and the need for harmonized data management systems.

The transition from technological development to standard practice is underway. However, widespread adoption requires technical solutions, organizational clarity, and contractual clarity. Collaboration among stakeholders, including infrastructure owners, service providers, and researchers, is essential to bridge the gap between advanced SHM technology and practical application. Every phase of SHM projects must include economic evaluation and quality assurance to ensure cost-effectiveness and reliability.

## 6.2 Outlook

The upcoming revision of the German bridge inspection standard, DIN 1076, is expected to accelerate the integration of monitoring into standard maintenance practice by incorporating SHM as a routine element. As SHM becomes more prevalent, the need for standardized data management and protocols for data sharing and ownership will grow. Future guidelines should address these topics in greater depth. Furthermore, future guideline editions must include regulations on personnel qualifications and calibration of monitoring hardware. Training programs and knowledge transfer initiatives should be developed to provide practitioners with the expertise necessary for the effective deployment of SHM. Guidelines should address differing expectations between practitioners (e.g., bridge operators) and SHM service providers to promote clear communication and user-friendly solutions.

A unified guideline or standard integrating technical, economic, and contractual aspects is needed to make it easier for practitioners to implement SHM, regardless of project size or complexity.

Future work should also focus on aligning German guidelines with European and international standards to facilitate cross-border projects and knowledge exchange. This includes adopting common terminology, data formats, and quality assurance procedures.

Additionally, future guideline issues should continuously integrate the results of ongoing research focusing on predictive analytics, integration with digital asset management systems, and the development of scalable, adaptable SHM solutions. SHM guidelines should support a shift from reactive to predictive maintenance by leveraging monitoring data to optimize infrastructure management and extend service life.

By fostering collaboration, harmonization, and continuous improvement, SHM guidelines can ensure the safety, reliability, and sustainability of critical infrastructure in Germany and Europe.

## REFERENCES

- [1] I. Hindersmann, BAST-Heft B 163: Dauerüberwachung von Bestandsbrücken – Quantifizierung von Zuverlässigkeit und Nutzen (Berichte der Bundesanstalt für Straßenwesen, Reihe B: Brücken- und Ingenieurbau - B 163), 2021.
- [2] DIN 1076:1999-11 - Ingenieurbauwerke im Zuge von Straßen und Wegen; Überwachung und Prüfung, D. D. I. f. Normung, 1999.
- [3] G. Marzahn *et al.*, Bauwerksprüfung nach DIN 1076, Bautechnik, vol. 100, no. 11, pp. 699-706, 2023, doi: 10.1002/bate.202300090.
- [4] DBV-Merkblatt Brückenmonitoring – Planung, Ausschreibung und Umsetzung, DBV, 2018.
- [5] DGZfP Merkblatt B 09 (2022) Dauerüberwachung von Ingenieurbauwerken, 2022.
- [6] BAST, Leitfaden – Strategischer Einsatz von Monitoring für Ingenieurbauwerke - Pre-publication, 2024. [Online]. Available: <https://www.bast.de/DE/Publikationen/Fachveroeffentlichungen/Ingenieurbau/Downloads/B-fv-15-0707.html>
- [7] Detektion von Spanndrahtbrüchen mit Schallemission, DGZfP, 2024.
- [8] Merkblatt B 12. Korrosionsmonitoring bei Stahl- und Spannbetonbauwerken, DGZfP, 2018.
- [9] B. Novák *et al.*, Monitoring für Brückenbauwerke - Erfahrungssammlung, Dokumentation 2021 - Schlussbericht, in Projekt-Nr. BMVI: StB 247192.7040-3418027, ed: Bundesministerium für Verkehr und digitale Infrastruktur, 2021.
- [10] F. Wedel *et al.*, Guideline for the strategic application of monitoring of road bridges in Germany, e-Journal of Nondestructive Testing, vol. 29, no. 7, 2024/07 2024, doi: 10.58286/29582.
- [11] F. Hille *et al.*, "Developing a guideline for structural health monitoring of road bridges in Germany," in Bridge Maintenance, Safety, Management, Digitalization and Sustainability, Copenhagen, Denmark, 24.06.2024 2024: CRC Press, pp. 2009-2017, doi: 10.1201/9781003483755-236.
- [12] M. Fiedler *et al.*, Detektion von Spanndrahtbrüchen mit Schallemissionsanalyse, Beton- und Stahlbetonbau, vol. 120, no. 2, pp. 150-164, 2025, doi: <https://doi.org/10.1002/best.202400098>.



# Structural Health Monitoring in the Italian Guidelines for bridges

Giancarlo Costa [0000-0003-3675-144X](https://orcid.org/0000-0003-3675-144X), Eleonora Morleo [0009-0002-5034-8833](https://orcid.org/0009-0002-5034-8833),  
Pier Francesco Giordano [0000-0003-0396-0253](https://orcid.org/0000-0003-0396-0253), Maria Pina Limongelli [0000-0002-9353-5439](https://orcid.org/0000-0002-9353-5439)  
Department of Architecture, Built Environment and Construction Engineering,  
Politecnico di Milano, Piazza Leonardo da Vinci, 32 - 20133 Milan, Italy  
email: [giancarlo.costa@polimi.it](mailto:giancarlo.costa@polimi.it), [eleonora.morleo@polimi.it](mailto:eleonora.morleo@polimi.it), [pierfrancesco.giordano@polimi.it](mailto:pierfrancesco.giordano@polimi.it),  
[mariagiuseppina.limongelli@polimi.it](mailto:mariagiuseppina.limongelli@polimi.it)

## EXTENDED ABSTRACT

**KEY WORDS:** Structural Health Monitoring; Italian Guidelines; Bridge management; Infrastructures.

### 1 INTRODUCTION

Bridge management plays a critical role in safeguarding transportation safety and functionality against aggressive environmental conditions, increasing load demands, and extreme events, making it an indispensable pillar of modern infrastructure systems. Recognizing the need for standardized practices, the Italian Ministry of Infrastructures and Transport issued the 2020 “*Guidelines for Risk Classification and Management, Safety Evaluation, and Monitoring of Existing Bridges*” [1]. These guidelines categorize bridges into five attention classes (ACs), determined by comprehensive assessments of structural and foundational conditions, as well as seismic, hydraulic, and landslide risks. Each attention class dictates specific analyses and Structural Health Monitoring (SHM) activities to enhance structural understanding and safety. This work provides a brief integrated overview of the 2020 Italian Guidelines in conjunction with the 2015 national “*Guidelines for Structural Health Monitoring*” [2], exploring their synergies and identifying key challenges in their application. The potential of SHM technologies is critically assessed, focusing on their role in evaluating structural performance and reducing uncertainties related to material properties and operational conditions.

### 2 THE ITALIAN GUIDELINES FOR BRIDGES

The Italian Guidelines for Bridges (IGB) are characterized by an innovative multi-level and multi-risk approach. The six levels of analysis present a progressive increment in complexity and detail, while the number of bridges that require this analysis should decrease. Level 0 consists of the collection of design information, structural and geometric data, road traffic information, and past maintenance interventions. This census and collection process involves the whole bridge portfolio, as well as levels 1 and 2. Level 1 corresponds to the visual inspection of bridges to verify the design geometry and evaluate the presence of defects, which are noted in the defectiveness sheets provided by the IGB for each structural element. The number of defects and their intensity establish the defectiveness level of the bridge. Further, level 2 evaluates the bridge AC, combining four risk types: structure and foundation, seismic, hydraulic, and landslide. For each risk type, a partial AC is defined as a combination of hazard, vulnerability, and exposure. The combination of the partial ACs leads to a total

AC for the bridge, which influences the application of the following level 3 and 4 analyses. Five ACs are defined, namely, low, medium-low, medium, medium-high, and high. Level 3 is a preliminary assessment of the bridge condition and is performed for bridges with a medium or medium-high AC to assess whether detailed analyses are needed. Level 4 represents a detailed structural analysis of the bridge according to the current standard, and it is mandatory for bridges in high AC. Structures are classified as: “adequate” if the analysis is satisfied for loads with a return period of 50 years, “operative” if the verification is satisfied for loads with a return period of 30 years, or “transitable” if it is verified for loads with a return period of 5 years. Transitable bridges need a maintenance intervention within 5 years, and during this period, can receive restrictions such as roadway partial closure or load limitations. Finally, level 5 corresponds to a resilience evaluation of roadways considering the consequences due to the loss of functionality of the bridge on the entire transport network. However, this level of analysis is not yet detailed in the current version of the IG.

### 3 THE ITALIAN GUIDELINES FOR MONITORING

The Italian Guidelines for Structural Health Monitoring (IGSHM) define the objectives and the minimum requirements for a monitoring system to be installed on a bridge. Two main objectives are identified: (i) the check of the structural performance with respect to specific limit states, e.g., collapse and serviceability, and (ii) the identification of a degrading effect in-act. Thus, based on the monitoring data, surveillance and maintenance activities can be planned, the service life of crucial assets can be evaluated (and extended), and innovative constructive methods or structural schemes can be investigated. Monitoring activities are distinguished in:

- occasional, when performed continuously for a limited period of time (from a few days to 1 or 2 years) to augment the knowledge of the structural performance before and after a rehabilitation activity,
- periodic, when performed continuously for a limited period of time (typically a few hours or days) every few years, to investigate specific degradation phenomena that may occur over time,
- continuous, when the monitoring system is permanently installed on the structure. This monitoring activity is

advised on complex structural systems (e.g., long-span bridges) or for structures that are subjected to rare, accidental, or exceptional actions (earthquakes, collisions, etc.).

While monitoring activities are defined depending on their scopes, the design process of an SHM system usually follows eight steps, herein illustrated in Figure 1.

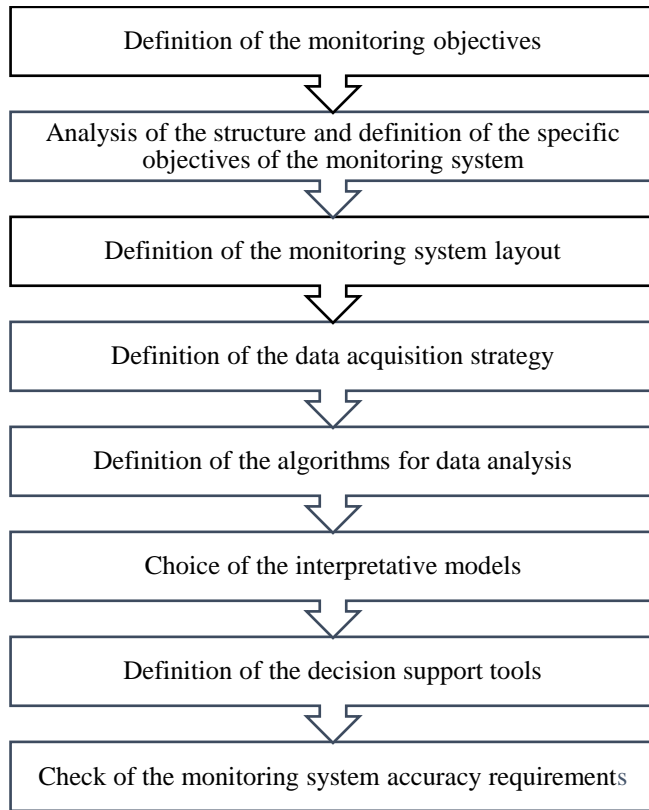


Figure 1: Steps in the design of a monitoring system according to [2].

The monitoring objectives, such as the knowledge of structural performance and the identification of in-act degrading phenomena, can be expressed in terms of an index (of damage, performance, or residual life) or through low-to-high classification (on damage or performance evolution). The estimation of such indices is based on the mechanical (both referring to the structural response and the actions that are applied to the structure), thermodynamic, chemical, or electromagnetic characteristics that are measured on the structure. The layout of the sensors is defined according to the structure types and static scheme, and the model that is used to interpret the collected data. In the case of a vibration-based monitoring system, the layout of the sensors should be conceived to effectively capture the mode shapes and natural frequencies. In doing so, the redundancy of the monitoring system is crucial to limiting the effects of malfunctions.

Therefore, the collected data are processed and interpreted. In some cases, the data already indicate the presence of damage (e.g., the scour depth or a crack size), while in some other cases, such as for a vibration-based monitoring system, data must be processed to estimate the natural frequencies and the mode

shapes. Damage can be detected by investigating the variation of such modal parameters.

Further, decision support tools can be developed based on the collected data by the definition of thresholds on the measured characteristics and associating them with warning alarms and/or interventions.

#### 4 THE ROLE OF SHM IN THE ITALIAN GUIDELINES FOR BRIDGES

Within the IGB, SHM is defined as an essential tool in the optimization of the management of critical infrastructure. Its role extends beyond data acquisition, as it augments structural understanding, reduces epistemic uncertainties, and enhances targeted maintenance scheduling. SHM systems are presented as complementary to inspections, destructive, and non-destructive testing methods, offering continuous information in bridge condition assessment. The real-time monitoring of stress responses, crack propagation, and displacements under operational and extreme load conditions, see Paragraph 6.2 of the IGB, can effectively support structural performance assessment and maintenance scheduling. Further, SHM data can allow for early warning by detecting anomalies and deterioration trends whenever periodic visual inspections are not performed. Emergency response planning can be supported by SHM, as for the cases of landslide (see Paragraph 4.4.2) or hydraulic (see Paragraph 4.5.1) hazards.

SHM is seen to contribute to both diagnosis and prognosis, aiding characterizing the current condition of the bridge and predicting its future behavior. As pointed out in Paragraph 6.3.3.5, SHM enables the calibration and update of bridge numerical models, reducing epistemic uncertainties related to material properties, loading conditions, and model assumptions. Also, as highlighted in Paragraph 7.6, SHM can optimize inspection scheduling by identifying zones of concern and providing long-term trends. The adaptive use of real-time data also supports the dynamic update of threshold values for alerts and interventions (see Paragraph 7.7), facilitating the transition from time-based to condition-based maintenance strategies. Furthermore, the integration of SHM data with Bridge Management Systems (BMS) can aid prioritizing interventions across a network of assets, enhancing long-term planning capabilities and aligning structural management with resilience and sustainability goals.

#### 5 MONITORABLE PARAMETERS IN THE ITALIAN GUIDELINES FOR BRIDGES

SHM can aid at Level 1, Level 2, and Level 4 of the IGB by automatically collecting data about the structural condition and refining the risk classification and the detailed analyses.

At Level 1, the automatic collection of data can both aid (i) detecting damage on bridge components that are not easy to inspect and (ii) investigating the evolution of defects in time.

Within Level 2, numerous parameters are considered in the definition of the attention class, which can be low, medium-low, medium, medium-high, and high. Defects that were detected during the inspections of Level 1, and other parameters proper to the four hazards (structural-foundational, seismic, hydraulic, and landslide) are examined, and an attention class is assigned to each bridge. SHM implementation is advised for medium-high and high attention classes.

A reclassification of the bridge attention class would consider the collected data from a monitoring system, therefore possibly repositioning the bridge in another attention class. Reclassifications are advised periodically or in the case interventions are implemented on the structure. Among the monitorable parameters that drive the risk-based classification, there are:

- Level of Defects, including all the possible defects that can be observed on bridge components,
- Average Daily Traffic, indicating the average number of vehicles that cross the bridge in a day,
- Frequency of commercial transit, indicating the average number of heavy loads, such as lorries, that cross the bridge in a day,
- Scour depth, indicating the erosion of soil or sediment by flowing water, particularly around bridge piers and abutments.

The level of defects is a primary parameter for the evaluation of the vulnerability within the structural-foundational risk, and it is characterized by gravity, intensity, and extension. As demonstrated in [3], the level of defects drives the attention classification – when the level of defects is high, the attention class is high regardless of the other parameters. Thus, the presence of defects with high or medium-high severity (and high intensity and extension) is defined as a critical condition for the attention classification [4]. Several monitoring techniques can be implemented to monitor the evolution of defects, such as extensimeters, tiltmeters, strain gauges, and accelerometers. Novel techniques include Interferometric Synthetic Aperture Radar (InSAR), video-based, and crowd-sensing [5].

The frequency of commercial transit is a parameter that characterizes the structural-foundational hazard within the attention class determination. Heavy loads, such as lorries, represent a criticality for bridge integrity management, as they may exceed the traffic load for which the bridge has been designed.

Further, the average daily traffic characterizes both the structural-foundational hazard and exposure. While together with the frequency of commercial transit is indicative of the traffic demand over the bridge, it is essential in estimating its exposure, i.e., the consequences in case of a collapse. Weight-in-motion systems can be implemented to investigate the load demand on bridges and eventually set limitations [6].

The scour depth is a crucial parameter in the hydraulic risk assessment, specifically for the evaluation of the hazard for the local scour. The scour depth can be monitored by, for example, a vibration-based monitoring system. A decrease in the natural frequency or a variation in the mode shapes may refer to a loss of stiffness in the support of a bridge pier caused by scour.

Noticeably, also the evaluation of the landslide hazard may be supported by SHM data, and its evolution may be monitored through several techniques, such as InSAR.

Within Level 4 of the IGB, SHM may be used to calibrate and update the numerical model that is built for the detailed analysis. Bridge components may be modelled accounting for the defect severity, extension, and intensity, as a local decrease of the component stiffness. Further, the traffic demand on the bridge can be evaluated and modelled to verify the bridge condition and impose traffic limitations. Digital twins (of

physical structures) can be created and continuously updated by SHM data.

## 6 CONCLUSIONS

This work provides a brief integrated overview of the Italian 2020 “Guidelines for Risk Classification and Management, Safety Evaluation, and Monitoring of Existing Bridges” (IGB) and the national 2015 “Guidelines for Structural Health Monitoring” (IGSHM). The role of Structural Health Monitoring (SHM) in the IGB is investigated. Monitorable parameters that can affect the attention classification of Level 2 and the detailed analysis of Level 4 are stated, and possible monitoring techniques are suggested.

## ACKNOWLEDGMENTS

Giancarlo Costa, Pier Francesco Giordano, and Maria Pina Limongelli were partially funded by the Italian Civil Protection Department. The study presented was carried out as part of the program of activities carried out as part of the agreement between the ReLUIS Interuniversity Consortium and the Superior Council of Public Works stipulated pursuant to art. 3 of the Decree of the Minister of Infrastructure no. 578 of 17 December 2020; however, this publication does not necessarily reflect the Council’s position and assessments.

## REFERENCES

- [1] Consiglio Superiore dei Lavori Pubblici, “Linee Guida per la classificazione e gestione del rischio, la valutazione della sicurezza ed il monitoraggio dei ponti esistenti,” 2020.
- [2] UNI Ente Italiano di Normazione, “UNI/TR 11634 ‘Linee Guida per il monitoraggio strutturale.’” 2015.
- [3] G. Santarsiero, A. Masi, V. Picciano, and A. Digrisolo, “The Italian guidelines on risk classification and management of bridges: Applications and remarks on large scale risk assessments,” *Infrastructures*, vol. 6, no. 8, 2021, doi: 10.3390/infrastructures6080111.
- [4] A. Miano, A. Mele, I. Della Ragione, A. Fiorillo, M. Di Ludovico, and A. Prota, “Impact of the Structural Defects on Risk Assessment of Concrete Bridges According to the Italian Guidelines 2020,” *Infrastructures*, vol. 8, no. 9, p. 135, Sep. 2023, doi: 10.3390/infrastructures8090135.
- [5] V. R. Gharehbaghi *et al.*, “A Critical Review on Structural Health Monitoring: Definitions, Methods, and Perspectives,” *Arch. Comput. Methods Eng.*, vol. 29, no. 4, pp. 2209–2235, Jun. 2022, doi: 10.1007/s11831-021-09665-9.
- [6] E. Oliveira Rocheti and R. Moreira Bacurau, “Weigh-in-Motion Systems Review: Methods for Axle and Gross Vehicle Weight Estimation,” *IEEE Access*, vol. 12, pp. 134822–134836, 2024, doi: 10.1109/ACCESS.2024.3461653.



## ANYTWIN - Characterization and standardization of monitoring data

Khadijah Basamad<sup>1</sup>, Oliver Mosig<sup>1</sup>, Matthias Koca<sup>1</sup>, Lakshanadevi Radhakrishnan<sup>1</sup>, Maria Walker<sup>2</sup>, Steffen Marx<sup>2</sup>

<sup>1</sup>Marx Krontal Partner, MKP GmbH, Germany

<sup>2</sup>Institute of Concrete Structures, Faculty of Civil Engineering, Dresden University of Technology, Dresden, Germany

email: khadijah.basamad@marxkrontal.com, oliver.mosig@marxkrontal.com, matthias.koca@marxkrontal.com,  
Lakshanadevi.Radhakrishnan@marxkrontal.com, maria.walker1@tu-dresden.de, steffen.marx1@tu-dresden.de

**ABSTRACT:** Aging bridges were not designed for today's higher traffic loads and often fail to meet current requirements. However, complete demolition or reconstruction is rarely feasible due to resource limitations, sustainability concerns and economic factors. A key issue lies in conservative assumptions regarding loads and resistance. Structural health monitoring (SHM) addresses this by providing real measurement data for a more accurate assessment.

Monitoring produces large volumes of data that must be well-structured and stored for reliable assessments. This requires collaboration between civil engineers, measurement specialists, IT experts, and data analysts. As Building Information Modeling (BIM) adoption grows, standardized monitoring methods must ensure consistency and comply with the Single Source of Truth (SSoT) principle, enabling an integration of monitoring data in a BIM environment.

The ANYTWIN research project aims to develop a framework for structured data storage and processing. It examines how measurement data relates to time and location, defines metadata and information for evaluation criteria and assigns responsibilities for data provision. A processing method ensures data preparation, analysis, and data mining, while quality indicators enhance reliability. These findings contribute to a tendering template, helping to structure monitoring tasks and improve maintenance strategies.

**KEY WORDS:** Structural health monitoring (SHM); Standardization; Monitoring data; Data Quality; Quality Indicator; Tendering template.

### 1 INTRODUCTION

Existing bridges age over time and were not designed for today's significantly higher traffic loads. Many of these structures no longer meet the current verification requirements of the Eurocode. However, complete demolition or new construction is not a practical solution—on one hand, the necessary resources for demolition and reconstruction are lacking; on the other hand, such an approach would be neither sustainable nor economically viable.

A primary shortcoming in meeting verification requirements arises from the conservative assumptions made regarding both loads and resistance. This is where structural health monitoring becomes crucial: by collecting measurement data, a more precise and realistic assessment of the bridge's condition can be made [1][2]. SHM allows for the adjustment of both load assumptions and structural resistance based on actual measurements, thereby enabling more accurate verification.

The monitoring process generates vast amounts of data, which must be well-organized and properly stored to ensure a clear understanding of the bridge's condition. This requires close collaboration among civil engineers, measurement experts, IT specialists and data analysts. As part of the ongoing digitalization effort and the adoption of Building Information Modeling (BIM), this collaboration should be enhanced while adhering to the Single Source of Truth (SSoT) principle. In a digital environment, such as a digital twin, various datasets and information sources converge, interconnect, and depend on each other. A structured representation of these relationships is essential for seamless integration. While the IFC model primarily serves as a static representation, it provides key

information for monitoring, including the positions of individual measurement points, cable routing and other infrastructure details.

However, the digital twin extends beyond this by dynamically reflecting the current sensor status, generating meaningful analyses of physical parameters at these points, and integrating diagnostic method data for a more comprehensive assessment. This approach enables a real-time, data-driven understanding of structural conditions. All of this should be guided by the principle that the digital twin serves as the SSoT, ensuring that all information is consistently structured, linked, and accessible within a unified system.

To achieve this, monitoring methods should be standardized and incorporated into data-based load-bearing safety checks in civil engineering [3].

This is precisely the aim of the ANYTWIN research project [4], [5], [6]. The goal of the project is to establish a clear structure for collecting, storing and processing monitoring data. Different types of measurement data are analyzed and classified to ensure systematic storage. The project investigates how measurement data is connected over time and space, identifies key details necessary for evaluation, and defines responsibilities for data provision. A processing method is also developed to ensure that the data is transformed into clean and usable time series. Finally, the project establishes the quality requirements that the data must meet for specific verification purposes and defines quality indicators for assessment.

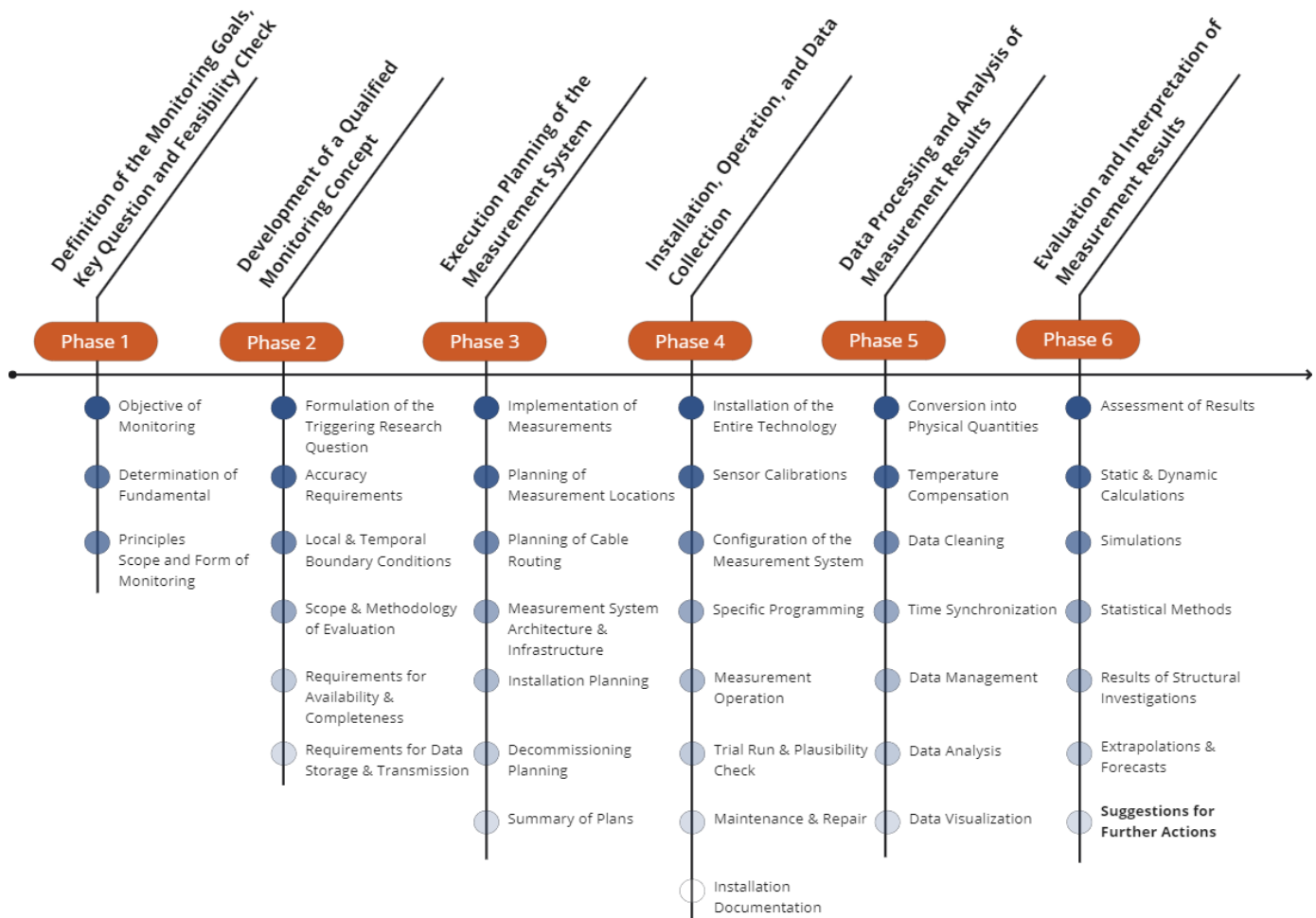


Figure 1. Representation of the individual phases of a monitoring process based on the DBV guideline [11], © MKP GmbH

All these findings will contribute to the standardization of tendering processes, providing project owners with a comprehensive overview of monitoring tasks and the respective responsibilities of all involved experts. The objective is to generate significant value for the future maintenance and management of bridges [7].

## 2 IMPLEMENTATION OF MONITORING IN BRIDGE CONSTRUCTION

The implementation of monitoring in bridge construction is still not a standardized procedure and is typically conducted on a case- by-case basis [8], [9], [10]. However, a structured approach has been established, based on the recommendations of the DBV guidelines [11]. According to these guidelines, the monitoring process consists of six phases, ranging from defining the objective, planning, installation, and operation of the monitoring system to the evaluation and assessment of measurement results (see Figure 1). In practice, these phases have not yet been fully standardized.

Regardless of the specific task, certain measurement parameters and objectives have been identified as crucial for the effective implementation of monitoring.

Specifically, for damage detection and computational verification in structural monitoring, the following measurement objectives are relevant:

**Temperature & Environment:** Measures temperature differences and climatic effects (e.g., temperature sensors, humidity sensors, thermocouples, resistance thermometers, infrared detectors). These parameters are crucial for assessing thermal loads on structures.

**Moisture Measurements:** Detects humidity levels and influences such as corrosion or mineral formation that can lead to durability issues (e.g., humidity sensors, multi-ring electrodes).

**Fatigue & Cracks:** Identifies stress, strain, and early cracks (e.g., strain gauges, DFOS [12], Acoustic Emission Sensors (AE Sensors) [13]), which are strong indicators of structural load-bearing capacity.

**Deformation & Movement:** Monitors settlements, vibrations and inclinations (e.g., displacement sensors, tilt sensors, acceleration sensors, distance sensors). By analyzing geometric changes at micro, meso and macro levels, insights into bearing movements, expansion behavior, creep & shrinkage, and crack formation can be derived.

**Load & Traffic:** Detects overloads and load distribution (e.g., pressure sensors, laser measurement systems), which are critical for understanding structural performance under varying traffic loads.

**Vibration Monitoring:** Assesses dynamic structural properties, such as natural frequencies and damping values, which provide insights into fatigue behavior and potential damage (e.g., accelerometers, vibration velocity sensors).

**Acoustic Monitoring:** Captures sound events to track damage progression caused by localized failure events (e.g., AE Sensors [13]).

The selection of sensors depends on the measurement objective, type of structure, and environmental conditions and is adapted to specific requirements. Figure 2 illustrates some examples of sensors and measurement systems used for bridge monitoring.

### 3 TYPES OF MONITORING DATA AND SENSORS

The efforts to standardize the handling of monitoring data obtained in the context of SHM require a comprehensive examination and description of the characteristics and typical features of such data. This foundational understanding enables subsequent classification and the formulation of universally applicable procedures for processing, evaluation, data manipulation, and establishment of quality requirements.

The term 'monitoring data' refers to the entirety of data generated in the context of SHM. In typical monitoring processes, sensor measurement data constitute the predominant volume of data. However, for effective information extraction, it is crucial to link these data with metadata, defined as all data describing the measurement.

In the initial phase of this study, the measurement data are examined. Measurement data include all data that originate directly from sensing devices on the structure. To account for the increasing technological capabilities of system-on-a-chip (SoC) solutions and edge computing, the term is also applied to data generated through automated process steps close to the sensor or hardware level, provided that their characteristics allow them to be treated as measurement data.

To illustrate the range of potential measurement data sources, typical measurement methods and their use cases briefly presented in Section 2, serves as a reference. The list focuses on recognized and proven methods without claiming to be exhaustive.

The classification of measurement data can be based on various criteria and is generally necessary to address both software-related aspects in the creation of a storage and processing infrastructure, as well as content-related aspects for the metadata to be collected.

One fundamental property describes the data in relation to a *measurement location*. Three main variants can be distinguished: point measurement methods, line measurement methods, and field measurement methods.

- **Point measurement methods** (e.g., strain gauges) provide information about a discrete measurement point with a very small spatial extent relative to the structure being monitored.
- **Line measurement methods** (e.g., distributed fiber optic sensing (DFOS) [12]) generate measurement data along a line with high spatial resolution.
- **Field measurement methods** (e.g., photogrammetry) can be used for measurements over a larger (surface) area.

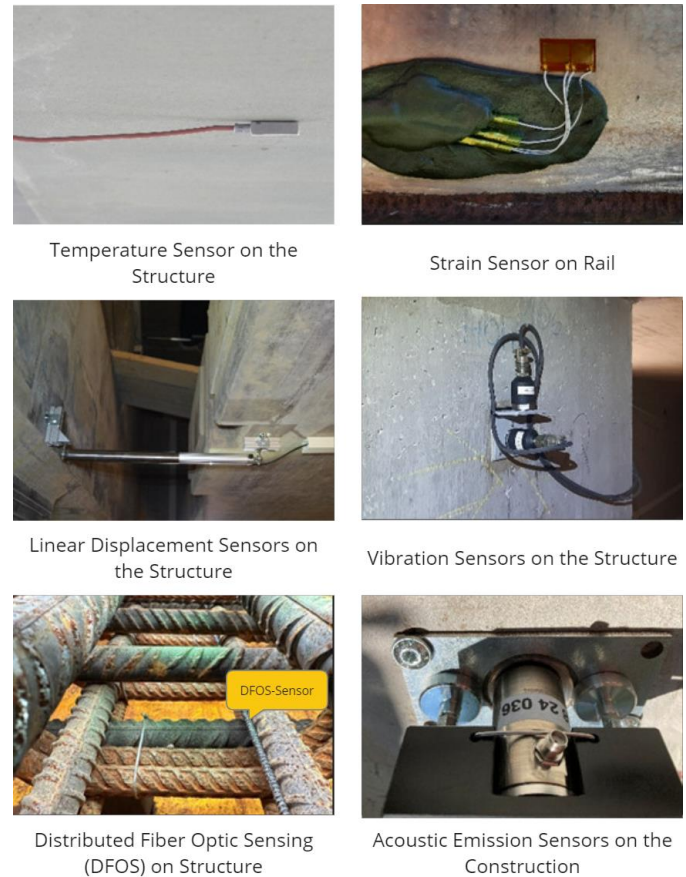


Figure 2. Example of Sensor Technology in Structural Monitoring in Use, © MKP GmbH

A second classification criterion characterizes *the temporal structure* of the measurement data. Continuous and discontinuous data can be distinguished:

- **Continuous data** are stored throughout the entire monitoring period with equidistant time intervals between consecutive data samples, typically with a low sampling rate (ranging from several minutes to hours).
- **Discontinuous data** are recorded over a typically short period of time at a high sampling rate. The recording time can be determined either by a predefined time pattern or by data-dependent trigger conditions.

Another classification option concerns *the temporal reference* of the measurement data. The simplest case is a direct assignment between the individual instantaneous value of the measurement signal and the timestamp. A further possibility is that the measurement data refer to a time-extended measurement interval, such as in the case of averaging. Even more complex time reference descriptions arise with methods like Rainflow counting or Fast Fourier Transform analysis (FFT).

A fundamental category of properties for the storage structure of measurement data is *the dimension of the index* required to address a measurement value. Besides storage, this also determines the programmatic interfaces to processing algorithms. The most common attributes in this category are:

- 1 index value per single measurement value,
- 1 index value per n measurement values, and
- 2 index values per 1 measurement value.



For time series, the index always includes at least the timestamp. Additional index values may be required, for example, to identify a location or direction.

Finally, a classification can be made based on *the underlying measurement instrument(s)* of the data. This is mainly used when assigning technical metadata. A key distinction is whether the data originate from a single, clearly identifiable sensor (element) or whether a sensor combination, a sensor array, or an automated/autonomous processing algorithm (e.g., a Weigh-In-Motion (WIM) system) should be considered as the data source.

Table 1 provides an overview of the key characteristics of the measurement data (measurement location, temporal structure, temporal reference, index dimension, and technical data source) and categorizes them into subgroups (a to c). Each subgroup was formed by identifying up to three distinct properties for each feature. This classification facilitates the systematic organization and comparison of different types of measurement data and supports further analysis and processing.

Table 2 provides an evaluation of the characteristics describing the generated measurement data based on the

established classification system for specific measurement methods and sensor technologies. It categorizes different sensors according to common characteristics and highlights potential groupings.

To facilitate abstraction, a '1' is assigned to applicable feature variants and a '0' to non-applicable ones. Gray shading is used to highlight transitions within a category. A gray mark appears in the feature column 1 to 5 whenever the assignment within a feature category changes from 0 to 1 or 1 to 0.

Through this visual grouping, at least seven sensor groups can be identified. Sensors sharing the same color pattern are classified into the same category. In this case, temperature sensors up to acceleration sensors (Table 2) are grouped together, as they exhibit identical feature combinations across the evaluated categories. In contrast, the multi-sensor system differs from these sensors, which typically measure a single physical quantity. Instead, a multi-sensor system can generate multiple independent measurement variables. As a result, its classification varies, particularly in Feature 5 (technical data source).

Table 1. Presentation and classification of characteristics for describing the generated measurement data

Classification option	Property 1 (a)	Property 2 (b)	Property 3 (c)
Feature 1: measurement location	Point measurement method	Line measurement method	Field measurement method
Feature 2: temporal structure	Continuous time-series-data	Discontinuous time-series-data, segments with fixed time interval	Discontinuous time-series-data with event-driven time interval
Feature 3: temporal reference	Single instantaneous value	(statistical) value derived from a time span	Indirect value based of underlying data
Feature 4: index dimension	1 index per 1 measurement sample	1 index per n measurement samples	2 indices per 1 measurement sample
Feature 5: technical data source	Direct data - sensor alignment	Indirect data-sensor alignment	-

Table 2. Evaluation of characteristics for describing the generated measurement data from various measurement systems

Examples of measurement systems	Feature 1			Feature 2			Feature 3			Feature 4			Feature 5	
	a	b	c	a	b	c	a	b	c	a	b	c	a	b
Temperature sensors	1	0	0	1	1	0	1	1	0	0	1	0	1	0
Strain gauges	1	0	0	1	1	0	1	1	0	0	1	0	1	0
Displacement sensors	1	0	0	1	1	0	1	1	0	0	1	0	1	0
Acceleration sensors	1	0	0	1	1	0	1	1	0	0	1	0	1	0
Multi-sensor	1	0	0	1	1	0	1	1	0	0	1	0	0	1
Corrosion sensor	1	0	0	1	0	0	1	0	1	0	1	0	1	0
Weigh-in-Motion (WIM)	1	0	0	0	0	1	1	0	1	0	1	0	1	0
AE Sensors	1	0	0	0	0	1	0	1	1	0	1	0	1	0
DFOS	0	1	0	0	1	0	1	0	0	0	0	1	1	0
Laser scan	0	0	1	1	0	1	0	0	1	0	0	1	1	0
Tachymeter-total station	0	0	1	1	0	1	0	0	1	0	0	1	1	0

Considering the goal of this grouping, it is crucial for data structuring to determine how measurement values should be assigned to their respective IDs or timestamps. Only Feature 1 and Feature 4, which are marked with bold borders in the table, are representative in this context.

These groupings reflect common classification features, allowing them to be treated as uniform types when assigning descriptive metadata, organizing data storage, and designing input and output interfaces for data processing.

For Feature 1, continuity on the spatial scale does not impact data structuring, thereby reducing the number of groups to two. For Feature 4, the key question is whether data should be structured as an array or a matrix. This decision is essential for grouping, as both Features (1 and 4) can be combined. The result is a definite grouping of sensors, which simplifies data structuring and enhances the readability of the stored data.

#### 4 RELEVANT METADATA AND ADDITIONAL INFORMATION IN BRIDGE MONITORING

In addition to the actual measurement data, another essential category of data exists: metadata and metainformation. For evaluations and measurement-based verifications, obtaining specific data and information from the measuring point on the structure and metadata from the installed measurement system or sensors is of great importance. This data is needed to apply the calculation method in data processing and evaluation while ensuring traceability of time-based trends, providing a comprehensive understanding of the structure's behavior over time and at specific locations.

According to the definition in the ANYTWIN research project, *metadata* refers to numerical, machine-readable values that can be assigned to sensors or measurement systems. In contrast, *metainformation* consists of structured, interpreted content and descriptions provided by actors, such as textual explanations. Both types of data are characterized by their stability, as they are generally static and determined once. An exception is when a sensor is replaced, which necessitates an update of the metadata and metainformation.

Metadata is defined either during the development of the measurement concept or determined after sensor installation. It can be divided into two main categories:

1. **General metadata for sensor types** – Cross-sensor information, such as the measurement method, the unit of the electrical signal, and the function used to convert the electrical signal into physical values.
2. **Specific metadata for installed sensors and measurement points** – These are unique to each installed sensor, its measurement system, and the respective measuring location. They include:
  - Sensor characteristics: such as conversion factors and calibration parameters
  - Measurement parameters: such as sampling rate, measurement ranges and spatial resolution
  - Measurement point characteristics: such as material properties like modulus of elasticity or thermal expansion coefficient
  - Technical properties of the measurement system: such as frequency range and filtering methods

- Additional evaluation parameters like installation values, calibration data and sensor orientation

In addition to metadata, additional informative metainformation is available, providing details about the installed sensors and measurement techniques. This data is not necessarily included in the metadata and is not directly relevant for data evaluation. However, it is important for traceability, quality assurance, and functional verification of the sensors, for example, in assessing their lifespan.

Unlike metadata, metainformation does not have to be stored in a machine-readable format. While it may include similar categories as metadata, it provides additional details that do not directly contribute to data analysis, such as:

- Measurement parameters: Additional metrics, such as the maximum measurement range or sensor frequency range
- Influencing factors: Environmental conditions, temperature compensation, background noise
- Technical properties of the measurement system: Connection type, measurement amplifier specifications
- Structural properties of the measurement points: Sensor protection mechanisms, material characteristics, installation date, expected lifespan

Table 3. Overview of metadata and metainformation categories and actors responsibilities

	Monitoring specialist planner	Structural monitoring service provider
<b>General metadata for sensor type</b>		
Measurement method (relative/absolute)	-	✓
Unit of the electrical signal	-	✓
Function model	-	✓
<b>Specific metadata from installed sensors and measurement points</b>		
Sensor characteristics	-	✓
Measurement parameters	-	✓
Measurement point characteristics	✓	-
Properties of the measurement system	-	✓
Additional parameters for evaluation	✓	-
<b>Informative data for documentation and traceability</b>		
Measurement parameters	-	✓
Influencing factors	✓	✓
Technical properties of the measurement system	-	✓
Structural properties of measurement points	✓	✓

Metadata and metainformation are provided and documented by different actors involved in various phases of the monitoring process. The monitoring specialist planner defines general sensor metadata and metainformation during the planning phase and in the creation of the measurement concept. This includes key parameters of the measurement point, such as surface area or modulus of elasticity. The specialized service provider for structural measurements is responsible for recording and providing specific sensor metadata and metainformation during installation. Additionally, they handle sensor calibration and update metadata and metainformation during maintenance or sensor replacement to ensure measurement accuracy and data consistency.

Table 3 provides an overview of common metadata types and the corresponding roles of actors.

## 5 DATA PROCESSING MODEL

Structural monitoring encompasses the processes of data acquisition, including data transmission and management, as well as data analysis, which involves evaluation, validation, and plausibility checks. Based on this, an assessment of the current structural condition or a forecast of future structural behavior can be conducted. This sequential process can also occur cyclically, with the system continuously receiving new data. Prior to this cyclical process, the preparation of the monitoring measures can be implemented. The success of a monitoring project largely depends on a structured workflow, where the monitoring objective remains the central focus [11].

This section introduces the data processing model developed in the ANYTWIN research project for monitoring data. This model aims to combine various sensor types, short-term, long-term, and continuous measurements, as well as different data processing methods, including machine learning, into a single process.

The model is based on well-known data processing models (CRISP-DM, SEMMA, Fayyad, DBV guidelines, Farrar) and consists of eight main steps [11], [14], [15], [16], [17], [18]. These steps are highlighted in orange in Figure 3. Additionally, the feedback loop, highlighted in blue, ensures that the

collected data meets the required quality standards and that the resulting maintenance recommendations are well-founded and reliable. All process steps are iterative. This means that it may be necessary to go back and repeat previous steps to refine the analysis and improve the results.

Quality management is an ongoing process that spans the entire monitoring workflow – from defining the research objective to planning and installing the system, and finally to analyzing the collected data.

In the first step, the objective of the monitoring measures is defined, specifying which aspects of the collected data should be analyzed and evaluated. This includes determining which parameters need to be monitored, what results are expected, and what resources are available for the monitoring process. This step involves developing the monitoring concept and preparing a tender. Additionally, success criteria for achieving the monitoring goals must be established, and suitable quality assurance methods (such as quality indicators, threshold values, and compensation methods) must be selected.

In the second step, the measurement system is installed on the structure. This step may also include retrofitting an existing measurement system. It is essential to conduct quality checks immediately after installation, such as function tests and plausibility checks, to ensure proper system performance.

In the third step, data collection is conducted to acquire the necessary information for subsequent analysis, which captures the impacts and/or responses of the structure. This step marks the beginning of the cyclical process of data collection, processing, and evaluation. At this stage, quantifiable quality measures are applied for the first time to ensure an objective assessment of data quality, independent of the specific task (these measures are detailed in Section 6). These quality indicators are also used in the next steps of data processing as they serve to monitor changes in data quality.

The fourth step, data selection, involves choosing the necessary and relevant data to answer the formulated question. This selection can be spatial (e.g., sensors in specific structural areas) or temporal (e.g., data from summer months). When applying machine learning methods, this step also includes

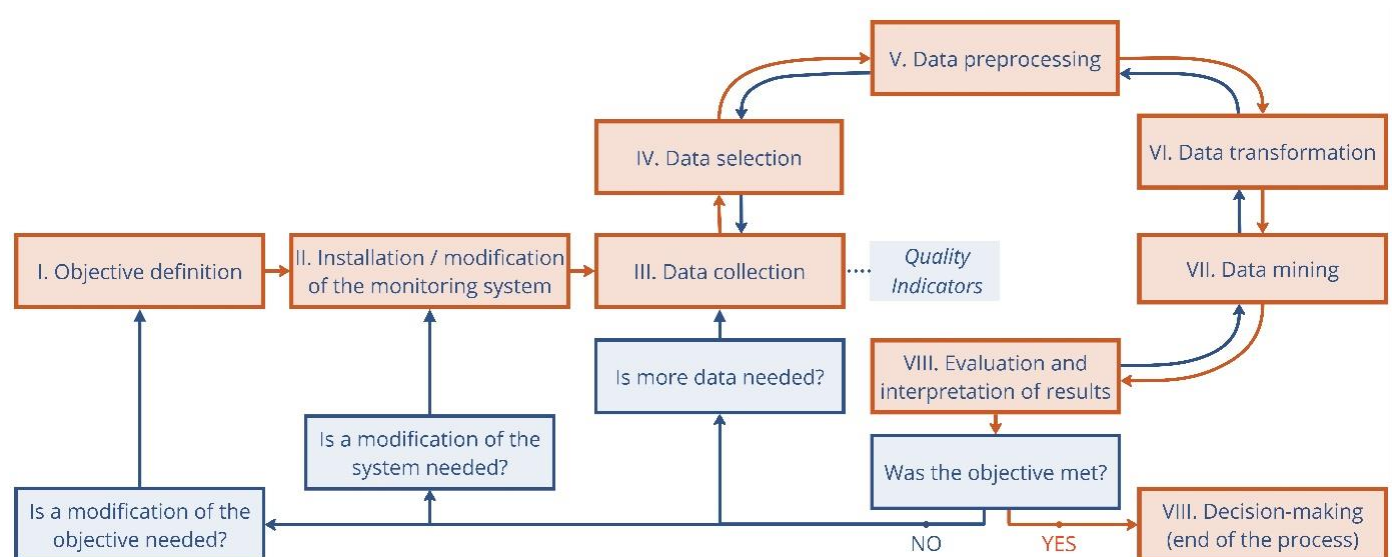


Figure 3. Data Processing Model in ANYTWIN project: Orange arrows represent the data processing workflow, while blue arrows illustrate the feedback loop, © Maria Walker, TUD.



selecting the data that will be used in the feature engineering process.

Data preprocessing follows (step five), which includes data preparation tasks such as converting electrical signals into physical measurements, temperature compensation, time synchronization, signal cleaning, and data normalization. After each preprocessing step, a new data quality assessment is performed. The goal of data preprocessing is to enhance the inherent (task-related) data quality [19].

In the sixth step, system-dependent data quality is addressed. Data from various sources and measurement systems are standardized into a common structure and enriched with metadata. This standardization ensures that the data can be automatically processed by data mining algorithms in the subsequent step.

The seventh step involves the actual data analysis or data mining, during which information is extracted from the data. This process may involve simple calculations, such as determination of mean values, maximum and minimum values, or counting algorithms, as well as the training and application of complex machine learning models to identify patterns in the dataset and to detect characteristic sequences in the data.

The final step involves the evaluation and interpretation of the data mining results in relation to the initial question and predefined success criteria. The findings are assessed based on their validity, novelty, usefulness, and understandability. Based on these insights, necessary actions are determined, such as rehabilitation, load reduction, maintenance, reconstruction, or further monitoring measures. Additionally, this step includes a final assessment of the entire monitoring process and of the installed monitoring system to ensure its overall effectiveness.

## 6 QUALITY ASSESSMENT OF DATA USING QUALITY INDICATORS

To ensure reliable analysis and evaluation of structural behavior, the quality of measurement data must be guaranteed. It is crucial to eliminate anomalies in measurement data and deviations in time signals to achieve precise data evaluation of the structure's performance. However, measurement anomalies and deviations are inevitable and can be caused by various factors, including:

- Electromagnetic interference, leading to signal noise or data distortion
- Direct interventions on-site, such as maintenance work or sensor replacements
- Transmission errors, resulting in incomplete or faulty data
- Malfunctions in the measurement system, caused by calibration errors or hardware defects

In monitoring systems, which encompass interconnected and complex structures of measurement technology, data transmission, and IT aspects, anomalies in measurement data can occur. Therefore, it is essential to implement appropriate quality assessment methods to detect measurement anomalies early, correct or remove them if necessary, and optimize the monitoring system to ensure the reliability of the measured values.

As part of the ANYTWIN project, the requirements from measurement-based verifications are considered to systematically assess data quality. For this purpose, quality indicators have been developed to enable a structured and

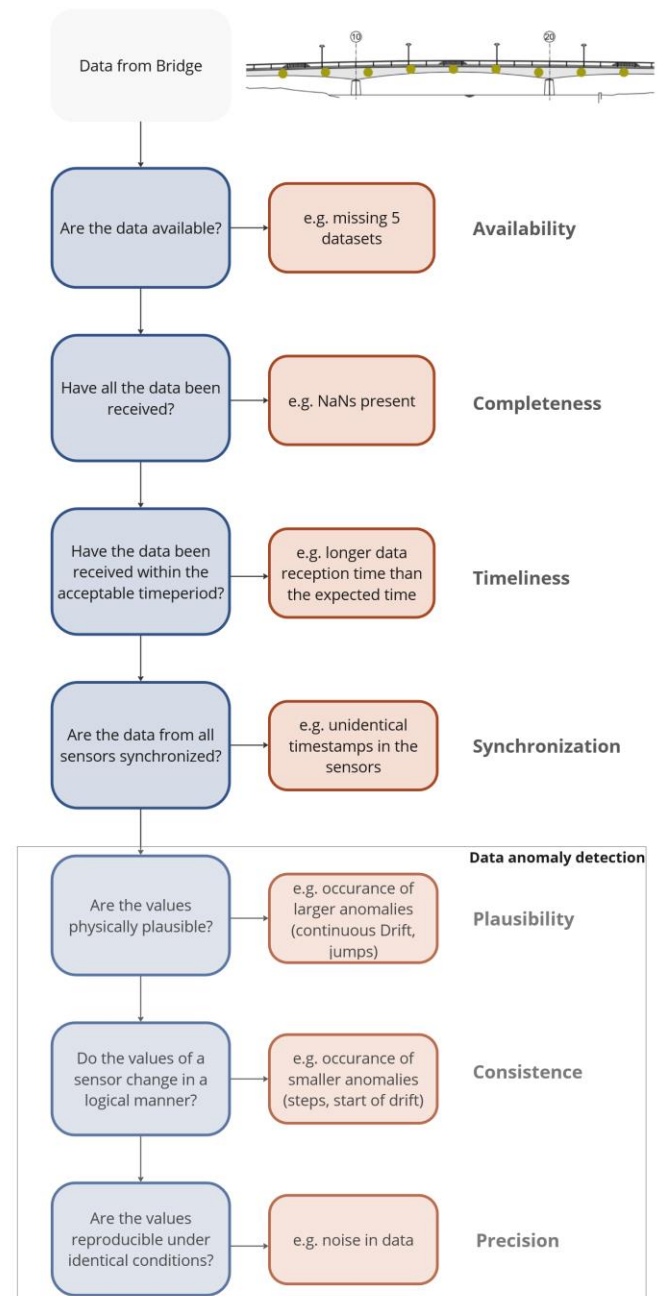


Figure 4. Overview of quality indicators and the addressed questions

objective evaluation of monitoring data in terms of its quality. The development of these indicators takes various use cases into account, including:

- Measurement-based verifications, allowing for a precise assessment of structural safety,
- Continuous monitoring with an integrated alarm system for early detection of deviations,
- Digital twins, enabling detailed modeling and data-driven evaluation of structural behavior.

For this purpose, both the status of the measurement system and the quality of individual time signals at the sensor level are analyzed. At the *dataset level*, key questions include:

- Are the data available, complete, and up to date?

- Are the measurements time-synchronized, ensuring that dependencies between two measured variables are reliably considered?

From these questions, the quality indicators availability, completeness, timeliness, and synchronization can be identified (see Figure 4).

**Availability:** Checks whether the expected measurement data has been received within a certain time window.

**Completeness:** Checks whether the received data contains all the required fields and sensor data records.

**Timeliness:** Checks if the measurement data arrives within an acceptable delay period.

**Synchronization:** Checks whether the multi-channel sensor data  $s$  is synchronized in time.

The indicators that assess the condition of the measurement system – availability, completeness, and timeliness – can be quantified by calculating the percentage of available and non-missing data points within a defined time-period. To evaluate synchronization, the timestamps of individually generated time series (each measurement system) are analyzed.

The second aspect, *the sensor level*, focuses on detecting potential measurement anomalies, such as outliers, jumps, unusual temporal trends, drift, or signal noise. Based on these possible signal anomalies, the following quality indicators can be identified:

**Plausibility:** Checks whether the received values fall within physically plausible limits, allowing the identification of measurement anomalies such as outliers or jumps that are visibly apparent.

To assess the plausibility of the data and determine whether it falls within a physically realistic range, initial filtering or thresholding can be used to define permissible limit values. Plausibility calculation involves verifying whether the measurement value lies within these physically plausible limits. In a second step, advanced regression methods can be applied to detect further apparent measurement anomalies in the signal.

**Consistency:** Evaluates whether the change in sensor values is consistent with respect to environmental changes. This enables the detection of drift and noticeable patterns in

temporal trends, such as step-like changes. While plausibility checks whether the data falls into a certain range, consistency compares current data with historical values and determines if the change in value is consistent with environmental changes (see Figure 5).

Consistency calculation is based on analyzing the differences between consecutive measurements. The standard deviation of these differences is determined and normalized by their mean value. A low standard deviation indicates high consistency, while a high standard deviation suggests irregular changes and, consequently, potential inconsistency. With consistency calculation, smaller or less apparent anomalies such as start of drift, step-formation can be detected.

**Precision:** Refers to the repeatability of measurements under identical conditions, ensuring the stability and reliability of sensor data. This helps to identify noise in the signal.

The precision of a measurement signal indicates the extent of value dispersion in repeated measurements. High precision means that the measured values are closely clustered, while low precision suggests random fluctuations and an increased level of noise. Mathematically, the precision assessment is based on the standard deviation of the measured values within a defined time window, relative to an acceptable variation range.

To quantitatively represent the indicators, the percentage of measured values that fall outside a defined tolerance range can be determined. Table 4 provides a comprehensive overview of the mathematical formulas used for detecting measurement anomalies, quantifying the indicators, and describing the relevant parameters.

The results of the quality indicators are also time series, but with a lower frequency than the actual measurement data, as they are based on aggregated time windows. Storing these indicators as time series allows for better integration into digital twins and facilitates the analysis of relationships between indicators, leading to a better understanding of the measurement data and its quality.

These indicators can be integrated into the partial safety factors of structural assessments as part of measurement-based verifications. This allows systematic consideration of

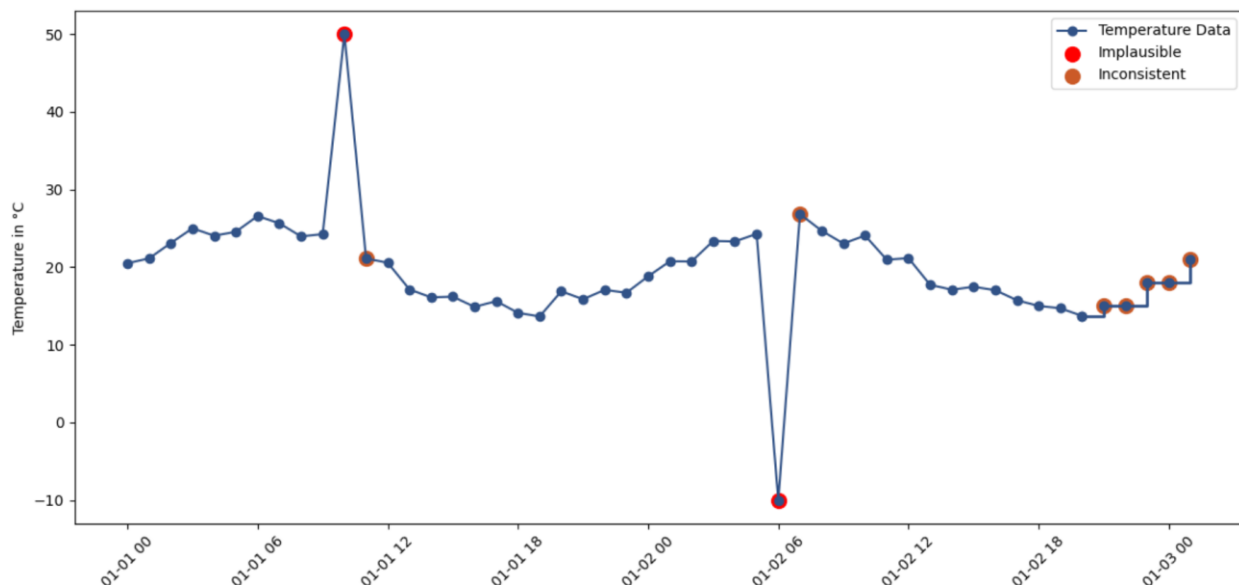


Figure 5. Example of temperature data containing implausible and inconsistent values

uncertainties related to measurement technology, data transmission, IT, and numerical aspects and quantification in the form of modified partial safety factors. However, further

research and development is needed to optimize these approaches and ensure their practical applicability.

Table 4. Overview of mathematical formulas for quantifying quality indicators

Indicator	Mathematical Formula for measurement errors detection	Quantification of the indicators	Description of the parameters
Availability	---	$\frac{N_{rec}}{N_{exp}} \cdot 100 \%$	$N_{rec}$ – Number of received data points $N_{exp}$ – Total number of expected data points
Completeness	---	$\frac{N_{comp}}{N_{exp}} \cdot 100 \%$	$N_{comp}$ – Number of complete data points (without missing fields) $N_{exp}$ – Total number of expected data points
Timeliness	$\Delta T = T_{now} - T_{last}$	$\frac{N_t}{N_{exp}} \cdot 100 \%$	$N_t$ – Number of data points received within the acceptable delay interval, $T_{max}$ with respect to current timestamp ( $\Delta T \leq T_{max}$ ) $N_{exp}$ – Total number of expected data points $T_{now}$ – Current time $T_{last}$ – Time of last received data
Synchronization	$\Delta T = T_{sync}$ $T_{sync} =  T_{S1,i} - T_{S2,i} $	$\frac{N_{sync}}{N_{exp}} \cdot 100 \%$	$N_{sync}$ – Number of synchronized data points $N_{exp}$ – Total number of expected data points $S_1$ & $S_2$ – Measurements from Sensor1 and Sensor2 $TS_{1,i}$ & $TS_{2,i}$ – Timestamp of Sensor1 and Sensor2 at row $i$ . $T_{sync} =  TS_{1,i} - TS_{2,i} $
Plausibility	Level 1: Filtering and thresholding Level 2: with/without ML-model	$\frac{N_{pl}}{N_{exp}} \cdot 100 \%$	$N_{pl}$ – Number of plausible data points $N_{exp}$ – Total number of received data points
Consistency	$1 - \frac{\sigma_{\Delta x}}{\mu_{\Delta x} + \epsilon}$ (or) with/without ML-model	$\frac{N_{con}}{N_{exp}} \cdot 100 \%$	$\sigma_{\Delta x}$ – Standard deviation of consecutive differences ( $\Delta x_i = x_i - x_{i-1}$ ) $\mu_{\Delta x}$ – Mean of consecutive differences $\epsilon$ – Small constant (to avoid division by 0, e.g. $10^{-6}$ ) $N_{con}$ – Number of consistent data points $N_{exp}$ – Total number of expected data points
Precision	$1 - \frac{\sigma}{R}$	$\frac{N_{pr}}{N_{exp}} \cdot 100 \%$	$N_{pr}$ – Number of data points without noise $N_{exp}$ – Total number of expected data points $\sigma$ – Standard deviation of the measurements $R$ – Acceptable variation range

## 7 SUMMARY

Bridge monitoring is a key component of structural assessment to ensure safety and longevity. Despite its growing importance, monitoring is not yet a standardized procedure and is mostly implemented on a case-by-case basis. A structured approach can follow the recommendations of the DBV guidelines.

The sensor market is expanding rapidly, with increasingly intelligent and complex technologies for measuring temperature, material fatigue, deformation, and traffic loads. Innovations such as System-on-a-Chip (SoC) and edge computing, including Weigh-in-Motion (WIM) systems, enable greater automation of data collection but require systematic storage and analysis.

A precise data classification and standardization are essential for efficiently processing monitoring data and making it usable for digital twins or measurement-based verifications. Classification is based on positional reference (point, line or field measurements), time-based structure (continuous or

discontinuous data), and time reference (instantaneous values, averaging or advanced methods such as Rainflow counting or FFT analysis).

Beyond the actual measurement values, metadata and additional information play an essential role in correctly interpreting the collected data. Metadata consists of machine-readable values assigned to sensors and measurement systems, while metainformation includes structured documentation details. A clear assignment of responsibilities for collecting and managing this data is necessary to maintain a consistent data foundation.

The ANYTWIN data processing model integrates various sensor types, measurement durations, and data processing methods, including machine learning, into a structured eight-step process. It follows established data processing frameworks (CRISP-DM, SEMMA, Fayyad, DBV guidelines, Farrar) and ensures data quality through an iterative feedback loop.

The process begins with defining the monitoring objective, followed by system installation and data collection. Next, data



selection, preprocessing, and standardization ensure structured and high-quality input for data mining and analysis. Finally, the results are evaluated and interpreted to support structural assessments and maintenance decisions. This structured workflow enables continuous monitoring and reliable decision-making in structural health management.

A key aspect of data analysis is the evaluation of data quality using quality indicators, which are categorized into system level (availability, completeness, timeliness, synchronization) and sensor level (plausibility, consistency, precision). At the system level, data is assessed for availability, completeness, timeliness, and synchronization. At the sensor level, the focus is on evaluating the quality of individual measurement series, particularly in identifying measurement deviations and anomalies. To detect and quantify measurement anomalies and uncertainties, statistical methods such as filter functions, regression analyses, and standard deviations are applied. These methods enable a precise assessment of measurement data, contributing to improved data evaluation.

By storing these indicators as time series, they can be integrated into digital twins. Furthermore, they could be incorporated into measurement-based verifications by serving as a foundation for modified partial safety factors, considering uncertainties in measurement technology and data processing. While these approaches are promising, further research is required to enable their practical implementation in structural monitoring.

## ACKNOWLEDGMENTS

This paper presents the findings of the ANYTWIN research project, which is funded by the German Federal Ministry for Digital and Transport (BMDV) as part of the mFUND funding program (Funding Reference Number: 19FS2248A-F). We sincerely acknowledge this support, which has enabled the advancement of research and innovation in this field.

## REFERENCES

- [1] S. Zhang, M. Käding, M. Wenner, M. Claßen, and S. Marx, Structural health monitoring (SHM) on a long semi-integral high-speed railway bridge (HSRB) under different traffic loads, *Engineering Structures*, 15 February 2025.
- [2] R. Herrmann, F. Hille, S. Pitters, E. K. Ramasetti, R. Schneider, F. Wedel and I. Hindersmann, Förderiertes Datenmanagement von Monitoringdaten aus Structural Health Monitoring Anwendungen und daraus gewonnenen Trainingsdaten bei Spannbetonbrücken, 11. Jahrestagung des DAfStb mit 63. Forschungskolloquium der BAM Green Intelligent Building, Berlin, S. 178 – 185, 16. – 17. Oktober 2024
- [3] A. Lazoglu, J.-H. Bartels, R. Stein, M. Maibaum, L. Puttkamer and L. Ulbrich, ANYTWIN – standardizing monitoring-based safety assessments of bridges and the integration into Digital Twins, In: Sandager Jensen, J.; Frangopol, D.M.; Wittrup Schmidt, J. (Hrsg.): Bridge Maintenance, Safety, Management, Digitalization and Sustainability, IAMBAS 2024, Kopenhagen, S. 808, 2024.
- [4] P. Esser, M. Walker, A. Lazoglu, L. Ulbrich, O. Mosig and S. Marx, Charakterisierung Digitaler Brückenzwillinge zur Integration messwertgestützter Tragsicherheitsnachweise, *Bautechnik*, 2025.
- [5] P. Esser, M. Walker, A. Lazoglu, L. Ulbrich and S. Marx, ANYTWIN – Charakterisierung Digitaler Brückenzwillinge zur Integration messwertgestützter Tragsicherheitsnachweise In: Müller, M. (Hrsg.): Tagungsband des 6. Brückenkolloquium. Fachtagung für Beurteilung, Instandsetzung, Ertüchtigung und Ersatz von Brücken, Technische Akademie Esslingen, S. 409 – 416, 01. - 02. Oktober 2024.
- [6] M. Walker, J.-H. Bartels, P. Esser and S. Marx, Integration of Monitoring-Based Safety Assessments of Bridges into Digital Twins, *fib International PhD Symposium in Civil Engineering*, 2024.
- [7] M. Wenner, Monitoring – Zukunft des Erhaltungsmanagements von Brücken Baukongress – Die Zukunft des Bauens, Aachen, 12. – 13. June 2024
- [8] F. Wedel, S. Pitters, F. Hille, R. Herrmann and R. Schneider, Leitfaden – Strategischer Einsatz von Monitoring für Ingenieurbauwerke Bundesanstalt für Straßenwesen (Vorabveröffentlichung)
- [9] F. Hille, R. Herrmann, S. Pitters, I. Hindersmann, R. Schneider and F. Wedel, Leitfaden für den strategischen Einsatz von Monitoring an Straßenbrücken 11. Jahrestagung des DAfStb mit 63. Forschungskolloquium der BAM Green Intelligent Building, Berlin, S. 186 – 191, 16. – 17. Oktober 2024.
- [10] F. Hille, R. Herrmann, R. Schneider, S. Pitters, F. Wedel and I. Hindersmann, Developing a guideline for structural health monitoring of road bridges in Germany, In: Sandager Jensen, J.; Frangopol, D.M.; Wittrup Schmidt, J. (Hrsg.): Bridge Maintenance, Safety, Management, Digitalization and Sustainability, IAMBAS 2024, Kopenhagen, S. 2009, 2024.
- [11] Deutscher Beton- und Bautechnikverein, DBV -Merkblatt Brückenmonitoring, 2018.
- [12] S. Kromminga, K. Zdanowicz, M. Käding and T. Howiacki, Zustandsüberwachung einer integralen, mehrfeldrigen Eisenbahn-Stahlverbundbrücke mit verteilten faseroptischen Sensoren In: Curbach, M.; Marx S.; Scheerer, S.; Hampel, T. (Hrsg.), Tagungsband des 12. Symposium Experimentelle Untersuchungen von Baukonstruktionen, Schriftenreihe konstruktiver Ingenieurbau Dresden, Heft 67, Technische Universität Dresden, S. 56 – 65, 01 Juni 2023.
- [13] M. Fiedler, S. Pirsawetz, F. Kaplan, R. Holst, K. Saloga, S. Schmidt and C. Sodeikat, Detektion von Spanndrahtbrüchen mit Schallemissionsanalyse Beton- und Stahlbetonbau, Volume 120, Issue S. 150-164, 2025,
- [14] J. Cleve and U. Lämmel, Data mining. 3rd edn. Boston: De Gruyter, 2020.
- [15] CORDIS, CROss-Industry, Standard Process for Data Mining, CRISP-DM Project, Fact sheet FP4 CORDIS, European Commission, 1998.
- [16] C. R. Farrar and K. Worden, Structural health monitoring: a machine learning perspective, Wiley, Chichester, UK, first edition, 2013.
- [17] H. Sohn et al, A Review of Structural Health Monitoring Literature: 1996 – 2001', Los Alamos National Laboratory, 2004.
- [18] SAS, *SAS Help Center: Introduction to SEMMA*. Available at: <https://documentation.sas.com/doc/en/emref/14.3/n061bzurmej4j3n1jn18bbj1a2.htm> (Accessed: 10 June 2024).
- [19] K. Hildebrand, M. Gebauer, H. Hinrichs and M. Mielke, Daten- und Informationsqualität – Auf dem Weg zur Information Excellence, Springer Vieweg, Wiesbaden, 2018.

## Inspection as a basis for structural health monitoring

Stefan S. Grubinger<sup>1</sup>, Stefan L. Burtcher<sup>2, 0000-0002-5469-9596</sup>, Peter Huber<sup>0009-0003-1935-4108</sup>, Morris Tutschku<sup>2, 0009-0007-0114-171X</sup>,  
Matthias J. Rebhan<sup>3, 0000-0002-0638-6202</sup>

<sup>1</sup>recordIT GmbH, Griesgasse 1, 8020 Graz, Austria

<sup>2</sup>Rocket NG GmbH, Austria

<sup>3</sup>Institute of Soil Mechanics, Foundation Engineering and Computational Geotechnics, Faculty of Civil Engineering Sciences,  
Graz University of Technology, Rechbauerstraße 12, 8010 Graz, Austria

email: grubinger@tugraz.at, stefan.burtcher@rocket-ng.at, peter.huber@rocket-ng.at, morris.tutschku@rocket-ng.at,  
rebhan@tugraz.at

**ABSTRACT:** To effectively monitor engineering structures such as bridges, tunnels, and retaining walls, comprehensive knowledge of load-bearing behavior and load transmission mechanisms is essential. This knowledge allows for the assessment of its behavior and the identification of damage mechanisms. A thorough and clear documentation of regular inspection forms the foundation for this. It is important not only to capture damage patterns and visible defects but also to determine their origin and precise location. This information aids in the development of monitoring processes, the selection of measurement variables, and the implementation of monitoring technologies. The paper addresses the progress on how a documentation process of inspections is carried out to serve as a basis for a valid monitoring of such structures. Therefore, the use of digital models and a standardized description of damage in combination with a precise localization on the structure is described in the beginning. Such documentation provides valuable insights into load-bearing behavior and possible underlying damage mechanisms. Additionally, the development of suitable monitoring systems that serve as key parameters for structural inspection is demonstrated. The interaction and exchange of information between inspection and monitoring are emphasized, including clear visualizations and meaningful data overlays, to offer valuable benefits for building owners and inspection personnel.

**KEY WORDS:** Inspection, SHM, monitoring data, structural behavior.

### 1 INSPECTION OF CIVIL ENGINEERING STRUCTURES

Inspections are an essential part of the maintenance strategy for residential and industrial buildings (see [1] & [2]) as well as for infrastructure such as bridges and tunnels (see [3] & [4]). While the former is usually carried out by the building owner, the latter are part of the responsibilities of the owners of the infrastructure (road or railway) or those responsible for maintenance. Due to its geographical location in the center of Europe and its alpine topography, Austria places special demands on the routing of its road and railway network and the associated infrastructure. Therefore, a large number of engineering structures to secure cuts and slopes (see Figure 1), cross mountains and span valleys.



Figure 1. Gravity wall along the Semmering railway line.

The majority of the routes required for this purpose, especially along the high-level road network, were built between 1960 and 1980, while other structures (e.g. along the Semmering railway line [5]) are already more than 150 years in service.



Figure 2. Visual inspection method.

Aside from the erection and the ongoing maintenance, inspections, as shown in Figure 2, are essential to ensure the reliability of these structures and, consequently, their roadworthiness, usability and safety. The principal task lays in generally on a manual visual inspection, which includes the load-bearing and non-load-bearing components and structural elements required for safety.



### 1.1 Goals, methods and guidelines

In general, for inspection, a distinction can be made between ongoing tasks by internal personnel and inspection and testing by trained specialist personnel. These inspection activities are carried out periodically and usually conclude with a report. Thus, providing information on the state of preservation, includes necessary steps for maintenance and serves as the basis for subsequent testing and inspection intervals.

Planning documents are required as the basis of inspection to define the scope and provide the necessary structural and safety-related information, defining the tasks for the inspection personnel. Furthermore, these documents provide the basis for recording information of the on-site activity during the inspection process. Examples hereof are damaged areas, image numbers, changes compared to the forerun inspections or in general changes in the state of preservation.

Depending on the asset to be analysed, different guidelines and regulations apply in Austria. These are issued by the FSV and are to be regarded as the state of the art:

- Road bridges - RVS 13.03.11 [6];
- Anchored retaining walls - RVS 13.03.21 [7];
- Road tunnel - RVS 13.03.31 [8];
- Gantries - RVS 13.03.51 [9];
- Retaining structures - RVS 13.03.61 [10];
- Noise barriers - RVS 13.03.71 [11], and
- Trough - RVS 13.03.81 [12].

In general, manual and visual inspections are carried out, which are performed by the inspection personnel directly on site. Various smaller tools and instruments are used to carry out such activities on structures. Depending on the type of structure and asset, these range from cameras and plans to observation instruments (binocular or crack magnifier) and tools such as hammers and spanners.

Digital tools for carrying out a structural inspection are generally not defined. Only specifications for integrating the inspection results into corresponding databases are given. Furthermore, within the area of monitoring [13] topics such as IoT (Internet of Things) and, briefly, the necessary digitalisation of measurement and monitoring tasks and the management of data and results are addressed.

### 1.2 Damage and damage symptoms

In order to enable a diagnosis of the structure and the resulting statement on the state of preservation, it is necessary to record defects and damage continuously on the structure to be inspected. Some examples are given in Figure 3.

Due to the wide-ranging and interdisciplinary approach to civil engineering structures, it is difficult to provide a schematic collection of damage patterns and defects in such structures. However, the literature (see [14] to [17]) provides comprehensive descriptions and lists that can be used as a basis. In such a categorisation, a general distinction must be made between damage and defects relevant to load-bearing capacity and those relevant to durability.

A distinction can be made between structural, geotechnical and geological damage patterns. In addition to a differentiation, however, an interdisciplinary and interactive approach is required in order to recognise the underlying causes of the damage so these can be addressed during maintenance.



Figure 3. Examples for damages found during inspection of civil engineering structures; reinforcement corrosion and concrete spalling (top); shift and misalignment within a construction joint (center); erosion and unguided surface flow (bottom).

### 1.3 Climate change

Austria's topography, the dense road and railway network and the increasing average age of the infrastructure are a major challenge for long-term maintenance. In addition to the approximately 2,300 km of high-ranking road network and 5,000 km of railway lines, there are also around 125,000 km of lower-ranking road network [3]. In terms of motorways, there are around 250 km per million inhabitants, which means that the high-ranking road network is around 50 % larger than the EU average.

In addition to an increase in loads and traffic, climate change will also have a direct impact on structures as a perceptible manifestation of climate change. These are superimposed by geological and geotechnical effects such as increasing water



supply due to heavy rainfall events or the increase in natural hazards such as mass movements and rockfalls.

The effects of climate change can be summarised as ‘*long-term changes in temperature and weather patterns*’ Figure 1. Gravity wall along the Semmering railway line. Among other things, this will have an impact on road and railway infrastructure. These changed boundary conditions influence the durability of the infrastructure substance due to increased thermal and hydraulic stress and changed environmental conditions. At higher temperatures, the saturation vapour pressure of the atmosphere increases and more and more water vapour can be held in the air (+ 7% per 1°C). This intensifies the greenhouse effect and increases the risk of short-term extreme precipitation (see [18] & [19]). The intensity of these events can for example exceed the capacity of existing drainage systems, leading to both direct damage to the structure and indirect damage with respect to surface erosion and sediment transport. Increased extreme precipitation is also accompanied by an increasing risk of gravitational natural hazards such as rockfall, which, in addition to the direct risk in the area along the infrastructure, can also have a corresponding impact on the functionality of engineering structures due to an impact. [20]

The increase in damage patterns, damage intensity and defects in combination with the increasing age of structures and the rise in traffic and loads pose new challenges for those responsible for maintaining structures. In 2021, the European Commission drew up a technical guideline to ensure the climate compatibility of infrastructure [21], which defines that the primary goal must be to make ‘*infrastructure climate-neutral and climate-resilient*’.

#### 1.4 Digital inspection

In addition to the advantages that a digitalisation can offer, it is also important to adapt working methods to newly created possibilities in order to generate a corresponding increase in time and quality. Preparation by the inspection staff will remain essential, but the approach will take a different form. For the most part, the collection and collation of (meta) data will no longer be necessary and a stronger focus on existing issues and damage will be possible.

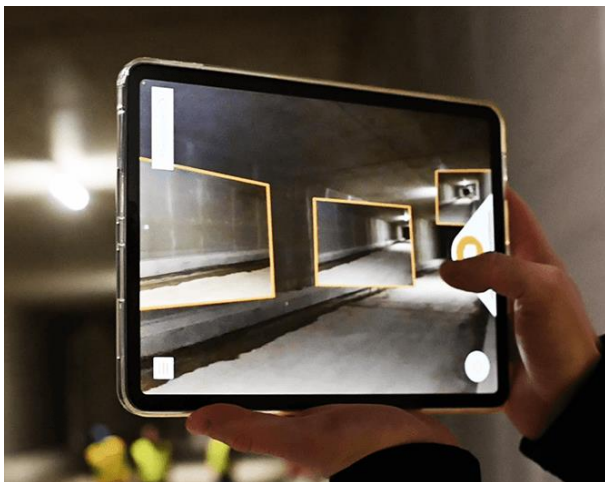


Figure 4. Using digital inspection tools to reduce workload and to improve information transfer.

However, it is not only the preparation that changes, the form of the inspection also changes when digital solutions are used. For example, due to standardisation and the use of existing inspection results, personnel will play a much stronger role as a controlling element. This results from the fact that a software-supported inspection specifies or can specify defects or damage and structures and thus provides a framework for recording in the field.

A number of benefits can be generated through the digitalisation of structural inspection. The biggest and usually most decisive point is the potential for savings in terms of on-site inspection time. In addition to the monetary savings, this can also result in shorter closure times, which could lead to massive improvements in route availability, especially if a total closure is required. In addition, software solutions using digital devices on site creates a standardised and less error-prone structural inspection, from which reports and documentations can be created with little effort or information and characteristic parameters can be further processed digitally. In addition, photorealistic 3D models (e.g. from photogrammetry) depict the current condition of a structure more comprehensively and allow a comparison between different inspection periods.

It should also be mentioned that structural inspections can provide the foundation for implementing structural health monitoring. Through the appropriate collection, evaluation, and interpretation of inspection results, it becomes possible, to have the fundamental information required for a structural health monitoring system readily available. Furthermore, based on the results of structural inspection and the analysis of findings over time, it is possible to determine whether the structure can remain in operation with monitoring, whether restrictions are necessary, or whether demolition, reconstruction, or strengthening are necessary.

In addition to these advantages, there are also disadvantages associated with a digitalisation measure - or generally a change and adaptation of existing processes. On the one hand, these relate to usability and the utilisation of digital solutions by users. However, this can be very easily remedied with an appropriate software solution (UX and UI design see Figure 4). On the other hand, the pervasive and sustainable use of digital solutions often requires adjustments to databases, data structures and standardisation. In Austria, there is largely a lack of specifications relating to the use of digital products for structural inspection of infrastructure. Nonetheless, a corresponding trend and a corresponding willingness to implement such solutions and procedures can currently be recognised among a number of structural owners and maintainers.

## 2 MONITORING OF CIVIL ENGINEERING STRUCTURES

An essential component of the safety assessment of civil engineering structures can be created by the systematic consideration of monitoring data. This can give an inclusive insight into the behaviour of the structure or the triggers responsible for damage or a change in the structures reliability.

However, in order to be able to utilise such information comprehensively, it is necessary to plan a monitoring system accordingly. The following briefly discusses possible measured variables, the timing of monitoring and the digitalisation of

existing measuring equipment. This serves to enable a holistic view between inspection and monitoring.

### 2.1 Behavior of the structure

The decisive factor when carrying out monitoring is the correct selection of the measured variable to be recorded. Due to the size and extent of engineering structures and the frequent interaction between the object and its surroundings, measurement data of the terrain is often the first choice. For example, data from satellite measurements or LIDAR measurements in the vicinity of the infrastructure can be used for this purpose. Such data offers information on areas that are otherwise difficult to access or overviews of the structure and the terrain, deformations can already be derived.

Monitoring is also usually carried out by attaching sensors or transducers. These are usually attached directly to the structure or to relevant component regions. A range of different measured variables [13] can be used to analyse the terrain, the structure or individual components. These are often also related to the requirements or statements from the structural inspection - such as questions regarding load-bearing behaviour or load transfer. In addition, the overall behaviour of the structure must be considered when selecting measured variables or generally when defining the monitoring concept.

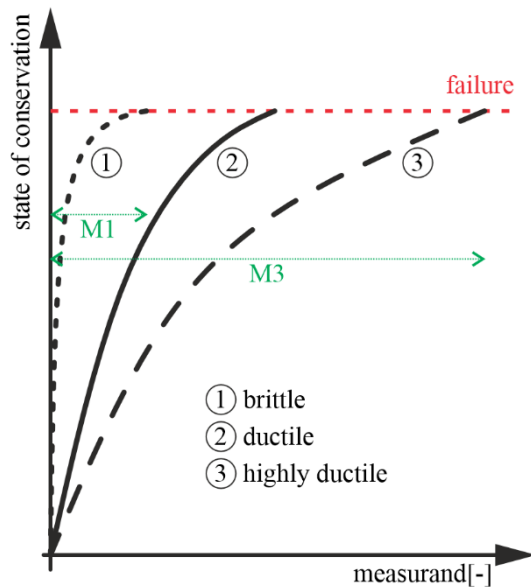


Figure 5. State of preservation with respect to a measurand depending on the behavior of the structure.

In addition to the arrangement of the sensors, the time component must also be thought of when planning a monitoring system. This is related to the behaviour of the structure and can be seen schematically in Figure 5. This shows the change in a possible measured variable depending on the state of preservation of the structure. The greater the damage to the structure - i.e. the greater the decrease in the state of preservation - the greater the change in a possible measured variable used for monitoring.

The extent to which a measured variable increases until the structure fails is strongly influenced by the behaviour of the structure. While all structures should exhibit ductile behaviour, this may only be the case to a limited extent, especially in the

case of brittle structures. An example of this is the reduction in the load-bearing capacity of a concrete cross-section that is damaged by corrosion of the main reinforcement [22].

This aspect means that the possible, recordable and detectable measured variable of a value is defined accordingly by the behaviour of the structure. As a result, during the planning of a monitoring, it is necessary to estimate how large the possible, still available supply of a measured variable is and whether the quantity is still sufficient to enable meaningful and accurate monitoring.

### 2.2 Timing of measurement

The behaviour of a structure in relation to the measurable value also results in a temporal influence on the monitoring. Similar to the quantity of the measurand to be recorded, a brittle or ductile structure also has an effect on the time available until failure occurs. This is shown schematically in Figure 6.

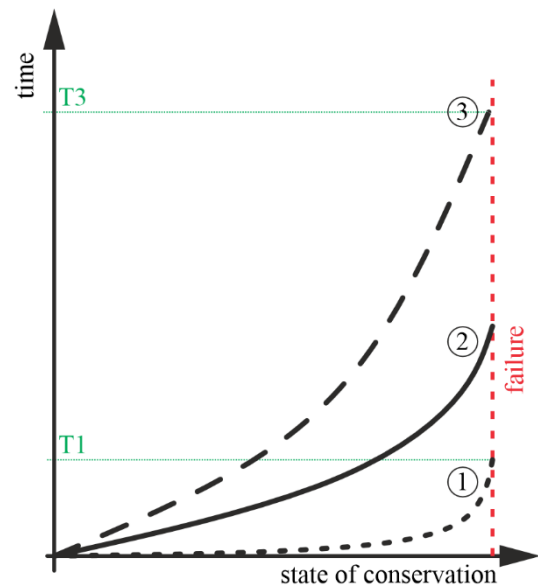


Figure 6. Timely installation of a monitoring system with respect to the state of preservation depending on the behavior of the structure.

This shows that, depending on the behaviour of the structure or the effects of damage, there are different time periods that indicate a decrease in the state of preservation. This can have a considerable influence, particularly with regard to the implementation of monitoring as a measure following a structural inspection. If the time period is too short, only a limited statement can be made about the behaviour of the structure. Meaning that it is not possible to differentiate between temperature-related and damage-related behaviour of the structure. This in turn means that a planned monitoring can only make a small contribution to the structural inspection.

### 2.3 Digitalization of existing measurement equipment

When implementing monitoring concepts, classic approaches applicable to new structures or the monitoring method can only be used to a limited extent. The subsequent installation and calibration of sensors and monitoring equipment on existing structures is often only possible to a limited extent due to accessibility. A particular problem with existing structures is the unknown construction effects and the limited observation

time compared to the age of the structure. In particular, the assessment of load-bearing behaviour, load redistribution and the delimitation of seasonal effects therefore usually requires a combination with redundancy and an overdetermination of the measurement concept in order to correctly characterise the structure's behaviour. Another aspect of monitoring tasks on existing structures is the reactivation or digitalisation of existing measuring equipment.

The aim of monitoring must always be to create a valid database which, in combination with appropriate testing and inspection of the structure, can be used to identify the load-bearing behaviour and possible damage mechanisms of the structure. One innovative application example is the digitalisation of hydraulic force measuring devices on prestressed grouted anchors. The current anchor force (see [23]) is one of the main parameters of an anchored structure. As a rule, force measuring devices have to be installed during the prestressing process of the tendon, making a retrofitting of such a measuring device not often possible.

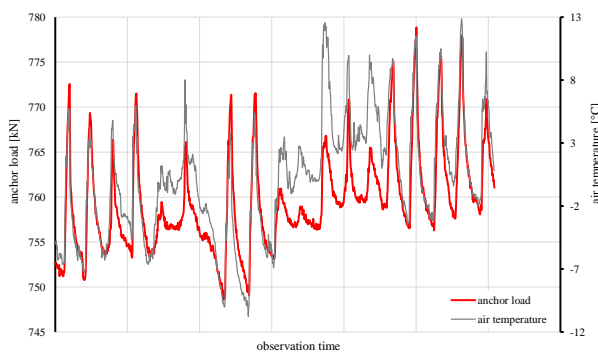


Figure 7. Time-period of a subsequently digitalized anchored load plate.

Digitising the measured value readings, as shown in Figure 7 and described in more detail in [24], enables permanent data recording and provision for existing force measuring systems. Temperature and seasonal anchor force changes and the resulting effects on the structure can be reliably recorded thanks to continuous recording. This makes it easier to interpret the measurement data and represents a significant improvement on the current practice of periodic and manual readings.

### 3 INTERLINK INSPECTION TO MONITORING

The previous chapters have attempted to provide a brief insight into the inspection and monitoring of engineering structures. These topics are usually directly linked, but are currently usually considered separately. While the inspection of the objects is carried out and documented regularly, monitoring is usually only used for structures that already show a deficit in their behavior or corresponding damage.

However, in order to be able to implement monitoring in a targeted manner, the content and results of inspection must be included. This can be seen schematically in the cycle in Figure 8. The cycle without monitoring refers to the classic inspection of a structure, in which the relevant data and information on the structure and its condition are collected in the course of an on-site activity in order to enable a subsequent assessment. This

usually takes place in a purely visual and manual manner. The data and information collected is therefore purely about damage patterns or changes in the state of preservation recognizable on the surface of the structure or its surroundings. If there is no major damage and no extensive changes in the behavior of the structure can be detected, the inspection process is completed for the period in question and no further activities are required.

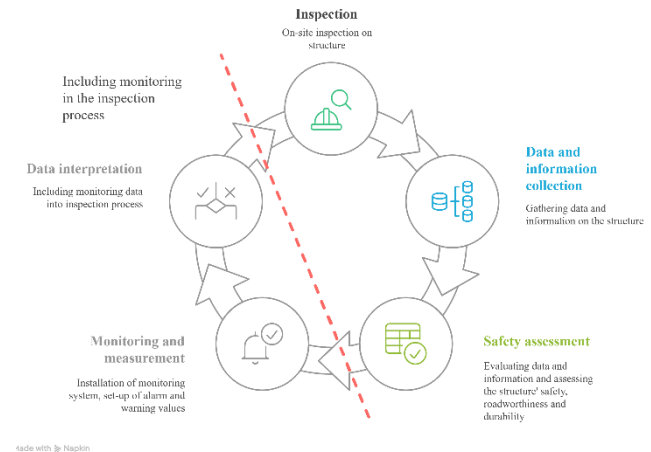


Figure 8. Schematic process of interlinking monitoring processes into the cycle of structural inspection.

The aim of the inspection is to be able to make a statement about the load-bearing behaviour of the structure and thus about its state of preservation. If this is not possible, special tests in the form of a material analysis or an in-depth inspection of the structure can be carried out. However, these often only provide information about the progression of damage (e.g. carbonation) or provide characteristic values for materials or components. A statement about the load-bearing behaviour of the structure and, for example, the interaction with the subsoil can only be given to a limited extent.

Monitoring of the structure can be used for this purpose. This can be used to make a statement about the behaviour of the structure by recording measured values and interpreting them accordingly. In relation to the building inspection or rather the assessment of the construction, a valid statement can be made about the load-bearing behaviour, load transfer mechanisms or, for example, a number-based assessment of the load and stress levels of components.

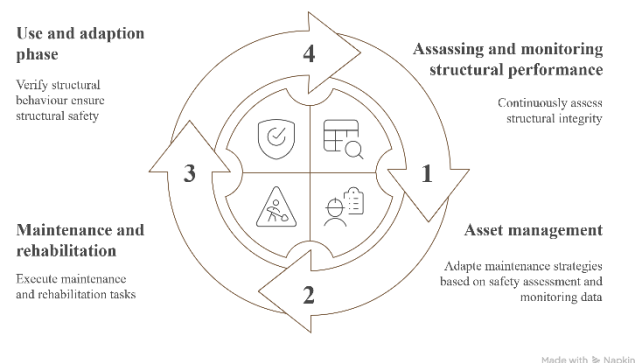


Figure 9. Ongoing circle on assessing data and information including asset management, maintenance and use phase.



If this relationship is now considered over the entire service life of a structure, it can be seen, as shown in Figure 9. Ongoing circle on assessing data and information including asset management, maintenance and use phase., that this results in a continuous process. Beginning after construction with a continuous recording and observation of the behaviour of the structure, which can be carried out either by inspection or supplemented by monitoring.

Based on this, the necessary processes are planned and implemented in the asset management in order to be able to carry out maintenance. Here, both smaller measures can be derived from the inspection (e.g. flushing the drainage) and larger measures (e.g. replacing the edge beam) can be implemented. The whole process is completed by a phase of utilisation which is not associated with any restrictions and in which the structure is in a sufficiently good condition to be used safely and reliably.

This brief and schematic illustration shows the possibilities in which the inspection of structures and their monitoring are linked. It also shows that monitoring is usually implemented as a measure or as a reaction to an inspection. It is therefore essential that the results are communicated and transferred to the monitoring of the structure in order to enable the two processes to interact and integrate with each other.

#### 4 EXAMPLE – ANCHORED STRUCTURES

The approach described in the previous chapter can be explained using a practical example. An anchored construction as shown in Figure 10, which has a height of 9.00 m and a total length of approx. 240 m. The wall was constructed in three stages, with individual concrete elements anchored by two anchors (diagonally). It is not possible to tell from existing planning documents whether there is a transverse force-locking connection between the elements in vertical and horizontal direction.



Figure 10. Segmented anchor wall.

In the course of an inspection of the wall, a number of damage patterns were identified, which primarily affect the durability of the entire structure as well as that of the concrete components. Two examples of this are given in Figure 11. These show two symbolically recorded cracks, which can be found in a similar way along the entire wall. The cracks have a width of 0.2 to 0.5 mm.

Some cracks are located in the area of the installed anchoring elements, as shown in the picture, while others are scattered across the entire surface of the wall. In general, the cracks are characterised by sintering and moss-like growth was also

visible, which indicates that the cracks have been present for some time.

No damage could be visually detected on the tensile elements of the structure (strand anchors), only slight signs of corrosion on the external components could be detected. In general, the structure was in an inconspicuous condition and only limited moisture damage, water leakage or other geological failure mechanisms could be found in the adjacent area.



Figure 11. Cracks along the concrete structure and adjacent to the anchors.

In general, this structure can be assumed to be in a good state of preservation, but there is a lack of information, particularly with regard to the anchorage, its function and the associated effects on the load-bearing behaviour. In order to obtain this information, special inspections [23] such as an endoscopic examination of the anchor head area and a lift-off check of the tension elements would be the first option. However, this is not possible on all structural anchors due to the non-liftable design of the tension elements, but it was possible to carry out subsequent digitisation on six structural anchors with existing force measuring equipment.

The monitoring data (Figure 7) shows that there is a clear correlation between the temperature and the anchor force, even over a longer period. This indicates that either the structure, the measuring device or both together exhibit temperature-



dependent behaviour. However, as there is no inexplicable change in the anchor forces, it can be assumed that there is no massive damage to the structure which is therefore behaving as it was designed intentionally.

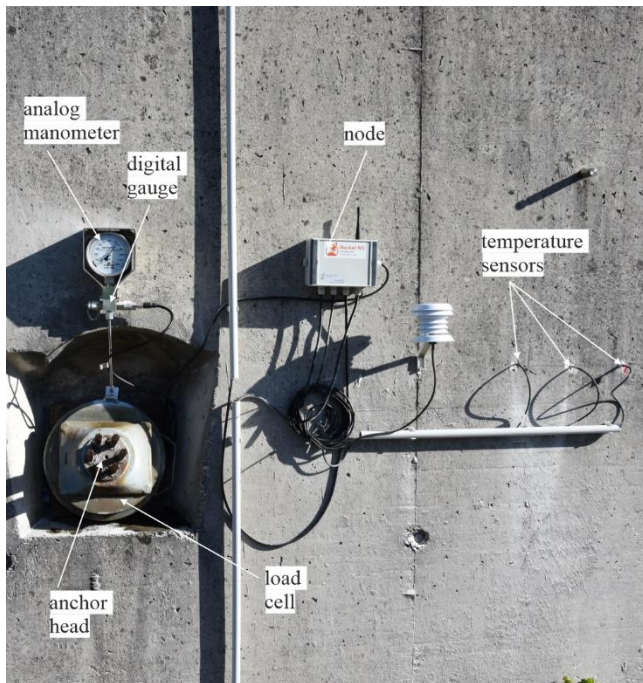


Figure 12. Anchor wall, anchor head and scheme of monitoring positions and sensors.

Such investigations were possible because the structure already had force measurement equipment (see Figure 12) that could be included in the monitoring. Whether this takes the form of digitisation or continuous readings is merely a question of the desired accuracy or a resource-related one. If this had not been possible, a variety of other measurement systems would have been applicable, which are briefly described below:

Classical deformation monitoring, for example by attaching measuring points, could possibly provide a statement about the temperature-related behaviour of the structure. However, this only provides a limited possibility of deducing an increase in damage, as only a limited distinction can be made between temperature-related fluctuations and a change in deformation. In particular, only periodic recording of the wall (e.g. on a weekly or daily basis) and not recording the entire surface of the structure means that only very limited detailed information can be provided. Current approaches such as full-surface monitoring of the wall surface and the resulting derivation of overall deformations could provide a remedy here, but are not yet considered state of the art.

As there were no signs of extensive deformation of the object in the course of an inspection of the rear area of the structure, no major changes in the stresses on the structure due to earth or water pressures can be assumed. On the one hand, this would rule out a change in the above-mentioned structural deformations and, on the other hand, would also put geotechnical measuring equipment such as inclinometers or extensometers in their place as far as the detection of a change in the structural behaviour as a result of damage is concerned.

As a result, only measured values that consider the structure itself remain possible. As this is an existing structure, the installation of earth pressure cells or the determination of the change in strain in the reinforcement, for example, is only possible to a limited extent, at great expense and with a possible falsification of the structure's behaviour. Nevertheless, the cracks already encountered on the front of the structure, for example, would be suitable for monitoring. Particularly with regard to a possible load redistribution between the tension element, which could indicate damage to these, would possibly manifest itself in the crack pattern of the structural components. Monitoring of the cracks on the front side would be recognisable in the event of a significant change in the cutting forces resulting from an anchor failure or a reduction in the prestressing force. A similar approach can also be used for corrosion-damaged angular retaining walls [24], for example, to show a redistribution between individual reinforcement elements.

## 5 CONCLUSIONS & SUMMARY

The aim of this article is to highlight the similarities between structural inspection and monitoring. The duality of this topic must be considered, which makes a significant contribution to a comprehensive understanding of the behavior of damaged infrastructure structures, whereby a distinction can be made between structural, geotechnical and geological damage patterns. In addition to a differentiation, however, an interdisciplinary and interactive approach is also required in order to recognize the underlying causes of the damage so that these can be addressed in the course of maintenance if necessary.

On the one hand, the structural inspection and the resulting information on damage and damage processes form the basis for the planning and implementation of monitoring and the interpretation of monitoring data. On the other hand, monitoring can significantly improve the level of data and information on the behaviour of a structure. This is a great added value in the assessment of the structure, especially for structures in a poor condition, but also for objects with missing documentation.

The aim of this article is to highlight the similarities between structural inspection and monitoring. The duality of this topic must be considered, which makes a significant contribution to a comprehensive understanding of the behaviour of defective infrastructure structures, and the relationships presented here are intended to show that considerable added value can only be generated through interdisciplinary and targeted cooperation and the exchange of information in both structural testing and monitoring. Only in this way it is possible to obtain a comprehensive statement about structures and thus subsequently guarantee their safety and reliability. Only in this way can a sustainable, durable and resilient infrastructure be made possible, which, in addition to appropriate usability, also has a certain resistance to climate change-related effects, whereby a distinction can be made between structural, geotechnical and geological damage patterns. In addition to a differentiation, however, an interdisciplinary and interactive approach is also required in order to recognise the underlying causes of the damage so that these can be addressed in the course of maintenance if necessary.

## REFERENCES

- [1] ÖNORM B 1300, 2018. Objektsicherheitsprüfungen für Wohngebäude - Regelmäßige Prüfroutinen im Rahmen von Sichtkontrollen und zerstörungsfreien Begutachtungen - Grundlagen und Checklisten. Austrian Standards. Wien.
- [2] ÖNORM B 1301, 2016. Objektsicherheitsprüfungen für Nicht-Wohngebäude - Regelmäßige Prüfroutinen im Rahmen von Sichtkontrollen und Begutachtungen - Grundlagen und Checklisten. Austrian Standards. Wien.
- [3] BMK (2023). Statistik Straße und Verkehr. Bundesministerium für Klimaschutz, Umwelt, Energie, Mobilität, Innovation und Technologie. Abteilung IV/IVVS1 – Planung, Betrieb und Umwelt. Vienna.
- [4] Rebhan, M.J., Grubinger, S.S., Schüppel A., Deutinger S., Schwarzenberger G. (2024). Advances in the digital documentation of railway tunnel. ITnA-reports – 12th international conference tunnel safety and ventilation. Volume 107, Graz.
- [5] <https://www.unesco.at/kultur/welterbe/unesco-welterbe-in-oesterreich/semmeringeisenbahn>
- [6] RVS 13.03.11, 2021. Überwachung, Kontrolle und Prüfung von Kunstbauten – Straßenbrücken. Richtlinien und Vorschriften für das Straßenwesen. Österreichische Forschungsgesellschaft Straße – Schiene – Verkehr (FSV). Wien.
- [7] RVS 13.03.21 Geankerte Konstruktionen. Verfügbar unter: <https://www.fsv.at/shop/produktdetail.aspx?IDProdukt=e65a7d2a-7e23-4312-a865-2f909c7b3c5c> [Abgerufen am 27.01.2025].
- [8] RVS 13.03.31, 2021. Überwachung, Kontrolle und Prüfung von Kunstbauten – Straßentunnel. Richtlinien und Vorschriften für das Straßenwesen. Österreichische Forschungsgesellschaft Straße – Schiene – Verkehr (FSV). Wien.
- [9] RVS 13.03.51, 2021. Überwachung, Kontrolle und Prüfung von Kunstbauten – Wegweiserbrücken. Richtlinien und Vorschriften für das Straßenwesen. Österreichische Forschungsgesellschaft Straße – Schiene – Verkehr (FSV). Wien.
- [10] RVS 13.03.61, 2021. Qualitätssicherung bauliche Erhaltung, Überwachung, Kontrolle und Prüfung von Kunstbauten, Nicht geankerte Stützbauwerke, Österreichische Forschungsgesellschaft Straße-Schiene-Verkehr, FSV, Wien.
- [11] RVS 13.03.71, 2021. Überwachung, Kontrolle und Prüfung von Kunstbauten – Lärmschutzbauwerke. Richtlinien und Vorschriften für das Straßenwesen. Österreichische Forschungsgesellschaft Straße – Schiene – Verkehr (FSV). Wien.
- [12] RVS 13.03.81, 2021. Überwachung, Kontrolle und Prüfung von Kunstbauten – Wannenbauwerke. Richtlinien und Vorschriften für das Straßenwesen. Österreichische Forschungsgesellschaft Straße – Schiene – Verkehr (FSV). Wien.
- [13] RVS 13.03.01, 2022. Überwachung, Kontrolle und Prüfung von Kunstbauten – Monitoring von Brücken und anderen Ingenieurbauwerken. Richtlinien und Vorschriften für das Straßenwesen. Österreichische Forschungsgesellschaft Straße – Schiene – Verkehr (FSV). Wien.
- [14] Stahr, M., 2011. Bausanierung: Erkennen und Beheben von Bauschäden, 5. Aufl., Wiesbaden: Vieweg+Teubner Verlag / Springer Fachmedien Wiesbaden GmbH Wiesbaden.
- [15] Weber, S., 2013. Betoninstandsetzung: Baustoff - Schadensfeststellung - Instandsetzung, 2. Aufl., Wiesbaden/s.l.: Springer Fachmedien Wiesbaden.
- [16] Deutscher Beton- und Bautechnik-Verein e.V., 2017. Ist-Zustandserfassung von Parkbauten in Betonbauweise: Merkblatt 39, Berlin: Eigenverlag DBV.
- [17] Schrepfer, T., Gscheidle, H., 2007. Schadenfreies Bauen: Schäden beim Bauen im Bestand, Zugriff im Juni 2019, [https://www.irb.fraunhofer.de/schadis/s\\_inhalt.jsp?band=Sfb41](https://www.irb.fraunhofer.de/schadis/s_inhalt.jsp?band=Sfb41)
- [18] ÖWAV 2020. ÖWAV-ExpertInnenpapier Klimawandelanpassung Wasserwirtschaft - Pluviales Hochwasser/Oberflächenabfluss. Wien: Österreichischer Wasser- und Abfallwirtschaftsverband (ÖWAV).
- [19] Stocker et. al., 2017. Klimaänderungen 2013, Naturwissenschaftliche Grundlagen, Beitrag der Arbeitsgruppe I zum Fünften Sachstandsbericht des zwischenstaatlichen Ausschusses für Klimaänderungen (Ipcc), Deutsche IPCC-Koordinierungsstelle.
- [20] Glade, Thomas & Bell, Rainer & Dobesberger, & Embleton-Hamann, & Fromm, & Fuchs, Sven & Hagen, & Hübl, Johannes & Lieb, & Otto, Jan-Christoph & Perzl, & Peticzka, Robert & Prager, & Samimi, Cyrus & Sass, O. & Schöner, & Schröter, Dagmar & Schrott, Lothar & Zangerl, & Zeidler, A., 2014. Der Einfluss des Klimawandels auf die Reliefsphäre. 10.1553/aar14s557.
- [21] Commission Notice 2021. Technical guidance on the climate proofing of infrastructure in the period 2021-2027. Verfügbar unter: [https://eur-lex.europa.eu/legal-content/EN/TXT/?uri=CELEX:52021XC0916\(03\)](https://eur-lex.europa.eu/legal-content/EN/TXT/?uri=CELEX:52021XC0916(03)). [Abgerufen am 27.01.2025].
- [22] Rebhan, M.J. (2019). Korrosionsschäden bei Winkelstützmauern. Dissertation. Graz University of Technology. Institute of Soil Mechanics, Foundation Engineering and Computational Geotechnics. Graz.
- [23] AP33 (2022). Arbeitspapier Nr. 33 – Sonderprüfmethoden für geankerte Konstruktionen und Zugelemente, Österreichische Forschungsgesellschaft Straße – Schiene – Verkehr. Vienna.
- [24] Rebhan et. al. 2024. Erfassung der Vorspannkraft bei bestehenden geankerten Konstruktionen – Abhebeversuche, Nachrüstung und Digitalisierung von Kraftmesseinrichtungen zu Monitoringzwecken. Mitteilung des Instituts für Geomechanik und Geotechnik, Technische Universität Braunschweig. Messen in der Geotechnik 2024. 22./23. Februar 2024. Heft Nr. 116.





# Advanced Filtering in Structural Dynamics

# Dynamic Monitoring using Hidden Markov Regression Model for Predicting Remaining Useful Life

Vincent Ifeanyi Ike<sup>1</sup>, 0000-0001-6560-812X, Andre Jesus<sup>1</sup>, 0000-0002-5194-3469, Mohamed Shaheen<sup>1</sup>, 0000-0002-9156-8827

<sup>1</sup>Loughborough University, School of Architecture, Building & Civil Engineering, Epinal Way, Loughborough LE11 3TU, UK  
email: v.ike@lboro.ac.uk, a.jesus@lboro.ac.uk, m.shaheen@lboro.ac.uk

**ABSTRACT:** This paper presents the remaining useful life (RUL) prediction problem in civil engineering applications using a hidden Markov regression model (HMRM), as a promising approach for model-based degradation. Unlike self-transition hidden Markov models for mass-produced components, where prior lifetime signals are available to estimate state information, the proposed HMRM formulates the conditional probability of RUL in terms of the estimated regressor parameters, after temporally fitting the damage model. The discrete property of state in HMRM makes it possible to handle heterogeneities in the degradation process. The HMRM can also synthesise multiple signals by adopting a decision-level fusion. An adaptive closed-form solution for RUL prediction is presented. The performance of HMRM is demonstrated on synthetic measurements and compared with a Bayesian extended Kalman filter (EKF) updating technique.

**KEY WORDS:** Hidden Markov chain; model-based degradation; remaining useful life prediction; damage model.

## 1 GENERAL GUIDELINES

The prediction of Remaining Useful Life (RUL) holds significant importance in both condition-based monitoring (CBM) and the formulation of maintenance strategies for structural components. RUL is defined as the time a structure has before reaching its design threshold, when it can no longer perform under its design function. In CBM, damage is characterised as a change in structural components due to the interaction between internal degradation and the working environment which adversely affects its current and future performance. The progression of damage is heterogeneous, and such heterogeneity can be due to *unit-to-unit variability* [1] of the material, *changing operational conditions* [2], or *periodic loading* [3].

Various damage models have been developed, ranging from empirical laws (such as Paris' laws) to continuum damage mechanics (CDM) methods [4], which requires stochastic-based approaches (such as Markov chain, Weiner processes) for predicting RUL [5]. However, these approaches suffer from parameter correlation. This study focuses on simple power and exponential laws suited in a hidden Markov chain, which, despite their simplicity, provide correlated, good curve fitting by: a linearised and automated regression segmentation and an adaptive parameter updates via a recursive Markov chain to improving accuracy. According to Si, et al. [5][6] hidden Markov models (HMMs) are suited for RUL prediction based on degradation state processes. HMM is composed of two state processes; an unobservable (hidden) Markov chain which accounts for the actual state of degradation such as fatigue at the grain level of a metallic component, and an observable process that interprets the monitoring information, for instance, crack width in a reinforced concrete beam.

Within a degradation process is multiple discrete-hidden states. Past studies [7][8] [9][10] focused on the transition probability matrix and state duration definition. They consider that these states can switch into each other under a predefined transition probability, which is specific to the lifetime datasets. Modelling degradation by this approach is limited to the Markov property

[11] which means that: a) the state at any given time step only depends on the previous state and not on any earlier states, b) and that shorter state durations are more likely than longer ones, i.e., state duration follows a geometric distribution. This can be a limitation for modelling real-world degradation processes. To remedy this weakness, hidden semi-Markov models (HSMM) have been proposed to explicitly model state duration distributions rather than assuming a geometric one [12][13]. Unfortunately, this improvement of modelling degradation in components with predefined transition probability and state duration does not extend to modelling the degradation processes on bespoke components that obeys damage laws.

To the best of the author's knowledge, this study frontier a premise of adopting a sequence of state in model-based degradation process. By this approach, the degradation process experiences a state switch at stages of damage triggered by the weighted state posterior distribution [14]. In addition, the proposed approach can handle multiple information of measured signals (i.e., multiple HMRM) earlier introduced in [13]. This improves the state identification since it captures the interacting factors of multiple signals, and reduces measurement noise uncertainty, leading to a more confident RUL prediction. The extended Kalman filter (EKF) is introduced in this study to recursively observe data in real-time, to compare with our inspection approach. As with HMM belonging to a finite-discrete set of states, the EKF is an optimal non-linear filter for finite-dimensional stochastic systems, for model-based analysis, where the states are continuous and described as parameters of the damage model [15].

Within the framework of modelling degradation presented in the paper, two case studies are considered: a fatigue crack growth process, and a multi-sensor beam degradation measurement. A decision-level fusion technique using fisher's weighted discriminant ratio [13] is considered to aggregate the multiple estimated parameters and predict the RUL.

## 2 HIDDEN MARKOV REGRESSION MODEL (HMRM)

This section provides the framework that captures the hidden state degradation processes.

### 2.1 HMRM Parameter estimation

The unobserved degradation processes  $u_t$  represent a sequence of  $K$  hidden states of data points, formulated at index time  $t$  in a particular state  $k$  as:

$$u_t = U_t \cdot \exp(\sigma_k^2 \dot{\varphi}), \quad (t=1, \dots, T) \quad (1)$$

where  $U_t$  represent the damage model that characterises the degradation process up till failure time  $T$ . To model the hidden Markov chain, we take the log-transform of equation 1 and put in matrix form as:

$$y_t = \log u_t = \mathbf{x}_t \boldsymbol{\beta}_k + \sigma_k^2 \dot{\varphi} \quad (2)$$

$y_t$  becomes degradation processes that follows a Gaussian distribution of mean  $\mathbf{x}_t \boldsymbol{\beta}_k$  and variance  $\sigma_k^2$ , the parameter vector  $\boldsymbol{\theta} = (\boldsymbol{\pi}, \mathbf{A}, \boldsymbol{\beta}_1, \dots, \boldsymbol{\beta}_K, \sigma_1^2, \dots, \sigma_K^2)$  defines the model of the degradation process.  $\dot{\varphi}$  is a random variable that follows the standard Gaussian distribution (zero mean and unit variance) representing an additive measurement noise with standard deviation  $\sigma_k$ .  $\mathbf{x}_t$  is the covariate vector at index time  $t$  that translates scatter due to environmental/operational conditions and  $\boldsymbol{\beta}_k$  is a  $\square^{2 \times 1}$  vector containing the regression coefficients. The hidden sequence  $\mathbf{k} = (1, \dots, K)$  is assumed to be a homogeneous Markov chain (as shown in Figure 1) of the first order and parameterised by an initial state distribution  $\boldsymbol{\pi}$  and a transition matrix  $\mathbf{A}$ .

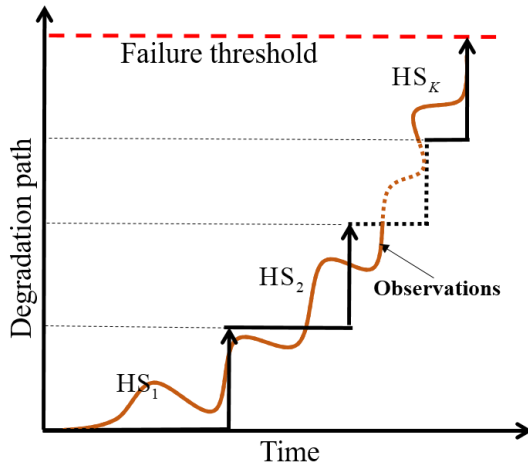


Figure 1. Schematic representation of the actual degradation process over a sequence of hidden states (HS), from 1 to  $K$ .

As shown in Figure 1, the hidden state discretises the observation that is continuously measured, in a sequence. This sequence of discretization is irreversible since degradation process is progressive, except when a maintenance action is implemented. Figure 2 describes the probability of stay in a hidden state is defined by the transition probability  $A_{k,k}$  in the transition matrix  $\mathbf{A}$ . Hence,  $A_{k,k}$  determines whether the degradation process is either staying or moving to the next degradation stage.

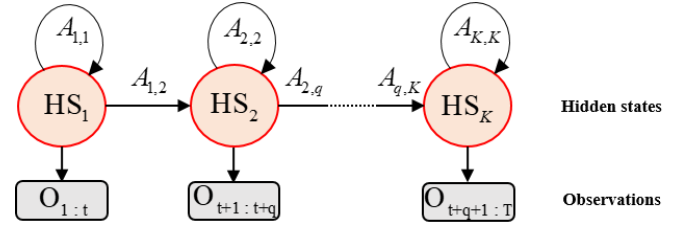


Figure 2. Illustration of the possible sequence of transition path between hidden states.

The vector  $\boldsymbol{\theta}$  can be estimated using the limiting properties of consistency, and asymptotic normality of the so-called maximum likelihood method. Its efficiency is subject to a considerable number of data points, so the sample size is suitable for taking advantage of the limiting properties of the likelihood estimator. The log-likelihood is presented in the form:

$$\begin{aligned} L(\boldsymbol{\theta}^{(m)}) &= \log p(\mathbf{y}_1, \dots, \mathbf{y}_T; \boldsymbol{\theta}^{(m)}) \\ &= \log \sum_{\mathbf{k}} p(\tau_1; \boldsymbol{\pi}) \times \prod_{t=2}^T p(\tau_t | \tau_{t-1}; \mathbf{A}) \prod_{t=1}^T N(\mathbf{y}_t; \mathbf{x}_t \boldsymbol{\beta}_k, \sigma_k^2) \end{aligned} \quad (3)$$

The Baum-Welch algorithm is referred to as the expectation-maximisation (EM) algorithm [11][16], which performs a recursive iteration over E-M steps while updating estimated parameters that govern the regression model. The regressor mean is:

$$\begin{aligned} \hat{\boldsymbol{\beta}}_k^{(m+1)} &= \left[ \sum_{t=1}^T \mathbf{x}_t' \gamma_{tk}^{(m)} \mathbf{x}_t \right]^{-1} \sum_{t=1}^T \mathbf{x}_t' \gamma_{tk}^{(m)} \mathbf{y}_t \\ &= [\mathbf{X}' \mathbf{W}_k^{(m)} \mathbf{X}]^{-1} \mathbf{X}' \mathbf{W}_k^{(m)} \mathbf{Y} \end{aligned} \quad (4)$$

where

$$\mathbf{X} = [\mathbf{x}_1, \dots, \mathbf{x}_T]' \quad (5)$$

is the  $\square^{T \times 2}$  regression matrix and  $\mathbf{W}_k^{(m)}$  is a  $\square^{T \times T}$  diagonal matrix of weights whose diagonal elements represent the posterior probabilities  $(\gamma_{1k}^{(m)}, \dots, \gamma_{Tk}^{(m)})$ . On the other hand, the covariance matrices are updated as a weighted variant of the estimation of a Gaussian density with the polynomial mean  $\mathbf{x}_t \hat{\boldsymbol{\beta}}_k^{(m+1)}$ :

$$\begin{aligned} \hat{\sigma}_k^{2(m+1)} &= \frac{1}{\sum_{t=1}^T \gamma_{tk}^{(m)}} \sum_{t=1}^T \gamma_{tk}^{(m)} (\mathbf{y}_t - \mathbf{x}_t \hat{\boldsymbol{\beta}}_k^{(m+1)})' (\mathbf{y}_t - \mathbf{x}_t \hat{\boldsymbol{\beta}}_k^{(m+1)}) \\ &= \frac{1}{\sum_{t=1}^T \gamma_{tk}^{(m)}} (\mathbf{Y} - \mathbf{X} \hat{\boldsymbol{\beta}}_k^{(m+1)})' \mathbf{W}_k^{(m)} (\mathbf{Y} - \mathbf{X} \hat{\boldsymbol{\beta}}_k^{(m+1)}) \end{aligned} \quad (6)$$

### 2.2 Multiple HMRM (M-HMRM)

Regarding the case of multiple signals, the model can be expanded as a set of  $q$  time-series:



$$\mathbf{y}_j = \begin{cases} \mathbf{x}_i \boldsymbol{\beta}_{1k} + \sigma_{1k}^2 \dot{\mathbf{0}}_i \\ \mathbf{x}_i \boldsymbol{\beta}_{2k} + \sigma_{2k}^2 \dot{\mathbf{0}}_i \\ \vdots \\ \mathbf{x}_i \boldsymbol{\beta}_{qk} + \sigma_{qk}^2 \dot{\mathbf{0}}_i \end{cases}, \quad \forall j=1, \dots, q, \quad (7)$$

where the latent degradation state  $k$  simultaneously governs all of the univariate time series components. Having observed the multivariate degradation process with the M-HMRM in equation (7) and obtaining the estimated posterior distribution, the weighted discriminant type fusion technique [13] is used to re-define the regression parameters to a univariate process, and consequently the sampled distribution. The core concept of discriminant function analysis is to determine whether groups differ in terms of the mean of a variable, and then use that variable to predict which group the sample distribution might belong to. When dealing with a single variable, the final test to assess whether the underlying assumption of homogeneity of variance (i.e. homoscedasticity) distinguishes between groups is the  $F$ -test. This test is calculated by comparing the variance between groups to the pooled (average) variance within groups. If the variance between groups is significantly higher, it indicates significant differences in the prediction. The weighting process is influenced by the respective  $F$ -values. The  $F$ -value indicates how statistically significant a variable is in distinguishing between groups, reflecting its unique contribution to predicting group membership or fusion.

Here, the estimated covariance ( $\hat{\sigma}_k^2$ ) of the M-HMRM is a  $q \times q$  matrix. Since  $F$ -value is a measure of the extent to which a variable makes a unique contribution to the prediction of group membership, one can easily obtain the  $F$ -value of the different sensors from ( $\hat{\sigma}_k^2$ ) to be:

$$F_{jk} = \frac{\text{variance between groups}}{\text{variance within groups}} \quad (8)$$

The final fusion becomes a weighted linear combination, as follows:

$$\{\hat{\boldsymbol{\beta}}_k, \hat{\sigma}_k^2\} = \frac{\sum_{j=1}^q F_{jk} \{\hat{\boldsymbol{\beta}}_{jk}, \hat{\sigma}_{jk}^2\}}{\sum_j F_{jk}} \quad (9)$$

and the estimated bivariate coefficients are then integrated into the failure function. Integrating these coefficients into the degradation process facilitates the consideration of time-varying dynamics of systems, making it a preferred approach among researchers.

### 3 REMAINING USEFUL LIFE PREDICTION

Having established the single and multiple signal HMRM degradation process, in this section the PDF of the RUL of their underlying damage models are formulated using a derived closed-form expression. As stated in the previous sections, the degradation is modelled by a random process  $\{\hat{u}_k(\tau); \tau \leq 0\}$ , assumed Gaussian for simplicity. Under the concept of first hitting time (FHT), the conditional RUL ( $\hat{\ell}_k$ ) of the system on the observation  $\hat{u}_k(\tau)$  at degradation rate  $\tau$  of state  $k$  is defined as the time from the initial state of performance

degradation until the failure threshold ( $\lambda$ ) is reached for the first time, as:

$$\hat{\ell}_k = \inf \left\{ \tau : \hat{u}_k(\tau + \hat{\ell}) \geq \lambda \mid \hat{u}_k(\tau) < \lambda \right\} \quad (10)$$

A simple system architecture of the approach is presented in Figure 3. The HMRM parameters are obtained by sampling the observed data over the underlying state-based damage model

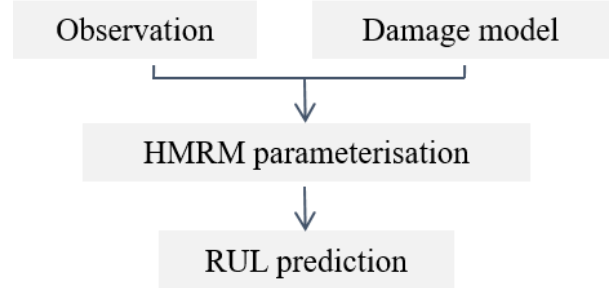


Figure 3. Remaining useful life flowchart.

#### 3.1 Power model

Consider that multiplicative measurement error in equation 1 can be approximated as  $\exp(\hat{\sigma}_k^2 \dot{\mathbf{0}}_\tau) \approx 1 + \hat{\sigma}_k^2 \dot{\mathbf{0}}_\tau$  and the variability in sampling the observation is very small, i.e.,  $(\hat{c}_k \tau^{\hat{b}_k} \hat{\sigma}_k^2 \sim \hat{\sigma}_k^2)$ , then the failure function becomes:

$$\hat{u}_k(\tau) = \hat{U}_k(\tau) + \hat{\sigma}_k^2 \dot{\mathbf{0}}_\tau = \hat{c}_k \tau^{\hat{b}_k} + \hat{\sigma}_k^2 \dot{\mathbf{0}}_\tau \quad (11)$$

$\tau$  controls switching between one degradation point  $u(\tau)$  and another across the  $K$  hidden states. From the log-linear transform,  $\mathbf{x}(\tau) = [1 \log \tau]$  and  $\hat{\boldsymbol{\beta}}_k = [\log \hat{c}_k \hat{b}_k]'$ . Since the FHT of the nonlinear degenerate model at the current rate  $\tau$  satisfies the inverse Gaussian distribution [17][18]. The degradation path upon hitting  $\lambda$  can be expressed as the PDF of the system RUL as:

$$f_T(\hat{\ell}_k \mid \hat{\theta}, \lambda) = \frac{\lambda - \hat{u}_k}{\sqrt{2\pi \hat{\ell}_k^3 (\hat{\sigma}_k^2 \hat{\ell}_k + \hat{\rho}_k)}} \times \exp \left[ -\frac{(\lambda - \hat{u}_k - \hat{c}_k \hat{\ell}_k^{\hat{b}_k})^2}{2 \hat{\ell}_k (\hat{\sigma}_k^2 \hat{\ell}_k + \hat{\rho}_k)} \right] \quad (12)$$

Where  $\hat{\rho}_k$  equal to one [19].

#### 3.2 Exponential model

Under the measurement error condition of log-normal distribution as assumed in the power model, the exponential failure function is presented as:

$$\hat{u}_k(\tau) = \hat{c}_k e^{\hat{b}_k \tau} + \hat{\sigma}_k^2 \dot{\mathbf{0}}_\tau \quad (13)$$

From the log-linear transform,  $\mathbf{x}(\tau) = [1 \tau]$  and  $\hat{\boldsymbol{\beta}}_k = [\log \hat{c}_k \hat{b}_k]'$ . The degradation path upon hitting  $\lambda$  can also be expressed in terms of the PDF of the system RUL:

$$f_T(\hat{\ell}_k | \hat{\theta}, \lambda) = \frac{\ln \lambda - \ln \hat{u}_k}{\sqrt{2\pi \hat{\ell}_k^3 (\hat{\sigma}_k^2 \hat{\ell}_k + \hat{\rho}_k)}} \times \exp \left[ -\frac{(\ln \lambda - \ln \hat{u}_k - \hat{b}_k \hat{\ell}_k)^2}{2 \hat{\ell}_k (\hat{\sigma}_k^2 \hat{\ell}_k + \hat{\rho}_k)} \right] \quad (14)$$

### 3.3 Performance error

The threshold  $\lambda$  is chosen based on expertise judgement. However, since this degradation dataset lacks historical data, as typical for bespoke components, the value of the last data point will be used as the threshold. In the second case study (for multiple sensor information), the mean of the signals' last data points is considered as the threshold.

Since the true internal states of degradation are not available, the number of states for the lifetime of either case is unknown. However, any chosen number of discrete states should be able to capture the degradation effects, encompassing material degradation, loading, environmental conditions and maintenance regimes. For prediction performance accuracy, we compute the root mean square error (RMSE) metric over each state  $k$  of the RUL, given as:

$$\text{RMSE} = \sqrt{\frac{1}{K} \sum_{k=1}^K (\ell_k - \hat{\ell}_k)^2} \quad (15)$$

where  $\ell_k$  and  $\hat{\ell}_k$  represents the actual and predicted RUL respectively.

## 4 FATIGUE CRACK GROWTH (FCG)

A FCG degradation process in a structural component has been simulated based on the Paris law of fracture mechanics described in [20], and the synthetic data is shown in Figure 4. The synthetic data will be used as the available data for the both models discussed in the previous section.

### 4.1 Results

Since RUL prediction solely depends on the available data, signals were continuously updated at every 25 cycles until failure. The advantage of this is to capture the heterogeneity of the degradation process. Typical for damage propagation in FCG, 2 and 3 state has been considered [21]. The parameter estimation procedure in section 2 and the PDF of RUL in section 3 is repeated recursively per inspection points.

The estimated PDF of RUL in terms of recursion in 2-state HMRM by power model is shown in Figure 5. At early stages of prediction (i.e., 25, 50 cycles), the prediction is dominated by uncertainty (high variance) due to limited degradation process, which does not clearly indicate the propagation trends. As failure approaches, the degradation process becomes more predictable and the variance shrinks. In addition, states switches is seen to adjust continuously as more data is introduced. However, the model seems to suffer a positive bias in predicting the RUL, as these models are conservative and obviously may not match the growth dynamics of Paris' law.

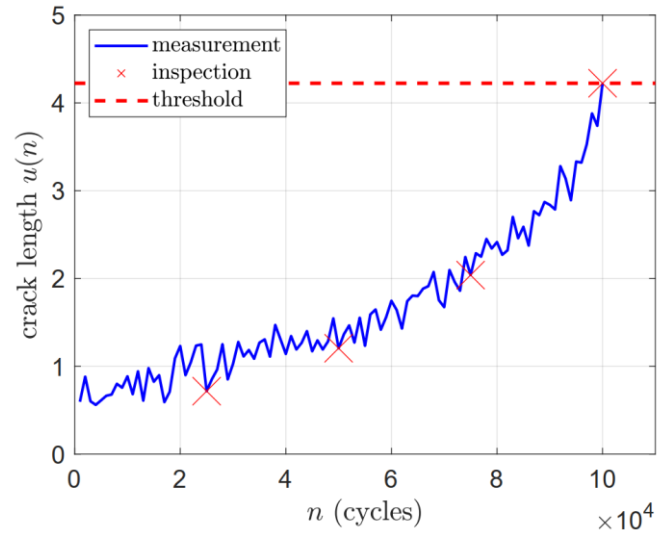


Figure 4. Fatigue crack length measurements  $u(n)$  versus magnitude of cycles  $n$ .

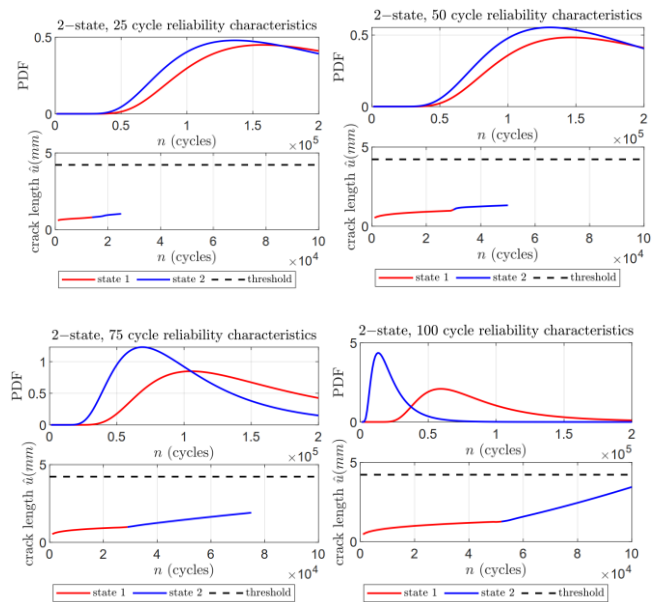


Figure 5. 2-state power HMRM reliability characteristics showing the predicted degenerate slope and the accompanying PDFs of RUL for real-time monitored information from the populated 25 initial cycles, updated by a populated 50, 75, and 100 cycle of monitored information.

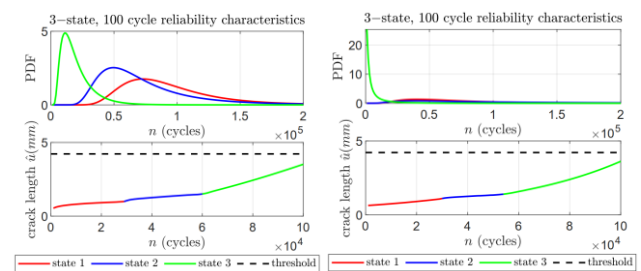


Figure 6. Reliability characteristics showing predicted degenerate slope and the accompanying PDFs of RUL for 100 cycles of monitored information in 3-state power (left) and exponential (right) HMRMs.

Figure 6 shows the complete (100 cycles of) predicted degenerate slope and the accompanying PDFs of RUL for 3-state HMRMs. It compares the prediction by power and exponential model. From the PDF plots, it shows that prediction from power model suffers more uncertainty than of the exponential model, especially at the late stage of damage propagation. This uncertainty is associated with the regressor parameter  $\hat{b}_k$ , which is gradual in the power model than in exponential model.

Figure 7 presents the RUL prediction based on the PDF of RUL plots. From the plot, it is observed that 2-state hidden states satisfy the heterogeneity in the datasets, and an additional state does not contribute to the dynamical distribution in the dataset. This is reasonable since FCG simulation is quasi-static, and rarely models the micro-cracks at grain levels. As time passes, it is shown that the predicted RUL converges towards the actual RUL in the absence of a prior degradation. The RUL distribution of the 2- state exponential model are observed to converge best than the power model. This is evident as the model follows damage accumulation scenario, which is a typical exponential. An EKF model based on the power model is also presented, for comparison. The EKF-power model converges to the true RUL better than 2-state power model. This is because, for an inspection routine with HMRM, the variance of estimating the regressor parameters over a sequence of observed data is higher than that of an EKF monitoring process. Along the true RUL is a 95% confidence interval.

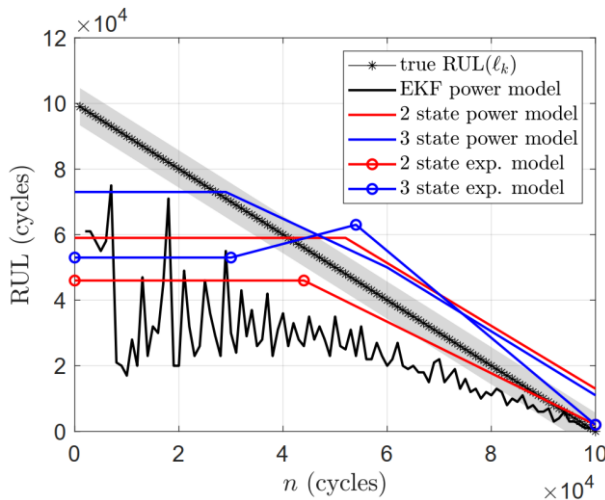


Figure 7. RUL prediction versus magnitude of cycles.

Figure 8 shows the corresponding RMSE using equation (15). Since error is cumulative, the model's performance is conditioned on state's discretisation and its ability to effectively capture the heterogeneity due to any dynamic effects by the switch operation mechanism of HMRM. The cumulative RMSE for 2–3 states of power model are  $2.51 \times 10^4$  and  $1.50 \times 10^4$  cycles; of exponential model are  $3.12 \times 10^4$  and  $2.60 \times 10^4$  cycles. The RMSE of EKF is  $2.86 \times 10^4$  cycles.

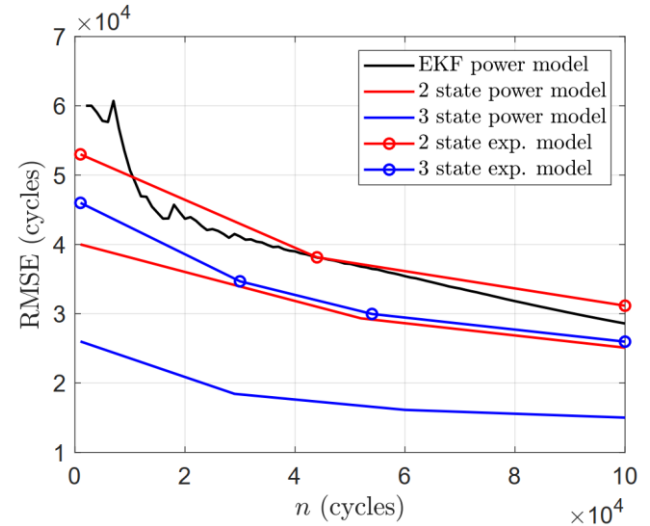


Figure 8. RMSE performance accuracy.

## 5 STRUCTURAL BEAM DEGRADATION

The second case study presents the corrosion degradation problem of a structural beam (see Figure 9). Sensors are deployed at intervals across the beam length to monitor the degradation process. For this study, synthetic measurements of signals from [20] were also considered which obey the power model in equation 11, with assumed log-normal state distribution and normal multiplicative measurement error as detailed in the mentioned reference.

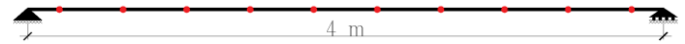


Figure 9. Multi-sensor condition monitoring scenario of a structural beam under progressive spatial varying damage accumulation, specific to the red "dotted" location.

Figure 10 illustrates the degradation distribution of the 10 sensor locations which were placed at 400mm sensor-sensor, numbered from left to right. Each degradation data point approximates the degradation level per year.

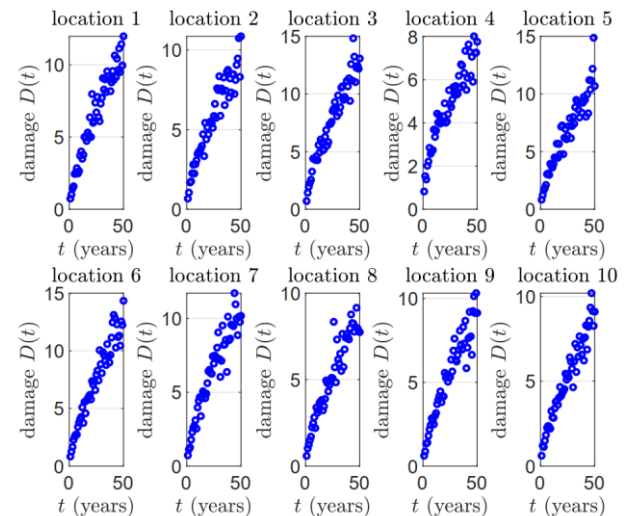


Figure 10. Synthetic sensor-based monitoring datasets of a structural beam subjected to damage accumulation. Observed dataset over the 10 sensor locations.



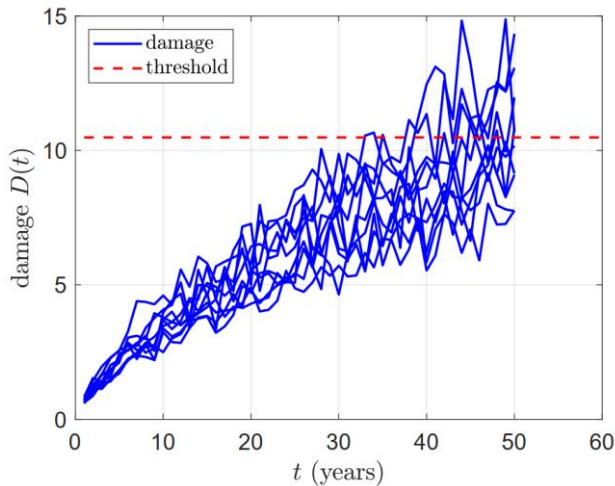


Figure 11. Combined distribution of the datasets.

As in the previous example, the sensor signals are inspected in 25 years' intervals until failure, when available, which was observed to be a minimum data points for a 2-state M-HMRM regression parameter estimation problem, according to the model. The same procedure of sequential updating of degraded sensor measurements applies to track the RUL change with time.

In Figure 11, the observed degradation in equation 7 is a  $t \times 10$  matrix for  $t$ -year cycle, which is used to estimate the degradation parameters by adopting the decision-level fusion in equation 9. A  $t \times 1$  predicted degenerate slope is obtained and the accompanying PDFs of RUL for 2 and 3-state M-HMRM are also obtained. The sensitivity of the concave degenerate slope is captured in the PDF distribution, in the hidden states, respectively. Whereas, a mean distribution of the  $j^{\text{th}}$  sensors is the assumed observation for the EKF.

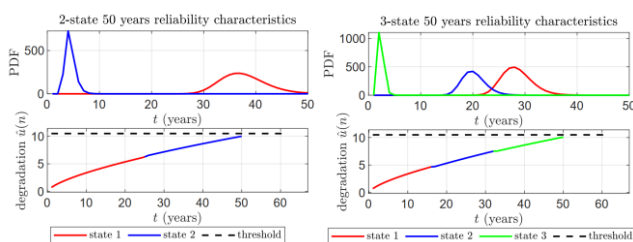


Figure 11. Multi-Sensory monitoring of a structural beam based on 2-state (left) and 3-state(right) segmentation process.

Figure 12 describes the RUL prediction at different times and its corresponding prediction performance accuracy. The prediction performance is influenced by the number of states used per observed cycle. The result shows that the 3-state predicted RUL converges better towards the actual RUL, consequently posing a better confidence of RUL prediction. The RUL for The RMSE for the prediction performance accuracy of both models is also presented. Figure 13 shows the cumulative RMSE for 2 and 3 states to be 10.47 and 10.94 years which is twice more accurate, in absolute terms, than 20.09 years of EKF.

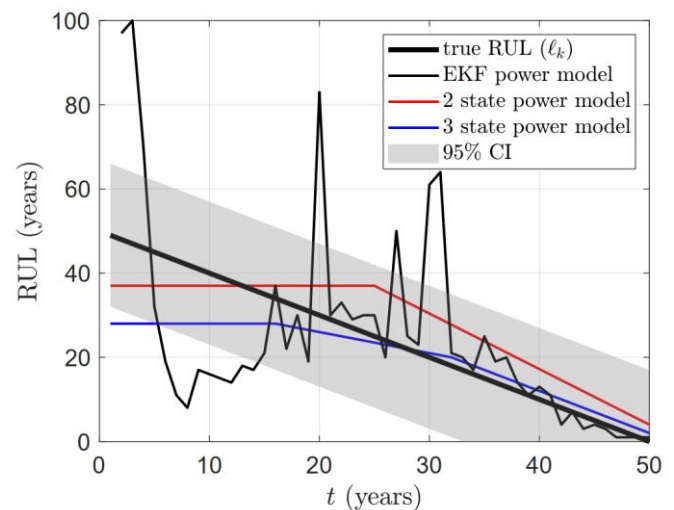


Figure 12. RUL prediction versus duration of degradation.

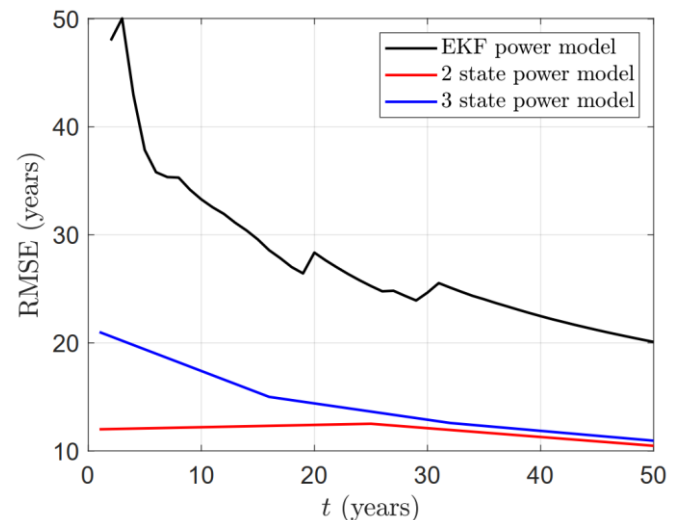


Figure 13. RMSE performance accuracy.

## LIMITATION IN PRACTICAL APPLICATION

The models discussed in this paper are generalized empirical power models to approximate self-accelerating crack growth behaviour and corrosion damage in a structural beam. While corrosion in reinforced concrete beam obey empirical power laws [22], crack growth may require differential or rate-based power laws, such in Paris or NASGRO equation [23], to capture multiple parameters (or uncertainties) which characterizes real-world systems. Crack growth phenomenon are influenced by multiple factors (or uncertainties) such as, material variability, environmental, and operational effects. Provided that these laws can be approximately linearised and adapted into hidden-state process to quantify these parameters or uncertainties, a closed form solution of it FHT to predict the remaining useful life distribution can be obtained. Although, the solution may not follow closely a similar trend as discussed in this paper, but the principle is the same.

## CONCLUSIONS

A framework to estimate the RUL of bespoke components was presented and illustrated on two examples. A regression-based hidden Markov model was proposed for degradation process prediction and two power failure functions were used to illustrate the state-dependent degradation scenarios for each problem. A case of multiple sensor measurements has also been presented.

Both cases presented address the situation where the system's prior lifetime dataset is unavailable, which makes it difficult to estimate RUL using traditional methods. The observations are modelled as sets of data that become available, and the parameters of the failure function are updated. Finally, the PDFs of RUL can be evaluated based on the re-estimated parameters of failure function, for each state. Compared to extended Kalman filter method, the model demonstrates its ability to estimate the RUL of a structural component in the absence of failure history.

## ACKNOWLEDGMENTS

The work was financially supported by the School of Architecture Building and Civil Engineering studentship of Loughborough University, UK.

## REFERENCES

- [1] C. J. Lu and W. O. Meeker, 'Using Degradation Measures to Estimate a Time-to-Failure Distribution', *Technometrics*, vol. 35, no. 2, pp. 161–174, May 1993, doi: 10.1080/00401706.1993.10485038.
- [2] V. v. s. Sarma, K. v. Kunhikrishnan, and K. Ramchand, 'A Decision Theory Model for Health Monitoring of Aeroengines', *Journal of Aircraft*, vol. 16, no. 3, pp. 222–224, Mar. 1979, doi: 10.2514/3.58508.
- [3] G. Perfetti, T. Aubert, W. J. Wildeboer, and G. M. H. Meesters, 'Influence of handling and storage conditions on morphological and mechanical properties of polymer-coated particles: characterization and modeling', *Powder Technology*, vol. 206, no. 1, pp. 99–111, Jan. 2011, doi: 10.1016/j.powtec.2010.03.040.
- [4] E. Santecchia *et al.*, 'A Review on Fatigue Life Prediction Methods for Metals', *Advances in Materials Science and Engineering*, vol. 2016, no. 1, p. 9573524, 2016, doi: 10.1155/2016/9573524.
- [5] D. Du, J. Zhang, X. Si, and C. Hu, 'Remaining Useful life Estimation: A Review on Stochastic Process-based Approaches', *Recent Patents on Engineering*, vol. 15, no. 1, pp. 69–76, Jan. 2021, doi: 10.2174/1872212114999200423115526.
- [6] X.-S. Si, W. Wang, C.-H. Hu, and D.-H. Zhou, 'Remaining useful life estimation – A review on the statistical data driven approaches', *European Journal of Operational Research*, vol. 213, no. 1, pp. 1–14, Aug. 2011, doi: 10.1016/j.ejor.2010.11.018.
- [7] T. Aggab, P. Vignat, M. Avila, and F. Kratz, 'Remaining useful life estimation based on the joint use of an observer and a hidden Markov model', *Journal of Risk and Reliability*, vol. 236, no. 5, pp. 676–695, 2022.
- [8] C. Bunks, D. McCarthy, and T. Al-ani, 'Condition-Based Maintenance of Machines using Hidden Markov Models', *Mechanical Systems and Signal Processing*, vol. 14, no. 4, pp. 597–612, Jul. 2000, doi: 10.1006/mssp.2000.1309.
- [9] W. Wang, 'A prognosis model for wear prediction based on oil-based monitoring', *J Oper Res Soc*, vol. 58, no. 7, pp. 887–893, Jul. 2007, doi: 10.1057/palgrave.jors.2602185.
- [10] W. Wang, 'A two-stage prognosis model in condition based maintenance', *European Journal of Operational Research*, vol. 182, no. 3, pp. 1177–1187, Nov. 2007, doi: 10.1016/j.ejor.2006.08.047.
- [11] L. R. Rabiner, 'A tutorial on hidden Markov models and selected applications in speech recognition', *Proceedings of the IEEE*, vol. 77, no. 2, pp. 257–286, 1989, doi: 10.1109/5.18626.
- [12] P. Juesas, E. Ramasso, S. Drujont, and V. Placet, 'Autoregressive Hidden Markov Models with partial knowledge on latent space applied to aero-engines prognostics', *PHME\_CONF*, vol. 3, no. 1, Jul. 2016, doi: 10.36001/phme.2016.v3i1.1642.
- [13] M. Dong and D. He, 'Hidden semi-Markov model-based methodology for multi-sensor equipment health diagnosis and prognosis', *European Journal of Operational Research*, vol. 178, no. 3, pp. 858–878, May 2007, doi: 10.1016/j.ejor.2006.01.041.
- [14] D. Trabelsi, S. Mohammed, F. Chamroukhi, L. Oukhellou, and Y. Amirat, 'An Unsupervised Approach for Automatic Activity Recognition based on Hidden Markov Model Regression', *IEEE Transactions on Automation Science and Engineering*, vol. 10, no. 3, pp. 829–835, Jul. 2013, doi: 10.1109/TASE.2013.2256349.
- [15] E. Benhamou, 'Kalman filter demystified: from intuition to probabilistic graphical model to real case in financial markets', Dec. 13, 2018, *arXiv: arXiv:1811.11618*. doi: 10.48550/arXiv.1811.11618.
- [16] G. J. McLachlan and T. Krishnan, *The EM Algorithm and Extensions*, 2nd ed. in Wiley Series in Probability and Statistics. Wiley-Interscience, 2008.
- [17] X.-S. Si, Z.-X. Zhang, and C.-H. Hu, *Data-Driven Remaining Useful Life Prognosis Techniques*. in Springer Series in Reliability Engineering. Berlin, Heidelberg: Springer, 2017. doi: 10.1007/978-3-662-54030-5.
- [18] X.-S. Si, W. Wang, M.-Y. Chen, C.-H. Hu, and D.-H. Zhou, 'A degradation path-dependent approach for remaining useful life estimation with an exact and closed-form solution', *European Journal of Operational Research*, vol. 226, no. 1, pp. 53–66, Apr. 2013, doi: 10.1016/j.ejor.2012.10.030.
- [19] X.-S. Si and D. Zhou, 'A Generalized Result for Degradation Model-Based Reliability Estimation', *IEEE Transactions on Automation Science and Engineering*, vol. 11, no. 2, pp. 632–637, Apr. 2014, doi: 10.1109/TASE.2013.2260740.
- [20] A. Kamariotis, L. Sardi, I. Papaioannou, E. Chatzi, and D. Straub, 'On off-line and on-Line Bayesian filtering for uncertainty quantification of structural deterioration', *Data-Centric Engineering*, vol. 4, p. e17, 2023, doi: 10.1017/dce.2023.13.
- [21] Y. Pan, Z. S. Khodaei, and F. Aliabadi, 'Online fatigue crack detection and growth modelling through higher harmonic analysis: A baseline-free approach', *Mechanical Systems and Signal Processing*, vol. 224, p. 112167, Feb. 2025, doi: 10.1016/j.ymssp.2024.112167.
- [22] W. Liu and M. E. Barkey, 'Prediction on Remaining Life of a V-Notched Beam by Measured Modal Frequency', *Shock and Vibration*, vol. 2019, no. 1, p. 7351386, 2019, doi: 10.1155/2019/7351386.
- [23] A.-H. I. Mourad *et al.*, 'Fatigue life and crack growth prediction of metallic structures: A review', *Structures*, vol. 76, p. 109031, Jun. 2025, doi: 10.1016/j.istruc.2025.109031.

# Identification of Damping Coefficients of Multi-degree of Freedom System

Mohammad Shamim Miah<sup>1</sup>, (0000-0001-9112-4049), Werner Lienhart<sup>1</sup>, (0000-0002-2523-4052)

<sup>1</sup>Institute of Engineering Geodesy and Measurement Systems, Faculty of Mathematics, Physics and Geodesy, Graz University of Technology, Steyrergasse 30, 8010 Graz, Austria  
email: miah@tugraz.at, werner.lienhart@tugraz.at

**ABSTRACT:** Structural dynamical properties are vulnerable to the dynamic loads because such loads can change those parameters significantly. It is not possible to halt the aforementioned issue as dynamic loads are entirely unpredictable. The changes in stiffness, mass, and damping can lead to minor to serious damage scenarios depending on the level of changes of those parameters. Typically, the displacements trajectories of any systems are unknown, and if any other physical parameters e.g. damping is unknown that will form a nonlinear problem. Herein, to deal with the early mentioned problem a nonlinear observer namely the unscented Kalman filter (UKF) is employed. In conventional practice, the partial or full stiffness matrix are identified but identifying damping matrix is rare due to inherent complicity. Hence, this study has focused on the identification of the entire damping matrix by adopting the UKF. The outcome of study shows that UKF is capable of identifying damping coefficients quite accurately. This outcome can play a vital role in the area of structural health monitoring and control applications.

**KEY WORDS:** Structural Health Monitoring, Unscented Kalman Filter, Dynamic Loads, Damage.

## 1 INTRODUCTION

System identification is a process that helps to estimate any desire quantities e.g. stiffness based on measured sensory data and develop an underlying mathematical model of the dynamical system. Typically, the goal of the system identification is to develop a representative model that can render the true behavior of the dynamical system. Modern structures are getting complicated to monitor due to many underlying uncertainties such as their form, adaptation of state-of-art technologies e.g. sensors, dampers, monitoring tools. Therefore, monitoring such structures require proper tools, scheme and knowledge to deal with hidden uncertainties. For instance, in order to keep track on any changes real-time monitoring could be an option [1], [5], [13] and [14]. On the other hand, system identification might assist to understand the structure better as it might help to update the virtual or mathematical systems real-time or offline.

System identification (SI) is a shared topic in many areas of science and engineering e.g. mechanical/civil engineering, robotics, process engineering [15][16]. However, in case of civil engineering application still the use and application of SI is limited due to associated problems, for instance, models are very large compare to a robot or mechanical tool. Dealing with large model require serious attention as many variables are unknowns along with inputs. To deal with the numerous uncertainties, typically, from the measured data, stiffnesses are identified and feed to the control loop to adjust and update the model. Thereby, the updated model can render the true system behavior better contrary to doing no update. If the aforementioned process is done in real-time, optimal control performances can be expected.

Many works can be found those who tried various methods to identify different parameters of various type of structures e.g. buildings, bridges. Among them, a new type black-box by the use of extended Kalman filter (EKF) is studied for SI [4], a

neural network and dead-zone Kalman filter algorithm has been reported in [6], SI for time-varying system [7], autoregressive models based frequencies and damping ratio identification by [8], new forms of EKF for SI [9], SI for medical image processing application [10], SI using stochastic filter techniques [12]. The fundamental concept of the Kalman filter was proposed by Rudolf E. Kalman in 1960 [17]. Later, many have been proposed and developed different nonlinear filters such as EKF and UKF [11], [18] and [19] and their modified version.

It is mentioned early that stiffness are often identified for civil engineering application due to the simplicity in contrast to identifying damping. For instance, a detail theoretical formulation and an experimental validation of semi-active control problem along with stiffness matrix identification has been carried out in [14]. In the aforementioned study, author did not perform the identification of damping matrix individually or linked to any control problem. Because, damping coefficients are extremely sensitive to inputs and material properties as a result dealing with the control problem makes things troublesome or even could lead to an uncontrollable situation. Therefore, not many studies have been conducted in case of damping coefficients/matrices in combination with states due to the underlying complicity. More specifically, when both states and damping coefficients are unknown simultaneously, it leads to a nonlinear problem that requires a nonlinear observer to solve. The aforementioned problem has been focused in [20] to identify damping matrix where main consideration was to see the effect of initial covariance of the observer. Another work [3] has tried to identify damping via sensitivity enhanced method linked to Principal Component Analysis. A more detail issues linked to nonlinear damping identification has been reported in [2].

From above discussion it is clear that identification of damping itself leads to a complicated problem and it gets more



complicated when both sates and damping coefficients are unknown. To handle this issue, this study has focused into the identification of damping coefficients along with unknown states. A 15 degree-of-freedom (DOF) dynamical system is consider for the numerical implementations. The system identification task is performed by employing the unscented Kalman filter (UKF). The overall outcome shows that the UKF is capable of identifying damping coefficients quite accurately. As a result, the dynamical response (e.g. displacements) of the system shows excellent match with the response of the true system. Rest of the paper contains, problem description & formulation, results and discussion and finally a summary of the study.

## 2 PROBLEM DESCRIPTION & FORMULATION

The numerical investigations are conducted by adopting a 15 storied dynamical system. The dynamical system is considered to be model as lumped-mass-spring system as depicted in Figure 1. A sample free-body diagram of the top floor and a typical floor is shown in the early mentioned figure along with the full structure. Typically, equation of motion (EOM) is derived for each floor from the free-body diagram of the structure. As for example, an EOM has been derived for the 1<sup>st</sup> DOF as shown below,

$$m_1 \ddot{x}_1(t) + c_1 \dot{x}_1(t) + k_1 x_1(t) - c_1 [\dot{x}_2(t) - \dot{x}_1(t)] - k_1 [x_2(t) - x_1(t)] = -\ddot{u}_1(t) \quad (1)$$

$$m_1 \ddot{x}_1(t) + [c_1 + c_2] \dot{x}_1(t) - c_1 \dot{x}_2(t) + [k_1 + k_2] x_1(t) - k_1 x_2(t) = -\ddot{u}_1(t) \quad (2)$$

Later, all those equations of motion are combined into one single equation in matrix-vector form. And the dynamical model can be expressed in vector-matrix form as,

$$M\ddot{X}(t) + C\dot{X}(t) + KX(t) = -\beta\ddot{u}_g(t) \quad (3)$$

where M, C and K are the mass, damping and stiffness matrices with a size of  $15 \times 15$ ,  $\dot{X}$ ,  $\ddot{X}$  and  $\ddot{X}$  are the displacement, velocity, and acceleration vector those have a size of  $15 \times 1$ ,  $\ddot{u}_g$  is the input excitation,  $\beta$  controls input excitations location,  $t$  is the time vector.

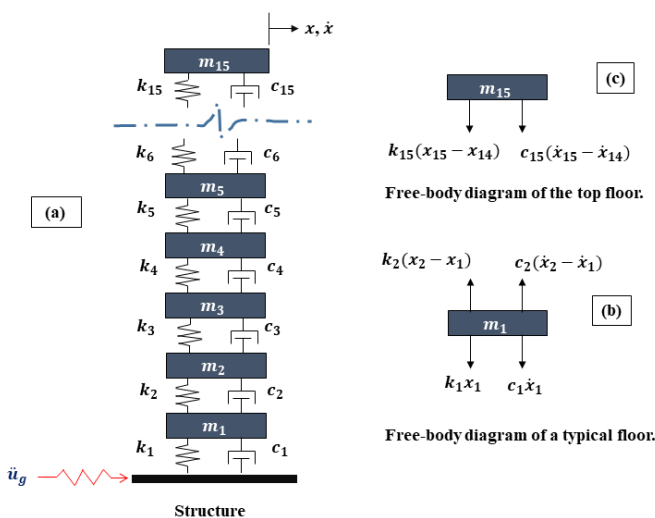


Figure 1. The structure and sample free-body diagram of a typical floor and top floor.

It is quite common that the dynamical system further formulated by adopting the state space (SS) formulation technique. The SS formulation contains two main equations, they called, (i) the process equation in Eq. (2), and (ii) the observation equation in Eq. (3).

$$x_{k+1} = Ax_k + Bu_k \quad (4)$$

$$y_k = Cx_k + Du_k \quad (5)$$

where  $x$  is the states vector that has displacement and velocity,  $A$  is the state matrix,  $B$  represents the input matrix, it can be with single of multi inputs,  $D$  is the feedthrough matrix,  $C$  is output matrix,  $u$  contains input and control force (if any),  $y$  is the output vector.

Step ahead, the noise terms (both process and observation) are added to the SS formulation to deal with the observer. Typical, formulation of the UKF would look like,

$$x_{k+1} = f(x_k, v_k) \quad (6)$$

$$y_k = h(x_k, n_k) \quad (7)$$

where  $v_k$  represent process noise and  $n_k$  is the observation noise. The dynamical systems are described via  $f$  and  $h$  functions [18]-[19]. UKF propagates random variables using a specific statistical procedure known as the unscented transformation (UT). Due the aforementioned procedure UKF is derivative free, as a result it is faster than its counterpart EKF [18]. In short, a structured transformation, distributed equally around the mean (also known as the sigma points) that propagate through early mentioned complex nonlinear functions. The sigma points ( $\hat{x}_k$ ) are estimated as follows,  $\hat{x}_k = [\hat{x}_{k-1}, \hat{x}_{k-1} + \sqrt{(L + \lambda)P_{k-1}}, \hat{x}_{k-1} - \sqrt{(L + \lambda)P_{k-1}}]$ , where  $L$  is the dimension of the states and  $\lambda$  is a scaling factor. There are two main steps for the UKF, they are known as (i) the prediction Eq. (6) and (ii) the measurement update Eq. (7).

$$\hat{x}_{k|k-1} = f(\hat{x}_{k-1}, u_{k-1}) + w_{k-1} \quad (8)$$

$$\hat{y}_{k|k-1} = h(\hat{x}_{k|k-1}) + v_k \quad (9)$$

A simplified flow-chart of the UKF is depicted in Figure 2. The overall estimation is done recursively until the simulation ends.

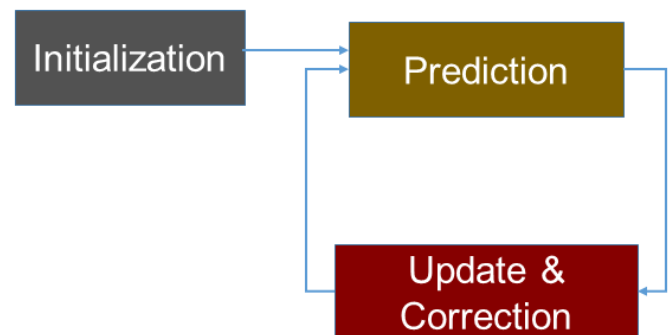


Figure 2. Basic steps of the UKF.

The estimation steps of the UKF is given below with more detail:

(i) The initialization step (setting the states and covariance):

$$\hat{x}_0 = E[x_0], P_0 = E[(x_0 - \hat{x}_0)(x_0 - \hat{x}_0)^T]$$

$$\hat{x}_0^a = E[x^a] = [\hat{x}_0^a \ 0 \ 0]^T, P_0^a = E[(x_0^a - \hat{x}_0^a)(x_0^a - \hat{x}_0^a)^T]$$

(ii) The Sigma Points estimation:

$$\gamma_{k-1}^a = \left[ \hat{x}_{k-1}^a, \hat{x}_{k-1}^a + \sqrt{(L + \lambda)P_{k-1}^a}, \hat{x}_{k-1}^a - \sqrt{(L + \lambda)P_{k-1}^a} \right]$$

(iii) The prediction or time update:

$$\gamma_{k|k-1}^x = f[\gamma_{k-1}^x, \gamma_{k-1}^v]$$

$$\hat{x}_k^- = \sum_{i=0}^{2L} [w_i^m \gamma_{i,k|k-1}^x]$$

$$P_k^- = \sum_{i=0}^{2L} [w_i^c (\gamma_{i,k|k-1}^x - \hat{x}_k^-)(\gamma_{i,k|k-1}^x - \hat{x}_k^-)^T]$$

$$\tau_{k|k-1} = h[\gamma_{k|k-1}^x, \gamma_{k|k-1}^v]$$

$$\hat{y}_k^- = \sum_{i=0}^{2L} [w_i^m \tau_{i,k|k-1}]$$

(iii) The measurement update & correction:

$$P_{\bar{y}_k \bar{y}_k} = \sum_{i=0}^{2L} [w_i^c (\tau_{i,k|k-1} - \hat{y}_k^-)(\tau_{i,k|k-1} - \hat{y}_k^-)^T]$$

$$P_{x_k y_k} = \sum_{i=0}^{2L} [w_i^c (\gamma_{i,k|k-1}^x - \hat{x}_k^-)(\tau_{i,k|k-1} - \hat{y}_k^-)^T]$$

$$\hat{x}_k = \hat{x}_k^- + P_{x_k y_k} P_{\bar{y}_k \bar{y}_k}^{-1} [y_k - \hat{y}_k^-]$$

where  $P_x$  is the process noise covariance,  $P_y$  is the measurement noise covariance,  $w_i$  is the weight parameters [462].

### 3 RESULTS AND DISCUSSION

The numerical investigations are conducted by adopting a 15 degree of freedom (DOF) dynamical system. Therefore, the mass, damping and stiffness matrices size are  $15 \times 15$ , while, the mass matrix is assumed to be fully-diagonal. The mass is assumed to be equal in each floor and the weight of every floor is around  $60 \times 10^3$  Kg. And the stiffness components of each floor are considered  $65 \times 10^5$  N/m. The damping coefficients are estimated using eigenfrequencies and a damping ration of 2%. The main goal here is to identify all of the 15 damping coefficients. To do this, UKF is employed as nonlinear observer and the numerical investigations are conducted for 160 sec with a sampling rate of 200 Hz. The harmonic type input excitation

( $\ddot{a}_g = 1 \times \sin(16.5t)$ ) is used to excite the structure (see Figure 3). The harmonic type input load has been selected due to the simplicity of the nature of the load in contrary to complex type input e.g. earthquake.

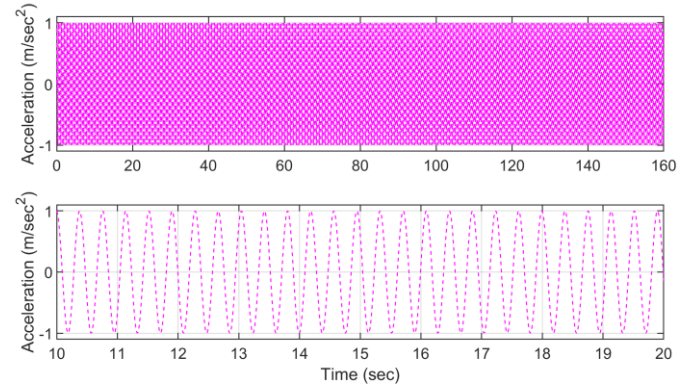


Figure 3. Input excitation: full-time series (top), zoomed view (bottom).

The comparison of the original versus identified damping coefficients are presented in Figure 4, Figure 5, and Figure 6. More precisely, the damping coefficients are separated as  $c_1 - c_5$  in Figure 4,  $c_6 - c_{10}$  in Figure 5, and  $c_{11} - c_{15}$  in Figure 6, respectively. The aforementioned separation is done for better visualization purpose. Additionally, the values are normalized with respect to the top floor's value for the same reason as mentioned earlier.

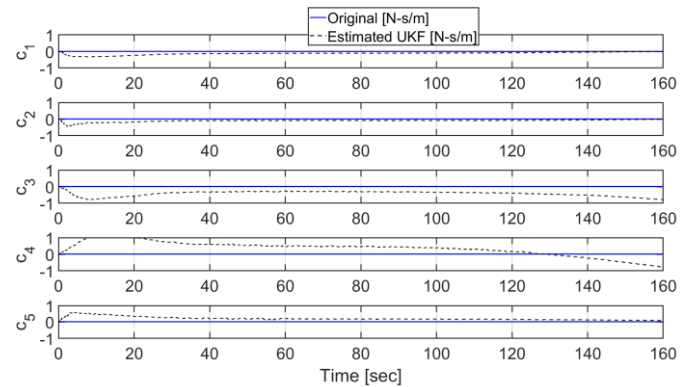


Figure 4. Comparison of the original and identified damping coefficients [ $c_1 - c_5$ ].

It is observed that the accuracy of the estimated damping coefficients is in generally good. However, few parameters have struggled than their peers, it is due to the size of model's variables, meaning, more parameters lead to complex tuning process (e.g. noise level, initial covariances, etc.), similar issues have been reported by many [12], [20] and [21]. However, even after hard tuning still at the end accuracy may not be as expected because it is mentioned earlier that the accuracy is not depended on any single variable.

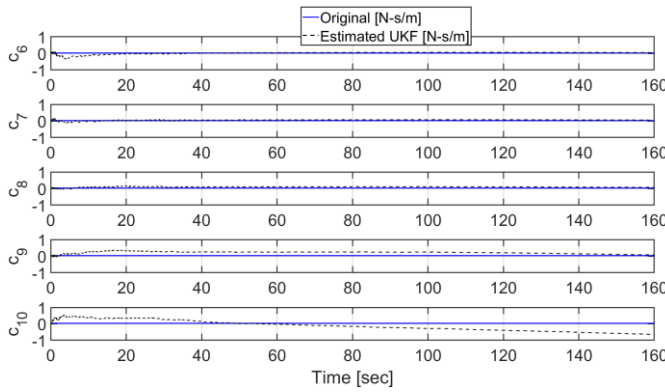


Figure 5. Comparison of the original and identified damping coefficients  $[c_6 - c_{10}]$ .

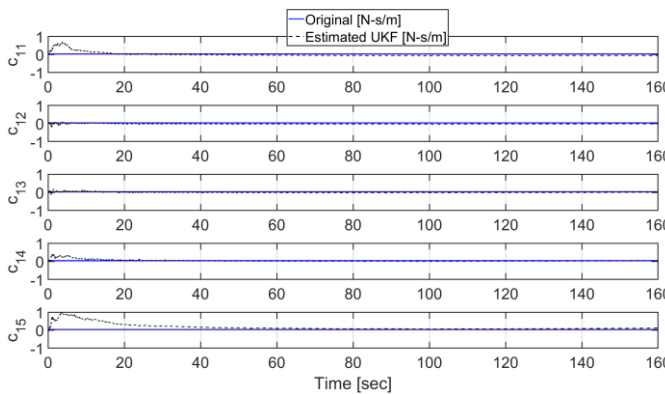


Figure 6. Comparison of the original and identified damping coefficients  $[c_{11} - c_{15}]$ .

There are many underlying uncertainties for parameters identification in general and it gets worse when it comes to damping. It is due to the nature of the damping itself and there are many influencing factors such as amplitudes of the inputs, initial covariances and noise. Additionally, the accuracy of the estimation/identification may change significantly if the sampling rate, duration of the simulation, initial states and covariances are not tuned properly. A summary of the identified damping coefficients is given in Table 1. Along with the early mentioned table a graphical representation of the data is shown in Figure 7. It should be noted that the normalized errors are estimated based on the last value at the end of the simulation. Hence for better understanding, Figure 4, Figure 5, and Figure 6 are recommended to see the whole time-series. As the parameters take some time to reach in stable or so-called steady-state condition hence errors are not isolation to a point of time of simulation (for example the identified value in the table).

Table 2. Summary of the identified damping coefficients.

Damping coefficients	Original	Identified*	Normalized Error (%)
$c_1$	1273.55	1665.95	0.016
$c_2$	3807.57	5017.11	0.048
$c_3$	6302.52	501131.164	19.78

$c_4$	8732.81	493153.22	19.36
$c_5$	11073.48	53097.78	1.68
$c_6$	13300.52	25630.01	0.49
$c_7$	15391.08	28422.90	0.52
$c_8$	17323.71	47258.82	1.19
$c_9$	19078.57	42974.68	0.95
$c_{10}$	20637.66	411245.85	15.61
$c_{11}$	21984.98	36596.87	0.58
$c_{12}$	23106.76	3977.92	0.76
$c_{13}$	23991.326	7640.00	0.65
$c_{14}$	24629.76	28217.52	0.14
$c_{15}$	25015.46	75434.76	2.01

\*absolute identified values belong to the end of the simulation

Further, the propagation of the uncertainties have evaluated and given as the root mean squared (RMS) and the standard deviations (STD), those values are estimated and illustrated in Figure 8 and Figure 9, respectively. Both the RMS values and STD shows that they are not constant and consistent throughout the simulation period. That also justify why the identified parameters may have different level of errors based-on at what point the parameters are considered.

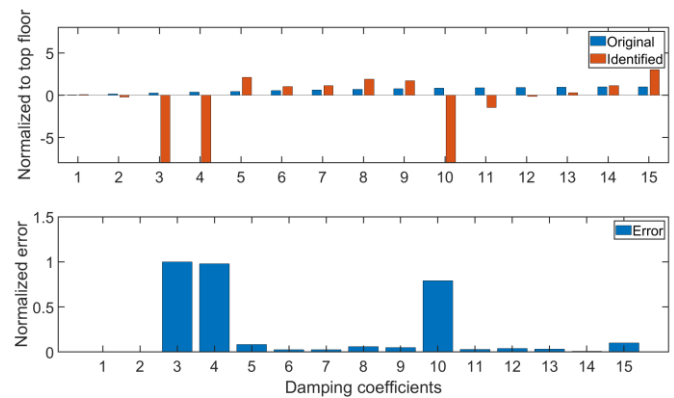


Figure 7. Comparison of the original and identified damping coefficients and their errors  $[c_1 - c_{15}]$ .

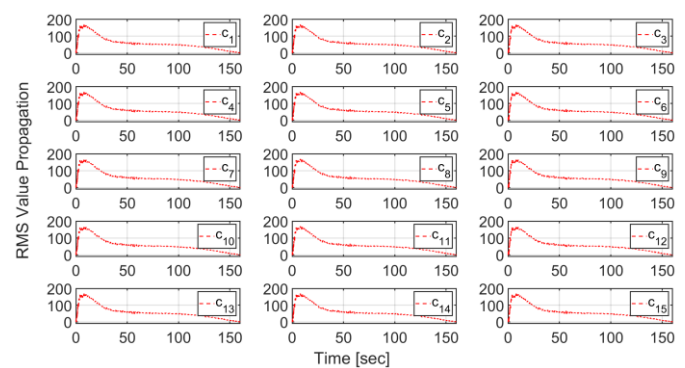


Figure 8. Point-to-point error changes during the simulation period  $[c_1 - c_{15}]$ .



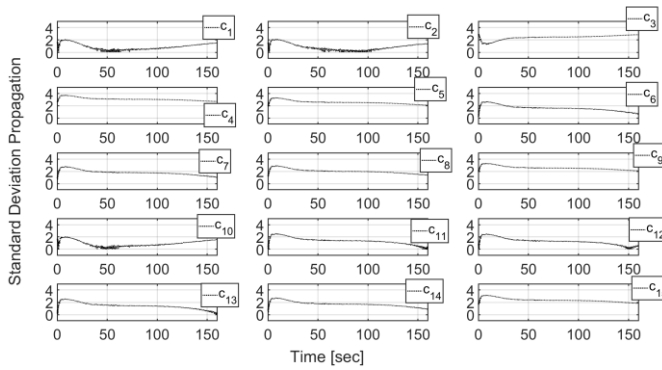


Figure 9. Standard deviation changes during the simulation period  $[c_1 - c_{15}]$ .

Furthermore, to understand the effect of the identified damping coefficients, the displacements trajectories of the 5<sup>th</sup>, 10<sup>th</sup> and 15<sup>th</sup> DOF is evaluated. The displacement of 5<sup>th</sup> floor is depicted in Figure 10, while Figure 11 has the 10<sup>th</sup> floor displacement and the 15<sup>th</sup> floor displacement is shown in Figure 12. All of the aforementioned figures have a full-time series (top sub figure) and a zoomed view (bottom sub figure). It can be observed that all of those figures show a very good accuracy in terms of rendering the original behavior of the system.

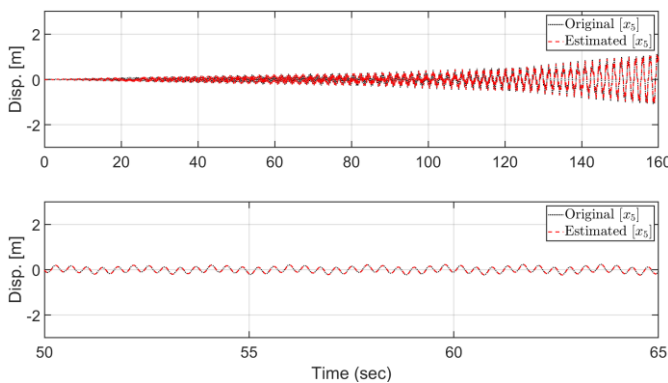


Figure 10. Original versus estimated displacement of the 5<sup>th</sup> floor.

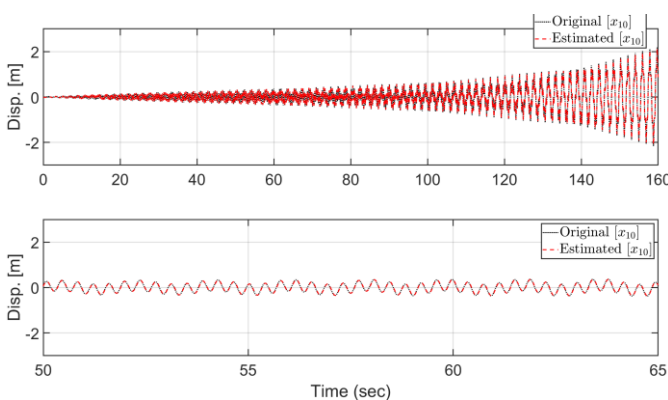


Figure 11. Original versus estimated displacement of the 10<sup>th</sup> floor.

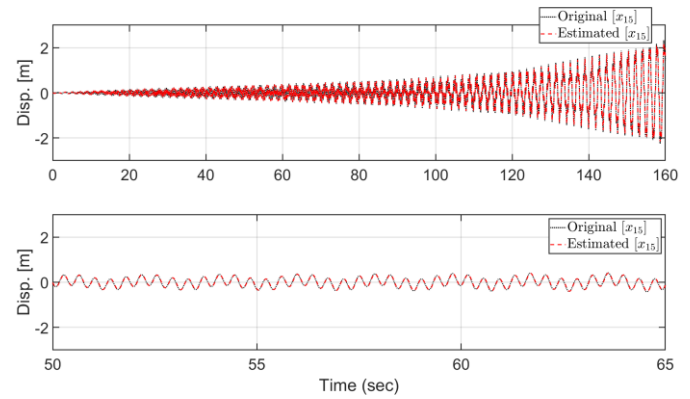


Figure 12. Original versus estimated displacement of the 15<sup>th</sup> floor.

Last but not least, the acceleration response of those early mentioned floors (e.g. 5<sup>th</sup>, 10<sup>th</sup> and 15<sup>th</sup>) has been evaluated and presented in Figure 13, Figure 14, and Figure 15, correspondingly. Similar to the earlier observation, it has been noticed that the estimated acceleration data render the original data quite accurately.

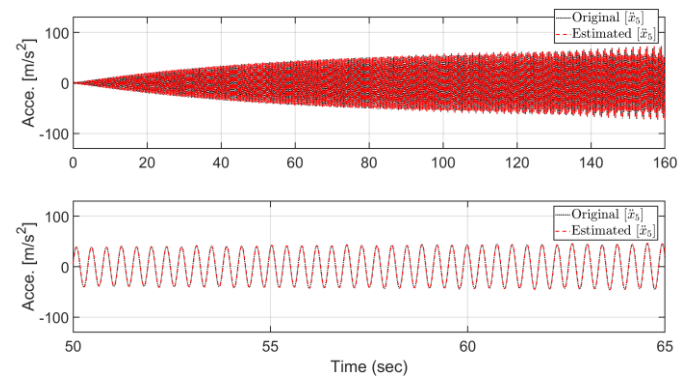


Figure 13. Original versus estimated acceleration of the 5<sup>th</sup> floor.

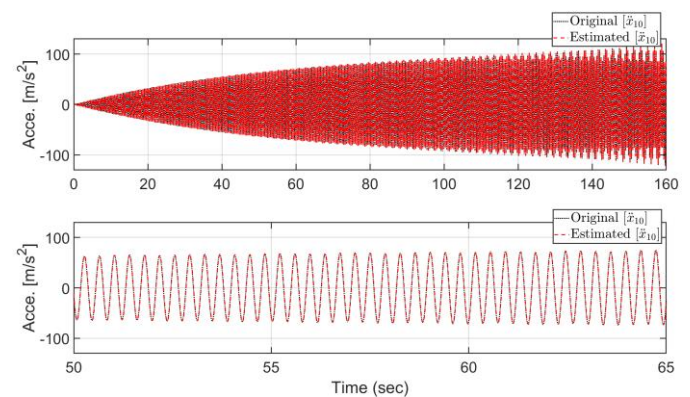


Figure 14. Original versus estimated acceleration of the 10<sup>th</sup> floor.

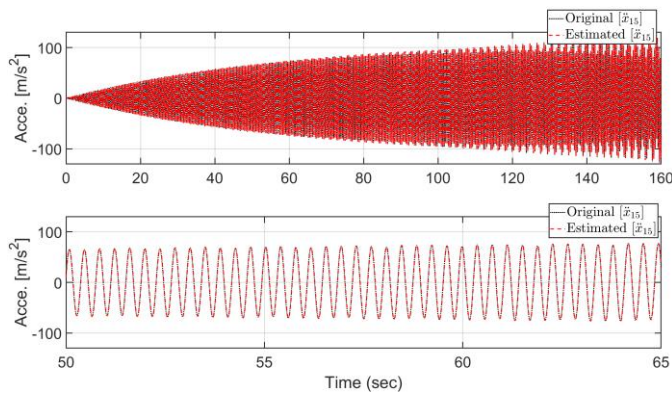


Figure 15. Original versus estimated acceleration of the top floor.

#### 4 CONCLUSION

This study investigates the possibility of identification full damping matrix of a 15 DOF system. The goal is achieved by adopting the UKF as an observer. The estimated parameter results show very good match with the original data. The displacement and acceleration comparison results confirm (due to their a very good match) that the identified damping coefficient are quite accurate. However, that doesn't mean that all 15 damping coefficients (e.g.  $c_1 - c_{15}$ ) are having same accuracy. UKF perform recursive estimation during the given time-span hence the error of the estimation is optimized by minimizing errors. In other words, the accuracy of the states (displacements and velocities) are not very much affected due to the individual damping coefficient accuracy. In a nutshell, the outcome of this study can be summarized that the investigated approach might be beneficial for structural health monitoring and vibration control applications as the states can be updated during the simulation in real-time.

#### ACKNOWLEDGMENTS

Authors appreciate the research supports and facilities provided by the Graz University of Technology, Graz, Austria.

#### REFERENCES

- [1] Z. Xie and J. Feng, Real-time nonlinear structural system identification via iterated unscented Kalman filter, *Mechanical Systems and Signal Processing*, 28, 309–322, 2012.
- [2] T. Al-Hababi, M. Cao, B. Saleh, N. F. Alkayem and H. Xu, A critical review of nonlinear damping identification in structural dynamics: Methods, applications, and challenges. *Sensors (Switzerland)*, 20(24), 1–41, 2020.
- [3] X. Wang, K. Liu, H. Liu and Y. He, Damping Identification with Acceleration Measurements Based on Sensitivity Enhancement Method. *Shock and Vibration*, 2018, 6476783, 2018.
- [4] K. Bogdanski and M. C. Best, A new structure for non-linear black-box system identification using the extended Kalman filter. *Proceedings of the Institution of Mechanical Engineers, Part D: Journal of Automobile Engineering*, 231(14), 2005–2015, 2017.
- [5] M. Wu and A. W. Smyth, Application of the unscented Kalman filter for real-time nonlinear structural system identification. *Structural Control and Health Monitoring*, 14(December 2005), 971–990, 2007.
- [6] J. Dejesusrubio and W. Yu, Nonlinear system identification with recurrent neural networks and dead-zone Kalman filter algorithm. *Neurocomputing*, 70(13–15), 2460–2466, 2007.
- [7] B. Weng and K. E. Barner, Time-Varying Volterra System Identification Using Kalman Filtering. *Information Sciences and Systems*, 2006 40th, 1617–1622, 2006.
- [8] H. Kosorus, M. Hollrigl-Binder, H. Allmer and J. Kung, On the Identification of Frequencies and Damping Ratios for Structural Health Monitoring Using Autoregressive Models. *2012 23rd International Workshop on Database and Expert Systems Applications*, 23–27, 2012.
- [9] S. Ghosh, D. Roy and C. Manohar, New forms of extended Kalman filter via transversal linearization and applications to structural system identification. *Computer Methods in Applied Mechanics and Engineering*, 196(49–52), 5063–5083, 2007.
- [10] J. Yin and V. Syrmos, System identification using the extended Kalman filter with applications to medical imaging. *American Control Conference*, June, 2000.
- [11] L. Jeen-Shang and Z. Yigong, Nonlinear structural identification using extended Kalman filter. *Computers and Structures*, 52(4), 757–764, 1994.
- [12] C. Myungjin and T. Sato, Structural Identification using Stochastic Filtering Techniques Based on Measurements from Wireless Data Acquisition System. *Steel Structures*, 6, 353–360, 2006.
- [13] M. S. Miah, E. N. Chatzi, V. K. Dertimanis and F. Weber, Real-time experimental validation of a novel semi-active control scheme for vibration mitigation. *Structural Control and Health Monitoring*, 24(3), e1878, 2017.
- [14] M. S. Miah, Semi-Active Control for Magnetorheological Dampers via Coupling of System Identification Methods. *ETH-Zürich*, 22776, 1–137, 2015.
- [15] L. Ljung, *System Identification: Theory for the User*. Second edition. PTR Prentice Hall, Upper Saddle River, NJ, 1999.
- [16] van Overschee, P., and B. De Moor. *Subspace Identification of Linear Systems: Theory, Implementation, Applications*. Springer Publishing: 1996.
- [17] R. E. Kalman, A new approach to linear filtering and prediction problems. *Journal of Basic Engineering*, 82(Series D), 35–45, 1960.
- [18] S. J. Julier and J. K. Uhlmann, A New Extension of the Kalman Filter to Nonlinear Systems. *Int. Symp. Aerospace/Defense Sensing, Simul. and Controls*, 3, 1–12, 1997.
- [19] E. Wan and R. Van Der, Merwe, The unscented Kalman filter. In S. Haykin (Ed.), *Kalman filtering and neural Network*, John Wiley and Sons, Inc, 5, 221–280, 2001.
- [20] M. S. Miah, M. Kaliske and M. J. Miah, Damping Matrix Identification for Structural Health Monitoring Considering Sensitivity of Initial Unknown Covariance. *Proceedings of the 4th World Congress on Civil, Structural, and Environmental Engineering (CSEE'19)*, 1–9, 2019.
- [21] K. Xiong, H. Y. Zhang, and C. W. Chan, Performance evaluation of UKF-based nonlinear filtering. *Automatica*, 42(2), 261–270, 2006.

# Integrated Motion Measurement – a Tool for Structural Health Monitoring?

M. Kohl<sup>1</sup>, 0009-0000-6512-6219, J. F. Wagner<sup>1</sup>, 0000-0002-8536-4668

<sup>1</sup>Chair of Flight Measuring Technology, University of Stuttgart, Pfaffenwaldring 31, 70569 Stuttgart, Germany  
email: michael.kohl@pas.uni-stuttgart.de, jfw@pas.uni-stuttgart.de

**ABSTRACT:** Integrated Motion Measurement Systems (IMMSs) are multi-sensor systems, based on the principle of integrated navigation with inertial sensors as central components and an aiding by, e.g., GNSS receivers. IMMSs can be used to track elastic motions as additional degrees of freedom (DOFs) that capture the deformations of the object. To support the estimation of elastic properties, additional internal aiding measurements like strain gauges can be implemented. In addition to the raw sensor data, the elastic DOFs in the time and frequency domain are possible indicators to be used for Structural Health Monitoring (SHM).

With the increasing availability of low-cost micro-electro-mechanical systems (MEMSs), combined with their ease of implementation, applications in large sensor quantities become feasible. To validate and experimentally test such an integrated motion measurement, a test rig with a movable, flexible pendulum beam was designed, to represent an idealization of a mast, rotor blade, or aircraft wing.

In this study a short categorization of possible SHM applications for IMMSs is given, based on previous work and state-of-the-art SHM approaches. In this context, the principle of IMMS is explained with the experimental realization, validation, and the resulting modal characteristics of the elastic DOFs as potential indicators for SHM. Furthermore, the importance of strain gauges is investigated with methods to reduce their number by redundant sensors and restricted aiding.

**KEY WORDS:** Sensor fusion; Kalman filter; Inertial sensors; Complementary Sensors.

## 1 INTRODUCTION

Integrated motion measurement of flexible structures is the expansion of conventional integrated navigation systems, typically employing an inertial measurement unit (IMU) aided by GNSS (global navigation satellite system) [1-3]. In contrast to the classic approach, the object of interest is now developed from a simple rigid point with six degrees of freedom (DOFs, three for the position and three for the attitude) to an elastic body with extra DOFs, capturing elastic deformations. Furthermore, additional sensors are distributed on the structure, enabling this model extension. Such additional sensors are, on the one hand, inertial sensors like accelerometers or gyroscopes to expand the system input to accommodate the extra DOFs. On the other hand, further GNSS receivers, strain gauges, or other sensor types are feasible for aiding [4].

With the ongoing development and miniaturization of micro-electromechanical systems (MEMSs), such integrated motion measurement systems (IMMSs) can now be realized with cost-effective sensors. A test rig [5], as well as a hybrid sensor system [6] was developed to validate the principle of IMMS on a flexible beam. The test rig and beam were designed to resemble an aircraft wing, mast, or rotor blade of a wind turbine. The validation proved that such low-cost sensor systems are suitable for IMMS applications and can reliably estimate structural deformations [7]. Concluding, IMMSs for flexible structures allow a comprehensive movement determination of the object including the rigid body part as well as elastic deformation of the structure itself.

The validation [7] so far relied on the usage of a quantity of strain gauges being the same as the number of characteristic deformations introduced as additional DOFs. This means that

with rising complexity of the structure and increased number of relevant mode shapes, more strain gauges are needed to complete the system requirements. Despite dominant advantages like high sensitivity leading to a reliable aiding of the selected deformations, certain disadvantages would benefit a reduction of these sensors. Such disadvantages are i.e. a complex installation process as well as maintenance. Installing strain gauges can be a lengthy and complex task that demands skill and accuracy. It requires specialized knowledge to ensure that the gauges are attached, wired, and calibrated correctly. Furthermore, strain gauges are vulnerable to environmental factors and therefore need to be shielded adequately. All these factors can add to the overall complexity of the project [8]. In contrast to that, the application of IMUs and Time-of-Flight distance sensors (ToF) is relatively easy. In the present setup, both sensors are located on a circuit board and screwed to the structure [6]. It can be beneficial to reduce the usage of strain gauges in favor of low-cost, easy to apply sensors like IMUs, ToFs, or GNSS receivers for installation and maintenance reasons.

The additional estimation of deformations by a distributed sensor network puts IMMSs in the spotlight as a potential application for vibration-based structural health monitoring (SHM) at a global approach. Unlike local methods, where a dense sensor network is setup around a perimeter of expected damage, the behavior of the complete structure is evaluated for damage diagnosis [9]. An abundance of methods exists in this field, however, to the knowledge of the authors, no existing method utilizes the estimation of elastic deformations via kinematic considerations:



In state-of-the-art SHM applications, accelerometers are widely used as sensors and typical parameters for damage evaluation are modal parameters like natural frequencies and mode shapes. Often, the input or output signals are further processed by methods like Fast Fourier transform (FFT), or Wavelet transform (WT) [10]. While several methods combine IMU or accelerometer data with GNSS measurements [11-13], the sensor network or node is treated as a rigid body and in practice, the displacement of the monitored location is extracted for signal evaluation. On the other hand, applications with distributed sensors, mostly accelerometers without any aiding exist. For example, a network of low-cost MEMS accelerometers is applied in a bridge structure for displacement and vibration analysis [14]. In this case, modal parameters like frequencies, damping ratios and amplitudes are estimated based on the model of a damped harmonic oscillator. Subsequently, the mode shapes are extracted from the calculated amplitudes of the involved sensor locations and modes. In other applications, the overall deflection of a bridge [15] or wind turbine [16] is reconstructed based on the calculated rotation angles of distributed IMUs or accelerometers, gyroscopes, and magnetometers respectively. The latter method proposes to use the obtained deflection to assess the occurring stresses via a Finite Element (FE) simulation for SHM.

Furthermore, many papers suggest the usage of Operational Modal Analysis (OMA). Here, only the measurement data with unknown system excitation is used to obtain modal parameters of the observed structure. A commercial OMA tool is for example used to identify different damage scenarios of an open-source benchmark system with distributed accelerometers [17]. In other OMA applications, simulated accelerometer data of distributed sensors are used to extract mode shapes [18] or natural frequencies, mode shapes, and curvature mode shapes [19] for floating offshore wind turbines and wind turbine blades respectively. Damage detection can then be applied by assessing the change of mode shape after applying damages [19]. Alternatively, distributed strain sensors in the form of Fiber Bragg Gratings (FBGs) can be used for damage detection by identifying the change of eigenfrequencies, obtained from OMA on a wind turbine structure [20].

In another approach, damage assessment is done by Finite Element Model Updating for a laboratory bridge structure equipped with accelerometers [21]. Based on the measurements obtained, the mass, damping, and stiffness matrices of the FE simulation are updated to match the characteristics of the measurements. To conclude, there exist a variety of SHM methods and applications which could potentially be adapted to an IMMS, which aims at a more complementary, integrated use of different types of sensors.

Thus, in this study, a preliminary classification and outlook on potential SHM applications by IMMS is conducted. Furthermore, the reduction as well as replacement of strain gauges with different sensor types and aiding approaches is investigated. For that, Section 2 introduces the concept of IMMS of flexible structures, including the general system equations and the kinematic equations for accelerometers and gyroscopes as central components. Section 3 provides the application of such a system for a flexible beam, introducing unit deformations as characteristic elastic deformations and

aiding models of different sensor types. The test rig for experimental implementation as well as a summary of the conducted validation are presented subsequently. Based on this, the experimental approach of this study is presented in Section 4, followed by the presentation and discussion of the results in Section 5. A conclusion and outlook finalize the paper in Section 6.

## 2 INTEGRATED MOTION MEASUREMENTS OF FLEXIBLE STRUCTURES

The main task of IMMSs is to track the propagation with time of the motion state vector

$$\mathbf{x}(t) = [\mathbf{r}(t) \quad \dot{\mathbf{r}}(t) \quad \boldsymbol{\Theta}(t) \quad \dots]^T, \quad (1)$$

which holds the classical navigation parameters position  $\mathbf{r}$ , velocity  $\dot{\mathbf{r}}$ , and attitude  $\boldsymbol{\Theta}$ . The state vector is further expanded by additional DOFs reflecting elastic deformations, which will be derived within this section. Other typical parameters like sensor biases are excluded for a better overview [4]. The dynamic behavior of  $\mathbf{x}$  can be modelled by a nonlinear, kinematical model

$$\dot{\mathbf{x}} = \mathbf{f}(\mathbf{x}, \mathbf{u}) + \mathbf{G}\mathbf{w}, \quad (2)$$

driven by the input vector  $\mathbf{u}(t)$ . In the case of IMMSs, the input consists of accelerations and angular rates, measured by an array of inertial sensors. Additionally, the stochastic measurement noise  $\mathbf{w}(t)$  of the input is mapped to  $\dot{\mathbf{x}}$  via the noise matrix  $\mathbf{G}$ . Inherent errors like sensor noise and bias of the input  $\mathbf{u}$ , in combination with numerical integration leads to a rising error if the system state  $\mathbf{x}$  is calculated from Equation (2). To reduce this error and ensure observability of the system, regular correcting measurements are necessary which are represented by the aiding vector

$$\mathbf{y} = \mathbf{h}(\mathbf{x}, \mathbf{u}) + \mathbf{v}. \quad (3)$$

The aiding vector  $\mathbf{y}(t)$  comprises measurements, e.g. from GNSS receivers, which can be modeled according to the current system state  $\mathbf{x}$ , input  $\mathbf{u}$ , and their stochastic measurement noise  $\mathbf{v}(t)$  [1].

The IMMS combines the calculated system state from Equation (2) with the aiding Equation (3) to merge different sensor types by using the advantages of each sensor type against the disadvantages of the other sensors. This so-called sensor fusion, as well as solving the differential Equation (2) is accomplished by an extended Kalman Filter (EKF). The system architecture and signal flow of an EKF, which works according to the observer principle, is depicted in Figure 1 [22].

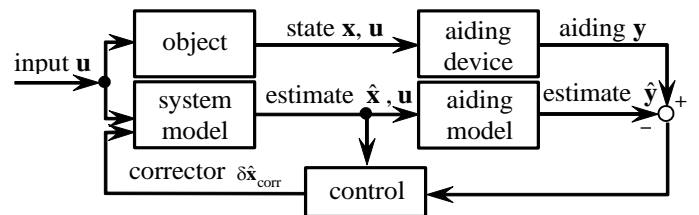


Figure 1. System architecture of IMMS. Adapted from Wagner and Wieneke [22].

The system state  $\mathbf{x}$  and therefore the aiding vector  $\mathbf{y}$  results from the accelerations and angular rates acting on the object,

which are measured by the input  $\mathbf{u}$ . Based on this input, an estimate of the system state  $\hat{\mathbf{x}}$  and measurement vector  $\hat{\mathbf{y}}$  is calculated. Conclusively, the difference between actual aiding measurements and their estimation  $\mathbf{y} - \hat{\mathbf{y}}$  is used to calculate an updated system state  $\hat{\mathbf{x}}$ .

### 2.1 Kinematic system model and input

To complete the state vector from Equation (1), to accommodate elastic deformations, and to give an overview of the involved input sensors within an IMMS, a simplified model of an aircraft fuselage with one wing as a beam is depicted in Figure 2.

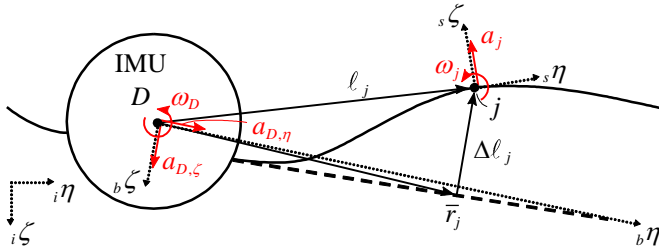


Figure 2. Simplified aircraft model with exemplary input sensors. Adapted from Örtel [4].

The wing is sketched in its deformed (solid line) and undeformed (dashed line) state. In this case, measurements of the input vector  $\mathbf{u}$  are indicated as red arrows, which are comprised of the accelerations  $a_{D,\eta}$ ,  $a_{D,\zeta}$ , and the angular rate  $\omega_D$  obtained from an IMU in the center of the system  $D$ . Furthermore, additional peripheral accelerometers or gyroscopes at arbitrary positions  $j$  measure either the acceleration  $a_j$  or angular rate  $\omega_j$ . Instead of single-axis accelerometers or gyroscopes, complete IMUs can be installed as peripheral sensors, however, only one of the signals shown is mandatory for the presented system model. The relevant coordinate systems are indicated by dotted arrows, which are the inertial coordinate system  $(i\eta, i\zeta)$ , the body coordinate system  $(b\eta, b\zeta)$ , and the sensor coordinate system  $(s\eta, s\zeta)$ . Accelerations and angular rates are measured with respect to the inertial coordinate system, in either the body coordinate system (IMU in the center  $D$ ) or the sensor coordinate system (peripheral sensor in  $j$ ). The lever arm  $\ell_j$  is the distance between  $D$  and  $j$ . In the case of peripheral accelerometers, the kinematic equation of motion of  $j$  is

$$\ddot{\mathbf{r}}_j = \ddot{\mathbf{r}}_D + \ddot{\ell}_j + 2(\boldsymbol{\omega}_{bi} \times \dot{\ell}_j) + \dot{\boldsymbol{\omega}}_{bi} \times \ell_j + \boldsymbol{\omega}_{bi} \times (\boldsymbol{\omega}_{bi} \times \ell_j), \quad (4)$$

with  $\ddot{\mathbf{r}}_j$  comprising  $a_j$ , which is therefore directly measured by the peripheral accelerometer (the left superscript indicates the reference system for differentiation). Furthermore,  $\ddot{\mathbf{r}}_D$  holds the accelerations  $a_{D,\eta}$ ,  $a_{D,\zeta}$ , whereas  $\boldsymbol{\omega}_{bi}$  contains the angular rate  $\omega_D$ , meaning both vectors are readily available from the IMU measurements in  $D$ . With lack of low-cost angular acceleration sensors,  $\dot{\boldsymbol{\omega}}_{bi}$  is calculated via numerical differentiation of  $\boldsymbol{\omega}_{bi}$ . Considering peripheral gyroscopes, the kinematic equation of motion becomes

$$\boldsymbol{\omega}_j = \boldsymbol{\omega}_{bi} + \frac{d(\text{rot } \ell_j)}{dt}. \quad (5)$$

Here,  $\boldsymbol{\omega}_j$  is directly measured by the peripheral gyroscope with  $\omega_j$ . Both Equations (4) and (5) contain the unknown lever arm

$\ell_j$  and its first and second derivative ( $\dot{\ell}_j$  and  $\ddot{\ell}_j$ ) in the case of peripheral accelerometers [4].

As indicated in Figure 2, the lever arm  $\ell_j$  is modeled by a rigid part  $\bar{\mathbf{r}}_j$  on the undeformed wing plus a time-dependent, elastic part  $\Delta \ell_j(t)$ . Under the assumption of small deformations, the lever arm is modeled by a series approach

$$\ell_j = \bar{\mathbf{r}}_j + \Delta \ell_j(t) \approx \bar{\mathbf{r}}_j + \sum_{\chi=1}^{\Gamma} (b_{\chi}(t) \cdot \mathbf{s}_{\chi}(\bar{\mathbf{r}}_j)), \quad (6)$$

with a selected number  $\Gamma$  of time-dependent deformation variables  $b_{\chi}(t)$  as a coefficient to their associated shape functions  $\mathbf{s}_{\chi}(\bar{\mathbf{r}}_j)$ . The deformation variables act as additional DOFs and reflect the current amplitudes of the shape functions, which spatially represent the structural deformations. For the latter, it is assumed that  $\mathbf{s}_{\chi}(\bar{\mathbf{r}}_j)$  only have components in  $b\zeta$ -direction, which justifies the usage of single-axis sensors (more components require more sensor-axes). Additionally, the shape functions are defined in a way that they have the maximum displacement value of 1 at least at one point. Due to this definition, they will be referred to as unit deformations, of which two exemplary selections  $\mathbf{s}_1(\bar{\mathbf{r}}_j)$  and  $\mathbf{s}_2(\bar{\mathbf{r}}_j)$  are sketched in Figure 3. In this case the rigid part  $\bar{\mathbf{r}}_j$  of the lever arm is aligned with the  $\eta$ -axis of the body coordinate system.

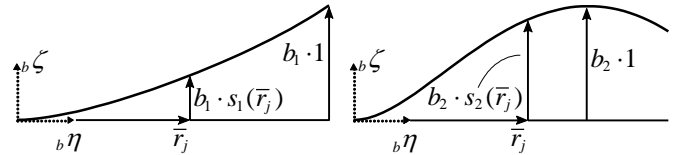


Figure 3. Typical unit deformations. Adapted from Örtel [4].

As a result, the superposition of all selected unit deformations multiplied with their current amplitudes should reflect the total deformation of the structure. Consequently, the choice of type and number of unit deformations is essential for a proper approximation of the structure. It has been proven that the eigenmode shapes are a reasonable, but not mandatory choice for the unit deformations [4,7].

Based on Equation (6), the first and second derivative of  $\ell_j$  can be formulated with

$$\begin{aligned} \dot{\ell}_j &= \sum_{\chi=1}^{\Gamma} (\dot{b}_{\chi}(t) \cdot \mathbf{s}_{\chi}(\bar{\mathbf{r}}_j)) \\ \ddot{\ell}_j &= \sum_{\chi=1}^{\Gamma} (\ddot{b}_{\chi}(t) \cdot \mathbf{s}_{\chi}(\bar{\mathbf{r}}_j)) \end{aligned} \quad (7)$$

With the abbreviation  $\mathbf{s}_{\chi}(\bar{\mathbf{r}}_j) = \mathbf{s}_{\chi,j}$ , Equations (7) are substituted into (4), to deliver the set of Equations

$$\ddot{\mathbf{r}}_j(t) = f(i\ddot{\mathbf{r}}_1, \dots, i\ddot{\mathbf{r}}_v, \dots, i\ddot{\mathbf{r}}_D, \boldsymbol{\omega}_{bi}, \dot{b}_1, \dots, \dot{b}_{\Gamma}, b_1, \dots, b_{\Gamma}, \mathbf{s}_{1,1}, \dots, \mathbf{s}_{\Gamma,v}), \quad (8)$$

for  $\chi=1, \dots, \Gamma$  selected unit deformations and  $j=1, \dots, v$  peripheral accelerometers. Substituting Equation (6) into (5) yields

$$\dot{\mathbf{r}}_j(t) = f(\boldsymbol{\omega}_1, \dots, \boldsymbol{\omega}_v, \boldsymbol{\omega}_{bi}, \text{rot } \mathbf{s}_{1,1}, \dots, \text{rot } \mathbf{s}_{\Gamma,v}), \quad (9)$$

for  $\chi=1, \dots, \Gamma$  selected unit deformations and  $j=1, \dots, v$  peripheral gyroscopes [4].

Depending on the type of peripheral sensor being either accelerometer (acc) or gyroscope (gyro), the state vector from Equation (1) becomes

$$\mathbf{x}_{\text{acc}} = \begin{bmatrix} {}_i\mathbf{r}_D & {}_i\dot{\mathbf{r}}_D & \Theta & \mathbf{b} & \dot{\mathbf{b}} \end{bmatrix}^T \quad (10)$$

or  $\mathbf{x}_{\text{gyro}} = \begin{bmatrix} {}_i\mathbf{r}_D & {}_i\dot{\mathbf{r}}_D & \Theta & \mathbf{b} \end{bmatrix}^T$ ,

according to the general form of Equation (2). All selected deformation variables  $b_1, \dots, b_\Gamma$  and their derivatives are summarized in the vectors  $\mathbf{b}$  and  $\dot{\mathbf{b}}$  respectively. The system input becomes

$$\mathbf{u}_{\text{acc}} = \begin{bmatrix} a_{D,\eta} & a_{D,\zeta} & \omega_D & \dot{\omega}_D & \mathbf{a} \end{bmatrix}^T \quad (11)$$

or  $\mathbf{u}_{\text{gyro}} = \begin{bmatrix} a_{D,\eta} & a_{D,\zeta} & \omega_D & \boldsymbol{\omega} \end{bmatrix}^T$ ,

with  $\mathbf{a}$  and  $\boldsymbol{\omega}$  holding all measured peripheral accelerations  $a_1, \dots, a_\nu$  and angular rates  $\omega_1, \dots, \omega_\nu$ . To maintain the observability of the IMMS, the number of peripheral sensors must be equal or higher than the elastic DOFs  $\nu \geq \Gamma$ . A further condition is that the chosen unit deformations need to be linear independent, and the sensor positions must be chosen adequately [4].

## 2.2 Aiding equations and measurements

The aiding Equation (3) relates the actual aiding measurements  $\mathbf{y}$  to their estimate  $\hat{\mathbf{y}}$ , to correct the state estimate  $\hat{\mathbf{x}}$  according to Figure 1. To achieve that, the measurements need to be reconstructed from the system state, which corresponds to the right-hand side of Equation (3). Aiding equations can be divided into two principles, with applications in Section 3:

**External aiding:** The systems providing the measurements are independent and located outside of the object. A prominent example of such an aiding system are GNSSs. If the system, i.e. provides a position or distance reference of a point  $j$ , the measurement can be related with a function including the position, orientation, and the deformations [4].

**Internal aiding:** The measurement systems are located on the structure. Strain gauges, for example, provide data which can be related to the elastic DOFs only [4].

## 3 IMMS APPLICATION OF A FLEXIBLE BEAM

For experimental validation and application of IMMS of flexible structures, the simplified aircraft model from Figure 2 was reduced to a suspended, elastic pendulum as shown in Figure 4. This setup should abstract the aircraft fuselage and one wing as the pendulum bearing  $D$  and the pendulum itself. This representation also holds for a rotor or mast of a wind turbine and is therefore generally applicable. Considering technical limitations and the desired realization, all inertial sensors are applied in the form of a six-axis IMU measuring three accelerations and three angular rates. This means, that an IMU is placed in  $D$ , measuring  $a_{D,\eta}$ ,  $a_{D,\zeta}$ , and  $\omega_D$ , as well as in  $j_s$ , measuring  $a_{j_s}$  and  $\omega_{j_s}$ . As a result of restricted GNSS visibility due to an indoor test rig, Time-of-Flight distance sensors (ToF) are placed alongside the peripheral IMUs, measuring the distance  $\rho_j$  from the point  $j_\rho$  towards a reflector plane, placed at the known location  $d_{\text{ref}}$ . Internal aiding is provided via strain gauges, which are applied as a wheatstone full bridge, measuring the bending strain  $\varepsilon_j$  in the location  $j_\varepsilon$  close to the IMU. The setup is completed by a high

precision distance sensor, providing the displacement of the bearing  $\rho_D$ . The Pendulum is a steel sheet of the material DX51D+Z, with the dimension 4 m x 0.2 m x 0.002 m [5,7].

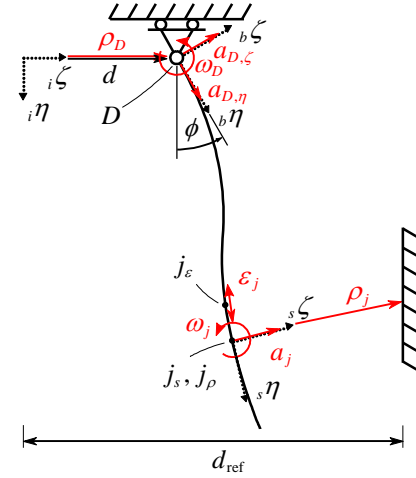


Figure 4. Experimental IMMS setup [7].

The state vector of the IMMS can be taken directly from Equation (10), with

$${}_i\mathbf{r}_D = \begin{bmatrix} d & h \end{bmatrix}^T, \quad \Theta = \phi \quad (12)$$

and  $h$  being the displacement of  $D$  in  $i\eta$ -direction. The input follows from Equation (11) without adjustments, including  $j_s = 1, \dots, \nu_s$  peripheral accelerometers or gyroscopes. Ultimately, the aiding vector becomes

$$\mathbf{y}_{\text{acc}} = \mathbf{y}_{\text{gyro}} = \begin{bmatrix} \rho_D & \dot{\rho}_D & \boldsymbol{\rho} & \boldsymbol{\varepsilon} \end{bmatrix}^T. \quad (13)$$

The vectors  $\boldsymbol{\rho}$  and  $\boldsymbol{\varepsilon}$  hold the data set of all measured distances  $\rho_1, \dots, \rho_\nu$  and bending strains  $\varepsilon_1, \dots, \varepsilon_\nu$  from  $j_\rho = 1, \dots, \nu_\rho$  utilized ToFs and  $j_\varepsilon = 1, \dots, \nu_\varepsilon$  strain gauges. The position measurement  $\rho_D$  contains the horizontal distance of the bearing  $\rho_D$  corresponding to  $d$  and a pseudo-measurement of 0 corresponding to  $h$  respectively. In the final application, not all available sensor signals are utilized, meaning that an IMU is used without the accompanying ToF or vice versa. Therefore a distinction between placement and number of the sensors at hand  $\nu_s$ ,  $\nu_\rho$ , and  $\nu_\varepsilon$  must be made.

### 3.1 Unit deformations

The unit deformations of the pendulum are acquired from the eigenmodes of the linearized structure. These were calculated with a Finite Element (FE) analysis in ANSYS®. As indicated in Figure 2 and 3, the unit deformations are relevant from the perspective of the object and therefore should be transformed into body coordinates. The first six transformed modes are plotted in Figure 5, where the first two modes of the structure have similar shape due to the transformation. As a result, these two modes are merged to a combimode, since their distinction by the system can not be guaranteed [4,7].

Consequently, the first six modes are represented by the first five unit deformations  $\Gamma = 1, \dots, 5$ , with the third mode corresponding to the second unit deformation, etc. The eigenfrequencies as well as the associated modes of each unit deformation are listed in Table 1.



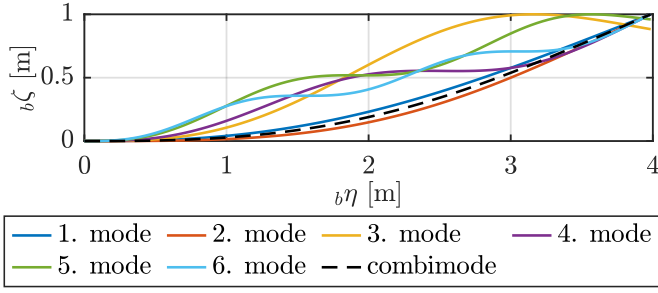


Figure 5. First six transformed modes shapes [4,7].

Table 1. Allocation of eigenmodes to unit deformations with corresponding frequencies [7].

Unit def.	1	2	3	4	5
mode	1	2	3	4	5
$f_i$ [Hz]	0.302	0.860	1.909	3.492	5.262

### 3.2 Beam deflection, curvature, and aiding equations

To give insight into the applied aiding measurements and equations, a sketch of the randomly deformed pendulum is shown in Figure 6. Furthermore, an arbitrary point (or sensor)  $j$ , placed at position  $\ell_j$  on the undeformed wing with deformation  $\Delta\ell_j$  is highlighted. The sensor coordinate system  $s$  is rotated relative to the body system  $b$  by the angle  $\phi_{j, sb}$ , whereas  $b$  is rotated by  $\phi$  relative to the inertial system  $i$ .

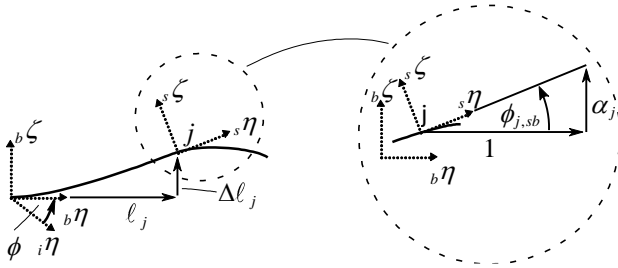


Figure 6. Relation between the local rotation and gradient of the bending line.

Considering  $j = 1, \dots, \nu$  arbitrary peripheral points, the elastic deformation of the object at each location can be reconstructed with

$$\begin{bmatrix} \Delta\ell_1 \\ \vdots \\ \Delta\ell_\nu \end{bmatrix} = \begin{bmatrix} s_{1,1} & \dots & s_{1,\nu} \\ \vdots & \ddots & \vdots \\ s_{\nu,1} & \dots & s_{\nu,\nu} \end{bmatrix} \cdot \begin{bmatrix} b_1 \\ \vdots \\ b_\nu \end{bmatrix} = \mathbf{S} \cdot \mathbf{b} \quad (14)$$

and the matrix of unit deformations  $\mathbf{S}$ . With the angle  $\phi$  being permanently calculated as part of the state vector, the location of  $j$  in the inertial coordinate system is given by the transformation

$${}^i\mathbf{r}_j = \begin{bmatrix} {}^i\eta_j \\ {}^i\zeta_j - d \end{bmatrix} = \begin{bmatrix} \cos \phi & -\sin \phi \\ \sin \phi & \cos \phi \end{bmatrix} \cdot \begin{bmatrix} \ell_j \\ \Delta\ell_j \end{bmatrix} \quad (15)$$

for small deformations. Under the same condition, the rotation  $\phi_{j, sb}$  from the body to the sensor coordinate system can be approximated by the gradient of the bending line  $\alpha_j$ . Considering the rotation of  $b$  relative to  $i$ , the total rotation of  $s$  relative to  $i$  can be formulated with

$$\begin{bmatrix} \phi_1 \\ \vdots \\ \phi_\nu \end{bmatrix} \approx \phi + \begin{bmatrix} \alpha_1 \\ \vdots \\ \alpha_\nu \end{bmatrix} = \phi + \begin{bmatrix} s'_{1,1} & \dots & s'_{1,\nu} \\ \vdots & \ddots & \vdots \\ s'_{\nu,1} & \dots & s'_{\nu,\nu} \end{bmatrix} \cdot \begin{bmatrix} b_1 \\ \vdots \\ b_\nu \end{bmatrix} = \phi + \mathbf{S}' \cdot \mathbf{b} \quad (16)$$

and

$$\frac{\partial s_{\chi,j}}{\partial b_\eta} = s'_{\chi,j} \quad (17)$$

being the gradient of the unit deformations [4].

While the aiding measurements  $\mathbf{p}_D$  and  $\dot{\mathbf{p}}_D$  directly correspond to the system states  $\mathbf{r}_D$  and  $\dot{\mathbf{r}}_D$ , the remaining aiding measurements have to be viewed in detail:

ToFs: The distance  $\rho_j$  is measured perpendicular to the local sensor position as sketched in Figure 7. With the location of the sensor, calculated from Equation (15), and the rotation  $\phi_j$  from Equation (16), the distance measurement can be modeled by the function

$$\rho_j = \frac{d_{\text{ref}} - {}^i\zeta_j}{\cos \phi_j} = h(d, \phi, \mathbf{b}) \quad (18)$$

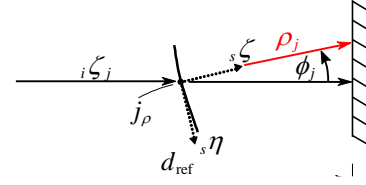


Figure 7. Distance measurement of peripheral ToF sensor.

Strain gauges: Considering the area moment of inertia and the moment of resistance, the bending strain of a rectangular beam of thickness  $h^*$  can be expressed for small deflections with

$$\begin{bmatrix} \varepsilon_1 \\ \vdots \\ \varepsilon_\nu \end{bmatrix} = -\frac{h^*}{2} \begin{bmatrix} s''_{1,1} & \dots & s''_{1,\nu} \\ \vdots & \ddots & \vdots \\ s''_{\nu,1} & \dots & s''_{\nu,\nu} \end{bmatrix} \cdot \begin{bmatrix} b_1 \\ \vdots \\ b_\nu \end{bmatrix} = \mathbf{S}'' \cdot \mathbf{b} = \mathbf{h}(\mathbf{b}) \quad (19)$$

for  $\nu_\varepsilon$  applied strain gauges.

### 3.3 Test rig

The implementation of the IMMS setup from Figure 4 is implemented by a test rig shown in the big picture of Figure 8. The movable pendulum 1 is suspended with a plain bearing 2 from a guidance rail 3. A reflector plane 4 for the ToFs completes the general structure. To impose movements  $d$  on the pendulum, a linear spindle actuator is mounted underneath the guidance rail and connected to the bearing suspension. The reproducible excitation of the system can then be used to provide comparability between different measurements and input for simulations [5].

The intended input and aiding measurements of Equations (11) and (13) are realized by a hybrid sensor system [6], developed for this application. The system consists of multiple interconnected printed circuit boards (PCBs) as shown in the small picture of Figure 8, which accommodate an IMU, a ToF, along with an analogue to digital converter (ADC) to connect the strain gauges. An additional PCB reads the measurements of the displacement sensor in the bearing. Controlled by a Master PCB, the measurement system provides simultaneous

measurements of the implemented sensor types at multiple, selectable positions.

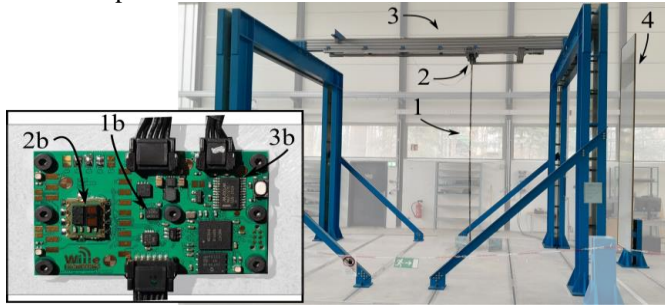


Figure 8. Test rig (big picture) and PCB (small picture) with IMU 1b, ToF 2b and ADC 3b [5].

### 3.4 Validation results

For validation, a practicable and realistic displacement function for the actuator was created. The displacement consists of back-and-forth movements, superimposed by frequency components up to the fifth eigenfrequency of Table 1. The resulting displacement  $d(t)$  is plotted in Figure 9, including an initial resting phase of 60 s for initialization purposes. As comparison parameters, the horizontal displacement  $d$  of the bearing, the angular orientation  $\phi$ , and the pseudo-elastic deformation  $e$  were chosen, the latter being the joint-related deformation and calculated by  $\Delta\ell$  according to Equation (14) at the lower tip of the pendulum. To evaluate the IMMS, the FE model from Section 3.1 was simulated with the displacement input measured by  $\rho_D$ . To create a realistic scenario, an artificial white noise is added to  $\rho_D$ , which is in the order of magnitude of the sensor noise of the ToFs.

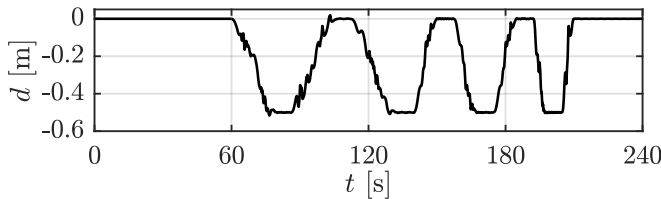


Figure 9. Displacement function  $d(t)$  [7].

It could be proven that for this excitation, the errors of attitude  $\Delta\phi$  and pseudo-elastic deformation  $\Delta e$  converge with four involved unit-deformations  $\Gamma=4$  and four peripheral sensors (accelerometers or gyroscopes)  $v_s = v_\rho = v_\varepsilon = 4$ . The position error  $\Delta d$  was insignificantly affected by the inclusion of the elastic DOFs. A comparison of the attitude  $\phi$  and pseudo-elastic deformation  $e$  is shown in Figure 10 for a time interval with relatively high dynamics. The simulated parameters (sim) are compared against the accelerometer (acc) and gyroscope (gyro) configuration of the converged case.

Despite time intervals with high dynamics, resulting in large deflections and other nonlinear effects, the results indicated that the IMMS delivers reliable estimates of the classical navigation parameters and the elastic deformation. A clear difference between the two sensor types in terms of the error values could not be determined, which can be explained by the relatively strong aiding of the deformation variables  $\mathbf{b}$  by the comparatively accurate strain gauges. This resulted in a convergence of the estimated deformation variables of both configurations towards the simulated values, as shown in

Figure 11. Furthermore, the plot shows that an excitation of four involved unit deformations from Table 1 could be registered, showing frequency components of the corresponding eigenfrequencies. Although higher unit deformations have less impact on the total deflection, their estimation in time and frequency domain can give valuable insight into the structural behaviour.

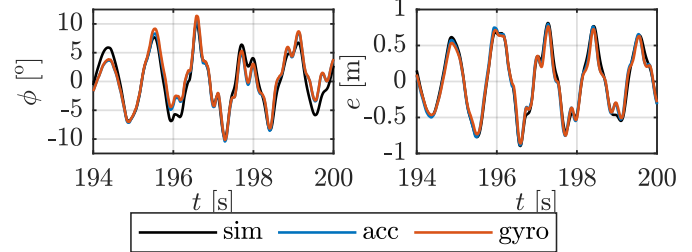


Figure 10. Attitude  $\phi$  and pseudo-elastic deformation  $e$  with nearly identical results for “acc” and “gyro”.

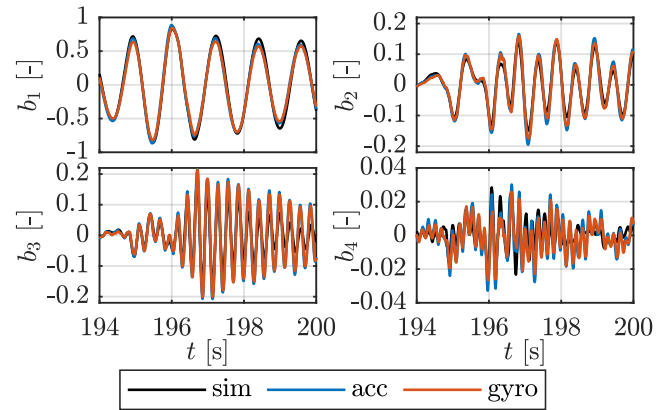


Figure 11. Deformation variables  $\mathbf{b}$  [7].

For the scenario at hand a sample rate of 200 Hz of the IMUs and strain gauges turned out reasonable, whereas the distance measurements were sampled with 33.33 Hz due to technical limitations.

### 3.5 Modal characteristics of deformation variables

In addition to the conducted validation, the modal characteristics of the deformation variables are shortly investigated in this Subsection, following the state-of-the-art criteria in SHM from Section 1. For that, the single-sided amplitude spectrum of the deformation variables of the time interval from Figure 11 are plotted in Figure 12 for the “acc” and “gyro” configurations. To obtain the amplitude spectrum, the according signals are processed via FFT with a Hamming window and zero-padding to smooth the results. The eigenfrequencies of Table 1 are highlighted with red dotted lines, whereas the eigenfrequencies of the according unit deformations are marked with red dashed lines.

While all amplitudes show distinctive peaks at their according frequencies, a coupling of the different mode shapes is clearly seen, especially for the fourth unit deformation. This can be explained by the multiple nonlinearities of the system, like the Coulomb-Friction in the bearing [7]. Furthermore, the displacement function of Figure 9 has components of the fourth eigenfrequency during the analyzed time interval, which explains the strong coupling of the fourth deformation variable. To minimize the nonlinearities, the bearing was fixed in a

purely simulative model, forcing the attitude  $\phi = 0$  at all times. Subsequently, the sensor data were obtained by the FE simulation with the same input of Figure 9. For a short overview of the fundamental changes by the linearization of the system, the deformation variables  $b_3$  and  $b_4$  are plotted in Figure 13 for the same selected time interval. Due to the system changes, a combimode according to Figure 5 is no longer necessary. Therefore the deformation variables  $b_3$  and  $b_4$  of Figure 13 correspond to  $b_2$  and  $b_3$  of Figure 11.

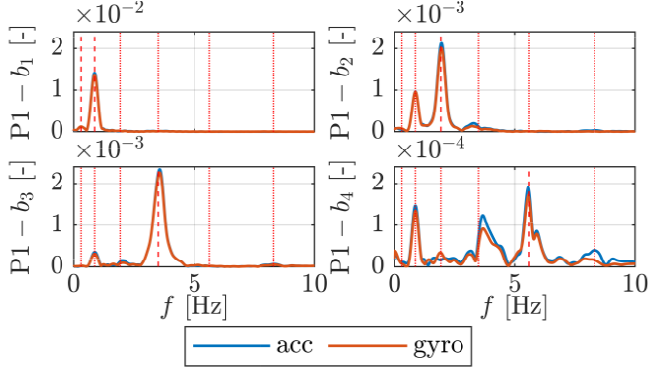


Figure 12. Single-sided amplitude spectrum of the deformation variables from Figure 11.

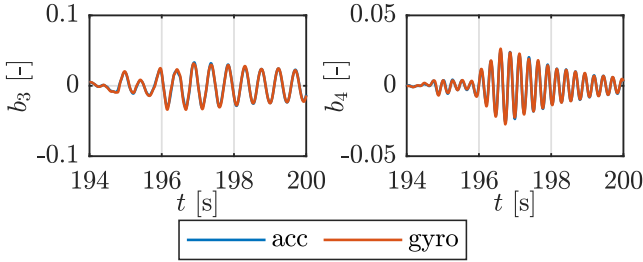


Figure 13. Deformation variables  $b_3$  and  $b_4$  for a simulated linearized system due to a fixed bearing ( $\phi = 0$ ).

Analogously, the single sided amplitude spectrum with the adapted eigenfrequencies is shown in Figure 14. Figures 13 and 14 show that a decoupling of the included deformation variables can be observed. This indicates that if the unit deformations are set according to the mode shapes of the structure, the deformation variables reflect the associated modal parameters of natural frequencies and modal damping. The prerequisite for this is, however, that the system is linear or at least linear during certain time intervals.

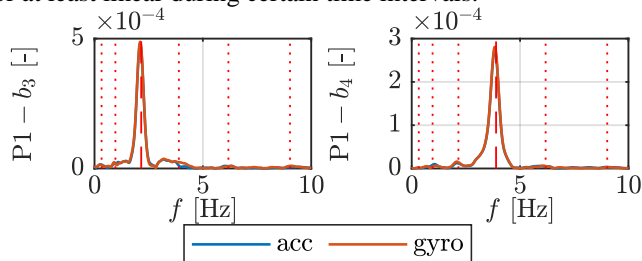


Figure 14. Single-sided amplitude spectrum of the deformation variables  $b_3$  and  $b_4$  from Figure 13.

#### 4 EXPERIMENTAL APPROACH

This part of the study follows the experimental validation of IMMS [7], which was recapped in Section 3.4, to assess the

importance of strain gauges. It is based on a pendulum equipped with 18 PCBs (holding IMUs and ToFs) and 12 strain gauge arrays (wheatstone full bridge), which were placed to investigate different configurations. According to each chosen sensor configuration, the optimal set of sensors is selected according to the method of Effective Independence [4,23] out of the available test beam. In analogy to the conducted validation, the system is excited by the displacement function of Figure 9. Furthermore, only configurations with four additional unit deformations  $\Gamma = 4$  are investigated. Due to the similarity of the results from Figure 10 and 12, the configuration with four unit deformations and four peripheral gyroscopes, strain gauges and ToFs (gyro:  $\nu_s = \nu_\rho = \nu_\varepsilon = 4$ ) serves as a new benchmark (bm) to compare and evaluate the acquired results. The comparative parameters are the attitude angle  $\phi$  of the bearing, the pseudo-elastic deformation  $e$ , as well as the deformation variables  $b_1, \dots, b_4$ . Of these, the error values are evaluated by calculating the root mean square error (RMSE) according to

$$\Delta x_{\text{rmse}} = \sqrt{\frac{1}{N} \sum_{i=1}^N (x_{\text{bm},i} - \hat{x}_i)^2} \quad (21)$$

for an arbitrary variable  $x$  with  $N$  samples. Again, the sample rate of the input vector and strain gauges (if used) is set to 200 Hz, while the ToFs and the linear distance sensor are set to 33.33 Hz as in Section 3.4.

To evaluate the importance of strain gauges, or more precisely the accurate aiding of the deformation variables in IMMS applications, the experimental procedure is divided into the following steps:

- Removing strain gauges:  
In the first step, an accelerometer and gyroscope configuration with four peripheral inertial sensors and ToFs (acc/gyro:  $\nu_s = \nu_\rho = 4$ ,  $\nu_\varepsilon = 0$ ) are compared against the benchmark.
- Extended aiding by redundant ToFs:  
To compensate for omitted strain gauges, configurations with varying number of peripheral ToFs  $\nu_\rho = 4, \dots, 13$  and redundant inertial sensors  $\nu_s = 4, 5$  are created.
- Aiding with reduced number of strain gauges:  
A reduced number of strain gauges  $\nu_\varepsilon = 1, 2, 3$  are employed. Even though measurement Equation (19) becomes underdetermined in this case, aiding can still be employed via the EKF. Based on the preceding results, a reduced set of deformation variables  $\mathbf{b}_{\varepsilon, \text{aided}}$  is aided by the strain gauges, leaving a remaining set of unaided deformation variables  $\mathbf{b}_{\varepsilon, \text{unaided}}$ . So, the strain gauges are selected in such a way that their placement is optimal with respect to  $\mathbf{b}_{\varepsilon, \text{aided}}$ . If the unaided deformation variables  $\mathbf{b}_{\varepsilon, \text{unaided}}$  are already accurately estimated by e.g. redundant ToFs, their contribution to the bending strain can be subtracted from Equation (19). Accordingly, the matrix  $\mathbf{S}_\varepsilon''$  is separated, resulting in the adapted aiding Equation

$$\boldsymbol{\varepsilon} - \mathbf{S}_{\varepsilon, \text{unaided}}'' \cdot \mathbf{b}_{\varepsilon, \text{unaided}} = \mathbf{S}_{\varepsilon, \text{aided}}'' \cdot \mathbf{b}_{\varepsilon, \text{aided}} = \mathbf{h}(\mathbf{b}_{\varepsilon, \text{aided}}) \quad (22)$$

Consequently, the left-hand side of Equation (22) is the adapted bending strain, associated to the aided deformation variables. The resulting configurations are supplemented by additional ToFs  $\nu_\rho = 4, \dots, 13$ .



Depending on the degree of observability and quality of aiding measurements, a careful filter tuning of the EKF can become a crucial task [24]. This applies especially to the cases of removed and reduced strain gauges. In these cases, the settings of the EKF are adapted in an appropriate range. However, by applying extensive filter tuning, the results can be further improved for any of the applied methods.

## 5 RESULTS

The results are presented in the order as they are introduced in Section 4. The configurations in the following subsections will be either with accelerometers (acc) or gyroscopes (gyro) as peripheral input sensors. If not specified otherwise, the number of peripheral sensors are set according to the case with removed strain gauges ( $\nu_s = \nu_\rho = 4$ ,  $\nu_\varepsilon = 0$ ).

### 5.1 Removing strain gauges

To demonstrate a general effect on the estimated system states by removing the direct aiding of the deformation variables, the estimates of attitude  $\phi$  and pseudo-elastic deformation  $e$  are displayed on the left side of Figure 15 for the whole time interval of excitation.

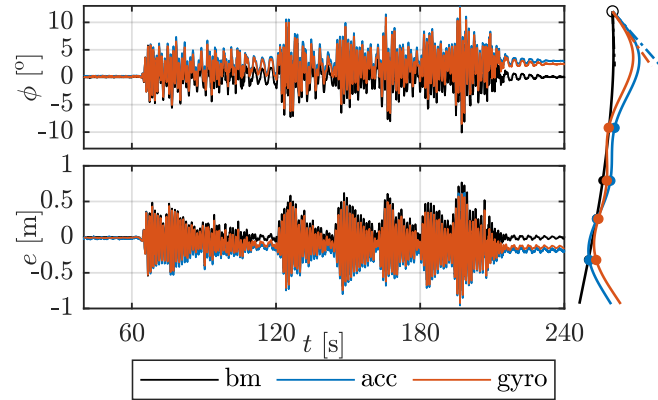


Figure 15. Estimated attitude  $\phi$  and pseudo-elastic deformation  $e$  (left), and overscaled beam deformation at  $t = 230$  s (right) for the acc and gyro configuration without strain gauges, compared to bm.

Both configurations show a gradual drift from the bm-values for both selected parameters in opposite directions, meaning that the attitude diverges contrary to the pseudo-elastic deformation. This behavior becomes apparent by visualizing the deformed, suspended beams at time  $t = 230$  s on the right side of Figure 15. The graph displays the three configurations including the bearing  $D$  indicated by the black circle. The deformations of the beam are overscaled to emphasize the occurring effect. Additionally, the positions of the involved ToFs are marked by dots on the deformed structures. The tangent lines on the beam origin is plotted by dash-dotted lines, visualizing the attitude  $\phi$  against an imaginary vertical line. Although the positions of the ToFs are accurate within the limits of their sensor error, the bending lines show a clear mismatch with respect to the benchmark. Without direct aiding of the elastic deformations and restricted accuracy of the ToFs, the aiding Equation (18) allows seemingly arbitrary combinations of  $\phi$  and  $\mathbf{b}$  to match the distance measurements. Ultimately, an overestimated attitude is compensated by an underestimated deformation.

In analogy to Figure 11, the deformation variables are plotted for the same time interval of high dynamics in Figure 16. The first deformation variable  $b_1$  is estimated accurately. This can be explained by its comparatively high amplitude, which can be resolved by the distance measurements. The deformation variables  $b_2$  to  $b_4$  display the observed drift, however in phases of high amplitude the estimations are partially corrected towards the bm values (especially  $b_2$  and  $b_3$ ). Furthermore, the gyro configuration displays a smoother and qualitatively more accurate representation of the deformation variables than the acc configuration.

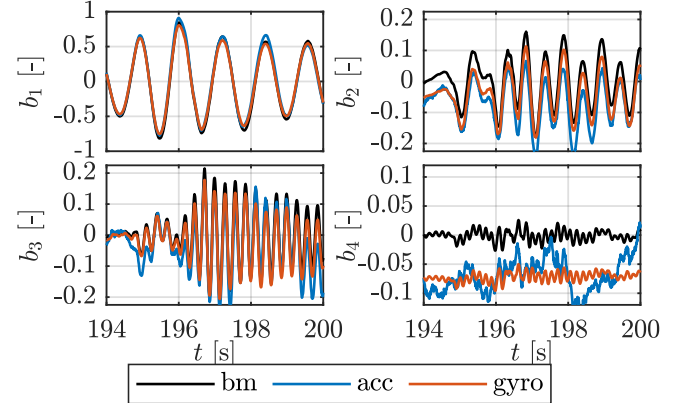


Figure 16. Estimated deformation variables  $b$  for the acc and gyro configurations without strain gauges, compared to bm.

### 5.2 Aiding by redundant ToFs

To compensate for the effects displayed in Figures 13 and 14, varying number of ToFs  $\nu_\rho = 4, \dots, 13$  are employed in combination with  $\nu_s = 4, 5$ . The RMSE of  $\phi$  and  $e$  according to Equation (21) is plotted in Figure 17 for the new acc and gyro configurations. With one additional ToF  $\nu_\rho = 5$ , both error values for both sensor types can be reduced significantly. By further increasing  $\nu_\rho$  the errors can be further decreased, however both error values converge towards a limit. Redundant inertial sensors show no positive effect, which is why they will be dismissed for further evaluation.

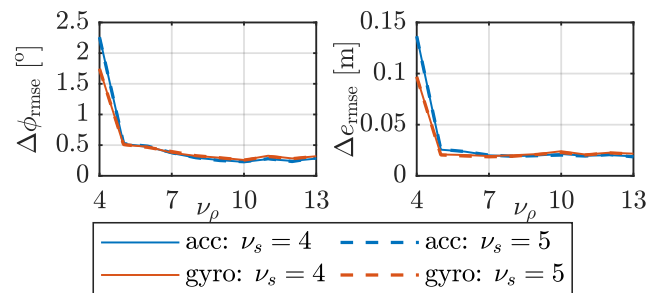


Figure 17. RMSE of the estimated attitude  $\phi$  and pseudo-elastic deformation  $e$  for the acc and gyro configuration with additional ToFs, compared to bm.

To show the reduced drift, the attitude  $\phi$  and pseudo-elastic deformation  $e$  for two exemplary acc and gyro configurations with  $\nu_\rho = 10$  is plotted in Figure 18 for the respective time interval. All cases display a satisfactory estimate, with the unwanted drift significantly reduced.

Accordingly, the deformation variables are displayed in Figure 19, analogously to Figure 16. While still displaying a reduced deviation,  $b_2$  to  $b_4$  are no longer shifted exclusively in

the negative direction. Again, the gyro configuration displays a superior behavior regarding the deformation variables.

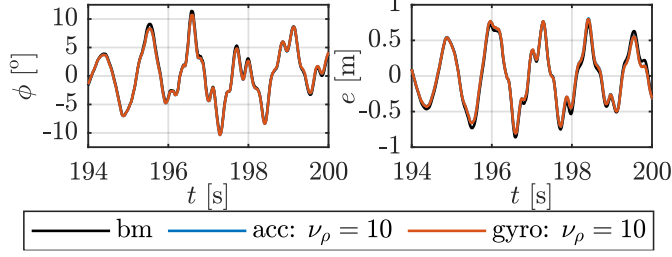


Figure 18. Attitude  $\phi$  and pseudo-elastic deformation  $e$  for exemplary acc and gyro configurations with additional ToFs, compared to bm.

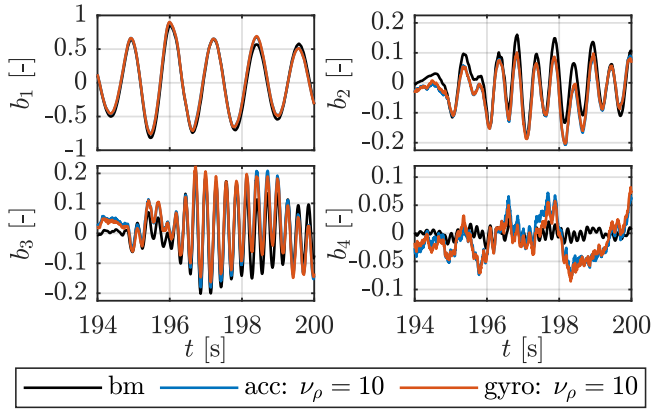


Figure 19. Estimated deformation variables  $b$  for the acc and gyro configurations with additional ToFs, compared to bm.

Overall, the negative effects of removing the direct aiding of the deformations can be significantly compensated (but not prevented by placing additional ToFs on the structure). This is because the aiding is carried out by Equation (18), which also involves deformation variables. However, the Equation is highly nonlinear, and the measurement accuracy and frequency are not sufficient to distinguish the low amplitudes of higher deformation variables. The higher accuracy of gyroscopes can be explained by the one-time integration of  $\mathbf{b}$  according to Equation (10) in comparison to the double integration of  $\ddot{\mathbf{b}}$  for accelerometers.

### 5.3 Aiding with reduced number of strain gauges

From Section 5.2 it becomes apparent that additional ToFs can not fully replace all removed strain gauges. However, it could be proven that the first deformation variable  $b_1$  is sufficiently aided by a system without strain gauges. Building on that, configurations with  $\nu_\epsilon = 1, 2, 3$  are created with the following specifications of Equation (22):

- $\nu_\epsilon = 1$ :  $\mathbf{b}_{\epsilon, \text{aided}} = [b_2 \ b_3 \ b_4]^T$ ,
- $\nu_\epsilon = 2$ :  $\mathbf{b}_{\epsilon, \text{aided}} = [b_3 \ b_4]^T$ ,
- $\nu_\epsilon = 3$ :  $\mathbf{b}_{\epsilon, \text{aided}} = [b_4]^T$ .

The selection is based on the observation that a set of aided variables equal to the number of the strain gauges used turned out to be beneficial. Nevertheless, aiding only one deformation variable was not feasible in the present setup.

In analogy to Figure 17, the RMSE of  $\phi$  and  $e$  are plotted in Figure 20 including the comparative values of the gyro configuration  $\nu_\rho = 10$  from the previous Section with a black, dash-dotted line. By employing at least one strain gauge, the

errors are comparable or better to the one achieved with additional ToFs. By increasing their number, the errors can be further decreased. Regarding the attitude and pseudo-elastic deformation, the gyro configurations with  $\nu_\epsilon = 2$  displays a superior behavior.

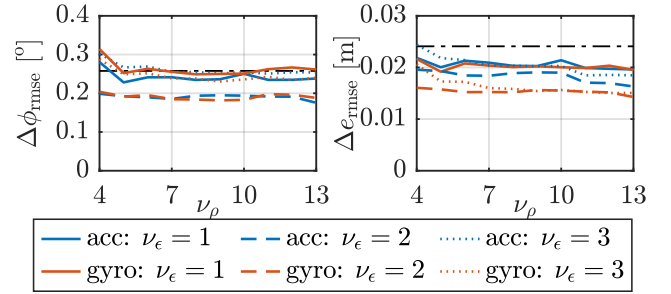


Figure 20. RMSE of the estimated attitude  $\phi$  and pseudo-elastic deformation  $e$  for the acc and gyro configuration with reduced number of strain gauges, compared to bm.

Assuming an adequate estimation of  $b_1$  and  $b_2$  according to the previous Sections, the RMSEs of  $b_3$  and  $b_4$  are further assessed in Figure 21. The errors decrease with increasing number of strain gauges, whereas the gyro configurations show superior characteristics for each number of strain gauges.

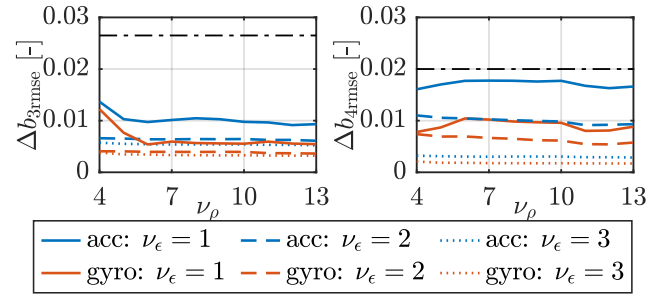


Figure 21. RMSE of the estimated deformation variables  $b_3$  and  $b_4$  for the acc and gyro configuration with reduced number of strain gauges, compared to bm.

The results suggest that a configuration with gyros and one strain gauge is comparable to accelerometers with two strain gauges and the same number of ToFs. Thus, the estimation of  $b_3$  and  $b_4$  for two corresponding configurations (acc:  $\nu_\epsilon = 2$ ,  $\nu_\rho = 10$ , gyro:  $\nu_\epsilon = 1$ ,  $\nu_\rho = 10$ ) is plotted in Figure 22 for the selected time interval. Despite comparable RMSE values, the estimation of the gyro configuration approaches the bm values significantly better.

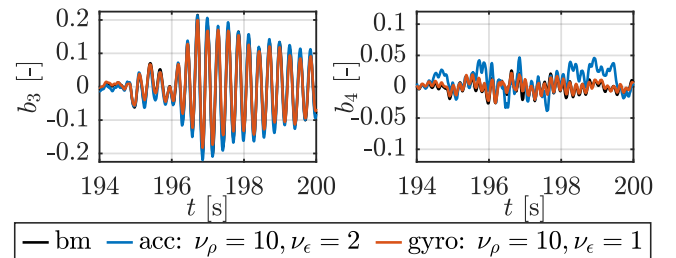


Figure 22. Estimated deformation variables  $b_3$  and  $b_4$  for the acc and gyro configurations with reduced number of strain gauges.

Concerning redundant ToFs and a reduced number of strain gauges, an attitude error of around  $\Delta\phi \approx 0.3^\circ$  corresponds to a

deflection of roughly  $\Delta e \approx 0.02\text{m}$ , which matches the error values of Figures 15 and 18. This error is within the limit of accuracy of the measurements and modelling errors. The gain in accuracy of the deformation variables is the result of their direct aiding through Equation 22. Nevertheless, the attitude and total deflection can not be further improved. Although the error  $\Delta b_{i,\text{rmse}}$  is roughly the same according to Figure 21 for the inspected case in Figure 22, the latter shows a superior performance of the gyro configuration. This can be achieved, even with fewer strain gauges than the accelerometer case.

## 6 CONCLUSIONS

In this study, IMMS are presented as a comprehensive tool for determining rigid and elastic movements of a wide range of possible structures. In addition to a general categorization within possible SHM applications, the reduction of high-maintenance sensors like strain gauges was investigated.

This study showed that the direct aiding of the deformation variables is crucial for a precise estimation of the state variables. It could be shown that redundant position aiding via distance sensors can not fully compensate for a loss of strain sensors, but the negative effects could be largely reduced. However, a reduction in strain gauges is feasible without an essential loss in accuracy. This can be achieved by aiding larger deformations with the available distance sensors and small deformations by the accurate remaining strain gauges.

With respect to the deformation variables, it could be shown that modal parameters are represented within the time and frequency domain. Even for a nonlinear system, the deformation variables show distinctive frequency peaks at their corresponding eigenfrequencies of the linearization. A linear simulated system holds the potential to estimate the modal amplitudes in the time domain during operation. With current SHM approaches using modal parameters like eigenfrequencies, mode shapes, or damping ratios, the estimation of the deformation variables in time and frequency domain are potential parameters to be analyzed. Eigenfrequencies could thus be extracted from the frequency, while the modal damping ratio could be extracted from the time domain. Both time and frequency domain of the deformation variables could also serve as an input for Finite Element Model Updating to localize simulated damage mechanisms. Additionally, the estimated deformation and curvature of the structure can indicate changes in the mode shapes due to damage. Furthermore, the precise movement analysis can give insight into loads and strains during operation and can therefore be included in the estimation of the remaining service life. In conclusion, this study could show the existing potential of IMMS for SHM.

Next steps will apply artificial “damages” in the form of additional masses or stiffeners to the test beam. Subsequently, the influence of these structural changes on the behavior of the deformation variables in time and frequency domain will be analyzed according to the presented state-of-the-art methods in SHM. Further steps could replicate the linearized system with a fixed bearing and a sensitivity analysis regarding sensor requirements like accuracy and noise in combination with quantity. Ultimately, the benefit of IMMS in relation to state-of-the-art methods needs to be proven experimentally.

## REFERENCES

- [1] J. A. Farrell and M. J. Barth, *The Global Positioning System and Inertial Navigation*, McGraw-Hill, New York, USA, 1999.
- [2] D. Titterton and J. L. Weston, *Strapdown Inertial Navigation Technology*, IET, Stevenage, UK, second edition 2004.
- [3] J. F. Wagner and G. Kasties, Improving the GPS/INS Integrated System Performance by Increasing the Distance Between GPS Antennas and Inertial Sensors, *Proc. 2002 Nat. Tech. Meeting Inst. Navigation*, pp. 103-115, Jan. 2002.
- [4] T. Örtel, *Integrierte Bewegungsmessung an flexiblen Strukturen*. Dr. Hut, München, Germany, 2010.
- [5] M. Kohl et al., Test Rig for Validating the Integrated Motion Measurement of Flexible Beam, *Proc. Appl. Math. Mechan.*, vol. 24, no. 4, pp. 1-11, 2024, doi: 10.1002/pamm.202400061.
- [6] J. F. Wagner et al., Hybrid Sensor System for Integrated Structural Motion Measurement, *IEEE Sensors Letters*, vol. 9, no. 3, pp. 1-4, March 2025, doi: 10.1109/LESENS.2025.3540358.
- [7] M. Kohl and J. F. Wagner, Validating the Integrated Motion Measurement of Flexible Beams, 2024 DGON Inertial Sensors and Applications, pp. 1-21, 2024, doi: 10.1109/ISA62769.2024.10786046.
- [8] S. Keil, *Dehnungsmessstreifen*, Springer, Wiesbaden, Germany, second edition, 2017.
- [9] C. P. Fritzen, *Vibration-Based Structural Health Monitoring – Concepts and Applications*, *Key Engineering Materials*, vol. 293-294, pp. 3-20, Sept. 2005, doi: 10.4028/www.scientific.net/kem.293-294.3.
- [10] D. Goyal and B. S. Pable, *The Vibration Monitoring Methods and Signal Processing Techniques for Structural Health Monitoring: A Review*, *Arch. Comput. Methods Eng.*, vol. 23, pp. 585-594, 2016, doi: 10.1007/s11831-015-9145-0.
- [11] W. Dai et al., DAI, Multi-Antenna Global Navigation Satellite System/Inertial Measurement Unit Tight Integration for Measuring Displacement and Vibration in Structural Health Monitoring, *Remote Sensing*, vol. 16, no. 6, p. 1072, doi: 10.3390/rs16061072.
- [12] N. Shen et al., Multi-route fusion method of GNSS and accelerometer for structural health monitoring, *J. Ind. Inf. Integr.*, vol. 32, p. 100442, 2023, doi: 10.1016/j.jii.2023.100442.
- [13] X. Qu et al., Real-time outlier detection in integrated GNSS and accelerometer structural health monitoring systems based on a robust multi-rate Kalman filter, *J. Geod.*, vol. 97, no. 4, p. 38, 2023, doi: 10.1007/s00190-023-01724-2.
- [14] M. Omidalizandari et al., A validated robust and automatic procedure for vibration analysis of bridge structures using MEMS accelerometers, *J. Appl. Geod.*, vol. 14, no. 3, pp. 327-354, 2020, doi: 10.1515/jag-2020-0010.
- [15] A. R. Al-Ali et al., An IoT-Based Road Bridge Health Monitoring and Warning System, *Sensors*, vol. 24, no. 2, p. 469, 2024, doi: 10.3390/s24020469.
- [16] A. M. Cooperman and M. J. Martinez, MEMS for structural health monitoring of wind turbine blades, 25th International Conference on Adaptive Structures and Technologies, pp. 1-6, 2024.
- [17] G. Faraco et al., Structural Health Monitoring by Accelerometric Data of a Continuously Monitored Structure with Induced Damages, *Structural Durability & Health Monitoring (SDHM)*, vol. 18, no. 6, pp. 739-762, 2024, doi: 10.32604/sdhm.2024.052663.
- [18] H. C. Kim et al., Structural health monitoring of towers and blades for floating offshore wind turbines using operational modal analysis and modal properties with numerical-sensor signals, *Ocean Engineering*, vol. 188, p. 106226, 2019, doi: 10.1016/j.oceaneng.2019.106226.
- [19] J. Pacheco-Cherrez et al., Operational modal analysis for damage detection in a rotating wind turbine blade in the presence of measurement noise, *Composite Structures*, vol. 321, p. 117298, 2023, doi: 10.1016/j.compstruct.2023.117298.
- [20] T. J. Arsenault et al., Development of a FBG based distributed strain sensor system for wind turbine structural health monitoring, *Smart Materials and Structures*, vol. 22, no. 7, p. 075027, 2013, doi: 10.1088/0964-1726/22/7/075027.
- [21] A. Haidarpour and F. T. Kong, Finite Element Model Updating for Structural Health Monitoring, *Structural Durability & Health Monitoring*, vol. 14, no. 1, pp. 1-17, 2020, doi: 10.32604/sdhm.2020.08792.
- [22] J. F. Wagner and T. Wienieke, Integrating Satellite and Inertial Navigation—Conventional and New Fusion Approaches, *Control Eng. Pract.*, vol. 11, no. 5, pp. 543-550, May 2003, doi: 10.1016/S0967-0661(02)00043-6.
- [23] D. C. Kammer, Sensor Placement for On-Orbit Modal Identification and Correlation of Large Space Structures, *J. Guid., Control, Dyn.*, 1991, vol. 14, no. 2, pp. 251-259, doi: 10.2514/3.20635.
- [24] J. F. Wagner et al., Reevaluation of Algorithmic Basics for ZUPT-Based Pedestrian Navigation, *IEEE Access*, vol. 10, pp. 118419-118437, 2022, doi: 10.1109/ACCESS.2022.3220629.



# Solving structural dynamics with uncertainty quantification via evidential neural operators

Pei-Lin Li<sup>1, 2, 3</sup>, 0009-0007-6195-6435, Yi-Qing Ni<sup>1, 2</sup>, 0000-0003-1527-7777, Jian-Ming Ling<sup>3</sup>, Shi-Fu Liu<sup>3</sup>, You-Wu Wang<sup>1, 2</sup>, 0000-0003-2293-4712

<sup>1</sup>Department of Civil and Environmental Engineering, The Hong Kong Polytechnic University, Hong Kong Special Administrative Region of China

<sup>2</sup>National Rail Transit Electrification and Automation Engineering Technology Research Center (Hong Kong Branch), Hung Hom, Kowloon, Hong Kong Special Administrative Region of China

<sup>3</sup>The Key Laboratory of Road and Traffic Engineering, Ministry of Education, Tongji University, Shanghai, 201804, China  
email: peilin.li@connect.polyu.hk, ceyqni@polyu.edu.hk, jmling@tongji.edu.cn, sflu@tongji.edu.cn, youwu.wang@polyu.edu.hk

**ABSTRACT:** Solving structural dynamic equations is crucial for evaluating the reliability and safety of civil infrastructures such as bridges, airport runways and railways under various loads. Currently, the Neural Operator (NO) shows great potential in solving structural dynamic equations under various excitations and boundary conditions without retraining and are capable of zero-shot learning. However, there has been a dearth of research into providing prediction errors and explicit uncertainty quantification of the operator-learned model for computing structural responses in different data regimes. This research aims to approximate the solution operator of structural dynamic equations with uncertainty quantification. Deep evidential learning is introduced to establish the Evidential Neural Operator (ENO) and the epistemic uncertainty of structural responses can be obtained. An illustrative example is given in this paper, which shows that the E-NO model can effectively identify the well-prediction condition and the worse-prediction condition. This work can provide an end-to-end framework for building surrogate models of real-world structures, which can rapidly compute structural responses with uncertainty.

**KEYWORDS:** Structural Dynamics; Uncertainty Quantification; Evidential Deep Learning; Neural Operator.

## 1 INTRODUCTION

The uncertainty analysis of structural systems is the key to ensuring the safety and reliability of structural design. The conventional physical model-based method can analyze the uncertainty of the forward computation under random material parameters, geometric dimensions or external excitation through the probabilistic or non-probabilistic framework [1]. Probabilistic uncertainty analysis methods such as Monte Carlo simulation [2], [3], stochastic finite element method [4], [5], etc., statistically sample uncertainty propagation on uncertainty parameters by calculating models or conducting experiments. Non-probabilistic methods such as interval analysis [6], [7] and fuzzy theory [8], [9], which are different from probabilistic methods, are suitable for analyzing the epistemic uncertainty caused by a lack of knowledge in the absence of deterministic prior information. The above methods are versatile and flexible in the form of the model, but the calculation cost would greatly increase to conduct the uncertainty analysis of large-scale and high-dimensional structures.

With the breakthrough of deep learning technology, neural operators [10], [11] can effectively learn the global mapping relationship of complex systems, especially for the cross-resolution solution of high-dimensional and nonlinear problems, which reduces the computational cost compared with traditional physical modeling methods. Chawit et al. established the vehicle-bridge interactive neural operator as a surrogate model of the bridge structure, which can more accurately predict the structural response under different structural damage fields than the traditional finite element model [12]. Ding et al. solved the coupled differential equations of structural dynamics based on the physics-informed neural operator (PINO-CDE). Also, PINO-CDE provides a higher resolution for uncertain propagation tasks, which takes less

than a quarter of the computing time compared to the probability density evolution method [13].

However, the neural operator mapping process is nonlinear and non-intuitive. The results are affected by multiple sources of uncertainty, such as aleatoric uncertainty and epistemic uncertainty [14], [15]. Most of the existing studies focus on the probability distribution of the output results of neural operators, but it is difficult to distinguish the sources of quantitative uncertainty. This fuzziness may lead to misjudgment in practical engineering based on computing results. While deep evidential learning provides a feasible path for aleatoric and epistemic uncertainty qualification of regression problems [16]. Therefore, how to integrate deep evidential learning and neural operators to build an efficient and interpretable computational uncertainty framework for dynamic structures is worth exploring.

In this work, we propose an evidential neural operator, extending evidential deep learning to a more flexible and complex neural network like the Fourier neural operator. For parametric structural dynamic systems with stochastic structural parameters and load excitation, ENO can quantitatively distinguish aleatoric uncertainty and epistemic uncertainty in the forward computation without retraining. The multi-task regularizer is introduced in ENO to improve adaptability to high-dimensional scenarios and complex structural systems, by flexibly controlling the weights of regularizer. A single-degree-of-freedom system is provided as a numerical example to verify the accuracy of uncertainty estimation and quantization distinction.

## 2 THEORETICAL BASIS

### 2.1 Fourier Neural Operator

Fourier Neural Operator (FNO) can capture high-frequency characteristics of dynamic systems by Fast Fourier Transform

and spectrum convolution operation and is suitable for solving structural vibration differential equations to simulate the dynamic behavior of structural systems.

Besides, performing convolution in Fourier space greatly reduces the computational complexity. For a single hidden layer (1), the Fourier neural operator utilize the kernel-integral operator, extend deep neural networks to infinite dimensions:

$$(N_l V)(x) = \sigma(A_l V(x) + B_l(x) + \int_D K_l(x, y) V(y) dy) \quad (1)$$

Due to,

$$K_l(x, y) = K_l(x - y) \quad (2)$$

$$\int_D K_l(x - y) V(y) dy = K_l \times V \quad (3)$$

Using the Fourier transform result in (4):

$$K_l \times V = f^{-1}(f(K) \cdot f(V)) \quad (4)$$

Hence, the computational complexity can be reduced from  $O(N^2)$  to  $O(N \log(N))$ . FNO shows great potential for fast and accurate computation of oscillatory differential equations.

## 2.2 Evidential Neural Operator

The sources of uncertainty can be divided into aleatoric uncertainty and epistemic uncertainty. Evidential theory assumes that the prediction target  $Z_i$  can be independently sampled from the Gaussian distribution. Then, a probabilistic estimate of its mean and variance is required.

The normal-inverse-gamma (NIG) prior distribution is introduced in evidential regression [16]. The mean  $\mu$  is assumed to follow a Gaussian distribution, and the variance  $\sigma$  is assumed to follow an inverse gamma distribution. By marginalizing  $\mu$  and  $\sigma$ , the model evidence can be expressed as a Student-t distribution (5):

$$p(z_i | \theta) = St(z_i; \gamma, \frac{(1+\tau)\beta}{\tau\alpha}, 2\alpha) \quad (5)$$

where  $\theta$  represents the combination of parameters of the NIG distribution.  $\gamma$  represents the expectation of the mean  $\mu$ .  $\tau$  is the precision parameter of the Gaussian distribution.  $\alpha$  and  $\beta$  are the shape parameters of the inverse gamma distribution.

Combining the high-dimensional computing capability of FNO and the ability of NIG high-order distribution for capturing data diversity and uncertainty. The evidential neural operator is proposed to convert the model output into four parameters of NIG distribution. The loss function (6) of the evidential neural operator is designed for uncertainty sources, which can be divided into two parts: negative log-likelihood loss and evidence regularizer.

$$\mathcal{L}_{ENO} = \mathcal{L}_{NLL} + \sum_{i=1}^n \lambda_i \mathcal{L}_{REGi} \quad (6)$$

where,

$$\mathcal{L}_{NLL} = \frac{1}{2} \log\left(\frac{\pi}{\tau}\right) - \alpha \log(\phi) + \left(\alpha + \frac{1}{2}\right) \log((z_i - \gamma)^2 \tau + \phi) + \log\left(\frac{\Gamma(\alpha)}{\Gamma(\alpha + \frac{1}{2})}\right)$$

$$\mathcal{L}_{REGi} = |z_i - \gamma| \cdot (2\tau + \alpha)$$

where,  $\phi = 2\beta(2\tau + \alpha)$ .  $n$  represents the number of regularizers for different outputs.

In this work, ENO adds multi-task regularization to ensure that each task has independent error and evidence constraints, and can better adapt to multi-task learning and complex scenarios by flexibly controlling regularization weights. The data normalization module is incorporated into the training process to normalize and denormalize the dataset to address the potential training instability and gradient explosions arising from differences in the scale of output variables.

## 3 ILLUSTRATIVE EXAMPLE

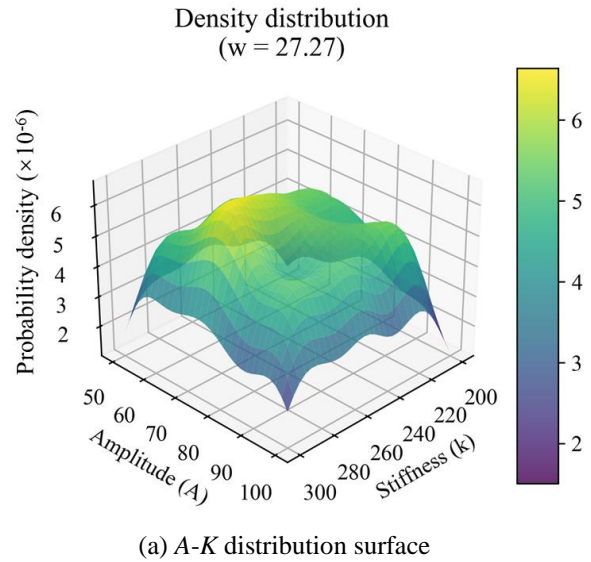
For validating the effectiveness of ENO, a single degree of freedom random vibration equation (7) with harmonic excitation is used as an example to solve the forward uncertainty of response prediction:

$$M\ddot{u} + C\dot{u} + Ku = A \sin(wt) \quad (7)$$

where,  $M$  is mass,  $M = 1\text{kg}$ .  $C$  is damping and  $K$  is stiffness.  $A$  represents amplitude and  $w$  represents the frequency of the harmonic force.  $u$ ,  $\dot{u}$ ,  $\ddot{u}$  represent the displacement, velocity, and acceleration, respectively.

$K$ ,  $A$ , and  $w$  are randomly sampled with a uniform distribution. The sampling interval of stiffness is  $[200, 300]$  N/m. The sampling interval of amplitude and frequency are  $[50, 100]$  N and  $[10, 45]$  rad/s, respectively. The probability density surface diagrams of three stochastic variables are shown in Figure 1. The Newmark- $\beta$  integral algorithm is used to solve equation (7) and generate the datasets. The proportions of the training set, verification set and test set are 70%, 20% and 10%, respectively. The network parameters, such as convolutional layer depth  $D_{\text{conv}}$ , convolutional layer width  $W_{\text{conv}}$ , fully connected layer depth  $D_{\text{fc}}$  and width  $W_{\text{fc}}$  of FNO were optimized by using the Bayesian optimization algorithm. The optimal network parameters were determined as follows:  $D_{\text{conv}}=4$ ,  $W_{\text{conv}}=32$ ,  $D_{\text{fc}}=3$ , and  $W_{\text{fc}}=64$ .

The ENO model is implemented in PyTorch and the Fourier modes of spectral convolution layers are 26. The weight parameters of the loss item are:  $\lambda_1 = 1$ ,  $\lambda_2 = 2$ ,  $\lambda_3 = 2$ . The total number of epochs is 300 and the Adam optimizer was used with a learning rate of  $10^{-3}$ .



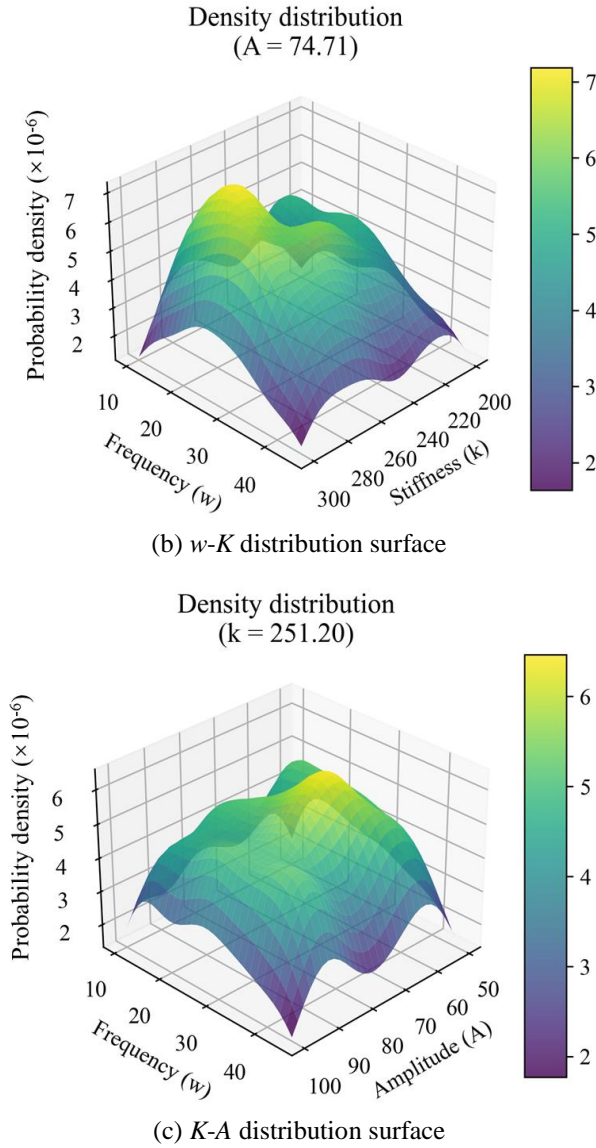


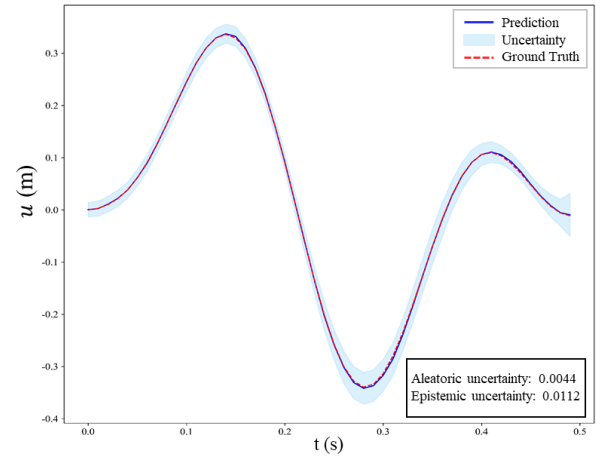
Figure 1. Probability density surfaces of stochastic variables.

The ENO model is validated against the state-of-the-art Deep Ensemble model presented in [17]. The baseline model is also embedded in the FNO framework (FNO-DE) to conduct ablation experiments, and the network parameters are consistent with those adopted by ENO. FNO-DE consists of five independently trained models with identical architecture but different random initializations. The evaluation metrics applied Root Mean Square Error (RMSE), Empirical Coverage Probability (ECP) and Pearson Correlation Coefficient ( $R_{pr}$ ). RMSE can evaluate the error level between the predicted mean and the ground truth. ECP monitors the proportion of samples falling into the predicted confidence interval to the total number of samples. In this work, 95% confidence is considered, and the ideal value of ECP should be close to 0.95. Besides, the Pearson Correlation Coefficient can evaluate the correlation between prediction error and uncertainty.

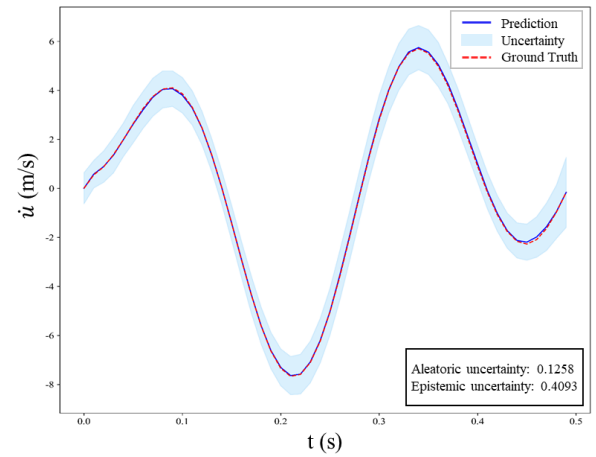
#### 4 RESULTS AND DISCUSSION

For solving the single-degree-of-freedom vibration equation, the ENO model performance was first tested by sampling test sets in the interval. The outputs of displacement, velocity and

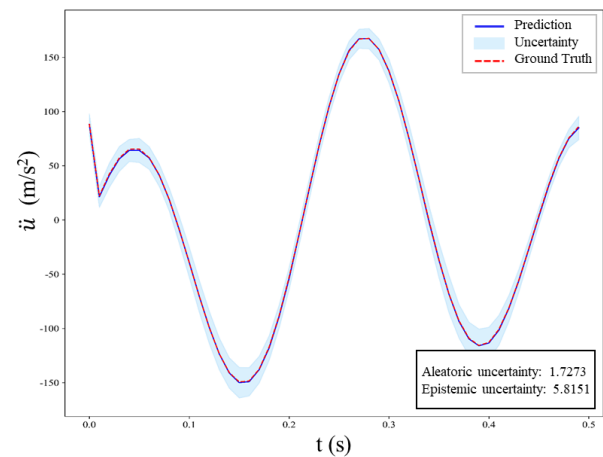
acceleration responses and their corresponding uncertainties are shown in Figure 2. Due to the high cognition level of the tested model within the interval, it can be seen that the aleatoric and epistemic uncertainty are both small, which are lower than  $10^1$ .



(a) Uncertainty prediction of the displacement



(b) Uncertainty prediction of the velocity



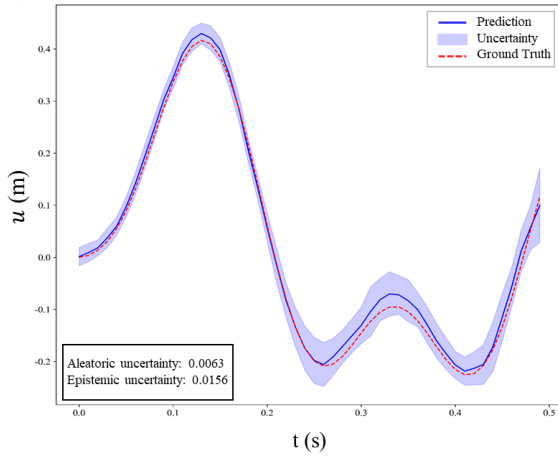
(c) Uncertainty prediction of the acceleration

Figure 2. Uncertainty prediction in the distribution (ENO).

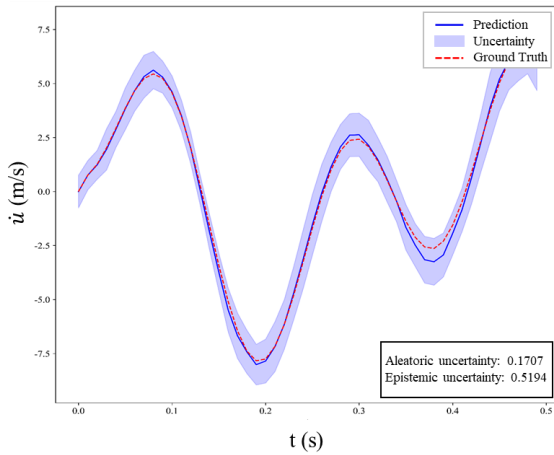
The out-of-distribution test evaluates the zero-shot learning ability and generalization of the ENO model. The results of out-of-interval testing are shown in Figure 3. The epistemic



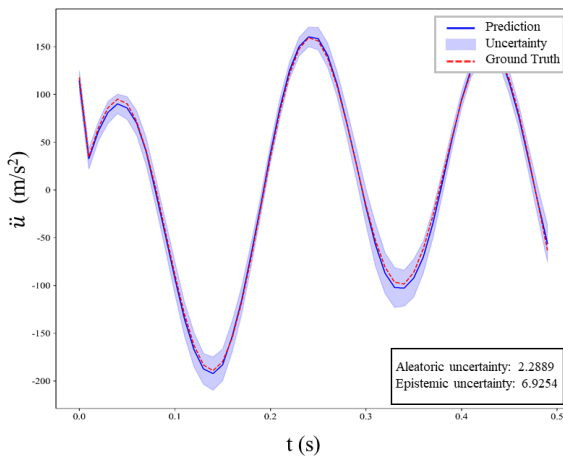
uncertainty of the model has increased by 20~40%, compared with that in distribution testing. And the epistemic uncertainty is always greater than the aleatoric uncertainty of the raw data, due to no extra noise added in the dataset for this illustrative case.



(a) Uncertainty prediction of the displacement



(b) Uncertainty prediction of the velocity



(c) Uncertainty prediction of the acceleration

Figure 3. Uncertainty prediction out of distribution (ENO).

The performance comparison between the ENO model and the FNO-DE model is shown in Table 1. The ENO model can achieve higher fitting accuracy than the FNO-DE model. The RMSE of ENO is less than that of FNO-DE, especially when

ENO is tested out of distribution. ENO has better generalization performance. In terms of uncertainty prediction, FNO-DE remains competitive in in-distribution testing, and the empirical coverage probability of both ENO and FNO-DE is relatively close to the nominal values. However, the uncertainty estimated by ENO shows a stronger correlation with prediction errors ( $R_{pr} \sim 0.86$ ) in interpreting out-of-domain data.

Table 1. Compared the metrics of ENO and FNO-DE models.

In distribution			Out of distribution		
Metrics	ENO	FNO-DE	Metrics	ENO	FNO-DE
RMSE	<b>0.35</b>	0.38	RMSE	<b>2.22</b>	2.41
ECP	<b>1.0</b>	1.0	ECP	<b>1.0</b>	0.82
$R_{pr}$	0.70	<b>0.79</b>	$R_{pr}$	<b>0.86</b>	0.67

## 5 CONCLUSION

In this paper, a novel evidential neural operator is proposed, which cooperates with the basic principle of deep evidential learning and the high-dimensional nonlinear mapping capability of the Fourier neural operator. ENO provides a scientific machine learning framework for the uncertainty quantification for the forward computation of structural vibration equations. This work solves the vibration equation of a single degree of freedom as a numerical example, indicating that the model has higher epistemic uncertainty when tested outside the interval. Compared to the evaluating metrics with the art-of-state ensemble model, the ENO shows superior uncertainty calibration and fitting accuracy in out-of-domain testing. Future works would consider the effect of data noise on the uncertainty qualification and expand the ENO to a more complex structural system.

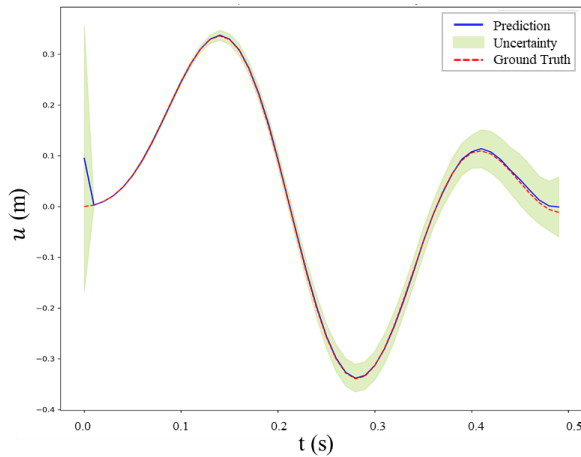
## ACKNOWLEDGMENTS

The work described in this paper was supported by a grant from the Research Grants Council (RGC) of the Hong Kong Special Administrative Region (SAR), China (Grant No. PolyU 152308/22E) and a grant from The Hong Kong Polytechnic University (Grant No. 1-WZ0C). The authors would also like to appreciate the funding support by the Innovation and Technology Commission of Hong Kong SAR Government to the Hong Kong Branch of National Rail Transit Electrification and Automation Engineering Technology Research Center (Grant No. K-BBY1).

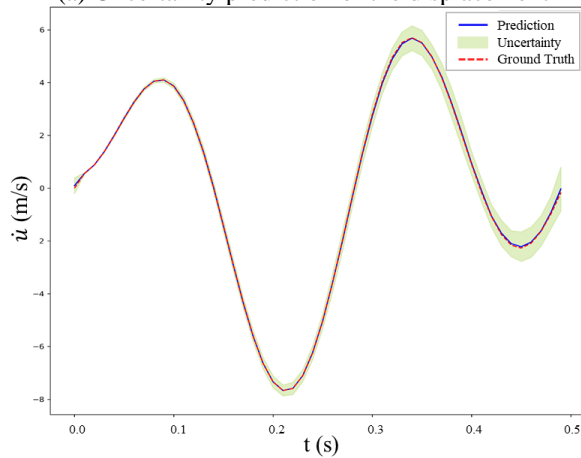
## APPENDIX: PREDICTION RESULTS OF FNO-DE

### A-1: Test results of FNO-DE within the interval

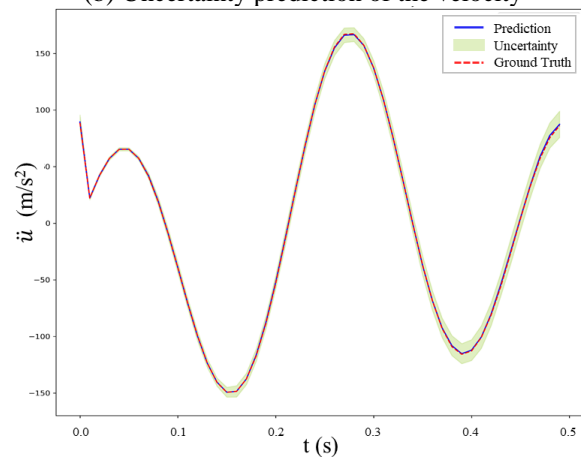
The test results of the baseline model (FNO-DE) within the sampling interval are also shown in Figure 4. The predicted responses are generally consistent with the ground truth, indicating the FNO-DE can capture the dynamic change trend of the displacement and its derivative. The regions with large uncertainties are mainly concentrated at the boundaries of time, such as around  $t = 0$  and  $t \approx 0.5$ , while the uncertainty distribution is narrow within the time interval. This demonstrates that the FNO-DE model is quite sensitive and can not comply well with the boundary conditions.



(a) Uncertainty prediction of the displacement



(b) Uncertainty prediction of the velocity

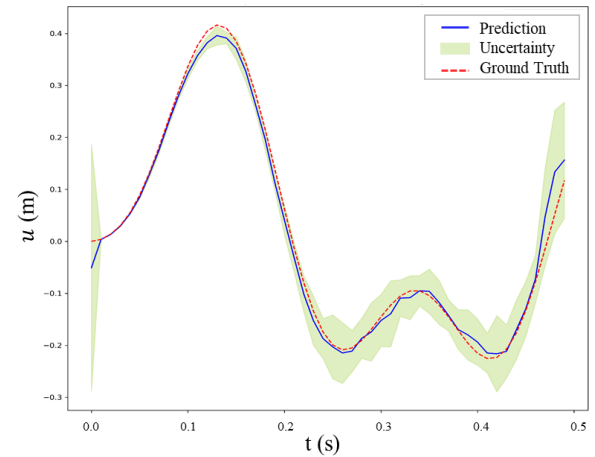


(c) Uncertainty prediction of the acceleration

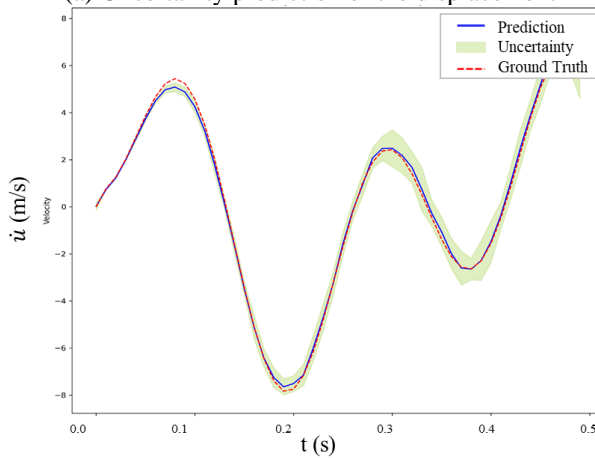
Figure 4. Uncertainty prediction in the distribution (FNO-DE).

#### A-2: Test results of FNO-DE out of the interval

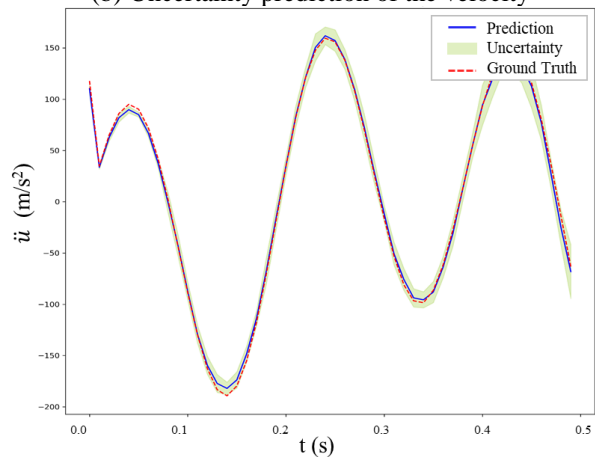
Outside the sampling interval (Figure 5), the deviation between the model prediction results and the Ground Truth increases, while the uncertainty region (green shadow) expands significantly, especially around the time period  $t = 0.4$  s, where the confidence interval of displacement  $u(t)$  increases from about  $\pm 0.1$  m to  $\pm 0.2$  m. This shows that the prediction confidence of FNO-DE for unseen data is greatly reduced.



(a) Uncertainty prediction of the displacement



(b) Uncertainty prediction of the velocity



(c) Uncertainty prediction of the acceleration

Figure 5. Uncertainty prediction out of the distribution (FNO-DE).

#### REFERENCES

- [1] K. Zhou, Z. Wang, Q. Gao, et al, Recent advances in uncertainty quantification in structural response characterization and system identification, Probabilistic Engineering Mechanics, 2023, 74, 103507.
- [2] C. Z. Mooney, Monte carlo simulation (No. 116), Sage, 1997.
- [3] P. Marek, J. Brozzetti, M. Gustar, et al, Probabilistic assessment of structures using Monte Carlo simulations, Applied Mechanics Reviews, 2002, 55(2), B31-B32.
- [4] S. Naskar, T. Mukhopadhyay, S. Sriramula, et al, Stochastic natural frequency analysis of damaged thin-walled laminated composite beams

- with uncertainty in micromechanical properties, *Composite Structures*, 2017, 160, 312-334.
- [5] H. Zhang, N. An, X. Zhu, Structural dynamic reliability analysis of super large-scale lattice domes during earthquakes using the stochastic finite element method, *Soil Dynamics and Earthquake Engineering*, 2022, 153, 107076.
- [6] M. Modares and R. L. Mullen, Dynamic analysis of structures with interval uncertainty, *Journal of Engineering Mechanics*, 2014, 140(4), 04013011.
- [7] K. Shariatmadar and M. Versteyhe, Numerical linear programming under non-probabilistic uncertainty models—interval and fuzzy sets, *International Journal of Uncertainty, Fuzziness and Knowledge-Based Systems*, 2020, 28(03), 469-495.
- [8] C. Wang and H. G. Matthies, Coupled fuzzy-interval model and method for structural response analysis with non-probabilistic hybrid uncertainties, *Fuzzy Sets and Systems*, 2021, 417, 171-189.
- [9] Z. Ni and Z. Qiu, Hybrid probabilistic fuzzy and non-probabilistic model of structural reliability, *Computers & Industrial Engineering*, 2010, 58(3), 463-467.
- [10] N. Kovachki, Z. Li, B. Liu, et al, Neural operator: Learning maps between function spaces with applications to pdes, *Journal of Machine Learning Research*, 2023, 24(89), 1-97.
- [11] Z. Li, N. Kovachki, K. Azizzadenesheli, et al, Fourier Neural Operator for Parametric Partial Differential Equations, In *International Conference on Learning Representations*, 2020.
- [12] C. Kaewnurachadasorn, J. Wang, C. W. Kim, Neural operator for structural simulation and bridge health monitoring, *Computer-Aided Civil and Infrastructure Engineering*, 2024, 39(6), 872-890.
- [13] W. Ding, Q. He, H. Tong, et al, Solving coupled differential equation groups using PINO-CDE, *Mechanical Systems and Signal Processing*, 2024, 208, 111014.
- [14] A. Der Kiureghian and O. Ditlevsen, Aleatory or epistemic? Does it matter?, *Structural safety*, 2009, 31(2), 105-112.
- [15] E. Hofer, M. Kloos, B. Krzykacz-Hausmann, et al, An approximate epistemic uncertainty analysis approach in the presence of epistemic and aleatory uncertainties, *Reliability Engineering & System Safety*, 2002, 77(3), 229-238.
- [16] A. Amini, W. Schwarting, A. Soleimany, et al, Deep evidential regression, *Advances in neural information processing systems*, 2020, 33, 14927-14937.
- [17] B. Lakshminarayanan, A. Pritzel, C. Blundell, Simple and scalable predictive uncertainty estimation using deep ensembles, *Advances in neural information processing systems*, 2017, 30.



# Nonparametric identification of structural nonlinear behavior based on extended Kalman particle filter and Chebyshev polynomial model

Ye Zhao<sup>1, 3</sup>, 0000-0003-2649-5673, Bin Xu<sup>2,3</sup>, 0000-0001-8336-3306, Yikai Yuan<sup>2</sup>

<sup>1</sup> School of Architecture and Civil Engineering, Heilongjiang University of Science and Technology, Puyuan Road 2468, 150022 Harbin, China

<sup>2</sup> College of Civil Engineering, Huaqiao University, Jimei Avenue 668, 361021 Xiamen, China

<sup>3</sup> Key Laboratory for Intelligent Infrastructure and Monitoring of Fujian Province (Huaqiao University), Jimei Avenue 668, 361021 Xiamen, China

email: zhaoye@usth.edu.cn, binxu@hqu.edu.cn, author3@tugraz.at

**ABSTRACT:** Describing the damage initiation and development of engineering structures during strong dynamic loadings such as earthquake is one of the most important topics in structural condition monitoring and identification. Structural nonlinear restoring force (NRF) can not only directly describe the initiation and development process of nonlinear behavior of the structure during strong dynamic loadings but also can be used to evaluate the energy dissipation of structural members or substructures. However, it is hard to measure structural dynamic responses at all degree of freedoms (DOFs) of a structure in practice, and to model the NRF with an accurate parametric mathematical model in advance due to the variability and individuality of structural materials and types. In this study, a Chebyshev polynomial model as a nonparametric model is employed to model the NRF of a structure and structural stiffness, damping, mass and NRF are identified based on the extended Kalman particle filter (EKPF) algorithm by using acceleration measurements at limited DOFs during the known external excitation. Then, two multi-degree-of-freedom (MDOF) numerical models equipped with different types of magnetorheological (MR) dampers are used as numerical examples to validate the performance of the proposed approach. Identified results show that the proposed method is effective for identifying the nonlinear MDOF structures with different nonlinearity with limited noise-polluted acceleration measurements.

**KEY WORDS:** Nonlinear restoring force; Extended Kalman particle filter; nonparametric identification; Chebyshev polynomial; MR damper.

## 1 INTRODUCTION

During the service of engineering structures, when subjected to severe loads, the structural characteristics may change abruptly or gradually, resulting in stiffness deterioration and increased damping. The problem of precisely detecting parameter changes has piqued civil engineering researchers' interest. Understanding changing structural parameters is crucial for designing, maintaining, and reinforcing structures, as well as selecting post-disaster rescue routes. When civil engineering structures are subjected to extraordinarily significant external excitations, such as earthquakes on buildings or heavy cars on bridges, they frequently exhibit nonlinear behavior.

Identification of structural parameters and nonlinear restoring force (NRF) of nonlinear structural systems using partial acceleration measurements from structural health monitoring (SHM) is crucial for structural condition assessment and damage identification[1, 2]. In the past decades, many researchers have developed many parameters and NRF identification methods of nonlinear system. It is difficult to measure the acceleration responses of all degrees of freedom in practical engineering, some methods based on Kalman filter (KF)[3, 4], extended Kalman filter (EKF)[5, 6], unscented Kalman filter (UKF) [7-9], and particle filter (PF) [10, 11] were proposed to tackle the problem. However, conventional methods are only suitable for nonlinear hysteresis model parameters that are known. Due to the diversity and individuality of nonlinear behaviors, it is crucial to propose a general nonparametric identification method for nonlinear behaviors that does not rely on nonlinear hysteresis models.

The idea of nonparametric identification of nonlinear behavior was first proposed by Masri and his collaborators[12,

13]. Based on the equivalent linear theory and least squares method, identified methods of the structural nonlinear restoring force were proposed by Xu et al. [14, 15] using external excitation and complete dynamic response information and verified the feasibility of the proposed method through dynamic test data of a multi-degree-of-freedom shear frame model equipped with a magnetorheological (MR) damper. Xu and his cooperators proposed nonparametric identification method of the NRF in the presence of the known or unknown input, where the NRF was expressed using different polynomial models[16-19]. Some researchers regarded the nonlinear restoring force as an unknown virtual input, proposing different NRF identification methods[20-22]. The effectiveness of the proposed method was verified by numerical simulation and experiment. However, as far as the author knows, there is no extended Kalman particle filter (EKPF) method that is suitable for nonparametric identification of structural nonlinear behavior under non-Gaussian measurement noise without the need of the known parametric model of nonlinear behavior.

Since the standard PF algorithm takes the transition probability of the system state as the importance density function, it does not use the updated observations. Therefore, the generated particle samples are concentrated at the tail of the posterior probability distribution, resulting in a large randomness in the selection of particles, which affects the filtering results. When there is a peak in the likelihood distribution, the prediction state is distributed at the tail of the likelihood distribution, which has a particularly serious impact on the filtering accuracy. The EKPF uses EKF as the posterior probability density function, which solves the problem of particle degradation in PF algorithm and improves the filtering

accuracy. For the EKF part of EKPF, when Kalman filter is applied in practice, model error, noise error and calculation error may cause the prediction error covariance matrix and gain matrix to weaken the modified state estimation with the increase of iteration times, which leads to filter divergence. Therefore, the fading memory filtering (MF) technology can be used for EKF to increase the proportion of new data, reduced the proportion of old data and the negative impact of old data on filtering [16].

In this paper, a model-free identification method for structural parameters and nonlinear restoring force under limited acceleration observation is proposed by using EKPF algorithm. Based on the equivalent linear theory and EKPF algorithm, the structural parameters, unknown dynamic response measurements and nonlinear locations are identified under limited acceleration observations. Based on the identification value, the Chebyshev polynomial model is used to characterize the nonlinear restoring force of the structure, and the nonparametric identification of the NRF is realized. To verify the feasibility of the proposed method, two four-degree-of-freedom shear frame models are established, and MR dampers with different numbers and different parameter models are introduced to simulate the nonlinear behavior of shear frame structures. Considering the influence of measurement noise in the observed acceleration signal, the structural stiffness, damping coefficient, mass, unknown dynamic response and NRF are identified. The feasibility of the proposed method is verified by comparing the identification results with the real values.

## 2 EXTENDED KALMAN PARTICLE FILTERING ALGORITHM

### 2.1 The state-space equation

In general, the nonlinear dynamic system of structures in civil engineering can be described as,

$$\begin{cases} \mathbf{x}_k = f(\mathbf{x}_{k-1}) + \mathbf{r}_{k-1} \\ \mathbf{y}_k = h(\mathbf{x}_k) + \mathbf{v}_k \end{cases} \quad (1)$$

where, the function  $f(\square)$  and  $h(\square)$  represent the state transition function and the measurement model function of the system respectively.  $k$  is the number of time steps,  $\mathbf{x}_k$  is the state value of step  $k$ ,  $\mathbf{y}_k$  is the observation value of step  $k$ ,  $\mathbf{r}_k$  is the process noise of step  $k$ ,  $\mathbf{v}_k$  is the observation noise of step  $k$ . Equation (1) describes the recursive relationship between the structural state vector and the structural response over time.

### 2.2 Bayesian theorem and Monte Carlo simulation

For the state space equation assumed by the formula (1), let  $\mathbf{x}_{0:k} = \{\mathbf{x}_0, \mathbf{x}_1, \dots, \mathbf{x}_k\}$ ,  $\mathbf{y}_{1:k} = \{\mathbf{y}_1, \mathbf{y}_2, \dots, \mathbf{y}_k\}$ , and given  $\mathbf{x}_{0:k}$ , when the measurement sequence  $\mathbf{y}_k$  is independent of each other, the prediction and update can be written recursively by the Bayesian formula,

$$p(\mathbf{x}_k | \mathbf{y}_{1:k-1}) = \int p(\mathbf{x}_k | \mathbf{x}_{k-1}) p(\mathbf{x}_{k-1} | \mathbf{y}_{1:k-1}) d\mathbf{x}_{k-1} \quad (2)$$

$$p(\mathbf{x}_k | \mathbf{y}_{1:k}) = \frac{p(\mathbf{y}_k | \mathbf{x}_k) p(\mathbf{x}_k | \mathbf{y}_{1:k-1})}{\int p(\mathbf{y}_k | \mathbf{x}_k) p(\mathbf{x}_k | \mathbf{y}_{1:k-1}) d\mathbf{x}_k} \quad (3)$$

For nonlinear models, the above analytical formulas are often unable to be obtained, and it is also very difficult to solve them

integrally. Therefore, the Monte Carlo simulation is considered to realize the recursion of Bayesian filter. The Monte Carlo simulation regards the problem to be solved as a random variable. By establishing a probability model and sampling a large number of samples, the integral value is regarded as the mathematical expectation of the random variable, and then the problem to be solved is estimated. That is to say, for the integrand  $f(x)$ , it can be decomposed into the product of the state variable  $g(x)$  and its probability density function  $p(x)$ , then the integral of  $f(x)$  can be regarded as the mathematical expectation of  $g(x)$ .

### 2.3 The sequential importance sampling

According to the Monte Carlo simulation, if we can sample from the posterior probability density function  $p(\mathbf{x}_{0:k} | \mathbf{y}_{1:k})$

and get the sample set  $\{\mathbf{x}_{0:k}^{(i)}, \omega_k^{(i)}\}_{i=1}^N$ , then  $p(\mathbf{x}_{0:k} | \mathbf{y}_{1:k})$  can be approximated by the sum of discrete samples, that is, the approximate solution formula of  $g(\mathbf{x}_{0:k})$  can be written as,

$$E(g(\mathbf{x}_{0:k})) = \sum_{i=1}^N \omega_k^{(i)} g(\mathbf{x}_{0:k}^{(i)}) \quad (4)$$

However, in practice, it is very difficult to extract samples from the posterior probability distribution. Therefore, the importance sampling method is introduced to extract samples from the importance density function  $q(\mathbf{x}_k^{(i)} | \mathbf{x}_{k-1}^{(i)}, \mathbf{y}_k)$ . Then the mathematical expectation of  $g(x)$  can be written as,

$$\begin{aligned} E[g(\mathbf{x}_{0:k})] &= \int g(\mathbf{x}_{0:k}) \frac{p(\mathbf{x}_{0:k} | \mathbf{y}_{1:k})}{q(\mathbf{x}_{0:k} | \mathbf{y}_{1:k})} q(\mathbf{x}_{0:k} | \mathbf{y}_{1:k}) d\mathbf{x}_{0:k} \\ &= \sum_{i=1}^N \hat{\omega}_k^{(i)} g(\mathbf{x}_{0:k}^{(i)}) \end{aligned} \quad (5)$$

where  $\hat{\omega}_k^{(i)}$  is the normalized weight, which can be written as,

$$\hat{\omega}_k^{(i)} = \frac{\omega_k^{(i)}}{\sum_{j=1}^N \omega_k^{(j)}} \quad (6)$$

For the weight  $\omega_k^{(i)}$  of each particle, it can be recursively expressed as,

$$\begin{aligned} \omega_k^{(i)} &= \omega_{k-1}^{(i)} \frac{p(\mathbf{x}_{0:k} | \mathbf{y}_{1:k})}{q(\mathbf{x}_{0:k} | \mathbf{y}_{1:k})} \\ &= \omega_{k-1}^{(i)} \frac{p(\mathbf{y}_k | \mathbf{x}_k^{(i)}) p(\mathbf{x}_k^{(i)} | \mathbf{x}_{k-1}^{(i)})}{q(\mathbf{x}_k^{(i)} | \mathbf{x}_{k-1}^{(i)}, \mathbf{y}_k)} \end{aligned} \quad (7)$$

Accordingly, the implementation steps of the PF algorithm are as follows,

(1) By sampling from the known prior probability distribution  $p(\mathbf{x}_0)$ , the initial sample  $\{\mathbf{x}_{0:k}^{(i)}, \omega_k^{(i)}\}_{i=1}^N$  is obtained, where  $\{\omega_k^{(i)}\}_{i=1}^N = 1/N$ .

(2) A new particle set  $\{\mathbf{x}_k^{(i)}\}_{i=1}^N$  is obtained by sampling from the importance density function  $q(\mathbf{x}_k | \mathbf{x}_{k-1}^{(i)}, \mathbf{y}_k)$ .

(3) Calculating the weight of each particle according to Equation (7).

$$(4) \text{ Normalized weights, } \left\{ \hat{\omega}_k^{(i)} = \omega_k^{(i)} / \sum_{j=1}^N \omega_k^{(j)} \right\}_{i=1}^N.$$

(5)  $k=k+1$ , and return to step (1) to continue the iteration.

#### 2.4 Resampling

Because the variance of the particle weight increases with time, the particle degradation in the basic PF is inevitable. After multiple iterations, most of the particle weights are so small that they can be ignored, while the weights of individual particles are too concentrated. To improve this situation, the resampling method is used to discard the particles with small weights, copy the particles with large weights and make them have equal weights, so as to reduce the phenomenon of particle degradation. The system resampling method is adopted to avoid particle degradation in this paper.

#### 2.5 EKF importance sampling density

At time  $k$ , according to the new observation, the EKF algorithm is used to calculate the particle mean estimation  $\bar{\mathbf{x}}_k^i$  and variance estimation  $\hat{\mathbf{P}}_k^{(i)}$ , and then the particles are extracted from the approximate Gaussian distribution  $N(\bar{\mathbf{x}}_k^{(i)}, \hat{\mathbf{P}}_k^{(i)})$ . This method of using EKF to generate importance density function is called EKPF. For a state vector  $\mathbf{X}(t)$ , the specific algorithm is as follows,

(1) The initial particle samples are obtained by sampling from the known prior probability distribution.

(2) The initial particles are updated by EKF,

$$\tilde{\mathbf{x}}_{k+1|k}^{(i)} = \mathbf{f}(\hat{\mathbf{x}}_{k|k}^{(i)}, 0) \quad (8)$$

$$\mathbf{P}_{k+1|k}^{(i)} = \Phi_{k+1|k}^{(i)} \mathbf{P}_{k|k}^{(i)} (\Phi_{k+1|k}^{(i)})^T \quad (9)$$

$$\mathbf{K}_{k+1}^{(i)} = \mathbf{P}_{k+1|k}^{(i)} (\mathbf{H}_{k+1}^{(i)})^T \left( \mathbf{H}_{k+1}^{(i)} \mathbf{P}_{k+1|k}^{(i)} (\mathbf{H}_{k+1}^{(i)})^T + \mathbf{R}_{k+1} \right)^{-1} \quad (10)$$

$$\hat{\mathbf{x}}_{k+1|k+1}^{(i)} = \tilde{\mathbf{x}}_{k+1|k}^{(i)} + \mathbf{K}_{k+1}^{(i)} \left[ \mathbf{y}_{k+1} - \mathbf{h}(\hat{\mathbf{x}}_{k+1|k}^{(i)}, 0) \right] \quad (11)$$

$$\mathbf{P}_{k+1|k+1}^{(i)} = (\mathbf{I} - \mathbf{K}_{k+1}^{(i)} \mathbf{H}_{k+1}^{(i)}) \mathbf{P}_{k+1|k}^{(i)} \quad (12)$$

where  $\Phi_{k+1|k}^{(i)}$  is the state transition matrix,  $\mathbf{H}_{k+1}^{(i)}$  is the observation coefficient matrix, there are,

$$\Phi_{k+1|k}^{(i)} = \frac{\partial \mathbf{f}_k(\mathbf{X}_k^{(i)}, \mathbf{y}_k)}{\partial \mathbf{x}_k^{(i)}} \bigg|_{\mathbf{x}_k^{(i)} = \hat{\mathbf{x}}_{k|k}^{(i)}} \quad (13)$$

$$\mathbf{H}_{k+1}^{(i)} = \frac{\partial \mathbf{h}_k(\mathbf{x}_{k+1|k}^{(i)}, 0)}{\partial \mathbf{x}_k^{(i)}} \bigg|_{\mathbf{x}_k^{(i)} = \hat{\mathbf{x}}_{k+1|k}^{(i)}} \quad (14)$$

Considering the cause of filtering divergence and the infinite growth of Kalman filter memory, the data error at the previous moment will cause the error covariance matrix  $\mathbf{P}$  and the gain matrix  $\mathbf{K}$  to lose the ability to correct the state estimation with the iteration, resulting in filtering divergence. To increase the weight of new data and relatively weaken the influence of old data, a fading factor is introduced to reduce the negative impact of old data on filtering estimation. The formula (9) is modified as follows,

$$\mathbf{P}_{k+1|k}^{(i)} = \Phi_{k+1|k}^{(i)} \mathbf{P}_{k|k}^{(i)} (\Phi_{k+1|k}^{(i)})^T S \quad (15)$$

Among them, the forgetting factor  $\lambda = 1/S$ , the literature suggests  $0.95 < \lambda < 1.0$ , then the weighted weight of the fading memory is  $1.0 < S < 1.05$ .

(3) Complete the sequential importance sampling with reference to Section 2.3.

(4) Complete system resampling with reference to Section 2.4.

### 3 PARAMETER-FREE RESTORING FORCE IDENTIFICATION METHOD BASED ON EKPF AND CHEBYSHEV POLYNOMIAL

#### 3.1 The equivalent linearization theory

For a multi-degree-of-freedom nonlinear dynamic system, the equation of motion can be written as,

$$\mathbf{M}\ddot{\mathbf{x}}(t) + \mathbf{K}\mathbf{x}(t) + \mathbf{C}\dot{\mathbf{x}}(t) + \mathbf{f}_{non}(t) = \mathbf{f}(t) \quad (16)$$

In the formula,  $\mathbf{M}$ ,  $\mathbf{K}$  and  $\mathbf{C}$  are the mass, stiffness and damping matrices of the system respectively.  $\ddot{\mathbf{x}}(t)$ ,  $\mathbf{x}(t)$  and  $\dot{\mathbf{x}}(t)$  are the acceleration, displacement and velocity vectors respectively.  $\mathbf{f}_{non}(t)$  is the nonlinear restoring force vector provided by the nonlinear element, and  $\mathbf{f}(t)$  is the excitation vector the system.

The dynamic equation of the equivalent linear system is,

$$\mathbf{M}_E \ddot{\mathbf{x}}(t) + \mathbf{C}_E \dot{\mathbf{x}}(t) + \mathbf{K}_E \mathbf{x}(t) = \mathbf{f}(t) \quad (17)$$

where  $\mathbf{M}_E$ ,  $\mathbf{C}_E$  and  $\mathbf{K}_E$  represent the equivalent linear mass, equivalent linear damping and equivalent linear stiffness, respectively. Since the structural mass does not change during the nonlinear development process,  $\mathbf{M}_E$  can be regarded as the identification value of the mass, that is, and  $\mathbf{M}$  is numerically equal  $\mathbf{M}_E$ . The nonlinear restoring force of the structure in the equation (17) will be reflected in the parameters  $\mathbf{C}_E$  and  $\mathbf{K}_E$  of the equivalent linear system, which is,

$$\mathbf{R}_{non}(t) = \mathbf{C}_E \dot{\mathbf{x}}(t) + \mathbf{K}_E \mathbf{x}(t) \quad (18)$$

#### 3.2 Model-free nonlinear restoring force representation based on Chebyshev polynomial

The Chebyshev polynomial is one of the most important function sets in mathematics. Any continuous function can be represented by a set of orthogonal function sequences on  $[-1, 1]$ , the expression is as shown in the literature[16].

Therefore, the restoring force of the nonlinear element between the two degrees of freedom of the structure can be expressed by a set of relative velocity and relative displacement between the stories,

$$\mathbf{R}_{i,i-1}^{non}(t) \approx \sum_{a=0}^A \sum_{b=0}^B c_{i,i-1,a,b}^{non} C_a(v'_{i,i-1}) C_b(s'_{i,i-1}) \quad (19)$$

where  $\mathbf{R}_{i,i-1}^{non}(t)$  denotes the NRF of the nonlinear member between the  $i$ -th and  $(i-1)$ -th degrees of freedom of the system, and  $c_{i,i-1,a,b}^{non}$  denotes the coefficient of the Chebyshev polynomial.  $C_a(v'_{i,i-1})$  and  $C_b(s'_{i,i-1})$  are Chebyshev polynomials.  $A$  and  $B$  are integers, and their values are related to the degree of nonlinearity of the structure. In this paper,



A+B=4.  $v'_{i,i-1}$  and  $s'_{i,i-1}$  denote the relative velocity and relative displacement between the  $i$ -th and  $i-1$ th degrees of the normalized system, respectively.

$$v'_{i,i-1} = \frac{v_{i,i-1} - \min(v_{i,i-1})}{\max(v_{i,i-1}) - \min(v_{i,i-1})} \quad (19)$$

$$s'_{i,i-1} = \frac{s_{i,i-1} - \min(s_{i,i-1})}{\max(s_{i,i-1}) - \min(s_{i,i-1})} \quad (20)$$

Among them,  $v_{i,i-1}$  and  $s_{i,i-1}$  are the relative velocity and relative displacement between the layers of the structure before normalization.

From Eqs. (17) and (18), the motion equation of the  $i$ -th DOF of the structure can be discretized as,

$$m_i \ddot{x}_i + \sum_{a=0}^A \sum_{b=0}^B c_{i,i-1,a,b}^{\text{non}} v_{i,i-1}^a s_{i,i-1}^b + \sum_{a=0}^A \sum_{b=0}^B c_{i,i-1,a,b}^{\text{non}} v_{i,i+1}^a s_{i,i+1}^b = f_i(t) \quad (21)$$

Therefore, the nonlinear member is introduced into the structure. After the complete structural parameters and dynamic response are obtained by the EKPF method, the Legendre polynomial coefficients are identified by the least square method, and the total nonlinear restoring force  $R_{\text{non}}(t)$  of the structure can be calculated. Finally, according to Eqs. (16) to (18), the damping force provided by the nonlinear member can be inversely derived.

## 4 NUMERICAL VERIFICATION

### 4.1 Example 1

To verify the effectiveness of the proposed method, numerical simulations are carried out to validate the four-degree-of-freedom shear-type frame with MR damper as an example. The nonlinear behavior of the structure is simulated by introducing the MR damper in the four-story concentrated mass shear-type frame shown in Figure 1. The mass of each layer of the structure  $m_i=150\text{kg}$ , the inter-story stiffness  $k_i=2.0 \times 10^5 \text{N/m}$ , and the damping coefficient  $c_i=160 \text{N} \cdot \text{s/m}$ , where  $i=1, 2, 3, 4$ . A horizontal external excitation  $f(t)$  with an action time of 2s is applied to the third story, and the time profile is shown in Figure 2. The structural response is obtained by the fourth-order Runge-Kutta method with a time step of 0.001s.

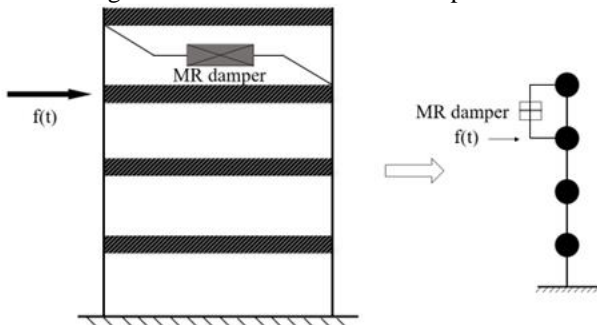


Figure 1. Nonlinear model equipped with MR dampers  
Define the structure state vector as,

$$X(t) = [x_1, x_2, x_3, x_4, \dot{x}_1, \dot{x}_2, \dot{x}_3, \dot{x}_4, k_{E1}, k_{E2}, k_{E3}, k_{E4}, c_{E1}, c_{E2}, c_{E3}, c_{E4}, m_{E1}, m_{E2}, m_{E3}, m_{E4}]^T \quad (22)$$

The MR damper introduced in the structure is a Bingham model with a damping force that satisfies the relation,

$$F_{\text{non}}^{\text{Bh}} = f_c^{\text{Bh}} \cdot \text{sgn}(v, v_{i,i-1}) + C_0^{\text{Bh}} \cdot v_{i,i-1} + f_0^{\text{Bh}} \quad (23)$$

where  $F_{\text{non}}^{\text{Bh}}$  is the damping force provided by the Bingham model,  $f_c^{\text{Bh}} = 20 \text{N}$ ,  $C_0^{\text{Bh}} = 600 \text{N} \cdot \text{s/m}$  and  $f_0^{\text{Bh}} = 0$  are model coefficients. The damping force calculated from Eq. (23) is accurately calculated by the mathematical relation equation and thus can be used as the theoretical damping force of the structure to evaluate the identified value.

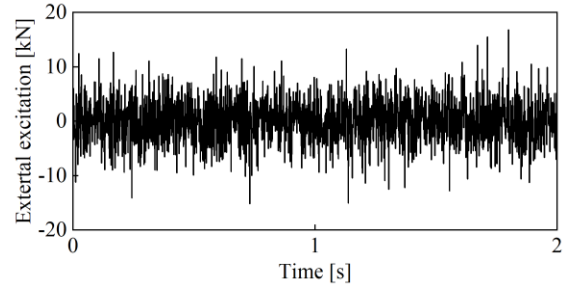


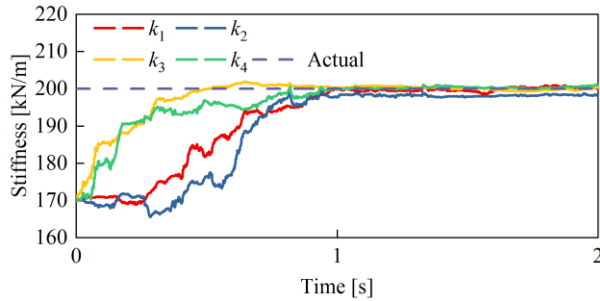
Figure 2. External excitation force time history

The setting range of the initial parameters of the structure is estimated based on the real parameters of the structure, and the number of particles is set to 20000, the initial value of the stiffness of each floor is  $130 \text{kN/m} \sim 210 \text{kN/m}$ , the initial value of the damping coefficient is  $0 \text{kN} \cdot \text{s} \cdot \text{m}^{-1} \sim 1000 \text{kN} \cdot \text{s} \cdot \text{m}^{-1}$ , and the initial value of the mass is  $100 \text{kg} \sim 160 \text{kg}$ . In fact, due to the use of EKF as the importance function for sampling, the identified range of particles after EKF update can exceed the setting range of initial parameters. Assuming that the acceleration of the second story of the structure cannot be measured, only the accelerations of the first, third and fourth stories of the structure are observed, and 5% non-Gaussian noise is added to the observations.

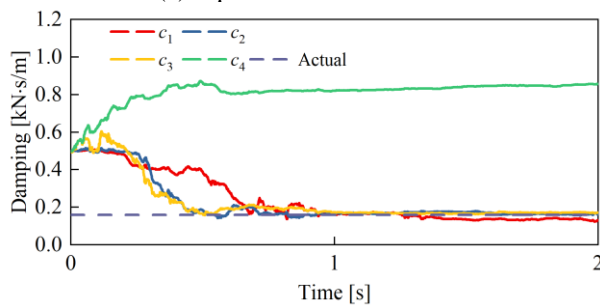
Taking the mean value of the last step in each iteration as the parameter identification result, the structural stiffness, damping, and mass are identified using EKPF, the convergence process of the equivalent linear parameter is shown in Figure 3. Figure 3(a) gives the convergence process of the identified equivalent stiffness of each story of the structure. It can be seen that from Figure 3(b) the equivalent damping identification value of the first to the third stories tends to the true value, but the identified value of the fourth story identifies with the other stories in the completely opposite direction, which can be judged that the structure has undergone a nonlinear behavior in the fourth story, which is also consistent with the actual installation of the damper. The convergence result of mass identification is shown in Figure 3(c), which can accurately converge to the actual value, which also shows that the nonlinear behavior of the structure does not affect the mass of the structure after it occurs. Table 1 and Table 2 give the identified results of the mass and the equivalent stiffness and equivalent damping, respectively. It can be seen from Table 1 that the identified result of the structural mass is better, and the error of each story is less than 1%. The equivalent linear parameters have also achieved good identification results.

Table1. Identified mass results

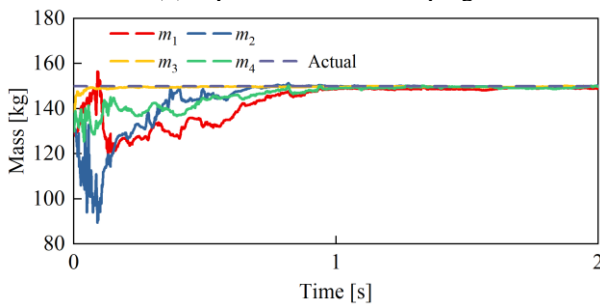
Mass	Identified [kg]	Actual [kg]	Error [%]
$m_1$	148.85	150	0.77
$m_2$	150.26		0.17
$m_3$	149.85		0.10
$m_4$	149.71		0.19



(a) Equivalent linear stiffness



(b) Equivalent linear damping



(c) Equivalent linear mass

Figure 3. Structural parameter convergence process

Table2. Identified equivalent stiffness and damping results

Parameter	Identified	Actual
$k_{E1}$ (kN/m)	200	200
$k_{E2}$ (kN/m)	198	200
$k_{E3}$ (kN/m)	200	200
$k_{E4}$ (kN/m)	201	200
$c_{E1}$ (kN·s·m <sup>-1</sup> )	0.13	0.16
$c_{E2}$ (kN·s·m <sup>-1</sup> )	0.16	0.16
$c_{E3}$ (kN·s·m <sup>-1</sup> )	0.17	0.16
$c_{E4}$ (kN·s·m <sup>-1</sup> )	<b>0.86</b>	0.16

Figures 4 and 5 show the comparison between the identified results and the actual values of the displacement and velocity response of each story of the structure, and Figure 6 shows the comparison between the identified values and the true values of the unobserved acceleration of the 2nd story of the structure. The identified results of displacement, velocity and acceleration of the second story are in good agreement with the true values.

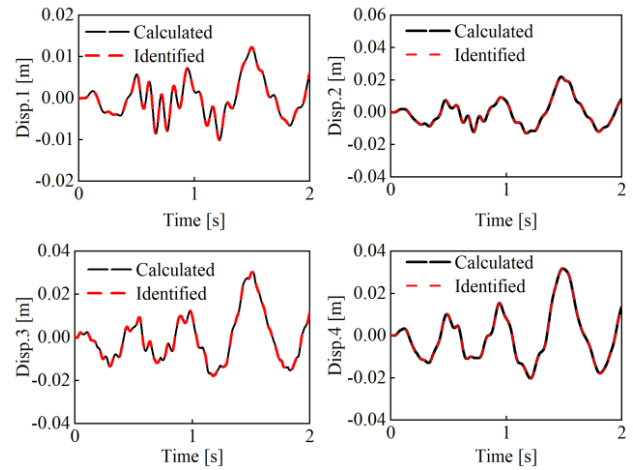


Figure 4. Identified structural displacement responses

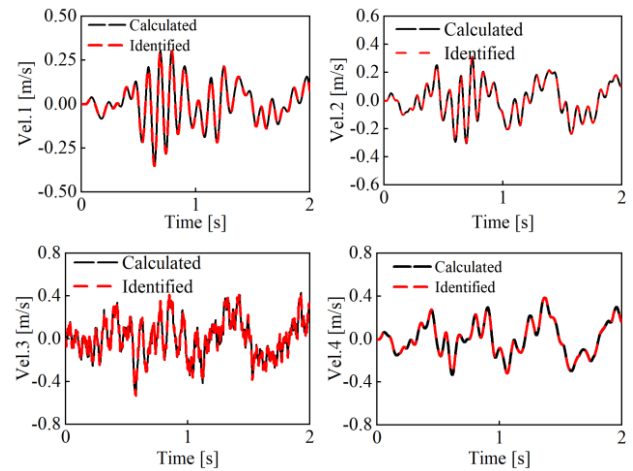


Figure 5. Identified structural velocity responses

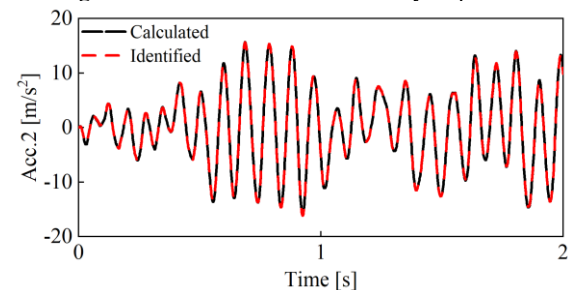


Figure 6. Identified structural acceleration responses on second floor

Based on the identified structural parameters, displacement and velocity responses, the NRF of the 4th floor of the structure can be further obtained using the least squares algorithm in a nonparametric manner, and the results of the comparison between the identified and the true values of the NRF of the 4th floor of are shown in Figure 7.

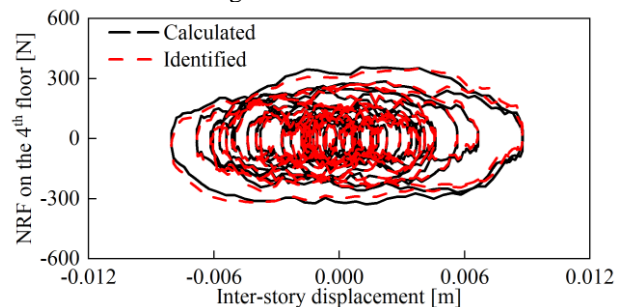


Figure 7. Identified MR damper force

The identified results of the unknown acceleration and NRF are quantified by the root mean square error (RMSE)[23], which are calculated to be 0.12m/s<sup>2</sup> and 12.59N for the acceleration of on the 2<sup>nd</sup> floor and NRF, respectively.

#### 4.2 Example 2

Considering the actual situation that the structure may have multiple damages under strong dynamic loading, in order to verify the generality of the proposed algorithm, MR dampers are introduced in the first and fourth stories of the structure, and horizontal external excitation is applied to the second floor, and the nonlinear structural model and the external excitation are shown in Figure 8 and Figure 9, respectively.

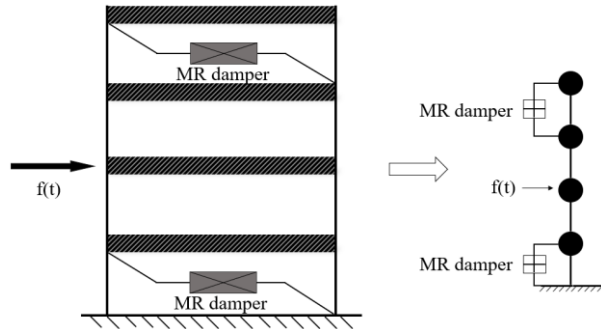


Figure 8. Four-story shear frame model with MR dampers

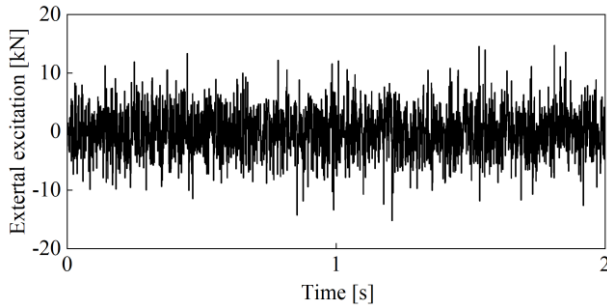


Figure 9. External excitation force time history

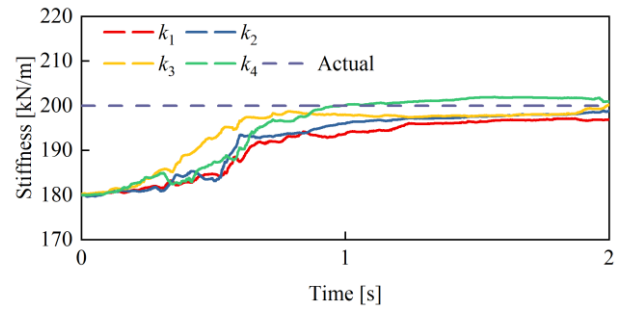
Distinguishing from the Bingham model in Example 1, the two MR dampers in this example use the modified Dahl model with the expression,

$$F_{non}^{Dh} = K_0^{Dh} s_{i,i-1} + C_0^{Dh} v_{i,i-1} + F_0^{Dh} Z + f_0^{Dh} \quad (24)$$

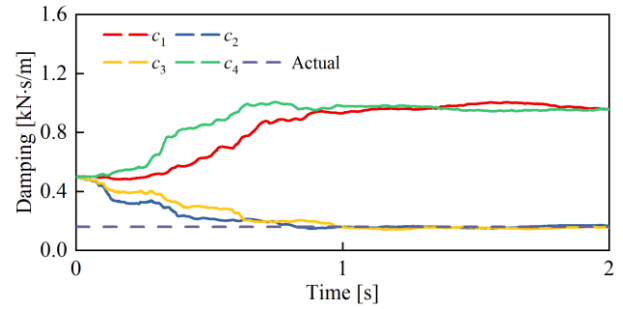
$$\dot{Z} = \sigma v_{i,i-1} (1 - Z \operatorname{sgn}(v_{i,i-1})) \quad (25)$$

where  $F_{non}^{Dh}$  is the damping force provided by the Dahl model,  $K_0^{Dh} = 30 \text{ N/m}$ ,  $C_0^{Dh} = 600 \text{ N}\cdot\text{s/m}$ ,  $F_0^{Dh} = 35 \text{ N}$ ,  $\sigma = 500 \text{ s/m}$  and  $f_0^{Dh} = 0$ ,  $f_0^{Dh} = 0$ ,  $C_0^{Dh}$ ,  $F_0^{Dh}$  and  $\sigma$  are model coefficients, and  $Z$  is the dimensionless hysteresis.

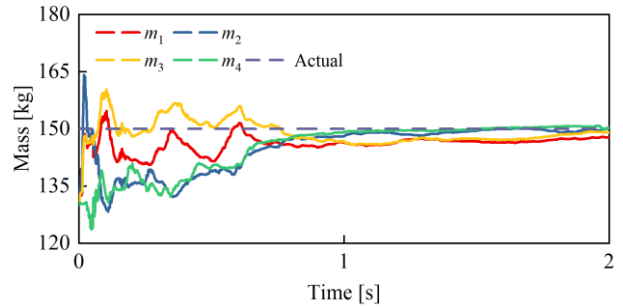
The settings of the initial parameters and the structural true values in Example 2 are the same as those in Example 1, and the identified process of the equivalent linear stiffness, damping and mass is given below. From Figure 10 the structural stiffness, damping, and mass parameters of the other floors converge to the actual value of the structure, except for the equivalent damping values of the first and fourth floors in Figure 10(b), which deviate from the actual value, and according to which it can be shown that the structure undergoes nonlinear behavior in the first and fourth floors. The identified results of the mass, the equivalent linear stiffness and damping are shown in Tables 3 and 4, respectively. The identified results of the parameters have small errors.



(a) Equivalent linear stiffness



(b) Equivalent linear damping



(c) Equivalent linear mass

Figure 10. Structural parameter convergence process

Table 3. Identified mass results

Mass	Identified [kg]	Actual [kg]	Error [%]
$m_1$	147.70	150	1.53
$m_2$	150.48		0.32
$m_3$	149.01		0.66
$m_4$	150.13		0.09

Table 4. Identified equivalent stiffness and damping results

Parameter	Identified	Actual
$k_{E1}$ (kN/m)	197	200
$k_{E2}$ (kN/m)	199	200
$k_{E3}$ (kN/m)	200	200
$k_{E4}$ (kN/m)	201	200
$c_{E1}$ (kN·s·m <sup>-1</sup> )	<b>0.96</b>	0.16
$c_{E2}$ (kN·s·m <sup>-1</sup> )	0.16	0.16
$c_{E3}$ (kN·s·m <sup>-1</sup> )	0.15	0.16
$c_{E4}$ (kN·s·m <sup>-1</sup> )	<b>0.95</b>	0.16

Figures 11 and 12 show the comparison of the identified results of displacement and velocity response of the nonlinear structure respectively, it can be found that the dynamic response of the structure in all floors are identified with good results.



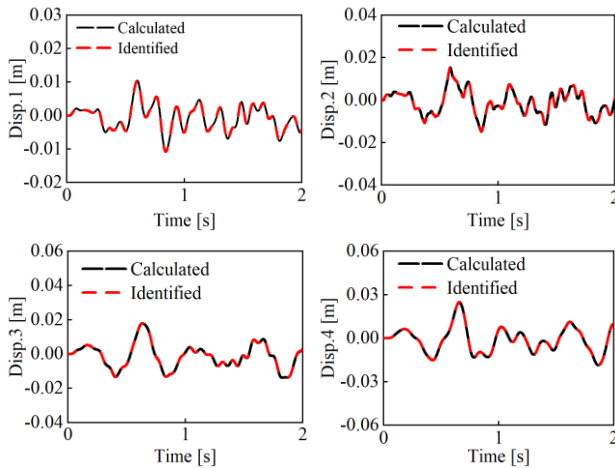


Figure 11. Identified structural displacement responses

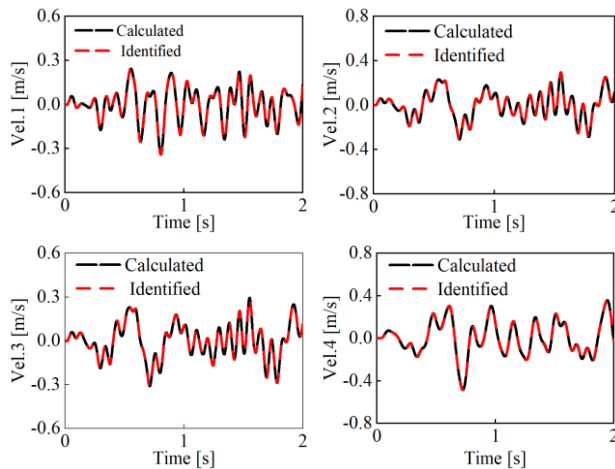
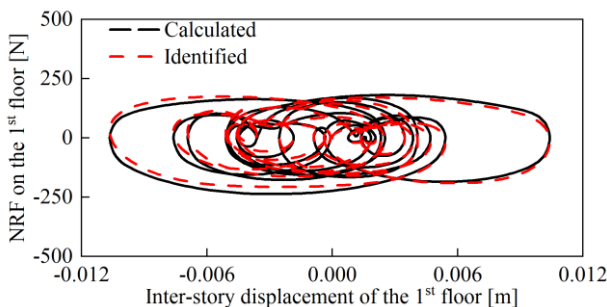
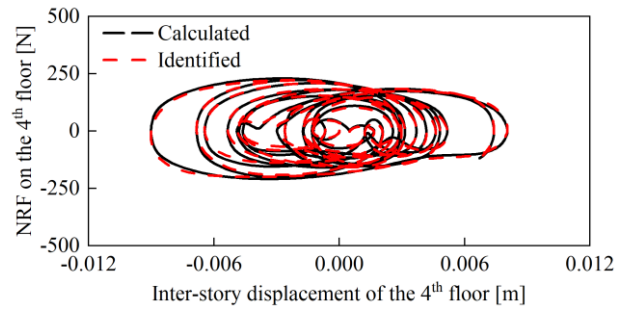


Figure 12. Identified structural velocity responses

The same as in Example 1, based on the parameters and responses identified by the structure, the NRFs between the first and fourth floors can be identified, as shown in Figure 13. The RMSE of the identified acceleration value of the second floor is  $0.30\text{m/s}^2$ , the RMSE of the identified value of NRF of the first floor is  $14.43\text{ N}$ , the RMSE of the identified value of NRF of the fourth floor is  $11.46\text{ N}$ . It can be seen in Figure 13 that the identified values of the first and the fourth floors of the damping force are in good agreement with the real values, which indicates that the proposed algorithm is not only able to effectively identify the nonlinear behavior of the structure at a single unknown location under strong dynamic loading, but also applies to the case of a nonlinear system where multiple nonlinear locations are unknown.



(a) Identified result of MR damping force on the 1st floor


(b) Identified result of MR damping force on the 4th floor  
Figure. 13 Identified MR damper force

## 5 CONCLUSIONS

In this paper, based on the EKPF algorithm and equivalent linear theory, the structural parameters and nonlinear locations are identified under limited acceleration observations, and a model-free identification of structural NRF is proposed based on Chebyshev polynomial.

Numerical simulations of a four-degree-of-freedom concentrated mass nonlinear shear frame model were performed. In two examples, different numbers and models of MR dampers (Bingham model vs. Dahl model) are sequentially introduced to the structure to simulate different nonlinear behaviors for different numbers and locations. Considering the effect of measurement noise and changing the location of horizontal external excitation application, the structural stiffness, damping, mass parameters, and the inter-story NRF at the arrangement of MR dampers are identified with limited observations of the acceleration response, and the validity and applicability of the proposed methodology are verified by comparing the identified values with the theoretical values.

The method proposed in this paper is general in that it does not need to utilize a parametric model of the NRF of the structure in the identified process. The identified NRF under strong dynamic loads such as earthquakes is an intuitive description of the hysteretic performance of the structure, and through the restoring force characteristics at different moments, it can reflect the occurrence and development of the damage of the structure or sub-structure at different moments in the process of dynamic loading, and can be used for the quantitative description of the energy dissipation of the structural components in the process of the loading. The method proposed in this paper is of great significance for damage localization, quantitative assessment and post-disaster structural performance evaluation of structures subjected to dynamic loads such as earthquakes.

## ACKNOWLEDGMENTS

The authors gratefully acknowledge the supports from National Natural Science Foundation of China (No. 52378301), and the Open Project Program of Key Laboratory for Intelligent Infrastructure and Monitoring of Fujian Province (No. IIM-02-01).

## REFERENCES

- [1] L. Liu, Y. Su, J. Zhu, et al. Data fusion based EKF-UI for real-time simultaneous identification of structural systems and unknown external inputs. *Measurement*, 88: 456-467, 2016.

- [2] D. Li, Y. Wang. Parameter identification of a differentiable Bouc-Wen model using constrained extended Kalman filter. *Structural Health Monitoring*, 20(1): 360-378, 2021.
- [3] J. He, XX. Zhang, N. Dai. An improved Kalman filter for joint estimation of structural states and unknown loadings. *Smart Structures and Systems*, 24(2): 209-221, 2019.
- [4] Y. Yang, T. Nagayam, K. Xue, et al. Displacement estimation of a nonlinear SDOF system under seismic excitation using an adaptive Kalman filter. *Journal of Risk and Uncertainty in Engineering Systems, Part A: Civil Engineering*, 8(1): 04021084, 2022.
- [5] J. He, MC. Qi, XG. Hua, et al. Substructural identification with weighted global iteration considering unknown interfacial forces and external excitation. *Measurement*, 180: 109537, 2021.
- [6] XX. Zhang, J. He, X. Hua, et al. Online identification of time-variant structural parameters under unknown inputs basing on extended Kalman filter. *Nonlinear Dynamics*, 109(2): 963-974, 2022.
- [7] T. Yu, Z. Wang, J. Wang. An iterative augmented unscented Kalman filter for simultaneous state-parameter-input estimation for systems with/without direct feedthrough. *Mechanical Systems and Signal Processing*, 205: 110793, 2023.
- [8] S. Wang, Y. Lei. An unscented Kalman filter under unknown input without direct feedthrough for joint input and system identification of structural systems. *Mechanical Systems and Signal Processing*, 208: 110951, 2024.
- [9] ZQ. Yuan, ZC. Wang, Y. Xin, et al. Synchronous identification of nonlinear structural parameters and unknown external excitation based on improved UKF. *Engineering Structures*, 298: 117094, 2024.
- [10] Z. Wan, T. Wang, S. Li, et al. A modified particle filter for parameter identification with unknown inputs. *Structural Control and Health Monitoring*, 25(12): e2268, 2018.
- [11] Y. Lei, J. Lai, J. Huang, et al. A generalized extended Kalman particle filter with unknown input for nonlinear system-input identification under non-Gaussian measurement noises. *Structural Control and Health Monitoring*, 29(12): e3139, 2022.
- [12] SF. Masri, TK. Caughey. A nonparametric identification technique for nonlinear dynamic problems. *Journal of Applied Mechanics*, 46: 433-447, 1979.
- [13] SF. Masri, H. Sassi, TK. Caughey. Nonparametric Identification of Nearly Arbitrary Nonlinear Systems. *Journal of Applied Mechanics*, 49: 619-628, 1982.
- [14] B. Xu, J. He, SF. Masri. Data-based Identification of nonlinear restoring force under spatially incomplete excitations with power series polynomial model. *Nonlinear Dynamics*, 67(3): 2063-2080, 2012.
- [15] B. Xu, J. He, SF. Masri. Data-based model-free hysteretic restoring force and mass identification for dynamic systems. *Computer-Aided Civil and Infrastructure Engineering*, 30(1): 2-18, 2015.
- [16] B. Xu, B. Deng, J. Li, et al. Structural nonlinearity and mass identification with a nonparametric model using limited acceleration measurements. *Advances in Structural Engineering*, 22(4): 1018-1031, 2019.
- [17] B. Xu, Y. Zhao, B. Deng, et al. Nonparametric nonlinear restoring force and excitation identification with Legendre polynomial model and data fusion. *Structural Health Monitoring*, 21(2): 264-281, 2022.
- [18] Y. Zhao, B. Xu, B. Deng, et al. Various damper forces and dynamic excitation nonparametric identification with a double Chebyshev polynomial using limited fused measurements. *Measurement*, 193: 110940, 2022.
- [19] Y. Zhao, B. Xu, B. Deng, et al. Generality of nonparametric nonlinearity identification approach with improved extended Kalman filter using different polynomial models. *Measurement*, 227: 114235, 2024.
- [20] J. He, X. Zhang, M. Qi, et al. Model-free identification of nonlinear restoring force with modified observation equation. *Applied Sciences*, 9(2): 306, 2019.
- [21] X. Yang, H. Su, L. Liu, et al. Identification of the nonlinear characteristics of rubber bearings in model-free base-isolated buildings using partial measurements of seismic responses. *Journal of Low Frequency Noise, Vibration and Active Control*, 39(3): 690-703, 2020.
- [22] Y. Lei, X. Yang, J. Mi, et al. Integration of locating baseline-free nonlinear elements and identifying model-free nonlinear restoring forces in structures. *Nonlinear Dynamics*, 111(14): 12855-12869, 2023.
- [23] YB. Du, B. Xu, Y. Zhao, et al. Nonparametric identification of structural nonlinear restoring force based on an updated cubature Kalman filter. *Journal of Vibration Engineering*, 36(2): 389-399, 2023. (in Chinese)



# Session 11

## Fibre Optic Sensing in Field Applications



# Insights into Rail Track Buckling from Distributed Fibre Optic Sensing Data

Neil A Hoult<sup>1, 0000-0002-2819-7410</sup>, Fuzheng Sun<sup>1</sup>, Liam J Butler<sup>2, 10000-0002-2777-5952</sup>, Merrina Zhang<sup>3</sup>

<sup>1</sup> Dept of Civil Engineering, Queen's University, 58 University Ave., Kingston, ON K7L 3N6, Canada

<sup>2</sup> Dept of Civil Engineering, York University, 4700 Keele St., Toronto, ON M3J 1P3, Canada

<sup>3</sup> National Research Council of Canada, Ottawa, ON, Canada

email: neil.hoult@queensu.ca, fuzheng.sun@queensu.ca, Liam.Butler@lassonde.yorku.ca, Merrina.Zhang@nrc-cnrc.gc.ca

**ABSTRACT:** As climate change leads to increasing temperatures around the globe, rail track buckling has become an increasing concern for rail operators. This paper provides an overview of the key outcomes from a four-year research program that sought to explore the use of distributed fibre optic sensors (DFOS), analytical modeling, and artificial intelligence techniques to aid in track buckling assessment and detection. Lab tests and field monitoring data were used to develop and evaluate two DFOS systems, one for short length dynamic buckling assessment due to train passage and the other for long length thermal buckling assessment. The data from each system was used to develop models for the detection of buckling using different techniques depending on the quality of the initial data and the required output. Finite element model (FEM) updating and statistical FEMs were explored to predict buckling response based on measurements at service loads. Beam on elastic spring models were used to estimate the influence of train passage on buckling capacity while Gaussian process regression (GPR) techniques provided insights into buckling indicators at the field sites.

**KEY WORDS:** Distributed fibre optic sensing; Rail track buckling; Lab tests; Field monitoring; Data-based modelling.

## 1 INTRODUCTION

Continuous welded rail (CWR) is used in most modern rail networks because of the enhanced ride quality it provides as well as reducing noise and wear on the rails. However, the removal of joints along the rail means that there is no room for the rail to expand when its temperature changes relative to the rail neutral temperature (RNT) resulting in the development of a state of self-stress within the rail. If the temperature increases to a critical value, the lateral load resistance system of the rail track, consisting of ballast, ties, and fasteners, can no longer provide adequate support and the rail track buckles laterally [1,2]. The critical temperature can change over the operational life of the rail network as deterioration lowers this buckling temperature and proper maintenance increases it [1,3].

Analytical models exist to account for buckling during the design stage [1,4] however there are a number of challenges with using these models for the assessment of in-service buckling such as variations in geometry and support conditions that are present in existing rail tracks. Numerical simulations can provide more accurate estimates of track behaviour since they can account for variations in geometry and support conditions with length [2,5]. But obtaining the measurements required to develop accurate models in the field is time consuming and expensive.

Structural health monitoring techniques represent a potentially useful approach for either detecting rail track issues directly or acquiring the data required to develop more accurate models. Researchers have previously explored the use of a variety of sensors to detect rail track issues such as strain gauges [6], accelerometers [7], ultrasonic and laser vibrometers [8,9], and digital image correlation [10]. The challenge with many of these techniques is that they only provide a local measurement of rail behaviour whereas buckling can occur anywhere along the length of the rail.

A potential solution to this challenge is the use of distributed fibre optic sensors (DFOS). For strain sensing, research has focused on the use of Rayleigh based systems when high-resolution (gauges lengths less than 1 mm are possible) and high-accuracy measurements (up to  $\pm 1$  microstrain at the fiber core for Rayleigh based systems) are required [11]. And Brillouin based systems when lower resolution (gauge lengths of 50 mm) and lower accuracy ( $\pm 15$  microstrain) [12] is an acceptable trade-off to achieve longer sensing lengths (100 m per channel for Rayleigh-based systems [11] versus up to 25 km and more for Brillouin-based systems [12]). Most of the current research using DFOS for rail applications has focused on the response of the rail due to vehicle loading [13,14]. Initial studies have been conducted on short lengths of rail to measure thermal strain due to free expansion using Brillouin Optical Time Domain Analysis (BOTDA) [15,16] as well as to measure strains due to thermal stress in the lab and the field [16].

The goal of the research campaign described in this paper was to evaluate the viability of using DFOS for the assessment of rail track buckling. The objective of this paper is to provide an overview of the entire research campaign starting with lab-based thermal buckling experiments that were used to update finite element models (FEM) as well as to explore the use of statistical FEM (StatFEM) with distributed sensing data for the first time. Three field tests were also undertaken on a tangent track and a curved track section in Ontario, Canada to acquire first of their kind data sets and to explore the use of DFOS data to inform improved models of rail track buckling.

## 2 LAB TESTING

### 2.1 Introduction

Before undertaking field tests, the first phase of this research involved a series of small-scale lab-based experiments to

explore the use of both Optical Frequency Domain Reflectometry (OFDR), and BOTDA measurements for assessing rail track buckling. The rails were subjected to both mechanical and thermal loading to induce buckling in the rail.

## 2.2 Specimens

An ASCE 5.95 kg/m (12 lbs/yd) mining rail specimen with the length of 3,048 mm (Hammer Steel Products, Canada) was used, as buckling of the member could be induced within the available lab constraints. The specimen had a specified elastic modulus ( $E$ ) of 207 GPa, cross-sectional area ( $A$ ) of 761 mm<sup>2</sup>, and coefficient of thermal expansion ( $\alpha$ ) of  $11.6 \times 10^{-6} / ^\circ\text{C}$ . The second moment of area was 53,000 mm<sup>4</sup> about the weak axis ( $I_y$ ) and 229,000 mm<sup>4</sup> about the strong axis ( $I_x$ ). The specimen was instrumented with eight nylon-coated single mode strain measurement optical fibres (F1 – F8) to measure the surface strain and a temperature measurement fibre to measure the distributed temperature as illustrated in Fig. 1. Further details about the specimens are provided in [17,18].

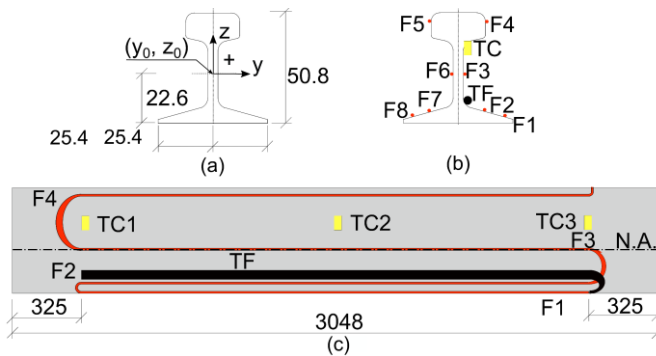


Figure 1. Lab buckling test specimen (in mm). (a) rail cross-section dimensions, (b) fibre locations on cross-section, (c) longitudinal dimensions and fibre layout.

## 2.3 Test setup

As shown in Figure 2, the testing frame consisted of two steel plates that were connected to four threaded rods using nuts. Two types of tests were conducted: (1) buckling due to applied load from an actuator with three different lateral support conditions and (2) thermal buckling caused by restraining axial elongation due to changes in temperature.

Figure 2(a) shows the schematic frame setup for the applied load buckling with no lateral restraint (NS) and thermal buckling tests. In the applied load tests with lateral restraint, the lateral restraint was provided by springs with a stiffness of 32.7 N/mm, and a maximum compressible length of 30.2 mm. Figure 2(b) illustrates the test setup for the applied load tests with one spring placed at the mid-length test, and Figure 2(c) shows the applied tests with two springs placed at 1/3 and 2/3 of the rail length, respectively, where weak-axis buckling occurs in the vertical direction.

For the thermal buckling tests, the rail temperature was adjusted by changing the temperature within a climate chamber where the specimen was placed. The steel frame experienced similar thermal expansion/contraction as the rail due to a temperature increase/decrease ( $\Delta T$ ), so to keep the length of the rail constant (e.g. full axial restraint), an axial load was applied to the rail to ensure the net axial displacement of the rail was 0 mm. For all tests, the axial load was applied by a hydraulic jack

with a capacity of 1010 kN and measured using a load cell with a 222 kN capacity. The actuator, supports, and the specimen could not be aligned perfectly, and axial loads with different eccentricities occurred in all tests. A linear potentiometer (LP) was placed at the mid-length of the rail to measure the lateral deflection during the test. The strain was measured using a LUNA ODISI 6104 analyzer (LUNA Innovation, USA) for the OFDR tests and an NBX-6050A Brillouin Optical Time Domain Analysis (BOTDA) analyzer (Neubrex, Japan) for the BOTDA tests.

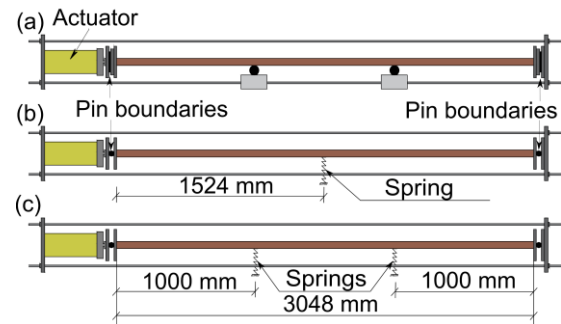


Figure 2. Lab buckling test setup. (a) no lateral restraint, (b) one spring, (c) two springs.

## 2.4 Results

The lab experiments were used to evaluate the potential for using DFOS measurements to assess buckling. Because 8 fibres were placed around the rail cross-section (see Figure 1), it was possible to define a fitted strain plane using the measurements at each point along the length of the rail as seen in Figure 3.

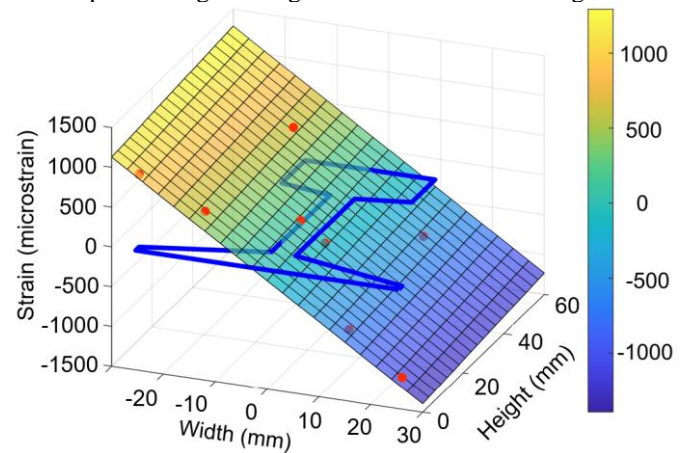


Figure 3. Strain measurements from 8 fibres on the rail forming a strain plane enabling calculation of axial strain and strong and weak axis curvature.

The strain plane seen in Figure 3 can be used to calculate the axial strain and weak and strong axis curvatures in the rail. The curvatures can then be numerically integrated twice to obtain a lateral deflection profile along the rail. One of the key conclusions from this part of the research was that both OFDR and BOTDA sensor systems could be used to measure the response of the rail using the strain plane approach although OFDR provided more accurate measurements, especially of the lateral restraint force provided by the springs [18]. While measurements of axial strain and displacement can be used as

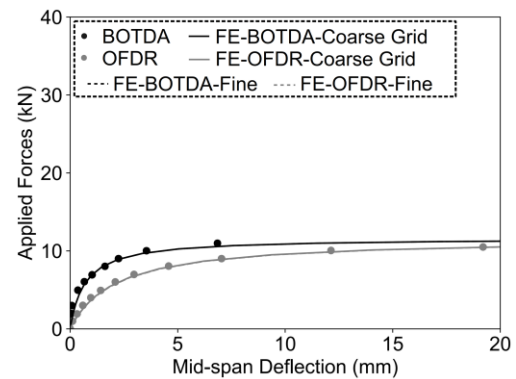
thresholds for assessing the impact of buckling, to provide predictions of future behaviour, a numerical model based on the experimental data is required as discussed in the next sections. Further details about the lab-based experimental campaigns can be found in [17,18].

### 2.5 Finite element model updating

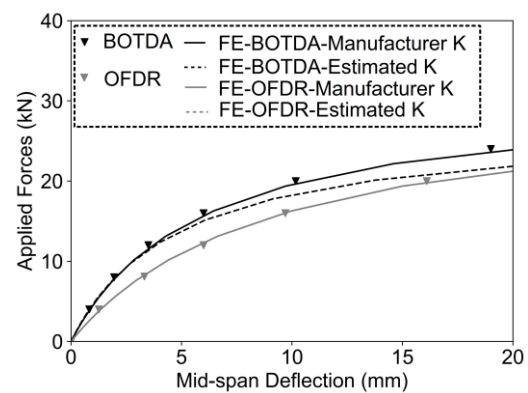
One challenge with using monitoring data to estimate the ultimate limit state behaviours of a structure is that the data is usually recorded at service loads. In this investigation DFOS data captured at service loads (i.e., applied loads and temperatures that were 50% of ultimate) were used to update finite element models to estimate the buckling capacity. A commercially available finite element analysis (FEA) program (i.e., Abaqus) was used to model the tests. The 3.048 m long slender member was modelled with 30 three-noded beam elements (B32), with the same cross-sectional and material properties as the rail. Connector elements with one degree of freedom perpendicular to the member were used to model the spring supports and were given one of two stiffnesses: (i) the manufacturer specified value (i.e., 32.7 N/mm) or (ii) the stiffness calculated from the DFOS measurement derived reaction force divided by the DFOS measurement derived displacement at the support location for each test [18]. Three steps of analyses were undertaken: 1. a linear buckling analysis to obtain the initial deflected shape, 2. a static general analysis considering geometric nonlinearity to determine the value of the mid-span imperfection and the end eccentricities through model updating and, 3. a static risk analysis to develop the buckling load-displacement response. Two approaches were taken to step 2: (a) a coarse grid and (b) a fine grid analysis. In the coarse grid analysis, the initial eccentricity parameters (at the supports and at midspan) were varied over a range of  $\pm 2.0$  mm with an increment of 0.5 mm and the optimum analysis was chosen based on the computed root mean square error (RMSE) between the modelled curvature values and the measured curvature values. In the fine grid analysis, each of the optimal eccentricity values from the coarse grid analysis were varied over a range of  $\pm 0.5$  mm with an increment 0.1 mm resulting in 1331 analyses.

Figure 4 presents the load-deflection responses from the finite element model updating investigation for (a) the NS tests and (b) the OS tests. Also plotted in the figure are the measured load and displacement at each load stage. Figure 4(a) shows the results from the tests using both the OFDR and BOTDA sensing systems. The difference in behaviour between the OFDR and BOTDA tests is not a function of the measurement systems but is due to the different axial load eccentricities present in each test. The results from the fine and coarse grid approaches plot on top of each other suggesting either approach to estimating the impact of eccentricities on the tests results is acceptable. Overall, the finite element model updated using the service load data was able to capture the ultimate behaviour of the rail accurately. In Figure 4(b) it can be seen that using the manufacturer or estimated spring stiffness provides the same result for the OFDR system. This is because the higher spatial resolution and accuracy of this system compared to the BOTDA allows for localized behaviour, such as lateral supports, to be resolved more accurately. Using the manufacturer's spring stiffness along with the BOTDA data at service loads enables the updated FEM to capture the full

behaviour. Though the estimated spring stiffness model is not as accurate, it is still conservative.



(a) No lateral restraint tests comparing BOTDA and OFDR data to FE models using Coarse and Fine Grid approach



(b) One spring restraint tests comparing BOTDA and OFDR data to FE models using both the Manufacturer and Estimated spring stiffness, K, from the data

Figure 4. FE model updating results compared to measured response from applied load tests.

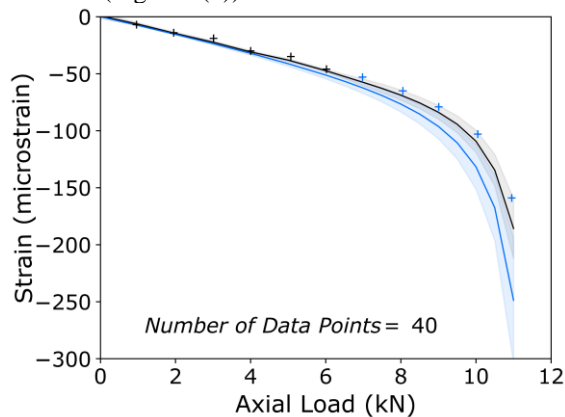
### 2.6 Statistical FEM model

The previous section highlighted that DFOS data could be used to support FEM updating but one limitation of the approach is that depending on the number of structural parameters to be optimized and the complexity of the model, model updating can have a high computational cost associated with finding the structural parameters that provide the optimum fit to the data. A second limitation is that traditional model updating assumes the model perfectly represents the true structural response whereas in reality the model always involves assumptions and idealization of the actual system (e.g., materials, boundary conditions, loading, etc.). To address these two limitations, a second FEM updating investigation was undertaken, exploring the use of the Statistical FEM (StatFEM) with distributed sensor data for the first time [19]. The basis of the StatFEM approach is that the measured structure response is composed of the true structure response and errors due to sensor measurement noise that have a known statistical distribution. The true structural response is assumed to be a combination of the FEM structural response and the model-reality mismatch due to model idealization and assumptions. The same approach was taken whereby data acquired at service

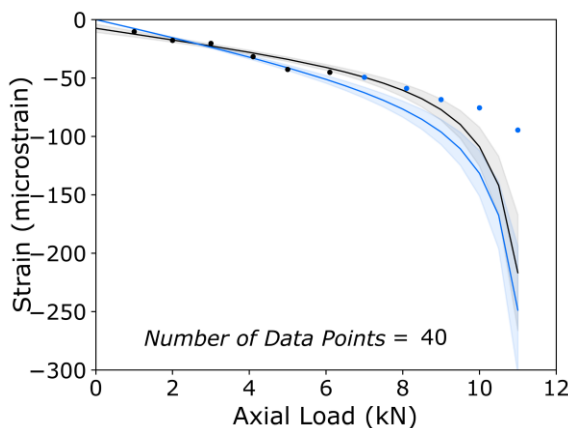


loads was used to update the model that was then used to predict ultimate capacity. In this investigation, polynomial chaos expansion (PCE) was investigated as an approach to generate the FE probability distribution prior to updating as opposed to the more traditional Monte Carlo simulation. This resulted in order of magnitude improvements in computation time from 16 hours and 40 minutes to 9 minutes with a less than 1% reduction in accuracy.

Figure 5 shows the strain versus load relationship for an (a) OFDR tests and (b) a BOTDA test for when 40 data points along the rail length (i.e.  $n_y = 40$ ) were used. It can be seen that the initial FE probability distribution overestimated the strain at a given load in the nonlinear range but that the StatFEM prediction of the ultimate limit state response incorporating the DFOS data collected in the service load range shows an excellent visual agreement with the measured ultimate limit state structural response. The model updated using the OFDR measurements (Figure 5(a)) demonstrates an excellent fit to the data over the entire measurement range and the error range (the grey shaded area) is smaller than the model updated using BOTDA data (Figure 5(b)).



(a) OFDR measurements



(b) BOTDA measurements

Figure 5. Strain versus load relationship where the blue line and shaded area represents the FE prediction, the black line and shaded area represent the StatFEM prediction, and the discrete points are measured strain.

The number of data points used to update the model was also found to play an important role in terms of prediction accuracy and the size of the error envelope. This shows the benefit of

using DFOS for FEM updating as the number of points enable much higher prediction accuracy. Further details on the use of DFOS with the StatFEM can be found in [19].

### 3 FIELD MONITORING

#### 3.1 Introduction

Having demonstrated the potential to use DFOS for monitoring of thermal buckling and development of robust numerical models using controlled lab-based experiments, the next phase of the research involved three separate field investigations to evaluate the use of DFOS to monitor rail track buckling in the field: (i) short term dynamic monitoring, (ii) long-term thermal monitoring and assessment of tangent track, and (iii) long-term thermal monitoring and assessment of curved track.

#### 3.2 Site installations

The site installations were similar in that three nylon-coated strain measurement fibres with a diameter of 0.9 mm were installed at the various heights in the cross section as illustrated in Figure 7 so that the strain plane in Figure 3 could be measured. The two long-term monitoring installations were similar with the major difference being one was on a tangent track and the other was on a curved track. In both cases, a 20 m long 8 mm diameter temperature fibre and 4 thermocouples were also installed on the rail as shown in Figure 7 to capture thermal effects. The long-term fibre optic data was acquired using an NBX-6050A Brillouin Optical Time Domain Analysis (BOTDA) analyzer with readings being taken every 30 minutes over the course of one month [20]. For the short-term dynamic monitoring, the installed fibre length was 9 m (as opposed to the 20 m shown in Figure 7) so that the data could be acquired at a rate of 13 Hz using a LUNA ODISI 6104 analyzer [21].

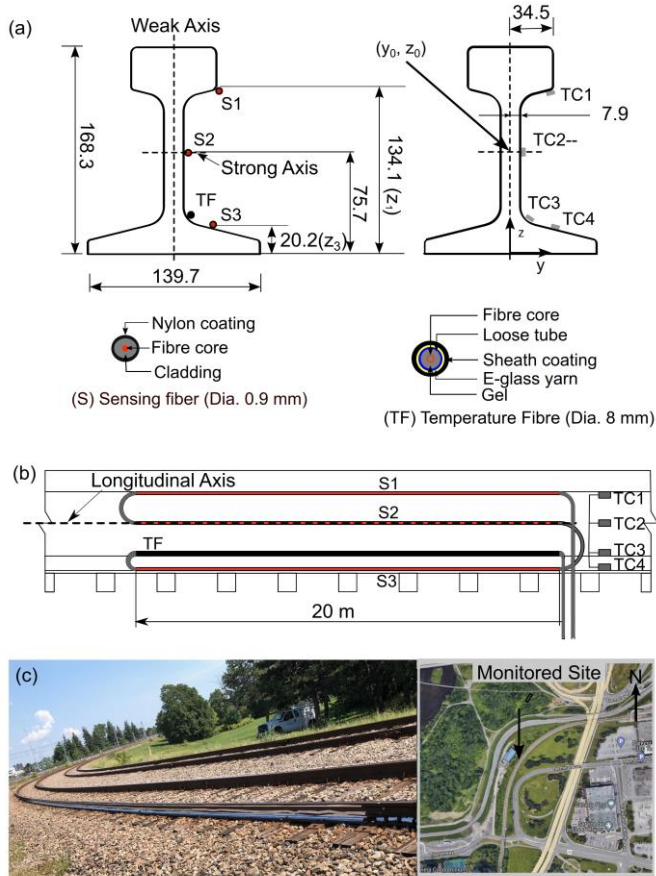


Figure 7. Field monitoring installation on curved track. Strain (S) and temperature fibre (TF), and thermocouple (TC) locations on (a) cross-section (in mm) and (b) rail length, and (c) site layout and location.

### 3.3 Impact of temperature and train passage

One of the key findings from the installation on the tangent track was that solar gain had an impact on rail strain measurements. Figure 8 shows the difference in temperature measurements from the thermocouples at various points on the rail cross-section relative to the location of the temperature fibre (TC3). It can be seen that at night (between midnight and 8 am in Figure 8) the difference in temperature measurements is less than 1°C and is within the noise of the thermocouple measurements. During the day this difference can be as high as approximately 2°C and depends on the position of the sun relative to the rail as well as the amount of cloud cover. The impact of this temperature difference is three-fold. First, it challenges the conventional assumption of constant temperature in the rail cross-section often used in buckling assessment. Second, the strain measurements from the fibres must be compensated for temperature with the correction factor being approximately 20 microstrain/°C for the BOTDA system [16]. Third, this differential temperature can cause rail bending if the rail is not adequately restrained, which could increase the likelihood of rail track buckling.

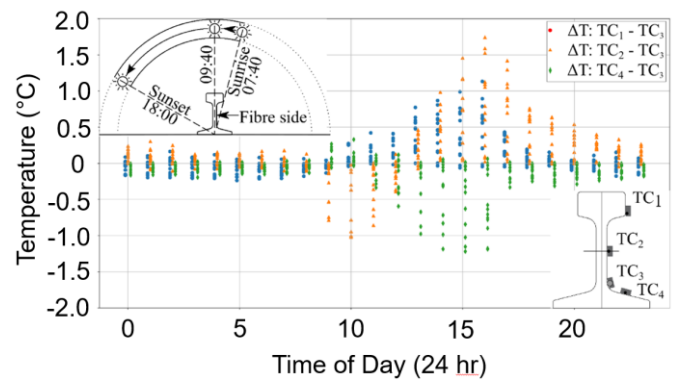


Figure 8. Difference in rail temperature at 4 different locations on the rail cross-section with time of day.

A second issue that affects the accuracy of long-term monitoring data is the passage of trains. Figure 9 shows three sets of consecutive measurements taken at the curved track site taken before any trains passed, after the position of Train 1, and after the passage of Train 2 at a constant temperature.

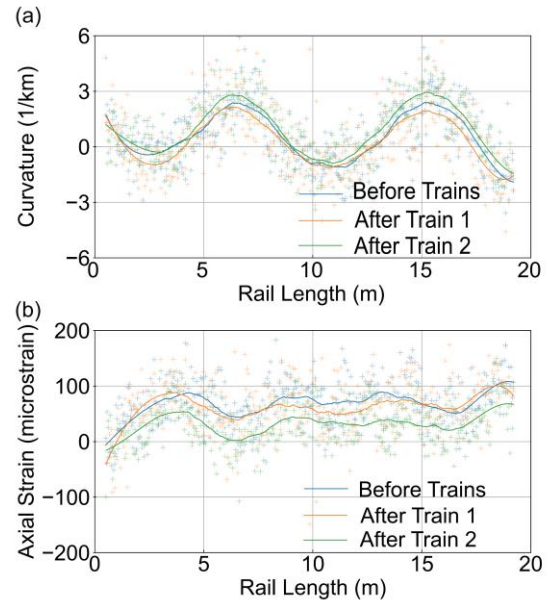


Figure 9. Effect of train passage on DFOS measurements at the curved rail site. (a) Curvature and (b) Axial Strain

One can see from Figure 9 that both the curvature and the axial strain are impacted by the passage of a train. While this might not be the case for a track that was properly restrained against lateral and longitudinal movement, previous research has demonstrated that rail tracks supported by wooden ties and gravel ballast can experience longitudinal movement and thus changes in axial strain due to the passage of trains [22]. Thus, when monitoring and assessing rail tracks for buckling using DFOS, temperature effects due to solar gain and the passage of trains are important issues that must be carefully addressed. In the case of thermal effects, a potentially straightforward solution is to use combined strain and thermal measurement fibres at all three measurement heights along the rail.

### 3.4 Dynamic thermal buckling models

Dynamic buckling occurs when the train wheel loads acting on the rail track cause a section of the track to lift off the ties and

become laterally unsupported. If that section of rail track is already prone to buckling due to being on a curve, having a small amount of misalignment along its length, or both then railway buckling can occur at lower temperatures than static thermal buckling.

DFOS measurements were taken with the OFDR analyser along a section of curved track as a passenger train travelled over the instrumented section. Because strains were measured at multiple heights on the rail, the curvature profile along the instrumented section could be derived. A beam on elastic foundation (BOEF) model, where the rail is modelled as a beam with the same flexural stiffness (EI) as the rail and the foundation is modelled as a series of elastic springs, was then created. The curvature pattern was then used to update the BOEF model to estimate the track modulus by adjusting the spring stiffness until the measured rail curvature matched the model beam curvature, which resulted in a track modulus of 13.6 MPa in this case.

To predict the dynamic buckling temperature, a finite element model was constructed in ABAQUS using two-noded beam elements. Two types of connector elements were used in the FE model to simulate the interaction between the rail track and the rail ties as well as between the ties and the ballast, respectively. The track modulus that affects the rail lifting-off behavior under train loading was derived from the DFOS measurements as noted above and the rest of the structural parameters that affect static thermal buckling behavior were obtained from the literature [21]. The FE modelling was conducted in two stages. First, a static nonlinear analysis was conducted to get the railway lift-off response under train loading. Afterwards, the impact of railway lift-off response on the lateral resistance provided by the ballast to the railway system was inputted into the railway FE model to simulate the railway dynamic buckling. A misalignment in the rail of either 20 mm or 34 mm was modelled and then an increasing temperature was applied to the model to determine the temperature increase above the rail neutral temperature versus lateral displacement response as seen in Figure 10. Further details of the model can be found in [21].

From Figure 10 it can be seen that the passenger cars had no impact on the buckling behaviour as the dynamic buckling curve for the passenger cars plots on top of the static thermal buckling curve. This was because the rail passenger cars were not heavy enough to cause the rail to lift off the ties and reduce the lateral resistance. The locomotives, on the other hand, were heavy enough to cause the track between trucks of the locomotive to lift off the ties. As a result, the temperature to cause thermal buckling while a locomotive is passing was found to be lower than the static case. By comparing Figures 10(a) and 10(b) one can also see that rail misalignment impacts both the static and dynamic buckling temperature where larger misalignments lead to lower critical buckling temperatures as would be expected. The combined effect of dynamic buckling and misalignment can be significant since in this case the critical temperature increase to cause buckling went from 42.6°C with a 20 mm misalignment and no train loading to 35.3°C with a 34 mm misalignment and locomotive loading.

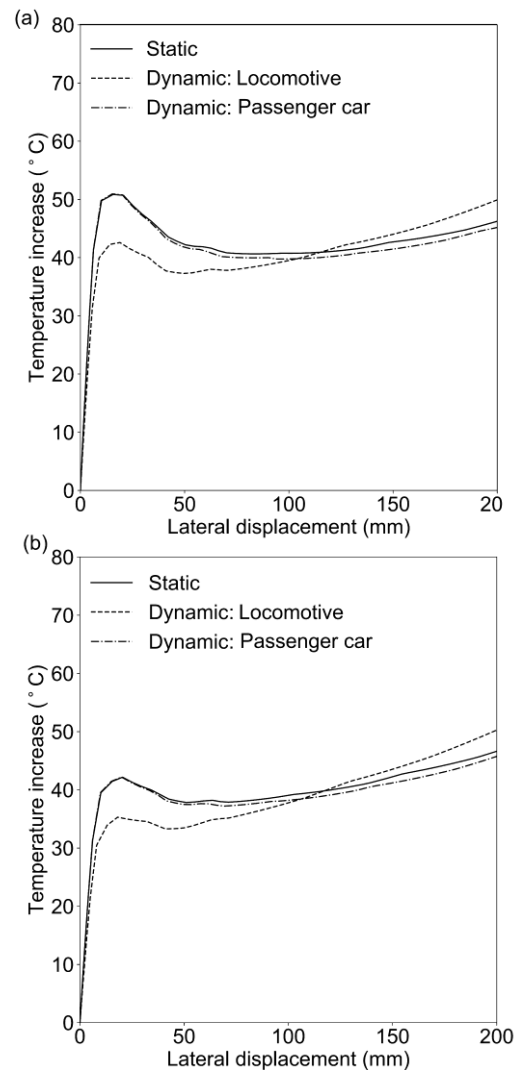


Figure 10. Static versus dynamic buckling response for monitored section of track. (a) 20 mm misalignment, (b) 34 mm misalignment

### 3.5 Data-driven thermal buckling models

In many infrastructure monitoring applications, the system being monitored is too complex to be accurately captured by a physics-based model. Such is the case for many rail buckling applications where the likelihood of buckling is a function of a complex system that involves interaction between the environment and a physical system with spatial varying geometric and material properties. As noted earlier in the paper, the position of the sun and cloud conditions affect the rail temperature and due to the lack of perfect rail restraint (e.g., due to gaps between the restraint plates and the rail) the rail experiences changes in the stress-state due to the passage of trains. Other issues such as variable support stiffness and rail track alignment further complicate the situation and make it essentially impossible to develop a comprehensive physics-based model.

One potential solution to this is to use a data-driven modelling approach. DFOS produces thousands of data points along the length of the rail to capture the spatial variability in both strain and temperature and allows for scans to be taken multiple times a day over the course of weeks to help resolve



the temporal variability. Gaussian process regression is a data-regression technique that allows for the uncertainty of the model to be calculated. The first step in the process is to select an appropriate kernel which defines the function and the relationships between variables. In the current work a Matern32 + linear kernel was selected based on a comparison of 12 different kernels to determine which one best fit the data. Each of the 12 models was trained using the first two weeks of data from the curved track monitoring site and then were used to predict the data from the last two weeks of monitoring.

Two different GPR models were developed: Model 1 defined a relationship between the axial strain and curvature along the rail and the input variables of rail surface temperature and location. Model 2 also considered train passage and non-uniform rail surface temperature as noise components that could impact the results based on the observations presented earlier. Figure 11 presents the GPR model results for axial strain versus temperature where the blue line represents the most likely relationship proposed by both models. The dark blue shaded region in the figure is the range of potential relationships according to Model 1 while the light blue region is the range of potential solutions for Model 2. It should be noted that the associated uncertainty for each model represents the range of potential models and should not be confused with other potential sources of error such as measurement error. If enough training data was available, it would be possible to have a GPR model with no uncertainty, but the actual measurements might not lie on the curve due to measurement noise. More details about the development of the models can be found in [20].

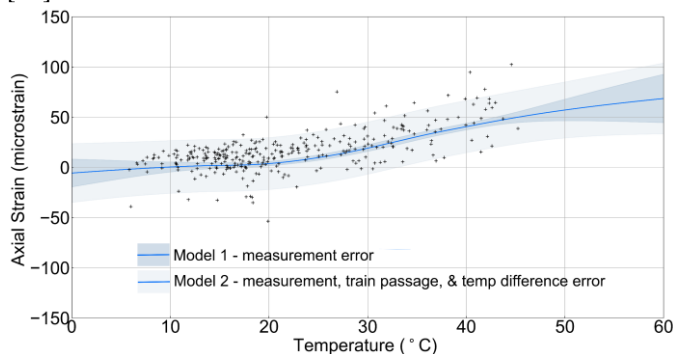


Figure 11. GPR model of the relationship between axial strain and temperature with and without consideration of train passage and differential rail temperature effects.

From Figure 11 it can be seen that the uncertainty band for Model 1 is smaller than for Model 2, due to the added potential uncertainty due to train passage and temperature variation around the cross-section of the rail. The uncertainty is also higher when the temperature is below approximately 7°C and above 45°C due to lack of training data in these regions. This presents a challenge as rail operators are most concerned about the behaviour above 40°C but there is inherently going to be less or even no training data at these critical temperature levels. Another important thing to note about Figure 11 is that many of the measured points do not match the proposed relationship or in some cases do not even fall within the uncertainty bounds. One reason for this is measurement error but there is another more fundamental issue and that is for this system there is more than one state of stress that can occur at a given temperature.

Because of variables such as gaps between the rail and the supports, train passage, and differential rail temperatures, the rail can actually take on a variety of positions at a given temperature. As such, a limitation of using GPR for systems such as these is that they are not accurately described by a closed-form solution. However, they do provide rail operators with guidance as to the overall relationship.

### 3.6 Future Work and Scalability

The initial results suggest that DFOS show promise as a rail track thermal buckling detection tool. However, three major issues still need to be addressed: (i) installation, (ii) improved thermal compensation, (iii) and automated detection. In terms of the installation, in a parallel study the research team developed a prototype robotic system that could install the fibre optic cables at various heights on the rail section an order of magnitude faster than human installers with improved placement accuracy. In the current work, temperature was only measured along the rail at one location on the cross-section, which meant that temperatures at other locations must be inferred from the single fibre optic measurement and thermocouple measurements. However, there are commercially available fibres that combine strain and temperature measurement fibres in a single housing that could be used to improve the temperature compensation. Finally, while the current research has shown that data driven techniques can be used to assist in modelling rail behaviour, further work is required to develop models and detection techniques that can be used by rail operators to automatically detect and provide warnings of thermal rail track buckling.

## 4 CONCLUSIONS

This paper presented the key findings from a four-year investigation into the use of distributed fibre optic sensing (DFOS) to support the monitoring and assessment of rail tracks that are susceptible to thermal buckling. The key conclusions include:

1. Installing three DFOS strain sensing fibres on the cross-section of the rail allows a strain plane at every sensor location along the length to be derived. Axial strain, and weak and strong axis curvature can then be determined and the curvature can be numerically integrated to obtain displacement along the length of the rail.
2. DFOS data can be used to update finite element models that are capable of predicting the ultimate response even when model updating is based on data acquired at service loads. Additionally, DFOS data can be used with the StatFEM to provide not only more accurate models but also error bounds associated with sensor noise.
3. The change in strains due to the passage of trains and due to variable heating of the rail cross-section due to solar effects are two of the challenges associated with using DFOS results for the assessment and modeling of buckling behaviour.
4. Dynamic DFOS measurements can be used with a beam on elastic foundation (BOEF) model to estimate the deflected shape of the rail and the track modulus. The deflected shape and track modulus can then be used in an FE model of the rail track to estimate the impact of vehicle load on the dynamic thermal buckling behaviour.

5. Data-driven models such as Gaussian process regression (GPR) offer a potential approach for developing models in situations where a physics-based model is intractable. However, if the system does not have a unique solution at a given temperature, e.g., due to poorly constrained degrees of freedom from gaps between the rail and sleepers, the GPR model may not capture this behaviour but can still serve as a guide for rail network managers.

## ACKNOWLEDGMENTS

This project was supported in part by collaborative research funding from the National Research Council of Canada's Artificial Intelligence for Logistics Program, and the Natural Sciences and Engineering Research Council of Canada. The authors would also like to acknowledge the support of Paul Montgomery and Andrew MacDonald from City of Ottawa in providing temporary access for placing the BOTDA analyzer, Paul Charbachi from VIA Rail Canada Inc., in assisting with coordinating field tests, and Heshan Fernando from Queen's University for assisting with the field tests. And finally the support of Fehmi Cirak of the University of Cambridge and Eky Febrianto of the University of Glasgow for their assistance with the StatFEM portion of the research.

## REFERENCES

- [1] Kish A, Samavedam G. Track buckling prevention: theory, safety concepts, and applications. John A. Volpe National Transportation Systems Center (US); Report for the US Department of Transportation. Report no. DOT/FRA/ORD-13/16. 2013.
- [2] Pucillo GP. Thermal buckling and post-buckling behaviour of continuous welded rail track. *Vehicle System Dynamics*. 2016; 54(12): 1785-1807.
- [3] Ngamkhanong C, Feng B, Tutumluer E, Hashash YMA, Kaewunruen S. Evaluation of lateral stability of railway tracks due to ballast degradation. *Construction and Building Materials*. 2021; 278: 122342.
- [4] Kerr AD. An improved analysis for thermal track buckling. *International Journal of Non-Linear Mechanics*. 1980; 15(2): 99-114.
- [5] Lim N-H, Park N-H, Kang Y-J. Stability of continuous welded rail track. *Computers & Structures*. 2003; 81(22-23): 2219-2236.
- [6] Tam HY, Lee T, Ho SL, Haber T, Graver T, Méndez A. Utilization of fiber optic Bragg Grating sensing systems for health monitoring in railway applications. *Structural Health Monitoring*. 2007; 2: 1824-1831.
- [7] Mori H, Tsunashima H, Kojima T, Matsumoto A, Mizuma T. Condition Monitoring of Railway Track Using In-service Vehicle. *Journal of Mechanical Systems for Transportation and Logistics*. 2010; 3(1): 154-165.
- [8] Vangi D, Virga A. A practical application of ultrasonic thermal stress monitoring in continuous welded rails. *Experimental Mechanics*. 2007 Oct; 47: 617-623.
- [9] Damjanović V, Weaver RL. Laser vibrometry technique for measurement of contained stress in railroad rail. *Journal of sound and vibration*. 2005; 282(1-2): 341-366.
- [10] Le Pen L, Watson G, Powrie W, Yeo G, Weston P, Roberts C. The behaviour of railway level crossings: Insights through field monitoring. *Transportation Geotechnics*. 2014; 1(4): 201-213.
- [11] Luna Innovations (2024) ODiSI 7100 Series data sheet Available from: [https://lunainc.com/sites/default/files/assets/files/data-sheets/ODiSI%207100%20Data%20Sheet%20oct2023a\\_CVS.pdf](https://lunainc.com/sites/default/files/assets/files/data-sheets/ODiSI%207100%20Data%20Sheet%20oct2023a_CVS.pdf). Date accessed: August 16, 2024.
- [12] Neubrex. Neubrex NBX-6026/NBX-6056 2018. Available from: [https://www.neubrex.com/pdf/NBX\\_6026&6056.pdf](https://www.neubrex.com/pdf/NBX_6026&6056.pdf). Date accessed: July 23, 2023
- [13] Minardo A, Porcaro G, Giannetta D, Bernini R, Zeni L. Real-time monitoring of railway traffic using slope-assisted Brillouin distributed sensors. *Appl Opt*. 2013; 52(16): 3770-3776.
- [14] Wheeler LN, Take WA, Hoult NA, Le H. Use of fiber optic sensing to measure distributed rail strains and determine rail seat forces under a moving train. *Canadian Geotechnical Journal*. 2019; 56(1): 1-13.
- [15] Gu L, Zhang L, Bao X, Zhang M, Zhang C, Dong Y. Detection of Thermal Strain in Steel Rails with BOTDA. *Applied Sciences*. 2018; 8(11): 2013.
- [16] Barker C, Hoult NA, Zhang M. Development of an axial strain measurement system for rails. *Journal of Performance of Constructed Facilities*. 2021; 35(1): 04020145.
- [17] Sun, F., Hoult, N.A., Butler, L.J. et al. Distributed monitoring of rail lateral buckling under axial loading. *J Civil Struct Health Monit* 12, 757–774 (2022).
- [18] Sun, F., Hoult, N. A., Butler, L., & Zhang, M. (2024). Monitoring and assessment of buckling in slender members with varying lateral restraint and thermal loading using distributed sensing. *Journal of Structural Engineering*, 150(1), 04023190.
- [19] Sun, F., Febrianto, E., Fernando, H., Butler, L. J., Cirak, F., & Hoult, N. A. (2023). Data-informed statistical finite element analysis of rail buckling. *Computers & Structures*, 289, 107163.
- [20] Sun, F., Hoult, N. A., Butler, L. J., & Zhang, M. (2024). Field monitoring and prediction of the thermal response of an in-service curved continuous welded rail using distributed fiber optic strain measurements. *Journal of Civil Structural Health Monitoring*, 1-15.
- [21] Sun, F., Hoult, N. A., Butler, L., & Zhang, M. (2024). Dynamic Monitoring of Rail Behavior under Passenger Train Loading Using Distributed Fiber Optic Sensors. *Journal of Performance of Constructed Facilities*, 38(4), 04024018.
- [22] Murray, C. A., Take, W. A., & Hoult, N. A. (2015). Measurement of vertical and longitudinal rail displacements using digital image correlation. *Canadian Geotechnical Journal*, 52(2), 141-155.

# Distributed Acoustic Sensing for Civil and Geotechnical Infrastructure Monitoring Applications

Cheng-Cheng Zhang<sup>1,2</sup> [0000-0003-2589-7160], Bin Shi<sup>1,2</sup>, Tao Xie<sup>1</sup>, Taiyin Zhang<sup>1</sup>, Zhuo Chen<sup>1</sup>, Zheng Wang<sup>1</sup>, Qi-Yu Xu<sup>1</sup>

<sup>1</sup>Department of Geoenvironment, Nanjing University, Nanjing 210023, China

<sup>2</sup>Center for Engineering Monitoring with Opto-Electronic Sensing (CEMOES), Nanjing University, Nanjing 210023, China  
email: zhang@nju.edu.cn

**ABSTRACT:** Distributed acoustic sensing (DAS) has emerged as a powerful technology for monitoring the health and integrity of civil and geotechnical infrastructure. This technology leverages existing fiber-optic cables as dense arrays of vibration sensors, enabling continuous, real-time monitoring over long distances. This abstract summarizes recent research advancements in applying DAS to various infrastructure monitoring challenges. We first provide a brief overview of the DAS technology and its working principles. Subsequently, we present several case studies demonstrating the versatility of DAS. These include: (1) monitoring and identifying geohazards, such as landslides and rockfalls, that threaten the stability of linear infrastructure; (2) detecting disturbance events, including drilling and excavation activities, near a high-speed railway tunnel; (3) identifying wire breaks in prestressed concrete cylinder pipes for early warning of potential failures; (4) measuring flow rates and detecting illicit flows in urban underground pipelines for improved water management; and (5) integrating DAS with deep learning for traffic monitoring, providing insights into traffic dynamics and patterns, particularly during the COVID-19 pandemic. These examples highlight the potential of DAS as a cost-effective and comprehensive solution for enhancing the safety, resilience, and operational efficiency of critical infrastructure.

**KEY WORDS:** Distributed acoustic sensing (DAS); Infrastructure monitoring; Geotechnical hazards; Artificial intelligence; Fiber optic sensing

## 1 INTRODUCTION

Civil and geotechnical infrastructure faces escalating risks from geohazards, structural degradation, and operational challenges. Traditional monitoring methods often suffer from sparse spatial coverage, high deployment costs, or limited real-time capabilities. Distributed acoustic sensing (DAS) revolutionizes infrastructure health monitoring by repurposing optical fibers as ultra-dense vibration sensor arrays [1, 2]. Through precise analysis of Rayleigh backscattered (RBS) phase changes, DAS achieves meter-scale spatial resolution over tens of km ranges, enabling simultaneous strain rate measurement across thousands of sensing channels [3, 4].

Recent advances integrate DAS with artificial intelligence to address critical applications: geohazard early warning (e.g., landslides), tunnel integrity protection, prestressed pipeline diagnostics, urban water management, and intelligent traffic systems. This work demonstrates DAS's dual capability as both physical sensor network and AI-driven data platform, providing cost-effective solutions for infrastructure resilience. Case studies validate its adaptability across energy, transportation, and water sectors, highlighting its transformative potential in smart city ecosystems.

## 2 DAS MEASUREMENT PRINCIPLE

A DAS system consists of an interrogator unit (IU) and a sensing fiber. The IU injects a continuous pulsed laser into the fiber and detects the RBS phase changes over specified gauge lengths (Figure 1). These scattering are caused by refractive index variations in the fiber. For the same pulsed (along the fast axis), the phase delay  $\Phi$  of the RBS between two points of the gauge length is:

$$\Phi = \frac{4\pi n L_g}{\lambda} \quad (1)$$

where  $n$  is the refractive index of the optical fiber,  $L_g$  is the gauge length, and  $\lambda$  is the wavelength of the incident laser.

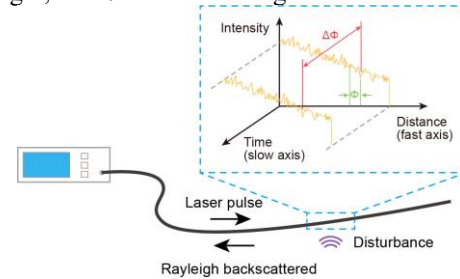


Figure 1. Schematic of DAS measurement principle.

Between adjacent pulse (along the slow axis), the change in phase delay  $\Delta\Phi$  over a gauge length is linearly correlated with axial strain rate  $\dot{\epsilon}_{xx}$ , following:

$$\dot{\epsilon}_{xx}(x, t) = \frac{\lambda f_s}{4\pi n L_g \psi} \Delta\Phi \quad (2)$$

where  $x$  and  $t$  determine the spatial and temporal information of the phase delay change,  $f_s$  is the sampling rate of the DAS IU, and  $\psi$  is the Pockels coefficient.

Commonly available commercial DAS IU offers a range of gauge length from 1 to 20 m, with channel spacing capable of reaching below 1 m and a sensing range that can extend up to 50 km. During DAS measurement, the sensing fiber is divided into dense sensing units based on the chosen gauge length. This approach enables each sensing unit to measure the axial strain rate of the fiber induced by vibration signals.



For the case studies described in this work, we utilized an OVLINK MS-DAS2000II DAS IU. This interrogator is based on the principle of phase-sensitive optical time-domain reflectometry ( $\Phi$ -OTDR), which allows for the high-sensitivity detection of dynamic strain events along the sensing fiber.

### 3 CASE STUDIES

#### 3.1 Automated rockfall classification

DAS enables continuous seismic monitoring, offering valuable insights into critical infrastructure hazards like rockfalls (Figure 2). However, automated real-time classification of extensive DAS datasets remains challenging. We developed an accurate and interpretable random forest classifier that achieved over 98.4% precision, recall, and F1-score in differentiating windowed DAS signals of rockfall events and various interferences (Figure 3) [5]. Rigorous training and validation on field-collected data leveraged waveform and spectral features for robust rockfall identification. Hyperparameter optimization further improved classification, reaching 99.3% accuracy through cross-validation. Importantly, the model generalized well to unlabeled test data, demonstrating its resilience for real-world deployment. This near real-time solution transforms distributed fiber networks into comprehensive seismic monitoring systems, unlocking their potential to enhance safety and resilience of critical infrastructure worldwide.

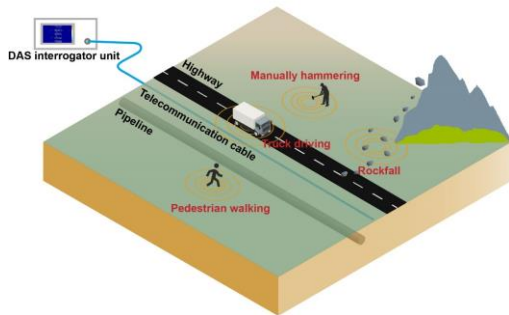


Figure 2. Conceptual overview of DAS for rockfall event monitoring along linear infrastructure.

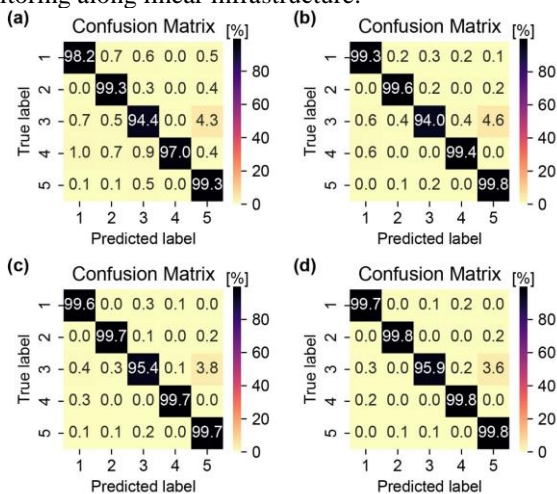


Figure 3. Confusion matrices comparing Random Forest classification performance for window lengths of (a) 2 s, (b) 4 s, (c) 6 s, and (d) 8 s. Five classes are shown: rockfall (1), pedestrian walking (2), hammering (3), truck driving (4), and background noise (5).

#### 3.2 Automatic identification of diverse tunnel threats

As the backbone of modern urban underground traffic space, tunnels are increasingly threatened by natural disasters and anthropogenic activities. Current tunnel surveillance systems often rely on labor-intensive surveys or techniques that only target specific tunnel events. We present an automated tunnel monitoring system that integrates DAS technology with ensemble learning (Figure 4) [6]. We develop a fiber-optic vibroacoustic dataset of tunnel disturbance events and embed vibroscope data into a common feature space capable of describing diverse tunnel threats. On the scale of seconds, our anomaly detection pipeline and data-driven stacking ensemble learning model enable automatically identifying nine types of anomalous events with high accuracy. The efficacy of this intelligent monitoring system is demonstrated through its application in a real-world tunnel (Figure 5a), where it successfully detected a low-energy but dangerous water leakage event (Figure 5b). The highly generalizable machine learning model, combined with a universal feature set and advanced sensing technology, offers a promising solution for the autonomous monitoring of tunnels and other underground spaces.

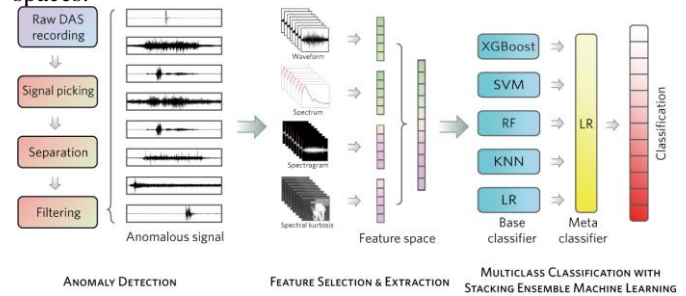


Figure 4. The framework of the DAS monitoring system for automatic tunnel threat identification.

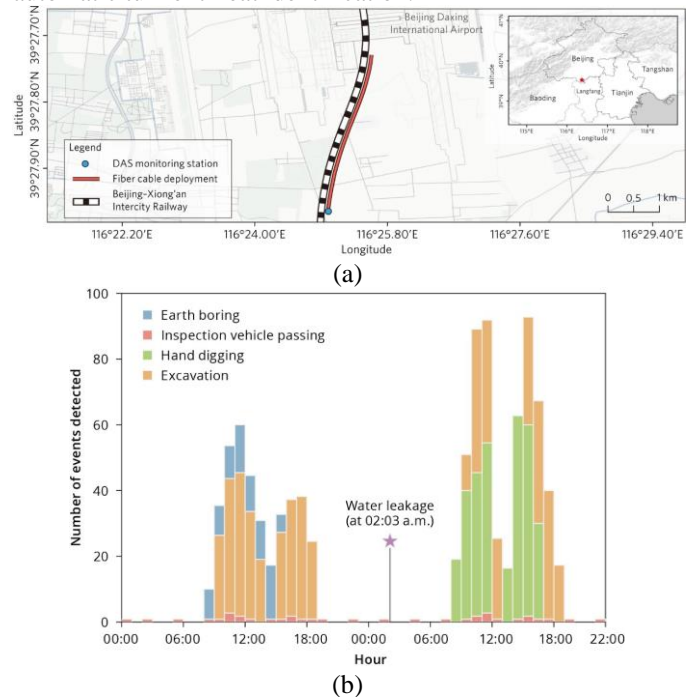


Figure 5. (a) DAS fiber deployment scheme along the Beijing-Xiong'an Intercity Railway tunnel; (b) Disturbance events

identified in the Beijing–Xiong'an Intercity Railway tunnel during a monitoring campaign.

### 3.3 Identifying wire breaks in prestressed concrete cylinder pipes

The inspection of broken wires in prestressed concrete cylinder pipes is crucial for ensuring the safety and reliability of the pipeline. Traditional point detection techniques always require labor-intensive periodic inspections and cannot be deployed along the entire pipeline, significantly limiting the development of the industry. Hence, there is an urgent need for more advanced and intelligent sensors that can achieve 100% coverage and provide sufficient accuracy assurance. Figure 6 presents an overview of the PCCP wire breaking test site. We develop a DAS-based automated monitoring system to accurately classify the rupture of prestressed wires (Figure 7) [7]. First, a computer vision approach is employed to primarily screen out potential vibrational signals from DAS array images. Then, a pre-trained support vector machine model is used to classify the vibrations as either wire breakages or non-wire breakages (Figure 8). This model's performance surpassed other classification strategies, achieving 99.62% accuracy, 99.41% precision, 98.82% recall, and 99.12% F1-score in a side-to-side comparison. Our innovative workflow provides a comprehensive solution for detecting broken wires and offers guidance for the application of artificial intelligence-based DAS to complex vibration systems with limited training data.

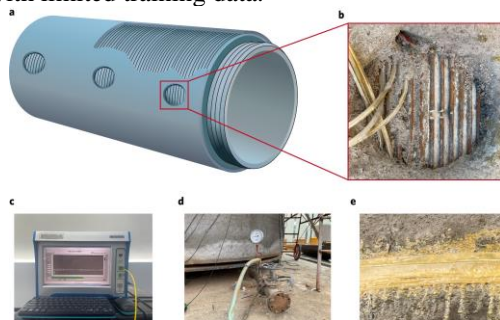


Figure 6. PCCP wire breaking test site; photos show the wires in a circular recess, DAS interrogation unit used, water pressure monitoring gauge within the PCCP, and optical fibers coupled to the outer wall of the pipe.

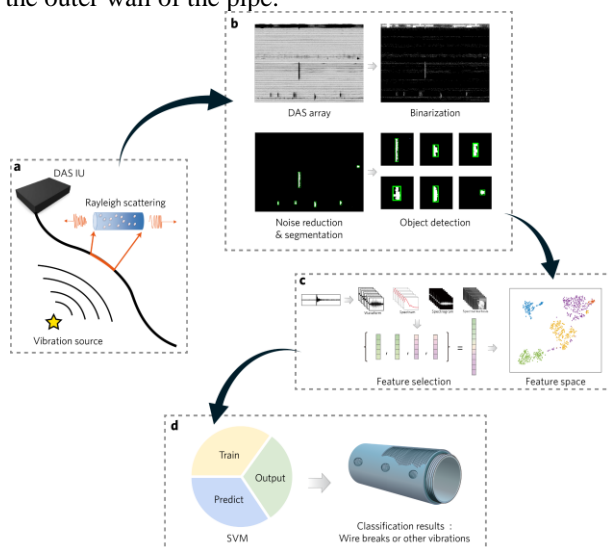


Figure 7. The framework for the autonomous monitoring of wire breaks using DAS data.

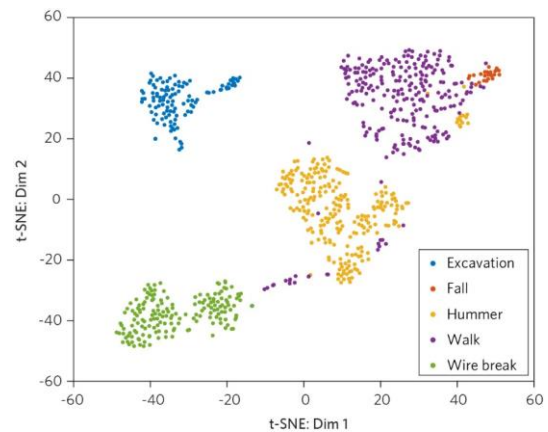


Figure 8. t-SNE is used to reduce the feature dimensionality from 15 to 2 dimensions for purpose of visualization. Five kinds of events are embedded in the same feature space, in which different types are distinguished with different colors.

### 3.4 Detecting illicit flows in urban underground pipelines

Wastewater discharge from outfall pipes can significantly impact river water quality and aquatic ecosystems. Effective outfall monitoring is critical for controlling pollution and protecting public health. We demonstrate a novel DAS approach for detecting wastewater discharge events from outfall pipes located along rivers [8]. Controlled field experiments were conducted in an industrial park river to systematically evaluate DAS performance (Figure 9). DAS detects vibrational signals imparted to suspended fiber-optic cables by turbulent wastewater flows, predominantly within 10–30 Hz, enabling continuous monitoring along entire river lengths. Vibrational power analysis locates outfalls with meter-level accuracy, while time–frequency techniques discern discharge timing and characteristics (Figure 10). Cable type and outfall–fiber separation influence on detection capability was assessed. Thermoplastic-jacketed cables optimized detection through enhanced vibrational coupling. Vibrational energy decreased exponentially with separation, highlighting benefits of proximal deployment for sensitivity. However, detection range scales with discharge flow rate. Frequency centroid proved a robust feature with potential for automated discharge identification. Overall, DAS enables high spatiotemporal resolution monitoring to pinpoint concealed outfalls minimally invasively. This positions DAS as a promising tool supporting improved water governance through early pollution warnings and rapid source localization via outfall vibrational signatures emanating across river networks.

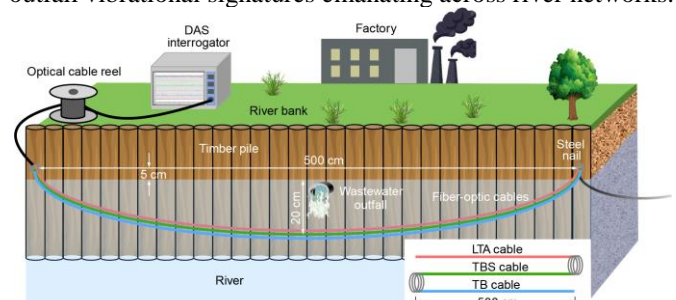


Figure 9. Layout of the DAS system used in field discharge experiments.



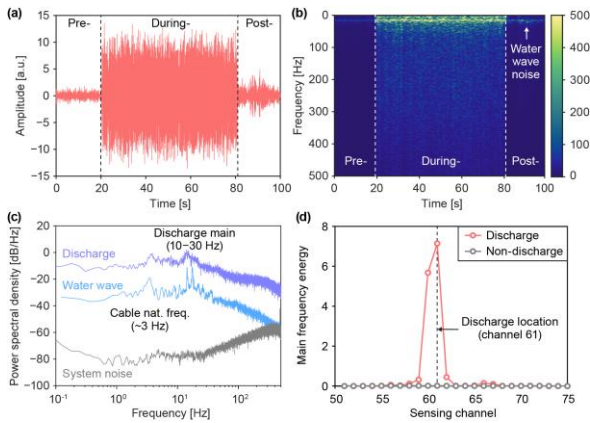


Figure 10. Wastewater discharge detection and localization. (a–b) Time series and short-term Fourier transform (STFT) plots showing pre-, during-, and post-discharge. (c) Power spectral density (PSD) comparison of the discharge signal, wave noise, and system noise. (d) Outfall location identified by calculating vibration power (10–30 Hz) along the cable.

### 3.5 Enhanced traffic monitoring

Traffic monitoring provides crucial data for intelligent transportation systems (ITS) but traditional sensors are expensive to deploy and maintain at scale. A field experiment was conducted using a section of telecommunications fiber-optic cable co-trenched with a natural gas pipeline in Yudu County, Ganzhou City, Jiangxi Province (Figure 11). We explore DAS using existing fiber-optic infrastructure as a cost-effective solution for traffic monitoring [9]. While DAS offers advantages, vehicle detection signals are susceptible to noise. To address this, we propose a novel approach combining DAS with deep learning object detection using YOLOv8. Pre-processed and labeled DAS data collected over two weeks on a highway during a COVID-19 lockdown were used to train the YOLOv8 network, achieving 92% classification accuracy. Applying the trained model revealed detailed hourly traffic patterns and vehicle compositions (Figures 12 and 13), demonstrating the potential of DAS for robust and cost-effective ITS. These findings highlight the effectiveness of combining DAS and deep learning for noise mitigation in traffic monitoring and provide valuable insights into traffic dynamics during the pandemic.

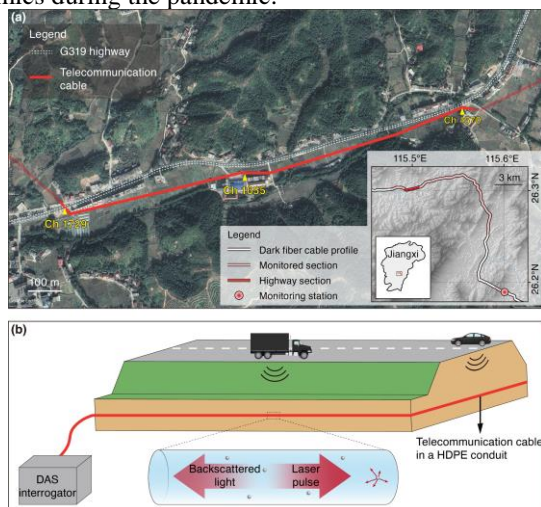


Figure 11. (a) Field experiment site for traffic monitoring and (b) Operating principle of DAS for measuring vehicle signals.

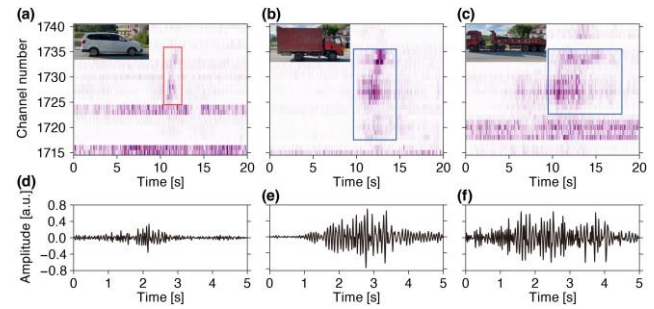


Figure 12. DAS signals from passenger (a, d) and commercial (b, c, e, f) vehicles. (a–c) Waterfall diagrams. (d–f) Time series.

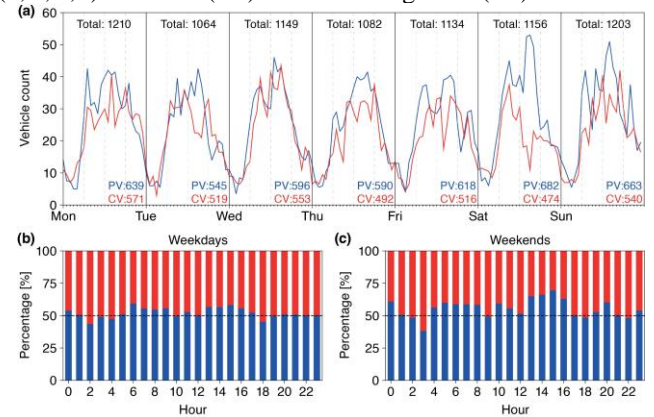


Figure 13. Comparison of passenger (blue) and commercial (red) vehicle traffic patterns determined via DAS. (a) Daily traffic volume trends. (b–c) Vehicle proportions on weekdays and weekends.

## 4 CONCLUSIONS

This overview demonstrates the transformative potential of DAS as a unified monitoring solution for heterogeneous infrastructure systems. Across geohazard monitoring, structural integrity assessment, and urban network management applications, DAS consistently proves its capacity to convert standard optical fibers into high-resolution vibration sensor arrays. By synergizing Rayleigh backscattering physics with machine learning architectures, the technology overcomes traditional trade-offs between spatial granularity, coverage range, and operational scalability.

The case studies reveal two paradigm-shifting attributes: First, DAS inherently operates as a cyber-physical transducer, simultaneously capturing mechanical wavefields and feeding AI-driven digital twins. Second, its compatibility with existing fiber networks enables rapid deployment at marginal cost, particularly advantageous for linear assets like pipelines and tunnels. While signal interpretation remains context-dependent, emerging standardization frameworks for DAS data annotation are reducing domain adaptation barriers.

As cities prioritize infrastructure resilience, DAS emerges as a strategic tool for converged monitoring of above-ground and subsurface environments. Future implementations could expand its use in decarbonization initiatives, such as CO<sub>2</sub> storage integrity verification and smart grid dynamics tracking. By bridging physical infrastructure with computational analytics, this technology redefines the boundaries of structural health monitoring in the era of ubiquitous connectivity.



## ACKNOWLEDGMENTS

The authors extend their sincere gratitude to all past and present members of Nanjing University's DAS research team whose intellectual contributions and persistent efforts shaped the ideas and projects described in this work. Particular appreciation goes to colleagues who participated in multi-year collaborations that made this decade-long research journey possible. This research was supported by the National Natural Science Foundation of China through grants 42107153 and 42030701, and the Young Elite Scientists Sponsorship Program of the China Association for Science and Technology through grant YESS20200304.

## REFERENCES

- [1] Lindsey, N. J., & Martin, E. R. (2021). Fiber-optic seismology. *Annual Review of Earth and Planetary Sciences*, 49(1), 309–336.
- [2] Zhang, C.-C., Shi, B., Yin, J., Xie, T., Wang, Z., & Zhang, S.-S. (2021). Seismic wavefield and strain recordings on a 20-kilometer dark fiber allow detecting mass movement events and anthropogenic activities threatening a natural gas pipeline. In *AGU Fall Meeting Abstracts* (pp. NS21-A06). New Orleans, LA, United States: American Geophysical Union.
- [3] Bao, X., & Wang, Y. (2021). Recent advancements in Rayleigh scattering-based distributed fiber sensors. *Advanced Devices & Instrumentation*, 2021, 1–17.
- [4] Shi, B., Zhang, D., Zhu, H., Zhang, C.-C., Gu, K., Sang, H., et al. (2021). DFOS Applications to Geo-Engineering Monitoring. *Photonic Sensors*, 11(2), 158–186.
- [5] Xie, T., Zhang, C.-C., Shi, B., Chen, Z., & Zhang, Y. (2024). Integrating distributed acoustic sensing and computer vision for real-time seismic location of landslides and rockfalls along linear infrastructure. *Landslides*, 21(8), 1941–1959.
- [6] Zhang, T.-Y., Zhang, C.-C., Xie, T., Xu, X., & Shi, B. (2025). Automatic identification of diverse tunnel threats with machine learning-based distributed acoustic sensing. *Structural Control and Health Monitoring*. (in press)
- [7] Zhang, T., Zhang, C.-C., Shi, B., Chen, Z., Zhao, X., & Wang, Z. (2024). Artificial intelligence-based distributed acoustic sensing enables automated identification of wire breaks in prestressed concrete cylinder pipe. *Journal of Applied Geophysics*, 224, 105378.
- [8] Chen, Z., Zhang, C.-C., Shi, B., Xie, T., Wei, G., & Guo, J.-Y. (2024). Eavesdropping on wastewater pollution: Detecting discharge events from river outfalls via fiber-optic distributed acoustic sensing. *Water Research*, 250, 121069.
- [9] Wang, Z., Zhang, T., Chen, H., Zhang, C.-C., & Shi, B. (2025). Enhancing traffic monitoring with noise-robust distributed acoustic sensing and deep learning. *Journal of Applied Geophysics*, 233, 105616.

# DFOS solutions covering full monitoring needs of an enlarged concrete deck viaduct

M. VILLAR<sup>1</sup>, M. FERRARIO<sup>2,3</sup>, J. MOROSI<sup>3</sup>

<sup>1</sup>FEBUS Optics SAS, 2 Avenue du Président Pierre Angot 64000 Pau, France

<sup>2</sup>Politecnico di Milano, Department of Electronics, Information, and Bioengineering, Via Giuseppe Ponzio, 34, 20133 Milan, Italy

<sup>3</sup>Cohaerentia Srl, Via Pinturicchio 5, 20131 Milan, Italy.

Corresponding email: miguel.villar@febus-optics.com

**ABSTRACT:** 60s economic boom led to spread construction of large transport infrastructures. Many of these steel reinforced concrete structures attain their end of lifespans on this and next decade. With no major renewing plan, repairing and retrofitting are explored alternatives. A good example is Milano's ring-road viaduct; while already repaired and its concrete deck enlarged, SHM begins nowadays. **Monitoring of thermal and mechanical induced strain, static and dynamic, brings access to permanent strain, thermal expansion, eigenmodes of each single road span and better understanding of the whole structure dynamic behavior.** Three trucks moving at 30 km/h load dynamically the enlarged deck, while real traffic is used for modal analysis. Often, this kind of comprehensive monitoring requires combining various measurement technologies, making their installation time-consuming and expensive. Thus, the number of sensors may be undercut, and measurement campaigns duration reduced, which may result in poorer monitoring results and mismatching between experimental results and model's ones. FEBUS SHM solutions based on DAS (Distributed Acoustic Sensing), DSS (Distributed Strain Sensing) and DTS (Distributed Temperature Sensing) provide quick instrumentation and easy monitoring. With long-range devices to address tens of km of infrastructure instrumented in a row, up to 400 kHz continuous monitoring, state-of-the-art DAS repeatability threshold of only 2 picoStrain/SquareRoot(Freq), FEBUS DFOS (Distributed Fiber Optics Sensing) solutions brings values for every node of the structure, remote monitoring and mastered opex and capex.

**KEY WORDS:** SHM; DFOS; DAS; Bridge monitoring; Dynamic strain monitoring; Fiber Optics instrumentation.

## 1 INTRODUCTION

DFOS begins to play a major role in SHM due to its outstanding combination of huge number of sensing points, sensitivity, repeatability, and easiness of very large instrumentation. In the past, DAS (Distributed Acoustic Sensing based on Rayleigh Backscattering in fiber optics) has been used to assess the dynamic behavior of a structure, while DSS/DTS (Distributed Strain Sensing / Distributed Temperature Sensing both based on Brillouin backscattering in fiber optics) focused on quasi-static strain and temperature monitoring.

The collapses of widely used infrastructures like the Morandi Bridge in Genoa and the Florida International University Pedestrian Bridge have highlighted the need of implementing monitoring strategies to prevent such disasters. These failures are often attributed to design flaws, material deficiencies, overloading, or insufficient maintenance. Following the Morandi bridge collapse, a substantial number of infrastructures were flagged for close inspection. DFOS monitoring can play a major role in detecting anomalies and raising early alerts to infrastructure operators and owners before collapses occur. Indeed, traditional point sensors have limitations, especially in urban environments with complex needs, stacked infrastructures and embedded networks [1 - 7]. When addressing Operative Modal Analysis, we can benefit from high sensitivity of DAS, and different kind of active and passive sources can be used. Indeed, Ambient vibration recordings provide valuable dynamic information on structural behavior. These vibrations stem from various sources such as traffic on the deck and ambient anthropogenic noise, including external traffic, construction activities, and industrial

operations, as well as natural elements like wind and earthquakes. They enable the estimation of dynamic parameters related to structural properties and serve as a valuable tool for monitoring structural condition [8 - 12].

This study shows how FEBUS Optics' DAS technology can be used for both dynamic (OMA) and quasi-static strain monitoring of an enlarged steel reinforced concrete bridge, which is a high-traffic viaduct.



Figure 1. Two in-parallel motorway steel reinforced concrete viaduct. Yellow lines show extended deck interface.

Indeed, the sensed structure is Milano's Ring-road, having a 12 km concrete viaduct with new bridge held by their own piles have been built parallel to each original viaduct and the road-

slabs have been joined together through steel bars (Figure 1, Figure 2).

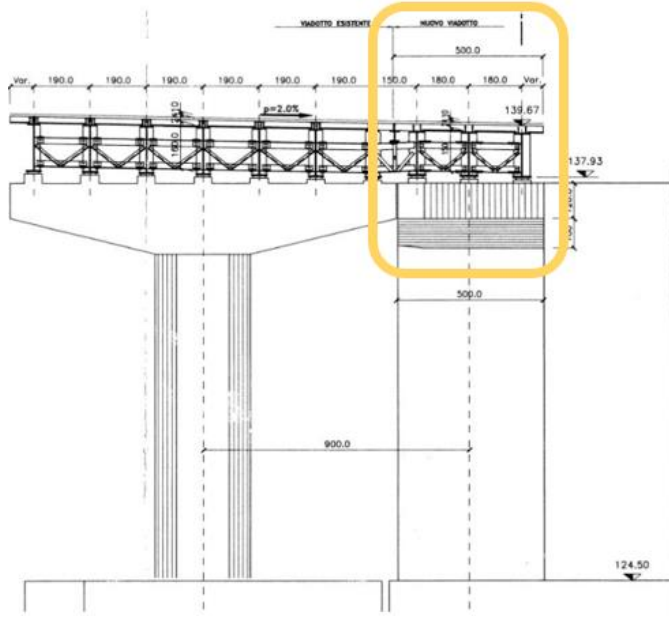


Figure 2. Transversal section. Extended deck in yellow frame

This viaduct is facing several issues and challenges. It is suffering from corrosion on its exposed rebars at several locations, not fully successful repair works, heavy traffic, and interferences with other infrastructures and buildings that complicate the attempts of structural retrofitting to improve safety and durability.

This study covers the first tests done with the initially instrumented parts of the viaduct and brought significant results to improve the understanding of the behavior of the structure, allowing to check the viability of the instrumentation for the entire viaduct, validating the numerical models, and highlighting the importance of monitoring and control of the structure to the asset operator (confidential).

## 2 METHODS

### 2.1 DAS. Distributed Acoustic Sensing

DFOS technologies rely on one of the three backscattering effects which are Rayleigh, Brillouin and Raman. The DAS (Distributed Acoustic Sensing based on Rayleigh backscattering technology) record high-frequency laser pulses sent into the fiber, analyzing backscattered light to detect heterogeneities along the cable.

Rayleigh backscattering, caused by defects in the fiber, is repetitive along its length and changes when the fiber is disturbed by external events. These changes grant access of physical parameters variations like vibrations coming from a leakage being energetic enough to propagate its related noise around. The optical phase shift between two positions along the fiber is related to the longitudinal strain using equation 1 below. Key acquisition parameters include fiber length, pulse rate frequency, spatial and temporal sampling intervals, and gauge length (GL).

$$\varepsilon_{yy} = \frac{\lambda \cdot d\theta}{4\pi \cdot n \cdot GL \cdot \xi} \quad (1)$$

Where  $\varepsilon_{yy}$  is the longitudinal strain,  $\lambda$  is the optical wavelength,  $d\theta$  is the phase shift,  $n$  is the optical fiber index and  $\xi$  is a correction factor.

As briefly introduced above, the optical principle of operation is based on the Rayleigh backscattering of a light pulse propagating through the fiber. As it progresses, a tiny fraction of the laser pulse is continuously returned to the interrogator by random heterogeneities present in the fiber. An acoustic interaction at one point of the fiber will alter this process allowing its detection and location by time of flight of light (Figure 3).

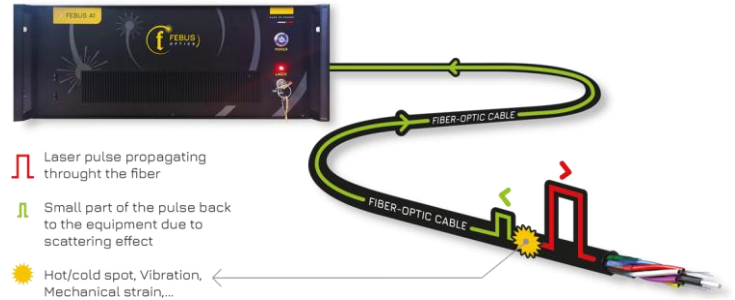


Figure 3. Principle of measurement via DFOS.

The information is contained in the optical phase of the received signal requiring interferometric detection. As the pulse propagates very quickly, the fiber can be repeatedly interrogated by sending a series of pulses, thus allowing to solve in frequency of acoustic vibrations (Figure 4) [13 – 17].

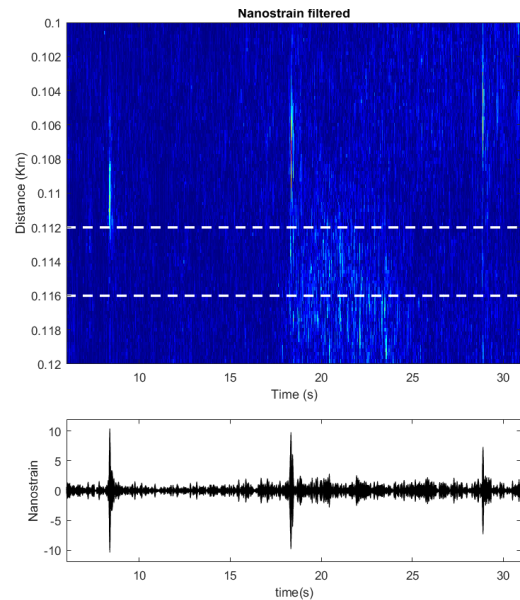


Figure 4. Distributed acoustic measurements. Filtered signal Bandpass @465Hz (Width 20Hz)

The achieved acoustic bandwidth can range from a few Hz to a few tens of kHz, the upper limit being a function of the length of the fiber used (the longer the fiber is, the longer the pulse will travel through the fiber and the lower the cut-off frequency is). This device performs highest state-of-the-art sensitivity,



which is an advantage but can also be a disadvantage by being subject to noise acoustic environment. Real-time digital processing of the data is required to extract the signals of interest, as well as correctly applying the technology and instrumenting in the right manner the structure to be sensed. [18]

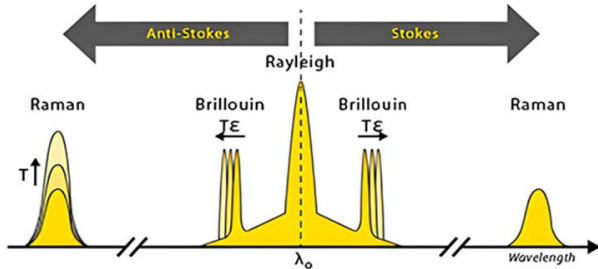


Figure 5. Fast Fourier Transform representation of Rayleigh, Brillouin and Raman backscattering [19]

## 2.2 Experimental Setup. Dynamic loading of the viaduct

Given the fact that the evolution of elastic modulus because of material ageing was not characterized and not having preliminary results from previous measurements at the beginning of this test campaign, one of the main challenges was to mobilize heavy enough loads to ensure the entire structure would strain as theoretically expected. To do so, up to three trucks were used to bend each span. The principle was very simple, each span was statically and dynamically strained by three trucks moving on single file at 30 km/h (Figure 6). Live tests were done overnight to be able to use these heavy trucks for loading.

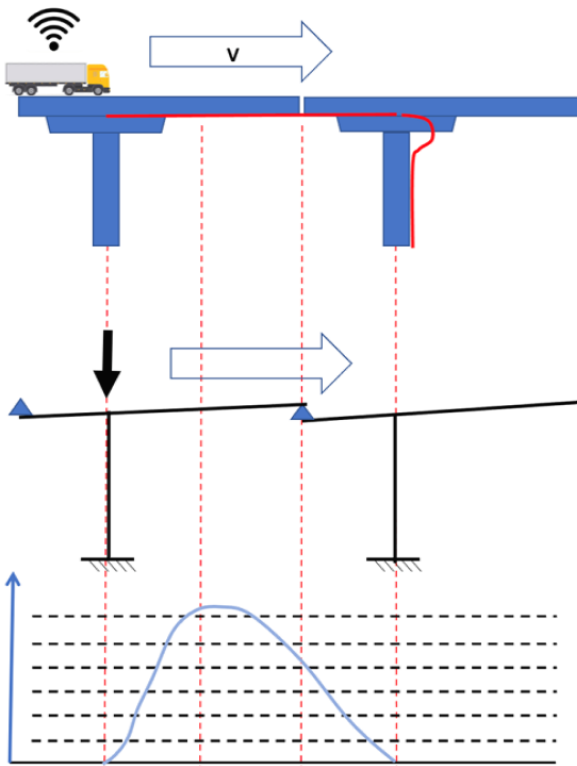


Figure 6. Principle of dynamic bending of viaduct's span.

Strain rate was measured by DAS. Both strain rate and dynamic strain were real-time plotted onsite. Indeed, time-integrated strain rate brings strain without need of classic DSS (Distributed Strain Sensing based on Brillouin). This use of Rayleigh backscattering technology (DAS) combines the best state-of-the-art repeatability of FEBUS A1 (DAS), the capability of measuring quasi-static strain and high frequency (up to 400 kHz) strain all along the sensing fiber optic cable which would be complex to match using Brillouin technology (DSS/DTS) going up to around 100Hz nowadays.

## 2.3 Sensors. Fiber Optic sensing cables

Three different fiber optic sensing cables were tested for this study.

- Strain sensing - Tight-buffered cable with steel reinforcement. Deemed the robust cable.
- Strain sensing - Tight-buffered cable without steel reinforcement. Lighter and less rigid providing more sensitivity but less protection.
- Temperature sensing - Loose tube cable. Essential to understand the thermal expansion of the viaduct. Not presented on this publication.

While choosing a robust (tensile, bending and torsion resistant) make sense for high demanding deployments, the downside is that cable reinforcements increase stiffness which tends to reduce sensitivity of the cable. That's why the second strain sensing tight-buffered cable without steel reinforcement is selected (Figure 7).

Additionally, temperature sensing loose tube cable is used for both assess the thermal behavior of the viaduct, typically sensing the temperature evolutions between day and night as well as seasons ones. This was used for a classic temperature compensation with other Brillouin interrogator used on the study but out of the scope of this paper.

## 2.4 Instrumentation

Different approaches were discussed during preparation phases. Indeed, one of the difficulties were to find a cost-effective method to instrument the entire viaduct in a durable and sensitive way. It is important to note that the instrumentation is done beneath the viaduct deck, under its bottom, so gravity is pulling down the whole cable/glue until fully cured. Prior the bonding, point-by-point attachments allow to place the cable at right position until the glue is spread and cured.

All the cables were bonded using three different glues:

- Fast crosslinking (*curing*) - Resin PPPO (2,5-diphenyl-p-phenylene oxide). Combining tenacity and vacuum effect to increase quick adherence (bonding strength).
- Strong - Thixotropic Polyurethane (undisclosed formulation). Extremely rigid after crosslinking. Specially designed for structural gluing.
- Medium Strong - Thixotropic Polyurethane (undisclosed formulation). Less rigid and quicker on crosslinking than the second one. Specially designed for structural gluing.

Fast curing adhesive is used for the first part of the instrumentation. Despite the use of temporary tape, uncured state viscosity remains too low and not perfectly fully suited to bottom instrumentation. Main goal was to deem if coupling is severely impacted by the type of Strong and Medium Strong adhesives (Figure 7).

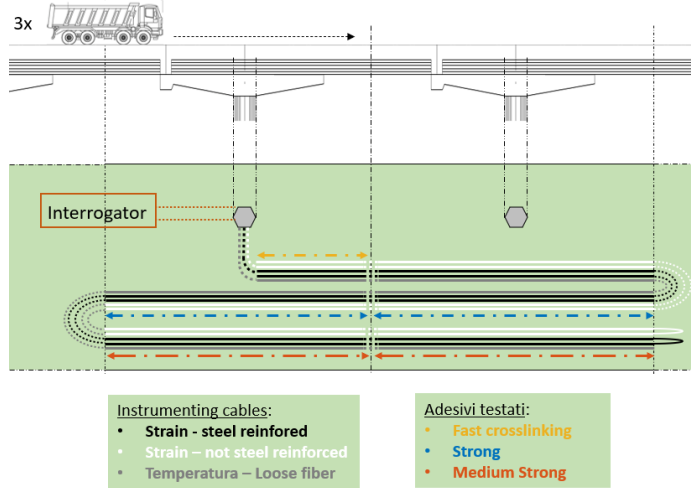


Figure 7. Sensors and Instrumentation.

Figure 7 shows the sensing fibers instrumentation in a single loop, so the full line is interrogated using only one channel. It is important to note during data interpretation that each cable passes three times through the same spatial point. This way, each truck will be seen three times.

### 3 RESULTS

#### 3.1 Strain Rate monitoring

The results are presented on a 3-axis diagram typically called inverted waterfall. Time on vertical axis (sooner time close to zero), distance on horizontal axis and magnitude of strain Rate on colour scale on the right side (Figure 8).

The bending of the viaduct is properly captured. As expected, the tension relative strain (positive, red) appears first then replaced by compression (negative, blue) as truck goes away from each sensing point. This is coherent with a bended deck sensed on its bottom (Figure 6).

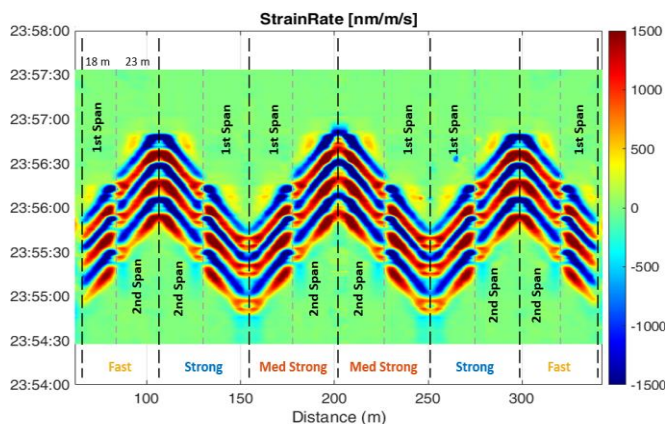


Figure 8. Longitudinal axis Strain Rate. Comparison of three different adhesives and two first instrumented spans.

It is noted the three trucks are equally captured. Indeed, three consecutive positive and negative loadings (related to (tension and compression respectively) are plotted. Furthermore, the amount of strain is the same, meaning the three trucks weigh the same. Since the loads are moving at constant speed, both tension and compression strain rate follow constat slope. Trucks are moving in the same direction and sense; the wavy shape is due to the sensing fiber loop instrumentation (Figure 7). Both spans respond qualitatively and quantitatively in the same way. The same slope and same amount of strain rate around  $\pm 1500$  nm/m/s. It is important to highlight the units (nanometers/meter/second) to understand the slight straining of the viaduct deck.

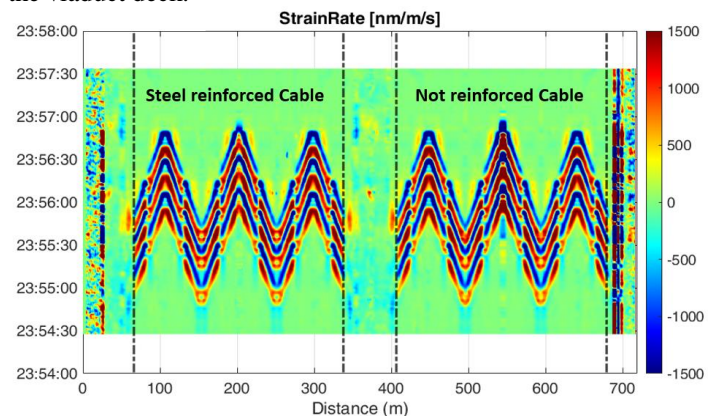


Figure 9. Longitudinal axis Strain Rate. Comparison of Steel reinforced and not reinforced cable.

Then, the adhesive and bonding are assessed. It is shown that all three adhesives show the same response. Indeed, there are no significant differences on the intensity of the strain rate which points to a similar coupling structure-sensors, leading *in fine* to a similar sensitivity. The same conclusion for the comparison between steel reinforced cable and not reinforced one, having similar sensitivity (Figure 9).

#### 3.2 Strain monitoring

From previous results, strain rate expressed in nm/m/s - typical dimension and units of vibration on DAS measurements - many useful information can be inferred.

Dynamic strain rate can be time integrated to obtain strain, expressed on  $\mu\text{m/m}$ . In this case, typical integration time is 1ms but can be adjusted thanks to the capabilities of FEBUS A1 (DAS) to modify all its measurement parameters like pulse rate frequency (number of laser pulses emitted per time) and time resolution.

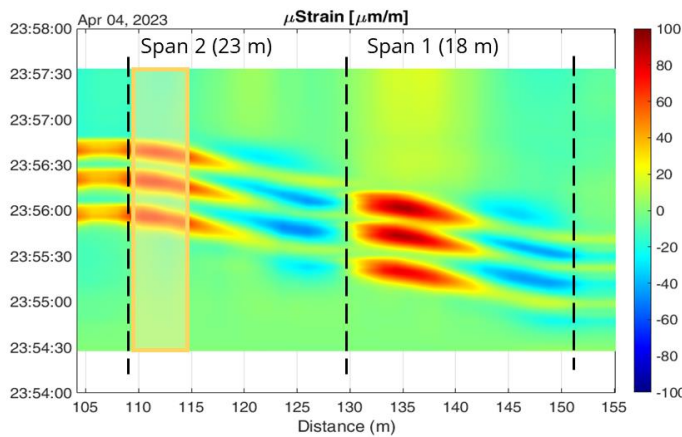


Figure 10. Longitudinal axis strain from time integrated strain rate

In the graph above (Figure 10), the strain is plotted in function of time (left axis) and distance (bottom axis), while intensity of the strain is represented by the color scale on the right. To enhance the result, only two first spans with strong glue are plotted. From 105 m to 155 m.

It is important to note the trucks are travelling from far distance to closer one, more precisely started on 155 m and go to 105 m, while the time is increasing on the left axis, so the trucks' movements is seen as diagonal from bottom right corner of the graph to the upper left corner.

It is observed in the figure above (Figure 10) the same patterns of positive and negative strain for each truck pass, as seen with strain rate. In contrast of strain rate results exploitation, we can note that the first span is reaching up to 100  $\mu\text{m/m}$  on tensile and -60  $\mu\text{m/m}$  on compression, while the second span is less strained on tensile, going up to 80 only  $\mu\text{m/m}$ , and the same compression strain of -60  $\mu\text{m/m}$ .

To go further in the quantification, we can see the pass of the trucks two and three on second span seemed to load 20  $\mu\text{m/m}$  more than the pass of the first truck.

### 3.3 Displacement monitoring

It is important to note that one the main aim of this study was to quantify the positive longitudinal displacement of the span because of the bending. To do so, a space integration was done at a particular point, where the strain was related to tensile, so positive. The region of this point is represented by the orange rectangle between 110 m and 115 m (Figure 10).

#### Longitudinal axis displacement

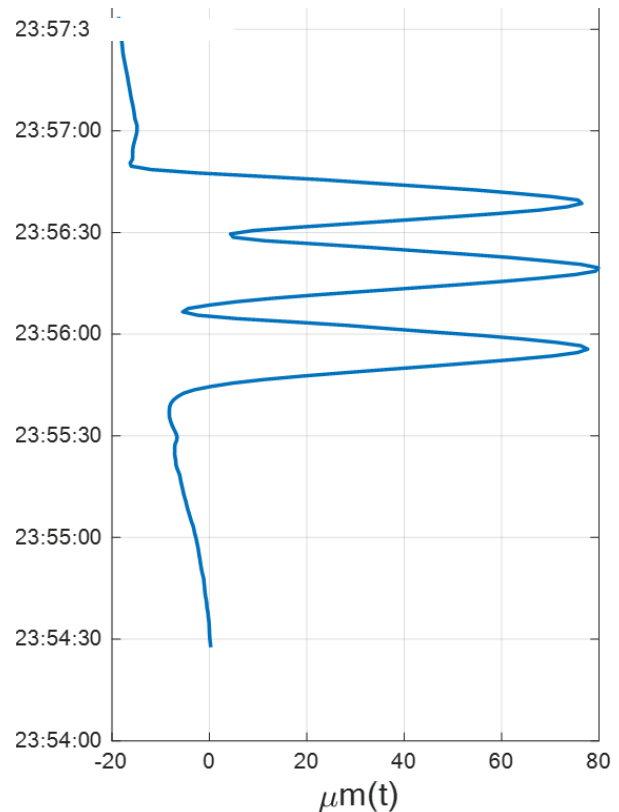


Figure 11. Longitudinal axis displacement from space integrated strain

In the graph above (Figure 11), we can see the result of the space integration of the strain rate, which is the longitudinal axis displacement created by the bending of the span. The length of integration was 1m, which can be tuned as wished with FEBUS A1. Thus, it is observed the amount of displacement is 80  $\mu\text{m/m}$  on first span. This matches the expectations from numerical modelling as confirmed by the technical direction of CaemATE Srl, the entity tasked of the mechanical modelling of the bridge for this study.

### 3.4 Modal analysis with DAS

FEBUS A1 DAS was applied for monitoring of strain rate, strain and displacement but also for its more common use, modal analysis. The same cable and interrogator were suited for this kind of acquisition, and the real traffic at a high load time of the day (rush hour) was used. This is widely used and bring plenty of acoustic signals. Since the sensitivity of DAS is very high, it is preferable to plot results at one single point but other FFT-based 3D representations allow to get info from the entire line at once. In this case, the choice is to represent time on left axis while the frequency is on the bottom axis, while color represents the signal energy, thus amplitude of the vibration (Figure 12).



### Modal Analysis of the viaduct

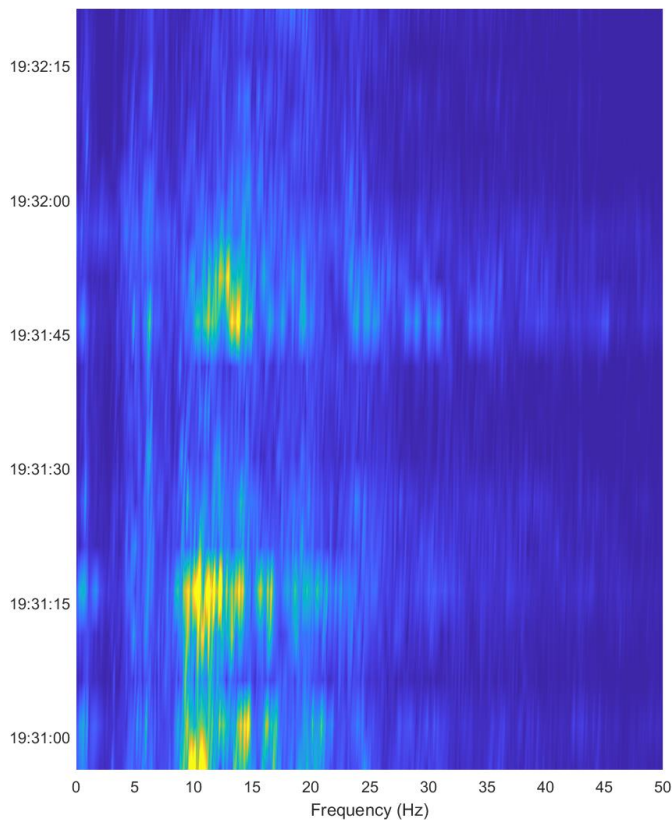


Figure 12. Vibrations from real traffic, frequency in function of time for a particular point

From previous information, the frequencies can be represented for a particular point and time, thus the amplitude of the vibration in function of the frequency, as shown on the figure below (Figure 13). In the aim of comparison of different states, two instants are plotted, on red the steady state to see the ambient noise when no vehicle on the instrumented spans, and blue for high intensity signals from traffic on the instrumented spans.

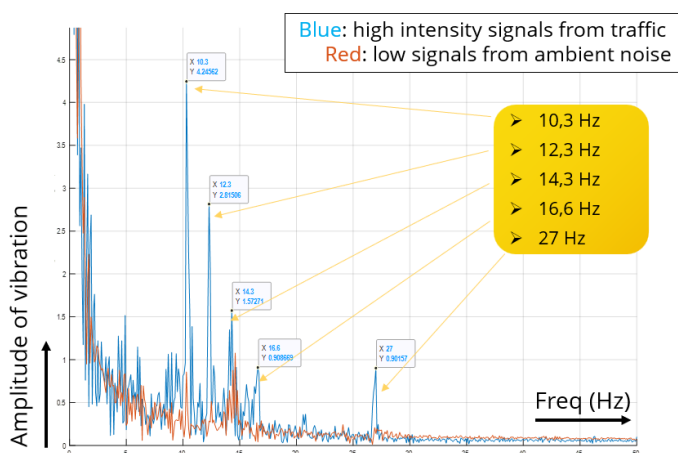


Figure 13. Modal frequencies of the viaduct

Up to five modal frequencies are detected clearly, between 10,3 Hz and 27 Hz.

It is important to note that this is plotted for one single point, thus one node identified previously on FFT over distance, but it is possible to do the same analysis for all the nodes of the structure, that are sensed simultaneously thanks to the properties of Distributed Acoustic Sensing, and its long range and fine resolution measuring capabilities.

## 4 DISCUSSION

It has been shown that DAS technology can be applied to both dynamic and quasi-static acquisitions addressing OMA and strain measurements with the same sensor (Fiber Optics) and DAS interrogator (FEBUS A1). Live data production - time and space integration - allowed to go from strain rate to strain and displacement during the acquisitions and check the quality of results and the coherence with the numerical models.

While this is mathematically well known, the application of this methodology to DAS acquisitions is a novelty that unlocks new applications of DAS in the context of SHM and Civil Engineering as well as other potential uses on sectors like Oil & Gas and Geophysics, for static and dynamic assessment of pipelines and ground movement for instance. Indeed, thanks to the capabilities of FEBUS A1, all measurement parameters can be easily modified to suit to the infrastructure length and acquisition demands.

Besides, one of the main advantages of Modal analysis of DAS monitoring is the possibility to combine high sensitivity and decide the position of nodes after instrumentation, allowing to overcome the difficulties of predicting the nodes of the vibration modes, and deciding the right positions to locate traditional point sensors without knowing how the structure behaves dynamically. For the selected position, 5 modal frequencies were located spectrally and quantified in terms of amplitude of vibration.

The measurements were achieved with all the combinations of cable and adhesive in the scope, two different cables, steel reinforced and not reinforced, and three different glues. Indeed, all cables and glues tested shown good properties in terms of coupling and sensitivity for the intended goal of longitudinal axis displacement and Modal Analysis.

## ACKNOWLEDGMENTS

Prof. Mario Martinelli, Maddalena Ferrario, Jacopo Morosi and their team for the work on preparation, instrumentation and sharing data.

University Politecnico di Milano and its Department of Electronics, Information, and Bioengineering, as well as Coherentia Srl for the logistics and support during the preparation and first data analysis.

CaeMATE Srl for assisting the overnight tests and giving feedback from their theoretical models.

The operator of the infrastructure (undisclosed name - confidential) for granting access to their viaduct and allowing the overnight measurements with heavy trucks.

## REFERENCES

- [1] Calvi, G. M., Moratti, M., O'Reilly, G. J., Scattarreggia, N., Monteiro, R., Malomo, D., ... & Pinho, R. (2019). Once upon a time in Italy: The tale of the Morandi Bridge. *Structural Engineering International*, 29(2), 198-

- 217.
- [2] Cao, R., El-Tawil, S., & Agrawal, A. K. (2020). Miami pedestrian bridge collapse: Computational forensic analysis. *Journal of Bridge Engineering*, 25(1), 04019134.
  - [3] Figueiredo, E., & Brownjohn, J. (2022). Three decades of statistical pattern recognition paradigm for SHM of bridges. *Structural Health Monitoring*, 21(6), 3018-3054.
  - [4] Maurey, H., Chaize, P., & Dagbert, M. (2019). Sécurité des ponts : Éviter un drame.
  - [5] Anastasopoulos, D., De Roeck, G., & Reynders, E. P. (2021). One-year operational modal analysis of a steel bridge from high-resolution macrostrain monitoring: Influence of temperature vs. retrofitting. *Mechanical Systems and Signal Processing*, 161, 107951.
  - [6] Khoo, L. M., Mantena, P. R., & Jadhav, P. (2004). Structural damage assessment using vibration modal analysis. *Structural Health Monitoring*, 3(2), 177-194.
  - [7] Snover, D., Johnson, C. W., Bianco, M. J., & Gerstoft, P. (2021). Deep clustering to identify sources of urban seismic noise in Long Beach, California. *Seismological Society of America*, 92(2A), 1011-1022.
  - [8] Peeters, B., & De Roeck, G. (2001). One-year monitoring of the Z24-Bridge: environmental effects versus damage events. *Earthquake engineering & structural dynamics*, 30(2), 149-171.
  - [9] Magalhães, F., Cunha, Á., & Caetano, E. (2008). Dynamic monitoring of a long span arch bridge. *Engineering Structures*, 30(11), 3034-3044.
  - [10] Farrar, C. R., Doebling, S. W., & Nix, D. A. (2001). Vibration-based structural damage identification. *Philosophical Transactions of the Royal Society of London. Series A: Mathematical, Physical and Engineering Sciences*, 359(1778), 131-149.
  - [11] Magalhães, F., Cunha, Á., & Caetano, E. (2012). Vibration based structural health monitoring of an arch bridge: From automated OMA to damage detection. *Mechanical Systems and signal processing*, 28, 212-228.
  - [12] Rodet J., Tauzin B., Amin Panah M., Gueguen P., Nziengui BA D., Coutan O., Brule S. (2024). Urban dark fiber Distributed Acoustic Sensing for bridge monitoring. *E-Journal of Nondestructive Testing* - July 2024. ISSN 1425-4934.
  - [13] Hartog, A. H. (2018) *An Introduction to Distributed Optical Fibre Sensors*. CRC Press 2018-06-28.
  - [14] Tanimola, F., & Hill, D. (2009). Distributed fibre optic sensors for pipeline protection. *Journal of Natural Gas Science and Engineering*, 1(4-5), 134-143.
  - [15] Fichtner, A., Bogris, A., Nikas, T., Bowden, D., Lentas, K., Melis, N. S., ... & Smolinski, K. (2022). Theory of phase transmission fibre-optic deformation sensing. *Geophysical Journal International*, 231(2), 1031-1039.
  - [16] Froggatt, M., Soller, B., Gifford, D., & Wolfe, M. (2004, February). Correlation and keying of Rayleigh scatter for loss and temperature sensing in parallel optical networks. In *Optical fiber communication conference* (p. PD17). Optica Publishing Group.
  - [17] Gifford, D. K., Kreger, S. T., Sang, A. K., Froggatt, M. E., Duncan, R. G., Wolfe, M. S., & Soller, B. J. (2007, October). Swept-wavelength interferometric interrogation of fiber Rayleigh scatter for distributed sensing applications. In *Fiber Optic Sensors and Applications V* (Vol. 6770, pp. 106-114). SPIE
  - [18] Huynh C. Real-Time Classification of Anthropogenic Seismic Sources from Distributed Acoustic Sensing Data: Application for Pipeline Monitoring
  - [19] <https://www.febus-optics.com/fr/page/technology>.

# Experimental study on two tunnel micro-leakage monitoring methods based on distributed fiber optic sensing technology

Junyi Guo<sup>1</sup>, Bin Shi<sup>1</sup>, Jinhui Fang<sup>1</sup>, Hongtao Jiang<sup>2</sup>, Mengya Sun<sup>3</sup>

<sup>1</sup> School of Earth Sciences and Engineering, Nanjing University, No.163 Xianlin Avenue, 210023 Nanjing, China

<sup>2</sup> School of Geographic and Oceanographic Science, Nanjing University, No.163 Xianlin Avenue, 210023 Nanjing, China

<sup>3</sup> School of Earth Sciences and Engineering, Hohai University, No. 8 Focheng West Road, 210098 Nanjing, China

email: gjy@smail.nju.edu.cn, shibin@nju.edu.cn, MF2129004@smail.nju.edu.cn, jianghongtao@nju.edu.cn, smy@hhu.edu.cn

**ABSTRACT:** Real-time monitoring and accurate localization of pipeline leaks are crucial for pipeline safety. Conventional methods often fail to detect micro-leaks and face issues such as low positioning accuracy, high false alarm rates, and inability to monitor long distances. This study proposes two innovative leakage monitoring methods based on distributed temperature sensing (DTS) and distributed strain sensing (DSS). The first method utilizes evaporation-induced relative humidity measurement. By measuring the temperature of DTS fiber optic cables wrapped in gauze, real-time detection and localization of leaks in pipelines carrying ambient-temperature liquids can be achieved. A significant temperature drop at the leakage location allows precise identification of micro-leaks. The second method employs fiber optic cables with water-swelling blocking yarns for localized strain sensing, combined with Optical Frequency Domain Reflectometry (OFDR). At the leakage location, the strain of the sensing fiber significantly decreases, providing a distinct signal for detection. Indoor experiments confirmed the feasibility of both methods, demonstrating their ability to achieve real-time monitoring and precise localization of micro-leaks. These methods offer novel solutions for addressing pipeline leakage challenges.

**KEY WORDS:** Micro-Leakage; Distributed Fiber Optic Sensing; Distributed Temperature Sensing; Distributed Strain Sensing.

## 1 INTRODUCTION

Pipeline transportation is a widely adopted technology for conveying fluids such as gases and liquids. In recent years, it has developed rapidly and has been extensively applied in sectors such as energy, municipal infrastructure, and water conservancy due to its advantages of high transport capacity, small land footprint, short construction cycles, and low operational costs. As one of the five major modes of modern transportation—alongside rail, road, waterway, and air—pipeline systems have become the predominant solution for transporting water, oil, and gas across land, playing a critical role in national economic development and public safety [1,2].

However, as pipelines age, they become increasingly vulnerable to damage caused by thermal expansion and contraction, fatigue, corrosion, foundation settlement, or accidental excavation. These factors frequently lead to failures such as rupture or leakage, resulting in significant resource loss and economic damage. Consequently, real-time monitoring and accurate localization of pipeline leakage are essential to ensuring safe operation, protecting public assets, and maintaining system reliability [2].

Conventional leakage detection methods—such as the negative pressure wave, mass balance, ground-penetrating radar (GPR), capacitive sensing, electromagnetic reflection, and acoustic emission (AE)—have been widely utilized, but each presents notable limitations. While some offer advantages like fast response or low cost, they often suffer from poor localization accuracy, high false alarm rates, limited sensitivity to small or slow leaks, and an inability to monitor over long distances. For example, the negative pressure wave method is effective only for large and sudden leaks; the mass balance method lacks precise localization capability; and GPR and AE techniques are heavily dependent on operator expertise and are

sensitive to environmental noise. These drawbacks significantly restrict their applicability in large-scale or complex pipeline systems.

In this context, distributed fiber optic sensing (DFOS) has emerged as a promising alternative, offering numerous advantages such as corrosion resistance, compact structure, high sensitivity, immunity to electromagnetic interference, and long-term operational stability [3]. By monitoring physical parameters such as temperature, strain, or vibration, DFOS enables distributed and real-time leak detection with high spatial resolution.

Among DFOS techniques, temperature-based methods have been most extensively studied. For instance, Vogel et al. [4] employed Distributed Temperature Sensing (DTS) to detect pipeline leaks by identifying abnormal temperature variations, a method that has since gained widespread adoption. Wang et al. [5] applied Brillouin Optical Time-Domain Reflectometry (BOTDR) for temperature-based leak detection and investigated how different installation methods influence sensing performance. However, these approaches typically rely on a significant temperature difference between the leaking fluid and the surrounding environment. To address this issue, some researchers have introduced active heating of the fiber to enhance detection sensitivity [6], though this introduces safety concerns in environments containing flammable gases. Commercial systems such as Omnisens DiTeST, which utilize both Brillouin and Raman scattering to monitor temperature and strain, can detect large-scale leaks but usually require the leakage volume to exceed 0.01% of the total flow to be identified [7].

Additional innovations include MacLean's polymer-embedded fiber design, which swells upon contact with leak fluids and causes signal attenuation detectable via Optical



Time-Domain Reflectometry (OTDR) [8]. While effective, this design is single-use and must be replaced after each leak event. Similarly, Jia et al. adopted Brillouin Optical Time-Domain Analysis (BOTDA)-based strain sensors, which exhibited significant accuracy degradation and poor reusability after leakage exposure. Interferometric methods such as Sagnac or Mach-Zehnder configurations offer high sensitivity but require complex signal processing. Moreover, Stajanca et al. [9] applied Distributed Acoustic Sensing (DAS) based on Rayleigh scattering to detect vibrations from gas leaks, but the method was highly susceptible to environmental noise, had low localization accuracy, and consumed large amounts of optical fiber.

Despite these advancements, current DFOS-based technologies still face three main challenges:

(1) limited ability to detect ambient-temperature liquid leaks without external heating;

(2) low sensitivity to small or slow leakage events, resulting in potential missed detections; and

(3) dependence on non-reusable sensing materials, such as polymer coatings that degrade upon fluid exposure.

To address these limitations, this study proposes two novel DFOS-based methods for micro-leakage monitoring in tunnel pipelines. The first method utilizes evaporation-induced humidity sensing, in which a gauze-wrapped DTS fiber detects localized temperature drops caused by water evaporation at leak points. The second method employs Optical Frequency Domain Reflectometry (OFDR)-based strain sensing, using fiber optic cables integrated with water-swelling blocking yarns that exhibit measurable strain changes upon contact with leaking fluid.

## 2 MATERIALS AND METHODS

### 2.1 Pipeline Leakage Sensing Principle Based on EETS-DTS

Distributed Temperature Sensing (DTS) technology measures temperature along an optical fiber by exploiting the temperature-dependent intensity ratio between Stokes and anti-Stokes components of Raman backscattered light. When a pump pulse is launched into the fiber by a DTS laser source, photon-molecule interactions generate backscattered Raman signals at two distinct frequencies—Stokes and anti-Stokes. The Stokes signal intensity is largely temperature-independent, while the anti-Stokes intensity is strongly temperature-sensitive, increasing with local fiber temperature.

The DTS interrogator calculates the temperature at each point by computing the intensity ratio of the anti-Stokes to Stokes signals and locates the scattering position using the round-trip travel time of the light pulse. The temperature  $T$  can be expressed as follows:

$$R(T) = \frac{I_F}{I_S} = \left(\frac{\nu_F}{\nu_S}\right)^4 e^{\frac{-h\nu}{KT}} \quad (1)$$

where  $R(T)$  is the temperature function,  $I_F$  is the anti-Stokes light intensity,  $I_S$  is the Stokes light intensity,  $\nu_S$  is the central frequency of the Stokes component,  $\nu_F$  is the central frequency of the anti-Stokes component,  $c$  is the speed of light in vacuum,  $\nu$  is the Raman shift,  $K$  is the Boltzmann constant,  $h$  is the Planck constant, and  $T$  is the absolute temperature.

The distance from the laser input to the scattering point can be determined by:

$$X = \frac{cT}{(2n)} \quad (2)$$

where  $X$  is the distance,  $v$  is the speed of light in vacuum,  $t$  the travel time of the light and  $n$  is the refractive index of the fiber. By combining Equations (1) and (2), the temperature at any point along the fiber can be measured in a distributed manner.

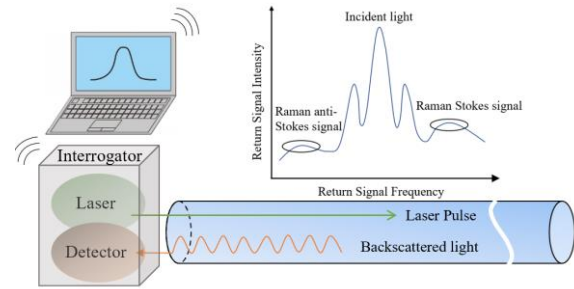


Figure 1. Principle of distributed temperature sensing (DTS) technology.

In unsaturated air, evaporation can occur at any temperature. When leakage occurs in a pipeline, the leaked liquid may come into contact with the sensing cable. However, conventional temperature-sensing cables have smooth outer surfaces, which inhibit significant evaporation, leading to minimal temperature drop. To enhance detection sensitivity, Sun et al. [10] proposed wrapping the fiber with porous gauze, which increases water absorption and promotes evaporation.

The proposed Evaporation-Enhanced Temperature Sensing DTS (EETS-DTS) method involves deploying a gauze-wrapped DTS cable beneath the pipeline. The gauze absorbs leaking water and facilitates capillary spreading due to its high porosity and large surface area. This promotes enhanced evaporation, resulting in a localized temperature decrease at the leak site, which is detected by the DTS system. Over time, a thermal equilibrium is reached between the heat loss due to evaporation and the heat supplied by ambient air, causing the gauze temperature to stabilize at a value lower than the surrounding dry areas.

For ambient-temperature water leakage, the temperature difference  $\Delta T$  between dry and wet cables can be estimated using the World Meteorological Organization (WMO) psychrometric formula:

$$\Delta T = T_1 - T_2 = \frac{e_w(t_2) - U/100 \cdot e_w(t_1)}{AP} \quad (3)$$

where  $e_w(T_1)$  and  $e_w(T_2)$  are the saturated vapor pressures corresponding to the dry and wet cable temperatures,  $U$  is the relative humidity (%RH),  $A$  is the psychrometric coefficient (related to air velocity and sensor design), and  $P$  is the atmospheric pressure (MPa). Hence, the temperature difference is mainly influenced by humidity and ventilation conditions.

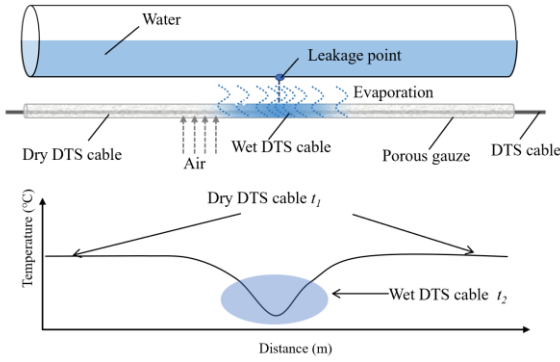
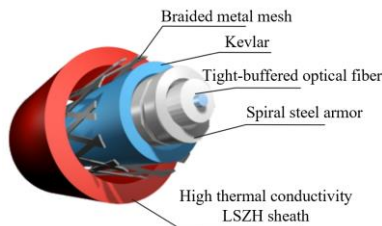


Figure 2. Schematic of the EETS-DTS leakage detection principle.

The DTS cable used in this study (model NZS-DTS-C09) has an outer diameter of 5 mm and consists of five structural layers: a tight-buffered optical fiber, spiral steel armor, Kevlar yarn, braided metal mesh, and a protective outer sheath (Figure 3). The spiral armor and braided mesh provide mechanical protection, the Kevlar layer enhances tensile strength, and the outer sheath offers good thermal conductivity and flame resistance. The cable operates reliably within a temperature range of  $-20^{\circ}\text{C}$  to  $85^{\circ}\text{C}$ .

Temperature data are collected using a DTS interrogator (model NZS-DTS-A03), manufactured by Suzhou Nanzee Sensing Technology Co., which provides high-resolution distributed temperature profiling along the fiber. The key specifications of the device are listed in Table 1.

(a)



(b)



Figure 3. Structure of the DTS temperature-sensing cable: (a) Schematic diagram; (b) Physical photograph.

Table 1. Specifications of the DTS interrogator.

Parameter type	Value
Measurement range (km)	1~16
Temperature range ( $^{\circ}\text{C}$ )	$-40\sim 120$
Fiber type	Multimode 62.5/125 or 50/125
Temperature accuracy ( $^{\circ}\text{C}$ )	$\pm 0.3$
Temperature resolution ( $^{\circ}\text{C}$ )	0.1
Response time (s)	2 s/channel
Spatial resolution (m)	0.5~3
Number of channels	4
Fiber connector type	FC/APC
Communication interface	USB / RS232 / Ethernet
Power supply	DC19V

## 2.2 Pipeline Leakage Sensing Principle Based on OFDR

Optical Frequency Domain Reflectometry (OFDR) is a high-resolution sensing technique based on frequency-swept continuous wave interferometry (FMCW). It employs a laser source with linear wavelength sweep combined with heterodyne detection. The optical signal is split into two arms: a reference arm and a signal arm. Due to differences in optical path lengths, the Rayleigh backscattered signal from the sensing fiber interferes with the reference signal, producing a beat frequency that is directly proportional to the scattering position. By applying a Fast Fourier Transform (FFT) to the interference signal, a spatially resolved Rayleigh scattering profile can be obtained.

Rayleigh scattering originates from random microscopic fluctuations in the refractive index of the fiber. Froggatt and Moore modeled these variations as a weak random Bragg grating. When external strain is applied to the fiber, the local spectrum of the Rayleigh scattering shifts. The magnitude of this spectral shift is linearly proportional to the applied strain. By comparing the shifted spectrum with a reference state, the strain distribution along the fiber can be quantified with high spatial resolution.

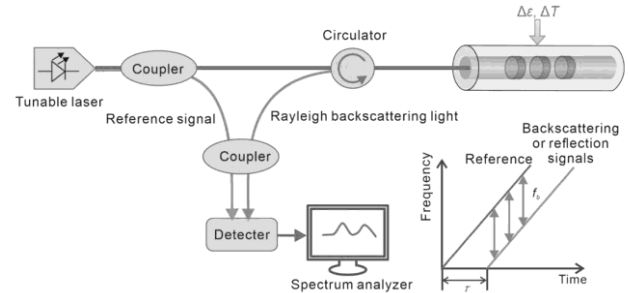


Figure 4. Measurement principle of OFDR.

Building upon the high-resolution strain measurement capability of OFDR, this study proposes a novel strain-sensing cable that incorporates water-swelling yarns into a fixed-point sensing structure. These yarns are made of polyester filaments coated with super-absorbent polymers (SAPs) and are commonly used as water-blocking fillers in optical cables. The SAPs contain abundant hydrophilic functional groups and a moderately cross-linked polymer network, enabling them to absorb water up to hundreds or even thousands of times their own weight. Once hydrated, the yarns expand into a hydrogel, maintaining structure under pressure and remaining functional under thermal cycling.

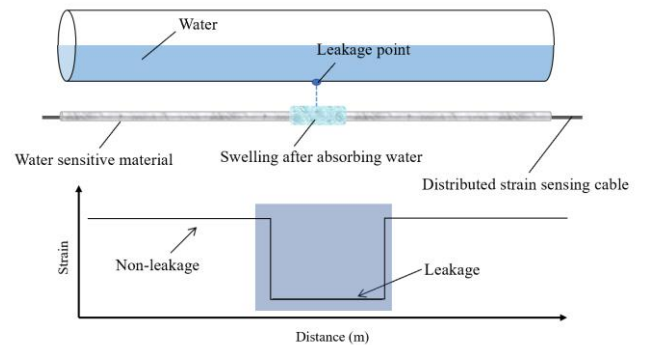


Figure 5. Schematic of pipeline leakage detection using OFDR and water-swelling yarns.

In the proposed sensing cable, the fiber is pre-tensioned between discrete fixed points. Upon contact with leaked liquid, the SAP yarns rapidly swell, reducing the tensile force acting between anchor points. This localized strain reduction is accurately captured by the OFDR system, allowing for precise leakage detection. The cable features a four-layer construction, consisting of: a 0.9 mm tight-buffered strain-sensing fiber, a spiral armored tube, water-swelling yarn, and an outer braided mesh (Figure 6).

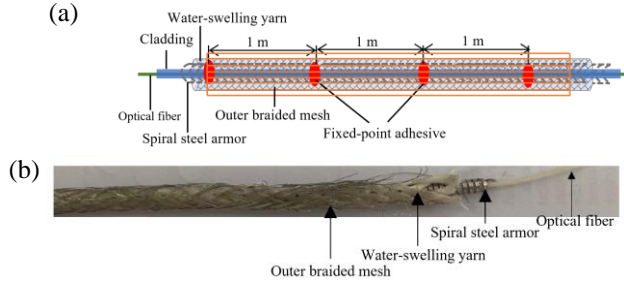


Figure 7. Structure of the strain-sensing cable with water-swelling yarns: (a) Schematic diagram; (b) Physical photograph.

The cable is fixed at 1-meter intervals, creating a structure with discrete sensing segments. The outer mesh ensures that the yarn remains in place during operation. The yarn itself consists of two components: a super-absorbent polymer (e.g., polyacrylate), which swells when exposed to water, and reinforcement fibers (e.g., nylon or polyester), which improve tensile strength and elongation properties. The key specifications of the water-swelling yarn and the OFDR interrogator (model OSI-S) are presented in Tables 3 and 4, respectively.

Table 3. Performance parameters of water-swelling yarn.

Property	Value
Yarn linear density (dtex)	3330
Basis weight (m/kg)	3000
Breaking strength (N)	≥100
Elongation (%)	15
Swelling rate (ml/g in 1st minute)	≥60
Long-term thermal swelling (150 °C, 24 h, ml/g)	≥65
Instant thermal swelling (230 °C, 10 min, ml/g)	≥65
Moisture content (150 °C, 1 min)	9

Table 4. Specifications of OSI-S OFDR interrogator.

Type	Specification
Portable enclosure dimensions (mm)	280×250×164
Portable enclosure weight (kg)	4.5
Spatial resolution (mm)	1-100
Maximum sampling resolution (mm)	1
Temperature accuracy (°C)	±0.1
Temperature repeatability (°C)	≤0.1
Measurement range (m)	100

### 3 RESULT

#### 3.1 EETS-DTS Monitoring

Based on the spatial resolution of the DTS system, the length of gauze wrapping on the EETS cable was set to 1.8 meters. To simulate leakage, a 2-meter-long PVC pipe with an inner diameter of 75 mm and a leakage hole at the bottom was used. The fiber optic cable was secured directly beneath the pipe using plastic zip ties. Before the experiment, the water inside the pipe was left to stand for 24 hours to allow its temperature to reach equilibrium with ambient conditions.

During the test, the PVC pipe was maintained in a fully filled state. A dual-probe PT100 thermometer was employed to continuously monitor and record both the water temperature inside the pipe and the ambient air temperature. As humidity can significantly influence evaporative cooling, a digital hygrometer was placed near the pipe to record ambient relative humidity throughout the experiment.

The DTS temperature-sensing cable was connected to a temperature calibration box, which in turn was linked to the DTS interrogator, enabling real-time acquisition of the distributed temperature profile along the fiber. The complete experimental setup is shown in Figure 8.



Figure 8. Photograph of the experimental setup.

Figure 9 presents the temperature variation trends at different positions along the bare DTS cable wrapped with gauze. The observed behavior is consistent with that of the sheathed cable: the temperature at each point decreases over time, and the closer a point is to the leakage location (located at 6.02 m), the greater the temperature drop. Furthermore, the temperature distribution is approximately symmetrical about the leakage point.

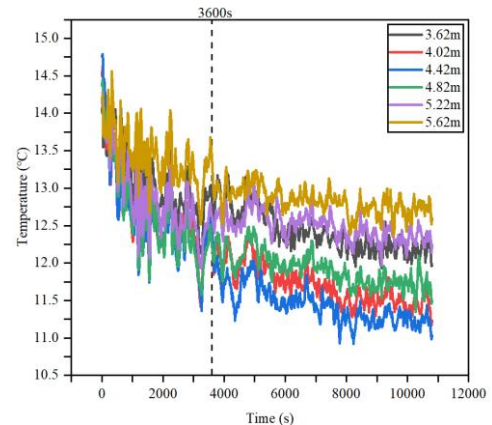


Figure 9. Temperature variation trends at different positions along the bare DTS temperature-sensing cable.



However, in contrast to the sheathed condition, where temperatures eventually stabilized, the bare cable setup exhibited a continuous temperature decrease over time, without reaching equilibrium. This indicates that the evaporative heat loss exceeded the heat replenishment from the surrounding environment, suggesting that a dynamic thermal balance was not achieved during the experiment. One possible explanation is that, in this configuration, the gauze was directly wrapped onto a copper mesh, enhancing the fluid contact efficiency and promoting stronger evaporation, which resulted in sustained cooling.

Figure 10 illustrates the temperature distribution profiles along the bare cable at different time intervals. Similar to the sheathed condition, the temperature profile forms a characteristic “arch-shaped” curve, indicating that the temperature is lowest near the leakage point at any given time. However, compared with the sheathed cable, the bare cable exhibits a sharper temperature gradient, with a maximum temperature difference of 2.8 °C observed at 3600 seconds.

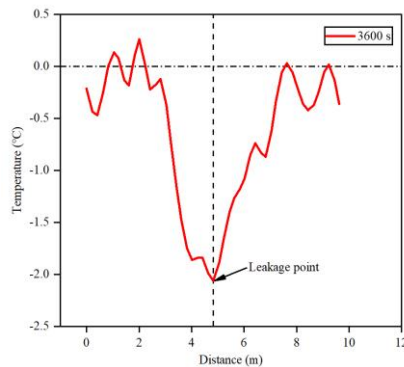


Figure 10. Temperature distribution along the bare DTS sensing cable at 3600 s.

These results indicate that the protective sheath has a noticeable effect on the EETS-DTS leakage detection performance. The bare cable yields clearer monitoring results, suggesting improved sensitivity. Therefore, the following sections focus on analyzing influencing factors for the bare EETS-DTS configuration.

### 3.2 OFDR-Based Monitoring

In this experiment, a peristaltic pump was employed to control the leakage rate, and both ends of the strain-sensing optical fiber cable—embedded with water-swelling yarns—were fixed in place. The leak outlet of the pump was precisely aligned with the sensing section of the cable. The selected leakage rate was 70 mL/min. The OFDR interrogator was connected to capture wavelength shift data corresponding to strain variations. The experimental setup is shown in Figure 11.

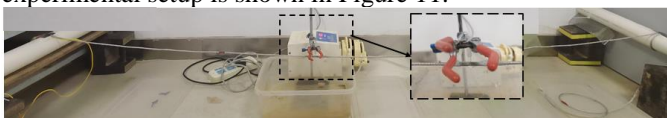


Figure 11. Experimental setup for OFDR-based leakage monitoring.

The measured strain distribution along the fiber is shown in Figure 12. Upon leakage, the strain recorded by the OFDR

system dropped sharply and then stabilized. Throughout the leakage process, the strain-affected segment—defined by a significant drop in measured strain—spanned from 3.36 m to 4.36 m. In contrast, the rest of the cable exhibited minimal strain change, resulting in a distinct step-like pattern in the strain profile.

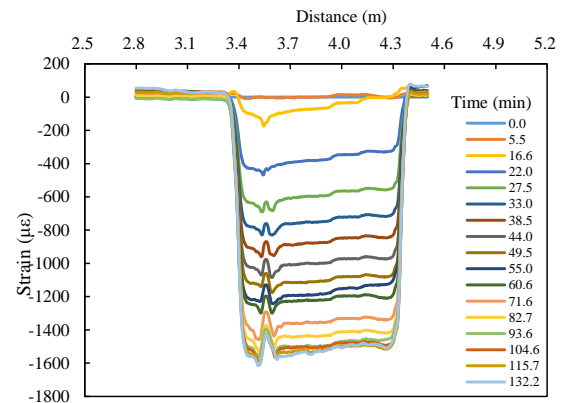


Figure 12. Strain magnitude measured by the fixed-point strain-sensing cable with water-swelling yarns.

To further analyze strain behavior, two points were selected: one located within the strain-drop region and the other outside it. Their strain variation over time is compared in Figure 13. It is evident that the strain at the leakage point decreased rapidly at first, followed by a gradual stabilization, while the unaffected region maintained a stable strain level throughout. The time required for the strain to stabilize was approximately 100 minutes.

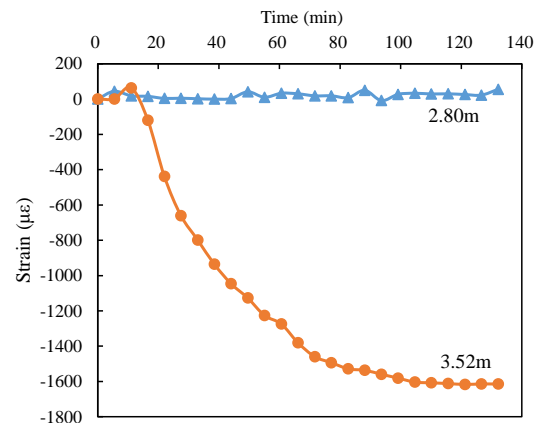


Figure 13. Strain variation over time at the leakage point of the strain-sensing cable with water-swelling yarns.

## 4 DISCUSSION

### 4.1 Applicability Analysis

This study presents two pipeline leakage monitoring methods: one based on evaporation-induced humidity sensing using DTS, and the other based on strain sensing using Optical Frequency Domain Reflectometry (OFDR) combined with water-swelling yarns. Both methods are suitable for detecting ambient-temperature liquid leaks in environments where the pipeline is exposed to air, such as underground utility corridors and aboveground pipelines. However, they are not applicable to

buried pipelines, where direct air contact is absent, and evaporation or swelling may be inhibited.

The current work focuses on leakage scenarios involving water as the leaking medium. The effectiveness of these methods for other fluid types (e.g., oils, chemicals) requires further study, as variations in fluid properties may affect evaporation behavior or interaction with swelling materials.

The first method, based on evaporation sensing (EETS-DTS), is generally applicable in a wide range of environments and performs especially well in conditions with low humidity and high airflow, which enhance evaporation and generate more distinct temperature differences. In high-humidity environments, however, evaporation may be limited or suppressed, leading to reduced sensitivity or loss of functionality.

The second method, based on OFDR strain sensing with water-swelling yarns, demonstrates broader applicability. It is insensitive to environmental variables such as humidity and wind speed and exhibits high sensitivity, enabling the detection of small-scale or micro-leaks with better reliability.

#### 4.2 Practical Application Analysis

Both methods offer distributed monitoring capabilities for pipeline leakage and are particularly advantageous for detecting small-volume, ambient-temperature liquid leaks. They are well-suited for underground utility corridors and open-air pipelines, where sensing cables can be conveniently installed beneath the pipelines.

The EETS-DTS method supports long-distance distributed measurement, but it offers relatively low measurement accuracy. In practical scenarios, elevated ambient humidity may cause natural temperature fluctuations, leading to false positives. Additionally, in harsh environments—such as acidic, dusty, or corrosive conditions—the gauze layer may degrade or fail over time, compromising the monitoring performance. For long-term or demanding applications, regular gauze replacement is recommended to ensure reliability.

The fixed-point strain-sensing cable embedded with water-swelling yarns also enables distributed leakage detection. However, given that standard OFDR systems are limited to approximately 100 meters, it is advisable to adopt alternative demodulation technologies such as Brillouin Optical Domain Frequency Analysis (BODFA) or Brillouin Optical Time-Domain Reflectometry (BOTDR) for longer-distance applications.

In practical deployment, a hybrid monitoring strategy is recommended: (1) Use the EETS-DTS method in well-ventilated, low-humidity environments to take advantage of its evaporation-based sensitivity. (2) In environments where the EETS-DTS method is inapplicable or limited, deploy the strain-sensing cable with water-swelling yarns to ensure continued leakage detection.

## 5 CONCLUSION

This study proposed and experimentally validated two novel pipeline leakage monitoring methods based on distributed fiber optic sensing (DFOS): an evaporation-enhanced temperature sensing method using DTS (EETS-DTS), and a fixed-point strain sensing method using OFDR combined with water-swelling yarns. Both approaches demonstrated effective

capabilities for detecting small-scale leaks of ambient-temperature liquids in tunnel or aboveground pipeline environments.

The EETS-DTS method leverages gauze-wrapped optical fibers to amplify evaporation-induced temperature differences, enabling distributed leak localization with a relatively simple setup. It is particularly effective in low-humidity, well-ventilated environments. The OFDR-based strain sensing method utilizes the swelling behavior of specially embedded yarns to detect leakage-induced strain changes with high resolution and sensitivity, and is less affected by environmental variables.

Laboratory experiments confirmed the feasibility and reliability of both methods. The EETS-DTS technique offers advantages in long-range monitoring, while the OFDR-based method provides high accuracy in micro-leak detection. A hybrid deployment strategy is recommended to combine the strengths of both approaches for broader practical applicability.

Overall, the proposed methods provide promising and complementary solutions for pipeline leakage monitoring, offering new perspectives for enhancing infrastructure safety and maintenance in complex pipeline networks.

## ACKNOWLEDGMENTS

This research was financially supported by the National Natural Science Foundation of China, NSFC (Grant Nos. 423B2704, 42177135, 42030701).

## REFERENCES

- [1] S. Beskhyroun, L.D. Wegner, and B.F. Sparling, Integral resonant control scheme for cancelling human-induced vibrations in light-weight pedestrian structures, *Structural Control and Health Monitoring*, vol. 22, no. 1, 2012, pp. 55–69.
- [2] L. Ren, T. Jiang, Z. Jia, D. Li, C. Yuan, and H. Li, Pipeline corrosion and leakage monitoring based on the distributed optical fiber sensing technology, *Measurement*, vol. 122, 2018, pp. 57–65.
- [3] B. Shi, D. Zhang, H. Zhu, C. Zhang, K. Gu, H. Sang, H. Han, M. Sun, and J. Liu, DFOS applications to geo-engineering monitoring, *Photonic Sensors*, vol. 11, 2021, pp. 158–186.
- [4] B. Vogel, C. Cassens, A. Graupner, and A. Trostel, Leakage detection systems by using distributed fiber optical temperature measurement, in *Smart Structures and Materials 2001: Sensory Phenomena and Measurement Instrumentation for Smart Structures and Materials*, vol. 4328, International Society for Optics and Photonics (SPIE), 2001, p. 23.
- [5] F. Wang, Z. Sun, F. Zhu, C. Zhu, Y. Pan, J. Dong, X. Zhang, and L. Gao, Research on the leakage monitoring of oil pipeline using BOTDR, in *Progress in Electromagnetics Research Symposium (PIERS)*, 2016, pp. 4907–4910.
- [6] W. Li, T. Liu, and H. Xiang, Leakage detection of water pipelines based on active thermometry and FBG-based quasi-distributed fiber optic temperature sensing, *Journal of Intelligent Material Systems and Structures*, vol. 32, 2021, pp. 1744–1755.
- [7] D. Inaudi and B. Glisic, Long-range pipeline monitoring by distributed fiber optic sensing, *Journal of Pressure Vessel Technology*, *Transactions of the ASME*, vol. 132, 2010, pp. 011701-1–011701-9.
- [8] A. MacLean, C. Moran, W. Johnstone, B. Culshaw, D. Marsh, and P. Parker, Detection of hydrocarbon fuel spills using a distributed fibre optic sensor, *Sensors and Actuators A: Physical*, vol. 109, 2003, pp. 60–67.
- [9] P. Stajanca, S. Chruscicki, T. Homann, S. Seifert, D. Schmidt, and A. Habib, Detection of leak-induced pipeline vibrations using fiber-optic distributed acoustic sensing, *Sensors (Switzerland)*, vol. 18, 2018.
- [10] M. Sun, B. Shi, D. Zhang, C. Feng, J. Wu, and G. Wei, Pipeline leakage monitoring experiments based on evaporation-enhanced FBG temperature sensing technology, *Structural Control and Health Monitoring*, vol. 28, 2021, pp. 3–6.



# Point Cloud Data Applications to evaluate Structural Conditions and Performances



## A PC based FE model as an innovative learning tool in structural mechanics

Yasunori Miyamori<sup>1</sup>, 0000-0003-2686-8062, Kakeru Komuro<sup>2</sup>, Soushi Suto<sup>2</sup>, Takanori Kadota<sup>3</sup>, 0009-0008-1645-3078, Takehiko Saito<sup>3</sup>

<sup>1</sup>Division of Civil Engineering, Faculty of Engineering, Hokkaido University,  
Kita 13 Nishi 8 Kita-Ku, 060-8628 Sapporo, Japan

<sup>2</sup>Division of Engineering and Policy for Sustainable Environment, Graduate School of Engineering, Hokkaido University,  
Kita 13 Nishi 8 Kita-Ku, 060-8628 Sapporo, Japan

<sup>3</sup>Division of Civil and Environmental Engineering, Faculty of Engineering, Kitami Institute of Technology,  
Koen-cho 165, 090-8507 Kitami, Japan

email: miyamori.y@eng.hokudai.ac.jp, komuro.kakeru.e7@elms.hokudai.ac.jp, suto.soushi.f2@elms.hokudai.ac.jp,  
kadotaka@mail.kitami-it.ac.jp, saitota@mail.kitami-it.ac.jp

**ABSTRACT:** Recent developments in digital technology make it possible to create interactive 3D models for structural analysis in a user-friendly software environment. In addition, the technology for creating 3D models of real structures using point cloud data for various users is also developing rapidly. Such rapid change may raise concerns about a developing gap between traditional structural mechanics education based on beam theory and the modern structural analysis scheme. However, if it becomes possible to efficiently perform structural analysis by recreating structures in cyberspace without special skills, it will be beneficial to cultivate a sense of structural mechanics for beginners. In this study, we investigated the feasibility and simplicity of constructing a point cloud-based structural analysis model to capture the general trend of deformation and stress in a structure. Specifically, we constructed a point cloud model from photographs of an approximately 2m long steel plate girder bridge using the SfM technique, meshing the model, and assembled a solid FE model using only general functions of packaged software without any special operations for model modification. We compared the strain in the constructed model under static loading with the actual measured values for the bridge. The model properly calculated the deflection shape, and it will help learners understand structural mechanics.

**KEY WORDS:** Structure from Motion, Point cloud model, Structural mechanics.

### 1 INTRODUCTION

Our predecessors have taught us that the history of structural mechanics is a repeated process of observing phenomena through experimentation, and then formulating and systematising them [1], [2]. Today, students can learn about systematised structural mechanics efficiently. In exchange for these fruits, many students are passive and just learn how to solve problems.

On the other hand, recent developments in structural analysis software have made it possible to precisely analyse structures' deformation and stress distribution with complicated shapes and materials. In addition, it has become possible to model even existing structures easily using point cloud technology[3]. Researches have been conducted on utilising point cloud data for structural analysis. However, they require advanced or complex procedures developed by each researcher[4], [5]. We have yet to fully benefit from them in structural engineering. Bridging the gap between cutting-edge structural analysis technology and traditional structural mechanics education or feeding back the latest technology to the learning of beginners will increase the attractiveness of this engineering area.

The authors investigated the technique of constructing precise structural models of actual structures from point cloud models using SfM (Structure from Motion) or photogrammetry techniques. We have also developed a method for converting point cloud models into 3D FE models that can be used for structural analysis. Through this research, it has become possible to model the damaged actual structures with a certain degree of precision and to evaluate the stress of damaged members. On the other hand, modelling point clouds into appropriate shapes of FE models requires a relatively

complicated procedure, and fine-tuning of parameters is also necessary individually. The precise evaluation of structural performance with automated procedures from point cloud data is the ambitious goal; however, even if the analytical accuracy is somewhat limited, more straightforward procedures will enhance the possibility of structural mechanics.

In this study, we investigated the feasibility and simplicity of constructing a point cloud-based structural analysis model to capture the general trend of deformation and stress in a structure. Specifically, we constructed a point cloud model from photographs of an approximately 2m long steel plate girder bridge using the SfM technique, meshing the model, and assembled a solid FE model using only general functions of packaged software without any special operations for model modification. We compared the strain in the constructed model under static loading with the actual measured values for the bridge.

### 2 FE MODEL FROM POINT CLOUD

#### 2.1 A model bridge and point cloud model

A simple steel girder bridge, an out-of-service railway bridge located on a test bed consisting of two main girders made of rolled I-shaped steel[4], was subject to study. The length of the girder is 2.4 m, and the total width of the bridge is 1.1 m. The steel surface was generally rusted, but there was no significant reduction in thickness. A damaged state was prepared by grinding a 200×68.5 mm area on the top surface of the lower flange at the mid-span of one girder.

The static loading experiment was conducted by placing steel plates on top of the main girders to create a two-point loading

condition as shown in Figure 1. The loading weight is 80 kN. Strain gauges measured strain at the mid-span of girders. The point cloud model of the bridge was constructed using SfM. A SONY  $\alpha 6500$  digital camera captured 2,969 images from around the bridge. The vertical and horizontal overlap rates were set to 80% or more. The Agisoft's Metashape (ver1.6.5.11249) loaded captured images and constructed a tie point cloud with high accuracy. Then, a point cloud model was constructed at medium quality and high-depth filter settings. Figure 2 shows the point cloud model of the bridge. There were no missing points in the entire point cloud. Table 1 shows the plate thickness of the damaged bridge at the center cross-section of the span. The average error was 1.1 mm, and the model was generally accurate. The reduction in plate thickness of the damaged area was also modeled.

## 2.2 Conversion method into FE model

Because the number of points in the point cloud model was enormous, a voxel grid was set on the point cloud, and a voxel downsampling was applied to create nodes. The grid size, which was set to 9mm or 18mm in this study, corresponds to the mesh size of the FE model. The centroid of the point cloud within the grid was then calculated as the node of the FE model.

The girders were divided into web and flanges using the maximum and minimum z-coordinates of the web. The maximum and minimum values were calculated by using the normal vector for each point.

To create a cross-section, align only the x-coordinate value of each point along the component's axis to the same plane. An outline of a section was created along the component's axis. The shape of the outline was controlled by a shrink factor determined by trial and error for each component.

Figure 3 shows the concept of element generation. A 2D Delaunay triangulation was first performed on each cross-sectional outline, dividing the 2D region into triangles using an arbitrarily set group of nodes. Next, the process of generating solid elements was applied to all cross-sections where 2D Delaunay triangulation was performed. For each triangular element on the  $S_n$  cross-section, the closest point on the  $S_{n+1}$  cross-section was found, and triangular solid elements were formed by connecting these points. Lastly, the web and flanges were reconnected using a similar way of generating the solid elements of each component.

The elements and node information were exported to a NAS file and then imported into the structural analysis software Midas NFX. The constructed FE model of the damaged bridge, which is called Model A, will be shown in Figure 4. The analytical result will be discussed in Chapter 4.

## 3 A SIMPLE METHOD FOR POINT CLOUD BASED FEM

The recent development of image processing technologies and laser ranging technologies have brought about several options to obtain point cloud models of structures. If more straightforward procedures can be utilized to construct the FE model from the point cloud model, structural analyses will be much more user-friendly for non-professional users. Therefore, the authors explored a method to compose an FE model using only general software without original codes. The proposed steps are as follows:



Figure 1. Static loading experiment.

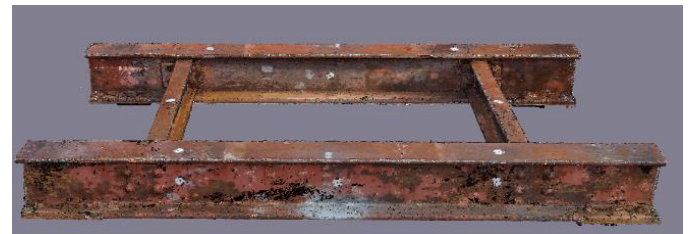


Figure 2. A point cloud model of a simple girder bridge.

Table 1. Plate thickness (mm).

		Real	P.C. model
Upper flange (G1)		20.0	19.6 (-0.4)
Web (G1)		15.0	13.1 (-1.9)
Lower flange (G1)	outside	15.0	12.6 (-2.4)
	inside	10.0	10. (+0.4)
Upper flange (G2)		20.0	19.7 (-0.3)
Web (G2)		15.0	12.2 (-2.8)
Lower flange (G2)		20.0	20.1 (+0.1)

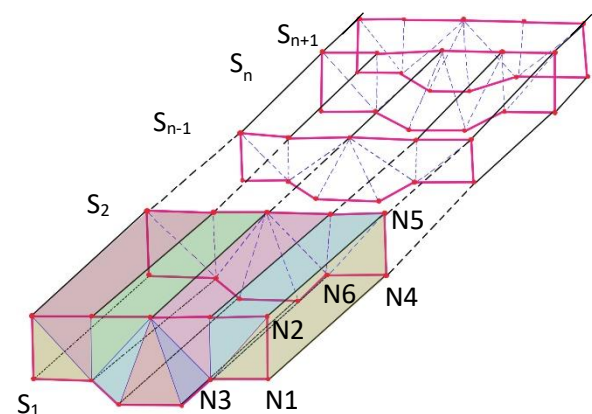


Figure 3. Concept of elements generation.

- I. Loading the point cloud data by scanning and meshing software for point cloud data.

In this study, Autodesk ReCap Pro loaded the same point cloud data in the previous chapter. Downsampling is also conducted in the software to 25% of the original point cloud model.

- II. The meshing of the point cloud model

Convert the point cloud to a mesh using the scan-to-mesh service from ReCap with the medium-quality setting.

- III. Converting the meshed data into a 3D object

Recap Photo converts the meshed data to 3D object data in an FBX format. The target face count is decimated by 90%.

- IV. Transformation of the mesh body into a solid body

Autodesk Fusion opens the FBX file and closes the mesh. The mesh body has mass and volume, and then the mesh body is converted into a solid body with the facet option.

The constructed FE model of the bridge, which is called Model B, will be shown in Figure 5, and the analytical result will also be discussed in Chapter 4.

#### 4 LINEAR STATIC LOADING ANALYSES

Linear static analysis is conducted for the constructed 2 FE models; Model A was originally developed by the authors [4], and Model B was the proposed simple model in this study. The boundary conditions in the FE models were applied to the points on the underside of the sole plate, assuming the simple support condition. For the loading conditions, vertical downward loads of 80 kN in total acted at 4 points 400 mm away from the midspan to the support. In Model A, distributed load acted on nodes within the experimental loaded area. On the other hand, 4 concentrated loads were applied in Model B because the size of the automated generated mesh was not uniform and was larger than that of Model A. Commercial software Midas NFX for Model A and Fusion for Model B calculated the stress and deformation of the model.

Figure 4 and Figure 5 show the longitudinal bending stress distribution and the enlarged deformation in Models A and B, respectively. Both figures show that stress distribution and deformation indicate positive bending in the structure.

In the damaged area of Model A, tensile stress increases due to the introduction of damage at the midspan of the lower flange, and compressive stress predominates in the loaded area. The error in the experimental result was about 6% for the nodal longitudinal stress at the damaged point.

On the other hand, the stress value of Model B is generally half of the stress of Model A. The thickness of plates was generally identical to the point cloud model and the actual structure in both FE models. However, the web plates of Model B have some thick parts due to rivets of connection and the roughness of the paint, and they may cause the reduction of stress. The error in the calculated stress is caused by such mesh configuration of Model B because both models are generated from the same point cloud data. Additionally, due to the low density of nodal points, a local torsional deformation occurs in the upper flange because of the eccentric loading at the upper flange, which was not observed in the experiment.

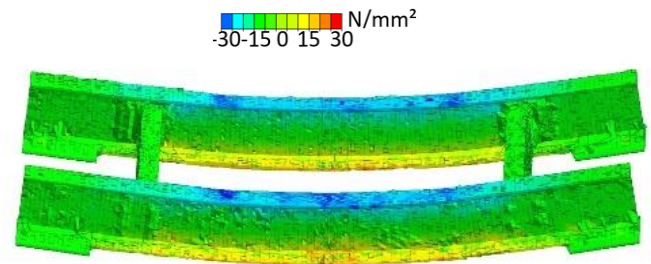


Figure 4. The analytical result of Model A.

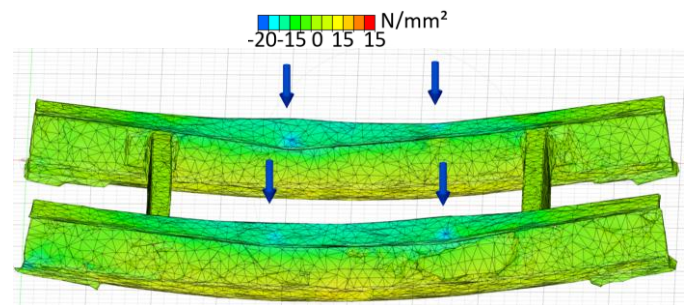


Figure 5. The analytical result of Model B.

#### 5 CONCLUSION

The authors have developed the construction method of the FE model from point cloud models. Because straightforward procedures will enhance the possibility of structural mechanics, we investigated the feasibility and simplicity of constructing a point cloud-based structural analysis model using only general functions of packaged software without any special operations for model modification. From the analytical results of a 2m long steel girder bridge, the global tendency of deformation and stress of the structure could be obtained, although the precision of calculated stress needs to be improved. The reproducibility and stability of composing mesh and solid are also subjects to be improved. However, future developments of this technique will provide a powerful tool for learners in structural mechanics and motivate the development of innovative construction design and effective maintenance methods.

#### REFERENCES

- [1] S. P. Timoshenko, History of Strength of Materials, McGraw-Hill Book Company, New York, USA, 1953.
- [2] F. Takabeya, History of Structural Mechanics (in Japanese), Shokokusha Publishing Co. Ltd., Tokyo, Japan, 1957.
- [3] H. Kim, J. Yoon, J. Hong, S.H. Sim, Automated damage localization and quantification in concrete bridges using point cloud-based surface-fitting strategy. *Journal of Computing in Civil Engineering*, 35(6), 2021.
- [4] K. Komuro, Y. Miyamori, M. Yoshida, T. Kadota, T. Saito, Construction of a point cloud FE model for a real structure with local damage and evaluation of its element shape, *Proceedings of the IABSE Symposium 2025*, pp.2925-2933, 2025.
- [5] A. Talebi, F. Potenza, V. Gattulli, Interoperability between BIM and FEM for vibration-based model updating of a pedestrian bridge, *Structures*, Vol. 53, pp. 1092-1107, 2023.



# RTK-Enabled UAV for Structural Health Monitoring Without GCPs

Hojune Ann<sup>1</sup>, Yong-Rae Yu<sup>1,2</sup>, Gi-Sang Kang<sup>1</sup>, Juheum Oh<sup>1</sup>, Jong-Jae Lee<sup>1,2</sup>, Ki-Young Koo<sup>3</sup>

<sup>1</sup>Department of Civil Environmental Engineering, Sejong University, Seoul 05006, Republic of Korea

<sup>2</sup>SISTech Co., Ltd., Seoul 05006, Republic of Korea

<sup>3</sup>Vibration Engineering Section, Faculty of Environment, Science and Economy, University of Exeter, Exeter, EX4 4QF, UK

email: [2015020674@korea.ac.kr](mailto:2015020674@korea.ac.kr), [pop9849@gmail.com](mailto:pop9849@gmail.com), [gisang772@gmail.com](mailto:gisang772@gmail.com), [juhm3078@naver.com](mailto:juhm3078@naver.com),  
[jongjae@sejong.ac.kr](mailto:jongjae@sejong.ac.kr), [k.y.koo@exeter.ac.uk](mailto:k.y.koo@exeter.ac.uk)

**ABSTRACT:** This study presents a structural shape monitoring system combining Real-Time Kinematic (RTK) technology with an Unmanned Aerial Vehicle (UAV) for georeferencing without Ground Control Points (GCPs). Traditional GCP-based methods, though accurate, require substantial field efforts, limiting efficiency. This approach employs RTK-enabled UAVs for direct georeferencing, achieving sub-2 cm positioning accuracy. Experiments involved detecting shape changes using a target structure with attached brick shapes of varying depths (8 mm, 20 mm, 44 mm, and 84 mm). Successful detection was achieved for depths of 20 mm or greater, with limitations for smaller depths due to sensor and resolution constraints. Depth and volume estimation errors, initially 11% and 3%, were reduced to 6% and 1% through point cloud registration, improving alignment and geometric accuracy. The study also identified challenges like occlusions and patternless surfaces, which impacted reconstruction quality. These findings highlight the system's potential to enhance structural health monitoring, offering an efficient, scalable solution for infrastructure inspections, with applications in civil engineering and beyond.

**KEY WORDS:** Structural health monitoring, Real-time kinematic positioning, Point cloud, Unmanned aerial vehicle, Photogrammetry, Change detection, Structure from motion, Civil engineering

## 1 INTRODUCTION

Recently, the integration of unmanned aerial vehicles (UAVs) with photogrammetry technology has been widely utilized across various fields. For example, it is used for large-scale 3D mapping of extensive areas such as terrain, forests, and coastal regions, as well as for the 3D mapping of individual objects such as buildings, bridges, and roads. Additionally, it is employed for monitoring construction progress and detecting deformations in roads, landslides, and ground subsidence. UAV-based photogrammetry has potential applications in structural health monitoring by detecting changes in structural geometry.

Traditional UAV-based photogrammetry lacks scale and orientation information, which has conventionally been compensated for by using ground control points (GCPs) to generate 3D models. Since the point cloud is aligned to a real-world coordinate system based on GCPs, the process requires installing GCPs around the target area and measuring their precise coordinates.

However, the use of GCPs is time-consuming and costly, which can hinder the efficiency of UAV-based photogrammetry. Additionally, in areas with difficult access, such as valleys and rivers, deploying GCPs can be challenging. To address this issue, recent advancements have enabled georeferencing without GCPs by utilizing UAVs equipped with Real-Time Kinematic (RTK) receivers (Figure 1: RTK UAV). UAVs equipped with RTK receivers have been reported to achieve terrain mapping accuracy of 2–10 cm without GCPs, making them suitable for various applications over extensive terrains [1-2]

In this study, structural health monitoring was conducted using a UAV equipped with RTK technology without the need for GCPs. The contribution of this research lies in the quantitative evaluation of monitoring accuracy in terms of the positional accuracy of the point cloud and the sensitivity to detecting structural deformations.

## 2 METHODOLOGY

### 2.1 Photogrammetry

Photogrammetry consists of Structure from Motion and Multi-View Stereo to reconstruct 3D structures from overlapping, unoriented, and uncalibrated images, producing sparse and dense 3D point clouds. Structure from Motion involves the simultaneous reconstruction of the unknown three-dimensional scene structure, as well as the estimation of camera positions and orientations, based on a given set of feature correspondences [3]. After successfully recovering the intrinsic and extrinsic parameters of the camera in the Structure from Motion process, Multi-View Stereo is employed to create a 3D densified reconstruction [4].



Figure. 1 RTK UAV

## 2.2 Georeferencing

Georeferencing is the process of aligning and scaling a generated 3D model to a real-world coordinate system. There are two approaches to georeferencing: rigid registration and non-rigid registration [5]. Rigid registration is applied after Structure from Motion, modifying the reconstructed point cloud to align with the RTK-surveyed coordinates of GCPs on the ground or GNSS-geotagged data from UAV-captured photos. Non-rigid registration, also known as adaptive registration, introduces a more dynamic approach. It utilises pose priors—the RTK-geotagged data in the UAV-captured photos—as flexible constraints during the Structure from Motion Bundle Adjustment phase.

## 3 EXPERIMENTS

The target structure is shown in Figure 2. A flight path was generated as a double-grid trajectory for 3D photogrammetry using the built-in app on the UAV's remote controller and deployed in all the survey cases.



Figure. 2 Target structure

Structure from Motion (SfM) and multi-view stereo processing were performed using Pix4Dmapper v4.56, as shown in Figure 3. These processes were employed to generate a dense point cloud representation of the target structure based on UAV-acquired images.



Figure 3. Target structure (Point cloud)

Figure 4 presents the comparison of two point clouds of the target structure acquired at different time intervals using the

Cloud-to-Cloud (C2C) absolute distance measurement in millimetres. This method quantifies the geometric differences between the two datasets by calculating the shortest distances between corresponding points in the point clouds. The resulting C2C distance values indicate structural deformations or displacements over time, allowing for an assessment of changes in the target structure's shape and stability.

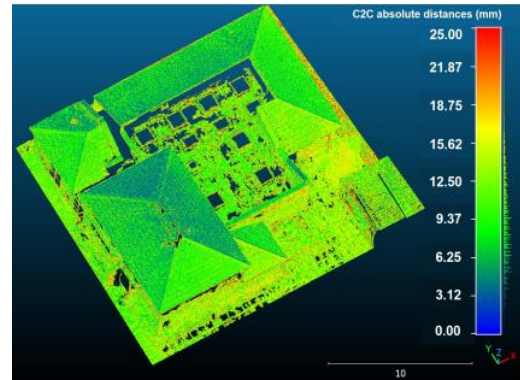


Figure 4. C2C absolute distance (mm)

## 4 CONCLUSION

This study evaluated the feasibility of using an RTK-equipped UAV with GCP-free georeferencing for structural shape monitoring. The results demonstrated that the generated point clouds achieved centimeter-level accuracy, with positioning differences of less than 2 cm compared to RTK rover measurements. The method successfully detected variations in brick depths down to 20 mm at a UAV altitude of 15 m, though it failed at 8 mm, suggesting that close-up images could improve detection but would introduce higher operational complexity. Point cloud registration was found to enhance alignment, reducing depth and volume estimation errors from 3% and 4% to 1% each. However, patternless surfaces and occlusions negatively impacted reconstruction accuracy, highlighting the need to consider such factors for effective structural shape monitoring.

## ACKNOWLEDGMENTS

This work was supported by the National Research Foundation of Korea(NRF) grant funded by the Korea government(MSIT)(RS-2021-NR059168)

## REFERENCES

- [1] F. Benassi *et al.*, 'Testing Accuracy and Repeatability of UAV Blocks Oriented with GNSS-Supported Aerial Triangulation', *Remote Sensing*, vol. 9, no. 2, Art. no. 2, Feb. 2017, doi: 10.3390/rs9020172.
- [2] M. Rabah, M. Basiouny, E. Ghanem, and A. Elhadary, 'Using RTK and VRS in direct geo-referencing of the UAV imagery', *NRIAG Journal of Astronomy and Geophysics*, vol. 7, no. 2, Art. no. 2, Dec. 2018, doi: 10.1016/j.nrjag.2018.05.003.
- [3] N. Snavely, S. M. Seitz, and R. Szeliski, 'Modeling the World from Internet Photo Collections', *Int J Comput Vis*, vol. 80, no. 2, pp. 189–210, Nov. 2008, doi: 10.1007/s11263-007-0107-3.
- [4] M. Innmann *et al.*, 'NRMVS: Non-Rigid Multi-View Stereo', in *2020 IEEE Winter Conference on Applications of Computer Vision (WACV)*, Snowmass Village, CO, USA: IEEE, Mar. 2020, pp. 2743–2752. doi: 10.1109/WACV45572.2020.9093583.
- [5] P. Moulon, P. Monasse, R. Perrot, and R. Marlet, 'OpenMVG: Open Multiple View Geometry', in *Reproducible Research in Pattern Recognition*, B. Kerautret, M. Colom, and P. Monasse, Eds., Cham: Springer International Publishing, 2017, pp. 60–74.

# Advanced and Efficient Monorail Facility Inspections Using Optical Measurement Technologies, Including Laser and Imaging

Motoki Nakamura<sup>1</sup>, Hirotohi Kurashige<sup>1</sup>, Hiroshi Yamazaki<sup>2</sup>, Ryohei Hayashi<sup>2</sup>, Kousuke Inoue<sup>2</sup>

<sup>1</sup>Keisoku Research Consultant Co., Creative Division, 665-1 Fukuda 1-chome, Higashi-ku, Hiroshima 732-0029, Japan

<sup>2</sup>Kanko Co., Ltd., 12-8Noe 1-chome, Joto-ku, Osaka 536-0006, Japan

email: nakamura@krcnet.co.jp, kurashige@krcnet.co.jp, yamazaki@kanko.cityis.co.jp, ghayashi@kanko.cityis.co.jp, inoue-k@kanko.cityis.co.jp

**ABSTRACT:** To support safe operation of monorail systems, periodic track inspections for line maintenance and structural inspections of the concrete girders and steel beamway that form the track are necessary, and efficient inspections and highly accurate inspection results are required. Since conventional inspections centered on manual measurement and visual inspection, there were issues in terms of the safety risk associated with work in high places and work efficiency. Furthermore, in visual inspections, it was not possible to gain an adequate understanding of deterioration over time due to the difficulty of quantitative evaluation. This paper presents an example of a non-contact inspection technique in which industrial area cameras, laser displacement sensor and a high-speed 2D laser profiler were installed on the inspection vehicle, and track displacement, visible deterioration trolley wire wear are measured while the vehicle is traveling. Although inspection work at the work site had required half a year with the conventional technique, the introduction of this technique shortened the inspection time to only 4 days, realizing improved efficiency and reducing the man-power required in site work. Future goals include sustainable infrastructure maintenance and improvement of track safety through efforts in trend analysis of the progress of deterioration based on an expanded range of inspection items and analysis of various types of accumulated data.

**KEY WORDS:** Structural Condition Assessment; Performance Evaluation; Laser Scanning; Non-Destructive Testing; Infrastructure Monitoring.

## 1 INTRODUCTION

### 1.1 Background and Issues of Monorail Inspection

Monorails are widely used as a key part of transportation infrastructure in urban areas and tourist destinations. Figure 1 shows a photograph of a monorail train traveling along the track beam above automobile street traffic. In proper maintenance management of this track structure, appropriate maintenance (line maintenance) is demanded from the viewpoints of safe operation and long service life. However, several issues arise in inspections of monorail systems.

Investigations of equipment degradation by conventional manual work center on judgments based on the experience and subjectivity of the inspection worker. However, in inspection work, objective and quantitative assessments are required for numerical management of the track condition. Manual inspection work is also extremely time- and labor-intensive, and securing work safety is also an issue because work is frequently performed in high places or at night. Although automation and digitization utilizing laser measurement and image analysis techniques have been promoted in recent years, techniques adapted to the structures and environmental conditions peculiar to monorails have not been adequately established[1][2][3].

### 1.2 Purpose and Significance of this Paper

In the current state of monorail inspections, the 3 issues of “Efficiency,” “Quantifiable Results” and “Safety” may be mentioned.

To solve these problems, this paper proposes a non-contact inspection technique utilizing industrial area cameras and laser displacement sensor. In addition to a very substantial reduction in work time achieved by mounting sensors on an inspection vehicle and performing measurements during vehicle travel,

the quantifiable results of the inspection results is also improved by quantification and visualization of the measured data. Cracks and other surface damage are detected using image analysis with the cameras, and displacement of the track beam and wear of the trolley wire are captured with high accuracy by analyzing the data acquired by the laser displacement sensor as point cloud data. Higher efficiency and improved safety in inspection work and more advanced maintenance management can be expected by introduction of this technique.



Figure 1. Photograph of a monorail

## 2 VISUAL AND MANUAL INSPECTION TECHNIQUES AND THEIR ISSUES

Since the track structures of monorail systems are subject to progressive deterioration in the forms of rail displacement and beamway deformation when used repeatedly day after day, railway operators are legally required to conduct periodic inspections and perform appropriate maintenance management. In particular, since monorails play a key role in urban transportation, securing their safety is an extremely important social obligation. However, the current inspection methods still



depend on visual inspections and manual work, and higher efficiency and more advanced methods are needed.

## 2.1 Conventional Inspection Techniques by Close Visual Inspection

In conventional inspections of monorails, the inspectors checked the structures directly, and the general method was judgment of abnormalities based on Close Visual Inspection. Concretely, inspectors conducted a “Visual Inspection” for structural deterioration by visually checking the structure surface for cracks, peeling, discoloration, etc., and “Track Displacement Measurement,” in which deviations in the height and levelness of the travel surface and misalignment of joints between beam segments and the gap between the beam segments were measured. The inspection items are shown in Table 1 and Table 2, and photographs of the conventional techniques used in rail displacement measurements are shown in Figure 2.

Table 1. Inspection items in Visual Inspections

Inspection equipment
PC track beams (including beam underside surface), steel track beams, lower part of steel beams, cross beams, PC track beam bearings, joint devices, signs, track circuit boundary markers
Inspection items
Cracks and other damage (fissures, etc.)
Paint peeling and deterioration (corrosion)
Paint peeling/corrosion of bearings (PC beams, steel beams)
Paint peeling/deterioration of lower part of steel beams and cross beams (except flange parts)
Other abnormalities (damage of resin mortar, presence/absence of damping materials, looseness of bearing anchor bolts and nuts, confirmation of signs and boundary markers)

Table 2. Inspection items in Track Displacement Measurements

Inspection equipment	
Position of expansion joints of PC/steel track beams (including branch beams, median lines and pullup lines)	
Inspection item	Content of inspection
Partial longitudinal level irregularity measurement	Measure changes in height of track beam
Partial horizontal alignment irregularity measurement	Evaluate linearity of track beam, and detect horizontal bending
Cross level irregularity measurement	Measure levelness (inclination) of beam
Vertical/horizontal misalignment measurement	Measure vertical level difference in joints and horizontal differences in the level of girder joints
Joint gap measurement	Measure gap between beams at beam joints

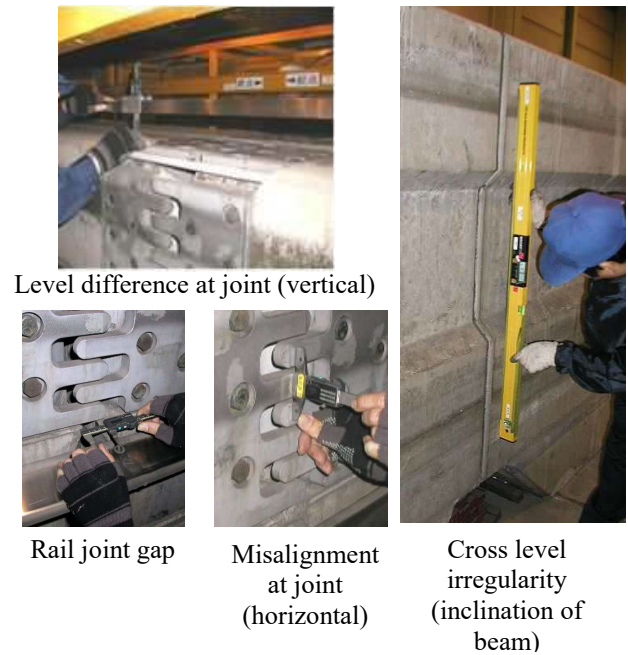


Figure 2. Conventional inspection techniques

## 2.2 Issues Related to Efficiency, Quantifiable Results and Safety

### 2.2.1 Issues related to efficiency

Many of the target sections of monorail inspections have been in service for more than 25 years, and since many lines were also constructed in the same period, demand for inspections and repairs is tending to increase. Because the target section in this paper has a total constructed length is 28.6 km and contains a large amount of infrastructure, enormous amounts of time and labor when an inspection is conducted. Thus, it is necessary to reduce the work load on inspection workers. However, a single inspection by the conventional method requires as much as several months, and securing speed (high efficiency) is an issue.

### 2.2.2 Issues related to quantifiable results

Partial deterioration of the track beam with age has already been confirmed from the inspection results, and further progress of deterioration is also expected in the future. Because inspection workers judge abnormalities by visual inspection and manual work, a large part of the conventional inspection method depends on the individual experience and senses of the inspectors. For example, when measuring the width of cracks, there are variations in the results depending on the measurement position and angle, and in some cases, there are differences in the evaluation depending on the inspector, even when inspecting the same damage. Since it is difficult to check for deterioration of facilities over the wide inspection area by a single standard, securing quantifiable results is an issue.

### 2.2.3 Issues related to safety

Because the track beam of monorails is generally installed in an elevated location, inspection worker must use a high-lift work vehicle or scaffolding to conduct inspections. Inspections

are frequently carried out at night, which increases the possibility of accidents due to fatigue or decreased concentration. Because this work involves a risk of falling or contact accidents, securing work safety is an issue.

### 3 PROPOSED NON-CONTACT INSPECTION TECHNIQUE

#### 3.1 Necessity of Digital Measurement Technique

In recent years, infrastructure inspections using non-contact measurement technologies have been widely adopted, and more accurate and efficient inspections are expected to be possible by utilizing laser measurement and image analysis techniques. This can achieve improved worker safety and labor-saving in inspection work. In addition, it can also contribute to predictions of long-term deterioration and sustainable infrastructure maintenance by accumulating and analyzing data.

This paper introduces a non-contact inspection technique utilizing laser displacement sensor and industrial area cameras and describes its effectiveness. The laser displacement sensor enable quantitative evaluations of the displacement of structures and wear of trolley wires. Highly accurate image analysis, without depending on visual inspection, is possible by using the industrial area cameras in combination with the laser displacement sensor. Although it was difficult to accumulate numerical data in conventional visual inspections, the proposed technique enables precise measurement and evaluation of visible deterioration and wear with high quantifiable results by combined use of the industrial area cameras and laser displacement sensor.

#### 3.2 Outline of the Technique and Sensor Configuration

As described in this paper, a non-contact measurement technique was constructed in order to gain a highly accurate understanding of the condition of the track beamway and the trolley wires of monorails and quantitatively evaluate the current condition of deterioration.

In this technique, sensors were mounted on a monorail inspection vehicle, and data are acquired while the vehicle was traveling. The main sensors and their inspection items were industrial area cameras (visible deterioration, joint gap measurement), laser displacement sensor (for longitudinal level irregularities, horizontal alignment irregularities and vertical and horizontal misalignment of joints) and a high-speed 2D laser profiler (for trolley wire wear).

The sensor installation arrangement was designed to extract the maximum possible measurement accuracy. The cameras were installed on the front of the vehicle, and photography was performed with a total of 16 units so as to cover the entire surface of the track girder, including the beamway, side surfaces, under beam area, bearing parts and track beamway substructure. The laser displacement sensor were installed at equal intervals under the vehicle and capture information on the distance to the beamway. A high-speed 2D laser profiler was also installed on the vehicle underbelly to capture information on wear of the trolley wire. Introduction of the cameras, lasers and various other sensor makes it possible to collect data continuously, and achieves more comprehensive deformation analysis than is possible with conventional spot measurements. The images of the installation positions of the industrial area

cameras and image of installation of the laser displacement sensor are shown in Figure 3 and Figure 4, respectively, and photographs of the installed sensor are shown in Figure 5.

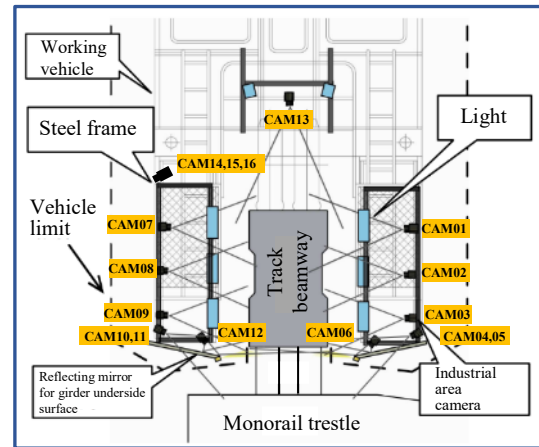


Figure 3. Image of installation positions of industrial area cameras

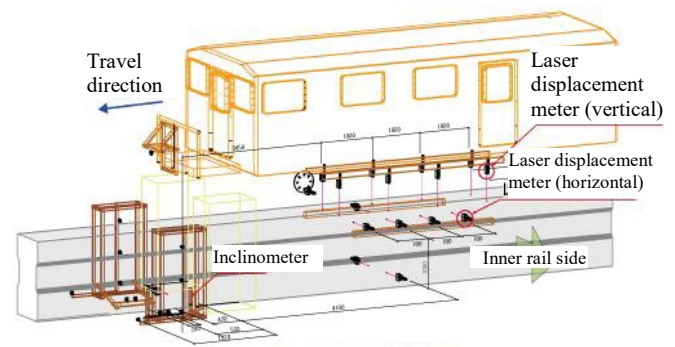


Figure 4. Image of installation positions of laser displacement sensor

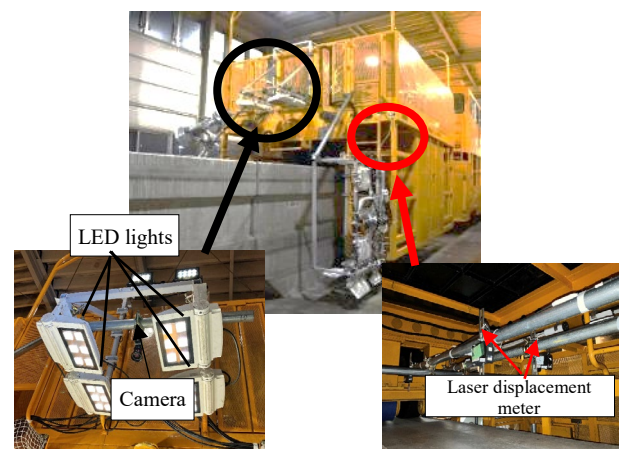



Figure 5. Photographs of site installation condition

### 3.3 Visual Inspection by Industrial Area Cameras

#### 3.3.1 Camera installation method and arrangement

In visual inspections for facility deterioration, industrial area cameras are employed to capture surface cracks and paint degradation. Compared to line scan cameras, area cameras offer greater flexibility in installation and imaging conditions, as they can capture full-frame images in a single exposure without requiring continuous motion of the object. A total of 16 compact area scan cameras with 2.35 megapixel resolution and a framerate (fps: frames per second) of 30 fps are used. A dedicated camera frame was designed to enable photography with the same quality from positions equidistant from the object of photography. An appropriate lighting arrangement and photographing distance for extraction of cracks with a width of 0.2 mm were planned. The cameras used to photograph the running surface and side surfaces of the beamway were arranged directly facing those objects, and the cameras used to photograph the bearings and underside of the steel beamway were arranged to photograph those objects from an oblique angle. Arranging the cameras so there is an overlap in the camera angle of view of the beam side surfaces enables sure data acquisition, with no gaps between the photographs of each image. Since it would be difficult to photograph the underside surface of the girder directly from within the vehicle limit width, a method of photographing images reflected by a mirror was adopted. Table 3 shows the specification of the cameras mounted on the vehicle.

Table 3. Specification of high-resolution cameras

Product name	GO-2400C-PMCL
Appearance	
Standard	1936 x 1216 px
Sensor	1CMOS
Sensor size	1/1.2 type
External dimensions	29 x 29 x 41.5 mm
Weight	46 g

#### 3.3.2 Issues in photography and countermeasures


Since photography while the vehicle traveling is affected by vehicle vibration and shaking, the shutter speed of the cameras used in this technique was set to 1/4 000 s. This made it possible to minimize the effect of blurring caused by vibration and shaking. On the other hand, if this setting is used, the images will be dark because the short exposure time limits the light available when photographing an image. In order to acquire high quality image data even in dark areas, multiple LED lights were arranged so as that the entire surface of the girder received an appropriate, uniform amount of light.

#### 3.4 Track Displacement Measurement by Laser displacement sensor

Track displacement, including unevenness, level differences, and inclination, is measured using a total of 14 laser

displacement sensors, each capable of high-precision, single-point distance measurements that enable the detection of subtle structural shifts. Since the sampling frequency is 2 000 Hz, measurement at a pitch of about 2 mm in the travel direction at a travel speed of 15 km/h. The spacing of the laser displacement sensor was adjusted to 400 mm, which is the median value of the measurement range, and were installed so as to enable capture of displacement of the upper limit value ( $\pm 100$  mm). The specification of the laser displacement sensor is shown in Table 4.


Table 4. Specification of laser displacement sensor

Product name	LK-G405
Appearance	
Measurement range	300 to 500 mm
Wavelength	655 nm (visible light) Laser class: 3Ror2
Sampling period	20 to 1 000 $\mu$ s
Protection structure	IP67 (IEC60529)
External dimensions	3.6 x 10.8 x 8.5 cm
Weight	Approx. 380 g (including cord)

#### 3.5 Trolley Wire Wear Inspection

To investigate wear of the trolley wire located on the side face of the beamway, a high-speed 2D laser profiler is used to perform continuous scanning of cross-sectional shapes, enabling precise visualization and quantification of wear, misalignment, and other geometric anomalies. As in the case of the above-mentioned laser displacement sensor, because the sampling frequency is 2 000 Hz, measurement at a pitch of approximately 2 mm in the travel direction is possible, assuming a travel speed of 15 Km/h. Since it is necessary to grasp the complete image of the trolley wire when investigating wear, the high-speed 2D laser profiler was installed so that the entire trolley wire can be scanned from a position directly facing the wire. The specification of the high-speed 2D laser profiler is shown in Table 5.

Table 5. Specification of high-speed 2D laser profiler

Product name	LJ-V7300
Appearance	
Measurement range	155 to 445 mm
Wavelength	405nm (visible light) Laser class: 2
Sampling period	Max. 16 $\mu$ s
Protection structure	IP67 (IEC60529)
External dimensions	5.7 x 17.3 x 8.8 cm
Weight	Approx. 1 000 g



## 4 ANALYSIS OF MEASURED DATA

### 4.1 Preparation of Composite Image and Investigation of Visible deterioration

After geometric correction, magnification correction and color correction, the images captured by the industrial area camera are composed as continuous composite images. Geometric correction is a type of correction processing in which images that contain distortion and deformation are adjusted to produce orthorectified images with an accurate shape and positional relationship. Creating composite images makes it possible to check each of the girders and beams of the track over a wide range, and at the same time, understand their actual positional relationships. Figure 6 shows composite images of the beamway running surface and side surface.

Damage is extracted using the crack drawing support software “k-TRACE” (Figure 7), which was developed by this company (KRC: Keisoku Research Consultants Co.)[4][5]. When the inspector clicks the line of a crack with the mouse, k-TRACE analyzes the shading of the color around the line joining the clicked points and automatically outputs the shape and width of the crack. Application of this tool is not limited to cracks, as the software can also extract the positions of peeling, water leaks and free lime at the same time. This processing makes it possible to obtain a comprehensive understanding of the exact position and scale of the damage from images, without going to the site, thereby securing “Safety” and “Quantifiable Results.”

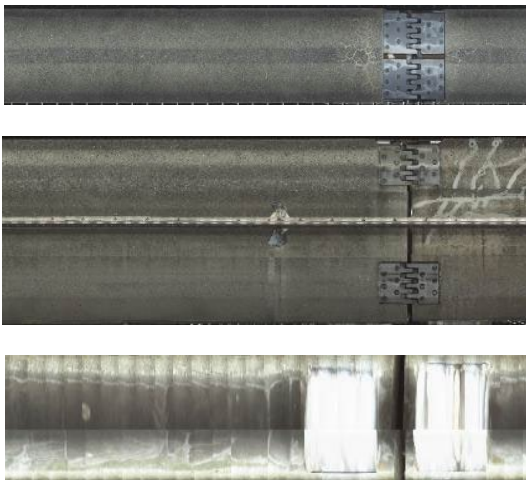


Figure 6. Composite images of beamway (top: running surface, middle: side surface, bottom: underside of girder)



Figure 7. “k-TRACE”: crack drawing support software

### 4.2 Joint Gap Measurements

For joint gap measurements, analysis is performed based on the photographed images. An image showing the joint part in the center is extracted from multiple images, and the width of the joint gap is calculated from the number of pixels at the gap position in the image. The calculated joint gap is standard value are then compared, and the locations of joints where the gap exceeds the control standard value are extracted. A photograph of the joint gap image is shown in Figure 8.

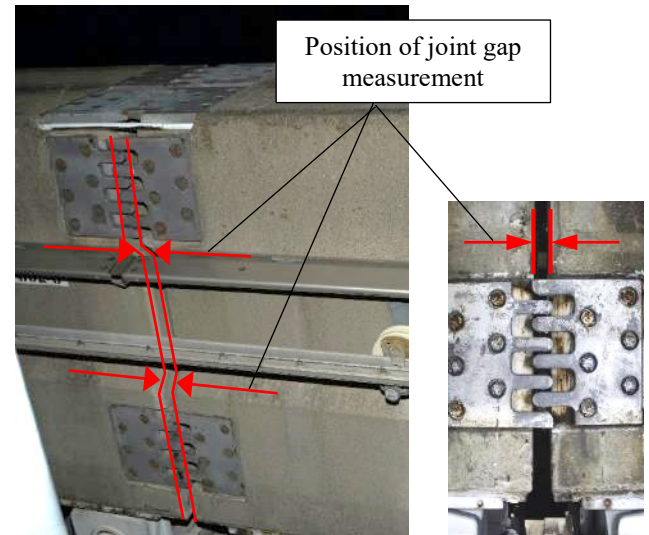


Figure 8. Position of joint gap measurement

### 4.3 Partial Longitudinal Level Irregularity Measurement

Displacement of the height of the beamway running surface (partial longitudinal level irregularity) is measured by using 3 laser displacement sensor (A, B, C) installed at 1 m intervals in the travel direction. The partial longitudinal height displacement  $h_d$  is calculated as the difference between the average distance measured by the first and last units  $(A+C)/2$  and the distance measured by the center unit B. The calculated values are arranged for each beamway segment, and locations that exceed the control standard value are extracted. An image of the height calculation method is shown in Figure 9.

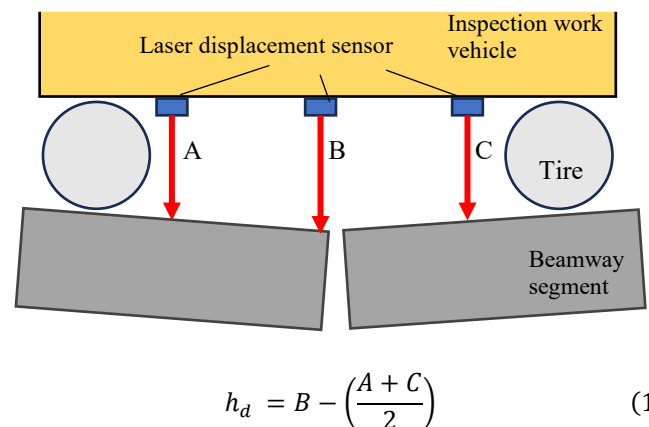


Figure 9. Image of height value calculation

#### 4.4 Partial Horizontal Alignment Irregularity Measurement

Similarly to the partial longitudinal level irregularity measurement method, lateral deviations of the beam side are measured by 3 laser displacement sensor installed at equal distances in the travel direction. The data calculation method is also similar to that used in partial longitudinal level calculations. The waveform obtained in a horizontal alignment irregularity measurement is shown in Figure 10.

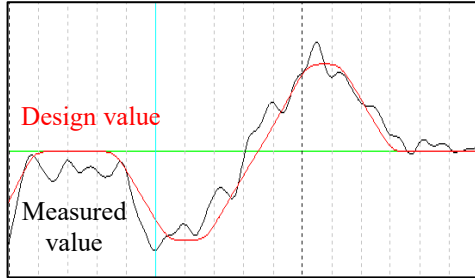


Figure 10. Waveform in horizontal alignment irregularity measurement

#### 4.5 Cross Level Irregularity (Inclination) Measurement

The inclination (cross level) of the beamway is measured by using an inclinometer and laser displacement meter. If the beam and the vehicle are parallel, the cross level  $\theta$  can be measured using only the inclinometer, but there will be a slight variation in the inclination. Therefore, displacement is measured by using laser displacement sensor installed on the guideway and the stability surface of the beamway side surface to correct for the difference in inclination, and the difference in the inclinations of the track beamway and the vehicle is obtained from the respective measured values of  $a$  and  $b$  and positional relationship  $l$  between the displacement meters. Since the measured values of the inclinometer are also affected by centrifugal force, the cross level  $\theta$  of the beam can be calculated by adding a corrected value  $\Delta\theta_c$ , which is calculated based on the beam linearity and speed values. An image of the relationship of the inclinometer and the beam side surface and the numerical expression are shown in Figure 11.

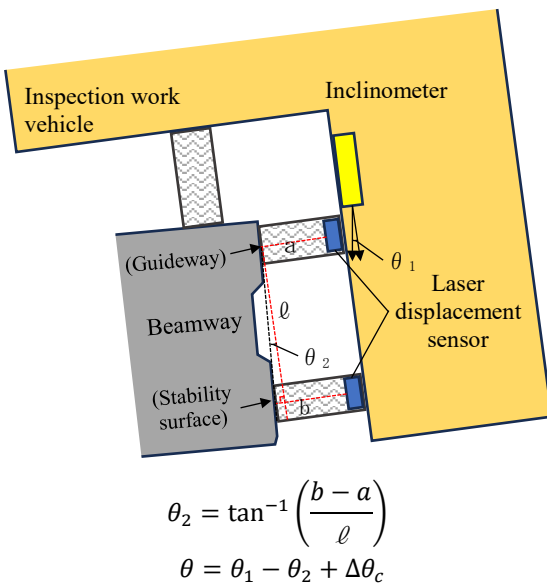


Figure 11. Relationship of inclinometer and beam side surface

#### 4.6 Vertical and Horizontal Misalignment Measurement

Vertical misalignment and horizontal misalignment are measured at beamway joints (total of 6 positions of the running surface, guideway and stability surface) using laser displacement sensor. The amount of displacement is calculated from height of the fingerplate surface measured before and after passing the joint, and the vertical and horizontal misalignment of each joint is evaluated. Figure 12 shows a position diagram of the laser displacement sensor when measuring vertical and horizontal misalignment, and Figure 13 shows the waveform of vertical misalignment measurement results.

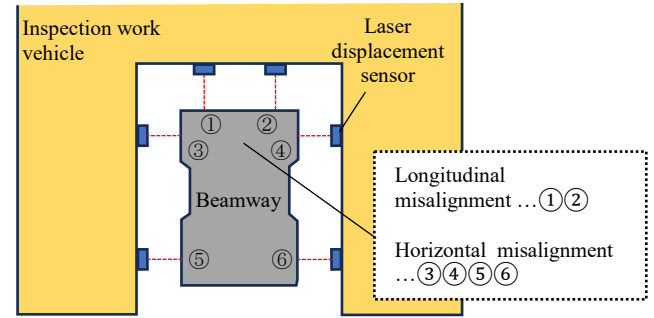


Figure 12. Position diagram of laser displacement sensor for vertical and horizontal misalignment

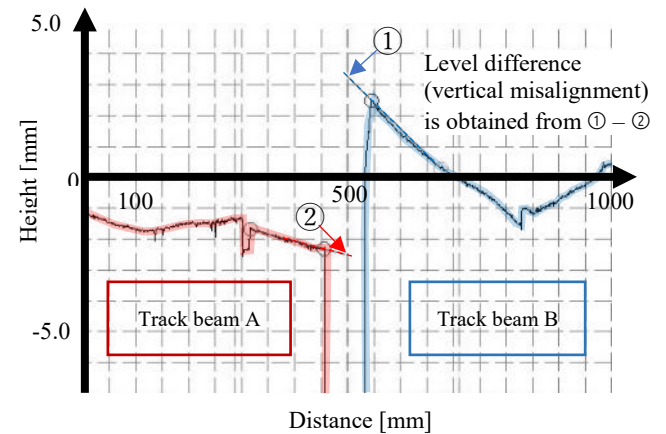


Figure 13. Result of vertical/horizontal misalignment measurement

#### 4.7 Trolley Wire Wear Measurement

In wear inspections, the cross-sectional shape of the trolley wire is measured using a high-speed 2D laser profiler, the result is compared with the design cross section, and the wear amount  $\Delta W$  is calculated. Here,  $\Delta W$  is the difference between the design value of the trolley wire thickness  $W_{design}$  and the measured thickness of the remaining part of the wire  $W_{meas}$ . The thickness of the remaining part  $W_{meas}$  is calculated by acquiring point information on 1 point (point A) at the tip, which is the wear zone of the trolley wire, and 2 corner points (points B and C) of the metal part where wear has not occurred, and calculating  $W_{meas}$  from the relationships of distances  $a$ ,  $b$  and  $c$  between the each of these points and the laser displacement meter.

Using the high-speed 2D laser profiler enables more complete, quantitative wear measurement than is possible by

conventional manual measurement. It is also possible to analyze the trend of wear progress and carry out systematic trolley wire maintenance and exchanges by accumulating measurement results over the long term. Figure 14 shows an image of the trolley wire and wear and the numerical expression for the wear calculation. Figure 15 shows the data used to create the composite waveform of the high-speed 2D laser profiler.

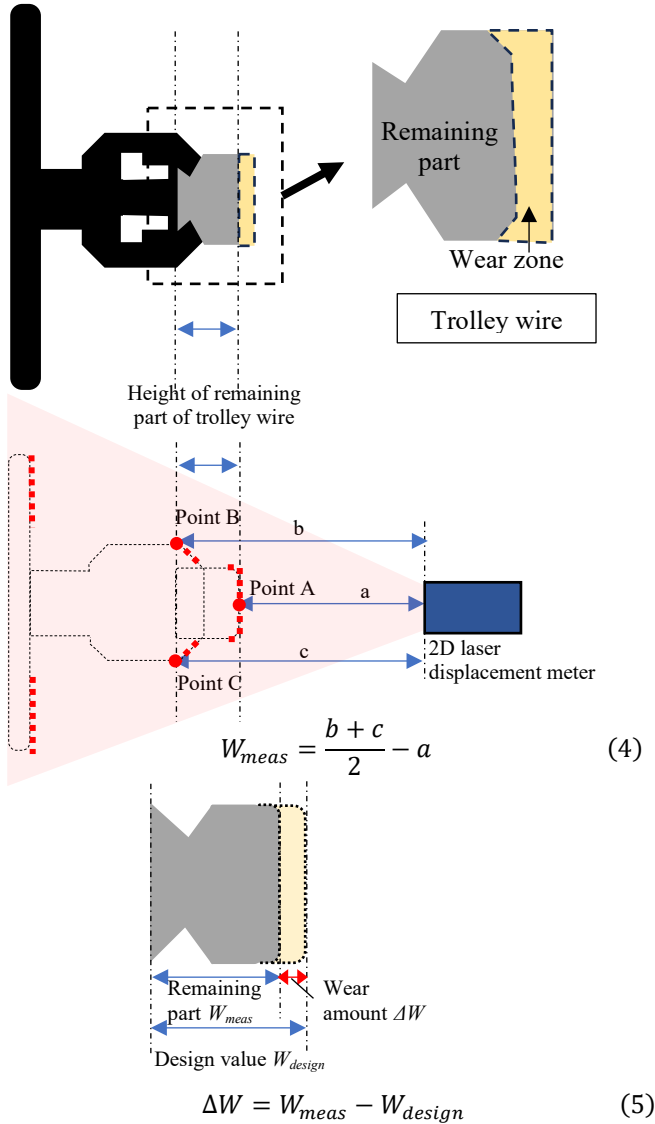


Figure 14. Image of trolley wire and wear

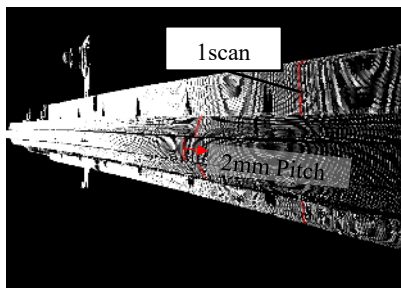


Figure 15. Point cloud composed using scan data from the 2D laser profiler

## 5 DISCUSSION

### 5.1 Improvement of Work Efficiency

With the proposed method, site working time was shortened from half a year by the conventional method to only 4 days because many types of measured data can be collected at one time while travelling. This shortening of site working time not only improves work efficiency, but also contributes to improved safety. On the other hand, the load of office work, such as processing and analysis of acquired data, is large, so efforts for improvement for reduction of the volume of work are necessary. Nevertheless, digitization of inspection results has lightened the work involved in arranging and managing measurement results and improved the convenience of data use.

### 5.2 Improvement of Quantifiable Results

By using the proposed technique, measured results with quantifiable results based on numerical values, and evaluations of damage based on those results, have become possible by using industrial area cameras and laser displacement sensor. In detection of cracks, semi-automatic measurement of the width and length of the damage is possible by utilizing image analysis, and quantitative comparison with past data is now easy. In measurements of track displacement, measurement results and evaluations with high quantifiable results have also become possible by using laser displacement sensor.

### 5.3 Improvement of Safety

With the proposed technique, it is no longer necessary for workers to enter dangerous areas because the sensors are mounted on the inspection vehicle and measurements are carried out while the vehicle is traveling. The use of non-contact sensors rather than contact-type measurement methods has not only reduced the loads on structures during measurements, but has also realized stable measurement.

## 6 CONCLUSION AND FUTURE OUTLOOK

### 6.1 Conclusion

The proposed technique is a system in which sensors are mounted on an inspection vehicle, and track displacement and visible deterioration are measured while the vehicle is traveling. Cracks and other surface damage are detected by utilizing image analysis of images acquired with industrial area cameras, and displacement of the track beamway is measured with laser displacement sensor. Highly precise evaluation of trolley wire wear has also become possible by applying an analysis technique utilizing point cloud data. Although conventional site inspection work had required half a year, the application of these techniques has shortened the site work time to only 4 days, realizing improved work efficiency and a reduction of the work load. Improved safety could also be secured by shortening the site work time of workers.

By using the industrial area cameras, creation of composite images, understanding the overall deterioration of facilities, and comparison of deterioration between two time periods have become easy, and in measurements of track displacement, it is



now possible to obtain measurement results with high quantifiable results as a result of the acquisition of high-accuracy data using the laser displacement sensor and establishment of methods for calculating the amounts of various types of displacement using that data. Likewise, in measurements of trolley wire wear, quantitative evaluation of the amount of wear has become possible by a technique using a high-speed 2D laser profiler. Based on the above, in comparison with conventional inspections, it can be said that improvement of the reproducibility of inspection results, understanding of changes over time and quantitative evaluations are now possible.

## 6.2 Future Outlook

The introduction of the proposed technique has realized high efficiency and improved quantifiable results in inspection work. However, we intend to address the following issues in order to develop more advanced techniques and enable long-term operation.

### 6.2.1 Reduction of the data processing load and automation

With the proposed technique, on-site measurements can be completed in significantly less time compared to conventional methods. However, the analysis of the acquired images and point cloud data still requires a certain amount of processing time. In particular, damage detection and evaluation by image analysis involve work that requires specialized knowledge. Therefore, the introduction of AI technologies is expected to improve the efficiency of post-processing and reduce reliance on expert interpretation.

- AI automation of image analysis:  
Analysis time can be shortened and variations in accuracy can be reduced by automatic recognition and classification of cracks and other damage by machine learning. We will also study a system for diagnosis and evaluation of structures from damage extracted for each girder/beam.

### 6.2.2 Further expansion of range of application

Although this technique has been applied mainly to evaluations of displacement and damage of the track beamway and trolley wire wear, application to other inspection items should also be studied in the future.

- Deployment to various structures on the track:  
The aim here is to realize comprehensive infrastructure monitoring by expanding the objects to inspections to include bridges on the track, peripheral equipment, stations, etc.
- Selection of the optimum sensor technologies:  
In addition to the existing image and laser technologies, LiDAR, thermal infrared camera technology, etc. will also be studied in order to establish a multifaceted deterioration detection technique.

### 6.2.3 Confirmation of linkage of individual inspection items

Causal relationships also seem to exist between respective inspection items such as longitudinal levelness, horizontal levelness, misalignment, etc. These will be utilized for

appropriate line maintenance by clarifying their relationships based on accumulated data.

### 6.2.4 Prediction of long-term deterioration risk

In the future, the establishment of a technology for predicting the future deterioration of structures by using accumulated data will be demanded.

- Creation of risk assessment model:  
Based on acquired data, a technique for assessing the rate of progress of deterioration and the range of its effects, and quantitatively judging the priority of repairs and maintenance, will be developed.
- Deterioration prediction using risk assessment model:  
Based on the risk assessment model, the progress of displacement and wear of the track beamway and trolley wire will be predicted to optimize maintenance management plans.

In the future, we promote higher efficiency and more advanced techniques by solving these issues, with the aim of realizing more sustainable and precise infrastructure maintenance management.

## REFERENCES

- [1] I. Matsumura, K. Nezu: Labor-saving inspection method for overhead contact lines using laser sensors and image analysis, RTRI Report, Vol.78, No.8, pp.4–7, 2021.
- [2] Y. Momoya: Research and development for improving operational efficiency in track maintenance, RTRI Report, Vol.79, No.7, pp.14–19, 2022.
- [3] K. Kajihara, H. Tanaka: Efficient maintenance method for rail surface irregularities caused by corrugation, RTRI Report, Vol.79, No.7, pp.32–37, 2022.
- [4] S.Nishimura and K. Hara and K. Kimoto and H. Matsuda, The Measurement and Draw damaged plans at Gunkan-Island by Using 3D laser scanner and Digital Camera, Journal of JSPPS, Japan, 2012.
- [5] S. Nishimura and K. Kimoto and N. Matsuoka and H. Otani and T. Ogata and H. Matsuda, The Development and Evaluation of Telemetry in Bridge Maintenance, Applied Surveying Papers, Japan, 2013.



# Application Method of SfM/MVS Technique Combined with Point Cloud Data for Inspection of Steel Bridges

Ko Yamashita<sup>1</sup>, Jun Kato<sup>1</sup>

<sup>1</sup> Keisoku Research Consultant Co., Kyushu Division, 665-1 Fukuda, Higashi-ku, Hiroshima-shi, Hiroshima, Japan  
email: k-yamashita@krcnet.co.jp, jun@krcnet.co.jp

**ABSTRACT:** The Structure from Motion/Multi-View Stereo (SfM/MVS) technique, which enables reconstruction of the three-dimensional shape of an object based on multi-view images, is a useful technique for inspection of infrastructure such as bridges in order to gain a comprehensive understanding of the state of damage. However, in SfM/MVS, the camera position and three-dimensional coordinates of the object are estimated based on feature points in images, making it difficult to apply this technique to steel structures, which have fewer feature points on surface textures due to coating. This paper presents a case in which SfM/MVS was successfully applied to a steel structure, specifically a steel bridge, by substituting the incomplete polygon model constructed in the conventional SfM/MVS process with a current-state CIM model created from existing drawings and point cloud data acquired with a terrestrial 3D laser scanner.

**KEY WORDS:** SfM/MVS; Terrestrial Laser Scanner; Point Cloud; Steel Bridge; Inspection; BIM/CIM.

## 1 INTRODUCTION

At present, aging of bridges in service and a shortage of inspection engineers have become problems in Japan [1], heightening the need for higher efficiency and labor-saving in bridge inspections. In this situation, preparation and wide use of Guidelines for Use of New Technologies [2], Delivery Manual for 3-Dimensional Deliverables [3] and other regulations are being promoted for image instrumentation technologies, including the Structure from Motion/Multi-View Stereo (SfM/MVS) technique [4], [5], which enables reconstruction of the three-dimensional shape of an object structure from images to gain an understanding of the state of damage, etc.

This study focuses on steel bridges as one type of bridge. As in other types of bridges, the problems associated with aging have also become apparent in steel bridges, as seen damage by corrosion of the steel materials [6]. However, it is sometimes difficult to apply the SfM/MVS technique to steel bridges since steel materials have fewer feature points, which are necessary for image processing, due to the uniform surface texture formed by coating film, and in such cases, reconstruction of the three-dimensional shape may be incomplete.

This paper examines the applicability of the SfM/MVS technique to steel bridges by using a method that utilizes a current-state CIM model (current-state CIM). This model was constructed by correcting existing drawings based on the current-state point cloud data (TLS point cloud) measured with terrestrial 3D laser scanners (TLS).

## 2 USE OF SfM/MVS AND POINT CLOUD DATA

### 2.1 Overview of SfM/MVS

SfM/MVS is a technique in which the three-dimensional geometry of an object is reconstructed from an image sequence (multi-view images) of the object by estimating the camera position and posture and the three-dimensional coordinates of the object by calculations based on feature points. Figure 1 is an image diagram of the reconstruction of a three-dimensional shape by SfM/MVS.

“Feature points” refer to points on the object appearing in the image that can be identified based on differences in color, brightness, etc., allowing its position to be determined. By detecting corresponding feature points between images, it becomes possible to estimate the relative camera position and posture with respect to the target structure, as well as the three-dimensional coordinates of each point. In general, the less uniform the surface texture of a structure, the greater the number of points detected as feature points. Accordingly, SfM/MVS technology can be effectively applied to structures with non-uniform surface textures and abundant feature points, such as concrete bridges.

### 2.2 Flow of Processing in SfM/MVS

The following describes the process of reconstructing the three-dimensional shape of an object by SfM/MVS and determining the three-dimensional location, size and other features of damage of the object structure. First, the point cloud data of the object structure is obtained by estimating the position and posture of the camera and the three-dimensional coordinates of the object structure based on the feature points described above. Next, a polygon model composed of surfaces is constructed based on the point cloud data, and a textured polygon model is obtained by applying textures sourced from photographic images onto the surface of that model. After this, it is possible to confirm the two-dimensional damage position and size by outputting orthoimages based on the textured polygon model. Figure 2 shows the general processing flow of SfM/MVS, including image acquisition.

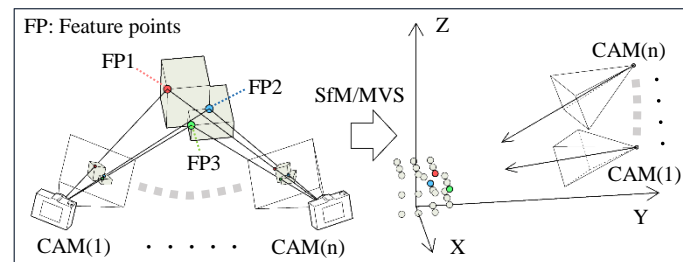


Figure 1. An image diagram of a three-dimensional shape reconstruction by SfM/MVS



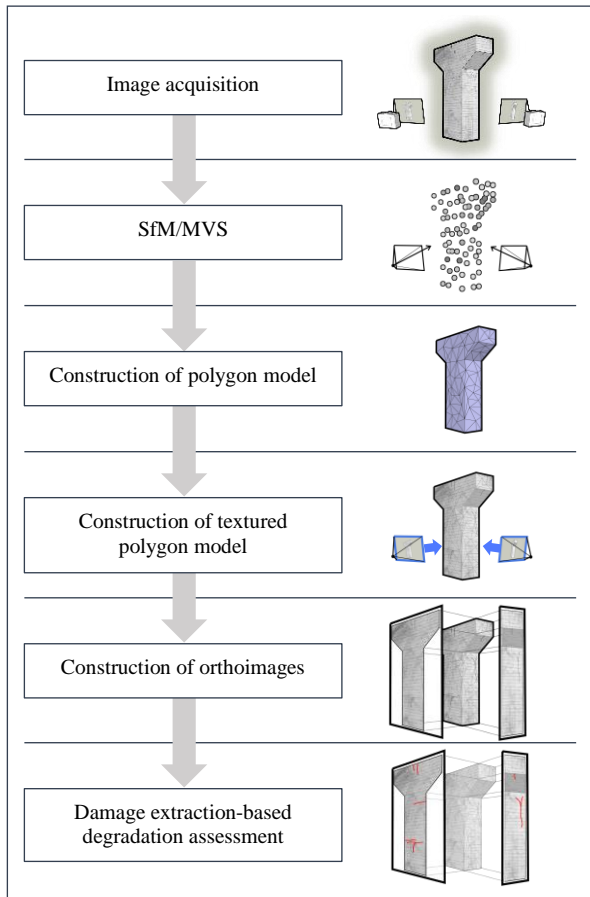


Figure 2. General Processing Flow for Applying SfM/MVS

### 2.3 Objects with Few Feature Points

The importance of feature points in SfM/MVS is as described above. However, when a paint film or other coating has been applied to the surface of the steel materials of a steel bridge, etc., the surface texture becomes uniform. This results in fewer points being detectable as feature points, making it difficult to apply SfM/MVS using general methods. Figure 3 shows a comparison of the detection status of corresponding feature points between objects with surface textures of varying uniformity. In the case of non-uniform surface texture, corresponding points are distributed across the entire surface. On the other hand, in the case of uniform surface texture, it is confirmed that corresponding points are not detected, except in distinctive areas such as corroded parts. Furthermore some manuals for general software products used in computational processing by SfM/MVS also recommend avoiding objects with a uniform texture or luster [7].

Figure 4 shows an example of constructing a point cloud data from SfM/MVS technique, targeting a steel bridge. In this example, there were many areas where the surface texture is uniform, and there were also areas where it was not possible to acquire a point cloud of the object structure at members that intrinsically have a flat surface due to the inadequate number of feature points. The inaccuracies in the shape of the polygon model and the improper placement of textures make it difficult to record the condition of damage of the entire object.

Figure 5 shows the processing flow for the problem that occur when SfM/MVS processing by the general technique is applied to an object with a uniform surface texture due to coating film.

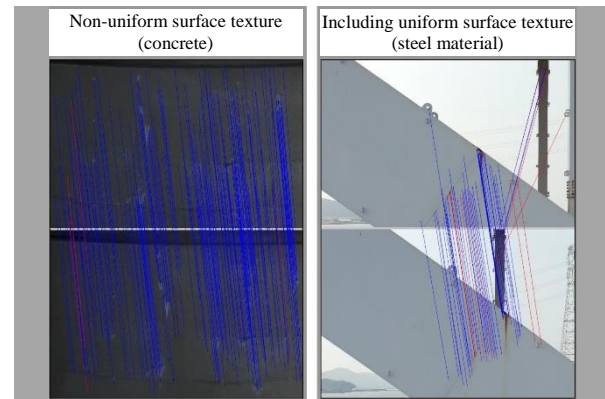


Figure 3. Comparison of the detection status of corresponding feature points

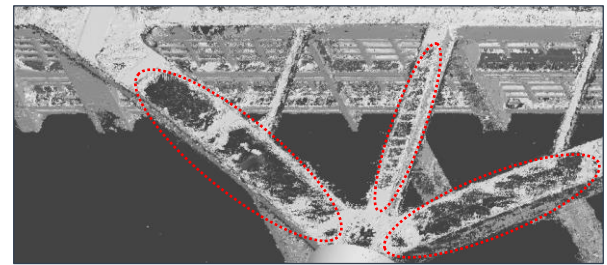


Figure 4. Point cloud where gaps occurred

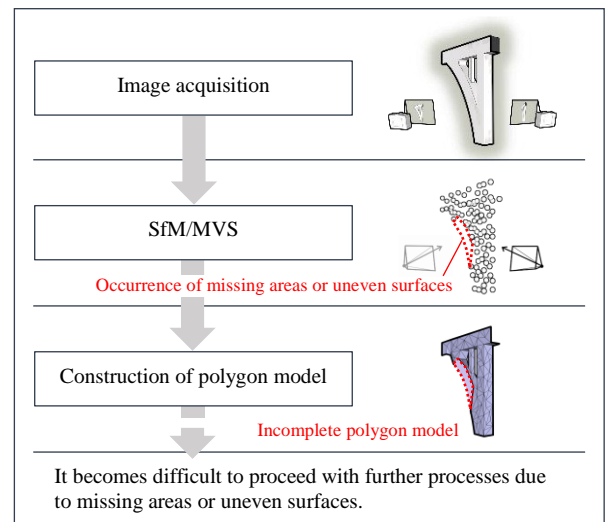


Figure 5. Problems in processing flow of SfM/MVS

### 2.4 SfM/MVS Combined with Measured Point Cloud Data

To solved the problems in application of SfM/MVS to steel bridges with few feature points, this paper examines a technique in which the object is measured with TLS, and the acquired measured point cloud data are used.

In this method, positions and posture of cameras, along with three-dimensional coordinates within the possible range, are first estimated using the conventional SfM/MVS approach.

Then, instead of the polygon model used in conventional methods, the current-state CIM, which reproduces the current shape of the object based on TLS point cloud and existing drawings, is utilized. Texture is projected onto this current-state CIM using camera images as sources, enabling the construction of textured models and orthoimages. Furthermore, even the incomplete polygon models created through conventional methods are used as a reference data for aligning the current-state CIM. UAV is employed for image acquisition, and during the SfM/MVS phase, GNSS data obtained during image acquisition is also used for analysis. This method is referred to as "SfM/MVS combined with TLS point cloud" and the processing flow is shown in Figure 6.

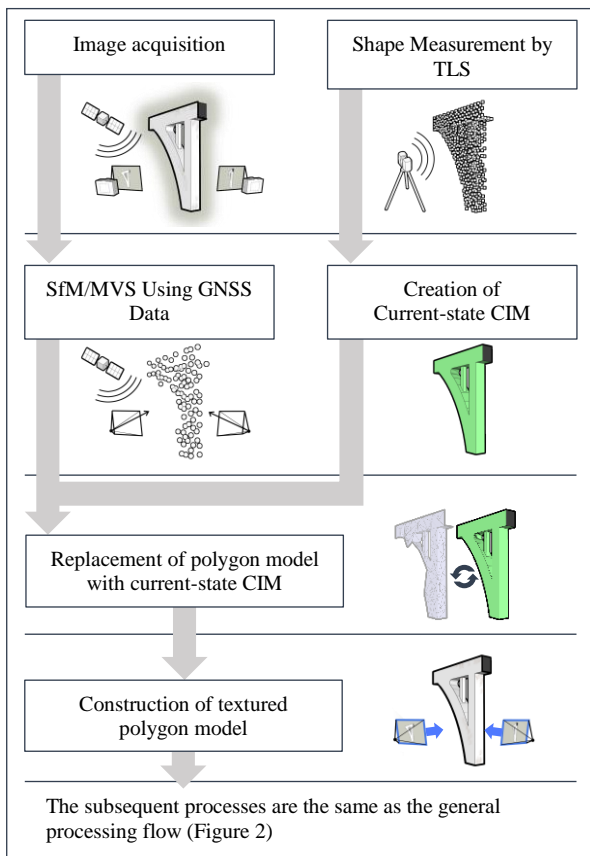


Figure 6. Processing flow of SfM/MVS combined with TLS point cloud

### 3 EXAMPLE OF APPLICATION TO AN ACTUAL STEEL BRIDGE

This chapter presents an example in which the proposed technique, SfM/MVS combined with TLS point cloud, was applied to an actual steel bridge. This verification is an attempt to apply SfM/MVS in work for investigation of the condition of corrosion and others of the steel materials of the object bridge.

#### 3.1 Overview of Steel Bridge

The object bridge is a bridge with a total length of 651 meters, in which the main bridge section is a mid-height-deck arch Lohse structure as shown in Figure 7. The object range of the inspection was the steel parts between piers P5 and P8, as

shown in Figure 8. The bridge is constructed over the sea, and the distance between the revetments on the origin and terminus sides is approximately 450 meters. Owing to the water depth directly under the bridge between piers P5 and P7, it was impossible to enter this area on foot, but the area between piers P7 and P8 could be entered on foot at low tide. The specifications of the bridge are shown in Table 1. As can be seen in Figure 9, the steel materials in this object range have a uniform surface texture due to paint film.



Figure 7. Object bridge

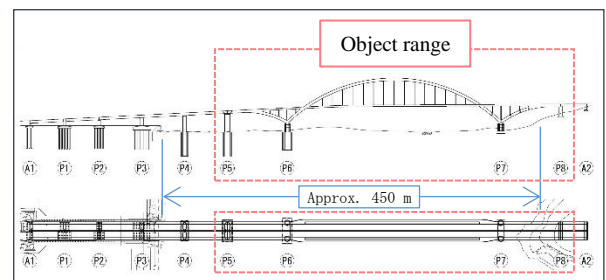


Figure 8. Object range

Table 1. Specifications of object bridge

Bridge name	Imari Bay Bridge
Date completed	2003
Location	Imari City, Saga Prefecture, Japan
Bridge length	651 m (over sea length: 420 m)
Width	Total width: 21.3 m
Space below girder	Height: 20.5 m, width: 200 m
Superstructure (main bridge part)	Steel 3-span continuous mid-height-deck Lohse bridge (70 m + 250 m + 70 m)



Figure 9. Steel with uniform surface texture

### 3.2 Equipment Used

Image acquisition was performed using two types of UAVs with an attached camera. A Matrice 300 RTK was mainly used, and a compact Skydio was used in some places. Table 2 shows the specifications of the UAVs and the attached cameras.

To acquire measured point cloud data on the current state of the object bridge, measurements were carried out with TLS. Two types were used in the measurements, a medium-range Focus S-350 (FARO) and a long-range SX10 (Trimble). Table 3 shows the specifications of the instruments

The software used in image analyzing by SfM/MVS was Metashape Professional (Agisoft).

Table 2. Specifications of UAVs and camera






Manufacturer	DJI	
Type	Matrice 300 RTK	
Appearance		
Device	Item	Specification
Main unit	Dimensions (length x width x height)	810 x 670 x 430 mm
	Weight	6.3 kg (approx.)
	Flight time (max.)	55 min
	Auto flight function	Yes
	Cruising speed (max.)	17 m/s
	Max. operational wind speed	12 m/s
Name	Zenmuse P1 (mounted on Matrice 300 RTK)	
Appearance		
Dimensions	198 x 166 x 129 mm	
Weight	800 g (approx.)	
Sensor dimensions	35.9 x 24 mm	
Photo size	8 192 x 5 460 pixels	
Shutter speed	1/8 000 to 1 s	
Aperture range	F2.8 to F16	
ISO sensitivity	100 to 25 600	
Manufacturer	Skydio	
Type	Skydio 2+	
Appearance		
Device	Item	Specification
Main unit	Dimensions (length x width x height)	229 x 274 x 126 mm
	Weight	0.8 kg
	Flight time (max.)	27 min
	Auto flight function	Yes
	Cruising speed (max.)	58 km/h
	Max. operational wind speed	11.1 m/s
Mounted camera	Photo size	4 056 x 3 040 pixels
	Shutter speed	1/1 920 to 1 s
	Aperture value	F2.8
	ISO sensitivity	100 to 3 200

Table 3. Instrument specifications of TLS

Manufacturer	FARO	Trimble
Name	Focus S-350	SX10
Appearance		
Ranging method	Phase shift	Time-of-flight
Measurement distance	0.6 to 350 m	1 to 600 m
Measurement range	V:320° H:360°	V:150° H:360°
Laser class	Class 1	Class 1M
Scan speed	122 000 points/s	26 600 points/s
Accuracy	Three-dimensional positional accuracy	Distance measurement accuracy
	2mm@10m, 3.5+0.1mm/m@25m or more	2 mm + 1.5 ppm
Unit weight	4.2 kg	7.5 kg

### 3.3 Condition of Measurement

The condition of image acquisition by UAV is shown in Figure 10. To prevent UAV crash accidents, the UAVs were not flown directly over the bridge, and images were acquired from positions where visual confirmation of the UAV by the operator was possible. In acquiring the images of the underside of the girders between P7 and P8, we entered the riverbed area of P7 during low tide, and used the compact Skydio UAV to photograph the structure due to the limited space under the girders. To prevent image blurring, the shutter speed was set to approximately 1/1 000 s during photography, and continuous images were taken at intervals after adjusting the focus. The purpose of this work was to understand the positions and surface areas of corroded areas. Image acquisition was performed at a resolution of approximately 3 mm/pixel with a 45 megapixel camera (8 192 x 5 460 pixels), as this is adequate resolution for confirming corrosion and image processing, and SfM/MVS can be performed more easily with a wider field of view per image. Image acquisition by UAV was conducted over a 4-day period, and a total of 10 232 images were captured. Figure 11 shows the cross-sectional positions of image acquisition.

Figure 12 shows the condition of shape measurement of the object bridge by TLS. The Focus S-350 was used in measurements on the bridge. The inner surface shapes of the arch ribs and suspension members were measured. Additionally, given that the distance between the revetments at the bridge origin and terminus sides of the bridge is approximately 450 meters, the entire side elevation of the bridge was measured using the SX10 laser scanner, which enables long-distance measurement from both revetments. Figure 13 shows the measurements positions of the two TLS.



Figure 10. Condition of image acquisition by UAV



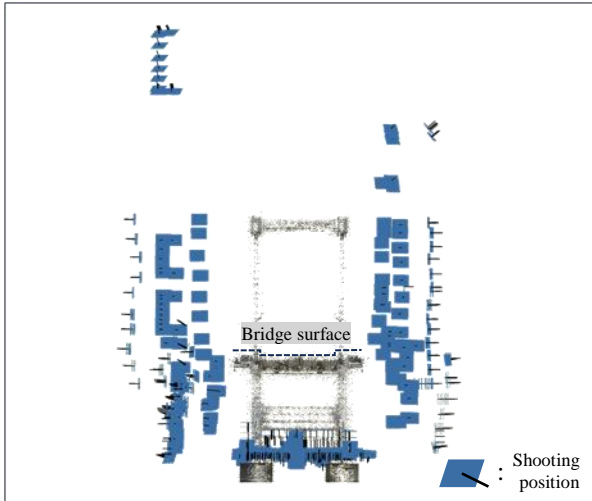


Figure 11. Positions of image acquisition by UAV (section view)



Figure 12. Condition of measurements by TLS (left: from revetment, right: on bridge)



Figure 13. Positions of measurements by TLS (Created using aerial photographs (by the Geospatial Information Authority of Japan))

### 3.4 Measurement Results

The TLS point cloud of entire bridge shape is shown in Figure 14. By precisely aligning the point cloud data measured from the various positions, the point cloud data representing the entire bridge shape were obtained.

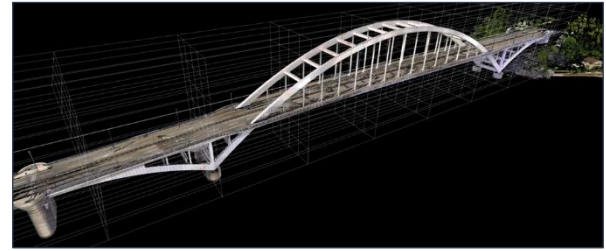


Figure 14. TLS point cloud of entire bridge shape

### 3.5 Creation of Current-state CIM Based on TLS Point Cloud

When the TLS point cloud was superimposed on existing drawings data, as shown in Figure 15, deviations were observed in the lateral shape of the arch rib members. Therefore, the linear data of existing drawings were corrected in accordance with the geometry of the TLS point cloud. The condition of correction of the drawing data is shown in Figure 16.

Next, based on the corrected drawing data, a current-state CIM of the bridge was created. The condition of creation of this current-state CIM is shown in Figure 17. The required level of performance for reproducing CIM models, based on their intended use, is defined as "Level of Detail (LOD)" in the Guidelines for Introduction of CIM [8], [9] issued by Japan's Ministry of Land, Infrastructure, Transport and Tourism. Excerpts of the definitions of each specified level of detail are shown in Table 4. In the range where point cloud data were acquired for steel materials, an LOD of approximately 300 was used, as it was possible to understand the external shape. However, in the range where point cloud data could not be acquired, for example, on the underside of girders, modelling was performed using LODs of 200 to 300, referring to the data in existing drawings, etc. The created current-state CIM created is shown in Figure 18.



Figure 15. Overlay of measured cloud point data and drawing data

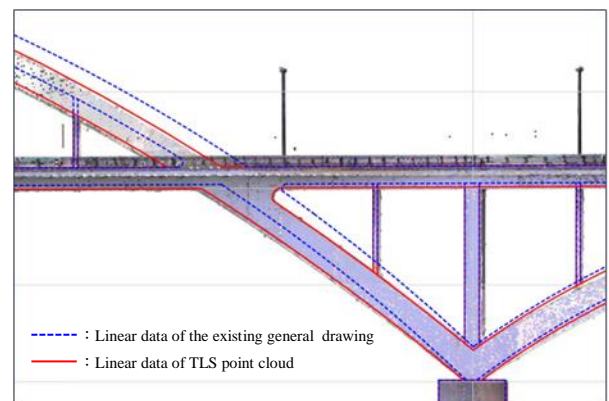


Figure 16. Correction of drawing data

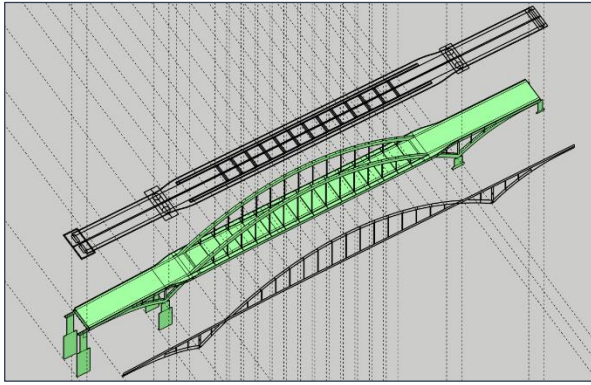


Figure 17. Creation of current-state CIM

Table 4. Definitions of levels of detail (LOD)

LOD	Common definition
100	Model showing the position of the object by symbols, lines or simple shapes.
200	Model with sufficient detail to understand the structural type. Cuts and fills are represented by standard transects, or in sufficient detail to sweep the standard transects of each structure in the general drawing in the object range.
300	Model accurately representing the external geometry of the object, with the exception of ancillary works and other detailed structures and the structure of connecting parts.
400	In addition to the requirements of LOD 300, accurate modeling is performed, including ancillary works, connecting structures and other detailed structures and the arrangement of reinforcing materials.
500	Model representing the actual geometry of the object.

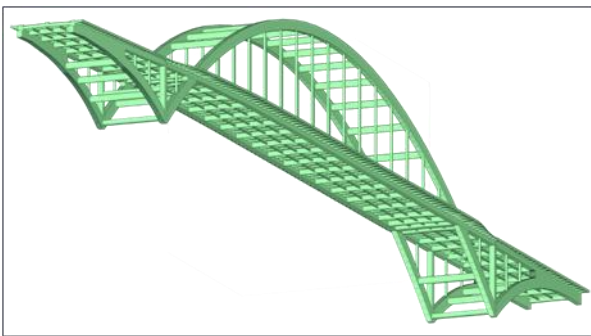


Figure 18. Created current-state CIM

### 3.6 SfM/MVS combined with TLS point cloud Application Process and Results

First, sparse point cloud data of the object bridge were obtained using location information from the GNSS data of UAV-captured images and camera posture information derived from SfM analysis. The results are shown in Figure 19.

Subsequently, for the dense point cloud data obtained through MVS analysis, a color map was created based on the number of depth maps used to generate each point cloud, as shown in Figure 20. A depth map is data that indicates the distance from the camera to each pixel in an image, and it is generally determined that the more depth maps used in the point cloud generation process, the higher the reliability of the

point cloud data. The number of point cloud for each confidence level is shown in Table 5. As shown in Figure 20, while a large number of depth maps were used in some areas, a decrease in the number of depth maps used was observed near areas with missing point cloud.

In the following step, in order to create textures based on camera images and construct a textured polygon model for the created current-state CIM, the current-state CIM and the cameras must be in the correct positional relationship. Therefore, to align the current-state CIM, a polygon model was first created based on the point cloud obtained through conventional SfM/MVS. As shown in Figure 21, although this model itself was an incomplete polygon model with missing areas and unevenness in originally flat sections, the point cloud derived from SfM/MVS with a confidence level of 10 or higher were superimposed on the TLS point cloud, and their differences were examined, as shown in Figure 22 and Table 6. As a result, 57.34% of the point cloud fell within a difference of 0.15 m and was distributed across the entire bridge. Note that 27.86% of the point cloud showed a difference of 0.3 m or more, which is thought to be primarily due to differences calculated at the lower parts of the girders where sufficient measurement using TLS was not possible.

Based on these results, the overall shape of the bridge and areas with high confidence were deemed to have a sufficient level of precision to serve as data indicating the positional relationship between the bridge and the camera. Therefore, the constructed incomplete polygon model was used as a reference for aligning the current-state CIM.

Subsequently, the aligned current-state CIM was imported into the SfM/MVS software, enabling the creation of an accurate textured polygon model. Figure 23 shows the data of the SfM/MVS application process using the current-state CIM, and Figure 24 shows the textured model created by this process. In addition to being able to confirm damage such as corrosion on the textured model, it became possible to output orthoimages, as shown in Figure 25, and accurately record the location, size, and other details of the damage by overlaying the orthoimages with drawings. Furthermore, the visualization of damaged areas using the 3D model enabled desk-based assessments of deterioration, as shown in Figure 26.

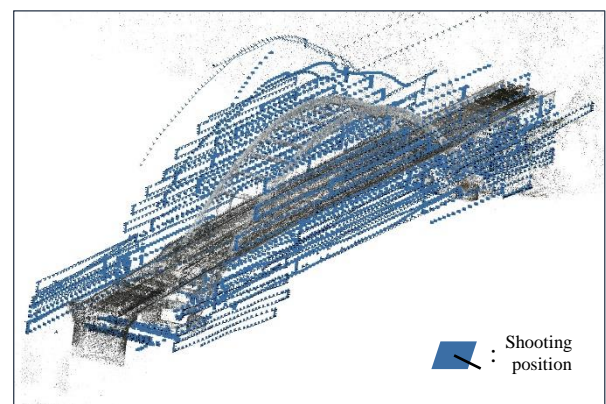


Figure 19. Estimation of camera position based on GNSS coordinate information



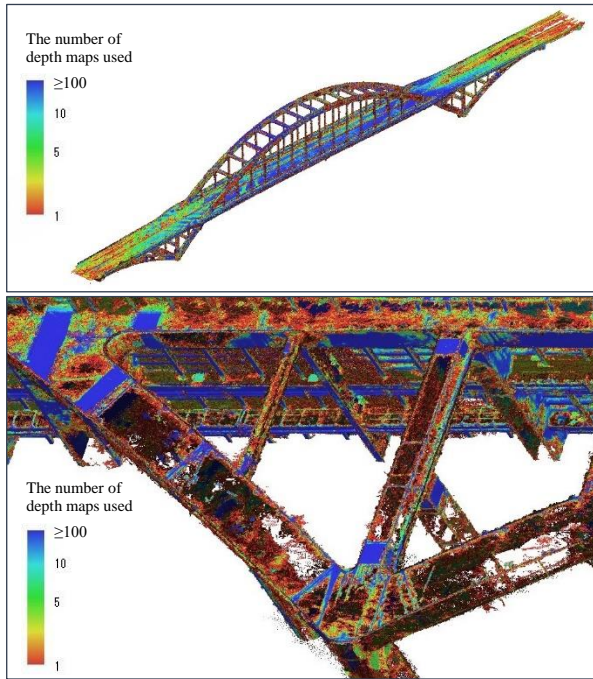


Figure 20. The confidence map of point cloud generated by SfM/MVS

Table 5. Number of point cloud for each confidence level

Confidence level (number of depth maps used)	Number and proportion of point cloud
1 to 4	150,509,599 points (54.38 %)
5 to 9	50,222,768 points (18.14 %)
10 to 99	75,733,315 points (27.36 %)
100 or more	330,028 points (0.12 %)

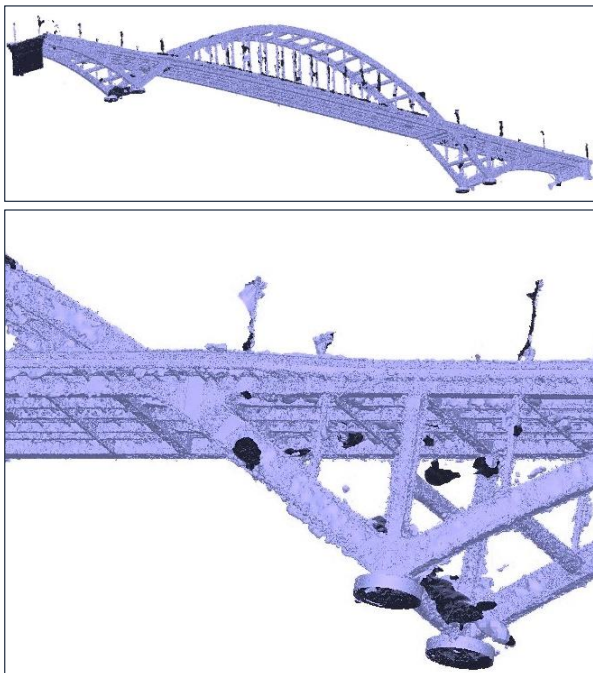


Figure 21. Results of SfM/MVS processing by the conventional technique

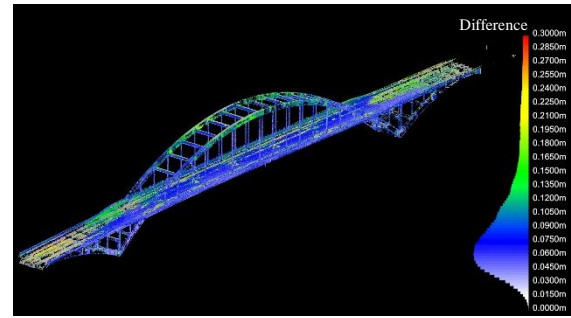


Figure 22. The difference color map between point SfM/MVS point cloud (high-confidence area) and TLS point cloud

Table 6. The difference verification results between point cloud generated by SfM/MVS (high-confidence area) and TLS

Statistics	Range of color map	0.000 m to 0.300 m
	Total point cloud (Sampled with an average point spacing of 10 cm)	2,819,768 points
	Point count in range	2,034,179 points
	Mean distance from base surfaces	0.1056 m (0.0655 std dev.)
Point Distribution	0.000 m to 0.075 m	836,198 points (29.66 %)
	0.075 m to 0.150 m	780,498 points (27.68 %)
	0.150 m to 0.225 m	247,846 points (8.79 %)
	0.225 m to 0.300 m	169,637 points (6.02 %)
	0.300 m or more	785,589 points (27.86 %)

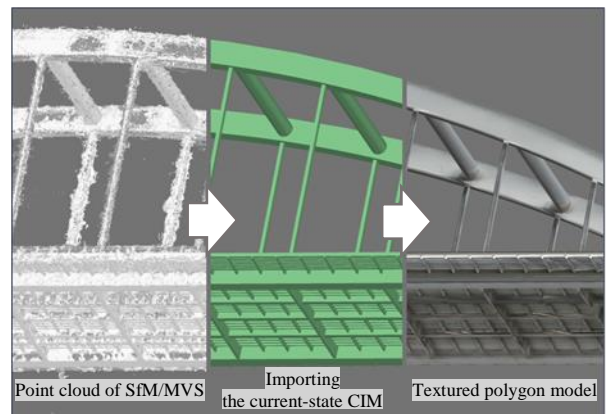


Figure 23. The application process of current-state CIM



Figure 24. Created textured polygon model



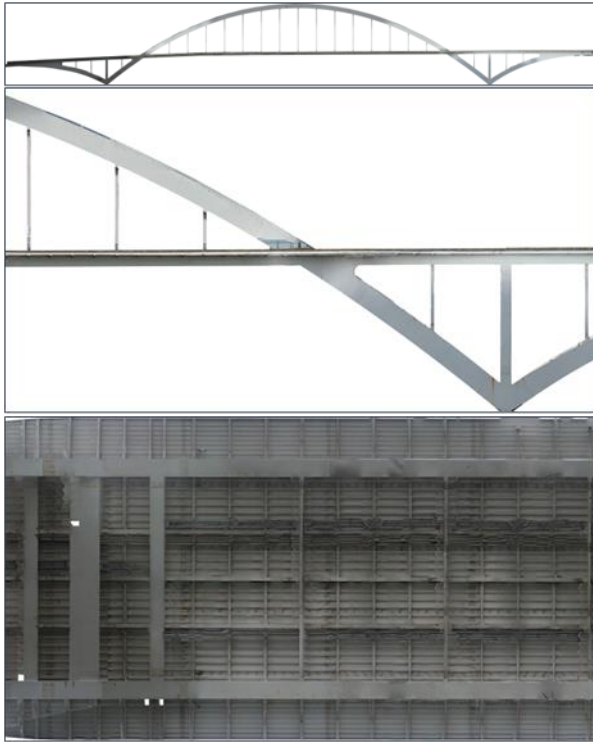


Figure 25. Examples of created orthoimages

(Top and middle images: bridge side view, bottom image: underside of the girder)

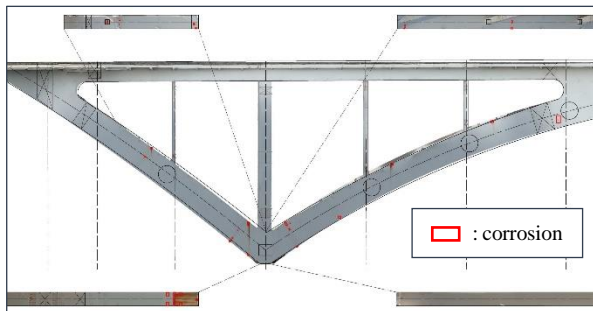


Figure 26. Example of a damage map created based on orthoimages

### 3.7 Issues

Four points may be mentioned as issues in the SfM/MVS combined technique using measured point cloud data described in this paper: i), Increase in costs associated with the construction of the current-state CIM, ii) Accuracy and level of detail of the current-state CIM, iii) Accuracy of alignment of the current-state CIM and camera positions and iv) Applicability of SfM/MVS to more difficult cases.

i) Cost incurred in construction of the current-state CIM

Compared to conventional SfM/MVS, the measurement of point cloud data aimed at understanding the current-state shape, the modification of drawing data to match the actual shape, and the creation of the current-state CIM lead to an increase in costs and workflow. It is necessary to plan accordingly to ensure efficient and sufficient data acquisition, based on the purpose of applying SfM/MVS techniques. This involves selecting appropriate equipment, preparing a measurement plan, and

considering factors such as the level of detail (LOD) of the 3D model, as described later.

ii) Accuracy and level of detail of the current-state CIM

The current-state CIM prepared in the proposed method will contain errors due to measurement accuracy, accuracy during model preparation and the setting of LOD. As the error in shape estimation increases, the accuracy of the positional relationship of the model and the cameras will decrease, leading to decreased quality of the textures to be projected. In actuality, even in the case described in this paper, it was confirmed that due to the difficulty in capturing detailed geometry using TLS, the quality of textures decreased in parts on the underside of the girders, where the level of detail of the current-state CIM was low, compared to other areas.

iii) Accuracy of alignment of the current-state CIM and camera positions

The point cloud obtained through conventional SfM/MVS processing was confirmed to be usable as reference data for alignment based on comparative verification with the TLS point cloud. Using the constructed incomplete polygon model as a reference, the alignment between the current-state CIM and the camera was performed. On the other hand, to ensure the accuracy and reproducibility of alignment, it is desirable to manage coordinates on public coordinate systems. This can be achieved by setting up multiple ground control points during UAV imaging and TLS measurements, and performing processes such as aligning the control points placed on the current-state CIM based on the TLS point cloud with the control point coordinates calculated by SfM/MVS.

iv) Applicability of SfM/MVS to more difficult cases

In the example described in this case, it was possible to estimate the camera positions by applying conventional SfM/MVS and perform polygon modeling, although incomplete. The factors in this successful result are thought to include the fact that image acquisition was performed by setting the angle of view to capture a wide range in photography by the UAVs, and corroded parts and fine irregularities on members could be detected and used as feature points. Thus, there is a possibility that the technique described in this paper may be inadequate for steel bridges and other structures with uniform surface textures or flat shapes over larger areas. Therefore, going forward, it will be necessary to consider combining SfM/MVS with other 3D model acquisition techniques, including improvements to the methods discussed in this paper.

## 4 CONCLUSION

As a technique for applying SfM/MVS to steel bridges, in which the steel materials have a uniform surface texture as a result of coating film, this paper examined a processing flow for projecting textures from camera images on a current-state CIM model based on measured point cloud data obtained with terrestrial 3D laser scanners. The technique was also verified at an actual bridge. Although the quality of textures differed depending on the accuracy and level of detail (LOD) of the current-state CIM model, the possibility of constructing a textured model and orthoimages with sufficient quality to identify overall damage could be confirmed.

On the other hand, various issues for application of the SfM/MVS technique verified in this paper may be mentioned.

These include the cost of creating the current-state CIM model, the accuracy and LOD of the model, the accuracy of alignment, and the applicability of the proposed technique to more difficult object structures. To overcome these problems, it will be necessary to plan methods corresponding to the purpose of applying SfM/MVS, the geometry of the object structure, and the surrounding environment. In the case described in this paper, the current-state CIM model was prepared based on existing drawings and the measured point cloud data of the current shape of the structure. In the future, the application of BIM/CIM, which has been actively promoted in recent years, may make it possible to substitute the current-state CIM with BIM/CIM models constructed at stages prior to inspections.

As future work on SfM/MVS application techniques, the authors intend to improve the accuracy and expand the range of application of the SfM/MVS technique, and study approaches for realizing higher efficiency and labor-saving in bridge inspections of steel bridges.

## REFERENCES

- [1] Ministry of Land, Infrastructure, Transport and Tourism (MLIT), Efforts for Aging Countermeasures, pp. 1–2, Japan, 2022, [Online], Available: <https://www.mlit.go.jp/road/sisaku/yobohozen/torikumi.pdf>
- [2] Ministry of Land, Infrastructure, Transport and Tourism (MLIT), Guidelines for Using New Technologies (Draft), Japan, 2019, [Online], Available: [https://www.mlit.go.jp/road/sisaku/yobohozen/tenken/yobo5\\_1.pdf](https://www.mlit.go.jp/road/sisaku/yobohozen/tenken/yobo5_1.pdf).
- [3] Ministry of Land, Infrastructure, Transport and Tourism (MLIT), 3D Product Delivery Manual Using Inspection Support Technologies (Image Measurement Technologies) [Bridge Edition] (Draft), Japan, 2023, [Online], Available: <https://www.mlit.go.jp/tec/constplan/content/001612927.pdf>.
- [4] K. Oda, Explanation: Structure from Motion (SfM) – Part 1: Overview of SfM and Bundle Adjustment, Photogrammetry and Remote Sensing, vol. 55, no. 3, pp. 206–209, Japan, 2016.
- [5] T. Fuse, Explanation: Structure from Motion (SfM) – Part 2: SfM and Multi-View Stereo, Photogrammetry and Remote Sensing, vol. 55, no. 4, pp. 259–262, Japan, 2016.
- [6] National Institute for Land and Infrastructure Management (NILIM), A Study on the Advancement of Environmental Evaluation Methods for Weathering Steel Bridges (I) — Examination of Environmental Evaluation Methods for Weathering Steel Materials —, NILIM Material No. 777, Japan, 2014.
- [7] Agisoft LLC, Agisoft Metashape User Manual, Professional Edition, ver. 2.2, pp. 9, 2025.
- [8] Ministry of Land, Infrastructure, Transport and Tourism (MLIT), CIM Introduction Guidelines (Draft) Part 1: Common Edition, Reference Materials, pp. 20–21, Japan, 2020, [Online], Available: <https://www.mlit.go.jp/tec/content/001334802.pdf>.
- [9] Ministry of Land, Infrastructure, Transport and Tourism (MLIT), CIM Introduction Guidelines (Draft) Part 5: Bridge Edition, pp. 12, Japan, 2020, [Online], Available: <https://www.mlit.go.jp/tec/content/001334799.pdf>.

# Re-meshing Method for Finite Element Model Updating based on Extracting Structural Anomalous Information from Point Cloud Data

Jiexiu Wang<sup>1</sup>, 0009-0008-7416-5656, Mayuko Nishio<sup>2</sup>, 0000-0003-1079-2577

<sup>1</sup>Department of Engineering Mechanics and Energy, University of Tsukuba, 1-1-1 Tennodai, Tsukuba, Ibaraki, Japan

<sup>2</sup>Institute of Systems and Information Engineering, University of Tsukuba, 1-1-1 Tennodai, Tsukuba, Ibaraki, Japan  
email: s2330203@u.tsukuba.ac.jp, nishio@kz.tsukuba.ac.jp

**ABSTRACT:** Finite element analysis (FEA) is widely used to evaluate civil structures' performance. To consider detected structural anomalies due to damage in FEA, it is required to represent the anomalous areas in the original finite element (FE) model and update the mesh configuration. This study proposes an approach for updating the shell-element FE models of thin-walled structures with anomalous areas by the point cloud data (PCD)-based CV method, focusing on surface planar anomalies. In this approach, the Iterative Closest Point (ICP) algorithm was used for the alignment of the point cloud with the FE model. The Density-Based Spatial Clustering of Applications with Noise (DBSCAN) on HSV values of PCD was used to extract points of anomalies. The anomalous region is denoted as its boundary points detected by the Alpha-shape algorithm. Constrained Delaunay Triangulation (CDT) generates the new meshes over a constrained area based on points related to anomalies. An experimental study was conducted for validation using a steel plate structure with various stickers attached to simulate the anomalies. The proposed CV-based FE model updating method was validated by comparing the PCD-based updated model and the manually updated model in terms of geometric and analytical accuracy. Most of the corresponding anomalous regions in the two models show a high degree of consistency, except for some areas affected by the low quality of the PCD, which, however, do not have a significant impact on the FEA results. With the same thickness reduction of anomalies, the analysis results indicate that there is only a minimal error between the two models. The proposed method is feasible as a substitute for manual rebuilding, facilitating the automation of the FE model updating with anomalies.

**KEY WORDS:** Finite element analysis; Point cloud data; FE model updating; Shell element; Anomalies detection; Registration.

## 1 INTRODUCTION

Since civil infrastructures, such as buildings, bridges, dams, and tunnels, in many countries have been in service for extended periods, various damage accumulated through aging in these in-service structures seriously threatens their safety. The damage assessment for aging structures is critical, considering the infrastructure's crucial role in supporting the quality of life and the economy.

Residual capacity assessment, based on simulation with finite element analysis (FEA), is one of the most widely used methods for evaluating damage to in-service structures. Computer vision (CV) techniques based on point cloud data (PCD) enable the identification and representation of real structural anomalies in computational models. However, current PCD-based modeling studies primarily focus on geometric reconstruction, while relatively limited attention has been given to their applicability in structural analysis. Moreover, there are far more studies related to mass solid structures such as concrete than shell structures like steel [1], [2], [3], [4], [5].

Considering that the PCD-based method of extracting anomalies can greatly facilitate the subsequent damage assessment based on numerical simulation, the purpose of this research is to propose a method for extracting anomalous information from the point cloud and incorporating it into the finite element (FE) model for analysis.

## 2 EXPERIMENT

This research conducted a full-scale steel structural mock-up test to simulate the actual inspection process of anomalies in steel structures. Shell element FEA was used to assess the structure's performance. The results of the manually built

model served as a reference to validate the proposed CV-based modeling method. The specific setup of the specimen and FEA will be elaborated on as follows.

The specimen was set up in this experiment as shown in Figure 1. It is based on a combined structure, consisting of three orthogonal SS400 steel plates welded together, with dimensions of 400 mm in height, 180 mm in length, and 180 mm in width. The thickness of all plates is 9 mm.

On the surface of the specimen, stickers of different shapes, sizes, and colors are arranged in various locations to indicate anomalies.

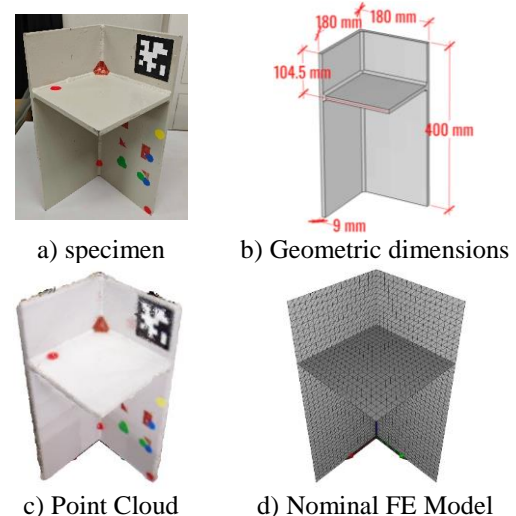


Figure 1. Setup and source data of specimen.

In this paper, A standard static analysis was conducted on the model using the commercial FEA software Abaqus. The reference model is manually imprinted with the outline lines of



anomalous regions in the geometric model, and the mesh generator tool included with the software is used to generate shell element (S3) meshes. Meanwhile, the test model is automatically remeshed based on the existing nominal FE model. The re-meshing is only executed within the local region specified by the proposed method. To introduce an observable amount of load capacity reduction, a uniform shell thickness of 3 mm is used in the anomalous regions for both models, representing a corrosion depth of 6 mm.

### 3 METHOD

We propose a PCD-based, CV-driven approach for updating the shell finite element model with anomalous information on the structure. This approach comprises three tiers.

The Perception Tier extracts geometry, features, and anomalous information from structures using point cloud data and establishes correlations between this information. The PCD of the steel structure was registered to the mesh through two steps: coarse (PCA) and fine (ICP) alignment. A clustering method that combines the Density-Based Spatial Clustering of Applications with Noise (DBSCAN) algorithm and the Support Vector Machine (SVM) was implemented to extract anomaly-related points based on the color information of points.

The Anomaly Description Tier processes anomalous information in the point cloud, extracting features to represent the anomalous area. We utilize the Alpha-shape algorithm for boundary detection. For a single anomalous area that may distribute across multiple planes, the points are further separated into corresponding planes by joint lines, allowing boundary detection to be conducted on each subset.

The Re-meshing Tier performs local mesh regeneration of the target area based on the feature extracted by the previous tier. The Constrained Delaunay Triangulation (CDT) algorithm is used to generate new meshes within the original edge lines of the remeshing region.

### 4 RESULTS

The original model, manually updated model, and PCD-updated model are shown in Figure 2.

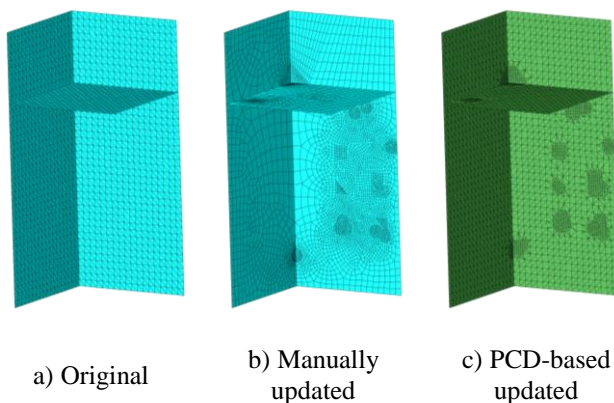


Figure 2. Results of the updated FE model

The locations of anomalous regions in the PCD-based updated model are generally consistent with those in the manually updated model.

Figure 3 presents the load-displacement curves at the loading point for the three models during the loading process.

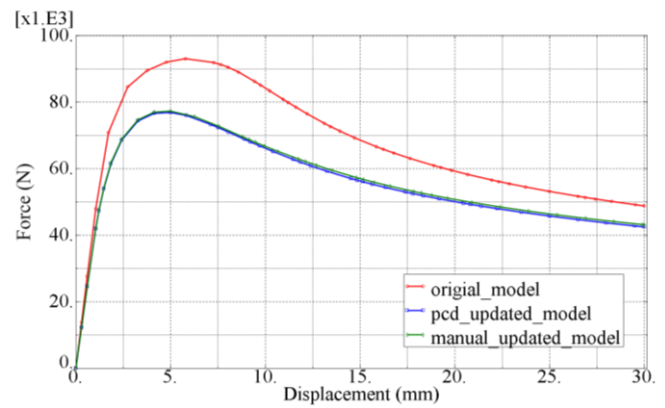


Figure 3. Load-displacement curve

### 5 CONCLUSION

This study proposed a method that utilizes PCD-based CV techniques to extract anomalous information from the structure and update it into an existing FE model. This paper focuses on surface anomalies commonly encountered in structures modeled by shell elements. The meshes corresponding to anomaly are locally updated based on geometric and color information contained in the point cloud.

The PCD-updated FE model was validated at the analytical level using a manually updated model created according to the design as the criterion. The following conclusions were drawn:

1. The PCD-updated model accurately captures the changes in the global distribution of stress and reduction in ultimate load capacity caused by anomalies in nonlinear analysis. Its results are in good agreement with those of the manually updated model, with a difference of less than 1% in the ultimate strength reduction.

2. The local stress distribution in the anomalous areas of the PCD-updated model is highly consistent with that of the manually updated model. However, due to limited detail in the extracted boundaries of anomalous regions, its local stress concentration effects do not perfectly match those of the manually updated model. Nevertheless, the level of accuracy is sufficient for evaluating structural load-bearing capacity.

### ACKNOWLEDGMENTS

This work was supported by JST SPRING, Grant Number JPMJSP2124.

### REFERENCES

- [1] Y. Lin, Z. Nie, and H. Ma, Structural Damage Detection with Automatic Feature-Extraction through Deep Learning, *Comput.-Aided Civ. Infrastruct. Eng.*, vol. 32, no. 12, pp. 1025–1046, 2017.
- [2] T.-C. Hou, J.-W. Liu, and Y.-W. Liu, Algorithmic clustering of LiDAR point cloud data for textural damage identifications of structural elements, *Measurement*, vol. 108, pp. 77–90, 2017.
- [3] E. Rúa, M. Cabaleiro, B. Conde, and B. Riveiro, First results of a methodology to obtain a 1D variable geometry model for the structural analysis of corroded steel beams from the point cloud, *Structures*, vol. 33, pp. 3257–3268, 2021.
- [4] G. Tzortzinis, B. T. Knickle, A. Bardow, S. F. Breña, and S. Gerasimidis, Strength evaluation of deteriorated girder ends. I: Experimental study on naturally corroded I-beams, *Thin-Walled Struct.*, vol. 159, p. 107220, 2021.
- [5] G. Tzortzinis, C. Ai, S. F. Breña, and S. Gerasimidis, Using 3D laser scanning for estimating the capacity of corroded steel bridge girders: Experiments, computations and analytical solutions, *Eng. Struct.*, vol. 265, p. 114407, 2022.

# Synthetic environment for close-range photogrammetry-based surface friction assessment of road infrastructures

Cheng Peng<sup>1</sup>, Yi Jiang<sup>1</sup>, Shuo Li<sup>2</sup>

<sup>1</sup>School of Construction Management Technology, Purdue University, 363 N Grant St., West Lafayette, IN

<sup>2</sup>Division of Research and Development, Indiana Department of Transportation, 1205 Montgomery St., West Lafayette, IN  
email: peng211@purdue.edu, jiang2@purdue.edu, sli@indot.in.gov

**ABSTRACT:** Quantification of friction demands is a major task in management of road infrastructures. The use of pavement texture measurement in friction assessment offers the potential for describing road frictional characteristic in a non-contact manner. However, surface macrotexture profiles tested by stationary measurements and high-speed laser systems provide limited range of texture information at high frequency scales. To achieve adequate outdoor road surface reconstruction at ultra-high resolution and low cost, this research develops a synthetic environment for ground truth reference and efficient generation of data and experiment. To illustrate the approach, a photo-realistic computer graphics model of asphalt pavement surface is produced and virtually scanned using candidate image acquisition plans. Then, in-depth quality assessment of the corresponding 3D point cloud reconstruction models is performed. In this way, suggest use of a close-range photogrammetric pavement surface scan method using Structure-from-Motion (SfM) technology and its requirements for friction-oriented texture quantification in terms of spatial resolution, camera movement, and illumination configuration is put forth. The effectiveness of the synthetic environment and the optimized experiment setup is demonstrated through a field survey on three roads. Finally, the obtained point cloud datasets are used in texture feature characterization and friction number prediction modeling processes.

**KEY WORDS:** Synthetic environment; Structure-from-Motion; Pavement texture measurements; Infrastructure friction performance.

## 1 INTRODUCTION

Pavement skid resistance is one of the most important properties among other highway surface characteristics. Demand for engineering interventions to restore friction of the aging and deteriorating highway network has been increased through years. Period assessment of pavement friction performance at the tire-road interaction has a pivotal role in developing the inventory of the condition of infrastructures at the highway network level. Current means of tire friction measurement devices and processes need calibration and harmonization for quality assurance. The use of pavement texture measurement in friction prediction offers the potential for describing highway frictional characteristic in a non-contact manner. To this end, such practices need to identify a comprehensive list of pavement macrotexture and microtexture attributes which contribute to friction. Both stationary measurements and high-speed laser systems are employed for sufficient reconstruction of macrotexture surface profiles [1]. However, a lower bound of microtexture wavelengths that relate to pavement skid resistance is not standardized. Furthermore, not all high frequency scales of microtexture are measurable. Criteria for sufficient spatial sampling rate and quality quantification of a pavement microtexture measurement approach, which includes all useful scales, is still vague [2].

In this paper, camera-based sensing of highway surface texture, using Structure-from-Motion (SfM) technique, is suggested for outdoor practices of high-resolution reconstruction of surface topography. In order to make fully use of the advantages provided by SfM technique while at the same time quantify and overcome limitations observed in previous studies, the investigation qualify SfM pipelines for pavement

texture measurements with three main contributions: (1) in-depth quantitative studies of the texture measurement accuracy influenced by the photogrammetric capturing quality of highway surfaces at high frequency scales; (2) comprehensive list of 3D texture characteristics contributing to the texture-friction correlation; (3) suggest use of an experimental setup using commercial off-the-shelf camera and its requirements for sufficient pavement texture quantification in terms of spatial resolution, camera movement, and illumination configuration is put forth. The works aims to optimize the use of outdoor photogrammetry techniques to friction-oriented road surface assessment, particularly for sufficient characterization of surface texture at micro-scales.

## 2 PAVEMENT SYNTHETIC ENVIRONMENT

Development of a synthetic test environment for close-range image acquisition of pavement surface topography is important for the proposed investigation for two main reasons:

1. Ground truth measurement: Evaluation of the SfM surface reconstruction quality in terms of texture characterization requires a well-defined ground truth model as the target reference. More often, camera-based approaches rely on a comparison to model from another costly technique such as a laser texture scanner or a microscopy. Therefore, the quality of such a comparison is limited by inevitable uncertainty in the reference model. Practices to mitigate this drawback include replication molding of the target surface and the use of 3D-print target objects [3]. In an approach using synthetic environment, the surface topography ground truth data is available. The

accuracy and quality of a SfM reconstructed surface digital elevation model (DEM) can be quantified using a direct comparison to the ground truth displacement map of the synthetic texture model. Subsequently, the pavement texture measurement performance from a photogrammetric survey can be optimized based on the observed variation in comparison results.

2. Efficient data generation and experiment: In the submillimetre, and micrometer range, quality of a photogrammetric surface reconstruction can be affected not only by the environmental and apparatus setups, but also by local characteristic variations of a target surface texture. Conducting a quantitative study of these factors in the field is time and cost consuming. In contrast, SfM surveys using images rendered in the synthetic environment can efficiently cover a wide variety of system configurations at any time without labor-intensive and site-sensitive field surveys.

A synthetic environment has been developed to test and quantify all influential factors regarding pavement macrotexture and microtexture measurements in a generalizable manner. To bring the close-range photogrammetric setup into the outdoor field environment, the image acquisition strategy should be developed, tested, and optimized for an efficient and robust performance.

Blender software is used to implement the synthetic modeling steps introduced herein. To extend the synthetic environment to a generalizable one, the high-resolution surface geometric details are modeled with a variation of texture characteristics using the Blender-Python API (Blender, 2024). The developed environment is used to produce survey images “captured” by a virtual micro-four thirds camera using different ground sampling distance (GSD). The resolution of each simulated image is  $4592 \times 3448$ , in which each pixel has a size of  $3.77 \mu\text{m}$ . This section describes the detail of each created texture model and the steps to develop the synthetic setup for pavement close-range photogrammetric texture measurement. First, a mesh of each solid object in the environment is created to represent the 3D geometric details of the target structure. Then, multiple texture maps and settings are imported to control base color, roughness, and shading effects of the object surfaces. Third, a simplified surrounding scene is configured, and a camera-light pair is positioned facing down at a determined height. Finally, a group of simulated images rendered from predetermined viewpoints are produced. An overview of the development is depicted in Figure 1.

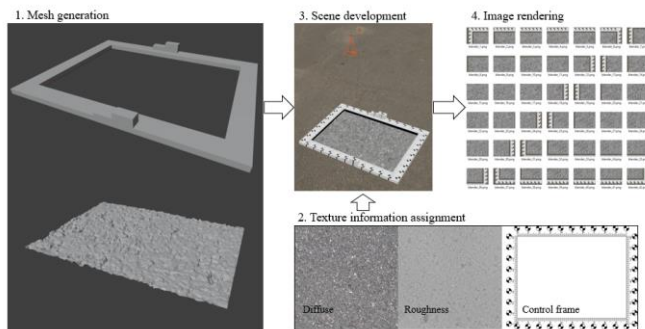


Figure 1. Framework for the synthetic approach of pavement texture photogrammetry.

## 2.1 Synthetic Data Generation

The synthetic environment developed in this research consists of a  $100 \text{ mm} \times 75 \text{ mm}$  patch of surface texture with four edges enclosed by a  $10 \text{ mm}$  wide rectangular control frame.

A solid object of control frame was generated in the synthetic environment. A cardboard thickness of  $3.175 \text{ mm}$  ( $1/16 \text{ in.}$ ) was selected to ensure flatness of reference surface for surveys in the field. The frame has a rectangular shape, and its inner and outer dimensions are  $100 \text{ mm} \times 75 \text{ mm}$  and  $120 \text{ mm} \times 95 \text{ mm}$ . The  $10 \text{ mm}$  width of four edges is selected so that the entire inner scanning area can be captured with at least two images (high overlapping). With a printed paper texture projected on the control frame top surface, a total of 40 reference marks of  $5 \text{ mm}$  diameter are horizontally distributed on the edges of the enclosed target scanning area. The edge distribution approach of ground control points (GCPs) is followed to have an optimized mapping accuracy [4] and to avoid texture occlusion. Previous studies have observed that the addition of a few vertically distributed GCPs can decrease the vertical reprojection error of a UAV surface mapping without influencing the planimetric accuracies [4], [5]. Therefore, additional heights ( $1/32 \text{ in.}$ ,  $1/16 \text{ in.}$ ,  $3/32 \text{ in.}$ ,  $1/8 \text{ in.}$ ) are added to four of the 40 edge marks so that they can be utilized as vertical GCPs.

A photogrammetry-based asphalt material downloaded from an public database [6] was adapted to generate a realistic pavement texture at a ultra-high level of resolution in the synthetic environment. The original data has a color map, a roughness map, a normal map, and a displacement map, each was represented by a  $16\text{K}$  image of  $1.2 \text{ m} \times 1.2 \text{ m}$  area. Several data processing steps were developed to the texture maps so that realistic ground truth textures with a variation of statistical characteristics can be tested in the synthetic environment.

1. The original maps have a resolution of  $186.4 \text{ p/mm}^2$ , equivalent to a pixel size of  $73.2 \mu\text{m}$ . Each of the three texture maps was refined to have an ultra-high resolution of  $1.68 \text{ Kp/mm}^2$  ( $24.41 \mu\text{m}$  pixel size) using bicubic interpolation. The 3D surface developed from a refined texture mesh has a smooth mesh geometry in the simulated images, in which unexpected edge artifacts in the high-frequency domain become invisible to the virtual camera pixels. Figure 2 shows a  $5 \text{ cm} \times 5 \text{ cm}$  patch of the surface color map before and after the interpolation. While increasing the synthetic surface smoothness enables a more realistic modeling of structure, it significantly increases the required computational power and time. The increased resolution of  $1.68 \text{ Kp/mm}^2$  in the geometry modeling of ground truth surfaces is selected to offer a tradeoff between model reality and tedious work. As a result, the ground truth power spectrum density (PSD) has a nominal high cutoff wavevector of:

$$\frac{2\pi}{\lambda_{min}} = \frac{2\pi}{4.882 \times 10^{-5} \text{ m}} = 1.287 \times 10^5 \text{ m}^{-1} \quad (1)$$



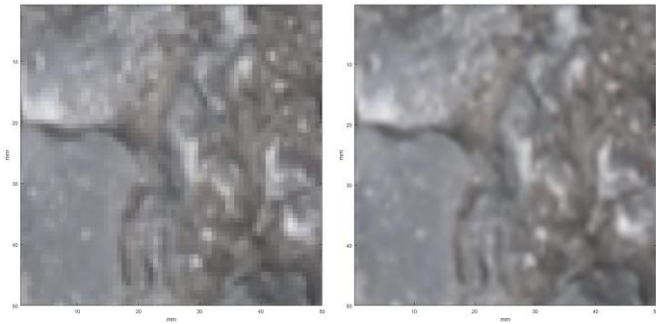


Figure 2. 5cm x 5cm patch of the asphalt texture model: original (left) and refined (right).

2. To enable real world applications of the system configuration with performance tested in synthetic simulations, the synthetic asphalt was scaled to have a middle level of average macrotexture MPD equal 0.83 mm. In this way, the target pavement shows realistic amplitude asperities over a large frequency range.

Using the Blender-Python API [7], gridded vertices, and triangulated faces of a mesh with displaced vertical coordinates is first created to represent the ground truth geometry of each synthetic pavement. Then, the generated 3D mesh is textured using a principle BSDF node in Blender, in which the base color and the light reflection roughness of the mesh surface are controlled and rendered using a physically based approach.

## 2.2 Rendering Synthetic Images

The length of the abstract is limited to 15 lines. The abstract should be self-contained and it must not refer to the other parts of the paper (such as the list of references). After the synthetic textured mesh of a pavement surface is created, an image acquisition plan including illumination condition and camera viewpoints is needed for optimization of tradeoff between spatial resolution and time/cost efficiency.

**Optics.** The critical parameters of a commercial off-the-shelf camera optics that influence the GSD of captured images on the target surface are: (a) the minimum focus distance, which is the closest capturing distance the camera can focus; (b) the depth of field (DoF), which is the vertical variability limit the survey can digitize. The reference project developed in the synthetic environment uses a virtual 4K camera of 30 mm focal length capturing at a height as low as 80-mm.

Macro camera lenses with a 1:1 or higher magnification ratio are widely used in applications of close-range photogrammetry [8]. The magnification ratio is the relationship of the size of a focused object in reality and the size of its reprojection on the camera image sensor. For a camera with pre-determined pixel size, a lens with higher magnification ratio enables capturing of images at a higher resolution. However, macro lenses exhibit a limited DoF without a time tedious process of focus stacking. According to the size of image sensor, most commercial off-the-shelf cameras can be categorized into three types: micro-four thirds (17.3 mm x 13 mm), APS-C (about 23 mm x 15 mm), and full frame (36 mm x 24 mm). Figure 3 compares the three types of cameras and the relationship between GSD and DoF. The focal lengths are selected for individual camera type, so that they achieve same level of image GSD at an equivalent object (focus) distance. Although large image sensor size cameras feature superior performance in cases that require low-

light (small aperture) and/or high-ISO settings, they result in shallower DoF assuming equivalent effective focal length. At a lateral resolution level of 10  $\mu\text{m}$ , the three cameras produce DoF results of 4.44 mm, 3.12 mm, and 2.03 mm, respectively. Therefore, micro-four thirds camera type is selected in both the synthetic environment and the field experiments to achieve sufficient DoF with cost efficiency.

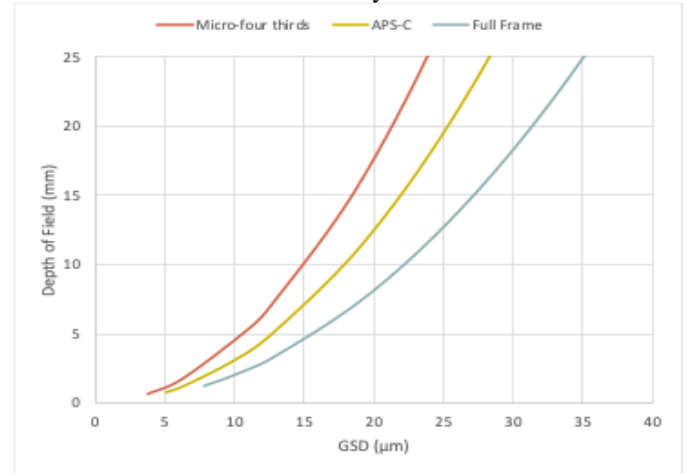


Figure 3. Depth of field (DoF) relationship with GSD for three camera types at a 60 mm equivalent effective focal length.

To capture full range of surface texture amplitudes in a targeting pavement, a DoF greater than the texture maximum height ( $S_z$ ) is preferred. Most asphalt pavements have an MPD of less than 2 mm. Thus, a minimum GSD of 10  $\mu\text{m}$  is selected for all configurations of image acquisition tested in the synthetic environment.

**Scanning Area and GSD.** The ground sampling distance (GSD) of captured images is a standard metric for the resulted spatial resolution of reconstructed point cloud, as it is the measured distance between two consecutive pixel centers on the ground. The determination of GSD depends on various factors including the camera focal length, the sensor pixel size, and the object distance (Figure 4a). A camera with fixed focal length captured at a higher height can result in larger GSD and lower spatial resolution (Figure 4b) compared to a closer range of photo capturing (Figure 4c). Ideally, a GSD is expected to be smaller than the smallest roughness horizontal scale to enable measurement of surface irregularities at the highest frequencies. However, the apparatus cost can be exponentially increased to have an image sensor with smaller pixel size and a macro camera lens that allows higher magnification ratio captured at a longer distance. While the synthetic environment is an effective tool enabling the use of simulated images “captured” by a virtual camera of any specifications at any distance, inevitable constraints on a low-cost field survey configuration should be taken into consideration.

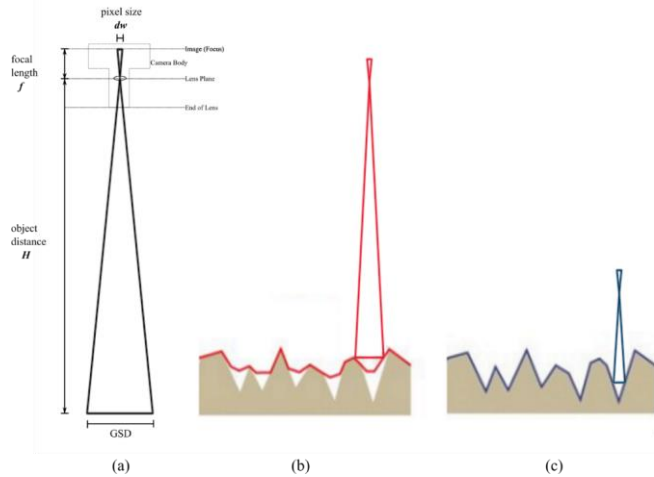


Figure 4. Determination of GSD (a), Large GSD – Low spatial resolution (b), and Small GSD – High spatial resolution (c).

Another factor that can affect the selection of GSD in a photogrammetric survey is the dimensions of target scanning area. A single 4K digital image can only capture about 16 mm in width if a  $4\ \mu\text{m}$  of GSD is used. Therefore, numerous numbers of images will be required for a single pavement texture 3D scan. This requirement can lead to tedious image acquisition work as well as long image processing time. Figure 5 shows the variation of the required number of images with GSD for a  $3.77\ \mu\text{m}$  pixel size 4K camera capturing a  $120\text{mm} \times 95\text{mm}$  surface area. The calculated number of required images include auxiliary images captured from multiple heights to ensure consistent mosaicking of partial scans. In the resolution range of  $10\ \mu\text{m}$  or smaller, the required number of images per survey is increased exponentially as GSD decreases. The minimum tested GSD of  $10\ \mu\text{m}$  enables not only enough DoF, but also reasonable image acquisition time. As the computational power grows and the cost per pixel decreases through time [9], the observed limitations can become negligible for future implementations.

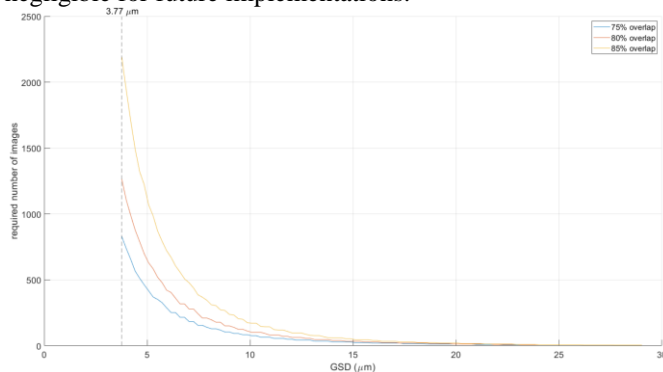


Figure 5. Required number of images with GSD for 4K camera scanning  $120\text{mm} \times 95\text{mm}$  area.

**Scene and Lighting.** The primary goal of lighting configuration is highlights while at the same time provide shadowless illumination. As discussed before, a camera with focus stacking technique may be needed if the aperture optimized for exposure provides insufficient DoF. In the proposed approach, fixed settings of F-stop ( $f/22$ ) and ISO 200 are selected for deeper DoF and smaller visibility of noise. As the target object is partially insulated from the environmental

illumination through set-ups including the surrounding control frame, close apparatus, and a very small aperture, a specific light source in conjunction with the sunlight is used towards proper exposure. In Figure 6, three images are rendered at 105 mm camera height with different energy settings of the added point light source. Therefore, proper adjustments of the light power output with object distance changes are required to prevent irreversible loss of data in the dynamic range.

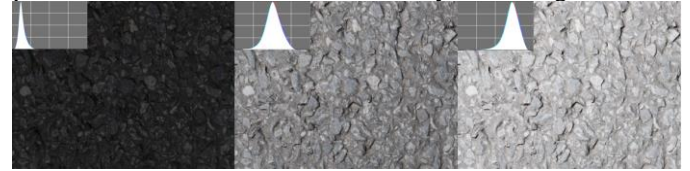


Figure 6. Synthetic rendered images of asphalt pavement texture with histogram at different light settings: (left) under exposed, (middle) proper exposure, and (right) over exposed.

Finally, a complete synthetic scene of pavement background and morning sunlight was used in image rendering processes. A 600mW power of diffused point light source moves along with the virtual camera is used to ensure shadowless and even imaging. In field studies, the shadow introduced by an imaging apparatus capturing at a close distance can be removed using a ring light installed around the camera lens. Figure 7 shows the rendered scene including a target object placed on the ground, a virtual camera facing down, and a diffused point light with pre-adjusted power output. Camera specifications and illumination configurations are set according to optimization of trade-off between cost, time, and resolution discussed in the above sections.

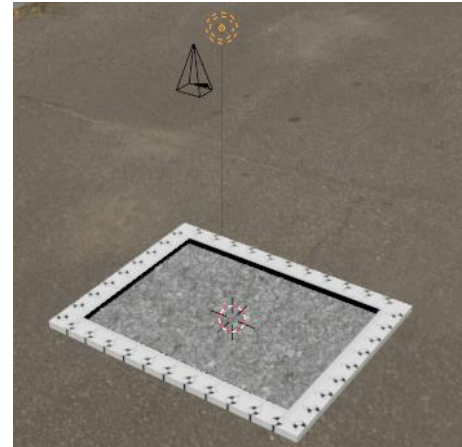


Figure 7. Scene and lighting configuration in synthetic environment.

**Camera Motion.** Images captured from numerous prescribed viewpoints are used in SfM technique to estimate the relative camera positions through feature matching, which is the start of triangulation processes. Both quantity and quality of the acquired images can greatly influence the feature detection performance. Following the principle of full coverage with high overlapping, two main strategies of shooting scenarios are widely used to obtain high quality of surface scanning: circular camera motion around the object, or viewpoints in a Cartesian lattice [8]. The former is preferred when the size of a single image footprint is greater than the target scanning area, whereas the latter is good for wider



surface scanning. A minimum net scan area width of 100 mm is required for measurements of pavement macrotexture MPD. Therefore, one standard 4K image cannot fully cover a scanning area of the required size at a GSD smaller than 25  $\mu\text{m}$ . However, the lowest wavelength of pavement roughness in rubber friction theory can be as small as a few micrometers [10]. This approach follows the Cartesian approach to avoid illumination artifacts and to achieve a lateral resolution as small as 10  $\mu\text{m}$ . In addition, a few auxiliary images captured at larger heights are collected so that the overall reconstructed surface structure is consistent through small partial scans.

The accuracy of 3D reconstruction outputs and their performance in texture characterization are tested at multiple levels of GSD: 10  $\mu\text{m}$ , 13  $\mu\text{m}$ , 15  $\mu\text{m}$ , and 38  $\mu\text{m}$  in the developed synthetic environment. As shown in Figure 8, a Cartesian approach is used in the first three image acquisition plans as it allows closer object distance for smaller GSD. The strategy of circular camera motion around the target, at a 22.5° rotation interval, is also tested for comparison. The number of images used in the texturing of the reconstructed surface in four different image acquisition plans are 80, 35, 20, and 13, respectively. At least 80% image overlap is employed in all four plans since photogrammetry in a close-range scenario requires larger overlapping of images [11].

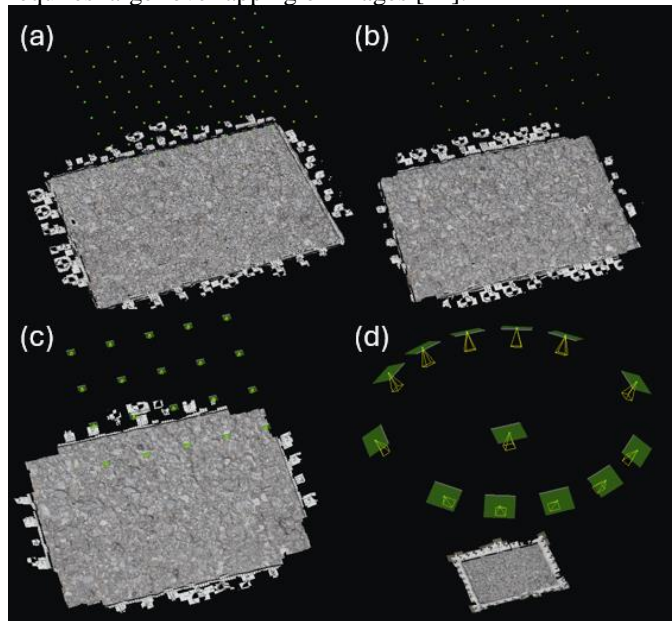


Figure 8. Image acquisition plans simulated in the synthetic environment tested at different GSD: (a) 10  $\mu\text{m}$ , (b) 13  $\mu\text{m}$ , (c) 15  $\mu\text{m}$ , and (d) 38  $\mu\text{m}$ .

### 2.3 Photogrammetric Process and 3D Reconstruction

All simulated images for each system configuration of pavement characteristics and camera viewpoints are imported in ContextCapture software [12] carrying out a photogrammetric process. The entire process includes three major stages: feature tracking, sparse reconstruction, and dense point cloud reconstruction.

First, the evenly distributed ground control points (GCPs) are detected in the images, either manually or automatically. An aerotriangulation process started from estimating the photogroup intrinsic and extrinsic properties. Taking into

account the world coordinates of GCPs for georeferencing, the aerotriangulation detects and tracks matched features in the overlapped area of consecutive images. As a result, numerous automated tie points are detected and an estimation of camera properties is provided. Figure 9 shows an example of 4,412 tie points detected in one image “captured” at a GSD of 13  $\mu\text{m}$  with a root mean square (RMS) reprojection error of 0.5 pixel. Enough tie points with sub-pixel parallaxes matched in the images is a good indicator of high precision in feature tracking.

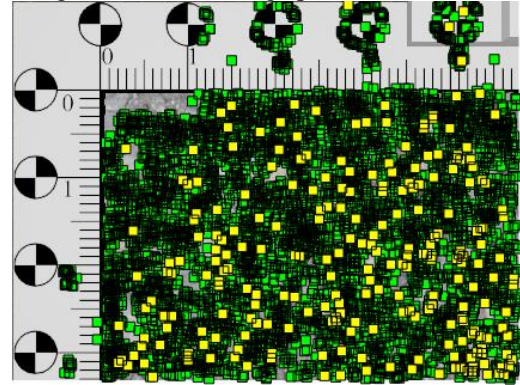


Figure 9. Example of 4,412 tie points detected in one rendered image by ContextCapture.

Next, the correspondence found between all tie points at the previous stage still contain errors and the camera pose estimates will be further refined in sparse reconstruction. At this stage, a bundle adjustment of camera internal and external parameters is employed for robust estimation. Taking advantage of redundancy in large number of detected tie points, this step estimates the geometry of the scene and obtains a sparse point cloud with robustness. Figure 10 shows the output of the sparse reconstruction stage of an asphalt surface texture modeled in the synthetic environment. The pavement model has an average MPD of 1 mm and was scanned at a GSD of 10  $\mu\text{m}$ . The control frame on the edges is only used to provide GCPs and will not be included in the reconstruction of dense point cloud. This stage marks the end of SfM technique applications.

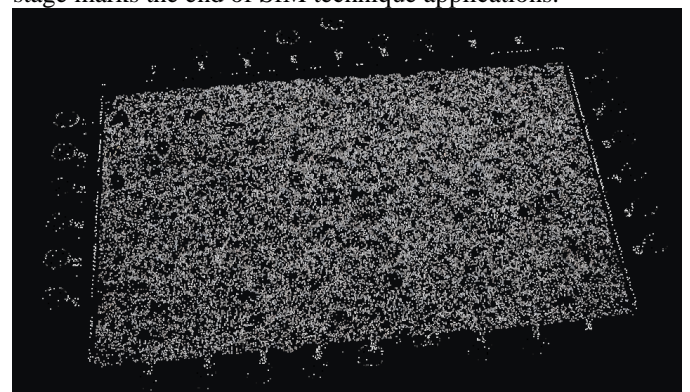


Figure 10. Sparse point cloud reconstruction output example.

The proposed photogrammetry approach requires a 3D reconstruction result of dense point cloud with a resolution equal or close to the determined GSD. Therefore, Multi-View Stereo is implemented to increase the point cloud density and reconstruct the 3D model with voxel color texturing according to stereo images of the scene captured with overlapping across different viewpoints. In both synthetic and laboratory



environments, the camera motion can be controlled precisely with accurate positioning data. However, to simulate the outdoor scenario that camera positions are not available to be used as initial estimate of camera extrinsic parameters. In the proposed method, the scene coordinate system of a developed output 3D reconstruction was initialized using at least three arbitrary GCPs of choice instead. Figure 11 compares the top view of a synthetic asphalt surface in Blender and its 3D reconstruction model produced by ContextCapture at a spatial resolution of 10  $\mu\text{m}$ . The original pavement model on the left is a mesh containing 1,567,362 vertices and 3,129,672 triangular faces. Due to the limited computational power (32Gb memory), the resulting resolution of the model is set as 24.41  $\mu\text{m}$ . Compared to the model ground truth, the 3D reconstruction on the right provides a top view picture with higher resolution. Although the two structures have different voxel resolutions, limited differences among the measurement of pavement texture parameters should be observed for a good photogrammetric texture reconstruction.



Figure 11. Synthetic asphalt pavement surface (left) and its 3D reconstruction with 10  $\mu\text{m}$  spatial resolution (right).

### 3 DATA QUANTIFICATION AND EVALUATION

The quality of each photogrammetric survey can be assessed by quantifying the difference between ground truth and 3D reconstruction and its Digital Elevation Model (DEM).

#### 3.1 3D Reconstruction Model Quality

Regardless of asperities in the surface topography, the modeling quality of a 3D reconstruction depends on the image acquisition plan, illumination, and camera intrinsic and extrinsic properties. Table 1 compares quality of 3D reconstruction outputs developed using different image acquisition plans. The density of the reconstructed point cloud remains uniform throughout the entire scanning area when a Cartesian approach is selected. Therefore, the resulted point cloud resolution of each Cartesian output is at the same level of the pre-determined image GSD (10  $\mu\text{m}$ , 13  $\mu\text{m}$ , and 15  $\mu\text{m}$ , respectively). However, if a circular camera motion is selected, the resulted point cloud will be distributed at a range of resolution because of the inclined orientation of camera viewpoints. In this case, a sampling rate equal to the highest resolution (37  $\mu\text{m}$ ) or one pixel size (38  $\mu\text{m}$ ) will be used in the creation of surface DEM model even if smaller resolution values were observed in partial areas.

Generally, a large number of tie points per image with a sub-pixel parallax for images used in the aerotriangulation process is desired for high quality 3D reconstruction. The automated tie points detected in each image of the circular camera motion model (GSD=38  $\mu\text{m}$ ) is significantly decreased compared to results from the Cartesian approaches. A reason of this change is that the target surface was not covering the whole

image footprint when the camera was capturing the entire object with a rotation in Z direction. An RMS reprojection error of less than one pixel size is observed for all four outputs, indicating that a satisfied precision in camera pose estimations can be obtained at various levels of point cloud resolution. As shown in Table 1, the average uncertainties found in estimation of image poses are less than 0.01 mm in all directions for three models with a  $\text{GSD} \leq 15 \mu\text{m}$ . For the model with 38  $\mu\text{m}$  of GSD, the observed image pose uncertainties are also less than one pixel size for quality assurance. For all four model outputs, the image uncertainty in the Z direction is smaller than ones in the two horizontal directions, as the camera was moving mostly in the X and Y directions.

Table 1. Quality summary of 3D construction at different GSD levels in image acquisition/

Point Cloud Resolution Range	Median Tie Points per Image	RMS Tie Points Reprojection Error
0.0099 mm – 0.01 mm	4,541	0.55 pixels
0.013 mm	5,395	0.5 pixels
0.015 mm	6,025	0.5 pixels
0.028 mm – 0.037 mm	1,263	0.68 pixels

#### 3.2 Digital Elevation Model Quality

Measurements of pavement texture only concern the height or elevation values of a target surface. Instead of conducting a direct comparison between voxels in two 3D structures, the 3D dense point cloud output of photogrammetry model will be rasterized to provide a surface DEM at one pixel sampling rate in MATLAB. The output map contains generalized height information of the input point cloud based on a local binning algorithm. As the GSD (one pixel size in mm) was selected as the fixed resolution of the grid element along X and Y axes, a few missing values are inevitable in the computed DEM and will be filled with linear interpolation. The corresponding percentage of the unfilled grids in DEM of the models with different grid resolutions are 0.099% (10  $\mu\text{m}$  resolution), 0.1% (13  $\mu\text{m}$  resolution), 0.15% (15  $\mu\text{m}$  resolution), and 0.00056% (38  $\mu\text{m}$  resolution) respectively. The number of unfilled grids in all four DEMs are neglectable compared to the matrix sizes. And the DEM of each 3D point cloud will be compared with the original displacement map of the synthetic asphalt pavement in terms of both residual errors and texture characteristics measurements. A visual comparison of the displacement (height) ground truth and the created model DEMs are displayed in Figure 12. According to the DEM surface plots, most of the height asperities of the structure are accurately scanned into the models. However, one deep pit was lost with a decreased absolute height in its 3D scans. The possible reason for this false is that occlusion happened when the optical paths were detecting the target point in valley.

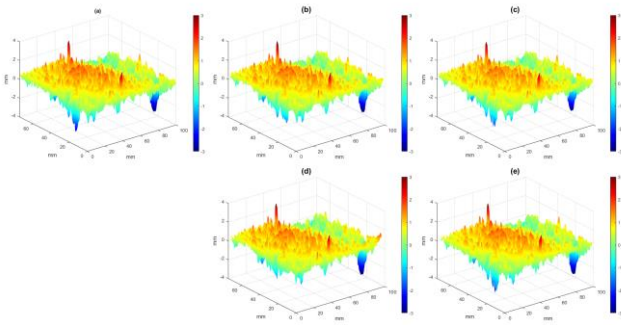


Figure 12. 3D surface plot comparison of surface ground truth (a) and DEMs of four 3D reconstructions of the synthetic pavement at different resolutions: 10  $\mu\text{m}$  (b), 13  $\mu\text{m}$  (c), 15  $\mu\text{m}$  (d), and 38  $\mu\text{m}$  (e).

Before comparing individual values in the ground truth matrix and the computed DEM of a 3D point cloud reconstruction, a spatial referencing process is needed to align the two matrices with different grid sizes. Then, the size of the matrix with a larger resolution is increased using linear interpolation. Finally, the residual errors of each DEM using the identical world coordinates are collected. Figure 13 shows the residual distribution of the DEMs compared to the ground truth. The shapes of residual histograms are close to normal distributions with zero means. It is observed that the RMS of all the residual distributions is within single digits of pixels. The general quality of a surface DEM is not improving with a decreased resolution. And the model sampled at 38  $\mu\text{m}$  resolution provides the highest quality because a tilt camera view helped in preventing the occlusion issue. However, a high DEM general quality only means that the texture roughness in the range of wavelengths greater than  $2 \times$  resolution was reconstructed accurately. The height asperity data in higher frequency ranges of the original structure was lost.

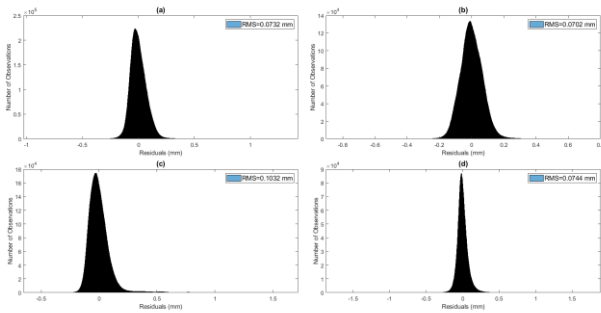


Figure 13. Residual distributions of DEMs of four 3D reconstructions of the synthetic pavement at different resolutions: 10  $\mu\text{m}$  (a), 13  $\mu\text{m}$  (b), 15  $\mu\text{m}$  (c), and 38  $\mu\text{m}$  (d).

After the spatial referenced comparison, the quality of a DEM needs to be further evaluated in terms of the characterization of pavement macrotexture and microtexture. To this end, a Butterworth filter was applied to both the pavement ground truth and the reconstruction DEMs to get: (iii) total texture roughness with wavelengths less than 50 mm, (ii) macrotexture with wavelengths within [0.5 50] mm, and (iii) microtexture with wavelengths  $\leq 0.5$  mm. Figure 14 illustrates the filtering process and its effects on the synthetic pavement

ground truth. As shown in Figure 14d, the original synthetic pavement contains waviness with wavelengths greater than 50 mm and it will be filtered out before the texture characterization processes.

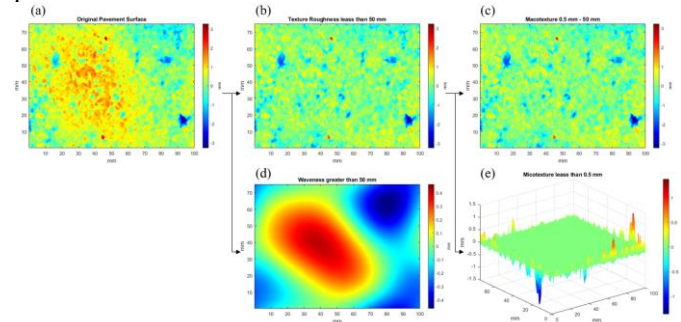


Figure 14. Butterworth filtering results on the synthetic pavement texture: (a) original surface; (b) total texture roughness; (c) macrotexture; (d) removed waviness; (e) microtexture.

### 3.3 Texture Characterization Quality

In this section, the macrotexture MPD and 3D areal parameters in total texture roughness measured from the 3D reconstructions will be evaluated.

First, the standard MPD is calculated from macrotexture of both the ground truth and the DEMs. Since different numbers of MPD measurements will be collected from data with different resolutions, the averaged MPD and the RMS MPD value will be compared as metrics. Since all four 3D reconstructions were sampled at a resolution much smaller than the microtexture lower bound wavelength (0.5 mm), the MPD measurements of DEMs are all accurate with small differences observed in the averages ( $<3.1\%$ ) and the RMS ( $<3\%$ ) compared to the ground truth, as shown in Table 2.

Table 2. Evaluation of the photogrammetric macrotexture MPD measurements.

Resolution	Average MPD		RMS MPD	
	mm	Diff (%)	mm	Diff (%)
<b>Ground Truth</b>	0.8305	-	0.8498	-
<b>0.01 mm</b>	0.8343	0.4596	0.8548	0.5910
<b>0.013 mm</b>	0.8048	-3.0875	0.8244	-2.9851
<b>0.015 mm</b>	0.8413	1.2991	0.8626	1.5069

Two pavements with the same macrotexture and microtexture amplitudes, e.g. MPD, can have different friction levels. A variety of supplemental variables have been used to represent the texture-friction correlation with improved performance. 3D areal parameters has been playing a significant role in tribological studies [13]. Adapted from the ISO 25178-3 [14] standard, a list of statistical quantitative texture measurements is used for comprehensive characterization of a 3D surface topography. Specifically, in total of 26 3D areal texture parameters were calculated across five categories: seven height parameters (arithmetic mean height  $Sa$ , RMS height  $Sq$ , minimum peak height  $Sv$ , maximum peak height  $Sp$ , skewness  $Ssk$ , and kurtosis  $Sku$ ), two hybrid parameters (root mean square gradient  $Sdq$  and developed interfacial area ratio  $Sdr$ ), three spatial parameters (autocorrelation length  $Sal$ , texture aspect ratio  $Str$ , and the texture direction in rad  $Std$ ), five

feature parameters (the density of peaks  $Spd$ , arithmetic mean peak curvature  $Spc$ , five-point peak height  $S_{5p}$ , five-point pit height,  $S_{5p}$ , and ten-point surface height,  $S_{10z}$ ), and nine functional parameters (peak material volume  $Vmp$ , core material volume  $Vmc$ , core void volume  $Vvc$ , dales void volume  $Vvv$ , peak extreme height  $Sxp$ , surface section difference  $Sdc$ , reduced peak height  $Spk$ , core height  $Sk$ , and reduced dale height  $Svk$ ).

The measurements of all seven height parameters were robust among four 3D models. The differences between the 3D measurements and the ground truth are less than 5%.

The two hybrid parameters are both good indicators of texture roughness in general. As  $Sdq$  increases, the surface is inclined steeply. The surface becomes more rough when the  $Sdr$  value increases. All three 3D models with a resolution smaller than the ground truth resolution (24.4  $\mu m$ ) provide good measurements of the hybrid parameters. However, significant errors (>10% difference) are observed for the model that has a larger resolution (38  $\mu m$ ).

Spatial parameters measure the surface horizontally. Therefore, the accuracy of 3D measurements varies depending on the influence of surface isotropy in the high frequency range. The strongest surface orientation was not accurately detected in the two 3D models of higher resolution (15  $\mu m$ , 38  $\mu m$ ).

Due to the sensitive nature of feature parameters, the difference observed between the ground truth and the 3D measurements in this category are large. Among the four 3D reconstructions, the circular camera motion model with a resolution of 0.038 mm has the best performance in feature parameters measurements. The reason is that a tilt camera orientation can help in capturing the actual value of points with the largest global peaks and pits heights. However, there is a trade-off between the sampling resolution and camera orientation. Therefore, feature parameters will not be used in the friction prediction modeling process utilizing the field texture measurements.

Most of the nine functional parameters are measured accurately in the four 3D models. Some error in  $Vmp$  measurement were observed in two models with the smallest resolutions (10- $\mu m$  and 13  $\mu m$ ). A possible reason is that redundant volume of extreme peaks are sampled in the two models as the result of linear interpolation. The significant differences in  $Spk$  and  $Sxp$  measurements for the 3D model with 15  $\mu m$  indicate that this model failed to scan some peak height values.

#### 4 FIELD EXPERIMENT

A low-cost commercial off-the-shelf camera (Lumix GX850) with a micro-four thirds 4K image sensor (4592×3448) installed with a macro lens is utilized in the field capturing images of pavement surface texture. The selected macro lens has a fixed focal length of 30 mm and a minimum focus distance of 105 mm (equivalent to a minimum working distance of about 22 mm). To minimize shake and achieve a spatial resolution of the order of tenth of micrometer, the camera was mounted on a tripod with a working height as low as 55 mm. In addition, a 180 mm rail nodal slider is fitted on the tripod to ensure consistent overlapping between consecutive images. Although the macro lens allows a maximum magnification ratio of 1:1, a smaller magnification (1/3) is selected to allow

larger DoF at f/22 aperture. The target three track roads have previous MPD measurements fall in the range of 0.1 mm – 2 mm. Therefore, a DoF of 5.63-mm should be sufficient to capture the asperities in amplitudes. As tested in the synthetic environment, a battery powered ring light is added to compensate for the low environmental lighting resulted from the shallow aperture.

A LTS measurement pair for each photogrammetric texture scans was recorded for initial validation purposes of field MPD measurements. The LTS Model 9200 by Ames scans enables selected number of 100 mm length 2D texture profiles at a horizontal resolution of 0.015 mm. The device needs approximately 15 minutes to complete 50 scans of profiles over a scan area of 107.95 mm by 72.01 mm.

Figure 15 shows all the apparatus utilized in field texture measurements as well as the LTS used for validation purposes. The total cost of all equipment listed in Figure 15b is less than \$1000. Specifications of the photogrammetry device used for field texture scan are listed in Table 3.



Figure 15. Apparatus of field texture scans: (a) LTS model 9200, (b) 4K camera, macro lens, tripod, slider, and ring light.

Table 3. Summarized specifications of texture scan using LTS and photogrammetry.

SfM-based Photogrammetry	
Total scan area	100 mm × 75 mm
Resolution	0.011 mm in X, Y, Z directions
Pixel Size	3.77 $\mu m$
Image Sensor Size	17.3 mm × 13 mm (4592×3448)
Aperture	f/22
ISO	200
Focal Length/GSD	30 mm/0.011 mm

Field data collection of pavement friction and texture was conducted on three track roads in Spring 2024. As shown in Figure 16, the research and development division of INDOT has three track pavements with distinct MPD levels: two hot-mix asphalt (HMA) pavements at the left and middle lanes, and one slick concrete pavement on the right. For each road, two longitudinal sections (each about 65 feet long) along with three locations: the left wheel-path, the center line, and the right wheel-path were selected as individual test locations. The three transversal locations are assumed to have different levels of traffic polishing. Consequently, the difference observed in friction data gathered from the three locations within each road will explain the influence of traffic polishing on road wet friction performance. On the other hand, two longitudinal sections for each road were selected for data argumentation,



assuming that the pavement surface texture in real world is not homogenous in real-world scenarios.



Figure 16. The test fields: three track roads in INDOT. Each road includes two longitudinal sections (left) and three transversal locations (right).

After texture data collection, a LWST was employed to obtain the pavement friction number (FN) at two vehicle speed levels with multiple repetitions. In total of 130 LWST measurements were completed in three days, and the test temperature of pavement varies between 45°F to 112°F.

The residual errors of GCPs during the reconstruction of the field surfaces increases compared to the synthetic test results. One important reason is the additional uncertainties caused by calibration of a real-world camera with lens distortion. To verify the method reliability in the field, a comparison of macrotexture MPD measurement distributions between the proposed photogrammetric method and its LTS counterpart is employed. Since the measurement sampling rates and locations in the transversal direction varies, two sample T tests are employed to compare the average MPD in the distributions provided by the two methods. All 41 tests failed to reject the null hypothesis that MPD measured by photogrammetry and LTS are from populations with equal means at a 5% significance level.

The R-square value of 0.7672 indicates that limited information in the road friction performance can be explained by the standard macrotexture MPD solely. Therefore, three alternative models are trained: stepwise linear regression, neural network (NN) model, and regression ensemble model (random forest). The optimized regression ensemble model contains 47 learners of all 25 predictors. And the model achieves better goodness-of-fit compared with both the stepwise linear model and the NN. As shown in Table 4, a R-squared (Test) of 0.98 is obtained. The RMSE (Test) has been reduced to 3.36, and the MAE (Test) is only 2.55. It is worth noting that the MAE statistic (mean absolute error) is less sensitive to outliers compared to RMSE and MSE.

Table 4. Performance of three texture-based FN prediction models.

Model	RMSE (Valid)	R-squared (Valid)	RMSE (Test)	R-squared (Test)
Stepwise LR	4.853	0.960	4.995	0.956
Neural Network	5.318	0.952	4.796	0.959
Ensemble	3.549	0.978	3.361	0.980

As discussed in the synthetic simulations, a selection of small image GSD leads to high spatial resolution in the 3D photogrammetric pavement texture reconstruction.

Consequently, the measurement quality of texture roughness characteristics is also changed with the sampling rate. The comparison results of an asphalt pavement surface scanned at multiple image GSD in the synthetic environment suggest that a DEM developed using the proposed 3D reconstruction method with a GSD/resolution of 0.011 mm – 0.013 mm can provide reliable measurements of 23 distinct texture parameters, as long as the maximum imaging DoF is sufficient for feature capturing of extreme peaks and pits. However, the highest frequency of pavement microtexture is undefined. Therefore, the minimum spatial resolution in surface texture scan required for reliable prediction of pavement friction performance is still debated.

The original 3D reconstruction of 41 field texture photogrammetric scans will be down sampled at a scale of 0.5 multiple times. Next, texture DEMs of the down sampled point cloud data are developed, among which there are five distinct resolution levels: 0.022 mm, 0.044 mm, 0.088 mm, 0.176 mm, and 0.352 mm. The 22 areal texture parameters are measured using the down sampled texture DEMs. The original speed, pavement temperature, and macrotexture MPD are kept as they were not affected by the down sampling process. Finally, new observations with changed values in 22 texture predictors are collected.

The optimal regression ensemble model is used to predict FN using the six test groups of data observations. The prediction performance in terms of resolution changes is measured using the test RMSE and R-squared values. High R-squared values are observed in test results of all five samples, indicating that most of the pavement performance can be explained by pavement macrotexture. However, the RMSE between predicted FN using input of 25 predictors and the true FN provided by a LWST increases as the spatial resolution in texture 3D scan increases. Therefore, the texture asperities at micro-scales have contributed to the friction performance of a pavement surface. According to the increasing rates of test RMSE shown in Figure 17, it is suggested that the spatial resolution of a comprehensive 3D texture scan for friction prediction should be smaller than 0.1 mm at the least.

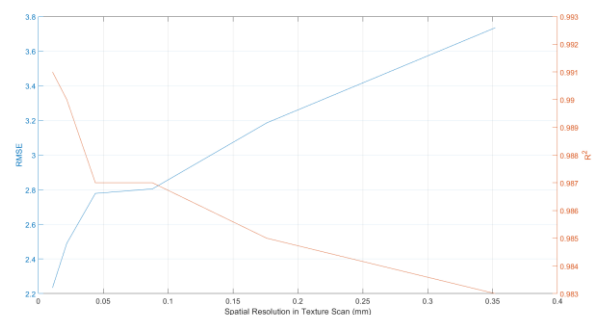


Figure 17. Relationship between the Model performance and spatial resolution in texture scans.

## 5 CONCLUSION

This paper develops a prototype of image-based pavement texture measurement for friction prediction in a non-contact manner. Towards the goal of data quality assurance, a synthetic environment is developed before field implementation. The

survey simulations evaluate sensitivities in texture measurements arising from different experimental designs and testing feature configurations. The minimum condition for optimized 3D surface reconstruction of pavement surface is discussed. Finally, a field experiment investigates the characterization of surface texture at different scales and their contribution to pavement friction performance.

## ACKNOWLEDGMENTS

The authors would like to thank Michael Sanders of INDOT for his input and technical guidance in the field road friction experiments.

## REFERENCES

- [1] S. Li, S. Noureldin, and K. Zhu, "Safety Enhancement of the INDOT Network Pavement Friction Testing Program: Macrottexture and Microtexture Testing Using Laser Sensors," 2010. doi: 10.5703/1288284314248.
- [2] M.-T. Do and V. Cerezo, "Road surface texture and skid resistance," *Surf. Topogr.: Metrol. Prop.*, vol. 3, no. 4, p. 043001, Oct. 2015, doi: 10.1088/2051-672X/3/4/043001.
- [3] M. S. Nielsen, I. Nikolov, E. K. Kruse, J. Garnæs, and C. B. Madsen, "Quantifying the Influence of Surface Texture and Shape on Structure from Motion 3D Reconstructions," *Sensors*, vol. 23, no. 1, Art. no. 1, Jan. 2023, doi: 10.3390/s23010178.
- [4] P. Martínez-Carricondo, F. Agüera-Vega, F. Carvajal-Ramírez, F.-J. Mesas-Carrascosa, A. García-Ferrer, and F.-J. Pérez-Porras, "Assessment of UAV-photogrammetric mapping accuracy based on variation of ground control points," *International Journal of Applied Earth Observation and Geoinformation*, vol. 72, pp. 1–10, Oct. 2018, doi: 10.1016/j.jag.2018.05.015.
- [5] D. S. Dharshan Shylesh, N. Manikandan, S. Sivasankar, D. Surendran, R. Jaganathan, and G. Mohan, "Influence of quantity, quality, horizontal and vertical distribution of ground control points on the positional accuracy of UAV survey," *Appl. Geomat.*, vol. 15, no. 4, pp. 897–917, Dec. 2023, doi: 10.1007/s12518-023-00531-w.
- [6] ambientCG, "ambientCG - CC0 Textures, HDRIs and Models." Accessed: Apr. 14, 2024. [Online]. Available: <https://ambientCG.com/>
- [7] Blender, "Blender 4.1 Python API Documentation." Accessed: Apr. 16, 2024. [Online]. Available: <https://docs.blender.org/api/4.1/#>
- [8] P. Koutlemanis, X. Zabulis, N. Stivaktakis, N. Partarakis, E. Zidianakis, and I. Demeridou, "A low-cost close-range photogrammetric surface scanner," *Front. Imaging*, vol. 3, Jan. 2024, doi: 10.3389/fimaging.2024.1341343.
- [9] Q. Alexander, V. Hoskere, Y. Narazaki, A. Maxwell, and B. Spencer, "Fusion of thermal and RGB images for automated deep learning based crack detection in civil infrastructure," *AI in Civil Engineering*, vol. 1, Aug. 2022, doi: 10.1007/s43503-022-00002-y.
- [10] B. N. J. Persson, "Theory of rubber friction and contact mechanics," *The Journal of Chemical Physics*, vol. 115, no. 8, pp. 3840–3861, Aug. 2001, doi: 10.1063/1.1388626.
- [11] G. Guidi, U. Shafqat Malik, and L. L. Micoli, "Optimal Lateral Displacement in Automatic Close-Range Photogrammetry," *Sensors*, vol. 20, no. 21, p. 6280, Nov. 2020, doi: 10.3390/s20216280.
- [12] Bentley, "iTwin Capture Modeler | Bentley Systems | Infrastructure Engineering Software Company." Accessed: Apr. 16, 2024. [Online]. Available: <https://www.bentley.com/software/itwin-capture-modeler/>
- [13] L. A. Franco and A. Sinatora, "3D surface parameters (ISO 25178-2): Actual meaning of Spk and its relationship to Vmp," *Precision Engineering*, vol. 40, pp. 106–111, Apr. 2015, doi: 10.1016/j.precisioneng.2014.10.011.
- [14] ISO, "ISO 25178-3:2012," ISO. Accessed: Oct. 14, 2024. [Online]. Available: <https://www.iso.org/standard/42895.html>

# Developing a Deep Learning-Based Method to Segment Bridge Members by using 2D Cross Sectional Point Clouds

Nao Hidaka<sup>1</sup>, Naofumi Hashimoto<sup>1</sup>, Ei Watanabe<sup>2</sup>, Daisuke Uchiyama<sup>1</sup>

<sup>1</sup> Nagoya Institute of Technology, Gokiso-cho, Showa-ku, Nagoya, Aichi, Japan

<sup>2</sup> Aichi Prefectural Government, 3-1-2, Sannomaru, Naka-ku, Nagoya, Aichi, Japan

email: hidaka.nao@nitech.ac.jp, n.hashimoto.704@stn.nitech.ac.jp, ei\_watanabe@pref.aichi.lg.jp,  
d.uchiyama.703@stn.nitech.ac.jp

**ABSTRACT:** For efficient maintenance and repair, 3D modeling of bridges for converting analytical models and visualizing deformation locations is being advanced. Instead of manually creating models from drawings and ledgers, automating model generation from point cloud data, capable of capturing as-is geometry quickly and widely, can improve efficiency. Generating 3D modeling of bridges from point cloud data requires segmenting each member, but dynamically setting thresholds for shape features and positional relationships is challenging due to point density and missing points. While deep learning can dynamically set thresholds, in the case of point cloud data, it is impractical to prepare sufficient training data, and the number of inputting points is inadequate for setting appropriate thresholds. Therefore, this research focuses on two aspects: most bridges consist of members with swept cross sections along longitudinal direction, and deep learning classification methods for 2D images are highly developed. The aim is to segment members based on deep learning on 2D cross-sectional point cloud data obtained by slicing along longitudinal direction. This reduces the number of inputting points and increases training data. Additionally, fine cross sections enable segmentation close to 3D. The multiple patterns of learning methods, training data processing, and procedures of segmentations are compared to identifying highly accurate segmentation methods.

**KEY WORDS:** Point cloud; Deep learning; Segmentation; Cross section; Steel truss bridge.

## 1 INTRODUCTION

A vast number of existing bridges are rapidly aging. Since it is not practical to rebuild all of them at the same time, strategic renewal through life cycle extension is required. To extend the life cycle of bridges, 3D models of bridges are created. These models can be converted numerical analysis models [1] and can visualize deformations [2]. However, in cases of old bridges, as-build drawings are often unavailable. In addition, conditions of bridges inevitably changed since its construction due to various factors. Therefore, it is necessary to construct 3D model based on dimensions data instead of relying on drawings, but manual measurement is time-consuming and prone to various human errors.

Therefore, a method to efficiently create 3D models from point cloud data, capable of capturing as-is 3D geometry as a set of points quickly and widely, has begun to attract attention. It can make a significant contribution to efficiency. Qin et al. [3] sliced the point cloud data of a PC box girder bridge vertically from the ground and used the density of each obtained point cloud as a threshold to divide the superstructure and substructure for Building Information Modeling (BIM). Schatz et al. [4] semi-automatically divided the point cloud data of a PC box girder bridge into substructure, girders, bearing pavement, drainage facilities, etc. based on template matching, and created an Industry Foundation Classes (IFC) model. The authors [5] performed Finite Element Method (FEM) modeling of a steel truss bridge by segmenting a fine section along a longitudinal direction and dividing the point cloud of the section based on Euclidean distance. The segmentation and component determination processes in these papers are a mixture of manual processing based on human visual judgment and automatic processing based on threshold values such as

shape features and positional relationships. In general, it is not easy to set the threshold dynamically in automatic processing because of the effects of point density, missing points, and other factors. In recent years, deep learning has attracted attention as a method for dynamically setting threshold values, and there are several cases where it has been applied to point cloud data processing [6, 7]. However, when targeting large-scale bridges with a wide variety of geometries, the classification is roughly divided into upper and lower structures, and the lack of training data and the number of input points are insufficient.

Therefore, this research focuses on the characteristics of bridges, which generally have many structures with swept cross sections of each member along a longitudinal direction, and the fact that classification methods for 2D images are relatively well-developed. In this research, point cloud data of 2D cross sections sliced along the longitudinal direction is used to classify members using deep learning. The number of input points can be reduced, and the number of training data can be increased by inputting point cloud data of cross sections. In addition, a finer cross-sectional view leads to an almost 3D segmentation. The optimal learning method, processing procedures, and multiple proposed patterns are compared and validated, and a highly accurate segmentation method is considered.

## 2 STRUCTURE OF THE MODEL

### 2.1 Literatures about segmentation by using deep learning

Deep learning-based image classification and segmentation often uses Convolutional Neural Network (CNN), which obtains features by convolving surrounding pixel features. If the number of pixels is reduced by convolution, the



segmentation results are restored to the original number of pixels by increasing the number of pixels based on the convolved features again. Typical models include U-Net [8], which performs domain segmentation at the pixel level; Feature Pyramid Networks (FPNs) [9] which combine high-resolution and low-resolution features to exploit multi-scale information; DeepLap v3+ [10] which applies convolution with different expansion rates in parallel. As an example of member segmentation of point cloud data of bridges, Saovana et al. [11] implemented segmentation of point cloud data by segmenting photographs of bridges from multiple viewpoints into members using U-Net and then projecting the results onto the point cloud data generated by Structure from Motion (SfM). The results are then projected onto the point cloud data generated by SfM to implement point cloud data segmentation.

On the other hand, point cloud data differs from images in that pixels are not arranged in a regular and continuous manner, the same shape and color data can be obtained even if the order of the points is changed, and the three-dimensional coordinates provide a large degree of freedom. To cope with these problems, a transformation matrix is obtained from the features and applied to control the posture, and MaxPooling is applied to eliminate the effect of reordering. The segmentation of point cloud data is similar to that of a CNN. Typical models include PointNet [12], PointNet++ [13], and Dynamic Graph CNN (DGCNN) [14]. PointNet does not perform convolution to obtain features for all input points. PointNet++, an advanced version of PointNet, reduces the number of points and obtains features from the points in the neighborhood of the point, which is similar to the convolution process. DGCNN also obtains features from neighboring points, but the number of points does not change at any layer.

## 2.2 Structure of the deep learning model in this research

Since the aforementioned PointNet++ [13] and DGCNN [14] are candidates for deep learning models in this research, the details of these model configurations are described in this section.

The model structure of PointNet++ is shown in Figure 1. First,  $c_1$  is obtained by randomly sampling  $n_1$  points from the cross-sectional point set  $c_0$ . Next, a point  $p_{c_1}$  in  $c_1$  is used to search  $k_1$  neighbor points within  $r_1$ , and then vectors from  $p_{c_1}$  to the neighbor points as feature values. The obtained feature values are convolved by using Conv1d, BatchNormize and Relu function. This process is repeated 4 times to obtain a set of cross-sectional points  $c_1$ ,  $c_2$ ,  $c_3$ , and  $c_4$  reduced by random sampling and the features associated with  $c_4$ . After that, 3 neighbor points from  $c_3$  to  $c_4$ , are detected and their feature values are convolved by using Conv1d, BatchNormize and Relu function. This process is repeated until the  $c_0$  features are updated, and finally they are convolved with the classified features and output as random variables by applying the Logsoftmax function.

The model structure of DGCNN is shown in Figure 2. In PointNet++, the neighbor points were obtained based on the position coordinates, but in DGCNN, the  $k_n$  neighbor points are obtained based on all the feature values changed by convolution, not limited to the position coordinates, and the vector from the reference point to the neighbor points and the original feature values are integrated and convolved. The

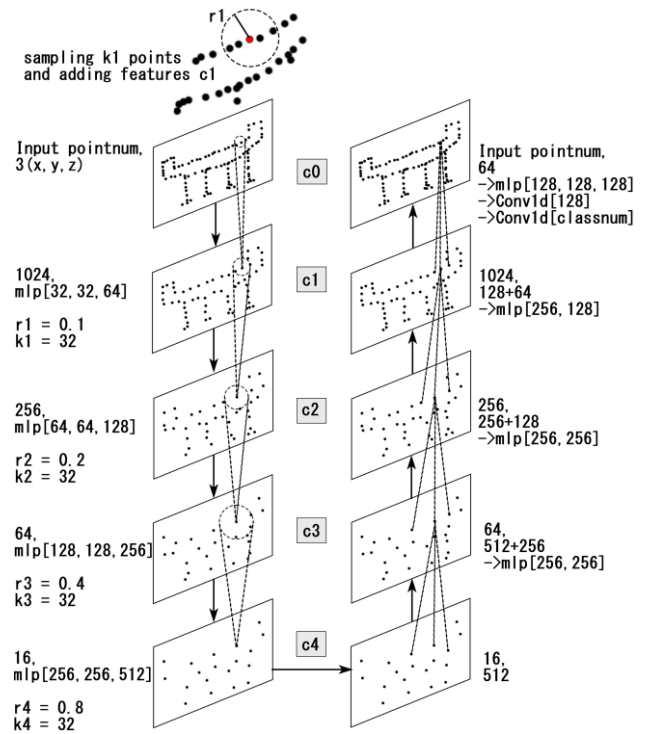


Figure 1. Model structure of PointNet++.

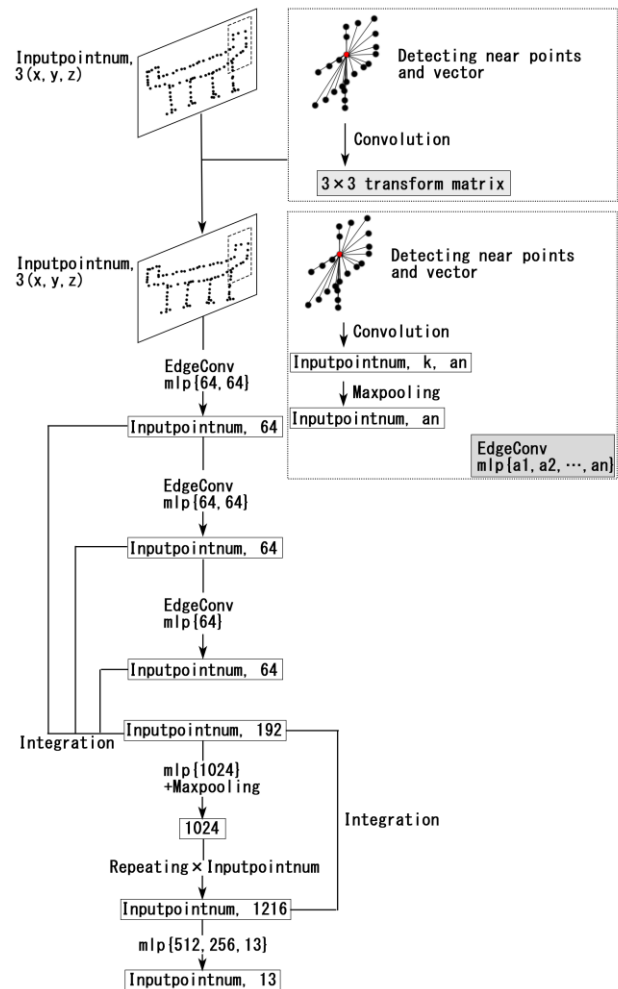


Figure 2. Model structure of DGCNN.

number of input points does not change in either layer, but the xyz coordinates also change due to convolution. After repeating this process 3 times, the feature values obtained in each step are integrated. Next, MaxPooling is applied, and replicated for the number of input points. Finally, after several convolutions, the number of classified features is obtained and output as a random variable by applying the Logsoftmax function. Although the paper [14] describes a categorical vector that provides labels for each input data as additional information, it is not used in this research.

### 3 PREPARING DATA FOR DEEP LEARNING

#### 3.1 Case study

A two-span continuous through-type truss bridge in Aichi Prefecture, Japan, is the case study. A photograph of the bridge is shown in Figure 3. The bridge length is 136.9m with a span length of 2@67.9m. A full width is 14.3 m with sidewalks on both sides. The effective width of the roadway is 7.5 m and that of the sidewalk is 2.0 m without widening. A slab thickness is 200 mm with a pavement of 80 mm thickness (roadway) and of 30 mm thickness (sidewalk). In addition, the bridge is straight and has a symmetric cross slope. A general bridge drawing is shown in Figure 4. The members to be segmented are "Upper chord", "Lower chord", "Brace (tensile)", "Brace (compression)", "Main girder", "Cross beam", "Upper lateral bracing", "Lower lateral bracing", "Sway bracing", "Gate", "Handrail", "Mounted components", and "Slab".

#### 3.2 Generating point cloud data from 3D CAD data

The 3D CAD data was manually created based on the drawings of the bridge shown in Section 3.1. Furthermore, for each 3D CAD component, point cloud data is obtained by randomly sampling points on its surface. In this case, noise and missing points are not generated. In addition, a uniform density (1 [pts./cm<sup>2</sup>] in this case) was set for all members in order to avoid extreme bias in density. It is also possible to assign to each point the normal vector of the plane from which it was generated as a parameter. The generated point cloud data is shown in Figure 5. Each point in the point cloud data has a label number that corresponds to only one of the 13 types of components mentioned above, and the colors of the points in the figure correspond to the labels of the components (Figure 6). The total number of points was 64,016,718.

#### 3.3 Creating cross sectional point clouds

The following shows the flow of the method for acquiring cross-sectional point clouds.

First, the line that corresponds to a longitudinal direction is determined. Since the bridge in this research has straight linear and the width is not widened, a line passing through the centroid of the point cloud data and having the direction of the first principal component vector obtained by principal component analysis is defined as the "longitudinal direction line".

Next, the point **p** is shifted pitch (0.1[m] in this case) from the starting point of the longitudinal direction line, and the plane that contains **p** and is perpendicular to the line along the longitudinal direction line is defined as the "cutting plane". Points within *d* (0.05 [m] in this case) of the cutting plane are detected, and these points are projected onto the cutting plane.

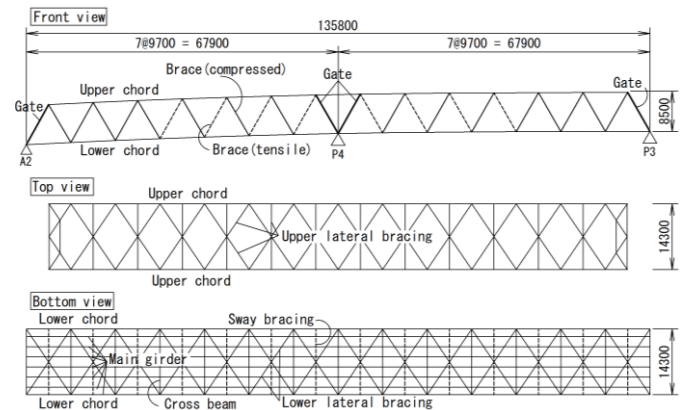


(a) Side view

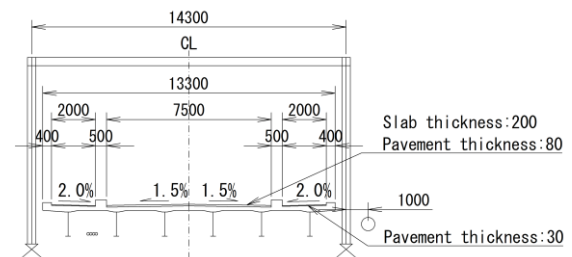


(b) Bottom view

Figure 3. Pictures of the case study bridge.



(a) Front, Top, Bottom view



(b) Cross sectional diagram

Figure 4. General bridge diagram (Unit: mm).

This process is repeated until **p** reaches the end point (Figure 7).

From the point cloud data described in Section 3.2, 695 cross-sectional point clouds were created. Examples are shown in Figure 8. The position of the braces differs depending on the cross section, and those irregular cross sections such as cross beams and sway bracings, are also included.

#### 3.4 Normalization process for deep learning

When training a cross-sectional point cloud, the coordinate system is modified. Define a local coordinate system for the cutting plane as shown in Figure 7. The cutting plane is the xy-coordinate plane of the local coordinate system. The world

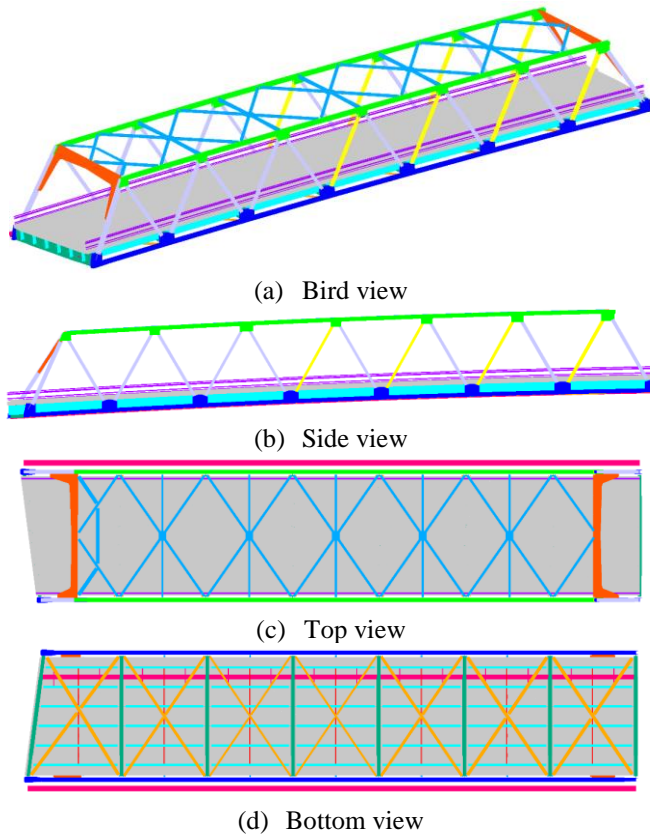


Figure 5. Point cloud generated from 3D CAD data.

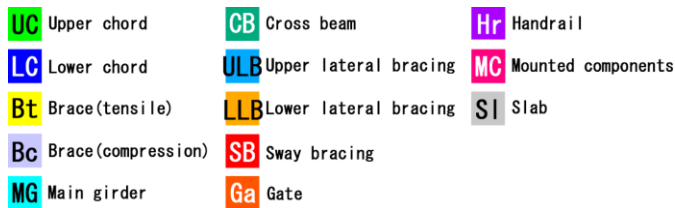


Figure 6. Legend of point colors.

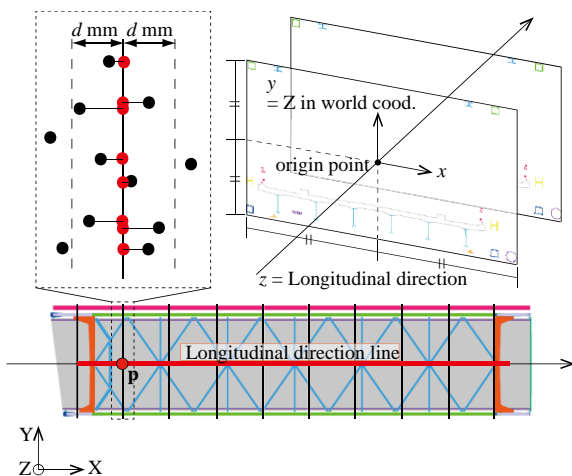


Figure 7. Detecting cross-sectional point clouds.

coordinate Z-axis corresponds to the y-axis of the local coordinate system. The origin point is adjusted so that the

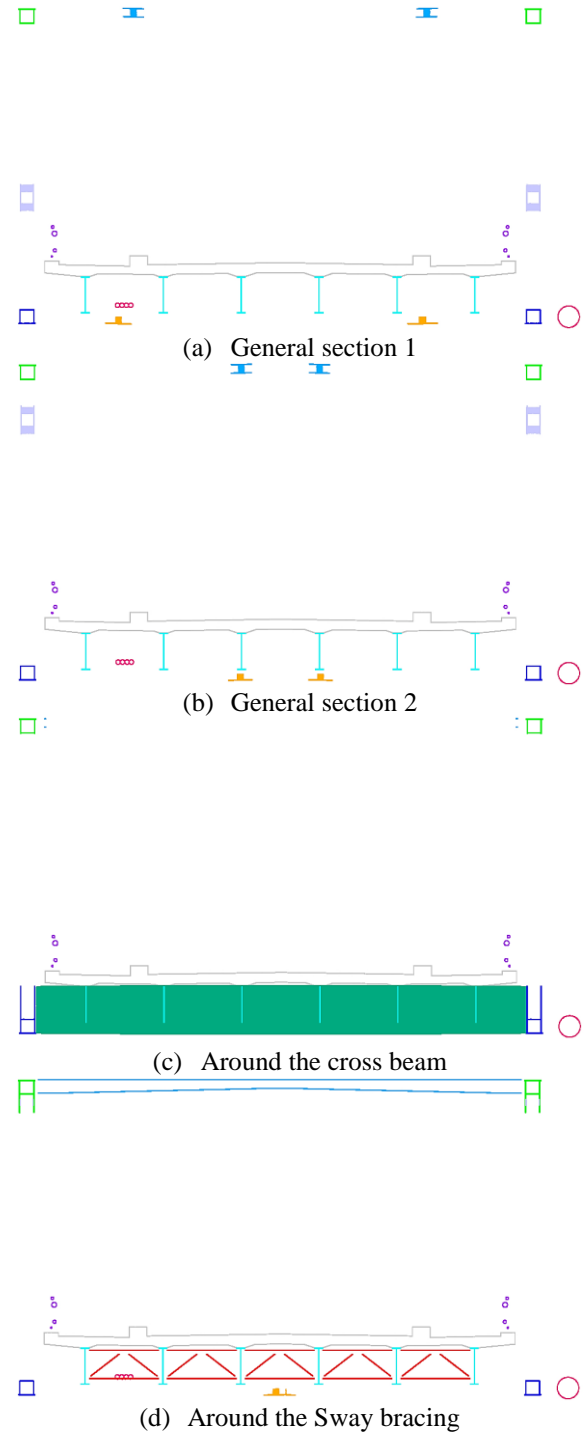


Figure 8. Examples of cross-sectional point clouds from 3D CAD data.

midpoint between min. and max  $x$ -coordinates and  $y$ -coordinates as shown in Figure 7. In order to prevent overlearning, the  $x$ -coordinate is flipped with respect to the  $y$ -axis with a probability of 50%.

## 4 IMPLEMENTATIONS AND DISCUSSIONS

### 4.1 Overview

In this chapter, several cases are implemented and discussed using training data described in Chapter 3 and test data obtained



from the actual steel truss bridge by the stationary laser scanner. The implementation environment is shown in Table 1, and the common parameters used for verifying multiple cases are listed in Table 2. The number of input points and the batch size must fit in the GPU's memory. If this limit is exceeded, computation is offloaded to the main memory, significantly increasing computation time. In addition, the batch size must be 2 or greater due to the use of BatchNormalize function as explained in Section 2.2. The number of training samples is 10,336, calculated by dividing the total number of points in the cross-sectional point cloud by the number of input points.

The implementation cases are organized in Table 3. During training, validation is included in each epoch. No fixed distinction is made between training and validation data; instead, 8,000 samples are randomly selected from the 10,336 available for each epoch. The Intersection over Union (IoU) for each member in the cases is shown in Figure 9. The values shown represent the results from the epoch in which the average IoU across all members was the highest. Computation times for each case are summarized in Table 4.

#### 4.2 Point cloud for using the implementation

In this section, the measured point cloud data of the actual bridge without member labels is mentioned. It is used for the test of the trained model. The point cloud data (1,065,353,413 points, Figure 10) measured with a stationary laser scanner Leica RTC360 (resolution: 3mm@10m, accuracy: 1.9mm@10m) from 27 locations on the underpass and road surface of one span of the bridge described in Section 3.1. 5,000 cross-sectional point clouds are created as the validation data by slicing at regular intervals (0.02 [m] in this case) along the longitudinal direction. Note that although this point cloud data contains color information, it is not used because there is no color information in the training data. Normals were obtained by calculating them with the Point Cloud Library [15], a point cloud data processing library. The normalization described in Section 3.4 is also applied to this cross-sectional point cloud.

#### 4.3 Comparing PointNet++ or DGCNN

First, the effectiveness of PointNet++ and DGCNN in segmenting point cloud data of cross sections sliced along the longitudinal direction is evaluated. The construction of model is shown in Figure 1 and Figure 2. As shown in the results of the application to the point cloud data presented in Section 4.2 (Figure 11 and Figure 12), PointNet++ was more accurate in the test. Although DGCNN resulted in a higher IoU and faster computation time during training, there were many places where other members were misidentified as the main girders in the test. PointNet++ was able to distinguish between two types of cross-sections of the braces with high accuracy, although in some cases the slabs were misidentified as the cross beams in areas where the data quality was low due to limitations of the measurement environment. This is likely due to the fact that DGCNN have over-trained the training data. In addition, it seems that PointNet++ is more versatile in handling 2D point cloud data with image-like features, as its behavior more closely resembles the convolution process used in image-based deep learning. For generality, PointNet++ is used in the subsequent validations, although it takes more time.

Table 1. Development Environment.

Common					
CPU	Intel(R) Xeon(R) Silver 4214R	CPU @	2.40GHz	2.39 GHz	(2 processors)
Memory	224GB				
GPU	NVIDIA GeForce RTX 3080 (10GB)				
OS	Windows 11 Enterprise 24H2				64bit
Slicing point cloud					
Platform	Microsoft Visual Studio Community 2022				64bit
Library	Point Cloud Library (PCL) 1.12.0				64bit [15]
Language	C++				
Deep learning					
Platform	Microsoft Visual Studio Code				
Library	Pytorch 2.5.1				cuda 12.1
Language	Python 3.10.5				

Table 2. Common parameters of deep learning.

Num. of input points	6164
Batch size	8
Num. of training data	10336
Num. of epoch	32
Optimization function	Adam
Loss function	Cross Entropy Loss

Table 3. Implementation cases.

Sec.	Model	Sampling	Scale Norm.	Normal vector	Weights for loss
4.3	*	sample	Yes	No	All 1
4.4	PointNet++	*	Yes	No	All 1
4.5	PointNet++	sample	*	No	All 1
4.6	PointNet++	sample	Yes	*	All 1
4.7	PointNet++	sample	Yes	No	*

\* is the comparing topic

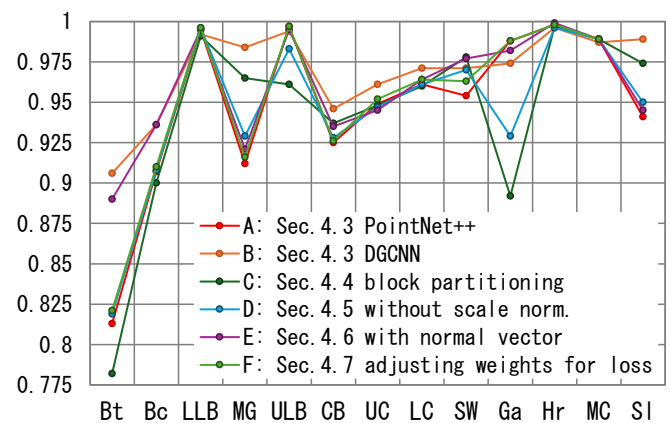


Figure 9. IoU of training in each case.

Table 4. Computation time of each case.

	Train	Test		Train	Test
A	18h.	6h.	D	16h.	9h.
B	9h.	4.5h.	E	15.5h.	11h.
C	16h.	36h.	F	15.5h.	9h.

#### 4.4 Comparing sampling methods as input data

The number of input points is 6144, but the number of cross-sectional point clouds is approximately 50,000 to 100,000 points. Therefore, sampling is required. Here, two types of sampling "block partitioning" and "random sampling" are selected and compared the accuracy. For block partitioning, one point is randomly selected from the cross-sectional point cloud, from which points within a 5 m block around it are extracted and sampled so that the total number of points is 6144. In addition, the coordinates that origin is at the center of the block are calculated and added as new features. Random sampling was performed by randomly selecting 6144 points from the entire cross-sectional point cloud and  $x$  and  $y$  coordinates are adjusted so that a distance to the farthest point from the origin point is 1. As shown in the test results (Figure 13), block partitioning is able to detect the slabs without misidentifying them even in areas where the quality of the measurement data is low, but the accuracy of other members such as the braces and the cross beams is low.

#### 4.5 Comparing presence or absence of scale normalization

According to Section 4.4, since block partitioning without scale normalization has a higher detection rate of the slabs, the additional case without scale normalization with random sampling is implemented. As shown in the test results (Figure 14), the accuracy of the slab segmentation was improved, but the accuracy of the braces was significantly reduced. The second span, where segmentation accuracy is low, was not originally intended to be measured. However, it was partially captured during scanning of the adjacent first span. As a result, the point cloud data is of poor quality, with low density and many missing points. Although it is necessary to develop a learning model that can be applied to point cloud data of low measurement quality as a future challenge, this paper concludes that random sampling and scale normalization are effective for segmentation accuracy in high measurement quality areas.

#### 4.6 Comparing presence or absence of normal vector

In the previous explanations, only  $xyz$  coordinates were used for the input point cloud data, but the case with additional normal vector was also verified. As shown in the test results (Figure 15), the reason for the poor results in the case where normals were added is that, as shown in Figure 16, normals were generated even where the laser scanner would not have been irradiated if generated from 3DCAD, which may have caused a discrepancy between the training data and the test data. Although it is useful to develop a sampling tool that simulates a laser scanner, it is more effective to create a learning model that does not use normal vector, considering the efficiency of training data generation.

#### 4.7 Adjusting weights for loss calculation

The equation for the CrossEntropyLoss function is shown below:

$$Loss = \sum_{n=1}^N -w_{yn} x_{n,y_n} \quad (1)$$

The loss is calculated each member and they are sum up.  $N$  is the number of points and  $x_{n,y_n}$  is a random variable in the output data. In the previous cases,  $w_{yn}$  was set to 1 for all members, but in this case, it is adjusted for each member. This



Figure 10. The point cloud data measured with a stationary laser scanner

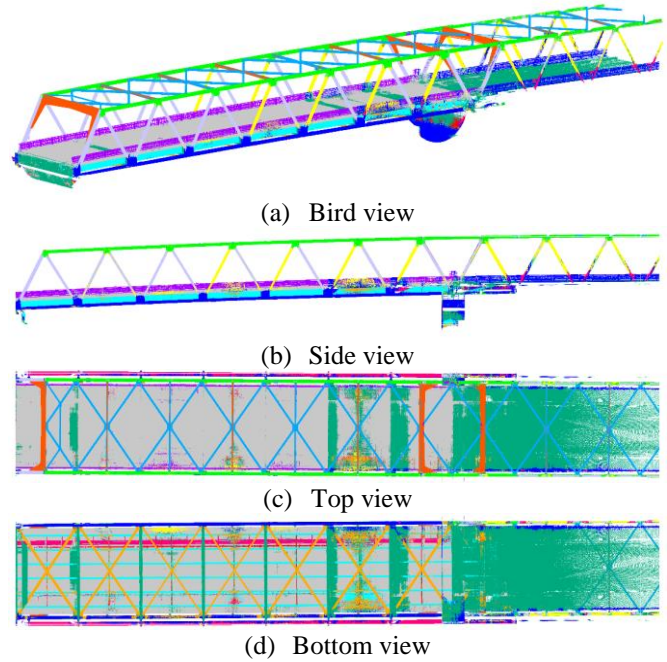


Figure 11. Result of case A: PointNet++.

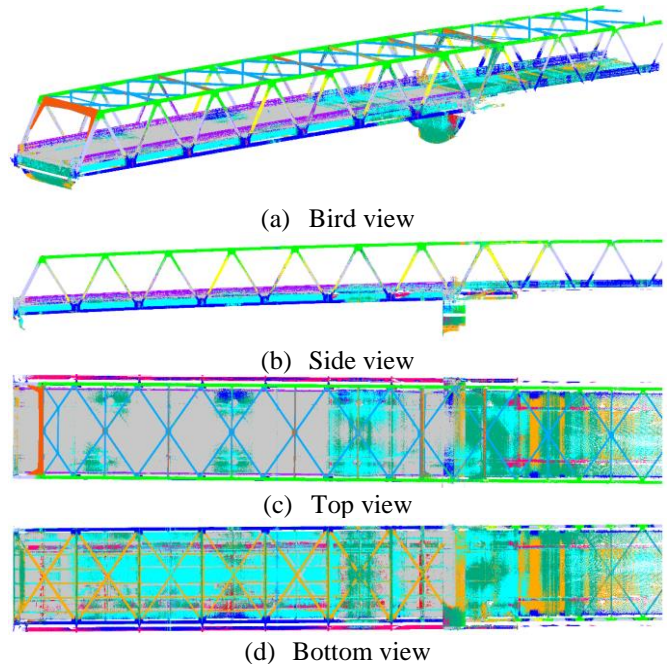


Figure 12. Result of case B: DGCNN.

parameter is used to prevent bias in the accuracy of the classification depending on the size of the member that is



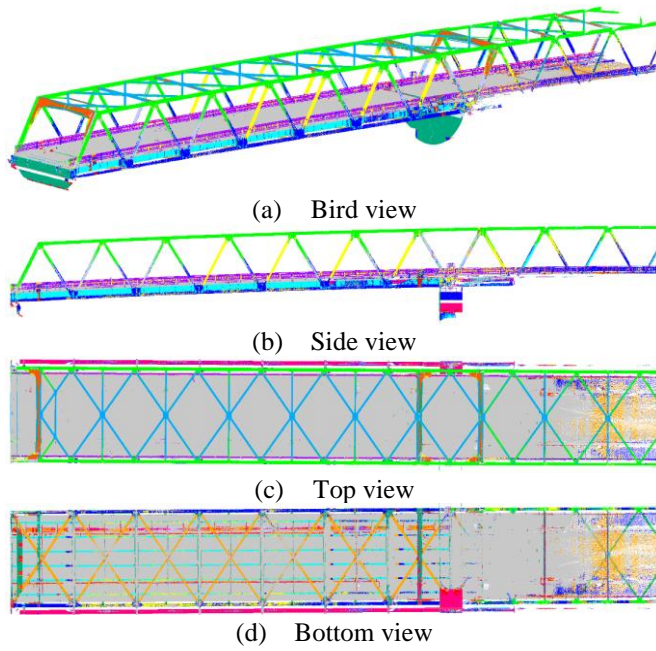


Figure 13. Result of case C: block partitioning.

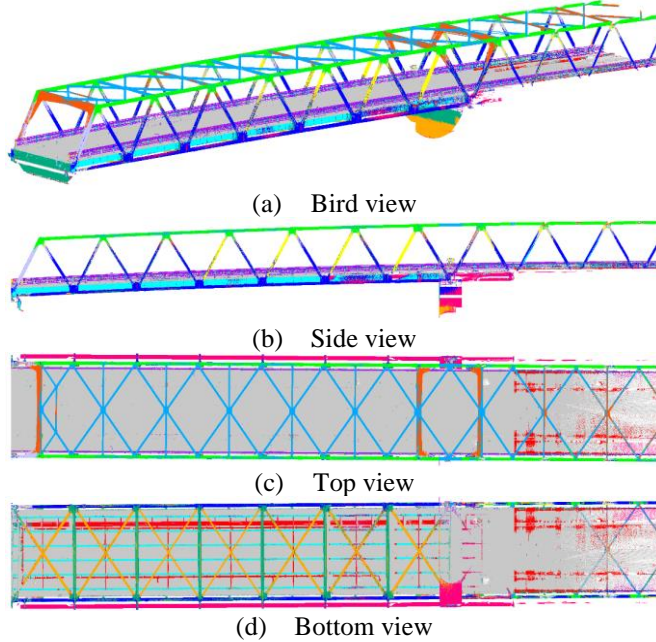


Figure 14. Result of case D: without scale normalization.

number of points. So, in this case,  $w_{yn}$  is set inversely proportional to the number of points in each member (Table 5). As shown in the test results (Figure 17), the outcomes were generally similar to the case in which all weights were set to 1. However, the segmentation accuracy for the braces was slightly lower. This is believed to be due to the increased weight assigned to members that appear in only a small number of cross-sectional point clouds, such as the gates and the sway bracings, which in turn reduces the accuracy for other members that appear in most cross-sectional point clouds. Therefore, it is more effective to set all weights to 1 without adjusting the weights between members.

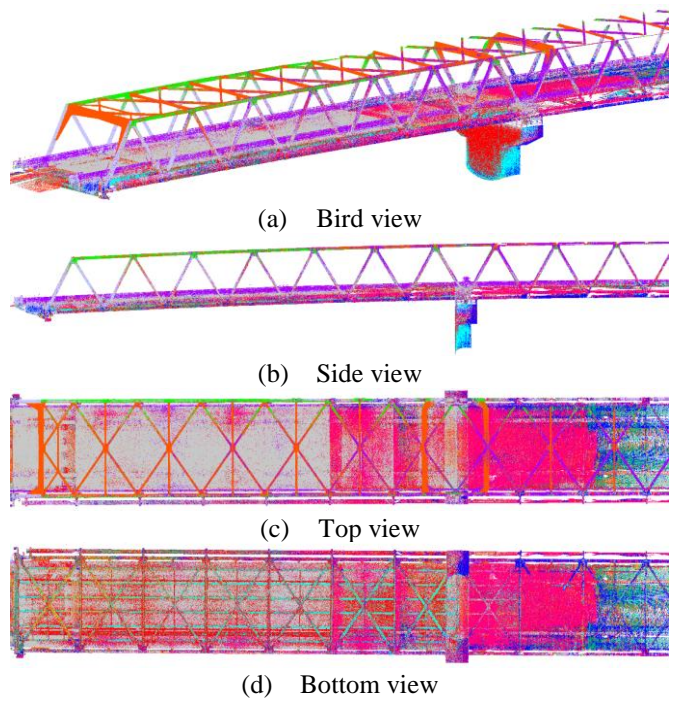


Figure 15. Result of case E: Using normals.

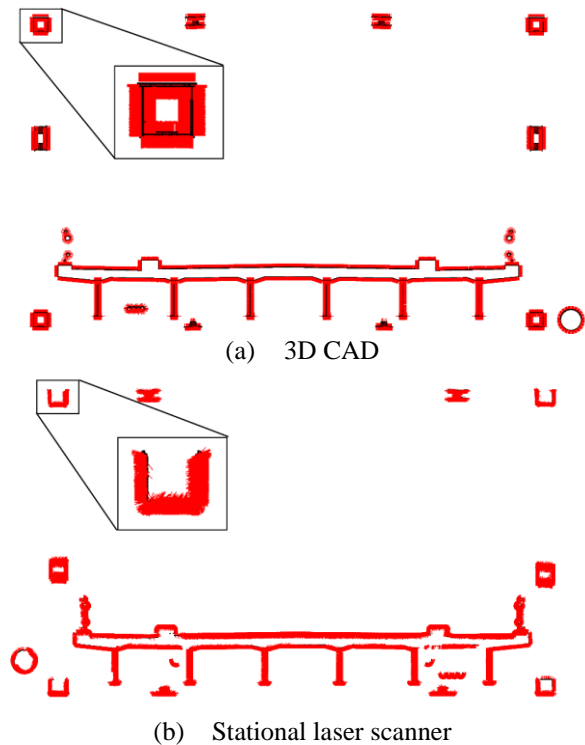


Figure 16. Normal vectors of the point clouds.

## 5 CONCLUSION

In this research, as a method for segmenting point cloud data of bridges into members using deep learning, using point cloud data of 2D cross sections sliced along the longitudinal direction. Several patterns are proposed and compared for validation to identify a highly accurate segmentation method.

Through the implementation of several cases, it was confirmed that the following settings were effective when point cloud data obtained by pseudo-sampling the surface of a 3D



Table 5. The weights inversely proportional to points.

UC	1.76	MG	1.19	SW	2.99	SI	1.00
LC	1.55	CB	1.60	Ga	2.51		
Bt	2.45	ULB	1.70	Hr	2.37		
Bc	1.63	LLB	2.10	MC	1.94		

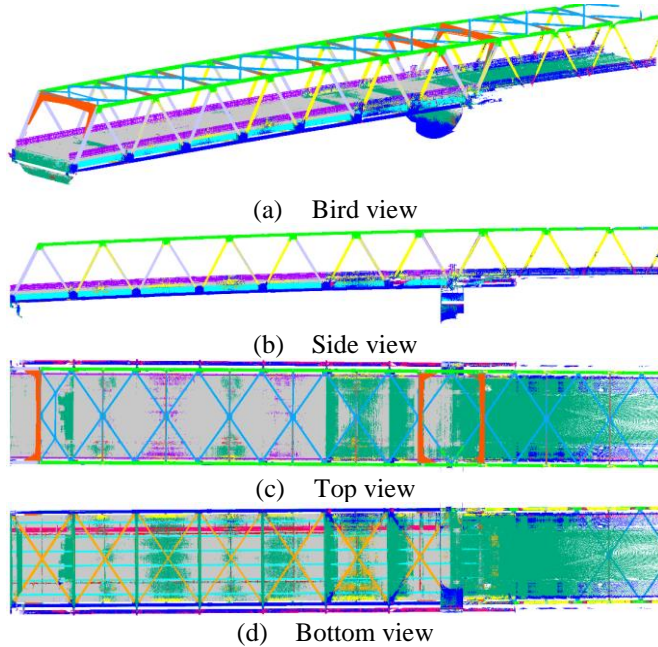


Figure 17. Result of case F: adjusting weights for loss.

model was used as training data and point cloud data obtained by measuring the same bridge with a laser scanner was used as test data:

- The learning model type PointNet++ is expected to be more versatile because of its higher segmentation accuracy of the test data.
- When the number of input points was reduced to about 5-10% of the total number of points, random sampling was more accurate and faster.
- To increase versatility, it was more effective to apply scale normalization at the time of training model input.
- Normal vectors can cause discrepancies between training data and test data depending on the calculation method, so care must be taken when generating them.
- Weight adjustments during the calculation of the loss function for each member did not have a significant effect.

As future work, training on multiple types of bridges (not limited to steel truss bridges) and performing segmentation across various bridge types is necessary, since the training and test data in this research are from the same bridge, although generated by different methods. In addition, since the bridges covered in this paper have straight liner and no width widening, it is desirable to conduct verification on bridges with curved liners or varying widths.

## ACKNOWLEDGMENTS

This research was supported by the Foundation of public interest of Tatamatsu (Nao Hidaka).

## REFERENCES

- [1] M. E. Mabsout, K. M. Tarhini, G. R. Frederick, and C. Tayar, Finite-Element Analysis of Steel Girder Highway Bridges, *Journal of Bridge Engineering*, Vol. 2, No. 3, pp. 83-87, 1997.
- [2] T. Yamane, P. Chun, J. Dang, and R. Honda, Recording of bridge damage areas by 3D integration of multiple images and reduction of the variability in detected results, *Computer-Aided Civil and Infrastructure Engineering*, Vol. 38, No. 17, pp. 2391-2407, 2023.
- [3] G. Qin, Y. Zhou, K. Hu, D. Han, and C. Ying, Automated Reconstruction of Parametric BIM for Bridge Based on Terrestrial Laser Scanning Data, *Advances in Civil Engineering*, Vol. 2021, No. 1, pp. 8899323, 2021.
- [4] Y. Schatz and B. Dömer, Semi-Automated Creation of IFC Bridge Models from Point Clouds for Maintenance Applications, *Frontiers in Built Environment*, Vol. 10, 2024.
- [5] N. Hidaka, N. Hashimoto, K. Magoshi, T. Nonaka, M. Obata, and E. Watanabe, Construction of a Practical Finite Element Model from Point Cloud Data for an Existing Steel Truss Bridge, *Proceedings of the 23th International Conference on Construction Applications of Virtual Reality (ConVR 2023)*, pp. 1155-1166, 2023.
- [6] T. Xia, J. Yang, and L. Chen, Automated Semantic Segmentation of Bridge Point Cloud Based on Local Descriptor and Machine Learning, *Automation in Construction*, Vol. 133, pp. 103992, 2022.
- [7] R. Pierdicca, M. Paolanti, F. Matrone, M. Martini, C. Morbidoni, E. S. Malinverni, E. Frontoni, and A. M. Lingua, Point Cloud Semantic Segmentation Using a Deep Learning Framework for Cultural Heritage, *Remote Sensing*, Vol. 12, No. 6, pp.1005, 2020.
- [8] O. Ronneberger, P. Fischer, and T. Brox, U-Net: Convolutional Networks for Biomedical Image Segmentation, *Medical Image Computing and Computer-Assisted Intervention (MICCAI 2015)*, pp.234-241, 2015.
- [9] T.Y. Lin, P. Dollár, R. Girshick, K. He, B. Hariharan, and S. Belongie, Feature Pyramid Networks for Object Detection, *Computer Vision and Pattern Recognition*, pp. 2117-2125, 2017.
- [10] L. C. Chen, Y. Zhu, G. Papandreou, F. Schroff, and H. Adam, Encoder-Decoder with Atrous Separable Convolution for Semantic Image Segmentation, *Computer Vision and Pattern Recognition*, pp. 833-851, 2018.
- [11] N. Saovana, N. Yabuki, and T. Fukuda, Automated Point Cloud Classification Using an Image-Based Instance Segmentation for Structure from Motion, *Automation in Construction*, Vol. 129, pp. 103804, 2021.
- [12] C. R. Qi, H. Su, K. Mo, and L. J. Guibas. PointNet: Deep Learning on Point Sets for 3D Classification and Segmentation, *Computer Vision and Pattern Recognition*, pp. 652-660, 2017.
- [13] C. R. Qi, L. Yi, H. Su, K. Mo, and L. J. Guibas. PointNet++: Deep Hierarchical Feature Learning on Point Sets in a Metric Space, *Proceedings of the 31st International Conference on Neural Information Processing Systems*, pp. 5105-5114, 2017.
- [14] A. V. Phan, M. L. Nguyen, Y. L. H. Nguyen, and L. T. Bui, DGCNN: A convolutional neural network over large-scale labeled graphs, *Neural Networks*, Vol. 108, pp. 533-543, 2018.
- [15] R. B. Rusu and S. Cousins, 3D Is Here: Point Cloud Library (PCL), *In 2011 IEEE International Conference on Robotics and Automation (ICRA)*, pp. 1-4, 2011.

# A 3D Virtual Assembly Method for Cable-Stayed Bridge Closure Using Laser Scanning

Yan Xu<sup>1</sup>, Zhenzhen Cao<sup>2</sup>

<sup>1</sup> Jiangsu Key Laboratory of Mechanical Analysis for Infrastructure and Advanced Equipment, Southeast University, Nanjing 210096, China.

<sup>2</sup> School of Civil Engineering, Southeast University, Nanjing 210096, China.  
email: [xuyan0909@live.com](mailto:xuyan0909@live.com), [czzl10909@163.com](mailto:czzl10909@163.com)

**ABSTRACT:** The mid-span closure segment assembly of a cable-stayed bridge after cantilever construction traditionally relies on using a total station to measure the longitudinal distances of key control points to determine the closure trimming length. This approach neglects the rotation of the cantilever section, reduces the inherently three-dimensional (3D) assembly problem to a one-dimensional (1D) longitudinal assembly. To overcome this limitation, this paper presents a 3D virtual pre-assembly method for the closure segment based on point clouds captured from a single station. An efficient and accurate two-stage registration method based on 2D image matching and 3D visibility simulation was developed to align incomplete measured point clouds with the design model. The estimated poses of the two cantilever ends were used for the virtual assembly of the closure segment. An optimization model for 5-DOF geometric information of the closure segment was established and calibrated using a particle swarm optimization. The proposed method was validated during the construction monitoring of a large-span railway cable-stayed bridge, demonstrating its reliability and practical effectiveness.

**KEY WORDS:** Virtual Assembly, Laser Scanning, Point Cloud Registration

## 1 INTRODUCTION

Cable-stayed bridge closure marks the moment when two independent cantilevers become a single, continuous load-carrying system. To achieve the desired stress redistribution and deck profile, engineers must monitor the closure joint during the 48 h immediately preceding installation, capturing temperature-induced movements and determining the match-cut length of the closure segment with millimetre-level precision. Traditional construction monitoring relies on total-station surveys of a handful of control points on each cantilever tip to estimate the longitudinal gap. Although well established, this point-wise procedure is labour-intensive, prone to human error, and often too slow for modern fast-track schedules. Terrestrial laser scanning (TLS), by contrast, can acquire a dense, full-field 3-D point cloud of the entire closure region in a single scan, providing sub-centimetre accuracy and a far more comprehensive geometric record.

Over the past decade, researchers have explored TLS-enabled “virtual pre-assembly” workflows in bridge construction, focusing on reducing geometric deviations and optimizing prefabricated component assembly. Zhou et al. [1] proposed the virtual trial assembly method for prefabricated steel components in scenarios like bridge construction. It integrates high-precision point cloud registration, reverse BIM construction, and finite element analysis to accurately predict geometric shapes and stress states in prefabricated components. Li et al. [2] developed an automatic modeling approach for creating as-built prefabricated component models from laser-scanned data, specifically for virtual trial assembly. Liu et al. [3] develops an automated virtual trial assembly framework for large and complex steel members, integrating terrestrial laser scanning and BIM to improve geometric accuracy, streamline assembly point extraction, and enable precise geometric quality inspection of bending and torsional deviations. Zhang et al. [4] introduced an automated virtual trial assembly framework for

large steel members with bolted connections, leveraging multiscale point cloud fusion to achieve submillimeter precision in feature extraction, registration, and assembly deviation analysis. Li et al. [5] proposed a virtual pre-assembly method utilizing 3D laser scanning technology to predict alignment of large-span segmental precast assembled concrete cable-stayed bridges under stress-free conditions, effectively shortening construction time, reducing complexity, and enhancing precision in the assembly process.

Despite the progress achieved in prior studies, significant challenges still remain. First, current fit-up calculations seldom account for the local downward deflection of the free cantilever tips under self-weight, thermal gradients, or wind loads, leading to non-vertical end faces at the time of measurement. Second, by collapsing millions of points into a few targets, valuable shape information is discarded. To address these gaps, this study introduces a 3D virtual-assembly method for cable-stayed-bridge closure that capitalises on high-resolution TLS. After all segments except the closure slab are erected, a TLS survey simultaneously captures the full geometry and relative pose of the two cantilever ends. A particle-swarm-optimisation-based virtual assembly routine then searches the point-cloud pair for the closure segment length and installation attitude that minimise global deck discontinuities. The method was validated during the closure of a cable-stayed bridge in Zhejiang Province, China, where it delivered rapid, centimetre-level predictions that aligned with field measurements. Ultimately, the goal is to leverage complete 3-D geometry and relative pose information to predict—before any on-site cutting—the optimal closure-segment length and pose, thereby streamlining cable-stayed bridge completion and enhancing construction quality control.

## 2 METHODOLOGIES

Traditional closure practice measures only the longitudinal gap between the two cantilever tips and match-cuts the segment vertically, reducing a fundamentally 3-D structural-assembly problem to a 1-D splice. Because this approach ignores the true pose of the cantilever end sections (rotations and offsets), it struggles to meet today's mm-level accuracy requirements.

To overcome these limitations, we develop a point-cloud-driven virtual pre-assembly workflow consisting of three core stages (Figure 1).

In the first stage, each cantilever tip is scanned in situ, yielding dense but incomplete point clouds that capture deck edges. A synthetic point cloud generated from the as-designed numerical model is then rigidly aligned to the measured data via an iterative closest-point procedure, producing a 3D transformation matrix that maps design space to the bridge's physical coordinate frame. This registration not only reconciles deviations due to construction tolerances but also embeds the design geometry in the same reference frame as the field measurements.

The second stage performs virtual pre-assembly. The meshed design models of the two cantilever tips are transformed with the previously obtained matrix and imported into a physics-aware simulation environment. A particle-swarm-optimization solver searches the six-degree-of-freedom space to minimize the surface misfit between opposing tips, rapidly converging to a sub-mm pose match. Because the algorithm explores both translational and rotational degrees of freedom concurrently, it reveals subtle misalignments that would otherwise remain undetected under one-dimensional gap measurements.

In the final stage, the optimized virtual pose is used to derive the manufacturing and installation parameters of the closure segment. After correcting for construction-stage temperature effects, the workflow outputs the optimal match-cut length, the required bevel angle of the end faces, and the spatial orientation necessary for installation. These data provide fabricators with precise cutting instructions and give field crews an accurate set-out for lifting and welding, thus shortening decision cycles while ensuring that closure is achieved within the stringent tolerances demanded by fast-track bridge construction.

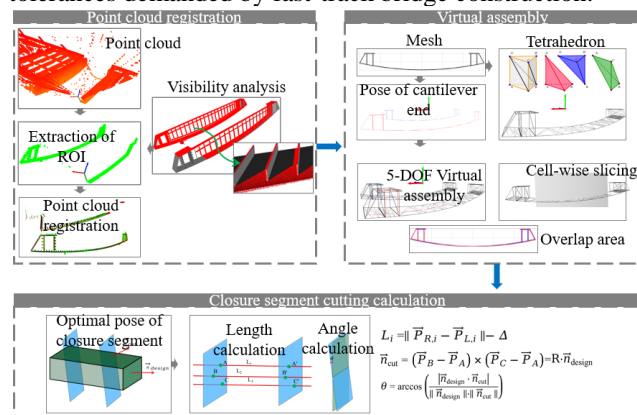


Figure 1. Flowchart of the proposed method for closure segment cutting calculation.

## 3 FIELD TEST ON A CABLE-STAYED BRIDGE

The proposed virtual-assembly workflow was validated on a cable-stayed bridge crossing on the Fuchun River in Hangzhou,

Zhejiang Province, China. The structure features a mixed-height, H-shaped pylon arrangement and a hybrid steel–concrete deck. Span configuration proceeds from the west abutment as 62.395 m + 97 m + 300 m + 46 m + 30 m, giving an overall length of 535.395 m. The downstream pylon rises 141.5 m above foundation level, whereas the upstream pylon is 92 m high (see Figure 2).

The 300 m main span employs a composite section in which a U-shaped steel box girder is integrally connected to a cast-in-place concrete deck slab, yielding both bending stiffness and fatigue durability. Construction of this span followed the free-cantilever method: modular box-girder segments were symmetrically erected from each pylon, forming two outward-growing cantilevers. When the remaining gap diminished to less than a single segment, a closure unit was installed using the thermal-expansion technique to create a continuous load path. The segments immediately adjacent to the closure piece are labelled MG15 on the south-east cantilever and MD09 on the north-west cantilever. This full-scale construction scenario offered a realistic test bed for examining the accuracy and efficiency of the TLS-driven virtual pre-assembly method under field conditions.



Figure 2. Tested bridge for closure in construction

A RIEGL VZ-400i terrestrial laser scanner was deployed to acquire high-density point clouds of the opposing cantilever tips. The instrument offers a ranging window of 0.5 – 800 m and a single-shot accuracy of  $\pm 5$  mm; for this test the pulse-repetition frequency was set to 1.2 MHz, while the full 360° horizontal and 100° vertical fields of view were enabled. To maximize coverage of the local cross-section, the scanner was rigidly mounted 1.6 m above the deck on the outboard edge of segment MD09 and levelled with its optical axis parallel to the bridge centerline. From this vantage, a single sweep captured the entire end face of the MD09 tip together with the mating surface of segment MG15 across the closure gap, yielding a unified dataset that preserves both geometry and relative pose for subsequent virtual pre-assembly processing.

Figure 3 depicts a representative time step of the raw point-cloud data. Because each sweep originates from a single scanner station, the TLS captures only the outward-facing portions of the two cantilever tips; one tip is almost complete, whereas the opposite tip contains only a narrow chord of the full cross-section. To isolate the geometric cues most relevant for alignment, the cloud is first segmented by fitting a best-fit plane to the deck-edge points of each tip and then retaining the points within a narrow band around that plane. The result shown in Figure 4 is a pair of sparsely sampled, partially visible cross-sections that serve as registration targets.



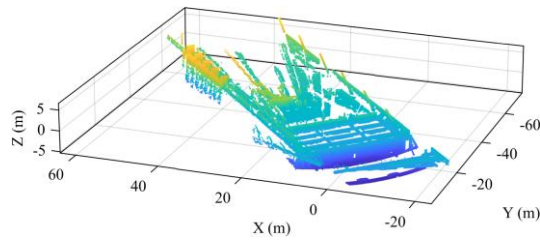


Figure 3. Raw point cloud of the cable-stayed bridge captured with the TLS.

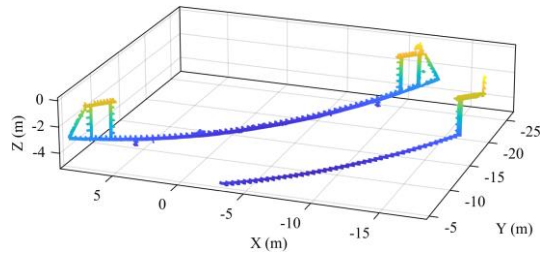


Figure 4. Filtered cantilever-tip cross-section extracted from the TLS data.

Iterative closest point (ICP) requires a reasonably accurate initial transform to avoid convergence to local minima. It is challenge to deal with the two targets share only limited overlap. To generate a robust starting estimate, the extracted cross-sections are orthogonally projected onto an image plane and converted to binary occupancy maps. A phase-correlation matcher is then applied to the two images, yielding translational shifts and in-plane rotations with sub-pixel precision; these parameters are back-projected into 3D space to construct the initial rigid-body transform.

Directly registering the measured cloud to the full design model is computationally inefficient and prone to bias because large portions of the as-designed surface are invisible in a single scan. We therefore employ a ray-casting routine to generate a virtual scan of the design model that mimics the scanner's actual position and field of view. The synthetic cloud retains only those facets that would be visible to the TLS under identical conditions, producing a down-sampled "design-congruent" dataset whose completeness closely matches that of the field measurement. ICP is then executed between the real and virtual point clouds, with the phase-correlation transform as its initialization. After registration, the measurements of control point distances were extracted from the TLS data and compared with those obtained from the total station. As shown in Figure 5, the distance errors for all 17 control points are within 10 mm.

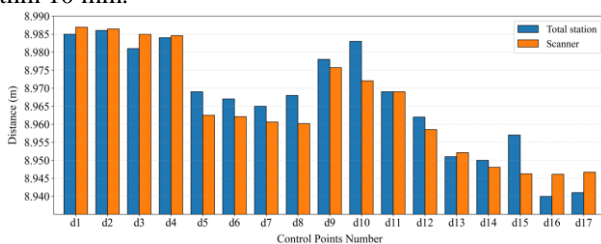


Figure 5. Comparison of control point distance measurements at cantilever beam ends using total station and TLS.

Once the spatial poses of the two cantilever tips have been fixed, the search for the best installation strategy can be formulated as a stand-alone optimization problem. A closure

segment of ample stock length is first inserted between the tips in a nominal configuration that deliberately intersects both end faces. Because high-quality welding demands near-perfect geometric agreement at each splice plane, we evaluate every candidate pose by the overlap area—the common surface shared by the closure-segment end face and its mating cantilever section.

To automate the search, we couple the point-cloud pose information with the 3D CAD model of the closure segment and cast the task as a 5-DOF optimization: three translational components and two rotational angles around the local horizontal axes. The remaining rotation about the longitudinal axis is fixed to maintain deck camber continuity. A PSO scheme explores the 5-DOF space, beginning from a physically reasonable initial guess derived from the measured gap and the nominal bridge geometry. During each PSO iteration the algorithm updates the candidate pose, clips the closure segment to the planes of the two cantilever tips, and computes the resulting overlap areas. The fitness function is defined as the negative sum of these areas.

Convergence of the swarm yields the pose that maximizes simultaneous overlap at both interfaces. From the converged configuration the algorithm extracts two quantities required for fabrication and erection: (i) the match-cut length, obtained by measuring the distance between the optimally aligned splice planes, and (ii) the six-parameter installation pose, which prescribes the precise translation and orientation of the trimmed closure segment in the bridge's global coordinate frame. In this way, the virtual pre-assembly routine provides construction crews with a complete, data-driven specification for manufacturing and installing the closure element.

## 4 CONCLUSIONS

This study presented a point-cloud-driven, 3D virtual-assembly method for cable-stayed-bridge closure that resolves the intrinsic shortcomings of one-dimensional match-cutting practices. By combining high-precision TLS acquisition, rigid registration of design geometry, and a particle-swarm-optimized pose-matching procedure, the workflow delivers sub-mm estimates of the closure gap and end-face attitude. Field trials conducted on the 300 m main span of the cable-stayed bridge verified the method's effectiveness.

## REFERENCES

- [1] Zhou Y, Han D, Hu K, Qin G, Xiang Z, Ying C, et al. Accurate Virtual Trial Assembly Method of Prefabricated Steel Components Using Terrestrial Laser Scanning. *Advances in Civil Engineering* 2021;2021. <https://doi.org/10.1155/2021/9916859>.
- [2] Li D, Liu J, Feng L, Zhou Y, Qi H, Chen YF. Automatic modeling of prefabricated components with laser-scanned data for virtual trial assembly. *Computer-Aided Civil and Infrastructure Engineering* 2021;36:453–71. <https://doi.org/10.1111/mice.12627>.
- [3] Liu J, Cui N, Cheng G, Li D, Ma X, Liao Y. Towards the automated virtual trial assembly of large and complex steel members using terrestrial laser scanning and BIM. *Engineering Structures* 2023;291:116448. <https://doi.org/10.1016/j.engstruct.2023.116448>.
- [4] Zhang Z, Liang D, Huang H, Sun L. Virtual trial assembly of large steel members with bolted connections based on multiscale point cloud fusion. *Computer-Aided Civil and Infrastructure Engineering* 2024;39:2619–41. <https://doi.org/10.1111/mice.13210>.
- [5] Li XX, Deng E, Wang YW, Ni YQ. 3D laser scanning for predicting the alignment of large-span segmental precast assembled



concrete cable-stayed bridges. Automation in Construction  
2023;155:105056. <https://doi.org/10.1016/j.autcon.2023.105056>.

# Short- and long-term monitoring of bridges using terrestrial laser scanning data

Thomas Moser<sup>1</sup>, Werner Lienhart<sup>1</sup>, [ORCID](#)

<sup>1</sup> Graz University of Technology, Institute of Engineering Geodesy and Measurements Systems,  
Steyrergasse 30, 8010 Graz, Austria

email: thomas.moser@tugraz.at, werner.lienhart@tugraz.at

**ABSTRACT:** Terrestrial laser scanning (TLS) is commonly used to capture 3D point cloud data of the environment. In this article we demonstrate that TLS data can also be used to measure long-term and daily deformations of bridges. On one hand full dome laser scanning is used to determine the deformations of entire bridge pillars whereas scanning total stations are well suited to capture segments and profiles of bridge pillars. We highlight that an accurate point cloud registration and appropriate processing algorithms are crucial to reliably determine deformations in the millimeter range. The capabilities of our approach are demonstrated on two large highway bridges where the bending of bridge beams due to temperature changes and one side sun illumination are investigated.

**KEY WORDS:** Terrestrial laser scanning, bridge monitoring, structural health monitoring

## 1 INTRODUCTION

Many large highway bridges in Europe were built in the 1960s and 70s. While the lifetime of these bridges was designed to be up to 100 years, reality shows that lots of bridges do not meet this expectation. One of the reasons is the increased load due to the rapid increase of traffic volume within the last decades (Figure 1 [1]).

As the replacement of the respective structures will take several years, aging objects need to be kept in service in the meantime. To ensure safe operation during this period, monitoring measures are often taken to obtain crucial data for decision making, e.g. prioritize structural measures, restrict traffic or similar.

One way to gather reliable data of bridges is to capture geometric changes of the structures. A geometric change can either be induced by loading of the bridge, by changing environmental conditions or by damages. Deformations can be measured with traditional geodetic sensors such as Robotic Total Stations (RTS), where one or multiple discrete points are measured and the absolute coordinates are determined in 3 dimensions with high accuracy. Another possibility is to capture multiple point clouds with Terrestrial Laser Scanners (TLS) over time. The different point clouds can be compared to each other and deformations can be computed throughout the entire object.

With these kind of remote sensors, not only static deformations can be captured but also dynamic changes during the pass of a load over a bridge. Modern RTS can track individual prisms with 20 Hz [2] and many TLS can also be operated in profile mode. The Profile Laser Scanner (PLS), works just as an TLS, but the rotation of the standing axes is suppressed. Therefore, the profile is measured multiple times per second and the relative deformations can be captured dynamically in 2D [3]. When using an RTS dynamically, the instrument stays with observing just one prism at the time but can take angle and

distance measurements with up to 20 Hz and therefore capture the dynamic 3D deformation of this prism. A study about the performance of both of the methods as well as Profile Laser Scanners can be found in [2] and [4]. Additionally, some modern RTS have also a scanning feature included. These so called Multi Stations (MS) have a slower scanning speed than conventional TLS and therefore are not well suited for full dome scanning but well applicable for scanning defined sections of a scene, e.g. a tunnel face or bridge pillars.

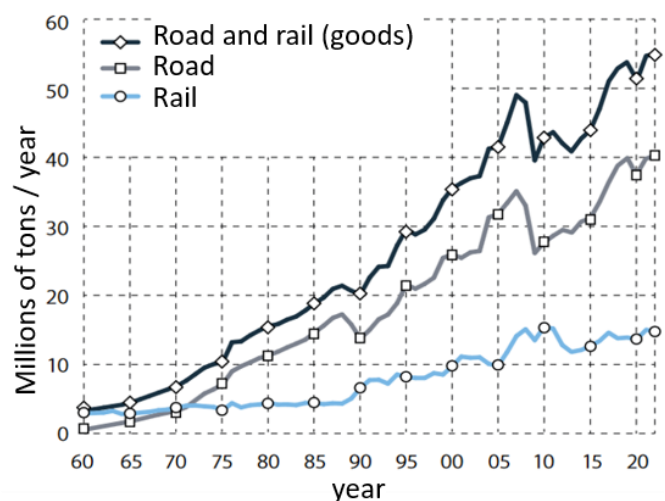


Figure 1. Exemplary trend of good transportation at the Brenner pass for Railway and road transportation from 1960 – 2022, translated to English after [1].

While dynamic measurements are mostly done to assess the deformations of structures due to dynamic loading, e.g. overpass of a truck or other dynamic excitation, static measurements are used to either determine the deformations



during static load tests or to observe changes due to environmental effects such as temperature or structural changes. One important criterion for the comparison of multi-epoch data is the registration of point cloud data to obtain reliable results. This is challenging as bridges do not always offer stable areas to connect multiple scan epochs.

In this paper we demonstrate that it is possible to compare multiple scanning epochs that are taken over several days with a scanning total station, as well as point cloud data captured by a classical TLS with target-based registration over a longer period of time on a real-life bridge object. This work focuses on the deformation of the bridge pillars. The deformation of the bridge decks e.g. during load tests are discussed in [2], [4] and [5].

## 2 BRIDGE OBJECTS

### 2.1 Aurachbrücke

The Aurachbrücke, is the highest bridge of the A1 Westautobahn in Austria, located between Linz and Salzburg. The observed bridge is a temporary building for the time of the replacement of the old bridge. The bridge is a concrete box girder structure with 5 spans and a total length of 420 m.

### 2.2 Gschnitztalbrücke

Situated in Steinach am Brenner in Tyrol, the Gschnitztalbrücke (Figure 2) is part of the most frequented alp passage in Europe, the Brenner highway. The bridge consists of 7 spans with a total length of 560 m. The deck is curved with an arch radius of about 600 m. The steel-concrete composite bridge was built as a continuous beam in the 1960s for two lanes in each direction.

## 3 MEASUREMENT SETUP

### 3.1 Aurachbrücke

The measurements at the Aurachbrücke were taken within 48 hours from 06.09.2024 to 08.09.2024 with a Leica MS60 RTS with scanning function. Every 15 minutes the following sequence of measurements was performed: First multiple prisms were measured within 3 sets of combined angle and distance measurements. Afterwards, parts of the pillars 3 and 4 were scanned, see Figure 3. The scans included areas pointing along and across the bridge's direction. This setup creates the possibility to derive the 3D bending line of the pillars. In this paper, only pillar 3 is considered.

Additionally, IoT tilt sensors were mounted on top of every pillar for long term monitoring. The measurement rate of these sensors was also set to 15 minutes. Hence, three different data types (3D prism coordinates, point clouds, tilt readings) are available for comparison.

### 3.2 Gschnitztalbrücke

At the Gschnitztalbrücke in Tyrol, TLS and RTS measurements are taken epoch-wise 4 times a year. The measurements are taken at night from 10 p.m. onward to avoid truck traffic affecting the measurements. In Figure 2 the setup with the laser scanner in span 7 and the setup of the static total station is shown. A Leica RTC360 was used as TLS. This instrument performs full dome scans and hence the captured 3D point cloud includes the whole bottom side of the girders as well as the pillar and end abutment of the bridge. The measurement time is about two and a half minutes per scan for the highest scanning resolution (without pictures). The RTS takes

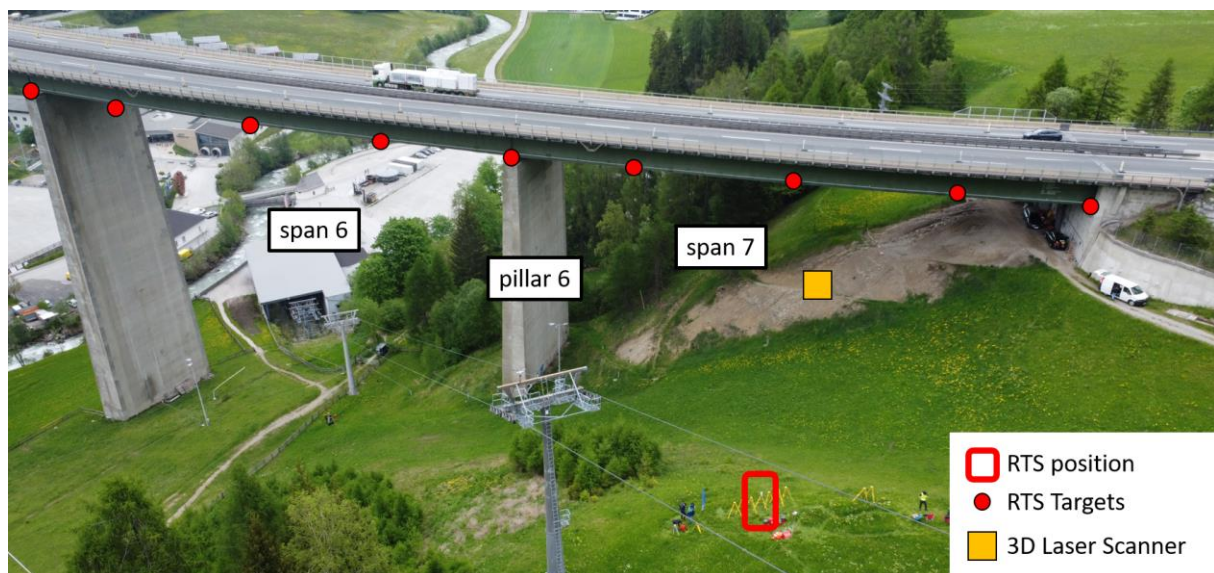


Figure 2. Overview at the Gschnitztalbrücke with span 6 & 7.

The measurement setup shows the prisms at the spans, as well as the RTS position and the TLS position.

In the 1980s an additional third lane was built in each direction due to upcoming traffic. One of the 7 spans is observed via TLS and RTS.

measurements of the prisms sequentially. Not only the prisms on the bridge are measured, but also control points are included in the measurements.

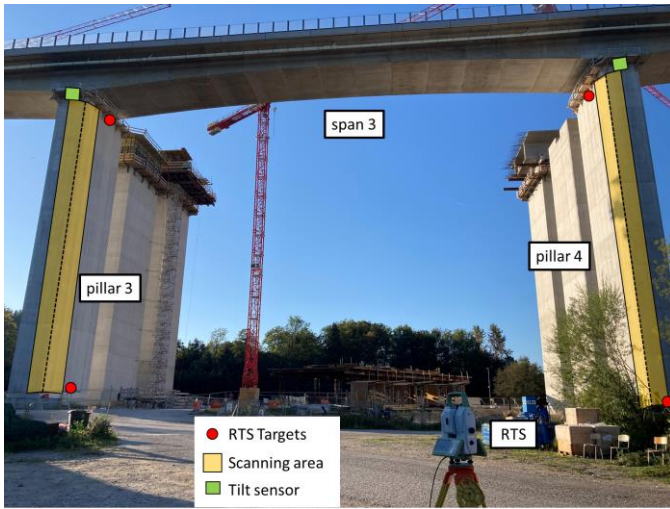


Figure 3. Setup of the RTS at Aurachbrücke.

The scanning areas can be seen in light yellow, as well as the measured prisms mounted at the pillars (red circles)

## 4 DATA ASSESSMENT

### 4.1 Aurachbrücke

The Leica MS60 is capable of not only measuring single points sequentially, but also capturing point clouds. Compared to a real TLS, the scanning speed is rather slow, but the advantage of the scanning total station is, that specific Regions of Interest (RoI) can be chosen which are scanned. This reduces the scanning time, and the definition of the scans can be used multiple times, so a time series of scans can be captured. All these measurements are triggered externally by a laptop using a python script and Leica GeoCom for communication. Combining the scanning function with classical point-wise measurements, the following data is available for every epoch (15 minutes):

- 3 sets of all prism points
- 1 scan of each of the two pillars 3 & 4

The scan resolution is about 5 cm in horizontal and 5 cm in vertical direction. To compute the deformations of the pillar, horizontal bands of 0.5m are cut from the point cloud along the Z-component for the longitudinal and cross section of the pillar. The points within each band are then averaged for every 5 cm in height and a moving average filter is applied to the remaining vector with a size of 0.2 m. To eliminate stationing errors, the bottom part (1 m) of the pillar is supposed to be fixed, so the mean value of the lowest meter is subtracted from every epoch. As reference epoch serves the first captured epoch on 06.09.2024 at around 20:00.

For the sequentially measured object points a free stationing is computed for every epoch and the polar points are derived from there. The coordinates can be transformed into along and across direction of the bridge to compare the results of both methods. A bending line can also be calculated, assuming, that the bending originates from the temperature differences of both sides of the pillar which is calculated by

$$\Delta T = \frac{d \cdot 2 \cdot B}{\alpha_T \cdot H^2} \quad (1)$$

whereas  $d$  is the displacement,  $B$  is described as the width of the pillar,  $\alpha_T$  is the temperature expansion coefficient of the material and  $H$  the height of the pillar. The biggest temperature differences are calculated to be less than 3 K.

Also, for the tilt sensor data, a theoretical bending line is calculated to be compared to the captured point cloud and pointwise prism data.

### 4.2 Gschnitztalbrücke

The scans at the Gschnitztalbrücke were taken at night with the Leica RTC360 while no heavy traffic was passing the bridge. Hence the load free state of the bridge was captured and only environmental effects are affecting the structure. The registration of the point clouds was target based, whereby four targets were setup and their positions determined via RTS measurements. Different approaches to register deformed point clouds are available and investigated by many researchers, one of the latest examples is stated in [6].

In this case the comparison of the point clouds of the pillars was done using a Cloud to Cloud (C2C) comparison directed to the surface plane of the examined pillar. So, it is possible to show the deformation of the pillar over the entire surface. Comparisons with the RTS data are not shown in this work but can be seen in [5]. Other state of the art methods of comparing point clouds are described in [7].

## 5 RESULTS

### 5.1 Aurachbrücke

The results of the 48 hours measurement reveal interesting significant temperature dependent deformations. The behavior of the pillar can be followed for every 15 minutes over 2 full days.

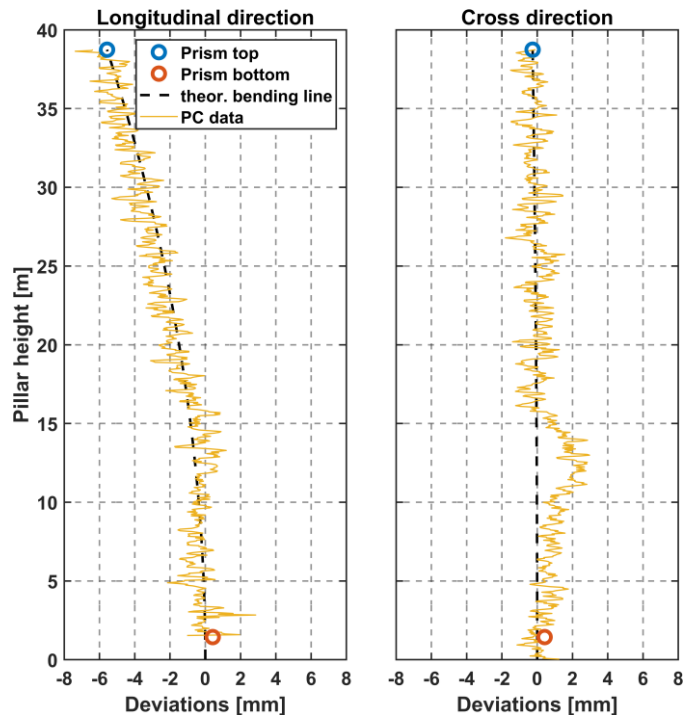


Figure 4. Deformation of Pillar 3 in longitudinal and cross direction for the epoch 07.09.2024 12:00 compared to the first captured epoch (06.09.2024 20:00)



In Figure 4, one epoch captured at noon is shown relatively to the first epoch measured in the evening. In longitudinal direction, the bending of the pillar is clearly visible and matches well the calculated theoretical bending line that is derived by the prism on top of the pillar.

Looking at the cross direction, the prism on the top as well as the scanning data do not show significant deformations at the height of the pillar. However, a strong deformation is noticeable at the height of about 10 to 15 m. The source of this anomaly was not clearly found, but it seems unlikely that the pillar deforms that way. Yet, looking at the waterfall Figures 5 and 6, it can be seen, that the apparent deformation occurs in both directions at the same time of day in the same height of the pillar. This indicates, that the deformations may occur due to a combination of angle of incident of the sun and the angle of impact of the laser distance measurement by the RTS.

Also, it can be seen in Figure 5 that the bending in longitudinal direction rises beginning on top of the pillar and grows with time over the day and peaks at about midday. After the deformation is widely dismantled, a short deformation in the other direction can be seen on the second day at around 16:00. But this coincides also with the described anomaly and therefore is not considered real deformation but rather a problem with the laser distance measurement due to the surface of the pillar.

The peak of bending on midday is explainable by the East-West alignment of the bridge which implies that the pillars are illuminated from one side before and from the other side after midday.

To further validate the quality of the point cloud acquisition, a band of 1 m is cut from the top of the point cloud and averaged for every epoch. This timeseries can be directly

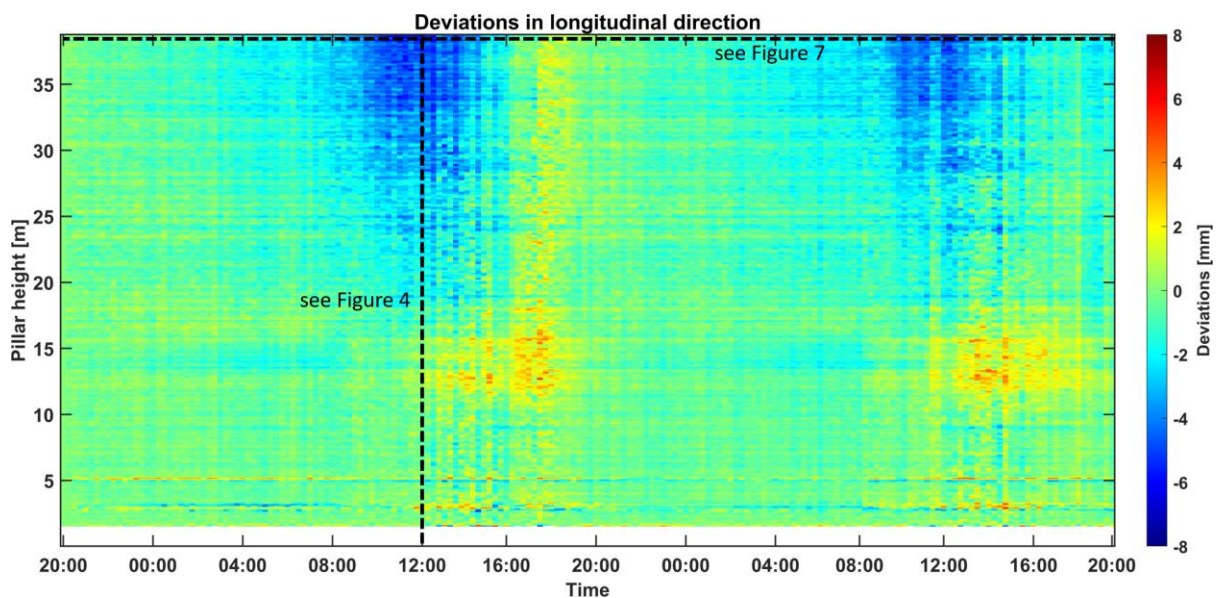


Figure 5. Deformations of pillar 3 in length direction of all measured epochs.

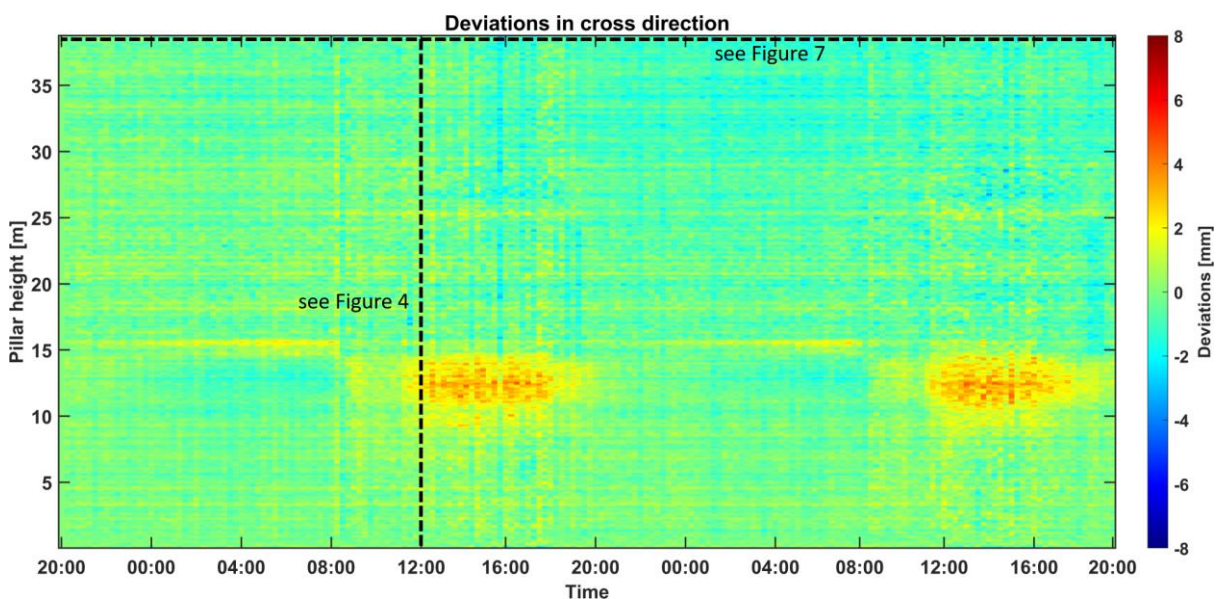


Figure 6. Deformations of pillar 3 in cross direction of all measured epochs.



compared with the time series of the prism on top and bottom of the pillar, but also with the calculated displacement by the tilt sensor data assuming a temperature induced bending. These results for both, longitudinal and cross direction can be seen together with the temperature and global radiation during the experiment in Figure 7. The measurement of global radiation is disturbed by the bridge's shadow that is casted onto the radiation sensor from 08:30 to 10:30 for both days. The missing parts are interpolated in Figure 7 (bottom).

The timeline of the prism at the bottom of the pillar shows deformations of less than 0.5 mm in both directions, which could be assumed as stable. The prism on top of the pillar shows a deformation over the day up to 6 mm with its minima at 12:00 at midday. The same deformation with small variations is also captured by the tilt sensor in longitudinal direction. In cross direction, the tilt sensor obviously captures deformations that are not recorded by any other sensor and may be caused by internal temperature dependent effects of the sensor itself but needs further investigation.

The calculated deformation of the point cloud data shows a higher noise than the other sensors in both directions. Nevertheless, the deformation derived from TLS fits well with the measured deformations using the RTS and the prism.

In cross direction, no clear diurnal variation can be seen, except for the tilt sensor. As the pillar is significantly wider in cross direction than in longitudinal direction, this seems to be plausible. Also, no force due to bridge expansion can act onto the pillar in cross direction, whereas the fixed bearing at the pillar may cause additional longitudinal deformations.

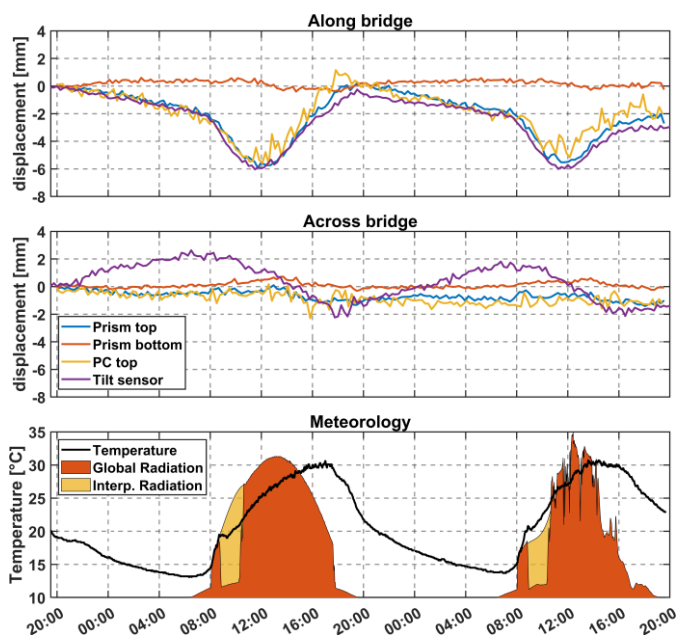


Figure 7. Deformation of the top part of the point cloud (PC), the prism on top and bottom and calculated deformation of tilt sensor on top in length direction (top figure), cross direction (central figure), and the temperature and global radiation during the experiment, while shadow is casted onto the sensor the global radiation is interpolated (bottom figure)

## 5.2 Gschnitztalbrücke

At the Gschnitztalbrücke multiple measurement epochs were taken, and two of them are shown here. While the comparison of pillar deformations at the Aurachbrücke was motivated by the behavior of the pillar due to one sided sun illumination over a rather short time and high measurement frequency, the concern at the Gschnitztalbrücke is the thermal expansion of the bridge deck and transfer of this deformation to the pillars. Usually the bearings between pillar and girder should absorb this deformation, but as long-term tilt measurements indicated, the bearings do not take the full deformation that is expected by thermal expansion.

In Figure 8, the deformations in plane direction of the pillar can be seen for the spring (2023/05) and summer (2023/08) epochs. The temperature difference between the epochs was only 1°C. Assuming a free thermal deformation of the bridge, and the length of 210 m to the zero point of thermal expansion, the deformation of the girder should sum up to 2.5 mm at the position of the pillar. Figure 8 shows deformations of up to 10 mm and therefore rather bigger deformations than expected.

Looking at the second epoch that is examined in Figure 9, the measured deformations are way bigger with up to 25 mm. The temperature difference on the other hand is 7°C compared to the reference epoch which results in a theoretical deformation of 17.5 mm. So, also in the second epoch, the deformation is way bigger than expected. The shape of deformation can also be seen in the figure and leads from the bottom left to the top right.

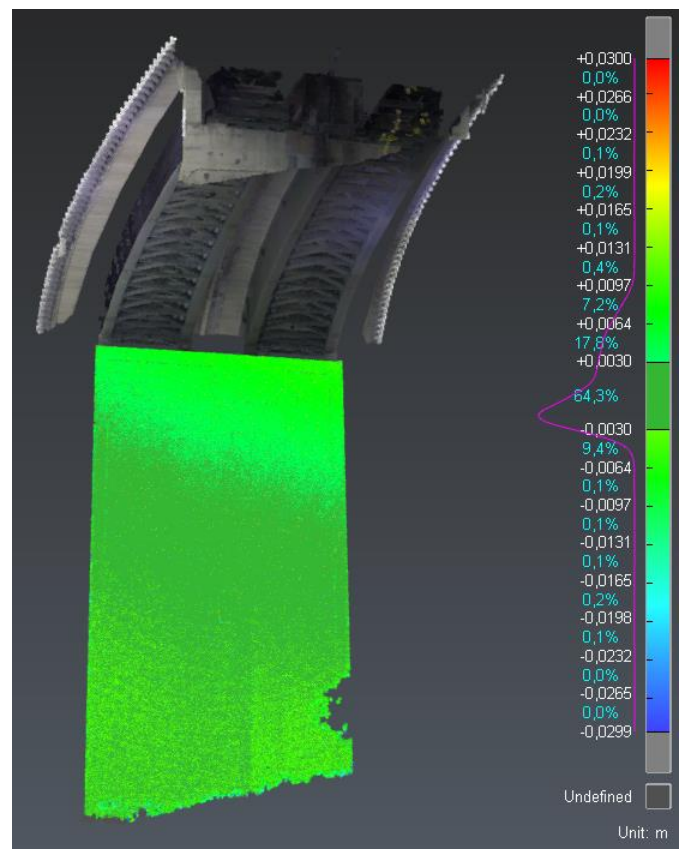


Figure 8. C2C comparison of pillar 6 seen from the end abutment below span 7 of reference epoch 2023/05 and the following epoch of 2023/08

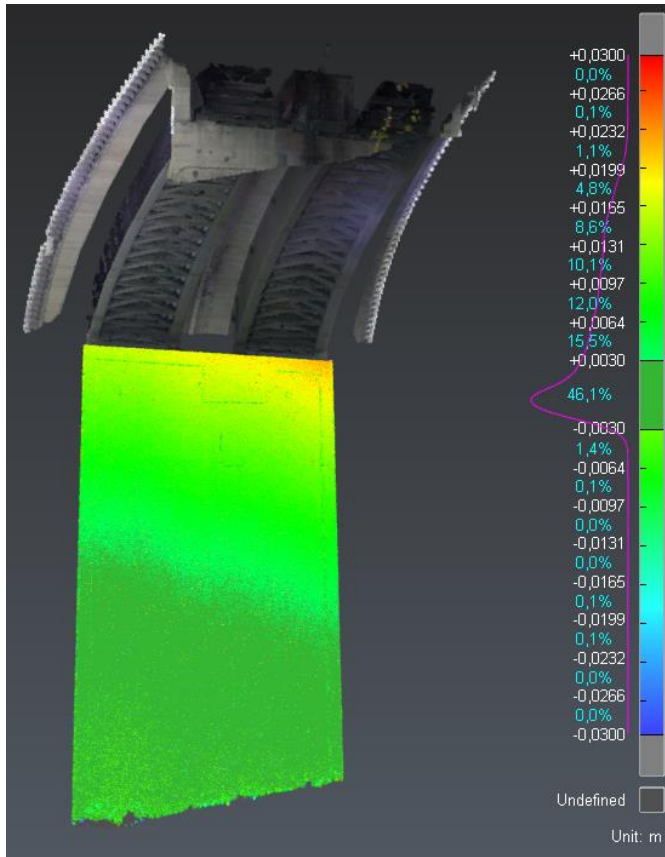


Figure 9. C2C comparison of pillar 6 seen from the end abutment below span 7 of reference epoch 2023/05 and epoch of 2023/11

While both epochs overshoot the expected deformation, the differences of the epoch can also be considered. The temperature difference is 6°C, and therefore a deformation of about 15 mm is expected. Taking the maximum values, which occur on top of the pillar, of 10 mm of the first epoch and 25 mm of the second epoch into account, the relative deformation adds up to 15 mm which is exactly the expected value between the epochs. The offset to the reference epoch has to be investigated further on as its source cannot be determined yet.

The results of the Gschnitztalbrücke show the potential of gathering valid data of the behavior of the structure and verifying the idea of nonconforming bearing transmission over a long period of time.

## 6 CONCLUSIONS & OUTLOOK

Conventional geodetic monitoring of bridges delivers deformation data only at a few distinct points. With modern laser scanners entire bridge decks and pillars can be observed and a tilting of a pillar can be well distinguished from bending.

The required point clouds can either be captured with full dome laser scanners or scanning total stations. Depending on the given situation the right type of instrument has to be chosen. Although a full dome laser scanner is much faster than a total station, the distance measurement noise is usually higher. Measurements to individual prisms with an RTS still deliver highest accuracy, see Table 1 and true 3D displacements [8].

Table 1. Performance of RTS measurements on prisms [9] and scanning of TLS RTC360 [10]

Instrument	Angle accuracy	Distance Accuracy
MS60 prism measurement	1"	1 mm + 1.5ppm
RTC360	18"	1 mm + 10 ppm

Furthermore, a scanning total station can register point clouds with a high accuracy by using RTS setup functionalities like free stationing.

Overall both techniques help to gain a better understanding of the overall behavior of large civil structures without the need to physically access the measurement location to install sensors on the structure.

## ACKNOWLEDGMENTS

We want to acknowledge the support of the Austrian Highway Agency (ASFINAG), for the possibility of performing a load test and taking measurement at their bridges.

## REFERENCES

- [1] Land Tirol, Verkehr in Tirol Bericht 2023, S. 41, [www.tirol.gv.at/fileadmin/themen/verkehr/verkehrsdatenerfassung/downloads/VB\\_2023\\_web.pdf](http://www.tirol.gv.at/fileadmin/themen/verkehr/verkehrsdatenerfassung/downloads/VB_2023_web.pdf), 2024.
- [2] T. Moser, W. Lienhart, F. Schill, Static and dynamic monitoring of bridges with contactless techniques. In J. S. Jensen, D. M. Frangopol, & J. W. Schmidt (Eds.), *Bridge Maintenance, Safety, Management, Digitalization and Sustainability: Proceedings of the 12th International Conference on Bridge Maintenance, Safety and Management, IABMAS 2024* (pp. 332-340). CRC Press/Balkema. <https://doi.org/10.1201/9781003483755-35>, 2024.
- [3] F. Schill, C. Michel, A. Firus, Contactless Deformation Monitoring of Bridges with Spatio-Temporal Resolution: Profile Scanning and Microwave Interferometry. *Sensors* 2022, 22, 9562. <https://doi.org/10.3390/s22239562>, 2022.
- [4] W. Lienhart, F. Schill, T. Moser, Dynamic Bridge Monitoring with Remote Sensing Techniques. In *Structural Health Monitoring 2023: Designing SHM for Sustainability, Maintainability and Reliability* (pp. 184-191). DEStech Publications, Inc. <https://doi.org/10.12783/shm2023/36736>, 2023.
- [5] W. Lienhart, T. Moser, L. Strasser, Large scale monitoring of a highway bridge with remote sensing and distributed fiber optic techniques during load tests. In *Proceedings of the 10th European Workshop on Structural Health Monitoring (EWSHM 2024)* (e-Journal of Nondestructive Testing; Vol. Special Issue). <https://doi.org/10.58286/29678>, 2024.
- [6] Y. Yang, C. Holst, Piecewise-ICP: Efficient and robust registration for 4D point clouds in permanent laser scanning. *ISPRS Journal of Photogrammetry and Remote Sensing*, Volume 227, Pages 481-500, ISSN 0924-2716, <https://doi.org/10.1016/j.isprsjprs.2025.06.026>, 2025.
- [7] C. Holst, B. Schmitz, H. Kuhlmann, Investigating the Applicability of Standard Software Packages for Laser Scanner based Deformation Analyses, *Proceedings of the FIG working week 2017*, ISBN 978-87-92853-61-5.
- [8] W. Lienhart, Geotechnical monitoring using total stations and laser scanners: critical aspects and solutions, *Journal of Civil Structural Health Monitoring*, 7(3): 315-324: <https://doi.org/10.1007/S13349-017-0228-5Ssf>, 2017.
- [9] Leica Geosystems, Leica Nova MS60 MultiStation Datasheet, 2015
- [10] Leica Geosystems, Leica RTC360 Product Specifications, 2018



# Non-destructive Test Methods used for Inspection and Damage Assessment of Concrete Structures



# External Magnetization based Elasto-Magnetic Sensing Technique for Tension Monitoring of Aged PSC Structures

Junkyeong Kim<sup>1</sup>

<sup>1</sup>Research Center for Disaster & Safety, Advanced Institute of Convergence Technology, Gwanggyoro 145, 16229 Suwon, Korea, Republic of  
email: junkyeong@snu.ac.kr

**ABSTRACT:** This study proposes a novel non-contact electromagnetic (EM) sensing system tailored to detect magnetic flux density changes associated with prestressed tendons embedded in concrete structures. The research emphasizes the optimization of sensor head geometry and coil configurations, including single, multi-solenoid, and Halbach array arrangements, to enhance external magnetic field detection at distances representative of real structural applications. Analytical formulations based on closed-form magnetic field equations were validated through finite element analysis (FEA) using ANSYS Maxwell. Results confirm that concentric Halbach-arrayed multi-solenoids outperform conventional configurations in delivering high-density magnetic fields beyond structural surfaces, particularly at target distances up to 30 cm. The verified modeling framework supports further development toward practical integration into structural health monitoring (SHM) systems.

**KEY WORDS:** External Magnetization; Tensile Force Estimation; Magnetic Sensor; Simulation;

## 1 INTRODUCTION

The long-term structural integrity of prestressed concrete (PSC) systems relies heavily on the performance and health of internal tendons, which bear the majority of tensile stresses in such structures. Over time, factors such as corrosion, overloading, or construction defects can compromise the tendon condition, potentially leading to severe degradation or even catastrophic failure of bridges, buildings, or other critical infrastructure. Accurate and efficient detection of tendon degradation is thus essential for ensuring public safety, extending structural service life, and reducing maintenance costs.

Conventional non-destructive testing (NDT) methods—such as ground-penetrating radar, ultrasonic testing, and magnetic flux leakage (MFL)—have shown limitations in terms of resolution, access requirements, or signal penetration through dense concrete media. Many existing approaches require contact or partial exposure of the internal tendon system, making them invasive, time-consuming, and impractical for routine inspection in large-scale infrastructure. In particular, methods that rely on internal access or cutting into protective sheaths can inadvertently introduce new vulnerabilities into the structure or disrupt service operations [1][2].

To overcome these limitations, recent research has shifted toward the development of non-contact electromagnetic (EM) sensing technologies capable of detecting magnetic field variations induced by internal steel tendons through external measurements. These techniques leverage the principle that magnetization induced in ferromagnetic tendons (such as carbon steel wires) generates measurable magnetic flux that extends beyond the concrete surface. However, accurately detecting and analyzing such flux from the outside remains challenging, especially at distances exceeding several centimeters from the embedded tendon.

This study proposes a new design and modeling approach for an external, non-contact EM sensor system specifically engineered to detect magnetic flux leakage fields generated by

prestressed tendons embedded in concrete. Central to this investigation is the optimization of the sensor head geometry, solenoid coil configuration, and magnetization arrangement to maximize field sensitivity and directional control. Theoretical modeling is performed using closed-form solutions based on vector potentials and elliptic integrals, while simulation validation is conducted through finite element analysis (FEA) using ANSYS Maxwell [3].

## 2 DERIVATION OF EXTERNAL MAGNETIC FIELD FOR NON-CONTACT EM SENSOR DESIGN FOR EXTERNAL SECTIONS

### 2.1 External Magnetization Trends by Sensor Head Geometry

Sensor head designs with varying top diameters (0.3 mm to 50 mm) were modeled in ANSYS Maxwell. The diameter of the upper surface was changed from 0.3 to 50 mm and finite element analysis was performed using ANSYS Maxwell software.

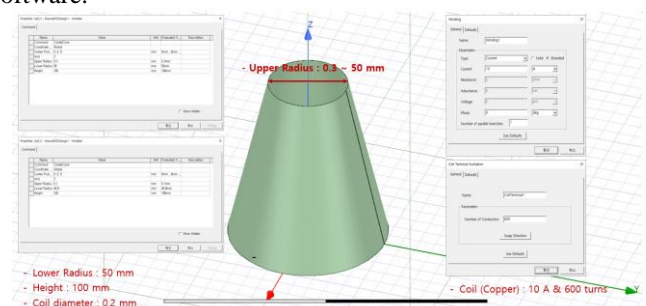
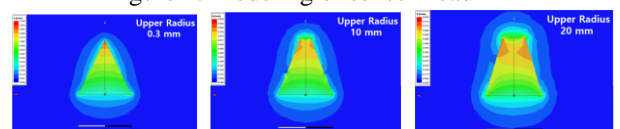


Figure 1. Modeling of sensor head



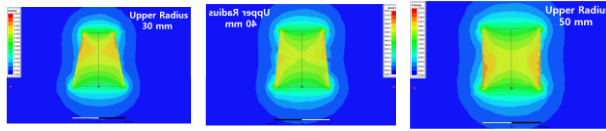


Figure 2. Magnetization according to the shape of head

As the upper radius of the cylindrical sensor increases, the magnetic field concentration effect at the upper part decreases, but the magnetic field dispersion effect into the external space increases.

A finite element analysis was performed on the space of 300 mm above and below the sensor head, and a graph of external magnetization by distance was obtained.

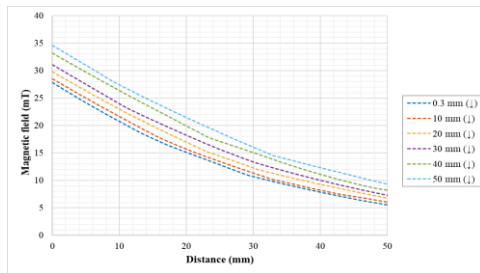


Figure 3. External magnetization according to distance by sensor head type

## 2.2 Generating an external magnetic field using multiple solenoids

The magnetization trend at heights of 10 cm, 20 cm, and 30 cm outside the solenoid was analyzed by changing the diameter of the solenoid (100 mm, 150 mm, and 300 mm) in the same area along the x-axis and y-axis.

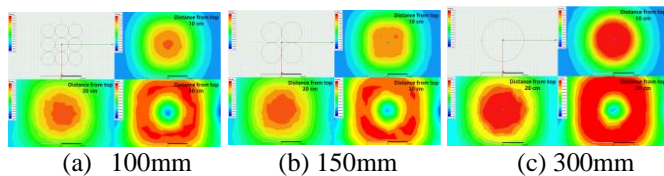


Figure 4. Magnetization degree at heights of 10 cm, 20 cm, and 30 cm for each solenoid diameter

In order to determine the optimal solenoid arrangement with the strongest magnetic flux density in the same area, various coil arrangements were analyzed. As a result, it was confirmed that the arrangement of three concentric circles showed the strongest magnetic flux density at a position of 30 cm.

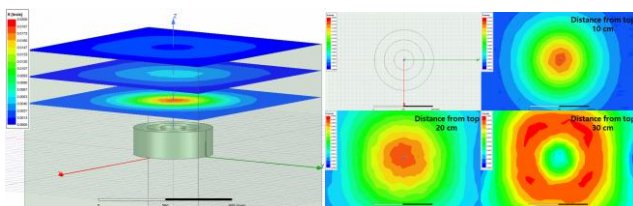


Figure 5. Magnetization degree at heights of 10 cm, 20 cm, and 30 cm for a solenoid arrangement with concentric circles

## 3 CONCLUSION

This study presented a comprehensive approach for designing, modeling, and validating a non-contact electromagnetic (EM) sensor system for external magnetic field detection, aimed at assessing the integrity of prestressed tendons embedded in concrete structures. Through the combination of theoretical modeling and finite element analysis (FEA), the work systematically explored the influence of sensor head geometry, solenoid arrangement, and coil dimensions on the resulting external magnetization performance.

In the early stages, parametric simulations were conducted to evaluate how varying the sensor head's upper surface diameter affects magnetic field distribution. The results revealed a trade-off between field concentration at the sensor surface and its dispersion into external space, and consequently, a cylindrical head with identical top and bottom diameters was selected as the optimal geometry for external flux detection.

Further investigation into solenoid coil diameter demonstrated that larger diameters yield significantly higher external flux densities. In particular, concentric arrangements of solenoids with increasing diameters (100 mm, 200 mm, and 300 mm) achieved approximately double the magnetization at a 30 cm height compared to a single solenoid of equivalent maximum diameter. These results support the use of concentric, multi-sized solenoid configurations for enhanced long-range sensing. Overall, the study has successfully established a robust design methodology for non-contact EM sensing tailored to the constraints of structural health monitoring in concrete infrastructures. The integration of analytical theory with numerical simulation provides a solid foundation for practical implementation. Future work will focus on experimental prototyping, performance evaluation in real structural environments, and integration with data acquisition and diagnostic systems to enable autonomous, continuous health monitoring of critical infrastructure components.

## ACKNOWLEDGMENTS

This work was supported by a grant (RS-2024-00402840) funded by the Ministry of Interior and Safety (MOIS, Korea).

## REFERENCES

- [1] J. Simpson and E. Weiner, Eds., The Oxford English dictionary, Clarendon Press, Oxford, UK, second edition, 1989. D. C. Jiles and D. L. Atherton, Theory of ferromagnetic hysteresis, *Journal of Magnetism and Magnetic Materials*, 61(1-2), 48–60, 1986.
- [2] H. Zijlstra, Experimental Methods in Magnetism. North-Holland Publishing Company, 1967.
- [3] J. C. Mallinson, One-sided fluxes—a magnetic curiosity?, *IEEE Transactions on Magnetics*, 9(4), 678–682, 1973.

# Development of SFCW Radar System for Concrete Structure Inspection

Sangho Lee <sup>1</sup>, Keunhee Cho <sup>1</sup>, Ji-Young Choi <sup>1</sup>, Joo-Hyung Lee <sup>1</sup>, Imjong Kwahk <sup>1</sup>, Changbin Joh <sup>1</sup>

<sup>1</sup>Korea Institute of Civil Engineering and Building Technology (KICT), Republic of Korea

email: slee0614@kict.re.kr, kcho@kict.re.kr, legion@kict.re.kr, leejoohyung@kict.re.kr, kwakim@kict.re.kr, cjoh@kict.re.kr

**ABSTRACT:** Ground Penetrating Radar (GPR) is commonly used for internal inspection of concrete structures. However, the fixed design parameters of commercial GPR limit adaptability for specific inspection conditions and integration with emerging technologies. This study presents the development of a Stepped-Frequency Continuous Wave (SFCW) radar for concrete structure assessment, based on numerical simulations and experimental validation. Parametric analysis was performed to evaluate the influence of frequency bandwidth, antenna spacing, synthetic aperture length, and beamwidth on imaging performance, particularly in detecting embedded reinforcing bars. B-scan data were generated and processed using Delay and Sum Algorithm (DSA) for an image focusing, and image resolution was evaluated in both azimuth and range directions. Based on the simulation results, an SFCW radar prototype was built, and its performance was assessed through tests on reinforced concrete specimens. The experimental results confirmed the system's capability to detect internal targets. The findings suggest that the proposed radar system offers improved flexibility and adaptability for concrete inspection compared to conventional commercial GPR.

**KEY WORDS:** Nondestructive Estimation; SFCW Radar; GPR; Image Focusing; Concrete Structure Inspection.

## 1 INTRODUCTION

In recent decades, the deterioration of civil infrastructure has become a growing issue in many countries. In addition, extreme climate events have introduced loading and environmental conditions that were not considered during the original design and construction phases. Under such conditions, accurate structural condition assessment and maintenance technologies are essential. For reinforced concrete structures, identifying internal features such as voids and rebar structure is necessary for reliable performance evaluation. Currently, Ground Penetrating Radar (GPR) is widely used for internal inspection of concrete structures [1, 2, 3, 4, 5]

GPR can be categorized into impulse-type and stepped-frequency continuous wave (SFCW) type depending on the signal transmission method [1]. Impulse-type GPR transmits short-duration electromagnetic pulses, while SFCW GPR transmits continuous waves by sweeping the frequency in discrete steps. SFCW has advantages in terms of signal-to-noise ratio and penetration depth [6], and is also used for concrete inspection applications [7, 8, 9, 10]

The image quality of GPR data depends on various radar design parameters such as waveform, frequency bandwidth, antenna characteristics, and scanning distance (synthetic aperture). These parameters affect the azimuth (scan direction) and range (depth direction) resolution and the overall imaging performance [6, 11]. However, most commercial GPRs have fixed configurations in terms of frequency range, antenna spacing, and polarization, which limits the ability to optimize inspections for specific applications. Additionally, integrating GPR with technologies such as drones or multi-channel antenna arrays is restricted. Therefore, it is necessary to develop a customizable radar platform for concrete inspection.

This study develops an SFCW radar for internal imaging of concrete structures through numerical simulations and experimental validation. The effects of key design parameters - frequency bandwidth, antenna spacing, synthetic aperture length, and beamwidth - on imaging quality were analyzed using simulation. Based on the results, a SFCW radar system was constructed and its performance was evaluated through experimental tests on reinforced concrete specimens.

## 2 DESIGN OF SFCW RADAR FOR CONCRETE SCAN

### 2.1 SFCW Radar

An SFCW radar transmits continuous waves while incrementally increasing the frequency from a minimum frequency ( $f_{min}$ ) to a maximum frequency ( $f_{max}$ ) at fixed intervals  $\Delta f$ , as expressed in Equation (1) [6]:

$$s_{tx,i}(t) = A_i \cos(2\pi f_i t + \phi_i) \quad (1)$$

Here,  $s_{tx,i}(t)$ ,  $f_i$ ,  $A_i$ , and  $\phi_i$  represent the  $i$ -th transmitted wave, its frequency, amplitude, and phase, respectively, and  $t$  is time. The received signal is a delayed version of the transmitted signal, with a round-trip delay ( $\tau$ ) due to the wave propagating to and from the target, as shown in Equation (2):

$$s_{rx,i}(t) = B_i \cos(2\pi f_i(t - \tau) + \phi_i) \quad (2)$$

In this equation,  $s_{rx,i}(t)$  is the received signal corresponding to the  $i$ -th transmission (A-scan),  $B_i$  is the attenuated amplitude. Due to spherical spreading and material attenuation,  $B_i$  is typically proportional to  $(\Delta t/\tau)^2$ .  $\Delta t$  is the time step between A-scans. The radar module demodulates the received signal into a baseband signal in frequency domain as in Equation (3):



$$S_{f,i} = (\Delta t/\tau)^2 C_i \exp(-j2\pi f_i \tau) \quad (3)$$

Here,  $C_i$  is a coefficient related to the amplitude and assumed to be 1. The time domain response is then obtained by applying the inverse Fourier transform to the frequency domain signal:

$$s_{t,m} = \mathcal{FFT}(S_f)_m \quad (4)$$

where  $m$  denotes the scan position. Performing this calculation across all scan positions yields the B-scan data.

## 2.2 GPR Image Focusing

To obtain focused images, image processing is applied to the acquired B-scan data. In this study, the Delay and Sum Algorithm (DSA) was used for image focusing [12]. The focused image  $g(x_i, z_j)$  is calculated as:

$$g(x_i, z_j) = \frac{1}{M} \sum_{m \in C_x} s_{t,m}(\tau)$$

where  $(x_i, z_i)$  denotes the azimuth and range coordinates of an image pixel,  $m$  is the number of A-scan positions,  $C_x$  is the set of A-scan positions.

To analyze the design parameters of SFCW radar for concrete inspection, a simulation was performed as illustrated in Figure 1. Two reinforcing bars were embedded 50 mm deep in concrete with a center-to-center spacing of 50 mm. This spacing was chosen based on the maximum aggregate size and typical cover thickness. The relative permittivity of concrete was assumed to be 10 [13], and the rebars were modeled as point targets.

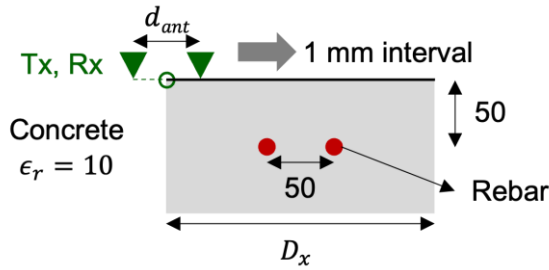


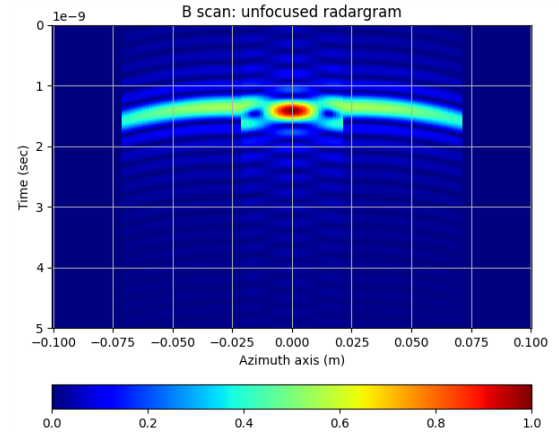
Figure 1. Numerical simulation model (unit: mm)

The frequency bandwidth used in the simulation was set to 1–5 GHz, based on typical GPR configurations for concrete inspection [7]. The transmitting and receiving antennas were placed on the surface of the concrete with a defined spacing, and moved horizontally with 1 mm step intervals to simulate scanning. The antenna was assumed to have a beamwidth ( $\theta$ ), and signals outside this angle were ignored for simplicity.

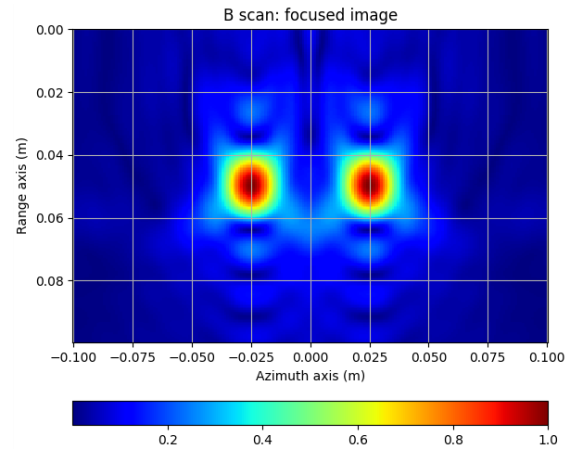
Figure 2(a) shows a representative B-scan image generated through the simulation ( $d_{ant} = 80$  mm,  $\theta = 120^\circ$ ). The amplitude values were normalized to a range of 0 to 1. The time interval was set to 5 ps, and the total time window was determined to be 20 ns based on the 50 MHz frequency step. Only the reflections from the rebars were considered, and surface reflections and direct waves were excluded, assuming that background removal would eliminate these components [14]. Background removal was performed by averaging the B-

scan data along the scan direction and subtracting it from the original signal.

Figure 2(b) shows the focused image obtained by applying DSA to the B-scan in Figure 2(a), also normalized from 0 to 1. The image shows a strong reflection at the rebar locations, with decreasing amplitude as the distance from the rebar increases, indicating that the imaging and focusing were successful.



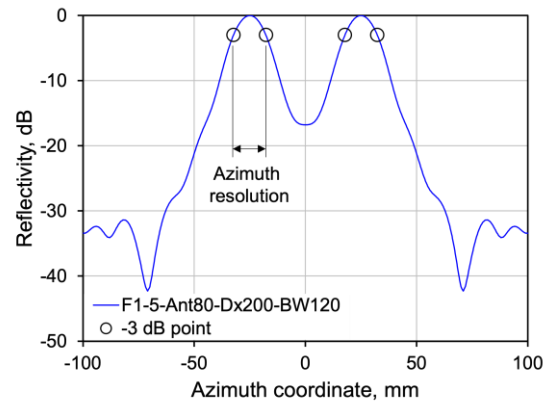
(a) B-scan data



(b) Focused image

Figure 2. Simulation results

Figure 3 shows the reflection amplitude in dB scale along a cross-section including the rebars, and the  $-3$  dB resolution was measured in both azimuth and range directions [15].



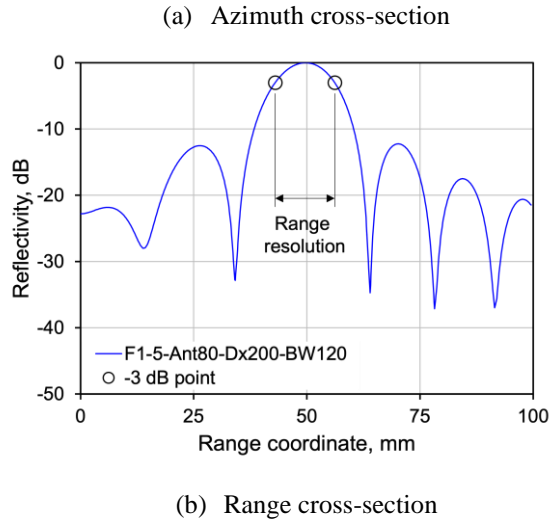


Figure 3. Distribution of reflectivity at rebar cross section

### 2.3 SFCW Radar Design Parameters

Based on the numerical simulations, several design parameters for SFCW radar in concrete scanning were considered. First, wide frequency bandwidth is required, and higher frequency components are preferred unless significantly attenuated. Vivaldi antennas, commonly used in wideband applications, can be applied [16]. However, electromagnetic attenuation in concrete increases with frequency [17], so optimal bandwidth selection should consider this trade-off.

Second, a smaller antenna spacing improves resolution, but mutual coupling effects must be considered. The simulation did not account for these effects, but in practice, closely spaced antennas may interfere with each other's radiation patterns and impedance [18,19]. Therefore, antenna spacing should be minimized without causing mutual coupling.

## 3 SFCW RADAR DEVELOPMENT AND VALIDATION

### 3.1 Radar Configuration

A vector network analyzer (VNA) is a device used to evaluate the frequency domain performance of RF components by sweeping a wide frequency range. When combined with appropriate antennas, it can function as an SFCW radar. In this study, the UVNA-63, the educational VNA by Mini-Circuits, was used as the SFCW radar module (Figure 4).

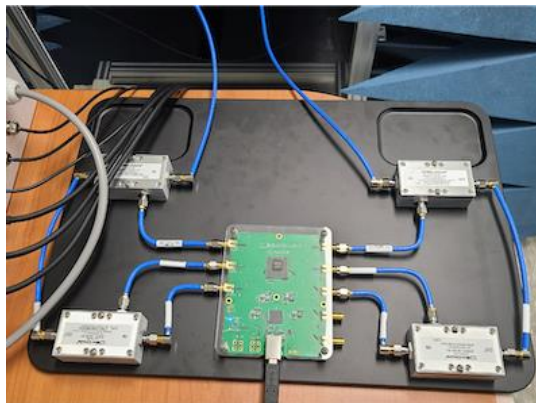


Figure 4. UVNA-63 (<https://www.minicircuits.com>)

The device provides a maximum output power of 0 dBm and operates in the frequency range from 0.1 to 6 GHz, which covers the frequency range of typical commercial GPRs [8, 9, 10]. The maximum receive input level is 10 dBm.

For transmission and reception, a wideband Vivaldi antenna (113 × 150 mm) was used (<https://www.craeca.com/antenna>).

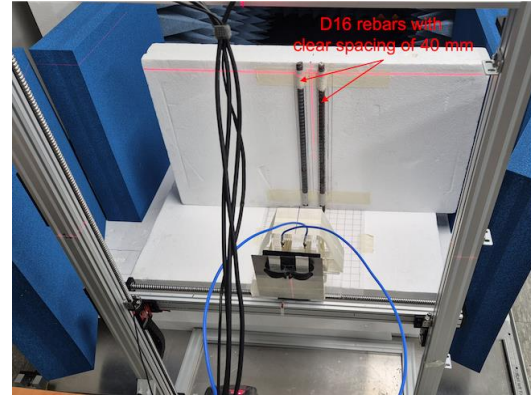


Figure 5. Preliminary test for antenna spacing

As shown in Figure 5, the antenna was mounted on a 2D motorized scanning frame that enables C-scan acquisition. The horizontal scan range was set to 1150 mm to secure a sufficient synthetic aperture length. This configuration ensures that concrete members located 100 mm away can be scanned up to approximately 1.2 m in depth. The antennas were oriented so that the scan direction aligned with the H-plane, which typically has a wider beamwidth. The antenna used in this study had a reduced beamwidth at higher frequencies, indicating the need for further development of antennas that maintain beamwidth across the full frequency range.

A preliminary experiment was conducted to determine the appropriate antenna spacing using two D16 rebars (SD400 grade) placed 40 mm apart in air, as shown in Figure 5. The antennas were spaced at 9, 50, and 88 mm during horizontal B-scan. The rebars were positioned 165 mm away from the antenna tips and fixed using Styrofoam, which has a relative permittivity of approximately 1.04 [20], making it nearly equivalent to air and minimally affecting the measurement. Electromagnetic absorbers were placed around the rebars to minimize environmental reflections.

The transmission bandwidth was set to 1–5 GHz based on antenna performance, with 50 MHz frequency steps. The transmit power was 0 dBm. A-scan data were acquired at 2 mm intervals over a scan distance of 600 mm. To enhance high-frequency components in the measured data, an amplification process was applied as defined in Equation (6), where R was empirically set to 1000:

$$S_{\text{enhanced},i} = S_{f,i} \exp \left[ \ln R \frac{f_i - f_{\min}}{f_{\max} - f_{\min}} \right] \quad (6)$$

Here,  $S_{\text{enhanced},i}$  is the amplified signal at frequency  $f_i$ , and  $f_{\min}$  and  $f_{\max}$  are the minimum and maximum frequencies, respectively.

The B-scan data were processed with background removal and DSA for image focusing. Figure 6 shows the experimental results. The white circles indicate the positions of the rebars.

Unlike the simulation results, lower resolution was observed when the antennas were placed too close together. At 9 mm spacing, the two rebars could not be distinguished. When the spacing was increased to 88 mm, the rebars were clearly resolved. This result indicates that at least 88 mm of antenna separation is required to suppress mutual coupling effects.

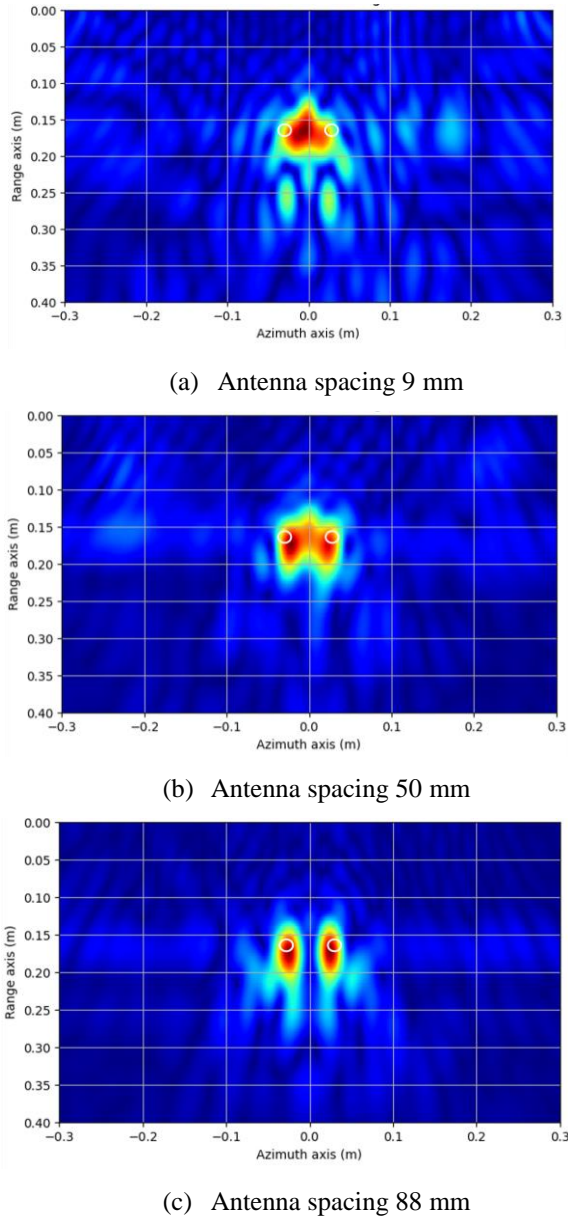


Figure 6. Preliminary test results

### 3.2 Validation Test

To validate the developed SFCW radar, an experiment was conducted using a reinforced concrete specimen. Figure 7 shows the geometry of the specimen. The concrete block measured  $160 \times 200 \times 260$  mm and included six D16 rebars (SD400) embedded in two layers. The vertical spacing between the two layers was 50 mm, and the horizontal spacing between rebars in the same layer was 50 mm and 70 mm. The compressive strength of the concrete was 30 MPa, a typical value for structural applications. The antenna spacing was set

to 100 mm to avoid mutual coupling effects. The scan length was 1000 mm with 2 mm measurement intervals. The standoff distance between the antenna and the specimen surface was 100 mm. The same high-frequency amplification process used in the preliminary test was applied to the acquired data.

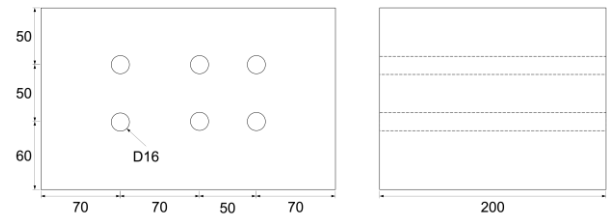


Figure 7. Concrete test specimen (unit: mm)

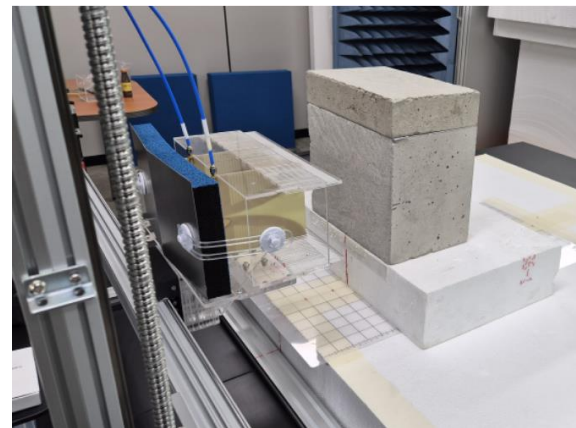


Figure 8. Verification test setup

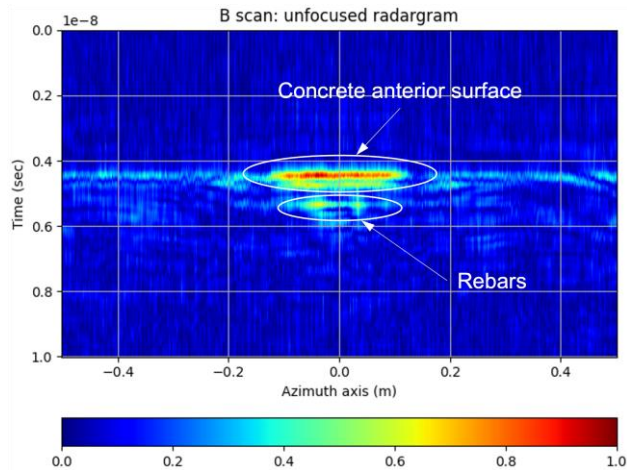
Figure 8 shows the experimental setup. To minimize environmental interference, only the concrete specimen was placed in the direction of wave propagation. The scan was performed on the surface with a concrete cover of 42 mm. The transmit frequency range was set from 0.1 to 6 GHz in 50 MHz steps, and the transmit power was 0 dBm.

The acquired B-scan data were processed using background removal and DSA. Figure 9(a) shows the time-domain B-scan after high-frequency amplification and background removal. A strong surface reflection was observed due to the large area of the concrete surface, exceeding the strength of the rebar reflections. DSA was applied with a relative permittivity of 7 for concrete. Refraction at the air-concrete interface was accounted for using Snell's law. Figure 9(b) shows the focused image in dB scale for the scan area (260 mm in azimuth, 160 mm in range). Strong reflections were observed at the positions of the front-layer rebars, and three distinct rebar signatures were clearly identified. The positions in both range and azimuth directions matched the actual locations of the rebars. These results confirm that the developed radar can detect and localize rebars located 50 mm deep in concrete.

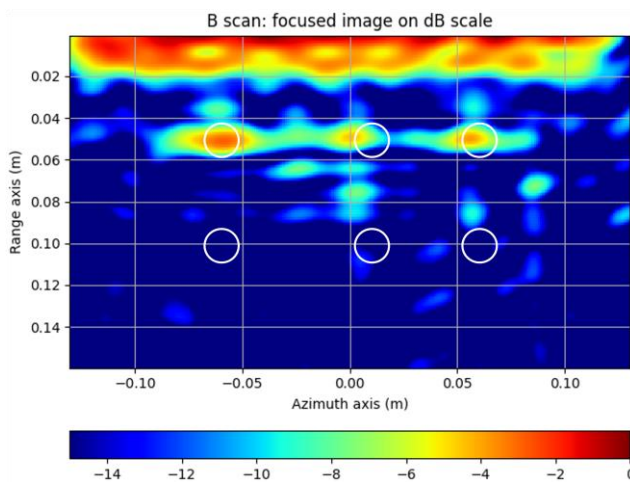
However, the rebars in the rear layer were not detected in the focused image. This is attributed to signal attenuation during propagation and interference from surface and front-layer reflections. Since the rear-layer signal becomes weaker and is partially masked by stronger reflections, detection is more difficult. To address this, future research is required on signal compensation techniques, clutter removal methods, and



antenna design that enhances high-frequency transmission for deeper penetration.



(a) B-scan data



(b) Focused image

Figure 9. Verification of test result

## 4 CONCLUSION

This study conducted numerical simulations and experimental tests to develop an SFCW radar system for internal inspection of concrete structures. The following conclusions were drawn:

1. To analyze the effects of SFCW radar design parameters on image quality, simulations and image focusing were performed using rebar-embedded concrete models. The results identified five key design parameters for an SFCW radar in concrete scanning:

(1) A wide frequency bandwidth is required, and higher frequency components should be used as long as attenuation is acceptable.

(2) The antenna spacing should be minimized without introducing mutual coupling effects.

(3) The synthetic aperture length should exceed the expected rebar spacing and target area.

(4) A larger antenna beamwidth improves resolution; therefore, the antenna should be oriented such that the scan direction aligns with the plane having a wider beam.

(5) Amplifying high-frequency components while maintaining overall bandwidth improves azimuth resolution without degrading range resolution.

2. An SFCW radar system was developed using a vector network analyzer. Ultra-wideband Vivaldi antennas were employed. Preliminary tests were conducted on exposed rebar with varying antenna spacing. The results showed that mutual coupling effects were avoided when the spacing was 88 mm or more.

3. A validation experiment was conducted on a reinforced concrete specimen using the developed radar. The focused image showed strong reflections at the locations of the front-layer rebars, and three rebars were clearly detected. This confirmed the radar's ability to identify and localize rebars embedded 50 mm deep in concrete. However, the rear-layer rebars were not detected due to signal attenuation and masking by front-layer reflections. To address this, further research is needed on signal compensation, clutter suppression, and antenna design for improved high-frequency transmission.

The developed SFCW radar offers greater flexibility than commercial systems, as its configuration can be freely modified by the user. This advantage makes it suitable for structure-specific inspection applications, integration with emerging technologies such as UAVs, multi-channel antenna arrays, and the development of new NDT techniques. With continued development, the proposed system has the potential to outperform existing commercial GPRs in terms of performance and applicability.

## ACKNOWLEDGMENTS

Research for this paper was carried out under the KICT Research Program (project no. 20250057-001, Concrete CT: Reinforcement Damage) funded by the Ministry of Science and ICT.

## REFERENCES

- [1] ACI Committee 228, Report on nondestructive test methods for evaluation of concrete in structures (ACI 228.2R-13), American Concrete Institute, Farmington Hills, MI, USA, 2013.
- [2] J.E. Baek, H.J. Lee, K.C. Oh, and B.S. Eom, "Evaluation of Concrete Bridge Deck Deterioration Using Ground Penetrating Radar Based on an Extended Common Mid-Point Method," *J. Korea Inst. Struct. Maint. Inspect.*, vol. 16, no. 6, pp. 82–92, 2012. (In Korean)
- [3] E.J. Kim, S.J. Cho, and S.H. Sim, "A Recent Research Summary on Smart Sensors for Structural Health Monitoring," *J. Korea Inst. Struct. Maint. Inspect.*, vol. 19, no. 3, pp. 10–21, 2015. (In Korean)
- [4] J. Rhee, J. Shim, S. Lee, and K.H. Lee, "A Consideration on the Electromagnetic Properties of Road Pavement Using Ground Penetrating Radar (GPR)," *KSCE J. Civil and Environmental Engineering Research*, vol. 40, no. 3, pp. 285–294, 2020. (In Korean)
- [5] C. Ozdemir, S. Demirci, E. Yigit, and B. Yilmaz, "A review on migration methods in B-scan ground penetrating radar imaging," *Mathematical Problems in Engineering*, vol. 2014, p. 280738, 2014.
- [6] C. Nguyen and J. Park, *Stepped-Frequency Radar Sensors: Theory, Analysis and Design*, Springer, Cham, Switzerland, 2016.
- [7] D. Huston, J.O. Hu, K. Muser, W. Weedon, and C. Adam, "GIMA ground penetrating radar system for monitoring concrete bridge decks," *Journal of Applied Geophysics*, vol. 43, pp. 139–146, 2000.
- [8] T. Lee, M. Kang, M. Choi, S.E. Jung, and H. Choi, "Development of Thickness Measurement Method From Concrete Slab Using Ground Penetrating Radar," *J. Korea Inst. Struct. Maint. Inspect.*, vol. 26, no. 3, pp. 39–47, 2022. (In Korean)
- [9] H.J. Lim, "Application of Ground Penetrating Radars (GPR) in Concrete Bridges: A Review," *Journal of the Korea Concrete Institute*, vol. 36, no. 4, pp. 329–336, 2024. (In Korean)

- [10] S. Park, J. Kim, W. Kim, H. Kim, and S. Park, "A Study on the Prediction of Buried Rebar Thickness Using CNN Based on GPR Heatmap Image Data," *J. Korea Inst. Struct. Maint. Inspect.*, vol. 23, no. 7, pp. 66–71, 2019. (In Korean)
- [11] C. Ozdemir, *Inverse Synthetic Aperture Radar Imaging with MATLAB Algorithms*, John Wiley & Sons, Hoboken, NJ, USA, 2021.
- [12] M. Schickert, M. Krause, and W. Muller, "Ultrasonic Imaging of Concrete Elements Using Reconstruction by Synthetic Aperture Focusing Technique," *Journal of Materials in Civil Engineering*, vol. 15, no. 3, pp. 235–246, 2003.
- [13] D.H. Chen and A. Wimsatt, "Inspection and Condition Assessment Using Ground Penetrating Radar," *Journal of Geotechnical and Geoenvironmental Engineering*, vol. 136, no. 1, pp. 207–214, 2010.
- [14] D.J. Clem, T. Schumacher, and J.P. Deshon, "A consistent approach for processing and interpretation of data from concrete bridge members collected with a hand-held GPR device," *Construction and Building Materials*, vol. 86, pp. 140–148, 2015.
- [15] M.A. Tolman, *A Detailed Look at the Omega-k Algorithm for Processing Synthetic Aperture Radar Data*, Master's Thesis, Brigham Young University, Utah, USA, 2008.
- [16] A.M.D. Oliveira, M.B. Perotoni, S.T. Kofuji, and J.F. Justo, "A Palm Tree Antipodal Vivaldi Antenna With Exponential Slot Edge for Improved Radiation Pattern," *IEEE Antennas and Wireless Propagation Letters*, vol. 14, pp. 1334–1337, 2015.
- [17] S. Kim, J. Surek, and J. Baker-Jarvis, "Electromagnetic metrology on concrete and corrosion," *Journal of Research of the National Institute of Standards and Technology*, vol. 116, no. 3, pp. 655–669, 2011.
- [18] R.G.S. Alsultan and G.O. Yetkin, "Mutual Coupling Reduction of E-Shaped MIMO Antenna with Matrix of C-Shaped Resonators," *International Journal of Antennas and Propagation*, vol. 2018, no. 1, p. 4814176, 2018.
- [19] C.A. Balanis, *Antenna Theory: Analysis and Design*, 3rd ed., John Wiley & Sons, Hoboken, NJ, USA, 2005.
- [20] M. Plonus, "Theoretical investigations of scattering from plastic foams," *IEEE Transactions on Antennas and Propagation*, vol. 13, no. 1, pp. 88–94, 1965.

# A Novel System Identification-Based Method for Rebar Radius Estimation in Radar SAR-Based Non-Destructive Testing

Kwang-Yeun Park, Joo-Hyung Lee, Changbin Joh

KOREA INSTITUTE of CIVIL ENGINEERING and BUILDING TECHNOLOGY, Korea, Republic of (South Korea)  
email: kypark@kict.re.kr, leejoohyung@kict.re.kr, cjoh@kict.re.kr

**ABSTRACT:** Non-destructive testing of reinforced concrete commonly utilizes electromagnetic waves, such as radar, to obtain internal structural information. When probing around rebars using electromagnetic equipment, hyperbolic-shaped images are often generated. Typically, image focusing techniques, including Hyperbolic Summation, Kirchoff Migration, Phase-shift Migration, Omega-k Migration, and Back-projection-based Focusing, which are based on Synthetic Aperture Radar (SAR) algorithms, are applied to analyze these hyperbolic images. However, these conventional methods cannot accurately determine the size of rebars and face limitations when inspecting doubly reinforced concrete due to shadow regions created by surface-layer rebars, which obscure the internal rebars. To address these challenges, this study proposes a novel approach that analyzes hyperbolic images based not on the image itself, but on the information related to wave propagation distances. In this method, the rebar cross-section is assumed to be a circle with an arbitrary radius, and a hyperbolic equation is established accordingly. The radius is determined by solving the equation using a system identification (SI)-based approach that minimizes the error between the measured hyperbola and the theoretical one. As with many conventional SI techniques, this problem is highly ill-posed, requiring the introduction of regularization methods to stabilize the solution.

**KEY WORDS:** System Identification (SI), Rebar Radius Estimation, Non-Destructive Testing (NDT), Radar SAR Imaging, Regularization Techniques.

## 1 INTRODUCTION

When non-destructive testing is performed on reinforced concrete using radar equipment, the result appears in a hyperbola as shown in Figure 1. Such hyperbola images can be processed using methods such as hyperbolic summation, Kirchoff migration, phase-shift migration, Omega-k migration, or back-projection-based focusing [1-5], or analyzed empirically to determine the position and size of the rebar. These methods are very useful for identifying the overall internal structure of concrete. They make it possible to detect the presence of materials other than concrete (e.g., rebar or voids) inside the concrete and to estimate their approximate size. However, only a relative size can be inferred; the exact size of the object remains unknown. While it is fairly easy to detect a missing rebar—omitted either by mistake or wrongdoing during construction—it is difficult to confirm whether a rebar with a smaller cross-sectional area than required was used. It is also challenging to verify significant reductions in effective cross-sectional area due to severe corrosion. Moreover, in cases such as double-layered reinforcement, shadowed areas may appear, making analysis difficult.

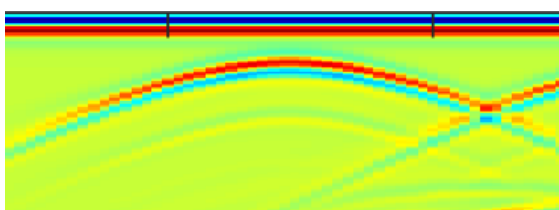


Figure 1. Hyperbola seen in a B-scan when rebar is present in concrete

To compensate for these shortcomings of image focusing methods, this study aims to develop an algorithm that determines the size of the rebar by analyzing the hyperbola seen in B-scan images—strictly speaking, this curve is not a perfect hyperbola but one that closely resembles it, and is commonly referred to as such.

## 2 PROBLEM DEFINITION AND SOLUTION

### 2.1 Definition of “Hyperbola”

When rebar is present inside concrete, a B-scan taken on a plane parallel to the rebar’s cross-section shows a hyperbola, as in Figure 1. If it is assumed that the rebar has a perfectly circular cross-section and that the transmitting and receiving antennas are located at the same position (mono-static), the principle behind the formation of this hyperbola can be explained by Figure 2.

In Figure 2, the gray area represents concrete and the white area represents the rebar. The variables  $r_r$ ,  $T$  and  $\bar{T}$  correspond to the rebar radius, the distance from the transmitter/receiver antenna to the surface of the rebar, and the rebar-related information actually recorded by the transmitter/receiver antenna in the B-scan, respectively.

Because the transmitter/receiver antenna transmits electromagnetic waves in all directions and receives waves from all directions, it only knows the time difference between transmission and reception; it does not know which direction the wave traveled. At each position of the antenna, the signal strength is recorded over time and plotted with the vertical axis as time (or distance) and the horizontal axis as the antenna’s location. By displaying signal intensity as color, one obtains a B-scan similar to Figure 1. Conventionally, the time axis in a



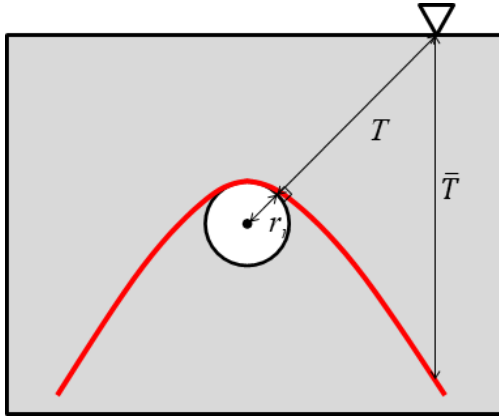


Figure 2. Principle behind hyperbola formation in the B-scan when rebar is present in concrete

B-scan represents half the round-trip time of the wave, effectively the one-way travel time. When the dielectric constant is known and assumed constant, this time can easily be converted into distance. For simplicity, the discussion here assumes the vertical axis represents the one-way travel distance of the electromagnetic wave.

In Figure 1, a hyperbola commonly appears in the B-scan. This hyperbola can be idealized by the red curve in Figure 2. For instance, when the transmitter/receiver antenna is located at the inverted triangle in Figure 2, the electromagnetic wave emitted by the transmitter reflects off the rebar and then returns to the receiver. Because the angle of reflection equals the angle of incidence, only the wave that follows the normal vector of the (assumed circular) rebar cross-section can return to the receiver. Therefore, the wave travels a distance of  $T$  to reach the rebar, reflects, and then travels the same distance  $T$  to reach the receiver. In the B-scan (Figure 1), the reflected signal from the rebar appears at a vertical distance of  $T$  beneath the antenna's position. If this vertical distance is denoted by  $\bar{T}$ , then in an ideal situation with no external interference and no measurement error,  $\bar{T}$  should be equal to  $T$ . The term  $T$  is the distance from the rebar center to the antenna minus the rebar radius; using Figure 3, it can be expressed as follows:

$$T(x, r_x, r_y, r_r) = \sqrt{(r_x - x)^2 + r_y^2} - r_r \quad (1)$$

Here,  $x$ ,  $r_x$ , and  $r_y$  denote the antenna's horizontal position, the rebar center's horizontal coordinate, and its vertical

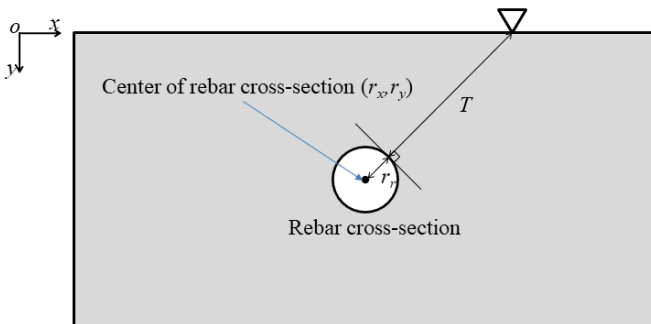


Figure 3. Travel distance of the electromagnetic wave upon reflection

coordinate, respectively. In Equation (1), if the rebar radius  $r_r$  is set to zero—in other words, if the cross-section of the material embedded in the concrete is assumed to be a point—the curve becomes a perfect hyperbola. It is for this reason that the curves in Figures 1 and 2 are commonly referred to as “hyperbolas.”

## 2.2 Estimation of the Rebar Radius in the Form of an Inverse Analysis

As explained above, in an ideal situation without any measurement error,  $T = \bar{T}$  holds in Figure 2. By substituting three pairs of  $(x, \bar{T})$  into Equation (1) and solve the simultaneous equations, the rebar radius  $r_r$  can be found. However, because actual measurements are subject to various errors, the measured  $\bar{T}$  inevitably includes some error. As a result, the value of  $r_r$  obtained using only three pairs of  $(x, \bar{T})$  can be extremely sensitive to even slight errors.

To reduce such errors, Multiple  $(x, \bar{T})$  pairs is used to solve an inverse problem defined by the following optimization equation:

$$\min_{r_x, r_y, r_r} \frac{1}{2} \int_A \|\bar{T} - T(x, r_x, r_y, r_r)\|_2^2 dx \quad (2)$$

In this equation, the integration domain  $A$  covers all  $x$  values where measurements were made. Discretizing this integral yield:

$$\min_{r_x, r_y, r_r} \frac{1}{2} \sum_{\text{for all } n} (\bar{T}_n - T(x_n, r_x, r_y, r_r))^2 \quad (3)$$

$\bar{T}_n$  and  $x_n$  denote the  $n$ -th measured  $(x, \bar{T})$  pair. Although Equations (2) or (3) can be solved by various methods, because the gradient vector and the Hessian matrix can be derived analytically, Newton's method provides an efficient way to obtain a solution.

## 3 NUMERICAL EXAMPLE

### 3.1 General Rebar Example

To analyze the error sensitivity of the proposed method, a numerical example was employed to verify Equation (3). In general, non-destructive testing equipment that uses electromagnetic waves discretizes the signals received by the receiver antenna. As shown in Figure 1, because only discrete points on the hyperbola can be recorded, the actual measurement cannot produce a smooth curve; instead, it is represented by quantized (or gridded) points. Such quantization becomes a significant source of error when using Equation (1) to fit to the measurement points for solving Equation (3). Various other errors that inevitably occur during the measurement process also contribute substantially to the instability of Equation (3).

To verify the stability against these errors, a numerical example was created using Equation (1), and then Equation (3) was solved using Newton's method to obtain a solution. The details of the example are as follows:

- Rebar radius: 12 mm

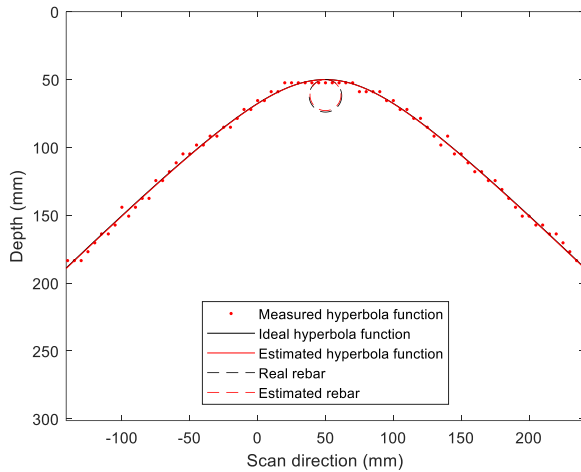


Figure 4. General rebar example and the resulting estimation of the rebar radius

- Concrete cover: 50 mm
- Rebar spacing: 50 mm
- Spatial sampling frequency: once per 5 mm
- Time sampling frequency: 20.48 GHz
- Relative permittivity of concrete: 5

It was assumed that the measuring device is Proceq's GP8800 [6]. The horizontal axis was discretized based on the number of scans per unit distance, and the vertical axis was discretized based on the temporal sampling rate and the relative permittivity. Up to 3% uniformly distributed white noise was added to the hyperbola generated by Equation (1), and the data were placed at the nearest discretized (grid) point.

Figure 4 shows the results of this example. The black dashed line indicates the actual rebar cross-section, and the black solid line represents the hyperbola derived from Equation (1). After adding white noise and mapping it onto the discretized grid, the red points appear in a stepwise manner rather than forming a smooth curve. It can also be observed that some points are distributed discontinuously because of the white noise.

Using the  $(x, \bar{T})$  pairs of these red points to solve Equation (3), the rebar radius was estimated to be 12.229 mm. The rebar radius and center location obtained from the estimation are plotted as a red dashed line in Figure 4, showing a good match with the actual location and radius.

### 3.2 Double-Layered Rebar Example

When the rebar is double-layered, as shown in Figure 5, information about the rebar behind the front one is obscured. Figure 5(a) shows the B-scan image, and Figure 5(b) illustrates a schematic representation. The obscured region is where the curve undergoes the most significant change, and thus contains the greatest amount of information. If a typical image-focusing post-processing method is applied to this image, almost no meaningful information about the rebar can be extracted. However, by employing the proposed inverse hyperbola analysis method, the rebar radius can still be estimated in such cases. The same conditions as the previous example were used, with the concrete cover doubled and a shadow region created extending five times the rebar radius from its center. As shown

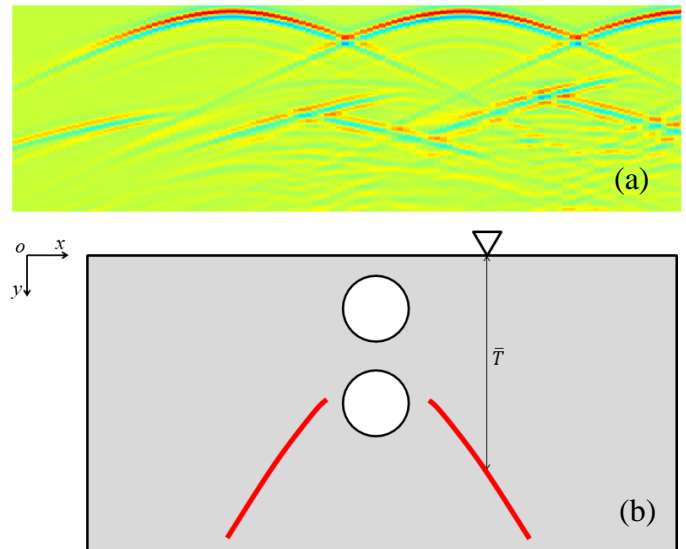


Figure 5. Double-layered rebar as seen via B-scan: (a) B-scan and (b) Schematic

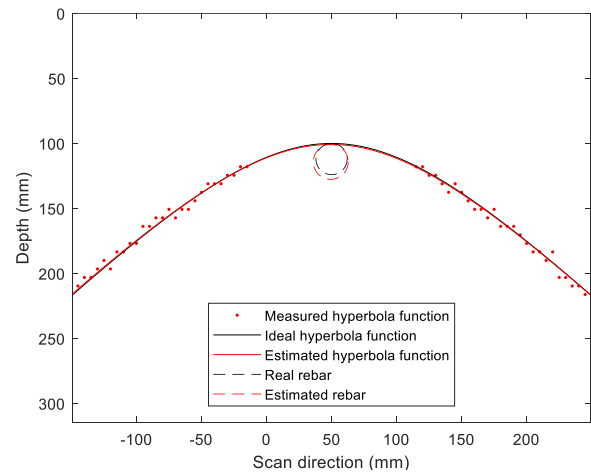


Figure 6. Simulation example of double-layered rebar and the resulting rebar radius estimation

in Figure 6, this setup is similar to the previous example but lacks measurement points near the rebar. By solving Equation (3), the rebar radius was estimated to be 13.42 mm. Although the accuracy is lower compared to the earlier example, it still represents a reasonably good estimation of the rebar radius

## 4 CONCLUSION

- An inverse-analysis-based method for estimating the rebar radius is proposed, which utilizes the hyperbolas observed in B-scans. By treating the rebar center coordinates and radius as unknown variables and formulating an optimization problem that minimizes the least-squares error, it becomes possible to determine the precise size of rebar cross sections—information that is difficult to obtain using conventional image-focusing techniques.
- The proposed rebar radius estimation method was verified through numerical examples. In a scenario with a typical rebar arrangement, the method accurately estimated the

rebar radius. It also performed well for the multi-layered rebar

- By presenting an inverse analysis approach for explicitly estimating the rebar radius, the proposed method overcomes limitations of existing non-destructive testing techniques. It can be effectively applied to detailed analyses of internal concrete structures. With ongoing research to refine  $(x, \bar{T})$  pair extraction and address numerical instabilities, even higher levels of accuracy can be expected in the future.

## ACKNOWLEDGMENTS

This research was funded by the Korea Institute of Civil Engineering and Building Technology (KICT) of the Republic of Korea, Project No. 2025-0057 (Concrete CT: Reinforcement Damage).

## REFERENCES

- [1] C. Özdemir, Ş. Demirci, E. Yiğit, and B. Yilmaz, A Review on Migration Methods in B-scan Ground Penetrating Radar Imaging. *Mathematical Problems in Engineering*, 2014.
- [2] J. Gazdag, Wave Equation Migration with the Phase-Shift Method. *Geophysics*, 43(7), 1978, 1342–1351.
- [3] Q. Yao and W. Qifu, Kirchhoff Migration Algorithm for Ground Penetrating Radar Data. In 2012 International Conference on Computer Science and Electronics Engineering (ICCSEE), vol. 2, IEEE, 2012, 396–398.
- [4] K. Dinh, T. T. Pham, T. T. Nguyen, and H. H. Vu, Application of Synthetic Aperture Focusing Technique to Visualize GPR Data from Reinforced Concrete Structures. *IOP Conference Series: Materials Science and Engineering*, 869(5), IOP Publishing, 2020, p. 052072.
- [5] H. Choi, J. Bittner, and J. S. Popovics, Comparison of Ultrasonic Imaging Techniques for Full-Scale Reinforced Concrete. *Transportation Research Record*, 2592(1), 2016, 126–135.
- [6] Proceq, Proceq GPR GP8000/GP8100/GP8800 User Manual (Version 1.0), Proceq SA, Schwerzenbach, Switzerland, 2024.



# Non-contact non-destructive monitoring of concrete structures using pulsed Laser and microphones

Subhra Majhi<sup>1</sup>, Abhijit Mukherjee<sup>1</sup>, Nihar Sane<sup>1</sup> and Siddhant Sharma<sup>1</sup>

<sup>1</sup> School of Civil and Mechanical Engineering, Curtin University, Kent Street, Bentley, WA:6012, Australia

email: [subhra.majhi@curtin.edu.au](mailto:subhra.majhi@curtin.edu.au) (for correspondence), [abhijit.mukherjee@curtin.edu.au](mailto:abhijit.mukherjee@curtin.edu.au), [n.sane@postgrad.curtin.edu.au](mailto:n.sane@postgrad.curtin.edu.au), [s.sharma6@postgrad.curtin.edu.au](mailto:s.sharma6@postgrad.curtin.edu.au)

**ABSTRACT:** Concrete structures are at several stages of deterioration across the world. The presence of chloride ions salts as in the case of marine infrastructure or due to the application of de-icing salts, can further aggravate the rate of deterioration. Inspections of large concrete structures are predominantly undertaken through visual inspections. Detailed inspections are undertaken using piezo-generated ultrasonics. These inspections can be time and resource-intensive as the piezo devices need to contact the structure during measurements and their energy outputs are limited. Rapid inspections of large civil engineering structures would require a non-contact, high-energy source means of measurement. In our approach, we used a high-energy pulsed laser for excitation and an acoustic microphone for reception towards monitoring concrete structures. Defects in concrete like debonding and honeycombing, were simulated in the concrete specimens. The pulsed laser was used to excite the concrete specimen and the resultant waves generated due to this excitation were measured using focused cardioid microphones. The characteristic features in a typical waveform were first identified in pristine specimen. Subsequently, features corresponding to defects are extracted from the acquired signals using the signals from the pristine signal as a reference. The variations in these features were localised and their veracity was associated with the embedded defects in the specimen. As a result, the location and the nature of the defect were inferred. Thus, through this work, a framework for using pulsed lasers and microphones for non-contact non-destructive detection of defects in concrete is demonstrated.

**KEY WORDS:** Concrete structures, Pulsed laser, acoustic microphone, non-contact Condition monitoring, damage detection.

## 1 INTRODUCTION

Australia has a road network of about 14,500 km of National highways and 265,000 km of major local roads. These roads are supported by 53,000 bridges which are predominantly made of concrete [1]. According to the National State of the Asset Report in 2024, councils across Australia have concrete bridges, buildings and stormwater drains worth \$66.5bn that are in poor condition, function and capacity [2].

Traditionally, built infrastructure assets have been inspected visually, depending on the expertise of the inspectors. These assets are predominantly inspected visually which is tedious, unreliable, and expensive. Moreover, asset owners find it difficult to allocate resources for their monitoring and maintenance. So, sensors can be embedded into the assets to improve reliability in reporting their condition. Fibre optic sensors have been embedded in concrete structural assets to measure strains and sense deterioration in them [3]. As these fibres are predominantly glass fibres, they are susceptible to deterioration due to alkali attack from the concrete. Ensuring the longer durability of these sensors is a challenge [4]. Radio Frequency Identification (RFID) sensors have been embedded in concrete assets to detect changes in humidity and temperature in assets [5]. However, RFID devices are a passive means of monitoring, requiring the sensors to be embedded during the construction phase of assets.

Ultrasonic sensors generate waves that travel through the asset and interact with any emanating deterioration in it. Ultrasonic sensors can be embedded in concrete, and the condition of the concrete asset is discerned through the recorded travelling waves [6]. However, they can deteriorate over time and are prone to vandalism, making them unreliable. Moreover, these sensors must be pre-embedded in the assets before the inception of any deterioration. Mobile sensors can be used to alleviate the shortfalls in embedded sensing [7].

Image analysis and its synergistic association with computer vision have also been attempted for mobile sensing of concrete assets [8]. However, using this method, sub-surface deteriorations in the assets cannot be detected until they emerge to the surface. Mobile piezo sensors are commonly used for the generation and reception of ultrasonic waves for condition monitoring. They have been used to detect corrosion in rebars [9] and subsequently when they are embedded in concrete [10]. Field instruments that can provide scans of concrete are now available. The compact modular design of these ultrasonic scanners makes them convenient for surface-based operations [11]. The data obtained from these scanning devices can be coupled with advanced imaging algorithms to understand hidden rebars [12], incipient corrosion and debonding [13]. However, the scanning area is rather limited (around 300 mm square). Moreover, it is a manual and contact device. Thus, generating ultrasonic scans for concrete assets using mobile piezo sensors can be time and labour-intensive with contact between the sensors and the asset imperative.

In Impact Echo (IE), the surface of the concrete asset being tested is impacted with a solenoid-based metallic impactor, and the response is measured using an accelerometer. Lower frequency waves are typically used in this inspection to develop rapid scans in concrete assets [14]. These waves can also be monitored by using an array of acoustic microphones on a mobile platform [15]. The limited energy of the impactor and high attenuation of waves in concrete restrict the inspection range of this method. This impactor can be replaced with a high-energy pulsed Laser to generate high-energy pulses for rapid inspections of large concrete assets.

The range of inspections can be extended by using a high-energy pulsed laser for excitation. A pulsed laser imparts high-energy laser pulses on the substrate being monitored, making them ideal for sub-surface inspections. The energy from the

Laser pulse ablates the substrate being monitored and subsequently generates waves in the substrate [16]. These generated waves can be monitored using a range of air-coupled sensors such as acoustic microphones and Laser Vibrometers [17,18]. The laser-generated waves, when received non-contact, would help improve the inspection capabilities for large concrete assets.

In this paper, we explore the capabilities of a non-contact pulsed laser-microphone system for inspecting large concrete assets. The results and discussion of the experimental works are presented in the subsequent sections of this paper. The embedded defects in the specimens simulate some of the common defects in concrete structures.

## 2 METHODOLOGY

### 2.1 Experimental setup

In the present scheme of experiments, an Nd-YAG pulsed laser was used to excite the concrete specimen. This pulsed laser, NL303 HT, was made by Ekspla and can operate at two wavelengths 1064 and 532 nm. In the present scheme, the Laser was operated predominantly at 1064 nm with a pulse duration

causes the generation of travelling mechanical stress waves in the material. A portion of the generated stress waves leaks into the air surrounding the concrete while the other part propagates in the concrete. In the present testing regime, the pulsed Laser is operated at a lower energy such that the pulsed laser, upon impact, results in an ablative region on concrete about 1 mm in diameter. The depth of penetration of this ablative region is on a sub-millimetre scale. This laser ablation results in the generation of stress waves in concrete. Visual observations reveal that the geometry of the ablation marks on concrete was of the order of some air voids which occur in concrete while it sets. Moreover, the imparted energy of the Laser wasn't of the order to cause any severance to the structure. Moreover, this approach doesn't involve the extraction of a core from the concrete specimen. Thus, as the inspection method is relatively void of destruction to the specimen, this approach is considered a non-destructive test for assessing concrete.

The stress wave propagation in concrete interacts with any defects in concrete in its travel path. Based on the differences in acoustic impedances of the defect and the surrounding concrete, a portion of the travelling wave gets reflected towards the free surface of the concrete, causing vibrations in the air

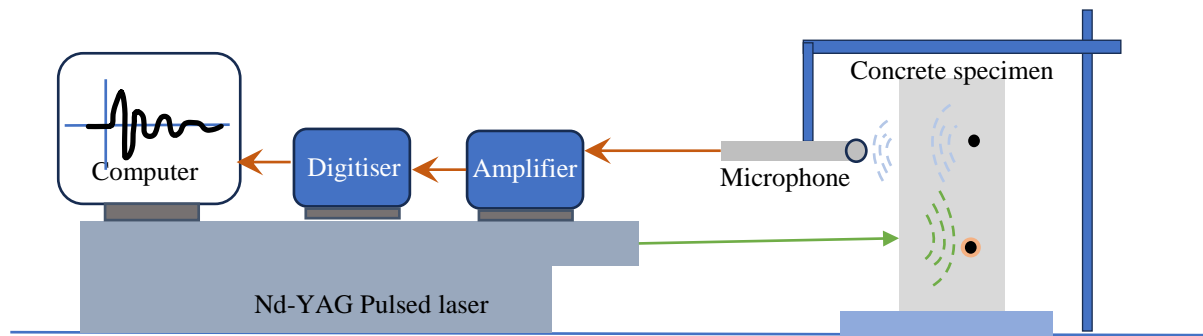


Figure 1 Experimental setup

of 3-6ns where the pulse was Gaussian in shape. The pulse repetition rate of this laser was 10 Hz. The maximum energy output from this laser was 800mJ. The waves generated from the laser impact were measured using a microphone and amplifier system. A representation of the experimental setup is shown in Figure 1. A matched pair of Røde Compact Cardioid ½'' condenser microphones was used as an air-coupled receiver. The received signals were amplified using a Yamaha MG06 mixer. The amplified signals were digitised using a Picoscope 2000 series modular oscilloscope, and subsequently, the digitised data was stored as .csv files on a personal computer. During the experiments, the specimens were securely placed on the measurement table on a positioner assisted by a guide. The Nd-YAG pulsed Laser was operated at 1064nm wavelength for excitation at an energy output of 480mJ. The microphones were placed on a rigid support and secured to the measurement table using screws as needed. An average of 32 signals is used for measurements made at any acquisition location.

As the Pulsed Laser impacts concrete, the temperature at the impact location rises to a few tens of thousands of degrees. The severe increase in temperature causes melting and ablation of material locally. As the ablation and molten material front moves ahead, it interacts with the surrounding material. This

surrounding the concrete. The vibrations in the air caused by the laser impact and subsequent reflections from embedded defects in the air surrounding the concrete are measured by acoustic microphones. The vibrations received at the microphones are digitised and amplified as required.

### 2.2 Specimen details

In this experiment, concrete specimens were cast for testing. All specimens were of the dimension 500 x 250 x 100 mm. Each specimen has two steel bars of 10 mm diameter embedded in it. The concrete specimens were prepared with a mix design by weight as shown in Table 1.

Table 1: Concrete Mix Design

Constituent	Cement	Fine aggregate	Coarse aggregate	w/c ratio
Ratio	1	1.44	2.32	0.5

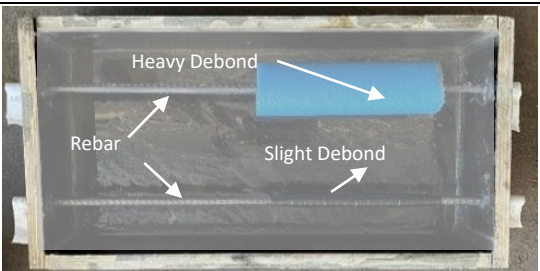
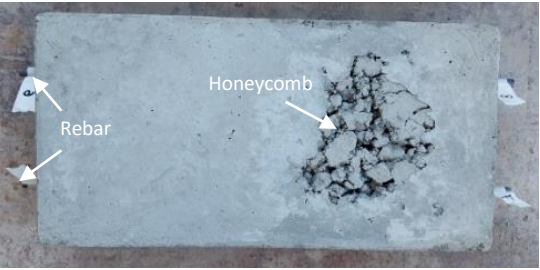
The nominal size of the coarse aggregate used was 10mm. The prepared moulds were filled in three layers, and a table vibrator was used to remove any air voids formed during casting of the specimen. After casting, the specimens were cured for 28 days in a water bath. Along with the specimen mentioned below,

cylinders of the specimen were also cast to test the cylinder compression test of the mix. The average compression strength of concrete obtained from this mix was 48.2 MPa. Table 2 demonstrates the details of the specimens used in the present study. In specimen D1, two types of debonds were created on the embedded rebars. One debond was created using a polystyrene foam wrap around the bar, representing severe debonding, and the other by wrapping several layers of insulation tape around the bar, representing slight debonding. In specimen H1, a region of honeycombing was simulated. This was created by placing aggregates of larger diameter mixed with cement without vibration in the mould and letting it set for one day before casting. Subsequently, the measurement points were marked on the specimen at distances of 50 mm. The microphones were placed 70 mm from the surface of the specimen for all measurements. As the Laser impacts on the specimen, due to ablation a travelling mechanical stress wave gets generated and is received by the microphones. The first arrival times of these waves are noted as the Time of Arrival (*ToA*). The *ToA* of the first positive peak was calculated using Equation 1.

$$ToA = \frac{d_a}{v} \quad (1)$$

Here  $d_a$  is the aerial distance between the microphone and the laser impact on the concrete specimen, and  $v$  is the velocity of sound in air. The specimens presented in Table 2 will now be tested, and the results will be reported in the subsequent sections of this paper.

Table 2 Details of specimens used in this experimental study

ID	Photograph
D1	
H1	

### 3 RESULTS AND DISCUSSIONS

#### 3.1 Specimen D1

On specimen D1, the pulsed laser was applied, and measurements were subsequently taken on three lines, namely A, B and C series. The measurement points were marked on the specimen at distances of 50 mm as shown in Figure 2. The

microphones were placed 70 mm from the surface of the specimen for all measurements. The distance between the point of laser impact and measurement using the microphone was set to 100mm. The impact and measurement locations were chosen such that they span undamaged and locations with embedded damage in the specimen. In the present study, the pulsed laser and microphone were placed on the same side of the concrete specimen while undertaking measurements. Thus, all measurements were taken in the reflection mode, where reflected waves were monitored.

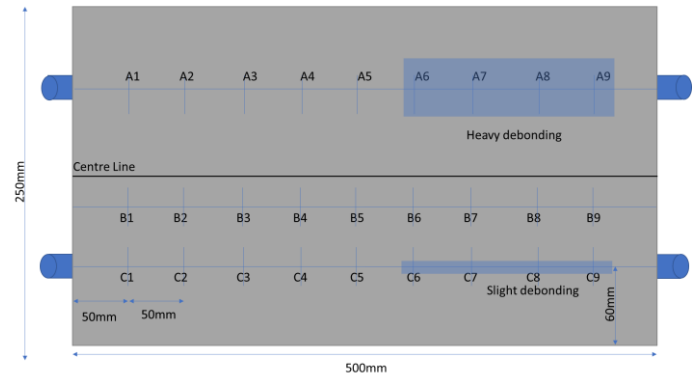


Figure 2: Specimen D1 with simulated debonding

Typical measurements from the laser-microphone acquisition setup are presented in Figure 3. This measurement is called A-Scan. Along line B, to develop an overview of the specimen condition, the laser was imparted at B8, B7, B6 etc., and the corresponding measurements were received by Microphones at positions B6, B5, B4, etc., ensuring a 100mm distance between the transmission and measurement points in the specimen. In Figure 2, the measurements' nomenclature is chosen so that it denotes the location of laser impact and microphone placement during measurements. The measurement, LaserB7\_MicB5, represents the measurement taken with a pulsed laser impacting at B7 and a microphone at B5. In Figure 3, the presented measurements denote the pristine location of the specimen. From here forth, this nomenclature will be followed for nomenclature. In these measurements presented in Figure 3, the first peak was observed between 0.3 and 0.4 ms. *ToA* of the first positive peak was calculated using Equation 1. Here, *ToA* accounts for the arrival of the Rayleigh wave to the microphone due to Laser impact on concrete.

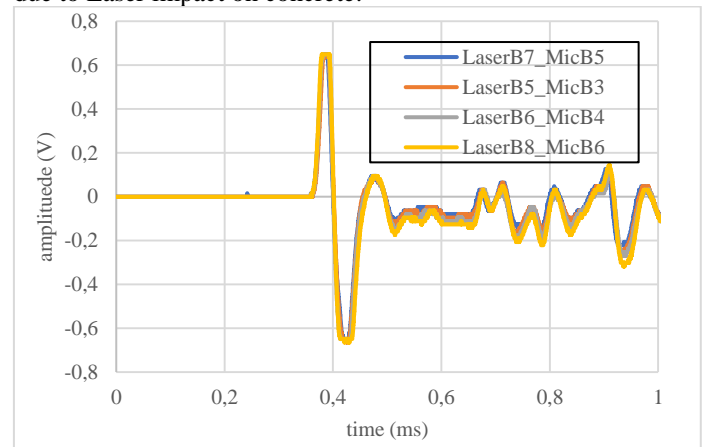


Figure 3 Repeatability of measurements



During the experiments, the Laser is aimed at a horizontal distance of 100 mm from the microphone on the concrete. The microphone is placed at a vertical distance of 70 mm from the concrete surface. For this configuration, the value of  $d_a$  was 122.06 mm. The value of  $v$  was assumed to be 343 m/s at a temperature of 25°C. Thus, the  $ToA$  was 0.35 ms as per Equation 1. As the Laser impacts the concrete surface, a stress wave is generated in the concrete due to its ablation. Upon impact, a stress wave travels in the air as well as in the concrete. The travelling stress waves in concrete have a higher velocity. The stress wave in concrete travels through the specimen and reflects from the concrete-air interface at the bottom of the specimen. The difference in acoustic impedance between concrete and air results in the generation of this reflected wave. The reflected wave now reaches the level where the laser had initially impacted. Subsequently, the reflected wave leaks into the air and reaches the microphone. The expected arrival time of this reflection is around 0.7 ms. The presence of any defects in concrete would result in a mismatch of acoustic impedances between the concrete and the defect. This acoustic impedance difference would result in the generation of a subsequent reflected wave. As the source of the reflected waves would lie before the bottom of the specimen, the reflection from embedded defects would occur before the arrival of the reflection peak. Thus, the first arrival and the arrival of the reflected peak would be considered as two markers in the measured signals. Further investigations will be undertaken to explore reflection signatures from defects in the subsequent sections.

The characteristic of this peak corresponding to the first arrival remains unchanged over the measurement undertaken on line B. Between 0.4 and 0.7 ms, several other reflections are observed. This corresponds to the arrival of the reflected waves in the specimen. Similarities in the character of the signal were observed across several measurements along line B, as presented in Figure 3. As the signals remain relatively unchanged across several locations on the specimen, the repeatability in measurements using the laser-microphone system is ascertained. Now, the variations in measurements over locations of embedded debonds will be explored to understand the capabilities of this technique for the detection of embedded damages.

Subsequently, measurements were undertaken on specimen D1 in a similar configuration. The laser-microphone measurements were taken over Lines A and C over the two rebars embedded in the specimen. Over these measurement lines, two different types of debonding were simulated. During casting, heavy debonding was simulated along line A by embedding a concentric low-density polyethylene foam of about 10 mm thickness over the rebar. Along line B, four layers of regular insulation tape were used to create the slight debonding case. The observed variation in measurements corresponding to the locations of defects is presented in Figures 4 and 5.

As observed in Figures 4 and 5, the measurements taken along lines A and C in principle have similar characteristics between 0.3 and 0.4 ms as those observed earlier over line B. This initial peak, corresponding to the arrival of Rayleigh waves, can be observed at 0.4 ms. They correspond to the measurements acquired over the simulated heavy debond and slight debond

regions are presented. In the measurements along line A, the signal amplitude varies between 0.5 and 0.7 ms in regions with the presence of an embedded heavy defect. Figure 4 shows the variation in the amplitudes in measurement LaserA6\_MicA8 in the heavy debond region over the measurement LaserA2\_MicA4. This variation is caused by the acoustic impedance introduced by the heavy *debond*.

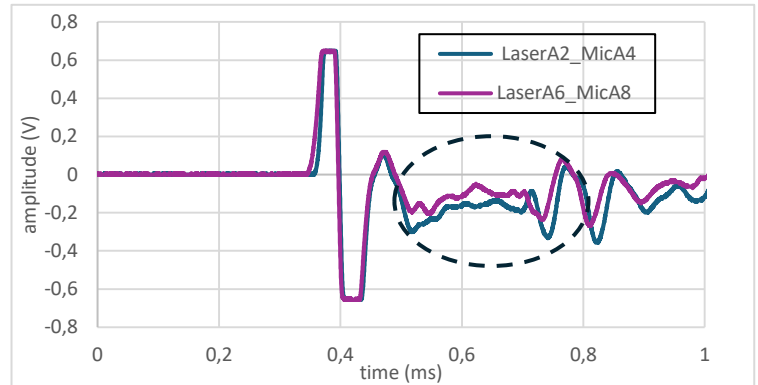


Figure 4 Measurements over simulated heavy debonding

On line C, a significantly different variation in the phase of the signal between 0.6 and 0.7 ms was observed. In the mentioned time interval, the measurement LaserC8\_MicC6, which is directly over the slight debond region, has a significantly different signature as compared to the pristine region in measurement LaserC3\_MicC1, as observed in Figure 5. This variation was on account of the change in acoustic impedance caused by the simulated slight debond that was embedded in the specimen. The variations in amplitude and phase as reflected in the signal characteristics due to the embedded effects were thus observed.

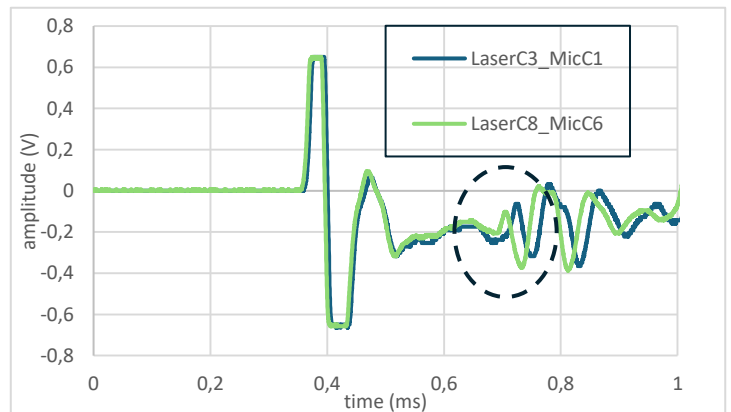


Figure 5 Measurements over simulated slight debonding

Thus, considerable changes in the waveform were observed in the specimen corresponding to the presence of embedded damages in the specimen. These changes in the waveform need to be identified and subsequently used to understand and classify the nature of damage in the specimens.

### 3.2 Specimen H1

The methodology discussed for specimen D1 will now be tried for specimen H1. Measurements are undertaken on lines A and C on this specimen as presented in Figure 6. In Figures 7 and

8, measurements taken along the lines B and C on the specimen are presented.

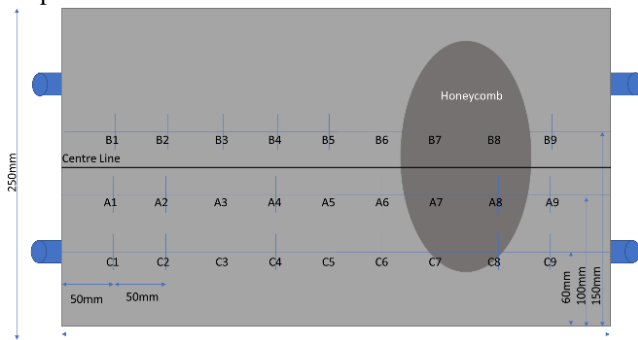


Figure 6 Specimen H1 with simulated honeycombing

The arrival time of the first peak across all measurements in this specimen is consistent with those observed in specimen D1. However, there is a considerable variation in the phase and magnitude of the signal after the first arrival between 0.4 and 0.8 ms. Along the line B, in the measurement LaserB6\_MicB8, there is a sharp rise in the amplitude and considerable variation in the phase of the signal compared to measurements at LaserB1\_MicB3. The increased difference in acoustic impedance due to air voids in the honeycomb around the LaserB6\_MicB8 points resulted in this variation in the signal. The variations in the signal between 0.4 and 0.7ms warrant further investigation to uncover details about hidden defects in the specimen (Figure 7).

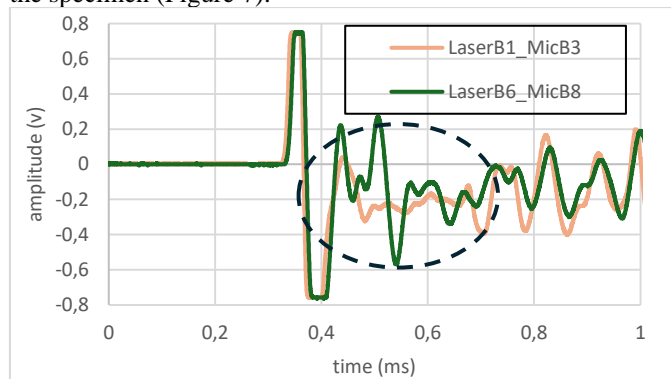


Figure 7 Signals in specimen H1 over the line B

In measurements along line C, the extent of variation in the signals is slightly lower compared to the ones over line B. In Figure 8, a variation in measurement over honeycomb, LaserC8\_MicC6, between 0.4 and 0.7ms over measurement LaserC3\_MicC1 can be observed. This trend is expected, and a plausible explanation surrounding this trend is the presence of line C further away from the core of the honeycomb. However, this variation is to be classified, and its extent is associated with the veracity of the damage in the specimen.

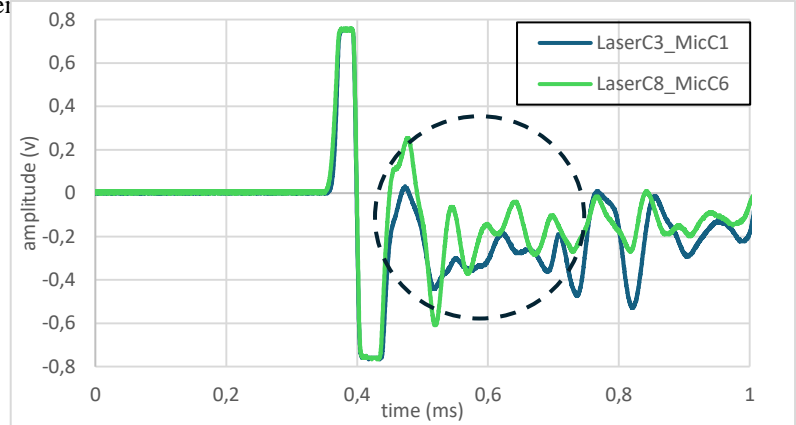


Figure 8 Signals in specimen H1 over the line C

### 3.3 Classification of defects

To further understand and classify the variations in the acquired signals due to embedded damages. The acquired signals are compared with the measurements at the pristine region. A Condition Index ( $CI$ ) is proposed to compare the signals acquired at various locations in the specimens. Though there are several approaches to compare two vectors, the proposed approaches are used for its simplicity and ease of computation. To undertake this comparison, the signals in the comparison are considered vectors. The vectors are unitised by dividing them by their magnitude. The process of unitising a vector is presented in Equation 2 by considering the example of a pristine signal. Here  $V_p$  is the signal and  $V_{pu}$  is its corresponding unitised vector.

$$V_{pu} = \frac{V_p}{\|V_p\|} \quad (2)$$

Subsequently, unitised vectors of measurements from other damage locations are also developed. Using scalar products, the similarities of the developed vectors are evaluated. The scalar product of these vectors is presented in Equation 3. The scalar product is captured in a parameter  $CI$ .

$$CI = V_{pu} \cdot V_{du} \quad (3)$$

Here  $V_{du}$  represents the unitised vector from an A-Scan acquired over a defect. This is compared with the  $V_{pu}$  calculated over the pristine region.

The outcome of Equation 3 is  $\cos \theta$ , where  $\theta$  represents the angle of the two unitised vectors. If  $CI = 1$ , the corresponding  $\theta$  between the vectors is 0, which implies the vectors are identical to each other. As the value of  $\theta$  increases, the value of  $CI$  decreases. Thus, the value of  $CI$  indicates the difference between the signal at a location with the pristine signals. Now,  $CI$  at several locations will be compared with the pristine signal to understand its association with the location of damage in the specimens.

To undertake the comparison, an average of three measurements recorded at LaserB5\_MicB3 on specimen D1 over line B was utilised and as  $V_{pu}$  as per Equation 2. Subsequently, three other pristine locations on this specimen were considered as  $V_{du}$  and their  $CI$ s calculated as per Equation 3. In Table 3, a comparison of  $CI$  values at various locations in the pristine region is presented. These values are very close to each other, indicating that the time signals are like each other.

Table 3 CI over the line C for pristine condition

Location	CI
Pristine1	0.993458
Pristine2	0.986087
Pristine3	0.990595

As the reliability of measurements was observed earlier over the pristine location, an average of the three measurements recorded at the pristine region will now be used as a reference pristine signal. The variation in *CI* at the damage will now be explored to understand the sensitivity of the proposed approach in detecting damage. This will be compared against the measurements taken over the defect regions. As seen in Table 4, a low *CI* value was observed at the debond region. This variation occurred because of the variation in the acquired signal due to the acoustic impedance difference between the surrounding concrete and the simulated debond in specimen D1. This variation in acoustic impedance causes the incident wave to reflect, thus the variation in the wave signature. The magnitude of *CI* further reduces over the honeycomb region in specimen H1. The air present in the simulated honeycomb results in further variation in acoustic impedance and thus a further decrease in *CI* value.

Table 4 Variation in signal similarities at various locations

Location	CI
Heavy debond	-0.08175
Slight debond	-0.08782
Honeycomb1	0.050011
Honeycomb2	0.001647

The veracity of the proposed methodology in detecting hidden damages in concrete is thus established. Further investigations are now underway to explore the capabilities of the proposed method to evaluate the veracity of this method in deciphering defects at various depths from the surface. This will be extended to detecting progressive deterioration. Monitoring long-term durability due to the actions of corrosion and freezing-thawing will be explored.

#### 4 FREQUENCY RESPONSE

To understand the variation in A-Scans due to defects, the acquired time signals will now be explored to understand the frequency content in them. The frequency content in the signal was developed through the Fast Fourier Transform algorithm implemented using the ‘fft’ function in MATLAB software [19]. The frequency content of signals is presented in Figure 9. A high-pass filter with a cut-off set at 2 kHz was used on the frequency response to remove any ambient vibrations in the signal. The frequency response of the pristine sample was compared with that of the defect cases discussed earlier. It can

be observed that the signal has considerable signal strength between 6 and 15 kHz across all measured signals. The magnitude of the frequency spectra across all the damage cases is higher than the pristine case. Moreover, there is an increase in the magnitudes of lower frequency components, particularly between 6 and 12 kHz and a damping down of frequencies higher than that range. This indicates a change in the vibration characteristic of the specimen. To explore the trends in the frequency responses, regions of interest will be identified, and the frequency content in the regions will be explored. Further information can be inferred from the inclusion of information about the phase spectra of the acquired signal.

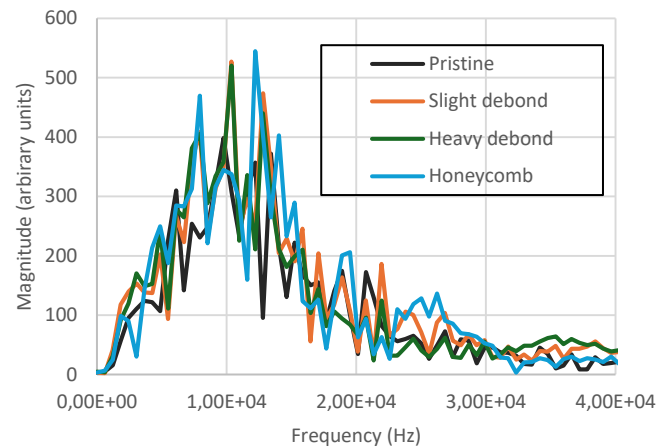


Figure 9 Frequency responses of A-Scan signals

#### 5 CONCLUSIONS

In this paper, we present a novel pulsed-laser microphone system to monitor deterioration in concrete. In this method, high-energy pulses are used to generate acoustic waves and microphones are used for reception. The efficacy of this non-contact, non-destructive method for monitoring hidden deterioration in concrete is explored in this study. The following are the key conclusions:

- In this study, the generation of acoustic elastic waves in concrete using a Pulsed Laser and their reception using an acoustic microphone was established.
- The variation in acoustic wave pressure due to laser impact was received by the microphone and digitised into an electrical signal.
- The signals were acquired on two specimens with embedded defects like simulated debonding and honeycombing.
- The variation of signals in the pristine region and the defects was identified.
- A Condition Index (*CI*) was developed to qualify the variation of signals due to the presence of defects.
- The efficacy of using a pulsed laser–acoustic microphone system in detecting embedded defects was established.



## ACKNOWLEDGMENTS

The authors would like to acknowledge the support from SmartCrete CRC on project number 21.PP.0112 titled 'Digital twin of reinforced concrete infrastructure for intelligent asset management'. The support from Curtin University technical staff in fabricating the moulds for the concrete specimens used in this work is kindly acknowledged.

## REFERENCES

- [1] C. Caprani. (2018, August 22, 2018) Are Australian bridges safe, and can we do better? *The Conversation*. Available: <https://theconversation.com/are-australian-bridges-safe-and-can-we-do-better-101825>
- [2] Australian Local Government Association. (2024). *2024 National State of the Assets Report*. [Online] Available: <https://alga.com.au/app/uploads/ALGA-2024-National-State-of-the-Assets-Technical-Report.pdf>
- [3] S. Villalba and J. R. Casas, "Application of optical fiber distributed sensing to health monitoring of concrete structures," *Mechanical Systems and Signal Processing*, vol. 39, no. 1-2, pp. 441-451, 2013.
- [4] H. Qiao, Z. Lin, X. Sun, W. Li, Y. Zhao, and C. Guo, "Fiber optic-based durability monitoring in smart concrete: A state-of-art review," *Sensors*, vol. 23, no. 18, p. 7810, 2023.
- [5] P. Pursula, I. Marttila, K. Nummila, and H. Seppä, "High frequency and ultrahigh frequency radio frequency identification passive sensor transponders for humidity and temperature measurement within building structures," *IEEE Transactions on Instrumentation and Measurement*, vol. 62, no. 9, pp. 2559-2566, 2013.
- [6] X. Wang, J. Chakraborty, A. Bassil, and E. Niederleithinger, "Detection of Multiple Cracks in Four-Point Bending Tests Using the Coda Wave Interferometry Method," *Sensors*, vol. 20, no. 7, p. 1986, 2020.
- [7] J. F. Scherr and C. U. Grosse, "Delamination detection on a concrete bridge deck using impact echo scanning," *Structural Concrete*, vol. 22, no. 2, pp. 806-812, 2021.
- [8] C. Koch, K. Georgieva, V. Kasireddy, B. Akinci, and P. Fieguth, "A review on computer vision based defect detection and condition assessment of concrete and asphalt civil infrastructure," *Advanced engineering informatics*, vol. 29, no. 2, pp. 196-210, 2015.
- [9] S. Majhi, A. Mukherjee, N. V. George, and B. Uy, "Corrosion detection in steel bar: A time-frequency approach," *NDT & E International*, vol. 107, p. 102150, 2019.
- [10] S. Majhi, L. K. Asilo, A. Mukherjee, N. V. George, and B. Uy, "Multimodal monitoring of corrosion in reinforced concrete for effective lifecycle management of built facilities," *Sustainability*, vol. 14, no. 15, p. 9696, 2022.
- [11] K. Hoegh, L. Khazanovich, and H. T. Yu, "Ultrasonic tomography for evaluation of concrete pavements," *Transportation Research Record*, vol. 2232, no. 1, pp. 85-94, 2011.
- [12] S. Majhi, A. Mukherjee, and A. Ganguli, "Enhanced ultrasonic imaging in concrete structures with spatial apodization filters," *Journal of Materials in Civil Engineering*, vol. 33, no. 10, p. 04021266, 2021.
- [13] Y. Wang, A. Mukherjee, and A. Castel, "Non-destructive monitoring of incipient corrosion in reinforced concrete with top-bar defect using a combination of electrochemical and ultrasonic techniques," *Construction and Building Materials*, vol. 360, p. 129346, 2022.
- [14] H. Azari, S. Nazarian, and D. Yuan, "Assessing sensitivity of impact echo and ultrasonic surface waves methods for nondestructive evaluation of concrete structures," *Construction and Building Materials*, vol. 71, pp. 384-391, 2014.
- [15] R. Groschup and C. U. Grosse, "MEMS microphone array sensor for air-coupled impact-echo," *Sensors*, vol. 15, no. 7, pp. 14932-14945, 2015.
- [16] S. Majhi, A. Mukherjee, N. V. George, V. Karaganov, and B. Uy, "Corrosion monitoring in steel bars using Laser ultrasonic guided waves and advanced signal processing," *Mechanical Systems and Signal Processing*, vol. 149, p. 107176, 2021.
- [17] J. F. Scherr, J. Kollofrath, J. S. Popovics, B. Bühling, and C. U. Grosse, "Detection of Delaminations in Concrete Plates Using a Laser Ablation Impact Echo Technique," *Journal of Nondestructive Evaluation*, vol. 42, no. 1, p. 11, 2023.
- [18] V. Vierhub-Lorenz, C. S. Werner, K. Weiher, C. Heinze, and A. Reiterer, "Laser-based measurement system for the detection of delamination in tunnel linings," in *Optical Measurement Systems for Industrial Inspection XIII*, 2023, vol. 12618: SPIE, pp. 526-531.
- [19] The MathWorks, Inc., MATLAB version: 9.7.0.1190202 (R2019b).



# Smart Sensing and Artificial Intelligence for Advanced Civil Infrastructure Monitoring and Management

# AI-Powered vehicle classification for scalable infrastructure monitoring

Leonardo Iacussi<sup>1</sup>, 0009-0007-5321-3826, Nicola Giulietti<sup>2</sup>, 0000-0001-9922-3201, Alessandro Lucci<sup>1</sup>  
Giuseppe Lucenti<sup>1</sup>, Emanuele Zappa<sup>1</sup>, 0000-0003-3320-9030, Paolo Chiariotti<sup>1</sup>, 0000-0001-6287-5521, Alfredo Cigada<sup>1</sup>, 0000-0001-6861-8374

<sup>1</sup>Politecnico di Milano, Department of Mechanical Engineering, Via Privata Giuseppe la Masa, 20156 Milano, Italy

<sup>2</sup>University of Pavia, Dipartimento di Ingegneria Industriale e dell'Informazione, 27100 Pavia, Italy

email: leonardo.iacussi@polimi.it, nicola.giulietti@unipv.it, alessandro.lucci@mail.polimi.it, giuseppe.lucenti@mail.polimi.it, emanuele.zappa@polimi.it, paolo.chiariotti@polimi.it, alfredo.cigada@polimi.it

**ABSTRACT:** Real-time monitoring of road infrastructure is crucial in addressing the challenges posed by the increasing volume of vehicles and the need for timely maintenance to manage structural aging. Traditional Weight-in-Motion (WIM) systems provide accurate measurements of vehicle load, axle configurations, and speed but are costly to install and require road closures, hindering widespread deployment. This study introduces an innovative method for estimating traffic load by repurposing acceleration-based Structural Health Monitoring (SHM) systems integrated with an AI powered vision system which enables to classify vehicles, estimate their weight, speed and finally assess traffic load over time with a scalable and cheaper solution. Vehicles have been classified into three macro classes: cars, lightweight trucks and heavy trucks. A comparative analysis has been performed between load estimation using only the AI-powered vision system, based on YOLO object detection, and an enhanced approach that integrates acceleration data. The combined method demonstrated significantly improved accuracy in weight estimation. The methodology was tested on an highway viaduct and the results validated by using a reference WIM system. The findings underscore the potential of this integrated approach to provide cost-effective and scalable solutions for traffic load estimation and structural health assessment.

**KEY WORDS:** SHM; Weight in motion; Road traffic monitoring; Sensor fusion

## 1 INTRODUCTION

In recent decades, highway infrastructure has been subjected to escalating stress due to the combined impacts of increasing traffic volumes and the aging of structural components. Transportation networks, which serve as vital conduits for economic activity and goods distribution, are facing growing demands. A major driver of this strain is the rapid expansion of road-based freight transport, fueled by the rising demand for efficient and adaptable logistics. In Europe, for instance, road freight accounted for more than 75% of all inland freight transport in 2023, with heavy-duty vehicles (HDVs) playing a central role in long-haul logistics and supply chains [1]. Bridges and viaducts are particularly susceptible to the combined effects of increased loading and structural aging. These assets often endure long service durations, facing environmental wear, and intensified mechanical stresses. Among the various contributors to their deterioration (e.g. material fatigue, environmental factors, seismic forces and inadequate maintenance) overloading by HDVs stands out as one of the most widespread and damaging. Numerous studies have identified overloading as a critical factor in both the progressive degradation and sudden failure of bridge structures across different contexts and typologies [2, 3].

Given this context, the need for effective and continuous traffic monitoring systems has become increasingly urgent. In particular, identifying and quantifying the load contribution from heavy vehicles is critical for estimating cumulative damage, supporting load rating decisions, and optimizing maintenance schedules. Traditional static weighing stations, while accurate, are inefficient for large-scale deployment due to their reliance on vehicle stops, high operational costs. Consequently, Weigh-In-Motion (WIM) systems have

emerged as a valuable alternative, capable of measuring axle loads, gross vehicle weight (GVW), and vehicle classification in real time without interrupting traffic flow [4]

WIM systems are generally classified into two main categories: Pavement-based WIM (P-WIM) and Bridge-based WIM (B-WIM). P-WIM systems involve the installation of strain or piezoelectric sensors within the roadway surface to directly record the forces exerted by passing axles. While effective in certain applications, these systems require a high installation cost and frequent maintenance and recalibration due to their direct exposure to traffic and weather. In contrast, B-WIM systems leverage the dynamic or static responses of bridge structures to estimate vehicle weights typically using strain, displacement, or acceleration sensors. This approach is advantageous as it utilizes existing infrastructure, minimizes road surface interventions, and offers spatial scalability over the entire highway network [5].

The concept of B-WIM was first introduced by Moses in 1979, where an inverse problem formulation was used to estimate axle weights based on strain measurements recorded during vehicle crossings [6]. This methodology laid the foundation for modern B-WIM systems and has since been refined through the integration of improved sensing hardware, robust signal processing algorithms, and advanced calibration procedures [7]. Strain-based B-WIM systems are currently the most widely adopted, offering high accuracy for vehicle weight estimation under controlled conditions. However, they still face limitations related to temperature sensitivity, sensor drift, and



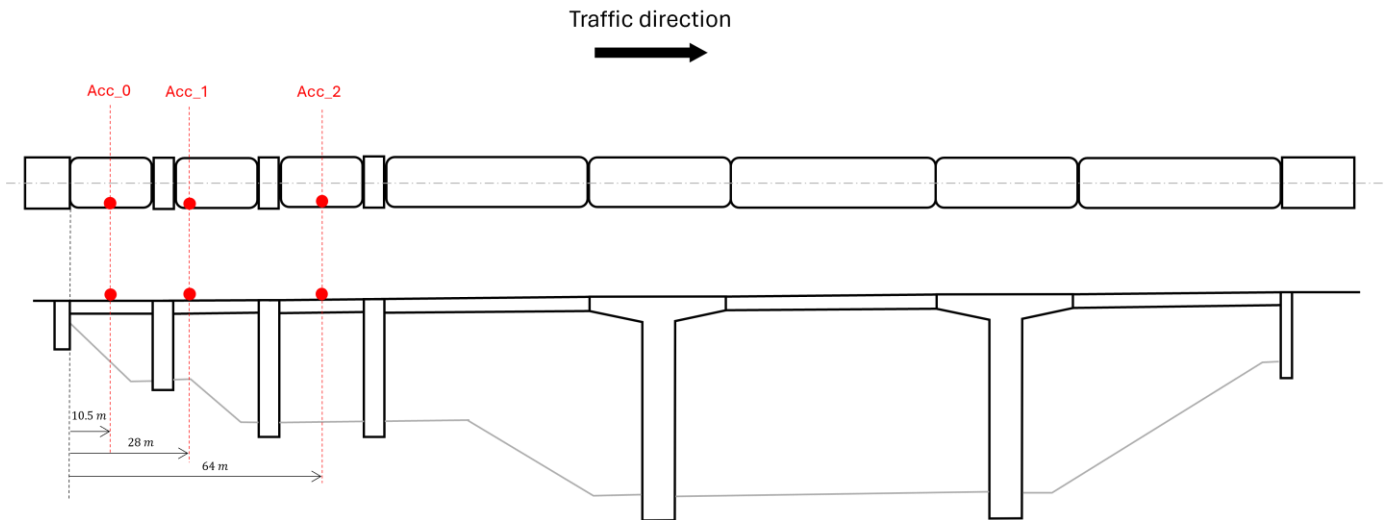


Figure 1: Viaduct schema and accelerometer position.

the need for detailed knowledge of bridge geometry and boundary conditions.

More recently, research has explored the use of acceleration-based B-WIM systems as a low-cost and scalable alternative. These systems utilize MEMS (Micro Electro-Mechanical System) accelerometers to measure bridge vibrations induced by vehicle crossings. Their non-intrusive nature and ease of deployment make them attractive for widespread monitoring applications. Nevertheless, acceleration-based systems introduce new challenges, particularly related to signal variability caused by vehicle dynamics, road roughness and environmental noise [8]. Despite these challenges, several promising studies have demonstrated the feasibility of such approaches. For instance, Sekiya et al. [9] deployed MEMS accelerometers on a steel bridge and demonstrated the potential to estimate GVW and axle positions from a single vehicle crossing. A follow-up study [10] extended this investigation to a year-long deployment, highlighting the need for temperature compensation and advanced data filtering techniques to ensure accuracy.

Further developments in the field have explored hybrid and data-driven methods. O'Brien et al. [11] used statistical analysis of acceleration signals to jointly estimate vehicle weight and assess bridge integrity. While effective for GVW estimation, the method struggled to resolve axle weights and spacings. Wang et al. [12] addressed some of these limitations by integrating vision-based systems with acceleration data to enhance vehicle detection and classification capabilities. The incorporation of transfer learning also demonstrated improved generalization across different bridge types.

These advancements underscore the growing interest in low-cost, scalable, and intelligent structural health monitoring systems. The evolution of WIM technologies, particularly B-WIM systems enhanced by MEMS sensors and machine learning algorithms, opens new possibilities for real-time infrastructure assessment. However, significant challenges remain in terms of robustness, environmental adaptability, and the reliable estimation of axle-level loads. As urban infrastructure continues to age and traffic volumes increase, the development of resilient and accurate WIM systems becomes

not only desirable but essential for the future of bridge

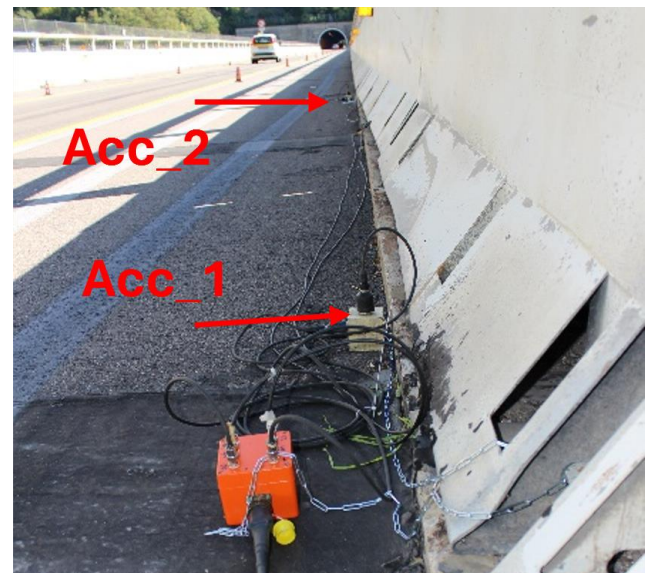


Figure 2: Piezoelectric accelerometers (Acc\_1 and Acc\_2) positioned on the viaduct spans.

maintenance and safety.

This study aims to demonstrate the feasibility of estimating highway traffic loads by utilizing existing structural monitoring systems installed on viaducts, offering a cost-effective alternative to conventional, high-cost systems such as P-WIM technologies. The proposed methodology integrates vision-based systems for vehicle detection and classification with acceleration data acquired using accelerometers positioned on the bridge spans of the viaduct. The effectiveness of this approach is illustrated through a case study involving an operational highway viaduct located in Italy (schematized in Figure 1) where a reference P-WIM system is present as a reference for the vehicle weight.

In this work, sensitive data regarding highway traffic and viaduct accelerations were used; therefore, the actual acceleration values will be masked in the figures, and no

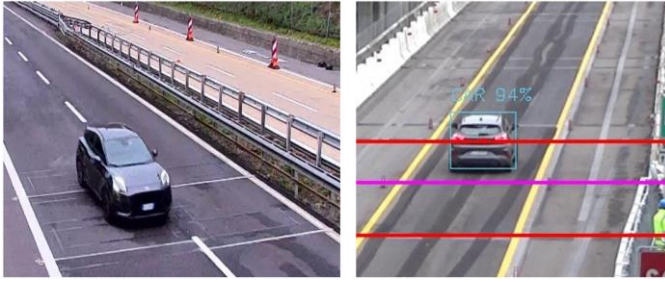


Figure 3: Vehicle detection when it crosses the P-WIM system (left) and while it crosses the first viaduct span (right).

absolute values will appear in the text. This does not affect the validity of the results.

## 2 MATERIALS AND METHODS

The viaduct features a simply supported beam configuration and consists of six spans. This study focuses on the first three spans, each measuring 21 meters, as they correspond to the direction of traffic flow. The primary structural components are made of conventional reinforced concrete, while the decks and pier caps are constructed using pre-stressed reinforced concrete to enhance load-bearing capacity and durability. Overhangs are located at piers 5 and 6, supporting the adjacent suspended spans through Gerber saddles, which facilitate simple support articulation and allow for structural continuity. The entire structure is founded on direct foundation systems.

The monitoring setup implemented on the viaduct includes three PCB 393A03 piezoelectric IEPE accelerometers positioned on the first three spans of the viaduct (see Figure 1 and Figure 2). The use of multiple accelerometers enables vehicle speed estimation by correlating the time delays between the signals captured by the sensors. Furthermore, it allows for a comparative analysis of acceleration responses at mid-span locations (Acc\_0 and Acc\_2), where the dynamic amplification of structural response is more significant and near the joint (Acc\_1), where vehicle impacts contribution on the acceleration data. Data acquisition was performed synchronously using a National Instruments CompactDAQ system (model cDAQ-9172 equipped with NI 9230 boards) with a sampling frequency of 1000 Samples/s.

For vehicle detection and classification, a vision system comprising a Sony Handycam HDR-CX405 camera was installed above the tunnel exit, providing a clear field of view of the traffic flow immediately following the tunnel (as shown in Figure 3). To establish a ground-truth reference, a P-WIM system located upstream of the viaduct was used. Given the absence of highway exits along between the P-WIM system and the viaduct, it was ensured that all vehicles recorded by the P-WIM system subsequently traversed the viaduct under investigation. To account for potential overtaking between the two locations, an auxiliary camera installed at the P-WIM site was used to reorder vehicles and ensure accurate matching with the viaduct observations.

The reference data provided by the P-WIM system included detailed vehicle information, such as speed, length, lane position, axle count and spacing, individual axle loads, gross vehicle weight (GVW), and vehicle classification based on the ASTM E1318-09 standard [13]. The vehicle flow was sparse

enough to ensure that only one vehicle crossed at a time, simplifying the analysis and reducing the complexity associated with multi-vehicle events. The dataset analyzed comprises a total of 96 vehicles that traversed the viaduct during the time period in which all monitoring systems were simultaneously acquiring data. Approximately 90% of the recorded vehicles were two-axle vehicles, with an average GVW of around 2 tonnes. This category includes not only passenger cars, but also vans, light trucks, and motorcycles. The remaining 10% consisted of heavier vehicles with three, four, or five axles, corresponding primarily to trucks, with an average GVW of approximately 20 tonnes. Regarding vehicle speed estimation, it was derived by correlating the data from the accelerometers with the output from the vision system. The velocity measurements provided by the P-WIM system could not be considered a reliable reference, as the system is located upstream of the viaduct and vehicle speeds may vary along the intervening highway segments.

### 2.1 Vision-based vehicle detection and speed estimation

Vehicle detection and classification within the region of interest were performed using a Python-based application that integrates OpenCV with a pre-trained object detection algorithm. Each video frame was processed to identify and localize vehicles using the YOLOv3 (You Only Look Once [14]) model, trained on the COCO dataset [15], which enables vehicle classification in only four classes: car, motorbike, bus, and truck. To achieve more stable classification and refine detections, post-processing was performed by applying a confidence threshold and non-maximum suppression. A tracking algorithm was then employed to assign persistent IDs to detected vehicles across consecutive frames by comparing the centroids of bounding boxes. This enabled consistent object identification throughout the video. Vehicle counting was carried out by monitoring object trajectories across a user-defined detection zone delimited by three virtual lines. When an object centroid crossed the designated thresholds, it was counted and classified accordingly (see Figure 3 (right)).

Given the relevance of vehicle speed as a parameter, a method for its estimation was also implemented. During video processing, the frame numbers at which each vehicle entered and exited the detection area is recorded. By combining this information with the known frame rate and the estimated physical distance ( $\Delta s$ ) between the entry and exit lines, the vehicle speed ( $v_{ID}$ ) was approximated using the following relation:

$$v_{ID} = \frac{\Delta s \times fps}{frame_1 - frame_0} \quad (1)$$

where  $frame_0$  and  $frame_1$  denote the frame indices corresponding to the vehicle entry and exit points, respectively, and  $fps$  (frame per second) corresponds to 50 for the camera used. The accuracy of this estimate depends on factors such as camera placement, resolution, and perspective distortion. Several limitations in the detection and classification process were addressed. First, the object class assigned by YOLOv3 may vary across frames, leading to misclassification. To

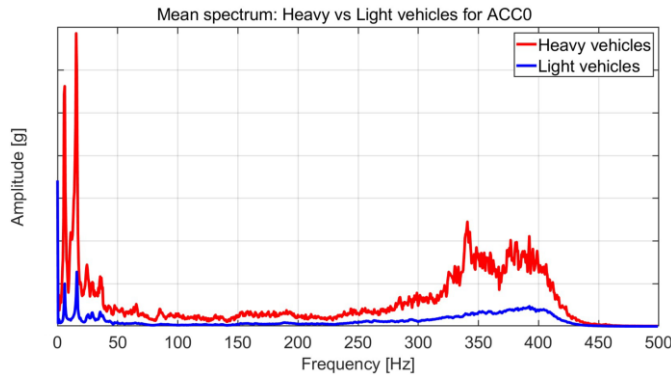


Figure 5: Average spectrum for heavy vehicles and light vehicles during their passage over the accelerometer Acc\_0.

mitigate this, all class labels assigned to an object during its passage were stored, and the most frequently assigned class (mode) was used as the final classification. Second, incomplete or intermittent detections, often due to low confidence scores, could cause the same vehicle to be assigned to different IDs, affecting both vehicle counting and speed estimation. To address this, the ID matching process was extended to compare across both temporary detection lists, improving continuity in object tracking. However, if a vehicle was detected only in the latter part of the detection zone, the estimated speed would be significantly overestimated. To prevent this, the system recorded the initial detection point for each object and suppressed speed calculations for vehicles detected too late in the zone, where time-distance correlation becomes unreliable.

## 2.2 Acceleration-based vehicle detection and speed estimation

This section focuses on vibration analysis using accelerometer data, aiming to correlate sensor-derived information with data obtained from video recordings. Specifically, the analysis addresses two objectives: (i) the identification of light and heavy vehicles using time-domain features extracted from acceleration signals, and (ii) the estimation of vehicle speed through the synchronization of signals from three accelerometers, followed by comparison with speed estimates derived from the vision-based system.

By analyzing the time histories from raw accelerometer data (see Figure 4), vehicle pass-by events were initially identified by observing distinct signal peaks. A representative segment of the vibration data, collected during one of the experimental campaigns, illustrates this concept. To improve detection clarity, a moving Root Mean Square (RMS) function was applied to the signal. The RMS provides a measure of signal energy over a defined time window and is particularly useful for distinguishing between light and heavy vehicles, as heavier vehicles are expected to induce greater energy in the structure. However, fixed thresholds for vehicle classification cannot be determined a priori, as they depend on the specific structure and sensor placement.

Frequency domain analysis (see Figure 5) reveals that the primary distinction between light and heavy vehicles lies in the low-frequency range, specifically below 50 Hz. Based on this observation, the signal energy within this band, quantified using the RMS of the band-pass filtered signal (5–50 Hz), was selected as the key feature for vehicle classification.

Vehicle speed can be estimated also correlating signals from different accelerometers, based on their spatial position and the time taken by a vehicle to traverse the corresponding distance. Several methods can be used to estimate the time lag between two signals; in this case, the cross-correlation method was used, which computes the time lag between two signals considering the well-known correlation function:

$$\text{Corr}(\tau) = \int_0^T a_{en}(t) a_{ex}(t + \tau) dt \quad (2)$$

where  $a_{en}(t)$  and  $a_{ex}(t)$  represent the signals from entry and exit sensors, respectively, and  $\tau$  denotes the time shift. The correlation was applied either directly to the moving RMS of the signal or to the envelope of the signal. These two acceleration-based methods will be compared to the vision-based estimates in the results section to evaluate their performance.

## 3 RESULTS

This section presents the results of the study, beginning with the comparison of speed estimations comparison between the two systems and subsequently discussing the outcomes of vehicle classification between light and heavy vehicles.

Although vehicle speed estimation is not the primary focus of this study, it remains a valuable parameter, as the velocity at which a load travels over a viaduct can significantly influence the dynamic response of the structure. Moreover, since speed is also estimated by P-WIM systems, utilizing existing infrastructure such as cameras or accelerometers for speed estimation can enhance the spatial coverage of traffic monitoring. This approach has the potential to provide a more comprehensive mapping of vehicle speeds across the highway network, contributing to a more accurate assessment of moving loads on the structure.

The comparison between the acceleration-based and vision-based vehicle speed estimation methods is summarized in Table 1.

Table 1. Vehicle speed estimation comparison between acceleration-based and vision-based methods.

Method	$\Delta < 20 \frac{\text{km}}{\text{h}}$	$\Delta \geq 20 \frac{\text{km}}{\text{h}}$
<b>Moving RMS</b>	91.7%	8.3%
<b>Envelope</b>	82.5%	17.5%

Both the Moving RMS and the Envelope methods have been used for speed estimation from the acceleration based system. The parameter  $\Delta$  represents the absolute difference in speed estimates between the two systems. Results are categorized based on whether this difference is less than or greater than 20 km/h. The Moving RMS method exhibited a high level of agreement, with 91.7 % of the estimates falling within a  $\Delta < 20$



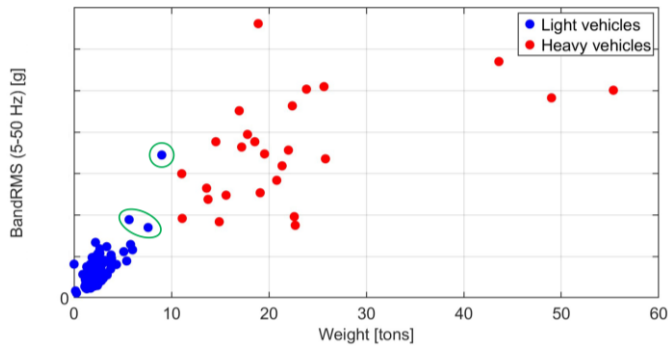


Figure 6: RMS value of the acceleration in the time window when the vehicle passes by the accelerometer Acc\_0.

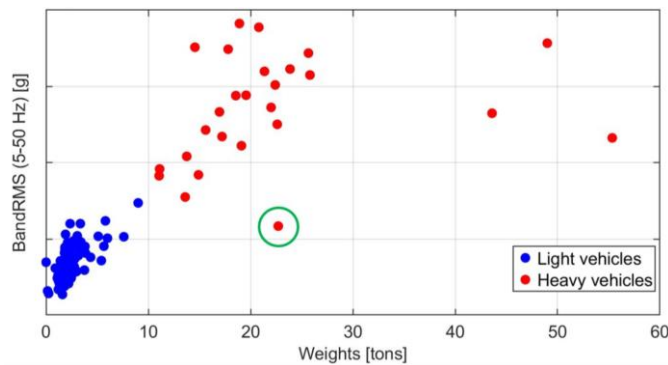


Figure 7: RMS value of the acceleration in the time window when the vehicle passes by the accelerometer Acc\_1.

km/h and only 8.3 % exceeding this threshold. Similarly, the Envelope method showed that 82.5 % of estimates were within the acceptable margin, while 17.5 % exceeded it. These findings suggest that both acceleration-based techniques, particularly the Moving RMS approach, demonstrate promising accuracy and consistency when compared with the vision-based system.

#### 4 CONCLUSION AND FURTHER DEVELOPMENT

This study presents a preliminary investigation into the feasibility of leveraging existing monitoring systems - , specifically, accelerometers installed on viaducts and highway surveillance cameras - to estimate traffic loads acting on highway infrastructure.

Although not the primary objective, traffic load estimation is highly relevant for informing maintenance strategies, forecasting potential structural damage and design new infrastructure.

Currently, P-WIM systems serve this purpose but are often associated with high installation and maintenance costs. As an alternative, the proposed methodology offers a low-cost, albeit less precise, approach by estimating vehicle loading by identifying the number of heavy vehicles (>10 tons) traversing the viaduct. A reference P-WIM system was used as ground truth for weight calibration, enabling a daily estimate of total traffic-induced load, potentially useful in design or assessment contexts where knowledge of acting loads is required.

Results demonstrate that employing an intelligent vision-based system (e.g. using pre-trained deep learning object detection models), can distinguish between light and heavy vehicles. However, intermediate vehicle categories (e.g., vans, minibuses, RVs) are occasionally misclassified. One inherent limitation is the high variability in heavy vehicle weights depending on loading conditions, making it challenging to detect overloading or estimate precise weight using classification alone. In this regard, the inclusion of structural acceleration data improves classification accuracy, as the energy transferred by the vehicle, expressed through the root mean square (RMS) of the acceleration signal, provides an additional informative metric for estimating vehicle mass.

Furthermore, the study compares vehicle speed estimates derived from both systems. By correlating signals from three accelerometers and cross-referencing them with visual detections, the comparison shows that in 90% of cases, the speed difference between the two methods is below 20 km/h, suggesting consistency and potential for dual-system validation.

Despite its promising results, the study faces several limitations that define avenues for future research. Most notably, the dataset includes only 239 vehicles, limiting the use of more sophisticated data-driven algorithms that could enhance load estimation using richer input features beyond RMS. Expanding the dataset would enable the exploration of machine learning models trained directly on raw acceleration signals.

Concerning vision-based algorithms, having a bigger dataset would allow model retraining with more vehicle classes specifically tailored for this application, enabling a more precise weight estimation. Additionally, while the present study analyzes the two systems separately, future work should consider integrating their outputs into a unified model, enabling sensor fusion to enhance overall system robustness and accuracy.

#### ACKNOWLEDGMENTS

The data in this article refer to the project "Argo Innovation Lab – Comparison of the metrological performances of measurement systems to get the cumulative damage by heavy traffic", funded by the private companies Movyon and Elis Innovation Hub. Both companies are respectfully acknowledged.

#### REFERENCES

- [1] Who is driving what, and where? EU road freight trends iru.org. <https://www.iru.org/news-resources/newsroom/who-driving-what-and-where-eu-road-freight-trends>, 2024. [Accessed 07-04-2025].
- [2] Lu Deng, Wei Wang, and Yang Yu. State-of-the-art review on the causes and mechanisms of bridge collapse. *Journal of Performance of Constructed Facilities*, 30(2):04015005, 2016.
- [3] Wanshui Han, Jun Wu, C. S. Cai, and Suren Chen. Characteristics and dynamic impact of overloaded extra heavy trucks on typical highway bridges. *Journal of Bridge Engineering*, 20(2), February 2015.
- [4] Rahim F. Benekohal, Yoassry M. El-Zohairy, and Stanley Wang. Truck travel time around weigh stations: Effects of weigh in motion and automatic vehicle identification systems. *Transportation Research Record: Journal of the Transportation Research Board*, 1716(1):135–143, January 2000.
- [5] Lu Cheng, Hongjian Zhang, and Qing Li. Design of a capacitive flexible weighing sensor for vehicle wim system. *Sensors*, 7(8):1530–1544, August 2007.

- [6] Fred Moses. Weigh-in-motion system using instrumented bridges. *Transportation Engineering Journal of ASCE*, 105(3):233–249, May 1979.
- [7] Myra Lydon, S. E. Taylor, D. Robinson, A. Mufti, and E. J. O. Brien. Recent developments in bridge weigh in motion (b-wim). *Journal of Civil Structural Health Monitoring*, 6(1):69–81, May 2015.
- [8] Enrico Oliveira Rocheti and Rodrigo Moreira Bacurau. Weigh-in-motion systems review: Methods for axle and gross vehicle weight estimation. *IEEE Access*, 12:134822–134836, 2024.
- [9] Hidehiko Sekiya, Kosaku Kubota, and Chitoshi Miki. Simplified portable bridge weigh-in-motion system using accelerometers. *Journal of Bridge Engineering*, 23(1), January 2018.
- [10] Hidehiko Sekiya. Field verification over one year of a portable bridge weigh-in-motion system for steel bridges. *Journal of Bridge Engineering*, 24(7), July 2019.
- [11] Eugene OBrien, Muhammad Arslan Khan, Daniel Patrick McCrum, and Aleš Žnidarič. Using statistical analysis of an acceleration-based bridge weigh-in-motion system for damage detection. *Applied Sciences*, 10(2):663, January 2020.
- [12] Haoqi Wang, Tomonori Nagayama, Takaya Kawakatsu, and Atsuhiko Takasu. A data-driven approach for bridge weigh-in-motion from impact acceleration responses at bridge joints. *Structural Control and Health Monitoring*, 2023:1–14, May 2023.
- [13] Standard specification for highway weigh-in-motion (wim) systems with user requirements and test methods, 2009.
- [14] Ultralytics. YOLOv3 — docs.ultralytics.com. <https://docs.ultralytics.com/it/models/yolov3/>. [Accessed 07-04-2025].
- [15] Tsung-Yi Lin, Michael Maire, Serge Belongie, Lubomir Bourdev, Ross Girshick, James Hays, Pietro Perona, Deva Ramanan, C. Lawrence Zitnick, and Piotr Dollár. Microsoft coco: Common objects in context, 2014.

# Structural condition monitoring through information transferring with dimensional expansion

Jaebeom Lee<sup>1, 2</sup>, Seungjun Lee<sup>3</sup>, Dong-Jin Yoon<sup>4</sup>

<sup>1</sup>Senior Research Scientist, Nondestructive Metrology Group, Korea Research Institute of Standards and Science (KRISS), 267 Gajeong-ro, Yuseong-gu, Daejeon 34113, Republic of Korea

<sup>2</sup>Assistant Professor, Precision Measurement Major, University of Science and Technology (UST), 217 Gajeong-ro, Yuseong-gu, Daejeon 34113, Republic of Korea

<sup>3</sup>Postdoctoral Researcher, Nondestructive Metrology Group, Korea Research Institute of Standards and Science (KRISS), 267 Gajeong-ro, Yuseong-gu, Daejeon 34113, Republic of Korea

<sup>4</sup>Principal Research Scientist, Nondestructive Metrology Group, Korea Research Institute of Standards and Science (KRISS), 267 Gajeong-ro, Yuseong-gu, Daejeon 34113, Republic of Korea

email: [jblee@kriss.re.kr](mailto:jblee@kriss.re.kr) & [jblee@ust.ac.kr](mailto:jblee@ust.ac.kr), [seungjun@kriss.re.kr](mailto:seungjun@kriss.re.kr), [djyoon@kriss.re.kr](mailto:djyoon@kriss.re.kr)

**ABSTRACT:** With the rapid development of sensor technologies and computational methodologies, real-time structural health monitoring (SHM) has gained significant attention in the field of civil engineering. Infrastructures, such as long-span bridges and dams, are often equipped with diverse sensor arrays to enable continuous monitoring of their structural conditions. However, conventional SHM typically require extended data collection periods post-sensor installation, which can delay their practical applications. To address this challenge, this study introduces a novel methodology termed information transferring with dimensional expansion, which leverages transfer learning principles to enhance anomaly detection capabilities in newly instrumented structures. By referencing datasets from similar existing infrastructures, this approach mitigates the dependency on extensive initial data while ensuring reliable anomaly detection. Validation through a case study on a long-span bridge in Republic of Korea demonstrates the method's efficiency and accuracy, highlighting its potential to revolutionize SHM practices by enabling immediate operationalization upon sensor deployment. This research contributes to advancing SHM systems, emphasizing scalability and adaptability for diverse structural applications.

**KEY WORDS:** Structural Health Monitoring; Transfer Learning; Anomaly Detection; Gaussian Process Regression.

## 1 INTRODUCTION

As sensor technology and computational capabilities have advanced, interest in structural condition monitoring has been steadily growing. In particular, there has been a noticeable shift toward real-time monitoring of infrastructures, such as long-span bridges and dams, utilizing a wide array of sensors including accelerometers, strain gauges, inclinometers, anemometers, thermometers, piezometers, and water level gauges. Consequently, the development of techniques capable of identifying structural anomalies based on sensor data has become important.

Previous studies have proposed various methods for detecting structural anomalies. For instance, Lee et al. (2018) dynamically adjusts anomaly detection criteria by considering environmental conditions' seasonal and daily variations [1]. Lee et al. (2019) integrates information from finite element simulations to build anomaly detection models of structures under construction [2]. Lee et al. (2022) explored the evaluation of railway bridge deflections under high-speed train loads to identify behavioral irregularities [3]. However, a common limitation of these methods is their reliance on extensive data collection before deployment, making them less viable for immediate application following sensor installation.

To address this challenge, our study seeks to develop an anomaly detection model for newly constructed structures by leveraging data from similar existing ones. We adopt the concept of transfer learning [4], enabling knowledge transfer

from previously monitored structures to new monitoring applications.

## 2 METHOD

To develop an anomaly detection model for structural condition monitoring, an information transfer approach with a dimensional expansion can be introduced. Traditional methods require extensive data collection before deployment, while the proposed approach aims to leverage data from existing structures with similar characteristics to enhance anomaly detection in newly instrumented structures. The methodology consists of the following steps:

- **Data collection:** This process involves acquiring data using sensors, such as accelerometers. A crucial aspect of this step is securing pre-existing sensor data from structural members and physical quantities similar to those of the newly installed target.
- **Dimensional expansion:** To address the issue of scale differences in data from different sensors, an additional feature via one-hot encoding is introduced, distinguishing data classes while maintaining comparability. For example, when temperature and response data are collected from two different sensors, the input dimension can be expanded, as shown in Figure 1, distinguishing between different sources of data.
- **Transfer learning implementation:** Instead of training separate models for each dataset, a unified *super-model*



that incorporates knowledge from well-established datasets which fine-tuning for new dataset is constructed.

- Probabilistic anomaly detection: A probabilistic anomaly detection model to identify deviations in structural behavior is constructed using Gaussian process regression, which is non-parametric Bayesian regression methods.

AS-IS		TO-BE			
X	Y	X1	X2	X3	Y
Temperature	Response	Temperature	ID 1	ID 2	Response
12.52	30	12.52	1	0	30
13.42	32	13.42	1	0	32
15.21	40	15.21	1	0	40
12.90	31	12.90	1	0	31
12.22	10	12.22	0	1	10
13.71	12	13.71	0	1	12

Figure 1. Dimensional expansion via one-hot encoding

### 3 RESULTS

The approach was validated using real-world bridge monitoring sensors: two accelerometers installed on the cables of an operational cable-stayed bridge. One accelerometer had been measuring data for two weeks in advance, while the other began recording approximately two weeks later, leaving only one day of available data for anomaly detection model construction. The acceleration measurements from the two sensors differed in scale by approximately 2 cm/s<sup>2</sup>. The objective was to detect anomalies in the sensor data over the subsequent 10-day period (Figure 2).

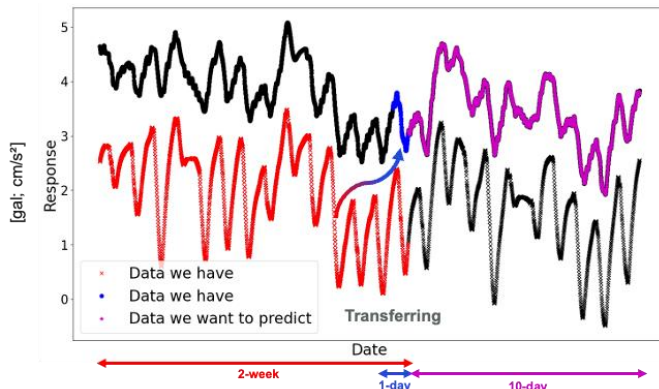


Figure 2. Dataset utilized to validate the approach

First, Figure 3 presents the anomaly detection results obtained using only one day of data without applying transfer learning. Although the 10-day prediction period corresponds to a normal state with no actual anomalies, the model incorrectly identifies multiple data points as anomalies. In contrast, Figure 4, which applies the proposed approach, successfully distinguished the normal state, even though the model was built with limited data from a newly installed sensor. This demonstrates that the proposed approach enables the construction and deployment of an anomaly detection model from the early stages of sensor installation.

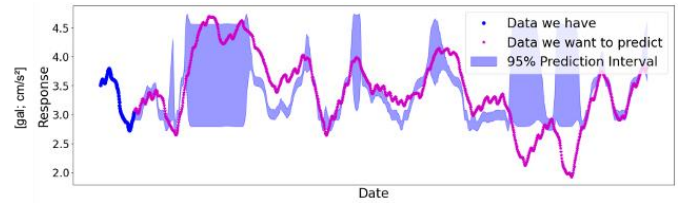


Figure 3. Anomaly detection without transferring information

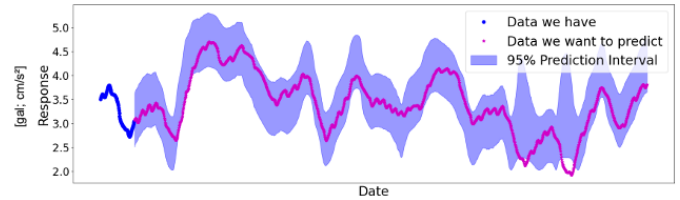


Figure 4. Anomaly detection with transferring information

### 4 CONCLUSION

This study demonstrates the effectiveness of a transfer learning-based approach for structural anomaly detection in newly monitored structures. Traditional anomaly detection methods require a substantial data collection period before deployment, limiting their immediate applicability. To address this challenge, leveraging pre-existing sensor data from similar structural members can be considered to enhance anomaly detection for sensors with limited initial data.

The results show that models built using only one day of data without transfer learning tend to misclassify normal conditions as anomalies. In contrast, the proposed method effectively distinguishes normal states, even when applied to a newly installed sensor. This confirms that transfer learning can improve anomaly detection accuracy from the early stages of sensor deployment.

### ACKNOWLEDGMENTS

This work was supported by the National Research Foundation of Korea (NRF) grant funded by the Korea government (MSIT) (2021R1C1C2008770), and also supported by “Developing digital safety measurement to enhance the availability of smart structural monitoring of facilities” funded by Korea Research Institute of Standards and Science (KRISS-2025-GP2025-0009).

### REFERENCES

- [1] J. Lee, K.-C. Lee, & Y.-J. Lee (2018). Long-term deflection prediction from computer vision-measured data history for high-speed railway bridges. *Sensors*, 18(5), 1488.
- [2] J. Lee, K.-C. Lee, S.-H. Sim, J. Lee, & Y.-J. Lee (2019). Bayesian prediction of pre-stressed concrete bridge deflection using finite element analysis. *Sensors*, 19(22), 4956.
- [3] J. Lee, S. Jeong, J. Lee, S.-H. Sim, K.-C. Lee, & Y.-J. Lee (2022). Sensor data-based probabilistic monitoring of time-history deflections of railway bridges induced by high-speed trains. *Structural Health Monitoring*, 21(6), 2518-2530.
- [4] T. Saida & M. Nishio (2023). TL-GPRSM: A python software for constructing transfer learning Gaussian process regression surrogate model with explainability. *Software Impacts*, 16, 100515.

# Unsupervised Anomaly Detection for Structural Health Monitoring: A Vibration-Based Approach Using Isolation Forest

Mr Emad Soltani<sup>1</sup>, Dr Florimond Gueniat<sup>2</sup>, Dr Mohammad Reza Salami<sup>3</sup>

<sup>1,2</sup> Faculty of Computing, Engineering and the Built Environment, Birmingham City University, 15 Bartholomew Row, Birmingham B5 5JU, UK

<sup>3</sup> Department of Civil Engineering, School of Engineering, University of Birmingham, Edgbaston, Birmingham, B15 2TT, UK  
email: emad.soltani@bcu.ac.uk, florimond.gueniat@bcu.ac.uk, m.r.salami@bham.ac.uk

**ABSTRACT:** Structural health monitoring (SHM) plays a crucial role in ensuring the safety and longevity of critical infrastructure, such as bridges. SHM refers to continuous, sensor-based, and automated monitoring that complements traditional inspection methods by providing real-time data on structural performance. This paper proposes an unsupervised machine learning approach to SHM using vibration data, aiming to address the challenges of data scarcity and the difficulty of collecting labelled damage examples. The methodology combines statistical and spectral feature extraction with an Isolation Forest anomaly detection model, trained solely on healthy data to identify potential damage. The feature extraction process includes key metrics such as root mean square, entropy, and spectral centroid, which capture both time-domain and frequency-domain characteristics of the vibration signals. The Isolation Forest model is trained on these features to distinguish between normal and anomalous patterns, making it well-suited for applications where labelled damage data is unavailable. Results from FE simulation show high accuracy (95.5%), precision (91.75%), and recall (100%), demonstrating the effectiveness of the method in distinguishing damage from healthy states. The proposed approach provides a scalable and data-efficient solution for real-time damage detection in civil infrastructure, with significant potential for deployment in large-scale monitoring systems. Future work will focus on experimental validation and improving the model's robustness in real-world conditions.

**KEY WORDS:** Structural Health Monitoring; Unsupervised Learning; Anomaly Detection; Vibration Data; Isolation Forest; Damage Detection; Bridges; Machine Learning; Feature Extraction; Real-Time Monitoring

## 1 INTRODUCTION

Structural health monitoring (SHM) is an essential aspect of maintaining the safety and integrity of civil infrastructure, particularly for critical structures like bridges. With the ageing of infrastructure, globally and increasing demands on transportation networks, the need for efficient, real-time monitoring systems has never been more pressing. SHM refers to continuous, sensor-based, automated monitoring that complements traditional inspection methods by providing real-time data on structural performance. This allows engineers to prioritise inspections and, in some cases, reduce their frequency, especially for hard-to-access structures such as long-span bridges or offshore platforms.

Machine learning-based approaches represent a more contemporary method for processing SHM data and developing models that enhance damage detection. These methods can improve both the speed and accuracy of detection and complement established techniques like system identification that are commonly used for real-time monitoring. Structural responses, such as acceleration, displacement and strain, provide quantitative measures of how a structure reacts to applied loads. Among machine learning approaches, unsupervised anomaly detection has gained interest for its ability to function without requiring labelled damage data. This is especially useful in civil infrastructure applications, where collecting labelled examples of damage is costly, time-consuming, and often impractical.

Unsupervised learning approaches are particularly advantageous in SHM applications where only healthy baseline data are available, as they do not require labelled damage examples for training. While unsupervised methods broadly include clustering and dimensionality reduction techniques, this study specifically adopts an anomaly detection approach trained solely on healthy data. This is especially relevant in large-scale infrastructure where controlled damage scenarios are infeasible [1]. Accelerometers, widely used for collecting vibration-based data in SHM, are valued for their simplicity, cost-effectiveness, and ability to capture overall structural response. Despite limitations such as temperature sensitivity and noise, they remain a preferred choice for large-scale deployment. While other sensors, such as Fibre Bragg Grating (FBG), can detect localised damage with higher precision, they require complex installation and costly equipment [2].

Soltani et al, provided a comprehensive review of machine learning techniques for SHM, highlighting the increasing use of unsupervised methods such as Principal Component Analysis (PCA), Isolation Forest, and autoencoders [3]. Their study emphasised the importance of real-time, data-driven monitoring frameworks in situations where model-based or supervised methods are limited by the lack of labelled damage data. Fernandez-Navamuel and Magalhães proposed an ensemble method that combines PCA and autoencoders for feature extraction and damage detection in bridge vibration data [4]. Their hybrid approach improved sensitivity to structural changes while maintaining robustness in noisy environments, making it suitable for long-term monitoring

applications. Boccagna, Bottini, Petracca, and Amelio also supported hybrid techniques by combining convolutional autoencoders with PCA and Isolation Forest to detect anomalies in railway bridge vibration data [5]. Their results demonstrated the potential of integrating deep learning and traditional unsupervised methods to detect complex structural changes in simulated datasets. This work further reinforces the value of hybrid models, particularly where conventional techniques may struggle to capture subtle anomalies. Recent work by Toufigh and Ranjbar explored a deep autoencoder–Isolation Forest framework for detecting damage in concrete structures using ultrasonic vibration responses [6]. Their method integrated automatic feature extraction with unsupervised anomaly detection, offering an efficient and scalable solution without the need for labelled damage data. Similarly, Bayane, Leander, and Karoumi developed an unsupervised SHM pipeline using vibration-based features and anomaly detection techniques to monitor bridges [7]. Their results illustrated the practicality of using data-driven methods for real-time monitoring, especially in preventing costly maintenance or failure events.

In contrast to these studies, the model developed in this paper focuses on vibration data from bridge structures, particularly using statistical and spectral feature extraction methods (e.g., RMS, entropy), combined with the Isolation Forest algorithm trained exclusively on healthy data. The novelty of this approach lies in its use of a sliding window technique to segment the signal, enabling localised anomaly detection over time. This is especially valuable for identifying slowly progressing damage, such as cracking or fatigue, which may not be visible in global features. Additionally, the implementation of a consecutive anomaly rule ensures that damage is only flagged when anomalies persist across multiple windows, which increases robustness against transient noise and false positives. Together, these design choices make the system well-suited for large-scale, real-time SHM applications where computational efficiency and scalability are essential.

In this study, a finite element (FE) model of a simply supported beam was developed to simulate the dynamic response under both healthy and damaged conditions. A moving load was applied to reflect real-world traffic scenarios, and acceleration data were collected at mid-span. The time-series signals were segmented using a sliding window, and statistical and spectral features were extracted. These were used to train an unsupervised Isolation Forest model, aiming to detect structural damage based solely on deviations from the healthy baseline vibration signature.

## 2 METHODOLOGY

### 2.1 Simulation Setup

The finite element model represents a simply supported beam subjected to a moving load, as illustrated in Figure 1. This configuration is used to emulate bridge structures, where the

pinned–roller boundary condition provides a simplified yet effective representation of real-world support systems [8]. To ensure the accuracy of the model and to validate the results, the initial simulation setup was based on the approach outlined in [8]. Specifically, the model was first validated by replicating their results, ensuring that the acceleration of the mid-span of the beam matched their findings before proceeding to select the range of velocities and forces for further simulations.

The beam is discretised into ten elements, with damage introduced in a single element for selected cases[8]. In the validation setup, the damaged element is positioned at 35% of the beam's total span from the left support.

In this study, damage was introduced by locally reducing the stiffness of a single finite element in the beam by 20 per cent. The damage location remained static across all damaged simulations and was fixed at 35 per cent of the beam span from the left support, following the setup used in Mousavi and Holloway [8]. This fixed location was chosen to allow consistent comparison of model predictions across simulations and to simplify the initial sensitivity analysis. The reduction in stiffness was chosen to represent a moderate-to-severe degradation, such as advanced cracking or corrosion. While 20 per cent is a relatively large value, it was selected to ensure the damage signal was sufficiently distinct to validate the effectiveness of the detection method. Future work will explore smaller reductions and varying damage locations to assess the model's robustness in detecting more subtle or distributed damage scenarios.

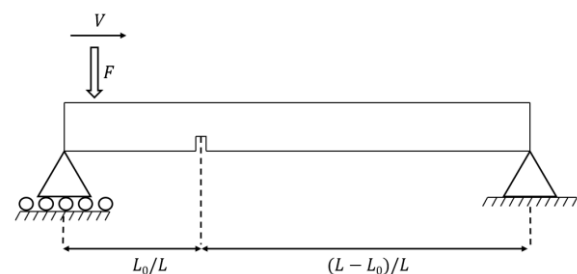


Figure 1. The schematic of the simply supported beam with a moving load

A total of 200 dynamic simulations were conducted to evaluate the beam's acceleration under varying loading conditions—100 with undamaged beams and 100 with damage applied. For each simulation, the magnitude of the vertical force and the moving velocity were randomly selected within specified ranges, using uniform random sampling. The vertical force was chosen randomly between 5000 N and 15000 N, and the velocity was selected between 13 m/s and 25 m/s. This approach introduces variability in the system, ensuring that a range of realistic vehicle loading conditions is tested.

Material properties for the beam were based on structural steel, assuming linear elastic behaviour. To simulate structural degradation, damage was introduced by locally reducing the stiffness of a single element. This modelling approach is used



in the literature to represent localised damage within a linear elastic framework [9]–[11].

Huner, Irsel, Bekar, and Szala demonstrate that explicit solvers provide advantages over implicit methods in both computational efficiency and accuracy when dealing with transient impact loads [12]. An explicit solver (LS-DYNA) was used to perform the simulations, selected for its effectiveness in modelling highly dynamic and nonlinear systems.

All simulations were sampled at a frequency of 1000 Hz, ensuring high-resolution capture of the system's dynamic response. The main modelling parameters are listed in Table 1.

Table 1. System Parameters for the SHM model.

Quantity	Value
Modulus of elasticity	200 GPa
Density	7800 kg/m <sup>3</sup>
Poisson's ratio	0.3
Beam length (L)	20 m
Cross-section width (w)	0.2 m
Cross-section depth (h)	0.2 m
Sampling frequency	1000 Hz
Load range (F)	5000 – 15000 N
Velocity range (V)	13 – 25 m/s
Number of simulations	200 (100 damaged, 100 undamaged)

## 2.2 Anomaly Detection with Isolation Forest

An unsupervised anomaly detection framework was developed to identify structural damage from acceleration time-series data obtained from simulations of both healthy and damaged beam conditions. The overall procedure is summarised in Figure 2, which presents a flowchart of the anomaly detection pipeline. Although each simulation lasts only 1.54 seconds at the lowest velocity (13 m/s), the signals were concatenated across 100 healthy and 100 damaged runs to emulate continuous traffic loading. The resulting dataset was divided into overlapping windows of two seconds, with 50% overlap. This approach enables the system to track localised signal variations while preserving frequency content and computational efficiency.

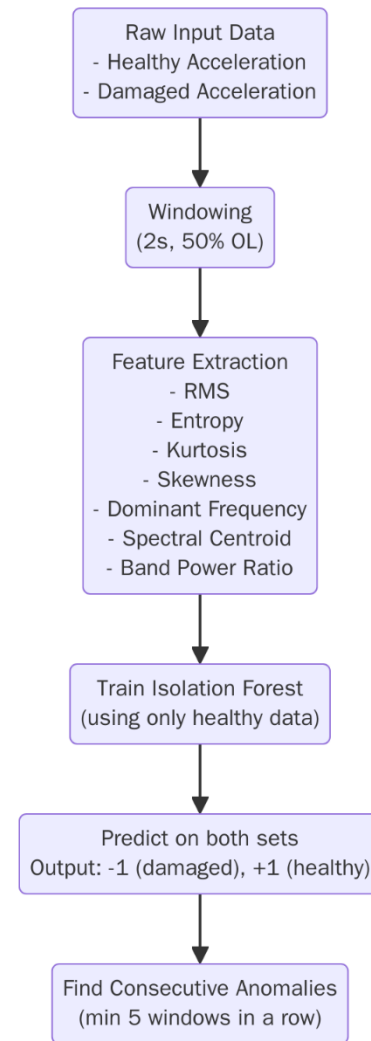


Figure 2. Flowchart of the anomaly detection model.

This configuration was selected to balance temporal and frequency resolution and improve the model's sensitivity to dynamic structural changes. While smaller window sizes were considered, they reduced the effectiveness of frequency-domain features and increased susceptibility to noise. The adopted strategy aligns with recent studies in structural health monitoring that use similar windowing to support reliable anomaly detection. An example of the sliding window approach used to segment the time-series data is illustrated in Figure 3.

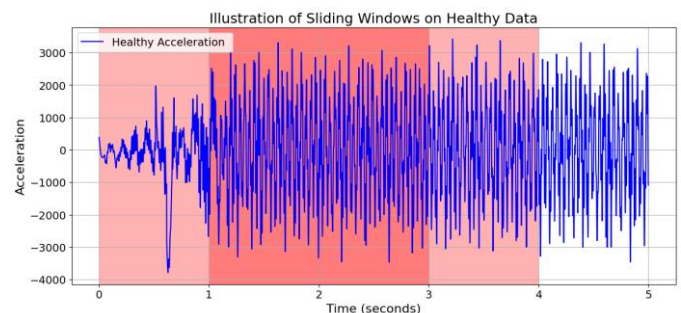


Figure 3. Sliding windows illustration

For each window, a set of statistical and spectral features was extracted to characterise the dynamic response. The features used in this study include root mean square (RMS), entropy, kurtosis, skewness, dominant frequency, spectral centroid, and band power ratio. These features were selected for their proven utility in vibration-based structural health monitoring and are supported by recent benchmark studies.

An Isolation Forest model was trained exclusively on the healthy feature set to establish a baseline for normal structural behaviour. This algorithm builds an ensemble of binary trees (isolation trees), each of which recursively partitions the data space using randomly selected features and split values. The key idea is that anomalies differ sufficiently from the bulk of the data to be isolated more quickly. For any input vector  $x$ , the anomaly score is computed as:

$$s(x, n) = 2^{-\frac{E(h(x))}{c(n)}}$$

where:

- $h(x)$  is the path length, that is, the number of splits required to isolate the data point within a tree.
- $E(h(x))$  represents the average path length of  $x$  across all trees in the forest.
- $c(n)$  is the expected average path length in a binary search tree built from  $n$  samples. It is approximated by:

$$c(n) = 2H(n-1) - \frac{2(n-1)}{n}$$

Here,  $H(i)$  is the  $i$ th harmonic number, approximated by  $\ln(i) + \gamma$ , with  $\gamma \approx 0.5772$  being the Euler–Mascheroni constant. Data points with short path lengths (i.e. those isolated quickly) receive anomaly scores close to 1, indicating a higher likelihood of being anomalous. Normal points, which are harder to isolate, tend to have longer path lengths and receive scores closer to 0.

In this study, the IsolationForest implementation from the scikit-learn library (v1.6) was used. The number of trees (`n_estimators`) was set to 100 to ensure a stable estimation of anomaly scores. The `random_state` was fixed at 42 to ensure reproducibility. The `contamination` parameter, which estimates the expected proportion of anomalies in the dataset, was tuned to 0.085 based on preliminary experiments. This value provided a good balance between capturing true positives and minimising false detections.

After training on the healthy data, the model was applied to both healthy and damaged datasets. The `.predict()` method classified each window as either normal (+1) or anomalous (−1), depending on whether its anomaly score exceeded the threshold determined by the `contamination` setting. To enhance reliability, only groups of five or more consecutive anomalous windows were treated as an indication of structural damage. This post-processing step helped reduce the risk of false positives caused by transient fluctuations or signal noise, ensuring that only sustained deviations from the healthy baseline were flagged as damage.

Once trained, the model was used to classify both healthy and damaged windows as either inliers (labelled +1) or anomalies (labelled −1). To enhance the robustness of the classification and reduce false positives, a post-processing step was applied whereby only groups of five or more consecutive anomalous windows were considered indicative of actual damage. This thresholding logic aligns with practices in unsupervised SHM where transient anomalies or noise could otherwise trigger misleading alerts [17].

This decision was motivated by the observation that isolated anomalous predictions frequently arose due to short-lived signal fluctuations or imperfect feature generalisation. By requiring a minimum streak of five consecutive anomalies, the model avoids false alarms while still being sensitive to sustained deviations caused by damage. Additionally, the simulation data were not shuffled during concatenation. Instead, the 100 healthy simulations were placed first, followed by 100 damaged ones, ensuring a continuous transition from undamaged to damaged conditions in the time series. This ordering reflects a realistic monitoring scenario in which damage develops after a prolonged healthy period and also allows for visual and algorithmic evaluation of detection accuracy at the transition point.

### 3 RESULTS

The system's performance was evaluated using accuracy, precision, recall and F1-score metrics, with the confusion matrix providing a summary of classification outcomes. Results

The performance of the anomaly detection framework was evaluated using both visual comparison of signals and quantitative metrics derived from classification results.

Figure 4 shows a side-by-side comparison of raw acceleration data from the damaged and undamaged simulations. It is evident that the damaged signal (red) exhibits a higher density of peaks and more abrupt variations in magnitude than the undamaged signal (blue). This variation highlights the physical impact of stiffness reduction on dynamic response.

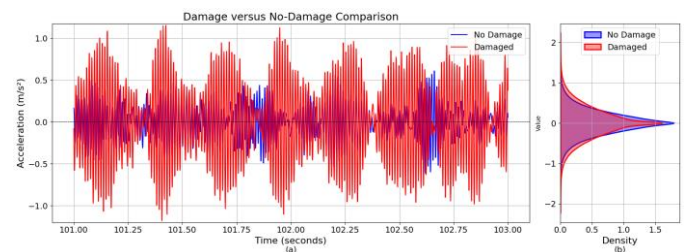


Figure 4. (a) Time-series comparison of acceleration signals between damaged and undamaged beams at mid-span from 101 to 103 seconds under a 10,000 N moving load at 15 m/s.

(b) Kernel density estimate of full signal distributions, showing increased spread in the damaged case.

Figure 5 illustrates the point of transition between healthy and damaged data in the concatenated signal, where the black dashed line marks the onset of damage. This figure does not represent a change in damage location, but rather demonstrates the model's ability to correctly identify the onset of anomalous behaviour. The Isolation Forest model successfully distinguishes between the two conditions, with no false

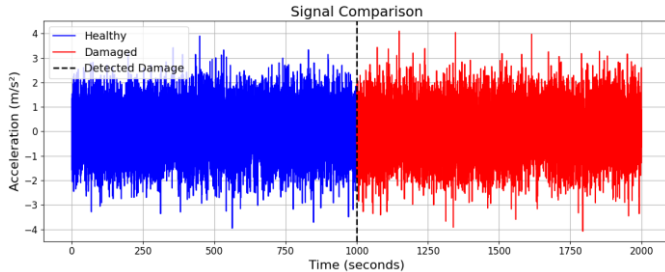


Figure 5. Mid-span acceleration response under moving load for healthy and 20% stiffness-reduced beam. Dashed line marks detected damage.

The confusion matrix in Figure 6 provides a quantitative view of the model's predictive accuracy. Out of 945 damaged windows, all were correctly identified, yielding a recall of 1.000. Meanwhile, 860 out of 945 healthy windows were correctly classified, producing a precision of 0.917. The overall accuracy of the model was 0.955, and the F1 score was 0.957, indicating a strong balance between precision and recall.

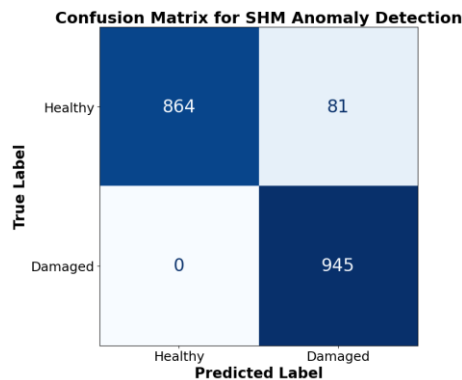


Figure 6. Confusion matrix for SHM anomaly detection.

Table 2. Anomaly detection performance metrics.

Metric	Value
Accuracy	0.955
Precision	0.917
Recall	1.000
F1 Score	0.957
True Positives (TP)	945
True Negatives (TN)	860
False Positives (FP)	85
False Negatives (FN)	0

These results, summarised in Table 2, demonstrate that the proposed combination of statistical and spectral features with an unsupervised Isolation Forest algorithm is effective in identifying structural damage using only healthy training data. The perfect recall of 1.000 confirms the model's ability to detect all instances of damage under the simulated conditions. While this result is promising, it may also reflect the relatively distinct nature of the simulated damage (a 20% stiffness reduction), which provides a clear contrast to the healthy baseline. In real-world scenarios, where damage may be more subtle or masked by noise, recall performance may vary. Nonetheless, achieving full sensitivity in this setup is an important step toward validating the model's potential for practical SHM applications.

The absence of false negatives indicates that the selected features, including root mean square, kurtosis and spectral centroid, are sensitive enough to detect changes in the mid-span acceleration response associated with damage. Permutation feature importance analysis in Figure 7 supports this, showing that RMS had the greatest influence on the model's predictions, while entropy, kurtosis and skewness contributed less. This highlights the importance of signal energy in distinguishing damaged from undamaged states and suggests that the model relied primarily on RMS to detect anomalies.

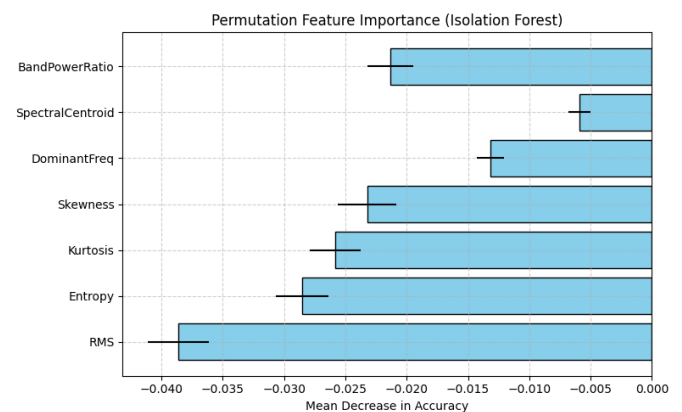


Figure 7. Permutation feature importance showing the relative contribution of all features to the Isolation Forest model's anomaly detection performance.

However, the presence of 85 false positives, reflected in a precision of 0.917, suggests that some healthy windows exhibited irregular but non-damaging patterns. These anomalies may be due to transient structural behaviours, elevated loads, or complex vibration modes that were not well represented in the training data.

This result reflects a trade-off between sensitivity and specificity. In structural monitoring applications, prioritising recall is often preferred, as missing damage poses a greater risk than raising a false alarm. The high F1 score of 0.957 supports the strength of this balance. Nevertheless, repeated false positives may reduce user trust in the system and increase inspection costs. To address this, further work is needed to



investigate the nature of these misclassifications and explore feature refinement or adaptive thresholding strategies that can improve specificity without compromising detection accuracy.

The simulations used in this study were designed to represent realistic bridge conditions, based on established finite element modelling techniques reported in structural health monitoring literature. A simply supported beam was subjected to a moving load, with force and velocity ranges chosen to reflect typical vehicle traffic scenarios. By randomly sampling these parameters across simulations, the model captures a level of variability comparable to that seen in practice. However, while the simulations reproduce essential structural behaviours, certain complexities that exist in real-world monitoring, such as sensor noise, thermal drift, and environmental changes, were not included. Although the method performs well in this controlled environment, additional validation using experimental or field data is needed to confirm its applicability in real conditions.

In this study, damage was introduced by reducing the stiffness of a single element in the finite element model by 20%. This level of degradation represents a significant structural change, such as might result from cracking or corrosion. The resulting increase in vibration energy was clearly detectable in the acceleration signal, particularly at the beam's mid-span. While the model achieved full sensitivity to this level of damage, its performance with smaller changes remains to be assessed. Reductions in stiffness of 5%-10%, for example, may produce more subtle variations in the signal, making them harder to distinguish from normal fluctuations. Future work will investigate how sensitive the model is to such smaller degradations and how well it performs under more realistic conditions that include noise and environmental variation.

All results presented in this study are based solely on finite element simulations. While these simulations provide a controlled and repeatable environment for evaluating the proposed method, they do not capture the full complexity of real-world monitoring scenarios. It is well known that vibration-based damage detection techniques often face challenges in practical applications due to noise, environmental variability, temperature effects, and operational conditions. These factors can introduce variability that may obscure subtle signs of damage or increase the rate of false positives.

We acknowledge this as a limitation of the current study and plan to address it in future work. Specifically, we aim to validate the approach using real-world sensor data collected from instrumented laboratory-scale bridge models or in situ field deployments. This would involve applying accelerometers to physical structures subjected to controlled damage and comparing the model's predictions against ground truth. Such validation is essential for assessing the robustness and transferability of the proposed method and would provide critical insights into how it performs under realistic operating conditions.

#### 4 CONCLUSION

This study set out to develop and evaluate an unsupervised machine learning framework for structural health monitoring (SHM), with the specific aim of detecting damage using only vibration data from healthy structural conditions. The motivation was to address the limitations of supervised approaches that rely on labelled damage data, which is often unavailable or impractical to collect in real-world scenarios.

The proposed method combined lightweight time-domain and frequency-domain features with an Isolation Forest anomaly detection model, further enhanced by a consecutive anomaly rule to reduce false positives. The approach was tested on simulated acceleration data from both healthy and damaged beam configurations. Results showed that the model achieved high detection accuracy, with perfect recall and no false negatives, indicating strong sensitivity to damage. Precision and F1 scores also demonstrated the model's ability to reliably distinguish between normal and abnormal structural behaviour, despite being trained exclusively on healthy data.

These findings confirm the method's suitability for low-cost, real-time deployment on civil infrastructure, particularly in settings where computational resources and data availability are constrained. Although this study relied on simulated data, it provides a solid foundation for future experimental validation using real-world sensor inputs. Further refinement may focus on improving robustness to environmental variability and exploring hybrid models to enhance detection performance.

#### REFERENCES

- [1] A. Calderon Hurtado, K. Kaur, M. Makki Alamdari, E. Atroshchenko, K.C. Chang, and C.W. Kim, Unsupervised learning-based framework for indirect structural health monitoring using adversarial autoencoder, *Journal of Sound and Vibration*, vol. 550, p. 117598, 2023.
- [2] D. Heider, Fibre Bragg grating sensors for aircraft structural health monitoring, in *Proceedings of SPIE 7292: Sensors and Smart Structures Technologies for Civil, Mechanical, and Aerospace Systems*, paper 72920H, 2009.
- [3] E. Soltani, E. Ahmadi, F. Gueniat, and M.R. Salami, A review of bridge health monitoring based on machine learning, *Proceedings of the Institution of Civil Engineers - Bridge Engineering*, 2022.
- [4] A. Fernandez-Navamuel and F. Magalhães, Deep learning enhanced principal component analysis for structural health monitoring, *Journal of Intelligent Material Systems and Structures*, 2022.
- [5] R. Boccagna, M. Bottini, M. Petracca, and A. Amelio, Unsupervised deep learning for structural health monitoring, *Big Data and Cognitive Computing*, 2023.
- [6] V. Toufigh and I. Ranjbar, A deep learning framework for ultrasonic-based distributed damage detection in concrete: integration of a deep auto-encoder and Isolation Forest for anomaly detection, *Journal of Intelligent Material Systems and Structures*, 2024.
- [7] I. Bayane, J. Leander, and R. Karoumi, An unsupervised machine learning approach for real-time damage detection in bridges, *Engineering Structures*, 2024.
- [8] M. Mousavi and D. Holloway, Using a moving load to simultaneously detect location and severity of damage in a simply supported beam,

- Journal of Vibration and Control, vol. 25, no. 19–20, pp. 2737–2752, 2019.
- [9] M. Najafgholipour and S. Dehghan, Finite element analysis of reinforced concrete beam with damage simulation, *International Journal of Civil Engineering*, vol. 18, no. 5, pp. 567–579, 2020.
- [10] M.A.S. Bahri, M.M. Ratnam, and H.P.S. Abdul Khalil, Functionally graded wood filler–recycled polypropylene composite: Effect of mechanical loading on deflection of cantilever beam, *Advanced Composites Letters*, vol. 29, pp. 1–9, 2020.
- [11] H. Luo, J. Fu, P. Wang, and W. Zhou, Design optimization of the ram structure of friction stir welding robot, *Journal of Mechanical Science and Technology*, vol. 33, no. 1, pp. 123–130, 2019.
- [12] U. Huner, G. Irsel, U. Bekar, and M. Szala, A comprehensive case study to the implicit and explicit approach in finite element analysis, *Cogent Engineering*, DOI: 10.1080/23311916.2024.2399737, 2025.
- [13] K.P. Anastasiadis, C.S. Sakaris, R. Schlanbusch, and J.S. Sakellariou, Vibration-based SHM in the synthetic mooring lines of the semisubmersible OO-Star Wind Floater under varying environmental and operational conditions, *Sensors*, vol. 24, no. 2, p. 543, 2024.
- [14] K. Eltoumy, M. Gomaa, and X. Liang, Unsupervised learning methods for data-driven vibration-based structural health monitoring: a review, *Sensors*, vol. 23, no. 6, p. 3290, 2023.
- [15] K. Kritikakos, X. Konstantinou, C.F. Lee, C.S. Sakaris, J.S. Sakellariou, and R. Schlanbusch, Vibration-based structural health monitoring of the mooring lines in a floating offshore wind turbine under varying environmental conditions: NN vs STS based methods, *ResearchGate*, 2025.
- [16] T. Buckley, B. Ghosh, and V. Pakrashi, A feature extraction & selection benchmark for structural health monitoring, *Journal of Intelligent Material Systems and Structures*, 2023.
- [17] K. Yang, T. Liu, Z. Yang, Y. Zhou, and Z. Tian, Baseline optimized autoencoder-based unsupervised anomaly detection in uncontrolled dynamic structural health monitoring, *Journal of Intelligent Material Systems and Structures*, 2025.

# Deep generative models to mitigate data scarcity in bridge structural health monitoring

Sasan Farhadi<sup>1</sup>, 0000-0002-9562-9199, Mauro Corrado<sup>1</sup>, Danilo Acquesta Nunes<sup>1</sup>, Giulio Ventura<sup>1</sup>

<sup>1</sup>Institute of Engineering Geodesy and Measurement Systems, Graz University of Technology, Graz, Austria  
email: sasan.farhadi@polito.it, mauro.corrado@polito.it, danilo.acquesta@polito.it, giulio.ventura@polito.it

**ABSTRACT:** Structural health monitoring is essential for ensuring the safety, reliability, and longevity of infrastructural assets. However, conventional monitoring measurements face significant challenges, such as being labor-intensive, costly, and time-consuming. In recent years, the rise of machine learning and deep learning has data analysis frameworks, offering a promising solution to these challenges. Despite this, developing reliable and robust approaches that generalize well to unseen scenarios often requires large amounts of training data. This presents a challenge, mainly with regulatory constraints and difficulties in collecting data, particularly for rare events. To address the issue of data scarcity, this study proposes a generative data augmentation approach using a Wasserstein Generative Adversarial Network (WGAN). This approach generates high-quality short-time Fourier transform (STFT) spectrograms, which are transformed into image-like data, from in-situ acceleration signals for model training. The collected signals, recorded from real-world bridges during various events such as hammering, drilling, environmental noise, and, most importantly, the rare event of wire breakage in prestressed concrete bridges, are processed and fed into the WGAN model to synthesize additional data. This improves the diversity and robustness of training datasets. Evaluation of the generated spectrograms using various performance metrics, such as Structural Similarity Index Measure, Peak Signal-to-Noise Ratio, and Fréchet Inception Distance, demonstrates that the proposed method offers a scalable and cost-effective solution for enhancing the training dataset, particularly in scenarios where event data is sparse, such as prestressing wire breakage.

## 1 INTRODUCTION

Bridges are critical infrastructures for transportation and economic development, but are increasingly vulnerable to deterioration caused by aging, traffic loads, and environmental impacts [1]. Structural Health Monitoring (SHM) is essential for the early detection of damage, as highlighted by failures such as the Reale Viaduct and Fossano Bridge collapses in Italy [2, 3]. However, conventional SHM methods, such as visual inspections, are often costly, labor-intensive, and ineffective at detecting subtle or internal damage. Although sensor-based methods offer improvements, they generate complex and noisy data, making manual analysis difficult [4]. As a result, recent advances in Machine Learning (ML) and Deep Learning (DL) have emerged as promising approaches, demonstrating strong performance across various domains, including structural damage detection [5, 6]. Nevertheless, real-world implementation of these methods still faces challenges, particularly data scarcity and class imbalance, which are especially essential for rare events like wire breakage, an internal form of structural damage that is difficult to capture.

Data augmentation (DA) techniques have been proposed to address these issues, but conventional methods like Mixup and time-shifting are insufficient for replicating the complexity of real-world events. In this study, Generative Adversarial Networks (GANs) are proposed as a powerful solution for generating realistic synthetic data. Prior work, mainly in speech and audio generation, has demonstrated the effectiveness of spectral-domain representations, such as STFT spectrograms, for improving generative models. However, applications of GANs in SHM, particularly for STFT-based augmentation, remain limited.

To address this gap, this study utilized Wasserstein GAN using gradient penalty (WGAN-GP), a GAN model designed to generate single-channel STFT spectrograms specifically for SHM applications. Unlike traditional three-channel approaches, the single-channel input maintains the spectral information of structural vibration signals. This study also

provides a unique real-world dataset from two operational bridges in Italy, offering realistic and challenging data for model training and validation. By enhancing dataset diversity and improving model robustness, the proposed approach aims to tackle key SHM challenges, advancing scalable, adaptive, and reliable monitoring frameworks. The methodology, experimental setup, evaluation strategies, and detailed analysis are presented to support future developments and replication steps.

## 2 METHODS

### 2.1 Generative Adversarial Networks

GANs are a type of generative model that learns patterns in data and generates new samples that resemble the original dataset [7]. GANs consist of two neural networks, competing in a zero-sum game: the generators, which create the synthetic data, and the discriminator, which distinguishes between the real and generated data (Figure 1). The generator aims to minimize the discriminator's ability to differentiate between real and fake samples, while the discriminator tries to maximize its ability to classify data correctly.

GANs' training can be challenging due to issues like mode collapse and gradient instability. To address this challenge, Wasserstein GAN (WGAN) was introduced [8]. In this approach, the Wasserstein distance (Earth Mover's distance) was utilized to measure the difference between the real and generated data. The WGAN replaces the discriminator with a critic network, which provides more stable gradients, avoiding the problem of vanishing gradients in traditional GANs.

To further improve training stability, WGAN with gradient penalty (WGAN-GP) was introduced [9], which added a gradient penalty in the loss function. This term makes the critic's gradient more stable and smooth and improves convergence. The WGAN-GP loss functions are:

$$L_D = \frac{1}{N} \sum_{n=1}^N [d(g(z_n)) - d(x_n)] + \lambda \cdot E[(|\nabla d(\hat{x})|_2 - 1)^2]$$



In this equation  $d(x_n)$  and  $d(g(z_n))$  are the critic's outputs for real and generated images, respectively.  $N$  is the batch size and  $\lambda$  is controlling the strength of the gradient penalty.

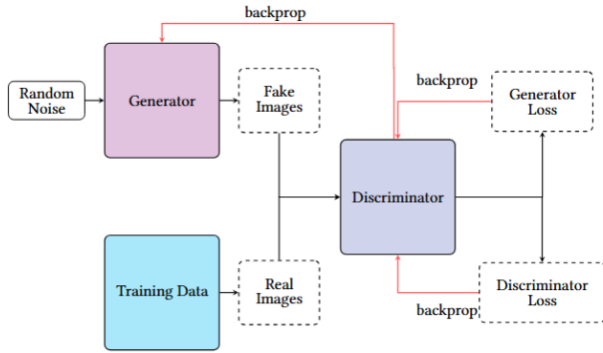


Figure 1. Overview of Generative Adversarial Networks.

## 2.2 Evaluation Metrics

### 2.2.1 Structural Similarity Index Measure (SSIM)

SSIM evaluates the similarity between two images by considering structural information, such as luminance, contrast, and structure. The SSIM score ranges from 0 to 1, with 1 being perfect similarity [10].

$$SSIM = \left( \frac{2\mu_x\mu_y + c_1}{\mu_x^2 + \mu_y^2 + c_1} \right) \cdot \left( \frac{2\sigma_x\sigma_y + c_2}{\sigma_x^2 + \sigma_y^2 + c_2} \right) \cdot \left( \frac{\sigma_{xy} + c_3}{\sigma_x\sigma_y + c_3} \right)$$

In this equation,  $x$  and  $y$  are image patches.  $\mu_x$  and  $\mu_y$  are the mean intensities of the image  $x$  and  $y$ .  $\sigma_x$  and  $\sigma_y$  are the standard deviations and  $\sigma_{xy}$  is the covariance, and  $c$  is the constant value to prevent division by zero.

### 2.2.2 Peak Signal-to-Noise Ratio (PSNR)

PSNR measures the similarity between two images by comparing the maximum pixel value to the noise in the image. Higher PSNR value indicates better quality [11].

$$PSNR(R, G) = 10 \log_{10} \left( \frac{MAX_I^2}{MSE} \right)$$

$R$  and  $G$  refer to the real and generated images, respectively.  $MAX_I$  is the maximum possible pixel value (set to +1 in this study due to normalization), and  $MSE$  is the mean squared error between the real and generated images.

### 2.2.3 Fréchet Inception Score (FID)

FID measures the distance between the feature distributions of real and generated images [12]. A lower FID score indicates better image quality.

$$FID = \|\mu_r - \mu_g\|^2 + Tr(\Sigma_r + \Sigma_g - 2(\Sigma_r \Sigma_g)^{\frac{1}{2}})$$

$\mu_r$  and  $\mu_g$  are the mean feature vectors of the real and generated images, respectively.  $\Sigma_r$  and  $\Sigma_g$  are the covariance matrices of the real and generated images.  $Tr$  refers to the trace of the matrix, which is the sum of its diagonal elements.

## 2.3 Acquisition Setup and Data Collection

The experimental framework was conducted on two post-tensioned concrete bridges in Italy, Le Pastena and Cerqueta. The data collection phase was performed during the deconstruction and maintenance phase with a collaboration between Politecnico di Torino and Strada dei Parchi S.p.A. Due to the bridges' height and limited access, a Mobile Elevated Work Platform (MEWP) was used for instrumentation setup. The wire cutting process, performed on twisted tendons, was carried out using an electric trimmer in a controlled setup after the prestressing tendons were exposed.

The primary dataset was acquired using two accelerometers (Model 805M1, DSPM Industria srl), placed 4.5 meters from the cutting point on the sides of the beams. This setup was chosen to ensure the signal could be reliably recorded, considering the effects of signal attenuation and dispersion along the propagation path. These propagation effects can influence the measured acceleration signals and, consequently, the generated spectrograms. These accelerometers recorded structural vibrations during wire cutting, with a high sampling rate of 96 kHz and a frequency response of 0.4 to 12 kHz. In addition to the rare event of wire breakage signals, other vibrational events such as hammering, electric trimmer, and traffic were captured. This comprehensive dataset ensures the development of a robust model for generating sound events and further development of more generalized automated systems (Figure 2).

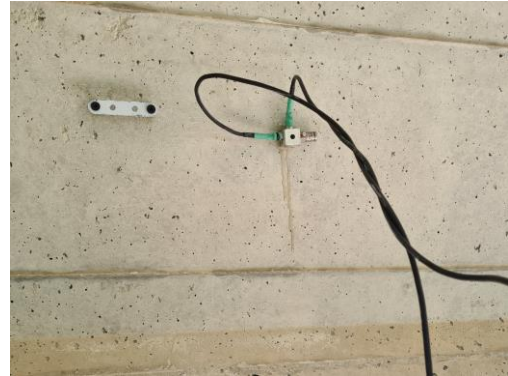


Figure 2. Sensor positions on La Patenda Bridge.

## 2.4 Experiments

### 2.4.1 Feature Extraction

The dataset used in this study comprises four signal classes: wire breakage (202 samples), hammering (264 samples), electric trimmer (459 samples), and traffic (415 samples). As it is evident, there is a class imbalance, with critical events like wire breakage being underrepresented, which may affect model performance. The signals were captured at a sampling frequency of 96 kHz, with each signal having 1000 samples over 0.0104 seconds (Figure 2). To ensure consistency and reduce bias from varying amplitudes, all signals were normalized before further processing.

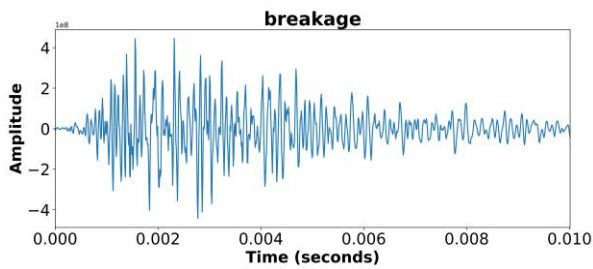


Figure 3. Time-domain representation of the wire breakage acceleration signal (units: m/s<sup>2</sup>).

This study uses Short-Time Fourier Transform (STFT) for feature extraction from in-situ acceleration signals to analyze event patterns. STFT transforms signals from the time domain to the two-dimensional time-frequency domain, keeping both temporal and spectral information. One important parameter in STFT analysis is the window size selection, which can affect the trade-off between time and frequency resolution. Smaller window sizes (e.g., 64) offer high time resolution but low frequency resolution, while larger windows (e.g., 512) provide better frequency resolution but less temporal precision. In this study, the optimal balance was achieved using window sizes of 128 and 256 (Figure 3). The extracted STFT spectrograms were used as single-channel images for model training, optimizing feature extraction and computational efficiency for event detection and structural health monitoring applications.

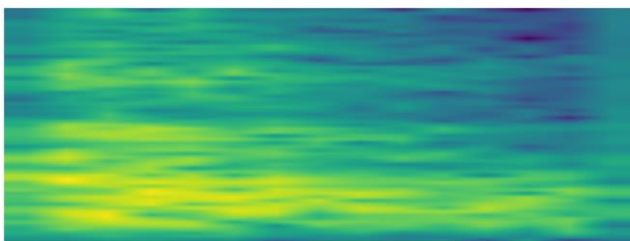


Figure 4. STFT spectrogram of a wire breakage signal. The x-axis represents time (seconds), the y-axis represents frequency (Hz).

### 2.4.2 Model Developments

The WGAN-GP was implemented as one of the most successful models for image generation. It improves on the standard GAN and WGAN models by using the Wasserstein loss function and adding a gradient penalty. The generator starts with a latent noise vector of size 100, a typical setting in GAN studies. This vector is reshaped into small feature maps and upsampled through transposed convolutional layers to generate spectrogram-like images. In this study, the generator consists of four transposed convolutional layers with kernel sizes of 5×5 and strides of 2, progressively reducing the feature map depth from 512 to 256, 128, and 64 before producing the final spectrogram. To ensure stable training and avoid vanishing or exploding gradients, batch normalization is applied after each layer. Leaky ReLU activation is used throughout the layers to add non-linearity, except in the final layer, where a tanh activation function normalizes the output values to the range [-1, 1].

The critic, unlike the discriminator, does not classify samples as real or fake; instead, it assigns real-valued scores to samples, helping to approximate the Wasserstein distance between real and generated data. The critic consists of several 2D convolutional layers, which progressively reduce the spatial dimensions of the input, followed by batch normalization and Leaky ReLU activations to improve learning stability. To enforce the Lipschitz constraint, a gradient penalty term with a coefficient of  $\lambda=12$  is added to the loss function. The selection of hyperparameters search space was based on a combination of recommendations from GAN literature and preliminary tuning experiments on dataset to achieve stable and high-quality spectrogram generation. The summary of hyperparameter selection for this model is in Table 1.

Table 1. Hyperparameter Selection for WGAN-GP Model

Parameter	Value	Search Space
Learning Rate (Generator)	$2 \times 10^{-5}$	$2 \times 10^{-5}$ to $2 \times 10^{-5}$
Learning Rate (Critic)	$2 \times 10^{-6}$	$2 \times 10^{-5}$ to $2 \times 10^{-5}$
Batch Size	16	16 to 64
Epochs	1500	1000 to 5000
Optimizer	Nadam	Nadam, Adam, RMSProp
Gradient Penalty Coefficient	12	1 to 25
Activation Function (Generator)	Leaky ReLU, Tanh	Leaky ReLU, ELU, Tanh
Activation Function (Critic)	Leaky ReLU	Leaky ReLU, ELU, Tanh
Generator Layers	4 Transposed Convolutions	3 to 8
Critic Layers	5 Convolutions	3 to 8
Kernel Size	5x5	3x3 to 5x5

To assess the performance of WGAN-GP and the quality of generated images, the model was evaluated using multiple metrics, including SSIM, PSNR, and FID. The results are shown in Table 2 for both window sizes of 128 and 256, which enable the determination of the effect of window sizes in generating STFT-based images.

Table 2. Performance Metrics of WGAN-GP

Metrics	Class	Window Size:128	Window Size:256
SSIM	Breakage	<b>0.367</b>	0.180
	Trimmer	0.342	<b>0.403</b>
	Hammer	0.208	0.232
	Traffic	0.170	0.186
PSNR	Breakage	13.409	11.972

	Trimmer	<b>13.424</b>	<b>13.621</b>
	Hammer	10.520	11.289
	Traffic	11.374	12.020
FID	Breakage	0.219	0.331
	Trimmer	<b>0.173</b>	0.270
	Hammer	0.221	<b>0.194</b>
	Traffic	0.179	0.237

For SSIM, WGAN-GP achieved the highest value for the Trimmer event at window size 256 (0.403), indicating better structural similarity compared to the other events. It is notable that for the breakage event at a window size of 128, the score dropped from 0.367 to 0.18, which suggests that the model is not able to preserve the pattern of more complex signals, such as wire breakage. For Hammer and Traffic events, the SSIM values were relatively lower, indicating that WGAN-GP had difficulty maintaining high structural similarity for these types of events across both window sizes.

In terms of PSNR, which measures image clarity and noise levels, the best performance was obtained for the Trimmer event with a PSNR of 13.424 at window size 128 and 13.621 at window size 256, indicating that WGAN-GP generated spectrograms with minimal distortion for this event. However, the Breakage event exhibited lower PSNR scores, particularly at window size 256 (11.972), highlighting a reduction in image quality for events with more intricate features. Hammer and Traffic events also showed similar trends, with Traffic performing better at window size 256 (12.020). For reference, higher PSNR values indicate greater similarity, with values above 20 generally considered good for images; however, in the context of generated spectrograms, PSNR values are typically lower, and values above 10 are commonly reported as acceptable in the literature for synthetic data with complex structures.

The FID metric, which evaluates the similarity between real and generated data distributions, showed that WGAN-GP performed well for the Trimmer event at window size 128 (FID of 0.173). However, it struggled with Breakage and Hammer, with higher FID scores indicating that the generated spectrograms deviated more from real data. Overall, Traffic also showed relatively low FID values at both window sizes, indicating good model performance for simpler events.

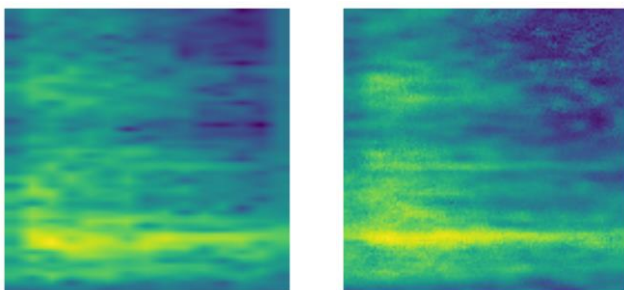


Figure 5. STFT Spectrogram images (window size 128) of wire breakage signal (Left) Real Sample, (Right) Generated by WGAN-GP. The x-axis represents time (seconds), the y-axis represents frequency (Hz).

In summary, WGAN-GP demonstrated strengths in generating synthetic spectrograms for certain events like

Trimmer and Traffic, especially at window size 128. However, the model faced challenges in generating high-quality spectrograms for more complex events such as Breakage and Hammer, particularly at larger window sizes. These results highlight the need for further development and utilization of GAN models to better capture fine spectral features and improve consistency across different types of events.

## 2.5 Conclusion and Future Developments

This study demonstrated the potential of GAN-based data augmentation in the context of structural health monitoring using STFT spectrograms from in-situ acceleration signals. The model showed promising performance, particularly for Trimmer and Traffic events. However, it is important to note that WGAN-GP showed some limitations in generating more complex STFT patterns, such as those associated with Wire Breakage events.

To further improve the model, future work will focus on addressing these limitations by refining and customizing the architecture. Additionally, integrating more advanced models, such as sequential models and attention mechanisms, which are robust for time-series data, will be explored to enhance the model's ability to capture intricate temporal dependencies and improve the generation of complex event patterns. Furthermore, future studies will systematically evaluate the impact of GAN-generated data on downstream event classification and detection models to better quantify the practical benefits of data augmentation for structural health monitoring.

## REFERENCES

- [1] Ko, J. M., & Ni, Y. Q. (2005). Technology developments in structural health monitoring of large-scale bridges. *Engineering Structures*, 27(12), 1715–1725.
- [2] Ferro, G. A., Restuccia, L., Falliano, D., Devitofranceschi, A., & Gemelli, A. (2022). Collapse of Existing Bridges: From the Lesson of La Reale Viaduct to the Definition of a Partial Safety Coefficient of Variable Traffic Loads. *Journal of Structural Engineering*, 148(11), 04022181.
- [3] Zingoni, A. (Ed.). (2019). *Advances in engineering materials, structures and systems: Innovations, mechanics and applications: Proceedings of the seventh International Conference on Structural Engineering, Mechanics, and Computation, 2-4 September 2019, Cape Town, South Africa*. International Conference on Structural Engineering, Mechanics and Computation, Boca Raton. CRC Press, Taylor & Francis Group.
- [4] Saleem, M. R., Park, J.-W., Lee, J.-H., Jung, H.-J., & Sarwar, M. Z. (2021). Instant bridge visual inspection using an unmanned aerial vehicle by image capturing and geo-tagging system and deep convolutional neural network. *Structural Health Monitoring*, 20(4), 1760–1777.
- [5] Farhadi, S., Corrado, M., & Ventura, G. (2024a). Acoustic Event-Based Prestressing Concrete Wire Breakage Detection. *Procedia Structural Integrity*, 64, 549–556.



- [6] Farhadi, S., Corrado, M., & Ventura, G. (2024b). Automated acoustic event-based monitoring of prestressing tendons breakage in concrete bridges. *Computer-Aided Civil and Infrastructure Engineering*, 39(24), 3700–3720.
- [7] Goodfellow, Ian, Jean Pouget-Abadie, Mehdi Mirza, Bing Xu, David Warde-Farley, Sherjil Ozair, Aaron Courville, and Yoshua Bengio. "Generative adversarial networks." *Communications of the ACM* 63, no. 11 (2020): 139-144.
- [8] Arjovsky, M., Chintala, S., & Bottou, L. (2017). Wasserstein GAN (No. arXiv:1701.07875). arXiv.
- [9] Gulrajani, I., Ahmed, F., Arjovsky, M., Dumoulin, V., & Courville, A. (2017). Improved Training of Wasserstein GANs (Version 3). arXiv.
- [10] Li, Y., Gan, Z., Shen, Y., Liu, J., Cheng, Y., Wu, Y., Carin, L., Carlson, D., & Gao, J. (2018). StoryGAN: A Sequential Conditional GAN for Story Visualization (Version 2).
- [11] Smith, S. W. (1997). *The scientist and engineer's guide to digital signal processing* (1. ed). California Technical Publ.
- [12] Heusel, M., Ramsauer, H., Unterthiner, T., Nessler, B., & Hochreiter, S. (2017). GANs Trained by a Two Time-Scale Update Rule Converge to a Local Nash Equilibrium.

# Smart adaptive triggering strategy for edge intelligence enabled energy-efficient sensing

Shuaiwen Cui<sup>1</sup>, 0000-0003-4447-6687, Xiao Yu<sup>1</sup>, 0009-0007-8294-5671, Yuguang Fu<sup>1\*</sup>, 0000-0001-7125-0961

<sup>1</sup>School of Civil and Environmental Engineering, Nanyang Technological University, 50 Nanyang Ave, Singapore, 639798  
email: SHUAIWEN001@e.ntu.edu.sg, XIAO004@e.ntu.edu.sg, yuguang.fu@ntu.edu.sg

**ABSTRACT:** Achieving both energy efficiency and high triggering accuracy is a critical multi-objective optimization challenge in Structural Health Monitoring (SHM), particularly for power-constrained wireless edge devices deployed in dynamic environments. Traditional empirical and static-threshold-based methods often struggle to simultaneously have low miss trigger and false trigger rate and lack adaptability to varying environmental and operational conditions. This study proposes a multi-stage adaptive triggering strategy built upon a Feedback Control (FC) framework, driven by Bayesian Optimization (BO) as the optimization engine, and accelerated by Digital Twin (DT) for data augmentation and Neural Networks (NN) for real-time contextual understanding and robust inference. The strategy dynamically refines triggering thresholds based on simulated insights and partial observations, enabling rapid adaptation and generalization across scenarios. Experimental validation through simulations and onboard deployments demonstrates that the proposed method improves F-beta performance by over 30% compared to conventional empirical methods. This approach provides a promising pathway toward intelligent, energy-efficient, and sustainable SHM sensing through fast feedback, reduced deployment cost, and minimized missed critical events.

**KEY WORDS:** Trigger Sensing, Energy-efficiency, Adaptive Sensing, Feedback Control, Bayesian Optimization, Structural Health Monitoring

## 1 INTRODUCTION

In Structural Health Monitoring (SHM) systems, triggering mechanisms are essential for determining when edge sensor nodes should initiate data acquisition to capture transient structural responses during events of interest [1]. In real-world deployments with limited energy resources, triggering directly affects both responsiveness and long-term system sustainability. A mechanism that is both energy-efficient and accurate allows the system to capture meaningful data while minimizing power consumption [2]. When continuous high-rate sampling is infeasible, intelligent triggering becomes critical for reliable and autonomous monitoring.

Conventional methods typically rely on fixed thresholds or handcrafted rules based on prior knowledge [3]. While easy to implement and low in computational cost, they lack adaptability. Triggering parameters (e.g., threshold and duration) set during deployment often remain static, making it difficult to respond to changes in structural behavior or environmental conditions. In practical deployments, these parameters are often conservatively configured to minimize the risk of missing events of interest. This conservative strategy prioritizes recall at the expense of precision, which, although effective in reducing missed detections, often leads to an increased rate of false triggers [1].

Practical SHM deployments present several challenges that complicate the design of effective triggering mechanisms. Structural events are typically rare, limiting the amount of available data and making it difficult to establish reliable patterns for triggering. The occurrence of events is also highly imbalanced, with most data corresponding to normal or inactive states, which biases learning-based methods and complicates threshold design. In addition, due to energy constraints, sensors

operate in low-power sentinel modes and only acquire data when a triggering condition is met. As a result, only responses associated with triggered events are recorded, leading to partial observability, where only a subset of structural behaviors is accessible for analysis [4]. These factors collectively call for a triggering mechanism that is adaptive, context-aware, and lightweight, while also possessing the capability to predict and infer unobserved structural responses.

To address these challenges, this study proposes a multi-stage adaptive triggering strategy primarily built upon a Feedback Control (FC) framework [5], which integrates a digital twin (DT) [6], onboard neural networks (NN) [7] [8], and Bayesian optimization (BO) [9]. FC enables the continuous refinement of triggering behavior through performance-driven feedback; BO operates as an optimization engine that seeks the global optimum and guides trigger parameters toward rapid convergence; DT facilitates data augmentation by simulating real deployment environments; NN provides real-time contextual awareness and accurate prediction, even under partial observability. This integration empowers the triggering system to adaptively and efficiently search for the optimal trigger parameters under uncertain event conditions.

The proposed strategy is validated upon a setup mimicking real-world deployment, showing clear advantages over empirical baselines. Specifically, it achieves over 30% improvement in  $F_\beta$  score, enhancing event detection without increasing unnecessary energy use. These findings demonstrate the effectiveness of the proposed strategy in simultaneously optimizing detection accuracy and energy efficiency, and further underscore the potential of integrating closed-loop control, Bayesian optimization, and digital twin to enable

adaptive and intelligent triggering in real-world SHM deployments.

## 2 SMART ADAPTIVE TRIGGERING

### 2.1 Basic triggering mechanism and baseline strategy

An example of a typical trigger sensing mechanism is the one implemented in Xnode [2], which combines a low-power, low-resolution sensor with a high-power, high-resolution sensor, as illustrated in Figure 1 and Table 1. The low-power sensor, such as the ADXL362 [10], is responsible for continuously monitoring motion and detecting events of interest based on predefined thresholds and durations. When the signal amplitude exceeds the configured threshold for a specified duration, an event of interest is deemed to have occurred, as shown in Figure 1. At this point, the low-power sensor activates the high-power sensor, transitioning the system from sentinel mode to working mode to capture detailed event data. This fundamental triggering mechanism forms the basis of the smart adaptive triggering strategy proposed in this study.

Table 1. Xnode sensor energy consumption.

Mode \ Sensor	ADXL362 (12 bit)	LIS344 (24 bit)
Sentinel Mode	Working 270nA	Sleeping 1uA
Working Mode	Sleeping 10nA	Working 680uA

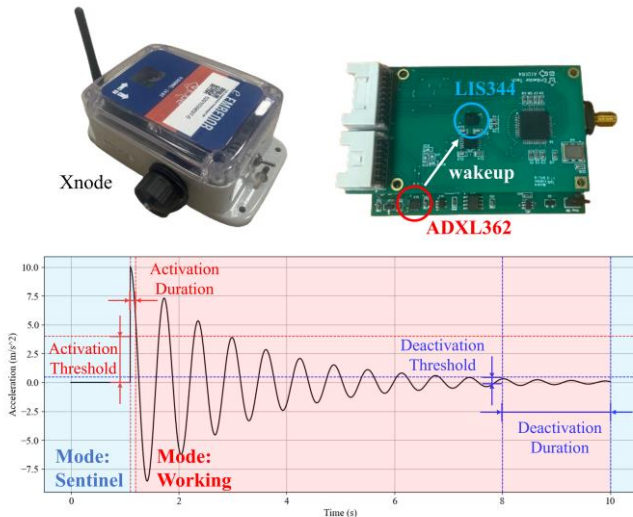


Figure 1. Xnode trigger sensing mechanism.

In SHM practice, the application of basic triggering mechanisms is typically accompanied by parameter configuration using empirical approaches. Engineers often perform preliminary sensing to gain insights into the target structure or environment, and subsequently configure the triggering parameters (i.e., threshold and duration) manually in a conservative manner to ensure low miss trigger rate [2]. This empirically tuned method also serves as the baseline for comparison in subsequent sections.

### 2.2 Feedback control powered by Bayesian optimization

As stated in the introduction, the goal of the triggering mechanism is to minimize missed triggers while keeping the false trigger rate at an acceptably low level, which constitutes a multi-objective optimization problem in its mathematical nature. To facilitate the analysis, the  $F_\beta$  score is introduced to

quantitatively and comprehensively evaluate the performance of the triggering mechanism, as defined in Equation (1). Note that with the use of  $F_\beta$ , the original multi-objective problem is transformed into a single-objective optimization problem, where the parameter  $\beta$  controls the relative weighting between missed and false triggers. In SHM context, usually more weight should be put on recall, which means  $\beta$  should be configured greater than 1. For situations where precision is more important than recall, e.g., false triggering can be quite costly,  $\beta$  should be smaller than 1.

$$F_\beta = (1 + \beta^2) \frac{\text{Precision} \cdot \text{Recall}}{\beta^2 \cdot \text{Precision} + \text{Recall}} \quad (1)$$

Based on the analysis presented in the introduction, smart adaptive triggering centers on two key questions: what are the optimal triggering parameters, and how they can be efficiently approached during system operation. The first question represents an optimization problem, while the second constitutes a control problem. A major limitation of most existing triggering mechanisms lies in their lack of adaptivity, which can be effectively addressed through a feedback loop. As illustrated in Figure 2(a), the triggering mechanism outputs a performance metric to the optimizer, which in turn determines the next parameter configuration to explore based on historical observations. To comply with modern control theory [5], the closed loop can be expressed as Figure 2(b). Figure 2(b) depicts the formal structure of feedback control, comprising four main components: the environment, the system, the estimator, and the controller. In the context of trigger-based SHM, the environment refers to the structural responses that sensors aim to observe. The system corresponds to the triggering mechanism itself, as shown in Figure 1. The estimator is responsible for monitoring or estimating the performance of the triggering mechanism, specifically, the  $F_\beta$  score in this study. The controller, in turn, utilizes iterative feedback to search for the optimal parameter configuration and to devise strategies for efficiently approaching the optimal values. In short, feedback control serves as a backbone to integrate necessary tools to provide adaptivity for triggering parameter fine-tuning.

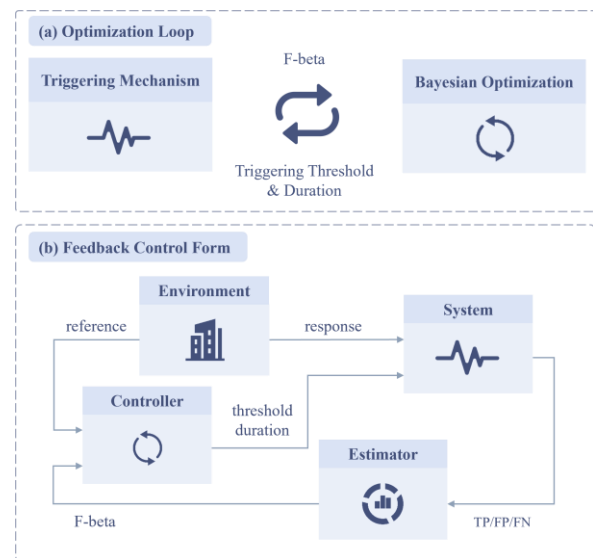




Figure 2. Feedback control framework for triggering parameter optimization: (a) optimization loop; (b) feedback control form.

At the core of the feedback control architecture is the controller, which governs the adaptation process through parameter adjustment. While various tools can be used to implement the controller, the choice must be carefully tailored to the characteristics of the target problem. In the case of trigger-based SHM, the controller takes the  $F_\beta$  score as input and outputs the triggering threshold and duration. However, there is no explicit analytical expression linking the input to the output, making it a black-box optimization problem. Moreover, each feedback iteration requires calculating the  $F_\beta$  score based on many events, resulting in considerable computational cost, in addition to the overhead of observation and estimation. Given these considerations, Bayesian optimization [9] is adopted as the controller due to its demonstrated effectiveness in solving black-box problems and its ability to efficiently converge toward the global optimum.

The algorithmic framework of BO is presented in Algorithm 1. As illustrated, the optimization process is driven by the observation dataset  $\mathcal{D}$ , which comprises input–output pairs, where the inputs are the triggering parameters, and the outputs are the corresponding  $F_\beta$  scores. The process begins with an initial sampling phase to obtain a preliminary understanding of the input–output relationship. Subsequently, the optimization proceeds iteratively, with each iteration updating the surrogate model  $\mathcal{M}$  and expanding the dataset with new evaluations. Typically based on Gaussian Process Regression (GPR), the surrogate model provides a non-parametric, probabilistic estimate of the objective function, offering both the predicted mean and associated uncertainty for any given input. This probabilistic nature enables GPR to model complex, non-linear relationships with relatively few samples, while maintaining analytical tractability and useful mathematical properties such as differentiability. To balance exploration of uncertain regions and exploitation of promising areas, an acquisition function  $\mathcal{S}$  is employed to determine the most informative point  $x_i$ . Common acquisition functions include Expected Improvement (EI), Probability of Improvement (PI), and Upper Confidence Bound (UCB), each offering a different strategy for leveraging the predictive mean and variance to guide sampling. Herein, UCB is used for simplicity. After evaluating the objective function to obtain the corresponding output  $y_i$ , the dataset  $\mathcal{D}$  is updated. Finally, the input  $\hat{x}$  associated with the best observed output in  $\mathcal{D}$  is selected as the optimum.

#### Algorithm 1 Bayesian Optimization Algorithm Framework

**Input:** Search space  $\mathcal{X}$ , objective function  $f$ , surrogate model  $\mathcal{M}$ , acquisition function  $\mathcal{S}$

**Output:** Dataset  $\mathcal{D}$  (set of sampled points and their evaluations)

Initialize dataset:  $\mathcal{D} \leftarrow \text{InitSamples}(f, \mathcal{X})$

**for**  $i = |\mathcal{D}|$  to  $T$  **do**

Fit the model:  $p(y|x, \mathcal{D}) \leftarrow \text{FitModel}(\mathcal{M}, \mathcal{D})$

Select next point:  $x_i \leftarrow \arg \max_{x \in \mathcal{X}} \mathcal{S}(x, p(y|x, \mathcal{D}))$

Evaluate objective function:  $y_i \leftarrow f(x_i)$

Update dataset:  $\mathcal{D} \leftarrow \mathcal{D} \cup \{(x_i, y_i)\}$

**end for**

Pick the best from  $\mathcal{D}$  as optimum:  $\hat{x} \leftarrow \arg \max_{(x,y) \in \mathcal{D}} y$

After introducing the algorithmic details, it becomes evident that the surrogate model  $\mathcal{M}$  plays a central role in addressing the black-box nature of the problem by providing a reliable approximation of the true input–output relationship along with favorable mathematical properties. Meanwhile, the acquisition function  $\mathcal{S}$  serves as the foundation for efficient convergence toward the global optimum, as it guides the search process in a principled manner rather than relying on random exploration.

As can be inferred by Algo. 1, the computational efforts required for BO for the following edge deployment is mainly determined by the size of observation dataset  $\mathcal{D}$ , and each sample in this dataset is only a pair of triggering parameters and performance metric, meaning it can be easily operated on edge devices.

### 2.3 Digital twin for data augmentation

Feedback control is a powerful tool to address the lack of adaptivity; however, it falls short in tackling another critical challenge—data scarcity, imbalance, and uncertainty. Digital twin technology offers a promising solution to augment data for a variety of purposes, such as simulation, optimization, and neural network training. To effectively construct a digital twin for trigger-based sensing for SHM, it is essential to accurately simulate both the structural response and the triggering mechanism. Specifically, this involves modeling the excitation–structure–response chain as well as the threshold–duration-based triggering logic, as shown in Figure 3.

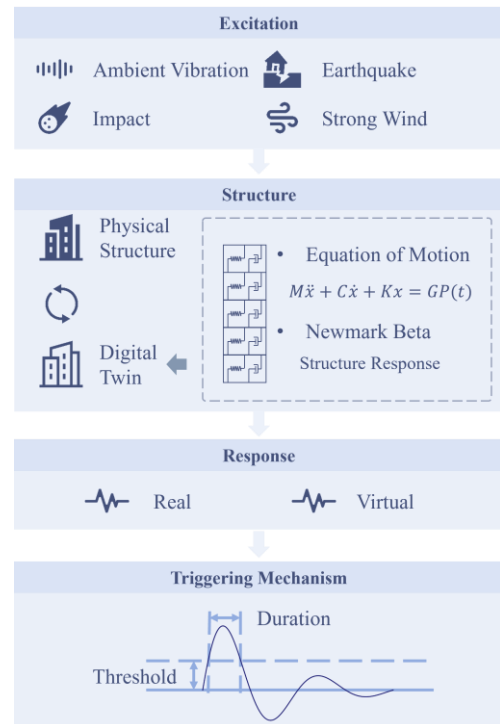


Figure 3. Digital twin for excitation-structure-response flow and triggering mechanism.

Excitation simulation is the first step in structural response modeling. To support the study, several common types of events are considered, including ambient vibrations, earthquakes, impacts, and strong winds. Each event type can be

generated using either external databases or simulation techniques. Ambient vibrations are typically modeled using Gaussian white noise, while earthquakes can be synthesized by superimposing harmonic waves based on a given spectrum. Impacts are represented as impulsive loads, and strong winds can be simulated using autoregressive models combined with time modulation.

Structure modeling is another crucial step in response simulation, achieved by formulating the equation of motion, as shown in Equation (2). In this equation,  $M, C, K$  represent the mass, damping, and stiffness matrices, respectively.  $G$  denotes the force allocation matrix, and  $P(t)$  represents the external force vector at time  $t$ . Equation (2) thus serves as a digital twin of the target structure to be monitored. Following structural modeling is the simulation of structural responses, which involves calculating the displacement, velocity, and acceleration of each degree of freedom in the constructed digital twin. A widely used and reliable numerical method for this purpose is the Newmark-beta method [11], which provides accurate structural response simulation.

$$M\ddot{x} + C\dot{x} + Kx = GP(t) \quad (2)$$

In addition to structural responses, the basic triggering mechanism must also be simulated to complete the digital twin, with implementation details provided in Algorithm 2. With a comprehensive digital twin that includes both the structural model and the triggering logic, data can be flexibly manipulated for various purposes, such as simulation, optimization, neural network training, and more.

---

**Algorithm 2** Triggering Mechanism

---

**Input:** signal value  $s$ , threshold  $\tau$ , duration  $d$

**Output:** trigger flag  $T$  (binary: 1 for trigger, 0 for no trigger; initialized as 0)

**Internal Variable:** counter  $c$  (initialized as 0, used to track consecutive time steps)

For each time step  $t$ :

if  $|s| \geq \tau$  then

Increment counter:  $c \leftarrow c + 1$

if  $c \geq d$  then

Set trigger flag:  $T \leftarrow 1$

Reset counter:  $c \leftarrow 0$

end if

else

Reset counter:  $c \leftarrow 0$

Set trigger flag:  $T \leftarrow 0$

end if

---

#### 2.4 Lightweight neural networks for onboard inference

Feedback from the triggering mechanism is essential for achieving adaptivity; however, its effectiveness is often hindered by challenges in real-world deployment. As shown in Equation (1), the computation of the  $F_\beta$  score relies on both precision and recall, each of which faces practical difficulties. Specifically, precision depends on the identification of true positives and false positives. In the absence of human intervention, ground truth labels for captured signals are typically unavailable, making it impossible to determine whether a triggered signal corresponds to an actual event of

interest. This uncertainty undermines the ability to accurately evaluate performance metrics such as precision and, consequently, the  $F_\beta$  score. The situation is even more challenging for recall, which relies on identifying both true positives and false negatives as shown in Equation (4). Estimating false negatives necessitates knowledge of missed events of interest—information that is inherently inaccessible in trigger-based sensing systems. These limitations present fundamental barriers to autonomous online adjustment of triggering parameters, underscoring the importance of developing effective solutions.

$$precision = \frac{TP}{TP+FP} \quad (3)$$

$$recall = \frac{TP}{TP+FN} \quad (4)$$

Edge intelligence, which integrates lightweight onboard computation with AI, offers a promising pathway for achieving online fine-tuning on edge devices, particularly for problems beyond the reach of traditional approaches. To address the issue of precision, the absence of ground truth can be mitigated by deploying an onboard AI classifier to infer signal labels. Similarly, for recall, an AI-based estimator can be employed to directly approximate the recall value, thereby facilitating more accurate performance evaluation. Most importantly, the onboard AI enables autonomous feedback generation without the need for human intervention, thereby streamlining operations and advancing full system automation. To meet the requirements of edge deployment, these neural networks should prioritize lightweight architecture and high computational efficiency.

Table 2. NN parameters summary.

Parameter Type	CNN	DNN
Total Parameters	142 (572.00 B)	209 (836.00 B)
Trainable Parameters	44 (176.00 B)	209 (836.00 B)
Non-trainable Param.	8 (32.000 B)	0 (0.00 B)
Optimizer Parameter	90 (364.00 B)	0 (0.00 B)

To effectively classify time series data, a 1D Convolutional Neural Network (CNN) combined with feature engineering is employed. Given an input signal of 6000 samples, the data is first transformed from the time domain to the frequency domain using the Fast Fourier Transform (FFT). Both time- and frequency-domain signals are then downsampled to 64 samples each. The resulting vectors are concatenated into a 128-dimensional feature vector, which serves as the input to a lightweight CNN classifier. Details of the network size and architecture are provided in Table 2 and Table 3, respectively. The training curves and classification results are presented in Figure 4.

Table 3. CNN classifier architecture.

Layer	Output Shape	Para. Number
Input Layer	128	0
Conv1D	128	16
BatchNorm	128	16
ReLU	128	0
GlobalAvgPooling	4	0
Dense	4	20

Table 4. DNN Recall estimator architecture.

Layer	Output Shape	Para. Number
Dense	16	64
Dense	8	136
Dense	1	9

Since false negatives cannot be directly observed in trigger-based sensing, a Dense Neural Network (DNN) is introduced to estimate recall based on noise level, trigger threshold, and duration. Utilizing the dataset generated from the digital twin, the DNN is trained to predict recall under various noise conditions and triggering configurations. The network size is detailed in Table 2, the architecture is provided in Table 4, and the training curves are shown in Figure 4. With both the CNN classifier and the DNN recall estimator trained, the feedback loop is fully established, completing the final component of the closed-loop control system.

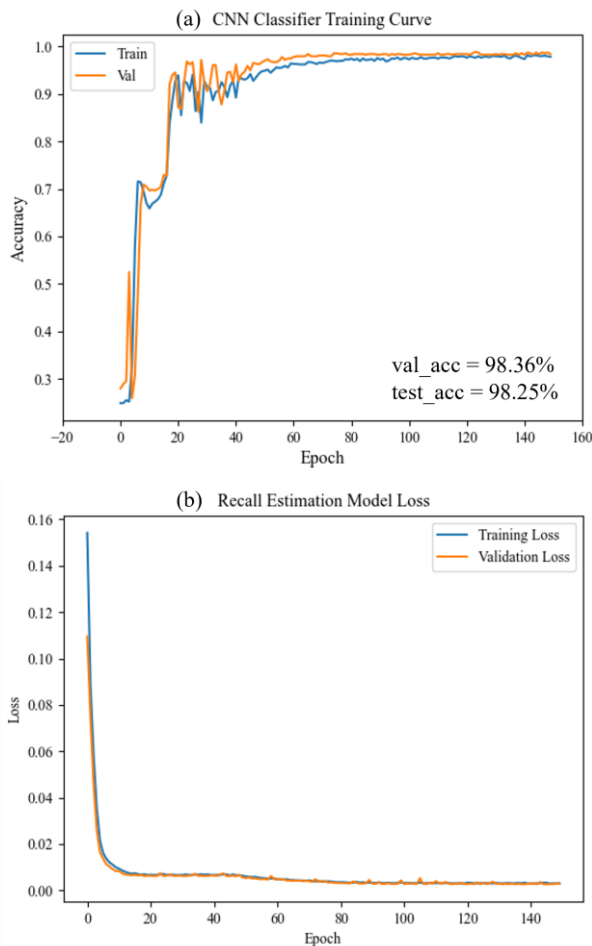


Figure 4. NN training curves: (a) CNN classifier (b) DNN estimator.

### 3 STAGED DEPLOYMENT

Despite the many advantages of edge intelligence, its most prominent inherent limitation lies in the constrained onboard resources, which restrict the efficiency of triggering parameter optimization. In the previous section, a feedback control approach was introduced for iterative optimization of triggering parameters. To further accelerate this process, a staged

deployment strategy is proposed, comprising a pre-deployment optimization stage and an onboard fine-tuning stage. The second stage inherits insights obtained during the first, allowing only lightweight fine-tuning on the device and thus minimizing computational overhead.

Figure 5 illustrates the concept of this staged optimization strategy. Both stages are built upon the same feedback control framework. The key differences lie in two components: the environment component, which refers to the excitation-structure-response flow, and the estimator component, which is responsible for providing performance metrics. In Stage I, the environment is simulated using a digital twin. Although the structural responses are not real, this fully controlled setting provides complete knowledge of all events, enabling accurate performance evaluation. In Stage II, the environment becomes real and uncertain. Since ground truth labels are unavailable, recall cannot be directly computed. To overcome this limitation, onboard neural networks including the CNN classifier and the DNN-based recall estimator are employed to complete the closed-loop feedback control. It is important to note that in the trigger sensing setup, the DT model is not required to be of high fidelity, as its primary role is to generate synthetic data for training the classification model.

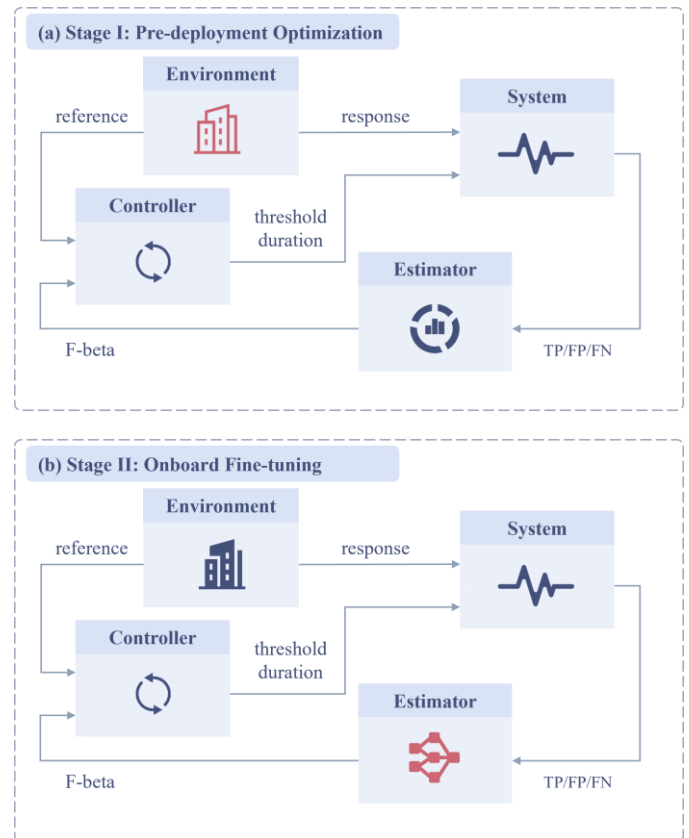


Figure 5. Staged deployment strategy: (a) pre-deployment optimization (b) onboard fine-tuning.



## 4 VALIDATION AND RESULTS

### 4.1 Dataset generation

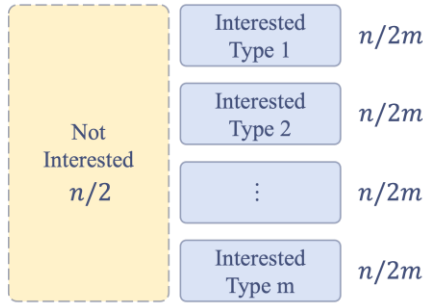


Figure 6. Dataset generation.

As previously discussed, the uncertainty of data distribution in real-world deployment makes it unsuitable for reliable evaluation of triggering mechanism performance. To enable consistent and controlled assessment, a synthetic dataset with a predefined distribution was constructed, as illustrated in Figure 6. Let  $n$  denote the total number of event samples, and  $m$  represent the number of event types considered as events of interest. Events of no interest, represented by ambient vibration in this context, account for half of the dataset ( $n/2$  samples), while the remaining half is evenly divided among the  $m$  types of events of interest. In this study,  $n$  is set as 1200 for validation. For ambient vibration signals, data is generated using a Gaussian distribution with a mean of zero and a standard deviation derived from real-world ambient data. This approach aims to closely approximate actual deployment conditions.

In this evaluation setup, three types of events are defined as events of interest: earthquake, impact, and strong wind, resulting in  $m = 3$  and  $n/6$  samples for each type. These signals are synthesized using a uniform distribution based on peak value ranges, allowing for diverse intensity levels within each event type. This structured and realistic data generation strategy ensures a balanced and reproducible dataset, enabling consistent evaluation of triggering mechanisms across a wide range of simulated scenarios.

### 4.2 Host Devices and Implementation Procedures

According to the proposed staged deployment strategy, the first stage focuses on preliminary optimization of triggering parameters using the digital twin in a resource-rich environment, such as a personal computer or workstation. The second stage is dedicated to real-time fine-tuning in real-world conditions on resource-constrained edge devices. To emulate this setup in the evaluation, Stage I was carried out on a personal computer, while Stage II was implemented on LiftNode, a low-cost microcontroller-based AIoT sensor node developed by the Laboratory of Intelligent Infrastructure at Nanyang Technological University. More specifically, the implementation is based on a dedicated middleware named TinySHM, which is currently under active development and features a hierarchical structure of basic utilities (e.g., time management, communication), mathematical operations, signal processing, and AI support (accelerated by ESP-DL library [12]). The specifications of the host devices, including main frequency and RAM capacity, are summarized in Table 5.

Table 5. Host devices specifications.

Layer	Main Freq.	RAM
PC	2.50 GHz	32 GB
LiftNode-ESP32	480 MHz	8 MB

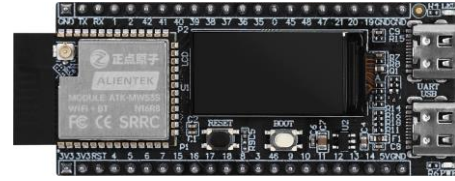


Figure 7. The main control board of LiftNode-ESP32.

ESP32 features the capability for Wi-Fi Connection designed for IoT applications. By combining onboard SD card module for large volume data storage and IoT capabilities, the proposed framework can achieve large dataset storage via Internet streaming and record-by-record onboard processing within limited onboard memory. In short, the implementation adopted a ‘more time for less space’ strategy, using longer time consumption to address the limits of restrained onboard resources. This is reasonable, as the appearance of interested events can be sparse during monitoring, leaving enough time for edge device to process. Besides, the event records are only used to provide classification label, the core part for adaptive optimization is BO, which only focuses on the observation dataset  $\mathcal{D}$ , simply data pairs of trigger parameters (threshold and duration) and performance metric ( $F_\beta$ ). Usually, it requires hundreds or thousands interested events to update the observation dataset  $\mathcal{D}$  once, which means low demand for computational capability on edge devices.

In this research, each record was formulated to 1 min long, assuming most events will not exceed this duration. Theoretically, even the time history data is longer than 1 min, the onboard NN can still easily provide the type of events using partial data, showing the robustness of the proposed framework design. For each triggered and recorded event, the host device determined its type, and update the counting variable. Only when there are enough number of events recorded, the host machine will conduct BO for triggering parameter updating.

### 4.3 Results

The detailed configurations for the optimization process is listed in Table 6, and the optimization process is recorded and visualized in Figure 8 and Figure 9. As illustrated in Figure 8, red dots represent Stage I optimization results and blue dots represent Stage II results. To accelerate convergence, a bonus factor of 1.1 is applied to the final  $F_\beta$  score for iterations where both precision and recall exceed 90%. The final results including the baseline approach and breakdown results of stage I and II are presented in Table 9.

Table 6. Validation configurations.

Parameter	Description	Value
noise std	ambient vibration	$2.92 \sim 3.57 \times 10^{-3} \text{ g}$
EQ peak val.	earthquake	$0.1 \sim 3.0 \text{ g}$
IP peak val.	impact	$0.1 \sim 3.0 \text{ g}$
SW peak val.	wind (x noise std)	$1.5 \sim 2.5$
beta	beta in Eq (1)	5
IniNum	# initial observation	15

IterNum1	# iteration in stage I	50
IterNum2	# iteration in stage II	20
bonus factor	for $p > 0.9$ & $r > 0.9$	1.1
$\tau_{lb}$	threshold lower bound	0
$\tau_{ub}$	threshold upper bound	0.01706
$d_{lb}$	duration lower bound	2
$d_{ub}$	duration upper bound	10

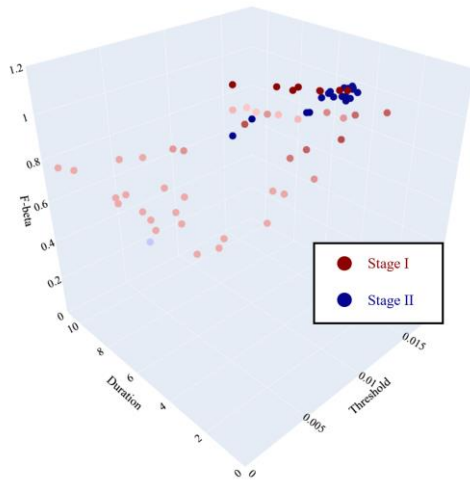


Figure 8. Optimization result overview.

Table 7. Validation results.

Item	F-beta	Precision	Recall
Baseline	0.8025	50%	100%
Stage I	1.0808	96.33%	98.37%
Stage II	1.0511	92.54%	95.72%

As shown in Figure 9 and Table 7, the baseline method, marked in black, reflects a conservative conventional configuration. While it achieves high recall, this comes at the cost of significantly reduced precision, resulting in a high false trigger rate. In contrast, the proposed staged optimization framework effectively addresses this limitation. Several key observations can be drawn from the results.

**Superior Performance of SATM.** The proposed SATM framework demonstrates clear advantages over the conventional approach, achieving  $F_\beta$  scores of 1.0808 during pre-deployment optimization and 1.0511 during onboard optimization, significantly outperforming the baseline score of 0.8025. These results highlight the effectiveness of SATM in optimizing triggering parameters for SHM applications.

**Strong Synthetic-to-Real Transferability.** The similarity between data distributions in the pre-deployment phase (based on the digital twin) and the real-world onboard phase indicates strong transferability of the optimization strategy. Although some deviations are observed due to inherent differences between synthetic and real data, such discrepancies are expected to decrease as real-world data continues to accumulate over time.

**Highly optimized energy-efficiency ratio.** For long-term, battery-powered monitoring, a trigger-based scheme is significantly more energy-efficient than always-on or duty-cycled approaches. By adaptively optimizing the triggering parameters, the overall performance can be quantitatively

evaluated using a dedicated performance metric. Depending on the initial parameter settings, energy consumption may decrease if the parameters are overly strict, or increase if they are too loose. However, one thing remains consistent: the energy-efficiency ratio improves, as reflected by the performance metric.

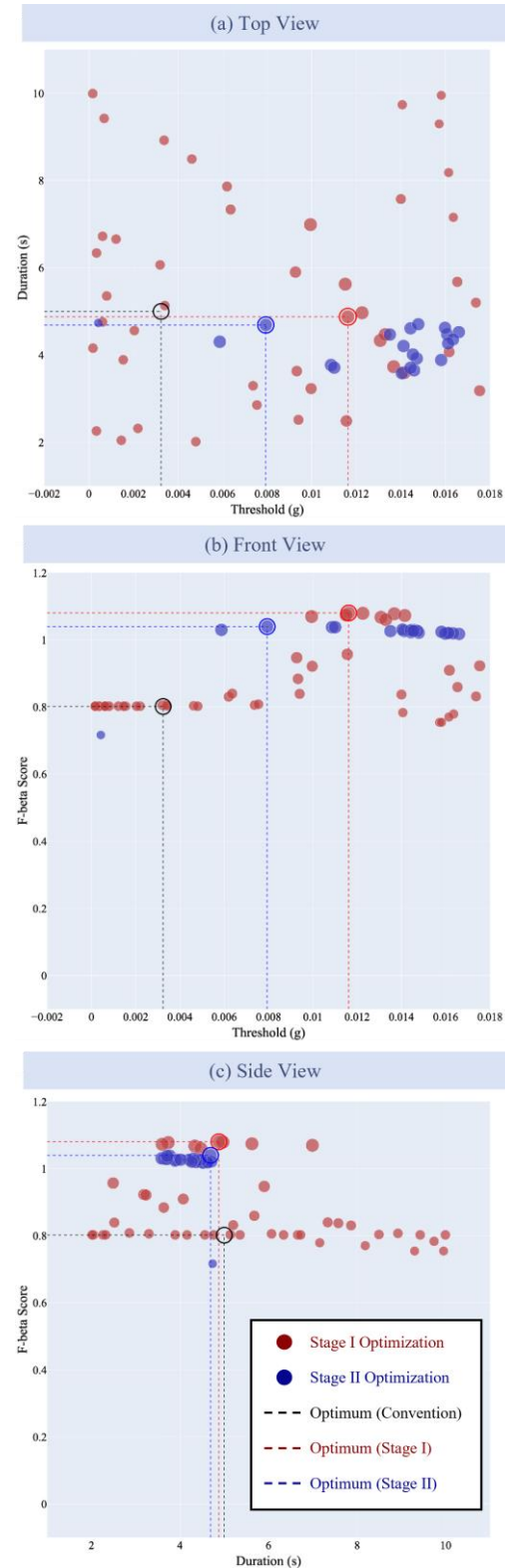


Figure 9. Optimization results: (a) top view, (b) front view, (c) side view.

**Efficiency of the Surrogate Model.** The surrogate model, trained within the digital twin environment, significantly enhances the efficiency of onboard fine-tuning. It enables the optimization process to converge in fewer iterations compared to the initial stage, achieving rapid progression toward high-quality configurations and yielding improved average performance during real-world deployment.

**Balanced Exploration and Exploitation.** The two-stage deployment strategy effectively balances the trade-off between exploration and exploitation. The first stage emphasizes exploration, exhibiting greater variability in performance metrics to thoroughly investigate the parameter space. In contrast, the second stage focuses on refining configurations based on prior knowledge, resulting in stable and robust system performance.

## 5 CONCLUSION

This study introduces a smart adaptive triggering mechanism that seamlessly combines feedback control, digital twin modeling, and Bayesian optimization. It is specifically designed to tackle key challenges such as limited adaptivity, multi-objective optimization, unknown event distributions, lack of ground truth, partial observability, and high data acquisition costs. SATM is structured around four core components: the environment, the system, the estimator, and the controller. The mechanism functions through two sequential phases: an initial pre-optimization phase utilizing a digital twin to identify a strong baseline configuration, followed by an onboard fine-tuning phase that adapts parameters under real-world deployment conditions. Evaluations confirm that SATM achieves substantial improvements in triggering performance, delivering approximately a 30% increase in the  $F_\beta$  score compared to traditional approaches. These results underscore the promise of SATM in enabling automatic, adaptive parameter tuning for trigger-based sensing systems across various application domains. In future, the proposed method will be used for long term monitoring uses and incorporate more types of events, e.g., structure failure.

## APPENDICES

### Excitation-Structure-Response Simulation:

<https://github.com/Shuaiwen-Cui/Research-Excitation-Structure-Response.git>

### Smart Adaptive Trigger Sensing:

<https://github.com/Shuaiwen-Cui/Research-Smart-Adaptive-Trigger-Sensing.git>

## ACKNOWLEDGMENTS

The authors want to gratefully acknowledge the financial support from NTU Start-up Grant (03INS001210C120), CoE Dean's Interdisciplinary Grant 2024 (03INS002320C120), and MOE AcRF Tier 1 Grants (RG121/21).

## REFERENCES

- [1] Y. Fu, "Sudden-event monitoring of civil infrastructure using wireless smart sensors," Thesis, University of Illinois at Urbana-Champaign, 2019. Accessed: Aug. 03,

2024. [Online]. Available: <https://hdl.handle.net/2142/106325>
- [2] Y. Fu, T. Hoang, K. Mechtov, J. R. Kim, D. Zhang, and B. F. Spencer, "Sudden Event Monitoring of Civil Infrastructure Using Demand-Based Wireless Smart Sensors," *Sensors*, vol. 18, no. 12, Art. no. 12, Dec. 2018, doi: 10.3390/s18124480.
- [3] Y. Ni, X. Liu, and C. Yang, "Sensor Scheduling for Remote State Estimation with Limited Communication Resources: A Time- and Event-Triggered Hybrid Approach," *Sensors*, vol. 23, no. 21, Art. no. 21, Jan. 2023, doi: 10.3390/s23218667.
- [4] S. Wang and K. Li, "Constrained Bayesian Optimization Under Partial Observations: Balanced Improvements and Provable Convergence," *arXiv.org*. Accessed: Sep. 04, 2024. [Online]. Available: <https://arxiv.org/abs/2312.03212v2>
- [5] K. Ogata, *Modern control engineering*. in Instrumentation and controls series. Prentice Hall, 2010. [Online]. Available: <https://books.google.com.sg/books?id=Wu5GpNAelzkC>
- [6] R. Ganguli, S. Adhikari, S. Chakraborty, and M. Ganguli, *Digital Twin: A Dynamic System and Computing Perspective*. Taylor & Francis Group, 2023. [Online]. Available: <https://books.google.com.sg/books?id=0o9RzwEACAAJ>
- [7] S. Cui, T. Hoang, K. Mechtov, Y. Fu, and B. F. Spencer, "Adaptive edge intelligence for rapid structural condition assessment using a wireless smart sensor network," *Engineering Structures*, vol. 326, p. 119520, Mar. 2025, doi: 10.1016/j.engstruct.2024.119520.
- [8] C. M. Bishop and H. Bishop, *Deep Learning: Foundations and Concepts*. Cham: Springer International Publishing, 2024. doi: 10.1007/978-3-031-45468-4.
- [9] T. Agrawal, "Bayesian Optimization," in *Hyperparameter Optimization in Machine Learning*, Apress, Berkeley, CA, 2021, pp. 81–108. doi: 10.1007/978-1-4842-6579-6\_4.
- [10] AnalogDevices, "ADXL362 Datasheet and Product Info | Analog Devices." Accessed: Dec. 25, 2024. [Online]. Available: <https://www.analog.com/en/products/adxl362.html>
- [11] N. M. Newmark, "A Method of Computation for Structural Dynamics," *Journal of the Engineering Mechanics Division*, vol. 85, no. 3, pp. 67–94, Jul. 1959, doi: 10.1061/JMCEA3.0000098.
- [12] Espressif, *ESP-DL*. (Feb. 25, 2025). Accessed: Feb. 25, 2025. [Online]. Available: <https://components.espressif.com/components/espressif/e-sp-dl>





# Fibre Optic Sensing for Damage Detection at Bridge Structures

# Post-tensioned wire breaks detection method using distributed acoustic sensing in bridges & viaducts.

Dinesh Lakshmanan <sup>[1,2]</sup>, Felipe Muñoz <sup>[1,2]</sup>, Javier Urricelqui <sup>[1]</sup>, Marco Jimenez-Rodriguez <sup>[1]</sup>

<sup>[1]</sup> Uptech Sensing, Pol. Ind. Mutilva Baja, 31192 Mutilva Baja, Navarra, Spain

<sup>[2]</sup> Universidad Técnica Federico Santa María, Valparaíso, Chile

Email: dinesh.lakshmanan@uptech-sensing.com, felipe.munoz@uptech-sensing.com,  
javier.urrichelqui@uptech-sensing.com, marco.jimenez@uptech-sensing.com

**ABSTRACT:** Monitoring the structural integrity of civil infrastructures, such as bridges and viaducts is crucial, as non-visible damage like post-tensioned wire breaks can lead to catastrophic failures, endangering public safety. In this study, we simulate post-tensioned wire breaks by generating controlled mechanical impacts using a sclerometer. These impacts are applied at varying distances from optical fibers cables attached to the tendons of two different structures. A novel detection framework is developed using distributed acoustic sensing (DAS) technology to identify post-tensioned wire breaks in a suspension and a concrete bridge while effectively distinguishing between vehicular noise, environmental noise, and actual wire break events. For suspension bridges, a spectrogram-based template matching approach is implemented, leveraging sub-band selection and image-based analysis to enhance sensitivity to break events while suppressing false positives from environmental noise. In concrete bridges, a deep learning-based convolutional neural network (CNN) model achieves 96% classification accuracy, outperforming traditional methods in detecting wire breaks with high precision. These approaches provide a real-time, reliable solution for structural health monitoring, offering significant advancements in distinguishing critical break events from background interference, improving bridge safety and maintenance strategies.

**KEY WORDS:** Distributed acoustic sensors, Distributed optical fiber sensors, Structural Health Monitoring, Bridge monitoring

## 1 INTRODUCTION

Bridge maintenance is crucial for infrastructure management, directly impacting public safety and economic stability. Among the key components of bridge structures, post-tensioned cables are essential for enhancing load-bearing capacity and ensuring structural integrity [1]. These high-strength steel tendons, tensioned after concrete curing, play a pivotal role in suspension and concrete bridges. However, wire breaks in post-tensioned systems present a serious risk to structural stability, potentially causing catastrophic failures [2]. Such failures have led to costly repairs and tragic accidents, emphasizing the need for advanced monitoring and detection methods.

Traditional detection methods for wire breaks include techniques such as visual inspections, electromagnetic testing, and strain gauges. While these approaches have served as the foundation for bridge maintenance, they have limitations. Visual inspections are subjective and often miss hidden defects, while electromagnetic testing is hindered by accessibility challenges and the need for specialized equipment [3]. Strain gauges, although effective in measuring tension, lack comprehensive coverage, particularly in inaccessible areas [4]. These limitations highlight the need for real-time, reliable systems for continuous monitoring of bridge infrastructure.

The detection of post-tensioned wire breaks has been investigated using Fiber Bragg Grating (FBG) sensors and acoustic emission (AE) techniques, both crucial for ensuring the structural integrity of bridges and wind turbines. FBG sensors, which are point-based, detect wire breaks by monitoring changes in natural frequency [5], while AE methods, utilizing piezoelectric transducers, capture signals associated with wire fractures [6]. Despite their effectiveness, these approaches face challenges in distinguishing wire break

signals from background noise. In contrast, Distributed Acoustic Sensing (DAS) technology presents a promising alternative by converting optical fibers into dense arrays of vibration sensors. DAS sensors offer continuous spatial coverage and capture spatiotemporal patterns, significantly enhancing the detection of wire breaks within noisy environments, particularly in large-scale structures. Additionally, DAS systems enable the tracking of event propagation along the entire length of the optical fiber, a capability absent in point sensors, which are limited to detecting localized signals and cannot monitor the full progression of an event.

DAS technology has emerged as an innovative technology that utilizes fiber optic cables to detect vibrations, enabling real-time data collection and analysis [7]. DAS technology, leveraging optical fibers, is currently used in various applications such as infrastructure monitoring [8], seismic data acquisition[9], security[10], and environmental research[11]. While DAS is typically employed for monitoring natural frequencies in Structural Health Monitoring (SHM)[12], this paper explores its use for detecting potential wire breaks in infrastructure. This technology addresses the shortcomings of traditional methods by providing reliable, continuous monitoring of the entire bridge, allowing for early detection and timely intervention to prevent minor issues from escalating into major problems.

Simulating wire breakages under controlled conditions is essential for thoroughly testing and calibrating the DAS system for detecting such failures. Field testing with actual wire breaks in post-tensioned tendons is inherently challenging and impractical, as it requires the intentional damage of structural elements, which is not a feasible approach for testing.

Controlled impact testing has been widely used in structural health monitoring to simulate damage events in prestressed concrete [13], as well as for detecting wire breakages in post-tensioned structures [14]. These methodologies substantiate the use of impact-induced stress waves as a reliable proxy for wire break simulations, enabling repeatable testing without causing irreversible structural damage. To generate these controlled impacts, a sclerometer was utilized, as it is a well-established industry method for producing stress waves that replicate those associated with actual wire failures.

The evolution of detection algorithms for post-tensioned wire breaks using DAS has been driven by the need for efficient and accurate monitoring. Traditional, labor-intensive methods have been replaced by automated systems that employ artificial intelligence, machine learning, and advanced signal processing for real-time detection, even in challenging environments. Although DAS has proven effective in controlled settings, it faces challenges such as external noise and unpredictable conditions [15]. As an example, in railway systems, DAS techniques like gradient analysis and convolution have been used for rail break detection but can struggle with varying track conditions or interference [16].

Machine learning algorithms, such as support vector machines and neural networks, have improved detection accuracy but rely on large, labeled datasets, limiting their effectiveness in dynamic environments [17]. DAS systems have been explored as a promising solution to overcome these limitations in detecting wire breaks in prestressed concrete pipes. For instance, one study introduced a DAS system combined with a pre-trained support vector machine model, achieving 99.62% accuracy in classifying vibrational signals, thus automating the detection process and improving pipeline safety [18]. Another research applied DAS to detect wire breaks by analyzing key parameters, such as zero-crossing rate and short-time energy, which allowed for precise identification and location of acoustic signals generated by wire breaks in large experimental pipelines [19]. While both studies demonstrate the effectiveness of DAS in wire break detection, they do not address other potential causes of structural failure or the influence of environmental factors and external noise, which may limit the accuracy of these systems in practical, real-world settings.

This study proposes a novel approach for detecting post-tensioned wire breaks in bridges using DAS technology. By strategically installing fiber optic cables along post-tensioned tendons, it enables continuous real-time monitoring and advanced signal processing to identify acoustic anomalies indicative of cable failures. This innovative methodology enhances bridge safety, reliability, and maintenance by addressing the limitations of current detection methods. The findings from this research demonstrate the potential of DAS to revolutionize structural health monitoring, offering a more efficient and cost-effective solution for premature failure detection and long-term infrastructure resilience.

## 2 INSTALLATION AND SETUP

An UTS-AS1000 DAS interrogator from Uptech Sensing was employed at two locations: a suspension bridge in Bear Mountain and a viaduct in Florida, both in the United States. A single-sensing optical fiber was used, and measurements were

recorded with different fiber installations. The two sites were chosen to evaluate the DAS system's performance in different structural environments.

### 2.1 Installation at Suspension Bridge

First, in the Bear Mountain suspension bridge installation, the optical fiber was structurally bonded to one of the suspension cables using epoxy resin, enabling distributed acoustic sensing along the cable. A schematic representation of the installation is provided in Figure 1, where the monitored cable is highlighted in red.



Figure 1: Schematic of the optical fiber (red line) installed at Bear Mountain bridge.

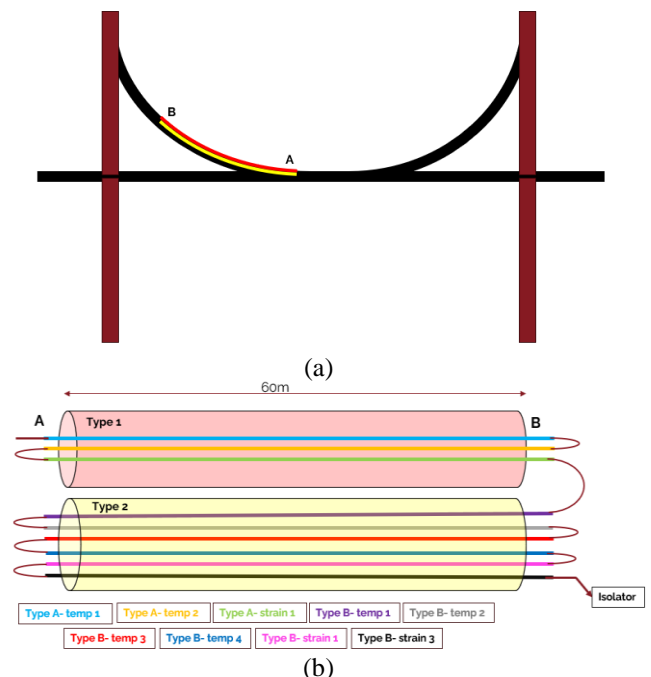


Figure 2: (a) Suspension bridge with fiber optics from Type 1 (red) and Type 2 (yellow), placed within 1 cm of each other. (b) Fiber arrangement in Type 1 (red) and Type 2 (yellow) cables with color-coded segments indicating their function.

Two fiber optic cables from different manufacturers were installed in the structure: one from Prysmian (Type 1) and one from Solifos (Type 2), both of them containing several fibers for strain sensing (tight fibers in the cable) and for temperature sensing (loose fibers). The fiber was glued to a suspension cable of the Bear Mountain metal bridge by means of an epoxy



resin. These two fibers, strain and temperature, are widely used in industry when measuring with distributed strain and temperature sensors (DTSS), being the first tight bonded, thus sensitive to temperature and mechanical deformations, while the latter loosely bonded, therefore only much less affected by strain variations. However, for DAS sensing, both fibers will detect the acoustic events, since the sensitivity is highly increased with respect to a DTSS, but it is expected to have higher attenuation levels in loose fibers (temperature) rather than in tight fibers (strain).

The schematic representation of the cable installed in the structure is shown in Figure 2(a). Type 1 is highlighted in red, while Type 2 is highlighted in yellow. The Type 1 cable contains three fibers—two temperature-sensitive and one strain-sensitive. The Type 2 cable contains six fibers—four temperature-sensitive and two strain-sensitive. Together, they form a total of nine segments, each of the 60-m-long. The figure drawn is scaled for a better representation of the scenario.

A 540 m composite fiber was formed by fusion-splicing the nine 60 m fiber segments in series. The purpose of creating this composite fiber was to investigate the impact of different fiber couplings on the measurements obtained by the DAS sensor, with the goal of determining whether significant differences in the results could be observed. The splicing at the different ends of fibers A and B is shown in Figure 2(b), with each fiber represented by a distinct color for clarity. In Type 1, the temperature-sensitive fibers are shown in blue and orange, while the strain-sensitive fiber is in green. In Type 2, the temperature-sensitive fibers are represented in purple, gray, red, and blue. The strain-sensitive fibers in Type 2 are shown in pink and black. The figure drawn is scaled for a better representation of the scenario.

After creating the 540 m composite fiber, two distinct cables, each incorporating two different fiber types, were employed to evaluate the performance of both the cables and the optical fibers. The fiber-cable combinations were assessed to evaluate their impact on the system's ability to minimize false positives, improving the reliability of event detection.

## 2.2 Installation at Concrete Bridge

Next, the interrogator was deployed at the Roosevelt Viaduct in Stuart, Florida, a major highway, where measurements were taken at the second location. It has a twin parallel drawbridge, one for northbound traffic and the other for southbound traffic. The interrogator was connected to a previously installed fiber for DTSS measurements in a road bridge in Florida. The sensing optical fiber is affixed to one of the tendons using an industrial-grade adhesive, ensuring strong coupling for effective vibration and acoustic sensing. This configuration enables the detection of structural responses to environmental and vehicular loads, facilitating distributed acoustic sensing along the bridge.

The optical fiber was installed inside the structure of the Roosevelt Viaduct, with its placement highlighted in red in both images in Figure 3: In Figure 3(a), the exterior of the viaduct is shown for reference, providing context for the installation. In Figure 3(b), the fiber was visibly integrated within the interior, demonstrating its positioning for structural monitoring. This setup was designed to optimize the detection, ensuring effective internal assessment of the viaduct's condition. Additionally, the impacts were generated at different

distances from the fiber to evaluate the influence of the distance of the impact from the fiber on the detection performance.



(a)



(b)

Figure 3: Optical fiber installation at Roosevelt Viaduct: (a) Exterior perspective from the structure, (b) Interior placement within the structure. Installed fiber is highlighted in red.

Suspension bridges like the Bear Mountain metal bridge rely on cable-supported flexibility, allowing vibrations to dissipate through tensioned cables and the deck, resulting in distributed and oscillatory wave propagation. In contrast, concrete bridges such as the Roosevelt in Florida, with their rigid structural elements, transmit vibrations more directly through the solid slab and supporting components, leading to localized wave reflections and attenuation. This fundamental difference affects how vibrations propagate through each type of bridge[20]. This distinction in vibration behavior underscores the need for tailored monitoring approaches for each bridge type. With this understanding in mind, the impacts on both structures are approached differently.

## 3 WIRE BREAK DETECTION

### 3.1 Experimental Design

As introduced before, a controlled approach was employed, utilizing a sclerometer to generate impact events, simulating the sound and vibrations generated by a post-tensioned cable break, at varying distances from an optical fiber sensing cable affixed to the tendons of two distinct structures. The study analyzed the DAS system's response to controlled impacts to assess its ability to detect, characterize, and locate potential tendon failures in real-world conditions, while minimizing the possible false cases generated due to other events that might produce similar sound patterns.

On one hand, the DAS sensor is configured with a spatial resolution of 2m, a gauge length of 2m, and an acquisition frequency of 2 kHz, monitoring a 540-meter-long optical fiber cable on the suspension bridge installation. On the other hand, for the concrete bridge tests, the system used spatial resolution and gauge length of 3m, with the same acquisition frequency of 2 kHz, to monitor a 3.5-kilometer-long optical fiber.

In the suspension bridge configuration, impact events were generated using a sclerometer to replicate the characteristic waveforms of wire breakage. These impacts were delivered at varying angles relative to the suspension cable axis, enabling the investigation of strike orientation on the propagation of acoustic signals through the structure. As depicted in Figure 4, the monitoring optical fiber, highlighted in red, was positioned along the cable to capture the resulting waveforms. A series of tests was conducted under controlled conditions, with the impact responses systematically recorded for each test. The waveform of the sclerometer hits were obtained for angles of 0°, 45° and 90° with respect to the position of the monitoring fiber. The resulting data were organized into a comprehensive dataset, facilitating further analysis of signal variations as a function of impact direction and intensity.

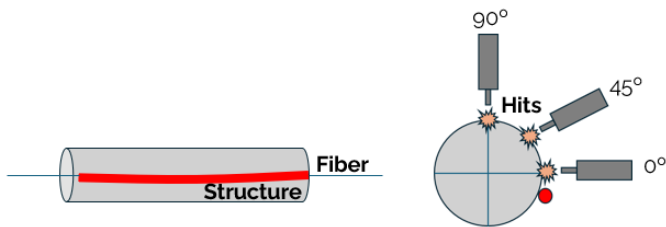


Figure 4: Fiber optic scheme (red line) in suspension cable and sclerometer strike angle diagram relative to the position of the monitoring optical fiber.

For the concrete bridge, impact events were generated at two carefully selected locations to assess the system's sensitivity to structural vibrations. As shown in Figure 5, the sensing fiber highlighted in red was positioned in the concrete slab to capture the resulting waveforms. The first set of impacts was applied at the midpoint of the 19th span, directly on the ground, to simulate the propagation of vibrations through the bridge deck. The second set of impacts was introduced on the ceiling, generating acoustic waves that traversed the upper structural elements. The impact events were generated at varying distances from fiber (0.7112m, 1.4224m, 2.032m, 3.3528m) in both cases. The resulting data were organized into a comprehensive dataset, facilitating further analysis of signal variations as a function of impact direction and intensity.

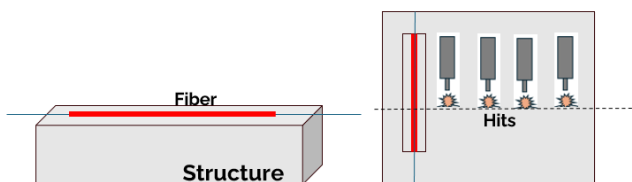


Figure 5: Fiber optic scheme (red line) in concrete slab and sclerometer strike diagram relative to the position of the monitoring optical fiber in the bridge.

## 3.2 Data Analysis

### 3.2.1 Data Analysis on Suspension Bridge

Data analysis plays a crucial role in monitoring suspension bridges, enabling the assessment of structural integrity and the identification of potential issues. Nine fiber segments were used to monitor the same region, arranged one after the other in parallel. This configuration results in repeated measurements, with the hit observed across all nine segments. The fiber runs from A to B, as shown in the Figure 2(a) and Figure 2(b).

In this study, the sclerometer hits were obtained for angles of 0°, 45°, and 90° with respect to the position of the monitoring fiber. The waveform of the sclerometer hits was recorded at an angle of 0° relative to the position of the monitoring fiber. Figure 6 presents the first two segments, where the x-axis range from 20 to 80 meters corresponds to the first fiber segment, and the range from 80 to 140 meters represents the second fiber segment. Signal amplitudes are represented by the color scale previously shown, where negative values (down to -2.0 a.u) are indicated by blue hues and positive values (up to 2.0 a.u) are depicted in red, with near-zero values shown in white. All the waterfall plots were generated using this fixed amplitude limit to ensure consistent visual comparison across different events. Distinct diagonal and vertical patterns can be observed in the data distribution.

Two segments monitor the same zone of the suspension cable, and the sclerometer hit was clearly visible in both, characterized by the diagonal pattern. This pattern was attributed to the propagation of the hit made at 0° angle respect to the structure, captured as the disturbance moves through the fiber. Notably, the second segment exhibits a reversed version of the pattern seen in the first segment, which results from the light in the second segment traveling in the opposite direction compared to the first, producing a mirror image of the hit's propagation.

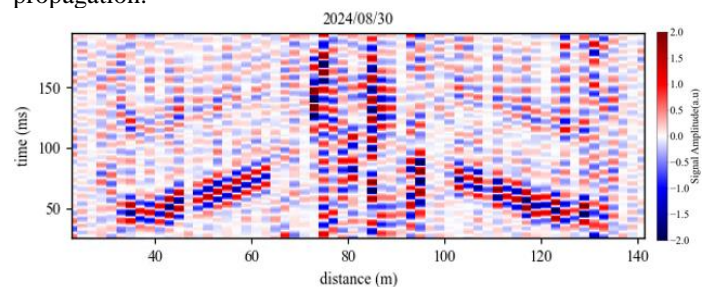


Figure 6: Waterfall data from two segments with the hits from the sclerometer.

Additionally, a fainter hit was observed closer to time 100ms, which was produced by the rebound of the sclerometer hit. It is important to note that whenever a hit is produced, it is usually followed by several rebounds, resulting in the consistent visibility of the secondary, fainter hit. Noise was also observed around the 80-meter mark as a vertical pattern, at the end of cable B, shown in Figure 2(a), is highly susceptible to wind exposure. This noise was not observed at end A, as this portion of the bridge was less affected by winds compared to the other end.

A waterfall diagram containing a sclerometer stroke for the entire length of the fiber is shown in Figure 7. Diagonals with opposite slopes were observed, which were repeated along the

spatial axis (x-axis) and were found to correspond to the acoustic signals acquired by the nine optical fiber segments connected in series. Additionally, multiple diagonals over time (y-axis) were identified, representing replicas of the blow that had been generated by the sclerometer.

When comparing the signals acquired from the center of each optical fiber region, it was evident that the strain fibers labeled as "c," "h," and "i" demonstrated the highest sensitivity. This was observed through both temporal and spatial replications, as each of these fibers consistently detected three replicates of the same event at different time intervals and locations. The repeated detection at multiple spatial points and across various times indicates that these fibers were particularly responsive to the transient events, highlighting their effectiveness in capturing the signal. In contrast, the temperature fibers had demonstrated variable sensitivity; fiber "d" had been able to detect the third replication slightly, whereas fibers "a," "b," "e," and "f" had not exhibited such detection capabilities. The consistency of the replicated patterns was observed to indicate a high degree of repeatability in the impact response of the sclerometer. This observation was found to highlight the reliability of strain-sensitive fibers in capturing high-frequency acoustic signals. Moreover, the periodic nature of the detected hits was noted, further reinforcing the consistency of the acquired signals. The temporal waveform at the center of each optical fiber region is presented in Figure 8.

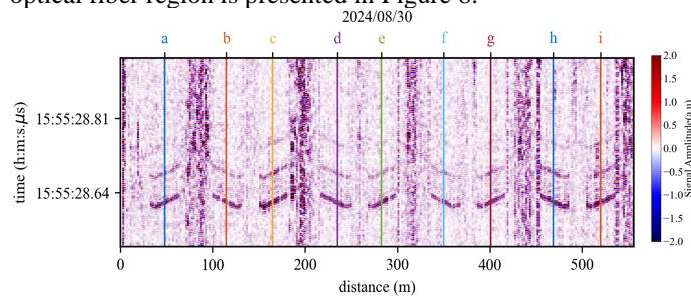


Figure 7: Waterfall diagram showing a sclerometer stroke hits obtained for angles of 0° acquired by the DAS sensor.

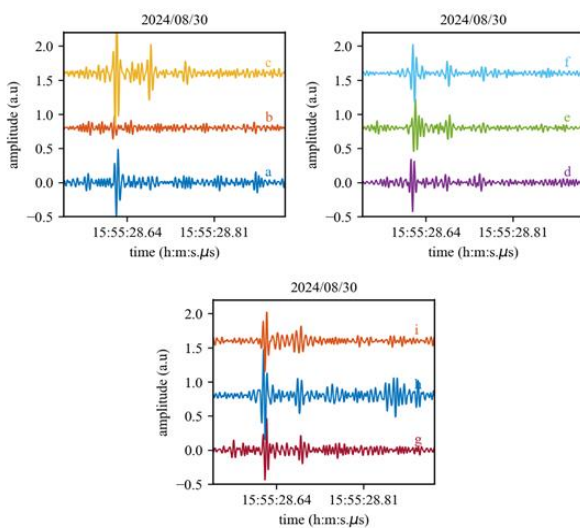


Figure 8: Waveforms at different spatial positions of the monitoring fiber. The spatial positions correspond to those indicated in Figure 7.

The comparison of the performance across the nine segments highlighted distinct differences between fiber types, but no significant differences between cable types. As seen in Figure 8, the strain fibers exhibited a pronounced detection pattern, while the temperature fibers showed a more subtle response. This difference is due to the tight bonding of strain fibers, which makes them highly sensitive to vibrations but also more prone to noise. In contrast, temperature fibers, with their loose bonding, produced less noise but were less effective at detecting vibrations. Therefore, the choice of fiber should depend on the specific application, with strain fibers ideal for high-sensitivity detection and temperature fibers better suited for scenarios where noise reduction is a priority. Additionally, as shown in Figure 7, the detection patterns were consistent across different cables when the same fiber type was used, indicating that cable type had a negligible impact on the overall detection performance.

A similar analysis was conducted for impact angles of 45° and 90° with respect to the cable, revealing variations in the acquired waveforms. At 90°, as shown in Figure 9. The amplitude of the diagonals was observed to be lower than at 0°, and the temporal replicas of the signal could no longer be detected. The corresponding temporal waveform at the center of each optical fiber region, depicted in Figure 10, indicated that the amplitude of the impacts was comparable to background noise, making detection challenging without spatial information.

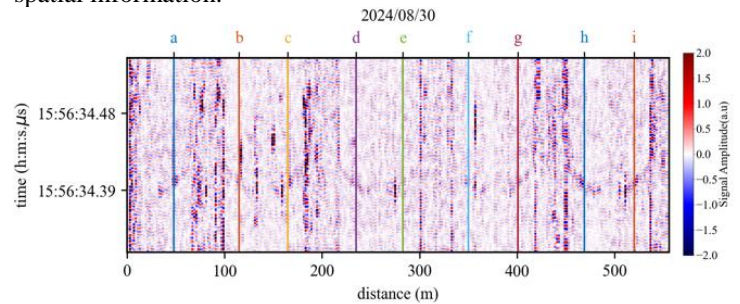


Figure 9: Waterfall diagram showing a sclerometer stroke hits obtained for angles of 90° acquired by the DAS sensor.

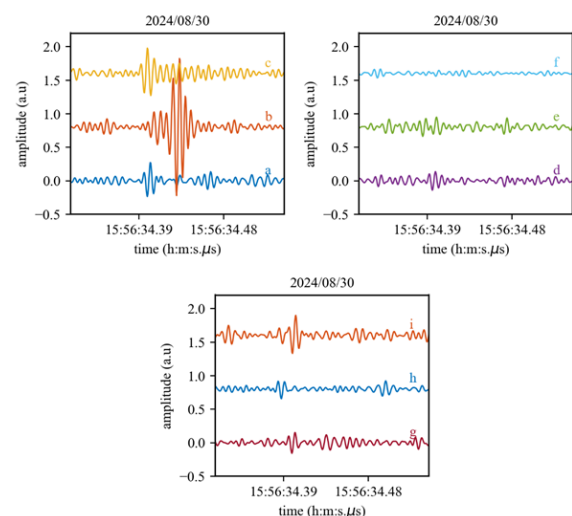


Figure 10: Waveforms at different spatial positions of the monitoring fiber. The spatial positions correspond to those indicated in Figure 9.



For the 45° impact, the amplitude of the diagonals, which represents the signal strength along the diagonal axis of the data, as shown in Figure 11, was found to be similar to that of the 0° impact but greater than that of the 90° impact. While temporal replicas were still visible, they appeared significantly attenuated. The temporal waveform at the center of each optical fiber region, presented in Figure 12, demonstrates that the amplitude of the initial impact was distinguishable from noise, whereas the replicas became indistinguishable. These findings indicate that while monitoring fiber effectively captured acoustic events at different impact angles, the detectability of replicated signals was highly dependent on impact orientation, with attenuation effects becoming more pronounced at higher angles.

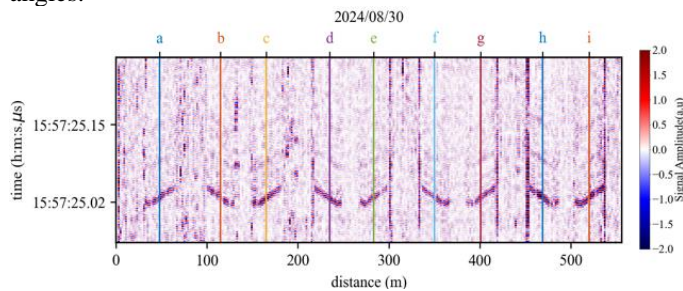


Figure 11: Waterfall diagram showing a sclerometer stroke hits obtained for angles of 45° acquired by the DAS sensor.

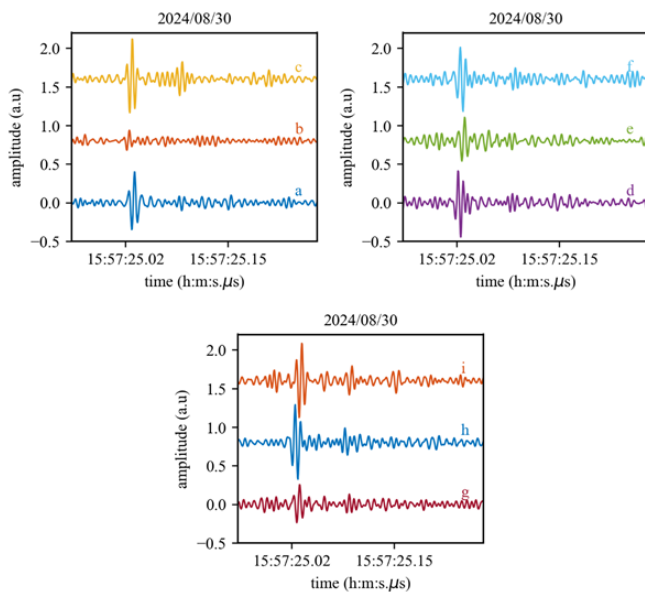


Figure 12: Waveforms at different spatial positions of the monitoring fiber. The spatial positions correspond to those indicated in Figure 11.

The monitoring composite fiber effectively captured acoustic events from different impact angles, although performance depended heavily on the impact orientation. Attenuation effects increased at higher angles, a phenomenon that field experts link to air gaps between the structure and cables at certain orientations, likely caused by installation flaws. Orientations where fibers were closer together experienced less gap interference, resulting in better event detection. This sensitivity profile indicates that high-energy events like tendon ruptures, especially in well-coupled areas, would produce strong, easily detectable signals similar to sclerometer impacts recorded

outside poor coupling zones. These findings strengthen the system's potential for reliably detecting critical structural events, boosting confidence in its monitoring ability for vital infrastructure.

### 3.2.2 Data Analysis on the Concrete Bridge

In the context of monitoring concrete bridges, data analysis plays a crucial role in assessing integrity and detecting potential issues. For this analysis, data were recorded from hits generated by a sclerometer, simulating events such as wire breaks. Unlike suspension bridges, where the fiber installation allows for repetition across multiple segments, the configuration of fibers in concrete bridges is unique, meaning repetition of patterns across segments is not expected. A typical hit pattern detected by the interrogator is shown in Figure 13. The pattern clearly shows a hit detected across multiple spatial points, with surface waves propagating from the point of impact to adjacent locations. This wave distribution aids in detecting the event at various points, crucial for assessing the damage's extent.

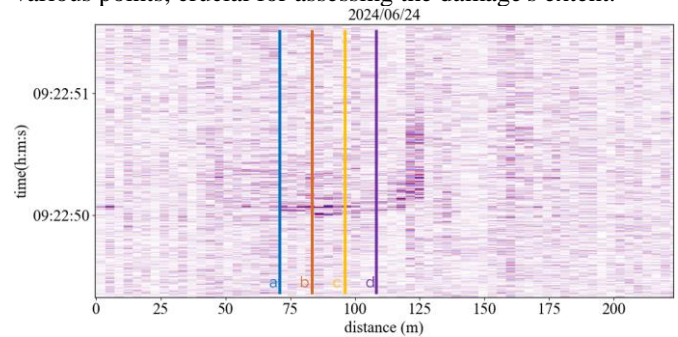


Figure 13: Waterfall diagram showing a sclerometer stroke acquired by the DAS sensor.

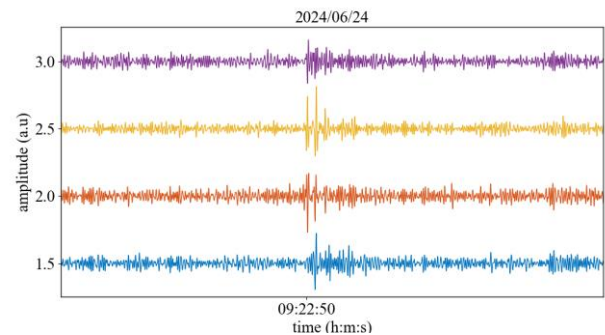


Figure 14: Waveforms at different spatial positions of the monitoring fiber. The spatial positions correspond to those in Figure 13.

A detailed analysis of the acquired signals was conducted, and the temporal waveform at points "a" to "d" was presented in Figure 14. The hits were distinctly observed, and the duration of each blow was measured at approximately the same time 09:22:50. Furthermore, variations in amplitude across different spatial points were identified, suggesting differences in their sensitivity and signal attenuation. The time-domain characteristics of the acquired signals were analyzed, revealing that certain spatial points were more effective at detecting transient events due to their proximity to the point of impact and the propagation of surface waves. It was observed that signals from these locations exhibited stronger and clearer responses. Optimizing fiber selection and positioning could enhance detection accuracy by placing fibers at strategic

locations where the signal propagation is most pronounced, thereby capturing more relevant data.

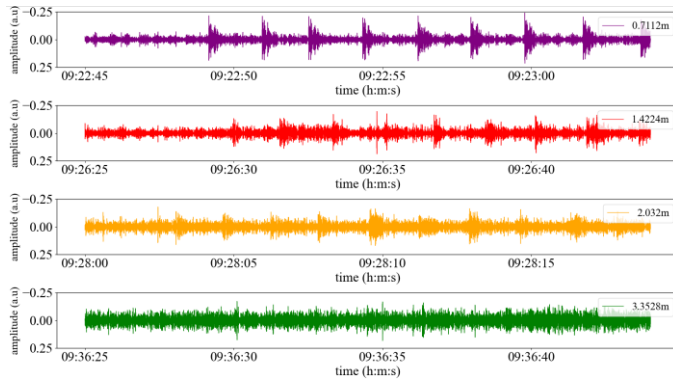


Figure 15: Waveforms at central positions of the fiber monitoring for different hitting lengths from the fiber.

The impacts from the sclerometer at the different distances from the fiber were taken, and the mid spatial point is chosen from all the impacts, and their temporal evolution is shown in Figure 15. The decrease in hit amplitude with increasing depth from the sensor is primarily due to the fundamental principles of seismic wave propagation in concrete. As acoustic waves travel through the slab, their energy disperses, leading to geometric attenuation. Additionally, material absorption within the concrete causes further energy loss. Scattering effects due to variations in the concrete's composition and microstructural heterogeneities also contribute to signal attenuation. These combined factors naturally result in a reduction in amplitude as the distance from the source increases.

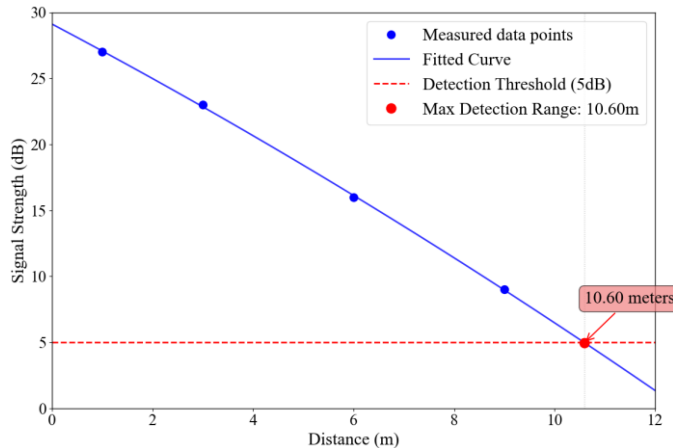


Figure 16 Maximum detection range estimation for tendon break monitoring.

To quantify the effective detection range for tendon break monitoring, the exponential attenuation relationship observed in Figure 15 was extrapolated using curve fitting analysis. The measured signal decay follows  $y = ae^{-bx} + c$ , with amplitudes decreasing from 27 dB at 1 m to 9 dB at 9 m due to geometric spreading, material absorption, and scattering effects in concrete. A minimum detection threshold of 5 dB was established to ensure reliable discrimination of tendon break signals from background noise. The fitted model, as shown in Figure 16 predicts a maximum effective detection range of 10.6 meters, beyond which the combined effects of wave

propagation losses render tendon break detection unreliable. This analysis provides essential parameters for determining sensor spacing in structural health monitoring systems, ensuring complete coverage for the early detection of prestressing tendon failures in concrete bridges.

In conclusion, this analysis highlights the influence of the distance between the sclerometer hits and the fiber on the amplitude of the detected signals. The decrease in hit amplitude with increasing distance is attributed to seismic wave propagation, material absorption, and scattering effects within the concrete. To enhance the sensitivity and reliability of the monitoring system, it is recommended that the sensing fiber be placed closer to the structure, allowing for more accurate detection of breaks and better signal capture.

### 3.3 Detection Algorithm

#### 3.3.1 Detection Algorithm for Suspension Bridges

The hits from the suspension and concrete bridge were clearly observed in the data, with the temporal traces from the relevant spatial points carefully explored to study the generated impacts. These impacts were analyzed in detail to understand their characteristics and temporal evolution. This was used effectively in designing the detection algorithm for the two structures.

As for the suspension bridge, in this study, a spectrogram-based method was proposed, utilizing only a single fiber segment. A spectrogram-based template matching approach was employed for the suspension bridge to detect transient events in time series data across multiple sensor channels. This method was chosen for its ability to detect transient events across multiple optical fiber segments by leveraging spectrogram-based template matching. The use of multiple optical fiber segments enhances the spatial robustness of the detection, reducing the likelihood of false positives and ensuring reliable identification of events. Additionally, the repetition of results across various fiber segments provides strong validation for detected events, reinforcing the reliability of the method. This approach is preferred over machine learning as it offers a clear, interpretable process that directly correlates spectral energy variations with event detection, without the complexity and data dependency often associated with machine learning models.

The methodology consisted of sequential steps, beginning with spectrogram computation. Given a time series  $x(t)$ , its time-frequency representation was obtained using the short-time Fourier transform (STFT), producing a spectrogram  $S(f, t)$ , where  $f$  represented frequency and  $t$  represented time. For the spectrogram computation, a window length of 256 samples and an overlap of 248 samples were used. This transformation enabled the localization of spectral energy variations over time, forming the basis for subsequent feature extraction.

To enhance sensitivity to specific frequency components, sub-band selection was performed by isolating predefined frequency ranges from the spectrogram. Two sub-bands were defined for analysis: Sub-band 1 ranged from 90 to 180 Hz, and Sub-band 2 ranged from 350 to 440 Hz. This process yielded refined sub-band spectrograms  $S'(f, t)$ , where only the relevant spectral components were retained. Each extracted sub-band spectrogram was then treated as an image  $I(f, t)$  in which pixel

intensities corresponded to spectral power. This conversion facilitated the application of image-processing techniques for event characterization.

The core of the detection methodology involved template matching, in which a predefined temporal template was convolved with  $I(f, t)$  to identify characteristic signal patterns. The template was designed with three consecutive time slots, where the first and third slots were assigned a weight of -1, and the central slot was assigned a weight of 1. This structure enhanced contrast by emphasizing transient spectral changes while suppressing background variations. The template extended across the entire frequency sub-band, ensuring comprehensive coverage of the targeted spectral range. Through convolution, a response function was obtained that highlighted localized temporal variations indicative of hits.

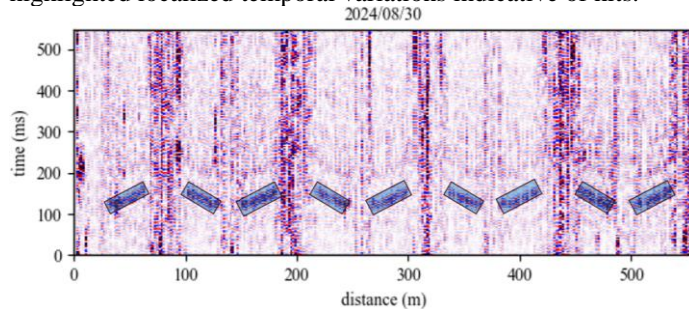


Figure 17: Detection of the hits in the suspension bridge.

To ensure spatial robustness, the template matching procedure was applied independently across multiple fiber sensor locations, generating a three-dimensional response matrix  $M(c, t)$  where  $c$  represented the sensor channel and  $t$  denoted time. Each entry in  $M(c, t)$  corresponded to the template matching response at a given location and time. A hit was considered when multiple sensor channels exhibited a significant response simultaneously, thereby reducing the likelihood of false positives caused by localized noise or isolated fluctuations. A thresholding operation was applied to  $M(c, t)$  to identify significant activations, ensuring that only strong and spatially correlated events were retained. The detection results are presented in Figure 17, where the significant activations identified through the thresholding operation are distinctly visualized across the sensor channels. The algorithm successfully identified the sclerometer impact points, which are highlighted in pale blue within the figure.

Despite the use of a single segment, minimal false-positive rates were achieved. The analysis was conducted exclusively on this segment, demonstrating the effectiveness of the proposed approach in reducing false positives. These results highlight the spatial and temporal correlations of the detected hits, demonstrating the effectiveness of the method in identifying true events while minimizing false positives. The figure provides a comprehensive overview of the detected impacts within the given time frame and sensor locations. By integrating sub-band selection, image-based template matching, and distributed sensor analysis, the approach provided a scalable and robust solution for detecting transient events in DAS applications. High sensitivity to localized perturbations was achieved while mitigating false positives, making the methodology well-suited for health monitoring and real-time monitoring for the suspension bridge.

### 3.3.2 Detection Algorithm for Concrete Bridges

This study presents a deep learning-based approach for detecting wire breaks in concrete bridges utilizing Convolutional Neural Networks (CNNs). Unlike suspension bridges, which benefit from repetition across multiple segments, allowing for template matching, concrete bridges lack this repeatability in optical fiber segments, necessitating a different method. Machine learning is preferred over traditional techniques because it can automatically learn complex patterns, eliminating the need for manual feature extraction. CNNs are ideal for this task as they efficiently learn complex patterns and features from data, making them highly effective for detecting wire breaks in concrete bridges.

The dataset consists of positive images showing a pattern from hits and negative images of patterns from vehicles and other patterns that are not hits. To generate a more robust dataset for training, a Generative Adversarial Network (GAN) was utilized for data augmentation, as it generated realistic synthetic data that enhanced the training dataset. GAN-based data augmentation techniques were employed here to create additional images, ensuring a larger and more diverse set of training data. The images were preprocessed and resized for uniformity, and the dataset was split into training and testing sets. Positive images were labeled as 1, and negative images as 0. This ensured the model could effectively learn to distinguish between the two classes.

The CNN architecture consists of five fully connected convolutional layers, each followed by a max pooling layer, which reduces the spatial dimensions while retaining key patterns. The number of filters increases progressively with the layers, to capture both low- and high-level features. The extracted feature maps are then flattened and passed through a fully connected layer, followed by a single neuron with a sigmoid activation to classify the images into two categories: breaks (1) or not possible breaks (0).

The training process and the model's learning progression are illustrated in Figure 18, which presents both training and validation loss trends throughout 15 epochs. Two side-by-side plots are shown: the left plot depicts a consistent decrease in loss values for both the training and validation datasets, while the right plot demonstrates an increase in accuracy metrics, which plateaued around 95%. The model was trained efficiently, and convergence was achieved with minimal overfitting, as indicated by the close alignment between validation and training performance throughout the training period.

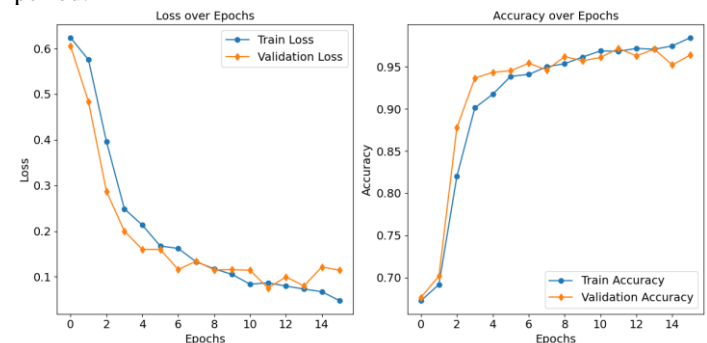


Figure 18 Training and validation loss curves over 16 epochs.



Post training, the model's performance was evaluated on the test set, where predictions were converted into binary labels. Standard evaluation metrics, including accuracy, precision, recall, and F1-score, were calculated. Performance metrics and the confusion matrix are presented in Table 1 and the classification report is presented in Table 2, offering a detailed overview of the model's effectiveness. Confidence scores and entropy were also calculated to measure the model's certainty in its predictions.

Table 1 Confusion Matrix

	Predicted Negative	Predicted Positive
True Negative	673	19
True Positive	18	313

Table 2 Classification Metrics

Type of Perturbation	Precision	Recall	F-score
Negative	0.97	0.97	0.97
Positive	0.94	0.95	0.94

The predicted labels were visually compared with true labels on a subset of test images to assess the model's accuracy. Based on the results obtained, the proposed deep learning-based model demonstrates robust performance in detecting wire breaks in concrete bridges. The model achieved an overall accuracy of 96%, as evidenced by the confusion matrix and classification report. Visual comparisons of predicted and true labels for a subset of test images highlighted the model's strengths in correctly identifying wire breaks, while also revealing some misclassifications that can be improved. These insights are crucial for refining the model and enhancing its performance. This method's potential to advance structural health monitoring, particularly in the context of bridge inspections, underscores its importance in improving the safety and maintenance of infrastructure.

#### 4 CONCLUSION

A comprehensive method was developed for detecting post-tensioned wire breaks in both suspension and concrete bridges using DAS. By tailoring techniques to each bridge type, the approach enabled real-time monitoring and effective detection, classification, and localization of cable break events. These advancements offer valuable applications in improving the safety and maintenance of critical infrastructure.

In the suspension bridge, the monitoring fiber captured acoustic events at various impact angles; however, signal detectability was strongly influenced by orientation. The comparison of performance across different segments revealed distinct differences between fiber types, though no significant differences were observed between cable types. The strain fibers exhibited a pronounced detection pattern, while temperature fibers showed a more subtle response. Based on these findings, a spectrogram-based template matching approach was developed, incorporating sub-band selection and

image-based matching. This method enabled accurate detection while maintaining low false positive rates, even when relying on a single fiber segment. Therefore, the choice of fiber should depend on the specific application, with strain fibers ideal for high-sensitivity detection and temperature fibers more appropriate for environments requiring minimal noise.

For the concrete bridge, a decrease in signal amplitude was observed as the distance from the fiber increased. This emphasized the need to place the fiber close to the structural surface. A CNN achieved 96% classification accuracy, outperforming traditional methods in both precision and false positive reduction. Data augmentation using a GAN further improved model generalization by creating a diverse training dataset.

These tailored methodologies provide effective, real-time monitoring strategies for both bridge types. Future efforts should focus on integrating the proposed techniques to improve system accuracy and adaptability in complex environments, and on exploring additional data augmentation strategies to further enhance model robustness.

#### FUNDING

This work has been partially funded by the following projects: PTQ2021-011958 Torres Quevedo Grant from Ministerio de Ciencia, Innovación y Universidades, Government of Spain, 0011-1408-2022-000020 and 0011-1408-2023-000026. Doctorados Industriales of 2022 and 2023 from the Government of Navarra.

#### REFERENCES

- [1] K. D. Bondy and B. Allred, *Post-Tensioned Concrete: Principles and Practice*, Second Edition, 2nd ed. Boca Raton, FL: CRC Press, 2015.
- [2] T. Vogel and S. Fricker, "Condition survey and evaluation of an early post-tensioned bridge verified after removal," *Structure and Infrastructure Engineering*, vol. 10, no. 3, pp. 359–374, 2013.
- [3] M. I. Silva, E. Malitckii, T. G. Santos, and P. Vilaça, "Review of conventional and advanced non-destructive testing techniques for detection and characterization of small-scale defects," *Prog. Mater. Sci.*, vol. 138, p. 101155, 2023.
- [4] W. Corte and P. Bogaert, "A case study on strain gauge measurements on large post-tensioned concrete beams of a railway support structure," *Insight*, vol. 45, pp. 822–826, 2003.
- [5] S. Mahmoudkhani, B. Algohi, J. Zhao, H. Ling, A. A. Mufti, and D. J. Thomson, "Acoustic emissions sensor and fuzzy C-mean clustering-based break detection in post-tensioning tendons," *IEEE Sensors*, 2019.
- [6] Xu, R., Lange, A., Käding, M., Ostermann, J., & Marx, S. (2024). Detecting wire breaks in post-tensioned tendons of wind turbines: A signal energy spectrum analysis approach. *Proceedings of the 10th European Workshop on Structural Health Monitoring (EWSHM 2024)*, June 10-13, 2024.
- [7] X. Zhang, J. Qi, X. Liang, Z. Guan, Z. Liu, C. Zhang, D. Chen, W. Deng, C. Xu, X. Wang, et al., "Fiber-optic distributed acoustic sensing for smart grid application," *Photonics*, 2025.
- [8] A. Kuttybayeva, A. Abdykadyrov, G. Tolen, A. Burdin, V. Malyugin and D. Kiesewetter, "Application of Distributed Acoustic Sensors Based on Optical Fiber Technologies for Infrastructure Monitoring," 2024 International Conference on Electrical Engineering and Photonics (EEExPolytech), Saint Petersburg, Russian Federation, 2024.
- [9] M. Li, H. Wang, and G. Tao, "Current and Future Applications of Distributed Acoustic Sensing as a New Reservoir Geophysics Tool," *Open Petroleum Eng. J.*, vol. 8, no. 1, pp. 272–278, 2015.
- [10] Ali Masoudi, Gilberto Brambilla; Distributed acoustic sensing with optical fibres: Fundamentals and applications. *J. Acoust. Soc. Am.* 1 October 2022.
- [11] Y. Shang, M. Sun, C. Wang, J. Yang, Y. Du, J. Yi, W. Zhao, Y. Wang, Y. Zhao, and J. Ni, "Research progress in distributed acoustic sensing techniques," *Sensors*, vol. 22, no. 16, p. 6060, 2022.

- [12] X. P. Zhang, Y. Y. Shan, Y. H. Zhang, J. Reng, M. M. Chen, and Y. X. Zhang, "An enhanced distributed acoustic sensing system based on the interactions between microstructures," *J. Phys. Conf. Ser.*, vol. 1065, no. 25, p. 252011, 2018.
- [13] C. R. Farrar and K. Worden, "An introduction to structural health monitoring," *Philos. Trans. A Math. Phys. Eng. Sci.*, vol. 365, no. 1851, pp. 303–315, Feb. 2007.
- [14] M. Maizuar, L. Zhang, S. Miramini, P. Mendis, and C. Duffield, "Structural health monitoring of bridges using advanced non-destructive testing technique," in *ACMSM25*, C. Wang, J. Ho, and S. Kitipornchai, Eds., *Lecture Notes in Civil Engineering*, vol. 37, Springer, Singapore, 2020.
- [15] R. Rueda-García, A. Pérez, and M. López, "Detection of wire break events in prestressed concrete pipes using Distributed Acoustic Sensing systems," *Journal of Structural Engineering*, vol. 150, no. 4, pp. 04023023, Apr. 2024.
- [16] A. Wagner, A. Nash, F. Michelberger, H. Grossberger, and G. Lancaster, "The effectiveness of distributed acoustic sensing (DAS) for broken rail detection," *Energies*, 2023.
- [17] M. Bublin, "Event detection for distributed acoustic sensing: Combining knowledge-based, classical machine learning, and deep learning approaches," *Sensors*, vol. 21, no. 22, p. 7527, 2021.
- [18] T.-Y. Zhang, C.-C. Zhang, B. Shi, Z. Chen, X. Zhao, and Z. Wang, "Artificial intelligence-based distributed acoustic sensing enables automated identification of wire breaks in prestressed concrete cylinder pipe," *Journal of Applied Geophysics*, Apr. 2024.
- [19] L. Rueda-García, D. Tasquer-Val, P. Calderón-Bofías, and P. A. Calderón, "Detecting wire breaks in prestressed concrete pipes: an easy-to-install distributed fibre acoustic sensing approach," *Structural Health Monitoring-an International Journal*, Mar. 2024.
- [20] N. J. Gimsing and C. T. Georgakis, *Cable Supported Bridges: Concept and Design*, 3rd ed. Chichester, UK: John Wiley & Sons, 2012.

# Detection of steel fractures in existing prestressed bridges with DFOS

Harald Burger<sup>1</sup>, Nicholas Schramm<sup>2</sup>, Oliver Fischer<sup>1,2</sup>

<sup>1</sup>Chair of Concrete and Masonry Structures, TUM School of Engineering and Design, Technical University of Munich,  
Theresienstraße 90, Building N6, 80333 München, Germany

<sup>2</sup>Büchting + Streit AG, Gunzenlehstraße 22 - 24, 80689 München, Germany

email: harald.burger@tum.de, nicholas.schramm@buechting-streit.de, oliver.fischer@tum.de

**ABSTRACT:** Prestressed concrete bridges are designed to limit cracking. Aging can lead to prestressing steel fractures with strain changes without visible cracks. To detect and locate fractures, long-term monitoring with distributed fiber optic sensors in combination with acoustic emission sensing is useful. This study focuses on fiber optic sensing based on Rayleigh backscattering. A long-term monitoring system was installed to ensure the service of two prestressed concrete bridges in Munich. Their prestressing steel is at risk of stress corrosion cracking. For reliable operation of the fiber optical measurements, tests were carried out both in the lab and in the field to investigate the measurement signal in conditions that are as isolated as possible. On the bridges data is collected at three-month intervals starting in 2021. Furthermore, strain changes caused by temperature fluctuations and traffic loads were captured. Moreover, valuable insights are being gained in a long-term operation. The investigations show that long-term fiber optical strain measurements are useful to assess the structural behaviour of existing prestressed bridges over several years and can ensure safety of structures.

**KEY WORDS:** SHMII-13; prestressed bridges, DFOS, stress corrosion cracking.

## 1 INTRODUCTION

The first standards and regulations for prestressing steel in Germany were developed after 1945 [1]. The first decades of the use of prestressing steel were the source of many structural problems in prestressed bridges. Due to the lack of knowledge at that time, some deficiencies can still be found in existing bridges today. One such material defect is the susceptibility of prestressing steel to stress corrosion cracking. This can lead to brittle failure of the steel without plastic deformation and subsequent collapse of the component without warning. Recently stress corrosion cracking led to the component failure of the Carola Bridge in Germany [2]. In this case, cracks were observed years before failure, but the existing crack widths were below the standard limits [3]. Acoustic emission (AE) monitoring is proposed for the remaining bridge components [4].

In Munich, a monitoring system with AE has been in operation since 2021 on two bridges with prestressing steel sensitive to stress corrosion cracking. Additionally, distributed fiber optical sensors (DFOS) are in usage for crack detection. On these bridges, DFOS can also be used to monitor structural behaviour. This application of DFOS for structural behaviour monitoring has been carried out in many cases. [5], [6], [7] and [8] are just a few examples. This case study provides some insights into the laboratory and field tests and shows selected results from the past years.

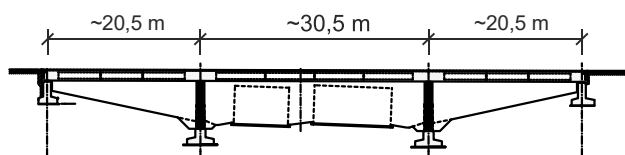
## 2 MONITORING KREUZHOF BRIDGES

German bridges with stress corrosion cracking sensitive steel must be reassessed according to the guideline HA SpRK [9]. This guideline recommends the numerical verification of sufficient warning behaviour as crack-before-failure. For both "Kreuzhof" bridges, the crack-before-failure criterion could not be verified in every section. But even in areas with sufficient warning behaviour, an object-related inspection instruction must be defined.

The bridges were built in 1967 and span a four-lane road. They are three-span slab bridges with longitudinal tubular voids and span lengths of about 20.5 m – 29.0 m – 20.5 m. The concrete slabs are prestressed by the bonded post-tensioning system according to the approval of the company "Polensky und Zöllner". There is a minimum of two and a maximum of six post-tensioning tendons in each web between these hollow bodies. Figure 1 shows the longitudinal and the cross-sectional profiles of bridge "BW40/45".

Acoustic emission sensors have been installed for direct detection of steel fractures. They are measuring continuously since 2021. The local and global structural response to fractures is measured as strain changes along the length of the bridge.

Longitudinal Section



Cross-Section

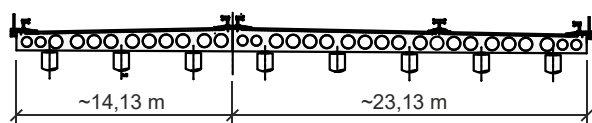


Figure 1. longitudinal and cross-section of the bridge „Kreuzhof“ BW40/45



Data is collected three to four times a year using BRUSens V9 distributed fiber optical sensors. Rayleigh backscattering technology is used with the ODiSI instrument manufactured by Luna Innovations Incorporated. The DFOS are applied in a groove milled into the structure and are located in every second web on the bottom of the slabs. In addition, 1.5 years of data acquisition was carried out using different sensor technologies for object-specific traffic load determination (B-WIM system). More details can be found in [10] and [11].

### 3 VERIFICATION OF STRAIN MEASUREMENTS

For verification of the measurements tests were performed in the laboratory using the same type of sensor. The BRUSens V9 is a layered sensor with an outer PA sheath, a stainless steel tube and a multilayer buffer to the optical fiber. In order to simulate the strain transfer from the host material to the sensor core in an equivalent way, the sensor was applied to a concrete specimen using the same method. The aim of these tests was to investigate conditions that were as isolated as possible. This was achieved by applying pure compressive, tensile or temperature loads, generating a specific crack width and performing a long-term test under constant conditions. In addition, different sensors with the same and different measurement principles were used for each test to validate the reliability of the strain signal.

Test loads were also applied to the bridges by trucks at the beginning of the monitoring and repeated after six months. The tests were carried out to assess structural behaviour and to analyse environmental effects on the measured data. For in-field verification, it was possible to compare the DFOS results with those from the B-WIM strain gauges.

### 4 RESULTS AND DISCUSSION

Laboratory tests show reliable results for compressive and tensile strains in the uncracked concrete. When cracks appear, due to the sensors layers a slippage can occur. In this case the crack width can no longer be determined exactly. Various studies have also analysed the measurement signal at crack opening with different sensors, i.e. [5], [12], [13], [14]. The appearance of a crack manifests itself always as a strain peak, even in the case of slippage. In prestressed structures already new formed small cracks are first signs of a deterioration.

If a test specimen is subjected to a constant temperature load, the DFOS BRUSens V9 will record the thermal expansion of the inner stainless steel jacket layer. In addition, the strain profile scatters over the sensor length with increasing temperature difference. In the tests, a value between  $15$  und  $19 \times 10^{-6}/K$  was determined for the thermal expansion coefficient of the sensor, whereby the average value is  $16 \times 10^{-6}/K$  according to the manufacturer Solifos AG [15].

Strain measurements on the bridges show that only very small strain changes of less than  $30 \mu m/m$  ( $0.03 \%$ ) occur when two trucks with a maximum vehicle weight of 42 tonnes are loaded. This means that the measurement signal from light vehicles such as cars is masked by the DFOS measurement noise. On both bridges no cracks have been detected since the start of monitoring.

In contrast, strain changes due to temperature variations are particularly pronounced. Figure 2 presents selected results from the mid-span of the 'Kreuzhof' bridges. The raw data taken on

twelve different days since November 2021 are shown. When these results are compared with the theoretical strain change at the given temperature, the same influence of thermal expansion on the data as in the laboratory results is observed. Furthermore, strain peaks in Figure 2 have a dominance of approx.  $200 \mu m/m$  ( $0.20 \%$ ). In laboratory tests, such peaks are an indication of the presence of a crack. A visual inspection of the bridge revealed an offset in the concrete surface in the location of the peak. This concrete offset results in a longitudinal offset of the sensor, which means that linear strain transmission between the concrete and the glass fibre core is not possible. When comparing all measurements over several years, the strain peaks appear in the same location. Provided a single measurement signal is referenced to a measurement taken at a similar temperature, no more pronounced strain peaks are visible. The conclusion is that no new strain change has occurred at these locations. In a theoretical case of a possible prestressing steel fracture, a local peak would appear that could be distinguished from the temperature.

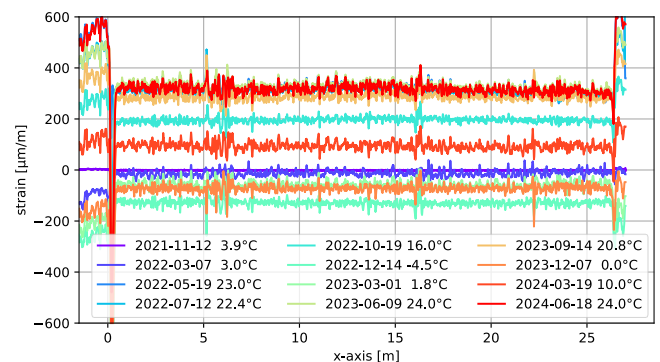


Figure 2. Raw data of the results and the corresponding temperature in the mid-span of bridge BW40/45 from November 2021 to June 2024

### 5 CONCLUSION

The long-term monitoring on the "Kreuzhof" bridges in Munich, employing acoustic emission sensors and distributed fiber optic sensors (DFOS), does guarantee a safe operation of the bridge service. Laboratory tests have been crucial in understanding the limitations and reliability of the DFOS measurements, particularly in the presence of cracking and temperature variations. While with in field tests object specific limitations are discovered.

The City of Munich decided to replace the bridges due to the risk of stress corrosion cracking in the prestressing steel and a future tram line which will pass under these bridges. In January 2025 destructive structural tests were carried out shortly before the partial dismantling to validate the monitoring system. The first results will be generated in the middle of the year 2025.

### ACKNOWLEDGMENTS

The authors would like to thank the Department of Civil Structures of the City of Munich for the project assignment and the pleasant cooperation.

## REFERENCES

- [1] S. Gefbner, R. Niedermeier, M. A. Ahrens, J. Hegger, O. Fischer und P. Mark, "Spannbetonbau – Entwicklung, Bemessung und Konstruktion," in Beton-Kalender 2017: Spannbeton, Spezialbetone. 2017
- [2] Marx Krontal und Partner GmbH. Carolabrücke - Schadensursache und Hergang des Teileinsturzes. Retrieved March, 2025, from [https://ratsinfo.dresden.de/si0056.asp?\\_\\_ksinr=14555](https://ratsinfo.dresden.de/si0056.asp?__ksinr=14555)
- [3] Landeshauptstadt Dresden. Carolabrücke. Retrieved March, 2025, from [https://www.dresden.de/de/rathaus/aktuelles/pressemitteilungen/2024/12/pm\\_024.php](https://www.dresden.de/de/rathaus/aktuelles/pressemitteilungen/2024/12/pm_024.php)
- [4] Marx Krontal und Partner GmbH. Vorläufige Erkenntnisse zur Ursache und Hergang des Teileinsturzes der Carolabrücke. Retrieved March, 2025, from [https://www.dresden.de/media/pdf/presseamt/2024\\_12\\_11\\_Carolabruেকে\\_Zusammenfassung-Ergebnisse.pdf](https://www.dresden.de/media/pdf/presseamt/2024_12_11_Carolabruেকে_Zusammenfassung-Ergebnisse.pdf)
- [5] Monsberger, C.M.; Lienhart, W. Distributed Fiber Optic Shape Sensing of Concrete Structures. *Sensors*, 21, 6098. 2021 <https://doi.org/10.3390/s21186098>
- [6] Bednarski L.; Sienko R.; Howiacki T.; Zuziak K.; The Smart Nervous System for Cracked Concrete Structures: Theory, Design, Research, and Field Proof of Monolithic DFOS-Based Sensors. *Sensors* 22, 8713. 2022 <https://doi.org/10.3390/s22228713>
- [7] Novák, B.; Stein, F.; Reinhard, J.; Dudon, A.: Einsatz kontinuierlicher faseroptischer Sensoren zum Monitoring von Bestandsbrücken. In: Beton- und Stahlbetonbau Volume 116, Issue 10, S.s 718-726. 2021 <https://doi.org/10.1002/best.202100070>
- [8] Herbers, M.; Richter, B.; Bartels, J.; Al-Zuriqat, T.; Smarsly, K.; Marx, S.: openLAB – A large-scale demonstrator for advancing digital twin developments of bridges. Ed.: Richard S. Henry, Alessandro Palermo: fib. The International Federation for Structural Concrete- ReConStruct: Resilient Concrete Structures. 2024
- [9] Bundesministerium für Verkehr, Bau und Stadtentwicklung: Regelungen und Richtlinien für die Berechnung und Bemessung von Ingenieurbauwerken (BEM-ING) – Handlungsanweisung Spannungsrisskorrosion - Handlungsanweisung zur Überprüfung und Beurteilung von älteren Brückenbauwerken, die mit vergütetem, spannungsrisskorrosionsgefährdetem Spannstahl erstellt wurden. Bonn, 2011.
- [10] Burger, H; Tephro, T.; Fischer, O.; Schramm, S.: Performance assessment of existing prestressed concrete bridges utilizing distributed optical fiber sensors. Biondini, F.; et al. [edit.] Life-Cycle of Structures and Infrastructure Systems. London: CRC Press. 2023
- [11] Burger, H; Tephro, T.; Fischer, O.; Schramm, S. Load testing on existing prestressed concrete bridges to determine long-term effects on strain measurement. Jensen, J. S. et al. [edit.] Bridge Maintenance, Safety, Management, Digitalization and Sustainability. London: CRC Press. 2024
- [12] Fischer, O., Thoma, S. & Crepaz, S.: Distributed fiber optic sensing for crack detection in concrete structures. In Civil Engineering Design, 1 (2019): 97-105. <https://doi.org/10.1002/cend.201900000>
- [13] Herbers M.; Richter B.; Gebauer D.; Classen M.; Marx S.: Crack monitoring on concrete structures: Comparison of various distributed fiber optic sensors with digital image correlation method. *Structural Concrete* Volume 24, Issue 5. 2023 <https://doi.org/10.1002/suco.202300062>
- [14] Bassil, A., Chapeleau, X., Leduc, D. & Abraham, O.: Concrete Crack Monitoring Using a Novel Strain Transfer Model for Distributed Fiber Optics Sensors. *Sensors*, 20, 2220. Basel, Switzerland. 2020 <https://doi.org/10.3390/s20082220>
- [15] Breuer, S. (Solifos): personal communication, June 16, 2022

# Distributed fiber optic sensing of bridges with stress corrosion cracking

Goldyn Michal<sup>1, 3</sup>, ORCID 0000-0002-7791-1940, Herbers Max<sup>2</sup>, ORCID 0000-0002-2187-1652, Richter Bertram<sup>2</sup>, ORCID 0000-0002-3833-8424, Zdanowicz Katarzyna<sup>1</sup>, ORCID 0000-0003-3847-3631, Marx Steffen<sup>2</sup>, ORCID 0000-0001-8735-1345

<sup>1</sup>FOLAB GmbH, Zum Hospitalgraben 2, 99425 Weimar, Germany

<sup>2</sup> Technische Universität Dresden, Institut für Massivbau, George-Bähr-Straße 1, 01062 Dresden, Germany

<sup>3</sup>Lodz University of Technology, al. Politechniki 6, 93590 Lodz, Poland

email: michal.goldyn@folab.de, max.herbers@tu-dresden.de, bertram.richter@tu-dresden.de, k.zdanowicz@folab.de, steffen.marx1@tu-dresden.de

**ABSTRACT:** Stress corrosion cracking (SCC) of prestressing steel represents a critical threat to the long-term safety and serviceability of aging bridge infrastructure. This phenomenon occurs within the cross-section and leads to the initiation and propagation of cracks, ultimately causing the rupture of the prestressing wires, which may ultimately result in sudden bridge failure. This underscores the need for reliable monitoring solutions. Traditional non-destructive testing techniques, while valuable, often lack high-resolution capabilities. In contrast, Distributed Fiber Optic Sensing (DFOS) has emerged as a transformative approach, offering high-resolution, continuous monitoring of strain distribution and crack development in concrete structures. This study demonstrates the practical application of DFOS technology for detecting and quantifying crack propagation in operational bridge structures affected by the risk of active SCC. By considering field investigations on four infrastructure projects the research evaluates DFOS performance for structures vulnerable to SCC. The paper demonstrates the technology's capability to monitor crack dynamics under operational conditions as anomalies in the crack pattern may indicate early symptoms of structural damage caused by SCC. By bridging knowledge gaps in the application of DFOS for infrastructure safety, the study advances the role of fiber optic sensing in addressing SCC challenges, ultimately contributing to the development of more resilient and sustainable bridge monitoring systems.

**KEY WORDS:** DFOS, distributed fiber optic sensing, stress corrosion cracking, bridge monitoring, SHM, structural health monitoring.

## 1 INTRODUCTION

### 1.1 Background and motivation

Stress corrosion cracking (SCC) is a critical degradation mechanism in prestressed concrete bridges. This phenomenon involves the initiation and gradual propagation of cracks in prestressing wires inside the cross-section, often remaining undetectable by conventional methods in early stages. As the process advances, stress concentrations may lead to surface cracking in prestressed elements. Progressive SCC results in sequential wire rupture, reducing structural capacity and potentially leading to sudden failure. This form of corrosion is particularly insidious due to its delayed manifestation and the absence of external indicators, making early detection extremely difficult. Numerous historical cases have shown that even well-constructed bridges can suffer unexpected failures due to SCC, emphasizing its relevance for long-term structural integrity [1]. As many existing bridges age and are subjected to increasing traffic loads, the risk posed by SCC continues to grow. Conventional inspection techniques often fail to capture early signs of SCC, prompting the need for advanced, reliable monitoring methods. Therefore, the development and implementation of modern evaluation and monitoring strategies are essential to ensure the safety and longevity of critical infrastructure.

### 1.2 Scope and objectives of the article

This paper focuses on the application of Distributed Fiber Optic Sensing (DFOS) in the monitoring of structures

susceptible to SCC, with examples of identifying structural response to loading, crack detection, and evaluation of crack width changes. The article also outlines the advantages of DFOS over conventional inspection methods, emphasizing its ability to provide continuous, high-resolution, and little-invasive monitoring.

## 2 FUNDAMENTALS OF STRESS CORROSION CRACKING IN BRIDGES

### 2.1 Mechanisms of SCC in prestressing steel

The phenomenon of SCC refers to the chemical and/or electrochemical corrosion of a material under the simultaneous influence of static tensile stress. Two primary types of SCC in steel can be distinguished: anodic and cathodic corrosion [2]. Anodic corrosion involves the decomposition of material at the surface through an electrolytic reaction. Cracks form deep inside the crystal structure and are not visible from the outside. In contrast, cathodic corrosion occurs when free hydrogen atoms penetrate the metal's crystal structure. As hydrogen molecules form, they cause internal expansion, which leads to crack initiation along the grain boundaries.

Microscopic corrosion scars are usually the points of crack initiation. Scanning electron microscope (SEM) studies have shown that microcracks begin at weak points in the grain structure and grow into a honeycomb-like pattern [2]. The visible signs of stress corrosion manifest as numerous microcracks, perpendicular to the axis of the prestressing strand, starting at the surface and progressing inward —



see Fig. 1. What makes SCC particularly dangerous is progression without visible deformation of the structure or expansive corrosion products, meaning failure often happens suddenly due to brittle fracture of the prestressing steel.

In Germany, high-strength steels with tensile strengths above 1700 N/mm<sup>2</sup>, used primarily in the 1960s and 1970s, are considered particularly susceptible to SCC. This includes steel types such as Neptun St 145/160 (FRG), Sigma St 145/160 (FRG), and Henningsdorf St 140/160 (GDR) [3].

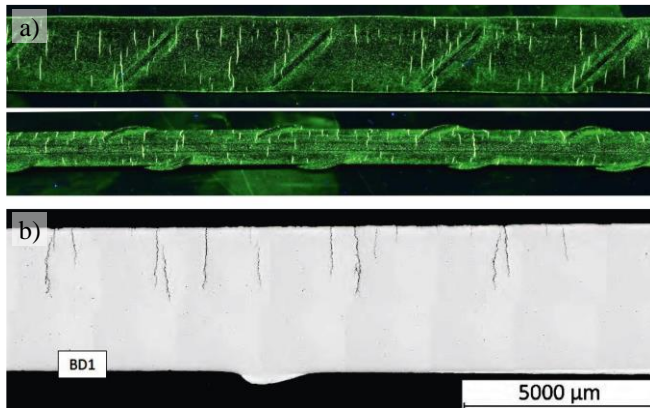


Figure 1. Inspection of the prestressing strand taken from the Carola Bridge (Dresden): a) microcracks visible by fluorescent magnetic particle method, b) longitudinal section [4]

## 2.2 Impact of SCC on structural integrity and service life

Several failures of well-designed and properly built structures have been linked to SCC. A prominent example is the partial collapse of a production hall in Mannheim in 1989, after 28 years of use. Investigations revealed that the primary cause was the loss of flexural capacity in the roof girders due to SCC. Despite proper grouting and maintained alkalinity, the prestressing wires showed numerous microcracks characteristic of SCC. Similar damage occurred in Mühlacker in 1992, where only rapid intervention prevented a collapse. Even with completely filled ducts, SCC-induced cracking was found in the prestressing steel. In some cases, such as the collapse of the Berlin Kongresshalle in 1980, SCC acted as an additional factor accelerating degradation, alongside moisture and chlorides.

Recent events underline the ongoing relevance of SCC: In September 2024, a 100-meter section of the Carola Bridge in Dresden collapsed due to severely corroded and fractured steel tendons [4]. The collapse caused major infrastructure and traffic disruptions in the city. Demolition of the remaining structure is currently planned. Similarly, in November 2024, the Elbe Bridge in Bad Schandau was immediately closed after inspections revealed longitudinal cracks in prestressed elements (particularly in the lower arch). The closure caused significant local transport disruptions, with temporary ferry services established. At the beginning of April 2025, load tests of the bridge were conducted. The collected results, including strain measurements using DFOS, were used to calibrate the computational model. Based on the performed analysis, authorities decided to temporarily reopen the bridge for use, with a restriction on the maximum allowed vehicle weight.

It is estimated that in Germany, there are at least 500 [5], [3] or even 1000 bridges [6] still in service that contain prestressing steel susceptible to SCC. Due to the considerable

costs and potential socio-economic consequences, it is essential to take actions aimed at extending the service life of these structures while maintaining an appropriate level of safety and considering the economic and environmental impacts.

## 2.3 Limitations of conventional monitoring technologies

Conventional monitoring methods have notable limitations in detecting and observing SCC. Visual inspection, though widely used, is time-consuming, costly, and limited to surface-level damage. Moreover, the reproducibility is limited due to the high dependency of crack localization on the observer's perception, as well as on environmental conditions at the time of inspection, such as temperature and humidity. It cannot detect microcracks or subsurface flaws, which often form due to localized stress concentrations – such as those caused by ruptured prestressing tendons [7].

Non-destructive testing methods like ultrasonic or radiographic testing offer deeper insight but still struggle with early-stage SCC, particularly in inaccessible areas or complex geometries [8]. These methods require skilled operation, offer limited scanning depth, and are significantly affected by the density of reinforcement. Early-stage SCC, which typically begins as microscopic damage below the surface, can avoid being detected until it becomes critical. Conventional techniques lack sensitivity to local stress concentrations, which are critical indicators of potential SCC initiation [9].

## 3 DISTRIBUTED FIBER OPTIC SENSING (DFOS) FOR STRUCTURAL MONITORING

### 3.1 Principles and advantages of DFOS

DFOS systems utilize the Rayleigh, Brillouin, or Raman scattering mechanisms in optical fibers to measure strain, temperature, or vibration continuously along the fiber length [10], [11]. Optical fibers serve both as the sensing element and the transmission medium, making them ideal for long-range, distributed measurements without the need for discrete sensors. Depending on the chosen scattering principle and instrumentation (e.g., OFDR, BOTDA), high spatial resolution (down to the millimeter scale) and varying sensing ranges (from 100 m to over 80 km) can be achieved [12].

The DFOS technology offers the following advantages:

- Provides high-resolution structural monitoring over time and along the full length of the sensor [13].
- Enables early detection of the cracks in reinforced and prestressed concrete structures, with the sensitivity allowing to detect even microcracks with very small widths [14].
- DFOS can be integrated into digital twin models and automated data analysis pipelines, supporting predictive maintenance and real-time infrastructure assessment [15].

### 3.2 Application of DFOS in crack detection and strain monitoring

Distributed Fiber Optic Sensing (DFOS) enable continuous, high-resolution strain measurements that are particularly effective for detecting cracks and evaluating their width changes in reinforced and prestressed concrete structures. Cracks are identified by localized strain peaks in the profile, which are analyzed based on parameters such as prominence, height, and width. The key challenge lies in

distinguishing these from peaks caused by noise or local deformation accumulations, which do not necessarily indicate cracks [16]. Crack detection is based on the algorithms employing a topographic approach, with peak height and prominence serving as key parameters. They quantify how distinctly a peak stands out from its surrounding strain environment. The careful selection of these parameters is critical: if set too high, adjacent cracks may be mistakenly interpreted as a single, broader crack, while if set too low, insignificant microcracks may be falsely detected, leading to overestimated number of cracks and underestimated widths of the real cracks at the same time. Additional parameters such as minimum peak width are employed to further filter out noise and ensure that only meaningful strain concentrations are considered.

The width of an identified crack is calculated as the integral of the strain distribution between local minima, which define the boundary of the strain peak – see Fig. 2. In reinforced concrete members, the tension stiffening effect reduces the apparent crack width, what is included by adjusting the area under the strain distribution curve according to the following equation

$$w_{cr,i} = \int_{x_{cr,i}-l_{t,i}^-}^{x_{cr,i}+l_{t,i}^+} \varepsilon(x) - \varepsilon^{TS}(x) dx \quad (1)$$

where:

- $x_{cr,i}$  – position of the crack,
- $l_{t,i}^-$  – distance to the preceding local minimum,
- $l_{t,i}^+$  – distance to the following local minimum,
- $\varepsilon(x)$  – measured strain,
- $\varepsilon^{TS}(x)$  – strain resulting from tension stiffening effect.

Practically, the effect of tension stiffening is accounted for in crack width calculations by subtracting the shaded regions, representing the contribution of concrete, from the total area under the strain distribution curve. These regions are typically approximated as triangular zones with peak values located at midpoints between adjacent cracks.

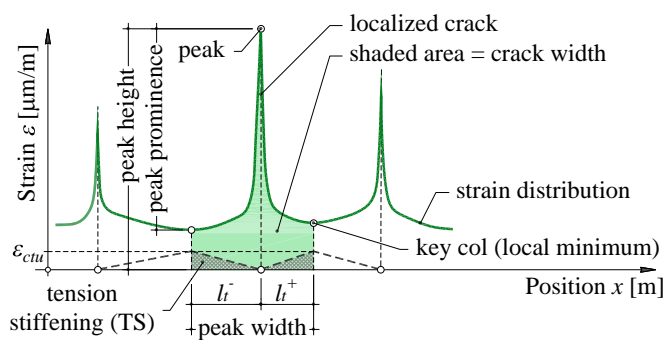


Figure 2. Parameters included in crack detection and estimation of crack width

The presented approach allows for accurate quantification of width changes as small as 0.02–0.05 mm [17]. Herbers et al. [18], [19] demonstrated that Rayleigh-based DFOS systems can reliably identify cracks across different fiber types and installation methods, achieving results

comparable to those obtained using high-resolution digital image correlation (DIC) techniques.

In addition to crack monitoring, DFOS is also effective in identifying prestressing wire or tendon failures. Abrupt strain changes – such as localized jumps or sudden deviations in gradient – are key indicators of tendon breakage events and can be detected with high spatial resolution [20]. Such events can be detected using DFOS, which is particularly well-suited for periodic measurements. To enhance diagnostic capabilities, it might be advantageous to integrate DFOS with complementary, continuous monitoring techniques such as Acoustic Emission (AE). In this configuration, AE signals can serve as event-based triggers, initiating high-resolution DFOS measurements to enable accurate spatial localization of damage. As DFOS provides a thorough strain distribution along the length of the sensor, it allows also to determine the anchorage length of prestressing tendons based on strain measurements along the tendon axis after cutting [21]. Furthermore, DFOS facilitates the creation of digital crack maps and enables the tracking of strain development under load and temperature fluctuations. These features support automated condition assessment, early damage detection, and risk-informed maintenance strategies [22].

### 3.3 DFOS Performance in Detecting Crack Initiation and Propagation

The initiation of cracking in concrete is typically associated with a localized strain concentration, which DFOS detects as a sharp and narrow strain peak along the fiber path. These peaks emerge even before visible cracking occurs and serve as early indicators of damage accumulation. Once cracks are initiated, DFOS allows for real-time tracking of their propagation. Lemcherreq et al. [23] applied DFOS under monotonic and cyclic loading, demonstrating that cyclic strain accumulation is directly correlated with the development of microcracks and that bond shear stresses progressively redistribute toward the unloaded end with an increasing number of load cycles. Importantly, the repeated loading (1 000 000 load cycles) did not impair the quality or reliability of the DFOS measurements throughout the test.

Based on the study by Broth and Hoult [24], it can be concluded that after 3 600 load cycles, strain profiles still captured distinct peaks at crack locations, with strain gradients evolving due to stress redistribution. Crack breathing was clearly visible in the strain signals across load cycles. The sensors enabled the recording of a gradual increase in strain peaks during successive loading cycles, particularly in deep beams, which suggested the widening of previously formed cracks. Initially, the strain values at crack locations reached approximately 1400–1500 μm/m, increasing to nearly 2000 μm/m by the final cycle of the test.

The DFOS system described by Galkovski et al. [25] achieved a measurement resolution of up to 10 μm/m (0.001%), allowing for detection of early-stage microcracking. Strain peaks exceeding 12 000 μm/m (1.2 %) were measured at crack locations—well above the steel yield strain (~2 000 μm/m), indicating DFOS capability to track yielding and post-yield bond behavior.

### 3.4 Limitations and Challenges

The application of DFOS in SHM of prestressed concrete structures susceptible to SCC offers comprehensive strain analysis. Conducting measurements that enable the acquisition of data essential for a reliable and unequivocal analysis necessitates careful consideration of the following aspect:

- interference from overlapping strains within the intensively cracked areas affected by superimposed long-term strains (from creep, shrinkage, or thermal gradients), complicating damage localization and potentially masking SCC-related events [26];
- proper choice of the sensor-adhesive combination and measurement settings are crucial for reliable measurement results and good quality data [19].
- quality of the installation – successful application of DFOS relies on the proper sensor installation. Adhesive selection, groove preparation, and embedding quality significantly influence data accuracy. Unsuitable adhesives or rough interfaces can introduce artificial strain peaks or suppress real ones [27];
- data interpretation – measurements, above all the 24/7 monitoring processes, produce large datasets requiring robust post-processing algorithms to distinguish true damage signs from noise, thermal effects, or adhesive degradation. Misinterpretation may lead to false alarms or overlooked damage [28], [29];
- sensor length affecting data quality – with longer sensors, optical device constraints lead to reduced spatial resolution and sampling rate [19]. This decline in performance is accompanied by increased measurement noise, which may obscure or distort strain events associated with SCC. In practical terms, a compromise must be made between coverage area and data fidelity, depending on the selected DFOS interrogation technology [11].

## 4 FIELD INVESTIGATIONS ON REAL INFRASTRUCTURE ASSETS

In the following section case studies demonstrating the application of DFOS for monitoring bridge structures susceptible to SCC are presented. The focus is on real-world infrastructure where DFOS enables early detection of microcracks, evaluation of changes in crack widths, and assessment of structural behavior under operational loading.

### 4.1 Considerations for DFOS Deployment at Bridge Structures

The installation of DFOS systems in existing bridge structures requires meticulous engineering, application-specific adaptation, and access to specialized equipment. Sensor routes must be defined with precision, targeting critical zones such as anchorage areas, webs, soffits, and coupling joints [30] – regions particularly vulnerable to hidden damage or prestressing wire fracture. For installations in existing structures reference measurements (“zero measurements”), ideally under constant loading conditions (no traffic), are used to initialize monitoring cycles and enable tracking of structural evolution over time.

The fiber optic sensors are typically bonded to prepared surfaces using adhesives. While exact details vary, the standard approach includes marking sensor paths, cutting grooves, and embedding the sensors with injection mortars, ensuring robust

strain transfer from the measured substrate to the sensor core. These operations are carried out with specialized cutting and cleaning tools. Due to the location of sensors on the underside of structural elements, auxiliary access equipment, such as scaffoldings, under-bridge platforms, or telescopic lifts, is often necessary – see Fig. 3.

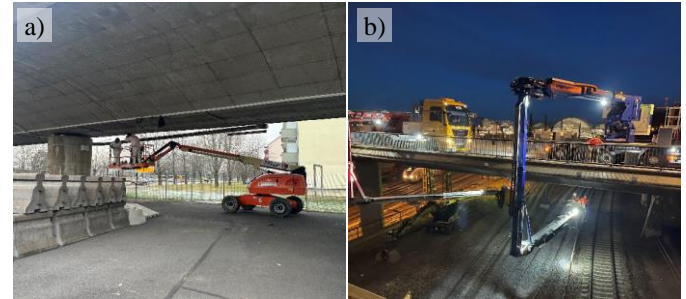


Figure 3. Examples of the special equipment for sensor installation: a) lifting platform, b) under-bridge inspection device

Furthermore, proper choice of the sensors used is crucial for meeting the demands of the monitoring purpose – for high-resolution crack assessment, monolithic fiber optic sensors provide the best results, while their consistent and rigid geometry ensures more direct strain transfer. This is essential for accurately capturing sharp strain gradients near cracks [19]. Environmental durability and system reliability are ensured not only by using robust sensors, but also by routing fiber leads in protective conduits and terminating them in sealed cabinets. Additionally, to distinguish mechanical strain from temperature-induced effects, several thermal compensation methods are employed in practice [31]. Temperature influence strain measurements through changes in the refractive index (which represents the dominant effect on the results) and the thermal expansion of the fiber. One approach involves interrogators based on Raman backscattering, which is sensitive to thermal effects only. Alternatively, two interrogators (e.g., Rayleigh and Brillouin) can be used on the same fiber, allowing for precise measurements but requiring laboratory calibration. Mechanically decoupled reference fibers, typically embedded in gel, may be affected by friction and are generally more suitable for shorter measurement sections. The simplest and most cost-effective, though less precise, solution involves pointwise temperature measurements using conventional resistance temperature sensors embedded in structural members – particularly suitable for applications with minimal temperature gradients. In such cases, compensation is performed by subtracting the strain resulting from the known temperature change.

In the following sections, four examples of monitoring bridges at risk of SCC using DFOS technology are presented. In all reported implementations, monolithic sensors EpsilonSensor Ø3 mm (manufacturer: Nerve-Sensors) were installed. These sensors featured single-mode (SM 9/125) optical fibers and an external braid that additionally enhanced adhesion. Measurements were carried out using Rayleigh backscattering technique, with a spatial resolution of either 1.3 mm or 2.6 mm, depending on the total sensor length. Thermal compensation was achieved based on discrete temperature measurements. These measurements accounted for the previously discussed effect of the temperature change and the associated thermally induced strain changes.



#### 4.2 Asset 1: Königsbrücker Str. Bridge in Dresden

The bridge at Königsbrücker Straße in Dresden, constructed in 1979, crosses railway infrastructure and consists of three structurally independent units: one for tram traffic and two for road traffic. Due to the use of Hennigsdorf's prestressing steel a dedicated structural health monitoring (SHM) system based on DFOS and AE combination was deployed to ensure continued structural safety and detect early signs of deterioration [32]. Fiber optic sensors were installed along the full length of each superstructure, embedded into grooves on the bottom surface and bonded with high-performance mortar, enabling high-resolution, distributed strain and crack monitoring – see Fig. 4. Measurements are being conducted since November 2023, including an initial zero measurement and further follow-up measurements under varying seasonal and operational conditions.

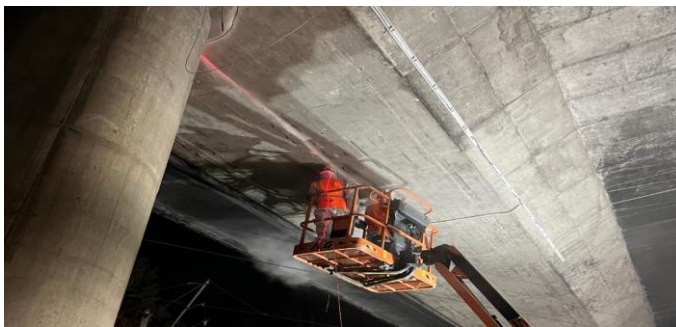


Figure 4. Installation of the optic sensor on the bottom surface of the girder

Across all monitored spans, the DFOS system consistently detected multiple microcracks, with crack width variations typically below 0.05–0.07 mm and strain peaks occasionally exceeding 1000–1600  $\mu\text{m}/\text{m}$  – see Fig. 5.

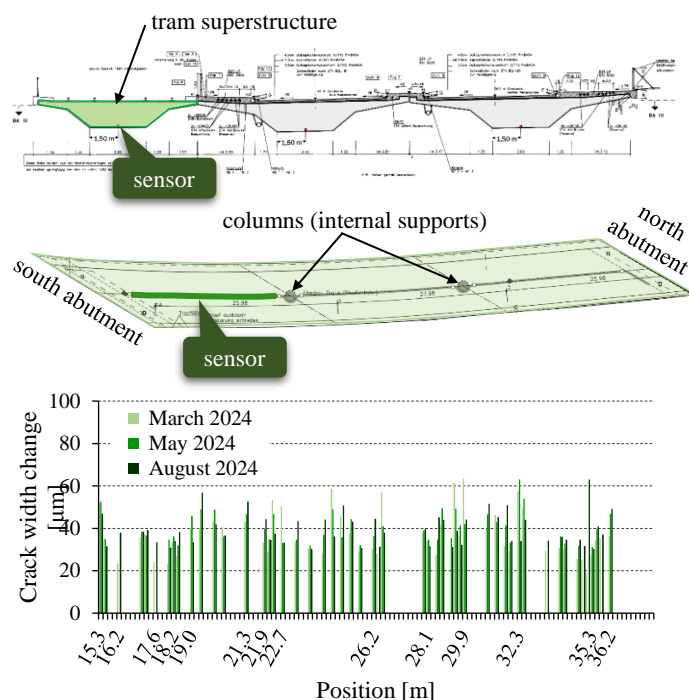


Figure 5. Comparison of the crack width change within the first span of the tram superstructure

In the latest, following measurement, only minimal crack width changes were noted compared to the previous measurements, suggesting no SCC-induced damage and confirming structural stability. The DFOS monitoring proved highly effective in characterizing microcrack evolution in SCC-susceptible girders and offers non-intrusive solution for long-term condition monitoring.

#### 4.3 Asset 2: Road bridge in Waren (Müritz)

The bridge on federal road B192 over the railway line in Waren (Müritz) is a continuous three-span structure consisting of two separate overpasses. Due to the use of high-strength prestressing steel prone to hydrogen-induced SCC, continuous monitoring has been in place since 2014. Long-term inclinometer measurements indicated a successive reduction in structural stiffness, suggesting progressive structural degradation, due to SCC.

In preparation for an upcoming replacement of the bridge, the south span - temporarily carrying all traffic – was equipped with a DFOS system to monitor potential crack propagation. Two sensor lines (10.5 m and 11 m) were installed on the underside of the deck to detect strain changes and localize microcracks in the mid-span section. Initial load tests in April 2024 with a 50-ton truck showed only minor strain changes (0–50  $\mu\text{m}/\text{m}$ ) and microcrack width changes below 0.01 mm, with no macroscopic damage detected – see Fig. 6. A second load test in October 2024 confirmed these results, with strain peaks up to 80  $\mu\text{m}/\text{m}$  and similar minimal crack width variations. The structural response remained consistent between both tests, and all observed strains were reversible after unloading.

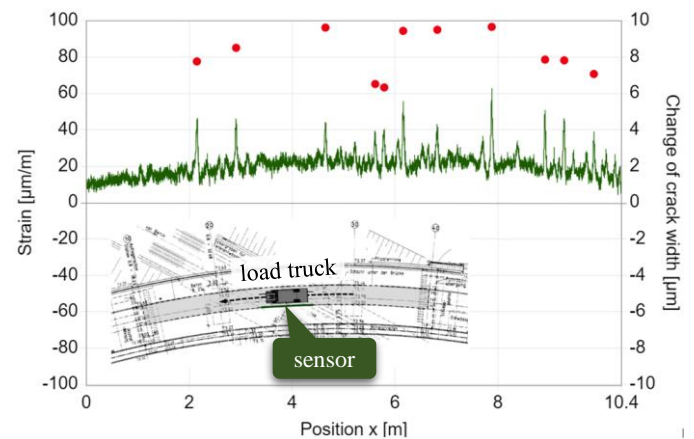


Figure 6. Strains (blue line) and change in microcrack (red points) resulting from truck load

Due to the results of long-term measurements, facing doubts about the condition and safety of the structure, it was decided to demolish and replace both spans, with the detonation of the north span scheduled for January 2025. Since the south span must carry all traffic during the construction period, DFOS measurements and load testing were carried out to assess whether the explosion on the north span had caused any damage to the south span and to ensure its safety for continued use. To this end, load testing was conducted using a 50-ton heavy-duty truck. Figure 7 presents the change in strains along the sensor segment at the mid-span, induced by the passage of

the test vehicle. A gradual increase in strains is evident along the monitored length. Distinct strain peaks correspond to the locations of pre-existing cracks. Under loading, local strain peaks of up to 40  $\mu\text{m/m}$  were recorded, while in the sections between the cracks, the strain values remained approximately constant at around 20  $\mu\text{m/m}$ .

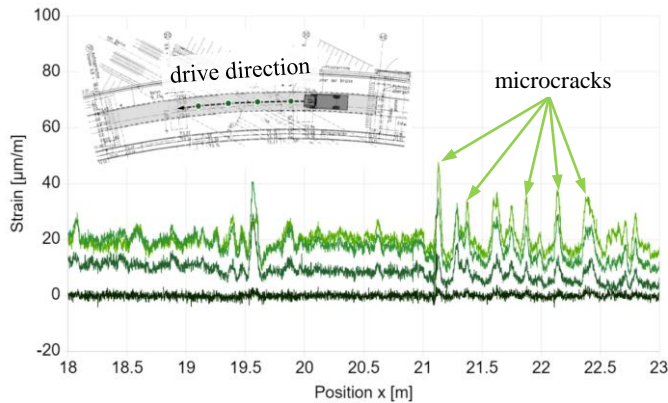


Figure 7. Strain change resulting from the passage of a test truck with distinct microcrack opening

DFOS measurements enabled the identification of crack locations at the very beginning of the loading test, even before the test vehicle reached the center of the monitored span. Strain development was most pronounced at the crack locations, with the progressive formation of peaks clearly visible. Due to the considerable stiffness of the structure, the variation in the microcracks, calculated according to the methodology described in Section 3.2, was minimal and did not exceed 0.01 mm.

The DFOS measurements, conducted before and after the controlled demolition confirmed no anomalies or damage to the monitored bridge segment. The consistent, low, and fully reversible strain values provide clear evidence that the structural integrity was not compromised by the blast or load tests.

#### 4.4 Asset 3: Bridge BW55b in Döbeln

The B169 bridge near Döbeln (BW55b), built in 1966, is a prestressed concrete structure consisting of two hollow box girders connected by a concrete deck, spanning approximately 67 m with a total width of 16 m [33]. The bridge forms part of a vital route connecting the A4 and A14 motorways and remains structurally safe but is classified as highly susceptible to SCC due to the use of prestressing steel made from over 200 fine wires per tendon. Instead of replacing the bridge, the Saxon State Authority for Road Construction and Transport (LASuV) implemented an advanced SHM strategy to prolong its service life. This included the installation of DFOS on the undersides of the four longitudinal box girder webs, in total around 100 m of sensing length. The sensors were installed in grooves and bonded using high-performance injection mortar – see Fig. 8.

The follow-up measurement performed under regular traffic revealed strain changes with peak values typically below 150  $\mu\text{m/m}$ , and extremely small variations of crack widths – generally not exceeding 0.01 mm. Several local strain peaks were detected, suggesting the presence of microcracks, but no signs of active or progressive damage were observed. Temporary changes during vehicle crossings indicated reversible crack width variations between 5 and 20  $\mu\text{m}$ , which

immediately returned to previous state after the load passed, demonstrating the high stiffness and resilience of the structure. All measurements were temperature-compensated, and sensor performance remained stable. No anomalies indicating structural issues were identified. The purpose of the long-term DFOS monitoring supported by AE is the continuous assessment of the structure's condition, ensuring safe operation without the need for costly replacement.



Figure 8. Layout of the sensors on the surface of hollow box

#### 4.5 Asset 4: Budapest Str. Bridge in Dresden

The Budapest Straße Bridge in Dresden, built between 1963 and 1968, is a critical urban infrastructure linking the city center with the southern districts. The 850-meter-long structure spans the main rail yard of Dresden Central Station, tram lines, and the Ammonstraße, and is composed of multiple monolithically constructed prestressed concrete sections. Its overpasses were constructed with longitudinal post-tensioning using oil-tempered Henningsdorf's prestressing steel, a material highly susceptible to hydrogen-induced SCC. Cracks between 0.1 and 0.5 mm wide (Fig. 9a) and visible rust staining (Fig. 9b) have raised concerns about latent internal damage.

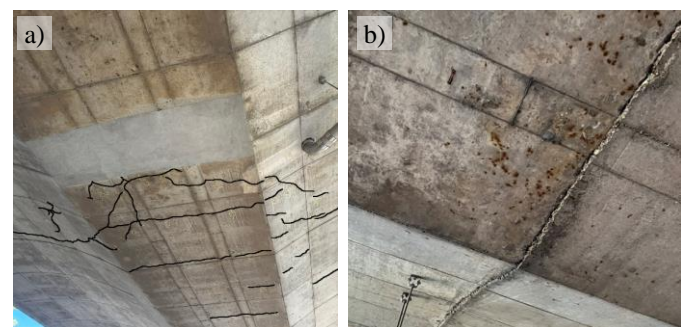


Figure 9. Visible damages: a) cracks with extensive widths, b) rust staining and displacement within coupling joint

To address the concerns and ensure long-term traffic safety without the necessity of a premature reconstruction, a comprehensive SHM system based on DFOS and acoustic emission is being installed – see Fig. 10. Around 880 meters of sensors are glued into the grooves along the underside of overpasses a and c. The system is designed to detect microcracks, localize strain peaks, and monitor changes over time under thermal and traffic-induced loading. Strain measurements are complemented by distributed temperature



fiber optic sensors, using Raman backscattering, to ensure reliable thermal compensation for longer sections. The main goals include detecting potential wires breakage, tracking crack formation near coupling joints, and providing high-resolution insights into the bridge's response to operational and environmental loads.

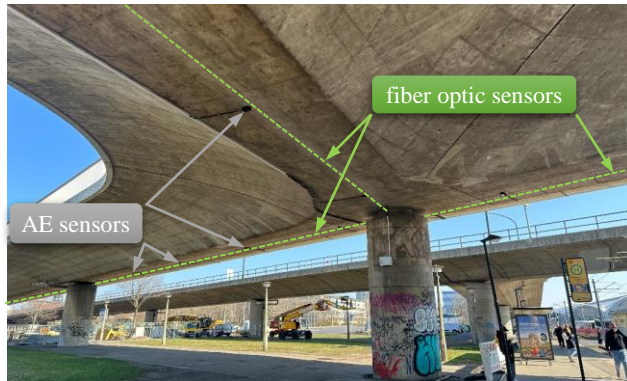


Figure 10. Localization of the sensors on the internal segment of the superstructure

The sensors are divided into 14 segments, each covering up to three spans, with data acquisition performed periodically using optical interrogators. This quasi-continuous monitoring allows localization of crack activity across the entire length of both overpasses. Although the installation in the existing structure obviously does not allow to monitor structural health from the “hour zero”, DFOS enables ongoing evaluation of crack development and possible early signs of structural deterioration starting directly after the installation.

## 5 DISCUSSION

### 5.1 Comparison with Traditional Monitoring Methods

DFOS offers several advantages over conventional monitoring methods such as strain gauges, vibrating wire sensors, and visual inspections. Unlike these techniques, DFOS enables continuous, high-resolution strain measurements over long sensor paths.

In a study on the Black River Bridge in Ontario, DFOS successfully identified localized cracking and strain concentrations – insights that were missed by traditional gauges spaced every meter. It also detected unintended semi-rigid restraint conditions at supports, demonstrating its ability to capture unexpected behavior [34]. DFOS strain resolution (typically 1–5  $\mu\text{m/m}$ ) is comparable or superior to that of foil strain gauges (5–10  $\mu\text{m/m}$ ), while covering thousands of data points simultaneously. In the project described in [35], discrete sensors were replaced by more than 1500 m of fiber optic sensors, with each individual sensor providing approximately 38 400 measurement points.

Compared to visual inspection, DFOS provides objective, quantitative detection of crack formation and width changes. With strain change exceeding 50  $\mu\text{m/m}$ , it can identify cracks smaller than 0.05 mm, well below the threshold of unaided visual assessment [20], [36]. Additionally, sensors can be embedded into structural components like tendons and rebar, enabling long-term monitoring of prestressing forces and

internal damage progression – tasks that are difficult or impossible with surface-mounted sensors or manual inspection.

### 5.2 Interpretation of Long-Term Structural Behavior including thermal compensation

DFOS enables precise interpretation of long-term structural behavior by continuously capturing strain distributions and tracking crack evolution under both mechanical loading and environmental influences. Based on DFOS measurements carried out by the authors on actual bridges during in-service operation, over several years of continuous monitoring, following findings can be pointed out. At the Königsbrücker Straße bridge in Dresden, fiber optic sensors recorded mechanical strain responses caused by tram and road traffic, with peak strain values near supports and midspans. These strain concentrations corresponded to microcrack openings predominantly between 0.01–0.05 mm. Changes in crack width over time indicated stable structural behavior under service loads. In the bridge on the road B192 over the railway in Waren, strain peaks of 50–100  $\mu\text{m/m}$  were recorded during staged loading under increasing traffic, allowing localization of microcracks with widths estimated around 0.02–0.05 mm. In both projects, thermal effects were observed as restrained strain patterns uniformly distributed along the spans, depending on exposure and structural response (imposed strains).

Thermal compensation is essential to distinguish thermal effects from mechanical responses. Rayleigh and Brillouin backscattering are sensitive to temperature-induced changes in the fiber, what needs to be considered in evaluation of mechanical strain readings [37]. Including the findings presented in [31], a temperature change of 1 K results in an additional strain of approximately 20  $\mu\text{m/m}$  in monolithic sensors embedded in concrete structures. To address this, multiple solutions can be utilized for dedicated temperature measurements, allowing separation of thermal and mechanical effects and thus enabling accurate compensation and interpretation of structural behavior over time [38]. For real use cases the most practical approaches to thermal compensation include utilizing distributed temperature measurements with Raman backscattering or even local spot temperature sensors.

### 5.3 Enhancing Predictive Maintenance Strategies

The integration of DFOS into SHM systems offers multiple advantages. One effective strategy is the use of hybrid monitoring systems, where DFOS is combined with technologies such as acoustic emission sensors. An example of such implementations is Kreuzhof bridge in Munich, where real-time detection of wire breaks via AE was supplemented by spatially distributed strain monitoring via DFOS, significantly improving damage assessment reliability [39].

Beyond external installations, DFOS can also be integrated directly into structural elements such as prestressing tendons or reinforcement cages. This embedded approach enables continuous internal monitoring of strain and prestressing forces, providing detailed insights from the initial loading stages through the entire service life of the structure. A practical demonstration of this concept was presented in a study on a prestressed concrete bridge girder, where fiber optic sensor was installed during fabrication to successfully



monitor strain development and crack formation under service and ultimate loads [40].

In addition, DFOS systems can be linked to digital twin platforms, enabling real-time data to support predictive maintenance, condition-based inspections, and system-wide risk assessments. This form of integration advances infrastructure monitoring from traditional inspection cycles toward proactive, data-driven management [15].

## 6 FUTURE RESEARCH DIRECTIONS

Despite significant progress in the deployment of DFOS for SHM, several open research questions remain, particularly addressed to:

- early-stage and automated SCC detection – future studies should explore enhanced DFOS signal interpretation methods, such as high-frequency dynamic strain analysis or modal-based decomposition, to identify signatures associated with early-stage wire degradation; the development of automated algorithms for the classification and localization of SCC-induced damage, based on DFOS strain gradients, could streamline monitoring and reduce the reliance on manual data interpretation; techniques such as anomaly detection, pattern recognition, and signal filtering are promising directions for algorithmic refinement.
- integration with predictive modelling – coupling DFOS data with finite element models and machine learning-based predictive tools would enable dynamic risk assessment by correlating measured strain patterns with probabilistic failure modes.

One of the most promising directions for the advancement of detecting tendon breakages is distributed acoustic sensing (DAS) technology. While distributed strain sensing excels in measuring quasi-static and low-frequency strain distributions with high spatial resolution, DAS extends the functionality of the same optical fiber network by enabling detection of dynamic, high-frequency acoustic signals along the entire fiber length. Mechanical disturbances, such as microcracking, prestress wire rupture, or acoustic emissions, alter the backscattering pattern, allowing the system to localize and characterize the source of dynamic events in real time. This makes DAS particularly suitable for detecting sudden or progressive failure mechanisms, including wire breakages or energy release events associated with SCC [41]. However, the use of this technology still requires extensive research to determine the effective detection range around the optic sensor – i.e., the distance between the event and the sensor at which the event can be reliably detected. Further studies are needed to establish the optimal application pattern and to develop automated methods for data analysis.

Combining DSS and DAS in a hybrid sensing system can significantly enhance the sensitivity, reliability, and redundancy of SHM strategies. For instance, a wire rupture may first be identified as a sharp acoustic signal via DAS and subsequently confirmed and quantified by correlated local strain changes registered by DSS. This fusion of datasets might support cross-validation, improve false positive rejection, and enable automated alert systems for infrastructure operators.

## 7 CONCLUSIONS

The application of distributed fiber optic sensing in the structural health monitoring of bridges vulnerable to stress corrosion cracking demonstrates clear advantages over traditional inspection and sensing methods. DFOS provides continuous, high-resolution strain data capable of detecting early-stage microcracks, quantifying crack width changes, and localizing damage with high spatial precision. The case studies presented confirm the efficacy of DFOS in operational environments, with successful deployment across multiple bridge structures. Monitoring results revealed that even microcrack width changes (typically below 0.01 mm) could be captured, and strain peaks were localized precisely at pre-existing damage sites. Multiple real-world case studies have shown that DFOS systems can effectively monitor the evolution of cracks under operational conditions, offering valuable insights into the structural integrity and residual service life of aging infrastructure. The ability to detect reversible strain patterns and correlate them with loading events supports informed decision-making regarding the continued safe use of SCC-affected structures.

The integration of DFOS with other sensing technologies, such as acoustic emission, further enhances damage detection capabilities and supports predictive maintenance strategies. While there are still challenges, such as sensor installation complexities and the need for robust data processing algorithms, the DFOS technology can be perceived as a transformative tool in advancing resilient, data-driven infrastructure monitoring practices.

## ACKNOWLEDGMENTS

This paper presents some of the results of the research project FOSSure - Faseroptische Sensoren zur sicheren Zustandsbewertung von Massivbrücken (Fiber Optic Sensors for the Reliable Structural Health Assessment of Concrete Bridges), funded by the Federal Ministry of Transport and Digital Infrastructure, Germany, within the innovation program mFUND (funding reference: 01FV2075C, 01FV2075A). The authors sincerely thank the funding agency for their support.

## REFERENCES

- [1] W. Podolny, 'Corrosion of Prestressing Steels and Its Mitigation', *pcij*, vol. 37, no. 5, pp. 34–55, Sep. 1992, doi: 10.15554/pcij.09011992.34.55.
- [2] J. Mietz, J. Fischer, and B. Isecke, 'Spannstahlschäden an einem Brückenbauwerk infolge von Spannungsrißkorrosion', *Beton- und Stahlbetonbau*, vol. 93, no. 7, pp. 195–200, 1998, doi: 10.1002/best.199800370.
- [3] T. Hampel, T. Bösche, S. Anker, S. Scheerer, and M. Curbach, 'Gefahr Spannungsrissskorrosion – Systematische Untersuchung des Brückenbestands in Mecklenburg-Vorpommern', *Bautechnik*, vol. 87, no. 1, pp. 12–18, Jan. 2010, doi: 10.1002/bate.201010002.
- [4] Silke Scheerer *et al.*, 'Die wechselvolle Geschichte der Carolabrücke in Dresden', in *Tagungsband zum 34. Dresdner Brückenbausymposium*, Dresden, 20.03 2025, pp. 15–33.
- [5] W. Macheleidt, 'Statische Untersuchung des Ankündigungsverhaltens von Spannbetonbrücken:

- Gefährdung durch Spannungsrisskorrosion', *Straßen- und Tiefbau*, vol. 56, no. 11, pp. 6–9, 2002.
- [6] FUNDSCENE, 'Bundesländer melden mehr als 500 Brücken aus gefährdetem Spannstahl - Politics, Economy & Finance'. Accessed: Apr. 09, 2025. [Online]. Available: <https://fundscene.com/bundeslaender-melden-mehr-als-500-bruecken-aus-gefaehrdetem-spannstahl/>
- [7] J. Broomfield, *Corrosion of Steel in Concrete: Understanding, Investigation and Repair, Second Edition*, 2nd ed. London: CRC Press, 2003. doi: 10.1201/9781482265491.
- [8] T. F. Mayer, C. Gehlen, and C. Dauberschmidt, 'Corrosion monitoring in concrete', in *Techniques for Corrosion Monitoring (Second Edition)*, L. Yang, Ed., in Woodhead Publishing Series in Metals and Surface Engineering. , Woodhead Publishing, 2021, pp. 379–405. doi: 10.1016/B978-0-08-103003-5.00016-3.
- [9] *Stress-Corrosion Cracking: Materials Performance and Evaluation*. ASM International, 2017. doi: 10.31399/asm.tb.sccmpe2.9781627082662.
- [10] M. F. Bado and J. R. Casas, 'A Review of Recent Distributed Optical Fiber Sensors Applications for Civil Engineering Structural Health Monitoring', *Sensors*, vol. 21, no. 5, p. 1818, Mar. 2021, doi: 10.3390/s21051818.
- [11] A. Barrias, J. Casas, and S. Villalba, 'A Review of Distributed Optical Fiber Sensors for Civil Engineering Applications', *Sensors*, vol. 16, no. 5, p. 748, May 2016, doi: 10.3390/s16050748.
- [12] C. M. Monsberger and W. Lienhart, 'Distributed Fiber Optic Shape Sensing of Concrete Structures', *Sensors*, vol. 21, no. 18, p. 6098, Sep. 2021, doi: 10.3390/s21186098.
- [13] M. F. Bado, J. R. Casas, and G. Kaklauskas, 'Distributed Sensing (DOFS) in Reinforced Concrete members for reinforcement strain monitoring, crack detection and bond-slip calculation', *Engineering Structures*, vol. 226, p. 111385, Jan. 2021, doi: 10.1016/j.engstruct.2020.111385.
- [14] R. Sieńko, M. Zych, Ł. Bednarski, and T. Howiacki, 'Strain and crack analysis within concrete members using distributed fibre optic sensors', *Structural Health Monitoring*, vol. 18, no. 5–6, pp. 1510–1526, Nov. 2019, doi: 10.1177/1475921718804466.
- [15] M. F. Bado, D. Tonelli, F. Poli, D. Zonta, and J. R. Casas, 'Digital Twin for Civil Engineering Systems: An Exploratory Review for Distributed Sensing Updating', *Sensors*, vol. 22, no. 9, p. 3168, Apr. 2022, doi: 10.3390/s22093168.
- [16] B. Richter, M. Herbers, and S. Marx, 'Crack monitoring on concrete structures with distributed fiber optic sensors—Toward automated data evaluation and assessment', *Structural Concrete*, vol. 25, no. 2, pp. 1465–1480, Apr. 2024, doi: 10.1002/suco.202300100.
- [17] X. Zhang, L. Long, W. Broere, and X. Bao, 'Smart sensing of concrete crack using distributed fiber optics sensors: Current advances and perspectives', *Case Studies in Construction Materials*, vol. 22, p. e04493, Jul. 2025, doi: 10.1016/j.cscm.2025.e04493.
- [18] M. Herbers, B. Richter, D. Gebauer, M. Classen, and S. Marx, 'Crack monitoring on concrete structures: Comparison of various distributed fiber optic sensors with digital image correlation method', *Structural Concrete*, vol. 24, no. 5, pp. 6123–6140, Oct. 2023, doi: 10.1002/suco.202300062.
- [19] M. Herbers, B. Richter, and S. Marx, 'Rayleigh-based crack monitoring with distributed fiber optic sensors: experimental study on the interaction of spatial resolution and sensor type', *J Civil Struct Health Monit*, Dec. 2024, doi: 10.1007/s13349-024-00896-5.
- [20] A. Paul, D. Sanio, and P. Mark, 'Monitoring tendon breaks in concrete structures at different depths using distributed fiber optical sensors', *eJNDT*, vol. 29, no. 7, Jul. 2024, doi: 10.58286/29598.
- [21] H. Burger *et al.*, 'Untersuchungen zur Verbundverankerung von durchtrennten Spanngliedern beim Brückenrückbau: Faseroptische Dehnungsmessungen im Diskontinuitätsbereich bei der Spannglieddurchtrennung', *Beton und Stahlbetonbau*, vol. 119, no. 10, pp. 753–763, Oct. 2024, doi: 10.1002/best.202400046.
- [22] J. Gómez, J. R. Casas, and S. Villalba, 'Structural Health Monitoring with Distributed Optical Fiber Sensors of tunnel lining affected by nearby construction activity', *Automation in Construction*, vol. 117, p. 103261, Sep. 2020, doi: 10.1016/j.autcon.2020.103261.
- [23] Y. Lemcherreq, T. Galkovski, J. Mata-Falcón, and W. Kaufmann, 'Application of Distributed Fibre Optical Sensing in Reinforced Concrete Elements Subjected to Monotonic and Cyclic Loading', *Sensors*, vol. 22, no. 5, p. 2023, Mar. 2022, doi: 10.3390/s22052023.
- [24] Z. Broth and N. A. Hoult, 'Dynamic distributed strain sensing to assess reinforced concrete behaviour', *Engineering Structures*, vol. 204, p. 110036, Feb. 2020, doi: 10.1016/j.engstruct.2019.110036.
- [25] T. Galkovski, J. Mata-Falcón, and W. Kaufmann, 'Experimental investigation of bond and crack behaviour of reinforced concrete ties using distributed fibre optical sensing and digital image correlation', *Engineering Structures*, vol. 292, p. 116467, Oct. 2023, doi: 10.1016/j.engstruct.2023.116467.
- [26] H. Burger, T. Tephö, O. Fischer, and N. Schramm, 'Performance assessment of existing prestressed concrete bridges utilizing distributed optical fiber sensors', in *Life-Cycle of Structures and Infrastructure Systems*, CRC Press, 2023, pp. 3134–3141.
- [27] M. F. Bado, J. R. Casas, A. Dey, and C. G. Berrocal, 'Distributed Optical Fiber Sensing Bonding Techniques Performance for Embedment inside Reinforced Concrete Structures', *Sensors*, vol. 20, no. 20, p. 5788, Oct. 2020, doi: 10.3390/s20205788.
- [28] M. F. Bado, J. R. Casas, and J. Gómez, 'Post-processing algorithms for distributed optical fiber sensing in structural health monitoring applications', *Structural Health Monitoring*, vol. 20, no. 2, pp. 661–680, Mar. 2021, doi: 10.1177/1475921720921559.
- [29] B. Richter, L. Ulbrich, M. Herbers, and S. Marx, 'Advances in Data Pre-Processing Methods for

- Distributed Fiber Optic Strain Sensing', *Sensors*, vol. 24, no. 23, p. 7454, Nov. 2024, doi: 10.3390/s24237454.
- [30] B. Novák, F. Stein, J. Reinhard, and A. Dudonu, 'Einsatz kontinuierlicher faseroptischer Sensoren zum Monitoring von Bestandsbrücken', *Beton und Stahlbetonbau*, vol. 116, no. 10, pp. 718–726, Oct. 2021, doi: 10.1002/best.202100070.
- [31] Ł. Bednarski, R. Sienko, T. Howiacki, and K. Badura, 'Thermal compensation of monolithic distributed fibre optic sensors: From the lab to the field', *Measurement*, vol. 238, p. 115280, Oct. 2024, doi: 10.1016/j.measurement.2024.115280.
- [32] Max Fiedler, Peter Deepe, Gregor Schacht, and Katarzyna Zdanowicz, 'Faseroptik und Schallemission bei Spannungsrisskorrosion – eine innovative Anwendung bei einer Spannbetonbrücke in Dresden', in *Tagungsband zum 13. Symposium Experimentelle Untersuchungen von Baukonstruktionen*, [Online]. Available: <https://tu-dresden.de/bu/bauingenieurwesen/imb/das-institut/veranstaltungen/SEUB/11-15>
- [33] Steffen Müller, Max Käding, Gregor Schacht, Andreas Gruner, and Ralf Seifert, 'Spannungsrisskorrosion in konzentrierten Spanngliedern–Erfahrungen aus einem gesamtheitlichen Bewertungsansatz für zwei Bauwerke in Döbeln (Sachsen)', in *6. Brückenkolloquium: Fachtagung über Beurteilung, Instandsetzung, Ertüchtigung und Ersatz von Brücken. Tagungshandbuch 2024*, expert verlag, 2024, pp. 233–243.
- [34] R. Regier and N. A. Hoult, 'Distributed Strain Behavior of a Reinforced Concrete Bridge: Case Study', *J. Bridge Eng.*, vol. 19, no. 12, p. 05014007, Dec. 2014, doi: 10.1061/(ASCE)BE.1943-5592.0000637.
- [35] B. Novák, F. Stein, J. Reinhard, A. Dudonu, and T. Zeller, 'Neues Potential im Structural Health Monitoring: Verteilte faseroptische Sensoren für Bestandsbauwerke', in *12. Symposium Experimentelle Untersuchungen von Baukonstruktionen*, Technische Universität Dresden, 2023, pp. 78–87. doi: 10.25368/2023.139.
- [36] M. K. Dhahir, B. Beckmann, and S. Marx, 'Utilizing the Distributed Fiber Optic Sensor (DFOS) Technology for Monitoring the Long-Term Behavior and Structural Performance of Carbon-Reinforced Concrete', Sep. 2024. doi: 10.1007/978-3-031-70145-0\_85.
- [37] A. H. Hartog, *An Introduction to Distributed Optical Fibre Sensors*. Boca Raton: CRC Press, 2017. doi: 10.1201/9781315119014.
- [38] Raymond M. Measures, *Structural Monitoring with Fiber Optic Technology*, 1st ed. Academic Press, 2001.
- [39] H. Burger, T. Tephro, O. Fischer, and N. Schramm, 'Load testing on existing prestressed concrete bridges to determine long-term effects on strain measurement', in *Bridge Maintenance, Safety, Management, Digitalization and Sustainability*, 1st ed., London: CRC Press, 2024, pp. 358–365. doi: 10.1201/9781003483755-38.
- [40] B. Richter *et al.*, 'Monitoring of a prestressed bridge girder with integrated distributed fiber optic sensors', *Procedia Structural Integrity*, vol. 64, pp. 1208–1215, 2024, doi: 10.1016/j.prostr.2024.09.168.
- [41] R. Xu, K. Hicke, S. Chruscicki, and S. Marx, 'Akustisches SpRK-Monitoring mit SEA und verteilten faseroptischen Sensoren', in *12. Symposium Experimentelle Untersuchungen Von Baukonstruktionen*, 2023, pp. 136–147. Accessed: Apr. 21, 2025. [Online]. Available: [https://fis.tu-dresden.de/portal/de/publications/akustisches-sprkmonitoring-mit-sea-und-verteilt-faseroptischen-sensoren\(fb941f96-af7a-435e-ab47-2aeadd9dc0a9\).html](https://fis.tu-dresden.de/portal/de/publications/akustisches-sprkmonitoring-mit-sea-und-verteilt-faseroptischen-sensoren(fb941f96-af7a-435e-ab47-2aeadd9dc0a9).html)



# Lifetime elongation of existing prestressed bridges with a lack of structural integrity using DFOS

Sören Neumann<sup>1</sup>, Harald Burger<sup>1</sup>, Sebastian Lamatsch<sup>1</sup>, Oliver Fischer<sup>1</sup>

<sup>1</sup>Chair of Concrete and Masonry Structures, TUM School of Engineering and Design, Technical University of Munich,  
Theresienstraße 90, Building N6, 80333 München, Germany

email: soeren.neumann@tum.de, harald.burger@tum.de, sebastian.lamatsch@tum.de, oliver.fischer@tum.de

**ABSTRACT:** Existing prestressed concrete bridges without minimum shear or flexural reinforcement are at increased risk of sudden failure, even if they appear undamaged. To prevent such a sudden failure surface mounted Distributed Fiber Optical Sensors (DFOS) can detect local strain changes prior to cracking and visible damage. Failure mechanism analysis, laboratory tests and numerical simulations are used to identify relevant strain indicators. These strain changes could be detected by DFOS even if the failure location is not known exactly in advance. From these results, limits for a universal monitoring concept could be derived considering the individual failure mechanisms and the limitations of the sensor system.

**KEY WORDS:** SHMII-13; distributed fiber optical sensors; existing prestressed bridges; shear failure; brittle failure; monitoring.

## 1 INTRODUCTION

Existing prestressed concrete bridges often no longer meet current safety standards, even though they were originally designed and constructed in accordance with the standards in force at the time, and show no visible damage. Particularly critical are structures lacking minimum shear or flexural reinforcement, where sudden failure without sufficient prior warning can occur [1].

Reassessments of such structures according to the German Reassessment Guidelines and their supplements increasingly reveal structural deficiencies [2][3]. Some of these affect shear capacity, transverse reinforcement between flanges and web, and the structures bending robustness. Due to these deficiencies, early indications of failure become less likely or may not occur at all when conducting structural inspections in accordance with current German standards (e.g., DIN 1076 [4]) [1].

A further challenge is the accurate measurement of local strain changes in existing structures, where irregular surface conditions, structural tolerances and limited accessibility significantly affect the reliable application of both established and innovative monitoring methods.

To ensure the long-term structural safety of this existing structures, it is essential to develop and implement tailored monitoring strategies. This requires the development of practical principles that provide engineering consultants, clients and inspection authorities with a sound basis for decision making.

## 2 FAILURE MECHANISM

The absence of minimum reinforcement or corrosion damage, especially stress corrosion cracking in prestressing steel, can lead to brittle, unannounced failures in prestressed concrete bridges.



Figure 1 Applied DFOS on the Hammelburg bridge girder web, taken from [6]

## 2.1 Shear

Previous test programs have shown that, despite low shear reinforcement, redistribution in the tension chord can result in a certain increase in shear capacity [5]. In contrast, shear tests at the Hammelburg bridge revealed early failure after initial cracking due to pre-damaged and unfavourably oriented tendons, as well as smooth reinforcement bars [6]. Figure 1 shows the girder web of the Hammelburg bridge after the shear test.

## 2.2 Bending Robustness

Significant problems on prestressed structures with a lack of flexural reinforcement became apparent with increasing operational experience. In Germany the introduction of robustness reinforcement was consequently introduced in 1995 [7]. In bridges that were built before this time, calculative proof of sufficient warning behavior as a crack before structural failure is not always given. Moreover, even with proven sufficient warning behavior, the implementation of condition monitoring is required to prevent sudden failure [8].

## 3 SURFACE MOUNTED DFOS ON PRESTRESSED CONCRETE BRIDGES

Fiber optical measurement technology based on Rayleigh backscattering offers advantages on prestressed concrete structures. As there is generally little or no tensile stress in the cross-section of existing prestressed concrete bridges, there is less likelihood of significant cracking. Nevertheless, it is possible to follow the stress under temporary loading and thus detect cracks that may have been overstressed by the prestressing. Strain changes are detected continuously and with high spatial resolution up to 0.65 mm along a bonded fiber optical sensor with lengths exceeding 100 m.

The application of DFOS on the surface of existing structures faces many challenges. Uneven adhesive layer thicknesses, rough formwork surfaces, and positional inaccuracies due to construction tolerances are just a few, which have to be considered in the data evaluation. Discontinuities in the adhesive or surface irregularities can lead to strain peaks in the signal, but these can be validated through visual inspections [9].

The early detection of localized strain changes long before the appearance of visible cracks enables innovative condition monitoring strategies, which can significantly extend the service life of existing structures and support more efficient and economical maintenance planning.

## 4 ACTUAL RESEARCH

The current research at the Chair of Concrete and Masonry Structures at the Technical University of Munich includes numerical simulations to identify strain fields associated with failure mechanisms. Various damage scenarios are analyzed to map critical strain zones for shear and flexural failure. The results serve as the basis for defining expected measurement quantities and developing robust sensor layouts.

Parallel experimental investigations are conducted. In small-scale tests different sensor-adhesive combinations, application techniques, and environmental influences are compared. Particular attention is given to overhead applications and the detection of strains over irregular surfaces. Long-term tests

examine the effects of temperature cycles and potential creep phenomena within the sensor.

Building upon these results, current research focuses on the development of a monitoring concept for prestressed concrete bridges with static and structural deficiencies. The study emphasizes the identification of suitable sensors, application methods, sensor placement, and the definition of meaningful measurement intervals. The outcomes are intended to provide consulting engineers, clients, and inspection authorities with a solid basis for developing and implementing individually adapted monitoring strategies.

Large-scale tests on prestressed concrete girders will be carried out based on the numerical and experimental results. The focus of these tests lies on the application of a developed monitoring concept to detect the initial signs of a shear or flexural failure described in chapter 2. The load cycles are designed to induce microcracking and pre-damage, which, although not visibly detectable after unloading, can still be measured by DFOS.

The outcomings should lead to a comprehensive guideline for the use of DFOS on existing prestressed bridges. It will include recommendations for sensor layouts, suitable adhesive and application techniques, and methods for determining appropriate measurement intervals. The guideline also provides information on installation requirements and data interpretation. Validation will be carried out on two bridges with different types of structural deficiencies: one suffering from shear capacity issues and another from missing robustness reinforcement combined with susceptibility to stress corrosion cracking.

## 5 CONCLUSION

Effective use of DFOS on bridges has already been demonstrated by several studies, i.e. [10][11][12][13]. This shows that the general and widespread use of this sensor technology can be useful for extending service life of existing bridges. Therefore, limits can be developed for a universal monitoring concept for prestressed concrete bridges with known deficiencies using DFOS. Therefore, reliable sensor layouts for typical failure mechanisms and recommendations for the selection of suitable sensor and adhesive combinations have to be analyzed. Moreover, the development of methodological approaches for defining measurement intervals, considering damage probabilities and degradation processes have to be considered.

Through practical validation, the feasibility of the developed concepts will be demonstrated. Thus, the project contributes significantly to the sustainable maintenance of existing prestressed concrete bridges and the extension of their service life.

## ACKNOWLEDGMENTS

The authors wish to express their gratitude to the German Federal Highway Research Institute. The research project FE 88.0221/2024/AE04 is funded by the German Federal Highway Research Institute on behalf of the Federal Ministry for Digital and Transport. The responsibility for the content lies solely with the author.

## REFERENCES

- [1] Marzahn, G.; Hegger, J.; Maurer, R.; Zilch, K.; Dunkelberg, D.; Kolodziejczyk, A.; Teworte, F. Die Nachrechnung von Betonbrücken – Fortschreibung der Nachrechnungsrichtlinie. In: Bergmeister, K.; Fingerloos, F.; Wörner, J.-D. [eds.] Beton-Kalender 2015. Berlin: Ernst&Sohn, (2015)
- [2] Fischer, O.; Lingemann, J.; Jähring, J.; Sonnabend, S.: Massivbrücken - Aktuelle Entwicklungen und Beispiele zu Neubau und Bestand. In: Bergmeister, K. et al. [eds.] Beton-Kalender 2023. Berlin: Ernst&Sohn. (2023)
- [3] Fischer, O.; Müller, A.; Lechner, T.; Wild, M.; Kessner, K.: Ergebnisse und Erkenntnisse zu durchgeführten Nachrechnungen von Betonbrücken in Deutschland, in: Beton- und Stahlbetonbau 109 (2), (2014).
- [4] DIN Deutsches Institut für Normung e.V. DIN 1076: Ingenieurbauwerke im Zuge von Straßen und Wegen. Berlin: Beuth Verlag GmbH, (1999)
- [5] Lamatsch, S.; Fischer, O.: Querkraftversuche an unterschiedlich hoch vorgespannten Balkenelementen mit baupraktischen Bauteilabmessungen. In: Bauingenieur 99 Heft 1/2, (2024),
- [6] Gehrlein, S; Fischer, O.: Großversuche zur Querkrafttragfähigkeit bestehender Spannbetonbrücken an der Saalebrücke Hammelburg. Teil 2: Messprogramm, Versuchsergebnisse, Vergleich mit verschiedenen Berechnungsansätzen. Beton- und Stahlbetonbau 113 Heft 10, S. 696-704. doi.org/10.1002/best.201800068 (2018)
- [7] Zilch, K.; Zehetmaier, G.: Bemessung im konstruktiven Betonbau: Nach DIN 1045-1 (Fassung 2008) und EN 1992-1-1 (Eurocode 2), Springer, Berlin, Heidelberg, (2010)
- [8] BMVBS: Handlungsanweisung Spannungsrisskorrosion - Handlungsanweisung zur Überprüfung und Beurteilung von älteren Brückenbauwerken, die mit vergütetem, spannungsrisskorrosionsgefährdetem Spannstahl erstellt wurden. Bundesministerium für Verkehr, Bau und Stadtentwicklung – Abteilung Straßenbau, (2011)
- [9] Burger, H; Tepfo, T.; Fischer, O.; Schramm, S. Performance assessment of existing prestressed concrete bridges utilizing distributed optical fiber sensors. Biondini, F.; et al. [eds.] Life-Cycle of Structures and Infrastructure Systems. London: CRC Press. (2023)
- [10] Wild, M.; Schmidt-Thrö, G.; Fischer, O.: Faseroptische Dehnungsmessung im Laborversuch und an Bauwerken – Anwendungsmöglichkeiten und -beispiele im Betonbau, in: Fischer, O. (ed.): 18. Münchener Massivbau Seminar, München, (2014)
- [11] Novák, B.; Stein, F.; Reinhard, J.; Dudon, A.: Einsatz kontinuierlicher faseroptischer Sensoren zum Monitoring von Bestandsbrücken. In: Beton- und Stahlbetonbau Volume 116, Issue 10, S.s 718-726. <https://doi.org/10.1002/best.202100070> (2021)
- [12] Bednarski, L.; Sienko, R.; Howiacki, T.; Zuziak, K.: The Smart Nervous System for Cracked Concrete Structures: Theory, Design, Research, and Field Proof of Monolithic DFOS-Based Sensors. Sensors, 22, 8713. <https://doi.org/10.3390/s22228713> (2022)
- [13] Strasser, L.; Lienhart, W.: Distributed fiber optic sensing during static and dynamic bridge loading. Jensen, J. S. et al. [edit.] Bridge Maintenance, Safety, Management, Digitalization and Sustainability. London: CRC Press. (2024)



# Concrete signature in long-term Distributed Fiber Optic Strain Sensing: Challenges and opportunities for Structural Health Monitoring

Lisa Ulbrich<sup>1</sup>, [ORCID](#), Alessia Abbozzo<sup>2</sup>, [ORCID](#), Frank Jesse<sup>1</sup>, [ORCID](#), Marco di Prisco<sup>2</sup>, [ORCID](#)

<sup>1</sup>Hentschke Bau GmbH, Department of Research and Development, Zeppelinstr. 15, 02625 Bautzen, Germany

<sup>2</sup>Department of Civil and Environmental engineering, Politecnico di Milano, P.za L. da Vinci, 32 – 20133 Milano, Italy.

email: Ulbrich.Lisa@hentschke-bau.de, Jesse.Frank@hentschke-bau.de, alessia.abbozzo@polimi.it, marco.diprisco@polimi.it

**ABSTRACT:** In recent years, Distributed Strain Sensing (DSS), utilizing optical frequency domain reflectometry of Rayleigh backscatter, has gained significant prominence in the realm of Bridge Structural Health Monitoring (BSHM). Its key advantage is its ability to provide continuous strain monitoring with high spatial resolution (0.65 mm) and an accuracy of up to 1  $\mu\text{m/m}$ . This capability facilitates the monitoring of deformations and defects, as well as precise crack detection, the assessment of crack width and others.

However, publications on DSS based on Rayleigh backscattering often report local effects that are not linked to disturbances caused by the measurement principle, such as noise or anomalies in strain readings. These effects can complicate the evaluation of DSS data, particularly concerning crack detection and width measurement, as well as tasks like detecting tension wire breakages. There have been theories, suggesting that these local effects may stem from micro-cracks or inhomogeneities within the concrete matrix, yet further investigations into this phenomenon are lacking.

Within this paper the phenomenon of local effects, henceforth referred to as the *concrete signature*, has been investigated on multiple time scales during. The analysis utilizes data from the openLAB research bridge in Bautzen, Germany. Possible reasons for the development and behavior of *concrete signature* are discussed, along with the challenges and opportunities associated with addressing it.

**KEY WORDS:** Concrete Signature, Distributed Fiber Optic Sensing, Distributed Strain Sensing, Bridge Structural Health Monitoring.

## 1 INTRODUCTION

Distributed fiber optic sensing (DFOS) has emerged as a pivotal technology in the realm of structural health monitoring (SHM) in recent years. The applications of DFOS can be broadly classified into three primary categories: distributed temperature sensing (DTS), distributed acoustic sensing (DAS), and distributed strain sensing (DSS). All these applications exploit backscatter effects arising from inhomogeneities within optical fibers. The principal types of backscatter effects include Raman, Brillouin, and Rayleigh backscattering [1, 2].

Within the scope of SHM of concrete structures, DSS has gained considerable attention, as it offers continuous strain measurements in structures, a significant advantage over traditional measurement systems such as strain gauges or inductive transducers [3]. DSS utilizing Rayleigh backscattering (optical frequency domain reflectometry) achieves a high spatial resolution of up to 0.65 mm with an accuracy of 1  $\mu\text{m/m}$  [4], albeit with a sensing range constrained to approx. 100 m [5]. Therefore, its principal applications lie in the evaluation of failures, damages and local effects in concrete structures, particularly in the realms of crack detection and crack width calculation [6, 7].

Crack detection with DSS is predicated on peak identification, while the subsequent quantification of crack width relies on minima or midpoint approaches to ascertain the influence length of the crack to find out the borders for linear integration. Hence, it is important to distinguish clearly

between peaks and minima attributable to cracks and those arising from other factors present in DSS readings [6, 7].

However, literature regarding DSS based on Rayleigh backscattering in concrete structures frequently reports local effects that do not correlate with disturbances originating from the measurement principle, such as noise or strain reading anomalies [8-11]. These local effects, subsequently referred to as the *concrete signature*, appear to evolve over time, maintaining a consistent position, thereby complicating the interpretation of DSS readings, particularly concerning crack detection and crack width evaluation, as well as for the identification of tension wire breakages [12].

Given that current publications on DSS employing Rayleigh backscattering predominantly rely on laboratory assessments or short-term field trials, this paper aims to investigate the phenomenon of evolving *concrete signature* in DSS readings over various time scales. To achieve this objective, DSS data from the openLAB research bridge in Bautzen, Germany, are analyzed [13, 14]. A picture of the openLAB research bridge is given in Figure 1.

The DSS dataset analyzed encompasses the production of precast elements, the installation phase, and the operational phase of the bridge, extending over a total sensor length of 1.5 km [13]. For the purposes of this analysis, a single beam will be selected to examine the development of the *concrete signature* along with the potential underlying factors and their implications. Ultimately, the study will elucidate the impact of *concrete signature* on DSS reading evaluation and its potential significance.



Figure 1. OpenLAB research bridge in Bautzen, Germany (Stefan Göschel)

## 2 CONCRETE SIGNATURE

Although *concrete signature* is recognizable in the majority of publications [12, 15, 16], only a few commented it briefly [8-11, 17]. For instance, Richter et al. highlighted the emergence of local effects that are not associated with disturbances in the measurement system [9]. Becks et al. reported fluctuations of up to 200  $\mu\text{m/m}$  in DSS readings from sensors adhered to the concrete surface, attributing these variations to local strain changes within inhomogeneous concrete [8]. Weisbrich et al. provided a similar explanation, conducting laboratory tests with concrete specimens that had Ormocer coated sensors glued to the surface, to reinforcement, and embedded in the concrete matrix [11]. They indicated that "inhomogeneities and imprecision of the concrete" could account for fluctuations in DSS readings observed during their tests [11]. Additionally, Sieńko et al. reported on micro-cracks resulting from thermal shrinkage during the concrete hardening process in laboratory tests, which correspond in size to the phenomena described by Becks et al. [8, 10]. Despite these effects being identified and illustrated in diagrams across numerous publications, there has yet to be a thorough investigation into their underlying causes and behaviors.

## 3 METHODOLOGY

To investigate the development and properties of *concrete signature* over various time scales, DSS readings from a fiber optic sensor placed in a 15 m prestressed bridge beam of the openLAB research bridge in Bautzen, Germany have been analyzed. The beam FT1.1 features a T-shaped cross-section and is prestressed. The beam is made from C20/25 standard

concrete using granite and quartzite aggregates, with a maximum aggregate size of 16 mm.

The fiber optic sensor analyzed is an EpsilonSensor, 3 mm, ripped from Nerve-Sensors [18], where the fiber itself is embedded within a monolithic core out of polyester fibers and epoxide. It is situated at the bottom of the beam within the concrete matrix and is securely fixed to the stirrups using cable ties. The sensor was interrogated by an ODiSi6100 system from Luna Inc. [5], utilizing a gage pitch of 1.3 mm.

Figure 2 and Figure 3 are showing the placement of the sensor within beam FT1.1. Figure 2 illustrates the sensor placement within the beam FT1.1 at openLAB, while Figure 3 is a picture of the fiber optic sensor (red) within the reinforcement cage during the production of FT1.1.

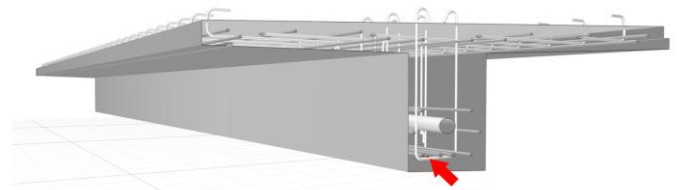


Figure 2. Sensor placement of the fiber optic sensor at beam FT1.1 in span 1 of the openLAB in Bautzen, Germany.

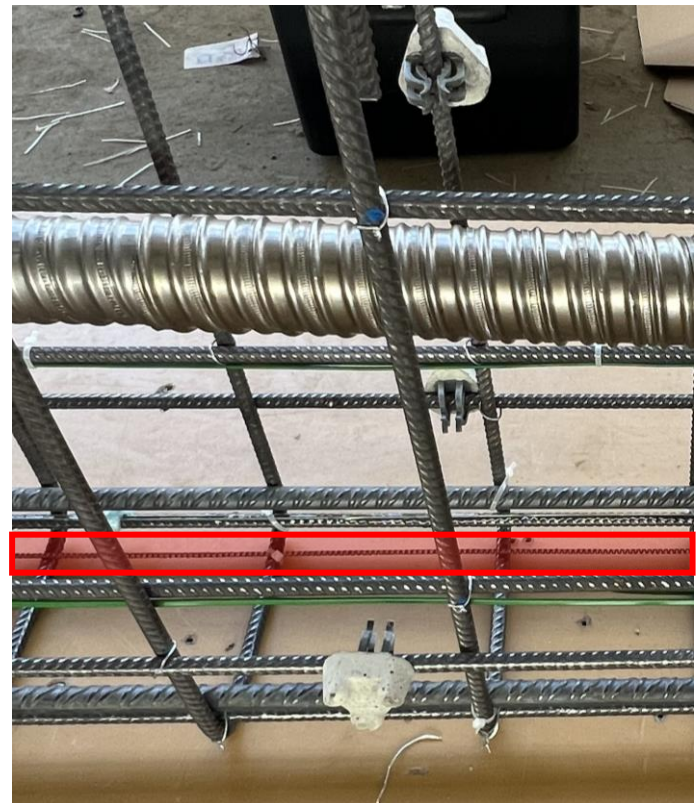


Figure 3. EpsilonSensor 3 mm ripped with the reinforcement cage of FT1.1 in span 1 of the openLAB in Bautzen, Germany.

In addition to DSS readings, temperature measurements with Gaia 200 of Maturix [19] using thermocouples type K inside the concrete took place during hydration. Later, during



prestressing and operation, the concrete temperature was measured using Testo 176T4 [20] with thermocouples of type K at five points inside the beam. In the operational phase, a combi-sensor continuously measuring air temperature and air humidity was installed next to the beam.

The DSS readings have not been compensated for temperature variations, either regarding optical or material effects. Compensation for material effects entails addressing the thermal expansion of both the sensor materials and the host material. In the case of concrete as the host material, this is typically accomplished by utilizing the overall thermal expansion coefficient of concrete [16]. For optical effects, temperature compensation related to changes in refractive index is achieved by applying the temperature calibration constant of the fiber and calculating the spectral shift based on the temperature difference [21]. Given that only gradual temperature changes occur within concrete elements, neither effect significantly impacts the local, distinctive manifestation of the *concrete signature*.

The analysis involved varying the DSS readings tare to examine the redevelopment of the concrete signature across different time scales and for comparisons. Thereby, tare defines the point where the DSS reading was set to zero line again.

#### 4 RESULTS

During the time scales under consideration, the global stress in the beam is changing several 100  $\mu\text{m}/\text{m}$  due to temperature changes, load, creep, and shrinkage. However, the focus of this study is the development of the local *concrete signature*. Thus, a representative segment of 2 meters from the DSS readings, collected at specific timestamps, is presented to elucidate the data. The diagram areas delineate a section of 200  $\mu\text{m}/\text{m}$ , visualized through a grid structured in increments of 50  $\mu\text{m}/\text{m}$ . The orientation of the readings was selected based on the mean value located at the midpoint of the y-axis to effectively showcase the manifestation of the *concrete signature*.

The investigation initiates with the first 24 hours of the hydration phase of concrete, aiming to analyze the initial development of the *concrete signature*. For that the DSS readings have been referenced to the beginning of the hardening.

Figure 4 depicts the evolution of the *concrete signature* throughout hydration. The timestamp 0 hours signifies the beginning of the hardening process and the tare for the following DSS readings; consequently, the DSS reading establishes a baseline of zero. After 2 hours, initial fluctuations are observed, although the DSS readings remain relatively smooth. After 6 hours, a pronounced signature emerges, exhibiting an increasing trend until 12 hours, ultimately reaching a value range around the mean of approx.  $\pm 80 \mu\text{m}/\text{m}$  and a standard deviation of approx. 22.6  $\mu\text{m}/\text{m}$ . Thereafter, the signature exhibits a decreasing trend until the concluding DSS reading at 24 hours with a value range of  $\pm 75 \mu\text{m}/\text{m}$  and a standard deviation of 20.4  $\mu\text{m}/\text{m}$ . Notably, significant peaks are apparent between 2 hours and 6 hours, with DSS readings at 24 hours remaining considerably elevated.

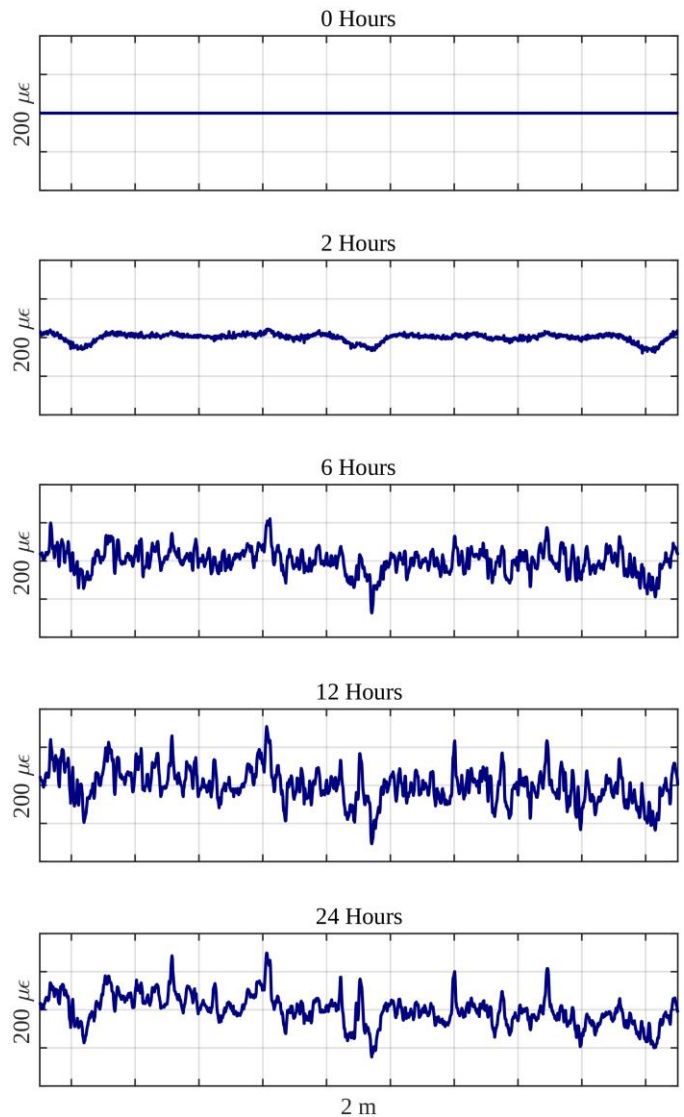


Figure 4. Distributed strain sensing readings during the first 24 hours of hydration.

During the hydration, a notable increase in the temperature of the concrete was observed, reaching a maximum temperature differential of 22.5 K relative to the tare readings at 0 hours. Figure 5 shows the temperature development during the hydration process as well as the temperature difference  $\Delta T$  for the selected DSS readings to the tare reading at 0 hours.



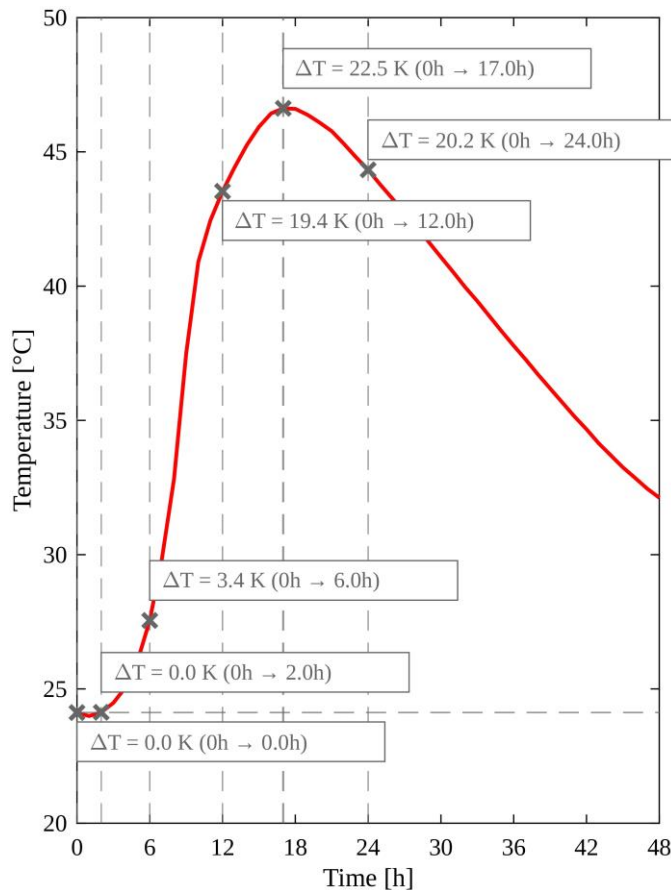


Figure 5. Temperature measurements during hydration.

The prestressing process was subsequently analyzed with respect to the tare prior to hydration and the tare prior to prestressing. This included assessments prior prestressing the tendon, after partial prestressing the tendon in subsequent bonding 33 % and after prestressing strands in immediate bonding at a concrete age of 5 days. Followed by DSS readings after full prestressing of the tendon 100 % in subsequent bonding at concrete age of 15 days.

Figure 6 illustrates the evolution of the *concrete signature* throughout the prestressing process. The red lines represent the DSS readings with tare before hydration, while the blue lines indicate the DSS readings with tare before partial prestress, marked by the zero line at the timestamp just prior prestressing. Regardless of the tare used, the *concrete signature* in both DSS readings shows an increase and noticeable similarities.

A comparison of DSS readings across the different tares reveals that primary features consistently re-emerge during the prestressing process, also after taring prior to prestressing. Specifically, the *concrete signature* with tare before hydration reaches a maximum value range according to the mean of  $\pm 69 \mu\text{m/m}$  and a standard deviation of  $22.1 \mu\text{m/m}$ , whereas the *concrete signature* with tare before prestressing reaches a maximum value range around the mean of  $\pm 31 \mu\text{m/m}$  and a standard deviation of  $11.8 \mu\text{m/m}$ .

During the prestressing process, the concrete temperature changed less than 1 K. Compared to the tare before hydration the temperature changed approx.  $-4.9 \text{ K}$ .

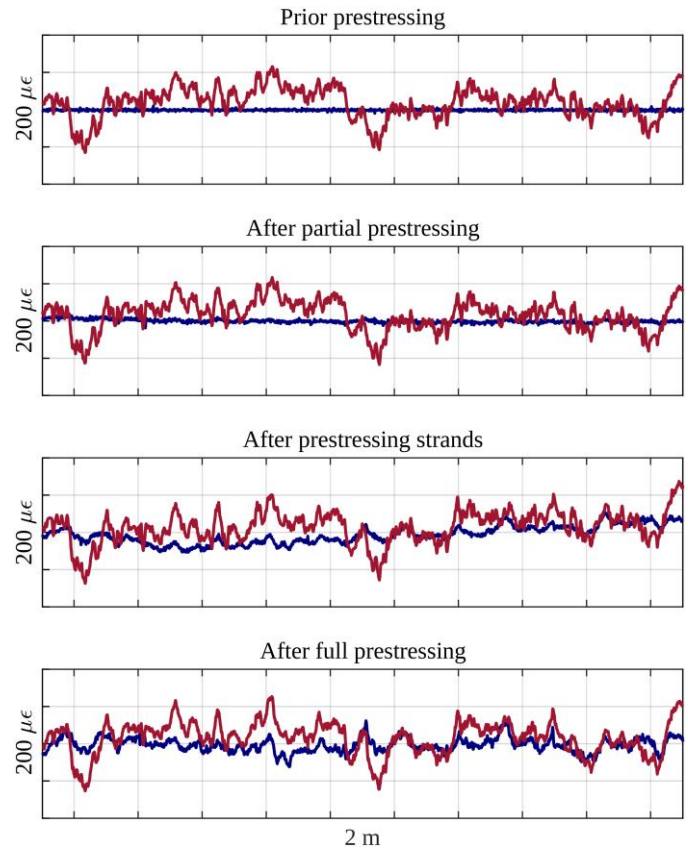


Figure 6. Distributed strain sensing readings during prestressing process (red: DSS readings with tare before hydration, blue: DSS readings with tare before partial prestress).

Finally, the *concrete signature* was assessed over one year with no traffic load during the DSS readings. The tare is established after finishing construction at the beginning of the operation phase (0 Months). Figure 7 illustrates the evolvement of the *concrete signature* during the operation. It is noteworthy that the *concrete signature* is already significantly redeveloped after three months. The increasing trend of the strain values from the left to the right side of the diagram in each DSS reading is due to the bending moment in the beam bearing on the columns. To quantify the *concrete signature* despite the bending effects, a sliding mean with a window of 380 (approximately 0.5 m at a gage pitch of 1.3 mm) was applied (Figure 7 dashed line). This approach yields a maximum value range of the concrete signature around the sliding mean of approximately  $\pm 29 \mu\text{m/m}$  at six months and a maximum standard deviation of  $8.1 \mu\text{m/m}$  at 12 months.

After two months, distinct patterns of regular increases and decreases, occurring approx. every 15 cm, become apparent and are clearly noticeable after six months.

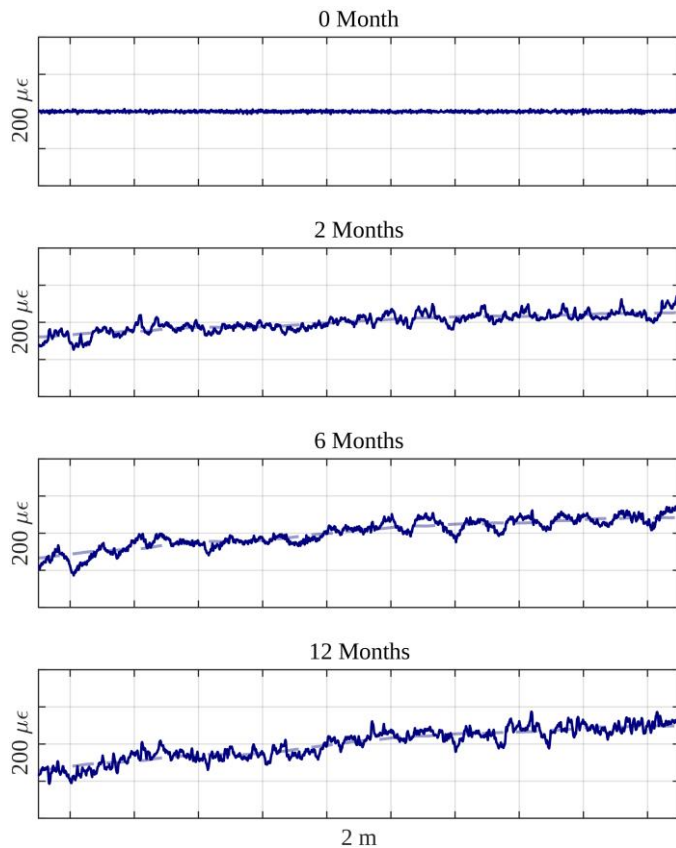


Figure 7. Distributed strain sensing readings during one year of operation.

During the operation, the beam was exposed to environmental conditions, resulting in permanent changes in air temperature and humidity. Concrete temperature, air temperature and air humidity changes regarding the tare measurement at 0 months are presented in Table 1.

Table 1. Temperatures and humidity changes during the selected DSS readings regarding to the tare at 0 months.

DSS reading	$\Delta T_c$ [K]	$\Delta T_a$ [K]	$\Delta rH_a$ [%]
0 months	0	0	0
2 months	+11.4	+17.0	+12.37
6 months	+10.5	+19.6	+6.81
12 months	-3.6	-1.54	+56.01

## 5 DISCUSSION

It has been demonstrated that the *concrete signature* begins to develop during the hydration process, with certain features remaining consistent over time. In the chosen DSS readings the most prominent signature occurs at 12 hours, which correlates with the highest temperature reached, leading to relation between the *concrete signature* and the temperature behavior of the concrete matrix. The temperature expansion coefficients of the various components of the concrete matrix—such as granite, quartzite, and cement stone—differ substantially (as shown in Table 2), thus the distinct expansions of these materials could be recorded by the sensor.

Table 2. Thermal expansion coefficients [22].

Component	Coefficient of thermal expansion $\alpha T$ [-]
Granite, Quarzporphyr	$7.4 \times 10^{-6}$
Basalt, Diorite, Gabbro	$6.5 \times 10^{-6}$
Quartz sand/gravel	$11.0 \times 10^{-6}$
Quartzite	$11.8 \times 10^{-6}$
Cement matrix (min)	$10.0 \times 10^{-6}$
Cement matrix (max)	$23.0 \times 10^{-6}$

A temperature increase of 19.4 K, like for the 12 hours DSS reading, induces a temperature strain of approx.  $140 \mu\text{m/m}$  for granite, about  $130 \mu\text{m/m}$  for basalt, and around  $200 \mu\text{m/m}$  for liquid cement. This results in strain variations of up to  $65 \mu\text{m/m}$ , close to the variation visible in the DSS reading at 12 hours. However, it is important to note that the thermal expansion coefficient of the cement matrix increases during hydration and decreases with diminishing humidity [22]. Additionally, throughout the hydration process, the modulus of elasticity, concrete strength, and, as a result, creep behavior exhibit continuous variations [23], which may also affect the signature.

The decrease of the signature at 24 hours might be due to the cooling as well as relaxation effects. The peaks observed after cooling can be attributed to the shrinkage of the cement matrix in relation to the aggregates. The more prominent peaks may be indicative of micro-cracks formed as a result of this shrinkage, as described by Sieńko et al. [10]. However, the regular spatial appearance of these peaks suggests the influence of structural elements such as stirrups or cable ties used for sensor fixation may also contribute.

During the prestressing process temperature remains almost constant. However, even after taring before prestressing, the *concrete signature* begins to redevelop. This suggests that the concrete signature is also influenced by load changes, leading to creeping effects. The creep behavior in concrete is affected by the Young's modulus, which varies based on age, aggregate size and shape, its deformation characteristics, and the ratio of cement paste or mortar to aggregates [23]. Considering the use of two aggregate types with differing shapes, sizes, and deformation characteristics, variations in their respective Young's moduli are expected. These differences can significantly influence their creep behavior, potentially affecting the DSS readings.

Similarly, the *concrete signature* continues to redevelop during the operational phase even after taring in the beginning. In this phase, all the potential influencing factors previously mentioned are at play. Environmental changes, such as fluctuations in temperature and humidity, contribute to swelling, shrinking, and thermal expansion. Additionally, there are creeping effects resulting from the prestressing and the dead weight of both the beam and the cast-in-place concrete slab.

The interaction of these effects, combined with the heterogeneous nature of the concrete matrix, leads to a continuous change in the *concrete signature*. Noteworthy is, that the maximum value range of concrete signature apparently increases with the concrete temperature. Additionally, the most significant fluctuations in the *concrete signature*, as indicated by the highest standard deviation, occur at an elevated relative air humidity level, which serves as an indicator of increased

moisture in the concrete. However, due to the multitude of simultaneous effects, it is challenging to isolate and quantify the impact of each individual factor on the *concrete signature*.

The observed regular increases and decreases every 14 to 15 cm in certain sections may be attributed to the placement of stirrups, which are distributed approximately every 15 cm in the corresponding section of the beam. It is important to note that the concrete analyzed here is still relatively young (with the last DSS reading taken at an age of 19 months), which may result in greater fluctuations in the *concrete signature* due to more pronounced creeping effects in younger concrete.

Conceivable would also be that there are also effects from the reaction of the sensor coating itself. Fluctuations in the concrete moisture and concrete temperature can lead to expansion effects in the material, which can be transferred to the fiber. This effect is for example used for polyimide-coated fibers in order to measure humidity [24]. However, for coating out of polyester fibers and epoxide these effects can be neglected, since epoxide (epoxy glue) is used to insulate fibers from the surrounding moisture [24].

Regardless of the specific time episode being analyzed, the manifestation of the *concrete signature* is always dependent on the selected tare. While the tare does alter the resulting *concrete signature* itself - such as the position of the peaks - it does influence the prominence (e.g. the height of the peaks), as illustrated in the prestressing process. This distinction is crucial during data evaluation, as an appropriately chosen tare can enhance the *concrete signature* for analysis or diminish it to isolate other factors under scrutiny, such as tension wire breakages. However, the ability to reduce the *concrete signature* in this manner is contingent upon DSS readings taken in temporal proximity to the effect being analyzed, given that the *concrete signature*, at least in the evaluated DSS readings, tends to redevelop rapidly.

## 6 CONCLUDING REMARKS

It has been shown that *concrete signature* develops over various time episodes, ranging from several hours to several months. Potential environmental factors influencing this phenomenon include temperature, humidity, and load, which can lead to thermal expansion, shrinkage, swelling, and creep, as well as localized disturbances from structural elements like cable ties or reinforcement. Additionally, it is crucial to consider factors intrinsic to the concrete matrix, particularly the differing responses of aggregates and the cementitious matrix to these environmental influences. The age of the concrete itself may also play a significant role, since creeping and shrinkage depend on concrete maturity.

In this study, *concrete signature* achieved a maximum value range of  $\pm 75 \mu\text{m/m}$ , which considerably affects crack detection and width calculation, as peak detection and minima approaches may not work accurately. Moreover, identifying micro-cracks or instances of tension wire breakage may prove challenging, as these phenomena produce effects smaller than those associated with *concrete signature*. Consequently, the priority will be to develop effective compensation methods to ensure the reliability of data from digital signature systems (DSS).

However, gaining insights into the causes and influences on *concrete signature* could provide a better understanding of

concrete behavior related to load, creep, shrinkage, and thermal expansion. This understanding would facilitate more accurate assessments of structural behavior, for instance, by refining calculations pertaining to creep effects as outlined in EC2. Moreover, *concrete signature* may present opportunities for quality assessment during production through the examination of material inhomogeneities like gravel nests.

To gain a deeper understanding of the causes and factors influencing *concrete signature* in DSS readings, systematic testing is currently underway. Initial experiments are designed to isolate these impact factors and observe the resulting responses of the concrete matrix at the meso-level. Building on this knowledge, compensation methods and knowledge extraction techniques can subsequently be developed and evaluated in field tests.

## ACKNOWLEDGMENTS

This paper outlines findings from the research projects FOSsure (Fiber optic sensors for reliable condition assessment of solid bridges) and IDA-KI (Automated evaluation of monitoring data from infrastructure structures) funded by the Federal Ministry for Digital and Transport, Germany, within the innovation program mFUND (funding references: 19FS2075B and 19FS2013C).

Additionally, it outlines findings from the Return (Multi-risk science for resilient communities under a changing climate) This Foundation, with headquarters in Corso Umberto I, 40 80138 Napoli (NA), is founded by National Resilience and Recovery Plan (NRRP).

## REFERENCES

- [1] Berrocal, C. G., I. Fernandez, and R. Rempling. 2020. "Crack monitoring in reinforced concrete beams by distributed optical fiber sensors" *Struct. Infrastruct. E.*, 17(1):124–139, doi:10.1080/15732479.2020.1731558.
- [2] Howiacki, T., R. Siénko, Bednarski, and K. Zuziak. 2023. "Crack Shape Coefficient: Comparison between Different DFOS Tools Embedded for Crack Monitoring in Concrete" *Sensors*, 23(2):566, ISSN 1424-8220, doi:10.3390/s23020566.
- [3] Monsberger, C. and W. Lienhart. 2021. "Distributed Fiber Optic Shape Sensing of Concrete Structures" *Sensors*, 21:6098, doi:10.3390/s21186098.
- [4] Janiak, T., H. Becks, B. Camps, M. Classen, and J. Hegger. 2023. "Evaluation of distributed fiber optic sensors in structural concrete". *Materials and Structures*, 56(9), 159, doi:10.1617/s11527-023-02222-9.
- [5] Luna Innovations Incorporated. 2021. "User's Guide ODISI 6" Tech. rep., Luna Innovations Incorporated.
- [6] Herbers, M., B. Richter, and S. Marx. 2024. "Rayleigh-based crack monitoring with distributed fiber optic sensors: experimental study on the interaction of spatial resolution and sensor type" *Journal of Civil Structural Health Monitoring*:1–25, doi:10.1007/s13349-024-00896-5.
- [7] Richter, B., M. Herbers, and S. Marx. 2023. "Crack monitoring on concrete structures with distributed fiber optic sensors—Toward automated data evaluation and assessment" *Structural Concrete*, 25:1465–, doi:10.1002/suco.202300100.
- [8] Becks, H., A. Baktheer, S. Marx, M. Classen, J. Hegger, and R. Chudoba. 2022. "Monitoring concept for the propagation of compressive fatigue in externally prestressed concrete beams using digital image correlation and fiber optic sensors" *Fatigue Fracture of Engineering Materials Structures*, 46, doi:10.1111/ffe.13881.
- [9] Richter, B., L. Ulbrich, M. Herbers, and S. Marx. 2024. "Advances in data pre-processing methods for distributed fiber optic strain sensing" *Sensors*, 24(23):7454.
- [10] Siénko, R., L. Bednarski, and T. Howiacki. 2021. "Distributed Optical Fibre Sensors for Strain and Temperature Monitoring of Early-Age Concrete: Laboratory and In-situ Examples" in F. Kanavaris, F. Benboudjema, and M. Azenha, eds., *International RILEM Conference on Early-Age and Long-Term Cracking in RC Structures*, Springer International Publishing, Cham, ISBN 978-3-030-72921-9, pp. 77–87.



- [11] Weisbrich, M., D. Messerer, and K. Holschemacher. 2023. "The Challenges and Advantages of Distributed Fiber Optic Strain Monitoring in and on the Cementitious Matrix of Concrete Beams" *Sensors*, 23(23), ISSN 1424-8220, doi: 10.3390/s23239477.
- [12] Richter, B., E. Will, M. Herbers, and S. Marx. 2025. "Detection of prestressing wire breaks in post-tensioned concrete structures using distributed fiber optic strain sensing" [submitted].
- [13] Herbers, M., B. Richter, J.-H. Bartels, T. Al-Zuriqat, K. Smarsly, and S. Marx. 2024. "openLAB - A large-scale demonstrator for advancing digital twin developments of bridges".
- [14] Technical University of Dresden. "openLAB". Accessed June 2025. [https://tu-dresden.de/bu/bauingenieurwesen/imb/forschung/grossprojekte/openLAB?set\\_language=en](https://tu-dresden.de/bu/bauingenieurwesen/imb/forschung/grossprojekte/openLAB?set_language=en)
- [15] Boros, V., A. Vorwagner, D. Prammer, and W. Lienhart. 2024. "Application of Embedded Distributed Fiber Optic Sensors on a Highway Bridge as a Support for Bridge Inspections".
- [16] Alj, I., M. Quiertant, A. Khadour, Q. Grando, and K. Benzarti. 2022. "Application of Distributed Optical Fiber Sensing Technology to the Detection and Monitoring of Internal Swelling Pathologies in Massive Concrete Blocks" *Sensors*, 22(20), ISSN 1424-8220, doi: 10.3390/s22207797.
- [17] Zdanowicz, K., T. Howiacki, R. Siénko, and S. Marx. 2021. "DFOS measurements of strain development in textile reinforced concrete slabs with expansive admixture during setting and hardening".
- [18] Nerve-Sensors. "EpsilonSensor". Accessed June 2025. [https://nerve-sensors.com/wp-content/uploads/2024/10/EpsilonSensor\\_DE.pdf](https://nerve-sensors.com/wp-content/uploads/2024/10/EpsilonSensor_DE.pdf).
- [19] Maturix. "Gaia 200". Accessed June 2025. <https://maturix.com/sensors/gaia-200/>
- [20] Testo Saveris GmbH. Accessed June 2025. <https://static.testo.com/image/upload/HQ/testo-176-t3-t4-datenblatt.pdf>
- [21] Luna Innovations Incorporated. 2014. "Distributed Fiber Optic Sensing: Temperature Compensation of Strain Measurement". [https://lunainc.com/sites/default/files/assets/files/resource-library/LT\\_TD\\_EN-FY1402\\_TempComp1.pdf](https://lunainc.com/sites/default/files/assets/files/resource-library/LT_TD_EN-FY1402_TempComp1.pdf)
- [22] Spilker, A. 2024. Zur experimentellen Bestimmung der Wärmedehnzahl von Beton im Straßenbau, Ph.D. thesis, Institut für Werkstoffe im Bauwesen der Universität Stuttgart.
- [23] Meyer, L. 2007. Zum Einfluss der Kontaktzone bei der Modellierung des Elastizitätsmodulus von Beton, Ph D. thesis, Rheinisch-Westfälische Technische Hochschule Aachen.
- [24] Wang, L., N. Fang, and Z. Huang. 2012. "Polyimide-coated fiber Bragg grating sensors for humidity measurements". InTech.



## Smart Integrated Sensors and Wireless Sensors (IoT)

# Integrated Sensor Technology for Basalt-Reinforced Segmental Lining Elements

Alexandros Evangelatos<sup>1</sup>, ORCID 0009-0000-7300-1686, Lukas Heindler<sup>2</sup>, ORCID 0000-0003-3951-8838, Robert Galler<sup>1</sup>, ORCID 0000-0002-1150-4525, Thomas Thurner<sup>2</sup>, ORCID 0000-0003-3783-1193

<sup>1</sup>Department Mineral Resources Engineering, Chair of Subsurface Engineering,  
Montanuniversität Leoben, Erzherzog-Johann-Straße 3/III, 8700 Leoben, Austria

<sup>2</sup>Department Product Engineering, Chair of Automation and Measurement,  
Montanuniversität Leoben, Peter-Tunner-Straße 25/II, 8700 Leoben, Austria  
email: alexandros.evangelatos@unileoben.ac.at, lukas.heindler@unileoben.ac.at

## ABSTRACT

Current climate protection goals are driving research toward large-scale structural health monitoring solutions for critical, long-lifespan infrastructure, alongside the usage of low CO<sub>2</sub> emission materials. In this work, we present an innovative approach that combines both aspects: the use of continuous basalt fibers assembled into sustainable reinforcement structures, and low-cost measurement systems for integrated long-term condition monitoring, specifically applied to tunnel segment monitoring. As a proof-of-concept for the integration of sensor elements into basalt reinforced concrete structures, we utilized stranded steel wire to create custom strain gauge sensors for integrated strain measurements, paired with a custom-designed resistive bridge-based measurement system to evaluate the feasibility of enabling low-cost condition monitoring. Mechanical tests were conducted on basalt-reinforced concrete specimens under both tensile and compressive loading. The results indicate that the system can measure even low strain values for the sensor-enhanced structures down to approximately 5  $\mu\text{m/m}$  and a standard deviation of 2.1  $\mu\text{m/m}$ , achieving a sensing performance close to state-of-the-art measurement systems and externally applied standard strain gauges. The study demonstrates the potential for cost-effective condition monitoring of individual tunnel segments with sustainable basalt reinforcement. Further optimizations of the system are anticipated in future projects.

**KEY WORDS:** Structural health monitoring; Strain measurements; Integrated stress monitoring; Crack detection; Basalt fiber reinforcement; Tunnel segment monitoring; Segmental lining element; Measurement system design; Low-cost electronics.

## 1 INTRODUCTION

The expansion of the European infrastructure network and the growth of international metropolises are increasing the need for major road and railway construction projects. Tunnelling and bridge construction are essential in this context. At the same time, the focus is shifting to climate protection and ambitious international targets. According to the Climate Act, the EU is committed to reducing net greenhouse gas emissions by 55% by 2030 and becoming climate-neutral by 2050 [1].

The construction and building sector is responsible for 38% of global CO<sub>2</sub> emissions and harbors great potential for innovation [2]. Cement production alone contributes 3.3% to Austria's and 4.5% to global emissions [3][4].

Structural steel in reinforced concrete is approx. 3 to 5 times more CO<sub>2</sub>-intensive per ton. According to a study on the Brenner Base Tunnel, one ton of structural steel emits 1,980 kg of CO<sub>2</sub>, while cement emits 576-622 kg of CO<sub>2</sub> per ton [5][6]. In segmental lining elements, concrete can contain approximately 150 kilograms of steel per cubic meter. The production of 150 kilograms of steel emits nearly the same amount of carbon dioxide as the cubic meter of concrete surrounding it. Consequently, a low-CO<sub>2</sub> material as an alternative to steel reinforcement offers great sustainability potential.

Due to these challenges, ongoing research projects are investigating the use of basalt fibers as a sustainable alternative for concrete reinforcement. The key advantages include significantly lower production intensity and CO<sub>2</sub> emissions compared to steel, as well as high corrosion resistance. Other beneficial properties include higher tensile strength than steel,

low weight, and fire resistance. Additionally, basalt reinforcement exhibits electrically insulating characteristics, resulting in longer lifespans of basalt-reinforced materials [7].

While the application of basalt fibers is also being researched in the form of macrofibers, this study considers continuous fibers with diameters of  $17 \mu\text{m} \pm 1 \mu\text{m}$  [8] bundled into multifilament yarns. These fibers can resemble structural steel in the form of Basalt fiber-reinforced polymer (BFRP) rebars or be woven into grid-like structures. Due to their processability, they can also be woven into 3D structures and precisely manufactured to meet specific load-bearing requirements. To maintain the stability of the reinforcement structure and ensure the stress distribution among the individual filaments within the bundle, they are impregnated with resin [9].

The manufacturing method allows for the processing of various fiber materials, leading to the concept of integrating a sensing fiber for strain measurements. The precise placement of fibers during the process enables the defined integration of measurement sensors, ideally within a fully automated manufacturing setup. The process combines sustainable and corrosion-resistant basalt fiber reinforcement with an efficient method for structural health monitoring. This offers significant potential in saving CO<sub>2</sub> emissions, particularly relevant in tunneling, where the required structural service life often exceeds 100 years [10].

The production of reinforcement structures using basalt fibers is considered to be particularly advantageous for prefabricated construction [7], placing the focus of our investigations on segmental lining elements. By equipping each



segment with an integrated, low-cost measurement device, continuous structural health monitoring could be extended beyond individual rings to cover the entire tunnel, enabling comprehensive long-term condition assessment. Building on this approach, we have extended our research to include the development of a cost-effective measurement system. Figure 1 shows the conceptual sketch of the combined basalt reinforcement and integrated strain gauges in a tunnel segment.

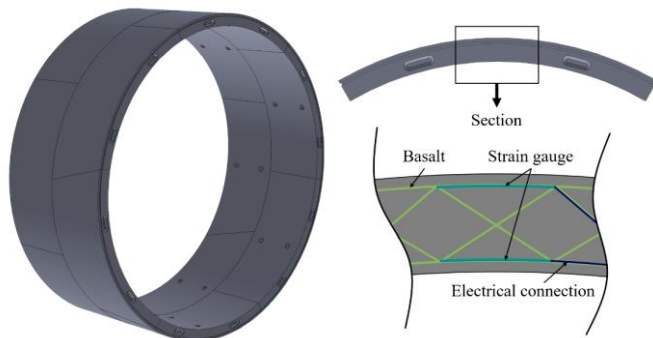


Figure 1. Segmental lining element ring and a conceptual sketch of the basalt reinforcement with integrated strain gauges in a tunnel segment.

The sensor's measuring length can be tailored to accommodate the desired spatial resolution and range. The strain sensor's integration into the reinforcement windings ensures precise measurement along the axis of maximum force, resulting in optimal measurement signals. An overlapping sensor configuration with varying measuring lengths is being evaluated for localized crack detection.

## 2 STATE OF THE ART METHODS

Current methods for ensuring structural safety and functional maintenance of tunnels rely on regular inspections. A distinction is made between destructive methods, core drilling, and non-destructive methods for condition monitoring.

The Austrian Federal Railways (ÖBB), for example, governs these inspections by the RW 06.01.02 regulations [11], focusing on crack formations in the tunnel linings. Tunnel scanners are used to create high-resolution images of the inner shell surface. Despite ongoing artificial intelligence integration, the process remains labor-intensive due to specialized equipment and manual evaluation [12][13].

In addition to condition assessments conducted through inspections, systems for continuous long-term monitoring (LTM) and structural health monitoring (SHM) are also employed. One focus is geotechnical monitoring, for which instrumentation, typically comprising extensometers, pressure cells, and convergence systems [14], are strategically installed in areas where geologically unstable zones, such as fault zones and swelling rock formations, are anticipated. The systems can be installed deep within the surrounding rock mass, extending behind the structural construction, in order to record data from the unaffected or stable rock formations.

To monitor the stress state of concrete structures, measurement systems are commonly embedded within the concrete matrix. These systems are typically attached to the reinforcement to ensure precise positioning, or alternatively,

they are mounted to separate structural elements, particularly in the case of unreinforced concrete. The two most common systems for SHM in tunnelling are based on strain gauges (SG) and distributed fiber optic sensing (DFOS). Both sensor types are applied in cast-in-place concrete, such as inner linings, as well as in precast elements, such as tunnel segments.

Vibrating wire sensors provide accurate measurement of strain and, consequently, allow for analytical prediction of stress within the tunnel lining. However, they are limited in their strain length, often below 250 mm. Therefore, they only provide localized data from a few selected points. Furthermore, data is manually collected on-site from individual measurement boxes, which often require road enclosures.

The more recent advancement in SHM with DFOS offers several benefits over SGs. One fiber optic cable enables multiple measurement points within the structural component, making it an ideal system for crack detection [15]. Additionally, data transmission can be performed over long distances without significant loss, allowing the measurement analysis to be conducted outside the tunnel. However, DFOS systems require careful installation and protective measures to ensure durability. To enhance robustness, they are often encased in a thick protective layer, compromising flexibility and being subject to strain incompatibilities with the material to be monitored. The complex setup and costly instrumentation are key reasons for the installation at only few locations [16].

An innovative alternative to conventional monitoring methods involves using carbon fiber reinforcement not only for structural support but also as a sensor [17]. Although carbon fibers offer greater durability and tensile strength, they are far less favorable than basalt fibers in terms of CO<sub>2</sub> emissions during production, production costs and handling during installation [7].

The presented disadvantages of the existing solutions speak in favor of the approach pursued in this work of a sensor system that can be fully and automatically integrated into the basalt reinforcement structure. This cost-efficient approach enables continuous SHM not only of sections, but the entire tunnel. A holistic SHM system is essential for detecting overstressing early, thereby enhancing safety, minimizing downtime of infrastructure, and reducing overall maintenance costs [12]. Particularly relevant for infrastructures such as tunnels with a projected and required long service life.

## 3 METHODOLOGY

Current state-of-the-art metrology solutions to measure strain on tunnel segments, like DFOS, offer precise measurement data and can, therefore, reliably monitor the few segments in which they are integrated. With this approach, the condition of other segments can only be estimated. Reliable condition monitoring of the whole tunnel system, however, depends on the condition monitoring of each segment. Therefore, more cost-effective and simpler solutions must be used. The following sections cover metrology, and the electronics used for this goal.

The Methodology section is divided into several subsections. It begins with the sensor conceptualization and the description of the hand-patterned steel wire strain gauge used in the devices under test. Next, the construction of the test device is discussed, including the design of the specimen. Following this, the

subsequent subsection describes the design of the custom electronic measurement system and the theoretical measurement principle behind the approach. In the final subsection, the test procedures that were conducted are explained.

### 3.1 Sensor Concept

Readily available strain gauges suitable for condition monitoring of tunnel segments are expensive and challenging to mount automated and securely on reinforcement or concrete surfaces. Additionally, the precise location and orientation of the strain gauges may become uncertain if they shift during the concrete pour. A more practical approach would involve integrating the strain gauges into the construction of the concrete reinforcement. One potential method involves integrating a resistance wire into the basalt reinforcement fabrication at predefined areas of interest and measuring the reinforcement's strain at those locations. This process can be automated using existing robots, simplifying the integration process. Prototype devices discussed in this work are equipped with hand-wound strain gauges glued to the basalt reinforcement. In future production processes, the resistance wire would be integrated between individual strands of the prefabricated basalt reinforcement of a concrete segment.

Accompanying electronics would need to be attached during this process. After concrete pouring and electronic verification, the segment would be ready for mounting inside a tunnel.

Because the anticipated operation duration is several years to decades, common issues such as creep and sensor degradation can affect long-term strain measurements. This may lead to false-positive or false-negative alerts regarding damage in the tunnel segment. These factors are a significant focus of our research and pose major concerns for the design and development of our condition monitoring system.

In this work, a stranded steel wire with 90 strands and a diameter of 14  $\mu\text{m}$  per strand is used. Electrical insulation between each winding is guaranteed due to the careful forming of meanders by hand. The specific resistance is approximately 70  $\Omega/\text{m}$ . 1.74 meters of wire are used, which results in 120  $\Omega$  resistance, accommodating standard bridge measurement systems.

The steel wire exhibits a gauge factor  $k$  of approximately 2, a typical value for metal strain gauges [18][19]. The gauge factor relation  $k$  is defined by

$$k = \frac{\Delta R/R_0}{\Delta l/l_0} = \frac{\Delta R/R_0}{\epsilon} \approx 2. \quad (1)$$

In the given equation the gauge factor  $k$  is defined as the ratio of the relative change in electrical resistance  $\Delta R/R_0$  to the technical strain  $\epsilon$ . The strain  $\epsilon$  is given by the relative elongation, where  $\Delta l$  is the change in length and  $l_0$  is the initial length. Similarly,  $\Delta R$  denotes the change in electrical resistance, while  $R_0$  is the initial resistance of approximately 120  $\Omega$ .

For clarity, relevant values of the steel wire material are presented in Table 1, the wire is a Bekinox® VN-fiber 14.1.9 from Bekaert [20]. The stainless-steel fiber bundle was chosen as the sensor material due to its corrosion resistance and the fact that the strands are not twisted. The individual strands are held together by a limited number of wrapped polyester filaments.

Table 1. Test strain gauge properties. [20]

Steel fiber: Bekaert Bekinox® VN-fiber 14.1.9			
Diameter	Strands	$\Omega/\text{m}$	k-factor
14 $\mu\text{m}$	90	70	2

Before concrete pouring and after curing, a digital multimeter was used to measure the wire's resistance and ensure proper installation and electrical connection.

### 3.2 Test Device Construction

Prior to the concrete tests, tensile tests using PET film were conducted to validate the measurement concept. The steel wire was mounted to a PET film strip over an approximate gauge length of 120 mm with seven meanders, using an epoxy adhesive. To verify the measurements, an additional reference strain gauge with the same length was attached adjacent. The promising results obtained justified further investigations in the context of the intended application on basalt reinforcements.

In the subsequent tests, the steel wire was attached by hand to the basalt rods using epoxy. Two types of reinforcement were used: basalt rebars with a diameter of 8 mm [21] and custom-manufactured basalt rods. The latter consisted of a total of 16 basalt fibers, each with a linear density of 2400 tex [8], bundled together. The 16-fiber configuration closely approximates the cross-sectional area of the basalt rebar and is intended to resemble the future application of fully automated placement of continuous basalt fibers into 3D reinforcement structures.

Figure 2 shows the steel wire strain gauge conceptual drawing and a BFRP rebar with the steel wire attached to the surface with epoxy, after a destructive compressive test.

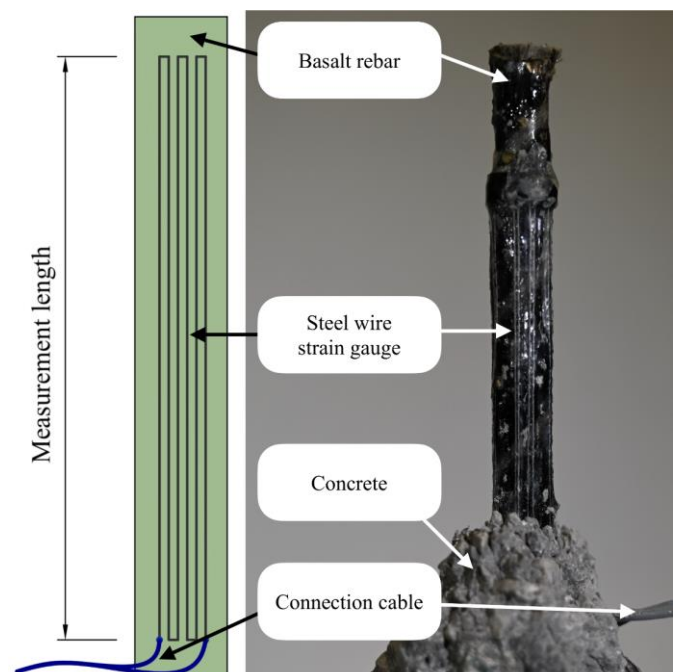


Figure 2. Steel wire strain gauge conceptual drawing and implementation on basalt-reinforced polymer rebar after destructive compressive test.

Due to the small test geometry, multiple meanders were required. After the test, pieces of concrete were additionally detached for inspection of the steel wire.

Two test arrangements were designed for both basalt materials, with only one basalt rod in the center of each specimen, to investigate the suitability of the test strain gauge applied to basalt reinforcement inside concrete elements. The designs were developed to account for the different directions of applied force or load, specifically in both tension and compression directions. Both concrete specimen designs are cylindrical with only one reinforcing basalt rod in the center. The dimensions of both designs can be viewed in Figure 3. PVC pipes were used as molds for the concreting process. The concrete mix of both designs was similar to typical formulations used in precast elements for tunnel construction.

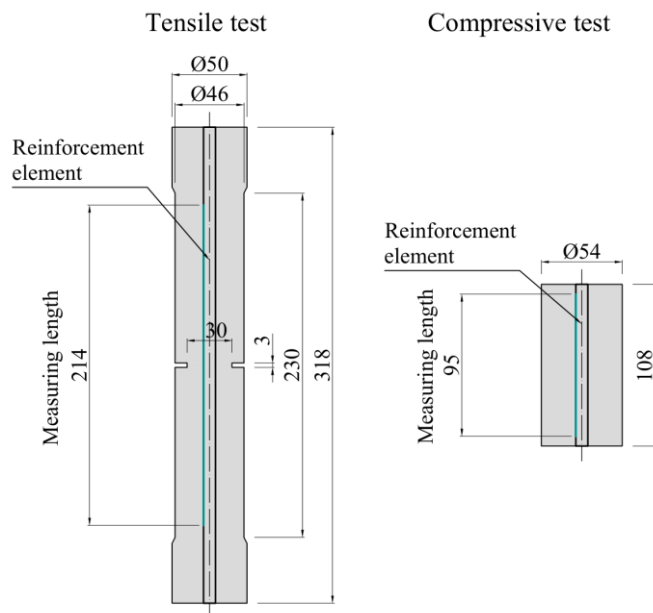


Figure 3. Specimen geometry for tensile (left) and compressive tests (right) with measuring length (in mm) and strain gauge (blue) on basalt reinforcement element.

The concrete mix design originates from the corresponding specification for precast tunnel segments but was adapted to suit the test specimen size. Specifically, aggregate fractions exceeding 8 mm were excluded and their mass proportions were redistributed among the other grain sizes. The cement used was CEM I 42.5 R-SR, and Dynamon NRG 1010 NK was employed as the superplasticizer and accelerator. Due to the slender design, the concrete was poured in layers with intermittent short compaction cycles on a vibrating table to minimize the formation of large pore spaces. Additionally, unreinforced specimens were produced for each mixing batch to determine the uniaxial compressive strength (UCS).

After demolding the tensile specimens, they were further modified by a 3 mm wide and 8 mm deep notch, achieved through four cuts with a stone saw, to ensure the formation of a central crack during the destructive tensile test. The central crack formation enables comparability of the strain gauges, as cracks near the fixtures, for instance, could occur outside the shorter measurement range of the reference strain gauge.

Due to the required length of the resistive sensor element of approximately 1.74 m to achieve a resistance of approximately

120  $\Omega$ , suitable for the commercially available bridge measurement devices, the steel wire test strain gauge had to be arranged in a meander pattern, resulting in varying effective gauge lengths between the tensile and compression tests. As a reference, a commercial strain gauge from the company Althen BV was applied to the outer surface of the concrete specimen after demolding. Two reference strain gauge types for concrete, mortar, and rock materials were applied: PL-120-11-3LJCT-F and PL-60-11-3LJCT-F. Both types feature a three-wire parallel vinyl cable configuration in a three-wire quarter-bridge setup [22]. The reference strain gauges were mounted on the surface with a 120 mm measuring length on the tensile and 60 mm on the compressive specimens, intended for the comparison of the inner strain on the basalt reinforcement to the strain on the outer concrete surface.

The specific steel wire gauge lengths and the required number of meanders for each test configuration was adjusted to the specimen length. For the tensile test setup, the measuring length was set to 214 mm with 4 meanders on the basalt reinforcement. The shorter compressive tests required 9 meanders of steel wire over the measuring length of 95 mm.

### 3.3 Electronic Design

The strain gauges' resistance is commonly not directly measured but rather utilized in a resistance measurement bridge. Therefore, a quarter bridge measurement to determine the strain of the specimen under test using the approximated strain relation presented in Equation (2) was used:

$$\varepsilon \approx \frac{4 \cdot V_d}{k \cdot V_0} \quad (2)$$

Here,  $V_d$  represents the amplified differential voltage of the two bridge arms,  $k$  is the gauge factor of the strain gauge, and  $V_0$  denotes the excitation voltage applied to the Wheatstone bridge.

As state-of-the-art measurement tools prove to be impractical for large-scale tunnel condition monitoring, a complementary, low-power, and compact electronic measurement system approach is being tested throughout the measurements. The block diagram of the developed prototype electronics is presented in Figure 4.

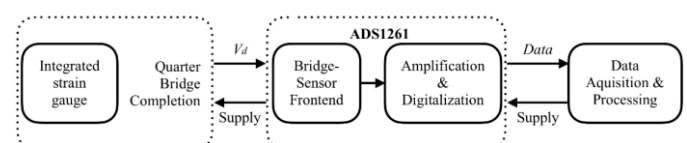


Figure 4. Block diagram of the developed measurement system. The device under test is employed in a quarter bridge. The ADS1261 IC measures the bridge voltage  $V_d$  and supplies the bridge with its internal voltage reference. An Arduino Uno R4 Minima reads the digitized data. Additionally, the Arduino exports its data to a PC for data storage.

The primary focus of this design is the sensor front-end section. This part is responsible for analog-to-digital conversion, amplification, filtering, and transmission of the digitized measured bridge voltage  $V_d$ . Furthermore, the resistance bridge must be supplied either by a current for absolute resistance changes or a voltage source for relative resistance changes. In addition to signal conditioning, the sensor front-end must



communicate with a microcontroller to transmit the measurement data to a PC for further signal processing. Given the significance of various key parameters, such as offset drift, linearity, potential supply outputs, the number of analog inputs, the number of samples per second, the possible integrated circuit (IC) supply ranges, package sizes, and recommended applications, the sensor front-end ADS1261 [23] (Texas Instruments, Inc.) was selected as the preferred choice. This sensor front-end incorporates a precision 40 kSPS Delta Sigma analog-to-digital converter ( $\Delta\Sigma$ -ADC), along with a programmable gain amplifier (PGA), an internal precision voltage reference, and an internal current source for bridge applications. Furthermore, the ADS1261 provides programmable registers to configure sampling rates, 4-wire or 6-wire measurements, current or voltage-driven bridge supply, PGA gain, filter modes, and read-only registers for data transmission over the serial peripheral interface (SPI). For the initial prototype, an Arduino Uno R4 Minima [24] (Arduino, Inc.) was used to read-in the digitized bridge level data. For this purpose, an algorithm to configure the ADS1261 registers for a predefined operating mode and a voltage-driven bridge circuit was developed. It then read the incoming data and displayed it on the Arduino's serial monitor for further storage and processing.

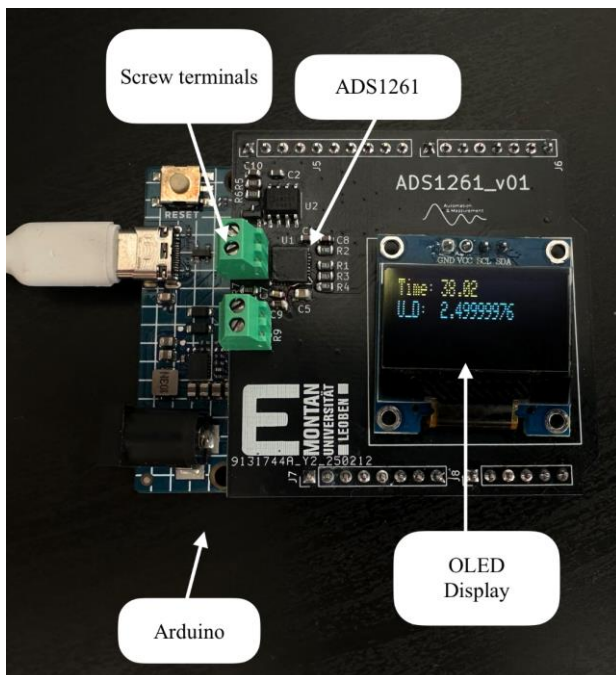


Figure 5. Developed Arduino shield incorporating the ADS1261 bridge front-end, screw terminals, and an OLED display for data visualization and debugging.

Furthermore, a printed circuit board (PCB) was designed and constructed. It integrates the ADS1261, connectors for the steel fiber strain gauge, and an OLED screen for data visualization, as shown in Figure 5. The printed circuit board was designed to fit seamlessly onto the Arduino pins, facilitating a direct connection. Such boards are commonly referred to as shields.

The strain gauge connection was realized with screw terminals as seen in light green and will be replaced by soldered connections in future revisions for a smaller contact resistance. These terminals form one half of the measurement bridge. This

approach enabled adaptation for every strain gauge resistance within certain linearity boundaries. Given a specific strain gauge resistance, either two strain gauges can be connected to form a temperature-compensating half bridge, or a resistor with an equal no strain resistance can be connected to the second terminal to form a quarter bridge circuit.

### 3.4 Test Configurations

Building on the success of previous proof-of-concept measurements that involved creating a test strain gauge by attaching a steel wire to a plastic foil for tension tests, handcrafted concrete test devices are used for the following evaluations. These devices are equipped with handcrafted meander-shaped strain gauges and serve as preparatory tools for future tests involving real segmental lining elements.

Figure 6 depicts the setup comprising the devices under test for tensile and compressive tests in the test stand, including the load cell in the tensile test arrangement, and the mechanical measurement connections that can be applied as tensile force or compression force by a servo-hydraulic actuator.

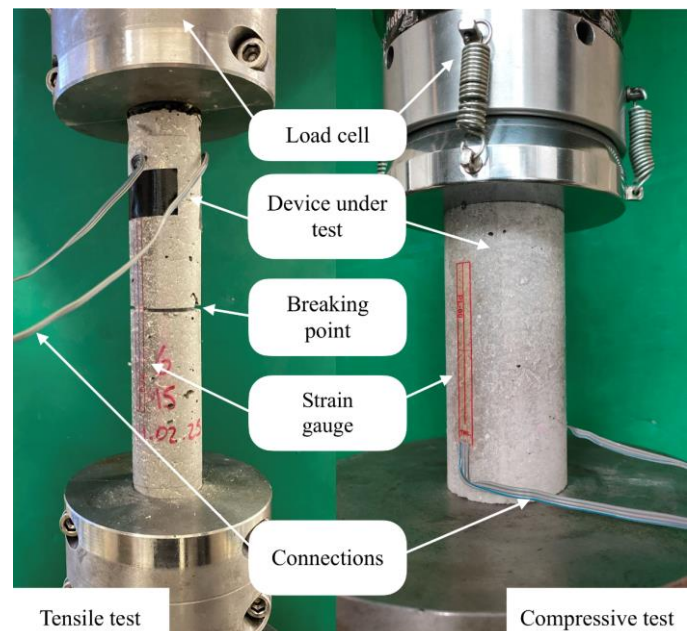


Figure 6. Test setup with the device under test mounted securely for tensile and compressive tests. Inside the device a steel fiber strain gauge is used. On the outside of the device, a standard strain gauge is installed. The load cell measures the applied force.

During measurements, the test stand applies and records force and travel distance in the longitudinal direction of the device under test. This force induces elongation or compression in the device and the strain gauges. Consequently, the strain gauges' resistances are anticipated to change. As a result, the strain/force relation can be quantified and visualized. As the resistance of the strain gauge also fluctuates in response to temperature, air pressure, magnetic field, and electromagnetic radiation changes, all of these factors were held constant to the extent practicable.

After constructing the devices under test and allowing a curing time of seven days, realistic test conditions were assumed. Special clamps to hold the devices, which are equipped with elastic rubber bands at the clamp edges were

used to ensure equal pressure around the circumference of each device. Once the devices were mounted in the clamps, the connection wires to the measuring devices were connected. At this stage, a small amount of pre-tension or pre-compression was applied to ensure that the test stand can directly apply force during movement without any forceless travel.

Due to a limited number of test devices resulting from the tedious manufacturing process, several measurements using non-destructive forces with half of the expected maximum force before failure were conducted. This approach allowed us to measure strain with multiple setups before any devices were destroyed. The testing control paradigm varied between the two test setups. The compression test was conducted in force-controlled mode with a linear increase in applied force over time. In contrast, the tensile test was performed in distance-controlled mode by linearly increasing the distance between the mounting positions of the device under test, due to easier test stand programming.

As the final step of a measurement session, a destructive test was conducted. During destructive tests, the applied force exceeded the load-bearing capacity of the concrete, leading to the formation of cracks. In the case of the displacement-controlled tensile test, the applied force drops rapidly after the expected initial crack in the pre-notched specimen center. Further cracks form along the length of the specimen. Depending on the arrangement, different reactions occur at the inner and outer measuring areas.

Table 2. Relevant specimen and test parameters.

	Tensile	Compressive
Number of samples	6	3
Number of tests	25	13
Nondestructive force (kN)	1.5	45
Destructive force (kN)	4	120

The experimental test program on the steel wire strain gauge with basalt fiber-reinforcement materials is structured into tensile and compressive tests as presented in Table 2. The

number of tests includes the number of repeated non-destructive variants and the final destructive ones for each test sample. Estimates of nondestructive and destructive loads are based on the results of tests with unreinforced concrete specimens.

## 4 RESULTS

Out of many test measurements, selected results based on their significance are presented in this section. Both for tensile and compressive tests on the reinforced concrete test objects, we present comparisons between the measurement signals recorded by a Quantum MX1615B [25] (HBK, Inc.) measurement system and the custom bridge measurement system. We organized the setups such that each strain gauge was measured with each measurement device, but for sequential and separate measurements. For instance, the inner strain gauge was connected to the MX1615B, and the outer strain gauge to the custom electronics during one non-destructive test. In the subsequent non-destructive test, we switch the connections. This method allows qualitative comparison of the results obtained by the MX1615B device and the results obtained by the custom electronics.

Using its accompanying software tool, we set a low-pass filter using a 4th-order Bessel filter, with a cutoff frequency of 10 Hz at a measurement rate of 50 Hz, for the Quantum MX1615B measurements.

For all signals recorded by the measurement systems, zero-phase digital filtering in the signal post-processing using Matlab's `filtfilt()` function was applied. In this case, an FIR low-pass filter with a cutoff frequency of 2 Hz and a length of 101 was implemented. This approach ensures no phase delays of different frequency components of the measurement signal.

### 4.1 Tensile tests

Based on previous test measurements conducted with unreinforced concrete test specimens, non-destructive tensile tests were performed with estimated tensile forces below 1.5 kN, less than half of the expected maximum load, as stated in Table 2. Given the relatively small forces, only minor strains

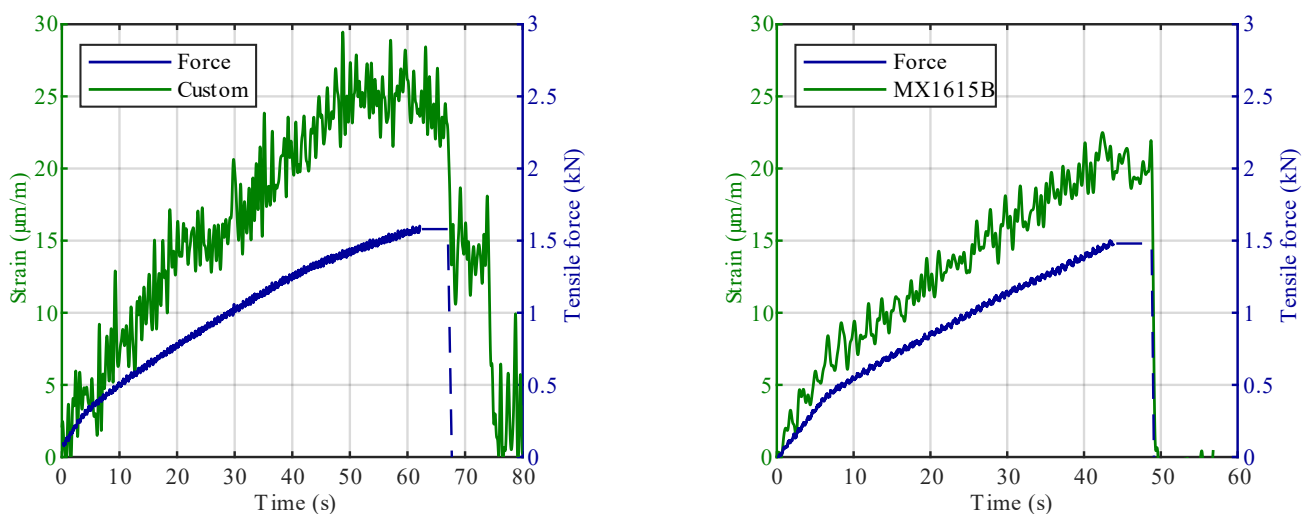


Figure 7. Two non-destructive tensile tests with an in-built hand-made strain gauge in green, measured with the custom-made electronics (left) and with the MX1615B (right). The applied tensile force is shown in blue.

of less than  $50 \mu\text{m/m}$  were anticipated, which was reflected by the executed measurements. Figure 7 shows two measurements of different test measurements using the same device under test for a qualitative comparison between the custom measurement system and the MX1615B. Each plot illustrates the tensile force resulting from uniform cylinder motion in blue and the low-pass filtered measurement signal from the measurement systems connected to the inner steel wire strain gauge in green. In the left plot, the measurement signal of the custom electronics is shown. On the right side, the measurement signal from the MX1615B instrument. Both measurement signals were digitally filtered with the aforementioned FIR low-pass filter with a filter length of 101 and a cut-off frequency of 2 Hz. As one can observe, at these strain values, even the reference measurement system MX1615B has significant signal variations.

Most non-destructive tensile tests were conducted over a duration exceeding 60 seconds, as the test stand exhibited a slow but consistent movement. It is evident from Figure 7 that the reduction of the tensile force signal precedes the end of the load sequence. The tests concluded at this point, and the force was set to zero manually after a few seconds, shown with the dashed blue line. The minor strain relaxation detected, prior to the manual movement, was observed in all tensile tests and is most likely attributable to displacements of the elastic rubber bands within the clamping device.

During destructive tensile tests, cracks in the concrete appeared, resulting in sudden force drops and elongation rises. Figure 8 shows this behavior in a comparable range for both, inner and outer strain gauges. As the force, due to the steadily moving test stand, increases, the device under test experiences more and more mechanical stress. At a certain point, the concrete rips and gives way for a relative movement between the concrete and the basalt reinforcement. This results in an overall elongation of the system, which is measured by the applied strain gauges, shown in Figure 8. During destructive tests, several cracks occur. For a more detailed insight into the destructive strain measurements, only one is shown here.

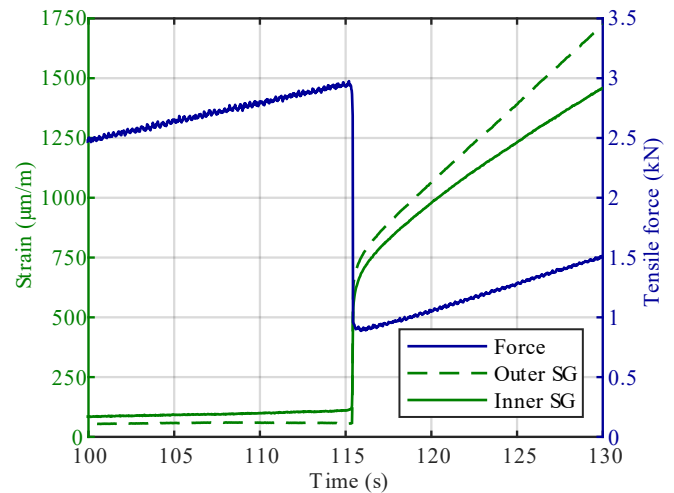


Figure 8. Concrete ripping apart during a destructive tensile test. The applied test stand force, shown in blue, drops due to the formation of a crack. The outer reference strain gauge in dashed green, and the inner steel wire strain gauge (green line) show the feasibility of crack detection. Both measurement signals were recorded with the MX1615B.

#### 4.2 Compression tests

Due to concrete's high compressive strength and previous unreinforced compression tests, a linearly increasing compression force of up to 60 kN was applied for non-destructive test measurements, again less than half of the expected maximum load, as stated in Table 2. Given the significantly higher forces during this measurement session, correspondingly greater changes in the signals were expected to be observed.

Figure 9 illustrates, similar to Figure 7, two separate compressive test measurements with the inner steel wire strain gauge. The compressive force is shown in blue, and the measurement signals from the custom electronics on the left and the MX1615B on the right are shown in green. Both strain signals were again filtered using the FIR low-pass filter with filter length 101 and a cut-off frequency of 2 Hz.

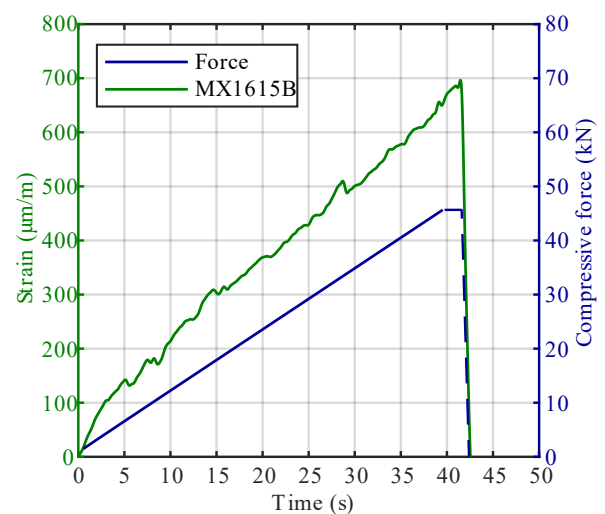
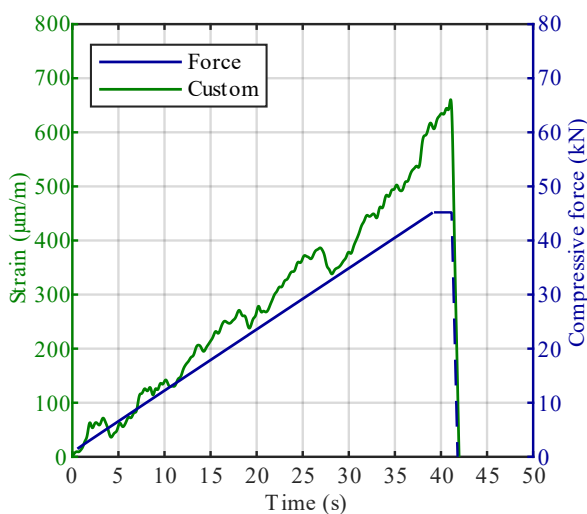


Figure 9. Two non-destructive compressive tests with an in-built hand-made strain gauge in green, measured with the custom-made electronics (left) and with the MX1615B (right). The applied compressive force is shown in blue.



Once again, the load was held at a specific point before manually setting it to zero after a few seconds, shown with the dashed blue line. The fluctuations in the strain measurement signals are believed to be a result of relative movement between the individual components of the composite material.

#### 4.3 Evaluation of Noise

During all tests, the Quantum MX1615B (accuracy class 0.1, linearity deviation 0.05) was used alongside the PL-120-11-3LJCT-F and PL-60-11-3LJCT-F strain gauges, which have a gain factor of  $2.1 \pm 1\%$ . According to the datasheet, the Quantum MX1615B produces less than  $0.6 \mu\text{V/V}$  noise at  $25^\circ\text{C}$  with a 5 V excitation.

In comparison, the ADS1261, used in the custom system, exhibits 30 nVRMS noise (gain 128, 20 SPS) and a linearity of 2 ppm. The stranded steel wire used in the setup is assumed to have a gain factor of 2. Throughout the tests, temperature and humidity were maintained constant, as the test stand is located in a sub-terrain basement. These factors lead to the standard deviations of the detrended measurement signals, as shown in Table 3.

Table 3. Standard deviations obtained from the reference Quantum MX1615B and the custom measurement system, both for tensile and compressive tests after low-pass filtering.

Standard deviations	Tensile ( $\mu\text{m/m}$ )	Compressive ( $\mu\text{m/m}$ )
MX1615B	0.769	0.563
Custom system	1.49	2.07

As is visible, after low-pass filtering, the standard deviations are in the same order of magnitude.

## 5 CONCLUSION

Our measurements aimed to demonstrate the feasibility of in-built strain gauges into the basalt reinforcement for future automated production processes.

Based on prior tests, tensile as well as compressive tests were conducted, using hand-patterned steel wire strain gauges mounted on basalt reinforcement to measure the device under test's elongation and compression. Both compressive and tensile tests showed promising results. Relative movement between the basalt reinforcement and the concrete is the same for wounded basalt fibers as well as basalt rebar. Furthermore, the adhesion between the hand-patterned strain gauge and the basalt rebar holds and the strain gauges endure the harsh concrete environment without failure, as seen in Figure 2.

These are promising findings for further development of automated basalt reinforcement construction. Additionally, it shows that the adhesion between the reinforcement and the concrete has to be improved in future revisions, giving valuable insight into the dynamic behavior of the compound material.

Our low-cost, custom-made, first prototype measurement device reaches acceptable sensitivity close to the range of the Quantum MX1615B measurement system. As a result, we demonstrated the viability of our low-cost, structural health monitoring concept, feasible for the instrumentation of a whole tunnel.

Future revisions of the electronics anticipate the replacement of the Arduino with an industrial-grade microcontroller, further reduction of component sizes, and the removal of the OLED screen for low-power operations within tunnel segments. Additionally, all metrics for improvement, concerning an integrated solution of both the electronics and sensors for the application in concrete elements, including temperature compensation actions, are being considered. These include half-bridge configurations, degradation compensation, and software measures to counteract false-positive and false-negative readings.

Moving forward, we anticipate further tests including bending beam tests as a precursor to tests on real tunnel segments due to more representative conditions of standard segment test scenarios. Furthermore, in the long term, we propose test arrangements with multiple measurement systems in segments, forming a tunnel ring, for real-world test environments.

## USE OF AI TOOLS

The authors acknowledge the use of AI-based grammar tools for language refinement.

## ACKNOWLEDGMENTS

The authors gratefully acknowledge the financial support of the Austrian Research Promotion Agency (FFG) through the FFG-funded project “EbiT – Endlosbasaltfaser als smarte Bewehrung im Tiefbau” (FO999913255) and the valuable contributions of the project partner Fiber Elements GmbH to this research.

## REFERENCES

- [1] European Council, Climate change: what the EU is doing, <https://www.consilium.europa.eu/en/policies/climate-change/>, retrieved March 2025.
- [2] UN environment programme, Global status report for buildings and construction, Global Alliance for Buildings and Construction, 2020.
- [3] GCCA – Global Cement and Concrete Association, GNR 2.0 – GCCA in Numbers, <https://gccassociation.org/sustainability-innovation/gnr-gcca-in-numbers/>, 2021.
- [4] J.G.J. Olivier, J.A.H.W. Peters, PBL Netherlands Environmental Assessment Agency, Trends in global CO<sub>2</sub> and total greenhouse gas emissions: 2020 Report, PBL publication number: 4331, 2020.
- [5] Sauer, J., Ökologische Betrachtungen zur Nachhaltigkeit von Tunnelbauwerken der Verkehrsinfrastruktur, Dissertation, Technische Universität München, Institut für Baustoffe und Konstruktion, Lehrstuhl für Massivbau, 2016.
- [6] EURAC RESEARCH, Ausbau Eisenbahnachse München-Verona - Brenner Basistunnel. Bereich Umweltplanung - Erstellung eines CO<sub>2</sub>-Haushalts, Untersuchung der Nachhaltigkeit des Brenner Basistunnels im Hinblick auf seine CO<sub>2</sub>-Emissionen, Innsbruck, Juni 2011.
- [7] Kromoser, B., Reichenbach, S., Stoiber, N., Preinstorfer, P. and Huber, T., Potentiale von nichtmetallischer Bewehrung im Infrastruktur-Betonbau NIMETBEW, Endbericht, Wien: E212-02 - Institut für Tragkonstruktionen - Forschungsbereich Stahlbeton- und Massivbau, [https://projekte.ffg.at/anhang/62790e46a3083\\_NIMETBEW\\_Ergebnisbericht.pdf](https://projekte.ffg.at/anhang/62790e46a3083_NIMETBEW_Ergebnisbericht.pdf), 2022.
- [8] DBF - Deutsche Basaltfaser GmbH, Technisches Datenblatt, BF-17/2400, 2024.
- [9] M. Egger, Gesticke Bewehrungen für Textilbeton, Dissertation, Universität Innsbruck, urn:nbn:at:at-ubi:1-103523, 2022.
- [10] ÖBB-Infrastruktur AG, Netzzustandsbericht 2022 - ÖBB, 2023.
- [11] ÖBB-Infrastruktur AG, Regelwerk 06.01.02, Konstruktiver Ingenieurbau: Instandhaltung – Instandhaltungsplan, 2012.
- [12] R. Matt, B. Moritz and T. Parapatich, Challenges and New Approaches for the Inspection of Railway Tunnels – Asset Safety Management,

- Geomechanics and Tunneling 17, Nr. 5, pages 473–81. <https://doi.org/10.1002/geot.202400048>.
- [13] AMBITION - Entwicklung eines integrativen Ansatzes zur Messung und Bewertung von Eisenbahn- und Straßentunnel, Ergebnisbericht. Ein Projekt finanziert im Rahmen der Pilotinitiative Verkehrsinfrastrukturforschung 2015, BMK, FFG, [https://projekte.ffg.at/anhang/5dd541860bcd3\\_VIF2015\\_AMBITION-Ergebnisbericht.pdf](https://projekte.ffg.at/anhang/5dd541860bcd3_VIF2015_AMBITION-Ergebnisbericht.pdf), 2018.
- [14] K. Bergmeister, U. Santa, and A. Strauss, Überwachung und Analyse der Lebensdauer von Tunnelbauwerken, Beton- und Stahlbetonbau 102, Nr. 1, pages 24–32, <https://doi.org/10.1002/best.200600528>, 2007.
- [15] Ł. Bednarski, R. Sieńko, T. Howiacki, and K. Zuziak, The Smart Nervous System for Cracked Concrete Structures: Theory, Design, Research, and Field Proof of Monolithic DFOS-Based Sensors, Sensors 22, Nr. 22, <https://doi.org/10.3390/s22228713>, 2022.
- [16] C. Monsberger, W. Lienhart, In-situ Deformation Monitoring of Tunnel Segments using High-resolution Distributed Fibre Optic Sensing, The 8th International Conference on Structural Health Monitoring of Intelligent Infrastructure, 2017.
- [17] T. Quadflieg, O. Stolyarov, and T. Gries, Carbonfaserbewehrung als Sensor für Bauwerke, Beton- und Stahlbetonbau, 112(8), pages 541–544, 2017.
- [18] P. Bajpai, Biermann's Handbook of Pulp and Paper - Process Control, pages 483–492, doi:10.1016/B978-0-12-814238-7.00024-6, 2018.
- [19] W. Bolton, Control Systems, pages 1–36, doi:10.1016/b978-075065461-6/50001-5, 2002.
- [20] Bekaert, Bekinox VN, [https://api.bekaert.cn/media/wysiwyg/files/basic\\_materials/CD035\\_Datasheet-VN-Bekiflex.pdf](https://api.bekaert.cn/media/wysiwyg/files/basic_materials/CD035_Datasheet-VN-Bekiflex.pdf), retrieved March 2025.
- [21] DBF - Deutsche Basaltfaser GmbH, Technisches Datenblatt, Basalt Rebar, 2024.
- [22] ALTHEN Mess- & Sensortechnik GmbH, P-Series - Polyester Strain Gauges, <https://www.althensensors.com/uploads/products/datasheets/plc-series-polyester-backing-wire-straingauge-for-concrete-material-en.pdf>, retrieved March 2025, 2021.
- [23] Texas Instruments, ADS1261 ADC, <https://www.ti.com/product/de-de/ADS1261>, retrieved March 2025.
- [24] Arduino S.r.l., Arduino Uno, <https://store.arduino.cc/en-at/products/uno-r4-minima>, retrieved March 2025.
- [25] HBK, Quantum MX1615B, Data Sheet, <https://www.hbm.com/fileadmin/mediapool/hbmdoc/technical/B03899.pdf>, retrieved March 2025, 2023.

# Wind Input and Acceleration & Displacement Outputs Monitoring System for High-Guyed Masts in ROSEHIPS Project

Miaomin Wang<sup>1</sup>, Duncan Gould<sup>2</sup>, Richard Stafford<sup>1</sup>, Ki-Young Koo<sup>1</sup>, James Brownjohn<sup>1</sup>

<sup>1</sup>University of Exeter, UK

<sup>2</sup>Arqiva Limited, UK

**ABSTRACT:** This paper presents a battery-operated wireless long-term response measurement system for high-guyed masts in the UK, as a part of ROSEHIPS project. The monitoring system aims to capture wind speed and direction as input and 3D accelerations and 3D displacements as outputs for a target period of three months. GNSS (Global Navigation Satellite System) based time-synchronisation methods were used in all subsystems for accelerometer, anemometer, and Computer Vision based cameras. Epson E-M352 sensors were used to measure triaxial accelerations with extreme accuracy 0.2 $\mu$ g/ÖHz at multiple points along the height of the mast, together with an anemometer. Low-power consumption features of ESP32 microprocessor unit was utilized to achieve a longer battery life. To remotely monitor its 3D displacement, a wireless stereo vision system was developed using Raspberry Pi. The displacement is measured in the image plane of each camera, and the data is then uploaded to the cloud for 3D reconstruction. The measurement accuracy was validated through an outdoor test, where the two cameras were approximately 100 meters apart, and the target was located about 200 meters from both cameras. The results showed a measurement error of approximately 1 mm. The time synchronisation between the accelerometer and the stereo vision system was also evaluated. By using the system to track an accelerometer mounted on a cantilever, the time-sync error was found to be less than 1 ms.

**KEY WORDS:** Structural Health Monitoring, Wireless Sensor, Accelerometer, Stereo Vision, Anemometer.

## 1 INTRODUCTION

High-guyed masts are critical infrastructure for telecommunications and broadcasting, yet their slender designs make them vulnerable to environmental loads, particularly wind-induced vibrations [1].

Effective monitoring of these structures is essential to ensure safety and reliability [2]. Traditional wired systems face challenges including high installation costs, power supply limitations, and maintenance difficulties. Wireless, battery-operated systems offer an attractive solution, providing flexibility and ease of installation.

This paper presents a wireless long-term monitoring system developed as part of the ROSEHIPS project, specifically targeting high-guyed masts. It integrates Epson E-M352 accelerometers for accurate acceleration measurements, an anemometer for wind monitoring, and a Raspberry Pi-based stereo vision system for remote displacement tracking. GNSS-based synchronization [3] ensures precise timing across all sensors.

## 2 WIRELESS INPUT-OUTPUT MONITORING SYSTEM

### 2.1 Accelerometer

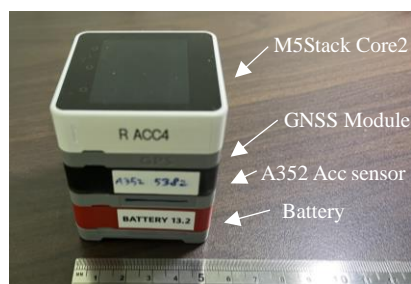


Figure 1. Accelerometer node

The accelerometer node consists of a M5Stack Core2 MPU based on esp32, a GNSS module, an accelerometer module for an Epson M-A352 sensor, and a battery module. M5Stack provides a convenient modular design, which an additional feature can be added a module layer stacked below the MPU. Light sleep was employed in esp32 to save power-consumption.

### 2.2 Stereo vision system

The wireless stereo vision system comprises two identical nodes (left and right), each equipped with a SONY IMX296 camera and lens, a Raspberry Pi 4B computer, a GNSS board and antenna, and a 4G communication module. The camera in each node is triggered by its Raspberry Pi via a jumper cable. To achieve synchronous image capture, both nodes use pulse-per-second (PPS) signals from the GNSS modules; upon receiving these PPS signals, the Raspberry Pi generates a synchronised 10 Hz trigger signal for the cameras.

First, the two nodes are positioned, and their geometric relationship is accurately determined using a GPS-RTK system for later 3D reconstruction. Users set an identical start time for both nodes, initiating synchronised 10 Hz image capture upon receiving the PPS signals. A measurement target is selected from the initial images of each node, ensuring the same target is tracked by both nodes. Each node independently measures the target's 2D displacement, and the data is uploaded to AWS. Finally, the 3D displacement is calculated in AWS using triangulation based on the uploaded 2D measurements and the known geometric relationship between the cameras

### 2.3 Anemometer

Anemometer used was a GILL 1350 ultrasonic anemometer, which measures wind speed and direction up to 10 Hz.



### 3 SYNCHRONISATION VALIDATION

#### 3.1 Setup

The time synchronisation between the accelerometers and the stereo vision system was validated. Three accelerometers (named ACC1, ACC2, and ACC3) were mounted on a cantilever beam. Two camera nodes (named CV1 and CV2) were placed 0.62 m from the structure, as shown in Figure 2. The validation consisted of three subtests: (1) synchronisation error between accelerometers, (2) synchronisation error between camera nodes, and (3) synchronisation error between accelerometers and cameras.

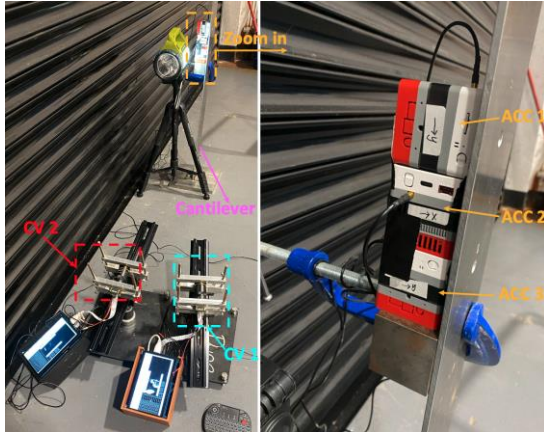


Figure 2. Experiment setup.

#### 3.2 Results

##### (1) Synchronisation error between accelerometers

The structure was manually excited, and the accelerometers recorded the structural acceleration. Figure 2(a) shows the measurement results, and Figure 2(b) shows a zoomed view. If the sensors were perfectly synchronised, the measured data from all three sensors should have no phase lag. The observed phase lags were considered as synchronisation errors. The synchronisation error was 40  $\mu$ s between ACC1 and ACC2, and 11  $\mu$ s between ACC1 and ACC3.

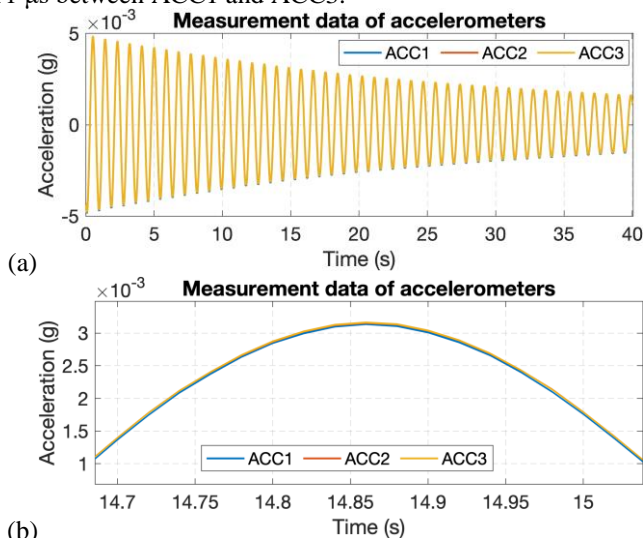


Figure 2 Measurement data of accelerometers.

##### (2) Synchronisation error between camera nodes

Figure 3(a) shows the measurement data from CV1 and CV2, and Figure 3(b) provides a zoomed view. The synchronisation error between the two camera nodes was 32  $\mu$ s.

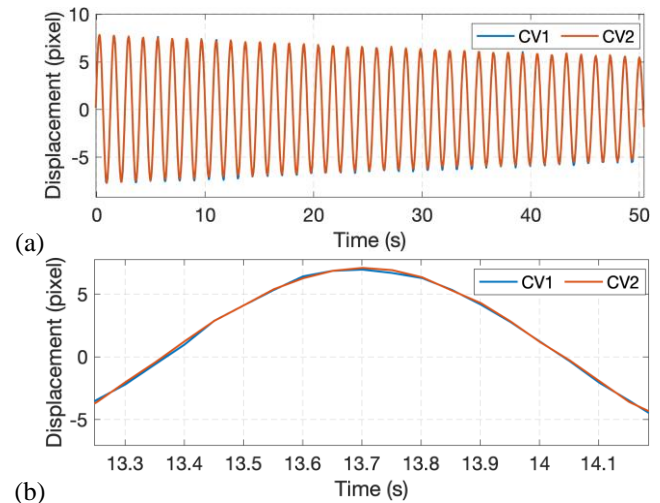


Figure 3 Measurement data of camera nodes.

##### (3) Synchronisation error between the accelerometer and camera

Acceleration and displacement are two different measurement units, but their waveforms are opposite when the signals are simple harmonic. The ACC1 data was multiplied by -1500 and then compared with the CV1 data. The synchronisation error between the two types of sensors was 309  $\mu$ s.

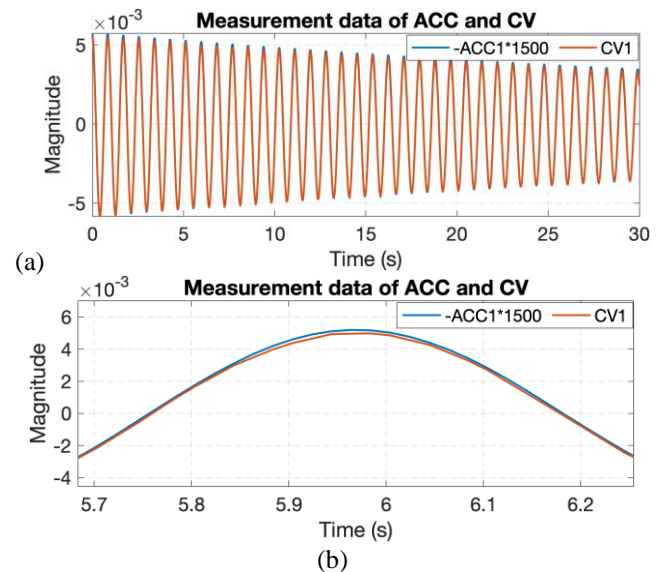


Figure 4 Measurement data of the accelerometer and camera.

### 4 CONCLUSION

The developed wireless sensors—including anemometers, accelerometers, and vision-based systems—help fill the gap in long-term input-output monitoring of high guyed masts at low cost. These heterogeneous sensors form a wireless sensor network, which also has potential for other structural health monitoring applications, such as using vision-based systems to capture vehicle input and accelerometers to measure structural response on bridges.



## REFERENCES

- [1] K. Koo, J.J. Capilla, J. Brownjohn, Innovative sensing solution and SHM for Moel-Y-Parc telecommunication high guyed mast, International Conference on Smart Infrastructure and Construction 2019 (ICSIC) Driving data-informed decision-making, ICE Publishing, 2019, pp. 589-594.
- [2] T. Höbbel, K. Thiele, M. Clobes, Wind turbulence parameters from three dimensional full-scale measurements at 344 m high guyed mast site Gartow 2, Journal of wind engineering and industrial aerodynamics, 172 (2018) 341-350.
- [3] K. Koo, D. Hester, S. Kim, time Synchronization for Wireless Sensors Using Low-Cost GPS Module and Arduino 2019 Frontiers of Built Environment, Vol. 4, Article 82.

## Wireless Multi Sensor Monitoring of Engineering Structures

Markus Rennen<sup>1</sup>, ORCID 0009-0002-5772-4205

<sup>1</sup>Senceive Ltd, Milton-Keynes, UK

**ABSTRACT:** Engineering structures are generally understood to be predominantly functional objects, such as bridges, tunnels, cranes, silos etc. Failure of these structures not only causes physical damage but can also lead to interruption of production, disturbance of infrastructure or traffic and thus disruption of operations with commercial impact for both the asset owner as well as concerned commuters or customers.

Therefore, in-situ monitoring is of major importance. The challenge lies in the need to observe specific parameters in difficult to access locations, under demanding environments, or with high data rate requirements. These conditions often exceed the capabilities of geodetic observation techniques. Wireless Condition Monitoring (WCM) nowadays can breach the gap by implementing a variety of sensors and maintenance-free hardware without the requirements of line-of-sight or cables. Compact Nodes with internal and external sensors and low power consumption are versatile and provide long battery life. Remote access allows adjustment or temporary changes of configuration settings (e.g. recording intervals). Automated data transfer to cloud-based visualization platforms enables continuous data access with configurable alerts, allowing for proactive evaluation of structural health.

The article presents a number of practical field examples that address the challenges mentioned above, while highlighting the specific requirements for interpreting the collected data – supported by examples of result validation using independent techniques.

**KEY WORDS:** Monitoring, Structural Health, Wireless Condition Monitoring, Multi Sensor System



Figure 1 : Installation of tilt sensors for monitoring a retaining wall in a track area with restricted access





Figure 2: Wireless Sensor Nodes: 3-Axes-Tilt-Sensor (Triaxial Tilt Sensor) (Foreground) and Laser Distance Sensor (Background)

## 1 MONITORING OF ENGINEERING STRUCTURES

### 1.1 Motivation

Per definition, the primary focus of engineering structures lies in fulfilling functional tasks. According to DIN 1076, engineering structures include relevant buildings, transportation systems, bridges, tunnels, trough and retaining structures, but also silos, masts, chimneys, cooling towers, industrial facilities, etc. If a structure can no longer fulfill its function, the damage is not limited to the structure itself but also includes the loss of its economic utility. In industrial plants, entire production lines can be affected if a single component fails. Naturally, structural safety is of fundamental importance and ensuring usability while avoiding failure-oriented maintenance is essential.

As an additional challenge, monitoring usually has to be conducted during full operation, which causes limited accessibility and demands an extraordinary robustness of the hardware.

### 1.2 Automation of Monitoring

Monitoring of engineering structures typically focuses on relatively small-scale structures. The motivation to automate monitoring usually stems from one or more of the following:

- The required sampling rate makes manual monitoring impractical or inefficient.
- Access to the monitored object is generally difficult, uneconomical, or dangerous (see Figure 1).
- The observation period is very long. Automation ensures that operations (e.g., traffic flow) remain undisturbed.

Moreover, smart automation of the monitoring process allows operational workflows (e.g. traffic flow) to remain undisturbed.

Monitoring, as a broad term can involve various parameters, including economic or statistical indicators characterizing industrial usage. It may also be necessary to record internal and external timeframes to synchronize operational influences with structural integrity parameters.



Figure 3: Solar powered cellular gateway, intermediately stores the sensor data and transmits it to the server



Figure 4: Sensor locations at the Südzucker Lime Kiln in Wabern/Germany

Automated systems collect data in regular or event-triggered intervals and transmit it to a platform, locally or via cloud-based interfaces accessible through a web browser.

## 2 WIRELESS MONITORING SYSTEMS

Various observation methods can be considered wireless (e.g., prisms, remote sensing). Generally, the term refers to what has become known as Wireless Condition Monitoring (WCM): active sensors with autonomous data acquisition units, or 'nodes', that integrate sensing, power supply, and data transmission. These nodes can incorporate external sensors with various signal types (analog or digital) and are highly compact. Miniaturized low-power MEMS (Micro-Electro-Mechanical Sensors) have opened the door to practical usage. For instance, tilt sensors consist of a chip-based nano-sized probe resting between capacity electrodes recognizing gravity related rotations. Available High-G versions offer considerable resistance to physical shock. Additionally, built-in mechanical as well as statistical filters help eliminate outliers. Some manufacturers include additional accelerometers that allow sensor values to be triggered by outside impacts which occasionally is utilized in slope and embankment monitoring as well as rockfall detection.

In Figure 2 examples for commercial 3-axis tilt sensors, and laser distance sensors, are shown, offering more than 10 years of battery life at half-hourly data sampling rate.

### 2.1 Communication and Operation

Data is typically encrypted and transmitted from nodes to a local gateway (Figure 3), and from there via cellular networks to an online platform. Internally, systems use 2.4 GHz Wi-Fi frequency for high bandwidth or LoRa for long range (868

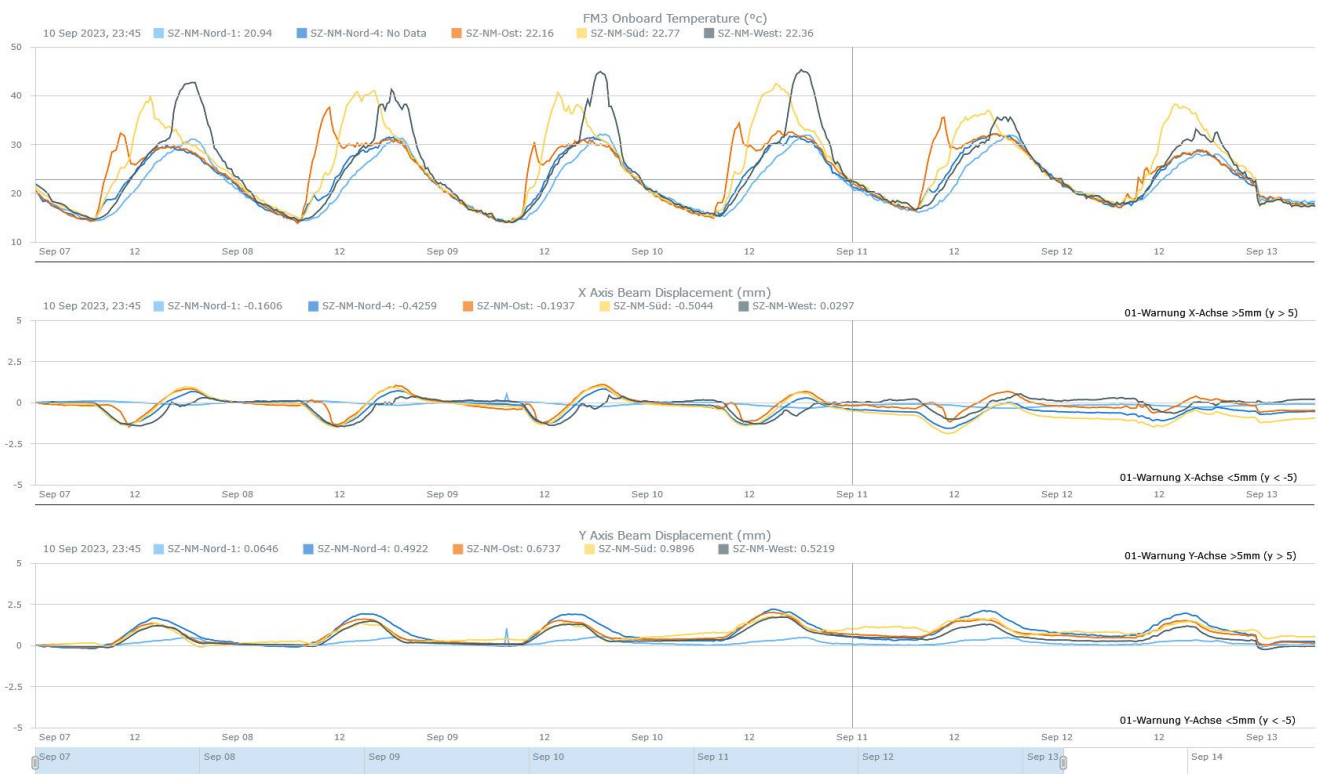


Figure 5: Correlation of Lime Kiln Deformation with diurnal Sun Exposure (Tilt Units in  $\text{mm/m}$ )





Figure 6: Installation of tilt sensors on the supports and longitudinal beams of the crane rails

MHz licensed in Europe). Due to short sampling intervals and small monitoring areas in structural applications, 2.4GHz is often preferred. LoRa only allows longer reporting intervals and has limited two-way communication, making remote configuration more difficult. 2.4GHz-based systems mitigate shorter range via node meshing, where neighboring nodes act as repeaters. Gateways can be solar powered, enabling flexible placement. Unlike geodetic methods, WCM does not require line-of-sight, allowing sensor placement on hard-to-reach structures. Sensors are maintenance-free and configurable remotely.

## 2.2 Applications and Interpretation

Interpreting WCM results can be challenging. While geodetic methods like Total Station observations provide 3D coordinates, tilt sensors only provide angular data, which must be interpreted cautiously. For instance, when converting angular units via trigonometric calculations, i.e. projection onto real respectively virtual beam lengths, into more intuitive metric values, (e.g. mm/m) structural stiffness and deformation behavior must be considered.

Sometimes, the mere indication of movement is enough to trigger further action. In inaccessible areas like rail zones, ease of installation and maintenance are crucial (see Figure 1). If models of deformation characteristics exist, tilt angles can be

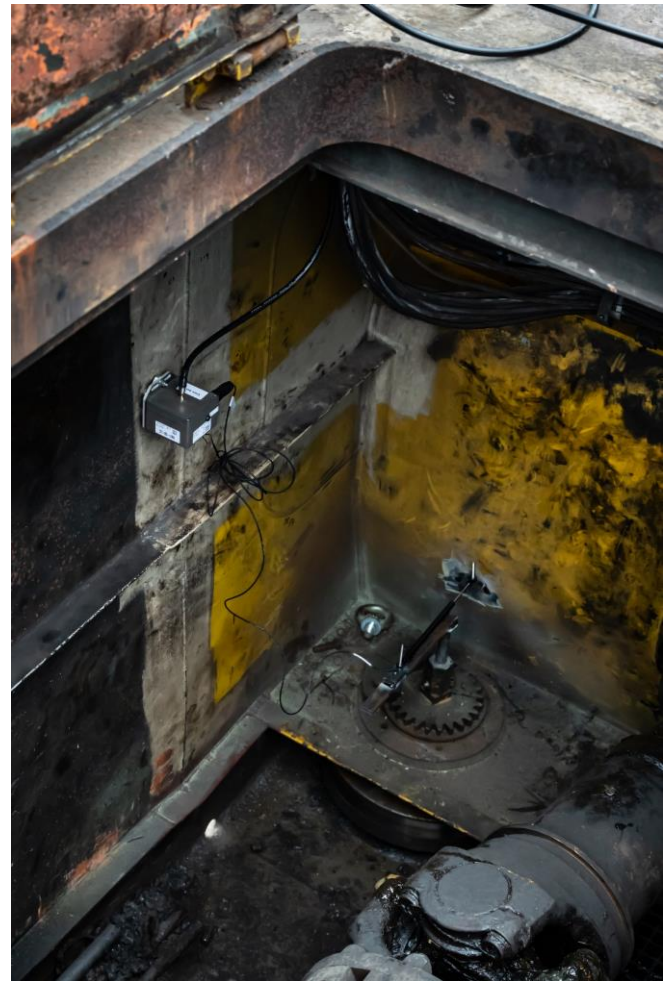


Figure 7: Crack sensor for detecting the internal deformation of the crane bridge

extrapolated to derive horizontal or vertical displacements of masts, walls, foundations, etc.

## 3 CASE STUDIES

### 3.1 Südzucker Lime Kiln, Wabern

#### 3.1.1 Situation

The lime kiln at the Südzucker site in Wabern/Germany was monitored to assess its behavior during operation, including firing and loading phases. The structure is a 48.5m tall cylindrical tower with a diameter of 2.66m. Tilt sensors were mounted in all four cardinal directions near the top of the tower. As mentioned above, extrapolating tilt measurements along the length of a structure requires the assumption that the structure is rigid. If the assumption holds, the recorded tilt values can be projected over the kiln's height to measure the horizontal displacement at the top of the structure. Model assumptions like this naturally must be validated.

As it was rather unlikely that the tower would tilt as a rigid body over the entire almost 50m, three additional sensors were installed in a vertical alignment on the north side from the foundation to the top (Figure 4).

Typically, MEMS tilt sensors provide resolution of approximately  $0.0001^\circ$  or less than  $0.002^{\text{mm}}/\text{m}$  with repeata-



Figure 8: Mobile crane bridge with centrally positioned gateway



bility of roughly  $\pm 0.0005^\circ$  (less than  $\pm 0.01 \text{ mm/m}$ ). Critical though is temperature correlated sensor behavior which can reach a magnitude of  $0.0017^\circ/\text{K}$  ( $0.03 \text{ mm/m je } ^\circ\text{K}$ ) [1]. Therefore, to achieve higher accuracy, temperature compensation is required, or the installation must be configured to separate deformation effects from temperature influences.

### 3.1.2 Interpretation

The installation took place in early September, at a time when temperatures fluctuated between approximately  $15^\circ\text{C}$  at night and, in some cases with strong sunlight, well over  $40^\circ\text{C}$  during the day. Since all nodes are equipped with an internal thermistor, the local temperatures were recorded directly at the sensor.

Figure 5 depicts the nodes' behavior for all four top nodes and the bottom one on the north side. The top graph shows the nodes' temperature recordings for roughly the first week of observations. Temperature peaks shifting from east to west throughout the duration of one day reflect the sun's path. Naturally, no temperature peaks occurred on the north side; however, the bottom and top sensor in the North i.e. the light and dark blue graphs still followed the general daily temperature pattern.

When examining the movements in the horizontal X and Y directions (Figure 5 lower two graphs in  $\text{mm/m}$ ), a temperature-correlated, oscillating motion pattern can be observed in all sensors located in the upper tower area. In contrast, the tilt sensor at the base of the tower showed virtually no movement). These observations essentially allow two conclusions to be drawn:

- The movement in the upper part of the tower is real and not caused by temperature effects on the sensor, as otherwise the sensor at the base would also show temperature-correlated movements.
- The tower deforms increasingly with height and does not tilt as a rigid body.

Therefore, the above demanded separation of temperature impact from the real signal could be achieved by appropriate sensor constellation. The derivation of realistic horizontal displacements at the various levels of the kiln would require more sophisticated differential models not conducted during this task (for comparison see 3.4).



3.2 Crane Track at Thyssen Krupp, Duisburg

Figure 9: Permanent Observation of Abutment Tilt and indicative vertical Displacement of the Bridge Deck

### 3.2.1 Task and Realization

According to the client, German Thyssen Steel Company in Duisburg/Germany, the crane track girders had previously exhibited wear damage with unknown causes in the past. It is suspected that crane movements while transporting heavy steel slabs induce short-term deformations, which remain detectable by geodetic methods among others due to their dynamic nature.

### 3.2.2 Data Considerations

Tilt sensors and crack sensors were installed on supports and beams (Figure 6 and Figure 7), with their positions measured geodetically.

Additional gateways were placed on each crane bridge to allow for independent, stable, yet mobile wireless mesh networks (Figure 8). Data was sampled every 2 seconds and transmitted via cellular network. Through an API-based database interface, approximately 400 MB of CSV data per day was transferred over several months to a local computer.

Moreover, the timestamp of the data allows synchronization between sensor behavior and crane position. This should enable the user to associate specific load cases and crane configurations with the corresponding sensor.



Figure 10: Bridge during load test with 48t mobile crane

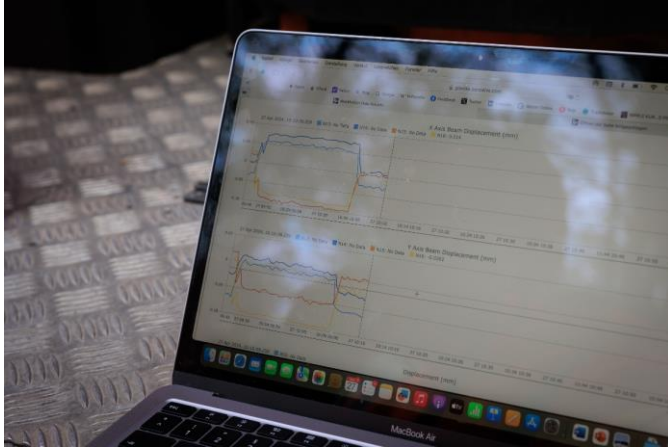


Figure 12: Visualization of the deformation during the load test via live access to the cloud portal

At the time of writing, the geometric evaluation of the combined data from sensor readings and crane positioning is still ongoing and will be the subject of a student master's thesis. Even ahead of that outcome, the project has already demonstrated that such high sampling rates can be handled wirelessly over extended periods of time.

### 3.3 Indicative Monitoring Bridge BAB43 Bochum

At a highway bridge in Bochum/Germany the asset owner expressed concerns that the cylindrical roller bearing might exceed its margins due to the abutment tilting outwards. In order to avoid dangerous vertical displacement ("drop") of the bridge deck, wooden supports were inserted that would only allow <10mm sag.

Since the question of whether the vertical displacement occurred was essentially binary - either it happened or did not - a low cost, indicative alarm solution was requested to run alongside the abutment tilt observations. A spring-loaded telescopic crack sensor was installed (Figure 9) that allowed for diurnal and seasonal horizontal movement of the deck while reliably indicating vertical displacement.

### 3.4 Bridge on Wittekindstraße, Dortmund

#### 3.4.1 Situation and Task

Compared to the above, this Dortmund bridge demanded more detailed i.e. quantitative observation. The case presented involves a slab structure built in 1957, consisting of two identical superstructures separated by a joint, each approximately 31 meters in length, with four individual bridge spans of about 15 meters each (Figure 10). At this location, two major traffic arteries of Dortmund intersect in an urban setting: the six-lane B1 and the four-lane Wittekindstraße.

An expert report prepared in 2023 confirmed the load-bearing capacity of the bridge. To ensure continued safe operation, permanent monitoring was recommended as a supplementary measure to the regular structural inspections. As a result, the Civil Engineering Department of the City of Dortmund, in collaboration with the Surveying and Cadastral Office, developed a monitoring concept that included the continuous observation of the structure using WCM sensors.

Following the layout of the prestressing tendons, tilt and strain sensors were installed across the four bridge spans

(Figure 11). The arrangement was designed to approximate the expected deformation trough using four tilt sensors per bridge deck, i.e. two tilt sensors at each shoulder and a strain sensor in the middle, where the greatest tensile stress was expected. In addition, transverse cracks were equipped with potentiometric crack sensors, and temperature probes were embedded in the concrete. The system was installed using a lifting platform within a single day and has been transmitting data to a browser-accessible cloud server at 30-minute intervals since October 2023.

#### 3.4.2 Load Test

The initial expert report had already recommended a dedicated load test, which was carried out in April 2024 using a 48-ton crane provided by the Dortmund fire department (Figure 10).

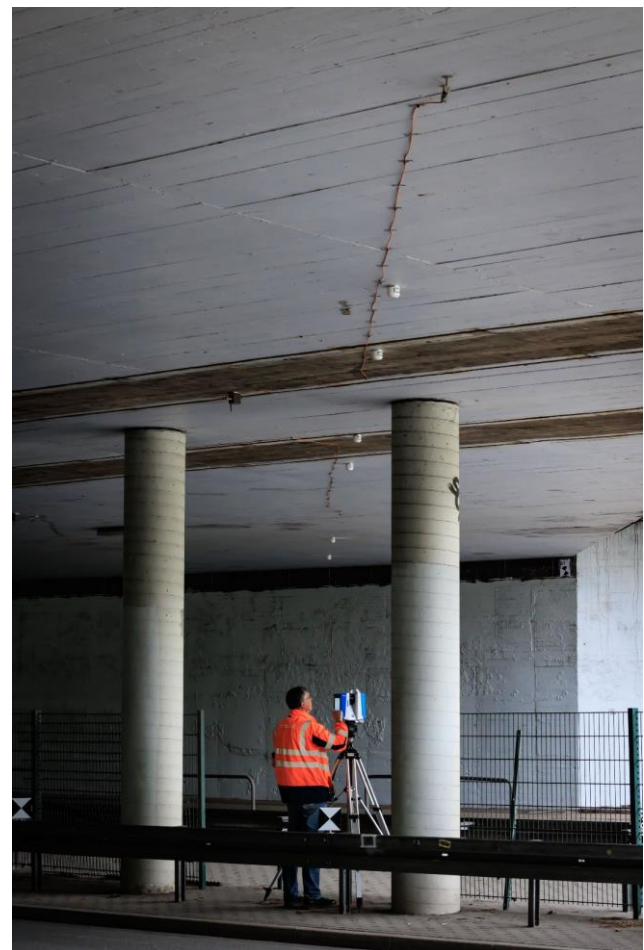


Figure 11: Arrangement of the WCM sensors (tilt, strain, and crack sensors) and operation of the laser scanner during the load test



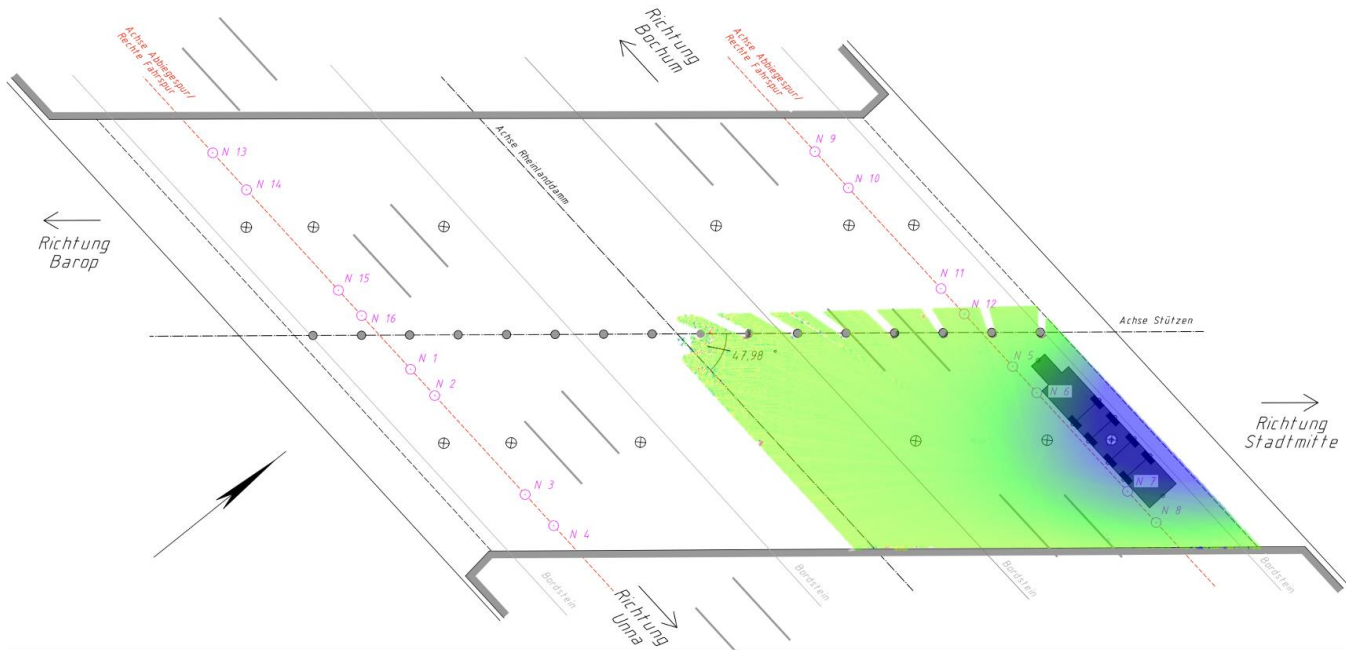


Figure 13: Example visualization of the load-induced deformation pattern of a bridge span from the surface scan  
(Graphic: [2] M.Róžański)

Specific loading points were defined by the Civil Engineering Department and marked by the Surveying and Cadastral Department<sup>1</sup>. For the test, the sensor system was remotely switched into a 30sec interval live mode. This was intended to ensure that the vehicle remained in position until the increase in deformation had subsided and stabilized at a constant level. It turned out that the full deformation occurred almost instantaneously (Figure 12). Accordingly, the crane was held in position for approximately 15 minutes before moving to the next position. This duration allowed precise evaluation of the sag dynamics while providing redundant observations to generate reliable, representative averages in order to avoid data noise bias.

The experts from the Civil Engineering Department of Dortmund predicted a load-induced deformation in the order of

magnitude of 2-4mm that can certainly be detected using geodetic methods. Accordingly, surface scans were carried out before, during, and after the loading using a high-precision geodetic Zoller & Fröhlich phase scanner (Figure 11), and the results were evaluated as part of a bachelor's thesis at the Department of Geodesy at Bochum University of Applied Sciences. Figure 11 shows the significant deformation of the bridge span around the load position by color coding.

To compare the two methods, a cross-sectional profile-spline was calculated through the scan-generated surface, following the layout of the prestressing tendons.

In order to get a comparable graph from the tilt nodes the resulting deformation trough was approximated by a higher order polynomial with the tilt values representing tangents at dedicated "chainage". The tangent gradient is obtained from the

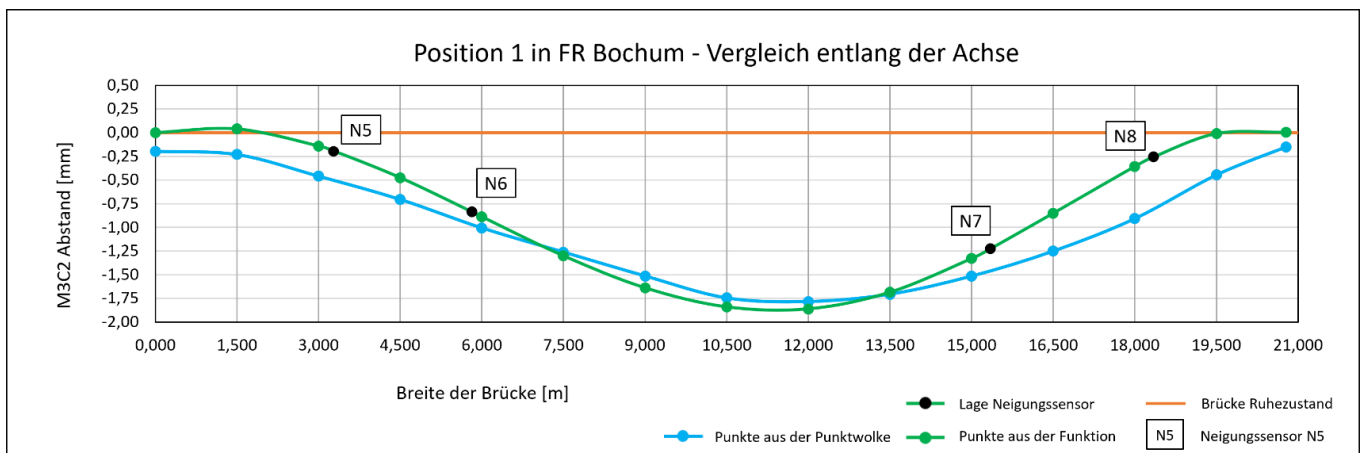


Figure 14: Comparison of the results from surface scanning and tilt sensor data along the course of the prestressing tendons  
(Graphic: [2] M.Róžański)

<sup>1</sup> Vermessungs- und Katasteramt



first derivative of the polynomial. Accordingly, the inclination values can be used to solve the system of differential equations and determine the coefficients of the polynomial. In this way, a deformation profile can be calculated from the inclination values. Thanks to the high data density - through the large number of surface-representing points in the Laserscan and the repeated measurements from the tilt sensors - both systems achieved sub-millimeter relative accuracy at the collocation points.

The resulting graphs are shown in Figure 13. Since a laser scanner profile includes significantly more sample points, local deformations that fall between the gaps of the WCM are only picked up by the scans. Nevertheless, both methods yield similar results, coinciding closely in shape and differing by approximately 0.2mm.

The observed result came reassuring to the local authority. Not only did the results confirm that the installed system provides correct and representative data. The observed deformation of around 2 mm, confirmed the prediction and as such do not indicate any cause for concern regarding the structural integrity of the bridge.

The results of both measurement methods aligned within the submillimeter range. This demonstrates that the automated system is well suited for capturing the deformation behavior in a representative manner. Continuous monitoring can therefore be entrusted to an automated system, which can then trigger more detailed laser scanning if warning thresholds are exceeded.

#### 4 CONCLUSION

Using several practical examples, the capabilities of Wireless Condition Monitoring (WCM) for monitoring complex engineering structures has been demonstrated. While the operation of the system is low-maintenance and the installation is quick and straightforward, interpreting the results requires a certain level of understanding regarding the behavior of the structure.

The versatility of WCM is evident not only in the wide range of sensors available or possible to integrate, but also in the installation possibilities on or within the structure without the need for line-of-sight connections. The sensors operate autonomously, making them suitable for hard-to-reach or inaccessible areas, and their long battery life enables them to be used for long-term monitoring tasks. High sampling rates could be achieved, as well as temporary adjustments via remote access.

It is important to emphasize that WCM should not be seen as a competitor to traditional geodetic methods. Rather, it fills the gap where conventional approaches are impractical or inefficient. For example, WCM enables high-frequency, continuous monitoring and, through automated alerts, trigger manual geodetic verification when needed.

Utilizing WCM sensor technology allows safe extension of the observed structures' life span while reliably identifying approaching deterioration, without compromising on safety or

risking disruptions to increasingly interconnected infrastructure systems.

#### ACKNOWLEDGMENTS

The author's sincere gratitude goes to all individuals, partners and companies involved who allowed and made it possible to present their projects.

#### REFERENCES

- [1] KALENJUK S., LIENHART W. (2020), Vortrag „*Performance of Senceive Triaxial Tilt Sensor Nodes - Insights from lab tests and a field study*“, Geodätisches Kolloquium Universität Graz 07.10.2020, Graz, Österreich
- [2] Róžański, M.: „Geodätisches Monitoring mittels terrestrischer Laserscans im Zuge einer lastinduzierten Verformungsmessung an der B1-Brücke über die Wittekindstraße in Dortmund“; Bachelorthesis, Department of Geodesy, University of Applied Science Bochum, 2024.

# Practical approach to calibrating wireless sensors for use in structural health monitoring in an outdoor environment

Michael Markus Petschacher<sup>1</sup>, Markus Krüger<sup>1</sup>, 0000-0003-3364-7874

<sup>1</sup>Institute of Technology and Testing of Construction Material, Faculty of Civil Engineering Sciences, Graz University of Technology, Inffeldgasse 24, 8010 Graz, Austria  
email: petschacher@tugraz.at, krueger@tugraz.at

**ABSTRACT:** When sensor systems are used on outdoor structures (bridges, tunnels, etc.), they are exposed to a wide range of environmental influences. In particular, temperature can significantly affect the quality and accuracy of measurements. While most commonly available sensors are calibrated at temperatures of around 20°C before use, but the influence of variable temperatures is rarely considered. Furthermore, the measuring systems used for these sensors, particularly wireless sensor systems, are often only calibrated for room temperature. For this reason, this paper presents calibration procedures for monitoring systems including the sensors used (here displacement sensors are used as an example). The aim is to provide a practical routine for structural monitoring applications. This involves simulating typical temperature changes in a climate chamber (-20°C to +50°C) while measuring the temperature-induced strain of steel, and analyzing the reproducibility and temperature response of the entire measurement system. Other external influences affecting measurement quality are also discussed, and these are considered when determining the overall measurement uncertainty. This helps to define the requirements and limitations of measurement systems for structural health monitoring, particularly for bridges. The resulting findings should support the standardization process for assessing the suitability of monitoring systems for future SHM applications.

**KEY WORDS:** Calibration; Wireless Sensors; Environmental Influences.

## 1 INTRODUCTION

Structural Health Monitoring (SHM) plays a vital role in maintaining the long-term stability and safety of civil infrastructure. Among the various SHM technologies, wireless sensor networks (WSNs) have emerged as an efficient solution for the real-time monitoring of structural integrity. However, WSNs present specific challenges, particularly when deployed outdoors, where they are exposed to a variety of environmental factors. Bridges, for instance, are subject to extreme temperatures, rapid temperature fluctuations, wind, rain, and vibration, all of which can significantly affect sensor performance and measurement accuracy. Despite these challenges, most calibration efforts focus solely on the sensor itself and are typically performed under laboratory conditions at around 20°C. The effect of variable influences on the entire measurement system is often not sufficiently considered. These include not only external influences, but also aspects such as the stability of the measurement system in relation to its power supply (e.g., wireless sensors are often battery-powered). Such limitations can lead to measurement inaccuracies and impair the reliability of SHM systems in outdoor applications.

This paper presents the calibration process for a wireless monitoring system that measures displacement and strain. This system will later be used on a building to determine changes in strain or crack width with high precision. It should be noted that precision must be defined before selecting the appropriate sensors and sensor system. For example, in the context of service limit states, crack width change may require an accuracy of 0.05 mm. The proposed approach involves placing the complete sensor system in a climate chamber to simulate real-life temperature conditions and fluctuations ranging from

-20 °C to +50 °C. Monitoring the temperature-induced strain of a steel plate under these controlled conditions enables the development of a more comprehensive and practical calibration routine for SHM applications.

It is expected that the findings of this research will enhance the accuracy and reliability of WSN-based SHM systems, particularly for bridges exposed to harsh environmental conditions, and to contribute to the standardization of calibration procedures in this field.

## 2 BACKGROUND AND BASICS

### 2.1 Wireless Sensor Systems in SHM Applications

WSNs for SHM offer a promising alternative to traditional wired sensor systems. The reliance on physical connections for power supply and data transmission in wired systems significantly increases the complexity, manufacturing costs and maintenance requirements of such systems. In contrast, wireless sensor systems integrate power supply or harvesting and wireless communication capabilities directly into the sensor units, enabling efficient data acquisition and real-time signal processing without the need for extensive cabling infrastructure. This self-sufficiency not only simplifies the deployment of SHM systems but also reduces the overall costs and logistical challenges associated with their maintenance [1].

WSNs can be applied to a variety of different use cases. The network usually consists of a series of motes (sometimes also referred to as nodes), each equipped with one or more sensors depending on the measurement task. For example, these sensors can measure temperature, humidity, strain, displacement, pressure, force, tilt, and other variables. The measured values are transmitted wirelessly to a central

processing unit, which primarily stores and pre-processes the data. From there, the data is transmitted to the user for post-processing. It should be noted, however, that WSN applications are only of limited use for high-frequency measurements (vibrations, high-frequency load changes, etc.) due to the limited data transmission via radio and the limited energy supply in battery-powered WSNs (sampling rate correlates with energy consumption).

Figure 1 shows a standard schematic of a sensor mote, which can be described as having four major components: a sensor unit, a processing unit, a communication unit and a power supply unit [2]. When connecting analogue sensors, a suitable signal conditioning device and an analogue-to-digital (A/D) converter are also required.

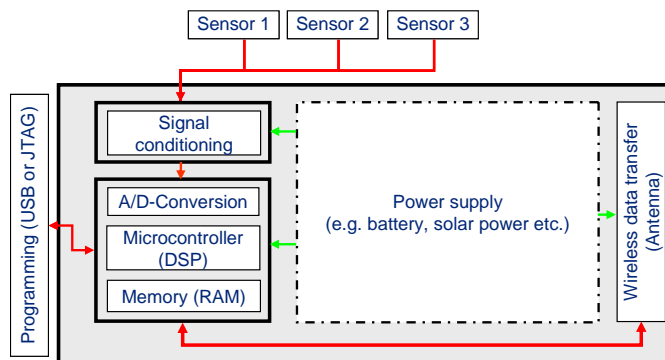


Figure 1. Block diagram of the hardware for a standard sensor mote [3].

While all these units vary depending on the application, they are subject to the same environmental influences when used outdoors. In this paper, the schematic in Figure 1 will be allocated with the components used in the calibration procedure and considered as a whole. Influences on the communication unit will not be discussed in order to focus on the sensors and the sensor mote themselves. Similarly, environmental influences on the power unit will not be considered, although fluctuations in the energy supply might affect the measurements.

## 2.2 External Influences on WSNs

A variety of external influences can affect both a wireless measurement system and the value being measured. As well as influences from the structure itself and how it is used (e.g. vibrations and deformations), environmental factors such as temperature and humidity also have a significant impact. The extent and nature of these influences depend largely on the structure's geographical location and the motes' specific positioning within it. It is essential to quantify these influences and take them into account when determining measurement results, as this is part of a highly recommended validation process.

For example, significant differences in environmental exposure can arise in the case of a bridge depending on whether sensors are mounted on the deck, beneath the structure, or within enclosed components such as hollow box girders. The Figure

primary influences affecting accuracy in wireless sensor systems can basically be categorized into two key factors, according to [3]:

- The transfer function between the physical quantity to be measured (stimulus) and the sensor system (specifically the sensor's response function). This defines how accurately and consistently the sensor converts the physical stimulus into a measurable signal.
- The cross-sensitivity of external disturbances on the measured quantity, which largely depends on the type of sensor and its underlying measurement principle. Such disturbances can introduce significant errors if not properly accounted for, particularly in environments with variable thermal, electromagnetic, or mechanical conditions.

Figure 2 shows an Ishikawa diagram of the many possible influences on a WSN node, which can impact the quality of the measurement. This categorization especially provides an overview of the basic influences, which are temperature [°K], relative humidity [%], shock [g] and vibration [mm/s]. Depending on the location of the WSN, disturbances due to electromagnetic fields might also be a significant factor (for example, near high-voltage lines). More detailed documentation on the classification of electrotechnical components according to environmental influences can be found in EN 60721/IEC 721 multi-part standard series of the International Electrotechnical Commission (IEC).

This article only considers temperature as a decisive factor influencing the measured value determined by a wireless sensor and the calibration of the sensor system, as the influence of temperature is often not adequately determined during calibration by the manufacturer.

Since the temperature on external structures fluctuates greatly, some assumptions must be made. For example, the climate in a tunnel is more constant than on a bridge, where wind, solar radiation and humidity also play a role in addition to the air temperature. In order to determine upper and lower limits for the air temperature, statistical results for the area in question should be analyzed beforehand.

As an example, for Austria, according to the annual climate report in [4], the minimum air temperature in 2024 was measured at -25.5 °C in mountainous regions and -21.1 °C in urban areas, with a maximum temperature of +36.9 °C.

Another approach could be to use the temperatures used to calculate the integrity of the structure in question, which are mostly regulated in national standards. In case of the European standard in the national appendix, set in [5], a two-day average of the maxima and minima, appearing all 50 years, is used as the dimensioning value. There the lowest temperature expected is set for -32 °C in Austria, while the highest is set for smaller than +39 °C, depending on the sea level.

These values, as can also be seen in Table 1, provide a rough estimate of the required range.

<sup>1</sup> With [g] being a common unit for acceleration with 1 g being the gravitational acceleration of Earth:  $1 \text{ g} \approx 9,81 \text{ m/s}^2$



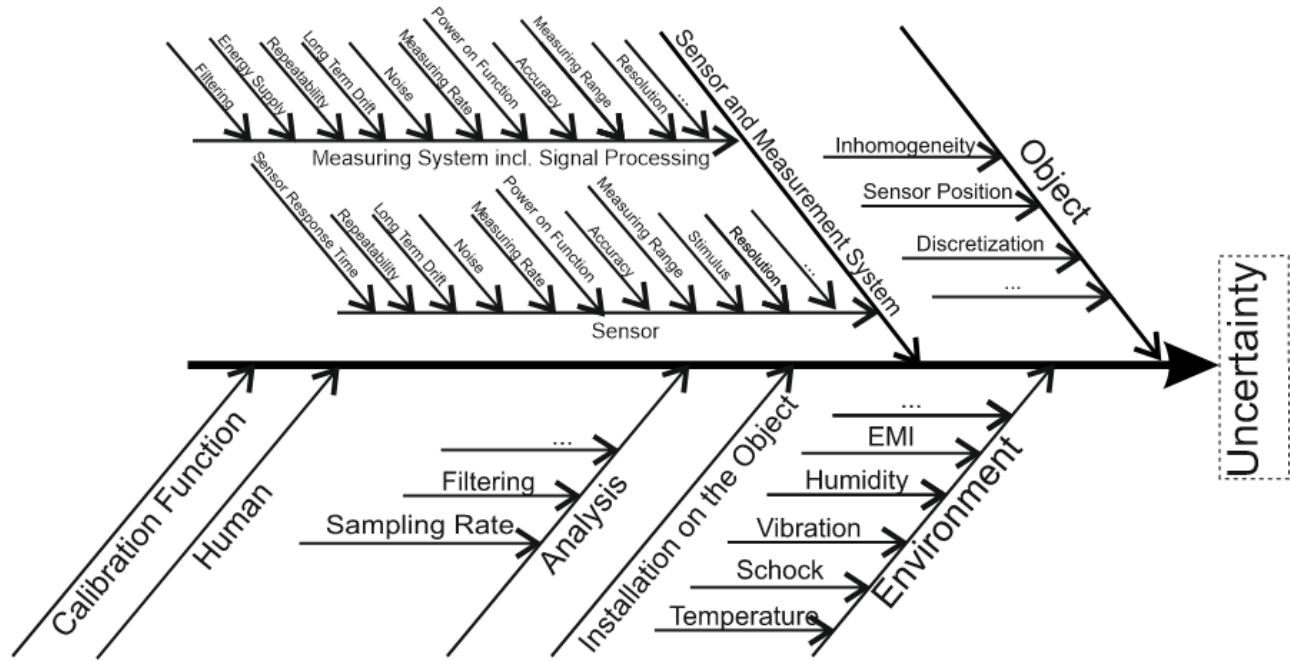


Figure 2. Ishikawa diagram showing the influences on the uncertainties of WSN nodes.

Table 1. Minima and maxima of air temperature in Austria.

Reference	$T_{\min}$ [°C]	$T_{\max}$ [°C]	$\Delta T$ [°K]
Austrian Measurement 2024	-25.5	36.9	62.4
Austrian Standard	-32	39	71
$T_{\min}$ ...	minimal temperature		
$T_{\max}$ ...	maximal temperature		
$\Delta T$ ...	difference of min and max		

The examples in Table 1 do not apply to every case. Firstly, the effect of direct sunlight is not considered. Depending on the medium, surface temperatures near motes can be much higher, depending on the intensity of the sunlight. Secondly, the values shown are extreme pinpoints of the whole country. They can vary considerably depending on the location. Nevertheless, they demonstrate that the estimated temperature range that a WSN has to endure for long-term SHM, can exceed 60 K, ranging from below -10°C to above 30 °C, depending on various factors.

### 3 PROPOSED CALIBRATION METHODOLOGY

#### 3.1 Experimental Setup

For experimental evaluation, an integrated sensor mote is placed in a climate chamber as a complete unit, including the sensors, but without the sensor mote housing. Approximately once per minute, measurement data is transmitted via a LoRa (Long Range) radio module to a receiver, which forwards the data to a remote database for storage and analysis.

The sensor mote provided by SmartMote [6] consists of two printed circuit boards (PCBs) and is referred to as Smartmote<sup>WS</sup>. The primary PCB contains a microcontroller that is responsible for signal processing and data management. It also contains a communication interface (LoRa – 868 MHz), a

power supply unit comprising two 3.6 V lithium thionyl chloride batteries, and several integrated measurement electronic components and digital sensors for measurement (see Figure 3). The second circuit board serves as a separate sensor interface card, which provides three ports for connecting analogue sensors. The card has a reference voltage and a voltage meter as well as 24-bit high precision analogue-to-digital conversion with adjustable gain for use with different sensor types (see Figure 4).

Table 2. Configuration of the Sensor Mote.

Sensor Mote Name:	SMUSE 143
Onboard measurements:	Acceleration x, y and z Temperature Relative humidity Battery voltage Illuminance
Port 1	Fixed resistors
Port 2	KG 2A – EFA231506
Port 3	KG 2A – EFA231507

Table 3. Specifications of the crack displacement transducers.

Transducer name	KG 2A – EFA231506
Capacity	2 mm
Rated Output	1480 $\mu\text{V/V}$ (2960 $\times 10^{-6}$ strain)
Non-linearity	0,2 %RO
Input resistance	351.6 $\Omega$
Transducer name	KG 2A – EFA231507
Capacity	2 mm
Rated Output	1430 $\mu\text{V/V}$ (2860 $\times 10^{-6}$ strain)
Non-linearity	0,2 %RO
Input resistance	351.2 $\Omega$

For this experiment, the sensor interface board is equipped with two crack displacement transducers (model KG-2A, Tokyo Measuring Instruments Laboratory [7]), which are connected in a mirrored configuration to a steel plate (see Figure 6 and Table 4) to measure the thermally induced strain. Additionally, the third input channel is connected to a fixed resistor network, which acts as a stationary reference input to periodically validate the stability and performance of the measurement system under varying environmental conditions (see Table 2,

Table 3 and Figure 5 for technical details).

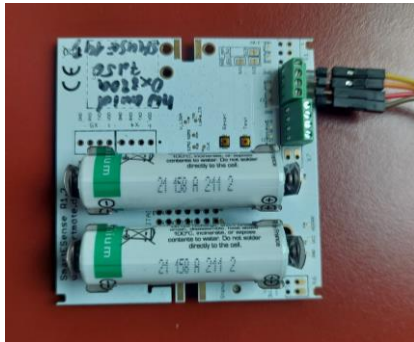


Figure 3. Primary PCB with power supply.



Figure 4. Secondary PCB with sensor ports.



Figure 5. Crack displacement transducers on a steel plate.

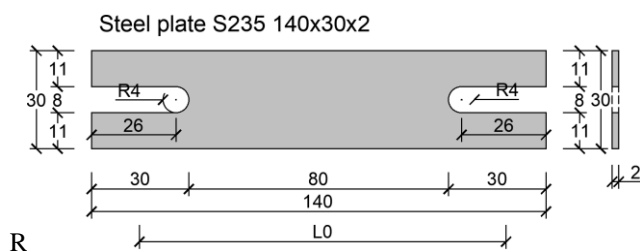


Figure 6. Steel plate S235 140x30x2 [mm].

A programmable climate chamber (model: VÖTSCH VT 4060) is used to determine the influence of environmental

temperature variations. It allows precise temperature control within the range of  $-40^{\circ}\text{C}$  to  $+180^{\circ}\text{C}$  and includes adjustable ramp rates and programmable dwell times at set points. This enables reproducible temperature profiles to be implemented that are tailored to sensor calibration procedures.

Table 4. Characteristics of the steel plate.

Steel plate grade	S235 JR
Length	140 mm
Width	30 mm
Thickness	2 mm
Temperature coefficient $\alpha_T$	$\sim 12 \cdot 10^{-6} \text{ } 1/^{\circ}\text{K}$
Base length of measurement $L_0$	103 mm

For the present calibration experiment, a temperature range of  $-20^{\circ}\text{C}$  to  $+50^{\circ}\text{C}$  is defined. This range is based on the boundary conditions discussed in section 2.2, with slight modifications to accommodate the technical limitations of the chamber. Although temperatures below  $-20^{\circ}\text{C}$  have historically occurred in the alpine regions of Austria, such extremes have become rare in recent years due to climate change. Conversely,  $+50^{\circ}\text{C}$  approximates the extreme surface temperatures that can be experienced by bridge components exposed to direct sunlight in summer.

The temperature setpoints selected for this calibration are  $-20^{\circ}\text{C}$ ,  $0^{\circ}\text{C}$ ,  $+20^{\circ}\text{C}$ ,  $+35^{\circ}\text{C}$ , and  $+50^{\circ}\text{C}$ , as recommended in [3] for the thermal characterization of wireless sensor motes and their attached sensors. Each setpoint is maintained for 30 minutes to allow sufficient time for data collection and to determine the response time of the sensor system, as well as for statistical evaluation of repeatability. Thus, a minimum of five readings is taken at each plateau.

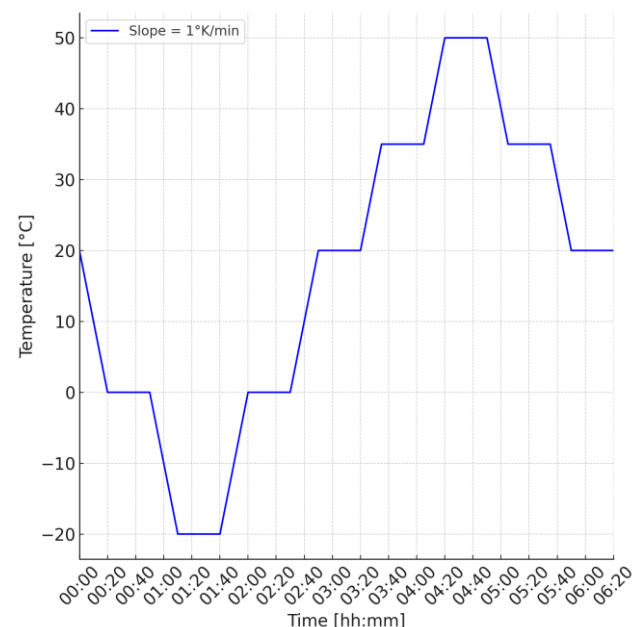


Figure 7. Temperature graph for one calibration cycle.

The full temperature profile is implemented as follows (see Figure 7 for the programmed profile): Starting from a reference temperature of  $+20^{\circ}\text{C}$ , the chamber performs a series of temperature ramps at a constant rate of  $1 \text{ K/min}$ . The temperature then drops to  $0^{\circ}\text{C}$ , falls further to  $-20^{\circ}\text{C}$ , returns

to 0 °C, rises to +20 °C, continues to +35 °C, and finally to +50 °C. It then returns to +20 °C via +35 °C. Each of these temperatures represents a holding period of 30 minutes.

This sequence defines one full temperature cycle, which is repeated ten times to increase the statistical significance of the results and to enable the observation of potential thermal hysteresis and time drift effects in the sensor system.

### 3.2 Calibration Procedure

To evaluate, calibrate and compare the performance of the two displacement sensors mounted on the steel plate (Figure 5), for which thermal expansion was calculated by using the chamber temperature and the characteristics of Table 4. It was decided to use ordinary structural steel for the application, rather than nickel-iron alloys (Invar steel) because the influence of steel strain on the uncertainty determination was expected to be minimal. Due to the homogeneous and predictable thermal expansion behavior of steel, its deformation under temperature change can be considered sufficiently uniform and it is therefore used as the “real” deformation value for comparison purposes.

The expected strain was calculated using the linear thermal expansion equation commonly applied in civil and structural engineering for practical application. The strain induced by temperature is defined as:

$$\Delta l = \alpha_T * \Delta T * l_0 \quad (1)$$

with:

- $\Delta l$  : absolute elongation or contraction [mm]
- $\alpha_T$  : coefficient of linear thermal expansion [1/°K]
- $\Delta T$  : temperature difference relative to a reference [°K]
- $l_0$  : original base length of measurement [mm]

For this experimental setup, the reference temperature is 20 °C and the base length of the steel segment between the two sensors is  $l_0 = 103$  mm. The coefficient of linear thermal expansion for structural steel is assumed to be  $\alpha_T = 12 \cdot 10^{-6}$  1/°K (Table 4) with an assumed standard deviation of  $\sim 0,3 \cdot 10^{-6}$  1/K. The expected median deformation values for the two temperature extremes in the calibration protocol are calculated using equation (1):

- Maximum elongation at +50 °C ( $\Delta T = +30$  K):  
 $\Delta l = 12 (\pm 0.3) \times 10^{-6} \times 30 \times 103 = \underline{0.037 (\pm 0,001) \text{ mm}}$
- Maximum shortening at -20 °C ( $\Delta T = -40$  K):  
 $\Delta l = 12 (\pm 0.3) \times 10^{-6} \times (-40) \times 103 = \underline{-0.049 (\pm 0,001) \text{ mm}}$

The calculated values serve as a reference line for the evaluation of the measurement results of both sensors. When functioning correctly, the cumulative deformation values recorded by the sensors should closely follow this curve, assuming a uniform temperature distribution and negligible mechanical disturbances.

The calibration procedure involves repeating the temperature cycle described in section 3.1 six times. During each cycle, measurements are recorded at a sampling rate of approximately one measurement per minute. It should be noted that this interval is shorter than is typical for long term monitoring applications, and therefore occasional inconsistencies in the data are to be expected as the system is optimized for lower frequency measurements.

Following the temperature programming, the sensors are subjected to controlled thermal load in the climate chamber.

The measurement output consists of a differential voltage signal relative to a reference voltage, which is continuously recorded and transmitted via the wireless mote system. A calibrated transfer function is then used to convert this voltage output into a displacement in millimeters [mm].

This conversion is based on the known sensitivity characteristics of the strain gauges (

Table 3), and the applied formula as shown in Equation (2):

$$X = \frac{main_{mvpv}}{(1000 - ref_{mvpv}) \cdot \frac{R_{sensor}}{R_5}} \cdot \frac{Cap_{sensor}}{RO_{sensor}} \cdot 1000 \quad (2)$$

with:

- $X$  : calculated displacement [mm]
- $main_{mvpv}$  : measured voltage at the sensor output [mV/V]
- $ref_{mvpv}$  : reference voltage equal to all supply voltages of the components [mV/V]
- $R_5$  : reference resistance of the measurement system being 100 in the apparent setup [ $\Omega$ ]
- $R_{sensor}$  : input resistance of the Wheatstone Bridge of the used sensor [ $\Omega$ ]
- $RO_{sensor}$  : characteristic value of the Wheatstone bridge for the measuring range [mV/V]
- $Cap_{sensor}$  : measuring span of the used sensor [mm]

Based on this formula, a data structure (see Table 5) is generated. To align the time domains of the two systems, the temperature measurements from the climate chamber are linearly interpolated to match the timestamps of the wireless sensor node. Figure 8 shows the results of the measurements at the set temperatures. The calculated cumulative displacement is set to zero for the first measurement at 20 °C.

Table 5. Data structure of experiment.

Column name	Description
__time	Datetime of the measurement [YYYY-MM-DD hh:mm:ss]
Ref_mV_per_V	reference voltage equal to all supply voltages of the components [mV/V] (see equation (2))
mV_per_V	measured voltage at the sensor output [mV/V] (see equation (2))
Displacement	Calculated displacement of each timestep in [mm] (see equation (2))
Delta displacement	Calculated displacement subtracted from each timestep before in [mm]
Cumulative displacement	Cumulative displacement started with the first timestep as zero in [mm]
Temperature	Measured temperature of the climate chamber interpolated for each measured timestep in [°C]
Reference temperature	Temperature which is programmed for the cycle (not measured) in [°C]
Cycle direction	Differentiated into cooling, heating and constant
Steel	Expected displacement of the steel plate with ideal strain in [mm] (see equation (1))
Error	Difference of cumulative measurement and steel in [mm]



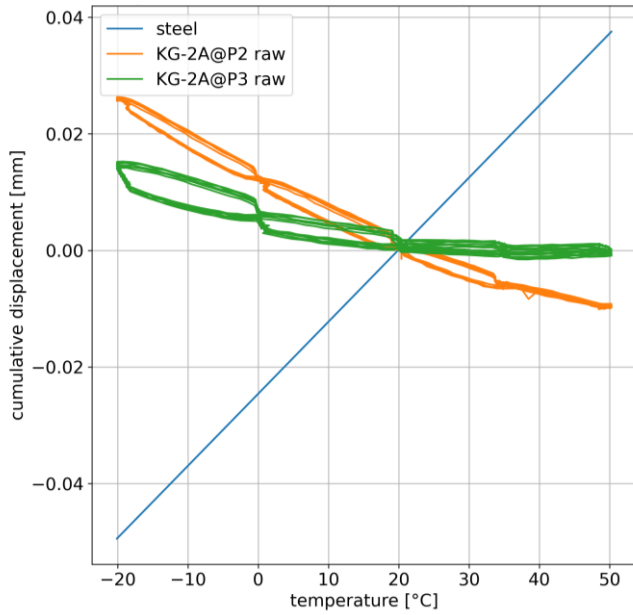


Figure 8. Raw data of cumulative displacement for both displacement transducers.

Figure 8 shows the results of the cumulative displacement of the two KG-2A sensors (Port 2 and Port 3) plotted against the temperature profile of the climate chamber and the theoretical elongation of the steel reference. Neither of the two sensor curves matches the expected thermal elongation of steel (blue line), which indicates a systematic error in the raw measurement data.

During heating and cooling phases, both sensors follow different curves. However, at the holding points where the temperature was kept constant, the cumulative displacement of both sensors converge to a common value. This behavior suggests that the response time of the sensors may need to be considered when higher accuracy requirements are specified.

### 3.3 System Temperature Compensation

It has not yet been clarified whether the measurement error (Figure 8) is due to the sensors themselves or to the measurement system. In order to isolate and correct the systematic temperature sensitivity of the wireless mote itself, a special reference arrangement was implemented using a full Wheatstone bridge composed of high precision 350  $\Omega$  (0.1%) resistors, which were connected to Port 3 of the sensor mote. This configuration allows sensor specific strain effects to be excluded and ensures that only thermal influences on the measurement electronics are detected.

The entire system was placed into the climate chamber and subjected to the same thermal cycling protocol. Since the strain gauges in the KG-2A sensors also operate with a Wheatstone bridge of approx. 350  $\Omega$ , this setup simulates the electrical behavior of such a sensor. Consequently, all recorded voltage variations can be attributed solely to temperature-related shifts in the signal conditioning circuit.

A correction function can therefore be derived from the resulting data set, which can be used to compensate the systematic temperature error of the wireless measurement system. This step is essential for improving measurement accuracy in an outdoor environment.

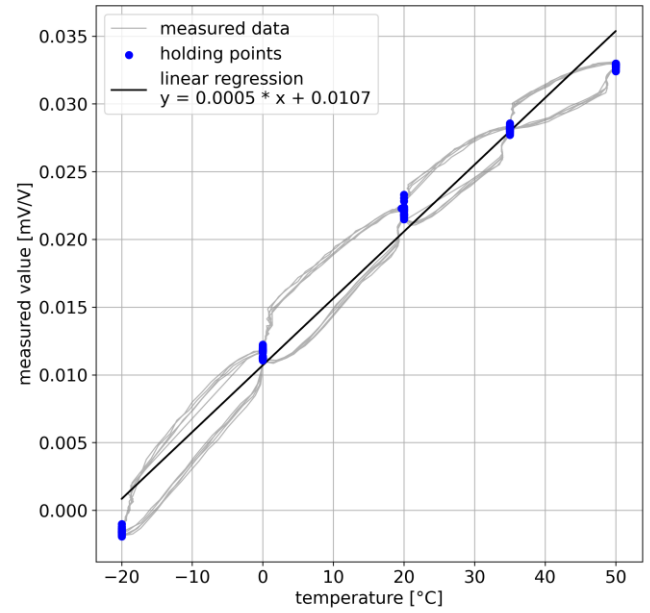


Figure 9. Results for the 350  $\Omega$  reference arrangement and linear regression for temperature compensation.

Figure 9 shows the results for the 350  $\Omega$  reference arrangement connected to Port 3. As can be seen, there is a systematic error in the measurement system over the investigated temperature range. To quantify the systematic thermal influence of the mote, a linear regression model was developed based on the stabilized measurement data at the holding points. Specifically, the final ten data points at each temperature plateau were extracted, equivalent to the final ten minutes of each holding phase. This time window was chosen to ensure that the system had reached thermal equilibrium, thereby minimizing transient effects caused by sensor response delays. The resulting data was used to fit a linear correction function with temperature as the independent variable, as shown in the following equation (3) below:

$$main_{corr} = main_{mvpv} - 0,0005 * T - 0,0107 \quad (3)$$

with:

$main_{corr}$  corrected measurement [mV/V]  
 $main_{mvpv}$  measured voltage at the sensor output [mV/V]  
 $T$  measured temperature [°C]

The corrected measurement is then inserted back into equation (2) to calculate the corrected displacement. The results of the corrected measurements can be seen in Figure 10 exemplary for KG-2A on Port 3.

As shown in Figure 10, correcting the error caused by the measuring system reduces the absolute error, but it is still relatively large. The deviation from the ideal strain curve of the steel is most likely due to the design of the sensor. The sensor itself consists largely of a steel construction, with the Wheatstone bridge presumably implemented inside the sensor via a type of spring mechanism. The steel construction therefore deforms almost identically to the steel rail in response to temperature, so that the Wheatstone bridge does not experience any significant strain.

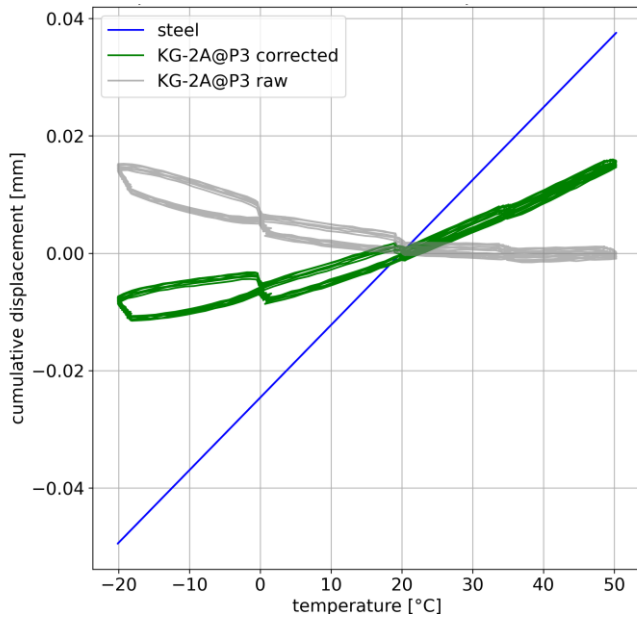


Figure 10. Corrected values on KG-2A@Port 3.

### 3.4 Sensor Temperature Compensation

The procedure for temperature compensation of the sensors is carried out in the same way as for determining the correction function for the temperature error caused by the measuring system. A linear regression over the last ten measurements at each hold point forms the basis for the correction formula for each individual sensor. The linear change in length of the steel plate is then also calculated using a linear function. From these two, a correction function (4) is created with temperature as the independent variable in order to calibrate the sensor with regard to its temperature behavior.

$$X_{cal} = X_{raw} + (k_{steel} - k_{lin.reg.}) * T - (d_{steel} - d_{lin.reg.}) \quad (4)$$

with:

$X_{cal}$	calibrated displacement [mm]
$X_{raw}$	corrected displacement acc. to equation (2) [mm]
$k_{steel}$	slope of the steel function [0.00123]
$k_{lin.reg.}$	slope of the linear regression of the raw measurements [0.0003]
$T$	measured temperature [°C]
$d_{steel}$	intercept of the steel function [-0.0244]
$d_{lin.reg.}$	intercept of the linear regression of the raw measurements [-0.0048]

Following calibration, the corrected measurement data clearly shows a trend towards the expected thermal elongation of the steel reference, as demonstrated in Figure 11 for the KG-2A sensor connected to Port 3.

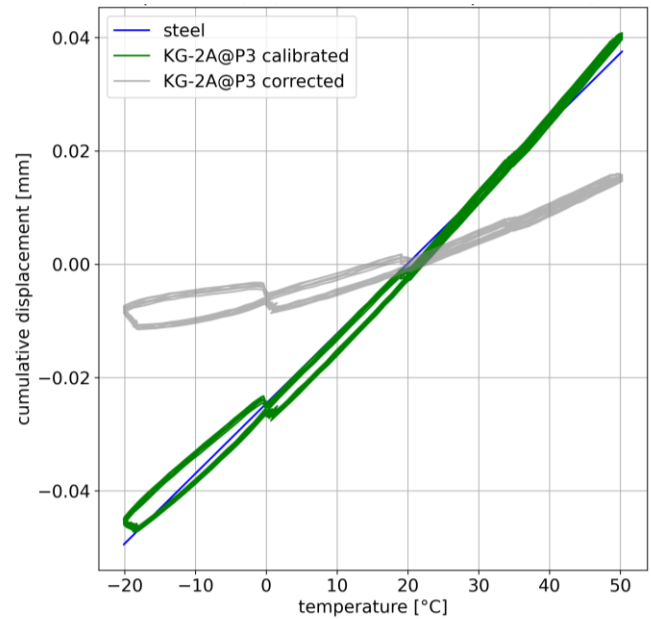


Figure 11. Calibrated displacements on KG-2A@Port 3.

### 3.5 Uncertainty Analysis

The uncertainty analysis involves evaluating each input parameter according to the classification defined in [8], distinguishing between Type A and Type B uncertainties. This procedure is also described for a comparable experiment in [9]. Type A evaluation is based on the statistical analysis of repeated measurements and is applied to the cumulative measurement value in this setup. Type B evaluation, on the other hand, relies on scientific judgement or prior information. Accordingly, the uncertainty associated with the elongation of the steel for example is classified as Type B. For practical purposes, the temperature is considered ideal. Consequently, rather than the actual temperature measured by the sensor mote, the temperature of the climate chamber (see Table 5) is used as a reference for this analysis.

Furthermore, the displacement calibration performed on a similar KG-2A sensor from [10] will be taken into account as an example.

#### Measurement error:

The measurement error is included in the data structure in Table 5 and is calculated using the following equation (5):

$$\varepsilon(t, T) = \Delta l_{measured}(t) - \Delta l_{steel}(T) \quad (5)$$

with:

$\varepsilon(t)$	error for each timestep [mm]
$\Delta l_{measured}(t)$	calibrated cumulative measurement for each timestep [mm]
$\Delta l_{steel}(T)$	expected steel elongation for each temperature [mm]

#### Type A uncertainty:

For the evaluation of Type A uncertainty, the methodology outlined in ([8], p. 22) is applied to each sensor port individually. This analysis assumes that the measurement deviations approximately follow a Gaussian (normal) probability distribution, which is a reasonable approximation for random fluctuations in sensor readings under stable

conditions. The arithmetic mean and the experimental standard deviation of the measurement error are calculated from the last ten measurements at each holding point to account for sensor response time. This allows for a detailed quantification of the repeatability and consistency of the sensor system under varying thermal conditions. Mathematically, the Type A uncertainty is expressed as follows:

$$u_i = s = \sqrt{\frac{1}{n-1} \sum_{i=1}^n (x_i - \bar{x})^2} \quad (6)$$

With:

$x_i$	individual error values in [mm]
$\bar{x}$	mean error
$s$	sample standard deviation, representing the Type A uncertainty

Following the Type A uncertainty evaluation for each port as shown in Table 6, Figure 12 illustrates the calibrated error including the standard deviation for each temperature holding point. Also shown in Table 6 is the final unweighted mean error and corresponding deviation across the entire temperature span. Figure 12 shows the error bands for raw, corrected, and calibrated data, highlighting the effect of each correction stage on measurement uncertainty.

Table 6. Type A uncertainty for each temperature holding point, after temperature compensation.

Temperature [°C]	KG-2A@Port2		KG-2A@Port3	
	$\bar{x}$ [mm]	$s$ [mm]	$\bar{x}$ [mm]	$s$ [mm]
$u_{t-20}$	0.0033	0.0002	0.0039	0.0004
$u_{t0}$	-0.0004	0.0002	-0.0011	0.0005
$u_{t20}$	-0.0020	0.0003	-0.0020	0.0006
$u_{t35}$	-0.0008	0.0004	-0.0001	0.0007
$u_{t50}$	0.0037	0.0002	0.0029	0.0004
$u_{temp\_full}$	0.00076	0.0001	0.00072	0.0002

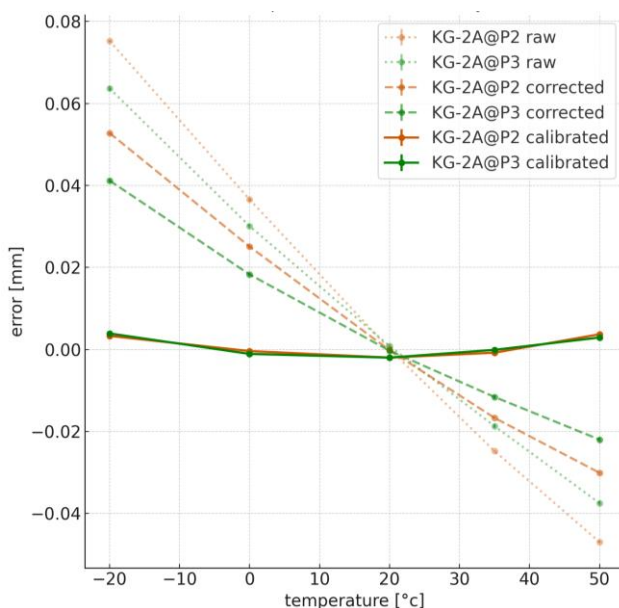


Figure 12. Error diagram for raw and compensated values.

The mean error at each holding point should be interpreted as a systematic bias (or also known as truthfulness) relative to the assumed real value. Since the total mean value of the errors across all temperatures after temperature compensation is relatively low, it is not considered in further uncertainty calculations. The decisive factor for the uncertainty assessment is therefore solely the combined consideration of the uncertainties at each hold point.

### Type B uncertainty:

In accordance with the methodology described in [[8], p. 23], Type B uncertainty is evaluated based on input quantities whose variability is derived from scientific judgement, manufacturer specifications or published data, rather than from repeated observations. As the aim of this paper is to establish a practical and field-adaptable calibration approach, not all parameter uncertainties are derived from formal traceable standards. Nevertheless, the main sources of Type B uncertainty in this setup are clearly identified and justified. Three factors are shown: the variance of the temperature coefficient of steel  $\alpha_T$ , assumed to be  $\pm 0.3 \cdot 10^{-6} \text{ 1/}^\circ\text{K}$ , the nonlinearity of each sensor (shown in

Table 3) and the displacement calibration given from an earlier analysis for a KG-2A sensor [10]. Given the variance of  $\alpha_T$  for a base length of 103 mm and a base temperature of  $20^\circ\text{C}$  the uncertainty of the elongation for every holding point is shown in Table 7 (calculated using Equation (1)).

Table 7. Uncertainty of elongation at holding points by variance of steel temperature coefficient.

Uncertainty by Temperature	$s$ [mm]
$u_{steel-20}$	0,0012
$u_{steel0}$	0,0006
$u_{steel20}$	0
$u_{steel35}$	0,00046
$u_{steel50}$	0,00092

According to the manufacturers' datasheet for the displacement sensors [7], the nonlinearity is specified as 0.2 % of the rated output (RO). Given the full-scale measurement range of  $\pm 2 \text{ mm}$  (i.e., a total span of 4 mm), the resulting nonlinearity can be interpreted as contribution to the uncertainty of  $u_{RO} = 0.002 \times 4 \text{ mm} = 0.008 \text{ mm}$ . However, the datasheet does not provide further details regarding the determination of this nonlinearity or whether the 0.2 % RO represents a standard uncertainty or a combined uncertainty with a coverage factor (e.g.  $k=2$ ). Therefore, in the absence of this information, the nonlinearity is conservatively treated as a Type B uncertainty contribution in accordance with the GUM framework.

Additionally, prior calibration using a similar KG-2A displacement sensor yielded a calibration uncertainty of  $u_{dis-cal} = 0.003 \text{ mm}$  based on measurements within a range of  $\pm 1.5 \text{ mm}$ . As no significant nonlinear behavior is expected beyond this range and there is no evidence to suggest otherwise, the same calibration uncertainty is assumed to be valid over the full range of  $\pm 2 \text{ mm}$ . This assumption is also incorporated into the Type B uncertainty budget.

The complete Type B uncertainty is calculated using equation (7) for general purposes and equation (8) for this demonstration, with the results shown in Table 8:



$$u_B = \sqrt{\sum_{i=1}^n u_i^2} \quad (7)$$

$$u_B(T) = \sqrt{u_{\alpha T}^2(T) + u_{RO}^2 + u_{dis-cal}^2} \quad (8)$$

with:

- $u_B$  combined uncertainty for Type B
- $u_i$  individual uncertainty of each factor falling in Type B,  $u_{\alpha T}(T)$  is the variation of the steel elongation depending on the temperature coefficient
- $u_{RO}$  nonlinearity given by the datasheet
- $u_{dis-cal}$  evaluated uncertainty due to displacement calibration

Table 8. Type B uncertainty by temperature.

Type B by Temperature	s [mm]
$u_{B-20}$	0.0086
$u_{B0}$	0.0086
$u_{B20}$	0.0085
$u_{B35}$	0.0086
$u_{B50}$	0.0086
$u_{Btemp-full}$	0.0086

Table 8 shows that the influence of uncertainty on the temperature coefficient is irrelevant in this experiment and will therefore not be discussed any further.

#### Combined uncertainty:

The combined standard uncertainty  $u_c$  is derived by aggregating the individual contributions of Type A and Type B uncertainties. Type A uncertainty reflects the statistical dispersion in repeated measurements, while Type B uncertainty accounts for systematic influences, such as variations in material properties and sensor nonlinearity. Assuming that these contributions are uncorrelated, the combined uncertainty is calculated using the root-sum-of-squares method, as recommended by the GUM framework [8]:

$$u_c = \sqrt{u_A^2 + u_B^2} \quad (9)$$

Substituting the Type A and Type B values for this experiment into Equation (9) the combined uncertainty for this setup is given in Table 9. It shows that for the temperature compensated values the uncertainty is determined by the factors of Type B.

Table 9. Combined uncertainty of the sensors on both ports.

[°C]	KG-2A@P2			KG-2A@P3		
	$u_A$ [mm]	$u_B$ [mm]	$u_C$ [mm]	$u_A$ [mm]	$u_B$ [mm]	$u_C$ [mm]
-20	0.0002		0.0086	0.0004		0.0086
0	0.0002		0.0086	0.0005		0.0086
20	0.0003	0.0086	0.0086	0.0006	0.0086	0.0086
35	0.0004		0.0086	0.0007		0.0086
50	0.0002		0.0086	0.0004		0.0086
Full Span	0.0001	0.0086	0.0086	0.0002	0.0002	0.0086

If the values for Type A and Type B for this experiment are inserted into equation (9), the combined uncertainty is obtained as shown in Table 9. It can be seen that the combined uncertainty for the temperature-compensated values is essentially determined by the Type B uncertainties.

#### Expanded uncertainty:

To express the measurement uncertainty with a defined level of confidence, the expanded uncertainty  $U$  is calculated by multiplying the combined standard uncertainty  $u_c$  by a coverage factor  $k$  as shown in Equation (10):

$$U = k * u_c \quad (10)$$

with:

- $U$  expanded uncertainty
- $k$  coverage factor chosen with
- $u_c$  combined uncertainty

In this study, a coverage factor of  $k=2$  is applied, which corresponds to an approximate 95% confidence level under the assumption of a normal distribution, as recommended in [8]. The resulting expanded uncertainty, as shown in Table 10, defines an interval around the measurement result within which the true value is expected to lie with a high degree of probability. This value is crucial for ensuring the reliability of decision thresholds and condition assessments in the presence of measurement variability, and serves as a practical limit for interpreting sensor data in structural health monitoring applications.

Table 10. Expanded uncertainty of the sensors on both ports

	$u_c$ [mm]	$U$ [mm]
KG-A2@Port 2	0.0086	0.0172
KG-A2@Port 3	0.0086	0.0172

## 4 DISCUSSION AND RESULTS

Previous studies have shown that sensor systems exposed to temperature fluctuations can exhibit irregular and inconsistent behavior with regard to the measured value to be recorded. In the present study, laboratory tests with wireless displacement sensors under the influence of temperature are carried out as examples. The displacement sensors are fixed to a steel plate in order to simulate guided deformation similar to an application on steel or reinforced concrete components with similar thermal expansion behavior.

Measurements (Figure 8) with wireless sensor nodes and displacement sensors have shown that the raw data on deformation deviates significantly from the expected thermal deformation of the steel. In addition, a temperature-dependent sensor response was observed during heating and cooling, which raises the question of how temperature influences and gradual changes can be handled and compensated for in on-site applications. Since convergence and reproducibility are achieved at different temperature holding points, it is possible to perform temperature compensation. In the present case, linear temperature compensation proved to be suitable for compensating for the influences from both the measuring system itself and the connected sensors. However, such temperature compensation is only possible if the sensors stabilize at a consistent value after reaching thermal

equilibrium. A special feature here is that the sensors under investigation themselves exhibit temperature expansion, which overlaps with the deformation to be measured on the component. It is therefore relatively difficult to carry out highly accurate measurements if the sensor temperature and the component temperature are unknown or even different, which can certainly occur in practice. This is particularly important when displacement transducers and discrete measuring paths of several centimeters are used to measure crack width changes in the hundredth of a millimeter range, as sensor and component expansion accompany the change in crack width. The same applies when displacement transducers are used to determine expansion with accuracies of approximately 10  $\mu$ strain. This article has explained that the influences on measurement uncertainty can be very diverse. These range from measurement uncertainties of the measuring system itself, including uncertainties from the power supply, to uncertainties of the connected sensors, to measurement uncertainty regarding the sensor mounting on the object and a wide range of other external influences.

In order to quantify and correct the influence of the measuring system, a special reference arrangement with a Wheatstone bridge consisting of identical high-precision resistors was implemented. This setup, which excludes mechanical components and deformations, shows the inherent temperature sensitivity of the mote and serves as the basis for a sensor node-specific correction function that ultimately also includes the individually connected sensors. For this purpose, temperature compensation functions were derived based on measurements at different temperature plateaus and measurement uncertainties were determined.

A comprehensive uncertainty analysis based on the GUM framework shows that, after calibration, the dominant contribution to the total uncertainty is of type B, provided that the uncertainty contribution of type A could be significantly reduced by applying temperature compensation functions (determined by calibration in temperature change tests). The final expanded measurement uncertainty for the measurement system shown with two displacement sensors is therefore less than 0.02 mm (20  $\mu$ m), whereby without temperature compensation, a measurement uncertainty of at best approximately 50 to 100  $\mu$ m can be assumed, depending on the temperature range.

## CONCLUSIONS

An important finding was that the thermal response of the sensor housing and mounting components largely matched that of the monitored steel structure. This resulted in a partial cancellation of thermally induced displacement, which highlights the need for proper system calibration and temperature compensation. A correction function derived from a temperature-controlled reference experiment and validated using stable measurement intervals effectively reduced systematic errors and extended uncertainty to less than 20  $\mu$ m. Furthermore, the comparison of the two identically installed sensors revealed distinct response behaviors in the raw measurements. This indicates that in this case individual calibration is recommended for each sensor, rather than relying on batch calibration procedures.

This study emphasizes the importance of considering the sensor and its mechanical integration as a unified measurement system. By demonstrating a reproducible calibration routine that considers electronic, mechanical and environmental influences, this study contributes to the practical standardization of wireless SHM devices. It therefore represents a step forward in providing information on the accuracy of sensors and sensor systems under real-world conditions. In the past, this was often not sufficiently taken into account, leading to misinterpretations of the measured values.

## REFERENCES

- [1] A. Deivasigamani, A. Daliri, C. H. Wang and S. John., A Review of Passive Wireless Sensors for Structural Health Monitoring, *Modern Applied Science* Vol. 7, No. 2 ISSN 1913-1844, <http://dx.doi.org/10.5539/mas.v7n2p5>, (2013).
- [2] Siew, Zhan & Wong, Chen & Kiring, Aroland & Chin, Renee & Teo, Kenneth. (2012). Fuzzy logic based energy efficient protocol in wireless sensor networks. *ICTACT J. Commun. Technol. (IJCT)*. 3. 639-645. 10.21917/ijct.2012.0091.
- [3] M. Krüger, W. Lienhart, Präventives Bauwerksmonitoring mit intelligenten, vernetzten Systemen PreMainSHM: Leitfaden Bauwerksmonitoring, Graz, Austria, (2025).
- [4] GeoSphere Austria, 2024: Monatlicher Klimabericht Österreich für das Jahr 2024, Vienna, Austria, 2025 URL: <https://www.zamg.ac.at/zamgWeb/klima/klimaruueckblick/archive/2024/wiewars24.pdf> (2024)
- [5] Austrian Standards International. ÖNORM B 991-1-5: Allgemeine Einwirkungen – Temperatureinwirkungen, Wien: Austrian Standards International, 2012.
- [6] TTI GmbH – TGU Smartmote, URL: <https://smartmote.de/joomla/de/>, Stuttgart, 2025
- [7] TML – Tokio Measuring Instruments Laboratory, URL: <https://tml.jp/e/product/transducers/kg.html>, Tokio, 2025
- [8] BIPM, IEC, IFCC, ILAC, ISO, IUPAC, IUPAP, and OIML. Evaluation of measurement data — Guide to the expression of uncertainty in measurement. Joint Committee for Guides in Metrology, JCGM 100:2008. doi:10.59161/JCGM100-2008E.
- [9] Zhao Y, Zhang F, Ai Y, Tian J, Wang Z. Comparison of Guide to Expression of Uncertainty in Measurement and Monte Carlo Method for Evaluating Gauge Factor Calibration Test Uncertainty of High-Temperature Wire Strain Gauge. *Sensors* (Basel). 2025 Mar 6;25(5):1633. doi: 10.3390/s25051633. PMID: 40096503; PMCID: PMC11902841.
- [10] H. Pongratz, IMBT-TU Graz, Calibration of displacement sensor KG-2A, 2023

# eNodes: GNSS Time-Synchronised Wireless Accelerometer Measurement Nodes capable of operating indoors

Ki-Young Koo, Miaomin Wang, Zuo Zhu, James Brownjohn  
<sup>1</sup>University of Exeter, UK

**ABSTRACT:** This paper presents time-synchronized wireless acceleration measurement nodes, named eNodes, capable of operating indoors by preserving timing information with a temperature-controlled crystal oscillator (TCXO). While GNSS-based time synchronization is commonly effective for outdoor measurements with available GNSS signals, it does not work indoors, such as inside high-rise buildings or box-girder bridges. To extend GNSS-based time synchronization to indoor applications, timing information is acquired outdoors both before and after the indoor deployment. The TCXO maintains this timing information accurately ensuring a stable and accurate frequency. Each eNode is equipped with an Epson M352 MEMS accelerometer, which offers extremely low noise of  $0.2 \mu\text{g}/\sqrt{\text{Hz}}$ , and an ESP32 microprocessor unit. Real-time data transmission is enabled by a Wi-Fi mesh network. A series of experiments were conducted to evaluate the time-synchronization accuracy of the eNodes.

**KEY WORDS:** Structural Health Monitoring, Wireless Sensor, Accelerometer.

## 1 INTRODUCTION

It is a challenging task to measure acceleration responses of large infrastructures such as long-span bridges, or high-rise buildings, due to long easy-to-tangle many wires between sensors and a DAQ system, up to several km's. As an alternative to the conventional wired DAQ system, the idea of wireless sensors emerged a few decades ago, but it has brought a side-effect, the time-synchronisation problem between the nodes for a proper identification of mode-shapes.

There have been a few wireless sensors developed and available commercially or academically. To the best knowledge of the authors, they were either not providing the accuracy of time-synchronisation, or not readily available to buy. Recently a few manufacturers emerged to provide time-synch'ed wireless nodes (from Sensquake, or Guralp), however their main application was not perfectly aligned with the task of campaign-type ambient vibration measurement of infrastructures.

This paper presents a realisation of wireless accelerometer nodes focusing on campaign type field measurement applications on civil infrastructures or high-rise buildings. The GNSS based time-synchronisation [1] method was used and extended to indoor measurements by combining the GNSS method with a stable clock source.

## 2 WIRELESS ACCELEROMETER NODES

### 2.1 Accelerometer

The accelerometer node, as shown in Figure 1, consists of a M5Stack Core2 based on esp32, a GNSS module (M5Stack GPS V2), an accelerometer module for an Epson M-A352 sensor, a battery module (M5Stack Battery 13.2), and battery charging module (M5Stack M5Go). The company M5Stack provides a convenient modular structure for their MPU and modules, so that a user can easily add a feature by added another layer of module stacked below the M5Stack Core2. The Core2 MPU provides a 320x240 pixels LCD and a touchpad, enabling a convenient control and operation of the sensor node.

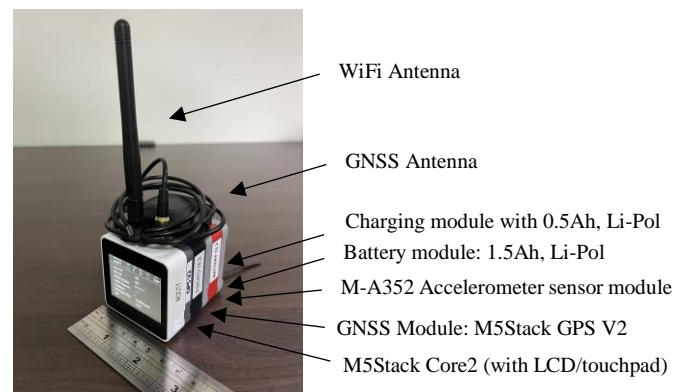


Figure 1. Accelerometer node eNode

Figure 2 shows Epson M-A352 sensor module, which is interconnected to Core2 MPU with 30 GPIO pins as well as the modules stacked together. Epson M-A352 provides the noise floor of  $0.2 \mu\text{g}/\sqrt{\text{Hz}}$ , which is extremely low, hence out-performing for low-vibration measurement of civil infrastructures. M-A352 is a digital sensor with a built-in ADC and output data rates range from 50 Hz to 1000 Hz.



Figure 2. Epson M-A352 Accelerometer module: (left) Top View, and (right) Bottom View





Figure 3. M5Stack GPS V2 module: (left) Top View, and (right) Bottom View

Figure 3 shows the M5Stack GPS V2 module, which plays the critical role for time-synchronisation. This outputs NMEA sentences and PPS (Pulse-Per-Second) signals to the Core2 MPU, which combines these outputs to get a highly accurate timestamping on each measured acceleration. Details method is shown in [1].

Espressif IoT Development Framework (ESP-IDF) was used, rather than the Arduino platform, mainly for the full control on the lower-level timing operations of esp32. In addition, Mesh-Lite was used to utilise a WiFi mesh network, extending maximum allowable distance between nodes, by multi-hops.

### 3 SYNCHRONISATION ACCURACY

Four different experiments were carried out from the ideal condition (Case #1), to the most realistic condition (Case #4) of the indoor capable eNodes with a temperature variation as shown in Table 1.

Table 1. Experimental Cases of timestamping error measurement

Case #	GNSS signal	Clock-Source	Temp. dev.
1	always	GPTimer (10MHz)	No
2	always	TCXO (32.768kHz) for RTC	No
3	limited	TCXO (32.768kHz) for RTC	No
4	limited	TCXO (32.768kHz) for RTC	Yes

#### 3.1 Case #1: Continuous GNSS signals with a GPTimer

Accuracy of time synchronisation for the hardware of the Core2 and the GNSS module was measured using the setup shown in Figure 4. This setup assumed that GNSS signals were always available with a high-frequency General Purpose Timer (GPTimer) of 10 MHz as the basis of the ideal time-sync performance for a comparison with the following Cases #2-4.

A common 10 Hz trigger signal was generated by a function generator, fed to the two identical nodes of Core2 and M5Stack GPS module. Each node was programmed to timestamp each trigger signal. GNSS signal was available all times during the experiment. In theory both nodes should produce the exactly same timestamps, but in reality they differ slightly. Their difference was measured and shown in Figures 5 and 6.

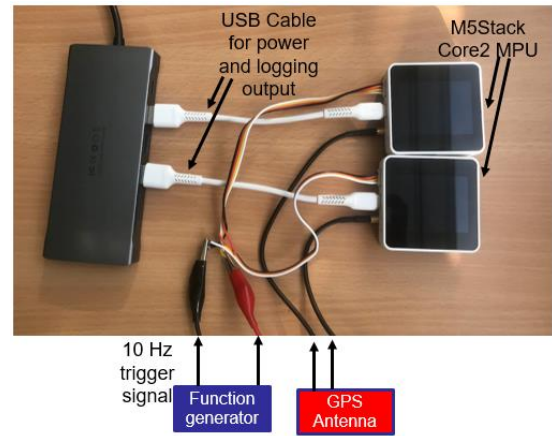


Figure 4. Experimental setup for measuring time-sync accuracy for eNode

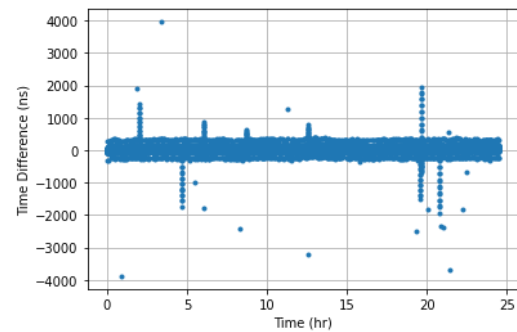


Figure 5. Case #1: Difference in timestamps by two identical nodes

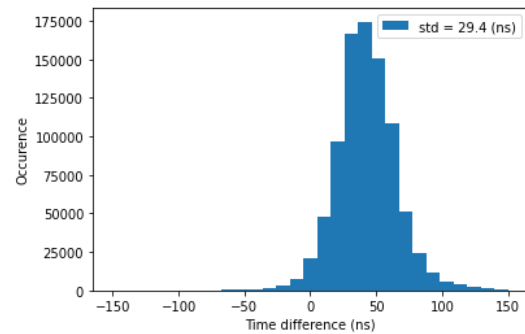


Figure 6. Case #1: Histogram of difference in the timestamps

#### 3.2 Case #2: Continuous GNSS signals with a TCXO

Frequency of General Purpose Timer used in Case #1 is influenced by temperature variation, which drastically reduces timestamping accuracy during the period without GNSS signals. There are different ways to improve this using OCXO (Oven Controller Crystal Oscillator) or TCXO. In this study, a TCXO with 32.768 kHz was used as the clock-source for the Real-Time Clock of ESP32 to replace GPTimer of Case #1.

Figure 7 shows the timestamping difference over 2 hours period, showing the step-wise errors between  $\pm 61$  usec. This can be explained two clock-oscillations error in the RTC clock-counter, which only increases by 2. One clock oscillation of a 32.768 kHz clock corresponds to 30.5 usec, and two clock oscillations correspond to 61 usec.

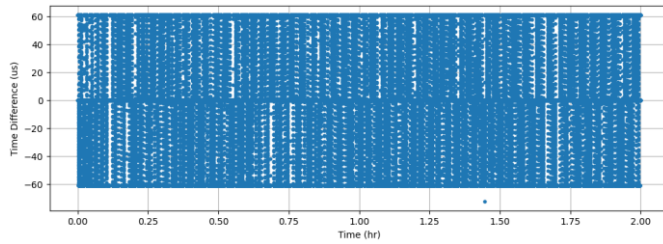


Figure 7. Case #2: Difference in timestamps by two identical nodes with TCXOs

### 3.3 Case #3: Limited GNSS signals with a TCXO

When eNodes are deployed indoors, GNSS signals becomes unavailable. In this Case #3, it was assumed that GNSS signals were missed for 1 hour in the beginning and becomes available again afterwards. Due to the deviation of TCXO, the two timestamps by the identical nodes differ slightly more than Case #1. Figure 8 shows the measured time-stamping difference in the beginning, followed by the normal pattern observed in Figure 7 in the last half hour.

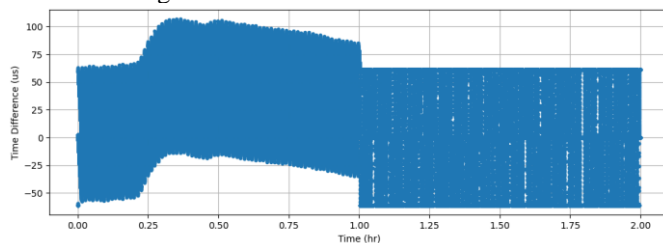


Figure 8. Case #3: Difference in timestamps by two identical nodes with TCXOs

### 3.4 Case #4: Limited GNSS signals with a TCXO under temperature variation

Temperature variation is a crucial factor to reduce timestamping accuracy in the nodes. TCXOs are designed to compensate the variation, but inevitably capable to do up to a certain degree. In this case, the timestamping difference under temperature variation was investigated.

In this Case #4, a temperature variation was imposed on one node by putting it into a refrigerator whilst the other node was kept in room temperature, resulting in 14°C temperature difference. The measured timestamp difference is shown in Figure 9. It was clearly seen that additional error was introduced by temperature variation to the maximum timestamp difference of about 250 usec.

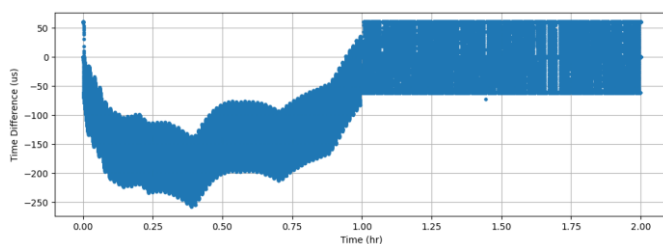


Figure 9. Case #4: Difference in timestamps by two identical nodes with TCXOs

## CONCLUSION

In this study, the time-sync accuracy of indoor capable acceleration nodes were measured. With the used hardware of 32.768 kHz TCXO and ESP32, it was found that the maximum of 250 usec timestamping difference was observed for an hour measurement under 14°C ambient temperature difference.

Further study will carry out to validation tests including a laboratory OMA on a shear building frame and a field OMA for a high-rise building.

## REFERENCES

- [1] K. Koo, D. Hester, S. Kim, time Synchronization for Wireless Sensors Using Low-Cost GPS Module and Arduino 2019 Frontiers of Built Environment, Vol. 4, Article 82.



# Smart Sensing Enhanced Resilient Civil Infrastructures



# Study on the Propagation Law of Magnetic Induction Signals for Wireless Communication in Underground Structures

Yiyan Zhang<sup>1</sup>, Dongming Zhang<sup>1,3</sup>, Jingkang Shi<sup>2</sup>, Mingtao Chen<sup>4</sup>, Erwu Liu<sup>4</sup>

<sup>1</sup> Tongji Univ, Dept Geotech Engr, Shanghai 200092, Peoples R China;

<sup>2</sup> Fuzhou Univ, Coll Civil Engr, Fuzhou 350108, Peoples R China

<sup>3</sup> Tongji Univ, Key Lab Geotech & Underground Engr, Minist Educ, Shanghai 200092, Peoples R China;

<sup>4</sup> Tongji Univ, Dept Informat & Commun Engr, Shanghai 201804, Peoples R China

email: 1710704@tongji.edu.cn.

**ABSTRACT:** Despite advancements in electromagnetic wave-based communication, challenges such as high attenuation, medium variability, and large antenna requirements persist. Magnetic induction (MI) communication has emerged as a promising alternative, offering stable transmission characteristics and reduced near-field path loss. While previous studies have explored MI waveguide models and relay coil applications, experimental validation of through-the-ground MI transmission, particularly in homogeneous media, remains limited. This study investigates magnetic signal propagation in uniform underground environments through numerical simulations and experimental validation. A finite element model was developed using COMSOL to simulate magnetic signal transmission, focusing on coil geometry and medium properties. Experimental validation was conducted using a custom-built outdoor platform, where mutual inductance coils were employed to measure signal transmission in both air and soil. Key parameters, including coil spacing and medium permeability, were analyzed to evaluate path loss. Results demonstrate excellent agreement between simulations and experiments, confirming that soil's air-like permeability results in minimal path loss over short distances. The study highlights permeability as the dominant factor in signal attenuation, with soil moisture and composition showing negligible effects. These findings validate the theoretical framework for MI transmission in homogeneous media and provide practical insights for optimizing MI-based communication systems in applications such as agricultural monitoring and underground utility networks. Future work should focus on long-distance transmission and the impact of enhanced power levels to further refine system performance in real-world scenarios.

**KEY WORDS:** Magnetic Induction; Signal Propagation; Underground Communication; Path Loss; Steel fabric.

## 1 INTRODUCTION

Despite advancements in electromagnetic wave-based communication, challenges such as high attenuation, medium variability, and large antenna requirements persist [1]. Magnetic induction (MI)-based communication has emerged as a promising alternative, demonstrating stable transmission characteristics and reduced near-field path loss [2][3]. Early studies proposed MI waveguide transmission models with relay coils to extend communication range, successfully applied in underground pipeline monitoring [4].

Subsequent research expanded MI communication models, exploring interactions with underground conductive structures [5] and developing adaptive environmental sensing networks. Studies have improved MI transmission devices by analyzing coil behavior and optimizing system parameters [6]. More recent advancements include rotating permanent magnet pair (RPMP) antenna arrays for extremely low-frequency transmission [7] and tightly wound helix-toroidal coils for underground structural monitoring [8][9].

While significant progress has been made, gaps remain in experimental validation of through-the-ground MI transmission, particularly regarding the impact of soil eddy currents and complex underground conductive structures like rebar networks. To address these gaps, this study develops a detailed finite element model of rebar mesh, analyzing key parameters such as spacing, influence range, and diameter on MI signal path loss. Comparative experiments through soil and

air further validate that soil's impact on MI transmission is minimal over short distances. This work highlights the need for expanded long-distance testing with enhanced transmission power to better understand soil's effect in practical scenarios.

## 2 METHODS

To investigate the propagation law of magnetic signals in underground structures, this study conducted a comparative analysis between numerical simulations and experimental investigations.

The research consists of two phases: (1) numerical simulation of signal transmission in homogeneous media, and (2) experimental validation of signal transmission in homogeneous media of signal transmission in homogeneous media.

### 2.1 numerical simulation

Firstly, this study performs parametric modeling of the magnetic signal transmission process based on COMSOL finite element software, establishes a magnetic induction signal simulation platform, and conducts multi-parameter analysis of the propagation characteristics of the magnetic signal.

First, a numerical simulation of magnetic signal propagation through a uniform medium is performed:

The coil domain consists of two concentric ring geometries: the primary coil and the secondary coil. These are controlled by the parameters: the Inner radius  $r_2$ , the Outer radius  $r_1$ , the

number of turns  $N$ , and the coil center-to-center distance  $d$ . The medium domain is a spherical region through which the signal is transmitted, and it is controlled by the parameter: region radius  $R$ .

The coil domain material is copper, while the material of the medium domain is the propagation medium (soil/air). The material parameters include relative permeability, relative permittivity, and electrical conductivity.

An excitation voltage  $V_0 = \sin(\omega t)$  is applied to the primary coil, where  $\omega = 2\pi f$ ,  $f = 50\text{Hz}$ . The geometric center of the coil set is placed at the center of the simulation domain, as shown in Figure 1 Numerical Model of Magnetic Signal for Mutual Inductance Coils.

Based on the equipment in the reference experimental platform, the model parameters are set as Table 1 Simulation parameter value table:

Table 1 Simulation parameter value table

Parameter	Value	Description
$r_1$	12cm	Outer radius
$r_2$	1cm	Inner radius
$N$	500	Number of coil turns
$d$	40cm	distance between coils
$R$	5m	Radius of the medium domain
$\mu$	1	Relative permeability of the medium

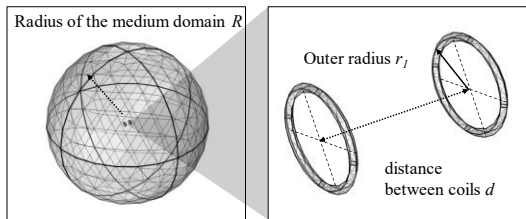


Figure 1 Numerical Model of Magnetic Signal for Mutual Inductance Coils

## 2.2 experimental validation

To investigate the propagation characteristics of magnetic signals in underground environments, validate the conclusions from theoretical and numerical simulations, and prepare for subsequent performance verification of magnetic signal equipment, an outdoor experimental platform for magnetic induction signal transmission was constructed, as shown in Figure 2.

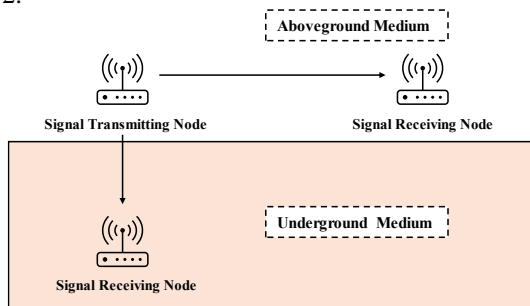


Figure 2 Schematic Diagram of Outdoor Transmission Experiment for Magnetic Induction Signal Using Mutual Inductance Coils

The equipment used in this platform includes

- (1) Coil 1: Diameter 24 cm, 500 turns
- (2) Coil 2: Diameter 24 cm, 500 turns
- (3) Signal Generator (RIGOL-DG2052)
- (4) Regulated Power Supply (ZHAOXIN-PS-23005D)
- (5) Oscilloscope (Tektronix-TBS 2000 SERIE)



Figure 3 Outdoor Transmission Experiment Platform for Magnetic Induction Signal Using Mutual Inductance Coils

First, we connect the signal generator to the primary coil as the signal transmission node and the oscilloscope to the secondary coil as the signal receiving node, placing them in an interference-free open field (as shown in Figure 3 Outdoor Transmission Experiment Platform for Magnetic Induction Signal Using Mutual Inductance Coils). The two coils are fixed on a flat surface using mounting devices, ensuring that the coil axes are aligned and the coil planes are parallel. The distance between the coils is measured before each experiment.

The signal generator is used to apply a 10V excitation to the transmitting coil (left side of Figure 3), which induces a current in the receiving coil that is captured by the oscilloscope.

By varying the coil spacing and recording the peak-to-peak voltage on the oscilloscope, the results can be calculated and visualized as shown in the figure.

To verify that the magnetic signal does not experience additional path loss when passing through soil, we conducted an underground experiment similar to the above-ground magnetic induction signal transmission experiment.

In the underground experiment, the excitation of the coil and the reception of the magnetic signal were the same as in the above-ground experiment. Here, we mainly describe the control of the transmission distance and coil attitude during the experiment.

First, a 31 cm deep pit was dug in the open field, and the bottom surface was leveled. The receiving coil was placed at the center of the pit, and a 1 cm thick layer of soil was added to ensure the receiving coil was just covered by the soil (with the receiving coil's small diameter of 1 cm). Then, a 10 cm thick layer of soil was added, and the surface was leveled again. The transmitting coil was placed at the center of the pit, excitation was applied to the transmitting coil, and the peak-to-peak value from the oscilloscope was recorded. This procedure was repeated for depths of 10 cm, 20 cm, and 30 cm to measure the magnetic signal path loss, as shown in Table 2 Path Loss Above and Below Ground with 10V Transmission Signal.

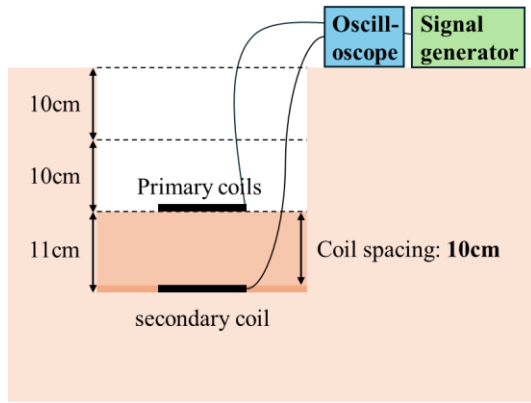


Figure 4 Schematic of the mutual inductance coil magnetic induction signal through-ground transmission experiment

An alternating signal generates a sinusoidal alternating magnetic field through the primary coil. The change in the magnetic field induces an electromotive force in the secondary coil, which in turn generates the corresponding induced signal. The voltage signal at the receiving end is recorded at different distances, and by combining the coil resistance, the induced power of the signal can be calculated, which allows for the calculation of magnetic signal transmission loss. The above-ground experiment is shown in Figure 4 Schematic of the mutual inductance coil magnetic induction signal through-ground transmission experiment.

### 3 RESULTS AND ANALYSIS

#### 3.1 Propagation in Homogeneous Media

First, a trial calculation is performed under the conditions of a coil spacing  $d=50\text{cm}$  and a uniform medium. The path loss is  $44.16\text{dB}$ , which is in good agreement with the theoretical value. The model performs well, producing the simulation cloud maps shown in Figure 5, Figure 6 Magnetic induction strength contour plot between coils

Next, the coil spacing  $d$  is scanned in the range of  $20\text{cm}$ - $200\text{cm}$  with a step size of  $10\text{cm}$ , keeping all other parameters constant. The path loss is calculated for the model and compared with experimental values (see Figure 8).

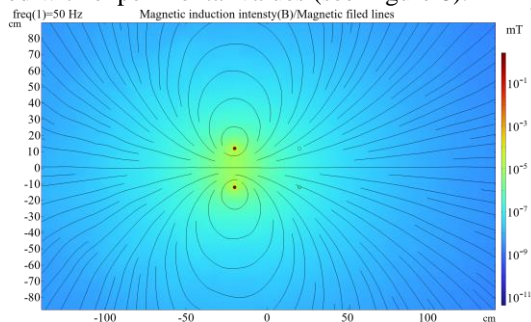


Figure 5 Magnetic induction strength contour plot of the coils cross-section

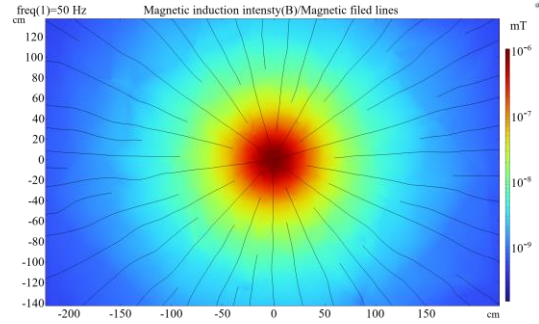


Figure 6 Magnetic induction strength contour plot between coils

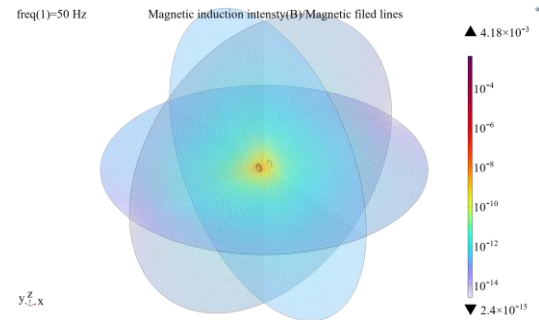


Figure 7 Magnetic Induction Intensity Cloud Map Between Coils

The simulation data of magnetic induction signal variation with coil spacing is shown in Figure 8 Path loss variation with coil distance.

The experimental values generally align well with the simulation results; however, some discrepancies are present due to the following reasons:

- (1) **Background noise interference:** At longer distances, unshielded noise added to the reception power calculation.
- (2) **Coil attitude:** During adjustments for distance, changes in coil angle affected the results.

As a result, the power path loss in the above-ground experiment follows a distance-based decay of approximately the fifth power, while the theoretical equation suggests a sixth power, resulting in some discrepancy. It is believed that with improvements to the filtering equipment, a better match can be achieved.

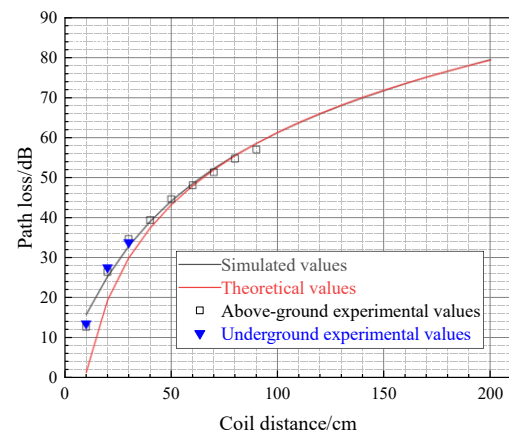


Figure 8 Path loss variation with coil distance



By comparing the path loss in the above-ground and underground experiments in Table 2 Path Loss Above and Below Ground with 10V Transmission Signal, and excluding experimental errors, it can be observed that the soil has no effect on the path loss of the magnetic signal, which is consistent with the theory.

Table 2 Path Loss Above and Below Ground with 10V Transmission Signal

Depth/d	Above Ground Experimental Value	Below Ground Experimental Value
10cm	12.70	13.50
20cm	26.40	27.51
30cm	34.65	33.79

#### 4 CONCLUSION

This study validates magnetic signal propagation theory in uniform underground media through numerical simulations and experimental measurements. The results demonstrate low path loss in soil environments due to their air-like permeability characteristics. Experimental data show excellent agreement with theoretical models, confirming permeability as the dominant factor in signal attenuation, while soil moisture and composition exhibit negligible effects. The consistent correlation between simulation and experimental results establishes a reliable framework for predicting magnetic signal behavior in homogeneous underground environments. These findings provide fundamental insights for developing magnetic induction-based communication systems in applications such as agricultural monitoring and underground utility networks.

#### REFERENCES

- [1] KISSELEFF, S., AKYILDIZ, I. F. & GERSTACKER, W. H. 2018. Survey on Advances in Magnetic Induction-Based Wireless Underground Sensor Networks. *IEEE Internet of Things Journal*, 5, 4843-4856.
- [2] SUN, Z. & AKYILDIZ, I. F. Underground Wireless Communication Using Magnetic Induction. 2009 IEEE International Conference on Communications, 14-18 June 2009 2009. 1-5.
- [3] SUN, Z. & AKYILDIZ, I. F. 2010. Magnetic Induction Communications for Wireless Underground Sensor Networks. *Ieee Transactions on Antennas and Propagation*, 58, 2426-2435.
- [4] SUN, Z., WANG, P., VURAN, M. C., AL-RODHAAN, M. A., AL-DHELAAN, A. M. & AKYILDIZ, I. F. 2011. MISE-PIPE: Magnetic induction-based wireless sensor networks for underground pipeline monitoring. *Ad Hoc Networks*, 9, 218-227.
- [5] TAN, X. & SUN, Z. On environment-aware channel estimation for wireless sensor networks using Magnetic Induction. 2017 IEEE Conference on Computer Communications Workshops (INFOCOM WKSHPS), 1-4 May 2017 2017. 217-222.J.
- [6] LIU, Z. & SHEN, L. 2018. Channel Modeling and Simulation of Wireless Underground Sensor Networks Based on Magnetic Induction Technology. *Journal of System Simulation*, 30, 1102-1108.
- [7] LIU, Y., XIAO, D., GONG, S., WU, J., JIANG, W. & HONG, T. 2024. Magneto-Mechanical Antenna Array for Extremely Low-Frequency Communication. *IEEE Antennas and Wireless Propagation Letters*, 23, 4189-4193.
- [8] MA, H., LIU, E., FANG, Z., WANG, R., GAO, Y., YU, W. & ZHANG, D. 2024. Fast-Fading Channel and Power Optimization of the Magnetic Inductive Cellular Network. *IEEE Transactions on Wireless Communications*, 23, 15096-15111.
- [9] MA, H., LIU, X., PAN, Y., SUN, Y. & HUANGFU, J. Pipeline Monitoring Based on Magnetic Inductive Coils Detection System. 2024 Photonics & Electromagnetics Research Symposium (PIERS), 21-25 April 2024 2024. 1-5.

# Smart Pavement Subsurface Monitoring with Distributed Embedded Passive RF Sensor Network

Kent X. Eng<sup>1</sup>, Zygmunt J. Haas<sup>2</sup>, Samir R. Das<sup>3</sup>, Petar Djurić<sup>4</sup>, Milutin Stanačević<sup>3</sup>, Branko Glisic<sup>1</sup>

<sup>1</sup>Princeton University, Department of Civil and Environmental Engineering, Princeton, NJ, 08544, USA

<sup>2</sup>University of Texas at Dallas, Department of Computer Science and Cornell University, School of Electrical and Computer Engineering, Richardson, TX, 75080, USA

<sup>3</sup>Stony Brook University, Department of Electrical and Computer Engineering, Stony Brook, NY, 11794, USA

<sup>4</sup>Stony Brook University, Department of Computer Science, Stony Brook, NY, 11794, USA

email: ke9722@princeton.edu, zjh130030@utdallas.edu, samir@cs.stonybrook.edu, petar.djuric@stonybrook.edu, milutin.stanacevic@stonybrook.edu, bglisic@princeton.edu

**ABSTRACT:** Pavement subsurface deterioration can lead to catastrophic road failures, often caused by long-term settlements and moisture accumulation. These effects develop gradually and are difficult to identify through manual inspection. Although structural health monitoring (SHM) systems have been developed to address these challenges, most are insufficient to collect 3D spatial information due to their limitations. Current systems primarily focus on surface and base courses, neglecting subsurface courses which sustain loads and provide stability. Therefore, it is essential to develop a long-term and scalable monitoring system for subsurface courses. Radio frequency sensing system has great potential to fill the gap.

This study aims to further quantify the uncertainty of using distributed embedded passive radio frequency (RF) sensors in pavement subsurface courses. Laboratory experiments were conducted to investigate the uncertainty sources of the relationships between channel information and structural changes. Key challenges include correlating collected data with subsurface changes and finding the sources of uncertainties.

The results demonstrate the effect of system topology on the relationships between channel information and structural changes. These prove the system's applicability in subsurface spatial monitoring. By addressing implementation challenges and decoupling monitored parameters, the system could be further advanced for real-world deployment

**KEY WORDS:** Structural health monitoring; Transportation monitoring; Pavement monitoring; RF sensing; Sensor network

## 1 INTRODUCTION

Pavement road structures are essential and critical infrastructure to the urban transportation system. However, aging, massive urbanization, and overuse contribute to distress and even catastrophic failure events. For example, part of California State Route 1, which was 150 feet long, was washed out in a landslide, which led to the total cost of repairing and clearing being \$11.5 million [1]. Meanwhile, the ASCE report card states that the grading evaluation on pavement roads is D+ [2]. Structural health monitoring systems can identify the pavement road's deterioration or damage at an early stage, which reduces economic loss and increases life safety.

Structural health monitoring (SHM) systems face a challenge in extracting large-scale spatial information in pavement subsurface courses at a reasonable cost. Current techniques are mainly limited to extracting one-dimensional or two-dimensional information from the structure [3]. However, extracting three-dimensional information gathered throughout the volumes of structural material, such as detection, location, and quantification of distress behaviors (e.g., damage, deterioration, or loss of performance) at an early stage is impossible using current SHM techniques. Meanwhile, most SHM systems primarily focus on the surface and base courses instead of the subsurface course, which sustains loads and provides stability. Therefore, it is essential to develop a 3D spatial monitoring system for long-term and scalable subsurface course monitoring. The recent developments in radio frequency (RF) sensing can be the potential solution to the challenges.

Recent research on radiofrequency (RF) sensing has resulted in hardware systems potentially suitable for the use in subsurface SHM [4]. RF sensors leverage channel information to monitor the 3D distribution of key parameters. A recent experiment demonstrates the feasibility of monitoring deformation and water content [5]. However, the uncertainty of monitoring deformation and water content has never been investigated. This study aims to investigate the uncertainty of monitoring deformation and water content using an RF sensing system.

## 2 UNCERTAINTY IN DECODING

Previous studies have shown that the displacement of sensors (measurand) is linearly related to the phase shift (encoding parameter) of the reflected signals. However, in the implementation scenarios, the exciter, which sends power to sensors, is mobile, and the sensors may have different initial mutual distances. The linear relationship, necessary to decode displacement from RF phase shift, can be affected by these different exciter locations and the initial distances between sensors. Therefore, the uncertainty in encoding function due to variable exciter locations and the initial distances between the sensors has to be investigated.

### 2.1 Method

A set of experiments was performed to determine the change of displacement between sensors in various 1D settings, where the backscatter RF signal propagated through the air. The goal of the experiment setup was to verify the effects of exciter locations and the initial distance of sensors. The 1D experiments consisted of two sensors and one exciter. The

exciter was used to power the two sensors wirelessly. One sensor was placed on the mobile tripod which was installed on a camera slider such that the mobile tripod was displaced by a linear actuator along the slider. Another sensor was placed on a stationary platform. The two sensors were set up with three different initial distances  $D$ : 30 cm, 60 cm, and 126 cm. At each setup of  $D$ , the mobile sensor was displaced by the linear actuator with a change in distance  $\Delta d = 1$  cm at a time while the static sensor remained stationary. After each 1 cm displacement, data were collected for 10 minutes with a sample rate of 30 seconds. The total displacement was 16 cm. After the experiments were conducted with three different  $D$ , the exciter was moved to a different location with repeated experiments of the different initial distances. By varying the initial distance, the effect of different initial distances between sensors on the linear (decoding) relationship could be investigated. By changing the exciter location, the effect of variable exciter location on the linear relationship could be investigated. These experiments can also show which effects have a larger impact on the linear relationship between displacement and phase shift. The experimental setup was shown in Figure 1. The antenna icon represents the location of the sensors, and the left sensor was the mobile sensor. The star represents the locations of exciters for each experiment. A total of 12 experiments were conducted (three initial distance setups with four different exciter locations).

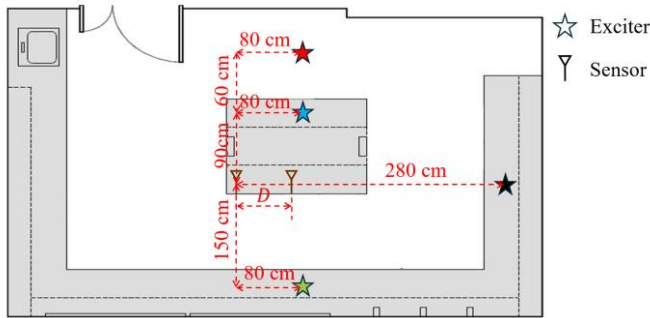


Figure 1. Location of the sensor and various exciters for the experimental setup in the indoor laboratory

## 2.2 Discussion

For each experiment, a linear relationship was obtained by fitting the median value of the recorded phase shift at each displacement, as shown in Figure 2. The slope of the linear fitting line represented the sensitivity of the system (the ratio between phase shift and displacement)  $\Delta\theta/\Delta d$ .

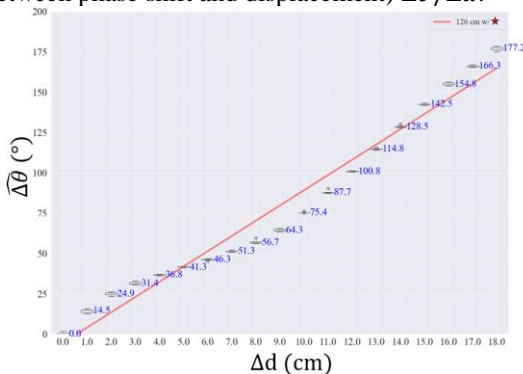


Figure 2. Experimental result of  $D = 126$  cm and the exciter location (red star); the red line indicated the linear fitting line

Table 1.  $\Delta\theta/\Delta d$  (°/cm) Comparison

$D$	Red Star	Blue Star	Green Star	Black Star	Max Min Diff. (%)
30 cm	10.17	10.45	10.11	10.34	3.4
60 cm	9.96	10.02	10.19	10.06	2.3
126 cm	9.54	9.86	11.48	10.87	<b>20.3</b>
Max Min Diff. (%)	6.6	5.98	<b>13.6</b>	8.05	

The results of 12 experiments are shown in Table 1. Maximum and minimum differences were also calculated across different exciter locations and sensor distances  $D$ . The maximum and minimum difference of each  $D$  showed that as  $D$  increased, the difference in  $\Delta\theta/\Delta d$  also increased. This demonstrated that the variation of  $\Delta\theta/\Delta d$  increased as the initial distance between sensors increased. The maximum and minimum difference of each location showed that the largest variation occurred when the exciter was located at the green star, perpendicular to the communication line between sensors. However, this phenomenon was observed only with the case of  $D = 126$  cm. If the case of  $D = 126$  cm was removed, the variation of  $\Delta\theta/\Delta d$  was similar across different exciter locations. The initial distance between sensors was more impactful to the variation of  $\Delta\theta/\Delta d$  comparing to the exciter location.

The linear fitting errors were also investigated in these experiments. As shown in Figure 2, the fitting error was presented in the linear fitting line. The variation of fitting errors across different  $D$  and exciter locations were shown in Table 2. The results showed that as the initial distance between sensors increased, the fitting error also increased. Meanwhile, the location of exciter had smaller effects on the fitting errors compared to the initial distances between sensors.

Table 2 Fitting error ( $\Delta\theta/\Delta d$  error) comparison

$D$	Red Star	Blue Star	Green Star	Black Star
30 cm	<b>5.34</b>	<b>4.16</b>	<b>5.93</b>	<b>4.22</b>
60 cm	8.99	6.29	14.74	6.19
126 cm	15.42	17.84	18.54	16.98

The fitting error and the discrepancy of  $\Delta\theta/\Delta d$  with various sensor spacing issues were potentially caused by the signal multipath effects. Since the experiments were conducted in an indoor laboratory, the surroundings reflected the backscattered signal from the transmitter sensor to the receiver sensor. The superposition of the backscattered signal and reflected signal can potentially affect the accuracy of the data collection. Additional experiments must be conducted to verify the causes.

In real applications, material inhomogeneity (e.g. moisture and density of fine aggregate) inside the structure can potentially affect the system's accuracy. Previous studies have demonstrated the capability of detecting the change of water content using an RF system [5]. Therefore, the material inhomogeneity due to moisture content can be further decoupled. Meanwhile, the effects from other sources of material inhomogeneity have to be further studied. Uncertainty quantification can be used to preliminarily quantify the effects of those sources.



### 3 CONCLUSION

This study investigates the uncertainties in the relationship between the channel phase (encoding parameter) and displacement (measurand) registered by RF sensors. Although distributed embedded passive radio RF sensors have great potential for 3D spatial pavement subsurface monitoring, the relationship between measurand and encoding parameter can be affected by the initial distances between sensors. As the initial distance between sensors increases, the uncertainty in the relationship also increases. Meanwhile, the location of the exciter has a smaller effect on the relationship. The reason behind this finding will be the subject of future work.

### ACKNOWLEDGEMENT

This research was funded by the National Science Foundation under Grants No. ECCS-2329800, ECCS-2329801, and ECCS-2329802. Any opinions, findings, and conclusions or recommendations expressed in this material are those of the authors and do not necessarily reflect the views of the National Science Foundation. The authors would like to thank Joseph Vocaturo Jr., Mauricio Pereira, Angel Dong, and Dane Utley for their help and contributions.

### REFERENCES

- [1] Caltrans, “Highway 1 at Rat Creek Reopened to Traffic at Noon on April 23,” California Department of Transportation. Accessed: Sep. 01, 2021. [Online]. Available: <https://dot.ca.gov/news-releases/news-release-2021-013>
- [2] “2025 Infrastructure Report Card | ASCE’s 2025 Infrastructure Report Card,” ASCE’s 2025 Infrastructure Report Card |. Accessed: Mar. 30, 2025. [Online]. Available: <https://infrastructurereportcard.org/>
- [3] S. Cola, V. Girardi, S. Bersan, P. Simonini, L. Schenato, and F. De Polo, “An optical fiber-based monitoring system to study the seepage flow below the landside toe of a river levee,” *J. Civ. Struct. Health Monit.*, vol. 11, no. 3, pp. 691–705, Jul. 2021, doi: 10.1007/s13349-021-00475-y.
- [4] A. Ahmad, X. Sha, M. Stanaćević, A. Athalye, P. M. Djurić, and S. R. Das, “Enabling Passive Backscatter Tag Localization Without Active Receivers,” in *Proceedings of the 19th ACM Conference on Embedded Networked Sensor Systems*, in SenSys ’21. New York, NY, USA: Association for Computing Machinery, Nov. 2021, pp. 178–191. doi: 10.1145/3485730.3485950.
- [5] K. X. Eng *et al.*, “A Vision and Proof of Concept for New Approach to Monitoring for Safer Future Smart Transportation Systems,” *Sensors*, vol. 24, no. 18, Art. no. 18, Jan. 2024, doi: 10.3390/s24186018.

# A Wireless Passive RFID Patch Antenna Strain Sensor

Chengkai Wei<sup>1</sup>, Jingkan Shi<sup>1</sup>, Zhenchang Guan<sup>1</sup>

<sup>1</sup>Department of Intelligent Construction, College of Civil Engineering, Fuzhou University,  
Fuzhou City, Fujian Province, China

email: Chengkai Wei, 240527093@fzu.edu.cn,

Jingkan Shi, jkshi@fzu.edu.cn,

Zhenchang Guan, zcguan@fzu.edu.cn

**ABSTRACT:** With the aging of civil infrastructures, strain monitoring is essential for predictive maintenance. However, current sensing technologies mainly rely on active battery powered sensors, leading to substantial expenses and low placement granularity. This paper proposes a wireless, passive RFID patch antenna strain sensor, characterized by a favorable linear relationship between its resonant frequency and the applied strain. In this paper, simulation is carried out by using the COMSOL multi-physics coupling software. The solid mechanics field is coupled with the electromagnetic field, and the frequency-domain scanning is conducted after the model generates strain. The simulation results are compared with the experimental results in the literature to determine their correctness. According to the simulation results of the scattering parameter  $S_{11}$ , a patch antenna sensor is designed and fabricated, and corresponding experiments are conducted to detect the variations of the spectral curve before and after the sensor is embedded in concrete, thereby verifying its validity. Finally, the sensor is optimized based on the experimental results.

**KEY WORDS:** Wireless; Passive; Strain Sensor; RFID; Patch Antenna.

## 1 INTRODUCTION

In the field of structural health monitoring (SHM), acquiring accurate, long-term, and stable monitoring data remains a core concern. Structural strain, a critical indicator reflecting the health status of structures, effectively characterizes local deformation and precisely reveals internal stress distributions and health conditions [1]. Traditional strain sensors typically employ wired connections using conductors or optical fibers as media. In large-scale structures, extensive cabling works are cumbersome, costly, and further exacerbated by the complexity of wiring and the need for relay devices, increasing economic burdens. Moreover, excessive cabling significantly amplifies resistance and introduces noise interference, severely degrading strain measurement accuracy and failing to meet high-precision monitoring requirements.

Digital image-based methods [2] leverage precision optical instruments and advanced image processing algorithms to obtain high-accuracy strain data. However, these methods have notable limitations: they impose stringent requirements on light source conditions, limiting adaptability in low-light environments such as tunnels; they also demand extreme equipment stability, making sustained and accurate measurements challenging in complex outdoor settings. The complexity of algorithms and harsh measurement conditions restrict their long-term monitoring applications.

Radio Frequency Identification (RFID) technology, a mature wireless information transmission method [3], has garnered substantial attention from scholars due to its compact size and low cost. Peng Guofeng et al. [4] proposed a wireless passive RFID humidity sensor based on U-shaped resonant units, achieving environmental humidity detection and encoding capabilities through grouped U-shaped resonators. Wang Xian et al. [5] designed a miniaturized wireless passive strain sensor array using split-ring resonators to detect strain magnitude and direction on metal surfaces. Wang Bo et al. [6]

developed a wireless passive metal crack sensor using RFID technology, detecting surface cracks by measuring radar cross-section (RCS) values.

Integrating RFID technology with sensors introduces a novel approach for structural strain measurement. This paper presents a rectangular patch antenna-based wireless passive strain sensor using RFID technology, simulated in COMSOL Multiphysics finite element analysis software. This sensor offers low cost, non-contact measurement, and passive operation, effectively addressing challenges such as cumbersome cabling, noise interference, and real-time power supply limitations in wired systems. Compared to other strain sensors, it features a simple structure and high sensitivity (4.45 kHz/ $\mu\epsilon$ ), demonstrating significant advantages and promising applications in SHM [7].

## 2 THE PRINCIPLE OF ANTENNA STRAIN SENSOR

### 2.1 Relationship Between Strain and Resonant Frequency

The patch antenna strain sensor achieves precise strain measurement by detecting shifts in the antenna's resonant frequency. The resonant frequency, as the optimal operating frequency of the antenna, exhibits distinct electrical characteristics: when the antenna operates at its resonant frequency, the backscattered energy reaches its minimum while the received energy attains its maximum. The resonant frequency shift of the patch antenna is closely linked to changes in antenna dimensions. Specifically, alterations in antenna geometry inherently modify the electrical length. An increase in electrical length leads to a decrease in resonant frequency, whereas a reduction in electrical length results in an increase in resonant frequency.

The RFID-based rectangular patch antenna wireless passive strain sensing structure is illustrated in Figure 1. The sensor consists of an upper radiating patch, a feed line, a dielectric

substrate, and a lower radiating patch. The upper radiating patch detects strain and facilitates signal transmission/reception, while the lower radiating patch grounds the sensor. The feed line serves dual purposes: providing electrical feed and impedance matching. Both radiating patches and the feed line are fabricated from copper. The dielectric substrate, positioned between the upper and lower radiating patches, is constructed from RO4003C material with a dielectric constant of 3.55.

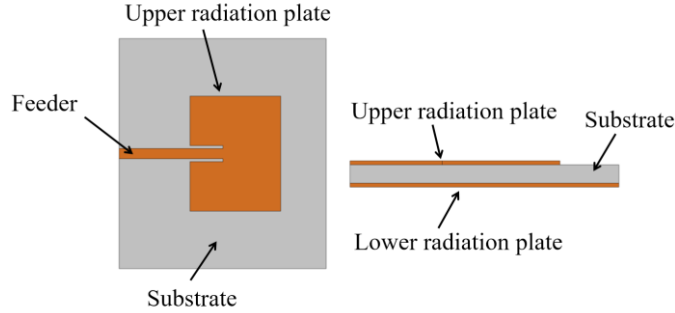


Figure 1. Sensor schematic diagram.

According to classical theory, the initial resonant frequency of a rectangular patch antenna can be expressed as:

$$f_{RO} = \frac{c}{4\sqrt{\epsilon_e} L_1 + 2\Delta L_1} \quad (1)$$

Where  $f_{RO}$  is the resonant frequency of the antenna under the initial condition;  $c$  is the speed of light in a vacuum;  $\epsilon_e$  is the equivalent dielectric constant of the dielectric plate;  $L_1$  is the length of the upper radiation patch;  $\Delta L_1$  is the additional length of the antenna, which is related to the antenna width, thickness and material.

When the antenna experiences strain  $\epsilon$  in the length direction, the resonant frequency  $f_R$  changes accordingly. For:  $\Delta L_1 \leq L_1$ ,  $f_R$  exhibits an approximately linear relationship with strain, expressed as:

$$f_R \approx \frac{c}{4\sqrt{\epsilon_e} L_1 (1+\epsilon)} = \frac{f_{RO}}{(1+\epsilon)} \approx f_{RO} (1 - \epsilon) \quad (2)$$

From equation (2), it can be seen that  $f_R$  is mainly affected by strain in the direction of antenna length, and  $f_R$  has a linear relationship with  $\epsilon$ , the slope is about equal to  $f_{RO}$ , that is, every  $1\mu\epsilon$  strain occurs, the resonant frequency of the antenna will decrease  $f_{RO} \times 10^{-6}$ .

Since the substrate thickness is much smaller than the length-width size, the dielectric constant of the antenna substrate is approximately the same as the relative dielectric constant:

$$\beta_r = \frac{\beta_{r0} + 1}{2} + \frac{\beta_{r0} - 1}{2} \left[ 1 + 12 \frac{h}{w} \right]^{-1/2} \cong \beta_{r0} \quad (3)$$

Where:  $\beta_r$  is the effective dielectric constant of the antenna substrate;  $h$  is the thickness of the substrate;  $w$  is the width of the substrate;  $\beta_{r0}$  indicates the relative dielectric constant of the substrate at room temperature.

## 2.2 Resonant Frequency and Echo Reflection Coefficient

With full The antenna's echo reflection coefficient ( $S_{11}$ ) is a metric that quantifies the ratio of reflected signal power to incident signal power at the antenna port, reflecting the degree of signal matching. A signal transceiver emits an

electromagnetic wave with frequency  $f$  and power  $P_{in}$ . The wave is reflected by the antenna and received by the transceiver with power  $P_{ref}$ . The echo reflection coefficient  $S_{11}$  at this frequency is calculated using Equation (4):

$$S_{11} = 10 \lg \left[ \frac{P_{in}}{P_{ref}} \right] \quad (4)$$

By transmitting an electromagnetic wave spectrum to the antenna and using a signal transceiver to record the echo reflection coefficient  $S_{11}$  at each frequency, the echo reflection curve (i.e., the  $S_{11}$  curve) across the frequency band is obtained. The minimum point of the  $S_{11}$  curve corresponds to the antenna's resonant frequency under the given conditions. As theoretically derived in the previous section, the minimum point of the  $S_{11}$  curve shifts when strain is applied, indicating a change in the resonant frequency, as illustrated in Figure X. Here,  $f_{RO}$  denotes the initial resonant frequency, and  $f_R$  represents the resonant frequency after strain application.

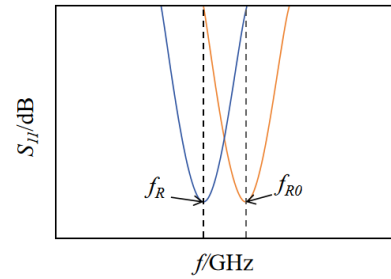


Figure 2. The shift of resonant frequency.

## 3 SIMULATION AND PARAMETER OPTIMIZATION

### 3.1 Finite element modeling of the antenna

The finite element analysis software used in this simulation is COMSOL. COMSOL's multiphysics coupling can accurately describe the interactions between different physical phenomena and achieve multi - field collaborative simulation by establishing and solving the coupled partial differential equations of each physical field.

Following optimization, the Geometric Dimensions of the Sensor in [Table 1] below:

Table 1. Geometric dimensions of the sensor.

Thickness of substrate/ $t_1$	0.8mm
Thickness of metal/ $t_2$	35 $\mu$ m
Width of patch/ $W_1$	20mm
Length of patch / $L_1$	16mm
Width of substrate/ $W_2$	40mm
Substrate length/ $L_2$	36mm
Width of feed line/ $W_3$	1.8mm
Length of feed line/ $L_3$	18mm

In addition, the dielectric constant of the dielectric substrate is 3.55.



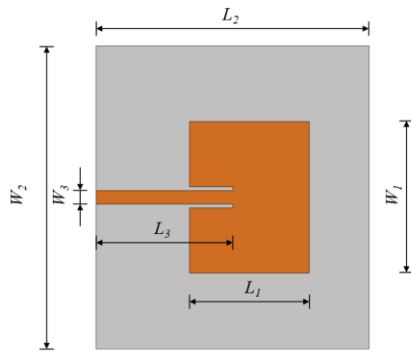


Figure 3. Dimensional schematic diagram of the sensor.

The simulation of the patch antenna strain sensor in this paper adopts the dual-physics-field coupling of the electromagnetic field and the solid mechanics field, enabling the calculation of the change in the resonant frequency of the antenna after strain occurs within a single model. The 3D model of this antenna is shown in the following figure. The outer shell-shaped structure is a perfectly matched layer (partially hidden), which serves to absorb the electromagnetic waves propagating outward, thereby simulating the open boundary conditions without reflection.

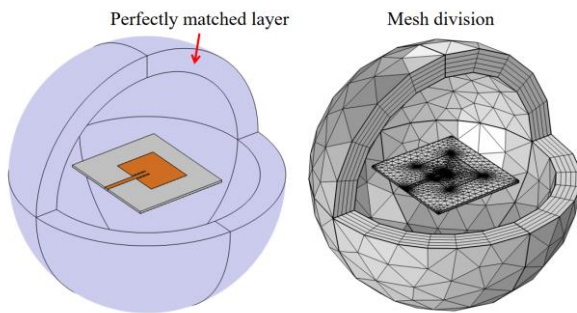


Figure 4. Sensor's finite element model.

First, an adaptive frequency sweep is performed on the antenna under strain-free conditions, and the curve is plotted to obtain its initial resonant frequency, as shown in the following figure.

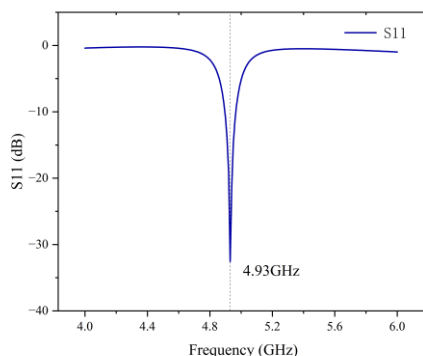


Figure 5. Initial resonant frequency.

Apply a specified displacement to the antenna in the length direction of the antenna through the solid mechanics field to simulate the generation of strain in the length direction

of the patch antenna. The total strain is set to  $4000 \mu\epsilon$ , and the step size of strain increase each time is  $400 \mu\epsilon$ . Obtain the curves under different strain values, and according to the obtained results, plot the linear regression curve of the relationship between the strain and the resonant frequency.

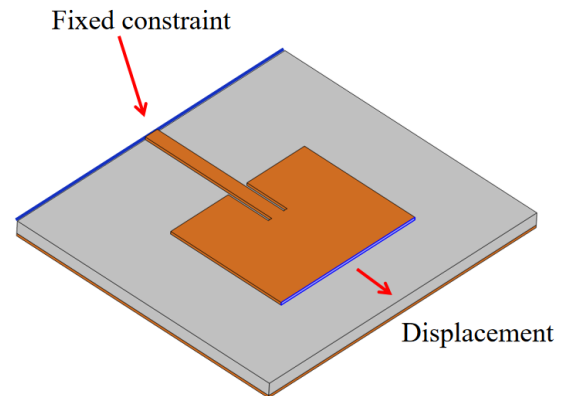


Figure 6. Schematic diagram of Strain.

### 3.2 Modeling Results

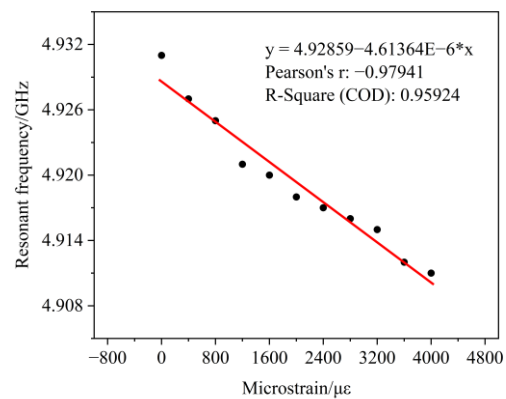


Figure 7. The relationship between resonant frequency and microstrain.

As shown in the figure, the regression coefficient is 0.979, indicating that there is a good linear relationship between the resonant frequency of the antenna and the strain in the length direction. The sensitivity of the antenna as a strain sensor is  $4.6136 \text{ kHz}/\mu\epsilon$ . The relative error between the simulation result and the theoretical calculation value of  $4.45 \text{ kHz}/\mu\epsilon$  is 3.68%.

## 4 CONCLUSION

In response to the imperative for wireless strain detection of building structures within the domain of structural health monitoring, leveraging the pronounced radiation efficiency, minimal power dissipation, and elevated quality factor characteristic of rectangular patch antennas, a wireless passive rectangular patch antenna strain sensor was meticulously devised. This design is firmly grounded in Radio - Frequency Identification (RFID) technology. Concurrently, a comprehensive finite - element analysis (FEA) simulation of the sensor was successfully executed.

The simulation outcomes unambiguously demonstrate that the sensor exhibits a sensitivity of  $4.6136 \text{ kHz}/\mu\epsilon$  along the lengthwise dimension of the patch, with a linearity regression

coefficient of 0.959. These strain - related simulation results incontrovertibly validate the viability of deploying an RFID - enabled rectangular patch antenna as a wireless passive strain sensor.

Looking ahead, the fabrication of the sensor will be expeditiously completed, and a series of well - designed tensile experiments will be carried out. These experiments are intended to rigorously verify the sensor's detection performance under diverse real - world working conditions. Post - experimentation, a secondary optimization of the sensor's structure will be implemented, with the explicit aim of further enhancing its sensitivity and thereby attaining a more superior strain - detection outcome.

## REFERENCES

- [1] Zhou Zhi, Ou Jinping. Intelligent Health Monitoring and Diagnosis System for Civil Engineering [J]. Journal of Transducer Technology, 2001(11): 1 - 4.
- [2] Li Xianbao. Measurement of Material Tensile Strain Based on Machine Vision [D]. Jilin University, 2020.
- [3] JIA X, FENG Q, FAN T, et al. RFID technology and its applications in internet of things (IoT)[C] The 2nd international conference on consumer electronics, communications and networks (CECNet), IEEE, 2012: 1282-1285.
- [4] Peng Guofeng, He Xingli, Li Peng, et al. Wireless Passive RFID Humidity Sensor Based on U-shaped Resonant Unit [J/OL]. Chinese Journal of Radio Science, 1 - 7 [April 16, 2025].
- [5] Wang Xian, Gao Shang, Yang Shangke, et al. Design of Miniaturized Wireless Passive Strain Sensor Array Based on Split Ring Resonators [J/OL]. Journal of Electronic Measurement and Instrumentation, 1 - 11 [April 16, 2025].
- [6] Wang Bo, Hou Rongrong, Wang Ke, et al. A Metal Crack Sensor Based on Wireless Passive RFID Technology [J]. Journal of Huazhong University of Science and Technology (Natural Science Edition), 2025.
- [7] Huang Cheng. Research on the Development of Passive Strain Sensors Based on RFID System [D]. Zhejiang University, 2020.

# 25-year Field Monitoring of the Tsing Ma Suspension Bridge in Hong Kong

Yong Xia<sup>1,2\*</sup>, Lu Zhang<sup>1,2</sup>, Tian Lu<sup>1,2</sup>, Xiaoyou Wang<sup>1,2</sup>

<sup>1</sup> Department of Civil and Environmental Engineering, The Hong Kong Polytechnic University, Hong Kong, PR China

<sup>2</sup> Joint Research Centre for Marine Infrastructure, The Hong Kong Polytechnic University, Hong Kong, PR China

email: ceyxia@polyu.edu.hk, lulzhang@polyu.edu.hk, tian1.lu@connect.polyu.hk, [cexiaoyou.wang@polyu.edu.hk](mailto:cexiaoyou.wang@polyu.edu.hk)

\* Corresponding author

**ABSTRACT:** The Tsing Ma Suspension Bridge in Hong Kong has been the world's first batch of bridges equipped with a long-term health monitoring system since 1997. For the first time, this study reports the first-hand field monitoring data of the bridge from 1997 to 2022. The 25-year data provide an invaluable and rare opportunity to examine the long-term characteristics of loads, bridge responses, and their relationships, thereby enabling the assessment of the bridge's load evolution and structural condition over time. The current status and recent update of the health monitoring system are also reported. This study is the first to report the one-quarter-century status of a structural health monitoring system and the behavior of a long-span suspension bridge. This research provides a benchmark for many other bridge monitoring systems worldwide.

**KEY WORDS:** Structural health monitoring, Long-span bridges, Long-term behavior, Load evolution.

## 1 INTRODUCTION

Large-span bridges are vital economic lifelines, and their failure can have catastrophic human and socio-economic impacts. Proactive maintenance is essential to ensure the serviceability and safety of long-span bridges that are subjected to complex loads (e.g., typhoons, earthquakes) and harsh environments (e.g., corrosion) during operation. Structural Health Monitoring (SHM) is essential for monitoring the health of bridges, assessing their safety, guiding their maintenance and providing early warnings. Although SHM systems are now being adopted in major bridges (e.g., Akashi Kaikyo Bridge, Runyang Bridge, etc.) and newly designed bridges around the world, there is a lack of long-term operational history data for SHM systems. This creates a research gap in analyzing long-term data, actual structural degradation, and service life assessment [1-11].

The Tsing Ma Bridge (TMB), operational since 1997 with a pioneering SHM system, offers a unique 26-year dataset (1997-2022). This study analyzes the long-term data, SHM system status of TMB and the health monitoring system, and investigating long-term trends in environmental loads and structural performance.

## 2 THE TSING MA BRIDGE

The Tsing Ma Bridge is a highway and railroad dual-purpose large-span suspension bridge with a main span of 1,377 m, a total bridge length of 2,160 m and a tower height of 206 m, which was opened to traffic in 1997. An elevation of the bridge is given in Figure 1.

## 3 MONITORING DATA

### 3.1 Temperature

The annual maximum bridge temperatures are given in Figure 2. A linear regression analysis shows that the maximum deck effective and ambient temperatures increase at rates of 0.51 °C/decade and 0.72 °C/decade, respectively. The bridge temperature in 2022 is 44.9 °C, close to bridge design limit of 46 °C.

### 3.2 Deflections

The bridge displacement is subject to the temperature and the traffic effects. The mid-span deflection without traffic load is shown in Figure 3, using data between 2:00 to 4:00 am to exclude the traffic effect.

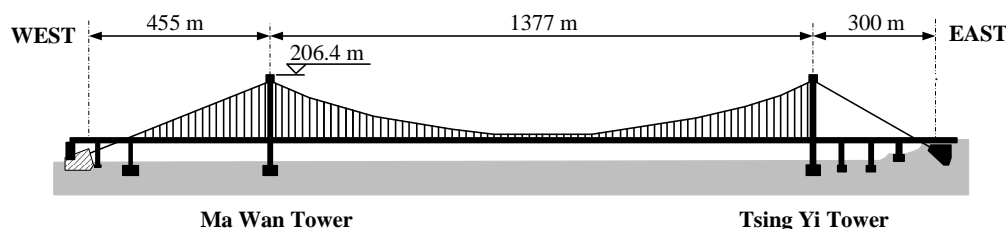


Figure 1 The elevation of the Tsing Ma Bridge



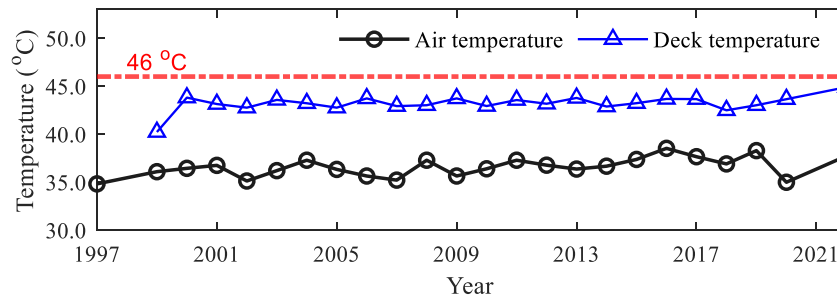


Figure 2 Annual maximum deck effective temperature of the Tsing Ma Bridge in 1997–2022

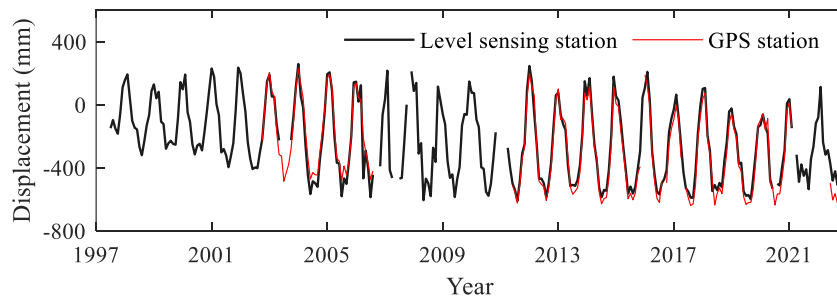


Figure 3 Monthly mean mid-span deflection of Tsing Ma Bridge in 1997–2022

## CONCLUSIONS

The operational condition of the Tsing Ma Bridge and its Structural Strength Monitoring (SHM) system has attracted much attention. In this paper, field monitoring data from the past 26 years are analyzed to study the long-term loading and response of the bridge. In addition, this paper discusses the current status and latest updates of the SHM system. The following conclusions are drawn from this study.

(1) Observed trends in bridge deck effective temperatures show significant increases over recent decades. Specifically, the maximum effective temperature has risen at a rate of 0.51 °C per decade, while the mean effective temperature increased at 0.16 °C per decade. Critically, the recorded maximum values are now approaching the original design thresholds for the deck.

(2) The monthly bridge midspan deflection show an increasing trend, the trend can be caused by the cracking and creep of materials.

## ACKNOWLEDGMENTS

**Funding:** This research was partially supported by the Collaborative Research Fund (Project No. PolyU C5004-23G). The authors also would like to thank the Hong Kong Observatory and the highways department for providing valuable data.

**Competing interests:** The authors have no relevant financial or non-financial interests to disclose.

## REFERENCES

- [1] Zhou Y, Xia Y, Chen B, Fujino Y. “Analytical solution to temperature-induced deformation of suspension bridges”, *Mechanical Systems and Signal Processing*, 2020, 139, 106568.

- [2] Xu YL, Xia Y. *Structural Health Monitoring of Long-Span Suspension Bridges*, CRC Press, 2012.
- [3] Li LF, Chen B, Zhou LR, Xia Q, Zhou Y, Zhou XQ and Xia Y. “Thermal Behaviors of Bridges – A Literature Review, *Advances in Structural Engineering*, 2023, 26 (6), 985-1010.
- [4] Zhang L, Lu T, Wang F and Xia Y, “Over 25-year Monitoring of the Tsing Ma Suspension Bridge in Hong Kong”, *Journal of Civil Structural Health Monitoring*, 2025, 15 (1), 263-283.
- [5] Xia Q, Zhang J, Tian Y, Zhang Y. Experimental Study of Thermal Effects on a Long-Span Suspension Bridge. *J Bridge Eng.* 2017;22(7):04017034. [https://doi.org/10.1061/\(ASCE\)BE.1943-5592.0001083](https://doi.org/10.1061/(ASCE)BE.1943-5592.0001083).
- [6] Xia Y, Chen B, Zhou X, Xu Y. Field monitoring and numerical analysis of Tsing Ma Suspension Bridge temperature behavior. *Struct Control Hlth.* 2013;20(4):560-575. <https://doi.org/10.1002/stc.515>.
- [7] Xia Y, Chen B, Weng S, Ni Y, Xu Y. Temperature effect on vibration properties of civil structures: a literature review and case studies. *J Civ Struct Health Monit.* 2012;2(1):29-46. <https://doi.org/10.1007/s13349-011-0015-7>.
- [8] Shan Y, Li L, Xia Q, Gao W, Jing Q, Xia Y (2023) Temperature behavior of cable-stayed bridges. Part I—global 3D temperature distribution by integrating heat-transfer analysis and field monitoring data. *Adv Struct Eng* 26(9): 1579-1599
- [9] Xia Q, Wu W, Li F, Zhou X, Xu Y, Xia Y (2022) Temperature behaviors of an arch bridge through integration of field monitoring and unified numerical simulation. *Adv Struct Eng* 25(16): 3492-3509
- [10] Wang X, Wu W, Du Y, Cao J, Chen Q, Xia Y (2023) Wireless IoT Monitoring System in Hong Kong–Zhuhai–Macao Bridge and Edge Computing for Anomaly Detection. *Ieee Internet Things* 11(3): 4763-4774
- [11] Zhou Y, Xia Y, Sun Z, Fujino Y (2022) Analytical formulation of the temperature-induced deformation of multispan suspension bridges. *Struct Control Hlth* 29(6): e2937.



# FBG and DFOS Applications for Infrastructure and Environmental Monitoring

# Towards Accurate Road Health Monitoring: A Damage Detection System Using FBG Sensors

Ali Golmohammadi<sup>1\*</sup>, 0000-0002-8144-2198, Navid Hasheminejad<sup>1</sup>, 0000-0002-0796-6321, Aliakbar Ghaderiaram<sup>2</sup>, 0000-0003-1947-4487, Wim Van den bergh<sup>1</sup>, 0000-0002-0897-1392, David Hernando<sup>1</sup>, 0000-0001-8284-5792

<sup>1</sup> SuPAR Research Group, Faculty of Applied Engineering, University of Antwerp, Antwerp, Belgium

<sup>2</sup> Materials & Environment, Faculty of Civil Engineering & Geosciences, Delft University of Technology, Delft, Netherlands

Email: seyedali.golmohammaditavalaee@uantwerpen.be, navid.hasheminejad@uantwerpen.be, A.Ghaderiaram@tudelft.nl, wim.vandenbergh@uantwerpen.be, david.hernando@uantwerpen.be

**ABSTRACT:** Advancements in road infrastructure health monitoring through sensor networks offer a transformative solution to the limitations of traditional inspection methods by enabling more accurate, real-time assessments of structural conditions. However, once appropriate sensors are selected and deployed, a key challenge remains: converting raw sensor data into meaningful health indicators (HIs) that effectively capture structural changes indicative of potential damage. A health indicator (HI) is a crucial metric derived from structural health monitoring (SHM) data, designed to reflect the current condition and damage state of a monitored structure. This study presents a machine learning-based approach leveraging principal component analysis (PCA) to develop a sensitive and damage-specific HI by extracting and ranking the most relevant current features. The proposed method is first validated through experimental fatigue testing using a four-point bending machine under random thermal conditions. To further evaluate its effectiveness and reliability in real-world applications, the approach is applied to field data collected from a network of fiber Bragg grating (FBG) sensors embedded in asphalt pavement. By analyzing strain measurements, the study demonstrates that the PCA-based HI successfully detects structural changes, providing a robust and data-driven solution for real-time infrastructure monitoring.

**KEYWORDS:** Health indicator, Structural health monitoring, FBG sensor networks, Principal component analysis, Fatigue damage detection.

## 1 INTRODUCTION

A significant amount of money is spent on maintaining infrastructure such as roads, bridges, and other critical structures. To reduce maintenance costs, various non-destructive testing (NDT) methods have been employed to enable predictive maintenance strategies. However, these methods have certain limitations. For instance, most NDT techniques operate offline, making continuous structural evaluation impossible [1].

To address this challenges, extensive research has been conducted to integrate advanced sensor technologies for continuous and real-time Structural Health Monitoring (SHM). Sensors such as accelerometers [2-4], piezoelectric sensors [5-7], and acoustic emission sensors [8-10] have been explored for their ability to collect SHM data continuously, providing valuable insights for early damage detection and improved maintenance planning.

Recently, optical sensors have emerged as a promising technology for infrastructure monitoring due to their unique advantages, such as immunity to electromagnetic interference, lightweight design, and, most importantly, the capability for distributed or quasi-distributed measurements. These features make optical sensors highly suitable for real-time structural health monitoring, enabling continuous and precise data collection over long distances. Additionally, their durability and resistance to harsh environmental conditions enhance their reliability for long-term deployment in critical infrastructure such as bridges, tunnels, and pipelines [11-17].

Although optical sensors offer these advantages, their application in large-span structures generates an enormous

amount of data, requiring specialized strategies for processing, compression, and reduction. Efficient data management techniques are essential to handle this influx of information while preserving critical insights for future interpretation and analysis. Developing advanced algorithms and intelligent data filtering methods can help optimize storage and computational efficiency without compromising the accuracy and reliability of structural health monitoring [18].

Various techniques can be integrated to accomplish this objective, including data reduction methods [19-20] and multi-sensor data fusion [21-22] at different processing levels. A structured approach involves organizing these steps to derive a health indicator (HI) that enables straightforward monitoring of a system's health status. HI is regarded as the most informative feature in SHM data [23] that can be obtained using different frameworks including statistical, signal processing, and machine learning. In the literature, different criteria have been proposed to define an optimal HI. First viewpoint (1VP) suggests that an ideal HI should exhibit monotonicity, which represents a consistent increasing or decreasing trend over time, prognosability, which reflects the distribution of a variable's final values, and trendability, which measures the similarity between different variable trajectories [24].

Alternatively, second viewpoint (2VP) emphasizes that an optimal HI should possess detectability, referring to its sensitivity in identifying the presence of faults, particularly the smallest detectable fault signatures at a given false-positive rate. It should also ensure separability, which is its ability to effectively distinguish between faulty and healthy states. Additionally, trendability is crucial, as the degradation trend of



the HI should maintain a positive correlation with operational time following an initial fault. However, identifying an optimal HI that satisfies all three properties is not a straightforward task. In practice, once an HI demonstrates both detectability and separability, it can already be considered optimal [25]. In this study, the second point of view is adopted as the criteria for defining an optimal HI. The first perspective requires extensive run-to-failure data, which is often challenging to obtain in real-world scenarios due to limited data availability. Ultimately, the developed HI can serve as an input for a prognosis model to estimate the remaining useful life (RUL), which will be explored in future studies.

## 2 OBJECTIVE AND OVERALL METHODOLOGY

The primary objective of this study is to propose a framework that integrates both data reduction and fusion techniques to construct health indicators that effectively represent the damage levels of infrastructures, such as roads, monitored using high-density FBG sensor networks. This method can be applied to individual FBG sensors or groups of sensors within a fiber, where data fusion can be performed at the data level.

In this approach (see Figure 1), following data acquisition via an embedded FBG sensor network and the management of large-scale collected data, a series of signal processing steps is applied to the raw data to prepare them for further analysis [26]. Subsequently, time-domain FBG signal features—including peak width, peak duration, and energy—are extracted from each segment of the pre-processed data.

After conducting long-term monitoring over a predefined period, these features are ranked based on their monotonicity metric to retain only the most significant ones. When new data arrive, the extracted features are normalized relative to the training dataset. Following normalization, a feature fusion technique based on principal component analysis (PCA) is implemented to project these features into a reduced-dimensional space. Since the first principal component captures the direction with the highest gradient in the feature space, it serves as a suitable indicator for representing the health status of the structure.

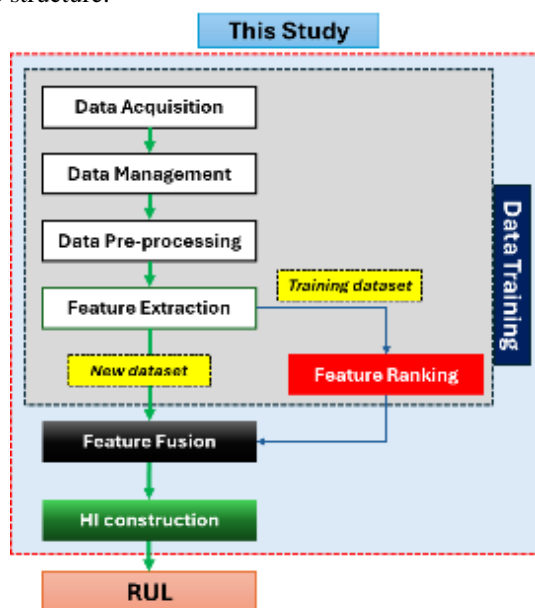


Figure 1. The overall framework of the study.

As no data is available on damage conditions from the embedded FBG sensor network, two approaches are used to evaluate the proposed framework. The first involves conducting an experimental fatigue test, while the second utilizes available FBG data to generate synthetic damage scenarios to validate its applicability. The following sections discuss these two approaches in detail.

## 3 METHODS

### 3.1 Data Acquisition

#### 3.1.1 Experimental Fatigue Test

An experimental test was conducted to validate the proposed framework for large-scale, real-world damage detection applications. To achieve this, a stress-control fatigue experiment was performed using a four-point bending machine (see Figure 2) on a standard asphalt beam with dimensions of 60×60×400 mm, made from the APO-A mixture. The loading frequency was 10 Hz, and the temperature was varied randomly to simulate real-world conditions.

For the experiment, strain gauge (SG) sensors (3×10 and 3×20 mm) were installed to monitor strain at the bottom of the beam throughout the fatigue test, in order to further investigate the effect of strain gauge length on strain readings in asphalt materials. However, a detailed analysis of this effect is considered outside the scope of the present study. These SGs glued using CC-33A×5 adhesive, provided by KYOWA, between two internal supports. Strain data were collected using a compact recording system (EDX-10) at a sampling frequency of 500 Hz and subsequently processed using DCS-100A software.



Figure 2. Four-point bending setup for fatigue test.

After the test ended, the sample was damaged at the SG2 location, as shown in Figure 3a. The temperature recorded during the test is also presented in Figure 3b. Temperature data were collected using a thermocouple placed near the beam during testing.

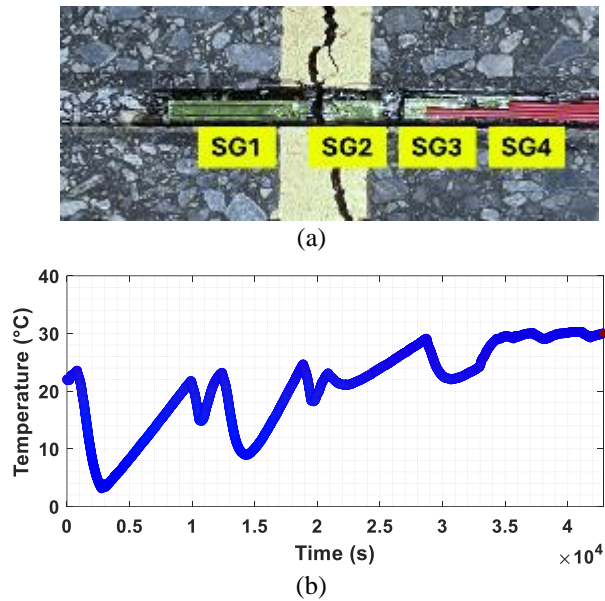


Figure 3. Fatigue test: (a) Damaged sample, (b) Temperature variations.

The strain data collected during the test using four strain gauges is presented in Figures 4a–4d.

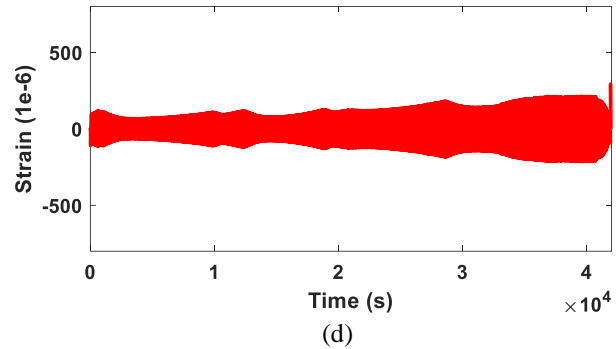
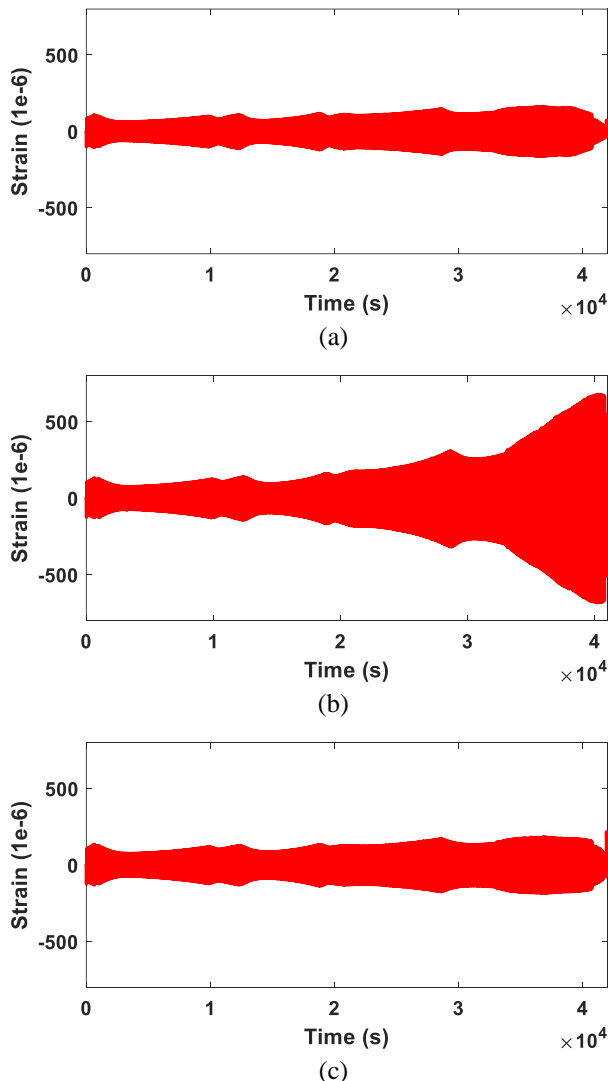


Figure 4. SG responses during fatigue test: (a) SG1, (b) SG2, (c) SG3, (d) SG4.

As shown in Figure 4, all SG responses exhibit load-induced strain signals after filtering out low-frequency components caused by temperature-induced strain. However, fluctuations in temperature can still influence the amplitude of the load-induced strain response due to temperature-dependent changes in material properties. As damage propagates, the responses of the strain gauges are affected depending on their location. If damage occurs at the sensor's location, an increasing trend will be observed due to strain concentration in that area. Conversely, if damage propagates near a sensor, its response will show a decreasing trend. However, this effect depends on the distance from the damaged region.

### 3.1.2 Field Test using FBG Sensor Network

In addition to the experimental fatigue test, strain and temperature data were collected using a FBG sensor network embedded in the asphalt layer at different locations on a constructed test track in the Port of Antwerp & Bruges. The sensor network configuration is shown in Figure 5, as can be seen this configuration includes 32 FBG in both lateral and longitudinal directions [27].



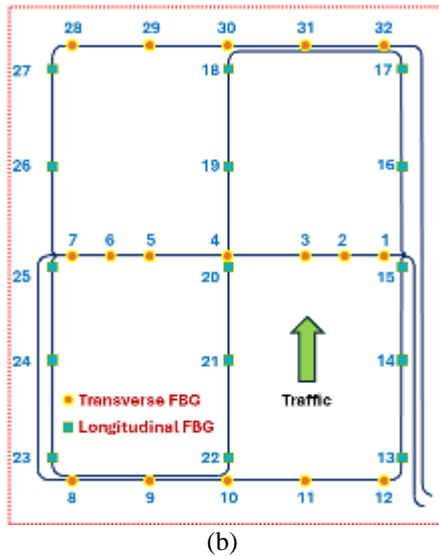


Figure 5. Monitoring system using FBG sensor network: (a) Test track, (b) FBG sensor configuration

After the construction of the test track, a continuous monitoring campaign was initiated from April 28, 2024, to October 17, 2024 (28/04/2024 to 17/10/2024), powered by a solar system and wind turbine. During this campaign, strain and temperature data were collected at a 100 Hz sampling frequency using an eight-channel, 2000 Hz FBG-Scan 708D interrogator. The collected data were then processed using ILLumiSense v2.3.5.5 software. Figure 6 shows the temperature variation in the asphalt during the monitoring campaign.

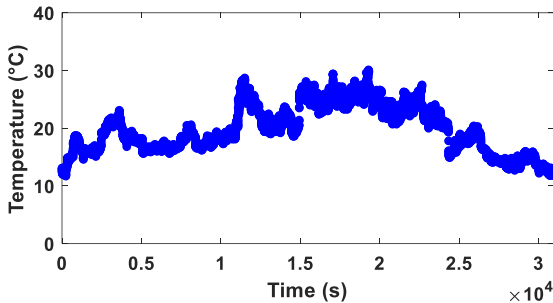


Figure 6 Temperature during the monitoring campaign collected by FBG sensor

### 3.2 Data Management and Pre-processing

During the monitoring campaign, 20 GB of data were generated daily, requiring efficient management to handle this large volume for future analysis. To address this, an automated system was developed to classify, merge, and prepare the data for subsequent steps, as outlined in Ref. [26].

Then, the data needs to be pre-processed using signal processing techniques to prepare it for the next steps. These steps include filtering, thresholding, concatenation, and windowing. Each technique is applied for a specific purpose: filtering removes strain caused by temperature variations, thresholding eliminates noise while preserving events, concatenation combines short-term monitored data into long-term datasets, and windowing ensures the data contains the same number of events for better comparison, as discussed in

Ref. [26]. Figure 7 shows an example of the daily collected data alongside the long-term pre-processed FBG data.

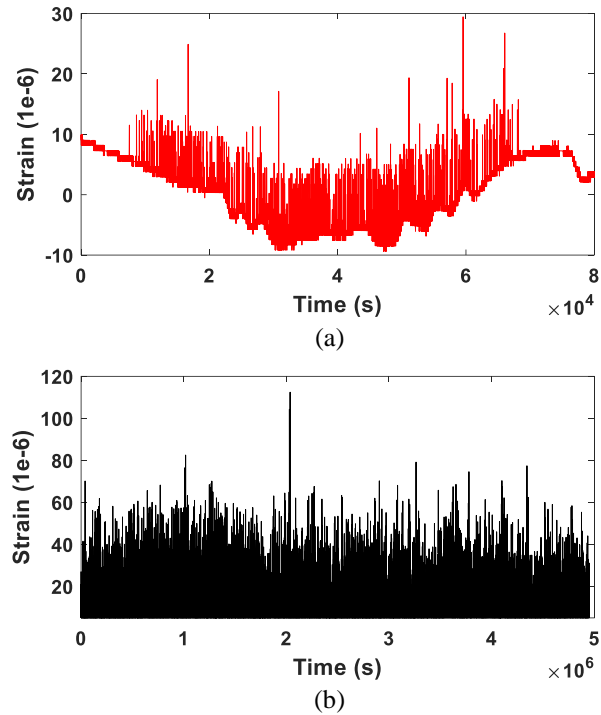


Figure 7 Collected FBG data during monitoring campaign: (a) daily data (17/05/2024), (b) long-term preprocessed data

### 3.3 Feature Extraction

Feature extraction plays a critical role in transforming raw data into meaningful, compact representations that can be efficiently used for analysis, classification, or prediction. As raw time-series or signal data is often too complex to interpret directly, extracting relevant features helps reduce dimensionality and focus on the most informative aspects of the data. This process not only improves model performance by providing more relevant input but also enhances the results, making it easier to identify underlying patterns or anomalies. In this study, several signal features in the time domain are calculated for each window of data [23], as listed in Table 1, along with peak width, peak duration, and energy. These features are essential for capturing the temporal characteristics of the signal and provide valuable insights into its behavior over time. Peak width and peak duration help describe the shape and spread of the signal's key events, while energy quantifies the overall magnitude of the signal, contributing to a more comprehensive understanding of its dynamics.

Table 1. Common statistical features in time-domain [23]

No	Equation	No	Equation
1	$X_m = \frac{\sum_{n=1}^N x(n)}{N}$	9	$X_{crest} = \frac{X_{peak}}{X_{rms}}$
2	$X_{sd} = \sqrt{\frac{\sum_{n=1}^N (x(n) - X_m)^2}{N - 1}}$	10	$X_{clearance} = \frac{X_{peak}}{X_{root}}$
3	$X_{root} = \left( \frac{\sum_{n=1}^N \sqrt{ x(n) }}{N} \right)^2$	11	$X_{shape} = \frac{X_{rms}}{\frac{1}{N} \sum_{n=1}^N  x(n) }$
4	$X_{rms} = \left( \frac{\sum_{n=1}^N (x(n))^2}{N} \right)^{1/2}$	12	$X_{impulse} = \frac{X_{peak}}{\frac{1}{N} \sum_{n=1}^N  x(n) }$



$$\begin{array}{ll}
5 & X_{rss} = \left( \sqrt{\sum_{n=1}^N |x(n)|^2} \right) \\
6 & X_{peak} = \max|x(n)| \\
7 & X_{skewness} = \frac{\sum_{n=1}^N (x(n) - X_m)^3}{(N-1)X_{sd}^3} \\
8 & X_{kurtosis} = \frac{\sum_{n=1}^N (x(n) - X_m)^4}{(N-1)X_{sd}^4} \\
13 & X_{p2p} = \max(x(n)) - \min(x(n)) \\
14-17 & X_{k\_cm} = \frac{\sum_{n=1}^N (x(n) - X_m)^k}{N} \\
18 & X_{FM4} = \frac{X_{4\_cm}}{X_{st}^4} \\
19 & X_{med} = \frac{\sum_{n=1}^N t(n)}{N}
\end{array}$$

$x(n)$  indicates the signal sequence for  $n = 1, 2, \dots, N$ .

$N$  indicates the number of data points.

$t(n)$  indicates the moments of occurrence of  $x(n)$

### 3.3.1 Feature Ranking

To determine the most relevant feature and develop an appropriate indicator, researchers have employed a specific metric in various studies [28]. This metric, known as monotonicity, captures the dominant increasing or decreasing trend of a feature concerning the target variable. It assesses how consistently a feature progresses in a specific direction. The monotonicity of the  $i$ th feature  $x_i$  is computed using the following equation:

$$\text{Monotonicity}(x_i) = \frac{\frac{1}{m} \sum_{j=1}^m \left| \frac{\text{number of positive diff}(x_i^j) - \text{number of negative diff}(x_i^j)}{n-1} \right|}{1} \quad (1)$$

Where  $n$  represents the number of windows, and  $m$  denotes the number of monitored systems or structures, which, in our case, is 1. In this study, the metric is computed using the training datasets to identify the most important features for subsequent steps.

### 3.4 Feature Fusion

In this step, the most important selected features need to be fused to create a more informative and compact representation in lower dimensions while preserving as much relevant information as possible. Feature fusion helps reduce redundancy and enhances the efficiency of subsequent analyses. In this study, PCA is employed as a dimensionality reduction technique to fuse the selected features. PCA transforms the original feature set into a new set of uncorrelated principal components, ranked by their ability to capture variance in the data.

Before applying PCA, it is crucial to standardize the data to ensure that all features contribute equally to the analysis. Standardization prevents features with larger magnitudes from dominating the principal components. As a best practice, features should be normalized to the same scale before performing PCA. The mean and standard deviation used for normalization using z-score function, along with the PCA coefficients, are derived from the training data and consistently applied to the entire dataset.

## 4 IMPELLIMENTATION ON EXPERIMENTAL DATA

Four strain data sets are available from the SGs for the experimental test, based on the proposed methodology. As the data has already been managed and pre-processed using the DCS-100A software, the next step is feature extraction. In this step, the features mentioned in Section 3.3 are calculated for

the SG signals by segmenting the signals into windows of 2,000 data points. Figure 8 presents examples of the features calculated for the SG signals.

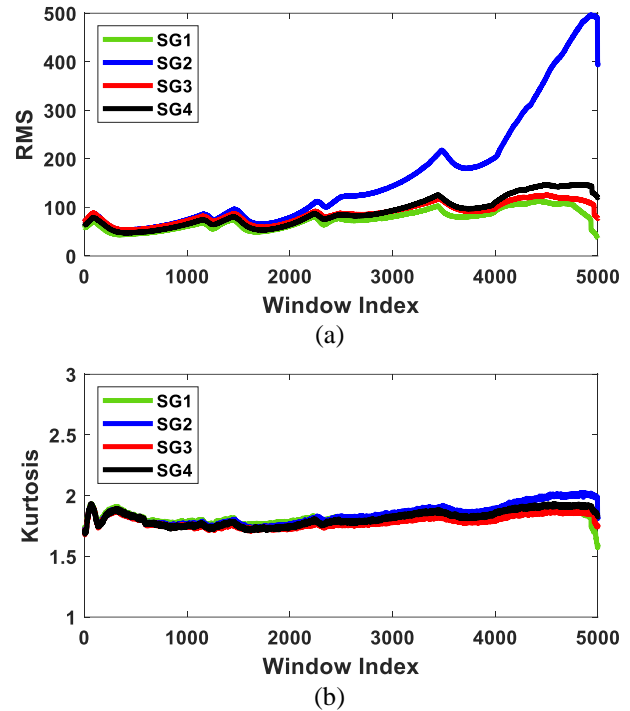
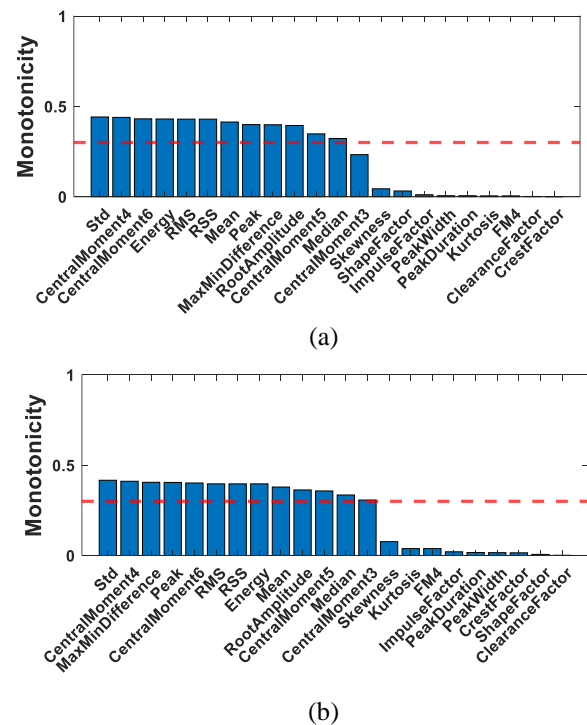
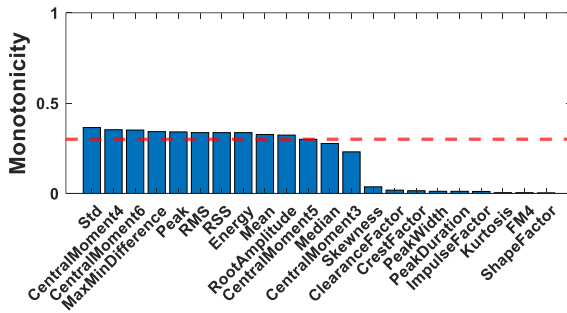


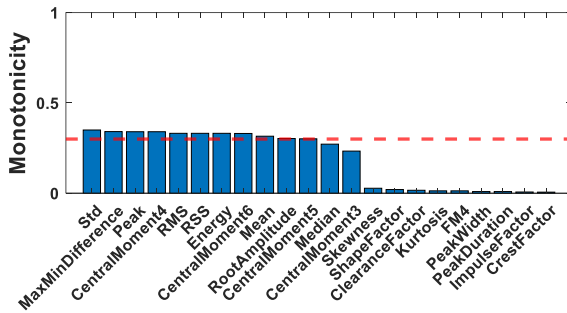
Figure 8 Examples of calculated features for SG sensors

After calculating these features, feature ranking is performed using Equation (1). However, the features are smoothed to enhance the performance of the monotonicity function. In this study, a threshold value of 0.3 is applied to select features for fusion. Figure 9 illustrates the feature importance for each SG. This feature ranking step is conducted using the training dataset, which represents 40% of the total lifetime.





(c)



(d)

Figure 9 Feature importance: (a) SG1, (b) SG2, (c) SG3, (d) SG4

Based on Figure 9, it can be concluded which features exhibit greater importance and maintain a more monotonic trend during the fatigue test. For instance, the standard deviation demonstrates the highest importance across all SG sensors. Therefore, all selected features that meet the predefined threshold will be utilized for fusion.

For each SG sensor, the selected features are transformed to a lower-dimensional space using PCA, with normalization applied relative to the training dataset. The first principal component (PC) is chosen as it captures the maximum gradient in the feature space. Figure 10 illustrates the first principal component for each SG sensor based on the selected features.

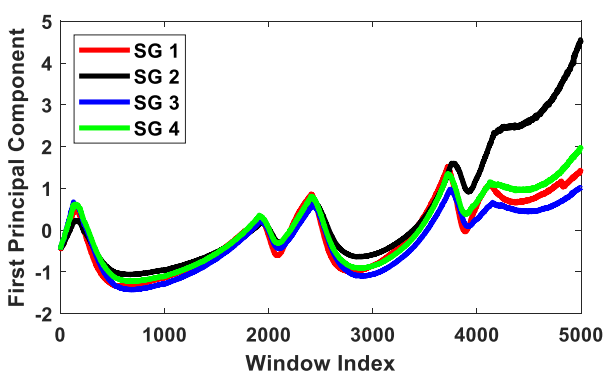


Figure 10 First principal component for each SG sensor

As shown in Figure 10, the first PC appears to be a promising HI derived from the fused features, offering greater robustness compared to any single feature. For better visualization of the first PC as a health indicator, an exponential function is fitted

to each curve, with all curves shifted to zero at the starting point, as shown in Figure 11.

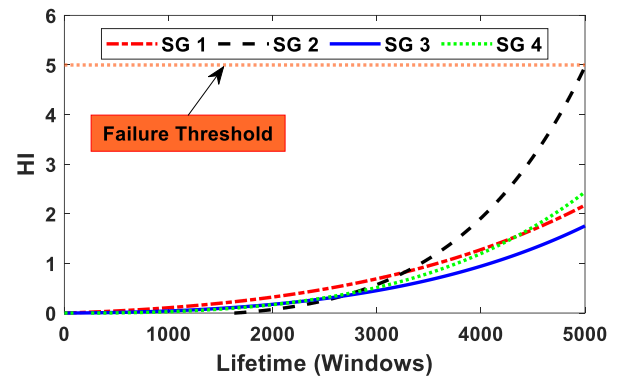
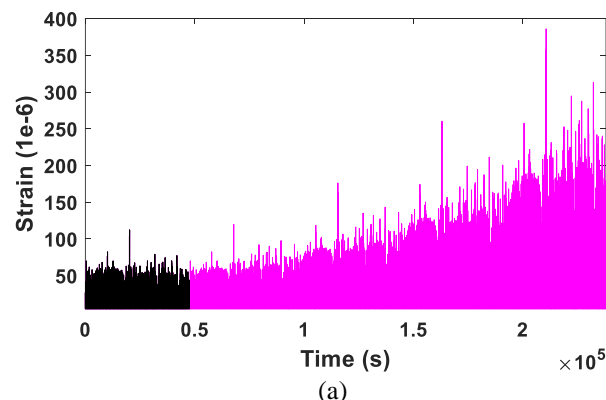


Figure 11 Constructed HI using SG sensor data

As shown in Figure 11, the HI for SG sensor 2 reaches level 5, which is recognized as the failure threshold. Therefore, this threshold can be used as a criterion for any new sample. However, due to the heterogeneous nature of asphalt, more experiments are required to establish a reliable threshold. Once validated, this HI can serve as an input to a prognosis model, such as an exponential degradation model, for estimating the remaining useful life. However, applying this approach in real field conditions remains challenging, as the exact failure point is still unknown.

## 5 IMPLEMENTATION ON IN-SITU DATA

Before implementing a method on in-situ data collected through an FBG sensor network embedded in the road, it is important to consider that, since the pavement is newly constructed, no damage is typically present, and the collected data can be labeled as "healthy." This dataset can then be used to generate synthetic data representing damaged conditions. Unlike experimental tests, where loading conditions are controlled, in this case, the loading is random, and no specific information about it is available. Based on experimental observations, damage affects sensor responses depending on its distance from the sensor. Therefore, two types of data can be generated: one where the damage occurs at the sensor location (G1) and another where the damage is not at the sensor location but within a detectable distance (G2). This can be achieved using an exponential function to generate synthetic data, as illustrated in Figure 12.



(a)

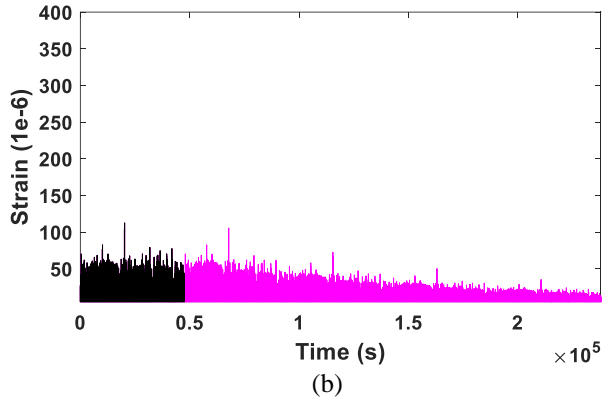


Figure 12 Generated synthetic data using available healthy data: (a) G1, (b) G2

Now, these data can be used to implement the proposed method, beginning with feature extraction. For example, Figure 13 shows the calculated features for both signals after segmentation into windows of 2,000 data points.

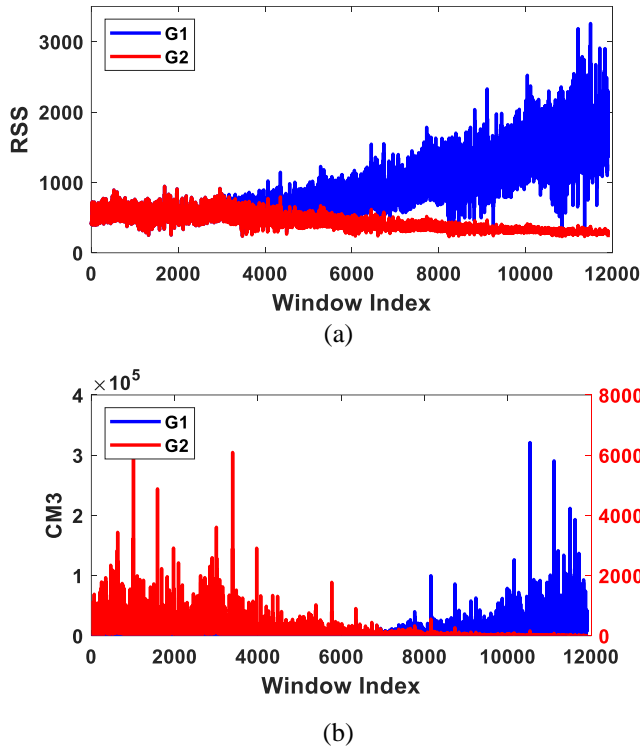


Figure 13 Examples of calculated features for G1 and G2

A threshold value of 0.3 is applied again to select features for fusion. Figure 14 illustrates the feature importance for G1 and G2. This feature ranking step is performed using the training dataset, which accounts for 40% of the total lifetime.

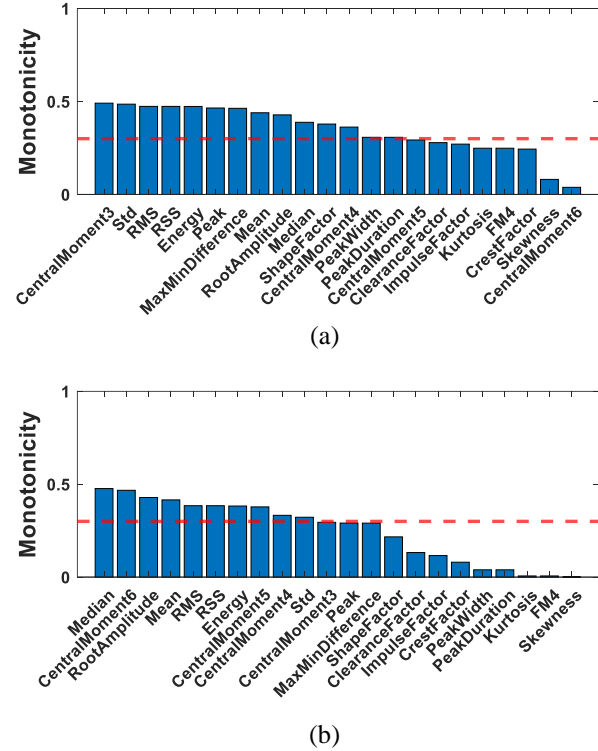


Figure 14 Feature importance: (a) G1, (b) G2

As shown in Figure 14, the important features vary in each case. For example, in the first case, central moment 3 is the top feature, whereas in the second case, it is not even among the selected features. This highlights the importance of feature ranking before fusion. Figure 15 illustrates the first principal component for each generated data based on the selected features.

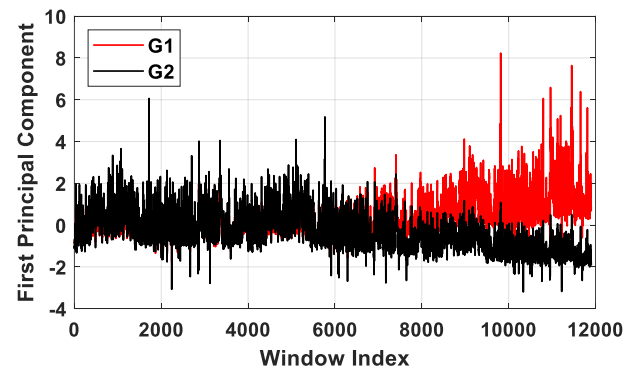


Figure 15 Feature importance: (a) G1, (b) G2

For clearer visualization of the PC as a health indicator, an exponential function is fitted to each curve, with all curves adjusted to start at zero, as shown in Figure 16.



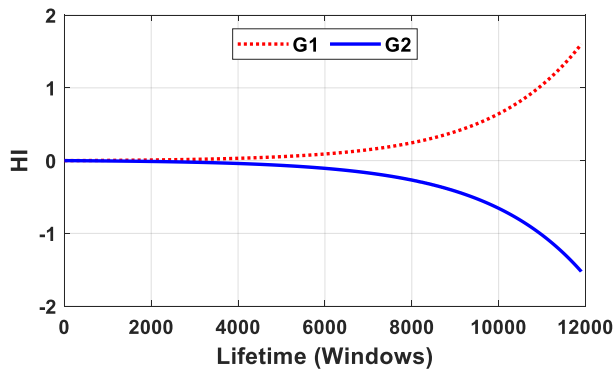


Figure 16 Constructed HI using generated data

As shown in Figure 16, the Health Indicator (HI) for G1 exhibits an increasing trend, while for G2, it shows a decreasing trend. This suggests that the HI can be used for health monitoring, even with real data. Although a specific threshold cannot be defined, an adaptive threshold could be a potential solution, requiring further investigation.

## 6 CONCLUSIONS

This study presents a framework to compress, reduce, and fuse raw data collected from a sensor network into a HI for monitoring road infrastructure using FBG sensor network that produces a sheer volume of data. The integration of sensor data processing, feature extraction, and machine learning methods enables the detection of damage in infrastructure, ensuring timely maintenance interventions. Key findings of this study are as follows:

- Based on experimental tests, it has been confirmed that the sensor response is dependent on its distance from the damage.
- The monotonicity metric is effective in identifying features sensitive to damage propagation and refining features before fusion.
- The use of the first principal component as a health indicator demonstrates its effectiveness in tracking damage progression. In experimental tests, the health indicator's trend helped identify damage once it exceeded a threshold, though further validation is needed to establish a universal failure threshold for real-world applications.
- The proposed HI meets the key criteria for an optimal HI, including detectability and separability, making it acceptable based 2VP. Additionally, trendability can be achieved by taking the absolute value of the HI if needed.
- The constructed HI can be used for RUL estimation using a prognosis model, provided the threshold is known. However, determining a reliable threshold remains a challenge for real-world applications.
- The proposed framework is sensor-independent, except for some specific pre-processing steps that vary for each sensor. This framework can be implemented for infrastructure monitoring using large-scale sensor networks for efficient SHM.

In conclusion, the methodology introduced in this study holds great promise for the future of infrastructure health

monitoring. With further refinement and validation, it has the potential to make road maintenance more efficient and cost-effective.

## ACKNOWLEDGMENTS

This study is funded by the Port of Antwerp-Bruges, project 48231 "Durable Pavements for Port area - Heavily loaded pavements: exploration and in-depth study". The research team also thanks Com&Sens for their technical support during installation and data collection.

## REFERENCES

- [1] Barbieri dm, Lou b. Instrumentation and testing for road condition monitoring—a state-of-the-art review. *NDT & E International*. 2024 Jun 12;103161.
- [2] Bajwa R, Coleri E, Rajagopal R, Varaiya P, Flores C. Pavement performance assessment using a cost-effective wireless accelerometer system. *Computer-Aided Civil and Infrastructure Engineering*. 2020 Sep;35(9):1009-22.
- [3] Memisoglu Apaydin N, Zulfikar AC, Cetindemir O. Structural health monitoring systems of long-span bridges in Turkey and lessons learned from experienced extreme events. *Journal of Civil Structural Health Monitoring*. 2022 Dec;12(6):1375-412.
- [4] Kavitha S, Daniel RJ, Sumangala K. High performance MEMS accelerometers for concrete SHM applications and comparison with COTS accelerometers. *Mechanical Systems and Signal Processing*. 2016 Jan 1;66:410-24.
- [5] Ghaderiaram A, Schlangen E, Fotouhi M. Structural Fatigue Life Monitoring with Piezoelectric-Based Sensors: Fundamentals, Current Advances, and Future Directions. *Sensors*. 2025 Jan 8;25(2):334.
- [6] Saafi M, Sayyah T. Health monitoring of concrete structures strengthened with advanced composite materials using piezoelectric transducers. *Composites Part B: Engineering*. 2001 Jan 1;32(4):333-42.
- [7] Alavi AH, Hasni H, Lajnef N, Chatti K. Continuous health monitoring of pavement systems using smart sensing technology. *Construction and Building Materials*. 2016 Jul 1;114:719-36.
- [8] Michalcová L, Bělský P, Petrusová L. Composite panel structural health monitoring and failure analysis under compression using acoustic emission. *Journal of Civil Structural Health Monitoring*. 2018 Sep;8(4):607-15.
- [9] Lovejoy SC. Acoustic emission testing of beams to simulate SHM of vintage reinforced concrete deck girder highway bridges. *Structural Health Monitoring*. 2008 Dec;7(4):329-46.
- [10] Carboni M, Crivelli D. An acoustic emission based structural health monitoring approach to damage development in solid railway axles. *International Journal of Fatigue*. 2020 Oct 1;139:105753.
- [11] Wang Y, Yao H, Wang J, Xin X. Distributed optical fiber sensing system for large infrastructure temperature monitoring. *IEEE Internet of Things Journal*. 2021 Jul 19;9(5):3333-45.
- [12] Chen B, Zhu Z, Su Z, Yao W, Zheng S, Wang P. Optical fiber sensors in infrastructure monitoring: a comprehensive review. *Intelligent Transportation Infrastructure*. 2023;2:liad018.
- [13] Velha P, Nannipieri T, Signorini A, Morosi M, Solazzi M, Barone F, Frisoli A, Ricciardi L, Eusepi R, Icardi M, Recchia G. Monitoring large railways infrastructures using hybrid optical fibers sensor systems. *IEEE Transactions on Intelligent Transportation Systems*. 2019 Nov 7;21(12):5177-88.
- [14] Chan TH, Yu L, Tam HY, Ni YQ, Liu SY, Chung WH, Cheng LK. Fiber Bragg grating sensors for structural health monitoring of Tsing Ma bridge: Background and experimental observation. *Engineering structures*. 2006 Apr 1;28(5):648-59.
- [15] Wang J, Han Y, Cao Z, Xu X, Zhang J, Xiao F. Applications of optical fiber sensor in pavement Engineering: A review. *Construction and Building Materials*. 2023 Oct 12;400:132713.
- [16] Golmohammadi A, Hasheminejad N, Hernando D. An Innovative Data Analysis Approach via Peak-Counting-Based Segmentation for Pavement Monitoring Using FBG Sensors. *Journal of Testing and Evaluation*. 2025 Mar 1;53(2).
- [17] Golmohammadi A, Hasheminejad N, Hernando D, Vanlanduit S. Performance assessment of discrete wavelet transform for de-noising of

- FBG sensors signals embedded in asphalt pavement. *Optical Fiber Technology*. 2024 Jan 1;82:103596.
- [18] Santos AD, Silva MF, Sales CS, Fernandes CS, Sousa MJ, Costa JC, Souza RM. Software development for acquisition and data management in optical sensor networks. In 2014 IEEE International Instrumentation and Measurement Technology Conference (I2MTC) Proceedings 2014 May 12 (pp. 96-101). IEEE.
- [19] Wang T, Bhuiyan MZ, Wang G, Rahman MA, Wu J, Cao J. Big data reduction for a smart city's critical infrastructural health monitoring. *IEEE Communications Magazine*. 2018 Mar 15;56(3):128-33.
- [20] Khoa NL, Zhang B, Wang Y, Chen F, Mustapha S. Robust dimensionality reduction and damage detection approaches in structural health monitoring. *Structural Health Monitoring*. 2014 Jul;13(4):406-17.
- [21] Hassani S, Dackermann U, Mousavi M, Li J. A systematic review of data fusion techniques for optimized structural health monitoring. *Information Fusion*. 2024 Mar 1;103:102136.
- [22] Wu RT, Jahanshahi MR. Data fusion approaches for structural health monitoring and system identification: Past, present, and future. *Structural Health Monitoring*. 2020 Mar;19(2):552-86.
- [23] Moradi M, Broer A, Chiachio J, Benedictus R, Loutas TH, Zarouchas D. Intelligent health indicator construction for prognostics of composite structures utilizing a semi-supervised deep neural network and SHM data. *Engineering Applications of Artificial Intelligence*. 2023 Jan 1;117:105502.
- [24] Coble J, Hines JW. Identifying optimal prognostic parameters from data: a genetic algorithms approach. In Annual Conference of the PHM Society 2009 (Vol. 1, No. 1).
- [25] Zhou H, Huang X, Wen G, Lei Z, Dong S, Zhang P, Chen X. Construction of health indicators for condition monitoring of rotating machinery: A review of the research. *Expert Systems with Applications*. 2022 Oct 1;203:117297.
- [26] Golmohammadi A, Hernando D, Hasheminejad N. Advanced data-driven FBG sensor-based pavement monitoring system using multi-sensor data fusion and an unsupervised learning approach. *Measurement*. 2025 Jan 1;242:115821.
- [27] Hernando D, Tavalaei SG, Hasheminejad N, Van Den Bergh W, Voet E. Exploring the use of fiber Bragg grating sensors for monitoring the structural response of asphalt pavements. In Bituminous Mixtures and Pavements VIII 2024 Jun 21 (pp. 708-716). CRC Press.
- [28] Saidi L, Ali JB, Bechhoefer E, Benbouzid M. Wind turbine high-speed shaft bearings health prognosis through a spectral Kurtosis-derived indices and SVR. *Applied Acoustics*. 2017 May 1;120:1-8.

# Etched fiber Bragg grating sensor-based groundwater salinity monitoring for seawater intrusion

Hongtao Jiang<sup>1</sup>, Junyi Guo<sup>2</sup>, Bin Shi<sup>2</sup>, Mengya Sun<sup>3</sup>, Guangqing Wei<sup>4</sup>

<sup>1</sup> School of Geographic and Oceanographic Science, Nanjing University, No.163 Xianlin Avenue, 210023 Nanjing, China

<sup>2</sup> School of Earth Sciences and Engineering, Nanjing University, No.163 Xianlin Avenue, 210023 Nanjing, China

<sup>3</sup> School of Earth Sciences and Engineering, Hohai University, No. 8 Focheng West Road, 210098 Nanjing, China

<sup>4</sup> Suzhou Nanzee Sensing Technology Co., Ltd, No.150 Renai Avenue, 215123 Suzhou, China

email: jianghongtao@nju.edu.cn, gjy@smail.nju.edu.cn, shibin@nju.edu.cn, smy@hhu.edu.cn, wgq@nzsensing.com

**ABSTRACT:** As global climate change drives rising sea levels, coastal regions face growing threats from seawater intrusion. This process increases groundwater salinity, accelerating steel corrosion and compromising the structural integrity of concrete infrastructure. However, addressing these challenges is limited by existing salinity monitoring technologies, which often suffer from slow response times and low sensitivity in in-situ conditions. This study proposes a salinity sensor based on Fiber Bragg Grating (FBG), enhanced by chemically etching the fiber cladding to create an etched FBG (EFBG). This modification improves sensitivity to external refractive indices for accurate salinity detection. A three-layer waveguide dispersion model simulated wavelength shifts during sensor etching and testing using MATLAB, revealing how etching diameters impact sensitivity and confirming a linear relationship between wavelength and seawater salinity. To improve EFBG durability and reduce hydrofluoric acid damage, the etching process was divided into rapid, stable, and fine stages. Results demonstrated that higher etching levels increased sensitivity, achieving a sensitivity coefficient of up to 29.432 pm/% in specific conditions. The EFBG salinity sensor offers high sensitivity, fast response, compact size, corrosion resistance, and interference immunity, making it ideal for in-situ groundwater salinity monitoring in aquifers and mitigating risks to coastal structural health.

**KEY WORDS:** Salinity; Fiber Bragg grating (FBG); Chemical etching; Seawater Intrusion.

## 1 INTRODUCTION

Excessive groundwater extraction in coastal areas disrupts the natural balance between freshwater and seawater, driving inland migration of the saltwater-freshwater interface — a phenomenon known as seawater intrusion [1,2]. This process significantly increases groundwater salinity, which accelerates corrosion of steel reinforcements and compromises the structural integrity of concrete infrastructure in coastal regions, posing severe risks to long-term structural health and safety [3].

Monitoring groundwater salinity is crucial for assessing seawater intrusion severity and protecting infrastructure [4,5]. Existing monitoring techniques include electrical conductivity sensors, microwave remote sensing, and fiber optic sensors. Electrical conductivity sensors offer high accuracy, but inductive types are vulnerable to electromagnetic interference, while electrode types suffer from fouling, limiting long-term performance [6,7]. Microwave remote sensing enables large-scale surface salinity observation, but it cannot penetrate below the surface or provide in-situ groundwater monitoring [8,9].

Fiber optic sensors have attracted increasing attention due to their compact size, immunity to electromagnetic interference, and high sensitivity [10]. Among them, Fiber Bragg Grating (FBG)-based salinity sensors can be divided into polymer-coated FBGs and etched FBGs (EFBGs). Polymer-coated sensors, such as those developed by Jun Cong et al. (2002) [11] and Ping Lu et al. (2008) [12], achieve moderate sensitivity, but suffer from slow response and poor repeatability due to polymer swelling and hysteresis.

To improve sensitivity, Kerstin Schroeder et al. (2001) [13] introduced a side-polished FBG, exposing the evanescent field for salinity detection, but the sensor exhibited non-linear response in varying temperature and salinity environments.

Pereira et al. (2004) [14] used hydrofluoric acid to etch FBGs, achieving a salinity sensitivity of 1.28 pm/%, but this approach lacked robust in-situ adaptation for groundwater monitoring.

Most existing EFBG sensors focus on biochemical sensing, with limited research targeting long-term groundwater salinity monitoring for seawater intrusion detection. This study develops a high-sensitivity, fast-response EFBG salinity sensor capable of salinity measurement, providing a compact and reliable solution for real-time in-situ groundwater salinity monitoring, contributing to the protection of coastal groundwater resources and infrastructure health.

## 2 FUNDAMENTAL PRINCIPLE OF EFBG FOR SEAWATER SALINITY SENSING

A Fiber Bragg Grating (FBG) is a reflective grating structure inscribed in the core of an optical fiber. When broadband light propagates along the fiber axis, the FBG reflects a specific wavelength, known as the Bragg wavelength, which is determined by the effective refractive index of the fiber core and the grating period, as shown in Figure 1 [15].

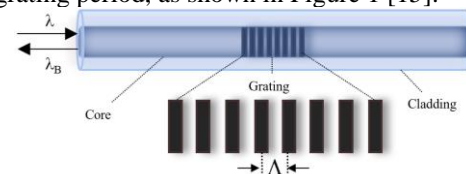


Figure 1. The schematic diagram of FBG sensing principle.

The Bragg wavelength  $\lambda_B$  satisfies the following relationship [16]:

$$\lambda_B = 2n_{eff}\Lambda \quad (1)$$



where  $n_{eff}$  denotes the effective refractive index of the fiber core, and  $\Lambda$  represents the grating period.

In conventional optical fibers, the presence of a complete cladding layer confines light within the fiber core, making the Bragg wavelength largely insensitive to changes in the external refractive index. However, by physically or chemically reducing the cladding thickness, a portion of the light propagating in the core extends into the surrounding medium as an evanescent field. This modification allows the effective refractive index  $n_{eff}$  to be influenced by the external refractive index, thereby shifting the Bragg wavelength  $\lambda_B$ .

As the cladding thickness decreases, the optical fiber gradually forms a three-layer waveguide structure, consisting of the external medium, the remaining cladding, and the core. The modal characteristics of light propagation change accordingly, and the propagation constant  $\beta$  is also affected. To quantify the influence of cladding etching on the propagation constant, the corrected propagation constant for different etched diameters can be expressed as [17]:

$$\beta = \beta_0 + \kappa \eta_P (n_{SRI} - n_{cl}) \quad (2)$$

where  $\beta_0$  represents the propagation constant under normal conditions,  $k$  denotes the wave vector, and  $\alpha$  is the power loss coefficient, representing the proportion of power loss in the etched region relative to the total guided power.  $n_{ext}$  and  $n_{clad}$  denote the refractive indices of the external medium and the cladding, respectively.

From the definition of the propagation constant, the effective refractive index  $n_{eff}$  can be derived as:

$$\partial n_{eff} = \partial n \partial \eta \quad (3)$$

At the end of the etching process, the effective refractive index reaches a stable value, denoted as  $n_{eff, final}$ . Combining this with Equations (1), (2), and (3), the relationship between Bragg wavelength shift and external refractive index can be obtained:

$$\partial \lambda_B = 2\Lambda \eta_0 (n_{SRI} - n_{cl}) \quad (4)$$

This indicates that after etching to a certain diameter, the Bragg wavelength becomes highly sensitive to changes in the external refractive index.

In practice, the primary salt component in seawater is sodium chloride (NaCl). Therefore, the salinity of seawater can be approximated using NaCl solution concentration. At constant temperature, the refractive index of NaCl solution exhibits a linear relationship with salinity [18]:

$$c(\%) = k_s n_{SRI} - k_0 \quad (5)$$

where  $k_s$  is the salinity coefficient, which remains constant under fixed external conditions when only salinity changes. In this study,  $k_s$  is set to 540.5405, and  $k_0$  is 720.5946.

### 3 NUMERICAL MODEL FOR EFBG SEAWATER SALINITY SENSING

To further establish the quantitative relationship between EFBG wavelength shifts and seawater salinity, a numerical analysis was conducted using MATLAB. The calculation of the effective refractive index requires a fiber waveguide model, which can be divided into two-layer and three-layer structures, as shown in Figure 2.

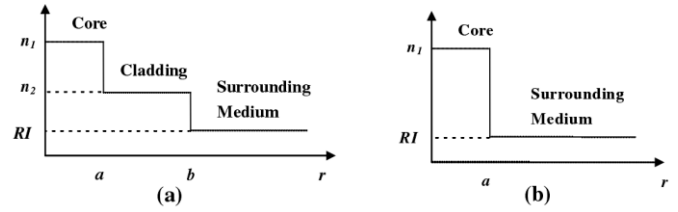


Figure 2. Two types of fiber waveguide models: (a) Three-layer structure; (b) Two-layer structure.

When the fiber cladding is fully etched away or the etching extends into the fiber core, the core and external medium form a simple two-layer circular waveguide model (Figure 2(a)). This type, known as the core-etched FBG, offers high salinity sensitivity. However, due to severe cladding removal, the mechanical strength is significantly reduced, resulting in poor robustness, which limits its suitability for long-term monitoring in harsh environments. To balance mechanical integrity and sensitivity, this study employs a partially etched FBG structure, modeled as a three-layer circular waveguide (Figure 2(b)). The dispersion equation for the three-layer fiber waveguide can be expressed as follows [19]:

$$\begin{cases} [\hat{J}_m(u) - \hat{Y}_m(u'c)][\hat{K}_m(v) - \hat{J}_m(u')] = \frac{J_{m+1}(u'c)Y_{m+1}(u')}{J_{m+1}(u')Y_{m+1}(u'c)} & (\beta < k_0 n_{cl}) \\ [\hat{J}_m(u) - \hat{J}_m(u'c)][\hat{K}_m(v) - \hat{Y}_m(u')] = \frac{J_{m+1}(u'c)Y_{m+1}(u')}{J_{m+1}(u')Y_{m+1}(u'c)} & (\beta < k_0 n_{cl}) \\ [\hat{J}_m(u) - \hat{K}_m(v'c)][\hat{K}_m(v) + \hat{I}_m(v')] = \frac{I_{m+1}(v'c)K_{m+1}(v')}{I_{m+1}(v')K_{m+1}(v'c)} & ((\beta > k_0 n_{cl})) \\ [\hat{J}_m(u) + \hat{I}_m(v'c)][\hat{K}_m(v) - \hat{K}_m(v')] = \frac{I_{m+1}(v'c)K_{m+1}(v')}{I_{m+1}(v')K_{m+1}(v'c)} & ((\beta > k_0 n_{cl})) \end{cases} \quad (6)$$

The mathematical symbols and parameters used in the equation are defined as:

$$\hat{Z}_m(x) = \frac{Z_m(x)}{xZ_{m+1}(x)} \quad (7)$$

$$u = a_1(k_0^2 n_1^2 - \beta^2)^{1/2} \quad (8)$$

$$u' = a_2(k_0^2 n_{cl}^2 - \beta^2)^{1/2} \quad (9)$$

$$v' = a_2(\beta^2 - k_0^2 n_{cl}^2)^{1/2} \quad (10)$$

$$v = a_2(\beta^2 - k_0^2 n_{SRI}^2)^{1/2} \quad (11)$$

$$c = \frac{a_1}{a_2} \quad (12)$$

where  $k_0$  denotes the vacuum wave number. The fiber parameters used in this model match the experimental optical fiber specifications discussed later.  $J_m$  and  $Y_m$  represent the first and second kind Bessel functions, respectively, while  $I_m$  and  $K_m$  denote the modified first and second kind Bessel functions.

Based on the above equations, MATLAB was used to calculate the relationship between FBG wavelength and fiber diameter during the etching process. Figure 3 illustrates the variation in Bragg wavelength as a function of fiber diameter when the external refractive index is set to 1.333.

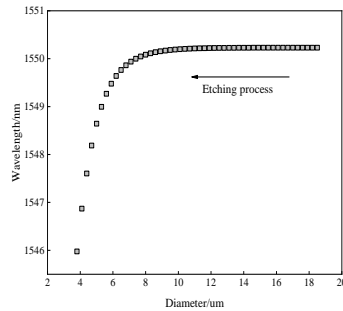


Figure 3 Diagram of wavelength variation as a function of diameter during etching.

As shown in Figure 3, at the initial stage of etching, the thick cladding confines the optical field within the core, making the wavelength almost insensitive to the external refractive index. As etching progresses and the cladding becomes thinner, the evanescent field begins to interact with the external environment. Due to the lower refractive index of the surrounding medium compared to the cladding, the Bragg wavelength decreases sharply as the diameter decreases. This trend provides a basis for real-time monitoring of fiber diameter during the etching process.

The surface salinity of seawater typically ranges from 3.4‰ to 3.7‰. To evaluate the feasibility of EFBG sensors for seawater salinity monitoring, MATLAB simulations were carried out to investigate the relationship between salinity and wavelength shift under low-salinity conditions. As shown in Figure 4, the smaller the fiber diameter, the higher the salinity sensitivity. Within the salinity range of 0–6‰, EFBG sensors with different diameters all exhibit a clear linear relationship between salinity and wavelength shift. Higher etching levels consistently lead to increased salinity sensitivity, providing important design and fabrication guidelines for EFBG-based salinity sensors.

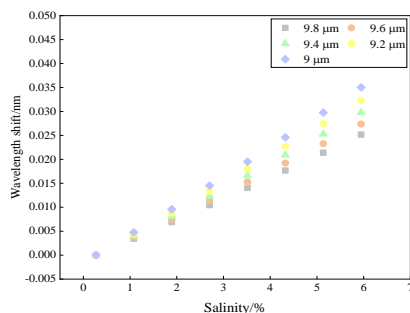


Figure 4 Relationship between wavelength variation and salinity at low salinity.

## 4 EXPERIMENTAL DESIGN AND SALINITY SENSING TESTS

### 4.1 Etching Process

The fiber optic sensing element used in this study is a single-point fiber Bragg grating sensor with a central wavelength of 1564 nm, a wavelength tolerance of  $\pm 0.2$  nm, and a grating length of 10 mm. The fiber is coated with an acrylate layer, with

a reflectivity of 88.3%, a 3 dB bandwidth of 0.23 nm, and a side mode suppression ratio of 22 dB. The core diameter is 9  $\mu\text{m}$ , cladding diameter is 125  $\mu\text{m}$ , and the coating diameter is 240  $\mu\text{m}$ , consistent with the parameters used in the numerical simulations.

Hydrofluoric acid (HF), known for its strong corrosive properties on glass and silicon-based materials, was used to etch the fiber cladding. The initial HF concentration was 40%, which was diluted with distilled water to prepare solutions of lower concentrations for staged etching. During the etching process, the non-grating sections of the fiber were covered with paraffin wax to protect them from unnecessary etching. The fiber was also connected to an NZS-FBG-A01 interrogator (Suzhou Nanzhi Sensing Technology Co., Ltd.) via patch cords to monitor real-time Bragg wavelength shifts, allowing precise control over the final cladding diameter. The interrogator operates in the wavelength range of 1528–1568 nm with a resolution of 1 pm. To ensure the reliability of etching rate measurements, three bare fibers were fixed in parallel on a T-shaped plastic holder and immersed in HF solutions for parallel etching experiments. Each etching session lasted 60 minutes, after which the fibers were thoroughly rinsed with deionized water to remove residual acid and air-dried in a ventilated area. The diameters of the fibers were measured under an optical microscope, and the average diameter of the three fibers was recorded for each condition. This process was repeated to determine etching rates at different HF concentrations.

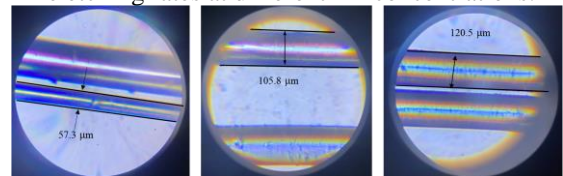


Figure 5. Microscope images of bare fibers etched by hydrofluoric acid at different concentrations: (a) 40% concentration; (b) 20% concentration; (c) 5.7% concentration.

The results show that higher HF concentrations lead to faster etching rates but also create rougher fiber surfaces, as shown in Figure 5. To reduce surface irregularities, minimize residual stress, and improve the wavelength stability of the sensor, a staged etching process was employed. In this process, high-concentration HF was first used for rapid bulk etching, followed by lower-concentration HF for gradual surface refinement. This method ensures a smoother grating surface and reduces unwanted stress-induced wavelength shifts.

### 4.2 Salinity Testing

To simulate coastal groundwater conditions, artificial seawater with salinities ranging from 0‰ to 6‰ (in 1‰ increments) was prepared by dissolving NaCl in distilled water. The EFBG sensor was sequentially immersed in these solutions, and the Bragg wavelength was recorded in real time to evaluate its response to salinity changes.

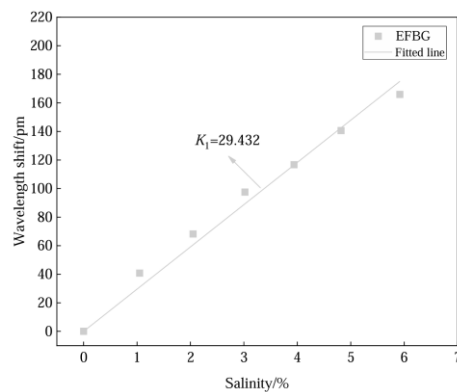


Figure 6. Bragg wavelength variation at different salinities.

The initial wavelength offset of the EFBG was 7.5 nm. Based on the diameter-wavelength relationship established through numerical analysis, the cladding diameter of the EFBG was calculated to be 14.82  $\mu\text{m}$ . The measured Bragg wavelength shifts at different salinity levels are shown in Figure 6. As illustrated, the Bragg wavelength shift increases significantly with rising salinity and demonstrates a clear linear relationship with salinity. The EFBG sensor achieved a salinity sensitivity of 29.432 pm/‰, confirming its potential for high-sensitivity salinity monitoring.

## 5 CONCLUSION

This study developed an etched fiber Bragg grating (EFBG) sensor for in-situ monitoring of groundwater salinity in coastal aquifers affected by seawater intrusion. A combination of numerical modeling, staged chemical etching, and salinity calibration experiments was used to evaluate sensor performance. The key conclusions are as follows:

(1) A three-layer fiber waveguide model was established to simulate the effect of cladding etching on Bragg wavelength shifts. Numerical results confirmed that reducing the cladding diameter enhances evanescent field sensitivity, significantly improving salinity response. A clear linear relationship between Bragg wavelength shift and salinity was observed within the 0–6‰ salinity range.

(2) A staged etching process using high and low concentrations of hydrofluoric acid was employed to optimize both the etching efficiency and surface smoothness. This approach minimized surface defects, reduced stress-induced wavelength drift, and ensured stable sensor performance.

(3) Experimental results demonstrated that the EFBG sensor with a cladding diameter of 14.82  $\mu\text{m}$  achieved a salinity sensitivity of 29.432 pm/‰, with excellent linearity between Bragg wavelength shift and salinity. This high sensitivity, combined with the sensor's compact size, corrosion resistance, and real-time monitoring capability, makes it well-suited for long-term in-situ groundwater salinity monitoring in coastal areas.

Overall, the proposed EFBG sensor offers a practical and effective solution for groundwater salinity monitoring, contributing to improved seawater intrusion early warning and the protection of coastal infrastructure and water resources.

## ACKNOWLEDGMENTS

This research was financially supported by the National Natural Science Foundation of China, NSFC (Grant Nos. 42177135, 42030701, 423B2704).

## REFERENCES

- [1] N. Kazakis, A. Pavlou, G. Vargemezis, K. S. Voudouris, G. Soulios, F. Pliakas, and G. Tsokas, Seawater intrusion mapping using electrical resistivity tomography and hydrochemical data: An application in the coastal area of eastern Thermaikos Gulf, Greece, *Science of the Total Environment*, vol. 543, pp. 373–387, 2016.
- [2] L. Shi and J. J. Jiao, *Seawater intrusion and coastal aquifer management in China: A review*, *Environmental Earth Sciences*, vol. 72, pp. 2811–2819, 2014.
- [3] S. Fadaie, M. Mehravar, D. J. Webb, and W. Zhang, *Nearshore contamination monitoring in sandy soils using polymer optical fibre Bragg grating sensing systems*, *Sensors*, vol. 22, pp. 1–19, 2022.
- [4] J. Safarov, F. Millero, R. Feistel, A. Heintz, and E. Hassel, *Thermodynamic properties of standard seawater*, *Ocean Science*, vol. 6, pp. 689–722, 2009.
- [5] I. Astin and Y. Feng, *Technical Note: Remote sensing of sea surface salinity using the propagation of low-frequency navigation signals*, *Ocean Science*, vol. 11, pp. 695–698, 2015.
- [6] C. Woody, E. Shih, J. Miller, T. Royer, L. P. Atkinson, and R. S. Moody, *Measurements of salinity in the coastal ocean: A review of requirements and technologies*, *Marine Technology Society Journal*, vol. 34, no. 2, pp. 26–33, 2000.
- [7] P. Grosso, M. Le Menn, J. L. De Bougrenet De La Tournaye, Z. Y. Wu, and D. Malardé, *Practical versus absolute salinity measurements: New advances in high performance seawater salinity sensors*, *Deep-Sea Research Part I: Oceanographic Research Papers*, vol. 57, pp. 151–156, 2010.
- [8] N. Vinogradova, T. Lee, J. Boutin, K. Drushka, S. Fournier, R. Sabia, D. Stammer, E. Bayler, N. Reul, A. Gordon, O. Melnichenko, L. Li, E. Hackert, M. Martin, N. Kolodziejczyk, A. Hasson, S. Brown, S. Misra, and E. Lindstrom, *Satellite salinity observing system: Recent discoveries and the way forward*, *Frontiers in Marine Science*, vol. 6, pp. 1–23, 2019.
- [9] C. Gabarró, J. Font, A. Camps, M. Vall-llossera, and A. Julià, *A new empirical model of sea surface microwave emissivity for salinity remote sensing*, *Geophysical Research Letters*, vol. 31, pp. 1–5, 2004.
- [10] B. Shi, D. Zhang, H. Zhu, C. Zhang, K. Gu, H. Sang, H. Han, M. Sun, and J. Liu, *DFOS applications to geo-engineering monitoring*, *Photonic Sensors*, vol. 11, pp. 158–186, 2021.
- [11] J. Cong, X. Zhang, K. Chen, and J. Xu, *Fiber optic Bragg grating sensor based on hydrogels for measuring salinity*, *Sensors and Actuators B: Chemical*, vol. 87, pp. 487–490, 2002.
- [12] P. Lu, L. Men, and Q. Chen, *Tuning the sensing responses of polymer-coated fiber Bragg gratings*, *Journal of Applied Physics*, vol. 104, 2008.
- [13] K. Schroeder, W. Ecke, R. Mueller, R. Willsch, and A. Andreev, *A fibre Bragg grating refractometer*, *Measurement Science and Technology*, vol. 12, pp. 757–764, 2001.
- [14] D. A. Pereira, *Fiber Bragg grating sensing system for simultaneous measurement of salinity and temperature*, *Optical Engineering*, vol. 43, p. 299, 2004.
- [15] K. O. Hill and G. Meltz, *Fiber Bragg grating technology fundamentals and overview*, *Journal of Lightwave Technology*, vol. 15, pp. 1263–1276, 1997.
- [16] J. Yang, H. Lee, and H. Sohn, *An optical fiber guided ultrasonic excitation and sensing system for online monitoring of nuclear power plants*, *AIP Conference Proceedings*, vol. 1430, pp. 1640–1647, 2012.
- [17] A. N. Chryssis, S. M. Lee, S. B. Lee, S. S. Saini, and M. Dagenais, *High sensitivity evanescent field fiber Bragg grating sensor*, *IEEE Photonics Technology Letters*, vol. 17, pp. 1253–1255, 2005.
- [18] M. Y. Sun, H. T. Jiang, B. Shi, G. Y. Zhou, H. I. Inyang, and C. X. Feng, *Development of FBG salinity sensor coated with lamellar polyimide and experimental study on salinity measurement of gravel aquifer*, *Measurement*, vol. 140, pp. 526–537, 2019.
- [19] M. Monerie, *Propagation in doubly clad single-mode fibers*, *IEEE Journal of Quantum Electronics*, vol. 18, pp. 535–542, 1982.



# Geo-hazard DFOS Monitoring and its Applications

Bin Shi<sup>1</sup>, Honghu Zhu<sup>1</sup>, Chengcheng Zhang<sup>1</sup>, Mengya Sun<sup>2</sup>, Wei Zhang<sup>1</sup>, Taiyin Zhang<sup>1</sup>, Junyi Guo<sup>1</sup>

<sup>1</sup>School of Earth Sciences and Engineering, Nanjing University, No.163 Xianlin Avenue, 210023 Nanjing, China

<sup>2</sup>School of Earth Sciences and Engineering, Hohai University, No. 8 Focheng West Road, 210098 Nanjing, China

email: shibin@nju.edu.cn, zhh@nju.edu.cn, zhang@nju.edu.cn, smy@hhu.edu.cn, wzhang@nju.edu.cn, zhangtaiyin@smail.nju.edu.cn, gjy@smail.nju.edu.cn

**ABSTRACT:** As the geological body on which humans depend, rock and soil are constantly moving under the action of natural forces and human activities. Their instability often triggers geo-hazards, posing severe threats to the environment, infrastructure safety, and sustainable development. High-quality data acquisition and effective monitoring are essential for geo-hazard prevention and mitigation. The stability of rock and soil is governed by mechanical discontinuous interfaces, which are classified into material, state, and movement interfaces. This paper focuses on distributed fiber-optic sensing (DFOS) technology as an advanced tool for geo-hazard monitoring and early warning. The paper summarizes the authors' achievements over the past two decades in DFOS-based geo-hazard monitoring theory, sensing techniques, and application systems. Key advancements include strain-sensing coupling theory, moisture and seepage monitoring methods, disaster identification and prediction models, and integrated fiber-optic sensing technology platforms. Three representative cases are presented, demonstrating the application of DFOS to monitor the material interface of slope overlying rock, the state interface of land subsidence, and the movement interface of a reservoir slope. Finally, future research directions for fiber-optic sensing in rock-and-soil disaster monitoring are outlined.

**KEY WORDS:** Rock-and-soil, Interface, Geo-hazard, Monitoring, Distributed fiber-optic sensing (DFOS), Application

## 1 INTRODUCTION

Earth habitability has become a critical scientific focus in the 21st century, with rock and soil providing the fundamental foundation for human survival and infrastructure development. These geological bodies are constantly subjected to natural forces, such as earthquakes, rainfall, and landslides, as well as anthropogenic disturbances, including excavation, construction, and resource exploitation. Such internal and external forces continuously reshape the physical and mechanical properties of rock and soil, leading to instability that can trigger a variety of geo-hazards. These disasters pose severe threats to the ecological environment, engineering safety, and the sustainable development of society.

The stability and evolution of rock and soil masses are primarily governed by mechanical discontinuity interfaces, which can be categorized into material interfaces, state interfaces, and movement interfaces, as shown in Figure 1. These interfaces play a decisive role in controlling the deformation, failure mechanisms, and overall stability of rock and soil systems under complex external loads. However, their concealed, heterogeneous, and dynamic nature makes real-time monitoring and early identification of potential disaster signals particularly challenging.

Traditional monitoring methods, such as discrete point sensors, geotechnical instrumentation, and geophysical surveys, often suffer from limitations in spatial coverage, resolution, and long-term reliability. These limitations hinder the accurate depiction of internal mechanical evolution and early identification of critical hazard precursors, especially in large-scale and complex geological settings.

To overcome these challenges, distributed fiber-optic sensing (DFOS) technology has emerged as a highly promising tool for in-situ, real-time, and continuous monitoring of geo-hazards [1].

DFOS enables the long-distance, high-resolution, and distributed acquisition of strain, moisture, temperature, and other critical parameters along the entire length of a sensing cable, offering unparalleled advantages in capturing the spatial evolution of mechanical discontinuities and hazard precursors in rock and soil masses.



Figure 1 Schematic diagram of rock and soil disasters and the three types of interfaces.

This paper summarizes the key advancements achieved in DFOS-based geo-hazard monitoring by the authors' research group over the past two decades, covering areas such as strain-sensing coupling theory, moisture and seepage monitoring techniques, disaster identification and prediction models, and integrated fiber-optic sensing technology platforms. Furthermore, three representative case studies are presented to demonstrate the practical application of DFOS in monitoring material interfaces, state interfaces, and movement interfaces in

complex geotechnical environments, highlighting its unique advantages and future potential in geo-hazard monitoring and early warning.

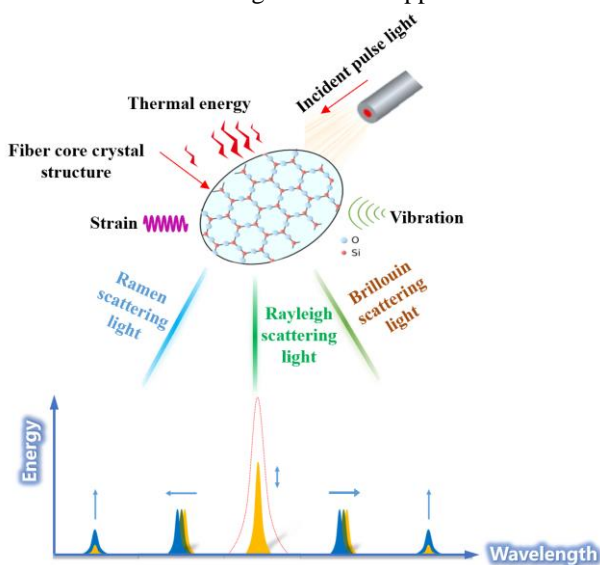
## 2 DISTRIBUTED FIBER-OPTIC SENSING TECHNOLOGY

DFOS enables continuous spatial and temporal monitoring by utilizing optical fibers as both transmission media and sensing elements. This technology encodes the measured parameter as a function of fiber length, allowing real-time data collection over large areas. By deploying sensing fibers in various configurations, DFOS effectively forms an integrated sensing network within geotechnical structures, providing critical insights into subsurface processes.

DFOS primarily encompasses three key techniques: Distributed Temperature Sensing (DTS) for thermal monitoring, Distributed Strain Sensing (DSS) for strain measurements, and Distributed Acoustic Sensing (DAS) for vibration detection [2], as shown in Figure 2. Additionally, Fiber Bragg Grating (FBG) sensing, including the advanced Ultra-Weak Fiber Bragg Grating (UWFBG) technology, offers high-resolution quasi-distributed measurements.

When embedded within soil and rock formations, DFOS enables real-time monitoring of stress, deformation, temperature, and fluid movement. This capability enhances the early detection of geo-hazards, supports infrastructure health monitoring, and improves disaster prevention strategies. Its ability to provide high-resolution, continuous data makes DFOS an essential tool for geotechnical applications.

(a)



(b)

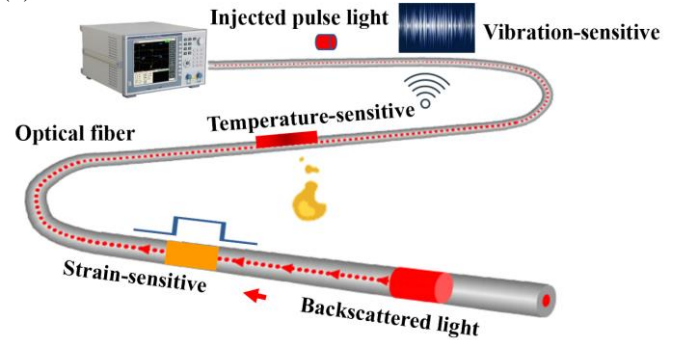


Figure 2 Schematic diagram of the distributed fiber optic sensing technology: (a) Optical principle of 3Ds; (b) 3Ds sensing scheme.

## 3 FIBER-OPTIC SENSING THEORY AND TECHNOLOGY FOR ROCK-AND-SOIL DISASTERS

The application of fiber-optic sensing technology in rock-and-soil disaster monitoring requires addressing several key theoretical and technical challenges. The primary difficulties lie in understanding and improving the strain coupling mechanism between optical fibers and geotechnical materials, effectively detecting and quantifying moisture infiltration and seepage processes, developing reliable methods for identifying and predicting disaster-related signal events, and constructing an integrated fiber-optic sensing system tailored for geo-hazard monitoring. These challenges must be overcome to enhance the accuracy and reliability of fiber-optic sensing technology in geotechnical applications. The following sections summarize the advancements achieved by the authors' research team in these areas.

### 3.1 Strain-Sensing Coupling Theory

The strain coupling mechanism between embedded fiber-optic sensors and surrounding geotechnical materials plays a crucial role in ensuring accurate deformation monitoring. Through extensive theoretical and experimental research, the authors have established a progressive failure model for fiber-soil interfaces, revealing the mechanisms governing interfacial bonding strength. On this basis, a criterion for evaluating fiber-soil interfacial adhesion was proposed, alongside a calculation method for determining critical confining pressure and the optimal embedment depth of borehole-installed fibers [3,4]. These findings provide essential guidance for improving fiber installation strategies in geotechnical applications.

To address the challenge of strain transfer in weak soil layers, a novel anchoring approach—fixed-point optical fiber technology—was developed. This technique enhances strain coupling by introducing controlled bonding points along the fiber, preventing signal attenuation due to excessive strain dissipation. By refining strain transfer mechanisms, these advancements have significantly improved the performance of DFOS in complex geological environments, ensuring the accuracy and stability of long-term geotechnical monitoring.

### 3.2 Moisture and Seepage Sensing Methods

Moisture and seepage are fundamental factors affecting the stability of rock and soil masses. Moisture primarily pertains to unsaturated soils, while seepage involves fluid movement

within porous media, often serving as a key trigger for geotechnical failures such as slope instability and land subsidence. Conventional monitoring methods, such as the active heating distributed temperature sensing (DTS) technique proposed by Selker et al., have limitations in accuracy and are only applicable in environments above 0 °C[5]. To overcome these constraints, we introduced the thermal pulse fiber-optic method, which leverages the thermal conductivity variations of geological materials under different moisture and seepage conditions. By integrating optical fibers as active heat sources, this technique enables high-precision, all-weather detection of subsurface moisture and seepage dynamics[6].

To further enhance measurement accuracy, ultra-weak fiber Bragg grating (UWFBG) technology was employed, embedding thousands of ultra-low reflectivity gratings along a single fiber-optic cable. Encapsulated with conductive heating materials, this advancement significantly improved sensing resolution, increasing accuracy from 5% F.S. to 1% and enhancing thermal response sensitivity compared to conventional methods[7]. Once embedded in geological formations, this fiber-optic sensing system enables continuous, high-resolution monitoring of dynamic changes in moisture content, capillary rise, groundwater levels, and seepage velocities. This innovation provides a powerful tool for tracking hydrological processes in unsaturated zones, improving geotechnical disaster prevention strategies, and supporting sustainable groundwater management.

### 3.3 Geo-hazard Identification and Prediction

Accurately identifying and predicting geo-hazards based on fiber-optic sensing data is essential for early warning and disaster prevention. The Random Forest algorithm, known for its efficiency and strong classification performance, has been applied to develop an intelligent multi-hazard classification system for underground engineering. Field tests in tunnels demonstrated its ability to distinguish construction activities (e.g., excavation, drilling) and sudden disasters (e.g., rockfalls, seepage) with 92.3% accuracy providing a reliable approach to geo-hazard detection [8].

For geo-hazard prediction, the Kalman Filter (KF) is widely used due to its precision and robustness. By integrating multi-physics data from fiber-optic sensors, it enhances anomaly detection accuracy. Since traditional KF models are limited to linear systems, an extended Kalman Filter (EKF) incorporating Taylor series expansion was developed to handle nonlinear geotechnical processes. Genetic algorithm optimization further improved prediction accuracy, enhancing the capability of fiber-optic sensing in forecasting disaster events and supporting proactive risk mitigation [9].

### 3.4 Fiber-Optic Sensing Technology Systems

Building on advancements in geo-hazard sensing theory and technology, the research team has developed an extensive fiber-optic sensing framework tailored for rock-and-soil disaster monitoring. Over 50 specialized fiber-optic sensing networks have been designed, alongside nearly 10 proprietary signal acquisition devices. Additionally, more than 10 intelligent geo-hazard recognition systems have been established, forming a comprehensive and systematic approach to fiber-optic sensing for geotechnical disaster detection and early warning (Figure 3). This integrated technology system enhances the accuracy,

efficiency, and applicability of distributed fiber-optic sensing in diverse geological environments, providing a robust foundation for large-scale geo-hazard monitoring and risk assessment [10,11].

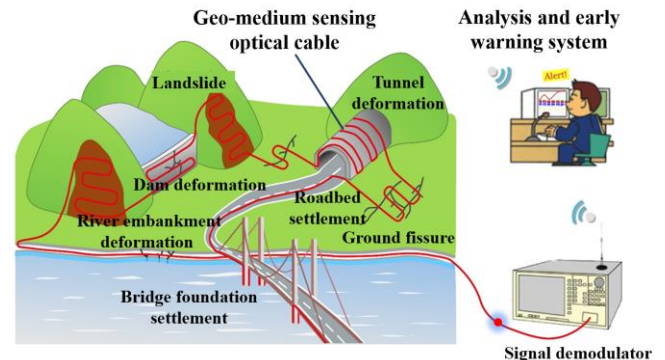


Figure 3 Fiber optic sensing system for rock-and-soil disasters.

## 4 APPLICATIONS OF DFOS IN ROCK-AND-SOIL DISASTER MONITORING

DFOS has emerged as a transformative technology for monitoring rock-and-soil disaster mechanisms by providing continuous, real-time, and high-resolution data over large spatial extents. Unlike traditional geotechnical monitoring systems that rely on discrete measurement points, DFOS allows for full-scale sensing of deformation, stress redistribution, and hydrological changes that contribute to geotechnical instabilities. This section highlights key applications of DFOS in monitoring material, state, and movement interfaces, with a focus on underground mining operations, land subsidence monitoring, and reservoir slope stability assessment.

### 4.1 Monitoring Material Interfaces in Slope Overlying Rock

In underground mining operations, the excavation process induces stress redistribution and fracture propagation within the surrounding rock mass. This often leads to instability in stope overburden, posing a significant risk of roof collapse, rock bursts, and ground subsidence. Material interfaces, such as the contact zones between ore bodies and surrounding rock or between different lithological formations, govern the mechanical response of the overlying strata and influence the failure mechanisms within the mine.

DFOS technology has been successfully deployed in longwall mining, sublevel caving, and room-and-pillar mining operations to monitor stress changes and detect potential failure zones [12,13]. Optical fibers installed along critical interfaces allow for real-time strain measurement, enabling the identification of stress concentrations and early warning of geotechnical hazards. By tracking localized deformation trends, strain redistribution, and fracture initiation, DFOS provides mine operators with actionable insights for optimizing roof support systems, adjusting mining sequences, and implementing safety measures to prevent catastrophic failures.

### 4.2 Assessing State Interfaces in Land Subsidence

Land subsidence is a widespread geo-hazard resulting from excessive groundwater extraction, soil consolidation, and hydro-mechanical interactions. The gradual settlement of soil layers due to subsurface compaction can cause structural



damage to buildings, differential ground deformation, and increased flooding risks, particularly in urban areas. State interfaces within subsiding soil formations represent the transition zones between stable and compacting soil layers, where changes in pore pressure, void ratio, and effective stress dictate the rate and extent of subsidence.

DFOS has been increasingly utilized for long-term land subsidence monitoring by embedding fiber-optic sensors in boreholes and along subsiding zones to capture real-time compaction trends. By measuring strain variations, DFOS allows for the early detection of compaction-related deformations, enabling timely intervention to mitigate damage [14]. For example, in cities experiencing significant subsidence due to groundwater depletion, DFOS networks provide high-resolution subsidence maps, allowing urban planners and engineers to develop effective groundwater management policies and infrastructure reinforcement strategies. Additionally, DFOS can be integrated with satellite-based InSAR (Interferometric Synthetic Aperture Radar) data to enhance the accuracy of subsidence monitoring by correlating surface deformation trends with subsurface strain variations.

#### 4.3 Detecting Movement Interfaces in Reservoir Slopes

Reservoir slopes are highly susceptible to landslides and slope failures triggered by hydrodynamic loading, seasonal water level fluctuations, and infiltration-induced weakening of slope materials. Movement interfaces within reservoir slopes define the boundaries between stable and actively deforming soil or rock masses, making them critical zones for monitoring slope stability and identifying potential failure mechanisms.

DFOS-based monitoring has been successfully applied in reservoir embankments, natural slopes, and engineered slopes near hydropower stations to track shear strain accumulation, deep-seated creep deformation, and progressive failure development [15–17]. Fiber-optic sensors embedded along potential slip surfaces and slope reinforcement structures provide continuous measurements of strain evolution, allowing engineers to identify precursory signs of instability before catastrophic failure occurs.

In large-scale reservoir projects such as the Three Gorges Reservoir in China, DFOS has been instrumental in monitoring slope deformation and evaluating landslide risks under varying hydrological conditions [18]. By integrating DFOS data with numerical slope stability models and geotechnical instrumentation, engineers can develop more reliable landslide prediction models, improve early warning systems, and implement targeted mitigation measures, such as slope drainage optimization and reinforcement design [19,20].

## 5 CONCLUSION

The integration of DFOS technology into geo-hazard monitoring has significantly enhanced the ability to detect, analyze, and mitigate geological and geotechnical disasters. By providing continuous, real-time, and spatially distributed data, DFOS effectively overcomes the limitations of traditional point-based monitoring techniques, enabling more comprehensive and proactive disaster prevention, early warning, and risk assessment. The case studies presented in this paper demonstrate the broad application potential of DFOS technology in underground mining stability evaluation, land

subsidence monitoring, and reservoir slope hazard management, highlighting its adaptability to complex geological environments and diverse hazard types.

Future research should focus on further enhancing sensor durability and environmental adaptability, developing more refined data interpretation and inversion models, and integrating DFOS with artificial intelligence (AI), remote sensing, and multi-source data fusion to build intelligent, automated, and predictive hazard monitoring systems. The continuous advancement and interdisciplinary integration of DFOS technology will play a key role in safeguarding geotechnical stability, infrastructure resilience, and sustainable land use under increasingly complex environmental and engineering challenges.

## ACKNOWLEDGMENTS

This research was financially supported by the National Natural Science Foundation of China, NSFC (Grant Nos. 42030701, 42177135, 423B2704).

## REFERENCES

- [1] B. Shi, D. Zhang, H. Zhu, C. Zhang, K. Gu, H. Sang, H. Han, M. Sun, and J. Liu, *DFOS applications to geo-engineering monitoring*, *Photonic Sensors*, vol. 11, pp. 158–186, 2021.
- [2] J. Yin, Z. W. Li, Y. Liu, K. Liu, J. S. Chen, T. Xie, S. S. Zhang, Z. Wang, L. X. Jia, C. C. Zhang, and B. Shi, *Toward establishing a multiparameter approach for monitoring pipeline geohazards via accompanying telecommunications dark fiber*, *Optical Fiber Technology*, vol. 68, p. 102765, 2022.
- [3] C. C. Zhang, H. H. Zhu, and B. Shi, *Interfacial characterization of soil-embedded optical fiber for ground deformation measurement*, *Smart Materials and Structures*, vol. 23, 2014.
- [4] C. C. Zhang, H. H. Zhu, S. P. Liu, and B. Shi, *Quantifying progressive failure of micro-anchored fiber optic cable–sand interface via high-resolution distributed strain sensing*, *Canadian Geotechnical Journal*, vol. 57, pp. 871–881, 2020.
- [5] C. Sayde, C. Gregory, M. Gil-Rodriguez, N. Tufillaro, S. Tyler, N. Van De Giesen, M. English, R. Cuenca, and J. S. Selker, *Feasibility of soil moisture monitoring with heated fiber optics*, *Water Resources Research*, vol. 46, 2010.
- [6] M. Y. Sun, B. Shi, C. Zhang, J. Liu, J. Guo, X. Zheng, Y. Wang, and G. Wei, *Quantifying the spatio-temporal variability of total water content in seasonally frozen soil using actively heated fiber Bragg grating sensing*, *Journal of Hydrology*, vol. 606, p. 127386, 2022.
- [7] X. Ye, H. H. Zhu, J. Wang, Q. Zhang, B. Shi, L. Schenato, and A. Pasuto, *Subsurface multi-physical monitoring of a reservoir landslide with the fiber-optic nerve system*, *Geophysical Research Letters*, vol. 49, 2022.
- [8] T. Y. Zhang, B. Shi, C. C. Zhang, T. Xie, and J. Yin, *Tunnel disturbance events monitoring and recognition with distributed acoustic sensing (DAS)*, *IOP Conference Series: Earth and Environmental Science*, vol. 861, 2021.
- [9] K. Liao, W. Zhang, H. H. Zhu, Q. Zhang, B. Shi, J. T. Wang, and W. T. Xu, *Forecasting reservoir-induced landslide deformation using genetic algorithm enhanced multivariate Taylor series Kalman filter*, *Bulletin of Engineering Geology and the Environment*, vol. 81, pp. 1–19, 2022.
- [10] S. P. Liu, B. Shi, K. Gu, C. C. Zhang, J. H. He, J. H. Wu, and G. Q. Wei, *Fiber-optic wireless sensor network using ultra-weak fiber Bragg gratings for vertical subsurface deformation monitoring*, *Natural Hazards*, vol. 109, pp. 2557–2573, 2021.
- [11] H. Sang, D. Zhang, Y. Gao, L. Zhang, G. Wang, B. Shi, B. Zheng, and Y. Liu, *Strain distribution based geometric models for characterizing the deformation of a sliding zone*, *Engineering Geology*, vol. 263, p. 105300, 2019.
- [12] G. Cheng, B. Shi, H. H. Zhu, C. C. Zhang, and J. H. Wu, *A field study on distributed fiber optic deformation monitoring of overlying strata during coal mining*, *Journal of Civil Structural Health Monitoring*, vol. 5, pp. 553–562, 2015.
- [13] G. Cheng, W. Xu, B. Shi, J. Wu, B. Sun, and H. Zhu, *Experimental study on the deformation and failure mechanism of overburden rock during coal mining using a comprehensive intelligent sensing method*, *Journal*

- of Rock Mechanics and Geotechnical Engineering*, vol. 14, pp. 1626–1641, 2022.
- [14] C. Liu, B. Shi, K. Gu, T. Zhang, C. Tang, Y. Wang, and S. Liu, *Negative pore water pressure in aquitard enhances land subsidence: Field, laboratory, and numerical evidence*, *Water Resources Research*, vol. 58, 2022.
- [15] Y. J. Sun, D. Zhang, B. Shi, H. J. Tong, G. Q. Wei, and X. Wang, *Distributed acquisition, characterization and process analysis of multi-field information in slopes*, *Engineering Geology*, vol. 182, pp. 49–62, 2014.
- [16] H. H. Zhu, B. Shi, J. F. Yan, J. Zhang, and J. Wang, *Investigation of the evolutionary process of a reinforced model slope using a fiber-optic monitoring network*, *Engineering Geology*, vol. 186, pp. 34–43, 2015.
- [17] H. H. Zhu, B. Shi, J. F. Yan, J. Zhang, C. C. Zhang, and B. J. Wang, *Fiber Bragg grating-based performance monitoring of a slope model subjected to seepage*, *Smart Materials and Structures*, vol. 23, 2014.
- [18] X. Ye, H. H. Zhu, G. Cheng, H. F. Pei, B. Shi, L. Schenato, and A. Pasuto, *Thermo-hydro-poro-mechanical responses of a reservoir-induced landslide tracked by high-resolution fiber optic sensing nerves*, *Journal of Rock Mechanics and Geotechnical Engineering*, vol. 16, no. 3, pp. 1018–1032, 2024.
- [19] C. C. Zhang, H. H. Zhu, S. P. Liu, B. Shi, and D. Zhang, *A kinematic method for calculating shear displacements of landslides using distributed fiber optic strain measurements*, *Engineering Geology*, vol. 234, pp. 83–96, 2018.
- [20] W. Zhang, R. Xiao, B. Shi, H. H. Zhu, and Y. J. Sun, *Forecasting slope deformation field using correlated grey model updated with time correction factor and background value optimization*, *Engineering Geology*, vol. 260, p. 105215, 2019.

# Structural Behaviors of Prestressed Double-T Slab under Loadings with Seasonal Effects

Yitian Liang<sup>1</sup>, ORCID (0009-0005-6376-0685), Branko Glišić<sup>2</sup>, ORCID (0000-0002-1852-5310)

<sup>1,2</sup>Department of Civil and Environmental Engineering, Princeton University, New Jersey, USA  
email: ytliang@princeton.edu, bglicic@princeton.edu

**ABSTRACT:** Understanding the effects of temperature on structural behavior is critical in structural health monitoring (SHM), especially for prestressed concrete components with complex geometries due to their complicated internal strain distributions. Temperature-strain relationships in structural components can offer valuable insights into various structural properties, such as the coefficient of thermal expansion (CTE), and boundary and continuity conditions of structures. However, these relationships can be influenced by variability of ambient environmental conditions, especially ambient temperature variations, which can create thermal gradients and complicate the interpretation of relationships and identification of structural properties.

This study presents a preliminary study on the structural behaviors of a prestressed slab with a double-T cross-section through a series of static and dynamic loading tests conducted across four seasons, with ambient temperatures ranging from 8°C to 24°C. The proposed approach utilizes long-gauge strain sensors embedded within the slab to continuously capture strain and temperature data. By analyzing the temperature-strain relationships derived from on-site loading test measurements, the study aims to evaluate how the structural behaviors of the prestressed double-T slab, which can reflect the structural properties, such as boundary and continuity conditions, change under different environmental temperatures.

The preliminary results show clear variations in strain changes for the same loading condition under different temperatures. These variations suggest that environmental temperatures and thermal gradients could affect load response and boundary restraints. Furthermore, the findings demonstrate that the embedded long-gauge strain sensors effectively capture the temperature changes and strain distribution under the loadings, enabling the assessment of structural behaviors of the slab with seasonal effects. This research highlights the importance of accounting for environmental factors in structural health monitoring and provides new perspectives for understanding and predicting the behavior of structures with complex geometrical properties (e.g., double-T slab) under varying conditions.

**KEY WORDS:** Prestressed concrete slab; Thermal behavior of structures; Temperature-strain relationship; Long-gauge fiber-optic strain sensors; Complex geometrical and boundary conditions; Structural health monitoring.

## 1 INTRODUCTION

Prestressed precast concrete components with complex cross sections, such as double-T slabs, are widely used in modern construction due to their high load-carrying efficiency [1]. However, their structural behavior is influenced not only by applied mechanical loading but also by environmental factors, most notably temperature [2,3]. Seasonal fluctuations in ambient temperature can cause significant strain variations within these components, even in the absence of mechanical loading, and complicate the interpretation of measurement data used in condition assessment and damage detection. In addition, temperature-strain relationships can provide valuable insights into material properties (e.g., help evaluate thermal expansion coefficient), restraint and boundary conditions, and the overall stiffness behavior of structural systems [4,5]. Understanding how these relationships evolve under different environmental conditions and loading scenarios is essential for assessing in-situ structural behavior and for developing reliable long-term monitoring strategies.

This project is developed based on the real-life case study. More specifically, it is based on observation of the structural behavior of a prestressed double-T slab located in the Stadium Drive Garage, Princeton University, with a particular focus on the influence of seasonal temperature variations. The slab is instrumented with long-gauge Fiber Bragg Grating (FBG) sensors embedded within the concrete during construction.

These sensors allow for simultaneous, continuous measurement of strain and internal temperature over extended periods.

To explore how environmental conditions influence the load response, four series of load tests were conducted over a period of nine months at different environmental temperatures. Each test series included static loading with various load cases, and dynamic testing. While the mechanical load applied during each test series remained similar, the environmental temperature varied significantly between tests, ranging from 8°C to 24°C. This variation provides a unique opportunity to assess the interaction between thermal conditions and mechanical response in a controlled yet realistic setting.

The aim of this study is to observe how strain responses in a prestressed double-T slab vary under similar loading scenarios across different ambient temperatures, and to explore the potential for identifying temperature-related effects on structural behavior. Preliminary observations confirm that the environmental temperature affects the measured strain distribution under mechanical load.

The originality of this study lies in the following aspects. It combines seasonal on-site testing under varying ambient conditions with embedded long-gauge FBG, which captures internal strain and temperature responses that surface-mounted sensors could miss. In addition, the study focuses on a prestressed double-T slab with complex boundary conditions, a



structural form that presents significant challenges for SHM yet has been underrepresented in previous literature.

While full analysis is ongoing, this extended abstract summarizes the current progress by describing the instrumentation and load configurations and presenting preliminary observations of temperature-influenced structural behavior.

## 2 METHODOLOGY

### 2.1 Sensor layout

The double-T slab of Stadium Drive Garage contains 14 embedded long-gauge FBG sensors, installed at locations denoted with A, B, C, E, F, D, G, and H, as illustrated in Figure 1. The sensors are mostly, but not only, installed in parallel and crossed topologies. For pairs of parallel sensors, such as sensors at locations A, B, C, E, F, the top sensor is denoted as “1” (e.g. “A1”), and the bottom one as “2” (e.g. “A2”). The gauge length of sensors at locations A, B and C was 60 cm (1'11.6”), and all the other sensors in the double-T slab had a gauge length of 25 cm (9.8”). The gauge length of sensors was determined using principles developed in Glisic 2011 [6].

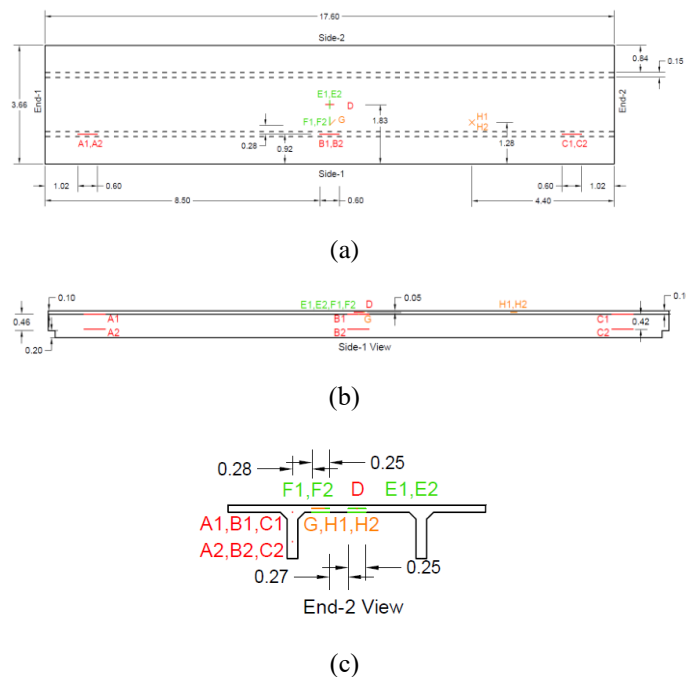


Figure 1. Locations of embedded long-gauge FBG strain and temperature sensors in the prestressed double-T slab: (a) plane view, (b) elevation view, and (c) cross-sectional view; all dimensions are in meters [7].

### 2.2 Experimental setup

The measurement data analyzed in this paper was collected from FBG sensors in the double-T slab during four series of load tests conducted between fall 2024 and spring 2025 at different environmental temperatures. These tests were performed using a truck provided by the Princeton University Facilities (Civil Engineering group), loaded with sandbags in the cargo bed to achieve a target weight of 10,000 lbs (4536 kg). This weight was selected to incur statistically significant

strain, according to the results of previous research on the slab [8]. Each test series included two types of load tests: static and dynamic. This paper focuses on results of static tests only, while dynamic tests are described only for the purposes of the completeness of presentation. In the static tests, the procedure began with the beam unloaded for approximately one minute. The truck was then driven onto a designated position on the beam and held stationary for another minute before being removed, after which the beam remained unloaded for an additional minute. During these static tests, sensors recorded strain at a rate of 1 hertz (Hz), or one measurement per second. An example of the truck with its cargo bed loaded with sandbags positioned on the beam during a static test is shown in Figure 2.



Figure 2. The truck on the slab in a static load test.

In the dynamic tests, the truck was driven across the width of the slab at variable speeds twice during each test series. After each impulse, the slab was allowed to vibrate freely for approximately one minute afterward. During these tests, the sensors measured at a rate of 100 Hz.

Table 1. Summary of load cases in four test series.

Load Case	Test 1 (15°C)	Test 2 (8°C)	Test 3 (10°C)	Test 4 (24°C)
V – center	✓	✓	✓	✓
V – web (w/ sensors)	✓	✓	✓	✓
V – web (w/o sensors)	×	✓	✓	✓
V – seam (closer)	✓	✓	✓	✓
V – seam (further)	×	✓	✓	✓
H – center	✓	×	✓	✓
H – neighbor slab center (closer)	✓	×	✓	✓
H – neighbor slab center (further)	×	×	✓	✓
Column test	✓	×	✓	✓
Dynamic test (mph)	15, 20	22, 25	25, 29	28, 30

Table 1 shows the environmental temperatures during four test series, all load cases each test series contains, and the speed of the truck during dynamic tests. For the load cases with the dash sign, the “V” and “H” before dash stand for “vertical” and “horizontal” respectively, which mean whether the centerline of the truck is along the length or the width of the slab; after the dash is the position of the rear wheels of the truck; “closer” means the side closer to the sensors, and “further” means the

side further away from the sensors. The tick mark “√” means the test series contains marked load case, and the cross “×” means the test series does not contain the load case.

### 3 PRELIMINARY OBSERVATIONS

Figure 3 presents the strain response recorded by FBG sensors embedded in the slab during Test2 with the load case “V – center”. The total strain changes  $\Delta\epsilon$  are plotted over time, with different colored lines representing individual sensors. Notably, sensors B2 shows significantly larger responses compared to others, due to its proximity to the applied load and its position at the midspan of the slab. This observation supports the effectiveness of the sensor network in capturing localized events while providing spatial context for interpretation.

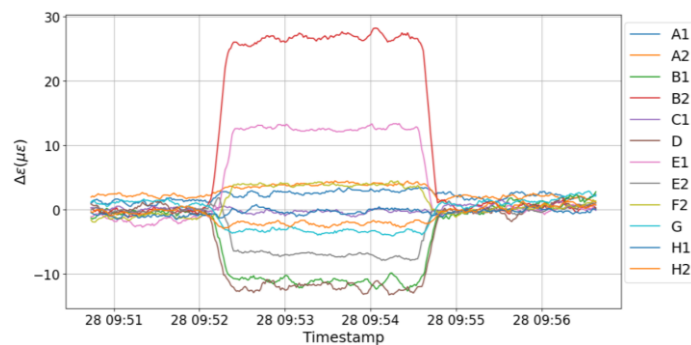


Figure 3. Total strain changes from slab-embedded FBG sensors during a static test.

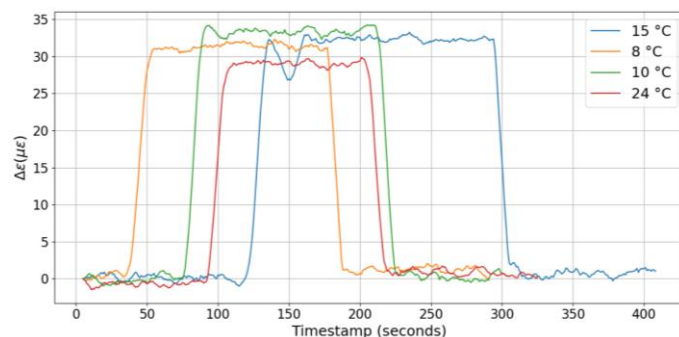


Figure 4. Total strain changes of sensor B2 under the same load case but at different ambient temperatures.

Figure 4 compares the strain measurement from one specific sensor (sensor B2) under the same type of load case but conducted under different ambient temperature conditions. Four curves represent four separate tests carried out when the slab was exposed to 8 °C, 10 °C, 15 °C, and 24 °C. Although all tests exhibit a similar response pattern (a rapid increase in strain during loading and a drop afterward), the magnitude of the peak strain differs across temperature conditions. This variation suggests that ambient temperature influences the sensor response—potentially due to changes in material stiffness, temperature gradient along cross section, or boundary restraint conditions. For example, the decrease in response with increase of temperature, for temperature higher than 10°C may reflect thermal expansion effects that result in higher stiffness of restrained slabs; inverse behavior for temperature lower than

10°C may indicate change in boundary conditions or interaction at connections. Yet combined effects can be in play in both cases.

These preliminary findings highlight two key observations: (1) the sensor network effectively captures localized strain patterns, and (2) environmental temperature influences the strain response, even under consistent loading scenarios. These effects will be further examined through more comprehensive analysis in future.

### 4 CONCLUSION AND FUTURE WORK

This study assesses the strain changes of a prestressed precast concrete slab with embedded FBG sensors under repeated localized loading and varying ambient temperatures. Through a series of static and dynamic load tests conducted across different seasons, it was observed that the same loading configuration caused different strain changes under varying ambient temperatures. The tests confirmed the effectiveness of the monitoring system and loading configuration. Furthermore, these preliminary observations highlight the significance of temperature as a factor affecting structural response and underline the importance of accounting for thermal effects in condition assessment and long-term monitoring.

Future work will focus on further examining the principles underlying the observed temperature-dependent strain variations, including the potential influences of thermal-induced stiffness changes and boundary conditions. Additional analysis will aim to quantify these relationships to better interpret long-term monitoring data. Moreover, the study will be extended to evaluate the dynamic behavior of the structure under different environmental temperatures to gain deeper insights into the stiffness evolution and structural performance with seasonal effects.

### ACKNOWLEDGMENTS

We would like to thank Gina Talt and Office of Sustainability of Princeton University for coordinating the project, Catherine Altadonna and Office of Capital Projects of Princeton University for providing funding and metadata related to project, George Hand, Ali Akber, and Jersey Precast, Hamilton, New Jersey, for their great assistance during the installation of sensors, Dan Polifroni and Whiting-Turner for their precious on-site help and coordination, Mauricio Pereira and Antti Valkonen, for installing the sensors, Elvis Le, for organizing, conducting, and recording the load tests, and for their contributions at various stages of the project.

### REFERENCES

- [1] Maguire, Marc, et al. "Structural Performance of Precast/Prestressed Bridge Double-Tee Girders Made of High-Strength Concrete, Welded Wire Reinforcement, and 18-Mm-Diameter Strands." *Journal of Bridge Engineering*, vol. 18, no. 10, Oct. 2013, pp. 1053–1061, [https://doi.org/10.1061/\(asce\)be.1943-5592.0000458](https://doi.org/10.1061/(asce)be.1943-5592.0000458).
- [2] Jiao, Yujie, et al. "Temperature Effect on Mechanical Properties and Damage Identification of Concrete Structure." *Advances in Materials Science and Engineering*, vol. 2014, Article ID 191360, 2014. <https://doi.org/10.1155/2014/191360>.
- [3] Teixeira Buttignol, Thiago Eduardo, and Telmo Nunes Bittencourt. "On the Effect of the Boundary Conditions of Plain Concrete Exposed to High Temperatures under Uniaxial Compression." *Structural Concrete*, vol. 23, no. 4, 2022, pp. 2030–2040. <https://doi.org/10.1002/suco.202000582>.
- [4] Lu, Lei, et al. "Application of Advanced Multi-Parameter Monitoring in Concrete Structure Defect Detection: Integrating Thermal Integrity

- Profiling and Strain Analysis." *Buildings*, vol. 15, no. 8, 2025, article 1350. <https://doi.org/10.3390/buildings15081350>.
- [5] Wang, Dong, et al. "Experimental Study and Numerical Simulation of Temperature Gradient Effect for Steel-Concrete Composite Bridge Deck." *Measurement and Control*, vol. 54, no. 5–6, 2021, pp. 681–691. <https://doi.org/10.1177/00202940211007166>.
- [6] Glisic, Branko. "Influence of the Gauge Length on the Accuracy of Long-Gauge Sensors Employed in Monitoring of Prismatic Beams." *Measurement Science and Technology*, vol. 22, no. 3, 2011, article 035206. <https://doi.org/10.1088/0957-0233/22/3/035206>.
- [7] Liang, Yitian, and Branko Glisic. Identification of Prestress Losses under Early-Age Cracking in Prefabricated Prestressed Slabs with Complex Cross Sections Using Long-Gauge Sensors. Manuscript submitted and under review, 2025.
- [8] Le, Elvis. Stadium Drive Garage: Analyzing Effects of Complex Boundary Conditions on a Prestressed Beam Using FBG Strain Sensors. Unpublished manuscript, May 2024.



## Vibration Analysis of Ship Hulls using Fiber Bragg Grating

Gethin Wyn Roberts<sup>1, 2</sup>, ORCID (0000-0002-3703-981X), Irena Åarberg<sup>2</sup>, ORCID (0000-0001-6978-6767), Werner Lienhart<sup>3</sup>, ORCID (0000-0002-2523-4052)

<sup>1</sup>Department of Land and Sea Mapping, Faroese Environment Agency, Tórshavn, Faroe Islands

<sup>2</sup>Geospatial Centre of the Faroe Islands, The University of the Faroe Islands, Tórshavn, Faroe Islands

<sup>3</sup>Institute of Engineering Geodesy and Measurement Systems, Faculty of Mathematics, Physics and Geodesy, Graz University of Technology, Steyrergasse 30, 8010 Graz, Austria  
email: gethinr@us.fo

**ABSTRACT:** The paper outlines an ongoing research project, incorporating Fiber Bragg Grating (FBG) systems to measure and detect the vibration in a ship's hull. The causes of such vibration are due to the various engines and motors on board, as well as the force induced by the movement of the sea, and the vibration induced into the hull by the propeller. Five ships in all have been monitored using the FBG system, using both 3 sensor rosettes, and chains of 10 sensors. All the sensors used were glued to the ships' hulls and various sea trials carried out. The tests included gathering data with the engines switched off, the engines running at various speeds, both whilst stationary in the harbour as well as whilst sailing.

Change detection is the main application of such monitoring, and such change is evident and detected due to a broken flange on one ship, and a new engine on one ship. Data were gathered before and after such effects were changed. The induced vibration due to the propeller is also evident.

**KEY WORDS:** Fibre Bragg Grating, Deflection monitoring, frequency analysis, SHM.

### 1 INTRODUCTION

Previous work conducted by the authors has focused on using RTK GNSS [1, 2] to monitor the long-term deformations of large bridges [3] as well as measuring the short-term deflections of such structures [4, 5, 6, 7, 8, 9] and extracting the frequencies of the movements [4, 7, 10]. Such deflection measurements and resulting frequency analysis can be used to detect movement characteristics of the structure due to damage or long-term deterioration. In parallel, the use of Fiber Bragg Grating (FBG) approaches was used to measure long term deformations of infrastructure such as roads and tunnels [11, 12, 13].

Both approaches were brought together by the authors [14] to use the high data rate and very precise data of the FBG system to measure dynamic characteristics of ship structures. Ships are structures that deform and deflect. Such deflections are caused by various external forces, such as the force induced on the hull by the sea as well as vibrations in the structure of the ship caused by various engines and motors on board. Ships, like all structures, can experience damage and long-term deterioration. These can result in deflections and vibrations in the ship's structure changing in characteristics over time or even instantly. The hypothesis of our research is that sudden changes in the characteristics of the ship's structure, caused by damage, can be detected by measuring changes in the frequencies observed in the vibration and deflection of the structure. The research objective of this current work is to be able to measure changes in the frequency response of the ship in relation to any damage or changes made to the ship. This was done by carrying out measurements using a FBG system on several ships, three of which exhibited damage or changes in engines, which resulted in the frequency responses changing. We gathered data on such vessels before and after any damage was fixed or engine changes were made.

FBG sensors were installed on a passenger ship in the Faroe Islands, and data were gathered at a rate of 1kHz during normal scheduled activity in 2017 and 2018 [14] and at a rate of 5kHz during the more recent tests. The frequency responses of the data were extracted to identify the frequency characteristics of the structure i.e. ship. The movements are caused by the ships' engines, motors and external factors such as weather and sea effects. In addition, vibrations are caused by the rotation of the propeller inducing force on the ship hull and causing vibrations. Further, change detection in these characteristics is possible, therefore detecting early damage to such infrastructure.

Following the initial sea trials, a three-year research project was undertaken to further this work.

### 2 FBG SENSORS

Fiber Bragg Gratings (FBGs) are patterns of refractive index changes inscribed in the core of a glass fiber with a typical length of about 1cm. When a broadband light source emits light into the fiber, the FBG behaves as a wavelength dependent mirror, meaning that only that portion of light with a wavelength corresponding to the spacing of the grating is reflected whereas other wavelengths can pass the grating unaltered, Figure 1. Hence, several gratings with different wavelengths can be placed along a single fiber enabling tens of sensor locations. The FBG sensors sample strain measurements at a rate of kHz with a precision of better than 1με (= 1 ppm = 1μm/m) and can be used for long term static monitoring as well as dynamic monitoring [11].

If local strain changes occur, the spacing of the patterns change and thus also the wavelength of the reflected signal peak changes. With appropriate calibration of FBG sensors [12] the recorded wavelength change can be reliably converted into a strain change. However, local temperature changes have an impact on the refractive index of the fiber and thus lead to a

wavelength change of the backscattered signal. A common method to numerically compensate the temperature impact is to place one or more FBGs along the sensing fiber, or to use a separate FBG, which are not coupled to the measurement object and thus only sensitive to temperature changes. The recorded wavelength changes of these gratings are in the processing subtracted from the measured wavelength changes from the rigidly connected FBGs. The remaining wavelength changes are then the real strains of the object.

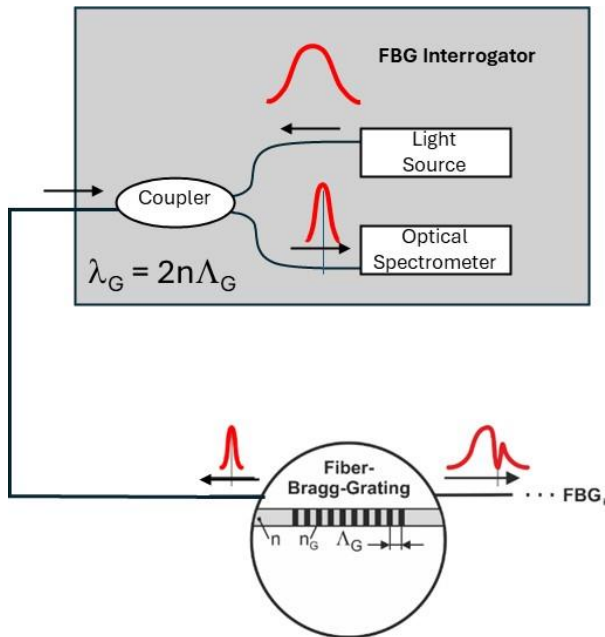


Figure 1. Principle of FBG measurements [14].

To monitor strains of the hull of the ship two different types of FBG sensor chains were used during the field tests. Firstly, a strain rosette, incorporating three FBG sensing elements, Figure 2. The rosette is an equilateral triangle, and the orientation of the three sensors of the strain rosette differs by 60°. Hence with this layout it is possible to determine the magnitude and direction of the principal strain. However, with one strain rosette these values can only be determined on one location.

In order to determine the strain distribution a secondary buffered FBG chain incorporating 13 FBG elements on the original Smyril tests conducted in 2017 and 2018, and 10 on all the more recent tests, Figure 3, were used. One of the sensors is loosely embedded in the chain and acts as temperature sensor, used for compensation measurements whilst the other 12 or 9 are rigidly embedded and capture the strain of the hull. The FBG chains were laid out in a meander shape glued on the inside of the ship's hull with sensors laid in the horizontal and vertical directions. Both the strain rosette and the secondary buffered FBG chain were installed on the inside of the hull of the ships in the engine room.

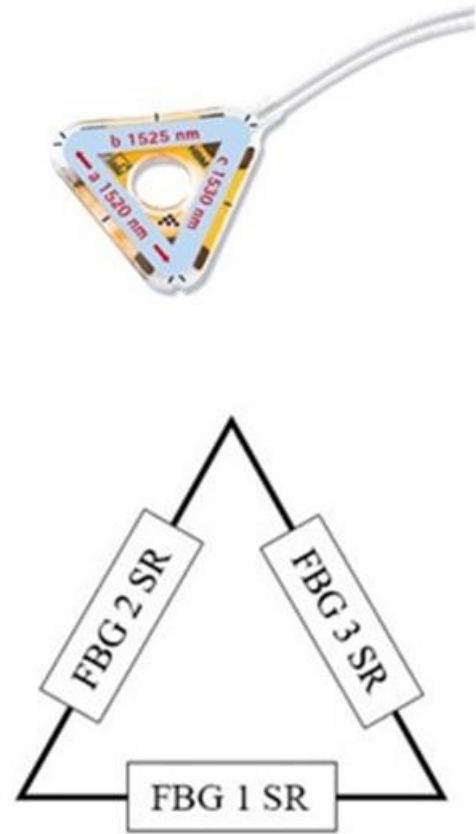


Figure 2. A strain rosette incorporating three FBG sensing elements [15].

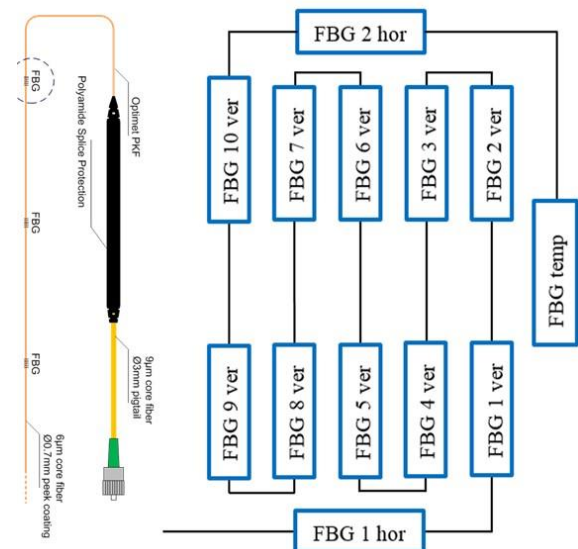


Figure 3. A secondary buffered FBG chain incorporating 1 temperature FBG sensor and 12 strain FBG element [15] positioned in both horizontal and vertical orientation.

### 3 FIELD TESTS

Five vessels were experimented upon, these being

- Smyril passenger ferry, operated by SSL (A 135m long passenger and vehicle ship, data were gathered before and after repairs were made to a flange)
- Jákup Sverri research vessel, operated by Havstovan (55m long research ship)
- Krosstindur, a fish farm vessel operated by Luna (15m long service vessel, we gathered FBG data before and after a new engine was installed)
- Samson, tugboat operated by MEST
- Gadus, a large fishing trawler owned by JFK (88.1 long ship with vibrations detected at high speeds)

The tests were conducted, where possible, under different conditions i.e. main engine on/off, propellor running/stationary, low speed passage and high-speed passage. The various parameters helped to identify the sources of the various vibrations detected using the FBG system. The data from Gadus, Smyril and Jákup Sverri were gathered whilst the ships were operational at sea, whilst the other vessels were gathered in and around the harbour areas but being able to vary the speeds and when the engines were switched on and off.

The sensors come in a number of different formats. They are glued onto a very clean surface on the body of the ship, such as the inside of the hull. The surface of the hull is thoroughly cleaned of grease using alcohol-based products, and the surface is also rubbed with sandpaper in order to create a good surface for the glue to work on. We used a rosette sensor, that incorporates three sensors in an equilateral triangle shaped housing, as well as a chain of 10 sensors. Figure 4 illustrates a rosette (left) and chain (right). Both cost around 1000 euros. However, the rosette is far easier and quicker to install, and the three measurements are at 60° to each other, whereas the chain takes 10 measurements, and each individual sensor along the chain are 1m apart, so it can cover a larger area. The chain also takes longer to install as each of the 10 sensors need to be attached individually using an epoxy resin glue.

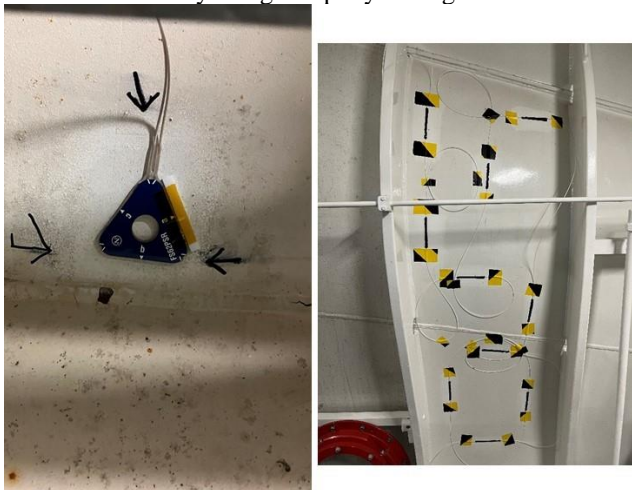


Figure 4. Rosette sensor on the Gadus (left) and chain sensor on the Jákup Sverri (right).

Figure 5 illustrates the interrogator unit (left) and the software used to gather the data, showing the real time data from 13 FBG sensors on a chain located on the Smyril (right). The interrogator costs around 30,000 Euros, and this version

gathers data at a rate of 5 kHz. Up to four sensors can be attached to the interrogator unit at any one time. The approach that we have is to install a number of FBG sensors on a number of vessels, and rotate the interrogator unit between them.

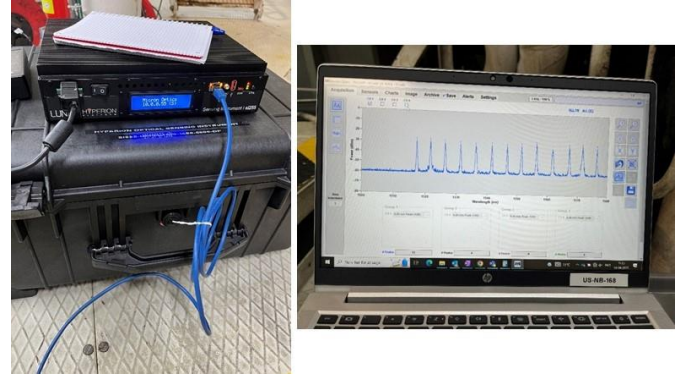


Figure 5. The interrogator unit (left) and a screenshot of the software used to gather the data (right).

A test rig was used in order to assess the precision of the system as well as the various sensor types. This is a rotating motor, with weights attached to the drive wheel in order to cause vibrations. Figure 6 illustrates the test rig used on a bench test with a rosette FBG sensor and an FBG chain attached to the table.

The chain was co-located with the FBG in order to compare results, and a couple of the chain sensors located on the chair away from the vibrating table as a baseline.



Figure 6. The vibrating test rig during a bench test, with a FBG chain and FGB rosette located on the table.

Possible applications are as follows. Once an initial installation of the sensors is carried out, subsequent data



collection can be compared to the initial data and change detection in the frequency response of the structure can be determined. Such changes in frequency response can be down to several factors, such as damage to the ship, damage to the propellers, or gradual deterioration of the vessel.

## 4 RESULTS AND DISCUSSION

### 4.1 Smyril

The Smyril data was compared to historical data that we gathered in 2017 and 2018 using a similar system belonging to TU Graz. During the initial tests, a flange was damaged at the stern of the ship, and vibration could be felt throughout the ship. We can see this in the data from 2017 and 2018, Figures 7 and 8, and it being absent in the new data we gathered during this current project, Figure 9.

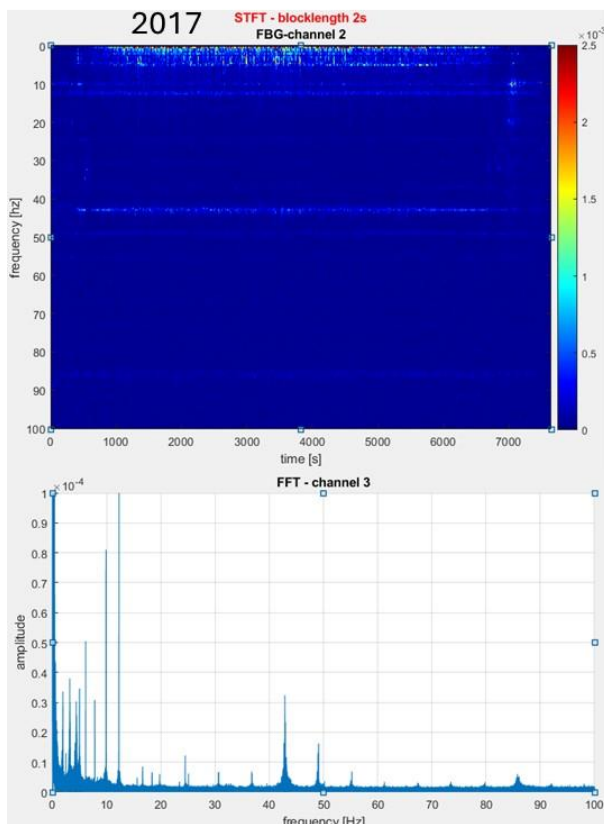


Figure 7. Waterfall and FFT plots from the tests conducted on Smyril in 2017.

The data from 2017 and 2018, Figures 7 and 8 respectively, illustrate the results showing more and noisier frequency characteristics than the more recent tests in 2023, Figure 9. This is especially true in the data in 2017 below 13Hz, Figure 7. The original setup consisted of a FBG rosette and a chain of 13 sensors glued to the inside of the ship's hull in the engine room. However, the connectors to the rosette had been cut off, for some reason sometime between the 2018 and 2023 tests, so this sensor couldn't be used in 2023. However, the FBG chain worked perfectly well. It is thought that the less frequency responses, and cleaner frequency characteristics are due to there being a broken flange at the rear of the vessel during the 2017 and 2018 tests.

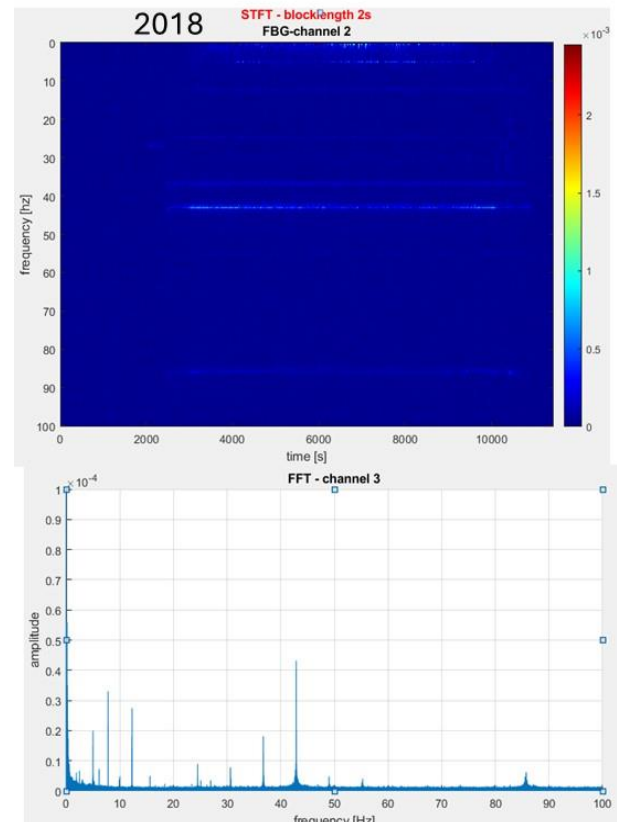


Figure 8. Waterfall and FFT plots from the tests conducted on Smyril in 2018.

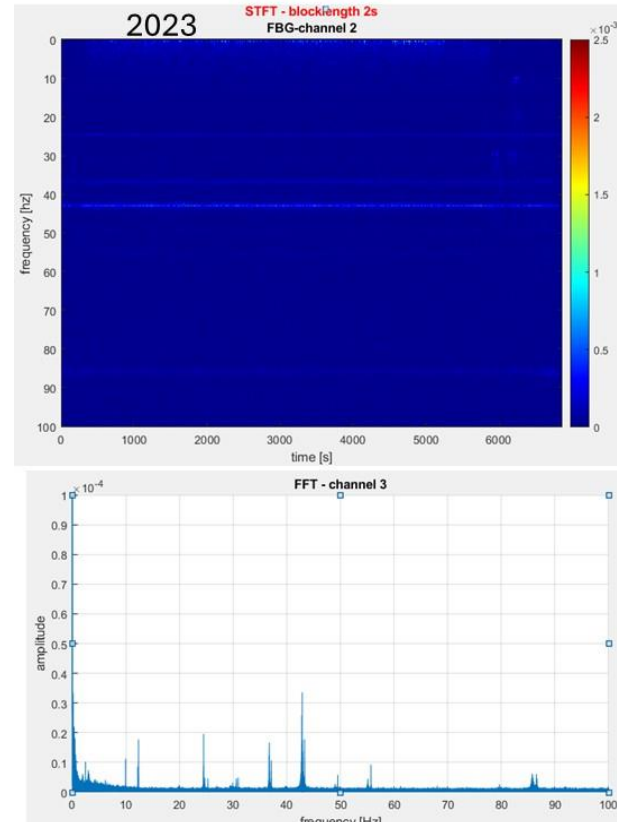


Figure 9. Waterfall and FFT plots from the tests conducted on Smyril in 2023.

#### 4.2 Krosstindur



Figure 10. The Krosstindur vessel.

The Krosstindur vessel, Figure 10, was suffering from vibration, and a new engine was installed with a lower vibration characteristic. Again, we gathered data before and after the engine was replaced, and we could see significant differences in the characteristics. More vibrations can be seen in Figure 11 (top) when the old engine was used, compared to the new engine, Figure 11 (bottom).

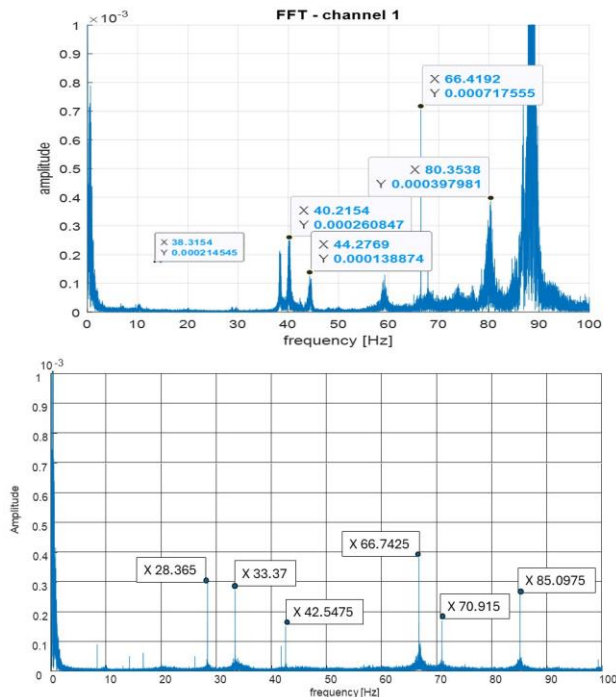


Figure 11. FFT results from the tests conducted on Krosstindur before (top) and after (bottom) the engine was replaced.

#### 4.3 Gadus

Gadus is a relatively new fishing trawler/factory. It is owned and operated by JFK. Rosette sensors were installed next to the rudder housing, Figure 12 (bottom), as well as in the bridge, Figure 12 (top right), and FBG chains were placed in the chief engineer's cabin, Figure 12 (top left), and in the engine room, Figure 12 (middle). The data were gathered during one of the ship tours in the Baren Sea. The interrogator spent periods of time attached to the various sensors during sailing and trawling, and notes were recorded of the ship speed, engine speed etc.

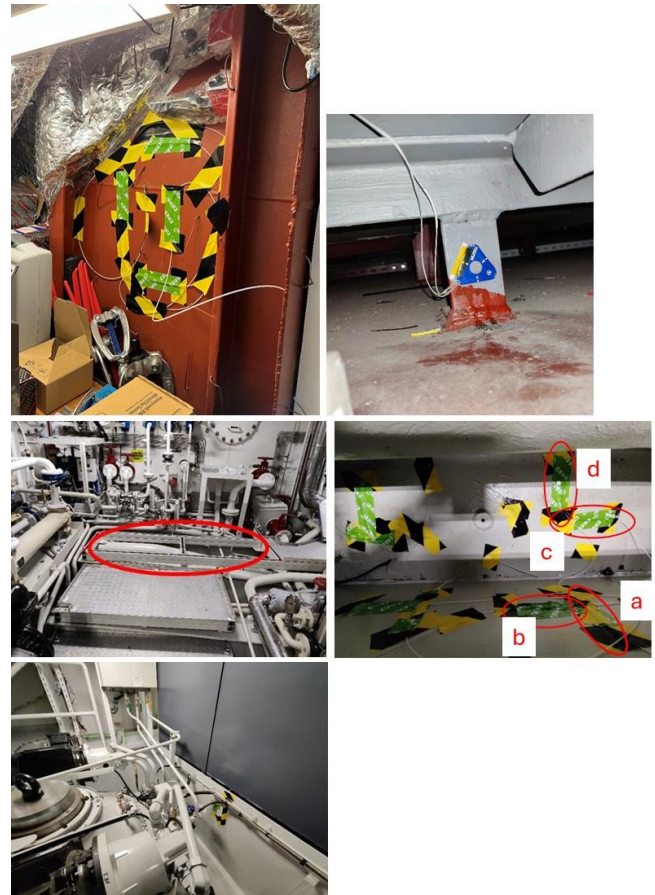


Figure 12. Sensor locations on the Gadus. FBG chain attached to a structural girder in the Chief Engineer's cabin (top left), Rosette attached to the structure in the bridge (top right), Engine room location of FBG chain (middle left) and the chain (middle right), Rosette located adjacent to the rudder (bottom).

Figure 13 illustrates a selection of FFT plots resulting from the FBG chain sensor in the engine room. All the results correspond to the same time series. The graphs show the FFT for the four locations, marked a-d in Figure 12 (middle right). It can be seen that there are different frequency response characteristics for the four locations, even though they are relatively close to each other. It is seen that the two horizontal results on the horizontal girder, a and b, show that there is a stronger vibration response in the bow to stern direction, and that the vertical girder results show that the vertical direction response has least vibration. All such responses have been shown to the chief engineer to help understand the vibration characteristics of the ship. These results illustrate that it is important to understand that the orientation of the sensor is important in order to measure specific frequencies.

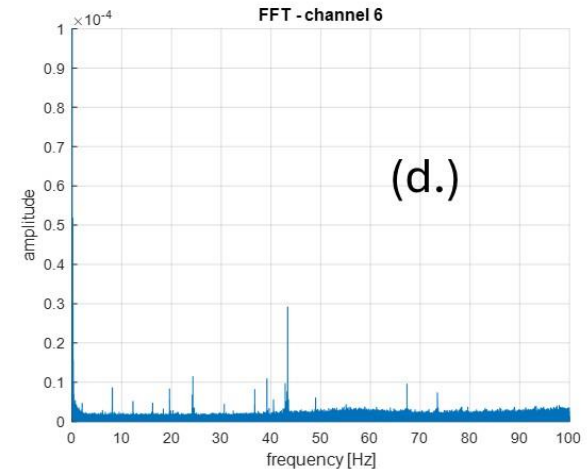
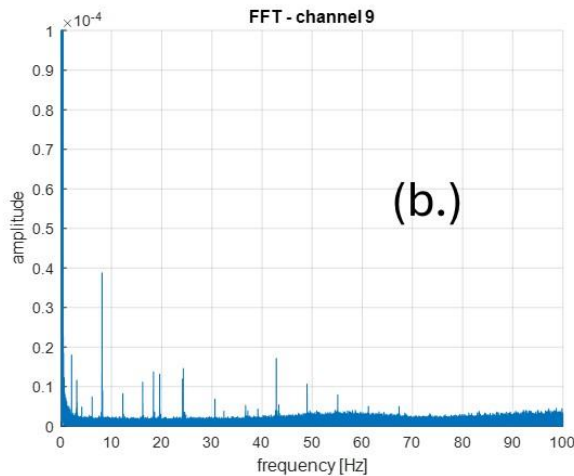
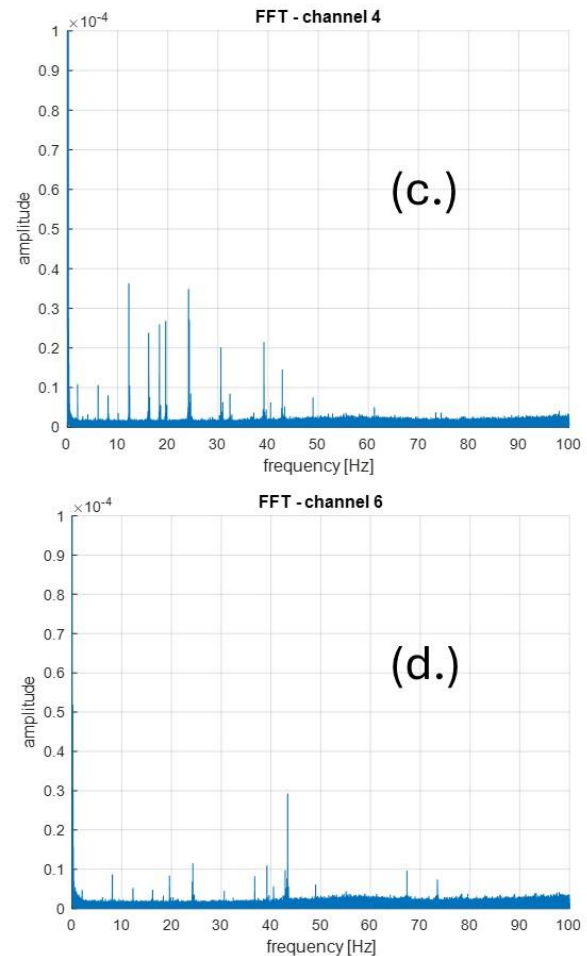
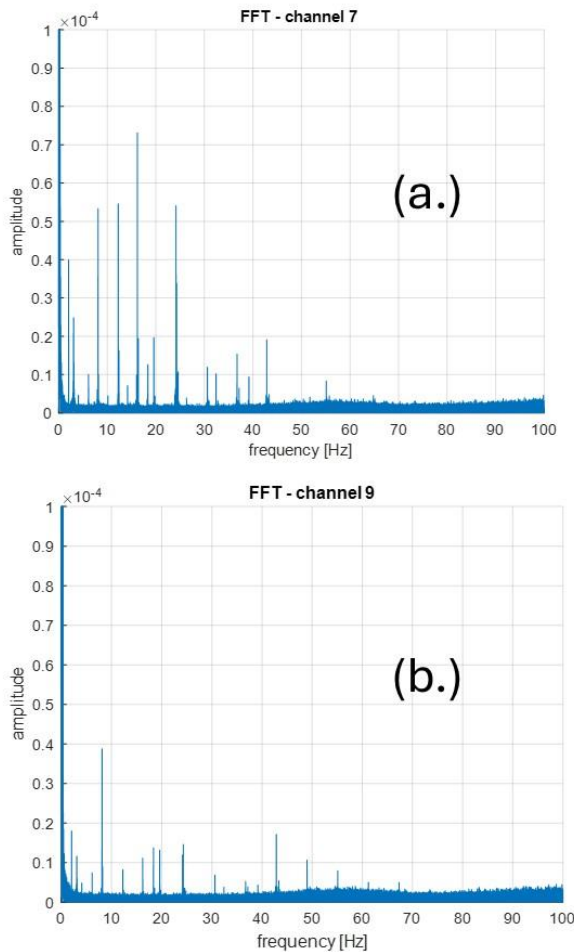


Figure 13. FFT results from the tests conducted on Gadus in the engine room. The graphs show the FFT response in the horizontal direction (stern to bow direction) on the horizontal girder (a.), the horizontal direction (port to starboard direction) on the horizontal girder (b.), the horizontal direction (port to starboard direction) on the vertical girder (c.), and the vertical direction on the vertical girder (left). Figure 12 (d.) a, b, c, d respectively.

Figure 13 (b.) illustrates the details of the FFT response at location b, Figure 12. The engine at this instance was operating at 735 RPM, and the propellor rotating at a speed of 122 RPM. The corresponding frequencies to these values are 12.25 Hz and 2.03 Hz respectively. These correspond well to the values of 12.24 Hz and 2.03 Hz in Figure 13 (b.). Further to this, the propellor has four blades, and  $4 \times 2.03$  Hz is equal to 8.1 Hz, again corresponding to the value of 8.1 Hz in Figure 13.

## 5 CONCLUSIONS

The paper outlines the field tests conducted using the FBG sensors to measure the frequency characteristics of ships. Two types of sensors are used, these being a FBG rosette and a FBG chain of 10 sensors. We can clearly detect changes in characteristics, as well as detecting the vibrations induced into the ship by various elements of the ship such as the engine and propellor.

The FBG sensors are relatively inexpensive, and can be installed on many vessels, then using a single interrogator to



gather data periodically, or when changes are thought to have occurred, in order to investigate any changes.

Gathering such data on a vessel can then be used as a blueprint to compare future data.

The measurements can be carried out at sea, so the vessel doesn't need to return to harbour, resulting in minimal down time in the vessel's activities.

Sudden changes due to damage or gradual changes due to deterioration can be detected.

## ACKNOWLEDGMENTS

The project was funded by the Research Council of the Faroe Islands, through the project (04589) HARMONISE - HeAlth and EnviRonmental MONItoring of Ships and Propellers.

The authors are also very grateful to the help of the staff at MEST, JFK, Luna, SSL and Havstovan for their help and assistance in obtaining access to the vessels and invaluable input to the project.

## REFERENCES

- [1] Hofmann-Wellenhof, B., Lichtenegger, H., Collins, J. (2001) Global Positioning System. 5th edition. Springer-Verlag Wien. ISBN 978-3-211-83534-0 DOI 10.1007/978-3-7091-6199-9
- [2] Leick, A., Rapoport, R., Tatarnikov, D. (2015) GPS Satellite Surveying, Fourth Edition. John Wiley and Sons, inc. ISBN:9781118675571 DOI:10.1002/9781119018612
- [3] Lovse JW, Teskey WF, Lachapelle G, Cannon ME (1995) Dynamic deformation monitoring of tall buildings using GPS technology. ASCE Journal of Surveying Engineering 121(1):35–40.
- [4] J.P. Montillet and M. Bos, Eds., Modelling Geodetic Time Series Analysis in Earth Sciences”, Springer Nature Switzerland AG 2020. [https://doi.org/10.1007/978-3-030-21718-1\\_12](https://doi.org/10.1007/978-3-030-21718-1_12)
- [5] Ashkenazi V, Dodson AH, Moore T and Roberts GW. (1996) Real time OTF GPS monitoring of the Humber Bridge. Surveying World4(4): 26–28. ISSN 0927-7900.
- [6] Brown CJ, Karuna R, Ashkenazi V, Roberts GW and Evans R. (1999) Monitoring of structures using GPS. Proceedings of the ICE – Structures34(1): 97–105. ISSN 0965-092-X.
- [7] Roberts GW, Brown CJ, Meng X, Ogundipe O, Atkins C, Colford B. (2012). Deflection and frequency monitoring of the Forth Road Bridge, Scotland, by GPS. Proceedings Institution of Civil Engineers; Bridge Engineering, 165(2), 105-123. DOI: 10.1680/bren.9.00022. ISSN: 1478-4637, E-ISSN: 1751-7664.
- [8] Roberts GW, Brown CJ, Tang X. (2017) Correlated GNSS and Temperature Measurements at 10-Minute Intervals on the Severn Suspension Bridge. Journal of Applied Geomatics, 9(2), pp 115-124. DOI: 10.1007/s12518-017-0187-x.
- [9] Roberts GW, Meng X, Psimoulis P, Brown CJ. (2019) In “Modelling Geodetic Time Series Analysis in Earth Sciences”, editors J.P. Montillet and M. Bos. Chapter: Time Series Analysis of Rapid GNSS Measurements for Quasi-static and Dynamic Bridge Monitoring, Springer Nature Switzerland AG 2020. [https://doi.org/10.1007/978-3-030-21718-1\\_12](https://doi.org/10.1007/978-3-030-21718-1_12).
- [10] Rao R, Li C, Huang Y, Zhen X, Wu L. (2018) Method for Structural Frequency Extraction from GNSS Displacement Monitoring Signals, Journal of Testing and Evaluation 47(3):2026-2043. <https://doi.org/10.1520/JTE20180087>
- [11] Klug F, Lienhart W, Woschitz H (2014) High resolution monitoring of expansion joints of a concrete arch dam using fiber optic sensors. In Proceedings of the 6th edition of the World Conference of the International Association for Structural Control and Monitoring (IASCM).
- [12] Klug F, Woschitz H (2015) Test and calibration of 20 FBG based strain transducers, In Proc. 7th Int. Conf. on Structural Health Monitoring of Intelligent Infrastructure - SHMII, Turin, Italy: 11p
- [13] Lienhart W, Lackner S, Moser F, Woschitz H, Supp G. (2013) Deformation Monitoring of Flood Prevention Dams Using Geodetic and Fibre Optic Measurement Techniques. In Proc. 6th International Conference on Structural Health Monitoring of Intelligent Infrastructure (SHMII-6). Hong Kong: CD-8p
- [14] Roberts GW, Hancock C, Lienhart W, Klug F, Zuzek N, de ligt H. (2021) Displacement and frequency response measurements of a ship using GPS and fibre optic based sensors. Journal of Applied Geomatics. 2021, 13, 51-61. <https://doi.org/10.1007/s12518-020-00338-z>
- [15] HBM. (2019) Product Manual: Optical Fiber Sensors. Online Resource: <https://www.hbm.com/en/4599/optical-fiber-sensors-fibersensing/>, Accessed 21. March 2019



# Risk Assessment and Monitoring of Civil Structures

# Structural monitoring of Zeeland Bridge - improved structural identification by combining a modular model updating framework with a mobile measurement setup during load tests

F. Besseling<sup>1,2</sup>, 0000-0003-4352-4536, C. Kortendijk<sup>2</sup>, J. de Bruijn<sup>2</sup>, E. Lourens<sup>1</sup>, 0000-0002-7961-3672

<sup>1</sup>Delft University of Technology, Stevinweg 1, Delft, The Netherlands

<sup>2</sup>Witteveen+Bos Consulting Engineers, Leeuwenbrug 8, Deventer, The Netherlands

email: f.besseling@tudelft.nl, coen.kortendijk@witteveenbos.com, janno.de.bruijn@witteveenbos.com, e.lourens@tudelft.nl

**ABSTRACT:** To reduce uncertainties associated with its structural re-assessment, the Zeeland Bridge in the Netherlands is currently the subject of a field lab, which will run for 2 years. In this contribution, the structural identification approach, the model updating concept and the first measurement campaign are presented, followed by some preliminary measurement results. The present stage focusses on load testing of the bridge to obtain insight into the possibly varying response in different spans of the bridge. Previously, parametric studies to expose input-output parameter dependencies were performed on a representative sub-system of the bridge, and the results are used to assist in the design of a measurement campaign and the development of a robust model updating strategy for the bridge. The results of the first measurements allow for evaluation of the actual performance of the bridge when subjected to heavy truck loads. This information will be used as a basis for further development of the updating approach.

**KEY WORDS:** Bridge monitoring; Structural identification; Concrete bridges.

## 1 INTRODUCTION

Bridges are vital infrastructure objects, with their availability critical for the operation of infrastructure networks. Many Western European bridges were built in the decades post WW-II, and therefore approach the end of their design lifetime. Depending on the function of a bridge and its location, loads may have substantially increased over the operational period due to increased traffic. Moreover, various time-dependent degradation processes may start to affect the state of a structure and therewith its safety. Examples of prestress loss related effects for prestressed concrete bridges are given in [1] and [2]. This necessitates structural reassessments of existing bridges in order to evaluate their structural reliability and remaining lifetime.

The models used for structural reassessments are developed based on design information, inspection results, and in some cases monitoring data. A key challenge in developing models for structural reassessments is uncertainty quantification. Bayesian techniques can be used to this end, combining data and expert knowledge to best estimate the actual state of a structure [7]-[10]. Where models are typically developed to predict the 'normal' structural response in the governing load scenarios, their results may not represent reality in cases where local deviations of structural response occur. Examples include bridges where the level of damage in for instance orthotropic steel decks varies significantly across spans, cable-stayed bridges suffering from damage concentrations in the deck structures at the location of specific cables, or concrete bridges showing regions with increased prestress losses. Response effects take place in such bridges, that seemingly result in load concentrations with locally increased damage potentials as a result. In such cases, tailored measurement campaigns might be needed to better understand the actual structural behavior.

In this contribution, the measurement strategy for the Zeeland bridge and a selection from the first measurement results are presented, followed by an outlook towards upcoming future measurements.

## 2 ZEELAND BRIDGE

The Zeeland bridge is a 5 km multi-span cantilever balanced prestressed concrete bridge, forming an important connection between the islands of Noord-Beveland and Schouwen-Duiveland in the Province of Zeeland in the Netherlands.



Figure 1. The Zeeland bridge in the local road network

The construction of the bridge was completed in 1964. The bridge spans are 95 m each, with a dowel connection at midspan connecting the two cantilever parts. Fig. 1 shows a picture of the bridge, with red ellipses indicating the locations of the dowel joints, the cantilevers, and



the foundations. These locations are related to the main sources of uncertainty in the bridge's load-response behavior, namely the forces transferred at the midspan joints (Fig. 2), shear stress levels in the cantilever, and foundation support stiffnesses.



Figure 2. The Zeeland bridge, showing the locations of main uncertainties.

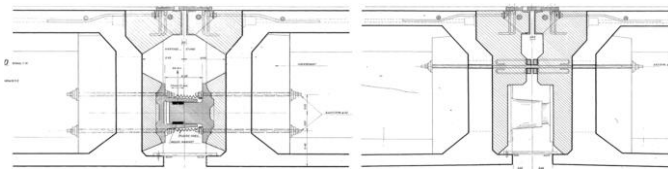


Figure 3. Longitudinal cross section of the Zeeland bridge sliding (left) and fixed (right) mid span joints.

In essence, the outcome of a structural reassessment is determined by both structural resistance and internal forces. For specifically balanced cantilever prestress concrete bridges, prestress loss and concrete time-dependent effects (e.g. creep) may occur, resulting in ongoing deformations with a potential effect on resistance as well as on internal force distributions. The potential development of extreme load concentrations in cantilevers depend on the relative stiffness of the cantilevers and midspan joints, and foundation support stiffnesses. Prestress loss in these type of bridges materializes as deformations increasing over time and reductions in shear capacity. According to Borges [1], the level of ongoing deformations can vary substantially per bridge, and is a function of concrete properties, the construction process, and environmental effects. For the Zeeland bridge specifically, potential long-term differential behavior between cantilevers in combination with additional deformations in the foundation or subsoil may contribute to internal loads in the cantilevers as well. Visual inspection of the mid-span joints of the bridge revealed signs of ongoing deformation and permanent load transfer between cantilevers. On the resistance side, the reduction of shear capacity due to time-dependent effects has been estimated in the range 1-5% [1]. Internal force variations due to variable loads, however, can reach levels up to 20%. Adding to these variations the additional internal loads due to possible long-term differential behavior between cantilevers and additional deformation in the foundation or subsoil, it can be concluded that for the Zeeland bridge the uncertainty associated with extreme internal loads is larger than the uncertainty associated with the loss of resistance. As such, we first focus on the identification of the actual load-deformation behavior of the bridge. Estimation of the actual degree of prestress loss per span will not be possible based on measured deformations under operational loads [2]. For specific spans of concern, localized destructive or non-destructive

measurements may at a later stage be considered to further investigate the actual degree of prestress loss.

### 3 MODEL UPDATING FRAMEWORK

In our project we intend to develop a Bayesian Network (BN) based model updating strategy. The BN forms the statistical model covering the dependency structures between model parameters of interest and measurable response quantities. The BN will be developed based on both finite element simulation results and measurement data. Finite element simulation results are used as a basis for parameter dependency evaluation of structural properties (parameters) and load-response characteristics (measurands), for which one is referred to [3]. Measurement data is used to check and optimize the BN structure.

Challenges and limitations that are associated with increasing numbers of model updating parameters in Bayesian inference are known as the curse of dimensionality [4]. In order to deal with this we follow the concept presented in [6], by defining a sub-system as a basis for our structural identification problem. This approach allows us to limit the number of parameters in the identification problem and focus on local measurements for the updating of local sub-system models. The sub-system includes one full span, existing of two connected cantilevers and their two supports, and the balancing cantilevers of this span. The sub-system, including parameters of interest and possible measurement variables, is shown in Fig. 3. The sub-system parameters are the concrete effective stiffness in bending ( $E_{c,i}$ ), the mid-span joint vertical stiffness ( $k_{d,2,3}$ ), and the support rotational stiffnesses ( $k_{s,ij}$ ). The sub-system boundaries are set at the mid-span joints of the two outer cantilevers, and the load transfer at these locations is accounted for using a vertical model boundary spring ( $k_{bc,ij}$ ). The total sub-system length is 190 m. In Fig. 3, the system parameters are shown in (a), and the possible measurement quantities in (b).

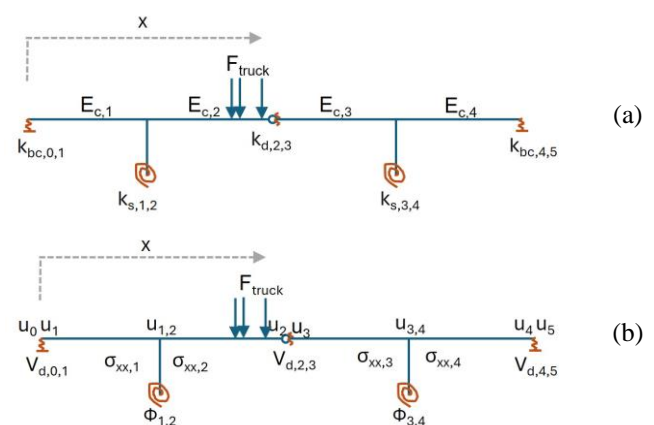


Figure 4. Sub-system schematization

The data used for model updating of the sub-systems is load-response measurement data from load tests on the bridge. Displacement response of the bridge is measured in various ways, from which displacement influence lines are constructed. The combined information of the known load, known load

position and measured response quantities serves as input for the updating problem, and overcomes typical issues associated with operational variability.

#### 4 MEASUREMENT CAMPAIGN

As a first test to identify the structural behavior of the bridge, a load test with two 50 tonnes 6-axle trucks and a mobile measurement setup is performed. The objective of this test is to obtain insight in the possibly varying response in different spans of the bridge. The measurement setup during the load test consists of measurements of the displacements at midspan relative to the supports, and the relative displacements of both cantilever ends at mid-span.

Absolute displacements are measured during the load test using Koherent's radio-based displacement measurement technology [12] and laser displacement measurements using GeoLaser L72 systems [13], verified by tachymeter measurements at some of the test locations. The results of the Koherent measurements are not yet included in this paper, because of time limitations and challenges associated with cleaning this data from radio wave reflections caused by the test vehicles.

Midspan joint relative displacements are measured by custom built joint displacement measurement devices (Figure 6). These systems provide high precision relative displacement monitoring of the joints, aiming to identify the load position where the direction of force transfer in the joints reverses. This is an indicator of permanent load transfer across a joint.



Figure 5. Laser receiver at midspan joint location



Figure 6. Midspan joint custom displacement sensor

The monitoring systems are applied in a mobile setup during the first phase load-test campaign, repositioning the systems repetitively across multiple spans of the bridge during a bridge closure by night (Figure 7).

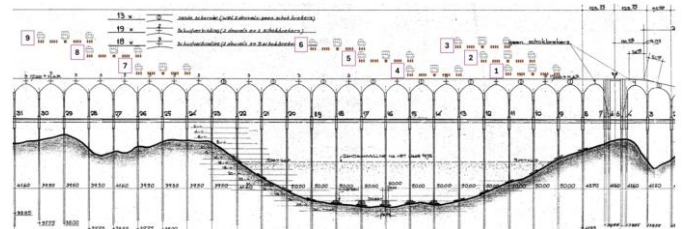


Figure 7. Multiple measurement locations in mobile load test setup

The load test is conducted by driving 1 and 2 trucks over a distance of 4 span lengths over the bridge at a speed of approximately 5 km/h. The setup with a load by both 1 and 2 trucks allows to evaluate the load level effect on the response. The 2 middle spans are equipped with the monitoring systems. By this means we generate influence lines of displacement response parameters for 2 spans.. This concept is illustrated by Figure 8. During 1 night a dataset consisting of load-response data for loads applied to 14 spans was obtained.

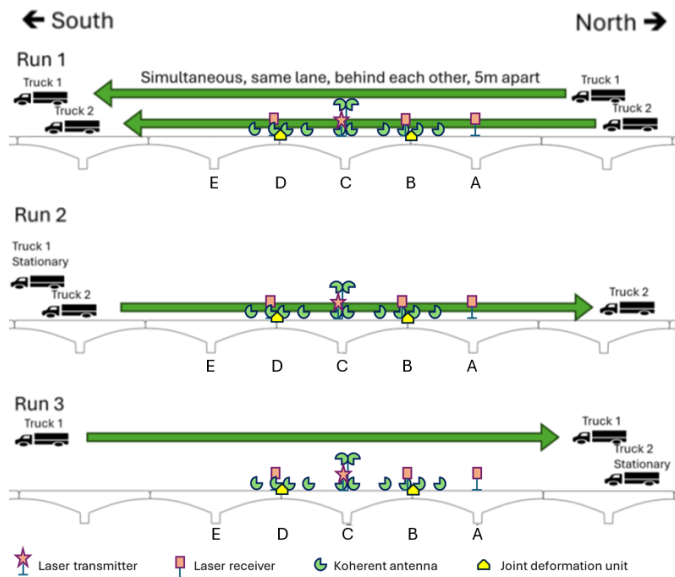


Figure 8. Mobile load test setup

## 5 PRELIMINARY MEASUREMENT RESULTS

### 5.1 Generation of response influence lines from measurement systems and GPS logging

The test trucks are equipped with the Witteveen+Bos GeoSaFence RTK-GPS tracking system. The GPS antennas are mounted on the outside top of the truck cabin, approximately above the first axle. Raw GPS measurement data comprises date and time and the location of the truck antenna in geographic coordinates (latitude and longitude in degrees). The positioning data are converted to geographic coordinates, and a coordinate transformation is applied to align the X-coordinate with the bridge's axis. Missing samples are filled by interpolation and the Rauch-Tung-Striebal Kalman Filter is applied to smoothen the positions and remove spurious jumps in the positions which occur during some of the runs. The result maps the bridge responses measured as function of time to the associated truck position on the bridge.

### 5.2 Laser based displacement influence lines

Laser measurements are performed to track the total displacements of the midspan joint relative to the adjacent pier at which the laser transmitter was positioned (see Figure 6). Figure 9 illustrates the laser measurement results for a single test run. The total displacement at midspan corresponded well with the model predictions. Displacements at the sliding joints are 10 to 30 % larger than the displacements at the fixed joints (Figure 3). Two trucks in convoy caused 10 to 20 % larger displacements than a single truck passage. It is interesting to note that displacements did not diminish to zero for trucks moving outside the test area: behavior was observed where the bridge deformations at some point do not seem to change with the truck position anymore, but rather some form of residual deformation remains. Possibly the trucks are not completely out of the zone where they influence the measurements, or time-dependent effects may be associated with the dampers present

in some midspan joints or effects in the soil-structure interaction response of the piers. All such effects may contribute to the observed behavior where displacements at the end of a test run did not return to zero.

Laser receiver E, positioned 1 full span away from the transmitter, was meant as a reference receiver, allowing for correction of measured displacements for support rotations. Rotation of the pier where the laser transmitter is positioned is observed from this receiver. In Figure 9 the blue curve represents the reference receiver positioned at pier 17. A vertical displacement of  $\pm 1$  mm are recorded by this receiver, for the truck moving backwards from pier 18 to pier 14. The data shows how the total midspan displacement consists of a bending component of the cantilever beam and a vertical displacement component associated with pier 'support' rotation, the latter being one order of magnitude smaller. The fact that the vertical displacement influence line for this reference receiver extends over a distance of 4 spans implies that the recorded vertical displacement in fact represents a rotation of the support where the laser transmitter is placed for this stage, and not an actual vertical deformation of the support where this receiver is positioned.

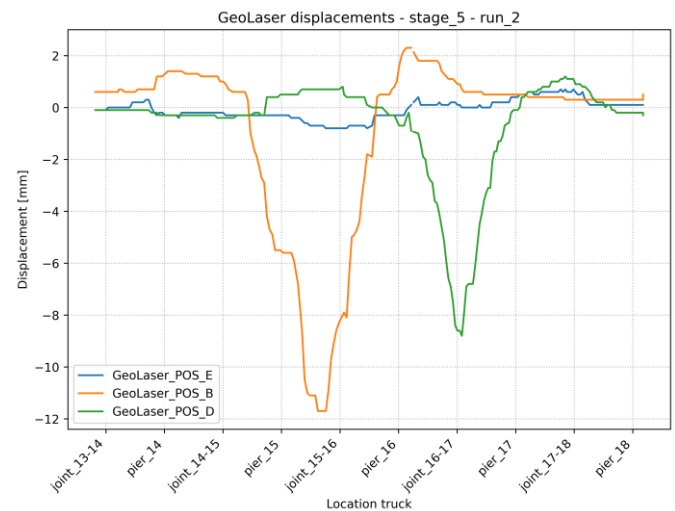


Figure 9. Total vertical displacements of midspan joints 15-16 and 16-17, and reference pier 17, measured by GeoLaser with transmitter positioned at pier 16

Evaluating the performance of the GeoLaser system, we conclude that the technology did perform quite well. The lasers' distance range was specified to be 100 m maximum. The 50 m measurements at the nearest midspan joints did generally perform well. The laser transmitter and receivers' glass screens however suffered from foggy circumstances during some measurement stages and runs, causing the reference receiver measurement to not be successful. For the adverse foggy conditions encountered during the test night the 100 m is concluded to be very much at the limit.



### 5.3 Joint deformation influence lines

The sliding and fixed joints depicted in Figure 2 are used in the Zeeland bridge in different configurations.. Going from North to South for pier 8 to 23 there are alternating sliding and fixed joints. This implies that this part of the bridge consists of sets of 2 coupled piers with balanced cantilevers forming a frame, having in the center a fixed dowel connection, and connected to the next part at the midspans of the outer cantilevers by sliding dowel connections. From pier 23 to 33 the pattern is different and all midspan joints are sliding joints. Figure 10 and Figure 11 show the joint relative displacements for joints 11-12 and 12-13 and for joints 15-16 and 16-17. Joints 11-12 and 15-16 are both sliding joints and 12-13 and 16-17 are fixed joints. In these figures the joint relative displacements at measurement location B and D (Figure 8), on both the East and West side of the bridge are presented.

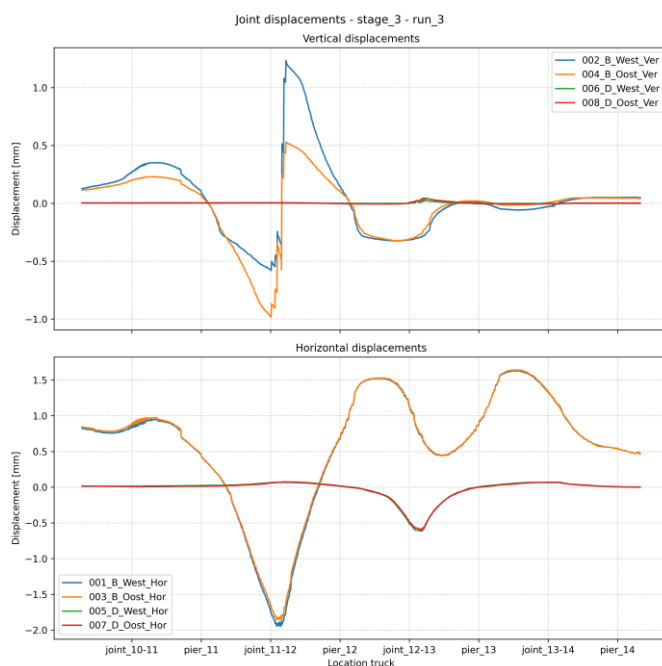


Figure 10. Joint displacements of joint 11-12 and joint 12-13

The different joint configuration affects both the total vertical displacements measured by the laser receivers and the joint relative displacements. Clearly, very different vertical relative displacement response is observed. Where in the first figure a more gradual increase of vertical joint displacements is recorded, the second figure shows more abrupt displacements when the truck is approaching and when the axles are passing the sliding joint. Also it is clear that the joint relative displacement sensors at joint 15-16 (B\_West and B\_East) do already record substantial negative vertical displacement when the test truck is still at joint 16-17, i.e. one span away from the sliding joint. This behavior deviates from the typical behavior observed at all the other measured spans (e.g. Figure 10). Apparently some displacement allowance is present in this joint which is mobilized by the test truck when it is on the center of the next span. Further research is ongoing to explain the locally deviating behavior around piers 14 to 16.

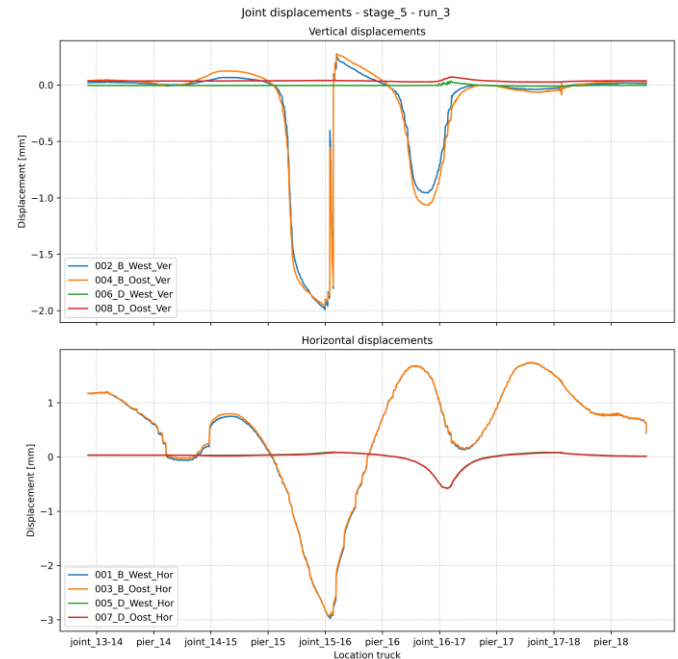


Figure 11. Joint displacements of joint 15-16 and joint 16-17

It is interesting to note that, as observed for the total displacements measured by the laser, residual displacements are present in the joints at the end of test runs. A certain degree of ‘memory’ seems to be present in the bridge system when it is subjected to heavy truck loads. It could not be established from the data which physical mechanisms causes this typical behavior. This will be further investigated in the upcoming phase.

From the figures it can also be observed that the fixed joint, where the two cantilevers are tied together with prestressed 32 mm steel bars, still show some vertical horizontal displacement allowance of approximately 0.5 mm. Vertical displacements for this joint configuration are limited to tens of millimeters. This is interesting because the same cast iron dowels are present at all joints, also the sliding joints where larger displacements are measured. This implies that the fixation point seems to take over the load transfer from the dowel at the fixed joints, which is an important insight from the perspective of load introduction in the concrete structure.

The part of the bridge with a joint configuration consisting of only sliding joints shows different behavior (Figure 12). The total vertical joint relative displacements are somewhat larger compared to the bridge part with alternating fixed-sliding joints. Horizontal joint relative displacements are much larger as well, up to 10 mm relative displacement amplitude, and shows, for both measured joints, a more or less symmetric response for the truck positioned at either side of the joint. The distance over which the joint relative displacement influence lines show substantial displacement is longer for the part of the bridge with only sliding joints. Especially the vertical joint displacement influence lines show comparable levels of relative joint displacement when the truck axles are passing the measured joint and when the truck is at midspan of adjacent spans.

The system of balanced cantilevers coupled by only sliding joints behaves much more like a continuous chain of rigid rotating elements. Relatively large horizontal compared to vertical displacements indicate the relevance of global rotation of the bridge superstructure and the need for modelling of the degrees of freedom at the supports. These need to be properly accounted for in models. The freestanding height of the foundation piles is around 15 m, which means that the characteristic of the substructure supporting the superstructure is determined by bending of foundation piles and soil-structure interaction of the bridge substructure and foundations. Both need to be integrated into lumped support springs in the model. The data of combined horizontal and vertical measured displacement allows to calibrate the model support characteristics.

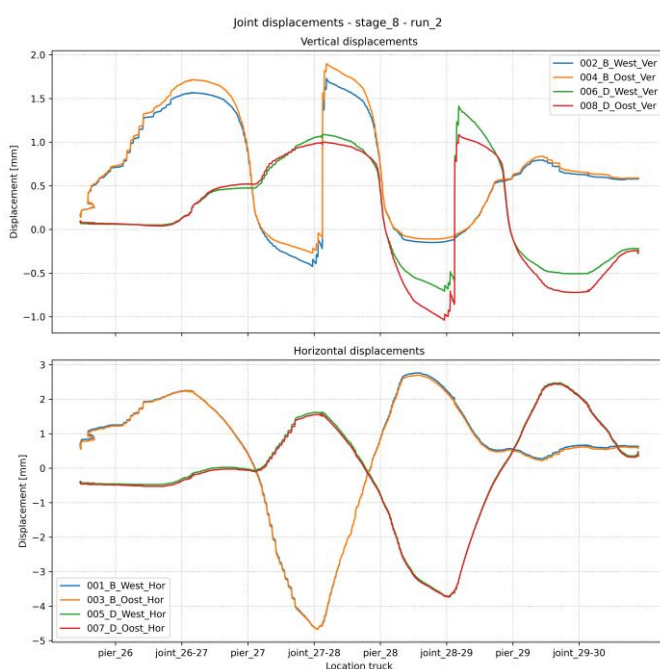


Figure 12. Joint displacements of joint 27-28 and joint 28-29

## 6 OUTLOOK TO UPCOMING MEASUREMENTS

The measurement results from the first tests have revealed interesting variations in the deformation response of certain cantilevers and spans, relative to others. These can be indicators for load concentrations in specific spans. In the next measurement campaign we will measure concrete stresses in the bridge indirectly by means of smart aggregates technology developed by TU Delft. These are installed in the box girder floor near 2 supports (locations indicated by  $\sigma_{xx,I}$  in Figure 4), which is in the compression zone of the cantilever gross cross section. Moreover, the mobile displacement measurements with laser and the custom joint sensors will be repeated at more spans to obtain a larger dataset and obtain insight in the response of more spans.

## 7 DISCUSSION

Load-deformation response is investigated for the Zeeland bridge to form a basis for full structural identification of the bridge. This paper builds on the previous paper [3] that introduced the model updating strategy for bridge structural identification. In the previous paper parameter dependencies between structural properties (parameters) and load-response characteristics (measurands) were investigated. The first phase measurement results that are now available form a basis for model updating of the sub-system models. However, given the quite different behaviour observed for the different spans one could question whether the model updating parameters set beforehand suffice to cover this spread in the observed behaviour. The measurement data indicates different ‘states’ of the sub-systems in terms of their neutral state, affecting their load-response behaviour when loaded by heavy test vehicles. It needs to be evaluated further how dependencies between input and output variables can contribute to the identification of the root cause or underlying mechanism that causes different behaviour of the spans. This will be one of the main topics considered in the upcoming phase of the project. Additional parameters that represent such different states might need to be added to the problem. In the upcoming phase it will be investigated how and through which parameters we can best represent the actual state in the updating problem formulation.

## 8 CONCLUSIONS

The present paper introduced the Zeeland bridge field lab and research project as well as an initial measurement campaign and the obtained load testing results. Structural re-assessment of the bridge requires a reduction of the uncertainty associated with internal forces in the bridge structure. The research project involves the development of a modular model updating approach for structural identification, based on load-response evaluation of sub-systems. Load-response influence lines constructed from measurement data are collected during the load tests with a mobile measurement setup. The developed mobile measurement setup performed well for the purpose of structural identification of the load-response behaviour. The total vertical displacements measured with lasers and the joint relative displacements measured with custom joint deformation monitoring systems were successful. It is concluded from the first phase measurement results that different spans exhibit different load-response behaviour. Differences in observed behavior can partially be assigned to different joint configurations across the bridge, but could possibly also be associated with a different ‘neutral’ state of the spans of this 5 km long multi-span bridge. In the upcoming phase of the project, this will be further investigated from both a theoretical (finite element model based) and experimental perspective (additional, more expensive measurements).

## ACKNOWLEDGEMENTS

The authors acknowledge the Dutch Ministry of Water and Infrastructure and the Dutch Provinces for their support to the ongoing research project on improvement of model updating strategies for structural reassessment. Especially we would like to acknowledge the Province of Zeeland for their contribution to this research for the Zeeland bridge and the commitment of their team when performing the first phase measurement campaigns.

## REFERENCES

- [1] Andrade Borges, E.A.: Long term effects of creep and shrinkage on the structural behaviour of balanced cantilever prestressed concrete bridges. (2023)
- [2] Chavez, A.A. and Gonzalez-Libreros, J. and Wang, C. and Capacci, L. and Biondini, F. and Elfgren, L. and Sas, G. : Assessment of residual prestress in existing concrete bridges: The Kalix bridge (2024)
- [3] Besseling, F., Lourens, E., Structural monitoring of the Zeeland Bridge for improved load - response evaluation and structural lifetime estimation, Proc. EVACES 2025, (2025)
- [4] Dashti M, Stuart AM. The Bayesian approach to inverse problems. In: Handbook of uncertainty quantification. Cham: Springer International Publishing; 2017, p. 311–428, [Chapter 10].
- [5] Zhou Y, Lu Z, Hu J, Hu Y. Surrogate modeling of high-dimensional problems via data-driven polynomial chaos expansions and sparse partial least square. *Comput Methods Appl Mech Engrg* 2020;364:112906.
- [6] Beck, J.L.: System identification methods applied to measured seismic response, Proc. 11th World Conference on Earthquake Engineering (1996)
- [7] Mendoza-Lugo, M.A. and Delgado-Hernandez, D.J. and Morales-Napoles, O.: Reliability analysis of reinforced concrete vehicle bridges columns us-ing non-parametric Bayesian networks, *Engineering Structures* 188 (2019) <https://doi.org/10.1016/j.engstruct.2019.03.011>
- [8] Jesus, A. and Brommer, P. and Westgate, R. and Koo, K. and Brownjohn, J. and Laory, I.: Bayesian structural identification of a long suspension bridge considering temperature and traffic load effects, *Structural Health Monitoring* (18-4), pp 1310-1323, (2019), <https://doi.org/10.1177/1475921718794299>
- [9] Koune, I-C. : Bayesian system identification for structures considering spatial and temporal dependencies, <http://repository.tudelft.nl/>, (2021)
- [10] Arangio, S. and Beck, J. L.: Bayesian neural networks for bridge integrity assessment, *Structural Control and Health Monitoring* 19-1, pp 3-12 (2012) <https://doi.org/10.1002/stc.420>
- [11] Barros, B. and Conde, B. and Riveiro, B. and Morales-Napoles, O., Gaussian Copula-based Bayesian network approach for characterizing spatial variability in aging steel bridges, *Structural Safety*(106) (2024), <https://doi.org/10.1016/j.strusafe.2023.102403>
- [12] Koherent Homepage, <http://koherent.io/>. Last accessed 3 March 2025.
- [13] Geolaser Homepage, <https://geo-laser.de/> Last accessed 7 April 2025.



## Scotiabank Saddledome Roof Structure Monitoring Program

Vidya Limaye<sup>1</sup>; Subharajit Roy<sup>1</sup>; Mark Leblanc<sup>1</sup>; Elizabeth Whittaker<sup>2</sup>; Atul Paranjape<sup>3</sup>; Lindsay Alleyne<sup>3</sup>

<sup>1</sup>SHM Canada Consulting Limited, Halifax, Nova Scotia, Canada

<sup>2</sup>Calgary Sports and Entertainment Corporation, Calgary, Alberta, Canada

<sup>3</sup>City of Calgary, Calgary, Alberta, Canada

email: [vidya.limaye@shmcanada.com](mailto:vidya.limaye@shmcanada.com), [subharajit.roy@shmcanada.com](mailto:subharajit.roy@shmcanada.com), [mark.leblanc@dal.ca](mailto:mark.leblanc@dal.ca),  
[ewhittaker@calgaryflames.com](mailto:ewhittaker@calgaryflames.com), [atul.paranjape@calgary.ca](mailto:atul.paranjape@calgary.ca), [lindsay.alleyne@calgary.ca](mailto:lindsay.alleyne@calgary.ca)

**ABSTRACT:** Scotiabank Saddledome, an indoor arena in Calgary, Alberta, constructed in 1983 with a hyperbolic paraboloid (saddle shaped) roof, has concave cables running in the east west direction to support gravity loads and convex cables in the north-south direction to support lateral loads. The stranded cables, encased in concrete and anchored into a ring beam, are not visible to detect the signs of corrosion. Events held in the arena require suspension of entertainment loads from the roof structure which, when coupled with snow loads, pose a major safety concern.

The installation of an acoustic monitoring system in 1999 to detect breaks in cable strands did not perform as intended. In 2014 the roof membrane was damaged by a significant hailstorm exposing concrete to moisture infiltration. In 2022, a Building Condition Assessment of the roof recommended further investigation of the bonded cable system.

Learning from strand failures at the Arizona Veterans Memorial Coliseum resulting in costly remediation work, a Structural Health Monitoring (SHM) system with strategically mounted sensors and a laser-based deflection measuring device, was implemented in July 2023. The objective of this SHM program is to collect data on monitoring parameters for roof movements continually over a period of 3 years in order to identify trends and implement an active alarm system based on data collected in the first year.

This paper presents the field application of SHM for risk management of a complex roof structure.

**KEY WORDS:** Hyperbolic paraboloid roof; Monitoring program; Parameters; Loads; Cables; Risk management; Analysis

### 1 INTRODUCTION

The Scotiabank Saddledome is a multi-use indoor arena located in Calgary, Alberta, Canada. Partnered with the City of Calgary, Calgary Sports and Entertainment Corporation (CSEC) maintains and operates the facility. The Saddledome was constructed in 1983 with a complex hyperbolic paraboloid (saddle) shaped roof. The arena hosts numerous events throughout the year requiring the suspension of entertainment loads from the roof structure. Event loads in combination with heavy snow loads during winter months lead to deformation of the roof structure. The roof structure's safety performance is correlated with the condition of its constituting components. As the facility ages and deteriorates reliable methods are needed to assess the overall condition of the structure.



Figure 1. Scotiabank Saddledome<sup>1</sup>

A Structural Health Monitoring (SHM) system was installed on the underside of the roof structure in July 2023 to monitor deflection and movement at key locations. The system sends an email alert when deflection at any of the key locations exceeds its preset threshold. In addition, the system detects changes in vibration characteristics which could indicate strand failure. This allows the condition of the roof structure to be monitored continually to manage risk while minimizing exploratory destructive testing and interruptions to the daily operation of the facility.

### 2 SADDLEDOME ROOF STRUCTURE

The roof of the Saddledome is a complex structure consisting of sagging (concave) cables running in the east-west direction to support gravity loads on the roof and hogging (convex) cables running in the north-south direction to support lateral loads on the roof. The cables are anchored into a ring beam around the perimeter of the roof, which is supported on thirty-two bearings, four of which are fixed A-frames at the low ends of the saddle. The sagging cables are spaced at 6 m on center and consist of two cables with twelve stainless steel strands each. The sagging cables in the center of the roof supporting the scoreboard consist of fifteen strands. The hogging cables consist of nineteen strands and are also spaced at 6 m on center. Precast panels are supported by intersecting cables to form the roof surface, as shown in Figure 2. Lightweight concrete was poured between the precast panels to encase the strands in concrete and form the ribs of the roof as shown in Figure 3. In addition to the bonded sagging and hogging cables, six unbonded post-tensioned strands are located within the ribs. These cables were most critical during construction and

contribute minimally to the roof's capacity. A catwalk system, scoreboard, and other rigging for event loading are suspended from the main cable system. Entertainment and concert events can impose up to 22,700 kg (50,000 lbs) of load on the roof.



Figure 2. Sagging and Hogging Cables<sup>2</sup>

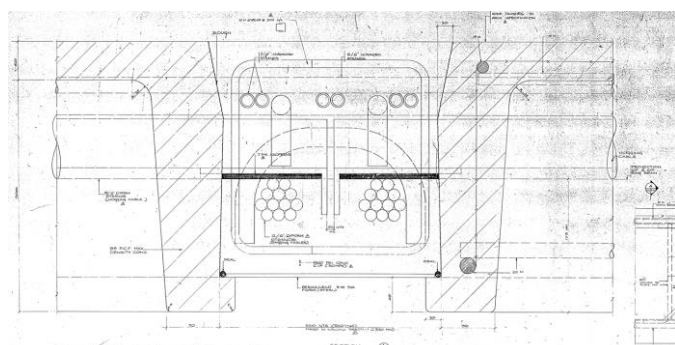


Figure 3. View of Embedded Cables in a Typical Rib<sup>3</sup>

The main risk to this type of roof structure is deterioration of the anchor connections at the ring beam or the loss of tension in the cables. Moisture infiltration at the anchor connection can result in corrosion of the anchor plate or cable strands. Loss of tension in the cables can occur if one or more strands were to break. The load would be redistributed to the remaining strands increasing and possibly exceeding their tensile stress. There are 4 main causes of strand failure:

- **Overloading of the structure**  
If the load imposed on the structure exceeds the design load the strands can become overstressed and fail.
- **Physical damage**  
During the life of a building new equipment may be installed requiring drilling or coring into the concrete. This can potentially cut or damage the strands.
- **Friction and wear**  
At the points where the cables cross, if a bearing pad is not present, the cables can rub against each other as the structure deflects under load or expands and contracts with changes in temperature. This cyclical rubbing can wear the strands down causing them to break.
- **Corrosion**  
The most common cause of strand failure is due to corrosion of the strand from moisture infiltration into the concrete or moisture build-up in void spaces.

### 3 CONDITION ASSESSMENT OF THE ROOF STRUCTURE

#### 3.1 Experience from Similar Structure

The Arizona Veteran's Memorial Coliseum, located in Phoenix Arizona, has a similar hyperbolic paraboloid shaped roof structure consisting of a grid of post-tensioned cables tied into a compression ring supporting precast roof panels. In 2006 a dip in the roof was discovered and further investigation revealed eleven cables had failed, one due to corrosion from past roof leaks and the others due to overloading. Costly emergency repairs were undertaken to replace the failed end anchorages. From the engineering team involved with the repairs it was understood that various non-destructive testing options to assess the condition of the cables were inconclusive. However, the change in shape of the roof surface was a sign that a loss of tension in the cables may have occurred.

#### 3.2 Saddledome Structural Assessment History

The Saddledome roof has experienced deterioration over the years. In 1999 an acoustic monitoring system was installed in the facility to record potential strand breaks. Since the system was installed, nine potential strand breaks were detected, four of which were in the sagging cables. In 2018 an unbonded post-tensioned strand failed and erupted through the concrete panel at the bottom of the rib where a void in the concrete had formed during construction. This event was not detected by the acoustic monitoring system. It was found that the wi-fi system in the building was interfering with the monitoring system and the event was not recorded.

In 2014 a significant hailstorm damaged the roof membrane exposing the system to moisture infiltration. Due to the strands being encased in concrete the condition of the strands could not be determined through visual assessment.

In 2020 a consultant was engaged to complete a condition assessment of the cable anchors and cable system. The cable anchors were assessed from the roof and found in good condition<sup>4</sup>. Ground Penetrating Radar (GPR) scanning was completed from the roof surface to assess the cables and locate other void spaces in the ribs that may be present however, due to the depth of the concrete and concentration of material in the ribs the results were inconclusive. Completing scanning from below was also challenging due to the access issues. Five locations were then selected to remove the concrete from the underside and expose the cables for visual assessment and penetration testing (two at the midspan of the sagging cables near the center of the building where moisture was likely to collect and three near the perimeter). The cables were found to be in good condition with no corrosion or tension deficiencies<sup>5</sup>.

A Building Condition Assessment (BCA) of the Saddledome completed in 2022 recommended further investigation of the bonded cable system to better understand the condition of the roof structure<sup>6</sup>. Given the inconclusive results of non-destructive testing completed in the past and the challenges of accessing the underside of the roof structure, options for monitoring the roof structure were explored. A monitoring plan was established to measure the shape and movement of the roof on a continuous basis over the next 3 years. This allows the City of Calgary and CSEC to manage the safety risks associated



with the roof structure and better understand how the roof structure behaves under varying loading conditions.

#### 4 MONITORING PROGRAM AND FIELD IMPLEMENTATION

SHM Canada Consulting Limited (SHM Canada) was engaged by CSEC to design, install, and operate a comprehensive structural health monitoring system at Scotiabank Saddledome to provide data on the performance of the saddle-shaped roof on an ongoing basis. The automated structural health monitoring system was installed and commissioned in late July 2023. It is currently active and provides valuable information to help maintain structural integrity of the roof.

##### 4.1 Instrumentation and Plan

The Scotiabank Saddledome roof monitoring system consists of a combination of wired and wireless sensors. The arena roof is divided into three main monitoring zones: Zone-1, Zone-2, and Zone-3. These monitoring zones are equipped with a total of twelve vibrating-wire strain gauges, twelve reflective target prisms, twelve triaxial tiltmeters, and nine triaxial accelerometers:

- *Vibrating-wire strain gauges*

Installed on the roof soffit, these gauges measure strain-related changes in the post-tensioned concrete beam network. These strain gauges are equipped with integrated temperature sensors that detect changes in the internal temperature of the arena. They are connected via signal cables to a datalogging system with highspeed acquisition modules capable of capturing burst strain data based on the required trigger points. The strain gauges were calibrated and set at the mid-range to ensure a sufficient offset for measuring both compression and tensile strain. Six strain gauges are installed in the direction of the two central sagging concrete ribs, while the remaining strain gauges are installed in the direction of the two central hogging concrete ribs.

- *Surveying system with reflective prisms*

The wireless system consists of a total station with a precision of 1 mm + 1 ppm and two types of reflective prisms. The target reflective prisms are installed in the roof soffit and the reference reflective prisms are installed along the peripheral wall. The total station measures the current baseline elevation and the roof elevation to provide precise roof deflection in the targeted regions. Six target reflective prisms track changes in roof elevation at the high-to-high direction along the two central sagging cables. The remaining six prisms record elevation changes at the low-to-low ends along the two central hogging cables. The approximate locations of the target reflective prisms are shown in Figure 4.

- *Triaxial tiltmeters*

Installed on the roof soffit, the wireless triaxial tiltmeters measure angular changes in two directions: in-plane and out-of-plane. Similar to the target reflective prisms, the tiltmeters are placed along both the central sagging and hogging directions. They are positioned near the prisms to measure in-plane and out-of-plane angular movements caused by event-specific loading arrangements.

- *Triaxial accelerometers*

Mounted on the roof soffit, the wireless triaxial accelerometers measure the acceleration in three orthogonal directions. The accelerations are recorded based on the ambient and induced acceleration of the arena roof under regular and event-specific vibrations, impacts, and other dynamic forces. The accelerometers are capable of measuring trigger data depending on their preset threshold limits. Out of the nine accelerometers, five are placed near other monitoring sensors, and the remaining four accelerometers are positioned near the non-axis boundary. Figure 5 demonstrates the axis orientation of triaxial monitoring sensors.

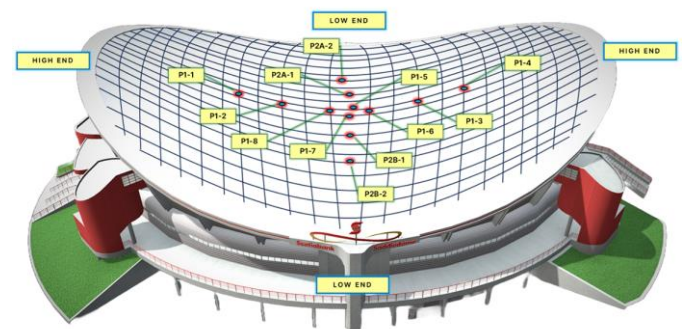


Figure 4. Approximate Positioning of the Survey Prisms

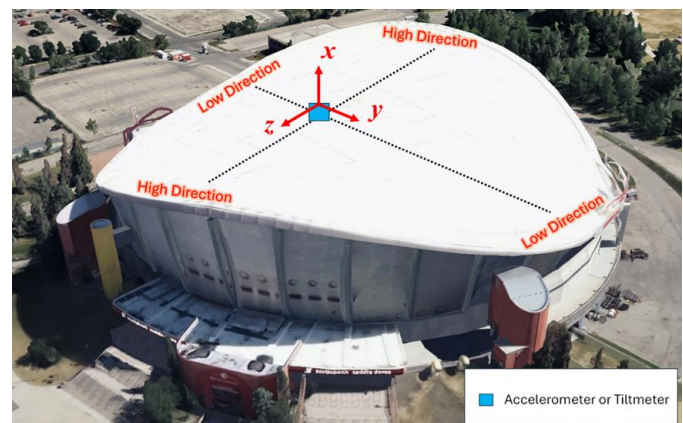


Figure 5. Orientation of the Triaxial Sensors

The monitoring sensors - strain gauges, reflective prisms, and triaxial sensors (including tiltmeters and accelerometers) - are installed in clusters positioned at the midpoint of cross ribs to maintain symmetry along the axes of the arena roof. The specific configuration of each cluster varies, allowing for tailored monitoring that addresses different structural requirements across the roof. This setup systemically provides comparative monitoring data based on the roof profile, helping identify any unbalanced loading effects and anomalies developing in the roof's structural system.

##### 4.2 Implementation

Implementing an effective monitoring program can be a complex task, especially when faced with challenges inherent in the arena and its environment. Several factors can influence the design, implementation, and ongoing management of the monitoring program. A few notable challenges faced by SHM



Canada team during the implementation and management of this monitoring system include access for installing the monitoring sensors due to unique roof geometry, the height of the roof, existing electrical and electronic fixtures, and tight project timelines.

One of the pressing challenges during the installation of monitoring equipment was the complex roof configuration and other hard to access areas. The limited access points, the concave and convex nature of the roof geometry, combined with existing fixtures on the arena roof, created significant complications in positioning, installing, calibrating, and maintaining proper line-of-sight (for reflective prisms) of the sensors. In addition to the roof geometry, sensor installation on the roof soffit of a significant height presented a time-consuming process and required a team of specialized rope access professionals.

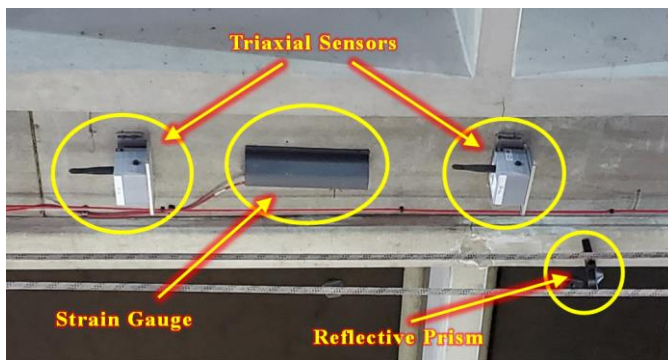


Figure 6. Typical Sensor Cluster

The Scotiabank Saddledome is considered the third busiest indoor arena in North America, hosting multiple professional

sports teams as well as a variety of concerts and events throughout the year. As a result, the timeline for implementing the monitoring system posed a significant challenge due to the need to avoid disruptions to the packed event calendar. The limited timeline and opportunities to install the monitoring systems, perform pre-commissioning tests, and commissioning a fully functioning monitoring system without interfering with the arena's operations were essential requirements.

Successfully addressing each of these obstacles required careful navigation and an understanding of each challenge to plan and prepare tailored solutions, ensuring the monitoring system provides accurate, reliable data without interfering with arena operations.

## 5 DATA ACQUISITION AND ANALYSIS

The Scotiabank Saddledome monitoring system collects four different types of SHM data: strain, deflection, tilt, and acceleration at varying acquisition rates. Therefore, data acquisition, communication, and management procedures depend on the capabilities and requirements of the different monitoring sensors. The unprocessed data from various sensors collected by data-logging systems is then transferred and stored in SHM Canada's server for reliability checks and further analysis.

Figure 7 illustrates a typical flow diagram for the Saddledome monitoring program protocol related to data collection, storage, and analysis. This diagram visually illustrates the steps, sequences, and decisions within the monitoring process. Data collected from strain gauges, target reflective prisms, and tiltmeters are processed both individually and collectively to identify data trends, establish relationships, and perform statistical analysis.

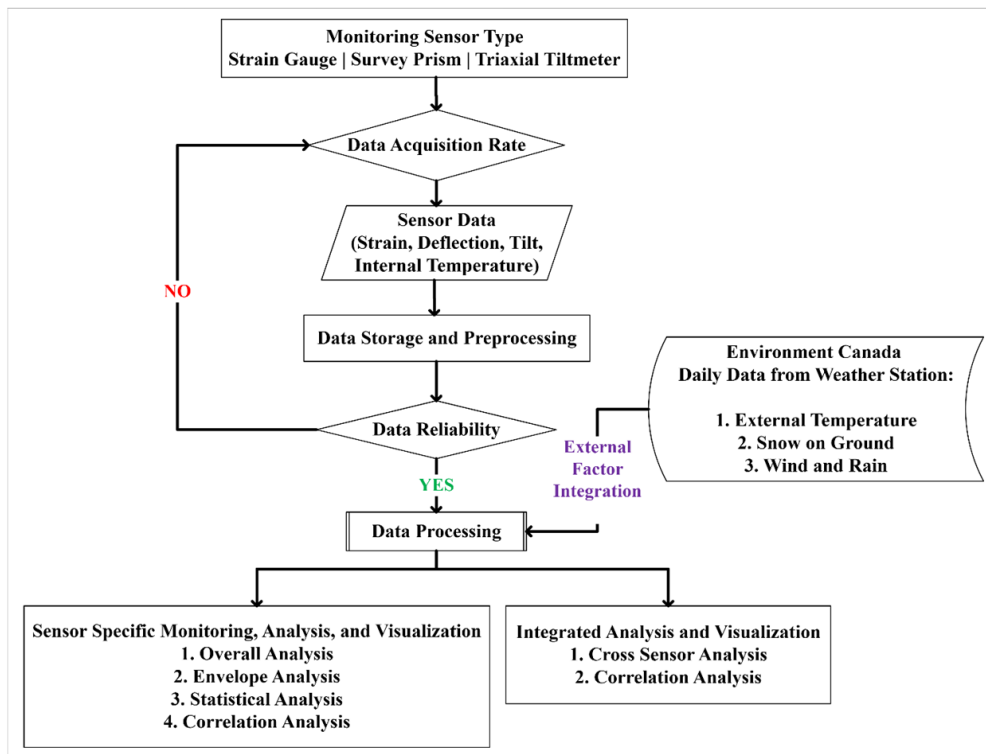


Figure 7. Data Acquisition and Analysis Process

The acceleration data is processed separately for peak-to-peak acceleration changes and spectral density analysis to understand the frequency response of the arena roof under ambient and excited conditions. The acceleration analysis helps to determine the overall performance and detect any significant changes in the dynamic behaviour of the arena roof.

Furthermore, the city of Calgary is known for its highly variable weather, often experiencing dramatic shifts in a single day. Located on the eastern slopes of the Canadian Rocky Mountains in Alberta, the city's proximity to the mountain system causes weather patterns to change quickly. During winter months, temperature can drop suddenly, while in the summer, warm spells can occur unexpectedly. Calgary "chinook" winds from the mountains, can raise temperatures by 20°C or more in a matter of hours, leading to a wide range of conditions throughout the year. Calgary's snowfall can be unpredictable, with snowstorms occurring any time during the winter months even as late as April. The city often experiences light and dry snow that accumulates rapidly but doesn't always accumulate for long. However, heavy snowfall can also occur, particularly in the winter and early spring.

Saddledome data analysis, therefore, integrates daily external weather data details (e.g., external temperature, snow on ground, rain, and wind) from the Environment Canada weather station near the Scotiabank Saddledome, along with different loading scenarios for major concerts and events hosted in the arena. This analysis protocol helps explore and incorporate all available internal and external factors that could influence the structural behavior of the arena roof.

The threshold limits are set based on the structure's age and history, combined with engineering judgment, allowing for a 10% increase or decrease over Year-1 recorded data. A notification system was implemented based on the established threshold limits to generate email alerts in the case of exceedance.

## 6 KEY MONITORING RESULTS AND DISCUSSION

This paper provides an overview of key monitoring results generated during the monitoring period from August 1, 2023, to January 31, 2025.

During this period, the Scotiabank Saddledome hosted a total of 51 major concerts and other events. This does not include minor events and other sporting events (such as hockey, lacrosse, skating etc.) The major events and concerts are indicated as vertical lines in Figure 8, 9, 10, 11, and 12. It is a well-established fact according to the National Building Code of Canada (NBCC) that the snow on ground data does not precisely represent actual snow accumulation on the arena roof. Actual snow accumulation on the arena roof and the nature of the accumulated snow plays a significant role in the roof's structural behavior. Due to limited information, the snow on ground data collected from the nearest weather station is integrated to provide context related to potential effects of heavy snow accumulation and snow drift. Any snowfall event is represented and incorporated by light-blue layers added in Figure 8, 9, 10, and 11.

The monitoring results presented as part of this study are referenced from their individual baseline readings and do not

account for preexisting conditions (strain, deflection, tilt) present on the arena roof. The sensor-specific data is primarily analyzed to understand the localized effects of changes related to the internal conditions inside the arena. In contrast, a comparative study of different types of sensors provides insights into the arena roof's structural performance based on both internal and external variations.

### 6.1 Strain

The strain gauges installed on the sagging concrete ribs primarily experience tensile forces, while those on the hogging concrete ribs experience compressive forces. Figure 8 presents differential strains in the most active strain gauges in both the sagging and hogging directions.

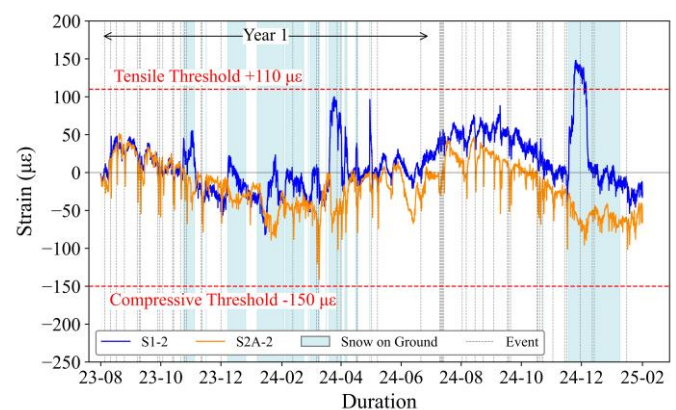


Figure 8. Strain Data from Different Zones

Analysis of the strain data revealed that the arena roof experiences event-specific changes in the strain levels both right before and after the events. These localized peak strain variations are primarily caused by the addition of event-specific mechanical and electrical fixture loads and their subsequent unloading from the arena roof. The strain levels are further increased due to snow accumulation and reduction in external temperatures. During these events, the internal temperature in the arena varied between 10°C and 22°C. The results also indicate that, during each scheduled event, the strain variations exhibited a similar pattern as the variation in the internal temperature inside the arena. The maximum tensile and compressive strain recorded by the strain gauge network is 148 µε and 140.5 µε, respectively against the threshold values of 110 µε and 150 µε. During this period, the absolute change in strain registered by a strain gauge was 230 µε.

### 6.2 Deflection

The deflection levels recorded by target reflective prisms are compared with prisms symmetrically positioned about the orthogonal axis of the dome to detect any unbalanced deflection conditions. The comparative differential deflection results showed some localized behavioral patterns. A steep increase in downward deflection is observed during the day of each scheduled event in the arena. When accompanied by snowfall events higher levels of deflection are recorded. Figure 9 provides an overview of comparative differential deflection results from three different zones.

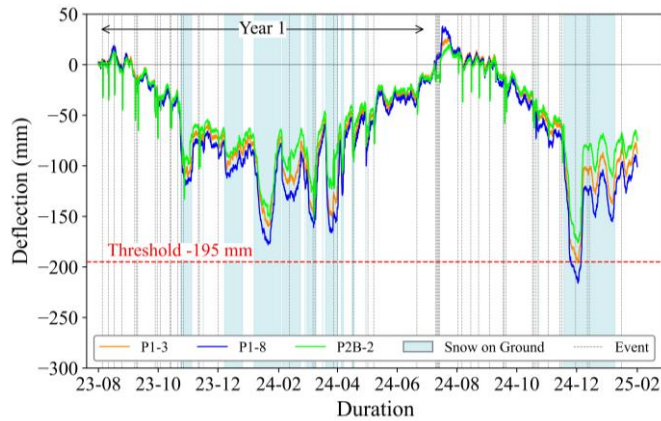


Figure 9. Deflection Data from Different Zones

The prisms located within the central region of the roof experienced higher deflection levels compared to the rest of the prisms. This phenomenon can be directly attributed to the consistent and balanced loading from the Jumbotron digital display system. The peripheral prisms in the hogging direction encountered a sudden increase in deflection levels during each major event. These specific changes in deflection levels are the result of the additional suspended loading. The maximum upward and downward differential deflections recorded by the survey prism network were 39 mm and 216 mm, respectively against the threshold values of 50 mm and 195 mm. The central prism recorded a maximum change of 254 mm in overall roof deflection during this period. The upward movement of the arena roof occurred during the removal of the old Jumbotron and the installation of the new Jumbotron of similar weight. A few hours after lowering the Jumbotron to the arena floor, the central region of the arena roof lifted upwards by 39 mm. With the installation of the new jumbotron, the deflection levels at the central zone returned to their previous deflection levels.

### 6.3 Tilt

The tilt levels are compared with respect to the in-plane and out-of-plane axes of the sensors at their symmetrical positions to infer any unbalanced rotation and its magnitude. The peripheral tiltmeters in both sagging and hogging directions recorded the maximum in-plane rotations. Steep changes in both the in-plane and out-of-plane tilt directions were observed mainly during the scheduled events. The maximum in-plane rotation for both high-to-high (sagging) and low-to-low (hogging) directional tiltmeters were 0.36 and 0.19 degrees, respectively. The absolute rotational range recorded by both high-to-high and low-to-low directional tiltmeters are 0.40 and 0.28 degrees, respectively. Similar to strain and deflection, the tilt is also influenced by event and environmental loading. Apart from the in-plane rotation, the Zone-2 tiltmeters experienced noticeable out-of-plane rotation during scheduled events, with the maximum rotation recorded at about 0.1 degrees. These out-of-plane rotations have primarily occurred due to the additional suspended loading and unloading during scheduled events. Figure 10 demonstrates the in-plane rotation in both the sagging and hogging directional tiltmeters. All the central tiltmeters showed a similar level of rotation on both planes when compared to the peripheral tiltmeters due to the consistent presence of Jumbotron loading. Similar to the deflection behavior, during the replacement of the Jumbotron,

the tiltmeters recorded a reverse angular shift but regained their normal levels after installation of the new Jumbotron.

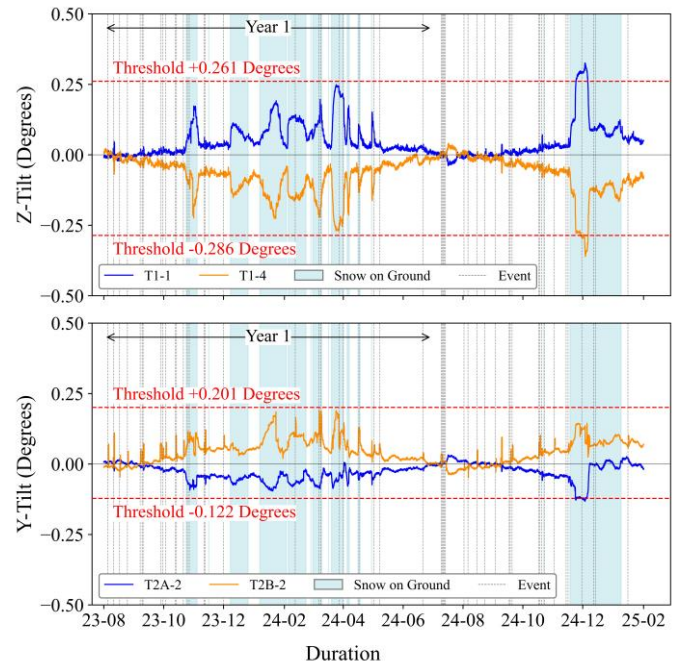


Figure 10. Tilt Data from Different Zones

### 6.4 Acceleration

The acceleration responses collected by triaxial accelerometers depending on two different acquisition modes: ambient and triggered, provided an understanding of the natural and induced frequency responses of the arena roof under different vibration levels and dynamic forces. The acceleration responses from different zonal accelerometers were analyzed using the Fast Fourier Transformation (FFT) and spectral density analysis. The peak frequencies were extracted and divided into four separate frequency bins based on their acquisition modes. Figure 11 presents the extracted ambient and induced frequency response from a Zone-2 accelerometer in the z-direction. Overall acceleration analysis showed that the natural frequency range of the arena roof is between 0 to 20 Hz. During an excited scenario, the frequency range of the arena roof lies primarily between 30 to 40 Hz.

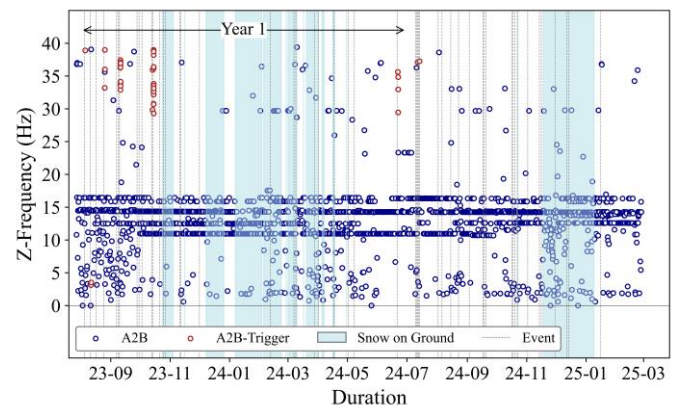


Figure 11. Typical Frequency Response of Arena Roof



## 6.5 Data Envelope and Discussion

The data acquired from various monitoring parameters, as well as other internal and external factors, are integrated into the analysis program to provide a comprehensive and global understanding of the Scotiabank Saddledome's roof behaviour under both environmental and operational conditions.

The first year of the roof monitoring program at Scotiabank Saddledome helped SHM Canada understand the response of the arena roof, create a monitoring data envelope, and establish threshold limits for individual sensor groups based on their locations. These threshold limits are set to study the performance of this unique roof structure in the coming years. Figure 12 presents an overall monitoring data envelope based on the most active sensors in the system, with respect to external weather conditions.

The global analysis shows that the arena roof experiences significant thermal-induced stresses and deformations, irrespective of their source being of internal or external origin. The changes in the concrete ribs' strain, the overall deflection profile, and the tilt variation at different locations in the arena are primarily driven by the external weather conditions (such as external temperature and snowfall) as seen in figure 9 and figure 10. However, the steep changes in the monitoring data are attributed to the internal conditions (such as event-related loadings and internal temperature of the arena).

In the later months of the year, primarily during the colder months, the monitoring sensors recorded significant variations in their monitoring ranges. The relationship between monitoring data (e.g., strain, deflection, and tilt), and outside

temperature greatly influences changes in the roof components due to its unique shape and internal load positioning.

The sagging concrete ribs in the arena roof are primary load-carrying members, and the tensile strain data recorded by those sensors installed on the sagging ribs showed elevated levels of strain. This period coincided with the increase in deflection and tilt levels observed by the central prisms and peripheral tiltmeters, respectively. In contrast strain gauges and tilt meters installed on the hogging ribs showed lower levels of strain and tilt respectively.

This behaviour can be attributed to movement in the arena roof caused by the temporary stretching of the sagging concrete ribs, the downward displacement of the central roof area, and the compressing of the hogging concrete ribs. In late 2024, accumulated heavy snowfall and additional event loading caused several deflection sensors to exceed their assigned thresholds, including a downward movement of up to 216 mm observed between November 25 and December 5. Upon clearing the accumulated snow, the roof rebounded to within acceptable threshold limits, indicating its elastic response to the loading conditions. The monitoring data indicate that changes related to external weather conditions are time-dependent rather than sudden. Additionally, the data analysis revealed a noticeable time lag between external weather changes and the corresponding monitoring data, likely due to the low thermal conductivity of the insulated concrete structure.

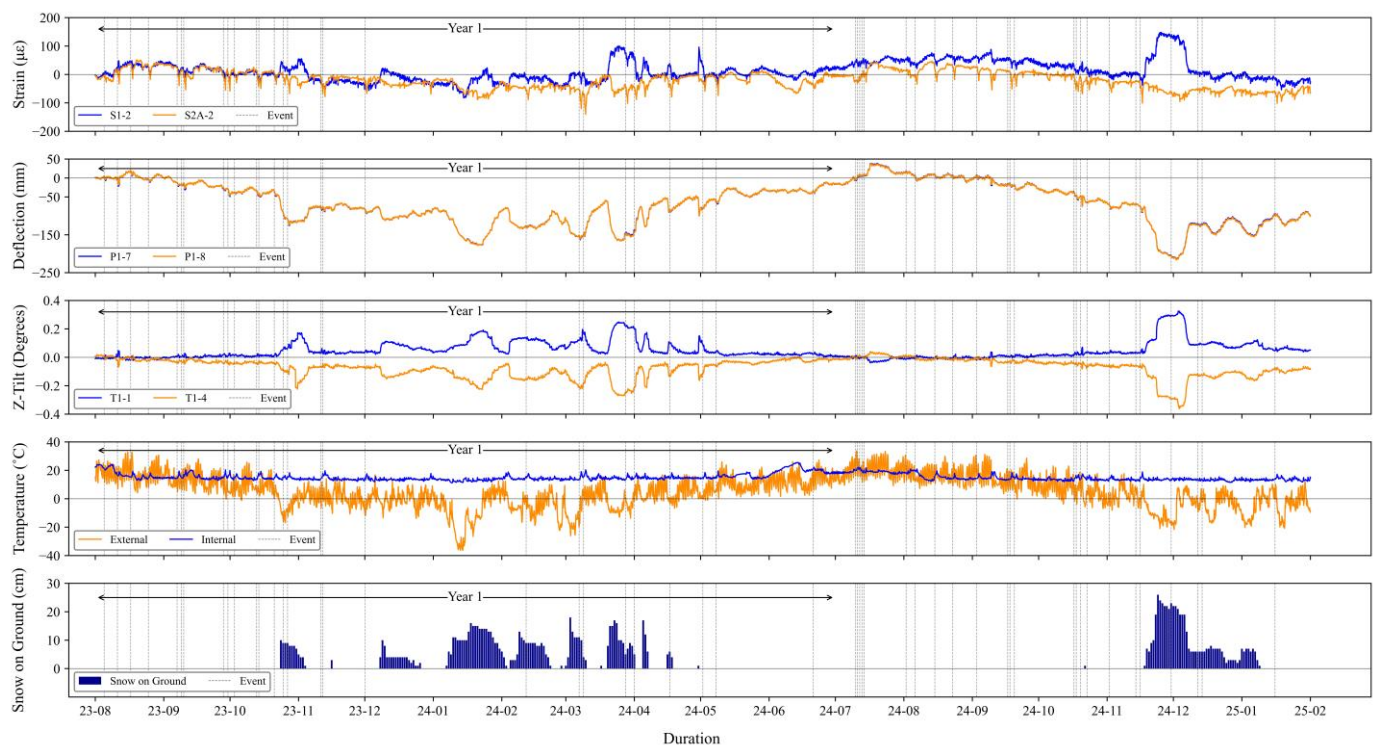


Figure 12. Monitoring Data Envelope for Strain, Deflection, Tilt, Temperature, Snow on the Ground

Figure 13 presents a Pearson correlation table between external temperature and deflection data from various reflective target prisms. Correlation analyses of other monitoring parameters not presented in this paper (strain and tilt) also show a high degree of correlation with external temperature.

The weather starts getting colder in October and remains cold until April of the following year. During the same period, starting in December, the City of Calgary experiences snowfall, which continues until the end of April. During Year 1 of the monitoring period, from August 2023 to July 2024, Calgary's lowest recorded temperature was  $-37^{\circ}\text{C}$ , and the highest was  $34^{\circ}\text{C}$ . So far, during the current period of 2024-25, the temperature has ranged between  $-28^{\circ}\text{C}$  and  $31^{\circ}\text{C}$ . However, the snow on the ground data for the current period shows that the city recorded higher levels of snow on the ground for consecutive days compared to the previous year. Due to the height of the arena roof, combined with heavy winds and adverse weather conditions, the snow removal process from the arena roof can be challenging. This becomes an important factor to consider, particularly when it coincides with an ongoing scheduled event or a concert.

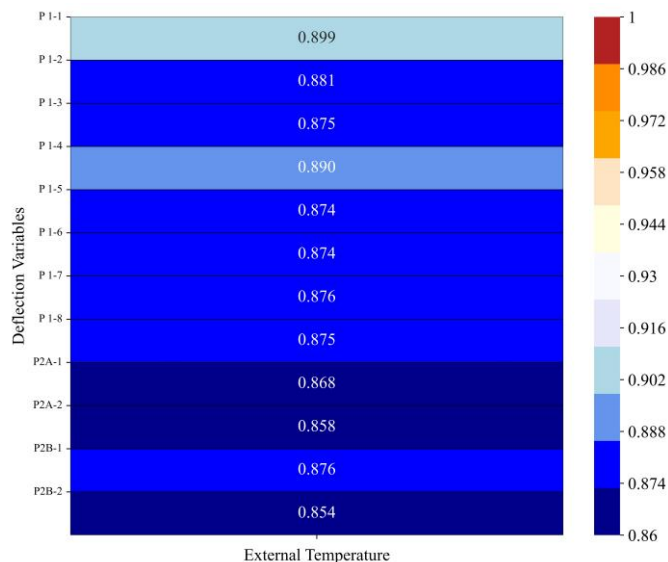


Figure 13. Relationship between Deflection and External Temperature

## 7 CONCLUSION

As asset owner, the City of Calgary is responsible for managing risk and ensuring safety of their assets. As the Scotiabank Saddledome ages the City of Calgary has taken proactive steps to assess the condition of the structure and mitigate potential risks. The monitoring program has provided CSEC and the City of Calgary valuable insight into the behavior of the roof structure under different loading conditions. It has ensured that necessary steps are taken to mitigate the risk of overloading the roof structure when environmental and entertainment loads are imposed on the roof. It has minimized the need to complete destructive exploratory assessments of the roof structure that are cost-prohibitive, disruptive to facility operations, and do not provide a thorough review of the system. In addition, the monitoring system has provided a method for identifying potential strand failures and thus reducing the risk of safety incidents. Structural Health Monitoring programs such as this

uphold the City of Calgary's commitment to engineering excellence, ensuring the highest standard of care in maintaining and operating its infrastructure.

Accounting for the effects of climate change, which is causing aggressive shifts in weather patterns, as well as the age of the arena and other contributing factors, the current monitoring program of Scotiabank Saddledome provides valuable insight into ensuring safety, functionality, and structural integrity, while also aiding in prolonging the lifespan of this iconic arena through proactive measures. Not only is it an important venue, but it also represents the pride, spirit, and cultural heritage of the City of Calgary.

## ACKNOWLEDGMENTS

Dennis Wipf with Gervasio and Associates provided valuable insights into the challenges and risks faced by the Arizona Veteran's Memorial Coliseum and methods for assessing and repairing a similar roof structure.

## REFERENCES

- [1] Photo source: Glenbow Archives NA 5654-401
- [2] City of Calgary / CSEC Archives
- [3] Calgary Olympic Coliseum. Drawing S3-2F Roof Panel and Joint Detail, prepared by Jan Bobrowski and Partners Ltd., dated September 15, 1982
- [4] Upper Ring Beam Inspection Report prepared by Entuitive, dated April 5, 2021
- [5] Roof Cable Anchor Inspection-Facility Structural Assessment prepared by Entuitive, dated March 25, 2020
- [6] Lifecycle Condition Assessment Report prepared by Entuitive, dated August 22, 2022

# Long-term monitoring and data processing of a continuous prestressed concrete bridge

Marc Savard, PhD, Eng., Jean-François Laflamme, MSc, Eng.

Direction de la gestion des structures, Ministère des Transports et de la Mobilité durable, Québec, Canada

email: marc.savard@transports.gouv.qc.ca, jean-francois.laflamme@transports.gouv.qc.ca

**ABSTRACT:** The Grand-Mère Bridge in the province of Québec, Canada, built in 1977, is a cast-in-place, segmental box-girder bridge measuring 285 m (935 ft) in length. Several problems arose during the construction of this bridge and an increasing deflection combined with localized cracking were noted after only a few months of operation. These defects were mainly due to insufficient prestressing, causing high tensile stresses in the deck and possible corrosion of the prestressing steel. A few years after strengthening of the bridge in 1992, a long-term monitoring program was implemented, including vibrating wire sensors (strain and crack sensors), inclinometers and temperature sensors. So far, more than 20 years of data have been collected and processed, leading to the recommendation of the rehabilitation of the structure using stay cables to ensure that the structure performs well until its scheduled replacement. This paper presents the instrumentation strategies, the various trends observed in the data and the relevant interpretations derived from them. In the context of damage detection, finite-element models have been developed and calibrated on measurements. Data indicate that the addition of stay cables eliminated the progression of permanent deflection and provided the structural system with added strength and redundancy. Lessons learned from this investigation are presented, along with a discussion of the conditions required for successful electronic monitoring.

**KEY WORDS:** Bridge monitoring; Bridge modeling; Data processing; Damage detection; Bridge rehabilitation.

## 1 INTRODUCTION

To manage all the structures under its responsibility, the Quebec Ministère des Transports et de la Mobilité durable (MTMD) has set up a periodic visual inspection program. The purpose of these inspections is to quickly detect defects that could reduce the strength of a structure or its durability. Defects that could jeopardize the safety of a structure are considered when assessing its theoretical load-bearing capacity.

Assessing the capacity of a concrete bridge is a complex task. It is very difficult to accurately assess the impact on capacity of a specific deterioration. The loss of capacity associated with a defect depends on its nature, location and extent. Moreover, the deterioration process evolves over time, often to the detriment of structural capacity.

The manager of a structure whose theoretical load-bearing capacity is inadequate can consider various approaches. Firstly, the structure can be reinforced or rebuilt in the very short term. Since financial resources are limited, this solution is only considered for structures with the most acute defects, or when the structure's reliability in the very short term is questionable. Secondly, restrictions on bridge exploitation may be imposed, for instance, reducing the number of lanes open to traffic or limiting maximum allowable loads. In the case of many highway bridges, restrictive measures are often unacceptable. The complete closure of a bridge is also unacceptable when no detour route can be considered or when the length of the detour is important.

When the reliability of a structure is questionable, it is possible, in some cases, to extend its useful life by placing it under electronic monitoring. One of the aims of such monitoring is to gather data that can be used to determine the rate of progression of the damage process. Monitoring may focus on structural properties such as equivalent stiffness, vibration frequencies or modal damping. It is also possible to

monitor the evolution of local parameters such as concrete crack width. Electronic monitoring can therefore be used to ascertain that the bridge is performing adequately under site-specific operating conditions.

Note that only slowly progressive failure modes can be properly monitored, and redundancy within the structural system is highly desirable, if not mandatory. In all cases where remote monitoring is being considered, the reliability of the structure must be ensured in the immediate future and cannot be adversely compromised by any subsequent worsening of the defects.

The Grand-Mère Bridge, in Québec, Canada, built in 1977 and measuring 285 m in length, consists of a three-span continuous prestressed concrete box girder of variable inertia. The central span is 181.4 m in length, while the two end spans are 39.6 m in length. Figure 1 shows an elevation view of the structure. At both ends of the three continuous spans and over one pier (at points B, D and E), roller supports have been chosen to allow the horizontal movement of the box girder. Pin supports are considered at the top of one pier (point C). Figure 2 illustrates cross-section geometry. Designed to limit deadweight stresses, this section depth variation does not meet current design recommendations regarding depth-to-length ratios. Another special feature of this bridge is that instead of prestressing cables, up to 216 longitudinal prestressing bars were distributed over tensioned portions of the box-girder cross section (mainly over the piers and at bottom of center span).

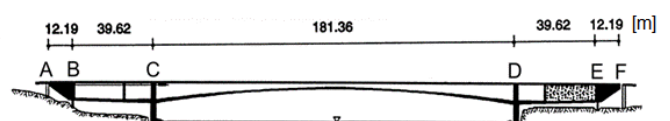


Figure 1. Elevation view of the bridge.



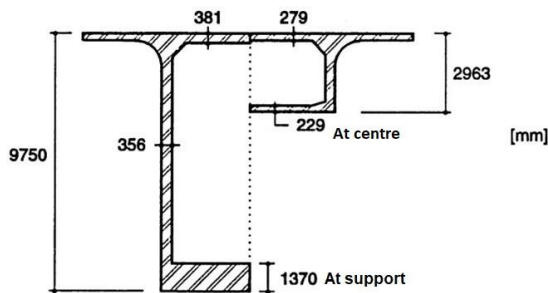


Figure 2. Cross-section geometry of the bridge.

Unfortunately, this bridge has experienced various problems resulting, among other factors, from many defects introduced during construction, such as poor quality of concrete between points B and C and the use of sleeves (joining end-to-end bars) that do not have the expected mechanical properties (many of them snapped). Also, the sheaths chosen were too tight around the prestressing bar, making grouting difficult. As a result, the prestressing bars are partially bonded to the surrounding concrete over undetermined portions of their length. Poor grouting can also lead to corrosion problems. The result of these defects is an asymmetric permanent stress distribution in the structure having a ballast at only one end of the bridge (instead of both ends, as initially designed) and additional compensating prestressing bars placed over pier C. In addition, as soon as the bridge was commissioned, a deflection at mid-span began to increase and shear cracking developed near the supports.

It has been recognized that many of the bridge's serviceability problems were due mainly to insufficient prestressing and limited knowledge at the time of design, especially regarding the estimation of creep and thermal stresses. While numerous studies showed that the short-term safety of the bridge was adequate, long-term integrity could be affected if short-term corrective measures were not taken [1]. Consequently, in 1992, the MTMD decided to strengthen the bridge by adding longitudinal prestressing cables in the box girder over piers C and D. Additional cables connected the bottom of the mid-span section of the bridge to the top of its ends. Since the deformation of the main span continued thereafter, a long-term monitoring program was initiated in 2001. The present paper briefly discusses a few of this program's findings, which led to the rehabilitation of the bridge using stay cables.

## 2 GENERAL CONSIDERATIONS FOR THE DESIGN OF THE BRIDGE'S STRUCTURAL HEALTH MONITORING SYSTEM

### 2.1 Overview

The design of an appropriate structural health monitoring (SHM) system must be tailored to the structure's behaviour under serviceability conditions. In the case of the Grand-Mère Bridge, in addition to its own weight, the dominant loads to which this structure is subjected are traffic loads and temperature variations. Traffic loads are transient loads acting over a short period of time, and fatigue problems associated with repeated loading cycles are not usually a concern for prestressed concrete bridges. Consequently, the bridge response under traffic loads is generally eliminated from long-term monitoring data. Thermal loads vary on daily and seasonal

basis and have a significant impact on the structure's behaviour. Therefore, assessment of the bridge's thermal response is mandatory prior to design and implementation of a suitable SHM program.

### 2.2 Bridge response to thermal loads

The internal temperature variation over the depth of a given cross-section can be broken down into three components: a mean value (TM), a linear vertical temperature gradient (GT) and a self-balancing non-linear component [2]. Given its nature, the latter component does not induce internal forces and global deformation of the structure. Therefore, the bridge response to thermal loads mainly results from variations of TM and GT. To perform data analysis such as linear regression, temperature sensors ought to be recorded simultaneously with measurements characterizing the bridge's response.

The following deformations occur in a structure subjected to temperature variations:

- The natural expansion and contraction of materials following a variation in the TM; these deformations are proportional and in phase with TM variations.
- The flexure strains induced by a thermal gradient GT.

Note that the presence of concrete cracks may lead to non-uniform thermal strain distribution along the structure.

As seen on Figure 2, the thickness of cross-section components is relatively uniform, varying from 279 mm to 381 mm, except for the bottom flange, which gradually increases from 229 mm at the centre to 1,370 mm at the piers. This infers a much greater thermal inertia near supports and a delay in the thermal response of thicker components.

In addition, the Grand-Mère Bridge is a complex hyperstatic structure having roller supports partially restrained that impede the free deformation of the structure. The partial restraint at the movable supports and the continuity of the spans above the piers at point C and D of Figure 1 give rise to additional thermal strains that may not be in phase with TM and GT variations.

Given the complexity of the bridge's thermal response, a finite element (FE) model has been developed (described at section 4) to predict its behaviour under specific loads. For instance, Figure 3 shows, schematically, the bridge deformation as predicted by the model of the Grand-Mère Bridge after a drop in the mean internal box girder temperature (TM). The restraint at roller supports generate axial tensile forces and associated positive strains. Consequently, sensor readings (such as extensometers or strain gauges) are expected to increase and are therefore out of phase with TM variations. In addition, as seen on Figure 3, a decrease in the TM also implies bending of the box girder and piers. Roller support restraint is responsible for these effects on the box girder. Pier bending causes a pair of horizontal forces (red arrows) acting in opposite directions at the bottom of the box girder and contributing to the lowering of the bridge profile. This pair of forces also induces axial tensile forces and bending moments in the girder. Depending on sensor location in the structure, the corresponding axial strains may or may not be in phase with TM variations.



Figure 3. Deformation (amplified) of the structure subjected to a drop in the mean temperature (TM) in the box girder.

Figure 4 presents the bridge profile predicted by the FE model of the Grand-Mère Bridge subjected to a thermal gradient (GT) developing in winter (corresponding to a cooling of top section fibres). The continuity of the spans above the piers causes non-uniform bending moments along the bridge and raising of the bridge centre. Depending on sensor location, the corresponding bending strains may or may not be in phase with GT variations. Also seen on Figure 4, a winter GT implies the bending of the piers and another pair of horizontal forces in opposite directions acting at the bottom of the box girder, which attenuates the raise of the centre of the central span. Note that these horizontal forces act in the same direction as those associated with a TM drop (as seen on Figure 3).



Figure 4. Deformation (amplified) of the structure subjected to a winter GT.

A third factor affecting bridge response to thermal variation is the lengthening or shortening of the piers. Figure 5 illustrates, schematically, the deformation of the box girder as the TM of the piers decreases, as observed in winter. As expected, the continuity of the spans gives rise to internal forces accompanying a drop in the centre of the main span and shortening of the top fibres along the entire length of the bridge. Note that temperature distribution across the width of a pier may not be uniform and might account for twisting movement of the box girder occurring over the piers.



Figure 5. Deformation (amplified) of the structure associated with a drop in mean temperature in both piers.

The Grand-Mère Bridge response to a specific profile of temperature variation is therefore the result of a combination of contributions that differ in importance from one another. The information provided by a numerical model enables a better understanding of bridge behaviour and the detection of possible damage processes.

### 2.3 Long-term effects

Among long-term effects that may affect this bridge, creep, shrinkage, prestress losses and concrete cracking are the main factors.

Creep, and to a lesser extent shrinkage, is a complex process that plays a major role in the gradual increase in deflection of such bridges [3]. Several models have been proposed in the literature [4] to predict the effects of creep over long periods of time. A suitable model ought to be adopted for long-term deflection and prestress losses predictions.

In prestress concrete members, prestress losses [2] can lead to cracking of fibres in tension, which may promote more prestress losses, water intrusion in the concrete mass and relaunch of creep. Passive steel rebars help control the development of cracks. Predicting crack location is difficult, and the possible addition of sensors must be anticipated when designing the monitoring system.

## 3 INSTRUMENTATION FOR THE STRUCTURAL HEALTH MONITORING OF THE BRIDGE

### 3.1 Objectives

The objectives of this SHM program were mainly to track the progression of mid-span vertical deflection and to collect information relevant to ongoing damage processes (mainly cracking, concrete delamination and spalling, corrosion, and breakage of steel tendons). As mentioned earlier, consideration of the evolution of these measurements helped in the management of the structure, to ensure user safety and bridge sustainability. During the more than 20 years of the monitoring campaign, sensors have been added, dictated by the necessity to validate and cross-check collected data, better understand bridge behaviour and detect initially unexpected progressive failure modes.

Considering the expected modes of failure of the Grand-Mère bridge and the selected structural health indicators, the SHM program features the following parameters.

### 3.2 Temperature measurement

Since the bridge profile and internal forces are strongly influenced by the vertical thermal gradient and the mean temperature, these parameters had to be recorded. In 2001, 24 resistance temperature detectors (RTDs) were installed at a cross-section located near the centre of the main span to measure internal temperature variations. Temperature sensors distributed over a section of the bridge allow for the calculation of the mean internal temperature as well as the thermal gradient (variation of internal temperature over the height of the section). Figure 6 presents TM and GT measured near the centre of the main span since 2001. Note the excellent performance of the monitoring system, which has experienced very few breakdowns over the past 24 years. As can be seen, GT is maximized in winter and TM and GT are almost perfectly out-of-phase.

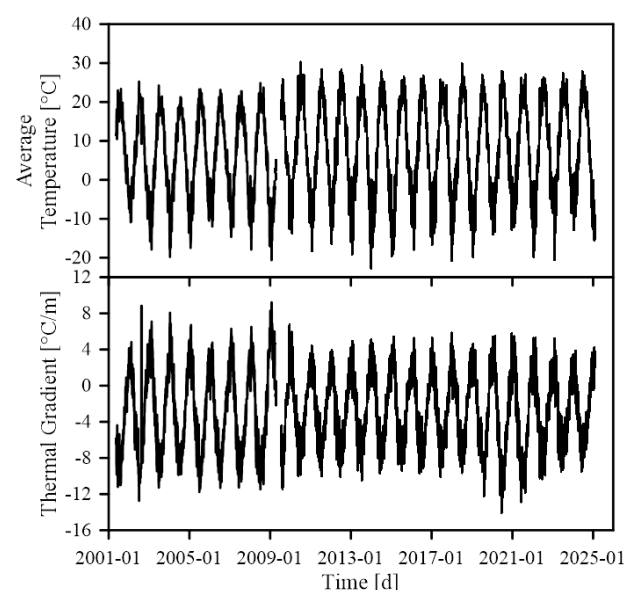


Figure 6. Internal average temperature and thermal gradient.

### 3.3 Estimation of mid-span deflection and box-girder torsion using tiltmeters

To estimate vertical deflection of the main span, a total of 17 biaxial tiltmeters (sensors measuring rotation in both vertical planes) were used. Figure 7 shows the tiltmeter layout. These sensors were spaced approximately 15 m apart along the first two continuous spans. They were installed in the centre of the lower flange of the box girder. A numerical integration procedure ([7] and [8]) enables the estimation of the vertical deflection at each rotation measurement point. Measurements in the other vertical plan give indications on torsional behaviour of the box girder.

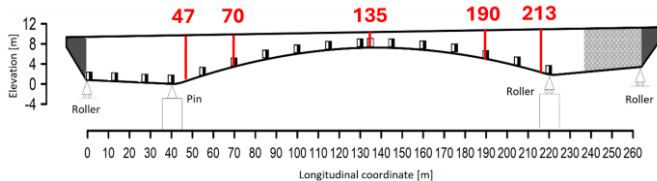


Figure 7. Tiltmeter layout and main cross-section identification.

### 3.4 Strain measurement

Thirty-two vibrating wire strain sensors located at the top and bottom of both webs allow the measurement of longitudinal strains at eight sections located in the central span at longitudinal coordinates 47, 70, 120, 125, 135, 140, 190 and 213 m. Figure 7 shows five of these sections. Figure 8 illustrates the layout of the vibrating wire sensors (VW\_i). Note that these sensors are set to zero when installed, so that only strain variations are measured.

Combining a realistic value of the concrete modulus of elasticity with four longitudinal strain measurements, the variation of the four internal forces present at a measuring section (axial force, two bending moments and distortion) can be estimated [5]. Note that these calculations are made using as-built section properties and measured elastic modulus is assumed constant over time. Also, given the small size of these sensors (125 mm in length), measurements are sensitive to cracks developing nearby. Therefore, care must be taken when interpreting the data. Localization of the neutral axis (NA) is useful in this respect.

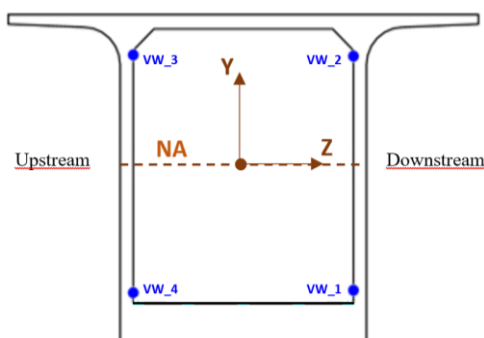


Figure 8. Typical vibrating wire sensor layout.

### 3.5 Rotation and displacement at abutments and at the top of piers

Potentiometers were installed to measure the relative horizontal movement between the box girder and supports at points B, C,

D and E. Tiltmeters were also added at the top of piers at points C and D to capture pier bending. A clockwise rotation at top of piers is considered positive. These sensors aimed to assess support mobility, as discussed at section 2.2. These restraints have an impact on main span vertical deflection.

### 3.6 Telescopic extensometers

A total of eight telescopic extensometers were installed at different locations where cracks are expected in concrete. In the case of this bridge, the sensors were between 5 m and up to 6.5 m in length. These sensors measure total longitudinal displacement and axial strains occurring between their anchor points. Should a new crack (oriented generally perpendicular to sensors' axis) appear between sensor anchor points, the associated movement will be added up with the breathing of other existing cracks and the total movement will be captured by the sensors. The concrete thermal expansion response is also measured by these sensors, and only sensor thermal response is eliminated from the recordings.

Four extensometers were installed in the main span on top of the box girder close to each pier (Extensio\_44 Upstream and Extensio\_44 Downstream, Extensio\_216 Upstream and Extensio\_216 Downstream) as tension may develop in those areas prone to concrete cracks. Two other sensors were also installed outside at the bottom of the box girder near the centre of the central span (Extensio\_130 Upstream and Extensio\_130 Downstream), since cracks may also appear in that area. Figure 9 shows four extensometers, two that are 6.5 m long (Extensio\_216) and two that are 5 m in length (Extensio\_232 and Extensio\_239), the latter installed under the top slab of the side-span girder.

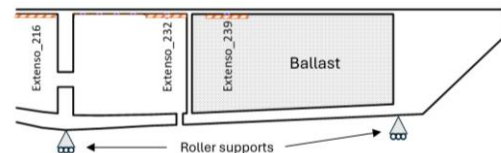


Figure 9. Telescopic extensometer layout.

## 4 FINITE ELEMENT MODEL

Concurrently with the SHM of the bridge, a numerical finite-element model of the crack-free structure has been developed to provide accurate estimates of expected behaviour under given load cases. Prestressing tendons were not explicitly included in the model, which means that total strain estimates are not available. However, concrete prestressing allows for the assumption of the linear and elastic behaviour of concrete, in both traction and compression areas. This assumption implies that under serviceability conditions, the largest compression stress in concrete shall never exceed 45% of concrete strength.

Moreover, prestressing forces are indirectly considered in the calibration process of the overall model. Calibration is done by adjusting the modulus of elasticity of different strategic structural components and the rigidity of the bearing devices. The objective of the calibration process is to have predicted vibration frequencies as close as possible to frequencies measured experimentally, in both bending and torsion. For instance, specific concrete properties have been established for certain portions of the webs, flanges and piers. Linear spring elements have been introduced to simulate actual support restraints. No rigidity is allocated for ballast weights.



The FE model has 48,830 nodes, 27,166 parabolic 20 noded brick elements for a total of 146,465 degrees of freedom. The piers have also been modelled (embedded at their base), since their flexibility significantly influences the overall behaviour of the structure, acting like elastic supports. Figure 10 presents a general view of the model, including the stay cables and the pylons that have been designed for the rehabilitation of the structure. Tensioning of all cables was completed in September 2022.

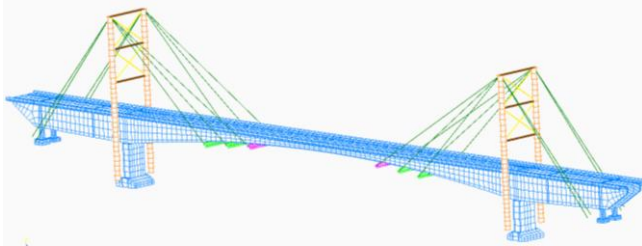


Figure 10. Isometric view of the rehabilitated bridge model.

## 5 DATA PROCESSING

This section presents some measurements gathered over the last 22 years with the various sensors presented above. A brief interpretation of the data is also provided.

### 5.1 Modal analysis and load tests

Modal analysis provides valuable information about the dynamic structural characteristics of a bridge. Recorded signals from accelerometers are analyzed and vibration frequencies and corresponding mode shapes are identified. A mode shape is a structural property that depends mainly on mass distribution and stiffness along the structure. Assuming mass remains constant over time, a change in the mode shapes or frequencies would indicate a change in rigidity resulting from cracks, concrete damage or changes to the support conditions.

A total of 12 modal analyses have been carried out at the Grand-Mère Bridge, the first one in fall 2003 and the last one in fall 2022. Since temperature affects support conditions and mode shapes, it is important to compare results under similar thermal conditions to detect damage or structural deficiencies. As reported by Cremona [6], measured frequencies may vary up to 5% for a 15°C (27°F) variation of the ambient temperature. Fall has been chosen for *in situ* modal analysis because thermal gradients are minimal during this season, thus limiting the effects of temperature on the behaviour of the structure. Vibrations have been measured under ambient traffic conditions.

Uniaxial and triaxial accelerometers individually connected to a data acquisition system have been distributed according to different schemes, for a total of 52 measuring points. The sampling frequency has been set at 200 Hz. In 2011, a wireless system was introduced, simplifying the data acquisition procedure. The location of the measuring points (schemes) has remained the same over the years. Representative results (flexural and torsional modes) of these modal analyses are gathered in Table 1.

Comparing the results for 2003 with those for 2021 at approximately the same internal temperature, a very slight decrease of the first seven frequencies of vibration is noted under normal traffic conditions. Those small variations may be caused by the thermal response of the structure, which affects

support conditions and internal forces, and are not necessarily the result of a damage process. In fact, the state of stress associated with thermal variations also depends on the weather conditions on the days preceding the *in-situ* modal analysis.

To assess seasonal temperature changes on the bridge behaviour, Figure 11 presents variations of the fundamental frequency of vibration (Flex.1 in Table 1) of the bridge along with TM as a function of time. The frequency is minimal in summer (approximately 1.02 Hz) and maximal in winter (around 1.07 Hz). Bridge response to thermal variations indicates that roller supports are partially restrained and incidental bridge internal forces have an influence on modal frequencies.

Structural rigidity has also been assessed through load testing. A total of eight load tests were performed in November of each of the following years: 2008, 2012, 2013, 2018 and each year thereafter until 2022. Load tests are intended to acquire data when the bridge is solely loaded by truck loads of known intensity. Generally, the loads consisted of semi-trailer trucks of about 40 tons each, for a total load never exceeding bridge service load. Measured data are used to validate the proper functioning of all sensors and provide valuable insight for FE model calibration.

The number of trucks and their relative position on the deck varied according to predefined load cases. Associated longitudinal and lateral force distribution in the structure can be established and bridge symmetry under symmetric loading conditions may be ascertained. The linearity of the bridge response under increasing loads is also verified and upon unloading, recordings indicate if the bridge returns to its initial profile. Detailed analysis of the test measurements showed that no significant changes in structural rigidity were detected from one year to the next, even with the seasonal support restraints above-mentioned.

Table 1. Measured frequencies [Hz] of some bridge's modes.

Modes	FE model estimates	Nov. 2003	June 2013	Nov. 2021
Mean temp.		1.5°C	20.4°C	1.0°C
Flex. 1	1,038	1,034	1,024	1,025
Flex. 2	2,177	2,134	2,117	2,124
Flex. 3	3,644	3,712	3,668	3,687
Tor. 1	4,625	4,665	4,605	4,639
Flex. 4	5,498	5,664	5,551	5,615
Tor. 2	6,794	7,102	6,966	7,056
Flex. 5	7,441	7,480	7,444	7,397

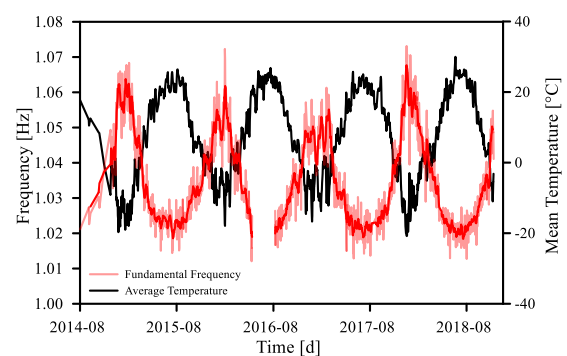


Figure 11. Variation of the fundamental frequency of vibration.

## 5.2 Tracking of roller support longitudinal movements and top of pier rotations

This section presents longitudinal movements recorded at each support. Figure 12 illustrates longitudinal support movement as a function of time. The dotted line added in many figures indicates when the stay cables have been tensioned. Very small relative movements are recorded at point C where a pin support is present. Maximum annual values are occurring in winter, as expected. Figure 13 shows top of piers rotations. Rotation recordings made at point C are the counterpart of those made at point D. Also, minimum rotation measurements at top of pier D occur in winter, as predicted by Figures 3 and 4.

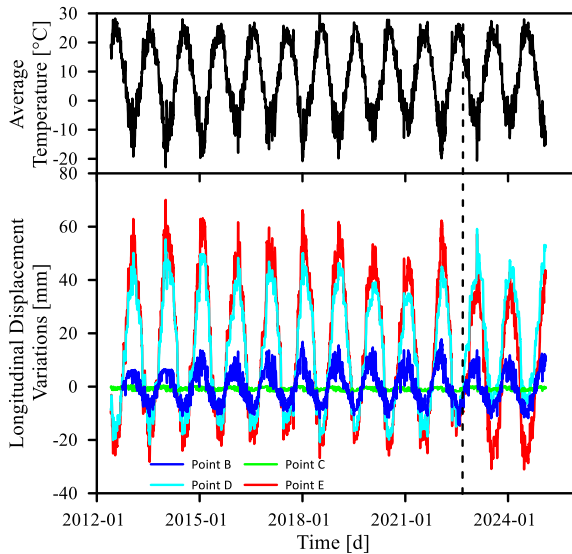


Figure 12. Box-girder longitudinal displacement relative to top of piers.

Under similar thermal loads year after year, the annual longitudinal displacement range decreases gradually from 2018 to 2022 (Figure 12), while top of pier rotation range is also decreasing (Figure 13). Measurements are linked together, and this result is in line with the gradual increase of mid-span deflection.

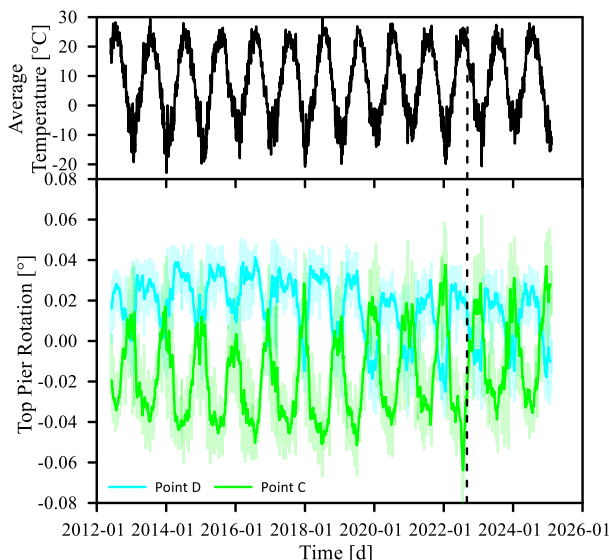


Figure 13. Top of piers rotation.

## 5.3 Tracking of mid-span deflection

Figure 14 shows mid-span daily average deflection as a function of time from November 2008, until February 2025. On the same figure, the blue dots represent bridge centre levelling and good agreement is observed.

Considering that temperature gradients have a greater influence on vertical deflection than average temperature, maximum mid-span deflection occurs early in winter. Regardless of creep, the annual deflection range is about 30 mm, close to the deflection caused by traffic serviceability loads (as confirmed by load tests). This result explains the significant variations that are observed in Figure 14, even with daily averages. This bridge is part of a freeway with an estimated average daily truck traffic of 1,600. The running average fit shown on the figure highlights the deflection trend over time.

Under similar thermal loads year after year, the mid-span deflection has been increasing since the sensors started recording. Furthermore, the process is accelerating.

Several factors have contributed to the increase in deflection at the centre of the bridge, including:

- concrete cracking under recurrent thermal loads and traffic loads.
- concrete shrinkage and creep.
- prestressing losses from steel relaxation, concrete long-term deformation, sleeve failure, bar corrosion, etc.

In addition to these phenomena, the bridge's response is influenced mainly by:

- the different thermal expansion coefficients of the various materials.
- the friction intrinsic to roller supports, which varies with temperature.
- the various thermal inertia of the structure's components (being a function of thickness and geometry).

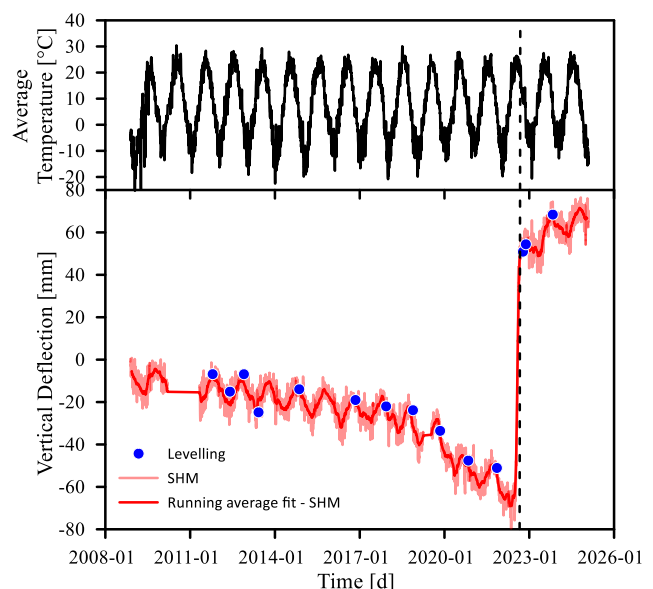


Figure 14. Mid-span deflection over the last 16 years.

In addition, 32 external prestressing tendons added to reinforce the structure in 1992 are exposed to ambient temperature inside the box girder, unlike the internal prestressing tendons, which are embedded in concrete.

Ambient temperature in the box girder varies more rapidly than internal concrete temperature, and this fact justifies the multiple oscillations observed even on the running average display, and to the deflection which is not perfectly in phase with TM or GT.

As seen on Figure 14, the tensioning of the cable stays caused the observed rise at the centre of the central span. The centre continues to rise months after tensioning, indicating a probable subsequent creep recovery.

#### 5.4 Tracking the breathing of groups of cracks using telescopic extensometers

As mentioned above, a total of eight telescopic extensometers were installed at longitudinal coordinates (length of the extensometer is indicated in parenthesis): two at coordinate 44 (6.5 m), two at coordinate 130 (6.5 m), two at coordinate 216 (6.5 m), one at coordinate 232 (5 m) and 239 (5 m) metres from B axis (Figure 1).

Figure 15 presents maximum seasonal response predictions at different locations where telescopic extensometers have been installed. These predictions have been made using the calibrated crack-free FE model. Two support conditions have been considered, whether the roller at point D is free to move horizontally or is partially restrained. Having the reference temperature set at 15°C, the annual mean temperature varies from 15°C (from Figure 6, the maximum temperature is about 30°C) to -35°C (the minimum temperature is approximately -20°C). As seen on Figure 6, the annual GT varies from 9°C/m in winter to -12°C/m during the summer.

Predictions indicate that a restraint at roller of point D (dark colours) reduces the annual total range of expected measurements. Also, a negative value is expected in summer for all sensors on the central span, meaning that these minimums are out of phase with mean temperature. For sensors of the side span (sections 232 and 239), expected maximum and minimum are in phase with mean temperature when roller at point D is restrained. With a free roller at D, maximum and minimum are out of phase with mean temperature. Depending on the stiffness of the restraint at the roller, a change in the sign of the bending moment can be observed from the central span to the approach span.

Figures 16 and 17 show twelve years of data recorded from extensometers 44 and 216. A positive recording corresponds to an extension of the sensor and crack opening. Note that in this figure, all sensors record their maximum value in winter, when the deck shortens. The contrary is noted in summer. Similar observations can be made at section 130.

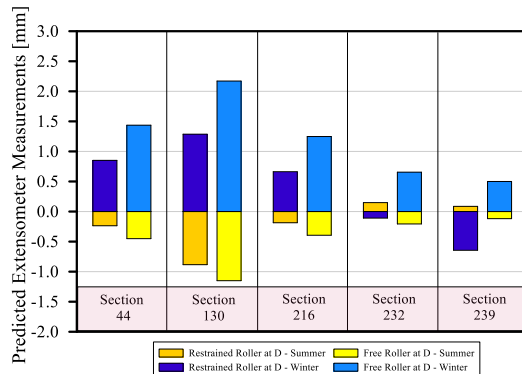


Figure 15. Maximum and minimum expected responses at five extensometer sections and different roller conditions.

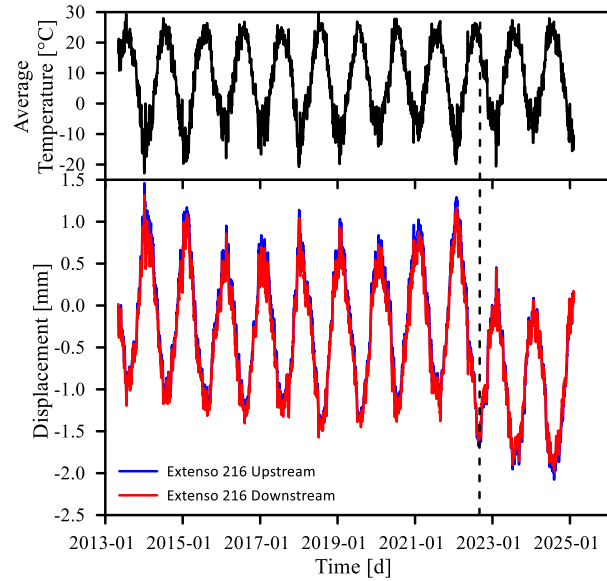


Figure 16. Recordings by extensometers 216.

At sections 44 and 216, measurements are therefore out of phase with concrete mean internal temperature, as predicted in Figure 15. However, the annual range of 2.5 mm is larger than expected with a crack-free model of the structure. This result seems to indicate the presence of active cracks. Recall that when a crack occurs, strain energy is released locally and thermal deformations along the prestressing bar are no longer uniformly distributed. Therefore, cracks may be considered as strain concentrators and if a sensor overlapped some of them, measurements can be amplified, especially when prestressing bars are not fully grouted.

Furthermore, sensors 44 and 216 experienced a permanent drop of approximately 0.75 mm following tensioning of the stay cables in September 2022. This result combines compressive strains and crack closures, since compression is induced in that area by the stay cable tensioning.

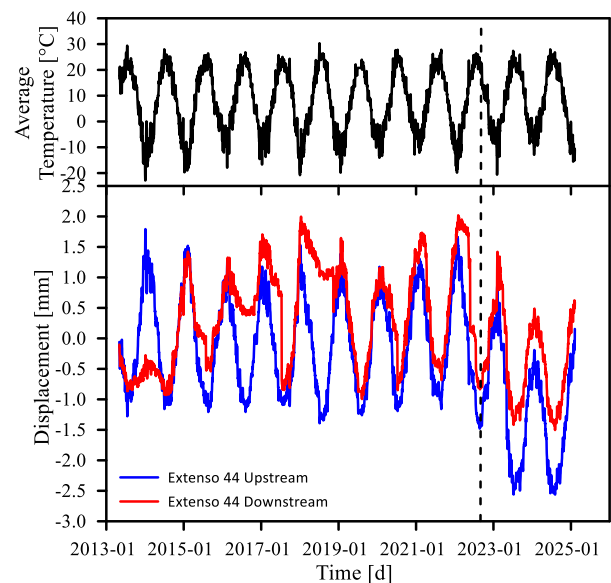


Figure 17. Recordings by extensometers 44.

Contrary to what can be seen in Figures 16 and 17, Figure 18 shows recordings from sensors 232 and 239 that are in phase



with internal temperature variations. In that area, side-span predictions (Figure 15) made with the roller partially restrained are confirmed. However, the recorded annual measurement range shown in Figure 18 are much larger than the range expected with the crack-free model of the structure. Once again, active cracks may be present, and the compression resulting from cable stays tensioning induced permanent closing of these cracks, as shown on Figure 18.

As seen in Figure 18, Extenso\_232 captured a permanent crack opening of 0.5 mm from the beginning of summer 2020 to fall 2021. This expansion is apparently not sufficient to eliminate the prestressing effect (decompressing crack lips). Also, as the stay cables were tensioned, Extenso\_239 experienced a 0.75 mm shortening, which is in line with the negative bending moment expected in this portion of the rehabilitated bridge.

Once cracks are closed, additional compression in concrete induces a minute variation in extensometer response. In winter, the deck shortens (see Figure 3), and compression in concrete decreases up to a point where the cracks re-open. The opening (breathing) of these cracks is captured by the extensometers and the measurements are amplified accordingly, as shown in Figures 16, 17 and 18. It should be emphasized that total or partial horizontal restraint at point D is mandatory for such crack breathing. Mean temperature and thermal gradient are then contributing.

Also, it should be kept in mind that when cracks widen and concrete decompresses locally, the mechanical properties of the box girder at crack surroundings are locally modified and the axial and bending rigidities are significantly reduced. This may invalidate the estimate of local stress from strain measurements in the vicinity of cracks, as discussed later in this paper.

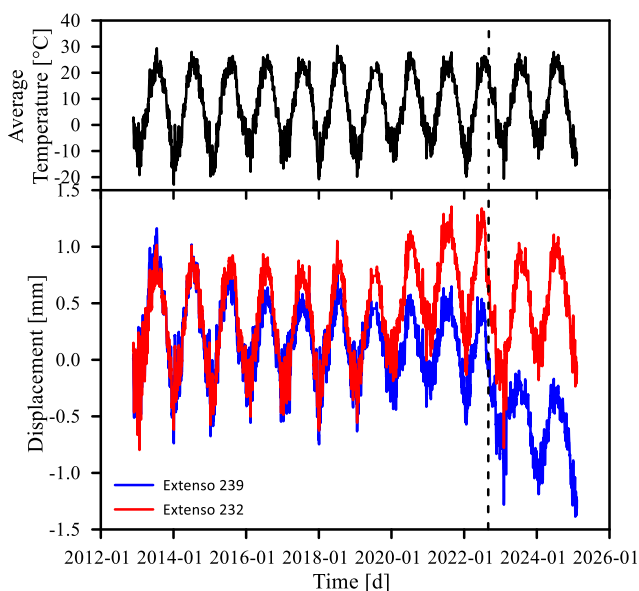


Figure 18. Recordings by extensometers 232 and 239.

### 5.5 Tracking of internal forces

In the case of the Grand-Mère Bridge, prestressing bars may be partially, if not fully, bonded to the surrounding concrete over most of their length. Consequently, the failure of a bar has generally a negligible effect upon vertical deflection and cannot be detected with strain sensors unless they are anchored close

to the failure. However, cracking and delamination of large portions of concrete may significantly affect the intensity and distribution of the forces within the structure. Therefore, to grasp the effects of concrete deterioration, internal forces can be good estimators. It should be emphasized that measured strains (and resulting calculated stresses) do not represent the total strain (including the permanent state), but rather the strain increase that occurred after the sensors were installed. Also, it should be kept in mind that the average elastic modulus of prestressed reinforced concrete may depend on local conditions such as cracks, delamination, corrosion, and other disorders.

Figure 19 shows the variation of bending moments computed at measuring sections 47 (near pier B), 70, 135 (near the centre), 190 and 213 (near pier D). As shown in that figure, although there were no significant permanent load variations, the bending moment gradually decreased at sections 47 and 70 between fall 2008 and summer 2022. At the opposite side of the main span, measurements at section 190 (the counterpart section) also decreased, while a surprisingly slight increase has been observed at section 213. At the centre of the main span, bending moments increased, as we expected them to. Meanwhile, less significant decreases have been observed at sections 120 and 140 (not shown on the figure). Note the large variations observed after the tensioning of the cable stays in September 2022. These measurements have been useful in confirming the adequacy of the cable stay arrangement.

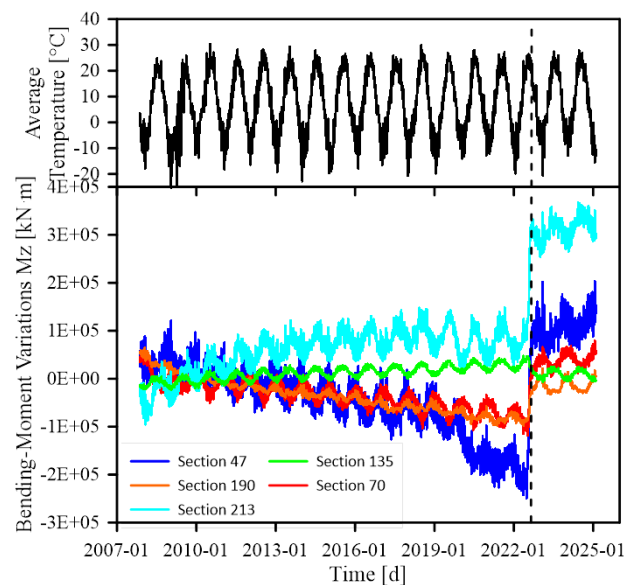


Figure 19. Bending-moment variations over time.

In a defect-free structure, bending moments vary according to the vertical deflection at the centre. To validate this statement and give insight to possible damage detection, a regression analysis has been performed between average daily bending moment  $M_z$  at a given cross-section and mean daily deflection at the centre as the explanatory variable. Figure 20 presents mean daily  $M_z$  at cross-section 47 as a function of mean daily deflection at the centre. The coefficient of regression for this distribution is equal to 0.85. Predictions from the defect-free numerical model are also presented. The comparison with the predicted behaviour indicates that for a given vertical deflection, the associated bending moment at section 47 is larger than expected.

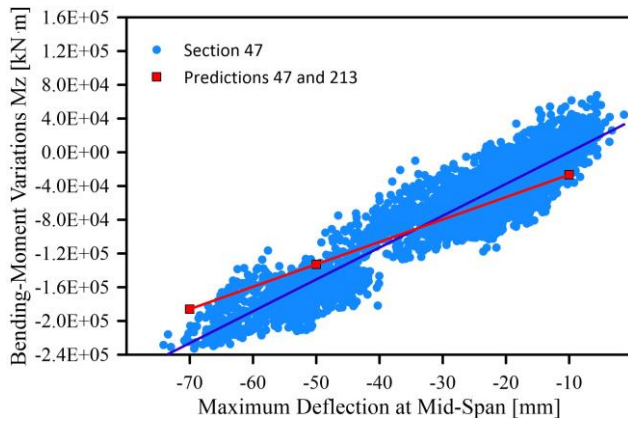


Figure 20. Bending-moment variations and predictions as a function of mid-span deflection.

The same regression analysis has been made with section 135 (near the centre) and section 213 (close to pier D). Figures 21 and 22 gather the results. At section 135, computed bending moments compare very well with predicted values, indicating that the bridge is behaving as expected under normal serviceability conditions. However, this is not the case at section 213 (Figure 22) where bending moments are not correlated with mid-span deflection (coefficient of regression for this distribution is less than 0.001). The comparison with the predictions (red line) makes this assessment apparent.

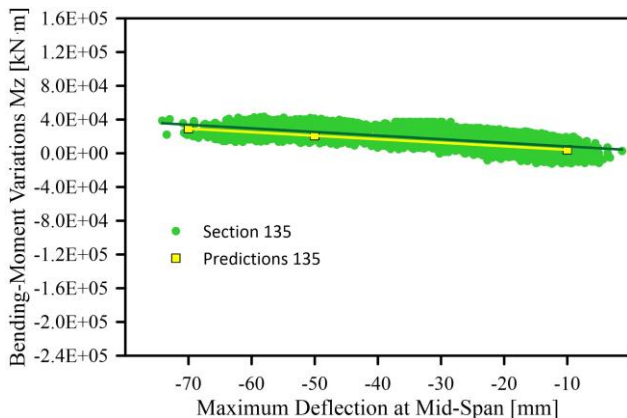


Figure 21. Bending moment variations and predictions as a function of mid-span deflection.

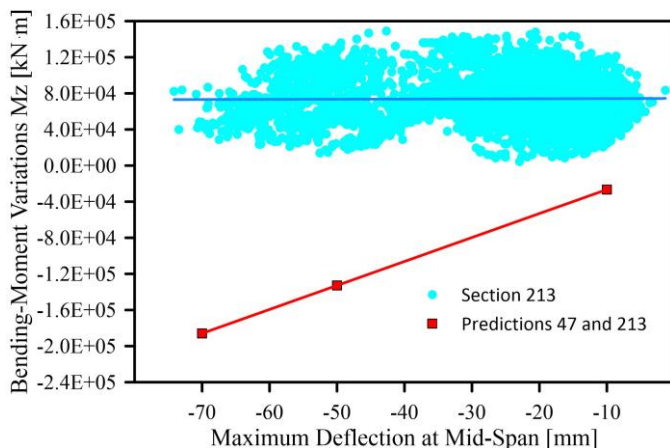


Figure 22. Bending moment variations and predictions as a function of mid-span deflection.

### 5.6 Tracking of mid-span box-girder torsional rotation

Figure 23 shows the recordings of the tiltmeter installed at the bridge centre, which measures box girder torsional rotation. A positive rotation is measured when the downstream web shifts downwards with respect to the upstream web, which may rise accordingly. In other words, a clockwise rotation around the bridge's longitudinal axis pointing east is assumed to be positive.

The data trend shown in Figure 23 indicates that girder torsional rotations are greatly correlated with internal temperature variations (the coefficient of regression being greater than 0.9). Also, an “event” may be noted around the end of April 2012, characterized by a rapid decrease of about  $0.012^\circ$  (from  $0.0055^\circ$  to  $-0.0065^\circ$ ) of the girder torsional rotation. Meanwhile, the internal temperature varies in the same way as in previous years. With permanent loads unchanged, this result suggests that structural damage took place, and the so-called event that occurred at the end of April 2012 may be the starting point of this apparent damage process. In fact, it can be shown that damage to a portion of a symmetrical cross-section (becoming unsymmetrical) induces such a torsional deformation. In Figure 19, the bending moment at section 213 became desynchronized from the bending moment at section 47 at approximately the same time.

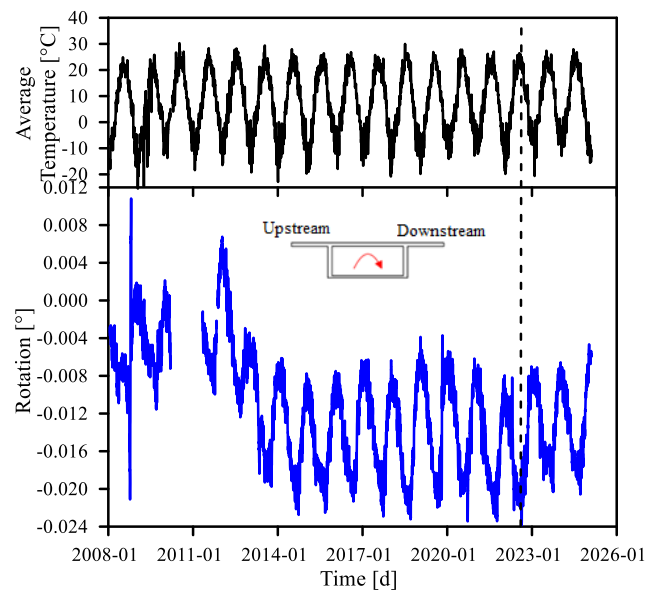


Figure 23. Box-girder torsional rotation at mid-span.

## 6 CONCLUSIONS

The structure under investigation was monitored for many years before it was strengthened. *In-situ* modal analysis and controlled load tests were conducted and recorded data were used to calibrate a representative numerical model of the bridge. Insights from a numerical model greatly helped bridge behaviour understanding and eventual damage detection. The model, in conjunction with long-term monitoring data, allowed for the identification of the following findings:

- Under ambient traffic conditions, 12 modal analyses have been carried out between 2003 and 2022. No significant changes were detected for the frequency of the first seven modes of vibration. Frequencies varied according to

internal concrete temperature and the sudden slips that may occur at the roller as the bridge expands or contracts. The numerical model showed that the rollers at points B, D and E needs to be partially restrained to fits the measured frequencies.

- Free relative longitudinal movement was expected at the roller between the box girder and the top of D axis pier. Sensors showed that such movement was partially restrained, and that the piers bend according to internal temperature changes. The C axis pier is topped with pin bearings. Consequently, an horizontal force developed in the box girder between points C and D—compression in summer when the deck lengthens and traction in winter when the deck shortens. Incidentally, a permanent and progressive tilting was detected in these piers, a result that is in line with the observed permanent mid-span deflection.
- In addition to a slow and progressive permanent mid-span deflection, there was no unexpected or spontaneous sag increase over time. Creep and prestress losses were the dominant parameters contributing to the permanent sag of the main span.
- A permanent box-girder torsional rotation was detected at mid-span. Along with longitudinal stresses estimated at different sections along the deck, these observations revealed structural damage over the support at point D. Structural damage may take different forms, such as concrete cracking (accompanied by tension stress relaxation) or prestress loss (breaking of a tendon, loss of anchorage, corrosion), the latter being accompanied by compression stress relaxation.
- Telescopic extensometers were used to track the breathing of groups of cracks. Recorded data indicate that concrete in the vicinity of some cracks is decompressed when the temperature is low. In winter, the deck shortens and compression in concrete reduces up to a point where cracks widen. Crack openings are picked up by extensometers and the detected amplitude is larger than expected. The frozen bearings mentioned earlier are mandatory for this behaviour to occur, and residual prestressing forces are not sufficient to prevent crack breathing. Consequently, prestress loss causes a reduction of the structure's load-carrying capacity. Moreover, breathing cracks and concrete decompression cause larger stress cycles in prestressed tendons. This phenomenon promotes the premature failure of tendons, especially those located in the top flange, which is a corrosion-friendly environment (de-icing salts are spread on the roadway). Note that this diagnosis is achieved with no information on total applied stress, only with the help of long-term electronic monitoring data.
- The addition of cable stays was the solution chosen to strengthen the bridge. Since the cables have been tensioned, no progress has been observed in the damage processes of this structure.

Given the low relative stiffness offered by the stay-cable structure compared to that of the prestressed concrete box girder, this reinforcement:

- has little impact on the bridge's overall live load and thermal load responses (deflections, stress distribution and intensity, etc.).
- contributes to the bridge's structural redundancy, by enabling alternative load paths in the event of failure or excessive deformation of the box girder.
- introduces permanent stresses in the box girder that reduced the intensity of stresses caused by gravity loads, thus enabling some cracks to close and subsequent creep recovery.
- does not contribute to segment joint decompression, though new cracks were visually detected near the centre of the bridge.

Given the deficient design and erection problems affecting the strength and durability of this bridge, its reliability was questionable. Since the initial reinforcement of the structure, the electronic monitoring program presented has played a crucial role in managing this structure and keeping it in service for almost 50 years. The program has also enabled us to validate the structural effects induced by the reinforcement of the structure using stay cables.

## ACKNOWLEDGMENTS

The authors would like to express their sincere thanks to all of those involved in this project, namely, Mr. Mathieu Lacoste, Eng., Ms. Geneviève David, Eng., and Mr. Éric L'Heureux, Tech., colleagues at the mobile laboratory team of the Direction de la gestion des structures of the MTMD, as well as the many dedicated engineers and technicians at Maurice-Centre-du-Québec regional office who have been involved in the project since 2001.

## REFERENCES

- [1] Massicotte, B., Picard, A., Ouellet, C., and Gaumond, Y. Strengthening of a Long Span Prestressed Segmental Box Girder Bridge. *PCI Journal*, 39(3), May-June, 1994.
- [2] Ghali, A., Favre, R. and Elbadry, M. *Concrete Structures: Stresses and Deformations: Analysis and Design for Sustainability*. Fourth Edition, CRC Press, 2005.
- [3] Bazant Z. P. and Qiang Y., Excessive Deflections of Record-Span Prestressed Box Girder, *ACI Concrete International*, Vol. 32, No. 6, June 2010.
- [4] Bazant Z.P. and Baweja S. *Creep and Shrinkage Prediction Model for Analysis and Design of Concrete Structures: Model B3*. Adam Neville Symposium: Creep and Shrinkage—Structural Design Effects, ACI SP-194, A.A. Manaseer, ed., Am. Concrete Institute, Farmington Hills, Michigan, 2000.
- [5] Massicotte, B., Halchini, C. and Labbe, J. Evaluation of the Capacity of an Existing Steel Truss Bridge. *IABSE Colloquium on "Remaining Structural Capacity,"* Copenhagen, Denmark, March 1993.
- [6] Cremona, C. Qu'est-ce qu'une évaluation dynamique? Principes et méthodes. *Revue européenne de génie civil*, 9(1-2), 2005.
- [7] Hou, X., Xueshan, Y. and Qiao, H. Using Inclinoimeters to Measure Bridge Deflection. *Journal of Bridge Engineering*, Vol. 10, Issue 5, 2005.
- [8] Easa, S. M. Area of Irregular Region with Unequal Intervals. *Journal of Surveying Engineering*, Vol. 114(2), 1988.



# Smart Structural Health Monitoring with Acoustic Emission

Dr. Michael Häuserer<sup>1</sup>, Horst Trattnig<sup>1</sup>

<sup>1</sup>Vallen Systeme GmbH, Bürgermeister-Seidl-Strasse 8, 82515 Wolfratshausen, Germany  
email: info@vallen.de

## ABSTRACT:

It is common sense that civil infrastructure like tunnels or bridges are coming in age and needs to be renewed in the next years. These issues are, amongst others, related to massive increased traffic load nowadays compared to the time of construction and material issues which turned out after many years of operation. In concrete structures with tendons, the stress corrosion cracking of the used steel is one of the main issues and leads to tendon failure with significant impact on the stability of the structure. SHM with Acoustic Emission is used successfully for many years to detect tendon failures. The products on the market have been adapted since many years to the needs of the customers and the full measurement chain from a self-checking smart sensor network, high performance and scalable data acquisition systems to automate data analysis, processing and alarming is available. A cloud-based dashboard rounds up the package and makes processed data available for customers. Since May 2024 a guideline from DGZfP “Richtlinie SE 05 Detektion von Spanndrahtbrüchen mit Schallemissionsanalyse” is available and give a general frame about the approach, definitions and help to specify tenders in a correct way.

**KEY WORDS:** Acoustic Emission, Structural Health Monitoring, Smart AE sensors, Wire break detection, SE 05

## 1 INTRODUCTION

Acoustic emission (AE) testing is a well-established nondestructive testing method for pressure vessel, pipeline and tank inspection in industry [1]. Integrity, leakage and corrosion tests are in the focus. Apart from these applications, the demand increases for continuous monitoring of civil structures like bridges and tunnels. The civil infrastructure e.g. in Germany is coming in age and was mainly constructed 50 or more years ago. The structures face nowadays a much higher traffic load than at the time of planning and it turned out that some of the materials used, especially the steel for tendons, had not the predicted quality in the long term perspective. The tendons are facing the risk of stress corrosion cracking which can lead to a catastrophic collapse of the structure in the worst case. To ensure the availability of the structure, operators often choose various inspection and maintenance strategies. Therefore, acoustic emission (AE) can be an outstanding tool to support the operators. Davies [2], Nakasa [3], Allevato [1] and others have shown that acoustic emission is a suitable method for permanent monitoring applications. In the last years, the number of projects increased especially in Germany and more than 25 structures were equipped with Acoustic Emission to detect wire breaks. The time period of the projects varies between a few months to several years. To fulfill the requirements the Acoustic Emission hardware and software had been improved significantly to enable a continuous, reliable and available permanent monitoring of the structure.

Civil infrastructure like bridges and tunnels are mainly in public hand and the size of monitoring projects requires tender processes. The community in Germany developed over the last years a guideline as general frame about the approach, definitions and help to specify tenders in a correct way. The guideline “Richtlinie SE 05 Detektion von Spanndrahtbrüchen

mit Schallemissionsanalyse” from DGZfP is available since May 2024 [4].

## 2 ACOUSTIC EMISSION AND TENDON FAILURE DETECTION

Acoustic Emission (AE) is a well-established NDT Methode and has been applied for many years in various applications in the industry like pressure vessel testing or testing of above ground storage tanks. The “passive” character of AE makes the method suitable for permanent monitoring of the structures and to “listen” for tendon failures. The available AE equipment was mainly driven by the requirements of the above-mentioned industrial applications, and it was the starting point for further investigations to adapt the AE equipment to the needs of permanent monitoring of civil infrastructures like concrete bridges. Several publications are available on the detection and location of wire breaks by Acoustic Emission [7-8]. Investigations were carried out to identify suitable AE sensors to detect wire breaks in concrete. In one internal feasibility study several sensors with different peak frequency sensitivities and preamplifications were mounted on a concrete beam (Figure 1) with tendons at different positions on the beam. Artificial AE was triggered with HSU-Nielsen source and several tendons were cut to see the behavior of the acoustic waves and the response of each individual sensor. It turned out that low frequency sensors around 30kHz peak frequency are suitable.



Figure 1: Evaluation of several AE sensors on a concrete beam to investigate the capability to detect wire breaks

During the investigation it turned out that the typical artificial AE source, a HSU-Nielsen source (Figure 2 (top)), is suitable to verify the sensor mounting quality close to the sensor but the artificial source is not strong enough to be detected by an AE sensor in several meters distance to the sensor due to the high attenuating properties of concrete for the propagation of acoustic waves. After several tests, it turned out that a rebound hammer, which is normally used by civil engineers to evaluate the quality of concrete, is a suitable tool to trigger artificial sources. The rebound hammer (Figure 2 (bottom)) is spring loaded and a reproducible source. Detection of a rebound hammer hit in 20 to 30m distance to the AE sensor is possible.



Figure 2: HSU-Nielsen source (0.5mm) to verify the sensor mounting quality (top).

Rebound hammer to trigger reproducible artificial AE sources on concrete structures (bottom)

Another difference between industrial applications and wire break detection is the preamplification of the sensor output. Observing the data after an artificial wire break, it turned out that measurement channels with a typical amplification for

industrial applications like 34dB or 40dB were saturated related to the high energy released by the wire break. Based on the results, preamplification with 0dB is beneficial and the preamplifier purpose is to convert the sensor output to be transported over long cable distances (approx. 600m) without significant losses.

## 2.1 Permanent monitoring of a concrete bridge in southwest Germany

The following example of the SHM is part of a bigger project and published in [5]. In autumn 2018, a concrete bridge in the southwest of Germany was equipped with a monitoring system consisting out of several NDT methods. A renewal of the bridge is required, and the existing structure should be permanently monitored during planning and approval phase. Apart from acoustic emission, various other parameters like temperature, displacement and strain (strain gauge) are part of the monitoring system. Acoustic Emission and temperature are recorded by an integrated system, whereas strain gauge and displacement parameters are fused and analyzed in post processing.

Bridge construction was finalized in 1950 and traverses the river Danube (Figure 3). It has a length of 96 m and a max. span of 81m. The width is 18m and the bridge has 4 lanes and 2 sidewalks. Damages caused by corrosion were found at the tendons of the bridge. Because the damage is unrepairable, a replacement of the bridge is planned. The bridge operator, an engineering office, a service provider and Vallen Systeme as measurement equipment provider are working together in this project [5].



Figure 3: Gänstorbrücke

The Acoustic Emission measurement system and data analysis must run automatically, recognize changes in the condition and trigger alarms if predefined criteria are fulfilled. Low frequency AE sensors with IP68 rating were used for the installation and the first version of a spring-loaded mounting mechanism which can be screwed to the concrete was used in this approach. The mounting mechanism has protection covers to protect the AE sensors against vandalism and animals (e.g. birds). AE sensors were installed in a linear setup on the beams with sensors distances between 12 to 14m and the line of sensors follows the course of the tendons in the concrete as good as possible. The acoustic emission measurement system AMSY-6 with 36 channels is stored in a cabinet which is installed in the bridge abutment at a height of 5m to guarantee flood protection. Besides acoustic emission measurement system, measurement

computer, communication equipment for a mobile network and additional measurement equipment for recording data of 71 temperature sensors are included in the cabinet. AE and temperature measurements are recorded with a synchronized time stamp and so data analysis is comfortable for the service provider. The other NDT methods were recorded with separate equipment, but all data is transferred to a cloud-based dashboard and the service provider can do further analysis across all data [5].

The project is still running, and the monitoring concept provides the security to operate the bridge in a safe way till renewal is properly planned.



Figure 4: First approach for a sensor mounting device including protection cover [5]

## 2.2 Tendon failure detection with AE and other NDT methods: “Altstädter Bahnhof”

The following example is part of a bigger project published in [6]. The bridge at the “Altstädter Bahnhof in Brandenburg an der Havel” was opened in the year 1969 and tensioned concrete structure was used. The used steel, “Hennigsdorfer” steel, was state of the art at this time. Today it is known that this type of steel has a high risk for stress corrosion cracking. Inspections and investigation on the bridge revealed significant and irreversible damages and a new construction was decided. In the meantime, a monitoring system including Acoustic Emission was installed as early warning system in case of detected tension breaks. Before final removal of the “old bridge” several measurement techniques were applied on the bridge to investigate their potentials on such objects during

artificial damaging of the structure. The approach was to cut parts of the bridge including the tendons with a “wire saw” (Figure 6). Two parts of the bridge were cut, one with known, existing damages and the other with no existing damages. The focus in this text is on Acoustic Emission results provided by Bilfinger Noell. The acoustic emission signals triggered by the wire breaks at the sensors are displayed by the acoustic emission system with a delay of a few milliseconds. The analysis of the acoustic emission data is carried out immediately on-site in monitoring and test mode. A classification of the data into the classes wire break, construction noise, background noise could be done immediately. The determination of the source location of the acoustic emissions was automatically done by the measuring system. The investigation showed that acoustic emission analysis is very well suited to detect wire breaks reliable and in real time.

### 2.2.1 Construction of the bridge

For the bridge at the Altstädter Bahnhof, the “clamping block method” was used on the main supporting structure in a longitudinal direction. Tension wires with a cross-sectional area of 35 mm<sup>2</sup> were used. Additionally, a larger tensioning box was necessary to accommodate the total of 392 individual wires and to be able to introduce a tension force of 12 MN per main girder. The 392 individual wires were installed in layers and secured in their position by spacers, as can be seen in Figure 5.

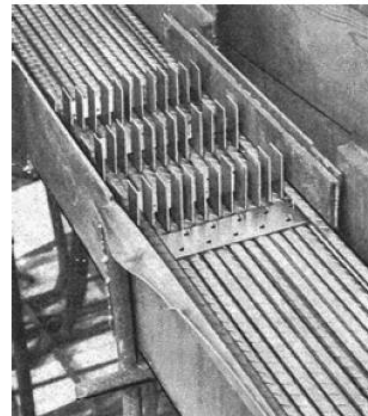


Abbildung 2.2a: Blick in den Hüllkasten an einer Umlenkstelle [Bautechnik 1969]

Figure 5: Photography of the open concentrated tendon before grouting [6]

The typical brand for such tendons at this time was “Hennigsdorfer” steel. The hardened and tempered tension wires were used as pretensioned steel.

### 2.2.2 Monitoring concept and results

Due to the described material properties of the tension wires, it was necessary to implement a monitoring strategy. This was the only way to ensure the safety of the traffic passing the bridge. The monitoring concept included a regular inspection combined with a permanent structural health monitoring. For the permanent monitoring, next to others, acoustic emission was selected as method to detect tendon breaks.



The acoustic emission system with 75 sensors was installed and put into operation in June 2020 by the company Bilfinger Noell. Until the demolition of the bridge in May 2021, 111 spontaneous tension wire breaks were detected. There were no technically related downtimes during the runtime of the system.

### 2.2.3 Comparison of NDT methods

Due to the condition of the bridge, it was decided that the bridge has to be removed and replaced by a new construction. The bridge was selected by the Federal Ministry of Transport and Digital Infrastructure to do an extensive case study to compare different NDT methods. The following NDT techniques were used: Strain gauging, geodesic measurement, vibration analysis, fiber optic measurements, photogrammetry and acoustic emission. The approach was to cut parts of the bridge, including the tendons, with a “wire saw” [6]. Two parts of the bridge were cut, one with known existing damage and the other with no existing damage.

Early-stage failure of this bridge, with concentrated tendons, is not indicated by flexural cracks at a span’s center. It was shown that for this bridge about one third of all wires in one concentrated tendon must fail before the cracks reach the concrete surface. One outcome of this evaluation study is that Acoustic Emission is the only technique that detects wire breaks in real-time and without the need to be close to the origin of the wire break. In addition, AE can locate the wire breaks origin. Vibration and geodesic measurements can detect changes in the rigidity of the structure if sensing elements are close to where failure occurs. Strain measurements, photogrammetry and fiber optic sensors are suitable for detecting cracks in the concrete structure [6]

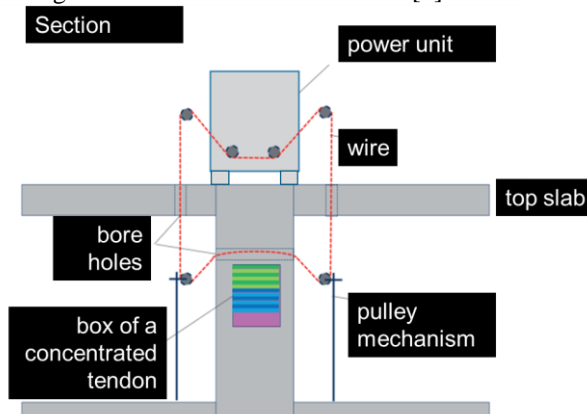


Figure 6: Wire saw to cut the concrete and tendons

## 3 IMPROVED ACOUSTIC EMISSION EQUIPMENT FOR SHM

It is necessary to provide a solution covering the entire measurement process, including data analysis, alerting and information dissemination workflows. Third-party acquisition modules need to be supported. Expandable and versatile monitoring systems can be configured using modular components and customized products where necessary.

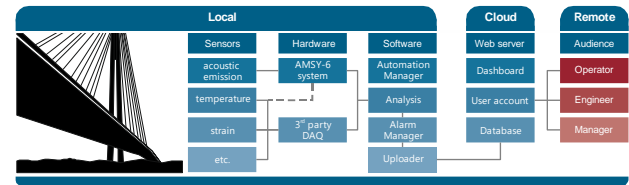


Figure 7: Example of a schematic Workflow of a monitoring system

### 3.1 AE sensors

Sensors need to work reliably 24/7 throughout the monitoring period, withstand varying and extreme conditions, moisture, and rain as well as excessive heat and frost. Special, low frequency sensors are available meeting the harsh demands of permanent monitoring. The sensors are optimized for the specific requirements of the application. Each AE sensor is connected to the AE data acquisition system with a single cable. The commonly used acoustic emission sensor for monitoring is e.g. VS30-SIC-V2-0dB sensor or the specifically developed SHM-MP1 measurement point for structural health monitoring. The SHM-MP1 (Figure 8) measurement point offers several advantages over conventional monitoring sensors: Vallen Smart Line™ sensor technology with automatic registration of the device at the monitoring hardware and reliable self-checking of its function and sensitivity that can be automatically triggered in regular intervals or on demand are some benefits. The reliable self-checking functionality enables the operator to verify the sensor mounting quality on a regular basis to proof the sensitivity of the sensor network without accessing the sensors personally which is beneficial in cases where the sensors are hard to access. The easy-to-install mechanical device, including strain relief and rugged protection lid is an additional improvement in sensor technology compared to the first approaches like in Figure 4. Both sensor types have integrated preamplifiers with 0dB amplification and the power for the preamplifiers is provided by the data acquisition system via phantom power along the sensor cable. The temperature range from -40°C to +85°C of both variants is designed for operation in all seasons of the year and covers cold and hot temperatures during winter and summer.



Figure 8: SHM-MP1 Vallen Smart Line™ sensor

### 3.2 AE hardware and software

The AE data acquisition hardware needs to be scalable and flexible in the number of channels to provide a suitable system size related to the structure. The AE system needs to be integrated into an enclosure specified for the environmental

conditions at the bridge. 19" racks are beneficial including data acquisition PC and mobile data communication.

A reliable and state-of-the-art software complements the measurement hardware. Flexible analysis is required to be adjusted to specific requirements of a job. Even user-specific evaluation routines need to be implemented and executed during the measurement. Fast online location, even at high data rates from many channels, is a key aspect of data analysis. Criteria for alarms and warnings can be set and notifications received via email or digital outputs.

On top of data analysis runs the Vallen Automation Manager software. It enables an autonomous operation of the data acquisition system and is an instance designed to inform the operator or other selected audience about alarms and the general status of the system. Amongst simple tasks is, for example, an automatic start-up of the monitoring system after a power outage, switching between data storage files in regular intervals and carrying out sensitivity checks of the installed sensors. Beneficial is the maintenance mode, which can be activated for a user defined time span. In this recording mode, all data is recorded but the alarm chain is blocked. It is used when, e.g. construction work is done on the bridge which will generate lots of activity and fails alarms.

Additional to the software running on site at the local PC, processed data can be uploaded to a cloud-based dashboard. The Vallen Dashboard is an important part of the software solution if the monitoring results need to be distributed to a broad audience. It provides an encapsulated and safe environment for viewing and analyzing data. Access and rights/privileges for this service can be restricted based on user roles. Data available in the dashboard has been transferred to it from the acquisition PC avoiding the necessity to log-in and possible manipulation of the running monitoring system.

It can be hosted on any Linux Ubuntu server. This may be rented services from local providers or a company-controlled internet server. Rented services can provide guarantees for accessibility, data safety (back up, but also storage locations in your own country) and security (access). An encrypted connection is established between the dashboard and the acquisition PC via internet.

Data upload from the acquisition PC is automated. If the connection is interrupted, upload data is cached and transferred once the connection is working again. The Dashboard engine informs selected users when the internet connection to the measurement system is lost.

Under the hood, the Vallen Export processor and Uploader program running on the data acquisition PC are responsible for supplying the dashboard with data. Both pieces of software can be configured according to the requirements of the scope/job/user. One has full control of what is uploaded and how frequently it is uploaded. The Vallen Dashboard displays the information in a user-defined layout.

The dashboard and layouts can be easily adapted and customized by the user. The administrator of the dashboard sets out the rules which information may be viewed, and which actions are available to certain users. Information can be displayed in bar charts, scatter plots, heat maps, line charts, tables, static images, and texts. Data can be downloaded for archiving purposes or offline analysis. The responsive design

of the front-end enables equally well access experience from PCs and mobile devices.

The open API of the Vallen Dashboard provides the possibility to integrate third-party time series measurement data to be uploaded, stored, and fused with acoustic emission data. This data does not even have to come from the acoustic emission data acquisition system or PC. The Vallen Dashboard is a true multi-source, multi-channel data management, visualization, and analysis tool from a single source.

#### 4 GUIDELINE TO "DETECT WIRE BREAKS WITH AE"

The increasing demand of monitoring post-tensioned concrete structures in Germany and the complexity of how to setup such projects and how to involve all required parties motivated the development of a guideline to solve the issue. The German Society of Non-Destructive Testing (DGZfP) published in May 2024 the guideline "Richtlinie SE 05 Detektion von Spanndrahtbrüchen mit Schallemissionsanalyse" [5]. The guideline is written by civil engineers, bridge responsible from the public authority, Acoustic Emission specialists and AE measurement equipment suppliers.

It is a detailed guideline with more than 30 pages on the planning, tendering, installation and operation of monitoring systems to detect wire breaks. One focus of this guideline is, of course, the description of the use of Acoustic Emission in order for successful monitoring

The guideline covers all required topics right from the beginning, like explanation of the terms e.g. how is a wire break defined or what artificial reference AE sources are available. It covers the topic Acoustic Emission and the capability for wire break detection, requirements for measurement equipment and data analysis as well as sensors, sensor distances and limitations. A summary of the requirements for the measurement technology is in Table 1 Next to the technical part another focus is on the project implementation and project participants, proposed sensor networks related to the different construction types like box girders, T-beams etc. It finally results in a guideline on how to set up the tender specifications.

NDT technique	Acoustic Emission (AE)
Codes	EN 1330-9, EN 13477, EN13554, EN 14584
Temperature Range for AE sensors	-40 °C to 60 °C
Type of AE sensors	Piezoelectric
Pre-amplification	0 dB or higher
Frequency range acquisition	5 kHz to 200 kHz
Resonant frequency AE sensor	20 kHz to 80 kHz
Sampling frequency AD converter	2 MHz or higher
Resolution AD converter	16 bit or higher
Dynamic range AD converter	65 dB or higher
Measured Features from Hits	RMS or equivalent Amplitude and/ or Energy Arrival Time (resolution µs) Frequency information Waveform recording
Analysis in time	Occurrence of wire breaks
Analysis with location	Position of wire breaks by linear or planar location
No. of sensors for wire break location	Linear: 3 or more Planar: 4 or more
Accuracy of location	+/- 2 m or better
Sensor cables	Coaxial cable (50 Ohm)
Reference sources	Hsu-Nielsen Source (0,5 mm 2H) Rebound Hammer Type N with an impact energy of 2.207 Nm

Table 1: Overview of the recommended measurement equipment [5]

It is common sense that each bridge is different, and it is not possible to copy one project 100% to another. It is recommended to do a feasibility study before tendering to evaluate amongst other parameters the noise level, the attenuation and the speed of sound. Artificial triggered AE can be used to evaluate the parameters and additionally it is recommended to open the concrete and remove a piece of the tendon for further analysis in the laboratory. In this case cutting of tendons are required and so a “real” wire break can be detected and the propagation of the waves in the structure evaluated. The target is to find a suitable sensor network with ideal sensor distances. It brings the public administration the position to make a clear and transparent tender specification about the size and dimension of the required monitoring system.

Figure 9 shows the peak amplitude in dB(AE) from one wire break of a post-tensioned concrete bridge. It is part of the guideline and gives an orientation on the relation between wire breaks and the artificial source from a rebound hammer. Sensors were positioned at three different distances from the location of the artificial wire break. The acoustic emission signals from the wire break and from the use of the reference source were recorded. The reference source was triggered in the closest possible proximity to the wire break location. Each position has its own value of K. It is recommended to use the smallest value of K to calculate the maximum possible sensor distance. For example, the signal from the wire break at a distance of about +200 cm in Figure 9 is saturated with a maximum amplitude of 134 dBAE, which means that the true peak amplitude cannot be determined. Therefore, the smallest value of K from Figure 9 with 101 dBAE - 121 dBAE results in -20 dB.

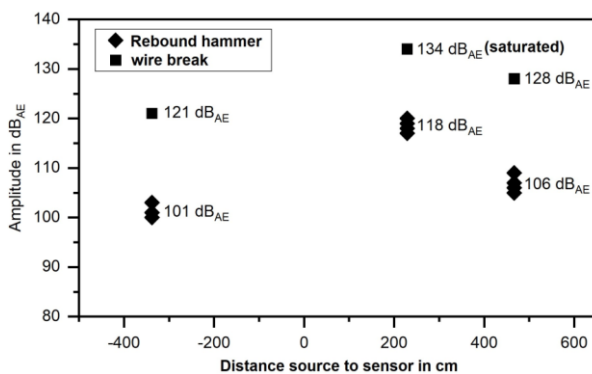


Figure 9: Representation of the peak amplitude(s) of a wire break and triggering of the reference source (rebound hammer type N) at three different distances in order to determine the value of K [4]

The method described here represents one possibility for determining the maximum possible sensor distance. However, other procedures or procedures based on this are also conceivable. The maximum possible sensor distance is the maximum distance between sensors to allow reliable detection and localization of sources (here: wire break). The wire breaks differ from the reference source by the value of K in dB. This

method is based on EN14584 [10], which describes the use of planar location for the testing of pressure vessels. The use of a fixed detection threshold is assumed. In contrast to EN14584, the reference source defined here is the rebound hammer type N and not the breakage of a pencil lead (Hsu-Nielsen source).

## 5 CONCLUSION

Wire break detection with Acoustic Emission is nowadays state of the art and a well-documented application. The NDT method AE has proved to be able to detect and locate wire breaks in concrete structures in many investigations and practical approaches and projects.

AE hardware and software have been optimized over the last years to the needs of the engineering companies and service providers to be a reliable tool. Easy to install, comfortable to use and stable in the long run. The automated alarming makes it possible to handle several projects in parallel and next to routine checks detailed analysis is required in case of alarms.

The alignment of more data sources in one platform like the dashboard gives more confidence and reduces the risk of false alarms.

Finally, guideline SE 05 was established to line up all approaches and to create a common sense of the application, the benefits and limits of AE and give public administrations a tool to formulate tenders in a way to get what they require.

## REFERENCES

- [1] Claudio Allevato, 'The use of acoustic emission testing on long term monitoring of damaged components', EWGAE 2010, 2010.
- [2] Ray Davis, 'AE as a Basis for Plant Integrity Monitoring', Progress in Acoustic Emission III - The Japanese Society of NDI, 1986
- [3] Hiroyasu Nakasa and Hiroaki Sasaki, 'Long-term continuous monitoring of structural integrity of steel storage tanks', IAES 1998
- [4] SE 05 – 2024 Detektion von Spanndrahtbrüchen mit Schallemissionsanalyse, Mai 2024 DGZfP Regelwerke, <https://publikationen.dgzfp.de/shop/detektion-von-spanndrahtbruechen-mit-schallemissionsanalyse/>
- [5] A. Müller, C. Sodeikat, J. Schänzlin, F. Knab, L. Alberecht, R. Groschup, P. Obermeier, Die Gänstorbrücke in Ulm – Untersuchung, Probelastung und Brückenmonitoring, Stahl und Betonbau 115 (2020), Heft 3
- [6] Bösche, T., Kaplan, F., Pirskawetz, S., Saloga, K., & Steinbock, O. (2021). B1—Brücke Altstädter Bahnhof in Brandenburg an der Havel—Bauwerksuntersuchungen vor dem Rückbau. Landesbetrieb Straßenwesen Brandenburg. [https://www.ls.brandenburg.de/sixcms/media.php/9/Brosch%C3%BCre\\_Bauwerksuntersuchungen%20B1%20%E2%80%93%20Br%C3%BCcke%20Altst%C3%A4dter%20Bahnhof%20in%20Brandenburg%20a.d.H.4172749.pdf](https://www.ls.brandenburg.de/sixcms/media.php/9/Brosch%C3%BCre_Bauwerksuntersuchungen%20B1%20%E2%80%93%20Br%C3%BCcke%20Altst%C3%A4dter%20Bahnhof%20in%20Brandenburg%20a.d.H.4172749.pdf)
- [7] Käding, M., Schacht, G., Marx, S.: Acoustic Emission analysis of a comprehensive database of wire breaks in prestressed concrete girders, Engineering Structures, Volume 270, 2022, ISSN 0141-0296. <https://doi.org/10.1016/j.engstruct.2022.114846>
- [8] Cullington, D. W., MacNeil, D., Paulson, P. and Elliot, J. (1999): Continuous acoustic monitoring of grouted posttensioned concrete bridges, Proc. 8th Int. Conf. Structural Faults & Repair-99, Commonwealth Institute, London, 13-15 July, Engineering Technics Press, ISBN 0-947644-41-5
- [9] M. Lühr (2023): SHM of wire breaks in concrete bridges by Acoustic Emission, APCNDT 2023, 2023





- [10] EN14584:2013-05, Non-destructive testing. Acoustic emission testing. Examination of metallic pressure equipment during proof testing. Planar location of AE sources

# The Collapse of the Carola Bridge – Forensic Engineering and Palliative Monitoring

Max Fiedler<sup>1</sup>, 0000-0003-1375-826X, Gregor Schacht<sup>1</sup>, Robert Ritter<sup>1</sup>, Steffen Marx<sup>2</sup>, Silke Scheerer<sup>2</sup>, Luise Clages<sup>1</sup>, Gino Ebell<sup>3</sup>, David Czeschka<sup>1</sup>, Chris Voigt<sup>1</sup>

<sup>1</sup>MKP GmbH, Altenzeller Straße 19, 01069 Dresden, Germany

<sup>2</sup>Institute of Concrete Structures, Technical University of Dresden, August-Bebel-Straße 30/30A, 01219 Dresden, Germany

<sup>3</sup>Federal Institute for Materials Research and Testing, Department 7.6 Corrosion and Corrosion Protection, Unter den Eichen 87, 12205 Berlin, Germany

email: Max.Fiedler@marxkrontal.com

**ABSTRACT:** The events of September 11, 2024, will remain etched in the collective memory of Germany's bridge engineering community. The sudden and unannounced partial collapse of a prestressed concrete bridge rightfully reverberated across society at large. The structure in question was the Carola Bridge in Dresden. This architecturally refined and exceptionally slender bridge is, with good reason, regarded by professionals as an icon of its time's structural engineering. Even by today's standards, its design and construction would pose a considerable challenge. This paper presents the main findings from investigations undertaken to determine the cause of the collapse and attempts to reconstruct the failure process. Additionally, the acoustic monitoring system implemented to safeguard the remaining superstructures is also presented.

**KEY WORDS:** Carola Bridge; Bridge Collapse; Prestressed Concrete; Stress Corrosion Cracking; Bridge Monitoring; Acoustic Emission Analysis; Forensic Engineering.

## 1 INTRODUCTION

The partial collapse of the Carola Bridge on September 11, 2024, sent shockwaves not only through the city of Dresden but also across the engineering community. The abrupt failure of an urban structure of such infrastructural importance raised fundamental questions: How could such an incident occur? What mechanisms led to the structural failure? At which location did the critical deficit manifest? And why did early indications of the developing failure remain undetected for so long despite routine structural monitoring?

These questions extend far beyond the technical assessment of a singular event. They also pertain to the derivation of potential implications for other structures that may be subject

to previously undetected load-bearing deficiencies. Moreover, they address the issue of accountability for this structural failure, although a definitive attribution of responsibility may prove elusive.

To investigate the incident, a comprehensive examination of both the collapsed section and the remaining superstructures was initiated. This paper presents the main findings of those investigations and elaborates on the subsequent failure analysis, with particular attention to the ad-hoc measures taken to assess the condition in the region of the fracture cross-section at axis D. In addition to material testing, an in-depth review and interpretation of the original construction documentation supplemented the analysis. This integrative approach enabled a reconstruction of the sequence of events leading to the collapse. Furthermore, the report outlines the monitoring that was enacted to ensure the continued operational safety of the remaining superstructures during their residual service life.

## 2 THE STRUCTURE

### 2.1 Overview

Based on the winning competition design, the new bridge over the river Elbe was designed by the state-owned VEB Design and Engineering Office for Road Construction (EIBS, Dresden division), under the leadership of Eckhardt Thürmer.

The Dr.-Rudolfs-Friedrich Bridge, inaugurated for traffic on 3 July 1971, was the longest-span prestressed concrete bridge in the German Democratic Republic (GDR) at the time [1], and has since become a defining feature of Dresden's cityscape (Figure 1). In 1992, it was renamed the Carola Bridge.

The approximately 400 m long structure, with five individual spans ranging from 44 to 120 m, has an overall width of 32 m and comprises three separate superstructures, each designed as a single-cell prestressed box girder (Figure 3). The fixed point is located at the pier in axis D, where the superstructure reaches its maximum structural height of 5.2 m. Towards the

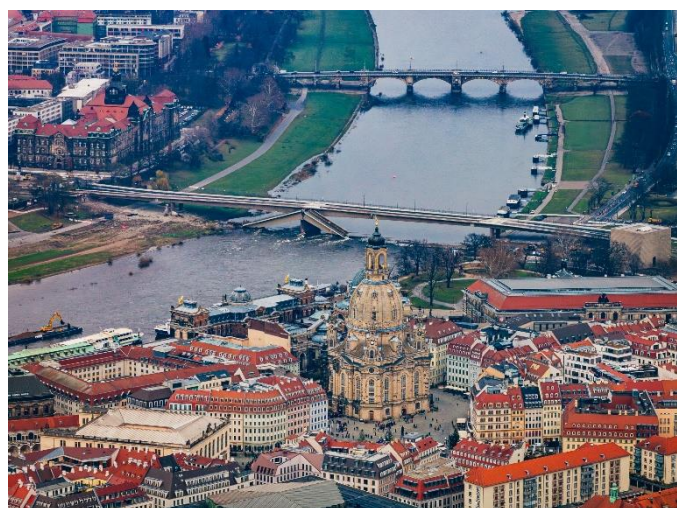


Figure 1. The Carola Bridge in the heart of Dresden's historic city centre, photographed on December 12, 2024, from a south-westerly perspective, with the Frauenkirche prominently in the foreground and the Albert Bridge visible in the background (Photo: Alex Burzik).

abutments, the cross-section tapers to 1.6 m and 1.8 m, respectively.

Due to pronounced moment variations under continuous beam conditions, the superstructure was subdivided by three hinges. This resulted in a two-span girder between axes A and C with a 12 m long cantilever towards the Elbe (hinge I). A single-span girder with two cantilever arms—44 m towards the Elbe (hinge II) and 10 m towards the Neustadt side (hinge III)—rests on piers D and E. A 64 m long suspended main-span beam bridges the gap between the cantilever arms. An additional suspended beam was placed in the edge span on the Neustadt side.

Superstructures a and b carried two-lane roadways in opposing directions (bridge class 60), while superstructure c accommodated a double-track tramway. The outer edges of superstructures a and c featured 3.2 m wide sidewalks for pedestrians and cyclists [3]. Utility lines for district heating, gas, electricity, and water were integrated into the interior of the box girders.

One of the design-specific challenges was developing an appropriate tendon layout. In the construction stage—before the installation of the suspended beams—positive bending moments prevailed in approximately 70% of the span between supports D and E. In contrast, the final state was characterised predominantly by negative bending moments. In addition, significant creep and shrinkage deformations were anticipated during the construction period. The chosen solution involved the use of three different types of tendons: permanent tendons to carry the dead load, construction-stage tendons for temporary stabilisation during erection, and post-tensioned tendons that were activated in the final state. From today's perspective, this tendon strategy represents a key construction-related contributing factor to the collapse, as some of the tendons were exposed to extended idle periods in ungrouted sheaths.

Another noteworthy structural feature was the transverse connection at the location of hinge II, where the three individual superstructures were interconnected via a cross-beam (Figure 2). During construction, vertical stressing jacks were used at this location to compensate for height differences between the successively erected superstructures. In the final state, the transverse connection equalised differential

deflections between the three very slender and separate box girders, which resulted from shrinkage, creep, thermal effects, and traffic loading. Furthermore, it enabled the redistribution of transverse loads, effectively enforcing load-sharing between adjacent superstructures.

### 3 MAINTENANCE AND REHABILITATION

#### 3.1 Monitoring of Structural Deformations

A prerequisite for the structural integrity of the bridge was sufficient prestressing of the coupling bolts between the steel hinges and the web tendons. Of the total 504 bolts installed across all joints, 121 were designed as measuring bolts. The existing bolt forces were inferred from the difference in elongation between the zero reading and the measurement under load, recorded using high-precision mechanical dial gauges. Data on bolt forces is available from the time of construction and subsequently from the years 1974, 1979, 1982, and the early 1990s.

Significant deflection at hinge II had been known since the 1980s. A measurement campaign conducted in the early 1990s aimed to determine the causes and assess the impact on the usability of the structure. Within the box girder of superstructure c, inclinations, displacements, vibrations, and temperatures were recorded using various measuring instruments at different locations, partly over a period exceeding one year. The absolute values of the coupling bolt



Figure 2. Building immediately after the collapse.

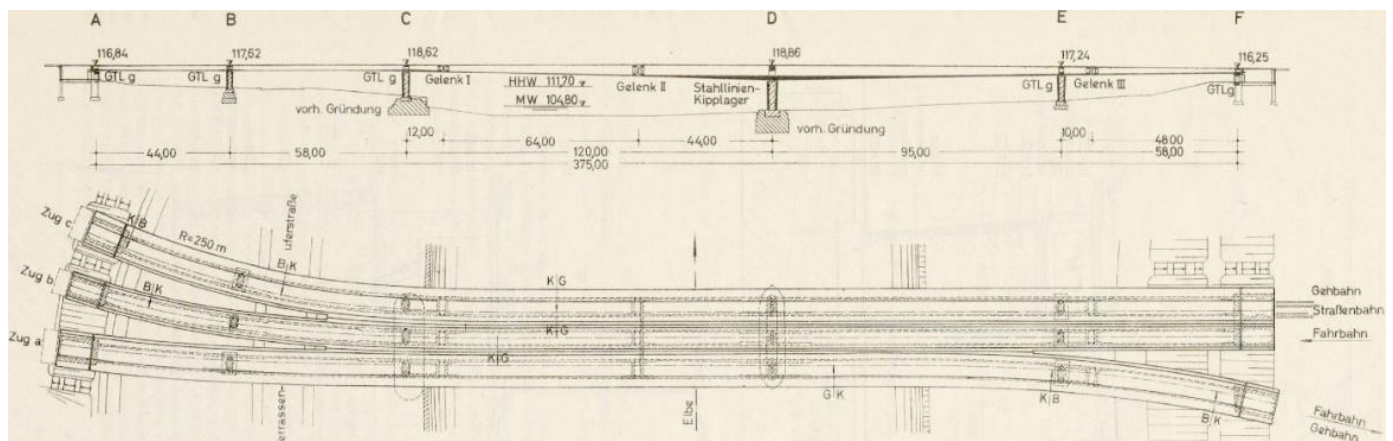


Figure 3. Longitudinal section and ground plan of the Carola Bridge, from [2].



forces exhibited large scatter and decreased continuously since the initial prestressing, though at a progressively slower rate. These force reductions were attributed to creep and shrinkage deformations and were thus considered explainable. At the time, damage to the prestressing tendons was not considered a possible cause. Nor was the structural safety called into question.

The passage of a tram caused vertical displacements at hinge II in superstructure c of approximately +12 mm (downward) and -3 mm (upward). Deformations due to temperature variations were significantly larger, reaching up to 65 mm within 1.5 days. Relative to the zero position, deflections ranged from -20 mm to +80 mm. Based on measured data and theoretical evaluations, it was estimated that by early 1993, hinge II had experienced an average downward deflection of approximately 30 cm, equivalent to roughly 80% of the total deformation expected over the entire 80-year design life.

In addition to long-term monitoring, short-term measurements were performed in 2004 as part of static and dynamic load testing on superstructure a, to assess the actual structural behaviour and the effective interaction with adjacent superstructures b and c. The tests did not reveal any plastic deformations. Movements of transverse cracks in the underside of the roadway slab remained minimal. Load redistribution through the transverse connection at hinge II was quantified at a maximum of 39–34–27% (superstructures a–b–c, respectively) under traffic loading applied to a. Neither the long-term nor short-term investigations indicated any critical implications for the global structural integrity.

### 3.2 Issue of Prestressing Steel

The issue of stress corrosion cracking (SCC) in prestressing steel was already known in connection with the Carola Bridge. Structural inspections were conducted regularly, following DIN 1076 [4], and initially revealed no abnormalities. A first recalculation was carried out in 1996, following [5], which successfully demonstrated the structure's failure annunciation behaviour.

Transverse cracks have been definitively documented since the year 2000. Two leading causes were considered: excessive creep deformations or failure of the prestressing reinforcement, e.g. as a result of SCC. Since high creep deformation was known, it was plausibly assumed to be the primary cause of the cracking. Potential tendon failures were not taken into account. The cracks showed only minor widths, within the permissible limits for prestressed concrete structures. As the failure annunciation behaviour had been analytically verified, larger crack widths would have been expected in the event of an actual pre-failure condition.

The limited rotational capacity of the cross-sections, caused by the high reinforcement ratio and high utilisation levels, was not sufficiently considered. Additionally, the transverse load distribution via the cross beam at hinge II was underestimated. The mutual support between superstructures resulted in minimal changes in crack width, even in the presence of critical damage in one of the superstructures.

From 2004 onwards, deformation monitoring was performed by measuring crack widths and joint openings at hinge II. From today's perspective, these measurements were not suitable for identifying early indicators of failure.

### 3.3 Chloride Exposure

Sections of the three superstructures—especially between axes D and E—were affected by chloride-induced corrosion. The failure of a drainage line was the cause of this. The resulting damage was repaired. Following a non-destructive electrochemical chloride extraction, the interior surfaces of the box girders were sealed with a crack-bridging protective coating.

During the structural investigation in autumn 2024, corroded prestressing steel and passive reinforcement were identified. However, these were not determined to be the cause of the collapse.

### 3.4 Other Aspects

Throughout the bridge's service life, numerous investigations were carried out. All irregularities were followed up, and the condition of the structure was continuously assessed. No serious deficiencies have been identified in the repair works.

As a result, a rehabilitation programme was initiated, beginning with the superstructure a in 2020/21. Due to chloride contamination, this superstructure was considered particularly critical. Rehabilitation of superstructure c was scheduled to start in early 2025. Measures to enhance the durability of this structure were also planned.

## 4 COLLAPSE

In the early hours of September 11, 2024, at approximately 02:58 a.m., the collapse of superstructure c of the Carola Bridge abruptly altered the Dresden cityscape. A camera operated by Sächsische Dampfschiffahrt, mounted on the bow of a ship,

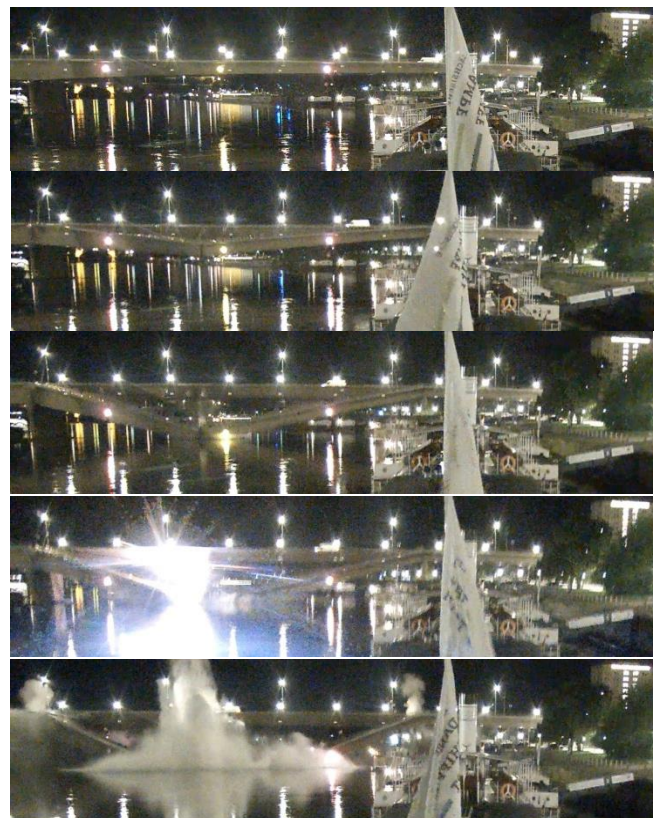


Figure 4. Recordings from a surveillance camera: initial state and moment of collapse.

captured the incident as it unfolded (Figure 4). Facing upstream, the camera recorded precisely the critical area—the river span between axes C and D.

A frame-by-frame analysis of the footage reveals the sequence of events: initially, the region around hinge II began to subside, while a crack opened at the support cross-section in axis D. Moments later, the overhead tram catenary came into contact with the river. A flash of light illuminated the night sky, accompanied by a column of spray erupting from the water's surface.

Just eight minutes before the failure, a tram had crossed this very span, likely initiating the kinematic chain leading to collapse. Fortunately, no pedestrians or cyclists were present on the structure at the time of failure. Only a delivery van travelling on superstructure a was crossing the river span as superstructure c gave way.

## 5 MATERIAL INVESTIGATIONS

### 5.1 Ad-hoc Measures for Assessing the Damage Condition of Superstructure c

In the very first hours following the collapse, an extensive photographic documentation of the general structural condition—and particularly of the fracture cross-section—was carried out. The aim was to ensure that the assessment of the exposed tendons and reinforcement would not be compromised by environmental influences or incipient corrosion. With the support of numerous contributors, nearly all components were documented on the day of the collapse itself.

The condition of the prestressing tendons was evaluated visually and classified into damage categories. It became evident that the post-tensioned tendons in the roadway slab area, in particular, showed advanced pre-existing damage and had failed long before the collapse. These post-tensioned tendons had only been stressed after a time delay, following the installation of the suspended main-span beam; see also [2]. This conclusion was drawn from the almost black fracture surfaces of many tendons (top right in Figure 6), indicating an oxygen-deficient environment within the still-intact sheathing. As such, these wire fractures occurred either during construction or shortly thereafter, but in any case, a considerable amount of time ago.

Later microscopic investigations of fractured wires, conducted by the Federal Institute for Materials Research and Testing (BAM), Berlin, revealed mortar residues on some fracture surfaces—clear evidence that these fractures had occurred before or during the grouting process. Fresh fracture surfaces appeared metallic and glossy, without signs of corrosion, and also showed no ductile necking in the failure zone (bottom right in Figure 6). Even the prestressing steels without pronounced crack initiation lenses showed signs of embrittlement.

A characteristic feature of the fracture cross-section—beyond the failed prestressing tendons—was the presence of reinforcement bars that had been pulled out from the concrete section in the upper reinforcement layers (Figure 5). In several cases, the reinforcing bars exhibited no signs of fracture, necking, or cross-sectional loss. Only isolated and minimal indications of chloride-induced corrosion were visible externally (e.g. slight pitting corrosion at the ribs).

Subsequent analyses of concrete samples taken from the fracture zone confirmed that chloride-induced pitting corrosion did not play a relevant role in this area. The tightly spaced arrangement of tendons and reinforcement bars likely impaired the bond performance, which may have contributed to the complete pull-out of some reinforcing bars from the roadway slab.



Figure 5. Failed cross-section in axis D with pulled-out steel reinforcement.

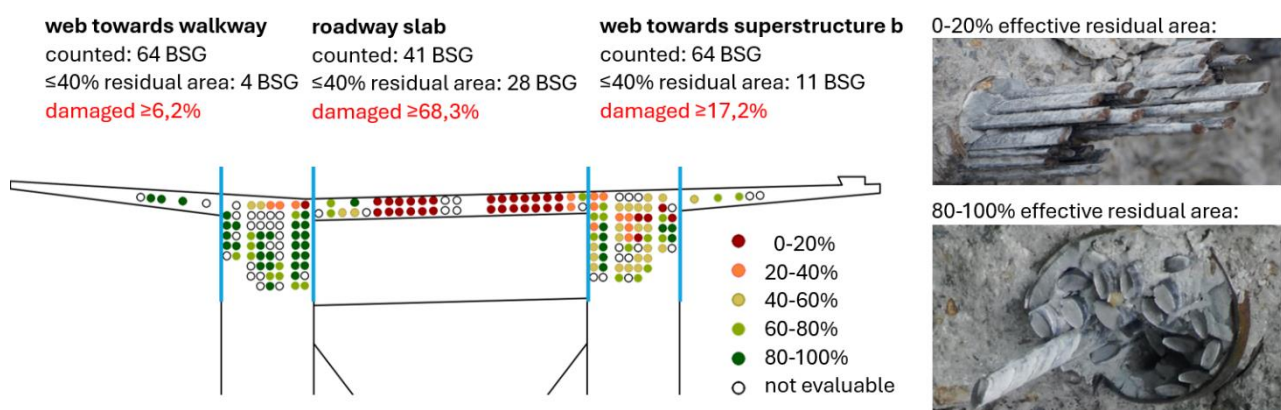


Figure 6. Results of photographic documentation of the condition of the broken prestressing wires at axis D of superstructure c, view direction Dresden-Neustadt (mid of December 2024).



## 6 ACOUSTIC MONITORING FOR THE SUPERSTRUCTURES A AND B

As the Elbe River and the southern (Altstadt-side) riverbank were gradually cleared of the remnants of superstructure c in December 2024, increasing attention was directed toward reopening the waterway and ensuring the safe underpassage beneath the remaining superstructures a and b. However, a general opening of the adjacent banks and associated roads, footpaths, and cycleways was not pursued, as these areas would soon have to be closed again for the dismantling of the remaining bridge sections. In contrast, due to its role as an international waterway critical to freight transport for the Czech Republic, the navigability of the Elbe was given priority.

An evaluation of the structural safety could not be guaranteed solely through static analysis under the prevailing conditions. Therefore, a prerequisite for reopening the Elbe to ship traffic was the implementation of acoustic emission monitoring to detect new wire break events [6], [7]. Shortly after the partial collapse, a small number of sensors were installed in the roadway slab above pier D in superstructures a and b to ensure safety during on-site diagnostic investigations. In January 2025, this system was expanded to cover the entire main river span and the support regions at axis C (Figure 7 and Figure 8).

As of February 3, 2025, controlled ship passages were permitted based on real-time monitoring data, solely for operationally critical transit (Figure 9). Initially, a ship-specific clearance protocol was applied. From 18 February onward, clearance was planned to be issued daily, allowing navigation within predefined time windows. However, on the morning of 18 February at 04:50 a.m., the first wire break events were recorded. Several additional events followed within hours, concentrated on the axes and adjacent roadway slabs. At axis D, up to six spatially correlated events were detected within 24 hours. This sudden development was most likely triggered by pronounced temperature differentials compared to previous days.

In preparation for the monitoring program, quantitative threshold values were determined through static analysis for the monitoring region. Engineering assumptions were made to estimate the loading condition that, with high confidence, had still been acting on the superstructure shortly before the partial collapse. Based on this load model, the equivalent number of prestressing wires available as structural reserve was determined. For axis D, a calculated reserve of 14 locally correlated wire breaks was established. Approximately 40% of this reserve was consumed within a very short period.

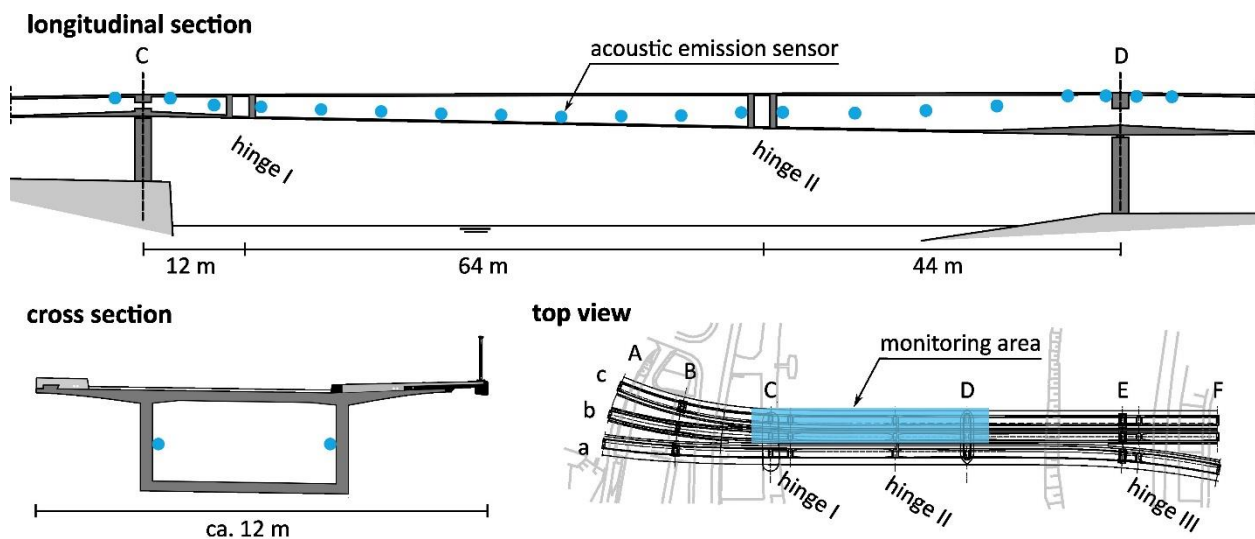


Figure 7. Overview of the monitoring area and the sensor layout for the acoustic emission monitoring system.

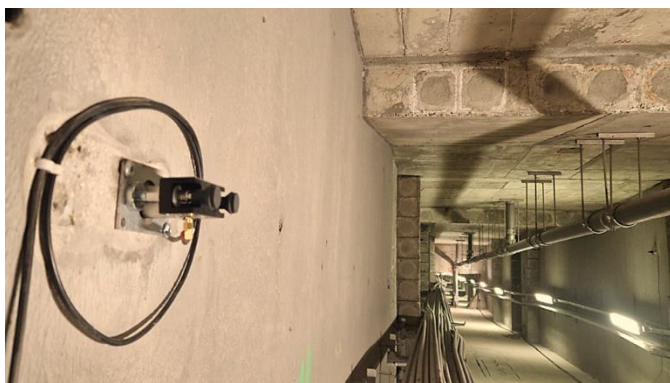


Figure 8. Acoustic emission sensor in superstructure b.



Figure 9. First ship passage after the collapse of the bridge and the installation of the monitoring system.



It was assumed that further significant temperature fluctuations would occur in the following weeks, which could again lead to an abrupt reduction in the remaining structural reserve. As an immediate response, a wire-break-free monitoring period of 72 hours was mandated before any further ship passages could even be considered. Subsequently, a day-by-day clearance protocol was reintroduced. Ship passages were permitted only under direct real-time monitoring using the installed measurement systems.

Ultimately, these events highlighted the vulnerable and undefined structural condition of the remaining bridge components, forming the basis for the decision to proceed with prompt deconstruction.

## 7 CONCLUSION

With knowledge of the brittle failure risk associated with the prestressing reinforcement, re-commissioning of superstructures A and B was deemed unacceptable. This decision was thoroughly examined and carefully weighed, as the Carola Bridge had represented an essential component of Dresden's road infrastructure. Among the options considered was a controlled load test. However, such a test would have only provided a snapshot of the current load-bearing capacity. Its predictive value for future performance would have remained uncertain, as the damage mechanism—stress corrosion cracking—may temporarily cease under the alkaline conditions of the grouting mortar. Still, the progression of fatigue-related damage could not have been reliably assessed at the observed level of deterioration, even if a load test had returned positive results, a residual risk would have persisted, one that could not be ethically or technically justified.

It must be acknowledged that the bridge had been inspected and monitored in accordance with established engineering standards. This highlights the need for a critical review and update of these standards. Current regulations prescribe recalculations, diagnostic investigations, and visual assessments from the exterior. However, it remains challenging to make definitive statements about the internal condition of structural components. Insights gained from the Carola Bridge investigations are now being systematically compiled and evaluated within the research initiative "Investigation and Verification of the Causes of the Carola Bridge Failure concerning the Review and Potential Revision of Concrete Bridge Design Codes" (Project No. FE-15.0729/2024/HRB). The objective is to assess the broader implications for similar structures and to initiate corresponding changes to design and inspection standards.

Measurement-based monitoring techniques—such as acoustic emission monitoring for detecting wire breaks in prestressed tendons—are playing an increasingly important role in this context and must be formally incorporated into regulatory frameworks. Ultimately, this method remains the only available approach capable of directly detecting and localising wire breaks at the moment of occurrence, thereby enabling meaningful insights into the progression of damage. Within the broader context of the tragedy resulting from the partial collapse, the successful application of this technique stands out: it was only through this method that navigation on the river Elbe could be safely resumed at minimal residual risk.

## REFERENCES

- [1] Schlimper, H.: Festansprache. In: Bau der Nord-Süd-Verbindung in Dresden : Erinnerungsschrift, Dresden, 1971, S. 1–3.
- [2] Berger, R.; Franke, M.; Thürmer, E.: Projektierung der Dr.-Rudolfs-Friedrich-Brücke. DIE STRASSE 11 (1971) 6, S. 266–277.
- [3] Kriesche, K.: Entwurfs- und Bauvorgaben für die Dr.-Rudolfs-Friedrich-Brücke. DIE STRASSE 11 (1971) 6, S. 264–277.
- [4] DIN 1076:1999-11: Ingenieurbauwerke im Zuge von Straßen und Wegen – Überwachung und Prüfung.
- [5] Bundesministerium für Verkehr (BMV, Hrsg.): Empfehlungen zur Überprüfung und Beurteilung von Brückenbauwerken, die mit vergütetem Spannstahl St 145/160 Neptun N40 bis 1965 erstellt wurden. 07/1993.
- [6] Fiedler, M.; Pirskawetz, S.; Kaplan, F.; Holst, R.; Saloga, K.; Schmidt, S.; Sodeikat, C.: Detektion von Spanndrahtbrüchen mit Schallemissionsanalyse – Die neue Richtlinie SE 05 der DGZfP. Beton- und Stahlbetonbau, online first: 18.12.2024 – DOI: 10.1002/best.202400098
- [7] Kädig, M.; Marx, S.; Schacht, G.: Schallemissionsmonitoring zur Spanndrahtbruchdetektion. In: Bergmeister, K.; Fingerloos, F.; Wörner, J.-D. (Hrsg.): 2023 BetonKalender, Berlin: Ernst & Sohn, 2023, S. 745–777 – DOI: 10.1002/9783433611180.ch15, 2022.



# Wind-Loaded Structures and Monitoring under Environmental Conditions

# Understanding the Dynamic Behavior of Large Sign Structures Under Wind Loading

Lauren E. Linderman<sup>1</sup>, Nicole Johnson<sup>2</sup>, Lam Nguyen<sup>3</sup>, Michele Guala<sup>1</sup>, Dominik Schillinger<sup>4</sup>, Catherine W. French<sup>1</sup>

<sup>1</sup>Department of Civil, Environmental, and Geo- Engineering, University of Minnesota, Minneapolis, MN, USA

<sup>2</sup>SSOE Group, Portland, Oregon, USA

<sup>3</sup>ANSYS, Livermore, CA, USA

<sup>4</sup>Institute for Mechanics, Department of Civil and Environmental Engineering, Technical University of Darmstadt, Darmstadt, Germany

email: llinderm@umn.edu, nicolejohnson0718@gmail.com, lam.nguyen@ansys.com, mguala@umn.edu, schillinger@mechanik.tu-darmstadt.de, cfrench@umn.edu

**ABSTRACT:** Dynamic Messaging Signs (DMS) are much larger and heavier roadside signs than typically placed on their respective support systems. The excess weight and size of these signs, in conjunction with their breakaway support systems, introduces wind-induced vibration problems not seen in the past. The AASHTO LRFD Specification for Structural Supports for Highway Signs, Luminaires, and Traffic Signals (SLTS), including interim revisions through 2022, does not yet address vibration design for these nontraditional roadside signs. The DMS support system, specifically the friction fuse connection, is susceptible to the formation of stress concentrations and potential fatigue issues. A DMS was instrumented with strain gages, accelerometers, anemometers, and temperature sensors to characterize both the wind loading and response of the structure. A dynamic numerical model was validated with experimental field data and used to evaluate the fatigue life of the DMS instrumented in the field. The results of the dynamic analysis performed with the validated FEM model differed significantly from the analysis with the equivalent static pressure equation for natural wind gusts prescribed in the AASHTO Specification, which highlights the importance of considering the dynamic behavior of these heavier sign panels. Extension of the dynamic method to models of other large DMS in service showed a greater fatigue stress and corresponding shorter estimate of the fatigue life.

**KEY WORDS:** Field Monitoring; Wind Loading; Sign Structures.

## 1 INTRODUCTION

Wind-induced vibrations are often a key consideration for the design of the structural supports of signs and signals. These vibrations introduce oscillations that can lead to fatigue concerns and potentially premature failure of the structure. The current AASHTO LRFD Specification for Structural Supports of Highway Signs, Luminaires, and Traffic Signals (SLTS) addresses fatigue design for overhead sign and signal structures and high mast light towers [1]. Fatigue design for roadside signs is not addressed because these are traditionally smaller and have not observed fatigue problems in the past. However, as roadside signs get heavier and larger, there is concern that these structures may be susceptible to fatigue under wind loading.

Dynamic messaging signs (DMS) include luminous elements that display words, numbers, or symbols to communicate real-time roadway and traffic information to drivers [2]. The roadside versions are often located in the clear zone alongside the roadway and as a result, must feature breakaway or yielding supports to limit injury to drivers and damage to vehicles that may swerve off the roadway [1], [3]. The DMS are much larger and heavier than signs typically placed on breakaway posts. The signs range from 1.8m x 4.3 m to 2.4m x 5.5m, weigh over 680 kg, and have post heights that range from 4.7m to 6.7m [4].

The 2025 interim revision of the AASHTO 2013 (ASD) Specification for SLTS acknowledges the potential impact of the mass of dynamic messaging signs and requires their cantilevered support structures to be designed for fatigue [5]. However, the revision states that design of these structures will require considerations beyond the specification. This ambiguity leaves the designer to determine if equivalent static

analysis or dynamic analysis is more appropriate to evaluate the fatigue life of the support structure.

In this work, the behavior of roadside dynamic messaging signs under wind loading was investigated to determine which analysis method should be considered in design. A DMS was instrumented in the field and the experimental field data were used to characterize the wind loading and response of the structure. The field data was further used to update a dynamic numerical model for comparison with an equivalent static pressure analysis. Ultimately these were used to evaluate the fatigue life of these DMS support structures.

## 2 DMS FIELD MONITORING

A post-mounted DMS (DMS 169-142.45NB) located in Brooklyn Park, MN with a Type A support detail was instrumented in the field to investigate its structural performance under wind loading. The Type A support featured a slip base and a friction fuse connection just below the sign panel (Figure 1). The friction fuse consisted of two plates used to splice two lengths of the support post: (1) a fuse plate with a weakened portion designed to fracture under impact, and (2) a hinge plate designed to yield.

The instrumentation consisted of two accelerometers, two cup and vane anemometers, one temperature probe, and 76 strain gages. Figure 2 provides an overview of the instrumentation. The single-axis accelerometers were used to identify the natural frequencies of the structure. The cup and vane anemometers measured the mean wind speed and direction. The strain gages were used to measure the dynamic response of the support and friction fuse connection under wind loading. The supports were expected to undergo strong-axis bending, weak-axis bending, and potentially torsion. The post



strain gages included two strain rosettes on each face of the web as well as strain gages at the tip of the flanges. These strain gage sets were located at four different locations along the two support posts. The field data was collected over five months from August 2017 through January 2018.

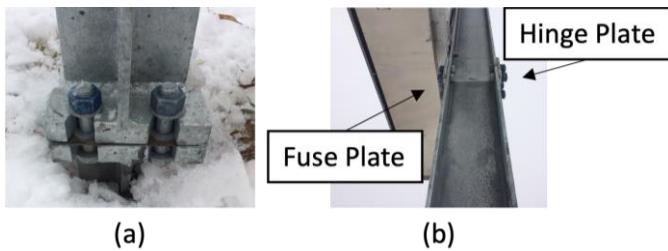


Figure 1. Type A breakaway connection: (a) slip base, (b) friction fuse.

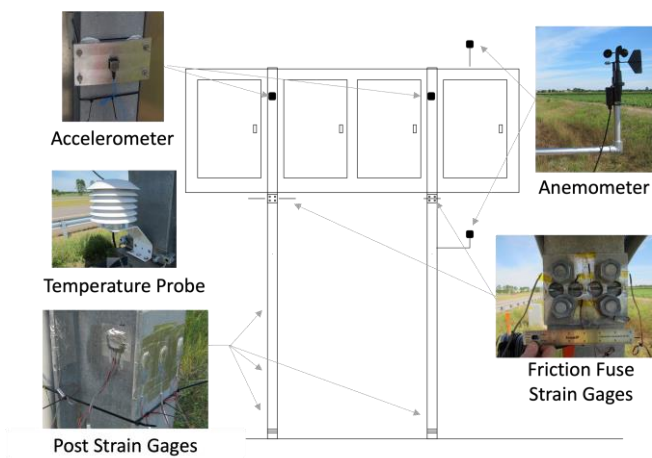


Figure 2. Overview of DMS field instrumentation.

### 3 ANALYTICAL MODELS

Three different models were used for analysis of the DMS structure: two simplified models and one finite element model. The simplified models consisted of a static beam model and a dynamic beam model. In the static beam model, the wind pressure applied to the sign was assumed to distribute evenly to the four panel support points. The resulting point loads on the cantilever posts were used to determine the stresses and the corresponding strains along the height. In the dynamic beam model, the inertial effects of the sign mass were considered by applying the mass of the sign to a rectangular prism that was supported by a cantilever beam with stiffness equivalent to the two columns. A single-mode dynamic model was used to capture the behavior of this system subjected to a dynamic drag forcing function due to the wind pressure on the sign face.

The third model featured a linear elastic finite element (FE) model created to evaluate the fatigue stresses generated in the friction fuse connection during wind loading. The friction fuse connection was modeled as a separate detailed three-dimensional component to capture stress concentrations, particularly in the fuse plate. The support posts were modeled with standard beam elements and the panel was modeled using standard four-node shell elements. The FE model was validated with the field data assuming the structure would have similar natural frequencies to those measured in the field.

All three analytical models assumed ASTM A36 steel with an elastic modulus of 200 GPa and yield strength of 248.2 MPa. The posts were W8x24 cross-sections with a moment of inertia of 3442.3 cm<sup>4</sup>. Additionally, the dynamic models assumed a damping ratio of 0.02.

### 4 RESULTS

The two simplified models were compared using the measured wind demand and corresponding strain response. A change in the measured wind speed normal to the sign face corresponded to a change in pressure that was applied as a drag force to the sign supports. For the simplified static model, the expected change in strain at the base of the post was determined and compared with the measured change in strain in the cross section. For the dynamic model, a transient drag force due to the measured wind speeds and corresponding pressure was applied to the single degree-of-freedom system. The change in strain at the base of the post between two times of interest was determined from the transient response for comparison. The strain distributions predicted by the dynamic response aligned better with the measured strains than those strains predicted by the static model (Figure 3). The comparison of the two simplified models demonstrated that considering the effects of the inertia of the sign panel is important to capture the behavior.

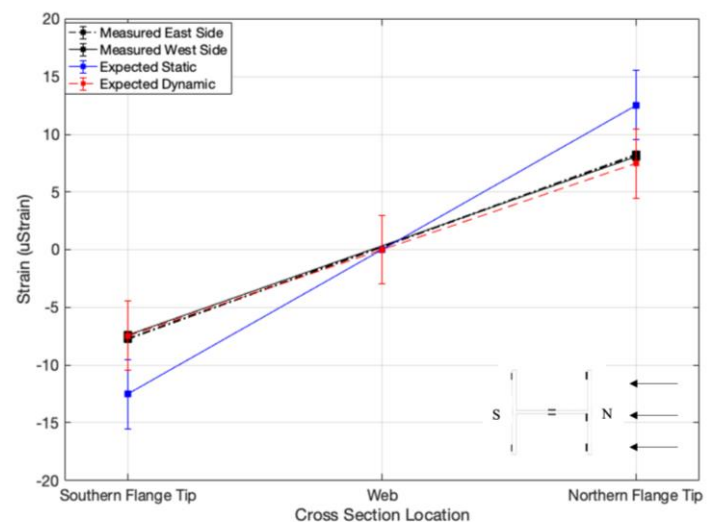


Figure 3. Comparison of the strains predicted by the simplified models and measured strains in the east post for a specific wind event. Error bars on predicted strains reflect the noise on the measured strains.

Based on the comparison, a dynamic FEM was used and required dynamic wind loading functions as inputs to the model for fatigue analysis. To generate the limit-state wind loading, a representative wind spectrum was used to generate zero-mean wind speed time histories. A Davenport spectrum with a terrain coefficient of 0.005 for open, unobstructed terrain best characterized the power spectrum of the measured wind data during the deployment [6]. The spectrum was scaled to the mean hourly wind speed of the region and a corresponding filter was applied to white noise inputs with unit covariance to generate wind speed time histories [7]. The pressure loading functions were generated from these simulated wind speed histories using a variation of the method presented in reference

[8]. Typically, the stress range only due to the fluctuating wind load would be considered in the fatigue analysis. However, because the gravity load of the sign was thought to play an important role in the resulting stresses within the connection, the wind pressure function included both the mean and fluctuating pressure. The combined mean and fluctuating pressure were thought to provide a more realistic representation of the magnitude of the fluctuating tension stresses and whether these would overcome the compressive stresses due to gravity. Five independent pressure functions were applied to the dynamic FEM to determine an average wind-induced stress range. The fatigue limit-state stress range was taken as the resulting amplitude of the tension stress within the friction fuse connection.

The fatigue demand in the connection was computed using two methods: (1) using the equivalent static pressure equations outlined in Article 11.7 of the AASHTO 2015 LRFD Specification for SLTS [1], (2) the dynamic FEM model with wind loading functions mentioned above. When using the equivalent static approach, the peak fatigue stress range was 49.6 MPa. The dynamic FEM model resulted in a peak fatigue stress range of 63.9 MPa. Both results exceed the constant amplitude fatigue threshold (CAFT) of 48.3 MPa for an infinite fatigue life. Further, the equivalent static approach underestimates the stress range predicted by the dynamic model.

## 5 CONCLUSION

The additional weight of dynamic messaging sign (DMS) panels requires fatigue under wind loading to be considered in design. However, the AASHTO 2015 LRFD specification does not address fatigue design for these nontraditional roadside sign structures. Field monitoring of a DMS structure was used to validate simplified and detailed numerical models and determine the fatigue life of the instrumented DMS structure. Additionally, the effectiveness of the different modeling approaches to capture the behavior of the sign structure to wind loading was evaluated.

A comparison of the modeling approaches to the field data highlighted the importance of considering the inertial effects of the sign panel mass on the response of the structure. Limit state pressure loading functions were generated as inputs to the validated dynamic FE model. The resulting fatigue stress demand in the breakaway connection was compared with the traditional equivalent static pressure analysis method. The peak stress demand from the dynamic FE model was 28% larger than the static approach further emphasizing the importance of using a dynamic model when evaluating these structures.

The resulting stress demands were used to calculate the fatigue life of the instrumented DMS. The dynamic modeling technique can be extended to other in-service DMS support structures to estimate their fatigue life.

## ACKNOWLEDGMENTS

Funding support was provided by the Minnesota Department of Transportation (MnDOT). Numerical computations were performed using resources provided by the University of Minnesota Supercomputing Institute (MSI). The work does not necessarily represent the views or policies of MnDOT or MSI.

## REFERENCES

- [1] AASHTO. (2015). LRFD Standard Specifications for Structural Supports for Highway Signs, Luminaires, and Traffic Signals. Washington, DC: American Association of State Highway and Transportation Officials (Interim Revisions 2022).
- [2] MnDOT. (2000). Guidelines for Changeable Message Signs (CMS) Use. Office of Traffic Engineering.
- [3] McGee, H.W. (2010). Maintenance of Signs and Sign Supports: A Guide for Local Highway and Street Maintenance Personnel. Washington, DC: Federal Highway Administration (FHWA).
- [4] Kimley Horn. (2015). Type A Sign Structure Detail. Plan set T.H. 94 DMS Moorhead to Alexandria, MnDOT.
- [5] AASHTO. (2013). Standard Specifications for Structural Supports for Highway Signs, Luminaires, and Traffic Signals. Washington, DC: American Association of State Highway and Transportation Officials (Interim Revisions 2025).
- [6] Davenport, A. G. (1961). The Spectrum of Horizontal Gustiness Near the Ground in High Winds. *Quarterly Journal of the Royal Meteorological Society*, 194-211.
- [7] Gawronski, W. (2002). Three models of wind-gust disturbances for the analysis of antenna pointing accuracy. *IPN progress report*, 42(149).
- [8] Dexter, R.J. and Ricker, M.J., (2002). NCHRP Report 469: Fatigue-Resistant Design of Cantilevered Signal, Sign, and Light Supports. *Transportation Research Board, National Research Council, Washington, DC*.

## 6-Component Operational Modal Analysis of wind turbines for damage detection

Laurin Müller<sup>1</sup>, Anjali Dhabu<sup>1</sup>, Felix Bernauer<sup>3</sup>, Stefanie Donner<sup>4</sup>, Kay Bode<sup>2</sup>, Céline Hadziioannou<sup>1</sup>

<sup>1</sup>Institute of Geophysics, Faculty of Earth System Sciences, University of Hamburg, Bundesstraße 55, 20146 Hamburg, Germany

<sup>2</sup>Vestas Wind Systems, Vestas Deutschland GmbH, Klostertor 1, 20097 Hamburg, Germany

<sup>3</sup>Department Earth and Environmental Sciences, LMU, Ludwigshöhe 8, 82256 München, Germany

<sup>4</sup>BGR, Stilleweg 2, 30655 Hannover, Germany

email: laurin.mueller@studium.uni-hamburg.de, anjali.dhabu@uni-hamburg.de, kabod@vestas.com, celine.hadziioannou@uni-hamburg.de, felix.bernauer@lmu.de, stefanie.donner@bgr.de

**ABSTRACT:** The rapid expansion of the wind energy sector has necessitated remote monitoring of wind turbines to ensure safe, reliable, and cost-effective operations. While traditional inspection methods remain in use, there is an increasing shift toward passively monitored, real-time solutions to detect and localize potential damage. The present study makes a novel attempt to explore the potential of 6-component seismic data for use in structural damage detection frameworks for wind turbine monitoring. Measuring both translational and rotational ground motions is a relatively recent advancement in Structural Health Monitoring, offering valuable insights into the dynamic behavior of towers.

In the present study, two 6-component (6-C) seismometers were placed at the foundations of two different wind turbine types in the wind park of Kirchheilingen, Germany. The monitoring campaign lasted 7 weeks and focused on capturing vibrational data during operation. By analyzing these signals, in conjunction with Supervisory Control and Data Acquisition (SCADA) Data from the turbine operator, the research aims to identify patterns indicative of structural damage, such as changes in modal frequencies, damping ratios, or signal coherences. It will contribute to the development of scalable, cost-efficient SHM systems tailored for the wind energy industry. Furthermore, the insights gained could inform future design improvements and predictive maintenance strategies, ultimately supporting the sustainable growth of renewable energy infrastructure.

**KEY WORDS:** Structural health monitoring; wind turbines; 6C-seismic data; damage detection; renewable energy; operational modal analysis; wind turbine tower

### 1 INTRODUCTION

Wind energy has become one of the key pillars in the global transition toward sustainable and low-emission power generation. As one of the most environment-friendly alternatives to fossil fuels, wind turbines contribute significantly to meeting international climate targets and reducing carbon footprints. However, as the number and size of installed wind turbines continue to grow, so do the demands on their structural integrity, operational efficiency, and service life. In this context, monitoring the condition and performance of wind turbines has emerged as a critical aspect for both industry and research. Modern sensor technology and data-driven analysis methods allow for the continuous observation of dynamic loads, vibration behavior, and early detection of potential damage. A particular focus lies on the measurement and analysis of vibration signals and the identification of structural eigenfrequencies, as changes in these parameters can indicate material fatigue, loosened connections, or structural weakening. The development of reliable and efficient monitoring techniques is therefore essential — not only for extending the lifetime of wind turbines but also for ensuring economically optimized and safe operation. Previous work on wind turbine monitoring has primarily focused on using SCADA data, strain gauges, accelerometers, and optical fiber sensors [1], [2]. Seismic observations have also been utilized to

assess the influence of wind turbines on ground motion and operational states [3]. However, to our knowledge, this study is the first to employ six-component (6C) seismic data — recording translational and rotational ground motion — specifically for the structural health monitoring of a wind turbine.

### 2 METHODS

#### 2.1 Location and instruments

The experiment was conducted in a wind park near Kirchheilingen, containing multiple wind turbines. Two turbines, differing in tower construction — a steel tower (LDST) and a concrete hybrid tower (CHT) — were selected for detailed analysis. The two turbines, each with a height of 166 meters, were commissioned in September 2022 and are therefore among the latest generation of models.

Their locations, highlighted in blue on the map in Figure 1, are situated only a few hundred meters apart.

Inside each of these turbines at the ground (on the top of foundation), a BlueSeis 3A and a Trillium Compact 120s Seismometer have been placed for a timespan of about seven weeks. The BlueSeis 3A station measures rotations about the three axes and the Trillium compact 120s measures translations providing 6 degree-of-freedom (DOF) data. Figure 2 shows the setup inside of the towers. The rotational seismometer on the



right as well as the translational seismometer directly next to it forming a 6-component (6C) station.

Additionally, two reference stations - marked in red in figure 1 - were used to characterize the local noise field. Each reference station was equipped with two Trillium Compact 120s seismometers. One station was placed directly next to the foundation of one of the turbines, while the other was located outside the wind park, behind a lake but near a road. During the days of setup of the two 6-component stations inside the tower these reference stations were setup to gain reference data.

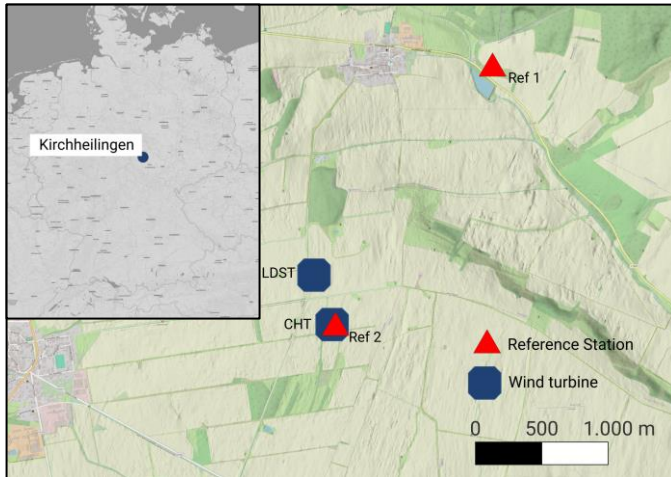


Figure 1. Location of the two wind-turbines in Kirchheilingen monitored using BlueSeis3A and Trillium Compact for 7 weeks.

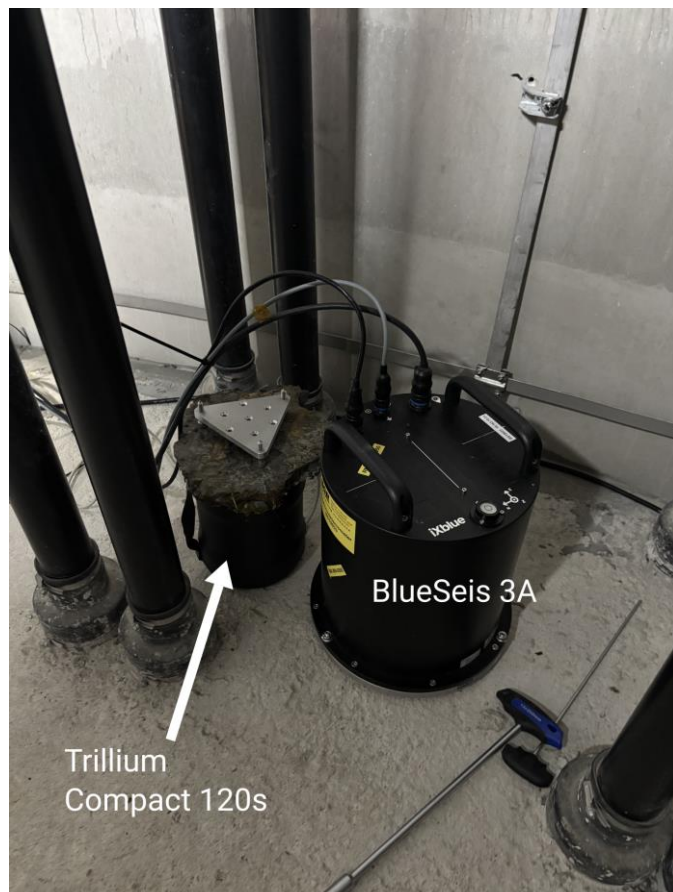


Figure 2. Example setup of instruments

## 2.2 Data acquisition

The experiment was carried out over a period of seven weeks, beginning on November 18, 2024, and concluding on January 9, 2025. This specific timeframe was chosen to coincide with a period of typically high wind activity, increasing the likelihood of capturing a wide range of operational states of the turbine. Additionally, we aimed to collect data during non-operational hours, hoping to observe the tower's behavior under different load conditions. The data of the 6-C stations was saved to local disks which were carried after the experiment. SCADA data (Supervisory Control and Data Acquisition) is collected by sensors at the turbine to provide engineers with valuable data for monitoring and maintaining the turbine. The data is collected in databases to which we have access. Data such as the rotor speed, windspeed and temperature are just a few of the environmental data. Combining these datasets, seismic and SCADA data might be good to get clearer insights into the dynamics of the tower and therefore for a setup on the structural health monitoring of the tower.

## 3 DATA ANALYSIS & RESULTS

The reference stations marked in Figure 1 already show expected results. The noise level at the outer station is significantly lower than at the directly next to the turbine. This meets the expectation. However, stable frequency bands are still observed between 1-10 Hertz and amplitudes are quite high for frequencies below 1 Hertz for the station which is far away. Figure 3 shows a spectrogram for the reference station which is near one turbine. The black line indicates the speed of the Rotor which lines up with the frequencies above 10 Hertz. There can be seen other frequencies such as this steady one between 25 to 30 Hertz which is likely to be caused by turbine operation. The short peaks over a wide frequency band between 22:30 and 23:00 local time could be related to the nacelle turning into the wind.

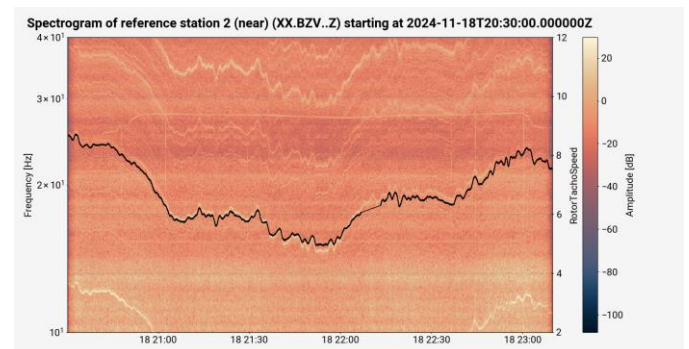


Figure 3. Frequencies rotor speed

To gain better insights into the frequencies recorded at the tower, Power Spectral Densities (PSDs) were calculated. The seismic signal from the Trillium Compact sensor was divided into two-minute time sections to ensure relatively constant conditions. For each of these sections, the corresponding rotor

speed was averaged and assigned to specific rotor speed ranges. The PSD for each time section was then calculated and colored according to its assigned rotor speed range. This approach allows differentiation of the PSDs based on the rotor speeds that drive turbine motion and induce seismic signals. Figure 4 shows the PSD peaks for all time sections. Differences in both amplitudes and frequencies can be observed. For instance, the frequency peak above 10 Hz appears to increase in amplitude with higher rotor speeds. Higher amplitudes, particularly at low frequencies, seem to be associated with elevated rotor speeds. The dominant peak at 1 Hz is clearly visible. Furthermore, a shift from lower to higher frequencies around 14 Hz with increasing rotor speed can be clearly identified and connected to the generator speed. Spectrograms also revealed sudden changes in frequency over time, likely related to variations in generator behavior.

Following the methodology of Neuffer et al. [1], we calculated hodograms for the translational seismic data at the bottom of the foundation. Hodograms provide a graphical representation of seismic motion in two dimensions over time. These hodograms illustrate the seismic movement of the turbine at the foundation, with time represented by color. By filtering for specific frequency bands, in this case between 0.9 and 1.1 Hz, which covers the dominant frequency, we observe smooth movement in particular directions.

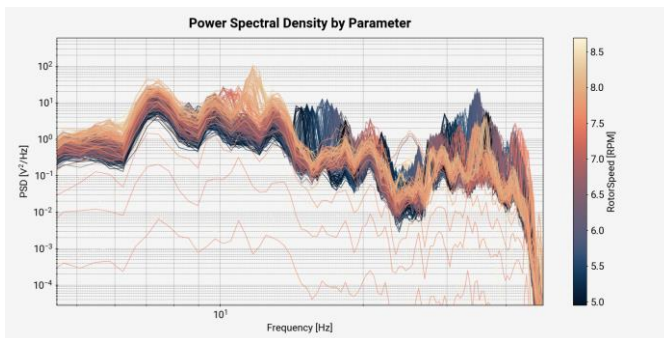


Figure 4. Power Spectral Density with respect to Frequency plot

The calculation was performed for all three planes: East-North, East-Vertical (Z), and North-Vertical (Z) directions. Figure 5 illustrates the corresponding hodogram. Focusing on the East-North (E-N) plane, which represents the bending of the tower, it becomes evident that the bending is predominantly polarized in one direction, but changes over time, in this case, within approximately 6 seconds. There is a main direction of bending, which raises the question of whether the tower predominantly bends in alignment with the wind direction. To further explore this, we calculate the covariance matrices along with their eigenvectors and eigenvalues, which allows us to determine a linearity factor with a directional component. The linearity index  $L$  is defined as 1 minus the ratio of these eigenvalues. A value close to 1 indicates high linearity, while a value close to 0 suggests circular motion for the respective time sections.

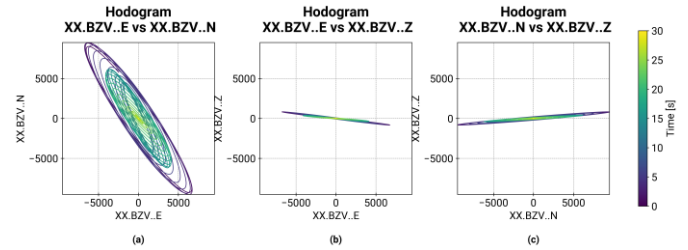


Figure 5. Hodograms for frequencies between 0.9-1 Hertz in the (a) East-North direction (b) Vertical-East direction and (c) Vertical-North direction.

We calculated linearity indices and vectors over short time windows during which translational motion was dominant. By filtering for high linearity values, we minimize the effects of whirling motions and identify the principal direction angles for each time section. Figure 6 displays the principal direction angles for the wind turbine tower alongside the measured wind direction. The wind direction is taken from the SCADA data, with the angle of the wind being subtracted by 180 degrees. This means that if the tower were to bend in the direction of the wind, we would observe that in the data. However, we instead see an offset of about 30–50 degrees for both towers. Furthermore, we notice that the principal direction angles align with the wind direction, but the tower seems to exhibit some inertia when the wind direction changes, as the principal direction angles do not increase as much as the wind itself. We also observe different principal direction angles across various frequency bands, though the reason for this remains unclear.

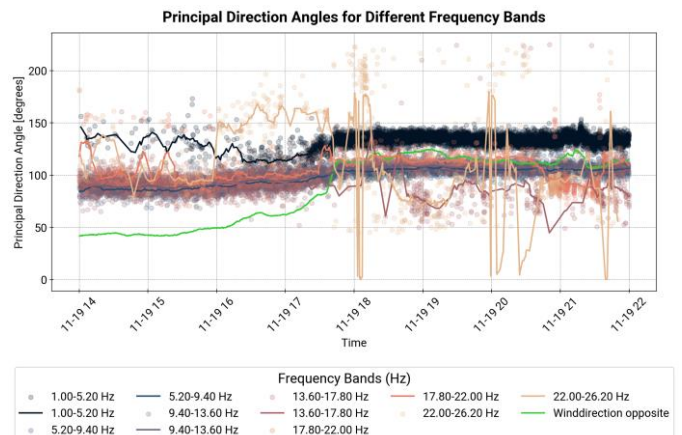


Figure 6. Principal direction angles for different frequency bands.

#### 4 FURTHER INVESTIGATION

As the present study is one of the first to leverage the three-component rotational ground-motions combined with translations for structural health monitoring of wind-turbines, we aim to determine how the 6-component measurements can be used to reliably replicate some of the SCADA data. One of the most important parameter measured as a part of SCADA data is the acceleration at the top of the tower. We aim to use this acceleration data from the top of the tower, located inside the nacelle, and compare it with the acceleration data at the bottom. By doing so, we may be able to predict the movement of the tower at the top. Additionally, we hope to extrapolate the

displacement at the bottom, assuming the stiff end is located inside or at the bottom of the foundation. This would allow us to measure the tower's eigenmodes. Given the extended time span of the data, we aim to detect any differences in the eigenfrequencies and modes over time. If successful, this approach could help identify structural damage using directional information. Previous studies [4], [5] have demonstrated such damage identification based on translational acceleration data through operational modal analysis.

To further investigate the dynamics of the wind turbine tower, we plan to use Campbell diagrams, wavelet transformations, and stabilization diagrams. We want to investigate more signal coherences, damping ratios and the advantage of rotation motion measurements for the structural health monitoring.

## 5 CONCLUSION

In this study, we identified significant eigenfrequencies in the seismic data and successfully correlated them with environmental changes. The Power Spectral Densities (PSDs) revealed distinct peaks corresponding to these eigenfrequencies. Hodograms further demonstrated the linear movement of the tower, with a slight offset relative to the wind speed and noticeable differences across various frequency bands. These observations suggest that the tower's behavior is influenced by both the wind and its structural dynamics. Ongoing investigations include the use of Campbell diagrams, wavelet transformations, and additional analyses to gain deeper insights into the tower's dynamic response.

## REFERENCES

- [1] B. Yang, X. Meng, and Y. Sun, "Wind turbine condition monitoring based on SCADA data using normal behavior models. Part 1: System description," *Applied Soft Computing*, vol. 13, no. 1, pp. 509–519, 2014.
- [2] F. Santos, A. Ribeiro, and J. Maia, "Structural health monitoring of wind turbines: A review," *Renewable and Sustainable Energy Reviews*, vol. 114, 109299, 2019.
- [3] T. Neuffer, S. Kremers, P. Meckbach, and M. Mistler, "Characterization of the seismic wave field radiated by a wind turbine," *Journal of Seismology*, vol. 25, no. 3, pp. 825–844, 2021.
- [4] Gustavo Miguel Cameira da Silva Oliveira. "VIBRATION-BASED STRUCTURAL HEALTH MONITORING OF WIND TURBINES". Universidade do Porto, 2016.
- [5] Pacheco, João, Gustavo Oliveira, Filipe Magalhães, Álvaro Cunha, und Elsa Caetano. "Wind Turbine Vibration Based SHM System: Influence of the Sensors Layout and Noise". *Procedia Engineering* 199 (2017): 2160–65.



# Estimation of Wind Turbine Foundation Settlement and Error Modeling Using High-Resolution Dual-Orbit Satellite Data

Veronica Dallari<sup>1</sup>, ORCID (0009-0005-0852-9763), Elisa Bassoli<sup>1</sup>, ORCID (0000-0002-4919-1421), Francesca Grassi<sup>1</sup>, ORCID (0000-0002-8493-0066),  
Francesco Mancini<sup>1</sup>, ORCID (0000-0002-8553-345X), Loris Vincenzi<sup>1</sup>, ORCID (0000-0003-2541-7104)

<sup>1</sup>Department of Engineering Enzo Ferrari, University of Modena and Reggio Emilia, Via Pietro Vivarelli 10, 41125 Modena, Italy

email: [veronica.dallari@unimore.it](mailto:veronica.dallari@unimore.it), [elisa.bassoli@unimore.it](mailto:elisa.bassoli@unimore.it), [Francesca.grassi94@unimore.it](mailto:Francesca.grassi94@unimore.it),  
[Francesco.mancini@unimore.it](mailto:Francesco.mancini@unimore.it), [loris.vincenzi@unimore.it](mailto:loris.vincenzi@unimore.it)

**ABSTRACT:** The demand for renewable energy sources is increasing, making it essential to develop effective maintenance plans for existing infrastructure. This study represents the initial step in a process designed to estimate the settlement of onshore wind turbine foundations, as well as its associated uncertainties. The method relies on high-resolution dual-orbit satellite data, which help to reduce cost and time required for instrument installation and on-site inspections. The turbine is modeled as a 1D rigid body and is assumed to be firmly constrained to the foundation slab. The proposed formulations allow for the estimation of the turbine motion components – translations in the W-E and vertical directions and rotation along the S-N axis –, which can be generally linked to foundation settlement. The components are determined by solving a linear system which accounts for the mean annual velocities of the Permanent Scatterers on the wind turbine surface, turbine height and incidence angles of satellite orbits. At the present stage, analytical formulations for the a posteriori estimation of the motion component uncertainties are proposed, with a particular focus on the positioning error in elevation of Permanent Scatterers. To assess the accuracy of these expressions, Monte Carlo numerical simulations are conducted. The strong agreement between numerical and analytical results demonstrates that the turbine motion components can be estimated with high accuracy.

**KEY WORDS:** Structural Health Monitoring; Foundation settlement; Wind turbines; Monte Carlo simulations; Uncertainty evaluation.

## 1 INTRODUCTION

As stated by the Global World Energy Council [1], the necessity to install new renewable energy sources grows stronger every year. In fact, to pursue the Paris Agreement goal – reducing greenhouse gas emissions by 43% by 2030 to limit global warming to 1.5°C – it was estimated that by 2030, 2 TW of wind energy will be installed. As for now, 78 GW of wind power capacity, of which 68.8 GW provided by onshore installations, were added globally in 2022.

In order to sustain the existing wind power structures, a solid maintenance plan is needed. Structural Health Monitoring (SHM) systems can contribute significantly to enhance wind turbines reliability and ensure their optimal performance, through different management approaches [2]. Various parts of the wind turbine, in fact, can be affected by structural issues, such as corrosion and cracks on the tower, or surface damage to the rotor blades [3]. Furthermore, particularly in the case of onshore installations, foundation settlement may occur: differential settlement, which manifests as tower rotation, can lead to a reduction in turbine efficiency, potentially resulting in economic losses. This phenomenon can take several months, or even years, to develop.

In [4], large vertical movements were observed in some onshore wind turbines, particularly in the case of concrete foundations in which embedded rings were used as connection systems, potentially leading to the sudden and catastrophic collapse of the turbine. Beyond the risk of structure failure, foundation settlement needs to be closely monitored for preserving the verticality of the tower and ensure an overall good health of the entire system. In particular, remote sensing

techniques enable the investigation of foundation settlement while ensuring an off-site and non-invasive monitoring of the turbines.

Satellite data based monitoring was largely applied to investigate landslides and ground deformation in non-urban areas [5, 6], but, in the past few years, it also gained popularity in the structural field [7, 8]. In fact, multi-temporal Differential Interferometric Synthetic Aperture Radar (DInSAR) techniques allow obtaining the displacement information of several points, called Permanent Scatterers (PSs) [9], both on the ground and on reflective elements with millimetric precision [10] – also thanks to the developments of X band SAR systems [11].

Combining displacement information from both satellite orbits – ascending (ASC) and descending (DES) – of PSs belonging to structure surfaces, it is possible to obtain displacement information about the structure itself [12, 13]. For instance, through the use of high-resolution dual-orbit satellite data, it is possible to estimate the 3D rigid motion components of buildings, which can be generally linked to their foundation settlement [14]. Specifically, rigid translations can be an indicator of total settlement, while rigid rotations may indicate a differential settlement.

Besides the potential to investigate displacements over large areas with high accuracy, advantages of satellite data use in SHM include the possibility of portraying off-site and non-invasive monitoring, thus reducing both time and costs of instrument installation. Moreover, traditional monitoring equipment does not allow for obtaining results in a reasonable time if the foundation settlement phenomenon is slow; on the

contrary, satellite techniques enable the analysis of past data - even 10 years before the time of analysis - proving to be effective when there is a need to obtain information from the past.

As part of a broader effort to detect potential foundation settlements in wind turbines, this paper introduces the initial stage of a procedure to estimate the 3D motion components of wind turbines using high-resolution dual-orbit satellite data. Formulations provided by Bassoli et al. [14] were adapted to the wind turbine case, which is modeled as a 1D rigid body. Also, analytical formulations for evaluating uncertainties regarding each motion component are presented. The main sources of error are related to measurement and positioning. Specifically, the measurement error includes the unavoidable uncertainties associated with measuring the displacements of PSs along the lines of sight. The positioning error refers to the uncertainties involved in placing the scatterers along the height of the turbine. At the present stage, a posteriori estimates of the uncertainties are presented and validated based on simulated data. Monte Carlo simulations were conducted to generate synthetic satellite data and obtain results under various conditions - detailed in section 3 - accounting for both primary sources of error. This allowed for a thorough assessment of the reliability of the proposed analytical expressions and supports their applicability to real-world scenarios. In future research, the procedure will be further developed by proposing a priori estimates based on simplified hypotheses and by applying them to real wind farms.

The paper is organized as follows. In section 777, analytical expressions relating 3D motion components of the turbine with displacement read along the line of sight are shown, as well as the procedure used to derive the uncertainties, with a specific emphasis on the positioning uncertainties. In section 3, the numerical simulations performed to verify the analytical expressions are outlined, while numerical and analytical results are presented and compared in section 4. Finally, conclusions are drawn.

## 2 IDENTIFICATION OF RIGID MOTION COMPONENTS FROM SATELLITE DATA

### 2.1 Geometry and satellite data definition

The wind turbine is modeled as a 1D rigid body firmly constrained to the foundation slab. Supposing that the slab-turbine connection happens at the exact center of gravity of the foundation, a reference system can be built as described: origin in the center of gravity (G), and  $x$ ,  $y$  and  $z$  axes along the W-E, S-N and vertical directions respectively. In Figure 1, satellite geometry as well as an example of the PSs placement along the turbine height are reported. Note that all PSs are assumed to be aligned along the turbine  $z$ -axis; therefore, the planar positioning error is not considered.

In this study, all satellite geometry parameters — such as heading angles, measurement accuracy, and ground resolution — were assumed to match those of the COSMO-SkyMed constellation operating in StripMap mode over Italian regions. Specifically, the heading angles  $\beta_A$  and  $\beta_D$ , representing the satellite orbit inclination with respect to the S-N direction, were set to  $\beta_A = 350^\circ$  and  $\beta_D = 190^\circ$ . The measurement accuracy was assumed to range from 1 to 2 mm/yr, and the ground resolution was taken as  $3\text{m} \times 3\text{m}$ .

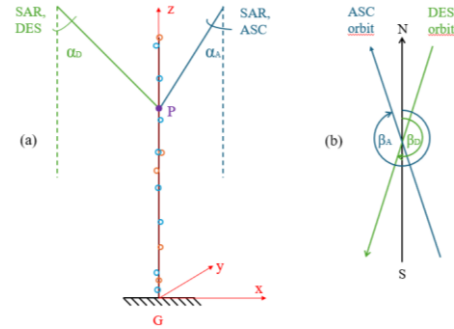


Figure 1. Satellite geometry: incidence angles and PSs positioning (a) and heading angles (b).

The same parameters were also used in the methodology to estimate rigid motion components and their associated uncertainties in [14]. The high resolution provided by this constellation makes COSMO-SkyMed data particularly well-suited for structural monitoring applications.

### 2.2 3D motion component estimation

In this study, the 3D rigid motion of wind turbines is estimated using the approach proposed by some of the authors in [14]. This method was originally developed to assess the motion of buildings modeled as 3D rigid bodies. Based on the structural geometry and satellite parameters, it allows for the evaluation of translations along the W-E and vertical directions, as well as rotations around the W-E, S-N, and vertical directions. The expressions proposed in [14] are adapted here to the case of wind turbines. Specifically, since the wind turbine is modeled as a 1D body, the rotation component along the  $z$ -axis was neglected. As with buildings, the translation along the S-N axis cannot be accurately assessed due to the limited sensitivity of SAR measurements in detecting displacements in the S-N direction [10, 15, 16].

It is important to emphasize that, to evaluate the full 3D rigid motion of the turbine, displacements of PSs measured in both orbits are required [15].

To avoid temporal misalignment of PSs displacements, the formulations are applied to the mean annual velocities of PSs (mm/yr), rather than to specific time instants. Additionally, due to the rigid motion assumption, spatial resampling to align PSs measured in ascending and descending orbits is unnecessary [17]: all permanent scatterers associated with the turbine contribute to the motion estimation.

Considering clockwise rotations as positive, the displacement of the generic point P with respect to G can be written as:

$$\begin{cases} v_{x,P} = v_{x,G} + \Phi_{y,G} D_{z,P} \\ v_{y,P} = v_{y,G} - \Phi_{x,G} D_{z,P} \\ v_{z,P} = v_{z,G} \end{cases} \quad (1)$$

where  $v_{x,G}$ ,  $v_{y,G}$ ,  $v_{z,G}$ , represent the translations along the three directions while  $\Phi_{x,G}$  and  $\Phi_{y,G}$  are the rotations around the  $x$ - and  $y$ - axes. Finally,  $D_{z,P}$  indicates the elevation of point P relative to G.

The displacement of point P is then projected along the ascending and descending lines of sight (LOSs) of the satellite constellation. Incidence angles  $\alpha_A$  and  $\alpha_D$  indicate the inclination of the satellite LOSs with respect to the vertical

direction, while  $\beta_A$  and  $\beta_D$  are the heading angles. Adopting the values reported in section 2.1,  $\sin \beta_A$  and  $\sin \beta_D$  can be approximated as 0 while  $\cos \beta_A$  and  $\cos \beta_D$  can be approximated as +1 and -1, respectively. Based on these considerations, and since that the translation component along the y-axis cannot be estimated due the limited sensitivity of SAR data in S-N direction, the displacement of point P projected onto the ascending and descending LOSs can be expressed as:

$$\begin{cases} d_{A,P} = v_{z,G} \cos \alpha_A - v_{x,G} \sin \alpha_A - \Phi_{y,G} D_{z,P} \sin \alpha_A \\ d_{D,P} = v_{z,G} \cos \alpha_D + v_{x,G} \sin \alpha_D + \Phi_{y,G} D_{z,P} \sin \alpha_D \end{cases} \quad (2)$$

A system of two equations in three unknowns – that are the translations in W-E and vertical directions and the rotation along the S-N direction – is obtained. To determine  $v_{x,G}$ ,  $v_{z,G}$  and  $\Phi_{y,G}$ , at least three PSs from the two orbits are required. Assuming  $n$  PSs are available for the ascending orbit and  $m$  for the descending one, the system can be expressed as:

$$\begin{bmatrix} d_{A,1} \\ \vdots \\ d_{A,n} \\ d_{D,1} \\ \vdots \\ d_{D,m} \end{bmatrix} = \begin{bmatrix} -\sin \alpha_A & \cos \alpha_A & (-D_{z,1} \sin \alpha_A) \\ \vdots & \vdots & \vdots \\ -\sin \alpha_A & \cos \alpha_A & (-D_{z,n} \sin \alpha_A) \\ \sin \alpha_D & \cos \alpha_D & (D_{z,1} \sin \alpha_D) \\ \vdots & \vdots & \vdots \\ \sin \alpha_D & \cos \alpha_D & (D_{z,m} \sin \alpha_D) \end{bmatrix} \begin{bmatrix} v_{x,G} \\ v_{z,G} \\ \Phi_{y,G} \end{bmatrix} \quad (3)$$

and can be synthesized as:

$$\mathbf{M} = \mathbf{S} \boldsymbol{\vartheta} \quad (4)$$

where  $\mathbf{M}$  is a  $Ns \times 1$  vector, being  $Ns=n+m$ , containing PSs displacements along the LOSs,  $\boldsymbol{\vartheta}$  is a  $3 \times 1$  vector containing rigid motion components of the turbine, and  $\mathbf{S}$  is a  $Ns \times 3$  matrix containing satellite geometries and the height of PSs.

Note that, due to measurement uncertainties thoroughly described in section 2.3, the theoretical displacement measurements in  $\mathbf{M}$  are never exactly equal to the ones directly obtained from the satellite  $\mathbf{M}^*$ . Thus, to obtain the best  $\boldsymbol{\vartheta}$  estimate, the least square operation must be applied:

$$\hat{\boldsymbol{\vartheta}} = (\mathbf{S}^T \mathbf{S})^{-1} \mathbf{S}^T \mathbf{M}^* \quad (5)$$

To assess the turbine motion relative to the ground, the terrain motion components must also be estimated and subtracted from the turbine motion. However, for the sake of simplicity, this study assumes the ground motion components to be zero.

### 2.3 Uncertainties estimation of rigid motion components

This section outlines the evaluation of the uncertainties associated to the above estimated motion components according to the procedure proposed in [14]. As previously stated, there are two main sources of error working with PS displacement data: measurement and positioning errors. Measurement error concerns the inevitable uncertainty committed when detecting the PS displacements along the LOSs, while positioning error regards the placement of the PS inside the resolution cell [14]. In this case, since PSs are supposed perfectly aligned to G, positioning uncertainties only regard the PS placement along the vertical direction. Using the product rule for derivatives, the variation of the  $\boldsymbol{\vartheta}$  vector can be expressed as:

$$\Delta \boldsymbol{\vartheta} = \Delta \mathbf{B} \mathbf{M} + \mathbf{B} \Delta \mathbf{M} = \sum_k \left( \frac{\partial \mathbf{B}}{\partial D_{z,k}} \right) \mathbf{M} \Delta D_{z,k} + \mathbf{B} \Delta \mathbf{M} \quad (6)$$

where  $\mathbf{B} = (\mathbf{S}^T \mathbf{S})^{-1} \mathbf{S}^T$  represents the pseudo-inverse of matrix  $\mathbf{S}$ ,  $\mathbf{M}$  contains the PSs displacements along the LOSs, and  $D_{z,k}$  is the elevation of the  $k$ -th PS. Lastly,  $k=1, \dots, n$  or  $k=1, \dots, m$  for the ascending or the descending PSs, respectively.

Assuming that measurement and positioning errors are not correlated [14], the total covariance matrix  $\Sigma(\boldsymbol{\vartheta})$  can be expressed as the sum of the measurement covariance matrix and the positioning covariance matrix as follows:

$$\Sigma(\boldsymbol{\vartheta}) = \Sigma_M(\boldsymbol{\vartheta}) + \Sigma_P(\boldsymbol{\vartheta}) \quad (7)$$

where the terms  $\Sigma_M(\boldsymbol{\vartheta})$  and  $\Sigma_P(\boldsymbol{\vartheta})$  indicate, respectively, contributions of measurement and positioning errors to the covariance matrix. Particularly, on the main diagonals, variances associated with each motion component can be found.

The covariance matrix associated to the measurement error  $\Sigma_M(\boldsymbol{\vartheta})$  can be obtained as:

$$\Sigma_M(\boldsymbol{\vartheta}) = \mathbf{B} \Sigma(\mathbf{M}) \mathbf{B}^T \quad (8)$$

Under the non-correlation hypothesis among the measures of PSs,  $\Sigma(\mathbf{M})$  can be assumed as a  $Ns \times Ns$  diagonal matrix with terms equal to  $\bar{\sigma}_M^2$  on the main diagonal, representing the measurement accuracy. Thus, eq. (8) can be written as follows:

$$\begin{aligned} \Sigma_M(\boldsymbol{\vartheta}) &= \bar{\sigma}_M^2 \mathbf{B} \mathbf{B}^T = \bar{\sigma}_M^2 (\mathbf{S}^T \mathbf{S})^{-1} \mathbf{S}^T ((\mathbf{S}^T \mathbf{S})^{-1} \mathbf{S}^T)^T = \\ &= \bar{\sigma}_M^2 (\mathbf{S}^T \mathbf{S})^{-1} \end{aligned} \quad (9)$$

According to section 2.1, typical values for  $\bar{\sigma}_M$  for COSMO-SkyMed data range from 1 to 2 mm/yr. However, to assess the applicability of the procedure, numerical simulations presented in the next section were conducted using values of 1, 2 and 5 mm/yr.

The positioning covariance matrix can be expressed as follows:

$$\Sigma_P(\boldsymbol{\vartheta}) = \left( \frac{\partial \mathbf{B}}{\partial \mathbf{D}} \mathbf{M} \right) \Sigma(\mathbf{D}) \left( \frac{\partial \mathbf{B}}{\partial \mathbf{D}} \mathbf{M} \right)^T = \mathbf{J} \Sigma(\mathbf{D}) \mathbf{J}^T \quad (10)$$

where  $\mathbf{J}$  is the  $3 \times Ns$  Jacobian matrix whose components can be expressed as:

$$\mathbf{J}_k = \frac{\partial \boldsymbol{\vartheta}}{\partial D_{z,k}} = \begin{bmatrix} \frac{\partial v_{x,G}}{\partial D_{z,k}} \\ \frac{\partial v_{z,G}}{\partial D_{z,k}} \\ \frac{\partial \Phi_{y,G}}{\partial D_{z,k}} \end{bmatrix} \quad (11)$$

$\mathbf{J}_k$  can also be written as:

$$\begin{aligned} \mathbf{J}_k &= \frac{\partial \boldsymbol{\vartheta}}{\partial D_{z,k}} = \frac{\partial [(\mathbf{S}^T \mathbf{S})^{-1} \mathbf{S}^T]}{\partial D_{z,k}} \mathbf{M} = \\ &= \frac{1}{|(\mathbf{S}^T \mathbf{S})|} \left[ -\frac{\partial |(\mathbf{S}^T \mathbf{S})|}{\partial D_{z,k}} \mathbf{I} + \frac{\partial [\text{adj}(\mathbf{S}^T \mathbf{S})]}{\partial D_{z,k}} \mathbf{S}^T \mathbf{S} + \right. \\ &\quad \left. + \text{adj}(\mathbf{S}^T \mathbf{S}) \frac{\partial \mathbf{S}^T}{\partial D_{z,k}} \mathbf{S} \right] \boldsymbol{\vartheta} \end{aligned} \quad (12)$$



with  $\text{adj}(\mathbf{S}^T \mathbf{S})$  and  $|\mathbf{S}^T \mathbf{S}|$  indicating the adjoint matrix and the determinant of  $(\mathbf{S}^T \mathbf{S})$ , respectively. Finally,  $\mathbf{\Sigma}(\mathbf{D})$  is a diagonal matrix with elements  $\bar{\sigma}_{Pz}^2$ , representing the positioning accuracy along the vertical direction.

Monte Carlo simulations were carried out for estimating  $\bar{\sigma}_{Pz}$ , considering the resolution cell size of the COSMO-SkyMed constellation, equal to  $3\text{m} \times 3\text{m}$ . The turbine tower can be divided into resolution segments  $RS$ s, which represent the projection of the ground resolution cell along the vertical direction. Random PS positions inside the ascending and descending resolution segments were simulated. The value of  $\bar{\sigma}_{Pz}$  was defined as the standard deviation of the distance of the PS from the segment centre. For this specific case, the formulations were applied to incidence angles of  $\alpha_A = 32.64^\circ$  and  $\alpha_D = 37.10^\circ$ . The obtained results are displayed in Table 1, while the trends of resolution segment lengths and standard deviations with the incidence angle are displayed in Figure 2. It is interesting to note that, since the resolution segment dimension depends on the incidence angles  $\alpha_A$  and  $\alpha_D$ , scatterers measured in the ascending orbit will display a different resolution than those measured in the descending orbit. In summary, the analytical formulation of the total uncertainty affecting each motion component can be derived by directly applying the error propagation law to both measurement and positioning errors:

$$\sigma_T(\vartheta_r) = \sqrt{\sigma_P^2(\vartheta_r) + \sigma_M^2(\vartheta_r)} \quad (13)$$

where  $\sigma_M(\vartheta_r)$  and  $\sigma_P(\vartheta_r)$  indicate, respectively, the measuring and positioning errors associated with the generic  $r$ -th motion component.

### 3 PROCEDURE FOR DATA SIMULATION

This section presents the numerical analyses designed to assess the performance of the procedure described in section 2. The analysis is based on: (i) applying rigid motion to an hypothetical turbine, (ii) simulating satellite measurements with incorporated measurement and positioning uncertainties, (iii) evaluating the rigid motion as outlined in section 2.2, (iv) comparing the imposed and estimated displacements, and (v) assessing the variability of the results.

The first step involved defining the geometric parameters of the wind turbine. A typical height of modern wind turbines is about 100 meters. For this reason, a maximum height  $D$  of 100 m was assumed. Next, the satellite characteristics of the COSMO-SkyMed constellation are chosen according to section 2.1. Incidence angles of the ascending and descending orbit are set equal to  $\alpha_A = 32.64^\circ$  and  $\alpha_D = 37.10^\circ$ , respectively.

To simulate PS mean annual velocities and positions, motion component values needed to be imposed to the turbine, thus defining vector  $\mathbf{\vartheta}$ . Matrix  $\mathbf{S}$  was reconstructed by incorporating

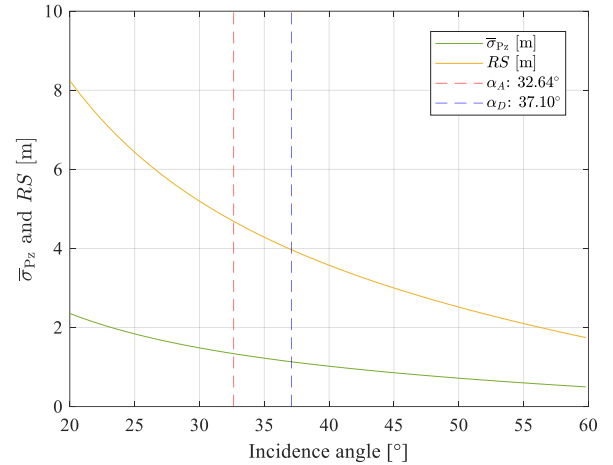


Figure 2. Trend of the standard deviation  $\bar{\sigma}_{Pz}$  and of the resolution segment  $RS$  with the satellite incidence angle.

the previously defined satellite geometries and a specific number of PSs, which was constrained by an upper limit based on the tower height and the resolution cells dimensions.

To simulate the measurement errors, quantities extracted from a Gaussian distribution with zero mean and a standard deviation of  $\bar{\sigma}_M$  were added to the velocities in vector  $\mathbf{M}$ . Measurement uncertainties were assessed in the cases of  $\bar{\sigma}_M=1$  mm/yr,  $\bar{\sigma}_M=2$  mm/yr and  $\bar{\sigma}_M=5$  mm/yr.

To clearly evaluate the impact of measurement and positioning errors, three scenarios are analyzed: the contribution of measurement errors alone, the contribution of positioning errors alone, and the effect of both. To account for the contribution of only measurement errors, the PSs were positioned at the exact center of each resolution segment. The PSs velocities along the lines of sight were then computed applying eq. (4). Instead, to account for only positioning errors, the PS velocities were kept without any uncertainties, while random errors were introduced into the PS heights within matrix  $\mathbf{S}$ . These errors shifted the PSs positions randomly within their resolution segments, displacing them from the center but ensuring they remained within the segment boundaries. Finally, the case where both measurement and positioning uncertainties are considered was evaluated. Total uncertainty for each motion component was numerically estimated by combining the two approaches: both the PS velocities in vector  $\mathbf{M}$  and the PS elevations in matrix  $\mathbf{S}$  were perturbed from their exact values by adding random quantities extracted as described above. For quantifying the analytical uncertainty, the measurement and positioning errors formulas were combined through the error propagation law (eq. (13)).

For each of these three scenarios, the analytical error formulations were compared to the numerical ones across three different cases:

- 1) The PS number was kept constant, while the motion components were varied in discrete steps, ranging from zero to their maximum values according to Table 2.
- 2) The motion components were kept at a constant value – equal to the maximum one – while the PS number was varied from a minimum of two per orbit up to the maximum one;

Table 1. Positioning accuracy.

Orbit	Incidence angle $\alpha$ [°]	Incidence angle $\alpha$ [rad]	Resolution segment $RS$ [m]	Standard dev. $\bar{\sigma}_{Pz}$ [m]
ASC	32.64	0.57	4.684	1.351
DES	37.10	0.65	3.967	1.144

Table 2. Ranges of variation of the imposed motion parameters.

Motion component	Min value	Max value	Step
$v_{x,G}$ [mm/yr]	0	10	0.2
$v_{z,G}$ [mm/yr]	0	100	2
$\Phi_{y,G}$ [mrad/yr]	0	2	0.04

- 3) The PS number was kept constant, while one motion component at a time was varied in discrete steps, as in case 1), with the others held at a constant zero value.

For each step of the three cases, Monte Carlo simulations were performed to characterize the rigid motion component uncertainties, which are then compared with the analytical ones obtained from in eqs. (9), (10) and (13).

## 4 RESULTS

In this section, the results obtained for each of the cases outlined above will be discussed and presented in the form of graphs and tables. Note that, for simplicity, only the results related to the vertical translation and rotation of the turbine are shown, as they are considered the most representative of foundation settlement. However, the procedure can also be applied to W-E translation.

### 4.1 Measurement uncertainties

The first scenario, which includes only measurement errors and excludes positioning errors, is presented in this subsection. The results are presented in terms of the uncertainty values of the rigid motion components as the value of the component itself and the number of PSs on the structure vary.

#### 4.1.1 Case 1: variation of the uncertainties with the motion amplitude

The results are presented in graph form (Figures 3 and 4) for the cases of  $\bar{\sigma}_M=1, 2$  and 5 mm/yr. Both the error and the coefficient of variation (CoV) associated with each motion component are shown as the corresponding motion component varies. For clarity, results for the maximum step are also provided in Table 3 for the case of  $\bar{\sigma}_M=2$  mm/yr, which is considered the most representative measurement precision for this specific case.

As expected, both numerical and analytical uncertainties decrease as measurement accuracy increases – namely, the value of  $\bar{\sigma}_M$  decreases. Additionally, it is important to note that the measurement uncertainty is independent on the motion component amplitude. This result is expected because eq. (8) states that the value of  $\sigma_M(\mathbf{\theta})$  is independent on  $\mathbf{\theta}$ . On the other hand, the coefficient of variation of the uncertainty decreases if the motion component increases. As observed from both the tables and graphs, the numerical uncertainty appears to be well approximated by the analytical formulations at each motion step, indicating that the motion entity does not affect the accuracy of the analytical models.

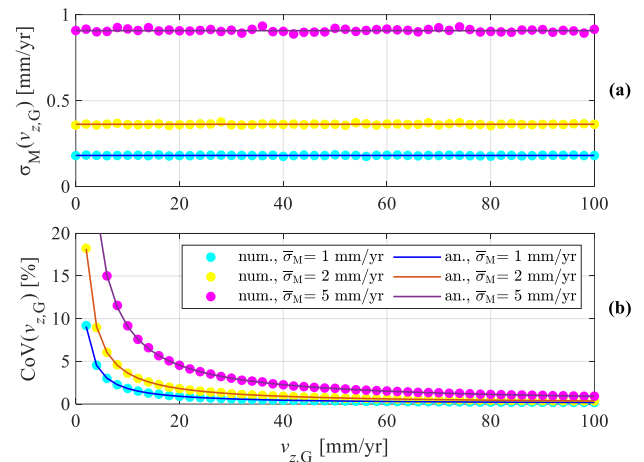
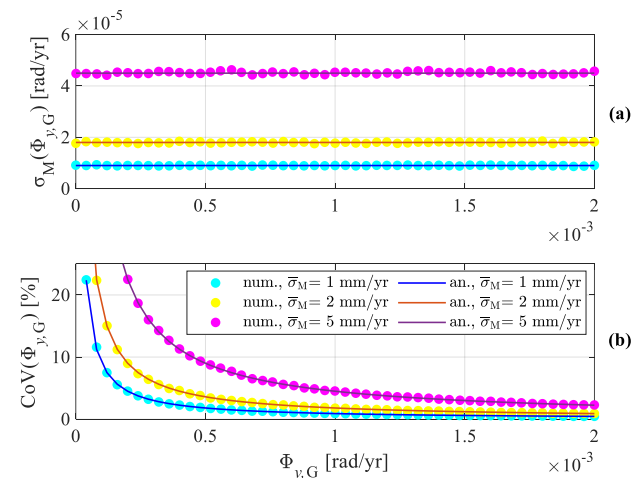
#### 4.1.2 Case 2: variation of the uncertainties with the number of PSs

The results are presented in Figures 5 and 6. The first graph depicts the values of  $\sigma_M(v_{z,G})$  and the CoV of  $v_{z,G}$  as a function

of the number of PS in the ascending and descending orbits for the cases of  $\bar{\sigma}_M=1, 2$  and 5 mm/yr, while the second one shows the values of  $\sigma_M(\Phi_{y,G})$  and the CoV of  $\Phi_{y,G}$  under the same conditions. For simplicity, the results are presented for the case where both orbits have the same number of PSs; in fact, the final step involves the use of 21 scatterers per orbit. Note that, as stated in section 2.2,  $n$  and  $m$  indicate, respectively, the number of PSs available for ascending and descending orbit.

Table 3. Measurement uncertainties on the rigid motion components -  $\bar{\sigma}_M=2$  mm/yr, last step.

Component		$v_{x,G}$ [mm/yr]	$v_{z,G}$ [mm/yr]	$\Phi_{y,G}$ [mrad/yr]
Imposed		10.000	100.000	2.000
Simulated		9.992	100.002	2.000
$\sigma_M(\mathbf{\theta}_r)$	Numerical	1.048	0.375	0.018
	Analytical	1.028	0.363	0.018
CoV( $\mathbf{\theta}_r$ )	Numerical	10.48%	0.375%	0.917%
	Analytical	10.29%	0.363%	0.900%


Figure 3. Influence of  $v_{z,G}$  on the measurement uncertainties: (a)  $\sigma_M(v_{z,G})$  and (b) CoV of  $v_{z,G}$ .

Figure 4. Influence of  $\Phi_{y,G}$  on the measurement uncertainties: (a)  $\sigma_M(\Phi_{y,G})$  and (b) CoV of  $\Phi_{y,G}$ .

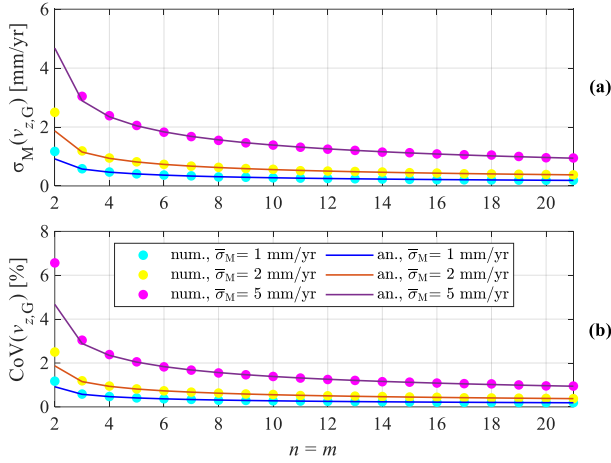


Figure 5. Influence of the PS number on the measurement uncertainties: (a)  $\sigma_M(v_{z,G})$  and (b) CoV of  $v_{z,G}$ .

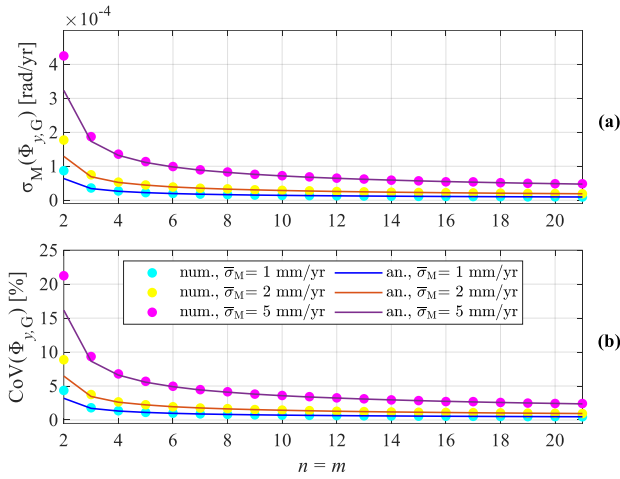


Figure 6. Influence of the PS number on the measurement uncertainties: (a)  $\sigma_M(\Phi_{y,G})$  and (b) CoV of  $\Phi_{y,G}$ .

To obtain uncertainties, at least two permanent scatterers are required per orbit. The results corresponding to the maximum number of permanent scatterers align with those shown in Table 3 for the  $\bar{\sigma}_M = 2$  mm/yr case. As expected, the uncertainties in the rigid motion parameters decrease as the number of PSs increases. For instance, in the case of S-N rotation  $\Phi_{y,G}$ , the coefficient of variation approaches nearly 20% if only 4 PSs are given and it decreases to a value less than 4% in the case of a number of PS greater than 18. Additionally, the numerical uncertainties appear to be well approximated by the analytical formulations, regardless of the PSs number. However, when only 2 scatterers per orbit are considered, the analytical formulations tend to underestimate the uncertainty, especially at lower measurement accuracy values. It can be observed that, to obtain significant results, at least five scatterers are needed in each orbit.

#### 4.2 Positioning uncertainties

In this subsection, the results including only the positioning error are presented as a function of the amplitude of the motion component as well as of the number of observed PSs.

##### 4.2.1 Case 1: variation of the uncertainties with the motion amplitude

Results are displayed in Figures 7, 8, and Table 4. The variation of  $\sigma_P(v_{z,G})$  and CoV of  $v_{z,G}$  with the value of  $v_{z,G}$  are shown in Figure 7, while the variation of  $\sigma_P(\Phi_{y,G})$  and CoV of  $\Phi_{y,G}$  with the value of  $\Phi_{y,G}$  are shown in Figure 8.

Numerical simulations were performed by introducing random perturbations to each PS position, as described in section 3. In contrast, analytical errors were computed using the method and parameters described in section 2.3.

The good agreement between the numerical and analytical uncertainties, as well as the CoVs for each motion component, demonstrates that the proposed analytical models provide a reliable approximation of the numerical errors, even in the case of positioning errors. It is also observed that, as predicted by eq. (12), positioning errors increase with the magnitude of the considered motion component, indicating that the positioning uncertainties do depend on the motion entity.

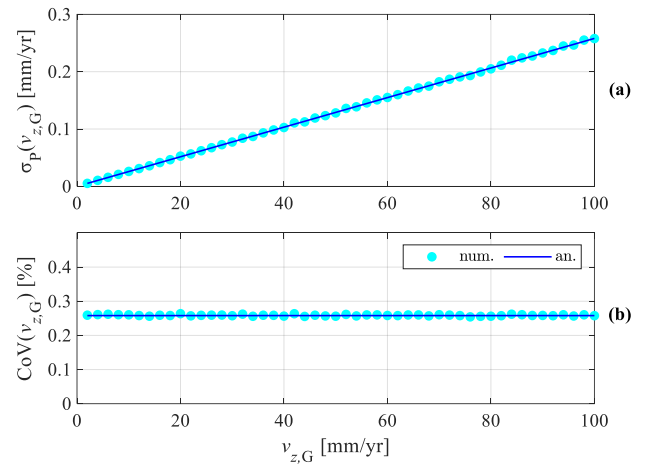


Figure 7. Influence of  $t v_{z,G}$  on the positioning uncertainties: (a)  $\sigma_P(v_{z,G})$  and (b) CoV of  $v_{z,G}$ .

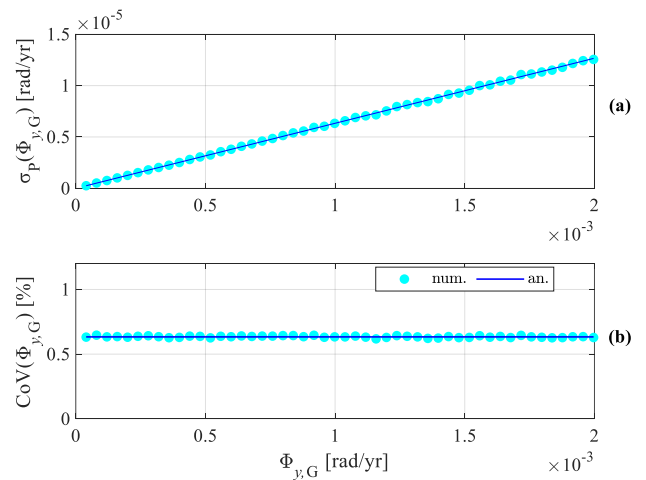
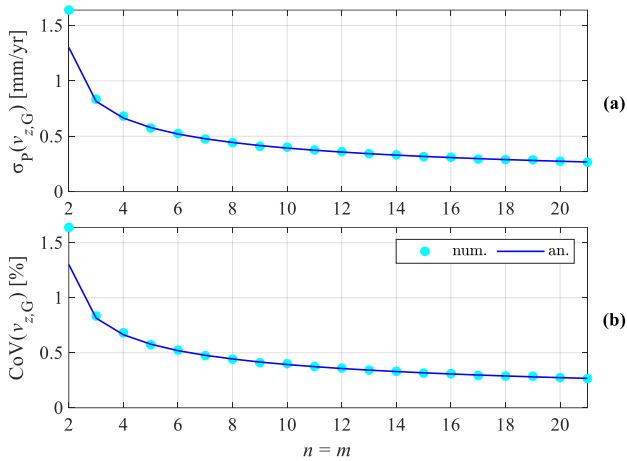
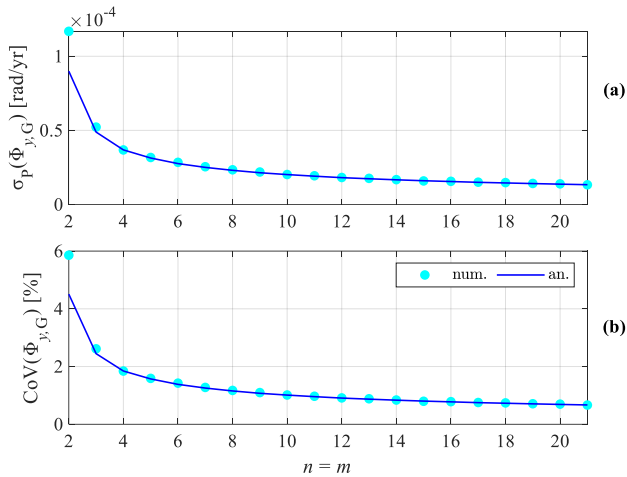


Figure 8. Influence of  $\Phi_{y,G}$  on the positioning uncertainties: (a)  $\sigma_P(\Phi_{y,G})$  and (b) CoV of  $\Phi_{y,G}$ .



Table 4. Positioning uncertainties on the rigid motion components, last step.

Component		$v_{x,G}$ [mm/yr]	$v_{z,G}$ [mm/yr]	$\Phi_{y,G}$ [mrad/yr]
Imposed		10.000	100.000	2.000
Simulated		10.166	99.999	1.997
$\sigma_P(\vartheta_r)$	Numerical	0.718	0.259	0.013
	Analytical	0.723	0.258	0.013
CoV( $\vartheta_r$ )	Numerical	7.06%	0.259%	0.634%
	Analytical	7.11%	0.258%	0.631%


Figure 9. Influence of the PS number on the positioning uncertainties: (a)  $\sigma_P(v_{z,G})$  and (b) CoV of  $v_{z,G}$ .

Figure 10. Influence of the PS number on the positioning uncertainties: (a)  $\sigma_P(\Phi_{y,G})$  and (b) CoV of  $\Phi_{y,G}$ .

#### 4.2.2 Case 2: variation of the uncertainties with the number of PSs

Figures 9 and 10 show the results as a function of the PS number. Specifically, Figure 9 illustrates the variation in positioning uncertainty  $\sigma_P(v_{z,G})$  and in the CoV of  $v_{z,G}$ , while

Figure 10 presents the variation in positioning uncertainty  $\sigma_P(\Phi_{y,G})$  and in the coefficient of variation of  $\Phi_{y,G}$ .

Note that, in line with the measurement error case, the values of  $\sigma_P(v_{z,G})$  and  $\sigma_P(\Phi_{y,G})$  tend to increase as the number of PSs decreases. Specifically, although the numerical uncertainty is generally well approximated by the analytical formulations, when only 2 PSs per orbit are considered, the analytical formulations underestimate both the uncertainties and the coefficients of variation.

#### 4.2.3 Case 1: variation of the uncertainties with the motion amplitude

As observed in the previous case, positioning error is indeed influenced by the motion entity. Therefore, it is crucial to identify which motion components have the greatest impact on the error. Figure 11, Figure 12 and Figure 13 show the variation in positioning uncertainty with the magnitude of the motion components. As shown, positioning errors seem to be uncorrelated with variations in  $v_{x,G}$  and  $v_{z,G}$ . Specifically, their values are in the order of  $10^{-10}$  mm/yr and rad/yr.

On the other hand, positioning errors appear to be strongly correlated with rotation; therefore, only the turbine's rotation can induce errors in the positioning of the PS.

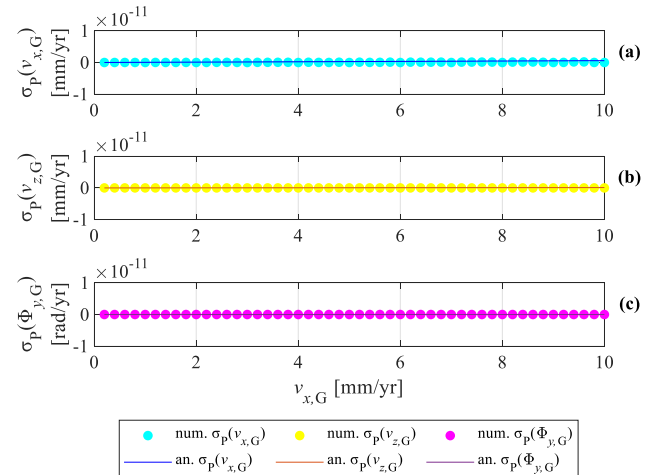
Regardless of the variations in motion components, analytical formulations appear to provide a good approximation of numerical errors.

#### 4.3 Total uncertainties

##### 4.3.1 Case 1: variation of the uncertainties with the value of the motion component

Figures 14 and 15 display the results in the form of graphs: as previously stated, the considered positioning precision is detailed in

, while for immediacy measurement precision is fixed at  $\bar{\sigma}_M = 2$  mm/yr. Particularly, Figure 14 details how the variation in  $v_{z,G}$  influences the total error  $\sigma_T(v_{z,G})$  and CoV of  $v_{z,G}$ , while Figure 15 illustrates the total error  $\sigma_T(\Phi_{y,G})$  and CoV of  $\Phi_{y,G}$  as a function of  $\Phi_{y,G}$ . For the sake of clarity, results regarding the maximum  $v_{z,G}$  and  $\Phi_{y,G}$  values are also displayed in table form in Table 5.


Figure 11. Influence of  $v_{x,G}$  on the positioning uncertainties:  $\sigma_P$  of  $v_{x,G}$  (a),  $v_{z,G}$  (b) and  $\Phi_{y,G}$  (c).

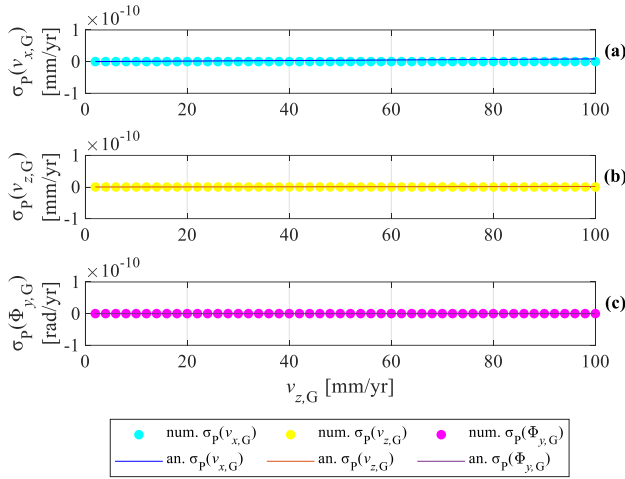


Figure 12. Influence of  $v_{z,G}$  on the positioning uncertainties:  $\sigma_p$  of  $v_{x,G}$  (a),  $v_{z,G}$  (b) and  $\Phi_{y,G}$  (c).

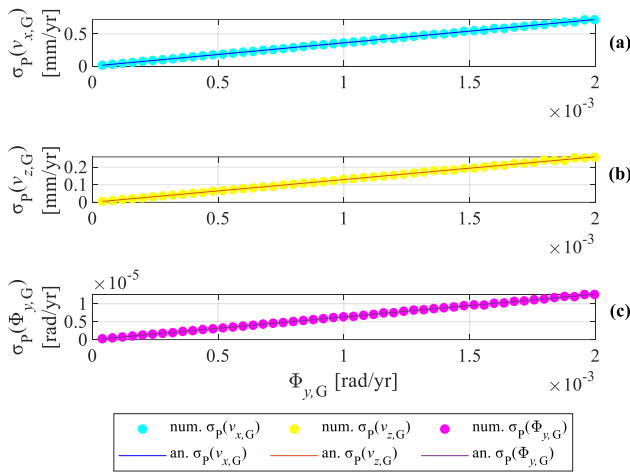


Figure 13. Influence of  $\Phi_{y,G}$  on the positioning uncertainties:  $\sigma_p$  of  $v_{x,G}$  (a),  $v_{z,G}$  (b) and  $\Phi_{y,G}$  (c).

Numerical simulations of uncertainties were performed as outlined in section 3. In contrast, analytical errors were computed using the method and parameters described in Section 2.3; in particular, adopting the formula described in equation (13). The good agreement between the numerical and analytical uncertainties, as well as the CoVs for each motion component, demonstrates that the proposed analytical models provide a reliable approximation of the numerical errors, even in the case of total errors. Note that measurement errors seem to be the largest contributor to the total uncertainty, while positioning error becomes a more significant factor as the motion component increases.

#### 4.3.2 Case 2: variation of the uncertainties with the number of PSs

In Figure 16, the variations of the total error  $\sigma_T(v_{z,G})$  and of the total CoV of  $v_{z,G}$  as a function of PSs number are displayed. Moreover, Figure 17 depicts the variation of the total error  $\sigma_T(v_{z,G})$  and of the total CoV of  $v_{z,G}$  as a function of PSs number. Note that, as anticipated, errors increase as the number of PSs decreases.

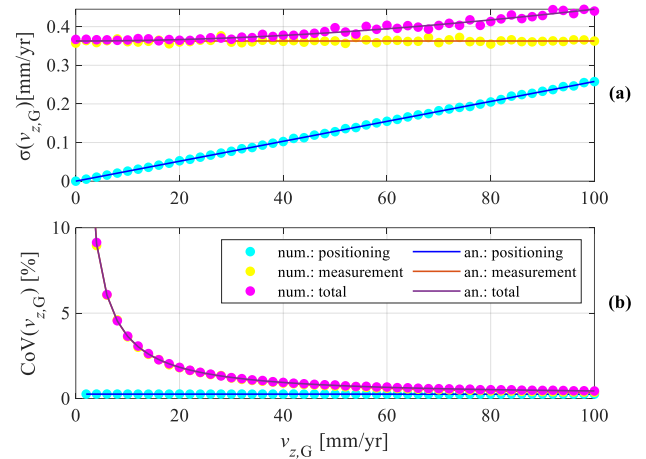


Figure 14. Influence of  $v_{z,G}$  on the total uncertainties: (a)  $\sigma(v_{z,G})$  and (b) CoV of  $v_{z,G}$ .

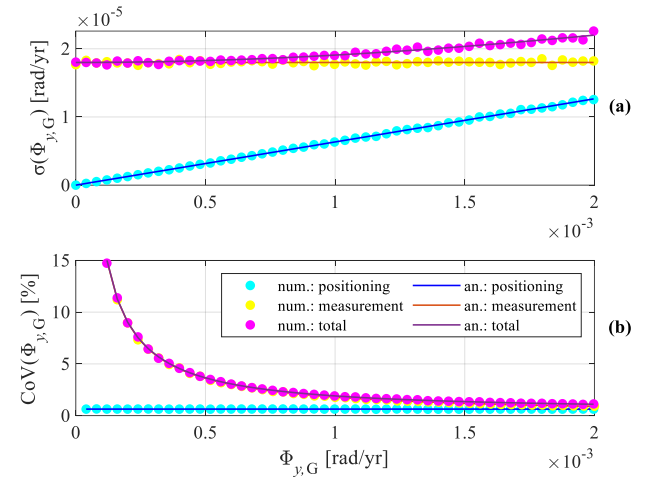


Figure 15. Influence of  $\Phi_{y,G}$  on the total uncertainties: (a)  $\sigma(\Phi_{y,G})$  and (b) CoV of  $\Phi_{y,G}$ .

Table 5. Total uncertainties on the rigid motion components -  $\bar{\sigma}_M=2$  mm/yr, last step.

Component		$v_{x,G}$ [mm/yr]	$v_{z,G}$ [mm/yr]	$\Phi_{y,G}$ [mrad/yr]
Imposed		10.000	100.000	2.000
Simulated		10.143	99.996	1.997
$\sigma_T(\vartheta_r)$	Numerical	1.273	0.447	0.022
	Analytical	1.248	0.444	0.022
CoV( $\vartheta_r$ )	Numerical	12.55%	0.447%	1.119%
	Analytical	12.31%	0.444%	1.092%

Similarly to the cases of measurement and positioning uncertainties, the numerical uncertainty is generally well approximated by the analytical formulations. The only exception occurs when 2 scatterers per orbit are considered, where the analytical formulations underestimate the numerical errors.

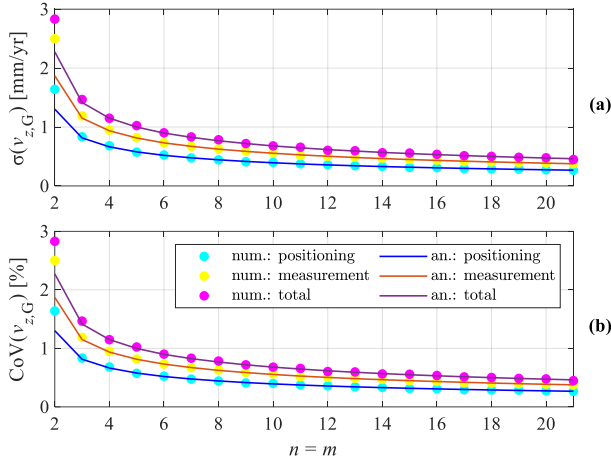


Figure 16. Influence of the PS number on the total uncertainties: (a)  $\sigma(v_{z,G})$  and (b) CoV of  $v_{z,G}$ .

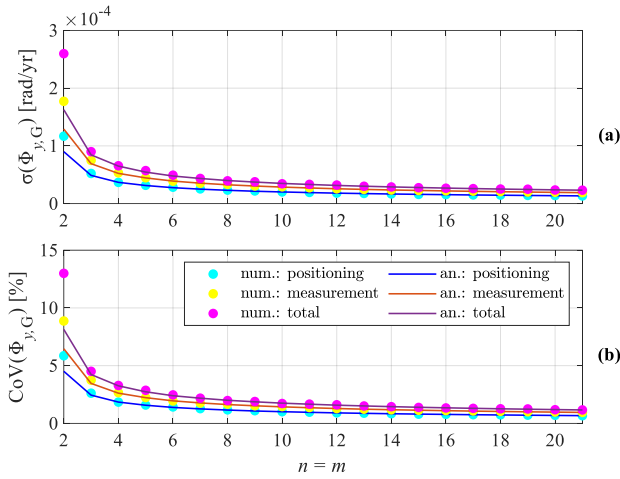


Figure 17. Influence of the PS number on the total uncertainties: (a)  $\sigma(\Phi_{y,G})$  and (b) CoV of  $\Phi_{y,G}$ .

#### 4.3.3 Case 1: variation of the uncertainties with the motion amplitude

Results are presented in Figures 18, 19 and 20. In particular, the three graphs depict how the variations in  $v_{x,G}$ ,  $v_{z,G}$  and  $\Phi_{y,G}$ , respectively, influence the total errors  $\sigma_T(v_{x,G})$ ,  $\sigma_T(v_{z,G})$  and  $\sigma_T(\Phi_{y,G})$ .

As already observed in the positioning uncertainties case, the rotation appears to be the only motion component affecting the uncertainty, while the translations have no effect on the error. Specifically, an increase in  $\Phi_{y,G}$  directly translates in an increase of the component total errors. In any case, the analytical formulations provide an effective approximation of the numerical errors: their quality is validated by their accurate approximation of numerical errors in each of the presented cases.

## CONCLUSIONS

This paper proposes a method for estimating the 3D rigid motion components of wind turbines and the corresponding uncertainties using DInSAR satellite data.

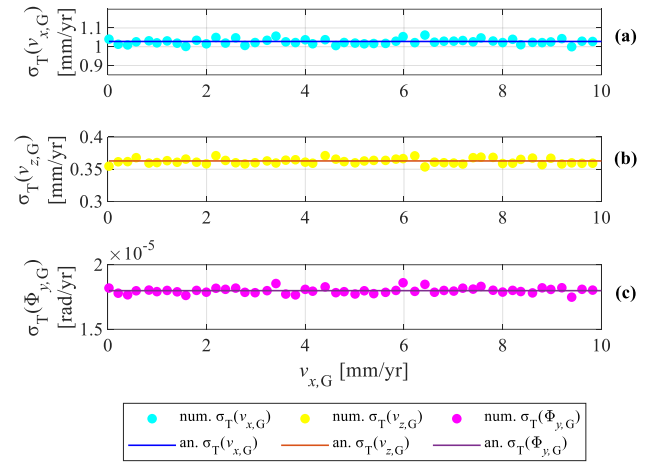


Figure 18. Influence of  $v_{x,G}$  on the total uncertainties:  $\sigma_T$  of  $v_{x,G}$  (a),  $v_{z,G}$  (b) and  $\Phi_{y,G}$  (c).

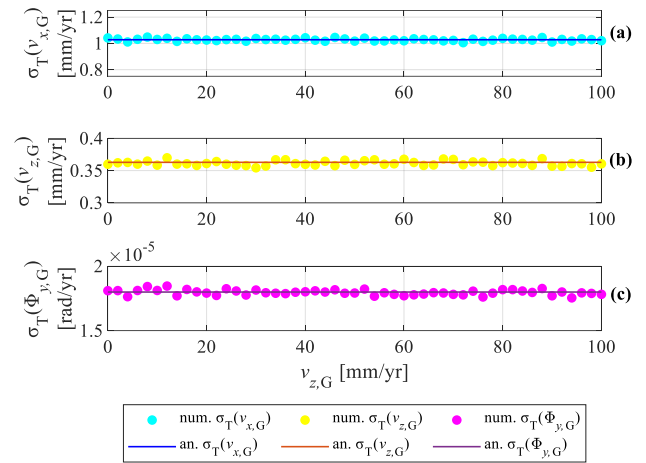


Figure 19. Influence of  $v_{z,G}$  on the total uncertainties:  $\sigma_T$  of  $v_{x,G}$  (a),  $v_{z,G}$  (b) and  $\Phi_{y,G}$  (c).

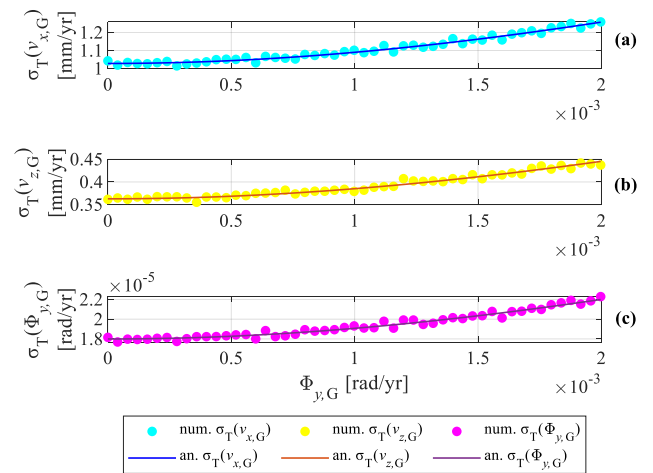


Figure 20. Influence of  $\Phi_{y,G}$  on the total uncertainties:  $\sigma_T$  of  $v_{x,G}$  (a),  $v_{z,G}$  (b) and  $\Phi_{y,G}$  (c).



Rigid motion of wind turbines can be generally associated with foundation settlement, a gradual phenomenon that can potentially cause damage to both structural and non-structural elements. Traditional Structural Health Monitoring techniques typically require extended acquisition times, making them economically impractical, particularly in foundation settlement cases. In contrast, satellite-based monitoring allows for the direct analysis of historical displacement time series without the need for on-site instrumentation, while enabling the monitoring of displacements over large areas with high accuracy. The proposed approach utilizes the mean annual displacement of permanent scatterers along the lines of sight, thereby eliminating the need for temporal and spatial resampling of satellite data.

The accuracy of the proposed approach was evaluated using Monte Carlo numerical simulations, in which satellite data were generated while accounting for uncertainties in both the displacement of the considered scatterers (measurement errors) and their vertical positioning along the wind turbine (positioning errors). The numerical results were then compared with those derived from the analytical expressions initially presented in [14] and adapted for application to wind turbines. The satellite data parameters were based on those of the COSMO-SkyMed constellation, which is particularly well-suited for structural monitoring applications. Numerical errors and analytical uncertainties were evaluated across various scenarios, including variations in the 3D motion components and the number of available PSs on the turbine. As expected, an increased number of available PSs leads to reduced uncertainties, while larger turbine rotations result in greater errors. In contrast, the uncertainties remain uncorrelated with both vertical and horizontal translations.

The method presents certain limitations, including the approximation of the turbine as a purely rigid body, which necessitates fitting the data to a rigid model without accounting for possible structural deformations. Additionally, the approach relies on Permanent Scatterers (PS), which – depending on the processing technique – can be affected by noise due to both decorrelation and atmospheric effects, potentially impacting the accuracy of the results. Nevertheless, the strong agreement observed between numerical simulations and analytical predictions confirms the robustness of the proposed procedure in estimating the rigid-body motion of wind turbines and the associated uncertainties. The method demonstrates high precision, with uncertainties on the order of tenths of millimeters and/or milliradians per year.

The next steps of the research involve attempting to obtain a priori estimates of the uncertainty based solely on the knowledge of the potential number of PS present, to assess whether satellite data can already provide the required accuracy during the phase of selecting the monitoring methodology. For this purpose, simplifications regarding the distribution of PS will be made. Additionally, data from a wind farm will be analyzed to evaluate the possibility of applying the methodology to real cases.

## ACKNOWLEDGMENTS

This study was carried out within the ReLUIIS-DPC 2024–2026 Project (Line WP6). The financial support of the Civil Protection Department of the Presidency of the Council of

Ministers and the Reluis Consortium is gratefully acknowledged.

## REFERENCES

- [1] Global Wind Energy Council, Global Wind Report 2023, 2023. Available at: <https://www.gwec.net/>.
- [2] M. Martinez-Luengo, A. Kolios and L. Wang, Structural health monitoring of offshore wind turbines: A review through the Statistical Pattern Recognition Paradigm, *Renewable and Sustainable Energy Reviews* 64: 91-105, 2016.
- [3] W. Liu, B. Tang and Y. Jiang, Status and problems of wind turbine structural health monitoring techniques in China, *Renewable Energy*, 35: 1414-1418, 2010.
- [4] M. Currie, M. Saafi, C. Tachtatzis and F. Quail, Structural integrity monitoring of onshore wind turbine concrete foundations, *Renewable Energy* 83: 1131-1138, 2015.
- [5] S. K. Gupta, D. P. Shukla and K. C. Niraj, Kortupi landslide deformation study in non-urban area using DInSAR and MTInSAR techniques on Sentinel-1 SAR data, *Advances in Space Research*, 70(12): 3878-3891, 2022.
- [6] M. Crosetto, L. Solari, M. Mróz, J. Balasis-Levinsen, N. Casagli, M. Frei, A. Oyen, D. A. Moldestad, L. Bateson, L. Guerrieri, V. Comerchi and H. S. Andersen, The evolution of wide-area DInSAR: From regional and national services to the European ground motion service, *Remote Sensing*, 12(12), 2020.
- [7] A. Miano, A. Mele, D. Calacaterra, D. D. Martire, D. Infante, A. Prota e M. Ramondini, The use of satellite data to support the structural health monitoring in areas affected by slow-moving landslides: a potential application to reinforced concrete buildings, *Structural Health Monitoring*, 20(6): 3265-3287, 2021.
- [8] D. Talledo, A. Stella, M. Bonano, F. Di Carlo, R. Lanari, M. Manunta, A. Meda, A. Mele, A. Miano, A. Prota e A. Saetta, Techniques for Structural Assessment Based on MT-DInSAR Data, Applied to the San Michele Complex in Rome, *European Workshop on Structural Health Monitoring. EWSHM 2022*, pp. 593-603, 2023.
- [9] A. Ferretti, C. Prati and F. Rocca, Permanent Scatterers in SAR Interferometry, *IEEE Transactions on Geoscience and Remote Sensing*, 39(1), 2001.
- [10] F. Mancini, F. Grassi and C. Nicola, A workflow based on snap–stamps open-source tools and gnss data for psi-based ground deformation using dual-orbit sentinel-1 data: Accuracy assessment with error propagation analysis, *Remote Sensing*, 13(753): 1-23, 2021.
- [11] M. Crosetto, O. Monserrat, R. Iglesias and B. Crippa, Persistent Scatterer Interferometry: Potential, Limits and Initial C- and X-band Comparison, *Photogrammetric Engineering & Remote Sensing*, 76(9): 1061-1069, 2010.
- [12] D. A. Talledo, A. Miano, M. Bonano, F. Di Carlo, R. Lanari, M. Manunta, A. Meda, A. Mele, A. Prota, A. Saetta e A. Stella, Satellite radar interferometry: Potential and limitations for structural assessment and monitoring, *Journal of Building Engineering*, 46: 103756, 2022.
- [13] F. Di Carlo, A. Miano, I. Giannetti, A. Mele, M. Bonano, R. Lanari, A. Meda e A. Prota, On the integration of multi-temporal synthetic aperture radar interferometry products and historical surveys data for buildings structural monitoring, *Journal of Civil Structural Health Monitoring*, 11(5): 1429-1447, 2021.
- [14] E. Bassoli, L. Vincenzi, F. Grassi and F. Mancini, A multi-temporal DInSAR-based method for the assessment of the 3D rigid motion of buildings and corresponding uncertainties, *Journal of Building Engineering*, 73: 106738, 2023.
- [15] A. Ferretti, G. Savio, R. Barzaghi, A. Borghi, S. Musazzi, F. Novali, C. Prati and F. Rocca, Submillimeter accuracy of InSAR time series: Experimental validation, *IEEE Transactions on Geoscience and Remote Sensing*, 45: 1142-1153, 2007.
- [16] S. Gernhardt and R. Bamler, Deformation monitoring of single buildings using meter-resolution SAR data in PSI, *ISPRS Journal of Photogrammetry and Remote Sensing*, 73: 68-79, 2012.
- [17] B. Zhang, L. Chang and A. Stein, Spatio-temporal linking of multiple SAR satellite data from medium and high resolution radarsat-2 images, *ISPRS Journal of Photogrammetry and Remote Sensing*, 176: 222-236, 2021.
- [18] J. A. Barros and A. Mathern, Recent and future trends of onshore wind turbine foundations, in *IABSE Symposium Prague 2022*, Prague, Czech Republic, 2022.

# Distributed fibre optic sensing of decommissioned wind turbine blades under bending

Chao Wang<sup>1</sup>, Shaoqiu Zhang<sup>1</sup>, Kieran Ruane<sup>2</sup>, Vesna Jaksic<sup>2</sup>, Zili Li<sup>1,3</sup>

<sup>1</sup>School of Engineering and Architecture, University College Cork, Cork, Ireland

<sup>2</sup>Civil, Structural and Environmental Engineering, Munster Technological University, Cork, Ireland

<sup>3</sup>Irish Centre for Research in Applied Geosciences, University College Dublin, Dublin, Ireland

email: chao.wang@ucc.ie, shaoqiu.zhang@ucc.ie, kieran.ruane@mtu.ie, vesna.jaksic@mtu.ie, zili.li@ucc.ie

**ABSTRACT:** The decommissioning of wind turbine blades (WTBs) presents significant environmental challenges due to their non-biodegradable composition. To promote sustainable reuse and repurposing, it is essential to establish effective structural health monitoring (SHM) techniques that can accurately assess the residual performance of decommissioned WTBs. This study investigates the feasibility and applicability of distributed fibre optic sensing (DFOS) as an advanced monitoring tool for evaluating the structural integrity of decommissioned WTBs intended for reuse in civil engineering applications. A four-point bending test was conducted on a WTB segment, with DFOS deployed alongside other monitoring techniques, including strain gauges, and digital image correlation (DIC). The DFOS measurements demonstrated strong agreement with those obtained from strain gauges and DIC, with negligibly small variations in strain magnitude, validating its accuracy and reliability for continuous strain monitoring. The results further confirmed sufficient load-bearing capacity of the WTB segment, indicating its potential for second-life structural applications. This study highlights the capability of DFOS in providing high-resolution, distributed strain measurements, offering a promising approach for assessing the suitability of decommissioned WTBs for reuse. Future research aims to incorporate material characterisation studies and long-term monitoring to establish standardised frameworks for the sustainable repurposing of WTBs, contributing to a circular economy in the wind energy sector.

**KEY WORDS:** Decommissioned wind turbine blades; Repurposing; Four-point bending test; Distributed fibre optic sensing.

## 1 INTRODUCTION

Wind energy has become a cornerstone of sustainable energy solutions worldwide, significantly contributing to the reduction of carbon emissions. In Ireland, the expansion of onshore and offshore wind farms is expected to play a critically significant role in achieving the country's 2030 renewable energy targets, potentially reducing its carbon emissions by 51% [1]. However, as wind energy industry grows and matures, a growing challenge is the decommissioning of the wind turbine blades (WTBs). By 2025, approximately 11,000 tons of WTBs are expected to be decommissioned in Ireland alone [2]. These blades are predominantly made from glass fibre reinforced polymer (GFRP) composites, which are non-biodegradable and pose significant disposal challenges, often ending up in landfills and leading to environmental degradation [3].

Despite the environmental challenges, WTBs possess unique structural properties, including high strength-to-weight ratios and resistance to harsh environmental conditions, making them promising candidates for reuse and repurposing in civil engineering applications [4]. Previous studies have explored various repurposing strategies. For example, Martini and Xydis (2022) reviewed the common practice of WTB reuse and recycling in the United States, which included whole and partial blade reuse, and grinding material reuse [5]. In another study, Hasheminezhad et al. (2024) further reviewed its reuse for construction and infrastructure applications [4], such as powerline poles [6], slow-traffic bridges [7], picnic tables [8], playground [9], etc.

However, despite the growing interest in repurposing WTBs, a critical challenge lies in understanding the residual structural performance after years of service. Long-term exposure to

environmental influences, such as UV radiation, moisture, and cyclic loading, can degrade the mechanical properties of the GFRP composites used in WTBs, which may influence their structural integrity and impact their long-term performance and suitability for reuse in civil engineering applications.

To enable the safe and sustainable reuse and repurposing of decommissioned WTBs, effective condition monitoring and structural health assessment is essential. While traditional monitoring methods, such as strain gauges, provide valuable insights, they are often limited to their discrete measurements. In contrast, distributed fibre optic sensing (DFOS) offers a high-resolution, continuous, and long-term monitoring solution capable of capturing detailed strain distributions over large structural elements. DFOS has been successfully implemented in various infrastructure applications such as tunnels [10], but its feasibility and applicability for monitoring the residual structural performance of decommissioned WTBs remains largely unexplored.

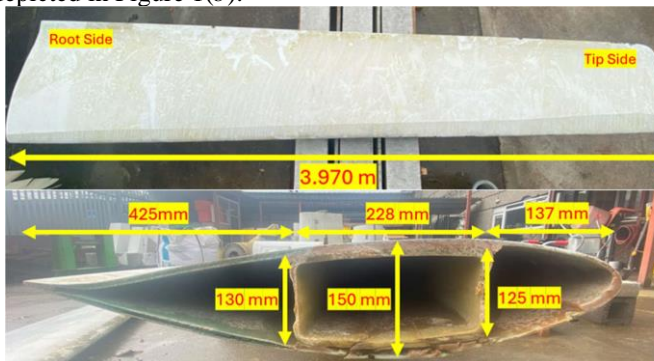
This study aims to evaluate the feasibility of DFOS as a monitoring technique for assessing the residual performance of a decommissioned WTB segment subjected to four-point bending tests. The segment was instrumented with DFOS, alongside other monitoring techniques such as strain gauges, linear variable differential transformers (LVDTs), and digital image correlation cameras to enable a comparative assessment of measurement accuracy and reliability. By examining the strain distribution and mechanical behaviour of the WTB segment, this study aims to determine the suitability of DFOS for structural health monitoring in second-life applications of decommissioned WTBs. The findings will contribute to the development of robust monitoring frameworks for WTB reuse

in civil engineering, supporting a circular economy in the wind energy sector and enhancing the sustainability of wind turbine decommissioning.

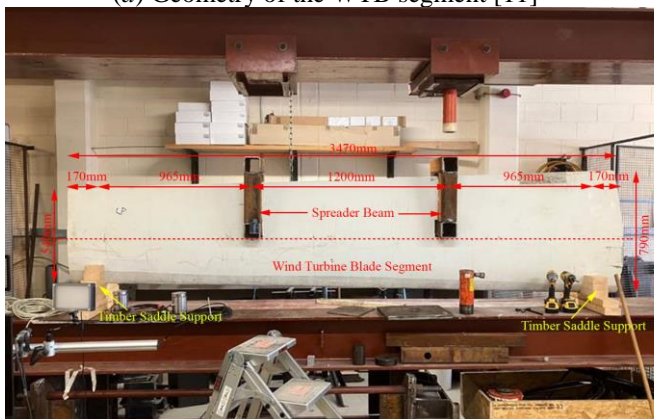
## 2 METHODOLOGY

### 2.1 Wind turbine blade preparation

The decommissioned wind turbine blade used in this study was sourced from a V42/600 wind turbine manufactured by Vestas in Denmark. Each turbine has a power rating of 600 kW and consists of three blades. The turbines have a rotor diameter of 42m, and each blade has a total length of 21 meters from root to tip. A 4-meter long segment was cut from the tip side for laboratory testing. In the initial preparation stage, the geometry of this blade segment was measured using vernier callipers, as illustrated in Figure 1(a). Surface stains were cleaned to facilitate a visual inspection for any potential damage. Subsequently, the blade segment was divided into 500 mm-long sections using a measuring tape and a chalk line. To accurately identify the location of the spar on the tip side, the final 500 mm portion at the blade tip was removed. The centre of the blade segment was then marked, with 600 mm measured on each side of the centreline to designate the positions for the spreader beams. A line was drawn connecting the top spar on the root side to the top spar on the tip side of the blade segment. To accommodate the installation of spreader steel beams, which are designed to transfer loads onto the spar cap, 110 mm square sections were cut from both the high-pressure and low-pressure sides of the blade aerofoil at the points where each 600 mm mark intersected with the spar cap line. This process is depicted in Figure 1(b).



(a) Geometry of the WTB segment [11]



(b) WTB segment preparation for testing  
Figure 1. Geometry of the WTB segment

### 2.2 Loading arrangement

The blade was positioned in the edgewise direction with the trailing edge facing upward and was supported by two timber saddles, each placed 170 mm from the ends to avoid areas of local skin damage. Loading was applied using two hydraulic jacks acting on both spreader beams, simulating a four-point bending test. Load cells beneath each jack recorded the applied force. Two four-point bending tests were conducted on the blade segment. In test 1, a total load of 30kN was applied, while in test 2, the total load reached 50kN. The objective was to maintain loading within the blade's elastic range, enabling multiple repetitions if necessary. In both tests, loading was applied stepwise: for the 30kN test, a designed step loading of 2-5kN was used, whereas for the 50kN test, increments of 10kN were used. Figure 2 illustrates the loading system. The four-point loading was carried out by manual handling of two hydraulic jacks due to the dysfunction of the automatic system. The loading details of both tests were shown in Figure 3.

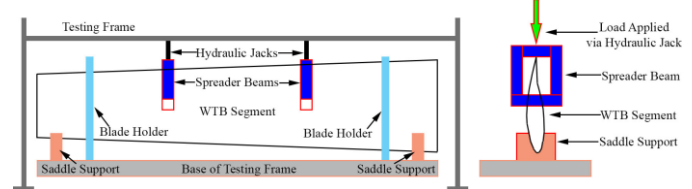
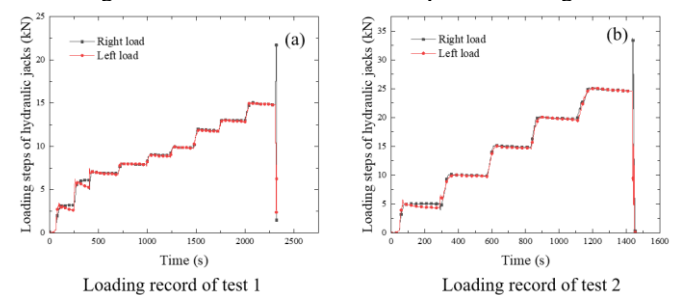


Figure 2. Illustration of the four-point bending test



Loading record of test 1

Loading record of test 2

Figure 3. Loading details of both tests

### 2.3 Monitoring system setup

To monitor the strain and displacement development of the WTB segment under four-point loading tests, a comprehensive monitoring system was implemented to capture multiple sets of displacement measurements, enabling a thorough assessment of its mechanical performance. This system incorporated diverse techniques, including strain gauges, LVDT, DIC) and DFOS. The setup of each monitoring system is detailed below. A general view of the installed monitoring systems on the WTB segment is shown in Figure 4.

**Strain gauge and LVDT:** Two strain gauges were deployed on the back of the WTB segment, as shown in Figure 4. The strain gauge fixed at the upper part of the blade segment is 80 mm from the top and the other gauge fixed at the lower level is 80mm from the bottom of the segment. Both strain gauges were deployed in the middle span of the blade segment. Three LVDTs were installed at three distinctive locations on the back of blade segment, as demonstrated in Figure 4. The LVDT mounted on the left was placed at a distance of 63mm below the bottom of the left spreader beam, while the one mounted on the right was at a distance of 70mm from the bottom of the right spreader beam. The middle one was fixed at 430mm from the top of the blade in the vertical direction.



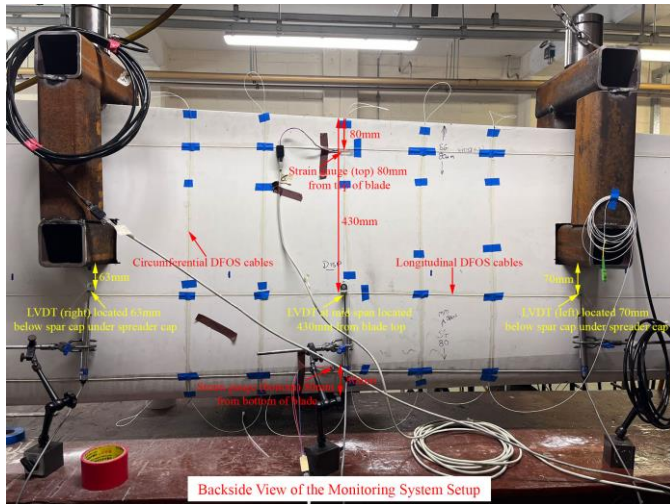


Figure 4. Monitoring system setup on the WTB segment

DIC and DFOS: One DIC camera was positioned to capture and monitor the deformation and displacement of the front side of the WTB segment. Line gauges and reference points were marked at key locations to facilitate deformation tracking. These markers were symmetrically aligned on the front face with the two strain gauges and three LVDTs positioned on the back of the segment, as shown in Figure 5. To get continuous strain measurements of the WTB segment, a Brillouin-based DFOS system was deployed. DFOS cables were installed on both the front and back surfaces of the segment, with two fixed loops: one horizontal and one vertical, as shown in Figures 4 and 5. The data logger used in this experiment was the VISION dual interrogator, manufactured by Omnisens, which integrates Brillouin Optical Time Domain Reflectometry (BOTDR) and Brillouin Optical Time Domain Analysis (BOTDA), enabling short- to long-distance strain measurements over a single fibre.

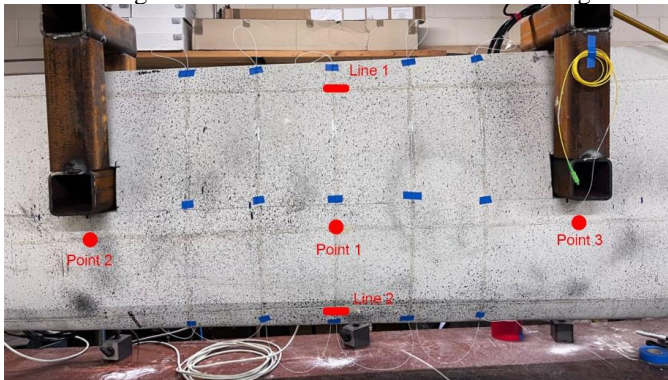
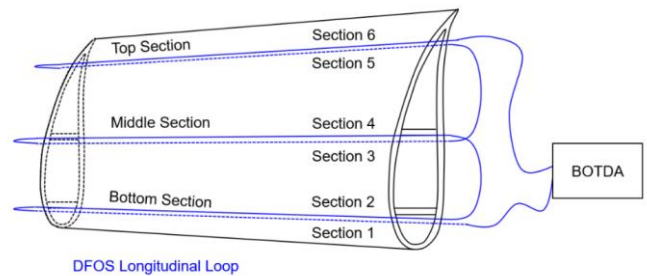


Figure 5. Line gauges and points to mark locations for DIC

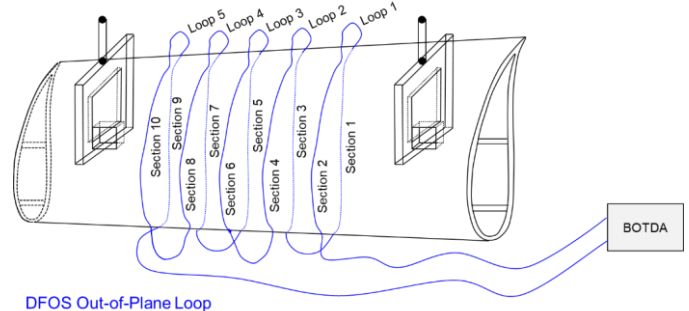
#### 2.4 DFOS instrumentation details

Theoretically, the four-point bending of the WTB segment is expected to induce the highest strain in its top and bottom regions, while the central portion is supposed to experience the lowest strain magnitude. Consequently, the monitoring systems are strategically positioned around the top and bottom areas to capture the most significant strain responses. To ensure consistency and comparability in the monitoring program, DFOS was deployed at locations corresponding to the strain gauges and LVDTs, as illustrated in Figure 6. The front and back surfaces of the WTB segment were instrumented with a single loop of longitudinal DFOS cable, which was virtually divided into three segments on the front and three on the back

(Figure 6(a)). In addition, an out-of-plane loop comprising five loops was installed at the mid-span of the segment and virtually segmented into ten sections on both the front and back surfaces (Figure 6(b)). Figure 6 provides a schematic representation of the DFOS instrumentation design for the WTB segment.



(a) Deployment of DFOS longitudinal loop



(b) Deployment of DFOS out-of-plane loop

Figure 6. DFOS deployment on the WTB segment

The DFOS cables used for monitoring strain development in the WTB segment are single-mode fiber optic cables. These cables were affixed to the front and back surfaces of the WTB segment using Loctite EA 3421 adhesive. For the longitudinal loop of DFOS cables, the top section was installed horizontally along DIC marker Line 1, as indicated in Figure 4-6, rather than being aligned parallel to the top edge of the WTB segment. The middle and bottom sections were also affixed horizontally. The vertical spacing between the top and middle section is 295 mm, while the distance between the middle and bottom sections is 210 mm, with the bottom section positioned 80 mm from the lower edge of the segment. The deployment sequence of the longitudinal loop followed the following order: Section 1-Section 2-Section 4-Section 3-Section 5-Section 6.

For the out-of-plane loop of DFOS cables, five sub-loops were installed on both the front and back surfaces of the WTB segment. The deployment sequence followed the order: Section 2-Section 1-Section 3-Section 4-Section 6-Section 5-Section 7-Section 8-Section 10-Section 9. The spacing between adjacent sub-loops was approximately 190 mm. Loop 1 was positioned 170 mm from the right load-spreader beam, while Loop 5 was located 188 mm from the left load-spreader beam.

Once the DFOS cables were installed, they were left undisturbed for approximately 48 hours to allow the adhesive to cure fully and ensure a secure bond between the cables and the segment surface, preventing slippage. Following the curing period, laser beams were used to verify the integrity of the DFOS deployment. Once the installation was confirmed to be intact, the formal testing phase commenced.

### 3 MONITORING RESULTS

#### 3.1 DFOS measurements

Figure 7 presents the monitoring results obtained using DFOS under test 1 and test 2 for the longitudinal loops, alongside the strain gauge (SG) and DIC measurements for comparison. As previously discussed, the middle section of the WTB segment (Section 3 and Section 4) is theoretically expected to exhibit the lowest strain magnitude, which is corroborated by the results in Figure 7. Given the minimal strain observed in these sections, their performance will not be further analysed in this paper.

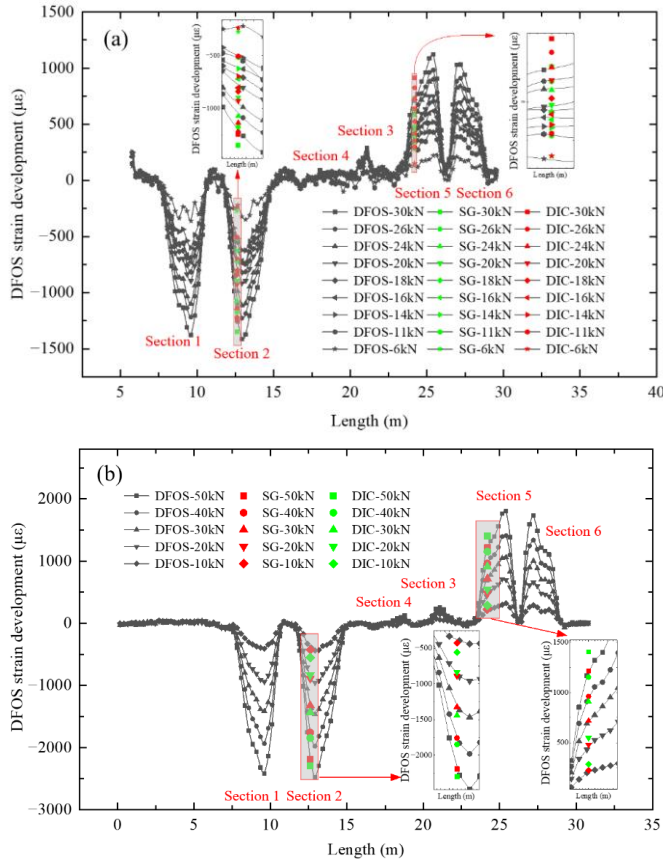


Figure 7. DFOS monitoring results of longitudinal sections under (a) test 1 and (b) test 2

Figure 8 presents enlarged graphs of the measurements obtained in Section 2 and Section 5, corresponding to locations where the DFOS sensors were positioned adjacent to two strain gauges. These graphs provide further insights into the bending behaviour of the WTB segment and facilitate a comparative analysis of different monitoring techniques. As illustrated in Figure 6, Section 1 and Section 2 were affixed to the back and front surfaces of the turbine blade, respectively, at the same height. Theoretically, the bending patterns observed in these areas should be similar under both test 1 and test 2, a hypothesis that is confirmed by the results presented in Figures 8(a) and 8(c). A comparable trend was observed in Sections 5 and 6, further validating this expectation. The consistency in bending patterns across these sections underscores the repeatability and reliability of the DFOS system employed in this study.

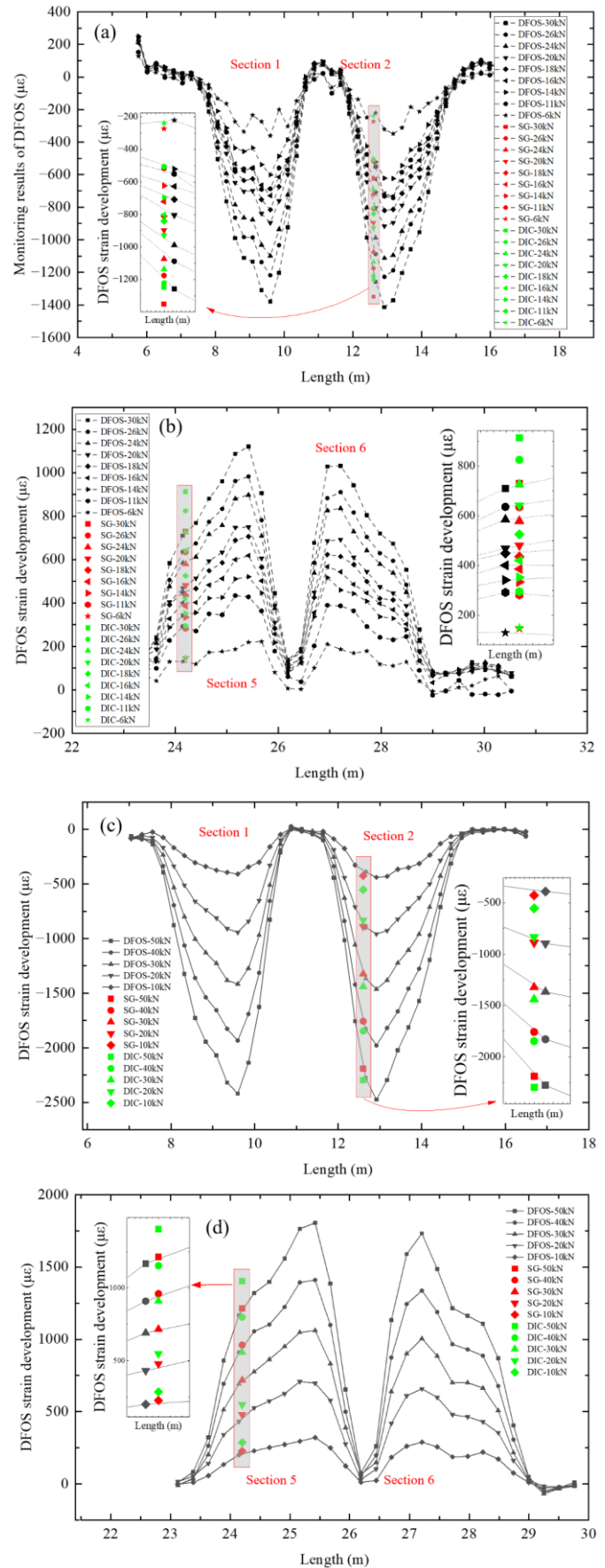


Figure 8. Enlarged graphs of section 2 and section 5 under test 1 (a and b) and test 2 (c and d)

### 3.2 Test results comparison

Figure 9 presents a comparative analysis of the monitoring results obtained using different techniques. The detailed values recorded by the strain gauge, DIC, and DFOS at the top and bottom area of the WTB under test 1 and test 2 are summarised in tables 1 and 2, corresponding to the conditions where total loadings of 30kN and 50kN were reached, respectively.

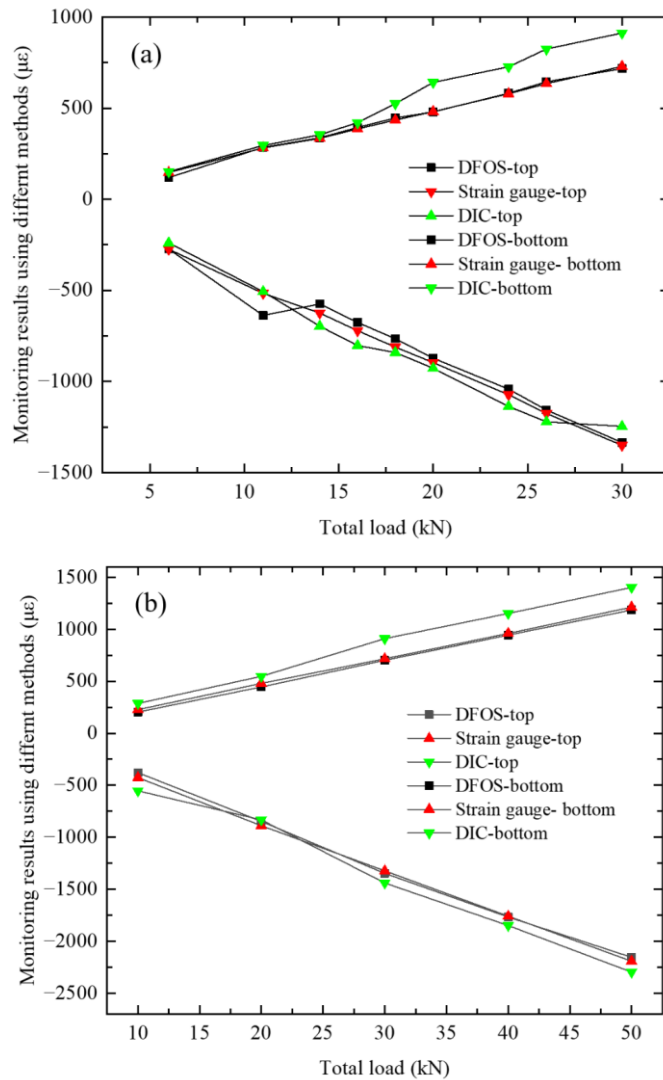


Figure 9. Comparison of monitoring results under (a) test 1 and (b) test 2

Table 1. Monitoring results under test 1

Strain/ $\mu\epsilon$	6kN	11kN	14kN	16kN	18kN	20kN	24kN	26kN	30kN
DFOS-top	-272.6	-637	-574.2	-675.8	-765.1	-871.5	-1041.4	-1155.9	-1334.4
SG-top	-274	-516	-624	-721	-811	-896	-1073	-1175	-1350
DIC-top	-239.6	-506.7	-696.2	-802.2	-840.5	-927.3	-1136.4	-1221.2	-1246.1
DFOS-bottom	119.6	284.7	337.4	393.8	446.4	479.5	581.8	644.7	717.2
SG- bottom	147	282	334	386	435	481	579	634	729
DIC-bottom	150.9	295.5	353.2	420.6	524.8	641.4	727.2	824.3	912.3

Figure 9 illustrates that measurements obtained using different monitoring techniques exhibit consistent deformation patterns in the turbine blade under both test 1 and test 2. The results indicate that the upper region of the blade experienced tensile stress, while the bottom region was subjected to compressive stress. Furthermore, as the external loading increased, the measured strain values exhibited an approximately linear increase, confirming the expected mechanical response of the WTB structure.

Overall, the DFOS measurements in both tests exhibited strong agreement with the results obtained from strain gauges and DIC, confirming its reliability. However, fluctuations were observed in the first two measurements of DFOS-bottom under test 1, which may be attributed to inaccuracies in the manual control of the loading increment. Despite these initial variations, the results affirm the effectiveness and reliability of DFOS as an innovative structural health monitoring technique for analysing the performance of decommissioned WTBs for repurposing.

Table 2. Monitoring results under test 2

Strain/ $\mu\epsilon$	10kN	20kN	30kN	40kN	50kN
DFOS-top	-379.0	-846.8	-1346.8	-1766.2	-2153.2
SG-top	-426	-888	-1323	-1758	-2191
DIC-top	-553.3	-832.1	-1439.7	-1847.9	-2296.4
DFOS-bottom	204.6	445.2	702.5	943.8	1185.1
SG-bottom	228	479	717	960	1213
DIC-bottom	286.6	548.1	909.7	1152.3	1403.1



## 4 CONCLUSION

This study evaluated the suitability and applicability of distributed fibre optic sensing for monitoring the second-life performance of decommissioned wind turbine blades in reuse and repurposing scenarios. Four-point bending tests were conducted on a decommissioned WTB segment, with DFOS deployed alongside strain gauges, digital image correlation, and linear variable differential transformers to assess its residual structural performance. The results revealed consistent strain measurements obtained from DFOS, strain gauges, and DIC, with only negligible differences in magnitude, confirming the accuracy and reliability of DFOS in capturing strain distributions in the WTB.

Through comparative analysis, this study confirms that DFOS is a viable and effective monitoring technique for assessing the structural behaviour of decommissioned WTBs, supporting their reuse in civil engineering applications. The tested blade exhibited adequate static load resistance and beam-like behaviour under bending loads, indicating its suitability for structural applications such as bridges and other load-bearing elements. Considering the growing demand for sustainable construction materials, the reuse of decommissioned WTBs, coupled with advanced sensing techniques like DFOS, can contribute to a circular economy in the wind energy sector, reducing waste generation and environmental impact.

However, to ensure the long-term reliability and safety of decommissioned WTBs in civil infrastructure, further research is recommended. Future studies should incorporate material characterisation tests to better understand the degradation effects of aging, UV exposure, and cyclic loading on GFRP composites. Additionally, long-term monitoring under real-world environmental conditions is necessary to validate the feasibility of DFOS for field applications. These steps will help establish standardised design and assessment frameworks, facilitating the widespread adoption of repurposed WTBs in civil engineering applications.

## ACKNOWLEDGMENTS

The authors acknowledge the financial support from the Science Foundation Ireland Frontiers for the Future Programme (21/FFP-P/10090) and the Research Ireland National Challenge Fund EirBLADE project (22/NCF/EI/11163G). The mobility support from the EU under the MSCA Staff Exchanges project 101182689 Geotechnical Resilience through Intelligent Design GRID is also greatly appreciated.

## REFERENCES

- [1] Climate Action and Low Carbon Development (Amendment) Act 2021.
- [2] Griffin, J., Ruane, K., Leahy, P., Jaksic, V. 2024. Physical testing and modelling of connections of steel brackets to decommissioned composite wind turbine blades. SAMPE Europe Conference 2024 Belfast – Northern Ireland.
- [3] Hasheminezhad, A., Nazari, Z., Yang, B., Ceylan, H., Kim, S. 2024. A comprehensive review of sustainable solutions for reusing wind turbine blade waste materials. *Journal of Environmental Management* 366, 121735.
- [4] Nagel, A. 2022. Sustainability assessment of the repurposing of wind turbine blades. PhD thesis, School of Engineering and Architecture, University College Cork, Cork, Ireland.
- [5] Martini, R., Xydis, G. 2022. Repurposing and recycling wind turbine blades in the United States. *Environmental Progress and Sustainable Energy* 42, e13932.
- [6] Alshannaq, A., Bank, L., Scott, D., Gentry, R. 2021. A decommissioned wind blade as a second-life construction material for a transmission pole. *Construction Materials* 1, 95-104.
- [7] Ruane, K., Soutsos, M., Huynh, A., etc. 2023. Construction and cost analysis of BladeBridges made from decommissioned FRP wind turbine blades. *Sustainability* 15, 3366.
- [8] Joustra, J., Flipsen, B., Balkenende, R. 2021. Structural reuse of wind turbine blades through segmentation. *Composites Part C: Open Access*, 5, 100137.
- [9] Medici, P., van den Dobbelsteen, A., Peck, D. 2020. Safety and health concerns for the users of a playground, built with reused rotor blades from a dismantled wind turbine. *Sustainability* 12, 3626.
- [10] Xiao, Z., Di Murro, V., Osborne, J., Zhu, H., Li, Z. 2024. Distributed fibre optic sensing and novel data processing method for tunnel circumferential deformation – A case study of an ageing tunnel at CERN. *Tunnelling and Underground Space Technology* 153, 106014.
- [11] O'Donovan, D. 2024. Assessing the suitability of decommissioned wind turbine blades for structural applications through digital image correlation. Master Thesis. Munster Technological University.

# Prediction of urban wind speed during tropical cyclones using a novel deep learning-based spatiotemporal model

Yuan-Jiang Zeng<sup>1,2</sup>, Zheng-Wei Chen<sup>1,2</sup>, Yi-Qing Ni<sup>1,2</sup>, Pak-Wai Chan<sup>3</sup>

<sup>1</sup>National Rail Transit Electrification and Automation Engineering Technology Research Centre (Hong Kong Branch), Hong Kong, China

<sup>2</sup>Department of Civil and Environmental Engineering, The Hong Kong Polytechnic University, Hong Kong, China

<sup>3</sup>Hong Kong Observatory, Hong Kong, China

email: yuanjiang.zeng@connect.polyu.hk, zhengwei.chen@polyu.edu.hk, ceyqni@polyu.edu.hk, pwchan@hko.gov.hk

**ABSTRACT:** Tropical cyclones (TCs) stand as one of the most destructive extreme weather events, posing significant threats to human safety and urban infrastructure. One critical phenomenon associated with TCs is the occurrence of strong winds; thus, accurate prediction of urban wind speed during TCs can provide essential information for decision-making, which is vital for enhancing urban resilience. This study proposes a deep learning-based model that accounts for the spatial and temporal dependencies of wind speed data collected from sensors of meteorological stations while addressing the impacts of climate change. The model integrates temporal and spatial encodings with measured time series data, enabling the capturing of long-term temporal dependencies that reflect periodic weather patterns and climate change through the attention mechanism of a Transformer architecture. The outputs derived from this computation are further utilized to identify dynamic patterns of wind speed during TCs. Additionally, a graph neural network (GNN) is integrated to capture spatial dependencies, considering the non-Euclidean distribution of meteorological stations. To evaluate the performance of the proposed model, wind speed measurements from Hong Kong between 2000 and 2023 are used for training and testing. Comparative analyses with sequence-to-sequence models and GNN-recurrent neural network or GNN-Transformer hybrid models demonstrate that the proposed model enhances prediction performance.

**KEY WORDS:** Tropical cyclones; Wind speed; Transformer; Graph neural network.

## 1 INTRODUCTION

Urban wind speed is a critical factor influencing human comfort, safety, and urban resilience [1] [2]. Its dynamics directly affect energy management systems [3], infrastructure durability, and ecological balance [4], while extreme wind events, such as tropical cyclones (TCs), pose significant threats to life and property. Rapid urbanization and climate change exacerbates these challenges by intensifying urban heat island effects and creating complex wind environments [5][7], further complicating prediction efforts. Accurate forecasting of urban wind speed, particularly during TCs, is thus essential for effective disaster mitigation, early-warning systems, and urban planning [8].

There are three primary methods for analyzing and predicting urban wind speed: physical models, statistical models, and hybrid models [9]. Physical models rely on geographic information and meteorological fields to solve complex physical equations. For instance, the Weather Research and Forecasting (WRF) model is often combined with complex urban canopy models to predict urban wind speed profiles during TCs [10] [11]. Additionally, WRF can be integrated with computational fluid dynamics (CFD) to investigate time-series wind speed data [12]-[14]. However, these models are typically time-consuming and computationally intensive, which may introduce time lags, and they are sensitive to parameter settings, particularly during extreme TCs.

In contrast, statistical models utilize historical data to develop statistical regressions for predicting future wind speeds. For example, autoregressive moving average (ARMA) models and generalized autoregressive conditional heteroskedasticity (GARCH) models have been employed to forecast seasonal [15]

or hourly [16] wind speed. Moreover, model decomposition methods are often integrated with ARMA to enhance wind speed predictions [17]. While statistical models offer rapid inference, they may sacrifice accuracy, especially when wind speed exhibits strong nonstationary behavior [18]. Hybrid models, which combine physical and statistical approaches, aim to leverage the strengths of both methodologies, though they also inherit the limitations of each model type.

Recent advancements in deep learning have attracted considerable attention across diverse fields, such as medicine, transportation, civil engineering, and aerospace, and the application of deep learning for predicting wind speed has also been explored. One approach treats wind speed prediction as a sequence-to-sequence task, employing recurrent neural networks (RNN)-based or convolutional neural networks (CNN)-based models. For instance, long short-term memory (LSTM), gated recurrent unit (GRU), CNN, and CNN-LSTM architectures have been assessed for their performance in long-term wind speed predictions, with forecast horizons ranging from 6 months to 5 years [19]. In addition to long-term predictions, LSTM models have been utilized to forecast 10-minute wind speeds using data from only two measurement sites [9]. Furthermore, ConvLSTM has been employed to predict 10-minute wind speeds based on weather-related images, considering six measurement sites [3]. Beyond RNN- and CNN-based models, Transformer has emerged as a popular alternative for sequence-to-sequence predictions. Various Transformer-based models have been compared for predicting 10-minute wind speeds at three meteorological stations [20].

Another approach incorporates spatiotemporal correlations, rather than treating the problem purely as a sequence-to-

sequence task. A notable example of this is the development of a temporal graph convolutional network (TGCN), which combines graph neural networks (GNN) and GRU to predict hourly wind speeds based on data from six measurement stations [21]. However, it is evident that the studies mentioned primarily focus on a limited number of measurement sites, with temporal resolutions typically set at 10 minutes or longer. The prediction of urban wind speed during TCs remains an area requiring further exploration, particularly regarding the application of Transformer-based models that account for spatiotemporal dependencies.

The contributions of this study are three-fold: Firstly, a dense meteorological station network that covers most urban areas is selected, enabling 1-minute resolution wind speed predictions during TCs—an improvement over existing sparse, low-frequency datasets. Secondly, the study develops a novel Transformer-GNN hybrid model that explicitly captures spatial topology through GNN while leveraging Transformer for temporal dependencies, thus advancing beyond conventional sequence-to-sequence approaches. Lastly, a comparison is conducted against current mainstream models, including pure sequence-to-sequence models, GNN-RNN, and GNN-transformer hybrids, demonstrating superior accuracy in extreme wind scenarios and providing valuable insights into spatiotemporal feature engineering for urban meteorology.

The remainder of this paper is structured as follows: Section 2 details the problem formulation, data source and processing, and model architecture. Section 3 presents experimental results with comparative analysis and ablation study, while Section 4 concludes the main findings of this study.

## 2 METHODOLOGY

### 2.1 Problem statement

The prediction of urban wind speed during TCs can be framed as a task where, given a series of wind speed measurements from the past  $P$  time steps  $X_P \in \mathbb{R}^{P \times C}$ , the wind speed for the future  $F$  time steps  $X_F \in \mathbb{R}^{F \times C}$  can be predicted by,

$$X_F = f(X_P) \quad (1)$$

where  $C$  represents the number of meteorological stations, and  $f(\cdot)$  denotes the deep learning-based models trained. Additionally, the meteorological station network can be described as a graph structure  $G = (V, E, A)$ , where  $V$  represents the nodes (the stations),  $E$  indicates the edges, and  $A$  denotes the adjacency matrix. The adjacency matrix is established based on the geographic distances between the stations.

### 2.2 Data source and processing

Hong Kong is located in the southeast of the Pearl River Estuary in southern China, facing the vast South China Sea to the south. It features a long coastline, with most of its low-lying areas concentrated along the coast. Additionally, Hong Kong has a high urbanization rate and is characterized by high-rise buildings, such as the International Finance Centre [22]. These urban and geographical characteristics make Hong Kong vulnerable to TCs [23]. In this study, urban wind speed data collected by 28 meteorological stations from the Hong Kong Observatory (HKO) is used to train and test model performance. It is important to note that the map and locations of the stations

shown in Figure 1 are for illustration purposes only; for official information, please refer to the HKO website. The 28 stations cover the main areas of Hong Kong and have maintained continuous data collection over a long period.



Figure 1. Schematic of distribution of meteorological stations.

The data is recorded at a 1-minute interval. A TC is considered to have an effect on Hong Kong if a TC signal has been issued by the HKO. Consequently, data from the entire lifecycle of each TC is extracted. The extracted data for the years 2000–2019 is used as the training set, for 2020–2021 as the validation set, and for 2022–2023 as the test set, as summarized in Table 1. Linear interpolation is employed to address missing data, while the mean and standard deviation are used for normalization and de-normalization.

Table 1. Summary of three data sets.

Data sets	No. of TCs	No. of samples	Rate
Training set	98	920,258	82%
Validation set	11	88,391	8%
Test set	10	115,210	10%

### 2.3 Model architecture

The model architecture is shown in Figure 2, and it is similar to the logic referenced in [21] [24]–[26]. However, urban wind speed is significantly influenced by TC intensity, which varies with climate change [27], as well as the distance between the TC location and the city. Therefore, this study incorporates long-term dependency, short-term dependency, and spatial dependency to effectively predict future 3-h urban wind speed during TCs using historical 3-h measurements from the meteorological station network. Specifically, both the input length and output horizon are set to 180.

**Patch embedding and positional encoding:** To improve computational efficiency, this study employs patch embedding to partition the input. Given the input  $X_P \in \mathbb{R}^{P \times N}$ , patch length  $L$  is used for patch embedding to obtain the patched sequence  $X^P \in \mathbb{R}^{L \times N \times C}$ , where  $N$  is the number of patched blocks. Positional encoding  $PE(\cdot)$  is added to the patched blocks using the commonly employed sinusoidal method in Transformer architectures [28], resulting in,

$$X_{enc} = X^P + PE(X^P) \quad (2)$$



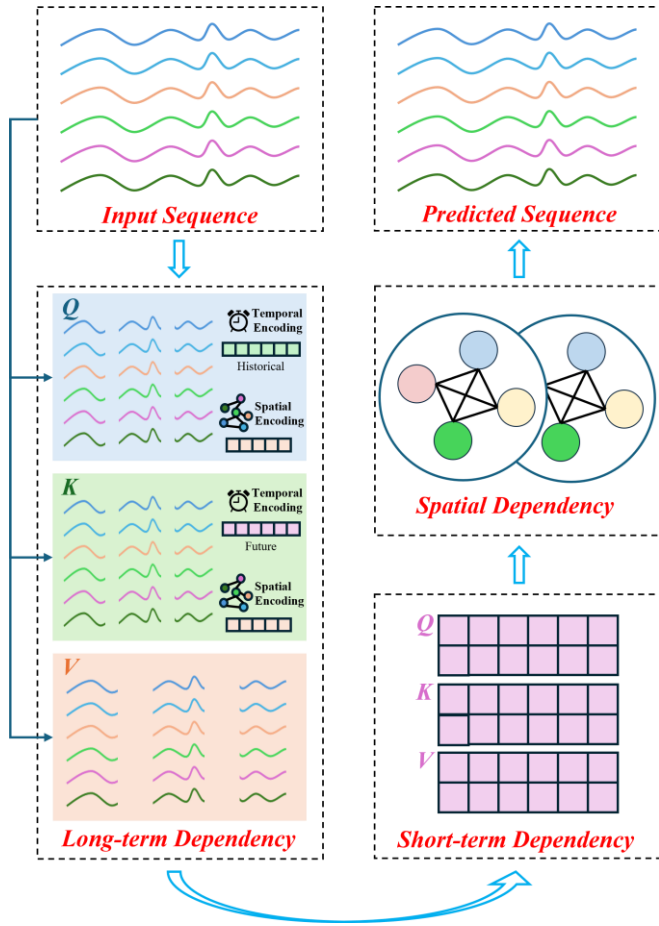


Figure 2. Overview of model architecture.

**Temporal encoding and spatial encoding:** Climate change [27] and the distance between the TC location and the city significantly influence TC intensity, which in turn affects urban wind speed. However, these factors are not explicitly incorporated into the training process. Regardless of climate change or distance, both are directly related to temporal evolution, which spans from days (for distance) to years (for climate change). Therefore, temporal encoding is necessary to account for both temporal scales.

In this study, temporal encoding is derived by considering various time components: the minute of the hour  $E^s$ , the hour of the day  $E^h$ , the day of the month  $E^d$ , the month of the year  $E^m$ , and the year  $E^y$ . This encoding embeds more time-related information using linear layers. The components of the temporal encoding are concatenated as follows,

$$E^T = \text{concat}[E^s, E^h, E^d, E^m, E^y] \quad (3)$$

where each  $E^s$ ,  $E^h$ ,  $E^d$ ,  $E^m$ , and  $E^y$  has a shape of  $L \times d/5$  (with  $d$  being the embedding dimension), resulting in a final temporal embedding  $E^T$  with shape  $L \times d$ .

Given that meteorological stations are located in various regions with different latitudes, longitudes, and altitudes, it is important to consider the spatial characteristics that may influence urban wind speed. In this study, spatial encoding is employed. Specifically, the normalized Laplacian matrix is calculated as,

$$\Delta = I - D^{-1/2}AD^{-1/2} \quad (4)$$

where  $I$  and  $D$  are the identity and degree matrices, respectively, and the adjacency matrix is calculated using the latitude, longitude, and altitude of each station. Following this, eigenvalue decomposition is performed as,

$$\Delta = U^T \Lambda U \quad (5)$$

where  $U$  and  $\Lambda$  are the eigenvector and eigenvalue matrices. The  $k$  smallest non-trivial eigenvectors are then used to generate the spatial encoding  $E^S \in \mathbb{R}^{C \times d}$  through linear transformation.

**Long-term dependency:** Based on the temporal and spatial encodings, temporal dependencies can be more effectively captured by the attention mechanisms of the Transformer architecture. It is important to note that the terms "long-term" and "short-term" differ from those used in the weather prediction field; they are merely used to distinguish between the different horizons considered in this study.

In addition to the long-term effects of climate change on urban wind speed, wind speed exhibits different characteristics across seasons, demonstrating periodic behavior [29]. Thus, long-term dependencies can be implicitly considered, as temporal information is encoded from minutely to yearly. Specifically, long-term dependency is addressed according to the temporal encoding as follows,

$$Q_l^h = w_{ql}^h(E_{his}^T + E^S) \quad (6)$$

$$K_l^h = w_{kl}^h(E_{fut}^T + E^S) \quad (7)$$

$$V_l^h = w_{vl}^h X_{enc} \quad (8)$$

where  $E_{his}^T$  is the temporal encoding derived from known historical temporal information, while  $E_{fut}^T$  is the temporal encoding derived from future temporal information. The attention mechanism, along with aggregation using the computed attention matrix, can be used to capture the long-term dependency as follows,

$$X_l^h = \text{softmax}\left(\frac{Q_l^h K_l^{hT}}{\sqrt{d_h}}\right) V_l^h \quad (9)$$

where  $w_{ql}^h$ ,  $w_{kl}^h$ , and  $w_{vl}^h$  are learnable parameters for heads  $h$ , and  $d_h$  is the scaling factor.

**Short-term dependency:** In addition to long-term dependency, urban wind speed during TCs may vary significantly within a short period as the TCs approach and make landfall in the city. Therefore, short-term dependency is also considered to capture these dynamics. The short-term dependency is addressed by the Transformer architecture based on the known sequence, enabling  $X_l^h$  to be used to derive the query, key, and value through commonly used linear layers as follows,

$$Q_s^h = w_{qs}^h X_l^h \quad (10)$$

$$K_s^h = w_{ks}^h X_l^h \quad (11)$$

$$V_s^h = w_{vs}^h X_l^h \quad (12)$$

where  $w_{qs}^h$ ,  $w_{ks}^h$ , and  $w_{vs}^h$  are learnable parameters. The short-term dependency can be computed as follows,

$$X_s^h = \text{softmax}\left(\frac{Q_s^h K_s^{hT}}{\sqrt{d_h}}\right) V_s^h \quad (13)$$

**Spatial dependency:** Spatial dependency is addressed using a graph convolutional neural network (GCN) as follows,

$$G = \delta[\alpha X_s + (1 - \alpha)(w_g \bar{A} X_s)] \quad (14)$$

where  $w_g$  are the learnable parameters and  $\bar{A}$  is the normalized adjacency matrix. After aggregating spatial information,  $\alpha$  balances the previous information with the aggregated information, and  $\delta$  is a function used to reduce overfitting.

Residual connections are then utilized as follows,

$$O^{(l)} = \text{SwiGLU}[\text{RMSN}(G^{(l)} + O^{(l-1)})] + G^{(l)} \quad (15)$$

where  $O^{(l)}$  and  $O^{(l-1)}$  represent the outputs of layer  $l$  and layer  $l-1$  of the aforementioned spatiotemporal dependency computation layer, respectively. Here, SwiGLU denotes the activation function, and RMSN represents the RMSNorm [30].

## 2.4 Experimental setup

In this study, three types of models are selected to compare their performance with the proposed model, representing three typical categories: statistical model, pure sequence-to-sequence models, and hybrid models combining GNN-RNN or GNN-Transformer architectures. The ARMA model is chosen as the baseline for statistical models, while LSTM, GRU, and vanilla Transformer models are selected as pure sequence-to-sequence models. For hybrid models, TGCN [26] is chosen for the GNN-RNN approach, and PDFormer [25] is selected for the GNN-Transformer approach.

The model setup for ARMA is derived from [16], where sensitivity analysis is performed. The configurations for TGCN and PDFormer follow the original papers [25] [26]. For GRU and LSTM, the number of RNN layers and embedding dimensions match those of TGCN [26], while the number of blocks and embedding dimensions for the Transformer align with the proposed model in this study. The specific configurations include an embedded dimension of 250, a Laplacian dimension for generating spatial encoding of 8, five heads for computing temporal dependency, a depth of 3 for spatiotemporal dependency computation, a drop rate of 0.1 for attention computation, and a linear drop rate within the range of [0, 0.1] for each depth.

## 2.5 Evaluation metrics

To evaluate the model's performance, three metrics are used: mean absolute error (MAE), root mean square error (RMSE), and the  $R^2$  score.

$$\text{MAE} = \frac{1}{n} \sum |y - \hat{y}| \quad (16)$$

$$\text{RMSE} = \sqrt{\frac{1}{n} \sum (y - \hat{y})^2} \quad (17)$$

$$R^2 = 1 - \frac{\sum (y - \hat{y})^2}{\sum (y - \bar{y})^2} \quad (18)$$

where  $y$ ,  $\hat{y}$ , and  $\bar{y}$  represent the target values, predicted values, and mean value of urban wind speed, respectively, while  $n$  denotes the total number of urban wind speed values. A lower MAE and RMSE signify superior model performance.

Additionally, a higher  $R^2$  score reflects improved model performance.

## 2.6 Optimization details

For each model, training is conducted three times, with the best result selected for performance evaluation. Each training session is set for a large number of epochs, and an early stopping mechanism is implemented to avoid overfitting. The batch size is set to 256, the learning rate is 0.0003, and *Adam* is employed as the optimizer. Mean squared error is chosen as the loss function. The programming is carried out using Python and PyTorch, with models trained on an RTX-6000 Ada GPU card featuring 48GB VRAM and 512GiB of system memory.

# 3 RESULTS AND DISCUSSIONS

## 3.1 Evaluation of model's performance

The model's performance is summarized in Table 2. It is evident that the conventional statistical model struggles to deliver reliable predictions in scenarios involving extreme wind speeds across the entire network of stations. The MAE of the ARMA model is approximately three times greater than that of the other deep learning models listed in Table 2, while the RMSE for ARMA is five times larger than that of the other models. Additionally, the  $R^2$  score indicates that the predicted results exhibit greater fluctuations compared to those generated by the deep learning models.

Table 2. Summary of model's performance.

Models	MAE	RMSE	$R^2$
ARMA	3.230	7.600	0.6539
LSTM	1.103	1.593	0.8638
GRU	0.990	1.464	0.8849
Transformer	0.909	1.376	0.8985
TGCN	0.919	1.372	0.8989
PDFormer	0.914	1.360	0.9007
Proposed	0.902	1.348	0.9026

Regarding the sequence-to-sequence models, the results indicate that the Transformer outperforms the other two models (GRU and LSTM) across all metrics, including MAE, RMSE, and  $R^2$  score. This demonstrates the Transformer's superior ability to capture temporal dependencies. However, compared to the GNN-RNN and GNN-Transformer hybrid models, the pure sequence-to-sequence models tend to yield less reliable predictions. This suggests that spatial dependencies are not adequately addressed in these models, leading to decreased performance. Notably, both LSTM and GRU exhibit larger errors compared to TGCN and PDFormer. While the Transformer has a smaller MAE, it also shows a larger RMSE and a lower  $R^2$  score compared to the two hybrid models. This indicates that, despite the Transformer's average performance being slightly better than that of TGCN and PDFormer, it may be less effective in predicting extreme values.

Regarding the hybrid models, the proposed model demonstrates superior performance in predicting urban wind speed across all metrics. It exhibits smaller errors compared to the other two hybrid models that also incorporate spatial dependency computation, as well as the pure sequence-to-sequence models. Notably, while TGCN and PDFormer have larger MAE values than the Transformer, the proposed model achieves smaller error rates than all other models listed in Table

2. This highlights the effectiveness of the proposed model in addressing both temporal and spatial dependencies in urban wind speed prediction.

### 3.2 Ablation study

To illustrate the role of the modules in the proposed model, an ablation study is conducted. The first experiment (Delete-LTD) involved removing the long-term dependency module, the second experiment (Delete-STD) removed the short-term dependency module, and the third experiment (Delete-SD) eliminated the spatial dependency module. In these three additional experiments, all other components (except for the deleted modules) are maintained exactly as in the proposed model (Full). The MAE, RMSE, and  $R^2$  scores from these experiments are presented in Figure 3.

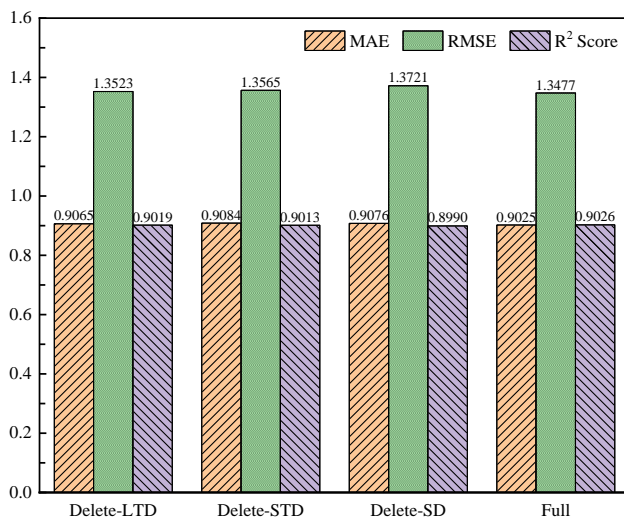


Figure 3. Performance comparison of ablation study experiments.

The results indicate that removing any component from the proposed model leads to a decrease in performance based on the evaluation metrics. This finding clarifies the contributions of each module to the overall effectiveness of the model, underscoring the significance of long-term, short-term, and spatial dependencies in achieving accurate predictions. Each module plays a crucial role in enhancing the model's ability to capture the complexities of urban wind speed dynamics.

When the GNN module is removed, the model resembles the vanilla Transformer, resulting in the outcome of experiment Delete-SD being closer to that of the vanilla Transformer listed in Table 2. However, the result of experiment Delete-SD is slightly better than the vanilla Transformer. This can be explained by the fact that the vanilla Transformer primarily focuses on correlations within the known sequence (the short-term dependencies in this study). When both short-term and long-term dependencies are incorporated, the performance improves slightly. On the other hand, the experiment Delete-SD does not perform as well as the proposed model due to the absence of the GNN module. This highlights the importance of the GNN in enhancing the performance of urban wind speed prediction. The presence of the GNN significantly contributes to capturing the spatial dependencies, resulting in more accurate predictions.

In the experiments Delete-LTD and Delete-STD, the results are similar, but neither provides better predictions than the proposed model. This indicates that both long-term and short-term dependencies are crucial for achieving accurate predictions. Furthermore, the results of these two experiments are better than those of the Delete-SD experiment, which further underscores the importance of spatial dependency in enhancing model performance. This highlights the necessity of integrating all three types of dependencies for optimal prediction accuracy in urban wind speed prediction.

### 3.3 Case study

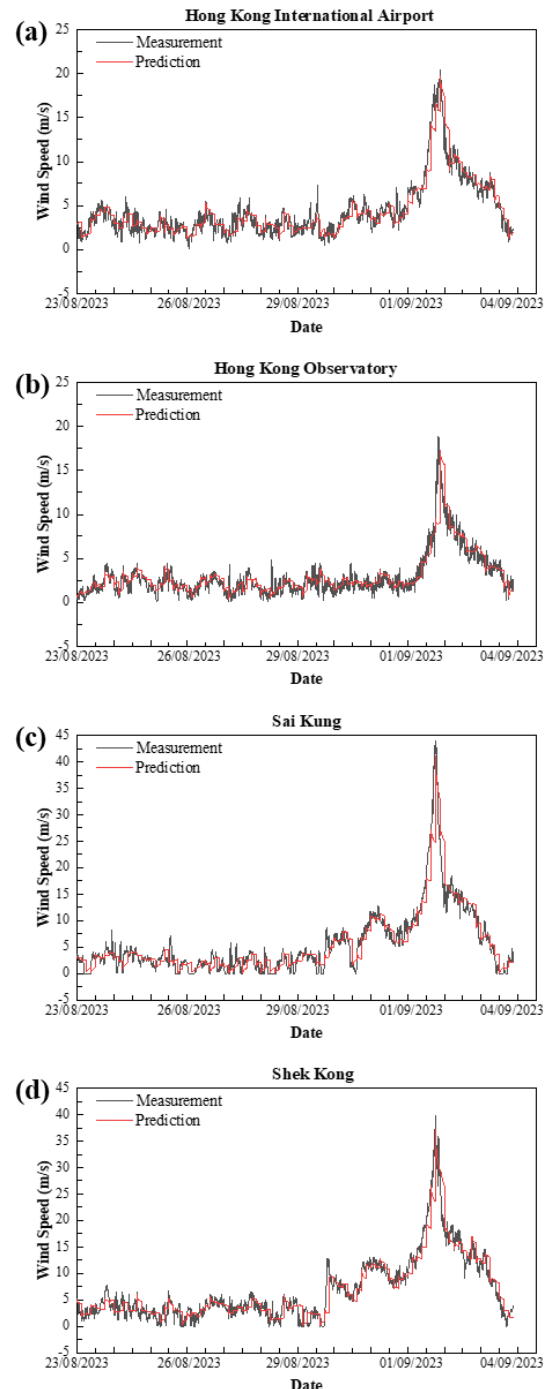


Figure 4. Wind speed prediction of four stations during Typhoon Saola.



To illustrate predicted urban wind speeds, two case studies are conducted: Typhoon Saola and Typhoon Koinu. Saola, the third TC in Hong Kong in 2023, prompted signal No. 10, the first since Super Typhoon Mangkhut in 2018. Koinu triggered signal No. 9 and brought heavy rain, with 369.7 millimeters recorded—over three times the normal monthly total and the highest daily rainfall for October.

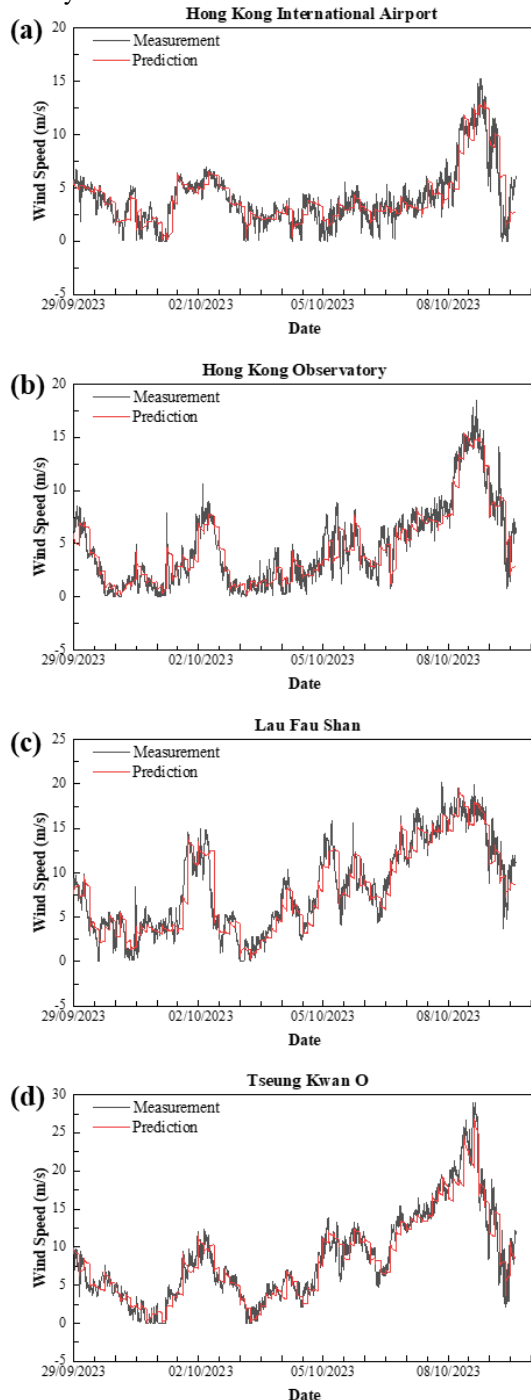


Figure 5. Wind speed prediction of four stations during Typhoon Koinu.

For Typhoon Saola, four stations—Hong Kong International Airport (HKA), HKO, Sai Kung, and Shek Kong—are selected to illustrate the predicted wind speed, as shown in Figure 4. The selection of these stations is based on two key principles: first, HKA and HKO were chosen for their strategic locations;

second, the remaining stations were selected due to their relatively higher measured wind speed during the cyclone, with an emphasis on decentralization. Similarly, for Typhoon Koinu, HKA, HKO, Lau Fau Shan, and Tseung Kwan O were selected to represent the predicted wind speed, as depicted in Figure 5.

The proposed model demonstrates strong predictive capabilities for the two selected cases. The trends in the predictions align closely with the target measurements, even as wind speeds increase when the TCs approach Hong Kong. However, it is evident that the model tends to underestimate the peak values, which may be attributed to the inherent tendency of neural networks to produce smoother outputs—a phenomenon commonly observed in many deep learning models. Additionally, the results for Typhoon Saola are more consistent with the measurements than those for Typhoon Koinu. This discrepancy may be partially due to the fewer local peaks observed during Typhoon Saola, as well as the model's limitations in effectively capturing peak wind speeds.

#### 4 CONCLUSIONS

In this study, a novel deep learning-based spatiotemporal model is proposed for predicting urban wind speed during TCs. The following key conclusions can be drawn:

- The proposed model achieves better prediction accuracy compared to the statistical model and pure sequence-to-sequence models, with a MAE of 0.902. This represents a 0.78% improvement over the vanilla Transformer, a 9.76% improvement over GRU, and a 22.28% improvement over LSTM. Additionally, it outperforms GNN-RNN and GNN-Transformer hybrid models by more than 1%.
- The vanilla Transformer demonstrates potential in predicting urban wind speed during TCs. The proposed model's integration of long-term, short-term, and spatial dependencies significantly enhances its performance compared to the vanilla Transformer. This improvement underscores the importance of considering various types of dependencies in achieving more accurate predictions in complex environments like urban areas during TCs.
- The proposed model effectively captures the trends in urban wind speed during TCs. Specific case studies reveal strong performance in predicting peak values for Typhoon Saola; however, some smoother predictions were observed for Typhoon Koinu.

#### ACKNOWLEDGMENTS

This work was supported by the Research Grants Council of the Hong Kong Special Administrative Region, China (Grant No. T22-501/23-R), and the Innovation and Technology Commission of the Hong Kong Special Administrative Region, China (Grant No. K-BBY1). The authors would like to express their gratitude for the computing platform provided by the University Research Facility in Big Data Analytics (UBDA) at The Hong Kong Polytechnic University, as well as for the data supplied by the Hong Kong Observatory, which was used solely for research purposes.

## REFERENCES

- [1] J. Ngarambe, J. W. Oh, M. A. Su, M. Santamouris, G. Y. Yun, Influences of wind speed, sky conditions, land use and land cover characteristics on the magnitude of the urban heat island in Seoul: An exploratory analysis, *Sustainable Cities and Society*, 71 (2021) 102953.
- [2] S. J. Low, V. S. Raghavan, H. Gopalan, J. C. Wong, J. Yeoh, C. C. Ooi, FastFlow: AI for fast urban wind velocity prediction, 2022 IEEE International Conference on Data Mining Workshops (ICDMW), 2022.
- [3] L. Zheng, W. Lu, Q. Zhou, Weather image-based short-term dense wind speed forecast with a ConvLSTM-LSTM deep learning model, *Building and Environment*, 239 (2023) 110446.
- [4] G. Liu, X. Wang, Q. Wu, D. Fang, Z. Wu, H. Liu, M. Lyu, Effect of urbanization on gust wind speed in summer over an urban area in Eastern China, *Environmental Research Letters*, 18 (7) (2023) 074025.
- [5] J. W. Wang, H. J. Yang, J. J. Kim, Wind speed estimation in urban areas based on the relationships between background wind speeds and morphological parameters, *Journal of Wind Engineering and Industrial Aerodynamics*, 205 (2020) 104324.
- [6] J. Allegrini, V. Dorer, J. Carmeliet, Influence of morphologies on the microclimate in urban neighbourhoods, *Journal of Wind Engineering and Industrial Aerodynamics*, 144 (2015) 108-117.
- [7] Y. Abbassi, H. Ahmadikia, E. Baniasadi, Impact of wind speed on urban heat and pollution islands, *Urban Climate*, 44 (2022) 101200.
- [8] P. Peduzzi, B. Chatenoux, H. Dao, A. De Bono, C. Herold, J. Kossin, F. Mouton, O. Nordbeck, Global trends in tropical cyclone risk, *Nature Climate Change*, 2 (4) (2012) 289-294.
- [9] Y. Hao, W. Yang, K. Yin, Novel wind speed forecasting model based on a deep learning combined strategy in urban energy systems, *Expert Systems with Applications*, 219 (2023) 119636.
- [10] Y. Zhang, S. Cao, L. Zhao, J. Cao, A case application of WRF-UCM models to the simulation of urban wind speed profiles in a typhoon, *Journal of Wind Engineering and Industrial Aerodynamics*, 220 (2022) 104874.
- [11] F. Salamanca, A. Martilli, M. Tewari, F. Chen, A study of the urban boundary layer using different urban parameterizations and high-resolution urban canopy parameters with WRF, *Journal of Applied Meteorology and Climatology*, 50 (5) (2011) 1107-1128.
- [12] J. Wang, L. Wang, R. You, Evaluating a combined WRF and CityFFD method for calculating urban wind distributions, *Building and Environment*, 234 (2023) 110205.
- [13] R. Kadaverugu, V. Purohit, C. Matli, R. Biniwale, Improving accuracy in simulation of urban wind flows by dynamic downscaling WRF with OpenFOAM, *Urban Climate*, 38 (2021) 100912.
- [14] Y. Miao, S. Liu, B. Chen, B. Zhang, S. Wang, S. Li, Simulating urban flow and dispersion in Beijing by coupling a CFD model with the WRF model, *Advances in Atmospheric Sciences*, 30 (6) (2013) 1663-1678.
- [15] Z. Guo, Y. Dong, J. Wang, H. Lu, The forecasting procedure for long-term wind speed in the Zhangye area, *Mathematical Problems in Engineering*, 2010 (1) (2010) 684742.
- [16] E. Grigonytė, E. Butkevičiūtė, Short-term wind speed forecasting using ARIMA model, *Energetika*, 62 (1-2) (2016).
- [17] H. Liu, H. Tian, Y. Li, An EMD-recursive ARIMA method to predict wind speed for railway strong wind warning system, *Journal of Wind Engineering and Industrial Aerodynamics*, 141 (2015) 27-38.
- [18] Z. Huang, M. Gu, Characterizing nonstationary wind speed using the ARMA-GARCH model, *Journal of Structural Engineering*, 145 (1) (2019) 04018226.
- [19] M. Yaghoubirad, N. Azizi, M. Farajollahi, A. Ahmadi, Deep learning-based multistep ahead wind speed and power generation forecasting using direct method, *Energy Conversion and Management*, 281 (2023) 116760.
- [20] C. Yu, G. Yan, C. Yu, X. Liu, X. Mi, MRformer: A multi-resolution interactive transformer for wind speed multi-step prediction, *Information Sciences*, 661 (2024) 120150.
- [21] Z. Chen, B. Zhang, C. Du, W. Meng, A. Meng, A novel dynamic spatio-temporal graph convolutional network for wind speed interval prediction, *Energy*, 294 (2024) 130930.
- [22] C. Song, C. Sun, J. Xu, F. Fan, Establishing coordinated development index of urbanization based on multi-source data: A case study of Guangdong-Hong Kong-Macao Greater Bay Area, China, *Ecological Indicators*, 140 (2022) 109030.
- [23] W. Chen, S. Yang, Z. Wu, F. Cai, Large-scale atmospheric features favoring the tropical cyclone activity affecting the Guangdong-Hong Kong-Macao Greater Bay Area of China, *Environmental Research Letters*, 17 (10) (2022) 104057.
- [24] Z. Li, L. Xia, L. Shi, Y. Xu, D. Yin, C. Huang, Opencity: Open spatio-temporal foundation models for traffic prediction, *arXiv preprint arXiv:2408.10269*, (2024).
- [25] J. Jiang, C. Han, W. X. Zhao, J. Wang, PDFformer: Propagation delay-aware dynamic long-range transformer for traffic flow prediction, *Proceedings of the AAAI conference on artificial intelligence*, 2023.
- [26] L. Zhao, Y. Song, C. Zhang, Y. Liu, P. Wang, T. Lin, M. Deng, H. Li, T-GCN: A temporal graph convolutional network for traffic prediction, *IEEE Transactions on Intelligent Transportation Systems*, 21 (9) (2019) 3848-3858.
- [27] I. J. Moon, S. H. Kim, J. C. Chan, Climate change and tropical cyclone trend, *Nature*, 570 (7759) (2019) E3-E5.
- [28] A. Vaswani, N. Shazeer, N. Parmar, J. Uszkoreit, L. Jones, A. N. Gomez, Ł. Kaiser, I. Polosukhin, Attention is all you need, *Advances in neural information processing systems*, 2017.
- [29] I. Deligiannis, P. Dimitriadis, O. Daskalou, Y. Dimakos, D. Koutsogiannis, Global investigation of double periodicity of hourly wind speed for stochastic simulation; Application in Greece, *Energy Procedia*, 97 (2016) 278-285.
- [30] N. Shazeer, GLU variants improve Transformer, *arXiv preprint arXiv:2002.05202*, (2020).



# Intelligent Sensing and Safety Assessment of Bridge Cluster Service Performance



# Graph network representation and intelligent evaluation for service performance of bridge clusters

Shunlong Li<sup>1\*</sup>, Jie Wang<sup>2</sup>

<sup>1</sup>School of Transportation Science and Engineering, Harbin Institute of Technology, 73 Huanghe Road, 150090 Harbin, China

<sup>2</sup>School of Transportation Engineering, East China Jiaotong University, 330013 Nanchang, China

email: lishunlong@hit.edu.cn, [wangjihit@163.com](mailto:wangjihit@163.com)

**ABSTRACT:** As the most vulnerable part of the infrastructure transportation network, bridges will inevitably encounter problems such as aging and degradation throughout their entire service life [1]. The maintenance costs for all bridges within the region are increasing year by year [2]. When the financial conditions are insufficient to fully cover the costs, many domestic provinces and cities adopt the maintenance and repair plans based on single bridges relying on experience and the "fire-fighting" post-event repair mode [3]. There are few scientific management models that focus on the overall service performance of the regional bridge clusters. This leads to either excessive or insufficient detection and maintenance. Therefore, there is an urgent need for a systematic intelligent assessment framework for existing bridge clusters. However, current research on service performance evaluation and prediction for large-scale bridge networks suffers from multiple limitations, such as limited research objects, simplified modeling forms, difficulty in quantitative assessment, generalized prediction outcomes, and insufficient consideration of maintenance decision-makings [4].

Therefore, this study focuses on graph network representation and intelligent evaluation for service performance of bridge clusters. Firstly, a systematic comparative analysis of two distinct graph network representation methodologies (undirected and directed network) is conducted based on actual bridge cluster cases of different scales. Secondly, tailored intelligent assessment frameworks of vulnerability are developed for each representation. Finally, benchmarking against evaluation outcomes reveals critical performance differentials across methodologies. This work thus establishes a theoretical foundation for intelligent operation and maintenance strategies in bridge network management.

## (1) For the undirected graph network representation methodology

As shown in Figure 1, the National highway (NH) network in the northeast of China connects 11 cities and 37 counties, and has 1772 bridges. It can be seen that the bridge assessment states are unevenly distributed. Funds for maintaining expressway bridges are abundant, and thus such bridges are in relatively good condition. Meanwhile, ordinary highway bridges, especially in poverty-stricken counties near the border, are underfunded.



Figure 1. NH network with evaluated bridges.

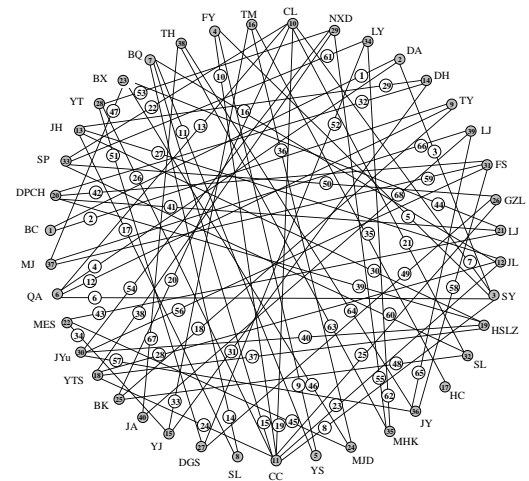


Figure 2. modelling result of the NH bridge network.

As a bridge network contains a significant amount of information, modelling a large-scale bridge network is complex. In this study, a undirected bridge network can be treated as an overlay of a topological graph and the corresponding information network. The nodes and edges in the topological graph of a bridge network represent intersections (or cities) and highways between nodes, respectively. Regarding the information group, a bridge network should contain the properties of nodes and edges, including the city (or node) name, the actual length of each edge (or NH) between nodes, and the assessment state of bridges on each edge. The NH bridge network is established as shown in Figure 2.

The intelligent assessment framework for the undirected bridge network adopts vulnerability as an indicator, utilizing backward thinking to evaluate network resilience. It methodology intentionally disrupts a portion of the network and quantifies

component importance by comparing pre- and post-damage performance indices. In detail, the proposed vulnerability index accounts for both bridge failures and their impact on bridge network performance from a probabilistic perspective. Additionally, the probability of bridge network connectivity, denoted as  $P(C)$ , is used to evaluate the performance of bridge networks with unreliable components. Therefore, the vulnerability index of the  $i$ th bridge  $V_{bridge}(i)$  and the bridge network  $V_{network}(G)$  are defined as:

$$V_{bridge}(i) = [P(C) - P(C | \bar{B}_i)] P(\bar{B}_i) \quad (1)$$

$$V_{network}(G) = \sum_{B_i \in G} [P(C) - P(C | \bar{B}_i)] P(\bar{B}_i) \quad (2)$$

Herein,  $G$  represents the undirected bridge network, and  $C$  and  $\bar{C}$  indicate the events of the bridge network being connected and disconnected, respectively.  $B_i$  and  $\bar{B}_i$  indicate the event of the  $i$ th bridge safety and failure, respectively.  $P(\bar{B}_i)$  and  $P(C | \bar{B}_i)$  are the  $i$ th bridge failure probability and the network connectivity probability given the  $i$ th bridge failure, respectively. Evidently,  $P(C | \bar{B}_i)$  demonstrates the effect of a bridge failure on network connectivity performance from a probabilistic view. The results indicate that vulnerability index of the NH bridge network is  $4.80 \times 10^{-3}$ , and the vulnerability of each equivalent bridge in the NH bridge network is shown in Figure 3. This approach effectively identifies critical bridges that elude detection by conventional indicators, a finding that should be emphasized in the future maintenance strategies formulated by the provincial management department.

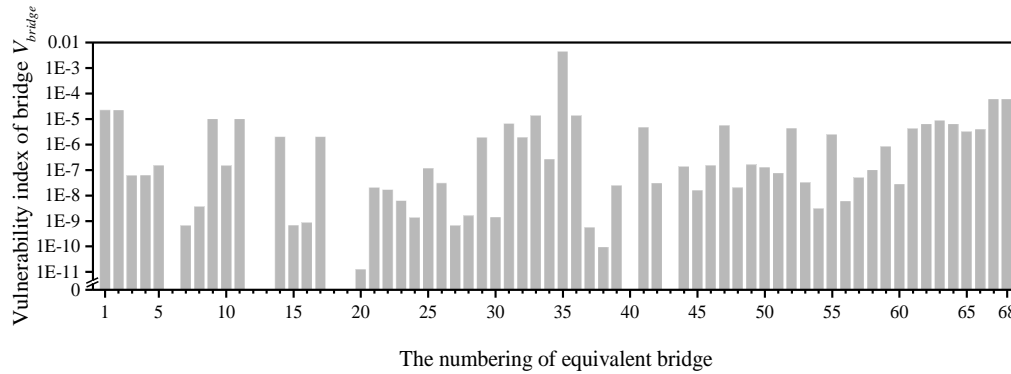


Figure 3. Vulnerability index of each equivalent bridge in the undirected NH bridge network.

## (2) For the directed graph network representation methodology

As shown in Figure 4, it considered a city located in the southern part of the Yangtze River Delta, China. As an important economic centre, a well-functioning transportation network is the foundation of regional economic development. Therefore, based on the inspection information of 299 actual bridges in the city, the directed bridge network was established by fully considering the direction of the streets (one- or two- way street) and bridge types (single- or double- deck bridge) between all nodes in the urban city. As shown in Figure 5, the topological model contained 63 nodes and 216 directed edges, including 107 two-way edge pairs and two one-way edges are constructed.

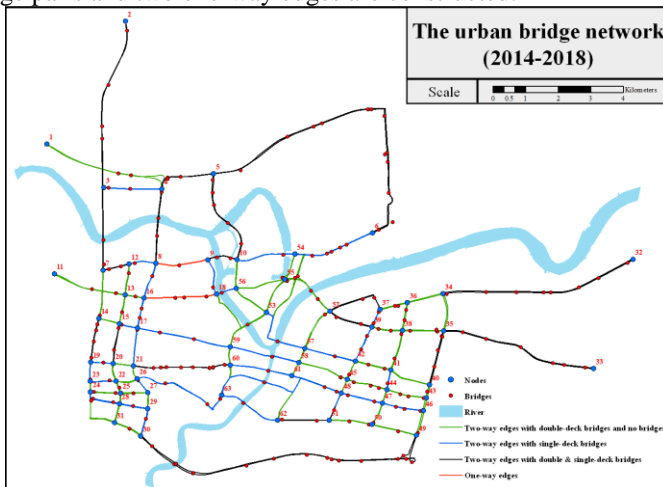


Figure 4. Physical location of the bridge network.

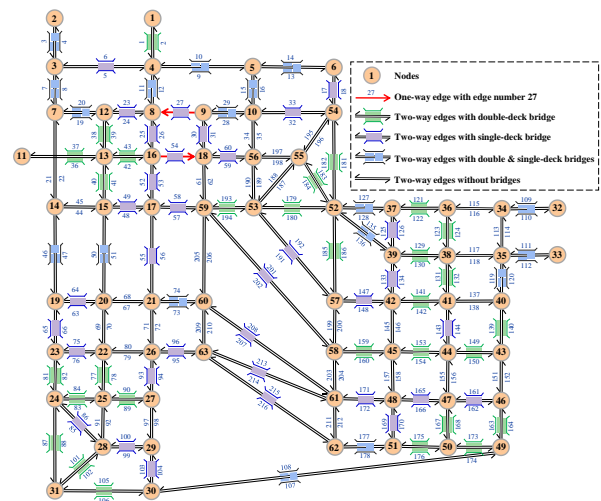


Figure 5. modelling result of the directed bridge network.

To describe the different edge dependencies in the directed bridge network, an extended network model and importance index  $\gamma(i, j)$  is proposed, and simulation methods are applied to calculate the results.

$$G_{\text{extended}} = (V, E_1, E_2, \dots, E_m) \quad (3)$$

$$\begin{aligned} \gamma(e_{i \rightarrow j}) &= P(G, \bar{e}_{i \rightarrow j}) = P(G | \bar{e}_{i \rightarrow j}) P(\bar{e}_{i \rightarrow j}) = \frac{\text{Num}(G | \bar{e}_{i \rightarrow j})}{N} P(\bar{e}_{i \rightarrow j}), m=1, 2, 3 \\ \gamma(e_{i \rightarrow j}) &= P(G, \bar{e}_{i \rightarrow j}, e_{j \rightarrow i}) + P(G, \bar{e}_{i \rightarrow j}, \bar{e}_{j \rightarrow i}) \\ &= P(G | \bar{e}_{i \rightarrow j}, e_{j \rightarrow i}) P(\bar{e}_{i \rightarrow j}, e_{j \rightarrow i}) + P(G | \bar{e}_{i \rightarrow j}, \bar{e}_{j \rightarrow i}) P(\bar{e}_{i \rightarrow j}, \bar{e}_{j \rightarrow i}) \\ &= \frac{\text{Num}(G | \bar{e}_{i \rightarrow j}, e_{j \rightarrow i})}{N} P(\bar{e}_{i \rightarrow j}, e_{j \rightarrow i}) + \frac{\text{Num}(G | \bar{e}_{i \rightarrow j}, \bar{e}_{j \rightarrow i})}{N} P(\bar{e}_{i \rightarrow j}, \bar{e}_{j \rightarrow i}), m=4, 5, 6 \end{aligned} \quad (4)$$

where  $\text{Num}(G | \cdot)$  represents the number of connected states to the bridge network, given the state of edge  $e_{i \rightarrow j}$  or edge pair  $(e_{i \rightarrow j}, e_{j \rightarrow i})$  in  $N$  samples.

Figure 8 shows the importance ranking of all edges (equivalent bridges) with non-zero failure probability in the directed bridge network during 2018. It can be observed that the importance of the upstream and downstream edges of an edge pair is not equal. It is related to the position and direction of the edge and the failure probabilities of single- and double-deck bridges. It is proved that the proposed index can effectively distinguish the relative importance of all edges in a network, thereby providing important guidelines for the designing novel network-level maintenance strategies.

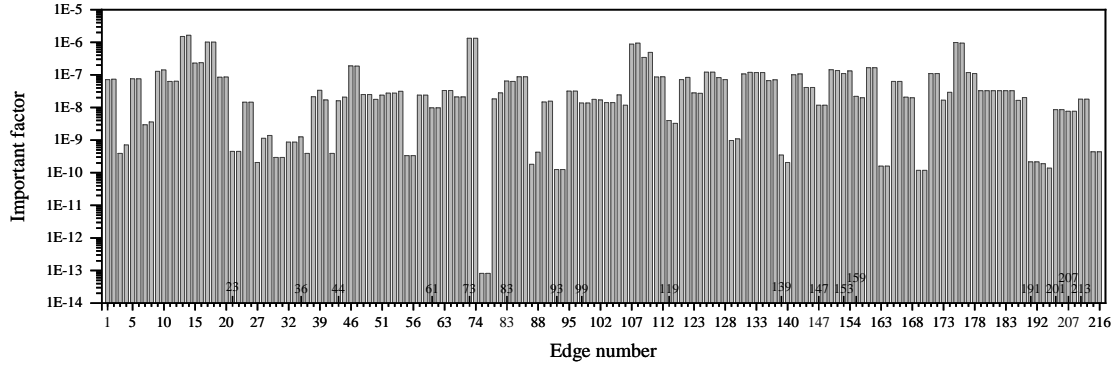


Figure 6. Important index of the directed urban bridge network.

**KEY WORDS:** Bridge clusters; Service performance; Graph network representation; Intelligent evaluation.

## REFERENCES

- [1] Frangopol, D. M., & Bocchini, P. (2012). Bridge network performance, maintenance and optimisation under uncertainty: accomplishments and challenges. *Structure and Infrastructure Engineering*, 8(4), 341-356.
- [2] Fiorillo G, Ghosn M. Risk-based life-cycle analysis of highway bridge networks under budget constraints. *Structure and Infrastructure Engineering*. 2022;18:1457-71.
- [3] Liu, D. (2009). Probability-based network-level performance assessment of exiting bridges. (master's thesis). Hnnan University, Changsha, China.
- [4] Wang X, Dai J Y, Liu X. A spatial-temporal neural network based on ResNet-Transformer for predicting railroad broken rails[J]. *Advanced Engineering Informatics*, 2025, 65: 103126.



# Lightweight vision fundamental model-based structural surface crack segmentation using model distillation

Yapeng Guo<sup>1</sup>, Shunlong Li<sup>2</sup>

<sup>1</sup>School of Transportation Science and Engineering, Harbin Institute of Technology, 150090 Harbin, China  
email: guoyapeng@hit.edu.cn, lishunlong@hit.edu.cn

**ABSTRACT:** Vision fundamental models demonstrate considerable competitiveness in structural surface crack segmentation due to their strong generalization ability. Vision fundamental models improve the fitting capacity for various objects by increasing image encoder complexity. However, for crack segmentation, the excessive number of these parameters leads to slow running speeds and large space occupation. This paper presents a lightweight Segment Anything Model (SAM)-based crack segmentation method using model distillation technology, aiming for consistent crack image embedding. Firstly, end-to-end automatic crack segmentation is achieved by modifying the SAM model through the addition of a crack segmentation head. Secondly, model distillation is employed to transfer features from the heavy-parametric encoder in SAM with minimal loss. Comparative analysis of cutting-edge crack segmentation techniques across eight frequently utilized datasets demonstrates their effectiveness and precision. The findings reveal the potential of mobile deployment of civil structure damage identification based on vision fundamental models.

**KEY WORDS:** Crack segmentation, vision fundamental model, model distillation, lightweight, deep learning, bridge damage

## 1 INTRODUCTION

Crack is a kind of critical apparent damages in civil structures, and crack identification serves as a fundamental basis for evaluating structural condition and determining maintenance strategies [1,2]. Currently, structural surface crack identification heavily relies on visual inspection by engineers, which suffers from limitations such as low efficiency and subjectivity. To address this issue, researchers have started to replace human eye inspection with visible light cameras, enabling the automatic identification of cracks through the acquisition of structural visual images and the design of corresponding algorithms. Common methods of image acquisition include portable digital cameras, fixed monitoring systems, smartphones, unmanned aerial vehicles, climbing or underwater robots, etc., which significantly reduce the cost and risk associated with obtaining apparent structural information [3,4].

After obtaining structural visual images, researchers employ digital image processing algorithms for structural surface crack identification. Considering the impressive advancements of deep learning (DL) in various fields, there is a gradual shift within the field of crack identification towards automatic feature extraction utilizing deep learning models [5,6]. Researchers have employed DL-based object classification algorithms to classify multiple patches cut from crack images to judge the presence or absence of cracks, achieving patch-wise crack identification [7-9]. Another important direction in this type of research is using DL-based object detection algorithms to find crack locations in crack images automatically, enabling box-wise crack identification [10-13]. However, the accuracy of patch-wise and box-wise crack identification may not meet the requirements for assessing the apparent condition of structures. As a result, DL-based pixel-

wise crack identification (i.e., crack segmentation), has emerged to address this limitation.

DL-based crack segmentation methods can be categorized into two main groups: convolutional neural network (CNN)-based and transformer-based. CNN-based crack segmentation mainly employs "encoder-decoder" architecture, including fully convolutional network (FCN) and its variants, as well as generative adversarial network (GAN). For FCN, Li et al. [14] proposed using FCN for pixel-to-pixel segmentation of various damages in civil structures. Chen and Jahanshahi [15] developed a rotation-invariant FCN to explicitly consider the rotational invariance of crack images. Hoskerc et al. [16,17] introduced a FCN-based multi-class semantic segmentation approach using multi-task learning, which achieved better results than training multiple tasks independently for multi-type structural materials and defects. To address the high noise and background interference in pavement crack images, Huyen et al. [18] established the CrackU-net framework with a modification on U-net, which also addressed the false-positive crack detection issue. Jiang et al. [19] applied attention mechanisms to U-net for detecting corrosion defects in steel box girders. Liu et al. [20] introduced a framework for concrete crack segmentation and quantitative calculation that considers the weight of crack boundaries. Xiang et al. [21] proposed a crack image augmentation method using active learning to enhance the accuracy of crack segmentation methods. Nguyen et al. [22] discussed the influence of different training loss functions using U-net on different crack datasets. Xu et al. [23] proposed a limited-supervised deep learning framework for damage segmentation (including cracks) using meta learning based on U-net.

For GAN, Zhang et al. [24] aimed to address the severe imbalance between cracks and backgrounds with a crack-patch-only GAN framework. Kim et al. [25] tackled the issue of data

scarcity in detecting cracks in steel structures using laser thermography for data augmentation by employing GAN. Similarly, to overcome the issue of limited training data, Ma et al. [26], Jin et al. [27], Li and Zhao [28], as well as Zhang et al. [29], utilized various variants of GAN to generate various crack images.

Transformer models have demonstrated significant progress in vision-based crack segmentation. Shamsabadi et al. [30] introduced Vision Transformer (ViT) into this area and attained higher detection accuracy in asphalt and concrete surface crack segmentation than CNNs. Wang and Su [31] developed a multi-level structure Transformer as an encoder to output multi-level features and fuse different levels of features. Ding et al. [32] analyzed the characteristics of crack recognition and proposed a boundary refinement Transformer for automatic segmentation of crack images obtained by drones. Guo et al. [33] used Swin Transformer to encode road crack images and employed UperNet to generate segmentation results. Tong et al. [34] combined Dempster-Shafer theory and Transformer network to construct a crack segmentation framework considering uncertainty and proposed a corresponding training strategy. Zhang et al. [35] proposed a segmentation Transformer framework called ShuttleNet v2, which can detect not only cracks but also multiple other diseases simultaneously. Furthermore, the amalgamation of CNNs' local modeling capability and Transformers' global modeling capability to build more powerful crack segmentation models is also an important research direction. Zhou et al. [36] fused Swin Transformer blocks and inverse residual blocks based on Deeplab v3 plus framework and combined channel attention mechanism to improve crack segmentation accuracy.

With the emergence of vision fundamental models, the inherent paradigm of object segmentation has been disrupted. These vision fundamental models, characterized by a massive number of network parameters and extensive training data, exhibit unprecedented robust generalization capabilities, allowing for precise segmentation of most common objects in zero-shot and few-shot forms [37]. However, when applied to crack segmentation tasks, vision fundamental models face two primary issues: (1) the need for specific prompts during application or a lack of semantic information for automatic segmentation; (2) the excessive number of network parameters in vision fundamental models leads to slow segmentation speeds and deployment difficulties in hardware-constrained environments.

This paper's primary goal is to significantly lighten the vision fundamental model while preserving its strong generalization ability, to achieve precise and efficient segmentation of cracks. To achieve this objective, this paper proposes the following two innovative approaches: (1) modifying SAM structure by adding a crack segmentation head to incorporate semantic information for automatic segmentation, and (2) utilizing model distillation techniques to substantially reduce the parameters of SAM and significantly improve its running speed, with only acceptable loss in segmentation accuracy.

This paper's primary contributions are twofold: (1) it represents an early attempt to apply vision fundamental models to automatic crack segmentation, providing a feasible approach for the application of such models in civil engineering, thereby offering valuable reference results for future research; (2) it

verifies the feasibility of lightweighting crack segmentation networks based on vision fundamental models, enabling effective transfer of the powerful generalization ability of these models under hardware-constrained conditions.

The remaining content of this paper are structured as follows. Section 2 provides an overview of the advancements in DL-based crack segmentation. Section 3 delves into the intricate framework of the proposed lightweight vision fundamental model-based crack segmentation approach. Section 4 outlines the implementation specifics. Section 5 offers the testing results under both full supervision and limited supervision, as well as the results evaluated on hardware-constrained platforms. Lastly, Section 6 concludes the paper.

## 2 METHODOLOGY

The proposed lightweight vision fundamental model-based crack segmentation method comprises a lightweight crack encoder and a crack segmentation head (shown in Figure 1). The former extracts the robust features of the crack image to generate crack image embeddings, while the latter uses high-quality embedding to complete pixel-level crack segmentation. The lightweight crack encoder's initialization weight originates from the SAM original heavy-parametric vision fundamental model through the utilization of model distillation technology (using common object segmentation dataset), the distillation objective is set to minimize the embedding difference of the image after the encoder. Finally, the crack segmentation model proposed here undergoes fine-tuning using the crack dataset.

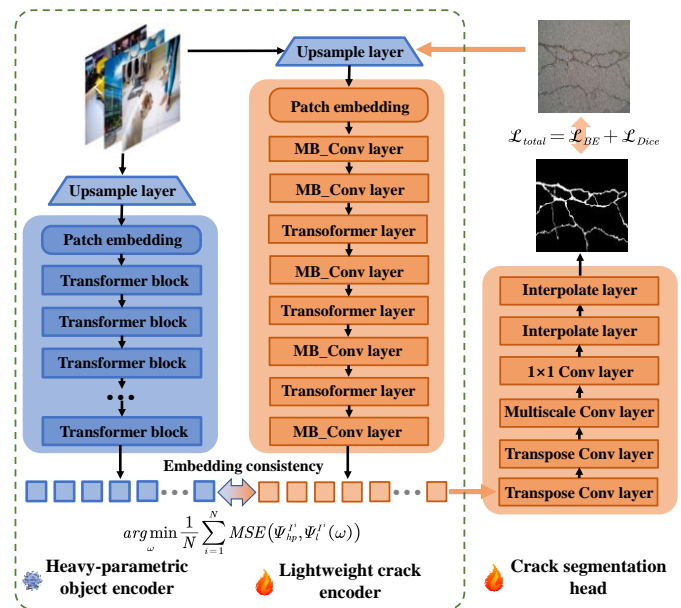


Figure 1. Overall architecture of the lightweight vision fundamental model-based crack segmentation method.

### 2.1 Lightweight crack encoder using model distillation

The heavy parameter encoder in SAM adopts the ViT model. To ensure the uniformity of the architecture, this study uses the lightweight TinyViT [38] as the crack encoder. TinyViT adopts a hierarchical vision transformer, serving as the foundational architecture, which can better integrate multiscale features for downstream tasks. TinyViT comprises four stages, leading to a gradual reduction in the resolution of the feature map. Each

stage includes a feature extraction (FE) layer and a down-sampling (DS) layer. The FE layer of stage 1 adopts MB\_Conv, and stages 2-4 adopt transformer. The DS layer of all stages adopts the MB\_Conv. TinyViT has been efficiently designed from three aspects: the sliding window mechanism corresponding to the FE layer (limiting the transformer attention mechanism to the window to reduce the computational complexity), the hierarchical design mechanism corresponding to the DS layer (taking advantage of the CNN to save the amount of calculation while extending the window attention to the global) and the model size control mechanism (customizing models of different sizes by adjusting the model control parameters).

To make full use of the effective information in the vision fundamental model SAM, this paper proposes to transfer the features in the heavy-parametric encoder of SAM to the proposed lightweight crack encoder by means of model distillation. That is, SAM is used as the teacher model, and the student model is employed as the proposed model. By setting the optimization goal, the knowledge in the teacher model is transmitted to the student model as lossless as possible.

It is assumed that the output image of the  $i^{\text{th}}$  image  $I^i$  after entering the SAM's heavy-parametric encoder is embedded as  $\Psi_{hp}^{I^i}$ , and the output image of the proposed lightweight encoder is embedded as  $\Psi_l^{I^i}$ . The crack segmentation head of the proposed framework directly uses image embedding as input, so it is not necessary to minimize the segmentation error after adding the crack segmentation head to SAM, but only to minimize the difference between the two embeddings [39] (illustrated in Equation (1)), where  $N$  represents the total count of training crack images required for model distillation, MSE is the least square error function, and  $\omega$  is the trainable weight parameters of the proposed lightweight encoder.

$$\arg \min_{\omega} \frac{1}{N} \sum_{i=1}^N \text{MSE}(\Psi_{hp}^{I^i}, \Psi_l^{I^i}(\omega)) \quad (1)$$

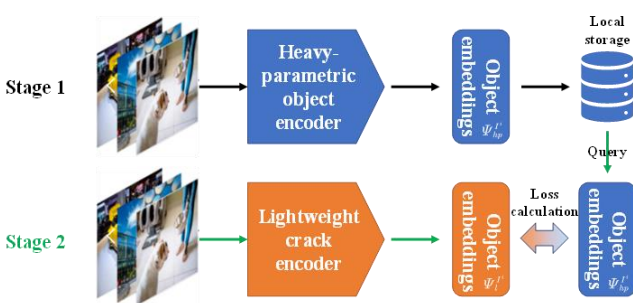


Figure 2. Processing procedure of model distillation.

Specifically, as shown in Figure 2, there are two stages during model distillation, the encoder parameters in the original SAM are frozen (untrainable), while the proposed lightweight encoder parameters are trainable. In stage 1 (embedding preparation), the image to be trained is input into the original SAM in advance to obtain the corresponding image embedding  $\Psi_{hp}^{I^i}$  and then stored locally. In stage 2 (lightweight encoder training), the image is fed into the proposed lightweight encoder to obtain the image embedding  $\Psi_l^{I^i}$ ,  $\Psi_{hp}^{I^i}$  can be

queried from the local storage. The optimization goal of training can be directly calculated. Taking such a training strategy will greatly reduce the time and cost of training while ensuring the distillation effect.

## 2.2 Crack segmentation head

To assist object segmentation, SAM employs prompts through the integration of incorporating prompt encoder and mask decoder into image embedding process. This encompasses the handling of image and prompt embedding, and output tokens subsequent to the image encoder. However, since the crack segmentation task in this study is automatic and does not require prompt input, the latter part of SAM needs to be modified. To address this, this paper introduces a crack segmentation head to fulfill the necessary functions.

The crack segmentation head is composed of several key components, including two transposed convolution layers, a multiscale convolution layer, a convolution layer with the size of  $1 \times 1$ , and two interpolation layers (shown in Figure 1). The transposed convolution layer is designed to increase the resolution of the encoded crack image embedding by a factor of 2, thereby restoring spatial information. The multiscale convolution layer is utilized to leverage feature fusion at different scales, enabling the model to learn information in various ranges around crucial pixels through backpropagation gradient. Figure 3 illustrates the detailed architecture of the multiscale convolution. According to the channel dimension, features from  $n$  channels of the transpose convolutional layer are partitioned into  $k$  groups. To retain features at the current scale, a  $1 \times 1$  convolution is applied to the first group. For the remaining  $k-1$  groups,  $3 \times 3$  convolutions with varying dilation rates are utilized to capture features at different scales, where the dilation rate is determined by the number of groups minus 1 [40]. The  $1 \times 1$  convolutional layer is responsible for integrating information from different channels and adjusting the output dimension accordingly. Finally, the interpolation layer further upsamples the output to fine-tune the output dimension.

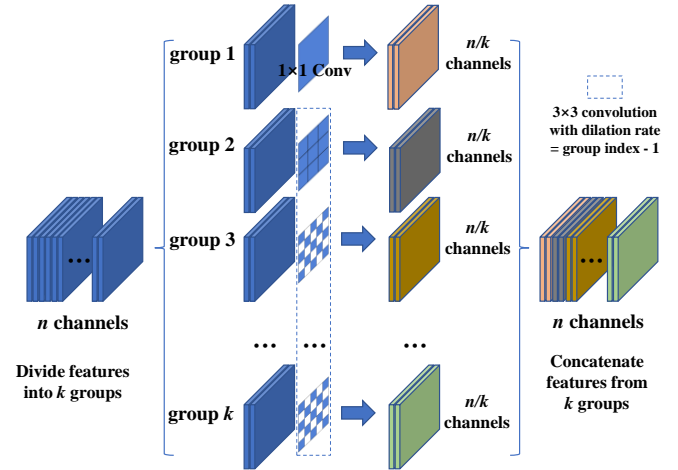


Figure 3. Architecture of the multiscale convolution.

A combined loss ( $\mathcal{L}_{total}$ ) comprising binary entropy ( $\mathcal{L}_{BE}$ ) and Dice ( $\mathcal{L}_{dice}$ ) is set as the objective of fine-tuning the proposed method, as illustrated in Equations (2)-(4). Here,  $N$  denotes the image's pixel number, while  $y_i$  and  $p_i$  respectively



denote the annotated label and predicted value for the  $i^{\text{th}}$  pixel. Additionally,  $Y$  and  $\hat{Y}$  represent the crack mask annotations and predictions, respectively.

$$\mathcal{L}_{total} = \mathcal{L}_{BE} + \mathcal{L}_{dice} \quad (2)$$

$$\mathcal{L}_{BE} = -\frac{1}{N} \sum_{i=1}^N y_i \log(p_i) \quad (3)$$

$$\mathcal{L}_{dice} = 1 - \frac{2|\hat{Y} \cap Y| + 1}{|\hat{Y}| + |Y| + 1} \quad (4)$$

### 3 IMPLEMENTATION DETAILS

#### 3.1 Dataset

**Distillation on common object dataset** SAM's powerful segmentation generalization ability comes from the large-scale segmentation dataset SA-1B. The dataset is generated by SAM's data engine and is divided into three stages: preliminary manual, semi-automated, and fully automated. During the initial stage, SAM aids the annotator to annotate the mask, akin to the traditional interactive object segmentation scenario. During the second stage, SAM is capable of autonomously producing the mask for certain objects by proposing their potential locations, and the annotator annotates the remaining objects, which helps to increase the diversity of the mask. In the last stage, the regular grid prompt SAM of the foreground point is employed to produce approximately one hundred high-quality masks for each image. Ultimately, SA-1B generates over 1 billion object masks across 11 million images. Since the proposed crack segmentation framework uses a lightweight encoder, the parameters are much smaller than the original SAM encoder. Therefore, 0.1% of the SA-1B dataset (11,000) is randomly sampled according to the literature results as the training dataset of the model distillation [39].

**Fine-tuning on crack dataset** Lately, crack recognition field have achieved significant progressions, and several crack segmentation datasets have been released to the research community. While many studies have trained and evaluated models on specific datasets, there is a lack of comprehensive testing across multiple datasets, which hinders our understanding of the generalization capabilities of crack segmentation models [41]. To address this limitation, this paper selected eight influential datasets for evaluating the proposed method. These datasets include CFD, Crack500, Cracktree200, DeepCrack, EugenMiller, GAPS, Rissbilder, and Volker (referred to as Datasets 1-8) [41]. These datasets exhibit significant variations in terms of structural materials, structural parts, image quality, and quantity, thereby enabling an effective evaluation of the generalization abilities of crack segmentation models. Figure 4 offers a summary of the quantity of training and testing images contained within each of the eight datasets. The entire set of training images, amounting to 7754, is partitioned into training subset (90%) and validation subset (10%). The testing images, collectively referred to as the testing subset, are employed to evaluate the segmentation methods proposed in this paper.

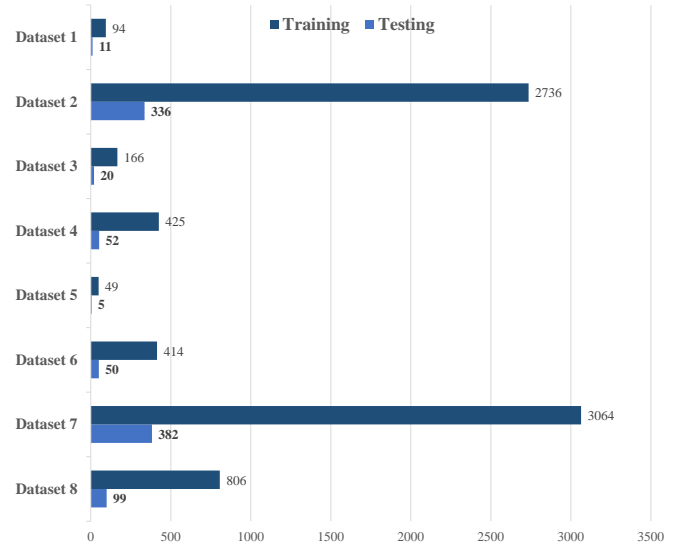


Figure 4. Numbers of training and testing images of eight datasets.

#### 3.2 Distillation and fine-tuning strategy

During the model distillation, the image embedding vector of the training image through the SAM heavy-parametric encoder has been calculated in advance and saved to the local storage. The training image only needs to go through the lightweight encoder to obtain the new image embedding vector, and then read the previously saved SAM embedding vector and calculate mean squared error (MSE). During the training, a single GPU was used, the batch size was 2, and a total of 50,000 iterations were performed. The MSE value obtained by the final convergence was 0.977, indicating the effectiveness and accuracy of the model distillation.

Throughout the proposed crack segmentation model fine-tuning, the initial learning rate was established as  $1e-5$ . The total training iteration count was determined as 24,000. A multi-step learning rate change approach was employed, where it was reduced to 0.1 times the previous value at the 16,000th and 20,000th iterations, respectively. The fine-tuning process implemented an early stopping strategy. The parameters at this iteration were taken as the final model weights. In addition, the batch size was 2.

The configuration utilized for fine-tuning and evaluating the proposed method comprised an Intel Xeon(R) E5-2620 v4 central processing unit (CPU), complemented by a robust Nvidia RTX 3090 graphics processing unit (GPU) offering 24GB memory. Additionally, the system was equipped with an ample 128GB of memory.

### 4 RESULTS AND DISCUSSIONS

The quantitative and qualitative results of the proposed lightweight crack segmentation method under full supervision and limited supervision conditions are illustrated in this section, and the state-of-the-art CNN-based method Deeplab v3 plus (with MobileNet v3) [42] and transformer-based Segformer [43] are employed to be comparison. Additionally, the weight file space occupation, the running speed on different hardware

platforms and the possibility of mobile deployment of the proposed method are discussed.

#### 4.1 Testing results under full supervision

Full supervision refers to training on the entire training subset (6,978 pairs of crack images and masks) and testing on the entire test subset (955 crack images). This condition facilitates the transfer of feature parameters from vision fundamental models to the domain of crack segmentation, enabling exploration of the segmentation accuracy limits across different models.

Table 1 elucidates the testing Dice scores ( $\times 100\%$ ) for eight datasets under full supervision, as well as the total parameter numbers of different algorithms and their GPU memory occupancy during training (with an input size of  $1024 \times 1024 \times 3$  and a batch size of 2). In Table 1, SAM represents the crack segmentation method based on vision fundamental models that employs the heavy-parametric encoder from the original SAM. Compared to Deeplab v3 plus, the proposed method significantly improves the Dice score by 13.6, and although the parameter count increases to twice that amount, the required GPU memory during training decreases to 36%, which is the most direct assessment of algorithm training expenses. Compared to Segformer, the proposed method is on par in terms of accuracy, but with a 45% reduction in parameter count and a 37% reduction in required GPU memory. Compared to the original SAM-based method, the proposed approach experiences a 5.4 decrease in Dice score, but with a parameter count reduced to 7% and at least an 85% reduction in required GPU memory. In summary, the proposed method not only maintains segmentation accuracy in comparison to other cutting-edge methods but also significantly reduces training costs.

Table 1. Testing Dice scores ( $\times 100\%$ ) on eight datasets, total parameter numbers and GPU memory occupation under full supervision

Method	DL v3p	Segformer	SAM	Proposed	
Dataset	1	52.6	51.8	68.5	56.1
	2	54.9	68.4	71.1	65.6
	3	24.3	24.4	37.6	24.4
	4	69.6	72.8	79.9	68.8
	5	36.2	56.1	57.7	53
	6	25.8	28.9	45.4	44.77
	7	30.9	50.1	54.9	50.8
	8	60	67.5	75.5	68.7
Average	44.4	58	63.4	58	
Params	3.2M	13.6M	89.8M	6.2M	
Mem	10.3G	10.1G	>24G	3.8G	

Figure 5 displays representative results of crack segmentation using different methods, where each row corresponds to a representative crack image from each dataset, and each column represents the original image, ground truth, and the test results using Deeplab v3 plus, Segformer, the original SAM-based method, and the proposed method, respectively. Whether they are concrete or asphalt surface cracks, whether they are dot-like, strip-like, or mesh-like, the

crack segmentation results of methods based on vision fundamental models are superior in terms of integrity and connectivity compared to CNN-based and transformer-based. While the proposed method's segmentation effect is slightly lacking in local detail handling compared to the original SAM-based crack segmentation method, it exhibits evident advancement over other methods, demonstrating the proposed method's efficacy in enhancing accuracy.

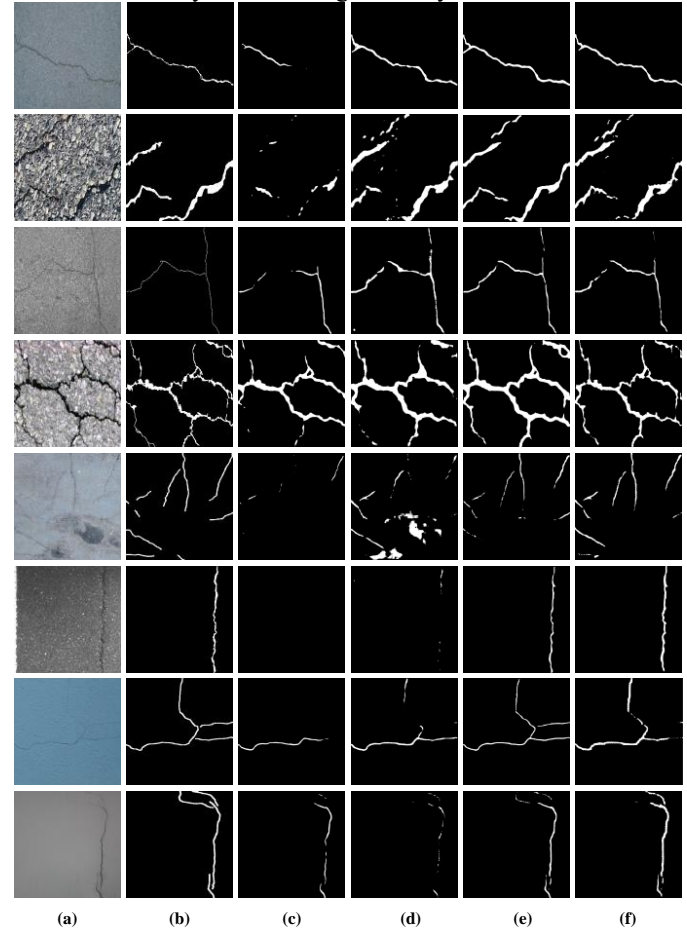


Figure 5. Representative testing results: (a) raw image, (b) annotation, (c) DL v3p, (d) Segformer, (e) SAM, (f) the proposed method.

#### 4.2 Testing results under limited supervision

In contrast to prior CNN-based and transformer-based object segmentation approaches, the primary advantage of object segmentation methods grounded on vision fundamental models is their robust generalization capability. This means that they can achieve high segmentation accuracy with minimal domain-specific supervision information. Hence, this part showcases the proposed method's strong generalization ability by comparing the test accuracy of different methods under two limited supervision cases (1%-shot and one-shot). The 1%-shot case refers to training with 1% of the training subset of full supervision (77 crack image-mask pairs), while the one-shot case refers to training with only one crack image-mask pair per dataset (a total of 8). These two cases provide an extreme test of the generalization capabilities of different methods.

The testing Dice scores of different algorithms under limited supervision are illustrated in Table 2. Consistent with

theoretical analysis, the crack segmentation method based on vision fundamental models significantly outperforms those based on CNNs and transformers in terms of segmentation accuracy in both the 1%-shot and one-shot cases.

Table 2. Testing Dice scores ( $\times 100\%$ ) on eight datasets under limited supervision

Data size		1%-shot			
Method	DL v3p	Segformer	SAM	Proposed	
Dataset	1	39.6	47.2	54.2	46.8
	2	53.7	60	65.8	57.4
	3	23	17.3	21.1	24
	4	66.4	65.6	70.5	63.2
	5	23.4	44.8	48.1	38.2
	6	9.7	23	32.9	19
	7	26.7	47	48.3	50.3
	8	54.5	64.2	66.8	66.1
Average		40.4	52.5	56.3	52.8
Data size		one-shot			
Method	DL v3p	Segformer	SAM	Proposed	
Dataset	1	35	47	44.8	49.2
	2	21.4	22.4	34.1	25
	3	20.1	22.2	16.5	20.3
	4	48	51.4	59.3	67.1
	5	46.1	48.7	54.2	53.9
	6	29.3	34.8	34.7	24.2
	7	24	36.1	39.3	42.8
	8	48.3	58.9	58	56.8
Average		27.4	34.3	39.9	38

Notably, in the one-shot case, the proposed method improved the Dice score by 3.7 compared to Segformer and only decreased by 1.9 compared to the original SAM-based method. Considering that the proposed method has fewer parameters and lower training costs, it is substantiated that the approach can reach high precision with maintaining operational efficiency. Former transformer models necessitated a substantial volume of supervised training data to attain elevated segmentation precision, although vision fundamental models are also based on transformer architectures. Preliminary judgments can also be made based on experimental results, the vision fundamental model-based crack segmentation method demonstrates good generalization capability even under extremely limited supervision conditions.

### 4.3 Deployment of the proposed method

Although the vision fundamental model has strong segmentation generalization ability, its deployment difficulty and cost are high, which aligns with the primary research concentration of this paper. Therefore, this subsection deploys the original SAM-based and the proposed lightweight vision fundamental model-based crack segmentation models on different hardware platforms to illustrate the advantages of the latter.

The weight file space occupancy serves as a metric for gauging the complexity of the model, encompassing all parameters and configurations stored on the disk. Table 3 demonstrates that the space occupancy of SAM-based models based on backbones of different sizes is 404MB, 1230MB, and 2665MB, respectively, while the proposed model is only 70MB (17% of the minimum SAM-based).

Table 3. Weight file space occupancy and running speed of the proposed method

Method	Space occupancy	Running speed	
		GPU	0.107s
SAM	ViT-B 404MB	x86	5.498s
		arm	/
	ViT-L 1230MB	/	/
	ViT-H 2665MB	/	/
Proposed	70MB	GPU	0.016s
		x86	0.637s
		arm	2.245s

The running speed is the most direct indicator to measure the complexity of a model. Although it is affected by factors such as code implementation, the relative speed of different models can still be compared after controlling variables. This paper tests on three common hardware platforms (GPU, x86 CPU and arm CPU), and the results are shown in Table 3. With  $1024 \times 1024$  images as input, the SAM-based model takes 0.107 s and 5.498 s on GPU and x86 CPU respectively. Because the model is too complex to be deployed on the arm CPU used in this experiment. Meanwhile, the proposed model consumes 0.016 s and 0.637 s on GPU and x86 CPU (15% and 12% of SAM-based, respectively), and 2.245s on arm CPU (twice as fast as SAM-based on x86 CPU).

It is worth noting that the arm CPU used in this experiment is Kirin 970, a consumer and low-cost chip released six years ago. Compared with the current mobile phone CPUs, the performance difference is huge. Employing the most cutting-edge chip would significantly enhance the performance of the proposed method. Figure 6 illustrates the exemplary testing outcomes of the deployed proposed method on a mobile phone.

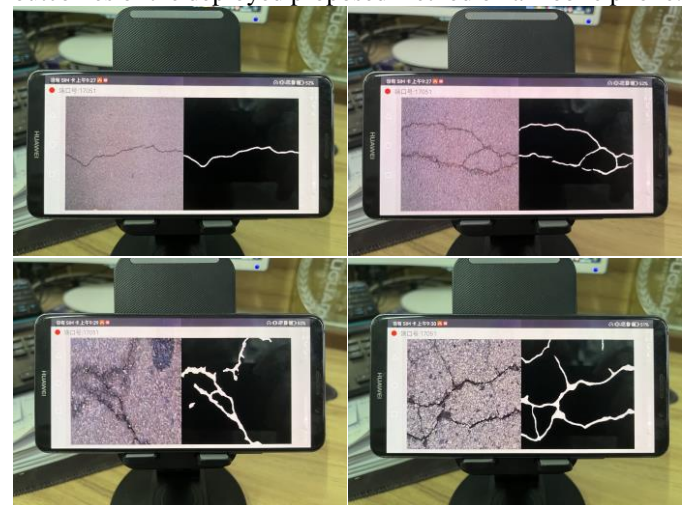


Figure 6. Representative testing results on mobile phones



## 5 CONCLUSIONS

A novel crack segmentation method using lightweight vision fundamental model is developed in this paper. The approach incorporates model distillation techniques to substantially decrease the model parameters and enhance operational speed while maintaining the robust generalization capabilities of the vision fundamental model to the greatest extent possible. In light of the findings, the following conclusions can be inferred: (1) By substituting the ViT encoder in the original SAM with the lightweight encoder TinyViT and using model distillation techniques with image embedding consistency as the optimization goal, effective transfer of the vision fundamental model's generalization ability is achieved. (2) Under full supervision, the proposed method surpasses current cutting-edge methods based on non-vision fundamental models, achieving a segmentation Dice score of 58.0. Moreover, relative to the original SAM, the model's parameter count is reduced to 7%, and the required GPU memory is decreased to 15%, with only a 5.4 decrease in Dice score. (3) Under limited supervision, the proposed method comprehensively surpasses methods based on non-vision fundamental models in terms of segmentation accuracy and algorithmic efficiency, with Dice scores reaching 52.8 (1%-shot) and 38.0 (one-shot). Furthermore, as the degree of available supervision information decreases, the proposed method demonstrates a heightened advantage, resulting in a diminished disparity with respect to the original SAM. (4) The proposed method achieves a sixfold and eightfold acceleration on GPU and x86 CPU, respectively, compared to the original SAM, and has been successfully deployed on cost-effective ARM CPUs.

The crack segmentation method developed from lightweight vision fundamental model serves as a reference for the efficient application of vision fundamental models in the field of automatic identification of civil engineering damages. Nevertheless, there remains potential for enhancing the detailed recovery of crack identification outcomes in this study. Future work will concentrate on incorporating crack boundary constraints into the loss function and bolstering the post-processing methodologies within the crack segmentation framework to enhance the precision of crack detail identification. To facilitate practical applications, follow-up research should further develop a quantitative measurement and evaluation module for crack dimensions.

## ACKNOWLEDGMENTS

This study received financial support from National Key Research and Development Program of China [2024YFC3015201], National Natural Science Foundation of China (NSFC) [52408324, U22A20230 and 52278299] and Natural Science Foundation of Heilongjiang Province of China [LH2024E056].

## REFERENCES

- [1] C. Koch, K. Georgieva, V. Kasireddy, B. Akinci, P. Fieguth, A review on computer vision based defect detection and condition assessment of concrete and asphalt civil infrastructure, *Advanced Engineering Informatics* 29 (2) (2015), pp. 196-210.
- [2] J. Guo, P. Liu, B. Xiao, L. Deng, Q. Wang, Surface defect detection of civil structures using images: Review from data perspective, *Automation in Construction* 158 (2024), p. 105186.
- [3] C.M. Yeum, S.J. Dyke, Vision-Based Automated Crack Detection for Bridge Inspection, *Computer-Aided Civil and Infrastructure Engineering* 30 (10) (2015), pp. 759-770.
- [4] Y. Xu, Y. Bao, Y. Zhang, H. Li, Attribute-based structural damage identification by few-shot meta learning with inter-class knowledge transfer, *Structural Health Monitoring* 20 (4) (2020), pp. 1494-1517.
- [5] Y. Hou, Q. Li, C. Zhang, G. Lu, Z. Ye, Y. Chen, L. Wang, D. Cao, The State-of-the-Art Review on Applications of Intrusive Sensing, Image Processing Techniques, and Machine Learning Methods in Pavement Monitoring and Analysis, *Engineering* 7 (6) (2021), pp. 845-856.
- [6] B.F. Spencer, V. Hoskere, Y. Narazaki, Advances in Computer Vision-Based Civil Infrastructure Inspection and Monitoring, *Engineering* 5 (2) (2019), pp. 199-222.
- [7] Y. Que, Y. Dai, X. Ji, A. Kwan Leung, Z. Chen, Z. Jiang, Y. Tang, Automatic classification of asphalt pavement cracks using a novel integrated generative adversarial networks and improved VGG model, *Engineering Structures* 277 (2023), p. 115406.
- [8] Y. Xu, Y. Bao, J. Chen, W. Zuo, H. Li, Surface fatigue crack identification in steel box girder of bridges by a deep fusion convolutional neural network based on consumer-grade camera images, *Structural Health Monitoring* 18 (3) (2018), pp. 653-674.
- [9] L. Chen, H. Yao, J. Fu, C. Tai Ng, The classification and localization of crack using lightweight convolutional neural network with CBAM, *Engineering Structures* 275 (2023), p. 115291.
- [10] X. Ye, T. Jin, C. Yun, A review on deep learning-based structural health monitoring of civil infrastructures, *Smart Structures and Systems* 24 (5) (2019), pp. 567-585.
- [11] H. Zhang, K. Gao, H. Huang, S. Hou, J. Li, G. Wu, Fully decouple convolutional network for damage detection of rebars in RC beams, *Engineering Structures* 285 (2023), p. 116023.
- [12] P. Wu, A. Liu, J. Fu, X. Ye, Y. Zhao, Autonomous surface crack identification of concrete structures based on an improved one-stage object detection algorithm, *Engineering Structures* 272 (2022), p. 114962.
- [13] L. Chen, W. Chen, L. Wang, C. Zhai, X. Hu, L. Sun, Y. Tian, X. Huang, L. Jiang, Convolutional neural networks (CNNs)-based multi-category damage detection and recognition of high-speed rail (HSR) reinforced concrete (RC) bridges using test images, *Engineering Structures* 276 (2023), p. 115306.
- [14] S. Li, X. Zhao, G. Zhou, Automatic pixel-level multiple damage detection of concrete structure using fully convolutional network, *Computer-Aided Civil and Infrastructure Engineering* 34 (7) (2019), pp. 616-634.
- [15] F.-C. Chen, M.R. Jahanshahi, ARF-Crack: rotation invariant deep fully convolutional network for pixel-level crack detection, *Machine Vision and Applications* 31 (6) (2020), p. 47.
- [16] V. Hoskere, Y. Narazaki, T.A. Hoang, B.F. Spencer Jr, MaDnet: multi-task semantic segmentation of multiple types of structural materials and damage in images of civil infrastructure, *Journal of Civil Structural Health Monitoring* 10 (5) (2020), pp. 757-773.
- [17] Y. Narazaki, V. Hoskere, T.A. Hoang, Y. Fujino, A. Sakurai, B.F. Spencer Jr, Vision-based automated bridge component recognition with high-level scene consistency, *Computer-Aided Civil and Infrastructure Engineering* 35 (5) (2020), pp. 465-482.
- [18] J. Huan, W. Li, S. Tighe, Z. Xu, J. Zhai, CrackU-net: A novel deep convolutional neural network for pixelwise pavement crack detection, *Structural Control and Health Monitoring* 27 (8) (2020), p. e2551.
- [19] F. Jiang, Y. Ding, Y. Song, F. Geng, Z. Wang, Automatic pixel-level detection and measurement of corrosion-related damages in dim steel box girders using Fusion-Attention-U-net, *Journal of Civil Structural Health Monitoring* 13 (1) (2023), pp. 199-217.
- [20] G. Liu, W. Ding, J. Shu, A. Strauss, Y. Duan, Two-Stream Boundary-Aware Neural Network for Concrete Crack Segmentation and Quantification, *Structural Control and Health Monitoring* 2023 (2023), p. 3301106.
- [21] Z. Xiang, X. He, Y. Zou, H. Jing, An active learning method for crack detection based on subset searching and weighted sampling, *Structural Health Monitoring* (2023), p. 14759217231183661.
- [22] Q.D. Nguyen, H.-T. Thai, Crack segmentation of imbalanced data: The role of loss functions, *Engineering Structures* 297 (2023), p. 116988.
- [23] Y. Xu, Y. Fan, Y. Bao, H. Li, Task-aware meta-learning paradigm for universal structural damage segmentation using limited images, *Engineering Structures* 284 (2023), p. 115917.
- [24] K. Zhang, Y. Zhang, H.D. Cheng, CrackGAN: Pavement Crack Detection Using Partially Accurate Ground Truths Based on Generative Adversarial Learning, *IEEE Transactions on Intelligent Transportation Systems* 22 (2) (2021), pp. 1306-1319.

- [25] C. Kim, S. Hwang, H. Sohn, Weld crack detection and quantification using laser thermography, mask R-CNN, and CycleGAN, *Automation in Construction* 143 (2022), p. 104568.
- [26] D. Ma, H. Fang, N. Wang, C. Zhang, J. Dong, H. Hu, Automatic Detection and Counting System for Pavement Cracks Based on PCGAN and YOLO-MF, *IEEE Transactions on Intelligent Transportation Systems* 23 (11) (2022), pp. 22166-22178.
- [27] T. Jin, X.W. Ye, Z.X. Li, Establishment and evaluation of conditional GAN-based image dataset for semantic segmentation of structural cracks, *Engineering Structures* 285 (2023), p. 116058.
- [28] S. Li, X. Zhao, High-resolution concrete damage image synthesis using conditional generative adversarial network, *Automation in Construction* 147 (2023), p. 104739.
- [29] T. Zhang, D. Wang, A. Mullins, Y. Lu, Integrated APC-GAN and AttuNet Framework for Automated Pavement Crack Pixel-Level Segmentation: A New Solution to Small Training Datasets, *IEEE Transactions on Intelligent Transportation Systems* 24 (4) (2023), pp. 4474-4481.
- [30] E. Asadi Shamsabadi, C. Xu, A.S. Rao, T. Nguyen, T. Ngo, D. Dias-da-Costa, Vision transformer-based autonomous crack detection on asphalt and concrete surfaces, *Automation in Construction* 140 (2022), p. 104316.
- [31] W. Wang, C. Su, Automatic concrete crack segmentation model based on transformer, *Automation in Construction* 139 (2022), p. 104275.
- [32] W. Ding, H. Yang, K. Yu, J. Shu, Crack detection and quantification for concrete structures using UAV and transformer, *Automation in Construction* 152 (2023), p. 104929.
- [33] F. Guo, J. Liu, C. Lv, H. Yu, A novel transformer-based network with attention mechanism for automatic pavement crack detection, *Construction and Building Materials* 391 (2023), p. 131852.
- [34] Z. Tong, T. Ma, W. Zhang, J. Huyan, Evidential transformer for pavement distress segmentation, *Computer-Aided Civil and Infrastructure Engineering* n/a (n/a) (2023).
- [35] H. Zhang, A.A. Zhang, A. He, Z. Dong, Y. Liu, Pixel-level detection of multiple pavement distresses and surface design features with ShuttleNetV2, *Structural Health Monitoring* (2023), p. 14759217231183656.
- [36] Z. Zhou, J. Zhang, C. Gong, Hybrid semantic segmentation for tunnel lining cracks based on Swin Transformer and convolutional neural network, *Computer-Aided Civil and Infrastructure Engineering* n/a (n/a) (2023).
- [37] A. Kirillov, E. Mintun, N. Ravi, H. Mao, C. Rolland, L. Gustafson, T. Xiao, S. Whitehead, A.C. Berg, W.-Y. Lo, P. Dollár, R. Girshick, Segment Anything, *arXiv e-prints* (2023), p. arXiv:2304.02643.
- [38] K. Wu, J. Zhang, H. Peng, M. Liu, B. Xiao, J. Fu, L. Yuan, TinyViT: Fast Pretraining Distillation for Small Vision Transformers, *arXiv e-prints* (2022), p. arXiv:2207.10666.
- [39] C. Zhang, D. Han, Y. Qiao, J.U. Kim, S.-H. Bae, S. Lee, C.S. Hong, Faster Segment Anything: Towards Lightweight SAM for Mobile Applications, *arXiv e-prints* (2023), p. arXiv:2306.14289.
- [40] J. Zhang, X. Chen, Z. Qiu, M. Yang, Y. Hu, J. Liu, Hard Exudate Segmentation Supplemented by Super-Resolution with Multi-scale Attention Fusion Module, *2022 IEEE International Conference on Bioinformatics and Biomedicine (BIBM)*, 2022, pp. 1375-1380.
- [41] E. Bianchi, M. Hebdon, Development of Extendable Open-Source Structural Inspection Datasets, *Journal of Computing in Civil Engineering* 36 (6) (2022), p. 04022039.
- [42] L.-C. Chen, Y. Zhu, G. Papandreou, F. Schroff, H. Adam, Encoder-Decoder with Atrous Separable Convolution for Semantic Image Segmentation, *arXiv e-prints* (2018), p. arXiv:1802.02611.
- [43] E. Xie, W. Wang, Z. Yu, A. Anandkumar, J.M. Alvarez, P. Luo, SegFormer: Simple and Efficient Design for Semantic Segmentation with Transformers, *arXiv e-prints* (2021), p. arXiv:2105.15203.

# Spatial-Temporal Graph Model for Environmental Temperature and Traffic Flow Prediction of City Regions

Chenglong Lin<sup>1,2</sup>, Yang Xu<sup>1,2</sup>, 0000-0002-8394-9224\*

<sup>1</sup>Key Lab of Smart Prevention and Mitigation of Civil Engineering Disasters of the Ministry of Industry and Information Technology, Harbin Institute of Technology, Harbin 150090, China

<sup>2</sup>School of Civil Engineering, Harbin Institute of Technology, Harbin 150090, China

\*Corresponding Author: Dr. Yang XU, xyce@hit.edu.cn

**ABSTRACT:** Recent research for correlation prediction from spatial-temporal monitoring data of bridge groups has explored graph neural networks and state space models, offering new angles and advanced algorithms. However, current research still faces significant challenges: (1) constructing suitable graph structures to accurately reflect complex spatial-temporal correlations, (2) designing an effective spatial-temporal neural network to capture spatial-temporal dependencies during the service state evolution of bridge groups, and (3) fully making use of spatial-temporal monitoring data to boost prediction accuracy and efficiency. To tackle these challenges, this study introduces a graph selective state space model for spatial-temporal prediction of environmental temperature and traffic flow for bridge groups. Firstly, a spatial-temporal graph structure is set up to account for data characteristics in both spatial and temporal aspects and forecast the dynamic evolution of bridge group system. Then, a state space model is built to produce a structured state space sequence and introduce a selective mechanism to dynamically adjust model behaviors and optimize computational resources. Lastly, through decomposing and reintegrating spatial-temporal features of monitoring data for bridge groups under different complexities, validation experiments are performed to show the efficacy, universality, and efficiency using multi-type, multi-scale, and multi-granularity spatial-temporal monitoring data of environmental temperature and traffic flow.

**KEY WORDS:** Spatial-Temporal Correlation; Time Series Prediction; Graph Model; Environmental Temperature; Traffic Flow.

## 1 INTRODUCTION

The rapid progression of urbanization in China has made the consistent serviceability of bridge groups a pivotal factor in determining the efficiency and safety of urban traffic. As urban transport system essentials, bridge groups consist of multiple interconnected bridges with interdependent serviceability. These bridges inside a city region are exposed to various related factors including environmental conditions and traffic flow, which can notably affect their structural integrity and operational efficiency. Accurately predicting the serviceability of bridge groups is crucial for traffic safety and maintenance strategy optimization. Traditional methods employed for predicting the service state of bridge groups often focus on individual bridges, neglecting the spatial-temporal correlations amongst different bridges in the group. This can cause inaccurate predictions and thus insufficient maintenance strategies, potentially causing significant safety risks and leading to considerable economic losses.

Recent deep learning advances have created new ways to predict the service state of bridge groups. Graph neural networks (GNNs) have shown great ability in dealing with data that has complex relational structures, like the interactions between different bridges in a group. Additionally, state space models (SSMs<sup>[1-4]</sup>) have drawn increasing interests due to their capability to model dynamic systems and capture the temporal evolution of structural service states. But even with these advances, current research faces big challenges. A main challenge is building a suitable graph structure that can truly reflect the complex spatial-temporal correlations embedded in the monitoring data of bridge groups. Another challenge is designing an effective neural network architecture that can

capture both spatial and temporal dependencies during the dynamic evolution of service states for regional bridges. Furthermore, it is crucial to leverage the abundant spatial-temporal data available for bridge groups to enhance prediction accuracy and efficiency.

To tackle these challenges, this study proposes a graph selective state space model for spatial-temporal prediction of environmental temperature and traffic flow for bridge groups. The model uses the core capacities of GNNs and SSMs to achieve comprehensive and accurate predictions of spatial-temporal variables. The main contributions of this study are as follows:

- An adaptive multi-granularity data fusion is designed to integrate multi-granularity data of recent, cyclic, and trend information from bridge groups. This fusion method not only captures various temporal patterns but also assesses their impacts on operational states of bridges. This approach strengthens the model's ability to handle complex spatial-temporal dependencies, thereby improving prediction accuracy.
- A novel spatial-temporal graph convolution module (STGCM) is introduced to consider the spatial-temporal correlation of environmental temperature and traffic flow.
- A graph selective state space module (GSSSM) is developed to model how spatial-temporal dependencies in regional monitoring data evolve for bridge group, which dynamically adjusts the model's learning behavior and optimizes computational resources. The GSSSM prioritizes the most relevant parts of regional monitoring data for environmental temperature and traffic flow,



thereby enhancing the model capacity to capture spatial-temporal correlations.

## 2 RELATED WORKS

### 2.1 Spatial-Temporal Graph Neural Networks

Most spatial-temporal graph neural networks (STGNNs) are categorized into three types: those based on recurrent neural networks (RNNs), those based on convolutional neural networks (CNNs), and those based on attention mechanisms.

Seo et al. (2018)<sup>[5]</sup> presented a graph convolutional recurrent network, capturing spatial-temporal dependencies by filtering inputs and hidden states in a recurrent unit via graph convolution. Later works adopted different strategies, for example, Li et al. (2017)<sup>[6]</sup> developed a diffusion convolutional recurrent neural network, integrating diffusion convolution with gated recurrent units (GRUs) to grasp spatial and temporal dependencies at the same time, and Zhang et al. (2018)<sup>[7]</sup> proposed gated attention networks, which combine GNNs with a convolutional subnetwork to assess the importance of each attention head. Another parallel work was that Jain et al. (2016)<sup>[8]</sup> used node-level and edge-level RNNs in their work to handle different aspects of temporal information. The main drawbacks of RNN-based approaches are that they become inefficient for long sequences and the gradients are more likely to explode when combined with graph convolution networks (GCNs). CNN-based approaches combine graph convolutions with standard 1D convolutions, for example, Yu et al. (2018)<sup>[9]</sup> proposed a spatial-temporal graph convolution network (STGCN), combining GCNs with temporal convolutional networks (TCN<sup>[10]</sup>) to capture spatial and temporal dependencies. A recent work about attention-based approaches is that Li et al. (2023)<sup>[11]</sup> proposed GCN-Informer, which combines GCNs with Informer to capture long-term dependencies in time series data. Although these three types of approaches are computationally efficient, they generally need to stack multiple layers or use global pooling to expand the neural network model's receptive field, which is a limitation that the proposed Spatial-Temporal Graph Selective State Space Model (STGSSSM) addresses by employing stacked dilated casual convolutions to capture temporal dependencies more effectively with fewer layers.

### 2.2 State Space Models

State Space Models (SSMs) are powerful tools for modeling dynamic systems, offering flexible frameworks to capture temporal evolution through state transitions influenced by external inputs. The recent fusion of SSMs with GNNs has achieved promising results in managing complex spatial-temporal graph-structured data.

For instance, Zhao et al. (2024)<sup>[12]</sup> proposed the graph state space network, the first model to incorporate SSMs into the spectral filter design of GNNs, thus overcoming the limitations of conventional methods in dealing with complex graph spectra. Behrouz et al. (2024)<sup>[13]</sup> introduced graph mamba (selective state space model) networks, an SSM-based framework for graph learning, which uses neighborhood tokenization, token ordering, bidirectional SSM encoder, and local encoding to efficiently handle long-range dependencies and heterophilic graphs. Wang et al. (2024)<sup>[14]</sup> presented graph-mamba, a novel graph model that uses a mamba module for efficient context

selection, achieving linear complexity and superior performance in long-range graph tasks. Yuan et al. (2024)<sup>[15]</sup> proposed dynamic graph-mamba, a dynamic graph structure learning framework that combines mamba and a kernelized dynamic message-passing operator to efficiently learn dynamic graph structures and capture long-range dependencies.

Although these approaches can dynamically adjust the learning behavior of the model and has high computational efficiency, they are relatively singular in feature extraction and lack in-depth extraction of spatial-temporal features, which is a limitation that the proposed STGSSSM addresses by utilizing STGCM to extract diverse spatial-temporal features.

### 2.3 Spatial-Temporal Traffic Forecasting

Traffic forecasting is crucial for optimizing urban transportation systems. Recent progress in spatial-temporal graph neural networks have greatly boosted the prediction accuracy by capturing complex spatial-temporal dependencies. Spatial-temporal traffic forecasting has been also investigated by RNN-based, CNN-based, and attention-based approaches.

For example, Zhao et al. (2019)<sup>[16]</sup> combined GCN with GRU to model temporal dynamics, effectively capturing long-term dependencies and achieving validation on the Los-loop dataset. Wu et al. (2019)<sup>[17]</sup> developed Graph WaveNet, using dilated causal convolutions to grasp long-term dependencies. Wu et al. (2020)<sup>[18]</sup> proposed the multivariate time series graph neural network (MTGNN), which integrated GCN and TCN for adaptive graph learning, delivering high performance on the large-scale METR-LA and PEMS-BAY datasets. In the attention-based approach, Zheng et al. (2020)<sup>[19]</sup> proposed graph multi-attention network, which utilized multi-attention mechanisms to weigh the significance of different nodes and time steps, achieving high accuracy on Xiamen and PeMS datasets. Guo et al. (2021)<sup>[20]</sup> developed an attention-based spatial-temporal graph neural network, combining dynamic GCN with transformers to adapt to dynamic traffic patterns, and showing robustness on the PEMS dataset.

### 2.4 Spatial-Temporal Temperature Forecasting

Environmental temperature greatly affects the service state of bridge groups, and spatial-temporal graph models can conduct highly efficient and accurate temperature predictions, which are summarized from RNN-based, CNN-based, and attention-based aspects.

Zhao et al. (2024)<sup>[21]</sup> presented an adaptive spatial-temporal graph recurrent network model. It used dynamic graph structures with a spatial-temporal recurrent network for sea surface temperature forecasting. Yang et al. (2023)<sup>[22]</sup> introduced a hierarchical graph recurrent network which utilized adaptive node embedding and hierarchical graph convolution to predict global sea surface temperatures accurately. Yu et al. (2021)<sup>[23]</sup> proposed a spatial-temporal graph neural network model that integrated graph attention networks and GRU for air temperature forecasting. Guo et al. (2025)<sup>[24]</sup> introduced spatial-temporal fusion graph neural networks with mixed adjacency, a model that leveraged spatial-temporal fusion GNNs with mixed adjacency and integrated GNNs with self-attention mechanisms to capture both long-term temporal periodicity and short-term spatial-temporal dependencies for temperature forecasting. Xu et al. (2024)<sup>[25]</sup> proposed the dynamic graph former model, a physics-guided

dynamic graph neural network for weather forecasting which combined GNNs and the Reformer architecture for temperature forecasting.

Despite the progress in traffic and temperature forecasting based on novel deep learning models, some challenges remain in multi-granularity data fusion, in-depth extraction of spatial-temporal features, dynamic adjustment of learning behavior and computational efficiency. This study addresses these limitations by integrating the multi-granularity data fusion, STGCM and GSSSM to enhance the prediction accuracy and efficiency.

### 3 METHODOLOGY

In this section, the mathematical definition is first formulated for the investigated issue of environmental temperature and traffic flow prediction of bridge groups in this study. Then, the overall schematic of the proposed STGSSSM is presented, along with detailed descriptions of its two core modules, i.e., spatial-temporal graph convolution module (STGCM) and graph selective state space module (GSSSM), which are combined together to capture the spatial-temporal dependencies.

#### 3.1 Problem Definition

A graph of bridge groups can be represented as  $\mathbf{G}_t = (\mathbf{V}, \mathbf{E}_t, \mathbf{A})$ , where  $\mathbf{V}$  denotes the set of nodes, representing bridges in a bridge group;  $\mathbf{E}_t$  denotes the set of edges (connections), describing the relationships between different bridges at time step  $t$ ; and  $\mathbf{A}$  denotes the adjacency matrix with elements  $A_{ij}$  representing the connection weight between nodes  $v_i$  and  $v_j$ . The input feature matrix of the bridge group at time step  $t$  is denoted as  $\mathbf{X}_t \in \mathbb{R}^{N \times D}$ , where  $N$  is the number of bridges in a bridge group, and  $D$  represents the number of feature dimensions, i.e.,  $D = 1$  represents the investigated variable of environmental temperature or traffic flow.

The graph-based spatial-temporal prediction task is to use the graph of bridge groups  $\mathbf{G}_t$  and feature matrix  $\mathbf{X}_t$  to learn a mapping function  $f$  (the proposed STGSSSM) which can accurately predict the prospective environmental temperature and traffic flow of bridge groups.

Assuming a future time step  $T$ , the prediction process can be expressed as:

$$[\mathbf{X}_{t+1}, \dots, \mathbf{X}_{t+T}] = f([\mathbf{X}_{t-T+1}, \dots, \mathbf{X}_t]; [\mathbf{G}_{t-T+1}, \dots, \mathbf{G}_t]) \quad (1)$$
 where  $[\mathbf{X}_{t+1}, \dots, \mathbf{X}_{t+T}] \in \mathbb{R}^{N \times D \times T}$  is the predicted environmental temperature or traffic flow in the future  $T$  time steps,  $(\mathbf{X}_{t-T+1}, \dots, \mathbf{X}_t) \in \mathbb{R}^{N \times D \times T}$  is the observed environmental temperature or traffic flow in the current  $T$  time steps.

#### 3.2 Overall Schematic of STGSSSM

The proposed STGSSSM comprises two primary modules of STGCM and GSSSM for environmental temperature and traffic flow prediction of bridge groups, as depicted in Figure 1.

Three temporal granularities of input data, recent data  $\mathbf{X}^r$ , cyclic data  $\mathbf{X}^c$  and trend data  $\mathbf{X}^q$  are individually fed into STGCM, which consists of  $N$  ST-Blocks and an output layer that consists of the *ReLU* activation function and a linear layer, each ST-Block employs a series of layers including  $1 \times 1$  convolution, gated temporal convolution (Gated TC), self-attention diffusion graph convolution (SADGC), residual

connection (Add), and batch normalization (BN); and adaptively fused after being passed through  $N$  layers of spatial-temporal graph convolution blocks (ST-Block) with skip connections and the output layer; In each ST-Block, the result of Gated TC is processed via a  $1 \times 1$  convolution, and the resulting output is skip-connected to the result of the last ST-Block.

Furthermore,  $\mathbf{X}^r$  is fed into GSSSM, which consists of  $M$  GSSS-Blocks. Each GSSS-Block incorporates a series of layers including layer normalization (Layer Norm),  $m$  parallel dynamic filter graph convolution (Dynamic Filter GC), concatenation and linear layer (Concat & Linear), graph state space selection mechanism (GSSS-Mechanism) which consists of two main algorithms of Parameter Calculation and Graph Selective Scan, linear layer and residual connection (Linear & Add).  $N$ ,  $M$  and  $m$  are hyperparameters.

The outputs of three STGCMs are first fused using an adaptive fusion module and then adaptively fused with the output of GSSSM. The final fusion result of STGCM and GSSSM is then passed through a fully connected layer to obtain the final output  $\mathbf{X}_{pred}$ .

The regularized mean squared error (MSE) is used for training the proposed STGSSSM and defined as

$$L = \frac{1}{B} \left( \sum_{b=1}^B \left( \frac{1}{TND} \sum_{i=t+1}^{t+T} \sum_{j=1}^N \sum_{k=1}^D (\hat{X}_{i,j,k}^b - X_{i,j,k}^b)^2 \right) + \lambda R(\Theta) \right) \quad (2)$$

where  $X_{i,j,k}^b, \hat{X}_{i,j,k}^b$  represents the model-predicted and ground-truth data for the  $b$ -th segment;  $i, j, k$  denote the indexes of time step, bridge node, and feature dimension;  $B$  and  $D$  denote the number of batch size and considered feature dimension (i.e.,  $D = 1$  represents environmental temperature or traffic flow);  $\lambda$  is the regularization coefficient, and  $R(\Theta)$  is the regularization term.

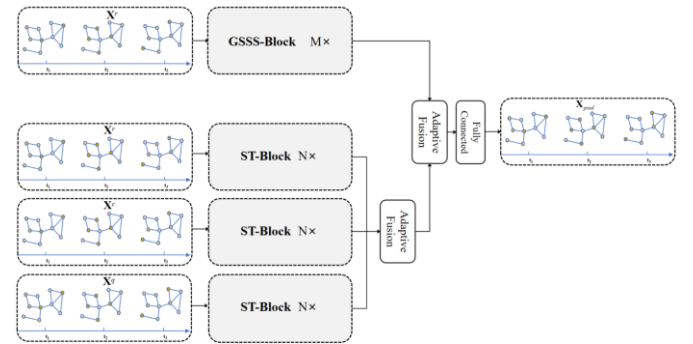


Figure 1. Overall schematic of the proposed STGSSSM.

### 4 EXPERIMENT STUDIES

#### 4.1 Datasets

Two real-world datasets are utilized here to assess the proposed approach for spatial-temporal prediction of environmental temperature and traffic flow for bridge groups. Training samples for time series are typically obtained by sliding a window of length  $P + T$  across the original time series. Here, the first  $P$  time steps are used as historical data, and the subsequent  $T$  time steps are used as future data; and the datasets are detailed as follows:

- **KnowAir<sup>[26]</sup>**: This temperature dataset contains spatial-temporal temperature data from weather stations across 184 main cities in China from September 1, 2016, to

January 31, 2017. It contains 184 nodes (weather stations) and 11688 time steps of temperature data with a 1-hour time interval; and the adjacency matrix of the graph is constructed based on the geographical locations of the weather stations. In the released KnowAir dataset,  $P = 7 \times 24$ , and  $T = 12$ .

- **PEMS04**<sup>[9]</sup>: This traffic dataset consists of spatial-temporal traffic flow data on California road network from January 1, 2018, to February 28, 2018. It contains 307 nodes (traffic monitoring stations) and 16992 time steps of data with a 5-minute time interval; and the adjacency matrix of the graph is constructed based on the geographical locations of the traffic monitoring stations. In the released PEMS04 dataset,  $P = 7 \times 24 \times 12$ , and  $T = 24$  or 36.

#### 4.2 Experimental Setup

All the datasets are split with a ratio of 7:1:2 for training/validation/testing sets, respectively. Before starting the model training process, all the data samples are normalized into range [0,1] with min-max normalization. The batch size is set as 48, and AdamW is employed as the optimizer. Model training epochs is set as 200. The number of ST-Blocks is set as  $N = 8$  with a sequence of dilation ratios  $R = 1$  or 2, and the number of GSSS-Blocks is set as  $M = 4$ . The diffusion step  $K = 2$  in Eq. (5), and the number of parallel Dynamic Filter GC,  $m = 3$  in Eq. (7). Hyperparameters in Eq. (3) of MSE loss function are set as the regularization coefficient  $\lambda$  of  $1e^{-2}$  and the learning rate of  $1e^{-4}$ .

All experiments are conducted under the software environment of PyTorch 1.12.1 and Python 3.8.10 with a NVIDIA GeForce RTX 3090 24GB GPU to accelerate neural computing. The training process requires nearly 4h for obtaining a well-trained model with acceptable accuracy.

#### 4.3 Comparative Studies with Baseline Models

Two recent Graph-based spatial-temporal predictive model of STGCN<sup>[9]</sup> and MTGNN<sup>[18]</sup> are utilized as baselines for comparative studies. STGCN integrates graph convolutional layers to model spatial dependencies and gated temporal convolutional layers to capture temporal dynamics in traffic data. MTGNN considers the features in the time-series to be multivariate and captures spatial dependencies through a learned graph structure, which uses a mix-hop propagation layer to handle spatial dependencies and a dilated inception layer for temporal dependencies.

In comparative studies with STGCN and MTGNN models, to ensure fairness, several trials are conducted to select an acceptable model with good accuracy though not necessarily optimal. For STGCN, the graph and temporal convolution kernel sizes are set to 3. Chebyshev polynomial approximation and first-order approximation are used in STGCN. For MTGNN, the propagation depth and dilation factor are set to 2 and 1, respectively. During training, the Adam optimizer is employed with a  $1e^{-3}$  learning rate, a regularization coefficient of  $1e^{-4}$ , and a dropout rate of 0.3. These adjustments made sure that the baseline models performed well on our datasets, which enable a fair comparison of model performances and a better evaluation of the proposed STGSSSM's strengths.

Evaluation metrics of mean absolute error (MAE), root mean squared Error (RMSE), and mean absolute percentage error

(MAPE) are utilized to measure and assess the accuracy of various methods.

The MAE is defined as

$$MAE_{test} = \frac{1}{TND} \sum_{i=t+1}^{t+T} \sum_{j=1}^N \sum_{k=1}^D |\hat{X}_{i,j,k} - X_{i,j,k}| \quad (3)$$

The RMSE is defined as

$$RMSE_{test} = \sqrt{\frac{1}{TND} \sum_{i=t+1}^{t+T} \sum_{j=1}^N \sum_{k=1}^D (\hat{X}_{i,j,k} - X_{i,j,k})^2} \quad (4)$$

The MAPE is defined as

$$MAPE_{test} = \frac{100\%}{TND} \sum_{i=t+1}^{t+T} \sum_{j=1}^N \sum_{k=1}^D \left| \frac{\hat{X}_{i,j,k} - X_{i,j,k}}{\hat{X}_{i,j,k}} \right| \quad (5)$$

Table 1 shows the performance comparison of the proposed STGSSSM with baseline models of STGCN and MTGNN. In the experimental results, 12 hours with a time interval of 1 hour corresponds to 12 time steps for temperature prediction; 6 hours with a time interval of 5 minutes corresponds to 72 time steps for traffic flow prediction; 9 hours corresponds to 108 time steps for traffic flow prediction.

Table 1. Performance comparison of the proposed STGSSSM with baseline models of STGCN and MTGNN.

KnowAir	12h		
	MAE	RMSE	MAPE
STGCN	0.35	0.51	3.77%
MTGNN	0.33	0.48	3.34%
STGSSSM	<b>0.28</b>	<b>0.44</b>	<b>3.02%</b>
PEMS04	6h		
	MAE	RMSE	MAPE
STGCN	14.21	20.85	12.95%
MTGNN	<b>13.28</b>	19.67	12.34%
STGSSSM	13.39	<b>19.47</b>	<b>12.12%</b>
PEMS04	9h		
	MAE	RMSE	MAPE
STGCN	17.60	26.39	14.96%
MTGNN	16.76	25.13	14.39%
STGSSSM	<b>16.37</b>	<b>24.01</b>	<b>14.23%</b>

#### 4.4 Ablation Study

To assess the effectiveness of each model component within STGSSSM, three kinds of model variants are first designed, and their forecasting performance is evaluated on the KnowAir and PEMS04 datasets: (1) the full model of STGSSSM, (2) GSSSM without STGCM, (3) STGCM without GSSSM.

To further evaluate the effects of three temporal granularities of recent, cyclic, and trend data, another three kinds of model variants are designed: (4) STGSSSM without cyclic and trend data, (5) STGSSSM without cyclic data, (6) STGSSSM without trend data.

Table 2. Model performances of ablation study for different modules of STGSSSM.

KnowAir	12h		
	MAE	RMSE	MAPE
STGSSSM	<b>0.28</b>	<b>0.44</b>	<b>3.02%</b>
GSSSM w/o STGCM	0.39	0.54	4.15%
STGCM w/o GSSSM	0.31	0.47	3.27%
STGSSSM w/o cyclic and trend	0.40	0.55	4.27%
STGSSSM w/o cyclic	0.30	0.45	3.16%
STGSSSM w/o trend	0.29	0.44	3.13%
PEMS04	6h		
	MAE	RMSE	MAPE



STGSSSM	<b>13.39</b>	<b>19.47</b>	12.12%
GSSSM w/o STGCM	18.86	28.94	15.72%
STGCM w/o GSSSM	14.48	21.46	12.29%
STGSSSM w/o cyclic and trend	13.94	20.25	12.22%
STGSSSM w/o cyclic	13.51	19.57	12.01%
STGSSSM w/o trend	13.45	19.63	<b>11.93%</b>
<b>PEMS04</b>			
	9h		
	MAE	RMSE	MAPE
STGSSSM	<b>16.37</b>	<b>24.01</b>	14.23%
GSSSM w/o STGCM	18.99	29.21	15.66%
STGCM w/o GSSSM	18.38	27.86	15.11%
STGSSSM w/o cyclic and trend	16.83	24.92	14.81%
STGSSSM w/o cyclic	16.39	24.36	13.95%
STGSSSM w/o trend	16.38	24.27	<b>13.93%</b>

The results in Table 2 show the contributions of each module to the overall performance.

(1) Influence of STGCM: The STGCM, which processes recent, cyclic, and trend data through a series of spatial-temporal graph convolution operations, is essential for capturing complex spatial-temporal dependencies. The results show that removing the STGCM leads to a substantial decline in performance across both datasets. For instance, on the KnowAir dataset, the MAE, RMSE, and MAPE increase from 0.28, 0.44, and 3.02% (full model) to 0.39, 0.54, and 4.15% (GSSSM w/o STGCM), respectively. Similarly, on the PEMS04 dataset, the MAE, RMSE, and MAPE rise from 13.39, 19.47, and 12.12% (6h prediction) to 18.86, 28.94, and 15.72% (GSSSM w/o STGCM). This shows that the STGCM greatly boosts the model's ability to handle multi-granularity data and extract meaningful spatial-temporal features.

(2) Influence of GSSSM: The GSSSM, which models the evolution of spatial-temporal dependencies and optimizes computational resources, also makes a significant contribution to the model's performance. Removing the GSSSM results in a significant decline in performance. On the KnowAir dataset, the MAE, RMSE, and MAPE increase to 0.31, 0.47, and 3.27%, respectively. On the PEMS04 dataset, the MAE, RMSE, and MAPE rise to 14.48, 21.46, and 12.29% (6h prediction). This demonstrates the importance of the GSSSM in dynamically adjusting the model's behavior and focusing on the most relevant parts of the data.

(3) Influence of Multi-Granularity Data Fusion: The fusion of recent, cyclic, and trend data is another critical aspect of the model. The results illustrate that removing both cyclic and trend data (STGSSSM w/o cyclic and trend) results in a significant decline in performance. On the KnowAir dataset, the MAE, RMSE, and MAPE increase to 0.40, 0.55, and 4.27%, respectively. On the PEMS04 dataset, the MAE, RMSE, and MAPE rise to 13.94, 20.25, and 12.22% (6h prediction). This shows that the fusion of multi-granularity data is crucial for seizing diverse temporal patterns and enhancing prediction accuracy.

(4) Influence of Individual Data Components: The results also illustrate the contributions of individual data components (cyclic and trend data). Removing only the cyclic data (STGSSSM w/o cyclic) or only the trend data (STGSSSM w/o trend) leads to moderate performance declines. On the

Temperature dataset, removing cyclic data results in MAE, RMSE, and MAPE of 0.30, 0.45, and 3.16%, while removing trend data results in 0.29, 0.44, and 3.13%. On the PEMS04 dataset, removing cyclic data leads to MAE, RMSE, and MAPE of 13.51, 19.57, and 12.01% (6h prediction), while removing trend data results in 13.45, 19.63, and 11.93%. These results indicate that both cyclic and trend data boost the model's performance, with cyclic data having a slightly more significant impact.

The proposed STGSSSM model gains from the integration of the multi-granularity data fusion, STGCM and GSSSM, which jointly deliver accurate and efficient spatial-temporal predictions for bridge groups.

## 5 CONCLUSION

This study introduced a Graph Selective State Space Model (STGSSSM) for predicting environmental temperature and traffic flow in bridge groups, integrating Graph Neural Networks (GNNs) and State Space Models (SSMs). The main contributions of the model include adaptive fusion of multi-granularity data, a Spatial-Temporal Graph Con-volution Module (STGCM), and a Graph Selective State Space Module (GSSSM). Experiments on real-world datasets (KnowAir and PEMS04) show STGSSSM outperforms state-of-the-art models like STGCN and MTGNN in prediction accuracy and efficiency. Ablation experiments validate that each component is effective, necessary, and enhances accuracy in capturing complex spatial-temporal dependencies. The proposed STGSSSM achieves overall prediction accuracy improvements of environmental temperature at the ranges of [13.70%, 20.00%] and [8.30%, 15.15%] and traffic flow at the ranges of [4.90%, 9.00%] and [1.02%, 4.46%] compared with STGCN and MTGNN, respectively. Specifically, the reported STGCM, GSSSM and multi-granularity data fusion decreases the relative prediction error at the ranges of [7.93%, 28.99%], [1.32%, 13.80%], and [0.49%, 29.50%], respectively.

Future work may extend the model to more complex data and other infrastructure systems.

## ACKNOWLEDGMENTS

Financial support for this study was provided by the National Key R&D Program of China [Grant No. 2023YFC3805700], Heilongjiang Provincial Natural Science Foundation [Grant No. LH2022E070], and Fundamental Research Funds for the Central Universities [Grant No. HIT.NSRIF202334].

## REFERENCES

- [1] G. Albert and D. Tri, Mamba: Linear-time sequence modeling with selective state spaces, arXiv preprint arXiv:2312.00752, 2023.
- [2] A. Behrouz and F. Hashemi, Graph mamba: Towards learning on graphs with state space models, in Proceedings of the 30th ACM SIGKDD Conference on Knowledge Discovery and Data Mining, 119-130, 2024.
- [3] Q. Haohao, N. Liangbo, A. Rui, F. Wenqi, D. Tyler, L. Hui, X. Xin and L. Qing, A survey of mamba, arXiv preprint arXiv:2408.01129, 2024.
- [4] S. Atitallah, C. Rabah, M. Driss, W. Boulila and A. Koubaa, Exploring Graph Mamba: A Comprehensive Survey on State-Space Models for Graph Learning, arXiv preprint arXiv:2412.18322, 2024.
- [5] S. Youngjoo, D. Michaël and V. Pierre, Structured sequence modeling with graph convolutional recurrent networks, neural information processing: 25th international conference, ICONIP 2018, Siem Reap, Cambodia, December 13-16, 2018, proceedings, part I 25. Springer International Publishing, 362-373, 2018.

- [6] L. Yaguang, Y. Rose, S. Cyrus and L. Yan, Diffusion convolutional recurrent neural network: Data-driven traffic forecasting, arXiv preprint arXiv:1707.01926, 2017.
- [7] Z. Jiani, S. Xingjian and X. Junyuan, Gaan: Gated attention networks for learning on large and spatiotemporal graphs, arXiv preprint arXiv:1803.07294, 2018.
- [8] J. Ashesh, Z. Amir R., S. Silvio and S. Ashutosh, Structural-rnn: Deep learning on spatio-temporal graphs, in Proceedings of the IEEE Conference on Computer Vision and Pattern Recognition, 5308-5317, 2016.
- [9] Y. Bing, Y. Haoteng, and Z. Zhanxing, Spatio-Temporal Graph Convolutional Networks: A Deep Learning Framework for Traffic Forecasting, in Proceedings of the 27th International Joint Conference on Artificial Intelligence, 3634–3640, 2018.
- [10] S. Bai, J. Kolter and V. Koltun, An empirical evaluation of generic convolutional and recurrent networks for sequence modeling, arXiv preprint arXiv:1803.01271, 2018.
- [11] L. Pengfei, Z. Tong and J. Yantao, A spatio-temporal graph convolutional network for air quality prediction, Sustainability, 15(9): 7624, 2023.
- [12] Z. Gongpei, W. Tao, L. Congyan, J. Yi, L. Yidong and L. Haibin, Grassnet: State space model meets graph neural network, arXiv preprint arXiv:2408.08583, 2024.
- [13] B. Ali and H. Farnoosh, Graph mamba: Towards learning on graphs with state space models, in Proceedings of the 30th ACM SIGKDD conference on knowledge discovery and data mining, 119-130, 2024.
- [14] W. Chloe, T. Oleksii, M. Jun and W. Bo, Graph-mamba: Towards long-range graph sequence modeling with selective state spaces, arXiv preprint arXiv:2402.00789, 2024.
- [15] Y. Haonan, S. Qingyun, W. Zhaonan, F. Xingcheng, J. Cheng, W. Yongjian, J. Bo and L. Jianxin, DG-Mamba: Robust and Efficient Dynamic Graph Structure Learning with Selective State Space Models, arXiv preprint arXiv:2412.08160, 2024.
- [16] Z. Ling, S. Yujiao, Z. Chao, L. Yu, W. Pu, L. Tao, D. Min and L. Haifeng, T-GCN: A temporal graph convolutional network for traffic prediction, IEEE transactions on intelligent transportation systems, 21(9): 3848-3858, 2019.
- [17] W. Zonghan, P. Shirui, L. Guodong, J. Jing and Z. Chengqi, Graph WaveNet for Deep Spatial-Temporal Graph Modeling, arXiv preprint arXiv:1906.00121, 2019.
- [18] W. Zonghan, P. Shirui, L. Guodong, J. Jing, C. Xiaojun and Z. Chengqi, Connecting the dots: Multivariate time series forecasting with graph neural networks, in Proceedings of the 26th ACM SIGKDD international conference on knowledge discovery & data mining, 753-763, 2020.
- [19] Z. Chuanpan, F. Xiaoliang, W. Cheng and Q. Jianzhong, GMAN: A graph multi-attention network for traffic prediction, in Proceedings of the AAAI conference on artificial intelligence, 34(01): 1234-1241, 2020.
- [20] G. Shengnan, L. Youfang, W. Huaiyu, L. Xiucheng and C. Gao, Learning Dynamics and Heterogeneity of Spatial-Temporal Graph Data for Traffic Forecasting, IEEE Transactions on Knowledge and Data Engineering, PP (99):1-1, 2021.
- [21] Z. Xingyu, W. Zhongyu and Z. Zhihao, Adaptive Spatio-Temporal Graph Recurrent Network for Sea Surface Temperature Forecasting, IEEE Transactions on Geoscience and Remote Sensing, 2024.
- [22] Y. Hanchen, L. Wengen, H. Siyun and G. Jihong, HiGRN: a hierarchical graph recurrent network for global sea surface temperature prediction, ACM Transactions on Intelligent Systems and Technology, 14(4): 1-19, 2023.
- [23] Y. Xuan, S. Suixiang and X. Lingyu, A spatial-temporal graph attention network approach for air temperature forecasting, Applied Soft Computing, 113: 107888, 2021.
- [24] G. Ang, L. Yanghe, S. Shiyu, S. Xiaowei and F. Zhenni, Spatial-Temporal Fusion Graph Neural Networks with Mixed Adjacency For Weather Forecasting, IEEE Access, 2025.
- [25] X. Zhewen, W. Xiaohui and H. Jieyun, DGFormer: a physics-guided station level weather forecasting model with dynamic spatial-temporal graph neural network, GeoInformatica, 28(3): 499-533, 2024.
- [26] E. Saleh, S. Al-Werfalli, T. Imbarak, S. Elakeili and H. Elmajpri, Know-Air: A Low-Cost PM2.5 Sensor Citizen-Based Air Pollution Monitoring System for Real-Time, International Conference for Information and Communication Technologies, Cham: Springer Nature Switzerland, 159-172, 2023.

# Ultimate flexural strength analysis of serving concrete main girders considering bridge deck pavement

Hongtao Cui<sup>1</sup>, ORCID (0000-0001-8470-2701), Zhonglong Li<sup>1</sup>, Yapeng Guo<sup>1</sup>, Shunlong Li<sup>1</sup>

<sup>1</sup>School of Transportation Science and Engineering, Harbin Institute of Technology, 73 Huanghe Road, 150090 Harbin, China  
email: cuihongtao@hit.edu.cn, lizhonglong@hit.edu.cn, guoyapeng@hit.edu.cn, lishunlong@hit.edu.cn

## ABSTRACT:

### Introduction:

Concrete girders are a type of widely used structures in small and medium span bridges. The ultimate flexural strength of concrete main girders serves as a critical foundation for assessing the structural performance of small and medium span simply supported girder bridges, and is essential for ensuring their safe operation. After the installation of prefabricated concrete girders, cement and asphalt concrete are sequentially poured on the top surface of the girders as bridge decks. The bridge deck pavement and concrete girder jointly bear the overall external loads. However, during the design and operation stages, the bridge deck pavement is typically regarded as secondary dead load when estimating bearing capacity, without considering its inherent reinforcement effect on the main girder. Thus, understanding the damage mechanism and destructive behaviour of concrete girders whilst considering the deck pavement effect is crucial for bridge safety assessment. The currently prevalent laboratory-based research method using scaled models can effectively elucidate the failure mechanisms of concrete girder members by controlling the experimental environment, the findings cannot be directly extrapolated to evaluate the service performance of actual bridge structures.

### Description of the serving concrete main girders:

This study focused on retired concrete main girders from real-world service environments, conducting ultimate flexural strength tests. The full-scale retired prestressed concrete girder used in this study was taken from a highway bridge in Northeast China. The bridge span, deck width, and structural form are typical representatives of medium and small-sized highway concrete girder bridges in this region. The superstructure is a post-tensioned prestressed concrete hollow slab girder with a calculated span of 17.60 m. The total width of the deck is 13 m, and the width of the motor vehicle lane is 12 m. The deck pavement is made of 10 cm thick cement concrete and 8 cm thick asphalt concrete. When the bridge was demolished, the top layer of asphalt concrete was milled off first, and then a cutting machine was used for longitudinal cutting to remove the cement concrete deck pavement along with the main girder as a whole. The research object of this paper is one of the middle girders, with a girder height of 90 cm and a width of 124 cm. Both the main girder and the deck pavement are made of C40 concrete. The stirrups of the top slab use HPB300 steel bars with a diameter of 12 mm, while the remaining stirrups and longitudinal bars use HPB300 steel bars with a diameter of 8 mm. The specification of the prestressed steel strands is  $1 \times 7 \phi^s 15.2$ , with a standard strength of 1860 MPa and a low-relaxation high-strength steel strand, and the initial tensile stress is 1178 MPa.

To study the crack development and failure mode of full-scale prestressed hollow slab girders in combination with the bridge deck pavement layer, the material properties of the test girders were tested. The compressive strength test of concrete was carried out in accordance with the "Technical specification for inspecting of concrete compressive strength by rebound method" (JGJ/T 23 - 2011). Before the failure test, rebound tests were conducted on the web and bottom slab of the girder. A total of 18 test areas were selected on the web and bottom slab of the test girder at intervals of 1 m, with 16 test points in each area. The average carbonation depth was tested using alcohol phenolphthalein solution, which was 2.5 mm. The rebound values of the concrete in each test area of the web and bottom slab of the test girder were basically the same, with an average value of  $R_{mc} = 52.2$ . The concrete strength was converted using a unified strength curve, which was 56.1 MPa.

During the test, to restore the boundary conditions as accurately as possible, fixed and sliding supports were respectively set up at both ends of the test girder, with a center distance of 17.30 m. The loading points were arranged at 7 m and 11 m away from the girder ends, and four-point bending loading was carried out using reaction frames and jacks. The 4 m range at the mid-span of the test girder was the pure bending section. A pressure sensor with a range of 2000 kN was installed between the jack and the reaction frame to monitor the pressure value in real time. To prevent the stress concentration effect from crushing the bridge deck pavement concrete, a  $0.5 \text{ m} \times 0.5 \text{ m}$  pad was placed between the jack and the test girder. Strain gauges and displacement transducers (Linear Variable Differential Transducers, LVDTs) were used to monitor the response of the test girder under static loading. Measuring points were arranged vertically at intervals of 20 cm on both side webs, and were densified at the variable cross-section positions. LVDTs were installed below the webs at 1/4 span, mid-span and 3/4 span of the test girder to monitor the deflection. Considering that the supports would deform downward during loading, LVDTs were arranged below the sliding and fixed supports to calibrate the actual deformation of the test girder. LVDTs were arranged along the longitudinal direction of the girder at the end of the sliding support, and a high-speed camera was placed in front of the web in the pure bending section to record the crack propagation process. Loading and sensor arrangement for flexural test can be seen in Fig.1.



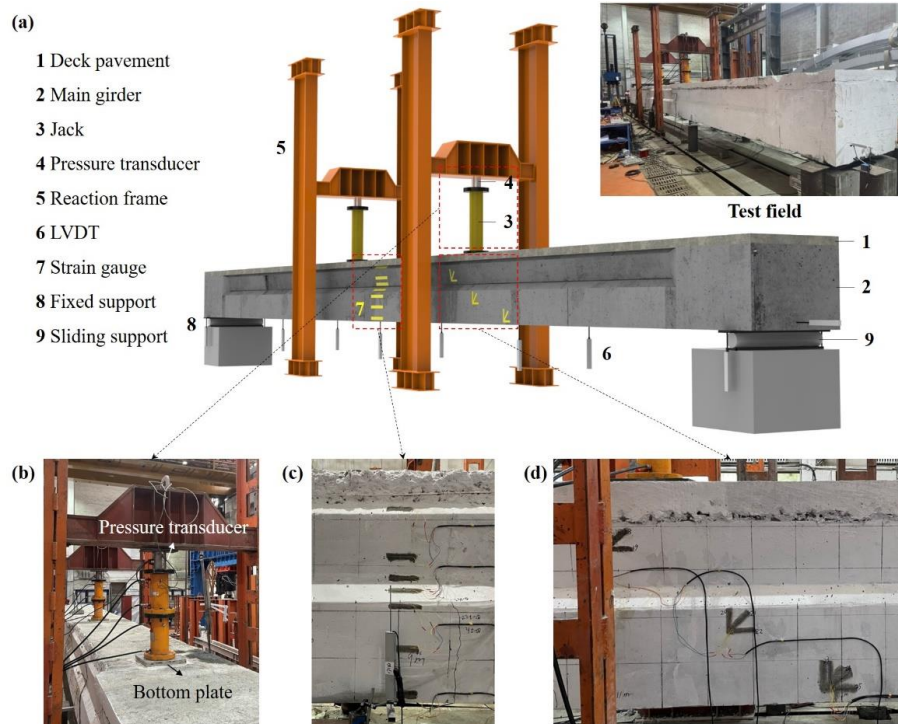


Fig.1. Loading and sensor arrangement for flexural test: (a) overall layout; (b) jack and pressure transducer; (c) strain gauge arrangement in mid-span; (d) strain gauge arrangement at shear position

### Establishing of FEMs:

To further investigate the mechanical behavior of the failure process of retired prestressed concrete girders and the influence of bridge deck pavement, two three-dimensional FEMs were established based on ABAQUS, namely the model with bridge deck pavement (Model 1) and the model without bridge deck pavement (Model 2). Then, the global response (deflection) and local response (strain and cracking) at each load level were calculated. The dimensions of each component in Model 1 were the same as those in the test field. Reference points were established and connected to the action surfaces of the supports and loading points through "coupling", and the boundary conditions and loads were controlled through the reference points. The main girder, bridge deck pavement, loading block and supports were simulated using continuous linear three-dimensional stress elements (C3D8R) with a mesh size of 5 cm. The prestressed steel strands were simulated using linear three-dimensional truss elements (T3D2), and the "embedded" constraint method was used to bond the prestressed steel strands with the surrounding concrete elements. The prestress was applied to the steel strands through the thermal stress method. Python scripts were used to batch establish line elements between the top plate of the main girder and the bridge deck pavement and specify them as sliding plane elements. The FEMs can be seen in Fig. 2.

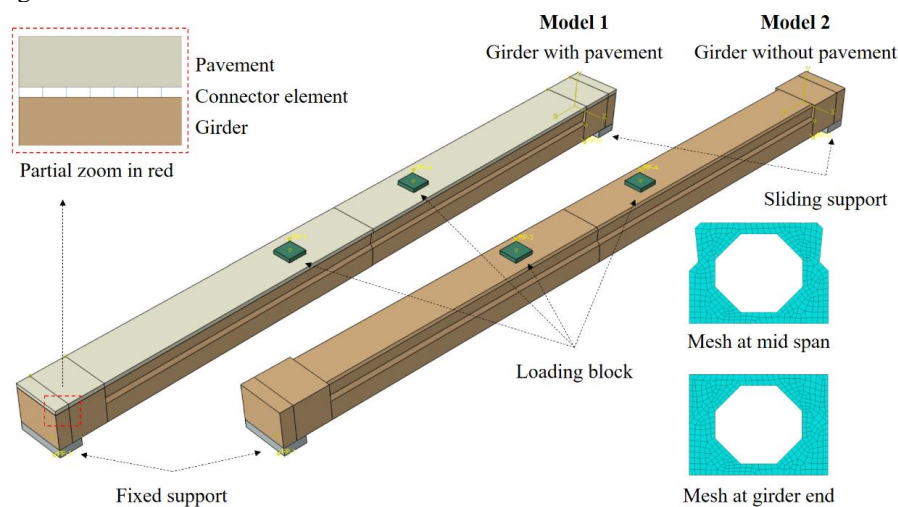


Fig.2. Establishing the FEMs

During the test, when a certain load was applied, a slip occurred between the bridge deck pavement layer and the main girder. This indicates that in the FEM, the connection between the bridge deck pavement and the main girder cannot be simulated by the

"binding" consolidation method. In this paper, the detachment of the bridge deck pavement is simulated by the failure of the connecting element. This study refers to the shear strength proposed by Mohama, considers the adhesive effect of concrete and the shear friction effect between components, and modifies the expression. Based on the results of experimental tests and FEM calculations, the coefficient corresponding to the peak bond force was derived according to the load at which the bridge deck pavement and the main girder cracked. The coefficient of concrete friction force was derived based on the load when the bridge pavement completely slipped. The derived formula is as follows:

$$\tau = \left(0.2378e^{0.237R_{pm}}\right)f_t + \left(0.5479R_{pm}^{0.3978}\right)\sigma_n$$

Through the observation of the test phenomena, the failure process of the test girder can be divided into three stages. The first stage is the elastic stage, during which the test girder is in an intact state as a whole, and the mid-span deflection increases linearly with the load. The second stage is the working stage with cracks. After reaching the cracking load, the cracks extend from the bottom plate to the web. As the load increases, the length and width of the cracks gradually increase, and they no longer extend when they approach the top plate. Cracks first appear between the bridge deck pavement and the main girder, and then they completely separate. The test girder enters the third stage of the failure process. At this time, the main girder mainly bears the load, and the strengthening effect of the bridge deck pavement on the main girder basically disappears. With the further increase of the load, the test girder completely breaks.

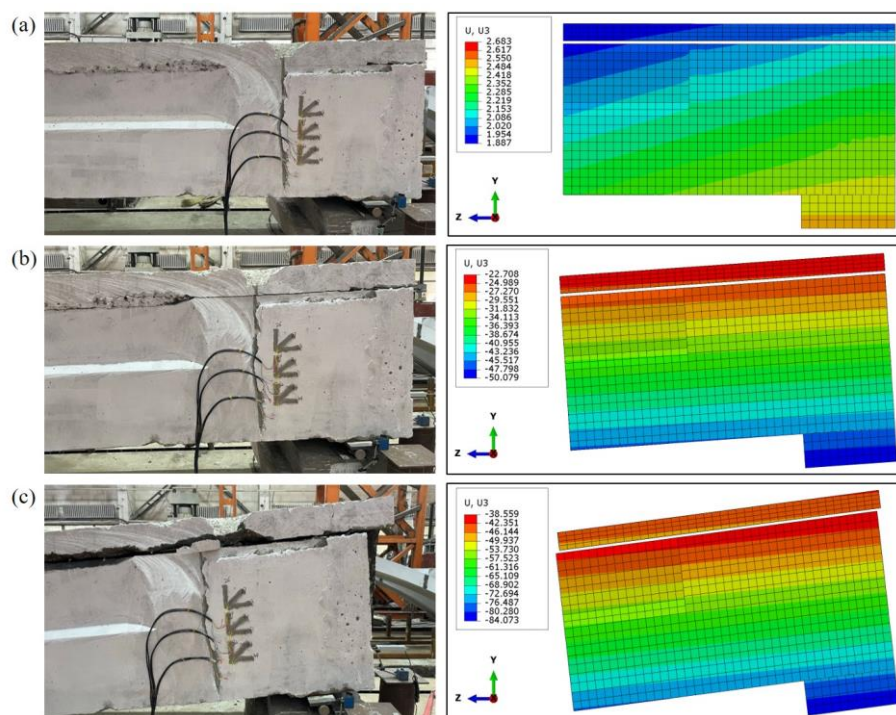


Fig.3. The three stages of main girder failure

## Results and analysis:

The load-deflection curve at mid-span is the most direct indicator for evaluating the bearing capacity of the test girder, which can be seen in Fig.4. The state of the test girder can be divided into three stages: the first stage is the elastic state, where the load is within the range of 0 to 200 kN, and the load-displacement curve is basically linear. When the load reaches 200 kN, the deflection-span ratio of the test girder is 1/1193; the second stage is the working state with cracks, when the load is greater than 200 kN, as the cracks extend towards the top slab, the stiffness of the test girder significantly decreases, and the mid-span displacement begins to increase at a larger rate. When the load reaches 541.5 kN, the bridge deck pavement layer completely detaches from the main girder, at which point the deflection-span ratio is 1/95. The structural system undergoes a sudden change, and the load suddenly decreases; in the third stage, the test girder enters the plastic state, loses its bearing capacity, and the mid-span displacement increases significantly before complete fracture. Without considering the effect of the bridge deck pavement, the bearing capacity of model 2 is significantly lower than that of model 1. Due to the reduction in section height, the displacements corresponding to the cracking point and the inflection point of the curve are slightly larger than those in model 1. Similar to model 1, the inflection point of the curve lags behind the cracking point. The slope of the load-deflection curve can be used to characterize the stiffness of the test girder. In the elastic stage, due to the strengthening effect of the bridge deck pavement layer, the overall stiffness of the test girder increases by 27.7%, the cracking load increases by 16.4%, and the load at the state inflection point increases by 16.7%. After the bridge deck pavement layer is completely separated from the main girder, the strengthening effect of the pavement layer disappears, and the load is mainly borne by the main girder. The load at the complete fracture of the test

girder is 496.7 kN, and the ultimate load before the bridge deck pavement detaches is 541.5 kN. Under the strengthening effect of the bridge deck pavement layer, the ultimate load of the test girder increases by 9.0%.

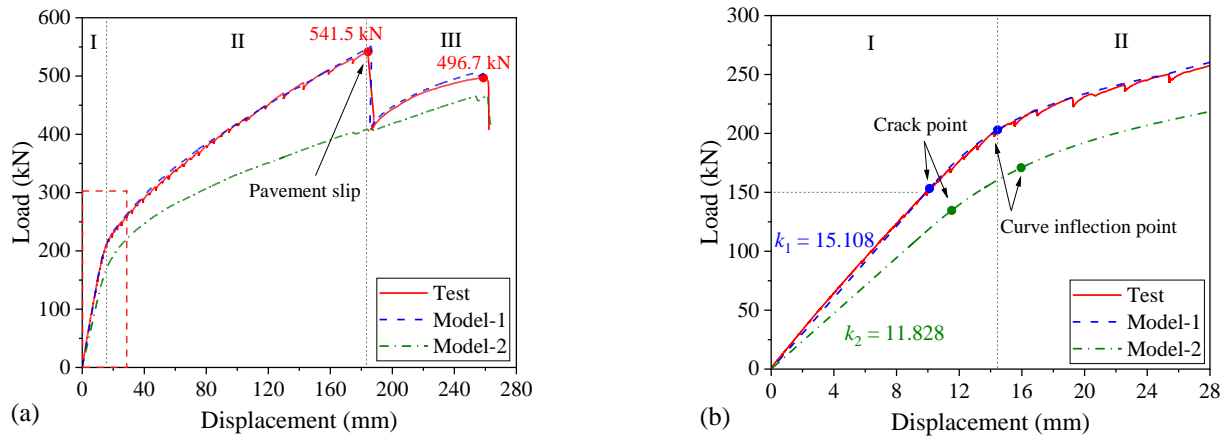


Fig.4. Load –displacement in mid span curves: (a) entire process; (b) local zoom in red box of (a)

The widths of key cracks under each loading step were recorded using a crack tester during the experimental process. Fig. 5 shows the maximum width of cracks under critical loads. According to the Specifications for design of highway reinforced concrete and prestressed concrete bridges and culverts (JTG 3362 – 2018), the maximum allowable crack width for PC components using steel strands in freeze–thaw areas under normal use is 0.10 mm. According to the test results, when the load was 170 kN (corresponding mid-span moment of 1190 ), the crack width reached the limit allowed by the specifications. The “condition rating” recommended by the International Atomic Energy Agency guidelines defines three types of damage levels based on the maximum crack width: grade I (minor damage: < 0.2 mm), grade II (moderate damage: 0.2–1.0 mm), and grade III (critical damage: > 1.0 mm). Based on the maximum crack width, the structure had minor damage when the load was 210 kN, when the load was approximately 210–320 kN, the structure was moderately damaged, and when the load exceeded 320 kN, the structure was critically damaged.

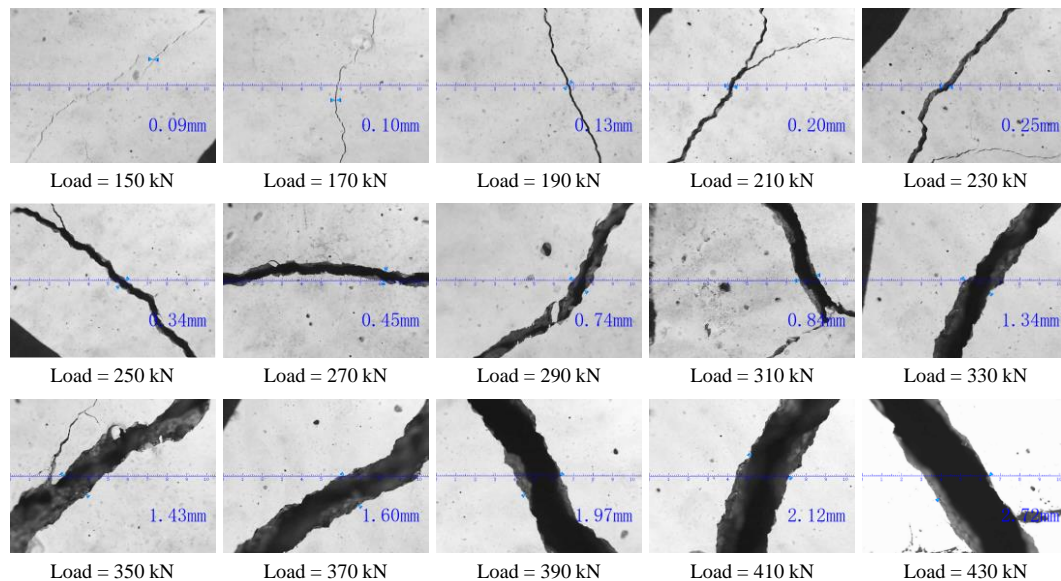


Fig.4. Maximum crack width in critical loads

In fact, for prestressed concrete girder bridges, whether in the design or inspection process, the strengthening effect of the bridge deck pavement on the main girder is not considered when calculating the bearing capacity of the main girder. Instead, it is applied to the main girder as a second-stage dead load. If its strengthening effect is taken into account, the design and inspection results are often overly conservative. The research on the strengthening effect of the bridge deck pavement on the main girder in this paper is not aimed at guiding the design optimization of prestressed concrete girder bridges. During the dynamic and static load inspection of prestressed concrete simply supported girder bridges in cold regions, the bridge deck pavement is also regarded as a second-stage dead load without considering its strengthening effect on the main girder. This will lead to an inability to grasp the true state of the main girder when inferring the bridge's bearing capacity from the inspection results, and thus an inaccurate assessment of its safety performance. If the structural state of the main girder does not meet the standards for normal use, the



inspection results may still meet the requirements under the strengthening effect of the bridge deck pavement, which will pose potential risks during the operation of the bridge. If the strengthening effect of the bridge deck pavement is considered in the simulation calculation, the threshold for the safety assessment of prestressed concrete girder bridges can be corrected, thereby more accurately evaluating the safety margin of the bridge structure. At this time, it is very necessary to consider the reinforcing effect of the bridge deck pavement.

**KEY WORDS:** Bridge engineering, Full-scale concrete main girders, Bridge deck pavement, Ultimate flexural strength, Numerical simulation



# Structural Health Monitoring of Transport Infrastructures using Drive-by Monitoring

# Data-Driven Monitoring Solutions for Concrete Structures: Long-Term Insights with CorroDec2G Sensors

Christian Steffes<sup>1</sup>

<sup>1</sup>Infrasolute GmbH, An den Kreuzen 3, D-56154 Boppard  
email: Christian.steffes@infrasolute.com

**ABSTRACT:** Passive sensor technologies offer a robust solution for monitoring concrete structures. These technologies utilize advanced methods to measure critical parameters such as moisture, corrosion, and temperature within the concrete. By employing RFID technology, the sensors operate wirelessly and require no maintenance. With a lifespan exceeding 80 years, passive sensors enable comprehensive and efficient long-term structural monitoring.

This article provides insights into the installation methods, the benefits of the cloud-based data platform, and how this technology contributes to improved safety, durability, and the preservation of infrastructure.

**KEY WORDS:** SHMII-13; Full paper; Corrosion monitoring; Moisture monitoring; Passive RFID sensors; Bridge rehabilitation

## 1 INTRODUCTION

### 1.1 *The importance of preventive monitoring of concrete structures*

In modern structural monitoring, the early detection of damage plays a central role.

Concrete structures such as bridges are exposed to extreme loads and environmental influences on a daily basis. The increasing demands on the safety and durability of such structures make continuous monitoring indispensable [1]. Preventive monitoring helps to identify potential damage at an early stage and to initiate appropriate measures before costly repairs or even critical failures occur [2].

In this context, the passive sensor technology CorroDec2G by Infrasolute offers innovative solutions. This technology enables long-term monitoring of structural integrity by capturing key parameters such as moisture, corrosion progression, and temperature within the concrete. Since 2018, these sensors have been used in various reinforced concrete structures and have established themselves as a reliable early warning system. The robust design of the sensors and their easy integration into existing structural elements facilitate their use in both new constructions and retrofit applications.

The advantages of this technology lie particularly in its passive nature—meaning it does not require an external power supply, which reduces maintenance costs. In addition, the sensors deliver precise long-term data that can be processed using modern data analysis systems to identify trends and potential damage patterns at an early stage.

This article uses two practical examples (Figure 1) to explain how Infrasolute's sensor technology works, how installation is carried out, and what kind of data is collected. These case studies demonstrate how the use of CorroDec2G technology

can extend the service life of structures and improve operational safety.

### 1.2 *Moisture as a risk factor*

In the case of durability-relevant bridge damage, moisture penetration is the most common cause, which can lead to corrosion-related damage to prestressing steel in older bridges [3]. Therefore, both the determination of the amount of moisture and the moisture condition are of great importance—on the one hand to monitor the long-term functionality of structures, and on the other to quantify the direction of moisture flow. This enables timely and effective decisions regarding necessary maintenance measures.

Moisture can be measured either directly or indirectly. Direct moisture measurement methods are usually based on extracting the amount of water from the material and determining it directly [4]. This approach allows for very accurate results; however, it is considered a destructive method and is therefore only suitable to a limited extent for use on bridges [5].

Alternatively, the moisture content can be determined indirectly by measuring certain material properties of the water that are functionally related to the moisture level. For example, by measuring the conductivity of the water, the actual moisture content can be inferred using specific calibration curves [5]. Indirect methods are well-suited for continuous measurements; however, the results can be influenced by various parameters such as temperature, density, material composition, and conductivity [4].



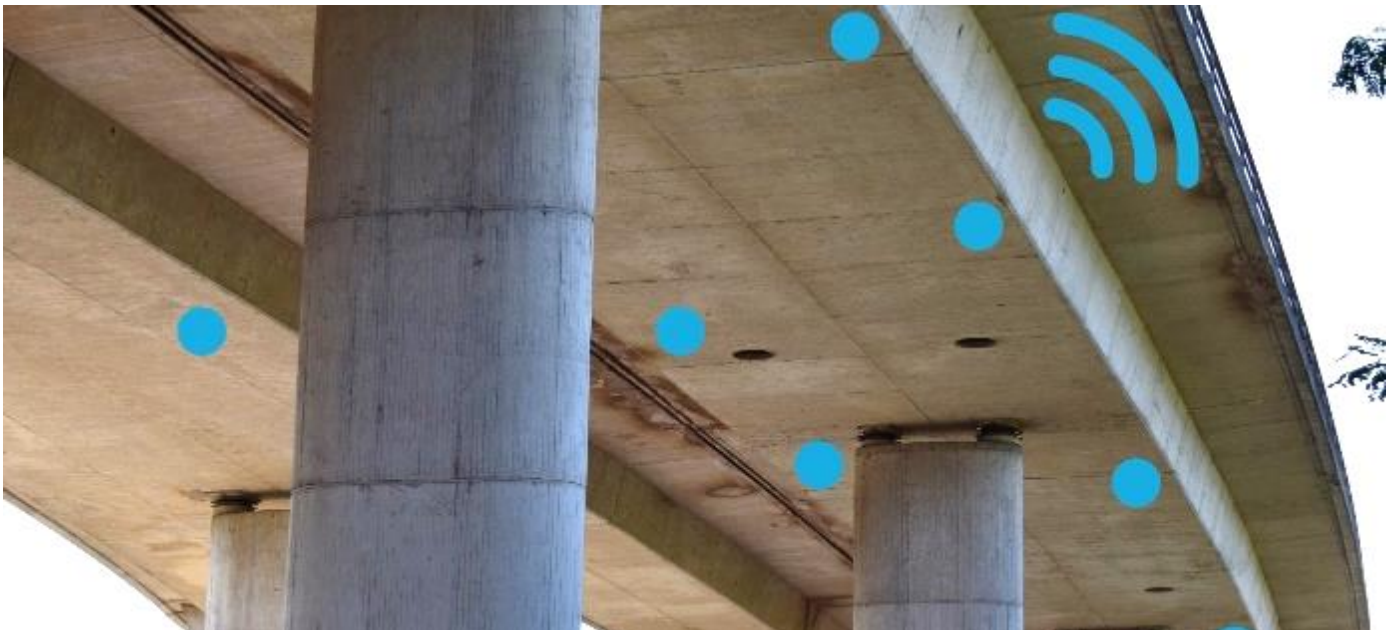


Figure 1. A selected practical example: Elevated Road Oberwerth, B327, in Koblenz (Copyright: Christian Steffes, Infrasolute).

## 2 FUNCIONALITY AND MEASUREMENT PRINCIPLE

The CorroDec2G sensors from Infrasolute are based on the indirect measurement method. They are characterized by their passive mode of operation. In contrast to active sensors, they do not require any cables or batteries to collect measurement data. Developed in cooperation with the Fraunhofer Institute for Microelectronic Circuits and Systems (IMS) in Duisburg, the sensors are designed to remain fully enclosed and maintenance-free within the concrete for the entire service life of a structure—at least 80 years—while transmitting data (moisture, temperature, corrosion) from within the structure [6].

The energy required for passive operation is supplied externally via RFID (radio-frequency identification) technology. RFID is a technology also used in everyday applications such as contactless credit card payments and enables wireless, contactless data transmission. With a reading range of up to 30 cm through concrete, the sensors can be reliably interrogated [10]. A specially designed antenna setup can extend this range up to 100 meters. In such cases, the measuring unit is embedded in the concrete, for example in the center of the roadway, while the reading unit is positioned in a strategically advantageous location outside the flow of traffic, allowing data retrieval without disrupting traffic.

The system's special design ensures that no component extends beyond the concrete surface, thereby eliminating potential weak points in the structure. This concept not only protects the structural integrity but also significantly extends the service life of the sensors by shielding them from environmental influences such as moisture, temperature fluctuations, and mechanical stress [5]. Such innovative RFID-based systems represent an important step toward sustainable structural monitoring, as they are cost-efficient in

the long term and do not interfere with the structure's operation.

## 3 INSTALLATION METHODS

### 3.1 New construction and rehabilitation

The installation of the sensors can be carried out both in new construction and during rehabilitation works. In new construction projects, as illustrated in Figure 2, the sensors are directly attached to the reinforcement using binding wires to ensure stable anchoring and to maintain their position during concreting—preventing, for example, floating within the fresh concrete. During rehabilitation works, such as after hydrodemolition (high-pressure water jet removal), the sensors can likewise be installed by affixing them to the exposed reinforcement. This allows for effective integration of the monitoring system even in existing structures without major modifications.



Figure 2. Attachment of moisture sensors in a new construction project using binding wires directly on the reinforcement (Copyright: Christian Steffes, Infrasolute).

Such precise installation procedures are particularly important to ensure accurate measurement data, which are crucial for condition assessment and maintenance planning [5].

### 3.2 Retrofitting installation

The sensors can be retrofitted into existing structures using core drilling. As shown in Figure 3, a core hole with a diameter of 100 mm allows the sensors to be embedded into the concrete without significantly affecting the structural integrity of the building. The sensor is placed in a thin layer of a special mineral-based, open-pored coupling mortar. This layer ensures optimal bonding with the existing concrete.

After installation, the coupling process begins. During this phase, moisture measurements can be used to monitor the drying of the surrounding coupling mortar. Once equilibrium moisture content is reached, the sensor can deliver precise data about the surrounding environment. The design of the coupling mortar ensures effective moisture migration from the existing concrete to the sensor.

To avoid creating a structural weak point, a sealing mortar is applied above the sensor after installation. This ensures a durable and secure integration into the structure while maintaining the mechanical and protective properties of the original concrete.



Figure 3. Core drilling with a diameter of 100 mm and installation of the sensor using coupling mortar (Copyright: Eugen Kronhardt, Infrasolute).

## 4 SENSORS AND DATA TRANSMISSION

### 4.1 Sensor variants

The **corrosion sensor** developed by Infrasolute can be identified by its characteristic red housing and the four surrounding wire layers (Figure 4).

The measurement method is based on the principle of proxy corrosion, in which the properties of the wires are specifically designed to closely replicate the corrosion behavior of reinforcement steel. Over time, the wires corrode in response to the surrounding environmental conditions [7].

The wire layers arranged around the sensor provide information about the presence and progression of corrosion, acting as indicators for the location of the passivation front. By analyzing the depth-wise arrangement of the wires, it is

possible to determine at what depth the passivation has broken down and how quickly the passivation front is advancing toward the reinforcement.

This data is critical for assessing the condition of the structure, planning further structural investigations, and initiating timely countermeasures to prevent the progression of corrosion [7].

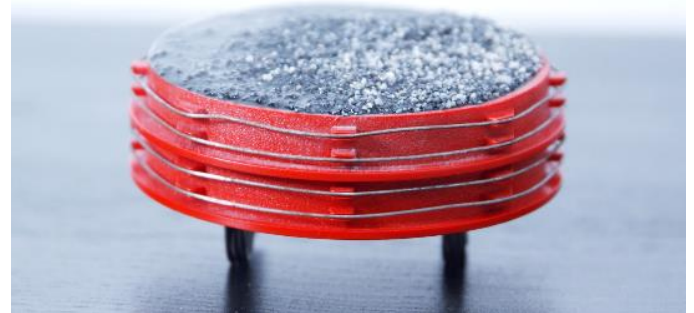


Figure 4. Corrosion sensor with two measurement wire layers (Copyright: Christian Steffes, Infrasolute).

The sensor operates using a redundant system, in which two circumferential wires form a single measurement layer. This design enhances the reliability of the measurement results and reduces potential sources of error. In addition, the corrosion sensor also measures temperature within the concrete, as temperature fluctuations can significantly influence corrosion dynamics [8]. The combination of corrosion monitoring and temperature measurement makes the corrosion sensor a vital tool for long-term monitoring and for implementing preventive maintenance strategies in reinforced concrete structures.

The **moisture sensor** (Figure 5) measures both moisture and temperature within the concrete. The moisture condition is a critical parameter in the formation of corrosion, as it affects the electrophysical environment required to initiate corrosion processes. By combining moisture and temperature data, it is possible to gain detailed insights into moisture development within the concrete. Early detection of moisture fluctuations allows for minimization of potential damage and contributes significantly to extending the service life of the structure.



Figure 5. Moisture sensor (Copyright: Christian Steffes, Infrasolute).

By combining a corrosion sensor and a moisture sensor placed approximately 15 cm apart, early information on corrosive processes and anomalies can be obtained. This spatial proximity enables detailed observation of the correlation between changes in moisture levels and the dynamics of corrosion processes, providing a deeper understanding of the environmental conditions that influence structural degradation.

#### 4.2 Data acquisition and transmission

There are two methods for retrieving data from the sensors embedded in the concrete. One option is to enable continuous data transmission, allowing the data to be accessed remotely at any time. For this purpose, a gateway, as shown in Figure 6, is installed near the sensor. This gateway both powers the sensor and transmits the collected data directly to the Infrasolute cloud platform.

Data transmission is carried out via NB-IoT (Narrowband Internet of Things), a communication standard specifically designed for reliable, energy-efficient data transfer in monitoring applications [7].



Figure 6. Solar-powered gateway (Copyright: Christian Steffes, Infrasolute).

As a low-bandwidth radio technology, NB-IoT (Narrowband Internet of Things) enables highly energy-efficient data transmission, allowing sensors and gateways to operate with minimal power consumption [10]. The technology also provides excellent building penetration, ensuring reliable signal transmission even through thick concrete structures (e.g., the new IT center in Koblenz, ground floor, wall thickness approx. 80 cm).

Thanks to support from existing mobile networks, NB-IoT is widely available, making it ideal for use in remote or hard-to-reach structures. Additionally, the low data transmission rate results in reduced operating costs, making NB-IoT a cost-effective solution for long-term monitoring applications.

The gateway is flexible in terms of power supply and can be operated via mains power, a long-life battery, or solar energy, depending on the construction site and local infrastructure. This flexibility enables deployment even in locations with limited access to conventional power sources. The combination of NB-IoT and energy-autonomous gateways represents a significant advancement in structural monitoring,

as it not only improves data quality but also reduces maintenance efforts.

Alternatively, there is the option of using a handheld reading device to manually retrieve sensor data on-site. The device shown in Figure 7 has been specially developed for this application. The process of collecting a sensor's measurement takes only a few seconds and is often carried out during routine bridge inspections by simply bringing the handheld device close to the sensor, enabling contactless and wireless data acquisition [7].



Figure 7. IoT handheld reader for manual sensor data acquisition (Copyright: Christian Steffes, Infrasolute).

The data collected by the handheld reader is transmitted directly to the cloud-based data platform via NB-IoT technology. This enables immediate verification and visualization of the measurement values on-site at the structure [8]. Both the gateway and the handheld reader transmit their data wirelessly via NB-IoT after sensor readout.

The sensor data is stored, referenced, visualized, and analyzed in the cloud platform by comparing it with previous measurements to enable precise trend analyses. Users can define threshold values, which—when exceeded—trigger automatic alerts, allowing potential issues to be identified at an early stage.

The platform also allows the integration of collected data into existing monitoring systems and can proactively send reports via email to all relevant project stakeholders. The data generated on the platform is presented in a user-friendly and easily understandable format, enabling all involved parties—regardless of their technical background—to effectively interpret the information.

## 5 SENSORS AND DATA TRANSMISSION

### 5.1 Südtangente in Koblenz – sensor variants

The Südtangente in Koblenz (Figure 8), constructed between 1972 and 1975, is a major traffic artery located just before the South Bridge crossing the Rhine River. It plays a key role in reducing urban traffic congestion. With a daily traffic volume of approximately 45,500 vehicles, including around 3% heavy goods traffic, it is considered part of the region's critical infrastructure [9]. The bridge connects important



transportation routes and is essential for both regional and long-distance traffic.



Figure 8. Südtangente in Koblenz (Copyright: Martin Lichtl, Infrasolute).

To meet the demands of increasing traffic volumes and to ensure the long-term durability of the bridge, the Südtangente in Koblenz has been undergoing comprehensive rehabilitation since 2020. As part of these measures, the roadway surface, structural waterproofing, guardrails, edge beams, and drainage systems have been renewed. In addition, all concrete surfaces have been repaired to enhance the load-bearing capacity and improve protection against environmental influences.

### 5.2 Sensor installation

As part of the rehabilitation, a comprehensive monitoring system was installed. The foundation for this was the execution of a potential field measurement, which enabled the precise localization of corrosion hotspots within the concrete. The results served as the basis for the targeted placement of sensors.

During the first two construction phases of the rehabilitation of the South Bridge in Koblenz, a total of 22 corrosion sensors and 62 moisture sensors were installed. The sensors were placed at critical and representative locations such as low points, expansion joints, waterproofing areas, structurally sensitive points, reference zones, and the corrosion hotspots identified by the potential field measurement. The final sensor placement was defined in coordination with the planning team. The installation layout is shown in Figure 9.

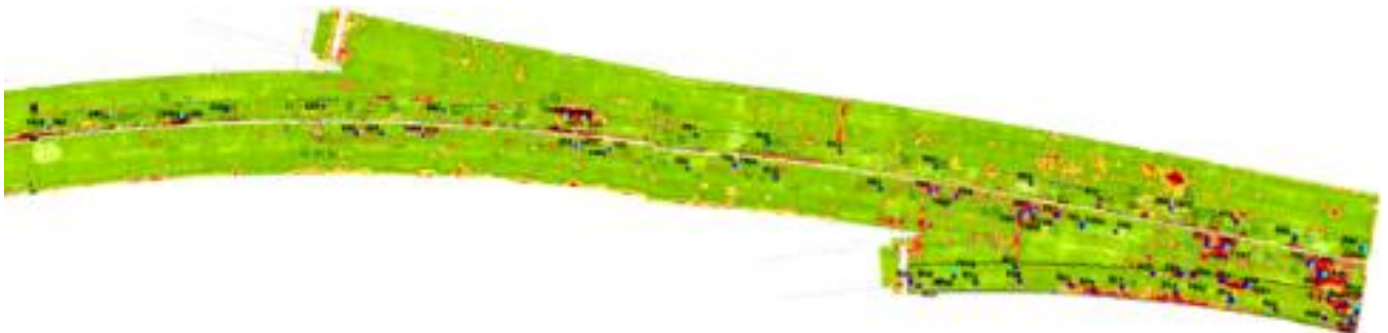


Figure 9. Potential field measurement and sensor positioning (Copyright: Christian Steffes, Infrasolute).

The sensors were installed into the existing concrete using core drilling (Figure 10). To optimize data retrieval, they were equipped with remote antennas. This allowed the readout units to be placed within the box girder of the bridge, providing protection from mechanical stress and weather conditions.

The gateways, which are connected to the existing power supply within the box girder, handle the data transmission. Each gateway collects the measurement data from four sensors and transmits the data wirelessly via NB-IoT to the Infrasolute cloud platform.



Figure 10. Installed sensors with remote antennas (Copyright: Benedikt Seuss, Infrasolute).

### 5.3 Measurement data and analyses

The continuous monitoring of the Südtangente in Koblenz, which has been carried out since the installation of the first sensors in the initial construction phase at the end of 2020, has so far shown no signs of corrosive activity.

An exception was one measurement point that reported corrosion on the first wire level three months after installation (Figure 11). The cause was identified as a construction-related weakness in the waterproofing, which was subsequently corrected during post-processing. Following this measure, the sensors detected no further corrosion progression.

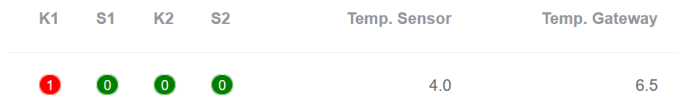


Figure 11. Data analysis in the software – display of a corrosion sensor showing corrosive activity at the first measurement wire level (Copyright: Christian Steffes, Infrasolute).

When corrosion is detected at the first wire level, the indicator K1 is no longer displayed within a green circle with a “0”, but instead within a red circle with a “1”. This provides a clear and unambiguous indication that corrosion has occurred at the first measurement wire level. The K2 value represents the status of the underlying wire level, allowing the progression of corrosion into deeper areas to be monitored and enabling a multi-layered condition analysis [7]. The values S1 and S2 serve the system’s internal self-referencing. These reference mechanisms ensure the accuracy and validity of the measurement data by automatically detecting any internal deviations or errors. This significantly enhances the reliability of the monitoring system and minimizes the risk of false diagnostics [8]. In addition, the sensor temperature within the concrete is shown under the indicator “Temp. Sensor”, providing essential information on the thermal conditions that may influence corrosion dynamics. The temperature of the gateway, located at the surface of the concrete inside the bridge’s box girder, is displayed separately as “Temp. Gateway”. In all other areas of the bridge, the moisture sensors showed a normalization to equilibrium moisture levels within the first six months after installation, without any notable irregularities or significant fluctuations. These results confirm both the effectiveness of the rehabilitation measures and the stability of the moisture conditions within the structure.

#### 5.4 Conclusion

By implementing sensor technology, the operator of the South Bridge gains the ability to monitor the success of rehabilitation measures in the short term. At the same time, the 24/7 online monitoring allows for the long-term observation of the internal condition of the structure, enabling the early detection of damage and the proactive initiation of maintenance actions. This minimizes the risk of unexpected damage and supports a preventive maintenance strategy that significantly enhances operational safety [7].

#### 5.5 Structure overview: Dieblich Bridge

The bridge along federal road B 411 near Dieblich serves as an important connection to the motorway network and

functions as a regional access route. Compared to the heavily trafficked South Bridge in Koblenz, the traffic volume on this structure is significantly lower. The two-lane bridge spans a length of 92 meters and is used by both passenger vehicles and agricultural traffic.

In 2023, a comprehensive concrete rehabilitation was carried out after elevated chloride levels were detected in the concrete. As part of the refurbishment, it was also necessary to partially replace the reinforcement to ensure the continued structural integrity and durability of the bridge.

#### 5.6 Sensor positions and installation

With a budget of under €10,000, an efficient moisture monitoring system was implemented to continuously provide data on the structural moisture content. This monitoring serves to track moisture levels following the rehabilitation measures and to draw conclusions about the success of the repair works and the containment of corrosive processes.

In the first step, the most critical areas of the structure were identified. This was achieved through a combination of a previously conducted potential field measurement and a detailed analysis of the structural topology. This comprehensive assessment allowed for the precise localization of potentially vulnerable zones.

Based on this analysis, it was jointly decided to install the moisture sensors at the lowest points of the structure, as these areas are particularly susceptible to moisture accumulation due to their proximity to the drainage system, as illustrated in Figure 12. The sensors were equipped with remote antenna configurations, allowing the actual measurement point to be positioned directly in the drainage area, while the readout unit was installed at a central, traffic-independent location behind the safety barrier near the expansion joint. This strategic positioning ensures easy maintenance and data retrieval without interfering with traffic.

For secure placement, the sensors were directly attached to the exposed reinforcement, as depicted in Figure 13.

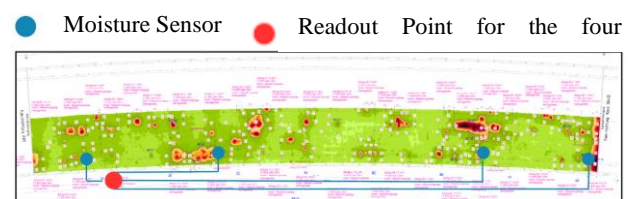


Figure 12. Potential field measurement and positioning of sensors and the readout point (Copyright: Christian Steffes, Infrasolute).





Figure 13. Installation of a moisture sensor on the reinforcement (Copyright: Eugen Kronhardt, Infrasolute).

### 5.7 Data acquisition and transmission

Data acquisition is performed using an IoT handheld reader. The readout process takes less than 5 seconds and can be carried out at any time on-site from a centralized location. In this project, the readout point was placed at the beginning of the bridge, behind the guardrail, at the height of the bridge cap.

By surveying and documenting the sensor installation positions on the structural plan, and marking them on-site with reference markers, the sensors and their readout points can be easily relocated during follow-up inspections.

Furthermore, the selected location allows for the optional retrofitting of a gateway to enable automated and remote data acquisition in the future. This ensures that the system remains flexible and scalable for long-term monitoring needs.

### 5.8 Measurement data and analyses

Since their installation, the moisture sensors have shown a continuous drying trend without any irregularities. The moisture levels are visualized on the data platform and can be correlated with precipitation data from the nearest weather station.

This type of analysis enables a deeper understanding of moisture changes within the structure and helps determine whether these changes are caused by temperature variations or external influences, such as heavy rainfall events.

## 6 SUMMARY

The CorroDec2G monitoring system developed by Infrasolute offers a durable and forward-thinking solution for the structural health monitoring of concrete. With a lifespan exceeding 80 years, the system operates entirely without batteries, cables, or external power sources, making it uniquely suited for both new construction and retrofit applications. It enables the measurement of moisture, actual temperature, and corrosion activity—without compromising the structural integrity of the concrete. The wireless and battery-free technology, based on RFID, enables long-term and maintenance-free monitoring of structural conditions. Particularly noteworthy are the system's high reliability and

energy efficiency, which are specifically tailored to meet the demanding requirements of structural diagnostics.

Thanks to its simple data retrieval process, the system is especially user-friendly. Measurement data can be collected within seconds, without the need for specialized expertise, and analyzed immediately. This significantly lowers the entry barrier for application and facilitates the integration into existing maintenance and monitoring workflows. Moreover, the data is presented in a clear and understandable format, enabling well-founded decisions regarding maintenance and repair actions to be made efficiently. This transparency benefits not only structure operators but also engineers and planners in ensuring the long-term safety and durability of concrete structures.

The primary advantages of CorroDec2G include its extremely long service life, energy independence, user-friendliness, and cost-efficiency. It supports condition-based maintenance strategies, contributes to the extension of structural service life, and helps optimize life-cycle costs by enabling the early detection of degradation mechanisms. Its rugged design and wireless operation allow for reliable performance in harsh environments such as underground garages or bridge structures. Moreover, its modular setup allows for flexible configurations and scalable integration into both small-scale and complex monitoring scenarios. Another key advantage of the CorroDec2G system is its cost-effectiveness. Continuous monitoring allows for the early detection of damage, minimizing expensive repairs and unforeseen failures. This not only contributes to the extension of the structure's service life but also supports sustainable resource use and optimizes maintenance costs.

Sensor data is accessible anytime and from anywhere, enabling efficient monitoring of multiple structures simultaneously. This is especially beneficial for critical infrastructure, where it supports effective prioritization of maintenance tasks and optimal use of resources [8].

Despite its strengths, CorroDec2G has inherent limitations. As a point-based early warning system, it provides localized data and does not offer full-surface or high-resolution spatial coverage. Strategic sensor placement - especially in critical zones identified by structural engineers - is therefore essential to obtain meaningful results. Furthermore, the system is not designed for high-frequency dynamic measurements but rather for long-term trends and early anomaly detection. Its value lies in its simplicity, reliability, and practical applicability in real-world construction environments

In an increasingly data-driven world, precise and reliable data collection plays a pivotal role. Advanced technologies such as Artificial Intelligence (AI), which are becoming more significant in the field of structural health monitoring, are also built upon such high-quality data. As a result, CorroDec2G serves as a bridge between traditional engineering and modern data science.

In summary, the CorroDec2G system provides an effective, forward-looking solution that actively promotes the safety,



functionality, and preservation of concrete structures over the long term.

## REFERENCES

- [1] DIN EN 1504-9:2008-11: Products and systems for the protection and repair of concrete load-bearing structures. Berlin: Beuth Verlag, 2008.
- [2] Federal Highway Administration (FHWA, Hrsg.): Bridge Preservation Guide: Maintaining a State of Good Repair Using Cost-Effective Investment Strategies. Washington, D.C., 2020.
- [3] Zilch, K.; Weiher, H.: Assessment of the condition of German prestressed concrete bridges, Universität München, 2006, p. 22–34.
- [4] Wischers G., Krumm E.: Moisture. In: Handbook of Concrete Surface Treatment (Ed.), p. 561–598, Bauverlag Wiesbaden, 2006.
- [5] Novák, B.; Stein, F.; Farouk, A.; Thomas, L.; Reinhard, J.; Zeller, T.; Koster, G.: Experience report on monitoring for bridge structures – Documentation 2021. In: Federal Highway Research Institute (BASt, Ed.): Reports of the Federal Highway Research Institute – Bridge and Structural Engineering, Issue B 197, Report on Research Project StB 247192.70403418027, Bergisch Gladbach, 2024 – <https://doi.org/10.60850/bericht-b197>.
- [6] GSMA: Narrowband IoT (NB-IoT): Accelerating the Internet of Things. London: GSMA, 2020. <https://www.gsma.com> (Accessed on 10.12.2024).
- [7] Homepage Infrasolute GmbH: CorroDec2G: Innovative sensor solutions for structural monitoring. <https://infrasolute.com/produkte/feuchtigkeitssensor-fuer-bauwerke/> Boppard: Infrasolute, 2020 (Accessed on 10.12.2024).
- [8] Fraunhofer IBMT (Ed.): Development report on long-term RFID sensors for concrete structures. In: Annual Report of the Fraunhofer Institute for Biomedical Engineering, St. Ingbert: Fraunhofer Verlag, 2020, pp. 89–92.
- [9] Homepage LBM: Südtangente Koblenz. <https://lbm.rlp.de/grossprojekte/b-327-suedtangente-koblenz> Koblenz, LBM, 2020 (Accessed on 10.12.2024).

# Numerical dataset for benchmarking of drive-by bridge monitoring methods

Daniel Cantero<sup>1</sup>, Zohaib Sarwar<sup>1</sup>, Abdollah Malekjafarian<sup>2</sup>, Robert Corbally<sup>2</sup>, Mehrisadat Makki Alamdari<sup>3</sup>, Prasad Cheema<sup>3</sup>, Jatin Aggarwal<sup>4</sup>, Hae Young Noh<sup>4</sup> and Jingxiao Liu<sup>4</sup>

<sup>1</sup>Structural Engineering, NTNU Norwegian University of Science and technology, Trondheim, Norway

<sup>2</sup>Structural Dynamics and Assessment Laboratory, School of Civil Engineering, University College Dublin, Ireland

<sup>3</sup>Centre for Infrastructure Engineering and Safety, School of Civil and Environmental Engineering, University of New South Wales, Sidney, Australia

<sup>4</sup>Department of Civil and Environmental Engineering, Stanford University

email: daniel.cantero@ntnu.no, muhammad.z.sarwar@ntnu.no, abdollah.malekjafarian@ucd.ie, robert.corbally@rod.ie, m.makkialamdari@unsw.edu.au, p.cheema@unsw.edu.au, noh@stanford.edu, liujx@stanford.edu, jatin08@stanford.edu

**ABSTRACT:** Publicly accessible vehicle measurements for testing and validating drive-by bridge monitoring techniques are currently insufficient. Although relevant monitoring campaigns have been conducted, their results are limited and generally inaccessible to the research community. Consequently, this paper introduces a numerical dataset designed to advance drive-by monitoring methods. The dataset is freely available and can be downloaded from an online repository. It comprises numerically simulated vehicle responses generated using an open-source vehicle-bridge interaction model. The repository includes over half a million individual vehicle crossing events, covering various monitoring scenarios, bridge spans, damage locations, damage magnitudes, road profile conditions, and vehicle properties. This dataset is intended to serve as a reference solution and benchmark for future developments in drive-by bridge monitoring.

**KEY WORDS:** Indirect Monitoring; Damage Detection; Vehicle-Bridge Interaction; Drive-By Inspection.

## 1 INTRODUCTION

To facilitate the advancement of data-driven drive-by bridge damage assessment techniques, this paper presents an openly accessible dataset [1]. The dataset consists of numerically simulated vehicle responses from crossings over diverse bridge spans with varying damage conditions. Additionally, it includes results that consider variations in road profiles, vehicle models, mechanical properties, and speeds. The objective is to offer the research community a valuable resource that serves as a reference for testing and benchmarking new developments in the field.

## 2 THE DATASET

This section offers an in-depth overview of the NuBe-DBBM dataset (Numerical Benchmark for Drive-By Bridge Monitoring methods), which is available to the public in [1]. The dataset encompasses vehicle response data from over half a million numerically simulated vehicle-bridge crossings, spanning a broad spectrum of road, bridge, and vehicle conditions. Furthermore, the repository provides additional materials to support users of the dataset.

The dataset was generated using VBI-2D [2], an open-source MATLAB tool designed to simulate vehicle-bridge interaction (VBI) for road traffic crossing bridges. This tool allows for the specification of various vehicle models, road irregularities, bridge characteristics, and structural conditions. In VBI-2D, bridges are modelled as beams within a finite element framework, while vehicles are represented as mechanical systems with multiple degrees of freedom. The coupled vehicle-bridge response is determined through direct integration of the corresponding equations of motion. For more detailed information on the numerical model, solution method, and user manual, readers are referred to [2]. Figure 1 provides a schematic overview of VBI-2D's simulation capabilities. Specifically for the dataset, simulations involved simply supported bridge configurations of single vehicles crossings at

constant speeds under varying road, vehicle, and bridge conditions.

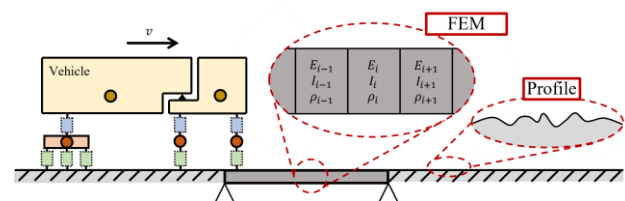


Figure 1. Illustration of VBI-2D model.

The dataset consists of individual MATLAB files, each containing information and vehicle responses for a single event. An event is defined as a single vehicle traveling at a constant speed over a specified road profile while crossing a bridge without any initial vibrations. The dataset includes five primary problem variables: Bridge length (B), Damage location (DL), Damage magnitude (DM), Vehicle type (V), and Profile (P). It is further divided into two subsets, named DSA and DSB, corresponding to two distinct monitoring scenarios. For each possible combination of problem variables and monitoring scenarios, 800 events are included, with vehicle properties randomly sampled.

The dataset comprises numerical results for six distinct simply supported bridges with span lengths varying from 9 m to 39 m, increasing in 6 m increments. These bridges are modelled as finite element representations using beam elements, each 0.25 m in length. The numerical properties of the beam models were chosen to represent typical bridges of these span lengths, with detailed values of the properties for the beam models provided in [3].

Bridge damage is modelled as a decrease in stiffness affecting either 2 or 4 elements, which equates to bridge lengths of 0.5 m or 1 m. The severity of the damage is expressed as a percentage reduction in stiffness, with the dataset providing results for three levels: 0% (undamaged bridge), 20%, and 40%. Furthermore, two damage locations are examined,

specified in relation to the bridge span  $L$ , namely at quarter-span ( $L/4$ ) and at mid-span ( $L/2$ ).

The dataset encompasses results for three distinct vehicle models, which are numerically represented through combinations of concentrated masses, rigid elements, springs, and dashpots. These models, generated using the open-source tool VEqMon2D [4], are schematically depicted in Figure 2, illustrating the names of all mechanical properties, relevant dimensions, and degrees-of-freedom (DOF) notation. The vehicles are classified based on their total number of axles: a 1-axle model (V1), a 2-axle model (V2), and a 5-axle model (V5). The V1 model, often referred to as a quarter-car model, has been extensively utilised in previous studies to evaluate the performance of drive-by methods. The V2 model represents a car or a 2-axle heavy vehicle, such as a van or truck. The V5 model characterises an articulated heavy vehicle, comprising a tractor and trailer connected by an articulation.

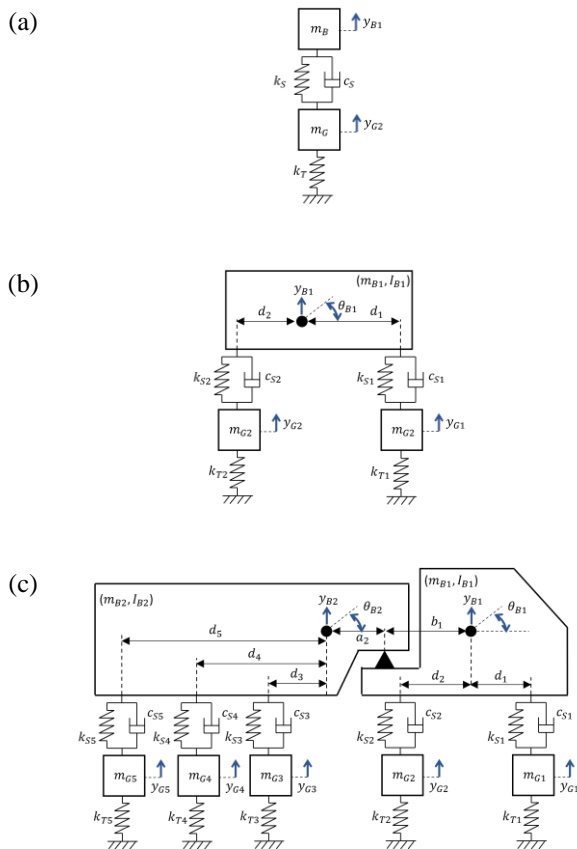


Figure 2. Vehicle models; (a) V1: 1-axle vehicle model; (b) V2: 2-axle vehicle model; (c) V5: 5-axle articulated vehicle model.

Each event in the dataset models the response of one of the vehicle types. For each simulation, the actual speed, along with the mechanical and geometrical properties, are randomly sampled based on probabilistic descriptions provided in the repository [1]. The variability in vehicle model parameters is intended to represent fleets of similar vehicles, although no two are identical. While the geometry of all vehicles within a specific model type remains consistent, their mechanical properties differ between simulations. This mirrors real-world conditions, where vehicles vary due to differences in payloads, suspension characteristics, and tyre pressures.

The dataset also incorporates the impact of road conditions. Some simulations assume a perfectly smooth road surface, labelled as P00. Additionally, the dataset features simulations with two randomly sampled Class A road profiles, generated according to the standardized procedure specified in ISO 8608. To simulate the actual wheel footprint, a moving average filter with a window size of 0.25 m is applied to the generated profiles. These profiles are 600 m in length, with their reference system centred at the midpoint. The profiles are consistently used across all bridge spans, with the left beam support positioned at the origin of the profile's reference system. For all simulations, vehicles include a 100 m long approach distance before crossing the bridge.

The dataset encompasses two distinct monitoring scenarios. Scenario A (DSA) depicts a situation where the target bridge has substantial damage, necessitating more controlled and detailed drive-by inspections while maintaining regular operational conditions. In this scenario, the bridge damage spans 4 elements (1 m), and the vehicle fleet gathers signals at high sampling rates while travelling at controlled, nearly uniform speeds. Scenario B (DSB), in contrast, represents normal operational conditions aimed at detecting early signs of bridge deterioration. Here, the damage spans only 0.5 m (2 elements), with vehicles travelling at varying permitted speeds (resulting in high variability) and signals collected at a lower sampling rate. Table 1 outlines the specifications for both scenarios, reflecting different levels of difficulty for drive-by methods. Scenario A, with more extensive bridge damage and less variability in vehicle speeds, is anticipated to enhance the performance of data-driven damage detection methods. Conversely, Scenario B presents a more challenging environment due to smaller damage and greater variability in operational conditions.

Table 1. Monitoring scenarios specifications.

Dataset code name	DSA	DSB
Number of damaged elements	4	2
Sampling rate of signals (Hz)	1024 (210)	256 (28)
Speed variation (km/h)	70 to 80	30 to 80

Table 2 gives an overview of all dataset dimensions together with their possible values.

Table 2. Summary of dataset's dimensions.

Property	Notation	Possible values
Monitoring scenario	DS + letter	DSA – DSB
Bridge	B + span in m	B09 – B15 – B21 – B27 – B33 – B39
Damage location	DL + location in % of span	DL25 – DL50
Damage magnitude	DM + % of stiffness reduction	DM00 – DM20 – DM40
Vehicle	V + number of axles	V1 – V2 – V5
Road profile	P + Class + Number	P00 – PA1 – PA2
Event number	E + number	E0001 – E0002 – ... – E0800



As mentioned earlier, the dataset consists of individual files containing numerical results and other relevant details for each vehicle crossing event. Each file is uniquely named to indicate the specific characteristics of the simulated event based on the dataset dimensions (see Table 2). The naming convention for each file is:

**DSa** + **\_** + **Bbb** + **DLcc** + **DMdd** + **Ve** + **Pfg** + **Ehhhh** + .mat

for:

**DSa** = Dataset name, where *a* indicates either A or B monitoring scenario

**Bbb** = Bridge type, where *bb* indicates span length

**DLcc** = Damage location, *cc* indicates the location as % of span length

**DMdd** = Damage magnitude, *dd* indicates % of stiffness reduction

**Ve** = Vehicle type, *e* indicates the number of axles of the vehicle model

**Pfg** = Profile, *f* indicates the class of profile (A), and *g* is the profile number

**Ehhhh** = Event number, *hhhh* indicates the event number

For example, the event file *DSA\_B15DL50DM20V5PA2E0327.mat* corresponds to event number 327. This event features a 5-axle truck traversing the 2nd Class A profile and a 15 m simply supported bridge, which has a 20% stiffness reduction at mid-span, under monitoring scenario A.

The dataset includes 518,400 events, totalling 52GB of files that are freely available for download [1]. These files are organised into compressed subfolders based on bridge span and monitoring scenario. Each event file contains the simulated acceleration responses from all degrees of freedom (DOFs) of the vehicle model, including both off-bridge and on-bridge responses, i.e., the vehicle's responses while approaching and crossing the bridge. The file also records the exact time the vehicle enters the bridge. Additionally, it includes the specific realisation of the vehicle's mechanical properties for the simulated event, along with the corresponding natural frequencies of the vehicle model.

Moreover, the repository includes supplementary files that detail the vehicle models and their DOF notation (*Vehicles\_DOF.zip*), the road profiles used in generating the dataset (*Profiles.zip*), and the bridge model parameters (*Bridges.zip*). It is important to note that the vehicle responses in the dataset are clean signals. To simulate real measurements, these signals should be corrupted with noise. To assist with this, the file *Noise.zip* offers two equivalent implementations (for MATLAB and Python) to add noise to the signals.

Readers are referred to the documents *ReadMe.pdf* available in the repository [1] for further information about the stored content and practical guidelines to read the event files. Also refer to the original publication [3] for additional details about the problem variables, vehicle property variability, and the stored information within the dataset.

### 3 CONCLUSION

This paper has introduced a publicly accessible dataset designed as a benchmark for drive-by monitoring techniques. The dataset comprises numerically simulated vehicle responses during bridge crossings. A wide array of configurations and conditions have been modelled and systematically stored in files, which are readily available at [1]. The dataset's variability includes different bridge spans, damage locations, damage magnitudes, road profile irregularities, monitoring scenarios, and vehicle properties. It contains over half a million files with vehicle responses and additional information for individual crossing events. This paper encourages the research community to employ this dataset to test and enhance drive-by monitoring methods.

### ACKNOWLEDGMENTS

The UNSW authors would like to thank Australian Research Council (ARC) for the provision of support under Discovery Early Career Researcher Award (DECRA) scheme with grant number DE210101625.

The UCD authors wish to express their gratitude for the financial support received from the Irish Research Council (IRC) GOIPD/2023/1588 and the financial support of Science Foundation Ireland under Grant number 20/FFP-P/8706.

### REFERENCES

- [1] D. Cantero, NuBe-DBBM: Numerical benchmark for drive-by bridge monitoring methods. Zenodo repository, 2023. <https://doi.org/10.5281/zenodo.7741091>
- [2] D. Cantero, VBI-2D - Road vehicle-bridge interaction simulation tool and verification framework for Matlab, SoftwareX, 26:101725, 2024. <https://doi.org/10.1016/j.softx.2024.101725>
- [3] D. Cantero, Z. Sarwar, A. Malekjafarian, R. Corbally, M.N. Alamdari, P. Cheema, J. Aggarwal, N.Y. Noh, J. Liu, Numerical benchmark for road bridge damage detection from passing vehicles responses applied to four data-driven methods, Archives of Civil and Mechanical Engineering, 24:190, 2024. <https://doi.org/10.1007/s43452-024-01001-9>
- [4] D. Cantero, VEqMon2D - Equations of motion generation tool of 2D vehicles with Matlab, SoftwareX, 19:101103, 2022. <https://doi.org/10.1016/j.softx.2022.101103>

# Indirect footbridge damage classification using explainable deep learning: A field-testing study

Zhenkun Li<sup>1</sup>, ORCID (0000-0002-1444-6017), Yifu Lan<sup>1,2</sup>, ORCID (0000-0002-8411-6507), Weiwei Lin<sup>1</sup>, ORCID (0000-0001-8486-6538)

<sup>1</sup>Department of Civil Engineering, Aalto University, 02150 Espoo, Finland

<sup>2</sup>School of Civil Engineering, University College Dublin, D04V1W8 Dublin, Ireland

email: zhenkun.li@aalto.fi, yifu.lan@ucd.ie, weiwei.lin@aalto.fi

**ABSTRACT:** Structural health monitoring (SHM) has gained significant attention in recent decades due to several structural failures and the increasing maintenance demands from stakeholders. This urgency has been further amplified by the impact of predictive climate changes worldwide. Footbridges, as critical components of modern transportation systems, play a vital role in daily life and therefore require meticulous attention to their health conditions. Traditionally, monitoring footbridge conditions involves installing many sensors directly on the structure, which is often cost-prohibitive in engineering applications. Recent advancements have highlighted the indirect method of bridge health monitoring, where sensors are mounted on passing vehicles rather than the bridge itself. This approach is not only more economical but also easier to implement in practical engineering scenarios. This paper further extends the indirect monitoring method to classify footbridge damage using the responses of shared scooters. Advanced deep learning techniques are utilized to predict the severity of damage to the footbridge based on the vibrations recorded from shared vehicles. The proposed method was validated through field tests involving scooters and a footbridge. Furthermore, to interpret the outputs of the deep learning model, SHapley Additive exPlanations (SHAP) values were calculated, offering insights into the decision-making process of the model.

**KEY WORDS:** structural health monitoring; footbridge; damage classification; convolutional neural networks; SHAP.

## 1 INTRODUCTION

The assessment of bridge health has gained significant attention over the past decades due to widespread aging and deterioration. This concern stems from the fact that many of these structures were built in the previous century, with a large proportion having been in service for over 50 years. For instance, in Finland, the Finnish Transport Infrastructure Agency reported that, as of 2023, 882 out of 17,351 highway bridges (5.1%) were in poor condition, with aging structures from the 1960s and 1970s accumulating a growing maintenance backlog [1]. The European Commission has noted that bridges constructed after 1945 were typically designed for a lifespan of 50 to 100 years. In 2001, it was reported that bridges in France, Germany, and the UK showed deficiency rates of 39%, 30%, and 37%, respectively [2]. These figures highlight the urgent need for effective health monitoring of in-service bridges, which can provide critical information on their condition and support informed decision-making by stakeholders.

Traditional bridge inspections rely heavily on human vision, requiring engineers to conduct on-site visits and determine whether maintenance is needed [3]. However, as modern bridge construction becomes more extensive and complex, this approach faces several limitations, including being labor-intensive, inefficient, and time-consuming. At the beginning of this century, structural health monitoring (SHM) systems gained popularity [4]. These systems involve installing various sensors on bridges to continuously collect different types of data. In practice, however, this approach has proven to be expensive. It typically involves a one-to-one setup, where the monitoring system is customized for a specific bridge and cannot be easily transferred to others. Moreover, the cost of installing numerous sensors can be high. As the number of

aging and newly built bridges continues to rise, there is an increasing need for cost-effective and scalable monitoring technologies.

In 2004, Yang et al. [5] proposed the indirect method, where sensors are installed on passing vehicles instead of the bridge itself. This approach is based on the vehicle-bridge interaction (VBI) process. During this interaction, the dynamic characteristics of the bridge are transferred to the vehicles equipped with sensors, allowing the vehicles to act as moving sensors that collect information about the bridge. In this pioneering study, the bridge was simplified as a simply supported beam, and the vehicle was modeled using a spring-mass system. Under these assumptions, the authors demonstrated that the fundamental frequency of the bridge could be extracted from the vehicle's response, laying the groundwork for future research in this area.

In recent studies, researchers have further investigated the extraction of bridge modal shapes and damping ratios from vehicle response [6,7]. For example, Yang et al. [8] proposed using the Hilbert Transform to extract mode shapes from filtered vehicle responses, while González et al. [9] introduced a method for retrieving damping ratios by minimizing the errors in identified road roughness between the front and rear axles. In 2018, Yang et al. [10] introduced the concept of contact-point (CP) response, which represents the response at the interface between the vehicle and the bridge. This response was found to be independent of vehicle characteristics, making it useful for identifying bridge properties from vehicle data [11]. In addition to vehicle influence, road roughness is another major source of interference when identifying bridge dynamic parameters from vehicle accelerations. This issue can be mitigated by using residual CP responses between vehicle axles,

which eliminates the effects of road roughness [12–14]. However, in practical applications, modal parameters often show limited sensitivity to structural damage and may be significantly affected by operational conditions. Moreover, most existing studies on the indirect method have focused on road bridges. Although footbridges play an essential role in modern transportation and logistics, they are rarely equipped with SHM systems and have received little attention in indirect monitoring research.

Over the past decade, advancements in computer science algorithms and hardware have significantly enhanced deep learning techniques, particularly through the widespread use of neural networks. Technologies such as large language models (LLMs) have transformed many aspects of daily life and have also made a notable impact on SHM for bridges. Researchers have increasingly applied machine learning and deep learning methods to assess bridge health using structural responses [15]. In the context of the indirect method, vehicle responses typically consist of three components: vehicle dynamics, road roughness, and bridge vibrations [16,17]. This complexity makes it challenging to isolate bridge-specific information for use as damage indicators. However, deep learning models are sensitive to subtle signal variations, making them well-suited for detecting damage-related changes in vehicle responses. For example, Li et al. [18] applied support vector machines and Mel-frequency cepstral coefficients (MFCCs) to predict the severity of bridge damage based on vehicle responses. Unlike earlier studies that focused only on low-frequency signals [19], this research also explored high-frequency responses. In addition, Corbally and Malekjafarian [20] used convolutional neural networks (CNNs) to classify the type, location, and severity of bridge damage using drive-by data. In their study, particle swarm optimization was employed to fine-tune the vehicle model, and the resulting simulated data were used to train the CNN. Laboratory experiments validated the framework, demonstrating its ability to accurately detect and classify damage in most cases. These studies highlight the promising role of deep learning in bridge health monitoring. However, most research to date has focused on road bridges, with footbridges largely overlooked [21]. Additionally, deep learning models are often applied without adequate explanation of how features are selected or interpreted, limiting the transparency and broader adoption of these approaches.

In this paper, an explainable deep learning-based method is proposed to detect and classify damage in footbridges. Shared scooters equipped with smartphones are used to assess the health condition of footbridges when they pass the footbridge structures and collect dynamic data. 2D CNN is employed to extract key features from the time-frequency representations (TFRs) of the scooter's response as it moves over the footbridge. A field test is conducted to validate the effectiveness of the proposed method. The structure of the paper is as follows: Section 2 introduces the fundamental scheme of the proposed method and architecture of the used 2D CNNs. Section 3 describes the field test setup and discusses the results. Finally, Section 4 presents the conclusions of the study.

## 2 PROPOSED METHODOLOGY

### 2.1 Data collection

In this study, smartphones were mounted on a scooter to record vibration data. The scooter first crossed the bridge multiple times when it was in a healthy state to establish a baseline. After the bridge had been in use for several months or years and potential damage had developed, the scooter was used again to collect vibration data. These recordings, from both healthy and possibly damaged states, were used to train neural networks for predicting the bridge's health condition.

### 2.2 Data processing

Before feeding scooter data into the 2D CNNs, signals are preprocessed in 3 steps: (1) synchronization: two smartphones on different scooter parts are synchronized using Unix time to align data collection; (2) channel formation: only vertical and pitch accelerations, the most relevant signals, are retained. Signals from misaligned sensors are combined to extract these components; (3) segmentation: only data collected while the scooter is on the footbridge is kept, removing unrelated signals before and after crossing. This ensures clean, relevant input for 2D CNN training.

### 2.3 2D CNN

CNNs are widely used for extracting damage-sensitive features from signals. In this study, the 2D CNNs based on a simplified Visual Geometry Group (VGG)-16 [22] architecture (with two instead of four fully connected layers) were developed to analyze scooter vibrations for footbridge monitoring. When sensors are mounted on a scooter, fewer measurement points are available, but key inputs: vertical body acceleration ( $\ddot{z}_s$ ), angular acceleration ( $\ddot{\theta}_s$ ), and front wheel acceleration ( $\ddot{z}_t$ ), can be collected using two smartphones. The 2D CNN uses TFRs of scooter vibrations as input. To standardize input size, signals are first truncated to a uniform time length (5 s in this study), then transformed into 2D representations using methods like short-time Fourier Transform [23]. Each CNN channel uses 2D kernels (kernel\_size=3) with zero padding to keep the input size. The max-pooling (kernel\_size = 2, stride = 2) is utilized to extract key features. Activation function was selected as rectified linear unit (ReLU), and the Cross-Entropy (CE) loss was employed [24]. The architecture of the 2D CNNs are shown in Table 1.

Table 1. Architecture of the 2D CNNs.

Layers	Output shape	Kernel size	Activation
Input	$3 \times 402 \times 257$	-	-
Conv 2D	$64 \times 402 \times 257$	3	ReLU
Conv 2D+MaxPooling	$64 \times 201 \times 128$	3	ReLU
Conv 2D	$128 \times 201 \times 128$	3	ReLU
Conv 2D+MaxPooling	$128 \times 100 \times 64$	3	ReLU
Conv 2D	$256 \times 100 \times 64$	3	ReLU
Conv 2D	$256 \times 100 \times 64$	3	ReLU
Conv 2D+MaxPooling	$256 \times 50 \times 32$	3	ReLU
Conv 2D	$512 \times 50 \times 32$	3	ReLU
Conv 2D	$512 \times 50 \times 32$	3	ReLU
Conv 2D+MaxPooling	$512 \times 25 \times 16$	3	ReLU
Conv 2D	$512 \times 25 \times 16$	3	ReLU
Conv 2D	$512 \times 25 \times 16$	3	ReLU
Conv 2D+MaxPooling	$512 \times 12 \times 8$	3	ReLU
Flattened	49152	-	-
Fully connected	4	-	-



### 3 FIELD TESTS AND DISCUSSIONS

#### 3.1 Field test setups

Field tests were carried out using scooters equipped with two smartphones to validate the proposed footbridge damage detection method (see Figures 1 and 2). Smartphone 1 (iPhone 12) was mounted on the scooter body, and Smartphone 2 (iPhone 8) on the front wheel. The scooter passed the footbridge multiple times under similar road roughness. A short acceleration zone was used for the scooter to reach a top speed of 20 km/h, which can be powered by an electric motor without human pedaling force. MATLAB Mobile was used on smartphones to collect data with sampling frequency of 100 Hz. The footbridge investigated in the field tests is shown in Figure 3. To simulate experimental damage cases (EDCs), different masses (people standing at the center) were used, which is a practical approach and has been validated in prior studies [25–27]. The added masses were 55 kg, 125 kg, and 185 kg for damage cases 1, 2, and 3, respectively. EDC 0 refers to the undamaged case with no added mass.



Figure 1. Scooter with two smartphones.



Figure 2. Scooter with a rider.



Figure 3. Experimental damage cases.

All EDCs and corresponding scooter runs are detailed in Table 2. Impulse excitation was applied by having a person

jump on the bridge to assess the effect of added mass. A smartphone placed at the 1/4 span of the footbridge recorded the resulting vibrations. For EDC 0, accurate natural frequencies cannot be obtained with this method, as at least one person is required to apply the excitation. Instead, an alternative approach using the bridge's free vibration after scooter crossing is utilized. Frequency values for all EDCs are listed in Table 2, where  $f_{b1} - f_{b4}$  represent the first four frequencies of the explored footbridge. It can be seen that when more people are standing on the footbridge, the first two frequencies of the footbridge  $f_{b1}$  and  $f_{b2}$  decrease apparently. However, for the third and fourth frequencies  $f_{b3}$  and  $f_{b4}$ , the frequency values sometimes remain unchanged due to the measuring accuracy. Even though the frequency changes can be observed from the first two frequencies, the change ratio can be minor, say 1.22% for the fundamental frequency in EDC 1 compared to that of EDC 0. It can be challenging to determine the damage condition only based on the changes in frequencies. Therefore, the following will investigate the use of data-driven methods for damage detection of the footbridge using scooter vibrations.

Table 2. Footbridge frequencies in all EDCs.

EDCs	People mass	$f_{b1}$	$f_{b2}$	$f_{b3}$	$f_{b4}$	Runs
EDC 0	0 kg	4.028 Hz	4.468 Hz	10.486 Hz	11.316 Hz	124
EDC 1	55 kg	3.979 Hz	4.443 Hz	10.486 Hz	11.304 Hz	65
EDC 2	125 kg	3.955 Hz	4.431 Hz	10.486 Hz	11.304 Hz	63
EDC 3	185 kg	3.918 Hz	4.370 Hz	10.437 Hz	11.304 Hz	60

#### 3.2 Results and discussions

For analysis, 63 runs were randomly selected from EDC 0, yielding a total of 251 runs in the experimental dataset. Of these, 70% were used for training and 30% for testing. The CNN configurations matched those used in simulations. Hyperparameters were set as follows: batch size = 32, optimizer = Adam, learning rate =  $1e^{-6}$ , weight decay =  $1e^{-5}$ , loss function = CE loss, activation = ReLU, and number of epochs = 400. CE loss and damage prediction accuracy are shown in Figure 4.

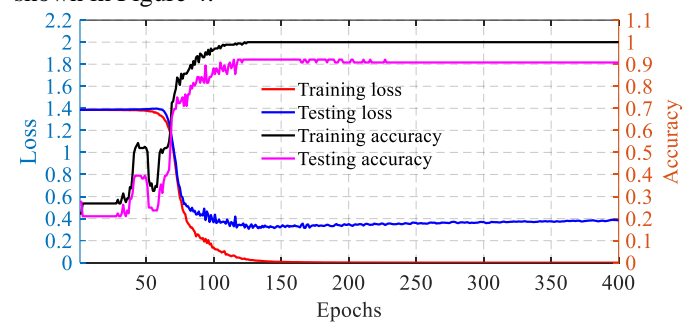


Figure 4. Loss and accuracy using 2D CNNs.

Figure 4 showed that the 2D CNN achieved early and sharp drops in both training and testing losses. The training loss nearly reached zero, and despite a minor rise in testing loss after 150 epochs, testing accuracy remained consistently above 90%.

To further interpret these findings, Shapley Additive Explanations (SHAP) were used to explain the 2D CNN's predictions. SHAP values reveal each feature's contribution to the model's output [28,29]. One sample from each EDC was analyzed to show how the 2D CNN classified bridge conditions. Figure 5 displays the SHAP values and predicted probabilities

for each TFR image. Red pixels (positive SHAP values) support the model's prediction, blue pixels (negative SHAP values) oppose it, and grey pixels have little impact.

The SHAP value images reveal that most significant features, those with strong positive or negative contributions, are concentrated in the 0–30 Hz range. This aligns with the fact that the bridge's natural frequencies, identified through impulse excitation (Table 2), also lie below 30 Hz. In EDC 0, for instance, image 2 shows that key features appear between 0.5–3.5 s as distinct non-horizontal lines and points, corresponding to peaks in the footbridge's frequency response. The 2D CNN confidently classified this sample as EDC 0 with a 99.98% probability. Images 4 and 5 contain blue regions indicating features that helped the model rule out EDCs 2 and 3. However, image 3 shows some overlap with EDC 1, resulting in a small 0.01% probability being assigned to that class. In EDC 1 (image 8), time-varying features near 1.5 s played a critical role, especially in distinguishing it from EDC 2. Because of the resemblance to EDC 0 around the same time, the model assigned a minor 0.08% probability to EDC 0. For EDC 2, distinct features were noted at 2.5 s and 4 s, while in EDC 3 (image 20), key contributions appeared around 4 Hz and 20 Hz. Although EDC 3 shared similar patterns with EDC 0 between 1.5–2.5 s, additional higher-frequency features around 1.5 s enabled the 2D CNN to correctly identify it as EDC 3.

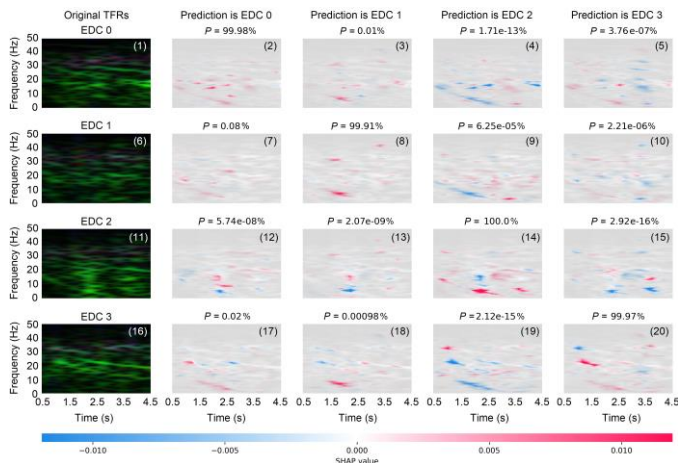


Figure 5. Explanation of 2D CNNs ( $P$ : Probability).

These observations confirm that the 2D CNN identifies damage-sensitive features based on both time and frequency information. Therefore, using TFRs as input to a 2D CNN provides good damage detection performance in the indirect method with vehicle-mounted sensors. This advantage stems from the inherently non-stationary dynamics of VBI systems, where both vehicle and bridge frequencies shift during interaction [30–32]. Therefore, by preserving time-varying characteristics, the 2D CNN in this study can effectively identify key features in scooter vibrations.

#### 4 CONCLUSIONS AND FUTURE WORK

This paper proposes a method for detecting and classifying footbridge damage by analyzing scooter vibrations collected via smartphones and processed through explainable deep learning. Specifically, TFRs of scooter vibrations were used with a 2D CNN to assess damage severity. The method was validated through real-world field tests. It was found that the

2D CNN can accurately predict the damage severity of the footbridge by using the TFRs of scooters. The 2D CNN's superior performance is linked to its ability to capture the non-stationary characteristics of VBI responses. SHAP analysis confirmed that damage-sensitive features vary over time in the scooter's vibrations.

Future work will focus on enhancing the practicality and robustness of the proposed method by exploring alternative smartphone placements (e.g., on the standing slab or handlebar), considering the behaviors of the drivers, incorporating influential factors such as temperature, road roughness variations, and pedestrian presence, and reducing reliance on labeled data through unsupervised learning. Furthermore, the authors understand that using standing people on the footbridge to simulate synthetic damage scenarios can not fully represent the real damage in practical engineering. In our future studies, we would like to test the proposed method on other bridges with real damage to evaluate the generalization.

#### ACKNOWLEDGMENTS

This research is financially sponsored by the Jane and Aatos Erkko Foundation in Finland (Decision number: 210018) and Aalto University (research project funding in ENG 2022). The help from colleagues on the field tests is highly appreciated.

#### REFERENCES

- [1] Finnish Transport Infrastructure Agency, Bridge maintenance, (2024). <https://vayla.fi/en/maintenance/road-network/bridge-maintenance> (accessed April 23, 2025).
- [2] Research and innovation in bridge maintenance, inspection and monitoring a European perspective based on the Transport Research and Innovation Monitoring and Information System (TRIMIS), Re-edition, Publications Office of the European Union, Luxembourg, 2019.
- [3] C.-Z. Dong, F.N. Catbas, A review of computer vision-based structural health monitoring at local and global levels, *Structural Health Monitoring* 20 (2021) 692–743. <https://doi.org/10.1177/1475921720935585>.
- [4] R. Hou, Y. Xia, Review on the new development of vibration-based damage identification for civil engineering structures: 2010–2019, *Journal of Sound and Vibration* 491 (2021) 115741. <https://doi.org/10.1016/j.jsv.2020.115741>.
- [5] Y.B. Yang, C.W. Lin, J.D. Yau, Extracting bridge frequencies from the dynamic response of a passing vehicle, *Journal of Sound and Vibration* 272 (2004) 471–493. [https://doi.org/10.1016/S0022-460X\(03\)00378-X](https://doi.org/10.1016/S0022-460X(03)00378-X).
- [6] H. Xu, X.Y. Chen, J. Chen, L.K. Shi, D.S. Yang, Z.L. Wang, Y.B. Yang, Review of vehicle scanning method for bridges from 2004 to 2024, *International Journal of Structural Stability and Dynamics* (2024) 2530003. <https://doi.org/10.1142/S0219455425300034>.
- [7] A. Malekjafarian, R. Corbally, W. Gong, A review of mobile sensing of bridges using moving vehicles: Progress to date, challenges and future trends, *Structures* 44 (2022) 1466–1489. <https://doi.org/10.1016/j.istruc.2022.08.075>.
- [8] Y.B. Yang, Y.C. Li, K.C. Chang, Constructing the mode shapes of a bridge from a passing vehicle: a theoretical study, *Smart Structures and Systems* 13 (2014) 797–819. <https://doi.org/10.12989/SSS.2014.13.5.797>.
- [9] A. González, E.J. O'Brien, P.J. McGettrick, Identification of damping in a bridge using a moving instrumented vehicle, *Journal of Sound and Vibration* 331 (2012) 4115–4131. <https://doi.org/10.1016/j.jsv.2012.04.019>.
- [10] Y.B. Yang, B. Zhang, Y. Qian, Y. Wu, Contact-Point Response for Modal Identification of Bridges by a Moving Test Vehicle, *International Journal of Structural Stability and Dynamics* 18 (2018) 1850073. <https://doi.org/10.1142/S0219455418500736>.
- [11] J. Li, X. Zhu, S. Chen, W. Ruan, Contact-point response reconstruction for indirect bridge monitoring via Bayesian expectation-maximization based augmented Kalman filter, *Engineering Structures* 309 (2024) 118066–118066. <https://doi.org/10.1016/j.engstruct.2024.118066>.
- [12] Z. Li, Y. Lan, W. Lin, Indirect Frequency Identification of Footbridges with Pedestrians Using the Contact-Point Response of Shared Scooters,



- Journal of Bridge Engineering 29 (2024) 04024036. <https://doi.org/10.1061/JBENF2.BEENG-6344>.
- [13] Z. Li, Y. Lan, W. Lin, Indirect damage detection for bridges using sensing and temporarily parked vehicles, *Engineering Structures* 291 (2023) 116459. <https://doi.org/10.1016/j.engstruct.2023.116459>.
- [14] Z. Li, W. Lin, Y. Zhang, Bridge Frequency Scanning Using the Contact-Point Response of an Instrumented 3D Vehicle: Theory and Numerical Simulation, *Structural Control and Health Monitoring* 2023 (2023) 1–23. <https://doi.org/10.1155/2023/3924349>.
- [15] L. Sun, Z. Shang, Y. Xia, S. Bhowmick, S. Nagarajaiah, Review of Bridge Structural Health Monitoring Aided by Big Data and Artificial Intelligence: From Condition Assessment to Damage Detection, *J. Struct. Eng.* 146 (2020) 04020073. [https://doi.org/10.1061/\(ASCE\)ST.1943-541X.0002535](https://doi.org/10.1061/(ASCE)ST.1943-541X.0002535).
- [16] A. González, K. Feng, M. Casero, Effective separation of vehicle, road and bridge information from drive-by acceleration data via the power spectral density resulting from crossings at various speeds, *Developments in the Built Environment* 14 (2023) 100162. <https://doi.org/10.1016/j.dibe.2023.100162>.
- [17] K. Feng, A. González, M. Casero, A kNN algorithm for locating and quantifying stiffness loss in a bridge from the forced vibration due to a truck crossing at low speed, *Mechanical Systems and Signal Processing* 154 (2021) 107599. <https://doi.org/10.1016/j.ymssp.2020.107599>.
- [18] Z. Li, W. Lin, Y. Zhang, Drive-by bridge damage detection using Mel-frequency cepstral coefficients and support vector machine, *Structural Health Monitoring* 22 (2023) 3302–3319. <https://doi.org/10.1177/14759217221150932>.
- [19] Y. Lan, Z. Li, K. Koski, L. Fülöp, T. Tirkkonen, W. Lin, Bridge frequency identification in city bus monitoring: A coherence-PPI algorithm, *Engineering Structures* 296 (2023) 116913. <https://doi.org/10.1016/j.engstruct.2023.116913>.
- [20] R. Corbally, A. Malekjafarian, A deep-learning framework for classifying the type, location, and severity of bridge damage using drive-by measurements, *Computer-Aided Civil and Infrastructure Engineering* 39 (2024) 852–871. <https://doi.org/10.1111/mice.13104>.
- [21] K. Feng, D. Hester, S. Taylor, C. O'Higgins, A. Ferguson, Z. Zhu, G. Zou, M. Lydon, J. Early, Experimental modal identification of a pedestrian bridge through drive-by monitoring integrated with shared-mobility vehicles, *Developments in the Built Environment* 20 (2024) 100562. <https://doi.org/10.1016/j.dibe.2024.100562>.
- [22] K. Simonyan, A. Zisserman, Very Deep Convolutional Networks for Large-Scale Image Recognition, (2015). <http://arxiv.org/abs/1409.1556> (accessed April 23, 2025).
- [23] M. Jamshidi, M. El-Badry, Structural damage severity classification from time-frequency acceleration data using convolutional neural networks, *Structures* 54 (2023) 236–253. <https://doi.org/10.1016/j.istruc.2023.05.009>.
- [24] O. Abdeljaber, O. Avci, M.S. Kiranyaz, B. Boashash, H. Sodano, D.J. Inman, 1-D CNNs for structural damage detection: Verification on a structural health monitoring benchmark data, *Neurocomputing* 275 (2018) 1308–1317. <https://doi.org/10.1016/j.neucom.2017.09.069>.
- [25] Z. Li, W. Lin, Y. Zhang, Real-time drive-by bridge damage detection using deep auto-encoder, *Structures* 47 (2023) 1167–1181. <https://doi.org/10.1016/j.istruc.2022.11.094>.
- [26] Z. Li, Y. Lan, W. Lin, Footbridge damage detection using smartphone-recorded responses of micromobility and convolutional neural networks, *Automation in Construction* 166 (2024) 105587. <https://doi.org/10.1016/j.autcon.2024.105587>.
- [27] Q. Mei, M. Gül, M. Boay, Indirect health monitoring of bridges using Mel-frequency cepstral coefficients and principal component analysis, *Mechanical Systems and Signal Processing* 119 (2019) 523–546. <https://doi.org/10.1016/j.ymssp.2018.10.006>.
- [28] F. Zhang, A. Cannone Falchetto, D. Wang, Z. Li, Y. Sun, W. Lin, Prediction of asphalt rheological properties for paving and maintenance assistance using explainable machine learning, *Fuel* 396 (2025) 135319. <https://doi.org/10.1016/j.fuel.2025.135319>.
- [29] S. Lundberg, S.-I. Lee, A Unified Approach to Interpreting Model Predictions, (2017). <https://doi.org/10.48550/ARXIV.1705.07874>.
- [30] Z. Li, Y. Lan, K. Feng, W. Lin, Investigation of time-varying frequencies of two-axle vehicles and bridges during interaction using drive-by methods and improved multisynchrosqueezing transform, *Mechanical Systems and Signal Processing* 220 (2024) 111677. <https://doi.org/10.1016/j.ymssp.2024.111677>.
- [31] J. Li, X. Zhu, S. Law, B. Samali, Time-varying characteristics of bridges under the passage of vehicles using synchroextracting transform, *Mechanical Systems and Signal Processing* 140 (2020) 106727. <https://doi.org/10.1016/j.ymssp.2020.106727>.
- [32] J. Li, J. Guo, X. Zhu, Time-Varying Parameter Identification of Bridges Subject to Moving Vehicles Using Ridge Extraction Based on Empirical Wavelet Transform, *International Journal of Structural Stability and Dynamics* 21 (2021) 2150046. <https://doi.org/10.1142/S0219455421500462>.



# Drive-by bridge modal identification under multi-source excitations

Jiantao Li, Jie Tan

School of Civil Engineering, Zhejiang University of Technology, Liuhe RD. 288, 310023 Hangzhou, China  
email:jjiantao@zjut.edu.cn

**ABSTRACT:** The drive-by bridge modal identification (BMI) method, which employs a sensory system mounted on a moving vehicle, offers an efficient and cost-effective alternative for monitoring the health of bridge structures, particularly for short- to mid-span bridges. This technique allows for real-time, large-scale bridge assessments without the need for stationary sensors or traffic disruptions. However, extracting accurate modal parameters, such as frequencies and damping ratios, from vehicle responses is challenging due to the influence of multi-source excitations, including road surface roughness, random traffic loads, and dynamic vehicle-bridge interactions. These factors introduce noise and complexity that can compromise the reliability of the BMI method.

To address these challenges, this study integrates an adaptive signal decomposition technique, Successive Variational Mode Decomposition (SVMD), with Operational Modal Analysis to accurately identify the modal frequencies and damping ratios from drive-by measurements. The impact of multi-source excitations on the vehicle-bridge interaction process is systematically investigated, and key factors affecting the accuracy and reliability of BMI under such conditions are analyzed. Based on these findings, recommendations are made to improve the robustness and precision of the drive-by BMI method. This work might contribute to advancing the practical implementation of BMI in real-world bridge health monitoring applications.

**KEY WORDS:** Drive-by Modal Identification; Vehicle-Bridge Interaction; Successive Variational Mode Decomposition; Operational Modal Analysis; Multi-source Excitations.

## 1 INTRODUCTION

Vehicular onboard sensing technology dynamically collects bridge response data through moving vehicles, offering advantages such as wide coverage and low cost (Yang et al. 2020). However, its application in bridge monitoring still faces multi-faceted challenges. On one hand, multi-source random excitations (e.g., road roughness, the simultaneous operation of multiple vehicles, and environmental loads) induce time-varying non-stationarity and strong uncertainty in the dynamic responses of the vehicle-bridge coupled system. On the other hand, the coupled interference from system transfer characteristics, speed fluctuations, and environmental noise results in multi-component mixing and quality heterogeneity in the collected data, significantly compromising the reliability of bridge vibration characteristic identification and condition assessment (Zhu and Law, 2015).

The extraction of bridge related dynamic information from the multi-component vehicle responses for bridge condition assessment is the key task of drive-by bridge monitoring (Tan et al. 2019).

Successive variational mode decomposition (SVMD) (Nazari and Sakhaei 2020) has been used to accurately extract the mono-component from the multi-component dynamic signal without much manual parameter setting or adjustment. Li et al. (2022) investigated its feasibility and effectiveness for the extraction of bridge related dynamic components from vehicle response considering a random Class A road surface roughness. This paper studies the feasibility of SVMD for the drive-by bridge modal identification considering the multi-source excitation.

## 2 VBI MODELING CONSIDERING RANDOM OPERATIONAL EXCITATIONS

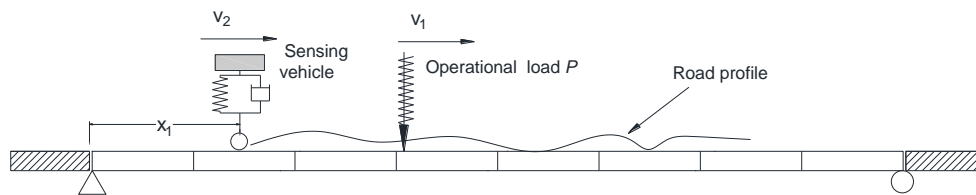


Figure 1 The model of drive-by bridge inspection in operational condition

The VBI model for the drive-by bridge modal identification is shown in Figure 1. The vehicle parameters are:  $m_v$  the mass of vehicle,  $k_s$  and  $c_s$  the stiffness and damping of suspension spring and damper, respectively. The equation of motion of vehicle can be expressed as

$$m_v \ddot{y}_v(t) + c_s \dot{y}_v(t) + k_s y_v(t) = F_{cp}(t) \quad (1)$$

where  $y_v$  is the displacement response of vehicle.  $F_{cp}(t) = k_v d_{cp}(t)$ , and  $d_{cp}(t) = w(\hat{x}_1(t), t) + r(\hat{x}_1(t))$  is the displacement input to the sensing vehicle at location  $\hat{x}_1(t)$ .

The multi-source excitations are considered as the road profile and a moving random operational load  $P$  (Sadeghi et al., 2020). The operational load enters the bridge ahead of the sensing vehicle with a moving speed  $v_1$  and the speed of the sensing vehicle is  $v_2$ . The road surface roughness is given as follows:

$$r(x) = \sum_{i=1}^{N_f} \sqrt{4S_d(f_i)\Delta f} \cos(2\pi f_i x + \theta_i) \quad (2)$$

where  $S_d(f)$  is the displacement power spectral density of road surface roughness;  $f_i = i\Delta f$  is the spatial frequency(cycles/m);  $\Delta f = \frac{1}{N_f\Delta}$ , and  $\Delta$  is the distance interval between successive ordinates of the surface profile;  $N_f$  is the number of data points;  $\theta_i$  is a set of independent random phase angle uniformly distributed between 0 and  $2\pi$ . The degree of road roughness is determined by the  $S_d(f_0)$  value, where  $f_0(=0.1$  cycles/m) is the reference spatial frequency. Class A road roughness defined using specified  $S_d(f_0)$  value in ISO specification is considered.

The flowchart of the proposed drive-by bridge modal identification is shown in Figure 2.

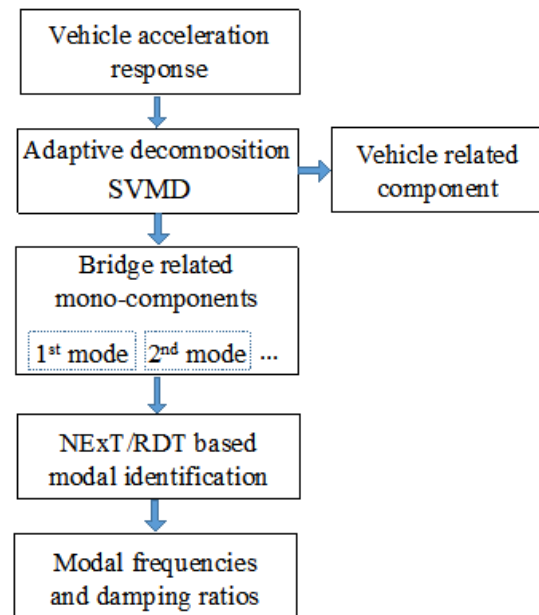


Figure 2 Flow chart of the bridge modal identification using moving test vehicle

### 3 DRIVE-BY BRIDGE MODAL IDENTIFICATION: NUMERICAL STUDY

Numerical study is conducted to analyze the effectiveness of the method for extracting mono-components from vehicle responses and drive-by bridge modal identification. The properties of the bridge are: length  $L = 35$ m, density  $\rho = 5000$  kg/m, and flexural rigidity  $EI = 2.178 \times 10^{10}$  Nm<sup>2</sup>. The damping ratio is set as 0.01 and the theoretical values of the first three bridge modal frequencies are 2.68, 10.71 and 24.09Hz, respectively. The properties of the sensing vehicle are: body mass  $m_v = 466.5$ kg, suspension stiffness  $k_s = 9.00 \times 10^5$  N/m, suspension damping  $c_s = 0.14 \times 10^3$  N s/m and its fundamental frequency  $f_v$  is 6.99Hz. The vehicle speed is set as 2m/s and the operational load to simulate the traffic on the bridge is a randomly generated load.

The dynamic modes decomposed by SVMd are used to estimate the bridge frequencies. To evaluate the accuracy of

the proposed drive-by bridge modal identification method, the Monte Carlo method with 50 simulations is used to generate the vehicle response dataset to simulate multiple passes of the sensing vehicle considering random operational load. Each of these responses is analyzed by SVMd, and the components related to the first two dynamic modes of bridge are used for the identification of frequency and damping ratio. Three different damping ratio values of bridge, i.e., 0.01, 0.02 and 0.03 are considered in simulating vehicle responses. The mean values and the standard deviation (std) of the identified frequencies for 50 passes are presented in Table 1. It can be seen that the mean values are very close to the theoretical values and the errors are all less than 1.5%. The results confirm that the bridge modal frequencies can be identified with high accuracy using the developed method.

Table 1 Identified frequency considering different damping ratios

Identified frequency (Hz)						
Damping ratio	0.01		0.02		0.03	
	mean	std	mean	std	mean	std
First mode	2.674	0.0561	2.667	0.0419	2.658	0.085
Second mode	10.589	0.0842	10.559	0.1012	10.549	0.182

### 4 CONCLUSIONS

This study investigates drive-by bridge modal identification under multi-source excitations based on the adaptive decomposition of vehicle responses using SVMd. The investigation confirms that the SVMd can be incorporated with the NExT/RDT to analyze the bridge related dynamic components to estimate the modal frequencies and damping

ratios. The bridge modal frequencies are identified accurately by computing the mean value of multiple tests to reduce the effects of the multi-source random excitations. A more sophisticated operational traffic model is required to meets more realistic situation in the simulation. Besides, experimental investigations on actual bridges in operational condition are necessary to further verify the effectiveness and robustness of the proposed method.

## ACKNOWLEDGMENTS

This research is supported in part by research funding of the National Natural Science Foundation of China (52108288) and China Postdoctoral Science Foundation (Grant No.: 2023M733407). The financial aid is gratefully acknowledged.

## REFERENCES

- [1] Yang, Y. B., Wang, Z. L., Shi, K., Xu, H., and Wu, Y. T. (2020). State-of-the-art of vehicle-based methods for detecting various properties of highway bridges and railway tracks. *International Journal of Structural Stability and Dynamics*, 20(13), 2041004. <https://doi.org/10.1142/S0219455420410047>
- [2] Zhu, X.Q. , Law, S.S. (2015). Structural health monitoring based on vehicle-bridge interaction: accomplishments and challenges. *Advances in Structural Engineering*, 18(12): 1999 - 2015. <https://doi.org/10.1260/1369-4332.18.12.1999>
- [3] Tan, C. J., Uddin, N., OBrien, E. J., McGetrick, P. J., and Kim, C. W. (2019). Extraction of bridge modal parameters using passing vehicle response. *Journal of Bridge Engineering*, 24(9), 04019087. [https://doi.org/10.1061/\(ASCE\)BE.1943-5592.0001477](https://doi.org/10.1061/(ASCE)BE.1943-5592.0001477)
- [4] Nazari, M., and Sakhaei, S. M. (2020). Successive variational mode decomposition. *Signal Processing*, 174, 107610. <https://doi.org/10.1016/j.sigpro.2020.107610>
- [5] Li, J. T., Zhu, X. Q., and Guo, J. (2022). Bridge modal identification based on successive variational mode decomposition using a moving test vehicle. *Advances in Structural Engineering*, 25(11), 2284-2300. <https://doi.org/10.1177/13694332221092678>
- [6] Sadeghi Eshkevari S, Matarazzo TJ and Pakzad SN. Simplified vehicle–bridge interaction for medium to long-span bridges subject to random traffic load [J]. *Journal of Civil Structural Health Monitoring*, 2020(10): 693–707. <https://doi.org/10.1016/j.istruc.2022.08.074>



# Field test on tunnel indirect damage identification from moving train response

Qi Li<sup>1,2</sup>, Xiongyao Xie<sup>1,2</sup>, Kun Zeng<sup>1,2</sup>

<sup>1</sup>Department of Geotechnical Engineering, School of Civil Engineering, Tongji University, Shanghai 200092, People's Republic of China

<sup>2</sup>Key Laboratory of Geotechnical and Underground Engineering of Ministry of Education, School of Civil Engineering, Tongji University, Shanghai 200092, People's Republic of China  
email: 2310026@tongji.edu.cn, xiexiongyao@tongji.edu.cn, zengkun\_tj@tongji.edu.cn

**ABSTRACT:** To explore the potential application of the tunnel damage identification method based on train acceleration, a three-axis accelerometer was installed on a metro train carriage to collect acceleration signals. The original signals are segmented and aligned according to the stations, with data analyzed in terms of station sections. Next, the probability density distribution, fast Fourier transform spectrum, and one-third octave spectrum of the signal are calculated. A time-frequency domain fast analysis software for acceleration data is then developed. By comparing changes in time-frequency domain features, the anomalous section of the tunnel is identified. The results confirm that the tunnel damage identification method based on train acceleration is applicable for real-world metro tunnels.

**KEY WORDS:** Field test; Probability density distribution; Fast Fourier transform; One-third octave.

## 1 INTRODUCTION

With the rapid pace of urbanization, metro systems are playing an increasingly vital role in alleviating urban traffic congestion [1]. As a critical support infrastructure for metro trains, metro tunnels can experience issues such as settlement, water leakage, and lining cracks during their operational period [2]. These problems can arise from the combined effects of geological conditions, material aging, dynamic loads from trains, and nearby construction activities, all of which can compromise the structural integrity of the tunnels [3]-[4]. Therefore, monitoring the health condition of metro tunnels and performing timely maintenance are crucial for ensuring the safe and efficient operation of the metro system [5].

Li [6] proposed a method that involves installing acceleration sensors on metro trains to identify tunnel damage or anomalies by analyzing changes in train acceleration. The feasibility of this approach was demonstrated theoretically. This method offers advantages such as high efficiency and low cost, providing a novel approach to metro tunnel health monitoring. Following this, damage indicators based on wavelet packet energy change rates [6], spectral kurtosis change rates [6], and relative entropy of wavelet packet energy [7] were introduced for analyzing train acceleration signals to identify tunnel anomalies. Deep learning techniques, including convolutional variational autoencoders (CVAE) [7], convolutional neural networks (CNN) [8], and long short-term memory (LSTM) [8] networks, have been applied to classify tunnel damage types, with their performance validated through model tests. Compared to traditional damage indicators, deep learning methods effectively reduce the interference from noise and data inconsistencies. Although the feasibility of the tunnel damage identification method based on train acceleration has been theoretically and experimentally verified, real-world acceleration data from metro trains have yet to be collected to assess the feasibility of the method in field conditions.

In this study, a three-axis accelerometer was installed on a metro train carriage to collect the train acceleration. The time-

frequency domain features of the acceleration signals are then calculated. By analyzing the changes in these features, the anomalous section of the tunnel is identified. The results confirm that the tunnel damage identification method based on train acceleration is feasible for real-world applications.

## 2 FIELD TEST

In this study, a field test was conducted on a complete metro line in a certain city, which includes two tunnels on the up and down lines, with a total of 19 stations. A wireless three-axis accelerometer, with a measurement range of 2g and a sampling frequency of 4000Hz, was installed under the seat in the middle of the train carriage to collect the train acceleration. The test, as outlined in Table 1, was conducted in three phases from April 16 to September 20, 2021, spanning a total of 24 days. For each test day, a set of acceleration data was recorded from the starting station to the terminal station, with separate data sets collected for both the up and down line tunnels.

Table 1. Test dates.

Phase	Dates
Phase 1	April 16 - April 28
Phase 2	May 12 - May 21
Phase 3	September 20

## 3 TEST DATA ANALYSIS

### 3.1 Original data

The original signal is segmented and aligned based on the 19 stations, dividing the line into 18 station sections for sectional data analysis. Taking a specific section as an example, the acceleration signal is shown in Figure 1. In this figure, the X direction represents the forward direction of the train, while the Z direction is perpendicular to the ground of the carriage. The acceleration in the X direction shows a clear ascending or

descending trend due to changes in train speed, whereas the acceleration in the Y and Z directions exhibits similar patterns of variation.

In this study, the Z direction is selected to analyze the changes in train acceleration. The acceleration in the Z direction for 18 sections is shown in Figure 2. The number above each curve corresponds to the section's serial number. Due to variations in tunnel length, geological conditions, and track irregularities across the sections, the time-domain waveforms of acceleration exhibit distinct differences.

The acceleration in the Z direction for 6 days in the same section is shown in Figure 3. The numbers above the curves in the figure represent the corresponding dates, with April 19 recorded as 4.19, and so on. Since the train's speed and the mass of the carriage vary slightly each day, the acceleration values in the same section show some differences in amplitude.

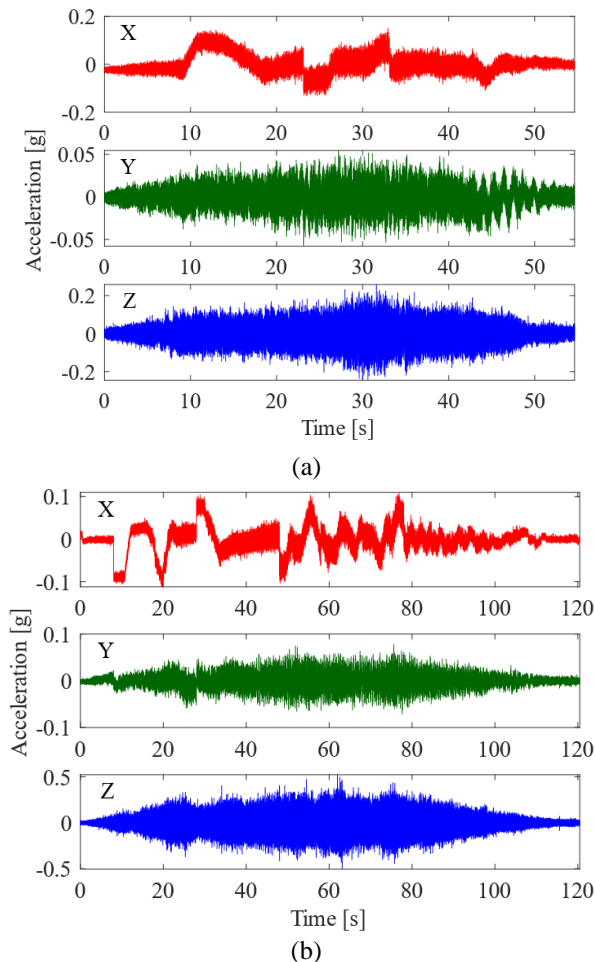


Figure 1. Acceleration signals in the X, Y, and Z directions:  
(a) Up line; (b) Down line.

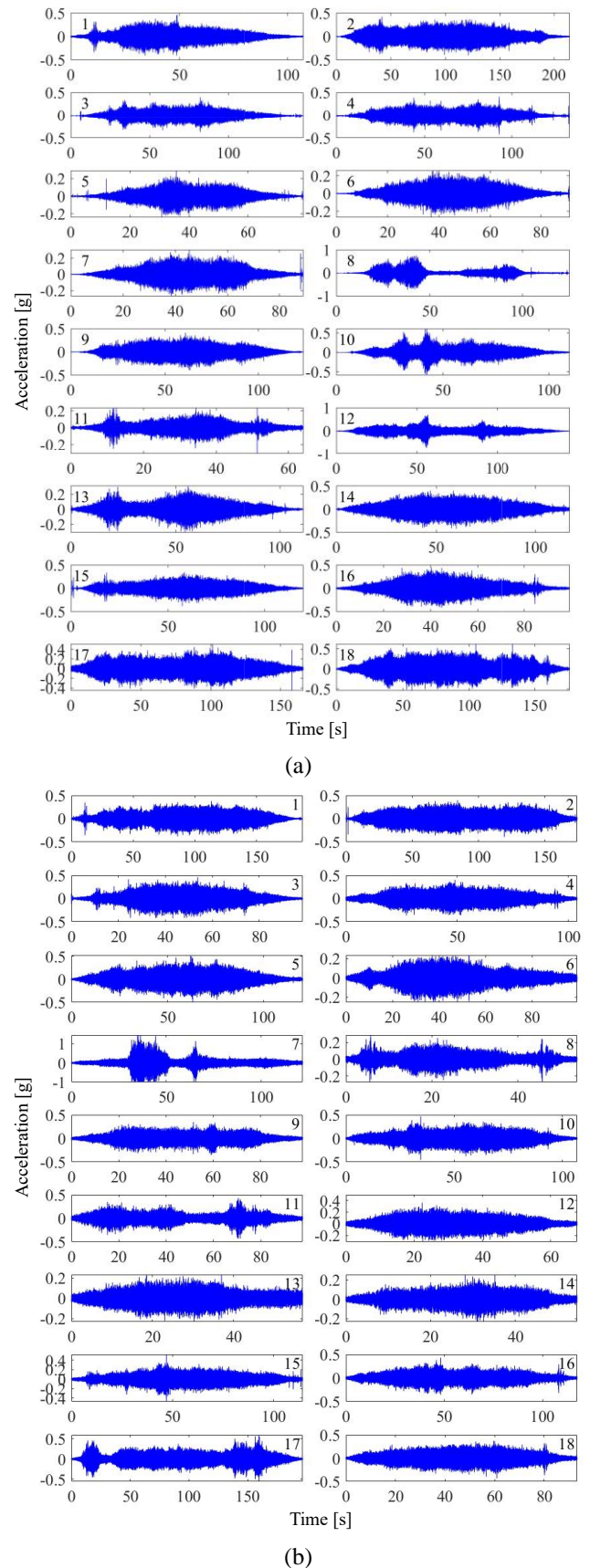
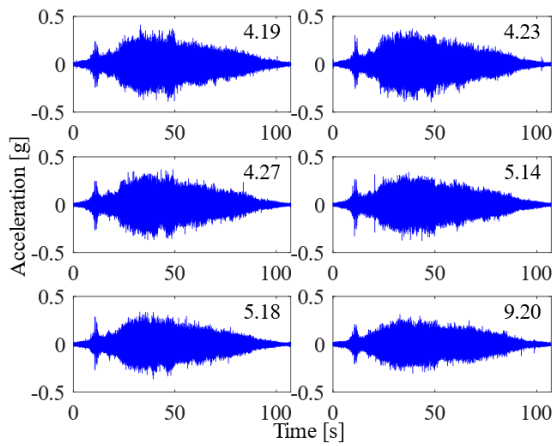
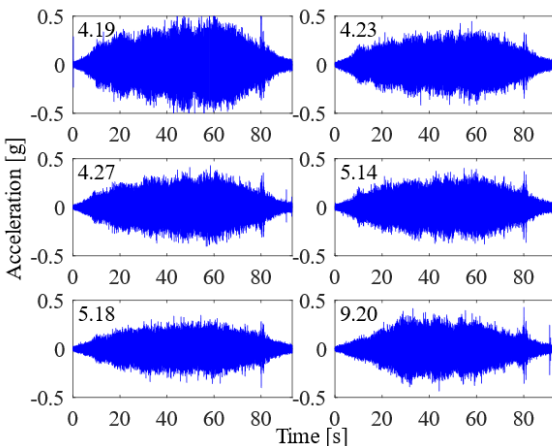


Figure 2. Acceleration signals in different sections: (a) Up line; (b) Down line.



(a)

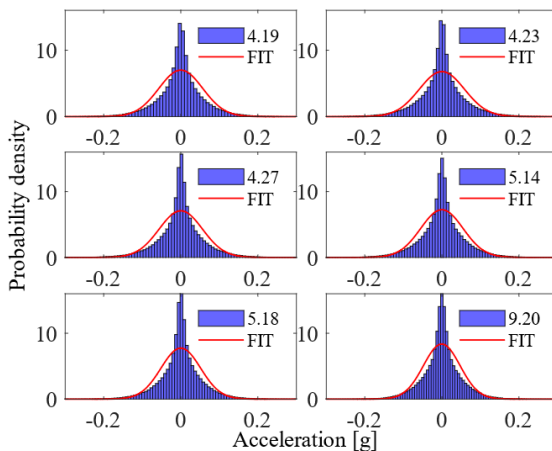


(b)

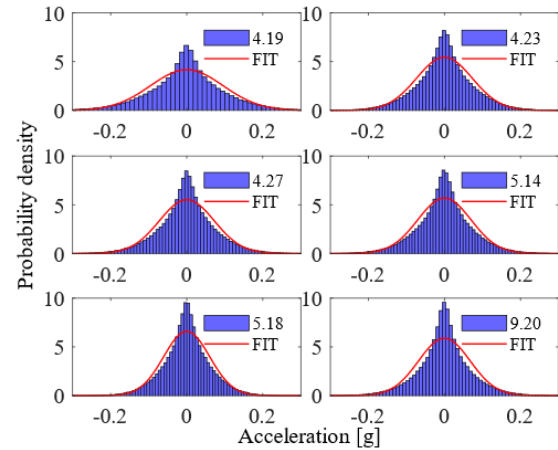
Figure 3. Acceleration signals on different dates: (a) The 1st section of the up line; (b) The 18th section of the down line.

### 3.2 Probability density distribution

The probability density distribution curve of the acceleration signals for 6 days within the same section is shown in Figure 4, with the FIT curve representing the normal distribution fit. The mean acceleration values within the same section are similar, while there are differences in variance.



(a)

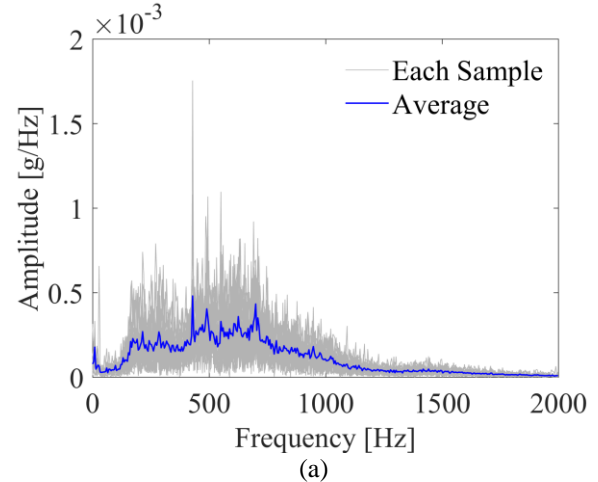


(b)

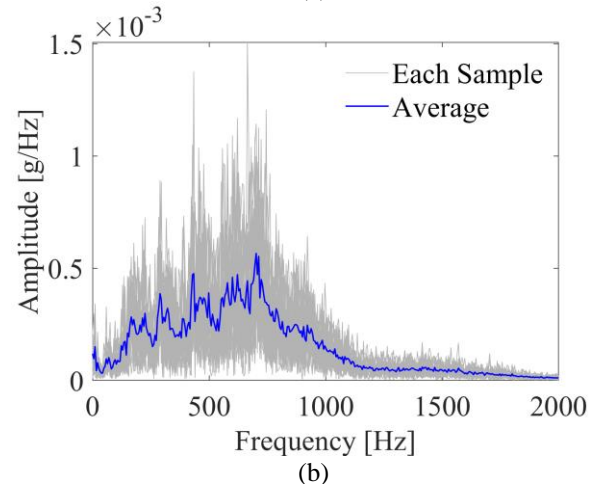
Figure 4. Probability density distribution curves of acceleration signals on different dates: (a) The 1st section of the up line; (b) The 18th section of the down line.

### 3.3 Fast Fourier transform

The acceleration signals from 24 days are analyzed using fast Fourier transform (FFT), converting the time-domain signals into the frequency domain. As shown in Figure 5, the blue curve represents the average of the FFT results from all the signals. The signal energy is concentrated between 200 and 800 Hz, with peaks around 450 Hz and 700 Hz.



(a)



(b)



Figure 5. Fast Fourier transform spectrum of acceleration signals: (a) The 1st section of the up line; (b) The 18th section of the down line.

### 3.4 One-third octave

Figure 6 shows the one-third octave spectrum of the acceleration signals over 24 days, illustrating the distribution of signal energy across different frequency bands. The blue curve in the figure represents the average energy of all the signals. Similar to the FFT spectrum, the signal energy exhibits a peak around 700 Hz.

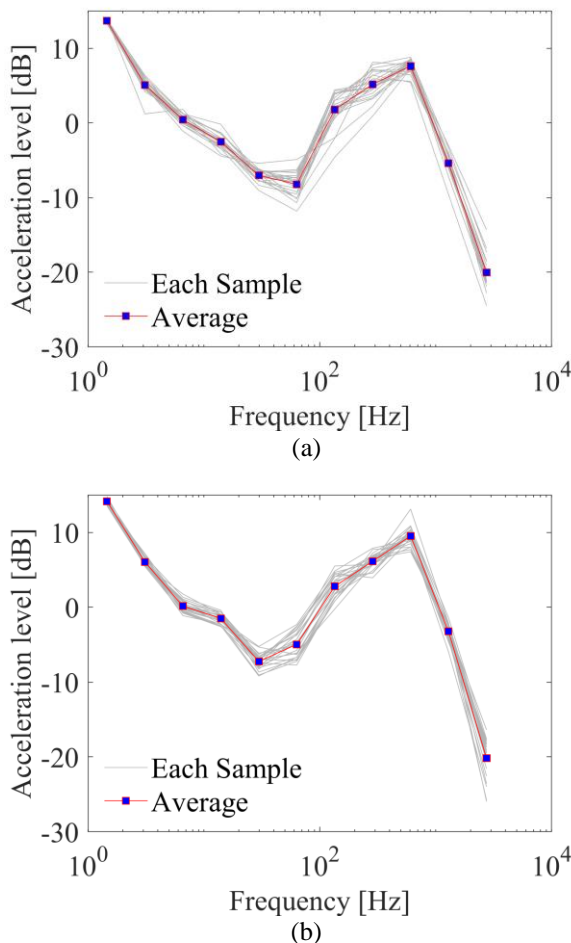


Figure 6. One-third octave spectrum of acceleration signals: (a) The 1st section of the up line; (b) The 18th section of the down line.

### 3.5 Time-frequency domain fast analysis software

As shown in Figure 7, a time-frequency domain fast analysis software for acceleration data is developed using MATLAB App Designer. First, click “Data loading” to read the train acceleration signal from the input “File name”. Next, select or enter the line direction (Left, i.e., Down, or Right, i.e., Up), section number, date, and acceleration direction (X, Y, or Z). Finally, by clicking the “Time domain data”, “Probability density curve”, “Fast Fourier transform”, and “One-third octave” buttons, users can quickly compute and visualize the time-frequency domain features of the signal, facilitating further comparative analysis.

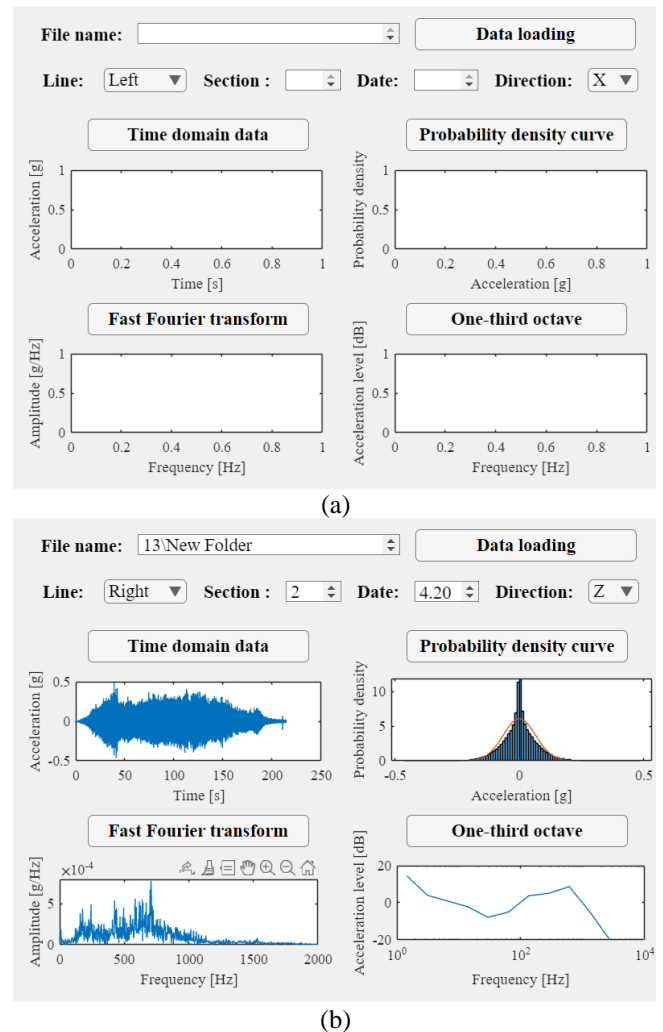
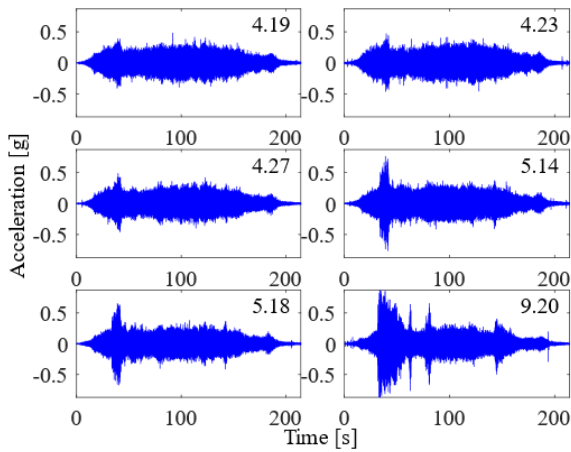


Figure 7. Time-frequency domain fast analysis software for acceleration data: (a) Software interface; (b) Visualization of analysis results.

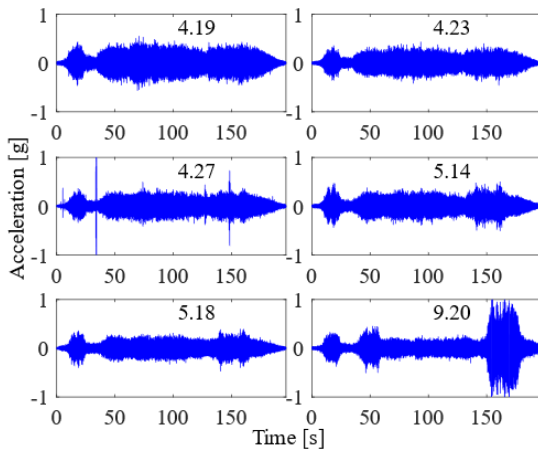
## 4 DATA ANALYSIS OF ANOMALOUS SECTION

### 4.1 Time domain analysis

As shown in Figure 8 and Figure 9, during the data analysis, it is observed that the acceleration signals in the 2nd section of the up line and the 17th section of the down line show significant changes over time. These two sections correspond to the left and right tunnels of the same station segment. Comparing this with the section's operation and maintenance records reveals that, during the field test, the tunnel linings of this station segment experienced excessive uplift, which altered the tunnel's stiffness and boundary conditions. This change is reflected in noticeable differences in the train's vibration signal waveforms. Additionally, on the test day, September 20, which was a rainy day, the tunnel's boundary conditions were further modified, resulting in a significant increase in the train's acceleration amplitude.

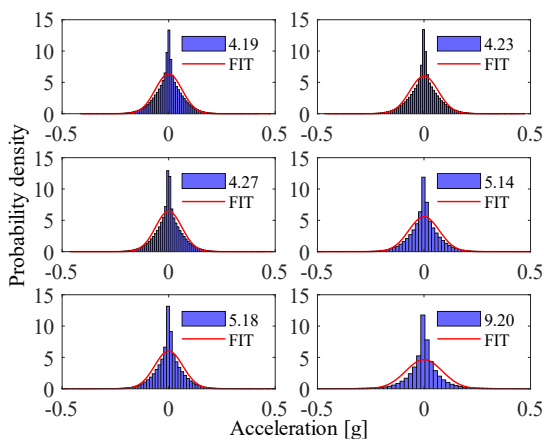


(a)

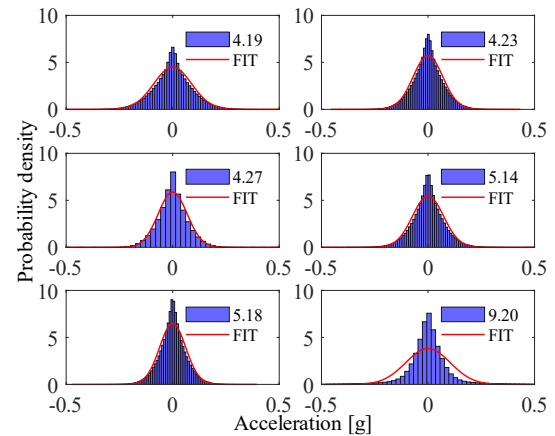


(b)

Figure 8. Acceleration signals of the anomalous section: (a) The 2nd section of the up line; (b) The 17th section of the down line.



(a)



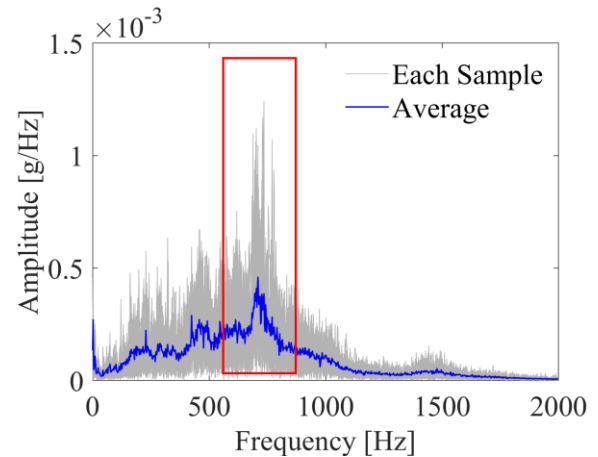
(b)

Figure 9. Probability density distribution curves of acceleration signals in the anomalous section: (a) The 2nd section of the up line; (b) The 17th section of the down line.

#### 4.2 Frequency domain analysis

Further analysis of the frequency domain features for the acceleration signals in the anomalous section, shown in Figure 10 and Figure 11, reveals an increase in energy around 700 Hz compared to the normal sections.

The discovery of the anomalous section validates the feasibility of tunnel damage identification method based on train acceleration for field applications. By analyzing the changes in the time-frequency domain features of the train's acceleration signals, tunnel anomalies can be indirectly identified.



(a)

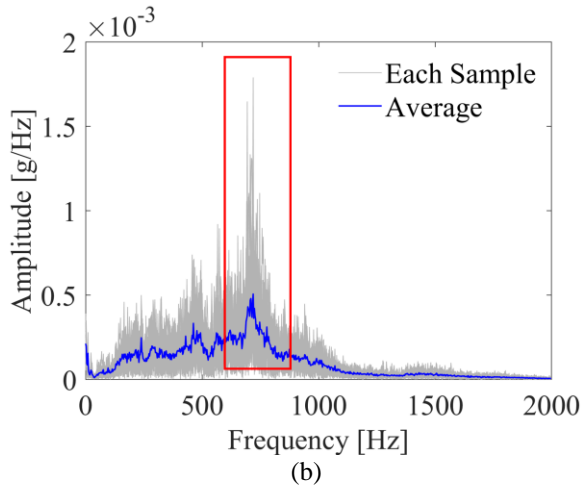


Figure 10. Fast Fourier transform spectrum of acceleration signals in the anomalous section: (a) The 2nd section of the up line; (b) The 17th section of the down line.

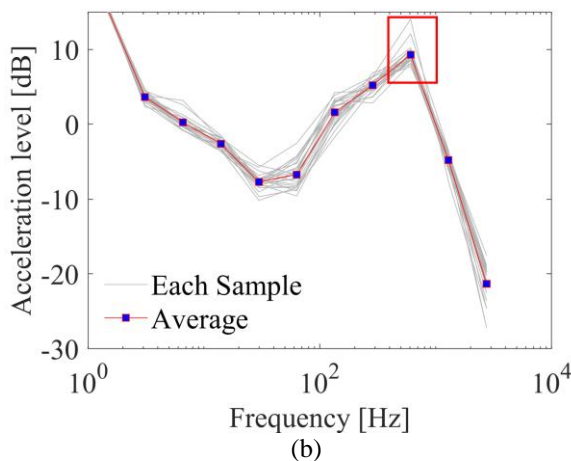
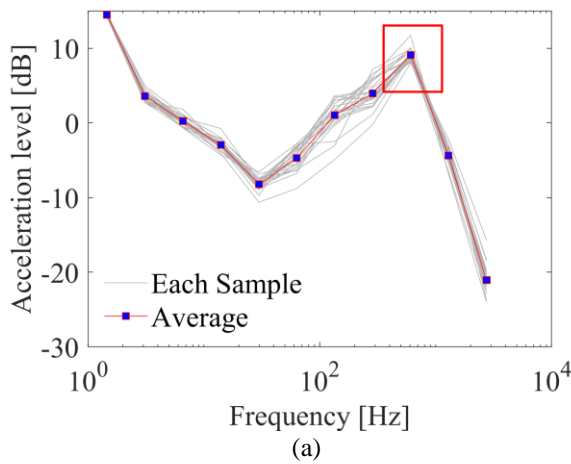


Figure 11. One-third octave spectrum of acceleration signals in the anomalous section: (a) The 2nd section of the up line; (b) The 17th section of the down line.

## 5 CONCLUSIONS

In this study, a three-axis accelerometer was installed on the train carriage to collect acceleration signals throughout the entire journey. The time-frequency domain features of the

signals are analyzed. The main conclusions of this study are as follows:

1) The acceleration in the direction of the train's motion shows distinct ascending or descending segments due to changes in train speed. The acceleration in the two directions perpendicular to the train's motion exhibits a similar trend.

2) The train acceleration signals in normal sections on different dates show slight differences in amplitude due to variations in train speed and carriage mass. In contrast, the train acceleration signals in anomalous sections on different dates exhibit significant differences in waveform, caused by changes in the tunnel's stiffness and boundary conditions, with more substantial fluctuations in signal amplitude.

3) By calculating the probability density distribution, fast Fourier transform spectrum, and one-third octave spectrum of the acceleration signals, changes in the time-frequency domain features can reveal anomalous sections of the tunnel. This analysis validates the feasibility of tunnel damage identification method based on train acceleration in real-world applications.

Future work will involve selecting additional metro tunnels, installing sensors on trains to collect field data, and building a comprehensive dataset. Machine learning or deep learning techniques will then be applied to further identify tunnel anomalies.

## ACKNOWLEDGMENTS

This work was supported by the National Natural Science Foundation of China (grant no. 52038008).

## REFERENCES

- [1] Zhou, C., Qin, W., Luo, H., Yu, Q., Fan, B., & Zheng, Q. (2024). Digital twin for smart metro service platform: Evaluating long-term tunnel structural performance. *Automation in Construction*, 167, 105713. <https://doi.org/10.1016/j.autcon.2024.105713>.
- [2] Zheng, A., Qi, S., Cheng, Y., Wu, D., & Zhu, J. (2024). Efficient Detection of Apparent Defects in Subway Tunnel Linings Based on Deep Learning Methods. *Applied Sciences*, 14(17), 7824. <https://doi.org/10.3390/app14177824>.
- [3] Yang, H., Wang, L., Pan, Y., & Chen, J. J. (2025). A Teacher-Student Framework Leveraging Large Vision Model for Data Pre-Annotation and YOLO for Tunnel Lining Multiple Defects Instance Segmentation. *Journal of Industrial Information Integration*, 100790. <https://doi.org/10.1016/j.jii.2025.100790>.
- [4] Lin, W., Li, P., Xie, X., Cao, Y., & Zhang, Y. (2023). A Novel Back-Analysis Approach for the External Loads on Shield Tunnel Lining in Service Based on Monitored Deformation. *Structural Control and Health Monitoring*, 2023(1), 8128701. <https://doi.org/10.1155/2023/8128701>.
- [5] Chen, X., Zhang, Q., Liu, R., Wang, X., & He, W. (2023). Maintenance strategies and life-cycle cost analysis of inspection robots in metro tunnels. *Tunnelling and Underground Space Technology*, 140, 105270. <https://doi.org/10.1016/j.tust.2023.105270>.
- [6] Li, H., Xie, X., Zhang, Y., & Wang, Q. (2021). Theoretical, numerical, and experimental study on the identification of subway tunnel structural damage based on the moving train dynamic response. *Sensors*, 21(21), 7197. <https://doi.org/10.3390/s21217197>.
- [7] Zhang, Y., Xie, X., Li, H., & Zhou, B. (2022). An unsupervised tunnel damage identification method based on convolutional variational auto-encoder and wavelet packet analysis. *Sensors*, 22(6), 2412. <https://doi.org/10.3390/s22062412>.
- [8] Zhang, Y., Xie, X., Li, H., Zhou, B., Wang, Q., & Shahrour, I. (2022). Subway tunnel damage detection based on in-service train dynamic response, variational mode decomposition, convolutional neural networks and long short-term memory. *Automation in Construction*, 139, 104293. <https://doi.org/10.1016/j.autcon.2022.104293>.





# Population Based Structural Health Monitoring (PBSHM)

# A methodology for data collection and aggregation in population-based structural health monitoring ecosystems

D. R. Lim<sup>1</sup>, <https://orcid.org/0009-0007-9068-9428>, A. J. Ferguson<sup>2</sup>, <https://orcid.org/0000-0002-3794-705X>, D. S. Brennan<sup>3</sup>, <https://orcid.org/0009-0001-7223-3431>, D. Hester<sup>2</sup>, <https://orcid.org/0009-0007-2280-4340>, R. Woods<sup>1</sup>, <https://orcid.org/0000-0001-6201-4270>

<sup>1</sup>School of Electronics, Electrical Engineering and Computer Science, Queen's University Belfast, Belfast BT9 5AH, U.K.

<sup>2</sup>School of Natural and Built Environment, Queen's University Belfast, Belfast BT9 5AG, U.K.

<sup>3</sup>Dynamics Research Group, School of Mechanical, Aerospace and Civil Engineering, University of Sheffield, Sheffield S1 3JD, U.K.

email: {dlim04, a.j.ferguson, d.hester, r.woods}@qub.ac.uk, d.s.brennan@sheffield.ac.uk

**ABSTRACT:** Population-based Structural Health Monitoring (PBSHM) provides insights based on data derived from comparing multiple structures' responses, providing a shift towards an integrated data domain. This presents significant challenges in data collection and integration of data across diverse structural populations, such as sensor systems, environmental data, and maintenance records and requires substantial engineering effort. This fragmentation of data across different formats and systems creates substantial engineering overhead when integrating new data sources, limiting the practical implementation of population-based approaches. This paper introduces a structured data flow architecture for systematic data collection and aggregation in PBSHM ecosystems by defining distinct functional components within the data collection process and enabling the structured integration of diverse data sources. The results establish a foundation for scalable PBSHM data collection, supporting the broader transition towards integrated structural health monitoring ecosystems.

**KEY WORDS:** Population-based Structural Health Monitoring (PBSHM); Data integration architecture; Data collection; Data aggregation

## 1 INTRODUCTION

Structural health monitoring (SHM) has the potential to reduce operational costs and increase infrastructure safety by augmenting existing primarily qualitative condition management processes using quantitative sensor data to track an asset's condition over time. More recently, population-based structural health monitoring (PBSHM) has been proposed to exploit the similarities between data from multiple structures to gain additional insights into their condition.

To date, the development of SHM sensing systems has largely been application-driven, such as in the Intersection Bridge 5 (IB5) [1] and the Telegraph Road Bridge [2] projects. As data acquisition (DAQ) systems were largely developed in isolation due to commercial interests, differing approaches to data measurement and transport for SHM exist. Consequently, there is no broadly agreed way to integrate these diverse, competing technical solutions into a PBSHM system. One potential approach is to develop a process that adapts all existing SHM sensing systems to support data representations compatible with current PBSHM data domains. However, this is largely impractical due to the complexity, cost, and time required to modify numerous existing systems.

To address this issue, this work proposes a methodology for the design, implementation, and operation of PBSHM data collection systems, allowing data to be merged from various sources to provide a unified view. This process is essential for analysing and making informed decisions based on comprehensive datasets in PBSHM.

A degree of data integration exists in existing SHM systems; for example, when utilising multiple vendors' sensors on a single structure. In this case, the operator may require that all the data be accessible from a single data system, therefore transforming data from multiple sources into a single database.

A common approach to transforming data makes use of an extract, transform, load (ETL) process, where the data is first

extracted from the original data source, transformed into the target format and loaded into the new data store. The methodology proposed here permits the integration of sensing systems for a wide variety of structures (incl. bridges, wind turbines, masts, etc.) into a collection system for PBSHM data, that allows the aggregation and translation of data from a given structure to the shared PBSHM standard, in a defined, consistent manner. Additionally, the methodology is applicable to both existing and future systems.

Our architecture proposes a PBSHM integration pipeline that offers a flexible, modular approach to aggregating data from multiple existing SHM data sources. To demonstrate our work, we present a design study based on the existing IB5 and Telegraph Road Bridge monitoring systems, that illustrates how these may be integrated with a wider PBSHM ecosystem. This design study is presented using UML component diagrams due to its widespread use in system modelling [3].

The main contributions of this work are:

- Introduction of the concept of PBSHM integration pipelines for systematic data collection and aggregation in PBSHM ecosystems;
- An architecture for these integration pipelines, including functional definitions for the mandatory and optional components within these; and
- Demonstration of the application of the design principles of our approach to integrate two existing bridge monitoring systems into a PBSHM system.

The paper is structured as follows: Section 2 describes the current landscape of PBSHM research and identifying key challenges; Section 3 describes data pipelines that enable the integration of individual structure data collection systems; Section 4 describes the functionality in the pipelines; Section 5 details a design study that demonstrates the efficacy of the proposed architecture with conclusions given in section 6.

## 2 BACKGROUND

To design a robust data architecture for supporting PBSHM, it is essential to first identify the benefits and requirements of PBSHM. Additionally, a thorough examination of the current landscape of SHM systems and existing data silos is necessary to pinpoint the needs and challenges for the data architecture.

### 2.1 PBSHM and the associated data ecosystem

As the availability of SHM data for a given structure is incomplete, a population-based SHM approach by collecting data from a group of similar structures to infer the condition of one structure. Bull et al. [4] showed that it is possible to represent the behaviour of these structures using a general form of the population that encapsulates behaviour of all structures within the population of "strongly homogeneous" or nominally identical structures. This is particularly useful for large populations that are manufactured identically and experience similar conditions, such as a farm of wind turbines where each turbine undergoes near-identical manufacturing and construction processes.

This concept, however, can be expanded to include structures that only share significant structural similarities otherwise known as homogenous populations [5], [6] with the challenge to identify those which are similar enough to transfer data between, without compromising model quality. Gosliga et al. [5] proposed an irreducible element (IE) model to represent such structures which solely captures the geometric properties of a structure, whereas a finite element (FE) model contains additional construction information. Brennan et al. [7] introduced an expanded IE model using a set of reduction rules which eliminate author ambiguity, ensuring that each is created using a consistent canonical form while maintaining all structural knowledge. Representing structures with IE models allows the creation of an attributed graph (AG) from the model, which can then be processed using a graph-matching algorithm to determine a "similarity score" between two structures.

Using this similarity score, it is possible to predict the possibility of positive data transfer across heterogeneous populations of structures. Gardner et al. [6] show that features and labels can be mapped from a source structure to a target structure, even among topologically different structures, by using IE and AG representations to extract the similarity between structures within a heterogeneous population.

Given the diverse and extensive data required for the successful realisation of PBSHM, meaningful comparisons between multiple data sources are needed. This requires the data to be standardised to allow large-scale analyses and efficient data processing. Attempts to extend open standards such as Bridge Information Management (BrIM) in Jeong et al. [8], look to address this shared-data problem within their specific regions, but extending to PBSHM is non-trivial.

As such, PBSHM has introduced a standard for its associated shared data. Brennan et al. [7] introduced a PBSHM technical ecosystem made up of the PBSHM Network, Framework, and Database. The Network is the shared data domain in which the similarity between structures is represented; the Database is the shared-data domain in which PBSHM data is stored in a common format and; the Framework is the computational domain in which all algorithms (both similarity and knowledge

transfer) exist. Each domain is valid in its own right, but independent from others.

This comprehensive PBSHM ecosystem integrates data storage and software but can be expanded to accommodate larger databases and additional software modules. It may store various data categories, including sensor data, IE and FE models, reports, features, information and similarity metrics. The authors use a NoSQL database for the PBSHM ecosystem due to its increased flexibility over relational ones allowing the expansion of the database to accommodate any data that may be used in the future to develop PBSHM. Brennan et al. implemented the database using MongoDB, using a detailed "PBSHM Schema" to standardise and store the aforementioned data categories, ensuring compatibility and allowing efficient data retrieval and analysis. The flexibility provided by these choices allow for current knowledge to be embedded within the schema, however, allows for the future needs of PBSHM by enabling the adaptation of the schema to include yet-unknown data at a future date.

### 2.2 SHM data acquisition systems for civil infrastructure

Many SHM systems collect data for civil infrastructure and are made up of either one or multiple data acquisition systems. Various vendors can be used and provide comprehensive DAQs that manage data capture and storage, but these cannot be integrated across vendors, requiring the creation of bespoke SHM systems. Whilst this has the potential of creating a comprehensive system for an SHM structure, it may produce data that is incompatible for the purposes of PBSHM and will not easily be shared.

To highlight this, two bridges, the Intersection Bridge 5 (IB5) and the Telegraph Road Bridge have been selected, due to their extensive sensor networks and well-documented cyber-physical systems.

**IB5** - IB5 is designed to continuously monitor the structural health of the bridge by recording and analysing various signals, using a variety of high-precision sensors that capture data on vibrations, strain, temperature, rotation, and other parameters. Data acquisition units collect the sensor data and convert it into a digital format suitable for real-time wireless transmission to a central server, which processes the data to detect any anomalies. The system includes an application programming interface (API) for authorized users to access the data remotely, facilitating ongoing monitoring and analysis. Additionally, power supply units ensure reliable operation of all components, even in harsh environmental conditions [1].

**Telegraph Road Bridge** - The Telegraph Road Bridge in Michigan employs a network of wireless sensors, including a variety of sensors that measure strain, acceleration, and temperature and are strategically placed to capture detailed data on the bridge's response to truck loading and thermal variations. Data acquisition units collect and digitize the sensor data, which is then transmitted to a central server. This bridge utilises a solar-powered wireless sensor network architecture that can also be used in hard environmental conditions [2].

Following the observations made on both systems [8], [9], [10], differences between the storage and representation between the two systems are described in Table 1.



Although both monitoring systems may appear very similar (each having a physical layer, cyber-physical layer and data storage/processing capability), the systems differ in their underlying data management technologies. Both display a well-thought-out, cyber-physical architecture; however, the systems have been developed largely in isolation, with differing goals leading to a clear difference in data representations. This presents a challenge when trying to compare both structures in a PBSHM context for reasons discussed in section 2.1. Therefore, for PBSHM to be effective, it can be deduced that data integration needs to occur across the two structures.

Table 1. Comparing data representation between IB5 and Telegraph Road Bridge monitoring systems

Structure	IB5	Telegraph Road Bridge
<b>Database Technology</b>	PostgresSQL	Apache Cassandra
<b>Sensor Information Storage</b>	Database Entry	OpenBrIM
<b>Sensor Information Schema</b>	“ID”, “Type” and “Location” fields in database	User-defined OpenBrIM Object

### 3 ARCHITECTURE

One of the key processes within SHM is gathering and capturing monitoring data to ultimately determine the health state of a structure. This is the same for PBSHM, but the process is compounded when considering the very nature of the population-based approach is to accumulate knowledge across multiple structures and types.

While the aforementioned PBSHM technological domains encompass knowledge when in a central ecosystem, they lack the understanding, definitions, and details of the procedures of migrating data from the SHM capture systems associated with the structures and the central system. This part focuses on proposing the missing link between the existing SHM systems – henceforth referenced as data generators – and the PBSHM technical ecosystem introduced by Brennan et al. [11].

#### 3.1 Data Generators

A data generator is any entity that can produce data potentially valid within the PBSHM schema. As data generators can consist of existing SHM data acquisition systems, data generators can produce many different possible representations of SHM data. Therefore, to preserve this, data representation within the PBSHM data domains needs to be facilitated. This gives two possible options: a) development of a process to adapt existing data formats to representations that are supported in the existing PBSHM data domains or, b) retroactive adaption of existing SHM capture systems to support this as well as every future representation. This is significantly hindered by the need for commercial systems to remain compatible with existing solutions.

Thus, we define data pipelines which allow the transport of data from these existing, and future, data generators to the PBSHM data-domains.

#### 3.2 PBSHM Integration Pipelines

The process of getting data from the aforementioned data generator into the PBSHM Framework is referred here to as a data pipeline. Pipelines describe the overall transmission of data from the location(s) at which the data is first introduced into the PBSHM domain to the desired end location.

#### 3.3 Pipeline organisation

Through this data pipeline, it is important to denote the responsibility of each actor within this pipeline, by dividing it into sections. These divisions will furthermore be referred to as scopes with their own set of responsibilities, purpose and defined goals for any data requirements, transformations, and formats that may occur within its remit.

Whilst we must acknowledge that each data pipeline will be unique to the requirements of the data generator(s), there is still an abstract delimitation between each scope area. As such, this paper proposes the following aspects (see Figure 1):

**Structure:** The structure scope describes all the cyber-physical infrastructure required to capture information regarding a physical attribute of a structure. This scope provides an interface that allows this information to be provided to the next scope in the pipeline. Any solution implemented to this scope is specific to the set of measurements desired for a given structure.

**Aggregation:** The aggregation scope is defined by a generic set of processes that universally apply to every application to allow the communication of data from the structure scope to the PBSHM database and vice versa. It receives data from the previous scope and transmits this to the next.

**PBSHM Network, Framework and Database:** This establishes the shared data domain for which the relationships between structures, the shared domain in which PBSHM-specific algorithms and computations reside and the database where PBSHM data resides.

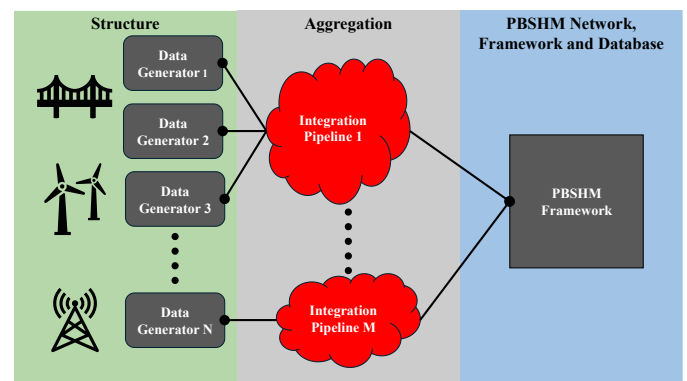


Figure 1. Pipeline flows through the aggregation scope from data generators to the PBSHM Framework

Due to the segregation of responsibility within the data pipeline, when acting within one scope, it is necessary to view the other scopes within the pipeline as black box systems. When implementing within the aggregation scope, it may not

be possible to modify or understand the implementations and behaviours within the structure and PBSHM server scopes.

## 4 FUNCTIONALITY

To describe the functionality required in the pipeline, a roles-based approach is used. Each role dictates the functionality that is required to produce a valid PBSHM data integration system. Each role provides an interface through which data is communicated. Data flows describe the transfer of data from one role to the next. By utilising the abstract form of a roles-based approach to describe the implementation of data flows, we can define a consistent terminology within the context of the PBSHM ecosystem, allowing the methodology to apply to not just existing technologies, but future technologies. In principle, roles can be described as actors, which perform some operation on data within the pipeline.

Figure 2 outlines mandatory and optional roles. Mandatory roles (which are denoted in grey) must be implemented to create a valid data pipeline from a data generator to the PBSHM server and the optional roles (denoted in pink) describe additional functionality that can be added to the system. Arrows are used to describe the data flows where the arrowhead indicates which direction the data flow is initiated.

### 4.1 Mandatory Roles

Initially, there is some required functionality that must be implemented to allow the movement of data from a given data generator to the PBSHM core. It is important to note that data generators may encompass a wide variety of data i.e. channel data, feature data, reports, etc.

A pipeline may be configured as follows: Initially, data is generated by the data generator contained within the structure scope. These roles provide some interface to the aggregation layer.

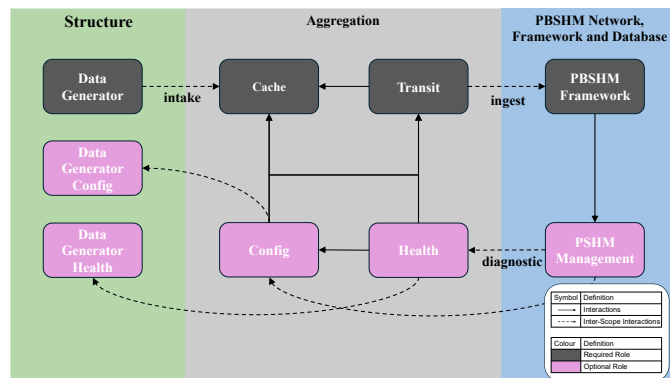


Figure 2. PBSHM data integration roles

Cache roles play a simple yet vital role in the PBSHM data integration pipeline. By utilising a buffer to store incoming data from data generators, we can aggregate multiple data streams at the cache to group the incoming data. In a PBSHM system where it can be expected to have many structures each with many data generators, it becomes infeasible to have each data generator directly interact with the PBSHM Framework.

Finally, the purpose of the transit role is to serve as the gateway between the data cache and the PBSHM Framework. Data provided by the transit role must be in the PBSHM schema

format to allow compatibility with the PBSHM database. This will then perform redundancy checks, parity checks etc.

### 4.2 Optional Roles: Config & Health

Additionally, there is potential within the PBSHM integration pipelines to anticipate the need for reconfigurability and insight into downstream aspects of the data pipeline from the PBSHM Framework to allow effective data infrastructure management and support decision systems. Therefore, it is possible to introduce the health and config roles. The function of the health role is to provide statistics and system state information to the PBSHM framework whereas config provides an interface of the components within the aggregation and structure scope to be modified with supported configuration options.

Both health and config roles pose a significant challenge due to the unending complexity of both existing and future technologies due to both differing configurable attributes of data generators and differing statistics provided by data generators. Furthermore, cache roles can take multiple technical forms, with a further set of differing configurable attributes and properties on which insight could be desired.

For the most part, these roles are beyond the scope of this work and will be covered in more depth in future work.

## 5 DESIGN STUDY

The objective is to validate and demonstrate the effectiveness of the proposed data integration architecture for PBSHM by demonstrating the integrity of live data transfer from various sensor systems to a central PBSHM server. Also demonstrated is interoperability by integrating different sensor types and data formats into a cohesive pipeline. To reflect the existing landscape of SHM deployments, the design study uses the two examples given in Section 2.2. We first establish the existing methods that the systems use to access collected data.

### 5.1 Existing data retrieval mechanisms and assumptions

IB5 supplies a representational state transfer (REST) API (built using Fast-API) that allows researchers or stakeholders to access both stored raw and processed data. This enables end-users to access stored data of the digital twin, including raw sensor data from the physical implementation [9]. Although the cyber-physical system supporting the IB5 bridge is a comprehensive and well-designed example of developing a digital twin for a bridge, the REST API implemented for the IB5 is not publicly documented, highlighting the data integration challenges in the current SHM landscape.

```

1 <?xml version="1.0" encoding="UTF-8"?>
2 <xs:schema xmlns:xs="http://www.w3.org/2001/XMLSchema">
3   <xs:element name="TimeSeriesCollection">
4     <xs:complexType>
5       <xs:sequence>
6         <xs:element name="TimeSeriesData" maxOccurs="unbounded">
7           <xs:complexType>
8             <xs:sequence>
9               <xs:element name="id" type="xs:string"/>
10              <xs:element name="data">
11                <xs:complexType>
12                  <xs:sequence>
13                    <xs:element name="DataPoint" maxOccurs="unbounded">
14                      <xs:complexType>
15                        <xs:sequence>
16                          <xs:element name="timestamp" type="xs:dateTime"/>
17                          <xs:element name="value" type="xs:float"/>
18                        </xs:sequence>
19                      </xs:complexType>
20                    </xs:element>
21                  </xs:sequence>
22                </xs:complexType>
23              </xs:element>
24            </xs:sequence>
25          </xs:complexType>
26        </xs:element>
27      </xs:sequence>
28    </xs:complexType>
29  </xs:element>
30 </xs:schema>

```

Figure 3. Assumed XSD of the API response from the IB5 monitoring system

As such, some assumptions have been made about the structure of their API queries and the resultant data that can be retrieved. The following fields are presumed necessary for the query: (1) Sensor IDs, and (2) Time window. It is assumed that the data is returned in an XML document is returned in the structure dictated by an XML schema definition (XSD) presented in Figure 3 where the values returned are:

- Sensor ID(s)
- An array of:
  - Timestamp
  - Value from sensor

An example of an object returned by the assumed API can be seen in Figure 4.

```

1 <TimeSeriesCollection>
2   <TimeSeriesData>
3     <id>sensor-1</id>
4     <data>
5       <DataPoint>
6         <timestamp>2025-03-28T15:51:18Z</timestamp>
7         <value>123.45</value>
8       </DataPoint>
9       <DataPoint>
10        <timestamp>2025-03-28T15:52:18Z</timestamp>
11        <value>125.67</value>
12      </DataPoint>
13    </data>
14  </TimeSeriesData>
15  <TimeSeriesData>
16    <id>sensor-2</id>
17    <data>
18      <DataPoint>
19        <timestamp>2025-03-28T15:51:18Z</timestamp>
20        <value>223.45</value>
21      </DataPoint>
22      <DataPoint>
23        <timestamp>2025-03-28T15:52:18Z</timestamp>
24        <value>225.67</value>
25      </DataPoint>
26    </data>
27  </TimeSeriesData>
28 </TimeSeriesCollection>

```

Figure 4. Example XML file based on the XSD of Figure 3

The monitoring system of the Telegraph Road also provides its own API to retrieve data. Its bridge information repository framework contains an Apache Cassandra database which provides the Cassandra Driver API for retrieving data. This used in conjunction with its “data mapper” (which maps the

time series data stored in the database with the BrIM sensor information) provides the data necessary by the PBSHM schema via the “Sensor data retrieval” service which provides a REST API. This allows the system to be integrated into the PBSHM ecosystem. Literature on the Telegraph Road Bridge both details the structure of the API queries and provides examples of data returned [10].

## 5.2 The proposed data integration system

Using the information supplied about the two systems’ APIs, and details inferred in section 5.1, it is possible to propose an integration system based on the architecture and roles detailed in sections 3 and 4. These roles are set out in Table 2.

This proposed integration system is defined in terms of a UML component diagram (shown in Figure 5). In this case, each component is a distinct software service. Relationships between the components which show how they interact, are drawn between each component. These components are grouped to detail in which deployment environment these would be implemented. Most have been implemented in the “PBSHM Integration Cloud Server”; however, an additional component has been added to the “PBSHM Integration Cloud Server” to show an additional module that could be added to the PBSHM Framework that would allow the insertion of records to the PBSHM Database over HTTP(S).

An important observation from Table 2 is the designation of the IB5 and TRB fetchers as data generators. Although these are part of the structure scope, in this case, they have been implemented in the “PBSHM Integration Cloud Server”. As data generators must be the actors of any data transaction to the cache (Figure 2), it is necessary to add a component that fetches from the existing APIs provided by both bridges and subsequently pushes the results to their respective RabbitMQ caches. To avoid changing the existing back-ends of both structures, these are implemented in the “PBSHM Integration Cloud Server”. However, this is an example of a deployment environment implementing roles across two scopes.

Table 2. Identifying how each role is fulfilled by components in the proposed PBSHM data integration system for IB5 and Telegraph Road Bridge

Role	IB5 Component	TRB Component
Data Generator	IB5 Fetcher	TRB Fetcher
Cache	IB5 Queue (RabbitMQ)	TRB Queue (RabbitMQ)
Transit	PBSHM Framework Loader	PBSHM Framework Loader
PBSHM Core	REST API	REST API

Within the proposed data integration system, most of the components could be implemented by a multitude of technologies. However, where new data transfer components are required, RabbitMQ has been chosen as the technology to represent to reception of these data transfers.



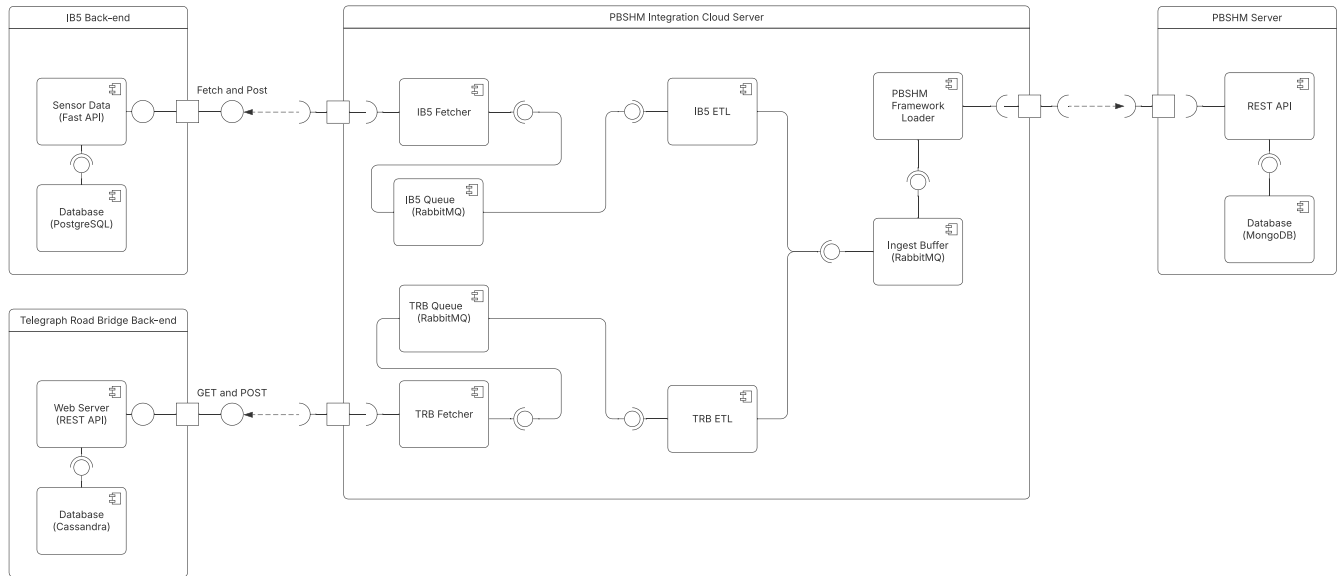


Figure 5. Universal markup language diagram showing the proposed population-based structural health monitoring data integration system for the Intersection Bridge 5 and Telegraph Road Bridge

Whilst these components could most likely be replaced with similar technologies or even a more traditional data transfer and storage method, RabbitMQ has been chosen as it both dictates the protocol in which messages are sent/read and provides a data store in the form of the message queue. Furthermore, it is open-source and well-documented, allowing ease of use without complications surrounding licensing [12], [13].

As stated, no changes have been made to the functionality provided by either the IB5 or Telegraph Road back-ends. Therefore, to bring data into the “PBSHM Integration Cloud Server”, two “Fetcher” components (each for their respective monitoring system) have been added which periodically sends requests to their respective APIs to check whether new data has been added to the databases and then fetches and loads it onto a RabbitMQ, therefore fulfilling the role of the data generator. An example application provided in [10] documents how automated data retrieval could be implemented for the Telegraph Road Bridge.

Once the sensor data from each bridge has been loaded into their respective message queues, sensor data from both bridges is then extracted from their message queues into ETL components. The purpose of these ETL components is to transform the data in the message queues from their respective data formats and schemas into a JSON format that follows the PBSHM schema. Whilst the data from both bridges is undergoing similar processes to be transformed into PBSHM schema, the underlying technologies will take significantly different methods to undertake this due to the difference in the data format and structure (schema) of the data generators. The key differences being:

- In IB5, data is assumed to be returned in XML format whereas Telegraph Road returns data in JSON format.
- It is assumed that IB5 returns data in a similar schema to that shown in Figure 3 whereas Telegraph Road produces data in its schema (examples given in [10]).

Once the data from either structure has been transformed into PBSHM Schema, this can then be loaded onto another RabbitMQ labelled the “Ingest Buffer”.

By transforming the data into the PBSHM schema data integrity and interoperability are ensured as the schema provides a unified way to represent sensor data and contains information about the origin of the data.

From this point, as the data from both bridges is in the same structure and format it can be manipulated by the same components through the rest of the pipeline. The data is then extracted by the ingest buffer and loaded onto “PBSHM Server” via a REST API with an HTTP(S) request at which point the “PBSHM Server” API will load the data onto the database.

## 6 CONCLUDING REMARKS

This paper presents a methodology for the design, implementation and operation of PBSHM data collection systems. By defining mandatory roles for data transfer from structure to PBSHM Network, Framework and Database scope and demonstrating their application to real-world, bridge monitoring systems, it is shown how diverse existing SHM data acquisition systems can be integrated into a PBSHM ecosystem, whilst maintaining data integrity and interoperability as provided by the standard PBSHM schema. Future work will focus on refining the optional components within the aggregation scope, particularly the config and health role which present significant challenges due to the variability in configurable attributes and operational performance. Robust reference implementations of the aggregation scope components will also be developed to provide practical guidance for SHM system operators seeking to integrate their monitoring systems with PBSHM systems, thereby accelerating the adoption of PBSHM. Furthermore, work will include the development of software modules for the PBSHM framework that allow for the use of external software tools by

providing interfaces to the data collected as defined by security policies.

## ACKNOWLEDGMENTS

The authors gratefully acknowledge the support of the UK Engineering and Physical Sciences Research Council (EPSRC) through the ROSEHIPS project (Grant EP/W005816/1). For the purpose of open access, the authors have applied a Creative Commons Attribution (CC BY) licence to any Author Accepted Manuscript version arising.

## REFERENCES

- [1] P. R. A. Fidler, F. Huseynov, M. Bravo-Haro, V. Vilde, J. M. Schooling, and C. R. Middleton, 'Augmenting an existing railway bridge monitoring system with additional sensors to create a bridge weigh-in-motion system and digital twin', Jul. 2022, doi: 10.17863/CAM.86738.
- [2] S. M. O'Connor, Zhang, Yilan, Lynch, Jerome P., Ettouney, Mohammed M., and P. O. and Jansson, 'Long-term performance assessment of the Telegraph Road Bridge using a permanent wireless monitoring system and automated statistical process control analytics', *Structure and Infrastructure Engineering*, vol. 13, no. 5, pp. 604–624, May 2017, doi: 10.1080/15732479.2016.1171883.
- [3] M. Ozkaya, 'Do the informal & formal software modeling notations satisfy practitioners for software architecture modeling?', *Information and Software Technology*, vol. 95, pp. 15–33, Mar. 2018, doi: 10.1016/j.infsof.2017.10.008.
- [4] L. A. Bull *et al.*, 'Foundations of population-based SHM, Part I: Homogeneous populations and forms', *Mechanical Systems and Signal Processing*, vol. 148, p. 107141, Feb. 2021, doi: 10.1016/j.ymssp.2020.107141.
- [5] J. Gosliga, P. A. Gardner, L. A. Bull, N. Dervilis, and K. Worden, 'Foundations of Population-based SHM, Part II: Heterogeneous populations – Graphs, networks, and communities', *Mechanical Systems and Signal Processing*, vol. 148, p. 107144, Feb. 2021, doi: 10.1016/j.ymssp.2020.107144.
- [6] P. Gardner, L. A. Bull, J. Gosliga, N. Dervilis, and K. Worden, 'Foundations of population-based SHM, Part III: Heterogeneous populations – Mapping and transfer', *Mechanical Systems and Signal Processing*, vol. 149, p. 107142, Feb. 2021, doi: 10.1016/j.ymssp.2020.107142.
- [7] D. S. Brennan, J. Gosliga, E. J. Cross, and K. Worden, 'Foundations of population-based SHM, Part V: Network, framework and database', *Mechanical Systems and Signal Processing*, vol. 223, p. 111602, Jan. 2025, doi: 10.1016/j.ymssp.2024.111602.
- [8] S. Jeong, R. Hou, J. P. Lynch, H. Sohn, and K. H. Law, 'An information modeling framework for bridge monitoring', *Advances in Engineering Software*, vol. 114, pp. 11–31, Dec. 2017, doi: 10.1016/j.advengsoft.2017.05.009.
- [9] D. Grdr Broo, M. Bravo-Haro, and J. Schooling, 'Design and implementation of a smart infrastructure digital twin', *Automation in Construction*, vol. 136, p. 104171, Apr. 2022, doi: 10.1016/j.autcon.2022.104171.
- [10] S. Jeong, Hou, Rui, Lynch, Jerome P., Sohn, Hoon, and K. H. and Law, 'A scalable cloud-based cyberinfrastructure platform for bridge monitoring', *Structure and Infrastructure Engineering*, vol. 15, no. 1, pp. 82–102, Jan. 2019, doi: 10.1080/15732479.2018.1500617.
- [11] D. S. Brennan, T. J. Rogers, E. J. Cross, and K. Worden, 'On calculating structural similarity metrics in population-based structural health monitoring', *Data-Centric Engineering*, pp. 1–24, Aug. 2024, doi: 10.1017/dce.2024.45.
- [12] M. M. P and S. Dixit, 'Distributing Messages Using Rabbitmq with Advanced Message Exchanges', *International Journal of Research Studies in Computer Science and Engineering*, vol. 6, no. 2, pp. 24–28, 2019.
- [13] G. Fu, Y. Zhang, and G. Yu, 'A Fair Comparison of Message Queuing Systems', *IEEE Access*, vol. 9, pp. 421–432, 2021, doi: 10.1109/ACCESS.2020.3046503.

# Towards a plug and play population-based structural health monitoring aggregation pipeline design for resource constrained systems

D. R. Lim<sup>1</sup>, <https://orcid.org/0009-0007-9068-9428>, A. J. Ferguson<sup>2</sup>, <https://orcid.org/0000-0002-3794-705X>, C. O'Higgins<sup>2</sup>, <https://orcid.org/0000-0001-7034-005X>, D. Hester<sup>2</sup>, <https://orcid.org/0009-0007-2280-4340>, R. Woods<sup>1</sup>, <https://orcid.org/0009-0007-2280-4340>

<sup>1</sup>School of Electronics, Electrical Engineering and Computer Science, Queen's University Belfast, Belfast BT9 5AH, U.K.

<sup>2</sup>School of Natural and Built Environment, Queen's University Belfast, Belfast BT9 5AG, U.K.

email: {dlim04, a.j.ferguson, c.ohiggins, d.hester, r.woods}@qub.ac.uk

**ABSTRACT:** The practical implementation of Population-based Structural Health Monitoring (PBSHM) often involves distributed which face challenges from limited compute resources, power budgets, and variable communication bandwidths, for example, IoT devices with battery-powered wireless sensor network gateways uploading data over metered connections. Building upon the data flow architecture presented in our first paper in this special session, this paper demonstrates how inherent state within data streams' can be leveraged for optimisation. This paper introduces a novel, plug-and-play aggregation pipeline specifically designed to address these limitations. We present an optimised data representation and transmission strategy that minimises computational and bandwidth requirements at the network edge. By leveraging efficient data serialisation techniques, our pipeline achieves a significant reduction in data payload size with negligible information loss, thereby enhancing the scalability and financial viability of PBSHM systems. This work validates an enabling technology for the real-world deployment of large-scale, low-power monitoring ecosystems. It does so by comparing two data formats, JavaScript Object Notation (JSON) and Concise Binary Object Representation (CBOR), using monitoring data from a long-term bridge campaign. The results show a reduction in the volume of transmitted data by up to 12.2 times.

**KEY WORDS:** Population-based Structural Health Monitoring (PBSHM); Resource-constrained systems; data optimisation; data serialisation.

## 1 INTRODUCTION

Infrastructure monitoring requires methods to track structural condition and optimise maintenance schedules. Structural health monitoring (SHM) has developed considerably in recent years [1]. Population-Based SHM (PBSHM) offers potential advantages over traditional SHM approaches by analysing data across multiple structures rather than analysing each independently. This approach enables knowledge transfer between similar structures, improving damage detection and diagnostic capabilities [2], [3], [4], [5].

While the definition of a computing framework for PBSHM is established [6], the practicalities of data logistics in heterogeneous, resource-scarce environments remain a significant research gap. Implementing PBSHM systems requires the integration of data from many different monitoring systems. Previous work has developed a methodology for the transmission of data from a data generator, to the PBSHM database [7].

Practical deployment faces challenges that haven't been fully addressed to date, for example, many monitoring scenarios such as wireless sensor networks, remote sites, and temporary deployments operate with limited resources. These systems must operate within constraints on bandwidth, computing power, energy supply, and storage capacity. These limitations become more significant as PBSHM networks expand to include more structures and sensors.

The focus of this work lies in the creation of a holistic and optimised data aggregation pipeline tailored for resource constrained systems on the network edge. We directly address the challenge of minimising data footprints prior to their arrival at a central repository, a critical step that has hitherto been underexplored. This paper thus provides a foundational

component for the next generation of truly scalable and deployable PBSHM systems.

This paper presents a stateful, connection-oriented approach to PBSHM data transmission designed for resource-constrained environments. Our transmission process establishes session contexts for data generators, handling metadata exchange during session initialisation rather than with each data sample for the period of the session. This reduces redundant information while maintaining schema compliance and plug-and-play functionality, allowing new data generators to join the system with minimal configuration. Functionality that becomes particularly useful for temporary monitoring campaigns or rapid PBSHM monitoring system rollout.

The main contributions of this work are:

- Development of a stateful, session-oriented pipeline architecture for PBSHM data transmission that reduces redundancy through session payload optimisation while retaining plug-and-play data generator integration.
- Demonstration and validation of a resource-efficient aggregation pipeline, using empirical evaluation with field monitoring campaign data to demonstrate its feasibility for real-world PBSHM applications.

The paper is organised as follows: Section 2 introduces the concept of a session-oriented pipeline; Section 3 details the case study used to validate the data and a proposed pipeline design; Section 4 analyses the results; and Section 5 concludes with a summary and future directions.

## 2 METHODOLOGY

To optimise data flow from a structure to a PBSHM server, a key aspect that must be considered is the data representation



used. The PBSHM schema defines the representation that must be provided to the PBSHM Framework.

The PBSHM data integration pipeline (Figure 1) segments the process from the data generator, which is an entity that produces data either already compliant with or transformable to the PBSHM schema, to the PBSHM Network, Framework, and Database, using defined scopes [7]. Using this definition, anything in and transmitted to the PBSHM Network, Framework and Database scope must be within the PBSHM schema representation. However, this approach allows data within scopes preceding the PBSHM Network, Framework, and Database to take any form, as long as it can be reconciled with the PBSHM schema, even if it does not initially conform to it. By exploiting this, we can attempt to optimise the data representation in the “structure” and “aggregation” scopes.

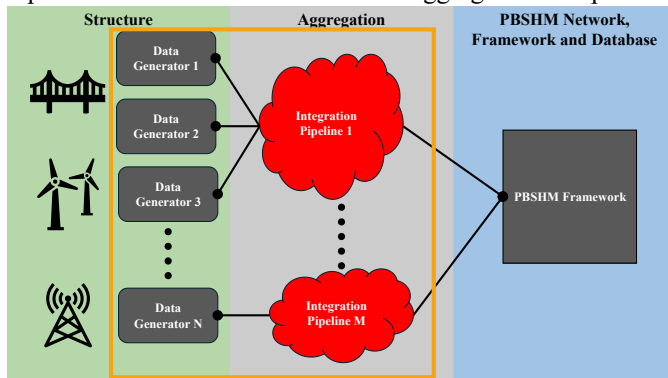


Figure 1. The PBSHM data integration system in which scopes where data representations are not enforced is highlighted

Although the data representation is not explicitly defined within these scopes, there are significant advantages to developing a reusable implementation, particularly for time series channel data. Optimising data representations is crucial when considering the application of streaming techniques to handle vast amounts of data efficiently. Given the potential for integrating multiple data generators to monitor a single system, such as data from various sensors in an SHM system, SCADA data, and weather data from an application programming interface (API) - a unified aggregation pipeline can provide a sensible solution. This approach would support all these sensors cohesively, ensuring efficient and effective data management. Creating a generic data representation that reduces redundancy within that data and therefore communications bandwidth utilisation would allow systems with resource constraints to share data integration pipelines which increases scalability while maintaining acceptable bandwidth utilisation.

A primary motivation for performing data reduction and standardisation directly on the sensor node is to achieve a truly 'plug-and-play' and interoperable system. While it is possible to offload metadata enrichment to a gateway or middleware server in its entirety, such an approach creates a dependency, binding the sensor node to a specific gateway with the requisite processing capabilities. This method, by contrast, ensures that each sensor node transmits a self-contained, efficient, and standardised data packet. This makes the capable of being integrated into any PBSHM ecosystem with a compatible endpoint, without requiring specialised intermediate hardware. This approach enhances deployment flexibility, as a node can

be replaced or relocated with the guarantee that it will function correctly with the central server, independent of the local network topology or available gateway resources. This is particularly advantageous in large-scale, heterogeneous deployments where multiple vendors and network types may coexist.

For a plug-and-play aggregation pipeline, enough information must be encoded into the data representation to enable compliance with the PBSHM schema when the data is transmitted to the PBSHM server whilst reducing the redundancy of information within said data representation. To achieve this, we must first identify the key aspects of the PBSHM schema that must be retained.

In this paper, we focus on time series channel data. Therefore, the key information that's encoded into a channel data object and must therefore be recoverable is:

- Structure name
- Population name
- Timestamp
- Channel name(s)
- Channel type(s)
- Channel unit(s)
- Channel value(s)

First, we must consider implementing this in such a way that all this information is explicitly stated for each timestamp. To illustrate this, consider two JavaScript object notation (JSON) objects compliant with the PBSHM schema that represent multiple sensor readings at two different time stamps one second apart as shown in Figure 2.

We can identify multiple items of redundant information across the two objects (i.e., structure name, population, channel names, channel types and channel units).

Many communication protocols incorporate mechanisms for tracking the origin of messages, enabling the inference of the communication state. For instance, protocols like TCP/IP and MQTT include metadata that identifies the sender and the context of the message. This capability allows us to avoid sending redundant information, as we can pair existing data with the sender's identity.

Therefore, we can split up the object into duplicated and non-duplicated data (when considering multiple objects from the same data generator) as shown in Table 1. As can be seen; by only transmitting updated data (or non-duplicated fields), we can significantly limit the number of fields that have to be transmitted for every object.

Table 1. Identifying duplicated and non-duplicated fields within the PBSHM Schema when considering multiple time series objects

Duplicated Fields	Non-duplicated Fields
Structure name	Timestamp
Population name	Channel value(s)
Channel name(s)	
Channel type(s)	
Channel unit(s)	

As such, we can define two new objects, the *initialisation* in which all the duplicated fields for a given data generator are

```

1 {
2   "name": "test-structure",
3   "population": "test-population",
4   "timestamp": 1756684800000000000,
5   "channels": [
6     {
7       "name": "test-channel-1",
8       "type": "acceleration",
9       "unit": "g",
10      "value": 10.5
11    },
12    {
13      "name": "test-channel-2",
14      "type": "tilt",
15      "unit": "radians",
16      "value": 22
17    }
18  ]
19 }

```

```

1 {
2   "name": "test-structure",
3   "population": "test-population",
4   "timestamp": 1756684801000000000,
5   "channels": [
6     {
7       "name": "test-channel-1",
8       "type": "acceleration",
9       "unit": "g",
10      "value": 10.6
11    },
12    {
13      "name": "test-channel-2",
14      "type": "tilt",
15      "unit": "radians",
16      "value": 21
17    }
18  ]
19 }

```

Figure 2. Two example JSON documents containing multiple sensor readings one second apart

represented and the *sample* in which we represent the non-duplicated fields.

With these new objects, we can define the process by which communications take place. For the data generator, first, we send the initialisation object, and then we send every sample object available as shown in Figure 3. These sample objects can optionally be added to a buffer to increase the efficiency of communications (i.e. only turning on radios for brief periods or trying to limit the number of packets sent). For the case in which each sample object is sent individually the buffer size would be one.

With these communication processes if there was a need to change the format of the sample objects (i.e. adding a channel, removing a channel or changing properties about a channel) this could also be achieved by closing the communication session and re-opening it with the new channel information in the same way the session is initialised as described previously. Furthermore, if the data generator was disabled for any reason the communications would be closed, and the process would also have to be re-initialised. In such cases, any incomplete sample objects and session state affected by the disconnection would be discarded. Any samples still in the send buffer would then need to be retransmitted where de-duplication would take place between the transit and the PBSHM framework, network and database.

Within the aggregation scope (shown in Figure 4), we then receive the initialisation message from the data generator and then receive the buffer (which fulfils the role of the cache from the PBSHM data integration system). From the buffer, we add the “redundant fields” to the sample to make a JSON object compliant with the PBSHM Schema and then transmit

said object to the PBSHM Framework. We then wait to receive a new buffer or close the communication.

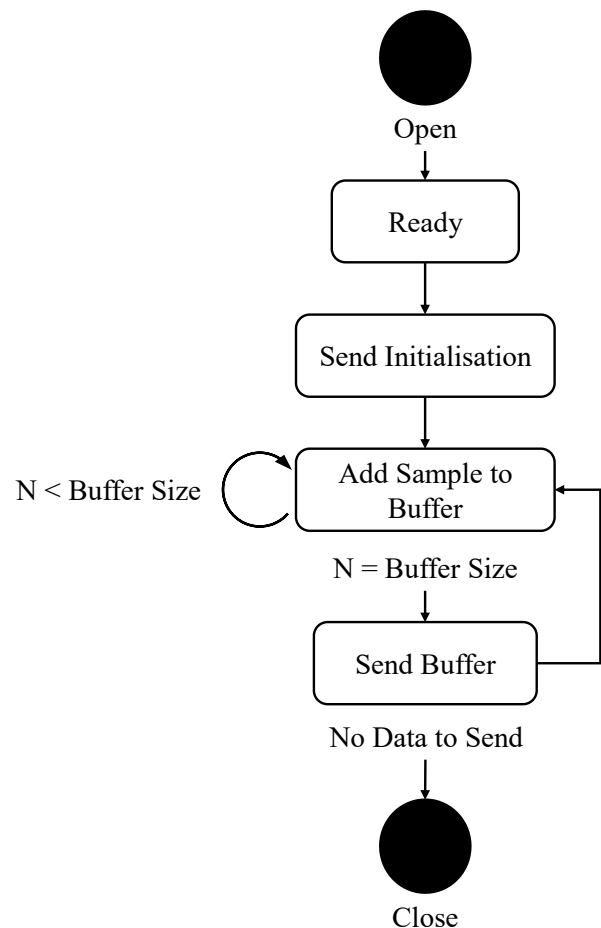


Figure 3. Data generator communications process

These two processes allow the use of a reduced communication schema to reduce the bandwidth utilised in the transmission of PBSHM data from a given data generator.

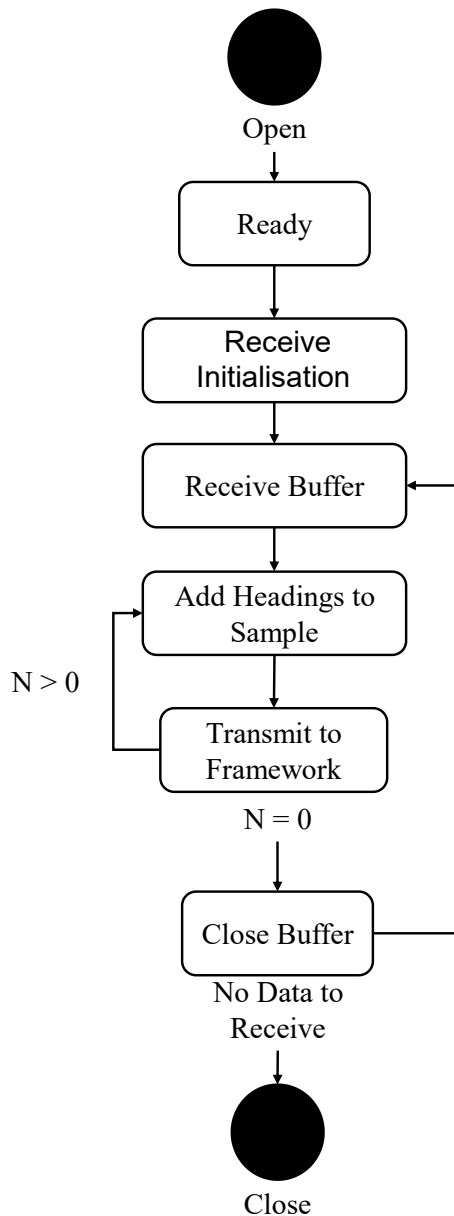


Figure 4. Aggregation pipeline communication process

### 3 CASE STUDY

The structure under test is a bridge that supports a dual carriageway, which consists of two lanes designated for one-way traffic, as well as a footpath for pedestrians. The structure of the bridge is composed of 13 concrete Y beams that provide support for a reinforced concrete deck. Adjacent is an older masonry arch bridge. These two bridges are constructed without any visible gap between them, making it unclear how much the concrete bridge deck is restrained on one side.



Figure 5. The structure under test in the case study

The SHM system implemented for this bridge was designed with versatility and ease of installation in mind. This system allows for the accelerometer to be installed directly on the surface of the bridge deck. The placement of the accelerometer is optimised by accounting for the variations in bridge types. It comprises a single MEMS accelerometer and an environmental sensor. The accelerometer employed is the Multifunction Extended Life (MEL) Data Logger from Gulf Coast Data Concepts. This device measures acceleration in three axes within a range of  $\pm 2$  g and includes a real-time clock to timestamp each acceleration measurement. The acceleration data collected by the sensor is stored locally on an SD card at a sampling rate of 128 Hz, and the sensor is powered by two D-cell batteries, which provide a run-time of up to 60 days of continuous recording. The MEL accelerometer is housed in an enclosure that is securely attached to the deck of each bridge. An example of one of these enclosures is shown in Figure 6.



Figure 6. MEL accelerometer and enclosure





Figure 7. MEL sensor in place

In addition to the accelerometer, the SHM system includes an environmental sensor that measures both air temperature and humidity. To ensure accurate temperature readings, the environmental sensors are not placed within the enclosure to avoid the effects of solar gain. Instead, these sensors are positioned out of direct sunlight, to provide a representative measurement of the local air temperature.

### 3.1 Data description

The data provided by the system is in a comma-separated values (CSV) format, of which an example showing ten values is shown in Table 2. Within the CSV document, the first 9 rows contain contextual information about the samples. The following rows contain time series data.

Table 2. Extract from the CSV data provided by the data logger containing headers and 15 samples

;Title	http://www.g cdataconcept s.com	x2-2	Kionix KXRB5 -2050		
;Version	1107	Build date	Oct 20 2015	SN:CC D C10022 6A4EB2	
;Start_time	2018-11-08	11:48:2 3.440 deg C	Vbat	3076	mv
;Temperature	13				
;Gain	high				
;SampleRate	128	Hz			
;Deadband	0	counts			
;DeadbandTimeout	0	sec			
;Headers	time	Ax	Ay	Az	
0.222	49	328	-13136		
0.229	28	314	-13129		
0.237	7	296	-13099		
0.245	21	296	-13101		
0.253	30	324	-13136		
0.261	33	341	-13161		

To evaluate the efficacy of the proposed pipeline architecture, a 30-minute window of the data has been selected. This can be seen represented in Figure 10.

### 3.2 Test pipeline models

As such, we can develop a pipeline that would allow transmission of data from the bridge under test to the PBSHM server which is shown at the top of the Universal Markup Language (UML) diagram of Figure 8. This model of the pipeline first extracts the data from the GCDC data store and converts it to the PBSHM schema format. Data in the PBSHM schema format is then loaded into the PBSHM Schema Cache on the Docker Server, where it is then loaded into the PBSHM server via a Representational State Transfer (REST) API.

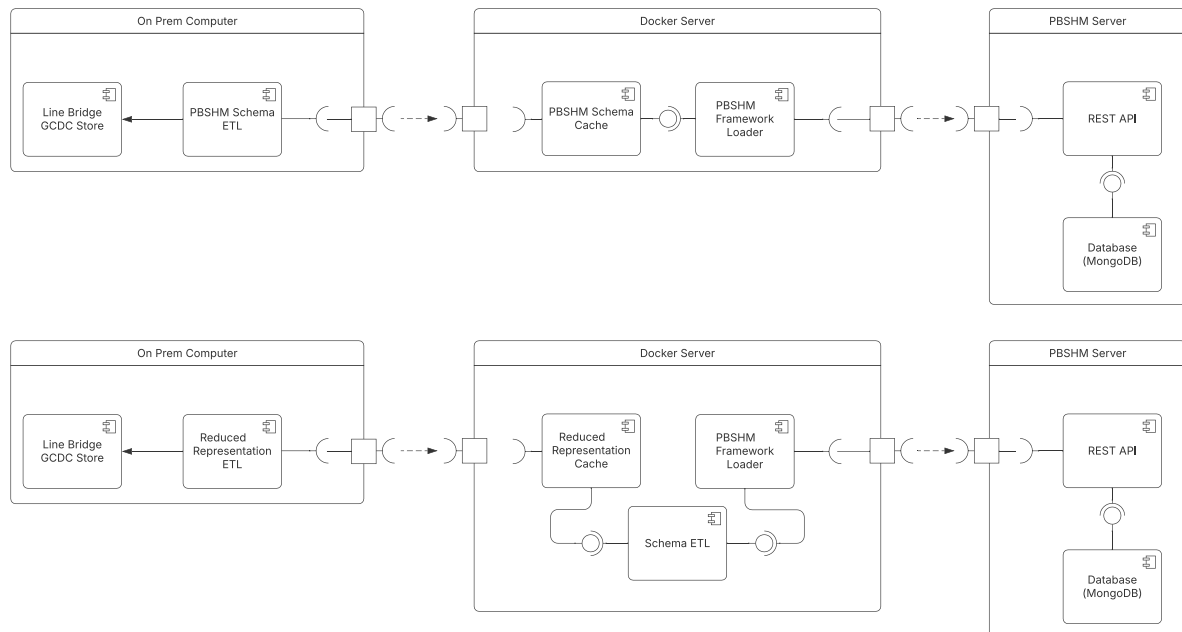


Figure 8. Universal markup language diagram showing two data integration pipelines (PBSHM Schema rep. above, reduced data rep. below)

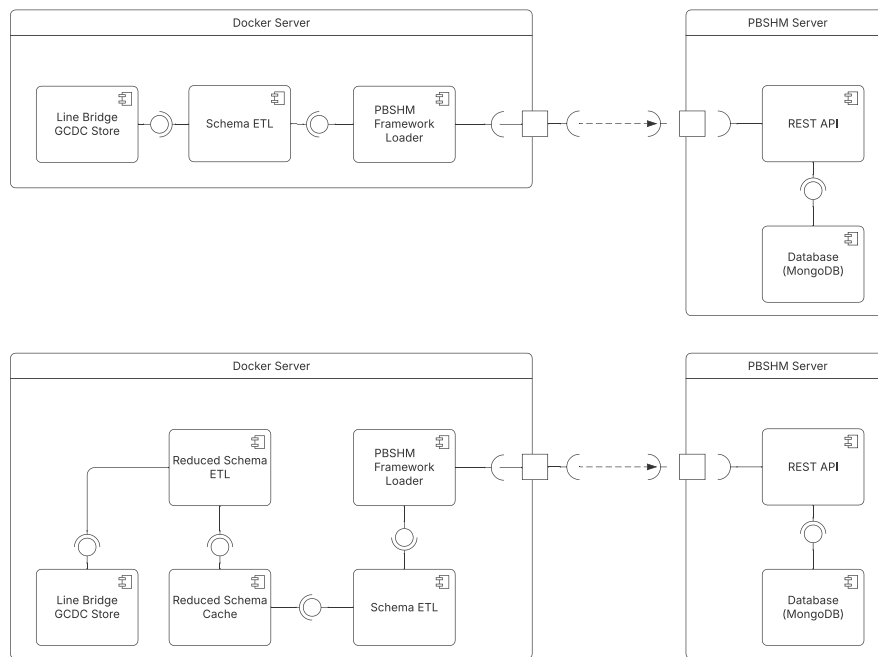


Figure 9. Universal markup language diagram showing the simulation test bench (PBSHM Schema rep. above, reduced data rep. below)

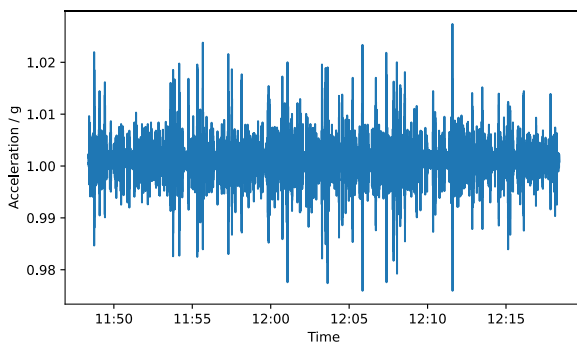


Figure 10. Single-axis raw acceleration over 30 minutes measured using the MEL accelerometer

The diagram at the bottom of Figure 8 shows a similar pipeline, however, this uses a reduced data representation as discussed in Section 2. Within the on-premises computer, data is extracted from the GDC store and transformed into an initialisation object (which contains all the duplicated fields shown in Table 1) and a set of samples objects. The initialisation object, of which an example is given at the top of Figure 11, is first transmitted to the Reduced Representation Cache which resides on the docker server. Samples, an example of which is shown in the bottom of Figure 11, are then transmitted to the Reduced Representation Cache. These samples are then transformed into PBSHM Schema compliant files which are then uploaded to the PBSHM server via the PBSHM server.

From these models, we can simulate the performance of the multiple data representations (namely the PBSHM schema in a JSON format and concise binary object representation (CBOR)

format as well as a reduced representation in both JSON and CBOR formats) using real-world data captured from the line bridge over a simulation test bench.

```
1 {
2   "name": "line-bridge",
3   "population": "bridge",
4   "channels": [
5     {
6       "name": "Accelerometer X",
7       "unit": "m/s^2"
8     },
9     {
10      "name": "Accelerometer Y",
11      "unit": "m/s^2"
12    },
13    {
14      "name": "Accelerometer Z",
15      "unit": "m/s^2"
16    }
17  ]
18 }
```

```
1 {
2   "1541677703440002650": [
3     -0.0021361000915471468,
4     -0.023954836740921574,
5     1.0016020750686603
6   ]
7 }
```

Figure 11. Initialisation object (above) and sample object (below) in the reduced data representation

## 4 RESULTS

To assess the performance of the methodology presented in Section 2 a simulation of the systems shown in Figure 8 was developed using individual docker containers running on a docker server (with the PBSHM schema version of the pipeline shown above in Figure 9 and the reduced representation version shown below).

This simulation test bench emulates all of the components in the systems described in Figure 8, however, integrates all the components that were shown to be implemented with on-premises equipment in the Docker Server to allow for greater control of the data pipeline and easy access to metrics.

In this paper, the size of the total payload for the selected 30-minute window is the metric used to evaluate the efficacy of the pipeline. This was chosen as within this setting, the size of the data transmitted over the period will likely impact bandwidth requirements and power requirements for resource-constrained systems.

This test bench was used to evaluate multiple data representations. The PBSHM Schema in JSON format was used as a benchmark data representation as it provides all the necessary context for the PBSHM server. This was then repeated by the reduced representation in JSON format. Finally, both tests were repeated with CBOR which allows a 1:1 mapping with JSON allowing it to be implemented with little to no modification to the existing PBSHM schema.

Table 3. Size of a 30-minute capture (230,400 samples of tri-axis acceleration data) in CSV, PSBHM Schema, and reduced representation data formats

Format	Size (MiB)	Ratio to CSV
CSV	5.14	1.00
PBSHM Schema (JSON)	131.42	25.58
Reduced (JSON)	34.30	6.68
PBSHM Schema (CBOR)	45.26	8.81
Reduced (CBOR)	10.77	2.10

From the results captured and presented in Table 3, it can be concluded that using the PBSHM schema in a JSON format dramatically increases the storage required for the 30-minute sample window compared to the original CSV data. This can be significantly reduced using a compressed format like CBOR, reducing the data size by 2.9x.

However, by using the reduced data representation, this can be further reduced. In the JSON format, the reduced data representation offered a 3.8x size reduction whilst the CBOR format of the reduced data representation offered a 12.2x size reduction when compared to the PBSHM Schema in JSON format. These results are plotted as shown in Figure 12.

By utilising the reduced data representation in the CBOR format, the ultimate size of data to be transmitted is 2.1x the original CSV data.

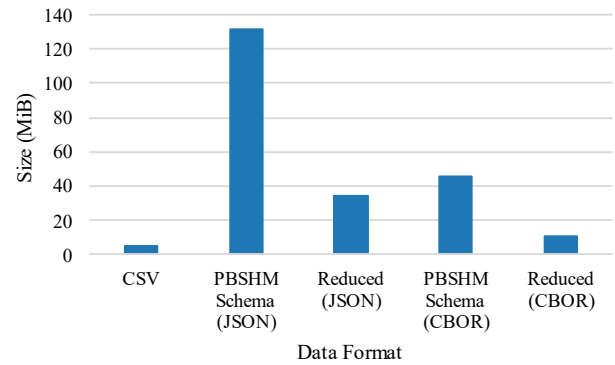


Figure 12. Bar chart plotting the different data representations and formats of a 30-minute capture (230,400 samples of tri-axis acceleration data)

## 5 DISCUSSION, LIMITATIONS AND FUTURE WORK

The findings presented in this paper provide a strong proof-of-concept for the proposed pipeline; however, several limitations should be acknowledged, and these point towards avenues for future research.

The results in Table 2 show a reduced file size from CSV format produced by the data acquisition system when compared to the schema under test. This shows that in situations in which an aggregation pipeline can be implemented on a case-by-case basis dependent tailored to the data produced by the data generator there is an inherent advantage to doing so. This will be true in almost all cases where this is possible as no extra information is required to allow the transformation of data produced by the data generator into the PBSHM schema format. However, as stated, this requires that each implementation of the aggregation scope be tailored to the specific data generator.

By utilising this plug and play aggregation pipeline design, it is possible, to reuse components across multiple data generators. This limits the effort required to develop new tailored aggregation components for each data generator as well as allows data from many data generators to be integrated into the PBSHM data ecosystem using few data aggregation components.

However, the validation was conducted using a homogenous set of accelerometer data. The “plug-and-play” architecture is designed to be extensible, yet its performance with a more diverse array of sensor modalities, such as strain gauges, acoustic emission sensors, or environmental sensors has not yet been empirically validated. Future work will focus on developing and testing data models for these sensor types within the pipeline.

Furthermore, while our work focuses on data representation, it does not currently incorporate specific protocols for secure data transmission. For deployment on critical infrastructure, ensuring data integrity and confidentiality through authenticated encryption schemes (e.g., using TLS/DTLS) could be employed.

A key focus of our future work will be on hardware-in-the-loop testing, further developing robust reference implementations of the technology demonstrated within the



aggregation scope to provide practical guidance for both current and future SHM system operators seeking to integrate their monitoring within PBSHM data domains.

## 6 CONCLUDING REMARKS

This paper has presented the potential of session-defined communication for PBSHM data within PBSHM data aggregation pipelines. By defining the processes that would be undertaken to achieve reduced bandwidth utilisation, we have demonstrated how to achieve reduced bandwidth requirements whilst maintaining plug-and-play functionality for PBSHM monitoring systems.

We demonstrate that it is possible to reduce the amount of data required to provide the necessary context for PBSHM when transmitting sample data providing a method to reduce the required data by 12.2x. This results in a transmission size that is 2.1x the original data size, which whilst a marked increase, allows for reasonable requirements for resource-constrained PBSHM monitoring systems.

## ACKNOWLEDGMENTS

The authors gratefully acknowledge the support of the UK Engineering and Physical Sciences Research Council (EPSRC) through the ROSEHIPS project (Grant EP/W005816/1). For the purpose of open access, the authors have applied a Creative Commons Attribution (CC BY) licence to any Author Accepted Manuscript version arising. The authors of this paper also gratefully acknowledge Daniel Brennan of The University of Sheffield for providing insights into the PBSHM ecosystem.

## REFERENCES

- [1] V. R. Gharehbaghi *et al.*, ‘A Critical Review on Structural Health Monitoring: Definitions, Methods, and Perspectives’, *Arch Computat Methods Eng*, vol. 29, no. 4, pp. 2209–2235, Jun. 2022, doi: 10.1007/s11831-021-09665-9.
- [2] L. A. Bull *et al.*, ‘Foundations of population-based SHM, Part I: Homogeneous populations and forms’, *Mechanical Systems and Signal Processing*, vol. 148, p. 107141, Feb. 2021, doi: 10.1016/j.ymssp.2020.107141.
- [3] J. Gosliga, P. A. Gardner, L. A. Bull, N. Dervilis, and K. Worden, ‘Foundations of Population-based SHM, Part II: Heterogeneous populations – Graphs, networks, and communities’, *Mechanical Systems and Signal Processing*, vol. 148, p. 107144, Feb. 2021, doi: 10.1016/j.ymssp.2020.107144.
- [4] P. Gardner, L. A. Bull, J. Gosliga, N. Dervilis, and K. Worden, ‘Foundations of population-based SHM, Part III: Heterogeneous populations – Mapping and transfer’, *Mechanical Systems and Signal Processing*, vol. 149, p. 107142, Feb. 2021, doi: 10.1016/j.ymssp.2020.107142.
- [5] G. Tsialiamanis, C. Mylonas, E. Chatzi, N. Dervilis, D. J. Wagg, and K. Worden, ‘Foundations of population-based SHM, Part IV: The geometry of spaces of structures and their feature spaces’, *Mechanical Systems and Signal Processing*, vol. 157, p. 107692, Aug. 2021, doi: 10.1016/j.ymssp.2021.107692.
- [6] D. S. Brennan, J. Gosliga, E. J. Cross, and K. Worden, ‘Foundations of population-based SHM, Part V: Network, framework and database’, *Mechanical Systems and Signal Processing*, vol. 223, p. 111602, Jan. 2025, doi: 10.1016/j.ymssp.2024.111602.

- [7] D. R. Lim, A. J. Ferguson, D. S. Brennan, D. Hester, and R. Woods, ‘A methodology for data collection and aggregation in population-based structural health monitoring ecosystems’, presented at the 13th International Conference on Structural Health Monitoring of Intelligent Infrastructure, Graz, Austria, Sep. 2025.

## Advancing PEAR: Development of a Bridge Benchmark Datasets for PBSHM Research

Connor O'Higgins<sup>1</sup>, 0000-0001-7034-005X, Tristan Gowdridge<sup>2</sup>, 0009-0008-9979-8396, David Hester<sup>1</sup>, 0009-0007-2280-4340,  
Keith Worden<sup>2</sup>, 0000-0002-1035-238X, Daniel S. Brennan<sup>2</sup>, 0009-0001-7223-3431

<sup>1</sup>School of Natural and Built Environment, Queen's University of Belfast, Stranmillis Road, Belfast, BT9 5AG, UK

<sup>2</sup>Dynamics Research Group, School of Mechanical, Aerospace, and Civil Engineering, University of Sheffield, Mappin Street, Sheffield, S1 3TD, UK  
email: c.ohiggins@qub.ac.uk

**ABSTRACT:** Population-Based Structural Health Monitoring (PBSHM) is an emerging field in Structural Health Monitoring that leverages data from multiple structures to enhance the assessment of individual structures. Unlike traditional SHM, which generally relies on data from a single structure, PBSHM utilises collective knowledge from a population to facilitate increasing the knowledge on an individual structure. Transfer learning enables the inference from a source structure to a target structure within the population. One of the limitations of this method is that a lot of transfer-learning methods require data models that are trained using substantial amounts of high-quality data which can be difficult to obtain. To support PBSHM research, the concept of the Population-based SHM Engineered Asset Resource (PEAR) has been introduced. PEAR is conceptualised as a benchmark dataset containing semi-realistic structures and associated data intended to drive the development and validation of PBSHM methodologies. This work advances the PEAR prototype by developing complete populations for two types of bridges, along with their associated data. The pipelines for generating these populations are presented, detailing how they produce structural data and PBSHM-specific models. Additionally, a simple analysis of the generated populations is conducted, demonstrating their utility in PBSHM research and showcasing the potential of PEAR as a resource for current and future PBSHM research.

**KEY WORDS:** SHMII-13; Population-based Structural Health Monitoring, Benchmark Dataset, Irreducible Element Model, Bridges

### 1 INTRODUCTION

In traditional Structural Health Monitoring (SHM), benchmark datasets such as the S101 [1] and Z24 [2] bridges have been pivotal in advancing the field. These datasets have provided researchers with common platforms to test, validate, and compare new SHM methods and algorithms. However, in the emerging field of Population-Based Structural Health Monitoring (PBSHM), data are leveraged from multiple structures to enhance the assessment of individual assets, no equivalent benchmark datasets currently exist. This gap is not only a reflection of the relative recency of PBSHM but also the inherent complexity of gathering multi-structure data necessitated to form a meaningful population.

To address this challenge, the Population-based SHM Engineered Asset Resource (PEAR) was devised as a potential solution. The foundational principles and envisaged structure of PEAR were outlined in a previous conference paper [3], laying the groundwork for a benchmark dataset that integrates curated synthetic populations. The envisioned PEAR dataset aims to serve as a standard for evaluating and advancing PBSHM methodologies by providing researchers with readily-accessible, semi-realistic data representative of various structural populations.

The fundamentals of the PEAR database have been established, this paper extends that work by developing two specific bridge populations for inclusion in the PEAR dataset. This work not only demonstrates the feasibility of generating synthetic populations but also how these populations can serve as a practical resource for PBSHM research.

The remainder of this paper is structured as follows. First, a background section provides an overview of PBSHM, detailing existing databases, schemas, and benchmark datasets, and highlighting the motivation for this work. This section is followed by an overview of the foundations of PEAR and the specific requirements for creating a benchmark dataset that is applicable for a population-based approach. Next, the "Developing Bridge Dataset" section describes the process of generating the two initial bridge populations, focussing on the design of semi-realistic bridge structures and the simulation of their structural response data. Subsequently, the "Bridge Datasets" section presents the developed populations, including a simple analysis to showcase their utility in PBSHM methods. Finally, the paper concludes with a discussion of the current dataset's limitations, potential avenues for future expansion, and the broader implications for advancing PBSHM research.

### 2 BACKGROUND

Population-Based Structural Health Monitoring (PBSHM) represents a shift from traditional SHM by focussing on the analysis of data from multiple structures within a related population. This approach not only provides valuable insights into the collective behaviour of the population but also enhances the understanding of individual structures. In contrast to conventional SHM methods that typically concentrate on a single structure, PBSHM enables the application of advanced techniques such as transfer learning, where knowledge gained from one task or structure is leveraged to improve performance on a related task in another structure. This methodology allows models to be adapted rather than built from scratch, thereby

enhancing efficiency and potentially making inferences about the condition of a structure that would otherwise be missed.

A critical aspect of implementing transfer learning in PBSHM is the careful identification of structural similarities across the population. Without a clear understanding of these similarities, there is an increased risk of negative transfer, where inappropriate model adaptation could degrade performance. To combat this risk, techniques such as Irreducible Element (IE) models combined with graph-based approaches have been developed [4], [5]. These methods are instrumental in identifying and quantifying both the similarities and variations among structures, ensuring that transfer learning is applied only where it is most appropriate. This framework for similarity assessment forms the foundation for effective knowledge transfer across structures.

Despite these methodological advancements, a significant challenge in PBSHM remains: the scarcity of comprehensive data representing populations of structures. Previous studies have attempted to address this gap by collecting data from similar populations, for example, one study collected data from four beam-and-slab bridges and two pedestrian footbridges [6]. Other research efforts have simulated populations using models with 10 degrees of freedom [7] or even toy structures to validate PBSHM transfer-learning methods and graph-matching algorithms [8]. However, these approaches have been limited in scope, so the developed datasets cannot always be used to test novel PBSHM methods.

It is within this context of data scarcity and the development of new PBSHM methods that the need for benchmark datasets in PBSHM becomes evident. A robust benchmark dataset would not only facilitate the testing and validation of new methodologies but also drive forward the development of PBSHM research. This motivation underpins the development of the Population-based SHM Engineered Asset Resource (PEAR) dataset, which aims to provide the PBSHM community with a dedicated set of synthetic populations that represent real-world structures and realistic structural behaviours for algorithm development and benchmarking.

### 3 PEAR OVERVIEW

This section gives an overview of the PEAR database, including its key requirements (Section 3.1), how the database is structured (Section 3.2), and the stages involved with producing populations of structures and data (Section 3.3).

#### 3.1 Requirements

##### Requirement 1:

The primary objective for the dataset is to function as a robust testbed for both established and emerging PBSHM methods. It must support the development and evaluation of methods and techniques across the entire remit of PBSHM. This remit includes the calculation of similarity scores and transfer-learning methods. Moreover, the dataset should facilitate structural comparisons via similarity metrics, including IE models and graph-matching algorithms, which are essential for guiding successful knowledge transfer. The datasets should also be compatible with various machine-learning techniques, ensuring high-quality data are available for training and validation purposes.

##### Requirement 2:

The dataset should be designed for ease of searchability, enabling users to quickly locate and extract relevant data subsets. To ensure this level of accessibility, the dataset must be thoroughly indexed so that key variables, such as the type of structure or, in the case of bridges, the number of spans, are easily queried and filtered.

##### Requirement 3:

The methodologies employed to generate the structures within the dataset must be transparent, clearly documented, and, whenever possible, grounded in real-world structural design practices. This approach guarantees that the simulated structures accurately reflect their real-world counterparts. Additionally, the dataset should capture the natural variability seen in practice, for instance, differences in span lengths, beam dimensions, and deck thicknesses in bridge designs, thus representing the diversity found in actual structural stocks.

##### Requirement 4:

A shared-data domain is fundamental to the success and broad adoption of PBSHM practices. Building on the work of Brennan et al. [5], the dataset will adhere to the PBSHM schema, a standardised format that ensures consistency in data storage and interpretation for PBSHM. All data and future additions to the dataset must comply with this schema. In cases where the current PBSHM schema does not accommodate certain data components, it will be necessary to propose and integrate an extension to the PBSHM schema to incorporate this data.

#### 3.2 Dataset Structure

Designing the dataset's structure is important to ensure effective data retrieval and utilisation. A well-structured dataset will facilitate users to quickly access the specific data they need, making it easier to perform tasks with the datasets and subsets of the data. In the context of PEAR, the structure is crafted not only to organise the data logically for easy retrieval but also to accommodate the addition of new data without disrupting existing records.

Figure 1 illustrates the four-level hierarchical organisation of the PEAR dataset: root category, subtype, dataset, and scenario. To illustrate how these levels interact, consider the analogy of a file system. At the highest level is a main "PEAR" folder. Inside this folder, there is a separate folder for each root category. Each root category folder contains folders for its various subtypes, which differentiate structures based on design or purpose. Within each subtype folder, there are individual dataset folders; each dataset represents a collection of structures forming the population. At this level of the database a descriptive file outlining the general forms of the population and allowable variations of these structures will be stored. The IE models and the meta data about each structure will also be stored at this level. The final level, scenario, is analogous to a load case in a structural model, for example, applying a 40-ton load to the mid-span of a bridge would constitute a single scenario.



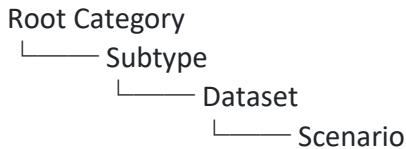


Figure 1: The hierarchical structure of the PEAR dataset

In this hierarchical structure, a root category groups structures that are typically classified together, such as aeroplanes and bridges. Within each root category, subtypes further differentiate the structures. For example, within the aeroplane category, subtypes may be single-engine and multi-engine, while the bridge category could be divided into truss bridges and suspension bridges.

During the initial planning phase for PEAR, three primary root categories were identified for inclusion: bridges, masts, and wind turbines. Figure 2 shows the initial dataset organised into root and subtype levels. This work specifically generates data for two bridge populations: a beam-and-slab bridge population and a ladder-deck bridge population, each accompanied by a corresponding scenario.

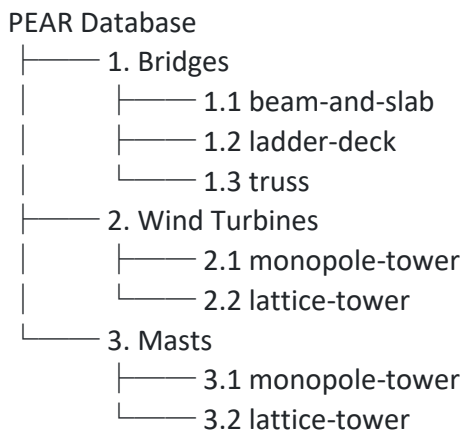


Figure 2: The initial 'root categories' and 'subtypes' for PEAR

### 3.3 Dataset Stages

PEAR has been designed from the ground up to develop over time by iterations and expansion of the data included within. Defined stages serve as clear milestones, enabling collaborative efforts across the diverse disciplines involved in PBSHM. The initial design of the structure within any population is undertaken in Stage 0, the development of IE models in Stage 1 and the simulation of structural responses in Stage 2+. By breaking the development into stages, different teams can contribute depending on their area of research. For example, one team can focus on constructing the IE models needed to derive similarity metrics (Stage 1) while another develops simulations for scenario data (Stage 2). Importantly, each stage builds exclusively on the data from the preceding stages; for instance, any Stage 2 processes rely only on the outputs from Stages 0 and 1.

For a dataset to be integrated into PEAR, it must, at a minimum, complete Stage 0 and Stage 1. Once a dataset reaches this milestone, it is assigned a unique reference within PEAR, and the structures it contains are fixed to ensure consistency and reproducibility of results. The specific processes of Stage 2 are left flexible, allowing researchers to select the most relevant structural responses for their research as well as the most appropriate simulation method. The overall staging structure is designed to be generic, applying to all datasets regardless of their root category or subtype.

#### Stage 0: Design of the Dataset Population

In this initial stage, realistic structures are generated with pseudo-random properties drawn from a predefined range of parameters. These parameters, along with the methods used for their selection, are detailed and stored in the dataset. For each structure, a Structural Information (SI) model is created alongside a structural report. The report offers a detailed, human-readable description, while the SI model provides a computer-interpretable format that facilitates indexing and querying.

#### Stage 1: IE Models

At this stage, Irreducible Element (IE) models are developed for each structure in the population, i.e. one IE model for each SI model in Stage 0. The typical workflow for producing IE models will be using the parameters defined in the SI for each structure to create detailed IE models. After the completion for Stage 1 the dataset may be included in PEAR.

#### Stage 2+: Scenario Data

Using the data from Stages 0 and 1, simulated scenarios are then produced using the information in the generated IE models. Although PEAR does not prescribe specific simulation methods, the simulation outputs must be saved back into the dataset as valid PBSHM Schema data. Scenarios might include, but are not limited to, static-load displacements, natural frequencies, mode shapes, or frequency response functions. Moreover; a scenario can simulate conditions where the structure is considered 'healthy' or introduce 'damage' prior to simulation, with the results documented accordingly.

## 4 DEVELOPING BRIDGE DATASETS

This section outlines the process by which the two initial bridge populations have been developed for the PEAR dataset. The development process is divided into two major phases. The first phase focusses on designing semi-realistic bridges and creating their associated Irreducible Element (IE) models, corresponding to Stage 0 and 1 of the dataset. The second phase involves simulating the structural responses of these bridges, which represents Stage 2. This section describes these processes to create both a beam-and-slab bridge population and a ladder-deck bridge population.

### 4.1 General Form of Population

For each population included in PEAR, the first step is to define the general form of the structure. This general form specifies the primary structural components and their arrangement, ensuring a consistent yet flexible framework for generating individual structures. Once the general form is established, a set of rules and parameters is defined to guide the creation of each structure within the population. These rules, grounded in engineering principles, ensure that the generated structures are

both realistic and representative of real-world variations. The diversity within each population is achieved by systematically varying these parameters, allowing for a range of structures that share a common form while exhibiting meaningful differences. The following subsections detail the general forms and parameterisation approaches for the beam-and-slab bridge population and the ladder-deck bridge population.

#### 4.1.1 Beam-and-Slab Bridge

The general form of a beam-and-slab bridge consists of precast concrete beams that serve as the primary structural components of the bridge. These beams are typically lifted into place, where they are supported by piers or abutments that have been constructed in advance. Once the beams are positioned, an *in situ* concrete deck is poured over them to form the main deck of the bridge. Below are the main components and a brief description of a typical beam-and-slab bridge:

- **Precast Prestressed Bridge Beams:** These are the primary load-bearing components of the bridge. Precast off-site and prestressed to increase their load-carrying capacity, these beams are designed to resist the main traffic loads of the bridge.
- **Reinforced Concrete Deck:** The reinforced concrete deck is poured *in situ* on top of the precast beams, forming the main surface of the bridge.
- **Diaphragm:** The diaphragm is a transverse structural element placed between the bridge beams. Its primary function is to distribute loads evenly across the bridge and provide lateral stability, and help transfer load to the supporting structure of the bridge.
- **Columns:** Columns are vertical structural supports that transfer the load from the bridge deck and beams down to the foundation.

#### 4.1.2 Ladder-Deck Bridge

The general form of a ladder-deck bridge consists of steel girder beams that serve as the primary structural components of the bridge. These beams are situated at the edge of the bridge with smaller steel girder beams spanning transversely, connecting the main beams. Once the beams are positioned and connected, an *in situ* concrete deck is poured over them to form the main deck of the bridge. Below are the main components and a brief description of a typical beam-and-slab bridge:

- **Longitudinal Girder Beams:** These are primary load-carrying members that run along the length of the bridge (parallel to the roadway). They bear the main loads from the deck and transfer them to the piers or abutments. These are typically made of steel and are placed at the two edges of the bridge.
- **Transverse Girder Beams (Cross Beams):** These are secondary beams that span between the longitudinal girders, providing lateral support and distributing loads from the deck to the longitudinal girders. These are also typically made of steel.
- **Concrete Deck:** The reinforced-concrete deck is poured *in situ* on top of the longitudinal and transverse beams, forming the main surface of the bridge.
- **Columns:** Columns are vertical structural supports that transfer the load from the bridge deck and beams down to the foundation.

## 4.2 Structural Parameters

This section outlines the parameters that can be adjusted within the general forms described in the previous section. These parameters are the tools used to create a varied population of structures while ensuring that each model remains realistic and grounded in sound engineering principles. Methods have been developed to select these parameters, ensuring that any variations still adhere to the constraints of real-world structural behaviour. For clarity, the parameters are divided into two groups:

1. **Generic Bridge Variables:** These parameters are common to all bridges, such as the number of spans and overall bridge length.
2. **Subtype-Specific Parameters:** These parameters are unique to each bridge subtype. For instance, in a beam-and-slab bridge, a key parameter might be the selection of the precast beam geometry.

By systematically varying these parameters, the PEAR dataset is able to generate diverse yet realistic bridge structures.

### Generic Bridge Parameters

The generic bridge parameters define common characteristics shared by both bridge populations, such as the number of spans, span lengths, deck dimensions, column details, and material properties. The selection process for these parameters combines random selection from predefined ranges with engineering constraints to ensure that the resulting structures remain realistic and consistent with real-world practices. For example, the number of spans is determined by randomly choosing a value within a range that typically mirrors actual bridge stocks, usually between one and five spans. Once the number of spans is set, the span lengths are similarly selected from a defined range. However, to avoid unrealistic configurations, such as pairing an exceptionally long span with an extremely short one, an additional constraint is imposed. All selected span lengths must fall within 70% of each other, ensuring a realistic design.

Other parameters, like the width and thickness of the deck, are also chosen from ranges that reflect standard practices in bridge construction. The inclusion of columns is treated as a variable feature; whether columns are present is determined randomly, and if they are included, further details, such as their height and quantity, are specified. These column characteristics are based on established engineering principles; for instance, the minimum column height adheres to government standards for bridge clearance. Material properties, too, are selected from realistic ranges that reflect common construction materials, contributing to the overall authenticity of the generated structures while proving realistic variation in the population.

### Subtype-Specific Parameters

Subtype-specific parameters are the parameters that are only relevant to each bridge subtype. For the beam-and-slab population, some key parameters include the beam centre-to-centre distance, the number of primary beams, the geometry of both primary and edge beams, and the diaphragm geometry. For the ladder-deck bridges, the parameters include the number of transverse beams and the geometry of both the primary and secondary girders. The methods for selecting these parameters tend to be more involved than those used for generic bridge variables to ensure that each choice results in realistic engineering practices.

The process of selecting these parameters is highly dependent on the subtype and the accepted process for designing the structure. For instance, when determining the primary bridge beam geometry for each beam-and-slab bridge, the process begins with a list of common bridge beam types. Beam types that are incompatible with the given span length or bridge width are eliminated using span tables provided by bridge beam manufacturers. From the remaining viable options, a beam type is then randomly selected. This method ensures that the chosen beam geometry is suitable for that span length while allowing for variation in the population.

Similarly, for the ladder-deck subtype, the main structural component is determined using a range of acceptable span-to-depth ratios sourced from the encyclopedia for UK steel construction (SteelConstruction.info). A random ratio is selected from this range and, together with the predetermined span length, used to set the depth of the girder. Additional properties such as flange width and thickness are subsequently determined using comparable ratios from the same source.

The parameterisation strategy for the two bridge datasets employs a total of 17 distinct parameters for beam-and-slab bridges and 23 for ladder-deck bridges. By integrating randomness while adhering to sound engineering principles, the established general form and corresponding parameter sets create a robust framework for generating a diverse yet realistic population of bridge structures. This approach not only mirrors real-world variability but also enables the production of thousands of unique and plausible structures, significantly enhancing the utility of the PEAR dataset for PBSHM research.

### 4.3 Dataset Scenarios

A scenario is defined as a specific set of actions applied to the generated structures within a given population. These scenarios are designed to simulate various conditions or loads to determine the structural responses. The scope of the scenarios is flexible and can vary considerably based on the intended requirements. There is no single prescribed workflow for transforming the generated population into simulated structural responses, provided that the outputs remain compliant with PBSHM standards. In this work, we implement a simple scenario for both bridge types by employing finite-element models (software: LUSAS) to simulate their structural responses. However, alternative approaches, such as computational fluid dynamics, might be more appropriate for other applications, leaving the choice of methodology to the scenario authors.

#### 4.3.1 Description of the Implemented Scenario

In this study, two simple scenarios were implemented to evaluate the structural response of the two generated bridge populations. Scenario 1 was the application of only the dead load on the bridge. Scenario 2 was the application of a point load of 40 kN at the mid-span of every span on each structure. After the mid-span load is applied, the maximum displacement and its corresponding location are extracted and recorded in a PBSHM-compliant format. This scenario is intentionally simple, which facilitates basic validation, such as comparing the self-weight of the structures with reaction forces of the FE models.

The implementation of this scenario can be defined using the following three actions.

1. The Irreducible Element (IE) models are converted into Finite Element (FE) models. This conversion uses the detailed information contained within the IE models to generate FE model files.
2. Loading parameters are defined by extracting necessary information from the Structural Information (SI) models. This step involves producing scripts for each load case, with one script generated per span for each bridge.
3. The generated loading scripts are integrated with the FE models to run simulations. Once the simulations are complete, the mid-span vertical displacements and reaction forces are extracted from the simulation results and stored in the output folder in the correct PBSHM format.

#### 4.3.2 Validation of Structures and Data

Validation of the populations ensures that the generated structures and associated data are reliable, accurate, and true to the design intentions. By confirming that both the individual models and the overall dataset behave as expected, researchers can trust the integrity of the PEAR dataset and confidently use it for their PBSHM research.

During Stage 0 (design of structures), there are two main validation checks. The first is to check if the produced IE models comply with the required PBSHM schema. They are required to comply with the format to ensure consistency and that the developed PBSHM methods can be used on the IE models. The second validation step during Stage 0 is the examination of dataset statistics. These statistics verify that the composition of the populations aligns with the predetermined design process. Analysing parameter distributions and other statistical metrics ensures that the variability within the population matches what is expected based on the defined ranges and engineering principles. A discussion of the two populations developed for this work can be found in Section 5.1.

Further validation is carried out during the scenario stage by comparing simulated structural responses with theoretical predictions. The specifics of this will depend on the workflow to obtain the structural responses of the structure. For illustration purposes, the validation methods that were used in this work will be described. These methods are expected to be applicable when FE models are used as part of the workflow. After converting the IE models to FE models, two key validation methods are employed. First, dead-load reaction forces are extracted from the FE models and compared with the calculated weights of the structures as determined in Stage 0. This comparison confirms that the transition from the IE model to the FE model has maintained the integrity of the original design, ensuring that the overall weight remains consistent. Figure 3 presents the percentage difference between the design self-weight and the reaction forces from the produced FE models. With the average percentage difference being 1.69% and 1.55% for the beam-and-slab population and the ladder-deck population, respectively, there is very good agreement between the design stage and the FE model stage. For the second validation, a point load was applied to the structures, and displacement across the deck was recorded from the FE



simulation. These displacements were checked to ensure there were no discontinuities in the deformed mesh. This comparison serves to verify that the FE models are simulating sensible structural behaviour.

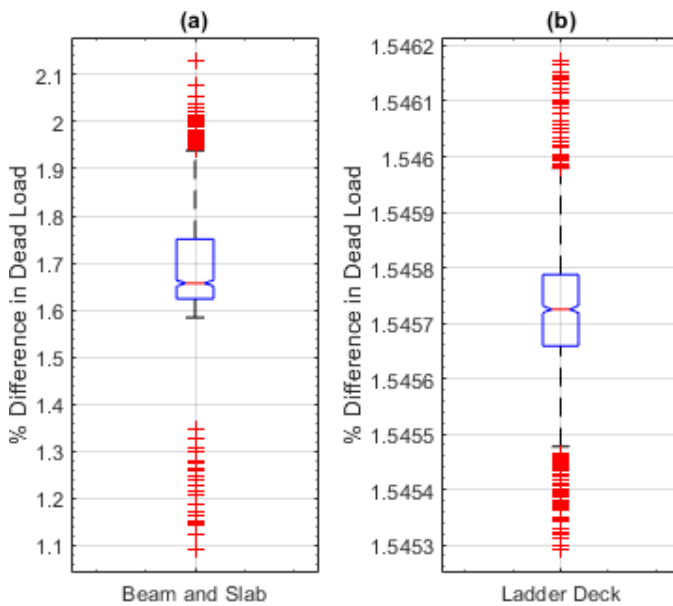


Figure 3: Percentage difference between the design self-weight of the bridges and the reaction forces from the FE models for (a) beam-and-slab population and (b) Ladder-deck population

As a further validation step data from all stages will go through a testing phase here the data will be accessible to the public for review and comments for a period of time. Following this review period it will be uploaded to the published version of the PEAR database.

## 5 BRIDGE DATASETS

In this section, the populations for both beam-and-slab bridges and ladder-deck bridges are presented. Firstly the structural composition of each population is examined, detailing how the individual structures come together to form a representative population of each bridge subtype. Following this, a simple analysis of the outputs from the scenario described in Section 4.3 is presented to demonstrate the practical application of these populations within the PBSHM framework. Finally, a similarity analysis of the populations is presented in section 5.3. This analysis serves to highlight how the PEAR dataset can be used as a valuable benchmark resource for evaluating transfer learning and other advanced PBSHM methods.

### 5.1 Dataset Statistics

Examining the overall composition of the two generated bridge populations provides insights and validation at the population level. By presenting a range of statistics, including the distributions of key parameters and variability, this analysis provides an insight into the composition of the populations. The main purpose of examining the dataset statistics is to ensure that the variations in the dataset reflect realistic engineering principles and expected real-world trends. Additionally, these statistical insights serve as a validation step, confirming that the

methods used to select the parameters yielded the expected set of structures.

For illustration, Figure 4 below displays the distributions of four key parameters for the beam-and-slab bridge dataset: the number of spans, the centre-to-centre spacing of the beams, the number of primary beams, and the width of the deck (subplots (a) to (d), respectively). The distribution of the number of spans is approximately even between one and five, which aligns with expectations, given that this value is selected randomly without influence from other design factors. In contrast, the distributions for the centre-to-centre spacing, the number of primary beams, and the deck width are less uniform because of their interdependent selection processes.

In Figure 4(b), the distribution of the centre-to-centre spacing reflects the specific weighting applied during parameter selection, following a ratio of 4:2:3:1:1, which is clearly visible in the resulting histogram. Figure 4(c), which shows the number of primary beams, indicates a skew towards higher numbers. Although the number of beams is randomly chosen between 4 and 10, this selection is further refined by ensuring that the combination of the number of beams and the centre-to-centre spacing produces a bridge width within the range of 6 to 20 meters. This constraint necessitates reselecting the number of beams when the initial combination falls outside the acceptable range, thereby skewing the distribution toward larger values. Finally, the distribution seen in Figure 4(d) for the deck width is a direct consequence of the deck width being determined by using the centre-to-centre spacing and the number of primary beams.

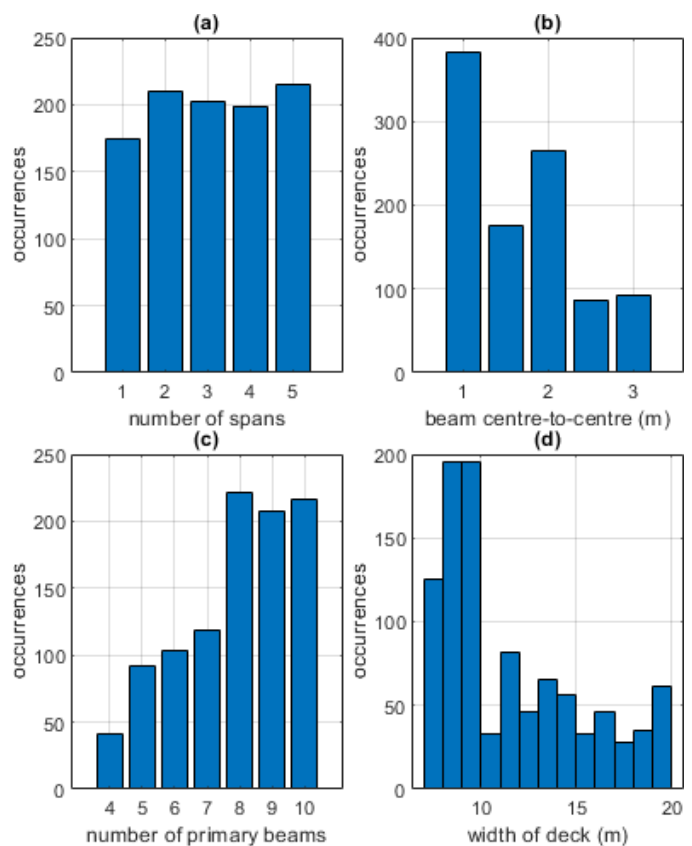


Figure 4: Beam-and-slab population statistics (a) the number of spans (b) the centre-to-centre spacing of the beams (c) the number of primary beams and (d) the width of the deck

Figure 5 presents the distributions of four key parameters for the ladder-deck bridge dataset: the number of spans, the width of the deck, the height of the main girder, and the height of the cross girders (subplots (a) through (d), respectively). The number of spans is distributed approximately evenly between one and five, similar to the statistics for beam-and-slab bridges. In contrast, the deck width, shown in Figure 5(b), displays a roughly even distribution as well; this is because of its independence from other design parameters in ladder-deck bridges, unlike in the beam-and-slab case.

The height of the main girders, illustrated in Figure 5(c), is determined using defined span-to-girder depth ratios and so is dependent on the length of the spans, with the span limitations setting clear upper and lower bounds for the distribution. Similarly, the height of the cross girders, depicted in Figure 5(d), is selected based on specific span-to-girder depth ratios, but with the additional constraint that they must not exceed the depth of the main girder.

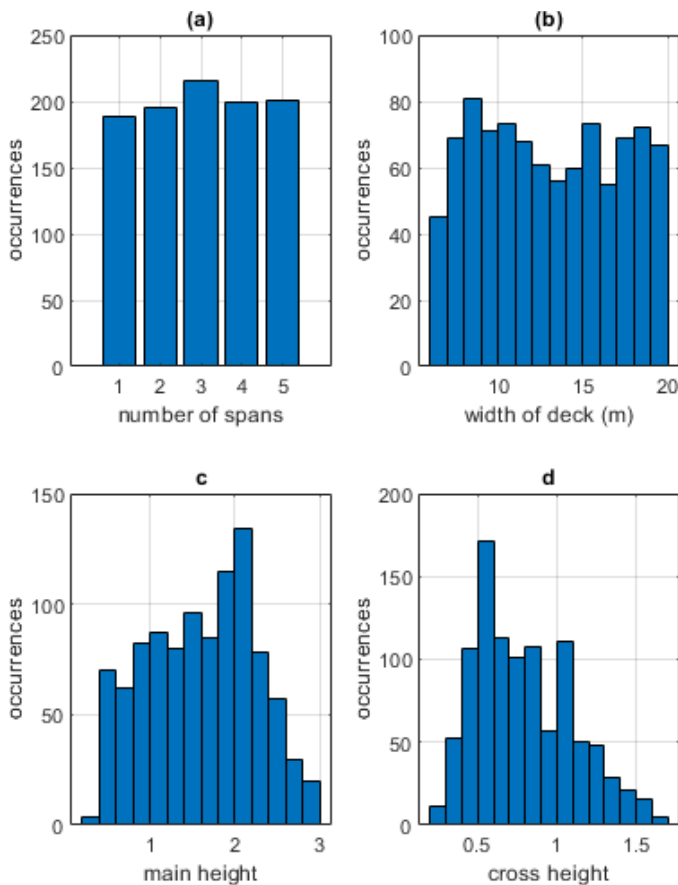


Figure 5: Ladder-deck population statistics (a) the number of spans (b) the width of the deck (c) the height of the main girder and (d) the height of the cross girders

## 5.2 Scenario Analysis

In this section, the results from the two implemented scenarios and conduct a simple analysis are presented. The aim is to provide the reader with a clear example of the types of data that can be generated from the populations, illustrating the applications of the PEAR dataset within PBSHM research.

Figure 6 illustrates the displacement responses of a representative ladder-deck bridge under the various loading

conditions simulated. In Figure 6(a) the vertical displacement of the bridge under dead load is presented. Figure 6(b) to (d) present the displacement responses when a 400 kN load is applied at the mid-span of each of the three spans, respectively. From the displacement results shown in Figure 6, the maximum displacement values for each load case were extracted. These values were then compared against the corresponding maximum displacements from the rest of the population.

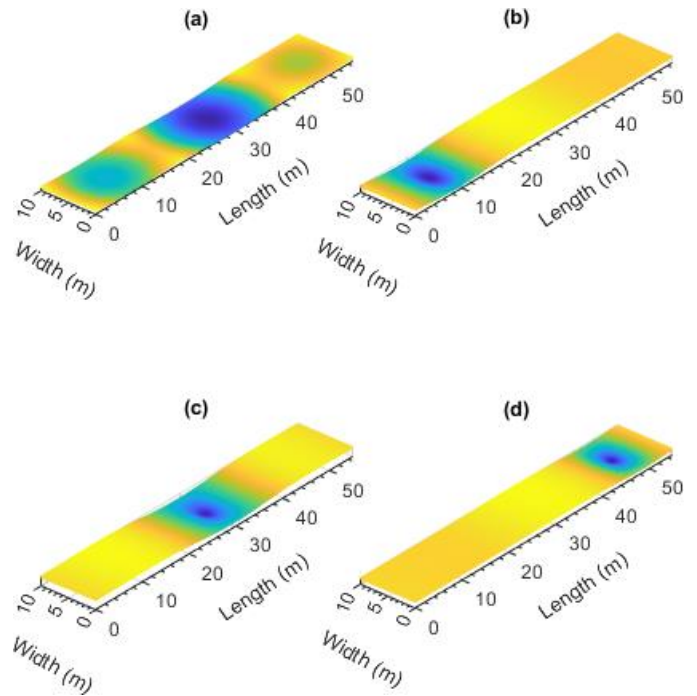


Figure 6: Vertical displacement output from FE model for (a) dead load (b) 400 kN applied to span 1 (c) 400 kN applied to span 2 (d) 400 kN applied to span 3

Figure 7 presents the combined maximum displacement values extracted from all of the FE models from the ladder-deck population, plotted against the span length where the point load was applied. In this figure, the colour of each data point represents the height of the main beam, with blue indicating the smallest beam depths and yellow indicating the largest. The displacements vary from 0.0018 m to 0.0653 m. This figure illustrates the relationship between the span length, the main beam depth and the displacement of the bridge. One of the key observations from the figure is the presence of distinctive bands. These bands show that as the span length increases, there is a corresponding increase in the depth of the beams, a trend that is consistent with design principles used for the ladder-deck bridges.

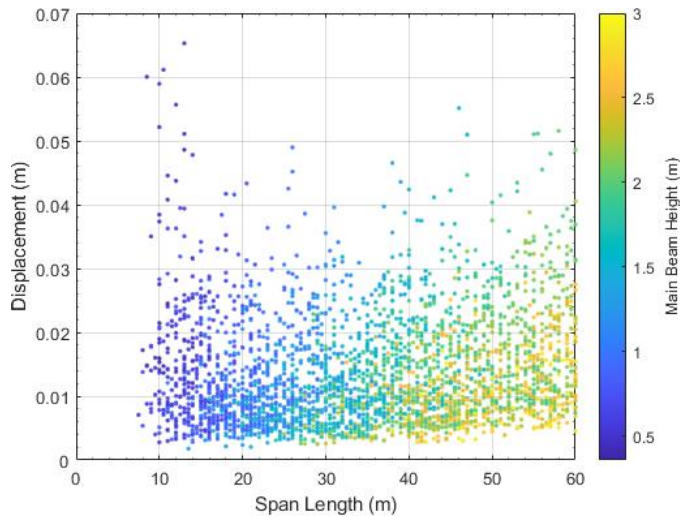


Figure 7: Span length vs the max displacement with the datapoints coloured with respect to main beam depth

### 5.3 Similarity Analysis

In this section, a basic similarity analysis between the populations will be presented. As stated in the prior, similarity assessments are key to PBSHM as they show where it is appropriate to undertake transfer learning between structures. In this work, the Jaccard index, a method used in graph theory [9], is employed to measure the similarity between IE models. The method used here will be slightly amended by embedding a geometry attribute of the elements in the IE model, specific details of this method can be found in [5]. The goal of this section is to highlight the suitability of the data in the PEAR being used for similarity analysis. Figure 8 shows the similarity matrix for a subset of 125 ladder-deck bridges. In the figure each pixel represents the similarity of one ladder-deck structure with another with dark blue representing least similar and yellow representing most similar. In this figure the structures are grouped by how many spans the bridges have; one-span bridges being grouped in the first 25 structures (indicated by the red box) and two-span bridges grouped in the next 25 positions and so on. Grouping in this way means that patterns can be observed about the relationship between the number of spans a bridge has and the similarity of other bridges with the same number of spans. In the case presented in Figure 8 it can be seen that the one-span bridges show a higher level of similarity with each other than with bridges of differing span. This pattern is repeated with the two-span bridges but the pattern seems to be diminished as the numbers of spans increase.

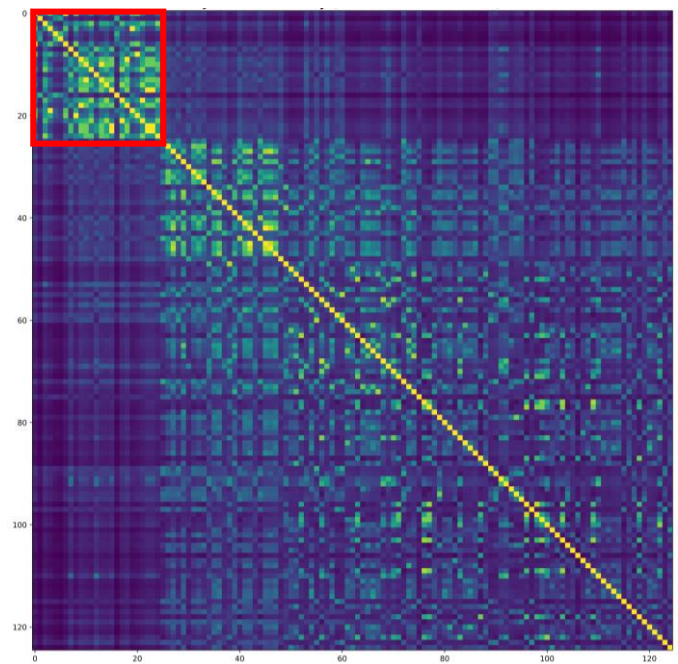


Figure 8: Similarity matrix for a subset of 125 ladder-deck bridges grouped by number of spans

To investigate this pattern further the similarity scores can be averaged across bridges with the same number of spans. This average is presented in Figure 9 and confirms the pattern seen in Figure 8. The bridges with the highest similarity are those with one span and as the number of spans increases the level of similarity decreases.

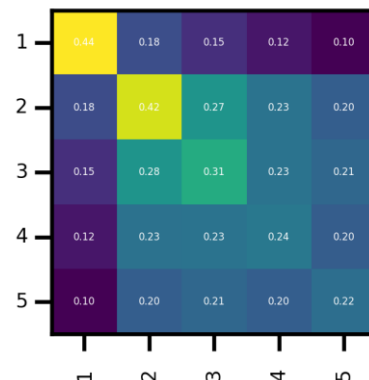


Figure 9: Similarity matrix for a subset of 125 ladder-deck bridges averaged by number of spans

This process was repeated for the beam-and-slab bridge population and the results are presented in Figure 10. This population largely follows the same pattern however the variability seems to be higher than that compared to the ladder-deck population this is most likely because of the other variations (other than number of spans) in the population affecting the similarity score.



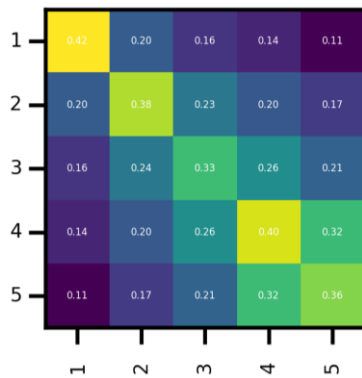


Figure 10: Similarity matrix for a subset of 125 beam-and-slab bridges averaged by number of spans

The similarity analysis in this section is the result of the question of how the number of spans of structures effects the similarity score between other members of the same population? This was chosen as an illustrative example of how a similarity analysis may be undertaken; however, it is only a single example of what may be considered in a similarity analysis. This produced dataset allows for a bespoke similarity assessment based on the needs of the specific research.

## 6 CONCLUSION

A fundamental challenge in Population-Based Structural Health Monitoring (PBSHM) is the need for data spanning multiple structures within a population. Ideally, these data would be sourced from real-world structures; however, acquiring comprehensive datasets across similar populations is challenging because of practical constraints, including data availability, monitoring costs, and access limitations. To address this issue, the database presented in this paper provides a synthetic dataset specifically tailored to the requirements of PBSHM research.

This work serves as a proof of concept for generating realistic populations of structures and associated data within a structured database. Two distinct bridge populations, beam-and-slab bridges and ladder-deck bridges, have been developed using engineering principles to maximise their realism. These structures have been validated via statistical analysis and comparison with theoretical expectations obtained from FE simulations. The FE models enabled structural responses under different loading conditions to be obtained.

The processes outlined in this work have been developed to be generalisable, meaning that aspects of engineering design can be incorporated into the population, such as varying material properties to adjust the material's strength. More complex design aspects, such as the amount of reinforcement or prestressed reinforcement, can be incorporated if the numerical simulation (e.g., an FE model) allows for it.

The results presented in this study demonstrate that it is feasible to create synthetic bridge populations that exhibit realistic structural behaviours, making them suitable for PBSHM development and validation. Although the analysis performed in this paper is relatively simple, it highlights the potential of the database for a range of PBSHM methodologies,

including data-driven condition assessment and transfer-learning applications.

The approach outlined in this paper has been intentionally designed to be flexible, allowing for the generation of both bespoke structural populations and corresponding datasets depending on specific research needs. Future work will build on this foundation by expanding the database with additional structural populations and scenarios, further enhancing its applicability for PBSHM research and facilitating broader adoption within the field.

## ACKNOWLEDGMENTS

The authors of this paper gratefully acknowledge the support of the UK Engineering and Physical Sciences Research Council (EPSRC) via grant reference EP/W005816/1. For the purpose of open access, the authors have applied a Creative Commons Attribution (CC BY) licence to any Author Accepted Manuscript version arising.

## REFERENCES

- [1] M. Döhler, F. Hille, L. Mevel, and W. Rücker, 'Structural health monitoring with statistical methods during progressive damage test of S101 Bridge', *Eng. Struct.*, vol. 69, pp. 183–193, Jun. 2014, doi: 10.1016/j.engstruct.2014.03.010.
- [2] B. Peeters and G. De Roeck, 'One-year monitoring of the Z24-Bridge: environmental effects versus damage events', *Earthq. Eng. Struct. Dyn.*, vol. 30, no. 2, pp. 149–171, Feb. 2001, doi: 10.1002/1096-9845(200102)30:2<149::AID-EQE1>3.0.CO;2-Z.
- [3] C. O'Higgins, D. Hester, K. Worden, and D. S. Brennan, 'Towards PEAR: a Benchmark Dataset for Population-based SHM', presented at the IMAC-XLIII, Orlando, Florida, Feb. 2025.
- [4] J. Gosliga, P. A. Gardner, L. A. Bull, N. Dervilis, and K. Worden, 'Foundations of Population-based SHM, Part II: Heterogeneous populations – Graphs, networks, and communities', *Mech. Syst. Signal Process.*, vol. 148, p. 107144, Feb. 2021, doi: 10.1016/j.ymssp.2020.107144.
- [5] D. S. Brennan, J. Gosliga, E. J. Cross, and K. Worden, 'Foundations of population-based SHM, Part V: Network, framework and database', *Mech. Syst. Signal Process.*, vol. 223, p. 111602, Jan. 2025, doi: 10.1016/j.ymssp.2024.111602.
- [6] A. Bunce *et al.*, 'On population-based structural health monitoring for bridges: Comparing similarity metrics and dynamic responses between sets of bridges', *Mech. Syst. Signal Process.*, vol. 216, p. 111501, Jul. 2024, doi: 10.1016/j.ymssp.2024.111501.
- [7] A. J. Hughes, R. J. Barthorpe, N. Dervilis, C. R. Farrar, and K. Worden, 'A probabilistic risk-based decision framework for structural health monitoring', *Mech. Syst. Signal Process.*, vol. 150, p. 107339, Mar. 2021, doi: 10.1016/j.ymssp.2020.107339.
- [8] Daniel S Brennan, Timothy J Rogers, Elizabeth J Cross, and Keith Worden, 'On calculating structural similarity metrics in population-based structural health monitoring', *Submitt. Data Centric Eng.*, 2024.
- [9] P. Jaccard, 'Distribution de la flore alpine dans le Bassin des Dranses et dans quelques régions voisines', 1901, doi: 10.5169/SEALS-266440.

# A Transfer Learning approach for damage identification in operational viaducts

Eleonora Morleo <sup>1</sup>, [0009-0002-5034-8833](#), Maria Pina Limongelli <sup>1</sup>, [0000-0002-9353-5439](#), Andrea Piscini <sup>2</sup>, [0000-0003-2786-1321](#), Edoardo Troielli <sup>2</sup>,  
[0009-0007-8761-4361](#)

<sup>1</sup>Department of Architecture, Built Environment and Construction Engineering, Politecnico di Milano, Piazza Leonardo da Vinci 32, 20133 Milan, Italy

<sup>2</sup>SINA S.p.A, Milan, Italy

email: [eleonora.morleo@polimi.it](mailto:eleonora.morleo@polimi.it), [mariagiuseppina.limongelli@polimi.it](mailto:mariagiuseppina.limongelli@polimi.it), [andrea.piscini@sina.it](mailto:andrea.piscini@sina.it), [edoardo.troielli@sina.it](mailto:edoardo.troielli@sina.it)

**ABSTRACT:** A major limitation in data-driven Structural Health Monitoring is the scarcity of labeled data for training machine learning models. Transfer Learning addresses this by enabling knowledge sharing across similar structures, reducing datasets distribution shift. This study proposes a novel Transfer Learning framework for damage identification in operational viaducts with similar spans, using modal frequencies as damage-sensitive features. Domain Adaptation is performed via Normal Condition Alignment, to map source and target features in a shared latent space. A baseline normal condition is established on source features through a linear regression model. Gaussian Mixture Models are trained on source residuals, and used to detect anomalies in the target domain, based on residual distributions. A real viaduct for which long-term monitoring data are available is used as a case study. The structure comprises two homogeneous datasets collected on the deck of similar spans. Source data pertain to a deck with extensive measurements, whereas target data refer to a second deck with a reduced dataset, due to sensor malfunctions. Damage is simulated in the target dataset by reducing the measured frequencies. Validation using data from real damaged scenarios will enable future scaling of the proposed framework to operational conditions, providing a practical tool for data-driven SHM of viaducts, enabling damage detection in under-instrumented areas by leveraging data from other spans.

**KEY WORDS:** Domain adaptation; transfer learning; operational viaduct; SHM; anomaly detection; GMM; linear regression; temperature variations.

## 1 INTRODUCTION

The deterioration of infrastructures poses a considerable challenge to the safety and efficiency of Europe's roadway network, as evidenced by the significant number of bridges that are nearing the conclusion of their service life [1]. The implementation of permanent monitoring systems, designed to observe the evolution of structural behavior over time, is imperative to support effective management of the structure, planning of maintenance activities and timely interventions. However, the financial implications associated with the deployment of such systems across an entire bridge network constitute a major obstacle to the widespread implementation of continuous monitoring campaigns. Consequently, less costly alternatives are often considered, as point-in-time monitoring campaigns or the selective installation of sensors in critical sections or structural components.

To tackle the limitations imposed by cost-saving measures and limited investments, while still guaranteeing an adequate level of safety, a promising solution involves transferring knowledge acquired from heavily instrumented structures or components to others with limited data availability to support the assessment of their structural behavior. This can be achieved through Transfer Learning (TL), a method which has recently gained significant attention among researchers in the field of civil infrastructure monitoring, as a means to overcome the issue of scarcity of labelled data for operating structures [2], [3], [4]. The concept of leveraging data – and, by extension, knowledge – from multiple structures to inform inferences about a target structure was introduced for the first time within the Population-Based SHM framework [5], [6], [7], [8], [9]. Notably, Poole et al. [10] proposed a domain adaptation

approach, referred to as Normal Condition Alignment (NCA), that aligns source and target datasets in a shared latent space, preserving the intrinsic meaning of damage-sensitive features, a capability not offered by other non-statistical approaches, such as DL. This statistical alignment technique has proven effective in several works concerning experimental and numerical datasets [11], [12], [13], in supervised settings with labelled data.

This paper investigates the application of NCA to an operational bridge equipped with a permanent monitoring system. Data from a well-instrumented span are leveraged to allow anomaly detection on a second span, where sensor failures have resulted in intermittent data acquisition.

The novelty of the proposed approach consists in the integration of a simple yet effective temperature compensation procedure following domain adaptation, to mitigate the confounding effect of temperature-induced variability on modal frequencies.

In the considered case study, no damage has been identified through field inspections, thereby the data from the source span are assumed to represent the undamaged state. For the target span, only the first year of monitoring data is considered representative of the undamaged configuration. Damage scenarios are synthetically introduced into the target dataset by increasingly reducing natural frequencies, to perform a sensitivity analysis of the proposed anomaly detection framework.

After domain adaptation is performed, a baseline normal condition for the source domain is established using a linear regression to model the relationship between temperature and natural frequencies. Residuals from this model are

subsequently employed to train a Gaussian Mixture Model (GMM) that is then used for anomaly detection in the target domain. The proposed approach is compared to a baseline method, where the GMM is trained directly on domain-adapted features of the source domain, and tested on domain-adapted features of the target. The results, evaluated in terms of F1-score, indicate that training the GMM on residuals improves performance, particularly when a moderate temperature-frequency correlation is present.

This study demonstrates the effectiveness of a simple domain adaptation technique and regression framework in enhancing novelty detection for bridge monitoring. The proposed framework offers a practical and cost-effective solution for optimizing the use of available monitoring data for critical infrastructure integrity management.

The remainder of the paper is organized as follows: Section 2 illustrates the methodology, Section 3 describes the case study and the datasets, Section 4 discusses the results, and the final section provides conclusion remarks.

## 2 METHODOLOGY

### 2.1 Domain Adaptation via NCA

Traditional machine learning algorithms rely on the assumption that training and testing data originate from the same underlying distribution [14]. When transferring knowledge from a source domain to a target domain, this assumption not necessarily holds, due to possible differences in the statistical distributions of the two domains. These differences may lead to degraded performance and increased generalization error. Domain Adaptation addresses this limitation mitigating the distribution shifts between source and target domains, aligning feature distribution into a shared latent space.

In this work, source and target domains are aligned into a common feature space exploiting NCA. This statistical alignment technique incorporates prior knowledge about the health state of the structure: alignment is achieved by matching both the mean and standard deviation of the normal-condition data distributions to effectively reduce domain discrepancy between the source and the target datasets.

Let  $D_S = \{\mathbf{x}_{s,i}, y_{s,i}\}_{i=1}^{n_s}$  be the source domain, with  $\mathbf{x}_{s,i}$  the source feature vector,  $n_s$  the number of observations and  $y_{s,i}$  the labels associated with each instance of the feature vector. Let also  $D_T = \{\mathbf{x}_{t,l}, y_{t,l}\}_{l=1}^{n_t}$  be the target domain, with  $\mathbf{x}_{t,l}$  the target feature vector,  $n_t$  the number of observations and  $y_{t,l}$  the labels associated with each instance of the feature vector in the target domain. NCA is developed in two steps. First, the source domain is standardized:

$$\mathbf{z}_{s,i} = \frac{\mathbf{x}_{s,i} - \boldsymbol{\mu}_s}{\boldsymbol{\sigma}_s} \quad (1)$$

being  $\boldsymbol{\mu}_s, \boldsymbol{\sigma}_s$  respectively the mean and the standard deviation of the source domain dataset. Then, the subset of the source domain consisting only of healthy instances  $\mathbf{x}_{s,n,i}$  is considered, and its statistics are computed  $\boldsymbol{\mu}_{s,n}, \boldsymbol{\sigma}_{s,n}$ .

Assuming that the target domain includes data associated with the undamaged configuration, reasonably identified as those collected from the start of the monitoring activity up to one year later, the statistics of this subset are computed and the following transformation is applied:

$$\mathbf{z}_{t,l} = \frac{\mathbf{x}_{t,l} - \boldsymbol{\mu}_{t,n}}{\boldsymbol{\sigma}_{t,n}} \boldsymbol{\sigma}_{s,n} + \boldsymbol{\mu}_{s,n} \quad (2)$$

being  $\boldsymbol{\mu}_{t,n}, \boldsymbol{\sigma}_{t,n}$  respectively the mean and the standard deviation of the target undamaged subset.

In this paper we assume that the entire source dataset is referred to the undamaged configuration of the structure, hence resulting in  $\boldsymbol{\sigma}_{s,n} = \mathbf{1}$  and  $\boldsymbol{\mu}_{s,n} = \mathbf{0}$ .

### 2.2 Linear regression

Natural frequencies are sensitive to the influence of environmental and operational fluctuations, being temperature the most significant source of variability. To filter out the effect of temperature on the modal properties of the structure, regression models have been widely proven effective, being able to characterize the relationship between temperature and eigenfrequencies [15], [16].

Considering the frequencies time history depicted in Figure 2, a linear dependency of the modal parameters on temperature can be appreciated. Hence, following the alignment of source and target data in the latent feature space, we train a linear regression model on the source features  $\mathbf{z}_{s,i}$  to learn the expected, temperature-dependent behavior of the structure. By doing so, the regression model establishes a baseline that characterizes the normal behavior of the source span. For each mode, the linear regression model reads as follows:

$$\hat{\mathbf{z}}_{s,i} = \beta_0 + \beta_1 \mathbf{T}_i \quad (3)$$

being  $\hat{\mathbf{z}}_{s,i}$  the predicted source feature in the latent space,  $\mathbf{T}_i$  the temperature corresponding to the  $i$ -th source feature  $\mathbf{z}_{s,i}$  in the latent space, and  $\beta_0, \beta_1$  the regression coefficients.

We then use this model to predict the features for both the source and the target domain, using the temperature values pertaining to each of them. The residuals, defined as the differences between the observed and predicted features values, are subsequently analyzed to detect potential anomalies or deviations from the expected structural behavior.

### 2.3 Gaussian Mixture Models for anomaly detection

Gaussian Mixture Models (GMMs) are probabilistic models employed in unsupervised machine learning for identifying clusters in data. They assume that data are generated from a mixture of multiple Gaussian distributions, each with unknown parameters. This assumption makes them suitable for modelling real-world monitoring data, which often exhibit multimodal distributions characterized by overlapping Gaussian components, due to changes in the data induced by factors such as temperature fluctuations and potential structural damage. Formally, the probability density function of the GMM is defined as:

$$p(\mathbf{x}) = \sum_{k=1}^N \pi_k N(\mathbf{x} | \boldsymbol{\mu}_k, \boldsymbol{\Sigma}_k) \quad (4)$$

where  $\pi_k$  is the mixing coefficient (the weight) for the  $k$ -th Gaussian component, satisfying  $0 \leq \pi_k \leq 1$  and  $\sum_{k=1}^N \pi_k = 1$ , and  $N(\mathbf{x} | \boldsymbol{\mu}_k, \boldsymbol{\Sigma}_k)$  is the  $k$ -th Gaussian distribution of the mixture, having  $\boldsymbol{\mu}_k$  mean vector and  $\boldsymbol{\Sigma}_k$  covariance matrix. The parameters of the GMM are estimated via the Expectation Maximization algorithm, which iteratively optimizes them by maximizing the likelihood of the observed data [14], [17].

GMMs are soft clustering algorithms, as they assign samples to a cluster based on the likelihood that each data point belongs



to that cluster in particular. In this paper we use the GMMs for anomaly detection. Specifically, for each mode, we train a GMM on the source domain residuals. Once the model is fitted, the log-probability density function (log-PDF) of each instance is evaluated and a detection threshold is established based on a low quantile of the log-PDF distribution, to distinguish normal from anomalous data points. The trained GMM is then applied to the target domain residuals and the log-PDF is computed and compared to the previously defined threshold. Instances falling below this threshold are identified as anomalies, indicating a deviation from the normal behavior modeled using source data.

Last, we compare the results of the proposed anomaly detection framework, combining linear regression and GMM, to those obtained using GMM alone. This is to assess the effectiveness of the integrated approach versus a direct application of GMM. More specifically, a separate GMM is trained, for each mode, using a dataset comprising the frequency and temperature vectors associated with the source domain in the latent space. Each GMM employs full covariance matrices to capture the correlations between frequency and temperature, and the optimal number of components for each model is selected based on the Akaike Information Criterion (AIC), to balance model complexity and goodness of fit. Then, for each mode, each GMM is tested against the target dataset in the latent space, including once again the frequency and temperature vectors associated with the selected mode.

#### 2.4 Performance evaluation

To assess the performance of the proposed anomaly detection framework, the number of true positives (TP), true negatives

### 3 CASE STUDY

#### 3.1 The viaduct

The structure under consideration in this study is an operational viaduct located in northern Italy. Constructed in 1968, the viaduct comprises 41 spans, extending for a total length of 1673.5 meters. The deck features continuous pre-stressed Gerber beams, each resting on two cast-in-place piers, and suspended Gerber spans (Figure 1). Of particular note is the monitoring of eleven spans that intersect with a river bed. In this section, the piers are spaced 61.5 meters apart, with a total length of 676.5 meters.

The instrumentation installed on the eleven monitored spans comprises a total of 219 biaxial MEMS inclinometers and 100 triaxial MEMS accelerometers, installed in 2020 to monitor the dynamic characteristics of the bridge and trigger alarms when fixed thresholds are exceeded. The accelerometers are not distributed uniformly across each span; rather, they are positioned on only half of each span.

The present study focuses on accelerometer data collected from May 2022 to December 2024. The structure is found to be in normal condition and is currently in service. Consequently, no damage configuration labels are available, as there is no evidence of damage to the structure. Temperature information is available for each of the set of eigenfrequencies obtained from the acceleration time histories.

#### 3.2 Description of the dataset

The objective of this study is to leverage the large volume of monitoring data available for a single span of the viaduct (the

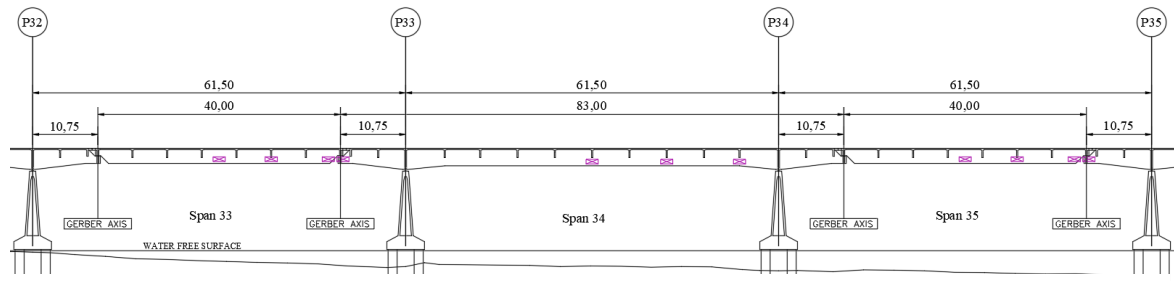


Figure 1. Part of the longitudinal section of the viaduct. Span 34 is the source one. In magenta the accelerometers installed.

(TN), false positives (FP), false negatives (FN) is computed. These quantities enable the evaluation of precision and recall metrics, which in turn are used to compute the F1 score. Precision measures the proportion of detected anomalies among all instances ( $TP / (TP + FP)$ ), while recall measures the fraction of correctly detected anomalies ( $TP / (TP + FN)$ ) [14]. Then, the harmonic mean of the two metrics is computed, resulting in the F1-score:

$$F1 - score = 2 * \frac{Precision * Recall}{Precision + Recall} \quad (5)$$

The F1-score is a commonly used metric to assess the performance of classification algorithms in presence of unbalanced dataset, a common issue in SHM datasets, where the number of healthy instances often exceeds the number of damaged ones by far.

source) to perform anomaly detection on another similar span (the target), with reduced data availability due to sensors malfunction. Two continuous spans are considered. Both the source and target dataset consist of time series observations that include the first three eigenfrequencies and the corresponding temperatures measured at each time step. Specifically, the source dataset comprises 4346 observations organized in a  $4346 \times 4$  matrix, while the target dataset includes 2143 observations structured in an analogous  $2143 \times 4$  matrix.

As previously stated, according to available inspection records, there is not any evidence of damage affecting the viaduct so far. Hence, both the source and target dataset considered contain observations which are reflective of the normal condition of the relative spans. For the source dataset, this condition is treated as factual throughout the study. Instead, we assume that only the observations acquired during the first year of monitoring of the target span are associated with its undamaged configuration. Additionally, we simulate the

occurrence of damage in the target by reducing the frequency values acquired from August 2024 by 2% and 5%. This enables us to conduct a sensitivity analysis on the performance of the anomaly detection procedure implemented.

The study is conducted in an unsupervised setting. However, to assess the performance of the framework in detecting anomalies in a real scenario, labels are assigned to the target dataset to mark the instances of reduced frequencies simulating damage, making it possible to compute the F1-score.

Figure 2 illustrates the first three natural frequencies for both source and target spans. The fundamental frequency  $f_1$  is approximately equal to 1.5 Hz for both the spans, and exhibits a similar trend for both domains. The second natural frequency  $f_2$  oscillates around 2.6 Hz. In this case, while there is a marked dependency of the source  $f_2$  on temperature, the corresponding target frequency displays a smoother trend. Finally, the third natural frequency of the two spans differs significantly, with  $f_3$  of the source domain having a mean value of 4.4 Hz, whereas  $f_3$  of the target dataset is lower, with a mean value of 3.6 Hz. Furthermore, a strong sensitivity to daily temperature fluctuations can be appreciated in the third eigenfrequency of the source span, with respect to the target one. Figure 3 depicts the temperature measurements recorded by the accelerometers installed on both spans. Figure 4 illustrates the time histories of  $f_1$ ,  $f_2$  and  $f_3$  of the target domain, highlighting the artificially reduced frequencies starting from August 2024 onward to simulate damage.

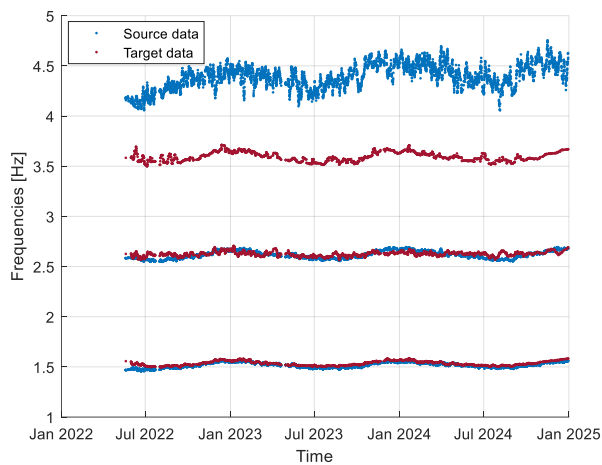


Figure 2. First three natural frequencies for source (in blue) and target dataset (in red). Frequencies  $f_1$  and  $f_2$  range around 1.5 and 2.6 Hz respectively, while  $f_3$  is around 3.6 Hz for the target domain and higher, around 4.3 Hz, for the source domain.

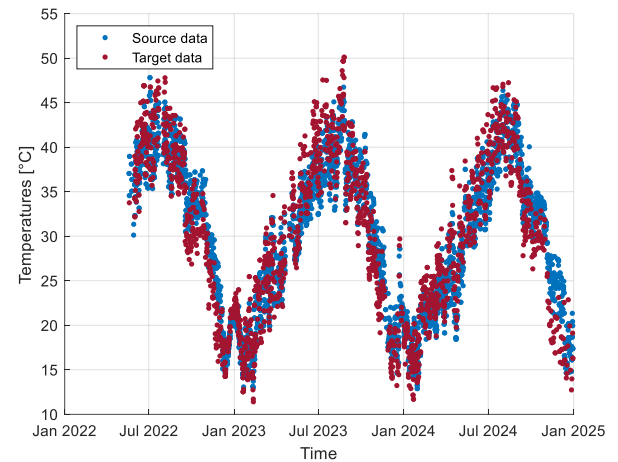
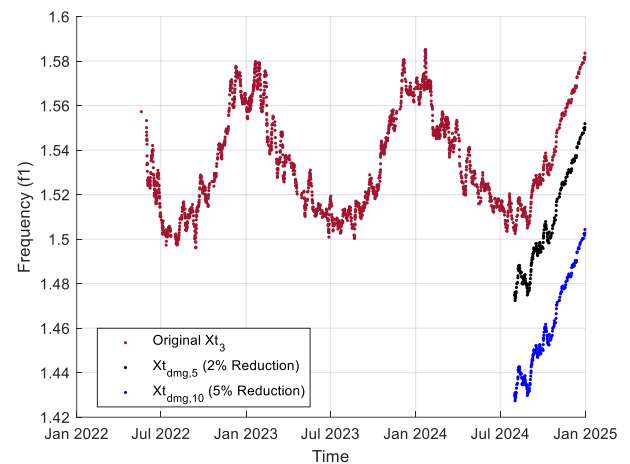
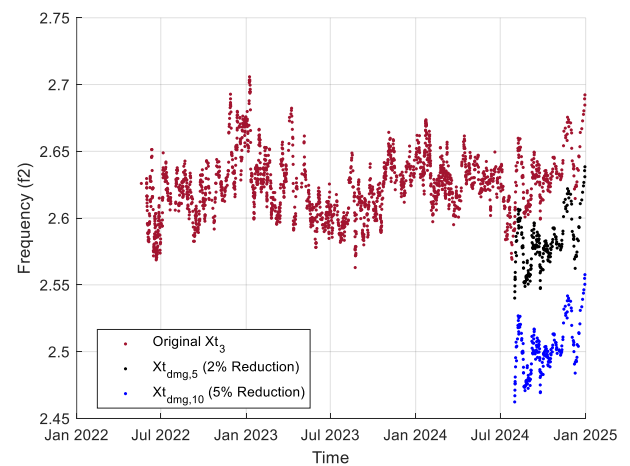


Figure 3. Source and target dataset temperature records.



a)



b)

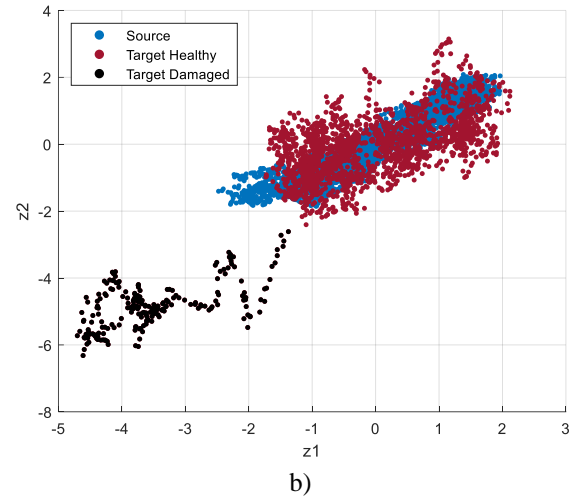
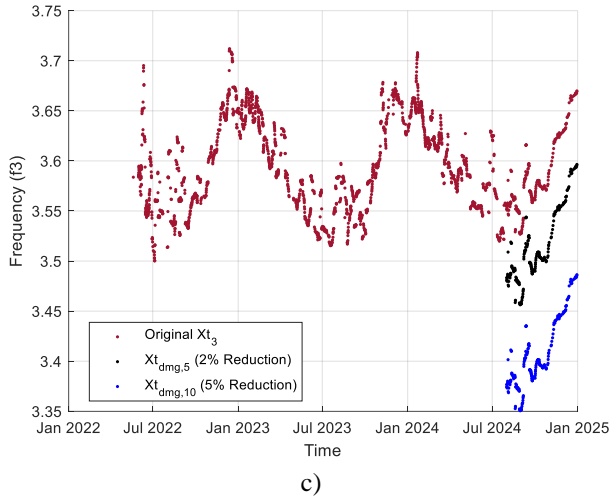


Figure 4. Original and synthetic data for the target domain. Frequencies of the target domain are reduced by 2% and 5% starting from August 2024 to simulate damage. Subfigures a), b), c) refer respectively to the first, second, and third natural frequencies.

Figure 5. Source and target features ( $z_1$  and  $z_2$ ) after domain adaptation. Figure 5a depicts the scenario in which damage is simulated through a 2% reduction in natural frequencies, whereas Figure 5b corresponds the case of a 5% frequency reduction.

#### 4 RESULTS

Normal Condition Alignment has been applied to the source and target datasets, and the resulting features in the latent space are depicted in Figure 5 and Figure 6. Figure 5a and Figure 6a are relative to the case where damage is simulated as a 2% reduction in natural frequencies, while Figure 5b and Figure 6b refer to a 5% frequencies reduction.

As a result of the application of NCA, when a 5% frequency reduction is introduced to simulate damage (Figure 5b and Figure 6b), we see that the normal instances of the target domain overlap the healthy features of the source. In contrast, the simulated damage instances tend to form distinct and distant clusters in the latent space. On the other hand, when damage is simulated through only a 2% reduction in frequencies, the corresponding damage instances of the target tend to cluster closely with, and even overlap, the healthy source and target features (Figure 5a and Figure 6a).

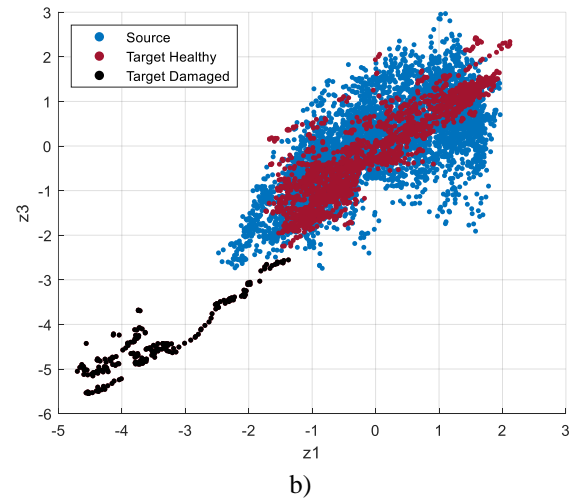
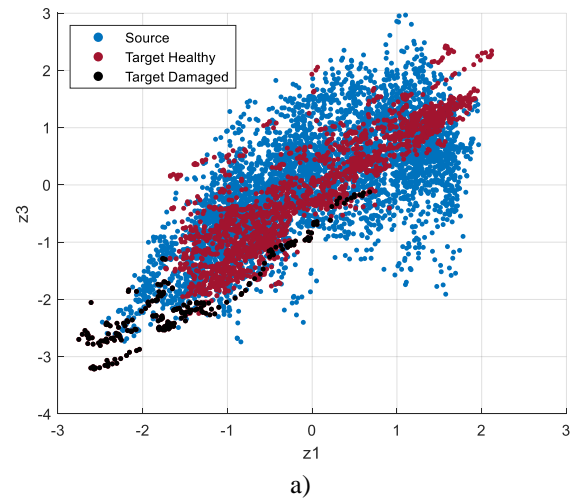
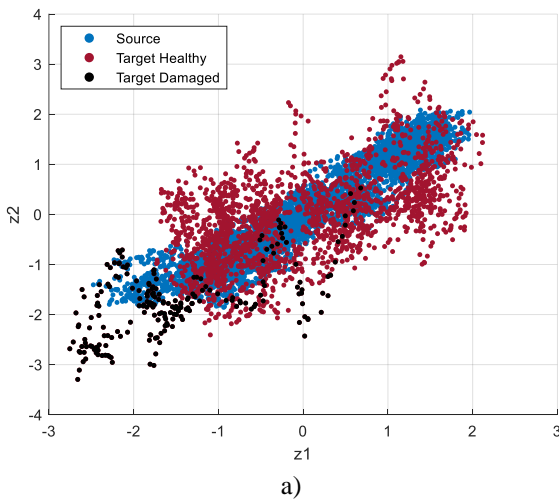


Figure 6. Source and target features ( $z_1$  and  $z_3$ ) after domain adaptation. Figure 6a depicts the scenario in which damage is simulated through a 2% reduction in natural frequencies,



whereas Figure 6b corresponds the case of a 5% frequency reduction.

In the following, the results associated with the 5% reduction in frequencies will be first illustrated, while those associated with the 2% frequency reduction for damage simulation will be discussed in the remainder of this section.

Separate linear regression models have been trained for each of the three source features (Figure 7, Figure 8, Figure 9) to capture their relationship with the corresponding temperature values. Each trained model has then been utilized to make predictions on both source data and target data, and the residuals between the actual feature values and the predicted ones have been computed.

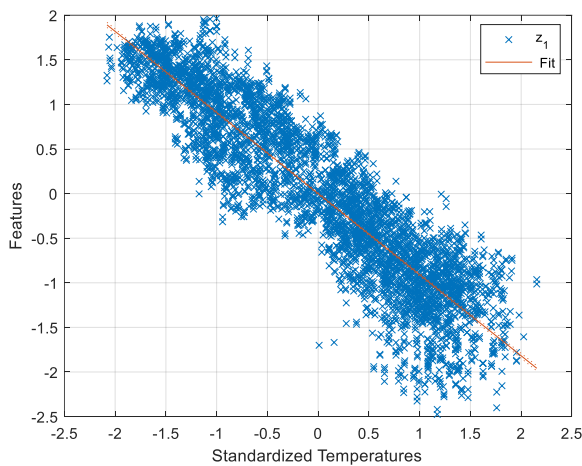


Figure 7. Linear regression of feature  $z_1$  of the source domain vs temperature.

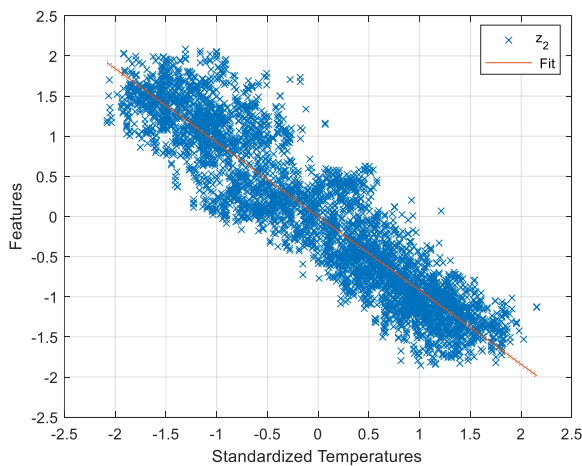


Figure 8. Linear regression of feature  $z_2$  of the source domain vs temperature.

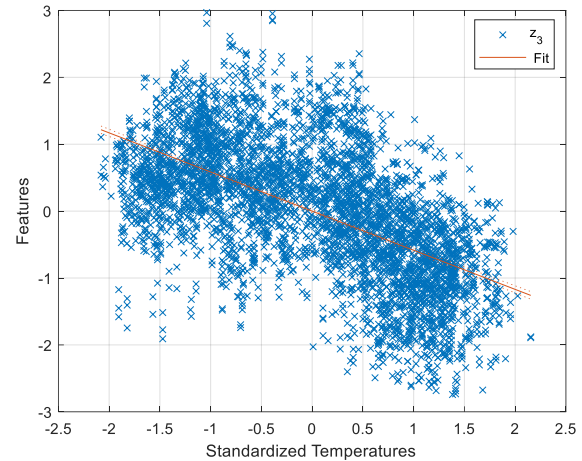


Figure 9. Linear regression of feature  $z_3$  of the source domain vs temperature.

A Gaussian mixture model has been independently trained on the source residuals for each mode. Following the training, the log-PDF of each GMM was evaluated, and a detection threshold was established at the 5th quantile for modes 1 and 3, and at the 1st quantile for mode 2. Subsequently, the trained GMMs have been applied to the target residuals for the corresponding modes, enabling anomaly detection by comparing the log-PDF values for the target against the predefined thresholds. The results are illustrated in Figure 10, Figure 11, and Figure 12, and the performance metrics are listed in Table 1.

Table 1. Anomaly detection results using GMMs trained on source residuals, evaluated on the target dataset with synthetic damage simulated by a 5% reduction in natural frequencies.

	TP	FP	FN	TN	Precision	Recall	F1 score
f1	219	95	0	1829	0.70	1.00	0.82
f2	219	475	0	1449	0.32	1.00	0.48
f3	219	14	0	1919	0.94	1.00	0.97

As we can see from the table, the GMMs tested on target residuals are in all cases able to detect the true damage instances, while detecting few false positives for  $z_1$  and  $z_3$ . In the case of  $z_2$ , the number of false positives is considerable, and this is probably due to the fact that frequency  $f_2$  of the target does not exhibit the same strong temperature dependence that is inherently present in the second natural frequency of the source domain.

Comparing these results with those obtained by training, for each mode, a GMM directly on the source features and temperatures (Table 3) in the latent space, a slight improvement in the F1-score can be appreciated when residual analysis is applied. As a matter of fact, from Table 2 we can see that, even though also in this case all the true anomalies are correctly identified, the baseline GMM produces a slightly higher number of false positives with respect to the residual-based approach. This demonstrates that the proposed framework can enhance the anomaly detection process by reducing the false alarms that would otherwise arise from applying the GMM to latent variables directly.

Table 2. Anomaly detection results using GMMs trained on source features directly, evaluated on the target dataset with synthetic damage simulated by a 5% reduction in natural frequencies.

	TP	FP	FN	TN	Precision	Recall	F1 score
f1	219	126	0	1798	0.63	1	0.78
f2	219	520	0	1404	0.30	1	0.46
f3	219	57	0	1867	0.79	1	0.88

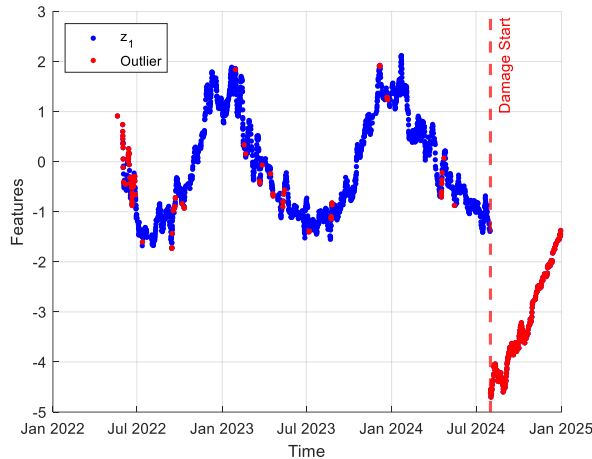


Figure 10. Target anomalies detected by GMM trained with source features residuals  $r_1$ . The threshold is set to the 0.05 quantile of the log-PDF.

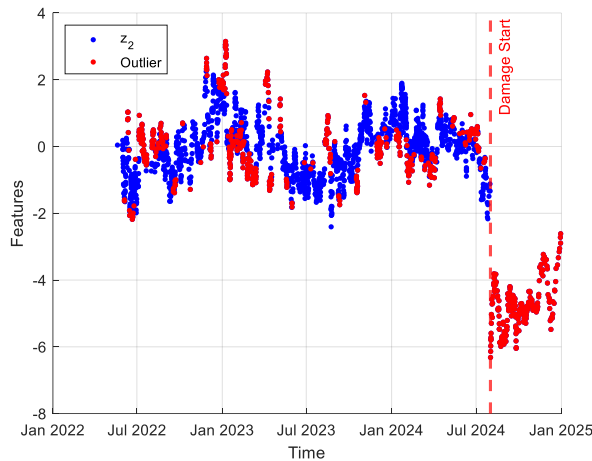


Figure 11. Target anomalies detected by GMM trained with source features residuals  $r_2$ . The threshold is set to the 0.01 quantile of the log-PDF.

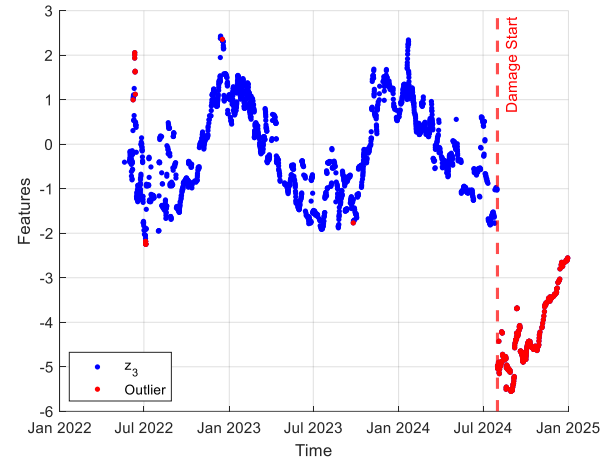


Figure 12. Target anomalies detected by GMM trained with source features residuals  $r_3$ . The threshold is set to the 0.05 quantile of the log-PDF.

Table 3. F1 scores comparison on the target dataset with synthetic damage data, reduction of 5%.

5% reduction	GMM trained on source features	GMM trained on source residuals	F1-score improvement
f1	0.78	0.82	5.13 %
f2	0.46	0.48	4.35 %
f3	0.88	0.97	10.23 %

Finally, Table 4 illustrates the results for the scenario where damage is simulated via a reduction of the actual target frequency values by 2%. In this case, we can see that the performances of the GMMs trained on source residuals are slightly worse than in the case with the 5% frequency reduction, standing the same detection thresholds. Nevertheless, the F1-scores computed for the residual-based anomaly detection approach still exhibit higher values than those achieved by GMMs trained on source latent features (Table 5), registering an increase in the F1-score value up to 10.5% for the third natural frequency (Table 6). This outcome highlights that the proposed framework is effective even when the damage is subtle, helping to mitigate the number of false positives that can occur in such cases.

Table 4. Anomaly detection results using GMMs trained on source residuals, evaluated on the target dataset with synthetic damage simulated by a 2% reduction in natural frequencies.

	TP	FP	FN	TN	Precision	Recall	F1 score
f1	202	94	17	1830	0.68	0.92	0.78
f2	178	472	41	1452	0.27	0.81	0.41
f3	168	14	51	1910	0.92	0.77	0.84

Table 5. Anomaly detection results using GMMs trained on source features directly, evaluated on the target dataset with synthetic damage simulated by a 2% reduction in natural frequencies.

	TP	FP	FN	TN	Precision	Recall	F1 score
f1	201	126	18	1798	0.61	0.92	0.74
f2	180	543	39	1381	0.25	0.82	0.38
f3	171	62	48	1862	0.73	0.78	0.76

Table 6. F1 scores comparison on target dataset with synthetic damage data, reduction 2%.

2% reduction	GMM trained on source features	GMM trained on source residuals	F1-score improvement
f1	0.74	0.78	5.41 %
f2	0.38	0.41	7.89 %
f3	0.76	0.84	10.53 %

## 5 CONCLUSIONS

In this paper, we have proposed a novel domain adaptation framework aimed at enhancing unsupervised anomaly detection in operational viaduct components. We have utilized the Normal Condition Alignment algorithm to leverage the extensive dataset available for a source span, to support anomaly detection in a target span with limited observations due to sensor malfunction. The novelty of this work lies in the use of a linear regression model to capture the dependency between frequency and temperature in the source domain after domain adaptation. This enables the establishment of a baseline normal condition for the source span in the latent space, which can then be “transferred” to the target span. Residuals from the source linear regression model have been used to train a Gaussian Mixture Model for each mode, enabling the detection of deviations from the expected normal behavior in the target domain when the trained models are tested against the target residuals.

We have compared the results of our residual-based framework against those obtained by training and testing the GMMs directly on domain-adapted features. The outcomes have highlighted that our method reduces the number of false positives, especially for modes where the natural frequencies are strongly influenced by temperature fluctuations, and even in the case in which the presence of damage is subtle, such as when frequencies from the normal condition are reduced by 2%. This is particularly relevant considering that even slight shifts in natural frequencies may correspond to severe structural damage.

Furthermore, from Figure 5a and Figure 6a we have seen that in the case of a 2% frequency reduction, the damaged instances of the target domain tend to overlap the healthy clusters of both source and target domains in the latent space. Relying solely on source features to train the GMM, without accounting for temperature in the establishment of a baseline normal condition, would have led to even poorer performances compared to using both features and temperatures. In fact,

overlapping damaged instances would likely be misclassified as healthy, thus increasing the number of false negatives.

In conclusion, the findings of this study underscore the significance of explicitly incorporating environmental variability into the knowledge transfer process. Future research will focus on examining the applicability of the proposed framework in contexts involving dissimilar source and target spans, as well as datasets with substantial data gaps. Additionally, validating the framework with data from actual damaged scenarios will pave the way for its future application to operational conditions. This will support the development of a practical, data-driven SHM tool for viaducts, capable of detecting damage even in under-instrumented spans by leveraging information from other ones.

## ACKNOWLEDGMENTS

The authors acknowledge SINA S.p.A. for sharing monitoring data and all relevant documentation related to the case study. Further, the authors thank Eray Temur for the development of the automated Operational Modal Analysis procedure used for extracting natural frequencies from the acceleration time histories.

## REFERENCES

- [1] Gkoumas, K. *et al.*, “Research and innovation in bridge maintenance, inspection and monitoring - A European perspective based on the Transport Research and Innovation Monitoring and Information System (TRIMIS),” vol. EUR 29650 EN, 2019, doi: 10.2760/719505.
- [2] M. Omori Yano, E. Figueiredo, S. Da Silva, and A. Cury, “Foundations and applicability of transfer learning for structural health monitoring of bridges,” *Mech. Syst. Signal Process.*, vol. 204, p. 110766, Dec. 2023, doi: 10.1016/j.ymssp.2023.110766.
- [3] L. Souza, M. O. Yano, S. Da Silva, and E. Figueiredo, “A Comprehensive Study on Unsupervised Transfer Learning for Structural Health Monitoring of Bridges Using Joint Distribution Adaptation,” *Infrastructures*, vol. 9, no. 8, p. 131, Aug. 2024, doi: 10.3390/infrastructures9080131.
- [4] E. Figueiredo, M. Omori Yano, S. Da Silva, I. Moldovan, and M. Adrian Bud, “Transfer Learning to Enhance the Damage Detection Performance in Bridges When Using Numerical Models,” *J. Bridge Eng.*, vol. 28, no. 1, p. 04022134, Jan. 2023, doi: 10.1061/(ASCE)BE.1943-5592.0001979.
- [5] L. A. Bull *et al.*, “Foundations of population-based SHM, Part I: Homogeneous populations and forms,” *Mech. Syst. Signal Process.*, vol. 148, p. 107141, Feb. 2021, doi: 10.1016/j.ymssp.2020.107141.
- [6] J. Gosliga, D. Hester, K. Worden, and A. Bunce, “On Population-based structural health monitoring for bridges,” *Mech. Syst. Signal Process.*, vol. 173, p. 108919, Jul. 2022, doi: 10.1016/j.ymssp.2022.108919.
- [7] P. Gardner, L. A. Bull, J. Gosliga, N. Dervilis, and K. Worden, “Foundations of population-based SHM, Part III: Heterogeneous populations – Mapping and transfer,” *Mech. Syst. Signal Process.*, vol. 149, p. 107142, Feb. 2021, doi: 10.1016/j.ymssp.2020.107142.
- [8] J. Gosliga, P. A. Gardner, L. A. Bull, N. Dervilis, and K. Worden, “Foundations of Population-based SHM, Part II: Heterogeneous populations – Graphs, networks, and communities,” *Mech. Syst. Signal Process.*, vol. 148, p. 107144, Feb. 2021, doi: 10.1016/j.ymssp.2020.107144.
- [9] G. Tsialiamanis, C. Mylonas, E. Chatzi, N. Dervilis, D. J. Wagg, and K. Worden, “Foundations of population-based SHM, Part IV: The geometry of spaces of structures and their feature spaces,” *Mech. Syst. Signal Process.*, vol. 157, p. 107692, Aug. 2021, doi: 10.1016/j.ymssp.2021.107692.
- [10] J. Poole, P. Gardner, N. Dervilis, L. Bull, and K. Worden, “On statistic alignment for domain adaptation in structural health monitoring,” *Struct. Health Monit.*, vol. 22, no. 3, pp. 1581–1600, May 2023, doi: 10.1177/14759217221110441.
- [11] V. Gligioni, J. Poole, R. Mills, I. Venanzi, F. Ubertini, and K. Worden, “Transfer learning in bridge monitoring: Laboratory study on domain adaptation for population-based SHM of multispan continuous girder



- bridges,” *Mech. Syst. Signal Process.*, vol. 224, p. 112151, Feb. 2025, doi: 10.1016/j.ymssp.2024.112151.
- [12] V. Giglioni, I. Venanzi, and F. Ubertini, “Supervised machine learning techniques for predicting multiple damage classes in bridges,” in *Sensors and Smart Structures Technologies for Civil, Mechanical, and Aerospace Systems 2023*, Z. Su, M. P. Limongelli, and B. Glisic, Eds., Long Beach, United States: SPIE, Apr. 2023, p. 48. doi: 10.1117/12.2664359.
- [13] V. Giglioni, J. Poole, I. Venanzi, F. Ubertini, and K. Worden, “A domain adaptation approach to damage classification with an application to bridge monitoring,” *Mech. Syst. Signal Process.*, vol. 209, p. 111135, Mar. 2024, doi: 10.1016/j.ymssp.2024.111135.
- [14] K. P. Murphy, *Machine Learning - A Probabilistic Perspective*. in Adaptive Computation and Machine Learning. Cambridge: MIT Press, 2014.
- [15] B. Peeters, J. Maeck, and G. D. Roeck, “Vibration-based damage detection in civil engineering: excitation sources and temperature effects,” *Smart Mater. Struct.*, vol. 10, no. 3, pp. 518–527, Jun. 2001, doi: 10.1088/0964-1726/10/3/314.
- [16] F. Ponsi, G. E. Varzaneh, E. Bassoli, B. Briseghella, C. Mazzotti, and L. Vincenzi, “Temperature effect on the modal frequencies of a steel railway bridge,” *Procedia Struct. Integr.*, vol. 62, pp. 1051–1060, 2024, doi: 10.1016/j.prostr.2024.09.140.
- [17] C. M. Bishop, *Pattern recognition and machine learning*. in Information science and statistics. New York: Springer, 2006.

# The future of conservation: Citizen Science models for the Photomonitoring of cultural heritage

Cosentino Antonio<sup>1,2</sup>, 0000-0002-7893-4693, Clementi Jessica<sup>1</sup>, 0000-0002-7576-4983, Molinari Antonio<sup>1</sup>, 0009-0001-9097-9640, Sanvito Veronica<sup>1</sup>, 0009-0000-9707-0248, Mazzanti Paolo<sup>1,2,3</sup>, 0000-0003-0042-3444

<sup>1</sup>Department of Earth Sciences, “Sapienza” University of Rome and CERI Research Centre for Geological Risks, P.le Aldo Moro 5, 00185 Rome, Italy

<sup>2</sup>IntelligEarth S.r.l.—Start UP, “Sapienza” University of Rome, Via V. Bachelet n. 12, 00185 Rome, Italy

<sup>3</sup>Nhazca S.r.l.—Start UP, “Sapienza” University of Rome, Via V. Bachelet n. 12, 00185 Rome, Italy

Email: antonio.cosentino@uniroma1.it, jessica.clementi@uniroma1.it, antonio.molinari@uniroma1.it, veronica.sanvito@uniroma1.it, paolo.mazzanti@uniroma1.it

**ABSTRACT:** This study investigates the effectiveness of photomonitoring as a remote sensing technique for cultural heritage conservation, focusing on the Aurelian Walls (Rome) and the Church of Santa Apollonia (Ferrara), Italy. Using mobile devices such as smartphones and tablets, structural changes—including brick detachment and vegetation growth—were detected through Structural Similarity Index (SSI) mapping. The results highlight both the advantages and limitations of mobile-based monitoring, emphasizing its flexibility and rapid deployment. Key challenges include variations in pixel size and lighting conditions, which influence data consistency. Despite these limitations, the study supports the potential of citizen science integration to enhance spatial and temporal data collection. By leveraging crowdsourced imagery, monitoring efforts can become more comprehensive and cost-effective. The findings align with broader citizen science initiatives, demonstrating how non-invasive, mobile-based techniques can contribute to sustainable heritage preservation. Future research should focus on optimizing data acquisition and processing methodologies to improve the robustness of this approach.

**KEY WORDS:** Photomonitoring, Structural Similarity Index, Cultural Heritage Monitoring, Mobile Sensing, Citizen Science, Remote Sensing, Image-Based Analysis

## 1 INTRODUCTION

The preservation of cultural heritage is a crucial endeavor, safeguarding the tangible expressions of human history and identity. The monitoring of immovable cultural assets—including monuments, archaeological sites, and historic buildings—is essential to ensure their longevity and structural integrity. While traditional monitoring methods have long been utilized in heritage conservation, recent advancements in image analysis techniques, coupled with the growing role of citizen science, have significantly enhanced these practices. Cultural heritage sites face numerous threats, including environmental factors such as weathering, pollution, and natural disasters, as well as human-induced damages such as vandalism and urban expansion. Regular monitoring is essential for detecting early signs of deterioration, enabling timely interventions to prevent further damage and preserve the historical value of these sites. Additionally, continuous assessment supports informed decision-making regarding conservation strategies and resource allocation.

Historically, cultural heritage monitoring has relied on several established techniques. Visual inspections remain a fundamental approach, with conservators and archaeologists conducting systematic assessments to identify surface anomalies, structural cracks, or material degradation. However, this method is inherently subjective and may fail to capture subtle changes over time. Standard photography has been widely used to document sites, facilitating comparative

analysis, yet it is often insufficient for detecting underlying structural issues or material compositions. Furthermore, environmental monitoring devices such as dataloggers provide valuable data on temperature, humidity, and vibrations affecting cultural assets. While effective, these sensors often require intrusive installation, which may pose risks to fragile structures.

In recent decades, the integration of advanced image analysis techniques has revolutionized cultural heritage monitoring, offering precise and non-invasive methods for assessing and preserving historical sites. The fusion of image analysis with geomatics and remote sensing technologies has significantly expanded heritage monitoring capabilities. The use of satellite imagery, such as data from Sentinel-2, allows for large-scale monitoring of archaeological sites, providing critical insights into environmental impacts and structural changes over time [1]. The incorporation of artificial intelligence (AI), particularly deep learning algorithms, has enhanced damage assessment accuracy in cultural heritage conservation. Automated detection and classification of deterioration patterns improve the efficiency of preservation efforts [2].

Moreover, linking hyperspectral imaging with other non-destructive analytical methods has further advanced research potential in this field. The integration of hyperspectral imaging with tensor-based learning models has improved the automated inspection of cultural monuments, allowing for detailed material characterization and defect classification, enhancing

the accuracy of preservation strategies [3]. The application of unsupervised clustering techniques to hyperspectral images has been explored for monitoring cultural heritage degradation, enabling the detection of decomposition and corrosion levels, providing valuable data for conservation efforts [4]. Deep learning methods, such as autoencoders and Generative Adversarial Networks (GANs), have been successfully employed for anomaly detection on ancient stone stele surfaces [5], while convolutional neural networks (CNNs) have been utilized to identify structural damage in heritage buildings [6]. By processing high-resolution images, these AI-driven techniques facilitate the timely detection of defects, supporting proactive conservation efforts.

These image-based techniques offer several advantages over traditional methods: they are non-invasive, minimize direct interaction with artifacts, and generate high-resolution data that can be quantitatively analyzed. Furthermore, their digital nature allows for the creation of permanent records that can be revisited for future studies or restoration initiatives.

In 2022, the Italian Ministry of Culture and the CERI Research Center at the University of Rome Sapienza entered into a collaboration agreement to develop new guidelines for the monitoring of deformations that affect cultural heritage sites. Within this framework, our research group is testing various innovative, non-invasive monitoring techniques, from the landscape scale down to individual cultural heritage buildings. Photomonitoring has emerged as a cost-effective, precise, and rapid alternative to traditional analytical methods [7; 8]. By leveraging low-cost tools such as smartphones and entry-level cameras, photomonitoring enables accurate multitemporal analysis to detect vegetation growth, mortar detachment, and structural deterioration. Based on Digital Image Processing principles, this approach extracts both qualitative and quantitative insights into structural changes by analyzing and comparing images of the same area taken at different time intervals [9;10]. This paper explores the potential of photomonitoring through case studies, including the Aurelian Walls in Rome and S. Apollonia Church in Ferrara. The results demonstrate its effectiveness in providing detailed insights into structural changes, offering a sustainable solution for heritage management.

Having established the reliability of photomonitoring, the next objective is to involve communities in data collection through mobile and web applications. Initiatives such as IntelligEarth exemplify the intersection of technology and citizen science. This startup aims to revolutionize heritage monitoring by integrating crowdsourcing systems and citizen participation, enabling real-time reporting and analysis of environmental risks to cultural sites.

Citizen science—the active involvement of non-professional researchers in scientific initiatives—has become an invaluable component of cultural heritage monitoring and conservation. Integrating citizen science not only complements traditional monitoring efforts but also democratizes the preservation process, fostering a sense of collective responsibility. Equipped with smartphones and digital cameras, individuals can capture

and upload images of heritage sites, contributing to large-scale monitoring databases. This approach significantly expands the spatial and temporal scope of data collection beyond what professional teams alone can achieve. Furthermore, engaging the public in heritage monitoring raises awareness about cultural preservation. Educational programs and workshops can empower communities to take an active role in conservation efforts.

Recent case studies highlight the effectiveness of citizen participation in heritage monitoring. The Tirtha project, launched in 2023, exemplifies the integration of technology and public engagement in cultural heritage preservation. This web platform enables crowdsourcing of heritage site images to generate detailed 3D models using advanced photogrammetry techniques. Contributors submit photographs that are processed to create accurate three-dimensional representations of cultural landmarks [11]. Monitoring and documenting remote heritage sites pose significant challenges for large heritage organizations. By encouraging tourists and local residents to share images captured during their visits, organizations can collect valuable data to assess the condition of sites, especially those that are unstaffed or in remote locations. This approach proved particularly valuable during the COVID-19 pandemic, ensuring continued monitoring despite travel restrictions [12].

The role of citizen science in cultural heritage conservation extends beyond data collection, fostering increased public awareness and community engagement. A compelling example of this dynamic is presented in the study of Kumar [13], which analyzed the response to the 1966 Florence flood and demonstrated how crowdsourcing efforts—long before the internet era—enabled effective heritage recovery through monetary donations, volunteer labor, and material support. The study further identified key motivational factors for public participation in such initiatives, including direct calls to action, media influence, and personal connections to affected cultural assets. These findings suggest that properly structured citizen science initiatives have the potential to mobilize extensive public participation in cultural heritage conservation, even in the aftermath of disasters.

The monitoring of immovable cultural heritage is a complex yet evolving field that has been greatly enhanced by technological advancements. While traditional methods have provided the foundation for conservation practices, the integration of sophisticated image analysis techniques has significantly improved the precision and efficiency of monitoring efforts. Simultaneously, the rise of citizen science has introduced a collaborative dimension, enriching data collection and fostering public involvement. Together, these advancements contribute to more effective and inclusive strategies for preserving the invaluable cultural legacies of humanity.



## 2 MATERIALS AND METHODS

### 2.1 Instrumentation and Source Data

In the frame of this work, the acquisitions have been performed with two different sensors, one for each site. In both cases, it has been chosen a multi-temporal approach to monitor the evolution of the phenomenon over time, providing a more comprehensive and accurate perspective.

The first dataset of images was taken using a Tablet Samsung Galaxy Tab S7+, whose features are shown in Table 1.

Table 1 - Samsung Galaxy Tab S7+ characteristics

Sensor	13 MP
Sensor size	1/3.4"
Focal length	3 mm

To acquire the second dataset, a Smartphone Samsung Galaxy A54 was used, whose characteristics are shown in Table 2.

Table 2 - Samsung Galaxy A54 characteristics

Sensor	12 MP
Sensor size	1/1.56"
Focal length	6 mm

As for the acquisitions, the images taken with the tablet were captured manually, while a tripod was used for those acquired with the smartphone. In order to keep the same position and the same camera orientation between one acquisition and another, it has been used the software of feature tracking CARE, that allows to obtain the same exact position of the previous acquisition. This is essential to ensure the best performance during the analysis, giving a more accurate result in the co-registration process.

Data collection lasted for more than a year. The tablet dataset has been collected in two phases, the first one from November to December 2022; the second one from December 2023 to November 2024. The smartphone dataset has been acquired over a period of one year, from February 2024.

Table 3 - Images characteristics

Subject	Date	Dimensi ons	Dista nce	Pixel Size
K11-K12 section	27-12- 2022/19-01- 2024	6.27 MB – 5.84 MB	30 m	19,3 mm
K12-K13 section	19-01- 2024/19-09- 2024	6.67 MB – 6.19 MB	32 m	20,6 mm

Sant' Apolloni a Church	13-06- 2024/26-09- 2024	9.56 MB – 8.39 MB	6 m	2,67 mm
-------------------------------	-------------------------------	-------------------------	-----	------------



Fig. 1 Map showing the Aurelian Wall cases of study and the positions of acquisition (a). Frame of the K12-K13 section (b). Frame of the K11-K12 section (c).

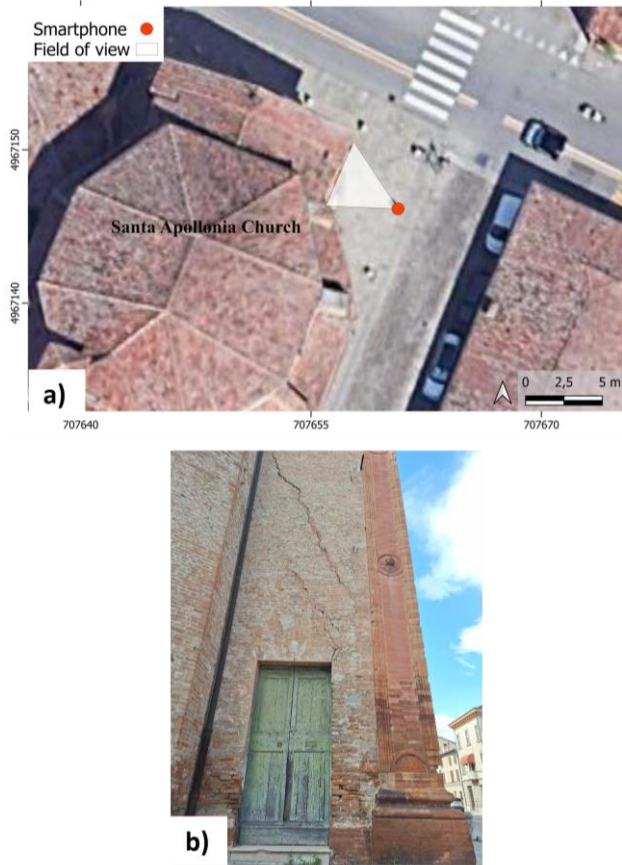


Fig. 2 Map showing Santa Apollonia Church case of study and the positions of acquisition (a). Frame of acquisition (b).

## 2.2 Methodology

The data acquired for this study were processed using Change Detection (CD) algorithms. Change Detection is a Digital Image Processing (DIP) technique that allows to identify variations between images acquired at different time intervals by comparing a reference image (master) with one or more successive images (slave) [14]. Digital images, represented as numerical matrices, enable the identification of features such as points, lines, patterns, color, brightness, and contrast. The comparison of these features between temporally successive images allows for the precise detection of changes within the area of interest [9]. Several Change Detection methods have been developed to date. Pixel-based approaches directly compare intensity values between successive images. Statistical approaches, such as the Mean Squared Error (MSE) and the Peak Signal-to-Noise Ratio (PSNR), quantify variations based on error metrics [14, 15]. Perceptual-based methods, such as the Structural Similarity Index (SSIM), analyze changes while accounting for human visual perception [16]. The accuracy of Change Detection, regardless of the method adopted, depends on the quality of the acquired images and the ability to distinguish actual structural modifications from variations induced by atmospheric conditions or illumination differences. Additionally, the presence of distinctive patterns or appropriate speckle models in the scene is also essential to ensure robust identification of corresponding features in successive images. Therefore, accurate image co-

registration is essential to guarantee proper spatial alignment between consecutive datasets, minimizing geometric distortions that could compromise the analysis [16]. The CD approach implemented within the software utilizes the Structural Similarity Index (SSIM) method [16; 17]. SSIM is an algorithm developed to quantify image similarity by analyzing three fundamental components: luminance, contrast, and structure [17]. Compared to conventional metrics such as MSE and PSNR, SSIM is based on a perceptual model, offering a more accurate assessment of visually perceptible modifications [16]. This method has demonstrated considerable potential for detecting changes due to its robustness and accuracy [18].

The SSIM index is defined by the following equation (Eq. 1):

$$SSIM(x, y) = [l(x, y)]^\alpha \times [c(x, y)]^\beta \times [s(x, y)]^\gamma \quad (1)$$

where  $l(x, y)$  represents luminance, which evaluates the difference in brightness between the two images,  $c(x, y)$  expresses contrast, which differentiates the intensity range between the brightest and darkest regions of the images, and  $s(x, y)$  represents structure, which compares the local luminance pattern between two images to assess similarity and dissimilarity. The exponents  $\alpha$ ,  $\beta$  and  $\gamma$  are positive constants that govern the weight of each component in the final computation. The algorithm is applied to local windows within the images and returns a value ranging from 0 to 1, where 0 indicates a complete change and 1 indicates an area where no changes have been detected. Intermediate values suggest partial variations, indicating potential structural modifications or illumination changes. The Change Detection analysis in the IRIS software begins with the selection and uploading of the master and slave images, followed by an additional image co-registration phase to achieve perfect dataset alignment [7]. The next step involves selecting the Window Size (WS) parameter. This parameter is crucial as the software employs a sliding window approach, computing the SSIM index on patches defined by the Window Size (WS) and assigning the calculated SSIM value to the central pixel of each patch.

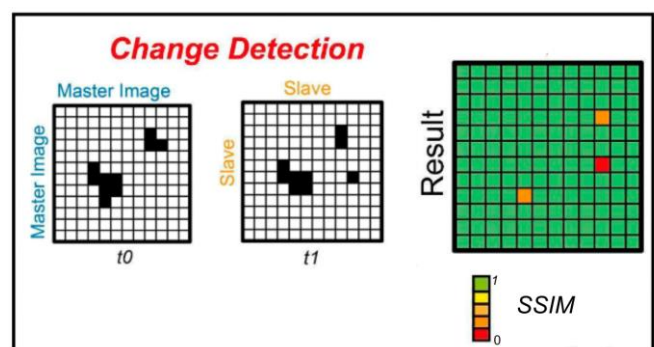


Fig. 3: Conceptual scheme illustrating the process of change detection (CD) analysis. Two images are compared to identify changes that occurred during the time interval  $t_0$ – $t_1$

Once the desired Window Size is selected, the next step involves assigning the weight of the individual contributions in the SSIM computation. This step is critical for ensuring the

correct execution of Change Detection. The software allows for adjustment of the  $\alpha$ ,  $\beta$  and  $\gamma$  exponents, exponentially increasing the analysis sensitivity based on specific cases. Operating at a local scale, the software iteratively evaluates image similarity within small pixel subsets defined by the WS, enabling the automatic detection of change regions.

The choice of the Window Size (WS) is fundamentally informed by the expected scale of detectable changes within the monitored structures. A properly defined WS allows the analyst to selectively filter out minor disturbances or non-structural changes that are not relevant to the analysis objectives. This tuning capability is particularly useful when addressing noise induced by lighting variations or acquisition-related inconsistencies, such as slight displacements, shadows, or differences in ambient conditions.

To further refine the detection process, the software supports semi-automatic calibration of the exponential weighting factors  $\alpha$ ,  $\beta$ , and  $\gamma$  within the SSIM algorithm. These parameters respectively control the contribution of luminance, contrast, and structural components, and their adjustment is essential for minimizing false positives caused by non-structural changes (e.g., shadow displacement or illumination shifts). By modulating these parameters in accordance with the selected WS, it is possible to enhance the robustness of the analysis, isolating meaningful structural variations while attenuating the influence of irrelevant fluctuations. This methodological flexibility is key to adapting photomonitoring workflows to diverse environmental and acquisition conditions.

The result of this analysis is a raster map that visualizes SSIM values for each individual pixel through a color gradient. Green indicates an SSIM value of 1, implying no change, while blue represents an SSIM value of 0, indicating a complete change.

### 3 CASE STUDY

One of the selected case studies is the Aurelian Walls in Rome, a monumental archaeological structure that once served as the primary defensive boundary of the city and now forms a significant part of Rome's UNESCO World Heritage designation. As the largest surviving monument in the city, the walls hold immense historical and architectural value. However, they are increasingly threatened by invasive vegetation, including species such as *Hedera helix* L., *Ficus carica* L., and *Capparis orientalis* Veill. (*Capparis spinosa* L.), with *Ailanthus altissima* emerging as the most invasive and difficult species to control [19, 20, 21, 22].

Geologically, the Aurelian Walls are located in an area characterized by Quaternary volcanic formations and Holocene alluvial deposits from the Tiber River. Constructed under Emperor Aurelian between 270 and 275 AD, with subsequent completion under Emperor Probus, the walls originally extended approximately 19 km, though only 12.5 km remain today due to partial demolitions. Structurally, they consist of a combination of tuff and brick masonry, with an inner core composed of loosely bonded tuff blocks. Over the centuries, conflicts and environmental factors have contributed to their deterioration, prompting numerous restoration interventions.

Notably, during the 16th century, Pope Pius IV commissioned extensive reinforcements to enhance their stability [23, 24]. More recently, the Capitoline Superintendence has undertaken conservation projects aimed at safeguarding the remaining sections and preventing structural collapses.

The second case study focuses on the Church of Santa Apollonia in Ferrara, a city recognized as a UNESCO World Heritage Site since 1995. Originally built in the 15th century, the church underwent significant reconstruction in 1612, transforming into an oratory with an expanded classical octagonal layout. Further modifications were made in 1662, including the incorporation of the portal from the Church of the Holy Spirit (*Chiesa dello Spirito Santo*), which had been demolished in 1839. The church remained closed since 1975 and was later deconsecrated. Over time, it has fallen into severe neglect and structural decay. Santa Apollonia has since been placed under state management as part of a broader restoration and redevelopment initiative aimed at repurposing its interiors into an exhibition space for the nearby National Archaeological Museum of Ferrara. The building, like many others in the region, is constructed on permeable fluvial sand deposits, which have contributed to significant water infiltration and accelerated degradation. Located north of the so-called Isola di Sant'Antonio, the structure exhibits pronounced signs of moisture-induced deterioration, with severe cracking observed along the left lateral wall, highlighting the urgent need for intervention.

## 4 RESULTS

Over a time span of more than a year, numerous changes have been identified in the two datasets. The changes observed during this period affect the vertical external curtain of the Aurelian Walls and the wall facing of Santa Apollonia church and consist mainly in detachments of bricks or mortar and vegetation growth. The product of the analysis is shown as a Structural Similarity Index Map where the changes are differentiated on the SSI values. Areas where no changes are present are highlighted in green, while changes are highlighted in red/purple, depending on their magnitude.

### 4.1 Aurelian Walls

**K11-K12 section:** The map in Fig. 4 c) shows some brick detachment on the external curtain. These bricks have a low similarity index value and are highlighted in red. Although the primary objective of the analysis was to detect structural changes, in this specific case the SSIM mapping also revealed variations associated with the growth of invasive vegetation (see upper-left portion of the image). These changes, while not structural in nature, contribute to the overall degradation of the wall surface and are thus relevant for conservation monitoring.



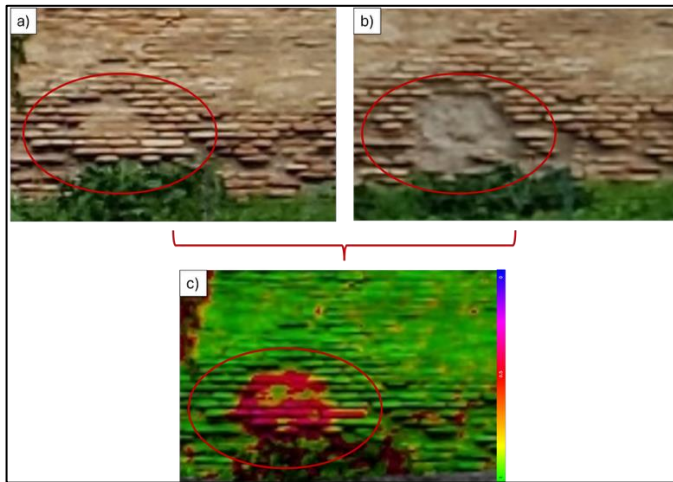


Fig. 4 - Detail of the Change Detection Map showing the bricks detachment from the K11-K12 section.

**K12-K13 section:** The map in Fig. 5 c) shows the vegetation growth. The areas of growth can be seen in red due to their low similarity index value.

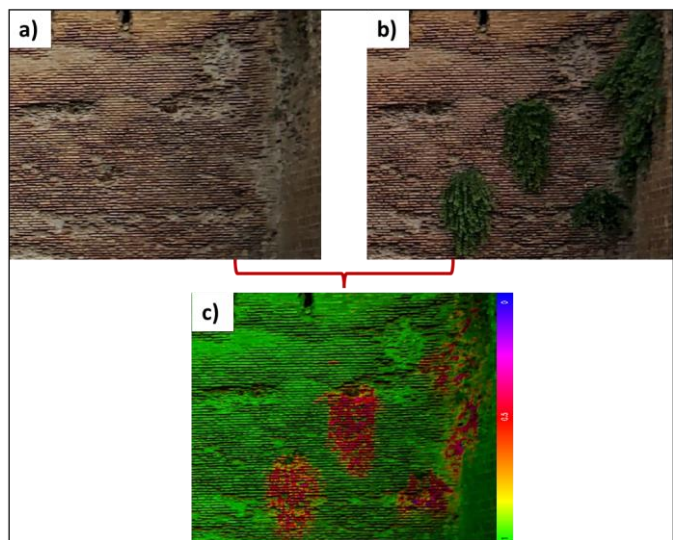


Fig. 5 - Detail of the Change Detection Map showing vegetation growth from the K12-K13 section.

#### 4.2 Sant'Apollonia Church

**Sant'Apollonia Church:** The map in Fig. 6 c) shows a brick detachment in conjunction with the pre-existing crack.

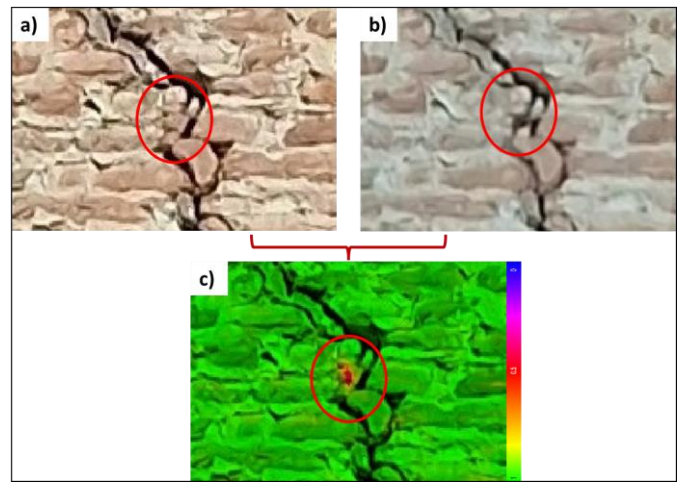


Fig. 6 - Detail of the Change Detection Map showing the brick detachment from the facing wall of Santa Apollonia Church.

**Sant'Apollonia Church:** In the Change Detection map in Fig. 7 c) it is shown, in purple, a mortar detachment connected to a pre-existing crack.

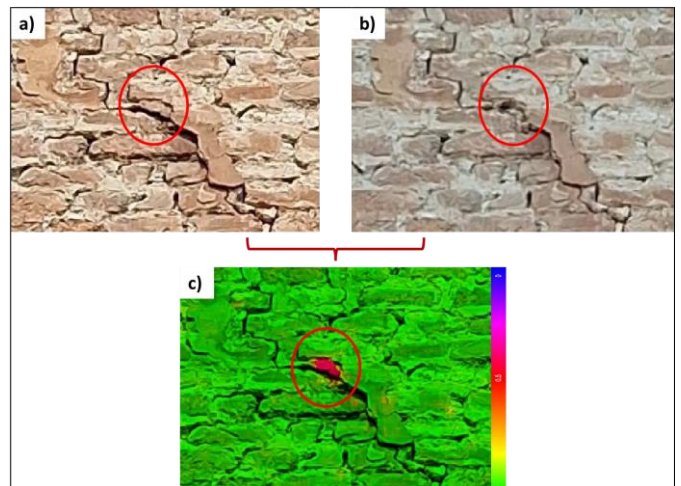


Fig. 7 - Detail of the Change Detection Map showing mortar detachment from the facing wall of Santa Apollonia Church.

## 5 DISCUSSIONS

The results of this study highlight both the effectiveness and the limitations of using mobile devices, such as smartphones and tablets, for environmental and cultural heritage monitoring. A key logistical advantage observed during field activities was the increased speed of repositioning and orienting the sensor when used manually compared to tripod-mounted systems. In this context, the tablet proved more efficient than the tripod-mounted smartphone, allowing for immediate sensor realignment and reducing the time required for data acquisition. This aspect is particularly relevant in scenarios where monitoring must be performed rapidly or in spatially constrained environments, confirming previous findings on the advantages of mobile device-based monitoring methodologies [12].

The type of changes detected by the two sensors was comparable, suggesting that smartphone and tablet cameras can provide similar results in image-based monitoring. However, a critical aspect to consider is pixel size, which depends not only on the intrinsic characteristics of the sensor but also on the distance from the observed object. In field conditions, this distance is often dictated by logistical constraints rather than experimental design, making it a variable that is not always controllable. Since pixel size directly affects the level of detail in image analysis, these factors must be carefully considered when designing a monitoring approach based on mobile sensors. Previous studies on cultural heritage monitoring through crowdsourcing emphasize the importance of such considerations, particularly when comparing images acquired with different devices under varying shooting conditions [13, 25].

Another critical factor influencing data quality was the variability in lighting conditions. Sudden changes in natural light posed challenges for image acquisition, affecting both processing and interpretation of results. This issue is well-documented in the literature, particularly regarding the impact of brightness variations on image-based analyses [25]. In some cases, excessive differences in lighting conditions between successive images introduced artifacts or inconsistencies in the final data, highlighting the need for adaptive calibration techniques or post-processing corrections to minimize these effects.

To address these lighting-related challenges, during this study we experimented with the adjustment of the  $\alpha$ ,  $\beta$ , and  $\gamma$  exponential parameters in the SSIM computation. Fine-tuning these parameters proved effective in minimizing the influence of illumination variation between successive image acquisitions. By reducing the contribution of luminance and contrast inconsistencies, the analysis becomes more sensitive to actual structural changes rather than to superficial alterations induced by light fluctuations. As a result, this approach enhances the robustness of the change detection process by suppressing noise and emphasizing the “true” changes that are structurally relevant to the monitored object.

An alternative but more computationally intensive strategy could involve the use of a redundant analytical framework, leveraging a broader image database for each observation. This would allow for comparative filtering and normalization across multiple acquisitions, thereby reducing the risk of localized errors introduced by individual source images. While this method could significantly improve result stability, it requires higher processing power and longer computation times, which may limit its applicability in real-time or field-based contexts.

Additionally, adjusting the Window Size (WS) also contributed to filtering the results based on the expected scale of the changes of interest. Smaller WS values allowed for detection of fine-grained alterations, while larger WSs enabled the system to disregard minor fluctuations and focus on broader structural modifications. This flexibility supports the customization of the methodology to different conservation goals, depending on whether fine detail or macroscopic patterns

are prioritized. Moreover, the application of photomonitoring for field-based heritage monitoring must also consider several site-specific environmental factors that may compromise the accuracy and interpretability of the results. As discussed in [26], there are a number of additional techniques and methodological improvements that can be adopted to enhance the overall accuracy, precision, and sensitivity of the analysis. However, the effective implementation of these advanced strategies requires careful calibration and expert knowledge, underscoring the importance of involving trained professionals in the design and interpretation of photomonitoring protocols.

Future studies should explore solutions such as High Dynamic Range (HDR) imaging or automated color correction algorithms to mitigate the impact of uncontrollable lighting variations and improve the robustness of mobile-based monitoring techniques. Alternatively, integrating the workflow presented in this study with Citizen Science approaches would enable the collection of large datasets with high temporal resolution, allowing for the calibration of AI models and mitigating the issue of varying lighting conditions and/or shadows.

Despite these challenges, the results demonstrate that effective monitoring can be achieved without the installation of fixed cameras or permanent sensors, relying solely on mobile devices. This outcome is particularly significant in the context of non-invasive cultural heritage monitoring, where minimizing physical interference is often a priority. Similar conclusions have been reached in Citizen Science studies, which emphasize how mobile technology can be leveraged for large-scale data collection while maintaining high methodological rigor [27, 28]. The ability to conduct fully contactless monitoring without requiring pre-installed instrumentation broadens the applicability of these methodologies, particularly in remote or sensitive sites where conventional instrument installation is impractical.

Overall, these findings support the potential of mobile device-based monitoring approaches as viable alternatives to traditional fixed-sensor systems, offering a flexible and scalable solution for environmental and cultural heritage analysis. However, further refinement of data processing techniques is needed to account for environmental variability and ensure consistency across different devices and observational conditions.

## 6 CONCLUSIONS

The primary objective of this study was to assess photomonitoring as a remote sensing technique for the monitoring and preservation of cultural heritage. The results demonstrate that photomonitoring represents an effective and non-invasive approach to detecting structural variations, such as mortar detachment in the masonry of the Aurelian Walls and the Church of Santa Apollonia in Ferrara. The use of widely accessible devices, including smartphones, tablets, and entry-level cameras, makes this methodology not only cost-effective but also adaptable to the specific requirements of different monitored sites.

The potential integration of citizen science into this framework presents a promising opportunity for expanding spatial and temporal data collection. Volunteers, acting as "sensor-visitors," could contribute images and observations that complement the work of professional conservation teams. This collaborative approach has the potential to enhance data coverage, bridging the gaps between scheduled professional surveys and ensuring more continuous monitoring of degradation dynamics. As noted by Bonney et al. [27], citizen science has been successfully implemented across various scientific fields, significantly improving data collection and public engagement. The economic implications of photomonitoring are particularly relevant, considering the extraordinary volume of images generated daily. It is estimated that in 2023, approximately 4.7 billion photographs were taken per day, predominantly using smartphones (93%), resulting in an annual total of approximately 1.8 trillion images. This statistic highlights an immense, yet largely untapped, visual resource that could be harnessed for cultural heritage monitoring. Through crowdsourcing and advanced data analysis, the simple act of taking a photograph can be transformed into a valuable tool for conservation. This approach not only reduces costs but also increases the frequency and geographical coverage of observations. As the quality of images and computational capabilities continue to improve, the integration of citizen-generated data into heritage conservation strategies could evolve into a sustainable and scalable solution [12].

The findings of this study align with a broader context of citizen science initiatives, which have demonstrated dual benefits: enhancing scientific productivity and democratizing research. Unlike basic crowdsourcing, citizen science projects are designed to achieve specific scientific objectives, involving non-expert volunteers in both data collection and analysis [26]. Contributions from participants are not limited to quantitative data but often include qualitative observations, reports of unauthorized interventions, and even personal narratives related to historic sites. As highlighted in studies such as that of Constantinidis [28], these elements provide valuable contextual information that can influence both short-term conservation decisions and long-term management strategies.

Looking ahead, the integration of photomonitoring with structured citizen science programs could be further explored through collaborations with other institutions (i.e. Superintendences for Cultural Heritage), and local governments. A promising development in this direction is the potential use of civil service programs for structured photomonitoring campaigns. By engaging volunteers through civil service initiatives, it would be possible to create systematic and large-scale monitoring efforts that ensure sustained data collection and improved methodological rigor. This approach could also provide training opportunities, fostering a new generation of conservation advocates equipped with digital skills relevant to heritage preservation.

As imaging technologies and computational capabilities continue to advance, the integration of citizen-generated data into professional conservation strategies could evolve into a

sustainable and idely adopted practice. Future research should focus on refining methodologies to optimize data acquisition and processing while exploring policy frameworks that support the ethical and effective implementation of citizen science in heritage conservation. By embracing photomonitoring as a collaborative tool, the preservation of cultural heritage can be made more accessible, inclusive, and resilient to emerging threats.

**Author Contributions:** **Antonio Cosentino:** Writing – original draft (§5), Software, Methodology, Conceptualization, Supervision. **Jessica Clementi:** Writing – original draft (§1; 3; 6), review & editing, Methodology, Conceptualization, Supervision. **Antonio Molinari:** Writing – original draft (§2), data acquisition and analysis, Methodology. **Veronica Sanvito:** Writing – original draft (§4), data acquisition and analysis, Methodology. **Paolo Mazzanti:** Supervision, Funding.

**Acknowledgments:** This study was supported by the Italian Ministry of Culture (MiC), General Directorate for the Safety of Cultural Heritage. The authors wish to acknowledge NHAZCA S.r.l for providing the IRIS software free-of-charge for academic research purposes.

## REFERENCES

- [1] V. S. Alfio, D. Costantino, M. Pepe, Monitoring of a cultural heritage site by Sentinel-2 images and change-detection analysis, *Proc. SPIE 11534, Earth Resources and Environmental Remote Sensing/GIS Applications XI*, 115340X (20 September 2020); <https://doi.org/10.1117/12.2573496>
- [2] M. Mishra, P. B. Lourenço, Artificial intelligence-assisted visual inspection for cultural heritage: State-of-the-art review, *Journal of Cultural Heritage*, 66, 536-550, 2024, ISSN 1296-2074, <https://doi.org/10.1016/j.culher.2024.01.005>.
- [3] Y. Tzortzis, I. Rallis, K. Makantasis, A. Doulamis, N. Doulamis, & A. Voulodimos, Automatic Inspection of Cultural Monuments Using Deep and Tensor-Based Learning on Hyperspectral Imagery, 3136-3140, 2022; 10.1109/ICIP46576.2022.9897527.
- [4] C. Zafeiropoulos, Y. Tzortzis, I. Rallis, E. Protopapadakis, N. Doulamis, & A. Doulamis, Evaluating the Usefulness of Unsupervised Monitoring in Cultural Heritage Monuments, 2021; 10.3233/FAIA210086.
- [5] Y. Liu, Y. Wang, & Ch. Liu, A Deep-Learning Method Using Auto-encoder and Generative Adversarial Network for Anomaly Detection on Ancient Stone Stele Surfaces, 2023; 10.48550/arXiv.2308.04426.
- [6] M. Bahrami, & A. Albadvi; Deep Learning for Identifying Iran's Cultural Heritage Buildings in Need of Conservation Using Image Classification and Grad-CAM, 2023; 10.48550/arXiv.2302.14354
- [7] A. Cosentino, A. Brunetti, M. Fiorio, M. Gaeta, & P. Mazzanti, IRIS a new powerful tool for Geohazards Assessment by PhotoMonitoring. In: *Proc. of ASITA Conf.*, pp. 119-122, 2022.
- [8] F. Mugnai, A. Cosentino, P. Mazzanti, G. Tucci, Vibration Analyses of a Gantry Structure by Mobile Phone Digital Image Correlation and Interferometric Radar, *Geomatics* 2, pp. 17-35, 2022; <https://doi.org/10.3390/geomatics2010002>



- [9] G. Mastrantoni, G. Santicchia, A. Cosentino, A. Molinari, G.M. Marmoni, & P. Mazzanti, Automatic Photomonitoring Analysis for Spatiotemporal Evaluation of Rockfall Failure Hazard, SSRN, 2024; <https://dx.doi.org/10.2139/ssrn.4824216>
- [10] A. Cosentino, G.M. Marmoni, M. Fiorucci, P. Mazzanti, G. Scarascia Mugnozza & C. Esposito, Optical and Thermal Image Processing for Monitoring Rainfall Triggered Shallow Landslides: Insights from Analogue Laboratory Experiments, Remote Sensing 15, 5577, 2023; <https://doi.org/10.3390/rs15235577>
- [11] J. Shivottam, & S. Mishra, Tirtha -- An Automated Platform to Crowdsourcing Images and Create 3D Models of Heritage Sites, 2023; 10.48550/arXiv.2308.01246.
- [12] R. Brigham, S. Orr, L. Wilson, A. Frost, M. Strlič, & J. Grau-Bové, Using Citizen Heritage Science to Monitor Remote Sites Before and During the First COVID-19 Lockdown: A Comparison of Two Methods. Conservation and Management of Archaeological Sites, 24, 1-16, 2022; 10.1080/13505033.2022.2147299.
- [13] P. Kumar, Crowdsourcing to rescue cultural heritage during disasters: A case study of the 1966 Florence Flood, International Journal of Disaster Risk Reduction 43, 2020, 101371.
- [14] D.Lu, P.Mausel, E. Brondizio, & E.Moran, Change detection techniques. International Journal of Remote Sensing, 25(12), 2365–2401, 2004, <https://doi.org/10.1080/0143116031000139863>.
- [15] A. Asokan, J.Anitha, Change detection techniques for remote sensing applications: a survey. Earth Sci Inform 12, 143–160, 2019, <https://doi.org/10.1007/s12145-019-00380-5>.
- [16] U.Sara, M.Akter, M.S.Uddin, Image Quality Assessment through FSIM, SSIM, MSE and PSNR - A Comparative Study. Journal of Computer and Communications 7, 8-18, 2019, <https://doi.org/10.4236/jcc.2019.73002>.
- [17] Z.Wang, A.C.Bovik, A universal image quality index. IEEE Signal Processing Letters 9, 81–84, 2002, <https://doi.org/10.1109/97.995823>.
- [18] D.Kim, A.S.Balasubramaniam, I.Gratchev, S.R.Kim, & S H.Chang, Application of image quality assessment for rockfall investigation. In 16th Asian Regional Conference on Soil Mechanics and Geotechnical Engineering (ARC 2019). Southeast Asian Geotechnical Society (SEAGS), 2019
- [19] G. Caneva, & A. Roccardi, Harmful Flora in the Conservation of Roman Monuments. In: Proceedings of the International Conference on Biodeterioration of Cultural Property, Lucknow (India). ICCROM-INTAC, pp. 212–218, 1989.
- [20] G. Caneva, G. De Marco, A. Dinelli, & M. Vinci, The wall vegetation of the roman archaeological areas. Sci. Technol. Cult. Herit. 1, 217–226, 1992.
- [21] F. Bartoli, F. Romiti, & G. Caneva, Aggressiveness of Hedera helix L. growing on monuments: evaluation in Roman archaeological sites and guidelines for a general methodological approach. Plant Biosystems-An International Journal Dealing with all Aspects of Plant Biology 151 (5), 866–877, 2017; <https://doi.org/10.1080/>
- [22] G. Trotta, V. Savo, F. Cicinelli, M. Carboni, & G. Caneva, Colonization and damages of Ailanthus altissima (Mill.) Swingle on archaeological structures: Evidence from the Aurelian Walls in Rome (Italy), International Biodeterioration & Biodegradation, Volume 153, 105054, 2020, <https://doi.org/10.1016/j.ibiod.2020.105054>.
- [23] D. Esposito, M. Fabbri, F. Giovanetti, M. Medri, [...] (eds.), Le Mura Aureliane nella storia di Roma-1. Da Aureliano a Onorio. Roma TrE-Press, 2017.
- [24] A. Molinari, D. Esposito, F. Pallottino, F.Giovanetti, [...] (eds.), Le Mura Aureliane nella storia di Roma. 2. Da Onorio a Niccolò V, Roma TrE-Press, 2023.
- [25] M. A. Barbero-Álvarez, J. M. Menéndez & J. A. Rodrigo, An Adaptive Colour Calibration for Crowdsourced Images in Heritage Preservation Science, in IEEE Access, vol. 8, pp. 185093-185111, 2020, doi: 10.1109/ACCESS.2020.3017390.
- [26] Cosentino, A., Brunetti, A., & Mazzanti, P. (2024). Photomonitoring as a Tool for Monitoring Landslides: A Technology within Everyone's Reach. Transportation Research Record, 2679(2), 1667-1675. <https://doi.org/10.1177/03611981241270173>
- [27] R. Bonney, C. B. Cooper, J. Dickinson, S. Kelling, T. Phillips, K. V. Rosenberg & J. Shirk, Citizen Science, A Developing Tool for Expanding Science Knowledge and Scientific Literacy, BioScience, Volume 59, Issue 11, 977–984, December 2009.
- [28] D. Constantinidis, Crowdsourcing Culture: Challenges to Change. In: Borowiecki, K., Forbes, N., Fresa, A. (eds) Cultural Heritage in a Changing World. Springer, Cham, 2016. [https://doi.org/10.1007/978-3-319-29544-2\\_13](https://doi.org/10.1007/978-3-319-29544-2_13)

# Correlation of natural frequencies of bridges that are under similar environmental conditions.

Ellie Swaile-Blemmings<sup>1</sup>, David Hester<sup>1</sup>, Connor O'Higgins<sup>1</sup>, Su Taylor<sup>1</sup>, Roger Woods<sup>2</sup>, Elizabeth J. Cross<sup>3</sup>

<sup>1</sup>School of Natural and Built Environment, Queen's University Belfast, David Keir Building, Stranmillis Road, Belfast, BT9 5AG, UK

<sup>2</sup>School of Electronics, Electrical Engineering, and Computer Science, Ashby Building, Stranmillis Road, Belfast, BT9 5AG, UK

<sup>3</sup>School of Mechanical Engineering, Sheffield University, Mappin Street, Sheffield, S1 3JD, UK

email: [eswaileblemmings01@qub.ac.uk](mailto:eswaileblemmings01@qub.ac.uk), [d.hester@qub.ac.uk](mailto:d.hester@qub.ac.uk), [c.ohiggins@qub.ac.uk](mailto:c.ohiggins@qub.ac.uk), [s.e.taylor@qub.ac.uk](mailto:s.e.taylor@qub.ac.uk),  
[r.woods@qub.ac.uk](mailto:r.woods@qub.ac.uk), [e.j.cross@sheffield.ac.uk](mailto:e.j.cross@sheffield.ac.uk)

**ABSTRACT:** While Structural Health Monitoring (SHM) has potential to aid bridge managers, its adoption has been limited, with one of the challenges being determining a bridge's condition without a historical reference point for that structure. Researchers have started investigating Population-Based Structural Health Monitoring (PBSHM) to tackle this, facilitating the sharing of data from comparable structures. The key advantage of PBSHM is that it potentially enables us to use data from one structure to make inferences about the health of another structure in the same population.

Whilst, to date, populations that have been used for PBSHM have been defined using structural similarities alone, you might be missing out on information that could be useful for bridge managers, which raises the question: Could we define populations in a different way? This research investigates if it is potentially useful to define a population of bridges based on whether they experience the same environmental conditions. To answer this, long-term natural frequency data from two bridges close to each other are analysed to determine the level of correlation between them. This work shows that it may be potentially useful to define populations based on factors other than structural similarities, which allows greater opportunities for PBSHM.

**KEY WORDS:** Structural Health Monitoring (SHM); Population-Based Structural Health Monitoring (PBSHM); Bridge Monitoring; Natural Frequencies; Environmental Effects; Correlation Analysis; Temperature Influence; Vibration Data; Graph-Based Structural Similarity; Machine Learning in SHM.

## 1 INTRODUCTION

### 1.1 Challenges in current bridge inspection

Bridges are vital pieces of infrastructure, enabling the movement of goods and people [1]. Currently, bridges are monitored primarily through periodic visual inspections, which provide valuable insights. However, these visual inspections can be subjective, and some defects, such as internal cracks or corrosion, may not be visible during routine inspections.

In the worst-case scenario, undetected structural deficiencies can lead to catastrophic bridge failures, resulting in substantial financial costs and loss of life. For example, in 2018 the Morandi Bridge failed, killing 43 [2]. Additionally, the subjectivity of visual inspections makes it challenging to efficiently allocate limited resources. In 2024, the Carola Bridge in Dresden, Germany, collapsed due to hydrogen-induced stress corrosion cracking in the bridge's steel components [3]. The aftermath of the collapse can be seen in Figure 1. This type of corrosion began during the bridge's construction between 1967 and 1971 and progressed internally over decades, remaining undetectable through standard visual inspections. The eventual collapse of the Carola Bridge is a good example of highlighting a significant limitation of traditional monitoring methods.

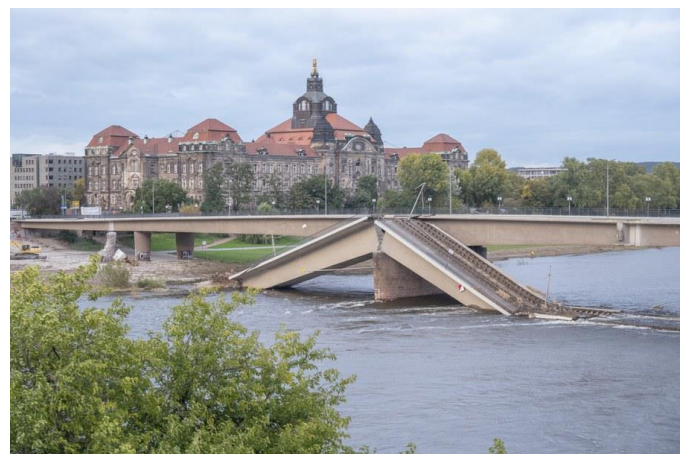


Figure 1. Carola Bridge (Dresden, 1971).

### 1.2 Background on Structural Health Monitoring (SHM)

Over the past 30 years, there has been increasing interest in using quantitative data, such as acceleration or displacement, to assess bridge health, a practice known as Structural Health Monitoring (SHM) [4]. Its widespread adoption has been limited, however, with one of the challenges being determining whether a bridge is healthy or damaged without a historical reference point for that structure. This process is challenging because SHM systems often rely on baseline data to detect structural deterioration. If you do not take measurements from the 'healthy' state, it is difficult to determine the difference between normal changes (caused by things like weather or traffic) and real damage, which raises the risk of false alarms or missed defects [4].

### 1.3 Overview of Population-Based Structural Health Monitoring (PBSHM) to date and current limitations

Researchers have begun exploring Population-Based Structural Health Monitoring (PBSHM) as a solution to address the challenges in traditional SHM, enabling the sharing of data across comparable structures. It allows data from one structure to be used to make inferences about the health of another structure within the same ‘population’ [5].

The foundations of PBSHM have been established through a series of published papers *Towards Population-Based Structural Health Monitoring* [6, 5, 7, 8, 9, and 10]. These papers examine methods for representing structures as graphs and developing similarity measures to compare them.

PBSHM extends traditional SHM by focusing on monitoring populations of structures rather than individual assets. Unlike conventional SHM, which relies on baseline data for a single structure, PBSHM enables the transfer of knowledge across a group of similar structures. By leveraging data from one structure, engineers can make inferences about the condition of others within the population, helping to mitigate the challenge of missing baseline data [5].

However, for PBSHM to be effective, the population must consist of sufficiently similar structures. If the differences are too significant, knowledge transfer may become inaccurate, leading to negative transfer; indeed, the application of insights from one structure can act to introduce error rather than improving understanding [7].

In practice, populations of bridges in PBSHM are typically formed by identifying structures that are structurally similar. For instance, Gosliga et al. [11] identified a pair of similar truss footbridges and a group of two beam-and-slab bridges. These bridges were represented as graphs, and using a graph matching algorithm, a high similarity metric was observed. Following field testing, the authors compared their dynamic responses and confirmed that the frequencies and mode shapes of bridges identified as similar through graph matching were indeed consistent [12].

If populations are defined solely based on structural information, potentially valuable factors that could aid in SHM might be overlooked. This raises the question: Could populations be defined differently? For example, a population could include bridges within the same geographical area, meaning they would be subject to the same environmental conditions. While populations in PBSHM have thus far been considered based on structural similarity, exploring alternative conceptualisations of populations may prove to be equally useful.

### 1.4 Contribution of this work

To explore whether bridges located in close proximity and therefore notionally experiencing the same environmental conditions could potentially form a population, long-term natural frequency data from two bridges 540 metres apart were analysed to determine the level of correlation between them. The results suggest that defining populations based on factors other than structural similarities could be potentially valuable, offering greater opportunities for PBSHM.

## 2 BRIDGE SITES USED AND TEMPERATURE CORRELATION BETWEEN SITES

### 2.1 Bridge selection and data collection

For this study, two bridges located 540 metres apart along the same river were selected. Bridge 1 is a 98-metre-long, 27-metre-wide bowstring girder bridge (Figure 2a), while Bridge 2 is a 76-metre-long, three-span composite concrete and steel bridge (Figure 2b). The proximity of these bridges allowed for a controlled investigation of how environmental factors influenced their dynamic behaviour.

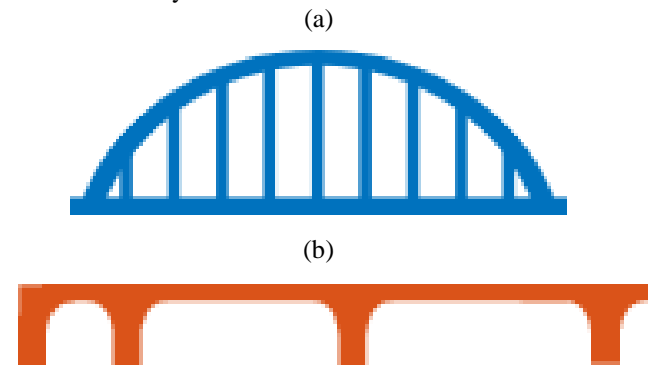


Figure 2. (a) Schematic of Bridge 1 (b) Schematic of Bridge 2.

As described by O’Higgins et al. [13], long-term vibration data was collected using a single accelerometer on each bridge. It was observed that positioning the sensor near the quarter-span point on both bridges allowed it to detect most modes and frequencies.

The Structural Health Monitoring (SHM) system used for long-term monitoring consisted of one MEMS accelerometer and one environmental sensor. The accelerometer employed was the Multifunction Extended Life (MEL) Data Logger from Gulf Coast Data Concepts. This accelerometer was housed in an enclosure, which was then attached to the deck of each bridge. One of these enclosures is shown in Figure 3.

The environmental variables were measured using an environmental sensor capable of recording both air temperature and humidity. To ensure accurate temperature readings, the sensors were not placed within the enclosure to avoid the effects of solar gain. Instead, they were positioned out of direct sunlight to provide a representative measure of the local air temperature. On each bridge, the temperature sensors were placed on the abutment shelf or at the base of an abutment, both out of direct sunlight.

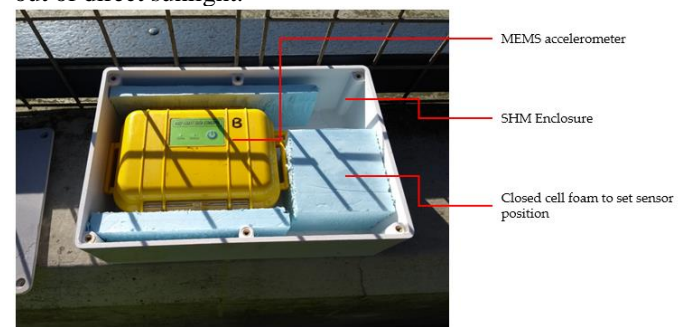


Figure 3. Monitoring enclosure and MEL data.



## 2.2 Correlation of temperature data

A key objective of this study was to determine whether the two bridges experienced similar environmental conditions. To assess this, temperature data from both bridges were compared using a hexbin plot (Figure 4). A hexbin plot is a 2D histogram where the bins are hexagonal, and the colour intensity represents the number of data points within each bin.

Figure 4 shows a strong positive correlation between the temperature measurements of both bridges, with a correlation coefficient of 0.98, indicating that higher temperatures on Bridge 2 correspond to higher temperatures on Bridge 1. This suggests that the two bridges experience nearly identical environmental exposure.

However, some variability was observed between January 6 and February 17, during which Bridge 1 exhibited slightly higher temperatures in the 0-5°C and 5-10°C ranges. The cause of these anomalies remains uncertain, but potential explanations include differential shading and differences in material thermal properties.

While these discrepancies are noticeable in the plot, they do not significantly impact the overall trend. There are up to 14,000 data points in the yellow bins and fewer than 2,000 data points in the dark blue bins, reinforcing the stability of the best-fit line. This indicates that most of the data follows a linear relationship, with only a brief period showing anomalous values.

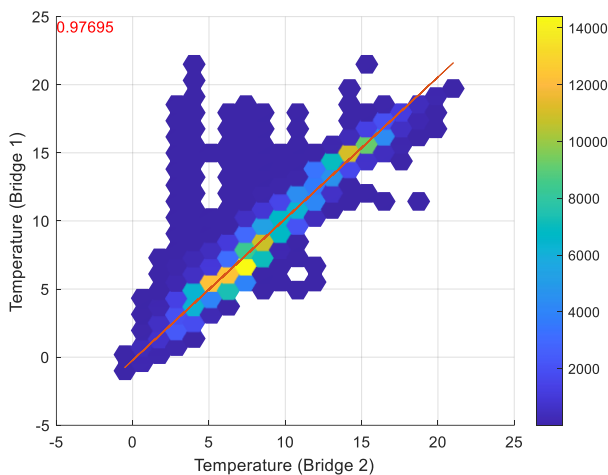


Figure 4. Temperature data from Bridge 1 versus temperature data from Bridge 2.

## 3 NATURAL FREQUENCY ANALYSIS

### 3.1 Extraction of Natural Frequency

As per O'Higgins et al. [13], acceleration data was segmented into 30-minute intervals and processed using the Stochastic Subspace Identification (SSI) method to extract the bridge frequencies. The data was recorded from October 2018 to May 2021, though some gaps occurred due to limited personnel availability for data collection and disruptions caused by the COVID-19 pandemic.

For this work, a simple outlier analysis was undertaken on natural frequency data so that the complexity of data analysis was reduced and data visualisation was clearer. Any data point that was more than three scaled median absolute deviations from the median of the data was removed.

### 3.2 Time-domain work

Figure 5 presents the time-series data for the natural frequencies of both bridges. Bridge 1 exhibits five natural frequencies ranging from approximately 1.2 Hz to 5.2 Hz, while Bridge 2 has five natural frequencies ranging from approximately 2.7 Hz to 9.3 Hz. Overall, Bridge 2 demonstrates higher frequency values compared to Bridge 1.

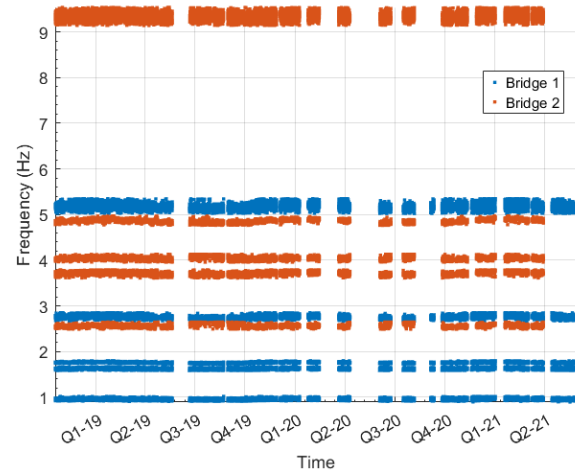


Figure 5. All frequency data over the whole monitoring period.

Figure 6 consists of two subplots, both illustrating the relationship between bridge frequencies and temperature over time. Frequency and temperature are plotted against the left and right vertical axes, respectively.

In plot (a), the temperature (purple line) exhibits seasonal variations, with distinct peaks and troughs. When analysing annual data, a seasonal trend is observed for frequency 5 of Bridge 1 and frequency 4 of Bridge 2, with evidence of an inverse correlation between the frequencies and temperature. Additionally, Bridge 1 and Bridge 2 appear correlated, with both bridges showing an inverse relationship with temperature on an annual scale.

In plot (b), which focuses on daily temperature cycles, there is some correlation between the two frequencies. As seen in plot (a), higher temperatures correspond to lower frequency values, a trend that is even more noticeable in plot (b). This aligns with expectations, as increasing temperature may cause a reduction in structural stiffness, leading to lower natural frequencies [14].

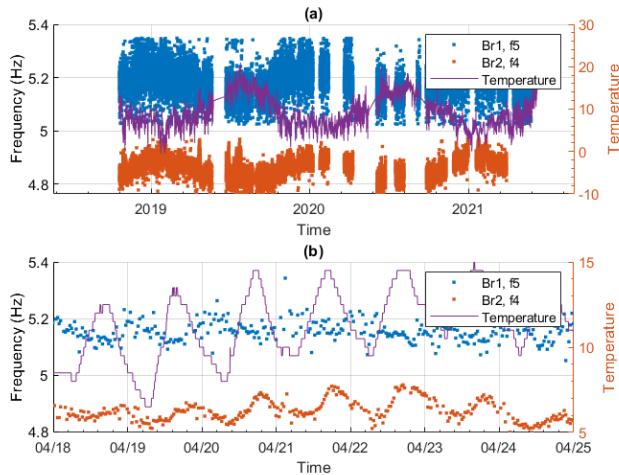


Figure 6. Frequency 5 of Bridge 1 and frequency 4 of Bridge 2 (a) Whole monitoring period (b) A week of monitoring data.

### 3.3 Frequency correlation work

Figure 7 presents hexbin plots for all the frequencies of Bridges 1 and 2, with the correlation coefficient displayed in the top left

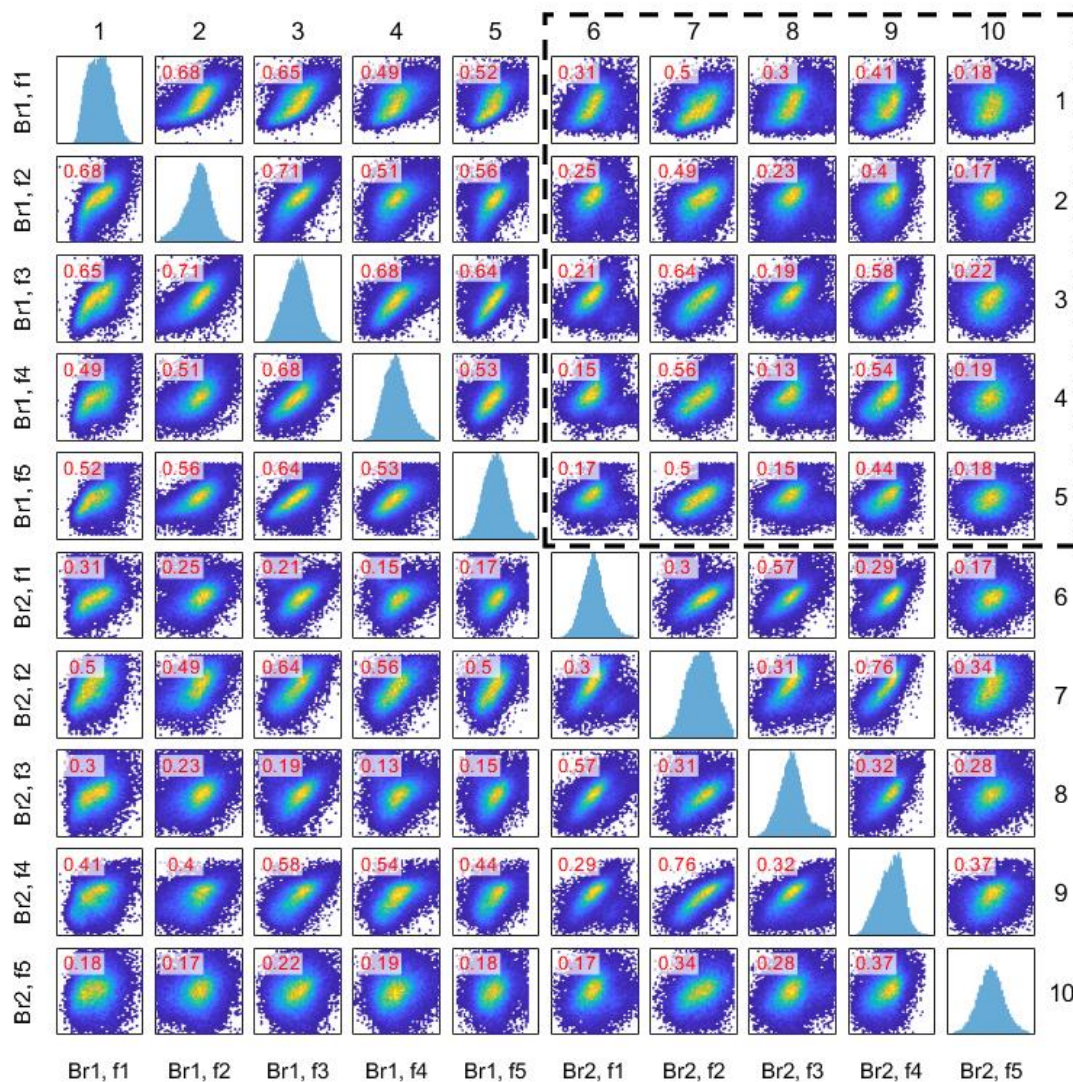


Figure 7. All correlation plots for all the frequencies.

corner of each plot. The histograms on the diagonal illustrate the distribution of each frequency.

The figure reveals a strong correlation between frequencies within the same bridge (rows 1-5, columns 1-5). However, the most relevant information is in the top right section of the figure, highlighted by a dashed black box, which shows the correlation between frequencies of Bridge 1 and Bridge 2. The column references (1 to 10) are displayed at the top, while the row references are shown on the right.

For example, the plot in row 1, column 6 represents the correlation between frequency 1 of Bridge 1 and frequency 1 of Bridge 2, with a correlation coefficient of 0.31, indicating a relatively weak correlation. Similarly, the plot in row 1, column 7 shows the correlation between frequency 1 of Bridge 1 and frequency 2 of Bridge 2, with a coefficient of 0.5. A zoomed-in view of the area inside the dashed black box in Figure 7 is shown in Figure 8. Figure 8 illustrates the varying correlations between frequencies, with correlation coefficients ranging from 0.13 to 0.64.



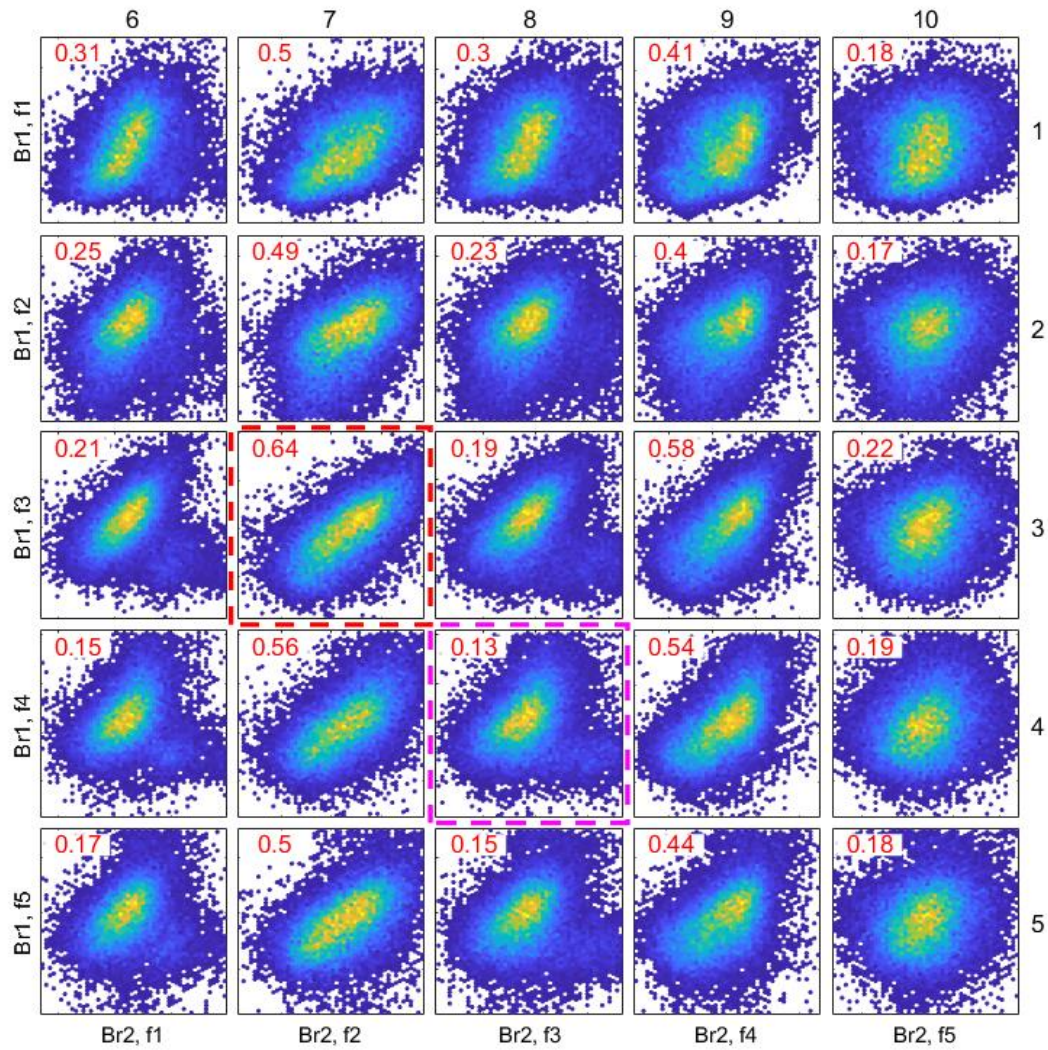


Figure 8. Correlation between pairs of frequencies in Bridge 1 and Bridge 2.

The highest correlation of 0.64 is observed between frequency 3 of Bridge 1 and frequency 2 of Bridge 2 (shown in row 3, column 7 in the dashed red box in Figure 8), and this is shown on a larger scale in Figure 9.

The lowest correlation of 0.13 is observed between frequency 4 of Bridge 1 and frequency 3 of Bridge 2 (shown in row 4, column 8 in the dashed magenta box in Figure 8), and this is shown on a larger scale in Figure 10.

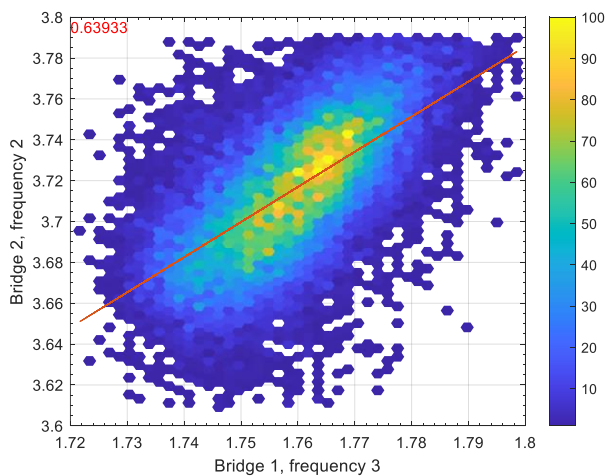


Figure 9. Most correlation between frequencies.

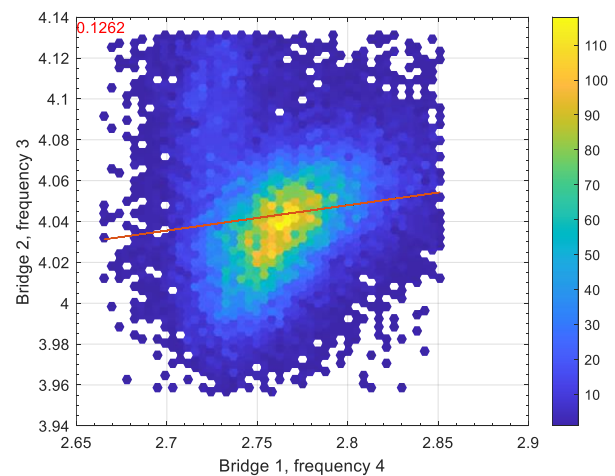


Figure 10. Least correlation between frequencies.



Having identified the pair of frequencies with the highest correlation (Figure 9) and the lowest correlation (Figure 10), we now look at the time series plots associated with these frequencies to try and get further insight into why some are better correlated than others. To this end, Figure 11 presents the pair of frequencies with the highest correlation, specifically frequency 3 of Bridge 1 (plotted against the left-hand vertical axis) and frequency 2 of Bridge 2 (plotted against the right-hand vertical axis). Plot (a) displays data spanning the entire monitoring period from October 2018 to May 2021, while plot (b) focuses on a 7-day period. The strong correlation between these frequencies is evident from the synchronised sinusoidal patterns observed in both bridges.

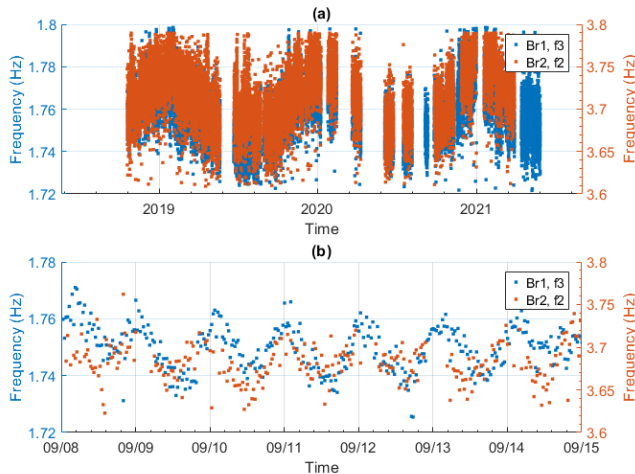


Figure 11. Frequency 3 of Bridge 1 and frequency 2 of Bridge 2 (a) Whole monitoring period (b) A week of monitoring data.

Figure 12 shows the least correlated frequencies between both bridges, specifically frequency 4 of Bridge 1 and frequency 3 of Bridge 2. This figure follows the same format as Figure 11, with the overall monitoring period shown in plot (a) and the same 7-day period shown in plot (b). When plotted as a time series, these natural frequencies exhibit a lower correlation to those shown in Figure 11, which is consistent with the expectations based on the hexbin plot in Figure 10.

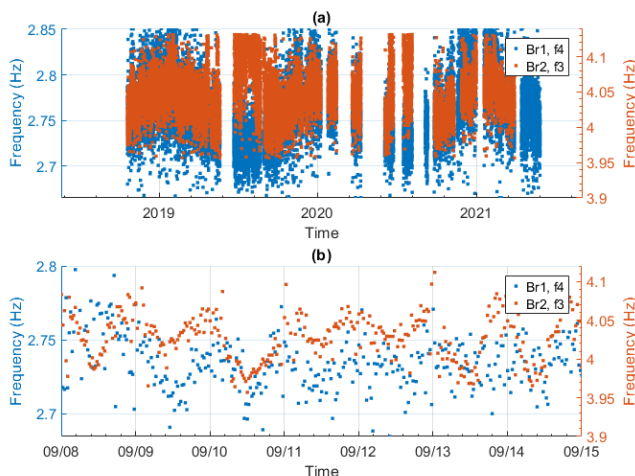


Figure 12. Frequency 4 of Bridge 1 and frequency 3 of Bridge 2 (a) Whole monitoring period (b) A week of monitoring data.

## 4 CONCLUSION

Temperature data from two bridges located near each other shows a strong correlation (with a correlation coefficient of 0.98), suggesting that the bridges experience similar environmental conditions. The natural frequencies of the two bridges also exhibit significant correlation, with coefficient values for some pairs of frequencies reaching up to 0.64. Traditionally, Population-Based Structural Health Monitoring (PBSHM) has defined populations based on structural similarities. This paper suggests the potential for defining populations based on shared environmental conditions. Given the sufficient correlation in temperature and frequency data, it may be possible to infer information about Bridge 1 based on the data collected from Bridge 2. This will be further explored in future work through correlation analysis, such as cointegration on the data.

Future studies will examine a wider range of bridge types to determine whether the same correlations apply. Additional research could also explore the conditions under which these correlations remain valid and when they begin to break down.

## ACKNOWLEDGMENTS

The authors gratefully acknowledge the support of the UK Engineering and Physical Sciences Research Council (EPSRC) through the full-time research studentship and the ROSEHIPS project (Grant EP/W005816/1).

## REFERENCES

- [1] Chen, W.-F., & Duan, L. (Eds.). (2014). *Bridge engineering handbook* (Second edition). Taylor & Francis.
- [2] Calvi, G. M., Moratti, M., O'Reilly, G. J., Scattarreggia, N., Monteiro, R., Malomo, D., Calvi, P. M., & Pinho, R. (2019). Once upon a Time in Italy: The Tale of the Morandi Bridge. *Structural Engineering International*, 29(2), 198–217. <https://doi.org/10.1080/10168664.2018.1558033>
- [3] Marx, S. (2024). Investigation Report on the Carola Bridge Collapse. Technical University of Dresden.
- [4] Farrar, C. R., & Worden, K. (2012). *Structural Health Monitoring: A Machine Learning Perspective*. John Wiley & Sons.
- [5] Gardner, P., Bull, L. A., Gosliga, J., Dervilis, N., & Worden, K. (2020). Towards Population-Based Structural Health Monitoring, Part IV: Heterogeneous Populations, Transfer and Mapping. In Z. Mao (Ed.), *Model Validation and Uncertainty Quantification, Volume 3* (pp. 187–199). Springer International Publishing. [https://doi.org/10.1007/978-3-030-47638-0\\_20](https://doi.org/10.1007/978-3-030-47638-0_20)
- [6] Bull, L. A., Gardner, P. A., Gosliga, J., Dervilis, N., Papatheou, E., Maguire, A. E., Campos, C., Rogers, T. J., Cross, E. J., & Worden, K. (2020). Towards Population-Based Structural Health Monitoring, Part I: Homogeneous Populations and Forms. In Z. Mao (Ed.), *Model Validation and Uncertainty Quantification, Volume 3* (pp. 287–302). Springer International Publishing. [https://doi.org/10.1007/978-3-030-47638-0\\_32](https://doi.org/10.1007/978-3-030-47638-0_32)
- [7] Gosliga, J., Gardner, P., Bull, L. A., Dervilis, N., & Worden, K. (2021). Towards Population-Based Structural Health Monitoring, Part II: Heterogeneous Populations and Structures as Graphs. In B. Dilworth & M. Mains (Eds.), *Topics in Modal Analysis & Testing, Volume 8* (pp. 177–187). Springer International Publishing. [https://doi.org/10.1007/978-3-030-47717-2\\_17](https://doi.org/10.1007/978-3-030-47717-2_17)
- [8] Worden, K. (2021). Towards Population-Based Structural Health Monitoring, Part VI: Structures as Geometry. In S. Pakzad (Ed.), *Dynamics of Civil Structures, Volume 2* (pp. 221–236). Springer International Publishing. [https://doi.org/10.1007/978-3-030-47634-2\\_26](https://doi.org/10.1007/978-3-030-47634-2_26)
- [9] Lin, W., Worden, K., Eoghan Maguire, A., & Cross, E. J. (2021). Towards Population-Based Structural Health Monitoring, Part VII: EOVS Fields – Environmental Mapping. In B. Dilworth & M. Mains (Eds.), *Topics in Modal Analysis & Testing, Volume 8* (pp. 297–304). Springer International Publishing. [https://doi.org/10.1007/978-3-030-47717-2\\_31](https://doi.org/10.1007/978-3-030-47717-2_31)
- [10] Brennan, D. S., Gosliga, J., Cross, E. J., & Worden, K. (2025). Foundations of population-based SHM, Part V: Network, framework and

- database. *Mechanical Systems and Signal Processing*, 223, 111602. <https://doi.org/10.1016/j.ymssp.2024.111602>
- [11] Gosliga, R. V. D., Worden, K., & Cross, E. J. (2022). Identifying similar structures for population-based structural health monitoring. *Journal of Bridge Engineering*, 27(1), 04021003. [https://doi.org/10.1061/\(ASCE\)BE.1943-5592.0001748](https://doi.org/10.1061/(ASCE)BE.1943-5592.0001748)
- [12] Bunce, A., Brennan, D. S., Ferguson, A., O'Higgins, C., Taylor, S., Cross, E. J., Worden, K., Brownjohn, J., & Hester, D. (2024). On population-based structural health monitoring for bridges: Comparing similarity metrics and dynamic responses between sets of bridges. *Mechanical Systems and Signal Processing*, 216, 111501. <https://doi.org/10.1016/j.ymssp.2024.111501>
- [13] O'Higgins, C., Hester, D., McGetrick, P., Cross, E. J., Ao, W. K., & Brownjohn, J. (2023). Minimal Information Data-Modelling (MID) and an Easily Implementable Low-Cost SHM System for Use on a Short-Span Bridge. *Sensors*, 23(14), 6328. <https://doi.org/10.3390/s23146328>
- [14] Farrar, C. R., & Worden, K. (2007). An introduction to structural health monitoring. *Philosophical Transactions of the Royal Society A: Mathematical, Physical and Engineering Sciences*, 365(1851), 303–315. <https://doi.org/10.1098/rsta.2006.1928>

# A Novel AI-Wavelet Based Framework for Benchmark Data Analysis in Structural Health Monitoring

Ahmed Silik<sup>1</sup>, [ORCID](#), Mohammad Noori<sup>1,2,5</sup>, [ORCID](#), Nabeel S. D. Farhan<sup>3</sup>, [ORCID](#), Tianyu Wang<sup>4</sup>, Wael A. Altabey<sup>1</sup>, Zhishen Wu<sup>1</sup>

<sup>1</sup>School of Civil Engineering and Architecture, Henan University of Technology, Zhengzhou, China

<sup>2</sup>Mechanical Engineering Department, California Polytechnic State University, San Luis Obispo, California

<sup>3</sup>School of Civil Engineering, Southeast University, Nanjing, China

<sup>4</sup>School of Urban Construction and Safety Engineering, Shanghai Institute of Technology, Shanghai, China

<sup>5</sup>School of Civil Engineering, University of Leeds, Leeds, UK

email: silikth@gmail.com, mnoori52@yahoo.com, eng.nabeel.saeed@gmail.com

**ABSTRACT:** Structural Health Monitoring (SHM) plays a vital role in ensuring the safety, durability, and operational efficiency of critical infrastructure. Traditional SHM methods often fall short in detecting subtle damage patterns, particularly when faced with noisy signals, missing data, or the complex, time-varying behavior of real-world structures. To address these challenges, this study presents a hybrid framework that integrates Discrete Wavelet Transform (DWT) with a deep learning architecture combining Convolutional Neural Networks (CNN) and Long Short-Term Memory (LSTM) networks. The proposed approach begins by segmenting long-duration acceleration signals into fixed-length windows and applying DWT to extract informative time–frequency features. CNN layers are then used to learn spatial representations from the transformed data, while LSTM layers capture temporal dependencies critical for detecting structural changes over time. The model is trained and evaluated using benchmark SHM datasets under both healthy and damaged states. Moreover, supervised learning is utilized for accurate damage severity classification, while unsupervised learning is used to facilitate anomalies detection without relying on labeled samples. Experimental results demonstrate improved performance in classifying damage conditions compared to conventional machine learning approaches. This framework offers a robust and scalable solution for data-driven SHM, supporting more accurate diagnostics and paving the way for predictive maintenance in complex monitoring environments.

**KEY WORDS:** SHM; Deep Learning; Damage Detection; Wavelet; Hybrid AI Models.

## 1 INTRODUCTION

Structural Health Monitoring (SHM) has become an essential field across civil, mechanical, and aerospace engineering, ensuring the functionality, longevity, and safety of critical infrastructure. SHM enables periodic or continuous assessment of structural performance and supports the early detection of system degradation. This allows for timely maintenance interventions and reduces the risk of unexpected failures. As infrastructure systems age and endure increasing stress from environmental and operational loads, effective SHM plays a crucial role not only in ensuring safety but also in optimizing life-cycle costs and extending service life.

Over the past few decades, SHM has evolved significantly, with numerous techniques developed to detect and assess damage and degradation in critical infrastructure. Conventional SHM approaches frequently rely on manual feature extraction, threshold-based anomaly detection, and classical signal processing techniques such as the Fast Fourier Transform (FFT) and Principal Component Analysis to extract frequency-domain features and reduce data dimensionality [1]. While these methods have demonstrated effectiveness in controlled environments or specific applications, they often struggle in real-world conditions where non-stationary signals, sensor noise, and data loss are prevalent. Moreover, they are often inadequate for capturing the complexity of real-world structures, particularly those exhibiting nonlinear and time-varying behavior. The reliance on expert-defined thresholds and manual feature selection further limits their scalability and suitability for automated or large-scale SHM deployment. These limitations underscore the need for more adaptive,

intelligent, and data-driven SHM methodologies capable of handling the dynamic behavior of structural systems.

To address these limitations, classical machine learning (ML) methods such as Decision Trees, k-Nearest Neighbors (k-NN), and Support Vector Machines (SVM) have been progressively applied to SHM tasks such as damage detection and anomaly classification [2]. These models offer greater adaptability than rule-based techniques and have shown effectiveness in certain SHM scenarios. However, they largely depend on handcrafted or engineered features, which may fail to capture the full complexity of structural responses. Also, classical ML algorithms often struggle with noisy, sequential data, or high-dimensional, limiting their scalability and generalizability in complex monitoring environments.

In response to the limitations of classical machine learning approaches, deep learning techniques have gained significant attention in SHM due to their ability to automatically learn hierarchical and abstract representations from raw sensor data. Models such as Convolutional Neural Networks (CNNs), Recurrent Neural Networks (RNNs), and their variants have shown promising results in tasks such as damage localization, classification, and prognostics. Unlike traditional methods, deep learning (DL) models can effectively capture nonlinear, time-dependent patterns in complex vibration signals without the need for manual feature engineering. Their robustness to noise, scalability to large datasets, and suitability for end-to-end learning make them especially well-suited for real-world SHM system operating under dynamic and uncertain conditions.

More recently, DL models, mainly CNNs and Long Short-Term Memory (LSTM) networks have demonstrated notable



success in processing spatial and temporal data for SHM applications. CNNs are well-suited for extracting spatial features from raw sensor data or transformed representations such as spectrograms [3], while LSTMs effectively model long-term dependencies in time-series signals [4]. Several studies have also proposed hybrid CNN–LSTM frameworks that jointly capture spatial and temporal patterns, resulting in improved damage detection accuracy, especially in complex structural systems [5].

Despite these advancements, significant challenges remain in applying AI to SHM, including the presence of noise, missing data, and the continued need for domain-specific feature engineering. Furthermore, many existing AI-based SHM approaches tend to overlook the advantages of time–frequency domain analysis an essential component for capturing complex, transient structural responses [6]. To address this gap, wavelet transforms have garnered significant attention in SHM due to their ability to localize features simultaneously in both the time and frequency domains. Unlike the FFT, which provides only a global view of frequency content, wavelet analysis enables the detection of localized, transient events such as those caused by impact damage or cracking [7]. The Discrete Wavelet Transform (DWT) has been widely used for feature extraction, denoising, and time–frequency characterization in structural vibration signals.

However, wavelet-based methods typically require the manual selection of proper mother wavelet and decomposition level, and often depend on thresholding heuristics. Also, wavelets are often used only as preprocessing tools, rather than being fully integrated into modern AI systems [8]. These limitations constrain their effectiveness in contemporary deep learning–based SHM frameworks. Although progress has been made, a clear gap remains in the integration of wavelet-based signal processing with advanced AI architectures. Existing approaches often either apply wavelets solely for noise reduction without enabling feature learning, or use DL models without exploiting the time–frequency structure inherent in SHM signals [9], [10].

To bridge these gaps, this study proposes a novel deep learning framework that seamlessly integrates the DWT with a hybrid CNN–LSTM architecture. The DWT is employed to extract multiscale time–frequency features from segmented acceleration signals, capturing both transient and stationary structural behaviors. These wavelet-derived features are then processed by a CNN to learn spatial patterns, followed by an LSTM network that models temporal dependencies across time steps. The framework supports both supervised damage classification and unsupervised anomaly detection, making it adaptable to a wide range of SHM scenarios and contributing to the advancement of intelligent, data-driven infrastructure monitoring.

## 2 PROPOSED FRAMEWORK

This section describes proposed SHM, which integrates wavelet-based signal processing with a hybrid deep learning combining CNN and LSTM networks as shown in Figure 1. The framework is designed to extract meaningful spatial and temporal features from structural vibration signals to enable reliable damage detection and anomaly identification under complex monitoring scenarios.

The process begins with long-duration signals, which are preprocessed and segmented into fixed-length time windows to standardize the input size and ensure consistency. Each segment is then processed using the DWT, which decomposes the signal into multiscale time–frequency components. These wavelet coefficients capture both localized and global signal characteristics and serve as rich input features for the deep learning model.

The CNN component s used to extract spatial features from the wavelet coefficients, while the LSTM network captures temporal dependencies across time window. This combination allows the system to recognize both long-term structural trends and transient events, improving its effectiveness in both damage classification and anomaly detection tasks. Both learning strategies are supported within the framework: supervised learning uses labeled damage states, while unsupervised learning applies autoencoders and clustering on latent features.

This integrated architecture leverages the strengths of both wavelet-based signal processing and DL: it enables automated feature learning from rich time–frequency data, enhances robustness to noise and nonstationary, and improves classification and anomaly detection performance across a variety of structural conditions. The following sections detail the data preprocessing, wavelet-based signal decomposition, and the architecture and training process of the DL model.

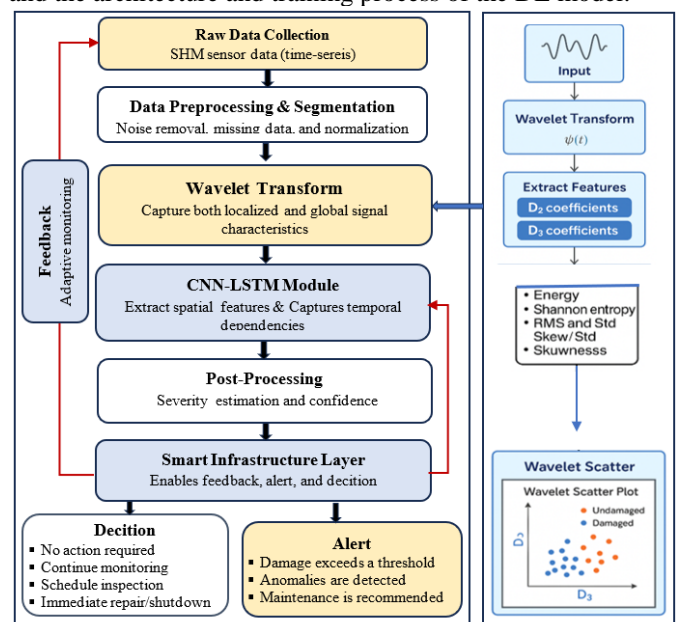


Figure 1. Hybrid methodology combining wavelet-based signal processing with deep learning.

## 3 EXPERIMENTAL VALIDATION USING TIANJIN YONGHE BRIDGE MONITORING DATA

The proposed framework was validated using data from the Tianjin Yonghe Bridge, a cable-stayed structure located in China connecting Tianjin and Hangu. The bridge spans 510 m, consisting of a 260 m main span and two 25.15 + 99.85 m side spans. The bridge wide is 11 m (9 m for vehicles and 2 x 1 m for pedestrians [21]). Originally constructed in 1983 and opened to traffic in 1987, the bridge began exhibiting structural degradation after nearly two decades of service, including the development of 2 cm cracks in the midspan and signs of

corrosion in the stay cables. To address these issues, major repairs were carried out between 2005 and 2007, including full replacement of all stay cables and reinforcement of the midspan girder [16], [17]. Following these repairs, a SHM system was installed by the Harbin Institute of Technology to monitor the bridge's condition under both undamaged (January 17, 2008) and damaged (e.g., July 31, 2008) states. The system included over 150 sensors at critical structural components such as the deck, towers, and cables including 14 single - axis accelerometers installed along the deck and a dual-axis sensor mounted at the top of the south tower.

The vibration data collected by this SHM system were used to evaluate the effectiveness of the proposed wavelet-based CNN-LSTM framework for damage detection and anomaly identification. The signals were segmented and preprocessed to ensure consistency, then processed using discrete wavelet transform before being fed into the hybrid deep learning model. This case study demonstrates the applicability of the proposed method to complex, real-world SHM scenarios and confirms its potential for robust damage classification and condition assessment.



Figure 2. General view of Tianjin Yonghe bridge

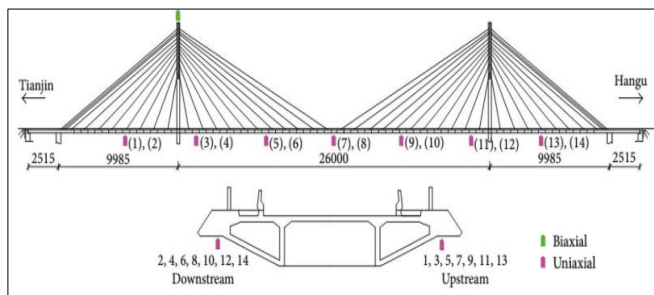


Figure 3. Tianjin Yonghe bridge elevation and health monitoring system

### 3.1 Visualization of structural acceleration data

To illustrate the structural vibration data characteristics, Figure 4 shows time-domain acceleration signals recorded from the bridge deck over a duration about 3600 s for healthy and damaged conditions state. These signals reflect the structure dynamic response under operational conditions. As shown, there is transient spikes, variations in amplitude and frequency content indicate changes in structural behavior, making them suited for SHM applications. Also, the acceleration data show nonstationary behavior that motivate the use of advanced time-frequency analysis. In this study, long-duration acceleration signals were segmented into fixed-length windows (15 minutes) to standardize input size and increase the number of training samples. Figure 5 shows segmentation of a 1-hour acceleration signal into four 15-minute windows. Each segment

is color-coded and vertically offset for clarity. This approach facilitates data preparation for time-series learning models and ensures consistency across training samples [4]–[6]. Also, these visualizations help highlight differences in dynamic response and support the need for data-driven SHM approaches.

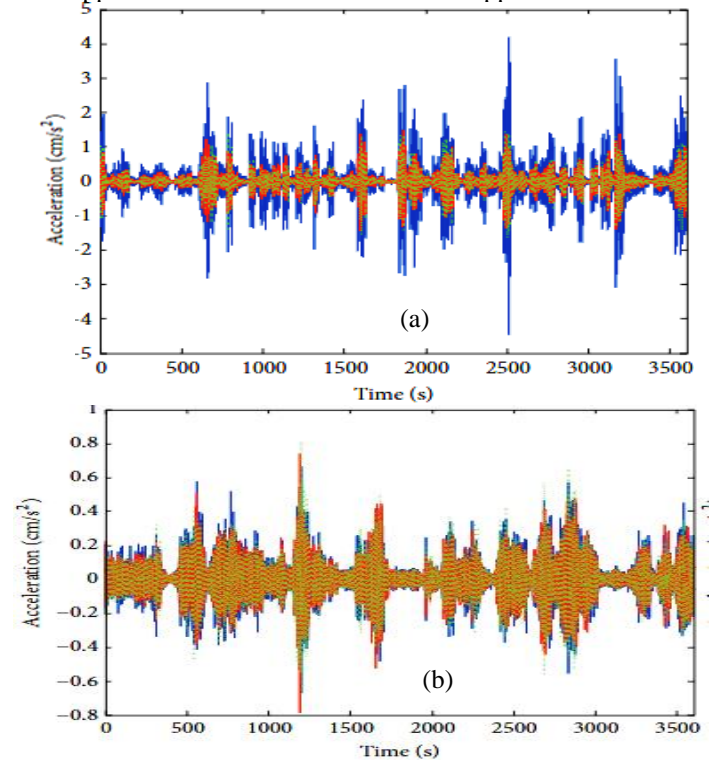


Figure 4. Acceleration signals for Sensor 1 (a) and Sensor 2 (b), showing healthy (bottom) and damaged (top) states.

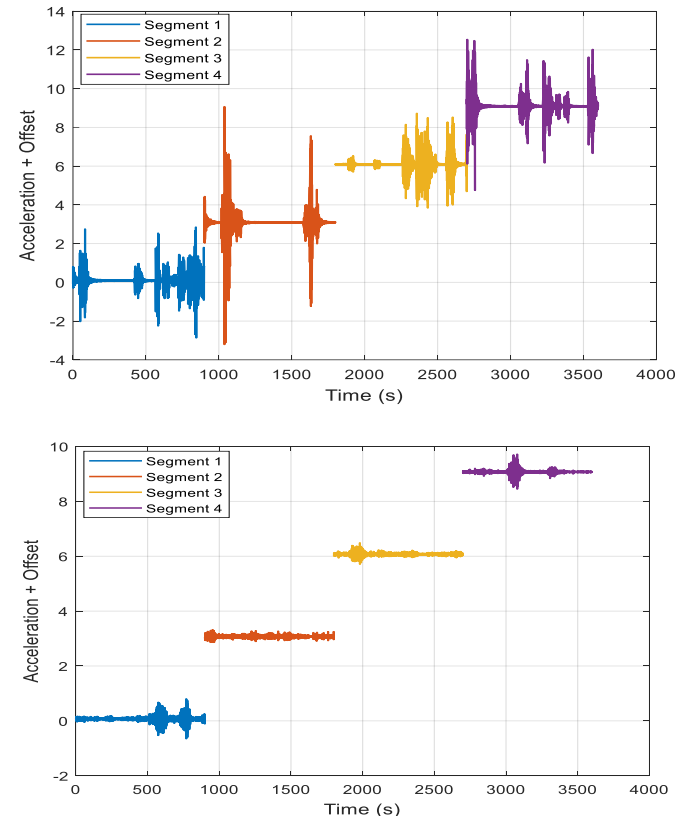


Figure 5. Segmentation of a 1-hour acceleration signals into four 15-minute windows

#### 4 SIGNAL DECOMPOSITION USING DISCRETE WAVELET TRANSFORM

To capture both time and frequency characteristics of structural vibration signals, the DWT was employed for signal decomposition. Unlike the FFT, which provides only global frequency information, DWT enables multiresolution analysis by breaking the signal into approximation and detail coefficients across multiple levels. This allows transient events and localized structural responses often indicative of damage to be effectively identified. In this study, each acceleration signal segment was decomposed using an appropriate mother wavelet and a predefined number of levels, facilitating the extraction of discriminative time–frequency features suitable for both supervised and unsupervised learning models. Based on our previous studies [11], [12], the db3 wavelet was selected as due to its effectiveness in capturing signal characteristics relevant to structural changes and level 4 was chosen as optimal level for further analysis based on optimal energy and classification performance observed in all extracted features Figure 5.

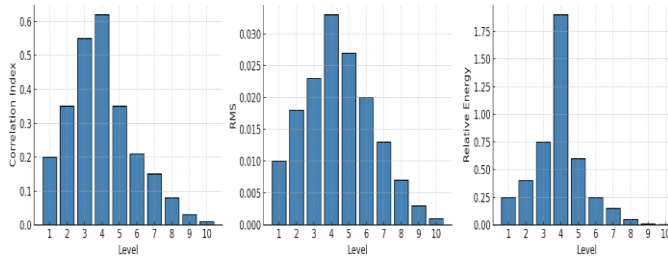


Figure 6. correlation index, root mean square and relative energy versus decomposition level

The signal is decomposed up to level 4, resulting in one approximation signal (A4) and four detail signals (D1–D4). In wavelet analysis, signal decomposition is carried out by projecting the signal onto subspaces of scaling and wavelets basis functions at different scales and their transmission. Figure 7 shows multi-level wavelet decomposition process of the signal. The original signal is recursively decomposed into approximation and detail components. Each approximation captures low-frequency trends (global behavior and long-term structure), while the corresponding detail captures high-frequency information related to transient events or damage. After 4 levels, the final detail and approximation components are used for damage detection and anomaly identification.

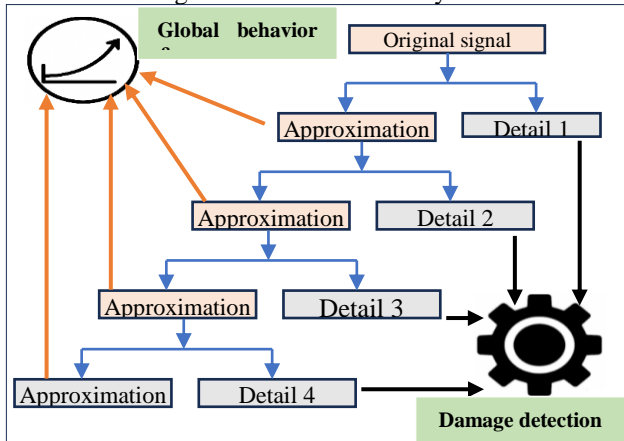


Figure 7. multi-level wavelet decomposition process of the signal.

Figure 8 illustrates the four-level wavelet decomposition of the second 15-minute segment of the acceleration signal using the db3 wavelet. The signal is decomposed into detail coefficients (CD1–CD4) capturing high- to low-frequency components, and an approximation (CA4) representing the global, low-frequency trend. This multilevel decomposition enables the extraction of both transient and long-term structural behaviors, supporting more effective damage detection and anomaly identification in SHM applications.

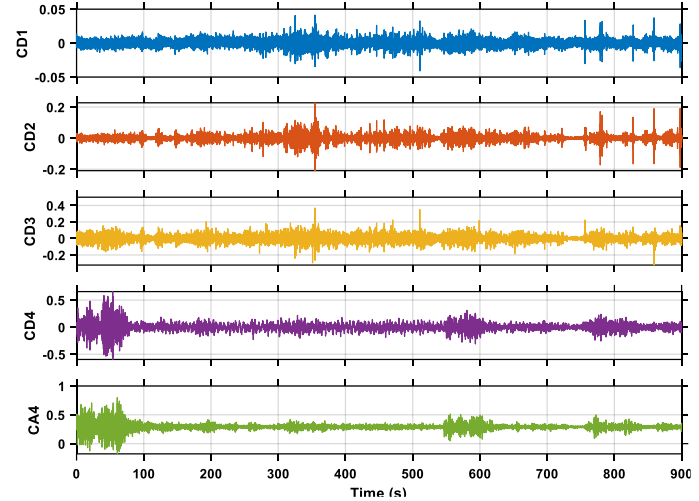


Figure 8. Multi-Level Discrete Wavelet Coefficients of the Acceleration Signal (db3, 4 Levels)

##### 4.1 Features extraction

Feature extraction is a vital step in data-driven structural health monitoring (SHM), converting raw acceleration signals into meaningful representations that support effective damage detection and classification. In this study, wavelet-based time–frequency decomposition is applied to one signal segment, and from each of the four detail sub-bands (D1 to D4), seven statistical features are computed: mean, standard deviation, root mean square, energy, skewness, kurtosis, and Shannon entropy. This results in 28 features for that segment, as summarized in Table 1. While additional segments and features were extracted in the full analysis from detail and approximation coefficients, only this representative example is presented here due to space constraints. These features serve as inputs to deep learning models, enabling them to learn complex structural dynamics and behavioral patterns.

Table 1. Extracted Wavelet-Based Statistical Features

Level	Sub band	Mean	Std. Dev	RMS	Energy	Skewness	Kurtosis	Entropy
Level 1	D1	D1_F1	D1_F2	D1_F3	D1_F4	D1_F5	D1_F6	D1_F7
Level 2	D2	D2_F1	D2_F2	D2_F3	D2_F4	D2_F5	D2_F6	D2_F7
Level 3	D3	D3_F1	D3_F2	D3_F3	D3_F4	D3_F5	D3_F6	D3_F7
Level 4	D4	D4_F1	D4_F2	D4_F3	D4_F4	D4_F5	D4_F6	D4_F7

To improve model interpretability and efficiency, feature importance analysis is carried out to select the most informative variables, allowing the AI model to concentrate on features with the highest predictive value. Figure 9 shows feature importance ranking showing the relative effect of each input variable on the model's prediction. Features with higher importance values contribute more to decision-making, highlighting the most critical parameters for accurate structural condition assessment.



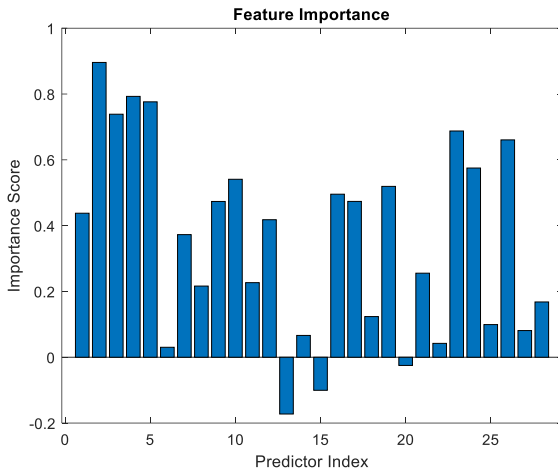


Figure 9. Feature importance ranking illustrating the relative influence of each input variable

## 5 NEURAL NETWORKS MODEL

Neural networks have widely used in SHM due to their ability to model complex data patterns. Deep architectures like CNNs and LSTMs are mainly effective for capturing spatial and temporal features. A CNN usually includes convolutional layers, pooling operations, and one or more fully connected layers. These components collaboratively extract and refine informative features from input data. The fully connected layers serve as the classifier based on the learned features. Through a sequence of operations, the CNN can reduce the dimensionality, which improves computational efficiency and support more effective model training [15]. LSTM is a variant of recurrent neural networks designed to learn long-term dependencies in sequential data. Its internal structure includes memory cells and gating mechanisms, exactly the input, forget, and output gates, which control the info flow through time. This architecture allows the LSTM to retain relevant time-based features and discard irrelevant ones, making it effective in time-dependent tasks [16]. Combining these models offers improved performance in analyzing dynamic, time-varying signals. This hybrid model is well-suited for SHM tasks, as it can capture both spatial features, such as vibration signatures, and temporal patterns, such as degradation over time both of which are critical for accurate classification and anomaly detection. A detailed summary of the proposed hybrid CNN-LSTM configuration is given in Table 2. Further architectural specifications and theoretical background can be found in [12].

Table 2. A detailed summary of the proposed hybrid CNN-LSTM configuration

Layer	Input Shape	Output Shape	Kernel Number	Kernel Size	Activation
Convolution 1-D	(500, 1)	(496, 32)	32	5	ReLU
Max Pooling 1-D	(496, 32)	(248, 32)	—	2	—
Convolution 1-D	(248, 32)	(244, 64)	64	5	ReLU
Max Pooling 1-D	(244, 64)	(122, 64)	—	2	—
LSTM	(122, 64)	(122, 64)	—	—	tanh
Dropout	(122, 64)	(122, 64)	—	—	—
Flatten	(122, 64)	-7808	—	—	—
Dense	-7808	-512	—	—	ReLU
Dense	-512	-5	—	—	Softmax

## 6 RESULTS AND DISCUSSION

All experiments were executed in MATLAB R2023a using built-in toolboxes for signal processing and deep learning. Signal processing tasks and wavelet analysis, were done using DWT with db3. Features were extracted from detail components obtained through decomposition, up to level 4. For supervised classification tasks, SVM, Random Forest, CNN, LSTM, and CNN-LSTM hybrids models were trained with appropriate layer configurations. A max of 100 epochs was used with early stopping if validation performance stagnated for 10 epochs. The Adam optimizer with a learning rate of 0.001, cross-entropy loss, mini-batch size of 64, and dropout (rate = 0.3) were used to ensure convergence and prevent overfitting. For unsupervised anomaly detection, autoencoders were trained using wavelet-based features extracted from database. MSE between reconstructed and raw signals was used as the reconstruction loss. Thresholds were determined from the 95th percentile of reconstruction error on training data. To assess performance, multiple evaluation metrics were used, accuracy, precision, recall, F1-score, and area under the ROC curve. Visual diagnostics such as ROC curves were generated for comprehensive interpretation. Model strength was validated using 5-fold cross-validation with stratified sampling to preserve balanced class distributions across damage states. The proposed WCNN-LSTM framework outdid existing SHM methods across many assessment metrics. The CNN-LSTM without wavelet achieved 86-accuracy, and wavelet-based models exceeded 89 accuracies, with notably higher F1-scores and. The WCNN-LSTM hybrid further contributed by capturing both spatial and temporal features, leading to better generalization across damage types and environmental conditions. As shown in Table 3, model assessment using metrics such as accuracy, precision, and recall confirms that the proposed framework's robustness.

Table 3. Model assessment using metrics such as accuracy, precision, and recall

Model	Accuracy (%)	Precision (%)	Recall (%)	F1-Score (%)
SVM (RBF kernel)	78.2	75.5	74.8	75.1
Random Forest	80.6	78.1	76.5	77.3
CNN Only	83.7	82	81.3	81.6
LSTM Only	84.1	82.5	82	82.2
CNN-LSTM Hybrid	86.4	85.1	84.2	84.6
Proposed Wavelet-CNN-LSTM	<b>89.2</b>	<b>88</b>	<b>87.4</b>	<b>87.7</b>

For unsupervised anomaly detection, autoencoders were trained using wavelet-based features extracted from database. To evaluate classification performance across five classes, we compared per-class ROC curves for the baseline CNN and the enhanced WCNN model. The comparison of ROC curves in Figure 10 highlights that the Wavelet-Combined CNN (WCNN) model offers more balanced and robust performance across all damage classes compared to the conventional CNN. While the CNN model achieves higher AUC values in some individual classes (e.g., Class 4), it performs poorly in others (e.g., Class 0). In contrast, the WCNN demonstrates more consistent AUC scores across all classes, indicating improved generalization and reliability for multi-class damage detection. This suggests that integrating wavelet-based time-frequency features enhance the model's ability to capture both transient

and global signal characteristics, leading to superior classification performance in structural health monitoring applications.

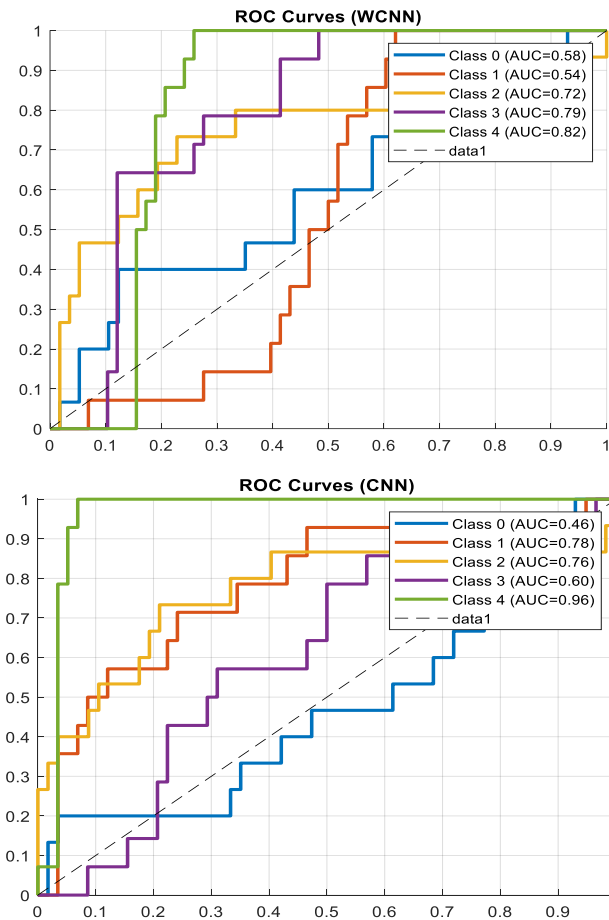


Figure 10. ROC curves for both CNN and WCNN models

Figure 11 shows the progression of training and validation accuracy over 100 epochs. While both curves show consistent improvement and reach above 93%, a slight performance gap remains, particularly toward the final epochs. The training accuracy marginally exceeds the validation accuracy, suggesting that some degree of overfitting may still be present. Also, the flattening of both curves indicates that the model has reached a learning plateau, beyond which additional training yields diminishing gains. This suggests that while the current architecture is effective, there is still room for enhancement, particularly in improving generalization, increasing robustness across classes, or reducing confusion between structurally similar samples. Future improvements could include techniques such as attention mechanisms, hybrid feature fusion, or advanced assembling strategies to push performance beyond the current ceiling.

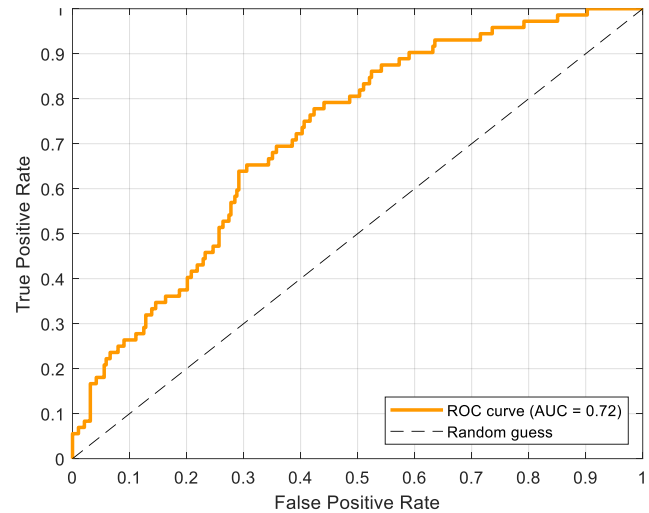


Figure 11. Receiver Operating Characteristic in Class 1 vs. Rest AUC = 0

Figure 12 shows the reconstruction errors distribution for normal and anomalous data. Normal samples exhibit low reconstruction errors, predominantly below the threshold of 0.03, indicating accurate reconstruction by the model. In contrast, irregular samples show higher reconstruction errors, with important portion exceeding the threshold. This separation reveals the effectiveness of reconstruction error as a discriminative feature for anomaly detection, with the threshold serving as a decision boundary between damaged and healthy states. The results confirms that error of reconstruction effectively separates anomalous and normal states, supporting its use as a reliable indicator for anomaly detection in SHM.

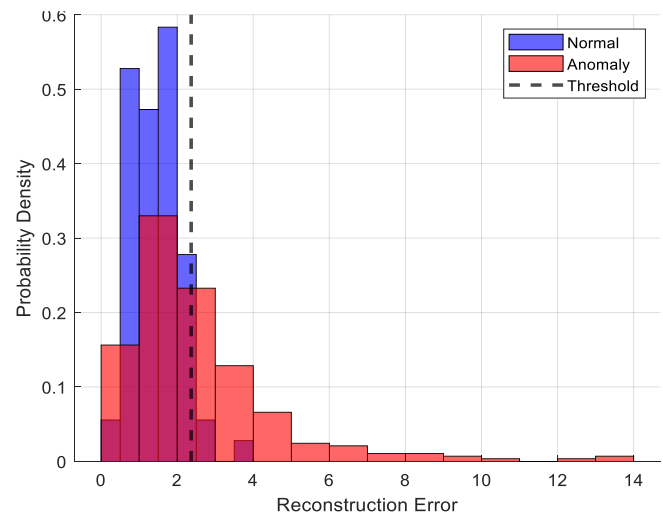


Figure 12. Wavelet-Autoencoder Reconstruction Error Distribution

## 7 CONCLUSION AND FUTURE WORK

This paper presented a wavelet-based deep learning framework for structural health monitoring (SHM) using benchmark data. By combining Discrete Wavelet Transform (DWT) for time-frequency feature extraction with a hybrid CNN-LSTM architecture, the method aimed to address some of the limitations in conventional SHM approaches, particularly under noisy and complex signal conditions. Experimental results showed that the proposed approach offered

improvements over baseline ML and standard DL models in terms of classification performance, including accuracy and AUC. The framework supported both supervised and unsupervised learning modes, making it adaptable to different data labeling scenarios.

Nevertheless, further research is needed to improve the framework's performance and adaptability under more diverse operational conditions, larger datasets, and real-time deployment constraints. Future work may focus on optimizing the model architecture, exploring additional feature representations, and validating performance under real-world deployment scenarios.

## REFERENCES

- [1] H. Sohn, C.R. Farrar, F.M. Hemez, J.J. Czarnecki, D.D. Shunk, A Review of Structural Health Monitoring Literature: 1996–2001, Los Alamos National Laboratory Report LA-13976-MS, 2003.
- [2] K. Worden, G. Manson, The application of machine learning to structural health monitoring, *Philos. Trans. R. Soc. A Math. Phys. Eng. Sci.*, vol. 365, no. 1851, pp. 515–537, 2007. <https://doi.org/10.1098/rsta.2006.1938>
- [3] Y.J. Cha, W. Choi, O. Büyüköztürk, Deep learning-based crack damage detection using convolutional neural networks, *Comput.-Aided Civ. Infrastruct. Eng.*, vol. 32, no. 5, pp. 361–378, 2017.
- [4] N.S. Gulgeç, M. Takáč, S.N. Pakzad, Convolutional neural network approach for robust structural damage detection and localization, *J. Comput. Civ. Eng.*, vol. 33, no. 3, p. 04019005, 2019.
- [5] S. Sony, K. Dunphy, A. Sadhu, M. Capretz, A systematic review of convolutional neural network-based structural condition assessment techniques, *Eng. Struct.*, vol. 226, p. 111347, 2021.
- [6] Z.P. Szewczyk, P. Hajela, Damage detection in structures based on feature-sensitive neural networks, *J. Comput. Civ. Eng.*, vol. 8, no. 2, pp. 163–178, 1994.
- [7] L. Deng, D. Yu, Deep Learning: Methods and Applications, *Found. Trends Signal Process.*, vol. 7, no. 3–4, pp. 197–387, 2014. doi: 10.1561/20000000039
- [8] R. Yan, R. Gao, X. Chen, Wavelets for fault diagnosis of rotary machines: A review with applications, *Signal Process.*, vol. 96, pp. 1–15, 2014. doi: 10.1016/j.sigpro.2013.04.015
- [9] A. Silik, M. Noori, R. Ghiasi, T. Wang, S.C. Kuok, N.S. Farhan, J. Dang, Z. Wu, W.A. Altabay, Dynamic wavelet neural network model for damage features extraction and patterns recognition, *J. Civ. Struct. Health Monit.*, vol. 13, no. 4, pp. 925–945, 2023.
- [10] E.P. Carden, P. Fanning, Vibration based condition monitoring: a review, *Struct. Health Monit.*, vol. 3, no. 4, pp. 355–377, 2004.
- [11] A. Silik, M. Noori, W.A. Altabay, R. Ghiasi, Selecting optimum levels of wavelet multi-resolution analysis for time-varying signals in structural health monitoring, *Struct. Control Health Monit.*, vol. 28, no. 8, p. e2762, 2021.
- [12] A. Silik, M. Noori, W.A. Altabay, R. Ghiasi, Z. Wu, Comparative analysis of wavelet transform for time-frequency analysis and transient localization in structural health monitoring, *Struct. Durab. Health Monit.*, vol. 15, no. 1, p. 1, 2021.
- [13] Z. Xue, C. Xu, D. Wen, Structural damage detection based on one-dimensional convolutional neural network, *Appl. Sci.*, vol. 13, no. 1, p. 140, 2022.
- [14] M.R. Kaloop, J.W. Hu, Stayed-Cable Bridge Damage Detection and Localization Based on Accelerometer Health Monitoring Measurements, *Shock Vib.*, vol. 2015, no. 1, p. 102680, 2015.
- [15] V. Ahmadian, S.B.B. Aval, M. Noori, T. Wang, W.A. Altabay, Comparative study of a newly proposed machine learning classification to detect damage occurrence in structures, *Eng. Appl. Artif. Intell.*, vol. 127, p. 107226, 2024.
- [16] H.N. Li, D.S. Li, G.B. Song, Recent applications of fiber optic sensors to health monitoring in civil engineering, *Eng. Struct.*, vol. 26, no. 11, pp. 1647–1657, 2014.
- [17] M.R. Kaloop, Assessment of bridge performance based on SHM system data, *Int. J. Civ. Struct. Eng.*, vol. 1, no. 2, pp. 138–147, 2010.
- [18] M.R. Kaloop, et al., Signal analysis for damage detection in cable-stayed bridges, *Meas.*, vol. 63, pp. 103–112, 2015. Pan, H., Azimi, M., Yan, F. and Lin, Z., 2018. Time-frequency-based data-driven structural diagnosis and damage detection for cable-stayed bridges. *Journal of Bridge Engineering*, 23(6), p.04018033.
- [19] N. Cristianini, J. Shawe-Taylor, An Introduction to Support Vector Machines and Other Kernel-Based Learning Methods, Cambridge University Press, Cambridge, UK, 2000.
- [20] S. Li, H. Li, Y. Liu, C. Lan, W. Zhou, J. Ou, SMC structural health monitoring benchmark problem using monitored data from an actual cable-stayed bridge, *Struct. Control Health Monit.*, vol. 21, no. 2, pp. 156–172, 2014.





# Advancements in Vibration-Based Bridge Health Monitoring

# Preliminary results from a field application of dynamic monitoring on three spans of a railway bridge

Eleonora Massarelli<sup>1</sup>, 0009-0001-5172-0804, Marco Civera<sup>1</sup>, 0000-0003-0414-7440, Giulio Ventura<sup>1</sup>, 0000-0001-5464-6091, Bernardino Chiaia<sup>1</sup>, 0000-0002-5469-2271

<sup>1</sup>Politecnico di Torino, Department of Structural, Geotechnical and Building Engineering (DISEG), Corso Duca degli Abruzzi 24, 10129 Turin, Italy

email: marco.civera@polito.it

**ABSTRACT:** Vibration-based Structural Health Monitoring is of the foremost importance for critical civil infrastructures, especially concerning the safety of the train transport network. In fact, even minor structural changes might cause derailment and potentially fatal accidents. This contribution reports some preliminary analyses carried out on 52 accelerometric recordings collected over two consecutive days from three spans of a railroad bridge. The acquisitions include several train passages and the quiet periods between them, when the structure was excited only by ambient vibrations (i.e. random microtremors), thus allowing Ambient Vibration Testing (AVT). Specifically, a newly developed Automated Operational Modal Analysis (AOMA) algorithm was applied. Its results are here compared to state-of-the-art commercial software (ARTEMIS). Some considerations regarding the effects of train passages are also briefly reported, as well as directions for current and future research work in this field.

**KEYWORDS:** automated operational modal analysis, railway bridge, structural health monitoring, operational modal analysis, vibration-based monitoring

## 1 INTRODUCTION

Railways are an essential component of civil infrastructures, representing one of the most critical parts of national and transnational transportation and communication systems. In particular, railway bridges are a crucial element in this context. Being affected by degradation processes of various natures and durations, they constitute the most vulnerable elements for the safety of the whole railway infrastructure, with potential consequences for the safety of goods and people.

In fact, considering that different parts of every railway infrastructure are connected from the superstructure, i.e. the ballast and the rails, even minor structural changes without complete structural failure might cause derailment and potentially fatal accidents.

For all these reasons, a robust understanding and awareness of the daily operations and safety concerns is required, given that many passengers use railway lines daily. In Europe, 35% of the more than 300,000 railway bridges, which are distributed over a total of 200,000 km of railways, exceed 100 years of operational life [1]. In particular, in Italy, the majority of railway viaducts built between the 1950s and 1970s consist of prestressed concrete bridges (PRC); hence, special attention should be granted to these ageing infrastructures [2].

Railway bridges are exposed to several factors which cause degradation. These include harsh environmental conditions, significant live loads – mainly due to the increase of traffic loads in the last decades, including high-speed trains – material ageing, and other rare or extreme events (i.e. impacts from accidents, earthquakes, etc.). Other than material ageing, PRC bridges are subjected to damages due to: corrosion of normal reinforcement steel bars as well as prestressing tendons; prestressing losses; construction errors (incorrect grouting of

tendons ducts, for example); and many other potential natural or human-made hazards [3]. Inadequate maintenance is also a practice that could result in further damages, often non-recoverable. Finally, hidden grouting defects of prestressing sheaths can lead to corrosion, reducing the area of prestressing steel with consequent bearing capacity decrease.

As a result, all these factors contribute to the potential development and growth of structural damage over time.

Per established tradition, visual inspection still plays an essential role in identifying superficial defects and evaluating the overall condition of the examined structure. However, visual inspections are labour-intensive, time-consuming, and often rely on the operator's experience level, which significantly impacts the accuracy, objectiveness, and reliability of structural condition evaluations.

Hence, the application of automated and objective anomaly detection is fundamental. This is the paradigm of Structural Health Monitoring (SHM) solutions [4]; their application to railway bridges is important to maintain operational safety, expand the structure's lifespan, and reduce maintenance costs. In particular, Vibration-Based SHM, which relies on analysing the vibrational response of structures to identify damage indicators, is one of the most used techniques to identify and monitor changes in the dynamic properties of a structure. In this framework, to identify such pathologies, the first step involves extracting the target structure's damage-sensitive features (DSFs) from the monitoring data – that is, natural frequencies, damping ratios, and associated mode shapes from acceleration time series. Possible changes in modal parameters over time could be a manifestation of both global and local damages.

In particular, natural frequencies are mainly sensitive to global damages and structural modifications. However, the global stiffness of a structure is often influenced by variations in normal environmental factors, such as temperature, and their influence (daily or seasonal gradients) can be significant enough to mask the presence of certain damages. Notably, local damage up to moderate severity has a minor influence on eigenfrequencies. On the other hand, mode shapes are more sensitive to local damages than natural frequencies and less sensitive to temperature variations [5], [6]. The main disadvantage is that a dense sensor grid is required to ensure effective damage localisation, a choice which is generally costly when conventional sensors, such as accelerometers, are employed.

Nevertheless, in both mode shape-based and natural frequency-based SHM, the key point is to extract high-quality modal parameters from the recorded time series; henceforth, accurate identifications are strictly required.

This short contribution presents the results of a novel output-only System Identification (SI) algorithm, applied to an experimental test campaign on a prestressed reinforced concrete railway bridge. In this context, the present study focuses on analysing the recorded accelerometric monitoring data of the viaduct's deck.

The case study presented here has been equipped with highly sensitive accelerometers on three spans, collecting data for two consecutive days. The acquired acceleration data are processed using the proposed Automated Operational Modal Analysis (AOMA) approach based on the SSI-COV algorithm [7] using a code developed in MATLAB environment. Dynamic identifications obtained considering ambient vibrations provide repeatable and directly comparable results between identical spans. Furthermore, as a benchmark, the results are compared to the ones obtained with the commercial software (ARTEMIS).

The remainder of this paper is organised as follows. Section 2 describes the structure, the dynamic monitoring system and the data acquired. In Section 3, the Automated Operational Modal Analysis procedure for dynamic monitoring is briefly described. The results obtained considering the environmental excitation of the structure are then reported in Section 4, followed by the analyses repeated with the commercial software ARTEMIS; such results are then compared. Finally, the conclusions of the study carried out for this structure follow in Section 5.

## 2 EXPERIMENTAL TEST CAMPAIGN

### 2.1 Description of the structure

The railway viaduct under investigation consists of 46 spans, each equal to 20 m, for a total length of 920 m. The individual spans are characterised by a simply supported static scheme and consist of eight prestressed concrete girders with I cross-sections, connected by a 20 cm thick upper slab, and four transversal beams having rectangular cross-sections. The main beams are 1.40 m high and have 1.20 m spacing, such that, considering the two lateral cantilever slabs supporting the parapets, the total width of the deck is approximately 12.40 m, allowing the support of two train tracks (see Figure 1 and Figure 2). The beams' prestressing reinforcement is arranged in the lower flange and, according to the original design drawings, consists of a total of 29 cables arranged in 3 rows, sheathed in

ducts at the supports. As mentioned, PRC beams are widely used in railway bridges, where dynamic loads from passing trains demand high stiffness and serviceability. The prestressing process introduces compressive forces into the concrete; these forces counteract tensile stresses, preventing cracking and the resulting stiffness reduction. This, compared to a beam of equivalent size in conventional (non-prestressed) RC, results in lower deflections under load and allows for larger spans. At the same time, lower amplitude vibrations are generated under working conditions, which is useful for safety and comfort in operating conditions but makes AVT and output-only identifications more challenging, requiring high-quality accelerometers.



Figure 1: View of a typical span of the railway viaduct.

The standard pier has a pseudo-rectangular reinforced concrete geometry (maximum dimensions 11.0 x 1.50 m). The 45 piers range from a minimum height of 2.5 m to a maximum of 5 m along the longitudinal direction. The foundation of the piers consists of a RC plinth lying on deep foundations (i.e. piles).



Figure 2: Intrados view of a typical span of the case study with the PRC beams.



## 2.2 Structural health monitoring (SHM) system

Because of the extension of the viaduct and its static scheme, with simply supported and nominally equal spans, only a part of the entire structure has been investigated. Specifically, three spans have been instrumented. Four uniaxial accelerometers were installed for each span under study in the positions showed in Figure 3 and with the numbering indicated. Measurements of only the vertical acceleration components were acquired for two consecutive days. This placement aimed to associate the obtained frequencies with both vertical and torsional vibrational modes.

Due to the high stiffness of prestressed reinforced concrete railway bridges, accelerometers with high sensitivity and low background noise are required. In the present case, PCB piezoelectric accelerometers model 393B12 were used, with a sensitivity of 10 V/g and a noise of  $0.32 \mu\text{g}/\sqrt{\text{Hz}}$  on the 10 Hz band.

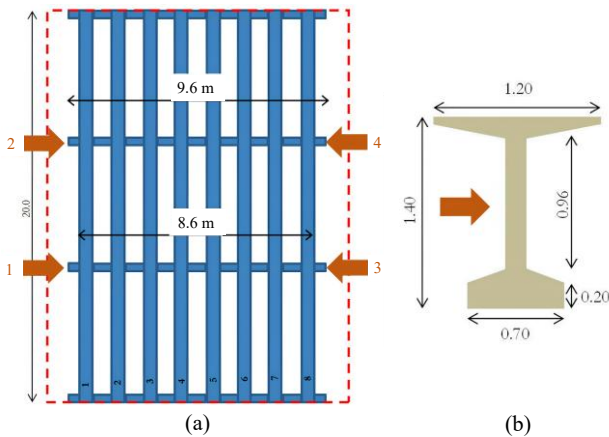


Figure 3: Scheme of the typical span (a) and position of the accelerometers on the main beams near the cross beams (b). The numbers in red (1 to 4) indicate the different output channels.

The instrumentation configuration differs between the spans as follows:

- in one span, the four accelerometers were installed at the end of the cross beams (transverse distance 9.6 m).
- in the other two spans, the four accelerometers were installed on the web of the main beams in proximity of the cross beams (transverse distance 8.6 m, see Figure 3 (b)).

The experimental tests were designed to identify the bridge's modal parameters and verify the structure's response under normal operating conditions. For this reason, some signals would inevitably contain train passages alongside ambient vibrations. 20 recordings were acquired for the first span; 16 other recordings were taken for the other two spans, referred to as numbers 2 and 3. All acquisitions were made with a sampling frequency  $f_s = 100$  Hz and a 24-bit acquisition system. That provides a wide margin with respect to the highest natural frequency of interest (16 Hz, as will be shown in the following Sections, thus well below the Nyquist limit  $f_s/2 = 50$  Hz). The duration of each measurement was about 15 minutes. Examples of recorded time series of the raw acceleration data for one of

the instrumented spans, showing all acquisition channels, are displayed in Figure 4.

The vertical acceleration signals acquired by the four acquisition channels for each instrumented span were analysed after the cleaning and pre-processing phase. In particular, after identifying the signals containing train passages, the corresponding signal portions were isolated and saved separately. The remaining parts, thus corresponding to ambient excitation, were likewise isolated, stored separately, and analysed in the subsequent steps. In this way, 80 signals were obtained, of which only those of appropriate length ( $> 4$  minutes) were used for the successive identification steps. The signal duration was found to be consistent with the range recommended in [8] for accurate damping estimation, i.e. 1000-2000 times the natural period of the first mode (2 to 4 minutes in the present case study), thus reliable results are ensured even when signals are segmented.

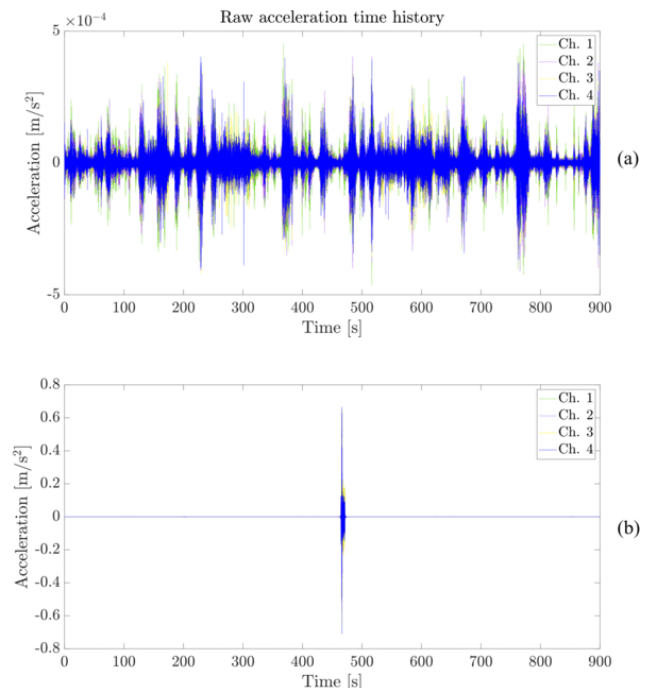


Figure 4: Example of a signal acquired in one of the spans under ambient vibration conditions (a) and with a passing train (b) after the pre-processing.

## 3 AUTOMATED OPERATIONAL MODAL ANALYSIS (AOMA) FOR SHM

The objective of any Automated Operational Modal Analysis (AOMA) procedure is the extraction of modal parameters through the analysis of vibration measurements. The procedure is a multi-stage process that involves several sequential steps. It begins with data pre-processing and the choice of the optimal algorithm parameters, followed by the system identification phase, then the sifting of the identified modal parameters, and finally, the estimation of cluster-wide values and their validation, as well-documented in [9] and [10]. In this context, the core of the procedure, i.e. the system identification phase, is carried out by applying the Stochastic Subspace Identification (SSI) method, which is a popular parametric time

domain algorithm based on state-space identification [7]. Several authors have proposed AOMA procedures to try to address the aspect of automating the interpretation of the stabilisation diagram and the following extraction of the physically meaningful modes of the structure [8], [11], [12].

### 3.1 AOMA algorithm and modal parameters' selection

In the present study, the dynamic identification of the structure decks was performed using the well-known SSI (Stochastic Subspace Identification) Operational Modal Analysis algorithm with clustering analysis (DBSCAN - Density-Based Spatial Clustering of Applications with Noise) to facilitate the identification of actual vibration modes [13], [14].

SSI returns all identified modal parameters, which are generally represented in a stabilisation diagram, which is a visual tool used to facilitate the interpretation of results showing the poles (modes) characterised by the natural frequencies, damping ratios, and eigenvectors identified in relation to the order of the dynamic system chosen a priori. However, these identified poles include the physical modes as well as many spurious modes; the latter ones, which are due to measurement noise misidentified as vibration modes, need to be disregarded to identify only valid results correctly. In the stabilisation diagram, poles aligned in a vertical line are stable as the model order changes and, therefore, are deemed to represent a physical mode. The automatic cleaning and interpretation phase of the stabilisation diagram consists of defining a set of criteria to distinguish physical poles from spurious and mathematical ones. The steps enabling this procedure are briefly outlined below:

- hard validation criteria (HVC), consisting of the elimination of poles with negative or excessively high damping ratios ( $> 20\%$ ) and those with eigenvectors not coming in complex conjugate pairs;
- soft validation criteria (SVC), concerning the introduction of comparison parameters between the modal parameters of the different poles (hence the distance in the stabilisation diagram) and elimination of those that do not fall within the selected thresholds, following the work done by Mugnaini et al. [15];
- application of the DBSCAN algorithm to group the poles with similar modal characteristics and discard any other outlier poles according to parameters that vary for each dataset. Each identified cluster individuates a set of probable physical modes; therefore, the modal parameters representative of an entire cluster are estimated as the average of the cluster values  $f_m$ ,  $\xi_m$  [10].

Determining the corresponding mode shape is essential to discern the modes with actual physical significance.

### 3.2 ARTeMIS software

The commercial dynamic identification software ARTeMIS was used as a benchmark to validate the results obtained from the developed AOMA code. ARTeMIS is a powerful operational and experimental modal analysis software. The results are obtained through a Data-Driven Stochastic Subspace Identification algorithm implementation.

## 4 DISCUSSION OF RESULTS

### 4.1 AOMA results

SSI needs the definition of two fundamental parameters:

- the range of model order, going from  $n_{\min} = 20$  to  $n_{\max} = 130$ ,
- the number of block rows of the Hankel matrix, defined as  $f_s/2$  [7].

For a fair comparison, these parameters were set once and kept untouched for all analyses (all signal tracts of all spans). The comparison parameters for the stabilisation diagram [13] reported above are set equal to:

- $df < 0.005$
- $0 < d\xi < 10\%$
- $(1 - \text{MAC}) < 0.05$

Figure 5 shows a 'cleaned' stabilisation diagram at the end of the clustering phase (in fact it can be seen how each cluster is identified by a different colour), taken by one example of one of the instrumented spans. In this particular case, the frequency range of interest goes from 8 to 20 Hz, where clear peaks can be observed. In the same way, a diagram of the damping ratios versus natural frequencies is represented in Figure 6. The identified clusters are linked to the ones in Figure 5, i.e. displayed with the same colours.

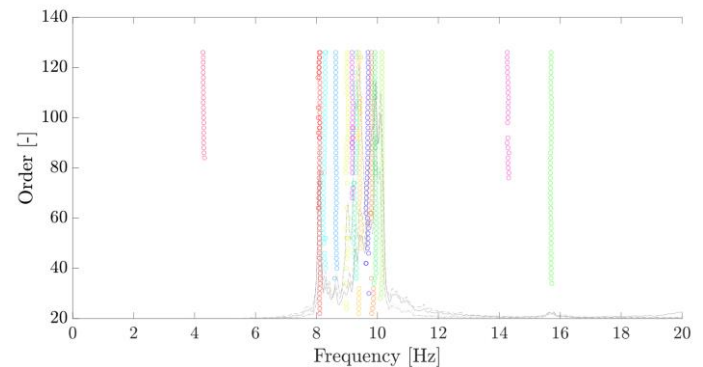


Figure 5: Example of stabilisation diagram with identified clusters.

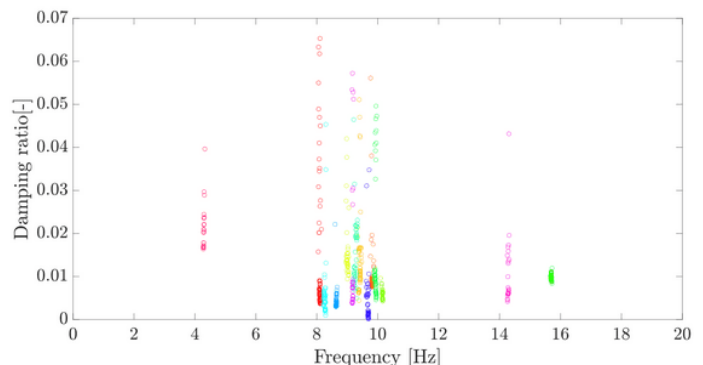


Figure 6: Example of frequencies vs damping ratios diagram with identified clusters.

Finally, Figure 7 shows the occurrence of the values of identified natural frequencies for the deck of one of the instrumented spans, considering all the ambient vibration signals used.

By comparing all the results obtained from the different signals, the natural frequencies with the highest occurrence and corresponding to mode shapes with physical significance were identified. The following figure (Figure 8) shows the experimental vibration modes of the structure, with distribution diagrams of the natural frequencies and an axonometric view of the mode shapes with an indication of measurement points for each identified mode.

Concerning the 2<sup>nd</sup> mode, it is noteworthy to point out the fact that it has been identified twice. Although the identified mode shape seems to indicate that it is the same mode, there is no certainty as to the exact corresponding frequency. One could conservatively assume that one of the two estimated modes corresponds to some residual effects of a lateral mode. Still, since all output channels are vertical, the algorithm can only extract the mode shape of the closest mode with vertical components, i.e., the first torsional. Here and for the rest of the article, these are referred to as modes ‘2a’ and ‘2b’. Instead, the 1<sup>st</sup> mode can be identified as the first flexural mode of the deck.

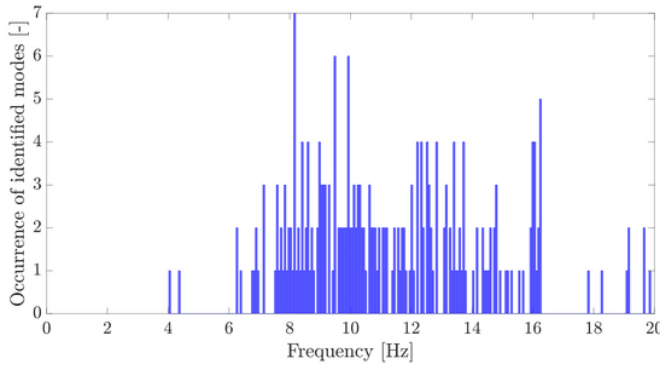


Figure 7: Histogram representing the occurrence of natural frequency estimates of probable physical vibration modes.

For the mode identified as ‘mode 3’ in Figure 8, given the positioning and limited number of sensors, the corresponding mode shape is similar to the first flexural one. It could be assumed that the mode in question is instead related to a local mode of the deck, whose shape could only be detected with a denser sensor network. However, it should be noted that for the practical purposes of detecting damage structural phenomena for this type of structure, the first two modes are generally significant, as they are also identifiable with greater accuracy and repeatability. The estimated damping ratios are around 2 % for most identifications, except for mode 3, for which it is about 1 %.

Table 1 shows the values of the identified natural frequencies for each span. The first torsional mode identified twice with different frequencies is reported as ‘mode 2a’ and ‘mode 2b’. Furthermore, the low standard deviation values confirm that the three instrumented spans, nominally identical, are very similar in terms of dynamic response (and thus mechanical properties). This suggests that any damage in one of them would be easily detected not only by comparing the historical and current response of the span in question but also by comparing it with the other spans contemporaneously monitored – i.e. a sort of population-based SHM [16]. Indeed, this approach falls into the concept of population-based SHM.

Table 1: Summary of the natural frequencies identified by the MATLAB code (all values in Hz) for the relevant modes in the three instrumented spans, with average and standard deviation values (St.Dev).

	Mode 1	Mode 2a	Mode 2b	Mode 3
Span 1	8.148	9.205	10.084	15.873
Span 2	8.117	9.181	10.112	16.020
Span 3	8.126	9.142	10.123	15.907
<b>Average</b>	<b>8.130</b>	<b>9.176</b>	<b>10.106</b>	<b>15.933</b>
<b>St.Dev</b>	<b>0.016</b>	<b>0.032</b>	<b>0.020</b>	<b>0.077</b>

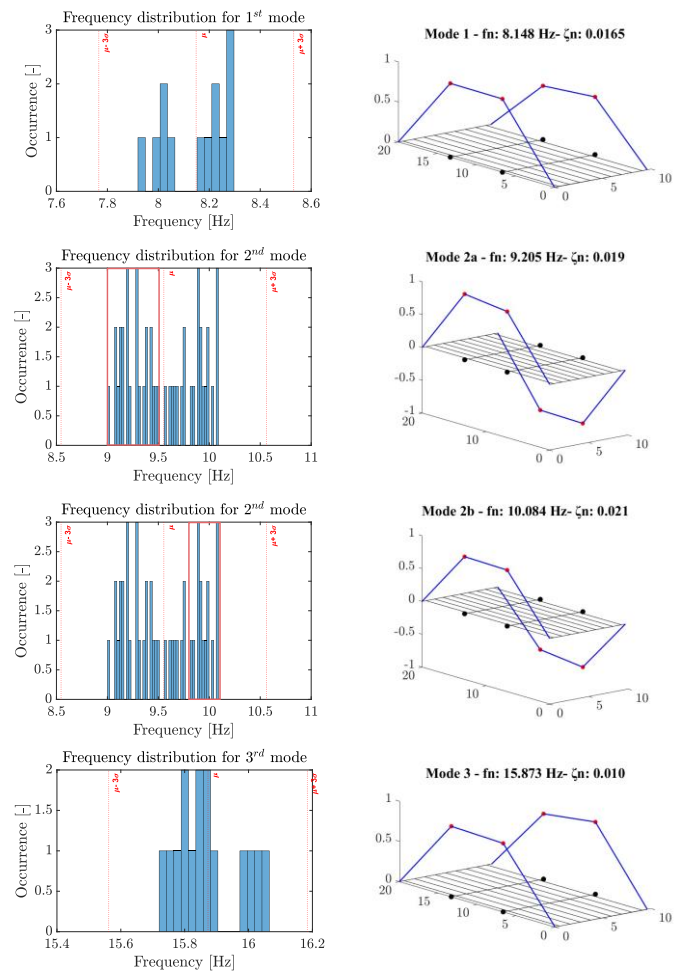


Figure 8: Distribution diagram of the identified natural frequencies and axonometric view of the identified mode shapes with an indication of the measurement points in red for mode 1 (a), modes 2a (b), and 2b (c), and local mode 3 (d).

Notably, the first mode shape was found to be slightly asymmetric, with the vibrations on one side ~20% larger than the other. This behaviour was confirmed in all acquisitions with both the MATLAB code and ARTeMIS (see next Section). Conversely, the other three mode shapes behave very symmetrically, with differences <4% between the two sides.

#### 4.2 ARTeMIS results comparison

The results from the ARTeMIS software were obtained by importing, via a .cfg text file, the geometric model of the



individual deck and the information regarding the actual position of the sensors, which was the same for the three instrumented spans. The acceleration time histories used are those from the pre-processing phase described in Section 2.2 and relative to ambient vibrations. The results showed in this section refer to a single example file belonging to one of the instrumented decks, but the overall outputs, analysed manually, are in line with those of the other acquisitions on the same span and the others. All results refer to the analysis with ambient noise, i.e. eliminating train passages.

At first, Frequency Domain Decomposition (FDD) was used, a frequency domain features extraction technique with manual peak selection to perform a preliminary analysis; the results obtained with this method are shown in Figure 9 on the left side. All natural frequency values estimated for the first three modes are very similar to those verified by MATLAB code on the entire dataset of available signals. As already observed through the AOMA code, there is a substantial similarity between the first and third modes. Moreover, as better detailed below, for each span, just one of the two modes named as ‘mode 2’ can be estimated by applying FDD.

Stochastic Subspace Identification with Unweighted Principal Component (SSI-UPC) [7] was then used. Regarding the definition of the SSI parameters, the same model order range as selected in the MATLAB code, i.e. from  $n_{\min} = 20$  to  $n_{\max} = 130$ , was set for direct comparability. Relative to the same example presented and discussed so far, the obtained results are shown in Figure 9 on the right side.

Although only the representation of the mode referred to above as ‘mode 2a’ is shown here, the results for both modes

2a and 2b are still identified with the same mode shape. Moreover, as can be noticed for the representative case here depicted, but is valid for all three instrumented decks, the estimated damping ratios for the first and second modes are slightly higher than those estimated and reported in the previous section.

At the bottom of the images in Figure 9 (d), (e), and (f) the Modal Assurance Criterion (MAC) can be observed to verify the similarity between the identified modes. As already observed through the MATLAB AOMA code, a substantial similarity is observable between the first and fourth (denoted as Mode 3) modes. Similarly, it is possible to visualise complexity plots, which make it possible to indirectly verify whether a mode is physical or, for example, due to numerical effects or acquisition noise, given its complexity.

Finally, the results in terms of identified frequencies for the different system identification approaches used are reported in Table 2. The analysis carried out on the signals of the three spans using commercial software ARTEMIS, using the FDD and SSI-UPC techniques and considering the first three modes, indicates a good correlation in terms of natural frequencies, while a discrepancy is noted in the estimation of modal damping, which on average is higher in ARTEMIS than in the MATLAB code. However, this parameter is known to be the most uncertain of those to be estimated [17] and, for this very reason, is generally not considered in terms of structural monitoring. Given the low standard deviation values, the same conclusions as in Section 4.1 can be replicated here.

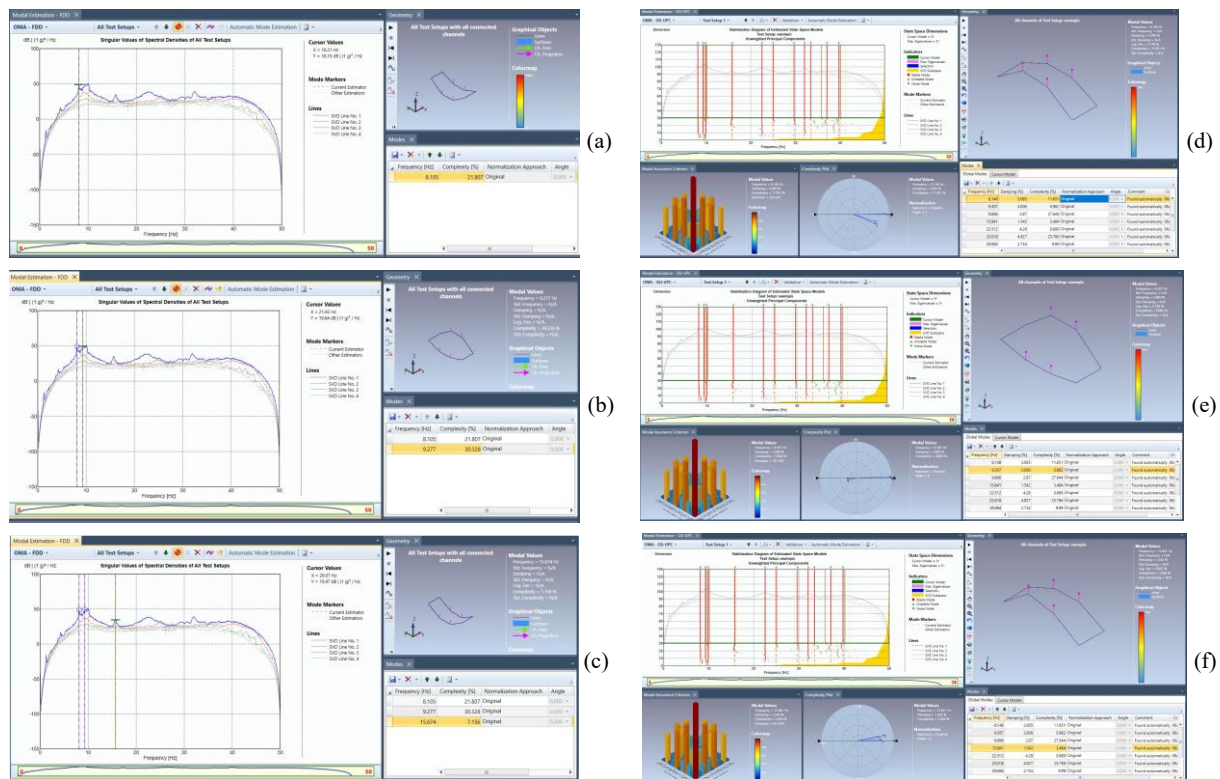


Figure 9: Results obtained in ARTEMIS by applying the FDD method on the left, reporting mode 1 (a), mode 2 (b) and mode 3 (c) manually selected from the signals PSD; and by applying SSI-UPC on the right, showing mode 1 (d), mode 2a (e) and mode 3 (f) estimated automatically.

Table 2: Summary of the natural frequencies identified by ARTeMIS (all values in Hz) for the relevant modes in the three instrumented spans with the FDD and SSI-UPC methods, with computation of the average and standard deviation values (St.Dev). The sign ‘-’ indicates unidentified modes.

		Mode 1	Mode 2a	Mode 2b	Mode 3
FDD	Span 1	8.562	9.684	-	15.789
	Span 2	8.255	9.365	10.101	16.034
	Span 3	8.297	-	10.108	16.219
	<b>Average</b>	<b>8.371</b>	<b>9.524</b>	<b>10.104</b>	<b>16.014</b>
	<b>St.Dev</b>	<b>0.166</b>	<b>0.226</b>	<b>0.005</b>	<b>0.216</b>
SSI-UPC	Span 1	8.461	9.631	10.030	15.777
	Span 2	8.171	9.168	10.197	16.092
	Span 3	8.125	9.231	10.320	16.217
	<b>Average</b>	<b>8.252</b>	<b>9.343</b>	<b>10.182</b>	<b>16.029</b>
	<b>St.Dev</b>	<b>0.182</b>	<b>0.251</b>	<b>0.145</b>	<b>0.227</b>

Finally, the mode shapes identified in Section 4.1 through the AOMA algorithm developed in MATLAB and those obtained with the two methods implemented in ARTeMIS, as in the present Section, are compared based on Modal Assurance Criterion (MAC), defined as [18]:

$$MAC(\phi_j, \phi_k) = \frac{[(\phi_j) * (\phi_k)]^2}{[(\phi_j) * (\phi_j)][(\phi_k) * (\phi_k)]} \quad (1)$$

The MAC correlation matrices for the instrumented span 1 are summarised in Table 3. The top part of the table shows the MAC values computed between the MATLAB-identified mode shapes and those obtained via the ARTeMIS SSI-UPC method, while the bottom section reports the MAC values with the FDD method. For the other couple spans the results are consistent with those presented.

The resulting MAC values for the modes indicated as 1, 2a, and 3 are reported, with the values of interest highlighted. Such values indicate a high correlation between the two sets of mode shapes.

Table 3: MAC correlation matrices of mode shapes identified for span 1 computed between MATLAB code vs ARTeMIS SSI-UPC (top part) and MATLAB vs ARTeMIS FDD (bottom part).

		MATLAB AOMA		
		Mode 1	Mode 2a	Mode 3
ARTEMIS SSI	Mode 1	0.9948	0.0202	0.9846
	Mode 2a	0.0455	0.9980	0.0046
	Mode 3	0.9667	0.0001	0.9958
ARTEMIS FDD	Mode 1	0.9846	4.44e-05	0.9882
	Mode 2a	0.0031	0.9697	0.0044
	Mode 3	0.9974	0.0189	0.9971

The results suggest that the modes obtained from the SSI-UPC automated method present excellent comparability with those obtained in MATLAB, showing a better reliability with respect to the FDD identifications.

It is noteworthy to notice the high MAC values between modes 1 and 3 in both cases, as expected by the nature of the mode shapes (see Figure 8 and Figure 9).

#### 4.3 Effects of train passages

The dynamic data recording included train transit events, presenting signals with much higher acceleration amplitudes but extremely short durations. The analysis of such portions of signals could be of particular interest in the case where less performing accelerometers are used, and as a consequence, are not able to detect vibrations due to environmental excitation, or in the case where load tests need to be performed on the structure, since in such loading conditions the identified modal parameters are in general more sensitive to longitudinal prestressing losses. These signals, if taken in their entirety (i.e. including train passages), become non-stationary and, therefore, difficult to analyse with algorithms intended for stationary analysis, such as SSI. For this reason, if one wants to exploit the excitation given by the passage of trains to extract damage-sensitive modal parameters, it is necessary to resort to other algorithms designed for modal identification and exploiting the excitation contained in the free vibration following a train passage. This aspect will be further explored as part of future developments of this project.

## 5 CONCLUSIONS

The primary aim of this study was to evaluate the applicability of a novel Automated Operational Modal Analysis (AOMA) algorithm for continuous Structural Health Monitoring (SHM) of a railway bridge. Three spans of this case study were instrumented with high-performance accelerometers. The workflow followed here, from the pre-processing phase of the ambient vibration measurements data to the Automated OMA, made it possible to identify natural frequencies, damping ratios, and mode shapes for the first relevant modes in the frequency range from 0 to 20 Hz, discarding spurious identifications.

The comparison between the AOMA algorithm developed in the MATLAB environment and the commercial software ARTeMIS shows that both approaches provide consistent and reliable results. The similarity in outcomes confirms the validity and robustness of the proposed method, ensuring its applicability. Since the bridge spans are nominally identical, the approach followed for this research study enables the estimation of the variability of the results under the same analysis methodology.

Overall, in view of a broader approach to infrastructure monitoring, maintenance, and management, these findings validate the feasibility of using AOMA for continuous SHM of railway bridges and damage detection.

## ACKNOWLEDGMENTS

The study presented here was carried out as part of the program of activities carried out within the MOST – Sustainable Mobility National Research Center and received funding from the European Union Next-GenerationEU

(PIANO NAZIONALE DI RIPRESA E RESILIENZA (PNRR) – MISSIONE 4 COMPONENTE 2, INVESTIMENTO 1.4 – D.D. 1033 17/06/2022).

## REFERENCES

- [1] B. Paulsson, J. Olofsson, H. Hedlund, B. Bell, B. Täljsten, and L. Elfgren, “Sustainable Bridges—Results from a European Integrated Research Project,” in *Proceedings of the IABSE Symposium Report*, International Association for Bridge and Structural Engineering: Zurich, Switzerland, 2010, pp. 17–24.
- [2] F. Biondini *et al.*, “BRIDGE|50 research project: Residual structural performance of a 50-year-old bridge,” *Bridge Maintenance, Safety, Management, Life-Cycle Sustainability and Innovations - Proceedings of the 10th International Conference on Bridge Maintenance, Safety and Management, IABMAS 2020*, pp. 3337–3344, Apr. 2021, doi: 10.1201/9780429279119-453.
- [3] M. D’Angelo *et al.*, “Bridge Collapses in Italy across the 21st Century: Survey and Statistical Analysis,” *Structure and Infrastructure Engineering (Accepted for publication)*, 2025.
- [4] C. R. Farrar and K. Worden, *Structural Health Monitoring: A Machine Learning Perspective*. 2013.
- [5] M. P. Limongelli, “Frequency response function interpolation for damage detection under changing environment,” *Mech Syst Signal Process*, vol. 24, no. 8, pp. 2898–2913, Nov. 2010, doi: 10.1016/J.YMSSP.2010.03.004.
- [6] D. Martucci, M. Civera, and C. Surace, “Bridge monitoring: Application of the extreme function theory for damage detection on the I-40 case study,” *Eng Struct*, vol. 279, p. 115573, Mar. 2023, doi: 10.1016/J.ENGSTRUCT.2022.115573.
- [7] P. Van Overschee and B. De Moor, *Subspace Identification for Linear Systems*. Boston, MA: Springer US, 1996. doi: 10.1007/978-1-4613-0465-4.
- [8] C. Rainieri and G. Fabbrocino, *Operational Modal Analysis of Civil Engineering Structures*. New York, NY: Springer New York, 2014. doi: 10.1007/978-1-4939-0767-0.
- [9] E. Reynders, J. Houbrechts, and G. De Roeck, “Fully automated (operational) modal analysis,” *Mech Syst Signal Process*, vol. 29, pp. 228–250, May 2012, doi: 10.1016/j.ymssp.2012.01.007.
- [10] F. Magalhães, Á. Cunha, and E. Caetano, “Online automatic identification of the modal parameters of a long span arch bridge,” *Mech Syst Signal Process*, vol. 23, no. 2, pp. 316–329, Feb. 2009, doi: 10.1016/j.ymssp.2008.05.003.
- [11] C. Rainieri and G. Fabbrocino, “Development and validation of an automated operational modal analysis algorithm for vibration-based monitoring and tensile load estimation,” *Mech Syst Signal Process*, vol. 60–61, pp. 512–534, Aug. 2015, doi: 10.1016/j.ymssp.2015.01.019.
- [12] F. Ubertini, C. Gentile, and A. L. Materazzi, “Automated modal identification in operational conditions and its application to bridges,” *Eng Struct*, vol. 46, pp. 264–278, Jan. 2013, doi: 10.1016/j.engstruct.2012.07.031.
- [13] M. Civera, L. Sibille, L. Zanutti Fragonara, and R. Ceravolo, “A DBSCAN-based automated operational modal analysis algorithm for bridge monitoring,” *Measurement*, vol. 208, p. 112451, Feb. 2023, doi: 10.1016/j.measurement.2023.112451.
- [14] M. Ester, H.-P. Kriegel, J. Sander, and X. Xu, “A density-based algorithm for discovering clusters in large spatial databases with noise,” in *Proceedings of the Second International Conference on Knowledge Discovery and Data Mining*, 1996, pp. 226–231.
- [15] V. Mugnaini, L. Zanutti Fragonara, and M. Civera, “A machine learning approach for automatic operational modal analysis,” *Mech Syst Signal Process*, vol. 170, p. 108813, May 2022, doi: 10.1016/j.ymssp.2022.108813.
- [16] L. A. Bull *et al.*, “Foundations of population-based SHM, Part I: Homogeneous populations and forms,” *Mech Syst Signal Process*, vol. 148, p. 107141, Feb. 2021, doi: 10.1016/j.ymssp.2020.107141.
- [17] E. Reynders, R. Pintelon, and G. De Roeck, “Uncertainty bounds on modal parameters obtained from stochastic subspace identification,” *Mech Syst Signal Process*, vol. 22, no. 4, pp. 948–969, May 2008, doi: 10.1016/j.ymssp.2007.10.009.
- [18] R. Allemang and David. L. Brown, “A Correlation Coefficient for Modal Vector Analysis,” in *Proc. 1st Int. Modal Analysis Conference*, 1982.



## A damage screening method of the concrete slab focusing on correlation of mode shapes

Takanori Kadota<sup>1</sup>, 0009-0008-1645-3078, Takuya Daigo<sup>2</sup>, Akihiro Tomioka<sup>2</sup>, Yasunori Miyamori<sup>3</sup>, 0000-0003-2686-8062, Toshiyuki Oshima<sup>1</sup>

<sup>1</sup>Division of Civil and Environmental Engineering, Kitami Institute of Technology, 165 Koen-cho, Kitami, Hokkaido, Japan

<sup>2</sup>Japan Aviation Electronics Industry, Ltd, 3-1-1 Musashino, Akishima, Tokyo, Japan

<sup>3</sup> Division of Civil Engineering, Hokkaido University, Kita 13, Nishi 8, Kita-ku, Sapporo, Hokkaido, Japan

email: kadotaka@mail.kitami-it.ac.jp, daigot@jae.co.jp, tomiokaa@jae.co.jp,

miyamori.y@eng.hokudai.ac.jp, t-oshima@iea.att.ne.jp

**ABSTRACT:** In Japan, visual inspections have been conducted as every five years duty since 2014. To improve the quality of inspections, it is necessary to record the evaluation of the structure's condition and its performance until the next inspection. However, methods and technical level depend on the judgement of the road administrator. A city of Kitami, Hokkaido, Japan where our university is located, was merged with one city and three towns in 2006, and has the largest area ranking in Hokkaido area and 4th in Japan. The total number of bridges, viaducts and functional culverts over 2.0 m length became more than doubled to 524 bridges compared to before the merger. Therefore, it is necessary to establish a labor saving and cost-effective method to assess the performance of bridge structures. In recent years, it has become possible to easily measure structural responses by the improvement of sensor performance, and more research has been conducted on maintenance management methods. Among those, vibration characteristics have a significant effect on the stiffness and mass of a bridge member and will be the index that grasps easily various damage effects. In this study, a damage location screening method was investigated for concrete slab bridges where segregation was suspected, based on correlation between mode shapes by using the COMAC. As a result, it is shown that these techniques will identify the damaged location and be used as an effective method to screen damaged locations.

**KEY WORDS:** Damage screening method; Mode shape; Concrete slab bridge; Maintenance.

### 1 INTRODUCTION

In Japan, visual inspections have been conducted as every five years duty since 2014. Under the established inspection specification, to improve the quality of inspections, it is necessary to record the evaluation of the structure's condition and its performance until the next inspection. However, methods and technical level depend on the judgement of the road administrator [1]. A city of Kitami, Hokkaido, Japan where our university is located, was merged with one city and three towns in 2006, and has the largest area ranking in Hokkaido area and 4th in Japan. Farmland is spread out in the suburbs and road network is expanding widely. The total number of bridges, viaducts and functional culverts over 2.0 m length became more than doubled to 524 bridges compared to before the merger [2]. Therefore, it is necessary to establish a labor saving and cost-effective method to assess the performance of bridge structures.

In recent years, it has become possible to easily measure structural responses by the improvement of sensor performance, and more research has been conducted on maintenance management methods [3], [4]. Among those, vibration characteristics have a significant effect on the stiffness and mass of a bridge member and will be the index that grasps easily various damage effects. Our research group has been studying a maintenance method using the COMAC focusing on a pedestrian bridge slab [5]. Consequently, it was shown that damage screening by co-relationship between mode shape is effective.

In this study, a damage location screening method was investigated for concrete slab bridges where segregation was suspected, based on correlation between mode shapes by using the COMAC.

### 2 TARGET BRIDGE

#### 2.1 Bridge specifications

The target bridge of this study is a reinforced concrete slab bridge. Since there is no detailed information such as construction records and drawing, shape measurements on site were taken as shown in Figure 1.

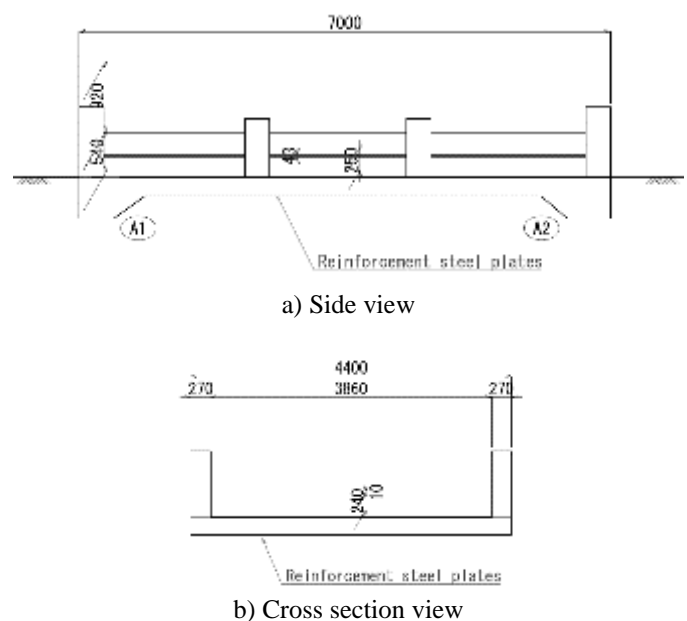


Figure 1. General arrangement drawing (unit: mm).



Figure 2. Inspection photos.

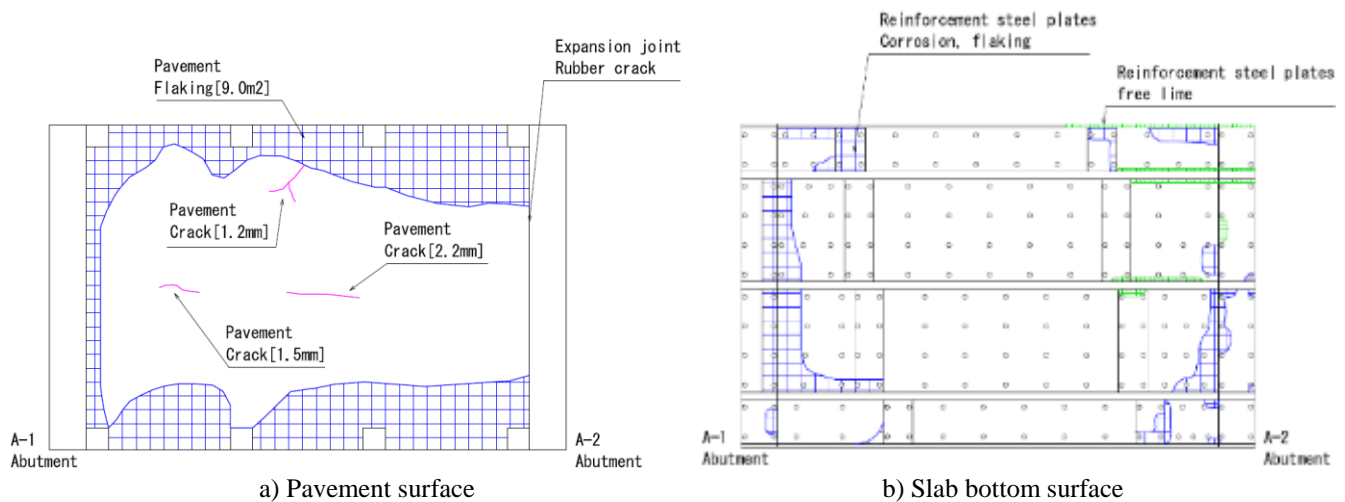


Figure 3. Inspection results.

## 2.2 Inspection results

Visual inspection was conducted to grasp degree of damage of each component by our research group in 2023. As a result of this inspection, widespread flaking has been found at the pavement on both sides, and corrosion and free lime can be seen on the reinforcement steel plates underside of the slab. Especially, icicle-like free lime has been found upstream side on the A2 abutment. Since this bridge does not have a waterproof layer on the concrete slab, it was suspected that segregation of the slab surface occurred more than in other areas. However, the pavement and steel plates make it difficult to see damage directly. A non-destructive survey by using electromagnetic waves was conducted on the pavement, but it did not obtain a clear waveform from the surface of the slab. Inspection status and results are shown in Figure 2 and Figure 3.

## 3 VIBRATION MEASUREMENT

### 3.1 Measurement conditions

Vibration characteristics were identified from acceleration data obtained by passing vehicle. The location of the accelerometer and passing situation of the vehicle are shown in Figure 4. Since this bridge has a short span and a roughly square planar shape, nine accelerometers were installed at equal spacing on the pavement surface to identify the bowl-shaped vibration mode shapes. In addition, accelerometers of number 1~3 and 7~9 were located under the tire lane, so they were moved 300mm outward.

Accelerometer is 3-axis MEMS type manufactured by Japan Aviation Electronics Industry, shown in Figure 5, with a sampling rate of 2000Hz. The vehicle passed over the bridge at 20km/h and measurements were taken 3 times in each direction.

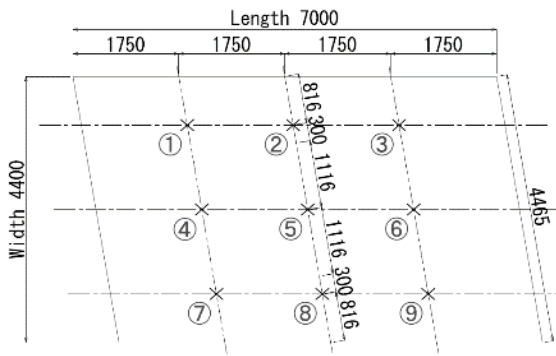


Figure 4. Measurement position and the test vehicle.



Figure 5. Accelerometer (JA-70SA).

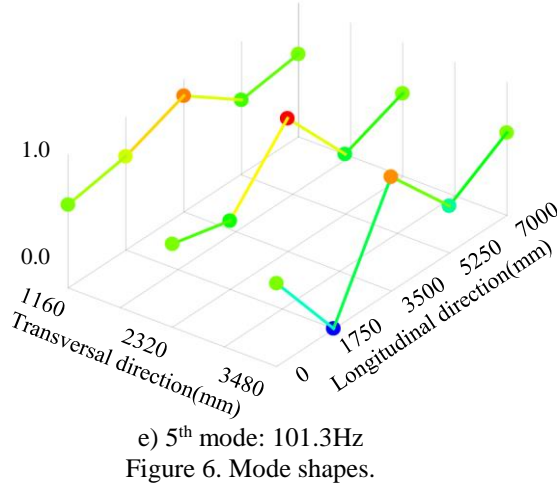
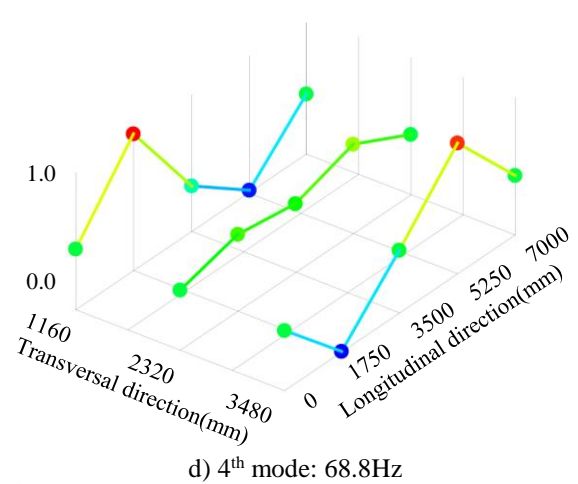
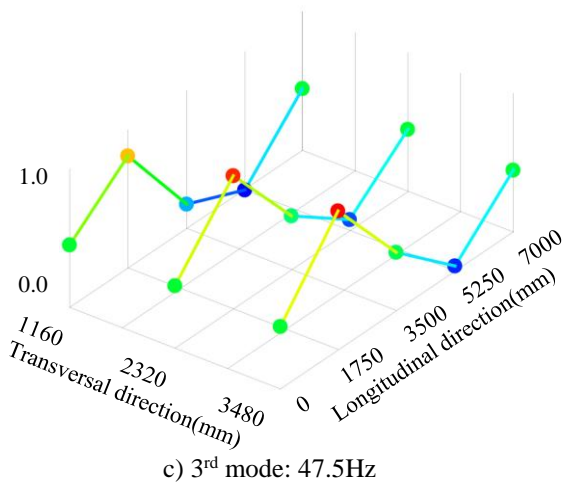
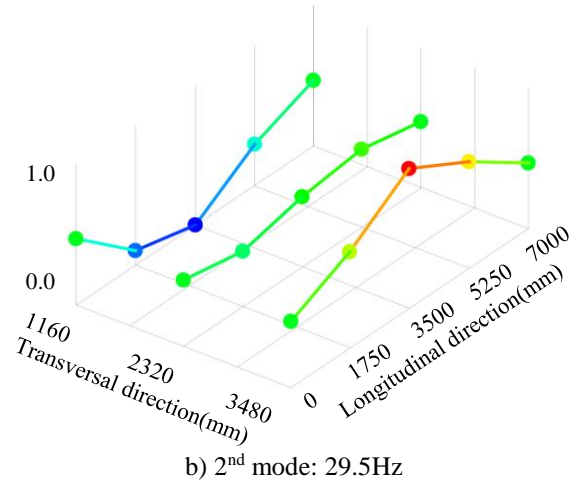
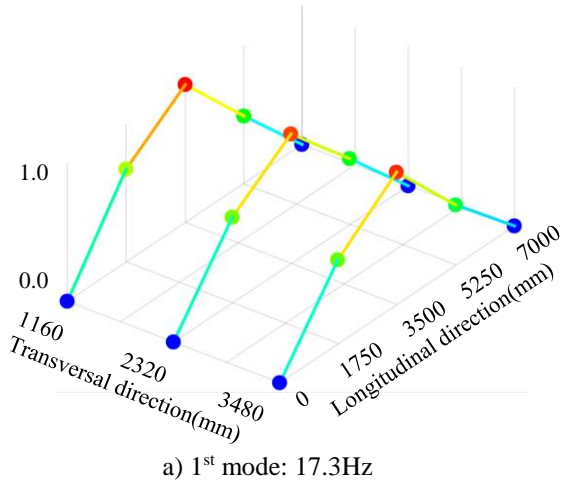


Figure 6. Mode shapes.



### 3.2 Conditions for data processing

The data processing was carried out by the following steps. First, the power spectrum of each set of acceleration data was obtained by Fast Fourier Transform (FFT). Next, natural frequencies were identified by the peak picking method. Finally, mode shapes were estimated from the filtered wave amplitude in each sensor node.

### 3.3 Measurement results

As shown in Figure 6, the five vibration modes were identified from the experiment. In addition, the points at both ends where no accelerometers are plotted as zero value to make the mode shape easier to understand.

As a result, the first mode was the lower vertical symmetric bending mode. The second mode was the lower torsional mode. The third mode was the unsymmetric bending mode. The fourth mode was the higher torsional mode. And the fifth mode was the higher vertical symmetric bending mode.

## 4 ESTIMATION OF DAMAGE AREA BY MODE SHAPE CORRELATION

### 4.1 Estimation method

As a result of the inspection shown in Figure 3, icicle-like free lime has occurred upstream side on the A2 abutment, then it is thought the segregation has progressed more than in other areas. At the relationship between sensor position and icicles position shown in Figure 7, it shows that the icicle-like free lime is near the sensor number 3. In this study, the COMAC (Coordinate Modal Assurance Criterion) [6] technique is adopted to try to

identify the damaged location. This technique is the calculation of correlation values at each coordinate over all the correlated mode pairs via the use of equation (1).

$$\text{COMAC}(j) = \frac{\sum_{i=1}^N |\{\phi_o\}_i^j \{\phi_D\}_i^j|^2}{\sum_{i=1}^N [\{\phi_o\}_i^j]^2 \sum_{i=1}^N [\{\phi_D\}_i^j]^2} \quad (1)$$

Where,  $j$  is sensor number,  $N$  is the number of the modes,  $\{\phi_o\}_a$  and  $\{\phi_D\}_i$  are the mode vectors in different situations respectively. In this study, the sensors were set at 9 locations, and the modes are 5 as total identified modes.

Now, there was no initial data for this bridge, it wasn't able to

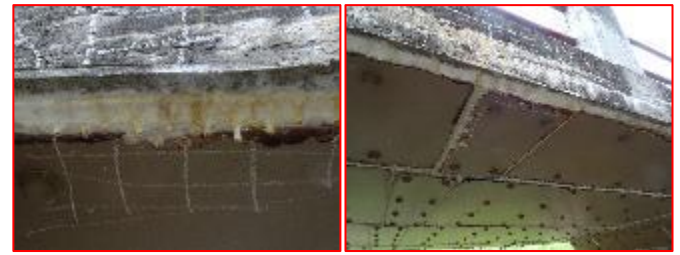


Figure 7. The icicle-like free lime and the position.

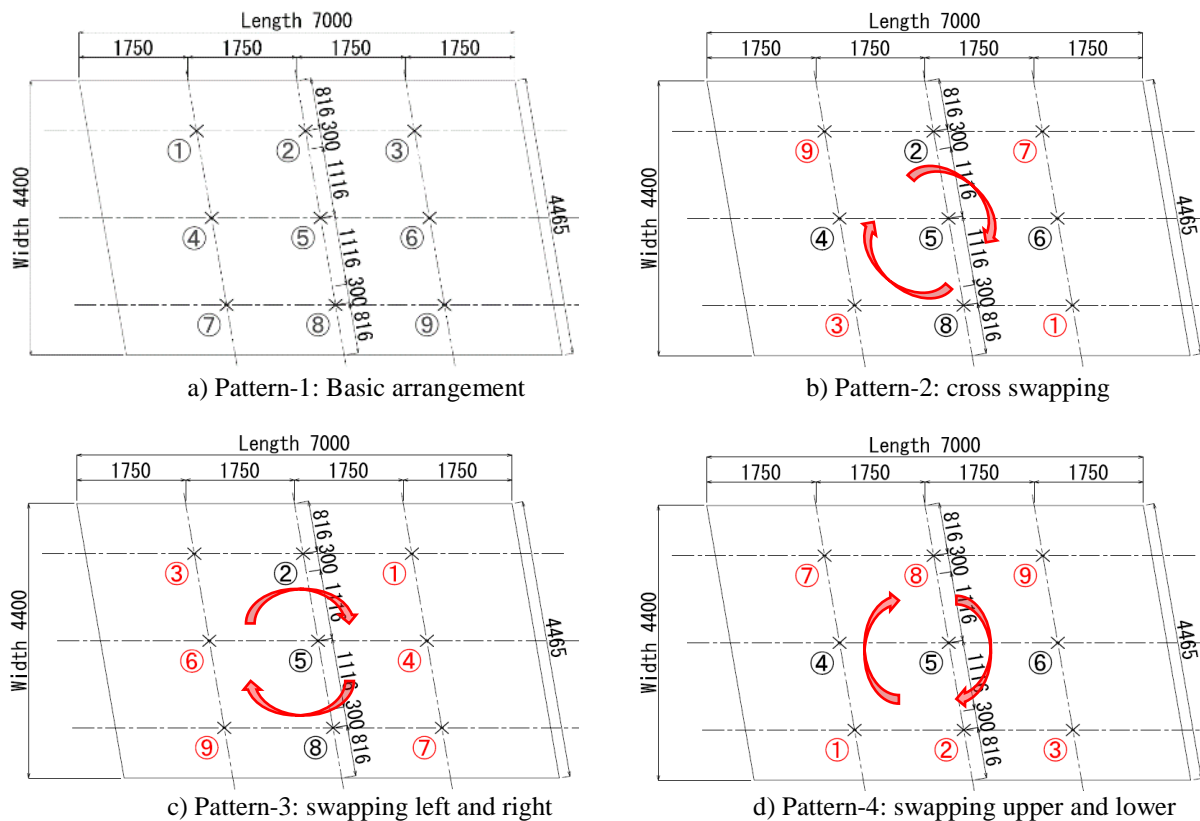


Figure 8. Swapping mode vectors.

calculate the COMAC. Therefore, the following assumption was assumed. Since the planar shape of this bridge is biaxially symmetrical, it was assumed that the mode vectors at the measurement points on the diagonal line can switch each other as shown in Figure 8b). The same assumption was also assumed for the axes at the center of the span and the center of the width as shown in Figure 8c) and Figure 8d). Hence, the COMAC was calculated by the four patterns combination as shown in Figure 8. However, since the sensor number 5 is located in the center, it cannot swap. And even numbered sensors are limited to only two patterns. Here, considering bridge shapes of small span concrete slab bridges that were managed by Kitami City. Since many of these bridges are almost symmetrical shape include skew angles, this swapping approach method is widely applicable. Many of bridge located on suburban routes with little traffic and cracks do not tend to occur on the underside of the slab. In addition, the cross section of the pavement has a 2% drainage gradient, and the ends of the girders are prone to damage due to pooled water. Therefore, simply identifying damaged areas at the four corners of the slab provides extremely useful information for maintenance.

#### 4.2 Result of estimation

The calculated results of the COMAC are shown in Figure 9. The vertical axis of this graph indicates the COMAC value, and the horizontal axis indicates the sensor number of the basic arrangement as shown in Figure 8a). As the COMAC approaches 1.0, it indicates that the correlation between these two different situations is high.

In the COMAC comparison between patterns 1 and 2, it shows the values at sensors 3 and 7 are relatively low. Also, in the COMAC comparison between patterns 1 and 4, it shows the values at the sensor number 3 and 9 are more clearly lower. On the other hand, the COMAC result between patterns 1 and 3 is less clear than the others, it barely lowered sensors 1 and 3. From these results, the COMAC value at sensor number 3 is generally low. Here, a graph of the three results multiplied together is shown in Figure 8d) in order to clarify the difference in the COMAC values for each sensor. The correlation at the sensor number 3 was the single lowest.

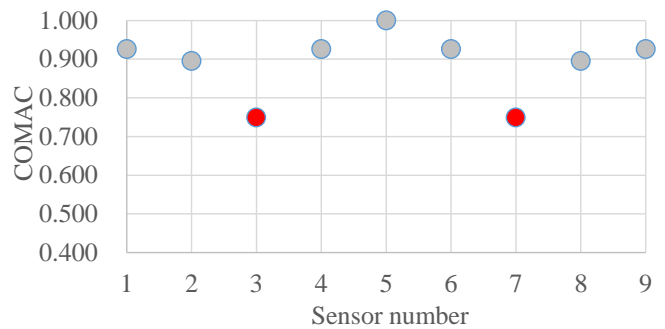
As a result of the above, it was considered that the COMAC value of sensor number 3 which was located near the icicle-like free lime was the lowest, the rigidity of the concrete slab may have been reduced by the pooled water at the invisible inside, it affected the mode shape of the sensor number 3. It was also shown that even without initial structural values or historical measurement data, it is possible to screen for the damaged locations by swapping vibration mode vectors, even the locations are limited.

#### 5 CONCLUSIONS

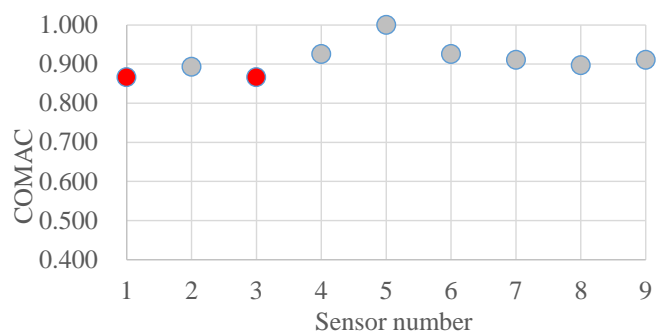
In this study, a damage location screening method was investigated for concrete slab bridges where segregation was suspected, based on correlation between mode shapes by using the COMAC. The results of this study are as follows:

- According to the inspection results for the reinforced concrete slab bridge, it was suspected that segregation of the slab surface at the upstream side on the A2 abutment.

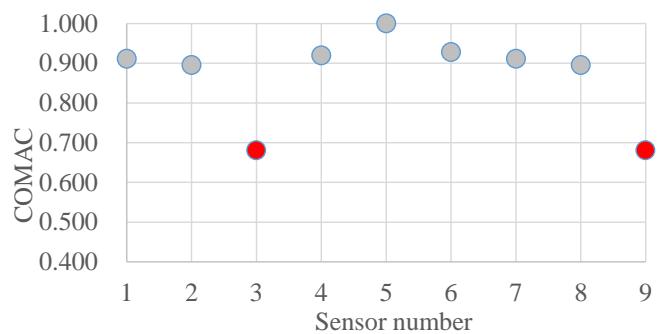
- Vibration characteristics were identified from acceleration measurement by vehicle passing, six vibration modes and natural frequencies were obtained.



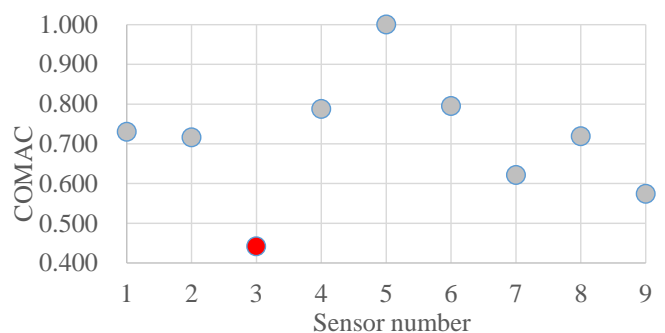
a) correlation Pattern-1 and Pattern-2



b) correlation Pattern-1 and Pattern-3



c) correlation Pattern-1 and Pattern-4



d) multiplication between a) - c)

Figure 9. COMAC results.

- From the results of COMAC, the sensor number 3 which was located near the icicle-like free lime was the lowest. The rigidity of the concrete slab may have been reduced by the pooled water at the invisible inside, it affected the mode shape of the sensor number 3.
- Since many of these small span concrete slab bridges that were managed by Kitami City are almost symmetrical shape include skew angles, this swapping approach method is widely applicable.

## ACKNOWLEDGMENTS

I would like to express my appreciation to Professor Emeritus Shuichi Mikami and graduate student Hitomi Onoda for their assistance in inspecting this bridge.

## REFERENCES

- [1] Ministry of Land, Infrastructure, Transport and Tourism, Periodic bridge inspection guideline, Tokyo, Japan, 2025 (in Japanese).
- [2] Kitami City, Bridge maintenance plan, Kitami, Japan, 2022 (in Japanese).
- [3] P. Tuttipongsawat, E. Sasaki, K. Suzuki, M. Fukuda, N. Kawada, K. Hamaoka, PC Tendon Damage Detection Based on Phase Space Topology Changes in Different Frequency Ranges, *Journal of Advanced Concrete Technology*, Vol.17, pp. 474-488, 2019.
- [4] T. Miyashita, D. Matsumoto, Y. Hidekuma, A. Kobayashi, Experimental study on CFRP strand sensor realizing repair/reinforcement and condition monitoring, *Journal of Structural Engineering*, Vol. 62A, pp. 537-548, 2016 (in Japanese).
- [5] T. Kadota, Y. Miyamori, T. Saito, Y. Shirakawa, T. Obata, Fundamental study on the structural health monitoring method to the pedestrian overpass with corrosion damage, *Journal of Structural Engineering*, Vol. 67A, pp. 261-272, 2021 (in Japanese).
- [6] NAJ Lieven, and DJ Ewins, Spatial Correlation of Mode Shapes, the Coordinate Modal Assurance Criteria (COMAC), 6th IMAC, 1988.



# Feasibility of micro-motion from SAR imagery for vibration-based SHM

Alessandro Lotti<sup>1</sup>, <https://orcid.org/0009-0000-5240-2122>, Aleksanteri B. Vattulainen<sup>2</sup>, <https://orcid.org/0000-0003-1898-600X>, Chiara Suppi<sup>1</sup>,  
Sebastian Diaz Riofrio<sup>2</sup>, Pietro Milillo<sup>3,4</sup>, Enrico Tubaldi<sup>2</sup>, Daniele Zonta<sup>1</sup>, Carmine Clemente<sup>2</sup>

<sup>1</sup> Department of Civil, Environmental and Mechanical Engineering, University of Trento, Trento, Italy

<sup>2</sup> Department of Electronic and Electrical Engineering, University of Strathclyde, Glasgow, UK

<sup>3</sup> Department of Civil and Environmental Engineering, University of Houston, Houston, TX, USA

<sup>4</sup> Visiting Scientist, German Aerospace Center, Munich, Germany

email: [alessandro.lotti@unitn.it](mailto:alessandro.lotti@unitn.it)

**ABSTRACT:** This paper explores the use of single-pass Synthetic Aperture Radar (SAR) images to remotely measure the vibrational response of reflective ground targets, aiming to support vibration-based Structural Health Monitoring (SHM) of civil infrastructure. A Sub-Pixel Offset Tracking (SPOT) technique is applied to SAR imagery to reconstruct the time history of radial velocity, using the principle of micro-motion (m-m) effects induced by vibrating targets. Validation is by comparing SAR-extracted velocity profiles with synchronous ground measurements of a vibrating Corner Reflector (CR). Three representative test cases—including single-frequency, and amplitude-modulated vibrations—with maximum displacement values of 24.1 mm, 1.1 mm and 0.5 mm are analyzed using SAR images collected by the Umbra X-band SAR constellation. The extracted vibrational features are evaluated through time-domain correlation, spectral accuracy, and error metrics. Results confirm that SPOT can reconstruct velocity time histories and frequency content reliably for medium-to-high velocity scenarios ( $> 10$  mm/s) and single-frequency signals. Even under low-velocity, complex signal conditions, the main frequency peaks are detectable, with negligible frequency errors and correlations of 0.61 (time) and 0.82 (frequency). This study demonstrates the potential of SAR m-m processing for fully remote vibration-based SHM, offering a scalable, installation-free alternative for assessing structural dynamics.

**KEY WORDS:** Structural Health Monitoring, Remote sensing, SAR-Imaging, Micro-Motion, Micro-Doppler, Modal Analysis.

## 1 INTRODUCTION

### 1.1 Background

Structural Health Monitoring (SHM) traditionally relies on contact-based sensors such as accelerometers to detect changes in a structure dynamic response [1]. While its claimed effectiveness in extracting the modal parameters—such as natural frequencies, damping ratios and modeshapes—they often face limitations in terms of costs, installation complexity, and sensor coverage [2], especially for large civil infrastructure. The need for prompt, scalable, and contactless sensing has led to increasing interest in remote sensing technologies [3]. Among these, spaceborne Synthetic Aperture Radar (SAR) stands out. SAR uses radar signals emitted from a sensor mounted on a satellite, to create images of the Earth surface. A SAR image appears as a complex matrix in range and azimuth coordinates, range corresponding to the radial direction (sensor to ground target) and azimuth to the direction of velocity of the platform (e.g., the satellite) motion [4].

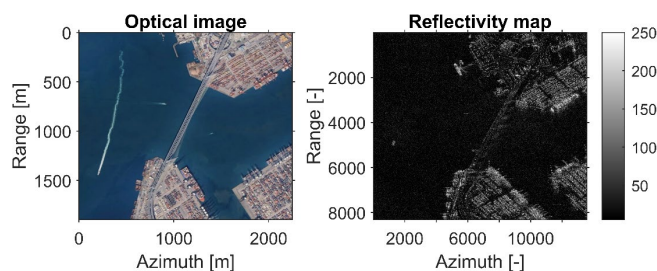


Figure 1.1. SAR image (from Umbra Sensor [5]) reflectivity map of the Stonecutters Bridge (Hong Kong harbor) compared to its optical image.

SAR has gained considerable attention thanks to its ability to cover large areas—ranging from 5 km to 200 km in width [6], [7]—and to detect ground movement through Interferometric SAR (InSAR), which reconstructs displacement trends by combining multiple images of the same area acquired over time [8]. Whilst InSAR is a widely recognized technique for measuring millimetric precision displacements [9], it requires a large dataset [10] and cannot extract SHM-related information from a single pass (i.e., single image). In contrast, recent literature shows that it is possible to overcome these limitations of InSAR and use single-pass SAR images to extract vibrational information from reflective ground targets, through different techniques based on the measurement of micro-motions (m-m) using the micro-Doppler (m-D) phenomenon [11].

### 1.2 Micro-motion in SAR images

In a SAR image, each pixel contains magnitude (reflectivity) and phase information. Targets with strong reflectivity, such as metallic objects with sharp geometries, are prominently visible in the reflectivity map. Figure 1.1 shows an example of a reflectivity map alongside its corresponding optical image of the Stonecutters Bridge in Hong Kong.

The spatial resolution of the SAR image—defined as the size of each pixel in meters along the range and azimuth directions—depends on several factors, particularly the acquisition time ( $t_a$ ) in the azimuth direction. Acquisition time refers to the duration over which the satellite observes the same ground target, from the start to the end of the collection. This duration can vary significantly depending on the type of satellite sensor and the acquisition mode employed.

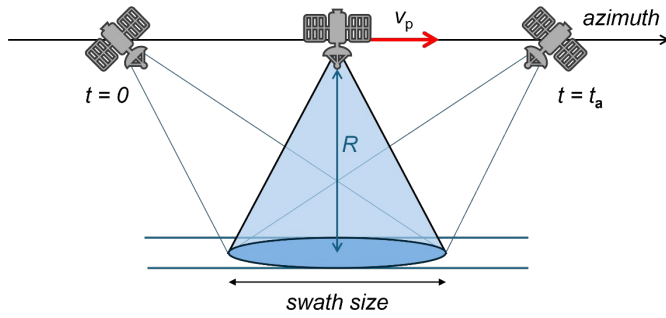


Figure 1.2. SAR acquisition geometry in case of spotlight acquisition mode.

In this work, SAR imagery collected in spotlight mode is studied. In this acquisition mode, the radar beam is continuously steered (or "squinted") to remain focused on the same ground area for an extended duration – typically between 5 and 20 seconds – greatly improving azimuth resolution. An example of the geometry of the SAR collection is shown in Figure 1.2. For spotlight acquisitions, the azimuth resolution  $\Delta x$  is given by Eq. (1):

$$\Delta x = \frac{\lambda R}{2 v_p t_a} \quad (1)$$

where  $\lambda$  is the wavelength of the SAR sensor (typically 25-40 mm for X-band radars),  $R$  is the radial distance to the ground target,  $v_p$  is the platform (satellite) velocity in the azimuth direction, and  $t_a$  is the acquisition duration (or illumination time). When generating a SAR image, the scene is typically assumed to be static – i.e., objects still on the surface. However, when a target is moving, its position in the image will be shifted in the range-azimuth plane due to uncompensated signal phase shift associated with the motion (imparted by the Doppler effect), causing a defocusing and smearing of the object. A point moving at constant speed, will be displaced mainly in the azimuth direction by a distance governed by Eq. (2) [12]:

$$x = \frac{v_r R}{v_p} \quad (2)$$

where  $v_r$  is the radial velocity of the object,  $R$  is the radial distance to the ground target, and  $v_p$  is the platform velocity in the azimuth direction. Since it is the change in radial velocity  $v_r$  relative to the moving satellite that produces this effect, the radial velocity is the key quantity of interest in this study.

Micro-motions of a target, such as vibrations, cause periodic fluctuations in the radar signal frequency due to the Doppler effect, where this is specifically referred to as micro-Doppler (m-D) [13]. In SAR imagery, this effect results in the formation of paired echoes along the azimuth direction around the real target [14], as shown in Figure 1.3. These effects are visible in the reflectivity image and can be exploited to measure the vibrations of reflective ground targets. The faster the velocity of vibration, the more evident these echoes appear. The earliest studies in this field, such as [15], explored how to extract vibrations and rotations from moving targets. Later works investigated the potential of employing this principle for SHM in civil engineering, applying it to a dam and a bridge, respectively [11], [16].

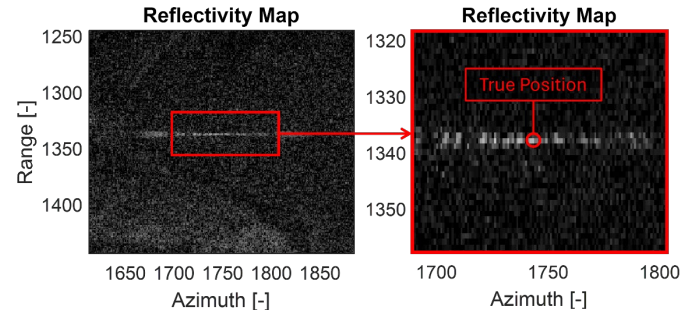


Figure 1.3. Micro-Doppler from an isolated target, vibrating vertically with an amplitude of 45 mm and frequency 0.8 Hz.

### 1.3 Research objective

The objective of this work is to assess the feasibility of using single-pass SAR images to extract vibration characteristics (i.e. micro-motions) from isolated reflective targets. Specifically, the performance and limitations of the extraction technique are assessed under different conditions of target vibrational amplitude, frequency, and movement time history complexity. Three representative test scenarios are used, and synchronous ground truth measurements are used as validation benchmarks.

The paper is structured as follows: Section 2 introduces the algorithm used to implement the m-m SAR method. Section 3 provides an overview of the experimental validation setup and the SAR datasets employed. Section 4 presents the results along with a detailed discussion. Lastly, Section 5 reports conclusions and summarizes the key insights of the study.

## 2 METHODOLOGY

### 2.1 Sub-Pixel Offset Tracking (SPOT)

The m-m SAR technique uses single-pass SAR imagery to estimate the radial velocity time history of a ground target within the observation window of the SAR image. The core algorithm used for this purpose is the Subpixel-Offset-Tracking (SPOT), as the one used in [11] and [16]. After cropping the area around the target (Region of Interest – ROI), SPOT segments the SAR image (full-aperture), into  $N$  sub-images (sub-apertures), each focused from a fraction of the full image observation time. To achieve this, a Fast Fourier Transform (FFT) is performed on the ROI along the azimuth dimension to convert the data from *range versus azimuth* to *range versus azimuth-frequency*. A segmentation in sub-apertures along the azimuth frequency axis is then performed using window lengths defined by the aperture fraction  $\alpha$  (see Figure 2.1):

$$\alpha = \frac{t_{\text{sap}}}{t_a} \quad (3)$$

where  $t_{\text{sap}}$  represents the duration in time of the sub-aperture, and  $t_a$  the acquisition duration (full aperture). Adjacent sub-apertures can share portions of the azimuth frequency domain (and therefore time); as controlled by the overlap ratio  $\Omega$ :

$$\Omega = \frac{t_{\text{ol}}}{t_{\text{sap}}} \quad (4)$$

where  $t_{\text{ol}}$  is the overlap duration between adjacent sub-apertures.

Given  $\alpha$  and  $\Omega$ , the total number of sub-apertures  $N$  can be computed as:

$$N = \frac{\alpha^{-1} - \Omega}{1 - \Omega} \quad (5)$$

The  $N$  azimuth-frequency sub-apertures are individually transformed into to  $N$  range versus azimuth images by means of an Inverse FFT. The target azimuth displacement  $x$  is then tracked across the sequence of sub-apertures using 2D cross-correlation. Each target azimuth shift  $x_k$  – given a specific  $k$ -th sub-aperture – depends on the instantaneous value of the radial velocity  $v_{r,k}$ . Therefore, it is possible to invert Eq. (2) to obtain the value of the radial velocity given the azimuth shift  $x_k$ :

$$v_{r,k} = \frac{x_k v_p}{R} \quad (6)$$

The time vector associated with the reconstructed velocity is a linearly spaced sequence of  $N$  values, starting at  $t_{\text{sap}}/2$  and ending at  $t_a - t_{\text{sap}}/2$ . The temporal resolution is then given by:

$$\Delta t = \frac{t_a - t_{\text{sap}}}{N - 1} \quad (7)$$

To ensure the desired frequency content is captured by the time series, the sampling frequency must satisfy the Nyquist criterion for the maximum frequency,  $f_{\text{max}}$ , to be observed:

$$f_s = \frac{1}{\Delta t} \geq f_{\text{max}} \quad (8)$$

There are two main ways to increase the sampling frequency: reduce the aperture fraction  $\alpha$ , or increase the overlap ratio  $\Omega$ . It should, however, be noted that reducing the aperture fraction shortens the illumination time for each sub-aperture and consequently worsens the azimuth resolution of each sub-aperture image. When the aperture fraction becomes too small, the target may no longer appear as a distinct feature, thereby degrading the tracking performance. This imposes a practical limit on how finely the aperture can be segmented, although this can be mitigated by increasing the overlap.

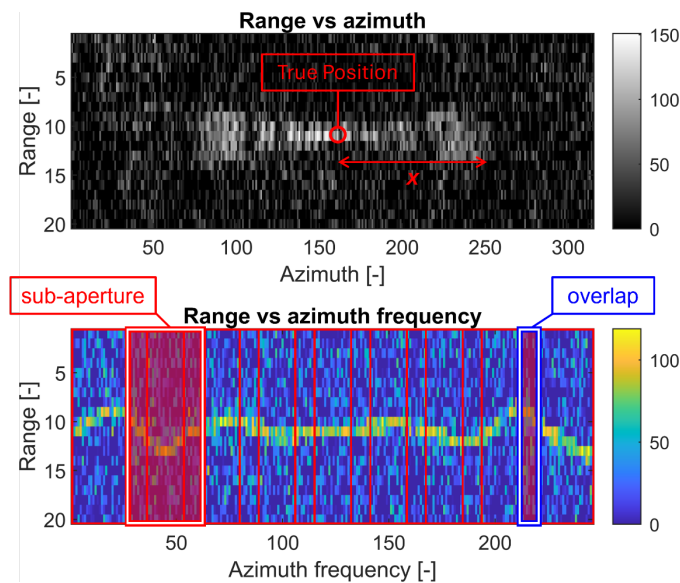


Figure 2.1. Top: range versus azimuth ROI (with highlighted and the azimuth shift  $x$ ); bottom: FFT of ROI along azimuth, yielding range versus azimuth frequency data, with the segmentation of sub-aperture data indicated.

The fundamental steps of the SPOT algorithm are as follows:

1. Crop the SAR image around the ROI;
2. Apply an FFT along azimuth to convert the ROI to the range versus azimuth-frequency domain;
3. Segment the azimuth-frequency spectrum into  $N$  sub-apertures according to selected parameters  $\alpha$  and  $\Omega$ ;
4. Apply IFFT to obtain  $N$  range versus azimuth sub-aperture images;
5. Track the azimuth pixel displacement of the target across sub-apertures;
6. Compute the velocity and the associated time-vector.

### 3 EXPERIMENTAL VALIDATION

#### 3.1 Tests sites and ground instrumentation

To evaluate the effectiveness of the m-m SAR technique, controlled experiments were conducted using artificially vibrating targets with ground truth data measured synchronously with the satellite passage. Tests took place in open fields in Trento, Italy, and Glasgow, UK, to avoid interference from nearby objects (see Figure 3.1).

The instrumentation setup included a Corner Reflector (CR) mounted on a shaker device, with motion captured using a Linear Variable Displacement Transducer (LVDT) (see Figure 3.2). The sensor recorded vertical displacement at a sampling rate of 50 Hz, where this was later projected onto the satellite radial direction and synchronized to match the satellite passage. As the m-m SAR algorithm measures velocity rather than displacement, the ground displacement signals were numerically differentiated to obtain the synchronized radial velocity profiles. This allowed for a direct comparison between SAR measured velocities and ground truth data. This study focuses on three representative test configurations, summarized in Table 1. The shaker was set to simulate various amplitudes and types of vibrational signals, including single-frequency sinusoidal oscillations and amplitude-modulated waveforms. In the context of civil engineering, the amplitude of structural vibrations can vary considerably depending on the structural type. For long-span bridges, typical displacements range from 0.1 mm to 5 mm, corresponding to radial velocities of approximately 1–10 mm/s or lower. To replicate these conditions, the test campaign was designed to progressively study vibrations beginning with well-defined, high-amplitude motions to those of lower-amplitude more relevant to SHM of bridges. The maximum target velocities for Tests 1, 2, and 3 were 95.5 mm/s, 10.8 mm/s, and 3.1 mm/s, respectively, corresponding to peak vertical displacements of 24.1 mm, 1.1 mm, and 0.5 mm.

To refine the analysis, the SAR measured velocity time histories were fitted using a model based on the superposition of multiple sinusoidal components. First, the SAR velocity spectra were upsampled by a factor of four, and dominant frequencies were identified from the FFT. For Tests 1 and 2, the frequency corresponding to the primary peak was selected, while for Test 3, being amplitude modulated, the three most dominant frequency components were extracted. These extracted frequencies were then used to fit sinusoidal models by optimizing amplitude and phase only. This procedure allowed for the reconstruction of refined, high-resolution velocity time histories.



### 3.2 SAR acquisitions

Satellite data were collected by the Umbra X-band SAR constellation, capable of high-resolution spotlight-mode imaging. Spotlight acquisition was selected to maximize the collection time, and therefore the azimuth resolution.

Commonly, SAR providers deliver Multi-Look Complex (MLC) images, which are generated by averaging multiple looks in the azimuth and/or range directions from the same observation in order to reduce speckle noise. While this averaging improves image interpretability, it also reduces the effective resolution (due to lower acquisition time) and suppresses the micro-motion effects (i.e., paired echoes), that are critical to this study. To preserve these effects, images were provided by Umbra in the form of Single-Look Complex (SLC) products, containing a single, unaveraged observation in both range and azimuth directions. These were processed using the polar format algorithm.

The three SAR images were acquired using sensors operating at a central frequency of 9.6 GHz, corresponding to a wavelength of  $\lambda = 31$  mm. The main characteristics of the SAR acquisitions used in the three tests are summarized in Table 1.

### 3.3 Evaluation of the performance

The ground-measured radial velocities served as a validation benchmark to quantify the performance of SPOT in reconstructing the time history of radial velocity of the target, during the SAR acquisition. To achieve this, the accuracy was evaluated according to the following metrics:

- Root Mean Square of the Error ( $RMSE$ ), computed in the time domain by comparing the SAR-reconstructed and ground-measured velocities at matching timestamps.
- Frequency error ( $\epsilon_f$ ), evaluated as the residual between the true frequency and the frequency measured with m-m SAR, corresponding to the highest peak of the FFT;
- Correlation in time ( $\rho_t$ ) and frequency ( $\rho_f$ ) domains.

Table 1. Test configurations. The table reports: type of signal tested (Signal type), principal frequency of vibration ( $f$ ), maximum ground vertical displacement ( $d_{max}$ ), maximum radial velocity value ( $v_{r,max}$ ), SAR sensor name (Sensor), Pulse Repetition Frequency (PRF), acquisition duration ( $t_a$ ), incidence angle ( $\theta$ ), platform velocity ( $v_p$ ), slant-range distance ( $R$ ), range resolution ( $\Delta x$ ), and azimuth resolution ( $\Delta x$ ).

Quantity	Test	1	2	3
Signal type	[-]	SIN	SIN	AM
$f$	[Hz]	1	2	1
$d_{max}$	[mm]	24.1	1.1	0.5
$v_{r,max}$	[mm/s]	95.5	10.8	3.1
Date	[d/m/y]	18/11/23	14/03/24	30/01/25
Time UTC	[H:M:S]	20:46:27	21:29:22	10:46:27
PRF	[kHz]	5.75	6.31	7.75
$t_a$	[s]	6.04	5.95	14.70
$\theta$	[°]	54.8	49.4	34.5
$v_p$	[km/s]	7.69	7.67	7.65
$R$	[km]	844	795	683
$\Delta y$	[mm]	0.18	0.17	0.13
$\Delta x$	[mm]	0.22	0.21	0.07

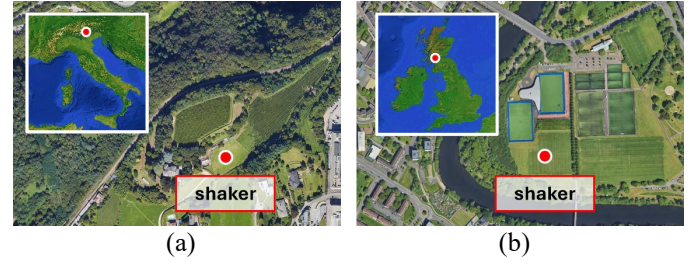


Figure 3.1. Tests Locations in (a) Trento, Italy; and (b) Glasgow, UK.

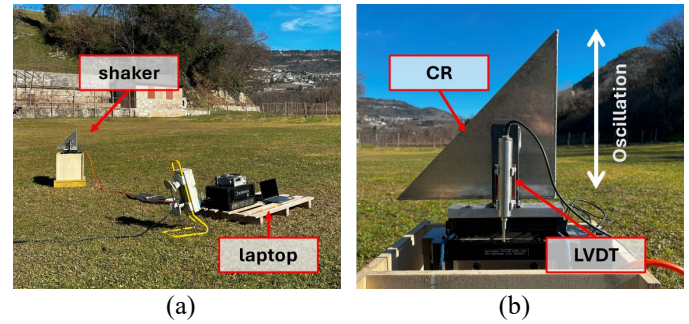


Figure 3.2. Instrumentation employed: (a) shaker and acquisition system, (b) Detail of CR and LVDT.

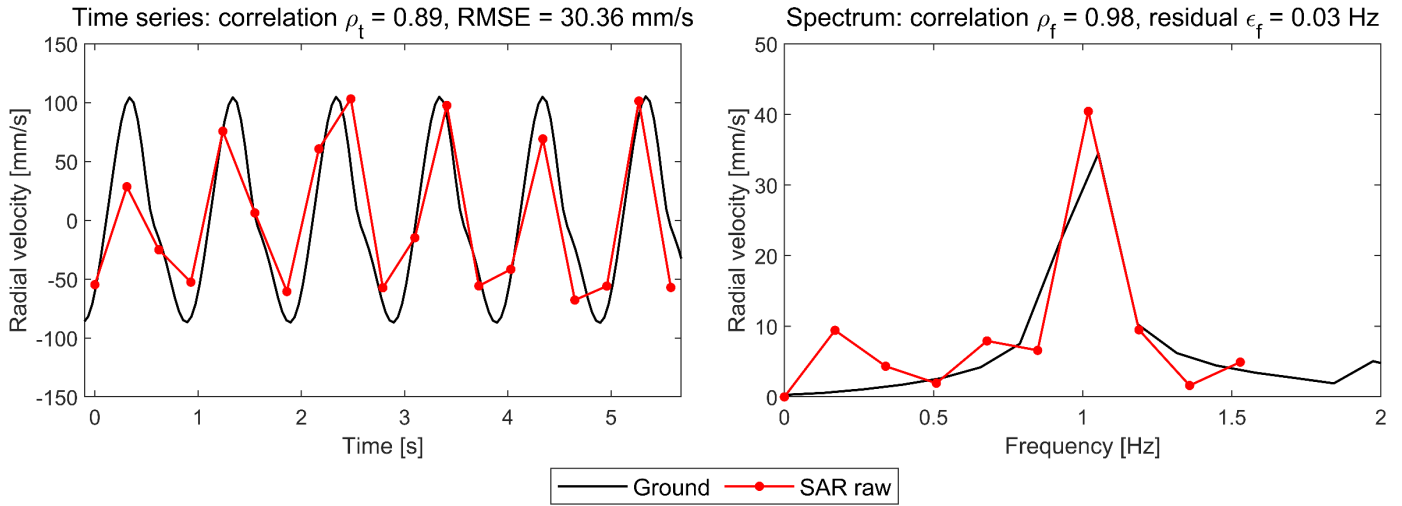
## 4 RESULTS AND DISCUSSION

This section highlights the results of the SPOT m-m measurement technique, as well as the performance evaluation through the comparison with ground data. The comparison is performed both graphically (see Figure 4.1, Figure 4.2, Figure 4.3) and numerically (Table 2), using error metrics such as  $RMSE$ , frequency error, and Pearson's correlation coefficients in time and frequency domains. Results focus on Tests 1, 2, and 3 as representative cases for varying vibration conditions. Each test was processed using the workflow described in Section 2, with extraction parameters summarized in Table 2.

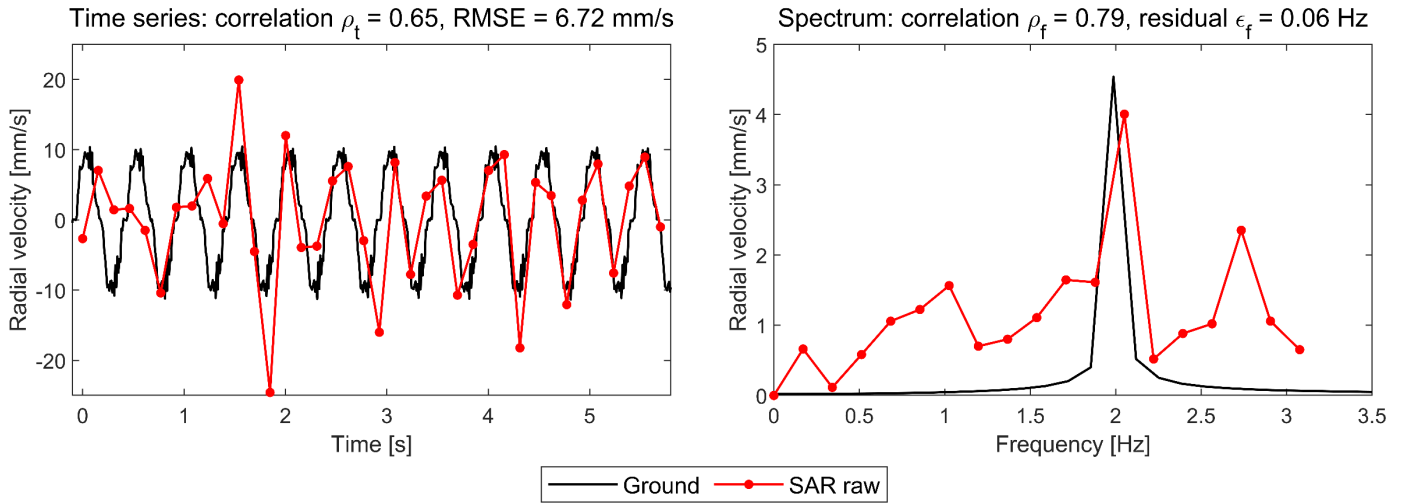
Table 2. Metric results. The table reports for each test: maximum radial velocity value ( $v_{r,max}$ ), acquisition duration ( $t_a$ ), aperture fraction ( $\alpha$ ), overlap ratio ( $\Omega$ ), number of sub-apertures ( $N$ ), sampling frequency ( $f_s$ ), frequency resolution ( $\Delta f$ ),  $RMSE$  and  $RMSE$  relative to max velocity value ( $RMSE\%$ ), frequency residual error ( $\epsilon_f$ ), correlations in time ( $\rho_t$ ) and frequency ( $\rho_f$ ) domains for the raw m-m SAR signal.

Quantity	Test	1	2	3
$v_{r,max}$	[mm/s]	95.5	10.8	3.1
$t_a$	[s]	6.04	5.95	14.70
$\alpha$	[%]	7.6	4.3	4.5
$\Omega$	[%]	35	40	49
$N$	[-]	23	38	42
$t_{sap}$	[s]	0.46	0.27	0.66
$f_s$	[Hz]	3.23	6.49	2.92
$\Delta f$	[Hz]	0.18	0.18	0.07
$RMSE$	[mm/s]	30.4	6.7	1.2
$RMSE\%$	[%]	31.8	62.0	38.7
$\epsilon_f$	[Hz]	0.03	0.06	0.02
$\rho_t$	[-]	0.89	0.65	0.66
$\rho_f$	[-]	0.98	0.79	0.71

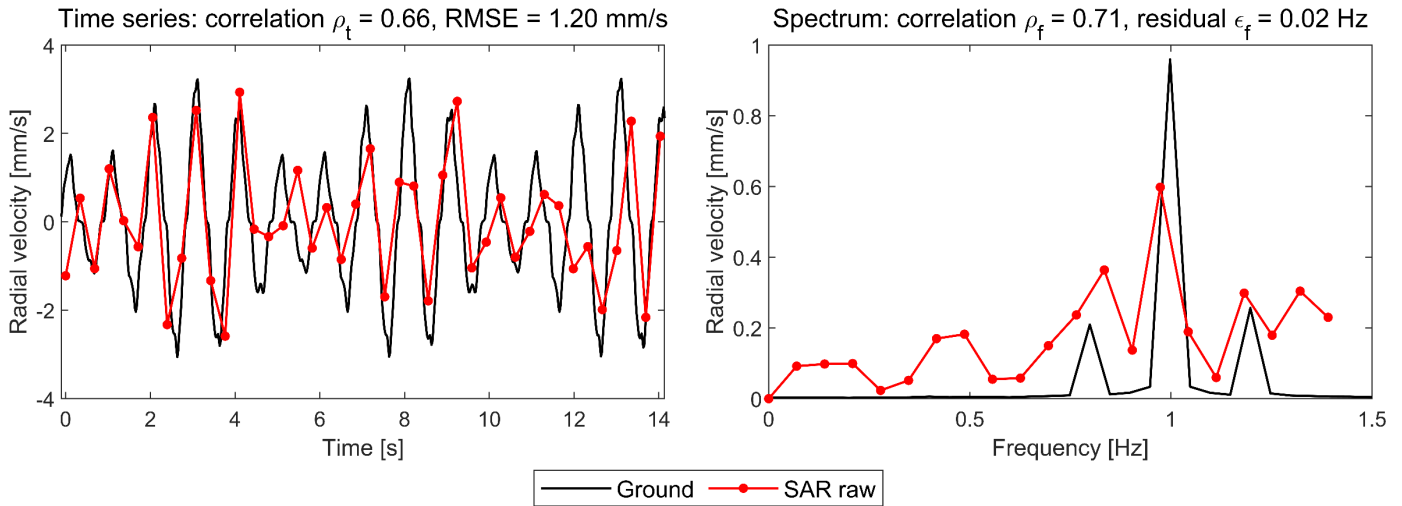
Test 1:  $\alpha = 7.6\%$ ,  $\Omega = 35.0\%$ ,  $N = 19$ ,  $f_s = 3.23$  Hz,  $t_{\text{sap}} = 0.46$  s,  $\Delta f = 0.18$  Hz



Test 2:  $\alpha = 4.3\%$ ,  $\Omega = 40.0\%$ ,  $N = 38$ ,  $f_s = 6.49$  Hz,  $t_{\text{sap}} = 0.27$  s,  $\Delta f = 0.18$  Hz



Test 3:  $\alpha = 4.5\%$ ,  $\Omega = 49.0\%$ ,  $N = 42$ ,  $f_s = 2.92$  Hz,  $t_{\text{sap}} = 0.66$  s,  $\Delta f = 0.07$  Hz



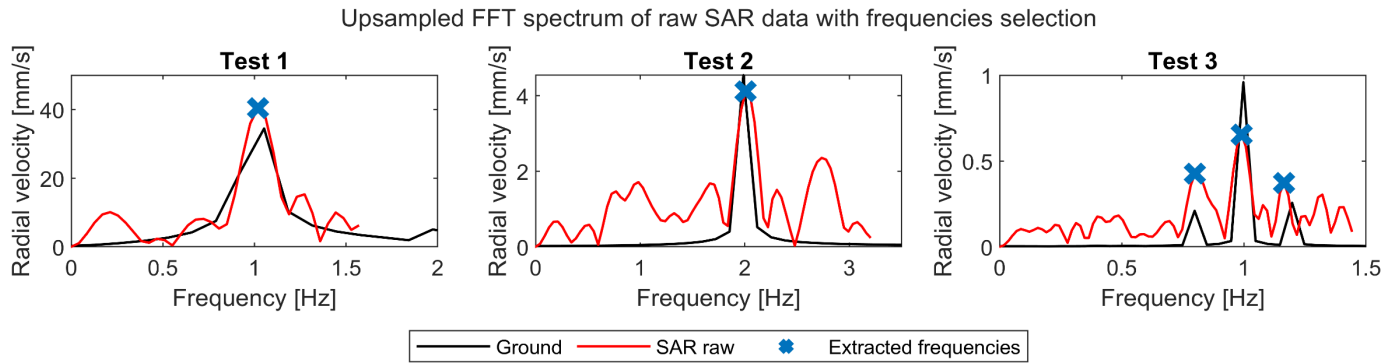


Figure 4.4. Upsampled SAR FFT spectra compared to ground truths. Plots shows the most dominant frequencies extracted.

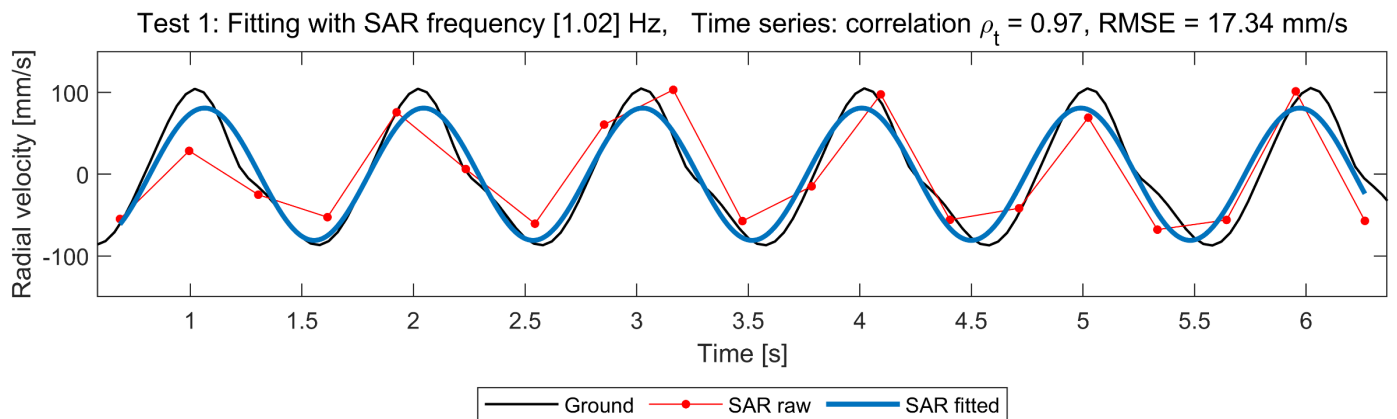


Figure 4.5. Test 1: results of model fitting on the SAR measurement, using a frequency of 1.02 Hz.

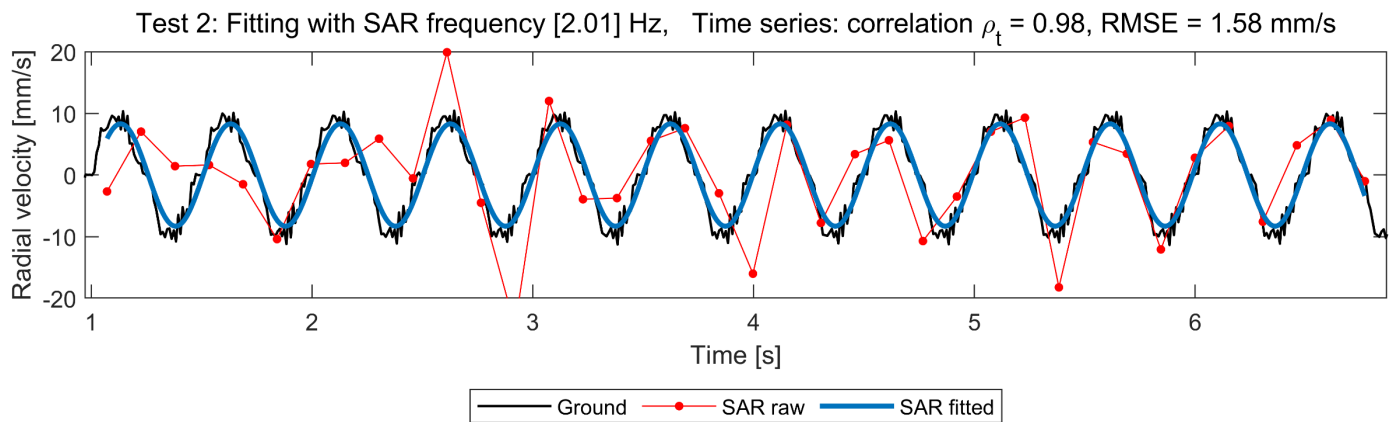


Figure 4.6. Test 2: results of model fitting on the SAR measurement, using a frequency of 2.01 Hz.

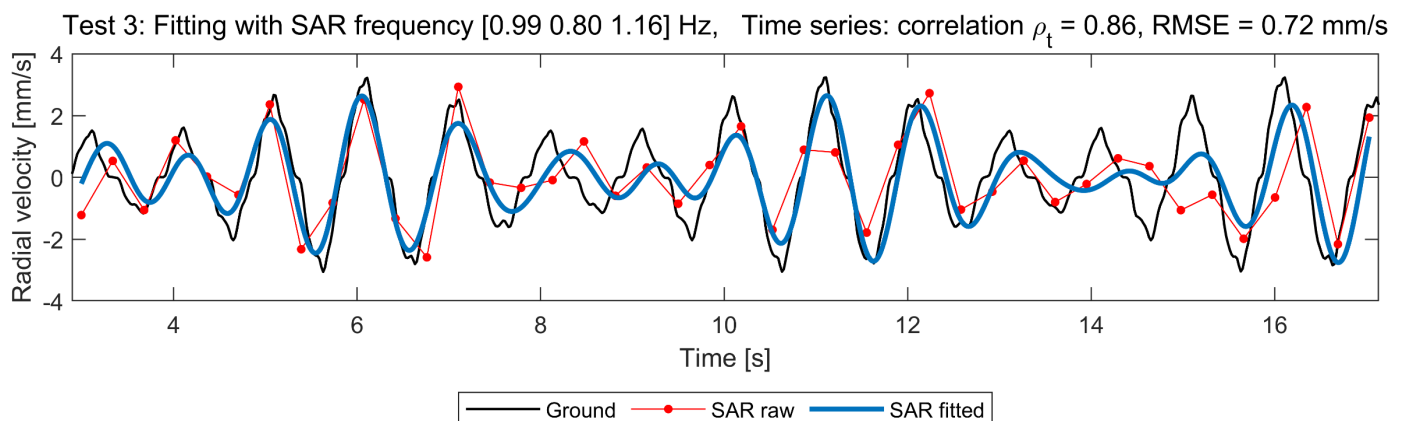


Figure 4.7. Test 3: results of model fitting on the SAR measurement, using frequencies of 0.80 Hz, 0.99 Hz, 1.16 Hz.



#### 4.1 Test 1 – High-velocity, single-frequency vibration

Test 1, presented in Figure 4.1, features the simplest case, with a low single-frequency oscillation (1 Hz) and relatively high vibration velocity ( $v_{r,max} = 95.5$  mm/s). The parameters to obtain the best extraction possible were an aperture fraction  $\alpha = 7.6\%$  and overlap ratio  $\Omega = 43\%$ , resulting in a sub-aperture duration of  $t_{sap} = 0.39$  s and sampling rate of  $f_s = 3.23$  (well above the Nyquist rate for the frequency of interest, 1 Hz). The limited acquisition time led to a spectral resolution of  $\Delta f = 0.18$  Hz. The extracted signal closely matches the ground truth in both time and frequency domains, proved by high Pearson's correlation coefficients, with  $\rho_t = 0.89$  and  $\rho_f = 0.98$  for time and frequency, respectively.

The dominant vibration frequency is accurately identified with frequency residual error of  $\epsilon_f = 0.03$  Hz (lower than the frequency resolution), as well as a correct estimation of the amplitude of the peak in the frequency spectrum. The RMSE in the extraction of the velocity time history is 30.4 mm/s (corresponding to a 31.8% relative to the true peak velocity value).

#### 4.2 Test 2 – Mid-velocity, single-frequency vibration

Test 2, shown in Figure 4.2, presents another constant frequency extraction, however with a frequency of 2 Hz and a vibration amplitude reduced by an order of magnitude to  $v_{r,max} = 10.8$  mm/s, making it a more challenging case. Here, the aperture fraction  $\alpha$  was decreased to 4.3%, and the overlap ratio  $\Omega$  set to 40%, resulting in a sub-aperture duration  $t_{sap}$  of 0.27 seconds and a sampling rate  $f_s$  of 6.49 Hz.

The main frequency component is correctly identified, being the error  $\epsilon_f = 0.06$  Hz (lower than the resolution  $\Delta f = 0.18$  Hz). Some local discrepancies appear in the time-domain signal, including underestimation and overestimation of peak values. Despite the lower absolute RMSE (6.7 mm/s), the relative error is 62.0% due to the lower ground truth amplitude. The time-domain correlation decreases significantly due to the impact of measurement noise, with  $\rho_t = 0.65$ , while frequency domain correlation remains satisfactory at  $\rho_f = 0.79$ . The spectrum also shows minor spurious peaks at 1 Hz and 2.7 Hz.

#### 4.3 Test 3 – Low-velocity, amplitude-modulated vibration

Test 3, represented in Figure 4.3, involved a more complex amplitude-modulated signal with significantly lower velocity magnitude of  $v_{r,max} = 3.1$  mm/s, which is more representative of vibrations from long span bridges or viaducts. An aperture fraction  $\alpha$  of 4.5% and an overlap ratio  $\Omega = 49\%$  were used. This configuration resulted in a sub-aperture duration of 0.66 seconds and a sampling frequency of  $f_s = 2.92$  Hz. In this case spectral resolution was finer, of 0.07 Hz, thanks to the longer acquisition time.

Despite the reduced signal energy, the algorithm extracts the carrier frequency, with a low residual error of  $\epsilon_f = 0.02$  Hz (within the frequency resolution  $\Delta f = 0.07$  Hz) and a frequency domain correlation  $\rho_f = 0.71$  – both comparable to Test 2. Time domain correlation is satisfactory at  $\rho_t = 0.66$ , while the RMSE for this extraction is 1.2 mm/s, with a relative error of 38.7%, the latter being more comparable to Test 1. This suggests that the dominant frequency of vibration has an impact on the quality of the extraction.

#### 4.4 SAR data fitting

Fitting the SAR-extracted data significantly improved the quality of the time-domain signal, both visually and quantitatively. As shown in Figures 4.5, 4.6, and 4.7, temporal resolution was enhanced through model-based fitting without altering the extraction parameters  $\alpha$  or  $\Omega$ . For each test, the dominant frequency components were identified from the upsampled FFT (upsampling factor = 4), and a sum of sinusoids with those frequencies was then fitted to the SAR data by optimizing only amplitude and phase. Results are as follows:

- *Test 1:* From the upsampled FFT, a frequency of 1.02 Hz was extracted. A single sinusoid was fitted, yielding an RMSE improvement from 30.34 to 17.34 mm/s, and a time-domain correlation increase from 0.89 to 0.97.
- *Test 2:* The extracted frequency was 2.01 Hz. After fitting, RMSE dropped from 6.72 to 1.58 mm/s, and  $\rho_t$  improved from 0.79 to 0.98.
- *Test 3:* Multiple dominant frequencies were identified at 0.80, 0.99, and 1.16 Hz. Fitting a sum of three sinusoids led to an RMSE reduction from 1.20 to 0.72 mm/s, and a correlation increase from 0.76 to 0.86.

These results demonstrate that using prior knowledge about the expected oscillatory behavior can significantly enhance the extraction quality. By narrowing the solution space to plausible signal shapes, fitting allows more accurate recovery of the target vibration profile.

### 5 CONCLUSIONS

This paper presented a feasibility study on the use of single-pass SAR images for extracting vibration characteristics from oscillating ground targets via the Sub-Pixel Offset Tracking (SPOT) micro-motion measurement technique. The algorithm was validated through a series of experimental tests, involving an isolated moving Corner Reflector (CR). The performance of the technique was assessed against synchronously acquired ground truth data.

Results demonstrate that SPOT can accurately reconstruct vibration-based information, capturing the dominant frequencies of motion with frequency errors well under the spectral resolution, even under varying conditions of signal amplitude, frequency, and complexity. The algorithm is also able to reconstruct the time histories of radial velocity with correlation values ranging from 0.65 to 0.98 (for the worst case, and best extraction case, respectively) and relative errors RMSE% from 31.8% to 62.0%. For high-velocity, single-frequency oscillations, SPOT achieves excellent correlation with ground truth in both time and frequency domains, respectively at 0.88 and 0.95, with relative RMSE values below 32%. When applied to more challenging low-velocity and amplitude-modulated cases, the method still proves effective in detecting the carrier frequency (with frequency correlations spanning 0.71 to 0.79) and producing meaningful velocity profiles, although the quality declines as vibration velocity decreases, and as frequency content becomes more complex.

Using prior knowledge about the expected oscillatory behavior can significantly enhance the extraction quality. Results from model fitting feature a significant reduction in RMSE and an improvement in correlation, even for the lowest velocity amplitude modulated case, improving from 1.20 mm/s to 0.72 mm/s (with a correlation increase from 0.66 to 0.86).

Limitations concerning m-m SAR measurements are primarily attributed to SAR acquisition constraints, such as short acquisition time, noise and image clutter. Alternative processing strategies could be explored to overcome these issues, particularly those using the phase information rather than the reflectivity. Additionally, the noise-affected velocity profile, in combination with limited acquisition durations, limits the application of m-m SAR for time domain modal extractions, to reconstruct not only the natural frequency but possibly the modeshapes and damping coefficients. On the other hand, the algorithm proves to be quite effective for extracting the frequency spectrum.

Despite these challenges, the study confirms that SAR m-m measurement opens new possibilities for remote vibration-based SHM. Future work will focus on refining the methodology by optimizing the extraction parameters, integrating phase-domain information, improving noise suppression models, and validating the algorithm on real-world bridge structures.

## ACKNOWLEDGMENTS

The study presented was funded by: the European Space Agency under the projects “Bridge Monitoring Based on Single Pass SAR Images” and “EO4Security- Innovative SAR Processing Methodologies For Security Applications-Topic B2: Micro-Doppler Processing”, the ReLUIS Interuniversity Consortium under the agreement DPC-ReLUIS 2020-2022 and DPC-ReLUIS 2024-2026 WP 6 “Monitoring and satellite data”, and the European Union- Next Generation EU, Mission 4 Component 2 - CUP E53D23003560006.

The authors would also like to acknowledge the collaboration of Umbra for providing satellite images, the Glasgow City Council for authorizing on-site tests., and the University of Trento and the University of Strathclyde for helping with the tests.

## REFERENCES

- [1] Wei Fan and Pizhong Qiao, ‘Vibration-based Damage Identification Methods: A Review and Comparative Study’, *Struct. Health Monit.*, vol. 10, no. 1, pp. 83–111, Jan. 2011, doi: 10.1177/1475921710365419.
- [2] J. M. W. Brownjohn, ‘Structural health monitoring of civil infrastructure’, *Philos. Trans. R. Soc. Math. Phys. Eng. Sci.*, vol. 365, no. 1851, pp. 589–622, Feb. 2007, doi: 10.1098/rsta.2006.1925.
- [3] A. Mardanshahi, A. Sreekumar, X. Yang, S. K. Barman, and D. Chronopoulos, ‘Sensing Techniques for Structural Health Monitoring: A State-of-the-Art Review on Performance Criteria and New-Generation Technologies’, *Sensors*, vol. 25, no. 5, p. 1424, Feb. 2025, doi: 10.3390/s25051424.
- [4] N. Earth Science Data Systems, ‘Synthetic Aperture Radar (SAR) | NASA Earthdata’. Accessed: Apr. 17, 2025. [Online]. Available: <https://www.earthdata.nasa.gov/learn/earth-observation-data-basics/sar>
- [5] Umbra Space, ‘Delivering Global Omniscience • Umbra’. Accessed: Jan. 22, 2025. [Online]. Available: <https://umbra.space/>
- [6] ‘Copernicus: Sentinel-1 - eoPortal’. Accessed: Apr. 17, 2025. [Online]. Available: <https://www.eoportal.org/satellite-missions/copernicus-sentinel-1>
- [7] ‘Umbra SAR Constellation - eoPortal’. Accessed: Apr. 17, 2025. [Online]. Available: <https://www.eoportal.org/satellite-missions/umbra-sar#orbit>
- [8] A. Ferretti, C. Prati, and F. Rocca, ‘Permanent scatterers in SAR interferometry’, *IEEE Trans. Geosci. Remote Sens.*, vol. 39, no. 1, pp. 8–20, Jan. 2001, doi: 10.1109/36.898661.
- [9] D. Tonelli, A. Valentini, A. Rocca, S. Zorzi, A. Lotti, and D. Zonta, ‘Uncertainty quantification of satellite InSAR-monitoring of bridges: a case study’, *ce/papers*, vol. 6, no. 5, pp. 900–906, Sep. 2023, doi: 10.1002/cepa.1991.
- [10] D. Perissin, ‘Interferometric SAR Multitemporal Processing: Techniques and Applications’, in *Multitemporal Remote Sensing*, vol. 20, Y. Ban, Ed., in Remote Sensing and Digital Image Processing, vol. 20., Cham: Springer International Publishing, 2016, pp. 145–176. doi: 10.1007/978-3-319-47037-5\_8.
- [11] F. Biondi, P. Addabbo, S. L. Ullo, C. Clemente, and D. Orlando, ‘Perspectives on the Structural Health Monitoring of Bridges by Synthetic Aperture Radar’, *Remote Sens.*, vol. 12, no. 23, p. 3852, Nov. 2020, doi: 10.3390/rs12233852.
- [12] R. Raney, ‘Synthetic Aperture Imaging Radar and Moving Targets’, *IEEE Trans. Aerosp. Electron. Syst.*, vol. AES-7, no. 3, pp. 499–505, May 1971, doi: 10.1109/TAES.1971.310292.
- [13] V. C. Chen, Fayin Li, Shen-Shyang Ho, and H. Wechsler, ‘Micro-doppler effect in radar: phenomenon, model, and simulation study’, *IEEE Trans. Aerosp. Electron. Syst.*, vol. 42, no. 1, pp. 2–21, Jan. 2006, doi: 10.1109/TAES.2006.1603402.
- [14] X. Li, B. Deng, Y. Qin, H. Wang, and Y. Li, ‘The Influence of Target Micromotion on SAR and GMTI’, *IEEE Trans. Geosci. Remote Sens.*, vol. 49, no. 7, pp. 2738–2751, Jul. 2011, doi: 10.1109/TGRS.2011.2104965.
- [15] M. Ruegg, E. Meier, and D. Nuesch, ‘Vibration and Rotation in Millimeter-Wave SAR’, *IEEE Trans. Geosci. Remote Sens.*, vol. 45, no. 2, pp. 293–304, Feb. 2007, doi: 10.1109/TGRS.2006.887025.
- [16] F. Biondi, P. Addabbo, C. Clemente, S. L. Ullo, and D. Orlando, ‘Monitoring of Critical Infrastructures by Micro-Motion Estimation: the Mosul Dam Destabilization’, 2020, *arXiv*. doi: 10.48550/ARXIV.2007.05326.

# Setting an optimal threshold for novelty detection in data-driven Structural Health Monitoring

Alessio De Corso<sup>1, 2</sup>, Carlo Rainieri<sup>2</sup>, 0000-0003-4854-0850

<sup>1</sup>Polytechnic University of Bari, via E. Orabona 4, 70125 Bari, Italy

<sup>2</sup>Construction Technologies Institute, National Research Council of Italy, corso N. Protopisani, 80146 Naples, Italy  
email: a.decorso@phd.poliba.it, rainieri@itc.cnr.it

**ABSTRACT:** The data-driven approach to vibration-based Structural Health Monitoring aims to detect anomalies in the monitored modal properties. A key step in this framework is compensating for the normal variability in the data, which is due to the strong influence of environmental and operational variables on the structure's dynamic behavior. The decision-making process is then formulated as a binary classification problem, supported by an appropriate alarm threshold to distinguish between normal and anomalous structural conditions. The threshold is typically set on the statistical distribution of the novelty index computed during the training phase, often assuming a Gaussian distribution of the data. However, anomaly detection requires a more refined modeling of the distribution tails. The present paper investigates the use of Extreme Value Theory for threshold setting, focusing on the Block Maxima sampling technique and the Generalized Extreme Value distribution. A comparison with conventional approaches demonstrates the significant accuracy achievable through the extreme value theory. The natural frequency time histories of the KW51 bridge are used as benchmark data to highlight the method's effectiveness in improving the reliability of early damage detection.

**KEY WORDS:** Data-driven Structural Health Monitoring; Novelty detection; Threshold setting; Environmental and operational variables; Extreme Value Theory.

## 1 INTRODUCTION

The remote and automated evaluation of the structural conditions through Structural Health Monitoring (SHM) is crucial in the modern management of civil engineering assets. SHM enables a transition from the traditional scheduled maintenance approaches to proactive strategies that exploit the early damage identification, thereby enhancing safety and reducing long-term maintenance costs [1]. In the context of SHM, damage detection is the first step of damage identification, and it is commonly approached through data-driven methodologies. In this framework, the damage detection problem is cast as a novelty detection one [2], [3]. This strategy involves extracting damage-sensitive features (DSFs) from sensor data through automatic Operational Modal Analysis (OMA) techniques, which are further analyzed to detect deviations from a baseline condition. As such, damage detection is framed as a binary classification problem, aiming to distinguish the anomalous structural behavior, caused by either progressive degradation or sudden events, from the normal operating state [4].

In vibration-based SHM the modal properties or other related parameters are often selected as DSFs. Several applications reported in the literature consider the natural frequencies as DSFs because they can be easily obtained from measurements of the ambient vibration response of structures by a few, appropriately located sensors. Even if natural frequencies are relatively easy to monitor and informative for the first level damage detection, they are also very sensitive to the influence of environmental and operational variables (EOVs), such as temperature changes over time. An accurate damage detection therefore requires the application of appropriate compensation techniques to isolate the changes in the structural behavior due

to damage or degradation phenomena from environmental and operational effects on the selected DSFs [5], and, as a consequence, enhance the reliability of the SHM outcomes. Such a compensation relies on setting data normalization models developed with reference to data collected in a training phase.

After the data normalization stage, the DSFs are transformed into novelty indexes (NIs), which are scalar indicators used to quantify how much a given observation deviates from the expected behavior. In order to assess whether the observed structural response should be considered anomalous, appropriate threshold values must be set, so that if the NIs overcome the threshold a warning can be issued. This is, therefore, another key step in the implementation of reliable modal based SHM strategies, in addition to the previously mentioned compensation of environmental and operational influence on DSFs (Figure 1).

A critical aspect in threshold setting is related to the need of defining it in an unsupervised context, that is to say, by using only data from the reference (nominally, healthy) condition of the structure. In the common practice, a Gaussian distribution for NIs is often assumed for the sake of threshold setting. However, this assumption is frequently inadequate for the novelty detection tasks [1]. As a result, setting the threshold based on a predefined data distribution can be misleading. Moreover, this approach does not take into account that detecting rare, extreme deviations is the focus of any SHM strategy, and, as such, an appropriate data-driven threshold setting approach should rely on the careful analysis of the tails of NI distribution.



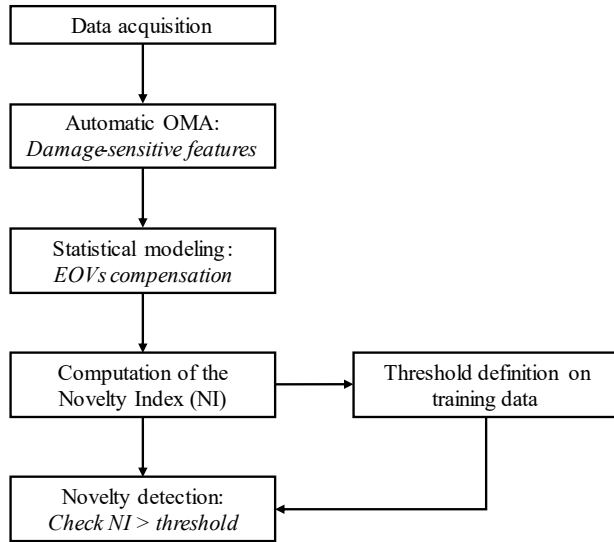


Figure 1. Flowchart of a typical data-driven SHM framework.

The Extreme Value Theory (EVT) represents a suitable alternative to the approaches based on the assumption of a Gaussian data distribution, as it focuses on the tail of the distribution – where anomalies are most likely to occur – thereby enabling a more precise threshold estimation [6].

This paper discusses the problem of the appropriate alarm threshold setting in the context of modal-based damage detection. A comparative assessment of different threshold setting strategies is presented by processing a benchmark dataset available in the literature. The analysis starts from the computation of NIs from natural frequency time histories through the combination of Gaussian Mixture Model (GMM) and Mahalanobis Squared Distance (MSD) to mitigate the influence of EOVs [7]. Afterwards, an EVT-based approach is applied for threshold setting. It resorts on the Block Maxima (BM) method to identify extreme observations and to model them according to the Generalized Extreme Value (GEV) distribution [8]. The effectiveness of the proposed approach in enhancing the robustness of novelty detection in modal-based SHM systems is demonstrated through quantitative comparisons with standard threshold setting methods.

The paper is structured as follows: after the introduction, Section 2 describes the methodological framework, detailing both the compensation strategy for data normalization with respect to the EOV influence and the computation of the NI time series. Moreover, Section 2 also outlines the EVT-based procedure for threshold setting. Section 3 presents the applicative case study and the characteristics of the benchmark dataset, followed by the analysis and discussion of results. The key findings of the study are finally summarized in the conclusions.

## 2 METHODOLOGY

### 2.1 Multivariate modeling of damage sensitive features under EOV influences

The present section describes the approach adopted for the compensation of EOV effects on DSFs and the computation of the NI. In this context, the matrix  $\mathbf{X} \in \mathbb{R}^{n \times m}$  represents the training dataset, holding  $n$  observations of the natural frequencies of  $m$  vibration modes. These are experimentally

collected under varying environmental and operational conditions at the beginning of the monitoring period or, more generally, in a reference monitoring period.

GMM is herein applied to represent  $\mathbf{X}$  as a finite mixture of multivariate Gaussian distributions. The objective of this data processing stage is the effective modeling of the dominant feature clusters associated with the reference states of the monitored structure. The mixture density function is formally defined as:

$$f_{mix}(\mathbf{x}) = \sum_{q=1}^Q \eta_q f_q(\mathbf{x}|\boldsymbol{\mu}_q, \boldsymbol{\Sigma}_q) \quad (1)$$

Here,  $f_q(\mathbf{x}|\boldsymbol{\mu}_q, \boldsymbol{\Sigma}_q)$  denotes the multivariate Gaussian probability density function of the  $q$ -th component, fully characterized by the mean vector  $\boldsymbol{\mu}_q$ , the covariance matrix  $\boldsymbol{\Sigma}_q$ , and the mixture weight  $\eta_q$ . The model parameters are obtained by the Maximum Likelihood Estimation (MLE) method, where the maximization of the likelihood function is achieved by the Expectation-Maximization (EM) algorithm [9].

The optimal number of components  $Q$  in Equation (1) is determined by minimizing the Bayesian Information Criterion (BIC), a standard model selection metric that penalizes model complexity to prevent overfitting [7]. This probabilistic framework supports the implementation of a robust anomaly detection methodology by leveraging the different components of the mixture model while inherently accounting for the influence of EOVs.

In order to obtain the NI time series for anomaly detection, the MSD is adopted as a multivariate metric to measure the distance between the observed DSFs and the GMM components. It incorporates both variable scales and correlations [10], and, given the generic test observation  $\mathbf{z}$ , its MSD relative to each GMM component can be computed as follows:

$$MSD_q(\mathbf{z}) = (\mathbf{z} - \boldsymbol{\mu}_q) \boldsymbol{\Sigma}_q^{-1} (\mathbf{z} - \boldsymbol{\mu}_q)^T \quad (2)$$

where  $\boldsymbol{\mu}_q$  and  $\boldsymbol{\Sigma}_q$  denote the mean vector and covariance matrix of the  $q$ -th GMM component, respectively. The NI corresponding to the generic test observation  $\mathbf{z}$  is then given by the minimum distance across all components:

$$NI(\mathbf{z}) = \min\{MSD_q(\mathbf{z})\} \quad (3)$$

Following the above-described approach, if a new observation is consistent with the reference structural condition, it will be close to one of the GMM components computed in the reference training period, and it will yield a low NI value. Conversely, if the structure has transitioned to a damaged state, the new observations will significantly diverge from all the GMM components in the training stage, resulting in larger NI values with respect to the undamaged condition.

### 2.2 Threshold setting methods for Novelty Detection

In the context of novelty detection, the EVT-based approach provides a robust statistical framework for threshold determination. This method is grounded in the theorem stating that the distribution of extreme values can converge only to one of three canonical forms: Gumbel, Weibull, or Fréchet distributions. To simplify the process, the GEV distribution is

employed, as it unifies all three types within a single parametric family. The GEV distribution is expressed as follows [8]:

$$G(Y) = \exp \left\{ - \left[ 1 + \xi \left( \frac{Y - \lambda}{\sigma} \right) \right]^{-\frac{1}{\xi}} \right\} \quad (4)$$

where  $\xi$ ,  $\sigma$  and  $\lambda$  are the shape, scale, and location parameters, respectively. It is defined on the set of maxima  $Y$ , satisfying the condition  $1 + \xi(Y - \lambda)/\sigma > 0$ , with  $\lambda$  and  $\xi$  real-valued parameters, and  $\sigma > 0$ . The unknown parameters are estimated by using the MLE method.

In order to define the population of extreme values to be fitted by the GEV distribution, the BM method is employed. Thus, the NI time series in the training period is divided into non-overlapping blocks of equal length, and the maximum value is selected in each block. Assuming that the structure is initially undamaged (null hypothesis), and selecting a significance level  $\alpha$ , the threshold can be defined as the corresponding quantile of the fitted distribution [8]:

$$t = \begin{cases} \lambda - \frac{\sigma}{\xi} [1 - \{-\log(1 - \alpha)\}^{-\xi}], & \xi \neq 0 \\ \lambda - \sigma \log\{-\log(1 - \alpha)\}, & \xi = 0 \end{cases} \quad (5)$$

In addition to the previously described approach based on EVT, in this study also a more conventional method for threshold setting is considered for the purpose of comparative assessment. It consists in setting a predefined False Alarm Rate (FAR), interpreted as the tolerable proportion of false alarms in the training data. The threshold  $t$  is then calculated as the cut-off value that satisfies [11]:

$$\frac{\text{number of false alarms } (t)}{n} = FAR \quad (6)$$

Another widely adopted strategy for threshold setting is based on the assumption of Gaussian distribution of the DSFs and the use of MSD as the novelty index. Under these assumptions, the NI follows a  $\chi^2$  distribution, and the threshold can be directly obtained as the quantile of the distribution at the significance level  $\alpha$  [7].

For the sake of the comparative performance assessment of the considered threshold setting approaches, the following parameters are computed: the number of false positives (FPs), the number of false negatives (FNs), and the Youden index. The latter, derived from the Receiver Operating Characteristic (ROC) curve, provides a measure of the balance between sensitivity (the true positive rate) and specificity (the true negative rate) and results in a single value that reflects the overall diagnostic performance of the considered approach [12].

### 3 ANALYSIS OF THE BENCHMARK DATASET

The data collected from the SHM system installed on the KW51 bridge in Belgium are processed for the objectives of the present study. The KW51 bridge is a steel bowstring railway bridge located in Leuven, Belgium (Figure 2). A detailed 15-month monitoring program was conducted between late 2018 and early 2020 to capture the dynamic behavior of the bridge under operational conditions [13]. Acceleration data collected during this period were processed using Operational Modal

Analysis techniques [14], allowing the identification of the first 14 natural frequencies of the bridge.



Figure 2. KW51 bridge in Leuven, Belgium [13].

During the monitoring period, the bridge was retrofitted to correct a construction defect identified during inspection. The intervention involved strengthening the connection between the diagonals, arches, and bridge deck by welding a steel box around each original bolted joint. Specifically, the bridge was monitored before the retrofit intervention between October 2<sup>nd</sup>, 2018, and May 15<sup>th</sup>, 2019, and after that in the period between September 27<sup>th</sup>, 2019, and January 15<sup>th</sup>, 2020.

In the application of the data processing and threshold setting approaches described in Section 2, the natural frequency time series corresponding to modes 1, 2, 7, 8, 10, 12, and 14 were excluded from the analysis due to significant data gaps that prevented successful monitoring of these modes. This was made in agreement with similar considerations reported in [13]. Thus, only the natural frequency time series of modes 3, 4, 5, 6, 9, 11, and 13 were considered for the present analysis. Minor data gaps in these time series were filled by linear interpolation.

In addition to mode selection, since the retrofit intervention introduced a significant shift in the considered natural frequency time histories, the difference in the average value of corresponding natural frequencies before and after the intervention was intentionally reduced to make more challenging the appropriate alarm threshold setting as a result of a reduced change in the observed structural behavior. Specifically, the frequency scatter was scaled down to 25% of its original value to avoid a straightforward or even trivial novelty detection (Table 1).

Table 1. Reduced scatter between average frequency before and after the retrofitting.

Mode	Frequency scatter	
	Original	Reduced
3	0.53%	0.13%
4	1.17%	0.29%
5	0.33%	0.08%
6	2.07%	0.52%
9	0.76%	0.19%
11	2.02%	0.51%
13	1.44%	0.36%

Indeed, without this correction, the frequency shift due to retrofit results in an overly obvious differentiation between pre- and post-intervention states, thereby undermining the relevance of the novelty detection process and threshold setting procedure.

A detailed inspection of the collected natural frequency time histories also reveals some sharp increases in frequency values in the first monitoring period (Figure 3). A detailed investigation about the occurrence of these particular patterns is reported in [13], where the correlation between the natural frequencies of the bridge and the measured temperature has been evaluated. That study showed that those singular patterns occur when the temperature falls below 0 °C. Indeed, before the retrofit intervention, the observed structural behavior is characterized by a bilinear trend in the frequency-temperature relationship, with a knee-point around 0 °C. The interpretation of this phenomenon has been guided by insights gained from similar previously analyzed case study where a similar relationship was observed and attributed to the freezing of the asphalt layer [15]. Further investigations specifically focused on the KW51 case study, also supported by finite element model updating, confirmed that the observed singularities in the natural frequency patterns were associated with the freezing of the porphyry ballast layer beneath the railway tracks.

Excluding the period during which the intervention took place, the dataset employed in this study comprises 6287 observations of the seven selected natural frequencies of the bridge, 3977 of which were collected before the retrofit

intervention, while the remaining 2310 were gathered after the completion of the works.

In the context of the present study, the first 3579 samples collected before the retrofit – approximately corresponding to 90% of the available observations in the same period – have been used to train the GMM and to define threshold values for the subsequent comparative analyses. The remaining 10% of the dataset collected before the structural intervention has been used as a validation set, in order to check that no structural changes are detected before the onset of the retrofit. The whole natural frequency time series collected after the retrofit intervention are instead employed as the test data (Figure 3) to assess the accuracy of the different novelty detection strategies.

The trained GMM has been specifically designed to model the variability induced by EOVs, including the effects of freezing conditions observed between late January and early February 2019. The optimal number of GMM components has been selected as discussed in Section 2.1, resulting in a five-component GMM, which has been identified as the appropriate representation of the training dataset. Once the model of the operational variability of natural frequencies has been established, the NI time series has been computed according to Equations (2) and (3). The resulting NI values, shown in Figure 4, demonstrate the model's capability to effectively account for the influence of EOVs. Specifically, the NIs computed over the training data exhibit a consistent and stable behavior, indicating that the model successfully captures the normal variability of data, even under freezing conditions. Moreover, the NIs

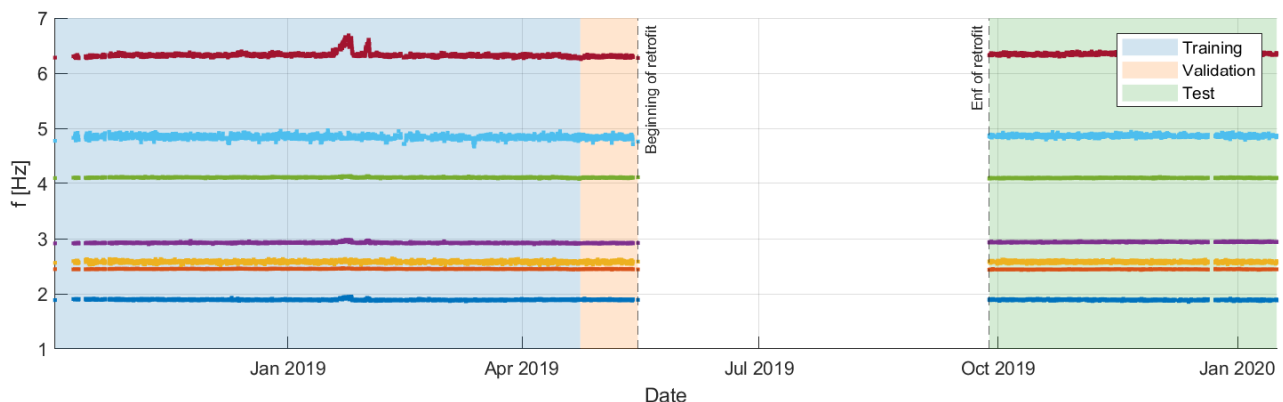


Figure 3. Time histories of the seven selected natural frequencies and partitioning of the dataset into training, validation and testing sets.

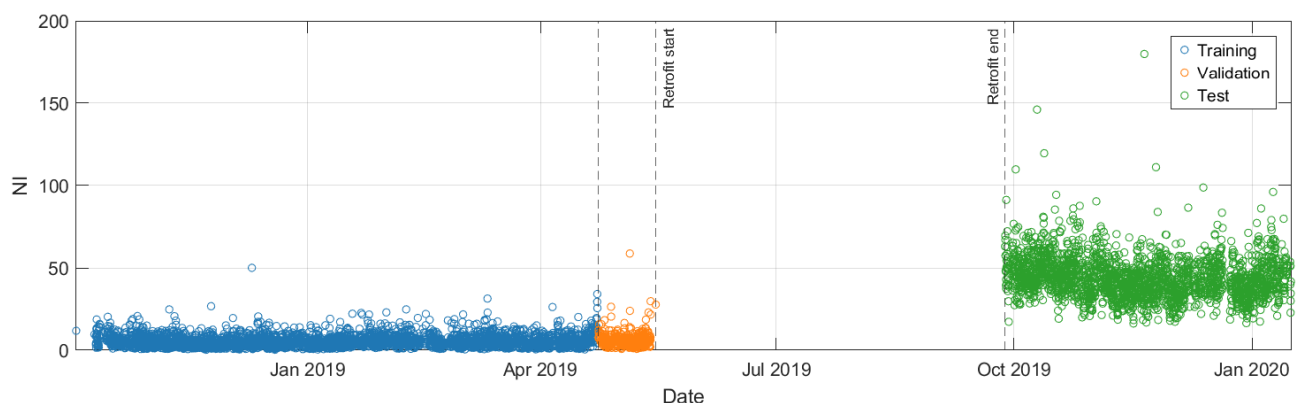


Figure 4. NIs time series during the entire monitoring period.



calculated on the validation set remain aligned with those obtained during the training period, thus confirming the generalization capability of the considered model.

In contrast with these results, a marked upward shift in the NI trend can be observed when data collected after the retrofit intervention are considered, clearly suggesting the transition to a different structural state. This result confirms the effectiveness of the proposed approach in distinguishing between the normal environmental and operational variability of the selected DSFs and that associated to the occurrence of changes in the structure as a result of damage or, as in the present case, of a retrofit intervention. In the context of the novelty detection framework, an alarm threshold has been established based on the NIs computed from the training data. To this aim, a combination of the BM method and the GEV distribution fitting has been applied, as further illustrated hereafter.

The training NI time series has been divided into consecutive, non-overlapping blocks, and the maximum value from each block has been extracted to collect a set of extreme values. The choice of the number of blocks plays a critical role in the process [8]. In this work, the number of blocks has set equal to 300.

Figure 5 shows the comparison between the empirical cumulative distribution function (CDF) of the extracted maxima and the CDF of the fitted GEV distribution. The close agreement between the two curves indicates that the GEV distribution effectively describes the statistical variability of the observed maxima.

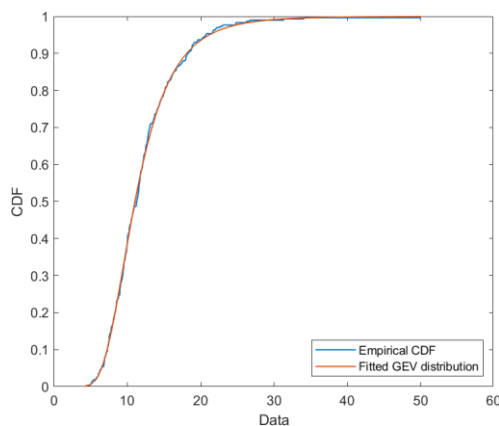


Figure 5. GEV distribution modeling: comparison between empirical CDF and fitted GEV distribution.

The fitted GEV model has been exploited to determine the alarm threshold corresponding to a significance level  $\alpha$  of 0.05, as per Equation (5). Figure 7a illustrates the application of the determined threshold for novelty detection analysis of the full dataset, highlighting the occurrences of misclassification. During the training and validation periods, corresponding to the structural condition before the retrofit intervention, only a few isolated points exceeded the threshold, indicating a low false positives rate and, therefore, a high specificity of the proposed approach in characterizing the structural behavior in this state. Notably, after the retrofit intervention, only a very limited number of observations remained under the threshold. This demonstrates also the high sensitivity of the method in detecting the transition to a new structural condition, as it

successfully identifies nearly all test data points, referring to the structural response after the retrofit intervention, as anomalous.

For the comparative assessment of the effectiveness of the method for threshold setting based on the GEV distribution, threshold values are also determined by means of the previously mentioned alternative procedures. The related results are presented in Figures 7b and 7c.

Table 2 summarizes the resulting threshold values, along with the corresponding number of misclassifications. Setting a fixed cut-off threshold is the most straightforward approach for the present task. For the considered application, a fixed cut-off threshold has been defined by setting the FAR to 0.05, meaning that up to 5% of the training data points are tolerated as FPs, in agreement with Equation (6).

As a second alternative approach, a threshold has been set based on the assumption of normal distribution of the natural frequencies in the training stage. As a result, the NIs derived through the MSD are expected to follow a  $\chi_m^2$  distribution, with  $m = 7$  degrees of freedom (with  $m$  corresponding to the number of modes considered). From this distribution, a threshold corresponding to a given significance level  $\alpha$  has been determined.

The analysis of the results reported in Table 2 indicates that, although the threshold values obtained as the 95% cut-off value or through the  $\chi^2$  CDF achieve a zero false negative rate – meaning that all observations in the testing stage are correctly classified as anomalous –, they still suffer from a relatively high number of FPs, which can jeopardize the reliability and practicality of the monitoring system (Figure 7b and 7c). On the other hand, the EVT-based method for threshold setting yields a small number of FPs as well as a small number of FNs. While this method might appear less conservative, it establishes a threshold that better approximates the optimal balance between FPs and FNs. This can be demonstrated by looking at the coordinates associated with the various thresholding strategies when they are plotted on the ROC curve (Figure 6).

Table 2. Number of misclassifications for the different threshold setting procedures.

Approach	Threshold	FPs	FNs
BM-GEV	21.2	24	29
Cut-off	12.4	199	0
$\chi^2$ CDF	14.1	120	0

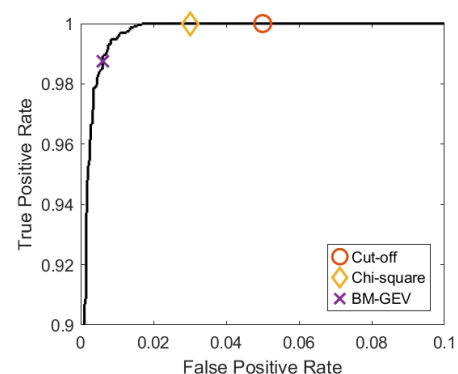


Figure 6. ROC curve and points corresponding to different threshold setting approaches.

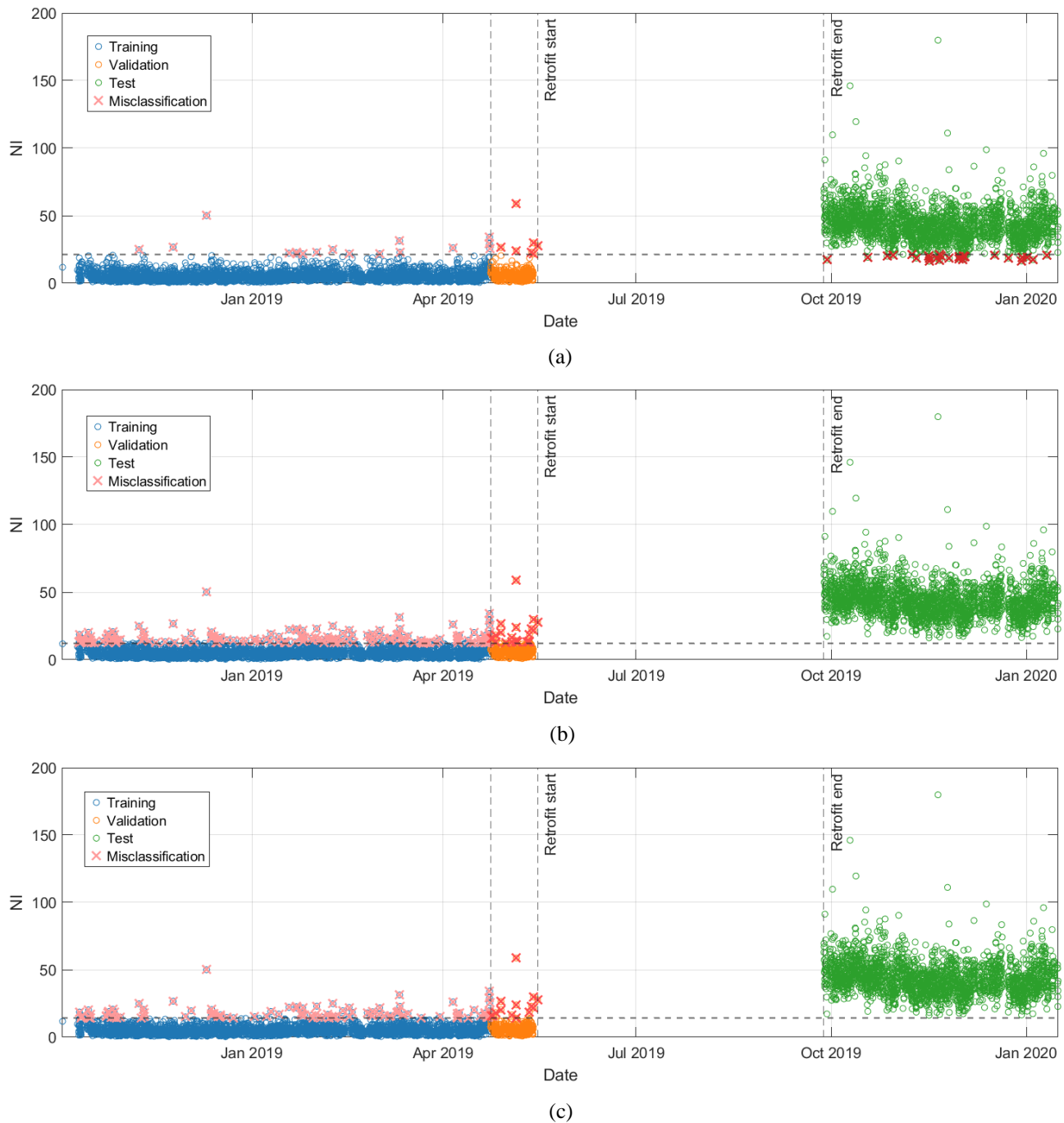


Figure 7. Novelty detection according to: EVT-based threshold (a), 95% cut-off threshold (b), and  $\chi^2$  distribution-based threshold (c).

Indeed, the proximity of a point to the top-left corner of the ROC space – representing a low false positive rate and a high true positive rate – serves as a qualitative measure of the model classification performance. In addition, the distance of each threshold point from the bisector (corresponding to the line of no-discrimination) quantified by the Youden index provides a quantitative measure for the selection of the most effective threshold value.

The Youden index values have been computed for each threshold setting method, and they are reported in Table 3. The results indicate that the threshold derived through the BM-GEV method lies very close to the optimum, corresponding to the maximum Youden index. Furthermore, it outperforms the other

considered approaches, confirming an excellent balance between sensitivity and specificity.

Table 3. Youden index values corresponding to different thresholds values.

Approach	Youden index
Max	0.987
BM-GEV	0.981
Cut-off	0.950
$\chi^2$ CDF	0.970

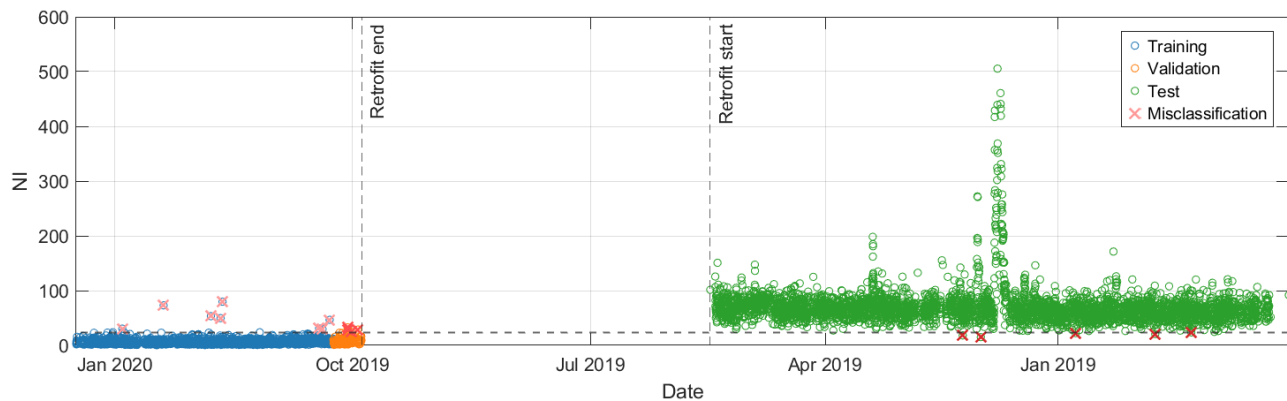


Figure 8. NIs time series during the entire monitoring period, considering the post-retrofitting condition as the healthy state for model training and validation, and EVT threshold-based novelty detection.

The analysis presented thus far follows the chronological order of data acquisition, corresponding to the subdivision of the dataset into training, validation, and testing sets. Since the retrofitting was intended to correct a construction defect, it led to an improvement in the structural condition of the bridge. As such, the post-retrofitting state can be regarded as the actual healthy condition.

An additional analysis is conducted by applying the proposed methodology using post-retrofitting data for model training and validation, and subsequently testing the model on pre-retrofitting observations. Once again, the novelty analysis results (Figure 8) confirm the model's ability to compensate for EOVs effects and demonstrate strong generalization performance, as evidenced by the NIs of validation data aligning closely with the training trend. The distinct structural condition characterizing the pre-retrofitting period is clearly revealed. Furthermore, a noticeable spike in the NIs time series during the freezing period highlights the presence of a transient condition within the pre-retrofitting state. In this case as well, applying EVT-based threshold yields an excellent balance between FPs (0.5%) and FNs (0.1%).

## CONCLUSIONS

The present study has focused on the comparative performance assessment of different methods for determining a reliable threshold for anomaly detection to be applied in the context of data-driven, modal-based SHM. The natural frequency time series of the KW51 bridge served as the benchmark dataset for the performance assessment. It has been processed using a method that combines GMM and MSD to compute the NI time series and compensate the normal variability of the selected DSFs due to changing environmental and operational conditions. An approach based on EVT has been applied and compared with alternative approaches for threshold setting. The EVT-based approach started from the identification of a set of maxima in the NI time series at the training stage according to the BM method; the GEV distribution was afterwards fitted to the collected maxima and used to define the alarm threshold. Comparing the performance of the EVT-based method with other approaches for threshold setting has shown that, for the considered dataset, the BM-GEV approach appears to be the most precise, with an optimal balance between FPs and FNs, as confirmed by the value of the Youden index derived from the ROC curve.

## ACKNOWLEDGMENTS

The present study is part of the research activities developed by the authors within the framework of the PNRR Program, CN00000023 National Center for Sustainable Mobility, SPOKE 7 “CCAM, Connected Networks and Smart Infrastructure” - WP4 (CUP B43C22000440001), and by the last author in the context of the PE00000005\_1 “MITIGATE - Monitoring built-up environment through dynamic Time series” Research Project (CUP E63C22002000002). Additional support from the STRIVE – INOSTRI FOE Project is also gratefully acknowledged. Finally, the KU Leuven Structural Mechanics Section is kindly acknowledged as the source of the data.

## REFERENCES

- [1] C. R. Farrar and K. Worden, *Structural Health Monitoring: A Machine Learning Perspective*. John Wiley & Sons, Ltd, 2012.
- [2] Q. Chen, J. Cao, and S. Zhu, Data-Driven Monitoring and Predictive Maintenance for Engineering Structures: Technologies, Implementation Challenges, and Future Directions, *IEEE Internet of Things Journal*, vol. 10, n. 16, pp. 14527–14551, 2023.
- [3] E. Figueiredo and J. Brownjohn, Three decades of statistical pattern recognition paradigm for SHM of bridges, *Structural Health Monitoring*, vol. 21, n. 6, pp. 3018–3054, 2022.
- [4] M. A. F. Pimentel, D. A. Clifton, L. Clifton, and L. Tarassenko, A review of novelty detection, *Signal Processing*, vol. 99, pp. 215–249, 2014.
- [5] Z. Wang, D. H. Yang, T. H. Yi, G. H. Zhang, and J. G. Han, Eliminating environmental and operational effects on structural modal frequency: A comprehensive review, *Structural Control and Health Monitoring*, vol. 29, 2022.
- [6] H. Sohn, D. W. Allen, K. Worden, and C. R. Farrar, Structural Damage Classification Using Extreme Value Statistics, *Journal of Dynamic Systems, Measurement, and Control*, vol. 127, n. 1, pp. 125–132, 2005.
- [7] E. Figueiredo and E. Cross, Linear approaches to modeling nonlinearities in long-term monitoring of bridges, *Journal of Civil Structural Health Monitoring*, vol. 3, n. 3, pp. 187–194, 2013.
- [8] S. Coles, *An Introduction to Statistical Modeling of Extreme Values*. London: Springer London, 2001.
- [9] J. Prawin and G. S. Vijaya Bhaskara, Outlier analysis combined with Gaussian mixture model for structural damage detection, *Materials Today: Proceedings*, 2023.
- [10] R. G. Brereton and G. R. Lloyd, Re-evaluating the role of the Mahalanobis distance measure, *Journal of Chemometrics*, vol. 30, n. 4, pp. 134–143, 2016.
- [11] E. Figueiredo, G. Park, C. R. Farrar, K. Worden, and J. Figueiras, Machine learning algorithms for damage detection under operational and environmental variability, *Structural Health Monitoring*, vol. 10, n. 6, pp. 559–572, 2011.
- [12] V. Giglioni, E. García-Macías, I. Venanzi, L. Ierimonti, and F. Ubertini, The use of receiver operating characteristic curves and precision-versus-





- recall curves as performance metrics in unsupervised structural damage classification under changing environment, *Engineering Structures*, vol. 246, 2021.
- [13] K. Maes, L. Van Meerbeeck, E. P. B. Reynders, and G. Lombaert, Validation of vibration-based structural health monitoring on retrofitted railway bridge KW51, *Mechanical Systems and Signal Processing*, vol. 165, n. 108380, 2022.
- [14] C. Rainieri and G. Fabbrocino, *Operational Modal Analysis of Civil Engineering Structures*, New York: Springer, 2014.
- [15] B. Peeters and G. De Roeck, One-year monitoring of the Z24-Bridge: environmental effects versus damage events, *Earthquake Engineering and Structural Dynamics*, vol. 30, n. 2, pp. 149–171, 2001.

# A Comprehensive Approach for Vision-Based Dynamic Monitoring of Structures and Infrastructure

Federico Ponsi<sup>1</sup>, 0000-0002-2808-4707, Ghita Eslami Varzaneh<sup>1</sup>, 0000-0002-2985-9359, Giorgia Ghirelli<sup>1</sup>,  
Elisa Bassoli<sup>1</sup>, 0000-0002-4919-1421, Loris Vincenzi<sup>1</sup>, 0000-0003-2541-7104

<sup>1</sup> University of Modena and Reggio Emilia, Department of Engineering “Enzo Ferrari”, Modena, Italy  
email: [federico.ponsi@unimore.it](mailto:federico.ponsi@unimore.it), [ghita.eslami@unimore.it](mailto:ghita.eslami@unimore.it), [giorgia.ghirelli@unimore.it](mailto:giorgia.ghirelli@unimore.it), [elisa.bassoli@unimore.it](mailto:elisa.bassoli@unimore.it),  
[loris.vincenzi@unimore.it](mailto:loris.vincenzi@unimore.it)

**ABSTRACT:** Structural monitoring is crucial for extending the service life of civil structures. Vibration-based monitoring is widely employed across various applications, leveraging both traditional and innovative sensing technologies. Among these, video-based methods have emerged as a promising and cost-effective approach for evaluating structural displacements at critical points. This paper presents a novel vision-based procedure enabling accurate three-dimensional structural displacement measurement using only a single camera. The method applies to assessing dynamic effects on bridges subjected to dynamic loads. The algorithm extracts displacements by tracking predefined targets over time. Special attention is given to reconstructing small 3D displacements from videos that inherently capture two-dimensional projections of the scene. The procedure is validated through experiments on a steel frame in a controlled environment, comparing displacement time histories with imposed vibrations from a shaking table. The originality of this work lies in achieving accurate 3D measurements with minimal equipment, offering a practical and innovative solution for structural health monitoring.

**KEY WORDS:** Vision-based monitoring; Structural vibrations; Displacement tracking; Laboratory tests; Experimental validation.

## 1 INTRODUCTION

Structural Health Monitoring (SHM) is a crucial component of modern infrastructure management, offering valuable insights into the condition of structures and helping prevent catastrophic failures while extending their service life. SHM utilizes a combination of sensors, data analysis methods, and computational models to evaluate the performance and safety of civil infrastructure such as bridges, buildings, dams, and other critical structures. The main objective of SHM is to detect changes in the structural integrity or behaviour of a structure, often before visible damage occurs, ensuring continued safety, preventing collapses, and reducing maintenance and repair costs.

SHM systems typically employ a range of sensors to monitor structural responses, such as strain, displacement, and acceleration. These sensors, including accelerometers, strain gauges, displacement transducers, and fibre optic sensors, generate reliable data but they often offer limited spatial coverage and necessitate the installation of dense sensor networks, requiring the structure to be accessible. This can pose challenges during extreme events or when access is restricted, such as during periods of heavy traffic, in remote locations, or unsafe structures. A significant advancement in SHM has been the integration of contactless technologies, which enable the installation of sensors without the need for extensive cabling and, therefore, without interrupting the operation of the structure [1, 2, 3].

These contactless systems allow for easier deployment, even in hard-to-reach or remote areas. With that premise, non-contact monitoring has become increasingly popular. Contactless technologies for civil monitoring encompass a range of methods, including global navigation satellite systems (GNSS) [4, 5], satellite remote sensing [6, 7], terrestrial radar interferometry [8], and vision-based techniques [9]. Among these, vision-based techniques stand out as the only remote sensing approach that can reduce dependence on expensive industrial products [10]. Indeed, these methods have shown

considerable promise even when using consumer-grade devices such as standard video cameras or smartphones [11, 12]. This progress is largely attributed to the development of low-cost technologies that provide high resolution and high frame rates, enabling accurate monitoring of large-scale structures in both static and dynamic fields.

These technologies use video feeds to track structural displacements, vibrations, and deformations, providing a flexible, cost-effective alternative to traditional methods and potentially eliminating the need for direct contact with the structure. The primary objective of such a system is to automatically and reliably transform video data into actionable insights. The fundamental concept behind vision-based monitoring is simple: a video of the structure being monitored is recorded, and the individual frames are analyzed, either in real-time or afterward, to extract motion data. This process generates displacement time histories, which can be further used to calculate strains, velocities, and accelerations. Vision-based methods offer several technical advantages, such as directly measuring displacements, which eliminates the need for the double integration of accelerations. Additionally, a single camera sensor can provide distributed monitoring, enabling the extraction of displacement data from multiple points on the structure within one video recording.

Beyond these technical benefits, the vision-based approach allows for substantial cost savings and significantly reduced setup efforts compared to traditional monitoring systems. Due to these advantages, vision-based techniques have garnered increasing attention in civil engineering research. Recent studies, including those by [13, 14, 15, 16], extensively review vision-based applications, including tests on bridges [17, 18, 19], and footbridges, [20, 21, 22].

A vision-based monitoring campaign and set up requires careful consideration and pre-planning, tailored to the specific structure being monitored. In civil engineering, two-dimensional measurements are typically favored because of their practicality and effectiveness. These measurements are

commonly employed to monitor vertical and transverse vibrations of bridges, as well as the horizontal displacements of buildings and towers. In vision-based applications, a-priori estimating the expected displacements of the structure is crucial for selecting the right camera parameters and determining the optimal camera-to-structure distance, ensuring accurate detection of displacements. While a single camera is usually sufficient for detecting in-plane movements, capturing the full 3D motion of all relevant points can be challenging. Typically, this requires the use of multiple synchronized cameras, each focusing on different parts of the structure. Differently, the proposed procedure enables the reconstruction of 3D motion using just a single camera. This approach simplifies the installation, eliminates the need for video synchronization and the geometrical merging required in stereovision.

In addition to the camera(s), it is essential to identify the sections of the structure to be monitored. In this regard, it is possible to choose intrinsic notable elements of the structure itself [15, 23], such as prominent details, corners, holes, or bolts, or install artificial high-contrast targets on the sections of interest. The first option does not require access to the structure, avoiding traffic disruption, but the second option generally provides more accurate results.

While highly effective in many applications, vision-based monitoring is featured by critical aspects that cannot be overlooked. A key limitation is the sensitivity to environmental conditions, such as vibrations of the camera or its support due to user intervention or wind, non-uniform air refraction caused by temperature differences between the camera and the monitored object, ambient light condition, weather, and visibility, all of which can affect data accuracy. Literature on the assessment of environmental uncertainties in vision-based monitoring includes theoretical analyses and laboratory testing [16, 24], but outdoor experiments are still limited.

The accuracy of measurements relies not only on the camera technical specifications (hardware) but also on video post-processing (software), which includes challenging tasks such as camera calibration, target tracking and pixel-to-metric conversion. This paper presents a vision-based approach for accurately assessing the condition of civil structures and infrastructure, with particular focus on the transformation of image units into real-world units, which is crucial in large-scale civil constructions where perspective distortions can significantly affect measurement accuracy. Aiming to propose a reliable and validated vision-based method for real-world applications, this study evaluates the procedure in a controlled environment, focusing on detecting the dynamic displacement of a laboratory steel frame subjected to controlled shaking. For validation purposes, the vision-based results are compared to reference displacements, highlighting the potential of this method for accurate monitoring.

The paper is organized as follows: Section 2 outlines the procedure framework, detailing each step of the proposed method, from the setup of the monitoring campaign to the post-processing of the recorded video. Section 3 presents the experimental test, specifically designed to assess the performance of the procedure across different camera-to-structure distances. Finally, Section 4 addresses conclusions and future perspectives.

## 2 PROCEDURE FRAMEWORK

The proposed vision-based procedure aims to determine the actual dynamic displacement of a structure within its reference system, effectively filtering out camera vibrations and ensuring independence from the camera position and orientation.

The vision-based procedure relies on different transformation of coordinates. To provide clarity, the reference systems involved are described progressively as follows:

1. The 2D image reference system ( $\pi$ ), which is related to camera sensor reference system by means of the focal length ( $f$ ) and optical center ( $o$ ) in a camera pinhole model. Specifically, the image reference system can be scaled and mirrored (with respect to the optical center) in order to obtain the sensor reference system. The image coordinates of this system are denoted as  $\eta$  and  $\xi$ .
2. The 3D real-world reference system ( $W$ ) located in the optical centre, which represents millimeter displacements, derived from pixel displacements via a three-dimensional mapping process. One axis of the system points in the viewing direction of the camera, along the optical axis. The remaining axes define the plane orthogonal to the optical axis, representing the front side of the camera.
3. The structure reference system defined by the coordinates ( $x, y, z$ ), which uniquely defines displacements along the main directions where structural motion occurs, ensuring that the results are independent of the camera pose.

The extraction of displacements within the image-plane ( $\pi$ ) is straightforward and it is carried out by comparing image coordinates ( $\eta, \xi$ ) across sequential frames. However, deriving the displacement time series in the structure reference system requires careful consideration of several key aspects.

These include the precise calibration of camera intrinsic parameters, accurate detection and frame-by-frame tracking of the target position within the image plane, establishing the correspondence between 2-D points in the image coordinate system ( $\pi$ ) and their corresponding 3-D points in the real-world coordinate system ( $W$ ) to account for potential perspective effects, roto-translating the results to align with the motion axes of the structure being analyzed, and filtering out unintended camera shaking to ensure measurement reliability.

To this end, a brief overview of the procedure is provided as follows:

- Stage 1: Monitoring set-up.
- Stage 2: Calibration of the camera.
- Stage 3: Post-processing of the recorded video, with the detection and the tracking of specific features.
- Stage 4: Perspective-3-Points method to establish the relationship between 2-D coordinates in the image-plane ( $\pi$ ) and their corresponding 3-D points in the real-world ( $W$ ).
- Stage 5: Transformation from real-world ( $W$ ) to structure ( $x, y, z$ ) reference system.
- Stage 6: Filtering of camera unintended vibrations.

### 2.1 Stage 1: Monitoring set-up

A vision-based monitoring system requires careful pre-planning based on the specific characteristics of the structure under observation. First and foremost, it is essential to identify the sections of the structure to be monitored, with each selected section being associated with distinguishing features to be



tracked. These may either be intrinsic, notable characteristics of the structure itself or artificial high-contrast targets placed in areas of interest, yielding more accurate results at the expense of the need to directly access the structure. Specifically, the procedure is designed for high-contrast artificial targets featuring a checkerboard pattern.

Additionally, it is crucial to estimate the expected structural displacements, as the magnitude of these displacements helps determine the necessary level of accuracy. This, in turn, guides the selection of the camera specifications, including the camera-to-structure distance, which depends on factors such as obstacles or finding a stable vantage point; the optical lenses with an appropriate range of focal length ( $f$ ) to ensure the desired field of view at that distance; and the frame rate, selected to adequately sample the expected vibration frequencies. For civil structures such as bridges and buildings, dominant modal frequencies typically lie below 10 Hz, indicating that frame rates of 30 frames per second (FPS) are generally adequate. This allows for the utilization of consumer-grade cameras, which is increasingly feasible thanks to recent technological advancements.

## 2.2 Stage 2: Calibration of camera parameters

Calibrating camera parameters is a crucial step for understanding how the sensor captures and processes visual data. In the current procedure, the calibration is performed according to the diffused approach proposed in [25]. This involves determining several parameters, including mm-to-pixel transformation factor (from sensor to image reference system), focal length ( $f$ ), and lens distortion coefficients (which account for geometric distortions introduced by the lens). Calibration outcomes will be employed in Stage 4 for the derivation of the relationship between 2-D points in the image-plane ( $\pi$ ) and their corresponding 3-D points in the real-world ( $W$ ).

## 2.3 Stage 3: Post-processing of the recorded video

Video post-processing is composed of three basic steps: definition of the Regions of Interest (ROIs), feature detection and feature tracking.

ROIs are defined in the first frame of the video as areas surrounding specific targets located on the structure or on the ground. Targets on the structure are key points of interest for dynamic characterization, while targets on the ground are used for camera vibration filtering. In the application case study, checkerboard targets are adopted.

The definition of a ROI for each target allows to narrow the operational area within the video frames, where the features of the targets are detected, thus accelerating the automated analysis. The defined ROIs are managed as matrices of pixels, where each pixel is characterized by its 2-D coordinates (expressed in pixels relative to the frame upper-left corner) and a unique RGB intensity value.

The next step involves the detection of sparse feature points, also known as key points, which characterize the digital representation of each target. A key point is generally a small region of the image characterized by unique and invariant features, described by a matrix or a vector that encodes its characteristics. A wide variety of key point types have been proposed in the literature, along with specific algorithms for

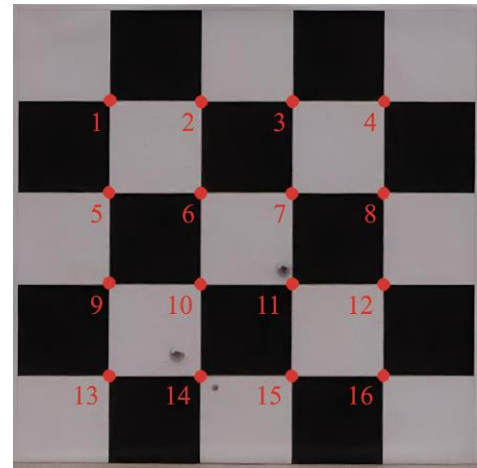


Figure 1. Feature detection via Harris function.

detecting and describing them [15]. In the presented procedure, the Harris-Stephens algorithm [26] is used to detect the internal corners of each checkerboard target (see Figure 1 for an illustrative example). A corner represents the intersection of two edges, where an edge is characterized by a sharp change in image brightness. In addition to their distinctiveness due to RGB intensity contrast, corners exhibit geometric invariance properties, making them robust features for various applications. Their stability under transformations such as translation, rotation, and changes in scale or illumination enhances their suitability for tasks like detection and tracking.

Once the checkerboard corners are identified in the initial frames of the video, their locations in the subsequent frames are tracked with the Kanade-Lucas-Tomasi algorithm [27, 28], a well-established technique for visual tracking applications. In this process, the movement of the key points is determined through optical flow estimation. The output of this stage consists of a time series of coordinates in pixel units, for each corner of every checkerboard target.

It should be carefully considered that the obtained displacement time series  $\eta$  and  $\xi$  solely represent the motion of the features within the image-plane ( $\pi$ ). To determine the actual displacements of the structure, additional analysis is required, such as establishing the relationship between 2-D points in the image-plane ( $\pi$ ) and their corresponding 3-D points in the real-world ( $W$ ), mapping the movements to the real-world coordinate system and accounting for any unintended camera shaking.

## 2.4 Stage 4: Perspective-3-Points method to relate the 2-D image-plane coordinates to 3-D the real-world position

The mapping of the observed 2-D image-plane ( $\pi$ ) coordinates into their actual 3-D real-world positions can be obtained by solving the so-called Perspective- $n$ -Point (PnP) problem for the target corner coordinates at each frame. This implies to determine the 3D position and orientation of the camera based on a set of  $n$  2D image points and their known corresponding 3D world coordinates. This is a fundamental problem that was first explored in the photogrammetry literature and later extended to the field of computer vision. The P3P method is a specific case of the PnP problem, where  $n = 3$ , namely the camera pose is computed according to the correspondence between 3 points.

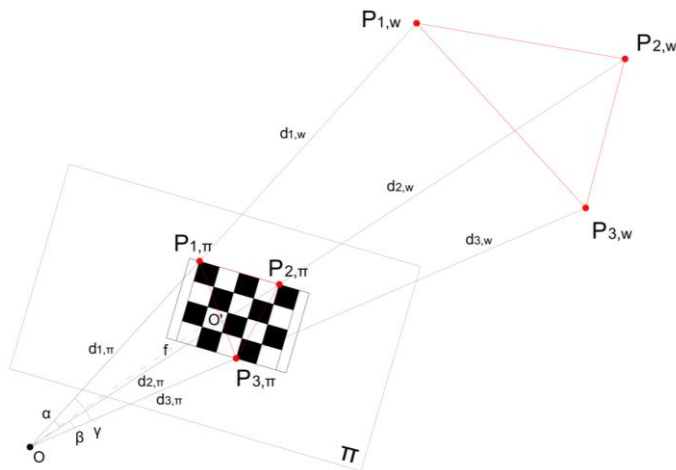


Figure 2. Geometric interpretation of the P3P method.

The solution of the P3P framework used here has its origins in the studies of Grunert [29], and for nearly two centuries it has remained relevant in various research and applications. In this paper, the  $P_nP$  method is used to define the position and orientation of both targets on a structure and the camera. The position of targets on the structure is determined by assuming the camera is not moving while the structure undergoes movement; the motion of the camera is obtained using a fixed target placed outside the shaking structure.

With reference to Figure 2, the intuitive procedure for solving the P3P problem is grounded in the resolution of the law of cosines, which is fundamental for calculating distances and angles in both the image-plane ( $\pi$ ) and the real-world ( $W$ ). The geometric interpretation of Figure 2 refers to a single triplet of checkboard corners, but it can be extended to every possible combination of corners. The law of cosines is first employed for the computation of the angles between the line of sight and the corners in the real-world system. In this phase, the results of Stage 2 and Stage 3 are exploited, namely the calibration outcomes and the coordinate time series of the corners. Then, the law of cosines is re-employed to compute the actual distances between the optical center and the corners of the physical target. This has been the subject of several studies due to the non-linear nature of the problem [30]. Here, the solution of Finsterwalder [31] is used for its high accuracy, as it does not involve any numerical approximations.

For each target, the P3P method is applied to every combination of triplets of corners, resulting in the distance between the optical center and each corner in real-world multiple times. Finally, the distance values related to the same corner are averaged to enhance the accuracy of the estimates. The procedure is repeated for each video frame, associated to a time instant through the frame rate, to obtain the target position at each time step. In this way, the reconstruction of the target displacement with respect to the camera optical center over time is carried out.

This approach is an alternative to the common approach relying on the simple scale factor for unit conversion. The latter only provides accurate results when the camera-to-target line of sight is perpendicular to the target plane. The proposed approach is more flexible, and it can adjust for perspective distortions caused by varying angles between the camera and

multiple targets. This is particularly common when monitoring civil structures due to their large scale and/or the presence of unavoidable restrictions on camera positioning.

## 2.5 Stage 5: Coordinate transformation to the structure reference system

At this stage, a transformation of coordinates into the structure reference system is proposed to ensure a rapid and clear interpretation of the structural behaviour. If the target is positioned in such a way that it aligns as closely as possible with the directions of the main structural movements, two axes of the structure reference system are considered to be parallel to the target directions, and the third one is perpendicular to the target plane. Once this reference alignment is established, a matrix-based change of basis is applied for coordinate transformation.

This involves roto-translating the real-world reference system  $W$  into the structure reference frame. The process includes both rotation and translation operations to account for the differences in orientation and position between the two coordinate systems. The core of the transformation is the least-square fitting of a plane to the coordinates of the checkboard corner in the real-world reference system. This transformation allows the representation of displacements in the structure reference system, which is independent of the location and orientation of the camera.

## 2.6 Stage 6: Filtering of camera unintended vibrations

Up to this stage, the procedure provides the relative displacements between the camera and each target, expressed in the world coordinate system. However, these displacement time series can be affected by camera shaking, which can arise from external factors such as wind or unintended user interactions. To obtain accurate estimates of absolute displacements, it is essential to account for and eliminate these camera-induced contributions. This is achieved by using reference targets placed on the ground in stable positions. These targets are assumed to remain stationary throughout the observation period. Consequently, any apparent displacement they exhibit in the world coordinate system reflects movement of the camera, rather than motion of the targets themselves.

The same tracking procedure outlined in the previous stages can be applied to the ground-based targets to quantify their apparent displacements. The absolute displacements of the targets on the structure can therefore be obtained by subtracting the apparent displacements of the ground-based targets from the relative displacements of the targets on the structure.

In laboratory settings, the camera can often be stably fixed, and the environment is controlled (e.g., no wind), which reduces the need for this correction. In the field, maintaining comparable stability is more challenging, making this filtering step essential. However, since this study focuses specifically on laboratory conditions, field-related considerations are not addressed further.

## 3 PROCEDURE ASSESSMENT PERFORMED UNDER CONTROLLED CONDITIONS

In this Section, the validation of the procedure described in Section 2 is performed through a laboratory test. The aim is to evaluate the performance of the designed vision-based monitoring procedure and to assess its potential applicability in

outdoor scenarios. The test involves the monitoring under controlled conditions of a scale steel frame subjected to excitation from a shaking table (see Figure 3). High-contrast artificial targets with a checkerboard pattern, measuring 250 mm by 250 mm, have been used. Two of them are connected to the base and the top floor of the frame, while a third one is located on the laboratory floor to identify potential camera movements.

The video-monitoring system consists of a Panasonic Lumix GH6 camera and Samsung S23 smartphone recording video in 4K and 8K resolution at 50 and 30 frames per second (FPS), respectively. The results presented below are based on videos captured by the camera, which has a lower resolution compared to the smartphone, making it more sensitive to the noise. Three different scenarios are considered by varying the location of the camera sensor. The distance between the camera and the steel frame for the three examined scenarios is listed in Table 1, measured using a laser meter. In both the scenarios, the angle of incidence between the line of sight and the target plane is nearly zero, implying an almost frontal view of the scene.

Several input excitations have been applied to the frame base during the tests. The results presented in the following refer to the Irpinia earthquake ground motion excitation [32], recorded on November 23, 1980, and reproduced by the shaking table along the  $x$ -axis of the structure, which is nearly horizontal to the recorded scene.

The accuracy of the vision-based monitoring system is assessed by comparing the estimated dynamic displacements with reference time histories. For the target at the base of the frame, the reference displacements are those imposed by the actuator of the shaking table. To validate the vision-based displacement for the target at the top of the frame, a Linear Variable Displacement Transducer (LVDT) is specifically positioned near the target for this purpose. The adopted LVDT measures displacements within the range [0, 100 mm], with sensitivity of 80 mV/V, excitation voltage equal to 10 V, and sampling frequency set at 200 Hz.

### 3.1 Results

The results of the monitoring conducted during the experimental test are discussed in this Section. Since the vision-based results for the target at the top of the frame exhibit similar accuracy, the following focuses on presenting the results for the target at the base of the frame.

The displacements of the frame base target in the 2-D image coordinate system, expressed in pixels and identified as detailed in Section 2.3, are shown in Figure 4 and Figure 5 for scenarios 1 and 2, respectively (similar conclusions can be drawn for scenario 3).

It can be observed that the vertical component of the motion,  $\xi$ , is approximately zero in both scenarios, since the imposed motion is horizontal to the structure and the camera is perpendicular to the target plane, implying no perspective effects. The difference between the amplitude of the horizontal displacement,  $\eta$ , in the two example scenarios is related to the distance between the camera and the frame, which is about 2 m for scenario 1 and 10 m for scenario 2, implying different pixel coverage on the examined target, as indicated in Table 1.

In this regard, it is specified that the target  $\eta$ -displacement time history in pixels (for example, Figure 5 for scenario 2) is



Figure 3. Laboratory experiment framework.

Table 1. Monitoring scenarios.

ID	Measured distance [m]	Target area [10 <sup>3</sup> pxl <sup>2</sup> ]
1	1.84	186.75
2	10.90	93.02
3	25.21	18.22

calculated by averaging the results obtained by separately tracking the motion of the corners of the checkerboard target (see Figure 6, which shows the motion of four out of sixteen monitored corners, specifically the outer ones: points 1, 4, 13, 16 with numbering following Figure 1), a step that allows for an increase in the accuracy. Indeed, this approach minimizes errors from individual tracking by leveraging multiple data for a more reliable measurement.

Afterwards, following the procedure indicated in Section 2.4, Section 2.5, and Section 2.6, pixel displacements related to the image system are converted into 3D real-world displacements, projected into the structure reference system, and cleared from uncontrolled camera shaking, measured by evaluating the apparent motion of the fixed ground-based target. The vision-based dynamic displacement along the  $x$ -direction in the structure coordinate system, expressed in millimeters, is represented in Figure 7 and Figure 8 for scenarios 1 and 2, respectively, along with a comparison to the corresponding reference displacement. In this, the reference is the known displacement time history set by the shaking table, which demonstrates excellent validation of vision-based results for all the scenarios.

As discussed in Section 2.4, a key aspect in determining the three-dimensional mapping between image and real-world systems is the evaluation of the distance between the optical center and the monitored target, determined by means of the P3P method. This method allows the calculation of the distances between the camera and any triplet of checkerboard corners within each frame, after which the time-varying



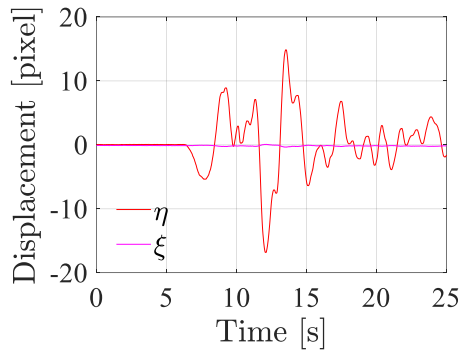


Figure 4. Scenario 1 - Image-plane horizontal and vertical displacements in pixel unit,  $\eta$  and  $\xi$  respectively.

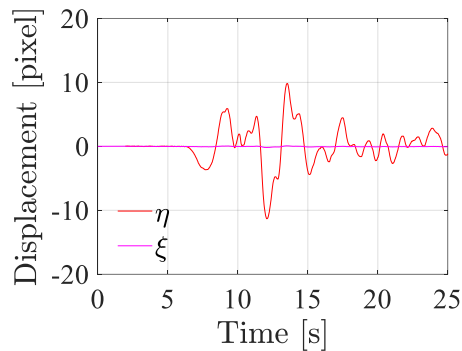


Figure 5. Scenario 2 - Image-plane horizontal and vertical displacements in pixel unit,  $\eta$  and  $\xi$  respectively.

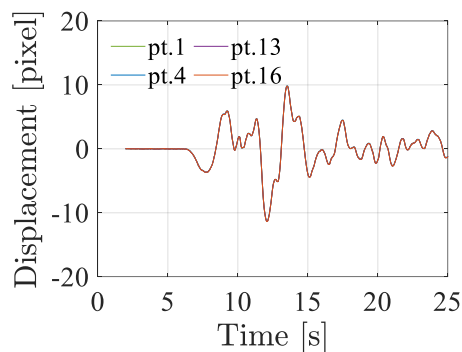


Figure 6. Scenario 2 - Image-plane horizontal displacement,  $\eta$ , obtained by tracking the four outer checkerboard key corners.

Table 2. Vision-based method accuracy.

ID	Estimated distance [m]	$\sigma_{(0-5)s}$ [mm]	$\sigma_{(5-25)s}$ [mm]
1	1.85	0.0072	0.2220
2	10.94	0.1033	0.1382
3	25.27	0.1904	0.3807

Table 3. Peak values compared with the scale factor approach.

ID	Reference displacement [mm]	Estimated displacement [mm]	Scale factor displacement [mm]
1	9.48	9.30	9.74
2	9.48	9.17	9.28
3	9.48	9.37	9.07

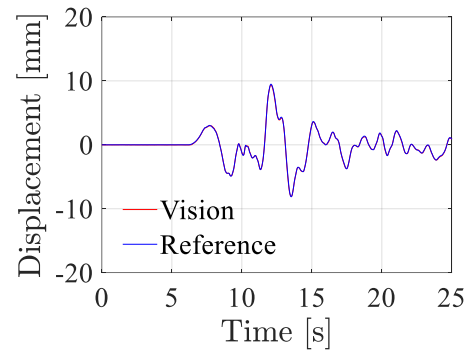


Figure 7. Scenario 1 - Horizontal displacement in the structure coordinate system.

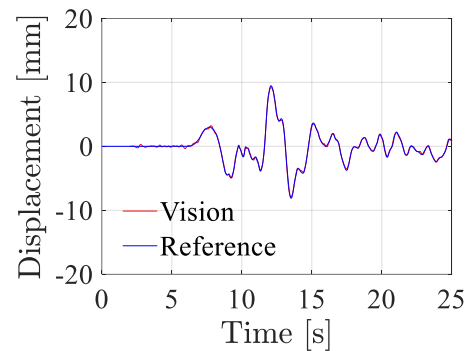


Figure 8. Scenario 2 - Horizontal displacement in the structure coordinate system.

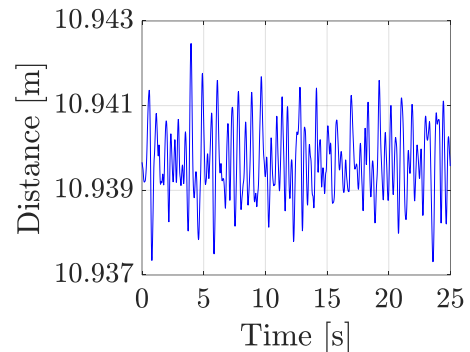


Figure 9. Scenario 2 - Variation of the estimated distance between the camera and the target centroid along time.

Table 4. Peak displacement relative error.

ID	Proposed method error [%]	Scale factor error [%]
1	1.90	2.95
2	3.27	2.11
3	1.05	4.32

distance between the target centroid and the camera is evaluated by averaging the triplet estimates.

The variation of the estimated camera-to-target distance along time is investigated in Figure 9, related to scenario 2. The estimation error is less than 1 mm, which is very small compared to the actual distance of 10.9 m. However, this error

is larger than the small change in the real distance caused by the maximum allowed horizontal displacement (about 10 mm). This explains why accuracy decreases as the distance camera-to-scene increases. The camera-to-target distance from the P3P method, averaged over time, is shown in Table 2. P3P-based estimates (Table 2) are in close agreement with the distances measured on-site using a meter laser (Table 1), with relative errors of 0.1, 0.4, and 0.2 % for scenarios 1, 2, and 3.

As a metric in evaluating the reliability of the method, Table 2 also presents the standard deviation  $\sigma_{(0-5)s}$  of the vision-based displacement time series in the first 5 seconds of the tests. During this interval, no excitation is transmitted by the shaking table, so the standard deviation reflects the signal noise and can be considered a measure of the accuracy. The obtained  $\sigma_{(0-5)s}$  is of the order of one-hundredth of mm for scenario 1, denoting a very high accuracy. It reduces to about one-tenth of mm for scenarios 2 and 3, highlighting the impact of the target-to-camera distance on vision-based results.

To further quantify the noise, the standard deviation  $\sigma_{(5-25)s}$  of the difference between reference- and vision-based displacement time histories is calculated for the time interval between 5 and 25 seconds, as reported in Table 2. The standard deviation of the error ranges between 0.1 and 0.4 mm including the three scenarios. Considering that the maximum displacement experienced by the examined (base) target is approximately 10 mm, the accuracy of the measurements is deemed satisfactorily high, with a standard deviation-to-amplitude ratio below 4%, even for the more distant case scenario, indicating reliable measurement accuracy.

Finally, a comparison of the results is presented to assess the accuracy of the P3P method in relation to the scale factor, a simpler and more widely used method in the literature. Scenario 1 is selected as an example, characterized by minimal uncertainty resulting from the (reduced) camera-to-target distance, allowing the error to be entirely attributed to the method employed. The scale factor is calculated as the ratio between the target side in metric units (250 mm) and its side in image units (432 pixel, based on the target area shown in Table 1), resulting in a value of 0.58 mm/pixel.

Using the scale factor method, the horizontal displacement  $\eta$  detected in the image system is simply scaled by the scale factor to obtain the physical displacement  $x$ . Thus, the peak absolute displacement of 16.83 pixels (see Figure 4) multiplied by the scale factor returns a physical value of 9.76 mm. As represented in Figure 7, the maximum absolute displacement detected by the P3P method is 9.30 mm, while the reference (i.e., imposed) value is 9.48 mm. This leads to relative errors with the reference peak displacement of 2.95 % for the scale factor approach and 1.90 % for the P3P method. Peak displacements obtained by the two methods for the other scenarios are shown in Table 3, leading to relative errors as indicated in Table 4. These results demonstrate a generally better performance of the P3P-based designed method compared to the scale factor approach. This indicates that the scale factor, which is designed for frontal views of small-scale objects, performs less effectively than P3P in its intended context. The discrepancy between the two methods is expected to become even more pronounced in the presence of inclinations in the line of sight relative to the structural displacement. These findings highlight the critical need for pixel-to-mm 3D mapping in real-world

case studies, underscoring the significance of the present research.

#### 4 CONCLUSIONS

This study proposes a vision-based approach for structural displacement monitoring, suitable for both dynamic and static conditions. It is a cost-effective, non-intrusive alternative to traditional sensing technologies. The approach involves the use of consumer-grade cameras and checkboard targets to be installed on the structure.

The reconstruction of the monitored target displacement is facilitated by computer vision algorithms, which detect the checkerboard corners in digital images and track their movement across consecutive frames. The proposed approach implements the Perspective-Three-Point (P3P) algorithm to establish a correspondence between the 2D image coordinates and the 3D world reference system coordinates. The flexibility of this approach makes it particularly suitable for a wide range of camera positions and orientations relative to the monitored structure. Additionally, unintended camera vibrations can be filtered out by tracking one or more targets placed externally to the structure, assumed to be stationary.

The methodology has been validated through a laboratory test on a steel frame excited by a shaking table. Specifically, performed tests focused on evaluating the impact of the camera-structure distance, or alternatively, the target area in the images to account for potential zoom variations, on the accuracy of the displacement estimates. The analysis considered two parameters: the standard deviation of the estimated displacements in the initial seconds of the test (where no excitation was applied) and the standard deviation of the difference between the estimated displacements and the reference values during the remaining part of the test. The first parameter represents the signal noise, whose order of magnitude increases from one-hundredth of a millimeter to one-tenth of a millimeter as the camera-target distance increases from 1.85 m to 25.21 m. Despite this variation, the second parameter, which measures the mean error of the displacement time series relative to the reference displacements, remains satisfactory in all the scenarios, with a standard deviation-to-amplitude ratio around 4 % in the greater structure-to-camera distance scenario.

In comparison, the scale factor approach, a simpler and more widely used method in the literature, was also considered. However, the P3P-based method demonstrated better accuracy in capturing displacement under laboratory conditions, suggesting that the scale factor may not be suitable for outdoor scenarios, which may involve non-frontal views and varying orientations of the targets. Additionally, the scale factor estimation requires user intervention, making it unsuitable for automated procedures.

These preliminary results underscore the potential of this vision-based approach for structural monitoring applications, paving the way for its broader adoption in civil engineering structures and infrastructure. Future research will focus on integrating these initial findings with further tests, particularly examining the effects of the inclination between the line of sight and the target, and refining the displacement accuracy.

## ACKNOWLEDGMENTS

This work was supported by the FAR 2023 Project - FOMO line (Vision-based approaches for the structural health monitoring of existing bridges, VIS4SHM). The financial support provided by the University of Modena and Reggio Emilia and the “Fondazione di Modena” is hereby gratefully acknowledged.

## REFERENCES

- [1] A. B. Noel, A. Abdaoui, T. Elfouly, M. H. Ahmed, A. Badawy and M. S. Shehata, Structural Health Monitoring Using Wireless Sensor Networks: A Comprehensive Survey, *IEEE Communications Surveys & Tutorials* 19(3): 1403-1423, 2017
- [2] M. Abdulkarem, K. Samsudin, F.Z. Rokhani, and M.F. A Rasid, Wireless sensor network for structural health monitoring: A contemporary review of technologies, challenges, and future direction, *Structural Health Monitoring*, 19(3): 693-735, 2019.
- [3] A. Sofi, J.J. Regita, B. Rane, and H.H. Lau, Structural health monitoring using wireless smart sensor network - an overview, *Mechanical Systems and Signal Processing*, 163: 108113, 2022.
- [4] L. Poluzzi, M. Barbarella, L. Tavasci, S. Gandolfi, and N. Cenni, Monitoring of the Garisenda tower through GNSS using advanced approaches toward the frame of reference stations, *Journal of Cultural Heritage*, 38: 231-241, 2019.
- [5] J. Yu, X. Meng, B. Yan, B. Xu, Q. Fan, and Y. Xie, Global navigation satellite system-based positioning technology for structural health monitoring: a review, *Structural Control and Health Monitoring*, 27(1): e2467, 2020.
- [6] D.A. Talledo, A. Miano, M. Bonano, F. Di Carlo, R. Lanari, M. Manunta, A. Meda, A. Mele, A. Prota, A. Saetta, and A. Stella, Satellite radar interferometry: Potential and limitations for structural assessment and monitoring, *Journal of Building Engineering*, 46: 103756, 2022.
- [7] E. Bassoli, L. Vincenzi, F. Grassi, and F. Mancini, A multi- temporal dinar-based method for the assessment of the 3d rigid motion of buildings and corresponding uncertainties, *Journal of Building Engineering*, 73: 106738, 2023.
- [8] C. Castagnetti, E. Bassoli, L. Vincenzi, and F. Mancini, Dynamic assessment of masonry towers based on terrestrial radar interferometer and accelerometers, *Sensors*, 19(6): 1319, 2019.
- [9] Y. Fradelos, O. Thalla, I. Biliani, and S. Stiros, Study of lateral displacements and the natural frequency of a pedestrian bridge using low-cost cameras, *Sensors*, 20(11): 3217, 2020.
- [10] Y. Xu, J.M.W. Brownjohn, and F. Huseynov, Accurate deformation monitoring on bridge structures using a cost-effective sensing system combined with a camera and accelerometers: Case study, *Journal of Bridge Engineering*, 24(1): 05018014, 2019.
- [11] H. Yoon, H. Elanwar, H. Choi, M. Golparvar-Fard, and B.F. Spencer Jr, Target-free approach for vision-based structural system identification using consumer-grade cameras, *Structural Control and Health Monitoring*, 23(12): 1405-1416, 2016.
- [12] X. Zhao, K. Ri, and N. Wang, Experimental verification for cable force estimation using handheld shooting of smartphones, *Journal of Sensors*, 2017(1): 5625396, 2017.
- [13] Y. Xu and J.M.W. Brownjohn, Review of machine-vision based methodologies for displacement measurement in civil structures, *Journal of Civil Structural Health Monitoring*, 8: 91-110, 2018.
- [14] B.F. Spencer Jr, V. Hoskere, and Y. Narazaki, Advances in computer vision-based civil infrastructure inspection and monitoring, *Engineering*, 5(2): 199-222, 2019.
- [15] C.Z. Dong and F.N. Catbas, A review of computer vision-based structural health monitoring at local and global levels, *Structural Health Monitoring*, 20(2): 692-743, 2021.
- [16] A. Zona, Vision-based vibration monitoring of structures and infrastructures: An overview of recent applications, *Infrastructures*, 6(1): 4, 2020.
- [17] D. Feng and M.Q. Feng, Experimental validation of cost-effective vision-based structural health monitoring, *Mechanical Systems and Signal Processing*, 88: 199-211, 2017.
- [18] M. Wang, W.K. Ao, J.M.W. Brownjohn, and F. Xu, Completely non-contact modal testing of full-scale bridge in challenging conditions using vision sensing systems, *Engineering Structures*, 272: 114994, 2022.
- [19] J.G. Chen, T.M. Adams, H. Sun, E. Santini Bell, and O. Büyükoztürk, Camera-based vibration measurement of the world war I memorial bridge in Portsmouth, New Hampshire. *Journal of Structural Engineering*, 144(11): 04018207, 2018.
- [20] Y. Xu, J.M.W. Brownjohn, and D. Kong, A non-contact vision-based system for multipoint displacement monitoring in a cable-stayed footbridge, *Structural Control and Health Monitoring*, 25(5): e2155, 2018.
- [21] C.Z. Dong, S. Bas, and F.N. Catbas, Investigation of vibration serviceability of a footbridge using computer vision-based methods, *Engineering Structures*, 224:111224, 2020.
- [22] D. Lydon, M. Lydon, S. Taylor, J. Martinez Del Rincon, D. Hester, and J.M.W. Brownjohn, Development and field testing of a vision-based displacement system using a low cost wireless action camera, *Mechanical Systems and Signal Processing*, 121: 343-358, 2019.
- [23] D. Tan, J. Li, H. Hao, and Z. Nie, Target-free vision- based approach for modal identification of a simply-supported bridge, *Engineering Structures*, 279: 115586, 2023.
- [24] X.W. Ye, T.H. Yi, C.Z. Dong, and T. Liu, Vision-based structural displacement measurement: System performance evaluation and influence factor analysis, *Measurement*, 88: 372-384, 2016.
- [25] A. Geiger, F. Moosmann, Ö. Car, and B. Schuster: Automatic camera and range sensor calibration using a single shot, *IEEE International Conference on Robotics and Automation*, pp. 3936-3943, 2012.
- [26] C. Harris and M. Stephens, A Combined Corner and Edge Detector, *Proceedings of the 4th Alvey Vision Conference*, pp. 147-151, 1988.
- [27] B.D. Lucas and T. Kanade. An Iterative Image Registration Technique with an Application to Stereo Vision. *International Joint Conference on Artificial Intelligence*, pp. 674-679, 1981.
- [28] C. Tomasi and T. Kanade. Detection and Tracking of Point Features. Carnegie Mellon University Technical Report CMU-CS-91-132, 1991.
- [29] J. A. Grunert. Das pothenotische problem in erweiterter gestalt nebst bber seine anwendungen in der geodasie, *Grunerts Archiv für Mathematik und Physik*, 238–248, 1841 (in German)
- [30] B. Wang, H. Hu, and C. Zhang, Geometric Interpretation of the Multi-solution Phenomenon in the P3P Problem, *Journal of Mathematical Imaging and Vision* 62: 1214–1226, 2020.
- [31] R.M. Haralick, C.N. Lee, K. Ottenberg, M. Nölle. Review and Analysis of Solutions of the Three Point Perspective Pose Estimation Problem, *International Journal of Computer Vision*, 13(3): 331-356, 1994.
- [32] L. Luzzi, R. Puglia, E. Russo, M. D’Amico, G. Lanzano, F. Pacor, and C. Felicetta. Engineering strong-motion database: a gateway to access European strong motion data. In *16th World Conference on Earthquake Engineering*, 2017.



# Model Updating and Damage Detection for Bridge Integrity Management

Eray Temur<sup>1</sup>[0000-0002-7560-7101], Maria Pina Limongelli<sup>1</sup>[0000-0002-9353-5439], Andrea Piscini<sup>2</sup>[0000-0003-2786-1321],

Edoardo Troielli<sup>2</sup>[0009-0007-8761-4361]

<sup>1</sup>Politecnico di Milano, Department of Architecture, Built environment and Construction engineering, Piazza Leonardo da Vinci 32, 20133 Milan, Italy

<sup>2</sup>SINA S.p.A., Viale Isonzo, 14/1, 20135 Milano, Italy

email: eray.temur@polimi.it, mariagiuseppina.limongelli@polimi.it, andrea.piscini@sina.it, edoardo.troielli@sina.it

**ABSTRACT:** The integrity management of bridges is crucial for ensuring public safety and economic stability. In practice, Structural Health Monitoring data recorded during bridge operation is increasingly used to guide maintenance decisions. However, incorporating structural damage information more effectively can lead to optimal strategies for integrity management. In this study, we employ Bayesian Model Updating to develop a more reliable structural model. The updated finite element model is then used to train a variational autoencoder-based surrogate model for damage detection, localization, and severity estimation. The variational autoencoder model establishes a link between damage-related features and the modal properties derived from SHM data. Damage information supports maintenance decision-making through a predefined decision rule.

**KEY WORDS:** Structural health monitoring, damage detection, surrogate models, structural integrity management, maintenance decision.

## 1 INTRODUCTION

Bridges and viaducts are fundamental components of transportation networks, ensuring connectivity and economic stability. However, their structural integrity is continuously challenged by aging, increasing traffic loads, and environmental stressors. Effective bridge health management can benefit from continuous monitoring and strategies to detect potential damage and mitigate the risks before they compromise safety.

Structural Health Monitoring (SHM) has emerged as a crucial tool for assessing bridge conditions in real-time, providing early detection of structural anomalies. The design and implementation of SHM systems for bridge integrity management were proposed in the study by Limongelli et al. [1]. SHM system provides continuous information about structural properties such as natural frequencies, damping ratios, and mode shapes. However, directly labeling the obtained modal properties as belonging to either damaged or undamaged states from data collected on real-world structures is challenging. This difficulty arises because the changes in modal features can also result from various factors not related to damage, such as environmental conditions, operational variability, or sensor noise. While some studies explored damage detection and localization through the modal properties [2], a fundamental part of damage detection strategies entails the use of physics-based models, which provide a basis for understanding the overall structural behavior under varying conditions. By integrating SHM data into physics-based formulations, the models are updated to represent the actual bridge conditions, enhancing structural integrity management, improving maintenance planning, and decision-making. However, the computational cost of updating a finite element model in real-time can be very high. Surrogate models provide a computationally efficient alternative to complex physics-based simulations.

In this paper, an approach based on Bayesian Model Updating (BMU) using Transitional Monte Carlo Markov Chain is implemented to update the structural model of a bridge using measured data. This approach refines the bridge model through the incorporation of modal properties extracted from SHM data, by reducing the discrepancy between measured and calculated modal properties. Thanks to the systematic updates of the structural parameters, the model accurately represents the bridge's current state. The high-fidelity and calibrated FE model is then used for training a surrogate model. Namely, the FE model is used to simulate several damage scenarios and generate the relevant response of the bridge, thus providing the necessary training data for the surrogate models. Several surrogate modeling approaches have been explored in the literature, with the most used ones including Kriging models, artificial neural network (ANN)-based surrogate models, and reduced order models [2], [3], [4], [5]. In this paper, a Variational Autoencoder (VAE) architecture is adopted to effectively capture complex, high-dimensional patterns in the structural response data. Unlike the other autoencoders, VAE provides a probabilistic latent representation, allowing better generalization, which is particularly valuable for long-term SHM tasks [6]. Furthermore, the use of fully connected layers in classifiers and regression blocks enables the estimation of damage severity and location directly from the latent space.

## 2 METHODOLOGY

The framework proposed in this paper integrates SHM information, a Bayesian finite element (FE) model updating approach, and surrogate modelling techniques to efficiently localize and quantify damage. A BMU framework is first employed to calibrate a high-fidelity FE model using SHM data, refining the model parameters to closely reflect the real structural behavior. Using the calibrated FE model, various damage scenarios are simulated to generate labeled datasets of

modal responses. These datasets are then used to train a Variational AutoEncoder (VAE)-based surrogate model, which learns a latent representation of the relationship between modal features and damage states. Subsequently, the trained VAE model is utilized to obtain fast and scalable predictions of damage scenarios during online monitoring, bypassing the computational burden of running FE simulations in real time. This integrated approach bridges the gap between accurate physics-based modeling and the practical demands of efficient damage diagnosis in SHM systems. The overall architecture of this framework, including the surrogate model construction and its application for decision support, is illustrated in Figure 1.

After being trained, the surrogate model is capable of mapping newly acquired experimental modal features to damage location and severity, providing damage scenario indicators that can be used for decision support. This hybrid approach combines physics-based model updating for data generation with data-driven surrogate modeling for inference. It ensures a computationally efficient yet robust damage detection system for bridges.

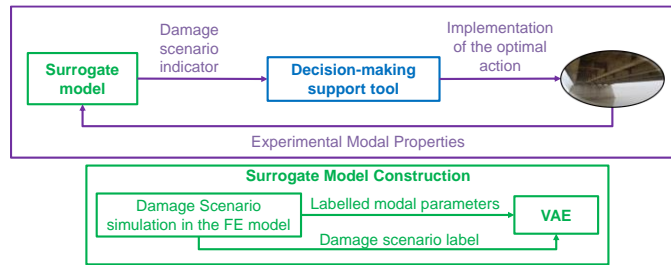


Figure 1: General workflow for online damage detection.

## 2.1 FE calibration and simulation of damage scenarios

Bayesian Model Updating (BMU) is employed to calibrate the FE model of the bridge using measured modal properties. The overall BMU workflow is indicated in Figure 2 that illustrates the step-by-step process of refining model parameters, from prior assumptions to the convergence of posterior distributions. The process aims to reduce discrepancies between experimental and simulated dynamic characteristics by updating uncertain model parameters, thereby enhancing the accuracy and predictive capabilities of the model. In this study, BMU is performed using Transitional Markov Chain Monte Carlo (TMCMC). TMCMC is a sampling-based Bayesian inference method that allows efficient estimation of the posterior distribution of model parameters, even in high-dimensional or nonlinear problems [7], [8].

### 2.1.1 Parameter Selection and Prior Definition

Parameters with high sensitivity to modal responses are selected for updating, specifically, the vertical stiffnesses of the girders. Each parameter  $\theta$  is assigned a prior distribution  $\pi(\theta)$ , representing the initial uncertainty in its value based on engineering knowledge.

### 2.1.2 Likelihood Function Construction

The likelihood function  $L(D|\theta)$  of data  $D$  quantifies the agreement between simulated and measured modal data, including both natural frequencies and mode shapes. Mode

shape similarity is evaluated using the Modal Assurance Criterion (MAC). The likelihood is defined as indicated in Eq. 1.

$$L(D|\theta) = \exp \left( -\frac{1}{2} \sum_i w_i \left( \frac{f_{m,i} - f_{s,i}}{\sigma_i} \right)^2 - \frac{1}{2} \sum_j w_j \log(1 - \text{MAC}_j) \right) \quad (1)$$

where  $f_{m,i}$  and  $f_{s,i}$  are measured and simulated frequencies,  $\sigma_i$  represents uncertainty, and  $w_i, w_j$  are weighting factors.

### 2.1.3 Transitional Sampling via TMCMC

TMCMC introduces a sequence of intermediate, tempered distributions shown in Eq. 2.

$$\pi_\beta(\theta|D) \propto \pi(\theta)L(D|\theta)^\beta \quad (2)$$

where  $\beta \in [0,1]$  gradually increases from 0 (prior only) to 1 (full posterior). At each state, samples are reweighted and resampled based on their likelihood, allowing efficient exploration of the parameter space. The process continues until the convergence is achieved.

### 2.1.4 Posterior Sampling and Model Updating

During the TMCMC process, the FE model is continuously evaluated as parameter samples are drawn and updated through each intermediate distribution. At every step, the simulated modal properties are compared with experimental data to assess the quality of the current model approximation. The iterative approach allows progressive refinement of the model, ensuring that the final set of posterior samples yields a calibrated model that reliably captures the dominant dynamic behavior of the structure. Despite the minor residual discrepancies (e.g. in higher modes), the updated model serves as a high-fidelity basis for generating synthetic damage scenarios, which provide the labeled data needed to train the surrogate model described in the following sections.

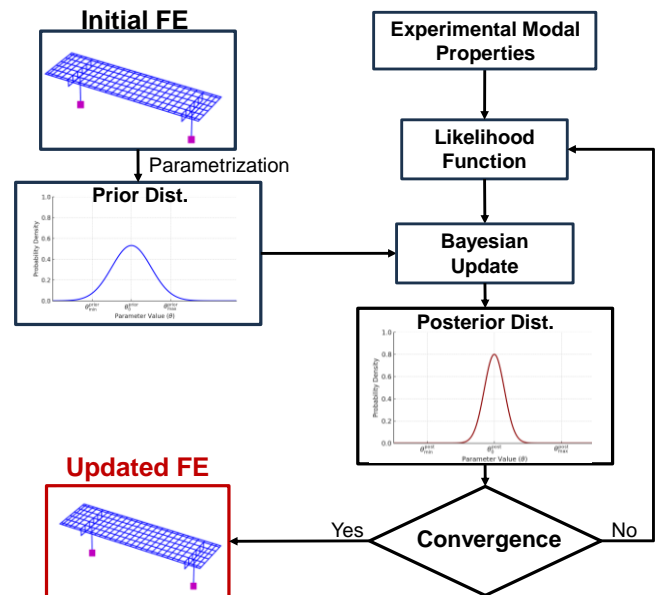


Figure 2: Bayesian Model Update diagram

In this study, vertical stiffnesses were chosen as updating parameters due to their high sensitivity to vertical and torsional modes identified in the experimental data. A total of 8 stiffness

parameters (one per each girder) were assigned uniform prior distributions with  $\pm 50\%$  bounds from nominal values. TCMC was implemented with 50 intermediate  $\beta$  steps and 1000 samples per step. Convergence was evaluated using the coefficient of variation of the likelihood, with a threshold of 5% at each stage.

## 2.2 Surrogate model

The calibrated FE model is used to generate labelled dataset for several damage scenarios, which constitute the training set for the surrogate model. In this work, a Variational Autoencoder (VAE) is employed to learn a latent representation of modal properties across the various damage scenarios. The model is trained on synthetic modal data representing damage states of increasing severity and is developed for real-time estimation of damage location and severity based on updated modal properties. While this structure supports unsupervised feature learning, it has incorporated supervised outputs, providing reconstructed modal properties and predicted damage features.

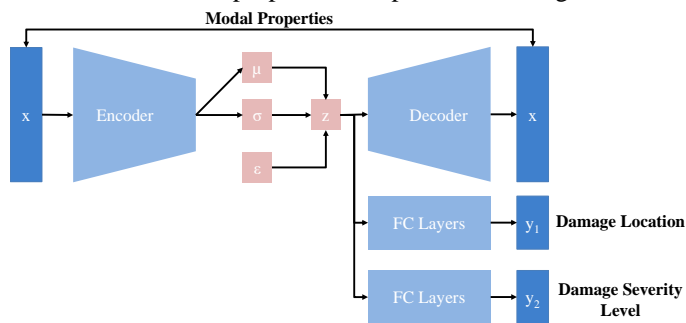


Figure 3: VAE architecture

The VAE consists of an encoder, which maps the modal properties ( $\mathbf{x}$ ) to a latent space ( $\mu, \sigma, \epsilon, z$ ), and a decoder, which reconstructs the modal properties while ensuring regularization through a Kullback-Leibler (KL) divergence term. This term, commonly used in VAE architecture, encourages the latent variables to follow a normal distribution and helps the model learn meaningful and general features [9]. In addition to the conventional VAE architecture, two fully connected layers (FC Layers) are incorporated as a part of supervised feature learning: one serves as a classifier for identifying the location of damage  $y_1$ , and the other functions as a regressor to estimate damage severity levels  $y_2$ , as illustrated in Figure 3.

The input to train the surrogate model comprises modal frequencies and normalized mode shapes, extracted from modal analysis. The encoder consists of three fully connected layers with Rectified Linear Unit (ReLU) as a nonlinear activation function mapping the input to a latent space of dimension 32. The ReLU is widely used for its simplicity and effectiveness in preventing vanishing gradients. Two separate fully connected layers use the mean and log variance of the latent distribution to establish a relationship between the latent features and the damage locations and severity levels. The decoder follows a symmetric structure to reconstruct the input. Additionally, two parallel output layers predict damage locations and severity. Similar to the approach proposed by Yessoufou and Zhu [10], who employed a convolutional neural

network-LSTM with distinct loss functions for damage classification and severity estimation, the proposed architecture treats damage location as a classification problem supervised with cross-entropy loss, while damage severity estimation is formulated as a regression task that predicts severity levels between 0 and 1 and is optimized using mean squared error.

The model is trained using a weighted loss function combining:

1. Reconstruction Loss: Mean Absolute Error (MAE) between input and reconstructed modal properties.
2. KL Divergence Loss: Enforcing latent space regularization.
3. Classification Loss: Cross-entropy loss for damage location prediction.
4. Regression Loss: Mean Squared Error (MSE) for damage severity estimation.

A cyclical KL annealing strategy is implemented, gradually increasing the weight of the KL term to improve latent space disentanglement [11]. To enhance the training performance, several incremental analyses were conducted, based on which the Adam optimizer was selected [12]. Additionally, the initial learning rate was set to 0.001 and configured to adaptively decrease throughout different phases of training to maintain stable convergence and improved generalization.

## 2.3 Decision-Making approach

A concept for a decision-making approach is proposed in Figure 4, drawing inspiration from existing SHM-informed response protocols proposed by Çelebi [13].

At the core of this approach lies a threshold-based logic that interprets the results produced by the VAE model. The VAE model identifies the most likely damaged locations and estimates the damage severity. For each identified component as the location of damage, the damage severity is evaluated individually through a decision-making layer that maps severity levels to specific actions. These outputs are contextualized through a decision-making layer that maps each damage severity level to a specific action. Namely, the outputs of the VAE (relevant to damage location and severity) are evaluated against predefined thresholds. The exceedance of a threshold triggers a specific action (continued monitoring, issuing a warning, or initiating a repair procedure). These layered interpretations add practical value to the detection results and allow for automatic mapping of evolving damage states into operational decisions. Exemplary actions are depicted in Figure 4. The VAE model provides two key outputs, which are the damage location and the damage severity. Each damaged component is associated with an evaluated damage severity ( $k_{red}$ ) and a warning indicator. Green indicates normal condition, yellow suggests the need for inspection, and red prompts immediate repair or closing bridge suggestions, depending on severity. The goal of this approach is to support a straightforward integration of SHM-informed, rule-based maintenance strategies into bridge integrity management, ensuring that timely and proportional interventions are triggered as the condition of the structure evolves. The definition of the threshold is a critical aspect of this approach and must be carried out based on reliability analysis for specific limit states defined for the bridge.



### 3 CASE STUDY

The procedure described in the previous section has been applied to a continuously monitored bridge located in northern Italy. The bridge consists of 15 spans, 11 of which are instrumented with acceleration sensors. Each monitored span is equipped with 5 to 6 acceleration sensors on the deck, strategically placed to capture the bridge's dynamic response under operational conditions.

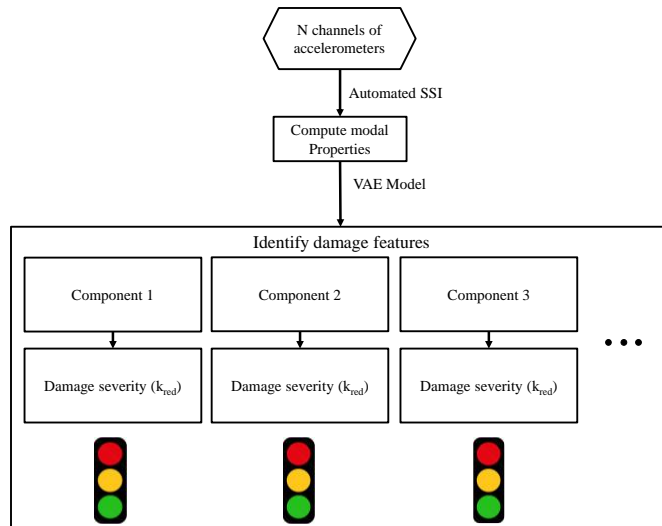


Figure 4: Decision-making framework based on damage level threshold

To identify the modal parameters from recorded responses, an online automatic Stochastic Subspace Identification (SSI) method has been developed. To ensure robust tracking of modal properties over time, a post-processing step involving modal clustering is employed. The identified modal properties are clustered using a hierarchical clustering algorithm based on a predefined Modal Assurance Criterion (MAC) and frequency similarity threshold. This process helps distinguish consistent modes from spurious ones, reducing uncertainties in the estimated modal parameters.

The approach follows the clustering methodology detailed in previous works by Magalhães et al. [14] which has demonstrated its effectiveness on SSI-based modal tracking in bridge monitoring applications.

A detailed finite element model of the bridge was built using the OpenSees software [15], and calibrated by applying the Bayesian model updating process. During the BMU, vertical bending stiffnesses were selected as updating parameters, based on their higher sensitivity. This choice was made since the experimental mode shapes of the selected bridge are predominantly in the vertical direction, including vertical and torsional modes. These stiffness parameters were iteratively updated using the Transitional Markov Chain Monte Carlo (TMCMC) algorithm described in section 2.1. The resulting frequencies and MAC values before and after the BMU are indicated in Table 1. The mode shapes obtained from experimental data and the updated FE model are shown in Figure 5 and Figure 6, respectively.

After updating, the FE model showed improved agreement with the experimental modal properties. The first and second modes reached MAC values of 99.8% and 94.2%, respectively.

However, the third mode retained a relatively low MAC value of 36.1%, which indicates limited consistency. This discrepancy is attributed to reduced sensitivity of vertical stiffness to higher terms not captured by the selected parameters.

Despite this, the updated FE model provides a sufficiently accurate representation of the bridge's dominant dynamic behavior, and it is used exclusively to generate synthetic damage scenarios for training the surrogate model. Since both training and test datasets are generated from the calibrated model, the surrogate model's performance reflects the behavior encoded in the updated FE model, while remaining independent of direct comparisons with experimental data.

Table 1: Modal properties comparison

	Experimental	FE Model before BMU	FE Model after BMU	
Mode Number	Frequency (Hz)	Frequency (Hz)	Frequency (Hz)	MAC value (%)
1	1.56	1.70	1.75	99.8
2	2.50	1.82	2.42	94.2
3	3.63	3.42	3.76	36.1

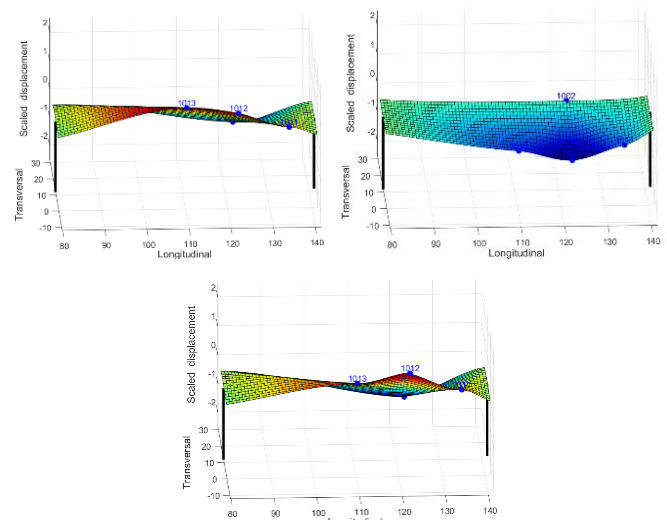


Figure 5: Experimental mode shapes

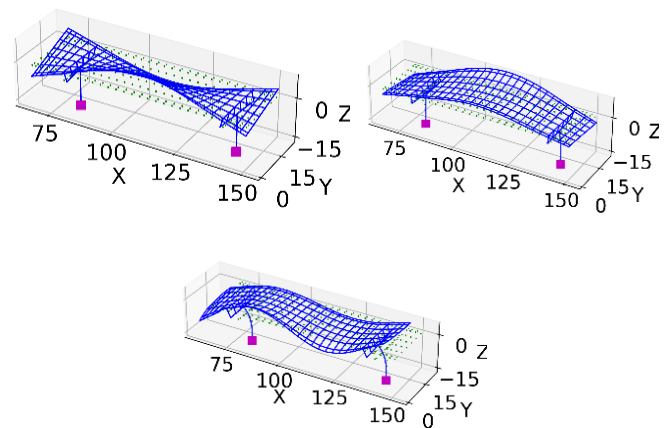


Figure 6: Updated FE mode shapes

### 3.1 Construction of the surrogate model and damage identification

The proposed damage identification framework is applied to a single span to demonstrate its effectiveness in damage detection and integrity assessment. The Variational Autoencoder (VAE) model was trained and applied using numerically simulated data representing various damage scenarios with different damage locations and severity. To generate the training dataset for the VAE model, damage was simulated in the FE model through the reduction in vertical rotational stiffness. For each damage scenario, the FE modal properties were obtained by dividing the span into 20 parts and applying the reductions to the corresponding vertical rotational stiffnesses.

Damage severity levels were defined as reductions ranging from 10% to 70% in the corresponding vertical rotational stiffness values. For each segment and each severity level, a separate damage scenario was created. In total, 140 damage scenarios were generated (20 segments  $\times$  7 severities). Table 2 summarizes the segments and the associated severity levels considered in the training data generation. To enhance the robustness of model learning, random noise was artificially added to the modal properties during the training data generation process. During the training phase, the surrogate model was trained using the labeled modal properties (natural frequencies and normalized mode shapes) corresponding to the various considered damage scenarios. The structural model was modified for each damage scenario, and a modal analysis was performed to obtain corresponding modal properties, enabling the VAE to learn patterns associated with different damage levels and locations. After the generation of the training dataset, it was divided into 80% and 20% portions, with 80% used to train the model, remaining 20% used to test the model, providing an unseen dataset to objectively evaluate the model's learning performance.

It is acknowledged that the damage scenarios used in this study are synthetically generated and not validated against experimental damage. While the applied stiffness reduction levels serve to explore the sensitivity and robustness of the surrogate model, such values may not reflect the typical damage progression in real-world structures. These scenarios are intended to span a wide range of conditions, including rare or extreme cases.

Table 2: Summary of the damage scenarios

Damage Scenario	Segment No	Reduction Factors
DS1	1	From 0.1 to 0.7
DS2	2	From 0.1 to 0.7
DS3	3	From 0.1 to 0.7
...	...	...
DS20	20	From 0.1 to 0.7

### 3.2 Damage identification

The capability of the surrogate model to identify damage was tested using unseen test data, that is, samples of modal parameters corresponding to the considered damage scenarios, not used in the training phase. Results are represented by the confusion matrix in Figure 7. The confusion matrix compares the true and predicted damage locations, where diagonal

elements represent correct predictions and off-diagonal elements indicate misclassification in the test datasets.

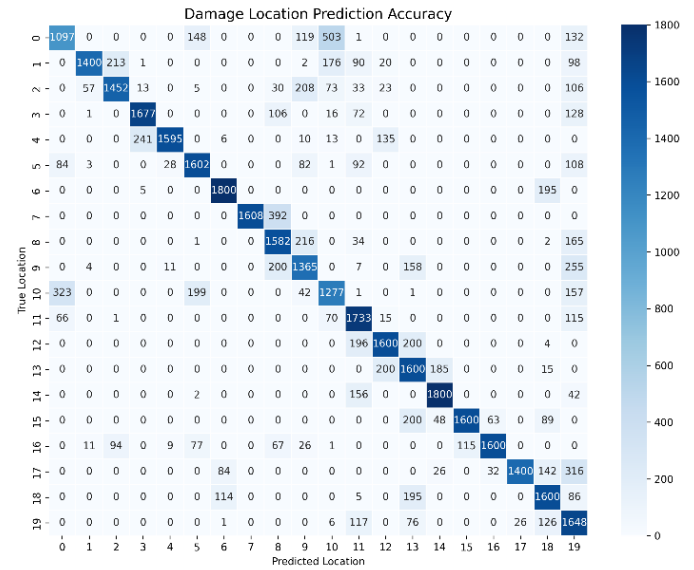


Figure 7: Confusion matrix for damage locations

In Figure 7, predicted and simulated (ground truth) damage locations are represented along the  $x$  and  $y$  axes by the element indices in the FE model. The diagonal elements of the matrix indicate the number of samples for which the damage location was correctly identified.

It is important to note that both training and testing datasets for the surrogate model were generated from the updated FE model, which was calibrated using experimental model properties. Although the updated model still presents some discrepancies, particularly in higher modes, the surrogate model operates entirely within the dynamic response space defined by the updated model. To enhance the robustness of the algorithm, artificial noise was introduced into synthetic modal data during both training and testing. This ensures that the model is not overfitted to idealized cases and can generalize across realistic measurement uncertainty, while maintaining consistency with the physical behavior captured by the updated FE model.

The model was tested on scenarios involving progressive damage evolution, effectively capturing and tracking the increasing severity over time. The data for the evolving damage severity was gathered from the unseen test dataset to indicate the model's performance in this context. The results are presented in Figure 8 where the vertical axis represents stiffness reduction factors. The predicted damage severity follows this predefined discretization to ensure the consistency between training and testing data. Additionally, Figure 8 illustrates the damage detection results over an evolving damage scenario, highlighting how the proposed framework translates predicted damage severity levels into actionable maintenance decisions. Each step in Figure 8 corresponds to a synthetic damage state generated by reducing the stiffness in the model. These steps represent hypothetical damage progression sequences, used to demonstrate the ability of the VAE model to track increasing severity.

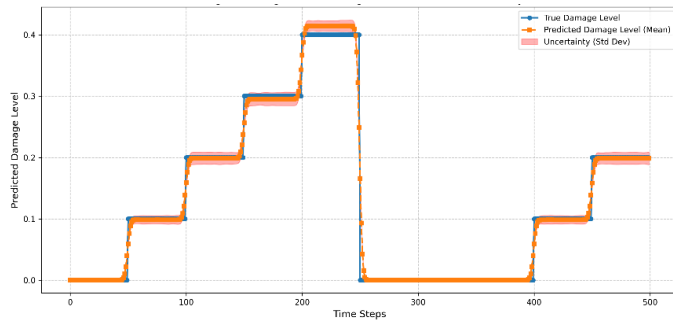


Figure 8: Damage level identification results

### 3.3 Decision Making

For the considered case study, the thresholds that trigger different management actions for each bridge component have been defined in terms of the stiffness reduction factor,  $k_{red}$ , and are reported in Table 3. To these thresholds correspond the damage scenarios considered for the training of the VAE model.

Table 3: Thresholds for stiffness reduction

$k_{red}$	Maintenance management action
0.1	normal condition
0.2	structural inspection
0.3	component repair
0.4	cautionary bridge closing

It is also worth mentioning that the maintenance actions proposed here are not intended to restore the load-bearing capacity but rather to compensate for localized stiffness reductions that may affect the bridge's dynamic behavior and long-term serviceability. The decision framework relies on stiffness reduction as a measurable proxy for damage progression, which triggers maintenance interventions aimed at preserving structural performance and reducing the risk of further deterioration. This approach reflects a conservative, condition-based strategy focused on sustaining system stiffness and structural continuity, even before reaching strength-based limit states.

## 4 CONCLUSION

This paper presents an online damage identification approach based on a Variational Autoencoder surrogate model. The proposed methodology combines model-based data generation with surrogate modelling to enhance the efficiency of the real-time data-driven damage identification without reducing accuracy.

To support timely maintenance decisions, a concept for a structured decision-making framework is proposed. The framework maps the structural condition into specific management actions. This structured, rule-based approach enables scalable, real-time decision support under varying operational scenarios.

Future work will explore the integration of stochastic deterioration models into the Finite Element model to refine long-term maintenance strategies, providing a more effective approach to bridge infrastructure management. The

investigation of threshold values consistent with pre-defined limit states of the bridge will be a further research step.

## REFERENCES

- [1] M. P. Limongelli *et al.*, "Bridge structural monitoring: the Lombardia regional guidelines," *Structure and Infrastructure Engineering*, vol. 20, no. 4, pp. 461–484, Jan. 2024, doi: 10.1080/15732479.2022.2107023.
- [2] X. Liu, F. Kang, and M. P. Limongelli, "Multi-zone parametric inverse analysis of super high arch dams using deep learning networks based on measured displacements," *Advanced Engineering Informatics*, vol. 56, p. 102002, Apr. 2023, doi: 10.1016/j.aei.2023.102002.
- [3] X. Yang, X. Guo, H. Ouyang, D. Li, "A Kriging model based finite element model updating method for damage detection," *Applied Sciences*, vol. 7, no. 10, p. 1039, 2017, doi: 10.3390/app7101039.
- [4] M. Vega, R. Madarshahian, and M. D. Todd, "A Neural Network Surrogate Model for Structural Health Monitoring of Miter Gates in Navigation Locks," *Conference Proceedings of the Society for Experimental Mechanics Series*, pp. 93–98, 2020, doi: 10.1007/978-3-030-12075-7\_9.
- [5] T. Simpson, N. Dervilis, P. Couturier, N. Maljaars, and E. Chatzi, "Reduced order modeling of non-linear monopile dynamics via an AE-LSTM scheme," *Frontiers in Energy Research*, vol. 11, 2023, doi: 10.3389/fenrg.2023.1128201.
- [6] K. Bacsá, W. Liu, I. Abdallah, and E. Chatzi, "Structural Dynamics Feature Learning Using a Supervised Variational Autoencoder," *Journal of Engineering Mechanics*, vol. 151, no. 2, 2025, doi: 10.1061/jenmdt.emeng-7635.
- [7] J. Ching and Y.-C. Chen, "Transitional Markov Chain Monte Carlo Method for Bayesian Model Updating, Model Class Selection, and Model Averaging," *Journal of Engineering Mechanics*, vol. 133, no. 7, pp. 816–832, 2007, doi: 10.1061/(ASCE)0733-9399(2007)133:7(816).
- [8] A. Lye, A. Cicirello, and E. Patelli, "Sampling methods for solving Bayesian model updating problems: A tutorial," *Mechanical Systems and Signal Processing*, vol. 159, p. 107760, Oct. 2021, doi: 10.1016/j.ymssp.2021.107760.
- [9] A. Pollastro, G. Testa, A. Bilotta, and R. Prevete, "Semi-Supervised Detection of Structural Damage Using Variational Autoencoder and a One-Class Support Vector Machine," *IEEE Access*, vol. 11, pp. 67098–67112, 2023, doi: 10.1109/access.2023.3291674.
- [10] F. Yessoufou and J. Zhu, "Classification and regression-based convolutional neural network and long short-term memory configuration for bridge damage identification using long-term monitoring vibration data," *Structural Health Monitoring*, vol. 22, no. 6, pp. 4027–4054, Nov. 2023, doi: 10.1177/14759217231161811.
- [11] S. R. Bowman, L. Vilnis, O. Vinyals, A. M. Dai, R. Jozefowicz, and S. Bengio, "Generating Sentences



- from a Continuous Space,” in *Proceedings of the 20th Conference on Computational Natural Language Learning (CoNLL 2016)*, Association for Computational Linguistics, Berlin, Germany, pp. 10–21, Nov. 2016, doi: 10.18653/v1/K16-1002.
- [12] D. P. Kingma and J. Ba, “Adam: A Method for Stochastic Optimization,” *arXiv preprint arXiv:1412.6980*, Dec. 2014.
- [13] M. Çelebi, “Real-time monitoring of drift for occupancy resumption,” in *Proceedings of the 14th World Conference on Earthquake Engineering (14WCEE)*, 2008.
- [14] F. Magalhães, Á. Cunha, and E. Caetano, “Online automatic identification of the modal parameters of a long span arch bridge,” *Mechanical Systems and Signal Processing*, vol. 23, no. 2, pp. 316–329, Feb. 2009, doi: 10.1016/j.ymssp.2008.05.003.
- [15] F. McKenna, “OpenSees: A framework for earthquake engineering simulation,” *Computing in Science & Engineering*, vol. 13, no. 4, pp. 58–66, Jul. 2011, doi: 10.1109/MCSE.2011.66.

# On a data compression technique for acceleration signals from a railway bridge

Pranav Yadav<sup>1</sup>, 0009-0003-9229-4797, Vaibhav Gupta<sup>1</sup>, 0009-0002-6651-4154, U. Saravanan<sup>1</sup>, 0000-0001-8565-0632

<sup>1</sup>Department of Civil Engineering, Indian Institute of Technology Madras, Adyar, Chennai 600036 Tamil Nadu, India  
email: pranavyadav23103@gmail.com, vaibgupta24@gmail.com, saran@iitm.ac.in

**ABSTRACT:** Structural health monitoring (SHM) is essential for ensuring bridge safety and longevity. Under dynamic loads, such as train traffic, acceleration data from sensors offers valuable insights into the condition of the structure. Vehicle bridge interaction models required to predict the acceleration time histories involve numerous parameters for rail traffic. Also, model-based methods have a trade-off between high-fidelity, computationally intensive, and less accurate models. To overcome these limitations, this study introduces a deep learning (DL) algorithm to identify changes in the bridge. However, large datasets resulting from high-frequency sampling and long observation periods pose computational challenges as the train passes over the bridge. To address this, down sampling is employed, reducing data complexity while preserving essential features of the signal. The approach is demonstrated using acceleration data recorded at a node point of a railway truss bridge during train passage. An Autoencoder is employed, compressing high-dimensional data into a low-dimensional latent space, and a deep neural network (DNN) is applied to the latent space, incorporating a measurement loss function to estimate the system parameters. This framework ensures computational efficiency and data integrity, enabling precise system parameter estimation and showcasing its effectiveness in real-life bridge SHM.

**KEY WORDS:** Data compression; Autoencoder; Deep neural network; Deep learning; Railway steel truss bridge; Structural health monitoring.

## 1 INTRODUCTION

Structural health monitoring (SHM) has advanced significantly with the development of sensing technologies and data collection capabilities [1],[2]. It plays a crucial role in ensuring the safety, durability, and reliability of critical structures, particularly railway bridges that experience continuous dynamic loading [3],[4]. Accurately estimating structural parameters such as cross-sectional area, damping coefficients, and stiffness properties is fundamental for detecting structural degradation, damage progression, and potential failures [5],[6]. Traditional methods, including finite element model (FEM)-based approaches, rely on high-fidelity models and experimental calibration, which are computationally expensive and susceptible to modeling inaccuracies [7],[8],[9]. These challenges necessitate data-driven approaches that leverage machine learning (ML) techniques for efficient and accurate structural assessment [10],[11].

Neural networks, a part of ML techniques, have emerged as powerful tools in SHM, enabling automated inspection processes and addressing the growing complexity of intelligent monitoring systems. Their primary advantages include automatic feature extraction, effectiveness in handling noisy datasets, and accurate modeling of nonlinear relationships [12]. Nevertheless, conventional artificial neural networks (ANNs) frequently encounter issues such as convergence to local minima, susceptibility to overfitting, and limited ability for deeper feature extraction due to shallow network architectures [13]. Recent advancements in deep learning (DL) have introduced data-driven SHM approaches, wherein structural parameters are inferred directly from measured vibration signals [14],[15] to overcome the above mentioned challenges.

Such DL frameworks effectively capture complex nonlinear relationships inherent in multi-sensor datasets, making them particularly suitable for classification and regression tasks [16]. Nevertheless, standalone DL models share several limitations commonly observed with traditional ANNs, including high computational efficiency, overfitting, and convergence issues, highlighting the need for hybrid DL methodologies [17]. Over the past decade, several hybrid DL approaches have been developed for bridge damage detection and condition assessment. One promising approach is the Autoencoder, which is known for its ability to perform dimensionality reduction and data compression effectively.

To highlight a few instances, an unsupervised Autoencoder approach proposed in [18] achieved real-time bridge damage detection directly from raw acceleration data, although it was limited to single-sensor applications without the capability for damage localization or quantification. In another study [19], a hybrid methodology combining statistical modeling, neural networks, and deep support vector domain description demonstrated effective real-time damage detection with minimal false alarms; however, this method lacked localization capability, exhibited reduced performance with multi-sensor datasets, and has not been tested on full-scale structures. [20] introduced an Autoencoder-based method emphasizing the relationships among natural frequencies and mode shapes. Further extending this concept, [21] proposed a deep sparse Autoencoder specifically used for structural damage detection using these vibration characteristics. [22] developed a two-level hybrid learning framework, employing unsupervised learning for preliminary damage detection followed by supervised validation, demonstrating its efficacy through

numerical simulations of concrete beams and experimental validation using laboratory frames. Additionally, [23] introduced an unsupervised deep neural network (DNN) method combining a deep Autoencoder with a one-class support vector machine (SVM), eliminating the reliance on extensive labeled datasets by utilizing only intact structural data.

While prior research has explored hybrid DL models involving Autoencoders for data compression, most studies have primarily addressed laboratory-scale experiments or relied on supervised learning methods. In contrast, this study introduces an integrated framework combining unsupervised Autoencoder-based compression and a supervised DNN model to effectively handle on-field acceleration signals coming in the form of latent space representation from the Autoencoder. The proposed Autoencoder-DNN framework is computationally efficient and provides an effective compression strategy that preserves the important structural characteristics of real-world acceleration data by extracting relevant features, facilitating accurate and reliable estimation of structural parameters in railway steel truss bridge members.

The methodology presented herein constitutes the preliminary phase of a comprehensive, multi-stage investigation to extend parameter estimation from an individual joint (node point considered in this study) to the entire railway steel truss bridge structure. By demonstrating the effectiveness and robustness of the developed approach through this single-node case study, the present work lays a solid foundation for data-driven SHM of complex infrastructure with relevance to railway bridge systems.

The structure of this paper is as follows: **Section 2** details the bridge type and instrumentation scheme. **Section 3** explains data collection and segmentation. **Section 4** presents the proposed methodology, including the Autoencoder and the DNN model. **Section 5** discusses the results, focusing on model accuracy, anomaly detection, and computational efficiency. Finally, **Section 6** concludes the key findings and explores potential directions for future research.

## 2 BRIDGE DETAILS AND INSTRUMENTATION SCHEME

The Pamban Bridge is a railway steel truss bridge linking Rameswaram on Pamban Island to mainland India, as shown in Figure 1. Commissioned in 1914, it was India's first sea bridge. Although most spans are conventional I-plate girders on concrete piers, the bridge features a notable double-leaf bascule section that pivots to let ships and barges pass. This movable portion, designed by Scherzer, is counterbalanced and pivots around a horizontal axis, with the superstructure rolling atop the track girder. Each leaf consists of a rigid jaw-and-tongue system to transfer shear without moments and is further subdivided into north and south trusses [24].

Since the bridge endures harsh marine conditions, corrosion is a significant concern, making it essential to evaluate any loss of cross-sectional area for structural assessments. A total of 40 uniaxial accelerometers have been installed at various bottom nodes in biaxial mode on the bridge's Mandapam and Pamban truss segments in both the north and south directions, as shown in Figure 2.



Figure 1. Orientation of the Pamban bridge.

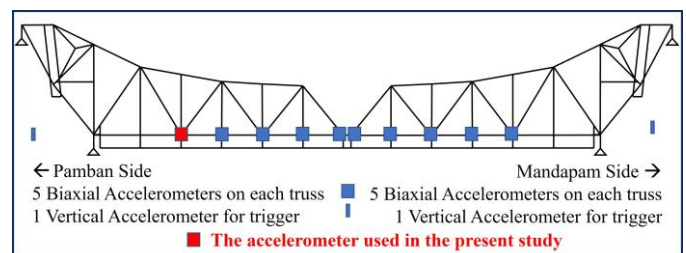


Figure 2. Location of accelerometers on the bridge.

## 3 DATA COLLECTION AND SEGMENTATION

The acceleration data used in this study was collected from a bottom node marked with a red box in Figure 2, where two uniaxial accelerometers were installed in biaxial mode. Measurements were taken in both the x and y directions, with the x direction corresponding to the direction of train movement and the y direction representing the direction of gravity. When detecting a train pass event, the DAQ system continuously recorded acceleration data for 480 seconds, which was sufficient to cover the train passage with an ample margin before and after the event.

The sampling frequency of the acceleration was set at 600 Hz, resulting in 288,000 data points for each recording session. After analyzing acceleration signals from 150 train passages for each direction, it was observed that the train-induced vibrations predominantly occupied the initial segment of the recorded signal. At the same time, the remaining portion primarily consisted of ambient noise. Based on this observation, a consistent segmentation approach was adopted, wherein the first 1,60,000 data points were extracted from each recording for further analysis. This segmentation ensured the retention of train-induced dynamic responses while excluding prolonged noise periods, thereby reducing the number of data points in the subsequent processing stages.

## 4 METHODOLOGY

This study adopts a multi-step methodology comprising data pre-processing and data compression to improve the performance, scalability and computational efficiency of the Autoencoder-DNN framework for parameter estimation. The overall flowchart is presented in Figure 3, which outlines the



key steps involved. Each step is further detailed in the following sections, explaining the implemented approach.

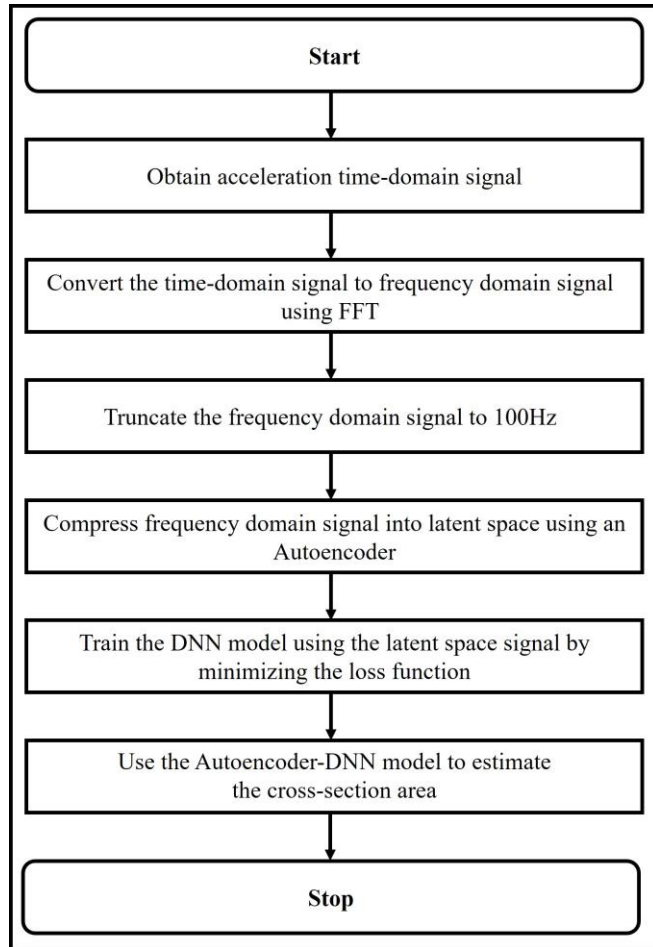


Figure 3. Flowchart depicting the methodology.

#### 4.1 Data Preprocessing

After obtaining the train pass signals, the time-domain data was converted into the frequency domain using the fast Fourier transform (FFT). This transformation was essential to facilitate efficient data processing, as the large dataset in the time domain posed computational challenges for subsequent analyses,

notably when applying the DNN model. The FFT utilizes the symmetric property of real-valued signals, reducing the adequate number of data points by half while retaining the qualities of the original signal, which optimizes storage and computational requirements. The amplitude spectrum of the transformed signal was carefully examined, revealing that frequency components beyond 100 Hz have acceleration amplitudes  $1/4^{\text{th}}$  less than the maximum amplitude. Therefore, a frequency threshold of 100 Hz was adopted to truncate the signal, effectively eliminating higher-frequency content while retaining the dominant spectral content. This transformation approach introducing symmetry and frequency truncation has resulted in a reduced dataset of approximately 26,666 data points. Figure 4 illustrates the process, where the time-domain acceleration signal is converted to the frequency domain and truncated up to 100 Hz. This significant reduction enhanced computational efficiency and preserved the essential dynamic characteristics of the train-induced vibrations. However, despite the reduction, the large dimensionality of the dataset still posed computational challenges, particularly concerning memory requirements and the convergence efficiency of the DNN model.

#### 4.2 Data Compression Using Autoencoder

To mitigate computational challenges, a data compression technique based on an Autoencoder is implemented. The Autoencoder used in this study consists of two key components: an encoder, which compresses the input data into a lower-dimensional latent space, and a decoder, which reconstructs the data from this compressed representation. Figure 5 illustrates the step-by-step application of the Autoencoder, detailing the transformation process at each stage.

Since acceleration signals exhibit distinct dynamic characteristics in the x and y directions, separate Autoencoders are implemented for each direction. The Autoencoders applied in both directions maintain an identical architecture, layer structure, and activation functions, as shown in Figure 5, but they are trained independently to capture the unique frequency and amplitude variations inherent to each direction. This ensures that the learned representations accurately reflect the direction-specific vibration behavior while preserving consistency in the latent space size.

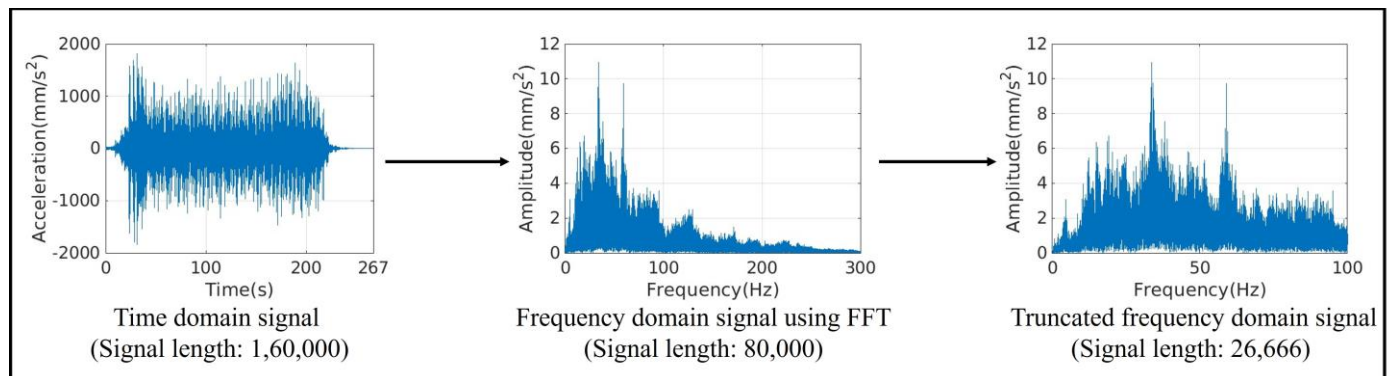


Figure 4. Data preprocessing workflow.

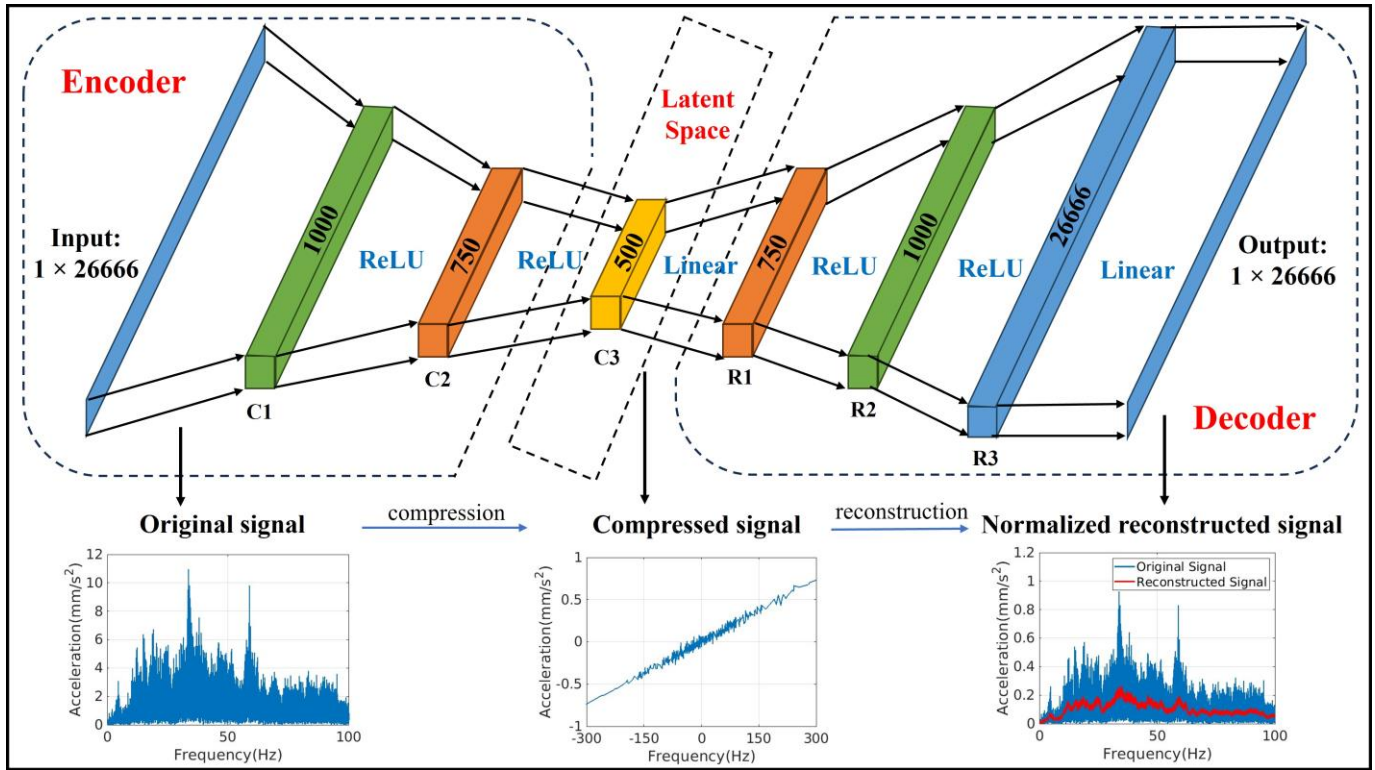


Figure 5. The architecture of the Autoencoder.

#### 4.2.1 Encoder network

It consists of three layers labeled C1 to C3. The ReLU activation function is applied in layers C1 and C2, while the linear activation function is used in layer C3. As described in the previous section, the network takes preprocessed input data of size  $1 \times 26666$  for one train pass. However, since the autoencoder is trained on data from 112 (75% of 150 train passes) train passes, the input data size becomes  $1 \times 26666 \times 112$  for each direction. The data is progressively compressed through each layer, reducing its dimensionality from  $1 \times 26666 \times 112$  in the input layer to  $1 \times 1000 \times 112$  in C1,  $1 \times 750 \times 112$  in C2, and finally to  $1 \times 500 \times 112$  in C3, which represents the latent space.

#### 4.2.2 Decoder network

The decoder network consists of three layers, labeled R1 to R3, designed to restore the compressed latent space to its original dimension. The ReLU activation function is applied in layers R1 and R2, while the linear activation function is used in the final layer R3. The input to the reconstruction network is the latent space representation of size  $1 \times 500 \times 112$ . The data is gradually reconstructed through each layer, expanding from  $1 \times 750 \times 112$  in R1, then to  $1 \times 1000 \times 112$  in R2, and ultimately restored to its original size of  $1 \times 26666 \times 112$  in R3 at the output layer.

#### 4.2.3 Dropout Regularization

To prevent overfitting and enhance the generalization capability of the Autoencoder model, dropout regularization is applied to each layer except the latent space layer. A 10% dropout rate is used, randomly deactivating 10% of the neurons to zero during each training iteration.

#### 4.2.4 Loss function

The Autoencoder is trained using the mean squared error (MSE) loss function, which measures the reconstruction error between the original input data and the reconstructed output. The MSE loss is defined as:

$$L_{MSE} = \frac{1}{N} \sum_{i=1}^N (x_i - \hat{x}_i)^2 \quad (1)$$

where  $x_i$  represents the original input data,  $\hat{x}_i$  represents the reconstructed output, and  $N$  is the total number of train passes. The loss function is minimized during training, ensuring that the reconstructed signal closely approximates the characteristics of the input signal. This optimization enables the Autoencoder to retain essential features of the input data, making the compressed representation more computationally efficient.

#### 4.2.5 Optimization

The Adam optimizer employed to train the Autoencoder is widely recognized for its effectiveness in various applications. It is well-suited for non-stationary objectives and problems with noisy or sparse gradients [25]. The optimization is performed over 30 epochs, minimizing the MSE loss to improve reconstruction accuracy while retaining the essential features of the input data.

#### 4.3 Integration with DNN Model

Integrating the compressed latent space representations of the frequency-domain acceleration data with the DNN model helps in parameter estimation. Figure 6 illustrates the step-by-step application of the DNN model.

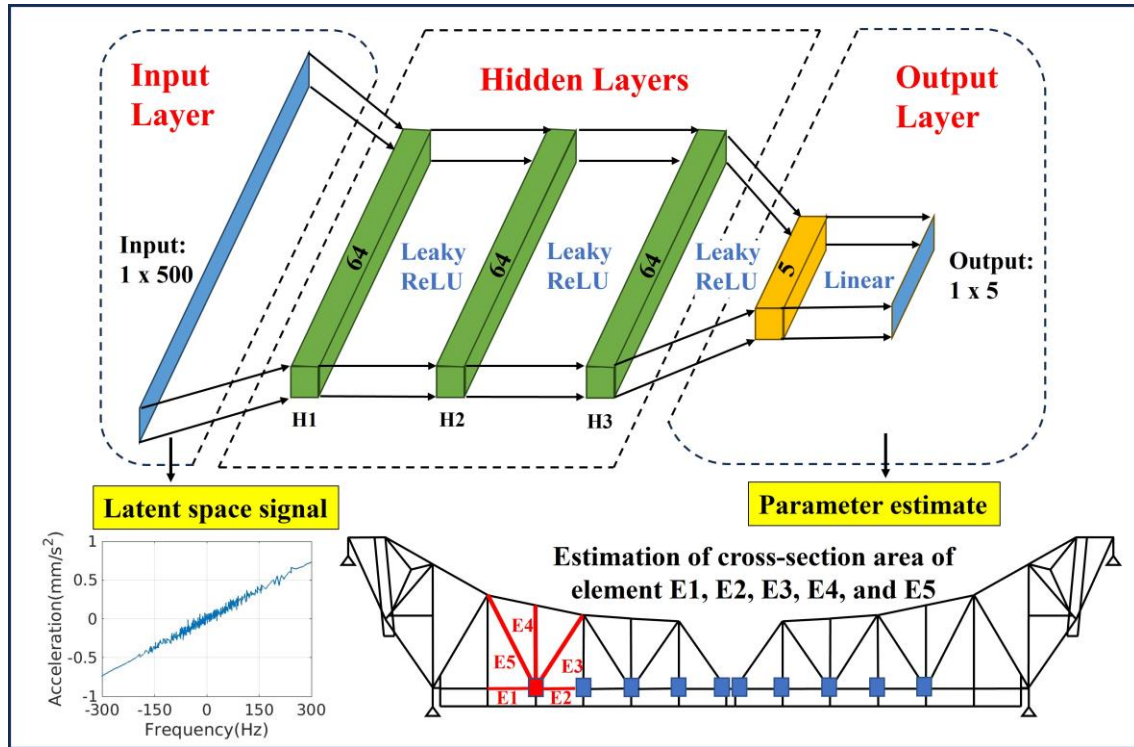


Figure 6. The architecture of the DNN model.

#### 4.3.1 Input to DNN model

The compressed latent space representations of the frequency-domain acceleration data in both the x and y directions are integrated within the DNN model to estimate the cross-sectional area of the truss members. Since acceleration responses exhibit distinct dynamic characteristics in different directions, the compressed x and y components are concatenated to form a combined  $500 \times 2$  input vector for each train pass.

This combined representation allows the DNN model to capture the full structural behavior influenced by both directional responses. The combined  $500 \times 2 \times 112$  input vector for all train passes is passed into the DNN model for training, enabling the model to learn the system's dynamics across multiple loading conditions.

#### 4.3.2 DNN architecture

As mentioned earlier, the DNN model receives compressed latent space representations of the acceleration data from the Autoencoder, presented in a concatenated format that includes data from both directions. After conducting hyperparameter tuning using the grid search method, Table 1 displays the final values of the parameters used in the DNN model.

Table 1. DNN model parameters and their values.

Parameter	Value
Hidden Layers	3
Hidden Neurons	64
Output Neurons	5
Hidden Activation	Leaky ReLU
Dropout Layer	0
Learning Rate	0.001
Optimizer	ADAM
Epochs	20000

The final output layer estimates the cross-sectional area of the truss members connected, which is highlighted by a red color line in Figure 6. The network effectively learns the mapping from the compressed input to the target output while integrating the measurement loss function to improve accuracy.

#### 4.3.3 Measurement loss function

The DNN model incorporates a measurement loss to improve the accuracy of the estimated area. This loss minimizes the difference between the true cross-sectional area (provided in Table 2) and the predicted area obtained from the DNN model using the MSE loss function defined as:

$$L_{MSE} = \frac{1}{N} \sum_{i=1}^N \sum_{j=1}^5 \left( (x_{true}^j)^i - (x_{predicted}^j)^i \right)^2 \quad (2)$$

where  $x_{true}^j$  is the true value of the  $j^{\text{th}}$  parameter of the system to be estimated – the cross-sectional area and  $x_{predicted}^j$  is the corresponding predicted value from the DNN model.

Table 2. The table shows the true values of the cross-sectional area.

Parameter	Value (mm <sup>2</sup> )
Element 1 (E1)	24400
Element 2 (E2)	12178
Element 3 (E3)	15800
Element 4 (E4)	20100
Element 5 (E5)	8700



#### 4.4 Hypothesis for Estimating Cross-Sectional Area from a Single Node Response

The study focuses on a single node among those where bi-axial accelerations are recorded. This node is structurally connected to five truss elements, each assumed to have known lengths ( $L_1, L_2, L_3, L_4$ , and  $L_5$ ) and elastic modulus, while the cross-sectional areas ( $A_1, A_2, A_3, A_4$ , and  $A_5$ ) are unknown and to be estimated. The arrangement of the members is as shown in Figure 7. The assumption that all five truss elements are fixed at the other end is not true in the actual truss structure. However, this assumption allows checking of the algorithm in a smaller setting.

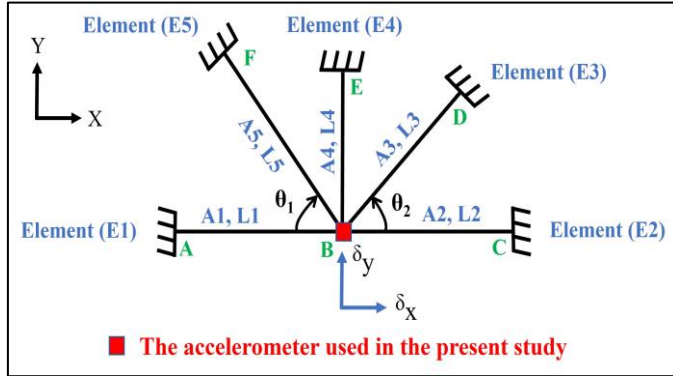


Figure 7. Schematic of the monitored truss node with five connected members. The bi-axial accelerometer is positioned at the node to record dynamic responses during train passages.

The mass matrix is formulated based on the shape functions that approximate the displacement. The consistent element mass matrix formulated in global coordinates for member AB is given by:

$$[M_{AB}] = \frac{\rho AL}{6} \begin{bmatrix} 2c^2 & 2cs & c^2 & cs \\ 2cs & 2s^2 & cs & s^2 \\ c^2 & cs & 2c^2 & 2cs \\ cs & s^2 & 2cs & 2s^2 \end{bmatrix} \quad (1)$$

where  $c$  and  $s$  denote  $\cos(\theta)$  and  $\sin(\theta)$ , respectively,  $\theta$  is the counter-clockwise angle measured with respect to the positive  $x$ -axis,  $\rho$  is the density of the material,  $A$  is the cross-sectional area, and  $L$  is the length of the element.

Meanwhile, the stiffness matrix is derived under the assumption of linear elastic behaviour. The stiffness matrix used in global coordinates for member AB is given by:

$$[K_{AB}] = \frac{EA}{L} \begin{bmatrix} c^2 & cs & -c^2 & -cs \\ cs & s^2 & -cs & -s^2 \\ -c^2 & -cs & c^2 & cs \\ -cs & -s^2 & cs & s^2 \end{bmatrix} \quad (2)$$

where  $E$  is Young's modulus,  $A$  is the cross-sectional area, and  $L$  is the element length.

Similarly, the global mass and stiffness matrices for all five connected truss elements are formulated and subsequently condensed by applying suitable boundary conditions according to the idealization results in a  $2 \times 2$  system of equations relating

the translational degrees of freedom at the monitored node to the forces acting on the node due to the train. During a train passage, this node undergoes dynamic displacement, and the bi-axial accelerometer captures its response along the train movement ( $x$ -direction) and gravity direction ( $y$ -direction).

Given that the displacement ( $u_x$  and  $u_y$ ) and acceleration ( $a_x$  and  $a_y$ ) responses are known, and the excitation is indirectly inferred from the train passage characteristics ( $f_x$  and  $f_y$ ), the cross-sectional areas, which influence the mass and stiffness of each member, leave a unique imprint on the node's dynamic response as reflected in:

$$\begin{bmatrix} K_{11} & K_{12} \\ K_{21} & K_{22} \end{bmatrix} \begin{Bmatrix} u_x \\ u_y \end{Bmatrix} + \begin{bmatrix} M_{11} & M_{12} \\ M_{21} & M_{22} \end{bmatrix} \begin{Bmatrix} a_x \\ a_y \end{Bmatrix} = \begin{Bmatrix} f_x \\ f_y \end{Bmatrix} \quad (3)$$

where  $K_{11} = \frac{EA_1}{L_1} + \frac{EA_2}{L_2} + \frac{EA_3c_2^2}{L_3} + \frac{EA_5c_1^2}{L_5}$ ;  $K_{12} = K_{21} = \frac{EA_3c_2s_2}{L_3} - \frac{EA_5c_1s_1}{L_5}$ ;  $K_{22} = \frac{EA_3s_2^2}{L_3} + \frac{EA_4}{L_4} + \frac{EA_5s_1^2}{L_5}$  and  $M_{11} = \frac{\rho A_1 L_1}{3} + \frac{\rho A_2 L_2}{3} + \frac{\rho A_3 L_3 c_2^2}{3} + \frac{\rho A_5 L_5 c_1^2}{3}$ ;  $M_{12} = M_{21} = \frac{\rho A_3 L_3 c_2 s_2}{3} - \frac{\rho A_5 L_5 c_1 s_1}{3}$ ;  $M_{22} = \frac{\rho A_3 L_3 s_2^2}{3} + \frac{\rho A_4 L_4}{3} + \frac{\rho A_5 L_5 s_1^2}{3}$ , are respective components of the effective stiffness and mass matrices. Here,  $c_1$  and  $s_1$  denote  $\cos(\theta_1)$  and  $\sin(\theta_1)$ ,  $c_2$  and  $s_2$  denote  $\cos(\theta_2)$  and  $\sin(\theta_2)$ , respectively, and  $\theta$  is the counter-clockwise angle measured with respect to the positive  $x$ -axis.

Equation (3) represents a possible relation between the acceleration and the cross-sectional area of connected elements. The proposed framework finds this relationship between the measured acceleration and cross-sectional areas in a data-driven manner.

## 5 RESULTS AND DISCUSSIONS

This section presents the performance evaluation of the Autoencoder-DNN framework, focusing on data compression, reconstruction errors, system parameter estimation, computational efficiency, and anomaly detection. The model is trained and tested using 150 train pass datasets for each direction, with a 75%–25% train-test split, ensuring the model generalizes well to unseen data.

### 5.1 Autoencoder Performance and Reconstruction Loss Behavior

The Autoencoder uses a validation set of a split ratio of 75%–25% instead of the test set during training to monitor the reconstruction loss and ensure that the model generalizes effectively to unseen data. This is important, as the loss terms for the autoencoder should remain consistent across the training and validation sets to facilitate accurate compression and reconstruction.

Figure 8 illustrates the training and validation loss curves, showing a smooth and stable convergence of order  $10^{-3}$ , which indicates that the latent space representation effectively captures the dominant structural features of the train-induced vibrations. The final loss values confirm that the compression process does not introduce significant deviations, making the latent representation reliable for subsequent DNN-based analysis.

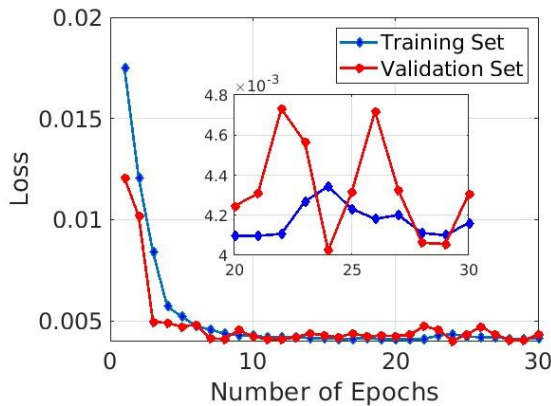


Figure 8. Comparison of loss in the training set and in the validation set.

Additionally, the method takes approximately 240 seconds to compress the acceleration data into the latent space for both directions, highlighting its effectiveness in data compression and computational speed.

## 5.2 DNN Model Parameter Estimation

Once the Autoencoder compresses the frequency domain acceleration data into the latent space, the DNN model is trained using 75% of the dataset and subsequently tested on the remaining 25% of unseen data. The primary objective of the DNN model is to estimate the cross-sectional area of the truss members by minimizing the measurement loss function. Figure 9 illustrates that during the training process, the MSE loss consistently decreases as the number of epochs increases, leading to stable convergence of the estimated parameters.

Once stable convergence is achieved, while observing the parameter values in the training dataset, it is noticed that the cross-sectional area of the truss members converges to their true values. To interpret this result physically, for an idealized truss structure without structural damage, the cross-sectional area values should remain constant across all train passes. Figure 10 shows the area estimation of element (E2) for five train passes. It can be observed that the cross-sectional area is converging to its true value (reported in Table 2). Similarly, for all the train passes and for all the truss members considered, the results across the entire training dataset confirm that the estimated area values closely align with the expected true values.

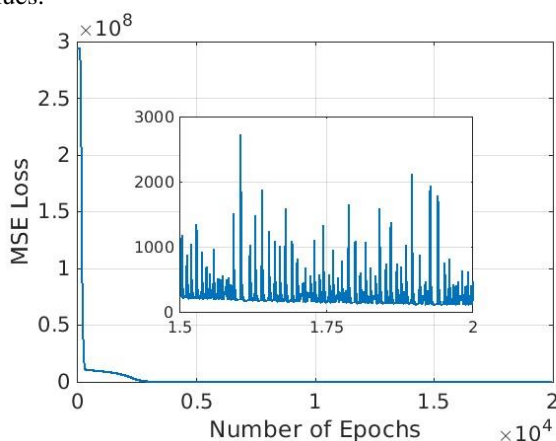


Figure 9. Convergence of measurement loss at each epoch.

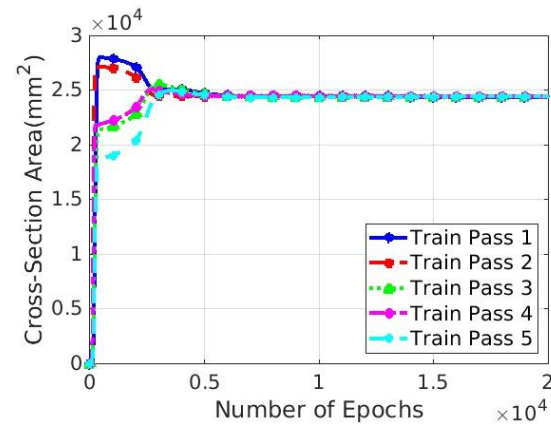


Figure 10. The cross-sectional area of element (E2) using the training data.

### 5.2.1 Performance Evaluation of the DNN Model on the Test Data

Once the DNN model is trained, its performance is evaluated using the test data. Figure 11 illustrates the values of the cross-sectional area obtained from the DNN model for all the test datasets. The coefficient of variation (CoV) is computed for the estimated cross-sectional area for all the truss members and tabulated in Table 3. It is observed that the CoV values for all the truss members are less and identical. This uniformity in CoV shows that the DNN model exhibits consistent relative variability in its predictions across different members. Such behavior indicates stable model performance under test conditions, with no bias or irregularity in estimating cross-sectional area. However, this observation also highlights the need for further analysis to ensure that the model is sufficiently sensitive to localized structural variations, and hence, the model is tested through false data simulating sensor fault, noise, and anomalies, as explained in the next section.

Table 3. The table shows the coefficient of variation of the predicted cross-sectional area under test data.

Parameter	Coefficient of Variation (%)
Element 1	0.18
Element 2	0.18
Element 3	0.18
Element 4	0.18
Element 5	0.18

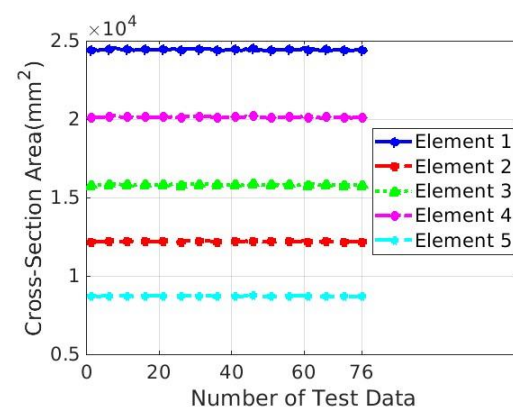


Figure 11. The cross-sectional area of the truss members for the test data.

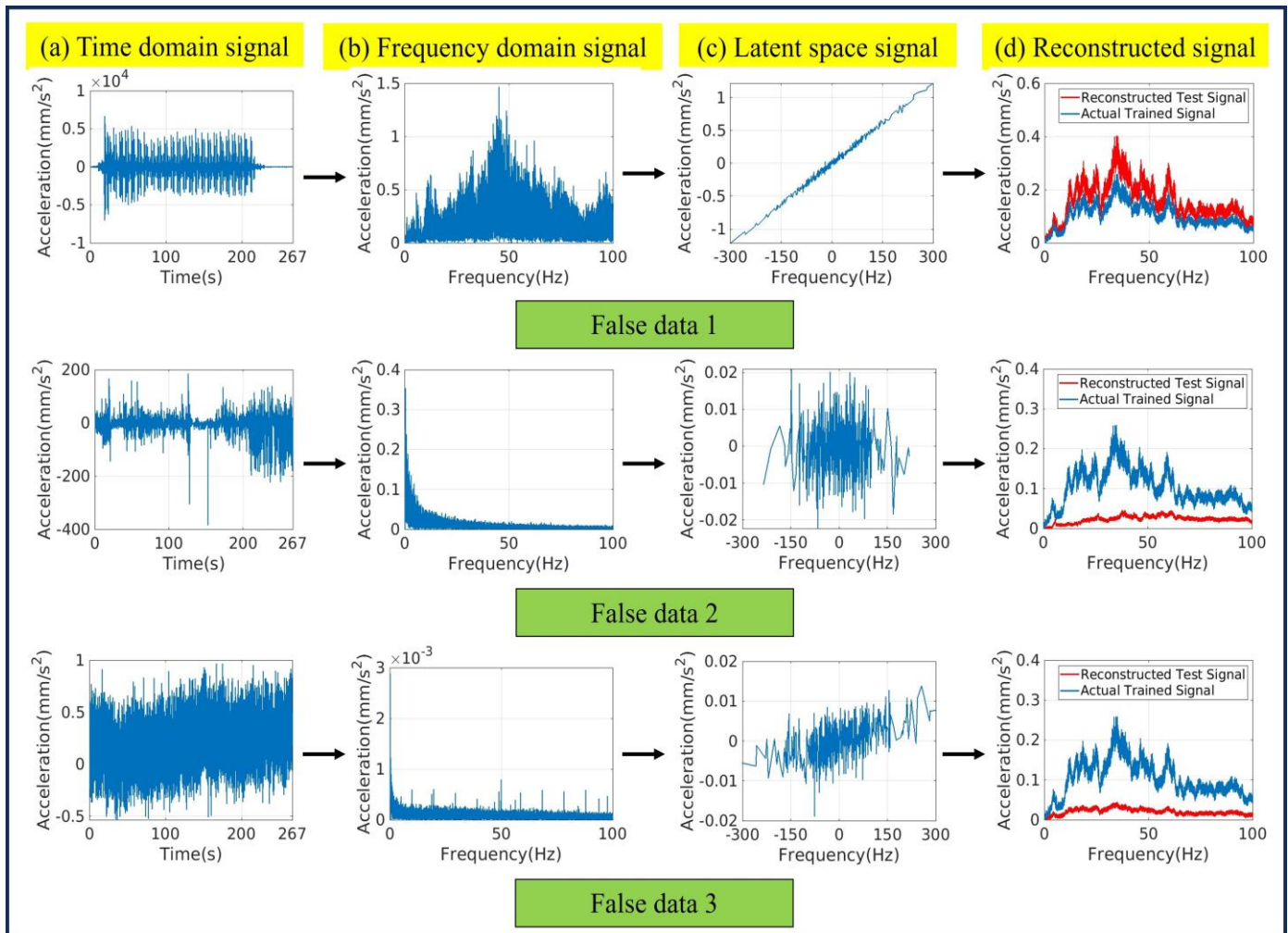


Figure 12. Illustration of the false data for the DNN model, showing (a) the time-domain acceleration signal, (b) its frequency-domain representation, (c) the latent space obtained from the Autoencoder, and (d) a comparison between the normalized reconstructed false data and original data, highlighting their differences.

### 5.3 Computational Efficiency

The DNN model employed in this study took approximately 100 seconds to estimate parameters involving 150 train passages in both directions, emphasizing the model's effectiveness in balancing accuracy and computational speed in parameter estimation.

### 5.4 Anomaly Detection Through False Data Injection

To evaluate the robustness of the Autoencoder-DNN framework and its ability to detect inconsistencies in the input data, three false datasets are used in this study. These false data are provided to check whether the proposed framework can detect potential structural anomalies, sensor noise, or environmental influences, which introduce variations in the acceleration response in the on-field conditions. To be specific, the first false data replaces the train pass signal with data collected from a different node point, the second exhibits a faulty sensor that fails to capture the correct train pass signal, and the third represents an anomaly where the sensor is unable to record any valid data—potentially caused by false triggers. Figure 12 illustrates the procedure followed for preparing these false datasets prior to their input into the DNN model. It sequentially presents (a) the acceleration signal in the time

domain, (b) its corresponding frequency-domain representation, (c) the latent-space representation obtained from the Autoencoder, and (d) a comparison between the reconstructed false data and original data from the trained Autoencoder, clearly highlighting differences between the two signals. When the latent space of the false data was passed onto the DNN model, the predicted cross-sectional area for all the truss members exhibited notable deviations, as shown in Table 4. It is observed that the percentage deviation of the cross-sectional area for all the truss members exhibits the same percentage change for the different false datasets, regardless of the specific member location. For false data 1, 2, and 3, the percentage deviation is approximately 4.30%, 1.10%, and 3.30%, respectively. The statistically significant percentage change across members highlights the framework's ability to detect gross inconsistencies in the input signals, though it also indicates a need for future enhancement to improve sensitivity to localize anomalies. It may be that localization would occur when multiple nodes are used. Thus, the proposed framework provides the identification of faulty sensor readings, environmental influences, or potential structural changes. However, the classification of the signal remains a challenge.



Table 4. The table shows the percentage deviation of the predicted cross-sectional area values with respect to the true cross-sectional area values for the false data.

Parameter	Percentage deviation from the true cross-sectional area value (%)		
	False data 1	False data 2	False data 3
Element 1	4.30	1.10	3.30
Element 2	4.30	1.10	3.30
Element 3	4.30	1.10	3.30
Element 4	4.30	1.10	3.30
Element 5	4.30	1.10	3.30

## 6 CONCLUSION

This study introduced an Autoencoder-DNN framework for data-driven structural parameter estimation using train-induced vibration responses. The Autoencoder effectively compressed high-dimensional acceleration data in the frequency domain into a lower-dimensional latent space, preserving critical structural features while significantly enhancing computational efficiency. The DNN model, trained on the compressed latent representation, allows for accurate estimation of the cross-sectional area of the truss members connected to the node point considered in this study. The model exhibited stable performance on test datasets, with low prediction errors and consistent coefficients of variation, indicating reliable and uniform estimation capabilities. Furthermore, the framework effectively detected inconsistencies when introduced with false datasets simulating sensor faults, noise, and anomalies. In all cases, uniform deviations in the estimated cross-sectional area confirmed the model's robustness in identifying global anomalies in the input data.

Overall, the proposed framework offers an Autoencoder-based compression, supervised DNN model, and automated anomaly detection, making it a scalable and computationally efficient tool for large-scale truss structures in real-world applications. Future work will focus on improving the framework's sensitivity to localize damage and integrating the full-scale truss bridge model and extended datasets to further examine the framework's generalization capability.

## ACKNOWLEDGMENTS

The authors thank Southern Railways for funding this work and allowing the utilization of the collected data for analysis.

## REFERENCES

- [1] S. Park, H. S. Park, J. H. Kim, and H. Adeli, 3D displacement measurement model for health monitoring of structures using a motion capture system, *Measurement*, 59, 352–362, 2015.
- [2] J. P. Amezquita-Sanchez and H. Adeli, Signal processing techniques for vibration-based health monitoring of smart structures, *Archives of Computational Methods in Engineering*, 23, 1–15, 2016.
- [3] V. Gupta, and U. Saravanan, Condition monitoring of steel truss bridge using acceleration data, In: *Proceedings of the Fourteenth International Workshop on Structural Health Monitoring (IWSHM)*, September 12–14, 2023.
- [4] V. Gupta and U. Saravanan, Comparative study on PSD and HHT techniques for condition assessment of steel truss bridge using acceleration data, *Proceedings of the 10th European Workshop on Structural Health Monitoring (EWSHM 2024)*, June 10–13, 2024 in Potsdam, Germany, *e-Journal of Nondestructive Testing Vol. 29*(7), 2024.
- [5] C. R. Farrar, S. W. Doebling, and D. A. Nix, Vibration-based structural damage identification, *Philosophical Transactions of the Royal Society of London, Series A: Mathematical, Physical and Engineering Sciences*, 359(1778), 131–149, 2001.
- [6] E. P. Carden and P. Fanning, Vibration based condition monitoring: a review, *Structural health monitoring*, 3(4), 355–377, 2004.
- [7] M. Azimi, A. D. Eslamlou, and G. Pekcan, Data-driven structural health monitoring and damage detection through deep learning: State-of-the-art review, *Sensors*, 20(10), 2778, 2020.
- [8] G. Gui, H. Pan, Z. Lin, Y. Li, and Z. Yuan, Data-driven support vector machine with optimization techniques for structural health monitoring and damage detection, *KSCE Journal of Civil Engineering*, 21, 523–534, 2017.
- [9] F. Wedel and S. Marx, Application of machine learning methods on real bridge monitoring data, *Engineering Structures*, 250, 113365, 2022.
- [10] C. R. Farrar and K. Worden, *Structural health monitoring: a machine learning perspective*, Chichester, West Sussex, UK; Hoboken, NJ: Wiley, 2013.
- [11] R. de Almeida Cardoso, A. Cury, and F. Barbosa, Automated real-time damage detection strategy using raw dynamic measurements, *Engineering Structures*, 196, 109364, 2019.
- [12] R. P. Bandara, T. H. Chan, and D. P. Thambiratnam, Frequency response function based damage identification using principal component analysis and pattern recognition technique, *Engineering Structures*, 66, 116–128, 2014.
- [13] O. Avci, O. Abdeljaber, S. Kiranyaz, M. Hussein, M. Gabbouj, and D. J. Inman, A review of vibration-based damage detection in civil structures: From traditional methods to machine learning and deep learning applications, *Mechanical systems and signal processing*, 147, 107077, 2021.
- [14] X. Jian, H. Zhong, Y. Xia, and L. Sun, Faulty data detection and classification for bridge structural health monitoring via statistical and deep-learning approach, *Structural Control and Health Monitoring*, 28(11), e2824, 2021.
- [15] D. Hajializadeh, Deep learning-based indirect bridge damage identification system, *Structural health monitoring*, 22(2), 897–912, 2023.
- [16] M. Z. Sarwar and D. Cantero, Vehicle assisted bridge damage assessment using probabilistic deep learning, *Measurement*, 206, 112216, 2023.
- [17] L. V. Jospin, H. Laga, F. Boussaid, W. Buntine, and M. Bennamoun, Hands-on bayesian neural networks—a tutorial for deep learning users, *IEEE Computational Intelligence Magazine*, 17(2), 29–48, 2022.
- [18] V. Giglioni, I. Venanzi, V. Poggioni, A. Milani, and F. Ubertini, Autoencoders for unsupervised real-time bridge health assessment, *Computer-Aided Civil and Infrastructure Engineering*, 38(8), 959–974, 2023.
- [19] S. Shi, D. Du, O. Mercan, E. Kalkan, and S. Wang, A novel unsupervised real-time damage detection method for structural health monitoring using machine learning, *Structural Control and Health Monitoring*, 29(10), e3042, 2022.
- [20] C. S. N. Pathirage, J. Li, L. Li, H. Hao, W. Liu, and P. Ni, Structural damage identification based on autoencoder neural networks and deep learning, *Engineering structures*, 172, 13–28, 2018.
- [21] C. S. N. Pathirage, J. Li, L. Li, H. Hao, W. Liu, and R. Wang, Development and application of a deep learning-based sparse autoencoder framework for structural damage identification, *Structural Health Monitoring*, 18(1), 103–122, 2019.
- [22] H. Sarmadi and A. Entezami, Application of supervised learning to validation of damage detection, *Archive of Applied Mechanics*, 91(1), 393–410, 2021.
- [23] Z. Wang and Y.-J. Cha, Unsupervised deep learning approach using a deep auto-encoder with a one-class support vector machine to detect damage, *Structural Health Monitoring*, 20(1), 406–425, 2021.
- [24] V. Gupta and U. Saravanan, Bridge condition monitoring using frequency domain decomposition method. In *International Operational Modal Analysis Conference*. Springer, 2024.
- [25] F. Ni, J. Zhang, and M. N. Noori, Deep learning for data anomaly detection and data compression of a long-span suspension bridge, *Computer-Aided Civil and Infrastructure Engineering*, 35(7), 685–700, 2020.



# Materials-Based Monitoring and Structural Health Assessment

# Intelligent Imaging: Transforming Concrete Assessment Methods with AI

A.Ahmad\_<sub>1,2</sub> <sup>0000-0001-9427-4296</sup>, V.Plevris\_<sub>3</sub> <sup>0000-0002-7377-781X</sup> M.ullah\_<sub>3</sub> <sup>0000-0002-7212-8826</sup> and J.Mir\_<sub>4</sub> <sup>0000-0002-4587-5121</sup>

<sup>1</sup>Department of Built Environment, Oslo Metropolitan University, Oslo, Norway

<sup>2</sup>Civil Engineering Department, University of Memphis, USA

<sup>3</sup>Department of Civil and Environmental Engineering, Qatar University, Qatar

<sup>4</sup>Department of Electrical Engineering, University of Engineering & Technology, Taxila, Pakistan

\*Email: afaq.ahmad@oslomet.no

**ABSTRACT:** This study uses novel image processing techniques to explore the effects of Cement Replacement Materials (CRM) like silica fume and fly ash on concrete's microstructure and durability. Cylindrical concrete specimens were prepared with mixed ratios of 1:2:4 and 1:3:6, incorporating water-cement (W/C) ratios of 0.4, 0.5, and 0.6 and CRM levels of 0%, 15%, and 25%. Images captured at various cylinder heights were analyzed using rectangle and nearest neighboring methods to quantify aggregate distribution and air void characteristics, including area, size, and spacing. Validation against manual measurements showed an error rate of less than 1.9%, underscoring the accuracy of these techniques. Results indicated that increasing CRM content reduced air void proportion and size, indicating improved durability. Additionally, CRM increased concrete homogeneity, with 25% of CRM samples exhibiting the lowest coefficient of variation (Cv) values (0.29–0.37), compared to higher Cv values (0.41–0.57) in non-CRM mixes. These findings highlight CRM's potential to enhance concrete mix design for better structural performance and sustainability in construction applications.

**KEY WORDS:** CRM, Concrete, Image Processing

## 1 INTRODUCTION

Concrete holds significant importance in civil infrastructure construction due to its favorable properties such as durability, strength, adaptability, and ease of availability. Concrete consists mainly of cement, aggregates, and water, making it a composite material. The cement paste, formed by mixing water with hydraulic cement, acts as a binding agent in concrete formulations. Cement is the most expensive component within the concrete matrix. Moreover, the escalating global demand for cement production contributes to the upward trend in environmental CO<sub>2</sub> levels [1]. To reduce both the economic and ecological impacts associated with cement production, the incorporation of cement replacement materials (CRMs) has gained prominence, leveraging waste materials like silica fumes (SF) and fly ash (FA) as viable alternatives to conventional cement [2, 3]. CRM can significantly affect the rheology of the mortar, which refers to its flow properties [4, 5]. FA particles are fine and spherical and act as ball bearings, reducing internal friction between cement particles and making the mix more workable in the concrete mixture [6]. SF particles are extremely fine with a high surface area, which enables them to fill the spaces between cement particles and create a dense matrix. This results in increased viscosity and reduced flowability in the concrete [7]. Therefore, aggregate distributions and air void content in concrete are affected by CRM due to the changes it induces in the rheological and microstructural properties of the concrete [8].

The distribution of aggregates and air voids in concrete offers valuable insights into the concrete sedimentation behavior, directly impacting its stability, structural serviceability, durability performance, and resistance to cracks [9, 10, 11]. Concrete petrographic analysis (ASTM C856) [12] is a commonly utilized method for assessing many concrete aspects, e.g., size and distribution of aggregates, porosity

levels, and bughole formations etc. [13]. Typically, concrete petrography entails the micro-structural examination of concrete components on a polished concrete section using imaging methods such as optical microscopy [14] or scanning electron microscopy [15]. In the past, human experts have conducted petrographic analysis by visually inspecting bugholes and aggregate distribution in cut sections of hardened concrete to evaluate its stability [16]. Determination of the size of aggregate particles has traditionally been done through mechanical sieving or manual clippers, but these methods are susceptible to human bias, errors, monotony, and inefficiency. Hence, there is a growing need for automated techniques and alternative methods to assess concrete stability.

In recent years, digital image processing has emerged as a widely employed tool in structural health monitoring (SHM) of concrete structures. [17]. Numerous studies have leveraged image processing techniques for the distribution analysis of aggregates within concrete. Aggregate size, area, and distribution within the concrete mixture are assessed to investigate the stability of self-compacting concrete [18]. Characteristics and distribution of coarse aggregate were computed in [19] by segmenting the concrete image into the background (cement paste) and foreground (aggregates). Characteristics and distribution of coarse aggregate are evaluated in [20] by an image analysis method using cross-sectional images. The consistency between 3D and 2D parameters is assessed, and a comparison of the ratio of mortar-to-coarse aggregate area with the mortar-to-coarse aggregate volume is presented. The aggregate distribution analysis in asphalt concrete was carried out by examining the aggregates' segmented images obtained through X-ray computed tomography in [21]. An aggregate classification approach that considers mesoscale angularity is proposed in [22].



This paper presents image processing-inspired techniques for assessing the impact of CRM on the concrete characteristics i.e., aggregate distribution, air void formation, and mixture homogeneity and segregation. To ameliorate this, concrete cylinders of different mix design ratios and percentages of SF and FA cut at the top and bottom sections were imaged to capture the internal concrete characteristics. Then, the images were annotated with pixel-level labels to facilitate quantitative analysis. Image processing-based methods are presented for aggregate and air void analysis to understand the impact of different CRM ratios in a concrete mixture. Subsequently, indicators for assessing concrete homogeneity are introduced by integrating aggregate size, roundness, and inter-aggregate distances. The study provides valuable insights into the segregation of aggregates and air void proportions within the concrete mixes and provides a comprehensive understanding of the sedimentation behavior induced by CRM.

## 2 DATABASE

### 2.1 Preparing Concrete Mixtures:

Two distinct designs of concrete were chosen, each with different proportions of cement, fine aggregates, and coarse aggregates for casting. These proportions were specified as

1:3:6 and 1:2:4. Mixes were formulated using different W/C ratios (0.4, 0.5, and 0.6) under the standards set by ASTM C 94 [23] and ACI 318 [24], since the variability in the water/cement (W/C) ratio plays a significant role in influencing the workability and distribution of aggregates within concrete. A total of six mix designs were included in the cast samples. Fly ash (FA) and silica fume (SF) were employed as Cement Replacement Materials (CRM) at varying replacement percentages of 0%, 15%, and 25% to assess their impact on the distribution of aggregate and air voids within the concrete mixtures. Two batches of 18 concrete cylinders were produced using the mix design ratios outlined in Table 1, and were allowed to cure for 14 and 28 days, respectively. These cylindrical samples were 300 mm in height (H) and 150 mm in diameter (D). They were then cut into three slices at 1/3rd and 2/3rd sections (approximately 100 mm from the bottom and top) using a stone cutting saw. The cutting procedure for acquiring concrete slices is depicted in Figure 4. Due to the fine materials accumulation on the bottom face of the third slice, and the top face of the first slice had minimal or no aggregate information and were thus excluded from imaging. This left four faces for imaging to generate the dataset.

Table 1. Detail of the samples with Mix Ratios

Sr. No.	Mix Ratio	W/C Ratio	FA %	SF %	Proportions in kg/m <sup>3</sup>					
					Cement	FA	SF	Fine Aggr.	Coarse Aggr.	Water
1	01:03:06	0.4	0	0	229.48	0	0	728.94	1505.78	91.8
2	01:03:06	0.5	0	0	229.48	0	0	728.94	1505.78	114.75
3	01:03:06	0.6	0	0	229.48	0	0	728.94	1505.78	137.69
4	01:02:04	0.4	0	0	327.79	0	0	694.27	1434.06	131.12
5	01:02:04	0.5	0	0	327.79	0	0	694.27	1434.06	163.9
6	01:02:04	0.6	0	0	327.79	0	0	694.27	1434.06	196.68
7	01:03:06	0.4	15	15	160.64	34.43	34.43	728.94	1505.78	91.8
8	01:03:06	0.5	15	15	160.64	34.43	34.43	728.94	1505.78	114.75
9	01:03:06	0.6	15	15	160.64	34.43	34.43	728.94	1505.78	137.69
10	01:02:04	0.4	15	15	229.45	49.18	49.18	694.27	1434.06	131.12
11	01:02:04	0.5	15	15	229.45	49.18	49.18	694.27	1434.06	163.9
12	01:02:04	0.6	15	15	229.45	49.18	49.18	694.27	1434.06	196.68
13	01:03:06	0.4	25	25	114.75	57.38	57.38	728.94	1505.78	91.8
14	01:03:06	0.5	25	25	114.75	57.38	57.38	728.94	1505.78	114.75
15	01:03:06	0.6	25	25	114.75	57.38	57.38	728.94	1505.78	137.69
16	01:02:04	0.4	25	25	163.9	81.95	81.95	694.27	1434.06	131.12
17	01:02:04	0.5	25	25	163.9	81.95	81.95	694.27	1434.06	163.9
18	01:02:04	0.6	25	25	163.9	81.95	81.95	694.27	1434.06	196.68

The image acquisition setup was organized in a closed room, depicting an experimental arrangement for capturing digital images of concrete specimens, as shown in Figure 1. To ensure high-quality images for effective processing, measures were taken to maintain a consistent environment and minimize external influences such as light variations, noise, and shadows. Black sheets were used to cover all entry points for light, and two 30-W LED bulbs provided controlled illumination from a

specific angle, resulting in a light intensity of 2000 lux. A digital camera (Nikon DSLR 3300) with a resolution of 24 megapixels and ISO value set at 1000 was employed to capture 192 high-resolution slice images, each measuring 6000→4000 pixels. A constant distance was maintained by mounting the camera on a stand at a distance of 600 mm from the surface of the sample. The image acquisition setup, for example slice image, is illustrated in Figure 1.



Figure 1. Preparation of Concrete Mixtures (Top Left), Casting and Cutting of Samples (Top Right), Image Acquisition (Bottom Left), Image Labeling (Bottom Right).

## 2.2 Casting and Cutting of Samples

Two batches of 18 concrete cylinders were produced using the mixed design ratios outlined in Table 1, and were allowed to cure for 14 and 28 days, respectively. These cylindrical samples were 300 mm in height (H) and 150 mm in diameter (D). They were then cut into three slices at 1/3rd and 2/3rd sections (approximately 100 mm from the bottom and top) using a stone cutting saw. The cutting procedure for acquiring concrete slices is depicted in Figure 2. Due to the fine materials accumulation on the bottom face of the third slice, the top face of the first slice had minimal or no aggregate information and was thus excluded from imaging. This left four faces for imaging to generate the dataset.

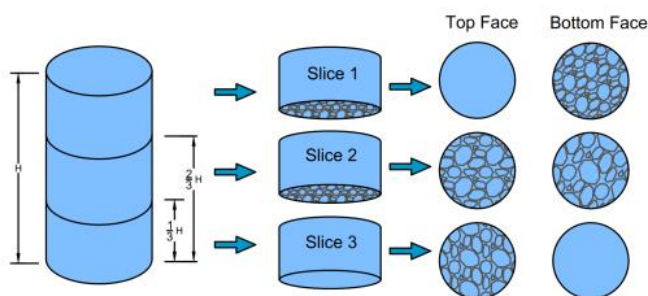


Figure 2. Cutting the concrete cylinders into three slices at top and bottom sections

## 2.3 Image Labeling

Each image was meticulously labeled at the pixel level to distinguish between non-aggregate suspension (e.g., air voids, sand-cement matrix) and aggregate pixels. Similarly, for air void analysis, image pixels were labeled as either air void pixels or non-air void suspension pixels (e.g., aggregates, sand-cement matrix). Binary images were generated for aggregates and air voids, respectively.

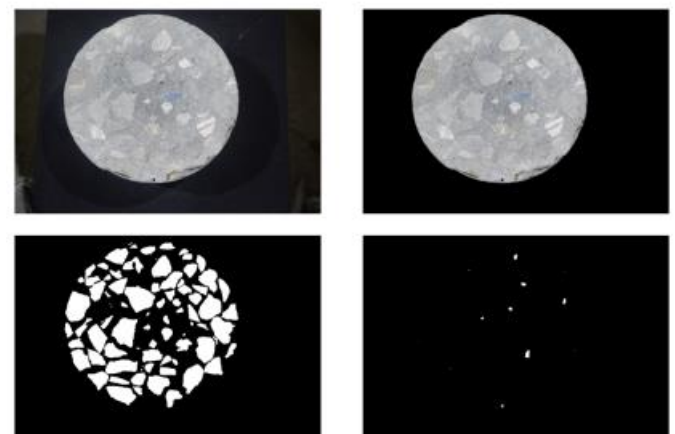


Figure 3. High-resolution images of concrete slices: The top left is the original image, the top right is the background removed image, the bottom left is the Aggregate ground truth and the bottom right is the Air void ground truth image

Figure 3 shows a concrete cylinder slice with background, the processed image with the background removed, and the corresponding ground truth images for aggregates and air voids. White pixels in these images indicate the presence of aggregates and air voids as per the ground truth labels. Among all the labeled pixels across 144 slice images, 41.3% were labeled as aggregate pixels and 58.7% as non-aggregate pixels. Similarly, 0.25% of labeled pixels were labeled as air void pixels, with 99.75% classified as suspension pixels. Among all the labeled images, 1.8% of the particles were found to be connected. On average, each connected component consisted of approximately 13 pixels. These connected components were separated with a Marker-controlled watershed transformation algorithm [25] enabling detailed analysis and quantification of characteristics of each aggregate and air void in concrete samples.

The aggregates and air voids proportions can significantly influence the rheology, stability, mechanical characteristics, durability, and cost-effectiveness of concrete. These proportions can be determined from annotated images. The overall area occupied by aggregates and air voids in a concrete cylinder was determined by counting the white pixels, representing aggregates and air voids, and then multiplying it by the unit pixel size. Then this pixel size is converted to 0.044 mm. To validate this method, the aggregate and air void characteristics were compared with measurements obtained manually and using AutoCAD [26]. For manual area measurement of aggregates and air voids, a transparent graph paper with a 1 mm square grid was placed on the cylinder surface to count squares covering aggregates and air voids, as illustrated in Figure 4. The numbers of squares fully and partially covering aggregates and air voids were counted and then finally summed to determine the area of aggregate and air void, respectively. The aggregate mean size and roundness

values were manually verified against a vernier caliper, as illustrated in Figure 4. In AutoCAD [26], the raster images were first scaled according to the standard diameter of the cylinder. Subsequently, the boundaries of the aggregates and air voids were then traced, and certain boundary points were marked to form polygons, as depicted in Figure 4. With the help of a built-in command, the area of these polygons was calculated based on the coordinates of the boundary points. This approach differs from the pixel-based method, enabling a meaningful comparison between the two techniques. The areas of these polygons were then summed to determine the total aggregate and air void area, respectively. A comparison of aggregate and air void characteristics measured using the proposed image processing method, manual measurements, and AutoCAD is presented in Table 2. The results demonstrate significant consistency, confirming the effectiveness of the proposed image processing method in precisely identifying characteristics of aggregates and air voids.

Table 2. Comparison of the computed areas

Parameters	Mix Ratio	Proposed Method	AutoCAD	Visual Inspection	Percentage Error
Aggregate Area (mm <sup>2</sup> )	01:02:04	9335.35	9297.12	9411.25	0.81
	01:03:06	10058.42	10083.88	10171.5	1.11
Aggregate Mean Size (mm)	01:02:04	14.84	14.53	14.75	0.61
	01:03:06	15.36	15.64	15.5	0.9
Aggregate Mean Roundness	01:02:04	1.73	1.81	1.75	1.14
	01:03:06	1.52	1.43	1.5	1.33
Air-voids Area (mm <sup>2</sup> )	01:02:04	5.19	5.31	5.25	1.14
	01:03:06	9.68	10.12	9.5	1.89
Air-voids Mean Size (mm)	01:02:04	2.53	2.42	2.5	1.2
	01:03:06	2.77	2.87	2.75	0.73

#### 2.4 Aggregate and Air Void Characteristics:

An object's characteristics, like size, shape, and orientation, can tell much about its concrete composition. Quantifying these characteristics can lead to size and distribution uniformity analysis, which in turn facilitates the examination of concrete mixture's consolidation, workability, compatibility, interlocking, and bonding. The Feret rectangle technique [27] was utilized in this study to measure the characteristics of the coarse aggregate and voids from the image. This technique entails drawing rectangles that enclose each object with the minimum area possible, according to their Feret diameter as depicted in Figure 5. The Feret diameter represents the greatest distance between points along the object's perimeter. To compute this, we iterated through pairs of points on the boundary line, calculating their Euclidean distances and

identifying the greatest distance as the Feret diameter. Subsequently, around each object, a rectangle was drawn, with its length corresponding to the Feret diameter and its width perpendicular to this direction. The orientation of these rectangles was optimized to minimize their area while encompassing the object. The dimensions, i.e., length and width of each Feret rectangle, were then determined and recorded as the corresponding object's length and width. The length of the object was considered as its size, and the mean aggregate size was calculated as the average of all aggregate sizes measured in the image. The roundness values of coarse aggregates were assessed by computing the ratio of the rectangle's longer side to its shorter side. A roundness value of one signifies a square-shaped rectangle. As the roundness increases, the shape of the object becomes more elongated.



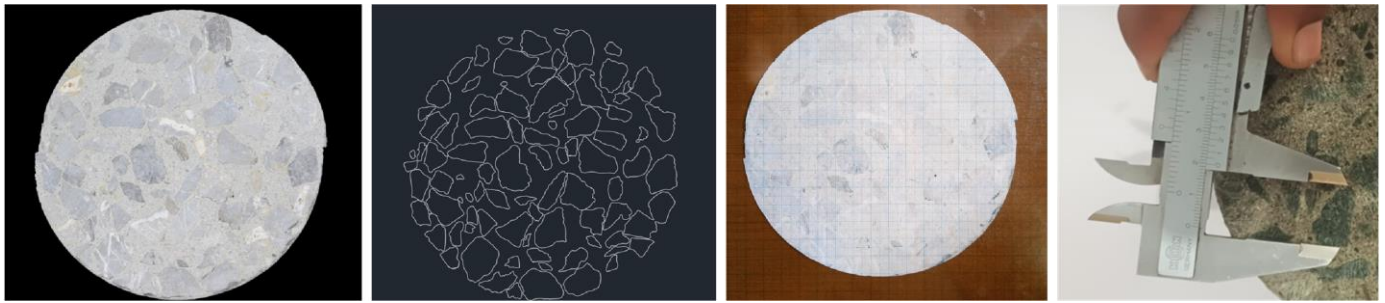


Figure 4. Concrete sample (1st image), traced boundaries using AutoCAD (2nd image), manual area measurements with graph paper (3rd image), and manual size measurement with vernier caliper(4<sup>th</sup> image)

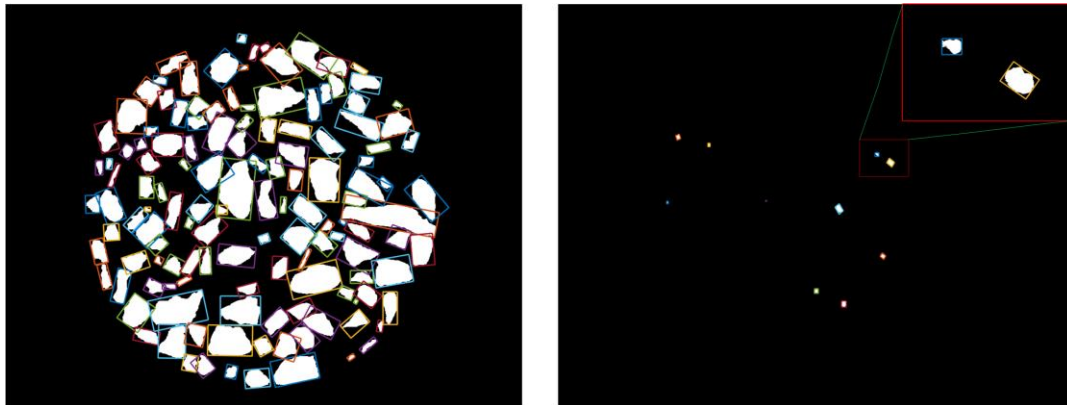


Figure 5. Concrete sample image showcasing minimum area rectangles derived from Feret diameter; Aggregate (Left), Air void (Right).

### 3 RESULTS AND DISCUSSION

#### 3.1 Aggregate Proportion

The proportion of aggregate in the concrete mixture is an essential factor in analyzing the structural health of a member and can be calculated using the image processing methodologies discussed previously. As presented in Table 1, in this study, two mix ratios, 1:2:4 and 1:3:6, were employed. These mix ratios denote the proportions of cement, fine aggregates (sand), and coarse aggregates in 1 m<sup>3</sup> volume of concrete. Initially, the proportion of coarse aggregates in the cylinder was quantified using the aggregate volume ratio (AVR) parameter. AVR represents the ratio of coarse aggregate volume to the total volume of a cylinder, as given by Eq. 1,

$$AVR = \frac{\text{Coarse Aggregate Volume}}{\text{Cement} + \text{Sand} + \text{Coarse}} \quad (1)$$

According to Eq. 1, the mix ratios of 1:2:4 and 1:3:6 correspond to AVR values of 0.57 and 0.60, respectively. The AVR values were then compared with the proportions of aggregates obtained from 2D cross-sectional images of the

cylinder. By analyzing concrete cross-sectional images and computing areas of aggregate, the proportion of aggregates in 2D images was quantified using the aggregate area ratio (AAR), given as Eq. 2,

$$AAR = \frac{\text{Area of Aggregate in Image}}{\text{total cross sectional area of cylinder}} \quad (2)$$

Here, the total cross-sectional area of the cylinder refers to the area encompassed by all pixels within the cylinder boundary. Figure 6 illustrates the AAR values obtained from the cross-sectional images for the two mix ratios across different CRM ratios. An observable trend emerges where an increase in the CRM ratio corresponds to a reduction in the variation of deducted AAR values. This may be because the incorporation of CRM results in a more uniform distribution of aggregates in concrete compared to normal concrete. It is noticeable that the calculated AAR values exhibit deviation from the AVR values. The disparity in AAR values may arise from several factors. Segregation can occur during mixing, transporting, and casting of concrete, leading to a nonuniform distribution of aggregates within concrete. These factors directly influence the calculated AAR values.

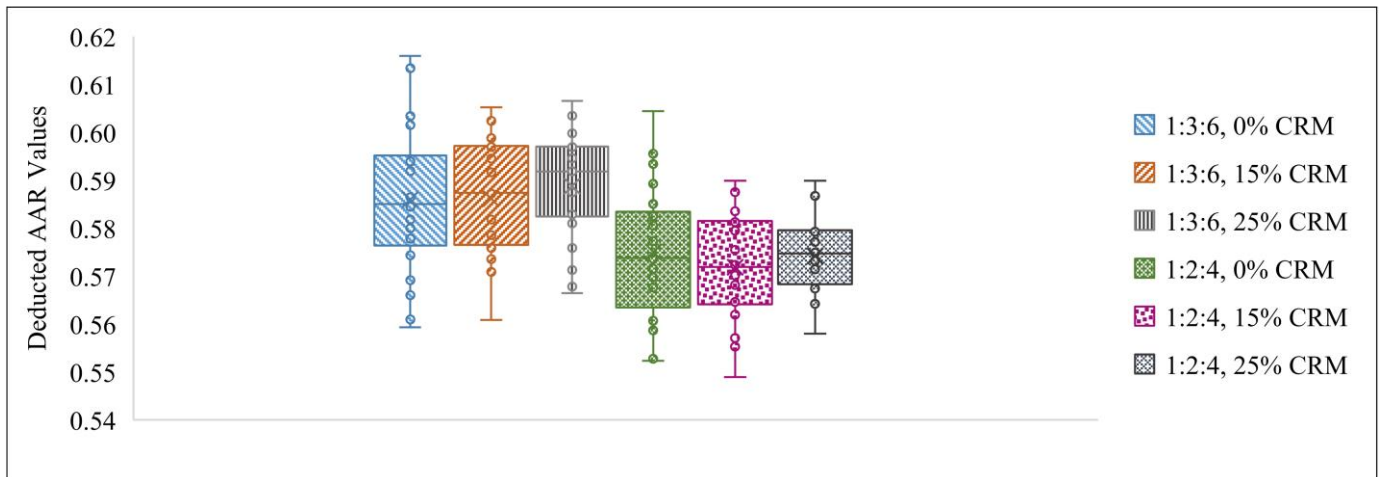


Figure 6. Box-Plots showing variation of calculated AAR values for the two mix designs with varying CRM ratios.

### 3.2 Aggregate Size

In segregation, the coarser aggregate particles tend to settle down, and the finer aggregate particles remain at the top. The sizes of aggregates at the bottom and top regions of concrete cylinders were analyzed (as detailed in Section 2.2) to assess the impact of different proportions of W/C ratio and CRM on segregation. Analysis of aggregate size involves examining cross-sectional images of the concrete cylinder at the top region (comprising the bottom face of the first slice and top face of the second slice) and the bottom region (comprising the bottom face of the second slice and top face of the third slice). The difference in aggregate mean size between these regions

indicates the extent of segregation and is shown in Figure 7 for different CRM Ratios. Within each mix ratio (1:2:4 and 1:3:6), generally, there is a slight increase in the difference in mean aggregate size with an increase in W/C ratio, which indicates the occurrence of segregation. This occurs because higher water content increases the mobility and fluidity of the concrete mix, making it more susceptible to segregation during handling, transportation, or placement. Excessive water can cause coarser particles to settle, increasing the size disparity between the aggregates.

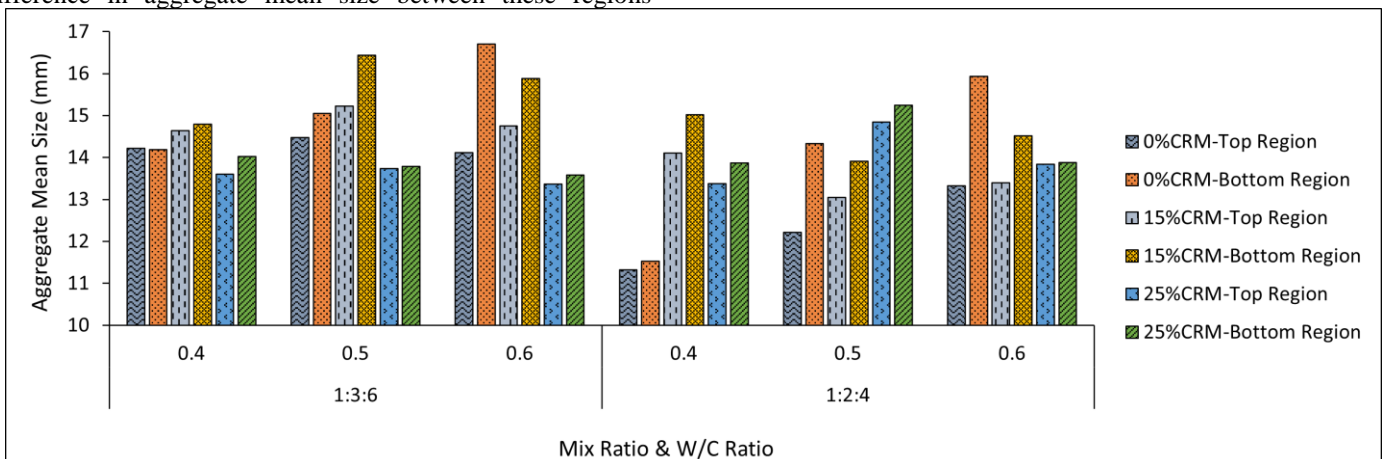


Figure 7. Mean size of coarse aggregates at bottom and top regions of the concrete cylinders bottom and top regions.

### 3.3 Aggregates Roundness

The roundness of aggregates significantly influences segregation in concrete. Less rounded aggregates have irregular shapes with sharp edges and corners. When these less-rounded particles come in contact, they interlock, creating a bridging effect in the concrete mix. This bridging effect minimizes the risk of segregation for the less-rounded particles. On the other hand, more rounded aggregates have a uniform shape, making

them less prone to interlocking and bridging. This can result in a higher likelihood of particle movement and segregation within the mix. The more rounded shape reduces the frictional forces between particles, allowing them to move more freely and potentially separate from one another. The mean roundness values of aggregates in the top and bottom regions of the concrete cylinders are calculated using a specified method. Figure 8 represents the analysis results of aggregate mean roundness values at the bottom and top regions of a concrete cylinder with 0%, 15%, and 25% CRM, respectively.

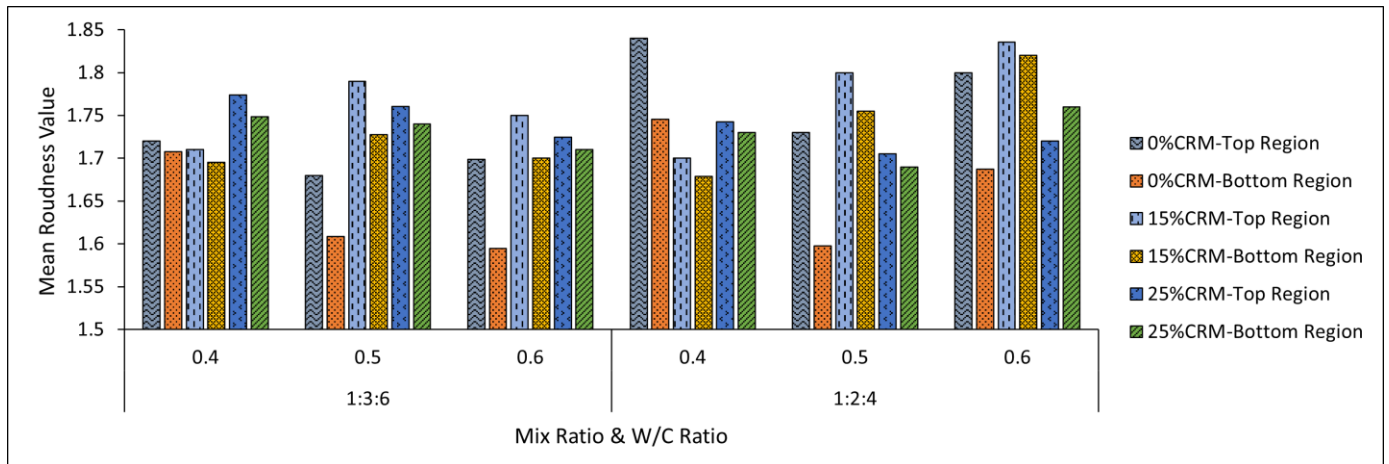


Figure 8. Mean roundness values of coarse aggregate at bottom and top regions of the concrete cylinders.

### 3.4 Distance Between Aggregates

The examination of the distribution of aggregates in the bottom and top regions of concrete specimens can provide valuable information about the concrete sedimentation behavior. To examine the effect of CRM and W/C ratios on the distribution of aggregates, the distance between centroids of coarse aggregate particles was determined by the nearest neighbor image analysis method. The frequencies of these distances for different range groups are then determined for each section. Figure 9 shows the frequencies of distances between the aggregate for the specified range groups at different CRM and W/C ratios. The frequencies of distances between coarse aggregates are shown separately for the bottom and top regions of the concrete cylinder specimens. Most aggregate distributions fall within the 10 mm- 20 mm distance

range in all specimens. Notably, the 0% and 25% CRM cylinders exhibit a high frequency within the range of 10 mm-20 mm spacing distances, indicating closer aggregate spacing compared to the 15% CRM specimens. Figure 13 also reveals that the frequency of distances between 10mm and 20mm is higher in the bottom region, suggesting a more compact arrangement of aggregates at the bottom. Additionally, the frequency of distances within the range of 30 mm- 40 mm and 40 mm- 50 mm is lower in the bottom region compared to the top region. This difference can be attributed to the settlement of heavier aggregate particles, which results in closer spacing of aggregates within the 10 mm- 20 mm range, consequently reducing the maximum spacing between aggregates, typically in the 30 mm- 50 mm range.

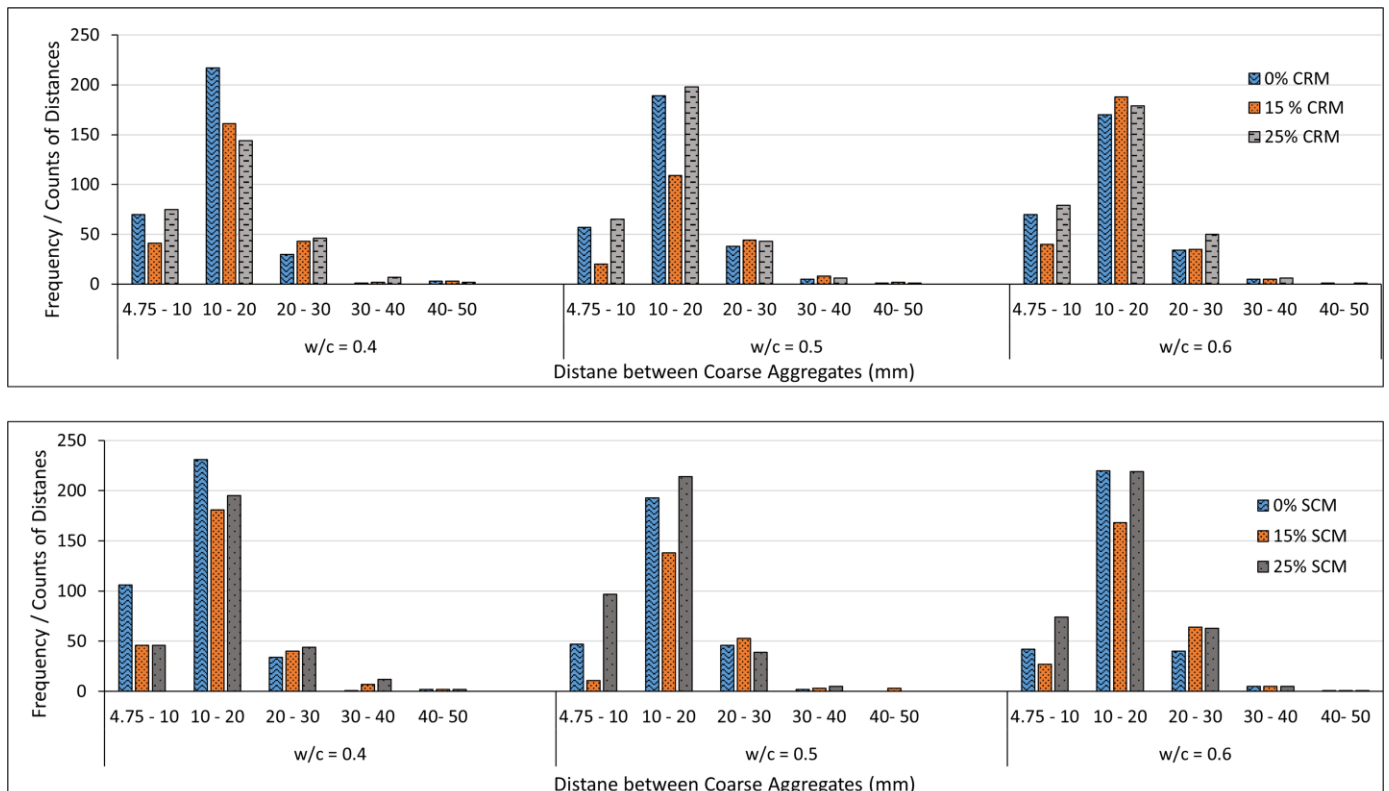




Figure 9. Frequency of distances between centriods of coarse aggregate particles; Top Cylinder Region (First row), Bottom Cylinder Region (Second row)

### 3.5 Air Void Proportion

Assessing the air void proportion within a concrete mixture is a crucial step for achieving the desired balance between durability and mechanical properties, and it can be determined using the image analysis techniques described above. The air void proportion in the 2D cylinder images was quantified through the area air void ratio (AAVR) parameter, which is calculated as Eq 3.

$$AAVR = \frac{\text{area of air void in image}}{\text{total cross sectional area of cylinder}} \quad (3)$$

Here, the total cross-sectional area of the cylinder slice refers to the area encompassed by all the pixels contained within the boundary of the Concrete cylinder. Figure 10 displays the AAVR values computed from the images of concrete cylinder

specimens for the two mix ratios with varying CRM ratios. Across varying W/C ratios and concrete mix ratios, a consistent trend emerges. Generally, as the percentage of CRM increases from 0% to 15% and 25%, the proportion of air voids tends to decrease. This suggests that incorporating CRM, such as FA or SF, can reduce the formation of air voids in concrete. This reduction in AAVR values can be attributed to the pozzolanic properties of FA and SF, which enhance the workability and cohesion of the concrete mix, reducing the likelihood of entrapped air and thus decreasing the number of air voids. These findings offer valuable insights into optimizing concrete mix designs with CRM to minimize air voids. It's also worth noting that the W/C ratio effects the influence of CRM on air void proportion, as the two factors interact to shape the entrapped air content, highlighting the importance of considering both factors when optimizing concrete mix designs for specific applications.

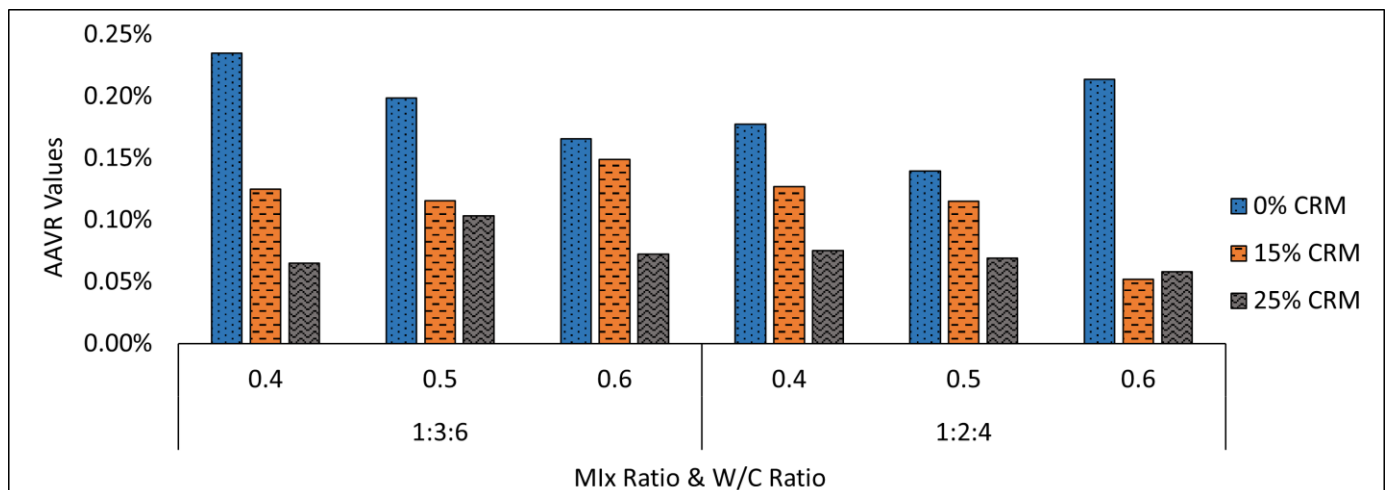


Figure 10. Influence of CRM on the area air void ratios

### 3.6 Air Void Size

The size of air voids significantly impacts concrete properties. Smaller air voids enhance the concrete's resistance to freeze-thaw cycles, enhancing durability. Larger air voids, on the other hand, can weaken the concrete's mechanical properties, making it more vulnerable to cracking and deterioration in challenging environmental conditions. Achieving the right balance in air void size is crucial in optimizing concrete for specific applications, ensuring a combination of strength, durability, and long-term performance. To understand the effect of different CRM and

W/C ratios on the size of air voids, the mean size of air voids in the concrete cylinder sections was calculated by the method discussed. The influence of CRM on the size of air voids can be observed by comparing the air voids' mean sizes at different CRM percentages, as shown in Figure 11. It can be seen that as the percentage of CRM in the mix increases, the mean size of air voids tends to decrease. For instance, in the 1:3:6 mix with a W/C ratio of 0.4, the air voids mean size is 1.97 mm when there is no CRM (0% CRM), whereas with 15% CRM, it reduces to 1.71 mm. The air void mean size further decreases to 1.55 mm with 25% CRM.

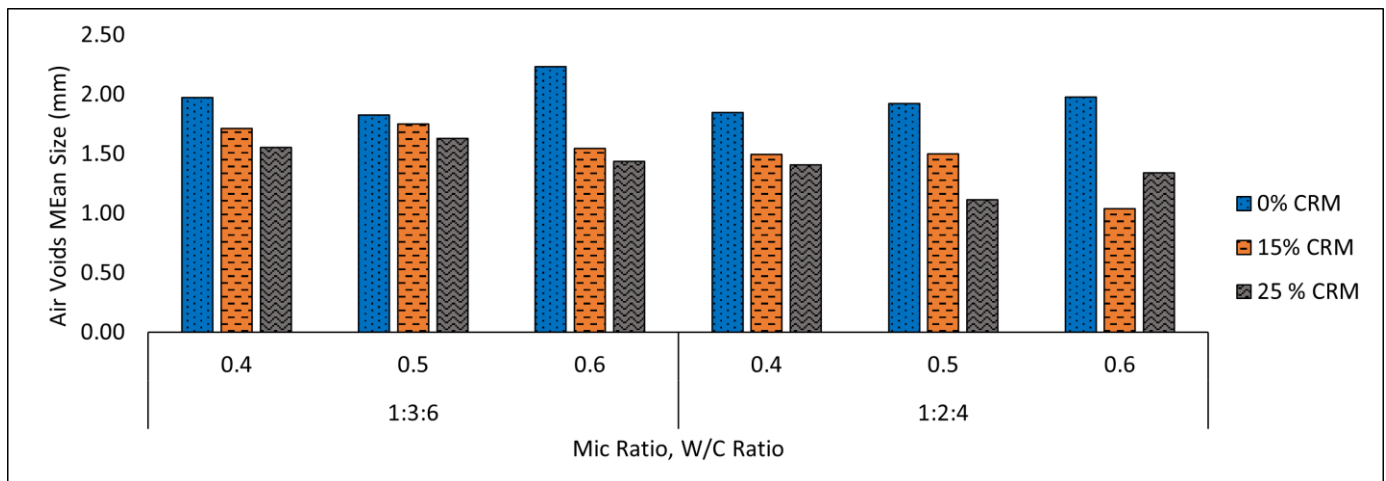


Figure 11. Influence of CRM on the mean size of air voids

#### 4 CONCLUSION

This study explored advanced image processing techniques to investigate the impact of CRM (Silica Fume and Fly Ash) on air void characteristics and aggregate distribution in concrete. Techniques such as the Feret rectangle method and nearest neighbor analysis provided detailed insights into the size, shape, and spatial distribution of aggregates. The following main conclusions can be drawn from the results of the study:

- The analysis of aggregate proportion, quantified through Aggregate Area Ratio (AAR), revealed a close correlation with Aggregate Volume Ratio (AVR) values. This correlation underscores the accuracy and effectiveness of the employed image processing methods in predicting the aggregate proportion.
- The incorporation of CRM led to a notable reduction in both the proportion and size of air voids. This decrease enhances concrete durability by improving resistance to freeze-thaw cycles and reducing cracking risks.
- Increasing CRM content significantly reduces segregation tendencies, leading to a more uniform aggregate distribution across the concrete mix. This improvement is evidenced by lower Cv values, indicating improved homogeneity.
- CRM improved the homogeneity of aggregates by providing more consistent results in terms of aggregate areas, sizes, and roundness, particularly in specimens with higher CRM content. Kurtosis analysis further showed fewer outliers, indicating a more even distribution of aggregates.

• The image processing techniques, including the Feret rectangle method and nearest neighbor analysis, showed an error rate of less than 1.90%, confirming their reliability and accuracy in predicting aggregate and air void properties.

This study primarily addressed rounded and angular aggregates. However, closely positioned elongated or flaky aggregates or irregular shapes aggregates may overlap, potentially leading algorithms to inaccurately identify them as a single aggregate. This could affect the analysis of parameters such as area, length, and roundness. While manual labeling ensures accuracy, it is labor-intensive and subjective, limiting scalability for large-scale or rapid analysis needs. In future work, we plan to use deep learning-based image processing methods, i.e., DeepLabv3+, UNET, and vision transformers, to

segment and quantify aggregate and air void characteristics. Additionally, we aim to validate the effect of different CRM ratios on homogeneity by analyzing the distribution of aggregates and air voids at various sections of other structural members in real-world applications.

#### ACKNOWLEDGMENTS

The authors are thankful to Oslomet University for investigating this research.

#### FUNDING

This is the part of the Project “Forensic Analysis of Concrete Through Image Processing” FACIP, funded by the EU against The Grant agreement ID: 101153307, <https://cordis.europa.eu/project/id/101153307>.

#### REFERENCES

- [1] H. Mikul'ci'c, J. J. Kleme's, M. Vujanovi'c, K. Urbaniec, N. Dui'c, Reducing greenhouse gasses emissions by fostering the deployment of alternative raw materials and energy sources in the cleaner cement manufacturing process, *Journal of Cleaner Production* 136 (2016) 119–132.
- [2] S. Vivek, G. Dhinakaran, Durability characteristics of binary blend high-strength scc, *Construction and Building Materials* 146 (2017) 1–8.
- [3] S. S. Nachiar, et al., A review on fly ash cenosphere as a solid waste in concrete application, *Materials Today: Proceedings* 68 (2022) 2072–2078.
- [4] T. Luo, C. Hua, F. Liu, Q. Sun, Y. Yi, X. Pan, Effect of adding solid waste silica fume as a cement paste replacement on the properties of fresh and hardened concrete, *case stud. constr. mater.*, 16 (2022) e01048.
- [5] A. I. Laskar, S. Talukdar, Rheological behavior of high-performance concrete with mineral admixtures and their blending, *Construction and Building Materials* 22 (12) (2008) 2345–2354.
- [6] T. Yang, H. Zhu, Z. Zhang, X. Gao, C. Zhang, Q. Wu, Effect of fly ash microsphere on the rheology and microstructure of alkali-activated fly ash/slag pastes, *Cement and Concrete Research* 109 (2018) 198–207.
- [7] D. Jiao, C. Shi, Q. Yuan, X. An, Y. Liu, H. Li, Effect of constituents on rheological properties of fresh concrete-a review, *Cement and concrete composites* 83 (2017) 146–159.
- [8] K. Kim, M. Shin, S. Cha, Combined effects of recycled aggregate and fly ash towards concrete sustainability, *Construction and Building Materials* 48 (2013) 499–507.
- [9] G. Wang, Y. Kong, T. Sun, Z. Shui, Effect of water-binder ratio and fly ash on the homogeneity of concrete, *Construction and Building Materials* 38 (2013) 1129–1134.
- [10] P. Nallathambi, B. Karihaloo, B. Heaton, Effect of specimen and crack sizes, water/cement ratio and coarse aggregate texture upon fracture toughness of concrete, *Magazine of concrete research* 36 (129) (1984) 227–236.

- [11] F. de Larrard, A. Belloc, The influence of aggregate on the compressive strength of normal and high-strength concrete, *Materials Journal* 94 (5) (1997) 417–426.
- [12] Standard practice for petrographic examination of hardened concrete (2020).
- [13] H. N. Walker, D. S. Lane, P. E. Stutzman, et al., *Petrographic methods of examining hardened concrete: A petrographic manual*, Tech. rep., United States. Federal Highway Administration. Office of Infrastructure . . . (2006).
- [14] J. Elsen, Microscopy of historic mortars—a review, *Cement and concrete research* 36 (8) (2006) 1416–1424.
- [15] P. E. Stutzman, Applications of Scanning Electron Microscopy in Cement and Concrete Petrography, *Petrography of Cementitious Materials* 1215 (1994) 74.
- [16] M. A. Esfahani, M. Kalani, Petrographic analysis method for evaluation and achieving durable hot mix asphalt, *Construction and Building Materials* 234 (2020) 117408.
- [17] C. Koch, K. Georgieva, V. Kasireddy, B. Akinci, P. Fieguth, A review on computer vision-based defect detection and condition assessment of concrete and asphalt civil infrastructure, *Advanced Engineering Informatics* 29 (2) (2015) 196–210.
- [18] C. Fang, S. Labi, Image-processing technology to evaluate static segregation resistance of hardened self-consolidating concrete, *Transportation research record* 2020 (1) (2007) 1–9.
- [19] X. Xu, S. Xu, L. Jin, E. Song, Characteristic analysis of Otsu threshold and its applications, *Pattern recognition letters* 32 (7) (2011) 956–961.
- [20] J. Han, K. Wang, X. Wang, P. J. Monteiro, 2D image analysis method for evaluating coarse aggregate characteristic and distribution in concrete, *Construction and building materials* 127 (2016) 30–42.
- [21] K. Zhang, Z. Zhang, Y. Luo, S. Huang, Accurate detection and evaluation method for aggregate distribution uniformity of asphalt pavement, *Construction and Building Materials* 152 (2017) 715–730.
- [22] J. Wu, X. Zhou, X. Zeng, Y. Xie, G. Long, R. Dong, H. A. Umar, G. Ma, L. Yao, Effect of aggregate morphology characteristics on the voidage of aggregate loose packing based on 3d discrete element method, *Construction and Building Materials* 348 (2022) 128598.
- [23] S. N. Abbas, M. I. Qureshi, M. K. Alkharisi, M. Alturki, Z. Ahmad, Combined effect of silica fume and various fibers on fresh and hardened properties of concrete incorporating HDPE aggregates, *Construction and Building Materials* 445 (2024) 137940.
- [24] D. G. Daniel, C. L. Lobo, *User's Guide to ASTM Specification C 94 on Ready-mixed Concrete*, ASTM International, 2005.
- [25] A. Committee, *Building code requirements for structural concrete (aci 318-08) and commentary*, American Concrete Institute, 2008.
- [26] AutoCAD software, version 2023. URL <https://www.autodesk.com/products/autocad/overview>
- [27] W. Wang, Image analysis of particles by modified ferret method—best-fit rectangle, *Powder Technology* 165 (1) (2006) 1–10.



# Monitoring of Non-Linearities in Fatigue Degradation of Metallic Materials Using Techniques beyond Stress and Strain

Christian Boller<sup>1</sup>, ORCID (0000-0003-1142-9390), Peter Starke<sup>2</sup>, ORCID (0000-0002-8033-0602)

<sup>1</sup>Chair of Non-Destructive Testing and Quality Assurance (LZfPQ), Faculty of Natural and Technical Science, Saarland University, Campus Dudweiler, Am Markt Zeile 4, 66125 Saarbrücken, Germany

<sup>2</sup>Materials Science & Materials Testing (WWHK), University of Applied Science Kaiserslautern,

Schoenstraße 11, 67659 Kaiserslautern, Germany

email: c.boller@mx.uni-saarland.de, peter.starke@hs-kl.de

**ABSTRACT:** Traditional fatigue assessment in metals is based on load sequences either measured or assumed, S-N (Wöhler) curves and the application of linearized damage accumulation rules. This requires a large amount of experimental effort to obtain materials data to be used for prognostics of which the result is often unsatisfactory. Furthermore, such assessment is mainly based on stress and strain as the loading parameters applied. However, materials fatigue degradation is a more complex process, far from being linear and not limited to stress and strain only. Material's degradation is an issue. Without knowing a material's prior loading history its degree of degradation can neither be assessed nor monitored on this basis. However, monitoring a material's degree of degradation is a prerequisite to preserve a structure's health over its Residual Useful Life (RUL). Available Non-Destructive Testing (NDT) techniques can be of a significant help. This paper shows how a metallic material's non-linear fatigue behaviour can be visualized in a 3D plot characterizing the loading applied as an input parameter, the NDT parameter recorded as a material response and the relative fatigue life, hence the degree of degradation, as a resulting parameter respectively. It is shown how this resulting 3D viewing plane can be used to determine a material's degree of fatigue degradation at virtually any stage of its operational life and it is demonstrated how this information can be used for a monitoring system in the sense of Structural Health Monitoring (SHM) to further track a structure's RUL in a much more precise way than traditionally done so far.

**KEY WORDS:** Monitoring, non-linear fatigue degradation, Residual Useful Life, metallic materials

## 1 INTRODUCTION

Degradation of materials due to fatigue is a concern scientifically elaborated on since around 150 years. Its traditional assessment is based on load sequences either measured or assumed, S-N (Wöhler) curves and the application of linearized damage accumulation rules. The approaches being applied to experimentally determine a material's fatigue degradation and to get this analytically and/or numerically evaluated has been described in a variety of textbooks (i.e. [1-3]). Although the principles described in those textbooks might be applicable to a variety of materials, these principles have been mainly developed and used so far best with metallic materials. The effort to get the respective materials characterized and data generated is relatively high. To sufficiently cover such materials' fatigue data a set of around 25 fatigue experiments needs to be performed at different loading levels, a significant effort in terms of time and cost. An attempt to optimize this effort has been achieved by collecting and evaluating materials' data for cyclic loading nearly 40 years ago [4,5]. This data has been based on stress and strain as the loading parameters, being the most relevantly used in engineering design today. A major application of this data is within the context of local strain approaches, where the fatigue life of a service loaded notched component is determined with the help of a notch-strain-relationship as proposed by Neuber and others [1-3]. Materials' fatigue data determined on unnotched specimens are therefore the basis to perform a fatigue life evaluation of notched components under service loading. This article will therefore focus on the material's fatigue response and how this could be monitored with

advanced sensing beyond the traditional parameters of stress and strain.

To further enhance the process of materials fatigue data generation in terms of time and cost Short Time Evaluation Procedures (STEP) have been developed, along which the material's stress-strain and S-N behaviour can be determined down to a single fatigue experiment only [6-8]. The logic of those STEP approaches in its earlier form and being applied here is shown in Figure 1. This is based on three fatigue experiments, where two are traditional Constant Amplitude tests (CAT) and one is a Load or a Strain Increase Test (LIT or SIT) respectively, all tests performed on unnotched specimens. A LIT or SIT is a fatigue test, where the specimen is loaded at a constant stress (LIT) or strain (SIT) amplitude for a defined number of time or loading cycles, starting at a small stress/strain amplitude within the material's full elastic range behaviour and then increasing the stress or strain stepwise while keeping the duration of each step in terms of either time or number of cycles constant.

What is determined from the LIT or SIT is a relationship between the load applied (i.e. stress or total strain) versus a respective material response. In traditional terms, this material response is often plastic strain, being one of the mechanisms associated with fatigue in metals. Morrow [9] was possibly one of the first who determined such a relationship in terms of the strain hardening exponent  $n'$  of a metallic material's stress versus plastic strain relationship proposed as

$$\varepsilon_{a,p} = \varepsilon_f' \cdot \left( \frac{\sigma_a}{\sigma_f'} \right)^{1/n'} \quad (1)$$

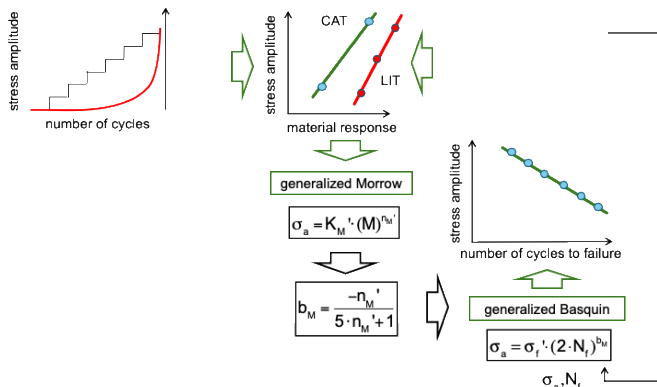


Figure 1 Logic of a STEP approach for the quick determination of an S-N curve

where  $\varepsilon_{a,p}$  represents the plastic strain amplitude,  $\sigma_a$  the applied stress amplitude, and  $\varepsilon_f'$  and  $\sigma_f'$  are constants referred to as the cyclic ductility and strength respectively similar to the true fracture ductility and strength under tensile monotonic loading. Morrow also used the two latter constants to describe a material's strain-life curve in the form of

$$\varepsilon_{a,t} = \frac{\sigma_f'}{E} (2N_f)^b + \varepsilon_f' (2N_f)^c \quad (2)$$

where  $\varepsilon_{a,t}$  is the total strain amplitude as an addition of elastic and plastic strain,  $E$  Young's modulus,  $N_f$  the number of cycles to failure and  $b$  and  $c$  the slopes of the life curves for elastic and plastic strain when being plotted in a double logarithmic scale respectively. What Morrow further did was to establish a relationship between the slopes  $b$  and  $c$  on the one side and the strain hardening exponent  $n'$  on the other resulting in

$$c = \frac{-1}{1+5n'} \text{ and } b = \frac{-n'}{1+5n'} \quad (3)$$

allowing a fatigue life (S-N) curve to be determined from a material's strain hardening response in the end. This relationship has also been used in the STEP procedures mentioned above in a slightly modified way, differentiating between the elastic and the plastic material behaviour.

Sensing and hence monitoring of a material's behaviour today can go far beyond monitoring stress and strain only. Non-Destructive Testing (NDT) has opened a large gamut of options considered in the past with respect to fatigue life evaluation and hence, residual life assessment of engineering structures, of which the potential has only been explored to a limited extent in the past. However, where this has been considered is in the context of STEP and here with respect to what has been considered as the 'material response' shown in the diagram in Figure 1. Examples presented in [6-8] and in various other publications do include techniques such as infrared thermography, electrical resistance and eddy current measurement. In this paper the case of thermography is presented and how this can be used for characterizing a metallic material's fatigue degradation behaviour. The information obtained is intended to be used for monitoring existing engineering structures, for which the degree of fatigue degradation due to a missing crack observation is unknown but where through monitoring an improved Residual Useful Life

(RUL) assessment of the metallic engineering structures is in need.

## 2 THERMOGRAPHY INSPECTION OPTIONS

Thermography is an electromagnetic NDT technique, along which a specimen is viewed with an infrared (IR) camera. The camera used here has been a thermoIMAGER TIM 450 from Micro-Epsilon, which is based on a bolometer-based pixelized image of 382 x 288 pixels with a sensitivity of  $\geq 40$  mK each. A view of such a set-up as well as a resulting image is seen in Figure 2. Temperatures are continuously recorded on the unnotched specimens in a fatigue test in the three zones indicated as  $T_1$  to  $T_3$ . From the data recorded a temperature difference  $\Delta T$  is then determined in accordance with the following equation:

$$\Delta T = T_3 - \frac{T_1 + T_2}{2} \quad (4)$$

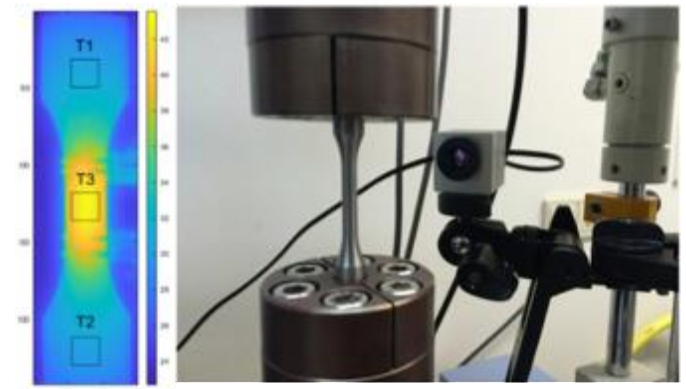


Figure 2 Thermographic monitoring on unnotched specimen under fatigue loading: View of the specimen through thermographic camera including measurement points (left), experimental set-up (right)

## 3 THERMOGRAPHY BASED FATIGUE DATA

Metallic materials' data for cyclic loading are traditionally determined under either stress or strain control and are represented in terms of stress-strain relationships and the number of loading cycles up to failure (S-N curves). This data may be used for fatigue life evaluation of engineering structures under cyclic service loading, where mainly linearized damage accumulation rules such as proposed by Palmgren [10] and Miner [11] are applied. Results obtained often show a certain randomness (scatter) and the reasons for this can be sought in non-linearities a material provides. A question therefore arises what additional material response information could be retrieved in case of data being recorded with an NDT technique. In the case shown here, unnotched specimens made of the unalloyed steel C45E (1.1191 or SAE 1045) have been fatigue loaded as CATs at different stress and strain amplitudes and a LIT and SIT respectively and this under stress as well as strain control and at partially different loading frequencies. The full test set-up is shown in Figure 3.

Three CATs were performed under stress control at amplitudes of 320, 340 and 360 MPa and resulting fatigue lives of 109 408, 14 957 and 16 294 cycles respectively were obtained. The reason why the fatigue life of the test run at  $\sigma_a =$

360 MPa is higher than the fatigue life for the test run at  $\sigma_a = 340$  MPa is due to scatter in the fatigue life and the proximity of the stress amplitudes. The  $\varepsilon_{a,t} - N$  curve shown in Figure 4 that the experimental results show a typical fatigue behaviour. In addition, a LIT was performed starting at a stress amplitude of 100 MPa and being increased by 20 MPa always after 9 000 cycles until it reached a stress amplitude of 380 MPa. All of those tests were operated at a loading frequency of 5 Hz. These experiments were part of a master thesis performed [12].

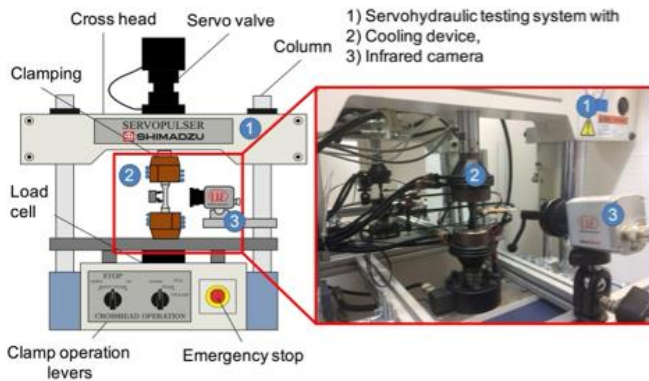


Figure 3 Test setup for recording thermographic data along fatigue experiments on unnotched specimens: 1) test frame, 2) clamped specimen, 3) IR camera

In addition, two CATs and a SIT were performed on the same material but now under a sinusoidal function in strain control mode and considering a constant average strain rate of 1.0 %/sec or a maximum strain rate of 1.57 %/sec respectively. The strain amplitudes for the CATs were  $\varepsilon_{a,t} = 1.0$  % and  $\varepsilon_{a,t} = 0.3$  % respectively while the SIT started at a strain amplitude of  $\varepsilon_{a,t} = 0.1$  % and was increased by 0.02 % after every step of 2 000 cycles until it fully failed at a strain amplitude of  $\varepsilon_{a,t} = 0.42$  %. The fatigue lives of the two CATs up to full fracture was 600 and 14 600 loading cycles respectively.

Based on this data STEP as described before was applied to determine the S-N data. Figure 4 shows the results in terms of the stress vs. plastic strain relationship as well as the strain-life curve. The exponent  $n'$  from Eq. 1 turned out to be -0.122 which allowed the exponents for the  $\varepsilon_{a,t} - N$  curve to be determined according to Eq.s 3. Coefficients  $\sigma_f'$  and  $\varepsilon_f'$  were determined from the results of the two strain-controlled CATs through averaging. The resulting  $\varepsilon_{a,t} - N$  curve very well matches the remaining experimental results used for validation.

A summary of the thermographic recordings is provided in Figure 5. It shows the relationship of the temperature difference  $\Delta T$  due to fatigue loading versus a normalized fatigue life. This normalization has been determined on the fatigue life of each of the experiments shown here. This can also be considered as the degree of degradation, specifically for the CATs, where the Palmgren-Miner rule applies per se. Why this has also been done for the LIT and the SIT is for reasons of comparison with some further explanation later. What can be seen at this stage is that the stress levels match fairly well between the stress-controlled CATs and the LIT. When looking at the strain-controlled tests the SIT generates higher temperature differences when compared with a CAT at the same strain level.

What is also to be observed from Figure 5 is, that the temperature difference  $\Delta T$  seems higher for the stress-controlled experiments than it is for the strain-controlled tests. However, it has to be kept in mind, that the loading frequency for the stress-controlled tests was always 5 Hz while the strain-controlled tests were done at a constant maximum strain rate of 1.57 %/sec and the loading frequency hence varied between 0.25 and 2.5 Hz only. Following these results, it might be worth to explore, which loading parameters do have an influence on the temperature difference  $\Delta T$ . The reason why the temperature drops after each loading step in the SIT is due to the fact that loading is briefly interrupted and the new loading step is started with a gradual increase of the load applied. This effect has not been further considered in the evaluation.

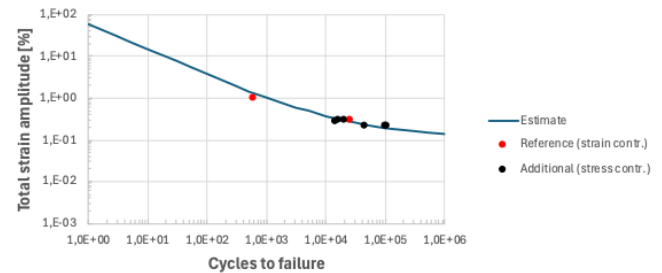
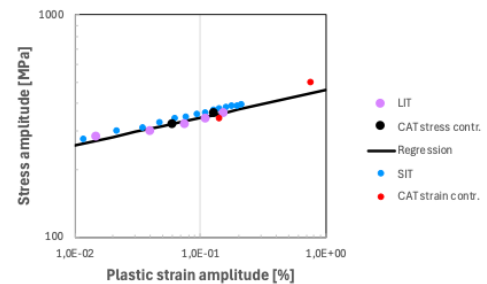


Figure 4 Results of fatigue tests performed presented as a stress vs. plastic strain relationship (top) and  $\varepsilon_{a,t} - N$  curve (bottom) both in a double logarithmic scale

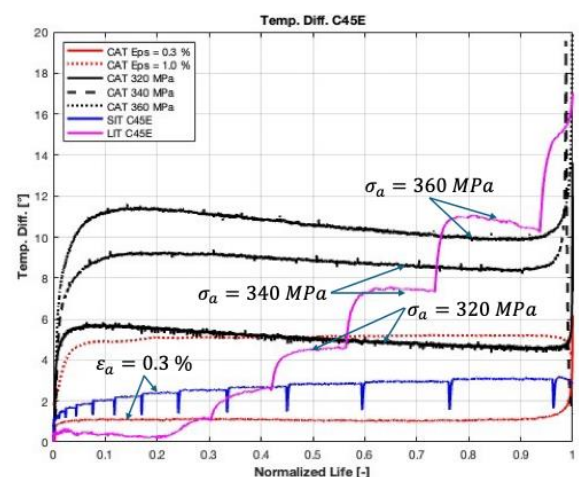


Figure 5 Development of temperature difference in three CATs and one LIT over normalized life of the CATs obtained under stress-controlled fatigue loading



All the experiments presented here were analysed with respect to stress amplitude and maximum strain rate vs.  $\Delta T$  and the result obtained is shown in Figure 6. It can be seen that as long as no plastic deformation occurs  $\Delta T$  remains marginal. Hence, any significant influence on  $\Delta T$  is governed by loading parameters in the plastic deformation region. The relationship between plastic strain and  $\Delta T$  can be linearized but this depends on the loading conditions (i.e. stress- or strain-controlled) and only when those are similar, a single function can be drawn, as to be seen from the fatigue test data shown in Figure 7.

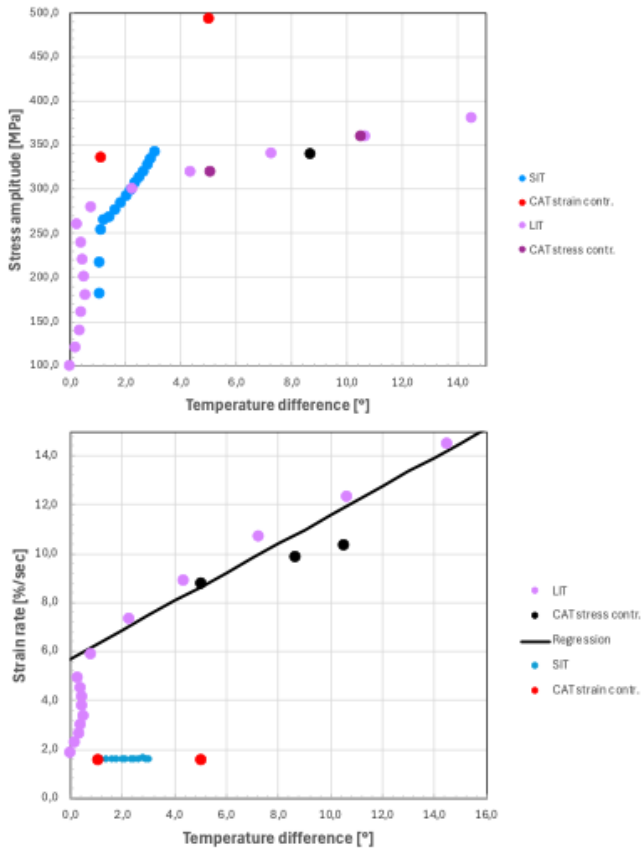


Figure 6 Stress vs.  $\Delta T$  (top) and strain rate vs.  $\Delta T$  (bottom) for all CATs, LIT and SIT performed

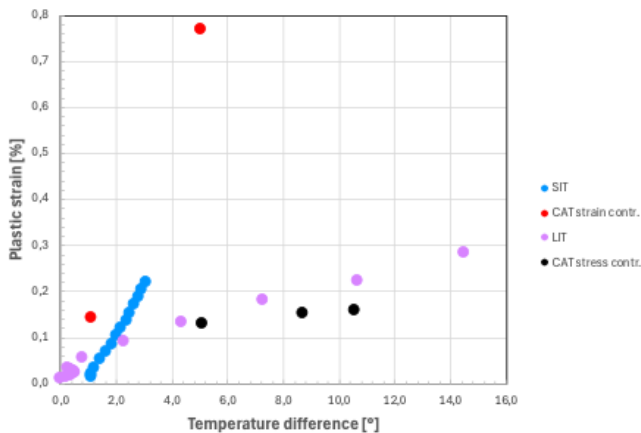


Figure 7 Plastic strain vs.  $\Delta T$  for all CATs, LIT and SIT performed

Energy is another parameter worth to be considered in that regard where the Smith-Watson-Topper (SWT) parameter [13] also known as the Neuber-parameter is widely used in the field of fatigue life evaluation of notched components and which is defined as:

$$P_{SWT} = \sqrt{\sigma \cdot \varepsilon_t \cdot E} \quad (5)$$

where  $\sigma$  represents the stress,  $\varepsilon_t$  the total strain and  $E$  Young's modulus respectively. If the fatigue results of this parameter are plotted versus  $\Delta T$  a result as shown in Figure 8 is obtained. The figure shows a lot of similarities to Figure 6 (top) and Figure 7 which is not much of a surprise. However, also in the case of energy no consistency in the thermographic material response can be observed. What can already be concluded here is that stress-controlled loading conditions can be better monitored with thermography than strain-controlled conditions can.

A question that might arise is, what would happen if a fatigue test could be performed where the energy applied could be permanently kept constant (controlled). First of all, this is a fairly complex fatigue test, which can be performed and has been specified as Neuber-controlled but which requires stress and strain to be controlled at the same time [14]. This could lead to some consistency between loading and the material's thermographic response and hence way of further validation. However, when looking plastic deformation in the roots of notched components, those plastic zones are mainly strain-controlled due to the elastic field around this plastic zone. Furthermore, energy conditions change along the life cycle of a material due to hardening and softening conditions resulting from the loading history.

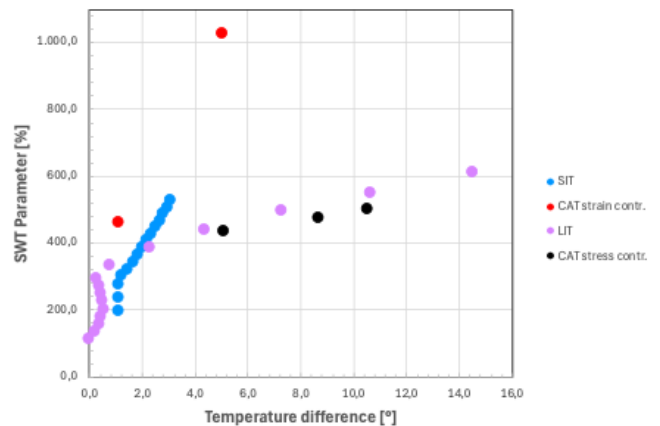


Figure 8 Energy expressed in terms of the Smith-Watson-Topper parameter vs.  $\Delta T$  for all CATs, LIT and SIT performed

As a consequence of all having been presented so far, the plastic strain rate as well as the stress range above the yield strength looks to be mainly influential on  $\Delta T$ . As such a thermography-related loading parameter  $P_T$  is defined as to the following:

$$P_T = \varepsilon_{a,p} \cdot \omega \cdot (\sigma_a - \sigma_y) \quad (6)$$

where  $\varepsilon_{a,p}$  is the plastic strain amplitude,  $\omega$  the circular frequency of the loading,  $\sigma_a$  the stress amplitude and  $\sigma_y$  the yield stress respectively, the latter determined as 255 MPa from the upper diagram in Figure 6. Plotting all the experimental results as  $P$  vs.  $\Delta T$  leads to the diagram shown as Figure 9, which allows a concise relationship to be determined in linear or close to linear format.

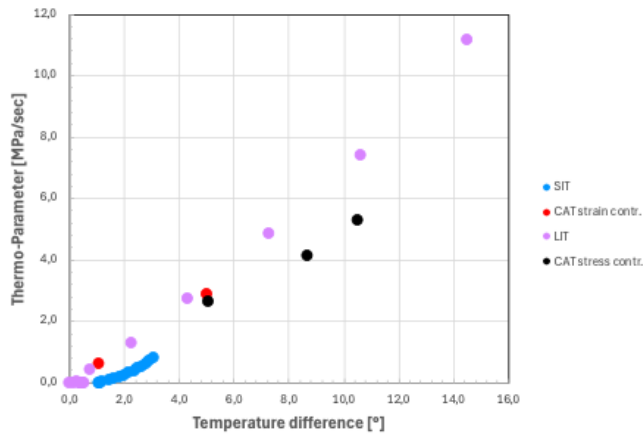


Figure 9 Loading parameter  $P_T$  vs. temperature difference  $\Delta T$  for all CATs, LIT and SIT performed

Since the temperature difference  $\Delta T$  recorded is a material response, its possible non-linear behaviour raises certainly the question what of a material's non-linear behaviour it represents and if the consideration of such non-linearity might better cover a metallic material's non-linear fatigue degradation than this has been possible to be covered in the past. To get this shown a 3D plot has been generated representing temperature difference  $\Delta T$  recorded (z-axis) versus the enforcement applied represented by the parameter  $P_T$  (y-axis) and the fatigue life for the CATs in a normalized form (x-axis). What the latter axis therefore represents is nothing else than the degree of degradation.

Such a result is shown in Figure 10 for the five CATs (stress and strain controlled) as well as the LIT and the SIT. In the case of the CATs the temperature increases immediately at the beginning since in all cases yield is passed and plastic deformation has occurred. Once plastified, the temperature increase looks fairly constant over the lifetime of the specimens until final fracture occurs. The strain-controlled tests show less of a temperature increase when compared to the stress-controlled tests. Principally they align well with the parameter  $P_T$  defined in Eq. 6. Furthermore, these test results can serve as a basis to generate a plane as shown in Figure 11 characterizing the material's fatigue as well as monitoring behaviour, which is discussed later.

When looking at the results from the LIT and the SIT a fairly different behaviour is observed. While the SIT due to its constant strain rate shows a relatively continuous behaviour with slight temperature increases observed due to the slight increases in strain amplitudes and loading in terms of the parameter  $P_T$ , the LIT and the way it has been performed shows a fundamentally different behaviour with significant changes in temperature due to the significant changes from loading step to loading step. However, the results of both tests fairly well align

in the plane described by the CAT results keeping potential scatter in materials' data in mind. It might therefore be worth considering such planes as a material's characteristic along which the results of any loading sequence might move. Further proof of those assumptions with more complex loading sequences might be advisable for the future.

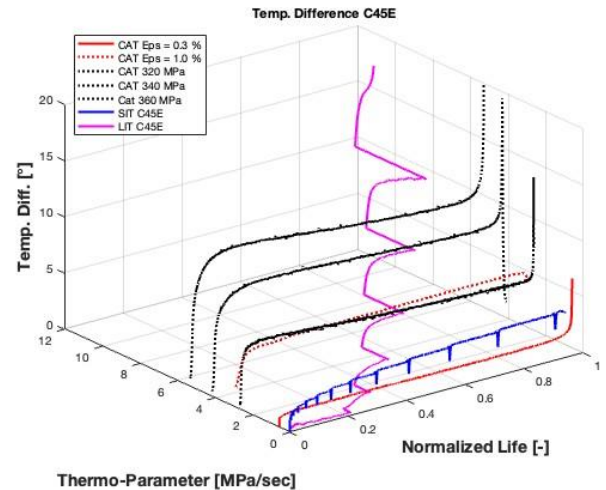


Figure 10 Development of temperature difference  $\Delta T$  in dependence of power rate applied and normalized fatigue life of CATs and comparison with the same relationship obtained from LIT and SIT

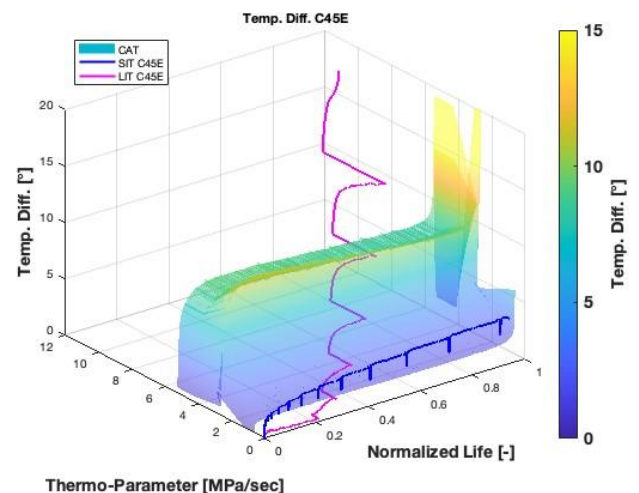


Figure 11 Topography of temperature difference  $\Delta T$  vs. power rate  $P$  and normalized life relationship for CATs and compared with similar results obtained from LIT and SIT

Since the stress, strain and loading frequency are the controlled and hence known input values related to the material's loading and  $\Delta T$  the material response monitored, the remaining unknown value is just the normalized life or in other words, the degree of degradation when talking in terms of the Palmgren-Miner rule, at least related to CATs. To get this degree of degradation obtained it has been assumed that the Palmgren-Miner rule applies for CATs and that as such the amount of degradation can therefore be calculated for each of the loading blocks or even loading cycles of the LIT and the

SIT. This leads to a description of the degradation development being very much different, as can be seen from Figure 12. The degradation process for the SIT and specifically for the LIT looks very much slower and the estimated fatigue life looks to be expired before plastic deformation even starts off in the case of the LIT. This contradicting result might be another proof of the lack of precision when applying Palmgren-Miner's rule. A conclusion is therefore, that monitoring the temperature emitted from a loaded structure might be the better information to determine a structure's degree of degradation than performing a Palmgren-Miner evaluation in traditional terms.

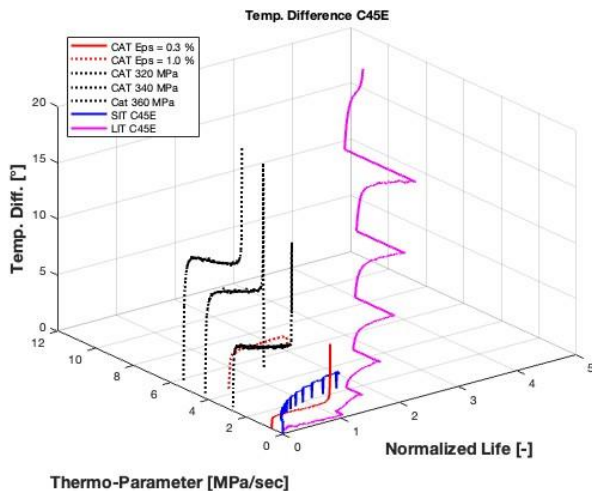


Figure 12 Development of temperature difference  $\Delta T$  over the CATs' normalized fatigue life and determining the respective fatigue life of the LIT and SIT through application of the Palmgren-Miner rule

#### 4 TEMPERATURE DIFFERENCE FOR MONITORING

SHM is based on using a material's response information to assess a structure's degree of degradation. Hence, the material's information provided through a diagram as shown in Figure 11 might therefore be a valuable tool to assess the structure as well as the monitoring principle being considered. A temperature difference resulting from a load applied on a structure and monitored through SHM could be principally used to be referenced to a diagram as shown in Figure 11. Assuming the respective value monitored on the structure could be determined as a single value on such a reference diagram, the degree of the structure's degradation could be easily determined. However, if such a value turns up more than once on the plane of the reference diagram, a conflict arises, which needs to be solved through more information to be retrieved. A help might be to mark the respective value positions on the diagram, which might even be described as isobars. Based on those isobars the appropriate solution needs to be found, which might be possible either through a variation (differentiation) in the direction of the power rate  $P_T$  and/or the normalized fatigue life.

As for the specific case of using thermography as the monitoring principle and the material as shown here, the situation in getting useful information from such a differentiation becomes tricky. The plane described in Figure

11 is mainly flat in the direction of the normalized life of the CATs. It looks like the material characterized becomes immediately plastified and this condition stays until fracture occurs towards the end of the tests. Thermography as a monitoring technique therefore clearly demonstrates, that it can identify plastic deformation but obviously not its contribution to fatigue degradation in the end. Also, the plane's inclination in the direction of the power rate  $P_T$  is fairly constant. Hence, the variation of loading parameters along the monitoring process might not provide the information to sufficiently identify the degree of material degradation.

However, the principle of a 3D plot as shown here in Figures 10 and 11 might be a useful instrument to collect and visualize data monitored as a combination of load, loading frequency and temperature on either a real structure or an unnotched specimen - of course of the same type of material. A summarized dataset shows in such a 3D plot if the data do represent a plane and which uncertainties might exist, to get this plane described or in other words how scattered the data recorded might be. Based on such scattered data allowance criteria might then be defined. Maybe that a longer-term monitoring on a structure to be assessed generating a larger database and combined with some advanced statistical evaluation might help to identify an appropriate location on the plane of the 3D plot and hence determine the degree of the structure's degradation. However, this requires further evaluation, which has not been performed so far.

In the context of the thermographic data presented here another aspect might be worth to be discussed. Thermography looks to be a method to allow plastic deformation in metals to be monitored well. This could make it interesting to identify plastic deformation in stress concentrated areas such as in notches. However, one needs to keep in mind, that fatigue loaded plastic zones in stress concentrated areas of notches are loaded in a strain-controlled mode. The reason for this is due to the elastic deformation occurring around the plastic zone. Hence, if those plastic zones might be monitored with thermography one should not be astonished if the signal might be weak, as concluded from results shown in Figures 5 and 6.

#### 5 CONCLUSIONS

The results presented here are far from claiming to be holistic. They are rather an additional extraction of data having been recorded along tests to establish S-N curves in accordance with the STEP approach. However, what proves to be interesting is to find out if an NDT method considered might be useful in terms of SHM and this in view of monitoring a material's and even a structure's degree of degradation with respect to fatigue. Compared to state-of-the-art approaches where monitoring is just possible in terms of detecting loads, strains and cracks, monitoring based on thermography at least allows plastic deformation to be identified additionally, a precursor to fatigue cracking.

While it has been shown here that loading, plastic deformation and of course also cracking can be measured through a temperature difference  $\Delta T$ , further parameters inherent in thermography signals might be worth to be explored. This may be achieved through higher sampling rates of the thermographic data and might allow the signal recorded to be better evaluated in terms of time domain information



including phase. Further extensions could be made in view of active thermography.

Generalizing the approach made here to virtually any monitoring and hence NDT technology to be considered for SHM could be a means to assess the NDT technology's potential with respect to SHM. A further step could be to differentiate the 3D plane obtained and shown in Figure 11 either in terms of the power parameter  $P_T$  or the normalized fatigue life. This would lead to a new 3D plot that would either characterize the material's sensitivity with respect to the loading or the fatigue life. In case of the fatigue life such differentiation might be a more sensitive parameter in identifying the degree of degradation and this also with respect to monitoring. However, this requires the 3D plane not to be as flat as in the case shown here, since a differentiation of this plane leading to a 3D gradient plot otherwise just scatters around zero. Such flatness of the 3D plane and scattering around zero in the 3D gradient plot might therefore also be an indication that the monitoring technique is possibly not suitable for monitoring a material's fatigue degradation in the pre-cracked stage.

The topography of the 3D plot shown in Figure 11 is also an indication of the non-linearity the monitoring parameter exhibits and this with respect to a potential non-linearity in the material. Hence, if the 3D plot is relatively 'flat' and constant in its height, this could mean that linearization of fatigue degradation for the respective material and hence the traditional Palmgren-Miner rule would be better applicable when compared to materials where such a topography of the 3D plane might be more uneven. However, in the case here it at least shows for the LIT and the SIT that irrespective of the smooth surface the predictions are not very consistent and the material response recorded might not work very well in combination with the Palmgren-Miner rule (c.f. Figure 12). Further corrections might therefore have to be done to get this improved. Or formulated inversely as a question: Would a 'wavy' or possibly more 'spiky' 3D plane characterize a monitoring technology as a more relevant technology for monitoring fatigue degradation? Furthermore, could a 'spiky' 3D plane possibly be used to enhance a component's fatigue life under service loading evaluation since it better covers the material's non-linearities in fatigue degradation than the Palmgren-Miner rule is able to do? Answers to these questions might be obtained through a further random load fatigue assessment.

Should any if not all of those questions be answered positively, then the diagrams as shown in Figures 10 and 11 might become future displays of materials' data for cyclic loading, representing a clear extension when compared to the traditional stress-strain and S-N curves provided in handbooks such as [4,5] in the past. Interesting additional questions in that regard are also if the 'life path' of a randomly loaded material follows the topography spanned by the CAT results. In case of a match every data recorded could be virtually added to the database, allowing the material's information to continuously grow.

What has been shown here with the SIT results is, that the temperature difference  $\Delta T$  mainly stays or marginally increases on an isobar during each loading step when the strain is increased from one strain level to another. However, what

happens with this path when the strain levels are decreased is still an open question to be answered.

The large amount of data being recorded might also become an interesting source for statistical evaluations. Monitoring an engineering structure under service loading with a thermographic camera combined with other loading parameters might provide an interesting data sample for a further statistical evaluation of which the statistical patterns might be correlated with patterns to be found in the material's general reference database.

The approach presented here intends to show how far thermography might be applicable in the context of SHM. At present the monitoring principle has been proven for a laboratory environment only. The major sensing device is the IR camera which has to stay as an external device. An interesting next step to explore would be to perform the same type of fatigue experiment but with larger, more complex, notched components and to see how well the fatigue behaviour in the notches could be monitored. A constraint might be the strain-controlled mode and the resolution of the IR camera system as well as the component's shape for which corrections might have to be made regarding the signals to be processed. Another aspect to be explored is the influence of the component's surface preparation. It is very likely that a quantitative validation of a component as is might not lead to satisfying results and that coatings might have to be removed and/or treated such that comparable conditions are achieved. This is an important step that has to be proven before considering any in field monitoring in terms of general applications. Potential first applications could be seen for fatigue loaded components being visually easily accessible and highly loaded, preferably considering a load spectrum to be 'sharp', hence, with a large number of high loads. Again, a potential application could be in the field of testing of fatigue loaded components and assessment of their degradation processes in a laboratory environment. Another field would be rotating machinery where the rotating rod is just fixed with bearings, but all other parts are visually easily accessible. However, a new challenge might arise between the rotating frequency of the machinery versus the frame rate of the IR camera.

A solution to all those challenges could be temperature sensors, that could be directly adapted onto the structure to be monitored but this is far from being realized at present. However, the approach presented here is not limited thermographic monitoring only. Eddy current or other electromagnetic sensors being commercially available are sensors that can already be attached in situ and where the 3D plot can be generated as the source of reference. In that case, civil infrastructure could be an interesting application field.

All what has been described here is related to passive thermography only. What active thermography would provide is an additional chapter being beyond the scope of this article.

A further challenge comes if those monitoring approaches might be applied in the field where a thermographic camera records a structure in service under general environmental conditions. In that case all environmental influences will have to be compensated such that only the true difference due to degradation becomes apparent in the thermographic analysis.

As such passive thermography in SHM of mechanically loaded structures is still limited to fundamental explorations that may provide the appropriate parameters to be considered for a more generalized application in structural life cycle management.

## REFERENCES

- [1] E. Haibach: Betriebsfestigkeit, Springer Berlin & Heidelberg, (2006) doi.org/10.1007/3-540-29364-7 (in German)
- [2] D. Radaj, M. Vormwald: Advanced Methods of Fatigue Assessment; Springer Berlin & Heidelberg (2013) doi.org/10.1007/978-3-642-30740-9
- [3] J. Schijve: Fatigue of Structures and Materials; Springer (2009)
- [4] C. Boller and T. Seeger: Materials Data for Cyclic Loading, Vol.s A to E. Elsevier Science Publ. (1987)
- [5] A. Bäuml jr. and T. Seeger: Materials Data for Cyclic Loading (Supplement); Elsevier Science Publ. (1990)
- [6] P. Starke, F. Walter and D. Eifler: PhyBaL – A new method for lifetime prediction based on strain, temperature and electrical measurements; Int. J. of Fatigue 28 (9), (2006), 1028-1036
- [7] P. Starke: Lebensdauerberechnung bei ein- und mehrstufig beanspruchten Proben aus vergütetem 42CrMo4; Dr.-Ing. thesis, TU Kaiserslautern (2007) (in German)
- [8] P. Starke, H. Wu, C. Boller: Advanced evaluation of fatigue phenomena using non-destructive testing methods, Materials Science Forum 879 (2016) 1841-1846
- [9] J.D. Morrow: Cyclic Plastic Strain Energy and Fatigue of Metals; ASTM STP 378, (1965) 45-87
- [10] A. Palmgren: Die Lebensdauer von Kugellagern, Z. VDI 68 (14), (1924), 339-341 (in German)
- [11] M.A. Miner: Cumulative damage in fatigue, J. of Appl. Mech. 12, (1945), A159-A164
- [12] B.D. Yesa: Analysis of the reproducibility of thermographic data under different external condition; Master thesis at Dresden Internat. Univ. (DIU) and LZfPQ Saarland Univ. (2022)
- [13] K.N. Smith, P. Watson, T.H. Topper: A Stress-Strain Function for the Fatigue of Metals, J. of Materials, IMLSA, Vol. 5, No. 4, (1970) 767-778
- [14] P. Heuler: Crack Initiation Life Prediction for Variable Amplitude Loading Based on Local Strain Approach; Doctoral thesis at Technische Hochschule Darmstadt (1983) (in German)

## Towards structural health monitoring of clay-printed structures

Jasper Vollmert <sup>0009-0001-6245-912X</sup>, Patricia Peralta <sup>0000-0002-1923-7142</sup>, Adel Alatassi <sup>0009-0006-2862-5530</sup>, Alexander Chmelnizkij, and Kay Smarsly <sup>0000-0001-7228-3503</sup>

Institute of Digital and Autonomous Construction, School of Civil and Environmental Engineering, Hamburg University of Technology, Blohmstraße 15, 21079 Hamburg, Germany

Email: jasper.vollmert@tuhh.de, patricia.peralta.abadia@tuhh.de, adel.alatassi@tuhh.de, alexander.chmelnizkij@tuhh.de, kay.smarsly@tuhh.de

**ABSTRACT:** Structural health monitoring (SHM) is a well-established practice to ensure safety and reliability of civil structures. With the increasing demand for environmentally responsible construction practices and the need to reduce the carbon footprint of construction projects, sustainable materials, such as clay, are gaining attention. Clay-printed structures introduce a novel domain to SHM that requires adaptations of established SHM strategies. Research on SHM strategies devised for clay-printed structures remains scarce, leaving a critical gap in understanding the long-term performance of clay-printed structures. Serving as a foundation for developing SHM strategies for clay-printed structures, this paper proposes a methodology to experimentally determine the structural behavior of clay-printed structures, including buckling, shrinkage, and load-bearing capacity, while identifying key factors critical for developing SHM strategies. The methodology proposed in this study incorporates condition assessment, constraint definition, design optimization, prototyping, and SHM strategy definition. The methodology is implemented for a wall component to experimentally determine shrinkage. Based on the structural behavior of the wall component, an SHM strategy is proposed that essentially consists of selecting appropriate SHM techniques, defining sensor placement, and establishing decision-making criteria. The results demonstrate the feasibility of constructing structurally stable clay-printed structures and provide key insights into SHM strategies for clay-printed structures, advancing sustainable construction practices.

**KEY WORDS:** Additive manufacturing; clay printing, structural health monitoring, sustainable construction.

### 1 INTRODUCTION

Digital fabrication techniques, particularly 3D printing (3DP), have witnessed increasing adoption across various industries in recent years [1]. The construction sector has been adopting 3DP technologies over the past two decades, scaling up 3DP processes to meet the demands of large-scale building projects and enabling environmentally responsible construction practices. The trend towards using 3DP in construction has encouraged research on automating construction processes, owing to well-developed digital-based construction methods as well as research on 3DP materials, such as concrete and clay [2].

Data on the long-term performance of 3D-printed structures and on the internal state of 3D-printed materials is essential for understanding relationships between 3DP processes, materials and geometries [3]. By monitoring structural aspects, such as buckling, shrinkage, and load-bearing capacity, the long-term performance of 3D-printed structures may be determined and assessed. Consequently, structural health monitoring (SHM) may facilitate data recording and analysis to monitor the long-term performance of 3DP structures. However, SHM methodologies tailored to 3D-printed structures, particularly clay-printed structures, barely exist [4].

Generally, embedded sensors may enhance monitoring of structural and material behavior of clay-printed structures. In 3DP applications, embedded sensors have been largely deployed for concrete printing and in a lesser extent for clay printing [5]. Since sensing in concrete printing is more mature compared to sensing in clay printing [6], synergies between concrete and clay printing may be exploited to monitor structural parameters (e.g., strain and deformation) and

material parameters (e.g., temperature and moisture content) of clay-printed structures. For example, lead zirconate titanate piezoelectric sensors, utilizing electro-mechanical impedance techniques, provide real-time insights into the stability of stacked layers and help assess potential structural weaknesses during printing [7]. Strain gauges and linear variable displacement transducers are used to evaluate buckling characteristics in complex 3D-printed walls under compressive loading [8]. Similarly, fiber Bragg grating sensors embedded in clay capture internal strain changes and allow measuring critical parameters, such as temperature and pressure variations [9]. However, current sensing techniques lack a systematic approach, hindering the development of SHM methodologies for clay-printed structures.

Latest studies in clay printing have primarily relied on visual inspection of in-situ tests, with limited emphasis on systematic evaluation techniques [10]. Moreover, sensor placement in clay-printed structures has been determined by trial-and-error testing rather than structured investigation. Hence, research on SHM methodologies specifically tailored to clay-printed structures remains limited. Thus, by deploying a generalized experimental testing methodology, SHM strategies may be defined to assess the behavior and improve the understanding of long-term performance of clay-printed structures. For example, shrinkage, which may cause structural instabilities [11], could be assessed by monitoring temperature and moisture content during the drying process to minimize desiccation cracks.

In this paper, a methodology for defining an SHM strategy for clay-printed structures is proposed. The methodology considers structural and material behavior, comprising



condition assessment, constraint definition, design optimization, prototyping, and, finally, SHM strategy definition.

The reminder of this paper is structured as follows. First, an overview of the proposed methodology is presented. The methodology is implemented by experimental testing to derive an SHM strategy. Next, the effectiveness of the SHM strategy is validated by embedding sensors to monitor moisture content. Finally, the paper concludes with a summary and a concluding synthesis of the key findings.

## 2 METHODOLOGY

The methodology is devised to propose a scientifically sound SHM strategy and it consists of five phases, condition assessment, constraint definition, design optimization, prototyping, and SHM strategy definition (Figure 1). In the first phase (*condition assessment*), initial conditions are determined to identify climate conditions, material characteristics, available equipment, and software applications. Climate conditions, such as temperature and humidity of the environment, provide insights for designing clay mixtures and for assessing drying processes. Clay mixtures are designed by mixing clay, aggregates, binders, and water, to achieve a material that is extrudable by the equipment (i.e., clay printer). The material characteristics of the clay mixtures are determined by material testing to assess extrudability, buildability, small-scale shrinkage, and cracking behavior based on established testing methods. For each material test, four specimens are tested. Specifically, in this study, shrinkage and cracking are assessed by non-standardized testing, where customized cylindrical specimens are printed and evaluated.

In the second phase (*constraint definition*), constraints are defined by identifying and categorizing limitations based on the initial conditions, including structural, fabrication, and sensing constraints. The structural constraints are based on the flowability, strength, buildability, and shrinkage performance of the material. The fabrication constraints (e.g., layer height, built height, overhang angle, and bridging length) are determined through process parameter tests [12-15]. For each process parameter test, two specimens are tested. The sensing constraints include sensor size and sensor type restrictions, which affect design decisions in the next phase.

In the third phase (*design optimization*), design variables are identified and optimized based on the structural constraints, the fabrication constraints, and the sensing constraints. Through parametric design, infill patterns and connections are optimized

for material reduction and structural integrity based on the structural constraints. The print path is then refined based on print speed and fabrication constraints, taking into account the process parameters previously defined to ensure the manufacturability of the optimized structure while considering the sensing constraints. The design process utilizes software applications for parametric design options, enabling efficient parameter adjustments without redesigning the workflow. In this study, the software application *Rhino 8* [16] is used for the parametric design, primarily motivated by the integrated visual programming tool *Grasshopper 3D*.

In the fourth phase (*prototyping*), physical prototypes are developed and evaluated to refine the design and to ensure structural integrity and manufacturability. The prototypes are fabricated to define the SHM strategy with emphasis on sensor positioning, with one prototype produced per clay mixture. The prototypes facilitate assessing changes in observable parameters (e.g., moisture content and drying direction), the respective structural behavior (e.g., shrinkage and desiccation cracking), and the related material testing (e.g., small-scale shrinkage tests).

In the fifth phase (*SHM strategy definition*), the SHM strategy is defined, based on the experimentally assessed structural behavior (e.g., shrinkage and desiccation cracking). The SHM strategy considers interactions observed between structural behavior and parametric design, when defining sensor type and sensor positions. For example, monitoring shrinkage includes selecting sensor types to observe temperature and moisture content and providing criteria for systematically determining sensor positions. The criteria determine sensor positions based on potential failure scenarios, ensuring comprehensive coverage of critical structural vulnerabilities, particularly those caused by desiccation cracks. Finally, a feedback loop facilitates adjusting the parametric design to fit the defined SHM strategy, where sensors are embedded into clay-printed prototypes to validate the SHM strategy. In the following section, the implementation of the methodology is presented.

## 3 EXPERIMENTAL TESTING

The methodology is implemented by experimental testing to derive the SHM strategy. The following subsections are structured in compliance with the aforementioned phases of the methodology, shown in Figure 1.

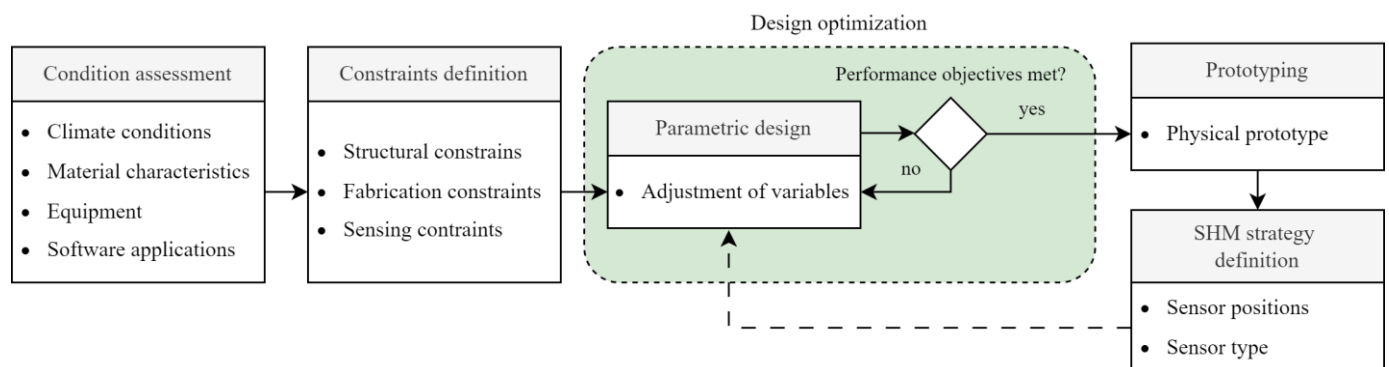


Figure 1. General workflow for determination of SHM strategies in clay printing.

### 3.1 Condition assessment and constraints definition

The tests are conducted in a laboratory container of the Institute of Digital and Autonomous Construction. The container is maintained at a constant temperature of 23 °C. The robotic system is a 3D Potterbot Scara v4, equipped with a linear ram extruder and 3.5 l extrusion tubes that can print plastic clays. As shown in Figure 2, material tests are performed on a designated testing area, while process parameter tests are conducted on a separate levelling board. The levelling board ensures a flat printing surface and enhances adhesion due to its rough texture.

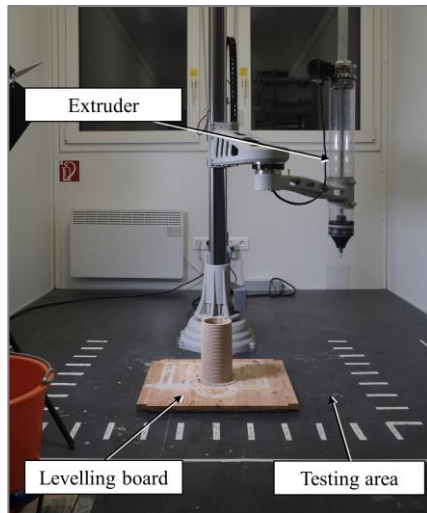


Figure 2. Experimental setup of the clay printer and print area in the laboratory container.

Clay mixtures are designed using two clay types, “clay A” representing a raw clay and “clay B” representing a milled clay. Quartz sand is added to the mixtures to increase stability and reduce shrinkage, and a starch binder is added to improve mechanical behavior. The residual moisture in the sand is below 0.3 %, with a grain size ranging from 0.062 mm to 0.3 mm. The binder, Optapix S 51, consists of modified starch with a bulk density of 0.5 kg/m<sup>3</sup>. The physical properties and the chemical composition of clay and sand are listed in Table 1.

Table 1. Physical properties and chemical composition for clay types and sand (percentages in M-%).

	Clay A	Clay B	Quartz sand
Density [g/cm <sup>3</sup> ]	2.65	2.65	1.3 ± 0.3
Drying shrinkage [%]	4.0	6.0	-
SiO <sub>2</sub> [%]	75.0	71.0	92.1
Al <sub>2</sub> O <sub>3</sub> [%]	19.8	24.0	2.7
TiO <sub>2</sub> [%]	1.4	2.0	0.0
Fe <sub>2</sub> O <sub>3</sub> [%]	0.9	1.0	0.1
CaO [%]	0.2	0.0	0.9
MgO [%]	0.3	0.0	0.2
K <sub>2</sub> O [%]	2.2	3.0	1.5
Na <sub>2</sub> O [%]	0.1	0.0	0.2

A detailed testing workflow is created (Figure 3), comprising material composition, material parameters, and process parameters. First, material composition tests are conducted for each mixture, to determine and evaluate viable ratios of clay, sand, binder, and water. The material composition tests consist of a simple extrusion test, where the consistency and extrudability of the clay mixtures are evaluated. Results achieved from the material composition tests, 19 viable clay mixtures are obtained.

Second, the material parameters of the viable clay mixtures are evaluated, including flowability, wet strength, buildability, and shrinkage. The tests to determine the flowability, strength, and buildability consist of a cylinder drop test according to [12] and a shape retention test according to [13]. For the (non-standardized) shrinkage test, customized cylindrical specimens are printed and observed for horizontal shrinkage, vertical shrinkage, and cracking behavior. The cylindrical specimens have a diameter of 150 mm and a height of 200 mm. As a result of the material parameter evaluation, 6 viable mixtures are selected from the previous 19 mixtures previously achieved.

Third, the process parameters are determined for each mixture via extrusion line tests, failure tests, double cone tests, and bridging tests, in compliance with [14] and [15]. The process parameters are utilized to determine the fabrication constraints for designing wall components. A clay content of

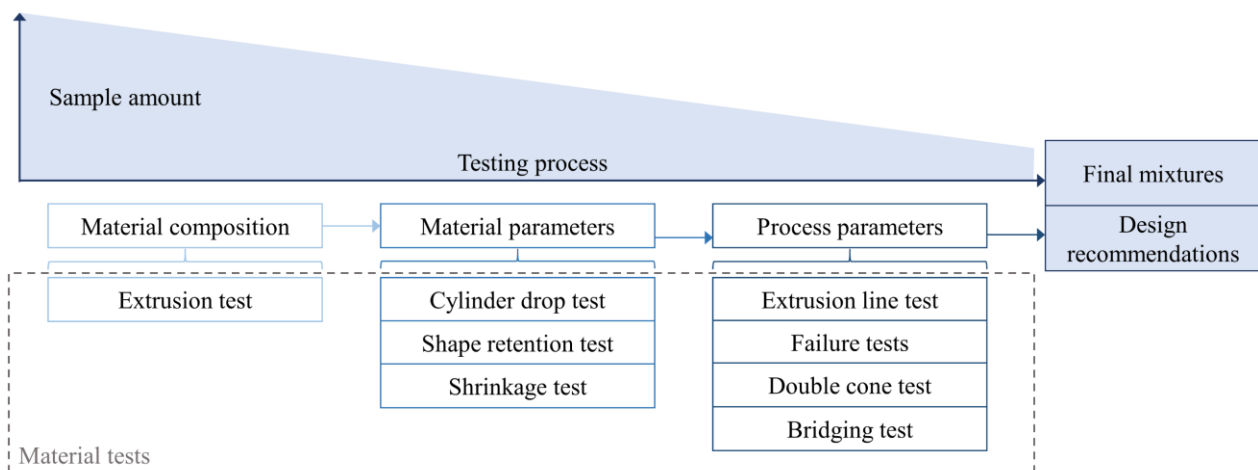


Figure 3. Material testing workflow.

Table 2. Material testing clay mixture proportions.

Name	Clay [M-%]	Sand [M-%]	Water [M-%]	Binder [M-%]
A_25.0C_36.0W_1.0B	32.9	29.0	15.1	0.8
B_25.0C_38.0W_1.0B	32.6	28.6	15.6	0.8

Table 3. Process parameters defined for design considerations.

Parameter	A_25.0C_36.0W_1.0B	B_25.0C_38.0W_1.0B
Layer height for 11 mm layer width	4.5 mm	4.0 mm
Maximum build height	243 mm	356 mm
Maximum inward angle	30.0°	27.5°
Maximum outward angle	27.5°	27.5°
Bridging length, adjacent layer spacing > 0 mm	40 mm	20 mm
Bridging length, adjacent layer spacing < 0 mm	80 mm	80 mm

25 % of the dry volume is observed to offer an optimal balance between shrinkage and stability, resulting in a suitable choice for prototyping applications. Therefore, two clay mixtures A\_25.0C\_36.0W\_1.0B and B\_25.0C\_38.0W\_1.0B are selected for prototyping; material composition is detailed in Table 2. The corresponding process parameters are listed in Table 3.

### 3.2 Design optimization

The design optimization includes design variable adjustments of infill patterns, segmentation, and connection design. The infill is optimized by reducing the total material volume and print speed. Through a curved geometry, the material is reduced while retaining stability. Intersection width of adjacent curves are increased to accommodate the sensor width. The process parameters defined in the fabrication constraints regarding overhang angle and build height influence segmentation and connection design. Additional factors, including layer height, determine the toolpath configuration. Furthermore, by defining toolpaths as continuous paths, print times are reduced as retraction points and non-printing moves are minimized.

### 3.3 Prototyping

Two prototype specimens of a wall component, prototype A (fabricated with the mixture using clay A) and prototype B (fabricated with the mixture using clay B), are devised respectively. Buckling, overhang angles, and surface quality are visually assessed immediately after fabrication. Following the fabrication, the prototypes are evaluated during and after the drying process on shrinkage and cracking.

The prototypes are observed to be printable with no failures or significant buckling of either the contour or the infill. Observations during the drying process reveal non-uniform drying patterns in the two prototype specimens. The drying process showcases a directional gradient, characterized by drying progressing from the top to bottom and from the exterior surfaces toward the interior infill.

Moisture content assessment, conducted after a six-day drying period, reveals variations between the prototype specimens. Figure 4 shows the moisture retention behaviors of the two prototype specimens. Prototype A demonstrates faster drying rate, with faster moisture dissipation across the specimen. Conversely, prototype B exhibits a slower drying

rate, as evidenced by a darker discoloration of the infill and contours, indicating retained moisture.

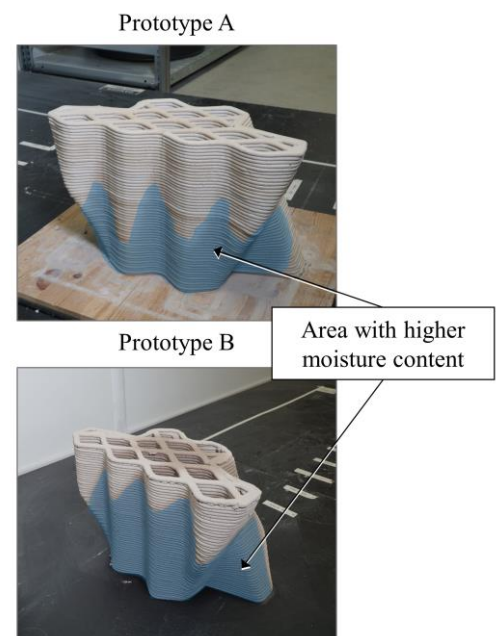


Figure 4. Prototype moisture content observed after a six-day drying period.

Desiccation cracks are documented during the drying process. On the one hand, prototype A develops multiple desiccation cracks (Figure 5). The first cracks appear after day four, primarily centered in the midline region advancing from bottom to top, with a final length of 226 mm and width of 2 mm. Further cracks appear in the midline and front region in days six and eight and increase in length during the following days, with a final length of 223 mm and 95 mm and a final width of 1 mm, respectively. The crack at the midline region may represent a protentional weak point due to the location, length, and width of the crack. On the other hand, prototype B exhibits significantly reduced desiccation cracks with only a single crack forming after eight days at the midline region observed to advance from bottom to top. The location of the crack is similar to the position observed in the first crack of prototype



A. However, the crack length and width are less severe, with a 140 mm in length and less than 1 mm in width.

Upon drying, shrinkage is evaluated by measuring the dimensions of the dry specimens and comparison with the initial dimensions. The measurements include the length on long side, length on short side, width, and height of each prototype specimen. Uneven shrinkage of the prototype is observed across the two specimens after two weeks of drying. For prototype A, a horizontal shrinkage of 5.34 % and a vertical shrinkage of 0.64 % is observed on average. Comparatively, for prototype B, a horizontal shrinkage is 6.76 % and a vertical shrinkage is 2.2 % is observed on average. The prototype A shows strong adhesion to the leveling board, resulting in reduced shrinkage at the base. In contrast, a free shrinkage at base of prototype B is noticeable due to low adhesion to the smooth bed plate. However, the prototype specimens are inaccurate for shrinkage material characterization due to the complexity of the geometry.

The difference in the shrinkage behavior of both prototypes may be attributed to the drying rate and to local errors, such as air bubbles in the extruded material, during printing. An increase in water content leads to increased shrinkage, as observed in the shrinkage evaluation, where prototype A showed less shrinkage than prototype B. Typically, increased shrinkage and faster drying processes are associated with increased desiccation cracking. However, errors during printing may cause additional cracking due to induced internal stresses, as observed by the strong adhesion to the leveling board showcased by prototype A. Special attention should be paid to the printing setup and drying rate to minimize desiccation cracking.

To define the SHM strategy, a second prototype iteration is conducted, where moisture sensors are embedded. Considering the shrinkage behavior exhibited by prototype B, the mixture using clay B is selected for the second prototype iteration (prototype B2). The prototype B2 serves to assess the effectiveness of the monitoring system and to refine the sensor

positioning that will be relevant to the SHM strategy to be proposed.

### 3.4 Sensor integration for SHM strategy definition

As a basis to define the SHM strategy, which will be proposed in the following section, sensor integration of varying sensor types and positions is investigated. A validation test is conducted to assess the performance of resistive and capacitive moisture sensors, as well as the effect of sensor positions. Resistive and capacitive moisture sensors are typically used to measure soil moisture content using different sensing principles. Therefore, by deploying both sensor types to monitor drying processes in clay printing, the sensitivity of the sensors for detecting changes in moisture content may be compared to assess performance. As shown in Figure 6, two sensor systems are used to monitor prototype B2,

- (i) sensor system I, a **commercial sensor system** consisting of a resistive moisture sensor typically used for discrete soil monitoring, and
- (ii) sensor system II, a **custom-made SHM system** consisting of a moisture sensor node (containing three capacitive moisture sensors) and an environmental sensor node for continuous monitoring of clay moisture content and the surrounding environment.

The resistive and capacitive moisture sensors are positioned at different embedment depths and distributed on the exterior and interior surfaces of prototype B2 to monitor the drying process following the observed drying gradient during the prototyping phase.

On the one hand, sensor system I is designed to measure soil moisture by outputting a value of resistance between the two probes. On the other hand, sensor system II is designed for recording real-time data of the prototype moisture content and the environmental conditions in the laboratory. The moisture sensor node of sensor system II comprises the three embedded capacitive moisture sensors v2.0 that are connected via cables to an Arduino ESP32 microcontroller to record moisture content by detecting changes in capacitance. The capacitive

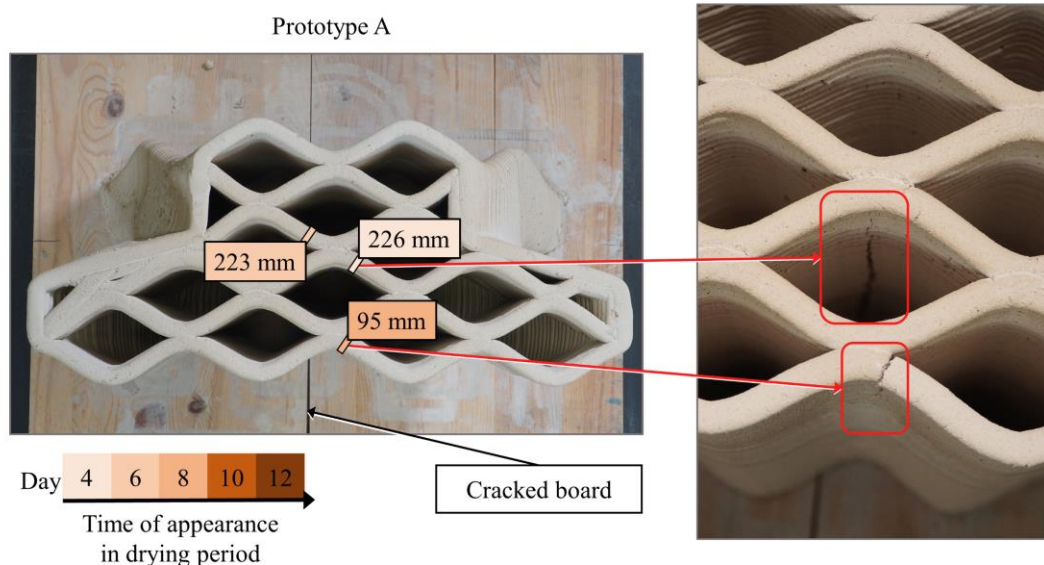


Figure 5. Desiccation cracks in prototype A.

sensors are embedded at a depth of two-thirds of the sensor length. The environmental sensor node consists of an Si7021 temperature and humidity sensor connected to a microcontroller for recording environmental conditions. The data recorded by both sensor nodes is transmitted via a cable connection to a base station (i.e. Raspberry Pi microcomputer) that serves as a datalogger for data management and storage. It should be noted that the capacitive moisture sensors are calibrated in both dry and fresh clay conditions using the pre-calibrated sensor system I as benchmark.

The positioning of the embedded moisture sensors of both sensor systems is determined by the respective geometric constraints. The resistive sensor of sensor system I consists of two probes, each 180 mm in length and spaced 30 mm apart. The capacitive soil moisture sensors of sensor system II measure 98 mm in length, 23 mm in width, and 4 mm in thickness. Considering a layer width of 11 mm, the sensors are embedded vertically at overlying points within the structure to minimize any impact on structural stability. Furthermore, to evaluate the effect of the sensor positions, three embedment depths are defined (Figure 7). The capacitive sensors of the moisture sensor node of sensor system II are positioned following the printing process, where Sensor 1 (printing time  $t = 60$  min) and Sensor 2 ( $t = 112$  min) are fully embedded during printing, while Sensor 3 ( $t = 147$  min) is partially embedded. The probes of the resistive sensor (Sensor 4) of sensor system I are also partially embedded at  $t = 147$  min. Due to the length of the probes of Sensor 4, Sensor 2, and Sensor 4 record moisture content at approximately the same height. A special consideration is given to the capacitive sensors, where a permeable membrane is wrapped around the sensing elements of the sensors that are in contact with clay to facilitate local moisture evaporation. Sensor cables are routed through the infill gaps, which serve as cable channels, and are connected to the microcontroller after the printing process.

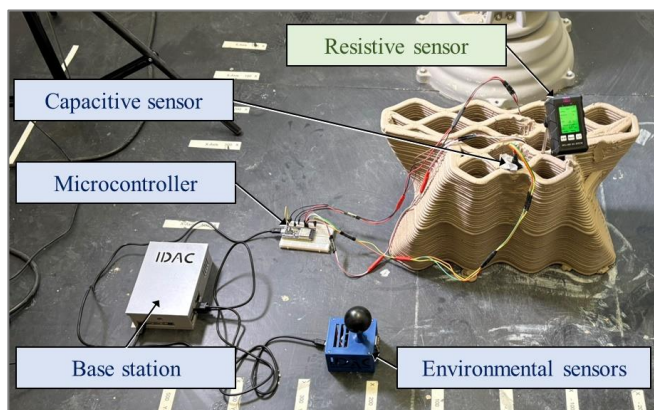


Figure 6. Components of sensor system I (blue) and sensor system II (green).

Prototype B2 is monitored over 10 days, and the moisture content is recorded continuously by sensor system II, while sensor system I is read manually three times daily. No structural instabilities or sensor-induced cracking are observed during this period.

The environmental data (Figure 8) shows humidity levels ranging from 15 % to 40 % and temperatures between 18.1 °C and 23.8 °C. The declining moisture content in the structure

(Figure 9) corresponds with these environmental changes. Capacitive sensors (Sensors 1-3) exhibit a stabilization phase of approximately 25 h, due to the membrane barrier. The fully embedded sensors (Sensor 1 and 2) reveal nearly identical trends, while partially embedded sensor 3 shows higher initial moisture levels during the first 160 h.

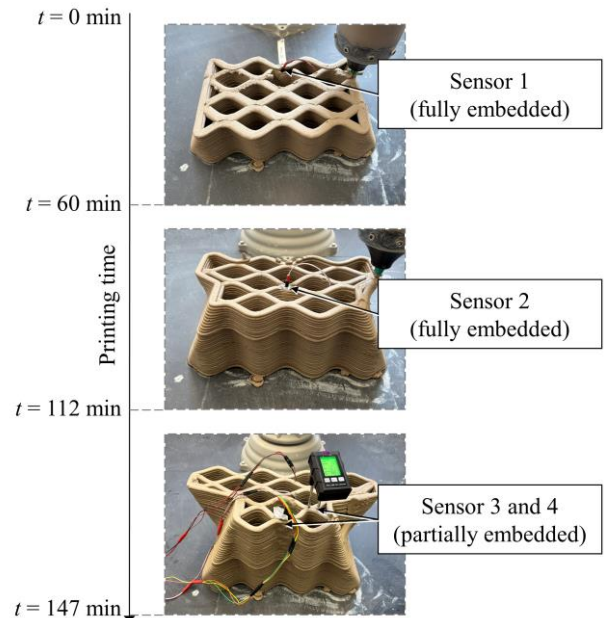


Figure 7. Embedded sensor integration during the printing process.

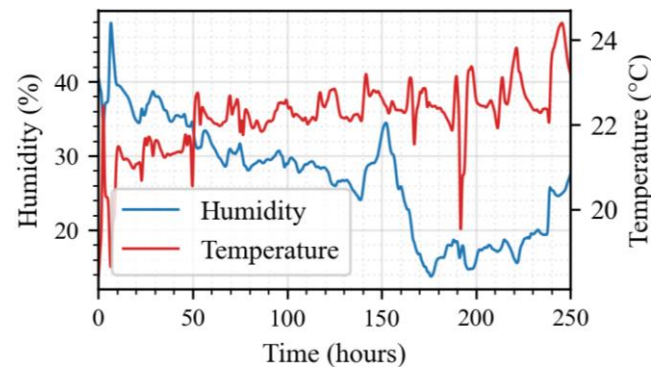


Figure 8. Environmental sensor readings.

Furthermore, as observed from Figure 9, the resistive sensor (Sensor 4) showcases higher values of moisture content compared to the capacitive sensors in the first 195 h of measurement, followed by a sharp drop of moisture content. Although a similar moisture content trend was expected between Sensor 2 and Sensor 4, the values observed for Sensor 4 indicate that the resistance-based sensing principle is not as sensitive to the change of moisture content compared to capacitive-based sensing principle. By observing the cumulative soil moisture loss over time (Figure 10), a total moisture loss ranging from 43 % to 48 % is observed. The measured cumulative moisture loss from Sensor 1 and Sensor 3 are comparable, while Sensor 2 deviates slightly in an acceptable range. In contrast, Sensor 4 deviates significantly, further indicating limited accuracy and responsiveness.



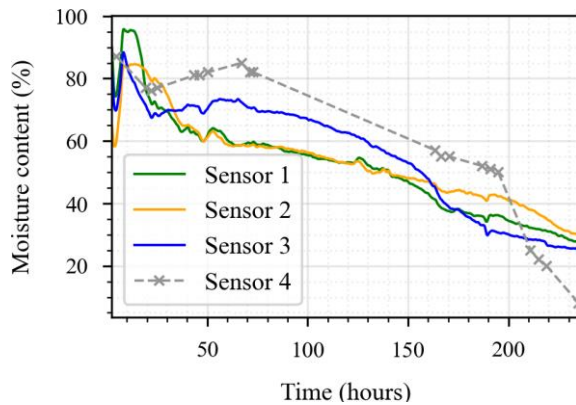


Figure 9. Moisture sensor readings (sensors are calibrated for dry mixture = 0%, wet mixture = 100%).

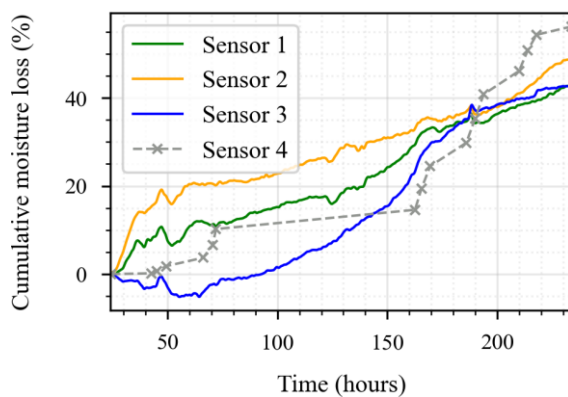


Figure 10. Cumulative moisture loss over time (starting at  $t = 25$  h).

## 4 DISCUSSION AND SHM STRATEGY DEFINITION

In this section, the results of the sensor integration are discussed as a basis for the SHM strategy definition, subsequently proposed in this section.

### 4.1 General discussion of the results

The moisture sensors have demonstrated varying accuracy. Fully embedded sensors have shown nearly identical values, while the partially embedded sensors have tended to record higher moisture levels. Following initial surface water loss, the sensor readings have aligned with the visual observations, reflecting the drying conditions of prototype B2. The absolute moisture readings have been inconsistent between sensor types and absolute measurement results have not been quantified by means of measuring the component weight over time. However, the recorded trends of capacitive soil moisture sensors have correlated with the expected structural performance and visual assessments, suggesting the suitability of capacitive measuring for relative monitoring. The permeable membranes have delayed the moisture penetration causing additional time for sensor stabilization. Capacitive changes have been detected by the embedded sensors with varying accuracy, depending on sensor type and position; however, measurements of capacitive moisture sensors have successfully captured the drying gradient within prototype B2. The environmental conditions have significantly influenced the

drying process, with accelerated moisture loss observed under lower humidity and elevated temperature.

Overall, the findings underline the applicability of moisture sensors for monitoring moisture loss in additively manufactured clay structures and form the basis for developing a tailored SHM strategy.

### 4.2 SHM strategy

Defining the SHM strategy for clay-printed structures requires careful selection and placement of sensors tailored to specific monitoring objectives. Clay moisture and environmental conditions must be assessed to evaluate structural integrity, while visual inspections aid in optimizing sensor placement. Different sensor types serve distinct monitoring purposes: Moisture sensors enable tracking of drying behavior, whereas stability sensors, such as strain gauges, allow detecting buckling and shrinkage, and provide long-term data on internal stress states. In this study, both capacitive and resistive moisture sensors have proven capable of capturing drying behavior in the conducted experiments. However, resistive sensors are more susceptible to corrosion and exhibit a high sensitivity to increased ion concentrations, such as salt, which are prominent in clay. Salts decrease the resistance between sensor nodes and, therefore, the sensors read comparatively increased moisture values. Capacitive sensors, by contrast, have shown greater reliability and resolution, rendering capacitive sensors a more promising choice for continued application in SHM strategies. Sensor placement should follow the observed (or expected) drying gradients, to enable accurate assessment of moisture migration and identification of zones prone to cracking. Due to the evolving geometry and temporal variability inherent to additive manufacturing, a fundamental decision must be made regarding the embedding time, i.e. whether the sensors are integrated during or after the printing process. Embedded wired sensors introduce challenges, including the risk of crack formation at cable transition points caused by clay shrinkage. The cracks may compromise structural stability or facilitate moisture ingress. Although infill gaps can serve as routing channels for sensor cabling, the geometrical complexity of 3D-printed components poses significant limitations for scaling wired sensor networks.

Therefore, wireless monitoring solutions are a prerequisite for scalable SHM in clay-printed structures. However, the physical properties of clay pose substantial challenges for embedded wireless communication. The high dielectric constant and moisture retention of clay lead to significant attenuation of high-frequency radio waves, thereby impairing signal transmission. Elevated moisture content intensifies the effect by increasing material conductivity and absorbing radio frequency (RF) energy, causing reduced transmission efficiency. Additionally, multipath interference, owing to RF signal reflection and scattering within the heterogeneous internal structure of clay, may lead to signal distortion and data loss. To ensure reliable wireless sensing, careful selection of operating frequencies and the implementation of adaptive communication protocols are required, to account for the variable electromagnetic properties of clay throughout the drying process. Furthermore, current technological limitations constrain the deployment of SHM systems: Low-cost capacitive sensors often lack the required accuracy, standard resistive sensors remain prone to corrosion, and both exhibit



limited sensitivity to gradual moisture changes. When implementing SHM strategies for clay-printed structures, attention must be paid to the aforementioned constraints by enhancing sensor robustness, measurement precision, and wireless operability. Particular attention should as well be given to the development of embedded, miniaturized wireless sensors capable of long-term, real-time data acquisition in the challenging environment of clay-printed structures.

## 5 SUMMARY AND CONCLUSIONS

With the increased attention on clay printing in research and practice, SHM strategies need to be tailored to fit clay-printing technologies. In this study, an SHM strategy has been proposed, and the structural properties of clay-printed structures, including buckling, shrinkage, and load-bearing capacity, have been experimentally determined. Prototyping and sensor placement validation have demonstrated the feasibility of constructing structurally stable clay-printed structures and provided key insights into material behavior (i.e., shrinkage) for deriving sensor positioning strategies.

The methodology proposed in this study has provided a structured approach to understanding clay as a 3DP material, incorporating both material characterization and an SHM strategy. The experimental results have demonstrated that effective sensor placement can be obtained through systematic analysis of material behavior, particularly focusing on drying patterns and potential fault locations. Moreover, the study has addressed relationships between small-scale laboratory tests and larger prototypes, establishing crucial scalability considerations for SHM sensor networks of large-scale structures. In summary, the findings contribute to advancing the field of sustainable construction by demonstrating the viability of clay printing based on a sound SHM strategy. Future research may include quantifying sensor results in respect to shrinkage and extending the SHM strategy from cable-based to wireless systems.

## ACKNOWLEDGMENTS

Financial support provided by the German Research Foundation (DFG) through grants SM 281/22-1 and SM 281/31-1 as well as by Hamburg University of Technology via the I<sup>3</sup> program under the junior project *Digitalization of Earth Printing to Advance Climate-Informed Engineering* is gratefully acknowledged. The authors express their gratitude to Goerg & Schneider GmbH & Co. KG for supplying the clay material. The opinions, findings, conclusions, and recommendations presented in this paper are solely those of the

authors and do not necessarily reflect the views of the sponsoring organizations.

## REFERENCES

- [1] Ponis, S., Aretoulaki, E., Maroutas, T. N., Plakas, G., and Dimogiorgi, K., 2021. A systematic literature review on additive manufacturing in the context of circular economy. *Sustainability*, 13(11), 6007.
- [2] Peralta, P. & Smarsly, K., 2022. Requirements analysis of additive manufacturing for concrete printing – A systematic review. In: *Proceedings of the 39th International Symposium on Automation and Robotics in Construction (ISARC)*, Bogota, Colombia, 07/12/2022.
- [3] Smarsly, K., Peralta, P., Luckey, D., Heine, S. & Ludwig, H.-M., 2020. BIM-based concrete printing. In: *Proceedings of the International ICCBE and CIB W78 Joint Conference on Computing in Civil and Building Engineering*, Sao Paulo, Brazil, 08/18/2020.
- [4] Peralta, P., Ahmad, M. E. & Smarsly, K., 2023. Printing information modeling (PIM) for additive manufacturing of concrete structures. *Applied Sciences*, 13(23), 12664.
- [5] Hong, C., Zhang, Y. & Borana, L., 2022. Performance investigation of 3D printed clay soil using fiber Bragg grating technology. *Acta Geotechnica*, 17(2), pp. 453-462.
- [6] Peralta, P., Heine, S., Ludwig, H.-M. & Smarsly, K., 2020. A BIM-based approach towards additive manufacturing of concrete structures. In: *Proceedings of the 27th International Workshop on Intelligent Computing in Engineering*, Berlin, Germany, 07/01/2020.
- [7] Ma, G., Li, Y., Wang, L., Zhang, J. & Li, L., 2020. Real-time quantification of fresh and hardened mechanical property for 3D printing material by intellectualization with piezoelectric transducers. *Construction and Building Materials*, 241(2020), 117982.
- [8] Tanapornraweekei, G., Jiramarootapong, P., Paudel, S., Tangtermsirikul, S. & Snguanyat, C., 2022. Experimental and numerical investigation of 3D-printed mortar walls under uniform axial compression. *Construction and Building Materials*, 360(2022), 129552.
- [9] Hassani, S. & Deckermann, U., 2023. A systematic review of advanced sensor technologies for non-destructive testing and structural health monitoring. *Sensors*, 23(4), 2204.
- [10] Panda, B. & Tan, M.J., 2019. Rheological behavior of high-volume fly ash mixtures containing micro silica for digital construction application. *Materials Letters*, 237(2019), pp. 348-351.
- [11] Tang, C.-S., Shi, B., Liu, C., Suo, W.-B. & Gao, L., 2011. Experimental characterization of shrinkage and desiccation cracking in thin clay layer. *Applied Clay Science*, 52(1–2), pp. 69-77.
- [12] Perrot, A., Rangeard, D. & Lecompte, T., 2018. Field-oriented tests to evaluate the workability of cob and adobe. *Materials and Structures*, 51(2018), 54.
- [13] Kazemian, A., Yuan, X., Cochran, E. & Khoshnevis, B., 2017. Cementitious materials for construction-scale 3D printing: Laboratory testing of fresh printing mixture. *Construction and Building Materials*, 145(2017), pp. 639-647.
- [14] Gomaa, M., Jabi, W., Veliz Reyes, A. & Soebarto, V., 2021. 3D printing system for earth-based construction: Case study of cob. *Automation in Construction*, 124(2021), 103577.
- [15] Curth, A., Pearl, N., Castro-Salazar, A., Mueller, C. & Sass, L., 2024. 3D printing earth: Local, circular material processing, fabrication methods, and life cycle assessment. *Construction and Building Materials*, 421(2024), 135714.
- [16] Robert McNeel & Associates, “Rhinoceros 3D,” [www.rhino3d.com](http://www.rhino3d.com).

## Icelandic turf houses: A one-year monitoring overview

Kathryn Ann Teeter<sup>1</sup>, ORCID (0000-0001-8760-375X), Björn Marteinsson<sup>2</sup>, ORCID (0000-0003-3368-0674), Ágústa Kristófersdóttir,<sup>1</sup> Alma Sigurðardóttir,<sup>1</sup> Dorotea H Sigurdardottir,<sup>1</sup>, ORCID (0009-0006-8496-4625)

<sup>1</sup>Department of Civil and Environmental Engineering, University of Iceland, Hjarðarhagi 2-4, 107 Reykjavik, Iceland

<sup>2</sup>Architect and Engineer, Reykjavik, Iceland

<sup>3</sup>National Museum of Iceland, Suðurgata 41, 102 Reykjavik, Iceland

email: [kat12@hi.is](mailto:kat12@hi.is), [bjomar@hi.is](mailto:bjomar@hi.is), [agusta.kristofersdottir@thjodminjasafn.is](mailto:agusta.kristofersdottir@thjodminjasafn.is), [alma.sigurdardottir@thjodminjasafn.is](mailto:alma.sigurdardottir@thjodminjasafn.is), [dorotea@hi.is](mailto:dorotea@hi.is)

**ABSTRACT:** Structural Health Monitoring (SHM) is employed to provide insights and conservation guidelines for Icelandic turf houses through periodic and continuous monitoring of hygrothermal and geometrical parameters. The turf houses are unique vernacular structures that were the primary dwelling form in Iceland from settlement (~ 874 A.D.) through the 20th century. These structures, now maintained predominantly by the National Museum of Iceland, represent a cultural legacy but suffer from limited research on their materials, structural behavior, and long-term maintenance requirements.

Key conservation challenges include water leakage, differential settlement, and geometrical distortion, highlighting the need to understand the hygrothermal performance of the turf roofs and the structural behavior of the timber frames carrying the roofs. To address these issues, a remote and unobtrusive SHM system was designed, tailored to the constraints of heritage buildings.

This paper provides a one-year overview of monitoring at two sites: Keldur farm in southern Iceland and Laufás in the north. The study details the monitoring strategy, system design, installation, and operation, presenting results such as 3D point scans, hygrothermal data, and comparative analyses between the two sites. Findings from the study contribute to understanding the behavior of Icelandic turf houses, offering insights for their long-term conservation and ongoing management.

**KEY WORDS:** Hygrothermal and geometrical monitoring, museum artifact, monitoring in remote locations, vernacular structures

### 1 INTRODUCTION AND MOTIVATION

Turf houses represent the vernacular architecture of Iceland. The tradition spans from the 9th-20th centuries, surviving far longer than turf architecture traditions in most other countries. Turf was historically an ideal building material in Iceland due to its ready availability, its excellent insulation properties, its ability to protect against wind and precipitation, and the lack of available timber in Iceland (Zöega et al 2023). It was used to build different types of houses, churches, stables, sheds, raised roads, and boundary walls by members of all social classes (Hafsteinsson and Jóhannesdóttir, 2024; Zoega et al 2023, Ágústsson, 2000).

The turf house developed alongside the inhabitants, serving as the main form of residence for most of the country's history. This declined rapidly into the 20th century as they were largely replaced by timber and concrete houses. By the 1950s, only 716 turf houses were registered, representing 3.6% of all residences in the country (Hagstofa Íslands, 1997). Most turf houses were either abandoned to decay or deliberately destroyed (Hafsteinsson and Jóhannesdóttir, 2024). The few remaining turf houses generally represent wealthy or influential farms that have been taken under the protection of the National Museum of Iceland through their Historic Buildings Collection, including Laufás and Keldur, monitored and presented in this paper (see Figure 1). There are also a handful of smaller houses under private ownership or owned by other institutions.

These surviving turf houses no longer function as homes, instead operating as museums intended to conserve this unique aspect of Iceland's cultural heritage. As no one lives in them, the buildings must be monitored and repaired to ensure their continued survival and operation. This can pose difficulties as the museums are not open year-round and funding is limited.

Damage is therefore not always immediately noticed and necessary repairs must be identified and prioritized. There are also few experts remaining who are experienced enough to undertake these repairs. While research has been done on traditional building methods and the cultural and historical importance of the turf tradition, little to no research has been done on the structural behavior of the buildings themselves, the properties of turf as a building material, or on the additional materials often used in turf roofs, leaving a large gap in the field of study.

This project seeks to fill this gap in research by studying the structural behavior and monitoring the structural health of several turf houses in the Historic Buildings Collection of the National Museum, including Laufás and Keldur. This research seeks to create a remote monitoring system that the museum can use to more effectively identify and prioritize repairs and keep track of the condition of the turf houses in their collection, many of which are very remote and far from the museum's headquarters in the capital region. This will be done through an interdisciplinary approach combining structural engineering, museology, and conservation studies. This comprises creating a monitoring strategy, 3D scan analysis, monitoring fluctuations in temperature and moisture in the turf roofs, modelling the hygrothermal behavior of turf, literary research, and interviews with experts actively working in the field. This paper provides a one-year overview of the monitoring process.

### 2 TURF HOUSES: LAUFÁS AND KELDUR

#### 2.1 Development of turf houses

The Icelandic turf tradition began with the settlement in the 9<sup>th</sup> century and can be divided into three main developmental

stages (National Museum of Iceland, 2011). The so-called Viking-Age longhouse represents the first stage of the turf tradition, featuring a long building made of turf, timber, and stone (Stefánsson, 2013 Abrecht, 2018). This first stage existed with relatively few changes until the 13<sup>th</sup> and 14<sup>th</sup> centuries, with the gradual emergence of the passageway farmhouse.

The passageway farmhouse represents the second stage of development. This did not replace the longhouse, and both forms as well as combinations of the two existed. The passageway farmhouse layout featured a long hall or passageway with individual rooms added to the sides and rear of the building (National Museum of Iceland, 2011).

The third and final stage of the turf tradition, the gabled farmhouse, emerged in the late 18<sup>th</sup> and early 19<sup>th</sup> centuries. The gabled farmhouse features individual but interconnected rooms, typically facing the front yard, with wooden gables and individual turf roofs (Abrecht, 2018). This is the version of the turf house that people are most familiar with today and serves as a physical representation of this aspect of Icelandic cultural heritage (Stefánsson, 2013).

Spanning over 10 centuries, the turf tradition represents the primary dwelling for Icelanders throughout its history. By the mid-20<sup>th</sup> century, the tradition had largely been abandoned, and a shift from residential buildings to museum buildings began to take place, largely under the supervision of the National Museum. Once representing a long-standing housing tradition, turf houses today serve a different function as museums to educate and conserve both the architectural tradition, but also cultural and social aspects of the nation's history.



Figure 1: Location of the monitored houses presented in this paper.

## 2.2 Turf roofs

The roofs of turf houses are mainly composed of turf blocks that rest on the top of an interior timber frame, as the turf walls themselves are typically not load-bearing (National Museum of Iceland, 2011, Zoega et al., 2023). There are two main roof types depending on the interior lining, either slate or thatch (Icelandic: hellupök eða tróðpök) (Ágústsson, 2000). Different types of turf can be used, and there are multiple ways of laying a turf roof (Sigurðardóttir, 2008). Additional materials and methods have also been introduced, particularly from the late 19th century onwards. The materials and methods were used based on material availability, the layout of the house itself, and decisions made by the craftsmen. This leaves much room for variation, and different layering can be found between locations

and within the same house, depending on the intended use of the specific room or building.



Figure 2: Example of dried birch twigs carried by purlins and rafters (thatched roof).

Turf roofs typically need to be steep to support moisture runoff and thick for insulation purposes and to allow absorption. If the top layer of turf in a roof is compromised, leaks are likely to occur (Zoega et al 2023, Sigurðardóttir, 2021). The problem of leaking with turf houses is not new, and people in the past dealt with this issue in a number of resourceful and creative ways. Layers of stone, brush, and straw were added in some places to support the turf, which can be seen in Figure 5. When corrugated iron and tar paper arrived in Iceland in the latter half of the 19th century, people almost instantly began adding these materials to their houses as a waterproofing layer in the roofs, examples of which can be seen in Figure 3 (Stefánsson, 2020, Hafsteinsson, 2024).



Figure 3: Examples of corrugated steel in turf roofs. A fishing net has also been added likely because the turf slides on the corrugated steel.

As turf houses began to transform from dwellings to buildings in a museum collection, their maintenance and upkeep changed as well. As the buildings were no longer lived in, the constant cycle of coexistence and repairs shifted. One of the biggest changes has been the roof itself; historically, the roof could be up to 1 meter thick, which promoted absorption and the correct conditions for the grass on the outermost layer to survive and hold itself up (Sigurðsson, 2025).

In the latter part of the 20th century, the roofs of many turf houses were significantly thinned, and a waterproofing layer of PVC or plastic was added as an attempt to prevent leaks and improve the aesthetics of the buildings, see examples in Figure 4 (Stefánsson, 2013). All turf houses in the Historic Buildings Collection of the National Museum have thinned roofs with PVC or plastic membrane, and many also have corrugated iron.



When constructing a turf roof today, the ideal thickness ranges from 40-70 cm (Sigurðsson, 2025). We have not yet seen a roof with this thickness in any of the buildings we are monitoring. Additionally, many of the roofs have holes or chunks of turf missing.



Figure 4: Examples of plastic membranes in turf roofs. Left: membrane visible from the inside. Right: membrane visible from the outside.

When the turf becomes too thin, it is unable to support itself and becomes more prone to damage from the elements. All additional roofing materials used in the past and in the present have been a response to problems, but these new materials have often had unexpected or unintended consequences, which is part of the focus of this study (Stefánsson, 2013).

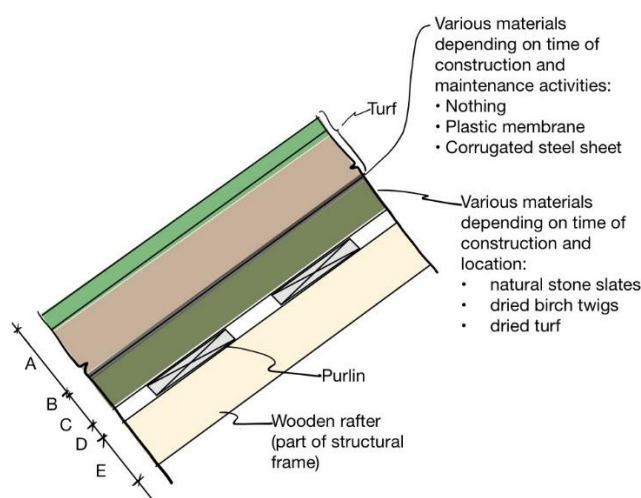


Figure 5: Typical cross-section of a turf roof.

Figure 5 shows a typical cross-section of a turf roof. As mentioned, the thickness of the different material layers can vary greatly from house to house and even within one house.

A: The turf layer itself can be divided into three sections: 1) the outermost layer is living grass serving as the first water barrier and provides possibilities for runoff from the roof, 2) root mesh serving as stabilizing layer that prevents the turf from sliding (this layer also has moisture absorption and insulation capabilities), and 3) the innermost layer is soil without roots, used to even out the surface for turf laying. B: The next layer, as discussed previously, was added when new materials arrived, such as corrugated steel and plastic membranes. These materials make it more challenging to keep the turf in place

since they are slippery. C: Various materials have been used under the membrane and turf depending on the time of construction and the local availability of materials. Natural stone slates, dried birch twigs and dried turf (Icelandic: nærtorf), are common materials. Some of them, like birch and turf, have some insulation properties, whereas stone is a poor insulator. D: These materials rest on purlins. E: The purlins are carried by a wooden rafter which is part of the structural frame carrying the whole roof.

### 2.3 Timber frame

The structural system of the turf houses is a timber frame which carries the roof, see for example Figure 6. The foundations for the frame are stone blocks resting on the ground. Each column in the frame is resting on individual blocks which are not connected to each other. Two columns are connected to each other by joists perpendicular to the walls. Parallel to the wall, columns are connected by beams. Sometimes the rafters only rest on the columns and sometimes the rafters are connected to beams between the columns. The walls, built by turf or stone, only carry their self-weight and do not support the roof.

All elements of the structural system are made from natural materials, that is timber and stone, making them susceptible to temperature and moisture fluctuations. Furthermore, the foundations, stones placed on the earthen floors, can suffer from differential settlements. However, the characteristics of the movements of the timber frames have not been studied in a structural context and are therefore not fully understood.



Figure 6: Structural system in the kitchen in Keldur.

### 2.4 Laufás

Laufás was a prosperous manor farm that also served as a priest's residence, see Figure 7. It is in Eyjafjörður in the North of Iceland. Its history dates back to at least the early 11th century, though the present buildings reflect 19th century building traditions (National Museum of Iceland, *Húsasafn*, Stefánsson, 2013). The farm entered the National Museum's collection in 1948 and has since undergone extensive renovations and repairs.

The farm consists of 12 interconnected houses and is approximately 29 meters long and 28 meters wide (Hafsteinsson, 2008). It is representative of the gabled farmhouse with older elements of a passageway farmhouse, and the roof falls under the thatched category as the inner lining is

turf. The room being monitored is called *dúnhús*, or down house, referencing the valuable down from eider ducks that was once an important source of income for the farm. The down house is on the western side of the farm facing the yard, with a door and three windows facing the yard.



Figure 7: Laufás in Eyjafjörður.

### 2.5 Keldur

Keldur was a prominent farm in the South of Iceland with a rich history dating back to the 12th century, see Figure 8. It is the largest turf farm in the south and is mentioned in several of the famous Icelandic sagas. The present buildings were primarily rebuilt in the 19th century, and the farm entered the National Museum's collection in 1946.

Keldur also represents a gabled-farmhouse with earlier elements of the passageway-farmhouse, but the roof is representative of the slate category. The inner layer of the roof is entirely slate, with an interior plastic membrane and turf as the outermost layer. Both the *skáli*, or longhouse, and the *eldhús*, or kitchen are monitored in Keldur.



Figure 8: Keldur in Rangárvellir.

### 2.6 Comparing Keldur and Laufás

The two farms are representative of turf building traditions in their respective regions. Laufás provides a classic example of the turf houses built in the north, with more turf used in the building and roof, and visible turf blocks in the walls. Keldur represents the turf building traditions in the south of Iceland, with more stone used in the building and roof and a grass covering on the top of the houses. These differences can be seen in Figure 7 and Figure 8, and relate to differences in climate in the north and south of the country.

The climate in the north of Iceland is more stable, with longer cold and dry periods providing better conditions for turf houses. This results in the northern turf houses having more turf and needing to be repaired and rebuilt less frequently. Historic records suggest that turf houses in the north lasted significantly longer before needing major rebuilding or repairs than those in the south, with one source reporting turf houses in the north lasted for 50-60 years, while those in the south lasted 10-20 years (Bald, 1897).

The climate in the south of Iceland fluctuates more in regard to both temperature and precipitation. Additionally, parts of the south do not have the same access to large amounts of good quality turf as in the north, and it is much more common to have higher amounts of stone in the buildings and the roofs.

The walls in Laufás are made from turf and rest upon a stone base. Different patterns of turf blocks can be seen from the interior and exterior of the building. The inner-most layer of the roof in the down house of Laufás is dried turf. In Keldur, the walls are layered with both turf and stone. The inner-most layer of the roof in the kitchen of Keldur is made of stone slates. It is not possible to see distinct patterns of turf blocks in the walls, and the exterior of the houses is grass.

## 3 MONITORING STRATEGIES, SYSTEM DESIGN, AND INSTALLATION

This project began in part as a response to reports from those working in close contact with the museum buildings. Issues with leaking roofs, moving timber frames and turf walls, losing turf from the roofs, and complications with the plastic membranes were reported. In order to research these issues, an unobtrusive monitoring system that could be utilized in a museum environment was employed. As these buildings are all active museums, any visible signs of research or monitoring must be limited, and museum activities and visitor access cannot be hindered.

Two monitoring strategies have been employed in the course of the research, targeting the pre-selected rooms at each location. One is continuous monitoring of the hygrothermal parameters in the turf roofs through sensors that were installed in both the exterior and interior layers of the roofs. The second is a periodic monitoring strategy where 3D scans are taken using LiDAR with an Artec Ray scanner. These scans are planned 3-4 times per year. Comparisons between the point clouds are planned in the open software CloudCompare.

### 3.1 Differential settlement and geometrical distortion

LiDAR scanning has been used to help monitor the structural health and behavior of buildings, bridges, roads, tunnels, and other forms of civil infrastructure (Kaartinen et al., 2022). LiDAR has also been implemented in the cultural heritage sector for a variety of purposes, including to detect and identify damage and degradation in wooden components of historic buildings (Liu et al., 2024) and documenting and assessing deformation (Yaagoubi and Miky, 2018).

LiDAR scanning was selected as a method in this study as a way to better understand the behavior of the interior timber frames of the turf houses. The reported displacements in the timber frames can impact the roof and the walls, which can lead



to accelerated decay and degradation, putting the overall health of the building at greater risk.

Some of these displacements can be seen with the naked eye, including tilt in passageways, halls, and door frames, warped wood, and compacted or deteriorating turf. Although this can cause strain on parts of the building, strain monitoring is not a feasible method, as the structural frames may be undergoing rigid body movement and displacement without deformation. While we know that movement is occurring, it is still unknown exactly why and how this movement happens. LiDAR scans and the subsequent point clouds that are created will be compared in CloudCompare. This will enable a greater understanding of the movement of the timber frames, particularly if the movement is related to the decay of the timber, seasonal fluctuations, or changes in weather.



Figure 9: Artec Ray scanner in operation in the kitchen of Keldur.

### 3.2 Turf monitoring

The hygrothermal behavior of turf is relatively unknown despite its usage in buildings for centuries and across the world. Turf is known for its insulation properties and its ability to absorb moisture, but the specifics are lacking. The usage of sensors in the indoor and outdoor climate of the turf roofs is a way to better understand the moisture and thermal characteristics of the turf.

Research into the hygrothermal properties and behavior of different earthen building materials has covered many types of materials, including earthen bricks (Cagnon et al., 2014), light-earth construction materials (Colinart et al., 2020), and various soil types (Kehrer and Pallin, 2017). A 2019 literary review provides a detailed overview on the research into hygrothermal properties of earthen construction materials, noting renewed interest in their sustainable building qualities and ability to support comfortable living environments, but turf and the turf tradition is not included (Giada et al., 2019). Therefore, research is needed to address this gap.

As mentioned earlier, the monitoring system needed to be unobtrusive and operable in remote locations. To that end, wireless sensors with Bluetooth connection to gateways that can connect and send the data to the cloud were chosen.

The first monitoring system was installed in Keldur. A monitoring system from SensorPush was chosen. The

SensorPush sensors are small, battery-operated devices with no wires, see left picture in Figure 10, making them ideal for this project. They measure air temperature and relative humidity. Eight sensors were installed in pairs, the inner laying on the plastic membrane and the outer very close to the surface of the turf. Two additional sensors were installed to measure the indoor and outdoor climate. In Keldur the thickness of the turf is approximately 10-12 cm. Figure 11 shows the monitored locations on the south side of the roof, one very close to the ridge, one close to the inside of the outer wall, and one in the valley where the gable house meets the longhouse.

In Keldur a service house is located close to the turf house making it possible to run an ethernet cable into the turf house for direct connection with the gateway. However, since the gateway was located inside the house and the sensors were installed inside the turf from the outside, it was challenging to connect to them through the turf. However, the installation was successful. Shortly after installation all the humidity sensors read a constant 100% RH and that did not change. Even though the moisture sensors did not survive the wet and cold Icelandic summer the temperature sensors kept operating until October 2024 when all sensors were unresponsive.



Figure 10: Left: Air temperature and humidity sensor from SensorPush. Middle: Soil moisture and temperature sensor from HOBO. Right: Air temperature sensor from HOBO.



Figure 11: Sensor locations on south side of roof in Keldur.

The next monitoring system was installed in Laufás. This time sensors for soil monitoring were chosen, see the middle picture in Figure 10. The sensors are from the MX series from HOBO. They have a robust casing, and the logger is connected to the sensors with wires, so the logger does not have to be buried into the turf. This makes the sensor more likely to survive harsh weather conditions, but it also makes it more visible.

Two pairs of sensors were installed in Laufás. Like in Keldur, the inner sensors were close to the plastic membrane and the outer sensors were near the surface. In Laufás the thickness of the turf was approximately 25-30 cm. The sensors were installed on the north side of the down house, close to the rear



gable wall, one upper location and one lower, which can be seen in Figure 12.



Figure 12: Sensor locations in down house roof in Laufás.

In Laufás an internet connection is established by SimCard WiFi Router which is then connected to the gateway. The gateway communicates with the dataloggers via Bluetooth. In Laufás the dataloggers were installed inside the house and the wires run through a small hole in the gable avoiding the problem with poor Bluetooth connectability through the turf. This was possible since the loggers were connected with wires to the sensors which were installed in the turf.

## 4 OPERATION AND SITE VISITS

### 4.1 Laufás

In October 2024, a research team undertook the first visit to Laufás to examine the building, photograph conditions, install sensors, and take the first round of 3D scans in the down house. Several issues were noticed with the roof, including holes, missing pieces of turf on the top layer, and degradation of the inner and outer layers of the turf roof, resulting in the plastic membrane showing. The back wall of the down house also had considerably higher moisture. The sensors were installed in the roof of the down house and the 3D scanning was performed.

The second trip to Laufás was taken in February 2025. Some small-scale repairs had been done to parts of the turf walls, but there were still holes in the roof of the down house. The back wall also had visibly more moisture than the other three walls. The sensors were still in place and actively logging data, and the second set of 3D scans were taken.

### 4.2 Keldur

Sensors were installed in the roof of Keldur in May 2024. The sensors were installed on the north and south side of the long-house. Several of the sensors went offline, so a second trip was taken in October 2024 to attempt to reconnect to the sensors. This was unsuccessful, and six out of ten sensors remained offline, unable to log data. This was thought to be related to the extreme weather conditions, as the sensors were unable to cope with the high amount of rain. Scans were not taken on either trip, as the 3D scanner is shared between departments at the National Museum and had been rented out.

Due to the remote location of Keldur, poor weather and road conditions prevented a return trip in the winter of 2024. The third trip took place in February 2025, where the kitchen was scanned. An additional trip is planned for the spring of 2025 to

take the next round of scans and install new sensors that can withstand the outdoor climate.

## 5 RESULTS FROM STUDY HOUSES

In this section current results from the monitoring strategies are presented.

### 5.1 Laufás

The down house in Laufás has been 3D scanned twice, once in October 2024 and again in February 2025. Comparative analysis of the scans is ongoing. Renderings of the scans are shown in Figure 13.

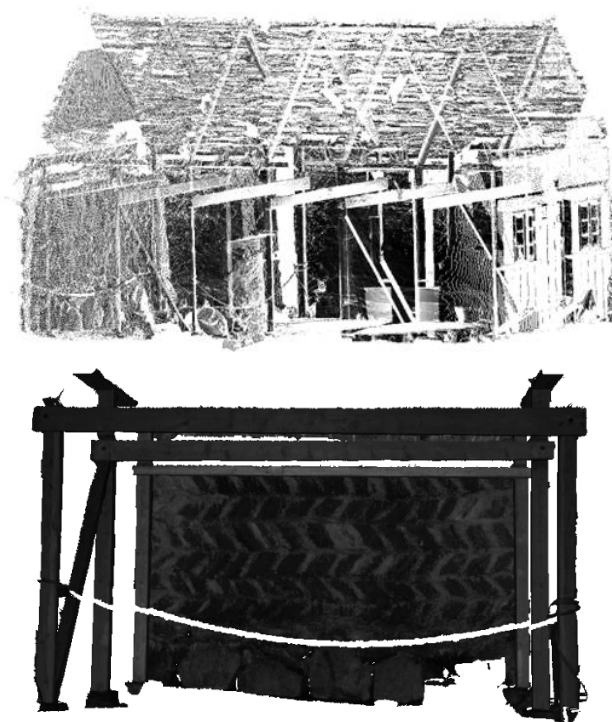


Figure 13: Renderings of 3D scans of the down house in Laufás.

Figure 14 shows the time series for temperature at Laufás. The blue shows the temperature measurements from the nearest weather station, Végeirsstaðir, approximately 12 km from Laufás. The orange shows the air temperature as measured outside by the monitoring system and the green shows the air temperature measurements from inside the house. The turf temperature close to the surface is shown in red and the turf temperature 20-24 cm deeper is shown in purple. The two monitored sections are shown, one upper and one lower, see Figure 12.

The temperature in the turf shows less fluctuations than the air temperature outside and inside the house. The difference between the outer and inner sensor is remarkably low, only 1-3°C, as shown in the lowest plot in Figure 14.

Figure 15 shows the turf moisture measurements in Laufás. In this first analysis the manufacturer calibration of the moisture sensor was used. That can have an effect on the absolute values but does not affect the trends. The moisture is plotted together with rainfall measurements from the weather station in Akureyri, 20 km from Laufás. Heavier rain can be correlated with higher moisture content.

Generally higher moisture content is measured in the lower location than in the upper location. This observation is consistent with that rainfall and moisture within the turf seeps downwards.

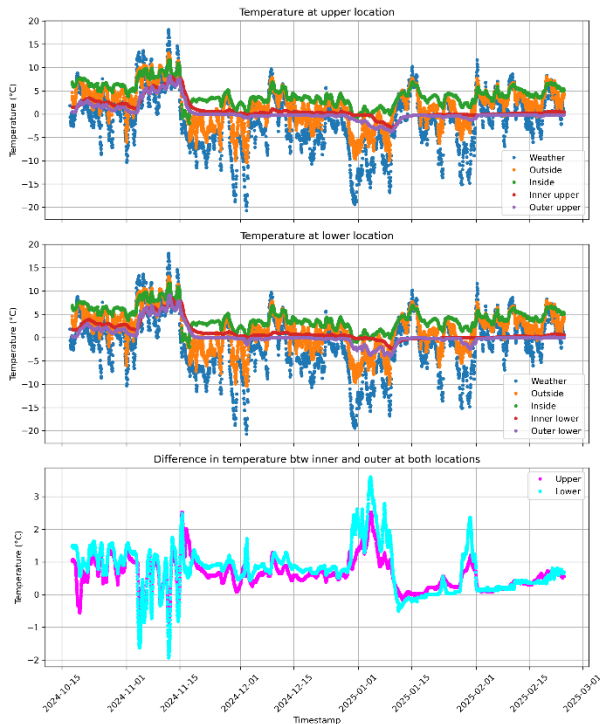


Figure 14: Temperature measurements in Laufás. Note: Weather refers to temperature from nearest weather station, Végeirsstaðir.

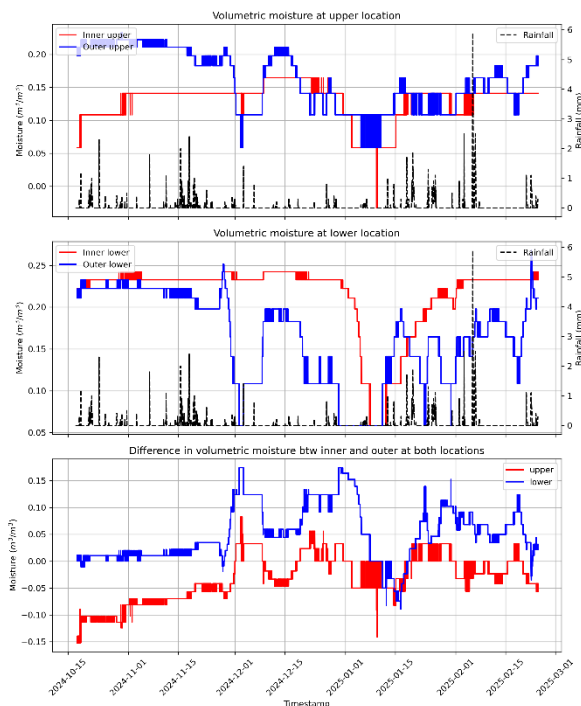


Figure 15: Turf moisture measurements in Laufás. Note: Rainfall measurements from weather station in Akureyri.

Moreover, the inner sensor at the upper location is drier than the outer sensor, also consistent with expected behavior. However, at the lower location the outer sensor is drier than the

inner. More investigation is necessary to fully explain this observation.

## 5.2 Keldur

Figure 16 shows the time series for temperature at Keldur. The blue shows the temperature measurements from the nearest weather station, Sámstaðir, approximately 5 km from Keldur. The orange shows the air temperature as measured outside by the monitoring system and the green shows the air temperature measurements from inside the house. The turf temperature close to the surface is shown in red and the turf temperature 10-12 cm deeper is shown in purple. Two cross sections are represented, one close to the ridge and the other in the valley.

In general, the temperature close to the surface (red) fluctuates more than the temperature deeper in the turf close to the plastic (purple). The temperature inside is more stable than outside. Close to the ridge the temperature increases significantly, even higher than the air temperature. This is most likely because this part of the roof is facing south and highly affected by the sun radiation.

In the valley, which has more shadow, the outer sensor measures higher temperatures than the inner. The lowest plot in the figure shows the temperature difference between the outer and inner sensor at both locations. The temperature difference is higher at the ridge than at the valley, showing that the surface of the turf is very prone to temperature fluctuations. It even indicates that the turf, albeit thin, exhibits good insulation properties and/or high thermal inertia.

Note that for less extreme temperatures, between 5°C and 10°C, the difference between the outer and inner measurements is not as pronounced.

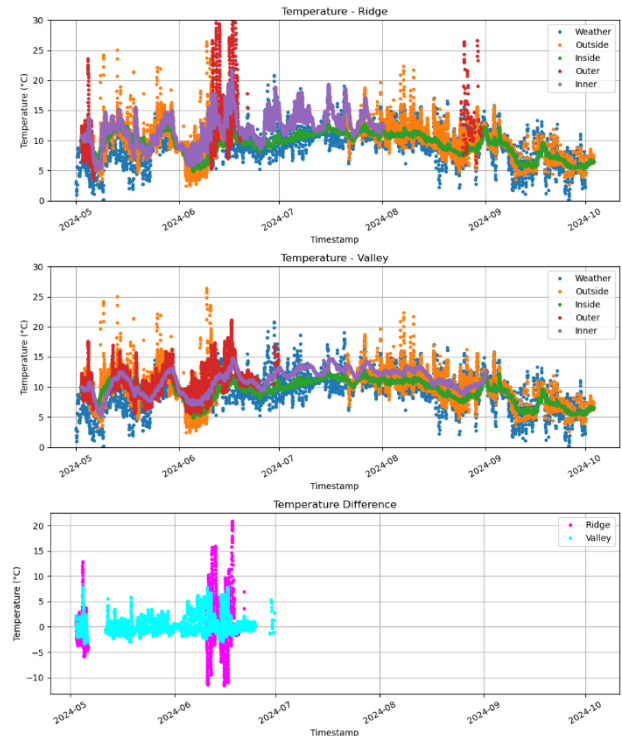


Figure 16: Temperature measurements in Keldur. Note: Weather refers to temperature from nearest weather station, Sámstaðir.

## 6 CONCLUSION

The implementation of this structural health monitoring system combines different methods and approaches to better understand the Icelandic turf buildings whose structural behavior has not been studied. One year into the monitoring reveals several details about working with these technologies in museum buildings and in the Icelandic weather conditions. Early results provide information on the buildings, but additional scans and continued monitoring with the sensors is necessary to provide a more complete picture.

The Artec Ray scanner had some difficulties operating in cold temperatures. While the interior temperature of the turf houses was just above the minimum operating temperature, some scans were incomplete and needed to be repeated.

Additional sets of 3D scans are necessary to perform a comparative analysis of potential displacement in the timber frames.

The first installation of sensors at Keldur revealed that the SensorPush sensors struggled to operate in wet conditions, resulting in a 100% RH reading before all sensors stopped logging data. Additionally, there were difficulties in getting the Bluetooth connection to work through the turf roofs.

These obstacles in the first round of sensors led to the selection of the HOBO sensors that were installed in Laufás. These sensors are better able to withstand harsh weather conditions and can connect to the gateway. Laufás has cellular reception, making it possible to send the data to the cloud. Multiple sensors can operate on the cellular internet with good reliability.

New sensors will be installed at Keldur this spring. Since Keldur has ethernet connection, good uploading capabilities are available. However, it is important that sensors in remote locations have internal memory in case the system goes offline.

The data from the sensors at Keldur shows that the turf roofs can get quite warm in the summer, well above the outdoor temperature. Smoother temperature readings by the inner sensors at Keldur also show the insulation capabilities of the turf. This difference is not as visible in Laufás, possibly because the sensors in Laufás are located on the north side and have only been monitoring during the wintertime.

Moisture content of the turf roof is correlated with the rainfall. The cross-section closer to the ridge is drier than the cross-section further down. At the upper location the outer sensor measures higher moisture content than the inner sensor. This is not the case at the lower location.

Monitoring of these two houses and more are planned for the next few years providing insights into long-term continuous monitoring strategies at remote locations.

## ACKNOWLEDGMENTS

Funding from the Icelandic Research Fund grant no. 2410205-051 is gratefully acknowledged.

## REFERENCES

- [1] G. Zöega et al., "Turf Building in Iceland – Past, Present, and Future," *Open Archaeology*, 9(1), 2023.
- [2] S.B. Hafsteinsson and M.G. Jóhannesdóttir, "Dirt Hovels' and Cultural Heritage: The Eradication and Inheritance of the Icelandic Turf House," *Vernacular Architecture* 54(1), 2024.
- [3] H. Ágústsson, *Íslensk byggingararfleifð I (Ágrip af húsagerðarsögu 1750-1940)*, Reykjavík: Húsafríðunafnd Ríkisins, 2000.
- [4] G. Jónsson and M.S. Magnússon, Eds., *Hagskinna: Sögulegar hagtölur um Ísland*, Reykjavík: Hagstofa, 1997.
- [5] National Museum of Iceland, "The Turf House Tradition," UNESCO World Heritage Convention, Tentative Lists, 2011, <https://whc.unesco.org/en/tentativelists/5589/>.
- [6] H. Stefánsson, *Af jörðu - íslensk torfhús*, Reykjavík, Crymogeia, 2013.
- [7] B. Abrecht, *Arkitektúr á Íslandi – Discover Icelandic Architecture – Entdecke Islands Architektur*, Reykjavík: Mál og Menning, 2018.
- [8] S. Sigurðardóttir, *Building with Turf, Sauðárkrúkur: Byggðasafn Skagfirðinga*, 2008.
- [9] Sigríður Sigurðardóttir, "Byggingarefnið torf: Meira en þúsund ára umgjörð íslenskrar mannvistar (Master's Thesis), Reykjavík, University of Iceland, 2021, <https://skemman.is/handle/1946/37431>.
- [10] H. Stefánsson, *Hvilikt torf—tóm steypa: Ur torfhusum í steypuhús*. Reykjavík: Haskolautgáfan, 2020.
- [11] K. Teeter, "Interview with Helgi Sigurðsson," Helgi Sigurðsson, February 20, 2025.
- [12] National Museum of Iceland, "Laufás í Eyjafirði," Laufás í Eyjafirði, Húsaafn, Þjóðminjasafnsins, [www.thjodminjasafn.is/soguleg-husasofn/laufas-i-eyjafirði](http://www.thjodminjasafn.is/soguleg-husasofn/laufas-i-eyjafirði).
- [13] National Museum of Iceland, "Keldur á Rangárvöllum," Keldur á Rangárvöllum, Húsaafn, Þjóðminjasafnsins, [www.thjodminjasafn.is/soguleg-husasofn/keldur](http://www.thjodminjasafn.is/soguleg-husasofn/keldur).
- [14] G.L. Hafsteinsson, "Byggingarlýsing 2008," Reykjavík, National Museum of Iceland, 2008.
- [15] F.A. Bald, "Um húsabætur á landskjálftasvæðinu og víðar," *Ísafold*, 24(10), 1897, <https://timarit.is/page/3945073#page/n0/mode/2up>.
- [16] E. Kaartinen et al., "LiDAR-Based Structural Health Monitoring: Applications in Civil Infrastructure Systems," *Sensors* 22(12), 2022.
- [17] H. Liu et al., "Precision detection and identification method for apparent damage in timber components of historic buildings based on portable LiDAR equipment," *Journal of Building Engineering*, 98(1), 2024.
- [18] R. Yaagoubi and Y. Miky, "Developing a combined Light Detecting And Ranging (LiDAR) and Building Information Modeling (BIM) approach for documentation and deformation assessment of Historical Buildings," MATEC Web Conf., 149, 2018.
- [19] H. Cagnon et al., "Hygrothermal properties of earth bricks," *Energy and Buildings*, 80, 2014.
- [20] T. Colinart et al., "Hygrothermal properties of light-earth building materials," *Journal of Building Engineering*, 29, 2020.
- [21] M. Kehrher and S.B. Pallin, "Hygrothermal Material Properties for Soils in Building Science," US Department of Energy, Technical Report: Hygrothermal Material Properties for Soils in Building Science, 2017.
- [22] G. Giada et al., "Hygrothermal Properties of Raw Earth Materials: A Literature Review," *Sustainability*, 11(19), 2019.



## Gas permeability under varying laboratory conditions

Damjan Grba<sup>1</sup>, Thomas Zimmermann<sup>2</sup>, Alfred Strauss<sup>1</sup>

<sup>1</sup>Institute of Structural Engineering, University of Natural Resources and Life Sciences, Peter-Jordan-Straße 82, 1190 Vienna, Austria

<sup>2</sup>Building Inspection Authority, Vienna City Administration, Dresdner Straße 73-75, 1200 Vienna, Austria  
email: damjan.grba@students.boku.ac.at, thomas.zimmermann@wien.gv.at, alfred.strauss@boku.ac.at

**ABSTRACT:** Durability is a critical factor in the long-term performance of concrete structures. Ensuring adequate surface quality – and thus extending the service life of concrete elements – relies significantly on proper curing during the hydration phase. To assess and monitor the effectiveness of the curing process, suitable testing methods are essential. Among these, gas permeability testing provides valuable insights into the porosity of the concrete, which directly affects its durability. This study investigates the influence of various curing methods on gas permeability using both laboratory and field testing. The results demonstrate that insufficient curing leads to higher gas permeability in the near-surface zone of concrete. Concrete specimens and structural components made from identical mix designs but subjected to different curing conditions are analyzed and compared. The findings also take into account the influence of concrete composition and environmental conditions on surface quality. Based on these insights, the study offers recommendations for a reliable evaluation of curing effectiveness through gas permeability as an indicator of surface integrity.

**KEY WORDS:** concrete curing; non-destructive testing; gas permeability testing; durability; quality control.

### 1 INTRODUCTION

The results of this study provide a differentiated understanding of how curing quality and external climatic influences interact to affect the permeability and thus the long-term performance of concrete structures. By isolating the effects of curing and environmental conditions, it becomes possible to derive targeted recommendations for construction practice and quality assurance, especially under conditions where optimal curing cannot be ensured. In particular, gas permeability is examined as a practical and sensitive indicator for the assessment of curing effectiveness and surface concrete quality, as highlighted in various previous studies [1–5, 7, 8, 10].

Several works have investigated the applicability of gas permeability as a diagnostic tool in both laboratory and field conditions [3, 4, 10, 11]. Moreover, the significance of environmental parameters during curing and their long-term implications for concrete performance has been documented [5, 6, 7, 9]. This study contributes to this ongoing research by systematically quantifying these influences under controlled yet variable conditions and by using a standardized testing approach (Permeator AC+), thereby ensuring comparability and reproducibility of the findings.

The remainder of this paper is structured as follows: Section 2 outlines the concrete material and details the specimen preparation, climatic conditioning, and measurement procedures. Section 3 presents the results of gas permeability testing under the different environmental scenarios. In Section 4, the results are discussed with regard to the interaction between curing quality and environmental exposure. Finally, Section 5 summarizes the key findings, draws practical implications, and suggests directions for future research.

**Objective:** This study involved a series of tests aimed at systematically quantifying the influence of time, temperature,

and relative humidity on the permeability of concrete. Three different concrete structures were examined under controlled climatic conditions. The resulting data make it possible to analyze the interactions between thermal effects, moisture ingress, and temporal changes in the diffusion behavior of concrete, thereby contributing to a deeper understanding of the long-term durability of concrete under varying environmental conditions.

**Relevance:** The study evaluated whether curing quality of concrete can still be clearly detected through gas permeability measurements, even under fluctuating environmental conditions. For this purpose, concrete specimens were exposed to different combinations of temperature and humidity, then analyzed for their gas permeability. The aim was to determine how variable environmental parameters influence the effectiveness of the curing process, allowing conclusions to be drawn about the durability of the concrete.

**Methodology and Approach:** Within the scope of this study, concrete specimens were systematically exposed to different temperature and relative humidity conditions in a climate chamber. The curing performance was assessed by measuring gas permeability, a reliable indicator of concrete tightness and therefore durability. For quantitative determination of gas permeability, the Permeator AC+ device was used, enabling standardized and reproducible measurements. The collected data provide a foundation for analyzing the relationships between specific climatic conditions and the diffusion properties of concrete.

This methodological approach ultimately allows for an assessment of how successful concrete curing is under varying environmental conditions, and which parameters significantly affect gas permeability a key criterion for assessing the durability of concrete.

As part of a study, nine identical concrete test specimens were initially produced to serve as the base material for examining curing quality. The specimens were divided into three equally sized groups of three units each to apply different curing methods. The curing was carried out as (a) optimal curing (b) neutral/no special conditions and (c) bad curing.

This approach enables a comparison of three different levels of curing quality derived from the same raw material.

Subsequently, all nine specimens were exposed to various environmental conditions in a climate chamber. Variable temperatures and relative humidity levels were simulated to evaluate the impact of these parameters on gas permeability. Gas permeability was measured using a Permeator AC+, ensuring precise and standardized determination of the concrete's diffusion properties.

This systematic investigation makes it possible to analyze in detail the influence of curing quality in conjunction with varying environmental conditions on the durability and impermeability of concrete.

## 2 CONCRETE MATERIAL

For the present investigation, nine concrete test specimens with dimensions of 15 cm × 15 cm × 15 cm each were produced. All specimens were made from the same batch of concrete to ensure a consistent starting point and to allow for isolated examination of the curing process. After demolding, the specimens were divided into three groups of three and subjected to different curing conditions. These differentiated curing procedures enabled a systematic investigation of how varying curing quality affects gas permeability and, consequently, the durability of the concrete.

### 2.1 Concrete Composition

All specimens were fabricated from a single concrete batch prepared in accordance with concrete type B3 as specified in ÖNORM B 4710-1. The binder used was a Portland composite cement of type CEM II/A-M (S-L) 42.5 N according to DIN EN 197-1. This cement contains, in addition to Portland clinker, ground granulated blast-furnace slag (S) and limestone (L) as main components, with a combined proportion of 6 to 20 m-%. The strength class 42.5 indicates a standardized strength between at least 42.5 MPa and at most 62.5 MPa after 28 days, while the "N" denotes normal early strength development. Table 1 summarizes the concrete mixture.

Table 1. Main Parameters of the Investigated Concrete Mixture (According to [8]).

Concrete parameter	value	unit
w/b	0.55	-
Slump-value	F52	-
Grain-size	22	mm
Air-content	3-5.5	%
Cement	CEM-II/A-M(S-L)	-

After demolding, the specimens were divided into three groups of three and subsequently subjected to different curing treatments. This systematic variation of curing conditions enabled precise analysis of how different curing qualities affect gas permeability and thus the durability of the concrete. The choice of concrete type in accordance with ÖNORM B 4710-1

and the use of composite cement aimed at a practice-oriented assessment of the interaction between curing, environmental conditions, and permeability characteristics.

### 2.2 Curing of the Specimens

The specimens were demolded 24 hours after production and then divided into three groups of three. Each group was subjected to the following differentiated curing procedures:

- **Good curing:** Immediately after demolding, the specimens were completely wrapped in foil to prevent moisture loss. For the first seven days, the specimens were stored at a temperature of  $20 \pm 2$  °C, a relative humidity of  $\geq 80\%$ , and no air flow due to the sealed foil environment. Afterward, they remained wrapped for an additional six days under the same conditions to ensure continued moist curing and optimal hydration.
- **No curing:** The second group received no further treatment after demolding and was stored under ambient laboratory conditions to simulate natural drying. The specimens were exposed to a temperature of  $20 \pm 2$  °C, a relative humidity of approximately  $50 \pm 5\%$ , and free air circulation. These conditions served as a reference for unprotected, natural drying in indoor environments.
- **Poor curing:** The third group was deliberately subjected to suboptimal curing conditions by being placed on a windowsill exposed to natural indoor light and airflow. This setup simulated increased drying conditions, resulting in accelerated surface moisture loss. The environmental conditions during this period were approximately  $25 \pm 3$  °C, relative humidity of  $40 \pm 10\%$ , and moderate to high air movement due to occasional ventilation and solar exposure. These conditions represent inadequate curing typical of poorly protected elements during early-age concrete exposure.

This methodological differentiation allowed for a systematic investigation of how different curing qualities influence gas permeability and, consequently, the durability of the concrete.

## 3 TIME-DEPENDENT TESTING

The concrete specimens were examined for gas permeability at 7, 14, 28, and 56 days after demolding. The  $k_T$  value was determined on four defined surfaces of each specimen: the troweled top surface, the bottom formwork surface, and two lateral formwork surfaces.

**Climate Chamber Testing:** The previously defined environmental conditions (temperature, relative humidity, and air flow) were maintained consistently in the climate chamber throughout the entire storage period, in accordance with the respective curing method. The specimens were removed from the chamber at the predefined testing ages, tested, and then returned to their respective environments. The remaining specimens continued to be stored under the assigned climatic conditions until their next scheduled testing.

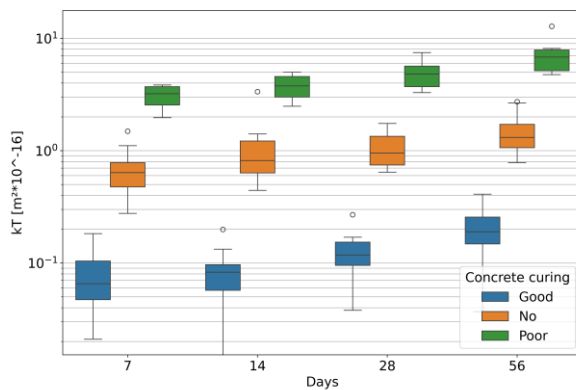


Figure 1. Change in  $k_T$  value over time..

Figure 1 illustrates a clear differentiation between the  $k_T$  values of the three different curing methods. The optimally cured specimens consistently show the lowest permeability values, while those with poor curing exhibit the highest. Furthermore, a marked increase in the  $k_T$  values is observed across all curing types over the observation period from 7 to 56 days. The distinctions between the individual curing classes remain, which can be attributed to continued surface drying of the concrete.

#### 4 CLIMATE CHAMBER TESTING

To further explore the effects of environmental conditions, additional tests were conducted in a climate chamber to assess their influence on the gas permeability of the concrete specimens. Each group was stored for 12 hours under varying combinations of temperature and relative humidity, as shown in Table 1. Subsequently, the  $k_T$  values were re-measured on the same surfaces as described in Chapter 3 (troweled top surface, bottom surface, and two sides).

Table 2. Climate chamber testing under different humidity and temperature conditions.

		Temperature in °C			
		25	30	35	40
Relative air moisture in %	60	x	x	x	x
	70	x	x	x	x
	80	x	x	x	x
	90	x	x	x	x

In addition to gas permeability, concrete moisture content was also measured at the same locations using a concrete moisture meter (Type: Tramex). This parallel measurement enables a more detailed analysis of the relationship between moisture content and the diffusion characteristics of concrete, and helps identify possible interactions between environmental conditions and concrete durability.

##### 4.1 Influence of Temperature on Gas Permeability

The results show that the overall impact of temperature on measured gas permeability is relatively minor. However, the

effect is most apparent in the optimally cured specimens. In general, a slight but noticeable increase in gas permeability with rising temperature can be observed (see Figure 2).

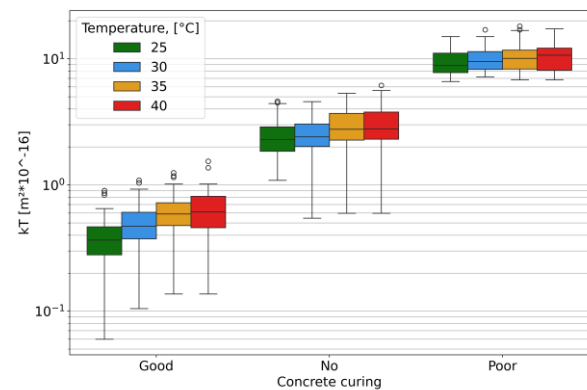


Figure 2. Gas permeability at different temperatures, grouped by curing method, for the corresponding relative humidity see Table 2.

This suggests that higher temperatures may accelerate surface drying, thereby enhancing the diffusion capacity for gases. Although this effect is present across all curing qualities, its magnitude varies significantly depending on the initial curing quality.

##### 4.2 Influence of Relative Humidity on Gas Permeability

As shown in Figure 3, relative humidity has only a minimal influence on the gas permeability of the concrete specimens examined. Across the studied range of relative humidity, the measured permeability values show little to no significant change.

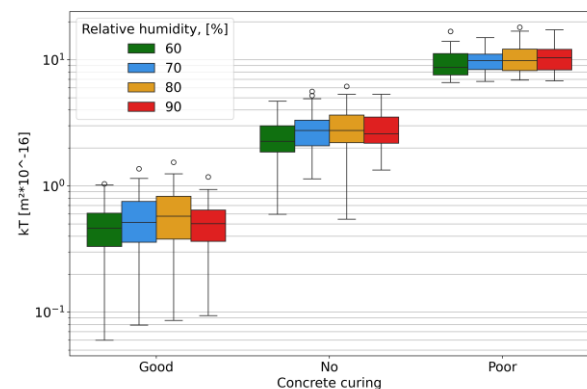


Figure 3. Gas permeability at varying relative humidity, grouped by curing method, for the corresponding temperature see Table 2.

##### 4.3 Influence of Relative Humidity on Concrete Moisture

Changes in relative humidity have a direct impact on measured concrete moisture. The data show a clear correlation: as relative humidity increases, so does the moisture content in the concrete. However, despite this relationship between environmental humidity and concrete moisture, the measured gas permeability remains almost unaffected.



#### 4.4 Comparison of Gas Permeability and Concrete Moisture

As illustrated in Figure 4, there is a clear inverse correlation between concrete moisture and gas permeability. Higher surface moisture levels correspond to lower  $k_T$  values, indicating reduced gas permeability—typically a sign of better curing quality. Conversely, lower surface moisture is associated with higher  $k_T$  values, suggesting insufficient curing and increased gas permeability.

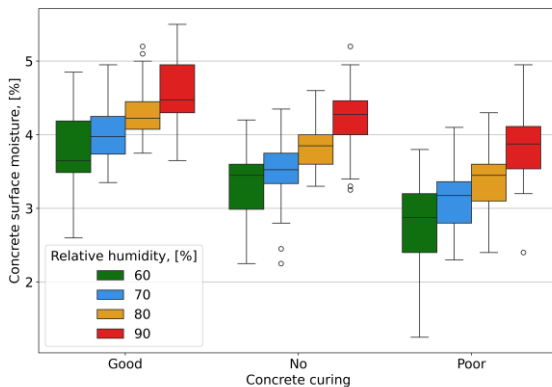


Figure 4. Moisture content of the material (in mass-%) as a function of curing conditions and different ambient humidity levels.

#### 4.5 Corrected $k_T$ Value

Referencing Torrent & Bueno et al. [12]: “Effect of surface moisture on air-permeability  $k_T$  and its correction”, it is well-established that moisture within concrete pores impedes gas flow and significantly affects gas permeability readings. While laboratory samples are often pre-conditioned through controlled drying, on-site measurements are typically performed under prevailing natural moisture conditions.

According to Swiss Standard SIA 262/1-E:2019, air permeability testing (Torrent method) on construction sites is only permitted if the concrete surface moisture ( $m$ ), as measured by electrical impedance, does not exceed 5.5%.

In this study, 50 data sets from five independent investigations were analyzed, showing a strong relationship between gas permeability ( $k_T$ ) and concrete moisture ( $m$ ). In 84% of the cases ( $R = 0.95$ ), this relationship could be described using an exponential function of the form:

$$k_T = k_{T_0} \cdot e^{d \cdot m} \quad (1)$$

with  $d$  typically ranging between 1.0 and 2.0 (median: 1.45). Based on these results, a practical correction method is proposed to mathematically adjust gas permeability measurements for moisture effects. For moisture levels between 4.5% and 5.5%, the correction is of minor practical relevance. However, incorporating such a correction into future versions of relevant standards is conceivable.

## 5 CONCLUSIONS

The presented research investigated the impact of various curing methods under otherwise nearly identical conditions.

The findings demonstrate that both the type and duration of curing significantly influence the gas permeability of concrete – and, by extension, the long-term durability of the structure. Therefore, gas permeability measurements can serve as an indirect indicator of curing quality.

This approach is notable for its straightforward and non-destructive application, suitable for both laboratory settings and on-site evaluations. The analysis of the collected data is efficient and uncomplicated. Existing recommendations, such as the representation of permeability values per test area according to Swiss Standard SIA 262/1:2019 [13], offer a useful framework for assessing surface quality.

However, since gas permeability is affected not only by curing conditions but also by concrete composition and other factors, it does not allow for a direct measurement of curing quality. One potential solution is to define a permeability threshold during the planning phase as a minimum standard for concrete performance. This threshold could be derived from reference measurements on similar concrete elements with the same composition. Implementing such a method would require extensive research to establish a statistically reliable dataset for defining acceptable limits.

A follow-up research project is currently underway, focusing on gas permeability testing of concrete structures with varying properties and exposed to different climatic conditions. Simultaneously, reference values are being gathered from test specimens with identical formulations and optimal curing to support the evaluation of site-specific results. While this approach shows promise, further research is essential to fully validate its effectiveness and reliability.

#### Summary of key findings:

- Laboratory investigations have confirmed that gas permeability measurement is a reliable and effective method for assessing the curing quality of concrete.
- A clear distinction in the permeability coefficient was observed between specimens with “good” curing and those with either “poor” or no curing. However, since gas permeability is also influenced by the specific concrete composition, it is not possible to define universal threshold values for curing quality evaluation.
- Inadequate curing leads to increased gas permeability and is also associated with a reduction in compressive strength compared to optimally cured concrete.
- Tests conducted on actual construction sites demonstrated that direct gas permeability measurements on structural elements yield valid insights into the quality of curing.
- Environmental conditions, such as wind, temperature, and humidity, significantly affect on-site measurements. These influences can either improve or impair concrete quality and must therefore be taken into account when choosing measurement locations, scheduling testing, and interpreting curing effectiveness.
- For field assessments, it is recommended – according to Swiss standard SIA 262/1:2019 – that at least six

individual  $k_T$  measurements be performed per testing area to ensure reliable results.

## ACKNOWLEDGMENTS

This work was carried out during VIF OptiNB activities. The authors would like to acknowledge Bundesministerium für Klimaschutz, Umwelt, Energie, Mobilität, Innovation und Technologie, ÖBB and ASFINAG als well as the Austrian Research Promotion Agency (FFG) for supporting this project.

## REFERENCES

- [1] Hayakawa, K.; Kato, Y. Effects of Construction Works and Mix Proportions on Quality of Cover-Concrete. J. Japan Soc. Civil Engs. 2012, 68(4), 399–409. (In Japanese)
- [2] Hayakawa, K.; Mizukami, S.; Kato, Y. A Fundamental Study for Quality Evaluation of Structural Cover-Concrete by Surface Air Permeability. J. Japan Soc. Civil Engs. 2012, 68(4), 385–398. (In Japanese)[SK1]
- [3] Kato, Y. Characteristics of the Surface Air Permeability Test and the Evaluation of Quality Variation in Cover Concrete due to Segregation of Concrete. J. Adv. Concr. Technol. 2013, 11, 322–332.
- [4] Kubens, S.; Wassermann, R.; Bentur, A. Non-Destructive Air Permeability Tests to Assess the Performance of the Concrete Cover. In Proceedings of the 15th Ibautil Intern. Baustofftagung, Bauhaus University, Weimar, Germany, 24–27 September 2003.
- [5] Kurashige, I.; Hironaga, M. Nondestructive Quality Evaluation of Surface Concrete with Various Curing Conditions. In Proceedings of CONSEC'10, Mérida, México, 7–9 June 2010.
- [6] Liang, J.; Maruya, T.; Sakamoto, J.; Matsumoto, J.; Shimomura, T.; Takizawa, M. Method for Compactability Evaluation of Concrete Based on Compaction Completion Energy. J. Japan Soc. Civil Engs. 2013, 69(4), 438–449. (In Japanese)[SK2]
- [7] Nakarai, K.; Shitama, K.; Nishio, S.; Sakai, Y.; Ueda, H.; Kishi, T. Long-Term Permeability Measurements on Site-Cast Concrete Box Culverts. Constr. Build. Mater. 2019, 198, 777–785.
- [8] Ptacek, L.; Grba, D.; Granzner, M.; Sattler, F.; Frangopol, D.M.; Strauss, A. Quality Control Criteria for Gas Permeability Testing of Concrete Structures. In Proceedings of Eurostruct 2023, Vienna, Austria, 26–28 September 2023.
- [9] Sakai, Y.; Nakamura, C.; Kishi, T. Correlation between Permeability of Concrete and Threshold Pore Size Obtained with Epoxy-Coated Sample. J. Adv. Concr. Technol. 2013, 11, 189–195.
- [10] Strauss, A.; Ptacek, L. Concrete Curing Performance Assessment Based on Gas Permeability Testing in the Lab and on Site. In Proceedings of the Conference on Durability of Infrastructure, Mendrisio, Switzerland, 25–27 March 2025.
- [11] Torrent, R.; Ebensperger, L. Studie über Methoden zur Messung und Beurteilung der Kennwerte des Überdeckungsbetons auf der Baustelle. Office Fédéral des Routes, Rapport No. 506, Bern, Suisse, Januar 1993, 119 p.
- [12] Bueno, V.; Nakarai, K.; Nguyen, M.H. et al. Effect of surface moisture on air-permeability  $k_T$  and its correction. Mater Struct 54, 89 (2021).
- [13] Swiss Standard SIA 262/1:2019 Betonbau - Ergänzende Festlegungen.

# Detailed material testing of adobe structures to complete a comprehensive SHM approach that includes laser scanning and ambient vibration studies

Shakhzod Takhirov<sup>1,0000-0002-4396-7946</sup>, Zukhritdin Ergashev<sup>2,0000-0002-9280-0616</sup>, Bakhodir Rakhmonov<sup>3,0000-0001-6285-2063</sup>, Amir Gilani<sup>4</sup>,  
Mirzokhid Akhmedov<sup>5</sup>, Ravshan Shamansurov<sup>6</sup>

<sup>1</sup>University of California - Berkeley, Berkeley, California, United States of America;

<sup>2</sup>Tashkent State Transport University, Tashkent, Uzbekistan;

<sup>3</sup>Urgench State University, Urgench, Uzbekistan;

<sup>4</sup>Miyamoto International, Sacramento, California, United States of America;

<sup>5</sup>Miyamoto International - Silk Road, Tashkent, Uzbekistan;

<sup>6</sup>Sigma Innovative Tech, Tashkent, Uzbekistan

email: [takhirov@berkeley.edu](mailto:takhirov@berkeley.edu), [ergashev33@gmail.com](mailto:ergashev33@gmail.com), [Rah-Bahodir@yandex.ru](mailto:Rah-Bahodir@yandex.ru), [agilani@miyamotointernational.com](mailto:agilani@miyamotointernational.com),  
[m.akhmedov@miyamotointernational.com](mailto:m.akhmedov@miyamotointernational.com), [shamansurov@rambler.ru](mailto:shamansurov@rambler.ru).

**ABSTRACT:** The research team, comprising international and local experts, has been studying heritage adobe buildings in Uzbekistan for several years. A few field studies were conducted at the heritage sites of Uzbekistan and Karakalpakstan: Toprak-Kala, Chadra Hauli, Ulli Hovli, and many others. As the first step of the comprehensive research strategy, laser scanning was used to generate accurate digital twins of the heritage structures. A non-destructive ambient vibration study of selected structures was conducted in the second step. This in-situ testing measures resonant frequencies and mechanical properties at very small excitations, which is insufficient for accurate numerical modeling. This study was conducted to address this shortcoming. A few adobe structures constructed of pakhsa were selected. Since the pakhsa is made of clay, which is available in the vicinity of the construction site, the exact georeferencing of each structure was considered. A few cylindrical samples were bored out from the walls of the structures and tested at the University of California, Berkeley. The samples were instrumented with strain gages, and they were investigated in compression and split tests. As a result of this study, Young's modulus, Poisson's ratio, and the strength of each test specimen were measured. These parameters will be used to generate more accurate numerical models of the structures and assess the advantages of reinforcement strategies for heritage structures.

**KEY WORDS:** Adobe heritage structures; structural health monitoring; pakhsa; numerical modeling; laser scanning.

## 1 GENERAL GUIDELINES

Buildings made of adobe materials are very common throughout the world. They represent a very affordable way of construction, utilizing local materials. In addition, the adobe buildings are environmentally friendly because their construction uses natural, renewable materials and energy-efficient construction methods. As a result, this construction has a smaller carbon footprint compared to conventional construction. In addition, the adobe buildings naturally retain heat inside longer during winter and preserve a cooler room environment on hot summer days.

The adobe construction is very common in Central Asian countries and is considered one of the traditional construction techniques in these regions. Adobe buildings can last a very long time. For example, the adobe structures of Toprak-Kala (Uzbekistan) are dated to the 2<sup>nd</sup> and 3<sup>rd</sup> centuries CE (Common Era). They still have an adequate structural health condition, as evaluated in a laser scanning study [1]. A recent discovery of previously unknown ancient cities, Tashbulak and Tugunbulak (Uzbekistan), revealed that these cities have adobe buildings dated to the 6<sup>th</sup>–11<sup>th</sup> century CE [2]. Another recent example is the four-story-tall Chadra Hauli in Uzbekistan, constructed in 1871 and still in excellent structural shape, as studied by using a laser scanner [3]. More than 200 Adobe buildings of more recent construction have been studied in rural areas of Tajikistan [4]. All of these structures are good representatives of pakhsa construction.

## 2 COMPREHENSIVE SHM APPROACH AND OBJECTIVES OF THIS PAPER

### 2.1 SHM of adobe buildings with performance prediction

A comprehensive approach is undertaken for the structural evaluation of the heritage structures and the prediction of their performance under various loading conditions. The structural evaluation and assessment are conducted using laser scanning technology to capture the current condition of heritage monuments in 3D accurately, as shown in Figure 1.

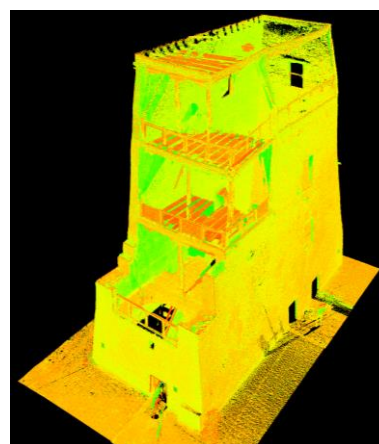


Figure 1. 3D point cloud of a heritage building collected by a laser scanner [3].



Based on the analysis of the point clouds collected by the laser scanner, all anomalies of the monuments are identified and studied in detail. Based on the 3D geometry captured by the laser scanner, an accurate finite element is created to investigate its structural performance under various loading conditions, as presented in Figure 2.

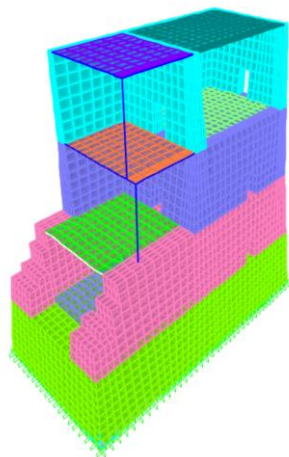


Figure 2. A finite element model of a heritage building was generated from the point cloud.

The finite element model requires input of the material properties of adobe to generate a realistic model. This information is difficult to obtain, as it relates to destructive testing, which is not permitted for heritage structures. Even if the collection of the sample is permitted, the benefits of the sample testing need to be investigated to optimize the sample set and the sample collection methods. This paper focuses on the development of a sample collecting procedure, a procedure for the preparation of collected samples for testing, and a procedure for testing to measure major material properties of the samples. These procedures are developed by investigating two buildings constructed of the same material as the heritage building, pakhsa. It is worth noting that there are a few standards focused on testing adobe samples, see [9], as a representative example. Still, their scope is very limited and does not provide any adequate guidance on reliable procedures for measuring the Young's modulus and Poisson's ratio.

## 2.2 Material properties of adobe: A brief review of the previous work

Adobe represents a man-made construction material that utilizes the raw earth material usually available close to the construction site. Hence, its mechanical characteristics depend on many parameters. These parameters can be as follows: the quality of earth material available for construction, the curing time of the clay before forming it into a wall or a brick, the way the clay was placed into the walls, bonding aggregates added to the earth material (if any), the quality of the craftsmanship work, the curing process after forming the wall, and many others. After the completion of construction, the mechanical properties can be affected by moisture. Therefore, there is substantial variability in the mechanical properties of adobe materials used in or taken from structures worldwide [5]. The mechanical properties are estimated by testing samples taken from adobe walls or created during construction (which is very rare). The samples can be collected in the form of cubes,

prisms, and cylinders, and the test results also depend on the shape of the test specimen [6]. For example, based on a comparative analysis of test results for cylinders [7] and [8], the Young's modulus of the adobe material varies by a factor of ten.

## 3 TESTING ADOBE CYLINDERS

### 3.1 General description of samples

The samples were collected from existing buildings at specific locations away from structurally critical areas. Two buildings were included in this study. One building was located in the Sabzovot region of Tashkent, Uzbekistan, and was estimated to be at least 60 years old. The second set of samples was collected from Sukok of the Tashkent Region. In both cases, the samples were bored out from the walls as presented in Figure 3.



Figure 3. Sample collection.

The hole in the wall after taking the bored cylinder out is presented in Figure 4.



Figure 4. Adobe wall after specimen collection

Since the specimens could break inside the bore during the boring process, their length varied from specimen to specimen, as shown in Figure 5. For consistency, only long specimens were used in the study, and the short ones were discarded. The long specimens were cut to a shorter length to maintain a similar length-to-diameter ratio.



Figure 5. Collected specimens before cutting them to the same length and selecting the best ones

The length and the diameter of each specimen are summarized in Table 1.

Table 1. Overall dimensions of adobe cylinders.

No	Length, mm	Diameter, mm	Geo-location
1	102	33	Sabzabot
2	110	52	Sabzabot
3	96	52	Sabzabot
4	105	52	Sabzabot
5	103	42	Sukok
6	104	44	Sukok
7	103	44	Sukok
8	103	43	Sukok

It is worth noting that the quality of the adobe material from these two geo-locations was noticeably different. The samples from Sabzovot were of a lighter color and were dense and uniform, whereas the samples from Sukok were of a darker color and had a few large voids, as shown in Figure 6. This difference played a significant role in the overall strength of the collected test specimens.



Figure 6. Adobe wall after specimen collection

### 3.2 Density results

The weight of each specimen was measured, and based on the calculated volume, the density was estimated as summarized in Table 2.

Table 2. Summary of density estimates.

No	Weight, g	Density, kg/m <sup>3</sup>	Average
1	148.4	1701.0	1541.0
2	343.4	1470.0	
3	303.6	1489.1	
4	335.3	1503.7	
5	218.9	1534.0	1468.5
6	219.3	1386.8	
7	217.8	1390.7	
8	233.7	1562.4	

As presented in the table above, the average density of specimens from Sabzovot was slightly greater than that of the specimens from Sukok.

### 3.3 Compression test: specimen preparation

As mentioned earlier, the specimens varied in length. All of them were cut to maintain the same length-to-diameter ratio. Since the specimens were quite brittle, they were cut in a special device, as shown in Figure 7.



Figure 7. Adobe specimen in a cutting device

To distribute the forces at the ends of the samples, the adobe specimens were sulfur-capped for the compression test as presented in Figure 8.



Figure 8. Adobe specimens with sulfur caps

Finally, the adobe specimens were instrumented by bi-axial strain gages as presented in Figure 9. The legs of the gage were

aligned with the longitudinal direction and the circumferential direction, respectively. A 40-mm long strain gage was used in this study.



Figure 9. Adobe specimen with bi-axial strain gage.

### 3.4 Compression test: strength

To measure the Young's modulus, Poisson's ratio, and strength of the specimens, they were tested using a compression test machine, as shown in Figure 10.



Figure 10. Adobe specimen in the compression test machine.

The compression load was applied at a constant rate of 25 N/s. A plot for Specimen No. 3 from the Sabzobot's geo-location showing the change of stress over time is presented in Figure 11.

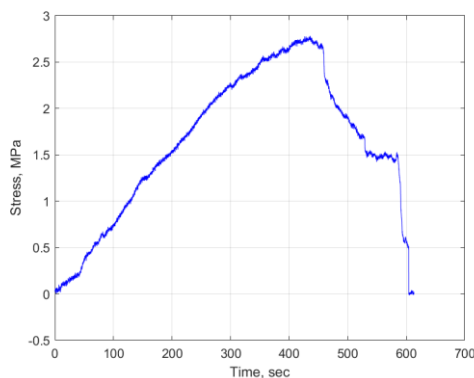


Figure 11. Force vs. time plot for Specimen No. 3.

As shown in the plot above, the stress steadily increases to the peak value, and there is a sharp decline in the compression stress capacity right after the peak value. A similar result was obtained for Specimen No. 4, as depicted in Figure 12. The peak load values were very close to each other, as summarized in Table 3. The table also shows the air humidity for each specimen on the day of testing.

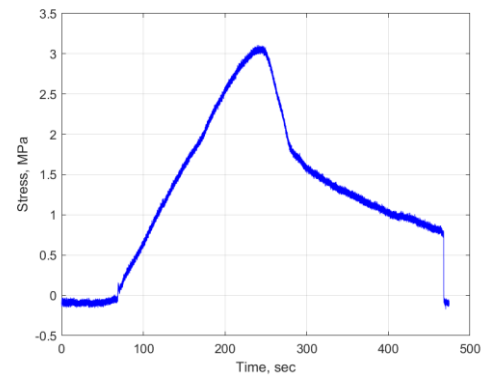


Figure 12. Stress vs. time plot for Specimen No. 4.

Table 3. Summary of compression strength (Sabzobot).

No	Peak load, N	Peak stress, MPa	Humidity, %
3	5911	2.78	30.0
4	6605	3.11	32.0

The results for the Sukok geo-location revealed different results. The strength capacity of the two tested specimens varied significantly, as presented in Figure 13 and Figure 14. The results are summarized in Table 4.

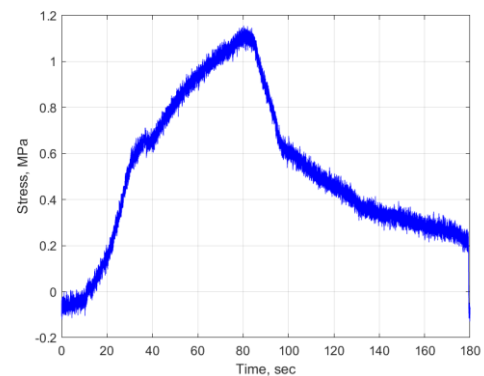


Figure 13. Stress vs. time plot for Specimen No. 6.

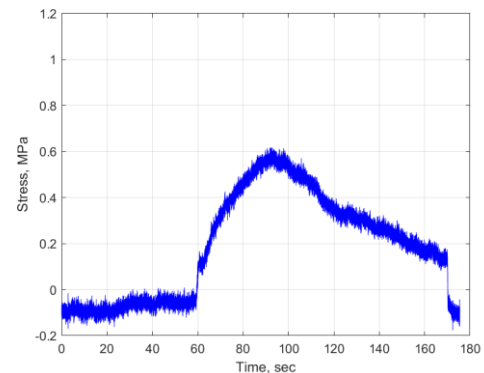


Figure 14. Stress vs. time plot for Specimen No. 7.



Table 4. Summary of compression strength (Sukok).

No	Peak load, N	Peak stress, MPa	Humidity, %
6	2456	1.16	32.0
7	1312	0.62	32.0

The larger variability in the test results was expected because the Sabzobot samples were more homogeneous than the Sukok samples, which had a few relatively large voids.

### 3.5 Compression test: Young modulus

Several approaches to measuring Young's modulus in compression for cylinder-shaped specimens have been previously proposed and utilized [6-8]. One of the primary objectives of this paper was to utilize existing methods and select the most suitable one for achieving consistency in data reduction; therefore, the following all three approaches were employed and evaluated. First, a slope of a secant line between the start and end of the linear portion of the stress-strain curve was used to estimate Young's modulus [6]. In this paper, the modulus based on this approach is denoted by  $E_{LR}$ . Second, the Young's modulus calculation was based on the slope of a secant line between 5 and 50% of the peak stress [8].  $E_{05-50}$  denotes the modulus based on this approach. Third, a slope of the secant between 33.3 and 66.6% of the peak stress was used for estimating Young's modulus [7].  $E_{33-66}$  denotes the modulus based on this approach. All three procedures were employed in this paper, and their results were compared to one another.

As mentioned earlier, a bis-axial strain gage was installed on each test sample. The longitudinal leg of the strain gauge was used to estimate Young's modulus. A plot showing stress ( $\sigma$ ) versus longitudinal strain ( $\epsilon$ ) for Specimen No. 3 is presented in Figure 15. The plot also displays the result of the linear regression, which was generated during the testing period, starting from loading and ending when the strain gage came out of the test specimen due to the gage's failure. It is worth noting that the latter point was very close to that when the peak stress occurs. The Young's modulus obtained from the linear regression ( $E_{LR}$ ) is also presented in the same plot. It is worth noting that the R-squared value of the linear regression is close to unity, indicating a good fit. It can also be observed visually that the stress-strain curve can be closely approximated with a straight line. To reduce the noise of the recorded data, which can be visually observed in Figure 14 and Figure 14, a running average over seven points was used to filter out the noise for the Young's modulus calculations.

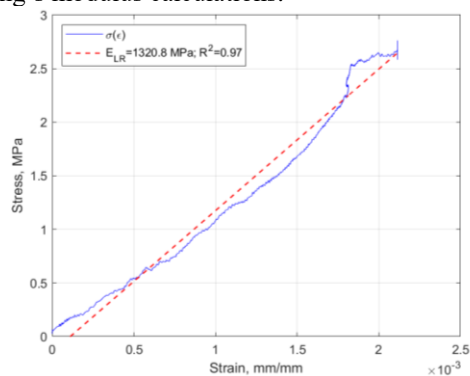


Figure 15. Stress vs. longitudinal strain plot for Specimen No. 3: Young's modulus from linear regression.

The results of the two other above-mentioned approaches for estimating Young's modulus are presented in Figure 16.

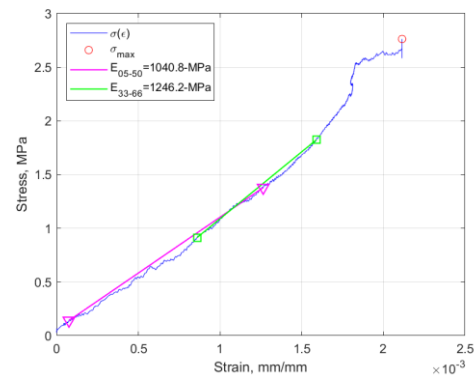


Figure 16. Stress vs. longitudinal strain plot for Specimen No. 3: two estimates of Young's modulus.

Similar results for Specimen No. 4 are presented in Figure 17 and Figure 18. As can be observed from the plots, the moment when the strain gage stopped working is very close to the moment when the maximum stress occurred.

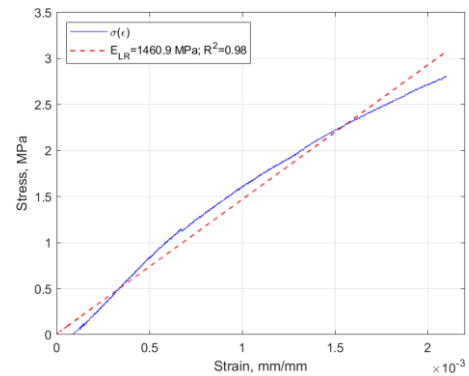


Figure 17. Stress vs. longitudinal strain plot for Specimen No. 4: Young's modulus from linear regression.

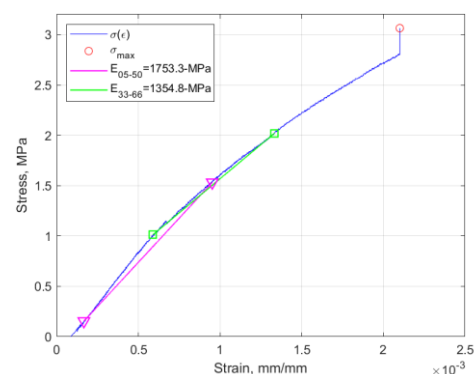


Figure 18. Stress vs. longitudinal strain plot for Specimen No. 4: two estimates of Young's modulus.

The results for the set collected from the Sabzobot geo-location show relatively large variation in the estimation of the Young's modulus, as summarized in Table 5. The variability of  $E_{05-50}$  is significantly greater than that of the other two modules. It depends on the overall trend of the stress-strain curve:  $E_{05-50}$  is less than  $E_{33-66}$  when the curve opens upwards (concave up), and  $E_{05-50}$  is greater than  $E_{33-66}$  when it opens downwards

(concave down). It is worth noting that the results for  $E_{33-66}$  in both cases are closer to those for  $E_{LR}$ , although slightly lower.

Table 5. Summary of estimations of Young's modulus (Sabzovot).

No	$E_{LR}$ , MPa ( $R^2$ )	$E_{05-50}$ , MPa	$E_{33-66}$ , MPa
3	1320.8 (0.97)	1040.8	1246.2
4	1460.9 (0.98)	1753.3	1354.8

The same calculation approaches were used for the sample set from the Sukok geo-location, and the results are summarized in Table 6. The stress-strain curves for Specimen 6, along with the respective values of Young's modulus, are presented in Figure 19 and Figure 20. It is worth noting that Specimen 7 data was very inconsistent with all other test results, and as such, it was considered an outlier.

Table 6. Summary of estimations of Young's modulus (Sukok).

No	$E_{LR}$ , MPa ( $R^2$ )	$E_{05-50}$ , MPa	$E_{33-66}$ , MPa
6	1258.5 (0.99)	1198.9	1361.6
7	671.9 (0.95)	547.3	1003.8

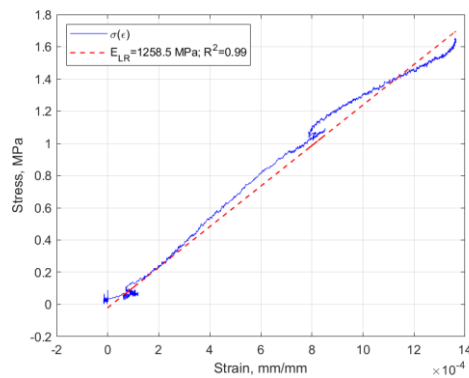


Figure 19. Stress vs. longitudinal strain plot for Specimen No. 6: Young's modulus from linear regression.

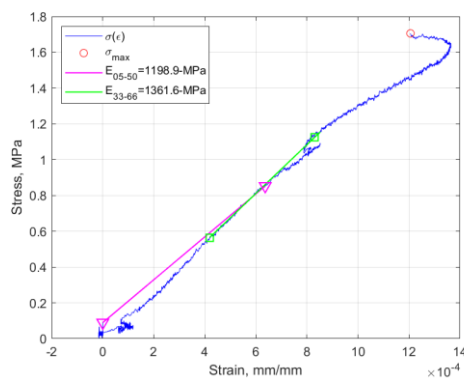


Figure 20. Stress vs. longitudinal strain plot for Specimen No. 6: two estimates of Young's modulus.

### 3.6 Compression test: Poisson's ratio

While the results for Young's modulus were reported for many locations worldwide [5], very limited information is available for the estimates of Poisson's ratio. This is especially true for the region of Central Asia. Therefore, one of the primary

objectives of this paper was to address this issue and to have a complete set of mechanical properties of some adobe buildings. For this purpose, a strain gage was installed to read the circumferential strain ( $\epsilon$ ) of the adobe cylinders.

Poisson's ratio ( $\nu$ ) was obtained by using the following expression:

$$\nu = -\epsilon/\epsilon \quad (1)$$

The results for Specimen No. 3 are presented in Figure 21. In this plot, only a portion of the data was used to ensure that both longitudinal and circumferential strain gages yield reasonable data. The portion of the plot in red corresponds to the data when the stress was between 33.3% and 66.6% of the maximum stress. The plot shows that the general trend of the change of Poisson's ratio with stress is very close to linear. In the red portion of the data, the values vary from 0.12 to 0.16 with an average of 0.14.

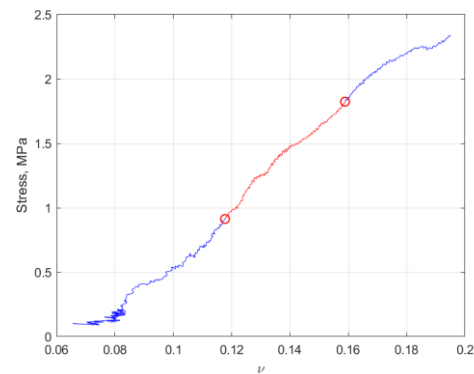


Figure 21. Stress vs. Poisson's ratio ( $\nu$ ) plot for Specimen No. 3: Sabzovot.

The respective results for Specimen No. 4 are shown in Figure 22. The plot shows that the general trend of the change of Poisson's ratio with stress is nonlinear. In the red portion of the data, the values vary from 0.12 to 0.18 with an average of 0.16.

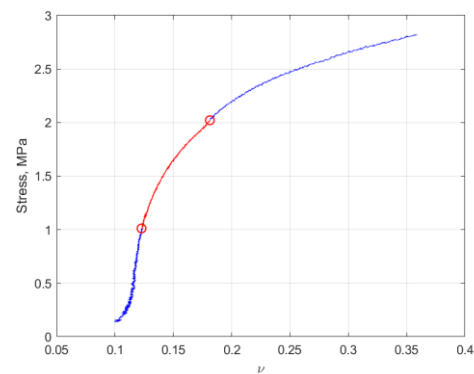


Figure 22. Stress vs. Poisson's ratio ( $\nu$ ) plot for Specimen No. 4: Sabzovot.

The test results for the specimens collected from Sukok geo-location are presented in Figure 23 and Figure 24. Specimen No. 6 (see Figure 23) yields stable results in the red portion of the data, where the value changes from 0.22 to 0.24 with an average of 0.23.

Specimen No. 7 was considered an outlier, and the results shown in Figure 24 serve as further evidence of this conclusion.

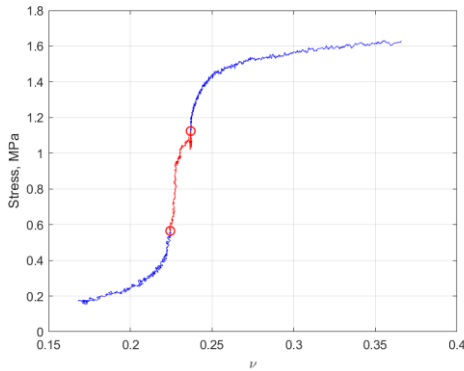


Figure 23. Stress vs. Poisson's ratio ( $\nu$ ) plot for Specimen No. 6: Sukok.

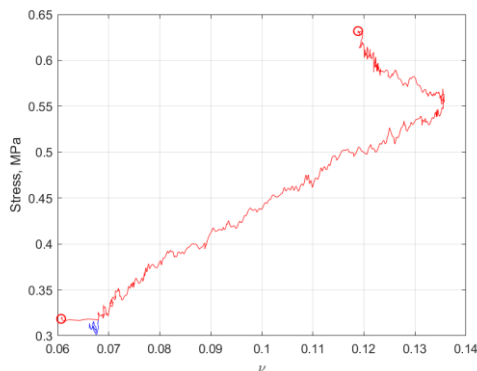


Figure 24. Stress vs. Poisson's ratio ( $\nu$ ) plot for Specimen No. 7: Sukok.

#### 4 DISCUSSION AND CONCLUSIONS

The results discussed in the paper show that the testing of adobe specimens can be challenging. It greatly depends on the procedures followed during specimen collection, handling from the collection site to the test site, and preparation for the test. In addition, it depends on the overall quality of the adobe wall from which the specimens are collected. The quality of the adobe wall is controlled by following parameters: the quality of earth material available at the construction site, the curing time of the clay before forming it into a wall or a brick, the way the clay was placed into the walls, bonding aggregates added to the earth material (if any), the quality of the craftsmanship work, the curing process after forming the wall, and many others.

Several cylinder-shaped samples were collected from two geo-locations in Uzbekistan. The density of all specimens was determined before the tests. Since some of the collected samples did not have a uniform and homogeneous structure, a total of eight samples (out of eleven total) were used in the density estimation. The compression tests were performed on four of them to estimate the following mechanical parameters: compression strength, Young's modulus, and Poisson's ratio. Based on previous studies, three approaches for calculating Young's modulus were employed. The correlation between the previously published results (only corresponding to cylinder-shaped specimens from the literature) and the results obtained in this study was as follows.

The comparison of the results of this paper to the previously published results on compressive strength of cylindrical

specimens is presented in Figure 25. As shown in the plot, the samples from Sabzobot geo-location were the greatest of all.

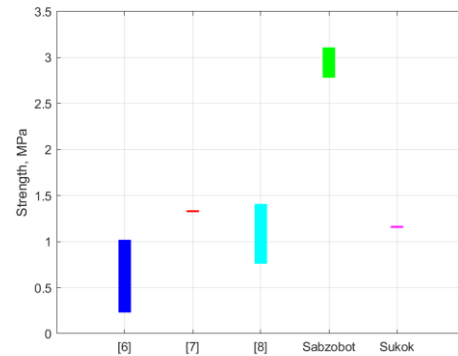


Figure 25. Compression strength results for Sabzovot and Sukok geo-locations compared to previously published [6], [7], and [8].

When comparing the Sabzovot and Sukok sets to [6], the compression strength of the adobe samples was slightly greater: the lowest value (excluding the outlier) is 1.16 MPa, versus 1.02 MPa [6]. Young's modulus was significantly lower: 1,461 MPa is the largest value obtained in this work, excluding the outlier, compared to 7,609 MPa reported earlier [6]. When compared to [7], the compression strength of adobe samples was slightly lower: the lowest value (excluding the outlier) is 1.16 MPa versus 1.33 MPa [7]. Young's modulus obtained in this study was significantly greater: 1,461 MPa is the largest value (excluding the outlier) versus 802 MPa reported earlier [7]. When compared to [8], the compression strength of adobe samples was slightly lower: the lowest value (excluding the outlier) is 1.16 MPa versus 1.71 MPa [7]. Young's modulus obtained in this study was significantly greater: 1,461 MPa was the largest value (excluding the outlier) versus 92 MPa published earlier [8].

The study showed that  $E_{0.5-50}$  depends on the direction of the overall curvature of the stress-strain curve and, as such, can have much larger variation. At the same time,  $E_{LR}$  and  $E_{33-66}$  yielded more similar results.

No literature references were found with respect to the experimental estimation of Poisson's ratio for adobe cylinders. The results of this study showed that Poisson's ratio is most likely stress-dependent, and for stress between 33.3% and 66.6% of the maximum stress, it can vary from about 0.12 to 0.24.

The results of this study will be used in finite element modelling of Chadra Hauily (Khorezm Region, Uzbekistan). The finite element mesh of the monument was generated by a laser scanner [3]; only the mechanical parameters of adobe were missing to generate a realistic model. This study fulfilled this need. The team is working on collecting more samples from other geo-locations to develop an extensive database of pakhsa properties in Central Asia.

It is worth noting that only a few test results are discussed here as representative examples. The research group is working on collecting more samples from other adobe buildings, including heritage buildings.



## ACKNOWLEDGMENTS

The authors would like to acknowledge the partial financial support and technical assistance of the Department of Civil and Environmental Engineering at the University of California, Berkeley.

## REFERENCES

- [1] Takhirov S., Rakhmonov B.S., Nafasov R., Samandarov A., Sultanova S., Akhmedov M.M., Shamansurov R.A. (2024). First Step Toward Preservation of Ancient Toprak Qala in Uzbekistan: Estimation of Erosion and Deterioration Rates by Laser Scanning. RILEM Bookseries, 47, pp. 581 - 590, Book chapter. DOI: 10.1007/978-3-031-39603-8\_47. [https://www.scopus.com/inward/record.uri?eid=2-s2.0-85170362061&doi=10.1007%2F978-3-031-39603-8\\_47&partnerID=40&md5=5d04041ade6b40f3983a6b064a8d5f78](https://www.scopus.com/inward/record.uri?eid=2-s2.0-85170362061&doi=10.1007%2F978-3-031-39603-8_47&partnerID=40&md5=5d04041ade6b40f3983a6b064a8d5f78).
- [2] Frachetti, M.D., Berner, J., Liu, X. et al. Large-scale medieval urbanism traced by UAV–lidar in highland Central Asia. *Nature* 634, 1118–1124 (2024). <https://doi.org/10.1038/s41586-024-08086-5>.
- [3] Takhirov S, Rakhmonov B, Akhmedov M, and Blondet M (2024) Structural Health Monitoring of Chadra Hauly (Khorezm, Uzbekistan) by Means of Laser Scanning. International Conference: Ensuring seismic safety and seismic stability of buildings and structures, applied problems of mechanics, Tashkent, Uzbekistan, May 27-29, 2024.
- [4] ADB (2025). Tajikistan: Case Study Report on Resilient Community Housing. Consultant's report (TA 6929-REG).
- [5] Silveira D et al. (2021). Mechanical Characterization of Adobe Bricks. In: Varum, H., Parisi, F., Tarque, N., & Silveira, D. (Eds.), *Structural Characterization and Seismic Retrofitting of Adobe Constructions. Building Pathology and Rehabilitation*, vol 20. Springer, Cham. [https://doi.org/10.1007/978-3-030-74737-4\\_3](https://doi.org/10.1007/978-3-030-74737-4_3).
- [6] Silveira D, Varum H, Costa A (2013) Influence of the testing procedures in the mechanical characterization of adobe bricks, *Construction and Building Materials*, Volume 40, Pages 719-728, ISSN 0950-0618, <https://doi.org/10.1016/j.conbuildmat.2012.11.058>.
- [7] Rodríguez-Mariscal JD, Solís M, Cifuentes H (2018) Methodological issues for the mechanical characterization of unfired earth bricks. *Constr Build Mater* 175: 804–814.
- [8] Illampas R, Ioannou I, Charmpis DC (2014) Adobe bricks under compression: experimental investigation and derivation of stress-strain equation. *Constr Build Mater* 53: 83–90.
- [9] ASTM (2023) ASTM C67/C67M-21: Standard Test Methods for Sampling and Testing Brick and Structural Clay Tile.

# Redundant Monitoring Strategies for Structural and Geohazard Assessment Using Wireless Tiltmeters and LiDAR on Linked Highway Bridges in Colombia

Víctor Restrepo<sup>1</sup>, Héctor Salazar<sup>2</sup>, Jean Piedrahita<sup>3</sup>

<sup>1</sup>Geoandina i SAS, Bogotá D.C., Colombia

<sup>2</sup>Geoandina i SAS, Bogotá D.C., Colombia

<sup>3</sup>Geoandina i SAS, Bogotá D.C., Colombia

email: vrestrepo@geoandina.net, hsalazar@geoandina.net, jpiedrahita@geoandina.net

**ABSTRACT:** The bridge system composed of Los Grillos, Puente Nuevo, and Chorro Blanco, located along the roadway connecting Sogamoso and Aguazul, near the municipality of Pajarito (Colombia), is founded on an active large-scale landslide in shale bedrock. This mass movement exhibits variable displacement rates depending on rainfall frequency over time. On August 20, 2023, the Los Grillos Bridge collapsed as a result of cumulative ground displacements that compromised its foundations and piers. Between July and December 2024, an integrated monitoring system was implemented, combining observations from an Automated Total Station (ATS), distance measurements using LiDAR, and tilt data obtained from inclinometers. The primary objective of this system is to establish correlations and track both ground and structural displacements, thereby supporting local stakeholders and decision-makers in the operational management of the remaining bridges still in service for civilian traffic. This paper presents the principal findings and illustrates how the integration of data from multiple sensor technologies enhanced the understanding of differential behavior between the ground and the structures. The analysis includes the collapsed bridge as well as the two remaining bridges in the affected area, providing timely and valuable information to support safe roadway operations.

**KEY WORDS:** Structural monitoring, Los Grillos Bridge, wireless sensors, landslide monitoring, Lidar ATS infrastructure monitoring, risk management.

## 1 INTRODUCTION AND GENERAL OVERVIEW

In Colombia, geological conditions present a wide range of engineering challenges, primarily due to the geodynamic behavior of the territory, which is heavily influenced by the presence of the Andes Mountain range across much of the country. These complex environments increase the risks that directly or indirectly affect social activities in these regions. Such risks may stem from seismic hazards, mass movements, among other factors, and have a direct impact on the design and construction of resilient and sustainable infrastructure.

In general terms and considering the current state of development in the country, one of the economic sectors most affected by geological conditions is freight transportation. Road corridors such as the one stretching from Sogamoso, Boyacá to Aguazul, Casanare—the focus of this study—are characterized by steep topography and high-mountain road networks, facing ongoing challenges in terms of mobility and connectivity.

Roadways with steep slopes, sharp curves, and unstable soils increase vulnerability to landslides, subsidence, and other impacts triggered by climatic phenomena such as heavy rainfall and thermal variability, including segments that traverse páramo ecosystems. These environmental factors significantly affect road safety, increase logistical costs, and prolong the time required for the transport of goods and personnel.

In the area located at station PR81 of the Sogamoso–Aguazul corridor, also known as the Cusiana Transversal, mass movement processes and geomorphological activity have been observed for more than two years and continue to occur to this day. These processes affect both the upper and lower zones of the surrounding slopes.

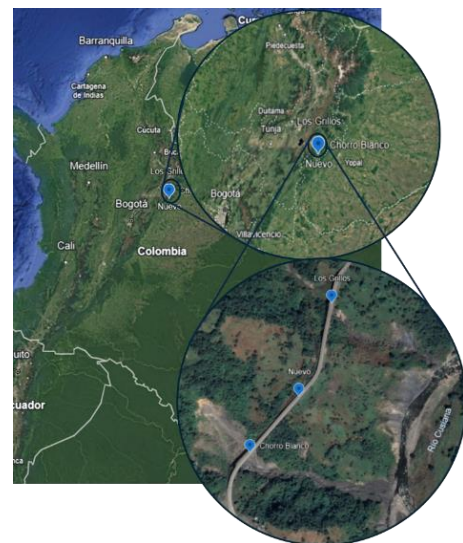


Figure 1. General location and panoramic view of the study area.

Given these geological conditions, a 666-meter-long viaduct was constructed, consisting of three consecutive bridges named Los Grillos (with a span of 261 meters), Nuevo (105 meters), and Chorro Blanco (300 meters from abutment to abutment).

Due to persistent landslides in the area, these structures are currently partially or completely out of service because of multiple evident structural pathologies. In the case of the Nuevo and Chorro Blanco bridges, significant deterioration has been observed, while the Los Grillos Bridge experienced a collapse of the structure.

Based on these geotechnical and structural conditions, and with the primary goal of providing continuous monitoring through an early warning system, two complementary monitoring systems were implemented.

The first system involved tracking three-dimensional displacements using automated readings of topographic prisms and virtual points with a GMS robotic LiDAR station (Geotech Monitoring Station).

The second system focused on structural monitoring of relative displacements and rotations through the use of triaxial inclinometers and wireless laser distance meters.



Figure 2. General overview of monitoring systems in sector PR81

In the face of these challenges, engineering plays a critical role in mitigating risks associated with road infrastructure and enhancing regional connectivity.

The application of advanced techniques for slope stabilization, pavement reinforcement, and geotechnical monitoring through automated methods contributes significantly to improving the safety and operational reliability of road corridors.

## 2 GEOLOGY AND GEOTECHNICAL INSTABILITY OF THE AREA

The study area is located between the municipalities of Sogamoso and Pajarito, in the department of Boyacá, Colombia. Hydrologically, the region where the monitoring points are situated is primarily influenced by the Cusiana River and the Chorro Blanco stream.

According to Sheet No. 192 of the regional geological map corresponding to the surroundings of Lake Tota, Department of Boyacá, Colombia, at a 1:100.000 scale [1], the sector known as PR81 lies within a geological unit referred to as the Macanal Shale Formation (Kilm), as shown in Figure 3.

This unit is predominantly composed of black shales interbedded with thin sandstone layers, which is indicative of a deep marine sedimentary environment typical of the Lower Cretaceous.

This paleoenvironmental interpretation is supported by field evidence, particularly the abundant presence of ammonite fossils, which serve as index fossils for this geological era.

The shales of this formation are fine-grained, rich in organic matter, and exhibit well-developed foliation, making them particularly susceptible to weathering processes and deformation under load or saturation conditions. These geomechanical characteristics significantly affect slope stability, subsoil behavior beneath structures, and the design of foundations or roadways that traverse such materials—factors that may account for the various active geotechnical processes currently observed in the area.

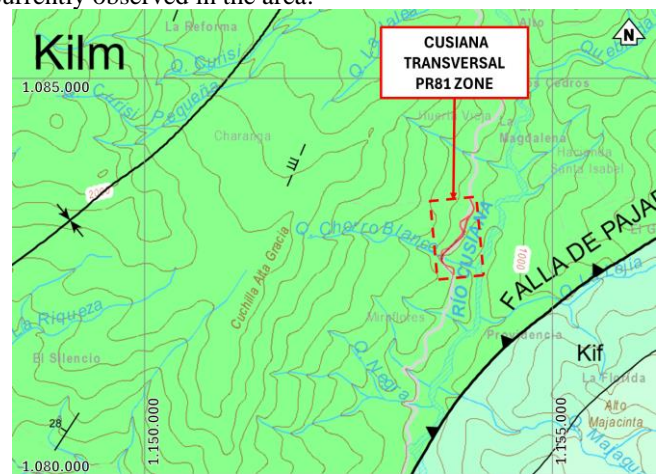


Figure 3. Regional geological map of the study area PR81 [1]

For years, the area has exhibited significant and progressive mass movement processes, particularly near the Chorro Blanco stream and along the slopes leading to the Cusiana River channel. This suggests that torrential flows from these tributaries may act as a triggering factor for the landslides and fissures observed on the slopes.



Figure 4. Evidence of geomorphological processes in sector PR81



### 3 STRUCTURAL COLLAPSE EVENT OF 2023 AT LOS GRILLOS BRIDGE

Due to the previously mentioned geodynamic conditions, among the three structures that comprise the viaduct, the Los Grillos Bridge exhibited the most significant deterioration. This was primarily attributed to its structural typology in conjunction with the landslides occurring in the area.

Since late 2022, multiple structural pathologies had been identified, raising concerns about the bridge's stability [2], with clear evidence of progressive structural degradation.

In 2023, following a series of seismic events with magnitudes ranging from 0.70 to 6.10, a collapse occurred on August 20 in a central section of the Los Grillos Bridge deck, located at the midpoint of the main span. This failure may have been influenced by a combination of factors, including material fatigue and cumulative effects of regional seismic activity.

The occurrence of these events underscores the critical importance of implementing continuous monitoring systems at the earliest signs of deterioration, integrating both geotechnical and structural data to enable comprehensive assessments and timely interventions.



Figure 5. Evidence of mass wasting processes near the foundations of the PR81 corridor bridges



Figure 6. Los Grillos bridge structural collapse.

### 4 IMPLEMENTED MONITORING SOLUTIONS

Considering the geotechnical challenges of the area, specific contingency measures were established to mitigate the risks faced by both the local population and construction personnel. Among these measures, a dual early warning system was implemented to monitor the displacement behavior of both the bridge superstructures and the surrounding slopes.

This dual system consisted of an automated total station based on LiDAR GMS technology, which conducted three-dimensional tracking of thirty (30) topographic prisms strategically installed in various sectors within the area of analysis.

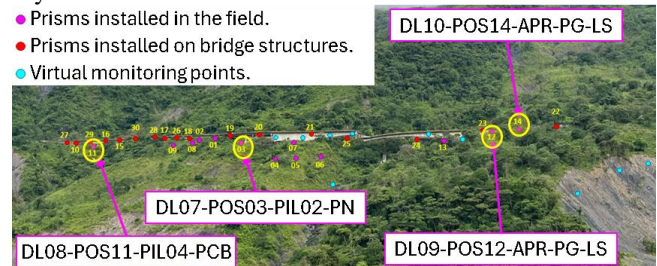


Figure 7. General location of measurement targets with GMS

Additionally, thirty-six (36) wireless sensors were installed. Of these, twenty-four (24) are triaxial clinometers used to monitor tilting at strategic locations on the viaduct bridges. The remaining twelve (12) sensors are laser distance meters equipped with triaxial clinometric sensors, designed to monitor relative displacements and inclinations.

These devices were mounted on poles located near exposed surfaces of the bridges, where topographic prisms were also installed to provide redundant data, monitored by the robotic GMS station.

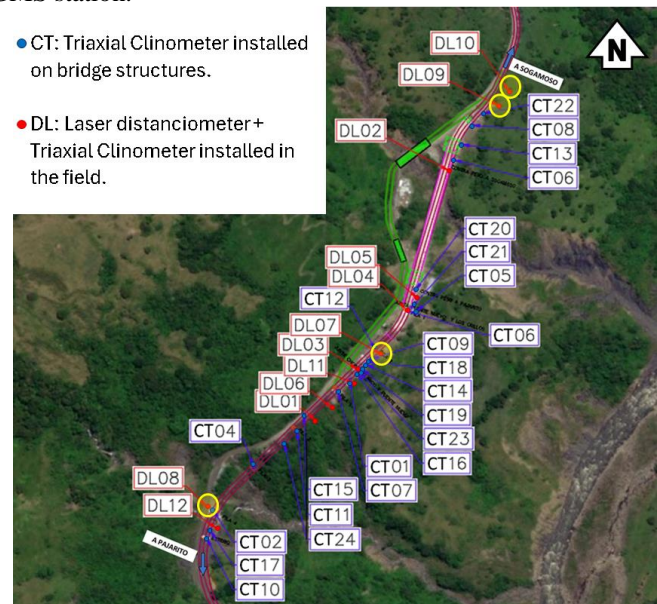


Figure 8. General location of wireless sensors

#### 4.1 Description of robotic lidar gms technology

This type of system consists of a state-of-the-art robotic total station capable of performing high-precision measurements of three-dimensional displacements on selected targets.

These targets may include both physical reference points, such as topographic prisms installed throughout the monitored area, and virtual points defined by pixel positions on images of exposed slopes or structural surfaces, using advanced image processing techniques.

This methodology enables continuous acquisition, processing, and analysis of displacement data within the area of interest. The resulting information facilitates the identification of incipient or progressive movements, as well as the establishment of behavioral trends in the short, medium, and long term.

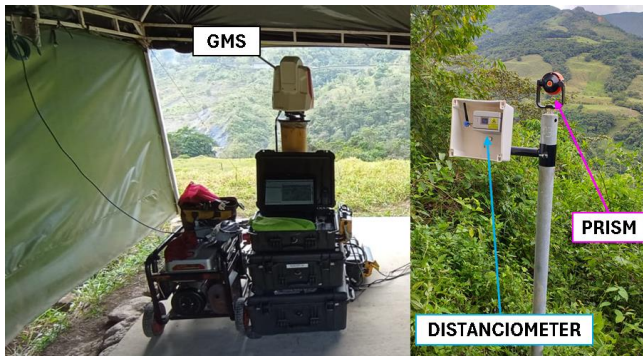
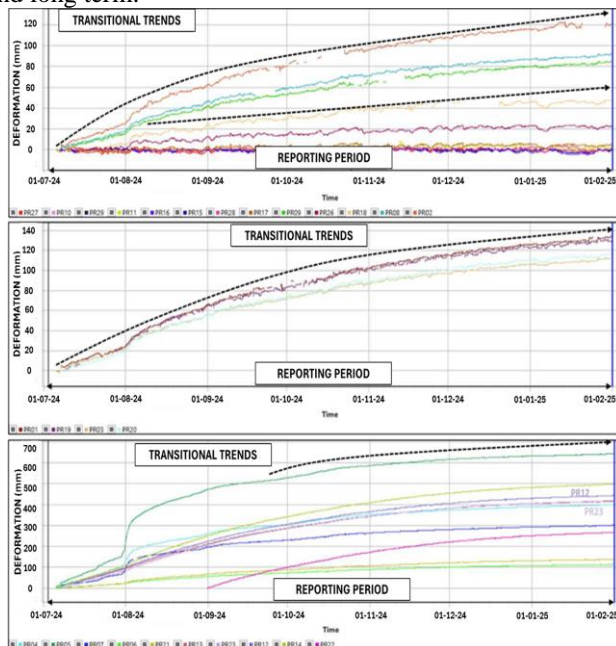


Figure 9. GMS Technology Implemented in Sector PR81

#### 4.2 Description of clinometric sensors and laser distance meters

This type of system enables the monitoring of displacements (via laser distance meters) and inclinations (via clinometers) at specific points on the structures.

Regarding the measurement of relative displacements, the laser distance meters project a light beam that allows for the measurement of the distance between the sensor location and a target surface, with high precision and under adverse environmental conditions.

On the other hand, the triaxial clinometers allow for the tracking of inclination angles, primarily along the two orthogonal axes, X and Y.

From this clinometric data, the displacement associated with the observed inclination can be calculated using trigonometric relationships.

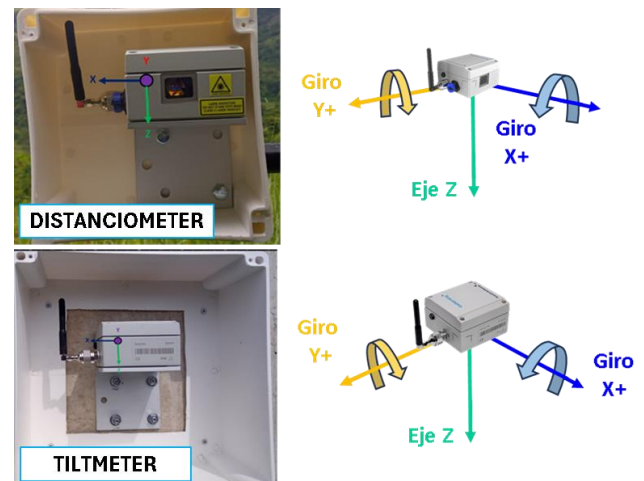
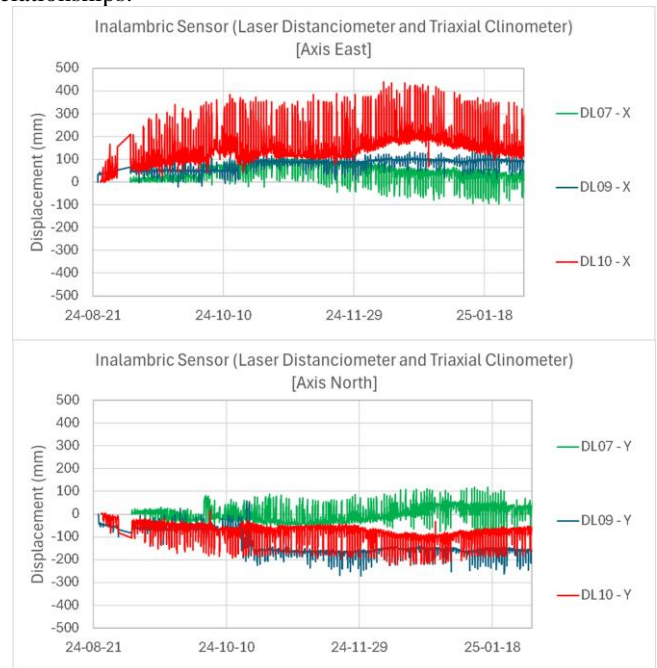


Figure 10. Sensor Technology Implemented in Sector PR81

### 5 RESULTS OBTAINED DURING THE GMS AND CLINOMETER MONITORING PERIOD

After nearly seven months of monitoring, primarily transient trends were observed in the study area PR81, both in the displacements recorded by the GMS equipment and in the inclinations measured by the triaxial clinometers.



It is important to note that, since the monitoring points reported movement data in their local axes ( $X'$ - $Y'$ ), the recorded values were transformed into local North-East coordinates. This transformation was performed through an orthogonal axis rotation (see Figure 11), as expressed in Equation 1.

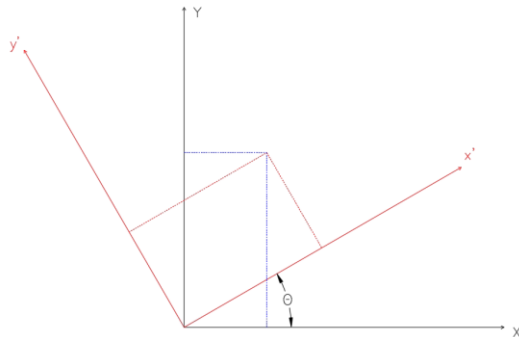


Figure 11. Diagram of orthogonal axis rotation

$$\begin{bmatrix} X \text{ (ESTE)} \\ Y \text{ (NORTE)} \end{bmatrix} = \begin{bmatrix} \cos(\theta) & -\sin(\theta) \\ \sin(\theta) & \cos(\theta) \end{bmatrix} \begin{bmatrix} x' \\ y' \end{bmatrix} \quad (1)$$

For each clinometer and laser distance meter, it was necessary to establish reference lines parallel to the bridge structures, as the instruments were installed following this alignment. Once these lines were defined, the angle between the local measurement axes and the global reference axes ( $X$ - $Y$ ), aligned with true north, was determined (Figure 12). By applying Equation 1, it was possible to transform the displacements recorded in local coordinates into the global coordinate system.

It is noted that, in the case of data obtained from the GMS (Geodetic Monitoring System), this transformation is performed automatically by the equipment, based on the predefined global axes and the relative orientation of each prism with respect to the measuring station, as determined by the laser projection



Figure 12. Axis diagram for the sensor DL02

Once the measurement results were transformed into global axes, it was possible to perform a comparative evaluation of the trends identified through both monitoring approaches (sensors and GMS).

As a summary, the data obtained for the following monitoring points are presented:

- Zone 1: Pile of Chorro Blanco Bridge (Prism PR11 – Sensor DL08).
- Zone 2: Pile of Nuevo Bridge (Prism PR03 – Sensor DL07).
- Zone 3: Sogamoso Abutment of Los Grillos Bridge (Prism PR12 – Sensor DL09).
- Zone 4: Sogamoso Abutment of Los Grillos Bridge (Prism PR14 – Sensor DL10).

For Zones 1 and 2, based on the data obtained from the dual monitoring system (GMS and sensor network), an initially positive incremental trend is observed along the X-axis (East), which subsequently tends to stabilize.

Similarly, although with an opposite pattern, the Y-axis (North) shows an initially negative incremental trend, also followed by a stabilization phase.

The global displacements recorded along both axes remain below 20 cm in magnitude, which aligns with field observations and with the presence of geomorphological indicators of slow-moving processes.

These behavioral patterns suggest a process of progressive deformation, followed by a decrease in displacement rates (as evidenced toward the end of the monitoring period), possibly associated with the seasonal transition from wet (winter) to dry (summer) periods.

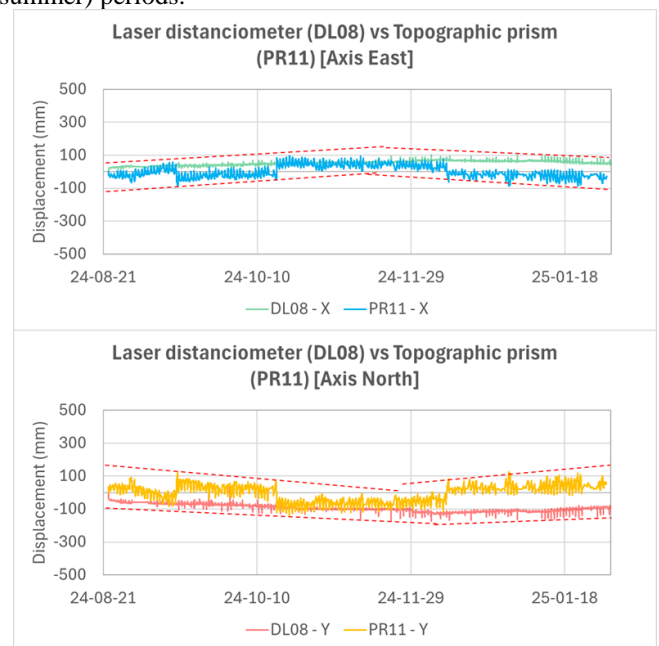


Figure 13. Location and historical record of horizontal displacements for Sector 1



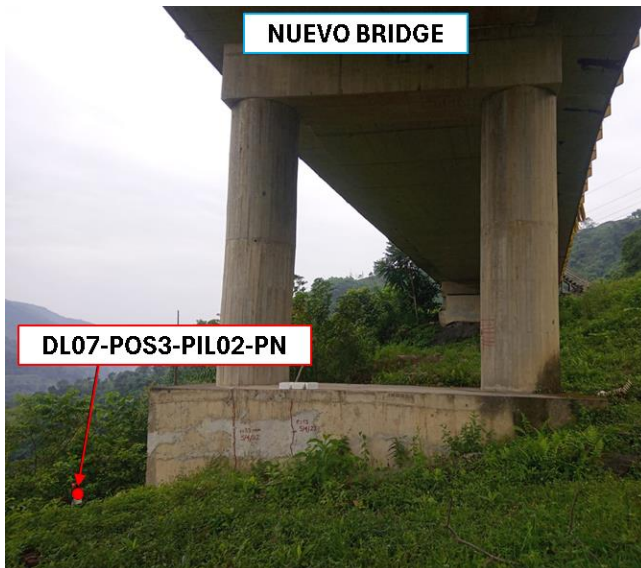
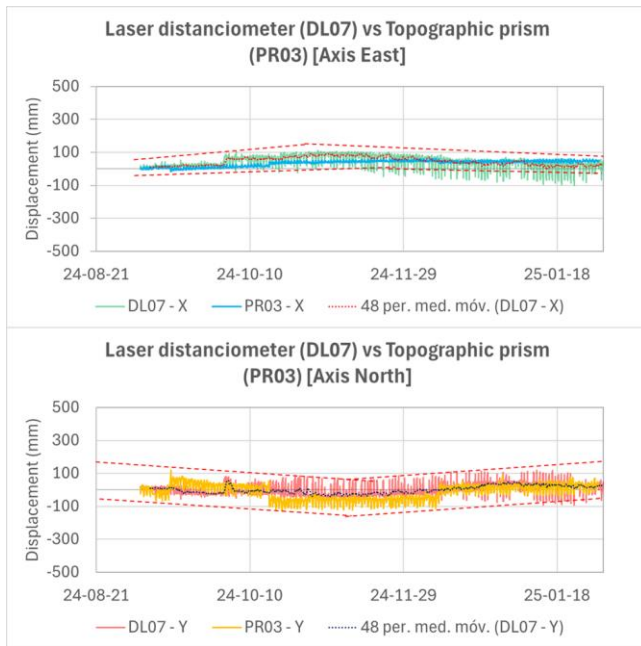


Figure 14. Location and historical record of horizontal displacements for Sector 2

On the other hand, for Zones 3 and 4, based on the information obtained during the monitoring period, mainly incremental displacement trends were identified, with more pronounced movement along the X-axis (East).

In contrast, the behavior along the Y-axis (North) tends to be more stable, exhibiting only minor variations.

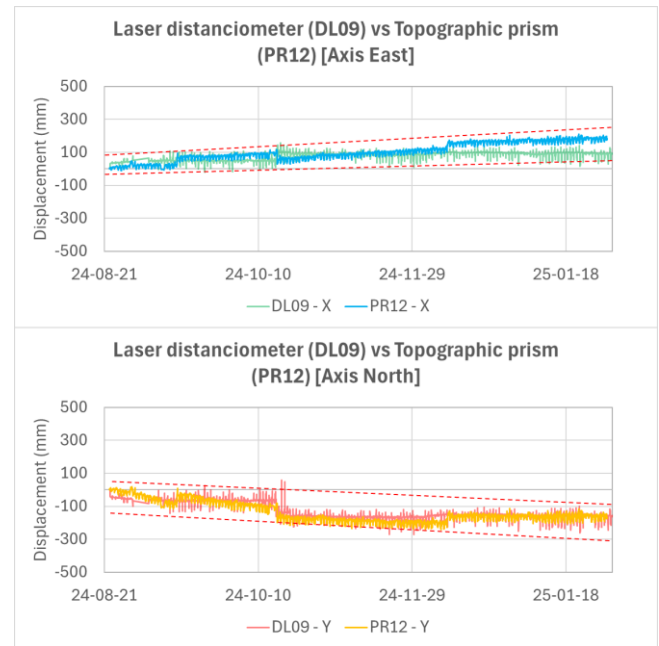


Figure 15. Location and historical record of horizontal displacements for Sector 3

The recorded displacements remained below 20 cm along the X-axis and below 25 cm along the Y-axis, values that are consistent with field observations and the documented surface morphological evolution in the area.

This behavior suggests a more active movement dynamic in the X-direction (East), possibly associated with the slope geometry, the orientation of the fracturing system, or the direction of the principal stress in the ground.

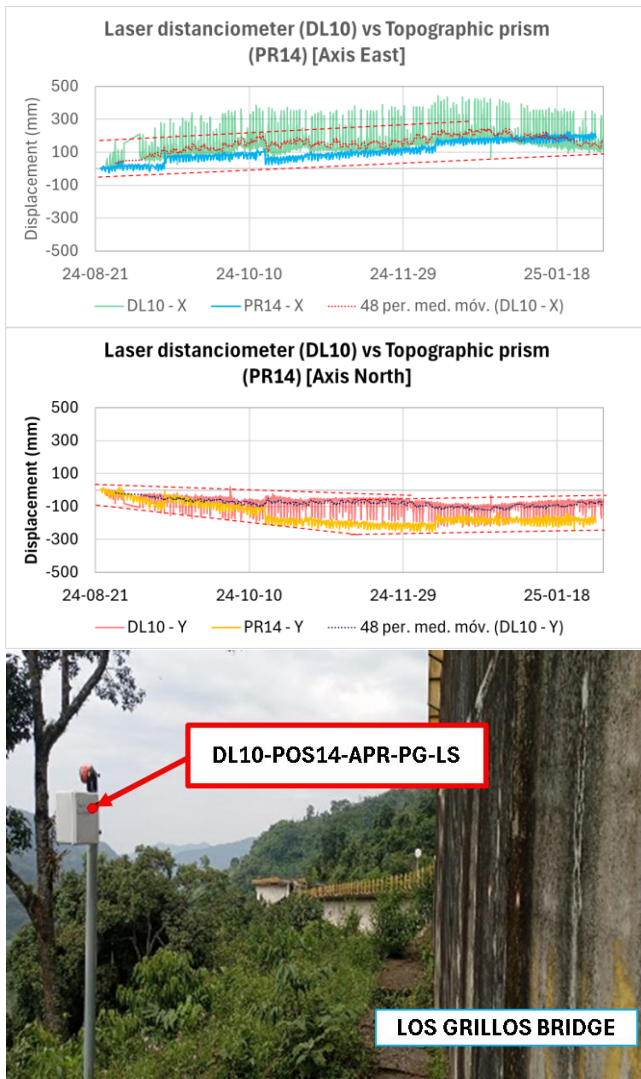


Figure 16. Location and historical record of horizontal displacements for Sector 4

### 5.1 Principal displacement directions identified

Regarding the displacement directions derived from the wireless sensors, it was observed that, as expected, movements recorded by devices installed directly on the ground exhibit greater magnitudes compared to those mounted on concrete structures.

This difference is primarily attributed to the foundation conditions of the structures, which tend to dissipate part of the deformation, as well as to the geological characteristics of the adjacent slopes, which favor greater displacement in the superficial soil layers.

Similarly, displacement behavior is also evident in the topographic prisms installed both on structural elements and on natural slopes. It is worth noting that, due to the specific conditions of the project, a higher density of prisms was installed in comparison to the wireless sensors deployed on the slopes.

This wider spatial distribution of topographic targets provides broader coverage of the monitored area, enabling a more detailed characterization of displacement patterns, particularly in critical zones of the terrain.

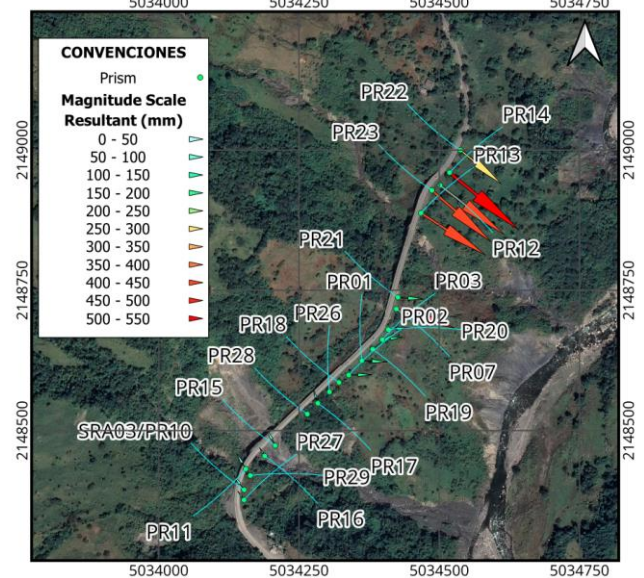


Figure 17. Principal Displacement Directions Identified Based on Measurements from Wireless Sensors

When comparing the results obtained from both monitoring systems, notable similarities are observed in the behavior of the monitored elements previously presented in this document.

These similarities suggest a degree of informational redundancy between the two systems.

The predominant displacement trends appear to be strongly influenced by the geomorphological characteristics of the area, which are generally aligned with the direction of the ongoing mass movement process occurring near the bridge foundation structures.

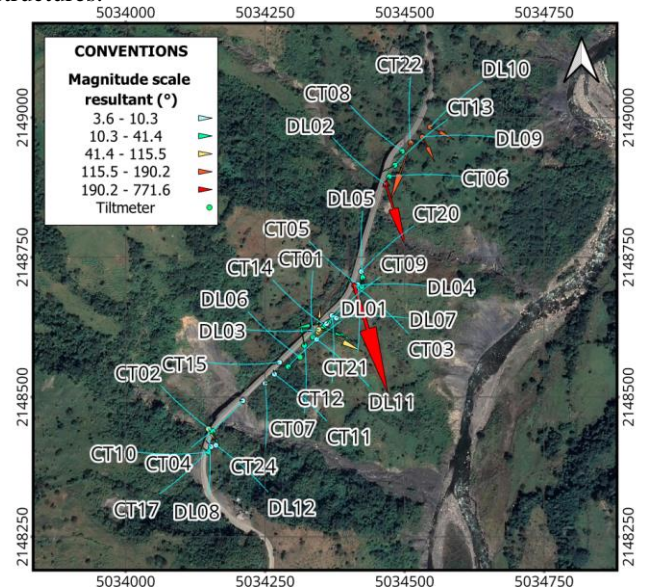


Figure 18. Principal Displacement Directions Identified Based on Measurements from topographic prism



The largest displacement magnitudes are concentrated around the abutment areas of the Los Grillos Bridge. It is important to highlight that, despite these observed similarities, the two monitoring systems are based on fundamentally different methodologies, each with its own limitations and advantages.

The convergence of results enhances the reliability of the data and supports the use of a hybrid monitoring strategy to improve interpretation, redundancy, and validation of both structural and geotechnical behavior over time.

## 6 DISCUSSION OF MAIN RESULTS

Based on the results obtained, an approximate correspondence can be identified between the displacement trends recorded by the wireless sensors (inclinometers) and those measured by the topographic prisms.

Likewise, a satisfactory agreement is observed in terms of the displacement magnitudes captured by both technologies.

It is important to highlight that the differences in magnitude can be attributed to the specific accuracy characteristics of each system. In this regard, the inclinometer-based methodology, being directly installed on the ground or the structural body, offers greater sensitivity and precision for detecting angular variations and relative displacements. It has been shown that, based on properly supervised studies conducted on buildings over 50 meters high, high-precision inclinometers provide optimal performance in the continuous monitoring of sub-millimetric displacements [3].

In contrast, monitoring through topographic prisms is subject to factors such as the distance between the GMS station and the target prisms, as well as atmospheric and visibility conditions, which may reduce its accuracy in detecting small-magnitude displacements. The precision of data obtained through geodetic equipment is mainly influenced by the atmospheric conditions along the measurement path. For example, in the case of a slope monitored in Austria, a variation of 1°C or 3.6 mbar resulted in measurement deviations of up to 10 mm over a 1 km measurement range [4]. Therefore, it becomes essential that the data acquisition system incorporates algorithms capable of applying atmospheric corrections in its operation, as is the case with the equipment used for monitoring sector PR81.

## 7 CONCLUSIONS

The results obtained through the implementation of a dual monitoring system—comprising wireless sensors (triaxial inclinometers and laser distance meters) and topographic prisms connected to the GMS (Geodetic Monitoring System)—provide a reliable and complementary framework for evaluating structural and geotechnical behavior in critical sections of the road corridor.

The identified displacement directions and magnitudes show an acceptable level of agreement between both monitoring methodologies, particularly in the analyzed sectors, which highlight the robustness and validity of the combined approach.

It was observed that the sensors installed directly on the ground recorded greater displacement magnitudes, which are consistent with local geotechnical conditions, slope geomorphology, and the foundation characteristics of the structures.

Additionally, although topographic prisms are more susceptible to external factors such as visibility and atmospheric conditions, they offer broader spatial coverage due to their higher installation density.

The convergence in displacement trends detected by both systems reinforces the reliability of monitoring data and enables a more comprehensive interpretation of the structural behavior in response to ongoing mass movement processes, especially in the vicinity of the Los Grillos Bridge.

This confirms the importance of integrating advanced sensor technologies with traditional geodetic monitoring methods to strengthen decision-making processes related to the design, maintenance, and risk management of critical infrastructure.

## ACKNOWLEDGMENTS

The authors express their sincere gratitude to all professionals, technicians, and the entire team who carried out the installation using high-access equipment in a complex geological setting. Special recognition is given to Alejandro Navarro and Cristhian Melo, whose work stood out for its passion and outstanding quality.

## REFERENCES

- [1] INGEOMINAS, Mapa de susceptibilidad a movimientos en masa: Plancha 192 Laguna de Tota 1:100.000, Instituto Colombiano de Geología y Minería (INGEOMINAS), Bogotá, Colombia, 2014. [Online]. Available: <https://recordcenter.sgc.gov.co/B4/13010010002291/mapa/pdf/0101022911300002.pdf>
- [2] Infobae, "Así quedó el puente Los Grillos tras el colapso: imágenes y videos muestran el estado de la estructura," Infobae, Bogotá, Colombia, agosto 21, 2023. [Online]. Available: <https://www.infobae.com/colombia/2023/08/21/asi-quedo-el-puente-los-grillos-tras-el-colapso-imagenes-y-videos-muestran-el-estado-de-la-estructura/>
- [3] G. De Roeck, S. Vanlanduit, M. Reynders, y B. Peeters, "Evaluation of high-precision sensors in structural monitoring," *Sensors*, vol. 10, no. 12, pp. 10870–10893, MDPI, 2010. [Online]. Available: <https://www.mdpi.com/1424-8220/10/12/10870>
- [4] P. Casagli, D. Tofani, F. Raspini, et al., "Geotechnical monitoring using total stations and laser scanners: critical aspects and solutions," *Journal of Civil Structural Health Monitoring*, vol. 7, pp. 415–428, Springer, 2017. [Online]. Available: <https://link.springer.com/article/10.1007/s13349-017-0250-4>





# Bridge Model Calibration and Validation Using Structural Health Monitoring Data

# Optimizing Bridge Recalculation: Uncertainty in SHM-Based Recalculation of Prestressed Concrete Bridges

Maria Walker<sup>1</sup>, Cedric Eisermann<sup>1</sup>, Jan-Hauke Bartels<sup>2</sup>, Steffen Marx<sup>1</sup>

<sup>1</sup>Institute of Concrete Structures, Faculty of Civil Engineering, TUD Dresden University of Technology, George-Bähr-Str. 1, 01069 Dresden, Germany

<sup>2</sup>LPI Ingenieurgesellschaft mbH, Völgerstraße 9, 30519 Hannover, Germany

email: maria.walker1@tu-dresden.de, cedric.eisermann@tu-dresden.de, bartels@lpi-ing.de, steffen.marx1@tu-dresden.de

**ABSTRACT:** There are several ways to incorporate SHM data into the structural assessment of existing bridges. Beyond conventional model calibration, SHM can improve environmental effects and load estimates, thereby reducing the model uncertainty. However, the measurement data itself is also affected by epistemic uncertainty. This paper investigates the influence of selected data quality characteristics on the recalculation of prestressed concrete bridges, focusing on the example of coupling joints. A research bridge serves as a case study, equipped with temperature sensors recording data since February 2024 until today. A numerical FE model of the bridge provides a solid basis for simulations. A sensitivity analysis was carried out to identify the key parameters influencing the results. This includes the effect of the temperature gradient on the fatigue stress of the coupling joint. The study demonstrates the impact of representativeness and coverage of measurements in a spatial and temporal context on the estimated remaining service life of the structure. It highlights the importance of the correct selection of the sensor number and placement, and of the data collection period length. The results confirm the suitability of the proposed methodology for the systematic evaluation of monitoring concepts. However, further research is needed to derive specific recommendations for the design of monitoring systems for coupling joints. This work contributes to optimized SHM-based bridge recalculation by providing a basis for assessing the quality of monitoring concepts and its influence on structural analysis.

**KEY WORDS:** Sensitivity analysis; Measurement uncertainty; Fatigue; Coupling joints; Temperature monitoring.

## 1 INTRODUCTION

A large number of bridges on Germany's federal highways were built in the 1960s and 1970s (see Figure 1) and have been exposed for more than 55 years to heavy traffic and other loads, for which they were not initially designed. About 47 % of these bridges are prestressed concrete bridges [1]. In addition to durability and overloading issues, fatigue is an important concern for many of these structures [2].

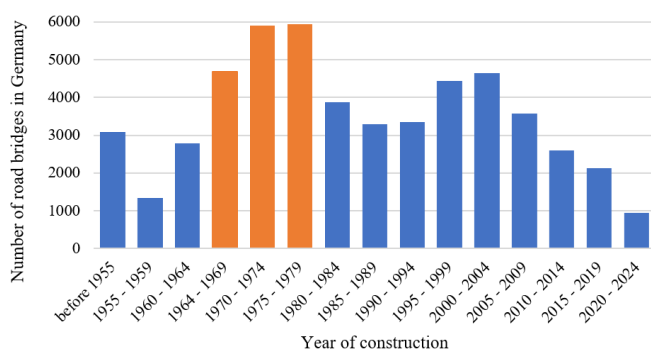


Figure 1. Bridge age along German federal highways, [1].

Long-span prestressed concrete bridges are typically constructed by concreting in sections (see Figure 2). Each section is prestressed as a partial structure to avoid the accumulation of frictional losses over the length of the superstructure. Each new section is prestressed against the previous one. The tendons are connected at the coupling joints by coupler anchors. One half of the fixed coupler anchor is embedded in the concrete of the previous section and serves as the end anchorage during the construction of this section. The

other half of the anchor is located in the new section (see Figure 2). The tendons are then connected by tying the tendons of the next section to the coupler anchor already embedded in the concrete [3].

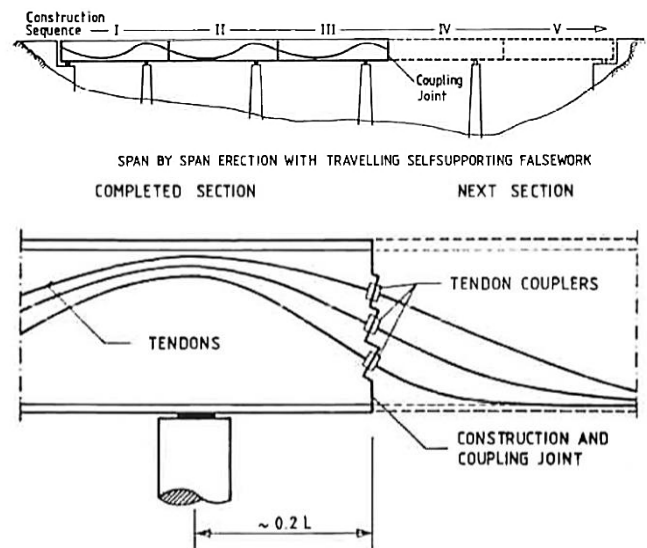


Figure 2. Section-by-section construction of a prestressed concrete bridge and a historical construction detail of a coupling joint, [4].

The first case of fatigue failure to coupler joints – and the only known fatigue failure to date – occurred in 1976 in the bridge “Hochstraße Prinzenallee” in Düsseldorf, Germany. This incident led to extensive theoretical and experimental research

[5; 6] as well as to the complementation of the technical rules for coupling joints in Germany. These regulations include the calculation of fatigue resistance, the more precise assessment of internal forces, and new design regulations. As a result of these regulations, it can generally be assumed that the coupling joints constructed from 1979 have no fatigue deficits [7]. The following causes of damage in coupling joints (vertical cracks and fatigue of tendons) were identified [3; 8; 9]:

- Concrete tensile strength in the joint is negligible;
- Neglect of temperature gradient over the height in the design stage;
- Position close to the points of contraflexure, where the temperature effects, and the scattering of the dead loads are important factors to consider;
- Non-linear strain distribution due to sectional prestressing;
- Internal stress states due to hydration heat;
- Increased prestressing losses in the coupling joint because of creep, shrinkage, and prestressing steel relaxation (CSR) due to the larger geometry of the couplers;
- Reduced fatigue strength of the tendons in the coupling joint due to fretting corrosion;
- Uneven distribution of tendons across the cross-section.

Consequently, infrastructure operators have routinely carried out recalculations of existing bridges based on advanced standards and guidelines. The recalculation guideline for existing road bridges [10] plays a key role in this context. After the introduction of this guideline in 2011, the results of the first recalculations were systematically evaluated in a research project on behalf of the Federal Highway and Transport Research Institute [11]. In this study, 43 % of the 126 investigated prestressed structures showed a calculational fatigue deficit at the coupling joints. This makes the fatigue verification of coupling joints the second most frequent failure mechanism that leads to calculational deficits. The recent evaluation of recalculations [7] took into account the first supplement to the recalculation guideline from 2015 [12]. The coupling joint fatigue was recalculated for 63 bridges, of which 33 showed deficits. In 37 % of the recalculations with coupling joint deficits, the fatigue resistance was exceeded by more than 50 % [7], see Figure 3.

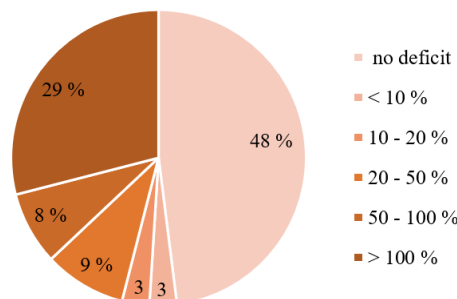


Figure 3. Fatigue deficits for coupling joints according to the German recalculation guideline after 2015, [7].

These calculational deficits do not necessarily indicate actual structural damage. However, they often lead to expensive external post-tensioning or even to a premature demolition of a bridge before the end of its intended service life. To improve

the assumptions about the actual impacts and resistances, the use of monitoring data is a powerful tool. The objective of monitoring is to reduce epistemic uncertainty, which arises from incomplete knowledge and can be reduced by increasing the amount of information or improving the model quality. In contrast, aleatory uncertainty – reflecting inherent randomness such as signal noise – is considered irreducible and is typically modeled stochastically [13–15]. In structural safety assessment, conservative assumptions are generally applied. Therefore, reducing epistemic uncertainty through monitoring data is expected to have a beneficial effect on the estimated load-bearing capacity and the predicted service life of the structure. This is especially true for bridges with high traffic volumes that exhibit considerable temporal variations in load, where incorporating measured daily temperature and traffic loads can yield more accurate results [16].

However, monitoring methods applied in practice are highly heterogeneous, with no standardized guidelines for the design of measurement systems, data evaluation, or data integration in the measurement-based recalculation. Standards for data quality requirements and quantifiable quality indicators are also missing. Consequently, monitoring concepts are often based on empirical knowledge, and the assessment of data quality remains subjective. The quality of the monitoring concept directly influences the quality of the resulting monitoring data, which in turn affects the reliability of structural condition assessments. Therefore, it is essential to consider both the data quality and the quality of the monitoring concept itself.

This paper presents a systematic methodology for the evaluation of an existing temperature monitoring concept, with regard to selected quality characteristics and their impact on the recalculation results using coupling joints as an example.

## 2 TEMPERATURE MONITORING FOR BRIDGE ASSESSMENT

The relationship between the bending moment  $M$  and the prestressing steel stress  $\sigma_P$  is described by the moment-stress diagram. The normal force, prestressing force, geometry of the cross section, material stiffness and tendon distribution influence the position and shape of the moment-stress curve, which is shown in Figure 4. It consists of three sections [17]:

- Linear-elastic behavior in uncracked state (Mode I)
- Transition area with concrete tensile strength  $f_{ct} = 0 \text{ N/mm}^2$
- Distinct cracked state (Mode II).

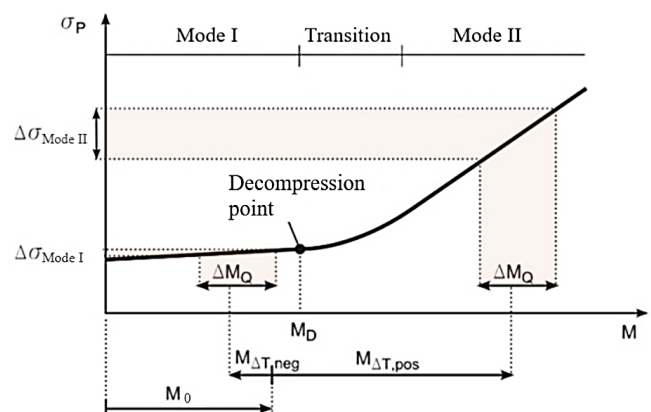


Figure 4. Moment-stress diagram for prestressing steel, [3].



In addition to the alternating moment  $\Delta M_Q$  due to traffic impact, the so-called base moment  $M_0$  has a substantial influence on the stress range  $\Delta \sigma_p$ . The base moment  $M_0$  is caused by the following components: dead weight of the structure, statically indeterminate part of the prestressing, losses due to CSR, redistributions from the construction to the final state, settlements as well as temperature loads. As long as the structure remains in Mode I, the stress range  $\Delta \sigma_{\text{Mode I}}$  is relatively low. However, once the decompression point is exceeded ( $M > M_D$ ) and the upper stress enters Mode II, fatigue-relevant stress ranges  $\Delta \sigma_{\text{Mode II}}$  are expected. The stress range  $\Delta \sigma_p$  in Mode II is considerably higher than in Mode I, despite the same impact through  $\Delta M_Q$ . The increase in the base moment  $M_0$  required for the Mode II can be caused, for example, by large vertical temperature gradients  $M_{\Delta T, \text{pos}}$  or prestressing losses [8]. For coupling joints, the moment component induced by temperature gradients is decisive in comparison to permanent loads, as they are typically located close to the points of contraflexure (points of zero bending moment). For older existing structures, variations of the base moment depend primarily on the temperature gradient, as redistributions, settlements and CSR are already completed [9].

For the reasons stated above, fatigue calculation of prestressed concrete bridges requires, in addition to the stress range  $\Delta \sigma$  in the prestressing steel from the traffic load  $\Delta M_Q$ , the knowledge of the magnitude of the base moment  $M_0$ . Therefore, the stress range monitoring in coupling joints is usually combined with temperature measurements. The temperature load  $M_{\Delta T}$  is a non-stationary variable influenced by environmental factors. While solar radiation and air temperature determine the general thermal input, wind speed and humidity affect the rate of heat exchange between the structure and the surrounding air. Additionally, the geographical orientation of the structure, height above ground, pavement thickness and other factors affect the temperature load [16].

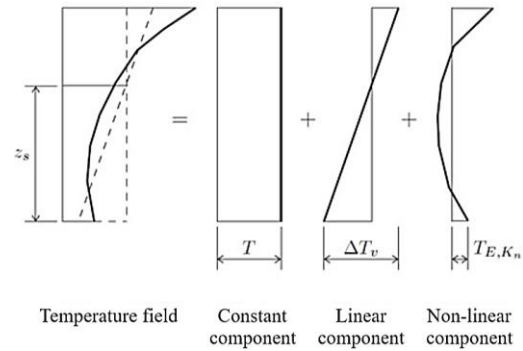


Figure 5. Temperature field components, [16].

The temperature field of a bridge cross-section can be divided into three components (Figure 5): (1) *The constant component*  $T$  induces no internal forces or stresses if the deformation of the structure is not impeded. (2) *The linear component*  $\Delta T_v$  causes a curvature that creates a constraining moment if the deflection is impeded. This component results in internal forces and therefore stresses in the cross-section. Only this component is considered in fatigue recalculations of coupling joints. (3) *The non-linear component*  $T_E$  is usually neglected in calculations of stresses [18].

In order to capture the linear temperature gradient over the entire cross-section, it is necessary to suitably distribute temperature sensors over the cross-section and to choose an appropriate monitoring period [16]. According to [2; 19], a measurement period of a whole year is sufficient to determine the structure-specific temperature load in the coupling joint. However, for Germany, the measurement period can be reduced to 3 to 6 months during the summer months (May to August), as both the highest positive and negative temperature gradients occur during this period [18]. Winter months are unsuitable for monitoring due to the low intensity of solar radiation. High gradients are especially observed when a cool, cloudy period is followed by a sunny day [9]. In [20] on the basis of measurements on a bridge and in [18] on the basis of simulation calculations, it was determined that the greatest temperature changes over the cross-sectional height occur in

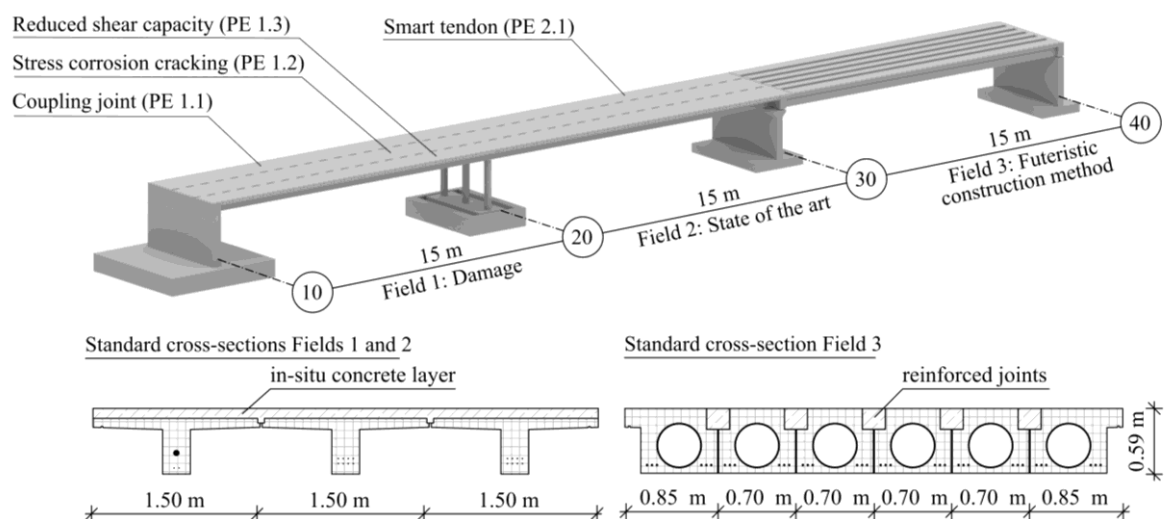


Figure 6. Illustration of the openLAB bridge including the standard cross-sections (Graphic: Fabian Collin, Max Herbers).

the slab, which requires a denser arrangement of temperature sensors in this area than in the webs.

The following section presents the existing measurement concept for recording temperature effects on a demonstrator structure – the openLAB research bridge located in Germany.

### 3 CASE STUDY: RESEARCH BRIDGE OPENLAB

#### 3.1 The structure and its coupling joint

The reference structure openLAB is a 45-meter-long and 4.5-meter-wide prestressed concrete bridge located in Bautzen, Germany. Constructed as part of the research project IDA-KI, it serves as a large-scale demonstrator for advancing structural health monitoring (SHM) and digital twin technologies. The bridge comprises three 15-meter spans, each meticulously designed to address specific research objectives [21].

Spans 1 and 2 consist of three precast elements (PE) with T-shaped cross-sections, which are transversely connected by a cast-in-place concrete layer, see Figure 5. Span 1 has been designed to replicate typical structural deficiencies of early tensioning methods, such as coupling joint problems, stress corrosion cracking, and areas with reduced shear capacity. Span 2 represents state-of-the-art construction methods and integrates innovative “smart tendons” which are equipped with integrated distributed fiber optic sensors [22]. Span 3 showcases a prefabricated construction system that eliminates the need for cast-in-place concrete. This system employs hollow precast elements that are transversely coupled by grouting joints, enabling the PE to be fully loadable immediately after installation.

All PEs are prestressed with strands that have an immediate bond. In addition, PE 1.1 and 2.1 are post-tensioned (see Figure 6 and Figure 7). The structural system features monolithic connections between the superstructure and substructure at axes 10 and 20. At axis 30, a connection between spans 2 and 3 with ultra-high-performance fiber-reinforced cementitious composite material (UHPFRC) is planned. However, the connection will be implemented at a later stage, after the first load tests planned for May 2025. Currently, span 3 remains statically decoupled from the other two spans.

The coupling joint under investigation is situated in PE 1.1, at the estimated point of contraflexure. The PE was constructed in multiple stages. Initially, a 4-meter segment of the element was fabricated and partially post-tensioned. Subsequently, the remaining 11-meter segment was cast, which also included the partial prestressing of the second tendon. The connection between the first and second tendons was achieved using a fixed coupler, certified under European Technical Assessment No. 13/0839. The first tendon was anchored in a manner consistent with the use of an anchor head for stressing anchors. In addition to a stress anchor, the coupler head provides a projecting ring collar with slots. The prestressing steel strands of the second tendon were placed in the slots and secured with a tensioning belt. Following this, the strands in immediate bond were prestressed, and the tendons in subsequent bond were tensioned to their final prestressing force. Finally, the tendon ducts were grouted to ensure proper bonding and corrosion protection of the prestressing steel.

#### 3.2 Temperature monitoring of openLAB

A comprehensive monitoring system has been installed at the openLAB since “hour zero” – the beginning of the construction phase. This monitoring system integrates global and local measurement techniques, providing detailed insights into the bridge’s structural behavior and environmental influences. Acceleration, inclination, and displacement sensors are employed to assess global structural behavior. Concurrently, environmental parameters such as air temperature, relative humidity, solar radiation, and precipitation are continuously recorded to account for external influences. Local measurements, in contrast, target areas susceptible to structural damage. These include strain gauges on reinforcement bars, distributed fiber optic sensors (DFOS) embedded in the concrete, and linear displacement transducers to monitor crack widths, e.g., in the coupling joint.

The component temperature is measured using temperature sensors, which were embedded into the PE 1.1 near the coupling joint during the construction phase. There are three temperature sensors (PT100) distributed over the height (see Figure 7). These sensors have been continuously recording data at 10-minute intervals since February 2024 until today.

To assess the influence of temperature measurement uncertainty on the recalculation results for the coupling joint, temperature data recorded by the component temperature sensors between January 31, 2024, and February 28, 2025, at 10-minute intervals, was used to calculate the linear temperature gradient. A reference dataset – Test No. 0.1 – was defined by using the full observation period (January 2024 to February 2025), a sampling interval of 10 minutes, and the complete sensor configuration including all three temperature sensors:  $T_{top}$ ,  $T_{middle}$ , and  $T_{bottom}$ .

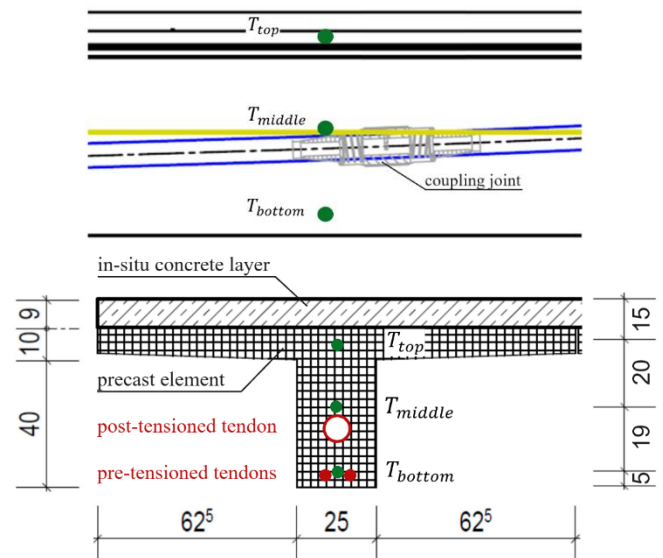


Figure 7. Installed temperature sensors embedded in the PE 1.1 of openLAB; all measures are given in cm.

The linear temperature gradient  $\Delta T_{M,y}$ , which induces a bending moment  $M_y$  in the coupling joint under consideration, is calculated using the following equation [23]:

$$\Delta T_{M,y} = \frac{h}{I_y} \cdot \sum_{i=1}^n T_i \cdot S_{y,i} \quad (1)$$

In this formulation,  $h$  denotes the total cross-sectional height,  $I_y$  is the second moment of area about the  $y$ -axis,  $T_i$  represents the temperature at a specific sub-area of the cross-section, and  $S_{y,i}$  is the first moment of area of the respective sub-area. The cross-section is conceptually discretized into  $n$  small sub-areas. The temperature values between the fixed-position sensors ( $T_{top}$ ,  $T_{middle}$ , and  $T_{bottom}$ ) are linearly interpolated or extrapolated to estimate the temperature distribution throughout the height of the cross-section. This approach is not limited to the number of available sensors but rather assumes a continuous distribution of temperature across the section.

### 3.3 Fatigue simulation

The residual fatigue life is predicted based on the accumulated fatigue damage  $D$ . Failure occurs at  $D = 1$ . The fatigue damage is calculated according to Miner's rule [24]:

$$D = \sum_{i=1}^m D_i = \sum_{i=1}^m \frac{n(\Delta\sigma_i)}{N(\Delta\sigma_i)} \leq 1 \quad (2)$$

The damage at a load level  $i$  is derived from the ratio of applied load cycles  $n$  to bearable load cycles  $N$ . The load cycles until failure are obtained from the S-N curve (Wöhler curve) according to the stress range  $\Delta\sigma_i$ . The progression of fatigue damage is simplified through extrapolation of the frequency of calculated stress ranges  $\Delta\sigma_i$  from varying traffic and temperature loads.

For traffic loads, the fatigue load model FLM 4, as defined by EN 1991-2, was applied. It consists of five standardized truck types which represent the characteristics of heavyweight traffic in Europe. To achieve relevant stress states up to the ultimate limit state with reasonable testing effort, only 25 % of Load Model 1 according to EN 1991-2 was considered for the design of the openLAB. Consequently, FLM 4 was appropriately scaled to ensure realistic stress amplitudes. Relevant load positions for the truck types were determined using influence lines.

For temperature loads, both the temperature gradients from the recalculation guideline and the temperature gradients from structural monitoring are considered (see Section 4.1).

The annual damage contribution  $D_{year}$  is calculated as the sum of partial damages  $D_{\Delta T,i}$ , incurred during the passage of a standard vehicle of type  $i$  under the simultaneous action of the temperature gradient  $\Delta T$ . The index  $i = 1 \dots 5$  covers the five vehicle types according to the FLM 4. Only high temperature gradients combined with heavy traffic lead to fatigue damage. The partial damage is weighted according to the relative frequency of individual vehicle types  $p_i$  in the annual traffic volume  $N_{obs}$  and the annual probability of occurrence of the temperature gradient  $\lambda_{T,\Delta T}$ :

$$D_{year} = N_{obs} \cdot \sum_{\Delta T=\min \Delta T}^{\max \Delta T} \left[ \sum_{i=1}^5 p_i \cdot \lambda_{T,\Delta T} \cdot D_{\Delta T,i} \right] \quad (3)$$

The calculation of internal forces in the cross-section of the coupling joint was performed using a linear-elastic finite element (FE) model developed in SOFiStiK (version 2024). Given the complete decoupling of spans 1 and 2 from span 3, the structural model was simplified to a two-span system. The

T-beams were modeled using beam elements with six degrees of freedom per node (three translations and three rotations). In the transverse direction, the three parallel beam axes were coupled using plate elements (see Figure 8).

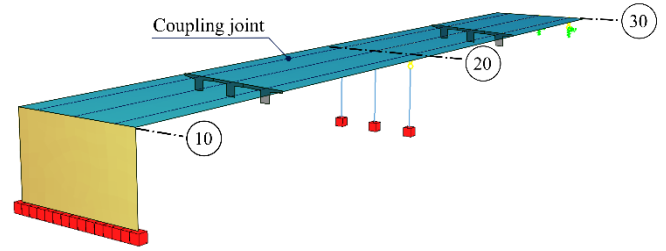


Figure 8: FE-Model of openLAB.

To accurately represent the load-bearing behavior of the integral structure, the abutment wall at axis 10 and the columns at axis 20 were modeled and rigidly coupled with the superstructure. Shell elements (abutment wall) and beam elements (columns) were used to idealize the substructures. At axis 30, the superstructure is supported on the substructure via a hinged connection. Thus, the pier wall at the support point was simplified using equivalent, linear-elastic springs. The tendons were integrated into the FE model according to their position in the construction plans. Prestressing forces were calculated internally by SOFiStiK and automatically applied to the intersected beam elements.

The structure was erected in various consecutive construction stages, which include the following: (1) manufacturing of the PEs in the factory; (2) construction of the substructures using cast-in-place concrete construction; (3) installation of PEs on temporary supports; and (4) production of the cast-in-place concrete layer for force-fit connection of PEs. The redistribution effects associated with this construction method, resulting from creep and shrinkage after the completion of the cast-in-place concrete addition, were accounted for in the FE model through different construction phases.

The calculation of the stress amplitudes  $\Delta\sigma_i$  were performed for the relevant cross-section also in SOFiStiK, considering the non-linear stress-strain relationships of concrete and steel.

## 4 IMPACT OF DATA QUALITY ON FATIGUE ASSESSMENT

### 4.1 Methodology

The collected measurement data only represents a sample from a total population. In this paper, three quality indicators were identified for the description of this property of measurement data at different levels: representativeness, coverage, and completeness. These quality indicators (for definition see Table 1) were originally presented by [25] for atmospheric measurements and adopted in the draft of VDI Guideline 3786 Sheet 1 [26]. These characteristics are adapted for the bridge monitoring and applied to the monitoring data of openLAB.

Completeness can be easily calculated as a percentage of the actual measurement data points relative to the expected measurement data points. This quality characteristic can be used to identify potential failures in the measurement system. In contrast, the other two quality characteristics – coverage and



representativeness – cannot be described with a simple formula and should already be considered when designing the measurement system. Therefore, the two characteristics – coverage and representativeness – are the subject of the following considerations.

Table 1. Quality characteristic for data of atmospheric measurements, [25; 26].

Quality characteristics	Definition according to [25; 26]
Representativeness	The ability of a series of observations to provide an unbiased estimate of a parameter of a specified statistical population.
Coverage	Spatial and/or temporal distribution of measurement locations in the area under investigation.
Completeness	The extent to which the information provided enables the data user to draw conclusions in accordance with the goal and scope definition.

Table 2 provides an overview of the definitions of these quality characteristics for bridge monitoring. Spatial representativeness refers to the areas of the bridge structure where sensors are installed. The temporal representativeness describes the period during which the data is collected. Spatial coverage describes the number of sensors distributed within the representative area of the structure and whether sufficient metrological redundancy is achieved. Temporal coverage refers to the sampling frequency of the measurements.

Table 2. Quality characteristics for bridge monitoring concepts.

Quality characteristics	Definition for bridge monitoring
Representativeness	Spatial: Local distribution of sensors
	Temporal: Period of data collection
Coverage	Spatial: Sensor density
	Temporal: Sampling frequency

Insufficient monitoring data completeness affects the coverage, which in turn affects the representativeness of the data. Furthermore, incorrect selection of monitoring areas and periods can render the monitoring results unusable for the intended use case, even if coverage and completeness are high. To address this problem, this paper presents a methodology using the openLAB research bridge as a case study. This methodology can be applied to identify sufficient representativeness and coverage of monitoring data.

The spatial representativeness is investigated by varying the local distribution of the sensors in the upper and lower area of the cross-section. To assess the temporal representativeness, the observation period for the temperature measurements at openLAB was systematically varied between two days and a whole year. Spatial coverage was analyzed by altering the number of sensors, while temporal coverage was assessed by applying different sampling frequencies. A total of four test

series were conducted in which only one of these three boundary conditions – observation period, sampling interval, sensor density, or local sensor distribution, – was varied at a time, while the others were held constant. This methodology corresponds to the one-at-a-time sensitivity analysis. The definition of the investigated test series is shown in Table 3.

Table 3. Definition of investigated test series.

No.	Description	Specification
0.0	Recalculation guideline	-
0.1	Reference measurement	12 months; 3 sensors
1.2	April – September	6 months; 3 sensors
1.3	May – August	4 months; 3 sensors
1.4	May – July	3 months; 3 sensors
1.5	June – July	2 months; 3 sensors
1.6	June	1 month; 3 sensors
1.7	08.07. – 09.07.2024	2 days; 3 sensors
2.2	0.00028 Hz (every hour)	12 months; 3 sensors
2.3	0.00002 Hz (every 12 hours)	12 months; 3 sensors
2.4	0.00001 Hz (every 24 hours)	12 months; 3 sensors
3.2	Upper and lower sensor	12 months; 2 sensors
4.2	Upper and middle sensor	12 months; 2 sensors
4.3	Middle and lower sensor	12 months; 2 sensors

Test Series 1 examines the impact of the temporal representativeness by shortening the observation period to six months (April - September 2024), four months (May - August 2024), three months (May - July 2024), two months (June - July 2024), one month (June 2024), and finally two days (July 8 - 9, 2024). The two-day period was selected according to the criteria that a cloudy day was followed by a sunny day [9]. This ensured a strong increase in air temperature and solar radiation within the observation period (Figure 9), which is expected to lead to high temperature gradients in the structure.

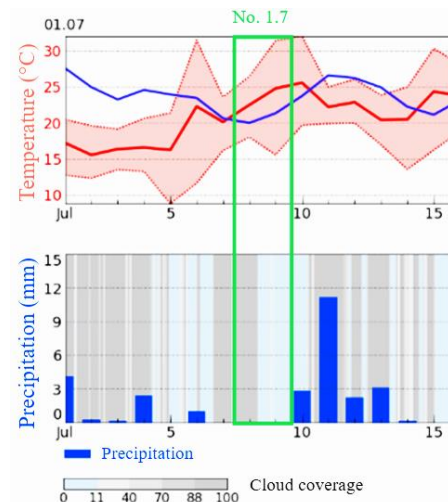


Figure 9. Meteorological data for the location Bautzen, Germany for the period from July 1<sup>st</sup> to July 15<sup>th</sup> 2024, [27].

Test Series 2 investigates the influence of the temporal coverage, i.e., sampling interval, by increasing it from the reference value of 10 minutes to 60 minutes, 720 minutes, and 1440 minutes.

Test Series 3 examines the effect of spatial coverage. In addition to the reference case using all three sensors ( $T_{top}$ ,  $T_{middle}$ ,  $T_{bottom}$ ), this scenario considers only two sensors:

$T_{top}$  and  $T_{bottom}$ . Due to the limited number of installed sensors, only one variation of spatial coverage was possible.

Test Series 4 addresses the spatial representativeness in two scenarios with two sensors each:  $T_{top}$  and  $T_{middle}$ , and  $T_{middle}$  and  $T_{bottom}$ , with the objective of concentrating the sensors primarily at the bottom or top of the cross-section.

The probability distributions for the temperature gradients were determined according to the methodology presented in Section 3.2. The results of the parameter study for the calculation of the linear temperature gradient  $\Delta T_{M,y}$  are illustrated in Figure 10. The linear temperature gradient determined for the openLAB is presented as a histogram of relative frequency  $f$  over  $\Delta T_{M,y}$  for each test case. The reference case exhibits an approximately normal distribution, whereas, for example, Test 1.7 (observation period from July 8 to July 9, 2024) shows a notable deviation from normality due to the limited number of temperature readings. Other histograms reveal distributions with varying degrees of positive or negative skewness when compared to the reference distribution.

In the next step of the analysis, these histograms derived from real-world temperature measurements will be used to estimate the remaining service life of the openLAB structure according to the Section 3.3.

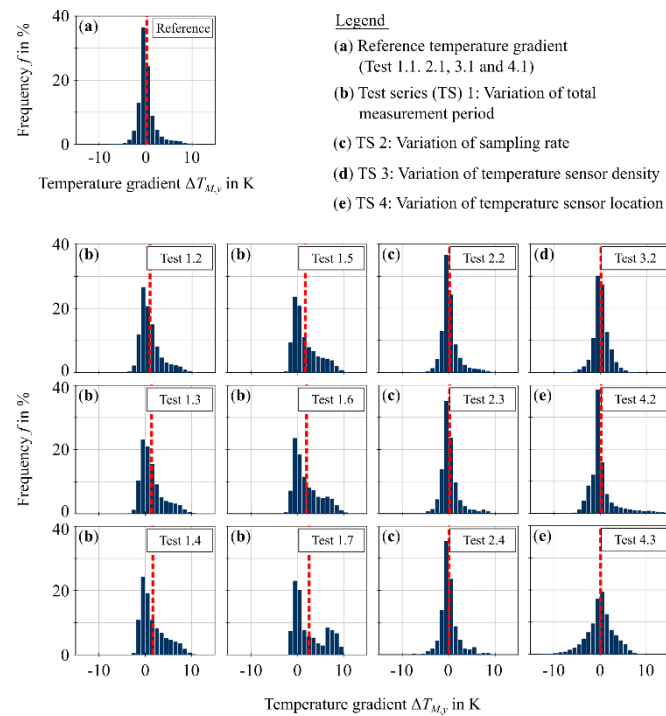


Figure 10. Parameter study on the influence of temperature measurement uncertainty on the linear temperature gradient. (a) Reference distribution; (b) Test series 1: Variation of total measurement period; (c) Test series 2: Variation of sampling rate; (d) Test series 3: Variation of temperature sensor density; (e) Test series 4: Variation of temperature sensor location.

In the German recalculation guideline [10], the temperature gradients are calculated in accordance with the reference standards DIN FB 101 and Eurocode DIN 1991-1-5. In addition, probabilities of occurrence for temperature gradients

are specified for the calculation with the fatigue load model FLM 4. The guideline states temperature gradients to be applied according to the probability of occurrence and the cross-sectional shape of the bridge (box girder, T-beam, or slab) for a pavement thickness of 50 mm. The probabilities of occurrence for the temperature gradients were determined based on extensive investigations in [16]. For this purpose, hourly weather data were collected over eight years for three typical bridge cross-sections and evaluated statistically. The distribution and the daily course of the temperature load given in the German recalculation guideline were derived from this data. This standardized probability distribution is compared to the bridge-specific measurements of openLAB in Section 4.2. This comparison enables a quantification of the uncertainty in  $\Delta T_{M,y}$  and its impact on the total service life assessment of the openLAB bridge.

## 4.2 Results

The results of the temperature gradient evaluation and the recalculation of the total service life for the coupling joint fatigue are summarized in Table 4. The first column corresponds to the test number. Test No. 0.0 represents the normative distribution given in the recalculation guideline, while No. 0.1 corresponds to the reference distribution, for which the entire temperature data set was utilized. The second and third columns contain the mean values  $\mu$  and the values of the standard deviation  $\sigma$  of the temperature gradients  $\Delta T$  in Kelvin. The third column provides the total service life in years for the respective data set about fatigue in the coupling joint. The last column shows the relative deviation of the service life compared to the reference distribution No. 0.1 in percent.

Table 4. Results of fatigue calculation.

No.	$\mu$ of $\Delta T$ in Kelvin	$\sigma$ of $\Delta T$ in Kelvin	Absolute service life in years	Relative deviation of service life in %
0.0	1.800	$\pm 2.619$	1077.583 (recalculation guideline)	+ 7.69
0.1	0.198	$\pm 1.887$	<b>1000.634 (reference)</b>	-
1.2	0.983	$\pm 2.289$	1051.303	+ 5.06
1.3	1.357	$\pm 2.463$	1075.903	+ 7.52
1.4	1.625	$\pm 2.698$	1092.141	+ 9.14
1.5	1.720	$\pm 2.731$	1098.567	+ 9.79
1.6	2.013	$\pm 2.873$	1117.958	+ 11.72
1.7	2.546	$\pm 3.334$	1147.002	+ 14.63
2.2	0.198	$\pm 1.887$	1000.509	- 0.01
2.3	0.176	$\pm 1.954$	998.609	- 0.20
2.4	0.082	$\pm 1.926$	992.569	- 0.08
3.2	0.184	$\pm 1.633$	1001.866	+ 0.12
4.2	0.220	$\pm 2.820$	989.575	- 1.11
4.3	0.146	$\pm 2.839$	985.031	- 1.56

Overall, the variations in the measured data result in only minor deviations in the service life, which was determined to be approximately 1045 years on average for all test series. The service life that was calculated on the basis of the reference configuration gave a result of approximately 1001 years. Relative values range from -1.56 % to +14.63 %. This observation indicates that the impact of the temperature

measurement uncertainty may not be a relevant factor for this structure with a relatively moderate influence on the fatigue of the coupling joint. The identification of relevant influence factors on the fatigue of the openLAB bridge will be systematically investigated in the further course of this study using a sensitivity analysis. It will enable a comparison of temperature influences with other relevant factors such as variation of traffic loads, prestressing losses or material properties.

It can be seen that the probability distribution of the temperature gradients from the recalculation guideline No. 0.0 leads to a slight overestimation of service life (+ 7.69 %) compared to the reference distribution No. 1.1 based on the complete measurement temperature data. In test series 1.2 to 1.7, in which the recording period becomes progressively shorter, there is a shift in the mean value towards high gradients and an increase in the standard deviation. Contrary to the expectation that this temperature gradient distribution would result in a reduced service life of the bridge, it continues to increase. This finding contradicts the information available in the literature (e.g. [9; 18; 20]), where the more frequent occurrence of positive temperature gradients (i.e., shorter measurement period in the summer months) normally leads to shorter service life. This unusual observation can be attributed to the initial stress state of the structure. Prestressing generates high negative bending moments in the coupling joint of the openLAB bridge (see Figure 11).

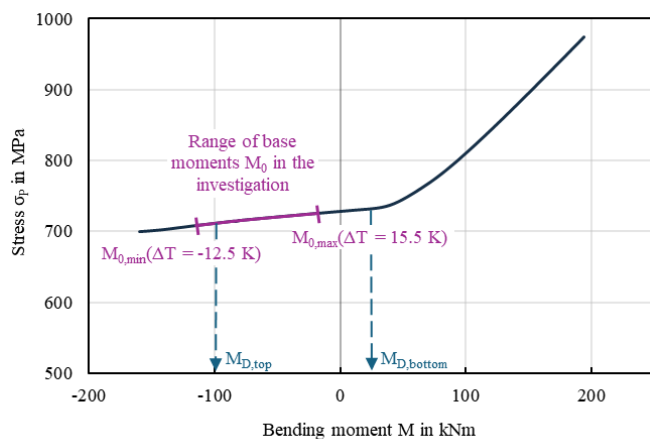


Figure 11. Moment-stress diagram for coupling joint of openLAB with moment impacts caused by applied temperature gradients.

The most extreme temperature gradients  $\Delta T$  determined from all test series in Figure 10 are  $-12.5$  K and  $+15.5$  K. The range of base moments  $M_0$  resulting from all measured temperature gradients between these values is represented as a purple section on the curve in Figure 11. The moments that lead to cracks in the cross-section  $M_D$  (exceeding the decompression point) are marked with blue arrows.  $M_{D,top}$  represents the base moment that causes the cross-section to crack at the top of the bridge cross-section.  $M_{D,bottom}$  represents the base moment that leads to cracking at the bottom edge. It can be seen that the calculated positive temperature gradients are not high enough to cause cracking at the bottom edge. Consequently, negative temperature gradients result in higher stress ranges in the prestressing steel and, therefore, greater partial fatigue damage

$D_{\Delta T,i}$  compared to positive temperature gradients of the same absolute magnitude. This explains why the positive gradients have a positive effect on the load-bearing capacity of the structure. In this case, the coupling joint tends to crack at the upper edge of the cross-section instead of cracking at the bottom edge, as is the case with conventional prestressed bridges [5].

The variation of sampling frequency (Test No. 2.2 – 2.4), sensor density (Test No. 3.2), and local distribution of sensors (Test No. 4.2 and 4.3) have a considerably lower influence on the service life span than the period of data collection (Test No. 1.1 – 1.7). Consequently, a reduced frequency of measurements, may suffice to reliably estimate the actual temperature distribution. A lower sampling frequency reduces the amount of data collected. The impact of variations in local distribution cannot be reliably assessed in this particular case due to the limited number of sensors available. To obtain reliable results, additional temperature sensors are required, particularly within the slab of the openLAB bridge and in the edge areas of the component, where the largest gradients occur. The installation and operation of additional sensors in the openLAB is carried out in April 2025. The same evaluation methodology will be applied again with the new data generated by additional sensors to prove the representativeness and coverage of the enhanced monitoring concept.

## 5 CONCLUSIONS AND OUTLOOK

This study provides a methodological approach for the systematic evaluation of the monitoring concept quality applied to a bridge structure. The fatigue recalculation of the coupling joint was utilized as an example for the implementation of the sensitivity analysis concerning the temperature data. It is based on a single case study of a research bridge, which limits the statistical significance of the results. It should be mentioned that the research bridge used in this study has considerably smaller dimensions and a different structural design compared to typical prestressed concrete bridges. Consequently, the findings cannot be directly generalized to conventional prestressed bridges. The primary focus of this work is the methodology itself, which requires further testing and validation on real-world, full-scale bridges. The introduced methodology can be applied to other sensor types and failure mechanisms.

The presented evaluation of temperature data indicates that, in this particular case study, the temporal representativeness expressed by the varied period of data collection has the most impact on the fatigue calculation of the coupling joint. The lower temporal coverage expressed by the lower sampling frequency does not notably affect the results of the recalculation. Spatial coverage and spatial representativeness could not be properly evaluated in this case study due to the limited number of sensors. It is not yet possible to derive universally applicable recommendations for the design of measurement systems for coupling joints based solely on this case study. Further investigations with a greater number of sensors are required to achieve this objective.

In addition to temperature monitoring, concrete strain or prestressing steel strain ranges are usually recorded at coupling joints. To determine an appropriate holistic monitoring concept for this specific structure, investigations are also required for



these measurements. The load tests that will be performed on the openLAB bridge in 2025 can be used to validate and update the existing FE model. The appropriate estimation of the base moment  $M_0$  and the determination of the moment-stress curve, which describes the transition of the coupling joint from Mode I to Mode II, play a key role in this context.

In summary, further research on the quality of monitoring concepts has the potential to refine existing monitoring approaches and to provide a more accurate assessment of impacts at coupling joints of prestressed concrete bridges. The quality control of monitoring concepts and data should be incorporated as a key component in relevant standards and regulations. This not only facilitates a more reliable condition assessment but also supports a potential extension of the service life of bridge structures.

## ACKNOWLEDGMENTS

This research was funded by the Federal Ministry for Digital and Transport within the research project ANYTWIN (Standardizing Monitoring Based Safety Assessments of Bridges and the Integration into Digital Twins, grant number: 01F2248B) and by the German Research Foundation (DFG) as part of the Priority Program 2388 (SPP 2388) "Hundred plus – Extending the Lifetime of Complex Engineering Structures through Intelligent Digitalization" (project number: 501808860). This article represents the opinions of the authors and does not mean to represent the position or opinions of the funding entities.

## REFERENCES

- [1] BASt, Brückenstatistik (Bundestfernstraßen), [https://www.bast.de/DE/Ingenieurbau/Fachthemen/brueckenstatistik/bruecken\\_hidden\\_node.html](https://www.bast.de/DE/Ingenieurbau/Fachthemen/brueckenstatistik/bruecken_hidden_node.html), 2024.
- [2] Treacy, M. A.; Brühwiler, E., A direct monitoring approach for the fatigue safety verification of construction joint details in an existing post-tensioned concrete box-girder bridge in: *Engineering Structures* 88, p. 189–202, <https://doi.org/10.1016/j.engstruct.2015.01.036>, 2015.
- [3] Geißler, K., *Handbuch Brückenbau*, first edition, Wilhelm Ernst & Sohn, Berlin, Germany, <https://onlinelibrary.wiley.com/doi/book/10.1002/9783433603437>, 2014.
- [4] Seible, F., Coupling Joints of Prestressing Tendons in Continuous Post-Tensioned Concrete Bridge in: *Structures and foundations, Transportation Research Record*, issue number 1044, p. 43–49, <https://onlinepubs.trb.org/Onlinepubs/trr/1985/1044/1044-007.pdf>, 1986.
- [5] König, G.; Gerhard, H.-C., Beurteilung der Betriebsfestigkeit von Spannbetonbrücken im Koppelfugenbereich unter besonderer Berücksichtigung einer möglichen Rißbildung in: *Deutscher Ausschuss für Stahlbeton*, issue number 370, Wilhelm Ernst & Sohn, Berlin, Germany, p. 85–123, 1986.
- [6] Zilch, K.; Zehetmaier, G.; Gläser, C., *Beton Kalender: Brücken und Parkhäuser - Ermüdungsnachweis bei Massivbrücken*, Wilhelm Ernst & Sohn, Berlin, Germany, 2004.
- [7] Maibaum, M.; Li, Z.; Puttkamer, L., ANYTWIN - Identifikation wesentlicher Einflussparameter für – auf Grundlage von Auswertungen des Nachrechnungsbestandes – ausgewählte Versagensmechanismen in: *Technische Akademie Esslingen 6. Brückenkolloquium*, Narr Francke Attempto Verlag GmbH + Co. KG, Tübingen, Germany, 2024.
- [8] Buba, R., Zur stochastischen Zuverlässigkeit bestehender Spannbetonbrücken gegen Ermüdung, Technische Universität München, Germany, 2005.
- [9] Zilch, K. et al., Bericht zum Forschungsprojekt 15.0652: Integration der Handlungsanweisungen "Spannungsrissskorrosion" und "Koppelfugen" in die Nachrechnungsrichtlinie, Heft B 186, Bergisch Gladbach, Germany, <https://bast.opus.hbz-nrw.de/opus45-bast/frontdoor/deliver/index/docId/2747/file/B186+Gesamtversion+BF.pdf>, 2023.
- [10] BASt, Richtlinie zur Nachrechnung von Straßenbrücken im Bestand (Nachrechnungsrichtlinie), Bergisch Gladbach, Germany, [https://www.bast.de/DE/Publikationen/Regelwerke/Ingenieurbau/Entwurf/Nachrechnungsrichtlinie-Ausgabe-5\\_2011.html](https://www.bast.de/DE/Publikationen/Regelwerke/Ingenieurbau/Entwurf/Nachrechnungsrichtlinie-Ausgabe-5_2011.html), 2011.
- [11] Fischer, O. et al., *Nachrechnung von Betonbrücken - systematische Datenauswertung nachgerechneter Bauwerke*, Bd. B 124, Bergisch Gladbach, Germany, [https://bast.opus.hbz-nrw.de/files/1609/B124\\_barrierefreies\\_ELBA\\_PDF.pdf](https://bast.opus.hbz-nrw.de/files/1609/B124_barrierefreies_ELBA_PDF.pdf), 2016.
- [12] BASt, 1. Ergänzung zur Richtlinie zur Nachrechnung von Straßenbrücken im Bestand (Nachrechnungsrichtlinie), Bergisch Gladbach, Germany, [https://www.bast.de/DE/Publikationen/Regelwerke/Ingenieurbau/Entwurf/1\\_Ergaenzung-Nachrechnungsrichtlinie-Ausgabe-5\\_2011.html](https://www.bast.de/DE/Publikationen/Regelwerke/Ingenieurbau/Entwurf/1_Ergaenzung-Nachrechnungsrichtlinie-Ausgabe-5_2011.html), 2015.
- [13] Kiureghian, A. D.; Ditlevsen, O., Aleatory or epistemic? Does it matter? in: *Structural Safety* 31, H. 2, p. 105–112, <https://doi.org/10.1016/j.strusafe.2008.06.020>, 2009.
- [14] Winnewisser, N. R. et al., How to Determine the Level of Epistemic Uncertainty and Exclude Faulty Sensors in Structural Health Monitoring Systems in: *IABSE Symposium, Tokyo 2025: Environmentally Friendly Technologies and Structures: Focusing on Sustainable Approaches*. Tokyo, Japan. International Association for Bridge and Structural Engineering (IABSE) Zurich, Switzerland, p. 745–752, 2025.
- [15] Richter, B. et al., Intermediately discretized extended  $\alpha$  -level-optimization – An advanced fuzzy analysis approach in: *Advances in Engineering Software*, volume 202, <https://doi.org/10.1016/j.advengsoft.2025.103865>, 2025.
- [16] Zilch, K.; Hennecke, M.; Buba, R., Kombinationsregeln für Ermüdung - Untersuchung der Grundlagen für Betriebsfestigkeitsnachweise bei Spannbetonbrücken, Bundesministerium für Verkehr, Bau- und Wohnungswesen, *Forschung Straßenbau*, volume 824, Bonn, Germany, 2001.
- [17] Sanio, D. et al., Bauwerksmessungen versus Rechenkonzepte zur Beurteilung von Spannstahlermüdung in Betonbrücken in: *Bautechnik*, issue number 95, H. 2, p. 99–110, <https://doi.org/10.1002/bate.201700092>, 2018.
- [18] Penka, E., Beurteilung der Ermüdungssicherheit von Koppelfugenquerschnitten bestehender Spannbetonbrücken durch Langzeitmessungen, Technische Universität München, Germany, 2004.
- [19] BASt, Erfahrungssammlung Monitoring für Brückenbauwerke - Dokumentation 2021. Fachverlag NW in der Carl Ed. Schünemann KG, Bergisch Gladbach, Germany, <https://bast.opus.hbz-nrw.de/files/2901/B197+Gesamtversion+BF.pdf>, 2024.
- [20] Weiher, H.; Runtemund, K.; Ullerich, C. (2015) Monitoringbasierter Nachweis der Spannstahlermüdung an den Koppelfugen der Köhlbrandbrücke in: *Beton- und Stahlbetonbau*, issue number 110, H. 8, p. 529–538, <https://doi.org/10.1002/best.201500029>, 2015.
- [21] Herbers, M. et al., openLAB – Eine Forschungsbrücke zur Entwicklung eines digitalen Brückenzwillings in: *Beton- und Stahlbetonbau*, issue number 119, H. 3, p. 169–180, <https://doi.org/10.1002/best.202300094>, 2024.
- [22] Richter, B. et al., Monitoring of a prestressed bridge girder with integrated distributed fiber optic sensors in: *Procedia Structural Integrity*, issue number 64, p. 1208–1215, <https://doi.org/10.1016/j.prostr.2024.09.168>, 2024.
- [23] Krohn, S., Messwertgestützte Ermüdungsnachweise an bestehenden Straßenbrücken – Entwerfen und Konstruieren Stahlbau, Shaker Verlag, Aachen, Germany, 2014.
- [24] Miner, M. A., Cumulative Damage in Fatigue in: *Journal of Applied Mechanics* 12, H. 3, p. 159–164, <https://doi.org/10.1115/1.4009458>, 1945.
- [25] Foken, T. (2021) *Springer Handbook of Atmospheric Measurements*, first edition, Cham: Springer International Publishing, University of Bayreuth Bayreuth, Germany, <https://doi.org/10.1007/978-3-030-52171-4>, 2021.
- [26] VDI 3786, *Umweltmeteorologie Umweltmeteorologie- Meteorologische Messungen - Grundlagen – Environmental meteorology - Meteorological measurements - Fundamentals*. DIN Media GmbH, Berlin, Germany, 2024.
- [27] Meteoblue, Wetterarchiv Bautzen für Juli 2024 – Saxony, Germany, [https://www.meteoblue.com/de/wetter/historyclimate/weatherarchive/bautzen\\_deutschland\\_2951881?fcstlength=1m&year=2024&month=7](https://www.meteoblue.com/de/wetter/historyclimate/weatherarchive/bautzen_deutschland_2951881?fcstlength=1m&year=2024&month=7) [last access on 9 April 2025].

# Hangar Stressing on the 6th Street Viaduct Replacement, Los Angeles, CA

Paul Thurlow<sup>1</sup>, Sergio Estrada<sup>2</sup>

<sup>1</sup>Vice President Western, Geo Instruments Inc, Ventura, California

<sup>2</sup>Project Manager, Geo Instruments Inc, Irvine, California

email: paul.thurlow@geo-instruments.com Sergio Estrada@geo-instruments.com

**ABSTRACT:** Spanning across Freeway 101, several rail roads and the LA river, the 6th Street Viaduct replacement project is one of the largest bridge projects in the City of Los Angeles. The original bridge was built in 1932 and became a backdrop to the film industry. The iconic bridge was demolished following the decision to replace it with the existing 6th Street Viaduct due to the structure becoming seismically vulnerable. At 3,060-ft-long and 100-ft-wide, the redevelopment of the new bridge – designed by Michael Maltzan, – includes 10 network arch spans, with a total of 388 hangers supporting the bridge deck. The bridge spans 101 Highway, the Los Angeles River. The hanger installation and stressing for the bridge was a complex procedure that would need careful attention to detail for loading the hangars before removal of formwork and for fine tuning the final load criteria. There were 18 load sequences per arch. The instrumentation and monitoring of the hangars while loading required a novel approach that started two years in advance of the works with development of a bespoke system, calibration and acceptance. During installation and works many lessons were learnt by all parties involved. The close working relationship with a desire to succeed between the site team and designers was as fascinating as the technical brilliance applied by all to deliver this section of the project in a safe manner, within the schedule and to the specification.

**KEY WORDS:** Bridge; structural monitoring; strain gauges, load verification, dataloggers, hangers

## 1. Introduction

The 6<sup>th</sup> Street Viaduct replaced the original, beloved bridge in 1932, which had been deteriorating for decades due to alkali silica reaction. This condition is caused by an aggregate in the concrete that drew in moisture and caused cracks. After repeated attempts to retrofit the old bridge the decision was made that it needed to be replaced. In 2012, after much outreach and consultation with the community, the Los Angeles Bureau of Engineering held an international design competition to select a design for the new viaduct. Michael Maltzan Architects, a local Los Angeles firm, and HNTB, were the winners with the design, called "The Ribbon of Light".

In 2016 the bridge was demolished completely, and construction on the new Sixth Street Viaduct began. Funded by the Federal Highway Transportation Administration, the California Department of Transportation, and the City of Los Angeles, the \$588 million Sixth Street Viaduct Replacement Project was led by the Los Angeles Bureau of Engineering under City Engineer Gary Lee Moore in partnership with the LA Bureau of Contract Administration.

The new Sixth Street Viaduct consists of 10 pairs of arches that range in heights from 30 feet to 60 feet tall. Each arch has a 9-degree outward cant, 10-foot width, and requires 260 cubic yards of concrete. Arches had to be poured at a rate of 4 vertical feet per hour for a total of 12-14 hours per arch due to the formwork and intricate support system.

The arches join into a Y-shaped column, and in total, the 23 columns and 2 abutments of the bridge use triple friction pendulum bearings for seismic base isolation. These bearings allow movement up to 30 inches in any lateral direction, not only ensuring earthquake survival, but making the Sixth Street Viaduct one of the largest base-isolated structures in the world. Generally, construction developed from east to west and was led by contractor Skanska-Stacy and Witbeck Inc. Arches were poured without cables in place, then cables 2 3/4 in. in diameter were added and tightened to create a network-tied arch structure.

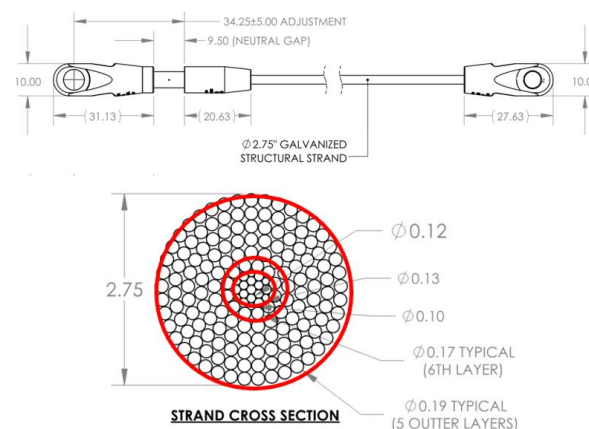


Figure 1. Typical strand construction



Figure 2. General view of the Sixth Street Viaduct Replacement

## 2. Development of a Custom Load Verification System.

Following an extensive series of interviews with manufacturers specializing in conventional load verification technologies, the contractor—Stacy Witbeck Skanska Joint Venture (JV)—engaged Geo Instruments to develop a bespoke load verification system tailored to the unique constraints of the Sixth Street Viaduct project. A key requirement was that instrumentation could not be integrated during strand manufacturing due to the complexity of the process. The system needed to be repeatable, allow for self-performed installation by the JV team following training, and support real-time data acquisition both on the bridge deck and remotely for review and approval by the design team based in Canada. Load measurements were required to achieve accuracy within 2 % of the target load for each loading cycle.

Traditional strand loading methods typically employ in-strand tensiometers or vibration-based devices. However, the project's emphasis on repeatability and operational simplicity led to the selection of vibrating wire strain gauges—recognized for their reliability and proven performance in structural load measurement.

Vibrating wire strain gauges operate by tensioning a steel wire between two fixed anchors within a stainless-steel housing. Electromagnetic coils induce oscillation in the wire via a brief voltage or swept frequency excitation. The wire vibrates at its resonant frequency, generating a sinusoidal alternating current. This frequency is captured by a readout unit or data logger equipped with a vibrating wire interface and converted into engineering units of strain. Changes in structural force alter the wire's tension, thereby shifting its resonant frequency. The square of the frequency change is directly proportional to the change in strain.

These gauges are cost-effective, durable, and compact, with the capability to record data at intervals as short as one second. For this application, low-profile vibrating wire strain gauges manufactured by Geosense (UK) were selected. The

chosen model had a maximum strain capacity of 3000  $\mu\epsilon$  which was deemed suitable for the expected load range.

To ensure consistent and accurate strain measurements, each vibrating wire strain gauge was mounted on a custom-engineered aluminum clamp designed to securely interface with the prestressing strands. The clamp assembly was developed to prevent slippage or misalignment during strand elongation, thereby preserving measurement integrity. A secondary carrier clamp, positioned above the primary clamp, housed the strain gauge and enabled reuse across multiple strands without compromising performance or structural integrity. The prototype assembly was presented to the client for review and approval.



Figure 3. Prototype strain gauge assembly.

## 3. Load Verification Tests.

An opportunity to conduct a destructive test on a single strand was utilized to validate the design. The initial test setup included two strain gauges mounted on opposite sides (top and bottom) of the test strand. The gauges were configured to record data at five-second intervals. The testing facility prepared and rigged the test frame to simulate loading conditions representative of field operations, in such a way that



there were not any incremental load stops to verify the load and strain alignment. The test was too fast, and load profiles generated on the test machine did not mimic the anticipated loading sequence anticipated on site. The initial destructive test provided limited insight into the load recording capabilities of the test frame. Unfortunately, the load data output was incompatible with standard data analysis platforms such as Microsoft Excel, which hindered post-processing and review. Following this session, and in consultation with the client, it was agreed to proceed with a single strain gauge per strand for subsequent tests. This decision was based on the observation that strand bending was negligible due to the strand's diameter and length, and that dual-gauge setups would unnecessarily slow down field operations.

The second test session comprised a series of ten proving tests, each requiring the strand to withstand a load of one million pounds prior to failure. Strain gauges were mounted at the mid-span of each strand, and data was recorded at two-second intervals. The resulting strain measurements demonstrated strong consistency and alignment with expected values, thereby validating the reliability of the system and increasing confidence in its field performance.

Despite the successful strain data acquisition, the load recording methodology employed by the testing facility remained a limitation. The format of the load data continued to be incompatible with standard analytical tools, presenting challenges for integration and review by the project team

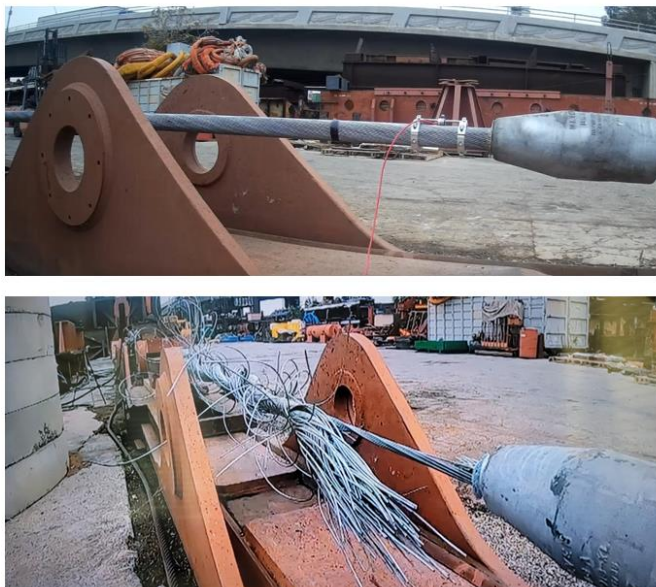


Figure 3. Testing hanger strands to destruction.

The third round of testing was conducted at the strand manufacturer's facility, enabling a more controlled environment and allowing tests to be performed at loading rates that closely matched field conditions. This controlled setup facilitated more accurate correlation between applied load and strain gauge measurements.

Following these tests, the client reviewed the results and verified the accuracy of the instrumentation system. Based on the successful performance and alignment with project requirements, the client approved the methodology and proceeded with the procurement and fabrication of the full instrumentation system.

#### 4. Field Work.

During the planning phase, the decision was made to utilize Campbell Scientific CR6 data loggers, equipped with the necessary number of multiplexers to accommodate strain gauge readings. The CR6 model was selected primarily for its integrated Wi-Fi capability, which enables real-time data visualization, an essential feature for the loading team during operations. Each arch structure required instrumentation of approximately 18 to 22 strands, with the optimal placement for the data loggers initially identified as the base of the arches, housed within secure enclosures.



Figure 4. Strain Gauge assembly and logger setup.

Strain gauge cables were procured based on the measured distances to the midpoints of each strand, with additional length included to ensure connectivity to the central logger. However, due to significant incidents of theft and equipment damage during the early stages of construction, the client mandated the relocation of the logger enclosures to the top of the arches. To accommodate this change in routing and cable length, pigtail with M12 connectors were added to both the loggers and multiplexers. Each pigtail was uniquely numbered to correspond with its respective strand, streamlining the installation process.

Although relocating the data loggers to elevated positions introduced logistical challenges—particularly related to working at height—the use of modular connectors proved to be a significant advantage. These connectors simplified installation and maintenance, especially under constrained site conditions.

To ensure all stakeholders were aligned with the revised installation procedures and loading protocols, the client organized a pre-installation workshop. This session brought together the site personnel, design team, and representatives from Geo Instruments to review the updated methods, including bracket installation, strain gauge handling, and the specific loading cycles planned for each arch. This collaborative approach helped streamline field operations and ensured consistency across the instrumentation process.

SPAN 15 NORTH																																	FORCE IN GABLE AT FOLLOWING CONNECTION WITH STAYS WELD																																																																																																																																																																																																																																																																																																																																																																																																																																																																																																																																																																																																																																																																																																																																																																																																																																																																																																																																																																																																						
FORCE IN GABLE AT INSULATION TAPED JOINT															FALGROUPE REMOVAL					FALGROUPE REMOVAL					FALGROUPE REMOVAL					FALGROUPE REMOVAL																																																																																																																																																																																																																																																																																																																																																																																																																																																																																																																																																																																																																																																																																																																																																																																																																																																																																																																																																																																																									
01	02	03	04	05	06	07	08	09	10	11	12	13	14	15	16	17	18	19	20	21	22	23	24	25	26	27	28	29	30	31	32	33	34	35	36	37	38	39	40	41	42	43	44	45	46	47	48	49	50	51	52	53	54	55	56	57	58	59	60	61	62	63	64	65	66	67	68	69	70	71	72	73	74	75	76	77	78	79	80	81	82	83	84	85	86	87	88	89	90	91	92	93	94	95	96	97	98	99	100	101	102	103	104	105	106	107	108	109	110	111	112	113	114	115	116	117	118	119	120	121	122	123	124	125	126	127	128	129	130	131	132	133	134	135	136	137	138	139	140	141	142	143	144	145	146	147	148	149	150	151	152	153	154	155	156	157	158	159	160	161	162	163	164	165	166	167	168	169	170	171	172	173	174	175	176	177	178	179	180	181	182	183	184	185	186	187	188	189	190	191	192	193	194	195	196	197	198	199	200	201	202	203	204	205	206	207	208	209	210	211	212	213	214	215	216	217	218	219	220	221	222	223	224	225	226	227	228	229	230	231	232	233	234	235	236	237	238	239	240	241	242	243	244	245	246	247	248	249	250	251	252	253	254	255	256	257	258	259	260	261	262	263	264	265	266	267	268	269	270	271	272	273	274	275	276	277	278	279	280	281	282	283	284	285	286	287	288	289	290	291	292	293	294	295	296	297	298	299	300	301	302	303	304	305	306	307	308	309	310	311	312	313	314	315	316	317	318	319	320	321	322	323	324	325	326	327	328	329	330	331	332	333	334	335	336	337	338	339	340	341	342	343	344	345	346	347	348	349	350	351	352	353	354	355	356	357	358	359	360	361	362	363	364	365	366	367	368	369	370	371	372	373	374	375	376	377	378	379	380	381	382	383	384	385	386	387	388	389	390	391	392	393	394	395	396	397	398	399	400	401	402	403	404	405	406	407	408	409	410	411	412	413	414	415	416	417	418	419	420	421	422	423	424	425	426	427	428	429	430	431	432	433	434	435	436	437	438	439	440	441	442	443	444	445	446	447	448	449	450	451	452	453	454	455	456	457	458	459	460	461	462	463	464	465	466	467	468	469	470	471	472	473	474	475	476	477	478	479	480	481	482	483	484	485	486	487	488	489	490	491	492	493	494	495	496	497	498	499	500	501	502	503	504	505	506	507	508	509	510	511	512	513	514	515	516	517	518	519	520	521	522	523	524	525	526	527	528	529	530	531	532	533	534	535	536	537	538	539	540	541	542	543	544	545	546	547	548	549	550	551	552	553	554	555	556	557	558	559	560	561	562	563	564	565	566	567	568	569	570	571	572	573	574	575	576	577	578	579	580	581	582	583	584	585	586	587	588	589	590	591	592	593	594	595	596	597	598	599	600	601	602	603	604	605	606	607	608	609	610	611	612	613	614	615	616	617	618	619	620	621	622	623	624	625	626	627	628	629	630	631	632	633	634	635	636	637	638	639	640	641	642	643	644	645	646	647	648	649	650	651	652	653	654	655	656	657	658	659	660	661	662	663	664	665	666	667	668	669	670	671	672	673	674	675	676	677	678	679	680	681	682	683	684	685	686	687	688	689	690	691	692	693	694	695	696	697	698	699	700	701	702	703	704	705	706	707	708	709	710	711	712	713	714	715	716	717	718	719	720	721	722	723	724	725	726	727	728	729	730	731	732	733	734	735	736	737	738	739	740	741	742	743	744	745	746	747	748	749	750	751	752	753	754	755	756	757	758	759	760	761	762	763	764	765	766	767	768	769	770	771	772	773	774	775	776	777	778	779	780	781	782	783	784	785	786	787	788	789	790	791	792	793	794	795	796	797	798	799	800	801	802	803	804	805	806	807	808	809	810	811	812	813	814	815	816	817	818	819	820	821	822	823	824	825	826	827	828	829	830	831	832	833	834	835	836	837	838	839	840	841	842	843	844	845	846	847	848	849	850	851	852	853	854	855	856	857	858	859	860	861	862	863	864	865	866	867	868	869	870	871	872	873	874	875	876	877	878	879	880	881	882	883	884	885	886	887	888	889	890	891	892	893	894	895	896	897	898	899	900	901	902	903	904	905	906	907	908	909	910	911	912	913	914	915	916	917	918	919	920	921	922	923	924	925	926	927	928	929	930	931	932	933	934	935	936	937	938	939	940	941	942	943	944	945	946	947	948	949	950	951	952	953	954	955	956	957	958	959	960	961	962	963	964	965	966	967	968	969	970	971	972	973	974	975	976	977	978	979	980	981	982	983	984	985	986	987	988	989	990	991	992	993	994	995	996	997	998	999	1000

Figure 5. Typical Load sequence of strands per arch.

The pre-installation workshops proved instrumental in resolving potential installation issues and allowed the team to simulate and troubleshoot scenarios that could arise during field operations. As is common with large-scale infrastructure projects, the introduction of a novel instrumentation method attracted attention from a wide range of stakeholders. In anticipation of this, the first week of loading operations was dedicated to comprehensive onsite training. This included verification of installation procedures, validation of data flow, and execution of trial runs to ensure system readiness.



Figure 6. View of typical strand hanging operation

During installation, each strand was secured to the top of the arch using custom holders, aligned with corresponding lower brackets, pinned, and subsequently tensioned. The strain gauge was connected to the strand and set to 1000 Hz manually using a GK404 VW readout to accommodate the expected loading tension. The strain gauges were factory calibrated in bulk to avoid any errors in this process. Given the length of the strands (up to 40 feet) significant initial curvature was observed prior to loading which forced a revision of the strain gauge loading

sequence to avoid strain gauge bending. A bedding-in phase was necessary to allow the strand to settle and align properly before the verification load was applied. A proving load of 10 tons was established as a baseline across the project to confirm system integrity. Operational loads for individual strands varied between 48 and 100 tons, depending on their location and structural role within the arch system. The contractor's jacking system consisted of a custom hydraulic setup featuring a yoke-style configuration designed to sit directly over each strand. This system included integrated load readouts and was operated via a tablet interface that displayed calculated load values derived from strain measurements at 30-second intervals.



Figure 7. Contractors strand loading system

Typical strain gauge readings, acquired through up to eight Campbell Scientific CR6 Wi-Fi data loggers with two number 32 channel multiplexers each, installed on the arches were recorded at one-second intervals per gauge and converted to load. During each loading sequence, the supervising engineer plotted the strain gauge load data against the hydraulic jacking system's load readings. These plots were reviewed and verified in real time by the City Engineer. Each strand's loading cycle was individually signed checked and signed off to ensure compliance with the performance criteria.

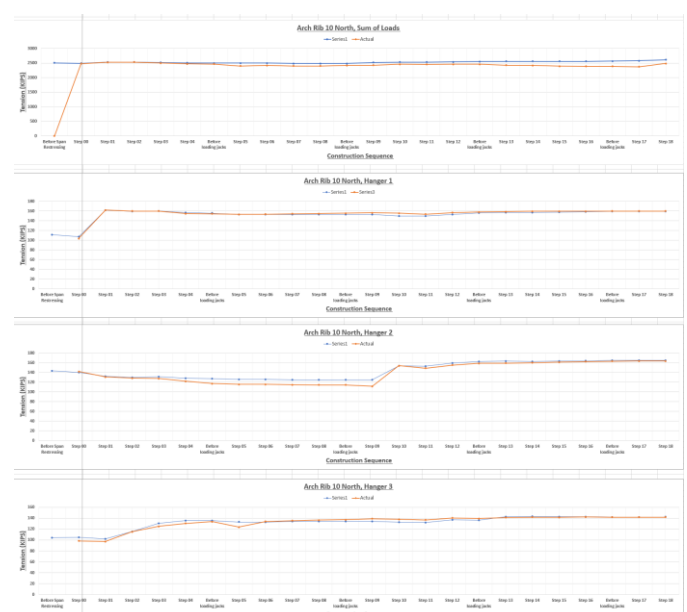


Figure 8. Hangar required load with applied load site plots



The data from the strain gauges was sent via modem and Wi-Fi to the Geo Instruments servers and in-house visualization software – Quickview.

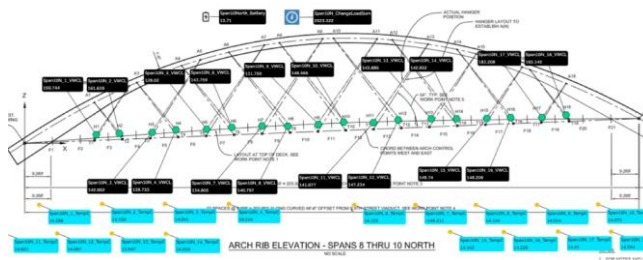


Figure 9. QuickView visualization platform

This software portal allowed the designers and contractors not on the bridge to view the loading sequence, one minute behind the actual site work. The data points on the site view showed digits, load and temperature for each strain gauge as well as the accumulative total load of the arch. Data was viewed and downloaded by consultant Ramboll for design verification and quality control reporting.

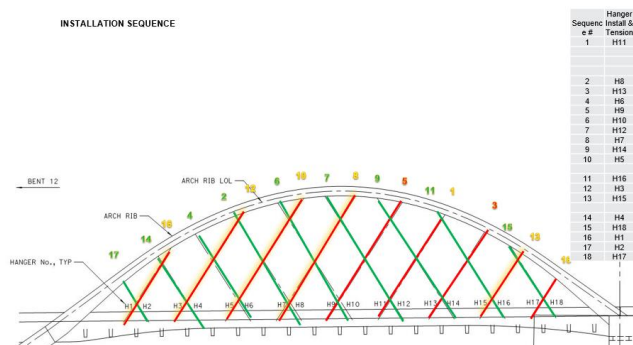


Figure 10. Sequence of strand installation.

### Temperature Effects and Adaptive Stressing Strategy

Temperature played a significant role in data interpretation and reduction throughout the project. Fortunately, the early phases of construction coincided with an unusually overcast period in Los Angeles, resulting in minimal temperature variation during the typical eight-hour workday. To further mitigate thermal effects, each strain gauge was wrapped in a heat-shielding material. While clamp-on heat shields were initially considered, they proved impractical for field use due to their bulk and handling complexity. Although the City of Los Angeles initially considered retaining the strain gauges for long-term monitoring post-commissioning, this plan was ultimately removed from the project scope during execution.

In the final three months of arch construction, weather conditions shifted unexpectedly, with unseasonably high temperatures becoming a concern. The combination of

intense solar radiation, the elevated position of the arches, the increased number of arches complete and the thermal mass of the concrete structure caused the bridge to act as a heat sink. This thermal buildup peaked during the same hours scheduled for hanger stressing, raising concerns about data reliability and structural behavior under elevated temperatures.

Rather than attributing delays or complications to any single party, the site team collaborated closely with the designers to analyze the data and identify the root cause of the discrepancies. With eight arches remaining to be instrumented, the team reviewed the sun trajectory and its impact on different arch segments. It became evident that larger arches and their associated strands were heating more rapidly and retaining heat longer than smaller ones, skewing strain readings throughout the day.

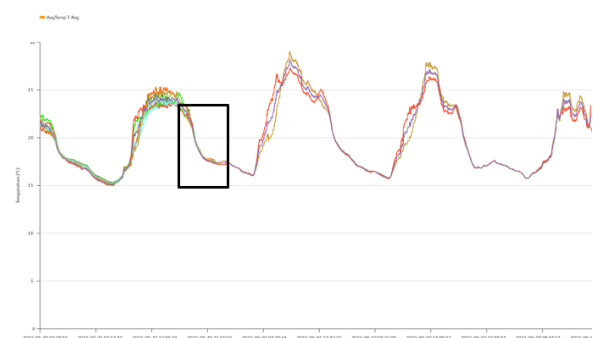


Figure 11. Temperature of strands on arch

To address this, the stressing schedule was revised. Work shifts were rescheduled to occur between midnight and 5:00 a.m., when ambient temperatures were more stable and thermal effects on the instrumentation were minimized. This proactive adjustment allowed the team to complete the stressing operations on schedule and within specification.

### 5. Conclusion.

All projects provide great feedback what went well and what could be improved on, it's how instrumentation and structural health monitoring evolves. In hindsight, the initial testing of the strain gauges should have been run under temperature variations, but as discussed, the testing locations were not suitably equipped up for long testing load cycles. The very fast load cycles in the testing locations and the ability to capture data in format that was compatible with instrumentation loggers turned out to be an issue. Such is the rarity of these large-scale tests; it would require some investment from all parties to get suitable outputs.





Figure 12. View of one completed arch.

The success of the Sixth Street Viaduct instrumentation program was driven by collaborative efforts, continuous feedback, and iterative improvement cycles among all stakeholders on site. The designer's clear articulation of data requirements, particularly the need for rapid and reliable access, guided the development of a robust instrumentation system, including the selection of strain gauges, bracket assemblies, and data loggers.

The site team played a critical role in refining installation procedures. Their feedback on bracket mounting techniques, bolt torque specifications, pre-connection verification methods, and data visualization strategies on the bridge deck significantly enhanced the practicality and reliability of the system.

Credit is due to the Los Angeles Bureau of Engineering for its foresight in supporting this novel testing approach. During early project meetings, concerns were raised regarding the lack of precedent for using this technique on large-scale strand bridges. Nevertheless, the Bureau's commitment to innovation enabled the development of a comprehensive and technically sound solution that instilled confidence across the project team.

The Sixth Street Viaduct replacement officially opened in June 2023, on schedule. It has since become an iconic structure within Los Angeles, earning multiple international awards for its design and construction excellence.

### Acknowledgments.

The authors would like to express their sincere gratitude to all those who contributed to the successful completion of this project. Special thanks are extended to the Stacey Witbeck Skanska Joint Venture and the management team: Emily Melkesian, Lee Pelton, and Robert Walent.

We acknowledge Geosense UK, particularly Tim and Martin Clegg, for their support, Tobias Petschke and his talented design team at Ramboll for their engineering insight. The authors further recognize the contributions of Geo Instruments and the Los Angeles Bureau of Engineering and HNTB for their collaboration and site support.

### References.

- [1] Carden, E. P., and Fanning, P. (2004). Vibration based condition monitoring: a review. *Struct. Health Monitor* 3, 355–377.
- [2] Li, H., and Ou, J. P. (2016). The state of the art in structural health monitoring of cable-stay bridges. *J. Civil Struct. Health Monitor.* 6, 43–67.
- [3] Das, S., Saha, P., and Patro, S. K., (2016). Vibration-based damage detection techniques used for health monitoring of structures: a review. *J. Civil Struct. Health Monitor* 6, 447–507
- [4] Geosense. V2.2a Vibrating Wire Strain Gauges 18/07/2024 Manual.

# SHM Application in Development of New Live Load Distribution factors for Timber Bridges

Limaye, V. <sup>1</sup>, Vickers, P. <sup>2</sup>, Hoseinpour, H. C. <sup>3</sup>, Memon, A. <sup>4</sup>, Clarke, J. <sup>5</sup>

<sup>1</sup>SHM Canada Consulting Limited, Halifax, Nova Scotia, Canada

<sup>2</sup>Public Services and Procurement Canada, Halifax, Nova Scotia, Canada

<sup>3</sup>CBCL Limited, Halifax, Nova Scotia, Canada

<sup>4</sup>Nova Scotia Department of Public Works, Halifax, Nova Scotia, Canada

<sup>5</sup>Halifax Regional Municipality, Halifax, Nova Scotia, Canada

email: [vidya.limaye@shmcanada.com](mailto:vidya.limaye@shmcanada.com), [phil.vickers@tpsgc-pwgsc.ca](mailto:phil.vickers@tpsgc-pwgsc.ca), [chhoseinpour@cbcl.ca](mailto:chhoseinpour@cbcl.ca), [amjad.memon@novascotia.ca](mailto:amjad.memon@novascotia.ca), [justin.clarke@halifax.ca](mailto:justin.clarke@halifax.ca)

**ABSTRACT:** The Nova Scotia Department of Public Works (NSDPW), based on their observations and research, believe that the simplified method of analysis of timber bridges included in the Canadian Highway Bridge Design Code (CHBDC) yields excessively conservative load ratings for typical timber girder bridges in the province. With over 2000 such bridges in their inventory, this study looks to improve conservative load ratings by developing more realistic live load distribution factors for timber bridges based on load testing and analytical work.

NSDPW engaged SHM Canada to conduct load testing of selected timber bridges and to develop a new regime of realistic live load distribution factors derived from the test data. Six timber bridges of various characteristics were selected for this study to cover as wide a range of bridge configurations as possible in the provincial inventory. The collected displacement and strain measurement data were analyzed and used to calibrate a large number of analytical models and followed by statistical and mathematical formulation of the proposed simplified method. The new method incorporates distribution factors specifically developed for timber bridges, by taking into consideration various parameters such as span length, girder spacing, and mechanical properties of the girders, to offer a fast, reliable, and cost-effective approach for evaluation and management of the province's timber bridge inventory.

**KEY WORDS:** Timber Bridge, Live load distribution factor, Load testing, Displacement transducer, SMA.

## 1 INTRODUCTION

The Nova Scotia Department of Public Works (NSDPW) inventory of bridges includes over 2000 timber bridges. These bridges are key components of the province's transportation infrastructure and are critical links on the local and collector roads. The majority of these bridges are short-span structures that have been in service for over 50 years [1].

Because of the size and importance of this inventory, substantial resources are dedicated for the inspection and load rating of these timber bridges. Currently, NSDPW uses the simplified method of analysis given in the latest editions of CAN/CSA-S6, the Canadian Highway Bridge Design Code (CHBDC/ the Code), for the load rating of in-service bridges and for the design of new timber bridges.

Based on their experience and research, NSDPW hypothesizes that load ratings determined through the CHBDC simplified methods are overly conservative for the types of timber bridges commonly found in the province. Comparison of results yielded by the CAN/CSA-S6-14 and -19 simplified methods to the results yielded by the preceding version (S6-06) show that the newer versions are relatively more conservative. This study has shown that even the simplified method in the 2006 edition of the Code yields more conservative load ratings for timber bridges than do the rigorous methods of analysis, [1-4]. Historically, NSDPW has used rigorous methods for analysis of its timber bridges. The application of these methods, however, is time-consuming and resource-intensive and would be too onerous to apply for the evaluation of NSDPW's timber bridge inventory. The overly conservative simplified methods, which have primarily been developed for steel and concrete bridges, also have a significant financial impact on the

province. The primary objective of this study, therefore, is to develop an easy to use, and efficient method of evaluation specifically for timber bridges.

SHM Canada Consulting Limited (SHM Canada) was engaged by NSDPW to carry out load testing of six preselected timber bridges, representing a significant portion of the inventory, and to develop new live load distribution factors for timber bridges in the Province of Nova Scotia that would offer a time- and cost-effective alternative to the more sophisticated analysis methods. The accuracy and efficacy of these factors will be critical to the continued safe operation of Nova Scotia's transportation infrastructure and for effective management of resources.

## 2 LITERATURE REVIEW

The current standard for the design and evaluation of bridges in Canada is CAN/CSA S6:19. Methods of calculation of live load distribution in CHBDC and its predecessor, the Ontario Highway Bridge Design Code (OHBDC), have been revised multiple times since 1983. These methods are categorized as either Simplified Methods of Analysis (SMAs) or Refined Methods of Analysis (RMAs).

RMAs emerged as the increasing availability and enhanced capabilities of computers in the 1980s and 1990s encouraged engineers to attempt more complex forms of analysis and to model bridges with a large number of structural elements. These methods are generally highly accurate but require significant modelling time [1], [5]. More time-efficient simplified methods are therefore required for analysis of large inventories of simpler structures (e.g. the NSDPW inventory of over 2000 timber bridges in Nova Scotia).

Finite Element Method (FEM), Semi-Continuum Analysis (SCA), Orthotropic Plate Theory, Grillage analogy, Folded plate theory... are some of the recognized RMAs in CHBDC, [1-4], however, only FEM and SCA were used in this study.

The Finite Element Method (FEM) is a powerful tool for analyzing simple to complex structures. The main challenge of this method remains a long modelling time [1] [5].

The semi-continuum analysis (SCA) method is useful for modelling timber bridges as it closely represents their structural configuration with slab on girder elements. The timber deck is modelled as a plate element supported on stringers, which are, in turn, modelled as line elements. The models generated by these methods are close to the reality of the nature of the bridge components and thus lead to more accurate results [1] [3] [4].

SMAs rely on the beam analogy, an equivalent-beam method in use since the 1930s, for longitudinal distribution of loads along the bridge, by calculating the maximum contribution of a single girder (or a unit width of a slab-type bridge) in resisting imposed loads. In all SMAs, transverse distribution of the longitudinal load effects is a result of multiplying a fraction coefficient provided by the formulas in the codes. Span length is a key parameter in deriving simplified method equations, as longer span length results in better transverse load distribution. Tighter spacing between girders leads to effective loads sharing among more number of girders across the width of the bridge, resulting in lower distribution factor values, [1-4], [8], [9].

As the Commentary for the current edition specifies, the CHBDC SMA equation should always produce load effects that are greater than those calculated using RMAs, as the RMAs used to develop the SMA equation are based on the most critical condition permitted by the Code [9]. In general, using RMA result in higher load rating values than those calculated from the three editions of the Code (06, 14, and 19). Using SMA will therefore lead to conservative designs and yield lower load ratings for the existing bridges.

The majority of the constants in the formulation of the CHBDC simplified method were derived from work by Smith, while the recent formulation of SMA in CAN/CSA-S6:19 benefits significantly from the work done by Théoret and Massicotte, [1]. These studies, however, relied primarily on analysis of concrete and steel bridges. Timber bridges differ considerably from the most concrete and steel bridges in their structural configuration, and the mechanical properties of timber are markedly different from those of concrete or steel.

The non-linear behavior of the girders beyond the proportionality limit, and before the point of failure, can result in redistribution of the load effects. The technical committee of the OHBDC, therefore, offered an 8% reduction in the live load moment effect due to the redistribution of the moment effect based on a number of analytical studies of bridges with a concrete slab-on-steel-girder design. This reduction was offered only for the evaluation of existing bridges, and not for the design of new bridges. Although it is recognized as applicable to other bridge types, it has not been investigated extensively for those bridge types [8].

Fanous et al. carried out extensive research on development of live load distribution factors for glued-laminated timber girder bridges with glued-laminated timber deck panels. With a verified numerical model created in ANSYS 11 based on four in-service bridges, more than 100 hypothetical bridge models

were produced and live load distribution factor's relation was obtained for various bridge parameters, such as span length, girder spacing, and bridge width. It was shown that the AASHTO LRFD Bridge Design Specifications are conservative compared to the results obtained from field tests and numerical models [10].

An analytical and experimental study of six sawn timber bridges showed that asphalt, which tends to be neglected in both SMAs and RMAs, contributes to better live load sharing between timber stringers. This conclusion was based on the finding that stringers in field tests contributed a 17% smaller value of load sharing than predicted through rigorous analysis using SECAN/SCA. This study also found that analytical results for deflection were 20% larger than values obtained in the field, suggesting a larger modulus of elasticity than assumed in the Code recommendation for that timber species [11].

A more recent study sponsored by NSDPW carried out analysis of timber bridges with multiple editions of CHBDC (CAN/CSA-S6-88 through CAN/CSA-S6-14). This project was aimed at understanding the evolution of the simplified method in CAN/CSA-S6 over time and to compare results of the simplified method with more rigorous analysis using SCA. The study employed SECAN4 software and a scaled-down laboratory mode of the timber bridge. The results showed that the load effects calculated using revised versions of the code had increased over time by up to 30% [1]. NSDPW currently recognizes a rate of increase of 22%. CAN/CSA-S6-06 was found to produce the most accurate results of the versions studied but still yielded more conservative load ratings than those determined from the rigorous analyses. The study recommended the use of the simplified method in CAN/CSA-S6-06 as a first step in evaluation. Where this analysis yields a live load capacity factor (LLCF) falling within the range of 0.7–1.0, as is the case for approximately 60% of bridges in the NSDPW inventory, a more rigorous method may yield a higher load rating [1].

### 3 INSPECTION AND LOAD TESTING

#### 3.1 Bridge Inspection Program

Prior to field load testing, detailed hands-on inspection of the six test bridges was carried out in accordance with CAN/CSA S6:19 [4]. The primary objective of these inspections was to identify any defects or deficiencies with the potential to affect load testing results.

The inspection program comprised three main components:

- Detailed visual inspection of the bridge superstructure and timber substructure where applicable;
- Non-destructive testing (NDT), including sounding and Stress Wave Timer (SWT) testing; and
- Timber grading.

Detailed measurements were taken with adequate detail to produce elevation and section sketches in AutoCAD format. The overall condition rating of the six bridges as determined during the inspection program is given in Table 1.



Table 1. Condition Rating of Six Test Bridges

Bridge ID	Overall Current Bridge Condition Rating
HFX 061	Good
COL 098	Fair, near to Good
HFX 334	Fair, near to Good
HFX 322	Good
HFX 325	Fair
HFX 099	Fair

### 3.2 Load Testing Program

Girder deflection under load from a static truck with a known weight was measured by displacement sensors under each girder of the bridge and by strain gauges installed at select locations. The quality of this data was improved by incorporating an array of strategically placed high-precision sensors in the load testing program.

#### 3.2.1 Data Acquisition System

All displacement sensors and strain transducers were connected to a data logger which acquired data at a speed of 3 Hz. Two 16-channel analog input modules were used to connect displacement transducers and strain transducers. The data acquisition system was housed in the monitoring vehicle located on site and powered by a high-capacity inverter. In order to avoid disruptions in power supply, the system was equipped with a rechargeable 12 V back-up battery.

#### 3.2.2 Displacement Transducers

In selecting the most appropriate type of displacement transducer, three main factors, under-bridge clearance; minimum environmental disturbance; and ease of installation, calibration, and removal of sensors; were considered in the selection of the draw wire displacement transducers. Under-bridge clearance varied between 1.2 m and 3 m, and special adjustable steel cable system was designed to facilitate easy installation.

#### 3.2.3 Strain Transducers

Strain measurements were recorded using strain transducers with a gauge length of 75 mm. The selected strain transducers provide improved accuracy in comparison to bonded foil-type strain gauges. Special mounting brackets were developed to eliminate the effect caused by local variations/imperfections in timber during installation of the transducers.

#### 3.2.4 Installation

For each bridge, draw-wire sensors were installed at mid-span on the soffit of all timber girders. Additional displacement sensors were installed near the supports on bridges where appropriate. Small steel plates were attached to the soffit of each timber girder with wood screws. Matching steel plates with high-power magnets attached to the displacement sensors allowed a quick, secure, and efficient installation and retrieval.

A custom-built sensor installations system, which incorporates a thin aircraft cable, was developed and fabricated to accommodate the varying distance between girder soffits and the stream bed. The draw-wire of the sensor was pulled down approximately 50% of the sensor range and attached to the thin aircraft cable, which was adjusted in the field to make up the

remainder of the distance to the stream bed. The aircraft cable was attached to steel hooks that were screwed on to a square timber beam supported on steel stools and ladders resting on the stream bed thus minimizing disturbance to the riverbed. The test setup for the bridge, HFX 099, is shown in Figure 1 below.

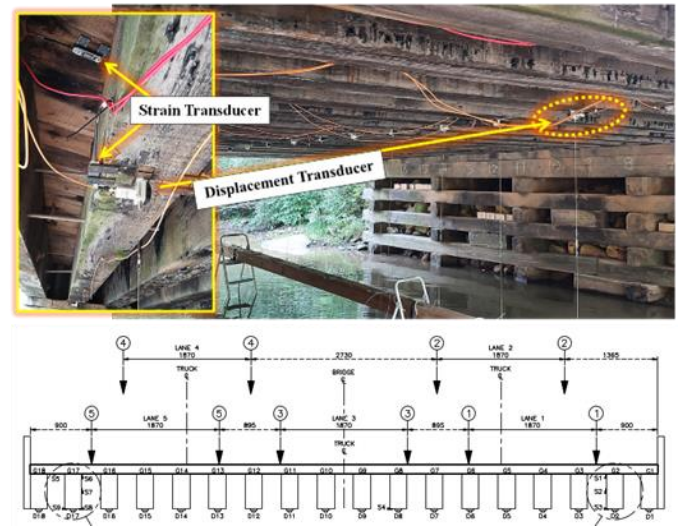


Figure 1. Test setup for HFX 099

Strain transducers were installed on selected timber girders, in close proximity to the draw-wire sensors as possible, in order to correlate strain measurements to the displacement measurements. On select bridges, strain transducers were installed on the deck soffit to determine load sharing characteristics of the timber deck.

#### 3.2.5 Test Vehicle

Bridges were tested using a single-unit tandem axle truck loaded near the legal maximum capacity (25880 kg). The truck was pre-weighed prior to commencing the load testing. A summary of the test vehicle axle loads and axle spacing is presented in Table 2 below for the bridge, HFX 322.

Table 2. Test Vehicle Axle Weight and Spacing

Front Axle Weight (kg)	Twin Rear Axle Weight (kg)	Axle Spacing (mm)	
		First to Second	Second to Third
7930	17950	4150	1360

#### 3.2.6 Load Testing Procedure

After all sensors were installed and tested for functionality, traffic control was implemented to close the bridge to all vehicular traffic. The load testing procedure consisted of the following steps:

- Demarcate travel lanes for each test run.
- Demarcate equally spaced lines at predetermined intervals depending on span length of the bridge.
- Record baseline readings of bridge prior to commencing load testing.
- Move the test truck to align with first travel lane and position centre point of second axles over the first stop as shown in Figure 2.

- Wait for one minute or longer for bridge to stabilize and then record data for 3 minutes.
- Review collected data to confirm consistency. If data were found to be inconsistent, repeat test before moving to the next load position.
- Move truck to next stop and repeat procedure at each transverse line.
- Collect data at end of each test and determine if any residual deflections remain in girders after removal of test truck from bridge.
- Move test truck to align with next travel Lane and repeat steps above until all travel lanes are completed.
- Once testing was complete in all lanes, confirm consistency of testing data by computing summation of girder deflections for similar stop points of different test lanes.
- Collect data for moving test truck over bridge in order to detect dynamic load effects.



Figure 2. Test Vehicle at COL 098

### 3.2.7 Load Testing Data Results

Collected data for each bridge was reviewed and processed prior to commencing data analysis. Maximum deflection values for each bridge are presented in Table 3. All bridges were well below the maximum deflection criteria of  $L/360$ .

Table 3. Summary of Load Testing Results

Bridge ID	Clear Span (m)	Maximum Recorded Deflection (mm)	Deflection-to-span Ratio
HFX 061	7.9	15.2	1/520
COL 098	6.7	11.3	1/591
HFX 334	5.1	9.4	1/543
HFX 322	6.2	8.5	1/729
HFX 325	3.9	8.8	1/443
HFX 099	8.4	14.1	1/596

## 4 DATA ANALYSIS AND DEVELOPMENT OF LOAD DISTRIBUTION FACTORS

Following the load testing phase, field-recorded data were processed to be used for validation of the computer models.

### 4.1 Data Processing and Preliminary Analysis

Data collected during the load testing were processed in this phase. For each bridge, data collected at each position of the

test truck were averaged. Initial recorded values from the gauges were then deducted from these averages. In bridges where displacement sensors were installed at the end of the girders, settlement of the abutments was noted. An average settlement of 3 mm was recorded for the tested bridges and was considered in the model calibration process. Data recorded after the truck was moved off the bridges showed that abutments rebounded to their original condition.

### 4.2 Material Properties of Timber

Material properties of timber are different in three orthogonal directions. Figure 3 shows a typical view of principal axes of wood relative to the direction of the wood grains.

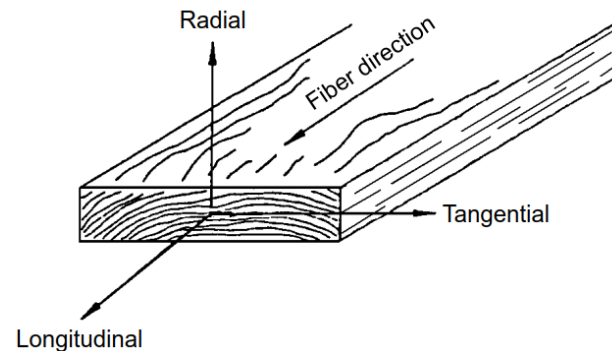


Figure 3. Principal axes of wood material, [12]

Material properties of timber also vary by species. According to the standard drawings for bridges in the province from 1959 and 2001, Douglas fir and hemlock have been extensively used as the material for stringers, and deck elements, respectively. Both are classified as soft [13], [14]. Multiple resources were consulted to determine a range of values for the material properties of these species [1], [11], [12], [15]. The wood material properties used in the initial analysis discussed in this section are presented in Table 4.

Table 4. Material properties of wood species used in Nova Scotia timber bridges.

Property (MPa)	Douglas Fir	Hemlock
Longitudinal ( $E_L$ )	1.06+E4	1.09+E4
Radial ( $E_R$ )	6.26+E2	4.85+E2
Tangential ( $E_T$ )	6.26+E2	4.85+E2
Longitudinal-Radial ( $G_{LR}$ )	7.53+E2	3.82+E2
Longitudinal-Tangential ( $G_{LT}$ )	7.53+E2	3.82+E2
Radial-Tangential ( $G_{RT}$ )	7.42+E1	3.27+E1
Modulus of Elasticity ( $E$ )		
Modulus of Rigidity ( $G$ )		

In an initial attempt to validate the girders' mechanical properties in the longitudinal direction, the recorded Strain-Displacement (converted to Moment-Displacement) values were compared with the equivalent results generated by an analytical MATLAB code, developed by Hoseinpour et al. and modified for the current study, [16]. This code uses the typical equations of the Strength of Material to calculate displacement diagrams for the timber beams to be compared and calibrated with the field-recorded displacement data. Strain-Displacement data from slow-speed dynamic load test were the key factors in carrying out the validation process. Figure 4 presents an

example of the analytical investigation of wood material properties where equivalent moments were determined using the recorded strain values for HFX 099, which has a clear span length of 8.40 m.

The resulting Moment-Displacement diagram was compared with the diagram generated by MATLAB for different span lengths and moduli of elasticity. Analysis showed that the closest relationship between the field data model and the analytical model is achieved by increasing the clear span length of the bridge by 3.5% (to account for the bearing span length) and by using a longitudinal modulus of elasticity of 1.0E4 MPa for the girders.

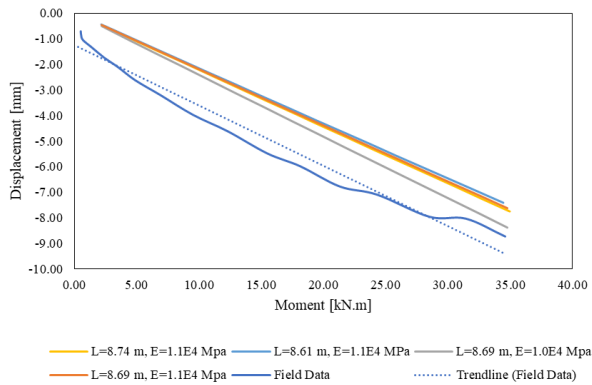


Figure 4. ST 3 on HFX 099

The final step in the process of validating material properties was examination of the values obtained with the 3D numerical model in midas Civil, and the generation of the deflection diagrams for comparison with the field recorded data. Due to the uncertainty associated with wood as an orthotropic material, multiple trials were performed to complete the validation of the wood material properties.

#### 4.3 Analysis Methods

Multiple methods were employed in analysis of the bridges under study, including the simplified methods of the codes CAN/CSA S6-06 and S6:19/14. Two different clauses of the SMAs in the newer versions of the Code were used where the method described in C5.6.6, generally applies to slab-on-girder bridges, and the simplified method outlined in C5.6.7, applies specifically to non-skewed timber bridges. Semi-Continuum Method of Analysis (SECAN4 in conjunction with CBridge) and Finite Element Analysis Method (midas Civil Software) were used for rigorous analysis and for evaluation of SMA results, which were then calibrated based on the field test data. The components of the modelled bridges via FEM were assigned appropriate element types, i.e., beam and plate elements for modelling girders and timber decks respectively, and appropriate links were created between them to represent nailed connections. In all analysis methods the timber bridges were assumed to act as a simple span beam.

The CHBDC standard loading truck was used in the analytical process, and the test truck “Test Vehicle” was used in the calibration of the computer models. A 3-D of the finite element model is shown in Figure 5.

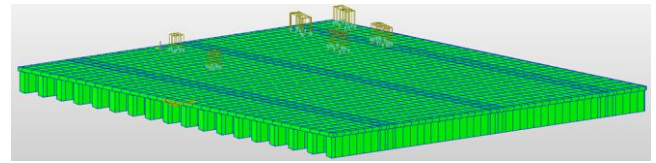


Figure 5. A FEM model of a skew bridge with truck load

The outcome of the final step of the calibration of the FEM models for two of the six bridges under investigation is presented in Figure 6 and Figure 7 below. The figures show the deflection profile across the bridge deck at the test vehicle stop that induced the maximum displacement under reference axle.

The small difference between experimental diagrams and numerical model can be attributed to the effect of other factors (e.g. abutment settlement, condition of the bridges, and presence of asphalt) which were taken into account while developing the distribution equations.

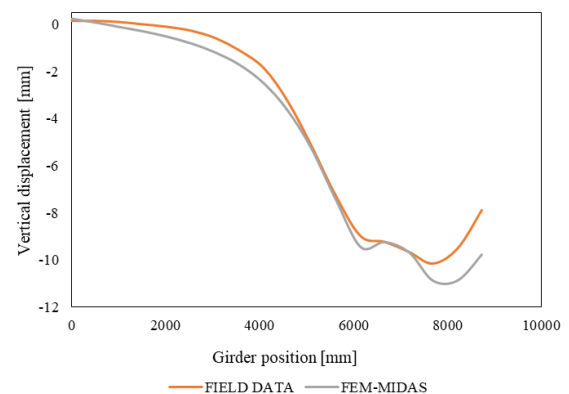


Figure 6. COL 098 – Lane 1: Transverse deflection profile

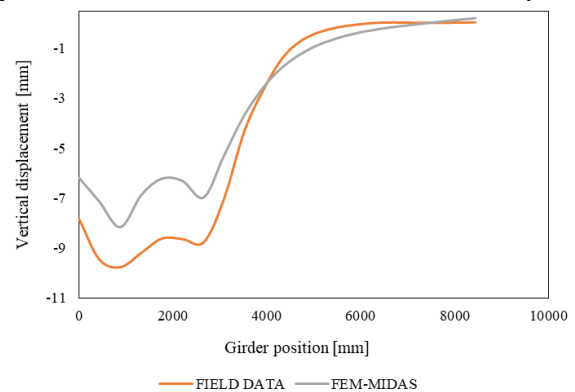


Figure 7. HFX 334 – Lane 5: Transverse deflection profile

#### 4.3.1 Comparison of Results

The results obtained by the mentioned methods are summarized in the Table 5 and Table 6, representing moment and shear effects respectively. Multi-lane reduction factor is multiplied in the results obtained by rigorous analysis as this factor is inherent in the code formulation. In both tables, all load factors have been excluded from the results; only net values of the maximum distributed effects are displayed.

#### 4.4 Loading Characteristics of the Hypothetical Models

The single unit truck of S6:19 (CL3\_625) was selected as the effective live loading on the hypothetical bridges shown in Figure 8, [4]. The selected truck was used to achieve uniform



loading and to eliminate any effect of additional axle loads. For the majority of timber bridges in Nova Scotia, given their defined range of span lengths, CL3\_625 is the governing truck for determining load effects.

CHBDC specifies that the minimum distance between the truck wheels and curb, railing, or barrier wall shall be 0.60 m. Standard drawings for Nova Scotia bridges include a typical barrier width of 0.30 m [13], [14], and are therefore in compliance with the Code. Some of the bridges studied, however, have a barrier measuring only 0.1 m. Therefore, a minimum 0.6 m distance from the edge of the bridge was used to establish the transverse location of the loading truck. To achieve maximum load effect, the truck wheels were also aligned directly over the nearest girder while maintaining a clearance of 0.6 m from the bridge edge.

Table 5. Moment effects comparison (all values are in kN-m).

Bridge	S6-06	S6:19/14, C5.6.7	S6:19/14, C5.6.6	SCA (SECAN)	FEM (MIDAS)
HFX322	41.76	53.89	44.58	46.92	47.95
HFX325	31.56	40.49	36.68	29.80	30.92
HFX334	30.32	38.91	33.51	31.53	30.50
HFX099	70.26	90.31	71.00	60.27	53.53
COL098	51.11	65.44	53.80	47.18	44.46
HFX061	57.86	82.77	58.49	62.56	60.40

Table 6. Shear effects comparison (all values are in kN).

Bridge	S6-06	S6:19/14, C5.6.7	S6:19/14, C5.6.6	SCA (SECAN)	FEM (MIDAS)
HFX322	47.27	59.19	46.61	57.43	55.58* (76.94)
HFX325	52.42	65.65	51.70	64.36	52.75* (78.48)
HFX334	43.72	52.17	41.09	61.41	48.20* (67.14)
HFX099	54.45	69.19	54.49	55.10	61.13* (82.69)
COL098	52.12	65.08	51.25	67.61	56.52* (72.85)
HFX061	50.77	66.59	49.35	80.31	68.34* (91.93)

\* These values represent shear effects when wheel load footprints are modelled as patch loads. The values shown in parentheses represent shear effects, when wheel loads are represented as point loads, representing an average increase of 1.35 over the patch load effects.

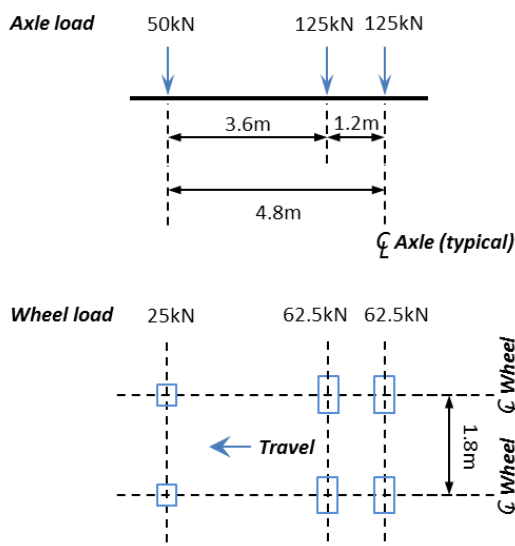


Figure 8. CL3 625 Single unit truck used in the hypothetical models, Source: CHBDC [4]

#### 4.5 Characteristics of the Hypothetical Models

Having the FEM models calibrated based on span length and material properties, 101 hypothetical bridges were created and used to generate the mass data required for statistical analysis. Typical values of the parameters of Nova Scotia timber bridge inventory, such as girder spacing and span length were considered when generation the models.

#### 4.6 Development of Moment Distribution Factor

Distribution of the moment effect between girders is known to be related to the girders' displacement. Based on the Theory of Timoshenko, however, it is critical to differentiate between displacement imposed on the girder by work moment and displacement imposed by shear effects. Lower maximum distribution factors indicate better distribution of load effects between girders.

##### 4.6.1 Parametric Analysis of Moment Distribution Factor

After the maximum distribution factor of each hypothetical bridge was obtained, those values were plotted against variable parameters, and relationships between distributions factors and each parameter was determined. Span length, for instance, which is a key factor in bridge analysis, appeared to have a negative linear relationship with the moment distribution factor, as shown in Figure 9 below.

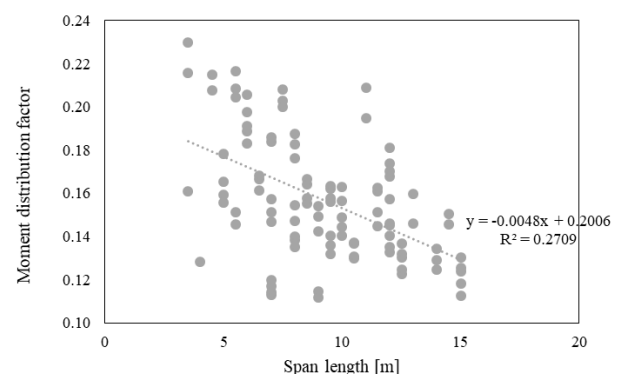


Figure 9. Span length in relation to the distribution factor

Girder spacing was also found to have a positive linear relationship with the distribution factors (Figure 10 below).

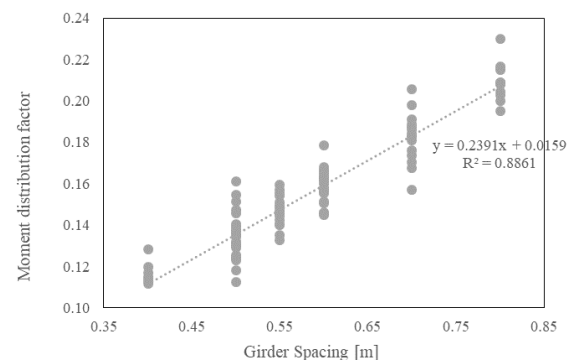


Figure 10. Girder spacing in relation to distribution factors

R-squared values showed that the spacing of girders correlates more strongly with the bridge distribution factor than do other parameters. The number and geometry of girders and

other parameters, however, did not play an important role in determining distribution factors and were tried to be imported to the equations as modification factors.

#### 4.6.2 Development of the Moment Distribution Factor Equation

The Moment distribution factor was formulated using MATLAB; in which the bridge's parameters were combined in different forms, i.e. separate linear combination and multiplication or division of parameters to different powers, to achieve highest correlation. The highest R-squared value (0.96) was found to belong to the simple linear summation of span length and girder spacing shown in Equation 1 below.

$$F_T = S/4.562 - L/394 + 0.051 \quad (1)$$

$$F_{T-min} = S/4.182 + 0.016$$

S: average girder spacing, center to center (metres)

L: bearing span length (metres)

When  $F_T > F_{T-min}$ :  $F_{T-modified} = F_T^2 / F_{T-min}$

When  $F_T \leq F_{T-min}$ :  $F_{T-modified} = F_{T-min}$

In cases where  $F_T$  is larger than  $F_{T-min}$ , a correction is required to account for the effect of different girder sizes. Therefore, the value obtained by the above equation shall be multiplied by the ratio of  $F_T / F_{T-min}$  as shown in the step 3 of Equation 1. Based on calibration process described in Section 4.2, the recommended bearing span length for timber bridges is 1.035 times of the measured clear span length.

#### 4.6.3 Effect of Skew Angle ( $\psi$ ) on Distribution Factors

Skew angle and span length are two important parameters used to determine skew effect in CHBDC. Bridge width, which was the dominant factor in the past editions of the code, plays an insignificant role in the current edition (S6:19).

Maximum moment effect is reduced in skewed bridges due to the decrease in the effective span length. Shear effect is subject to increase in the obtuse corner of skewed bridges, as a result of decreasing stiffness of the girders at the points on the axle line toward the acute edge and a corresponding reduction in load carrying of the far girders, [9].

The Mohr circle concept was employed to generate deck material properties for bridges with different skew angles. Analysis of the hypothetical skewed models also demonstrated that shear effects are increased, and moment effects are decreased in skewed bridges. The results for skewed bridges were close to those obtained by multiplying the CHBDC skew equation with the results of non-skewed bridges. The CHBDC skew effect equation should therefore be used to magnify shear effects and reduce moment effects. The shear modification coefficient determined from the CHBDC skew effect equation is denoted as  $F_S$  in relevant formulations.

$$F_S = 1.2 - (2.0/(\epsilon + 10)) \quad (2)$$

$\epsilon = (L/S) \tan \psi$  for  $\psi \leq 45$

L = Bearing span length

S = Girder spacing

#### 4.6.4 Effect of Girder Dimension on Distribution Factors

Mechanical properties of different girder sizes for each bridge configuration showed low correlation with the obtained

moment distribution factors and made it difficult to find a simple formulation to determine the effect of girder dimension. Given its partial correlation with the distribution factors, the effect of the mechanical properties of the girders is reflected in the original expression with  $F_{T-min}$  and the proposed increase in the moment distribution factors.

#### 4.6.5 Effect of Multiple Traveling Lanes on the Distribution Factors

Nova Scotia timber bridges are typically limited to two travelling lanes. Deflection diagrams showed that the effect of a single truck on one side of a wide bridge has an uplift effect on the far girders at the opposite side. Having three trucks on the specified lanes of the timber bridges would therefore lower distribution factor values; therefore, only two-lane bridges were considered in the modelling process. To account for multilane effect, the Number of Lanes factor,  $F_L$ , was included in Equation 4, with the values displayed in Table 7 below.

Table 8. Number of Lanes factor ( $F_L$ )

Single Lane Bridge	Two-Lane Bridge
1.00	1.21

The Code's statistical factor to account for multi-lane effects is still applicable and is presented in the current research as well. Per sections 3 and 14 of the Code, respectively, the modification factor is 0.90 for design of a two-lane bridge, and 0.85 for evaluation. This factor is denoted by  $R_L$  in Equation 3.

#### 4.6.6 Effect of Bridge Condition on the Distribution Factors

Live load testing results in conjunction with inspection findings and analytical modelling suggest that the bridge condition may affect the load distribution factor. In some cases, field-validated loading responses of the bridge structures differed from those expected based on the calibrated FE model. In order to align the FE model with recorded field data, the condition rating of the bridges under investigation was considered (See Section 3.1). The values provided in Table 9 below were assigned as the factor  $F_C$  to reflect the overall condition of the bridges in the load distribution formulation, Equation 4.

Table 9. Bridge Condition factor ( $F_C$ )

Good	Fair to Good	Fair
1.00	1.12	1.20

None of the bridges included in the current study were rated in lower than Fair condition. Local decays in bridges in Poor condition has the potential to significantly affect the load distribution factor. No  $F_C$  factor, therefore, is provided for evaluation of bridges rated at Poor condition and it has to be concluded based on professional judgment.

#### 4.6.7 Effect of Asphalt Surface on the Distribution Factors

Asphalt pavement of varying thickness was found on four of the six bridges in the current study. Thicker asphalt would result in better load distribution and therefore lower load distribution factors. The effect of asphalt surface is designated as  $F_A$  in Equation 3 and Table 10. Linear interpolation shall be used to find an equivalent factor for different asphalt thickness.

Table 10. Asphalt surface factor ( $F_A$ )

90 mm	150 mm	250 mm
1.08	1.15	1.25

A gravel surface, in contrast to an asphalt surface, is inconsistent in thickness/distribution over the bridge deck and has low elastic properties. Furthermore, only one of the bridges under investigation had a gravel surface, and it appeared to be loose and uneven near the edge of the bridge. Therefore, the contribution of a gravel surface to the load distribution, could not be evaluated in this study, and  $F_A$ , shall be assumed as 1.0.

#### 4.6.8 Generalized Moment Distribution Factor Equation

Equation 3 below presents the overall distribution factors for moment effects. This equation includes coefficients that account for the effects of other parameters, as discussed earlier in this chapter.

$$F_M = F_{T-modified} F_L F_C R_L / F_A F_S \quad (3)$$

$F_{T-modified}$  = Moment distribution factor

$F_S$  = Skew angle coefficient

$F_L$  = Multiple lane effect factor

$R_L$  = Statistical multilane coefficient

$F_C$  = Bridge condition factor

$F_A$  = Asphalt effect factor

#### 4.7 Shear Distribution Factor

Shear distribution factor was obtained by dividing the maximum contribution of the girders by the maximum shear effect of the same loading on a single beam with the same span length, where the single beam was analyzed using CBridge. In order to produce maximum shear in a simple beam, the heavy truck axles must be located as near as possible to the supports where, due to the minimum deflection of the girder, the girder closest to the wheel load absorbs much of the shear effect. Shear distribution does not, therefore, follow the same pattern as the moment distribution, and a separate distribution factor is required.

##### 4.7.1 Parametric Analysis of Shear Distribution Factor

Like the moment distribution factor, shear distribution factors showed a stronger correlation with girder spacing than with span length. In general, weaker correlations (i.e. R-squared values) were established between the shear distribution factor and variable parameters of the timber bridges than between the moment distribution factor and those parameters.

##### 4.7.2 Development of the Shear Distribution Factor Equation

The shear distribution factor in the 2019 version of the Code is only a function of girder spacing, magnified by a modification factor. Using this factor in the current study yielded an R-squared value well below the expected value.

MATLAB was used to combine the effects of different parameters and to develop a formulation for the shear distribution. Multiple trials, however, failed to yield correlations (i.e. acceptable R-squared values) that would suggest sufficient accuracy for these formulas.

A method similar to that used for determination of the moment distribution factor, was therefore applied to generate a

modification coefficient to account for the shear distribution factor. As shown in Equation 4, the shear distribution factor was obtained by modifying the moment distribution factor, the use of which can produce shear effects having an acceptable correlation with an R-Squared value of 0.71.

$$F_v = F_S^2 F_M / (1.35 \gamma_v \gamma_{lv}) \quad (4)$$

Where,  $F_S$  is the skew angle factor, and the shear modification factor  $\gamma_v$  is obtained from the following equation:

$$\gamma_v = S/2.532 - L/134 + 0.247 \quad (5)$$

The correction factor,  $\gamma_{lv}$ , of the shear effect for two-lane bridges is equal to 1.14. See Equation 1 and 3 for the notations.

In an attempt to create maximum load effects, the longitudinal wheel line of the loading truck was aligned over the girder closest to the bridge edge, while respecting the minimum 600 mm clearance. This was the governing case specifically for determining the shear effects.

Considering the low potential for transverse load distribution at the end of the bridges' span it would be safe to assume that the loaded girder absorbs the entire wheel load on the support.

On the other hand, analyzing the standard truck of CL-625 on a short span bridge has the potential of eliminating the effect of the heavier axle load in the shear analysis as it remains off the bridge span in the critical shear loading case. As a result, there is always a possibility to disregard the heavier axle loads with wide spacing in the shear analysis, where they have no potential to be transversally distributed when acting on the support. Therefore, the minimum unfactored shear effect shall be taken as the largest of the wheel load of the loading truck divided by the patch load correction of 1.35.

#### 4.8 Comparison of the results of the developed SMA to the loading tests and CHBDC results

Table 11 presents distribution factors obtained from live load tests, different versions of the Code, and the developed SMA in this study to validate the results of newly developed formulations.

Table 11. Comparison of the moment distribution factor derived using new formulation with other methods

Source	HFX322	HFX325	HFX334	HFX099	COL098	HFX061
(1)	0.1722	0.2563	0.1758	0.2167	0.2142	0.1938
(2)	0.1367	0.1986	0.1296	0.1460	0.1503	0.1347
(3)	0.1281	0.1708	0.1172	0.1444	0.1428	0.1292
(4)	0.1282	0.2117	0.1309	0.1668	0.1440	0.1270
(4-1) %	-25.6	-17.4	-25.5	-22.8	-32.8	-34.5
(4-2) %	-4.5	17	6.1	10.9	-3.6	-5.7
(4-3) %	0.1	23.9	11.7	15.5	0.8	-1.7
(5)	0.1273	0.2099	0.1309	0.1631	0.1624	0.1374
(5-1) %	-26.1	-18.1	-25.5	-24.5	-24.1	-29.1
(5-2) %	-5.1	16	6.1	8.4	8.7	2
(5-3) %	-0.6	22.9	11.7	13	13.7	6.3

(1) S6-14/ S6:19 C5.6.7

(2) S6-14/ S6:19 C5.6.6

(3) S6-06

(4) Live Load Test

(5) Developed SMA



This comparison established a close relationship between the live load test results and the results of the developed SMA here. Compared to the results obtained with CHBDC S6-14 and S6:19, C5.6.7, both live load tests and the new SMA show a decrease of between 17.4% and 34.5% in moment distribution factors across all timber bridges studied, which is consistent with NSDPW's hypothesis that the Code-specified analysis method for timber bridges leads to more conservative design and evaluation criteria.

## 5 CONCLUSION

Results of this study show that the current SMAs in the Canadian bridge codes are overly conservative, and the congruence of analytical and load test results supports the hypothesis that the newly developed equations are sufficiently accurate for the simplified analysis of typical timber bridges in Nova Scotia. The equations presented in this report can be used for both design and evaluation purposes, using appropriate factors and subject to the following parametric limitations:

- Span range: 3 m to 15 m.
- Girder spacing: 350 mm to 800 mm.
- Girder width: 150 mm to 300 mm.
- Girder depth: 250 mm to 800 mm.
- Girder spacing: Uniform or with less than 10% variation.
- Skew angle: Less than 45°

Bridges with characteristics outside the above ranges will require additional study.

## ACKNOWLEDGMENTS

The authors would like to acknowledge Nova Scotia Department of Public Works for initiating this study and their active support during all stages of its completion. The authors also acknowledge Dr. Baidar Bakht, P. Eng., for his help in determining load sharing factors for the six timber bridges evaluated during this study.

## REFERENCES

- [1] G. A. Smith, *The Impact of the Evolution of Simplified Methods of Analysis in Canadian*, Halifax, NS: Dalhousie University, 2018.
- [2] J. N. Reddy, *An Introduction to the Finite Element Method*, New York: Third Edition. McGraw-Hill, 2006.
- [3] A. Mufti, B. Bakht, L. G. Jaeger and J. Jalali, *SECAN4 User Manual: Incorporating the Semi-Continuum Method of Analysis for Bridges*, Halifax, NS, 1998.
- [4] L. G. Jaeger and B. Bakht, "Bridge analysis by the semicontinuum method," *Can. J. Civ. Eng.*, vol. 12, pp. 573-582, 1985.
- [5] B. Bakht and L. G. Jaeger, "Simplified methods of bridge analysis for the third edition of OHBDC," *Can. J. Civ. Eng.*, vol. 19, no. 4, p. 551–559, Feb 1992.
- [6] Commentary on CAN/CSA-S6-14, Canadian Highway Bridge Design Code, Toronto: Canadian Standards Association, 2014.
- [7] F. Fanous, J. May and T. Wipf, "Development of live-load distribution factors for glued-laminated timber girder bridges," *J. Bridg. Eng.*, vol. 16, no. 2, p. 179–187, Mar 2011.
- [8] A. Mufti and B. Bakht, "Diagnostic testing of six sawn timber stringer bridges in Nova," Unpublished Report to the Nova Scotia Department of Transportation and Public Works, Halifax, 1999.
- [9] CAN/CSA S6:19 Canadian Highway Bridge Design Code, Toronto: Canadian Standards Association, 2019.
- [10] Forest Products Laboratory, *Wood handbook—Wood as an engineering material*, Madison, WI: U.S: Department of Agriculture, Forest Service, Forest Products Laboratory, 1999.
- [11] NSTIR, *Standard Design Drawings of Timber Bridges of Nova Scotia*, Halifax: Department of Highways, 1959.
- [12] NSTIR, *Standard Design Drawings of Timber Bridges of Nova Scotia*, Halifax: Nova Scotia Transportation and Public Works, 2001.
- [13] Ontario Wood WORKS!, *Ontario Wood Bridge Reference Guide*, North Bay, Ontario: Ministry of Natural Resources and Forestry, 2017.
- [14] H. C. Hoseinpour, M. R. Valluzi, E. Garbin and M. Panizza, "Analytical investigation of timber beams strengthened with composite materials," *Constr. Build. Mater.*, vol. 192, pp. 1242-1251, 2018.
- [15] CAN/CSA-S6-06 Canadian Highway Bridge Design Code, Toronto: Canadian Standards Association, 2006.
- [16] CAN/CSA-S6-14 Canadian Highway Bridge Design Code, Toronto: Canadian Standards Association, 2014.

[Note: Nova Scotia Department of Public Works (NSDPW) was formerly known as Nova Scotia Transportation and Infrastructure Renewal (NSTIR)]

# Full-Scale Bridge Testing: Lessons from the Demolition of the Steinavötn Bridge

Sigurdardottir, Dorotea H<sup>1</sup>, 0009-0006-8496-4625, Tsai, Ching-Yi<sup>1</sup>, 0000-0002-0122-2575, Guðmundsson, Guðmundur Valur<sup>2</sup>

<sup>1</sup>Faculty of Civil and Environmental Engineering, University of Iceland, Sæmundargötu 2, 102 Reykjavík, Iceland

<sup>2</sup>Division of Development, The Icelandic Road and Coastal Administration, Suðurhraun 3, 210 Garðabær, Iceland  
email: dorotea@hi.is, cytsai@hi.is, gudmundur.v.gudmundsson@vegagerdin.is,

**ABSTRACT:** Structural engineers, particularly bridge engineers, rarely have the opportunity to test full-scale bridges to failure due to the high costs involved. Such experiments are typically conducted on scaled-down specimens in controlled settings, which can introduce challenges in accurately correlating results to real-world full-scale behavior. In 2019, a unique opportunity arose when the Steinavötn bridge in southern Iceland was irreparably damaged by flooding. Built in 1964, the 102-meter-long reinforced concrete continuous beam bridge had two abutments and five piers and was part of Iceland's national road system, connecting the ring road around the island. One of its piers suffered scour damage beyond repair, leading to the decision to demolish the structure. Before its demolition, a measurement campaign was conducted using long-gauge fiber-optic sensors to capture the bridge's response to ultimate loading. This study presents the findings from the measurement campaign and bridge modelling, providing valuable insights into the ultimate load behavior of a full-scale bridge and advancing the understanding of structural performance under extreme conditions.

**KEY WORDS:** Full-scale testing, Bridge modelling, Continuous beam bridge, Long-gauge fiber-optic sensors, Reinforced concrete.

## 1 INTRODUCTION

In 2017, a unique opportunity arose when the Steinavötn bridge in southern Iceland was irreparably damaged by flooding. Built in 1964, the 102-meter-long reinforced concrete continuous beam bridge had two abutments and five piers (Figure 1) and was part of Iceland's national road system, connecting the ring road around the island. One of its piers suffered scour damage beyond repair, leading to the decision to demolish the structure. Before its demolition, extensive load testing and vibration measurements were conducted on it during the summer of 2019. These tests were carried out as a collaborative effort involving the Icelandic Road and Coastal Administration (IRCA), Reykjavik University, ETH Zurich, and Osmos Monitoring Group. Various sensors were used during the measurements, including force gauges, displacement sensors, accelerometers, and different types of strain sensors. The bridge response was recorded under various load scenarios, such as excitation from natural environmental vibrations, controlled traffic loads on the bridge, impact loads, and gradually increasing vertical loads on one bridge span far into the non-linear regime.

The events leading up to and the causes of the bridge's destruction have been examined in a master's thesis written at the University of Iceland [1]. A bachelor's thesis at Reykjavik University documented the setup of the load tests on the bridge and the data collection process. It presented results from material tests on concrete and reinforcement steel. Furthermore, preliminary numerical computational models of the bridge were developed, deflections were calculated, and the load-bearing capacity was compared with measurement data as well as with design calculations [2]. The dynamic behavior of the bridge has also been analyzed based on vibration data by a research group at Reykjavik University and the Technical

University of Denmark [3], [4]. A comparison between non-linear beam-truss models with different boundary conditions was conducted at the University of Iceland [5].

Structural engineers, particularly bridge engineers, rarely have the opportunity to test full-scale bridges to failure due to the high costs involved. Such experiments are typically conducted on scaled-down specimens in controlled settings, which can introduce challenges in accurately correlating results to real-world full-scale behavior. It is therefore important to seize the opportunity and conduct full-scale experiments to improve knowledge and understanding of structural behavior as well as validating numerical models. Data analysis methods and numerical models developed in these rare settings provide valuable insights into structural behavior, numerical modelling, and structural health monitoring methods.

In this paper insights from data measured by the long-gauge fiber-optic strain sensors and LVDT displacement sensors during the ultimate load test at Steinavötn bridge are presented.



Figure 1. The Steinavötn bridge. Photo from ICRA, 2019.

## 2 THE STEINAVÖTN BRIDGE

### 2.1 Description of the bridge

The Steinavötn Bridge on National Road 1 was built by the IRCA in 1964 and was located in the Suðursveit region of Southeast Iceland, south of Vatnajökull, about 61 km west of Höfn in Hornafjörður. The bridge was a 102-m-long concrete beam bridge, single-lane and with six spans. The bridge was an important link in completing the ring road, and 10 years after its construction, the road was fully connected [6]. Figure 1 shows the bridge over Steinavötn.

The span from the abutment to the first intermediate pier was 14 m on both sides and the inner spans were 18.5 m (see Figure 2). The intermediate piers rested on timber piles that went approximately five meters into the ground.



Figure 2. A view of the Steinavötn bridge from the ICRA's drawing set.

### 2.2 Bridge cross-section

The bridge superstructure had two different cross-sections. Four meters on either side of every pier, the cross-section was a hollow box girder shown in Figure 3. The remaining 10.5 m and 6 m in the inner and outer spans, respectively, were double T-beams illustrated in Figure 4. The bridge deck was monolithically cast and reinforced with the piers.

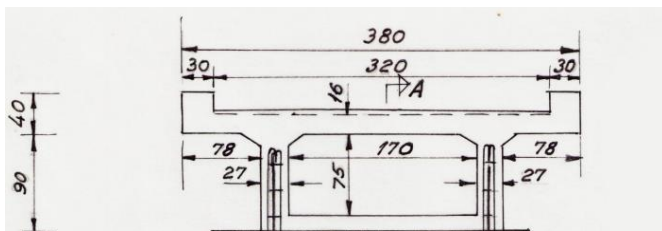


Figure 3. Bridge cross-section at pier. Hollow box girder. Measurements in cm. From the ICRA's drawing set.

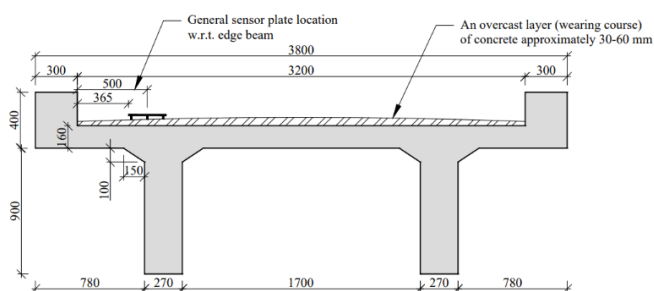


Figure 4. Bridge cross-section at midspan. Double T-beam. Measurements in mm. From the ICRA's drawing set.

### 2.3 Materials

Three concrete samples were extracted from the bridge using core drilling, taken from its longitudinal beams. The cylindrical samples had a diameter of 100 mm and an initial length of 270 mm, which was reduced to 200 mm by BM Vallá ehf. concrete plant, who also leveled the ends with additional concrete. The

compressive strength was tested in collaboration with Mannvit hf. consulting firm following the ÍST EN 12390-3:2009 standard, applying an axial load increasing at 0.6 MPa/sec until failure. The average compressive strength was 37.7 MPa [2].

Ultra-sonic measurements were performed on the side beams of the superstructure to determine the dynamic modulus of elasticity of the concrete. The average dynamic modulus of elasticity was 39 GPa [7]. Note that the dynamic modulus can be approximately 20-30% higher than the static one [8]. According to Eurocode EC2, the static modulus of elasticity for concrete strength 37.7 MPa is 33 GPa [9]. This is 15% of the measured dynamic modulus.

Three samples were taken from the longitudinal reinforcement and three from the shear reinforcement of the bridge. The steel strength was determined through tensile testing in collaboration with Mannvit, following the ÍST EN ISO 15630-1:2019 standard, with a 200 mm anchorage length at each end for proper grip. Due to challenges regarding the equipment, only the yield and ultimate strength were recorded [2].

Table 1 shows the material properties that were recorded and the values used in the subsequent analysis.

Table 1. Material properties.

	Measurements			
	Compr. strength [MPa]	Dyn. E [GPa]	Yield stress [MPa]	Ultim. stress [MPa]
Concrete	37.7	39	-	-
Steel stirrup	-	-	290	439
Steel longit.	-	-	405	758
	Used in analysis			
	$f_{ck}$ [MPa]	$f_{yk}/f_{uk}$ [MPa]	$E_c$ [GPa]	$E_s$ [GPa]
Concrete	38	-	33	-
Steel	-	400/760	-	210

### 2.4 Bridge after scour damage

In September 2017, there was a large increase in water in the river, resulting in scouring at intermediate pier 2, measured from the western end of the bridge. The settlement of the pier was measured at about 200 mm, but it also deviated and tilted by 70 mm/1000 mm, or 7%, from the vertical [1]. Figure 5 shows how the bridge pier has subsided. Cracks could be seen on the bridge superstructure above the seats of intermediate piers 1 and 3, which extended 5 m into the water. Since the bridge piers were cast and reinforced with the bridge deck, rotation of a pier therefore caused rotation of the bridge deck. Crack formations above the intermediate piers strongly indicated that floating elements had formed at these locations. After a site visit by the Icelandic Road Administration and stress tests in early October 2017, the bridge was deemed unusable [10]. Subsequently, a temporary bridge was built to allow traffic to reopen, and in September 2021, a new double-lane bridge over Steinavötn was inaugurated.





Figure 5. The intermediate pillar of the bridge has sunk [10].

### 3 BRIDGE TESTS

This section offers a comprehensive overview of the monitoring experiments conducted on the old Steinavötn bridge during the summer and fall of 2019, prior to its demolition. The IRCA chose to utilize the bridge as an educational and research resource prior to its demolition and commenced comprehensive experiments on it in collaboration with various Icelandic and international partners. Multiple experiments were carried out on the bridge, measuring acceleration, deflection, strain, and static loading.

#### 3.1 Short overview of tests

Figure 6 illustrates a side view of the Steinavötn bridge, highlighting the test span subjected to various structural analyses. The bridge, spanning the Steinavötn river, is depicted with five piers (labeled Pier 1 through Pier 5) and six spans (Span 1 through Span 6).

Notably, Figure 6 identifies "plastic hinge" locations in Span 1 and Span 3, indicating potential areas of structural weakness. The bridge is further divided into "Damaged Structure" and "Undamaged Structure". A note points to a pier damaged during a flood in September 2017, contributing to the "Damaged Structure" classification.

Researchers from ETH Zürich used single-axis accelerometers to measure the vertical acceleration response of the Steinavötn bridge within the test span. They installed sensors during the summer to monitor long-term ambient background vibrations and conducted damage detection experiments in September.

The OSMOS Group employed Fiber Bragg Grating sensors, including OSMOS Optical Strands, a Thermal Probe, and the OSMOS Expert Data Acquisition System, to measure strain in real-time within the test span. The sensors were installed on the bridge beams in July 2019. The sensors recorded mostly strain, but also some temperature data, evaluated through remote activation, until the ultimate load test in September 2019. The sensors were uninstalled prior to the bridge demolition.

Reykjavik University conducted two measurement campaigns on the bridge, utilizing five 3-axial accelerometers and two LVDT displacement sensors within the test span. The data from those measurements have been used to analyze the response of the bridge, and more details and results can be found in [3].

In September 2019, IRCA and Reykjavik University jointly performed a shear capacity test on the test span of the bridge, monitoring both strain and displacement.

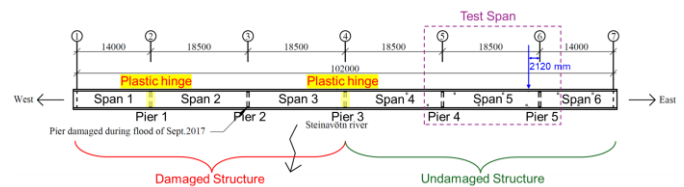


Figure 6. Side view of the Steinavötn bridge illustrating the test span (between Piers 4 and 5) used for structural analysis, including shear capacity testing.

#### 3.2 Detailed description of incremental point load test

The purpose of this test is to assess the structural integrity and load capacity of the bridge component, specifically related to the Steinavötn bridge's shear capacity. The steel structures supporting the hydraulic jacks were designed to withstand a minimum bearing capacity of 3000 kN, considering steel availability and on-site assembly. According to a 2018 master's thesis [1], the Steinavötn bridge's local shear capacity is approximately 2200 kN. The experiment aims to validate these calculations and ensure the safety and reliability of the bridge structure under realistic loads.

Figure 7 depicts the test setup designed to evaluate the load-bearing capacity of the bridge structure. The setup utilizes two hydraulic jacks, each capable of applying a maximum force of 200 tons, which is distributed through 300x300 mm plates onto the bridge deck. These jacks are supported by a 5-meter-long HEA1000 beam, which transfers the load to HEB100 columns. The columns, in turn, are bolted to lower HEA1000 beams, which are restrained by two HEB300 beams and connected to piles via  $\phi 25$  mm rebars. Each rebar pair is clamped to a single pile using UNP100 profiles and M20 bolts. Each pile group consists of four piles, approximately 11 meters deep.

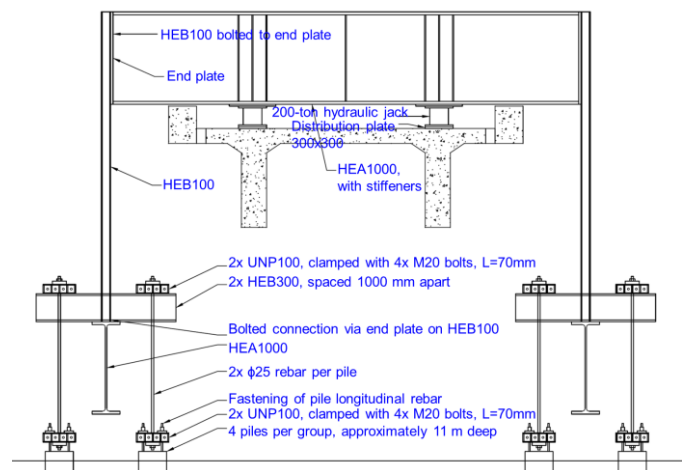


Figure 7. Test Setup

The test analyzed in this paper was performed on the 17<sup>th</sup> of September 2019. Loads were applied using the hydraulic jacks in steps, starting at approximately 500 kN and reaching approximately 2300 kN. The load as measured by the load cells is shown in Figure 8.

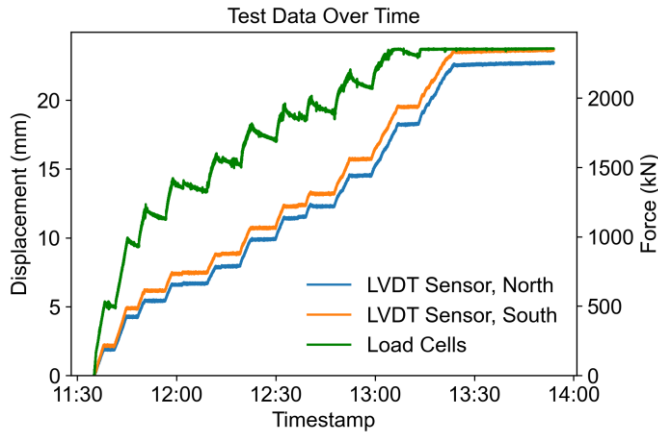


Figure 8. Displacement and force measurements during incremental point load test.

#### 4 FIBER-OPTIC AND DISPLACEMENT SENSORS

Before the load tests were conducted, long-gauge fiber-optic strain sensors from the technology company OSMOS were installed on the bridge in axial, parallel, and crossed topologies; see Figure 9. During the incremental point load test, an LVDT sensor was placed under each T-beam in the center of the tested span.

##### 4.1 Long-gauge fiber-optic strain sensors

Fiber-optic sensors emerged several decades after the invention of electrical strain gauges. Fiber-optic sensors are primarily made of silica, an inert material resistant to chemical exposure, and electromagnetic interference [11]. This makes silica highly suitable for measurements in harsh environments like concrete. The fiber optic serves both as the sensor and the transmission medium for the measurement. Depending on its configuration, a fiber-optic sensor can measure strain, tilt, acceleration, movement, temperature, humidity, corrosion, and more [12]. Additionally, multiple types of sensors can be linked together and transmit measurements through the same medium. Moreover, signals can be transmitted over long distances (several kilometers) without requiring electrical power [11], [13].

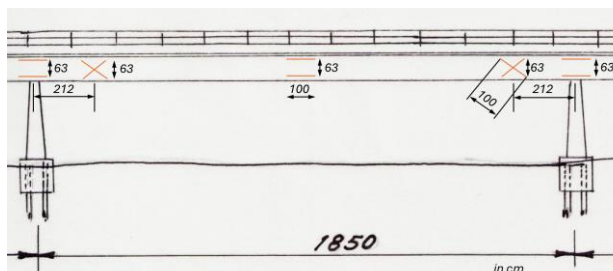


Figure 9. Long-gauge fiber-optic strain sensor locations on the south side of the monitored span. Note: sensor locations are the same on the north side of the span except lower sensors in parallel topologies over piers are not present.

Discrete strain gauges are either short (approximately 10–100 mm) or long (250–10,000 mm) [13]. Short- and long-gauge sensors provide similar results in homogeneous materials. Common construction materials, particularly concrete, are far

from homogeneous, as they are characterized by aggregates, cracks, and pores [14]. The properties of concrete are thus discontinuous, and while short strain gauges can provide accurate information about localized strains, it is nearly impossible to accurately represent the overall strain state of a concrete structure with short gauge sensors. However, long gauge strain sensors measure the average strain over their gauge length, offering a better overview of the behavior in heterogeneous materials. In other words, it is often less relevant to know the strain in the individual components of concrete (cement paste, aggregates, phase boundaries) but far more relevant to measure the overall behavior and response of the material referred to as concrete. Further discussion on the accuracy and applicability of long-gauge fiber-optic strain sensors can be found in the literature, f.ex. [15], [16], [17].

Parallel strain sensors provide information about the average curvature of the cross-section [13], specifically,

$$\kappa = \frac{\varepsilon_1 - \varepsilon_2}{h} \quad (1)$$

where:

$\kappa$  is the average curvature of the cross-section in  $\mu\text{ε}/\text{mm}$

$\varepsilon_1$  is the axial strain measured by the lower sensor in a parallel topology in  $\mu\text{ε}$

$\varepsilon_2$  is the axial strain measured by the upper sensor in a parallel topology in  $\mu\text{ε}$

$h$  is the distance between the two sensors in mm

Crossed strain sensors are intended to measure the average shear strain over the height of the cross [13], specifically,

$$\gamma = \frac{\varepsilon_1 - \varepsilon_2}{2 \cos(\alpha) \sin(\alpha)} \quad (2)$$

where:

$\gamma$  is the average shear strain in  $\mu\text{rad}$

$\varepsilon_1$  is the axial strain measured by sensor 1 in the crossed topology in  $\mu\text{ε}$

$\varepsilon_2$  is the axial strain measured by sensor 2 in the crossed topology in  $\mu\text{ε}$

$\alpha$  is the angle between the sensors in the cross

The curvature over the east pier and shear under the load, as measured by the parallel and crossed sensors respectively, are shown in Figure 10 and Figure 11.

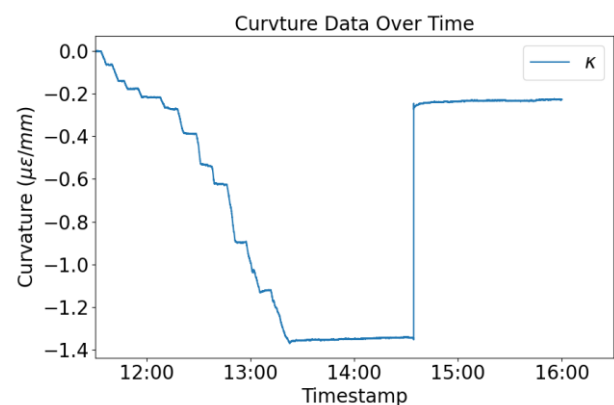


Figure 10. Average curvature over east pier during the incremental point load test.

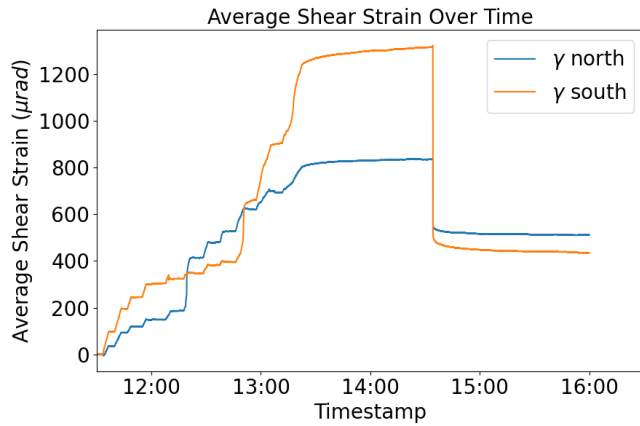


Figure 11. Average shear strain under the load during the incremental point load test.

#### 4.2 LVDT displacement sensors

Linear Variable Differential Transformers (LVDT) are known for their precision, dependability, and adaptability in measuring linear displacement [18]. The measurements from the middle of the span during the incremental point load test are shown in Figure 8 along with the load measurements.

### 5 LINEAR APPROXIMATIONS

Linear approximations for deformation at midspan, curvature and shear strain are provided in the following sections. These linear approximations become increasingly inaccurate as the load increases, more cracks form, and the structural behavior becomes more nonlinear.

#### 5.1 Deformation

The deformation is estimated using handbook equations for deformation of beams with different boundary conditions [19]. The true behavior of the span is somewhere between these two as the boundary conditions are stiffer than for the simply supported beam and softer than the fixed-fixed beam. Thus, the true deformation is a weighted average of the two equations.

Simply supported beam:

$$\Delta_x = \frac{Pbx}{6EI} (l^2 - b^2 - x^2) \quad (3)$$

Beam with fixed-fixed supports:

$$\Delta_x = \frac{Pb^2x^2}{6EI} (3al - 3ax - bx) \quad (4)$$

where:

$\Delta_x$  is the deformation at location  $x$  in mm.

$P$  is the load in N

$a$  is the location of the load from the left support in mm

$b$  is the location of the load from the right support in mm

$l$  is the total length of the span,  $l = a + b$ , in mm

$E$  is the elastic modulus in MPa

$I$  is the moment of inertia of the cross-section in mm<sup>4</sup>

#### 5.2 Curvature

When assuming linear behavior the curvature in the cross-section is

$$\kappa = \frac{M}{EI} \cdot 10^6 \quad (5)$$

where:

$\kappa$  is the average curvature in  $\mu\text{e}/\text{mm}$

$M$  is moment in the section in Nmm

$E$  is the elastic modulus in MPa

$I$  is the moment of inertia of the cross-section in mm<sup>4</sup>

#### 5.3 Shear

When assuming that the material behaves within the linear elastic range, the shear stress in a hollow box cross-section can be expressed as:

$$\gamma = \frac{VA\bar{y}}{2GI} \cdot 10^6 \quad (6)$$

where:

$\gamma$  is the average shear strain in  $\mu\text{rad}$

$V$  is the shear force acting on the section in N,

$A$  is the area above the point where the stress is calculated in mm<sup>2</sup>,

$\bar{y}$  is the distance from the centroid of  $A$  to the centroid of the cross-section in mm

$G$  is the shear modulus in MPa

$I$  is the moment of inertia of the cross-section in mm<sup>4</sup>

$t$  is the thickness of the web (total thickness  $2t$ ) in mm

### 6 NONLINEAR NUMERICAL MODELS

#### 6.1 OpenSees

OpenSees (Open System for Earthquake Engineering Simulation) is a software framework for developing applications in earthquake engineering using finite element methods [20]. It is designed to simulate the behavior of structural and geotechnical systems subjected to earthquakes. The flexibility of OpenSees allows researchers and engineers to create customized models that can accurately reflect the unique characteristics of various materials and structural configurations. This capability makes it an invaluable tool in assessing the performance of structures during seismic events and informing design improvements.

The Beam Truss Model (BTM) proposed by Lu and Panagiotou [21] and Lu et al. [22] is a design-oriented analysis method used to model reinforced concrete (RC) structures, efficiently computing the force and deformation capacity of RC components. It represents a wall component as an assemblage of horizontal, vertical, and inclined line elements with a beam formulation and a fiber section, capturing nonlinear out-of-plane flexural resistance and its coupling with axial and in-plane flexural/shear resistance. This method makes it possible to get a more accurate picture of how the structure will behave under different loads, which makes design predictions more reliable. The BTM also makes it easier to include advanced material models, which helps engineers better understand how the different parts of reinforced concrete structures interact with each other.

There is a biaxial truss element in OpenSees called Truss2. It is meant to consider biaxial effects in a uniaxial element when it is used with the ConcretewBeta material. The ConcretewBeta material is a uniaxial concrete material model in OpenSees that considers the effect of normal tensile strain on the compressive behavior of concrete, using a tri-linear compressive stress-strain envelope to model strength degradation in tension. This interaction allows for a more accurate representation of how



concrete structures respond under various loading conditions, particularly when subjected to simultaneous axial and lateral forces. By utilizing the Truss2 element with the ConcretewBeta material, engineers can better predict potential failure mechanisms and optimize the design of reinforced concrete elements for enhanced safety and performance.

## 6.2 OpenSees model of Steinavötn bridge

In this study, the test span of the Steinavötn bridge was modeled utilizing OpenSees with the BTM approach. The span was discretized into 60 units along its length. As illustrated in Figure 12, the blue lines, parallel to the bridge's longitudinal axis, were modeled as longitudinal elements. These dispBeamColumn elements are particularly suited for capturing nonlinear material and geometric behavior. Thirteen dispBeamColumn elements with fiber sections were used, totaling 780 elements. The fiber sections incorporated Steel02 material for rebar and Concrete04 material for concrete. Hollow boxed girder and double T-beam sections have been considered with different fiber sections at the bottom of the cross-section (this distinction is not visible in Figure 12). This fine discretization allowed for a detailed representation of the nonlinear material behavior under the incremental point load test. The red lines, representing the transverse elements of the deck, were modeled. In contrast, elasticBeamColumn elements model beams and columns with linear elastic material properties. Twelve elasticBeamColumn elements were used per cross-section, totaling 732 elements. The piers, located on both sides, were modeled with two elasticBeamColumn elements each, bringing the total number of elasticBeamColumn elements to 736. These elasticBeamColumn elements considered only the concrete's Young's modulus, assuming linear elastic behavior. The green lines, representing the diagonal elements of the triple-layer grid structure (Truss2 elements), a key component of the Beam-Truss model, totaled 1440 elements, incorporating the ConcretewBeta material to model the concrete's tensile and compressive response. The total number of elements used in the OpenSees model was 2952. Fixed boundary conditions, denoted by magenta squares in Figure 12, were applied at the base of the piers to simulate the support constraints.

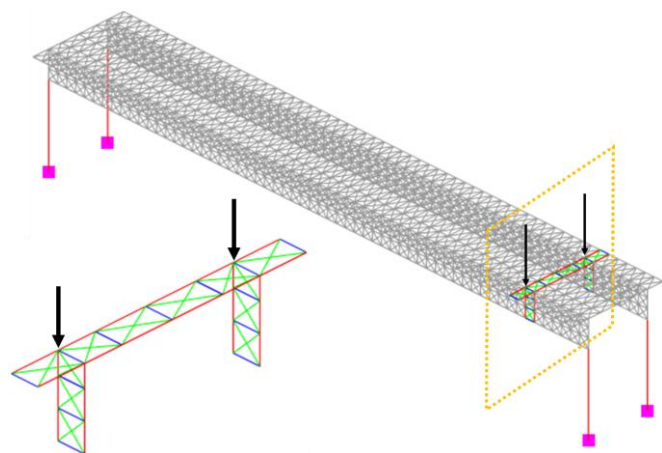


Figure 12. OpenSees model of the Steinavötn bridge with applied loads, highlighting the structural discretization.

Information on deformation is extracted directly from the midspan of the model. For evaluation of the curvature and shear, strains are extracted at the sensor locations, and the curvature and shear strain are calculated using Equations (1) and (2).

## 7 RESULTS

The results from measurements, linear approximations, and nonlinear numerical modelling are presented in Figure 13 to Figure 15. The results are presented as force-response diagrams highlighting the nonlinearity of the bridge behavior at high loads. The measurement results are shown in yellow and red, with measurements on the north side of the bridge in yellow and on the south side in red, the linear approximations in dot-dashed gray, and the nonlinear OpenSees results in dashed black.

The load-displacement at midspan is reported in Figure 13. The measurements fall between the linear approximations of the fixed beam and the simply supported beam, as was expected. The weighted average is calculated by combining 30% of the response from the fixed beam and 70% from the simply supported beam. However, the measured displacement is never truly linear. The nonlinear model has the same slope as the simply supported beam and starts to deviate from that line when the load reaches approximately 1500 kN. The model appears to have more capacity than the real structure.

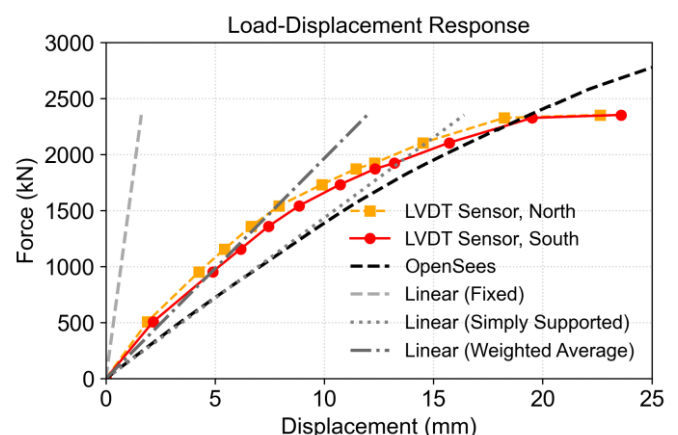


Figure 13. Load-displacement diagram. Results from measurements, linear approximations, and nonlinear numerical modelling at midspan.

The load-curvature at the east pier is shown in Figure 14. The curvature is calculated from strain measurements and nonlinear numerical modelling strains using Equation (1). The linear approximation is calculated using Equation (5). The measured curvature exhibits linear behavior very close to the linear approximation until the load reaches approximately 1500 kN. The nonlinear numerical model changes stiffness (slope) when the load reaches 500 kN and then again when the load reaches 1500 kN. The nonlinear numerical model shows less stiffness than the measurements. This is reasonable since the numerical model is a single span supported by piers, not including the adjacent spans that will increase stiffness. However, despite this minor difference in stiffness, the model successfully models the measured behavior.

The load-shear strain relationship close to the east pier is shown in Figure 15. The average shear strain from fiber-optic strain measurements in crossed topologies on the north and south side of the bridge is calculated using Equation (2). The same equation is used to calculate the simulated shear strain using strains from the Truss2 element in the OpenSees model. Note that  $\alpha = 45^\circ$  in the model whereas  $\alpha = 39^\circ$  for the fiber-optic strain sensors.

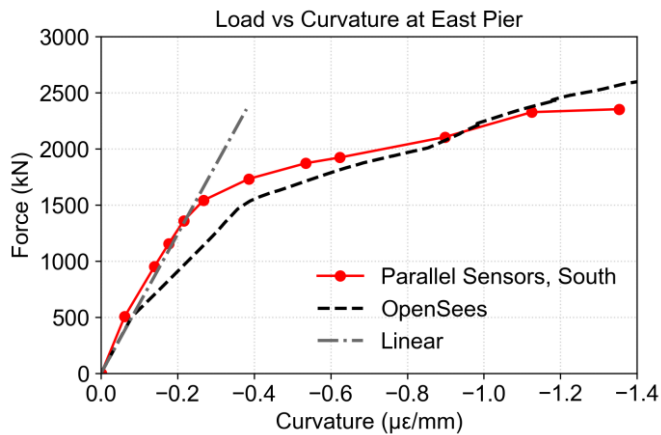


Figure 14. Load-Curvature diagram. Results from measurements, linear approximations, and nonlinear numerical modelling at the east pier.

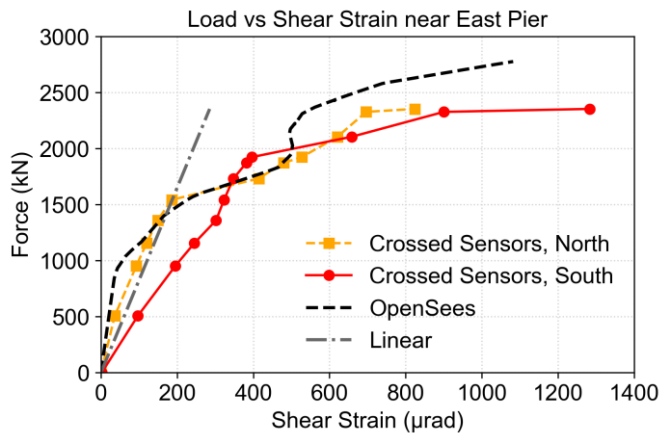


Figure 15. Load-Shear Strain diagram. Results from measurements, linear approximations, and nonlinear numerical modelling near the east pier.

In the incremental point load test the load is applied directly above the crossed fiber-optic strain sensors. The internal shear diagram for the bridge thus has a sharp discontinuity exactly at the sensor location. Additionally, according to St. Venant's principle the strain field directly under the force is heavily perturbed. However, despite these circumstances the average measured strain on the north side is in good agreement with the linear approximation until the load reaches 1500 kN. On the south side the stiffness seems to be less than on the north side and the stiffness changes before the load reaches 1500 kN. More detailed analysis is needed to explain the difference between the response on the north and south side of the bridge.

The nonlinear numerical model shows stiffer behavior under low loads than the fiber-optic measurements and changes stiffness when the load reaches 1000 kN. Generally, the numerical results are in good agreement with measurements on the north side of the bridge.

## 8 DISCUSSION

Simple linear approximations are able to describe the linear behavior of this concrete structure. When the load reaches 1500 kN, a nonlinear response is observed in all studied parameters. The load-displacement behavior at midspan demonstrates that measured displacements fall between the linear approximations of a fixed and simply supported beam, with an estimated weighted response of 30% fixed and 70% simply supported. While the nonlinear numerical model captures the general trend, it predicts a higher load capacity than observed in measurements.

The load-curvature relationship at the east pier exhibits good agreement between measurements and the linear approximation up to approximately 1500 kN. The nonlinear numerical model changes stiffness at 500 kN and 1500 kN and generally shows less stiffness than measured values. This difference is attributed to the model's exclusion of adjacent spans, which would otherwise contribute to the bridge's overall stiffness. Nonetheless, the nonlinear model successfully replicates the measured strain behavior at sensor locations, validating its reliability.

An important factor to keep in mind is that Equation (1) is based on the assumption that plain sections remain plain and that the strain distribution over the height of the cross-section is linear. This assumption is true in the linear elastic range of the materials, demonstrated by the excellent agreement between the linear approximation and the measurements. However, after the materials enter the nonlinear regime, plain sections do not necessarily remain plain and the assumption that the strain varies linearly between the two parallel sensors is not necessarily correct. In other words, the slope of the line between the two strain measurements in the parallel sensor topology does not necessarily accurately describe the curvature of the cross-section when the bridge starts to behave nonlinearly. The fact that the curvature obtained by this method from the strain measurements and the nonlinear model are similar demonstrates that nonlinear model successfully simulates the strains at the sensor locations.

The load-shear strain relationship near the east pier reveals a strong correlation between measured strains and the linear approximation up to 1500 kN on the north side. However, the south side exhibits lower stiffness and an earlier stiffness change, necessitating further investigation to understand these discrepancies. The nonlinear numerical model shows higher stiffness at low loads and a change in stiffness at 1000 kN but aligns well with measurements on the north side. Strains as simulated by the nonlinear OpenSees model are similar to the measurements from strain sensors, resulting in curvature and shear strain with similar behavior. This result highlights the strength of the Truss2 elements in OpenSees in conjunction with crossed fiber-optic sensors.

## 9 CONCLUSION

This paper presents the Steinavötn bridge that was damaged during flooding in 2017. Subsequently, before demolition, the bridge was instrumented with long-gauge fiber-optic strain sensors and LVDT sensors, and tests carried out far into the nonlinear regime. This paper presents the load-response behavior of the bridge under the incremental point load test using the fiber-optic and LVDT measurements, linear approximations, and nonlinear numerical modeling in OpenSees.

The analyzed parameters were displacement at midspan, curvature at the east pier and shear strain near the east pier (under the load). All analyzed parameters exhibit linear behavior up to an approximate load of 1500 kN. The results highlight the bridge's nonlinear response at high loads and provide valuable insights into its structural behavior.

More in depth analysis of the nonlinear strain field from the OpenSees model is necessary to evaluate the error caused by the linear assumptions made in the data analysis of the sensor and numerical data. Overall, the nonlinear numerical model effectively captures key aspects of the bridge's nonlinear response, despite minor discrepancies in stiffness predictions.

Future research should focus on refining the numerical model, exploring differences between the north and south side responses, and evaluating the effects of adjacent spans to enhance predictive accuracy.

## ACKNOWLEDGMENTS

Funding from the Icelandic Road and Coastal Administration (IRCA) research fund (grant no. 1800-1068) is gratefully acknowledged, as is the cooperation with IRCA staff members, E. Óskarsson and Ó. S. Haraldsson. Also, thanks to OSMOS staff and J. Snæbjörnsson at Reykjavik University.

## REFERENCES

- [1] H. Bogason, "Tjónagreining á brúnni yfir Steinavötn í Suðursveit," MS, University of Iceland, Reykjavík, 2018.
- [2] A. G. Ragnarsson, "Burðarþolsrannsókn á brú yfir Steinavötn í Suðursveit," BSc, Reykjavik University, Reykjavík, 2020.
- [3] Þ. V. Jónasdóttir, "The Steinavötn Bridge (translated: Steinavotn Broen)," Master Thesis, DTU, 2021.
- [4] T. Jonasdottir, J. Snæbjörnsson, and R. Brincker, "Modelling a Damaged Multi-span RC Bridge Based on Structural Monitoring Data," 2023, pp. 134–143. doi: 10.1007/978-3-031-07258-1\_15.
- [5] Þ. J. Tryggvason, "Ólínuleg töluleg greining á brotmörkum steinsteyptar brúar yfir Steinavötn," MS, University of Iceland, Reykjavík, 2023.
- [6] Vegagerðin, "Brýr og vegur yfir Skeiðarársand, 40 ár frá opnun lokaáfangna Hringvegarins," *Framkvæmdaféttir*, vol. 22, no. 16, Jul. 2014.
- [7] Þ. V. Jónasdóttir and J. Þ. Snæbjörnsson, "Structural analysis and modelling of a reinforced concrete bridge based on full scale data," Reykjavík, 2021.
- [8] W. de A. Thomaz, D. Y. Miyaji, and E. Possan, "Comparative study of dynamic and static Young's modulus of concrete containing basaltic aggregates," *Case Studies in Construction Materials*, vol. 15, Dec. 2021, doi: 10.1016/j.cscm.2021.e00645.
- [9] European Committee for Standardization, "Eurocode 2: Design of concrete structures - Part 1-1: General rules and rules for buildings," 2004, *Staðlaráð Islands*.
- [10] G. V. Guðmundsson, Ó. Einar, Ó. S. Haraldsson, A. Bjarnason, and A. G. Ragnarsson, "Burðargetumat steyptra brúa Álagspröfun brúa á Steinavötn," 2019.
- [11] E. Udd and W. B. Spillman Jr., *Fiber optic sensors. An introduction for engineers and scientists*, 2nd ed. Hoboken, New Jersey, USA.: Wiley, A John Wiley & Sons, Inc., Publication, 2011.
- [12] R. M. Measures, *Structural monitoring with fiber optic technology*. San Diego, USA.: Academic Press; A Harcourt Science and Technology Company, 2001.
- [13] B. Glisic and D. Inaudi, *Fibre optic methods for structural health monitoring*. Chichester, England: John Wiley & Sons Ltd, The Atrium, Southern Gate, 2007.
- [14] J. F. Young, S. Mindess, R. J. Gray, and A. Bentur, *The science and technology of civil engineering materials*. Upper Saddle River, New Jersey, USA: Prentice Hall, International Series in Civil Engineering and Engineering Mechanics, 1998.
- [15] B. Glisic, "Influence of the gauge length on the accuracy of long-gauge sensors employed in monitoring of prismatic beams," *Meas Sci Technol*, vol. 22, no. 3, 2011.
- [16] D. H. Sigurdardottir, J. Stearns, and B. Glisic, "Error in the determination of the deformed shape of prismatic beams using the double integration of curvature," *Smart Mater Struct*, vol. 26, no. 7, 2017, doi: 10.1088/1361-665X/aa73ec.
- [17] D. H. Sigurdardottir and B. Glisic, "Detecting minute damage in beam-like structures using the neutral axis location," *Smart Mater Struct*, vol. 23, no. 12, 2014, doi: 10.1088/0964-1726/23/12/125042.
- [18] A. Sivasuriyan *et al.*, "Emerging Trends in the Integration of Smart Sensor Technologies in Structural Health Monitoring: A Contemporary Perspective," Dec. 01, 2024, *Multidisciplinary Digital Publishing Institute (MDPI)*. doi: 10.3390/s24248161.
- [19] B. Chr. *et al.* Jensen, *Teknisk Ståbi*, 19th ed. Copenhagen: Nyt Teknisk Forlag, 2007.
- [20] F. McKenna, G. L. Fenves, M. H. Scott, and B. Jeremic, "OpenSees," 2000, *Berkeley, Univ. of California: 2.3.2*.
- [21] Y. Lu and M. Panagiotou, "Three-Dimensional Cyclic Beam-Truss Model for Nonplanar Reinforced Concrete Walls," *Journal of Structural Engineering*, vol. 140, no. 3, Mar. 2014, doi: 10.1061/(ASCE)ST.1943-541X.0000852.
- [22] Y. Lu, M. Panagiotou, and I. Koutromanos, "Three-dimensional beam-truss model for reinforced concrete walls and slabs – part 1: modeling approach, validation, and parametric study for individual reinforced concrete walls," *Earthq Eng Struct Dyn*, vol. 45, no. 9, pp. 1495–1513, Jul. 2016, doi: 10.1002/eqe.2719.



# Advancing high-fidelity Digital Twin Technology for Structural Health Monitoring

Ihar Antonau<sup>1,2</sup>, Suneth Warnakulasuriya<sup>3</sup>, Talhah Ansari<sup>3,6</sup>, Roland Wüchner<sup>3</sup>, Rainald Löhner<sup>4,6</sup>, Facundo Nicolas Airaud<sup>4</sup>,  
Habir Antil<sup>5</sup>

<sup>1</sup>Cluster of Excellence SE<sup>2</sup>A -- Sustainable and Energy-Efficient Aviation, Technische Universität Braunschweig, Germany,  
[www.tu-braunschweig.de/en/se2a](http://www.tu-braunschweig.de/en/se2a)

<sup>2</sup>Institute of Structural Analysis, Technical University of Braunschweig, Beethovenstrasse 51, 38106, Braunschweig, Germany

<sup>3</sup>Chair of Structural Analysis, Technical University of Munich, Arcisstr. 21, 80333, Munich, Germany

<sup>4</sup>Center for Computational Fluid Dynamics and Department of Physics and Astronomy, George Mason University, Fairfax, VA  
22030, USA

<sup>5</sup>Center for Mathematics and Artificial Intelligence (CMAI) and Department of Mathematical Sciences, George Mason  
University, Fairfax, VA 22030, USA

<sup>6</sup>Institute for Advanced Study, Technical University of Munich, Lichtenbergstr. 2a, 85748 Garching, Germany  
email: [ihar.antonau@tu-braunschweig.de](mailto:ihar.antonau@tu-braunschweig.de), [suneth.warnakulasuriya@tum.de](mailto:suneth.warnakulasuriya@tum.de), [talhah.ansari@tum.de](mailto:talhah.ansari@tum.de), [wuechner@tum.de](mailto:wuechner@tum.de),  
[fairaud@gmu.edu](mailto:fairaud@gmu.edu), [rlohner@gmu.edu](mailto:rlohner@gmu.edu), [hantil@gmu.edu](mailto:hantil@gmu.edu)

**ABSTRACT:** This study addresses the need for high-fidelity system identification in Digital Twin (DT) applications for Structural Health Monitoring (SHM). As infrastructure ages, its material properties may degrade due to various factors, including damage, corrosion, and fatigue. Accurate assessment of material properties is critical for ensuring safety and reliability. High-fidelity identification enables the detection of localized damages that traditional methods may not detect, directly impacting maintenance strategies and public safety. In this work, we present a formulation of the optimization problem that minimizes errors between observed and simulated displacements by varying material properties. Additionally, we utilize adjoint-based sensitivity analysis, combined with regularization techniques such as Vertex Morphing, to enhance the efficiency and robustness of the optimization process. Our case studies, which include detailed analyses of 2D and 3D structures using real-world data, demonstrate the effectiveness of our methods in accurately inferring material properties and revealing structural integrity. By implementing this advanced methodology, practitioners can achieve timely and accurate assessments of structural integrity, leading to better-informed decision-making regarding maintenance and safety protocols. This research contributes to the ongoing advancement of Digital Twin technology, promoting safer and more efficient infrastructure management.

**KEYWORDS:** High-fidelity Digital Twin, Inverse Problems, Regularization, Adjoint sensitivity analysis.

## 1 INTRODUCTION

Throughout the lifecycle of structures, their material properties can deteriorate due to various factors, including damage, corrosion, and fatigue. Advances in sensor technology and numerical simulation techniques now enable the creation of Digital Twins (DT) — dynamic digital representations of complex structures. DT can be defined as follows [7-10]:

*“A set of virtual information constructs that mimic the structure, context, and behavior of an individual/unique physical asset, or a group of physical assets, is dynamically updated with data from its physical twin throughout its life cycle and informs decisions that realize value.”*

A key component in developing DT is system identification, which involves evaluating the current state of material properties and identifying areas of weakness. This process often requires solving inverse problems through appropriate parameterization, typically framed as an optimization challenge. The formulation steps of the system identification problem can be outlined as follows:

1. *System Description:* Analyze all available information about physical objects and numerical models, including documentation, numerical models, or data from the design phase, for instance, testing data from wind tunnels or experiments with material samples.

2. *State Information:* Collect and analyze available sensor data, measurements, load tests, and visual inspections to inform the assessment.

3. *Definition of Optimization Problem:* Define the objective function that incorporates the available measured data and select system parameters to minimize the errors between measured and computed data points.

Figure 1 illustrates the “twinning” process schematically. In real-world applications, the structure can be used under various conditions. A digital model can predict performance and provide feedback about the structure, indicating whether it requires maintenance or can be safely used further. To enhance the feedback provided by the digital model, the system identification process aligns the real and virtual worlds.



Figure 1. Twinning real and digital worlds.

In system identification, various fidelities can be applied, which can be categorized into two main types: analysis and identification, as shown in Figure 2. Low-fidelity analysis is represented by simplified finite element (FE) models, such as using beam elements to describe the structure. In contrast, high-fidelity models incorporate detailed geometry, complex material laws, and other intricate characteristics.

Similarly, low-fidelity identification involves a limited number of parameters that typically reflect the overall structural behavior of the system. Low-fidelity system identification is well solved using artificial neural networks. For instance, in [14], the identification parameters are the coordinates of the damaged regions and the stiffness reduction factor. This setup allows for the localization of damage, but it is limited to a single region. In [16], the three-floor structure is studied, where each floor has its own set of global identification parameters, which describe the structure's properties. As a result the damage localization is limited to the floor.

In high-fidelity identification, however, many system parameters need to be determined, for example, a unique set for each finite element in the model. Consequently, while low-fidelity identification can indicate an average weakening in the structure, high-fidelity identification can localize many damaged regions with different shapes and damage intensity. In this work, we focus on high-fidelity FE models and high-fidelity identification as the most challenging case. However, the proposed methodology can also be applied to other fidelity cases.

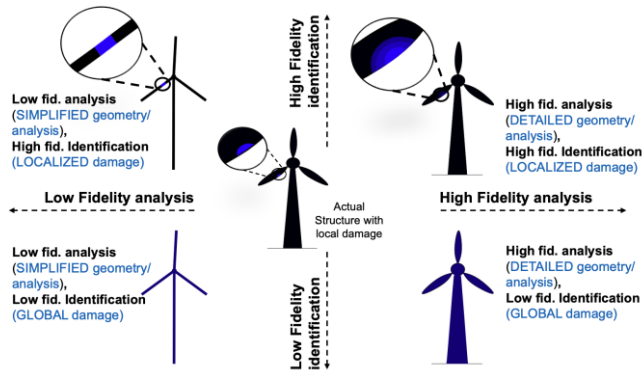


Figure 2. Fidelity levels in the FE model and system identification.

An adjoint analysis is an essential component of solving high-fidelity system identification problems with many parameters. The adjoint-based technique for localizing damages in structures using displacement and strain measurements is presented in [1]. A combination of several sensor approaches would also appear highly promising in future applications [11], including risk measures and uncertainty quantification [12]. Additionally, recent research has demonstrated the potential for restoring the temperature field based on displacement and strain measurements [13].

Frequent updates between numerical and physical assets are an essential property of the digital twin in practical applications. Live monitoring requires a fast solution to the system identification problem to analyze and update the system. In [3], the authors studied the possible computational cost reduction using various optimization algorithms.

This study addresses the minimization problem associated with identifying material properties within numerical models. The cost function is formulated based on the aggregated errors between observed and simulated displacements across multiple locations. To enhance the robustness of the minimization process, we employ various smoothing and filtering techniques, including the Vertex Morphing approach, which helps regularize the optimization problem.

We present both 2D and 3D structural case studies, where one of the cases are represented by a testing bridge “Concerto”. Our examples utilize real-world data alongside numerical simulations to demonstrate the effectiveness of our methods in accurately inferring material properties and revealing structural integrity. This work contributes to the ongoing advancement of Digital Twin technology for effective structural health monitoring, ultimately promoting safer and more reliable infrastructure.

## 2 METHODOLOGY

The system identification of material properties, such as damage, can be formulated as an optimization problem involving unknown material parameters  $\mathbf{p} = [p_1, p_2, \dots, p_n]$ . Depending on the applied material model, the unknown material parameters can be Young's modulus, Poisson's ratio, or other, at each of the elements in the finite element model (FEM). Figure 3 illustrates the components of generalized system identification, which includes a digital twin and the optimization problem.

The digital twin comprises a physical object, measured data, and a numerical model. The key components of the optimization process are material parameters, a regularization technique, an optimization algorithm, and the formulation of the objective function, which incorporates the available measured data. The following sections describe details of each component and its challenges.

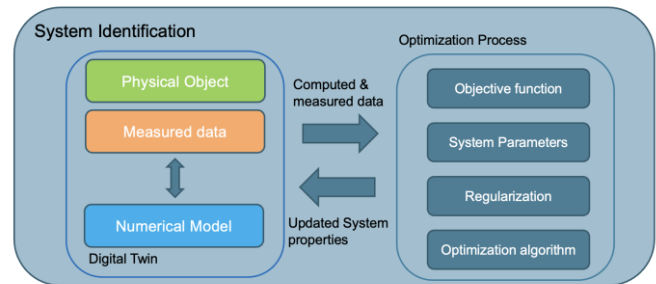


Figure 3. System identification process.

### 2.1 Objective function

One of the key components in setting up the optimization process is defining the objective function. Based on the available data, the generalized objective function can be formulated as a weighted sum of the errors between measured and computed quantities. Given  $l$  number of the different sensor types and  $n$  given load cases  $\mathbf{F}_i, i = 1..n$ ;  $n \cdot l$  corresponding measurements at  $m$  measuring points of their respective data  $\varphi$ . The variable  $\varphi$  can represent different quantities based on the sensor type, for instance, displacement, strain, temperature, acceleration and etc. The generalized objective (cost) function is formulated as:

$$J(\mathbf{p}, \boldsymbol{\varphi}(\mathbf{p})) = \sum_{k=1}^l \sum_{i=1}^n \sum_{j=1}^m \Phi(\omega_{kij}, \boldsymbol{\varphi}_{kij}^{md}, \mathbf{I}_{kij}^d \boldsymbol{\varphi}_{ki}(\mathbf{p}), \mathbf{p}) \quad (1)$$

where  $\omega_{kij}$  are the measurement weights;  $\mathbf{I}_{kij}^d$  are interpolation matrices that are used to obtain the computed value from the finite element mesh at the measurement locations.  $\Phi(\omega_{kij}, \boldsymbol{\varphi}_{kij}^{md}, \mathbf{I}_{kij}^d \boldsymbol{\varphi}_{ki}(\mathbf{p}))$  is a weighted aggregation function, for instance, weighted square sum:

$$\Phi = \frac{1}{2} \omega_{kij} [\boldsymbol{\varphi}_{kij}^{md} - \mathbf{I}_{kij}^d \boldsymbol{\varphi}_{ki}(\mathbf{p})]^2 \quad (2)$$

In case, only one load case is considered with one sensor type with displacement measurements, and the material parameter of interest is Young's modulus, then the objective function defined in Equation (1) simplifies to:

$$J(\mathbf{u}(\mathbf{E})) = \frac{1}{2} \sum_{j=1}^m \omega_j (\mathbf{u}_j^{md} - \mathbf{I}_j^d \mathbf{u}(\mathbf{E}))^2 \quad (3)$$

## 2.2 Sensitivity analysis

An important step in the optimization process for identifying material parameters is computing the derivative of the objective function with respect to the material parameters. Considering the objective function introduced in Equation (3), we can apply the chain rule:

$$\frac{dJ}{d\mathbf{E}} = \frac{\partial J}{\partial \mathbf{E}} + \frac{\partial J}{\partial \mathbf{u}} \frac{d\mathbf{u}}{d\mathbf{E}} \quad (4)$$

where  $\frac{\partial J}{\partial \mathbf{E}} = 0$  because  $J$  does not depend directly on  $\mathbf{E}$ , Equation (4) can be further developed:

$$\frac{dJ}{d\mathbf{E}} = \frac{\partial J}{\partial \mathbf{u}} \frac{d\mathbf{u}}{d\mathbf{E}} = - \left( \sum_{j=1}^m \omega_j (\mathbf{u}_j^{md} - \mathbf{I}_j^d \mathbf{u}) \right) \frac{d\mathbf{u}}{d\mathbf{E}} \quad (5)$$

In general,  $\frac{dJ}{d\mathbf{E}}$  can be computed using either the finite difference approach or the adjoint approach. Due to a large number of material parameters to identify, the adjoint approach is preferred because it is computationally more efficient by avoiding the direct computation of  $\frac{d\mathbf{u}}{d\mathbf{E}}$ . Adjoint approach requires first solving a primal problem, which is depicted in Equation (6) in the residual form, where  $\mathbf{K}$  is the stiffness matrix,  $\mathbf{u}$  is the displacement vector, and  $\mathbf{F}$  is the load vector:

$$\mathbf{R} = \mathbf{K}\mathbf{u} - \mathbf{F} \quad (6)$$

Then, the adjoint problem is solved for  $\boldsymbol{\lambda}$  Lagrange multipliers:

$$\left( \frac{\partial \mathbf{R}}{\partial \mathbf{u}} \right)^T \boldsymbol{\lambda} = - \left( \frac{\partial J}{\partial \mathbf{u}} \right)^T \quad (7)$$

and the Lagrange multipliers are used in a post-processing step to compute the final sensitivities:

$$\frac{dJ}{d\mathbf{E}} = \frac{\partial J}{\partial \mathbf{E}} + \boldsymbol{\lambda}^T \frac{\partial \mathbf{R}}{\partial \mathbf{E}} \quad (8)$$

We would like to note that the Equation (7) is independent of the choice of the material parameter. Hence, the adjoint approach can be used for various material parameters and Young's modulus  $\mathbf{E}$  has been used as an example. A lot of performance and implementation optimization can be achieved by solving the adjoint system, because  $\left( \frac{\partial \mathbf{R}}{\partial \mathbf{u}} \right)^T = \mathbf{K}^T$  and  $\mathbf{K}$  is symmetric, hence we can re-use the existing left-hand side of

the primal problem and only have to change the right-hand side (i.e. pseudo-load) to obtain  $\boldsymbol{\lambda}$ .

## 2.3 Regularization

Similarly to node-based shape and topology optimization, to avoid high-frequency noisy results, we need to apply appropriate regularization techniques [2]. Therefore, one option is to subject the raw gradients to smoothing using filters. In [1], the authors reviewed various gradient smoothing techniques for material identification problems, such as simple element averaging, weak Laplacian smoothing, and pseudo-Laplacian smoothing, where the last one has been chosen as a better technique. In [3], the authors apply an explicit filter called Vertex Morphing to smooth material gradients. In the context of Vertex Morphing, thus, the physical material properties, for instance, Young's Modulus  $\mathbf{E}$  are indirectly controlled by an unsmoothed control field  $\mathbf{p}$  and a kernel (or filter) function  $\mathcal{F}$ , for example, on the surface  $\Gamma$  with surface coordinates  $(\xi, \eta, \zeta)$ :

$$(\xi_0, \eta_0, \zeta_0) = \int_{\Gamma} \mathcal{F}(\xi - \xi_0, \eta - \eta_0, \zeta - \zeta_0) \mathbf{s}(\xi, \eta, \zeta) d\Gamma \quad (9)$$

After discretization of the structural geometry  $\mathbf{E} = [E_1, E_2, \dots, E_n]$  and control function  $\mathbf{s} = [s_1, s_2, \dots, s_n]$  by standard techniques such as the finite element method, Vertex Morphing appears as:

$$\mathbf{E} = \mathbf{A}\mathbf{s} \quad (10)$$

Where  $\mathbf{E}$  is Young's modulus of elements, and they are arranged sequentially.  $\mathbf{A}$  is the filter operator matrix, and  $\mathbf{s}$  is the vector of discrete control field parameters, again arranged sequentially. The most straightforward approach is to add control parameters to every element.

The entries  $A_{ij}$  of the filter matrix  $\mathbf{A}$  reflect the filter effect as the interaction between two different centers of the elements  $i$  and  $j$ , their center's spatial position vectors  $\mathbf{x}_i$  and  $\mathbf{x}_j$ , and their Euclidean distance  $\|\mathbf{x}_i - \mathbf{x}_j\|$ . For the case of the Gauss distribution as kernel function and approximating integration by summation, it holds:

$$A_{ij} = \mathcal{F}(\mathbf{x}_i, \mathbf{x}_j) / \text{sum} \quad (11)$$

$$\text{sum} = \sum_j \mathcal{F}(\mathbf{x}_i, \mathbf{x}_j)$$

$$\mathcal{F}(\mathbf{x}_i, \mathbf{x}_j) = \begin{cases} e^{-\|\mathbf{x}_i - \mathbf{x}_j\|^2 / 2r^2}, & \|\mathbf{x}_i - \mathbf{x}_j\| \leq r \\ 0.0, & \|\mathbf{x}_i - \mathbf{x}_j\| > r \end{cases} \quad (12)$$

and  $r$  is the filter radius. By changing the filter radius, one can adjust the filtering intensity.

## 2.4 Generalized workflow

Figure 4 shows the generalized workflow of the optimization process for system identification. Every optimization iteration, we need to evaluate objective function value and its gradients. Then, we apply Vertex Morphing (or other filtering technique) on the computed gradients and compute the control parameter update using optimization algorithm. Then, we apply one more time Vertex Morphing on the computed control parameter update to compute new model parameters state. This process continues till the convergence criteria are met or maximum number of optimization iterations are reached.



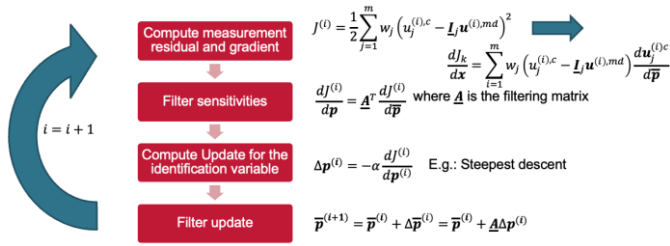


Figure 4. Generalized system identification workflow as an optimization process.

Relevant optimization convergence criteria for system identification are:

1. Relative reduction of objective function:

$$\frac{J(\mathbf{p}^i)}{J(\mathbf{p}^0)} \leq \varepsilon \quad (13)$$

2. Absolute reduction of objective function:

$$J(\mathbf{p}^0) - J(\mathbf{p}^i) \geq \varepsilon \quad (14)$$

3. Maximum sensor error:

$$\max_j \text{abs}(\mathbf{u}_j^{md} - \mathbf{L}_j^d \mathbf{u}(\mathbf{p})) \leq \varepsilon \quad (15)$$

In general, a lot of standard techniques from optimization theory can be apply to solve system identification problems, including convergence criteria, optimization algorithms, aggregation techniques, variable scaling, line search techniques and globalization strategies.

### 3 CHALLENGES IN SYSTEM IDENTIFICATION

In this section main challenges of the method are summarized.

#### 3.1 Modeling the objective function

The choice of the objective can play a crucial role in system identification because various types of measured data have to be combined. That require a proper scaling of the measured information to keep the objective function dimensionless and it allows to find a “correct” solution. Additionally, in minimization of the sum of the errors, the component with the highest error would have the highest contribution to the search direction. The sensor with highest error may change in the sequential optimization iterations leading to zig-zagging behavior. In [1], authors reviewed few weighting strategies to combine strains and displacements. In case of Equation (3), these techniques compute weights for displacements as follows:

1. *local weighting*:

$$\omega_j = (\mathbf{u}_j^{md})^{-2}$$

This method may lead to an ‘over-emphasis’ of small displacements, that are in regions of marginal interest.

2. *average weighting*:

$$\omega_j = \left[ \frac{\sum_{j=1}^m |\mathbf{u}_j^{md}|}{m} \right]^{-2}$$

This method may lead to an ‘under-emphasis’ of small displacements that may occur in important regions.

3. *max weighting*:

$$\omega_j = \left[ \max_j |\mathbf{u}_j^{md}| \right]^{-2}$$

This method may lead to an ‘under-emphasis’ of smaller displacements that can occur in important regions;

4. *local/max weighting*:

$$\omega_j = \max \left[ \varepsilon \max_j |\mathbf{u}_j^{md}|, |\mathbf{u}_j^{md}| \right]^{-2}$$

where  $\varepsilon = [0.01, 0.1]$ . This method works best of all, as it combines local weighting with a max-bound minimum for local values.

The weights for strain components (or other measured values) can be computed in a similar manner.

#### 3.2 Large design space

In our approach, we aim to identify the material parameters for each element individually. As a result, there are various spatial distributions of material properties that can produce similar or identical deformations under a fixed load case. This type of optimization problem is known as “multimodal,” meaning it has multiple optimal solutions with the same objective function values. Consequently, engineering expertise is necessary to “narrow” down the design space. For example, if the material is expected to weaken over time, we can impose an upper limit on Young’s modulus to prevent stiffening of the structure, as illustrated in Figure 5.

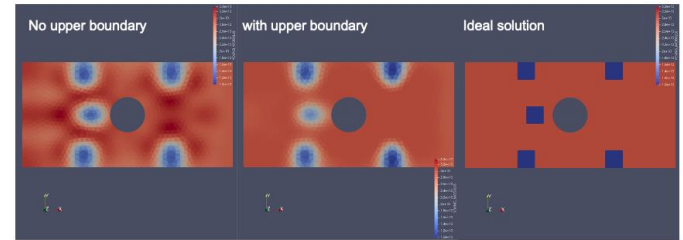


Figure 5. Results of the system identification problem with (right) and without (middle) stiffening in the material.

To improve the convergence of the system identification process, authors in [4] suggest using a zoom-in approach, where they start with a limited number of design variables and then gradually reparametrize the problem to zoom into the damaged region by switching from low-fidelity identification to high-fidelity. This approach improves the robustness of the method by better finding the weak areas globally and afterward identifying damages on a smaller scale.

#### 3.3 Discrete gradients

To localize damage effectively, it is necessary to consider many material parameters, such as modifying Young’s modulus for each element. This results in a large number of parameters and the need for gradient-based optimization algorithms. Consequently, adjoint analysis is essential. Section 2.2 discusses the use of adjoint analysis to compute the gradients of the objective function.

The gradients obtained through adjoint methods can be discrete and noisy, which may lead to high-frequency solutions. To address this issue, regularization techniques are required. One such technique is Vertex Morphing, which is introduced in Section 2.3. Figure 6 illustrates the effect of Vertex Morphing.

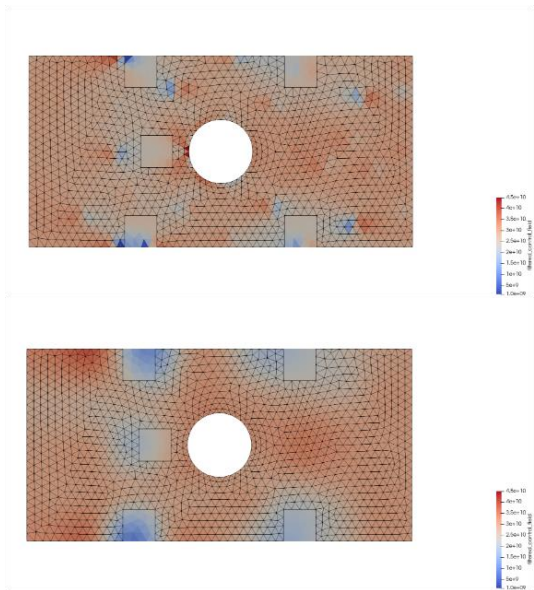


Figure 6. Young's Modulus distribution: top – without, bottom – with Vertex Morphing.

### 3.4 Optimization algorithm

The difference between classical mathematical optimization problem and system identification problem is that evaluation of the objective value typically requires solving the FEM-based structure analysis. Therefore, robust and efficient optimization algorithms are required with minimal functional and gradient evaluations. In [3], the authors compare various optimization algorithms and their performance. It has been shown that a significant amount of computational cost can be avoided by selecting a well-suited algorithm.

Figure 7 shows the performance of the various algorithms. 2D Plate with a hole (Section 4.1) has been used as a benchmark to study the performance. The tested algorithms are: SciPy Broyden-Fletcher-Goldfarb-Shanno (BFGS), SciPy Limited memory Broyden-Fletcher-Goldfarb-Shanno bounded algorithm (L-BFGS-B), SciPy conjugate gradient algorithm (CG), SciPy Trust-Region Constrained Algorithm (TRC), PyRol the steepest descent method with back-tracking line search, PyRol Lin-More trust region algorithm (LM-TR) and Kratos Nesterov accelerated gradient method with Quasi-Newton Barzilai-Borwein correction line search (NAG-QNBB).

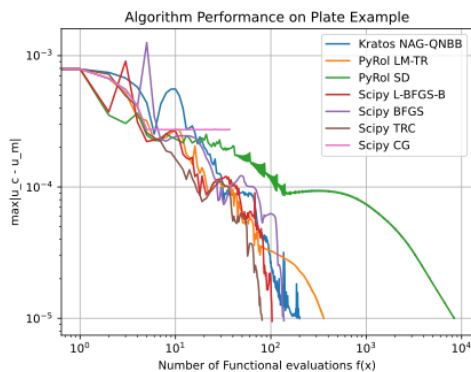


Figure 7. Convergence rate of the tested algorithms [3].

## 4 NUMERICAL EXAMPLES

This section demonstrates two examples of the system identification process. A simple 2D plate with a hole example is a numerical benchmark from [3], which is introduced to help the reader better understand the introduced methodology. The second example demonstrates the usability of the method on a real-world structure, and its measured performance is shown. The measured data were obtained from [5].

### 4.1 2D Plate with a hole

The FE model of the 2D plate with a hole is shown in Figure 8, where the left side is fixed, and the distributed force is applied on the right side. Figure 9 (left) shows displacements of the damaged model and the mapped displacements to the sensors. These displacements are used as “measured” displacements to identify the given damage. The virtual sensor is modeled as a point with  $x$ - and  $y$ - spatial coordinates, and the measured value is associated with its location. The damaged material is visible in Figure 9 (right).

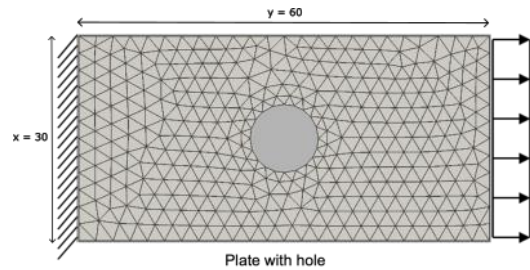


Figure 8. FEM model [3].

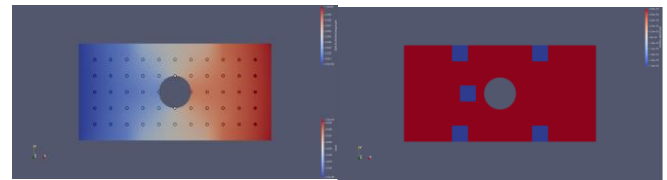


Figure 9. Measured displacements (left) and predefined damage (right) [3].

The objective function is defined similarly to Equation (3), and it is based on the measured and computed displacements in the  $x$ -direction:

$$J(\mathbf{u}(\mathbf{E})) = \frac{1}{2} \sum_{j=1}^m \omega_j \left( u_{x_j}^{md} - u_{x_j}(\mathbf{E}) \right)^2 \quad (16)$$

The filtering radius is chosen to be constant, and  $r = 5$ , covering approximately 4 FE elements. The optimization process stops when the maximum error in the sensor reaches  $10^{-5}$ , Equation (15).

Figure 10 shows the found damaged areas using the system identification process. Due to the applied filtering, the found damage areas have smoothed boundaries in contrast to the ideal predefined damage model (Figure 9).

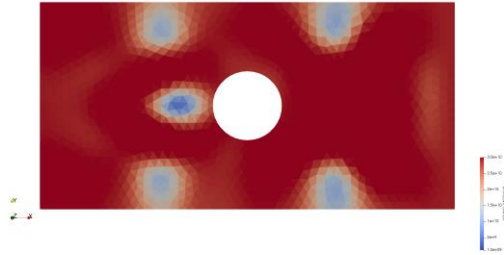


Figure 10. Found damaged areas using the NAG-QNBB algorithm [3]

#### 4.2 Concerto bridge

For the long-term evaluation of innovative Structural Health Monitoring (SHM) techniques, the experimental plate girder bridge "Concerto" was constructed in 2005. The bridge measures 17.5 m in total length, 4.0 m in width, and 0.8 m in height [5, 6]. Figure 11 shows the support positions (A, B), the ground anchors (C), the transducers (C, D), and the cantilever arm (E). In the lower part of Figure 11, the instrumentation and reference point signalization are depicted.



Figure 11. Experimental Bridge "Concerto". Upper part: indication of support (A, B), ground anchor (C), Deformation transducer positions (C and D), and cantilever arm (E). Lower part: instruments (UAV, laser scanner, and transducer) and signalization of reference points [5].

Figure 12 shows the deformation of the bridge under the load from photogrammetric measurements. For more details on the measurement techniques, an interested reader is referred to [5]. In this study, we utilized data obtained through photogrammetric measurements. However, data from other measurement techniques can also be applied. We chose photogrammetric measurements because they provide continuous data, in contrast to the limited number of points obtained from tachymetry and transducer measurements. It is important to note that laser scanner measurements exhibit a gap between 12.5 meters and 15 meters.

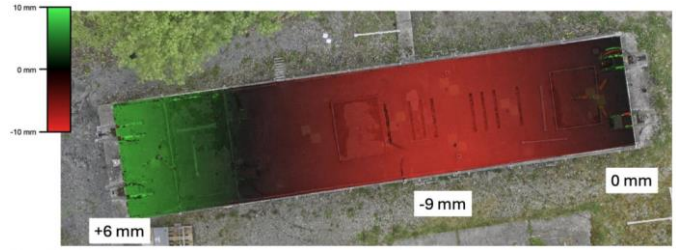


Figure 12. According to photogrammetric measurements, the deformation of "Concerto" under load is seen from the top. Lowered areas are colored in red, elevated areas in green, and no elevation change in black [5].

A finite element (FE) model has been created to model the bridge, as shown in Figure 13. This model consists of 77,000 small-displacement 3D elements that represent the concrete domain (depicted in gray), 800 truss elements representing the tendons (shown in blue), and 107 small-displacement 3D elements that represent the elastomers (illustrated in yellow). The load is applied to the red surfaces.

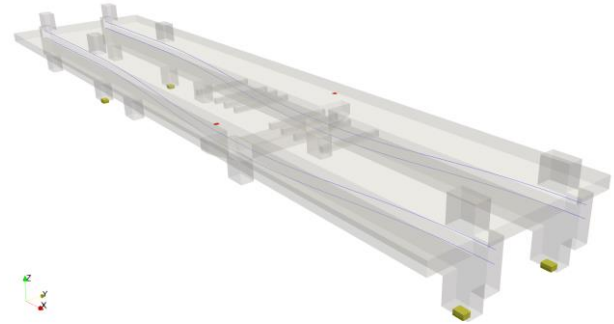


Figure 13. FE-model of the Concerto bridge: concrete part (gray), steel tendons (blue), elastomers (yellow), applied force (red).

To utilize the measured data, we create a series of virtual sensors positioned along the x-axis at the midpoint of the bridge. Figure 14 illustrates the locations of these virtual sensors, represented as spheres, along with their corresponding values (displacement in the z-direction) that have been derived from the measured data.

The objective function is defined similar to Equation (3) and it is based on the photogrammetric measurements and computed displacements in the z-direction:

$$J(\mathbf{u}(\mathbf{E})) = \frac{1}{2} \sum_{j=1}^m \omega_j \left( u_{z_j}^{md} - u_{z_j}(\mathbf{E}) \right)^2 \quad (17)$$

There are three various material domains to identify in the model. The largest domain is concrete, where we set the valid Young's modules range to  $E = [1e9, 1e11] Pa$  and as the initial parameter  $E^0 = 3e10 Pa$ . In this model, we set the upper boundary higher than the initial value because we want to keep large identification freedom. The second material domain is steel tendons, with parameter ranges  $E = [1e10, 1e12] Pa$  and  $E^0 = 2.1e11 Pa$ . The last model part is elastomers, which model the rubber supports with unknown material properties. We set  $E = [1e6, 1e8] Pa$  and  $E^0 = 1e7 Pa$ . All material



parameters are identified through a single system identification process.

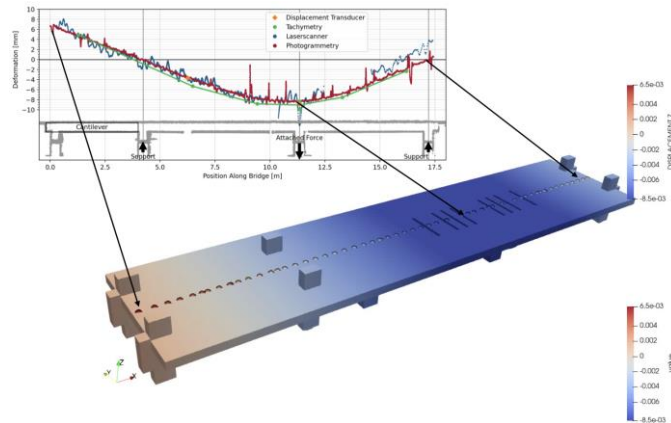


Figure 14. Applying the measured data to its numerical model: measured data at the center line (top graph), virtual sensors with mapped data (small circles).

Figure 15-18 shows the final Young's modulus of the materials. The results show that steel tendons are not damaged, and the elastomer material converges to  $1e8 Pa$ . In Figure 16, we highlight the areas with damaged concrete and provide photos of these areas. Figure 17 shows the graph comparing the measured and computed displacement at the middle line before and after system identification.

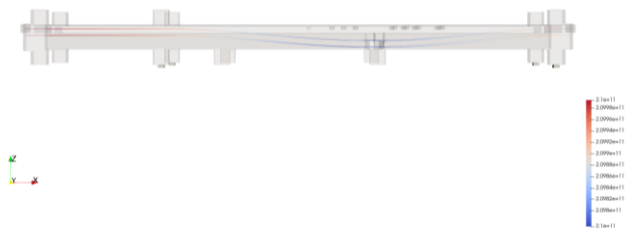


Figure 15. Young's modulus of steel tendons shows no damage.



Figure 16. Young's modulus of elastomers converged to upper bound ( $1e8$ ).

The optimization process took 30 optimization iterations to reduce the objective function by 98.9 %. Further optimization iterations lead to overfitting the parameters (see Figure 19), where the material parameters converge to unphysical values, while the reduction of the cost function stays at similar level 99.1 %.



Figure 17. Top: Young's modulus of concrete. Bottom: Pictures of the current state of the bridge in the weakened regions.

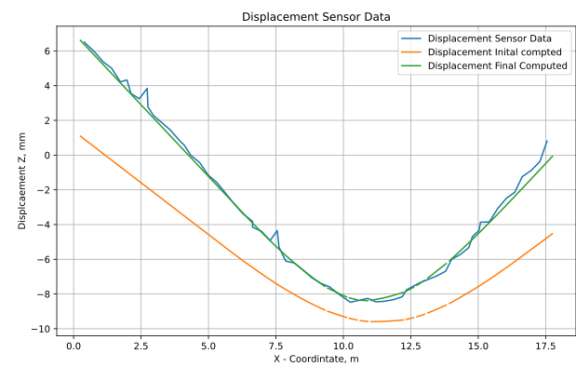


Figure 18. Comparing z-displacements along the x-axis in the middle of the bridge: measured data (green), initial computed data (orange), final computed data (blue).



Figure 19. Overfitted material parameters. Young's modulus of concrete reaches upper and lower bounds.

## 5 DISCUSSIONS

In this study, we explored the system identification process for structural health monitoring using adjoint-based optimization techniques. Our findings highlight the effectiveness of employing high-fidelity Digital Twin models to accurately infer material properties and detect weaknesses in structures. The method has been applied to the "Concerto" bridge with real-world measured displacement. We have found damaged areas that are confirmed by visual inspection of the real state of the bridge.

However, the results are not without limitations. One significant challenge is the dependence on sensor configuration, which can strongly affect the accuracy of the identified material properties. Additionally, the multimodal

nature of the optimization problem complicates finding a “true” solution during the identification process, as multiple identified states can yield similar results. Another significant challenge is the convergence criteria, which, on one hand, should stop the optimization process before overfitting the material parameters, and on the other hand, shouldn’t stop it too early before all damaged regions are found.

## 6 OUTLOOK

Moving forward, we recommend several directions for future work:

- 1) How can we identify the crucial measured locations / optimal sensor placement?
- 2) How to load the structure? How many load scenarios are required to identify all damaged regions?
- 3) How can we include the probability of sensor failure and inaccurate measurement?
- 4) How can we check which damage can be found by a given sensor configuration on the structure?
- 5) How to circumvent the overfitting of the data?

## ACKNOWLEDGMENTS

We would like to acknowledge the funding by the Deutsche Forschungsgemeinschaft (DFG, German Research Foundation) under German's Excellence Strategy - EXC 2163/1 - Sustainable and Energy Efficient Aviation - Project-ID 390881007. NSF grant DMS-2408877, Air Force Office of Scientific Research (AFOSR) under Award NO: FA9550-22-1-0248, and Office of Naval Research (ONR) under Award NO: N00014-24-1-2147. We would like to acknowledge the funding by the Institute of Advanced Studies, Technical University of Munich, under the Hans Fischer Senior Fellowship.

## REFERENCES

- [1] Airaudo, F. N., Löhner, R., Wüchner, R., and Antil, H., “Adjoint-based determination of weaknesses in structures,” *Computer Methods in Applied Mechanics and Engineering*, Vol. 417, 2023, p. 116471. Doi: [10.48550/arXiv.2303.15329](https://doi.org/10.48550/arXiv.2303.15329)
- [2] Antonau, I., Warnakulasuriya, S., Bletzinger, KU. *et al.* Latest developments in node-based shape optimization using Vertex Morphing parameterization. *Struct Multidisc Optim* **65**, 198 (2022). <https://doi.org/10.1007/s00158-022-03279-w>
- [3] Ihara Antonau, Suneth Warnakulasuriya, Roland Wüchner, Facundo Airaudo, Rainald Löhner, Harbir Antil and Talhah Ansari. "Comparison of the First Order Algorithms to Solve System Identification Problems of High-Fidelity Digital Twins," AIAA 2025-0285. AIAA SCITECH 2025 Forum. January 2025.
- [4] Rainald Löhner, Facundo Airaudo, Harbir Antil, Roland Wuechner, Suneth Warnakulasuriya, Ihara Antonau and Talhah Ansari. "High-Fidelity Digital Twins: Zooming in on Weaknesses in Structures," AIAA 2025-0286. AIAA SCITECH 2025 Forum. January 2025.
- [5] Maboudi, Mehdi & Backhaus, Jan & Ghassoun, Yahya & Khedar, Yogesh & Lowke, Dirk & Mai, Inka & Riedel, Björn & Bestmann, Ulf & Gerke, Markus. (2024). Very High-Resolution Bridge Deformation Monitoring Using UAV-based Photogrammetry. 10.48550/arXiv.2410.18984.
- [6] Budelmann, H., Hariri, K., & Holst, A. (2006). A real-scale PC bridge for testing and validating monitoring methods. In *Proceedings of the Third International Conference on Bridge Maintenance, Safety and Management*, Porto, Portugal.
- [7] American Institute of Aeronautics and Astronautics (AIAA), Digital Engineering Integration Committee, “Digital twin: Definition & value,” AIAA and AIA Position Paper, 2020. [https://www.aiaa.org/docs/default-source/uploadedfiles/issues-and-advocacy/policy-papers/digital-twin-institute-position-paper-\(december-2020\).pdf](https://www.aiaa.org/docs/default-source/uploadedfiles/issues-and-advocacy/policy-papers/digital-twin-institute-position-paper-(december-2020).pdf).
- [8] National Academies of Science, Engineering, and Medicine, “Foundational research gaps and future directions for digital twins,” <https://tinyurl.com/cx77p8hd>, 2023.
- [9] Willcox, K., Ghattas, O., and Soga, K., “Crosscutting Research Needs for Digital Twins,” 2024. <https://www.santafe.edu/events/crosscutting-research-needs-digital-twins>.
- [10] Antil, H., “Mathematical Opportunities in Digital Twins (MATH-DT),” arXiv preprint arXiv:2402.10326, 2024.
- [11] Löhner, R., Airaudo, F. N., Antil, H., Wüchner, R., Meister, F., and Warnakulasuriya, S., “High-Fidelity Digital Twins: Detecting and Localizing Weaknesses in Structures,” *International Journal for Numerical Methods in Engineering*, 2024. <https://doi.org/10.1002/nme.7568>.
- [12] Airaudo, F., Antil, H., Löhner, R., and Rakhimov, U., “On the Use of Risk Measures in Digital Twins to Identify Weaknesses in Structures,” AIAA SCITECH 2024 Forum, American Institute of Aeronautics and Astronautics, 2024. <https://doi.org/10.2514/6.2024-2622>, URL <https://dx.doi.org/10.2514/6.2024-2622>.
- [13] Ansari, T. S. A., R. Löhner, R. Wüchner, H. Antil, S. Warnakulasuriya, I. Antonau, & F. Airaudo (2025). Adjoint-based recovery of thermal fields from displacement or strain measurements. *Computer Methods in Applied Mechanics and Engineering* 438, 117818, <https://doi.org/10.1016/j.cma.2025.117818>.
- [14] Torzoni, M., Manzoni, A., Mariani, S. (2023). A multi-fidelity surrogate model for structural health monitoring exploiting model order reduction and artificial neural networks. *Mechanical Systems and Signal Processing* 197, 110376, <https://doi.org/10.1016/j.ymssp.2023.110376>
- [15] Wu, Rih-Teng, and Mohammad Reza Jahanshahi. 2018. "Data Fusion Approaches for Structural Health Monitoring and System Identification: Past, Present, and Future." *Structural Health Monitoring* 19, no. 2: 553–591. <https://doi.org/10.1177/1475921718765174>
- [16] Kim, J., Lee, S., & Park, H. (2023). Damage detection method using finite element model updating and deep learning for structural dynamic characteristics. *Scientific Reports*, 13, 18694. <https://doi.org/10.1038/s41598-023-46141-9>

# Advancing High Fidelity Finite Element Model Updating Using Cooperative Game Theory: A Novel Framework for Structural Optimization

Suzana Ereiz<sup>1,2</sup> 0000-0001-8485-0587, Ivan Duvnjak<sup>2</sup> 0000-0002-9921-1013, Javier Fernando Jiménez-Alonso<sup>3</sup> 0000-0002-4592-0375, Marko Bartolac<sup>2</sup> 0000-0002-5330-736X, Janko Koščak<sup>2</sup> 0000-0001-6677-6635, Domagoj Damjanović<sup>2</sup> 0000-0002-3565-1968

<sup>1</sup> Politecnico di Milano, Department of Architecture, Built Environment and Construction Engineering (DABC), Piazza Leonardo da Vinci, 32, Milano 20133, Italy

<sup>2</sup> University of Zagreb, Faculty of Civil Engineering, Fra Andrije Kačića-Miošića 26, Zagreb 10 000, Croatia

<sup>3</sup> Universidad de Sevilla, Escuela Superior de Ingeniería, Avenida Camino de los Descubrimientos s/n, 41092, Sevilla, Spain

email: [suzana.ereiz@polimi.it](mailto:suzana.ereiz@polimi.it), [ivan.duvnjak@grad.unizg.hr](mailto:ivan.duvnjak@grad.unizg.hr), [jfjimenez@us.es](mailto:jfjimenez@us.es), [marko.bartolac@grad.unizg.hr](mailto:marko.bartolac@grad.unizg.hr), [janko.koscak@grad.unizg.hr](mailto:janko.koscak@grad.unizg.hr), [domagoj.damjanovic@grad.unizg.hr](mailto:domagoj.damjanovic@grad.unizg.hr)

**ABSTRACT:** High fidelity finite element model updating plays a critical role in ensuring the accuracy and reliability of structural models for complex infrastructure systems. This study focuses on the application of a cooperative game theory model to update high fidelity finite element model of a pedestrian suspension bridge. By treating the model updating process as a cooperative game model, game theory provides a novel framework for distributing and balancing multiple objectives inherent in this process. The proposed approach is compared with conventional finite element model updating methods to assess its efficiency, accuracy, and robustness. Key performance indicators, such as the reduction in discrepancy between experimental and numerical modal parameters and computational efficiency are evaluated. The cooperative game theory framework is shown to enable an optimized and balanced resolution of conflicting requirements in high fidelity model updating, resulting in improved alignment with observed structural behavior. The primary objective of this research is to demonstrate the potential of game theory as an innovative and effective tool for solving optimization problems in high fidelity FE model updating. The findings are expected to contribute to advancements in structural health monitoring by providing a robust methodology for enhancing the reliability of numerical models.

**KEY WORDS:** High Fidelity Finite Element Model Updating; Cooperative Game Theory; Structural Optimization; Structural Health Monitoring, Dynamic parameters

## 1 INTRODUCTION

High-fidelity numerical modelling has become essential in modern structural engineering for simulating complex physical behavior with a high degree of accuracy. High-fidelity finite element (FE) models are characterized by detailed geometric definitions, fine mesh discretization, and many physically meaningful parameters. These models enable precise structural simulations but also significantly increase computational effort and sensitivity to modelling assumptions. Despite their accuracy, high-fidelity FE models often fail to perfectly represent real structural behavior due to uncertainties in boundary conditions, material properties, and idealizations made during the modelling process. To reduce these discrepancies, the Finite Element Model Updating (FEMU) procedure is employed. FEMU involves adjusting selected model parameters based on experimental data—typically obtained from static tests, dynamic modal analysis, or continuous structural health monitoring—to improve correlation between the numerical model and the actual structural behavior [1]. The updating process becomes particularly challenging for high-fidelity models, where computational demands are high, and the solution space is large. In such cases, effective and reliable optimization strategies are critical. FEMU methods can be broadly classified into direct (non-iterative) and indirect (iterative) approaches [2]. Direct methods update the numerical model by modifying mass or stiffness matrices in a single step but may lack physical

interpretability [3][4]. In contrast, indirect (iterative) methods adjust physical parameters through successive approximations until numerical predictions align with experimental data [5]. One of the most widely used formulations is the Maximum Likelihood Method, which treats FEMU as an optimization problem (Eq. (4)) aimed at minimizing the difference between predicted and measured structural responses (Eq. (1)-(3)) [6].

$$r_t^f(\theta) = |\Delta f_t| = \left| \frac{f_t^{num} - f_t^{exp}}{f_t^{exp}} \right| \quad (1)$$

$$\text{MAC}(\phi_t^{exp}, \phi_t^{num}) = \frac{|(\phi_t^{num})^T \phi_t^{exp}|^2}{((\phi_t^{num})^T (\phi_t^{num})) \cdot ((\phi_t^{exp})^T (\phi_t^{exp}))} \quad (2)$$

$$r_t^m(\theta) = \sqrt{\left( \frac{(1 - \sqrt{\text{MAC}})^2}{\text{MAC}} \right)} \quad (3)$$

These residuals are then combined into a single-objective function (Eq. (4)) using weighting factors:

$$F(\theta) = \sum_{t=1}^{n_r} w_t F_t(\theta)^2 \quad (4)$$

$$F(\theta) = (\sum_{t=1}^{n_f} w_t^f r_t^f(\theta)^2 + \sum_{t=1}^{n_m} w_t^m r_t^m(\theta)^2),$$

$$\theta_l < \theta < \theta_u$$

This discrepancy is mathematically expressed using residuals based on modal parameters—most commonly natural



frequencies (Eq. (1)) and mode shapes (Eq. (3)). The residuals are defined as: optimization problem into a cooperative game structure, enabling a more robust and adaptive solution process suitable for updating complex and high-fidelity FE models.

The performance of this approach is highly dependent on the proper selection of the weighting factors and, which balance the influence of different types of residuals. However, determining these weights is non-trivial—typically requiring trial-and-error procedures, sensitivity analyses, and expert judgment [7–11]. This process is especially inefficient and unreliable when applied to high-fidelity FEMU, where each function evaluation involves high computational cost. To overcome these limitations, this paper proposes a novel formulation of the single-objective FEMU problem using Cooperative Game Theory (CGT). In the proposed approach, each residual is modelled as a player in a cooperative game. Instead of manually assigning weights, the optimization seeks a compromise solution by introducing a weighted objective function and a super-criterion that captures collective performance. This eliminates the need for manual tuning of weighting factors and enables a more automated and adaptive updating process. The optimization is performed using the Harmony Search (HS) algorithm—a population-based metaheuristic known for its balance between exploration and exploitation, and for its computational efficiency in solving nonlinear problems [12]. The proposed CGT-based method is applied to the updating of a high-fidelity finite element model of a pedestrian suspension bridge, providing a relevant and demanding benchmark for testing performance. The results are compared to those obtained using conventional optimization algorithms, highlighting the benefits of the proposed approach in terms of accuracy, robustness, and efficiency.

The paper is structured as follows. Section 2 introduces the cooperative game theory model applied to single-objective optimization in the context of high-fidelity finite element model updating (FEMU). Section 3 describes the case study structure, including numerical modelling and experimental testing that define the target structural behavior. Section 4 presents the FEMU process, including sensitivity analysis and comparison between conventional and game theory-based optimization. Section 5 discusses the results, and Section 6 provides concluding remarks based on the findings.

## 2 COOPERATIVE GAME THEORY MODEL FOR HIGH FIDELITY FINITE ELEMENT MODEL UPDATING

Game theory (GT) is a mathematical framework used to model decision-making, conflict, and cooperation among multiple agents, or "players" [13]. Recent trends in optimization highlight the transformation of classical optimization problems into game-theoretic formulations [14]. Within this framework, the fundamental components include players, strategies, utility, information, and equilibrium [15]. In the context of optimization, objective functions can be interpreted as players, with their design variables acting as strategies, and their respective function values as utilities [16]. Cooperative game models are particularly suitable for complex engineering problems, where conflicting objectives need to be aligned into a compromise solution through a negotiation model or a super-criterion [17]. This study applies the cooperative game theory (CGT) approach to high-fidelity finite element model updating

(FEMU)—a process characterized by computationally intensive models and the need for precise alignment with experimental data. CGT has been successfully combined with various soft computing techniques in the literature: Dhingra and Rao [18] integrated CGT with fuzzy set theory; Xie et al. [19] developed a four-step GT-based multi-objective method; Monfared et al. [20] formulated Pareto-optimal equilibrium (POE) points via two-player games; and Cheng and Li [21] incorporated genetic algorithms into the CGT framework. Annamdas and Rao [22] proposed a modified CGT model using Particle Swarm Optimization (PSO), which is adapted in this work for single-objective optimization.

### 2.1 Single-Objective optimization using Cooperative Game Theory

To update high-fidelity FEM models without explicitly analysing the impact of weighting factors, this study uses a single-objective optimization approach based on the CGT model introduced by Annamdas and Rao [22]. In this adapted method, Harmony Search (HS) is used instead of PSO to reduce computational cost [23]. The procedure includes four main steps:

- definition of the objective function;
- minimization, maximization, and normalization of objective function residuals;
- formulation of a weighted objective function;
- optimization of the weighted objective function.

Initially, the HS algorithm is used to minimize the objective function and obtain optimal residual values -  $f_t(\theta_t^*)$ . Next, maximization via HS yields the worst-case residuals -  $f_t(\theta_t^{**})$ . These results are used to normalize the residuals:

$$f_{nt}(\theta) = \frac{f_t(\theta) - f_t(\theta_t^*)}{f_t(\theta_t^{**}) - f_t(\theta_t^*)} \quad (5)$$

The normalized values are then used to define a weighted objective function:

$$F_{w,t} = K_1 f_{n1}(\theta) + K_2 f_{n2}(\theta) + \dots + K_{k-1} f_{n(k-1)}(\theta) + (1 - K_1 - K_2 - \dots - K_{k-1}) f_{nk}(\theta) \quad (6)$$

with the constraints

$$0 \leq K_t \leq 1, \sum_{t=1}^k K_t = 1 \quad (7)$$

To ensure that residuals are as far as possible from their worst-case values, a super-criterion is introduced:

$$SC = \prod_{t=1}^k [1 - f_{nt}(\theta)] \quad (8)$$

The final optimization problem is thus defined as:

$$F_{w,t}(\Phi) = FK - SC, \quad \Phi = [\theta_1 \ \theta_2 \ \dots \ \theta_n \ K_1 \ K_2 \ \dots \ K_{k-1}]^T \quad (9)$$

Minimizing  $F_{w,t}(\Phi)$  yields the optimal set of design parameters and weighting factors, effectively enhancing the correlation between the high-fidelity FEM predictions and experimental observations.

### 3 CASE STUDY ON REAL STRUCTURE

Suspension bridges, though efficient for spanning long distances and visually striking, are prone to damage mechanisms such as corrosion and fatigue, especially in their main cables and hangers. Due to limitations in traditional local damage detection methods, global vibration-based approaches combined with high-fidelity finite element model updating (FEMU) have proven to be a promising solution for monitoring such complex structures.

#### 3.1 Description of the structure

To evaluate the proposed model updating methodology presented in the previous section, a pedestrian suspension bridge over the Drava River in Osijek (Figure 1.) was selected as the case study. Constructed in 1980, the bridge features a single span of 209.5 m, suspended by a parabolic cable anchored behind 24 m high steel pylons.

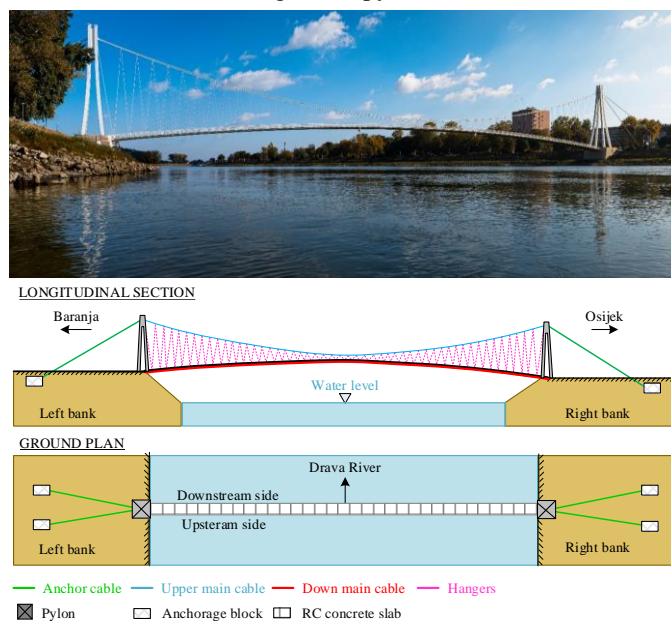


Figure 1. a) View on the bridge from the right bank b) Longitudinal section and the ground plane of the bridge

The 5 m wide pedestrian deck is composed of 50 prefabricated concrete slabs of three different types, characterized by reinforced longitudinal and transverse ribs. The slabs are supported by inclined hangers ( $\phi$  21 mm) on one side and longitudinally movable connections ( $\phi$  28 mm) on the other, allowing for limited displacement and load redistribution.

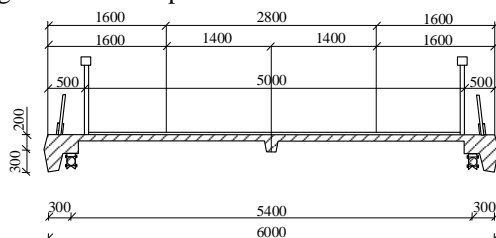


Figure 2. Cross section of the bridge (all dimensions are in millimetres)

The structural system includes two  $\phi$  61 mm pre-tensioned cables on each side, anchored at the base of the pylons to reduce deck deformations and mitigate vibrations (Figure 2.). During

the 1990s war, the bridge sustained damage to its hangers and several slabs. It was subsequently rehabilitated to its original state. In 2009, an asphalt layer was added and the slab connections repaired. Further rehabilitation work in 2022 included replacement of upper cable connections, reprofiling of slab beams, sealing of joints, corrosion protection renewal, and repair of the handrail. This real-world example, with its complex structural behavior and history of interventions, provides an ideal scenario for applying and validating advanced model updating techniques within a structural health monitoring context.

#### 3.2 Initial numerical model

An initial finite element (FE) model of the pedestrian suspension bridge was developed using ANSYS software, consisting of 20,787 elements (Figure 3.). The structural components were modelled as follows: main and transverse beams, handrails, and rigid joints with BEAM188 elements; concrete slabs with SHELL181 elements; cables and hangers with LINK180 elements; and interconnections via COMBIN14 spring-damper elements. Boundary conditions were applied to restrict translations at anchor points and pylons in all directions.

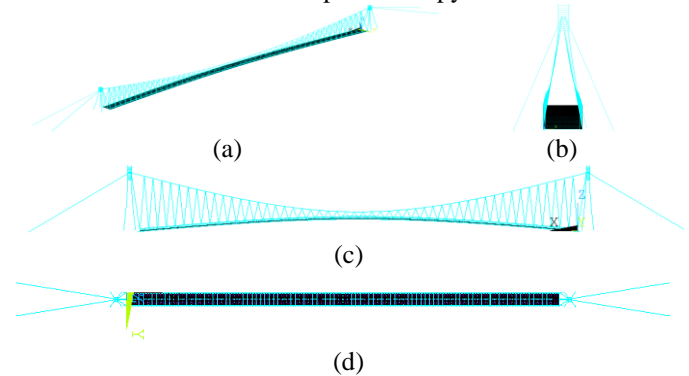


Figure 3. Initial numerical model of pedestrian suspension bridge over Drava River a) 3D view b) y-z plane c) x-z plane d) x-y plane

Material properties and cross-sectional dimensions were assigned based on project documentation, and initial tensile forces in cable elements were derived from previous experimental measurements. Hangers were grouped into four categories based on mean axial force values and standard deviations (ranging from 30.4 kN to 52.1 kN), while the upper main cables were divided into four groups with forces between 4744 kN and 4852 kN. The lower main cables were assigned a prestress force of 1300 kN. A numerical modal analysis was performed to extract natural frequencies and mode shapes (Figure 4).

$$\begin{array}{lll} \phi_1^{num} - \text{torsional} & \phi_2^{num} - \text{vertical} & \phi_3^{num} - \text{torsional} \\ f_1^{num} = 0.335 \text{ Hz} & f_2^{num} = 0.428 \text{ Hz} & f_3^{num} = 0.641 \text{ Hz} \end{array}$$

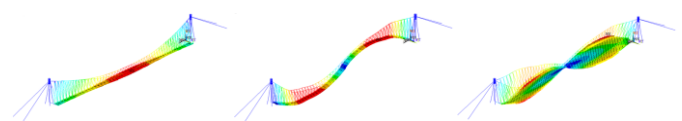


Figure 4. First three numerically determined natural frequencies ( $f_t^{num}$ ) and mode shapes ( $\phi_t^{num}$ ) of pedestrian suspension bridge over Drava River ( $t=1, \dots, 3$ )

These results served as a reference for subsequent model updating and were compared with experimentally obtained modal parameters to assess the model's initial accuracy.

### 3.3 Experimental campaign

A comprehensive experimental campaign was conducted to identify the dynamic properties of the pedestrian suspension bridge and its key structural components. The investigation included determination of axial forces in all hangers (Figure 5.) and main anchor cables, natural frequencies of the down main cables and pylons, as well as dynamic parameters of characteristic edge and span slabs.



Figure 5. Calculated force values in the hangers on the upstream and downstream side of the bridge

Global dynamic properties of the entire bridge were determined under ambient excitation from pedestrian walking. Axial forces in the hangers were determined using the resonant vibration method [24] by measuring the natural frequency of each hanger following a manual excitation. These frequencies were correlated to tensile force using string vibration theory [25]. The results showed highest force values in the mid-span hangers and noticeable deviations between upstream and downstream pairs. A similar procedure was used to determine force magnitudes in the main anchorage cables on both banks, with calculated values showing good agreement with historical measurements and design data. Dynamic testing of the down main cables and pylons was performed using impulse excitation with a rubber hammer. Natural frequencies were identified using frequency domain decomposition based on acceleration measurements in orthogonal directions. To assess local behavior, dynamic parameters of a representative edge slab and a central span slab (Figure 6.) were identified through ambient vibration testing induced by random pedestrian walking [26].

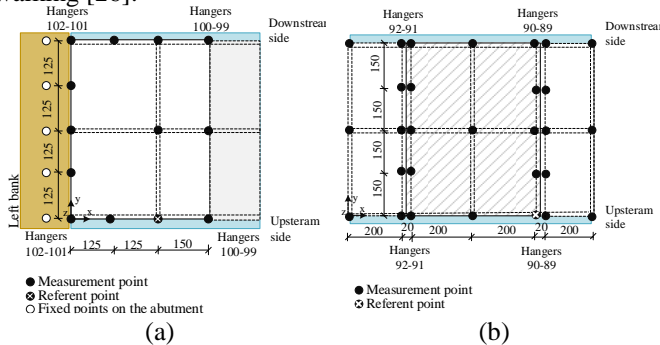


Figure 6. Arrangement of the measurement points on characteristic slab (a) edge (b) span

Acceleration responses were recorded at 13 and 29 measurement points, respectively, and modal properties were extracted using FDD. For global structural identification, vertical excitation due to pedestrian traffic was used to excite the entire structure. Acceleration was measured at 100 nodes (50 upstream and 50 downstream) in two directions, resulting in 200 degrees of freedom. Natural frequencies, mode shapes, and damping ratios (Figure 7.) were extracted using Enhanced Frequency Domain Decomposition (EFDD).

$$\phi_1^{exp} - \text{Torsional} / X; f_1^{exp} = 0.337 \pm 0.011 \text{ Hz}; \zeta_1^{exp} = 3.83 \pm 1.23$$

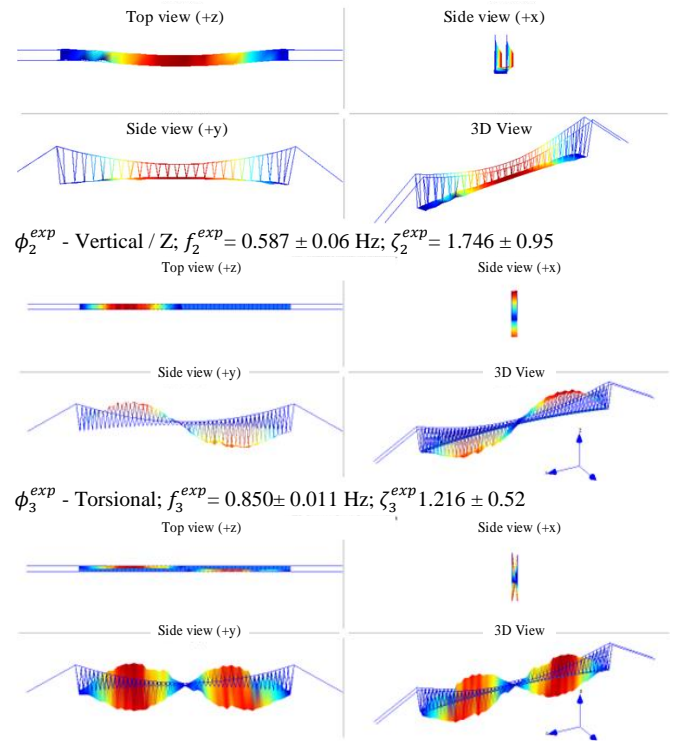


Figure 7. First three experimentally determined natural frequency ( $f_t^{exp}$ ), damping ratio ( $\zeta_t^{exp}$ ) with their standard deviation ( $\sigma_t^f, \sigma_t^z$ ) and mode shapes ( $\phi_t^{num}$ ) of pedestrian suspension bridge over Drava River ( $t=1, \dots, 3$ )

The analysis revealed distinct global mode shapes consistent with the expected behavior of a suspension bridge, providing essential input for finite element model updating (FEMU). These experimentally obtained dynamic parameters form the basis for calibrating and validating the numerical model, as described in the following chapter.

### 3.4 Comparison of Numerical and Experimental Results

A comparison between the initial numerical model and experimental results was conducted to evaluate model accuracy. Natural frequencies and mode shapes were compared using relative differences and the MAC coefficient (Table 1.). While the initial model showed acceptable agreement, some deviations indicated the need for refinement. To improve accuracy, finite element model updating (FEMU) was performed using two approaches: a conventional multi-objective (MO) optimization method and a Cooperative Game Theory (CGT)-based method.



Table 1. Comparison of the pedestrian suspension bridge modal parameters predicted by initial numerical model and its actual modal parameters based on the absolute relative difference between the natural frequency values ( $\Delta f_t$ ) and modal assurance criterion MAC ( $\phi_t^{exp}, \phi_t^{num}$ )

Mode shape t	$f_t^{num}$ [Hz]	$f_t^{exp}$ [Hz]	$ \Delta f_t $ [%]	MAC ( $\phi_t^{exp}, \phi_t^{num}$ ) [/]
1	0.335	0.337	0.597%	0.995
2	0.569	0.587	3.163%	0.967
3	0.862	0.850	1.392%	0.960
4	1.170	1.013	13.419%	0.937
5	1.142	1.150	0.701%	0.845
6	1.530	1.400	8.497%	0.870
7	1.694	1.663	1.830%	0.964
8	1.791	1.925	7.482%	0.802
9	2.061	2.188	6.162%	0.974
10	2.582	2.475	4.144%	0.967
11	2.661	2.737	2.856%	0.953
12	2.881	3.037	5.415%	0.812
13	3.197	3.313	3.628%	0.943

#### 4 FINITE ELEMENT MODEL UPDATING

##### 4.1 Sensitivity Analysis

To identify the most influential parameters for the model updating process, a sensitivity analysis was performed using the ratio of modal strain energy (MSE) associated with each physical parameter to the total MSE of the structure. Initially, 17 parameters were considered, but based on the analysis results (Figure 8.), 13 were selected for updating. The selected parameters include material properties (e.g., Young's modulus of concrete and handrails), connection stiffnesses, and cable pretension forces (down main cables, hangers, and upper main cables).

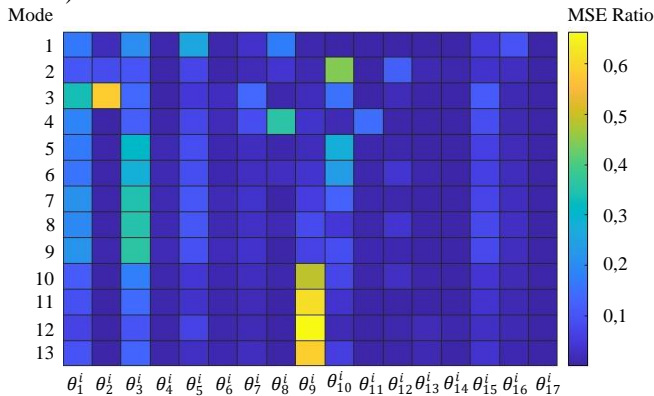


Figure 8. Results of sensitivity analysis performed on the pedestrian suspension bridge finite element model for initial selected ( $\theta_{1,...,17}$ ) 17 updating parameters

To ensure physical feasibility, each parameter was constrained within predefined lower and upper bounds. Following parameter selection, the optimization problem was structured by partitioning the residuals of natural frequencies and mode shapes. Using a sorting-based approach [14], the influence of each parameter was quantified, and two strategy spaces were defined: for natural frequency,  $S_f = \{\theta_1, \theta_2, \theta_3, \theta_4, \theta_5, \theta_6, \theta_7, \theta_8, \theta_9, \theta_{11}\}$  and for mode shape,  $S_{ms} = \{\theta_{10}, \theta_{12}, \theta_{13}\}$ . This

selection guided the subsequent model updating process to achieve more accurate and efficient calibration of the FE model.

##### 4.2 Solution of the MO FEMU problem based on the conventional optimization method

To assess the computational efficiency of the proposed CGT-based model for high-fidelity FEMU of complex structures, a benchmark analysis was conducted using a conventional multi-objective optimization method since previous research [23] has confirmed its effectiveness and accuracy. The Harmony Search (HS) algorithm was adopted for this comparison. The optimization process was implemented by coupling ANSYS for FE analysis with MATLAB for optimization. Key HS parameters were population size (PS = 50), maximum iterations ( $I_{max} = 100$ ), objective function tolerance ( $10^{-4}$ ), pitch adjustment rate (PAR = 0.3), and harmony memory consideration rate (HMCR = 0.9). The resulting Pareto front of the two objective function residuals is shown in Figure 9, highlighting the “knee point” as the most balanced solution. This optimal solution corresponds to a set of updated model parameters that improved the accuracy of the numerical model. The total computational time required to reach this solution using HS was approximately 192,783 seconds, providing a reference for evaluating the performance of the CGT approach.

##### 4.3 Solution of the FEMU problem based on the CGT model

Following its proven efficiency and accuracy on a laboratory-scale bridge model, the Cooperative Game Theory (CGT) model was applied to solve the high-fidelity FEMU problem of a complex pedestrian suspension bridge. The optimization began from an initial strategy vector  $\theta_{initial\_PSBO}^0 = [1 \ 1 \ 1 \ 1 \ 1 \ 1 \ 1 \ 1 \ 1 \ 1 \ 1 \ 1 \ 1 \ 1 \ 1 \ 1 \ 1 \ 1]$  and iterations were carried out until the convergence criterion  $\xi = 0.001$  was met. Cooperation weights were set symmetrically  $w_{11} = w_{22} = w_{12} = w_{21} = 0.5$  based on the established rules. Upon convergence, the optimal parameter set  $\theta_{CGT\_PSBO}^* = [0.9997 \ 0.8917 \ 1.0585 \ 1.0305 \ 0.8686 \ 1.2281 \ 1.7530 \ 1.0488 \ 0.8219 \ 1.0221 \ 1.0086 \ 0.9969 \ 1.0020]$  showed strong alignment with physical properties, leading to significantly improved correlation with experimental data. The CGT model completed the optimization in 89,758 seconds, demonstrating both computational efficiency and robustness in handling the multi-objective FEMU problem for a real-world, large-scale structure.

#### 5 DISCUSSION

To evaluate the performance of the proposed Cooperative Game Theory (CGT) method for multi-objective finite element model updating (FEMU), a comparative analysis was conducted against a conventional Harmony Search (HS) multi-objective optimization approach. Two main criteria were considered: solution accuracy and computational time. As illustrated in Figure 9, the solution obtained using the CGT method closely matches the optimal solution (“knee point”) identified by the conventional HS method. Importantly, this level of accuracy was achieved with significantly lower computational effort. The CGT model required 89,758 seconds, compared to 192,780 seconds for the HS algorithm—demonstrating a reduction in computational time of over 50%, without compromising result quality. This efficiency is

achieved through the direct identification of the knee point using game theory principles, eliminating the need to compute the entire Pareto front, as required in conventional methods.

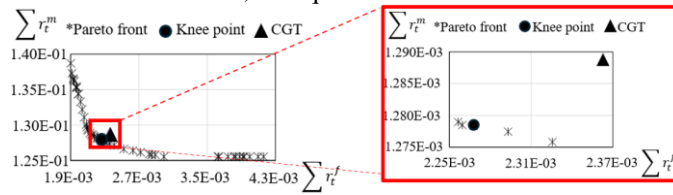


Figure 9. Comparison of the “knee” point obtained based on the Pareto front (conventional method) with the position of the optimal solution obtained using CGT model

Furthermore, Table 2 and Table 3 presents the updated natural frequencies and MAC values for both methods. The CGT approach (Table 3.) yields comparable accuracy in terms of relative frequency differences and mode shape correlation (MAC factors), confirming its robustness and suitability for high-fidelity FEMU of complex structures such as suspension bridges.

Table 2. Correlation between experimental and updated natural frequencies and mode shapes using conventional HS

Mode t	$f_t^{exp}$ [Hz]	$f_t^{upd,HS}$ [Hz]	$\Delta f_t^{HS}$ [%]	$MAC_t^{HS}$ [/]
1	0.337	0.335	-0.46	0.997
2	0.587	0.596	1.53	0.985
3	0.850	0.842	-0.94	0.984
4	1.013	1.025	1.18	0.954
5	1.150	1.142	-0.70	0.986
6	1.400	1.386	-1.01	0.982
7	1.663	1.634	-1.74	0.957
8	1.925	1.896	-1.51	0.972
9	2.188	2.215	1.23	0.996
10	2.475	2.427	-1.94	0.987
11	2.737	2.692	-1.64	0.993
12	3.037	3.054	0.56	0.964
13	3.313	3.258	-1.65	0.993

Table 3. Correlation between experimental and updated natural frequencies and mode shapes using CGT model

Mode t	$f_t^{exp}$ [Hz]	$f_t^{upd,CGT}$ [Hz]	$\Delta f_t^{CGT}$ [%]	$MAC_t^{CGT}$ [/]
1	0.337	0.334	-0.89	0.997
2	0.587	0.597	1.70	0.984
3	0.850	0.843	-0.82	0.984
4	1.013	1.025	1.18	0.954
5	1.150	1.141	-0.78	0.987
6	1.400	1.384	-1.14	0.982
7	1.663	1.635	-1.68	0.957
8	1.925	1.898	-1.40	0.971
9	2.188	2.223	1.60	0.996
10	2.475	2.425	-2.02	0.987
11	2.737	2.692	-1.64	0.993
12	3.037	3.042	0.16	0.964
13	3.313	3.269	-1.33	0.992

These results validate the CGT method as a computationally efficient and accurate alternative to traditional optimization

approaches for model updating in structural engineering applications.

## 6 CONCLUSION

This research presents a novel and efficient framework for high-fidelity finite element model updating (FEMU) by leveraging the principles of Cooperative Game Theory (CGT). The proposed approach was applied to a real-world pedestrian suspension bridge, providing a rigorous testbed to evaluate the effectiveness of the method in handling the complexity and precision demands of high-fidelity finite element analysis. Key contributions and findings include:

- By formulating FEMU as a cooperative game, the method enables a targeted and efficient resolution of conflicting objectives, such as matching both natural frequencies and mode shapes, without the need to compute the entire Pareto front. This aspect is especially beneficial in complex, high-fidelity models with many interdependent parameters.
- Compared to the conventional Harmony Search (HS) method, the CGT approach achieved equivalent or better accuracy with a reduction in computational time of over 50%. This demonstrates that high-fidelity analysis does not necessarily come at the cost of efficiency when advanced optimization strategies are applied.
- The CGT-based method improved the correlation between the numerical and experimental modal parameters, confirming its suitability for high-fidelity finite element analysis where accuracy and detail are critical. The updated model captured the structural behavior of the bridge with remarkable precision, addressing discrepancies in natural frequencies and mode shapes.
- The method was validated using extensive experimental data from a real suspension bridge, including local and global dynamic characteristics. The updated model reflects the true structural behavior with a high level of fidelity, even in the presence of structural uncertainties and historical modifications.

In summary, the CGT-based FEMU framework proves to be a robust, accurate, and computationally efficient solution tailored to the needs of high-fidelity finite element analysis. Its adaptability and performance make it a promising tool for advancing structural health monitoring in complex and intelligent infrastructure systems.

## ACKNOWLEDGMENTS

This project has received funding from the European Union’s Horizon 2020 research and innovation programme under the Marie Skłodowska-Curie grant agreement No [101151734].

## REFERENCES

- [1] J. Mottershead and M. Friswell, *Finite Element Model Updating in Structural Dynamics*, 1995.
- [2] M. I. Friswell and J. E. Mottershead, *Finite Element Model Updating in Structural Dynamics*, Springer, Dordrecht, Netherlands, 1995.
- [3] M. Baruch, “Optimization procedure to correct stiffness and flexibility matrices using vibration tests,” *AIAA Journal*, vol. 16, pp. 1208–1210, 1978. <https://doi.org/10.2514/3.61032>.
- [4] H. Jensen and C. Papadimitriou, “Bayesian finite element model updating,” 2019. [https://doi.org/10.1007/978-3-030-12819-7\\_7](https://doi.org/10.1007/978-3-030-12819-7_7).
- [5] W.-M. Li and J.-Z. Hong, “Research on the iterative method for model updating based on the frequency response function,” *Acta Mechanica*

- Sinica*, vol. 28, pp. 450–457, 2012. <https://doi.org/10.1007/s10409-012-0063-1>.
- [6] T. Marwala, *Finite-Element-Model Updating Using Computational Intelligence Techniques*, Springer London, London, 2010. <https://doi.org/10.1007/978-1-84996-323-7>.
- [7] S. Ereiz, I. Duvnjak, and J. F. Jiménez-Alonso, “Review of finite element model updating methods for structural applications,” *Structures*, vol. 41, pp. 684–723, 2022. <https://doi.org/10.1016/j.istruc.2022.05.041>.
- [8] D. S. Jung and C. Y. Kim, “Finite element model updating on small-scale bridge model using the hybrid genetic algorithm,” *Structure and Infrastructure Engineering*, vol. 9, pp. 481–495, 2013. <https://doi.org/10.1080/15732479.2011.564635>.
- [9] J. W. Park, S. H. Sim, and H. J. Jung, “Displacement estimation using multimetric data fusion,” *IEEE/ASME Transactions on Mechatronics*, vol. 18, pp. 1675–1682, 2013. <https://doi.org/10.1109/TMECH.2013.2275187>.
- [10] S. Kim, N. Kim, Y.-S. Park, and S.-S. Jin, “A sequential framework for improving identifiability of FE model updating using static and dynamic data,” *Sensors*, vol. 19, p. 5099, 2019. <https://doi.org/10.3390/s19235099>.
- [11] J. Naranjo-Pérez, J. F. Jiménez-Alonso, A. Pavić, and A. Sáez, “Finite-element-model updating of civil engineering structures using a hybrid UKF-HS algorithm,” *Structure and Infrastructure Engineering*, vol. 17, pp. 620–637, 2021. <https://doi.org/10.1080/15732479.2020.1760317>.
- [12] D. Manjarres, I. Landa-Torres, S. Gil-Lopez, J. Del Ser, M. N. Bilbao, S. Salcedo-Sanz, and Z. W. Geem, “A survey on applications of the harmony search algorithm,” *Engineering Applications of Artificial Intelligence*, vol. 26, pp. 1818–1831, 2013. <https://doi.org/10.1016/j.engappai.2013.05.008>.
- [13] J. von Neumann and O. Morgenstern, *Theory of Games and Economic Behavior*, 5th ed., Princeton University Press, Princeton, 1953.
- [14] S. Ereiz, J. F. Jiménez-Alonso, I. Duvnjak, and A. Pavić, “Game theory-based maximum likelihood method for finite-element-model updating of civil engineering structures,” *Engineering Structures*, vol. 277, 115458, 2023. <https://doi.org/10.1016/j.engstruct.2022.115458>.
- [15] S. Ereiz, I. Duvnjak, and J. F. Jiménez-Alonso, “Structural finite element model updating optimization based on game theory,” *Materials Today: Proceedings*, 2022. <https://doi.org/10.1016/j.matpr.2022.04.401>.
- [16] M. Jin, X. Lei, and J. Du, “Evolutionary game theory in multi-objective optimization problem,” *International Journal of Computational Intelligence Systems*, vol. 3, pp. 74–87, 2010. <https://doi.org/10.1080/18756891.2010.9727754>.
- [17] S. Özyildirim and N. M. Alemdar, “Learning the optimum as a Nash equilibrium,” *Journal of Economic Dynamics and Control*, vol. 24, pp. 483–499, 2000. [https://doi.org/10.1016/S0165-1889\(99\)00012-3](https://doi.org/10.1016/S0165-1889(99)00012-3).
- [18] A. K. Dhingra and S. S. Rao, “A cooperative fuzzy game theoretic approach to multiple objective design optimization,” *European Journal of Operational Research*, vol. 83, pp. 547–567, 1995. [https://doi.org/10.1016/0377-2217\(93\)E0324-Q](https://doi.org/10.1016/0377-2217(93)E0324-Q).
- [19] N. Xie, N. Shi, J. Bao, and H. Fang, “Analysis and application of multi-object decision design based on game theory,” *6th World Congress on Structural and Multidisciplinary Optimization*, 2005.
- [20] M. S. Monfared, S. E. Monabbati, and M. Mahdipour Azar, “Bi-objective optimization problems with two decision makers: refining Pareto-optimal front for equilibrium solution,” *OR Spectrum*, vol. 42, pp. 567–584, 2020. <https://doi.org/10.1007/s00291-020-00587-9>.
- [21] F. Y. Cheng and D. Li, “Genetic algorithm and game theory for multiobjective optimization of seismic structures with/without control,” in *11th World Conference on Earthquake Engineering*, Pergamon, Oxford, England, 1996, pp. 1–8.
- [22] K. K. Annamdas and S. S. Rao, “Multi-objective optimization of engineering systems using game theory and particle swarm optimization,” *Engineering Optimization*, vol. 41, pp. 737–752, 2009. <https://doi.org/10.1080/03052150902822141>.
- [23] J. F. Jiménez-Alonso, J. Naranjo-Perez, A. Pavić, and A. Sáez, “Maximum likelihood finite-element model updating of civil engineering structures using nature-inspired computational algorithms,” *Structural Engineering International*, pp. 1–13, 2020. <https://doi.org/10.1080/10168664.2020.1768812>.
- [24] M.-H. Nguyen, T.-D.-N. Truong, T.-C. Le, and D.-D. Ho, “Identification of tension force in cable structures using vibration-based and impedance-based methods in parallel,” *Buildings*, vol. 13, p. 2079, 2023. <https://doi.org/10.3390/buildings13082079>.
- [25] G. Nugroho, H. Priyosulistyo, and B. Suhendro, “Evaluation of tension force using vibration technique related to string and beam theory to ratio of moment of inertia to span,” *Procedia Engineering*, vol. 95, pp. 225–231, 2014. <https://doi.org/10.1016/j.proeng.2014.12.182>.
- [26] J. S. Jensen, D. M. Frangopol, and J. W. Schmidt, *Bridge Maintenance, Safety, Management, Digitalization and Sustainability*, CRC Press, London, 2024. <https://doi.org/10.1201/9781003483755>.



# Efficacy of decoupling techniques to extract the static strain response from the dynamic response of a bridge under a moving vehicle using a low pass filter

Sarath R.<sup>1,0000-0001-6208-253X</sup>, Saravanan U.<sup>1, 0000-0001-8565-0632</sup>

<sup>1</sup>Department of Civil Engineering, Indian Institute of Technology Madras, Chennai 600 036, Tamil Nadu, India  
email: sarathramesh09@gmail.com, saran@iitm.ac.in

**ABSTRACT:** Structural Health Monitoring of bridges is being used increasingly to ensure safe operation of bridges. Non-iterative and mechanics-based algorithms that were developed in the past to find the material property of a bridge or the live load moving over the bridge use the static strain response of the bridge. However, the field strain measurement of these response quantities has both static and dynamic components. To apply these non-iterative methods for live load or material property estimation, it is important to decouple the static components of the strain from its dynamic components. Hence, in the current study, the dynamic components of the bridge strain response are filtered to extract the static components using a low-pass filter. The adequacy of filtering is then measured based on the probability of the static maximum axial strain and average shear strain contained in the probabilistically determined dynamic response corresponding to different road roughness. The idea of relating the cutoff frequency to the bridge natural frequency is investigated. It is concluded that using a cutoff frequency of half the bridge natural frequency, one can sufficiently filter out the dynamic components under any case of vehicle speed, road roughness, and bridge natural frequency.

**KEY WORDS:** System identification; Dynamic response filtering; Monte Carlo simulation; Vehicle bridge interaction; Low-pass filter.

## 1 INTRODUCTION

Bridges play a critical role in a country's development. The bridges built in the past are deteriorating due to degradation from the environment and varying operational conditions. Although the current method of visual inspection is simple in procedure, it has some disadvantages when dealing with many bridges. It is time-consuming and subjective. Hence, structural health monitoring (SHM) is emerging as a viable alternative. SHM uses technology to access the current state of the bridge. The current state of the bridge here refers to either the current stiffness or the strength of the bridge. The strength is determined by non-destructive testing, like the rebound hammer and ultrasonic pulse velocity. In contrast, stiffness is determined by knowing the material parameters, boundary conditions, geometric parameters, and live load spectrum.

In the present study, the focus is on determining the current stiffness of the bridge. This can be computed by finding the current material properties and geometrical quantities like the moment of inertia and the cross-sectional area. To do so, the usual approach is to minimize the error between the measured response and the computed response using an optimization algorithm. But this involves computational costs, the problem being ill-posed, and other disadvantages. So, a mechanics-based non-iterative algorithm was proposed [1] to estimate the material property. This method has been proven effective for quasi-static loading conditions, neglecting vehicle-bridge interaction (VBI) dynamics. However, when it comes to realistic traffic scenarios and road roughness profiles, VBI is present and leads to a deviation of the measured response from the actual static response. So, one needs to filter out the dynamic components to arrive closer to the static response.

Now, the input to the material parameter estimation algorithm can be given in two ways. Either a known vehicle load will move over the bridge, as in [1] or the vehicle load also needs to be found using some appropriate measured response quantity [2]. The latter is more advantageous than the former in the case of continuous monitoring. So, identifying the moving load is also focused on. In general, moving load identification literature again involves optimization-based algorithms with the above-mentioned disadvantages. The numerous vehicles and bridge parameters must be known or optimized to find the axle loads. Such an approach increases the uncertainty involved in fixing the parameter values or ill-posed problem and hence reduces the accuracy of the identification. Instead, an algorithm for load estimation in a railway bridge was proposed by [2], which uses a composite strain response for estimating the moving load. An important property of this composite response is that it remains constant over a period for a single vehicle to pass over the bridge. But once again, the field-measured value of this composite strain response quantity can potentially include the dynamic components due to VBI and does not remain constant.

To overcome the above-mentioned difficulties, one of the approaches followed is to filter out the dynamic components from the measured response to get the static response. Few works on filtering can be found in the literature. For instance, in [3], a digital filtering technique was employed to obtain the static bridge response from the dynamic weigh-in-motion data. A low-pass filter of frequency ranging from 0.25 Hz to 1.0 Hz was used. But later it was shown that no proper criteria can be found for cutoff frequency, and a new technique called the equivalent digital filtering technique (EDFT) was proposed [4]. This uses the pseudo-static response of the bridge and the fact

that the dynamic response (pseudo-static response + dynamic effects) and the static response in the frequency domain are approximately equal at 0 Hz. It was shown to be highly accurate in estimating static vehicle weight on dynamic response untainted by other miscellaneous vibrations. [5] used an 11-point and 21-point moving average low-pass filter to improve the accuracy of identified moving loads by eliminating the noise effect. It was found that the percentage errors were significantly reduced, and hence filtering was highly recommended. [6] used a low-pass filter to filter out the dynamic components from the identified bridge influence lines. In [7], the noise and dynamic components are removed to get static strains for moving load identification. It was found that when the cutoff frequency is equal to six to eight times the fundamental frequency of the train load, the peaks of the second derivative of the strain measurements can be identified. Recently, [8] used a low-pass filter to isolate the bridge response from the vehicle dynamics and other excitation sources (the asphalt roughness). The acceleration signal from a vehicle moving at 140 km/h was filtered to obtain the static response for identification of the bridge's elastic modulus using the correlation method. A cutoff frequency of 0.5 Hz, much less than the vehicle's first natural frequency of 2 Hz, was used. It was shown that proper filtering could adequately filter out the vehicle dynamics and other excitations. Now, even though many studies on filtering are available, there are not many studies that extensively deal with measuring the efficacy of filtering algorithms for various vehicle bridge parameters.

Hence, in the present study, a methodology to filter out the dynamic components from the measured strain response is developed. A numerical simulation is performed by modeling the vehicle bridge interaction dynamics. Using a half-car model and a classical Euler-Bernoulli beam model, the dynamic characteristics of the bridge strain response are obtained. Then, using a low-pass filter based on a cutoff frequency, the high frequency components are filtered out. The degree of closeness of the static response is measured using a probabilistic measure. The working of the proposed method is checked for the practical range of vehicle and bridge parameters.

In this paper, the methodology adopted in the study is explained in Section 2, followed by the implementation details of VBI modelling, code validation, numerical data taken in the study, and modal convergence in Section 3. The investigation relating the cutoff frequency to the bridge natural frequency and the effect of various VBI parameters is illustrated in Section 4. Finally, the study is summarized, and the findings from the study are listed in Section 5.

## 2 METHODOLOGY

The Fast Fourier Transform (FFT) of the bridge response was computed to understand its various frequency components. The FFT of the mid-span bridge acceleration response and the bridge mid-span axial strain response is shown in Figure 1. It is observed that the dynamic components are predominant in the acceleration FFT, whereas the static components are predominant in the strain FFT. Hence, it can be observed that when one uses strain response, the feasibility of getting the static response is much higher than that of using the acceleration response. So, through a threshold frequency called

“cutoff frequency”, one can segregate the static and dynamic components. First, the dynamic analysis is performed using a half-car vehicle model. The dynamic responses of concern in the study are the maximum mid-span axial strain and the mean of the sum of shear forces at the quarter span and the three-quarter span. The reason for choosing them is because of their applicability in non-mechanics-based SHM algorithms. The maximum mid-span axial strain is used in finding the material property of the bridge [1] and the average shear strain is used in estimating the moving load [2]. A Monte Carlo simulation of 1000 random trials is performed to account for the random nature of road roughness. Assuming a typical population standard deviation of 2 to 3 micro-strain, a 95% confidence interval yields an estimated margin of error of approximately 0.1–0.2 micro-strain. The best fit distribution and the maximum likelihood estimate parameters for the filtered dynamic response are then found using the Kolmogorov–Smirnov (KS) test in MATLAB. The adequacy of filtering is then measured using the value of the probability for the filtered signal to contain the static response. A bound of  $\pm 1$  micro-strain is considered as a tolerance value for the static response, since it is the least resolution one can achieve in the field for electrical strain gauges.

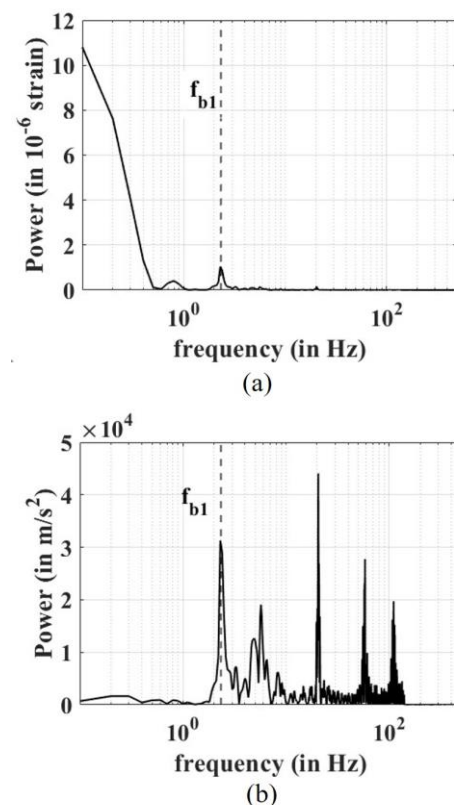


Figure 1. FFT plots of (a) bridge dynamic strain response (b) acceleration response.

## 3 IMPLEMENTATION DETAILS

### 3.1 Vehicle Bridge Interaction Modeling

The vehicle is modeled using a half-car model (HCM) as shown in Figure 2. The bridge is modeled as a simply supported Euler-Bernoulli beam. In HCM, four degrees of freedom are considered – vertical displacement ( $z_v$ ) and pitching rotation

( $\theta_v$ ) of the vehicle's center of gravity (CG), vertical displacement of the front ( $z_{tf}$ ) and rear tires ( $z_{tr}$ ). The vehicle's sprung mass is represented by  $M_v$ , pitching moment of inertia as  $I_v$ , front and rear suspension stiffness  $k_{sf}$  and  $k_{sr}$  and front and rear suspension damping as  $c_{sf}$  and  $c_{sr}$  respectively. The axle spacing between the two axles is ' $s$ ' and the distances of CG from the front axle and the rear axle are denoted by  $s_1$  and  $s_2$ . The displacements of the bridge at the contact points corresponding to the front and rear tires are  $u_{cf}$  and  $u_{cr}$  respectively. The road roughness profile at the contact points is represented by  $r_{cf}$  and  $r_{cr}$ . The equation of motion for the vehicle's bouncing motion can be given by taking vertical force equilibrium as,

$$M_v \ddot{z}_v + c_{sf} (\dot{z}_v + \dot{\theta}_v s_1 - \dot{z}_{tf}) + k_{sf} (z_v + \theta_v s_1 - z_{tf}) + c_{sr} (\dot{z}_v - \dot{\theta}_v s_2 - \dot{z}_{tr}) + k_{sr} (z_v - \theta_v s_2 - z_{tr}) = 0 \quad (1)$$

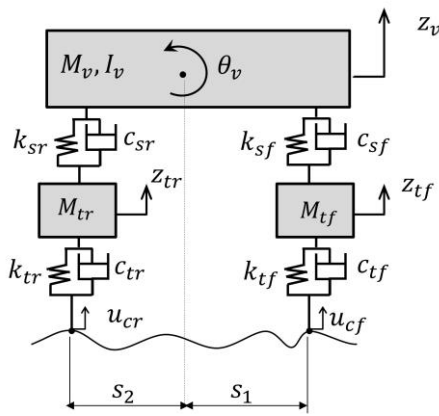


Figure 2. Half car model.

The equation of motion for the vehicle's pitching motion can be found by taking moment equilibrium about the vehicle's CG axis as:

$$I_v \ddot{\theta}_v + c_{sf} (\dot{z}_v + \dot{\theta}_v s_1 - \dot{z}_{tf}) s_1 + k_{sf} (z_v + \theta_v s_1 - z_{tf}) s_1 - c_{sr} (\dot{z}_v - \dot{\theta}_v s_2 - \dot{z}_{tr}) s_2 - k_{sr} (z_v - \theta_v s_2 - z_{tr}) s_2 = 0 \quad (2)$$

The equation of motion for the vertical displacements of the front and rear tires can be found as:

$$m_{tf} \ddot{z}_{tf} - c_{sf} (\dot{z}_v + \dot{\theta}_v s_1 - \dot{z}_{tf}) - k_{sf} (z_v + \theta_v s_1 - z_{tf}) + c_{tf} (\dot{z}_{tf} - \dot{u}_{cf} - v r'_{cf}) + k_{tf} (z_{tf} - u_{cf} - r_{cf}) = 0 \quad (3)$$

$$m_{tr} \ddot{z}_{tr} - c_{sr} (\dot{z}_v - \dot{\theta}_v s_2 - \dot{z}_{tr}) - k_{sr} (z_v - \theta_v s_2 - z_{tr}) + c_{tr} (\dot{z}_{tr} - \dot{u}_{cr} - v r'_{cr}) + k_{tr} (z_{tr} - u_{cr} - r_{cr}) = 0 \quad (4)$$

Finally, the bridge's flexural vibration equation is given by,

$$EI u^{iv}(x, t) + m \ddot{u}(x, t) + c \dot{u}(x, t) = \left[ -\frac{M_v g}{2} - m_{tf} g + c_{tf} (\dot{z}_{tf} - \dot{u}_{cf} - v r'_{cf}) + k_{tf} (z_{tf} - u_{cf} - r_{cf}) \right] \delta(x - vt) + \left[ -\frac{M_v g}{2} - m_{tr} g + c_{tr} (\dot{z}_{tr} - \dot{u}_{cr} - v r'_{cr}) + k_{tr} (z_{tr} - u_{cr} - r_{cr}) \right] \delta(x - (vt - s)) \quad (5)$$

Using the modal superposition technique, the displacement  $u(x, t)$  can be represented using,

$$u(x, t) = \sum_{n=1}^N q_n(t) \varphi_n(x) \quad (6)$$

where  $q_n(t)$  is the modal coordinate and  $\varphi_n(x)$  represents the  $n^{\text{th}}$  mode shape of the simply supported beam, and  $N$  represents the total number of modes used. Now, substituting Equation (6) in Equations (1), (2), (3), (4), and (5), and then using the modal orthogonality principle, the vehicle bridge interaction system can be represented in a matrix form as follows:

$$[M]\{\ddot{X}\} + [C]\{\dot{X}\} + [K]\{X\} = \{R\} \quad (7)$$

where  $[M]$ ,  $[C]$  and  $[K]$  represent the mass, damping, and stiffness matrix of the VBI system of size  $(N + 4) \times (N + 4)$ .  $\{R\}$  represents the force vector and  $\{\ddot{X}\}$ ,  $\{\dot{X}\}$  and  $\{X\}$  represents the acceleration, velocity, and displacement vector, respectively, of size  $(N + 4) \times 1$ . This equation is coded in MATLAB and solved using Newmark's technique (constant acceleration). In this study, road roughness is modeled as a random process with a normal distribution. The wavelength characteristics are characterized using the spectral density of the profile height. The power spectral density coefficients from [10] are adopted to represent various classes of road roughness. A typical roughness profile is shown in Figure 3.

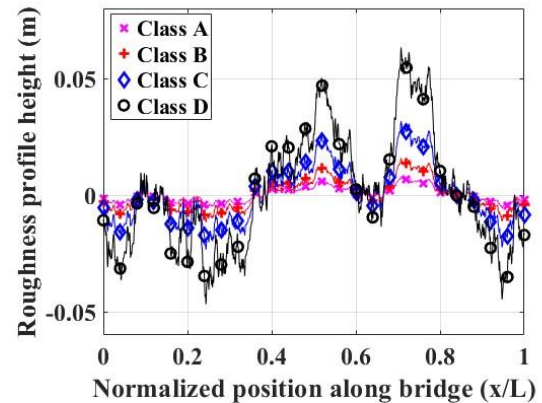


Figure 3. A typical roughness profile.

### 3.2 Validation of the HCM code

The code for vehicle bridge interaction is validated using data from the literature [9]. The values of the VBI parameters taken are as follows.

Vehicle:  $M_v = 1794.4$  kg;  $m_{tf} = 87.15$  kg;  $m_{tr} = 140.4$  kg;  $s_1 = 1.271$  m;  $s_2 = 1.713$  m;  $I_v = 3443.03$  kgm<sup>2</sup>;  $k_{sf} = 66.824$  kN/m;  $k_{sr} = 18.615$  kN/m;  $k_{tf} = k_{tr} = 101.12$  kN/m;  $c_{tf} = c_{tr} = 0$  Ns/m;  $c_{sf} = 1190$  Ns/m;  $c_{sr} = 1000$  Ns/m;  $v = 40$  km/h; Bridge:  $m = 20000$  kg/m;  $L = 100$  m;  $E = 207$  GPa;  $I = 0.174$  m<sup>4</sup>; Roughness: Smooth. The mid-span displacement of the bridge obtained using the developed code matched well with that from the literature, as shown in Figure 4.

### 3.3 Numerical data taken in the study

The half-car vehicle model values are taken from the representative vehicle data set from TruckMaker software. For the bridge, the values of a typical 50m span prestressed box



girder for three lane traffic are considered. And, for road roughness, the parameter values were taken from [10], [11] and [12]. The numerical values are given below.

Vehicle:  $M_v = 22700$  kg;  $m_{tf} = m_{tr} = 1500$  kg;  $I_v = 71,761.1$  kg/m<sup>2</sup>;  $s_1 = 3.133$  m;  $s_2 = 1.667$  m;  $k_{sf} = 25000$  N/m;  $k_{sr} = 30000$  N/m;  $k_{tf} = k_{tr} = 1.273 \times 10^6$  N/m;  $c_{tf} = c_{tr} = 6000$  Ns/m. Bridge:  $m = 11880$  kg/m;  $L = 50$  m;  $A = 4.87$  m<sup>2</sup>;  $I = 4.923$  m<sup>4</sup>;  $E = 31.62$  GPa;  $\nu = 0.2$ ;  $f_{b1} = 2.31$  Hz

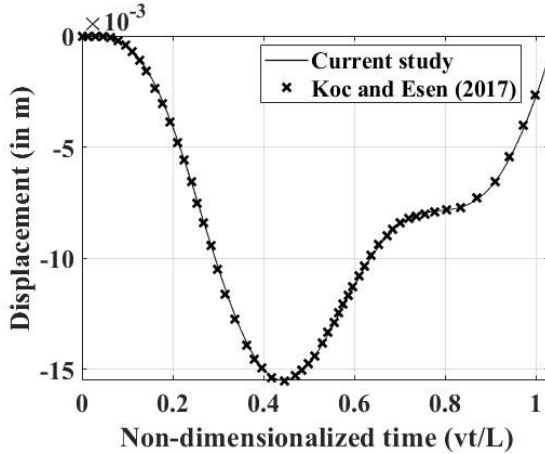


Figure 4. Validation of HCM code.

### 3.4 Modal Convergence study

As the method uses modal superposition, the minimum number of modes required to accurately represent the results are found using a convergence study. Towards this, absolute ( $\delta_{abs}$ ) and relative ( $\delta_{rel}$ ) convergence is checked wherein the definition used is,

$$\delta_{abs} = \| \epsilon_{N=N_{max}} - \epsilon_{N=1} \| \quad (8)$$

$$\delta_{rel} = \| \frac{\epsilon_{N=N_{max}} - \epsilon_{N=1}}{\epsilon_{N=N_{max}}} \| \times 100\% \quad (9)$$

where  $N$  represents the number of modes used;  $N_{max}$  represents the maximum number of modes used;  $\epsilon$  represents the maximum strain value at the given number of modes. The tolerance limit was kept at 0.01 micro-strain for absolute convergence and 0.01% for relative convergence. The convergence study was performed for various vehicle speeds ranging from 20 km/h to 120 km/h and for four roughness classes as per [10]. The minimum number of modes required to achieve convergence of the maximum axial strain response is shown in Table 1 and Table 2 respectively. It was found that 53 modes were adequate to satisfy the tolerance. Hence, further in the study, 60 modes were considered for all the computations.

Table 1. Modal convergence study based on absolute convergence for maximum axial strain at L/2.

Roughness Class	Speed (in km/h)					
	20	40	60	80	100	120
Class A	31	27	17	23	11	27
Class B	29	19	11	23	13	27
Class C	27	11	11	21	11	29
Class D	27	11	13	11	29	15

## 4 RESULTS

### 4.1 Filtered and Unfiltered response

To demonstrate the filtering process, as a reasonable estimate, a cutoff frequency of half the bridge's natural frequency is taken. The dynamic response of the bridge is simulated for 1000 random trials of road roughness. Assuming the velocity to be 50 km/h and road roughness as class D, the maximum midspan axial strain and average shear strain sum of the unfiltered and filtered signals are shown in Figure 5 and Figure 6 respectively.

Table 2. Modal convergence study based on relative convergence for maximum axial strain at L/2.

Roughness Class	Speed (in km/h)					
	20	40	60	80	100	120
Class A	31	29	17	31	15	29
Class B	31	31	17	31	31	31
Class C	29	19	13	31	29	31
Class D	29	11	31	17	29	15

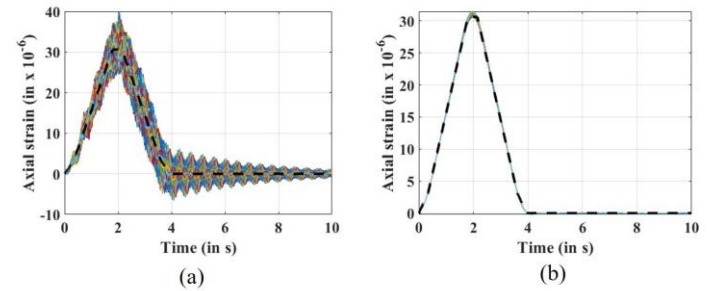


Figure 5. Monte Carlo simulation of (a) unfiltered and (b) filtered dynamic response of 1000 random trials for maximum axial strain at L/2 (dashed line represents the static response).

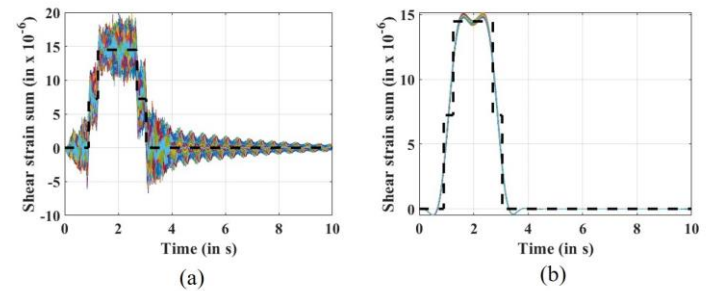


Figure 6. Monte Carlo simulation of (a) unfiltered and (b) filtered dynamic response of 1000 random trials for average shear strain sum at L/4 and 3L/4 (dashed line represents the static response).

The histogram plot for the maximum axial strain and average shear strain sum for 1000 trials is shown in Figure 7(a) and Figure 7(b) respectively. One can observe that filtering makes the unfiltered response come closer to the static response. This observation was not much in the case of the average shear strain sum. Various probability distributions that can sufficiently fit the filtered histogram data were checked using the maximum log likelihood values in MATLAB. The plot of various distributions fitting the histogram data is shown in Figure 8.

A Kolmogorov-Smirnov (KS) test is used to check whether two samples come from the same distribution or not. Here, one sample is from the Monte-Carlo simulation data, and the other sample is from the fitting distribution (Normal, Lognormal, Logistic, Weibull, Gamma, etc.). The null hypothesis is that both come from the same distribution, and the alternative hypothesis is that both come from different distributions. A p-value of 0.05 is used to denote the significance level for the null hypothesis to be true. The distribution that gives the highest p-value and the log likelihood value is chosen as the best fit distribution, and its probability density value at the static response is calculated.

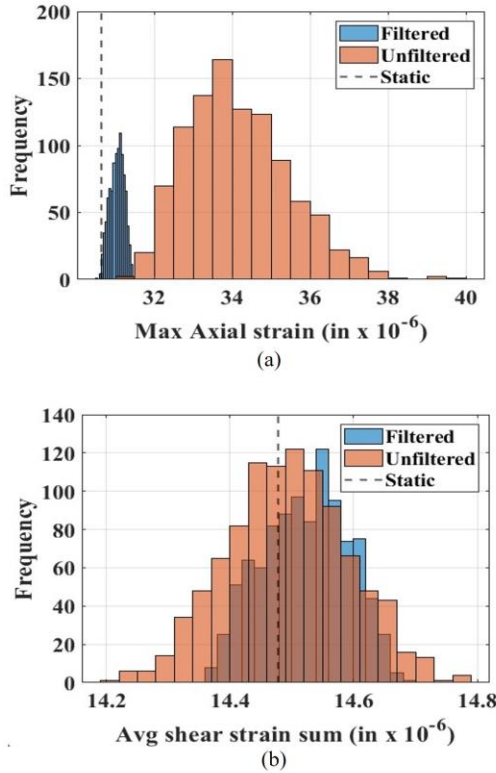


Figure 7. Histogram plot for the (a) Maximum axial strain (b) Average shear strain sum data.

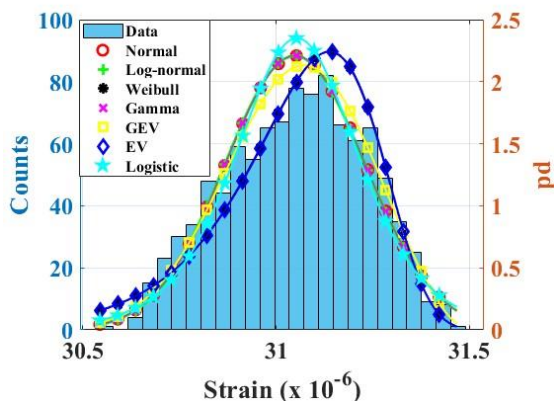


Figure 8. Best fit probability distribution for strain data.

The maximum likelihood estimates (MLE) parameters, KS test results, and their corresponding p-value for various distributions are shown in Table 3 and Table 4. One can observe that for the unfiltered response, the Generalized

Extreme Value (GEV) distribution has passed the test with the highest p-value of 0.9104. For the case of filtered response, all the distributions tested gave the pass results, but again, GEV has the highest p-value of 0.7167. Hence, the probability that the GEV distribution contains the static response  $\pm 1$  micro-strain for the filtered and unfiltered response will be 1.0000 and 0.0086, respectively.

#### 4.2 Study of static response probability for different cutoff frequency coefficients

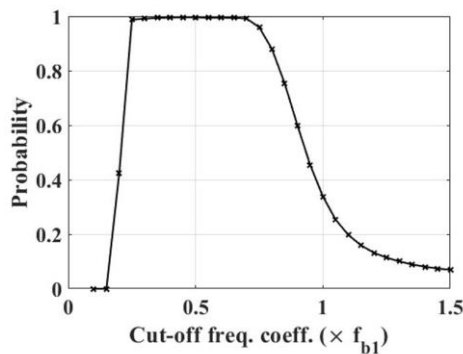
The cutoff frequency was taken as a multiple of the bridge's natural frequency. This multiple will be referred to as the cutoff frequency coefficient. The range of coefficients from 0.2 to 1.5 was studied. The variation of the probability value of the static response for this range of coefficients is shown in Figure 9(a) and Figure 9(b) for a given vehicle speed of 50 km/h and road roughness class D. For the case of axial strain in Figure 9(a), it is observed that the probability value becomes zero at very low cutoff frequency (here for 0.1 and 0.15). This implies that there are not enough frequency components in the filtered response to represent the static value. Hence, the distribution of the filtered response will lie much farther away from the static response. A typical histogram plot for this case is shown in Figure 10(a) and Figure 10(b) for a cutoff frequency of  $0.15f_{b1}$ . One can observe that the filtered values are much lower than the static value. For all the values after 0.1, the probability becomes greater than 0. This means that the probability of static response lying in  $\pm 1$  micro-strain bound of the filtered response is greater than that of the unfiltered response. This demonstrates the effect of filtering. The maximum effect is observed at the one with the highest probability value. i.e., in this case, for a cutoff frequency of  $0.45 f_{b1}$ . For the case of shear strain sum shown in Figure 9(b), the static response probability becomes almost close to 1.0 for all the cutoff coefficients above 0.1. This is because, for shear strain sum, the average value was taken. Even for the case without filtering, one can achieve a response value closer to the static value, as evident from Figure 7(b). Hence, filtering doesn't have much of an effect in this case.

Table 3. Maximum Likelihood Estimates, KS Test results, and probability values to contain the static response for various distributions of unfiltered responses.

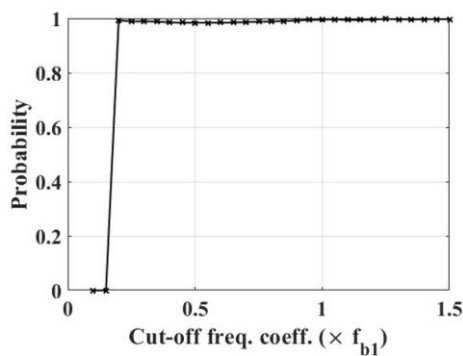
Distribution	MLE parameter	KS test	p-value	Probability
Normal	$\mu=34.13$ $\sigma = 1.311$	Pass	0.1768	0.0282
Log-normal	$\mu=3.527$ $\sigma = 0.038$	Pass	0.3078	0.0240
Weibull	$a=34.79$ $b = 23.82$	Fail	$9.8e-6$	0.0773
Gamma	$\alpha=686.3$ $\beta = 0.049$	Pass	0.2580	0.0253
GEV	$\mu=-0.1005$ $\sigma = 1.146$ $\xi = 33.57$	Pass	0.9104	0.0086
EV	$\mu=34.82$ $\sigma = 1.494$	Fail	$4.6e-7$	0.0815
Logistic	$\mu=34.07$ $\beta = 0.750$	Pass	0.3078	0.0351

Table 4. Maximum Likelihood Estimates, KS Test results, and probability values to contain the static response for various distributions of filtered response.

Distribution	MLE parameter	KS test	p-value	Probab ility
Normal	$\mu=31.05$ $\sigma=0.18$	Pass	0.5295	0.9994
Log-normal	$\mu=3.435$ $\sigma=0.006$	Pass	0.4938	0.9994
Weibull	$a=31.14$ $b=189.7$	Pass	0.2355	0.9999
Gamma	$\alpha=29566$ $\beta=0.0011$	Pass	0.5295	0.9994
GEV	$\mu=-0.368$ $\sigma=0.187$ $\xi=30.99$	Pass	0.7167	1.0000
EV	$\mu=31.14$ $\sigma=0.164$	Pass	0.2145	0.9999
Logistic	$\mu=31.03$ $\beta=0.106$	Pass	0.2355	0.9959



(a)



(b)

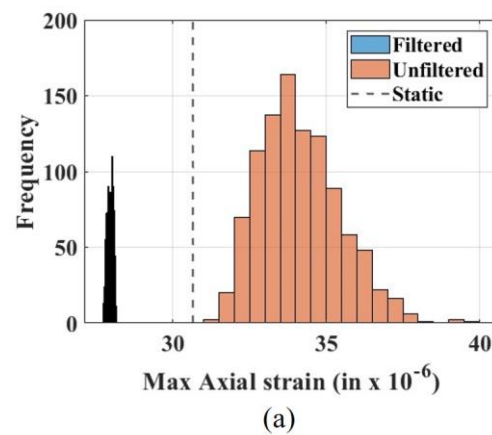
Figure 9. Variation of cutoff frequency coefficients with the static response probability of the filtered signal – (a) Maximum axial strain at L/2 (b) Average shear strain sum at L/4 and 3L/4.

### 4.3 Effect of vehicle speed

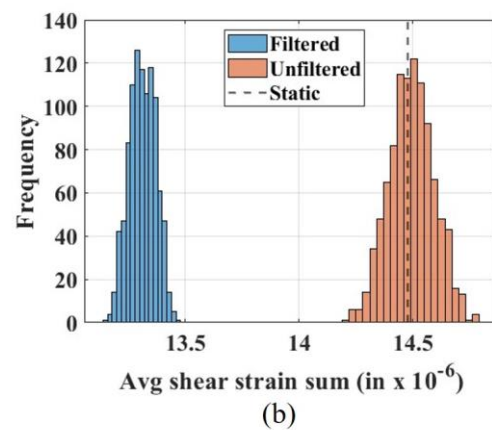
The effect of vehicle speed is studied by taking speed values as 10 km/h, 25 km/h, 50 km/h, and 100 km/h. The road roughness and bridge natural frequency were kept constant at class D and 2.31 Hz. The static response probability values for different cutoff frequencies are shown in Figure 11 for maximum mid-

span axial strain and in Figure 12 for the average shear strain sum. We can observe that the minimum cutoff required to attain a probability value of 1.0 increases with increasing speed. For instance, the minimum cutoff coefficients for speed values of 10, 25, 50, and 100 km/h are  $0.1f_{b1}$ ,  $0.15f_{b1}$ ,  $0.25f_{b1}$ , and  $0.4f_{b1}$ , respectively. This is because of the shifting of the driving frequency with the increase in speed. Also, the region from  $0.45 f_{b1}$  to  $0.75 f_{b1}$  has the probability value of 1.0 in all the cases and is hence recommended.

For shear strain sum, the effect of speed is observed in Figure 12. Again, the effect of driving frequency on the minimum cutoff coefficient can be observed. Also, after the minimum cutoff, at all the cutoff coefficients, the static response probability is maintained at 1.0, which was not observed in the axial strain case. This is because of the same advantage of taking the average value in the case of shear strain sum, as explained previously.



(a)



(b)

Figure 10. Histogram plot for filtered and unfiltered response corresponding to cutoff frequency of  $0.15f_{b1}$  for (a) Maximum axial strain at L/2 (b) Average shear strain sum at L/4 and 3L/4.



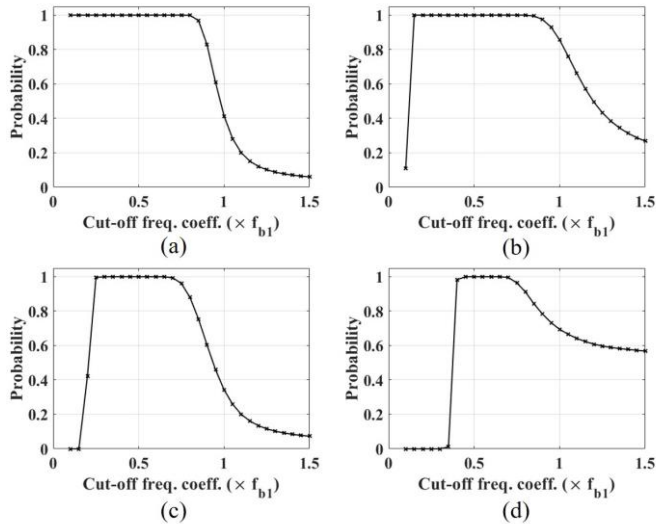


Figure 11. Effect of vehicle speed (a)  $v=10$  km/h (b)  $v=25$  km/h (c)  $v=50$  km/h (d)  $v=100$  km/h – Maximum axial strain at L/2 for  $f_{b1} = 2.31$  Hz and roughness class D.

#### 4.4 Effect of road roughness

The effect of road roughness is studied by varying the road roughness from class A (Very Good) to class D (Poor). The vehicle velocity is kept constant at 50 km/h, and the natural frequency is at 2.31 Hz. The static response probability values for different cutoff frequencies are shown in Figure 13 and Figure 14 for maximum mid-span axial strain and average shear strain sum, respectively. It can be observed that for low roughness classes, the probability is 1.0 even at higher cutoff frequencies. As the roughness class increases, the static response probability decreases. This is because a higher degree of roughness corresponds to increased dynamic noise in the signal and hence a decrease in the static response probability value. For the case of the average shear strain sum in Figure 14, there was not much observation. The probability value reaches 1.0 for all the cutoff coefficients above 0.15.

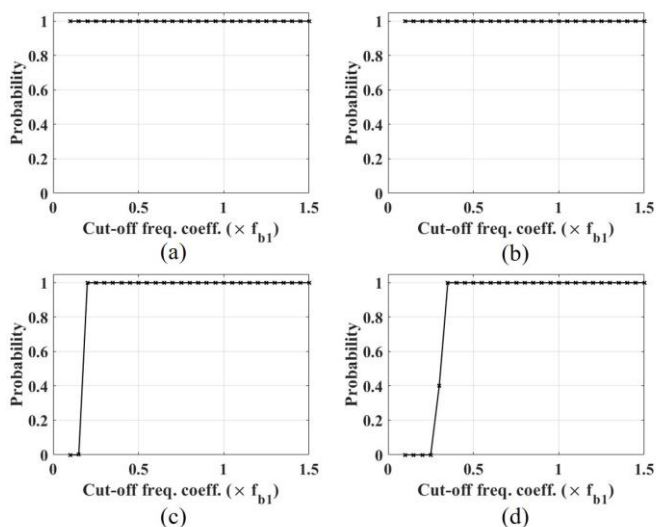


Figure 12. Effect of vehicle speed (a)  $v=10$  km/h (b)  $v=25$  km/h (c)  $v=50$  km/h (d)  $v=100$  km/h – Average shear strain sum at L/4 and 3L/4 for  $f_{b1} = 2.31$  Hz and roughness class D.

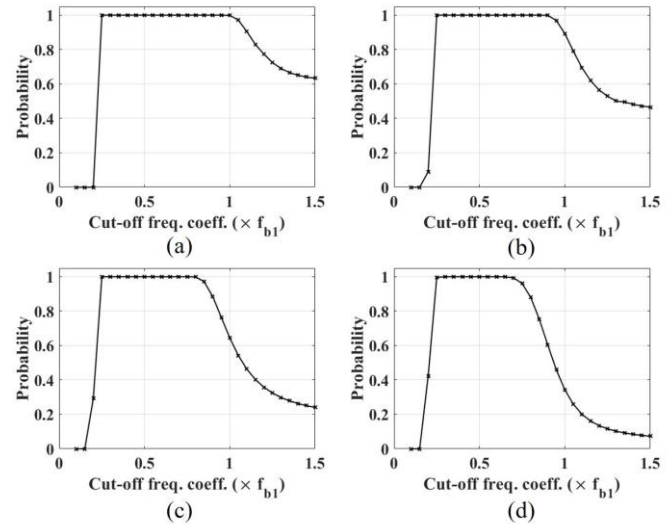


Figure 13. Effect of road roughness (a) Class A (b) Class B (c) Class C (d) Class D – Maximum axial strain at L/2 for  $f_{b1} = 2.31$  Hz and  $v=50$  km/h.

#### 4.5 Effect of bridge natural frequency

Finally, the effect of various bridge natural frequencies is studied. The natural frequency of the bridge is varied by changing the value of the flexural rigidity of the bridge. Four values of natural frequency – 2.31 Hz, 5 Hz, 7.5 Hz, and 10 Hz were studied, corresponding to four EI values – 157 GNm<sup>2</sup>, 753 GNm<sup>2</sup>, 1693 GNm<sup>2</sup>, and 3008 GNm<sup>2</sup>.

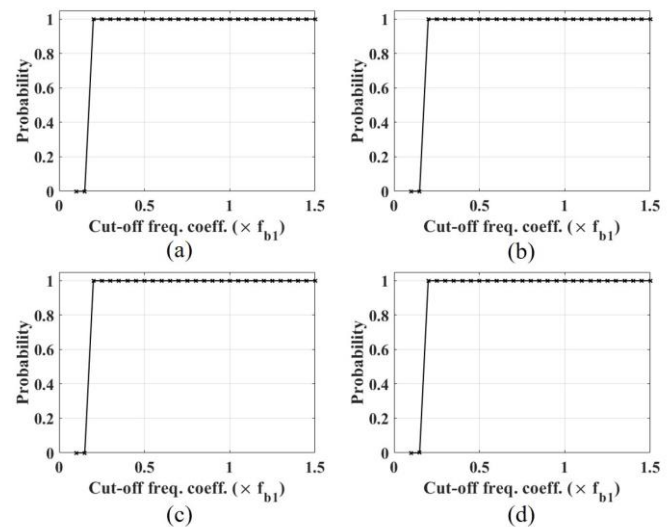


Figure 14. Effect of road roughness (a) Class A (b) Class B (c) Class C (d) Class D – Average shear strain sum at L/4 and 3L/4 for  $f_{b1} = 2.31$  Hz and  $v=50$  km/h.

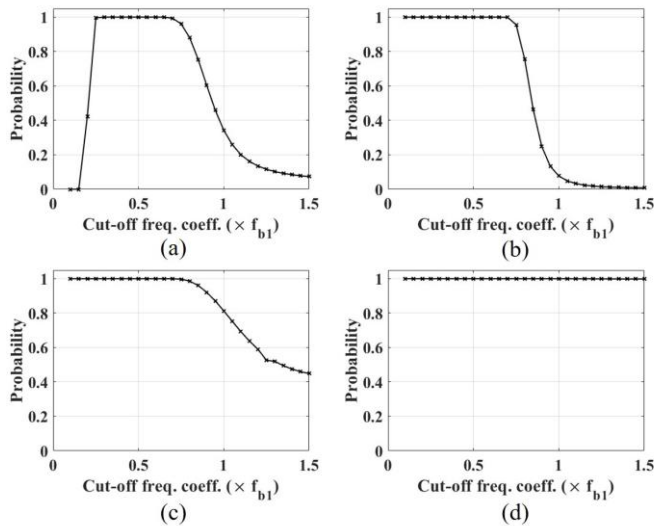


Figure 15. Effect of bridge natural frequency (a)  $f_{b1} = 2.31$  Hz (b)  $f_{b1} = 5$  Hz (c)  $f_{b1} = 7.5$  Hz (d)  $f_{b1} = 10$  Hz – Maximum axial strain at  $L/2$  for  $v = 50$  km/h and roughness class D.

For all the coefficients between  $0.25 f_{b1}$  to  $0.7 f_{b1}$ , the static response probability for the case of maximum axial strain is 1.0, irrespective of different natural frequencies, as shown in Figure 15. Also, it can be observed that for a given case of a cutoff frequency closer to the bridge's natural frequency, the static response probability depends upon the relative distance between the driving frequency and the bridge's natural frequency. If this difference is high, the probability value becomes 1.0; otherwise, the value reduces. The figure for the average shear strain sum is shown in Figure 16. As observed previously, the probability value for most of the cutoff coefficients is 1.0.

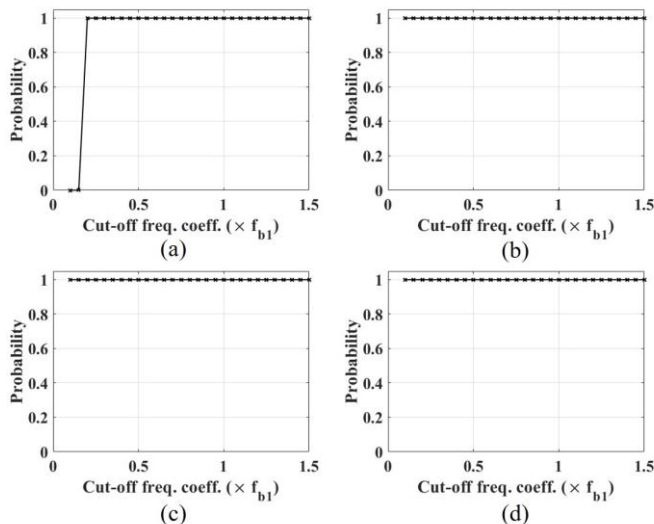


Figure 16. Effect of bridge natural frequency (a)  $f_{b1} = 2.31$  Hz (b)  $f_{b1} = 5$  Hz (c)  $f_{b1} = 7.5$  Hz (d)  $f_{b1} = 10$  Hz – Average shear strain sum at  $L/4$  and  $3L/4$  for  $v = 50$  km/h and roughness class D.

## 5 CONCLUSION

The idea of cutting off the higher frequencies from the bridge strain response to get the static response of the bridge is

investigated. A half-car vehicle bridge interaction model was used to simulate the motion of a moving vehicle. Newmark's constant integration scheme was used to solve the program in MATLAB.

A Monte Carlo simulation of 1000 trials is performed for random values of road roughness. A low-pass Butterworth filter is used to cut off higher frequencies. Contrary to the literature studies wherein the cutoff frequency was related to the driving frequency, in this study, it is related to the bridge's natural frequency. A detailed study on the influence of the cutoff frequency so that the filtered signal contains the static response  $\pm 1$  micro-strain is undertaken. And finally, the effect of VBI parameters – vehicle speed, road roughness, and natural frequency was studied. From the study, the following is inferred:

- The cutoff frequency of 0.5 times the bridge natural frequency seems to have the highest probability of containing the static strain response across different vehicle speeds, road roughness, and natural frequency of the bridge.
- The higher the vehicle speed, the higher is the driving frequency, and hence the cutoff frequency to contain the static response increases.
- The higher the road roughness, the higher the dynamic noise in the response, and hence, the static response probability decreases for a given cutoff frequency.
- Both the driving frequency and the bridge natural frequency determine the cutoff frequency, which would contain the static strain response.

Further efforts are required to validate the study using field data.

## ACKNOWLEDGMENT

Sarath R. gratefully acknowledges the Ministry of Education, Government of India, for supporting this work through the Prime Minister's Research Fellowship scheme.

## REFERENCES

- P. Pitchai, U. Saravanan, and R. Goswami, Mechanics-based algorithms to determine the current state of a bridge using quasi-static loading and strain measurement. *Structural Health Monitoring*, 18 (5-6), 1874-1888, 2018.
- T. M. Deepthi, U. Saravanan, and A. Meher Prasad, Algorithms to determine wheel loads and speed of trains using strains measured on bridge girders. *Structural Control and Health Monitoring*, 26(1), e2282, 2019.
- M. I. S. Elhelbawey, Definition of improved modeling procedures for the analysis of bridge structures under truck loading using Weigh in Motion. PhD Thesis, University of Maryland, College Park, USA, 1991.
- G. Thater, P. Chang, D. Schelling, and C. Fu, Estimation of bridge static response and vehicle weights by frequency response analysis. *Canadian Journal of Civil Engineering*, 25(4), 631-689, 1998.
- T. H. Chan and T. Yung, A theoretical study of force identification using prestressed concrete bridges, *Engineering Structures*, 22(11), 1529-1537, 2000.
- C. Mustafa, I. Yoshida, and H. Sekiya, An investigation of bridge influence line identification using time-domain and frequency domain methods. In *Structures*, 33, 2061-2065, Elsevier, 2021.
- H. Wang, Q. Zhu, J. Li, J. Mao, S. Hu, and X. Zhao, Identification of moving train loads on railway bridges based on strain monitoring, *Smart Structures System*, 23(3), 263-278, 2019.
- A. Aloisio and R. Alaggio, Experimental estimation of elastic modulus of concrete girders from drive-by inspections with force balance accelerometers. *Shock and Vibrations*, 2021(1), 1617526, 2021.
- M. A. Koc and I. Esen, Modelling and analysis of vehicle-structure road coupled interaction considering structural flexibility, vehicle parameters,



- and road roughness. *Journal of Mechanical Science and Technology*, 31, 2057-2074, 2017.
- [10] ISO 8608, Mechanical vibration road surface profiles – reporting of measured data, 2016.
- [11] J. Oliva, J. M. Goicolea, P. Antolin, and M. A. Astiz, Relevance of a complete road roughness description in vehicle bridge interaction dynamics, *Engineering Structures*, 56, 466-476, 2013.
- [12] Y. Zhan and F. Au, Bridge surface roughness identification based on vehicle bridge interaction. *International Journal of Structural Stability and Dynamics*, 19(07), 1950069, 2019.



## Laboratory Testing of Old Bridge Girders: Preliminary Results

Maja Kreslin<sup>1</sup>, Mirko Kosič<sup>1</sup>, Aljoša Šajna<sup>1</sup>, Andrej Anžlin<sup>1</sup>, Doron Hekič<sup>1</sup>, Vladimir Požonec<sup>1</sup>, Petra Triller<sup>1</sup>

<sup>1</sup>Slovenian National Building and Civil Engineering Institute, Dimičeva ulica 12, 1000 Ljubljana, Slovenia  
email: [maja.kreslin@zag.si](mailto:maja.kreslin@zag.si), [mirko.kosic@zag.si](mailto:mirko.kosic@zag.si), [aljosa.sajna@zag.si](mailto:aljosa.sajna@zag.si), [andrej.anzlin@zag.si](mailto:andrej.anzlin@zag.si), [doron.hekic@zag.si](mailto:doron.hekic@zag.si),  
[vladimir.pozonec@zag.si](mailto:vladimir.pozonec@zag.si), [petra.triller@zag.si](mailto:petra.triller@zag.si)

**ABSTRACT:** This paper presents key results on the laboratory testing of old girders removed from a flood-damaged bridge located near Ljubljana, Slovenia. The structure was widened in 1989 to accommodate pedestrians and cyclists by integrating prefabricated prestressed reinforced concrete T-girders. To assess the structural behaviour of the bridge, six girders were subjected to a rigorous testing program involving bending and shear tests in a laboratory setting. The tests were performed on girders with static lengths of 12.20 meters and 9.90 meters. The program aimed to evaluate the structural performance of the girders. Preliminary results indicate satisfactory structural behaviour of the prestressed T-girders under the applied loads, with insights into their performance under both bending and shear stresses. This study contributes valuable data for assessing the long-term behaviour of bridges. The outcomes are particularly relevant for optimising resource allocation in bridge rehabilitation projects and ensuring safety and functionality in transportation networks.

**KEY WORDS:** laboratory testing, prestressed girders, assessment, load test, operational modal analysis, damage, acoustic emission

### 1 INTRODUCTION

Bridges are a key component of transport infrastructure, ensuring connectivity and traffic flow at both regional and national levels. However, as they age, they become susceptible to damage due to material degradation, traffic loads, and extreme weather events. Regular condition assessment through visual inspections and different structural monitoring systems is therefore essential to ensure the safety of both the structures and their users.

Bridge replacement typically entails significant financial costs, long execution times, and considerable logistical challenges. Consequently, it is crucial to leverage all available knowledge to accurately assess the actual safety and remaining service life of existing bridges. In this context, experimental data plays a vital role, as it provides direct insight into the structural behaviour [1, 2, 3].

This paper presents the ReNos project, a research initiative by the Slovenian National Building and Civil Engineering Institute (ZAG), which involved laboratory testing of prestressed concrete girders recovered from an existing bridge structure that had been exposed to flooding. The main objectives of the research were: (i) to determine the actual load-bearing behaviour and (ii) to monitor damage development using various sensor types, and (iii) to develop a protocol for potential reuse of the girders.

First, the bridge and the girders are described, including the entire process of the adapted demolition and transportation of the girders to the laboratory. This is followed by a description of the experimental program, preliminary results, and the future work plan.

### 2 DESCRIPTION OF THE BRIDGE, GIRDERS, AND DISASSEMBLY PROCESS

#### 2.1 Bridge and girders

The five-span bridge with a total length of 52.6 m and width of 8.2 m was located on a state road near Ljubljana, Slovenia. The original superstructure consisted of a ribbed reinforced concrete slab with brick inserts, supported by thin walls.

In 1989, the bridge was widened on both sides to accommodate pedestrian and cyclist traffic. The extension incorporates prefabricated prestressed concrete T-girders supported by additional wall piers aligned with the existing substructure. These girders were connected transversely by a cast-in-place reinforced concrete slab. The extended bridge from the upper stream side is shown in Figure 1.



Figure 1. Existing bridge before the collapse (downstream).

Following the catastrophic 2023 floods in Slovenia, the bridge partially collapsed, as shown in Figure 2 from the downstream side. While the intermediate supports were damaged, an inspection confirmed that the longitudinal girders remained in good condition. In agreement with the infrastructure manager and demolition contractor, selected girders were salvaged for laboratory testing (Figure 3).



Figure 2. Partly collapsed bridge after floods (upstream).



Figure 3. Lifting the girders with cranes.

## 2.2 Disassembly process

The process of disassembling the girders proved to be highly challenging. Nevertheless, all stakeholders involved, including the infrastructure management authority and the demolition contractor, demonstrated a commendable level of flexibility by adapting the demolition procedure to enable the safe recovery of the girders for further purposes, such as experimental testing or potential reuse.

The girder disassembly process comprised the following key steps: identification of reusable elements; preparation of the demolition method by the contractor; cutting of the concrete slab between the girders; removal of the edge girders; lifting of the girders using cranes; transportation of the girders; and placement at designated storage or testing locations.

## 3 EXPERIMENTAL PROGRAM AND TEST SETUP

The investigation program was based on the testing of six girders, focusing on the following parameters: the influence of girder length (span lengths of 9.9 m and 12.2 m), the influence of the load application point (shear/flexural test), the influence

of the presence of a reinforced concrete (RC) slab on the girder (girders with and without slabs), and the impact of pre-existing damage to the girder.

In addition, supporting activities were carried out, including visual inspections of the girders, destructive and non-destructive testing of the girder materials/aggregates and laser scanning of specimens.

The test setup is presented in Figure 4. The girder was simply supported, with a pinned support at one end and a roller support at the other side. Both supports were rigidly anchored to the laboratory's strong floor. Lateral stability of the girder was ensured using a rigid steel frame. The load was applied by means of a hydraulic actuator, which was clamped into the steel reaction frame.

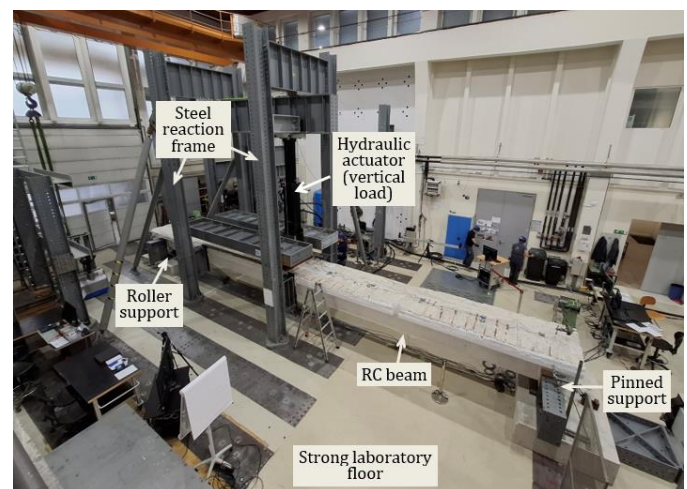


Figure 4. Experimental setup at ZAG's Laboratory for Structures.

The essential instrumentation for each test included a force transducer, displacement transducers, strain measurement devices (extensometers, strain gauges, digital image correlation (DIC) system, optical sensors), accelerometers, and acoustic emission sensors.

The testing procedure for the static cyclic tests was generally divided into two stages. The first stage was load-controlled, while the second stage was displacement-controlled. Each stage comprised several phases, defined either by force levels (in the first stage) or displacement increments (in the second stage). The load, whether force- or displacement-controlled, was progressively increased until the girder failed.

## 4 PRELIMINARY TEST RESULTS

Due to the limited scope of the paper, in the following, the preliminary results of only the flexural test on the B4 girder is presented. This girder, with a span length of 9.9 m, was loaded at mid-span during the test. It was tested without the top RC slab and had no pre-existing damage prior to the testing.

### 4.1 Flexural behaviour of girder

The flexural behaviour of the girder is represented by the hysteretic curve, which shows the relationship between applied force and mid-span displacement, as illustrated in Figure 5. The triangles indicate the state at initial cracking and the state just before failure. The labels S1, S2, and S3 denote engineering-



defined states employed for damage detection accelerometers, as described in Section 4.2.

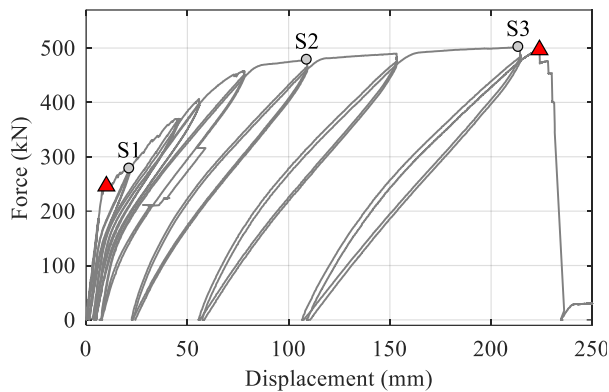


Figure 5. Hysteretic response of the girder at the middle.

The initial cracks appeared during the second loading phase, forming in the load application area with an initial width of approximately 0.1 mm (Figure 6). Cracking began at an applied force of 246.1 kN and a corresponding displacement of 10 mm. These cracks closed completely upon unloading. As the loading progressed through subsequent phases, the cracks widened and propagated, increasing both in number and extent. Inclined (shear) cracks also began to appear in supports' region.

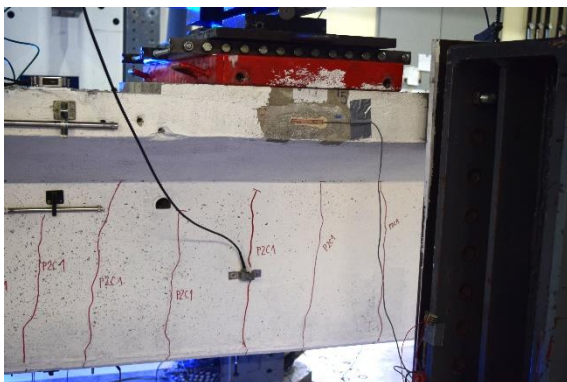


Figure 6. Damage state at the peak of the cycle when the first cracks appeared.

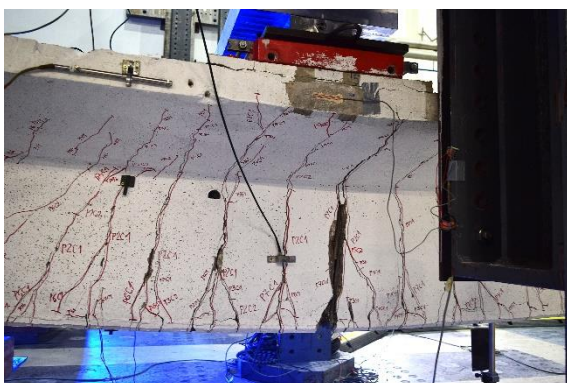


Figure 7. Damaged girder in the failure stage.

In the phase immediately preceding failure, the maximum observed crack width reached 4.5 mm, with a residual width of 3.0 mm after unloading. In the following phase at displacement of 22,4 mm and force 497 kN, the girder experienced flexural

failure, accompanied by the rupture of the prestressing tendons in the load application zone (Figure 7).

#### 4.2 Monitoring of damage with accelerometers

The damage of the girder at the end of individual loading cycles was monitored using 18 DEWESoft 3-axial MEMS accelerometers [4], placed on the top flange. This part of the experimental program aimed to evaluate the limits of acceleration-based monitoring systems to detect structural damage based on changes in the specimens' dynamic characteristics.

Damage progression was monitored through ambient vibration measurements conducted after each load cycle on fully unloaded girders, ensuring consistent initial boundary conditions. The specimen's dynamic properties, including natural frequencies, mode shapes, and damping ratios, were identified using Operational Modal Analysis (OMA) performed with the DEWESoft ARTEMIS OMA software [5].

This study presents and discusses the changes in natural frequencies of the first two vertical bending modes, shown in Table 1. A schematic illustration of the corresponding mode shapes is provided in Figure 8.

Table 1. Change in mode shape natural frequencies during experimental phases.

B4	$f_1$ [Hz]	$f_2$ [Hz]	$\Delta f_1$ [%]	$\Delta f_2$ [%]
Reference	12.4	45.8	\	\
S1: after crack phase	12.0	45.2	-3.2	-1.3
S2: after yield phase	10.3	43.8	-16.9	-4.4
S3: near collapse	8.0	40.8	-35.5	-10.9

The reference natural frequencies of the first and second vertical bending modes amounted to 12.38 Hz and 45.81 Hz, respectively. As damage accumulates during load cycles, the girder's stiffness diminishes, which is reflected in the corresponding reduction of natural frequencies in Table 1. A reduction of 3% to 36% in the first natural frequency was observed as the damage evolved from cracking (S1) to near-collapse limit state (S3). Smaller decrease was obtained for the second vertical bending mode (1% to 11%), which is due to the applied load causing more damage near mid-span, where the amplitude of the second mode is nearly zero (see Figure 8b).

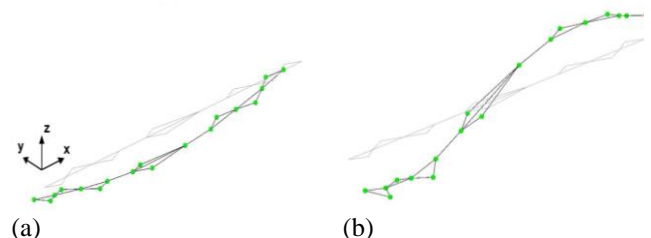


Figure 8. First (a) and second (b) vertical bending modes of B4 girder.

Initial findings indicate that acceleration-based monitoring can be used to detect structural damage in a controlled environment.



### 4.3 Monitoring of damage with acoustic emission

During the load test, the evolution and propagation of damage were also assessed using acoustic emission methods (AEM). Three Physical Acoustic Corporation type PK6I sensors were mounted half height of the girder's web. Physical Acoustic Corporation AEWin for Sensor Highway Smart Monitor Ver. E5.00 software was used to record the acoustic emission parameters and the load. The threshold was set to 40 dB.

General acoustic emission activity, represented by the amplitude of each hit, the applied load, are time-dependent and presented in Figure 9. Nevertheless, The AE activity, i.e. damage evolution during loading and unloading phases, is visible. In addition, the b-value and the damage parameter as used by Vidya Sagar and Raghu Prasad [6] and Elbatanouny et al. [7] in similar investigations were calculated to evaluate the damage evaluation. The decrease of b-value and the increase of damage parameter with increased load are clearly visible.

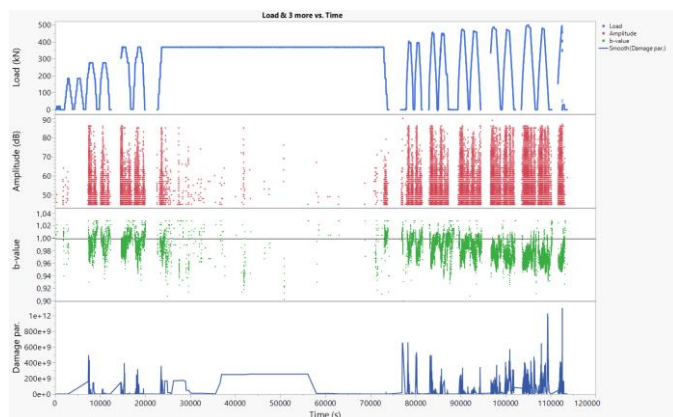


Figure 9: Load and amplitude of individual hits, and b-value and damage parameter as a measure of damage evolution and propagation.



Figure 10: Maximum loads (Max - blue), and number of hits (N - purple), total energy (Sum - red) and mean count (Mean - green) of the hits for individual phases (P1, P2, P3), cycles (C1, C2) and stages (loading L and unloading U).

As an example of a more detailed analysis the number of hits, total energy and mean counts of the first three phases are presented in Figure 10. Each phase consists of two cycles of loading and unloading. A significant difference in AE activity between different phases, cycles within individual phases and

loading/unloading stage was recorded. A more detailed analysis is foreseen. It must be noted that some data of the phase 3, cycle 1, loading stage (marked L\* on graph), was unfortunately lost.

## 5 CONCLUSION

The experimental investigation carried out within the ZAG's research project ReNos provides valuable insights into the structural behaviour and bearing capacity of prestressed concrete bridge girders recovered from a flood-affected structure. Preliminary results demonstrate that acceleration-based monitoring systems as well as acoustic emission can identify the progression of damage and help identify critical states in the girder's response. This confirms that such systems are suitable for structural health monitoring applications.

Additionally, the study highlights that, with coordinated stakeholder involvement, dismantling procedures can be executed in a way that preserves structural components for further testing and potential reuse.

Future work will focus on the analysis of remaining test results taking into account the main objective of the study: (1) to determine the actual load-bearing behaviour and compare it with the original design assumptions, (2) to monitor damage development using various sensor types, and (3) to develop a protocol for the potential reuse of the girders in line with circular economy principles.

Acoustic emission techniques can clearly detect and monitor damage evaluation, but a more detailed analysis of the results is needed.

## ACKNOWLEDGMENTS

The research was funded by the Slovenian Research Agency (ARIS) through the research programme No. P2-0273 and the infrastructure programme No. Z2-7431. Additional support was provided by the European projects CIRCUIT and BIM4CE. The authors sincerely acknowledge all individuals and institutions involved in various phases of the research.

## REFERENCES

- [1] C.S. Pettigrew, P.J. Barr, M. Maguire, and M.W. Halling, Behavior of 48-year-old double-tee bridge girders made with lightweight concrete, *Journal of Bridge Engineering*, Volume 21, Issue 9, 2016.
- [2] A. Znidarič, F. Moses, and M. Ghosn, System behavior of post-tensioned beam bridges – an experimental study, in *Structural Safety and Reliability*, Corotis et al. (eds.), *ICOSSAR '01*. 8th International Conference on Structural Safety and Reliability, Newport Beach, California, USA, 17-21 June 2001.
- [3] P. Savino, F. Tondolo, D. Sabia, A. Quattrone, F. Biondini, G. Rosati, M. Anghileri, and B. Chiaia, Large-scale experimental static testing on 50-year-old prestressed concrete bridge girders, *Applied Sciences*, vol. 13, 2023.
- [4] DEWESoft, “DEWESoft IOLITEi 3xMEMS-ACC.” [Online]. Available: <https://dewesoft.com/products/iolitei-3xmems>
- [5] DEWESoft, “Dewesoft ARTEMIS OMA software.” [Online]. Available: <https://dewesoft.com/blog/announcing-the-new-dewesoft-artemis-oma-solution>
- [6] Vidya Sagar, R., and B. K. Raghu Prasad. 2013. “Laboratory investigations on cracking in reinforced concrete beams using on-line acoustic emission monitoring technique.” *J. Civ. Struct. Heal. Monit.*, 3 (3): 169–186. <https://doi.org/10.1007/s13349-013-0036-5>.
- [7] Elbatanouny, M. K., P. H. Ziehl, A. Larosche, J. Mangual, F. Matta, and A. Nanni. 2014. “Acoustic emission monitoring for assessment of prestressed concrete beams.” *Constr. Build. Mater.*, 58: 46–53. Elsevier Ltd. <https://doi.org/10.1016/j.conbuildmat.2014.01.100>.

## Investigation of the causes of the unusual gap between the bridge and abutment using long-term monitoring

Sunao Iwabuchi<sup>1</sup>, Tomohisa Takehara<sup>1</sup>, Yasunori Miyamori<sup>2</sup>, 0000-0003-2686-8062, Takanori Kadota<sup>3</sup>, 0009-0008-1645-3078, Yoichi Hinata<sup>4</sup>, Toshiyuki Oshima<sup>3</sup>

<sup>1</sup>Koken Engineering Co., Ltd., 1-1, Kita 4, Higashi 4, Chuo-ku, Sapporo, Hokkaido, 060-0034, Japan

<sup>2</sup>Hokkaido University, Kita 13, Nishi 8, Kita-ku, Sapporo, Hokkaido, 060-8628, Japan

<sup>3</sup>Kitami Institute of Technology, 165, Koen-cho, Kitami, Hokkaido, 090-8507, Japan

<sup>4</sup>Nihon Kasetu Co., Ltd., 6-50, 16-14, Hassamu, Nishi-ku, Sapporo, Hokkaido, 063-0836, Japan

email: s.iwabuchi@koken-e.co.jp, t.takehara@koken-e.co.jp, miyamori.y@eng.hokudai.ac.jp, kadotaka@mail.kitami-it.ac.jp, hinata@nihonkasetu.co.jp, t-oshima@iea.att.ne.jp

**ABSTRACT:** Unusual gaps at the ends of bridge girders can occur due to the displacement of abutments or insufficient initial gaps during construction. However, when such irregularities arise, it is difficult to estimate the cause through visual inspection alone. As analyses on the causes of these gaps and their expansion are needed, investigations into appropriate remedial measures have become important. For these analyses, we developed a device called the Expansion-Gap Measurement System (EGMS), which enables the causes of unusual gaps to be estimated based on continuous monitoring for temperature-related changes in gap distance. By capturing seasonal variations in gap distance, the system allows us to estimate the progression in abutment movement and the causes of damage. This paper presents the case study of a simple bridge made with H-shaped steel girders with unusual gaps where the EGMS was installed for approximately three years to investigate the causes of a gap. It was found that during the high-temperature summer months, the gap closed completely, whereas in winter, the gap remained. Furthermore, it was confirmed that the abutment saw no lateral movement during the winter, indicating the minimal progression of displacement. Based on these findings, the cause of the unusual gap was attributed to either an error in the abutment's initial placement during construction or to previous lateral displacement of the abutment.

**KEY WORDS:** Unusual expansion gap; Expansion-Gap Measurement System; Long-term monitoring; Girder bridge.

### 1 INTRODUCTION

At bridge girder ends, cases where the main girder is in contact with the abutment have been frequently observed [1]. This phenomenon is a type of damage known as 'an unusual gap', which occurs when there is insufficient clearance to accommodate the temperature-related expansion and contraction of the main girder. As a result, unexpected and harmful axial forces develop in the main girder. Additionally, it is suspected that some form of horizontal displacement is occurring in the substructure.

The horizontal displacement of the substructure can arise from various causes, and in some cases, it may continue over time. If such displacement persists, the restoration of the gap will be done by cutting off the end of the main girder to shorten, but it may lead to the recurrence of the unusual gap. Therefore, it is crucial to identify the cause of the substructure's horizontal displacement, to assess its persistence, and to formulate an appropriate repair strategy for the unusual gap.

However, identification of the cause of horizontal displacement in the substructure is not straightforward. When such displacement is suspected, typical approaches to determine the cause are to investigate the ground and foundation conditions. This process often requires geological investigations, such as boring surveys, but it can be costly. Generally, it is difficult to estimate the cause of horizontal displacement solely through visual inspections.

To address this issue, the authors have developed the Expansion-Gap Measurement System (EGMS) for girders [2]. This system continuously measures the gap distance and the temperature of the main girder, enabling the cause of horizontal

displacement in the substructure to be estimated. The details of the EGMS are described in Chapter 2.

In this study, in order to verify the effectiveness of the EGMS, we installed the system on a simple steel girder bridge composed of H-shaped steel where an unusual gap had been observed. Over the course of approximately three years, we used the EGMS to determine the cause of the unusual gap.

### 2 OVERVIEW OF THE EXPANSION-GAP MEASUREMENT SYSTEM (EGMS) FOR GIRDERS

#### 2.1 Configuration of the EGMS

The EGMS for girders primarily consists of linear displacement sensors and thermometer installed at the gap section. Figure 1 provides an overview of the EGMS. The linear displacement sensors are placed on the upper and lower sections of the main girder to continuously measure the gap distance at each location. These sensors can detect changes in the gap distance caused by the temperature-induced expansion and contraction of the main girder. Additionally, the thermometer attached to the main girder provides data for calculations on the theoretical expansion/contraction amount and the corresponding gap distance.

The collected data is stored in a data logger for retrieval approximately once every two months. Since the data logger supports wireless data transfer, data can be collected from the bridge deck even if the data logger is installed underneath the main girder. The system is powered by either a solar battery or an 12V deep-cycle battery. A DC/DC converter is used to adjust the voltage to 5V, which is required for the linear displacement sensors and other components. The data logger,

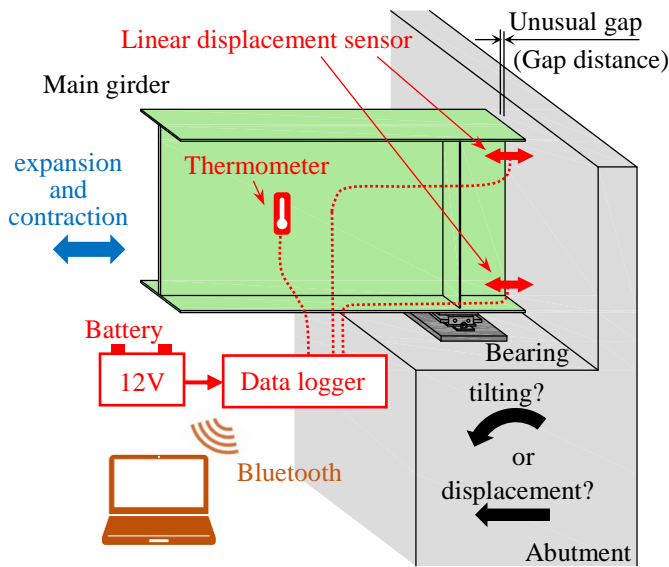


Figure 1. Overview of the EGMS.

battery, and DC/DC converter are housed in a compact, insulated box (approximately  $15 \times 25 \times 20$  cm) for protection.

Additionally, to verify the system's performance in cold environments, an operational test was conducted at  $-35^\circ\text{C}$  [3]. The system was confirmed to function properly even at extremely low temperatures.

The system is designed to determine the cause of unusual gaps simply and efficiently, without relying on large-scale equipment. As described above, it is composed of readily available devices.

## 2.2 Causes of Deformations Determined by the EGMS

In the EGMS, the gap distance at both the upper and lower sections of the main girder at each support, together with the temperature of the main girder, are continuously measured. Since the system records the temperature of the main girder, the theoretical gap distance at each support can be calculated (Figure 2(a)). At the same time, the EGMS measures the actual gap distance at the upper and lower sections of the main girder, allowing for a comparison between the theoretical and actual gap distance.

For example, in the case of a simple girder, if the gap distance becomes 0 mm during summer, when the main girder temperature is high, and recovers in winter, when the temperature is low (Figure 2(b)), then it can be assumed that the abutments remain stationary and that the gap reduction is stable due to an initially insufficient clearance between the abutments. In such a case, cutting off the end of the main girder would prevent further reductions in gap distance.

On the other hand, if one of the abutments (fixed bearing) undergoes horizontal displacement and continuously pushes the superstructure, the gap distance at the movable bearing remains 0 mm regardless of temperature changes (Figure 2(c)).

Additionally, if tilting occurs, a difference in the gap distance between the upper and lower sections of the main girder can be expected. In this scenario, since the horizontal displacement of the abutment is ongoing, cutting off the end of the main girder would lead to another reduction in the gap distance. Therefore, measures to stop the horizontal displacement of the abutment

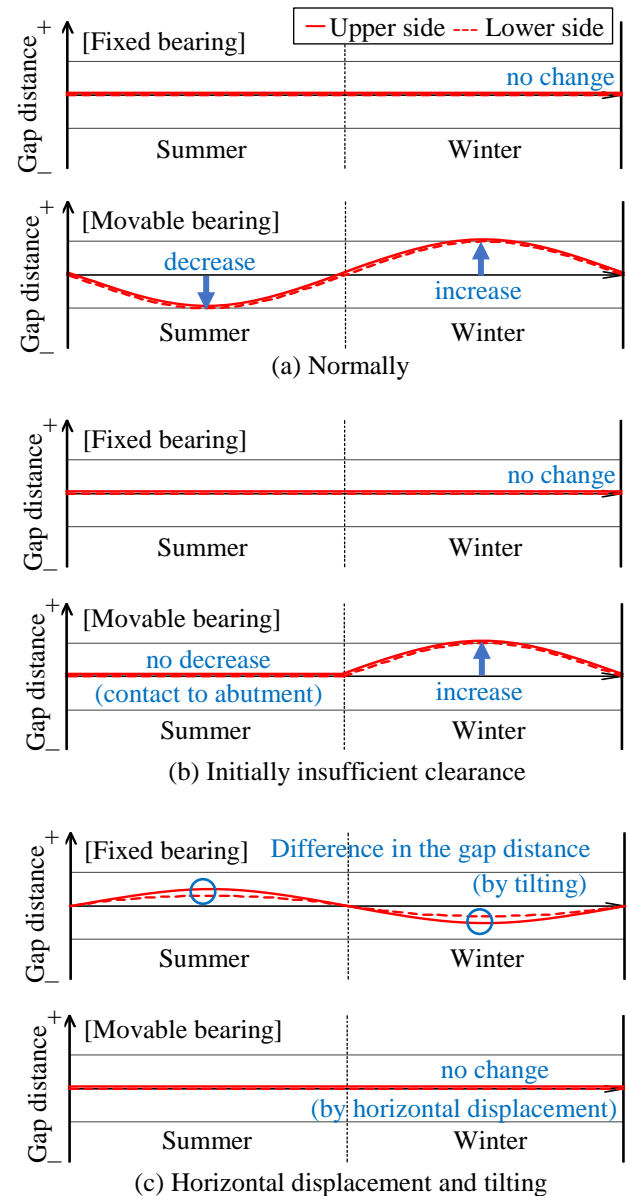


Figure 2. Example of theoretical and actual gap distance of a simple girder.

are necessary.

Although based on a classical approach, the Expansion-Gap Measurement System for girders enables the determination of the cause of unusual gaps by analyzing the horizontal displacement of the substructure. Furthermore, it facilitates the development of an appropriate repair strategy.

## 3 OVERVIEW OF EGMS INSTALLATION

### 3.1 Bridge Covered by the Study

Figure 3 provides an overview of the bridge investigated in this study. The target bridge is a simply supported non-composite H-shaped steel girder bridge in Hokkaido, Japan, with a total length of 14.6 meters. Each of the four main girders has the dimensions of  $H800 \times 300 \times 14 \times 26$  mm. The deck is a 19 cm-thick reinforced concrete slab with a 70 mm-thick asphalt pavement. The abutments are of the reversed T type and are



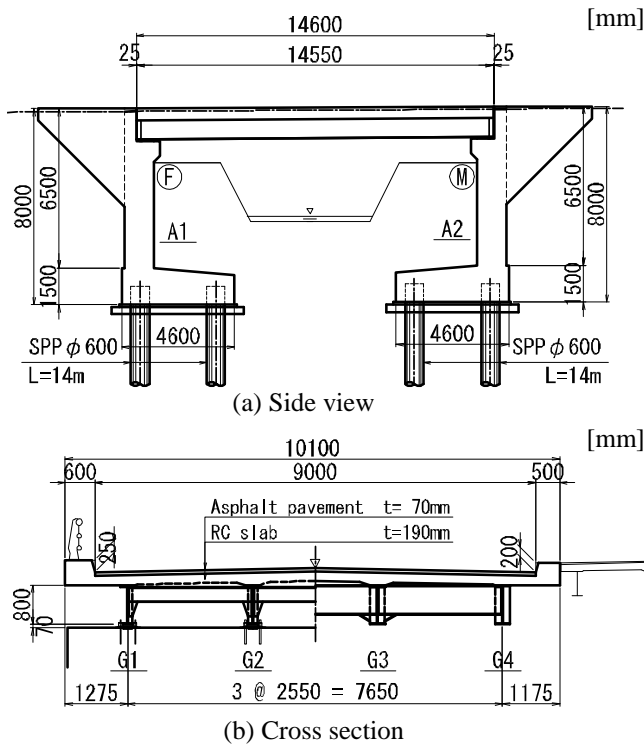


Figure 3. Overview of the target bridge.

constructed of concrete. The foundation consists of six steel pipe piles each with a diameter of 600 mm and a length of 14 meters. The lowest winter temperature in the region where the bridge is located is approximately  $-30^{\circ}\text{C}$  [4].

Regarding the ground conditions, the soil to a depth of 4 m below the road surface consists of a gravel layer with an N-value of approximately 10. Below this, from the depth of 4 to 18 m, clay layers with N-values ranging from 2 to 11 are distributed. Beneath the clay layers, a sandy layer with an N-value of 30 or higher (bearing layer) is present. According to the design drawings, the pile foundation reaches the bearing layer.

The bridge was completed in 1971, but a periodic inspection in 2012 found the gap at both abutments to be 0 mm. However, there were no indications of lateral movement, and the cause of the unusual gap remained unknown, posing challenges to the selection of appropriate remedial measures.

### 3.2 Installation Status of the EGMS

Figure 4 illustrates the installation locations of the EGMS for girders. The linear displacement sensors were installed at both the upper and lower sections of the girder ends on the north-side main girder (the G4 girder), with one sensor placed at each location. These sensors exhibited a measurement range of 50 mm, with an accuracy of  $\pm 0.3\%$  at full scale. Figure 5 shows the installation of the linear displacement sensors. Additionally, a thermometer was installed on the web of the G4 girder to measure the temperature of the main girder. Various devices, including the data logger, were installed on the bearing seat surfaces of each abutment.

The measurement interval for the gap distance and the temperature was set to 30 minutes. Continuous measurements were conducted from September 30, 2021, to October 21, 2024.

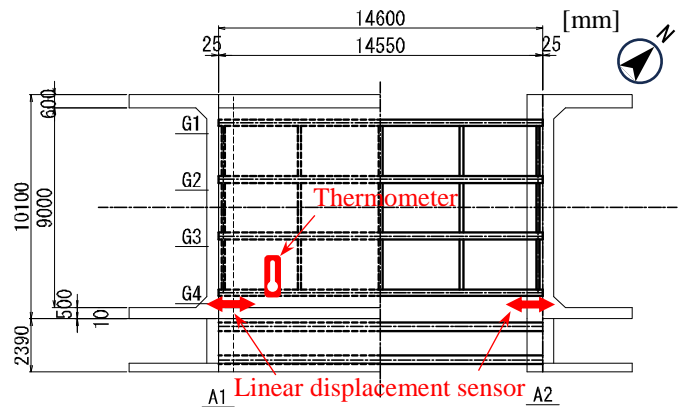


Figure 4. EGMS installation locations.

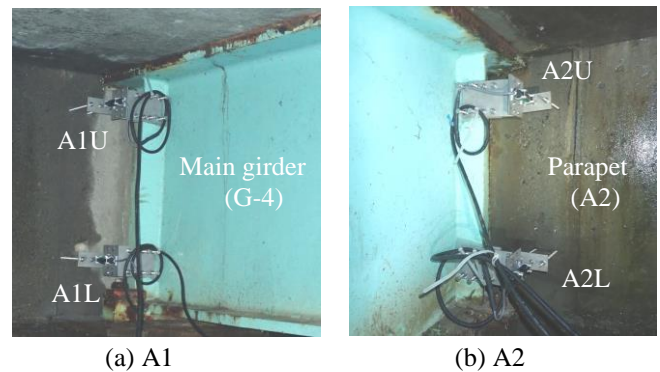


Figure 5. Installation status of the linear displacement sensors.

## 4 MEASUREMENT RESULTS AND DISCUSSION

### 4.1 Gap Distance Measurement at the Fixed Bearing

Figure 6 shows the measured gap distance at the A1 abutment, which serves as the fixed bearing. The gap distance is displayed with the initial measurement value set to 0 mm. Figure 6 also includes the temperature of the main girder for reference.

At the fixed bearing, the variation in gap distance was minimal, remaining within the range of  $\pm 0.7$  mm. Since the bearing at the fixed support has a 2 mm clearance, it is presumed that movement within this range occurred at the bearing. This confirms that the fixed bearing is functioning properly.

On the other hand, a difference in gap distance between the upper and lower sections of the main girder was observed over time. This discrepancy suggests that the abutment may have tilted. Therefore, a more detailed investigation of this issue is conducted in Section 4.5.

### 4.2 Gap Distance Measured at the Movable Bearing

Figure 7 shows the measured gap distance at the A2 abutment, which serves as the movable bearing. As for the A1 side, the gap size is displayed with the initial measurement value set to 0 mm. The temperature of the main girder is shown as a blue line, while the theoretical gap distance, calculated based on the girder temperature, is indicated in gray.

At the movable bearing, significant variations in the gap distance are observed in response to temperature changes. During the winter, when temperatures were low, the main girder contracted, and the measured gap distance closely

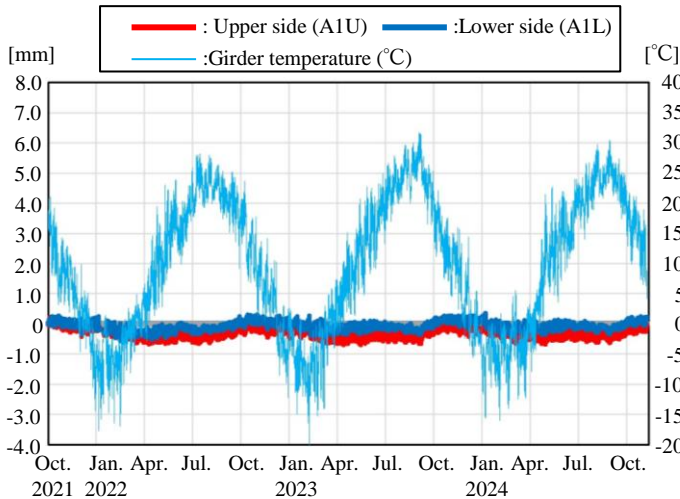


Figure 6. Variation in clearance (A1 abutment).

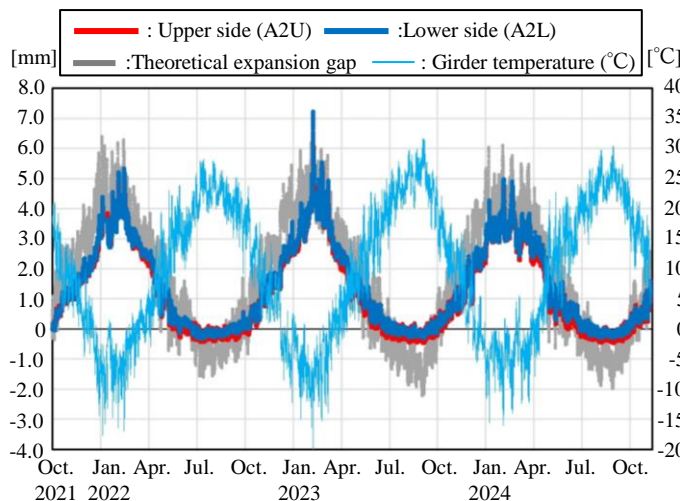


Figure 7. Variation in clearance (A2 abutment).

matched the theoretical gap distance. In the summer, when the temperatures were high, the gap distance decreased. However, the gap reduction was less than the theoretical value. Onsite inspection confirmed that the main girder was in contact with the abutment parapet. A more detailed investigation into the gap distance behavior during warmer periods is discussed in Section 4.6.

### 4.3 Temperature Measurements

To verify the accuracy of the temperatures measured by the thermometer installed on the main girder, a comparison was made with the temperatures recorded by thermometer at a nearby station of the Japan Meteorological Agency's Automated Meteorological Data Acquisition System (AMeDAS) [4]. Figure 8 presents this comparison. The bridge and the AMeDAS thermometer are approximately 15 km apart.

As shown in Figure 8, the temperature measured by the thermometer on the main girder closely approximates the temperature recorded at the AMeDAS station. However, the temperature variations observed on the main girder are smaller than those recorded by AMeDAS. This is likely due to the fact that the main girder is made of steel, which takes time to

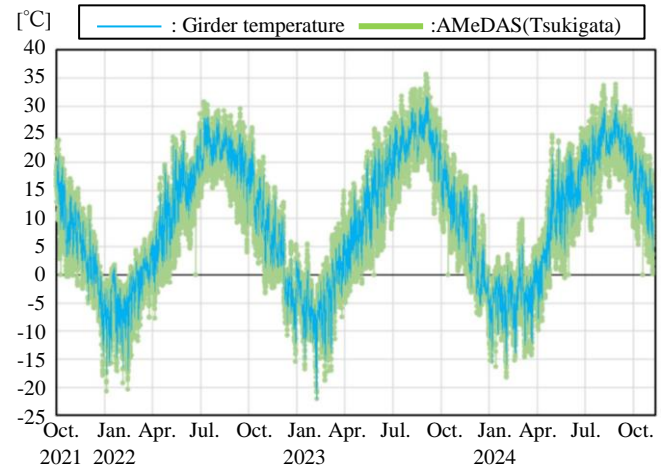


Figure 8. Comparison of temperatures measured at the main girder with those measured by nearby thermometer.

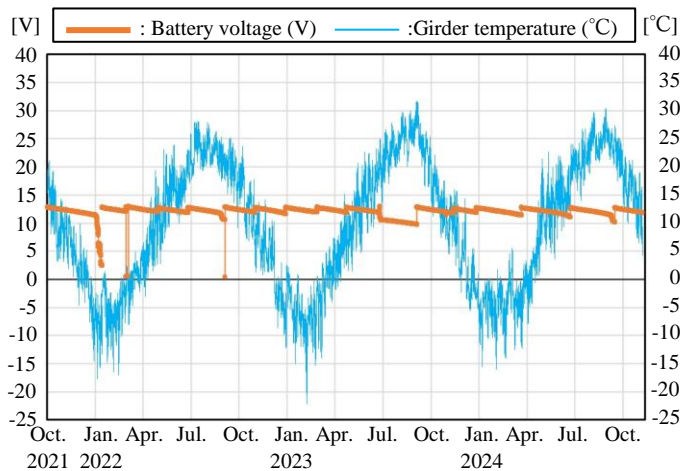


Figure 9. Battery voltage variation (A1 abutment).

respond to changes in ambient temperature. Since the measured values were generally consistent with the nearby temperature data, the measurement results are considered valid.

### 4.4 Transition of Battery Voltage

The battery used for the displacement sensors may experience voltage drops at low temperatures. Since the displacement sensors output data based on voltage, a drop in input voltage makes accurate displacement measurements difficult. Therefore, the battery voltage was also monitored. Figure 9 shows the changes in the voltage of the battery installed in the system at the A1 abutment.

The battery voltage decreases due to system operation, so periodic replacements were planned. However, at the end of 2021, the battery voltage dropped sharply, causing the system to shut down. This was attributed to power consumption by the system and to the cold temperatures. Therefore, from 2022 onward, the battery was replaced approximately every two months to prevent system shutdowns.

Except for the period at the end of 2021, the battery voltage remained above 10 volts. Since the 5 volts that is required to operate the displacement sensors and other components was maintained, the gap measurements obtained by the system were

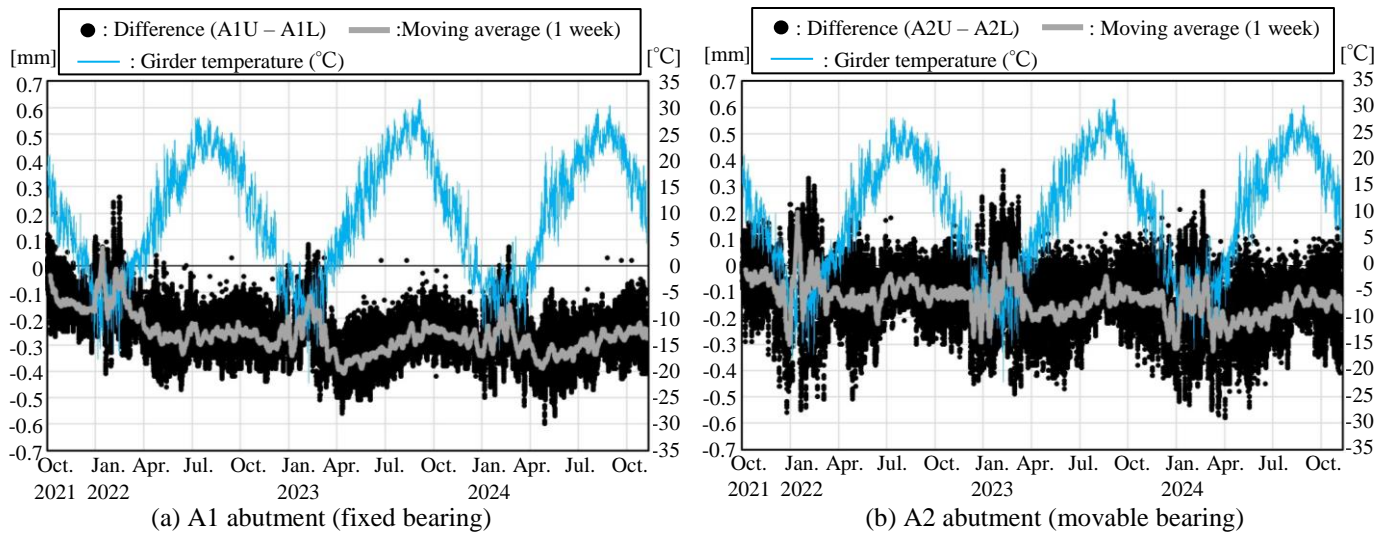


Figure 10. Variation in the difference of clearance between the upper and lower parts of the main girder.

confirmed to be accurate. Additionally, by replacing the battery regularly, it was confirmed that this system can be applied even in cold environments where temperatures drop below  $-20^{\circ}\text{C}$ .

#### 4.5 Evaluation of the Abutment Inclination using the Difference Between the Upper and Lower Displacement Sensors

To investigate the cause of the difference in gap distance between the upper and lower segments of the main girder at the fixed bearing over time, Figure 10 illustrates the transition of that difference for each abutment.

As shown in Figure 10a, at the A1 abutment (the fixed bearing), the difference became negative and that negative difference continued to increase over time. It is noted that the difference fluctuated significantly during the cold winter season, likely due to girder deflection caused by snow accumulation and the impact of snow removal. In contrast, the change in the difference at the A2 abutment (the movable bearing) remained minimal.

Referring to Figure 6, while the lower gap distance of the main girder remained around 0 mm, the upper gap distance showed a decreasing trend. This indicates that the increase in negative difference is caused by a decrease in the upper gap distance. Since the lower gap distance remained unchanged while the upper gap distance decreased, it is assumed that the A1 abutment is tilting toward the main girder. Therefore, it is presumed that the cause of the unusual gap lies in the A1 abutment.

However, since the decrease in the upper gap measurement was approximately 0.5 mm over three years, it is considered to have no immediate impact on the safety of the bridge.

#### 4.6 Determination of Damage Causes Using the Correlation Between Temperature and Gap Distance

To examine in detail the condition of girder gaps during periods of rising temperatures, Figure 11 shows graphs for each linear displacement gauge, with temperature on the horizontal axis and gap displacement on the vertical axis. To show the transition of gap distance, data points are color-coded by year,

and the theoretical gap distance is represented in gray.

At the A1 abutment (the fixed bearing) (Figures 11a and 11b), the gap distance fluctuates within the range of  $\pm 0.4$  mm regardless of temperature. Additionally, while the gap distance of the lower segment of the girder changes linearly with temperature, no distinct trend is observed in the upper segment. This is likely because the lower segment primarily undergoes thermal expansion and contraction due to the steel material of the girder, whereas the upper segment is constrained by the concrete deck, which has a different specific heat capacity. However, since the overall variation in displacement is small, it is confirmed that the A1 abutment is functioning as a fixed bearing.

At the A2 abutment (the movable bearing), it is observed that the gap distance increases as the temperature decreases. However, when the temperature exceeds  $15^{\circ}\text{C}$ , the decrease in displacement plateaus. The difference between the theoretical and measured gap distances increases, and at  $30^{\circ}\text{C}$ , this discrepancy reaches approximately 2 mm.

Since gap distance is maintained during periods of temperature decrease at the A2 abutment, it is unlikely that the abutment is consistently leaning against the girder. In contrast, as noted in Section 4.5, a slight tilt was observed at the A1 abutment. This suggests that one possible cause of the unusual gap is the gradual tilting of the A1 abutment after the bridge was completed. However, since no significant inclination is visible on the front of the abutment, another potential cause could be past abutment movement or an insufficient distance between abutments during construction.

In any case, since no ongoing horizontal displacement of the abutments was detected and the average annual tilt of the upper part of the A1 abutment is approximately 0.1 mm, cutting off the girder ends is expected to be effective in preventing axial force from being input into the main girder.

## 5 CONCLUSION

We have presented a case study in which the authors utilized their Expansion-Gap Measurement System (EGMS) for girders to identify the cause of unusual girder gaps in a simple steel



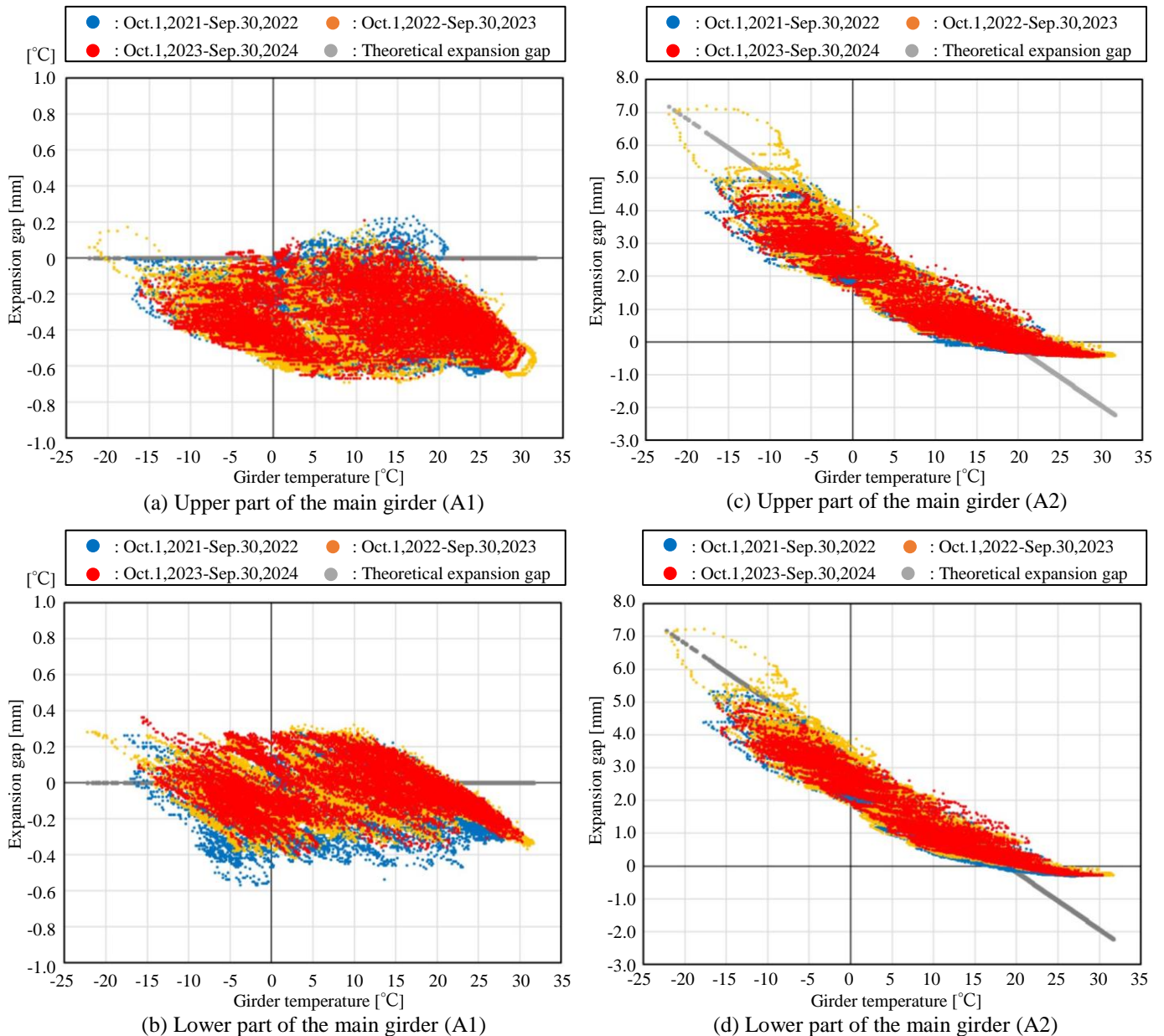


Figure 11. Relationship between temperature variation and clearance.

girder bridge composed of H-shaped steel. The following findings were obtained.

- (1) The EGMS enables the long-term monitoring of girder gap variations.
- (2) In the investigated bridge, the A1 abutment was found to be tilting toward the main girder, suggesting that the cause of the unusual gap lies in the A1 abutment.
- (3) As the temperature rises, the gap displacement at the A2 abutment decreases, and when the girder temperature reaches 30°C, the difference between the theoretical and measured gap distance is approximately 2 mm. Since the tilt of the A1 abutment on this bridge is gradual, cutting off the girder ends is considered effective to prevent axial force from acting on the main girder.

## ACKNOWLEDGMENTS

We would like to express my appreciation to the Hokkaido Regional Development Bureau for kindly providing the field for this study. We would also like to extend my gratitude to Mr. Takuya Nitta of Nihon Kasetsu Co., Ltd. for his assistance in the installation and adjustment of the equipment.

## REFERENCES

- [1] National Institute for Land and Infrastructure Management Ministry of Land, Infrastructure, Transport and Tourism, Japan, Reference to MLIT's Bridge Inspection Manual, 2013 (in Japanese).
- [2] T. Takehara, Diagnostic Device and Method for Bridges with Unusual Gaps, Japan Patent JP2020-094475, Japan, 2020.
- [3] S. Iwabuchi, Y. Miyamori, T. Takehara, T. Saito, Y. Hinata and T. Oshima, Performance test at low temperature of the Expansion Gap Observation System, 76th Proceedings of the Annual Conference of the Japan Society of Civil Engineers, 2021 (in Japanese).
- [4] Japan Meteorological Agency, Past weather data, <https://www.data.jma.go.jp/stats/etrn/index..>

## Monitoring the dynamic sensitivity of the Solkan footbridge to user-induced excitation

Mirko Kosič<sup>1</sup>, ORCID 0000-0001-8543-8009, Doron Hekić<sup>2</sup>, ORCID 0000-0001-5667-9129, Izabela Joanna Drygala<sup>2</sup>, ORCID 0000-0003-2051-0318

<sup>1</sup>Slovenian National Building and Civil Engineering Institute (ZAG), Dimičeva ulica 12, 1000 Ljubljana, Slovenia

<sup>2</sup>Cracow University of Technology, Faculty of Civil Engineering, Warszawska 24, 31-155 Krakow, Poland

email: [mirko.kosic@zag.si](mailto:mirko.kosic@zag.si), [doron.hekic@zag.si](mailto:doron.hekic@zag.si), [izabela.drygala@pk.edu.pl](mailto:izabela.drygala@pk.edu.pl)

**ABSTRACT:** This paper presents a comprehensive monitoring study of the dynamic sensitivity of the Solkan footbridge in Slovenia, with a focus on its response to user-induced actions. An extensive ambient vibration measurement campaign was carried out, during which 26 triaxial accelerometers were strategically deployed along the bridge to capture its modal characteristics in all three spatial directions. The structure's dynamic response was monitored under both regular pedestrian traffic and elevated loading conditions during a local marathon event, allowing for the assessment of its behaviour across a broad spectrum of real-world scenarios. Preliminary measurements revealed reduced pedestrian comfort, primarily due to resonance effects resulting from bridge–user interaction. The study highlights the importance of field-based dynamic assessments in diagnosing performance issues and informing mitigation strategies. The findings contribute to the advancement of resilient and dynamically efficient design and maintenance practices for pedestrian bridges.

**KEY WORDS:** Modal model validation; Footbridges; Ambient vibrations; Dynamic sensitivity; User-induced excitation.

### 1 INTRODUCTION

Pedestrian footbridges are particularly challenging structures to design due to their pronounced susceptibility to dynamic issues resulting from bridge–user interaction [1]. These interactions can lead to serviceability concerns such as excessive vibrations, which in turn affect user comfort and, in some cases, may even raise long-term durability concerns [2] [3]. Addressing these challenges requires going beyond conventional static checks and incorporating advanced dynamic analyses aimed at identifying and mitigating resonance-related problems [4].

Current standards and guidelines provide recommendations for the frequency ranges typically excited by pedestrians and runners and require dynamic analysis when a bridge's natural frequencies fall within these ranges [5-8]. The critical frequency range for vertical vibrations is between 1.5 and 3.5 Hz, while for horizontal vibrations, it is between 0.5 and 1.5 Hz [5]. According to Sétra guidelines [6], resonance risks are particularly high for vertical vibration frequencies between 1.7 and 2.1 Hz, and for horizontal vibration frequencies between 0.5 and 1.1 Hz. To prevent resonance, the fundamental frequencies of footbridges should ideally exceed these ranges. However, achieving this is often challenging in lightweight and flexible structures, such as suspension or cable-stayed footbridges. Therefore, detailed dynamic assessments are essential to ensure acceptable levels of pedestrian comfort. For instance, Eurocode [7,8] mandates dynamic analysis for footbridges with predominant vertical frequency below 5 Hz and horizontal frequency below 2.5 Hz.

Given the complexity of structural dynamic response, post-construction measurements are crucial to verify performance in real-world conditions. Ambient vibration testing, combined with operational modal analysis (OMA), offers a non-invasive and effective means of identifying a bridge's dynamic characteristics [2]. These data can be used to calibrate

numerical models and support robust methodologies for evaluating and improving dynamic performance.

In addition to typical service conditions, there is growing recognition of the need to monitor the structural response of footbridges under extreme user-generated actions, such as dense crowds, synchronized movements, or dynamic events like running or jumping. Long-term dynamic structural health monitoring (SHM) enables the detection of changes in modal properties, transient amplification effects, and possible structural degradation under such rare but critical loading scenarios. Integrating SHM strategies into bridge management enhances safety, informs maintenance decisions, and supports the development of resilient infrastructure that can withstand both everyday usage and exceptional dynamic demands.

This paper investigates the dynamic behaviour of a pedestrian footbridge spanning the Soča River in Slovenia, which has shown reduced pedestrian comfort during regular use. The bridge's dynamic response and its sensitivity to user-induced excitation are evaluated through an experimental monitoring campaign utilising strategically placed triaxial accelerometers [9].

### 2 METHODOLOGY

#### 2.1 Bridge description

The Solkan footbridge is a single-span cable-stayed suspension structure crossing the Soča River in Slovenia with total span 120.0 m (see Fig. 1). It features an open-section steel deck suspended from two main parabolic steel cables anchored on both riverbanks. The main cables are supported by two steel A-shaped pylons mounted on reinforced concrete abutments. Vertical hangers, spaced at 6.0-meter intervals, connect the deck to the main cables. The deck is additionally laterally and longitudinally stabilised by a parabolic cable anchored to the abutments, along with four straight bracing cables attached at one-quarter of the span length from each end. The deck is

supported at both ends by four elastomeric bearings, two of which allow for longitudinal movement to accommodate thermal expansion.

The material of the pylons is S235 steel according to EN-1993-1-1, while the material of all deck members is S355 steel. The cables are constructed with high-strength steel ropes with tension strength  $f_u = 1500$  MPa and modulus of elasticity  $E = 165$  GPa. The cross-section and material characteristics of the bridge are summarized in Figure 1. Footbridge over the Soča River (Slovenia).

Table 1.



Figure 1. Footbridge over the Soča River (Slovenia).

Table 1. Characteristics of footbridge's structural parts (FLC – Full Coil Rope, OSS – Open Spiral Strands,  $D$  - Outside diameter,  $t_w$  - Wall thickness)

Element	Property	Material
Main cables	FLC, $D = 72$ mm	High-strength steel
Hangers	FLC, $D = 16$ mm	High-strength steel
Stabilising parabolic cables	FLC, $D = 60$ mm	High-strength steel
Stabilising straight cables	FLC, $D = 38$ mm	High-strength steel
Connecting cables	OSS, $D = 12$ mm	High-strength steel
Pylon (legs)	Circular hollow section, $D/t_w = 355/10$ mm	S235
Pylon (traverse)	Hollow circular section, $D/t_w = 254/10$ mm	S235
Long. girders	IPE400	S355
Trans. girders	IPE270	S355
Bracing diagonals	IPE200	S355

## 2.2 Concept of investigation

The experimental campaign aimed at investigating the bridge's dynamic characteristics and its sensitivity to user-induced loads was conducted in November 2024. The measurements included:

- ambient vibration measurements,
- controlled pedestrian loading tests to assess its dynamic performance under user-induced excitation,
- monitoring of the bridge's response during a marathon event, to evaluate its behaviour under dense, real-world extreme pedestrian traffic.

Under controlled pedestrian loadings, the program included pedestrian sweeps, running, and synchronized marching tests with both small and large groups. This methodology allowed for evaluating the structure's general susceptibility to user-induced excitations.

Overall, the investigation was guided by two primary objectives:

- identification of the structure's modal properties,
- evaluation of the bridge's dynamic sensitivity to user-induced excitation.

## 3 MODAL MODELS

### 3.1 Monitoring setup

The footbridge's reference modal model was established based on experimental data obtained through ambient vibration measurements. For this purpose, the acceleration response of the bridge was recorded at multiple control points distributed across the structure. In total, 26 accelerometers were used in the campaign. Measurements were taken in all three global directions at each control point, with a sampling rate of 500 Hz. The sample of the measured acceleration signals consists of 1 hour of ambient vibration data. A representative control point with a tri-axial accelerometer is depicted in Figure 2.



Figure 2. Representative control point.

The measuring system was composed of twelve MonoDAQ-E-gMeter MEMS accelerometers and fourteen IOLITEi-3xMEMS-ACC accelerometers, both connected with EtherCAT cables to an industrial PC running the DewesoftX acquisition system. Both types of sensors are triaxial accelerometers, featuring low-noise performance (96 dB dynamic range and  $25 \mu\text{g}/\sqrt{\text{Hz}}$  spectral noise density), integrated data acquisition, and EtherCAT connectivity. The MonoDAQ-E-gMeters were mounted on aluminium plates and were attached to the deck's transverse girders via magnets, while the IOLITEi-3xMEMS-ACC were attached to steel tripods and were placed directly on the bridge deck.



Data acquisition and initial processing were carried out using DewesoftX software, which enabled signal recording, real-time analysis, and visualization. The collected data were subsequently exported for further analysis in FlexPro, Simcenter Testlab (LMS Test.Lab), and Dewesoft Artemis OMA, supporting both time- and frequency-domain evaluations.

### 3.2 Experimental modal models of the footbridge

Based on data collected during ambient vibration monitoring, the modal models of the footbridge were extracted using methods belonging to two main methodological groups that are strongly oriented towards OMA, namely [9]:

- Frequency Domain Decomposition (FDD),
- Stochastic Subspace Identification (SSI).

Accordingly, the following approaches were compared: Enhanced Frequency Domain Decomposition (EFDD), Curve-fit Frequency Domain Decomposition (CFDD), Unweighted Principal Component (SSI-UPC), and Extended Unweighted Principal Component (SSI-UPCX). Figure 3 presents an example of data recorded in the mid-span of the footbridge during ambient vibration testing, shown in the time-frequency domain. The experimental modal models were validated using the Modal Assurance Criterion (Eq. 1), with the AutoMAC matrix employed for this purpose [10].

$$MAC_{ij}(\psi_i^A, \psi_j^B) = \frac{(\{\psi_i^A\}^T \{\psi_j^B\})^2}{(\{\psi_i^A\}^T \{\psi_i^A\})(\{\psi_j^B\}^T \{\psi_j^B\})} \quad (1)$$

The modal models obtained from different identification techniques are summarized in Table 2. Figure 4 illustrates the 3D AutoMAC matrix for the SSI approach, and Figure 5 provides a comparison of the damping ratio estimates across the various methods.

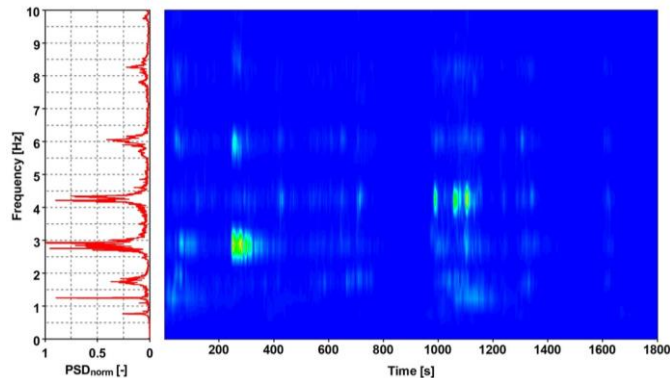


Figure 3. Acceleration and frequency time histories for ambient vibration (mid-span, vertical direction).

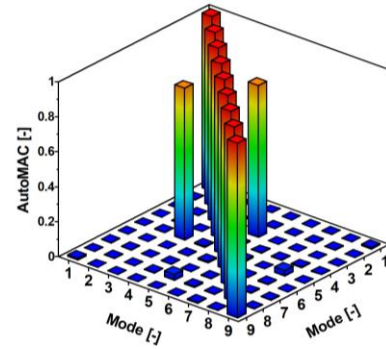


Figure 4. AutoMAC matrix for SSI OMA.

Table 2. Natural frequencies of the footbridge obtained with different OMA techniques.

Mode*	Frequency [Hz]			
	FDD	CFDD	EFDD	SSI
1V	0.574	0.570	0.569	0.571
2V	0.764	0.764	0.765	0.770
3H	0.847	0.843	0.843	0.844
4V	1.052	1.054	1.054	1.053
5H	1.096	1.096	1.097	1.098
6T	1.145	1.144	1.145	1.142
7V	1.743	1.740	1.741	1.735
8T	1.819	1.804	1.804	1.818
9V	2.202	2.196	2.201	2.194

V – vertical; H – horizontal; T – torsional

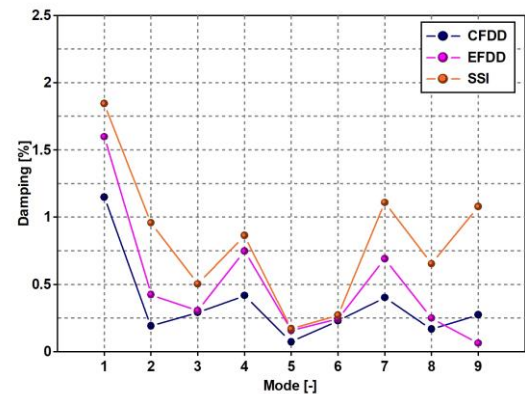


Figure 5. Damping ratios for the identified modes.

## 4 SENSITIVITY OF THE BRIDGE TO USER-INDUCED EXCITATION

### 4.1 Controlled pedestrian loading tests

The primary objective of the field tests involving pedestrians and runners was to evaluate the footbridge's susceptibility to resonance effects. Therefore, a series of experiments was carried out, during which various dynamic scenarios were considered, including walking and synchronized group movement, to identify critical excitation frequencies and assess the resulting vibration levels in different structural locations. The responses were evaluated using acceleration and frequency time histories obtained from Short-Time Fourier Transform (STFT) analysis with a window size of 0.54 s and 50% overlap.

Based on dynamic responses, a series of resonant frequencies induced by various human activities were observed. In the random walk case, the dominant response frequency in the horizontal direction was 0.84 Hz (see Fig. 6b). This resonance was exciting by walking-induced dynamic loading at a frequency of 1.64 Hz in the vertical direction, as shown in Fig. 6a. This suggests that the excitation falls within the resonance range of the first horizontal mode, which also contributes to the vertical response, particularly evident in the 7V mode (see Tab. 2). The excitation frequency (1.64 Hz) corresponds to approximately 95% of the mode's natural frequency (1.74 Hz). This is a significant observation, as both the 1.64 Hz and 0.84 Hz components originate from the same pedestrian passage, corresponding to the vertical and horizontal components of the walking-induced forces, respectively.

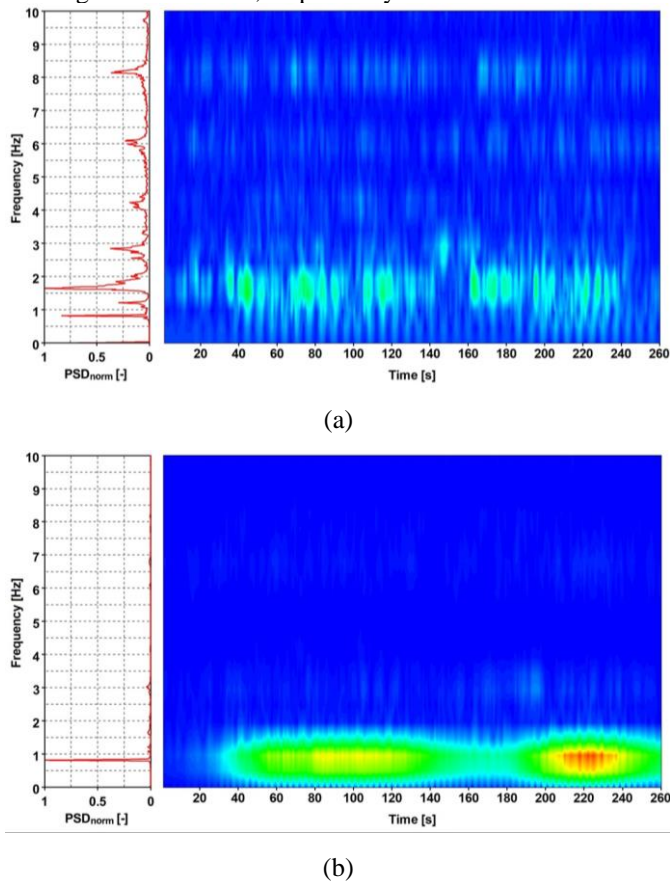


Figure 6. Acceleration and frequency time histories for random walking (mid-span) for vertical (a) and (b) horizontal direction.

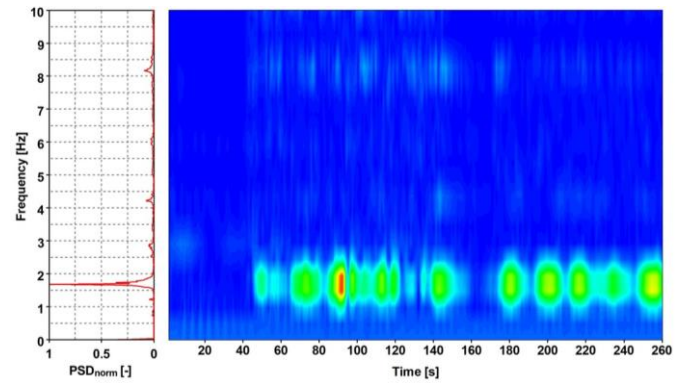


Figure 7. Acceleration and frequency time histories for marching group of people (mid-span, vertical direction).

Figure 8 presents the time-domain response recorded during the user-induced frequency sweep, ranging from 1.50 to 3.50 Hz. This was performed by three volunteers moving in synchrony, guided by a preprogrammed metronome recording. MP3 files with impulse sounds have been generated (intended to synchronize volunteers' stomping on the bridge). Each file contains a sweep of frequencies from 1.5 Hz to 3.5 Hz, in 0.1 Hz increments (i.e., 1.5, 1.6, 1.7, ..., 3.5 Hz), with smooth transitions between frequencies (no pauses) and an approximate total duration of 385 seconds.

The Short-Time Fourier Transform (STFT) analysis, represented in terms of normalized Power Spectral Density ( $PSD_{norm}$ ), revealed that several natural frequencies were excited over the course of the experiment, indicating a dynamic interaction between the excitation and the structure's modal characteristics. Notably, the most prominent response occurred in the frequency range between 0.8 and 1.70 Hz, which corresponds to the range of several resonant frequencies of the structure (3H to 7V, see Table 2). This suggests that the system exhibits a strong sensitivity to excitation near these frequencies. The largest amplification occurred at a frequency of approximately 1.2 Hz, which is close to the first torsional mode of the footbridge (6T). A clear amplification of the response in the range of resonant frequencies confirms the effectiveness of the frequency sweep in exciting the relevant modal behaviour.

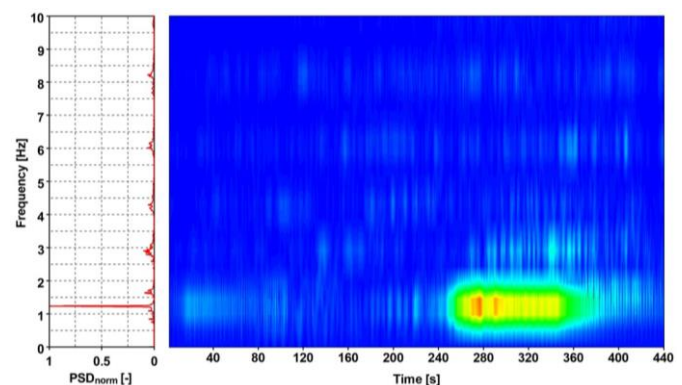


Figure 8. Acceleration and frequency time histories for user-induced frequency sweep (mid-span, vertical direction).

#### 4.2 Footbridge's response during a marathon event

The monitoring campaign also included continuous data acquisition during a marathon, allowing for the assessment of

the structure's dynamic behavior under dense pedestrian loading. Figure 9 presents the time-domain response recorded during the marathon at mid-span in the horizontal direction. STFT analysis revealed that several natural frequencies were excited during this large-scale social event, which represents an extreme loading scenario. This indicates a dynamic interaction between the excitation and the modal characteristics of the structure. The most significant response was observed at a frequency of approximately 1.10 Hz in the horizontal direction.

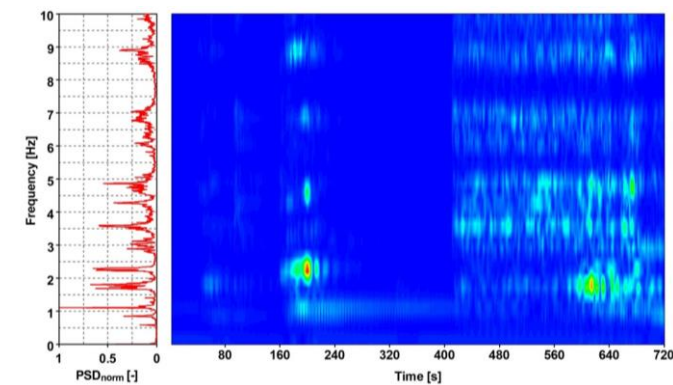


Figure 9. Acceleration and frequency time histories for marathon (mid-span, horizontal direction).

## 5 CONCLUSIONS

Based on the presented study, several key conclusions were drawn. Within the frequency range of 0–2.50 Hz, nine vibration modes were successfully identified. Among them, two modes belonged to the commonly recognized critical set for footbridges, including one vertical (1.74 Hz) and one horizontal mode (0.84 Hz), which suggests sensitivity of the bridge to user-induced excitation. Notably, both modes were excited by a single pedestrian passage, making the response particularly concerning. This is further amplified by the fact that the random walk scenario, responsible for triggering both modes, is the most frequent type of loading expected during regular bridge use. A high level of consistency was achieved across all developed modal models, with a mean error of less than 2%, confirming the reliability of the applied identification techniques.

The analysis of dynamic responses revealed a dominant resonant frequency of 1.64 Hz under both random walking and marching activities, indicating a strong excitation associated with the vertical component of pedestrian loading. Additionally, during random walking, a significant response was observed at 0.84 Hz, which corresponds to the horizontal component of the same excitation. These results demonstrate that human-induced vibrations can simultaneously activate multiple modal components of the structure. Furthermore, during the marathon event, extreme horizontal vibrations were recorded, to the extent that participants were unable to continue running across the footbridge. This highlights the severity of the dynamic response under real, large-scale crowd loading. The use of user-induced frequency sweeps during experimental testing proved to be an effective method for capturing a wide range of vibration modes and natural frequencies.

These findings underscore the importance of considering both vertical and horizontal components of pedestrian-induced

loading in the dynamic analysis, design, and safety assessment of footbridges. The observed variation in identified modal parameters across different load scenarios highlights the need to account for uncertainty in vibration-based evaluations. Future research should address this aspect more systematically by following established best practices in pedestrian bridge monitoring and incorporating statistical methods to quantify confidence levels in the extracted modal data.

## ACKNOWLEDGMENTS

The authors would like to acknowledge the support of the Municipality of Nova Gorica (Slovenia), Rok Mesar from the company Dewesoft (Slovenia), and Prof. Chiara Bedon, Marco Fasan and Michele Dilella from the University of Trieste (Italy) in the execution of the field measurements. The first and second authors would like to acknowledge the support of the Slovenian Research Agency, obtained through Research core funding No. P2-0273 and Infrastructure funding IO-0032.

## REFERENCES

- [1] H. Bachmann, 'Lively' footbridges – A real challenge, in: *Proceedings of Footbridge 2002*, 2002.
- [2] C. Bedon, I.J. Drygala, J.M. Dulinska, D. Jasinska, Application of optimized spring-mass-damper pedestrian load models for vibration assessment of footbridges: numerical and experimental investigation of a cable-stayed system, *Archives of Civil and Mechanical Engineering*, 25 (2025), 86.
- [3] X. Wei, J. Russell, S. Živanović, J.T. Mottram, Measured dynamic properties for FRP footbridges and their critical comparison against structures made of conventional construction materials, *Composite Structures*, 223 (2019), 110956.
- [4] C. Moutinho, A. Cunha, E. Caetano, J.M. Carvalho, Vibration control of a slender footbridge using passive and semiactive tuned mass dampers, *Structural Control and Health Monitoring*, 25 (2018).
- [5] International Organization for Standardization, ISO 10137:2007(E) – Bases for design of structures – Serviceability of buildings and walkways against vibrations, ISO, Geneva, Switzerland, 2007.
- [6] SETRA, Assessment of Vibrational Behaviour of Footbridges under Pedestrian Loading. Technical Guide, Technical Department for Transport, Roads and Bridges Engineering and Road Safety, Paris, France, 2006.
- [7] CEN, Eurocode 1: Actions on structures – Part 2: Traffic loads on bridges, European Committee for Standardization, Brussels, Belgium, 2003.
- [8] British Standards Institution, BS NA EN 1991-2: UK National Annex to Eurocode 1 – Actions on structures – Traffic loads on bridges, BSI, London, UK.
- [9] Structural Vibration Solution (SVIBS). ARTEMIS Modal. Operational Modal Analysis. Online: <https://www.svibs.com/operational-modal-analysis/>
- [10] D.J. Ewins, *Modal Testing: Theory, Practice and Application*, 2nd edition, Research Studies Press Ltd., Philadelphia, PA, USA, 2000.





## Monitoring applications using InSAR

# InSAR as a Component of Geotechnical Monitoring During Subway Construction in Prague

Ivana Hlaváčová<sup>1</sup>, <https://orcid.org/0000-0002-0620-2098>, Jan Kolomazník<sup>1</sup>, Juraj Struhár<sup>1</sup>, <https://orcid.org/0000-0001-6329-936X>, Erika Orlitová<sup>1</sup>

<sup>1</sup> Dept. of remote sensing, GISAT s.r.o. Prague, Czechia

email: [ivana.hlavacova@gisat.cz](mailto:ivana.hlavacova@gisat.cz), [jan.kolomaznik@gisat.cz](mailto:jan.kolomaznik@gisat.cz), [juraj.struhar@gisat.cz](mailto:juraj.struhar@gisat.cz), [erika.orlitova@gisat.cz](mailto:erika.orlitova@gisat.cz)

**ABSTRACT:** A new subway line is under construction in Prague, Czechia. The drilling and construction potentially affect the structural health of buildings and infrastructure in the zone of influence. As part of geotechnical monitoring for the Metro Line D construction, subsidence is monitored through satellite interferometry (InSAR). Measurements from TerraSAR-X/PAZ are analysed using a customised PS-InSAR algorithm to capture evolving deformation patterns during construction. In addition, several add-on methods have been developed to provide targeted trend analysis and geotechnically relevant metrics. The retrospective “passportization stage” has been followed by standard monitoring stages with adaptive stage duration and frequency of satellite acquisitions. The nonlinear characteristics of displacement trends present challenges for InSAR. Particularly in X-band data, phase unwrapping errors compromise spatial interpretation, elevate noise levels, and diminish the reliability of results. Issues are addressed by tailored enhancements to the InSAR methodology, including advanced time series segmentation considering statistically significant differences in displacement velocities or noise levels. Validation confirms strong agreement between displacement trends measured through InSAR and conventional geotechnical methods.

**KEY WORDS:** InSAR; Subway; Subsidence; Structural health.

## 1 INTRODUCTION

### 1.1 *MT-InSAR as a tool to monitor tunnel drilling impacts in an urban environment*

Urban tunnelling projects, particularly those involving mechanised excavation methods such as Tunnel Boring Machines (TBMs), are known to induce subsidence ground deformations that can compromise the structural integrity of buildings and infrastructures above the tunnel alignment. Monitoring and assessing these effects is crucial for mitigating risk in densely built environments. Interferometric Synthetic Aperture Radar (InSAR), particularly advanced multi-temporal techniques (MT-InSAR), has emerged as a reliable and cost-effective method for monitoring such deformations with millimetric precision over extensive spatial and temporal scales.

Recent studies have demonstrated the efficacy of InSAR in tracking surface displacements due to tunnelling activities in various urban contexts. For example, [1] utilised InSAR to monitor tunnel-induced ground movements and demonstrated its value in complementing conventional geotechnical instrumentation during tunnelling operations in Turin, Italy. Similarly, [2] applied InSAR to assess accumulated settlement related to highway tunnel construction in Genoa, Italy. The [3] showcased a novel integration of MT-InSAR and the relative stiffness method to assess structural damage during the London Crossrail project, highlighting the role of soil-structure interaction in deformation modelling. These approaches allow for better estimation of tensile strains and more accurate prediction of damage potential compared to greenfield assumptions.

The [4] emphasised the integration of InSAR in all phases of tunnelling—from planning to post-construction monitoring—noting its advantage in detecting both anticipated and unexpected deformations across large urban sectors. Meanwhile, [5] applied retrospective PSI analysis in East London during the Lee Tunnel construction, revealing previously undetected geotechnical anomalies and advocating for InSAR's role in early risk identification.

Beyond deformation detection, translating InSAR-derived ground displacement data into actionable insights for building vulnerability assessment is gaining traction. Damage level on buildings and infrastructure caused by subsidence depends on the asset's position in the subsidence bowl, displacement direction and magnitude [6]. The [7] and [8] successfully derived empirical fragility curves by correlating InSAR-derived displacements with in-situ damage surveys, enabling probabilistic assessments of structural risk across extensive building inventories. These methods have proven especially pertinent in older urban centres, where subsidence impacts are compounded by complex underground networks and historical constructions, such as in Madrid [9] and Pistoia [6].

### 1.2 *MT-InSAR supporting geotechnical monitoring during subway construction in Prague*

In this context, the present study describes the operational use of MT-InSAR as a component supporting complex geotechnical monitoring during the construction of the Prague D line subway. Spatially dense and temporally resolved deformation data from MT-InSAR complement traditional operational monitoring techniques, providing additional

insights about the extent and chronology of tunnelling-related hazards.

A new subway line is under construction in Prague, Czechia, traversing from the city's peripheral regions to its central districts through geologically complex and challenging conditions. The influence of subway construction potentially affects the structural health of buildings and infrastructure in the zone of influence, which is being monitored by standard geotechnical and geodetic techniques, including precise levelling. A network of more than 900 static measurement points has been established in the zone of influence between planned stations Pankrac and Olbrachtova by the client. Measurements identify deformation trajectories reaching or exceeding pre-established hazard warning levels to allow early and timely mitigation during construction.

InSAR complements the monitoring in two ways:

- Stage 0: Provision of passportization status documenting the level of (in)stability within and beyond the zone of influence before the construction started as of April 2022.
- Stage 1-8: Regular monitoring during construction with variable monitoring interval lengths (6 – 12 months) and satellite data acquisition frequency (11 – 33 days). The InSAR monitoring set-up has been designed to be efficient and cover periods with the highest expected deformation rates and measurement frequencies.

As of the end of 2024, the fifth monitoring stage has been completed, with stages 6-8 planned for 2025-2026 (refer to Figure 1). The overall size of the core area of interest (AOI) along the zone of influence is approximately 0.5 km<sup>2</sup>. InSAR monitoring covers the area of the AOI extended by a 0.5 km wide buffer.

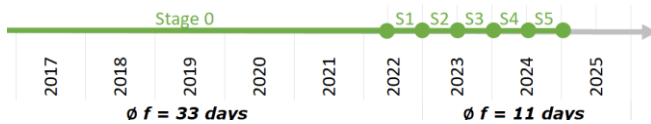


Figure 1: Passportization (Stage 0) and subsequent monitoring stages (up to Stage 5). The average frequency of TSX imagery acquisition is indicated below the graph. From 2025 on, additional stages follow up after Stage 5.

## 2 SATELLITE DATA

TerraSAR-X data (X-band, wavelength 3.08 cm) in StripMap mode (spatial resolution 3x3 m) are being used for InSAR monitoring. The images cover the monitoring period 2016-2024, and their total number is 129.

As a supplementary dataset, freely available Sentinel-1 (C-band, wavelength 5.6 cm) data were processed for the same area of interest from three tracks (ascending 146 (looking from West) and descending 22 and 95 (looking from East)). The look angle is flatter than that of TerraSAR-X and, therefore, more sensitive to the horizontal (East-West) displacements. Sentinel-1 images were processed from 2015 to the end of 2024, amounting to 430-450 images per track. An overview of satellite datasets is listed in Table 1.

Digital terrain models (DTMs) and digital surface models (DSMs) obtained from open data sources [10] were used to

estimate the location of each PS point (ground, facade, roof, etc.) and to determine its height above ground.

Table 1. Baseline and supplementary satellite datasets.

Satellite/mode / track	Images used	Inc angle [deg]	Spatial resolution [m]
TerraSAR-X / SM / D2	129	22	3x3
Sentinel-1 / IW / D95	441	32	20x5
Sentinel-1 / IW / D22	436	44	20x5
Sentinel-1 / IW / A146	429	39	20x5

## 3 METHODOLOGY

### 3.1 MT-InSAR analysis

The InSAR processing was performed using the persistent scatterers algorithm (PS-InSAR) in the SARproZ(c) software, which is tailored for infrastructure monitoring. For Sentinel-1, all pixels within the area of interest were processed to reach the highest possible point density. In contrast, for TerraSAR-X, point selection was based on local amplitude maxima to streamline the processing timeline. A reference point was selected in another stable part of the city to avoid being influenced by the construction works.

Subsequently, proprietary post-processing techniques have been employed to enhance results from the standard PS-InSAR algorithm. In particular, the detection of temporally coherent targets and time series segmentation has been used to retain a higher density of candidate PS measurement points.

The time series of each PS point was segmented into intervals with constant velocity and noise, and abrupt movements were excluded within a single segment. The segmentation method is data-driven, based on statistical tests to compare principal values for subsequent segments (such as velocity and noise). The segmentation enables us to more accurately estimate the quality of the time series for PS points experiencing highly non-linear displacement. In conventional InSAR workflows, the estimated reliability expressed by coherence “averaged” over the whole monitoring period is low for these points, resulting in their discarding in the candidate selection phase. For each segment, displacement noise was estimated, and if it was too high, that segment was considered unreliable. However, if a point is reliable for at least part of the monitoring period, it can be interpreted for that period. The tolerable noise level was calculated based on statistical simulations, considering ambiguous fundamentals of InSAR, and depends on the SAR wavelength and the length of a segment. Generally, the allowed noise level is around 2.8 mm for TSX for long segments, and slightly lower for shorter segments. This is particularly important in areas with ongoing construction work, where a point may become unreliable for shorter periods and then regain reliability. These periods may repeat frequently. The



segmentation is performed for each PS point individually; therefore, the segments vary between points.

With special attention, the displacement velocity in the last reliable segment (i.e. the most recent displacement velocity) is estimated, together with its standard deviation, at the end of each monitoring stage.

### 3.2 Estimation of horizontal component

The TSX dataset, featuring a steep incidence angle in the area of interest, is particularly suitable for detecting displacements with a dominant vertical component. In addition, due to suspicions of displacements with strong horizontal components in certain zones of the drilling influence zone, the Sentinel-1 dataset has been employed. Measurements from opposite ascending and descending orbits feature flatter incidence angles and are more sensitive to horizontal displacements in the East-West direction. Standard decomposition using a custom grid size was implemented to convert displacement rates from the LOS (radar line-of-sight) to vertical and horizontal deformation components. Sentinel-1 measurements at the end of Stage 3 and Stage 5 from their most recent reliable displacement rates (in mm/year) were used. This option turned out to be less noisy compared to processing options utilising stage-wise or cumulative displacements (in mm).

### 3.3 Estimation of buildings affected by geotechnical hazard

Geotechnical hazards and the structural health of buildings can be assessed using PS-InSAR results through various methodologies. For the pilot demonstration of technology utility for the D line subway in Prague, we focused on testing existing approaches, their customisation, and developing a new one.

The [11] combined PS-InSAR with damage surveys to develop empirical building fragility curves. The approach focuses on monitoring settlement-induced damage through parameters summarily ranked as SRI (Subsidence-Related Intensity), such as differential settlement and relative rotation (deflection ratio), calculated from a cloud of PS points for building polygonal footprints or their immediate vicinity. Ancillary metrics (length, width, buffer) are computed from the polygonal geometry. SRI proxies the potential damage risk for different classes of building construction materials.

The [9] employ PS-InSAR to monitor deformation in urban environments, particularly in historical city centres, where underground activities may induce ground subsidence. Their method applies novel classification indices, including deformation velocity, dispersion, and acceleration indices, as a proxy for assessing the structural health of buildings.

To complement the above methodologies for specific types of buildings in dense residential urban stock (tall and with a small footprint area), we developed an additional index to indicate the potential tilt of the building. It is based on the correlation between the estimated height of a PS point (above ground) and the estimated displacement velocity. Figure 2 displays the simple model of the situation.

Supposing the correlation exceeds the threshold and the difference between the highest and lowest PS points in the footprint exceeds the set value, then the rate between the displacement velocity and height is estimated and converted to tilt angle, assuming that the differential displacements are horizontal (East-West direction). In our case, the tunnel's

orientation is ideal for InSAR, as the expected East-West displacements are most sensitive to this technique.

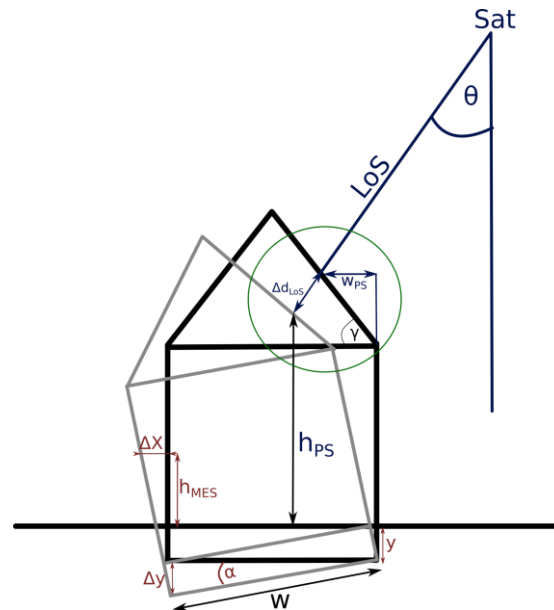


Figure 2: Illustration of the relation between the measured line-of-sight displacement and height for a tilted building.

To estimate the tilt angle, the least squares method accounting for errors in both x and y axes (i.e., height and displacement velocity) was used [12], as both values were estimated from the original InSAR data. Practically, the stochastic model is not precise as it does not consider the relation between the estimated height and displacement velocity. This is because the relationship is not straightforward, as the height is calculated from all the SAR data, while the displacement velocity is not. Moreover, outliers were excluded from the adjustment. Finally, the tilt angle was confirmed only if it was higher than its standard deviation; the tilt angles are overall smaller than, e.g., 2.5 times the standard deviation.

The correlation method can only be used for X-band data. Sentinel-1 data have a high standard deviation in height, which leads to a too-high standard deviation of the estimated tilt angle.

### 3.4 Cross-validation

Total displacements measured converted to vertical direction were compared with geodetically measured settlements for a set of buildings in the zone of influence.

## 4 RESULTS

At the end of each monitoring stage, results with a standardised structure and formatting are delivered to the construction monitoring committee. These include maps of ground displacements in LOS from the baseline TSX dataset complemented by additional metrics derived by analysis of segmented deformation time series (refer to Figure 3):

- Displacement rates – average, last reliable velocity (mm/yr)
- Stage-wise and cumulative displacement (mm)
- Acceleration
- Classification of displacement trend typology
- Classification of reflecting target type

In total, more than 4,000 temporally coherent PS measurement points are being detected for each monitoring stage in the core AOI from the TerraSAR-X dataset, and over 22,000 measurement points for the extended AOI.

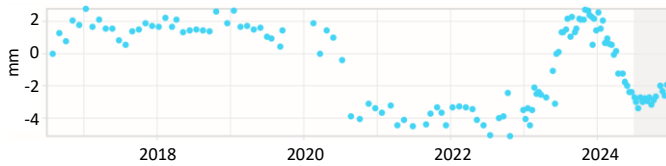


Figure 3. Example of PS points' displacement time series from a building affected by repeated drilling-induced settlements and injecting-induced uplifts in the meantime.

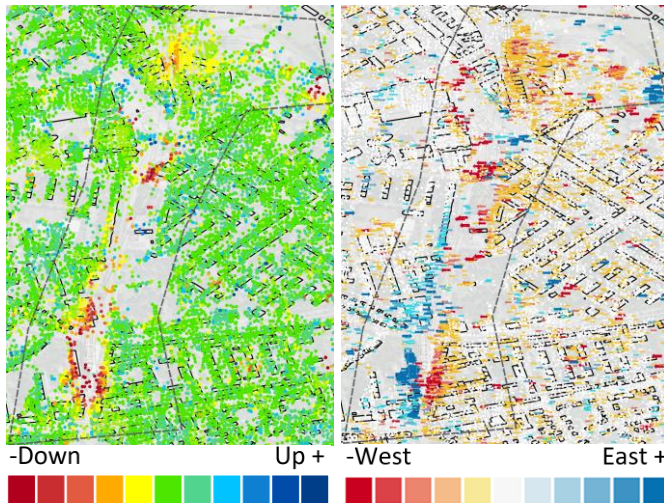


Figure 4. Ground displacement velocity (from at least a 1-year-long reliable time-series segment) in the core AOI from the Sentinel-1 dataset decomposed from LOS to (a) vertical and (b) East-West direction, which is roughly perpendicular to the subway drilling axis (please note: displacement velocity magnitude could not be disclosed).

Validation revealed discrepancies between InSAR displacements from TSX converted to vertical direction and geodetic measurements by levelling. These discrepancies in measured settlements amounted up to 3-4 mm over a comparable measurement period for a line of tall buildings at the east side of the settlement zone, while being negligible in other areas. After a thorough analysis, we can attribute these discrepancies to the influence of horizontal displacements – the buildings are slightly leaning away from the satellite in LOS. These displacements increase the displacement magnitude in the LOS and subsequently in the vertical direction, if projected without considering the horizontal component. Furthermore, the horizontal component estimated from InSAR for tall multi-storey buildings is higher than the magnitude measured trigonometrically at the buildings' foot or first storey level. As a result of tilting, the horizontal displacement is more pronounced at the rooftop level, where most of the PS measurements are located, than at the ground.

After realising the occurrence of horizontal displacements (accompanied by building tilting), the ground displacements map from the TSX has been complemented by MT-InSAR analysis of the Sentinel-1 dataset, followed by decomposition

of LOS velocities into vertical and horizontal displacement components for selected monitoring stages. These results (refer to Figure 4) confirm the existence of horizontal displacements and show the extent and heterogeneity of the phenomena.

The methodology of [8] was found helpful in detecting differential settlements for larger buildings as an indicator of potential damage risk. Buildings need to have enough PS points detected within the building footprint. Furthermore, the distance between PS points with minimum and maximum deformations, which is used to calculate the deflection angle, needs to be sufficiently long. The method is applicable to buildings regardless of their height; however, the deflection angle is estimated more reliably for buildings elongated parallel to the settlement sloping gradient vector.

Similarly, [9] provides a means for more complex assessment by considering aggregated displacement velocities complemented with their acceleration and spatial dispersion within a building polygon. This is an indicative proxy metric for building tilting regardless of height; however, buildings must have enough PS points within the footprint.

The correlation-based tilting indicator supplemented the above techniques by pointing to tilts of high buildings with relatively small footprints, which are common in the residential urban fabric.

## 5 CONCLUSIONS

During its operational execution, InSAR proved to provide highly valuable and complementary insights into the spatial and temporal context of settlement phenomena during Prague's Metro D line construction.

The most pronounced advantages and benefits of InSAR identified by its practical and operational application are listed below:

- High density of measurements that allows more precise delineation of the zone of influence.
- Delineation of the real extent of the zone of influence. Assessment of specific drilling-induced trend patterns in measurement time series and their spatial distribution reveals that this extent is larger in some areas compared to the projected zone of influence.
- Delineation of additional settlement zones within and beyond the core AOI. The geotechnical and hydrogeological interpretation indicates their association with groundwater withdrawal in the aquifers.
- Differentiation between drilling-induced settlement and subsidence caused by other drivers. This may turn instrumental for assessment and passportization of damages and as evidence in potential legal disputes.

Furthermore, results showcase that:

- The use of the temporally coherent targets variant of the PSI algorithm is instrumental in maintaining a high density of measurements during different monitoring stages.
- TSX data are indispensable to obtaining the highest measurement density, allowing detailed settlements and uplift impact assessment at the level of individual buildings.
- TSX measurements from single track suffer from biased displacement rate magnitude in LOS when buildings tilt

in a direction parallel to LOS. The bias is propagated in a vertical direction after simple reprojection.

- The monitoring should be complemented by InSAR measurements from ascending and descending paths of Sentinel-1 and their decomposition to map the extent of the horizontal deformation field.
- Appropriate geotechnical methodologies and metrics need to be selected, customised, and combined to indicate risk and tilting for a broader spectrum of different building sizes and heights. The reflective position of the PS measurement point (on the roof, facade, or from the ground) needs to be estimated and considered.

## ACKNOWLEDGMENTS

We would like to express our sincere gratitude to Jakub Bohátka and Jiří Bárta from SG Geotechnika, a.s. for their invaluable assistance with validation, geotechnically oriented insights, and interpretation, which contributed to the quality of the InSAR outputs.

## DISCLAIMER

Detailed results and scales of vertical or horizontal displacement velocities could not be disclosed due to their sensitive nature.

## REFERENCES

- [1] Barla, Giovanni & Tamburini, Andrea & Del Conte, Sara & Chiara, Giannico. InSAR monitoring of tunnel induced ground movements. *Geomechanics and Tunneling*. 9. 15-22. 2016.
- [2] Roccheggiani, Matteo et al, Detection and monitoring of tunneling induced ground movements using Sentinel-1 SAR interferometry. *Remote Sensing* 11.6, 2019.
- [3] Milillo, Pietro et al, Multi-temporal InSAR structural damage assessment: The London crossrail case study, *Remote Sensing* 10.2, 2018
- [4] Del Conte, Sara et al, Satellite InSAR monitoring in urban tunneling projects, [https://site.tre-altamira.com/wp-content/uploads/2018\\_InSAR-monitoring-in-urban-tunneling-projects\\_DelConte-et-al\\_Tunneling\\_Trenchless-Conference.pdf](https://site.tre-altamira.com/wp-content/uploads/2018_InSAR-monitoring-in-urban-tunneling-projects_DelConte-et-al_Tunneling_Trenchless-Conference.pdf), accessed 7.4. 2025
- [5] Scoular, Jennifer et al, Retrospective InSAR analysis of East London during the construction of the Lee Tunnel, *Remote Sensing* 12.5, 2020.
- [6] Saeidi Ali, Olivier Deck, and Thierry Verdel, Development of building vulnerability functions in subsidence regions from empirical methods, *Engineering Structures* 31.10, 2009.
- [7] Ezquerro, P., M. Del Soldato, L. Solari, R. Tomás, F. Raspini, M. Ceccatelli, J. A. Fernández-Merodo, N. Casagli, and G. Herrera, Vulnerability Assessment of Buildings due to Land Subsidence Using InSAR Data in the Ancient Historical City of Pistoia (Italy). *Sensors* 20 (10): 2749, 2020.
- [8] Peduto, Dario et al, Full integration of geomorphological, geotechnical, A-DInSAR and damage data for detailed geometric-kinematic features of a slow-moving landslide in urban area, *Landslides* 18, 2021.
- [9] Garcia, Adrian Jesus et al, Building health monitoring in the old town of Madrid: applicability of SAR Imagery to the monitoring of underground works through classification indexes, *International Journal of Digital Earth* 14.3, 2021.
- [10] Geoportál Praha, <https://geoportalpraha.cz/data-a-sluzby/clanky-a-projekty/3D-model/3D-model-dtm>, accessed 4.4.2025.
- [11] Nappo N., Peduto D., Polcari M., Livio F., Ferrario M.F., Comerci V., Stramondo S., Michetti A.M., Subsidence in Como historic centre (northern Italy): Assessment of building vulnerability combining hydrogeological and stratigraphic features, *CosmoSkyMed InSAR and damage data*, *International Journal of Disaster Risk*, 2021.
- [12] Cantrell, C. A, Review of methods for linear least-squares fitting of data and application to atmospheric chemistry problems. *Atmospheric Chemistry and Physics*, 8.17, 2008.



# Utilizing PSDefoPAT<sup>®</sup> to analyze surface deformation of embankment dams

M. Evers<sup>1,2</sup> A. Thiele<sup>1,2</sup>

<sup>1</sup>Fraunhofer IOSB, Gutleuthausstraße 1, 76275 Ettlingen, Germany

<sup>2</sup>Karlsruhe Institute of Technology, Kaiserstraße 12, 76131 Karlsruhe, Germany  
email: madeline.evers@iosb.fraunhofer.de, antje.thiele@iosb.fraunhofer.de

**ABSTRACT:** Dams are used worldwide to, e.g., manage flooding, generate energy, or secure the freshwater supply. They play an essential role in the local economy. However, an operational or structural failure also poses a significant threat to the environment and the local economy. Therefore, it is vital to ensure their structural health and functionality.

In this study, we present the ground surface deformation of the Parapeiros-Peios Dam during the later stages of its construction, first filling, and shortly afterwards. Since data services, such as the European Ground Motion Service, surfaced and provide freely available ground motion datasets, one might think that in-house processing of SAR data for surface deformation monitoring of critical infrastructure is obsolete. In order to explore the advantages of in-house processing, we compare ground motion datasets generated by Fraunhofer IOSB and the European Ground Motion Service based on advanced differential synthetic aperture radar interferometry techniques. The dataset consists of sets of measuring points, their mean deformation velocity, and the associated displacement time series. Based on the mean velocity maps, we present a spatial analysis of the observed deformation patterns. In addition, we analyzed the temporal deformation pattern of individual measuring points by employing the Persistent Scatterer Deformation Pattern Analysis Tool (PSDefoPAT<sup>®</sup>). This tool can be used to fully automatically identify the statistically best fitting model to describe the temporal deformation pattern of a persistent or distributed scatterer (i.e., linear, quadratic, piecewise linear, or periodic) and provides insight into the dynamics of the surface deformation. It can aid with the analysis of changes in the structural health of the dam.

**KEYWORDS:** Embankment Dam; Persistent Scatterer Interferometry; European Ground Motion Service; Deformation PSDefoPAT<sup>®</sup>.

## 1 INTRODUCTION

Dams are large engineering structures used for centuries to stop the surface water flow. They have at least two components: a dam body and a reservoir. The dam body is used to either redirect or impound surface water. The impounded water creates an artificial lake, which is referred to as a reservoir. The main purposes of these structures are storing water for irrigation or human consumption, energy generation, flood control, fish farming, and storing tailings. Thus, they have a significant influence on the local economy. They can have a positive impact on the region, but a failure of the dam body or an operational failure can also be detrimental to the local economy, human settlements, and the environment. Therefore, it is essential to ensure their structural health and functionality [1]. Depending on the construction type of the dam body, the set of parameters that need to be monitored varies. In the case of an embankment dam, which is the most common type used worldwide, the International Commission on Large Dams (ICOLD) stipulates monitoring structural deformations, movements, and temperature of the dam body, as well as uplift pressure, seepage, drainage rates and the chemical composition of the seepage water [2,3].

This study will focus on the surface deformation of embankment dams. Those dams are subject to numerous loads during their lifetime, which can result in the deformation or displacement of the entire or parts of the dam body [4]. Recent studies have demonstrated that Synthetic Aperture Radar Interferometry (InSAR) techniques, such as Persistent Scatterer

Interferometry (PSI), can be used to map and analyze the surface deformation of dams for short phases of their lifetime [5,6].

In this study, we map and analyze the deformation of the Parapeiros-Peios dam during the time of the first filling of its reservoir and shortly after. The dam is located in southern Greece on the Peloponnese Peninsula. Its construction finished in early 2019, and the reservoir filling process started in September 2019. We acquired two different datasets of the area of interest. The first dataset, Dataset A, consists of 119 Sentinel-1 (S1) Synthetic Aperture Radar (SAR) images and was processed in-house. The second dataset, Dataset B, was obtained from the European Ground Motion Service (EGMS), which provides ground surface deformation measurements for most European countries based on S1 SAR images and advanced DInSAR processing. Dataset B covers the time from January 2019 to December 2023. Since data services, such as the EGMS, are freely available, one might think that in-house processing of SAR data for surface deformation monitoring of critical infrastructure is obsolete. However, the EGMS does not provide customized datasets for specific events or time spans and is delayed by at least three quarters of a year. In order to explore the advantages of in-house processing, we compare our own results with those generated by the EGMS regarding the observable spatial and temporal deformation patterns. Both datasets provide maps with the mean deformation velocities and displacement time series for individual measuring points (MP). The mean deformation velocity maps were used to

analyze the spatial deformation pattern of the Parapeiros-Peios dam, while the individual displacement time series were analyzed using the Persistent Scatterer Deformation Pattern Analysis Tool (PSDefoPAT<sup>®</sup>) developed at Fraunhofer IOSB, which automatically assigns each time series a best-fitting model [7]. The estimated time series models offer information on the temporal deformation pattern, which is not directly visible in the mean deformation velocity maps.

This paper is structured into five sections. The Parapeiros-Peios dam and the data used to monitor it are described in Section 2. Section 3 provides an overview of the methods used to analyze the data. The results are presented and discussed in Section 4, and finally, our conclusion is presented in Section 5.

## 2 PARAPEIROS-PEIROS DAM

The Parapeiros-Peios dam is located in the municipality of Patras in the northwest of the Peloponnese Peninsula (Greece). It consists of an embankment dam, a diversion dam, and a reservoir. The total capacity of its reservoir is 44 million m<sup>3</sup> of water. The impounded water is intended to supply more than 2 million people in three regions (Patras, Erymanthos, and Dytiki Achaia) with fresh water. While the diversion dam reroutes the Peiros River, the embankment dam impounds the water of the Peiros and Parapeiros rivers. In detail, the dam is about 75 m high and 900 m long. Its construction finished in early 2019, and the filling process of the reservoir started in September 2019 [8,9] and is estimated to take about three years.

The first reservoir filling is particularly interesting, since the construction is subject to all the loads it was built to withstand for the first time. The dam body is expected to deform as a consequence. At this point, only the most significant deformation phenomena will be mentioned. A detailed description of the many deformation phenomena was provided by Evers [10]. The deformation phenomena can be sorted into three patterns:

- (1) subsidence,
- (2) uplift and
- (3) horizontal displacement.

The building and foundation materials of the dam body are compressed by the weight of the construction, resulting in partial or complete subsidence of the dam body. The dead load

of the increasing amount of impounded water only fosters this process [11]. Moreover, collapse compression on the upstream shoulder can add to the subsidence rates. A partial uplift of the dam body can be caused by a decrease in the effective stress in the upstream shoulder resulting from the increasing water load during the filling process. The third deformation category is the horizontal displacement of the entire or parts of the dam body. The cause for horizontal displacement is the increased lateral tension within the dam body during the filling process [4].

Two advanced DInSAR datasets were used to analyze the spatial and temporal deformation of the Parapeiros-Peios dam. The goal is to explore whether it is obsolete to process SAR images in-house for surface deformation monitoring of critical infrastructure such as dams, since ground motion datasets are freely available and updated regularly.

Dataset A consists of 119 S1 SAR images recorded with a descending acquisition geometry and Interferometric Wide Swath mode. The time series extends from September 2019 to November 2022, which corresponds to the time of the first filling of the reservoir. The images depict the area surrounding the Parapeiros-Peios dam, allowing for the mapping and analysis of the deformation of the dam body and the surrounding slopes. Dataset B is a ground motion dataset of the same area provided by the EGMS. The EGMS provides ground motion measurements at a millimeter scale using persistent scatterer (PS) and distributed scatterer (DS) techniques. The service was first made available at the beginning of 2022 and documented in its first edition the ground motion of most European countries from 2015 to 2020 based on all available S1 images from this time span. The dataset is regularly updated, always considering S1 images of the past five years [12]. The new dataset is made available in the following fall. For this study, a dataset covering the period from January 2019 to December 2023 was used, which corresponds to the time immediately preceding the first filling, the first filling itself, and approximately two years afterward. The chronology of the datasets and the time of the construction and commission phase of the Parapeiros-Peios dam they cover are illustrated in Figure 1. The goal is to explore whether

## 3 METHODS

### 3.1 Persistent Scatterer Interferometry (PSI)

InSAR and PSI are techniques used to map surface deformation

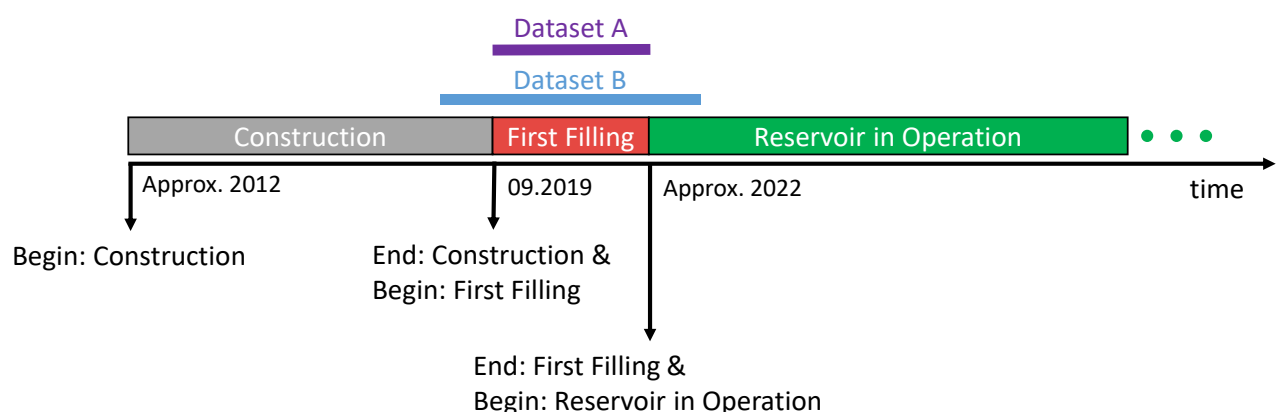
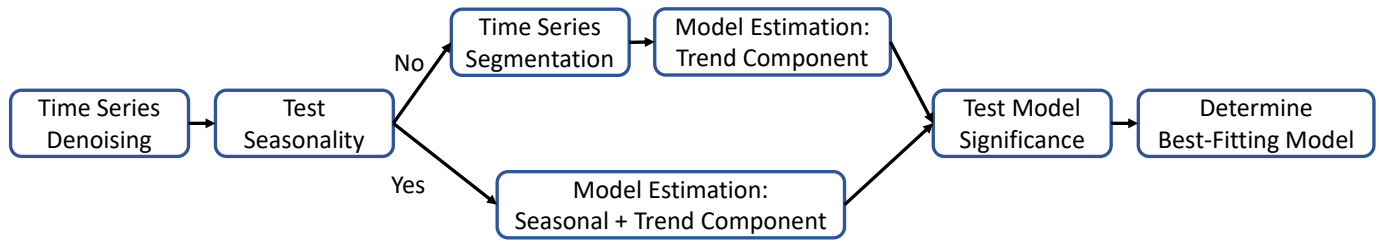


Figure 1. Timeline of the construction and commission phase of the Parapeiros-Peios dam and the Datasets A (S1 images processed by Fraunhofer IOSB) and B (provided by EGMS).


Figure 2. Workflow of PSDefoPAT<sup>®</sup> [7].

over a wide area. In contrast to InSAR, PSI uses a time series of SAR images to identify pixels with a low noise level to reduce the influence that phase decorrelation and the atmospheric phase delay have on the deformation estimates. The algorithms that implemented this concept were developed by, e.g., Ferretti and Hooper [13, 14]. An adapted version of the StaMPS PSI algorithm, which can be used in a Windows-based framework, was used in this study to process Dataset A.

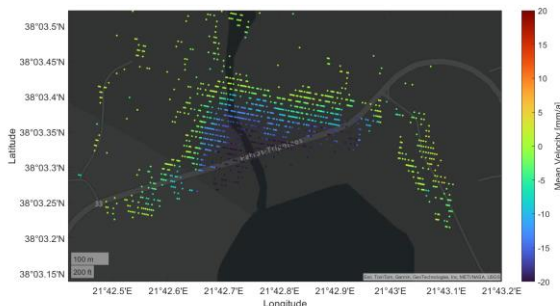
As stated previously, Dataset B was obtained from the EGMS. Processing the S1 SAR images for the EGMS with advanced DInSAR algorithms was carried out by four different companies, e-GEOS, TRE Altamira, NORCE, and GAF, who each have their own well-established processing chains. DSs were not taken into consideration for all regions processed in the EGMS. The type of scatterer, PS or DS, is indicated by the attribute field “mp\_type” in the downloaded EGMS datasets [15]. In the case of the northwestern region of the Peloponnese Peninsula, no MPs marked as DS were identified in the EGMS dataset. The service distributes several InSAR products at different processing levels: (1) Level 2a (L2a), (2) Level 2b (L2b), and (3) Level 3 (L3). The L2a datasets are precise InSAR displacement measurements in the line-of-sight (LOS) of the sensor. The displacements are relative values calculated with a local reference point. The L2b displacements were calibrated with a Global Navigation Satellite System (GNSS) model and are no longer relative measurements. L2b datasets in ascending and descending geometry were used to calculate the horizontal and vertical displacements for the L3 datasets [12]. For this study, we used an L2a dataset.

In addition to an analysis of the spatial deformation pattern, based on mean deformation velocity maps, both datasets were processed with the Fraunhofer IOSB tool PSDefoPAT<sup>®</sup> [7] to analyze temporal deformation patterns. PSDefoPAT<sup>®</sup> extracts

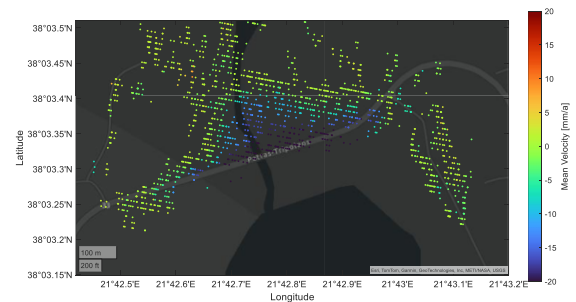
relevant information on the temporal deformation patterns not directly visible in the typically presented mean deformation velocity maps.

### 3.2 Persistent Scatterer Deformation Pattern Analysis Tool (PSDefoPAT<sup>®</sup>)

The tool PSDefoPAT<sup>®</sup> was developed at Fraunhofer IOSB to ease the analysis of the individual displacement time series of a large set of PS [7]. Most PSI algorithms provide a map of the mean velocity of each PS found in the area of interest and the associated displacement time series for each PS. The advantage of the mean velocity maps is that areas of active deformation are easily recognizable. Also, their spatial expansion and the direction of the deformation in the LOS of the sensors are provided. However, the mean velocity is calculated assuming the deformation is linear. More complex deformation patterns are not considered, such as a periodically varying surface deformation or an accelerating or decelerating deformation pattern. Thus, information on the dynamic nature of the deformation is completely lost to the analyst. PSDefoPAT<sup>®</sup> estimates the best-fitting model to describe the deformation pattern of each PS over time and thus provides information on the dynamic nature of the deformation. PSDefoPAT<sup>®</sup> separates the long-term trend, periodic, and noise components of each displacement time series in six steps. The order of these steps is illustrated in Figure 2. The displacement time series is first denoised using wavelet transformation. Afterward, the periodogram of the remaining time series is calculated, and a Fisher’s g-test is conducted to determine whether or not the time series has a significant seasonal component. If the time series has such a component, the seasonal and trend components are estimated in one step.



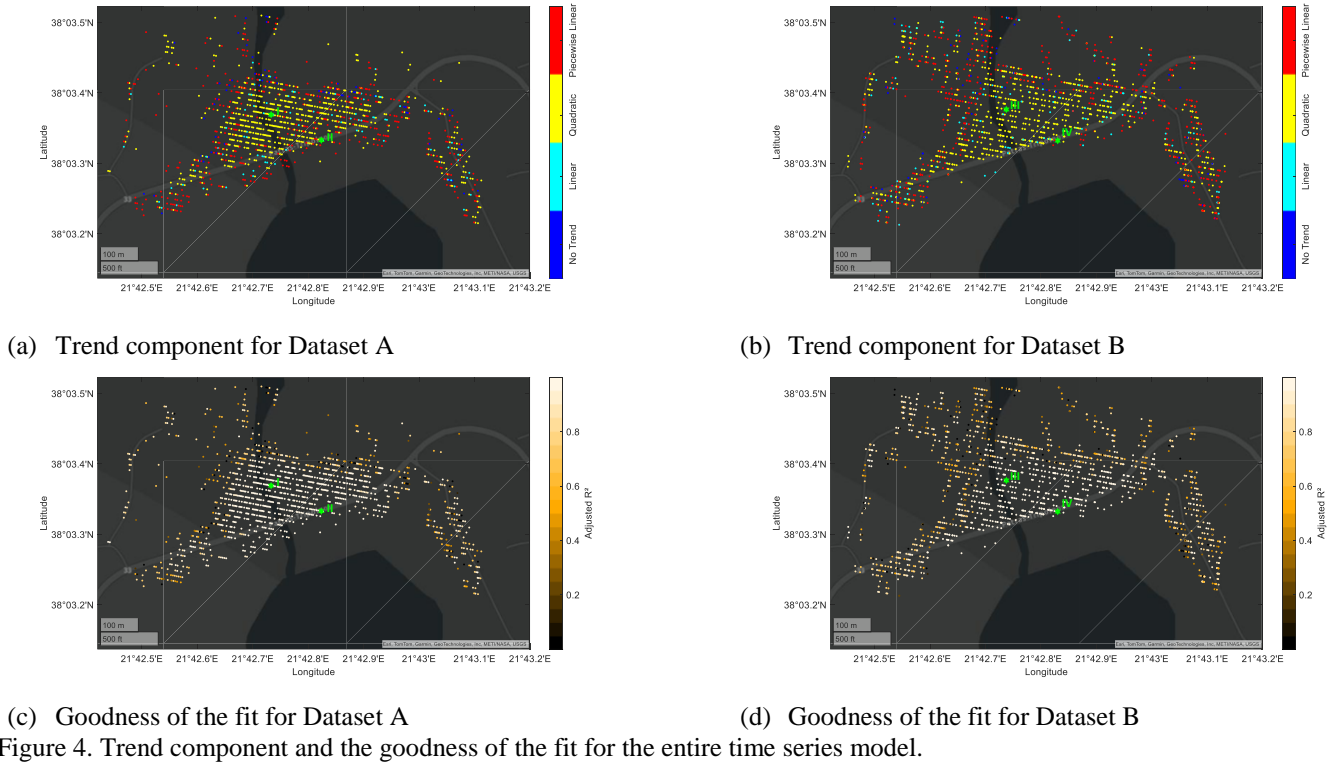
(a) Dataset A



(b) Dataset B

Figure 3. Mean deformation velocity for MPs on the dam body of the Parapeiros-Peios dam in Greece.





Valid time series models are (1) purely seasonal, (2) seasonal with a linear trend, and (3) seasonal with a quadratic trend. Only the trend component is estimated if the time series has no significant seasonal component. Applicable models for the trend component are (1) linear, (2) piecewise linear, and (3) quadratic time series models. Before the different models are estimated, the time series is segmented using a top-down segmentation algorithm to provide change points for a piecewise linear model. Lastly, the best-fitting model is determined using the Bayesian Information Criterion (BIC) and the value for the adjusted coefficient of determination  $R^2_{adj}$ . Both parameters provide information on the goodness of the fit, taking into consideration the complexity of the model and, therefore, preventing overfitting [7]. PSDefoPAT<sup>®</sup> automatically generates four plots by default to visualize its results. The plots indicate: (1) the type of trend component, whether or not the time series features a periodic component, (3) the amplitude of the periodic component, and (4) the goodness of fit for the entire time series model. A practical example of these plots is presented in Figure 4 and Figure 5, which visualize the results for the Parapeiros-Peiros dam. With these plots the temporal deformation pattern, not directly visible in the typically presented mean deformation maps, of the MPs in the AOI can be analyzed. For example, MPs effected by a periodic behavior can be easily spotted.

#### 4 RESULTS AND INTERPRETATION

In the following section the results generated with PSDefoPAT<sup>®</sup> for Dataset A processed by Fraunhofer IOSB and Dataset B obtained from the EGMS are presented and the fit of exemplarily displacement time series and the estimated time series models of individual MPs are discussed.

The mean deformation velocities for the measuring points (MP) in Dataset A and Dataset B located on the dam body of the Parapeiros-Peiros dam are presented in Figure 3. The color map ranges from red, indicating a deformation velocity larger than 20 mm/y in the direction towards the sensor, to blue, indicating a deformation velocity larger than -20 mm/y in the direction away from the sensor. Both images show that the mean deformation velocity on the dam body varies along the downstream shoulder, with more -20 mm/y at the crown and close to zero at the toe of the dam body. This is a typical spatial deformation pattern observed for embankment dams [16]. In order to analyze the temporal deformation pattern, the displacement time series of Dataset A and Dataset B were processed with PSDefoPAT<sup>®</sup>. The results are visualized in Figure 4 and Figure 5. Figure 4 (a) showing Dataset A and (b) Dataset B indicate whether the processed displacement time series exhibit a linear (cyan), quadratic (yellow), piecewise linear (red) trend, or no trend (blue). In both cases, the majority of MPs at the center of the downstream shoulder of the dam body exhibit a quadratic trend, and MPs located closer to the edges or adjacent to the dam exhibit a piecewise linear trend. This pattern is mirrored in Figure 4 (c) and Figure 4 (d), which present a measure for the goodness-of-fit in the form of the adjusted coefficient of determination  $R^2_{adj}$  for the estimated time series model for Dataset A and B, respectively. The estimated time series model for MPs at the center of the dam body fit the displacement time series better than those estimated for MPs at the edge of the dam body, for both Datasets.

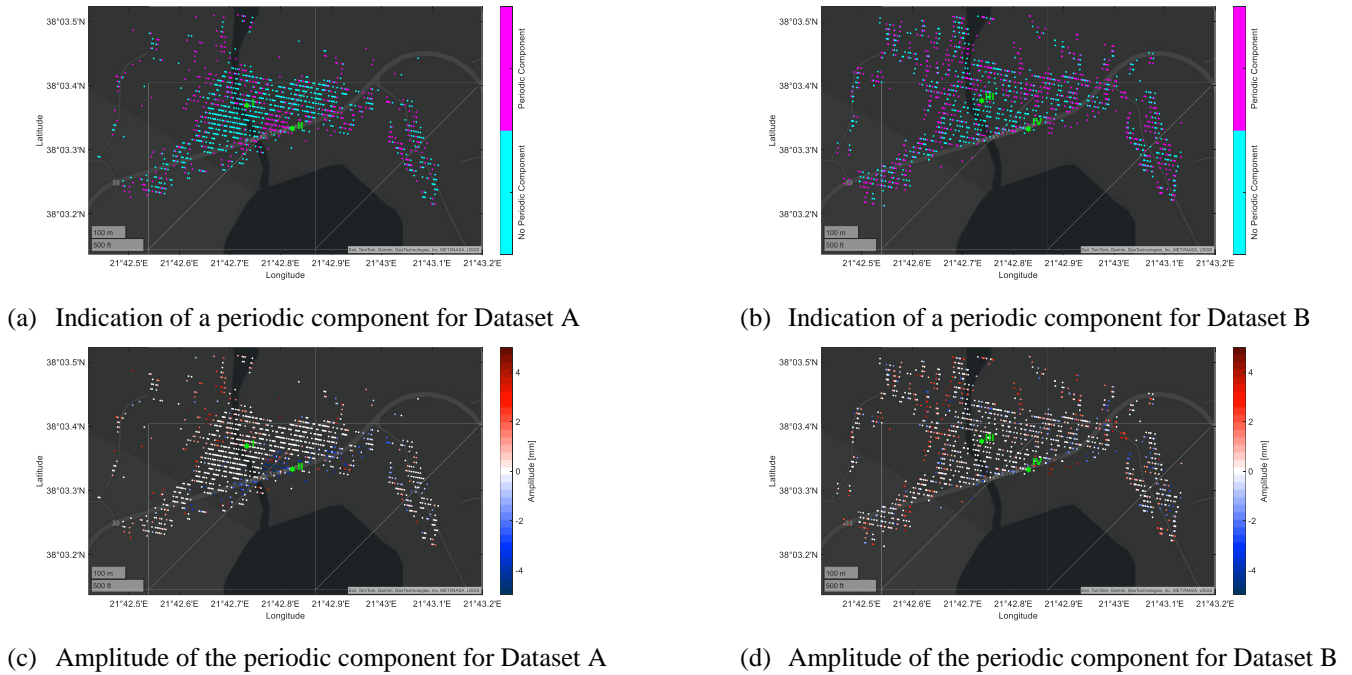


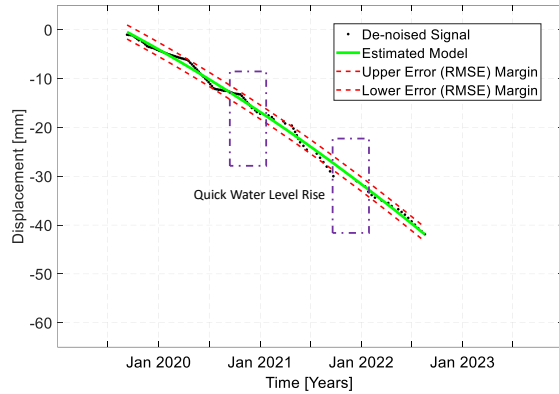
Figure 5. Periodic component and the corresponding amplitude of the periodic component.

Figure 5 indicates whether the estimated time series model includes a periodic component (magenta) or not (cyan), along with the corresponding amplitude of the periodic component. While the estimated time series models for Dataset A, see Figure 5 (a) and Figure 5 (c), show that only some MPs exhibit a periodic behavior, in the case of Dataset B, see Figure 5 (b) and Figure 5 (d), significantly more MPs exhibit periodic behavior. This may be due to the different time spans that Dataset A and Dataset B cover. In order to investigate the displacement time series and estimated time series models further, we examined four exemplary MPs located at the downstream shoulder (MP I and MP III) and crown (MP II and MP IV) of the dam body for both datasets. The MPs are marked in green in Figure 4 and Figure 5. The selected MPs for both datasets are not identical, however, they were picked as closely together as possible to ensure comparability. Their displacement time series (black dots), overall estimated time series model (green), and the lower and upper error margins

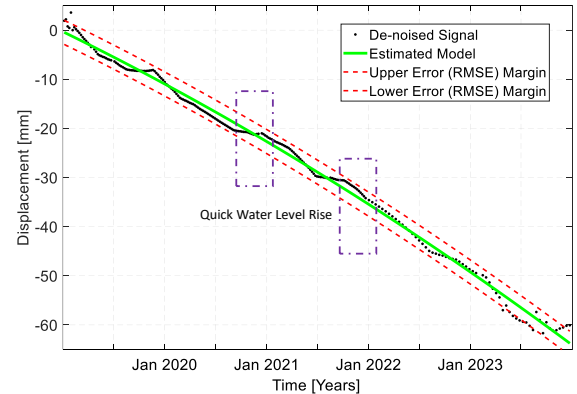
(red) are presented in Figure 6 and Figure 7. The estimated parameters for the time series models are also summarized in Table 1. Figure 6 displays the displacement time series for MP I and MP III, which are located on the downstream shoulder of the dam body. Both estimated time series models exhibit a quadratic trend. While the linear coefficients of both models are similar, with  $-11.1 \text{ mm/y}$  for MP I and  $-10.1 \text{ mm/y}$  for MP III, the scaling parameter of quadratic time series model differs. The scaling parameter is estimated to be  $-1 \text{ mm}^2/\text{y}^2$  for MP I and  $-0.5 \text{ mm}^2/\text{y}^2$  for MP III. A smaller value for the scaling parameter leads to a wider opening for the parabola, approximating the displacement time series. This difference in the scaling parameter might be influenced by the slightly different time spans that Dataset A and Dataset B cover. While Dataset A covers only the time of the first filling of the freshwater reservoir, Dataset B covers a short time before the first filling and about a year afterwards.

Table 1. Model parameters and estimated mean velocity of the selected MPs.

	Mean Velocity	Best-Fitting Model	$R^2_{\text{adj}}$
Downstream Crown:			
Dataset A	$-25.1 \text{ mm/a}$	$d = -29.7 \text{ mm/a} \cdot t + 2 \text{ mm}^2/\text{a}^2 \cdot t^2 - 4.6 \cdot \sin(\frac{2\pi}{798.3d}(t - 391.9 \text{ d}))$	0.99
Dataset B	$-28.1 \text{ mm/a}$	$d = -26.6 \text{ mm/a} \cdot t - 0.3 \text{ mm}^2/\text{a}^2 \cdot t^2 - 1.6 \cdot \sin(\frac{2\pi}{519.9d}(t - 119.4 \text{ d}))$	0.99
Downstream Shoulder:			
Dataset A	$-16.1 \text{ mm/a}$	$d = -11.14 \text{ mm/a} \cdot t - 1.0 \cdot t^2 \text{ mm}^2/\text{a}^2$	0.99
Dataset B	$-17 \text{ mm/a}$	$d = -10.1 \text{ mm/a} \cdot t - 0.5 \text{ mm}^2/\text{a}^2 \cdot t^2$	0.99



(a) MP I in Dataset A



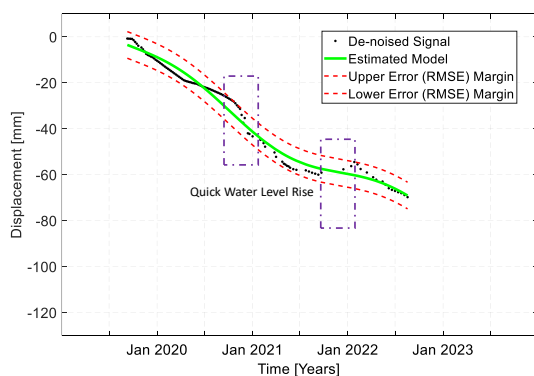
(b) MP III in Dataset B

Figure 6. The displacement time series (black dots), overall estimated time series model (green), and the lower and upper error margins (red) for MP I and MP III, which are located on the downstream shoulder of the Parapeiros-Peiros dam.

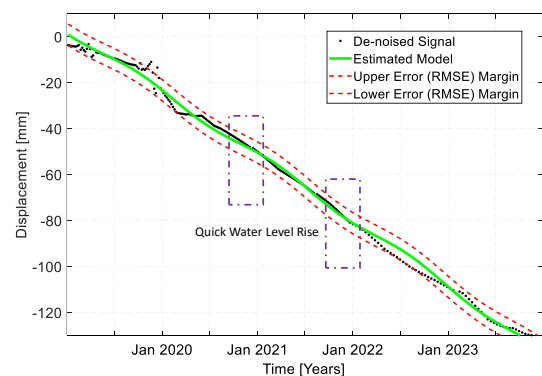
The estimated time series model of MP II and MP IV, which are located on the downstream side of the crown, are presented in Figure 7. Again, both displacement time series are approximated by a quadratic model for the trend component. The values of the linear coefficient are significantly higher than those estimated for MP I and MP III. The coefficients were estimated to be  $-29.7$  mm/y for MP II and  $-28.1$  mm/y for MP IV. The observed varying deformation rates from the crown of the dam body, along its shoulder to the toe, are common for embankment dams [16]. Additionally, both time series models have a periodic component. However, the estimated amplitude and cycle length of the periodic component for MP II and MP IV diverge from one another. The amplitude is  $-4.6$  mm for MP II and  $-1.6$  mm for MP IV, and the corresponding cycle lengths are 798.3 d and 519.9 d, respectively. These differences are again possibly influenced by the varying time span the datasets cover. Two events of quick water level rise in the reservoir occurred during the filling process [17]. The first one occurred in late 2020 and the second one in late 2021, both time spans are marked in purple in Figure 6 and Figure 7. The displacement time series of MP II diverges significantly from the quadratic during this time, see Figure 6(a). The displacement time series of MP IV also diverges from its trend during this time, see Figure 7(b). However, the periodic component is not as prominent as in the time series model of MP II. This might be due to the more

extended time span that the displacement time series of MP IV covers. The displacement time series includes data from 2022 and 2023, in addition to 2020 and 2021. The events of accelerated water level rise from fall and winter 2020 and 2021 did not repeat in the same severity at the end of 2022 and 2023. Therefore, the displacements due to these events have been smoothed over in the longer displacement time series and thus have led to different estimations for the periodic component of MP IV in comparison to MP II.

Based on the analysis of the mean deformation velocity maps, presented in Figure 3, the spatial deformation pattern of both datasets for the Parapeiros-Peiros dam are very similar. Using PSDefoPAT<sup>®</sup> in post-processing to analyze the temporal deformation pattern reveals that short-term temporal deformation patterns are not only smoothed over in the mean deformation map but also in cases where longer time series, such as Dataset B, are used. Highlighting the advantage of customizing the dataset to a specific time span that needs to be examined. For infrastructure monitoring, both long-term trends and short-term events are of interest. Thus, in-house processing of SAR images for surface deformation monitoring is still necessary.



(a) MP II in Dataset A



(b) MP IV in Dataset B

Figure 7. The displacement time series (black dots), the overall estimated time series model (red), and the lower and upper error margins (red) for MP II and MP IV, which are located on the downstream crown of the Parapeiros-Peiros dam.



## 5 SUMMARY

In this study, we examined the surface deformation of the Parapeiros-Peios dam during its first filling and shortly after, based on two datasets. The first dataset consists of 119 S1 SAR images and was processed in-house. The second dataset was downloaded from the EGMS. The observable spatial and temporal deformation patterns of both datasets were compared to explore the necessity for in-house advanced DInSAR processing for surface deformation monitoring of critical infrastructure, such as a newly built dam. An analysis of the spatial deformation patterns based on the mean deformation velocity maps showed good agreement between both datasets and that the highest deformation rates can be observed at the crown of the dam body, which agrees with the spatial deformation pattern typically observed in embankment dams [15]. The analysis of observable temporal deformation patterns, not directly visible in the mean velocity maps, was aided by the post-processing tool PSDefoPAT<sup>®</sup> developed by Fraunhofer IOSB. The tool extracts relevant information on the temporal deformation pattern of advanced DInSAR datasets by automatically determining the best-fitting time series model for each displacement time series of the dataset. In the case of the two datasets examined in this study, it was revealed that short-term displacement events are not only smoothed out in the mean deformation velocity maps but also in cases where longer time series are examined, e.g., Dataset B. Both long-term displacement trends and short-term events of diverging displacements are important to document and analyze in infrastructure monitoring. Pointing out a disadvantage of using the EGMS for infrastructure monitoring, which always examines a time span of five years. Another disadvantage is the time delay in providing the data, which is currently at a minimum of three-quarters of a year. Both of these aspects led us to the conclusion that the possibility of customizing the dataset to the deformation phenomena in question and the timelier fashion of processing still render in-house processing of SAR images for surface deformation monitoring of infrastructure necessary.

## REFERENCES

- [1] Scaioni, M., Marsella, M., Crosetto, M., Tornatore, V., Wang, J. "Geodetic and remote-sensing sensors for dam deformation monitoring", *Sensors*, vol. 18, no. 11, p. 25, 2018.
- [2] ICOLD, CIGB. "Automated dam monitoring systems: guidelines and case histories", *International Commission on Large Dams*, vol. 151, 2000.
- [3] Icold-cigb.org. "International Commission on Large Dams", (2022), <https://icold-cigb.org/> (22.12.2022).
- [4] Hunter, G., Fell, R., "The deformation behaviour of embankment dams", *University of New South Wales, School of Civil and Environmental Engineering*, 2003.
- [5] Sousa, J. J., Bastos, L., "Multi-temporal SAR interferometry reveals acceleration of bridge sinking before collapse", *Natural Hazards & Earth System Sciences*, vol. 13, no. 3, pp. 659-659, 2013.
- [6] Tomás, R., Cano, M., Garcia-Barba, J., Vicente, F., Herrera, G., Lopez-Sanchez, J. M., Mallorquí, J. J., "Monitoring an earthfill dam using differential SAR interferometry: La Pedrera dam, Alicante, Spain", *Engineering Geology*, vol. 157, pp. 21-32, 2013.
- [7] Evers, M., Thiele, A., Hammer, H., & Hinz, S. (2023). PSDefoPAT—persistent scatterer deformation pattern analysis tool. *Remote Sensing*, vol. 15, no. 19, 4646.
- [8] Demetrakopoulos, A. K., Dimas, A. A., Kaleris, B. K., Yannopoulos, P. X., Manariotis, I. D., Chasiakos, A., Podimata M., Lepidas, F., "Dam operator of the water project 'Water supply of Patras city, Patras Industrial Zone and Northwest settlements of Achaia prefecture via the Peiros and Parapeiros Rivers'", *University of Patras, Patras*, pp. 1-136, 2013 (in Greek).
- [9] Podimata, M. V., Yannopoulos, P. C., "A road map for resolving conflicts in dam's administration: The case of Peiros - Parapeiros dam in Greece", *European Water*, vol. 60, pp. 415-421, 2017.
- [10] Evers, M., Kyriou, A., Thiele, A., Hammer, H., Nikolakopoulos, K., Schulz, K., "How to set up a dam monitoring system with PSInSAR and GPS", *Proc. SPIE 11534, Earth Resources and Environmental Remote Sensing/GIS Applications XI*, vol. 11534, pp. 98-114, 2020.
- [11] Corns, C. F., "Gravity Dam Design and Analysis", in Jansen, R. B. (ed.) *Advanced dam engineering for design, construction, and rehabilitation*. Springer Science & Business Media, pp. 466-492, 2012.
- [12] Costantini, M., Minati, F., Trillo, F., Ferretti, A., Novali, F., Passera, E., Andersen, H., "European Ground Motion Service (EGMS)", *2021 IEEE International Geoscience and Remote Sensing Symposium IGARSS*, pp. 3293-3296, 2021.
- [13] Ferretti, A., Prati, C., Rocca, F., "Permanent scatterers in SAR interferometry", *IEEE Transactions on Geoscience and Remote Sensing*, vol. 39, no. 1, pp. 8-20, 2001.
- [14] Hooper, A., Zebker, H., Segall, P., Kampes, B. "A new method for measuring deformation on volcanoes and other natural terrains using InSAR persistent scatterers", *Geophysical Research Letters*, vol. 31, no. 23, L23611, 2004.
- [15] Capes, R., Passera, E., "End-to-end implementation and operation of the European Ground Motion Service (EGMS)", vol. 2, p. 33, 2023, <https://land.copernicus.eu/en/technical-library/egms-product-description-document/@download/file>
- [16] Kutzner, C. (2018). *Earth and rockfill dams: Principles for design and construction*.
- [17] Dounias, G.; Lazaridou, S.; Sakellariou, S.; Somakos, L.; Skourlis, K.; Mihos, S. The behavior of Asteri Dam on Parapeiros River during first filling, Greece. In *Proceedings of the 91st International Commission of Large Dams Annual Meeting, International Commission of Large Dams, Gothenburg, Sweden, 20 June 2023*; pp. 1–10.

# Exploring InSAR Capabilities for Bridge structural health monitoring using TerraSAR-X and Sentinel-1 Data

Maciej Kwapisz<sup>1</sup>, Vazul Boros<sup>1</sup>, Karl Heinz Gutjahr<sup>2</sup>, Ivana Hlavacova<sup>3</sup>, Cesar Martinez<sup>4</sup>, Stefan Schlaffer<sup>5</sup>, Juraj Struhar<sup>3</sup>, Alois Vorwagner<sup>1</sup>

<sup>1</sup>AIT, Giefinggasse 2, 1210 Vienna, Austria

<sup>2</sup>Joanneum Research, Steyrergasse 17, 8010, Graz, Austria

<sup>3</sup>GISAT, Milady Horakove 57, Praha 7, Czechia

<sup>4</sup>Red Bernard, Ernst-Melchior-Gasse 24, 1020 Vienna, Austria

<sup>5</sup>GeoSphere Austria, Hohe Warte 38, 1190 Vienna, Austria

email: maciej.kwapisz@ait.ac.at, vazul.boros@ait.ac.at, karlheinz.gutjahr@joanneum.at, ivana.hlavacova@gisat.cz, cesar.martinez@bernard-gruppe.com, stefan.schlaffer@geosphere.at, juraj.struhar@gisat.cz, alois.vorwagner@ait.ac.at

**ABSTRACT:** Remote sensing, in particular multi-temporal Synthetic Aperture Radar interferometry (MT-INSAR), is becoming an operational technique for landslide and subsidence monitoring, and it shows significant potential as an effective tool for bridge monitoring as well. In this case study, the possibilities of MT-INSAR-based structural health monitoring were demonstrated on a motorway bridge in Austria. The bridge is a perfect test object to compare the achieved accuracy due to the availability and good coverage of TerraSAR-X and Sentinel-1 data in combination with an in-situ deformation monitoring system. Due to the overlapping period of one year, a statistical evaluation of the obtained deformations along the bridge could be made. Another topic addressed in this contribution is the modelling of typical bridge deformation patterns, which are primarily caused by thermal expansion of the bridge. To detect critical displacement patterns, it is therefore necessary to separate the thermal component from the critical one. After completing this step, we applied and evaluated newly developed algorithms that detect changes in bridge deformation patterns and raise alarms when necessary. Furthermore, an interesting comparison was made between processed Sentinel-1 time series as provided by the Copernicus Land Monitoring Service via the European Ground Motion Service (EGMS) and the custom processing of the area of interest exclusively, utilizing site-specific temperature data.

**KEY WORDS:** Bridges, InSAR, MT-InSAR, Structural Health Monitoring, Sentinel, TerraSAR-X, thermal displacement.

## 1 INTRODUCTION

The transport infrastructure and its structures must be functionally intact, provide reliable performance and guarantee the safety of road users. Above all, this requires high standards for engineering structures such as bridges in terms of resistance to impacts, durability and sufficient fulfilment of requirements on structural safety. Other important aspects include low maintenance costs, few service interventions and cost-efficient operation over the entire life cycle.

In addition, the tasks of infrastructure operators with regard to their facilities have shifted from new construction to the maintenance and repair of existing structures or their replacement with new ones. The combination of an ageing infrastructure with limited financial resources makes this a very challenging task. For example, 50% of Austrian/German/Swiss motorways are now over 40 years old and most bridges are about to undergo major maintenance.

As of today, the condition of bridges is mainly determined by on-site inspections (visual inspections and close on examination). The main advantage of this method is the use of experienced personnel with knowledge of the historical development of the structural condition. Bridge monitoring systems with sensors are only used in special cases. A comprehensive, sensor-based examination of all structures is currently too time-consuming and costly to be used across the entire transport network.

### 1.1 InSAR for bridges

Remote sensing, particularly multi-temporal synthetic aperture radar interferometry (MT-INSAR), has a strong potential to be utilized for bridge monitoring. In this context,

the advantages of MT-INSAR are the large spatial and the dense temporal coverage (4-12 days, in the case of the Sentinel-1 constellation) of SAR data, the possibility of retrospective bridge monitoring and the fact that many bridges can be semiautomatically monitored at the same time. Furthermore, MT-INSAR techniques allow for the monitoring of slow movements that are often not apparent in visual inspections. But it is precisely the slowly occurring deformation patterns that play a major role in the assessment of the structural health of bridges. This could be shown by retrospective InSAR-based measurements of the bridge in Genoa (Italy) [1] after its collapse. First signs of critical deformation were identified several months/years in advance. However, [2] analyzed the same data sets as in [1] with two independent MT-INSAR methods and found no pre-collapse displacements in their consistent results, leading them to deeply disagree with the findings of [1]. In the reply, the importance of innovative research in the emerging field of InSAR applications to civil engineering structures is highlighted.

### 1.2 Motivation

The main focus of the study is to demonstrate the case study of the accuracy of the vertical deformation measurement of bridges based on MT-InSAR processing using Sentinel-1 and TerraSAR-X data. This was achieved by direct comparison with in-situ measurements for a selected motorway bridge in Austria. Although several such studies have been carried out [3], there is still a need to include more examples to increase their statistical significance. The conceptual basis of a flagging system to distinguish between normal bridge movement behavior resulting from environmental conditions and

abnormal behavior that may indicate structural damage is described here. Accurate bridge temperature is an important issue for this task. Therefore, different data sources on environmental conditions have been investigated and their influence has been analyzed.

### 1.3 Description of the chosen bridge and its in-situ measurement system

The bridge structure G46 is an integral bridge on the A2 Süd Autobahn of Austria, located in the south of Graz consisting of two identical structures, each carrying one traffic direction. It was built in 1969 and has a steel structure: a box girder with an orthotropic deck. The bridge is designed as a single-span composite frame, where the reinforced concrete columns support a steel beam with a span of 88 meters. It rests on non-inspectable lead bearings, presenting a challenge for direct inspection and assessment. Shortly after the completion, a sloping on the longitudinal beams was noticeable. A hydrostatic leveling monitoring system was installed in 2015 to monitor the structural integrity over time. Together with geodetic measurements, there was a confirmation of this sloping that is particularly relevant in the northern beam. A second monitoring system was then installed in 2018 which was complemented in 2020 with a redundant hydrostatic leveling system.

Hydrostatic levelling is a monitoring system used to measure relative displacements in the vertical direction. By interconnecting different liquid vessels, it is possible to use fluid pressure sensors to measure the movements of these vessels and the structures that these are attached to. This allows for very precise measurements over long distances and obstacles, that provides the relative vertical position between the sensors with accuracy under the millimetric scale.

RED Bernard installed two independent hydrostatic levelling systems each in one of the independent structures. These are installed in the abutment and the midspan of the bridge, which provides data about the displacement of the center of the bridge, taking the abutments as fixed points. An overview of the bridge and the sensors installed is shown in Figure 1.

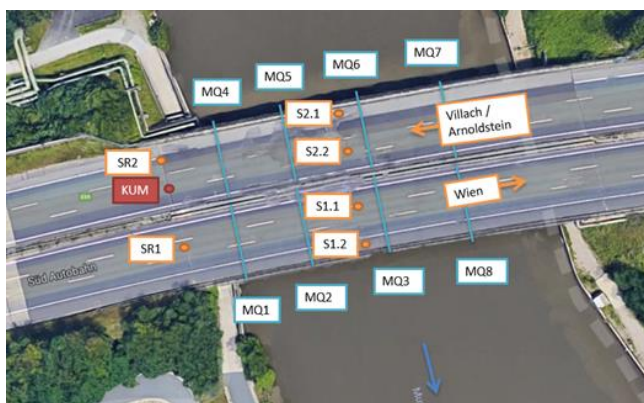


Figure 1. Highway bridge selected for the case study with schematic layout of the measurement system.

### 1.4 InSAR Data

One of the aims of the study was to compare the results obtained using different satellites and different processing methods. Both Sentinel-1 (C-band) and TerraSAR-X (X-band) data were used for this purpose. Sentinel-1 data was processed

specifically for the area of interest, but the centrally processed level 2a data from the EGMS platform [4] was also employed. Knowledge of the local temperature can improve the accuracy of custom processing. To evaluate this effect, processing was carried out separately using different temperature sources. Those used included global meteorological models, such as ERA5 [5], estimated structure temperature through Virtual Sensing [7][8], based on raster weather data from the GeoSphere data hub [6], and in situ temperature measurements from sensors installed on the bridge surface. TerraSAR-X data was available only from a single orbit and for a limited amount of images/acquisition dates, while Sentinel-1 data is available long-term and from three orbits. For a fair and direct comparison, it was decided to use only one ascending Sentinel-1 orbit (ASC146) for an initial comparison of the quality and quantity of data points. A large stack of data was processed for Sentinel-1 and the final (short) monitoring period was then cropped. An overview of the data used, including time frame, spatial resolution and orbit direction, is given in Table 1.

Table 1. Overview of satellite data used

Satellite (mode)	Sentinel-1 (Interferometric Wide Swath)	TerraSAR-X (StripMap)
Image no.	135	25
Timeline	08/20-08/23	05/22-03/23
Spatial resolution	5x20 m	3x3 m
Orbit direction	Ascending 146	Ascending

## 2 METHODOLOGY

### 2.1 Processing of the Sentinel and TerraSAR-X data

MT-InSAR processing was performed in SARproZ(c) software, independently for Sentinel-1 and TerraSAR-X data, listed in Table 1. Topography signal was subtracted using Copernicus DEM [9] and temperature effects were estimated based on in-situ measured, Virtual Sensing or ERA5 temperatures.

After thermal effect subtraction, Sentinel-1 time series (each point individually) were divided into segments with linear displacement and for each temporal segment, the noise level was estimated and segments with too high noise level were indicated as unreliable. Points which are not reliable for at least 3 years were discarded. After the segmentation, the thermal effects were re-added to the data, which was necessary for a direct comparison with the bridge deformations based on the EGMS and with the in-situ measurement, since in both of them the temperature effect is not compensated.

For TerraSAR-X data, the segmentation could not be performed because of too short timeline. As a quality criteria, interferometric temporal coherence was used, and points with coherence lower than a threshold of 0.8 were discarded. Unfortunately, the separation of thermal and permanent displacement was erroneous at the bridge center due to the short timeline: the minimum recommended timeline to reliably separate the permanent and thermal displacement is around 1.5 years [10].



It shall be noted that in spite of the fact that Sentinel-1 and EGMS resources are calculated using the same satellite data, the processing methodology slightly differs, as well as the criteria for point dropping.

MT-InSAR displacement time series were converted from SAR line of sight direction to vertical direction geometrically, based on the assumption that the displacement is purely vertical. If some points move in a horizontal direction, such a conversion gives incorrect results.

## 2.2 Clustering of the persistent scatterer (PS) Points on the bridge

The PS points for each of the three configurations (EGMS, Sentinel, TerraSAR-X) were first filtered to contain only points on the bridge based on their geo-location. As expected, the number of obtained PS points varied widely ranging from 34 (EGMS Figure 2a), 86 (Sentinel Figure 2b) up to 368 (TerraSAR-X, Figure 2c). To calculate the vertical deformations of the bridge with respect to its longitudinal coordinate, the PS points were clustered into 7 groups, which were distributed evenly along the bridge axis as shown in Figure 2.



Figure 2. PS Points with the background form OpenStreetMap (OSM), a) EGMS, b) Sentinel-1, c) TerraSAR-X

A time history of the deformation for each cluster was obtained as an average of these points, corresponding to the bridge deflection for that area. This approach is based on the

assumption that the points in this area move together, which is approximately true for a bridge deck, neglects however the effects of torsion along the bridge axis. This has been additionally testified with TerraSAR-X data, as there are enough PS points to divide each area further into three clusters across the width of the bridge. If the bridge had been subject to torsional deformations, it would have been visible, but none were observed.

Once the clustering was complete, the PS points were reselected based on the correlation matrix, which is a table showing the correlation coefficients between all PS points within a zone. The correlation coefficient is a statistical measure that expresses the extent to which two PS points are related. It ranges from -1 to +1, where +1 is a perfect positive correlation, -1 is a perfect negative correlation and 0 means no predictable relationship between the points. We estimated, that to classify a PS point as correlated with the others, it must be correlated with at least 1/3 of all points with a threshold of 0.5. It should be noted that this approach is case sensitive and must be carefully adapted when used for other bridges.

This step would be particularly important for bridges with many PS points underneath, as it would help to distinguish which points were on the bridge. In this case there is mostly water, where no PS points are present. Nevertheless, the use of this criteria helped to discard single points without any correlation to the others, which could be caused by the reflection of a non-structural element with some additional movement that does not reflect the deformation of the bridge.

The next step was to calculate a median value for each cluster based on the selected data points, including time series. This greatly reduced the noise of the PS points, removed the outliers and produced a smooth time series as can be seen in Figure 3.

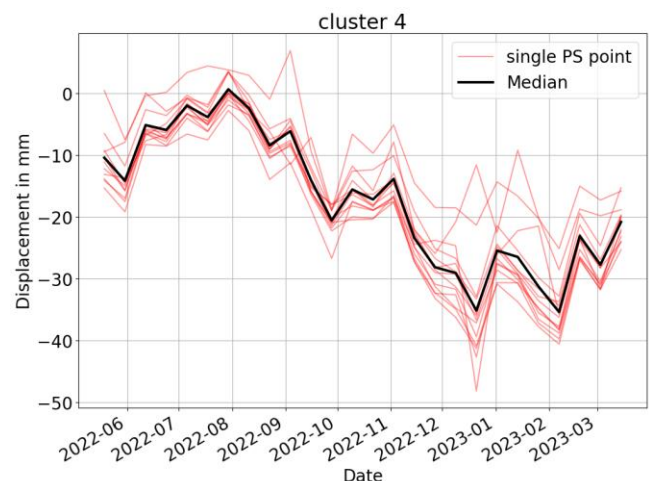


Figure 3. Calculation of the time – series for a cluster in the mid span for EGMS data.

## 2.3 Normal bridge deformation patterns

A critical task for MT-InSAR bridge monitoring and damage identification is the recognition of normal bridge deformation patterns resulting from environmental influences. This movement must subsequently be subtracted from the measured deformations to obtain a clear pattern. This step is not required when using the SARproZ(c) software mentioned above, as the estimation (and subtraction) can be performed within MT-

InSAR processing. However, it is essential for EGMS data or other MT-InSAR processing algorithms that do not automatically include it.

There are two common approaches to achieve this: data-driven and model-based. Both are effective in achieving the goal, but each has some advantages and limitations. Mostly, the first one is used and only when the time series is not long enough, the model-based one is employed.

In this study, we combined these approaches by identifying the normal bridge deformation pattern from the data and cross-checking it with an adapted finite element (FE) model. In this way, a link can be established between the single PS point approach and the whole bridge deformation shape. This approach requires two steps, which are described below.

The first step is to relate the deformation values calculated for each zone, as described in the previous section, to the structural temperature. If the data set is too short (less than 1.5 years), as may easily happens with commercial data (such as TerraSAR-X), this can be done with EGMS data (Figure 4). The structural temperature can be obtained either from in-situ measurements, if available, or by using the Virtual Sensing method developed by AIT [7][8]. If none of the above is accessible, the air temperature can be used, but a lower accuracy has to be accepted.

In the second step, a simple FE model was created, although only limited information about the cross-section geometry was available. In case of the examined integral bridge the longitudinal extension was restrained on both sides by very stiff elastic spring elements. To verify the temperature induced deformations, a uniform temperature was applied to the model and the deformations in vertical and horizontal directions were extracted for the same zones as defined for MT-InSAR processing. This was valuable for the decomposition of the Line of sight (LOS) deformation described in the next chapter and for the plausibility validation of the MT-InSAR results.

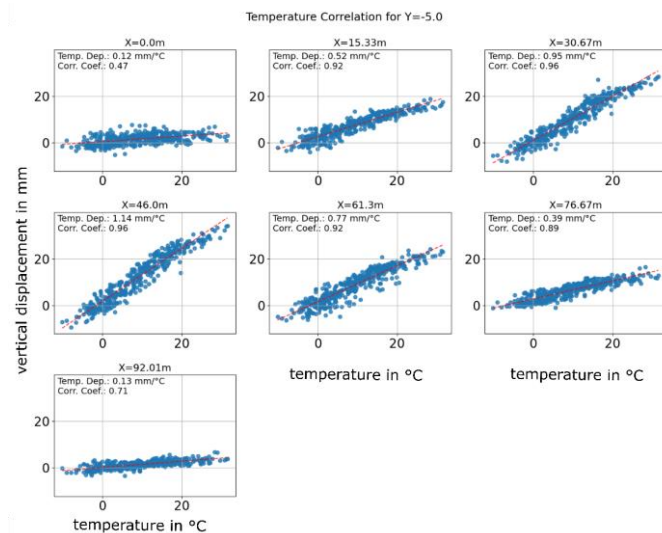


Figure 4. Thermal bridge deformation for each cluster based on EGMS.

In this way, not only the influence of temperature on the movement of each PS point was identified, but also the bridge deformation shape. The latter can be used to validate the

deformation over the entire length of the bridge if enough PS points are available.

## 2.4 LOS decomposition

The decomposition of  $d_{los}$  into  $d_{vertical}$  requires in general either both ascending and descending orbits or prior knowledge of the horizontal bridge movement based on normal bridge deformation patterns [3]. The analysis described in the previous section has shown that the temperature induced movement of the bridge is almost exclusively in the vertical direction. Therefore, the decomposition of  $d_{LOS}$  into  $d_{vertical}$ , which is of interest in this case, can be simplified to equation (1).

$$d_{vertical} = \frac{d_{LOS}}{\cos(\alpha_{incidence})} \quad (1)$$

## 2.5 Flagging system

In this study, we developed a method to detect abnormal bridge deflection. The purpose of this system is to identify bridges that require additional on-site inspection, rather than immediately triggering an alarm or leading to bridge closure based solely on MT-InSAR results. This approach ensures that potential structural issues are carefully evaluated before taking further action.

The flagging system was based on a data-driven approach in order to be flexibly adaptable to different types of bridges. The proposed system is designed to distinguish different classes of bridge displacement behaviors based on the time series of  $d_{vertical}$ :

- no trend or breakpoint,
- linear trend,
- one or more breakpoints,
- accelerating trend (i.e. at least one breakpoint and two different downward trend slopes  $\beta_{t2} < \beta_{t1}$ , where  $t_2 > t_1$  and  $\beta_{t1}, \beta_{t2} < 0$ ).  $\beta_{t1}, \beta_{t2}$  denote the slopes of the model segments before and after the breakpoint.

A data-driven approach assumes that normal bridge deformation patterns can be derived from the deformation time series as described in section 2.3. However, this may not always be the case as MT-InSAR time series may be too short to assume a pattern to be stable. In this study, only the Sentinel-1 time series was used as the displacement time series derived from TerraSAR-X was too short. Additionally, the flagging system provides for the possibility of applying user-specified thresholds on linear trends and total displacement. In order to minimise noise the PS points were grouped according in seven segments along the length of the bridge.

## 3 RESULTS

### 3.1 Influence of the temperature accuracy on MT-InSAR results

For data-driven methods to estimate/subtract temperature effects, temperatures at the acquisition times are necessary and their accuracy directly influences the (temporal) noise of the final time series of each point, and in some cases (especially those with shorter timeline), also other results, such as the displacement or estimated thermal dilation coefficient.

Results achieved using in-situ and Virtual Sensing temperatures are comparable, as the average differences between these two temperature sets is 0.7 degrees and the

maximum difference is 3.1 degrees (acquisition time for this data is 5PM UTC).

The differences between Virtual Sensing and ERA5 temperatures, on the other hand, (compared in a different processing not considered here), are much higher: average of 2.5 degrees and maximum 5.2 degrees (even if the acquisition time for this case was 5AM UTC).

If the number of images is high enough and the monitoring period long enough to provide numerical stability of separation between linear and thermal displacement components (at least 1.5 years according to [10]), the temperature inaccuracies (if not systematic in time) influence only the noise, i.e. the estimated point quality, which may slightly influence point density.

If temperature accuracy is lower but the number of points is high enough to provide for statistical processing, and the thermal dilation is also significant, higher accuracy can be achieved by temperature refinement procedure [10].

### 3.2 Comparison with in-situ measurements

To compare the accuracy of the three data sets considered, the recalculated values of vertical bridge deformation in the mid-span (zone 4) were compared with the in-situ measurement. A period of time from May 2022 to April 2023 was selected, which was common to all data sets. The direct comparison is shown visually in Figure 5, where green dots represent the in-situ measurements, while the red curve shows EGMS, black Terra-SAR-X and blue custom processed Sentinel-1 data. The normal bridge deformation patterns were not removed from either the reference in-situ or the InSAR data. If it was already subtracted during the MT-InSAR processing, it was added afterwards for the purpose of this comparison.

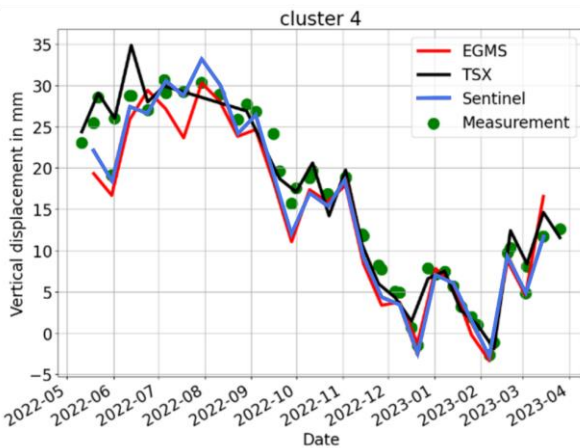


Figure 5. Comparison between the reference measurement (green dots), EGMS (red line), TSX (black line) and Sentinel (blue line) for the central segment of the bridge

The differences between each InSAR data set (EGMS, Sentinel-1 and TSX) and the reference were statistically analyzed and the resulting standard deviations are shown in Table 2. To compare the InSAR data with the reference measurements, first the mean value is calculated for all the Persistent Scatterer (PS) points belonging to the cluster associated with the location of the reference measurement. This mean value represents the average displacement derived from

the InSAR dataset for that area. Next, any offset between the two datasets is removed to align both to the same baseline. Once aligned, the mean value obtained from the selected InSAR cluster is then subtracted from the corresponding reference measurement. This difference reflects the deviation between the two datasets at the reference location. Finally, the standard deviation of these differences is calculated to quantify variability and assess consistency between InSAR-derived values and reference data.

Table 2. Comparison with in-situ measurement

data set	Std. deviation in mm
EGMS	3.8
Sentinel	2.1
TSX	1.7

The bridge deformations from the in-situ measurement are only given for the mid-span, so only these values were available for comparison. Therefore, a FE model of the bridge was used to perform a plausibility check on the deformed bridge shape that results from the MT-InSAR analysis. First, it was slightly updated to match the deformation in the center of the span by adjusting the stiffness of the constraining springs at the bridge abutments. Next, several TerraSAR-X acquisition times were selected and structural temperatures were calculated for each date and time. These temperatures were then applied to the FE model and the resulting bridge deformations were extracted and plotted as a solid line in Figure 6. Equivalent bridge shapes resulting from the TerraSAR-X data were plotted with the dashed line and the in-situ measurements with a point. The colors were kept the same for each date to enhance visual comparison. Not only does the mid-span deformation match very well between the FE model, reference measurement and MT-InSAR, but also the shape over the entire length of the bridge is similar. This demonstrates very high quality of the bridge deformation measurement obtained by MT-InSAR processing.

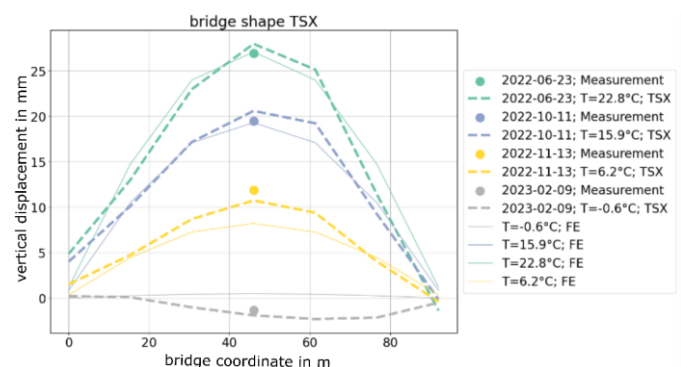


Figure 6. Comparison of the bridge shape according to FE Model (solid line), TSX (dashed) and reference (dots)

Once the direct comparison of the three datasets was complete, the analysis was repeated for the remaining two Sentinel-1 orbits. To obtain the total vertical deformation for each zone, the average of the results from each orbit was calculated after interpolation between acquisition times. In this way a combined EGMS and Sentinel-1 solution was obtained.



In addition, a combination of Sentinel-1 and TerraSAR-X data was derived for a total of four orbits. All three options for zone 4 (mid-span) were again compared with the reference measurement and the resulting standard deviations are shown in Table 3.

Table 3 Comparison with in-situ measurement for all available orbits

data set	Std. deviation in mm
EGMS	1.7
Sentinel-1	1.4
Sentinel-1 + TSX	1.3

The use of multiple orbits greatly improved accuracy, especially for EGMS. It is also evident that locally processed Sentinel-1 data can give better results than centrally processed EGMS, although both are based on exactly the same radar data. This is particularly true for the single orbit approach shown in Table 2. A novel combination of Sentinel-1 and TerraSAR-X data could improve the quality even more, but as the standard deviation is already very small, it does not bring that much improvement. It is expected that for bridges with scarce Sentinel-1 coverage the enhancement would be much more significant.

### 3.3 Flagging system

The developed algorithm for the flagging system was then applied to the processed data for each zone. This step allowed us to automatically evaluate potential anomalies in the bridge deflection and determine if the bridge may require further field inspection.

Figure 7 and Figure 8 show linear displacement rates up to 0.6 mm per year. Displacement rates of this magnitude were deemed too small to flag any of the anomalous behaviors listed in section 2.5. Breakpoints along the time series were detected, e.g., in zone 5, however, the overall displacement trend along the time series is close to zero. Overall, no flags were raised for any of the bridge segments.



Figure 7 Overview of annual displacement rates for each of the seven bridge segments. OSM is used as background map.

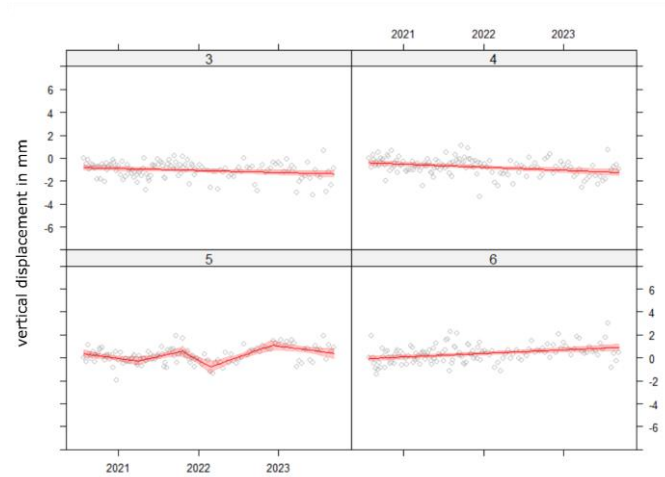


Figure 8 Displacement time series for four segments with fitted trend lines and 95% confidence intervals of the fitted lines.

## 4 CONCLUSIONS

While MT-InSAR bridge monitoring has certain limitations, it also offers unique advantages. One key advantage is its ability to provide retrospective monitoring when historical data are available, with Sentinel-1 data being available globally from 2015. However, due to its limited spatial resolution, Sentinel-1 data typically provides reliable results only for larger structures. For higher point density and improved accuracy, high-resolution satellite data from sources such as TerraSAR-X or Cosmo-SkyMed are required.

In this study, deformations from in-situ measurements of a highway bridge in Austria were compared with three different InSAR datasets: EGMS, processed Sentinel-1 and TerraSAR-X. As can be expected the number of PS points on the bridge is significantly higher for X-band radar compared to C-band. Nevertheless, the result show, that for the investigated bridge a remarkable accuracy, with standard deviations lower than 2 mm, can be achieved with all three datasets, especially if all available Sentinel-1 orbits are taken into consideration. This result not only highlights the great potential of MT-InSAR-based monitoring for detecting bridge deformations with high accuracy, but also raises the question whether expensive X-band data is required for bridge monitoring or often the freely available Sentinel-1 data is sufficient for this purpose.

To accurately assess actual bridge displacements and distinguish them from normal deformation patterns, thermal effects are estimated and subtracted from the MT-InSAR results. This correction helps to refine the analysis, ensuring that detected displacements more accurately reflect structural behavior rather than temperature-induced variations.

Finally, by implementing the flagging system, an automated method for identifying potentially problematic bridges was developed and demonstrated. However, it is important to emphasize that this approach is not intended to replace on-site inspections. Rather, it serves as a complementary tool that provides additional information to assist in the assessment of bridges that may require further investigation.

## ACKNOWLEDGMENTS

This research was funded by the Austrian Space Applications Programme (ASAP) through the project BOOST (FFG project number 892659).

## REFERENCES

- [1] Milillo, P.; Giardina, G.; Perissin, D.; Milillo, G.; Coletta, A.; Terranova, C. Pre-Collapse Space Geodetic Observations of Critical Infrastructure: The Morandi Bridge, Genoa, Italy. *Remote Sens.* 2019, 11, 1403.
- [2] Lanari, R., Reale, D., Bonano, M., Verde, S., Muhammad, Y., Fornaro, G., Casu, F., & Manunta, M. (2020). Comment on “Pre-Collapse Space Geodetic Observations of Critical Infrastructure: The Morandi Bridge, Genoa, Italy” by Milillo et al. (2019). *Remote Sensing*, 12(24), 4011. <https://doi.org/10.3390/rs12244011>
- [3] Giordano, P. F., Kwapisz, M., Miano, A., Liuzzo, R., Vorwagner, A., Limongelli, M. P., Prota, A., & Ralbovsky, M. (2025). Monitoring of a multi-span prestressed concrete bridge using satellite interferometric data and comparison with on-site sensor results. *Structural Concrete*, 26(1), 1-24. <https://doi.org/10.1002/suco.202400881>
- [4] <https://egms.land.copernicus.eu/>, accessed on 12.2024
- [5] Muñoz Sabater, J. (2019): ERA5-Land hourly data from 1950 to present. Copernicus Climate Change Service (C3S) Climate Data Store (CDS). DOI: [10.24381/cds.e2161bac](https://doi.org/10.24381/cds.e2161bac)
- [6] <https://data.hub.geosphere.at/dataset/inca-v1-1h-1km>, accessed 12.2024
- [7] Vorwagner, A., Kwapisz, M., Leopold, P., Ralbovsky, M., Gutjahr, K. H., & Moser, T. (2024). Verformungsmonitoring von Brücken mittels berührungsloser Satellitenradarmessungen. *Beton- und Stahlbetonbau*, 119(0005-9900), 636-647. <https://doi.org/10.1002/best.202400017>
- [8] Schlögl, M., Dorminger, P., Kwapisz, M., Ralbovsky, M., & Spielhofer, R. (2022). Remote Sensing Techniques for Bridge Deformation Monitoring at Millimetric Scale: Investigating the Potential of Satellite Radar Interferometry, Airborne Laser Scanning and Ground-Based Mobile Laser Scanning. *PFG-JOURNAL OF PHOTOGRAMMETRY REMOTE SENSING AND GEOINFORMATION SCIENCE*, 2022. <https://doi.org/10.1007/s41064-022-00210-2>
- [9] Copernicus DEM – Global and European Digital Elevation Model, <https://dataspace.copernicus.eu/explore-data/data-collections/copernicus-contributing-missions/collections-description/COP-DEM>, accessed 20.3.2025
- [10] M. Lazecky, I. Hlavacova, M. Bakon, J. J. Sousa, D. Perissin and G. Patricio, "Bridge Displacements Monitoring Using Space-Borne X-Band SAR Interferometry," in *IEEE Journal of Selected Topics in Applied Earth Observations and Remote Sensing*, vol. 10, no. 1, pp. 205-210, Jan. 2017, doi: 10.1109/JSTARS.2016.2587778

# Satellite-based InSAR for monitoring and safeguarding high-voltage power pylons amid the energy transition

Markus Dörfler<sup>1</sup>, Markus Keuschnig<sup>1,2</sup>, Ingo Hartmeyer<sup>2</sup>

<sup>1</sup>AUGMENTERRA GmbH, Urstein Süd 15, 5412 Puch bei Hallein, Austria

<sup>2</sup>GEORESEARCH Forschungsgesellschaft mbH, Urstein Süd 15, 5412 Puch bei Hallein, Austria

email: markus.doerfler@augmenterra.com, markus.keuschnig@georesearch.ac.at, Ingo.hartmeyer@georesearch.ac.at

**ABSTRACT:** Resilient high-voltage grids are essential for ensuring energy supply and preventing. However, climate change, the energy transition and the required expansion of electricity grids pose growing challenges for infrastructure operators in the energy sector. In Austria, landslides in alpine regions and decreasing groundwater levels in flat areas represent significant potential risks to power pylons. The Austrian Power Grid AG (APG), which operates the Austrian transmission grid, faces growing demands to detect damage at an early stage and to guarantee grid security amid changing climatic conditions. Satellite-based Interferometric Synthetic Aperture Radar (InSAR) potentially provides millimeter-precise, area-wide monitoring of ground motion and structural deformations. Periodic InSAR data updates (e.g. semi-annually) enable a complete and continuous analysis of all single structures such as power pylons and thus facilitate an assessment of the structural integrity of the entire grid. This allows the early identification of risks such as landslides or structural changes and the implementation of predictive maintenance. This paper highlights previous experiences and future potentials of integrating the InSAR technology into APG's workflows and risk management, which contributes to sustainable planning and increased grid stability in an increasingly complex system.

**KEY WORDS:** Wide-area InSAR; Power Grids; Monitoring; Predictive maintenance.

## 1 INTRODUCTION

The Austrian Power Grid AG (APG) plays a central role in Austria's energy infrastructure. As the operator of the Austrian electricity transmission network, APG is responsible for ensuring a continuous and reliable power supply. A critical factor in maintaining efficient and secure grid operations is the early detection of potential disruptions or structural changes in the transmission infrastructure.

APG manages an extensive network of power lines, substations and more than 12.000 power pylons in Austria, that require regular monitoring. Identifying ground movements, structural deformations, and other potential risk factors is essential to minimize unplanned outages and enhance operational security. In this context, a feasibility study is being conducted to evaluate the integration of satellite-based InSAR technology into APG's monitoring strategy, aiming to enhance early-warning capabilities and risk mitigation.

## 2 BASICS OF INSAR TECHNOLOGY

Synthetic Aperture Radar (SAR) satellites use radar signals to generate high-resolution images of the Earth's surface, independent of weather conditions or daylight. The principle is based on transmitting microwave pulses, which are reflected by the Earth's surface or manmade objects and received by the satellite. These signals are processed to create detailed images through complex signal processing techniques.

### 2.1 Reflection of Radar Waves

The reflection of radar waves follows the physical principles of electromagnetic wave propagation. The strength of the reflected signal depends on two main factors:

- **Geometry of the Reflector:** When incoming radar waves are reflected at an appropriate angle, a significant portion of the signal returns to the satellite. Smooth, metallic surfaces or structural elements enhance reflection.
- **Material Properties of the Surface:** Materials with high electrical conductivity, such as metals, reflect radar waves effectively, whereas natural surfaces like vegetation or snow scatter waves in various directions, reducing the returned signal strength.

### 2.2 Different Frequency Bands for Various Applications

SAR satellites operate at different frequency bands to serve specific applications:

- **L-Band (1-2 GHz):** Commonly used for agricultural and forestry monitoring due to its ability to penetrate vegetation.
- **C-Band (4-8 GHz):** Frequently used by Earth observation satellites like Sentinel-1, offering a balance between resolution and penetration depth.
- **X-Band (8-12 GHz):** Employed in high-resolution applications such as infrastructure monitoring and military surveillance, providing high spatial resolution but limited penetration capability.

### 2.3 Orbit and Imaging Geometry

SAR satellites typically follow a polar or sun-synchronous orbit, capturing data in both ascending (ASC) and descending (DSC) imaging geometries. In the ascending geometry, the satellite moves from the South Pole toward the North Pole, while in the descending geometry, it moves from the North Pole toward the South Pole. A schematic representation of the flight



directions can be seen in Figure 1. This configuration allows for continuous monitoring of the Earth's surface.

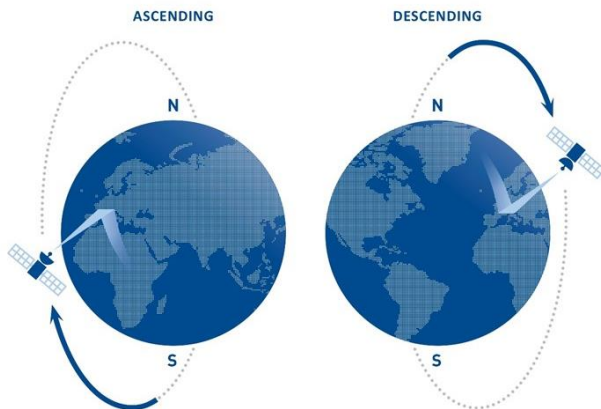


Figure 1. Ascending (ASC) and descending (DSC) geometry [2].

#### 2.4 Line of Sight (LOS) and Incidence Angle

The SAR system's viewing direction (azimuth angle) is typically oriented sideways ( $90^\circ$  to the flight path). In the ASC geometry, the satellite looks eastward, while in the DSC geometry, it looks westward. The incidence angle is the angle between the vertical and the incoming radar beam, varying depending on the satellite system and terrain conditions. A larger incidence angle occurs further from the nadir (directly below the satellite), affecting shadowing, measurement accuracy, and displacement detection.

Since SAR images capture displacements along the LOS, movements perpendicular to this direction remain partially undetected. This limitation can be mitigated through multi-orbit analysis (see chapter 2.6) or integration with ground-based data sources.

#### 2.5 From SAR to InSAR

As SAR satellites repeatedly capture images of the same area over time, they provide insights into surface changes. Each SAR acquisition records two essential parameters: (a) Amplitude, representing the energy of the reflected signal, and (b) Phase, related to the distance between the sensor and the target.

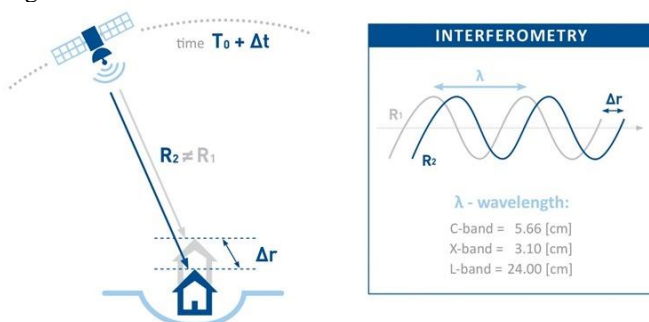


Figure 2. Schematic representation of how InSAR (interferometric SAR) works. The phase shift ( $\Delta r = R_2 - R_1$ ) results from the phase information ( $R$ ) of two or more images of the same area at different times or different positions [2].

Interferometric SAR (InSAR) compares phase differences between two or more SAR images to detect changes in distance

between the satellite and the Earth's surface along the LOS-vector. [1] This technique enables millimeter-accurate measurements of slow ground movements, such as landslides, earthquakes, and subsidence. Figure 2 shows the phase calculation that is performed for each individual measurement pixel.

#### 2.6 Displacement Vectors and 2D Decomposition

InSAR primarily measures displacement along the LOS. To derive vertical or horizontal displacement components, a 2D decomposition technique is applied using data from both ASC and DSC imaging geometries. This method allows for estimating movement in the east-west and vertical directions, while north-south displacement remains largely undetectable or at least underestimated and requires complementary data sources, such as GNSS measurements.

### 3 DATA PROCESSING

#### 3.1 SqueeSAR® Analysis

In this study, the applied SAR data was processed using the multi-interferogram technique known as SqueeSAR® [1]. SqueeSAR®, a patented method developed by TRE ALTAMIRA, improves the reliability of InSAR measurements in heterogeneous environments by reducing phase decorrelation in areas with vegetation or urban structures. It combines Persistent Scatterers (PS) and Distributed Scatterers (DS) to achieve a high spatial density of measurement points.

To ensure high precision and accuracy, SqueeSAR® requires a dataset of at least 15 to 20 SAR images acquired over the same area using the same acquisition mode and geometry. By combining PS, which are stable and well-defined radar reflectors, with DS, which represent diffuse scattering signals, SqueeSAR® can extract reliable movement data even in areas with low signal stability. This enables comprehensive monitoring of ground deformations.

#### 3.2 Precision and Accuracy

Precision and accuracy are crucial in measurement science:

- Precision refers to the consistency of repeated measurements. A measurement series is precise if repeated observations under the same conditions yield similar values, regardless of their deviation from the true value.
- Accuracy describes how close a measurement is to the actual (true) value, meaning a measurement is accurate if systematic errors are minimal.

#### 3.3 Determining Precision in InSAR Data

The precision of InSAR results is influenced by:

- Measurement Point Locations: The geolocation accuracy of measurement points depends on the SAR coordinates and the derived height from the InSAR analysis. Higher resolution sensors improve geocoding precision.
- Displacement Time Series: The standard deviation ( $\sigma$ ) of individual measurements quantifies the variation around the mean displacement rate. Lower  $\sigma$  values indicate higher precision, while higher values suggest greater measurement variability.

For a dataset of at least 30 SAR images covering a two-year period, measurement points within 1 km of a reference point typically exhibit a standard deviation of less than 1 mm/year. The average standard deviation for a single measurement is usually  $\pm 5$  mm. While InSAR precision is statistically derived, measurement accuracy is usually validated with ground-based reference data, such as geodetic surveys, achieving accuracy in the sub-millimeter range [1].

### 3.4 MatchSAR® - Transformation of InSAR measurements into objects

MatchSAR® is an advanced algorithm developed by AUGMENTERRA in collaboration with TRE ALTAMIRA. It transforms millions of InSAR measurement points across Austria by aligning them with physical structures such as buildings, power pylons, dams, roads, and railways.

The transformation process consists of several key steps. First, a spatial analysis and quality control of all available InSAR measurement points are conducted to ensure accurate attribution of ground movements to the corresponding structures. Additionally, the algorithm integrates InSAR data with other terrain and structural datasets, creating a comprehensive, multidimensional view of each object. As a result, every object processed by MatchSAR® is assigned a displacement time series covering at least two to three years, enabling in-depth movement analysis (e.g., steady vs. accelerating displacement).

MatchSAR® is a core component of the 'AUGMENTERRA Observer', a Software-as-a-Service (SaaS) platform featuring state-of-the-art 3D visualization. The 'AUGMENTERRA Observer' is accessible via various devices, including PCs, smartphones, and tablets, allowing users to retrieve structural and ground movement data within seconds. By automatically updating measurement data every six months, MatchSAR® ensures continuous tracking of structural movements, significantly reducing manual processing efforts and improving long-term risk assessment capabilities.

## 4 USE CASE: WIDE-AREA MONITORING OF STRUCTURAL MOVEMENTS AT APG

For the APG power pylon monitoring use case, Sentinel-1 data is automatically reprocessed every six months for all locations. Using a three-year moving window, updated measurement data is consistently incorporated into structural stability assessments. This approach ensures up-to-date risk evaluations, with new measurement pixels available every six to twelve days depending on Sentinel-1A/B availability. This guarantees a consistent and up-to-date analysis of structural stability over time. The results are implemented directly into APG's internal GIS using an API solution to ensure maximum availability and up-to-date information. Data access and visualization in the customer interface is displayed in Figure 3. A detailed time series of a moving pylon with an average movement of about 19 mm/year is shown in Figure 4.

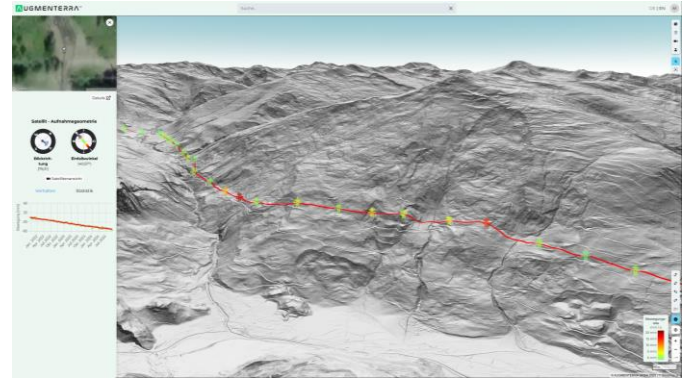


Figure 3. Structural movement measurements from InSAR and locations of the APG power pylons, visualized using the 3D WebGIS application 'AUGMENTERRA Observer'.

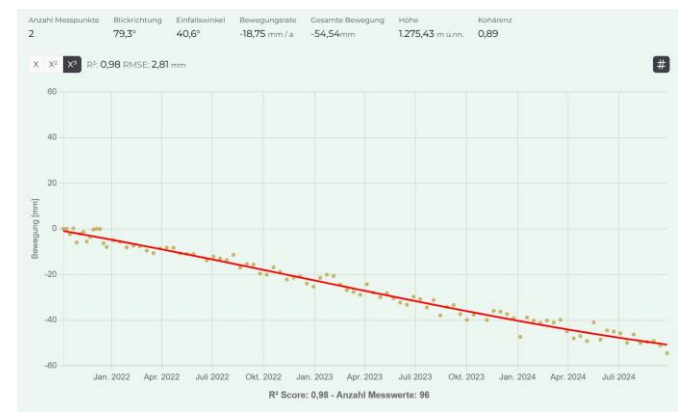


Figure 4. Time series of a power pylon located in Figure 3. The pylon shows an average movement of approx. 19 mm/year in the LOS direction. The movement behavior is homogeneous.

### 4.1 Monitoring Ground Deformation and Stability

One of the primary applications of InSAR for APG is detecting and analyzing ground deformations that could compromise the stability of power pylons. Subsidence, landslides, and soil compaction can lead to shifts in foundation structures, potentially endangering the transmission network. This allows the definition of hotspots that can be subjected to more intensive monitoring. A distinction is made between two main processes:

- Landslide and erosion detection: InSAR can identify gradual slope movements that may threaten pylon stability.
- Subsidence monitoring: Infrastructure near mining areas, groundwater extraction zones, or soft soil regions can be monitored for ground subsidence.

### 4.2 Structural Health Monitoring of Power Pylons

In addition to assessing ground stability, InSAR can also detect internal deformations of transmission pylons. While traditional structural monitoring relies on ground-based sensors, satellite-based InSAR provides:

- Large-scale coverage: Continuous monitoring of the entire power grid, including remote areas.

- Millimeter-level accuracy: Detection of slight tilting or deformation of pylons over time.
- Historical data comparison: Analysis of past SAR images to identify long-term structural trends.

#### 4.3 *Integration with Other Monitoring Technologies*

For optimal monitoring, InSAR data can be combined with:

- Ground-based sensors: Combining InSAR with GPS, inclinometers, and strain gauges enhances measurement reliability.
- Drone and LiDAR surveys: High-resolution aerial surveys provide additional validation of deformation patterns detected via satellite.

#### ACKNOWLEDGMENTS

We extend our gratitude to the Austrian Power Grid team, particularly Alois Ammerer, Christian Laister, and Gabriel Stollhof, for their continued collaboration and trust in our data. Their expertise and insights have played a key role in refining our automated monitoring system to meet the evolving demands of the energy sector.

#### REFERENCES

- [1] Ferretti, Alessandro; Fumagalli, Alfio; Novali, Fabrizio; Prati, Claudio; Rocca, Fabio; Rucci, Alessio (2011): A New Algorithm for Processing Interferometric Data-Stacks: SqueeSAR. In IEEE Trans. Geosci. Remote Sensing 49 (9), pp. 3460–3470. DOI: 10.1109/TGRS.2011.2124465.
- [2] TRE ALTAMIRA (2024): TRE ALTAMIRA. Company. TRE ALTAMIRA. Available online at <https://site.tre-altamira.com/>, updated on 8/16/2024, checked on 12.03.2025.



## Remote Sensing for Stability Assessment of River Bridges: Case Study of the Red River Bridge in Winnipeg, Canada

D. Cusson<sup>1</sup>, H. Stewart<sup>2</sup>, C. Regoui<sup>1</sup>, J. Zhao<sup>3</sup>, K. Helmi<sup>4</sup>, B. Telehanic<sup>3</sup>, E. Murison<sup>5</sup>, D. Thomson<sup>3</sup>, A. Mufti<sup>3</sup>, S. Clark<sup>3</sup>

<sup>1</sup>National Research Council Canada, Ottawa, Ontario, Canada

<sup>2</sup>Fugro, Houston, Texas, USA

<sup>3</sup>University of Manitoba, Winnipeg, Manitoba, Canada

<sup>4</sup>Arab Academy for Science, Technology and Maritime Transport, Alexandria, Egypt

<sup>5</sup>Manitoba Transportation and Infrastructure, Winnipeg, Manitoba, Canada

Emails: daniel.cusson@nrc-cnrc.gc.ca, hstewart@fugro.com, chaouki.regoui@nrc-cnrc.gc.ca, junhui.zhao@umanitoba.ca, kareem.helmy@gmail.com, telehanb@myumanitoba.ca, evangeline.murison@gov.mb.ca, douglas.thomson@umanitoba.ca, aftar.mufti@umanitoba.ca, shawn.clark@umanitoba.ca

**ABSTRACT:** With Canada's transportation infrastructure aging, compounded by the effects of climate change, the need to enhance condition assessment through structural health monitoring is increasingly critical to ensure integrity, performance, public safety, and cost-effectiveness. Bridge pier scouring, caused by high river flow and turbulence that erode the surrounding bed material, poses a significant threat to bridge stability and can potentially lead to failure. Conventional scouring inspections are often time-consuming and costly. This paper presents a case study on the Red River Bridge in Winnipeg, Canada, where an innovative, multidisciplinary assessment of bridge stability was performed, including both environmental and structural investigations. The environmental investigation utilized multispectral satellite imagery and optical-band unmanned aerial vehicle (UAV) imagery, combined with large-scale particle image velocimetry (LS-PIV), to assess river flow and turbulence. An anomalous condition near a bridge pier, detected in multispectral satellite imagery, was confirmed by UAV photogrammetry and LS-PIV river current patterns. The structural investigation, detailed in this paper, incorporated Persistent Scatterer Interferometric Synthetic Aperture Radar (PS-InSAR) deformation measurements from satellite imagery, in-situ measurements on the bridge deck, and numerical bridge model predictions. This provided an assessment of the bridge's structural behavior and its potential connection to the condition observed near one of the bridge piers.

**KEY WORDS:** Satellite PS-InSAR; Remote sensing; Bridge deformation; Case study.

### 1 INTRODUCTION

#### 1.1 Background and motivation

Canada's transportation infrastructure, especially its bridges, is facing significant challenges due to aging and environmental stresses. Many bridges across the country are nearing the end of their design life, necessitating substantial investments in maintenance and upgrades [1]. The aging infrastructure is further strained by increasing traffic loads and environmental impacts, such as extreme weather events and temperature fluctuations [2]. These factors accelerate the deterioration of bridges, affecting their safety, performance, and economic viability. The need for innovative solutions to ensure long-term sustainability and reliability is more urgent than ever [3].

Bridge pier scouring is a major issue impacting river bridges. It occurs when fast-flowing water erodes the bed material surrounding bridge piers, leading to instability and potential structural failure [4]. This problem is compounded by climate change, which is causing more frequent and severe flooding events [5]. Such conditions accelerate the scouring process, increasing risks to bridge safety and necessitating advanced monitoring and mitigation strategies [6]. Research has shown that various factors, including water velocity, bed material type, and pier shape influence the extent of scouring [7]. Effective countermeasures, such as pier modifications and protective structures, are essential to mitigate these risks [8].

In response to these challenges, there is a growing need to assess bridge safety and performance through structural health monitoring technologies. Remote Sensing for Structural Health Monitoring (RS-SHM) is an emerging field that uses multispectral and radar satellite remote sensing, combined with

low-footprint in-situ measurements, to monitor bridge structures between routine inspections. This approach, which does not require bridge closure or create traffic disruption, provides early awareness of developing risks and understanding of how environmental changes may affect structural behaviour and safety. By integrating satellite data with in-situ measurements, engineers can gain comprehensive insights into bridge structural behaviour, enabling proactive maintenance and risk management. This approach enhances safety by providing early detection of risks while improving cost-effectiveness through optimized maintenance plans and extended bridge lifespan.

The integration of advanced sensor technologies and cloud-based platforms in SHM systems allows for continuous real-time monitoring of bridge conditions. These systems can detect even minor structural changes, such as vibrations and displacements, which are critical for assessing the health of aging infrastructure. The use of SHM technologies not only improves the accuracy of bridge assessments but also facilitates timely interventions, thereby preventing catastrophic failures and extending the service life of bridges. As Canada continues to face environmental and economic pressures, the adoption of innovative SHM solutions will be crucial in maintaining the integrity and safety of its transportation infrastructure.

Additionally, the implementation of predictive maintenance strategies, supported by SHM data, can significantly reduce maintenance costs and extend the lifespan of bridge structures, which are typically designed for 75 years in Canada. Predictive maintenance involves analyzing data from SHM systems to forecast potential issues before they become critical, allowing for timely and targeted interventions.

This proactive approach enhances safety and optimizes resource allocation, ensuring that inspection, maintenance and rehabilitation efforts are focused on areas with highest risk.

Ultimately, aging transportation infrastructure requires substantial investments to address increasing traffic loads and environmental impacts. Adopting advanced SHM technologies and predictive maintenance strategies offers a promising solution to improve safety, performance, and longevity.

### 1.2 Case study site

The Red River is a shallow meandering river flowing north through the city of Winnipeg in Manitoba, Canada. The 258-m long Red River Bridge, with four lanes of vehicle traffic and one lane of foot traffic, crosses the Red River south of Winnipeg. Figure 1 shows a satellite view of the bridge, with annotations for bridge piers (P1 to P6), and west and east abutments (WA, EA). Piers P3, P4, and P5 are located in the permanent river channel, while Piers P1, P2, and P6 may become inundated at their base during periods of high flow.

From west to east, the bridge structure consists of a total of seven spans, including two simply-supported spans between WA and P2, where the longitudinal movement is fixed at P1, followed by four continuous spans between P2 and P6, where the longitudinal movement is fixed at P4, and a last simply-supported span between P6 and EA, where the longitudinal movement is fixed at the east abutment. This detail will explain the direction and extent of thermal expansion of deck along the bridge length. Ambient temperature data for this site was acquired from a local weather station located at the Winnipeg international airport, as given in Figure 2.



Figure 1. Bridge structure over Red River in Winnipeg, MB.



Figure 2. Ambient air temperature measured at Winnipeg international airport during the bridge monitoring period.

## 2 METHODS

### 2.1 Environmental investigation summary

In 2023-2024, a multimodal RS-SHM environmental investigation (not yet published) was conducted to detect and monitor potential hazards at the Red River Bridge and its surroundings from multispectral satellite imagery and optical-band UAV imagery. Eight Maxar Worldview mono orthoimage scenes acquired during the ice-free spring and summer months of 2022 were evaluated for river flow conditions that may affect the bridge structure stability. UAV photogrammetry of the riverbanks was conducted in November 2023, and two UAV-based Large Scale Particle Image Velocimetry (LS-PIV) collections were acquired in Spring 2024. These investigations did not require bridge closure or disrupt normal traffic, nor did they necessitate unsafe surveying practices. The findings are used to inform the structural investigation in order to verify if a correlation with the monitored bridge deformations do exist.

### 2.2 Georeferencing of SAR satellite imagery

Accurate positioning of SAR satellite imagery data, including the integration of up-to-date elevation data, is essential for precise georeferencing during the PS-InSAR analysis [9]. This process ensures that measurements are correctly aligned with real-world coordinates, which is critical for detecting subtle ground deformations. A reliable Digital Surface Model (DSM) plays a pivotal role in this step by accounting for topographic variations. Inaccuracies in the DSM can lead to misplacement of Persistent Scatterers (PS), introducing errors in phase interpretation and ultimately compromising the reliability of deformation estimates. Furthermore, an accurate DSM supports the separation of topographic and displacement signals, enhances phase unwrapping, and improves the 3D localization of PS, particularly in complex urban or mountainous terrains.

The horizontal coordinate reference frame for this project is the North American Datum of 1983 Canadian Spatial Reference System (NAD 83 CSRS). The horizontal geographical units were projected into planar coordinates in the Universal Transverse Mercator (UTM) system, Zone 14 North with a central meridian of 99° W. The vertical coordinate reference system is the Canadian Geodetic Vertical Datum of 2013 (CGVD-2013).

A stereo pair of 50-cm resolution panchromatic-band Airbus Pleiades 1-B satellite images acquired on 14 June 2021 was used to create a 1-m resolution Digital Surface Model (DSM) of the Red River in the Winnipeg metropolitan area, inclusive of the Red River Bridge. Image selection criteria included clear views of the river surface in the vicinity of the bridge, with no clouds, cloud shadows, or aerosols. The source images of the stereo pair were georeferenced using a sparse RTK survey of tie points (bases of lampposts on the pedestrian walkway of the bridge) on the bridge deck conducted by the University of Manitoba with a DJI D-RTK 2 mobile positioning system, orthorectified using the High Resolution Canadian Digital Elevation Model (HR-CDEM), and used to produce the DSM (Figure 3) and image stack with horizontal coordinates and elevations in the project coordinate reference system described previously. Horizontal and vertical accuracies of a DSM derived from satellite imagery in this manner is estimated at +/- 0.5 m horizontal (CE 90) and +/- 1.5 m vertical (LE90) [10].



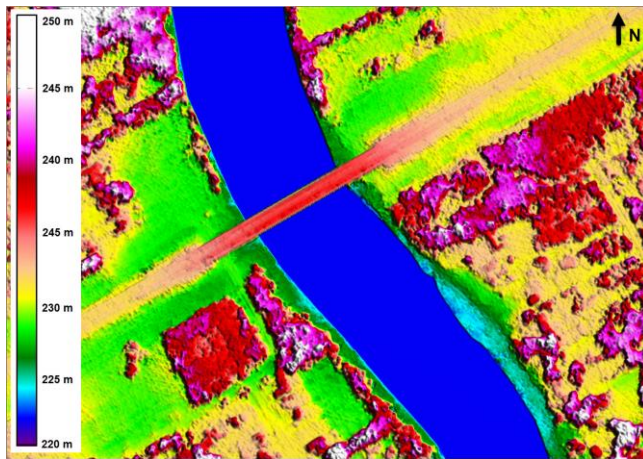


Figure 3. Digital surface model created for the Winnipeg bridge and its surroundings.

### 2.3 PS-InSAR satellite measurements

Persistent Scatterer Interferometric Synthetic Aperture Radar (PS-InSAR) is a satellite-based remote sensing technique used to monitor ground deformation over time. It involves analyzing a series of SAR images acquired at different times to measure the motion of stable ground features (or objects), known as persistent scatterers (PS). This method allows the detection of subtle movements and deformations on the Earth's surface or man-made structures by comparing the phase information (e.g., phase change and intensity) of the radar signals across multiple temporal acquisitions. More details on the PS-InSAR technique are available elsewhere [11][12], along with its applications in preventing bridge collapses [13][14].

The technique was applied to two image stacks of SAR satellite imagery (Figure 4) acquired over the Winnipeg metropolitan area from C-band satellites of the RADARSAT Constellation Mission (RCM), including one stack acquired in ascending viewing geometry (i.e., satellite travelling from south pole to north pole, looking to the East) with an incidence angle of  $45^\circ$  and a satellite track heading of  $350^\circ$ , and a second stack acquired in descending viewing geometry (i.e., satellite travelling from north pole to south pole; looking to the West) with an incidence angle of  $42^\circ$  and a satellite track heading of  $190^\circ$ . The bridge heading angle was measured at  $62^\circ$ . The RCM imaging mode was the Spotlight mode with a nominal pixel resolution of  $1 \times 3$  meters (range vs. azimuth). The minimum and maximum satellite revisit times were four days and twelve days, respectively. The image acquisition period covered in this paper spans approximately one year from May 2023 to June 2024. Table 1 provides the details on the two satellite image stacks processed for this study.

Table 1. Features of RCM satellite image stacks.

Look direction	Ascending	Descending
Beam mode	Spotlight	Spotlight
Incidence angle	$45^\circ$	$42^\circ$
Satellite track heading	$350^\circ$	$190^\circ$
Resolution (range x azimuth)	$1 \times 3$ m	$1 \times 3$ m
Swath (range x azimuth)	$20 \times 5$ km	$20 \times 5$ km
Number of scenes	29	55
Stack start date	1 May 2023	2 May 2023
Stack end date	16 June 2024	17 June 2024

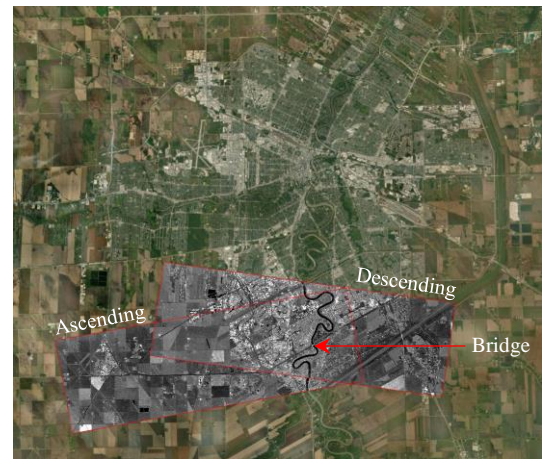


Figure 4. Winnipeg metropolitan area showing footprints of the ascending and descending satellite image stacks.

### 2.4 In-situ displacement measurements

Figure 1 above illustrates some structural parameters of the bridge, such as the connection details between girders and piers. Permanent survey positions were identified on the bridge deck for the in-situ measurements using a total station (TS) and GPS. These positions were located on the deck and aligned with abutments, piers and mid-spans. Matching markers were added to the metal handrail beside the pedestrian walkway so that the reflection prism for TS and the GPS Antenna could be precisely mounted on the same positions with good repeatability (within  $\pm 1$  mm error) during the measurement period.

The position measurements using the total station were taken from each abutment. The two sitting positions for the TS were fixed, and their origin coordinates were determined using a real-time kinematic (RTK) global positioning system (GPS). The coordinates of the position marks were determined by moving the 360-degree prism from the WA position to the centre of the bridge when the measurements were conducted from the west abutment, and by moving the prism from the EA position to the centre of the bridge when the measurements were taken from the east abutment.

The measurements using the GPS instrument were conducted using a base station and a rover. The base station was mounted at the WA position, and the rover was moved to all positions from WA to EA. The position measurements from the rover can achieve a horizontal positioning accuracy of 6 millimetres with a signal correction from the base station, while a vertical positioning accuracy of 10 millimetres can be achieved. The RTK correction signal was communicated between the rover and the base using a radio link. To ensure accuracy, data were collected with correction times of 1-2 seconds. The thermal movement of the marked positions on the handrail was measured against temperature during a period of a few months.

### 2.5 Numerical bridge model simulations

Figure 5 shows the finite element model (FEM) of the bridge using the SAP 2000 software, assuming linear elastic material behaviour. It was used to study the dynamic vibrations of the bridge and the ambient temperature dependence of bridge displacements. The bridge's steel girders and concrete slab were modelled using thin shell elements connected by stiff link elements.



The bracing system, brackets, and edge beams supporting the sidewalk were modelled using frame elements. The bridge abutments were modelled using thick shell elements, and the bearings between abutments and girders were modelled with special link elements to allow rotation only or rotation and relative displacement depending on bearing type.

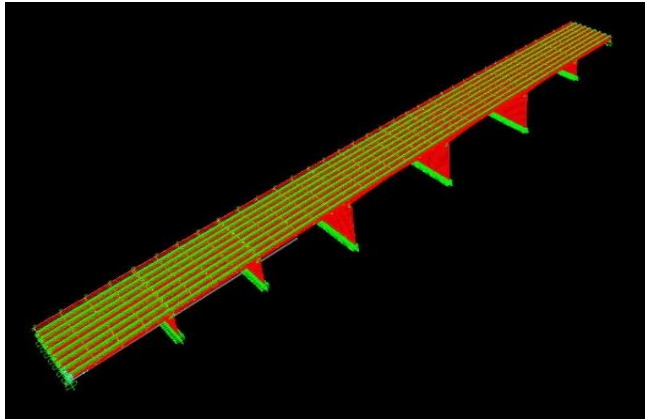


Figure 5. The numerical finite element model of the bridge.

An element size of up to 600 mm was chosen after comparing the results from several mesh sizes for a portion of the bridge. The complete model consists of 85,526 nodes, 2,268 frame elements, 6,912 thick shell elements, 75,133 thin shell elements and 12,704 link elements.

A FEM simulation is a component of a digital twin, but it does not constitute a digital twin on its own. Our work extends beyond the mere simulation by continuously updating and predicting the structure's performance using real-time data. Human intervention plays a crucial role in this process, modifying results by comparing outputs from FEM simulations, remote satellite imagery, and in-situ GPS, and TS.

### 3 RESULTS AND ANALYSES

#### 3.1 Environmental observations

The findings of this case study demonstrate how spatio-temporal environmental information is used to provide context to bridge deformation measurements in an RS-SHM study. Unexpected river turbulences observed in three different datasets (mono ortho satellite imagery, UAV imagery, LS-PIV vectors) acquired over a 2-year period indicate the presence of unexpected river behaviour upstream of Pier P5. The very high-resolution UAV photogrammetry collection provided particularly interesting contextual information for PS-InSAR monitoring, notably that riverbank sediment loss was occurring upstream of the bridge and a persistent pile of woody debris was present at the base of Pier P5 in all LS-PIV video collections but not at any other piers. The LS-PIV results confirmed the presence of a subsurface obstruction to river flow observed in the satellite image stack and revealed an area of unexpectedly high currents near the east bank of the river. These observations are sufficient to indicate that more detailed assessment of pier stability using other methods is required.

#### 3.2 PS-InSAR displacement results

PS-InSAR analysis was conducted independently on each stack of ascending and descending satellite images. The resulting

time series include measurements projected in the one-dimensional line-of-sight (LOS) of the satellite.

Three types of displacement measurements were obtained: (i) displacement linear rate (or velocity) derived from linear regression against time, (ii) displacement thermal sensitivity (or unit thermal displacement) obtained from linear regression against ambient temperature taken at times of image acquisitions, and (iii) cumulative displacements over the acquisition period (one year so far).

Figure 6 illustrates the ascending (top) and descending (bottom) sets of LOS linear displacement rates measured over the bridge deck, where the bridge concrete barriers with steel railings are perfect natural reflectors of SAR energy. However, due to the shallow incidence angle and the satellite look direction, not all sections of the barriers reflected valid persistent scatterers. Most ascending-pass PS concentrated on the north-west barrier while most descending-pass PS concentrated on the south-east barrier, making it challenging for the 2D decomposition analysis (explained next). Nevertheless, the study of these datasets reveals no excessive LOS displacement linear rates observed in the ascending or descending satellite data. Different viewing geometries (i.e., ascending and descending) were specifically selected to allow for a 2D decomposition calculation of the vertical and horizontal (east-west) components of displacement, noting that pole-orbiting satellites are not sensitive to pure north-south movement [11][12].

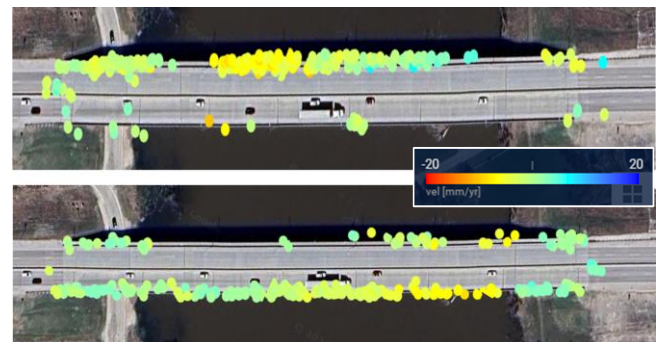


Figure 6. PS-InSAR LOS displacement linear rates (mm/year) measured over the bridge deck from ascending viewing geometry (top) and descending viewing geometry (bottom).

Figure 7 shows a horizontal grid of nine consecutive bins along the deck centreline, which was used for averaging displacement measurements from each viewing geometry. The bins were used to calculate the average vertical and horizontal components of displacement at the centre of each bin by trigonometry. The size of the bins was carefully selected to get representative values of displacement for each span of the bridge considering the different support conditions at the piers and abutments (free, pinned or fixed). The advantage of large bins is that each bin can contain multiple persistent scatterers from both ascending and descending satellite passes, enabling accurate 2D decomposition. A 2<sup>nd</sup> set of 18 consecutive bins was also created for comparison purposes, where the length of each bin was exactly half that of the 1<sup>st</sup> set (i.e., 14.4 m), with the aim to get a well-distributed set of average displacements, perhaps at the expense of having a few empty bins for either ascending or descending viewing geometry.

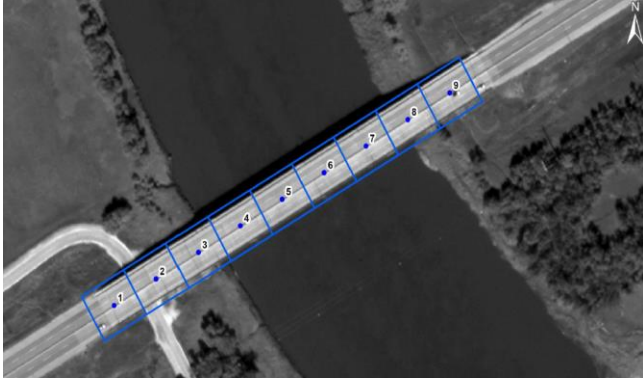


Figure 7. 2D decomposition grid over the bridge deck, showing nine regularly-spaced bins. Each bin is 28.8 m long.

Figure 8 illustrates how 1D LOS displacement measurements from two opposite satellite viewing geometries can be combined for a 2D decomposition of the vertical and horizontal components of displacement.

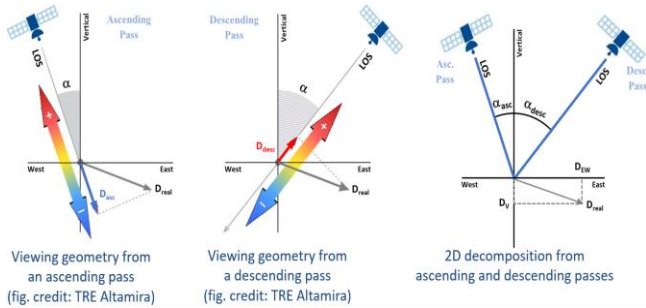


Figure 8. Satellite viewing geometries and 2D decomposition.

Equation 1 was adapted for a bridge-centric coordinate system [15]. If both the vertical and transverse components of displacement can be assumed to be small compared to the longitudinal component, then Equation 1 can reduce to Equation 2. The east-west component of displacement can then be projected onto the longitudinal direction of the bridge for direct comparison with other measurement and prediction methods. Similarly, if both longitudinal and transverse components of displacement can be assumed to be small in comparison to the vertical component, then Equation 1 can reduce to Equation 3, as follows:

$$D_{LOS} = D_V \cos \alpha - D_L \sin \alpha \sin \beta + D_T \sin \alpha \cos \beta \quad (1)$$

$$D_L = -D_{LOS} / (\sin \alpha \sin \beta) \quad \text{if both } D_V \text{ and } D_T \sim 0 \quad (2)$$

$$D_V = D_{LOS} / (\cos \alpha) \quad \text{if both } D_L \text{ and } D_T \sim 0 \quad (3)$$

where  $D_{LOS}$  is the line-of-sight displacement toward the satellite sensor,  $D_V$  is the vertical component in the upward direction,  $D_L$  is the horizontal component in the longitudinal direction of the bridge from west to east,  $D_T$  is the horizontal component in the transverse direction of the bridge,  $\alpha$  is the incidence angle of the satellite LOS, and  $\beta$  is the angle measured clockwise from the satellite track heading to the bridge longitudinal axis.

However, if the vertical and transverse components of displacement are not negligible, Equation 4 should be used to calculate the longitudinal displacement:

$$D_L = \left[ \frac{D_{LOS,d}}{\cos \alpha_d \tan \alpha_a \sin \beta_a} - \frac{D_{LOS,a}}{\sin \alpha_a \sin \beta_a} \right] / \left[ 1 - \frac{\tan \alpha_d \sin \beta_d}{\tan \alpha_a \sin \beta_a} \right] \quad (4)$$

Similarly, if the longitudinal and transverse components of displacement are not negligible, Equation 5 should be used to calculate the vertical displacement:

$$D_V = \left[ \frac{D_{LOS,d}}{\cos \alpha_d} - D_{LOS,a} \frac{\tan \alpha_d \sin \beta_d}{\sin \alpha_a \sin \beta_a} \right] / \left[ 1 - \frac{\tan \alpha_d \sin \beta_d}{\tan \alpha_a \sin \beta_a} \right] \quad (5)$$

where subscripts  $a$  and  $d$  represent the components calculated from the ascending or descending image stacks, respectively.

### 3.3 Comparison between PS-InSAR and other methods

In-situ measurements were conducted on the bridge, as described previously in Section 2.4. The distances from all marks to Mark 1 (located at the west abutment) were calculated, and the distance changes against ambient temperature variation during the measurement period were obtained (Figure 9). It can be seen that both in-situ measurement methods agree well with each other and to the FEM predictions of unit thermal displacement along the bridge, as expected. A small 0.2 mm/°C mean error is observed between the two sets of in-situ measurements and the FEM predictions.

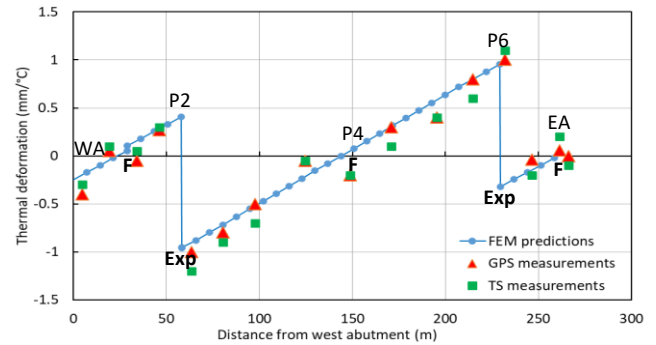


Figure 9. In-situ thermal displacements of bridge along the longitudinal direction compared to FEM predictions. (Notation: F = fixed joint; Exp = expansion joint).

In addition, the bridge unit thermal displacement in the vertical direction was also predicted with the FE model and measured with the total station and GPS instruments, for which the results are presented in Figure 10.

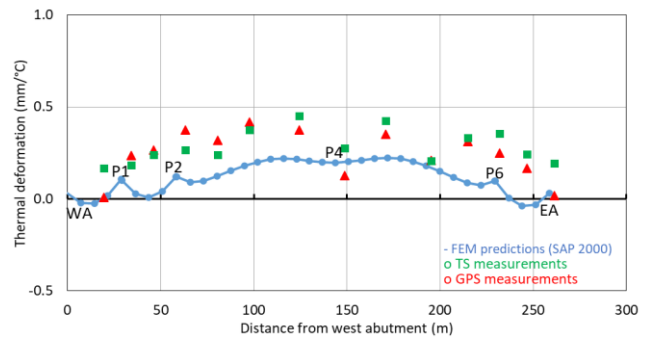


Figure 10. In-situ thermal displacements of bridge along the vertical direction compared to FEM predictions.

It can be observed that both types of field measurements agree well with the FEM predictions of vertical displacement.

Given that the FEM predictions of thermal displacements appear to be valid based on the horizontal and vertical field measurements, the PS-InSAR measurements will be compared to and validated against the FEM predictions in the next figures.

Figure 11 illustrates the average longitudinal thermal displacement measured by the RCM satellites for each set of bins along the bridge deck from West to East, using the detailed Equation 4. The expected movement direction (eastward vs. westward) and extent of thermal displacement are well characterized, with gradually increasing thermal displacements between the two expansion joints (at P2 and P6) and the expected sign reversal on either side of each expansion joint due to opposite directions of thermal movement going away from the pier. The comparison between the thermal displacements obtained from each bin size illustrates excellent agreement between the results of the two bin sizes, except that the smaller bin size returned no data at two locations near P6.

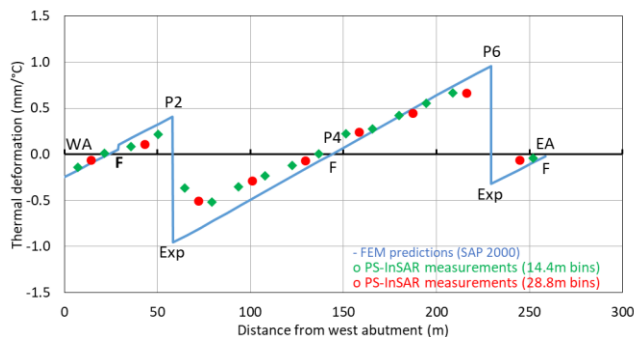


Figure 11. PS-InSAR thermal displacement along the longitudinal direction of bridge compared to FEM predictions.

Similarly, Figure 12 illustrates the PS-InSAR data for the vertical component of thermal displacement calculated along the bridge using Equation 5 for the two sets of bins. The comparison from either set of bins with the FEM predictions shows a good match, where the difference ranges from 0.1 mm/°C to 0.2 mm/°C. These PS-InSAR measurements also compare very well with the field measurements in Figure 10 above.

Overall, the satellite-monitored bridge thermal displacements are observed to be consistent with and very similar to both in-situ measurements and FEM predictions, confirming satellite-based PS-InSAR as a promising SHM tool for displacement measurements.

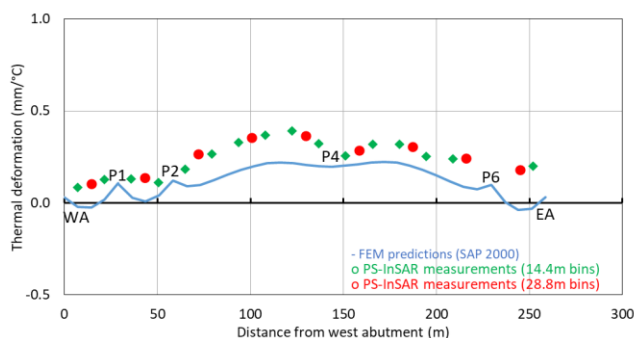


Figure 12. PS-InSAR thermal displacement along the vertical direction of bridge compared to FEM predictions.

### 3.4 Assessment of PS-InSAR calculation method accuracy

As mentioned in the previous section, the PS-InSAR measurements of the longitudinal thermal displacement shown in Figure 11 were calculated using Equation 4. These results show a maximum difference of 0.3 mm/°C at the expansion peaks (P2 and P6) compared with the FEM predictions. This difference is believed to be due to an averaging effect from the relatively large size of the bins used for 2D decomposition, especially around the P2 and P6 discontinuities. Shorter averaging bins would have been desired if the density of the ascending PS on the downstream barrier and the descending PS on the upstream barrier were higher (Figure 6). At P3 and P5, where the averaging effect is negligible, a small difference of 0.2 mm/°C is observed when compared to the FEM predictions.

Table 2 presents standard deviation and point count statistics for the PS results obtained from the 2D decomposition depending on pass direction and bin size. It is shown that the bin size did not have a significant impact on the accuracy of the averaged results, except that the smaller bin size had two empty bins around P6 due to the low density of PS for the ascending pass. The ascending data exhibited slightly higher standard deviations than the descending data, which is likely due to the lower PS density in the ascending pass, which also had fewer images in its stack (29 vs. 55, as shown in Table 1) compared to the descending stack.

Table 2. Standard deviation and point count statistics for PS-InSAR results from ascending and descending passes.

Bin no.	Bin centre distance from WA (m)	Ascending pass		Descending pass	
		St. dev. within each bin (mm/°C)	PS point count in each bin	St. dev. within each bin (mm/°C)	PS point count in each bin
9-bin grid:					
1	14.4	0.09	42	0.08	37
2	43.2	0.07	24	0.09	24
3	72.0	0.10	16	0.08	25
4	100.8	0.09	55	0.07	47
5	129.6	0.11	27	0.04	27
6	158.4	0.07	40	0.06	41
7	187.2	0.10	24	0.05	30
8	216.0	0.01	2	0.03	15
9	244.8	0.05	5	0.07	43
18-bin grid:					
1a	7.20	0.10	19	0.05	19
1b	21.6	0.07	23	0.05	18
2a	36.0	0.07	21	0.04	16
2b	50.4	0.01	3	0.13	8
3a	64.8	-	1	0.12	11
3b	79.2	0.10	15	0.05	14
4a	93.6	0.09	25	0.04	19
4b	108.0	0.08	30	0.06	28
5a	122.4	0.07	15	0.04	10
5b	136.8	0.11	13	0.03	17
6a	151.2	0.06	27	0.05	24
6b	165.6	0.08	13	0.04	17
7a	180.0	0.09	18	0.05	23
7b	194.4	0.05	5	0.04	7
8a	208.8	0.01	2	0.03	10
8b	223.2	-	0	0.04	5
9a	237.6	-	0	0.04	13
9b	252.0	0.05	5	0.07	30



This study was fortunate to have access to two stacks of satellite imagery over the bridge from opposing viewing geometries, which allowed the full 2D decomposition of movement for the correct determination of horizontal (east-west) and vertical components of movement. This is convenient when one needs to compare and validate results with field measurements and/or numerical simulations for which displacement results are typically determined in the vertical and horizontal directions.

There are cases where satellite imagery is only available for one viewing geometry (ascending or descending). While it is possible to estimate the horizontal or vertical displacement components by simple trigonometry (Equation 2 or 3, for example), one needs to ensure that the unknown variable is small enough to be safely neglected. Case studies on SAR satellite-monitored highway bridges have been successfully conducted using SAR imagery obtained only from one viewing geometry [16][17].

In this study, however, it was found that the vertical component of displacement could not be neglected. For example, Figure 13 presents the PS-InSAR measurements of unit thermal displacement in the longitudinal direction of the Red River Bridge, which were calculated separately for each viewing geometry using the simplified Equation 2, which comes with the assumption of negligible vertical displacement. The results actually show a poor match with the FEM predictions, especially for the descending set of displacement data, where differences with the FEM predictions of up to 0.8 mm/°C can be observed.

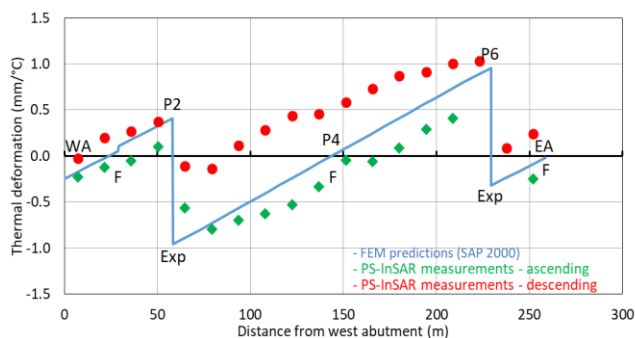


Figure 13. Longitudinal PS-InSAR thermal displacement for either ascending or descending passes compared to FEM predictions, using the inappropriate assumption of negligible vertical displacements. Dotted lines indicate lack of PS data.

The inferior match with the FEM predictions for the descending image stack is unique to this case study and depends on several factors – one of them being the orientation of the bridge with respect to the satellite tracks on the ground. As mentioned earlier, SAR satellites are not sensitive to movement along the satellite track heading (roughly N-S). This is because they are typically right-looking polar-orbiting satellites.

In this study, the angle between the satellite look direction (satellite track heading + 90°) and bridge heading is much larger for the descending stack ( $190^\circ + 90^\circ - 62^\circ = 218^\circ$ ) than it is for the ascending image stack ( $350^\circ + 90^\circ - 62^\circ - 360^\circ = 18^\circ$ ). Consequently, the ratio of vertical movement to the reduced observable longitudinal movement from the descending viewing geometry becomes apparently larger. This confirms the fact that SAR satellites are most sensitive to movement aligned with the look direction of the satellite [11][12].

### 3.5 Interpretation of results based on environmental context

As mentioned in the introduction section, the RS-SHM approach is meant to provide bridge operators with early awareness of developing risks and context to understand how changes in the surrounding environment may affect structural behaviour and safety.

The environmental investigation actually identified such a risk to bridge stability: a subsurface bluff-body obstruction to river flow and unexpectedly high currents near the east bank of the river close to Pier P5 of the bridge. These observations were sufficiently significant and clear to trigger a more detailed structural assessment of bridge stability using other methods.

The structural investigation, indeed, focused on two major aspects of structural behaviour of the bridge. The first aspect included the vibration measurements of bridge piers reported elsewhere [18]. The vibration study identified the fundamental natural vibration frequencies of the bridge piers and will keep monitoring them to detect changes where a reduction of the fundamental natural frequency is expected to indicate the weakening of the pier foundation as a result of scouring. Damping is another indicator but is not being considered.

The second aspect of the structural investigation included the thermal behaviour of the bridge, which was obtained by four different measurements and prediction methods (PS-InSAR, TS, GPS and FEM). The remote PS-InSAR and in-situ measurement methods agreed well with the expected bridge thermal deformation predictions from the bridge FE model.

Given the above, there is currently no evidence or signs of pier scouring at the bridge. However, due to observations from the environmental investigation, the deformations and ambient vibrations of the bridge piers, particularly at Pier 5, will remain under close scrutiny.

## 4 CONCLUSIONS

As part of a case study conducted on the Red River Bridge in Winnipeg, Canada, a structural investigation combining PS-InSAR deformation measurements from satellite imagery, in-situ measurements on the bridge deck, and numerical bridge model predictions was conducted. It provided an assessment of the bridge's structural behaviour with insight obtained from a prior environmental investigation. The following conclusions can be drawn:

1. This case study demonstrated the importance of combining key environmental observations with structural health monitoring data in an RS-SHM approach to provide comprehensive risk assessments for river bridges.
2. The environmental investigation identified unexpected river behaviour, including riverbank sediment loss, flow contraction during high-water periods, and persistent woody debris near Pier P5 of the bridge, suggesting potential risks to bridge stability, thus warranting further assessment of pier stability.
3. PS-InSAR displacement measurements were found to be consistent with in-situ and numerical model predictions, confirming its reliability as a monitoring tool, and have proven effective in this case study for assessing bridge stability and detecting subtle deformations over time.

4. The successful 2D decomposition of PS-InSAR displacement data allowed for accurate determination of both vertical and horizontal components, emphasizing the value of having satellite imagery from two opposing satellite viewing geometries.
5. It was demonstrated that, under some specific conditions, analyzing SAR images from only one viewing geometry might induce measurement inaccuracies if the simplifying assumptions on expected displacements cannot be met.
6. Although no current evidence of scouring was detected, the findings of the environmental investigation highlight the importance of remaining vigilant due to the potential scouring risks observed at Pier P5.

## ACKNOWLEDGMENTS

The PS-InSAR work detailed in this paper has been supported by collaborative research funding from the National Research Council Canada's Artificial Intelligence for Logistics Program with funding from Defence Research and Development Canada's Canadian Safety and Security Program (DRDC/CSSP).

The environmental investigation summarized in this paper was financially supported by the National Research Council Canada's Initiative on Climate Resilient Built Environment.

The authors would also like to acknowledge the Canadian Space Agency for providing the RCM satellite imagery and TRE Altamira for performing the PS-InSAR analysis.

The work related to the in-situ bridge displacement measurements and numerical bridge simulations was conducted by SIMTReC at the University of Manitoba, which was financially supported by the National Research Council Canada and Manitoba Transportation and Infrastructure.

## REFERENCES

- [1] Transport Canada, Overview of Canada's Transportation Sector, 2021. Retrieved from [Transport Canada](#).
- [2] Transport Canada, Outlook, Trends and Future Issues, 2011. Retrieved from [Transport Canada](#).
- [3] Senate Committee on Transport and Communications, Critical Transportation Infrastructure Vulnerabilities Place Lives and Economy at Risk, 2024. Retrieved from [Senate of Canada](#).
- [4] A. Baranwal, B.S. Das, Scouring Around Bridge Pier: A Comprehensive Analysis of Scour Depth Predictive Equations for Clear-water and Live-bed Scouring Conditions, *Journal of Water Supply: Research and Technology-Aqua*, 73(3), 2024.
- [5] R. Farooq, A.R. Ghumman, Impact Assessment of Pier Shape and Modifications on Scouring around Bridge Pier, *Water*, 11(9), 2019.
- [6] Kistler Group, Structural Health Monitoring (SHM), 2024. Retrieved from [Kistler](#).
- [7] P. Dubey, Bridge Protection and Traffic Safety at Its Finest. Informed Infrastructure, 2024. Retrieved from [Informed Infrastructure](#).
- [8] Smartec, Bridge Structural Health Monitoring Systems, 2024. Retrieved from [Smartec](#).
- [9] H. Stewart, D. Cusson, Digital Surface Models from Satellite Imagery for Improving the Geolocation of InSAR Deformation Measurements on Bridge Structures, 7<sup>th</sup> International Conference on Smart Monitoring, Assessment and Rehabilitation of Civil Structures (SMAR), Salerno, Italy, 4-6 September, 2024.
- [10] Airbus Defense and Space, 202 Pleiades Neo User Guide, V3.0, Toulouse, France, 2021.
- [11] M. Crosetto, O. Monserrat, M. Cuevas-González, N. Devanthery, B. Crippa, Persistent Scatterer Interferometry: A review. *SPRS Journal of Photogrammetry and Remote Sensing*, 115, 2016.
- [12] A. Ferretti, A. Monti-Guarnieri, C. Prati, F. Rocca, D. Massonnet, *InSAR Principles: Guidelines for SAR Interferometry Processing and Interpretation*, European Space Agency Publication TM-19, Noordwijk, The Netherlands, 2007.
- [13] S. Selvakumaran, S. Plank, C. Geiß, C. Rossi, C. Middleton, Remote Monitoring to Predict Bridge Scour Failure Using Interferometric Synthetic Aperture Radar (InSAR) Stacking Techniques, *International Journal of Applied Earth Observation and Geoinformation*, 73, 2018.
- [14] P. Milillo, G. Giardina, D. Perissin, G. Milillo, A. Coletta, C. Terranova, Pre-Collapse Space Geodetic Observations of Critical Infrastructure: The Morandi Bridge, Genoa, Italy, *Journal of Remote Sensing*, 11, 2019.
- [15] S. Samieie-Esfahany, R.F. Hanssen, K. van Thienen-Visser, A. Muntendam-Bos, On the Effect of Horizontal Deformation on InSAR Subsidence Estimates, *Fringe 2009*, Frascati, Italy, Nov. 30–Dec. 4, 2009.
- [16] D. Cusson, H. Stewart, Satellite Synthetic Aperture Radar, Multispectral, and Infrared Imagery for Assessing Bridge Deformation and Structural Health – A Case Study at the Samuel de Champlain Bridge, *Journal of Remote Sensing*, 16(4), 2024.
- [17] D. Cusson, C. Rossi, I. Ozkan, Early Warning System for the Detection of Unexpected Bridge Displacements from Radar Satellite Data. *Journal of Civil Structural Health Monitoring*, 11, 2020.
- [18] J. Zhao, K. Helmi, B. Telehanic, E. Murison, D. Cusson, C. Regoui, A. Mufti, D. Thomson, Bridge scour Detection and Displacement Monitoring using Vibrational Analysis and Radar Satellite Imagery, *CSCE Structures Specialty Conference*, Winnipeg, Canada, May 28-30, 2025.

# Potential of InSAR for Structural Health Monitoring of Flood Protection Systems

Petr Dohnalík<sup>1</sup>, Vazul Boros<sup>1</sup>, Maciej Kwapisz<sup>1</sup>, Philip Leopold<sup>1</sup>, Alois Vorwagner<sup>1</sup>, Antje Thiele<sup>2</sup>, Madeline Evers<sup>2</sup>

<sup>1</sup>Transportation Infrastructure Technologies, Austrian Institute of Technology,  
Giefinggasse 4, 1210 Vienna, Austria

<sup>2</sup>Fraunhofer Institute of Optonics, System Technologies and Image Exploitation,  
Fraunhoferstraße 1, 76131 Karlsruhe, Germany

email: Petr.Dohnalik@ait.ac.at, Vazul.Boros@ait.ac.at, Maciej.Kwapisz@ait.ac.at, Philip.Leopold@ait.ac.at,  
Alois.Vorwagner@ait.ac.at, Antje.Thiele@iosb.fraunhofer.de, Madeline.Evers@iosb.fraunhofer.de

**ABSTRACT:** Extreme weather events that cause flooding endanger people, economic goods, and the environment. Flood protection systems, such as dams, dikes, and levees, defend these valuable assets and therefore their structural health should be monitored. The goal of this project is to investigate the potential of Interferometric Synthetic Aperture Radar (InSAR) satellites for the monitoring of dams and dikes. The ability to monitor flood protection systems depends on the availability of a sufficient number of measurement points. This is influenced by several factors, such as the type of the scanned surface area (e.g. vegetation cover, concrete), the orientation of the dike with respect to the satellite's orbit, the temporal and spatial resolution of the SAR sensor, and the period for which the European Ground Motion Service (EGMS) provides the data. It is also of interest to study the differences between persistent scatterers and distributed scatterers. Furthermore, the correlation between surface subsidence detected by InSAR and the changes in water level, which pinpoint flood events, is also investigated. The use of Corner Reflectors or satellites with higher spatial resolution, are also some of the aspects to be explored in the next steps to investigate how to maximize the potential of InSAR satellites for the monitoring of flood protection systems.

**KEYWORDS:** InSAR, Structural Health Monitoring, Flood Protection, Dike, Levee, Earth dam

## 1 INTRODUCTION

### 1.1 Motivation

The occurrence and intensity of flooding constantly increases due to climate change and more frequent heavy rainfall events. Urban areas, often located near rivers, are threatened in particular by this natural hazard. Therefore, sustainable natural hazard management and structural health monitoring is essential to protect human lives, and their environment. Since the catastrophic floods of 2002 in Austria, a shift towards integrated flood risk management has been observed. In this context, the flood protection measures are complemented by the assessment and monitoring of existing protection structures such as dikes and levees.

Currently the condition of flood protection structures is mostly monitored by means of "close-up inspection" or by conducting geodetic surveys with theodolites along the dams. Only in rare exceptional cases are fully automated total stations with installed prisms or locally referenced Global Navigation Satellite System (GNSS) sensors permanently installed. Initial investigations into the use of drones for surveying dams have also revealed various limitations, turning these methods uneconomical.

The aim of the project "Flood protection monitoring via satellites" (HoSMoS) is to investigate the potential of structural health monitoring by means of satellites for flood protection systems. Based on multitemporal Interferometric Synthetic Aperture Radar (InSAR), long-term deformations on the earth's surface can be monitored under certain conditions [1]. The special feature of this indirect monitoring method is not only the fact that no additional sensors need to be attached to the structure, but depending on the mission, it can also offer the unique possibility to analyze data retrospectively,

e.g. Sentinel-1 data goes back to the year 2015. The accuracies currently achieved with InSAR are sufficient for monitoring trends of mass movements or glacier retreat, for example. There are promising results for the use of this technology in the monitoring of bridges, where the accuracy can be increased significantly by compensating for environmental conditions [2].

The innovation of the HoSMoS project consists of investigating the fundamental applicability of the InSAR technology for flood protection. The aim is to investigate whether monitoring by satellites is possible in principle under the special circumstances that typically prevail at such structures. For example, the influence of natural vegetation, construction materials, the presence of roads and paths and the orientation of linear structures on the satellite monitoring are to be investigated. The accuracy achievable with advanced differential InSAR (DInSAR) products provided by the European Ground Motion Services (EGMS) [3] is to be compared with the requirements for monitoring. Seasonal effects and relevant environmental conditions that require compensation are to be identified.

Remote sensing by satellites promises a great potential for the monitoring of flood protection systems. It would enable the simultaneous monitoring of deformations for many different structures in a large territory, with a higher temporal and spatial resolution than is currently possible. Long-term trends may be recognized through the retrospective evaluation of deformations. The definition of warning thresholds would allow the rapid, systematic identification of potentially critical areas and sections that require closer monitoring or inspection.



## 1.2 Remote sensing with InSAR

The publication of the first differential interferogram related to an earthquake in the United States in the 1990s marked the beginning of exploiting DInSAR to observe surface deformation [4]. Since then, the technique has undergone significant advances, including the development of more refined approaches such as Persistent Scatterer Interferometry (PSI) [5], [6].

The key idea of DInSAR is to combine the phase of at least two SAR images of the same area of interest (AoI) taken at different times and slightly different geometry in an interferometric manner to form an interferogram. The interferometric phase needs to be corrected for the phase contribution induced by the topography of the illuminated scene to extract information on the ground surface displacement that occurred between image acquisitions [1], [4].

SAR images from the Sentinel-1 satellites commissioned by the European Space Agency (ESA), can be processed with InSAR technology to produce displacement maps. They orbit the Earth at an altitude of 693 km, whereby the points on the Earth's surface are flown over in an approximately synchronous polar orbit in two orbital directions, once from south to north (ascending orbit) and once from north to south (descending orbit). The SAR images are taken in a skewed Line of Sight (LOS) with respect to the Earth's surface, see Figure 1, left. The return time to the same orbit is 12 days [2], [7]. Originally, Sentinel-1A and 1B satellites were used together, which doubled the temporal resolution. Unfortunately, satellite 1B has been out of service since December 2021 due to a solar storm. However, Sentinel-1C has been successfully deployed end of 2024 as a replacement.

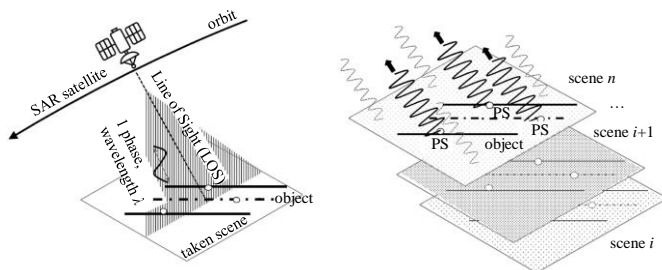


Figure 1. Left figure: The deformation measurement of the Earth's surface is recorded in so-called scenes during overflight; the direction of measurement is right-looking in the direction of flight of the satellite (= Line of Sight, LOS); right figure: Coherent reflectors (Persistent Scatterers, PS) of the recorded pixels are used as reference values and differential displacements are observed after approx.  $n$  recordings and analyzed, source: [8].

The basic idea of advanced DInSAR techniques, such as Persistent Scatterer Interferometry (PSI) is to identify pixels with low noise in a time series of differential interferograms. Relevant information about the observed deformation of the ground surface is then extracted from the backscattered radar signal of only these pixels, also referred to as Persistent Scatterer (PS). The backscattered signal of these pixels is characterized by the response of a single reflector in the corresponding ground resolution cell, which remains stable over time, as illustrated in Figure 1, right. The radar signal

reflected from the Earth's surface is detected, and the relative phase change of the PS pixels in between image acquisitions can be determined using interference, with the wavelength of  $\lambda = 54$  mm in the case of Sentinel-1 operating in C-band, see Figure 1 right. Displacement rates in the range of a fraction of the wavelength  $\lambda$  can be derived based on the comparison of the phase values of corresponding pixels from different consecutive differential interferograms [5], [6], [8]. With Sentinel-1, the images are taken at a time interval  $\Delta t$  of 6 or 12 days [8]. In principle, no additional man-made reflector is required on site; instead, the already present natural and man-made scatterers can be used, which provide a coherent signal for at least approx. 20 to 25 images. Sentinel-1 satellites acquire SAR images of the Earth's surface in a  $5 \times 20$  m ground resolution cell (Figure 1, left), which slightly limits the spatial resolution. Other satellites, such as TerraSAR-X, can also resolve ground cells down to 1.0 m in High Resolution Spotlight mode. The accuracy of the information obtained from Sentinel-1 data can be further increased by additionally attaching man-made Corner Reflectors (CR) to the Area of Interest (AoI). The CRs also be utilized in landscapes without already established PS for better object assignment [2].

Within the scope of this paper and the HoSMoS project, the focus is on the analysis of ground motion data provided by the EGMS. The EGMS generates fully processed PSI datasets based on Sentinel-1 SAR images for all European Countries supporting the Copernicus Initiative. The datasets are updated yearly using all Sentinel-1 data acquired in the past five years [3], [8].

## 2 MONITORING OF FLOOD PROTECTION SYSTEMS

### 2.1 Overview of satellite-based monitoring in flood protection

Before the potential of satellite-based monitoring of flood protection systems is analyzed, a brief overview of previous research on the topic is given. Comprehensive work was conducted within SAFELevee project organized by the Dutch Research Council (NWO) between 2014 and 2019, focusing on better understanding of the behavior patterns and situations that can lead to a failure of the flood protection structures, establishing an International Levee Performance Database [9], [10]. In this context, InSAR was investigated for the purpose of documenting surface deformations of flood protection systems in the Netherlands as a function of hydrodynamic loading and examine these deformations in relation to failure mechanisms [10]. In addition, the application of PSI was evaluated in several case studies in the Netherlands using SAR data from the high-resolution satellite TerraSAR-X, the medium-resolution satellites ERS-1/2 and Envisat, and the surface deformations were documented [11]. The analysis of the case studies showed that it was possible to document surface deformation with sufficient spatial coverage in all cases. The accuracy of the values depends on the orientation of the flood protection system and its slope. Based on the given temporal sampling rate, the authors see the potential for applying PSI for flood protection not in the area of real-time monitoring, but in an early warning system that indicates unusual deformation behavior.

The evaluation of images of Delft from TerraSAR-X in [12] showed that not only the density of the selected Persistent Scatterer (PS) pixels is sufficient to document surface

deformations, but also that the comparatively narrow temporal sampling rate can be used to observe the expansion and contraction of the flood protection barriers. In addition, it was shown that this short-term deformation pattern correlates with metrological data.

Further studies focused on the flood protection systems along the Mississippi River in the United States. A fully polarimetric L-band SAR mounted on an airplane and the X-band SAR satellite, TerraSAR-X, was investigated in [13] in order to show that weak points can be identified by means of analyzing the backscatter responses of the different polarizations and texture features. The same L-band SAR airborne system was also used in [14] and [15] to examine dike in California for subsidence and seepage in the Sacramento-San Joaquin Delta and the lower Mississippi River. Moreover, the polarimetric SAR (POLSAR) technique was used to detect seepage from multi-polarization images [14].

## 2.2 Conventional monitoring methods in flood protection

To analyze the potential of satellite monitoring methods, it is essential to create a base line for comparison. With this in mind, the currently available methods of monitoring flood protection systems were collected and are briefly systematically analyzed.

### 2.2.1 Geodetic surveying

The most commonly used method of monitoring is traditional geodetic surveying. In this process, selected points on the structure are marked and measured at regular intervals (e.g. monthly or yearly) using a theodolite. The accuracy of this method is approximately  $\pm 1$  mm [16].

### 2.2.2 Hydrostatic settlement cells

A very precise option for monitoring settlements is offered by hydrostatic settlement cells [17]. The principle of this device is based on liquid-level that consists of connected tubes filled with liquid causing liquid-level height difference or pressure differences (when using electronic liquid-level). The difference between two or more measurement points can be determined even over large distance.

### 2.2.3 Magnetic settlement tubes

Another solution for monitoring settlement is provided by magnetic settlement tubes, which allow the simultaneous monitoring of numerous vertically distributed measuring points located inside a dam [18], [19]. For this purpose, a tube is installed in the structure, with magnets placed on the bottom and in the wall at the locations, which are to be measured. A probe equipped with a reed switch is pulled up through the pipe in a controlled manner, starting from the bottom, and is activated each time it reaches a magnet, so that its relative height with respect to the bottom can be measured. The measurement accuracy is approximately  $\pm 3$ -5 mm [20].

### 2.2.4 Inclinometers

Inclinometers can also provide valuable information about geometric changes in a dam [17]. Inclinometers or tilt sensors measure the angular rotation related to the direction of the gravitational force. In principle, inclinometers can be designed for single-axis or for dual-axis measurements. There is a wide variety of different operating principles for inclinometers. The simplest inclinometers use a solid-state pendulum, the

deflection of which can be measured either by inductance or by a potentiometer [21].

### 2.2.5 Piezometers

Piezometers can be used to determine the water or earth pressure inside an earthfill dam, but they must be placed at the intended location already during construction [16], [22]. Tensiometers can also be used for continuous measurement of soil moisture in dams [23].

### 2.2.6 Electrical resistivity tomography

Electrical resistivity tomography (ERT) is a geoelectric method for imaging subsurface structures based on measurements of electrical resistivity at the surface or through electrodes in one or more boreholes. Possible applications of ERT on dams include: the localization of cracks, animal burrows, seepage points and leaks, the monitoring of water saturation, and the determination of geometric dimensions and internal properties [24], [25]. The measurements require extensive preparation and are very expensive. However, ERT also allows automated continuous monitoring of entire dam sections [26].

### 2.2.7 Fiber optic sensors

Fiber optic sensors (FOS) make it possible to measure physical quantities of the external world such as temperature, strain, vibration, magnetic field, etc. along the sensor fiber [27]. In the case of earth dams, they can be used primarily to detect seepage points by measuring the resulting temperature differences [28], [29].

### 2.2.8 Acoustic emissions sensors

Acoustic waves in a test object can be detected by piezoelectric sensors that convert surface displacements (or vibrations) caused by the acoustic emission into electrical signals. This technology can also be used to monitor piping causing seepage failure in dams and dikes [30].

### 2.2.9 GNSS

A second option for satellite-based monitoring of settlements in addition to InSAR is GNSS (Global Navigational Satellite System). The main difference to the InSAR technology is that a receiving device of the GNSS signal must be positioned on the structure to carry out measurements. In order to achieve greater accuracy, an additional reference station is required, the exact location of which is usually determined by classical surveying methods. The main advantage over InSAR is that not only long-term deformations but also dynamic processes can be observed. The two satellite technologies can also be combined. As an example, global positioning system was employed for monitoring of river embankment in [31].

### 2.2.10 Terrestrial laser scanning and Photogrammetry

Another alternative for capturing the geometry of flood protection structures is Terrestrial Laser Scanning (TLS), also referred to as terrestrial topographic Light Detection and Ranging (LiDAR). A TLS device scans its surrounding by means emitting light pulses in raster-like fashion. The distance between the scanner and the object is recorded and, depending on the scanning mode, one or two angles are recorded between the light and the vertical and horizontal axes. The scanning device can also be mounted on Unmanned Aerial Vehicles

(UAVs), i.e. aircraft that can operate autonomously or remotely and do not need to carry a human crew. When the UAV is expanded to form a complete system with recording technology, a control unit, a communication method, etc., it is referred to as an unmanned aerial system (UAS). Among UAS, drones are the most common because they can fly in confined spaces and are able to hover and take off and land vertically [32]. Drones can be equipped with various types of sensors, such as cameras [33] or LiDAR [34]. A study on the achievable accuracy for an earth fill dam showed an accuracy of approximately 1-2 cm for TLS and 2-4 cm for drone-based photogrammetry [35].

### 2.3 Comparison of monitoring methods in flood protection

The satellite monitoring of flood protection is now compared to the conventional methods described above in order to highlight the potential of the latter. In this context, important aspects are not only the spatial (density of measurement points) and the temporal resolution (measuring frequency), but also the accuracy of the measurement as well as required effort in terms of working hours and costs needed for carrying out a measurement and installation of the monitoring system.

Geodetic surveying requires significant effort due to the need of trained personnel to carry out measurements and operate a theodolite in the field. Another consequence of the *modus operandi* of this method is that the spatial and temporal resolution is low. This is noticeable particularly for large structures where scanning the surface's structure with InSAR has significant advantage.

Hose leveling system installation requires more planning and some kind of intervention into the structure as the theodolite surveying method. The very high effort needed to set up the measuring system is compensated with very high measurement accuracy and very high temporal resolution since the measurements can be automatized without the necessity of human supervision. As regards spatial resolution, the installation of this system is limited to a number of measurement cells and length that is bonded to a particular structure.

Electromagnetic settlement tubes require similar effort for setting up the measurement system as the hose leveling, needing a dedicated sensor for one measurement point. The advantage of this measurement system is high level of accuracy. The spatial and temporal resolution are average when compared to other methods.

One receiver device per measurement point is also required when using GNSS. If higher precision measurements are required, an additional reference station has to be in place, making the required effort very high and offering low spatial resolution. On the other hand, displacement monitoring with GNSS provides very high temporal resolution when compared to InSAR measurements.

Laser scanning offers very high spatial resolution stemming from the principle of this method when many measurement points around the TSL device are acquired. However, when aerial vehicles are used to increase scanned area in shorter time the accuracy of this method is compromised. Similar to the geodetic surveying, the measurements have low temporal resolution due to the trained labor that is necessary each time a measurement is taken.

Monitoring inclination is unique in measuring angular changes rather than displacements, which provide a slightly different viewpoint on the health status of the flood protection structure, that is obtained from InSAR data. The inclinometers also provide very high temporal resolution since the device is permanently located at the measurement point. However, the fact that one measurement device is needed for one measurement point limits the spatial resolution and increases the required effort for installation of the measurement system. Water or soil pressure measurements by means of piezometer sensors share the same levels of temporal and spatial resolution as with the inclinometers. The accuracy of this method is high, although the effort required to employ this method is also high since they have to be installed during construction of the dam. The advantage of using this measurement technique is that it offers information that cannot be directly obtained from any InSAR measurements.

Another technique that provides unique insight into health status of a flood protecting structure in comparison to SAR satellites is electrical resistivity tomography (ERT). However, it is very expensive to carry out ERT measurements, which require elaborate preparation. In comparison to other measurement techniques, ERT provides good accuracy and average spatial resolution, but low temporal resolution.

An excellent spatial and temporal resolution with high accuracy is provided by fiber optic sensors. However, in comparison to SAR satellites the installation of the fiber requires rather high amount of effort.

Similarly demanding on effort is acoustic emission method. This measurement technique also allows for high temporal resolution, but rather low spatial resolution and an average accuracy in comparison to the InSAR measurements.

The comparison of InSAR and other monitoring methods for flood protection systems in terms of effort for the operator of the infrastructure, accuracy, spatial and temporal resolution is summarized in Table 1.

## 3 RESULTS

Satellite based monitoring is particularly suitable for types of failure that develop over a longer time period and affect medium or large areas, such as subsidence, tilting or sliding. The accuracies and repeat-pass periods achievable through InSAR measurements are sufficient for monitoring these types of failure and the low cost compared to other monitoring methods makes this method particularly attractive. However, the question that arises based on the basic evaluation is whether and under what conditions a sufficient number of natural reflection points are available on dikes and other flood protection structures to carry out meaningful satellite monitoring.

In the present project analyses are carried out to answer this question, mostly based on selected representative AoIs, but in some cases also considering all flood protection systems in Lower Austria region along Danube River. Occasionally comparable systems abroad, where more suitable data is already available, are analyzed. The various investigations are explained individually and thematically separated below, and the results of each are briefly presented.



Table 1. Comparison of monitoring methods for flood protection systems in terms of measured property, effort, accuracy, measurement point density, and frequency

Method	Measured property	Effort required	Accuracy	Spatial resolution	Temporal resolution
InSAR	Displacement	Low	High	Medium-low	Medium
Geodetic surveying	Displacement	High	Very high ( $\pm 1$ mm)	Low	Low
Hose levelling	Displacement	Very high	Very high ( $\pm 1$ mm)	Low	Very high
Electromagnetic settlement tubes	Displacement	Very high	High ( $\pm 3$ -5 mm)	Medium	Medium
GNSS	Displacement	Very high	High	Low	Very high
TLS / LiDAR	Displacement	High	Medium-high	Very high	Low
Inclinometers	Inclination	High	High	Low	Very high
Piezometers	Pressure	High	High	Low	Very high
ERT	Damaged area	High	Medium	Medium	Low
Fiber optic sensors	Temperature	High	High	Very high	Very high
Acoustic Emission	Flow	High	Medium	Low	Very high

### 3.1 Point density depending on surface type and orientation

The flood protection structures in the Lower Austria region were divided into eight surface type categories based on characteristic locations, or structures in which they are integrated or surrounded. The typical surface types are the following:

- highways and roads,
- buildings (e.g. a house on a dam),
- green areas with asphalt paths,
- green areas with gravel paths,
- green areas without gravel,
- residential areas,
- foreign objects (e.g. electrical poles),
- miscellaneous (everything that does not fit above).

It is noteworthy that majority of the investigated dikes are situated in green areas, amounting to 60 %. The second and third most common surface type groups are highways with roads, and residential areas representing 22 % and 10 % of all analyzed dikes, see Figure 2.

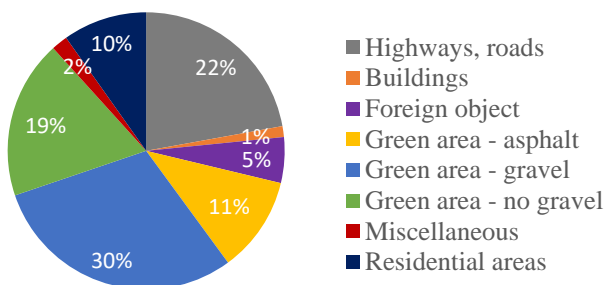


Figure 2. Distribution of surface types on or in the immediate vicinity of the investigated flood protection structures.

Orientation is a characteristic aspect of a flood protection structure since its length is usually significantly longer than the other two dimensions. The orientations of the 155 km of investigated dikes in Lower Austria along the Danube River were analyzed with respect to the cardinal directions. The results show that the dikes are predominantly aligned with the Danube River as evidenced by 43 % of the total dike length being oriented in the east-west direction, which matches the

river's course in this region. In contrast, the shortest dike orientation of is north-south, accounting for only 18 km or 12 % of the total analyzed length, see Figure 3.

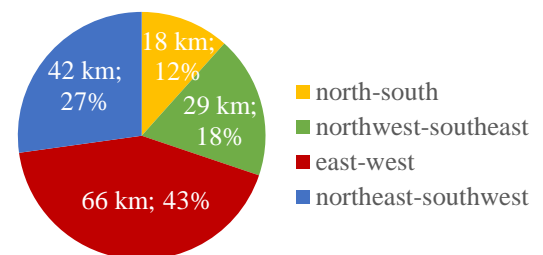


Figure 3. Orientation distribution of the 155 km-long flood protection structures in the investigated area with respect to cardinal directions.

Since the LOS direction of the SAR satellite is related to the cardinal direction, the number of available points also depends on the orientation of the observed object, such as dike. Based on the analysis of the investigated dikes, most of the PS points are obtained for dikes that are oriented in north-south direction for all surface types except highways and roads, as can be seen in Figure 4. Therefore, the number of points in the other directions are shown in relation to this most favorable orientation. Exceptionally high numbers of points are also obtained for all cardinal directions in highways and roads. An important finding is that in case of all types of green areas the number of reflection points drops significantly for unfavorable orientations. Particular low number of points is obtained for east-west and northwest-southeast directions, see Figure 4.

The results of the analysis regarding reflection point density with respect to the surface type are unfavorable for the investigated flood protection structures. The green areas, where the most dike sections belong to, have the smallest point density per 100 m. On the other hand, the surface types with the highest density are buildings, residential areas, and highway and roads as can be seen in Figure 5.

The number of available reflection points depend also on the date release of the postprocessed InSAR database. The EGMS database, used in this study, contains three different releases varying in the different time periods (epochs), 2015-2021, 2018-2022, and 2019-2023. Except for the newest data release in “highways and roads” surface type, the number of available measurements points slightly increases with later release time, see Figure 5. This is probably caused by better and more efficient data processing algorithms.

### 3.2 Comparison of persistent and distributed scatterers

Having a high number of reliable reflection points on the object or in the AoI is crucial for drawing reliable conclusions on the state of the flood protection structure. The potentially higher density of reflection points provided by additional distributed scatterers (DS) was examined, in order to investigate if their

inclusion could remedy the situation regarding scarcity of reflection points in green areas and unfavorable orientation of the investigated objects when using PS.

In contrast to PS pixels, DS pixels do not stand out due to a high coherence over a long period. They rather often exhibit a moderate coherence but show a statistically similar behavior as their neighboring pixels, since they often belong to the same object. This statistical similarity can be exploited to improve the signal-to-noise ratio of DS pixels by spatially averaging them. Thus, allowing a joint processing of DS and PS pixels. While PS pixels are often associated with point-wise bright scatters, such as dihedral or trihedral reflectors on buildings or naturally occurring boulders, DS pixels are often found in desert-like areas, areas covered by debris, and on non-cultivated land with short vegetation. [5], [36].

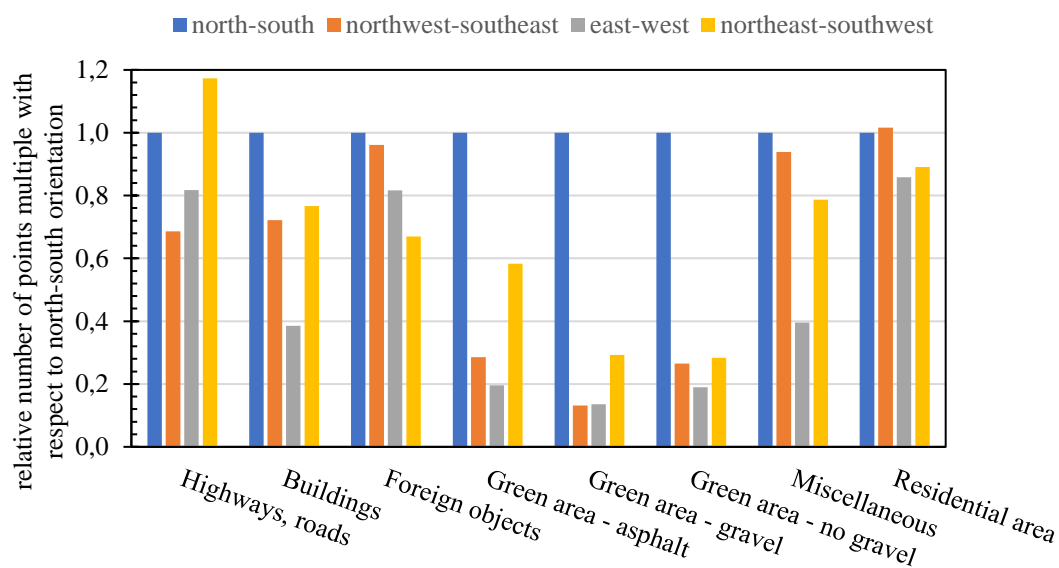


Figure 4. Relative number of points for different surface types with respect to the north-south orientation.

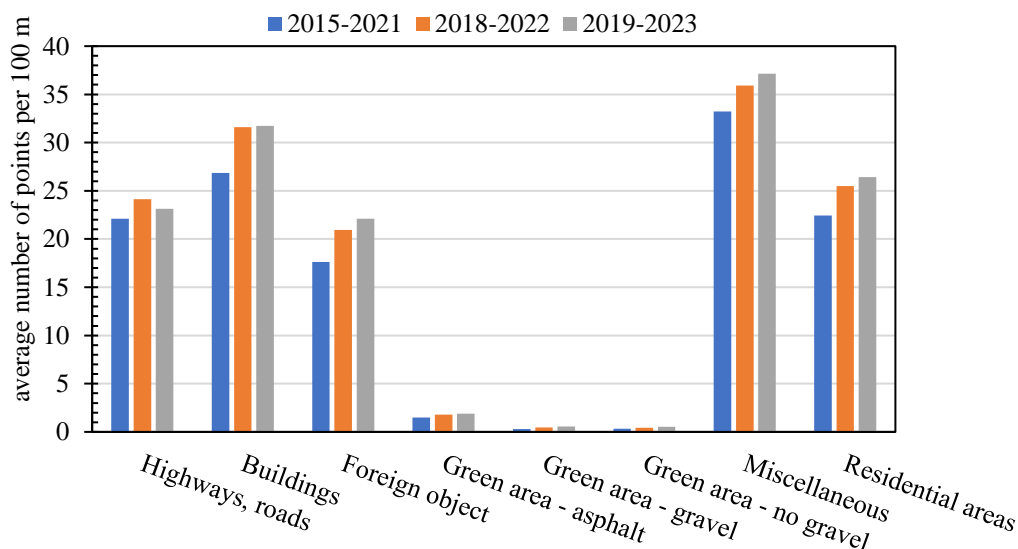


Figure 5. Comparison of the point density for different EGMS database releases and surface types on or in the immediate vicinity of the investigated flood protection structures.

The EGMS data are processed by four consortia using slightly different algorithms. While only the PS points are evaluated in Austria, the DS are also processed in Spain and France, among other countries. Since these are particularly suitable for non-urban areas, it was verified within the project whether a significantly higher number of data points along the dikes can be expected with a joint PS and DS processing.

For this purpose, a dike section in France, approximately 30 km long, was selected and examined. This is located on the La Loire River between Orleans and Jargeau. Analogous to the investigations on the Danube River, all points within 20 m of the dam crest, as illustrated in Figure 6, were considered and statistically evaluated. It was found that the DS points account for only 4.5% of all available points. The added value of such data processing is therefore not very high. A small part of this section with a particularly high density of PS and DS points was discovered and examined more closely. This section is almost free of vegetation, the surroundings are flat and treeless. The embankment section consists of coarse gravel and has a slope of approx. 20° to 30° and is seen from both orbit directions, the orientation is NW-SE. These findings are well in line with the observations obtained in the Vienna and lower Austria area.

### 3.3 Correlation of water level with InSAR measurement

As an example of the potential of using InSAR for flood protection structures in Vienna region was showcased for a lock in Greifenstein during high water periods. The object of interest was the end part of a pier of a lock. Here, three reflection points obtained from EGMS data for a period between the beginning of 2018 and the end of 2022 were analyzed and compared with water level measurement stations in Bärnsdorf and Nussdorf. The data from water level measurement stations shows periodical increases of water level in the Danube River depending on the seasons. In the available time period four prominent peaks marking extraordinary high-water level are visible on 30.05.2019, 04.02.2020, 05.08.2020, and on 19.07.2021. Analysis of the InSAR data revealed a settlement of approximately 8 mm (shown in red) at one reflection point and 12 mm (shown in light and dark green) at the other two points, at the beginning of 2020, see Figure 7 for a visual representation of the mean values and standard deviations. When compared to the water level during this period (shown in blue), it seems plausible that this change was related to the high-water level event on February 4<sup>th</sup>, 2020.

However, this showcase analyzed a rather local effect. Interesting results may be obtained after the analysis of the floodings in September 2024 in central Europe, once the EGMS data for this period becomes available.

## 4 DISCUSSION – FUTURE OUTLOOK

Corner reflectors provide a possibility to introduce a stable measurement point in areas or on structures that are absent of any reflective elements for L, S, C, or X-band waves. The corner reflectors can be also used as a reference to the other natural reflectors, to which they can be related to. The

disadvantage of the corner reflectors is that they require additional effort for installation. On the other hand, the installation is easy, there is no need for maintenance, and the service life is long. The benefit of a corner reflector is that it provides a stable reflection point.

The use of low-cost corner reflectors suited for dikes has been investigated and will also be a focus of future research. To this date, two couples of concrete corners with edge length of 40 cm were installed on a dike along the Danube River. Each couple was oriented in opposite directions so that the corner reflectors face directly to the LOS of the Sentinel-1 satellite descending and ascending flight trajectory, see Figure 8. Thin aluminum plates were glued onto the inner surfaces of one couple of the concrete corner reflectors as shown in Figure 8 a). The other couple of concrete corner reflectors was left untreated, see Figure 8 b). The two couples of low-cost concrete corner reflectors do not reflect enough signal back to the InSAR Sentinel-1A satellite and there would likely be no PS points corresponding to these four corner reflectors in the Sentinel-1 dataset. The reason for this may be small reflective surface or slightly obtuse angle between two neighboring inner surfaces. In addition to the experimental concrete corner reflectors, a standard double-headed corner reflector, shown in Figure 8 c), was installed near a dike next to the Danube River as a reference. The standardized corner reflector works as expected and a new measurement point is recorded by Sentinel-1A and is likely to appear in the EGMS dataset. This will be used as a reference measurement point in the future research.

As already mentioned, the choice of the SAR sensor also influences the monitoring results that can be achieved on the AoI. In addition to the theoretical maximum value of displacement rate, factors such as spatial resolution also play an important role. There are currently at least six SAR satellite missions (e.g. Sentinel-1, RADARSAT, PALSAR-2, TerraSAR-X, COSMO-SkyMed, SAOCOM) that generate SAR images capable of interferometry and at least two other missions (e.g. NASA-ISRO, ROSE-L) that are currently being implemented. The missions differ greatly in the wavelength used, the achievable spatial resolutions, the temporal sampling rate, as well as the general availability and the underlying data policy. In addition, commercial micro-satellite providers (e.g. ICEYE and Capella Space) are also striving for InSAR capability. Hence, it can be assumed that, as already shown in some studies [11], based on multi-resolution, multi-temporal and multi-frequency approaches the combination of InSAR measurements from different SAR constellations will significantly increase the added value of this measurement method.

Next research step is an analysis of the areas in lower Austria and in Vienna region flooded in September 2024. In comparison to correlation of the water level with the settlement of the pier, this research will exploit the full potential of InSAR that is particularly suitable for examining of middle to large areas.



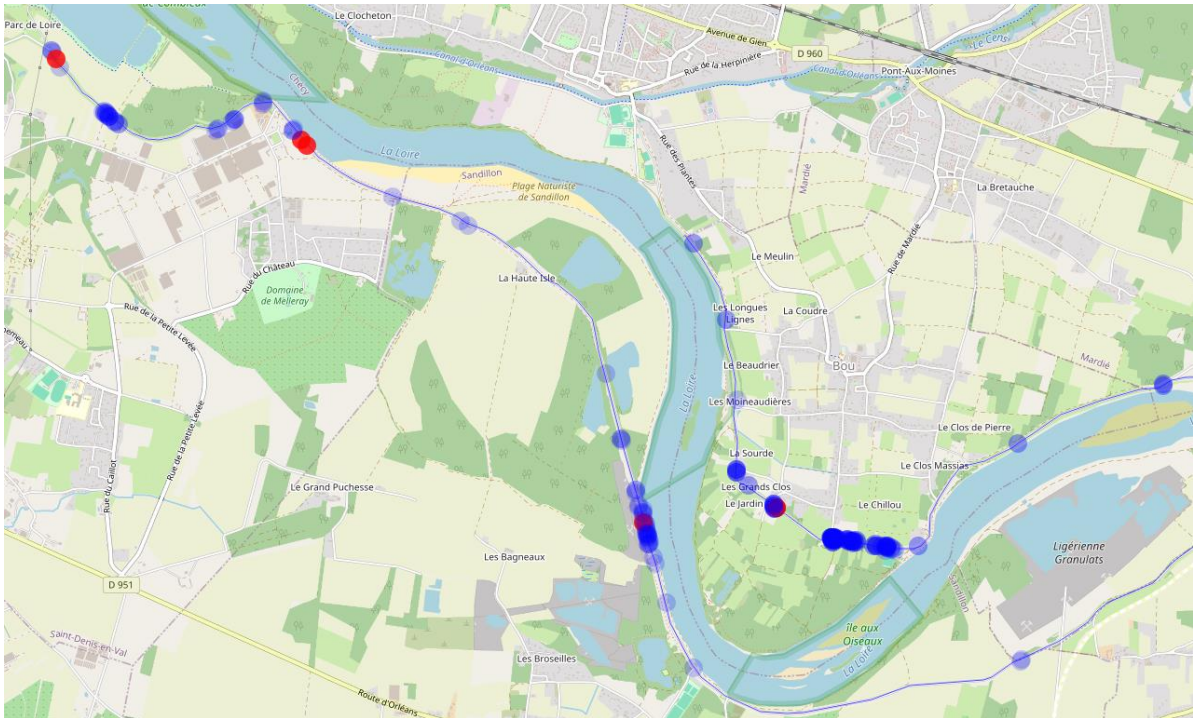


Figure 6. Overview of PS (blue) and DS (red) points along the embankment of the La Loire, France (thin blue solid line).

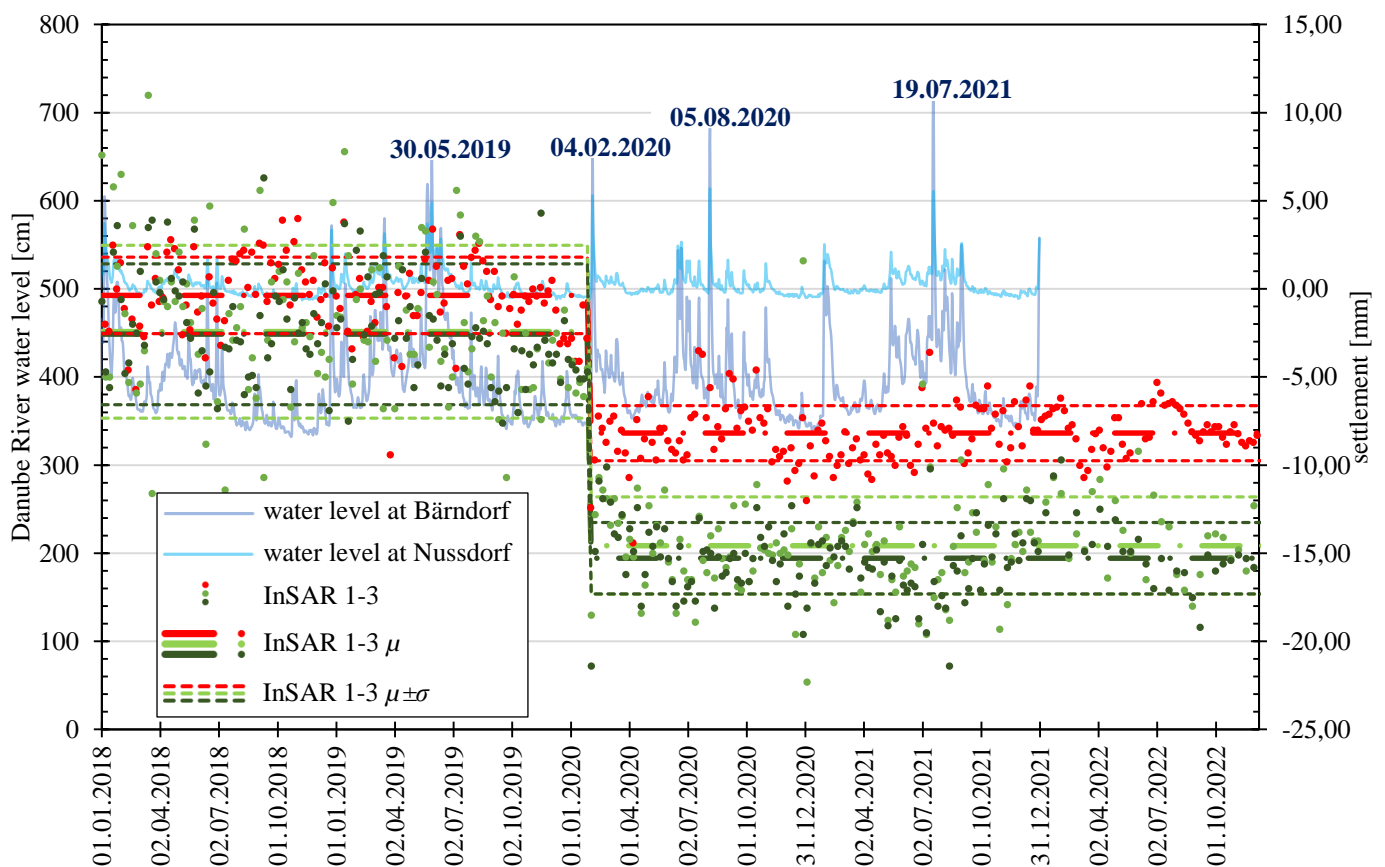


Figure 7. Settlement records from the EGMS database for three points (marked by red, light and dark green points, referring to the right vertical axis) at the endpoint of a river lock pier in Greifenstein, compared with water levels in the Danube River, as measured at stations in Bärndorf and Nussdorf (light and dark blue solid curves, referring to the left vertical axis), plotted as a function of time. The settlement mean trend lines,  $\mu$ , are indicated by bold dash-dotted lines and their standard deviations,  $\sigma$ , are plotted by thin dashed lines. The dates in blue font near the water level peaks mark high-water events.

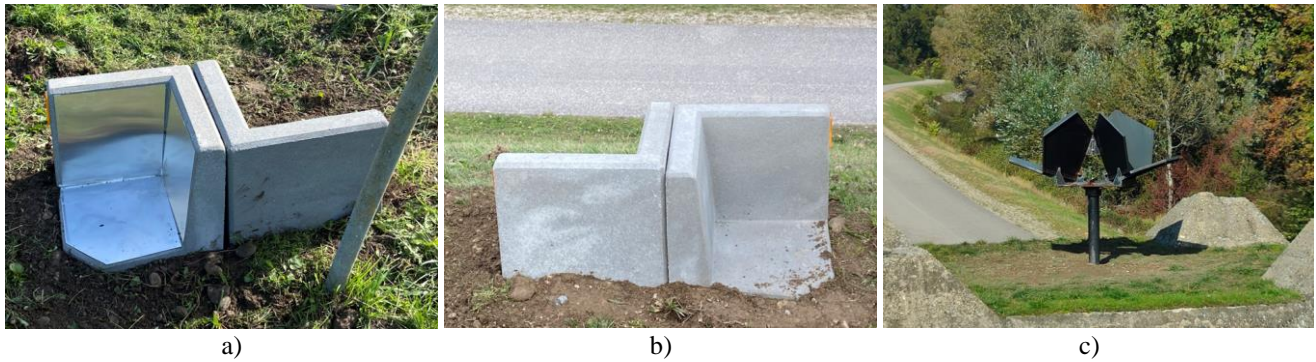


Figure 8. Corner reflectors installed on the dike at the Danube River: a) cement corner reflectors with aluminum sheets, b) plain cement experimental corner reflectors, and c) standard double-headed corner reflector.

## 5 CONCLUSION

The present paper provides a brief overview of the potentials of InSAR monitoring of flood protection structures comparing it to conventional monitoring methods. In this context, the EGMS data provide high accuracy of displacement measurements with low required effort. However, the temporal and spatial resolution is limited.

The temporal resolution is dependent on the number of satellites and their repeat-pass periods. Since the return time of the Sentinel-1A to the same orbit is 12 days, the resulting EGMS data is suitable for monitoring slowly occurring changes. With the successful launch of Sentinel-1C in December 2024, the temporal resolution will double in the future. The spatial resolution can be increased by using commercial SAR satellites, which, however, increases required costs effort.

The spatial resolution of the Sentinel-1 satellites, with respect to the measurement point availability, was extensively investigated in this study. The EGMS database was used to examine several aspects of the measurement point availability in selected AoIs. First investigated aspect was number of obtained reflection points based on surface type and orientation. Green areas with gravel, asphalt, and no-gravel which constitute 60% of dike length in the investigated area (Figure 2), have the lowest point density out of all considered surface types (Figure 5). The number of available points is also dependent on orientation of the observed object. In this context, the most points in investigated AoIs are obtained for objects oriented in north-south (Figure 4). Unfortunately, 43 % of dikes in the investigated area along the Danube River are oriented to east-west direction (Figure 3).

The number of available reflection points also depends on the database release. EGMS provide access to three databases of InSAR measurement points, 2015-2021, 2018-2022, and 2019-2023. With the exception of highways and roads the newer the database, the more available points there are for each surface type category (Figure 5).

Since most of the dikes are located in green areas and the distributed scatterers are known to be more suitable for natural landscape, the potential use of DS was examined. To this end, the PS and DS were extracted from EGMS database for approximately 30 km dike section. This analysis showed that only 4.5 % of all available points are DS (Figure 6), rendering usability of the DS points rather low.

The settlement at a pier of a ship lock could be linked with high probability the flood of the Danube River. This case study showcased the potential of InSAR utilizing Sentinel-1 satellites for monitoring the condition of flood protection structures along the Danube River in the aftermath of flood events.

InSAR is an excellent method to monitor surface displacements of large areas in all-weather conditions, providing useful insights on the structural health of infrastructure assets. This study shows the potential of this method for monitoring dikes along Danube River, but also highlights the limitations, stemming from the low number of available reflection points. Therefore, future research will focus on increasing the number of available reflection points, by employing low-cost, highly-available corner reflectors, and investigating the availability of InSAR data from other existing or upcoming InSAR satellite missions.

## ACKNOWLEDGMENTS

The authors and partners of this research project are grateful for support from the Austrian Research Promotion Agency (Forschungsförderungsgesellschaft; FFG). Without its funding and support it would not be possible to conduct this research. Furthermore, we would also like to acknowledge the support from the Danube Flood Control Agency (DHK) during this research.

## REFERENCES

- [1] R. Bamler und P. Hartl, „Synthetic aperture radar interferometry“, *Inverse Problems*, vol. 14, no. 4, pp. R1, 1998, doi: <https://doi.org/10.1088/0266-5611/14/4/001>.
- [2] A. Vorwagner, M. Kwapisz, P. Leopold, M. Ralbovsky, K. H. Gutjahr, und T. Moser, „Verformungsmonitoring von Brücken mittels berührungsloser Satellitenradarmessungen“, *Beton- und Stahlbetonbau*, vol. 119, no. 9, pp. 636–647, 2024, doi: <https://doi.org/10.1002/best.202400017>.
- [3] M. Costantini u. a., „EGMS: Europe-Wide Ground Motion Monitoring based on Full Resolution Insar Processing of All Sentinel-1 Acquisitions“, in *IGARSS 2022 - 2022 IEEE International Geoscience and Remote Sensing Symposium*, 2022, pp. 5093–5096. doi: <https://doi.org/10.1109/IGARSS46834.2022.9884966>.
- [4] D. Massonnet u. a., „The displacement field of the Landers earthquake mapped by radar interferometry“, *Nature*, vol. 364, no. 6433, pp. 138–142, 1993, doi: <https://doi.org/10.1038/364138a0>.
- [5] A. Ferretti, C. M. Prati, und F. Rocca, „Permanent scatterers in SAR interferometry“, *IEEE Transactions on Geoscience and Remote Sensing*, vol. 39, no. 1, pp. 8–20, 2002, doi: <https://doi.org/10.1109/36.898661>.
- [6] A. Hooper, H. Zebker, P. Segall, und B. Kampes, „A new method for measuring deformation on volcanoes and other natural terrains using



- InSAR persistent scatterers“, *Geophysical Research Letters*, vol. 31, no. 23, 2004, doi: <https://doi.org/10.1029/2004GL021737>.
- [7] P. Potin u. a., „Copernicus Sentinel-1 Constellation Mission Operations Status“, in *IGARSS 2019 - 2019 IEEE International Geoscience and Remote Sensing Symposium*, IEEE, 2019, pp. 5385–5388. doi: <https://doi.org/10.1109/IGARSS.2019.8898949>.
- [8] A. Hooper, P. Segall, and H. Zebker, „Persistent scatterer interferometric synthetic aperture radar for crustal deformation analysis, with application to Volcán Alcedo, Galápagos“, *Journal of Geophysical Research: Solid Earth*, vol. 112, no. B7, 2007, doi: <https://doi.org/10.1029/2006JB004763>.
- [9] „SAFELevee project“, TU Delft. Accessed: March 25, 2025. [Online]. Available: <https://www.tudelft.nl/citg/over-faculteit/afdelingen/hydraulic-engineering/sections/hydraulic-structures-and-flood-risk/research/safelevee-project>
- [10] I. E. Özer, M. van Damme, T. Schweckendiek, and S. N. Jonkman, „On the importance of analyzing flood defense failures“, *E3S Web Conf.*, vol. 7, pp. 03013, 2016, doi: <https://doi.org/10.1051/e3sconf/20160703013>.
- [11] I. E. Özer, F. J. van Leijen, S. N. Jonkman, and R. F. Hanssen, „Applicability of satellite radar imaging to monitor the conditions of levees“, *Journal of Flood Risk Management*, vol. 12, no. S2, pp. e12509, 2019, doi: <https://doi.org/10.1111/jfr3.12509>.
- [12] I. E. Özer, S. J. H. Rikkers, F. J. van Leijen, S. N. Jonkman, and R. F. Hanssen, „Sub-seasonal Levee Deformation Observed Using Satellite Radar Interferometry to Enhance Flood Protection“, *Sci Rep*, vol. 9, no. 1, pp. 2646, 2019, doi: <https://doi.org/10.1038/s41598-019-39474-x>.
- [13] J. V. Aanstoots u. a., „Earthen levee monitoring with Synthetic Aperture Radar“, in *2011 IEEE Applied Imagery Pattern Recognition Workshop (AIPR)*, 2011, pp. 1–6. doi: <https://doi.org/10.1109/AIPR.2011.6176370>.
- [14] C. E. Jones, G. Bawden, S. Deverel, J. Dudas, S. Hensley, and S.-H. Yun, „Study of movement and seepage along levees using DINSAR and the airborne UAVSAR instrument“, in *SAR Image Analysis, Modeling, and Techniques XII*, SPIE, 2012, pp. 76–83. doi: <https://doi.org/10.1117/12.976885>.
- [15] K. An, C. Jones, D. Bekaert, and V. Bennett, „Radar interferometry offers new monitoring approach for critical flood control infrastructure“, Accessed: March 25, 2025. [Online]. Available: <https://www.authorea.com/users/543806/articles/601411-radar-interferometry-offers-new-monitoring-approach-for-critical-flood-control-infrastructure>
- [16] J. Luo, Q. Zhang, L. Li, and W. Xiang, „Monitoring and characterizing the deformation of an earth dam in Guangxi Province, China“, *Engineering Geology*, vol. 248, pp. 50–60, 2019, doi: <https://doi.org/10.1016/j.enggeo.2018.11.007>.
- [17] R. Sukkarak, P. Jongpradist, and P. Pramthawee, „A modified valley shape factor for the estimation of rockfill dam settlement“, *Computers and Geotechnics*, vol. 108, pp. 244–256, 2019, doi: <https://doi.org/10.1016/j.compgeo.2019.01.001>.
- [18] B. Beiranvand, T. Rajaei, and M. Komasi, „Spatiotemporal clustering of dam settlement monitoring using instrumentation data (case study: Eyvashan Earth Dam)“, *Results in Engineering*, vol. 22, pp. 102014, 2024, doi: <https://doi.org/10.1016/j.rineng.2024.102014>.
- [19] Y. Li, K. Min, Y. Zhang, and L. Wen, „Prediction of the failure point settlement in rockfill dams based on spatial-temporal data and multiple-monitoring-point models“, *Engineering Structures*, vol. 243, pp. 112658, 2021, doi: <https://doi.org/10.1016/j.engstruct.2021.112658>.
- [20] rst instruments, „Magnetic Settlement Systems“. 2025. Accessed: March 26, 2025. [Online]. Available: <https://rstinstruments.com/wp-content/uploads/Magnetic-Settlement-Systems-SSB0001-2.pdf>
- [21] Q. Han and C. Chen, „Research on Tilt Sensor Technology“, in *2008 IEEE International Symposium on Knowledge Acquisition and Modeling Workshop*, 2008, pp. 786–789. doi: <https://doi.org/10.1109/KAMW.2008.4810608>.
- [22] I. Balan, D. Topa, C. Flaviana, I. Balan, and C. Loredana, „Numerical analysis of pore water pressure changes of an earth dam and monitoring of vertical deformations Case study – Plopi Dam IASI County“, 2023. [Online]. Available: <https://repository.iuls.ro/xmlui/handle/20.500.12811/4026>
- [23] Z. Illés and Ö. Antal, „Installation of a flood protection embankment’s monitoring system“, gehalten auf der 11th International Symposium on Field Monitoring in Geomechanics, London, 2022, pp. 1–9.
- [24] C. Comina, F. Vagnon, A. Arato, F. Fantini, and M. Naldi, „A new electric streamer for the characterization of river embankments“, *Engineering Geology*, vol. 276, pp. 105770, 2020, doi: <https://doi.org/10.1016/j.enggeo.2020.105770>.
- [25] R. Norooz, A. Nivorlis, P.-I. Olsson, T. Günther, C. Bernstone, and T. Dahlin, „Monitoring of Älvkarleby test embankment dam using 3D electrical resistivity tomography for detection of internal defects“, *Journal of Civil Structural Health Monitoring*, vol. 14, no. 5, pp. 1275–1294, 2024, doi: <https://doi.org/10.1007/s13349-024-00785-x>.
- [26] G. Jones, P. Sentenac, and M. Zielinski, „Desiccation cracking detection using 2-D and 3-D Electrical Resistivity Tomography: Validation on a flood embankment“, *Journal of Applied Geophysics*, vol. 106, pp. 196–211, 2014, doi: <https://doi.org/10.1016/j.jappgeo.2014.04.018>.
- [27] J. Li und M. Zhang, „Physics and applications of Raman distributed optical fiber sensing“, *Light: Science & Applications*, vol. 11, no. 1, 2022, doi: <https://doi.org/10.1038/s41377-022-00811-x>.
- [28] H. Su, S. Tian, Y. Kang, W. Xie, und J. Chen, „Monitoring water seepage velocity in dikes using distributed optical fiber temperature sensors“, *Automation in Construction*, vol. 76, pp. 71–84, 2017, doi: <https://doi.org/10.1016/j.autcon.2017.01.013>.
- [29] H. Li und M. Yang, „Application Study of Distributed Optical Fiber Seepage Monitoring Technology on Embankment Engineering“, *Applied Sciences*, vol. 14, no. 13, pp. 5362, 2024, doi: <https://doi.org/10.3390/app14135362>.
- [30] P. Ming, J. Lu, X. Cai, M. Liu, und X. Chen, „Experimental Study on Monitoring of Dike Piping Process Based on Acoustic Emission Technology“, *Journal of Nondestructive Evaluation*, vol. 40, no. 1, pp. 23, 2021, doi: <https://doi.org/10.1007/s10921-021-00752-2>.
- [31] Q. Zhao, K. Li, P. Cao, Y. Liu, Y. Pang, und J. Liu, „A Study on the Influence of Double Tunnel Excavations on the Settlement Deformation of Flood Control Dikes“, *Sustainability*, vol. 15, no. 16, pp. 12461, 2023, doi: <https://doi.org/10.3390/su151612461>.
- [32] A. A. Ab Rahman u. a., „Applications of Drones in Emerging Economies: A case study of Malaysia“, in *2019 6th International Conference on Space Science and Communication (IconSpace)*, 2019, pp. 35–40. doi: <https://doi.org/10.1109/IconSpace.2019.8905962>.
- [33] G. Morgenthal, V. Rodehorst, N. Hallermann, P. Debus, und C. Benz, *Bauwerksprüfung gemäß DIN 1076 – Unterstützung durch (halb-) automatisierte Bildauswertung durch UAV (Unmanned Aerial Vehicles – Unbemannte Fluggeräte)*. in Berichte der Bundesanstalt für Straßenwesen, no. B 171. 2021. Accessed: March 25, 2025. [Online]. Available: <https://bast.opus.hbz-nrw.de/frontdoor/index/index/docId/2551>
- [34] D. Roca, J. Armesto, S. Lagüela, und L. Díaz-Vilariño, „Lidar-equipped UAV for building information modelling“, in *The International Archives of the Photogrammetry, Remote Sensing and Spatial Information Sciences*, Copernicus GmbH, 2014, pp. 523–527. doi: <https://doi.org/10.5194/isprsarchives-XL-5-523-2014>.
- [35] D. Bolkas, M. O’Banion, J. Laughlin, und J. Prickett, „Monitoring of a rockfill embankment dam using TLS and sUAS point clouds“, *Journal of Applied Geodesy*, 2024, doi: <https://doi.org/10.1515/jag-2023-0038>.
- [36] A. Ferretti, A. Fumagalli, F. Novali, C. Prati, F. Rocca, und A. Rucci, „A New Algorithm for Processing Interferometric Data-Stacks: SqueeSAR“, *IEEE Transactions on Geoscience and Remote Sensing*, vol. 49, no. 9, pp. 3460–3470, 2011, doi: <https://doi.org/10.1109/TGRS.2011.2124465>.



# ISABHEL (Integrated SATellite and ground-based monitoring for Bridge HHealth Lifetime assessment)

Vera Costantini<sup>1</sup>, Bernardino Chiaia<sup>2</sup>, Marco Civera<sup>2</sup>, Alberto Ciavattone<sup>4</sup>, Davide Ambrosio<sup>3</sup>, Carlo Ranalletta<sup>3</sup>, Emanuele Del Monte<sup>4</sup>; Roberta Marini<sup>1</sup>, Paolo Mazzanti<sup>1</sup>

<sup>1</sup>NHAZCA, Italy; <sup>2</sup>Politecnico di Torino, Department of Structural, Geotechnical and Building Engineering (DISEG), Italy; <sup>3</sup>Nplus, Italy; <sup>4</sup>S2R, Italy;  
email: [vera.costantini@nhazca.com](mailto:vera.costantini@nhazca.com)

**ABSTRACT:** This paper presents ISABHEL (Integrated SATellite and ground-based monitoring for Bridge HHealth Lifetime assessment) project, which demonstrates an integrated approach to Structural Health Monitoring (SHM) by combining satellite InSAR data, contact sensors, Photomonitoring™, and Finite Element Modeling (FEM). The system is implemented on two bridges over the Po River in Turin, Italy: the Amedeo VIII and the Regina Margherita bridges. Each technology complements the others, providing a comprehensive understanding of bridge behavior. The InSAR analysis using high-resolution COSMO-SkyMed data revealed slight asymmetric deformation in the Regina Margherita Bridge, with the western lane exhibiting higher deformation rates. Contact sensors were strategically designed to be positioned based on each bridge's specific vulnerabilities, with the Amedeo VIII bridge focused on static monitoring and the Regina Margherita bridge on dynamic monitoring. The calibrated FEM models will enable prediction of structural behavior and establish critical thresholds. A web platform integrating all data sources will provide real-time visualization and alerts. This paper presents the initial results of this ongoing project funded by ESA, which will be completed in the next months.

**KEY WORDS:** Bridges; InSAR; Contact Sensors; Photomonitoring; Finite Element Modeling; Data Integration; 5G Communication

## 1 INTRODUCTION

The bridge infrastructure across Europe is aging, with many structures approaching or exceeding their design lifetime. This aging infrastructure requires consistent monitoring to ensure safety, optimize maintenance schedules, and extend its operational life. Traditional monitoring methods often rely on periodic visual inspections, which may miss early signs of deterioration and are labor-intensive [1]. Modern Structural Health Monitoring (SHM) approaches offer continuous data collection, but often focus on a single technology, providing only a partial view of the structure's condition [2]. The ISABHEL (Integrated SATellite and ground-based monitoring for Bridge HHealth Lifetime assessment) project, funded by the European Space Agency (ESA), and with the support of the Municipality of Turin, demonstrates an innovative approach to bridge monitoring by integrating multiple technologies: satellite Interferometric Synthetic Aperture Radar (InSAR), contact sensors, Photomonitoring™, and Finite Element Modeling (FEM). This integration leverages the strengths of each technology to create a comprehensive monitoring system capable of detecting various deterioration mechanisms at different scales.

The project focuses on two river bridges in Turin, Italy: Amedeo VIII bridge and Regina Margherita bridge (Figure 1). These structures were selected due to their strategic importance, different structural characteristics, and potential vulnerability to scouring phenomena. Additionally, the Regina Margherita Bridge may be affected by slope movements on the nearby hillside.

The project aims to demonstrate how multi-technology integration can provide a more comprehensive understanding of bridge health and support evidence-based maintenance decisions.



Figure 1. Location of bridges under study

## 2 PROJECT OVERVIEW AND METHODOLOGY

### 2.1 Case studies in Turin

The Amedeo VIII bridge is a reinforced concrete structure with post-tensioned cables added during a retrofit intervention in recent years. The bridge also features Gerber saddles (i.e. half-joints) which were strengthened during the same renovation (Figure 2).

The Regina Margherita bridge is a reinforced concrete structure with prestressed cables. It consists of two parallel carriageways that can be treated as separate bridges (Figure 3).

Both bridges are subject to potential scouring phenomena due to their superficial foundations. The Regina Margherita Bridge, moreover, is potentially subject to phenomena induced by slope movements on the hillside, which are difficult to perceive by on-site measurements but could be easily identified by satellite measurements over an extended area.



Figure 2: Overview of Amedeo VIII bridge



Figure 3: Overview of Regina Margherita Bridge

The Amedeo VIII and Regina Margherita bridges are examples of modern infrastructures, built respectively in 1933 and between 1970-1972, constructed in reinforced concrete, and that experience substantial daily traffic (2,164 and 2,715 vehicles per day, respectively). Notably, the Regina Margherita bridge falls within Class 1 (High) attention level as per current Guidelines. The project, conceived on these typologies of infrastructures, represents an important chance to develop reliable procedures that can be applied to a significant number of similar infrastructures, which are very common on the Italian territory.

This aspect is even more important since, in the last years, significant attention has been focused on the monitoring and safety assessment of bridges, due to the recent problems that occurred on some infrastructures because of maintenance problems [1]. As evidenced by the publication by the Ministry of Infrastructure and Transport, of the document "*Linee Guida per la Classificazione e Gestione del Rischio, la Valutazione della Sicurezza ed il Monitoraggio dei Ponti Esistenti*," in April 2020, surveillance and monitoring of bridge infrastructures should be provided especially for bridges ranked in the high attention class, which need continuous update of the structural model.

## 2.2 Integrated monitoring approach

In this project a comprehensive, multi-technology approach to bridge monitoring is adopted, ensuring a detailed and accurate assessment of structural health. At the core of this methodology is the integration of satellite-based and ground-based technologies, allowing for a continuous and complementary evaluation of deformation patterns and structural behavior.

The satellite-based component is represented by Interferometric SAR analysis (InSAR), which relies on high-resolution COSMO-SkyMed data to provide both historical deformation analysis and long-term monitoring of millimeter-scale displacements across the entire area of interest. This technology provides important information on long-term deformation trends and enables the detection of anomalies that might indicate structural degradation.

To complement the satellite data, a network of contact sensors is installed on the bridges, providing real-time measurements of key structural parameters. These sensors include biaxial inclinometers, triaxial accelerometers, strain gauges, displacement transducers and temperature probes, all of which contribute to acquiring data on both the static and dynamic behavior of the structures. The data collected from these sensors is transmitted via 5G technology, ensuring fast and reliable communication with the central monitoring system.

In addition to sensor-based measurements, the project incorporates an advanced Photomonitoring system. Camera installations near the bridges capture regular image sequences, which are then processed using Digital Image Correlation (DIC) and Change Detection (CD) techniques. These methods allow for the identification of visual modifications in the structure over time, facilitating the detection of potential issues such as cracks, material degradation, or unusual displacements. To further enhance the monitoring capabilities, Finite Element Modeling (FEM) is employed to create digital twins of the bridges. These virtual models are continuously updated and calibrated using real-world data obtained from satellite observations, contact sensors, and Photomonitoring. By simulating different loading conditions and environmental factors, FEM enables predictive analysis of structural performance.

All collected data is integrated into a centralized web-based platform, which serves as the primary interface for monitoring and analysis. This platform not only visualizes the structural health status in real time but also tracks changes over time and issues alerts when predefined thresholds are exceeded. By providing an intuitive and comprehensive overview of bridge conditions, the system facilitates informed decision-making for infrastructure management, ultimately enhancing safety and optimizing maintenance efforts.

This holistic monitoring approach ensures that all critical aspects of bridge health are continuously assessed, from large-scale deformations detectable by satellite to localized structural issues identified through sensor data and image analysis. The combination of these technologies provides a robust framework for long-term monitoring and early warning capabilities, supporting proactive maintenance and extending the lifespan of the infrastructure [2,3,4].



### 3 CONTACT SENSORS CONFIGURATION

#### 3.1 Monitoring strategy and sensor selection

Based on field inspections and analysis of bridge documentation, the project implemented a differentiated monitoring approach for the two bridges. The Amedeo VIII bridge focuses on static monitoring, while the Regina Margherita bridge incorporates both static and dynamic monitoring. This differentiation is due to the different structural characteristics and vulnerabilities of each bridge. The contact sensor system, developed by Nplus, integrates IoT-enabled sensors with advanced data analytics to provide a comprehensive assessment of bridge health. The selection criteria included sensitivity, durability, reliability, and suitability for the specific monitoring objectives of each bridge.

The Vittorio Infrastructure system by Nplus employs a wired architecture with a 2 Mbit/s digital data bus, ensuring 24/7 reliability in power and data acquisition. The system integrates various sensors connected via a fiber optic backbone, which also powers the devices.

#### 3.2 Regina Margherita bridge sensor layout

The Regina Margherita Bridge, constructed between 1970 and 1972, spans the Po River in Turin, Italy. It is a modern three-span arch bridge with a total length of 123.0 meters and runs primarily along a North-South axis.

The structure consists of two separate half-bridges, one for each carriageway, which are structurally independent and connected only at the mid-lane. This 3-meter-wide section between the decks was originally a tram line, later became a recreation park, and is currently a green area.

The bridge is made of prestressed reinforced concrete, while the decks are reinforced concrete box girders with variable height and six webs. They rest on steel-made fixed bearings on the south abutment and double-pendulum roller bearings on the north abutment and piers.

The piers lie on reinforced concrete caisson foundations that were sunk by self-weight rather than deep foundations, which makes the bridge susceptible to scouring and classifies it as high hydraulic risk, according to Italian guidelines.

The bridge was designed with spans ballasted with lean concrete and tie rods anchored in rock at the two abutments to reduce total downward deflection at the midspan.

For this bridge, both static and dynamic monitoring were implemented. The sensor layout was designed to detect potential scour-related issues using inclinometers and assess the deck's load-bearing capacity through accelerometers and strain gauges (Figure 4). While inclinometers and strain gauges monitor static behavior, accelerometers analyze dynamic behavior, providing a comprehensive assessment of the bridge's structural health.

- Inclinometers/accelerometers installed on piers and at deck mid-spans and quarters, respectively to:

- Measure static rotations to check plastic drift and reconstruct the deformed span
- Measure accelerations to perform Operational Modal Analysis (OMA), check mode drift, and identify natural frequencies, mode shapes and damping

- Strain gauges at mid-spans to monitor axial deformation, which can indicate excessive loading, prestressing cable relaxation, or changes in restraint effectiveness
- Temperature sensors on different spans to correlate environmental conditions with structural responses.

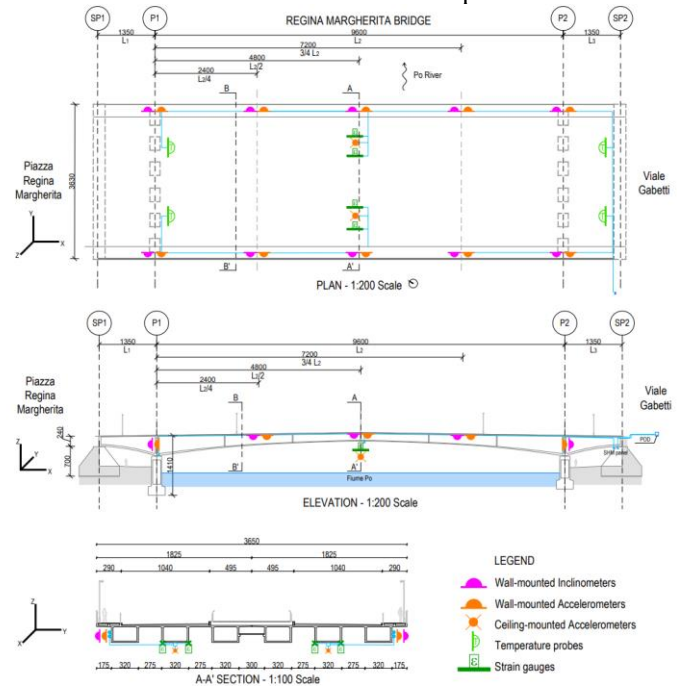


Figure 4: Contact sensors configuration for Regina Margherita Bridge

#### 3.3 Amedeo VIII bridge sensor layout

The Amedeo VIII Bridge, constructed in 1933, crosses the Stura River, a major tributary of the Po River, which it meets in Turin. This five-span bridge has a total length of 153.3 m, and its main axis lays in a southwest-to-northeast direction.

The bridge has a single carriageway, consisting of two lanes in each direction plus two large walkways - one on each side. The girder bridge has a regular grid of reinforced concrete (R.C.) transverse and longitudinal beams (these latter ones with variable thickness along the bridge's main axis) with the addition of post-tensioned cables during a recent structural retrofit intervention.

The deck is simply supported on the R.C. piers and clamped at the two abutments. On the second and fourth spans are located two half joints (i.e. the so-called Gerber saddles), which carry two simply supported half-spans.

Exactly as in the case of the Regina Margherita Bridge, all piers lie on self-sunk R.C. caisson foundations, not deep foundations. For the same reasons as before, this classifies it as high hydraulic risk according to Italian guidelines. For the Amedeo VIII bridge, static monitoring was preferred in order to track displacements and rotations (Figure 5). The sensor configuration includes:

- Biaxial inclinometers installed on piers and deck span extremes to monitor:
  - Static rotations of individual spans to check plastic drift
  - Static rotations of piles to check differential settlement
  - Rotations of Gerber saddles to check for potential failures



- Strain gauges installed on Gerber saddles to monitor expansions and detect potential saddle failures
  - Temperature sensors installed on different spans to correlate environmental conditions with structural responses.
- This configuration focuses on the bridge's main vulnerabilities: scouring phenomena (monitored through inclinometers) and the Gerber saddles (monitored through inclinometers and strain gauges).

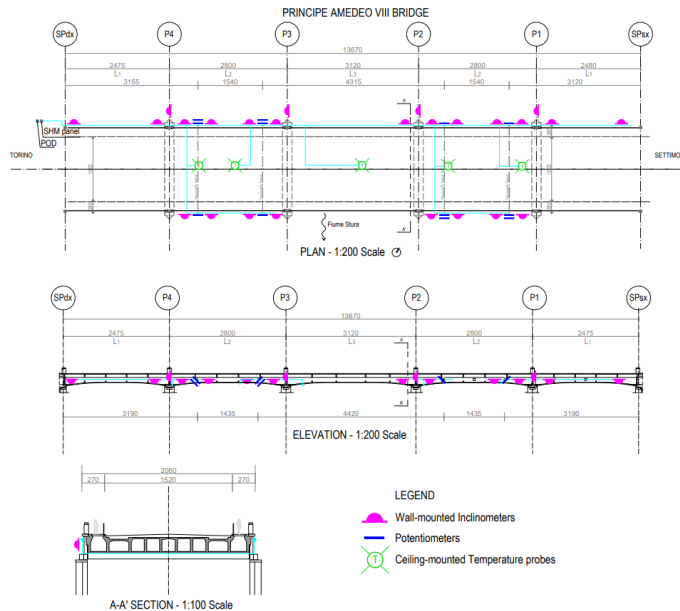


Figure 5: Contact sensors configuration for Regina Margherita Bridge

## 4 A-DINSAR ANALYSIS

### 4.1 Satellite radar interferometry technique

In this study, the Advanced Differential Synthetic Aperture Radar Interferometry (A-DInSAR) technique [5] is used to analyze historical ground displacement rates within the Turin municipality. A-DInSAR detects surface deformations by analyzing phase differences between successive radar satellite observations of the same area. These variations in the RADAR signal phase, reflected from objects on the Earth's surface, are directly correlated with ground movement, enabling the generation of high-resolution deformation maps [6,7]. Specifically, this technique is widely utilized for studying the temporal evolution of ground displacement of Persistent Scatterers (PS), which are objects within the SAR resolution cell (3x3 m<sup>2</sup> for CSK) that maintain consistent reflectivity over time [8].

The applied InSAR methodology follows the Persistent Scatterer Interferometry (PSI) approach, as described in reference articles [9] and [10]. The PS-InSAR technique extracts deformation information from an interferometric stack of SAR images, allowing for detailed pattern analysis. SAR datasets from the Cosmo-SkyMed (CSK) mission, operated by the Italian Space Agency (ASI), were utilized, which has provided archived data since 2009 and are free for research purposes. The CSK system is equipped with an X-band sensor (about 3.1 cm wavelength) that allows for millimetric displacement measurement precision. In STRIPMAP mode, it

offers a spatial resolution of 3m×3m. Over Italy. The revisiting time is 16 days with occasional gaps due to the dual use of the constellation for civilian and military applications.

For this study, a total of 460 SAR images were processed covering the period from 2011 to 2024, acquired in ascending and descending orbital geometries:

- Ascending orbit: 231 Single Look Complex (SLC) images acquired between January 18, 2011, and August 23, 2024.
- Descending orbit: 229 SLC images acquired between May 18, 2011, and September 24, 2024.

The A-DInSAR derived deformation rate values (expressed in millimeters per year) were estimated relative to a designated reference point. To ensure accuracy, our results were calibrated and validated using displacement data from the GNSS station located in the municipality of Turin.

To evaluate the reliability of our results, an error analysis was conducted, estimating the standard deviation of deformation rates, and assessing temporal coherence levels, considered only the points with temporal coherence up to 0.4.

In addition, complementary remote sensing techniques were integrated, including ground-based leveling data, to cross-validate our results. The Turin municipality is characterized by complex subsurface conditions, including sandy-gravelly alluvium and clayey alluvial soil, which contribute to varying deformation patterns. These geological factors were taken into account in our analysis to improve the interpretation of observed displacement trends.

### 4.2 Post-Processing and Analysis of Satellite Interferometry Data

The post-processing of satellite interferometry data is carried out using the PS-ToolBox Suite, developed by NHAZCA S.r.l. and integrated into QGIS. This suite enables the visualization of time series, decomposition of line-of-sight displacements, and the creation of various data representations to identify significant structural movements.

The vector decomposition process of the data allows the generation of velocity maps for the Synthetic Measurement Points (SMPs) in both vertical and horizontal (East-West) directions. These maps are derived from the decomposition of measurements along the sensor's line of sight (LOS) obtained through both ascending and descending orbital geometries.

It is essential to note that displacement and velocity measurements are calculated along the sensor's LOS. Therefore, the detected displacements represent the projection of actual displacements along the sensor-target line. Indeed, the observed displacement is the combination of the vertical and slightly east-west movement. Combining the observation from two looking geometries it's possible to decompose the signal along the vertical and horizontal components.

The data vector decomposition process was performed using proprietary algorithms to extract displacement vectors in both horizontal and vertical directions. The study area was discretized into hexagonal cells with a 5 m radius, arranged on a regular grid. The results were displayed only for cells containing at least one measurement point for both orbital

geometries, referred to as "Synthetic Measurement Points" (SMPs).

PS times series tool allows the interactive visualization and analysis of time series derived from satellite datasets, providing a detailed representation of the displacement evolution over time. The analysis of this time series helps identify patterns of progressive subsidence, seasonal variations, or sudden displacement changes, which could indicate structural anomalies or external influences.

The Interferometric Section tool creates interferometric sections using data analysis from different orbital geometries. The sections follow the road alignment and intersect the Measurement Points (MPs) of the monitored bridges, allowing the visualization of displacement distribution along a topographic profile.

#### 4.3 A-DInSAR Results

The results of the A-DInSAR analysis are presented through maps overlaid on orthophoto-based backgrounds, illustrating the annual average velocities of the measurement points (MP) across the study area, including the two bridges under investigation. A color scale, expressed in mm/year, is used to represent the average displacement velocity along the satellite line of sight (LOS): colors ranging from yellow to red indicate movement away from the sensor, while shades from cyan to blue denote movement towards it. Green areas correspond to measurement points with negligible or non-significant displacement variations, with an estimated instrumental accuracy of approximately  $\pm 1.0$  mm/year. The analysis provided a well-distributed spatial coverage of MPs across the entire study area in both ascending and descending geometries, ensuring redundant observation of potential deformation processes. A higher density of MPs is observed in urbanized areas, whereas a lower density is found in regions with dense vegetation or agricultural land.

A detailed analysis follows, focusing on the bridges, where time series of displacement for some measurement points, based on the A-DInSAR analysis, are shown for both ascending and descending geometries, plotted with the cumulated rain over time.

The final products are represented by velocity maps of the measurement points (MP) in the vertical and horizontal directions. These maps are obtained from the vector decomposition of measurements along the satellite line of sight (LOS) for the MP data collected in both ascending and descending orbital geometries.

#### 4.4 REGINA MARGHERITA BRIDGE Results

The Regina Margherita Bridge exhibits moderate deformation in the area where it is structurally stable, characterized by a localized movement at the midspan that is clearly visible in both satellite acquisition geometries. In Figure 6, the A-DInSAR analysis for the descending geometry shows that, while the bridge's abutments and piers at the ends remain stable, there is a non-negligible deformation ( $>2$  mm/yr) in the LOS direction, away from the sensor. In this geometry, the western carriageway seems to be more affected by the deformation, but possibly this is an artefact due to the satellite's line of sight. The up-down (UD) component, instead, is limited to  $<2$  mm/yr. However, from an engineering perspective,

considering the uncertainties associated with SAR technology, these outcomes will require further analyses to be accepted beyond any reasonable doubt. Figure 7 presents three representative time series for this carriageway, showing that measurement point MP2 at midspan accumulates up to 50 mm of displacement over the analyzed period.

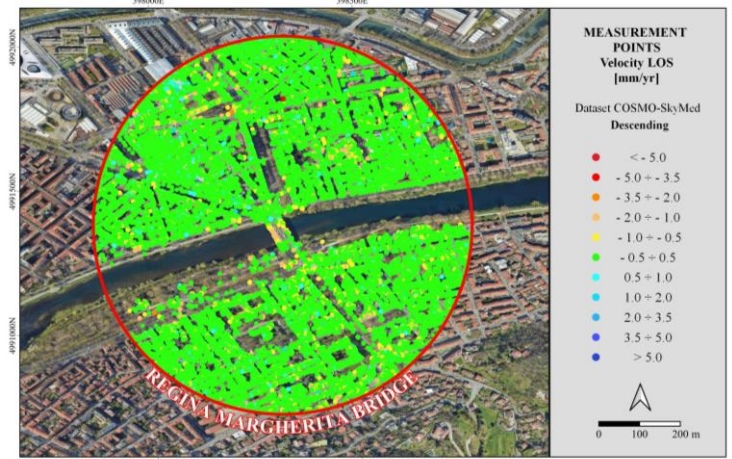


Figure 6 Velocity map of Measurement Points (MPs) obtained from A-DInSAR analysis in descending geometry for the Regina Margherita bridge area.

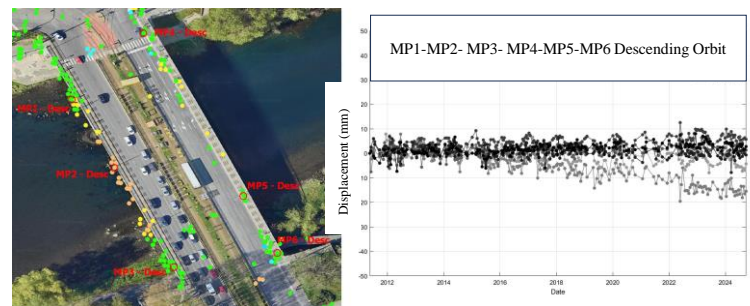


Figure 7 Time series of three measurement points for descending orbit on Regina Margherita bridge

Figure 8 shows the results from the ascending geometry, which display a deformation with rates of 2–3 mm/yr on both carriageways.



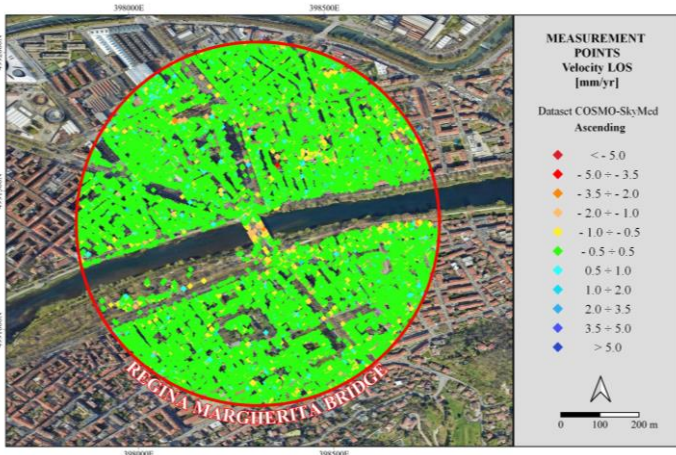


Figure 8 Velocity map of Measurement Points (MPs) obtained from A-DInSAR analysis in ascending geometry for the Regina Margherita bridge area.

From vector decomposition of the two LOS analyses, velocity maps for the vertical and horizontal components of displacement in the bridge area were produced (Figure 9).

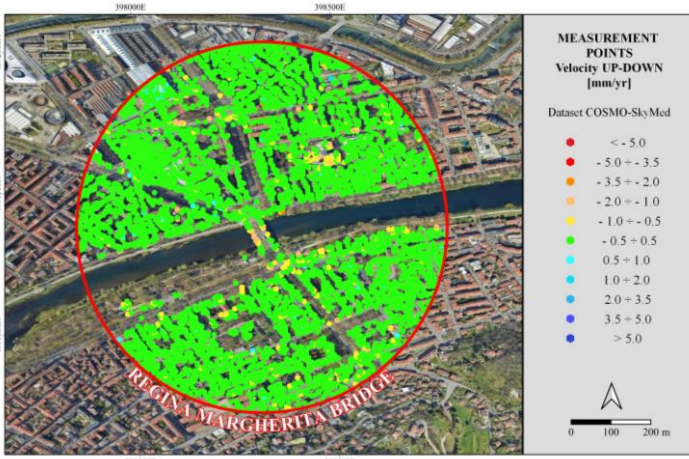


Figure 9 Velocity map of the Synthetic Measurement Points in vertical direction for Regina Margherita Bridge

The most representative outputs from the complete post-processing analysis of the satellite data are presented in Figure 10, which shows the cumulative vertical displacement along both the facade and plan view of the bridge, sampled at 5-meter intervals, to detail the deformative behavior in space and time. The interferometric section, which illustrates the evolution of the bridge's deformation over time and space, is presented in Figure 11.

#### 4.5 AMEDEO VIII BRIDGE Results

The Amedeo VIII Bridge exhibits deformation values within the stable range along its entire length, while the surrounding area shows minimal deformation. In figure 12, the descending geometry A-DInSAR analysis confirms that the bridge remains stable throughout its span, in contrast to adjacent areas that display displacement rates on the order of -2 mm/yr. Moreover, the time series presented in figure 13 clearly delineates the

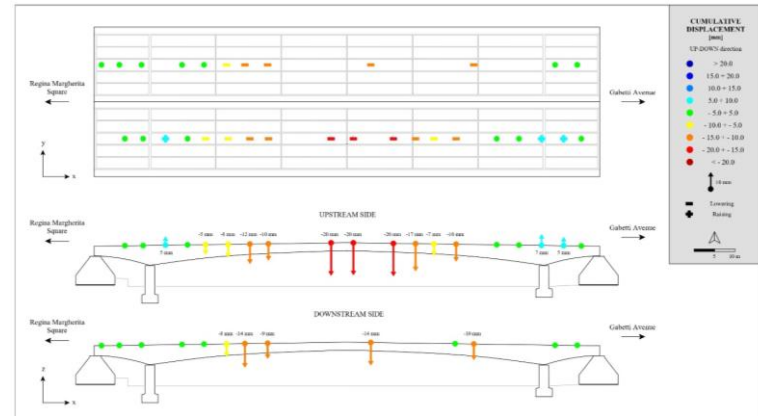


Figure 10 Cumulative vertical displacement on Regina Margherita Bridge

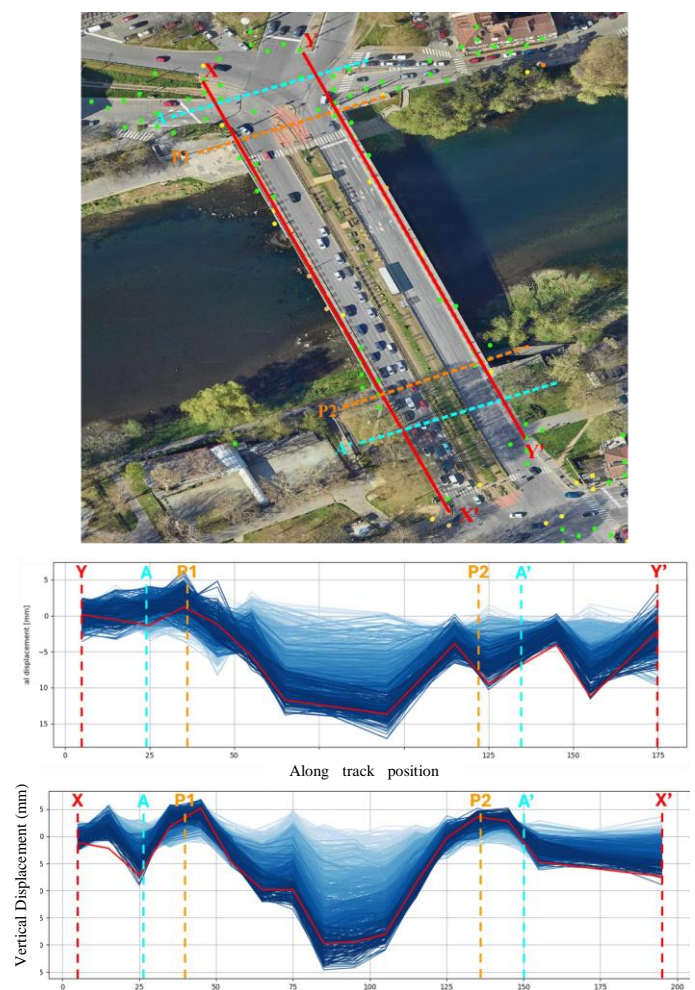


Figure 11 Interferometric section over the vertical deformation along the longitudinal path double way of the Regina Margherita bridge.



seasonal cyclic trend, with an average displacement of approximately zero.

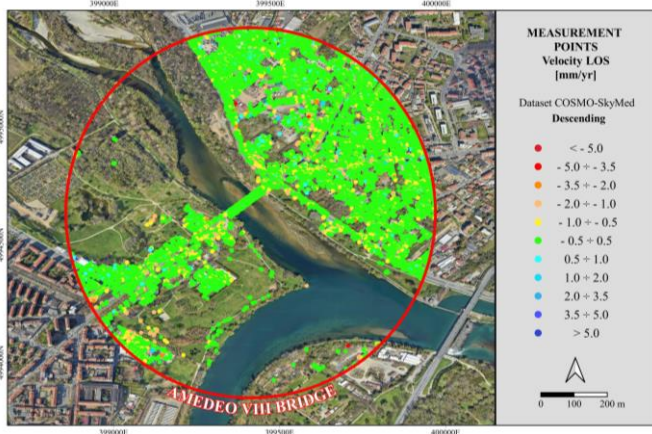


Figure 12 Velocity map of Measurement Points (MPs) obtained from A-DInSAR analysis in descending geometry for the Amedeo VIII bridge area.

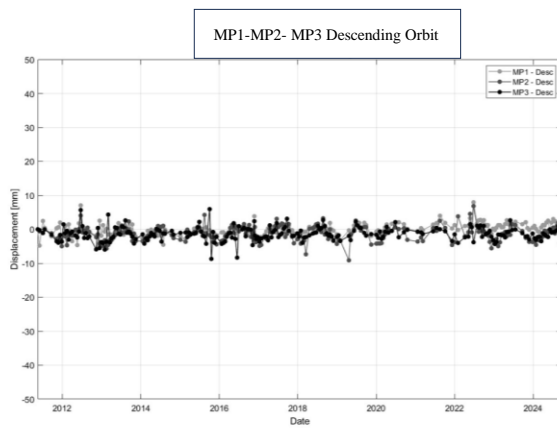


Figure 13 Time series of three measurement points for descending orbit on Amedeo VIII bridge

From the vector decomposition of the two LOS analyses, velocity maps for the vertical and horizontal components of displacement in the bridge area were produced, as shown in figure 14 and 15.

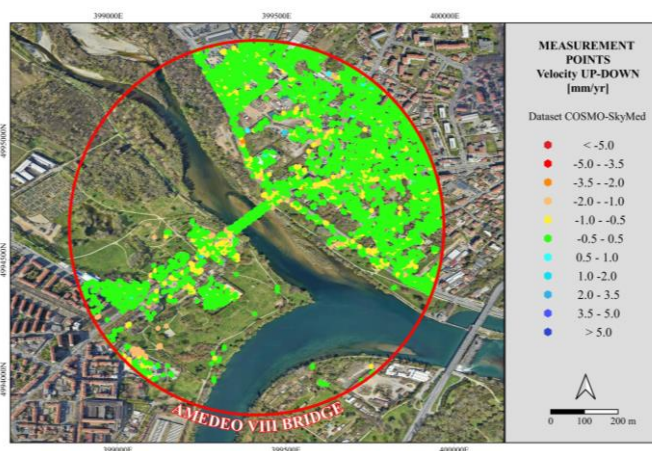


Figure 14 Velocity map of the Synthetic Measurement Points in vertical direction for Amedeo VIII bridge

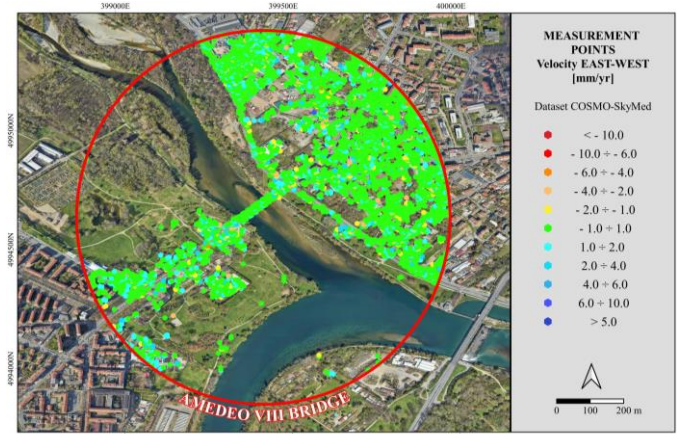


Figure 15 Velocity map of the Synthetic Measurement Points in horizontal direction for Amedeo VIII bridge

Finally, the most representative outputs from the complete post-processing analysis of the satellite data are presented in Figure 16, which shows the cumulative vertical displacement along both the facade and plan view of the bridge, sampled at 5-meter intervals, to detail the deformative behavior in space. The interferometric section, which illustrates the evolution of the bridge's deformation over time and space, is presented in figure 17.

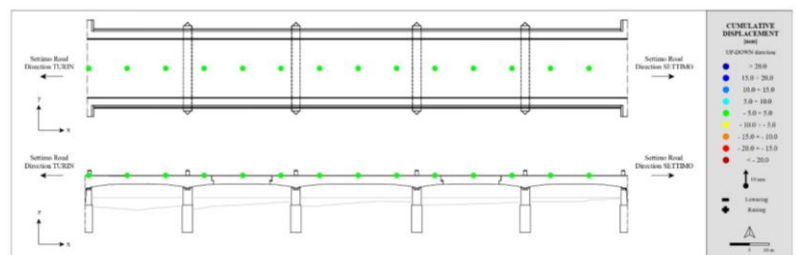


Figure 16 Cumulative vertical displacement on Amedeo VIII bridge

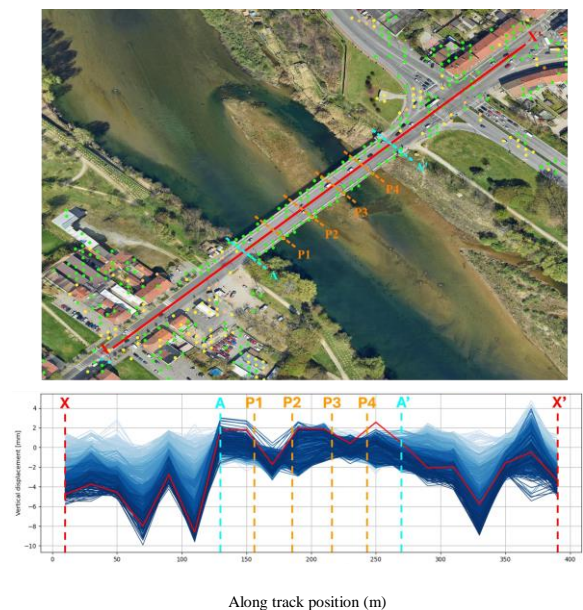


Figure 17 Interferometric section over the vertical deformation along the longitudinal path of the Amedeo VII bridge

It is clear from the interferometric sections, which illustrate the deformation behavior over time and space, that the bridge is stable, both the piers and the deck show minimal deformation.

## 5 PHOTOMONITORING

### 5.1 Introduction to technology

Photomonitoring<sup>TM</sup> is an innovative monitoring technique that can exploit any kind of raster data. Photomonitoring<sup>TM</sup> is based on the identification and analysis of terrain elements and structures and their possible variations through examining images acquired at different times. The analysis uses Digital Image Correlation (DIC) and Change Detection (CD) techniques implemented through NHAZCA's proprietary IRIS software. IRIS is conceived to work with terrestrial, aerial and satellite imagery of any datatype (Optical, Thermal, Near-Infrared, etc.). The technique allows to reach millimeter accuracy in displacement monitoring and can be used separately or combined with other monitoring systems [11,12].

### 5.2 Monitoring strategy

In the ISABEL project, the images will be acquired by cameras installed at the site.

For both bridges, MOBOTIX cameras with dual-lens configuration were deemed as the optimal choice: a wide-angle lens providing a global view and a telephoto lens focused on a specific pier (Amedeo bridge) or for monitoring crack evolution (Regina Margherita bridge).

On Amedeo bridge a single MOBOTIX M73 camera will be installed. The primary focus for the Amedeo VIII bridge is to monitor hydraulic action that can cause scouring of the piers and overall movement of the structures. The camera will be installed on the west riverbank, approximately 60 meters from the central area.

In particular, the wide-angle lens will capture a big part of the bridge, including all piers, providing an overview of the structure and detecting movements through DIC analysis. A telephoto lens will target a specific pier to monitor material accumulation (change detection analysis) and scouring caused by river flow (displacement of the pier).

For Regina Margherita bridge, a MOBOTIX S74 camera will be installed. The main monitoring objectives for the Regina Margherita bridge are crack detection, structural deformation, scouring and material accumulation at the base of the piers, and monitoring during high water levels or flooding conditions. The telephoto lens will be pointed at the nearest span to monitor the evolution and appearance of cracks (change detection). The wide-angle lens will detect displacements of the entire structure, with particular attention to the middle section.

### 5.3 Image acquisition and analysis workflow

For both bridges, image acquisition follows these specifications: Static images captured every 5 minutes for continuous monitoring; Automated trigger mechanism that switches to video recording (30 frames per minute) when significant changes are detected; Data processing using the IRIS software, which compares images within a 10-15 minute buffer to select the best quality for analysis.

The analysis workflow includes the following tasks:

- Feature Monitoring: Images processed using the IRIS software to assess changes in targeted areas, particularly cracks in the nearest arch and scouring at the base of piers; continuous comparison of images within a 10-15 minute buffer to select the best quality for analysis.
- Change Detection: Identifies structural changes while eliminating noise caused by lighting, water turbulence, or environmental conditions; specific attention to crack propagation and material accumulation.
- Displacement Analysis: Determines the extent and direction of structural movement, especially in the arches and piers. The system continues analysis until the structure returns to a stable state.



Figure 18: Example of monitoring of cracks evolution in a viaduct; the image below shows the result of change detection analysis.

## 6 FINITE ELEMENT MODELLING AND THRESHOLDS DEFINITION

### 6.1 FEM generation

Before beginning the bridge's structural modelling, two essential preliminary activities need to be conducted. First, all technical documentation concerning the bridge's structural aspects were gathered. Second, on-site inspections were performed to evaluate the current site conditions, confirm that the built structure matches the original designs, assess the current state, and collect other important observations.

The two bridge models were developed using CSI Bridge, a software specialized in the structural analysis of bridges, compliant with regulations for moving loads. The models enable linear analyses for comparison with data from contact-based sensors to be installed.

The modelling evolved from a simplified "frame" model, with the superstructure condensed into a single element, to a more detailed "shell" model, discretizing the deck with two-dimensional elements for greater accuracy, also allowing the modelling of the complex layout of the prestressed cables.

The validation phase has begun, with progressive verification of the models' accuracy and stability. This iterative approach ensures that potential discrepancies are addressed early, enhancing the robustness and reliability of the results as the



project advances into more sophisticated modelling phases. As the monitoring campaign progresses, the experimental data will be integrated into the digital twins, minimizing error propagation in critical areas of structural performance and enhancing the models' predictive capabilities for real-world scenarios. In later work stages, the numerical model is thought to be updated with material testing results and with the results from the ongoing monitoring system. Creating a reliable model that delivers consistent results is essential to be able to compare and potentially reproduce the phenomena detected through satellite monitoring (fig. 19).

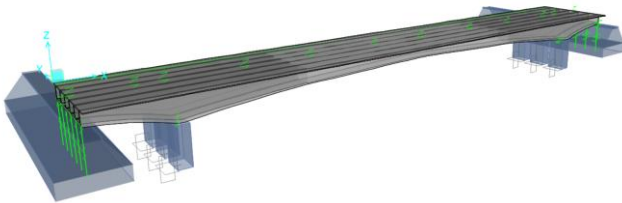


Figure 19: FEM model of the Regina Margherita bridge

## 6.2 SHM Parameters and Thresholds

The SHM system monitors several key parameters that indicate bridge structural health:

### 1. Static Parameters:

- Rotational measurements from inclinometers at pier bases, deck spans, and Gerber saddles
- Displacement measurements from transducers at expansion joints and Gerber saddles
- Strain measurements from gauges at mid-spans
- Deformation maps and displacement values from InSAR and Photomonitoring™
- Surface Damage (Cracks Evolution/Appearance) through Photomonitoring
- Debris material accumulation through Photomonitoring

### 2. Dynamic Parameters:

- Acceleration measurements for modal analysis (natural frequencies, mode shapes)
- Vibration characteristics in response to traffic and environmental loads

### 3. Environmental Parameters:

- Temperature measurements for correlation with structural responses
- Environmental conditions that might affect monitoring results

A multi-level threshold approach has been established to evaluate the monitored parameters:

1. Level 1 (Operational Conditions): Defined according to evaluations based on preliminary models. This represents normal operational conditions.

2. Level 2 (Statistical Deviation): Based on a data-driven model trained on the first period of continuous monitoring. This represents a significant (but not ultimate) deviation from normal behavior.

3. Level 3 (Ultimate Limit State): Derived from numerical simulations of the FEM models, representing the expected ultimate limit state before structural failure.

These thresholds are calibrated using the multi-source data from the integrated monitoring system. The temperature data is particularly important, as understanding the structural behavior induced by temperature variations is crucial for distinguishing normal responses from anomalies.

## 7 WEB PLATFORM

The ISABHEL web platform has been designed to provide a seamless, real-time interface for infrastructure monitoring, offering a user-centric approach to data visualization and interaction. Built using Next.js, the front-end ensures high performance through server-side rendering and static site generation, enhancing both responsiveness and search engine optimization. The modular, component-based architecture leverages React, allowing for reusability and scalability across various interface elements.

A key feature of the platform is its interactive dashboard, which aggregates real-time structural data from multiple sources, including contact sensors, Photomonitoring cameras, and satellite-based SAR analysis. The dashboard dynamically updates through WebSockets, ensuring that users have immediate access to the latest structural health indicators (figure 20).

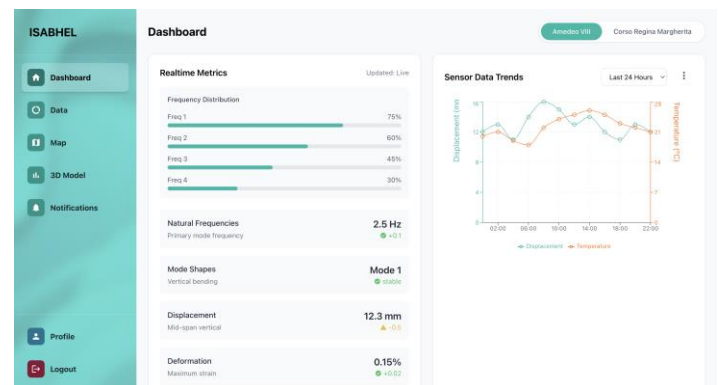


Figure 20: Dashboard of the web user interface

Another core component is the interactive GIS map, which integrates geospatial data through TileServerGL. This feature enables precise visualization of deformation patterns, historical trends, and real-time alerts. Users can navigate the bridge structures in detail, overlaying sensor readings and risk assessments to gain a comprehensive understanding of potential vulnerabilities.

To further enhance the analysis capabilities, the platform incorporates an advanced 3D bridge model rendered using WebGL technologies such as Three.js. The 3D model of the monitored bridge will be presented with a series of "traffic lights" to highlight any anomalies, using the three standard colors (green, orange, red) depending on whether the signal exceeds the predefined thresholds. "Local" traffic lights will be placed directly at the sensor's location (for example, the rotation of a pile or the movement of a Gerber saddle), while "global" traffic lights could refer to analyses at the entire structure level (such as generalized movement of the bridge,



variation in the fundamental vibration periods, etc.), helping the end user understand the nature of any anomalies (21).

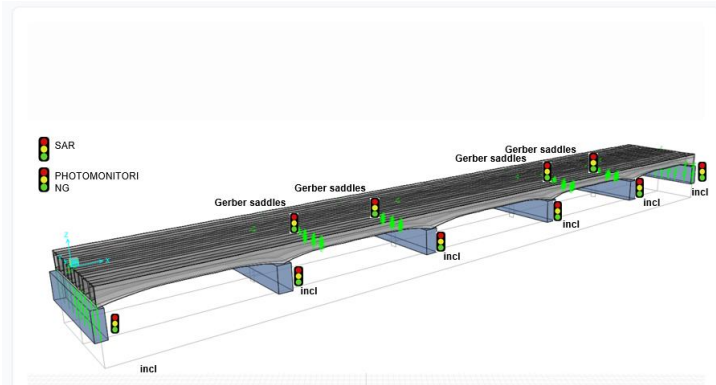


Figure 21: 3D model viewer with color-coded traffic lights

The design choices behind the ISABHEL front end prioritize usability, speed, and scalability. The use of Supabase for database management and authentication streamlines data retrieval and ensures secure access to user-specific functionalities. Additionally, the real-time notification system provides immediate alerts for threshold breaches, ensuring that stakeholders can take timely action when necessary.

## 8 CONCLUSIONS

The work is in its initial phase and ground-based acquisition have not started yet. However, thanks to an in-depth study of raw FEM models and based on A-DInSAR results, first-level thresholds for the bridge's structural health parameters have been estimated, which will need to be confirmed during monitoring. Based on the A-DInSAR analysis, the Regina Margherita Bridge shows localized deformation at midspan, while its abutments and piers remain stable. In contrast, the Amedeo VIII Bridge exhibits minimal deformation throughout its entire structure, with measurements remaining within the stable range ( $\pm 1.0$  mm/year) and displaying only seasonal cyclic variations with average displacement of approximately zero.

## 9 REFERENCES

- [1] M. Aimar, M. Civera, S. Foti, and B. Chiaia, "Preliminary Insights from Surveys of Bridges at High Scouring Risk in West Piedmont," in II Fabre Conference – Existing bridges, viaducts and tunnels: research, innovation and applications (FABRE24), Genoa, 2024.
- [2] Miccinesi, L., Giacomelli, G., Viviani, F., & Pieraccini, M. (2023). "Bridge Safety Monitoring Using Satellite and Multi-Technology Ground-Based Approaches in Italy." *Journal of Bridge Engineering*, 28(3), 04022094.
- [3] Bonfiglioli, B., Pascale, G., & Pezzetti, F. (2020). "Digital image correlation and digital twin for bridge monitoring: Benefits and limitations." *Structure and Infrastructure Engineering*, 16(12), 1768-1784.

- [4] Calvi, G. M., Moratti, M., O'Reilly, G. J., Scattarreggia, N., Monteiro, R., Malomo, D., & Pinho, R. (2019). "Once upon a time in Italy: The tale of the Morandi Bridge." *Structural Engineering International*, 29(2), 198-217.

- [5] Hanssen, R. F. (2001). *Radar interferometry: data interpretation and error analysis (Vol. 2)*. Springer Science & Business Media.

- [6] Wang, S., Mei, L., Liu, R., Jiang, W., Yin, Z., Deng, X., & He, T. (2024). Multi-modal fusion sensing: A comprehensive review of millimeter-wave radar and its integration with other modalities. *IEEE Communications Surveys & Tutorials*.

- [7] Hamzaoui Y., Civera M., Miano A., Bonano M., Fabbroncino F., Prota A. and Chiaia B. Hierarchical Clustering and Small Baseline Subset Differential Interferometric Synthetic Aperture Radar (SBAS-DInSAR) for Remotely Sensed Building Identification and Risk Prioritisation. *Remote Sens.* 2025, 17(1), 128;

- [8] Ferretti, A., Prati, C., & Rocca, F. (2002). Permanent scatterers in SAR interferometry. *IEEE Transactions on geoscience and remote sensing*, 39(1), 8-20.

- [9] Kampes, B. M. (2006). *Radar interferometry (Vol. 12)*. Dordrecht, The Netherlands: Springer.

- [10] A. Ferretti, C. Prati, and F. Rocca, "Permanent scatterers in SAR interferometry," *IEEE Trans. Geosci. Remote Sens.*, vol. 39, no. 1, pp. 8–20, Jan. 2001

- [11] Cosentino, A., Brunetti, A., Mazzanti P., Photomonitoring as a Tool for Monitoring Landslides: A Technology within Everyone's Reach *Journal of transportation Research board*. August 28, 2024

- [12] Mastrantoni G., Santicchia G., Cosentino A., Molinari A., Marmoni G.M., Mazzanti P. 2024. "Automatic photomonitoring analysis for spatiotemporal evaluation of rockfall failure hazard". *Engineering Geology Volume 339*, September 2024, 107662,

# SGAM – Smart Geotechnical Asset Management: Enhancing predictive maintenance with data-driven insights and Earth Observation technologies

Alessandro Brunetti<sup>1</sup>, Maria Elena Di Renzo<sup>1,2</sup>, Michele Gaeta<sup>1</sup>, Paolo Mazzanti<sup>1,2</sup>, Giandomenico Mastrantonio<sup>2</sup>, Emanuela Valerio<sup>1</sup>

<sup>1</sup> NHAZCA S.r.l., Via Vittorio Bachelet, 12 ,00185 Rome

<sup>2</sup> Sapienza Università di Roma, Dipartimento di Scienze della Terra, Piazzale Aldo Moro, 5 – 00185 Roma  
email: alessandro.brunetti@nhazca.com; mariaelena.direnzo@nhazca.com; michele.gaeta@nhazca.com;  
paolo.mazzanti@nhazca.com; giandomenico.mastrantonio@uniroma1.it; emanuela.valerio@nhazca.com

**ABSTRACT:** Natural hazards such as landslides, subsidence, and liquefaction represent growing threats to critical infrastructure. Building upon the methodological foundation presented in the SGAM project, this work introduces enhancements to the Smart Geotechnical Asset Management (SGAM) framework, with particular emphasis on its hazard assessment component. The SGAM system integrates geotechnical monitoring, Earth Observation (EO) data, and machine learning techniques to support predictive maintenance of linear infrastructure. In this paper, we present methodological refinements, expanded geohazard integration, and new insights from recent applications. A synthesis geospatial layer supports proactive risk mitigation by highlighting high-priority intervention zones. These developments aim to improve data-driven infrastructure management.

**KEY WORDS:** Infrastructure resilience, geohazards, EO data, AI algorithms

## 1 INTRODUCTION

Infrastructure systems worldwide are increasingly vulnerable to natural hazards, including seismic events and landslides, resulting in significant economic and social impacts. Prior studies estimate that around 0.5% of global assets are exposed to such hazards annually [1]. These threats often disrupt vital services such as transport and logistics, emphasizing the need for resilient infrastructure planning.

In the literature, several frameworks have been developed to support multi-hazard risk management, particularly in relation to linear assets. These approaches are generally developed for integrated and quantitative frameworks capable of modelling multi-hazard scenarios, infrastructure vulnerability, and resilience. This type of analysis is inherently multidisciplinary and typically requires high-resolution input data, including detailed fragility curves and comprehensive ancillary datasets [2][3]. To overcome the challenges associated with data availability, other studies [4][5] adopted index-based methodologies, offering a more qualitative approach that emphasizes the exposure and vulnerability components of risk rather than detailed hazard modelling. In this context, SGAM (Smart Geotechnical Asset Management) framework was introduced as a semi-automated decision support system integrating EO data, geotechnical monitoring, and data fusion algorithms [6]. The original SGAM methodology, laid the groundwork for a multi-hazard approach to infrastructure risk analysis.

This paper advances that framework by expanding the hazard models, improving the integration of InSAR-derived movement data with hazard assessments, and streamlining the generation of prioritized summary layers.

## 2 METHODOLOGY

The present study builds upon the SGAM framework previously introduced in [6], refining its methodology for the hazard assessment of linear infrastructure. SGAM remains a semi-automated decision support system that leverages satellite

Earth Observation (EO) data, machine learning techniques, and geological knowledge to support asset management and predictive maintenance. In this paper, we present methodological advancements with specific focus on the characterization of landslide, subsidence, and liquefaction hazards.

This version includes a development for individual hazard types, aiming to improve interpretability and accuracy at the asset level. While the geodatabase architecture and structure have already been described in detail in [6], here it is referenced as a resource for hazard data management.

SGAM employs a multi-hazard workflow, integrating ground motion data from satellite InSAR with thematic layers (e.g., topography, geology, land use) through supervised learning algorithms. The spatialized outputs are then segmented and intersected with infrastructure elements to enable the classification of asset segments into risk levels. Key enhancements include differentiated processing for slow and fast landslides, velocity-based subsidence scoring, and refined soil classification for liquefaction susceptibility.

In addition, this study introduces a summary geospatial layer, which was not present in the earlier framework. This integrative product consolidates hazard-specific outputs into a unified decision-support layer, providing a risk-informed prioritization of intervention areas along the infrastructure network.

### 2.1 Hazard assessment

The SGAM project is instrumental in identifying geohazards, which are of paramount importance for ensuring infrastructure safety, as already mentioned in [6]. The framework was tested in a pilot area encompassing a 110 km-long highway located in northern Italy. As a preliminary step in the hazard analysis, the

available ancillary data were compiled and organized, as summarized in Table 1.

Input Data	Dataset
Topography	DTM (Tinitally 10 m) for slope, curvature, and roughness
Geology	National Lithological Map 1:100.000
Land Use	Regional databases
Seismicity	PGA and Vs30 for liquefaction analysis
InSAR (PS)	EGMS Ortho Dataset (EW and UD)

Table 1: Input data for SGAM application in the pilot area

These datasets represent the foundational layers from which each hazard-specific analysis is developed, as illustrated schematically in Figure 1.

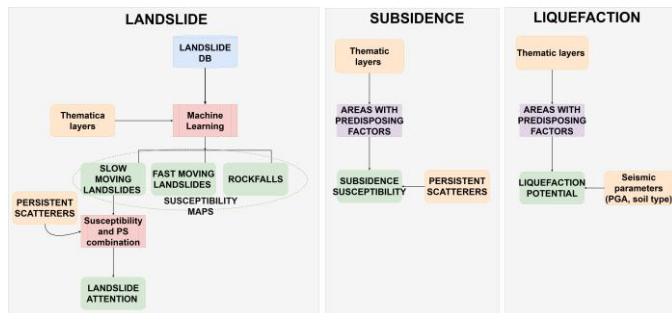


Figure 1: Workflow of SGAM application

### 2.1.1 Landslides

Building on the susceptibility analysis presented in [2], this study introduces a more detailed approach to characterize landslide hazards affecting linear infrastructure. The methodology refines both the input data structure and the classification logic, with particular attention to the kinematic behaviour of slope movements.

Susceptibility is evaluated as the intrinsic propensity of terrain to generate landslides, based on factors such as slope angle, lithology, land use, and morphometry. As in [2], machine learning algorithms trained on available inventories are employed to model landslide density and generate susceptibility maps.

Persistent Scatterers (PS) from satellite InSAR data are incorporated more systematically than in [2], serving as a proxy for activity status. These data support the validation and enhancement of susceptibility outputs by highlighting zones with active deformation. The improved pipeline also includes a Landslide Attention Index, which scores infrastructure segments based on hazard level and PS data velocities.

Figure 2 represents the combination of susceptibility classes and PS velocities, considering a threshold of 2.5 mm/years.

	No PS	$V <  2.5  \text{ mm/yr}$	$V >  2.5  \text{ mm/yr}$
Hazard class 1	Low	Low	Medium - high
Hazard class 2	Medium - Low	Low	Medium - high
Hazard class 3	Medium	Low	High
Hazard class 4	Medium	Medium - Low	High
Hazard class 5	Medium - high	Medium	High

Figure 2: Landslide attention matrix

### 2.1.2 Subsidence

The assessment of ground subsidence hazards in this study builds upon the foundations described in [6], introducing a more robust integration of vertical ground motion data with thematic geological and topographic layers. Subsidence is defined as the slow downward movement of the ground surface due to natural or anthropogenic causes, such as compaction or groundwater withdrawal.

This analysis integrates lithological characterization, slope thresholds, and PS InSAR measurements to identify and classify regions affected by subsidence.

While [6] included initial mapping efforts, the current approach incorporates a classification along the infrastructure into hazard classes based on maximum vertical velocities and contextual geomorphological settings. This classification allows infrastructure managers to identify critical zones where maintenance or reinforcement actions may be needed.

### 2.1.3 Liquefaction

The liquefaction hazard model presented here extends the susceptibility mapping approach introduced in [6], offering a more detailed evaluation of geotechnical and seismic parameters. Liquefaction occurs when saturated soils lose cohesion during seismic shaking, compromising ground stability.

The new model introduces a segmentation-based hazard index that aligns with infrastructure elements. In contrast to the more generalized susceptibility zoning described in [6], this version includes quantitative thresholds for seismic acceleration and susceptibility reclassification, enabling improved spatial resolution.

Additionally, the workflow supports continuous refinement as new geophysical or seismic datasets become available, facilitating dynamic hazard re-evaluation over time.

## 2.2 Summary layer

A key innovation introduced in this study—absent from the framework outlined in [6]—is the development of a summary geospatial layer that consolidates the outputs of the hazard-specific models into a decision-support product. This synthesis layer serves as a comprehensive tool for identifying high-hazard zones along linear infrastructure, prioritizing them for monitoring, maintenance, or intervention.

The summary layer integrates the results from landslide susceptibility (including activity-based scoring from PS data), subsidence hazard classification (based on vertical deformation velocity), and liquefaction potential (based on seismic-geotechnical analysis) (Figure 3). These individual assessments are spatially combined through a rule-based approach to assign a composite risk score to each infrastructure segment.



The results are made available within a GIS environment, enabling interactive visualization of the hazard assessments for each segment of the infrastructure network. By visualizing hazard in a single layer, decision-makers can easily identify critical areas where multiple hazards converge or where the severity of a single hazard justifies immediate action. This tool enhances operational readiness and resource allocation, offering a practical output directly usable by infrastructure managers and planners.

The introduction of this summary layer represents a major step forward in the SGAM methodology, improving its usability, interpretability, and impact in real-world applications.

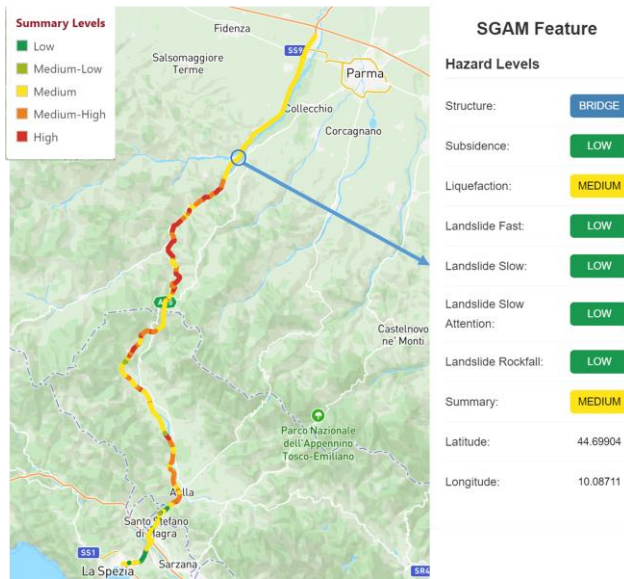


Figure 3: Example of SGAM result on linear infrastructure.

### 3 CONCLUSIONS AND FUTURE OUTLOOK

This study expands upon the foundational SGAM methodology presented in [6], delivering key enhancements in hazard modeling, data integration, and operational usability. While the previous version laid out the general framework for a semi-automated, EO-based geohazard assessment system, the current work provides a more refined and implementable approach by detailing the modeling procedures for landslides, subsidence, and liquefaction.

One of the most significant contributions of this study is the introduction of a summary geospatial layer, which enables an integrated and view of infrastructure vulnerability. This addition makes SGAM not only a robust analytical framework but also a decision-ready platform for operational use in infrastructure management and planning.

Future developments will aim to expand the temporal and spatial scope of SGAM through the integration of multi-temporal EO datasets, including LiDAR and drone-based surveys, and the adoption of automated change detection techniques. Additionally, work will continue incorporating vulnerability and exposure metrics to complement hazard-based assessments, building a more comprehensive picture of infrastructure resilience.

The SGAM system, as further developed in this work, offers a scalable and adaptable solution, capable of supporting

infrastructure managers in making informed decisions in the face of complex and evolving natural hazards.

- [1] Koks, E. E., J. Rozenberg, C. Zorn, M. Tariverdi, M. Voudoukas, S. A. Fraser, J. W. Hall, and S. Hallegatte. "A Global Multi-Hazard Risk Analysis of Road and Railway Infrastructure Assets." *Nature Communications* 10, no. 1 (June 25, 2019): 1-10.
- [2] Argyroudis, S. A., Mitoulis, S. A., Hofer, L., Zanini, M. A., Frangopol, D. M., and Tubaldi, E. "Resilience Assessment Framework for Critical Infrastructure in a Multi-Hazard Environment: Case Study on Transport Assets." *Science of The Total Environment* 707 (2020): 135575.
- [3] Argyroudis, S. A., Mitoulis, S. A., Gkoumas, K., and Christodoulou, S. E. "A Framework for the Resilience Assessment of Transportation Networks under Extreme Hazards." *International Journal of Disaster Risk Reduction* 39 (2019): 101230.
- [4] Joshi, A., Kumar, R., and Singh, P. "Multi-Hazard Risk Assessment for Critical Infrastructure Systems in Data-Scarce Regions." *Natural Hazards* 121, no. 2 (2024): 1123-1145.
- [5] Arvin, S., Lee, J., and Kim, H. "Climate-Informed Risk Evaluation of Infrastructure Assets under Cascading Hazards." *Journal of Infrastructure Systems* 29, no. 1 (2023): 04022047.
- [6] Di Renzo, M.E., Belcecchi, N., Brunetti, A., et al. (2024). *SGAM (Smart Geotechnical Asset Management)*. 11th European Workshop on Structural Health Monitoring (EWSHM). <https://doi.org/10.58286/29729>



# Smart Embedded Sensors and Non-destructive Test Methods for Quality Control

# An EMI-based approach for Structural Health Monitoring of a Space Reinforced Concrete Frame Structure

George M. Sapidis<sup>1</sup>, 0000-0002-0240-5699, Maria C. Naoum<sup>1</sup>, 0000-0002-2262-8267, Nikos A. Papadopoulos<sup>1</sup>, 0009-0007-1183-4616, Maristella E. Voutetaki<sup>2</sup>, 0000-0003-2420-9696, Constantin E. Chaliotis<sup>1</sup>, 0000-0001-8283-1382, Theodoros C. Rousakis<sup>1</sup>, 0000-0002-6384-1451

<sup>1</sup>Laboratory of Reinforced Concrete and Seismic Design of Structures, Civil Engineering Department, School of Engineering, Democritus University of Thrace – Xanthi 67100, Greece

<sup>2</sup>Structural Science and Technology Division, Architectural Engineering Department, School of Engineering, Democritus University of Thrace – Xanthi 67100, Greece

email: [gsapidis@civil.duth.gr](mailto:gsapidis@civil.duth.gr), [mnaoum@civil.duth.gr](mailto:mnaoum@civil.duth.gr), [nikpapad@civil.duth.gr](mailto:nikpapad@civil.duth.gr), [mvouteta@arch.duth.gr](mailto:mvouteta@arch.duth.gr), [chalioti@civil.duth.gr](mailto:chalioti@civil.duth.gr), [trousak@civil.duth.gr](mailto:trousak@civil.duth.gr)

**ABSTRACT:** The electro-mechanical impedance (EMI) method represents a promising approach to structural health monitoring (SHM), attributable to its ability to simultaneously employ piezoelectric transducers for both actuation and sensing purposes. As a result, an extensive volume of literature has surfaced recently, analyzing the efficacy of the EMI method in reinforced concrete (RC) structural elements subjected to quasi-static loading sequences. Nevertheless, the investigation into applying the EMI method in dynamic loading environments must be more robust within the current body of research. This study evaluates the effectiveness of the EMI method for SHM of a one-bay, one-story RC space frame structure under the influence of earthquake excitations. Therefore, a shaking table was used to excite the RC frame with progressively increased ground excitation, wherein piezoelectric patches are strategically embedded in meticulously chosen locations. The embedded PZT sensors facilitate promptly diagnosing earthquake-induced damage to the RC frame. The experimental outcomes reveal that the EMI method effectively and expeditiously identified damage formation within the RC frame.

**KEY WORDS:** Structural Health Monitoring (SHM), Electro-Mechanical Impedance (EMI), damage diagnosis, dynamic loading, Reinforced Concrete (RC) frame.

## 1 INTRODUCTION

In recent years, the secure extension of the service life of existing Reinforced Concrete (RC) structures has become critically significant due to the aging of a substantial portion of the European building stock, some of which have attained their original design life [1]. Therefore, Structural Health Monitoring (SHM) methods have emerged as an indispensable instrument for achieving this objective by evaluating their seismic performance and structural integrity [2]. Compared to conventional methods, such as visual inspection, SHM systems offer continuous inspection, enabling the detection of even slight internal damage initiation, by covering the 3D space of the structural mass in real-time rather than only after it becomes visibly apparent. These systems are permanently installed on the structure, allowing for ongoing monitoring without the need for manual inspections. Furthermore, the energy renovation of existing buildings increases the challenges associated with implementing conventional methods, given that the RC members are inaccessible due to the insulating materials. In contrast to traditional methods, the newly developed SHM techniques enable continuous monitoring and prompt damage identification. Consequently, these limitations have catalyzed SHM advancement in recent decades, during which several methodologies have emerged [3,4].

The electro-mechanical impedance (EMI) technique, recognized as one of the emerging methods in SHM, utilizes the coupling properties inherent in piezoelectric materials, notably lead zirconate titanate (PZT), to identify the deterioration of the assessed structure's mechanical properties. Furthermore, the damage within RC structures initially presents as distributed microcracks that localize to form significant visible cracks [5]. Additionally, a concentration of strain is observed within the material medium, accompanied by a

decrease in the material stiffness matrix, before the emergence of visible cracks [6,7]. Consequently, the deterioration of the mechanical properties of the structure material is manifested in the EMI response of an affixed PZT transducer. Within the extensive body of literature, two primary methodologies are identified for the application of PZT transducers in RC structures: the utilization of externally bonded patches [8,9] or their integration as smart aggregates within the RC structures [10,11]. According to Naoum et al., embedded PZT sensors, like smart aggregates, exhibit increased sensitivity to damage formation and stress fields of the host structure compared to externally bonded PZT patches [12].

Consequently, many research papers have been published investigating the efficacy of EMI-based monitoring of RC elements. The EMI method has been widely utilized in studies for prompt load-induced damage detection of RC and FRC beams. Furthermore, research initiatives have examined the viability of the EMI method for SHM of full-scale subassemblies of RC structures, including RC beams [13–16] and RC joints [17,18] under quasi-static loading, yielding promising outcomes. In addition, research implements machine learning techniques to increase the robustness of the EMI method in high-complexity scenarios, such as retrofitted RC members [19–22]. Nevertheless, prior research has predominantly concentrated on damage identification utilizing quasi-static loading conditions, and research regarding the SHM of RC structures under dynamic loads remains notably limited.

As aforementioned, SHM methods, particularly the EMI method, have been widely investigated in RC subassemblies. However, there has been a dearth of research concerning entire RC structures. Kaur et al. examine the effectiveness of the EMI method in evaluating the pre-stressing force losses in the Sarey



Kale Khan Bridge in New Delhi [23]. Moreover, Liao and Chiu investigate a PZT-based active sensing system designed for SHM of a one-bay, two-story RC space frame structure subjected to seismic loads [24]. A distributed array of PZT SAs was utilized, with specific units designated as actuators while others function as sensors. This approach contrasts with the EMI method, which employs the smart aggregates in dual roles as both actuators and sensors concurrently. Consequently, the EMI method requires fewer PZT transducers to monitor the same structure.

In this work, PZT transducers were embedded as smart aggregates in a one-bay, one-story RC space frame structure. Specifically, three PZT sensors were strategically positioned along the height of the RC columns for EMI-based SHM. Subsequently, the RC space frame underwent testing on a shaking table, with the Peak Ground Acceleration (PGA) level incrementally increased. To attain this incremental loading, a spectrogram of the substantial ground motion that significantly impacted Thessaloniki in 1978 was meticulously altered and determined the dynamic motion of the shaking table. Between the seismic sequences, the EMI responses of the PZT transducers were captured via a novel autonomous monitoring device. The obtained EMI signatures were utilized to expedite the identification of damage within the RC columns during the shake table test. The results underscore the viability and sensitivity of the EMI-based methodology for SHM of RC space frame structures subjected to seismic excitations.

## 2 ELECTROMECHANICAL IMPEDANCE METHOD

As previously indicated, the EMI method capitalizes on the unique characteristics of piezoelectric materials to generate surface electric charges when these materials are subjected to mechanical stress and experience mechanical deformation in response to an electric field [25,26]. Consequently, the reduction in mechanical impedance, associated with the formation of damage in RC members, significantly impacts the electrical impedance of a mounted piezoelectric transducer under harmonic excitation [27]. Furthermore, the EMI signatures of the attached piezoelectric transducers are frequently measured within a predefined frequency band. Any alteration in the EMI signature of each piezoelectric transducer signifies the development of structural damage in its vicinity. Therefore, numerous studies examine the interaction between an attached PZT transducer and the host structure, as exemplified in the work of Liang et al., who model this interaction [28].

In this study, a custom impedance analyzer excites the PZT transducers within a wide frequency range while simultaneously capturing the corresponding signals. Expressly, the EMI signature's frequency range was set between 10 and 250 kHz, with a resolution of 1 kHz. Initially, a set of measurements was taken before any seismic excitation to document the signatures of the PZTs in the healthy condition of the RC space frame structure. Subsequently, the EMI response of the PZT patches was recorded subsequent to the conclusion of each seismic excitation, while the specimen remained at rest. Then, each alteration of the EMI signature indicates the formation of damage in the monitoring area of each PZT sensor.

The interaction between the monitored structure and the PZT transducer significantly influences the EMI signature of the PZT. Consequently, the mechanical properties, including mass, damping, and Young's modulus, are reflected in the EMI signature of PZT due to these interactions. According to Bhalla and Soh, the interaction between the PZT transducer and the RC structure is depicted as an impedance signature that consists of resistance (the real component) and reactance (the imaginary component), as specified in Equation (1) for the complex impedance,  $Z(\omega)$ , of the affixed PZT transducer [29].

$$Z(\omega) = \frac{h}{2L^2\omega j} \left[ \bar{\epsilon}_{33}^T - d_{31}^2 \bar{Y}^E + \left( \frac{Z_a}{Z_s + Z_a} \right) d_{31}^2 \bar{Y}^E \left( \frac{\tan kL}{kL} \right) \right]^{-1} \quad (1)$$

h	PZT Thickness	k	wave number
L	Half-length of the PZT	$Z_a$	Effective mechanical impedance
$\omega$	Angular frequency	$Z_s$	Effective structural impedance
j	Imaginary unit	$d_{31}$	Piezoelectric strain coefficient
$\bar{\epsilon}_{33}^T$	Complex electric permittivity	$\bar{Y}^E$	Complex Young's modulus of the elasticity

Consequently, as indicated by Equation (1), any alterations observed in the electrical impedance of the connected PZT transducer arise from variations in the mechanical impedance of the monitored area, given that the other components of Equation (1) remain unaltered. Thus, notable variations in the EMI response measurements suggest the possibility of structural degradation in the monitored structure.

Researchers usually employ statistical scalar indices to quantify the damage from the EMI responses of the smart aggregates. This study uses the widely utilized damage index, Root Mean Square Deviation (RMSD). The RMSD quantifies the variations between the output signals at the pristine condition and after each loading sequence, according to Equation (2).

$$RMSD = \sqrt{\frac{\sum_{i=1}^N (|V_p(f)|_D - |V_p(f)|_H)^2}{\sum_{i=1}^N (|V_p(f)|_H)^2}} \quad (2)$$

Where:  $|V_p(f)|_H$  represents the absolute value of the voltage output signal extracted from the smart aggregate under the pristine condition of the RC structure,  $|V_p(f)|_D$  denotes the absolute value of the corresponding voltage output signal measured from the same smart aggregate at damage level D, and  $N$  is the discrete number of measurements taken within the frequency band of 10-250 kHz.

## 3 EXPERIMENTAL PROGRAM

### 3.1 Materials and Specimen

This experimental investigation entails casting a one-bay, one-story RC space frame structure, with four RC columns, four beams, a slab, four cantilevers and four infill masonry walls, all designed in accordance with old code provisions (1970s), before the adoption of current Eurocodes 2 and 8 or the New Greek Seismic Code for Concrete Structures. Furthermore, the specimen was scaled at a ratio of 1:3 in accordance with the capacity of the laboratory's shake table,

which possessed a maximum tested structure mass of 8 tons and a maximum overturning moment of 8 ton-m. Therefore, the mass of the specimens was adjusted to 4.3 tonnes, which is less than the maximum bearing capacity of the shake table. The clear span of the specimen's beam measured 1.24 meters, and the clear height of the specimen's columns was 1.0 meters. The concrete utilized in this study was of a C20/25 grade, and the reinforcement employed was referenced as B500C for the slab and foundation and for the longitudinal reinforcement of the columns and S220 for the column stirrup. The column cross-section was set to 13×13 centimeters, and the reinforcement of the specimen was four longitudinal reinforcement bars, each measuring 8 millimeters in diameter, strategically positioned at each corner. Additionally, a closed smooth steel stirrup measuring 5,5 millimeters in diameter was placed every 6 centimeters to serve as transverse reinforcement. A reinforced concrete (RC) slab, which incorporates four balconies and four hidden beams, was constructed with a thickness of 20 centimeters on top of the columns. This heavily reinforced slab was utilized to drive the potential damage in the RC columns and the brick infill panels as well as to allow for additional mass due to renovations involving greenery (with special reference to Thessaloniki metropolitan area). Although the occurrence of damage in vertical structural components is undesirable under current seismic regulations, it is prevalent in existing buildings constructed under older standards (strong slab or beams and weak columns). Figure 1 illustrates the specimen positioned on the shake table in the pristine condition.



Figure 1. RC frame test setup.

### 3.2 Adopted SHM Scheme

As mentioned above, this study investigates a PZT-enabled EMI-based SHM approach for the SHM of a one-bay, one-story RC concrete structure. Thus, several PZT transducers were embedded as smart aggregates in the RC frame specimen. The fabrication of smart aggregates involves several stages. Initially, two lead wires were welded to the two poles of the PZT patch, and the functionality of the sensors was duly verified before further action steps. Subsequently, the PZT transducers were coated with a waterproof layer of epoxy resin, as illustrated in Figure 2. Then, the smart aggregates were positioned in meticulously selected locations of the RC

specimen prior to the pouring of concrete. Although various PZT sensors were employed to monitor different aspects of the specimen's structural integrity, this study focuses on the prompt diagnosis of the formation of bending cracks in the critical regions of the columns. Therefore, two piezoelectric sensors were placed at various heights along the RC columns. The PZT Up and PZT Down were positioned within the critical region, where bending cracks were expected to develop, of the RC columns for the prompt detection of bending-associated crack formation, as depicted in Figure 2. As mentioned earlier, the EMI response of each PZT was recorded using portable EMI-based monitoring devices capable of capturing the EMI response of PZT transducers within the frequency spectrum of 10-250 kHz.



Figure 2. Ready to implement Smart Aggregate.

### 3.3 Shake Table Test Setup

The shake table tests were conducted at the laboratory of Reinforced Concrete and Seismic Design of Structures of Democritus University of Thrace, located in Xanthi, Greece. The shake table has dimensions of 3.4 m by 3.4 m and a maximum velocity of 1.2 m/sec. Furthermore, it possesses a maximum uniaxial acceleration capacity of 1.6g for a payload mass of eight tons and 2.9g for a payload mass of four tons. The maximum displacement capacity of the shaking table was 23 centimeters, and the range of response frequencies extended from 1.0 to 50.0 Hertz. Additionally, a dynamic capability data acquisition system acquired the data of twelve accelerometers, eight-string potentiometers, and 20 strain gauges. Three out of the 12 accelerometers were used to measure the out-of-plane acceleration of the infills. Four-string potentiometers were used to calculate the story drift of the RC structure, while the



remaining devices were used to evaluate the deformation associated with the in-plane response of the infills. Furthermore, appropriate markers for vision-based SHM were strategically positioned on the surfaces of the specimens and employed to extract the displacement field from videos captured by two cameras positioned perpendicularly.

The dynamic loading involved the gradual increment of PGA levels up to 1.1g peak acceleration, based on the employed earthquake component from Thessaloniki in the north-south direction (peak acceleration of 0.14g with main excitation frequencies ranging from 2 Hz to 10 Hz and minor excitation frequencies beyond 26 Hz). The seismic event occurred on 20 June 1978 at 20:03:21 in the epicenter 30 kilometers east of Thessaloniki, revealing the susceptibility of urban centers to such natural disasters. According to Theodulidis et al., 4000 buildings experienced serious, 13000 moderate, and 49000 minor damage [30]. The north-south component of the strong ground motion record at the Thessaloniki-City Hotel station, situated 29 kilometers from the epicenter, offered the ground excitation time history utilized during the dynamic tests, as illustrated in Figure 3. Subsequently, this sequence has been meticulously adjusted to stimulate the specimen with peak accelerations of up to 0.1g, 0.2g, 0.5g, 0.8g, and 1.1g, following a dynamic pushover approach. The ultimate level of the first phase of testing of the as-built structure (presented herein) was characteristic of a structure with RC members at Serviceability Limit States (SLS), where no yielding of steel rebars occurred and brick infills with damage initiation but no collapse. Thereafter, the EMI response of all the PZT sensors was recorded following each excitation.

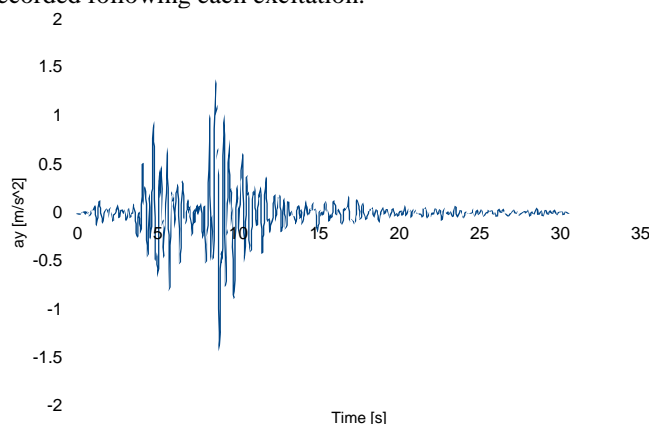


Figure 3. Ground acceleration time history.

## 4 TEST RESULTS

### 4.1 Cracking patterns of RC columns

This sub-section addresses the earthquake-induced damage of the specimen and its observed cracking pattern. The specimen underwent five progressively enhancing sequences of ground excitation. After the third test run, which corresponds to a peak acceleration of 0.5g, some slight surface cracks were observed in the lower region of the RC columns. Therefore, the EMI response captured after the first and second test runs was designated as pre-crack, in conjunction with the EMI response measured under pristine structural conditions. Conversely, the EMI response obtained following the third test run, and the formation of the first cracks, was classified as post-crack. The

cracks were further propagated during the subsequent loading sequences. Figure 4 illustrates the damage condition of the RC column Y1 after all the loading sequences. A bending crack was formed in the lower region of the column, in proximity to the PZT Y1B. Despite the crack propagating through the entirety of the column's cross-section, the measured width of the crack along with the recorded reinforcement strain suggests that the damage sustained was not severe.

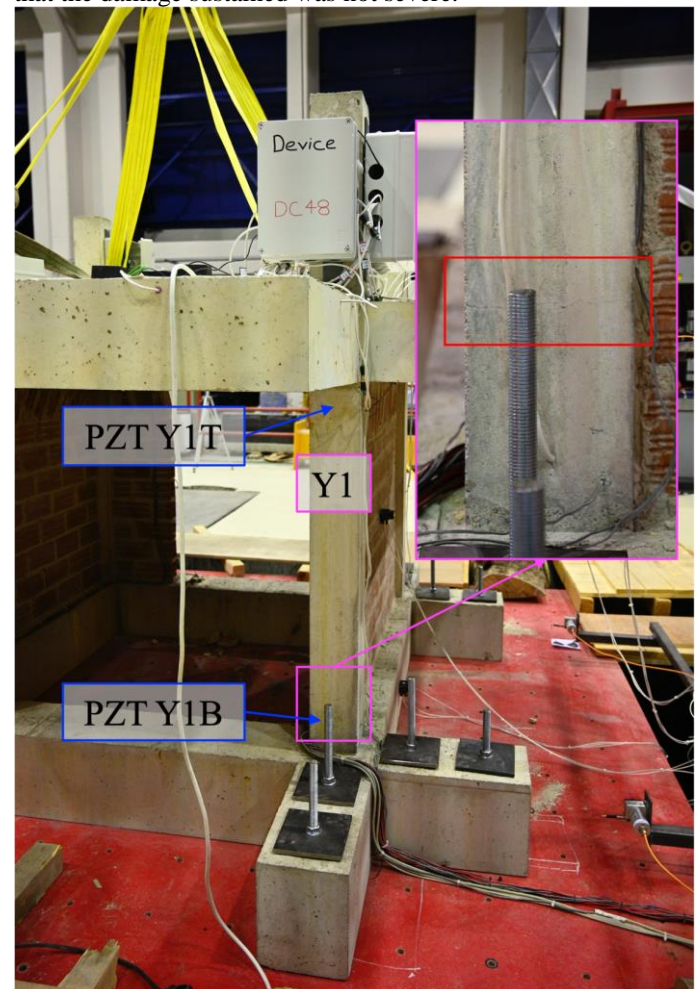


Figure 4. Damage state of RC column Y1

Furthermore, Figure 5 depicts the damage condition of the reinforced concrete column Y2 following the completion of the final loading sequences. In contrast to column Y1, column Y2 was in contact with infills in the biaxial direction. Notwithstanding the fact that the in-plane infill did not encompass the entire span, it nonetheless merely enhanced the load-bearing capacity and the overall stiffness of the specimen. A minor bending crack has developed in the lower region of column Y2, which was sustained in a portion of the column's cross-section, in contrast to the bending crack of column Y1. This may have been attributed to the beneficial contribution of the brick infill. Similarly to column Y1, the crack width and the steel reinforcement strain indicate that the damage sustained was not severe. Therefore, although cracks developed in the RC columns and the brick infill, the structural condition of the space RC frame specimen is categorized within the SLS, as determined by the experimental design for the initial testing phase, as previously noted.



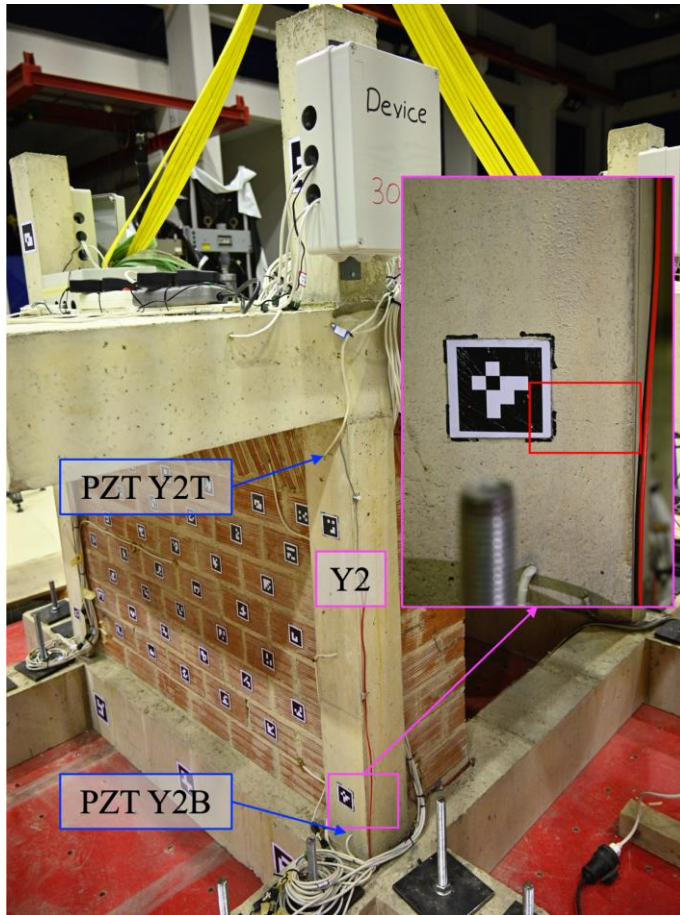


Figure 5. Damage state of RC column Y2

#### 4.2 The EMI response of smart aggregates

This sub-section presents the EMI response of each PZT transducer in terms of  $V_p$ —excitation frequency, as captured with the RC specimen at rest. The EMI responses were measured across a broad frequency spectrum from 10 to 250 kHz. Figure 6 illustrates the EMI response of PZT Y1B, which was placed in the lower region of column Y1. The EMI response of PZT Y1B demonstrated a leftward shift subsequent to the formation of a bending crack in its vicinity. Furthermore, the EMI response does not demonstrate any additional alterations, which aligns with the observed cracking pattern, where the crack width remains constant. Thus, the proposed SHM scheme promptly identifies the formation of the bending crack in the lower region of the column through the alterations of the PZT Y1B EMI responses.

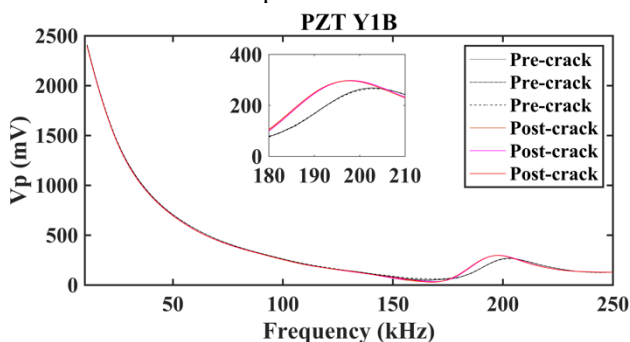


Figure 6. The EMI response of PZT Y1B

Figure 7 shows the EMI response of PZT Y1T, which was placed in the upper region of column Y1. In contrast to the smart aggregate PZT Y1B, the EMI response of PZT Y1T does not vary significantly, as verified by the RMSD values in the following subsection. These findings are consistent with the column's observed crack patterns, wherein the fissure developed in its lower region, as depicted in Figure 4.

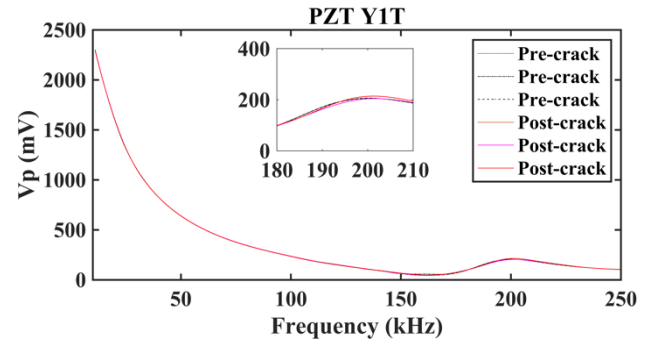


Figure 7. The EMI response of PZT Y1T

Figure 8 depicts the EMI response of PZT Y2B, which was placed in the lower region of column Y2. The EMI response exhibits a subtle peak shift resulting from the development of a bending crack in proximity to the smart aggregate. This is in line with the observed crack patterns of column Y2, as illustrated in Figure 5.

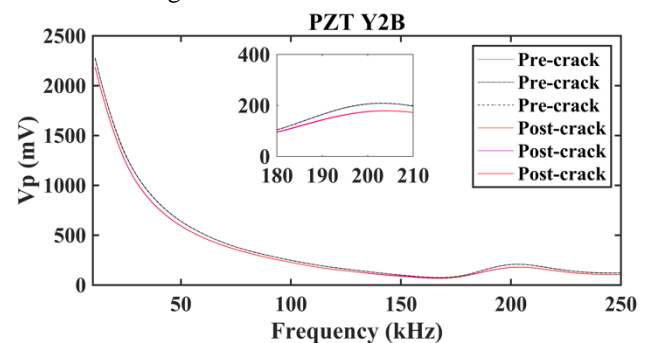


Figure 8. The EMI response of PZT Y2B

Figure 9 illustrates the EMI response of PZT Y2T, which was placed in the upper region of column Y2. No observable alterations in the EMI response of the smart aggregate PZT Y2T, which may be attributed to the distance of the formed bending crack.

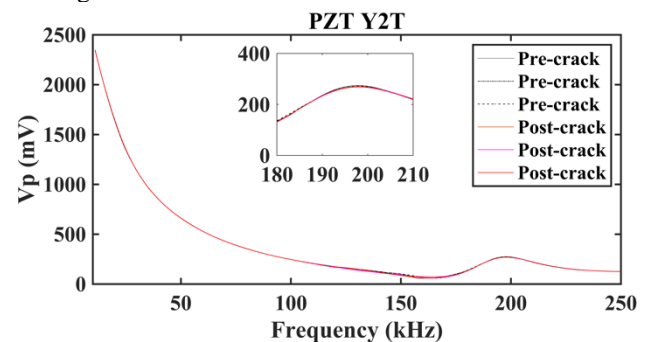


Figure 9. The EMI response of PZT Y2T

#### 4.3 The RMSD

As previously mentioned, the RMSD damage index utilized to quantify the variations in the EMI responses of PZTs in this

study. Figure 10 illustrates the RMSD values of the smart aggregates situated in the upper and lower sections of Column 1. Evidently, the development of a bending crack in column Y1 initiates a significant increase in the RMSD values of PZT Y1B, escalating from 0.5% to 3.2%. On the contrary, the RMSD values of PZT Y1T remain around 0.5 throughout the seismic sequences.

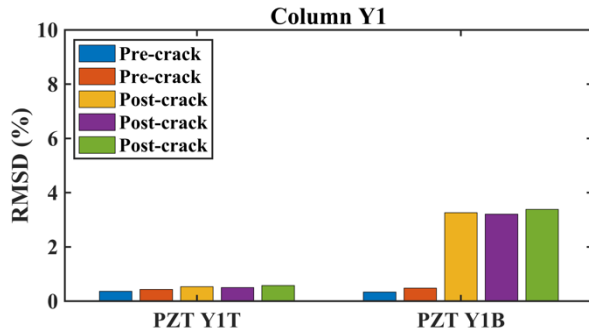


Figure 10. RMSD damage index values pertaining to the smart aggregates in Column Y1

Additionally, Figure 11 depicts the RMSD values of the corresponding smart aggregates of column 2. Similarly, the RMSD values of PZT Y2B demonstrate a significant increase, rising from 0.4% to 6%. Thus, PZT Y2B has effectively identified the development of a bending crack in the lower section of column Y2. Furthermore, RMSD values of PZT Y2T fluctuated between 0.5 and 0.7 during the seismic sequences. Consequently, the SHM scheme indicates that damage has occurred in the lower region of both columns, which aligns with the observations.

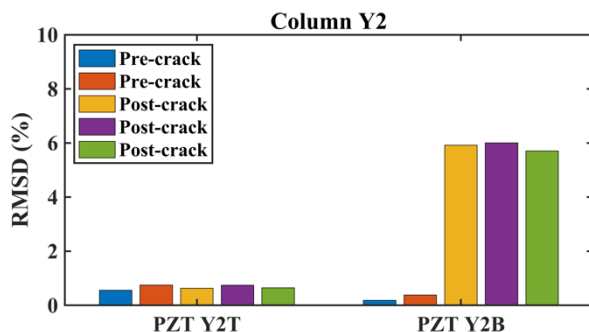


Figure 11. RMSD damage index values pertaining to the smart aggregates in Column Y2

## 5 CONCLUSIONS

This study addresses the feasibility of the EMI method for SHM of a one-bay, one-floor space RC frame structure subjected to earthquake excitations. The specimen was subjected to various percentages of PGA of a strong seismic event, resulting in bending cracks in the lower regions of the specimen's RC columns. The structural integrity has been classified into two distinct categories, referred to as pre-crack and post-crack. The EMI method effectively identified the formation of cracks through the variation induced in the EMI responses of the smart aggregates, indicating its feasibility for the SHM of RC structures. Additionally, it successfully localized these cracks within the lower regions of the specimen's columns. SHM was successful even though this

study was limited to minor damage conditions, relatively close to SLS of RC structures. Such RC damages are hard to detect as the residual drift of the structure is negligible. Subsequent research should further explore the efficacy of the EMI method under conditions approaching the near-collapse damage condition of RC structures as well as the effects due to additional mass after innovative renovations.

## ACKNOWLEDGMENTS

The research project is implemented in the framework of H.F.R.I call “Basic research Financing (Horizontal support of all Sciences)” under the National Recovery and Resilience Plan “Greece 2.0” funded by the European Union—NextGenerationEU (H.F.R.I. Project Number: 015376). <https://greenergy.civil.duth.gr/>

## REFERENCES

- [1] Palermo, V.; Maio, R.; Sousa, M.; Tsionis, G. Framework for resilience analysis of EU buildings. [Internet]. LU: Publications Office European Commission. Joint Research Centre.; 2017 [cited 2025 Mar 23]. Available from: <https://data.europa.eu/doi/10.2760/923762>
- [2] Kassem MM, Beddu S, Ooi JH, Tan CG, Mohamad El-Maissi A, Mohamed Nazri F. Assessment of Seismic Building Vulnerability Using Rapid Visual Screening Method through Web-Based Application for Malaysia. Buildings. 2021 Oct 18;11(10):485.
- [3] Farrar CR, Jauregui DA. Comparative study of damage identification algorithms applied to a bridge: I. Experiment. Smart Mater Struct. 1998 Oct 1;7(5):704–19.
- [4] Nagarajaiah, Satish, Erazo, Kalil. Structural monitoring and identification of civil infrastructure in the United States. Structural Monitoring and Maintenance. 2016 Nov 25;3(1):51–69.
- [5] Narayanan A, Subramaniam KVL. Sensing of damage and substrate stress in concrete using electro-mechanical impedance measurements of bonded PZT patches. Smart Mater Struct. 2016 Sep 1;25(9):095011.
- [6] Surendra P. Shah and Sushil Chandra. Critical Stress, Volume Change, and Microcracking of Concrete. ACI Journal Proceedings. 1968 Jan 9;65(9).
- [7] V. S. Gopalratnam and Surendra P. Shah. Softening Response of Plain Concrete in Direct Tension. ACI Journal Proceedings. 1985 Jan 5;82(3).
- [8] Sapidis G, Naoum M, Papadopoulos N, Voutetaki M. Flexural Damage Evaluation in Fiber Reinforced Concrete Beams Using a PZT-Based Health Monitoring System. In: Jędrzejewska A, Kanavaris F, Azenha M, Benboudjema F, Schlicke D, editors. International RILEM Conference on Synergising Expertise towards Sustainability and Robustness of Cement-based Materials and Concrete Structures [Internet]. Cham: Springer Nature Switzerland; 2023 [cited 2023 Jul 3]. p. 957–68. (RILEM Bookseries; vol. 43). Available from: [https://link.springer.com/10.1007/978-3-031-33211-1\\_86](https://link.springer.com/10.1007/978-3-031-33211-1_86)
- [9] Sapidis GM, Naoum MC, Papadopoulos NA. Electromechanical Impedance-Based Compressive Load-Induced Damage Identification of Fiber-Reinforced Concrete. Infrastructures. 2025 Mar 10;10(3):60.
- [10] Ai D, Li H, Zhu H. Flexure-critical stress and damage identification in RC beam structure using embedded piezoelectric transducers: 2D modelling and experimental investigations. Construction and Building Materials. 2023 Dec;409:134017.
- [11] Papadopoulos NA, Naoum MC, Sapidis GM, Chalioris CE. Resilient and Sustainable Structures through EMI-Based SHM Evaluation of an Innovative C-FRP Rope Strengthening Technique. Applied Mechanics. 2024 Jun 21;5(3):405–19.
- [12] Naoum MC, Sapidis GM, Papadopoulos NA, Voutetaki ME. An Electromechanical Impedance-Based Application of Realtime Monitoring for the Load-Induced Flexural Stress and Damage in Fiber-Reinforced Concrete. Fibers. 2023 Apr 11;11(4):34.
- [13] Ai D, Luo H, Wang C, Zhu H. Monitoring of the load-induced RC beam structural tension/compression stress and damage using piezoelectric transducers. Engineering Structures. 2018 Jan;154:38–51.
- [14] Naoum MC, Papadopoulos NA, Sapidis GM, Chalioris CE. Advanced Structural Monitoring Technologies in Assessing the Performance of Retrofitted Reinforced Concrete Elements. Applied Sciences. 2024 Oct 12;14(20):9282.

- [15] Angeli GM, Naoum MC, Papadopoulos NA, Kosmidou PMK, Sapidis GM, Karayannis CG, et al. Advanced Structural Technologies Implementation in Designing and Constructing RC Elements with C-FRP Bars, Protected Through SHM Assessment. *Fibers*. 2024 Dec 5;12(12):108.
- [16] Papadopoulos NA, Naoum MC, Sapidis GM, Chalioris CE. Cracking and Fiber Debonding Identification of Concrete Deep Beams Reinforced with C-FRP Ropes against Shear Using a Real-Time Monitoring System. *Polymers*. 2023 Jan 17;15(3):473.
- [17] Divsholi BS, Yang YW, Bing L. Monitoring Beam-Column Joint in Concrete Structures Using Piezo-Impedance Sensors. *AMR*. 2009 Aug;79–82:59–62.
- [18] Naoum M, Sapidis G, Papadopoulos N, Golias E, Chalioris C. Structural Health Monitoring of Reinforced Concrete Beam-Column Joints Using Piezoelectric Transducers. In: Jędrzejewska A, Kanavaris F, Azenha M, Benboudjema F, Schlicke D, editors. *International RILEM Conference on Synergising Expertise towards Sustainability and Robustness of Cement-based Materials and Concrete Structures* [Internet]. Cham: Springer Nature Switzerland; 2023 [cited 2023 Jul 6]. p. 945–56. (RILEM Bookseries; vol. 43). Available from: [https://link.springer.com/10.1007/978-3-031-33211-1\\_85](https://link.springer.com/10.1007/978-3-031-33211-1_85)
- [19] Perera R, Torres L, Ruiz A, Barris C, Baena M. An EMI-Based Clustering for Structural Health Monitoring of NSM FRP Strengthening Systems. *Sensors*. 2019 Aug 31;19(17):3775.
- [20] Ai D, Mo F, Han Y, Wen J. Automated identification of compressive stress and damage in concrete specimen using convolutional neural network learned electromechanical admittance. *Engineering Structures*. 2022 May;259:114176.
- [21] Sapidis GM, Kansizoglou I, Naoum MC, Papadopoulos NA, Chalioris CE. A Deep Learning Approach for Autonomous Compression Damage Identification in Fiber-Reinforced Concrete Using Piezoelectric Lead Zirconate Titanate Transducers. *Sensors*. 2024 Jan 9;24(2):386.
- [22] Sapidis GM, Naoum MC, Papadopoulos NA, Golias E, Karayannis CG, Chalioris CE. A Novel Approach to Monitoring the Performance of Carbon-Fiber-Reinforced Polymer Retrofitting in Reinforced Concrete Beam–Column Joints. *Applied Sciences*. 2024 Oct 10;14(20):9173.
- [23] Kaur N, Goyal S, Anand K, Sahu GK. A cost-effective approach for assessment of pre-stressing force in bridges using piezoelectric transducers. *Measurement*. 2021 Jan;168:108324.
- [24] Liao WI, Chiu CK. Seismic Health Monitoring of a Space Reinforced Concrete Frame Structure Using Piezoceramic-Based Sensors. *J Aerosp Eng*. 2019 May;32(3):04019015.
- [25] Ha SK, Keilers C, Chang FK. Finite element analysis of composite structures containing distributed piezoceramic sensors and actuators. *AIAA Journal*. 1992 Mar;30(3):772–80.
- [26] Ikeda T, Ikeda T. *Fundamentals of piezoelectricity*. 1. issued in paperback with corr. Oxford: Oxford University Press; 1996. 263 p. (Oxford science publications).
- [27] Liang C, Sun F, Rogers CA. Electro-mechanical impedance modeling of active material systems. *Smart Mater Struct*. 1996 Apr 1;5(2):171–86.
- [28] Liang C, Sun FP, Rogers CA. An Impedance Method for Dynamic Analysis of Active Material Systems. *Journal of Intelligent Material Systems and Structures*. 1997 Apr;8(4):323–34.
- [29] Bhalla S, Soh CK. Electromechanical Impedance Modeling for Adhesively Bonded Piezo-Transducers. *Journal of Intelligent Material Systems and Structures*. 2004;15(12):955–972.
- [30] Theodulidis N, Roumelioti Z, Panou A, Savvaidis A, Kiratzi A, Grigoriadis V, et al. Retrospective Prediction of Macroseismic Intensities Using Strong Ground Motion Simulation: The Case of the 1978 Thessaloniki (Greece) Earthquake (M6.5). *Bull Earthquake Eng*. 2006 May;4(2):101–30.



# Tactile Pressure Sensors to analyse Anchor Wall Behaviour in mid-scale Experiments

Julian Schleicher<sup>1</sup>, 0009-0005-7379-5937, Matthias J. Rebhan<sup>1</sup>, 0000-0002-0638-6202, Hans-Peter Daxer<sup>1</sup>, 0009-0006-7216-4348, Vera Pamminger<sup>2</sup>, 0009-0008-2295-0134, André Arnold<sup>3</sup>, 0009-0006-0653-5518, Franz Tschuchnigg<sup>1</sup>, 0000-0002-4279-7703

<sup>1</sup>Institute of Soil Mechanics, Foundation Engineering and Computational Geotechnics, Faculty of Civil Engineering Sciences, Graz University of Technology, Rechbauerstraße 12, 8010 Graz, Austria

<sup>2</sup>sendance GmbH, Pulvermühlstraße 3, 4040 Linz, Austria

<sup>3</sup>Lucerne University of Applied Sciences and Arts, School of Engineering and Architecture, Institute of Civil Engineering, Technikumstraße 21, 6048 Horw/Lucerne, Switzerland

email: julian.schleicher@tugraz.at, rebhan@tugraz.at, daxer@tugraz.at, vera.pamminger@sendance.at, andre.arnold@hslu.ch, franz.tschuchnigg@tugraz.at

**ABSTRACT:** Material ageing, such as corrosion of reinforcements or damage to geotechnical tension elements, can lead, among other effects, to load redistribution mechanisms at the interface of structure and the adjacent soil. These mechanisms are difficult to capture, as analytical calculations are not practical and three-dimensional numerical simulations, utilizing advanced constitutive laws require sufficient monitoring data to validate the calculations. Consequently, it is difficult to determine the reliability of damaged structures. To improve existing knowledge in this field, a test setup simulating an anchor wall was developed, to provide calibration data for numerical studies and to evaluate load redistribution mechanisms at the soil-structure interface in general. In this context, newly developed Tactile Pressure Sensors (TPS) were tested for their suitability as an additional monitoring tool, to record changes in compressive stress at the interface and consequently, to complement conventional monitoring devices used for deformation and force measurements. Such TPS can enable the visualization of an approximate compressive stress distribution across the entire interface, utilizing 576 individual sensing elements over an area of 1.50 m<sup>2</sup> to monitor changes in stress. Thus, additional data is provided to improve the evaluation of load redistribution mechanisms and to be used as validation data for numerical models.

**KEY WORDS:** tactile pressure sensors, piezoresistive sensors, geotechnical testing, experiment, validation.

## 1 INTRODUCTION

Anchored retaining structures are commonly used as an economical solution for the long-term stabilization of steep slopes or deep cuts along infrastructure routes. To ensure their reliability - encompassing durability, serviceability and load-bearing capacity - regular maintenance and inspection is essential throughout their intended service life [1][2]. These inspections often reveal damage, and in some cases, failure of the metallic tension elements. Corrosion represents the most significant challenge for pre-stressed ground anchors and reinforced concrete structures in general, which can lead to significant damage (up to failure) of the tension elements, affecting the load-bearing behavior of the structure. This may lead to a redistribution of forces, both within the retained soil and the structure itself. This redistribution can ultimately result in the failure of additional (adjacent) ground anchors and unexpected deformations of the retaining structure.

Currently, engineers are dealing with limited guidelines and regulations to assess such effects, caused by damage or failure, impacting the load-bearing capacity and, consequently, the safety of the structure. In this context, complex three-dimensional numerical models, regardless of their resource intensity, are inevitable to provide a reliable safety assessment. Such models are essential to determine the probability of critical failure mechanisms and their location within the soil body, which is mandatory for many existing anchored structures. To provide valid calculation data, these numerical models must be calibrated accordingly and therefore require a suitable amount of measurement data, e.g. on deformations and stresses. As such data is usually not sufficiently available for

existing structures, it is necessary to evaluate the expected behavior of the structure in the event of an anchor failure differently. For example, in mid-scale experiments, which combined with numerical models allow for an upscaling of the results to come up with recommendations concerning the assessment of existing structures possibly at risk. Based on this consideration, it would also be highly beneficial to consider an appropriate monitoring concept for future structures.

This paper describes a mid-scale test facility for simulating anchor failures and investigating the resulting load redistribution effects in the soil body and at the soil-structure interface. The studies provide more information on the sensitivity of anchored structures to tension element failure and help identify critical areas for potential future monitoring. To improve the quantity and quality of data obtained from the experiments, a newly developed measurement system is presented. These, so called Tactile Pressure Sensors (TPS), should enable an approximate two-dimensional recording of the stress field at the soil-structure interface and thus provide an extended amount of data for the calibration of numerical models and the interpretation of the experiment itself. The content includes an initial assessment of the capabilities of the TPS mentioned. Accordingly, an investigation of the sensors' performance under geotechnical constraints, considering the boundary conditions in the test setup, took place. Additionally, first results for the simulation of an anchor failure, monitored by classic load cells and displacement transducers, are presented.

## 2 TACTILE PRESSURE SENSORS

Standard earth pressure cells only provide a punctual recording of the compressive stress at the soil-structure interface, whereas the pressure distribution itself ideally needs to be monitored in a two-dimensional way. Thus, the evaluation of the problem in its entirety requires an alternative measurement system which provides a higher measurement resolution and consequently a better database to examine load redistribution effects due to anchor failure.

Tactile Pressure Sensors have been used in geotechnical experiments since the 1990s [3] and have been part of many experiments and publications since [4][5][6]. Due to their low-profile architecture and the amount of measurement points per area, they can be generally applied to determine the stress distribution between two structures. In geotechnical engineering such measuring equipment is used to determine the soil-structure interaction or the load transfer between two soil bodies in various setups, especially in geotechnical centrifuge testing [7][8]. According to previous experiences made with such sensors, the technology seemed to be suitable for the given task. Unfortunately, well-known TPS, although applicable in terms of metrological performance, did not meet the requirements of the planned testing series. Mainly caused by limitations in terms of geometry, robustness and high costs. Thus, it was necessary to find an alternative system which better addresses the requirements resulting from soil-structure interaction within the mid-scale experiment.

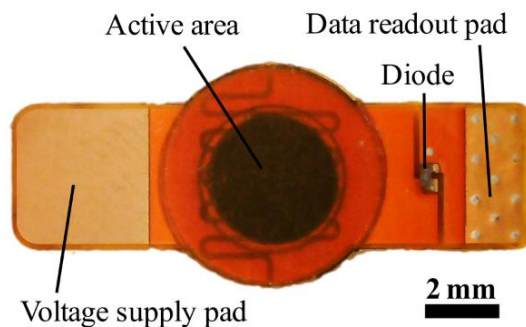


Figure 1. Sensor design.

The chosen TPS, developed by sendance GmbH, leverages the physical principle of piezoresistivity for pressure detection. The core sensing element consists of a circular 0.1 mm thin layer of piezoresistive material, with a diameter of 3.5 mm, that electrically connects two electrodes. The simplified sensor design is shown in Figure 1. Under compressive stress, the sensor's electrical resistance diminishes from values exceeding MΩs to tens of kΩ. During measurement, a 3.3V supply voltage is applied to one electrode. The other electrode is connected to a microcontroller with a 12-bit Analog-to-Digital Converter (ADC) and a 20 kΩ reference resistor connected to ground (GND). This voltage divider configuration allows the microcontroller to measure the voltage change resulting from the sensor's resistance variation, caused by the compressive stress acting on the piezoresistive material. To ensure a more uniform pressure distribution on the piezoresistive material and enhance the system's robustness, the TPS and its wires are encapsulated in a silicone coating, achieving a total thickness of 1 mm. To compensate for the production variability of sensors and to achieve more accurate readings, each sensor is

individually calibrated. The sensors are usually calibrated by 36 load-steps spread over the range of 0 to 500 kPa or lower, depending on the area of interest. At each load-step, the corresponding ADC value, and the acting compressive stress in kilopascals are recorded. These calibration data pairs each define one calibration point, which collectively form the calibration curve.

This data is subsequently stored within the readout electronics, and linear interpolation between the individual calibration points is used to determine the pressure corresponding to any measured ADC value not directly provided by the calibration points themselves. As the devices are tailor-made, the sensors can be arranged in any formation, limited only by the space required for wiring. Figure 2 shows a TPS example with a 4x4 grid formation, used for small-scale testing to evaluate sensor performance. In general, each sensor row (horizontal) shares one supply line and each column (vertical) shares one readout line to minimize wiring amount and complexity. Only one supply and one readout line are active at any given time, allowing for a sequential readout of the sensors with a rate of up to 150 Hz using Bluetooth®. To prevent crosstalk between sensors, which means they would influence each other's readings, a diode is added to each sensor.

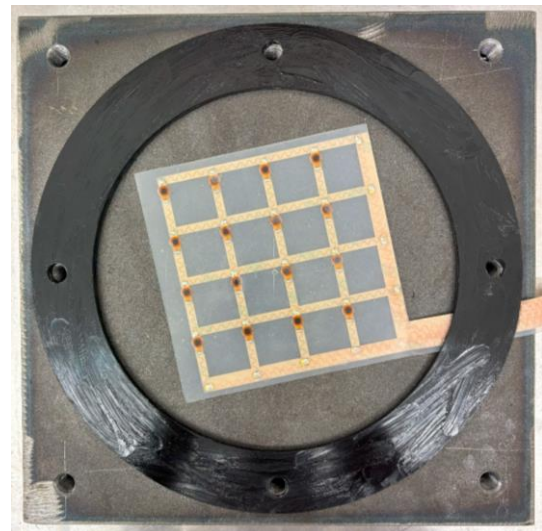


Figure 2. TPS for performance testing (small-scale), placed on pressure chamber baseplate.

The accuracy of the TPS is influenced by several factors, including the homogeneity of the applied pressure, the utilized pressure range, and the duration of the applied load. Consequently, the accuracy of the system must be determined within the field of application.

To evaluate the performance of the sensors under geotechnical conditions and to confirm the suitability of the TPS for the intended application within the mid-scale tests, some information on performance evaluation is provided in the following chapters. The focus is on the precision (repeatability) of the system's measurements, including soils.



### 3 TEST SETUP & METHODS

Mid-scale model tests on anchor failure are conducted in a test box (see Figure 3) with dimensions of 1.00 m (width), 1.50 m (height) and 3.00 m (length). Within the test box, a retaining wall is constructed using nine individual steel elements arranged in a 3 x 3 grid, rigidly connected in both horizontal and vertical directions. The retaining wall is backfilled with gravel (4/8 mm rounded grains). To simplify the assembly process, the ground anchors are represented by horizontally installed bracing units (struts) placed outside the soil body. These struts, which are subjected to compressive loads, rest on a horizontal abutment in front of the retaining wall. Each strut can be individually pre-stressed by applying torque, allowing for different test configurations. Individual struts are released to observe the system's response during the failure simulation. Force measurements, using load cells, are taken at each of the nine contact points between the retaining wall and the struts to capture the resulting force redistribution. Additionally, displacement transducers were installed to monitor wall deformation. These measurements have not been incorporated into this study, as the primary focus lies on the load redistribution.



Figure 3. Test setup during assembly.

Figure 3 illustrates the test set-up during the assembly process. The labelling scheme is as follows: from left to right, the axes are labelled A to C, while from bottom to top, the anchor rows are designated 1 to 3. For example, the central anchor is labelled B2. Additional details on the set-up can be found in [9].

Although the change in force, measured by the installed load cells, already allows some interpretation of the mechanical processes during the experiment, providing more data, to e.g. validate a numerical model for post-processing purposes,

would be highly beneficial. Furthermore, more data would be crucial to come up with a comprehensive conclusion about the occurring load redistribution effects.

Consequently, it was decided to integrate the previously described TPS into the testing facility, positioned at the soil-structure interface (see Figure 3), to analyze the acting compressive stresses. For this purpose, a sensor arrangement was designed which allows for 64 sensors on each of the nine individual steel elements (see Figure 4) which results in 576 individual measurement points evenly distributed over the entire back-side of the retaining wall, covering an area of 1.50 m<sup>2</sup>. Compared to the force measurements with just nine load cells, the TPS enables an approximately two-dimensional analysis of the stress field at the soil-structure interface and therefore allows a detailed interpretation of spatial mechanisms caused by the load redistribution within the soil body (e.g. arching effects) due to anchor failure.

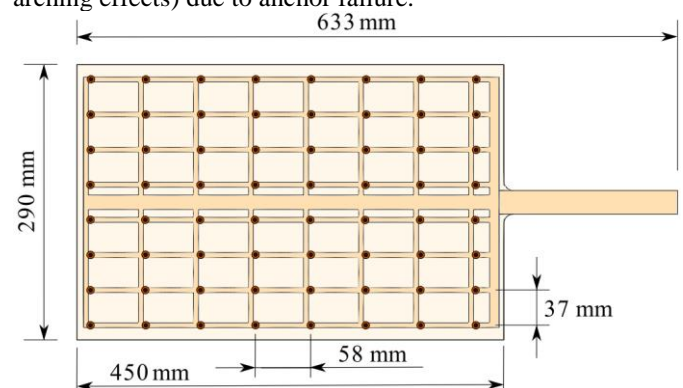


Figure 4. TPS configuration for mid-scale test.

The TPS system must be calibrated and tested in the geotechnical environment to obtain accurate sensor readings within the mid-scale model. While the entirety of the grid is encapsulated in silicone, the sensors are exclusively present in specific regions of the sensor grid, which causes the TPS to be inhomogeneously stiff. Areas where sensors are situated exhibit a higher stiffness than areas without any sensors present. Thus, applying stress to the TPS by e.g. a stiff loading plate doesn't allow for an accurate calibration or repeatable testing. Single-point calibration/testing on the other hand, with e.g. a load-stamp, would result in a significant testing effort. In addition, the use of a load stamp would prevent reliable repeatability, as the stamp would have to be positioned at the same spot on the sensor (diameter = 3.5 mm) each time, which cannot be guaranteed with a manual process, as was observed in preliminary studies.

Therefore, the testing and calibration is performed using a calibration chamber, designed to apply air pressure to the sensor grid. This approach satisfies the need for an evenly distributed compressive stress on the system (isobaric stress state), which is not affected by any inhomogeneities in the system's stiffness, which could possibly lead to a misinterpretation of the applied stress. Additionally, air pressure is well controllable, and the calibration steps can be chosen flexibly. Concerning measurements incorporating soils, a membrane was introduced to enhance the calibration chamber's suitability. This advancement allows air pressure, distributed by the membrane, to act across the soil grains, onto the TPS. This prevents additional air pressure being applied to



the system, which could act between the grains, although all loads should only be transferred by the soil grains themselves.

First tests to evaluate the TPS' accuracy were performed under load application by air pressure only - without any soils incorporated - to assess the sensors' performance under fully controllable and repeatable conditions. This ensured benchmark measurements that reflect the pure performance of the TPS in the pressure chamber, without the effects of uneven loading from soil grains, etc. This data can later be used for comparison with measurements of the TPS in soils to put the sensors' performance in different environmental conditions into perspective.

Subsequently, the systems suitability for application in the geotechnical environment was evaluated. Thus, soil samples with different grain size distributions (GSDs) were prepared to investigate the maximum grain size ( $D_{max}$ ) suitable for the TPS, as well as to generally analyze differences in performance due to the GSD. Sample preparation aimed for very narrow GSDs to isolate the critical grain size. Furthermore, angular grains were utilized for the tests, as these may cause more distortion in the sensor readings compared to round grains and thus represent a 'worst-case' scenario in terms of sensor performance and robustness, which provides the most information concerning the overall performance of the TPS.

#### 4 FIRST TESTS AND RESULTS

Preliminary studies concerning the TPS performance are shown below. All described tests were executed in the previously mentioned pressure chamber, using a 4x4 grid (16 sensors), which is illustrated in Figure 2. To characterize the TPS for the use under geotechnical constraints, the systems accuracy must be investigated in terms of precision and trueness, according to [10]. The outlined experiments mainly focus on the precision of the TPS, also defined as the repeatability of measurements. In addition to the studies concerning the TPS, initial experiments simulating anchor failure within the mid-scale test facility were carried out. The results of these tests are also presented and discussed below.

##### 4.1 Preliminary studies - TPS

In the following, the term 'representative sensor' always refers to one and the same sensor on the grid to ensure comparability of different measurements. The presented measurements were carried out by applying air pressure on the sensors.

First, all 16 sensors were calibrated, according to the calibration procedure, described in chapter 2. Afterwards the first test series was performed, which consisted of four individual tests with 10 load cycles – loading and unloading – of the entire sensor grid.

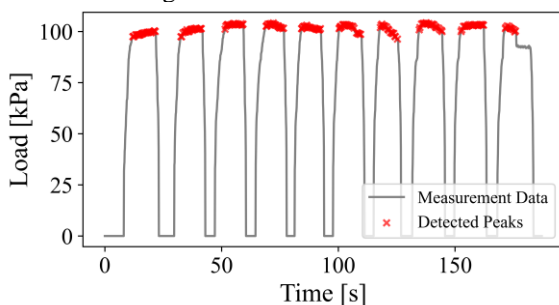


Figure 5. Recorded load-cycle for a representative sensor.

Figure 5 illustrates the recorded measurements for a representative sensor at a maximum pressure of 100 kPa, for one individual test.

Peak values were detected and marked with a red cross. Determining the mean value of the peak values per load-cycle, results in 10 measurements per sensor, per test, which corresponds to 160 values for the entire TPS. To simplify these results, only one mean value was calculated per sensor and test across all peak values. Subsequently, an average value was calculated from the measurements of all 16 sensors, representing the entire system, assuming a smeared performance as relevant. This approach represents an evaluation of the overall performance of the TPS, while studies on individual sensors are presented later.

Table 1 shows the mean value  $\bar{p}$  (measured compression stresses) for each individual test, as well as the global mean value  $\mu$ , the standard deviation  $\sigma$ , and the relative error  $\delta$  across all tests, at certain pressure levels  $PL$ , for the entire TPS.

Table 1. Preliminary evaluation of TPS performance

$PL$ [kPa]	$\bar{p}$ [kPa]	$\mu$ [kPa]	$\sigma$ [kPa]	$\delta$ [%]
100	98.56	96.31	4.01	3.69
	91.20			
	100.31			
	95.18			
200	195.30	195.27	2.85	2.37
	193.32			
	199.86			
	194.58			
300	290.73	295.51	3.42	1.50
	297.81			
	294.72			
	298.79			

First tests showed good results with a maximum relative error of 3.69 % at a pressure level of 100 kPa as well as 2.37 % and 1.50 % at 200 and 300 kPa respectively. Furthermore, the calculated standard deviations show a good consistency of the measurements.

To extend these first investigations, additional studies were conducted. As part of these studies, predefined load steps were performed and the corresponding ADC outputs from the TPS were analyzed. This allowed for a more descriptive interpretation of the sensor performance and avoided any distortion of the measurements due to linear interpolation and statistical processing of the test results. Thus, six tests were performed with load steps evenly distributed over a range of 0 to 300 kPa, resulting in one curve per sensor per test (run).

Figure 6 shows the measurement results for a representative sensor for all six runs labeled Run 1 to Run 6. The results can be considered promising as the curves show good repeatability, which is consistent with the results shown in Table 1. Especially at higher pressures, from 200 kPa onwards, the agreement of the individual measurement points is good, while at pressures below 100 kPa a certain deviation can be observed, which, however, is not critical. These results agree well with the previous observations, which confirms the initial assessment of the overall TPS' precision.

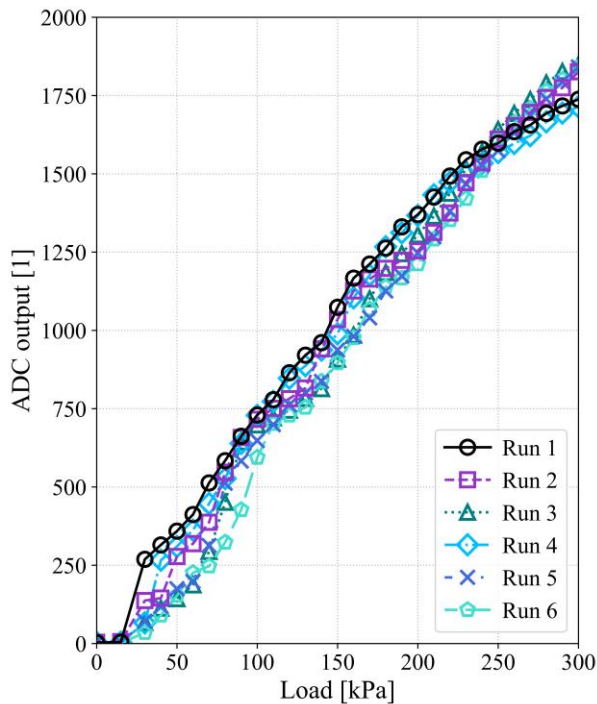


Figure 6. Precision test without soil for a representative sensor.

Proceeding with the test series, the TPS' performance was evaluated incorporating soils, simulating the application of the system at the soil-structure interface. The aim of these investigations was to evaluate the influence of soils with different maximum grain sizes on the accuracy of the sensors and to compare these findings with the results shown in Figure 6. To allow for comparison between the different test series the following studies were performed in line with the previously described procedures, apart from including a membrane, as explained in chapter 3. This test series should allow a statement related to the maximum tolerable grain size without a drastic reduction in sensor performance, which is considered mandatory to evaluate the applicability of the TPS in the mid-scale experiments. All tests were carried out with the same TPS system used previously.

Five samples with different grain size distributions were utilized, allowing a continuous increase in  $D_{max}$ . The samples were mainly coarse grained (angular grains) and contained little to no fine grains. All samples were artificially prepared by sieving a large soil sample into different GSDs, which ranged from 0/0.8 mm, with  $D_{max} = 0.8$  mm, to 2/4 mm, with  $D_{max} = 4$  mm and  $D_{min} = 2$  mm.

Figure 7 illustrates the results for this test campaign, comparing a representative air pressure curve (Run 1), labelled as 'Air', from Figure 6, with five curves including soils with different GSDs. The curves differ in the lower load range, up to  $\sim 100$  kPa, whilst the repeatability seems to improve with pressure levels above 100 kPa. Both effects have also been identified in the previous tests.

The results show good repeatability, and the influence of grain size appears to be negligible up to a  $D_{max}$  of 2 mm. Though, grain sizes above 2 mm seem to cause a change in sensor performance. Curve 2/4 (orange) shows significantly lower ADC outputs, from 150 kPa and onwards, than all other

curves. In general, it is assumed that the silicone coating of the TPS acts like a thin load distribution layer, which provides good sensor performance if  $D_{max} \leq 2$  mm, as these measurements agree well with the air pressure reference curves. However, the load distribution effect of the silicone doesn't appear to be suitable for dealing with larger grain sizes.

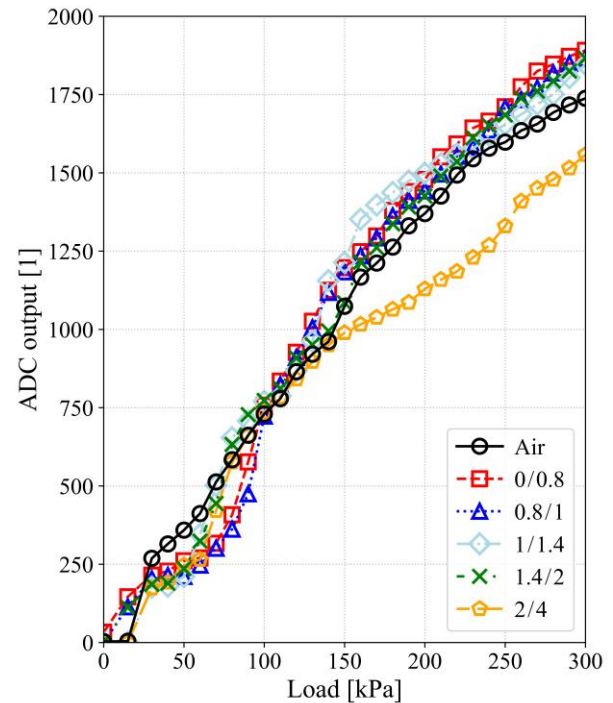


Figure 7. Influence of grain size (angular grains) on sensor curve for a representative sensor.

To summarize, the preliminary investigations on the sensor performance have shown the potential of the system for its application in the geotechnical environment. Soil with a grain size below 2 mm does not seem to negatively affect the sensor performance. However, it will be necessary to implement some kind of load distribution layer to improve the TPS for the application in larger grain sizes. As the material used in the mid-scale tests has a grain size above 4 mm, it is essential to adapt the TPS accordingly. This allows its application within the setup and enables the collection of more spatial information on load redistribution mechanisms.

#### 4.2 Mid-scale test facility

Figure 8 and Figure 9 present the initial evaluations of anchor failure simulations, conducted by setting the compressive load along individual struts to zero. Both figures show the modelled retaining wall, with the steel elements arranged in a 3 x 3 grid, following the labelling scheme from Figure 3. The failed anchor is marked with a red cross, and the changes in load, both in percentage and absolute terms, are shown for all remaining anchors. The failure simulations started from nearly identical stress states, with anchor rows 1, 2 and 3 pre-stressed to approximately 7 kN, 5 kN and 2 kN, respectively.

Figure 8 illustrates the first failure simulation, which assumed the central anchor B2 to fail. The results clearly show that the load redistribution following the failure of anchor B2 is almost symmetrical. In absolute terms, the majority of the redistributed load is transferred to the adjacent anchors on the

left (A2) and right (C2), rather than those above (B3) or below (B1). The largest increase, considering absolute terms, occurs at anchor A2, which increases by 0.95 kN, a 20% rise from its pre-stressing load of about 5 kN. However, in percentage terms, the largest increase is observed at anchor B3, which experiences a 24% increase from its pre-stressing force of approximately 2 kN (equivalent to an absolute increase of 0.52 kN). The anchors located in the corners (i.e. A1, C1, A3 and C3) play a minor role in the load redistribution.

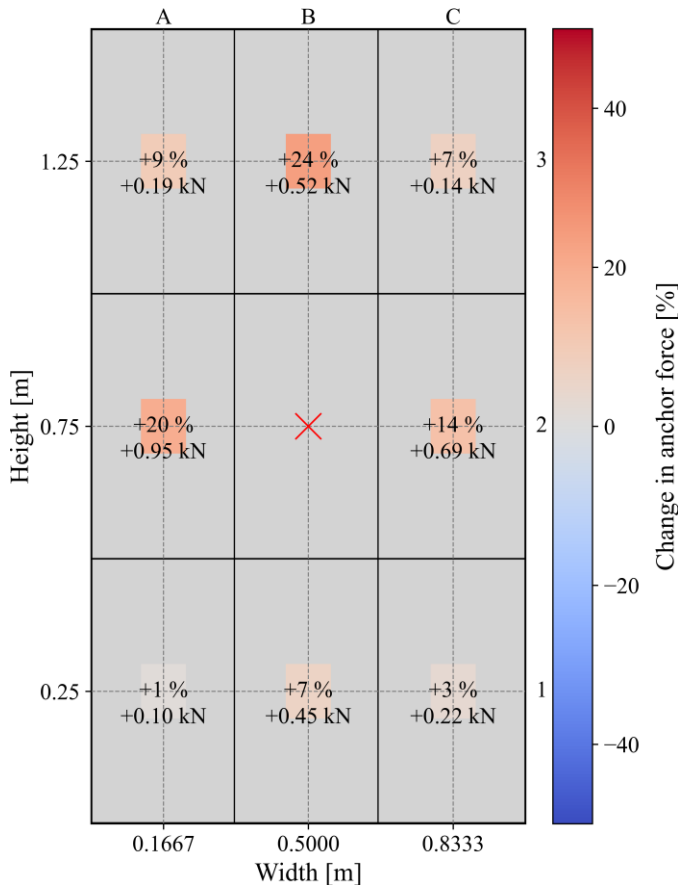


Figure 8. Failure simulation of anchor B2, adapted from [11].

In contrast, Figure 9 shows that the load redistribution following the failure of anchor A2 is more complex. The majority of the redistributed load is again transferred to the adjacent anchor on the right (B2), which increases by 1.23 kN, corresponding to a 28% increase from its pre-stressing load. However, anchor C2 experiences a significant load decrease of 1.04 kN, or -24%, from its pre-stressing load. Similar to the load redistribution pattern of the failed anchor B2 (see Figure 8), the maximum percentage increase occurs at the anchor directly above the failed element. In this case, anchor A3 shows a 50% increase from its pre-stressing load, which corresponds to a 0.60 kN increase.

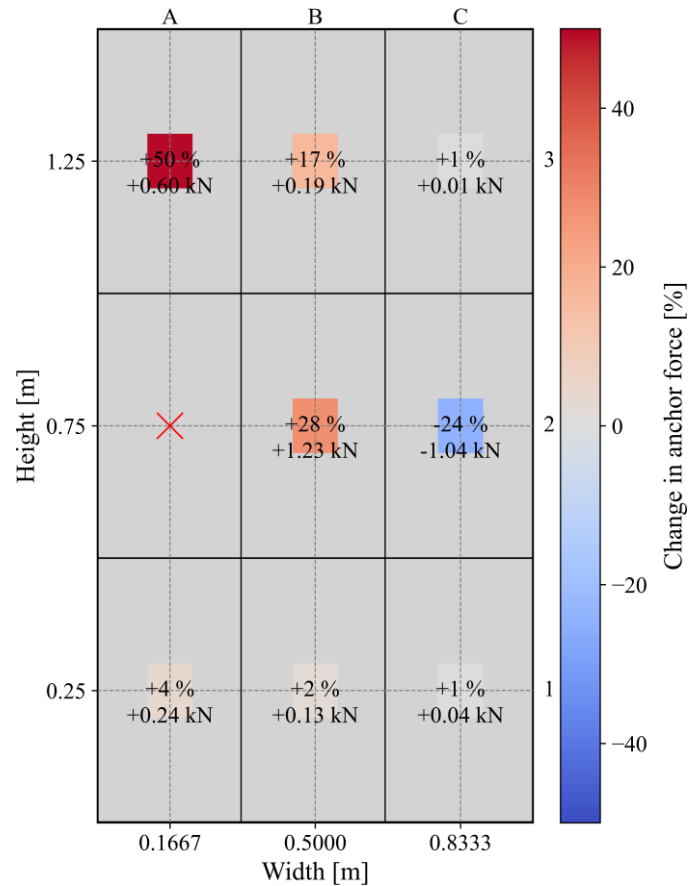


Figure 9. Failure simulation of anchor A2, adapted from [11].

As the measurement concept of the previously described tests only allowed for the evaluation of total force acting on the nine steel elements, future experiments need to conduct additional instrumentation to evaluate load redistribution effects in its entirety. It is therefore planned to integrate 576 Tactile Pressure Sensors to analyze the compressive stress distribution at the soil-structure interface. This will not only allow the experiments to be evaluated in a comprehensible way but also provides enough data to calibrate a numerical model of the setup. and to perform a robust back analysis. As a result, parameter and sensitivity studies can be carried out within the numerical model. Additionally, it is also possible to adjust the model scale if required.

## 5 CONCLUSIONS & SUMMARY

Preliminary tests of the presented Tactile Pressure Sensors (TPS) showed good sensor performance in terms of precision, with a maximum relative error of 3.69 % and a standard deviation of 4.01 kPa at a compressive stress of 100 kPa and even better results at 200 and 300 kPa. Based on these results, the TPS was further tested with soils to evaluate the applicability of the system for the planned experiments. On the one hand, these tests showed promising results, as soil grains up to a size of 2 mm could apparently be handled very well. On the other hand, larger soil grains unfortunately led to distortions in the measurements. As a result, in its current state, the stand-alone TPS did not appear to be suitable for the mid-scale experiments with 4/8 mm rounded grains. Consequently, simulations of anchor failure in the mid-scale test facility were not yet carried out as planned, which meant that first trials were



monitored with only nine load cells. The performed simulations led to the observation of the following load redistribution mechanisms.

Loads released by a failing anchor were mainly redistributed to the adjacent anchors, while others did not show significant increases in load. Furthermore, some anchors experienced significant changes in their pre-stressing loads. Considering the design process of such retaining structures and the determination of the required bearing capacity of the anchors, increases in anchor force of up to 50 %, as observed, may be critical for the safety assessment of such structures.

Although these experiments have provided important information on the behavior of the anchor wall in the event of anchor failure, the test setup had some limitations that need to be addressed. In particular, the presented approach of monitoring experiments with only nine load cells considerably limits the possibilities for interpreting the tests, as the amount and resolution of measurement data is not sufficient to spatially evaluate load redistribution effects. Furthermore, these effects should ideally be evaluated in terms of stress, not force, at the entire soil-structure interface to observe mechanisms such as e.g. arching effects within the soil body. Although this cannot be achieved completely, even with the presented TPS, the approximate area coverage with 576 sensors is a considerable improvement compared to point measurements and may allow for an assumed stress field.

Though the Tactile Pressure Sensors were not yet applicable, further trials are planned to prepare them for the upcoming experiments. To reduce the TPS' sensitivity to grain size, the concept of an additional load distribution layer between the TPS and the soil will be focused. For this purpose, a variety of elastomers with different thicknesses and stiffnesses will be considered. The aim of these studies is to identify an elastomer which offers good load distribution effects if applied to 4/8 mm rounded grains but also allows for a good measurement resolution. Additionally, it will be important to gain more knowledge concerning the sensors' performance, not only in terms of precision but also concerning trueness. Consequently, new testing rigs are in progress to allow for an appropriate testing procedure. As the TPS is fully characterized and the necessary load distribution layer is identified, the mid-scale testing will continue as planned.

## ACKNOWLEDGMENTS

The contents provided in this paper have been developed as part of the research project SG4SSI (Sensor Grid for Soil-Structure Interaction). The authors express their gratitude to the VÖBU (Association of Austrian Drilling, Well Construction and Specialized Civil Engineering Companies) as project leader and initiator, as well as to the Austrian Research Promotion Agency (FFG) for the funding provided.

## REFERENCES

- [1] FSV, Qualitätssicherung bauliche Erhaltung – Überwachung, Kontrolle und Prüfung von Kunstbauten – Geankerte Stützbauwerke, RVS 13.03.21, Vienna, Austria, 2022.
- [2] FSV, Sonderprüfmethoden für geankerte Konstruktionen und Zugelemente, RVS Arbeitspapier Nr. 33, Vienna, Austria, 2022.
- [3] S.G. Paikowsky and E.L. Hajduk, Calibration and Use of Grid-Based Tactile Pressure Sensors in Granular Material, *Geotechnical Testing Journal*, Vol. 20, No. 2, pp. 218-241, 1997.
- [4] M.C. Palmer, T.D. O'Rourke, N.A. Olson, T. Abdoun, D. Ha, M.J. O'Rourke, Tactile Pressure Sensors for Soil-Structure Interaction Assessment, *Journal of Geotechnical and Geoenvironmental Engineering*, Vol. 135, No. 11, pp. 1638-1645, 2009.
- [5] Y. Gao and Y.H. Wang, Calibration of tactile pressure sensors for measuring stress in soils, *Geotechnical Testing Journal*, Vol. 36, No. 4, pp. 568-574, 2013.
- [6] C. Deng and S.K. Haigh, Earth pressure mobilised in dry sand with active rigid retaining wall movement, *Géotechnique Letters*, Vol. 11, No. 3, pp. 202-208, 2021.
- [7] S.M. Springman, P. Natter, R. Chikata Maria, J. Laue, Use of flexible tactile pressure sensors in geotechnical centrifuges, *Physical Modelling in Geotechnics*, 1<sup>st</sup> Edition, Routledge, London, UK, 2002.
- [8] G. Madabhushi, *Centrifuge Modelling for Civil Engineers*, 1<sup>st</sup> Edition, CRC Press, London, UK, 2015.
- [9] H.-P. Daxer, G.O. Flatscher, F. Tschuchnigg, M.J. Rebhan, Simulation and numerical back analysis of the load redistribution associated with degrading anchor structures, *Proceedings of the 5<sup>th</sup> European Conference on Physical Modelling in Geotechnics*, Delft, the Netherlands, 2-4 October 2024.
- [10] ISO, Accuracy (trueness and precision) of measurement methods and results – Part 1: General principles and definitions, ISO 5725-1, Vernier, Geneva, Switzerland, 2023.
- [11] G.O. Flatscher, Versuchstechnische Betrachtung zu Änderungen der Vorspannkraft bei geankerten Konstruktionen, Master's Thesis, Graz University of Technology, Graz, 2025.

## Long term monitoring of the Balladelaan bridge using smart Aggregates

C.N. Kortendijk<sup>1</sup>, A. Hoekstra<sup>1</sup>, F. Besseling<sup>1</sup>, Y. Yang<sup>2</sup>, H. Cheng<sup>2</sup>

<sup>1</sup>Witteveen+Bos Consulting Engineers, Leeuwenbrug 8, 7411TJ Deventer, Netherlands

<sup>2</sup>Department of Engineering Structures, Faculty of Civil Engineering and GeoSciences, Delft University of Technology, Stevinweg 1, 2628CN Delft, Netherlands

email: coen.kortendijk@witteveenbos.com, Anke.Hoekstra@witteveenbos.com, Floris.Besseling@witteveenbos.com, Yuguang.Yang@tudelft.nl, H.Cheng-2@tudelft.nl

**ABSTRACT:** The Balladelaan Bridge is a key bridge in the city of Amersfoort. The city has asked us to investigate the construction quality and remaining lifespan of this 5 span statically indeterminate cast-in-place concrete plate bridge, which was built in 1946. For this a pioneering long-term Structural Health Monitoring (SHM) initiative has been implemented in the form of a Field lab employing Smart Aggregates (SA's) using Coda-Wave Interferometry (CWI), augmented with extensive temperature measurements, and a short-term measurement using Acoustic Emission (AE) sensors. This study represents an extensive application of Smart Aggregates for continuous monitoring of a bridge's structural health over an extended period. The study aims to address the suitability of SA's for long term monitoring and accounting for environmental influences such as temperature and humidity on the wave speed in the concrete. Preliminary findings demonstrate a significant influence of temperature on wave speed readings, underscoring the necessity of temperature compensation in SHM analysis. After accounting for these environmental influences, the study generates critical insights into the bridge's integrity and performance. The outcomes of this research will not only enhance the understanding of the Balladelaan Bridge's condition but also establish a benchmark for future SHM projects utilizing Smart Aggregates and CWI technology.

**KEY WORDS:** SHMII-13; Smart Aggregates; Structural Health Monitoring; Concrete; Bridges; Coda Wave Interferometry; Environmental Variability.

### 1 INTRODUCTION

Concrete slab bridges designed and built in the post WWII era, are relatively sensitive to shear failure. This raises concerns about the structural capacity of these bridges and the associated remaining service life.

Structural Health Monitoring (SHM) focuses in monitoring the variation of the structural performance a given structure with respect to selected dominant failure mechanisms. When it is properly designed, it enables asset managers to continuously track the evolution of the structural integrity of the bridge from the status without acquiring all the key information of the monitoring structure. This offers a significant advantage over traditional inspection methods, which often only involve periodic visual inspections.

For this a new monitoring solution using Smart Aggregates (SA's) has been installed on the Balladelaan bridge. SA sensors can be embedded or drilled into concrete to measure (changes in) stress and crack formation between sensor pairs. The installation of this field-lab has earlier been described by Cheng et al [1]. This paper describes the results of well over 1 year of continuous monitoring using SA's.

### 2 THE BALLADELAAN BRIDGE

The bridge in the Balladelaan in Amersfoort was built in 1946. It is a cast-in-place concrete bridge with 5 spans, which together form a statically indeterminate deck system. The bridge has one bus lane (1 lane), a cycle path and a pedestrian path. The bridge was chosen for its suitability:

- The multiple span configuration of the bridge allows to focus monitoring + data analysis on local response variations over time, as an indicator of damage.
- Because there is no normal car traffic on the bridge except a bus with known schedule, there is more certainty regarding the traffic load on the bridge. This makes calibration of models easier.
- Compared to new construction, lifespan extension with risk management by means of a monitoring system results in significantly lower costs and sustainability benefits.
- The bridge represents many equivalent concrete bridges in the Netherlands, so the knowledge gained here can be used more widely.



Figure 2-1 Side view of bridge (source: Google Streetview)



Figure 2-2 Top view of bridge (source: Google Maps)

### 3 SENSOR AND MONITORING SYSTEM

#### 3.1 Smart aggregates

Smart aggregates (SA's) are embedded piezoelectric sensors that can measure (changes in) stress and formation of cracks in concrete between two sensors using interferometry of waves through the concrete. An example of such a system is shown in Figure 4-5. They were first introduced by Song et al[3], designed for long term monitoring of concrete structures. These sensors are embedded within concrete structures. This can be prior to casting for new constructions or afterwards through a drilled hole. They generate high-frequency elastic waves and receive them within the concrete. The received wave signals are logged and eventually analyzed. There is a relation between the wave propagation velocity and the stress on the concrete. Also, there is a relation between the shape of the waves and the existing cracks in the concrete. Smart aggregates should be able to detect this.

In a typical measurement, one SA functions as the transmitter while the remaining SA's in the cluster act as receivers. When a measurement begins, the measurement order is assigned remotely, and a high-voltage electric pulse is sent to the transmitter to initiate vibration. This electric pulse is converted into a mechanical wave that propagates through the concrete. Upon reaching the receivers, the wave signals are converted back into electrical signals, recorded as 1D time-series data, and stored locally at the data station.

#### 3.2 Temperature sensors

Due to the static indeterminate structure of the bridge, it is expected that vertical temperature gradients due to sunlight will significantly influence the internal stress distribution in the bridge. The wave velocity in concrete is also temperature dependent. As these 2 factors will influence the signals measured by the smart aggregates, a significant amount of temperature sensors was installed to investigate this relationship, and in a later stage, compensate for this. Two systems were used in this particular setup:

- 1 PT1000 sensors. These are resistance-based sensors. They require a relatively short cable to a sensitive analog-to-digital converter.

- 2 DS18B20 sensors. These are digital sensors that support longer cables and can be read from a cheap microcontroller.

Both systems have a resolution of  $0.01^{\circ}\text{C}$ , and have been pre-calibrated in the lab to within  $0.1^{\circ}\text{C}$  accuracy. Part of this project was also to test the durability and reliability of both kinds of temperature sensors.

#### 3.3 Acquisition system

The monitoring system comprises a data acquisition (DAQ) system for signals received by the SA's, an ARM embedded board for temperature measurements, and a 4G router with a SIM card for communication. The DAQ system, designed and patented by Delft University of Technology (TU Delft), is optimized for ultrasound-based monitoring of concrete structures.

The DAQ system includes a pulser, pre-amplifiers, and multiplexers. Thanks to the specialized circuit board design, the pulser can generate square pulses with a magnitude of up to 300 V without interfering with the received signals. For this project a single square-wave pulse with a duration  $< 20 \mu\text{s}$  was used.

The data acquisition system supports a sampling rate of 3 MHz, enabling the recording of wave signals with frequencies up to 300 kHz without aliasing or loss of dynamics. This is well-suited for the requirements of ultrasound-based concrete monitoring applications. Each measurement lasts for 4 milliseconds from the moment the transmitter receives the electric pulse.

### 4 INSTALLATION AND DATA PROCESSING

#### 4.1 Sensor locations

Sensors have been installed in both the center span, and an end-span of the bridge. Sensor positions are shown in Figure 4-1 to Figure 4-4. Distributed data acquisition systems are below the bridge with a main station including 4G router on shore.

The distance between the top and bottom SA's in each hole is fixed at 300 mm. During installation the top SA's are consistently positioned 175 mm beneath the top surface of the bridge slab, while the bottom SA's are set 475 mm below the top surface.

Sensors are grouped in three clusters of 3-4 holes, with 2 sensors per hole. The first cluster (hole A-D) is positioned to detect flexural crack development in midspan, which is crucial for detecting bridge flexural failure. The second (E-H) monitors stress changes or crack opening at intermediate supports. The third cluster (I-K) is placed to detect the initialization or progression of diagonal cracks in shear critical zones.



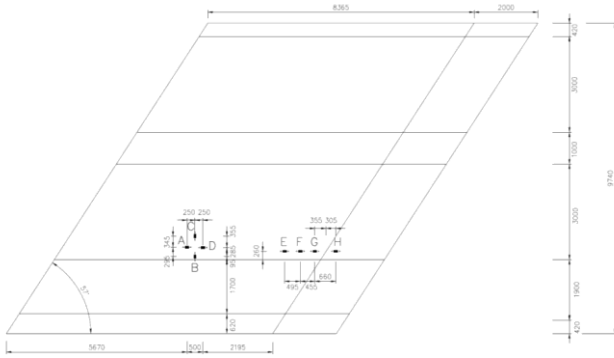


Figure 4-1 Top view SA-sensor locations center span

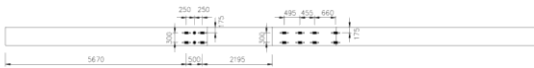


Figure 4-2 Side view SA-sensor locations center span

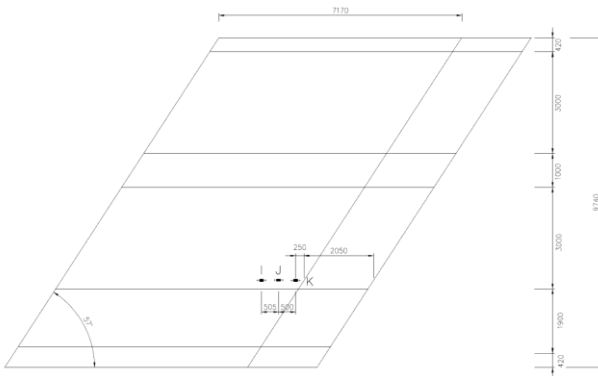


Figure 4-3 Top view SA-sensor locations end span



Figure 4-4 Side view SA-sensor locations end span

#### 4.2 Installation process

Sensor preparation was conducted at TU Delft. SA's were affixed to copper wires using glue to ensure their alignment with the specified orientation and spacing, as illustrated in Figure 4-5. At select locations mentioned in Section 4, temperature sensors were also glued adjacent to the SA's on the copper wires to measure temperatures in close proximity to the sensor positions, as depicted in Figure 4-6.

The entire installation process followed these steps:

- Determining the rebar layout using a radar-based rebar detector.
- Identifying drilling locations based on the rebar layout.
- Drilling holes at the designated sensor locations
- Installing sensors into the drilled holes
- Filling the holes with high-strength mortar

- Installing the data acquisition systems and organizing cables
- Installing the main station on the bank.

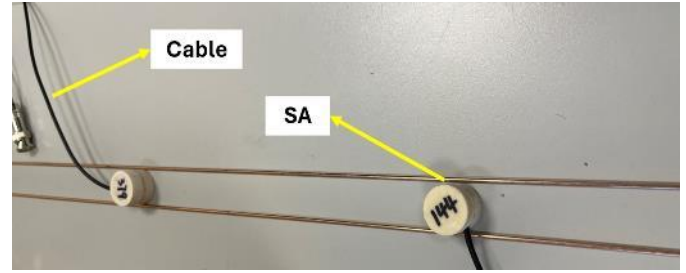


Figure 4-5 SA sensor at lab.

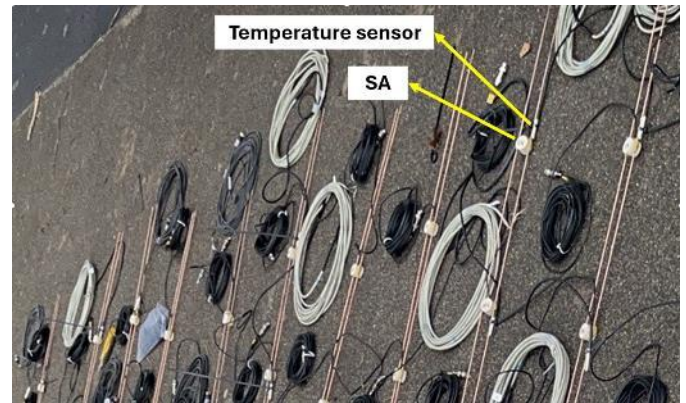


Figure 4-6 SA sensor in the field with added temperature sensors

#### 4.3 Wave velocity processing

Changes in wave velocity are related to changes in stress-state of the concrete. The wave-velocity change can be determined by comparing the two signals in time. When the velocity changes are small (which we can assume here), we can assume a linear relation between travel time and wave velocity:

$$\frac{dv}{v} = -\frac{dt}{t}$$

This means that an increase in travel time is directly related to a decrease in velocity. We use the stretching technique to find this relative shift in time between two signals. With this technique the new signal is stretched in the time domain, relative to  $t_0$ , which starts at the departure of the wave from the sending sensor, such that it fits the other signal (reference signal). Then this shift of the time axis between the signal and the reference signal is equal to the change in velocity.

With the stretching technique, we calculate correlation coefficients of windowed signals for the different delays.

$$CC(t_c, T, \epsilon) = \frac{\int_{t_c-T}^{t_c+T} u(t)u'(t(1-\epsilon))dt}{\sqrt{\int_{t_c-T}^{t_c+T} u(t)^2 dt} \sqrt{\int_{t_c-T}^{t_c+T} u'(t(1-\epsilon))^2 dt}}$$

$t_c$  is the center of the time window,  $2T$  is the duration of the time window and  $\epsilon$  is the stretching factor. When there is an

uniform velocity change in the medium, one can assume that the correlation coefficient is maximum at the stretching factor that corresponds to the relative velocity change.

The stretching window can be chosen in different ways. It depends on the wave frequency: a window that is too short will not contain enough information. The window should also not be too large, because in that case you can no longer assume a constant time shift within the stretching window.

In this research, we limited ourselves to direct waveforms. These are the waves that travel in a straight line from one sensor to the other. One can assume that this is mainly the longitudinal / compression wave, because their wave speed is higher. Therefore, we selected a window containing only the first part of the signal, which contains approximately 2 cycles.

## 5 MEASUREMENT RESULTS

### 5.1 Initial measurements

Figure 5-1 presents a typical trace in the time domain from a measurement obtained from SA's. Similar patterns are observed for other sensor pairs but are not displayed here. The data shows a high signal to noise ratio, indicative of high quality.

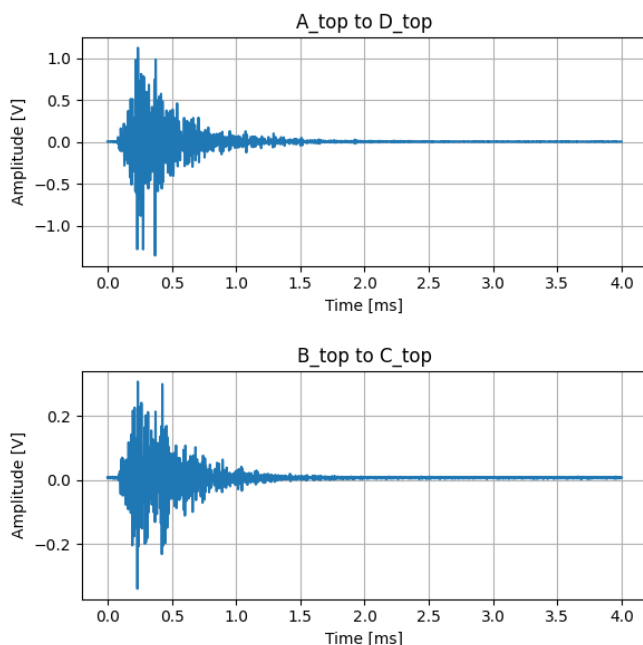


Figure 5-1 Trace of 2 sensor pairs

Figure 5-2 shows how on sunny days, a large temperature gradient between the top and bottom of the deck is observed, where the top of deck heats (and cools) faster than the bottom of the deck, which lags behind. All top temperatures show similar temperatures, with 1 sensor deviating. This sensor is on the end span, where the deck has some shade from neighboring trees.

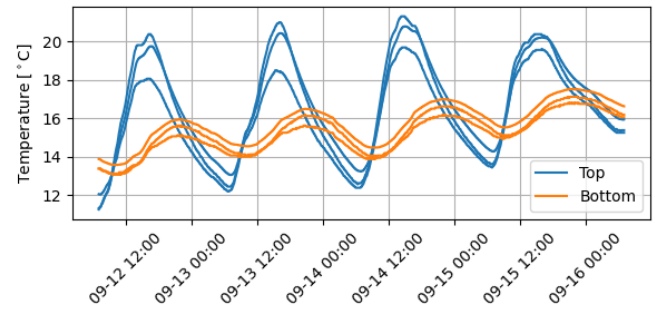


Figure 5-2 Temperatures in top and bottom of slab over 7 days

### 5.2 Wave velocity change

The resulting velocity change over time for a selected period is shown in the figure below. This period is chosen because it shows a large fluctuation in the measured temperature. The calculations are performed for two sensor pairs: A\_top to D\_top (Figure 5-3) and B\_top to C\_top (Figure 5-4). The velocity change is plotted together with the mean temperature measured in the bridge in this cluster by the temperature sensors.

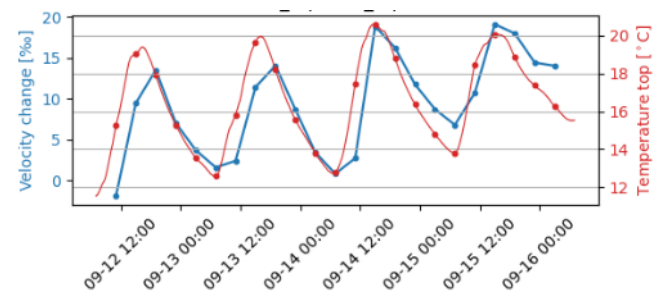


Figure 5-3 Temperature and velocity change A-D

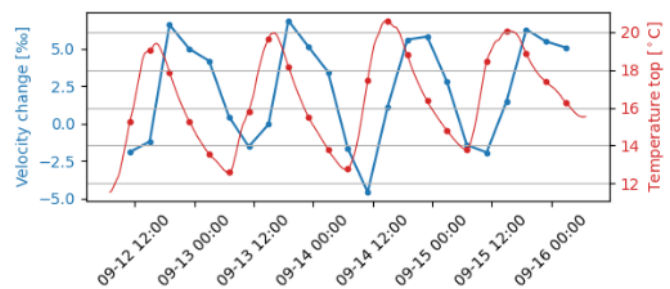


Figure 5-4 Temperature and velocity change B-C

The velocity changes in Figure 5-3 and Figure 5-4 are obtained by stretching a measurement signal until the maximum correlation between this signal and a predetermined previous signal is obtained. The resulting correlation coefficients as shown in Figure 5-5 are Figure 5-6 are an indicator of signal quality and may also indicate crack-opening. It can be seen that for the period shown the correlation coefficient is high (well over 0.8), indicating no significant crack change or deterioration of measurement equipment.

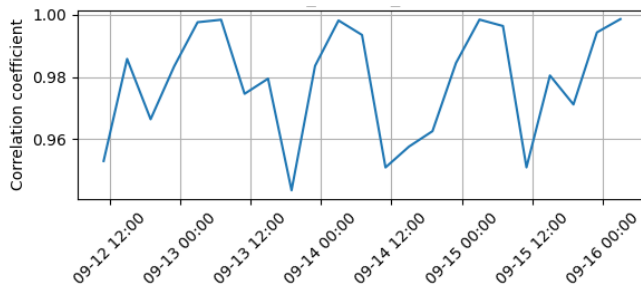


Figure 5-5 Correlation Coefficient A-D

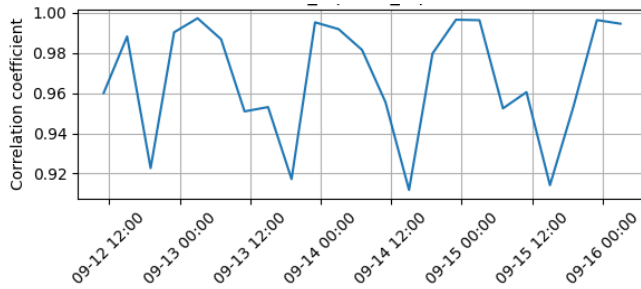


Figure 5-6 Correlation Coefficient B-C

Figure 5-3 implies a correlation between the velocity change of sensor pair A-D (and therefore the stress state of the material) and the temperature. This correlation is also seen in the scatter from Figure 5-5. It shows that with a higher temperature, there is an increase in the velocity.

This relation can also be observed in sensor pair B-C, but with an approximately 4-hour delay. After shifting the signal by four hours, a strong correlation is found, as shown in Figure 5-8.

The relation between temperature and velocity change and the accompanying time shift is not easily understood, as the velocity change is not only directly related to average concrete temperature. Due to the 5-span static-indeterminate system, the temperature gradients also induce stress which induces a velocity change. This will be different in the different directions that the sensor pairs have (A-D and B-C). Moreover, there is an overall temperature gradient within the bridge that fluctuates over time. The delay might be explained by the combination of different temperatures in the bridge. Further work will be to further analyze the temperature-induced changes in wave velocity.

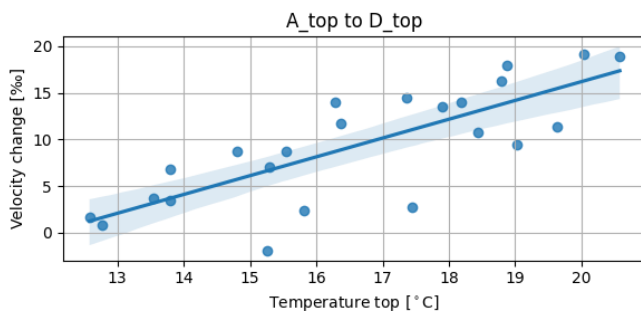


Figure 5-7 Temperature vs Velocity change A-D

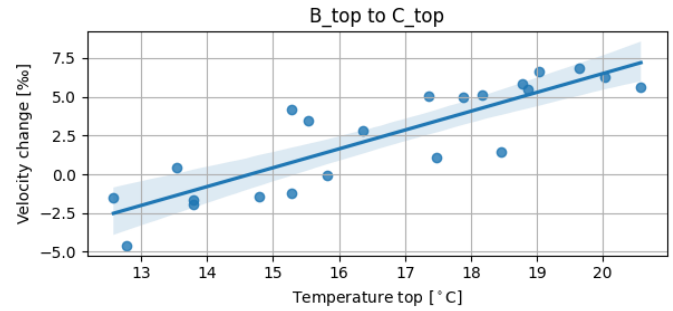


Figure 5-8 Temperature vs velocity change B-C after 4hr shift

### 5.3 Long term stability

The temperature sensors perform as expected. During well over one year of measurements, the concrete temperature has varied between  $-2.62^{\circ}\text{C}$  and  $+42.20^{\circ}\text{C}$ , see Figure 5-9.

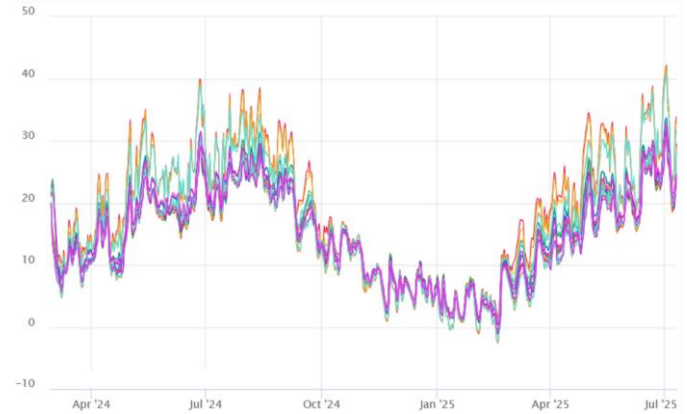


Figure 5-9 One year of temperature measurements

The digital DS18B20 sensors were unavailable for a short period of time due to a broken microcontroller, but this was easily fixed. In general, both types of sensors seem suitable for long term monitoring.

The SA-aggregates also perform well. After approximately 17 months of measurements each SA has sent and received approximately 500 days\*6 daily runs\*7 receiving SA's \* 10 stacks = 210000 pulses. The sensors have been exposed to both freezing ( $-2.62^{\circ}\text{C}$ ) and high ( $+42.20^{\circ}\text{C}$ ) temperatures, without failure. Proving the system is viable and stable for long-term measurements. Due to the nature of the system, no calibration of the built-in sensors is needed (or possible), while other sensor types may significantly degrade over time impacting repeatability.

As mentioned in 4.3 the change in wave velocity is calculated by finding the time stretching factor that results in maximum correlation coefficient between the current measurement and a specific previous measurement. The specific previous measurement may (in general) be chosen in two ways:

1. A(n average of a set of) reference measurement(s) just after installation is taken as the reference signal for all future measurements.



2. Each measurement is compared against its direct predecessor (in our case 4 hours earlier), or an average of a few direct predecessors.

After one year of measurements these two methods may be compared. Method 1 is shown in Figure 5-10. Here specific drops can be seen in early January for sensor pair A-D, and early March for pair B-C. In the first quarter of 2025 the wear-layer on the deck was replaced in multiple stages, which may have directly or indirectly caused this drop. The lower correlation coefficients may also negatively affect the accuracy of the time stretching.

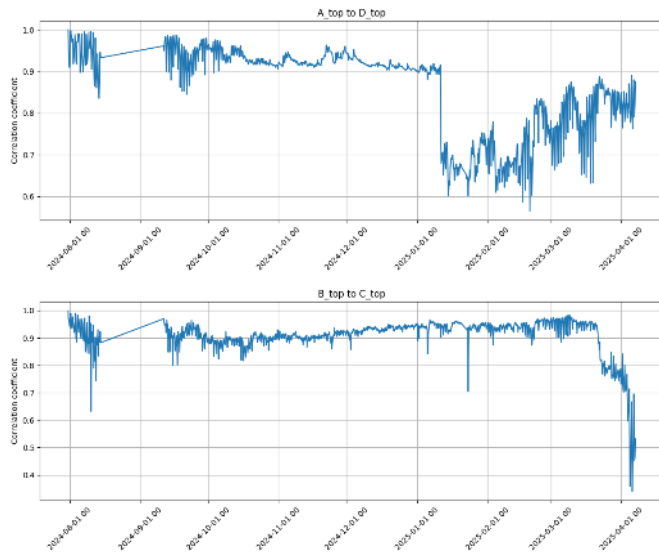


Figure 5-10 Correlation coefficient relative to first measurement

To obtain the optimal time stretching high correlation coefficients are preferred. This may be achieved by method 2, comparing each signal to its direct predecessor. In our case 4 hours earlier, as shown in Figure 5-11. Here high coefficients are obtained for most of the year. But during days with large temperature changes and accompanying temperature gradients (March-October as shown in Figure 5-9) the correlation coefficients also show variation. This variation is larger than it was in previous periods with similar temperature gradients, such as August 2024. A possible explanation might be that the replacement of the wear layer has induced (micro-)cracking in the high-strength mortar that was used to fill the drilled holes of the SA's.

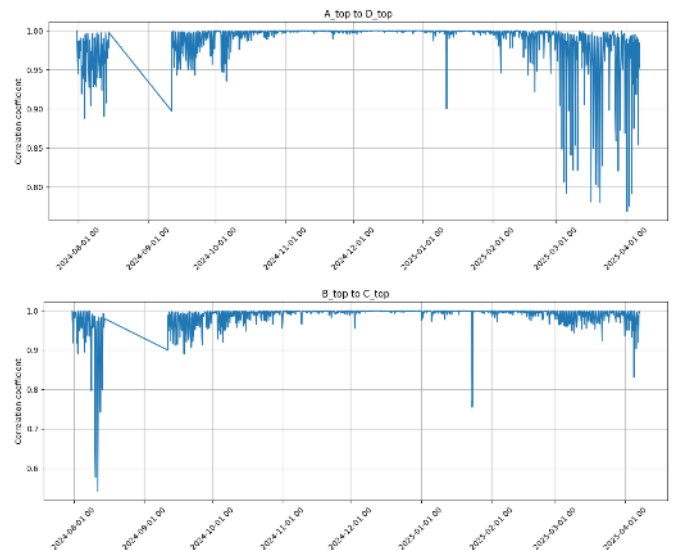


Figure 5-11 Correlation coefficient to 4hrs earlier

Both methods have their own advantages and disadvantages. Method 2 shows consistently high correlation coefficients, resulting in accurate stretch factors. But information about slow progressive changes over time are lost. Method 1 gives information relative to date of installation, but if the system is changed, correlation coefficients drop, and the stretch factors may be less accurate.

A solution may be found by combining both methods. Use method 1 until a significant drop in correlation coefficient is visible, indicating a change in the system which might be indicative of structural damage. Mark this point in time, and then apply all future processing relative to just after this event.

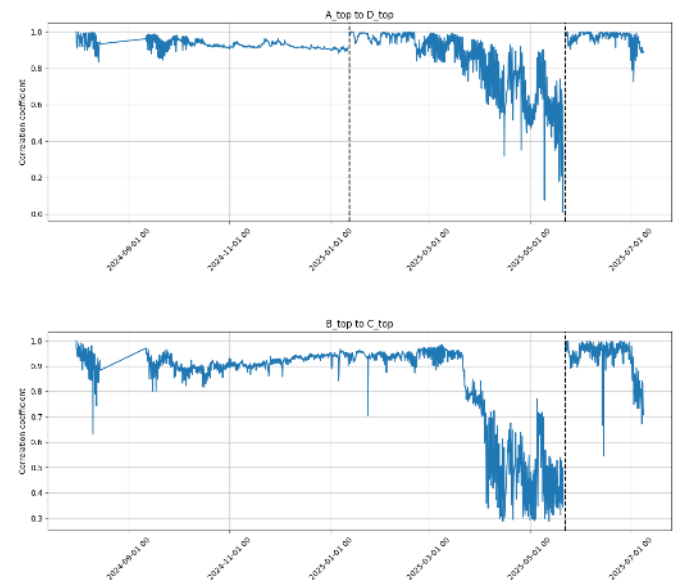


Figure 5-12 Correlation coefficient relative to previous event.

An example is shown in Figure 5-12. For 2024 the graphs are identical to method 1 as shown in Figure 5-10. For sensor pair A-D a sudden and significant change occurred in January 2025, which is marked with a vertical dashed line. Just after this

change a new reference measurement was selected, and the correlation coefficients after this time are calculated relative to this new reference. There's also a vertical dotted line in early May 2025. On this day the triggering system was reconfigured to improve time-accuracy. Therefore all measurements after this reconfiguration are compared to the first measurements since reconfiguration.

With this new processing it is clear that the low correlation coefficients of Figure 5-10 are not due to sensor degradation, since a new reference measurement can significantly improve the results. It is likely that the sudden drops in correlation coefficients are caused by structural changes in the bridge, and may be indicative of damage.

Further research is needed to determine the cause of some the low correlation outliers. A load tests with a known vehicle might be informative to relate the calculated stretch-coefficients to stress & strain. Further modelling of measured temperature gradients with a heat-flow model might also give a better understanding of the internal stress due to temperature gradients.

## 6 CONCLUSION

After well over a year of measurements, both types of temperature sensors remain operational. Suggesting there is no need for expensive analog temperature sensors and related cabling and AD converters. Cheap DS18B20 are accurate and reliable.

The Smart-Aggregate system has also performed well. While SA's are mainly used in short-term tests in the lab, our results show a life expectancy of at least 210 thousand pulses transmitted and/or received.

Work on the wear-layer of the deck is clearly visible in the correlation coefficient of sensors that are placed well below deck. Suggesting the sensors work well for long-term monitoring of structural changes. After the replacement of the wear-layer the daily variation in correlation coefficients has increased.

The selection of the reference measurement for stretching calculation has a significant influence on the resulting correlation coefficients and stretch factors. Using a fixed baseline is unfeasible because the correlation coefficient slowly degrades. Using a moving baseline however decreases insight in progressive changes. It is suggested to use a piecewise approach, where significant degradation of the correlation coefficient triggers a new reference measurement.

Results are strongly influenced by temperature, and this requires further study to separate the effects of temperature gradients from effects due to structural changes. It is advised to study this using a (simpler) statically determinate structure, where temperature gradients only result in strains, and not in stress. In this way the phenomena can be decoupled.

## REFERENCES

- [1] H. Cheng, Y. Yang, F. Besseling, C. Kortendijk, A. Hoekstra, Monitoring the concrete slab bridge on Balladelaan in the Netherlands using embedded ultrasonic sensors, Proceeding of the IABSE Congress Gent, 2025
- [2] Cheng, H.; Weemstra, C.; Hendriks, M. A. N.; Yang, Y., Comparing the stretching technique and the wavelet cross-spectrum technique for measuring stress-induced wave-velocity changes in concrete. *Autom. Constr.* **2024**, 158, 105221.

- [3] Song G, Gu H, Mo YL (2008) Smart aggregates: multi-functional sensors for concrete structures-a tutorial and a review. *Smart Materials and Structures* 17(3). <https://doi.org/10.1088/0964-1726/17/3/033001>

# Structural Health Monitoring of Composite Plate using Piezoelectric Transducer

Thanh-Canh Huynh<sup>1</sup>, Chan Ghee Koh<sup>2</sup>

<sup>1</sup> Department of Civil and Environmental Engineering, National University of Singapore, Singapore  
email: huynhtc@nus.edu.sg (T.C.H.); cgkoh@nus.edu.sg (C.G.K.)

**ABSTRACT:** This research proposes an approach for detecting damage in composite structures using the cost-effective electromechanical (EM) impedance method. By employing a piezoelectric transducer driven at high frequencies, the technique facilitates localized damage identification by tracking changes in EM impedance signatures that correspond to alterations in the structural properties caused by damage. A numerical model of a composite plate with a surface-mounted piezoelectric patch is constructed to simulate EM impedance responses under different damage conditions within the composite layers. Damage is represented by localized reductions in stiffness, simulating common failure modes such as delamination or matrix cracking. The simulation results indicate that the EM IMPEDANCE response is highly sensitive to damage within the composite plate across a wide frequency range.

**KEY WORDS:** Damage detection; Composite plate; Impedance technique; PZT; SHM

## 1 INTRODUCTION

Composite materials are increasingly adopted across various critical engineering sectors, including aerospace, marine, wind energy, and automotive, due to their exceptional strength-to-weight ratio, resistance to corrosion, and versatility in design. Despite these advantages, the complex, heterogeneous, and anisotropic characteristics of composites pose significant challenges for damage detection, as many types of damage such as delamination, matrix cracking, and fiber breakage typically begin within the material and remain hidden from surface inspection.

To maintain continuous health assessment of composite structures, a variety of structural health monitoring (SHM) strategies have been investigated, ranging from vibration analysis and acoustic emission techniques to guided wave inspection and piezoelectric-based sensing methods. Among these, the electromechanical (EM) impedance approach has emerged as a particularly effective tool for damage detection, especially in civil engineering systems [1]. This technique leverages the capabilities of a compact and economical piezoelectric sensor, which is directly attached to the surface of the structure and driven by high-frequency voltage inputs. The resulting high-frequency actuation enables the system to monitor local variations in structural behavior with high resolution, facilitating real-time identification of damage [2].

When damage occurs, it alters the local mechanical properties such as stiffness and damping, which in turn induces detectable changes in the impedance spectrum of the sensor. The short wavelengths associated with ultrasonic excitations make the method highly responsive to subtle or early-stage damage [3]. Additionally, EM impedance sensing is relatively immune to ambient low-frequency disturbances, enhancing its reliability in environments characterized by complex or fluctuating dynamic conditions. This resilience and sensitivity make the EM impedance method a strong candidate for practical SHM deployment in composite systems in complex real-world conditions.

This work presents a numerical study to evaluate the capability and sensitivity of the EM impedance approach for damage detection in composite structures. Utilizing a detailed finite element model developed in ABAQUS that incorporates

accurate material characteristics and simulates local damage effects, the study assesses the detectability of different damage severities. The findings contribute valuable understanding of the practical applicability of this cost-efficient SHM technique and set the stage for future experimental verification.

## 2 COST-EFFECTIVE EM IMPEDANCE METHOD

As shown in Fig. 1, a standard EM impedance measurement setup typically consists of a piezoelectric transducer, such as a PZT, bonded to the surface of the structure and an impedance analyzer that drives the transducer while recording its impedance response.

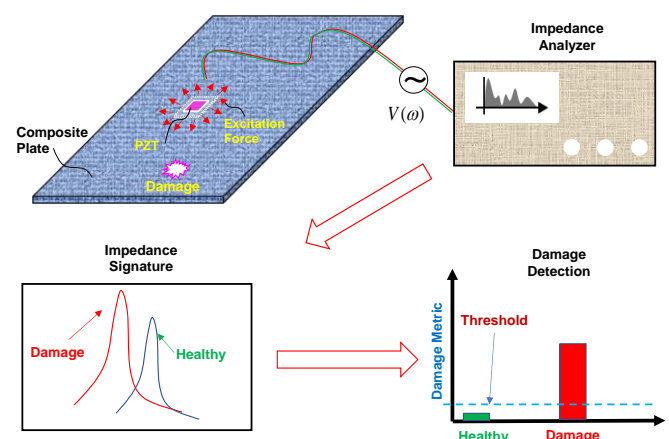


Figure 1. The EM impedance technique for composite plate

When a harmonic voltage  $V$  is applied across a range of frequencies  $\omega$ , the transducer undergoes mechanical vibrations due to the piezoelectric effect, thereby exciting the host structure (Park et al., 2003). The measured EM impedance response depends on the combined effects of the transducer's intrinsic impedance  $Z_a$  and the mechanical impedance of the structure  $Z_s$ , and it varies as the structural condition changes. For a simplified one-dimensional model, the theoretical EM impedance response  $Z$  can be described by the following relationship (Park et al., 2005):



$$Z = \left\{ i\omega \frac{h_a l_a}{t_a} \left[ \hat{\epsilon}_{33}^T - \frac{1}{Z_a/Z_s + 1} d_{31}^2 \hat{Y}_{11}^E \right] \right\}^{-1} \quad (1)$$

where  $\hat{\epsilon}_{33}^T$  is the complex dielectric permittivity, and  $d_{31}$  is the piezoelectric coupling coefficient;  $h_a$ ,  $l_a$ , and  $t_a$  represent the width, length, and thickness of the transducer, respectively;  $\hat{Y}_{11}^E$  denotes the Young's modulus of the transducer;  $\eta$  corresponds to the structural damping loss factor of the transducer; and  $i$  is the imaginary unit.

The EM impedance response is inherently sensitive to the mechanical properties of the host structure, such as its mass, stiffness, and damping characteristics. When damage occurs, these mechanical parameters are altered, which in turn leads to measurable variations in the EM impedance signal. By monitoring such changes using the damage metric, it is possible to reliably detect damage within composite materials (Fig. 1). Furthermore, due to the short wavelengths associated with high-frequency excitation, EM impedance measurements are particularly adept at identifying small-scale defects and early-stage damage in composite structures.

### 3 NUMERICAL STUDY

A detailed finite element (FE) simulation of a clamped composite laminate was carried out using ABAQUS to investigate the EM impedance response, as shown in Fig. 2. The FE model replicates an experimental model of composite plate with dimensions of 290 mm × 200 mm × 3 mm, rigidly fixed along all four edges, as depicted in Figs. 2a and 2b [4]. The laminate structure consists of 12 layers of T700/M21 carbon/epoxy, arranged in a symmetric stacking sequence of [45/-45/0/90/0/90]S, as shown in Fig. 2c.

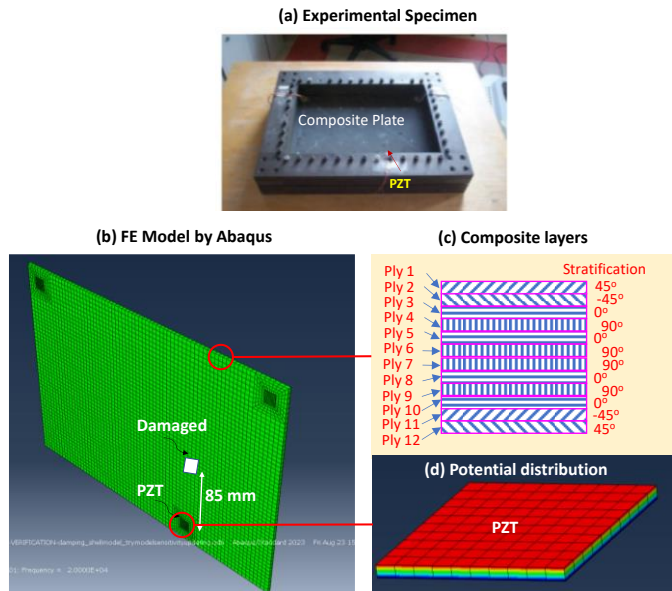


Figure 2. FE modeling

A square piezoelectric patch measuring 10 mm × 10 mm × 0.5 mm is surface-mounted at the center of the plate via a thin adhesive film of 0.04 mm thickness [4]. As shown in Fig. 1b, the composite laminate is discretized using 8-node continuum

shell elements (SC8R), while the adhesive layer is represented with 8-node linear brick elements (C3D8). The bonded piezoelectric transducer is modeled using 8-node coupled-field piezoelectric elements (C3D8E), capable of simulating electromechanical interactions.

The material parameters for both the piezoelectric patch and adhesive layer are adopted from established literature [4], and a structural damping ratio of 0.02 is incorporated to simulate energy dissipation. To evaluate the EM impedance response, a sinusoidal voltage excitation of 1 V is applied across the piezoelectric patch, specifically, the upper electrode is subjected to the harmonic signal  $V(\omega)$ , while the lower electrode is grounded. The potential distribution across the transducer's thickness is shown in Fig. 2d. The frequency sweep defined in ABAQUS spans from 10 kHz to 30 kHz with a frequency resolution of 50 Hz to capture relevant impedance dynamics.

To assess damage sensitivity, a localized defect scenario is introduced: a 10 mm × 10 mm square damage zone positioned 85 mm from the piezoelectric transducer. Variations in damage severity are simulated by incrementally reducing the stiffness of the plies to 0.1 Pa within the defect region, mimicking progressive internal damage such as delamination or matrix cracking.

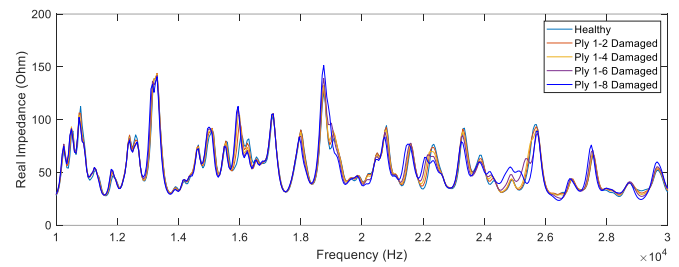


Figure 3. Real part of the EMI response under damage

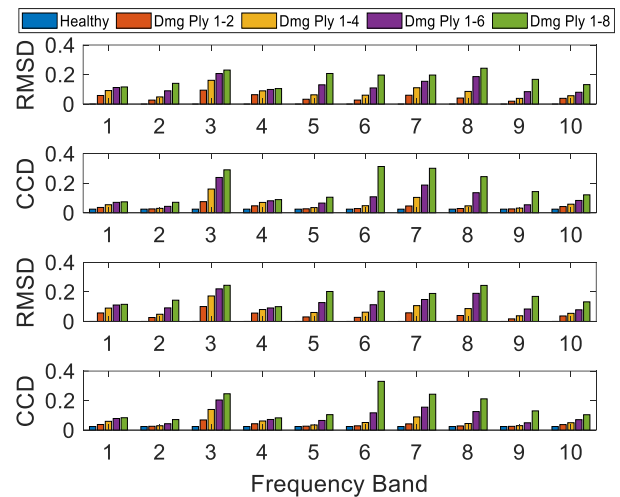


Figure 4. Damage detection results using RMSD and CCD metrics

As illustrated in Fig. 3, the EM impedance spectra recorded between 10 kHz – 30 kHz display multiple well-defined resonance peaks. Upon the introduction of damage to the

composite plate, these peaks exhibit noticeable shifts, predominantly toward lower frequencies, as the number of compromised plies increases. This frequency shift reflects a decline in local stiffness and a modification of the structure's dynamic behavior.

To systematically capture these changes, statistical damage indices, specifically, the root-mean-square deviation (RMSD) and cross-correlation deviation (CCD) [1] are employed. These indices are calculated across ten 2-kHz-wide sub-bands (see Fig. 4), enabling localized frequency analysis and heightened sensitivity to subtle damage.

The outcomes presented in Fig. 4 clearly illustrate that both RMSD and CCD values increase significantly under damaged conditions, with the magnitude of these indices growing in proportion to the severity of the damage. This trend reinforces the sensitivity of the EM impedance technique not only for detecting the presence of structural degradation but also for quantifying its extent. Such capability is critical in composite materials, where damage often initiates internally and may not be easily visible through traditional inspection methods.

Moreover, the identification of multiple damage-sensitive frequency sub-bands provides additional insight into the damage localization process. These sub-bands exhibit distinct impedance shifts, suggesting that the structural response to damage is frequency-dependent. By isolating and analyzing these sub-bands individually, the detection resolution is substantially improved. This is particularly valuable in real-world SHM scenarios where environmental and operational variability may obscure global trends in the impedance spectrum. The sub-band approach thus offers a practical means to enhance robustness and reduce false positives in damage detection systems.

#### 4 DISCUSSIONS AND CONCLUDING REMARKS

This study presents a preliminary numerical investigation into a low-cost SHM approach for composite structures using the EM impedance technique. A FE model of a clamped composite plate with a bonded piezoelectric transducer is developed to simulate EM impedance responses under different damage conditions, introduced as localized stiffness degradation at the ply level. To enhance sensitivity, the analysis applies frequency sub-band decomposition combined with RMSD and CCD damage indices. Results show that the EM impedance signatures are highly responsive to structural damage, with clear impedance shifts and increasing index values correlating with damage severity. These findings validate the effectiveness of combining EM impedance-based sensing with sub-band analysis and statistical damage indices.

The EM impedance technique offers a low-cost and sensitive approach for real-time damage detection, particularly suited to laminated composite structures in aerospace panels, and turbine blades, where internal damage is often undetectable by surface methods. Its compact size and high-frequency resolution make it ideal for embedded sensing in such systems.

While the current numerical model assumes fixed boundary conditions to isolate damage effects, real-world applications may involve boundary variability due to thermal or operational effects. Future work will therefore include parametric studies accounting for changes in boundary conditions, plate deformation, and internal stress states, to assess the robustness

of EM impedance-based damage indicators under practical uncertainties.

Future efforts will also focus on experimental validation to confirm the numerical findings under realistic conditions. Parametric studies involving different layouts, damage types, and sensor placements will help generalize the method. Additionally, integrating EM impedance features with machine learning could improve damage classification and quantification. Extension to complex geometries and real-world structures is also planned to support practical SHM applications.

#### ACKNOWLEDGMENTS

This study was funded by the National Research Foundation (Singapore) under the Singapore-China Joint Flagship Project on Clean Energy (grant no. 24-0128-A0001).

#### REFERENCES

- [1] Na WS, Baek J. A review of the piezoelectric electromechanical impedance based structural health monitoring technique for engineering structures. *Sensors*. 2018;18:1307.
- [2] Yu X, Fu Y, Li J, Mao J, Hoang T, Wang H. Recent advances in wireless sensor networks for structural health monitoring of civil infrastructure. *Journal of Infrastructure Intelligence and Resilience*. 2024;3:100066.
- [3] Park G, Sohn H, Farrar CR, Inman DJ. Overview of piezoelectric impedance-based health monitoring and path forward. *Shock and vibration digest*. 2003;35:451-64.
- [4] Selva P, Cherrier O, Budinger V, Lachaud F, Morlier J. Smart monitoring of aeronautical composites plates based on electromechanical impedance measurements and artificial neural networks. *Engineering Structures*. 2013;56:794-804.



## Hazard, Disaster and Damage Detection for Infrastructure



# Study on Methods for Identifying and Evaluating Damage to Cross-Sea Bridges Subjected to Ship Collisions

Jian Guo<sup>1</sup>, Yuhao Cui<sup>2</sup>, Zheng Wang<sup>2</sup>, Jiahui Wu<sup>2</sup>

<sup>1</sup>State Key Laboratory of Bridge Intelligent and Green Construction, Southwest Jiaotong University, Chengdu, Sichuan 610000, China

<sup>2</sup>School of Civil Engineering, Southwest Jiaotong University, Chengdu, Sichuan 610000, China  
email: guoj@swjtu.edu.cn, cuiyuhao@my.swjtu.edu.cn, wzhang@my.swjtu.edu.cn, wujiahui@my.swjtu.edu.cn

**ABSTRACT:** Cross-sea bridges are crucial transportation links, ensuring smooth maritime traffic and protecting public safety and property. However, ship collisions pose a serious threat, potentially causing extensive damage to bridges, disrupting traffic, polluting the environment, and leading to casualties. Therefore, it is extremely important to develop methods for identifying and evaluating damage to cross-sea bridges caused by ship collisions. A study has been conducted utilizing a combined approach of numerical simulation and experimental validation to analyze the structural dynamic responses of bridges subjected to ship collisions. Based on the insights gained, a structural damage assessment method combining response surface method and Monte Carlo simulation has been introduced. This method takes into account factors such as the impact height and kinetic energy during ship-bridge collisions, establishing a comprehensive evaluation index system. This approach offers a holistic view of the damage state of bridges subjected to ship collisions, providing a scientific foundation for subsequent emergency response and repair strategies. Ultimately, the research aims to mitigate the adverse effects of ship collisions on the structural integrity of cross-sea bridges.

**KEY WORDS:** Ship-bridge Collisions; Damage Assessment; Impact Test; Response Surface Method.

## 1 INTRODUCTION

Currently, the safety issues related to bridge ship collisions have garnered widespread attention. However, relevant research primarily focuses on impact force estimation and studies on bridge anti-collision facilities (Chen et al., 2022; Nian et al., 2016). However, previous studies have struggled to capture the damage evolution characteristics of bridges under varying ship kinetic energy impacts. Conducting fragility analysis for bridge ship collisions can predict the probability of structural damage at various levels, providing practical engineering value for structural design, reinforcement, and maintenance decision-making.

The seismic fragility analysis of bridges has garnered extensive attention from scholars both domestically and internationally. Song et al. (2024) conducted a comprehensive brittleness assessment of specimen viaducts under various ground motion excitation schemes in order to evaluate the impact of modeling detail and analysis complexity on estimating seismic performance. Wang et al. (2025) established an analysis model of the degradation state of a large cantilever cap bridge, and studied the seismic vulnerability of the bridge structure under different service times based on the OpenSees platform. Li et al. (2025) proposed a copula-based approach proposed for seismic vulnerability analysis by incorporating the uncertainty of scour depth into the assessment of bridge seismic performance. However, research on the fragility of bridges under ship collisions is very limited. Kameshwar et al. (2018) developed a meta-model to estimate the force requirements and vulnerability of bridge pillars under barge impact. Fu et al. (2024) proposed a new brittleness assessment framework based on the residual bearing capacity of piers. Zhong et al. (2024) propose a fragility based framework to determine the most

unfavorable position of a bridge column for collision with a barge.

However, there is currently no widely accepted and convincing damage indicator for assessing pier damage under ship collisions. Fan et al. (2021) proposed a bridge ship collision vulnerability analysis method combining a simplified finite element model with a response surface agent model, and obtained the bridge vulnerability curves under two types of typical ship impacts. In recent years, some scholars have also applied the response surface method to the parameter analysis and reliability analysis of bridges under impact, significantly improving computational efficiency. Fan et al. (2018) conducted an extensive parametric study using the response surface method to investigate the effects of reinforcement ratio, UHPFRC sheath thickness, UHPFRC strength, and initial impact velocity. Duan et al. (2024) proposed an efficient hybrid response surface method to study the system reliability of pile-reinforced slopes.

In this study, the stress-strain behavior at the base of the pier under ship impact was investigated through a combined experimental and finite element comparative analysis. Based on the response surface, a new bridge impact damage index is proposed and applied to bridge brittleness assessment. By establishing a full-scale finite element model of the bridge, a multi-factor ship collision simulation analysis was conducted. Fragility curves of the pier under different influencing factors were obtained, providing a reference for the fragility analysis of bridges subjected to ship collisions.

## 2 EXPERIMENTAL OVERVIEW

The non-navigational spans of the prototype bridge are 60-meter span continuous concrete girder bridges, with the main body of the bridge constructed using marine-grade concrete

C40. Based on the scale ratio, the overall schematic diagram of the bridge model structure, as shown in the Figure 1, was established by fully considering the interaction relationships between the pile caps, pile foundations, bearings, and girder segments. Hollow circular steel pipes with a diameter of 89 mm and a wall thickness of 2.5 mm were used to simulate the pile foundations. The pile length was determined to be 75 cm using the 8-times equivalent pile diameter method, and the piles were embedded into the pile cap to a depth of 5 cm.

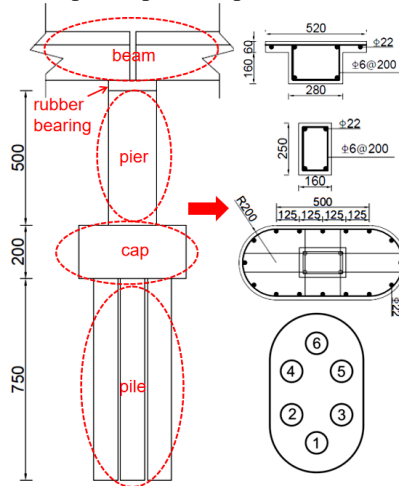


Figure 1. The dimensional drawing of the scaled full-bridge model (mm).

To simplify the design, the ship model consists of a bow model and a stern model, connected by a force sensor in between. Since the stern model does not directly contact the bridge model during the collision process, it is primarily responsible for accommodating sand and stone ballast to achieve different mass conditions. The bow model mainly comprises an internal structure and an external shell structure. The external shell structure is constructed by assembling 1 mm steel plates. Given the difficulty in replicating every detail of the actual bow's internal structure, the internal structure of the bow is composed of two equivalent supports, which are fabricated by welding steel bars with a diameter of 6 mm.

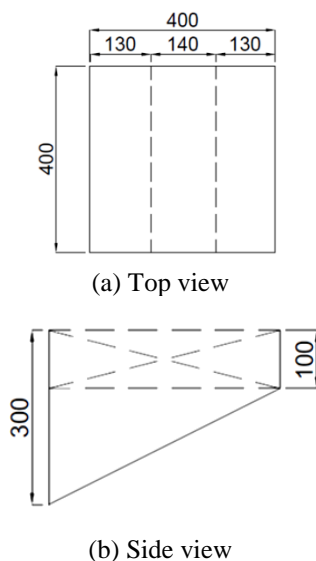


Figure 2. The dimensional specifications of the scaled bow model (mm).

Considering the test site conditions, a pendulum-type loading device powered by gravitational acceleration was employed. The frame of the loading device was constructed by welding I-beams, and its base was securely anchored to the ground trough using anchor bolts. A movable beam was installed at the top of the frame, equipped with universal wheels. The ship model was suspended at a pre-calculated height and released by a triggering mechanism. Utilizing gravitational acceleration, the ship model attained a certain horizontal velocity upon impact with the bridge model. The pile foundations were fixed to the steel plates in the ground trough using clamps and further secured with bolts, as illustrated in Figure 3.

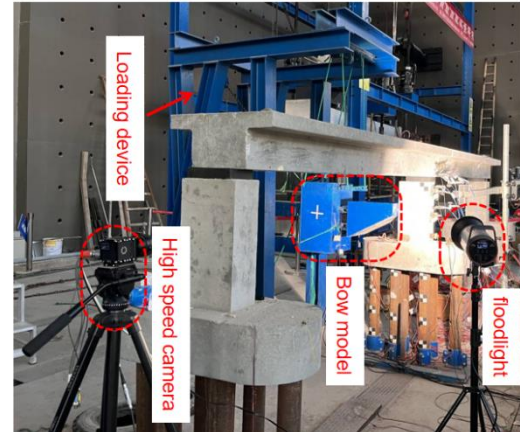
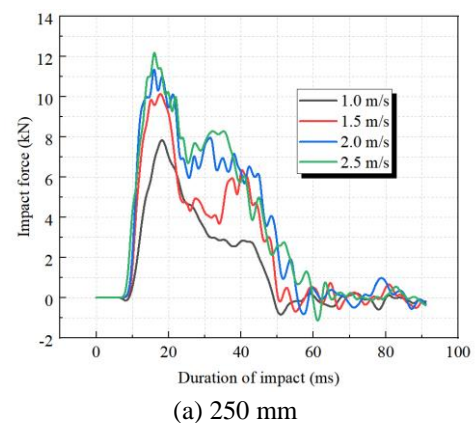


Figure 3 Scaled bridge collision test.

The ship-bridge collision process involves complex elastoplastic deformation of the bow. As the velocity increases, the deformation of the bow becomes more significant. This study conducted collision tests at two different heights, with impact points located 250 mm and 350 mm above the base of the pier, respectively. Analyzing the time-history curves of impact forces under different impact velocities at these two heights reveals that the change in impact location has almost no influence on the impact force. This is because the magnitude of the impact force is primarily determined by the contact area, and the change in impact location does not affect the contact area, as illustrated in Figure 4. Moreover, when the impact velocity exceeds 1.5 m/s, the peak impact force increases very slowly with further increases in velocity. This phenomenon is mainly attributed to the internal structure of the barge bow. Additionally, the stiffness of the barge bow is relatively high compared to other types of bows, resulting in the maximum impact force being reached almost immediately at the onset of collision.



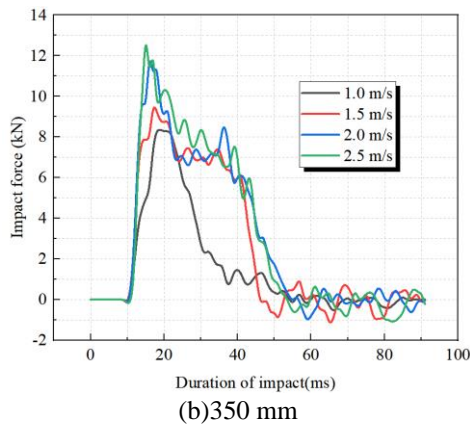


Figure 4. Time-history curve of ship-bridge collision force

After being subjected to impact, fine cracks appeared at the base of the pier. The cracks generated under the most critical impact condition are shown in Figure 5. At this stage, the cracks have not yet penetrated the entire cross-section of the pier, and their widths remain very small. Additionally, the strain values at the base of the pier caused by impacts at two different heights with a velocity of 2.5 m/s were recorded, as presented in Table 1.



Figure 5. Comparative analysis of damage at the base of bridge piers

When the impact velocity is the same, a higher impact height results in greater strain. Larger strains are more likely to induce cracks at the base of the pier, indicating that a higher impact location increases the likelihood of damage to the pier base.

Table 1. Strain data at the base of bridge piers

Impact velocity (m/s)	Height of impact (250 mm)	Height of impact (350 mm)
2.5	113	171

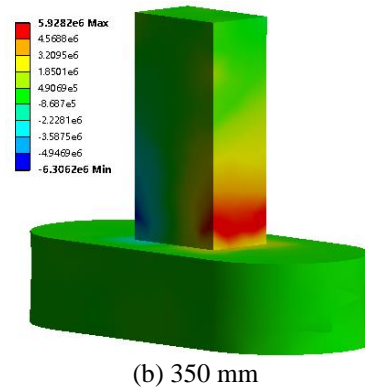
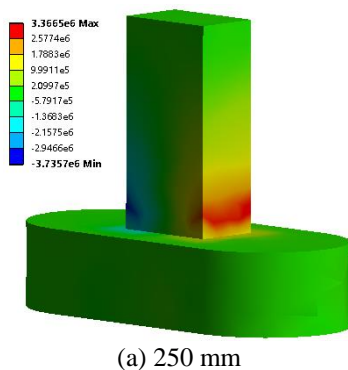


Figure 6. Stress simulation at the base of bridge piers

A finite element model corresponding to the experimental model was established, and the stresses at the base of the pier under two impact heights with a velocity of 2.5 m/s were calculated, as shown in Figure 6. The strain values obtained from the experiments were converted into stress values, and the results showed minimal discrepancies compared to the finite element results. This indicates that the finite element modeling approach in this study aligns well with the actual conditions. When the stress at the base of the pier exceeds the tensile strength of the concrete, cracks begin to form. As the stress at the base gradually increases, the cracks progressively penetrate the entire cross-section of the pier. According to the Chinese building industry standard Code for Design of Concrete Structures (GB 50010-2010), the standard tensile strength of reinforced concrete can be calculated. When the stress at the base exceeds the standard tensile strength of reinforced concrete, it indicates that the pier has suffered severe damage.

### 3 DAMAGE CLASSIFICATION THEORY

The Box-Behnken Design (BBD) method was employed for sampling value calculations. Taking a three-factor design as an example, the distribution of sampling points is illustrated in Figure 7. Here,  $E$  represents the kinetic energy during ship impact,  $h$  denotes the impact height, and  $f_c$  indicates the concrete strength grade. Subsequently, an actual ship-bridge collision model was established, and sampling value calculations were performed using the Box-Behnken Design. The obtained data were fitted to a surface, yielding the stress data at the base of the pier under the influence of the three factors in ship-bridge collisions.

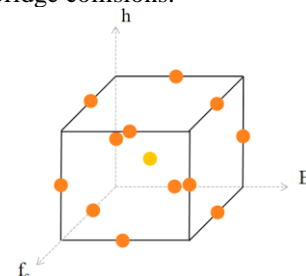


Figure 7. Sampling points for Box-Behnken Design

In the bridge ship collision fragility analysis studied in this paper, parameter  $A$  is defined as the impact kinetic energy of the ship. Specifically, the ship collision fragility is defined as the conditional failure probability that the structure reaches or exceeds a certain limit state ( $L_s$ ) when subjected to a ship



collision with impact kinetic energy  $A$  equal to  $E$ , as shown in Equation (1).

$$F_R(a) = P[Ls|A = E] \quad (1)$$

The polynomial response surface surrogate model is a commonly used form of surrogate model in response surface analysis. In this study, a polynomial surrogate model is employed to fit the stress at the base of the pier caused by barge impact. The impact force generated by the barge collision increases with the kinetic energy of the ship. However, when the kinetic energy exceeds a certain threshold, the growth of the impact force slows down. Consequently, the tensile stress at the base of the pier follows the same trend, necessitating a segmented calculation approach for the tensile stress. Here,  $\sigma_t$  represents the tensile stress at the base of the pier,  $E_0$  denotes the critical segmentation point of kinetic energy, and  $E_C$  represents the maximum kinetic energy used in the calculations.

$$\sigma_t = p_1 + p_2 f_c + p_3 h + p_4 E + p_5 f_c h + p_6 f_c E + p_7 h E + p_8 f_c^2 + p_9 h^2 + p_{10} E^2 \quad (2)$$

$$\sigma_t = \begin{cases} \sigma_1(f_c, h, E), & E \in (0, E_0) \\ \sigma_2(f_c, h, E), & E \in (E_0, E_C) \end{cases} \quad (3)$$

The fragility curve of the pier is obtained by performing Monte Carlo sampling on the normally distributed random variable  $f_c$  and plotting the failure probabilities corresponding to different kinetic energies, thereby generating the fragility curve. The probability distribution of C30 concrete strength is shown in Table 2.

Table 2 Distribution of concrete strength grades

Concrete strength	Nominal value	Mean value	Coefficient of variation (%)
$f_c$	30 MPa	30 MPa	15

#### 4 FAILURE PROBABILITY CALCULATION

A finite element model of the actual bridge was established, with the pier having a width of 3 m, a length of 6.5 m, and a height of 20 m. The hull was modeled using the AASHTO barge model. A comparison of the impact force and the tensile stress at the pier base under different ship kinetic energies reveals that the trends of change in impact force and tensile stress are remarkably similar. Furthermore, the installation of collision protection devices was considered to further verify whether the trends of change in impact force and tensile stress remain consistent.

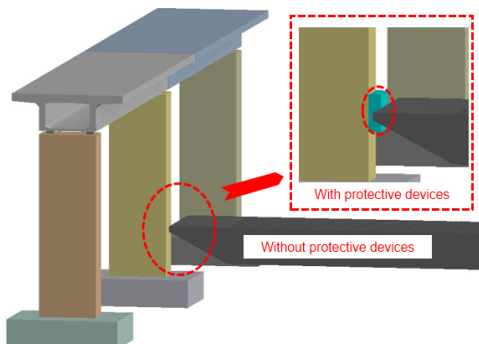
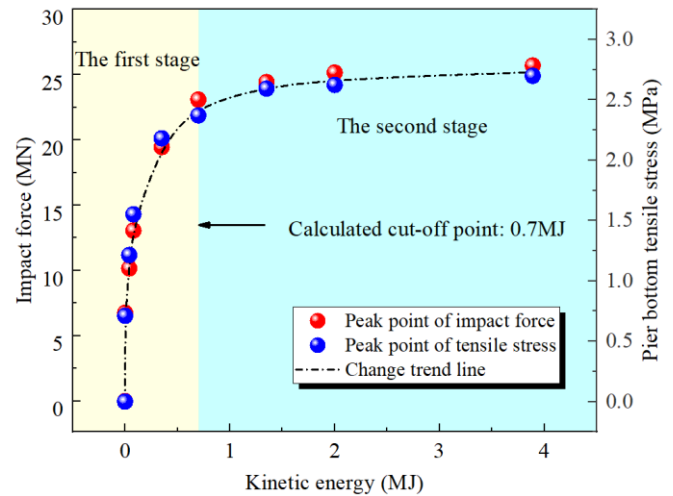
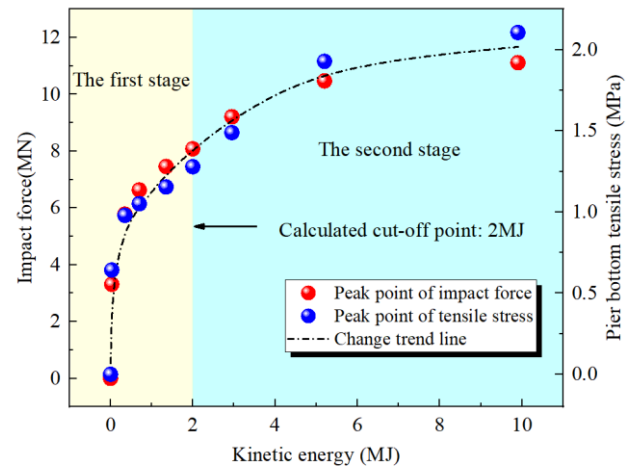


Figure 8. Full size bridge collision model

The results indicate that the trends of change in the impact force caused by ship-bridge collisions and the tensile stress generated at the pier base are consistent. Even with the addition of protective devices, this regularity remains unaffected. Therefore, the trend of change in barge impact force with respect to ship kinetic energy can be used to describe the trend of change in tensile stress with respect to ship kinetic energy. Moreover, both the peak impact force and the peak tensile stress increase with the rise in ship kinetic energy, but the trend of change exhibits a segmented pattern. When the ship's kinetic energy is below a critical threshold, the trends of change in impact force and tensile stress are rapid. Once the ship's kinetic energy exceeds the critical value, the trends of change in impact force and tensile stress become more gradual, as illustrated in Figure 9.



(a) Without protective devices



(b) With protective devices

Figure 9. The trend of impact force-tensile stress variation

According to the calculated results, it can be determined that the kinetic energy segmentation point for ship-bridge collisions without protective devices is 0.7 MJ. According to the sampling method of Box-Behnken Design, the tensile stresses at the base of the pier under different influencing factors were obtained through finite element calculations, as shown in Table 3.

The obtained tensile stresses at the base of the pier under different influencing factors were fitted to a surface, yielding the values of the undetermined coefficients for the two segments, as shown in Table 4.

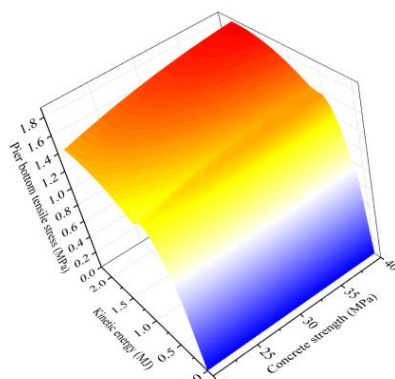
Table 3. Sampling values for numerical simulation

Concrete strength (MPa)	Height of impact (m)	Kinetic energy (MJ)	Pier bottom tensile stress (MPa)	Kinetic energy (MJ)	Pier bottom tensile stress (MPa)
20	3	0.35	1.303	1.35	1.468
40	3	0.35	1.441	1.35	1.806
20	9	0.35	2.299	1.35	2.678
40	9	0.35	2.607	1.35	3.104
20	6	0	0	0.7	2.178
40	6	0	0	0.7	2.587
20	6	0.7	2.178	2.0	2.457
40	6	0.7	2.587	2.0	2.864
30	3	0	0	0.7	1.466
30	9	0	0	0.7	2.798
30	3	0.7	1.466	2.0	1.808
30	9	0.7	2.798	2.0	3.022
30	6	0.35	2.181	1.35	2.593
30	6	0.35	2.185	1.35	2.598
30	6	0.35	2.178	1.35	2.587
30	6	0.35	2.182	1.35	2.588
30	6	0.35	2.184	1.35	2.592

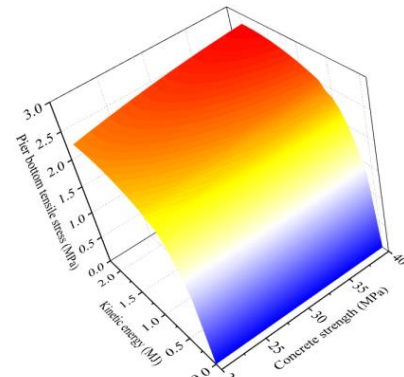
The obtained tensile stresses at the base of the pier under different influencing factors were fitted to a surface, yielding the values of the undetermined coefficients for the two segments, as shown in Table 4.

Table 4 Sampling values for undetermined parameters

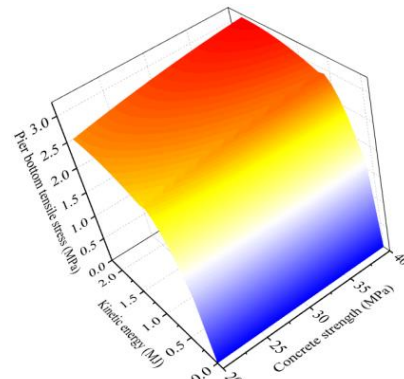
Coefficient value	$E < E_0$	$E \geq E_0$
P <sub>1</sub>	-0.6629	-1.1001
P <sub>2</sub>	0.0266	0.0385
P <sub>3</sub>	0.2600	0.5611
P <sub>4</sub>	3.0525	0.6283
P <sub>5</sub>	0.0017	0.0011
P <sub>6</sub>	0.0143	0.0016
P <sub>7</sub>	0.1978	0.0032
P <sub>8</sub>	-0.0005	-0.0005
P <sub>9</sub>	-0.0187	-0.0326
P <sub>10</sub>	-3.7999	-0.1819



(a) The impact height was 3 m

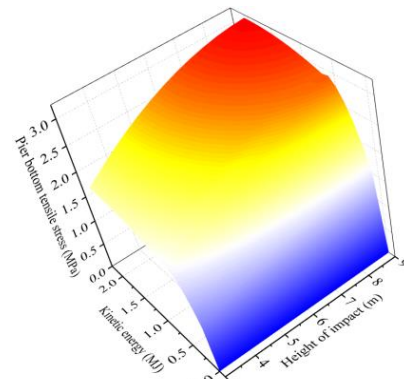


(b) The impact height was 6 m

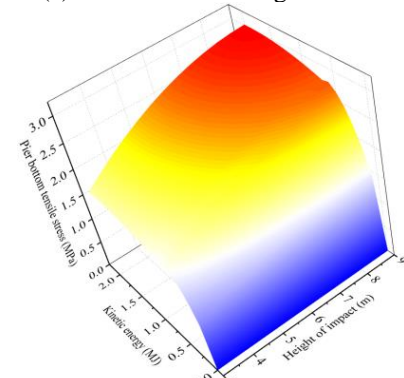


(c) The impact height was 9 m

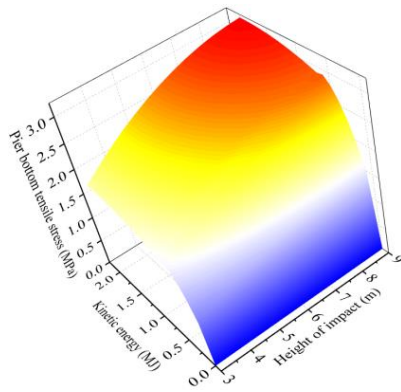
Figure 10. The combined effect of kinetic energy and concrete strength



(a) The concrete strength is C20

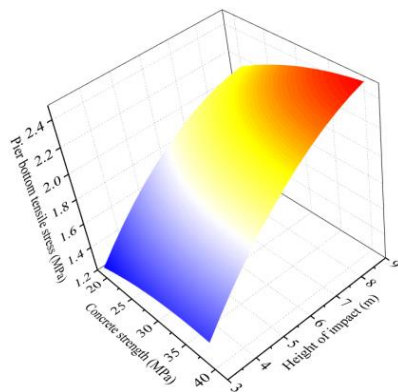


(b) The concrete strength is C30

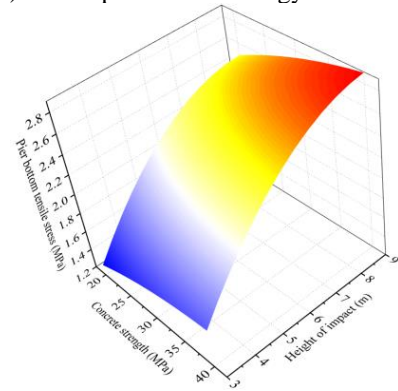


(c) The concrete strength is C40

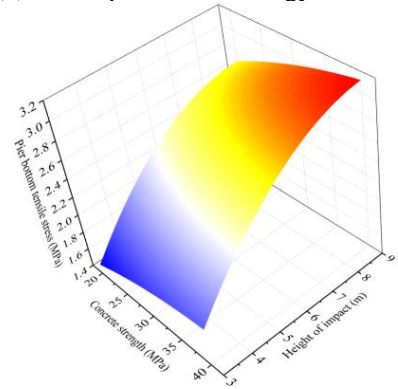
Figure 11. The combined effect of kinetic energy and impact height



(a) The impact kinetic energy is 0.35 MJ



(b) The impact kinetic energy is 0.7 MJ



(c) The impact kinetic energy is 1.35 MJ

Figure 12. The combined effect of concrete strength and impact height

The impact height and impact kinetic energy have a significant influence on the tensile stress at the pier base, whereas the concrete strength has a relatively minor effect on the tensile stress at the pier base. Therefore, in the subsequent vulnerability calculations, the primary considerations will be the effects of impact kinetic energy and impact height.

The fragility curves of the pier under three impact height conditions were obtained through Monte Carlo sampling, as shown in Figure 13. Since the tensile strength of C30 concrete is 2.01 MPa, the condition where the tensile stress at the base of the pier exceeds 2.01 MPa is considered as the onset of minor failure, the initiation of cracks in the pier.

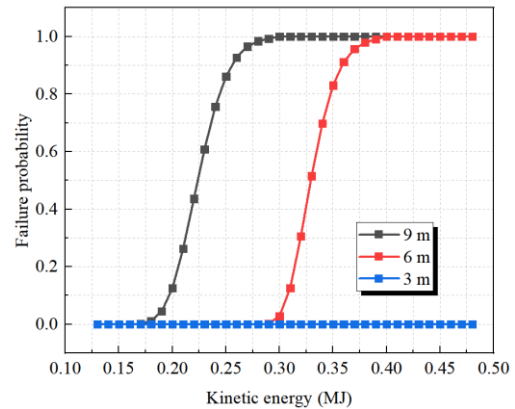


Figure 13. Fragility curves for different impact heights

As the tensile stress at the base caused by the impact does not reach the standard tensile strength of reinforced concrete, only minor failure conditions of the pier need to be considered. For the impact height of 9 m, there is a probability of minor failure when the barge's kinetic energy reaches 0.18 MJ, and direct failure occurs when the kinetic energy exceeds 0.3 MJ. For the impact height of 6 m, minor failure begins to occur when the barge's kinetic energy reaches 0.3 MJ, and direct failure occurs when the kinetic energy exceeds 0.4 MJ. For the impact height of 3 m, failure is almost negligible.

## 5 CONCLUSIONS

In this study, the magnitude of tensile stress at the base of the pier caused by barge impact is used as the damage assessment indicator. A fragility analysis method for bridge ship collisions based on the response surface method is proposed. This method enables rapid fragility assessment of the pier when subjected to barge impact.

The established high-precision response surface model can replace structural models that require complex nonlinear calculations. The developed response surface surrogate model can be utilized for extensive sample analysis in bridge ship collision fragility studies. When subjected to barge impact, the trend of tensile stress at the base of the pier is closely related to the critical barge kinetic energy, exhibiting a segmented characteristic similar to the impact force. Therefore, to accurately reflect the true response characteristics of the pier under barge impact, the sample design should be segmented based on the critical barge kinetic energy. Through a comparative analysis of the individual effects of the three factors on the fragility of the pier, it is evident that the magnitude of tensile stress at the base of the pier is significantly influenced by the impact height and impact kinetic energy,



while changes in concrete grade have a relatively minor effect on the tensile stress. However, the higher the concrete strength grade, the greater the standard tensile strength of the pier, enhancing its resistance to impact and reducing the likelihood of severe damage.

## ACKNOWLEDGMENTS

**Funding:** This work was supported by the National Key R&D Program of China [Grant Numbers. 2024YFC3015200], and National Natural Science Foundation of China [Grant Numbers. U1709207].

## REFERENCES

- [1] Chen, T. L., Wu, H., & Fang, Q. (2022). Impact force models for bridge under barge collisions. *Ocean Eng*, 259, 111856.
- [2] Nian, Y., Wan, S., Wang, X., Zhou, P., Avcar, M., & Li, M. (2023). Study on crashworthiness of nature-inspired functionally graded lattice metamaterials for bridge pier protection against ship collision. *Eng Struct*, 277, 115404.
- [3] Song, S., Xie, Y., Wang, Y., Zhang, W., Kurtulus, A., Apaydin, N. M., & Taciroglu, E. (2024). Seismic fragility and vulnerability assessment of a multi-span irregular curved bridge under spatially varying ground motions. *Soil Dyn Earthq Eng*, 180, 108585.
- [4] Wang, L., Che, J., Dou, C., Li, X., Zhu, Y., Wang, R., & Wu, T. (2025). Seismic vulnerability evolution of large cantilever cap bridges due to material degradation. *Structures*, 72, 108303.
- [5] Li, Y., Chen, H., Yi, M., Li, J., & Fang, C. (2025). Seismic vulnerability analysis of bridges incorporating scour uncertainty using a copula-based approach. *Ocean Eng*, 323, 120598.
- [6] Kameshwar, S., & Padgett, J. E. (2018). Response and fragility assessment of bridge columns subjected to barge-bridge collision and scour. *Eng Struct*, 168, 308-319.
- [7] Fu, J., Wang, W., Wang, X., Zhao, W., Zhou, R., & Lu, Z. (2024). Fragility assessment of RC bridge piers subjected to vehicle collision based on residual load-bearing capacity. *Structures*, 68, 107103.
- [8] Zhong, Z., Fan, W., Liu, B., Huang, X., & Geng, B. (2024). A fragility-based framework for identification of unfavorable impact location for bridge columns under barge collisions. *Ocean Eng*, 294, 116839.
- [9] Fan, W., Sun, Y., Shen, D. J., & Liu, b. (2021). Vessel-collision vulnerability analysis method of bridge structures based on simplified model with girders and response surface. *J Hunan Univ*, 48(03), 34-43.
- [10] Fan, W., Xu, X., Zhang, Z., & Shao, X. (2018). Performance and sensitivity analysis of UHPFRC-strengthened bridge columns subjected to vehicle collisions. *Eng Struct*, 173, 251-268.
- [11] Duan, X., Zhang, J., Liu, L., Hu, J., & Xue, Y. (2024). Hybrid response surface method for system reliability analysis of pile-reinforced slopes. *J Rock Mech Geotech Eng*, 16(9), 3395-3406..

# An automatic system for the rapid post-earthquake safety assessment of bridges

Marlon Agüero<sup>1</sup>, Derek Skolnik<sup>1</sup>, Mauricio Ciudad-Real<sup>1</sup>

<sup>1</sup>Kinematics, Pasadena, CA 91107, USA

email: mai@kmi.com, das@kmi.com, mcr@kmi.com

## ABSTRACT:

This paper presents the development of an advanced system for the rapid post-earthquake safety assessment of bridges using advanced sensor technology. Upon completing the assessment, the system generates an automated report on bridge condition. To evaluate the serviceability of bridges, engineers frequently employ sensors, such as accelerometers, strain gauges, and tiltmeters to measure accelerations, displacements, strain, tilt, and deflections. The obtained data are essential for theoretical and practical reasons. Engineers analyze the data to gain insights into real-world bridge dynamics and to develop and validate models that inform design codes. On the practical level, the data are used in structural health monitoring (SHM) systems to enhance public safety by providing reliable data about bridge conditions, both long-term and after unexpected events, such as disasters and earthquakes. Traditionally, bridge inspections are conducted every two years to detect potential deterioration. However, these inspections are expensive and may need to be done more frequently following extreme events like earthquakes, fires, or bridge strikes. To reduce costs, we propose an innovative automatic rapid assessment system that uses measured bridge response data to initiate and minimize re-evaluation efforts. The system works by converting the acceleration data to displacements; subsequently, a threshold that defines the serviceability of the bridge is established. When one of the thresholds is exceeded, a report on bridge condition is automatically generated. This system is particularly useful in post-earthquake events and after other emergencies. In such situations, fast and reliable decision-making is a strong necessity, but also a serious challenge due to common human conditions, such as panic and fear. Rapid, automated generation of reports ensures accurate assessments of damage, which are crucial for the reduction of serious economic losses and the maintenance of reliable infrastructure access. In the paper we will discuss two case studies which illustrate the deployment of automatic, real-time assessment systems. As will be shown, these systems enhance the preparedness for disaster scenario and considerably improve bridge safety.

**KEY WORDS:** SHM; Disaster; Earthquake; Bridge Safety; Sensors; Automatic System; Safety Report.

## 1 INTRODUCTION

Bridges are vital components of transportation infrastructure, serving as critical links that facilitate the movement of goods and people. Their safety and serviceability are essential for public well-being, economic stability, and emergency response capabilities. The integrity of bridges must be maintained to prevent catastrophic failures that could lead to significant loss of life and disruption of transportation networks. This is particularly crucial in seismic-prone regions, where earthquakes pose a constant threat to bridge structures [1].

Following an earthquake, assessing bridge conditions rapidly and accurately is essential to prevent further damage, ensure public safety, and maintain transportation continuity. Earthquakes can induce severe structural damage, including cracks, joint displacements, bearing failures, and even complete collapses. Immediate post-earthquake assessments are necessary to determine whether a bridge can remain in service, requires immediate repair, or must be closed to avoid endangering the public. However, conducting these evaluations efficiently is challenging due to the scale of transportation networks and the inherent risks associated with manual inspections in post-disaster environments [2], [3].

Traditional inspection methods, which involve manual visual evaluations conducted every two years, are often inadequate in emergency scenarios. These assessments typically require trained personnel to physically inspect bridges, document damages, and make qualitative judgments about their structural integrity. Such methods are time-consuming, labor-intensive, and prone to human error, potentially delaying critical

decisions about bridge usability. Additionally, access to bridges following an earthquake may be restricted due to debris, road blockages, or structural instability, further complicating manual inspection efforts [4].

To address these challenges, this paper presents an advanced system that leverages modern sensor technology and data analytics to facilitate rapid post-earthquake safety assessments of bridges. The proposed system integrates a network of sensors, including accelerometers, strain gauges, and tiltmeters, to continuously collect structural response data before, during, and after seismic events. By automating data acquisition, the system eliminates the need for labor-intensive manual inspections and provides real-time insights into the bridge's condition.

## 2 SENSOR TECHNOLOGY IN STRUCTURAL HEALTH MONITORING

Structural Health Monitoring (SHM) relies on various sensors to evaluate bridge conditions (see Figure 1).

Commonly used sensors include [5], [6]:

- Accelerometers: Measure vibrations and dynamic responses to external forces.
- Strain Gauges: Detect strain variations within bridge components.
- Tiltmeters: Monitor angular displacements and inclination changes.

The sensors such are strategically installed on key elements of the bridge, including the superstructure, bearings, and substructure. These sensors continuously or periodically record

physical responses like vibrations, strains, and movements caused by traffic loads, environmental changes, or seismic events. Each sensor generates analog signals that reflect changes in the measured parameter, serving as the raw input for the monitoring system.

These analog signals are transmitted to a local data acquisition system (DAQ), which is typically housed in a weatherproof enclosure on or near the bridge. The DAQ performs several crucial functions: it converts analog signals to digital data through analog-to-digital converters, applies filtering and signal conditioning, and timestamps each measurement for synchronization across multiple channels. Depending on the configuration, the DAQ may operate in real time or in scheduled bursts, and it often includes onboard memory for local storage. Some systems also include edge processing capabilities to perform preliminary diagnostics or event detection directly at the site.

Once the data is digitized and preprocessed, it is transmitted from the DAQ to a local or remote data center using communication methods such as cellular networks (4G/5G), Wi-Fi, satellite uplinks, or fiber-optic lines. The data center acts as the central hub for data management, enabling long-term storage, advanced analysis, and integration with cloud platforms. Here, engineers and transportation agencies can access the data remotely via secure web portals or custom dashboards. Real-time data streams enable continuous monitoring, while automated algorithms can trigger alerts when structural anomalies are detected. This end-to-end system supports rapid decision-making, improves maintenance planning, and enhances the resilience of critical bridge infrastructure.

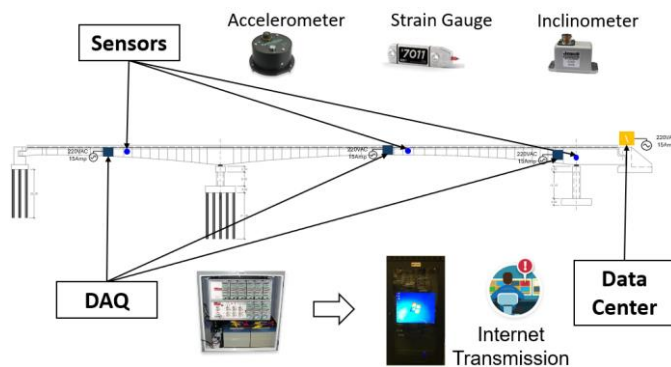


Figure 1. Typical instrumentation in bridge monitoring.

By continuously recording bridge responses, these sensors help engineers assess structural integrity, detect anomalies, and validate theoretical models that guide design and maintenance strategies.

### 3 CHALLENGES OF TRADITIONAL BRIDGE INSPECTION

Traditional bridge inspections are conducted biennially to identify potential deterioration. However, after extreme events such as earthquakes, additional inspections become necessary. Some key challenges include (see Figure 2) [7]:

- **High Costs:** Manual inspections require significant financial and human resources, including specialized personnel, equipment, and logistical support.
- **Time Constraints:** Evaluations can take days or weeks, delaying crucial transportation access and prolonging disruptions in emergency response efforts.
- **Human Limitations:** Panic, fatigue, and cognitive overload can impair decision-making during crises, leading to inconsistent or inaccurate assessments.
- **Safety Risks:** Inspectors working in post-disaster environments face significant hazards, including aftershocks, unstable structures, and difficult-to-access areas.
- **Limited Coverage:** Manual inspections may not comprehensively assess structural integrity, particularly in large-scale bridge networks where resources are constrained.



Figure 2. Challenges of Bridge Inspection.

The introduction of automated systems can significantly mitigate these challenges by providing rapid and accurate assessments without the need for extensive human intervention. Advanced technologies, such as sensor networks, computer vision, and artificial intelligence, enable continuous monitoring and real-time analysis, enhancing decision-making and improving overall safety and efficiency in bridge assessment processes [8].

By minimizing reliance on manual inspections, these automated systems not only reduce labor costs and human error but also allow for more frequent and consistent data collection. This continuous stream of high-quality data enables a shift from reactive maintenance to predictive maintenance strategies, where potential issues can be identified and addressed before they escalate. As a result, bridge management authorities can prioritize interventions more effectively, allocate resources efficiently, and extend the service life of critical infrastructure.

The collected sensor data is processed using advanced algorithms, to identify damage patterns, quantify structural deterioration, and predict the bridge's residual load-carrying



capacity. This automated analysis enables the generation of detailed condition reports, which provide decision-makers with critical information needed to implement timely and effective mitigation measures. Furthermore, integrating this system with geographic information systems (GIS) and cloud-based platforms enhances accessibility and facilitates coordinated emergency response efforts.

#### 4 PROPOSED AUTOMATIC RAPID ASSESSMENT SYSTEM METHODOLOGY

Structural Health Monitoring (SHM) is a critical tool for assessing the safety of bridges after an earthquake. The methodology involves 5 steps: pre-event preparation, real-time data acquisition during earthquake, post-event structural evaluation, decision-making process and reporting and action plan (see Figure 3).

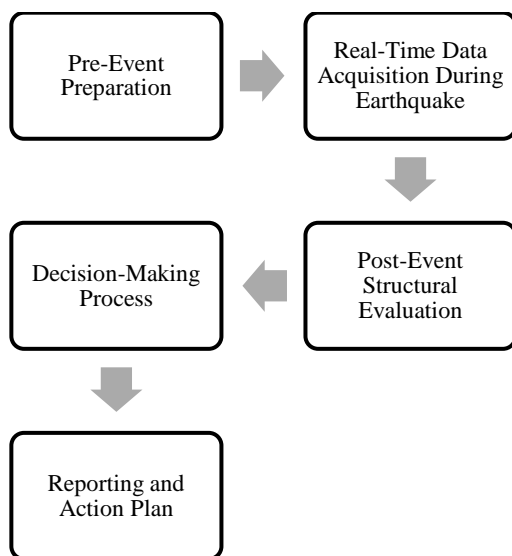


Figure 3. Proposed Automatic Rapid Assessment System Methodology.

##### 4.1 Pre-Event Preparation

Effective rapid assessment begins with thorough pre-event preparation, which includes identifying critical bridges within a transportation network and prioritizing them based on factors such as structural vulnerability, traffic volume, and strategic importance. Engineers conduct baseline assessments to understand the bridge's current condition and develop models that simulate its response to different seismic scenarios. These models form the reference point for interpreting data during and after seismic events.

Sensor deployment is a key part of preparation. Various sensors including accelerometers, strain gauges, and tiltmeters are installed on structural components most susceptible to damage. The placement is informed by structural analysis and past performance data. In addition to physical installation, sensors are calibrated to ensure accuracy and synchronized with the local data acquisition system (DAQ), which includes real-time clocks and backup power sources to maintain continuity during power loss.

Finally, a communication framework is established for transmitting sensor data to remote servers or data centers. The infrastructure includes reliable network connectivity (e.g., cellular, satellite, or wired connections) and cybersecurity measures to protect data integrity. Pre-event simulations and drills are also conducted to validate the system's performance and ensure all stakeholders, engineers, emergency responders, and transportation officials are familiar with the protocols in the event of a real earthquake.

##### 4.2 Real-Time Data Acquisition During Earthquake

When an earthquake occurs, the sensor network activates automatically or continues uninterrupted if running continuously. Force balance accelerometers capture ground and structural accelerations in three dimensions, while strain gauges and displacement sensors measure localized deformations. These signals are digitized by the DAQ and time-stamped to ensure synchronization across multiple channels and locations.

The DAQ processes the raw data using onboard algorithms to filter noise and detect events that exceed pre-set thresholds. Once significant shaking is detected, the system flags the event and immediately begins streaming prioritized data packets to the central server. Some systems also include edge computing capabilities, allowing for initial damage classification and triage to be performed locally and transmitted as summaries, reducing bandwidth requirements and accelerating response.

During this real-time acquisition phase, data flows continuously or in event-driven bursts to a central data center. There, automated software correlates input from multiple bridges, maps the earthquake's effects regionally, and compares the measured response with known damage thresholds from the pre-event models. This allows emergency management teams to quickly determine which bridges may be compromised and require immediate inspection or closure.

##### 4.3 Post-Event Structural Evaluation

After the shaking subsides, the system transitions to post-event evaluation. This involves aggregating the seismic response data and analyzing it against the bridge's baseline condition and predicted performance models. Engineers can assess the magnitude of forces experienced by each structural component and detect anomalies such as excessive displacements, residual vibrations, or sensor signal losses, which may indicate potential damage.

The evaluation process uses advanced algorithms. These tools identify patterns in the data that correlate with specific types of damage (e.g., joint failure, deck uplift, or bearing dislocation). By automating this analysis, the system reduces reliance on manual inspections and accelerates decision-making, particularly when multiple bridges are affected over a large geographic area.

Visualizations such as shake maps, bridge health dashboards, and risk scores are generated for each bridge. These outputs are reviewed by structural engineers and decision-makers to confirm automated findings. In high-priority cases, the system may recommend sending an inspection team or deploying drones for visual assessment, thus focusing on limited resources where they are most needed.

#### 4.4 Decision-Making Process

The decision-making process combines sensor-derived analytics with predefined action thresholds to classify bridge conditions into categories such as “safe,” “needs inspection,” or “likely damaged.” This triage helps agencies prioritize their response efforts, enabling the reopening of safe routes and the timely closure or detour of potentially unsafe bridges.

A critical component of this process is the decision support system, which integrates real-time sensor data, historical performance, and geographic context to recommend next steps. The system presents stakeholders with actionable insights, supported by confidence levels and potential consequences, empowering transportation officials to make informed, defensible decisions under pressure.

Human oversight remains essential. While the system automates much of the analysis, expert engineers review key findings to validate system outputs, especially in cases of high uncertainty or critical infrastructure. Collaboration between departments of transportation, emergency response, and engineering is coordinated through centralized platforms to ensure consistent, fast communication and execution of response plans.

#### 4.5 Reporting and Action Plan

Once the structural condition of each bridge is assessed, the system generates standardized reports that summarize sensor readings, algorithmic evaluations, and recommended actions. These reports include timestamps, structural response graphs, and comparison with design-level seismic criteria. They are shared through secure digital platforms with transportation authorities, emergency managers, and relevant stakeholders.

For bridges flagged as potentially compromised, the system issues automated alerts accompanied by suggested action plans. These may include full closures, restricted traffic use, or on-site inspection. In more advanced deployments, the system integrates with traffic management infrastructure to redirect traffic automatically, display warnings on digital signage, and update navigation systems.

The final component of the action plan involves post-event documentation and learning. All data and actions taken are archived for forensic analysis, regulatory compliance, and refinement of future response protocols. This feedback loop allows the system to improve over time, helping bridge operators become more resilient to future seismic events and more effective in their emergency response.

### 5 CASE STUDY 1: YUCAIPA EARTHQUAKE IMPACT ON BEAUMONT - I10/60 INTERCHANGE BRIDGE

In this case study, the automatic assessment system was deployed on Beaumont - I10/60 Interchange Bridge (see Figure 4). The bridge is located in Riverside County, California, near the city of Beaumont, where Interstate 10 (I-10) and State Route 60 (SR-60) converge (see Figure 5). This critical interchange lies in Southern California’s Inland Empire region and serves as a major transportation corridor linking Los Angeles to the Coachella Valley and beyond. Positioned in a seismically active area near the San Andreas Fault, the bridge plays a vital role in regional mobility and freight transport, making its structural integrity and seismic resilience essential for public safety and economic continuity.



Figure 4. Beaumont - I10/60 Interchange Bridge.

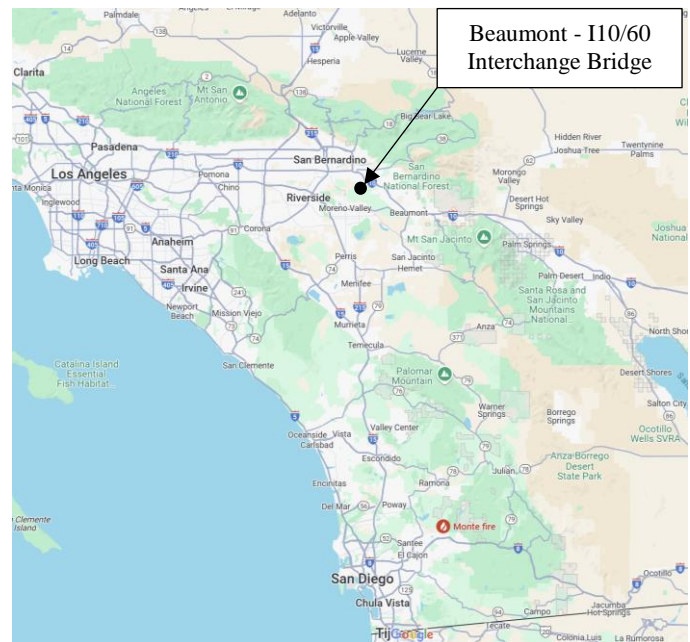


Figure 5. Bridge Location.

The bridge is composed of 2 abutments and 3 bents; the span of the bridge is 112.78 m (370 ft) and a height of 8.23 m (27 ft). In 1992, the bridge was instrumented with six force balance accelerometers as part of a seismic monitoring initiative (See Figure 6). This instrumentation was implemented through an interagency agreement between the California Department of Transportation (Caltrans) and the California Department of Conservation (DOC). The collaboration aimed to enhance the structural health monitoring capabilities of critical transportation infrastructure in seismically active regions, enabling the collection of high-quality acceleration data to support seismic performance assessment and emergency response efforts.

On June 16, 2005, the bridge was exposed to the Yucaipa Earthquake. The epicenter of the earthquake was located 3.39 km (2.1 mi) NE of Yucaipa, CA, USA; had a magnitude of 4.9 and a depth of 12.6 km (see Figure 7). The Yucaipa earthquake was a moderate seismic event and occurred at approximately 8:05 PM local time. Its epicenter was located within a seismically active zone influenced by the complex interactions between the San Andreas Fault and other nearby fault systems in the eastern Transverse Ranges. The event was widely felt throughout the Inland Empire and greater Los Angeles area, prompting temporary evacuations and raising concerns about infrastructure resilience in the region.

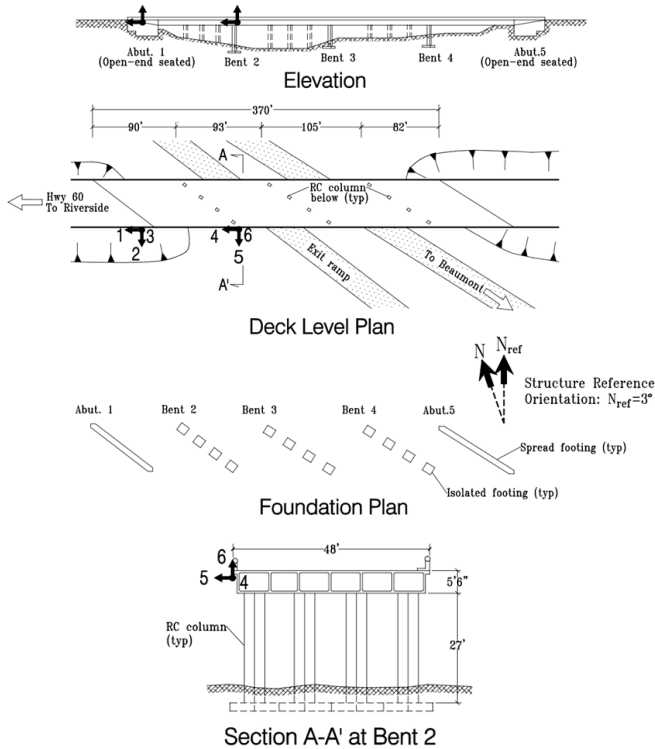


Figure 6. Instrumentation on the bridge (Source: Center for Engineering Strong-Motion Data -CESMD).

Although the 2005 Yucaipa earthquake did not result in any fatalities or major structural damage, it caused minor non-structural damage, such as cracked walls, fallen ceiling tiles, and items displaced from shelves in homes and businesses. The shaking intensity reached Modified Mercalli Intensity (MMI) level VI in the immediate vicinity, indicating strong shaking. The event highlighted the seismic hazard in this part of Southern California and reinforced the importance of earthquake preparedness and monitoring. For researchers and agencies, the earthquake served as a valuable data point for evaluating the performance of early seismic instrumentation, ground motion characteristics, and local soil amplification effects, especially in areas with vulnerable infrastructure such as bridges, schools, and hospitals.

In this context, the instrumentation installed on the bridge provided a critical opportunity to assess structural performance during the 2005 Yucaipa earthquake. The sensors captured real-time data on ground motion and structural response, offering insights that would have been difficult to obtain through visual inspections alone. This event demonstrated the practical value of instrumented bridges in seismic regions, as the recorded data allowed engineers to verify the integrity of the structure without interrupting service. The success of this monitoring effort laid the foundation for more advanced automated assessment systems, capable of rapidly analyzing sensor outputs, identifying potential damage, and supporting immediate post-earthquake decision-making—thus addressing many of the challenges associated with traditional inspection methods.

CISN Rapid Instrumental Intensity Map Epicenter: 2.1 mi NE of Yucaipa, CA  
Thu Jun 16, 2005 01:53:26 PM PDT M 4.9 N34.06 W117.01 Depth: 11.8km ID:14155260

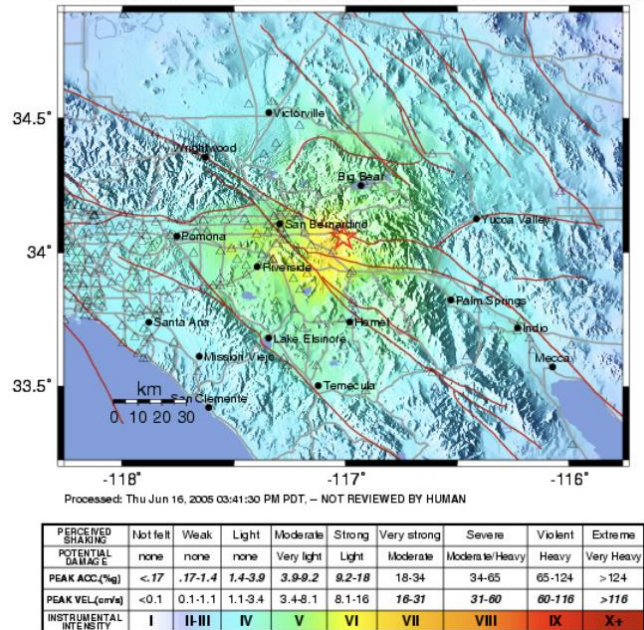


Figure 7. Yucaipa Earthquake (Source: Center for Engineering Strong-Motion Data -CESMD).

Traditional inspections required extended closures and significant financial investment. Following an earthquake, the system could successfully:

- Detected abnormal vibrations exceeding the established serviceability threshold.
- Generated an automatic report, recommending immediate structural reinforcement.
- Enabled engineers to assess the damage remotely, reducing the need for manual inspections.

As a result, the system significantly decreased bridge downtime and ensured rapid decision-making for emergency response teams.

## 6 CASE STUDY 2: CALEXICO EARTHQUAKE IMPACT ON BEAUMONT - I10/60 INTERCHANGE BRIDGE

In this case the Beaumont - I10/60 Interchange Bridge was exposed to the Calexico Earthquake on April 4, 2010. The epicenter of the earthquake was located 49.57 km (30.8 mi) SSE of Calexico, CA, USA; had a magnitude of 7.2 and a depth of 10.0 km (see Figure 8). The Calexico earthquake and the Yucaipa earthquake differed significantly in both magnitude and regional impact. The Yucaipa earthquake registered a magnitude of 4.9 and occurred in the inland region of Southern California, near the San Andreas Fault system. It resulted in minor non-structural damage and served primarily as a data point for evaluating local ground motion and instrumentation performance. In contrast, the Calexico earthquake, also known as the El Mayor-Cucapah earthquake, was a much larger event with a magnitude of 7.2. It struck near the U.S.-Mexico border, affecting both countries and causing extensive structural damage in the city of Calexico and surrounding areas.



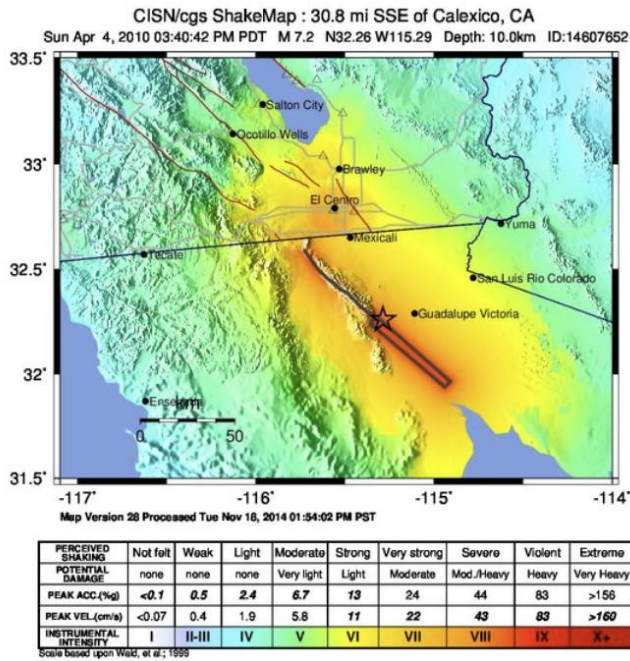


Figure 8. Calexico Earthquake (Source: Center for Engineering Strong-Motion Data -CESMD).

The automatic rapid assessment system showed higher displacements in the bridge for the Calexico Earthquake (see Figure 9 and Figure 10).

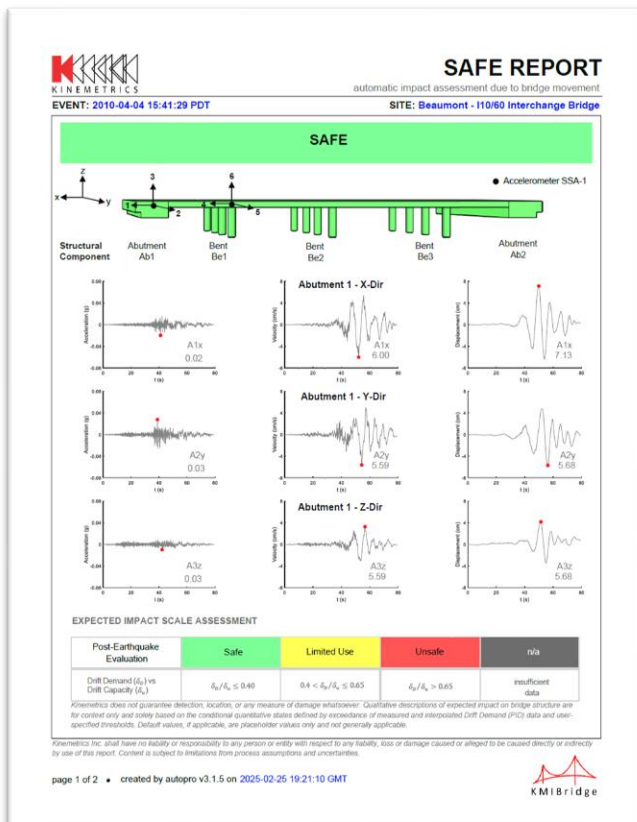


Figure 9. Automatic Rapid Assessment System 1/2.

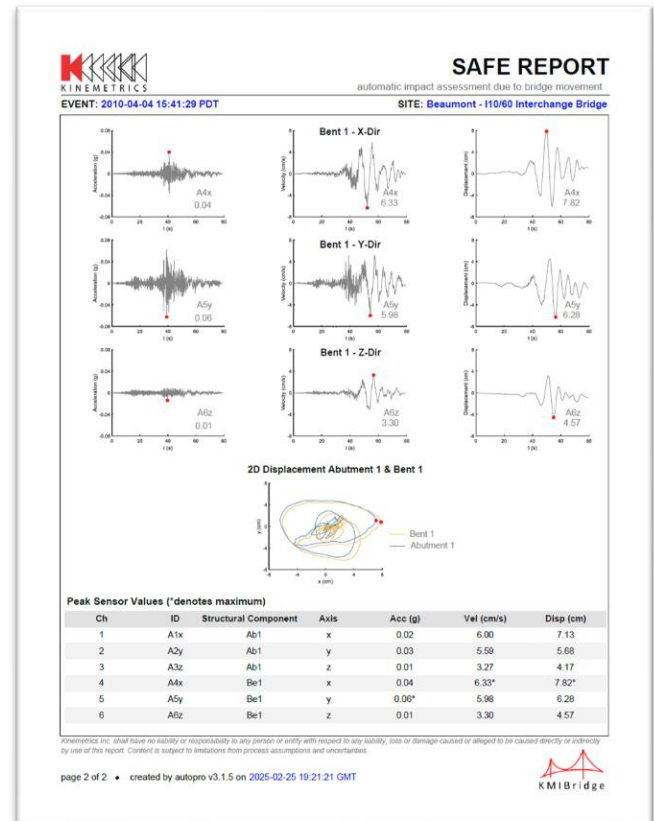


Figure 10. Automatic Rapid Assessment System 2/2.

What sets the proposed automatic rapid post-earthquake evaluation system apart from existing automated solutions is its ability to collect and process real-time acceleration, velocity, and displacement data immediately following a seismic event. Unlike conventional systems that primarily rely on periodic assessments or post-processed sensor data, this approach enables near-instantaneous evaluation of structural performance during and after an earthquake. By integrating high-frequency data acquisition with advanced algorithms, the system provides a more accurate and timely understanding of potential damage, allowing for faster decision-making and more effective emergency response.

Importantly, this system is designed to support, not replace, structural engineers. By delivering actionable data in real time, it empowers engineers to make informed decisions more quickly and confidently after events. The tool enhances professional judgment with rapid, data-driven insights, improving both the efficiency and reliability of post-earthquake assessments while maintaining the essential role of expert evaluation.

## 7 CONCLUSIONS

The proposed advanced system for rapid post-earthquake bridge safety assessments integrates sensor technology, automated data processing, and real-time reporting to enhance disaster response capabilities. By replacing traditional, labor-intensive inspections with automated evaluations, the system ensures timely, cost-effective, and reliable infrastructure

assessments. The case study illustrates its effectiveness in different bridge settings, reinforcing its applicability in both urban and rural environments. Future advancements in SHM technology, including artificial intelligence integration, could further improve the accuracy and predictive capabilities of such systems, ultimately leading to safer and more resilient bridge infrastructure.

By adopting this technology-driven approach, transportation agencies and emergency management teams can significantly improve the efficiency and accuracy of post-earthquake bridge assessments. The implementation of modern sensor-based monitoring systems enhances safety by enabling early detection of structural vulnerabilities, reducing the reliance on subjective visual inspections, and expediting repair and maintenance actions. Ultimately, the integration of these advancements contributes to more resilient transportation infrastructure and ensures the continued functionality of bridges in the aftermath of seismic events.

## ACKNOWLEDGMENTS

The authors of this paper thank the Center for Engineering Strong-Motion Data (CESMD) for the data collected on the field to inform this proposed method. The conclusions of this research solely represent those of the authors.

## REFERENCES

- [1] C. Karakostas, G. Quaranta, E. Chatzi, A. C. Zülfiqar, O. Çetindemir, G. De Roeck, M. Döhler, M. P. Limongelli, G. Lombaert, N. M. Apaydın, V. Pakrashi, C. Papadimitriou, and A. Yeşilyurt. Seismic assessment of bridges through structural health monitoring: a state-of-the-art review. *Bull Earthquake Eng*, 22(3), 1309–1357, 2024.
- [2] P. F. Giordano, C. Iacovino, S. Quqa, and M. P. Limongelli. The value of seismic structural health monitoring for post-earthquake building evacuation. *Bull Earthquake Eng*, 20, 4367–4393, 2022.
- [3] B. López-Castro, A. G. Haro-Baez, D. Arcos-Aviles, M. Barreno-Riera, and B. Landázuri-Avilés. A Systematic Review of Structural Health Monitoring Systems to Strengthen Post-Earthquake Assessment Procedures. *Sensors*, 22(23), 9206, 2022.
- [4] Z. Deng, M. Huang, N. Wan, and J. Zhang. The Current Development of Structural Health Monitoring for Bridges: A Review. *Buildings*, 13(6), 1360, 2023.
- [5] P. Rizzo, and A. Enshaieian. Challenges in Bridge Health Monitoring: A Review. *Sensors*. 21(13), 4336, 2021.
- [6] H. Wenzel. *Health Monitoring of Bridges*. Chichester: John Wiley & Sons. 2009.
- [7] J. O'Connor, and S. Alampalli. Post-earthquake bridge inspection guidelines for New York state. *Bridg. Maintenance, Safety, Manag. Life-Cycle Optim. – Proc. 5th Int. Conf. Bridg. Maintenance, Saf. Manag.* 160–160, 2010.
- [8] R. T. Ranf, M. O. Eberhard, and S. Malone. Post-earthquake prioritization of bridge inspections. *Earthquake Spectra*. 23(1), 131–146, 2007.

## Bridge superstructure vibrational analysis as means to detect scour in a medium span bridge

Junhui Zhao<sup>1</sup>, Kareem Helmy<sup>2</sup>, Boris Telehanic<sup>1</sup>, Evangeline Murison<sup>3</sup>, Aftab Mufti<sup>1</sup>, and Douglas Thomson<sup>1</sup>

<sup>1</sup>Department of Electrical and Computer Engineering, University of Manitoba, Winnipeg, MB, R3T 5V6, Canada

**ABSTRACT:** Scour around bridge piers is a leading cause of failure but detecting it reliably and cost-effectively remains a challenge. Vibration analysis offers a potential solution by monitoring changes in vibrational mode frequencies, as scour reduces a bridge's natural frequencies. This study measures traffic-induced vibrations on both bridge piers and decks, enabling continuous monitoring without disrupting traffic. An important consideration in using vehicle-induced vibrations is that each vehicle tends to preferentially excite certain vibrational modes, influenced by factors such as vehicle speed and span length. Therefore, obtaining a representative vibrational spectrum requires the passage of many vehicles. In this work, we found that the passage of 10 to 50 vehicles is necessary to reduce errors to the level required for robust vibrational analysis. Continuous monitoring of vibrational frequencies also enables compensation for seasonal variations in environmental factors such as temperature. In this study, a medium-span bridge was monitored over approximately 10 months. By correlating frequency data with temperature, we can account for environmental influences. After compensating for temperature, frequency changes exceeding  $\pm 1.7\%$  can be detected and may indicate the presence of scour. The measured frequencies closely matched predictions from finite element model calculations.

**KEY WORDS:** SHMII-13; field measurement, superstructure, vibrational analysis

### 1 GENERAL GUIDELINES

Scour can cause collapse of bridges by eroding the pier foundation systems and lead to large economic losses due to loss of infrastructure and transportation routes [1], [2]. There has been progress in solutions for mitigating scour [3], [4], but it remains critical that there is early detection so that rehabilitation and maintenance measures can be applied before scour reaches the point causing bridge failure [5], [6].

Scour is a process that excavates and removes the soil and sediments by the flowing water, particularly by the flooding. Natural scour is a degradation process of the level and conditions of waterbed due to the flow along the waterway; contraction scour is associated with the varying velocity and shear stresses of the flowing streams due to the bridge foundation structures; the formation of horseshoe vortex around pier structures is a localized scour process. These scour processes can reduce the rigidity of the surrounding earth foundation thus degrade the stiffness and the stability of the pier structures. In addition to the direct visual inspection of scour, many detection methods and instruments have been extensively explored to detect scour depth around piers and abutments, such as float-out devices and tethered buried switches, time-domain reflectometry (TDR) and ground-penetrating radar (GPR) devices, gravity-based magnetic and positioning sensors, electromagnetic and acoustic wave-based pulse-echo devices, fiber-Bragg grating sensors, and electrical conductivity-based devices [5]. However, the installation and operation of these instruments are practically very challenging in the harsh underwater environments, and measurement efficiency is restricted by the complex interfaces between the waterbed and the flowing streams. Due to the large size of

structures, some local scour holes are not easily detected with these measuring approaches. Different from these methods that measures the scour depth by installing the instruments under water, the dynamic response of bridge structures to scour progression has been investigated as a means of detecting scour [7], [8], [9], [10], [11]. The principle of detection is that structural vibrations depend on the mechanical properties and boundary conditions existing around bridge piers. The pier length, stiffness and its foundation rigidity are affected by scour depth and scour holes around a pier and its abutment as well as the supporting earth. The variation in vibration modes of a pier will hence signal the structural problems related to scour progression. The dynamic vibrations can be measured using sensors such as accelerometers. The measured acceleration signals can be processed and analyzed using spectral analysis tools. Observing frequency change provides an avenue to detecting the scour occurrence. An advantage of this method is that the instrument installation on a bridge above water is much cost-effective in practice and measurement operation is more efficient comparing to those measuring systems underwater. It could potentially become a less expensive and efficient tool for diagnosing scour related structural damage of a bridge.

There are many examples of laboratory and numerical simulations of scour comparing vibrational frequencies with depth of scour around bridge piers [11]. The vibrational frequencies are predicted to decrease as scour progresses. The field observation of changes in vibrational frequencies due to scour is very challenging. However, there are some examples of field observations that are relevant to this study. In one example, during the repair of scour damage, an additional 3 m was excavated from around the pier. The ambient bridge



vibration before and after the excavation was measured and a drop in vibrational frequencies near 1.5 Hz of 11 % was observed [12]. In another example, the frequencies of lower order vibrational modes were observed to drop by ~20% over a 3-year period due to scour. Kong and Cai also predicted a ~20% decrease in lower order vibrational mode frequencies before and after scour [12]. Tubaldi et al. also found in a 3 m x 3 m field tested scale model of spread footing a change of ~ 20% with scour under the footing [13].

In this paper, we examine the extraction of vibrational mode frequencies on a medium span bridge over the full seasonal temperature swings (Figure 1). The vibrational excitation was traffic induced, and this study also examines the improved accuracy of vibrational frequency determination by averaging over many vehicle passages. Finally the minimum frequency change that can be reliably determined after vehicle averaging and correction for environmental changes is determined.

## 2 METHODS

### 2.1 Accelerometer measurements

The vibrational measurements of pier structures were performed using a data acquisition device consisting of an accelerometer (ADXL355) and a microcontroller (Arduino Giga). The 3-axis accelerometer has low noise density, low offset drift, low power consumption, and selectable measurement ranges. It can be used for cost-effectively low-level vibration measurement applications such as structural health monitoring (SHM). The microcontroller was programmed to sample the vibrational signals sensed by the accelerometer in x, y, and z directions, and the collected acceleration signal was processed and stored in a USB drive. About once a week, the logged data was retrieved, and frequency domain analysis with Fast Fourier Transform (FFT) was performed offline using Python programming.

Our preliminary tests were conducted by placing the data acquisition device on three pier caps of the selected bridge as shown in Figure 2. The pier vibrations were excited by the passing vehicles. The sampling rate for the vibration signal is chosen as 100 Hz which is sufficient to capture the vibrational frequencies, as expected to be less than 25 Hz. The peak-to-peak acceleration of the pier due to traffic is typically about 20 mg.

The acceleration was sampled in blocks of 8192 readings and an FFT was used to produce a signal spectrum. This block length provides the necessary frequency resolution of  $200\text{Hz}/8192 = 0.024\text{ Hz}$ . Each block was stored as a data file. Individual spectrums were not consistent due to the variety of excited vibrations in different time slots. To improve the accuracy of the vibrational frequencies, more datasets are required for doing FFT analysis to obtain average frequency spectrums. The measurements were first carried out on three pier caps, pier 2, pier 3 and pier 4 as in Figure 1. Then the measurements were carried out on the bridge deck directly over pier 4.

Since the vibrations of the pier were easily observed by putting the sensor on the pier caps, it was also decided to investigate if the pier vibrations could be observed from the bridge vibrations by putting the sensor on the bridge deck. Therefore, in addition to the measurements on the pier caps, vibration data were also acquired using the accelerometer

device installed on the bridge barrier wall directly above pier 4. The measurements were carried out by collecting about 1014 data files each day, typically, about 507 files the during the period of daytime (8 am - 8 pm) were chosen for doing the FFT analysis considering the traffic is considerably reduced during night.

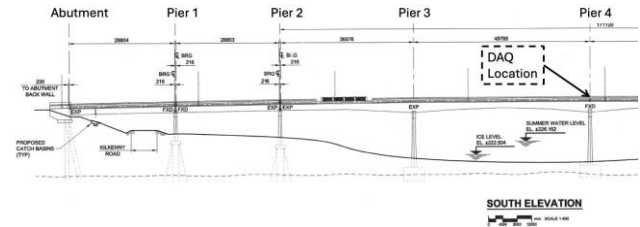


Figure 1. Schematic diagram of the bridge under observation



Figure 2. A) The data acquisition device on a bridge pier cap. B) View from the bridge deck of the DAQ system sitting on the pier cap.

When dealing with the bridge vibration, the peak frequencies of the averaged FFT spectrum were determined using a peak-finding algorithm in Python library SciPy. The found peak frequencies represent the vibration modes of the bridge. To determine the number of data files needed to adequately locate the individual peak frequency, the data processing for obtaining averaged frequency spectrum was conducted by randomly selecting subpopulations with the bootstrap approach. From the 507 data files, 10 files, 25 files, 50 files, 100 files, 250 files and 500 files were chosen for doing spectrum analysis, respectively. The simple linear average of the spectrums was calculated for each subpopulation of files, for instance, using  $N = 400$  subpopulations of 10 files to find peak frequency distributions for each observed vibrational mode. The histogram of the peak-frequency distribution of each mode was plotted against the subpopulation of data files.

### 2.2 FEM modelling

Figure 3 shows a bridge model for finite element analysis (FEA) using the SAP2000 software, it was used to simulate the dynamic behaviors of the bridge vibrations and to determine the expected vibrational modes of the bridge in addition to the effect of the scour on the vibration properties of the bridge. The bridge's steel girders and concrete slab were modeled using thin shell elements. The girders and the slab were connected

using stiff link elements. The bracing system, brackets and edge beams supporting the sidewalk were modeled using frame elements. The bridge abutments and foundations were modeled using thick shell elements. The bridge bearings between the abutments and the girders were modeled special link elements to allow for rotation only or rotation and relative displacement depending on the type of bearing. Rotational and vertical springs were added to the bottom of piers 3, 4 and 5 to simulate the effect of the soil at the foundation level. Horizontal area springs were also added to footing and pier shafts to simulate the effect of the soil on the sides of the piers. A maximum element size of 600 mm was chosen after comparing several mesh sizes for a portion of the bridge consisting of a girder and part of the concrete slab. In total the model consisted of 88643 nodes, 2268 frame elements, 7764 thick shell elements, 75529 thin shell elements and 12704 link elements.

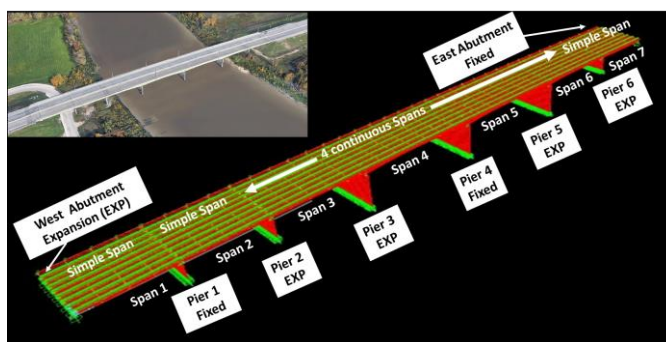


Figure 3. The bridge simulation model for dynamic analysis

### 3 RESULTS AND DISCUSSION

#### 3.1 Traffic induced vibration of piers

The accelerations of the piers were measured as the vehicles passed. A typical example of vibrations is shown in Fig. 4A, which is for the sensor mounted on the cap of pier 4. In this example, it appeared several vehicles passed during the measurement. The passing vehicles excited vibrations, and the vibrations were then damped and decayed. The vibration amplitudes cover a span from 5 mg for smaller vehicles to 40 mg for larger vehicles. Each data file (a block signal) contains the sampled acceleration readings of 8192 at the rate of 100 samples per second. The average FFT spectrum of many data files was calculated to achieve higher and smoother signal amplitudes over background signals. A typical example is shown in Fig. 4B, the data was collected from pier 4 cap. There are obvious vibrational peaks at approximately 2.28 Hz, 9.0 Hz and 12.9 Hz. The obtained frequency spectrums show that only vibrations along the direction of the traffic flow were observed. The vibrations in the other two directions were not observable above the noise level from their FFT spectrums. This is physically reasonable when the geometrical shape and mechanical properties of the piers are considered, the pier structure in a thick-shell-shape is very long and sturdy in the direction perpendicular to the traffic flow and in the up-down direction, the vibrations in these two directions are barely excited and observable, only flexural vibrations in the traffic flow direction are easily excited and observable from the frequency spectrums.

#### 3.2 Traffic induced vibration of the bridge superstructure

Accessing the pier caps is difficult. As part of this study, we also explored measuring the vibrational frequencies on the bridge deck, which is much easier to access. In the case of this bridge, the deck can be accessed via a walkway. Our hypothesis is that the pier vibration will be coupled to the deck and therefore the pier vibration can be accessed via the superstructure. In this case, the accelerometer was attached to the impact barrier. The details are given in Fig. 5A and 5B. The location is also noted in Fig. 1. In this case, a larger capacity battery could be used and vibrational signals could be gathered for approximately 24-48 hours. These signals were gathered periodically over 10 months. The vibrations of the bridge deck were observed in all three directions since the bridge deck is free to vibrate. A typical example is shown in Fig. 6A, where the acceleration signals in the direction of traffic flow were processed using FFT to produce spectrums. A simple algorithm was used to find an estimate of the frequency peak positions. These peaks are labelled with a black dot in Fig. 6A.

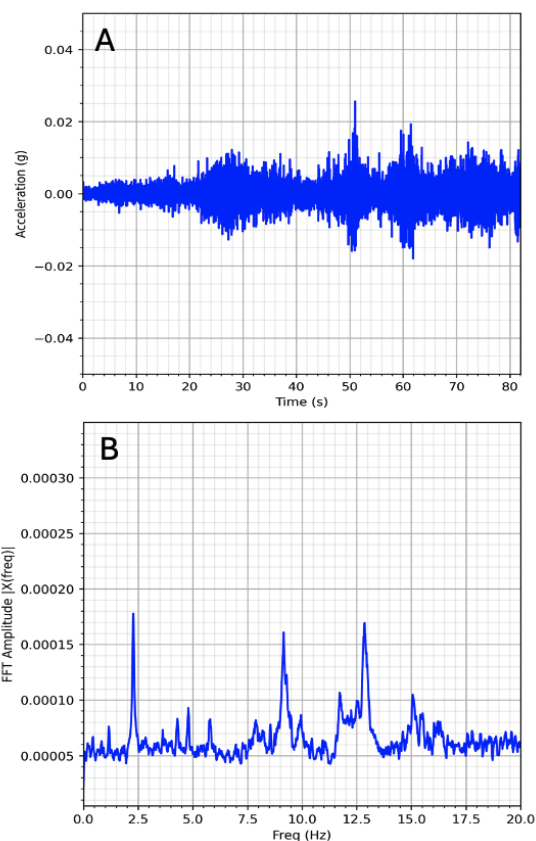


Figure 4. (A) Vibration measured on the cap of pier 4. (B) FFT spectrum of sampled acceleration from (A)

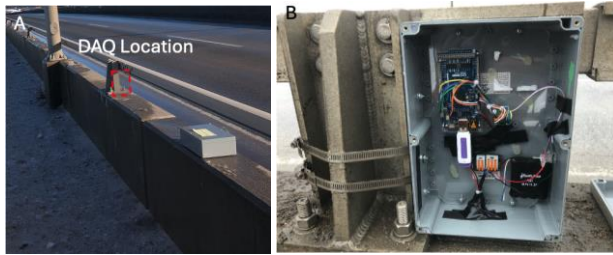


Figure 5. Location and mounting of DAQ apparatus on bridge

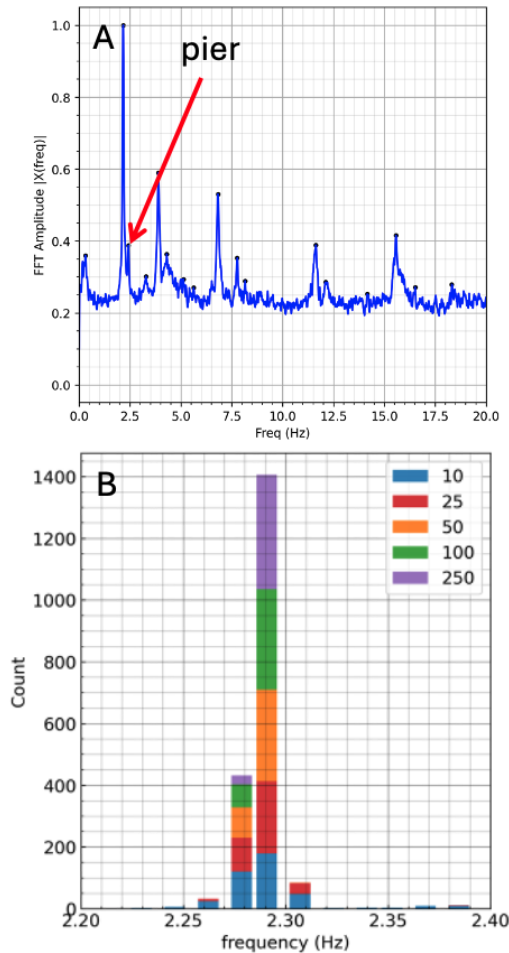


Figure 6. Vibrations measured on the bridge deck. (A) FFT spectrum. (B) Stacked frequency histogram

Table 1. Frequency estimates versus sample size

Sample size	Mean frequency	Median frequency	SD frequency
10	2.286	2.289	0.026
25	2.286	2.289	0.013
50	2.285	2.289	0.007
100	2.286	2.289	0.004

Single vibrational spectrum cannot produce good estimates of the vibrational frequencies with uncertainties that are small enough for this application. Therefore, multiple frequency

spectrums are averaged to produce better results. We have investigated the uncertainty of the frequency estimates versus the number of the frequency spectrums being averaged. The outcome is presented as a stacked histogram in Figure 6B. The number of data files for frequency averaging used 10, 25, 50, 100 and 250. With 10 averages, the peak frequency estimates fall into several bins. As the number of averages increases, the estimates fall into fewer bins. As shown in Table 1, for each block signal consisting of 8192 acceleration readings at a slightly higher sampling rate of 125 Hz, frequency estimates were done using different numbers of the block signal (sample sizes) by repeating FFT calculation of 400 trials, and the stacked frequency histogram was obtained by calculating the mean, median and standard deviation of a certain number of burst signals. For the averages of 10 spectrums, the standard deviation was 0.026 Hz. This would give a 95th percentile confidence limit of  $\pm 0.052$  Hz. As we will show later, this is greater than the uncertainty remaining after temperature compensation is applied, which is  $\pm 0.040$  Hz. Using 25 averages, the standard deviation was 0.013 Hz. This would give a 95th percentile confidence limit of  $\pm 0.026$  Hz. This is less than the uncertainty remaining after temperature compensation is applied and would be suitable for the detection of scour. Finally, the average number of 50, 100 and 250 provides better estimates well below the variability remaining after temperature compensation is applied.

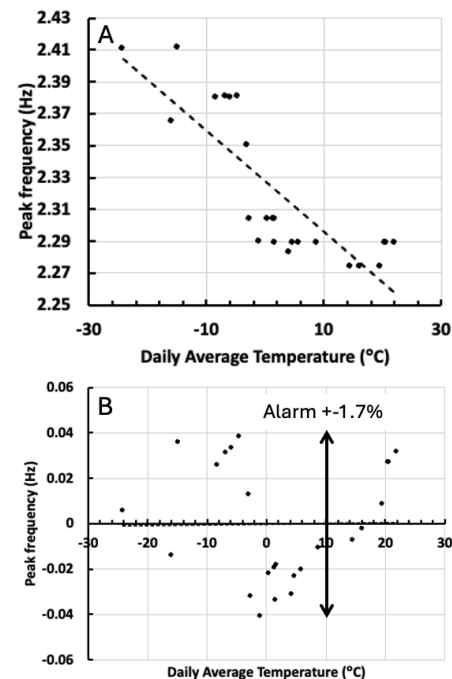


Figure 7. (A) vibrational frequency versus temperature. (B) residuals versus temperature for compensation.

### 3.3 Temperature induced changes to vibration and temperature compensation

Temperature is one of the main sources of environmentally induced vibrational change [14]. The mechanical properties of materials can change with temperature as well as the boundary conditions. Bearing restraint can also be influenced by



temperature [15]. The extracted peak frequencies were plotted against temperature to determine if the effects of temperature could be compensated for. The temperature used in this case was the average daily ambient temperature. This was used because the heat capacity of the bridge superstructure is relatively large and the change of bridge thermal properties with daily temperature is considered insignificant.

The vibration frequencies were extracted from the sampled data over a 10-month period, covering the full seasonal temperature swings expected for this structure. Each data point in Fig. 7 represents the vibrational average over a 24-hour period and was derived from an average of greater than 250 spectrums. According to the results of the uncertainty estimates as stated in section 3.2, here the uncertainty of each measurement point is expected to be less than 0.01 Hz.

Fig. 7A is the plot of vibrational frequency versus temperature. There is an obvious dependence of the vibrational frequency on temperature. The dependence was modelled using simple linear dependence. The linear dependence model was then used to compensate the measured frequency data for temperature.

The residuals versus temperature are plotted in Fig. 7B. Over the entire temperature range and period, the residuals fall within  $\pm 0.04$  Hz. This result is similar to that observed on other bridges [16]. Therefore, if a vibrational frequency was to fall outside this range, it would indicate that a structural change had occurred. The significant frequency change beyond the temperature compensation range could be due to several factors, but one possible factor would be the change in boundary conditions due to scour. Because a field experiment using excavation to simulate scour on this structure is not feasible, numerical calculations using a FEA model will be helpful for studying the vibrational modes of the bridge and scour effect.

### 3.4 Comparison of FEM calculations to measured response

A finite element model was developed as outlined in section 2.2. This model was used to simulate the dynamical vibration behavior of the bridge superstructure. Table 2 presents a few vibration modes obtained from the FEM model, where the corresponding frequencies from the measurements are also listed for comparison. The simulation agrees with the measurement very well for those modes. Modes #2 and #3 are not presented and could not be compared to the measured frequencies because they correspond to the bending of piers 5 and 3 respectively where the connection with the superstructure allows for relative displacement and therefore the vibration transferred to the superstructure is very weak. Additionally, no direct vibration was measured on those piers.

There are many vibration modes derived from simulation, such as, the rocking mode, the flexural and twisted modes of the bridge deck together with the piers, here the modes listed in Table 2 are of most interest to this study since these vibration modes were also observed from the field measurements. Some simulated lower vibrational modes and higher modes were either insignificant or unobservable in the field measurements, and they were either not excited or quickly damped out. Table 2 shows that the match between the calculated and observed frequencies is within 8%. In addition, the frequency of 2.289 Hz is the same as the measured for the sensor on pier 4 cap in Figure 4B, this vibration mode can be considered the coupling

between the pier 4 and the bridge deck. It provides a convenient way to monitor the pier vibration without accessing the pier.

The FEM model was also used to estimate the effect of the scour on the natural frequencies of the bridge. The scour was simulated by removing the top lateral springs representing the effect of the soil at the top of the pier. Scour values of 1 and 2 meters were simulated for piers 3, 4, and 5. Table 3 shows a comparison of three natural frequencies representing the bending of the piers with and without scour. It is apparent that the scour has a significant effect on the natural frequencies and therefore could be used to detect scour. The pier natural frequencies are not easily observed in the vibrational spectra. This may be due to the traffic induced vibration not preferentially exciting the pier natural frequencies. The more easily observed vibrational modes appear to be associated with the bridge superstructure. However, since the pier-superstructure system is a coupled mechanical system scour will affect both the pier and superstructure natural frequencies.

Table 2. Comparing the simulated and measured frequencies

Mode	#1	#4	#5	#6
Measured	0.26	2.06	2.29	2.81
FEM calculated	0.29	1.98	2.12	2.75

Table 3. Scour effect on first modes of three piers

Mode	Natural frequency Hz		
	Without scour	1 m scour	2 m scour
1 bending of Pier 4	0.292	0.282 (-3.5%)	0.277 (-5.17%)
2 bending of Pier 5	0.431	0.264 (-38.8%)	0.146 (-66.2%)
3 bending of Pier 3	1.384	1.278 (-7.67%)	1.204 (-13.04%)

### 3.5 Impact of truck mass on estimated vibrational frequencies.

One issue with the use of traffic induced vibration is that the presence of the vehicle will perturb the vibrational frequencies. When the truck passes over a span, the mass of the truck will perturb the vibrational frequency [17]. After the truck passes, the vibration will continue. This can be thought of as a driven vibration time and a free vibration time. In our case, we are using the complete time sequence and the signal would be a mixture of driven and free vibrations. If the driven vibrational frequency and the free vibrational frequency are significantly different, then one might expect the vibrational peak to be broadened out as it would be a mixture of driven and free vibrations. In this case, the peaks are well defined, and any broadening does not appear to be significant. In future work, the time variation of vibrational frequency as vehicles pass over will be examined more closely.

## 4 CONCLUSIONS

For this medium-span bridge, vibration measurements of the piers and the bridge deck were performed, and the corresponding frequency spectra were derived. The dynamic behavior of the bridge was also simulated using Finite Element Analysis (FEA). The major vibration modes identified from field measurements were found to match those obtained through FEA simulation. A common vibration mode at approximately 2.289 Hz was observed in both Pier 4 and the bridge deck above it, attributed to dynamic coupling between the structural components. With compensation for temperature-

induced frequency changes, frequency shifts of less than 1.7% can be reliably detected. FEA simulations showed that scour of 1–2 meters around the base of the pier resulted in natural frequency shifts greater than 10%. In future work, finite element model predictions of traffic-induced vibrations will be compared with the 1.7% detection threshold. This combined approach of in-situ measurements and numerical simulations is expected to provide a viable alternative for monitoring bridge scour.

## REFERENCES

- [1] B. W. Melville and S. E. Coleman, *Bridge scour*. Highlands Ranch, Colo: Water Resources Publications, 2000.
- [2] B. Maddison, “Scour failure of bridges,” *Proceedings of the Institution of Civil Engineers - Forensic Engineering*, vol. 165, no. 1, pp. 39–52, Feb. 2012, doi: 10.1680/feng.2012.165.1.39.
- [3] A. Pizarro, S. Manfreda, and E. Tubaldi, “The Science behind Scour at Bridge Foundations: A Review,” *Water*, vol. 12, no. 2, p. 374, Jan. 2020, doi: 10.3390/w12020374.
- [4] B. W. Melville and A. J. Sutherland, “Design Method for Local Scour at Bridge Piers,” *J. Hydraul. Eng.*, vol. 114, no. 10, pp. 1210–1226, Oct. 1988, doi: 10.1061/(ASCE)0733-9429(1988)114:10(1210).
- [5] L. J. Prendergast and K. Gavin, “A review of bridge scour monitoring techniques,” *Journal of Rock Mechanics and Geotechnical Engineering*, vol. 6, no. 2, pp. 138–149, Apr. 2014, doi: 10.1016/j.jrmge.2014.01.007.
- [6] G. Crotti and A. Cigada, “Scour at river bridge piers: real-time vulnerability assessment through the continuous monitoring of a bridge over the river Po, Italy,” *J Civil Struct Health Monit*, vol. 9, no. 4, pp. 513–528, Sep. 2019, doi: 10.1007/s13349-019-00348-5.
- [7] N. Boujia, F. Schmidt, C. Chevalier, D. Siegert, and D. Pham Van Bang, “Effect of Scour on the Natural Frequency Responses of Bridge Piers: Development of a Scour Depth Sensor,” *Infrastructures*, vol. 4, no. 2, p. 21, May 2019, doi: 10.3390/infrastructures4020021.
- [8] T. Bao, Z. L. Liu, and K. Bird, “Influence of soil characteristics on natural frequency-based bridge scour detection,” *Journal of Sound and Vibration*, vol. 446, pp. 195–210, Apr. 2019, doi: 10.1016/j.jsv.2019.01.040.
- [9] C.-C. Chen, W.-H. Wu, F. Shih, and S.-W. Wang, “Scour evaluation for foundation of a cable-stayed bridge based on ambient vibration measurements of superstructure,” *NDT & E International*, vol. 66, pp. 16–27, Sep. 2014, doi: 10.1016/j.ndteint.2014.04.005.
- [10] A. Elsaid and R. Seracino, “Rapid assessment of foundation scour using the dynamic features of bridge superstructure,” *Construction and Building Materials*, vol. 50, pp. 42–49, Jan. 2014, doi: 10.1016/j.conbuildmat.2013.08.079.
- [11] S. Foti and D. Sabia, “Influence of Foundation Scour on the Dynamic Response of an Existing Bridge,” *J. Bridge Eng.*, vol. 16, no. 2, pp. 295–304, Mar. 2011, doi: 10.1061/(ASCE)BE.1943-5592.0000146.
- [12] Y. Y. Ko, W. F. Lee, W. K. Chang, H. T. Mei, and C. H. Chen, “Scour Evaluation of Bridge Foundations Using Vibration Measurement,” in *Scour and Erosion*, San Francisco, California, United States: American Society of Civil Engineers, Oct. 2010, pp. 884–893. doi: 10.1061/41147(392)88.
- [13] E. Tubaldi *et al.*, “Field tests and numerical analysis of the effects of scour on a full-scale soil–foundation–structural system,” *J Civil Struct Health Monit*, vol. 13, no. 8, pp. 1461–1481, Dec. 2023, doi: 10.1007/s13349-022-00608-x.
- [14] B. Peeters and G. D. Roeck, “One-year monitoring of the Z24-Bridge: environmental effects versus damage events,” 2001.
- [15] B. Algohi, D. Svecova, A. Mufti, B. Bakht, and D. Thomson, “Long-term study on the effect of temperature on composite action and variation of neutral axis in slab on girder bridges,” *Structural Health Monitoring*, vol. 19, no. 5, pp. 1577–1589, 2020, doi: 10.1177/1475921719890588.
- [16] F. Magalhães, A. Cunha, and E. Caetano, “Vibration based structural health monitoring of an arch bridge: From automated OMA to damage detection,” *Mechanical Systems and Signal Processing*, vol. 28, pp. 212–228, Apr. 2012, doi: 10.1016/j.ymssp.2011.06.011.
- [17] D. Cantero, D. Hester, and J. Brownjohn, “Evolution of bridge frequencies and modes of vibration during truck passage,” *Engineering Structures*, vol. 152, pp. 452–464, Dec. 2017, doi: 10.1016/j.engstruct.2017.09.039.

## 2D sonar techniques for monitoring the canal bed morphology of entrances to navigation locks

Mohsen Bastani<sup>1</sup>, ORCID : 0009-0006-9977-7419 , Rolands Kromanis<sup>2</sup>, ORCID: 0000-0003-3477-1666

<sup>1</sup>High-Tech Business and Entrepreneurship Department, Industrial Engineering and Business Information Systems, Faculty of Behavioural, Management and Social Sciences, University of Twente, Drienerlolaan 5, 7522 NB Enschede, the Netherlands

<sup>2</sup>The Department of Civil Engineering and Management, Faculty of Engineering Technologies, University of Twente, Drienerlolaan 5, 7522 NB Enschede, the Netherlands  
emails: m.bastani@utwente.nl, r.kromanis@utwente.nl

**ABSTRACT:** Navigation locks are essential components of inland waterways. They enabling vessels to traverse sections with differing water levels. These structures are increasingly vulnerable to damages caused by (1) scour i.e., erosion of sediment due to natural water flow and ship-induced currents, and (2) sediment or debris obstructing lock gates. Scour-induced damage threatens the structural integrity of locks, leading to costly maintenance, prolonged closures, and economic and environmental consequences. Traditional monitoring methods, including visual inspections and fixed instrumentation, are often hampered by water turbidity, high costs, and susceptibility to debris damage. Sonar technologies provide a non-invasive, cost-effective alternative for detailed underwater imaging, even in challenging environments. This paper explores the application of 2D sonar imaging for monitoring navigation lock approaches, with a focus on bed morphology and scour progression. Using the Prinses Beatrix Lock in the Netherlands as a case study, the paper demonstrates the effectiveness of 2D sonar systems in (i) detecting morphological changes such as scour and sediment transport from bed protection layers and (ii) estimating ship drafts. The findings underscore the importance of integrating sonar-based structural health monitoring systems to extend the lifespan of navigation locks, enhance safety, and optimize maintenance strategies for aging waterway infrastructure.

**KEY WORDS:** sonar technologies; navigation locks; morphological changes; ship draft.

### 1 INTRODUCTION

Inland waterway transport is significantly more efficient than land-based (i.e., road and rail) transport, as waterways allow for the movement of large cargo volumes with low energy consumption and reduced environmental impact [1]. Navigation locks play a critical role in facilitating inland waterway transport, enabling vessels to traverse sections of canals or rivers with varying water levels. These structures are subjected to various environmental and operational stressors, which can lead to structural deterioration over time. One of the primary concerns in the maintenance of navigation locks is scouring, which is the removal of sediment caused by hydrodynamic forces [2]. Scouring can lead to morphological changes in the bed protection layer, potentially compromising the stability of the lock foundation. The interaction between ship-induced currents and the lock bed remains a significant challenge, particularly for older lock chambers that were not originally designed for large and high-powered vessels [3,4]. The issue is exacerbated by increasing global shipping activities, where vessel sizes and engine power have also grown, leading to intensified hydrodynamic forces in lock approaches [5]. The propeller wash from these vessels accelerates bed degradation, increasing maintenance demands and potential structural risks. The existing bed protection layers, designed decades ago, may not effectively withstand these forces induced by modern vessels.

Traditional monitoring techniques for scouring in navigation locks rely heavily on periodic visual inspections, divers, or stationary sensors. These methods are often costly, labour-intensive, and ineffective in real-time damage detection, particularly in turbid waters where visibility is poor [6]. Some advanced techniques, such as 3D sonar imaging, provide high-

resolution data but are prohibitively expensive for widespread implementation. The lack of an affordable and continuous monitoring system leaves lock operators and maintenance teams with limited options for proactive maintenance strategies [7]. The necessity for continuous monitoring of scouring in locks has been well established in existing literature [8], particularly in cases where the structural integrity of the lock foundation is at risk due to progressive erosion.

The issue of sediment transportation in lock complexes, originally designed for smaller vessels, becomes more pronounced with the use of large modern cargo ships. These vessels have a deeper draft, which brings their propellers close to the canal bed. As the vessel moves through the lock, the propeller's interaction with the sediment can cause stones or debris to be displaced and rolled toward the lock chamber. This can result in blockages that obstruct the closure of the lock gates. The presence of such obstructions can cause damage to critical components of the lock system, such as the de-icing pipes [5], which are essential for preventing freezing in cold climates. To prevent such incidents, a continuous monitoring system is essential for detecting these "rolling stones" at an early stage. Such monitoring system is also anticipated to provide insights into how the depth of the ship's draft, which can be correlated with sediment displacement.

To address these issues, an affordable and scalable monitoring system employing 2D sonar imaging has been designed to continuously assess the approach to a lock complex. This novel approach offers scour monitoring, detection of *rolling stones* and estimation of ship's draft in navigation locks. The monitoring system incorporates an image processing algorithm to detect bed morphology changes and provides assessment of vessel-induced impacts on the lock bed.



By enabling early detection of bed morphology changes, the system allows for timely interventions and mitigation measures to prevent further degradation of the lock complex. This approach aligns with the broader objectives of structural health monitoring of navigation locks, which aims to extend infrastructure longevity while reducing maintenance costs, thereby enhancing maintenance strategies. The findings of this study can be applied to other navigation locks facing similar challenges, offering a scalable solution for sustainable lock maintenance and improving the overall reliability of inland waterway infrastructure.

## 2 BACKGROUND

This section explains causes of scour, particularly, in lock complexes, scour monitoring techniques and sonar technologies.

### 2.1 Scouring

Scour can be categorized into three forms: local scour, contraction scour, and general scour. General scour typically happens as a result of alterations in the natural flow of water, causing the river/canal bed to experience both aggregation and degradation. Contraction scour, on the other hand, is a result of an increase in the flow velocity in conjunction with a reduced cross-sectional area of the waterway. The consequence is the removal of sediment from the waterway's bottom and side [9]. Local scour, the third form, takes place due to turbulent vortices generated by the flow of a current impacting the bed or foundation of the waterway, leading to erosion of surrounding sediment [10].

Local scour is a gradual process that evolves through multiple stages. The initial stage is characterized by the occurrence of erosive effects and damage due to extremely high velocity. Subsequently, scour transitions to the development stage, where the rate of erosion slows down compared to the initial stage. Finally, it reaches the equilibrium stage, where the depth of scour remains stable, and any changes in its depth become imperceptible [11]. The depth of the scour hole in the equilibrium stage is compared with the critical depth of the lock slab or foundation. Local scour takes place in two distinct forms: clear-water and live-bed flow conditions. Differentiating between the two can be determined by observing whether sediment is eroded and replenished (live-bed) or eroded without replenishment (clear-water flow) [10]. The latter condition is often investigated in scour studies.

Local scour is generally linked to turbulent vortices [12–15]. Unlike in cases of bridges, where this turbulence arises from a change in the cross-sectional area of the watercourse due to bridge piers, in locks, the turbulence is caused by the change in the bed roughness introduced by the weir or lock floor. Therefore, structures like locks and weirs, constructed on a soft bed in watercourses, tend to induce local scour, especially in the surrounding bed. To counteract this, a bed protection layer is applied to stabilize the adjacent loose bed.

The intensity of the turbulent vortices generated by this change is directly proportional to the velocity of water flow, higher velocities resulting in greater intensity. In the navigation locks, two factors influence the water flow velocity. Firstly, during the emptying of the lock chamber through small openings, the velocity increases. The intensity of this effect

depends on the water level difference between the two sides of the lock. The second factor affecting velocity is the passage of large vessels through the navigation locks. The propeller wash from these large vessels significantly increases water flow velocity, expediting morphodynamical changes in the surrounding bed through scouring. Ships, especially during the initial movement or acceleration, exert the most stress on the bed. Figure 1 (top) illustrates a schematic of a scour hole due to the currents from the emptying of the chamber, and Figure 1 (b) depicts a schematic of a scour hole due to the currents from the propeller wash of entering ships.

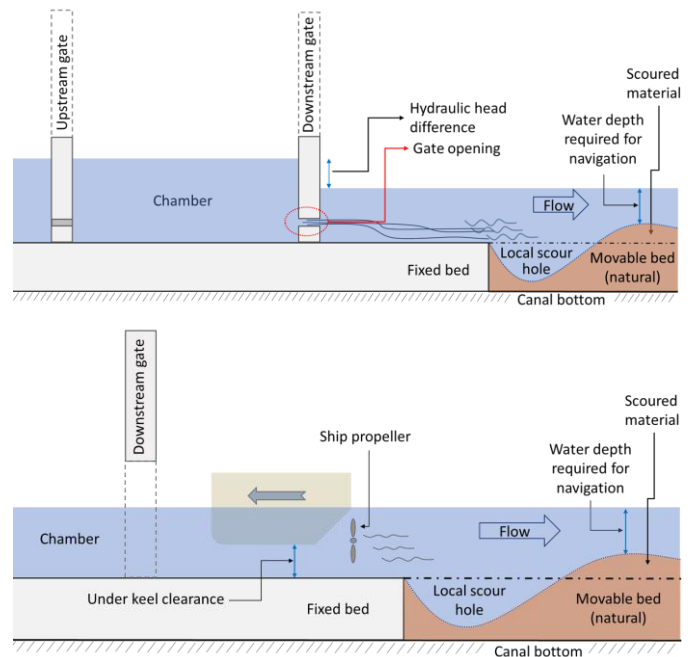


Figure 1. Development of a scour hole downstream of the lock head resulting from (top) currents caused by emptying the chamber, and (bottom) propeller wash of entering ships

When the propellers and thrusters initiate spinning, they set the previously stagnant water in motion. Consequently, they need to overcome the water's initial inertia, leading to the creation of localized vortices and high shear stresses. This shear stress is the cause of bed erosion or scouring. However, once the inertia is surmounted, the stress levels tend to diminish over time [16]. The scour hole generated by the propeller wash can be described as a combination of three polynomial components, including (1) a small scour hole located directly beneath the propeller, (2) a primary scour hole downstream of the initial one, and (3) a deposition mound situated farther downstream of the primary scour hole. This description is based on a setup with non-cohesive sediment [17].

The erosive process of scouring creates a depression in the immediate bed area, and if the slab/foundation's critical depth is surpassed, it can ultimately lead to the undermining and collapse of the foundation. On the other hand, the scoured material can alter the required depth for the navigation of ships. Therefore, in old navigation locks, the scour holes need to be refilled quite often and the sedimentations dredged, otherwise, countermeasures such as a bed protection layer have to be applied. Both scenarios, reduce the efficiency and operability of the lock, causing considerable economic loss [4]. Accordingly, scour holes induced by propeller wash of the

ships turned into one of the most prominent concerns for the design and maintenance of the waterways system.

Scour is a complex physical phenomenon involving interactions between flow, structures, and soil. Predictive models for scouring remain unreliable, contributing to the inherent uncertainty in its understanding. Therefore, there is a pressing need for the regular monitoring of scour at critical infrastructures that face a higher risk of scour-induced failure [8]. Continuous monitoring of areas prone to scouring is crucial due to the time-dependent nature of this phenomenon. This helps prevent scour-induced damage from becoming severe and causing critical failures.

## 2.2 Scour monitoring

The most widespread incidents of scouring in wet infrastructures are related to bridges, which is one of the main causes of bridge collapse [18]. An economically applicable and effective method to combat scouring is to monitor its progress over time and apply countermeasures before poses problems to the structure. The most prevalent monitoring scheme that is commonplace in engineering is visual inspection. In the case of wet infrastructures, visual inspections usually are undertaken by the divers. However, the risk of this inspection method during the flood is high. There is also one important fact about scouring that scour holes might be refilled, accordingly, the strength of the bed is not what it shows in the inspection [7]. Therefore, an effective method could offer continuous monitoring of the depth of scouring. As scour monitoring techniques are relatively well developed for bridge structures, and the origin of failure in locks is the same, the treatment can be generalized to these wet infrastructures as well.

As for bridge scour monitoring, some sensors have been employed that can measure the depth of scour holes such as single-use, pulse or radar, fibre-Bragg grating, driven or buried rod, and sound wave devices [7]. All these sensors are applicable in monitoring the progress of scouring in navigation locks. Among the mentioned methods, the last one; sound wave devices, provides region-wise monitoring, while the rest are spot-wise. In an extensive area such as a lock entrance bed, since the exact spot of scouring is hard to determine, the most promising method is using sound waves or so-called sonar devices [6].

## 2.3 Sonar techniques for scour monitoring

Sonar is a vital technology used to explore the underwater environment. Sound waves propagate and penetrate more effectively than light through water, especially in conditions of high turbidity. This feature makes it an ideal tool for underwater mapping and detection. Moreover, sound reflection shares similarities with light reflection; surfaces with different textures reflect varying fractions of the incidence of sound. For instance, textured surfaces cause reflection, scattering, and absorption. Surfaces with low reflection have more absorption [19]. The reflecting surface also determines the direction of the reflection. On smooth surfaces, the angle of reflection, measured from the normal to the surface, is equal to the angle of the incident of the wave [20]. However, rough surfaces scatter the waves or reflect them in all directions [19].

Based on the principles of sonar, sonar images can provide information about the location of bed surfaces with (i) strong

reflectivity, such as rocks, that (ii) are normal to the sonar transducer (hot/light-coloured pixels). These surfaces may include the uphill side of projections or depressions in the bed. On the other hand, the location of surfaces with low or no reflectivity is also known in the sonar images (cool/dark-coloured pixels). For example, surfaces that are parallel with the sonar transducer, silt or mud-covered areas, areas overshadowed by rocks, or the downhill side of depressions and projections. Figure 2 schematically demonstrates reflection intensities against surfaces of the seabed in different directions such as the uphill/downhill facing of projections/depressions.

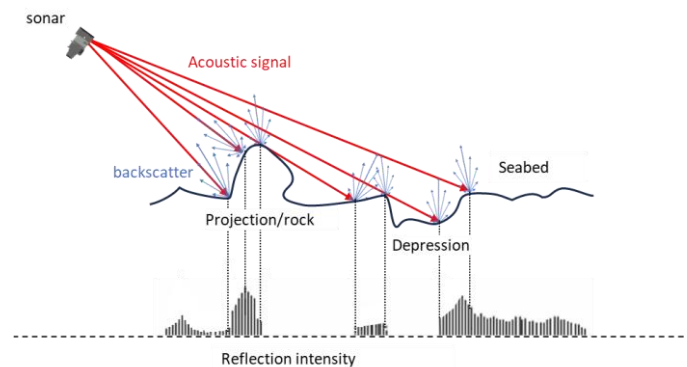


Figure 2. Reflection intensity of acoustic signals

When a rock resting on the waterbed is subjected to a force from high-velocity currents, depending on the weight of the rock, it may undergo displacement from its previous location. In this case, the intensity of signal reflection received by the sonar alters in a specific time interval that is related to a certain location. These alterations occur due to variations in the incident angle of the signals, resulting in modification of the sonar image at that particular location. Additionally, the presence and shape of shadows may undergo changes that indicate a change in the location or orientation of its source. Therefore, by placing a 2D imaging sonar underwater at a suitable altitude and a fixed position facing toward the area of interest on the bed, the changes in the bed features can be captured.

## 3 THE BEATRIX LOCK COMPLEX

The Princess Beatrix Lock is the largest monumental inland navigation complex in the Netherlands. The lock complex, with three chambers, is located within the Lekkanaal, connecting the Lek River and the Amsterdam-Rhine Canal. This connection is the main and shortest freight corridor and inland waterway between the North of the Netherlands/Amsterdam and Rotterdam/Antwerp. Around 50,000 vessels pass through the lock every year [21]. The Beatrix lock is positioned in the north-south direction, the water flow is northwards. Filling and emptying the lock system is performed via the gates. That means water is brought into or leaves lock chambers through openings in gates, instead of bypassing culverts or stilling chambers. The hydraulic head differences between the two sides of the lock can exceed two meters. Two of the chambers; the twin chambers, with a length of 225 m and a width of 18 m were built in 1938. These chambers can host ships with a maximum draft of 3.5 m. However, the third chamber, built in 2019, is designed to accommodate vessels of CEMT class Vb

with a draft of 4 m. The length of the third chamber is 276 m and its width is 25 m. Figure 3 shows an annotated aerial view of the Beatrix lock complex.



Figure 3. Aerial photo of The Beatrix lock [22]

The filling and emptying system of all three chambers of the Beatrix lock is the opening gate. The gates of the twin chambers have six openings at a height of one meter from the floor of the chamber. The hydraulic head differences between the two sides of the opening are variable and sometimes reach two meters. This difference affects the flow velocity of the opening outlet. In fact, the high-velocity currents from emptying of the chambers (levelling downward) accelerate the progress of scouring at the downstream side of the lock. This is potential damage that occurs due to the operation of the lock by itself, without any ships.

The effect of ship propeller wash on the scouring is intensified by reducing the distance between the ship propeller altitude and the bed. To minimize this effect, a minimum under-keel clearance needs to be considered when the ships pass through the lock. According to the waterways guideline of Rijkswaterstaat, which is the executive agency of the Dutch Ministry of Infrastructure and Water Management, the water depth in navigation canals should be at least a factor of 1.4 times the loaded draft of a passing ship relative to the normal low water level [21]. For example, for ships with a draft of 4 m, the water depth should be at least 5.6 m. This consideration is to minimize the scouring effect of ships' propeller wash on the canal bed. Also, the guideline provides a minimum keel clearance above the chamber floor in locks for different ship categories. For the ships in classes I, II, and III, keel clearance above the chamber floor is 0.6 m, for classes IV to Vb 0.7 m, and for classes VIa and VIb 1.0 m. This consideration needs to be met to minimize the erosion effect of propeller wash related to passing ships.

It is important to know whether the required water depth in the Beatrix lock is in accordance with the guidelines or not. Consequently, the minimum under-keel clearance of the passing ships from the Beatrix lock during the past years of 2019 and 2020 is investigated. To compute the water depth at the moment of passage of ships, the water level and level of the canal bed are needed. By subtracting these two levels, the water depth is determined. In the Rijkswaterstaat database, all the

passing ship's details are registered. These details include the date and time of ship entry to the lock, lockage time duration, chamber, direction of passing, and ship category. It is good to mention that ships within the same category have the same loaded draft. However, the status of the ships (loaded/unloaded) is unknown in this dataset.

The level of the canal bed is extracted from a bathymetry map of the lock and surrounding canal. The bathymetry is conducted by Martens en Van Oord in the year 2021. Figure 4 shows a segment of the bathymetry map of the chambers and the approach at the downstream side of the lock. Bed levels at the twin chambers and approach are estimated at -4.62 m and -4.95 m respectively (these numbers are circled in the figure). Therefore, the water depth of the old chamber during the passage of class VIa ships is on an average between 4.24 m and 4.56 m for the chamber and approach of the lock respectively. However, according to the guidelines, in this case, the water depth should be at least 5.6 m.

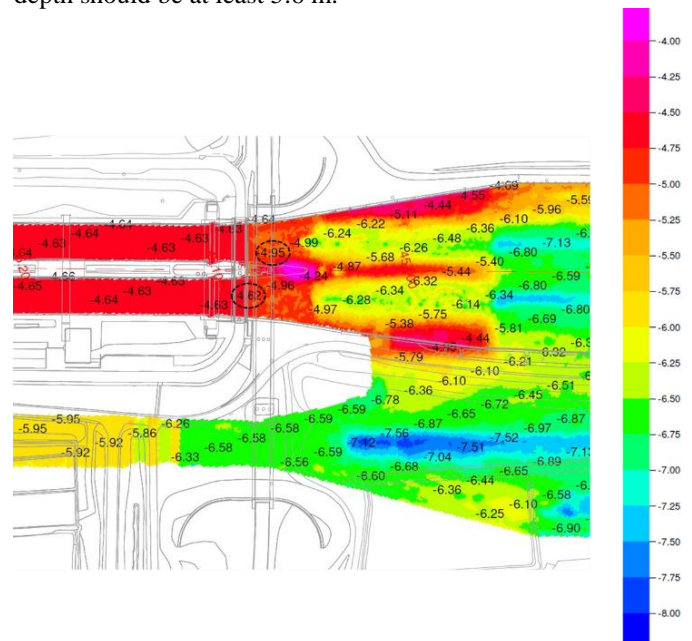


Figure 4. The bathymetry map of the north side of the Beatrix lock (downstream)

To gain insight into the condition of the approach bed of the Beatrix lock, the bathymetry data of the lock is investigated. According to the available drawing from the Beatrix lock in combination with the bathymetry of the canal around the lock structure, there are two changes in the roughness of the watercourse bed along its approach. The first change is related to the junction of the lock head and the bed protection layer of the canal, which is implemented immediately after the lock head. The second change is associated with the junction of the bed protection layer and the natural bed of the canal. Therefore, the junction of these two beds with different roughness is the area where local scour takes place. According to a diver inspection report on the bed protection layer of chambers 1 and 2, the layer is composed of pieces of rock affixed with a cement paste. However, the cement paste does not fully cover the rocks, resulting in a rocky finishing surface.

The point cloud data in Figure 4 from the north side of chamber 1 indicates degradation of the protection layer at its intersection with the natural bed, revealing the progress of the



scour hole. While the protection layer on the south side of this chamber shows signs of degradation, the intensity or depth of degradation is not as high as observed on the north side. This difference could be attributed to the lower water depth on the downstream (north side) resulting in more pronounced effects of the ship's propeller wash. The bed protection of the north side of chamber 2 and the south side of chamber 3 have not experienced any significant degradation. However, on the south side of chamber 3, a scour hole has formed at the natural bed of the canal, which could be an initial indication of degradation in the protection layer.

## 4 SONAR FOR THE LOCK MONITORING

### 4.1 Selection of sonar device

A variety of sonar devices are available for marine applications such as seafloor mapping, underwater structure inspection, navigation, and commercial fishing [23–26]. Given the cost constraint of under €25,000, a 2D sonar was selected for its affordability compared to 3D alternatives.

To identify the most suitable option, 12 commercially available 2D sonar devices were evaluated using a rating system based on criteria including price, frequency, range, power consumption, weight, resolution, casing, field of view, and beam angles. Each device was scored, normalised, and expressed as a percentage. All criteria were equally weighted, as established through requirement analysis. The ISS360 imaging sonar emerged as the optimal choice. Details of the scoring method are provided in Table 1, while the performance results and corresponding ranking are presented in Table 2.

Table 1. The scoring system and the description of the criteria

Score	Field of View (°)*	Score	Frequency (kHz)
5	360	3	>= 900
4	140	2	> 500
3	130	1	<= 500
2	120		
1	90		
	<b>Horizontal Beam Angle (°)</b>		<b>Casing</b>
3	<= 0.6	1	Titanium
2	<= 1.2	0	Aluminum
1	> 1.2		
	<b>Vertical Beam Angle (°)</b>		<b>Weight (kg)</b>
5	> 28	3	< 0.5
4	>= 26	2	>= 0.50
3	>= 24	1	>= 1.00
2	>= 22	0	>= 3.00
1	>= 20		
0	< 20		
	<b>Operating Range (m)</b>		<b>Resolution (mm)</b>
5	>= 120	2	< 5 mm
4	> 85	1	<= 10 mm
3	> 70	0	> 10 mm
2	> 55		
1	> 40		
0	<= 40		
	<b>Power Consumption (W)</b>		<b>Price (€)</b>
5	< 4	4	< 4,000
4	< 5	3	< 7,000
3	< 6	2	< 10,000
2	< 7	1	< 13,000
1	< 10	0	>= 13,000
0	>= 10		

Table 2. Evaluation results for sonar device selection

Brand (Model)	Field of View	Vertical Beam Angle	Horizontal Beam Angle	Operating Range	Power Consumption	Frequency	Casing	Weight	Range Resolution	Price	Total Points	Score (Out of 100)
1 ImpactSubsea (ISS360)	5	1	2	4	5	2	1	3	1	2	26	72.2
2 Echologger (MRS900)	5	1	3	2	4	3	0	2	1	3	24	66.7
3 Echologger (RS900)	5	2	5	2	2	3	0	1	1	1	22	61.1
4 BlueRobotics (Ping360)	5	1	3	1	3	2	0	2	0	4	21	58.3
5 Trittech (Micron Gemini)	1	1	1	1	1	2	0	3	1	1	12	33.3
6 Trittech (Gemini 720iik)	2	2	1	5	0	2	0	1	2	0	15	41.7
7 Trittech (Gemini 1200iK high-resolution)	2	3	0	1	0	3	0	1	2	0	12	33.3
8 Trittech (Gemini 1200iK)	2	2	1	5	0	2	0	1	2	0	15	41.7
9 Kongsberg (1171 high resolution)	5	3	5	3	0	3	0	0	1	0	20	55.6
10 Kongsberg (M3)	2	2	5	5	0	1	0	0	0	0	15	41.7
11 TeledyneMarine (SeaBat F50-R)	4	3	3	5	0	1	0	0	0	0	16	44.4
12 Blueview (S M900 Mk2)	3	2	0	5	0	3	0	1	0	0	14	38.9

### 4.2 2D Sonar system

The ISS360 2D imaging sonar from ImapctSubsea is selected as the sonar device for the lock monitoring system. This sonar is a single-beam rotary sonar that scans the area by rotating a transducer via an in-built stepper motor. The transducer emits an acoustic beam with a height of 23° and a width of 2.2° at a central frequency of 700 kHz. It operates within a bandwidth of 600 kHz to 900 kHz and has a range performance ranging from 0.15 m to 90 m. Frequencies below 700 kHz are employed for distances greater than 35 m. Figure 5 shows the geometry of the ISS360 imaging sonar sensor and its fan-shaped acoustic beam.

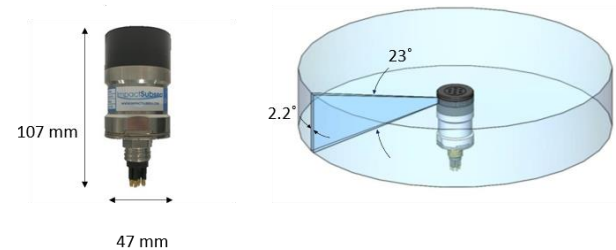


Figure 5. ISS360 imaging sonar sensor and with its principal dimension (left) and beam angles of the sonar (right) [27]

The sonar's power consumption is 150mA at 24V DC during scanning. The sonar device is powered by the Mean Well AC/DC PSU - LRS-75-24 - PSU 1, which outputs 24V/0-3. To enhance its ingress protection (IP) rating, the power supply is enclosed in a (150×110×70 mm) junction box with an IP56 rating. This protective case ensures the power supply can operate in wet environments and raises its IP rating to IP56.

The sonar must be firmly kept in its desired location with minimal vibrations. The sonar mount is specifically designed for this purpose. It restrict the displacement of the sonar to a maximum of 1 mm. This necessitates the mount to be rigid enough to prevent any vibrations or displacement caused by intense ship-induced currents. Another requirement for the sonar mount, associated with the selected sonar device, is to ensure electrical isolation from the housing of the sonar.

Considering the diameter of the sonar (47 mm), two scaffold clamp sizes of 50 mm, coupled with two brackets, are employed as the sonar mount. In one clamp, the sonar is fixed,

while in the other clamp, the mount pipe is fixed. The mount pipe can then be affixed to a wall using another clamp and bracket. This coupled clamp system allows the sonar to be positioned and fixed in all orientations. Figure 6 (left) presents the clamp system with sonar and the pipe. To meet the isolation requirement of the mount, a non-conductive spacer (Figure 6 (right)), made of Polylactic Acid, was designed. It is installed between the sonar and the clamp.

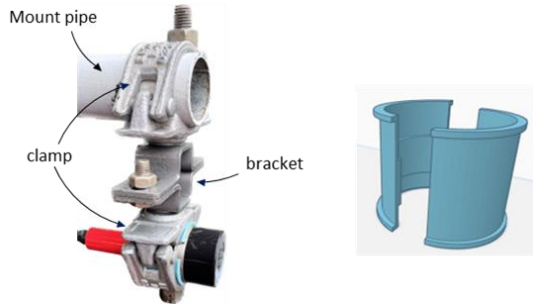


Figure 6. A coupled clamp system with sonar and the mount pipe (left) and a 3D sketch of the spacer (right)

The thickness of the spacer was considered to be 1.5 mm so that, when placed around the sonar, the total diameter of the sonar and the spacer is 50 mm, fitting the size of the clamp. To minimize the risk of the sonar slipping off the mount under high-pressure currents caused by ship propellers, the spacer was designed to provide a firm grip between the sonar and the clamp. The grip between the sonar and the clamp is facilitated by a projection in the spacer that fits into a recess in the sonar housing. Additionally, two teeth were added to the outer side of the spacer to ensure the grip between the spacer and the clamp. Figure 7 shows the detailed design of the spacer. To dampen vibrations between the sonar and the spacer, anti-vibration damper strips were affixed to the spacer. Shows the printed spacer placed between the sonar and the clamp. To prevent self-loosening of the clamp nut and ensure that the sonar remains securely in its place, a spring washer with a double nut configuration is being considered for the clamp



Figure 7. Detailed parts of the spacer

#### 4.3 Sonar location

The north side of chamber 1 is found to be the critical area of concern in the approach bed of the Beatrix lock. The sonar is installed to cover this area. Long-term monitoring of this area may reveal changes in the scour hole in the bed protection layer. The weakness of the protection layer in that region makes it susceptible to further growth, i.e., erosion. The concrete floor of the lock chamber also needs to be included in the sonar's field of view. Such configuration is expected to verify the capability of the monitoring system to capture the deposits on the threshold. If rolling stones/deposits on the concrete floor can be captured, it implies that they can also be captured on the

gate threshold. Situating the sonar system between these critical areas ensures comprehensive coverage while considering the trade-off between range limitations and image resolution. Figure 8 provides a top-down view of the point cloud from the north side of chamber 1 superimposed on the drawing of this region. Both the concrete floor of the chamber and the scour hole are illustrated. The location of the sonar is on the east side of the chamber in between the critical areas.

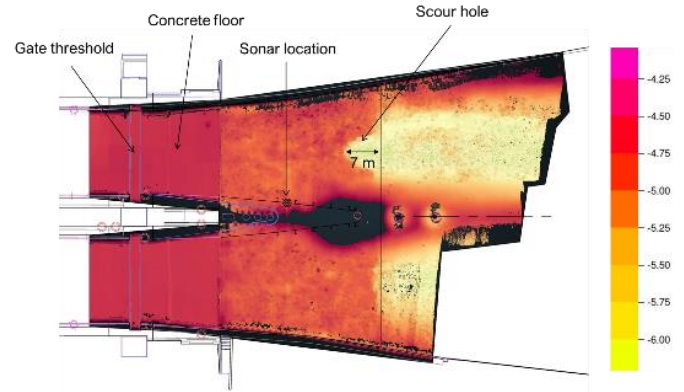


Figure 8. The top-down view of the point cloud of the north side of chamber 1 superimposed on the drawing indicating the sonar location.

The system must not disrupt the operation of the lock. This requirement prohibits any projection of the sonar installation into the track of passing ships. Consequently, the sonar is installed behind the fendering wood of the canal wall. Another requirement is to restrict the sonar displacement to a maximum of 1 millimetre. For this purpose, a galvanized steel pipe 6 m long with a diameter of 50 mm is used for the sonar mount. The mount pipe is clamped at two points to the fendering timbers with a distance of 1 m to provide the required rigidity for restricting vibrations caused by the turbulence of the ship's propeller. Figure 9 (a) depicts a schematic of the sonar installation, providing information about dimensions, while Figure 9 (b) shows an above-water view of the sonar location. Additionally, Figure 9 (c) offers a cross-sectional view of the canal, demonstrating that the outward projection of the sonar does not obstruct the ship's path.

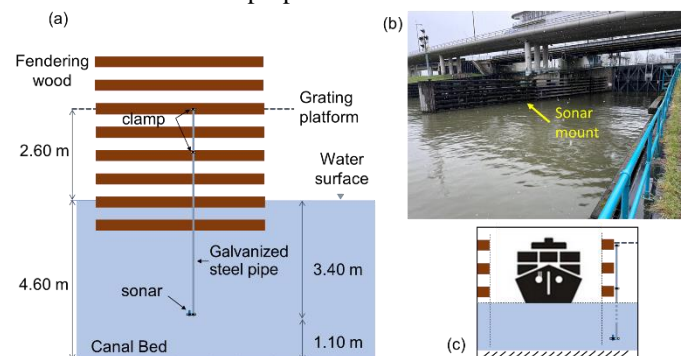


Figure 9. A schematic of sonar installation with some principal dimensions (a), the view of sonar location (b), and projection of sonar toward the ship track (c).

## 5 MONITORING RESULTS

### 5.1 Changes in the canal bed

The image rendered by the sonar contains two distinct parts; the bed protection layer, where the change in its feature is being sought, and the concrete floor, where the presence of sediment or rolling stone is sought. This section focuses on the bed protection part of the image to evaluate the ability to capture change in bed.

To verify the bed scanning subsystem, over a period of 7 days, the sonar continuously scanned the bed area of interest. Sequential images were acquired by capturing a screenshot from the software window every minute. These images were subsequently compared to evaluate the subsystem's effectiveness in capturing changes in the bed. Effective functionality necessitates, firstly, the absence of any changes in the sequential images as long as no source of excitation, such as the passage of ships or emptying the chamber, occurs. Secondly, changes are expected to occur in the images following a severe excitation.

It is important to note that the emphasis is on changes resulting from the removal of spots with high-intensity reflection, rather than changes due to the appearance of new spots. The removal of spots that have endured for an extended period, signifies their resilience against relocation by heavy ships. The longer a pattern of spots remains in place, the more assuredly it is considered fixed parts of the protection layer. In the event of such changes, it signifies that the initially heavy and securely fixed spot has been relocated due to severe excitation, interpreted as degradation of the protection layer, allowing for the identification of problematic passages. Conversely, the emergence of a new spot suggests a stone coming from elsewhere (probably as a result of removal from somewhere else).

To facilitate image comparison, each sequential image is divided into small ROIs, and each ROI is then compared with the corresponding ROI in the subsequent images. Focusing on only a ROI of this image, for instance, an 8.5 m × 10.5 m area near the scour hole (see Figure 10), numerous green/reddish spots can be seen with specific locations and sizes.

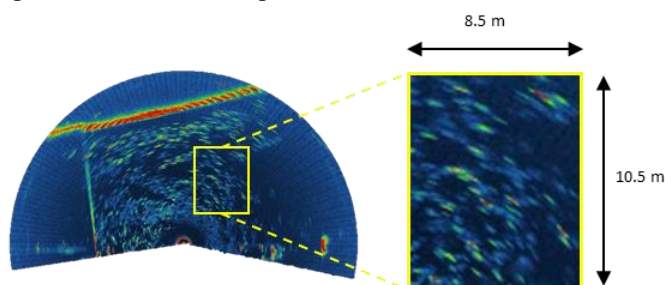


Figure 10. A magnified ROI (yellow box) of the sonar image near the scour hole.

These green spots represent the rock pieces of the bed protection layer. They constitute the distinctive features of the layer, forming a specific pattern depicted in Figure 11 with connected white circles of varying sizes and locations. Upon comparing this pattern in sequential images spanning a 2-day period, no changes are observed. This ongoing steadiness serves as evidence that the level of noise does not compromise image details, thereby satisfying the requirement of a signal-to-

noise ratio greater than 1.45. Furthermore, the consistent presence of these green spots, despite various excitations such as ship passages and chamber emptying during this period, indicates that they are fixed components of the protection layer.

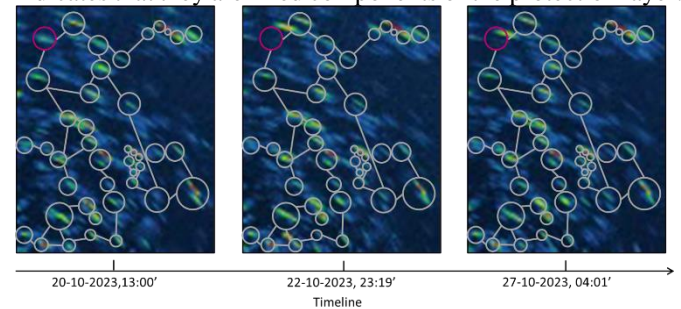


Figure 11. A region of interest in the at three different times, illustrating changes in the fixed pattern of the bed protection.

However, after a ship passage following this period, one of the green spots within this pattern changed its location. Subsequently, the pattern remained unchanged for 5 days. Interestingly, another ship passage after this period led to the same green spot undergoing a change once again. This suggests the presence of a loose stone in the bed protection, potentially indicating degradation of the protection layer. Figure 11 illustrates the initial location of this green spot circled in pink at the measurement's outset and its two new locations after the severe excitations. This serves as compelling evidence of the bed scanning subsystem's functionality, successfully capturing changes in the bed protection layer induced by specific excitations.

It is also possible to identify weak parts of the bed protection layer. For instance, upon an examination of the collected sonar images, specific locations in the bed protection layer exhibited a consistent pattern of spots for 6 days. However, numerous changes in the arrangement of spots, deviating from the fixed pattern, occurred after each passage. This observation indicates the presence of loose stones that are not securely fixed in their location or the void left by a detached stone, subsequently filled with sand. Both scenarios signify a weak section in the bed protection layer.

All constraints of this requirement have been satisfied, specifically, that the system captures changes occurring in at least 3 min within a minimum area of at least 0.5 m<sup>2</sup>. The scanning time for the area of interest at the highest resolution of the sonar device is 1 minute, ensuring the system can capture changes within a 3-minute timeframe. Upon examining the detected change on 27-10-2023, at 04:02', it was found that the change occurred within one minute. In the preceding image, the location of the green spot differed. This change is attributed to a shift in the location of a stone in the bed protection layer, measuring 0.5 m<sup>2</sup>. Figure 12 illustrates the stone in two different locations in two sequential images with a 1-minute interval.



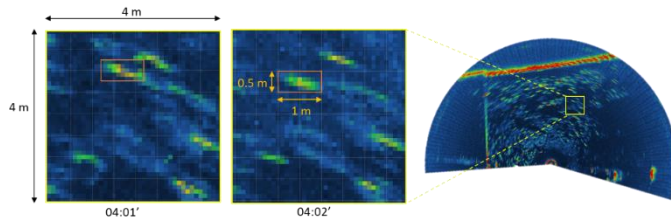


Figure 12. Detected change in the bed protection layer within an area of 0.5m<sup>2</sup>

### 5.2 “Rolling stones” on concrete floor

This section concentrates on the concrete floor part of the sonar image, aiming to evaluate the subsystem’s capability in capturing rolling stones. Upon examining sequential images in this part, a green spot is consistently evident in all images, situated in the north-western part of the concrete floor. This reflection indicates the presence of a projection at that location, as a significant amount of signal is reflected compared to its surroundings, where such reflection is not expected. To confirm this assumption, an underwater drone was sent to that location to capture a video from the concrete floor. The video revealed a substantial piece of rock resting on the concrete floor. Figure 13 (left) presents the identified green spot circled in yellow, and Figure 13 (right) shows a drone-captured image revealing the presence of a substantial rock.

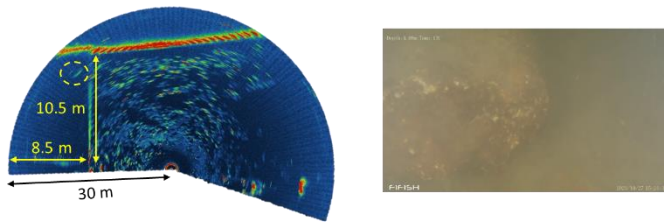


Figure 13. A green spot (circled in yellow) on the concrete floor (left) is a rolling stone, which is captured in an image taken by an underwater drawn (right).

Additionally, certain images display sporadic green spots on the concrete floor, appearing in one image and disappearing in the next. This fleeting presence suggests they are likely fish or other lightweight objects in that area. Contrarily, in many instances, these green spots endure for more than an hour, remaining unchanged in shape and location across many images. This extended presence indicates a heavier object, like stones, in those locations. Figure 14 depicts three incidences of stones observed on the concrete floor. Reviewing images collected over three days of scanning revealed the presence of stones on the concrete floor in multiple instances.

It is noteworthy that the system can capture hills/projections from a distance of 30m. However, the height of the projection cannot be measured due to the lack of access to the stones on the concrete floor captured by the sonar.

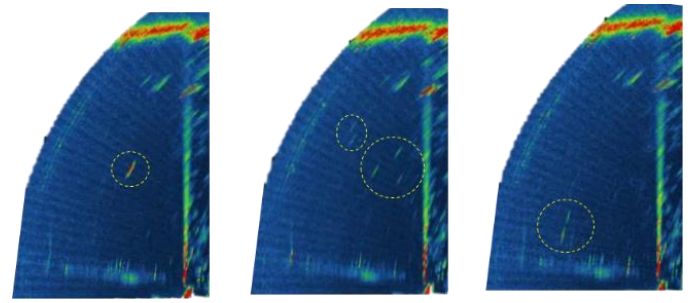


Figure 14. Incidents of persistent green spots (circled in dashed yellow line) suggesting the presence of rolling stones on the concrete floor

### 5.3 Ship’s draft

the draft measuring subsystem shares the same components as the bed scanning subsystem. To evaluate the draft measuring subsystem’s capability in measuring the actual draft of ships, the sonar was positioned in the same location with a slight modification in its orientation. Due to the inherent limitations of 2D imaging sonar in capturing vertical faces underwater, the sonar mount was tilted 90°, as illustrated in Figure 14 (right), allowing it to render vertical surfaces underwater. In this horizontal orientation, the sonar captures a cross-sectional view of the canal, including the canal bed, wall, and water surface. Figure 14 (left) illustrates the sonar image, overlaid onto the background image, presenting a cross-sectional view of the canal outlined by the red lines. The water surface in the background image is partially cut to reveal a point cloud view of the underwater canal from the same angle. This view allows the observation of the canal wall and bottom.

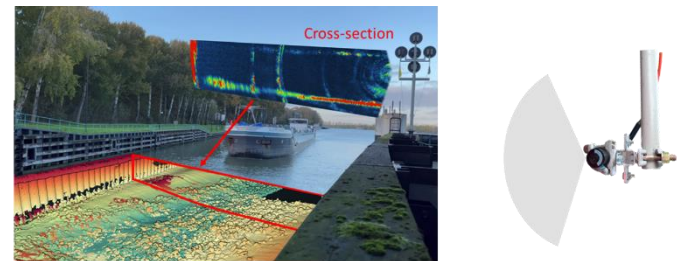


Figure 67 An illustration of a phot combined with 3D point cloud data and the sonar image of the cross-sectional of the canal (left), and the sonar tilted 90° (horizontally mounted) for measuring the ship’s draft (right)

When a ship passes the sonar, its hull blocks the sounds, causing a strong reflection due to its surface being perpendicular to the sonar. Consequently, its draft is expected to be captured in the sonar image. Figure 15 (left) presents the sonar image illustrating a cross-sectional view of the canal while a ship is passing the sonar. In this figure, the ship’s draft, depicted in red, signifies the extent to which it extends toward the canal bed, providing the dimension of the under-keel clearance. Considering the sonar’s depth of 3.5 m, if the ship hull’s bottom is not rendered in the image, it implies a draft greater than 3.5 m. Figure 15 (right) displays two passages of large ships with drafts of approximately 3.5 m and 3.6 m. The bottom image, suggesting a larger ship with more draft, blocks the opposite wall completely compared to the top image, despite their equal distance from the sonar.

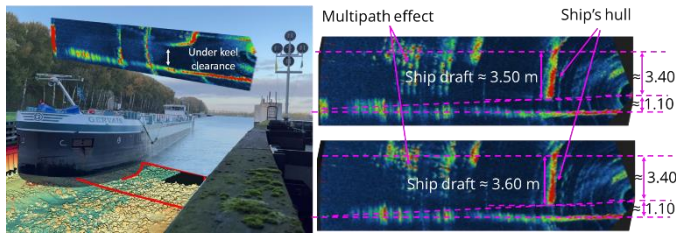


Figure 15. Sonar images rendering the cross-sectional view of the canal during a ship's passage (left) introducing the ship's hull in the sonar image, and estimated draft of two large ships at the same distance from the sonar (right).

Analysing historical traffic data before system design revealed a significant number of large ships passing through the old chambers with drafts of 3.5 m and 4 m. However, this data, obtained from Rijkswaterstaat, did not specify whether the ships were loaded or empty. The difference between loaded and unloaded ships can be up to 2 m. Examining the collected data from measuring ship drafts over 50 hrs uncovered 22 passages of ships with drafts exceeding 3 m, indicating a notable frequency of loaded ships in groups IV and V. Therefore, it is important to note that not all ships with large drafts were necessarily empty.

## 6 CONCLUSIONS

This project aims to investigate underwater dynamics and ship interactions with the canal bed by visualising changes in the bed protection layer near the lock structure. Reports indicate that this layer consists of large stones fixed with cement, some of which may detach due to excessive water pressure or excitation. Detached stones can obstruct the lock gate, risking damage. Monitoring their movement and understanding the causes i.e., chamber emptying and ship propeller wash, is crucial. The system is designed to detect changes in the bed protection layer, track rolling stones, and measure passing ship's drafts to prevent structural degradation and operational hazards.

The study draws the following conclusions:

- The sonar-based system successfully detects changes in the bed protection layer by capturing consistent images over time. A low noise-to-signal ratio ensures reliable detection, while variations in high-intensity reflections indicate potential degradation caused by ship passages.
- The system can identify and track stones on the concrete floor of the lock chamber. The size of the stones can be estimated using benchmarks, and their movement can be monitored to assess potential risks to lock infrastructure.
- Some ship passages generate significant turbulence, leading to the displacement of stones from the bed protection layer. By correlating these events with sonar images, the system provides evidence that specific passages contribute to degradation.
- Tracking the origin of rolling stones is difficult due to the limited field of view of the sonar. However, adjusting sonar placement and analysing traffic data can help determine whether stones move due to ship passages or chamber emptying.
- By measuring ship drafts and turbulence profiles, the system reveals how propeller wash affects the bed

protection layer. High air bubble concentrations in sonar images indicate strong disturbances, which may accelerate degradation of the canal bed.

Future studies should collect a comprehensive dataset using the monitoring system, with at least six months of continuous data to identify change patterns. The current limited dataset provided evidence of bed protection degradation but lacked a complete understanding of the underlying causes. Expanding the investigation to other chambers of the Beatrix lock will reveal trends in scouring and improve detection of loose stones. Implementing automated detection and event correlation will help categorise ship passages, clarifying their role in bed protection degradation.

## ACKNOWLEDGMENTS

This research was supported by Heijmans in collaboration with the University of Twente. The authors are pleased to express their gratitude to Dr. ir. Jasper Caerteling for his valuable supervision and to Heijmans Company for their financial and technical support, including facilitating the sonar testing at the Beatrix Lock.

## REFERENCES

- [1] European Commission. Inland waterways 2025. [https://transport.ec.europa.eu/transport-modes/inland-waterways\\_en](https://transport.ec.europa.eu/transport-modes/inland-waterways_en).
- [2] U.S. Army Corps of Engineers. Engineering and Design: Strength Design for Reinforced Concrete Hydraulic Structures. Engineer Manual\* 1110-2-2104. 2023.
- [3] Lauth T, Gordon D, Rector M, Moeller W. Scour and subsequent repair at lock & dam 25. 2015.
- [4] Mujal-Colilles A, Gironella X, Sanchez-Arcilla A, Puig Polo C, Garcia-Leon M. Erosion caused by propeller jets in a low energy harbour basin. *J Hydraul Res* 2017;55:121–8. <https://doi.org/10.1080/00221686.2016.1252801>.
- [5] Bastani M. Designing monitoring system for condition assessment of locks. University of Twente, 2024.
- [6] Negi P, Kromanis R, Dorée AG, Wijnberg KM. Structural health monitoring of inland navigation structures and ports: a review on developments and challenges. *Struct Heal Monit* 2023. <https://doi.org/10.1177/14759217231170742>.
- [7] Prendergast LJ, Gavin K. A review of bridge scour monitoring techniques. *J Rock Mech Geotech Eng* 2014;6:138–49. <https://doi.org/10.1016/j.jrmge.2014.01.007>.
- [8] Yousefpour N, Downie S, Walker S, Perkins N, Dikanski H. Machine Learning Solutions for Bridge Scour Forecast Based on Monitoring Data. *Transp Res Rec J Transp Res Board* 2021;2675:745–63. <https://doi.org/10.1177/03611981211012693>.
- [9] Liu W, Zhou W, Li H. Bridge scour estimation using unconstrained distributed fiber optic sensors. *J Civ Struct Heal Monit* 2022;12:775–84. <https://doi.org/10.1007/s13349-021-00510-y>.
- [10] Rogers A, Manes C, Tsuzaki T. Measuring the geometry of a developing scour hole in clear-water conditions using underwater sonar scanning. *Int J Sediment Res* 2020;35:105–14. <https://doi.org/10.1016/j.ijsrc.2019.07.005>.
- [11] Koken M, Constantinescu G. An investigation of the flow and scour mechanisms around isolated spur dikes in a shallow open channel: 2. Conditions corresponding to the final stages of the erosion and deposition process. *Water Resour Res* 2008;44:1–16. <https://doi.org/10.1029/2007WR006491>.
- [12] Sui J, Fang D, Karney BW. An experimental study into local scour in a channel caused by a 90° bend. *Can J Civ Eng* 2006;33:902–11. <https://doi.org/10.1139/106-037>.
- [13] Park SW, Hwang JH, Ahn J. Physical Modeling of Spatial and Temporal Development of Local Scour at the Downstream of Bed Protection for Low Froude Number. *Water* 2019;11:1041. <https://doi.org/10.3390/w11051041>.
- [14] Elnikhely EA, Fathy I. Prediction of scour downstream of triangular labyrinth weirs. *Alexandria Eng J* 2020;59:1037–47. <https://doi.org/10.1016/j.aej.2020.03.025>.

- [15] Chang C-K, Lu J-Y, Lu S-Y, Wang Z-X, Shih D-S. Experimental and Numerical Investigations of Turbulent Open Channel Flow over a Rough Scour Hole Downstream of a Groundsill. *Water* 2020;12:1488. <https://doi.org/10.3390/w12051488>.
- [16] Crowley R, Bloomquist D, Sande S van de, Lescinski J. Characterization of Bed Stresses near Quay Walls Due to Ship Thruster and Propeller Wash. *Geo-Congress 2020, Reston, VA: American Society of Civil Engineers*; 2020, p. 788–97. <https://doi.org/10.1061/9780784482810.082>.
- [17] Hong J-H, Chiew Y-M, Cheng N-S. Scour Caused by a Propeller Jet. *J Hydraul Eng* 2013;139:1003–12. [https://doi.org/10.1061/\(ASCE\)HY.1943-7900.0000746](https://doi.org/10.1061/(ASCE)HY.1943-7900.0000746).
- [18] Lin C, Han J, Bennett C, Parsons RL. Case History Analysis of Bridge Failures due to Scour. *Clim. Eff. Pavement Geotech. Infrastruct.*, Reston, VA: American Society of Civil Engineers; 2014, p. 204–16. <https://doi.org/10.1061/9780784413326.021>.
- [19] Photinos P. *The Physics of Sound Waves (Second Edition)*. IOP Publishing; 2021. <https://doi.org/10.1088/978-0-7503-3539-3>.
- [20] Christ RD, Wernli RL. *Sonar. ROV Man.*, Elsevier; 2014, p. 387–424. <https://doi.org/10.1016/B978-0-08-098288-5.00015-4>.
- [21] Rijkswaterstaat. *Richtlijnen Vaarwegen 2020* 2020.
- [22] Google Maps. *The Princess Beatrix Lock arial view* 2025.
- [23] Stepnowski A, Bikonis K, Moszynski M. 3 D seabed reconstruction from 2 D side-scan sonar images. *Forum Acusticum Budapest 2005 4th Eur Congr Acustics* 2005:2–6.
- [24] Park C, Kim Y, Lee H, Choi S, Jung H. Development of a 2 MHz sonar sensor for inspection of bridge substructures. *Sensors (Switzerland)* 2018;18:1–9. <https://doi.org/10.3390/s18041222>.
- [25] Manoj A, Aravind H, Varma K, Nair NP, Vivek A, Arjun D, et al. Sonar for Commercial Fishing. *2022 Int Conf Wirel Commun Signal Process Networking, WiSPNET 2022* 2022:28–32. <https://doi.org/10.1109/WiSPNET54241.2022.9767171>.
- [26] Horner DP, Healey AJ, Kragelund SP. AUV experiments in obstacle avoidance. *Proc MTS/IEEE Ocean* 2005 2005:2005. <https://doi.org/10.1109/OCEANS.2005.1639962>.
- [27] IMPACT SUBSEA. *IMPACT SUBSEA ISS360 Imaging Sonar Installation & Operation Manual* 2021.





## SHM of Tendons and Pipelines

# On-Line Health Monitoring of Underground Pipelines by Source Localization of Leak Damages

Dong-Jin Yoon<sup>1,\*</sup>, Sun-Ho Lee<sup>1</sup>, and Choon-Su Park<sup>1,2</sup>

<sup>1</sup>Korea Research Institute of Standards and Science, 267 Gajeong-Ro, Yuseong-Gu, Daejeon, 34113, Republic of Korea.

<sup>2</sup>University of Science and Technology, 217 Gajeong-Ro, Yuseong-Gu, Daejeon, 34113, Republic of Korea

Email : [\\*djyoon@kriss.re.kr](mailto:djyoon@kriss.re.kr), [sh.lee@kriss.re.kr](mailto:sh.lee@kriss.re.kr), choonsu.park@kriss.re.kr

**ABSTRACT:** This study aims to perform leak detection on an old oxygen underground pipeline in operation. The target pipe is a 220-meter section of nominal diameter 80A steel pipe that supplies oxygen for welding in heavy industrial facilities. In order to observe the response characteristics of the coupled vibration propagating through the pipe, an impact experiment was conducted to experimentally derive the frequency band and propagation velocity of the coupled vibration in the tested compressible fluid transportation pipe. Conventional leak detection methods mainly depend on frequency-domain filtering because it is difficult to improve the signal-to-noise ratio through averaging in the time domain due to the random nature of the leak signal. In this study, we propose a leak detection algorithm with improved detection performance by utilizing an ensemble cross-correlation function that applies averaging in the  $\tau$ -domain based on the deterministic arrival time difference characteristics of the leak signal. In addition, leak detection using two sensors is likely to misjudge the leak source near the sensor due to noise propagating outside the detection range, and a single damage positioning result is insufficient to determine the leak damage. Therefore, this study proposes a distributed measurement-based leak detection technique and a decision map based on multiple damage localization results. The experimental results confirmed that damage localization using coupled vibration is possible in compressible gas transport pipelines, and experimentally verified that leakage can be effectively detected with a location error rate of approximately 1.37% in industrial sites that are always in operation.

**KEY WORDS:** On-line monitoring; Underground pipelines; Leaks; Source localization; SHM.

## 1 INTRODUCTION

Acoustical and vibrational signals can be generated by a number of different damage sources in underground pipelines such as growing cracks, corrosion progress, connection part movement, third party interference, direct impact and leakage etc.. On-line monitoring technology for buried pipeline is one of the main concerns for most underground pipeline management systems that maintain buried structures that are difficult to access. There are many factors that can threaten the health of buried pipelines, but among them, leakages by aging and damages by third-party interference are known to be one of the main causes of failure, and it is emerging as a major social problem that causes safety problems such as leakage and ground subsidence due to damage. Ultimately, the pipeline failure owing to these kinds of damage lead to economic loss and huge accidents such as a ground collapse by a sinkhole, an eruption by leakage. Hence, it is extremely important to detect and localize such damages at the very early stage in order to prevent catastrophic failures. However, most of underground pipelines are located in very noisy urban areas, and these harsh conditions inflicted on practical difficulties in measuring meaningful acoustic vibratory signals. Especially, several kinds of background noise such as traffic, natural environment and sound pollution causes difficulty in signal analysis. Therefore, this study proposes a distributed measurement-based leak detection technique and a decision map based on multiple damage localization results and monitoring range information, and implements an algorithm to improve the reliability of damage localization in industrial sites where noise is frequent.[1-6]

## 2 WAVE PROPAGATION AND EXPERIMENT

In this study, acoustic wave propagation coupled with surrounding boundaries including cast iron and steel pipes is theoretically analyzed and the wave speed was confirmed with experiment.

When the impact by foreign damage occurs on a fluid filled pipe, a structural pipe vibration as well as a fluid-pipe coupled vibration will occur. That is, a pipe vibration mode appears in various mode shapes in shown in Figure 1. Also the fluid borne wave, non-dispersive wave in free space, is changed to dispersive wave by coupled vibration. This role is executed by “ $n=0$ ” mode. In other words, the ‘Breathing’ mode creates a new wave in the fluid filled pipe domain. This “Breathing” mode is important for detecting a damage sources.[1]

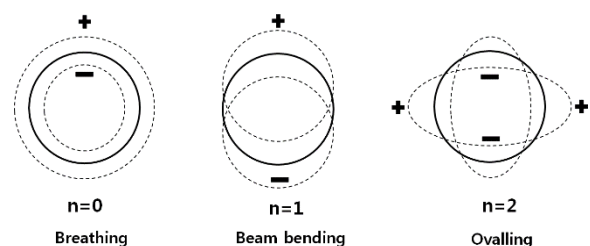


Figure 1. Mode shapes of a circular cylindrical shell [1].

In this study, the buried pipe used in the field experiment was an oxygen supply pipe for welding process, and seven sensors

were installed in a 220 m section. Several types of impact hammer and accelerometer were used as the artificial impact source and sensors. To examine the possibility of damage location markers in compressible fluid transport pipelines, the velocity change characteristics were compared for compressible and incompressible fluids. Steel pipes with a nominal diameter of 80A, which is the diameter of actual pipelines installed in the field, were used. Basically, one-dimensional source location algorithm was used to estimate the time delay with the cross-correlation method.

In order to experimentally verify the speed of the coupled vibration propagating in the compressible fluid transport pipe, an impact hammer(086D20, PCB Piezotronics, United States of America) was used to generate coupled vibration at an arbitrary location to reproduce the impact damage situation, and vibration accelerometers(393A03, PCB Piezotronics, United States of America) were installed at distances of 42.15 m and 220 m from the damage location, respectively. Additionally, the pressure applied to the buried pipe during the experiment was 55.154 Pa. Theoretically, it can be confirmed that incompressible fluids exhibit propagation velocity dispersion characteristics starting from a lower frequency band than compressible fluids. The velocities at 0 Hz are approximately 1381 m/s, 1319 m/s, 444 m/s, and 326 m/s, respectively. At this time, the theoretical propagation speed of the coupled vibration is approximately 326.5 m/s.

### 3 VERIFICATION AND RESULTS

First, we defined a ‘time history frame’ as each separated intrinsic parameter of input time signal. Then we obtained a couple of parameters such as frequency and intensity from time signal. We proposed a leak detection algorithm with improved detection performance by utilizing an ensemble cross-correlation function that applies averaging in the  $\tau$ -domain based on the deterministic arrival time difference characteristics of the leak signal. Figure 2 shows typical raw signal based on ensemble cross-correlation function.

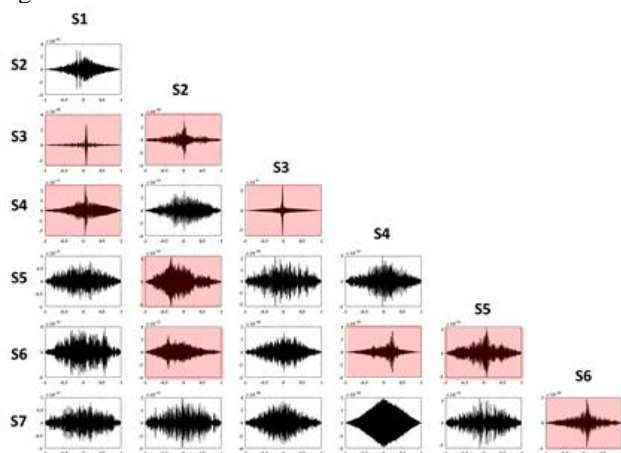


Figure 2. Typical raw signal based on ensemble cross-correlation function.

In addition, leak detection using two sensors is likely to misjudge the leak source near the sensor due to noise propagating outside the detection range, and a single damage

location positioning result is insufficient to determine the leak damage. Therefore, this study proposes a distributed measurement-based leak detection technique and a decision map based on multiple damage localization results and monitoring range information, and implements an algorithm to improve the reliability of damage localization in industrial sites where noise is frequent. Among these results, in the case of 100 m, the possibility of an abnormal location is ambiguous because the result is from only a single combination, whereas in the case of the range of 55~60 m, the result is judged to be significant because the results from multiple combinations are the same. Figure 3 shows that the result of a distributed measurement-based source localization.

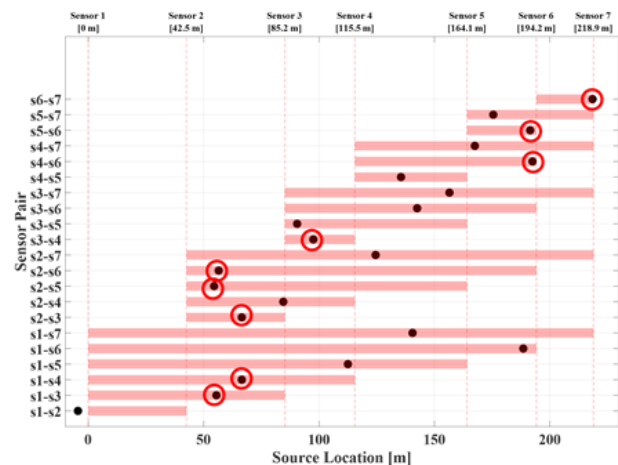


Figure 3. Distributed measurement-based source localization.

### 4 CONCLUSIONS

In this study, seven sensors were installed in a 220 m section, and micro-leakage was detected in a 55-60 m section by applying the proposed algorithm. The experimental results confirmed that damage localization using coupled vibration is possible in compressible gas transport pipelines, and experimentally verified that micro-leakage can be effectively detected with a location detection error rate of approximately 1.37% in buried pipelines in industrial sites that are always in operation.

### ACKNOWLEDGMENTS

This work was supported by the Korea Research Institute of Standards and Science (KRISS-2024-24011216) as a project “Development of structural health monitoring technology for infrastructures safety” and supported by the Korea Innovation Foundation (2023-DDRD-0153).

### REFERENCES

- [1] J. M. Muggleton, M. J. Brennan and R. J. Pinnington, “Wavenumber prediction of waves in buried pipes for water leak detection”, *Journal of Sound and Vibration*, vol. 249, pp. 939-954. 2002.
- [2] Adegboye, M. A., Fung, W.-K. & Karnik, A. (2019), Recent Advances in Pipeline Monitoring and Oil Leakage Detection Technologies: Principles and Approaches, *Sensors*, 19(11), 2548
- [3] Chen, C.-H., Sheen, Y.-N. & Wang, H.-Y. (2016), Case Analysis of Catastrophic Underground Pipeline Gas Explosion in Taiwan, *Engineering Failure Analysis*, 65, 39-47.



- [4] Lee, S.-H., Park, C.-S. & Yoon, D.-J. (2024), Source Location and Anomaly Detection for Damage Identification of Buried Pipelines Using Kurtosis-Based Transfer Function, *Structural health monitoring*, 23(3), 1742-1765.
- [5] Shen, Y., Ye, G., Zheng, F., Ye, Z. & Yu, Z. (2024), Intelligent Identification Method for Pipeline Leakage Based on Gpr Time-Frequency Features and Deep Learning, *AQUA—Water Infrastructure, Ecosystems and Society*, 73(7), 1421-1436.
- [6] Zuo, Z., Ma, L., Liang, S., Liang, J., Zhang, H. & Liu, T. (2022), A Semi-Supervised Leakage Detection Method Driven by Multivariate Time Series for Natural Gas Gathering Pipeline, *Process Safety and Environmental Protection*, 164, 468-478.

# Effects of grout-strand interface modelling on the degradation of external grouted post-tensioning tendons

Belén Vecino<sup>1</sup>, 0009-0002-9234-4005, Carlos M.C. Renedo<sup>1</sup>, 0000-0003-1014-0878, Luis Chillitupa-Palomino<sup>1</sup>, 0009-0001-5274-0436, Iván M. Díaz<sup>1</sup>, 0000-0001-9283-5109

<sup>1</sup>Department of Continuum Mechanics and Theory of Structures, ETSI Caminos, Canales y Puertos, Universidad Politécnica de Madrid, Calle Profesor Aranguren 3, Madrid, 28040, Comunidad de Madrid, Spain

email: b.vecino@alumnos.upm.es, carlos.martindelaconcha@upm.es, luis.cpalomino@upm.es, ivan.munoz@upm.es

**ABSTRACT:** In recent years, relevant brittle fractures of external grouted post-tensioning tendons in bridges have been reported due to corrosion damage, compromising the structural safety and stability of the bridges. A previous detailed finite element (FE) modelling approach for grouted tendons has been developed by the authors and compared with experimental results presented in the literature, ensuring an accurate reproduction of experimental results by accounting for steel plasticity and large deformations. This modelling approach considered a bonded contact to model the strand-grout interface. That is, an immediate re-anchoring of the strands in the grout is assumed in case of failure and, consequently the influence of the bond stress-slip behaviour is not considered in the modelling approach. This paper presents an alternative FE modelling strategy where the differences with the previous one are: i) the modelling of the strands as beams instead of solid bodies, ii) the presence of the sheathing duct, and iii) a non-linear model to reproduce the strand-grout bond stress-slip behaviour. The objective is to investigate the influence of different models to define the grout-strand interface: a bonded model or a bond stress-slip model, while validating the author's previous FE approach. These models are also compared with the experimental results from the literature. Normal stresses along the strands and in the grout are studied, and degradation curves are derived, that is, the effective tensile force and natural frequencies versus damage (defined as the percentage of broken strands). These degradation curves serve as a key performance indicator of the structural performance of the tendon for structural health monitoring systems, anticipating to severe damage and potentially dangerous scenarios.

**KEY WORDS:** Damage detection; Corrosion damage; Post-tensioning tendons; Finite element modelling.

## 1 INTRODUCTION

External post-tensioning tendons are key structural elements in bridge engineering, offering advantages like the ease of inspection, re-tensioning and substitution; however, they are also vulnerable to corrosion. Since the 1990's, relevant brittle fractures of external grouted post-tensioning tendons have been reported in bridges due to corrosion damage [1],[2]. This situation significantly compromises the structural integrity and safety of these bridges.

In externally grouted post-tensioning tendons, strand breakage does not necessarily lead to a significant reduction in the overall tensile force of the tendon. This is because the surrounding grout prevents the movement of the broken strand, effectively re-anchoring it and enabling the transfer of its tensile force to adjacent strands. As a result, the adjacent non-broken strands experience a localised increase of their tensile stress near the breakage region [3]. This stress redistribution occurs over a defined transfer length, which is the distance needed for the strands to nearly recover their original tensile force [3]. However, if a considerable number of strands are affected by corrosion, the resulting stress concentration may exceed the remaining strands' capacity, potentially leading to a brittle failure of the tendon.

Numerical research on the mechanical behaviour of external post-tensioning tendons affected by corrosion remains limited. Aparicio et al. [3] studied the re-anchoring phenomenon in monostrand tendons. A numerical model validated with experimental tests was developed to assess the sensitivity of parameters such as the grout elastic modulus, the mesh, or the

friction coefficient in stress redistribution when there is wire breakage. However, they did not consider the constitutive non-linear behaviour of the tendon materials. Subsequently, Vecino et al. [4] (the authors of the present paper) proposed a numerical modelling approach of external grouted post-tensioning tendons to be used within a parametric study to evaluate tendon failure. The grout-strand contact was modelled as bonded (that is, no sliding between them is allowed), but accounting for a prescribed re-anchoring length, plasticity was considered for the high-strength steel of the strands, and the grout was considered perfectly elastic in such a way that the sheathing duct was not explicitly modelled. The modelling approach presented in the previous paper was validated through the experimental results obtained by Lee & Kang [3]. They carried out a laboratory experimental campaign to analyse the variation in dynamic parameters and the tensile force of tendons subjected to progressive corrosion.

Thus, this study focuses on modelling strategies for the grout-strand interface to carry out numerical approaches that are both efficient and accurate. The numerical results obtained are compared against experimental data available in the literature and previous numerical studies performed by the authors, which assume a bonded contact between the strand and the grout. The accuracy of this modelling assumption is assessed to determine whether it serves for practical purposes or if a more complex contact approach, such as incorporating a non-linear bond stress-slip relationship, is required.

Establishing an appropriate modelling strategy for grouted tendons and the re-anchoring behaviour of strands is essential

for the reliable analysis of their structural performance. Accurate numerical models can support comprehensive risk assessments in the context of structural health monitoring (SHM) and serve as a tool for engineers and practitioners to complement inspections and prevent safety-critical situations.

The present paper is organised as follows. Section 2 provides a detailed description of the finite element (FE) model developed here and present a former model previously validated by the authors to study tendon degradation. Section 3 provides a discussion of the results obtained by the proposed modelling approach and using different grout-strand contact laws. Finally, Section 4 outlines some conclusions from the study.

## 2 FINITE ELEMENT MODEL

### 2.1 Experimental tests carried out by Lee & Kang

The experiment conducted by Lee & Kang [3] is used as a reference to compare their experimental results and the numerical results obtained in this investigation in terms of the degradation curves, which are: i) the tensile force with damage, and ii) the natural frequencies with damage. Damage is defined as the quotient between the number of broken strands and the total number of strands of the tendon:  $D = N_B/N$ , where  $N_B$  is the number of broken strands and  $N$  is the total number of strands.

This experiment was also used to validate the detailed FE modelling approach previously carried out by the authors [2], whose results on degradation curves are also contrasted with the ones obtained in this paper.

The Lee & Kang experiment stresses a 10 m tendon at approximately 70% of the ultimate load of a prestressing strand. Then, five strands are broken successively by accelerated corrosion in 24 hours. To carry out the breakage of the strands, the grout is retired in the 30 cm central section, leaving the strands exposed.

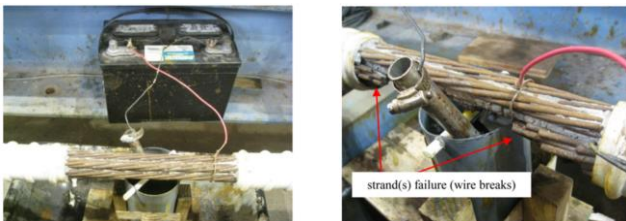


Figure 1. Strands subjected to accelerated corrosion [3].

### 2.2 FE model 1: 3D elements and bonded strand-grout interface

The Lee & Kang experiment was reproduced by the authors [4] using a FE detailed model of a seven-strand tendon surrounded by grout, except for the central section of 60 cm, which is modelled without grout to reproduce the Lee & Kang experiment, and to consider the re-anchoring length. This parameter was prescribed in the model due to the grout-strand contact considered, which will be explained hereafter.

The stress state reached by the stressing of the strands is modelled by a thermal load, at 70% ultimate stress,  $f_{pu}$ , which is 1900 MPa. Then, the stressing force of the tendon is 1241

kN. The strands' breakage due to corrosion damage is represented by the elimination of elements. The FE model was developed in ANSYS Mechanical using 3D SOLID185 elements for the grout and the steel strands. The duct (which has the main function of confining the grout to prevent its breakage) was neglected by assuming a perfectly elastic material for the concrete with a higher density (to include the duct weight). Sweep meshing method was used so that the positions of the nodes of the grout match with those of the strands in each section. Both ends of the seven strands were modelled with fixed support, that is, rotation and translation were restrained at both supports. A linear elastic surface-to-surface contact model was assumed between the grout and the strands; specifically, a bonded contact, which prevents separation and sliding. The bonded contact model does not capture the re-anchoring effect; a re-anchoring length had to be predefined in the model to simulate this behaviour. Plasticity of steel strands is considered. The elastoplastic model used presents the following characteristics: i) Bilinear isotropic hardening law, defined in Table 1, ii) Von Mises yield criterion, and iii) Associated flow rule.

Table 1. Bilinear isotropic hardening model parameters.

$E_s$ [GPa]	$f_{py}$ [MPa]	$\epsilon_{py}$ [%]	$f_{pu}$ [MPa]	$\epsilon_{pu}$ [%]
195.5	1760	0.9	1900	6

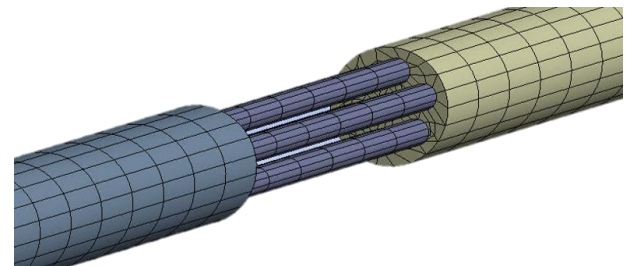


Figure 2. FE tendon model developed previously by the authors in [4] (FE model 1).

### 2.3 FE model 2: beam elements for strands and non-linear springs for the interface

The bonded contact employed in the FE model 1 for the grout-strand interface may not accurately capture the re-anchoring phenomenon, as this process involves bond mechanisms such as adhesion, friction, and mechanical interlock [6]. A bond stress-slip law has been proposed and validated by Wang et al. for strands. Thus, a new modelling approach that considers a bond stress-slip law to model the strand-grout interface is developed. The implementation of this law in the model eliminates the need to introduce the re-anchoring length as an input parameter, as in the FE model 1, allowing it to be intrinsically determined.

The Model Code [7] proposes a bond stress-slip relationship for ribbed bars, considering the bond stresses between concrete and reinforcing bar for pull-out. This relationship is defined in Figure 3 and its defining parameters are listed in Table 2.



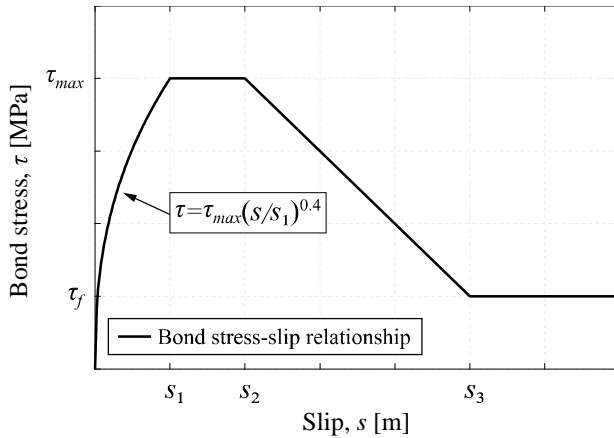


Figure 3. Bond stress-slip relationship [7].

Table 2. Parameters defining the bond stress–slip relationship [7].

$\tau_{max}$	$\tau_f$	$s_1$	$s_2$	$s_3$
$2.5 \sqrt{f_{cm}}$	$0.4 \tau_{max}$	1 mm	2 mm	$c_{clear}$

Parameter  $f_{cm}$  is the concrete compressive strength (a typical value of 30 MPa is considered), and  $c_{clear}$  represents the spacing between the ribs of a deformed bar. Considering the similarity in bond behaviour between steel strands and deformed bars embedded in concrete, the parameter  $s_3$  is defined as half of the distance between the concrete interlock region and the adjacent wires [8], and it is taken as 10 mm.

To introduce the bond stress-slip law in the FE model, non-linear springs are defined in every grout-strand coincident node. The elements used to create the non-linear springs are COMBIN39, with one degree of freedom in the longitudinal direction. COMBIN39 is defined by two nodes and a non-linear generalised force-deflection relationship.

The main purpose of this paper is to validate and critically discuss the interface modelling approach developed previously by the authors when considering bonded behaviour (FE model 1) [4]. For that, a new approach to numerically model the Lee and Kang experimental campaign has been developed (FE model 2). This new approach differs from the previous one in the following aspects:

- 1) Modelling of the HDPE sheathing duct, which is considered elastic. 3D SOLID186 elements are used for the duct, and the duct-grout contact is modelled as bonded. The grout is also modelled with these elements.
- 2) BEAM188 elements are used to model the strands. This simplifies the introduction of non-linear springs node-to-node to model the grout-strand interface. Also, considering beams for the strands reduces considerably the number of nodes and elements of the model, reducing the computational demand as well, which is one of the main limitations of the previous modelling approach.
- 3) Considering a non-linear bond stress-slip model to characterise the strand-grout interface. The Model Code bond stress-slip is introduced using non-linear springs (COMBIN39) in the longitudinal direction, whereas linear springs (COMBIN14) of high stiffness ( $k = 10^{12}$

N/m) are modelled in the transversal directions. The first branch of the bond stress-slip model (from  $s=0$  to  $s=s_1$ ) is considered linear for simplification.

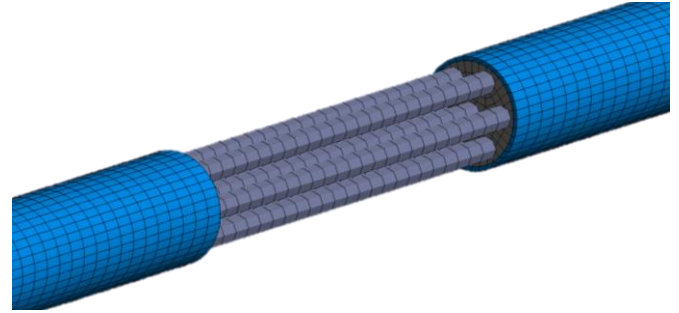


Figure 4. FE tendon model developed (FE model 2).

The differences between the modelling approaches are compiled in Table 3.

Table 3. Comparison of modelling approaches: FE model 1 and FE model 2.

	Sheathing duct	Strand elements	Strand-grout interface
FE model 1 [4]	Not modelled	SOLID186	Bonded contact
FE model 2	SOLID186 elements	BEAM188	Non-linear springs (bond stress-slip/bonded)

Then, four different results are compared:

- (i) Lee and Kang experimental results.
- (ii) FE model 1 with bonded contact between strands and grout.
- (iii) FE model 2 with bonded contact between strands and grout.
- (iv) FE model 2 with non-linear bond stress-slip behaviour.

## 2.4 Analysis description

A non-linear static analysis by load steps is performed. A sparse direct solver and the Newton-Raphson algorithm with convergence in forces, displacements, and moments are used. The non-linearity is caused by the activation and deactivation of elements. The influence of strands' plasticity, large displacement analysis, the grout-strand contact modelling (re-anchoring effects), and the mechanical properties of the grout on the FE modelling are studied. The FE analysis follows these steps (Figure 5):

- i) Stressing of the strands by applying a thermal load. The stressing of the strands was executed at 70% of their ultimate stress,  $f_{pu}$ . The temperature decrease  $\Delta T$  is equal to:

$$\Delta T = \frac{0.7 f_{pu}}{E_s \alpha}, \quad (1)$$

where  $E_s$  is the elastic modulus of the strands, and  $\alpha$  is the thermal expansion coefficient, taken as  $1.2 \cdot 10^{-5} \text{ } ^\circ\text{C}^{-1}$ .

- ii) Activation of the grout to simulate injection.

iii) Successive breakage of five strands in five different steps by eliminating elements. The order of strand breakage is from 1 to 5, the strands numeration is illustrated in Figure 5.

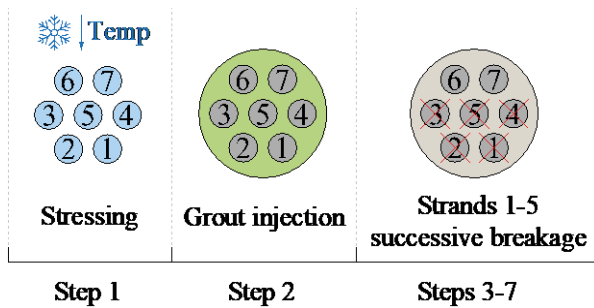


Figure 5. Steps of the FE non-linear static analysis performed.

Furthermore, a modal analysis is performed after each strand breakage step to assess the progressive reduction in the tendon's natural frequencies, which are useful as performance indicators (PIs) when performing vibration-based SHM of these elements. The characteristic stress state corresponding to each load step is incorporated into the modal analysis through the application of a preload state.

### 3 RESULTS DISCUSSION

#### 3.1 Tensile force degradation with damage

The evolution of tensile force,  $T$ , with damage,  $D$ , in the anchorage (outside the transfer length) is shown in Figure 6. The re-anchoring effect is captured by the proposed modelling approach (FE model 2), with a similar trend to the experimental and previous numerical results (FE model 1). It must be noted that the re-anchoring length in the FE model 1 was an adjusted parameter to replicate the experimental results, whereas in the FE model 2, it is a result of the implemented contact law. Thus, FE model 2 can replicate the phenomenological behaviour without requiring any preliminary calibration, as opposed to FE model 1. However, the differences observed in the most recent modelling approach compared to the previous one are noticeable. This may be due to modelling the strands as beam elements instead of solid bodies, which may not adequately capture the internal stress distribution within the strand volume.

When comparing the two grout-strand interface models (represented by the green and blue curves), the results are almost identical, indicating that the influence of the interface model used does not affect the accuracy of the results in reproducing the re-anchoring of the strands. However, these results also suggest that the interface modelling for ribbed bars exhibits greater stiffness compared to that for strand re-anchoring in grout.

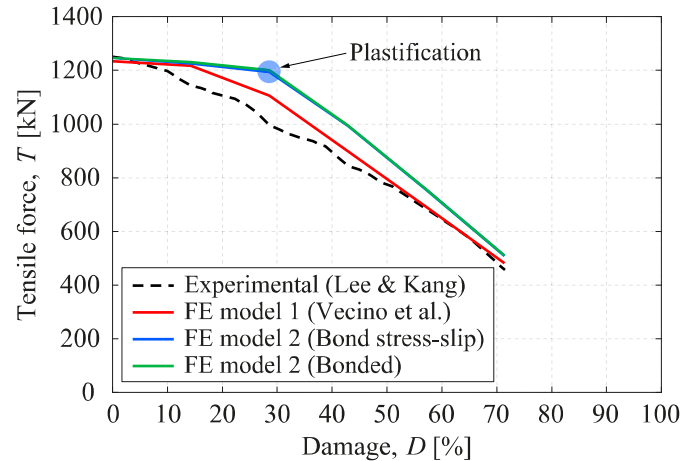


Figure 6. Tensile force degradation with damage.

#### 3.2 Natural frequencies degradation with damage

The evolution of the first four natural frequencies,  $f_i$ , of the tendon as damage progresses is also analysed in Figure 7. In this figure,  $f_{i,exp}$  refers to the frequencies obtained in the Lee & Kang experiment,  $f_{i,num}$  to the ones corresponding to the FE model 1, whereas the other two frequency groups refer to the FE model 2 with bonded and bond stress-slip models.

A behaviour similar to that observed in the tensile force degradation is noted when comparing the FE model results with the experimental data. While the overall trend is consistent, the natural frequencies predicted by the models are slightly higher than the experimental values, and the new modelling approach exhibits more pronounced discrepancies. However, the results obtained using the different interface models remain phenomenologically similar.

The degradation of natural frequencies becomes more pronounced at higher damage levels and is more significant in absolute terms for the higher modes. Accurately quantifying the absolute reduction in frequencies is important for their effective use as a PI in structural health assessment [4].

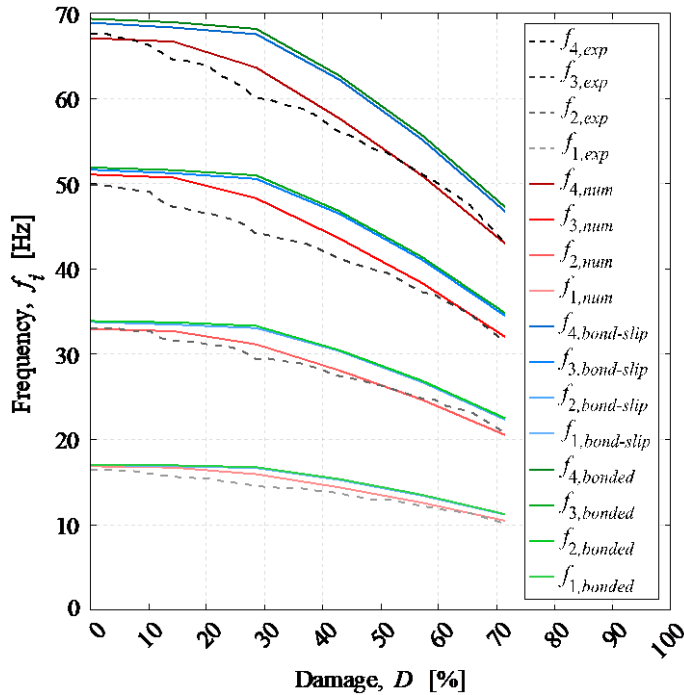


Figure 7. Frequency degradation with damage.

### 3.3 FE model 2: normal stresses along the strands

Two strands are considered for the study of the normal stresses along the strands: i) Strand 5, which is the central strand and is the last to break (Figure 8), and ii) Strand 6, which is a central that remains continuous throughout the entire analysis (Figure 9). The two interface models (bonded and bond stress-slip) are also compared.

Strand 5 exhibits a local increase in stresses as a result of the successive breakage of strands, becoming more pronounced as damage progresses, with fewer continuous strand remaining to carry the stresses of the broken ones. Additionally, the re-anchoring effect is observed in both models, where, in regions distant from the vicinity of breakage, the stress along the strand remains constant. Along the re-anchoring length, a transition occurs between the constant stress away from the breakage zone and the increased stress near the breakage. Both models effectively represent the re-anchoring effect; however, the primary difference lies in the re-anchoring length. The bond stress-slip model (Figure 8 (a)) shows a larger re-anchoring length, approximately 1.9 m, with a smoother transition in stresses, while the bonded model (Figure 8 (b)) exhibits a shorter re-anchoring length, around 0.9 m. This results in a difference of approximately 1 m in the re-anchoring length between the two models.

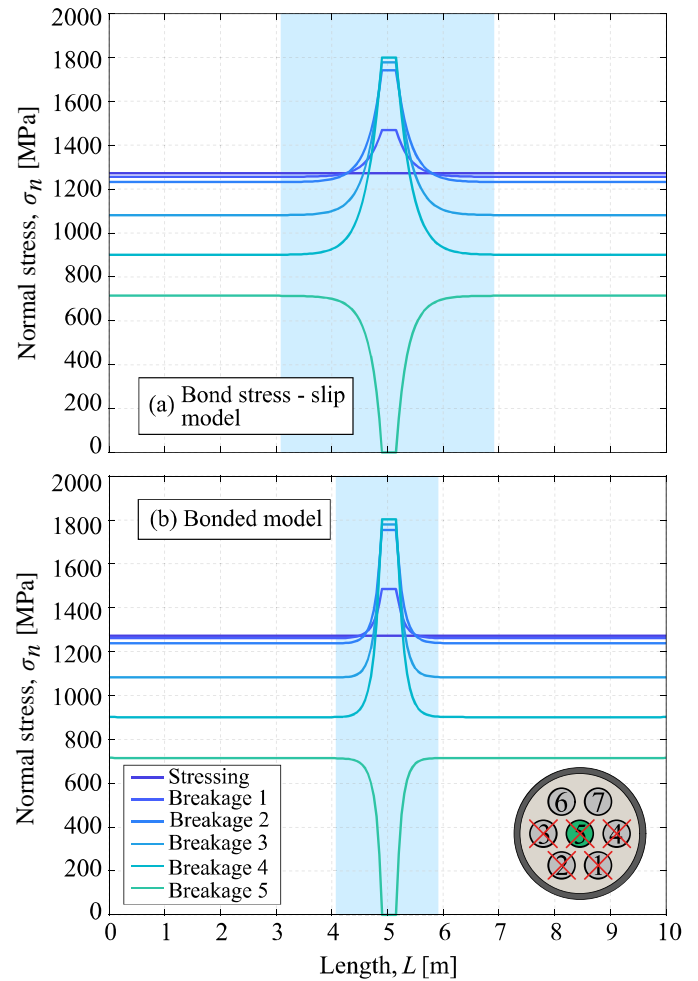


Figure 8. Normal stresses along strand 5 for different strand-grout interface modelling. (a) Bond stress-slip model. (b) Bonded model. Blue shadowed areas indicate the re-anchoring length.

Similar results are observed for strand 6. The stress evolution along the strand demonstrates the stress redistribution resulting from the successive breakage of strands. In a similar manner as for strand 5, the re-anchoring length is greater for the bond stress-slip model, where it is 2.2 m, compared to 1.9 m for the bonded model. The difference of 0.3 m is smaller in this case, as this strand does not break during the analysis. Given the exponential nature of the re-anchoring phenomenon, the re-anchoring length is a highly sensitive parameter to the point at which complete re-anchoring is achieved.



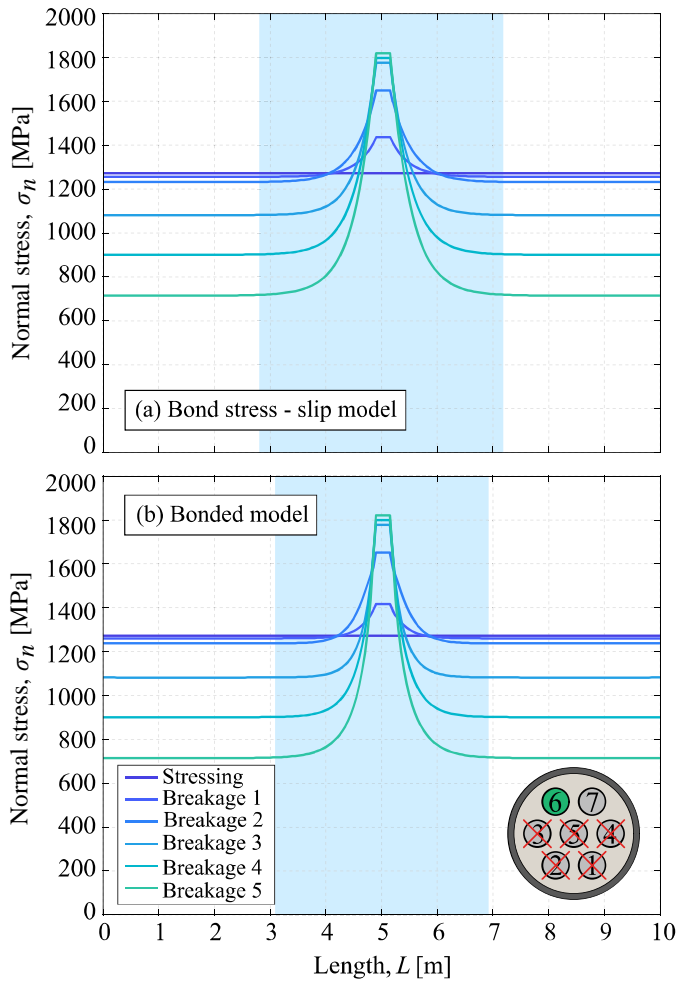


Figure 9. Normal stresses along strand 6 for different strand-grout interface modelling. (a) Bond stress-slip model. (b) Bonded model. Blue shadowed areas indicate the re-anchoring length.

### 3.4 FE model 2: normal stresses in the grout

The normal stresses in the grout as a function of damage are shown in Figure 10 for the two interface models studied, obtaining similar results for both. The grout normal stresses are analysed to characterise the grout's mechanical response, given that it has been modelled as perfectly elastic, which may not accurately represent the typical grout constitutive behaviour.

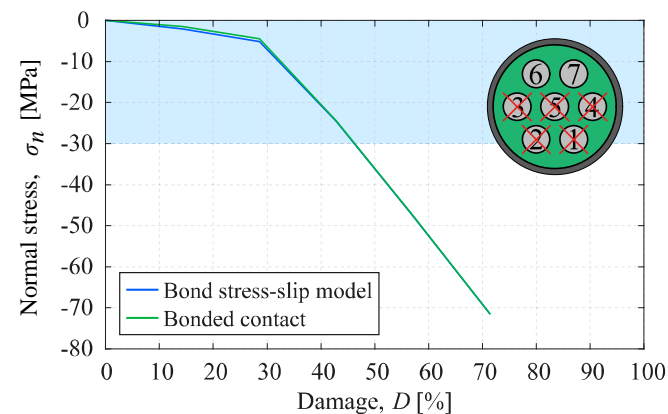


Figure 10. Normal stress in the grout with damage progression.

The compressive strength of the grout is 30 MPa, this value is reached for approximately a 45% of damage. Beyond this point, crack formation and propagation are expected to start. For the maximum damage value studied (71%), the stresses reach 70 MPa, which are considerably high, more than twice the compressive strength of the material. These stress values are not realistic; this highlights the limitations of the linear elastic assumption and suggests the need for a more accurate non-linear constitutive model.

## 4 CONCLUSIONS

The following conclusions are drawn:

1. The tensile force and the natural frequencies serve as PIs for damage detection within the context of SHM, provided that their degradation due to damage is accurately reproduced numerically. It can support early identification of deterioration mechanisms, complement fieldwork, and contribute to a more effective maintenance.
2. The new FE modelling approach shows discrepancies compared to the authors' previous numerical results, which may be attributed to the modelling of strands as beam elements instead of solid bodies. This also may explain the increased deviations from experimental results. However, the use of beam elements reduces computational demands, which was a limiting factor in the previous modelling strategy.
3. The influence of different literature-based grout-strand interface models is minimal compared to a bonded interface behaviour, as the results obtained are nearly identical. The primary difference lies in the re-anchoring length, which is approximately 1 m longer for broken strands when using the bond stress-slip model.
4. The interface models used to simulate ribbed bar pull-out may not be directly applicable to prestressing strands in external grouted tendons. The results indicate that the stiffness of the grout-strand interface may be considerably lower.
5. Future research aimed at improving the FE modelling of grouted tendons should focus on incorporating a non-linear constitutive model for the grout and a more realistic bond stress-slip behaviour with much less stiffness than those used for internal tendons or rebars.
6. In previous work [4], the authors applied the modelling strategy to conduct a parametric study to identify the critical number of strands broken leading to tendon failure. A reliable and efficient FE modelling approach can serve as a valuable tool in SHM applications, enabling risk assessment and early damage detection.

## ACKNOWLEDGMENTS

Research project PID2021-127627OB-I00 funded by MCIN/AEI/10.13039/501100011033/FEDER, EU. Belén Vecino acknowledges the Fundación Agustín de Betancourt for the financial support provided for the development of her doctoral thesis.

## REFERENCES

- [1] Kretz T, Lacombe J-M, Godart B. (2007). Note de sensibilisation sur les ouvrages existants à précontrainte extérieure protégée par du coulis de ciment au contact des armatures. Sétra.
- [2] Lau, K., Permeh, S., & Vigneshwaran, KK. (2016). Corrosion of post-tensioned tendons with deficient grout: Final report. Florida Department of Transportation.
- [3] Lee JK, Kang JW. (2019). Experimental evaluation of vibration response of external post-tensioned tendons with corrosion. *KSCE Journal of Civil Engineering*, 23, 2561–2572. <https://doi.org/10.1007/s12205-019-0735-5>.
- [4] Aparicio J, Hoang T, Cumunel G, Forêt G, Jeanjean Y, Saint Martin JC. (2023). Experimental and numerical study on the re-anchoring of wire in grouted prestressed tendons. In: Istanbul IABSE Symposium (ISTBR 2023) LONG SPAN BRIDGES.
- [5] Vecino B, Renedo CMC, García-Palacios JH, Díaz IM. (2025). Degradation modelling of external grouted post-tensioning tendons: Numerical assessment under corrosion conditions. *Engineering Structures*, 327, 119620.
- [6] Wang L, Yuan P, Zhang X, Dong Y, Ma Y, Zhang J. (2019). Bond behavior between multi-strand tendons and surrounding grout: Interface equivalent modeling method. *Construction and Building Materials*, 226, 61–71. <https://doi.org/10.1016/j.conbuildmat.2019.07.242>.
- [7] Fédération Internationale du Béton. (2020). Model Code 2020: Final version. Vol. 1–2.
- [8] Wang L, Zhang X, Zhang J, Yi J, Liu Y. (2017). Simplified model for corrosion-induced bond degradation between steel strand and concrete. *Journal of Materials in Civil Engineering*, 29(4), 04016257.

# Autonomous peak-picking procedure for tension force estimation in cables and external post-tensioning tendons

Luis Chillitupa-Palomino<sup>1</sup>, 0009-0001-5274-0436, Carlos M.C. Renedo<sup>1</sup>, 0000-0003-1014-0878, Jaime H. Garcia-Palacios<sup>2</sup>, 0000-0003-4336-5520, Iván M. Díaz<sup>1</sup>, 0000-0001-9283-5109

<sup>1</sup>Department of Continuum Mechanics and Theory of Structures, ETSI Caminos, Canales y Puertos, Universidad Politécnica de Madrid, Calle Profesor Aranguren 3, Madrid, 28040, Comunidad de Madrid, Spain

<sup>2</sup>Department of Hydraulics, Energy and Environmental Engineering, ETSI Caminos, Canales y Puertos, Universidad Politécnica de Madrid, Calle Profesor Aranguren 3, 28040 Madrid, Spain

email: luis.cpalomino@upm.es, carlos.martindelaconcha@upm.es, jaime.garcia.palacios@upm.es, ivan.munoz@upm.es

**ABSTRACT:** Cables and external post-tensioning tendons are key elements of modern strategic bridges; however, their structural integrity has been questioned due to some structural collapses registered during the last decades. In this context, cost-effective vibration-based monitoring strategies can be implemented to improve their maintenance by continuously estimating their tension force (a key damage indicator) from their natural frequencies. These frequencies may vary in time due to environmental changes, modification of the service loads, and tensioning processes produced during cable substitution manoeuvres. In monitoring systems that only use one accelerometer per cable (the most common situation in practice), a robust and accurate peak-picking method is required to adequately identify which are their actual almost harmonic natural frequencies and to which modal order they correspond to. Ideally, this method should be automated (to run continuously), autonomous (with as few hyperparameters as possible) and self-regulating (to discard poor quality spectra and outliers). Additionally, the method must be able to cope with two well-known phenomena experienced in practice that dirt cable spectra: i) the double peak effect, and ii) the presence of bracing belts between cables. Thus, this paper works on developing an autonomous peak-picking procedure to cope with the aforementioned phenomena for enabling a reliable tension force estimation method in cable structures. This methodology has been applied to a one-week monitoring data set of measurements of real external post-tensioning tendons of a road bridge in Spain.

**KEY WORDS:** Cable dynamics, Tension estimation, Post-tensioning tendons, Automatic peak-picking, Condition monitoring

## 1 INTRODUCTION

Cables and tendons are crucial elements in bridge engineering but also are vulnerable structural elements because they are usually subjected to fatigue and corrosion problems. Thus, vibration-based non-destructive techniques have been used for external post-tensioning tendon assessment. The main parameter to assess in these cases is the tension force, as this performance indicator can give a clear idea of the condition of the cable and thus, the overall condition of the structure. The tension force is usually estimated from the measured natural frequencies, which are used to inversely solve the dynamic equation of an elastic tensioned cable.

The higher the number of natural frequencies identified, the better the tensile force estimation. Indeed, the estimation of several natural frequencies results compulsory when the bending stiffness of the cable is not negligible. However, this frequency identification is especially challenging when only one accelerometer is employed for monitoring the element, as in these cases, it has to be performed by detecting peaks on the vibration signal's power spectral density (PSD). In the case of simply-supported cables, when their bending stiffness is negligible, the frequencies of these peaks should be perfectly periodical (which corresponds to the blue straight line in Figure 1, where the frequency values are represented against their modal orders). When the bending stiffness has a considerable influence on the cable dynamics, these frequencies are quasi-periodical, gradually increasing the distance between

consecutive peaks. This effect can be clearly seen in the orange line of Figure 1.

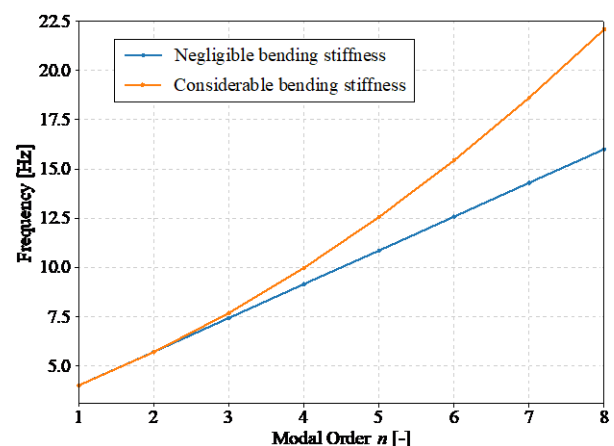


Figure 1: Effect of bending stiffness on natural frequencies.

Although peak-picking may appear to be simple, some issues make difficult the identification procedure and its automatization. First, the variation over time of the natural frequencies to be identified makes more suitable methods that do not use initial guessing values to detect these peaks. Second, the presence of double peaks (doublets) within the PSD. This is caused due to the fact that the cable section may not be perfectly symmetric and thus, certain bending modes may decompose in couples of closely-spaced peaks. Third, the presence of bracing



belts between homologous cables may couple their similar but not identical vibration, also contributing to create doubles. Fourth, in external post-tensioning tendons running through several spans, the vibration of the different sections of the cable between deviators (with different span lengths) may be coupled, providing dirty spectra in which harmonics of neighbouring cable segments are mixed. Finally, interactions between the measured cable and other structural elements may dirt the PSD signals, thus, perturbing the frequency identification process and provoking an unreliable tension estimation. A typical situation of this type occurs in cable stayed bridges, when the vibration of the deck is transmitted to the stay cables or hangers.

Some authors have faced in the past the problem of developing a real-time and automatic frequency identification methodology for performing an accurate tension estimation in cable elements. This automatization has been solved in a variety of ways within the literature. Most of them detect these frequencies by performing an automatic peak-picking process from the signal's PSD. Initially, Cho et al. [5] belowproposed a simple iterative process that lacked the necessary robustness. Then, Sim et al. [6] studied a frequency tracking method based on providing reference initial guessing values around which the peak search is performed. They claim its validity based on two facts: i) the frequencies variation due to environmental changes are small, and ii) the searched peaks are well-separated.

Regarding deep learning applications, Kim et al. [7] have developed a tool based on object detection for performing automatic peak-picking from PSDs images with a region based convolutional neural network (a similar method is researched by Chen et al. [9]). The main advantage of this approach lays on the fact that no guessing values need to be provided, although the robustness of these tools rely on their training data set. Later, Jeong et al. [8] applied this latter method for performing automatic tension estimation on cables. They worry about the detection of undesired peaks not corresponding to cable natural frequencies. For that, they use the frequency distance between peaks, also named as 'interval'. The main drawbacks of such a methodology will be discussed later. However, they do not cover issues as: i) how to correctly assign the modal order to each peak, ii) how to manage missing peaks that interrupt a series of consecutive frequencies, and iii) how optimize the computational cost for its proper in-line implementation in continuous monitoring systems.

One of the most revealing contributions is the one by Zhang et al. [10] that provided a clear explanation of the main challenges arising when performing tension estimation from cable vibration data, namely: i) detection of useful PSDs with recognizable peaks, ii) automatic and robust identification of frequency peaks, and iii) assignation of modal orders to the identified frequencies. They proposed a simple methodology based on updating a threshold prominence value till a minimum number of peaks has been identified. After this, they discard fake peaks if their frequency is not a multiple of the most common value for the interval. With this same principle, they assign the modal order to the peaks. This method results quite applicable to cables with low-bending stiffness ( $EI$ ), however, when  $EI$  is remarkable, its applicability is limited, as proportionality is lost for higher modes. Another important contribution is the one of Jin et al. [2] in which the automated

peak-picking is covered in detailed, remarking important facts such as the necessity of removing the baseline from the PSD curve to assess all the peaks with the same floor level. Their proposal is based on the application of a breakthrough multiscale-based peak detection algorithm (previously developed by [1]) combined with a criterion based on the median absolute deviation of the detected peaks. They compared this method with the one developed by Jeong et al. [8] confirming a substantial enhancement. Despite this, they do not provide any strategy to detect false peaks apart from the robustness of the method.

The present research provides a modified methodology for performing autonomous peak-picking detection based on the findings by Jin et al. [2]. To the authors knowledge, all the contributions covering autonomous tension estimation of cable structures have dealt with long cables of cable-stayed bridges with  $EI$  not influencing their dynamic. This paper, for the first time, addresses this automatization problem in much shorter external post-tensioning tendons with non-negligible  $EI$  influence.

This paper has been structured as follows: after the present section, Section 2 presents the autonomous peak-picking methodology. Section 3 illustrates a variation of the methodology for its in-line integration into a continuous monitoring system. Section 4 demonstrates the application of the methodology to data obtained from a week-long continuous monitoring measurement in an in-service post-tensioning tendon. Finally, Section 5 provides some conclusions and future works.

## 2 AUTONOMOUS PEAK PICKING METHODOLOGY

As mentioned before, an autonomous peak-picking method is an essential previous element to continuously estimate the tension force of cables from a single vibration measurement registered within a continuous monitoring application. The present paper proposes a method for that, based on the contribution of Jin et al. [2] in which the main innovation is the implementation of the so-called multi-scale peak detection algorithm previously developed by [1]. This algorithm, which is the core of the method, was conceived to detect periodic peaks within signals (indeed, it has been applied to detect heart beats). This is done through building the so-called local maximum scalogram (LMS) of the signal being analysed. A scalogram is a graphical representation of a given signal's magnitude, resulting from analysing it using moving windows of different scale (number of samples). With the LMS, it can be detected the particular scale related to the interval of the periodic peaks being searched. Jin et al. [2] applied this concept to successfully analyse the PSDs of cable vibrations.

On the one hand, for smoothly detecting environmental changes on the natural frequencies of cables, a great frequency resolution,  $\Delta f = 1/T$  ( $T$  being the duration of the time-domain measured signal) and high sampling frequencies are required to detect a significant number of harmonics, are needed within the PSDs to be analysed. On the other hand, if these PSDs are such long vectors, the computational cost and memory involved on computing their LMS matrices may prevent from performing this process in real time within a continuous monitoring loop (the complexity of the problem is  $O(n^2/2)$ ). To cope with this issue, a two-step procedure has been proposed: i) developing

the LMS of a low-resolution PSD for roughly detecting the frequencies of the harmonic peaks. Then, frequency bands for later searching them more precisely are created, and ii) searching the final frequency values within a high-resolution PSD using these bands. Apart from these aspects, the following sections cover other considerations which are capital for successfully implementing the methodology in practice when dealing with post-tensioning tendons.

### 2.1 Signal pre-processing

This process has been depicted in Figure 2. First, the time signal obtained from the monitoring system is detrended to eliminate any drifting caused by many factors, such as instrumental nonlinearity or signal offsets. Then, a low-pass filter is applied to eliminate peaks belonging to unimportant high frequency vibration that might shadow the actual peaks of interest. Furthermore, the filter cutoff frequency should be in accordance with the higher frequency order of interest for the posterior tension force estimation. Finally, the data is resampled (first interpolated and then decimated) to convert the original low-filtered signal to a lower rate in accordance with the low cutoff frequency.

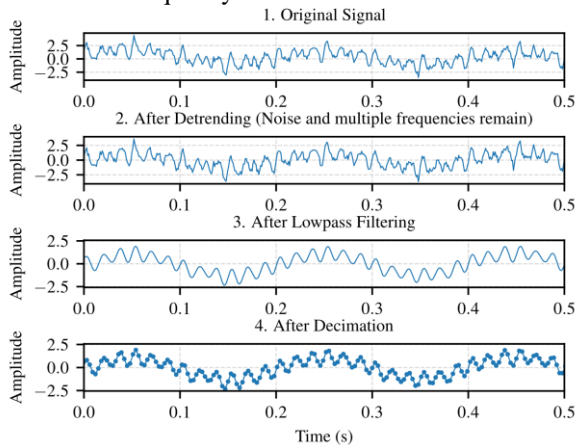


Figure 2: Signal pre-processing steps.

### 2.2 Low-resolution PSD of the signal

As previously mentioned, a low-frequency-resolution PSD is employed as a workaround to mitigate the high computational cost associated with generating a LMS from a PSD with sufficient frequency-resolution to capture the variation of natural frequencies with temperature. This first PSD is obtained applying the Welch's method using a high averaging of short time windows.

### 2.3 Baseline correction

Baseline correction is a crucial step in the methodology, as the shape of the spectrum can affect the algorithm's ability to detect certain peaks. Figure 3 provides an example of this process for a cable PSD. To ensure optimal performance, various methods such as polynomial-based, morphological, and asymmetric least squares have been investigated within the literature.

For the baseline correction there are many alternatives such as using the Savitsky-Golay filters, as mentioned in [2], but as indicated in [3], a better alternative is to rely on the use of asymmetric least squares smoothing.

The idea is that for a signal vector  $\bar{y}$  with a number of samples equal to  $m$ , there should be a 'baseline' signal  $\bar{z}$  of equal length that meets the two following characteristics: i) being enough faithful to  $\bar{y}$ , and ii) being smooth. Hence, the following least squares function,  $S$ , can be built to add together these two effects:

$$S = \sum_i^m \omega_i (y_i - z_i)^2 + \lambda \sum_i^m (\mathcal{A}^2 z_i)^2, \quad (1)$$

where  $i$  is an index corresponding to each sample of the signal, and  $\omega_i$  and  $\lambda$  are a penalty parameter, and a smoothing parameter, respectively, both controlling the balance between these two characteristics. The first term of this equation measures the baseline 'fidelity' to the original signal, while the second one regulates the 'roughness' of the baseline.

The higher the value of  $S$ , the less these two requirements are fulfilled. Thus,  $S$  must be minimized in terms of  $\bar{z}$ , to find an optimal baseline ( $dS/d\bar{z} = 0$ ). After that, the following matrix expression can be derived, from which the vector  $\bar{z}$  can be obtained:

$$(\mathbf{W} + \lambda \mathbf{D}' \mathbf{D}) \bar{z} = \mathbf{W} \bar{y}, \quad (2)$$

where  $\mathbf{D}$  is a backward second-order-finite-difference matrix and  $\mathbf{D}'$  its transpose.  $\mathbf{W}$  is a weighted penalty diagonal matrix composed of  $\omega_i$  values obtained as follows:

$$\omega_i = \begin{cases} p & , y_i > z_i \\ 1 - p & , y_i < z_i \end{cases}, \quad (3)$$

where  $p$  is a small value between  $[0.1, 0.001]$  which represents an asymmetry factor to consider the fact that a PSD baseline is usually underneath the original PSD. This factor determines a low penalty for positive residuals ( $y_i > z_i$ ) compared to a high penalty applied to negative residuals ( $y_i < z_i$ ).

The baseline correction is an iterative process that starts assigning initial values to  $\omega_i$ . After that,  $\bar{z}$  and  $\omega_i$  are iteratively computed using (2) and (3) till achieving convergence. Among all,  $\lambda$  is the most influential factor in this process. Its value must be manually set between  $[10^2, 10^9]$ .

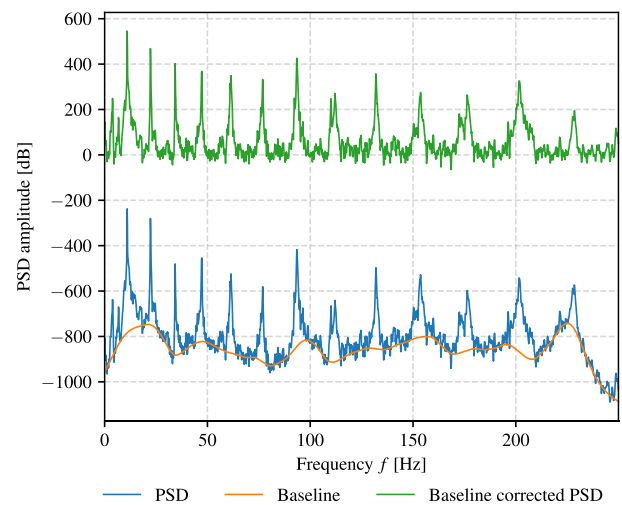


Figure 3: Baseline and baseline corrected PSD.

#### 2.4 Local maxima scalogram and optimal scale selection

From the low-resolution baseline-corrected PSD a LMS is created. This is done by analysing the PSD with a series of moving windows with different number of samples  $w_k$ , defined as two times the ‘scale’ of the window  $k$  ( $w_k = 2k$ ). This scale is a natural number ranging from 1 to  $L$ , being defined as  $L = \text{ceil}(N/2) - 1$ , being  $N$  the total length of the PSD.

Every window of scale  $k$  runs through the signal sample by sample. Considering  $j$  as the sample index on which the window is centrally positioned, for a given scale  $k$ ,  $j$  will vary from  $[k + 1, N - k]$ . The LMS is a matrix of dimensions  $L \times N$  composed of  $m_{k,j}$  elements resulting from moving different windows along the PSD samples. Each  $m_{k,j}$  is obtained using a subset of three samples contained within a given window, namely, the two window edges and the central sample  $[y_{j-k}, y_j, y_{j+k}]$  (see Figure 4). Thus,  $m_{k,j}$  is computed as follows:

$$m_{k,j} = \begin{cases} 0, & \text{if } y_j = \max(y_{j-k}, y_j, y_{j+k}) \\ r + 1, & \text{otherwise} \end{cases} \quad (4)$$

where  $r$  is a random number between 0 and 1. Finally, the LMS matrix,  $\mathbf{M}$ , gets the form:

$$\mathbf{M} = m_{k,j} = \begin{bmatrix} m_{1,1} & \cdots & m_{1,N} \\ \vdots & \ddots & \vdots \\ m_{L,1} & \cdots & m_{L,N} \end{bmatrix} \quad (6)$$

Thus,  $\mathbf{M}$  is a matrix whose elements  $m_{k,j}$  indicate whether the current PSD  $j^{\text{th}}$  value is higher than the neighbours at the edges of the corresponding window with scale  $k$ . A graphical representation of  $\mathbf{M}$  is given in Figure 5 (white colour corresponds to zero values around the peak regions).

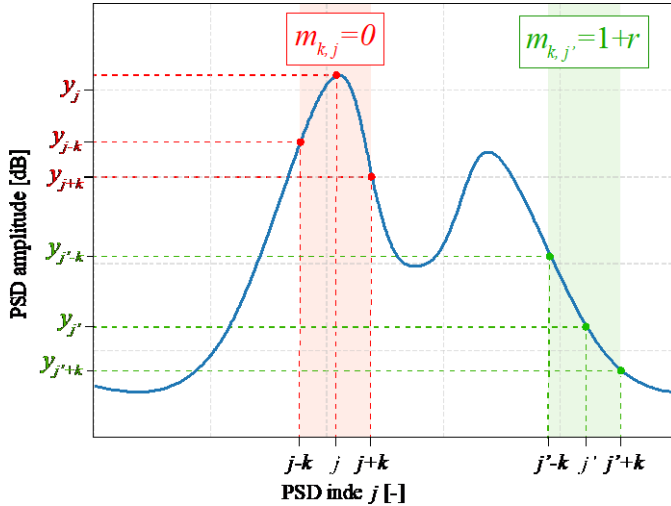


Figure 4: Subset value.

Once the LMS has been created, a row-wise summation is performed in the matrix to obtain the vector  $\bar{\gamma}_k$  (represented in Figure 6 as a function of  $k$ ) as follows:

$$\bar{\gamma}_k = \sum_{j=1}^N m_{k,j}. \quad (6)$$

The scale for which the value of this vector is minimum,  $k_{min}$  is the one accounting with more zero values, thus, it corresponds to the rate of appearance of quasiperiodic peaks in the PSD. This value is obtained as follows:

$$k_{min} = \{k \in \mathbb{N} \mid \gamma_{k_{min}} = \min(\bar{\gamma}_k)\} \quad (7)$$

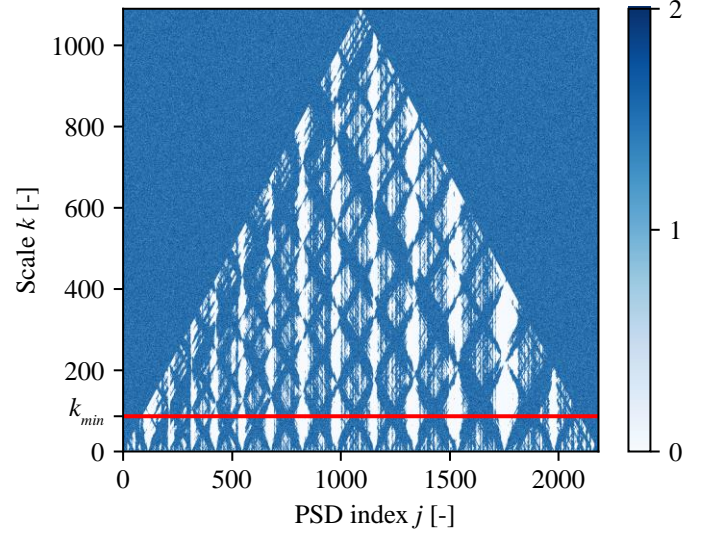


Figure 5: Complete scalogram of baseline-corrected low-resolution PSD.

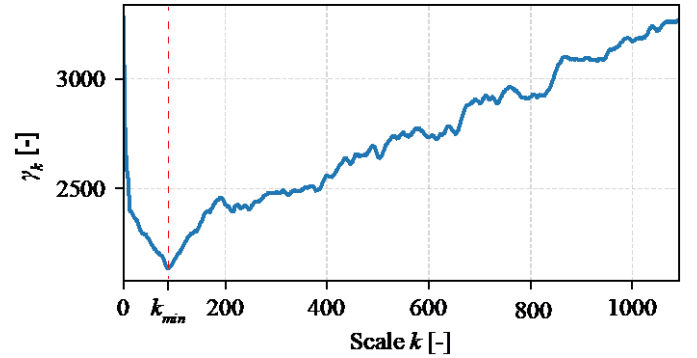


Figure 6: Minimum k scale identification.

Although the methodology works reasonably well, there might detect fake peaks near the PSD borders. To address this issue, it is recommended to add zero-padding to each side of the baseline-corrected-PSD. The extension of this padding must be in proportion with the length of the PSD.

#### 2.5 Rescaled LMS and column-wise sum

After obtaining  $k_{min}$  the scalogram is ‘cut’ only considering scales ranging from 1 to  $k_{min}$ . In this reduced version of the LMS a column-wise summation is performed to identify PSD samples whose overall sum is zero. This means that for every scale from 1 to  $k_{min}$  these particular samples with index  $j_{n,low}$  have a zero value in the scalogram, and therefore, they can be identified as peaks corresponding to cable’s natural frequencies  $f_{n,low} = j_{n,low} \Delta f$  in the PSD. Figure 7 shows the reduced LMS with red vertical lines indicating the columns where the  $j_{n,low}$  values are located.



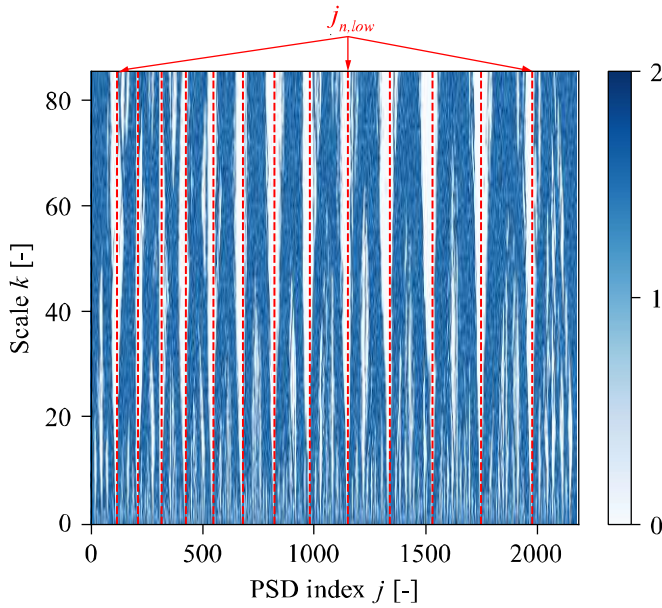


Figure 7: Rescaled LMS.

### 2.6 High-resolution PSD peaks identification

Once the peak regions have been located within a low-resolution PSD, the final peaks positions need to be precisely identified within a high-resolution PSD. This high-resolution PSD is computed using the Welch's method, considering much longer window lengths (half of the overall signal length) with a 50% of overlapping. Additional zero-padding is applied to each signal segment to improve the frequency resolution.

Within the high-resolution PSD, a precise search is performed in frequency bands associated to each  $f_{n,low}$  within the intervals  $\left[ f_{n,low} - \Delta f \cdot \left( \frac{k_{min}}{4} \right), f_{n,low} + \Delta f \cdot \left( \frac{k_{min}}{4} \right) \right]$ . The final natural frequency  $f_n$  is the one associated to the maximum of the high-resolution PSD value within the above interval. Figure 8 illustrates the aforementioned high-resolution PSD peak identification procedure.

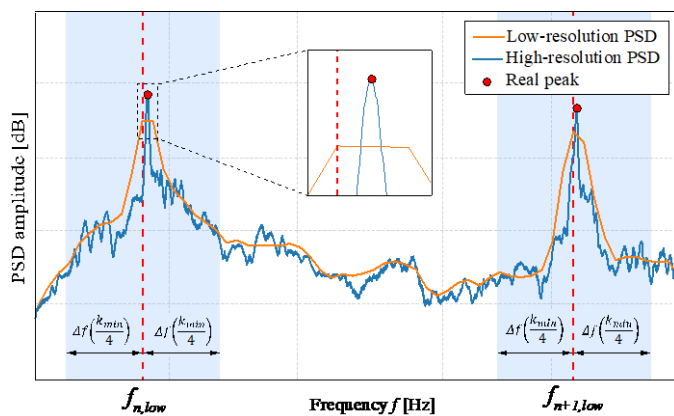


Figure 8: High-resolution PSD peaks identification scheme.

Applying this methodology to a PSD resulting from the vibration measurement of a cable, the results obtained are displayed in Figure 9.

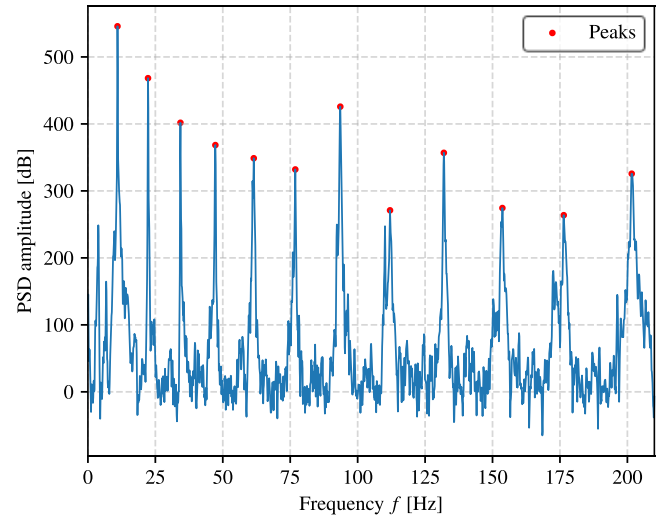


Figure 9: High-resolution PSD with the identified peaks.

## 3 EXAMPLE OF APPLICATION

The procedure presented in the previous section has been performed using the data obtained during 7 days of continuous monitoring of an external post-tensioning tendon belonging to a highway road bridge in Spain. The bridge monitored is a precast segmental externally post-tensioned bridge consisting of simply supported spans. The tendons monitored were grouted tendons made of 31 high-strength steel post-tensioning strands, each one made of 7 twisted wires of 6 mm of diameter. These strands were embedded inside a HDPE duct of 140 mm of diameter. Once tensioned, the duct was filled with grout to provide corrosion protection. This grout provides a monolithic effect to the tendon's section, which confers it a non-negligible bending stiffness. The accelerometers used were PCB-393B12 and were mounted using a clamp system attached to the tendon duct with bolts. Figure 10 depicts the bridge object of the study. The cable section being monitored is highlighted in red. Figure 11 shows the accelerometer mounted on the tendon.

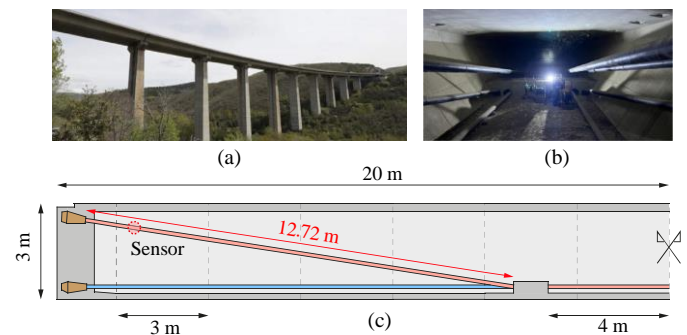


Figure 10: Description of the tendon being monitored

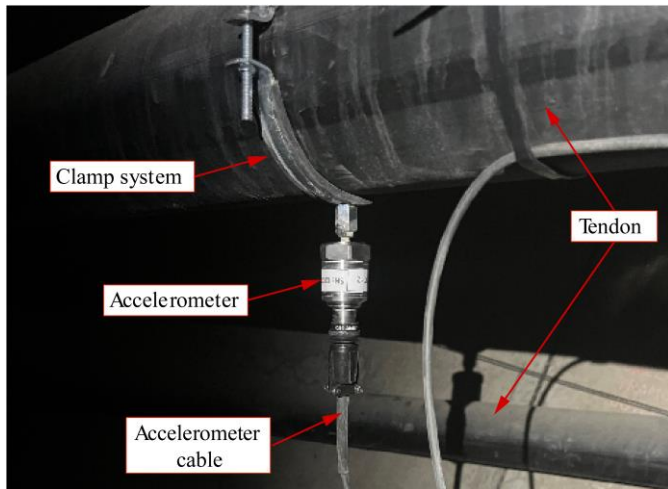


Figure 11: Accelerometer mounted on a tendon.

### 3.1 Analysis of a single data block

A single 10-minute data block has been analysed here to demonstrate the usefulness of the presented autonomous peak-picking methodology. The signal was acquired with a sampling frequency of 1651 Hz. The time-history and the corresponding PSD of this data block is shown in Figure 12.

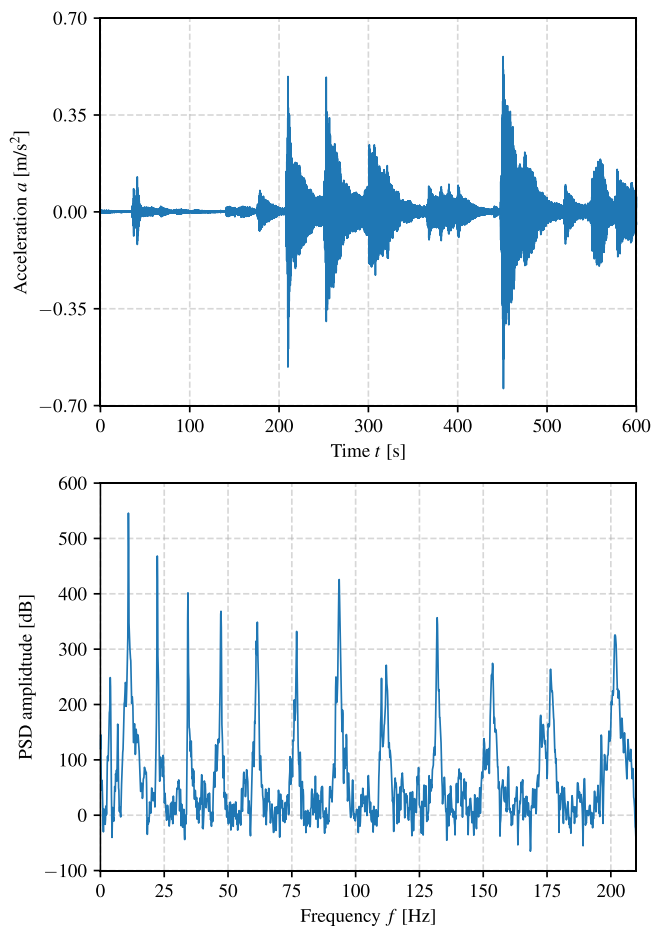


Figure 12: Analysis of a 10-minute data block.

The peaks detected present the noticeable effect of the bending stiffness, this effect can be seen in Figure 13, where the first 4 natural frequencies show a linear trend while starting

from the fifth natural frequency the data starts to show a non-linear trend.

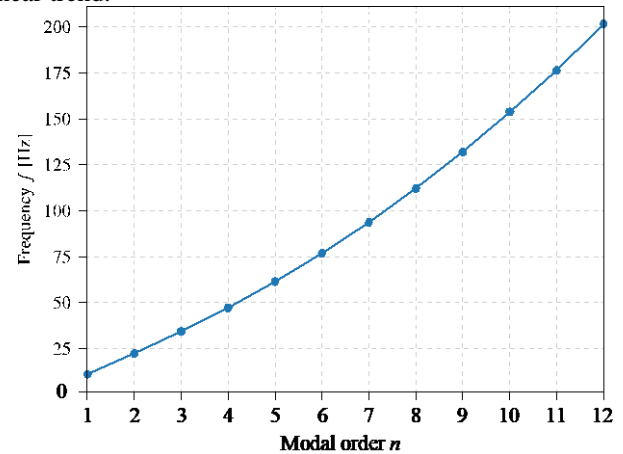


Figure 13: Modal order vs Frequency of a single data block.

### 3.2 Analysis of a one-day long data set

The variation of the different natural frequencies on the cable due to the temperature effect through one day has been firstly analysed. For that, the absolute frequency variation with respect to the initial frequencies being identified (those of the first 10-minutes record at 00:00) has been computed. Figure 14 shows this variation. It can be appreciated that the 4<sup>th</sup> modal order presents a slightly different behaviour this is due to its associated doublet. From this analysis, it can be also recognized how this variation is higher for higher modal orders.

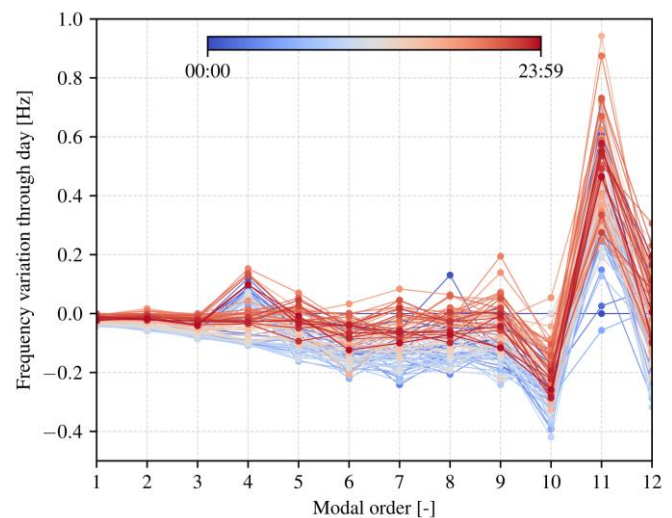


Figure 14: Temperature variation relative to the ones recorded at 00:00.

### 3.3 Analysis of a one-week long data set

Figure 15 shows the first 12 natural frequencies identified using the presented methodology. From the analysed data set, it can be confirmed the influence of temperature variation over frequency. While this variation is small, knowing its magnitude is fundamental to distinguish between environmental or damage variations. These results confirm the validity of the methodology applied and its use within a continuous monitoring loop.

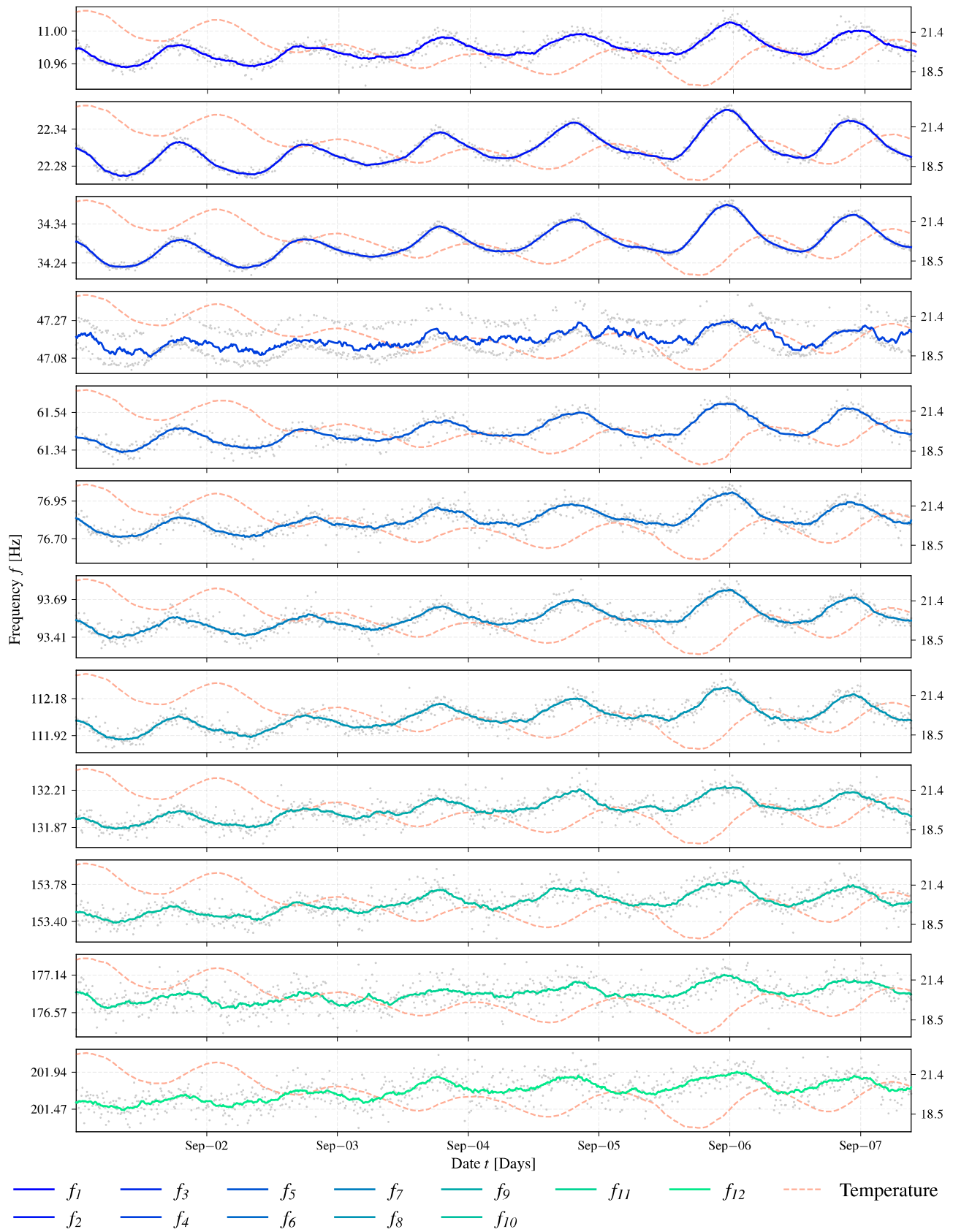


Figure 15: Complete frequency distribution along the week-long continuous monitoring.



## 4 CONCLUSIONS

An autonomous pick-picking procedure based on two PSDs (low and high resolution PSDs) combined with the use of a LMS procedure has been presented. The methodology has been conceived for its inclusion in continuous monitoring systems and to perform in-line tension force estimation since computation costs have been considered within the proposed methodology. From the results obtained from the one-week long monitoring data, it has been shown the performance of the proposed methodology.

Finally, some future works may include the autonomous identification of missing frequencies by the method, which can difficult cable tension estimation as this calculation depends on the natural frequencies and their corresponding modal orders correctly identified. Aside from this, the inclusion of the optimized asymmetric least squares (O-ALS) [4] baseline correction method which does not need hyperparameters fine tuning could be included.

## ACKNOWLEDGMENTS

Supported by Research project PID2021-127627OB-I00 funded by MCIN AEI/10.13039/501100011033/FEDER, EU and Fundación Agustín de Betancourt.

## REFERENCES

- [1] Scholkmann, F., Boss, J., & Wolf, M. (2012). An Efficient Algorithm for Automatic Peak Detection in Noisy Periodic and Quasi-Periodic Signals. *Algorithms*, 5(4), 588–603. <https://doi.org/10.3390/a5040588>
- [2] Jin, S.-S., Jeong, S., Sim, S.-H., Seo, D.-W., & Park, Y.-S. (2021). Fully automated peak-picking method for an autonomous stay-cable monitoring system in cable-stayed bridges. *Automation in Construction*, 126, 103628. <https://doi.org/10.1016/j.autcon.2021.103628>
- [3] Eilers, P. H. C. (2003). A Perfect Smoother. *Analytical Chemistry*, 75(14), 3631–3636. <https://doi.org/10.1021/ac034173t>
- [4] Dong, Z., & Xu, J. (2024). Baseline estimation using optimized asymmetric least squares (O-ALS). *Measurement*, 233, 114731. <https://doi.org/10.1016/j.measurement.2024.114731>
- [5] Cho, S., Lynch, J. P., Lee, J.-J., & Yun, C.-B. (2010). Development of an Automated Wireless Tension Force Estimation System for Cable-stayed Bridges. *Journal of Intelligent Material Systems and Structures*, 21(3), 361–376. <https://doi.org/10.1177/1045389X09350719>
- [6] Sim, S.-H., Li, J., Jo, H., Park, J.-W., Cho, S., Spencer Jr, B. F., & Jung, H.-J. (2014). A wireless smart sensor network for automated monitoring of cable tension. *Smart Materials and Structures*, 23(2), 025006. <https://doi.org/10.1088/0964-1726/23/2/025006>
- [7] Kim, H., & Sim, S. (2019). Automated peak picking using region-based convolutional neural network for operational modal analysis. *Structural Control and Health Monitoring*, 26(11). <https://doi.org/10.1002/stc.2436>
- [8] Jeong, S., Kim, H., Lee, J., & Sim, S.-H. (2021). Automated wireless monitoring system for cable tension forces using deep learning. *Structural Health Monitoring*, 20(4), 1805–1821. <https://doi.org/10.1177/1475921720935837>
- [9] Chen, Z.-W., Ruan, X.-Z., Liu, K.-M., Yan, W.-J., Liu, J.-T., & Ye, D.-C. (2022). Fully automated natural frequency identification based on deep-learning-enhanced computer vision and power spectral density transmissibility. *Advances in Structural Engineering*, 25(13), 2722–2737. <https://doi.org/10.1177/13694332221107572>
- [10] Zhang, M., He, H., Li, G., & Wang, H. (2021). Fully Automated and Robust Cable Tension Estimation of Wireless Sensor Networks System. *Sensors*, 21(21), 7229. <https://doi.org/10.3390/s21217229>
- [11] Wu, W.-H., Chen, C.-C., Lin, S.-L., & Lai, G. (2023). A Real-Time Monitoring System for Cable Tension with Vibration Signals Based on an Automated Algorithm to Sieve Out Reliable Modal Frequencies. *Structural Control and Health Monitoring*, 2023, 1–25. <https://doi.org/10.1155/2023/9343343>
- [12] Yuan, Y., Au, F. T. K., Yang, D., & Zhang, J. (2024). Active learning guided automated cable force monitoring based on modified S-transform. *Measurement*, 224, 113880. <https://doi.org/10.1016/j.measurement.2023.113880>

# Field monitoring and mitigation for high-mode vortex-induced vibrations of cables in cable-stayed bridges

Yuxuan Yan<sup>1,2</sup>, Xin Wang<sup>3</sup>, Hao Hu<sup>1,2</sup>, Hua Guan<sup>4</sup>, Kai Wang<sup>5</sup>

<sup>1</sup>Zhejiang Scientific Research Institute of Transport, Hangzhou, China

<sup>2</sup>Zhejiang Provincial Key Lab for Detection and Maintenance Technology of Road and Bridge, Hangzhou, China

<sup>3</sup>Quzhou Highway and Transport Management Center, Quzhou, China

<sup>4</sup>Zhejiang Zhoushan Sea Crossing Bridge Co. Ltd., Ningbo, China

<sup>5</sup>CCCC Highway Consultants Co., Ltd., Ningbo, China

email: yanyuxuan\_2022@163.com, 83702075@qq.com, hhu@zjjtkyy.com, 9580520@qq.com, 514586067@qq.com

**ABSTRACT:** With the increase in the span of cable-stayed bridges, stay cables tend to become more flexible and longer, which leads to lower damping and structural natural frequency. Therefore, it is more vulnerable to wind load effects. This study aims to investigate the characteristics and mechanisms of vortex-induced vibrations (VIVs) of stay cables based on long-term field monitoring for a sea-crossing cable-stayed bridge. First, a vibration monitoring system with a high sampling frequency for cables was established. On this basis, the time history data of vibration acceleration for cables with different lengths were collected to study the vibration characteristics, such as vibration amplitudes and frequency distributions of cables. For the longer stay cables, the cable vibrations with over-limit acceleration amplitudes were observed in a wind velocity region of 6–9m/s with very high vibration frequencies, and the wind directions that caused the vibrations were almost vertical to the stay cables. The mechanism of cable vibrations was discussed and investigated based on the relationship between wind characteristics parameters and the vibration response of cables. VIV occurred because the control frequencies of the cable vibrations coincided with the high-mode vortex shedding frequencies of the cables. Finally, the effects of different types of dampers on suppressing VIV were compared and investigated.

**KEY WORDS:** Cable-stayed bridge; cable vibration; bridge health monitoring; vortex-induced vibration.

## 1 INTRODUCTION

In the past few decades, cables have been widely used in long-span bridges. The cables of bridges tend to be more flexible, longer, and prone to vibrate due to low damping and structural natural frequency. The wind-induced vibration of stay cable can be roughly categorized as rain-wind-induced vibrations (RWIV), vortex-induced vibrations (VIV), and dry galloping (DG) classified by different vibration mechanisms and characteristics.

VIV of cables is a common form of cable aerodynamic instability phenomena with limited vibration amplitudes. When flow passes around cables, vortices are generated along the profiles of cylinder cables, alternatively on the upper and lower sides, and induce forces perpendicular to the wind direction[1]. As the length of stay cables grows, the structural natural frequency tends to be much smaller, indicating a much lower critical wind velocity corresponding to the classical vortex shedding. For a long cable, a high-mode VIV can be easily excited even under a moderate wind speed.

Field monitoring is meaningful for investigating the vibration characteristics of cables. Based on continuous half-year data from the bridge structural health monitoring system (SHMS), Ge found the frequency of the in-plane VIV is around 9.6 Hz for a 577m cable, and then validated that the cable is mainly subjected to high-frequency VIV[2]. Matsumoto conducted a field observation for a cable model of the Meiko West Bridge and discovered rain-wind-induced vibrations by comparing the vibration characteristics under different weather conditions [3]. Cable vibrations of the Fred Hartman Bridge were also investigated and studied by field monitoring. RWIV requires a much higher reduced velocity than that required by

VIV[4], and the high-order modes play the dominant role in the VIV of cables[5].

The vibrations of cables may cause fatigue or service problems if the vibration amplitudes are not mitigated by dampers or other countermeasures[6]. Therefore, aerodynamic and damping countermeasures were employed to mitigate cable vibrations. To optimize the aerodynamic profile of cables, the effects of helical strakes on suppressing VIV are studied by field measurements [7] and wind tunnel tests [8]. In addition, various types of dampers are usually installed near the anchor end of the cables to mitigate cable vibrations, including oil dampers, high-damping rubber dampers, viscous shear dampers [9], Magnetorheological (MR) dampers [10] and eddy current dampers [11]. The mitigation theories of various types of dampers for suppressing cable vibrations are different. Furthermore, it is still lacking an in-depth study regarding the effects of dampers on suppressing cable vibrations based on the field observation data of the bridge SHMS.

In this study, field monitoring was conducted on a cable-stayed bridge. The time history data of vibration acceleration for cables were collected to study the vibration characteristics and mechanism. Various types of dampers are adopted on symmetrical cables to compare the effects of different dampers on suppressing cable vibrations.

## 2 VIBRATION MONITORING SYSTEM FOR CABLES

The field monitoring was conducted on a cable-stayed bridge (Figure 1) located in Zhoushan of Zhejiang Province in China. As part of an important cross-sea passage, the Ningbo-Zhoushan Expressway between the island and the mainland,

this bridge is a cable-stayed bridge with twin towers and a semi-floating system, and the main span of this bridge is 580m. The height of the bridge tower is 151m. The bridge girder is supported by a total of 168 stay cables, and the length of the cables is 63-298m.



Figure 1. Bridge for field monitoring.

In the construction stage of the bridge, viscous shear dampers were pre-installed near the anchor of every cable of the bridge. However, on sunny and no precipitation days, obvious cable vibrations can still be found on this bridge. The cable monitoring system, as an important part of the SHMS, is shown in Figure 4. In total, 52 groups of acceleration sensors were installed on the cables at a height of 5m. To analyze the vibration characteristics of cables, the time history monitoring data of cable acceleration sensors and wind speed sensors were analyzed.

### 3 DYNAMIC CHARACTERISTICS OF CABLE VIBRATIONS

#### 3.1 Vibration characteristics of cables with different lengths

According to a 5-day period of monitoring data for cables, the dynamic characteristics of different cables were investigated and compared. In this study, cables are roughly categorized based on their lengths: short cables (<100m), medium-length cables (100~200m), and long cables(>200m).

For the short cables, the vibration amplitude is quite small (Figure 2(a)). Based on the power spectral density (PSD) of acceleration, the vibration frequencies are mainly between 5-10 Hz, which is quite average and not concentrated on one or several typical frequencies (Figure 2(b)).

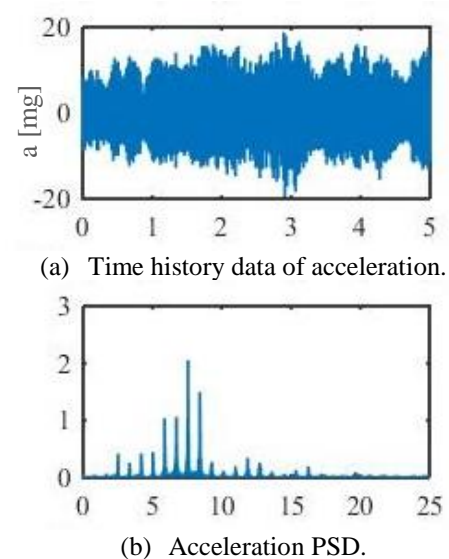


Figure 2. Vibration data and frequency distributions of a short cable.

According to Figure 3(a), for the medium cables, the vibration amplitude is larger than short cables but still smaller than the warning value defined in “Technical specifications for structural monitoring of highway bridges” (JT/T 1037-2022) [12]. The vibration frequencies are mainly between 5~20 Hz, which is quite average and not concentrated on one or several typical frequencies (Figure 3(b)).

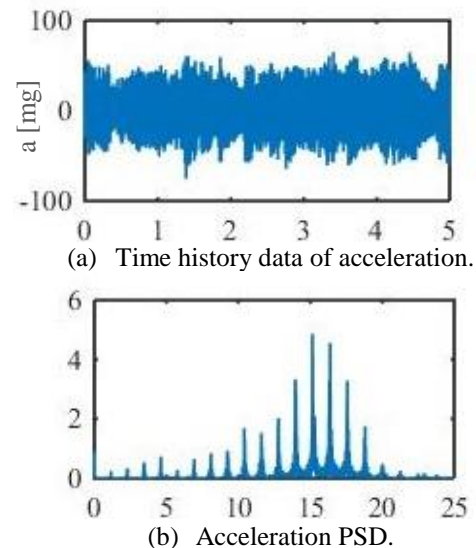


Figure 3. Vibration data and frequency distributions of a medium cable.

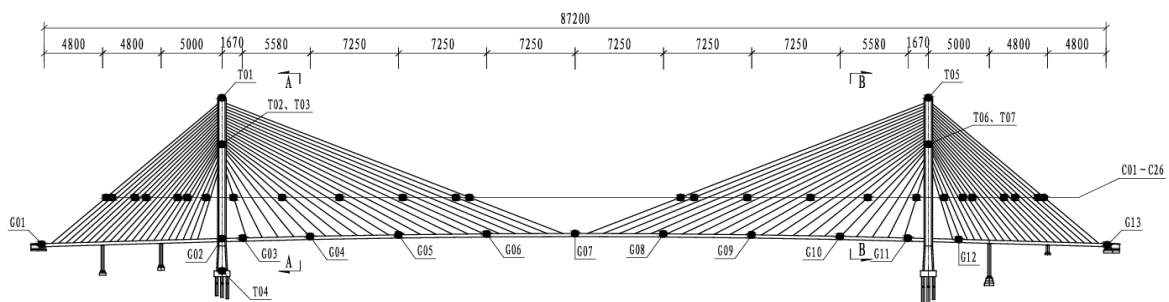


Figure 4. Cable monitoring system of the bridge.



For the long cables, abnormal vibrations are excited (Figure 5(a)). During the vibration period, the vibration amplitude is quite large, and the energy is mainly concentrated in the high-frequency region (Figure 5(b)).

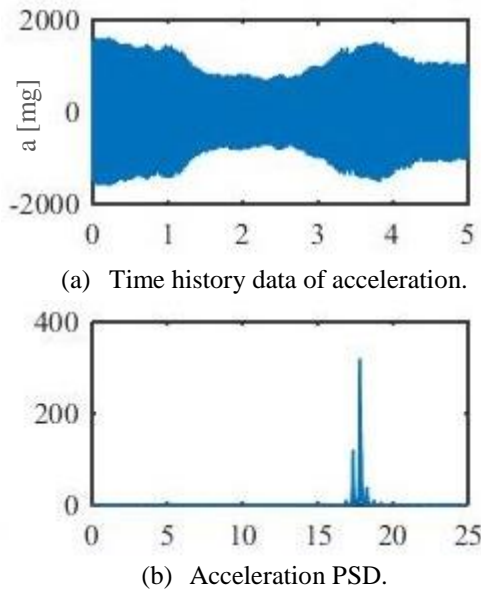


Figure 5. Vibration data and frequency distributions of a long cable.

Therefore, the length of the cables is a crucial parameter that determines whether abnormal vibrations will be excited or not. This is because long cables with lower structural natural vibration frequencies and damping are more vulnerable to the wind effects and are more easily excited into large amplitude vibrations.

### 3.2 Vibrations of long cables and mechanism analysis

A typical large amplitude vibration event of a long cable is analyzed to further analyze the vibration characteristics of long cables.

As shown in Figure 6(a), a continuous cable vibration event in the period of August 2<sup>nd</sup> and 5<sup>th</sup> was recorded by the cable vibration acceleration sensors. The root-mean-square (RMS) values of every ten-minute acceleration are calculated (Figure 6(b)), and the maximum value is 723 mg, which is far greater than the allowable limit for cable vibrations defined in “Technical specifications for structural monitoring of highway bridges” (JT/T 1037-2022) [12].

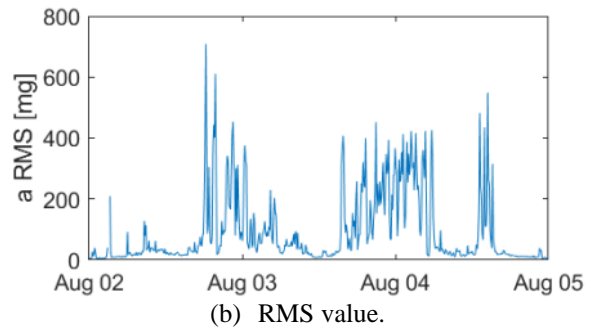
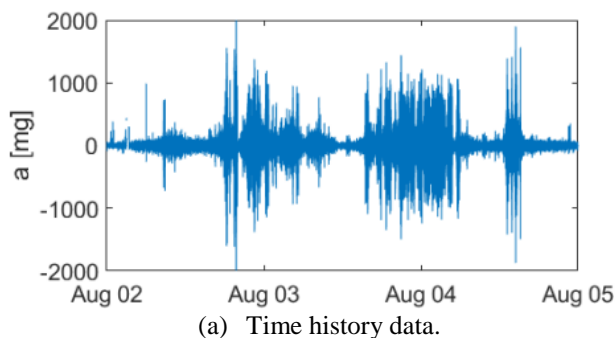


Figure 6. Time history data and RMS value of acceleration.

Figure 7 shows the average power spectral density calculated using every 10-minute acceleration. The vibration was found to be concentrated in high-frequency regions, and the main frequency of vibration is 17.9 Hz.

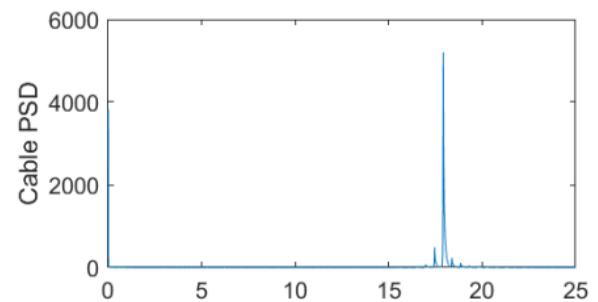


Figure 7. Acceleration PSD.

To analyze the vibration mechanism, the relationship between the vibration amplitude and wind characteristics was studied. The wind velocity and wind angle in this period are recorded by the wind speed sensors (Figure 8). Therefore, it can be inferred that the cable vibration may be excited under nearly north-south wind conditions.

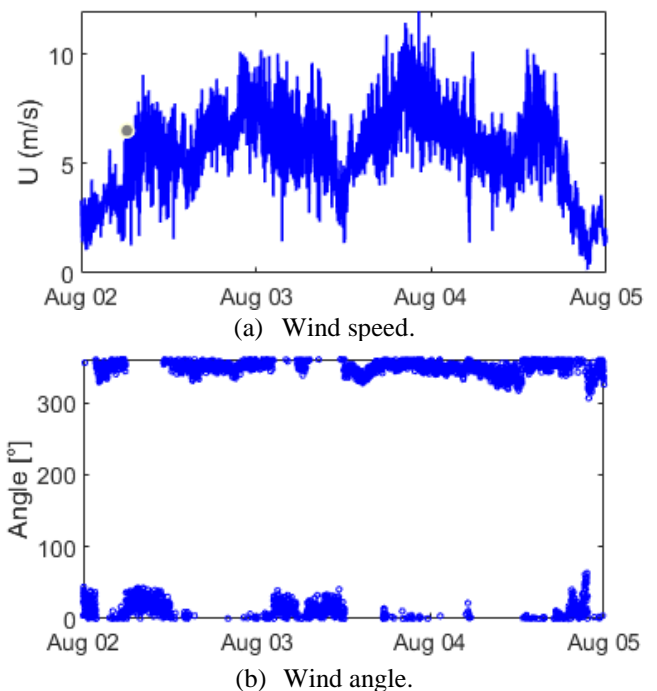
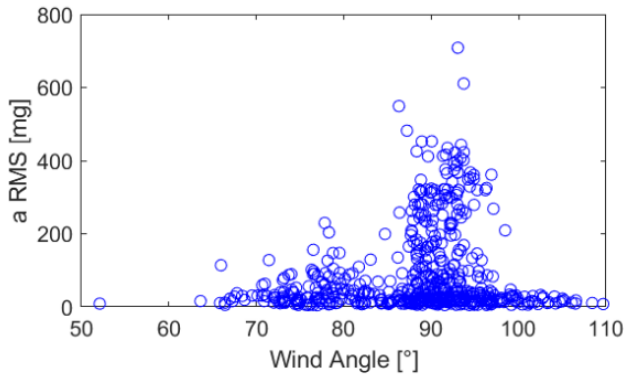
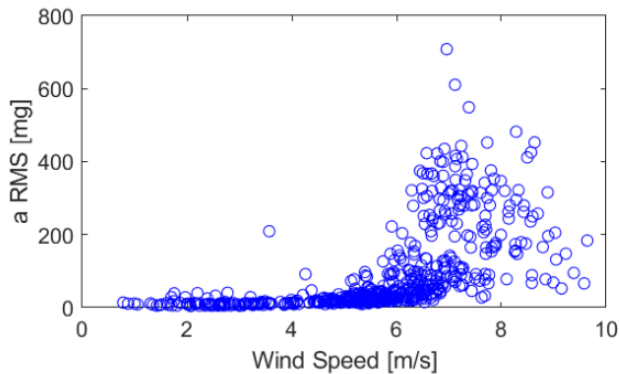


Figure 8. Time history data of wind.

Considering the installation direction of the bridge wind speed sensors as well as the angle between the stay cable and pylon, the wind yaw angle between the stay cable and wind was recalculated. The relationship between the acceleration vibration amplitudes and wind angles is shown in Figure 9(a). Large vibration amplitudes occur when the wind angle is around 90°, which means the wind direction is vertical to the cable plane. In addition, the wind speed vertical to the cable plane was also calculated (Figure 9(b)). It can be concluded that vibrations are maximized at a wind velocity of 6 to 9 m/s.



(a) Acceleration response under different wind yaw angles.



(b) Acceleration response under different vertical wind speeds.

Figure 9. Relationships between acceleration responses and wind characteristics.

For the VIV of cables, when the flow passes around the section of stay cables, vortex shedding emerges on the upper surface and lower surface alternatively, and the frequency of vortex shedding  $f_v$  can be defined as equation (1) [13]

$$f_v = \frac{US_t}{D} \quad (1)$$

Where  $U$  is the average wind speed.  $S_t$  is the Strouhal number, which is related to the section configuration, for a circle section,  $S_t = 0.2$ .  $D$  is the diameter of the cable. When vortex shedding frequencies of cables are close to the structural natural frequencies, cables will be excited into VIV resonance.

The vibration frequencies are calculated to investigate the vibration mechanism. In Figure 10, the x-axis represents the wind speeds, and the y-axis represents one-minute vibration frequencies. The maximum frequency calculated by the PSD of acceleration is selected as the main frequency of cables in one minute. Therefore, the scatters indicate different main vibration frequencies of cables under different wind conditions.

However, as the height increases, the wind speed apparently increases. Therefore, considering the overall speed of the wind profile passing around cables, the height of the cable and the wind field landform, the wind speed measured on the bridge deck should be multiplied by a factor of 1.3. Based on the dimensions of stay cables, the fundamental frequencies of vortex shedding can be calculated. Therefore, the relationships between different orders of vortex shedding frequencies and bridge wind speeds can be drawn as a red line (Figure 10). For the long cables, the micro-vibrations are mainly concentrated in the frequency range of 17~20 Hz, and 2~5 Hz (Marked as circles). The micro-vibrations are mainly catalogued into the vehicle-bridge coupled vibration and the vehicle load. Except for these scatters. The main distribution of scatters coincides with the line, especially in the wind speed region of 6~9 m/s, which indicates that the vibration frequencies are consistent with various modes of vortex shedding frequencies, and thus proves that the vibrations of the cable are dominated by VIV.

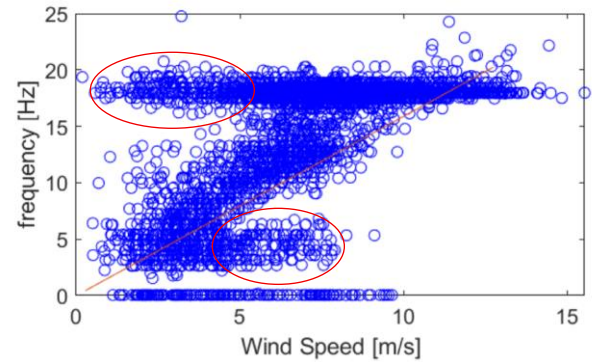


Figure 10. Relationship between vibration frequencies and vortex shedding frequencies of cables.

#### 4 MITIGATION OF CABLE VIBRATIONS

Different dampers are utilized to compare their effects in mitigating the cable vibrations. The damping ratios are set to achieve the optimal dimensionless damping coefficient 1.5~2.0 for different cables to minimize the large vibrations under lower frequencies. According to previous monitoring history data, under a certain wind field condition, the VIV responses of the cables symmetric along the bridge axis are quite similar because the structural parameters and natural frequencies of cables are almost the same. Therefore, different dampers are adopted for the symmetric long cable groups to investigate their effects on suppressing VIV. An eddy current damper (Figure 11(a)) is mounted on the cable R-20, and an MR damper (Figure 11(b)) is mounted on the cable R-21, respectively. For the sake of comparison, the new viscous shear dampers (Figure 11(c)) are employed on the symmetric cables L-20 and L-21. The parameters of dampers are designed with the consideration of the suppression of low-mode rain-wind vibrations.



(a) Eddy current damper.



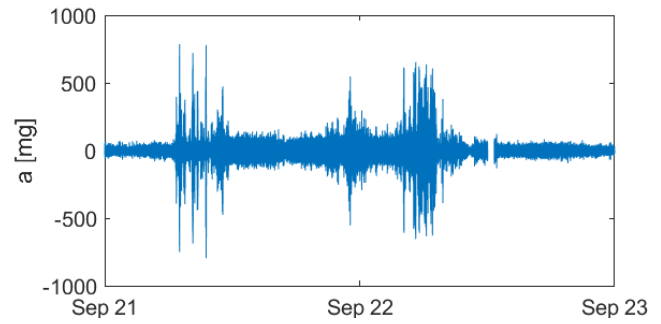
(b) MR damper.



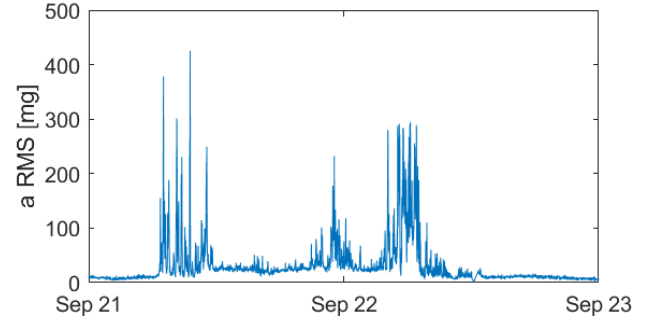
(c) Viscous shear damper.

Figure 11. Three types of dampers on cables.

Because the excitation of cable vibration under high frequencies ( $f > 15\text{Hz}$ ) is quite difficult, field monitoring is conducted under the condition of the ambient excitation of natural wind. A typical VIV response occurred in September of 2024 after the replacement of dampers was selected to study the effects of dampers on suppressing VIV. By comparing the time history data and RMS value of acceleration for the symmetric cables of R-20 (Figure 12) and L-20 (Figure 13), the VIV response of cable R-20 is significantly larger than that of L-20, which proved that the viscous shear damper is more effective in suppressing the high-mode VIV than the current eddy damper. When the high-mode (30<sup>th</sup>-40<sup>th</sup>) VIV of cables occurs, the position of the damper is close to the stagnation point of vibrations, and thus, it needs a large damping coefficient to suppress vibrations [14]. However, for the current eddy damper, as the vibration frequencies increase, the equivalent damping coefficients decrease [15], which is disadvantageous to the suppression of a high-mode VIV.

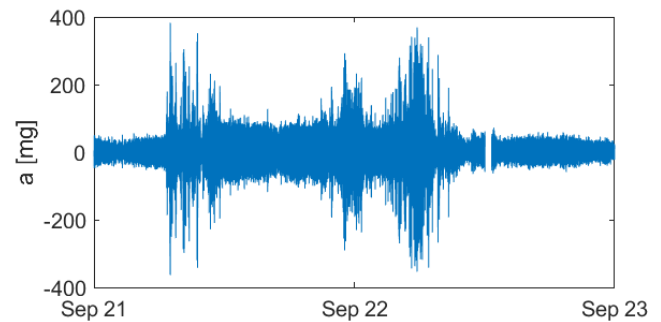


(a) Time history data of acceleration.

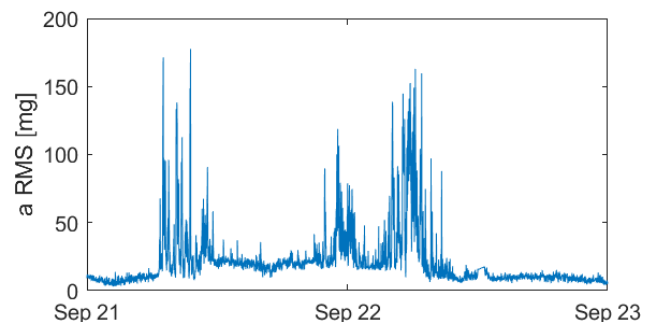


(b) RMS value of acceleration.

Figure 12. Vibration data of Cable R-20.



(a) Time history data of acceleration.



(b) RMS value of acceleration.

Figure 13. Vibration data of Cable L-20.

By comparing the time history data and RMS value of acceleration for the symmetric cables R-19 (Figure 14) and L-19 (Figure 15), the VIV amplitude of cable R-19 is a little smaller than that of L-19, which proved that the MR damper is slightly better than the viscous shear damper in suppressing the high-mode VIV. The initial stiffness of the MR damper may provide additional damping effects [16].



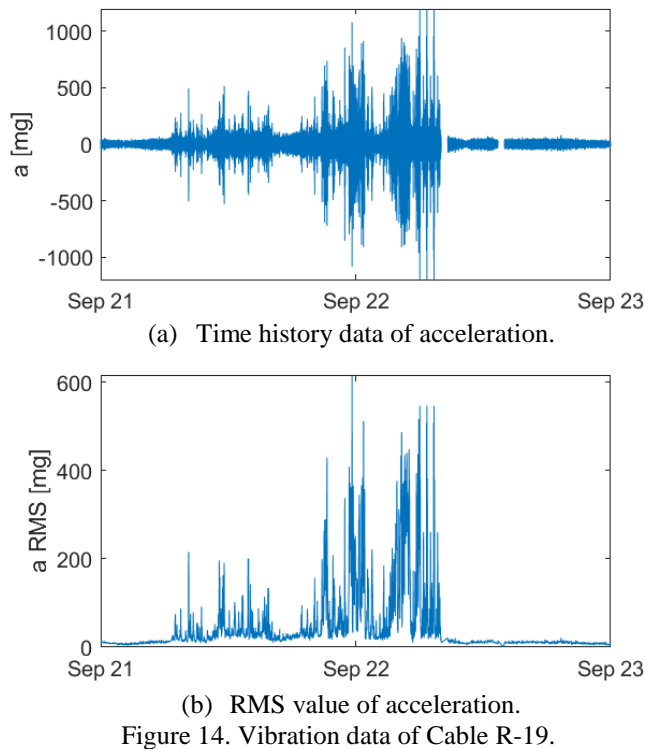


Figure 14. Vibration data of Cable R-19.

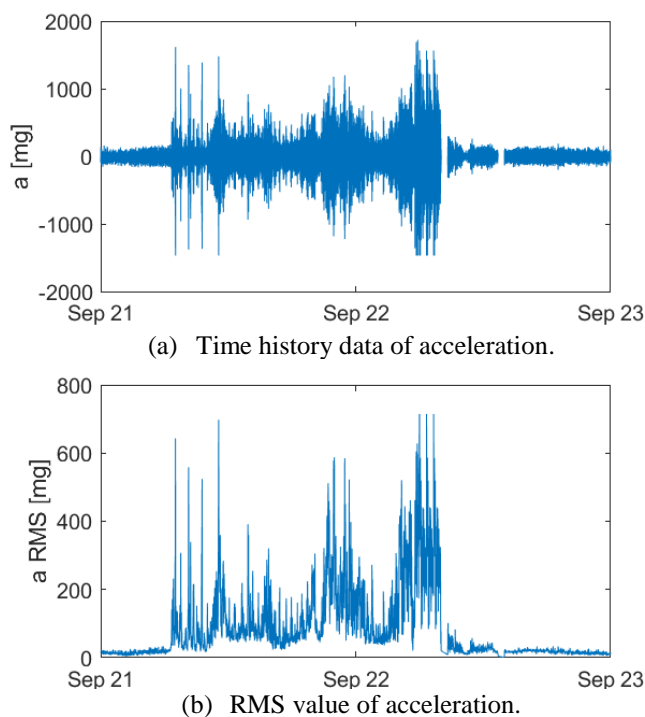


Figure 15. Vibration data of Cable L-19.

However, for these three types of dampers, the high-mode VIV cannot be entirely suppressed. Because the high-mode vibration may have multiple stagnation points along the cables, the installation positions of dampers tend to be close to the stagnation points. Therefore, stock-bridge dampers should be installed at suitable positions of cables as complementary dampers to mitigate the specific high-mode VIV [14].

## 5 CONCLUSIONS

In this study, continuous field monitoring is conducted to investigate the vibration characteristics of stay cables for a cross-sea cable-stayed bridge. Different dampers are mounted to compare their effect on suppressing vibrations. The conclusions are as follows:

- (1) According to the field monitoring data, the long cables of this long-span bridge are easily excited into a high-mode vibration under the vertical wind in a speed region of 6–9 m/s.
- (2) For the high-mode vibrations of long cables, the vibration frequencies of cables under different wind speeds are consistent with various modes of vortex shedding frequencies, proving that the vibrations of the cable are dominated by VIV.
- (3) For the mitigation effects of high-mode VIV of cables, MR damper > viscous shear damper > current eddy damper. However, the effects of the three types of dampers on controlling high-mode VIV are limited. Stockbridge dampers should be designed to mitigate the specific high-mode vibration.

## ACKNOWLEDGMENTS

The authors would like to acknowledge the support of the Independent Research and Development Projects of Zhejiang Scientific Research Institute of Transport (ZK202401, ZK202405, ZK202501).

## REFERENCES

- [1] M. Virlogeux, State-of-the-art in cable vibrations of cable-stayed bridges. *Bridge Structures*, 1(3): 133–168, 2005.
- [2] C. Ge and A. Chen. Vibration characteristics identification of ultra-long cables of a cable-stayed bridge in normal operation based on half-year monitoring data. *Structure and Infrastructure Engineering*, 15(12): 1567–1582, 2019.
- [3] M. Matsumoto, H. Shirato, T. Yagi, et al. Field observation of the full-scale wind-induced cable vibration. *Journal of Wind Engineering and Industrial Aerodynamics*, 91(1–2): 13–26, 2003.
- [4] D. Zuo, N. P. Jones, and J. A. Main. Field observation of vortex- and rain-wind-induced stay-cable vibrations in a three-dimensional environment. *Journal of Wind Engineering and Industrial Aerodynamics*, 96(6–7): 1124–1133, 2008.
- [5] J.A. Main, N. P. Jones, Full-scale measurements of stay cable vibration. In: *Proceedings of the Structures Congress*, Philadelphia, Pennsylvania, 2000.
- [6] Z. Liu, Z. Zhu, C. Wei, et al. Observation of vortex-induced vibration and wind characteristics of cables across the Yangtze river bridge. *Journal of Railway Science*, 17, 2020.
- [7] J.K. Vandiver, S. Swithenbank, V. Jaiswal, et al. The effectiveness of helical strakes in the suppression of high-mode-number VIV. In: *Offshore Technology Conference*, Houston, Texas, U.S.A., 2006.
- [8] T. Zhou, S. Razali, Z. Hao, et al. On the study of vortex-induced vibration of cylinder with helical strakes. *Journal of Fluids Structure*, 27, 903–917, 2011.
- [9] L. Sun, H. Zhou, A. Chen. Classification and performance of vibration control device for cables of long span cable-stayed bridge. *Journal of World Bridge*, 4:36–40, 2001.
- [10] P. Zhou, M. Liu, W. Kong, et al. Modeling and evaluation of magnetorheological dampers with fluid leakage for cable vibration control. *Journal of Bridge Engineering*, 26(2):04020119, 2021.
- [11] X. Lei, H. Niu, Z. Chen, et al. Development and Application of a New-type Eddy Current TMD for vibration control of Hangers of Long-span Steel Arch Bridges. *China Journal of Highway and Transport*, 28(4), 2015.



- [12] Ministry of Transport of the People's Republic of China. Technical specifications for structural monitoring of highway bridges: JT/T 1037-2022, 2022.
- [13] Z. Chen. Bridge wind engineering. China Communications Press, Beijing, China. 2005.
- [14] C. Yang. Theoretical and experimental studies on higher multi-mode vibration control of cables. PhD thesis, Hunan University. 2022.
- [15] Z. Wang, Z. Cheng, H. Wang, et al. Eddy-current inertial mass damper for cable vibration control. China Civil Engineering Journal, 12 (54): 53-63, 2021.
- [16] M. Wang, F. Wang, R. Zhao, et al. Application Research of Passive Magnetorheological Dampers for Vibration Suppression of Stay Cables in Real Bridges. Journal of North China University of Water Resources and Electric Power (Natural Science Edition) 11, 2024.

# Field Application of TFC-based Electromagnetic Sensors for Monitoring Cross-sectional Loss in Tendons of Bridges

Lee, Joo-Hyung<sup>1</sup>, Park, Kwang-Yeun<sup>1</sup>, Choi, Ji-Young<sup>2</sup>, Lee, Sangho<sup>1</sup>, Joh, Changbin<sup>1</sup>

<sup>1</sup>Korea Institute of Civil Engineering and Building Technology, Department of Structural Engineering Research, 283, Goyang-daero, Ilsanseo-gu, Goyang-si, Gyeonggi-do, Republic of Korea

<sup>2</sup>Korea Institute of Civil Engineering and Building Technology, Department of Highway & Transportation Research, 283, Goyang-daero, Ilsanseo-gu, Goyang-si, Gyeonggi-do, Republic of Korea

email: leejoohyung@kict.re.kr

**ABSTRACT:** External tendons in prestressed concrete (PSC) bridges are essential for structural performance and durability. However, internal damage to strands within grouted ducts is difficult to detect through visual inspection. To address this issue, the Korea Institute of Civil Engineering and Building Technology (KICT) developed a non-destructive testing (NDT) sensor based on the Total Flux Change (TFC) principle, derived from Faraday's law of electromagnetic induction. The TFC-based electromagnetic (EM) sensor was designed for field use, featuring a lightweight, detachable frame and wireless data acquisition system. The sensor generates an alternating magnetic field via a primary coil and measures the induced voltage from a secondary coil. A reduction in strand cross-sectional area alters the magnetic flux, resulting in a measurable variation in the induced voltage. Field tests were conducted on the Jeongneungcheon Overpass in Seoul, targeting external tendons between piers. The sensor successfully measured voltage variations along the tendon length. In tendons with suspected damage, the voltage amplitude showed distinguishable reductions, unlike in undamaged control cases. Results were consistent with previous laboratory experiments on specimens with artificially induced strand loss. The findings confirm that the developed EM sensor enables efficient and intuitive detection of internal tendon damage with practical field applicability, even in actual bridge environments. This study demonstrates the feasibility of the TFC-based EM sensor for practical field applications and highlights its potential for integration into long-term bridge monitoring systems.

**KEY WORDS:** Prestressed concrete bridge; External tendon; Electromagnetic sensor; Total flux change; Non-destructive testing

## 1 INTRODUCTION

Prestressed concrete (PSC) bridges have been widely adopted in modern road bridge due to their advantages in structural safety, aesthetics, serviceability, cost-effectiveness, and ease of maintenance. Among various structural components of PSC bridges, external tendons play a critical role by enhancing structural performance, allowing for flexible prestress control, facilitating maintenance, and providing design versatility.

However, since external tendons contain prestressing strands – typically seven-wire strands – embedded within ducts, it is inherently difficult to directly inspect them for damage during the service life of the structure. A notable example of such a limitation occurred in February 2016 with the failure of an external tendon in the Jeongneungcheon Overpass, constructed in 1999 in Seoul, Korea. The failure was attributed to undetected strand damage caused by grout defects inside the duct, which could not be identified through visual inspection.

Following this incident, the Korea Institute of Civil Engineering and Building Technology (KICT) initiated extensive research to develop non-destructive testing (NDT) sensors capable of detecting internal damage to the strands within the duct. As a result, a novel electromagnetic (EM) sensor based on Faraday's law of electromagnetic induction was developed. This sensor allows for effective detection of cross-sectional losses in the strands embedded within external tendons.

However, many of the existing NDT sensors developed for detecting cross-sectional loss in external tendons face limitations in actual bridge sites. These systems often require complex installation procedures, specialized equipment, and

controlled conditions, making them less suitable for field environments. In particular, external tendons located in narrow or elevated areas pose significant challenges for sensor installation and measurement. As such, not only the accuracy of damage detection, but also the workability and field applicability of the sensing system become crucial factors for successful deployment in practice. The aim of this study is to evaluate the field applicability and damage detection performance of the developed EM sensor through field tests on actual PSC bridges.

## 2 PRINCIPLE OF TFC-BASED ELECTROMAGNETIC (EM) SENSOR

### 2.1 Principle of cross-sectional loss detection

The EM sensor operates on the principle of electromagnetic induction, as governed by Faraday's law. According to this law, a change in magnetic flux induces an electromotive force (EMF) in a closed loop. The induced voltage  $V$  is proportional to the number of coils turns  $N$  and the time rate of change of magnetic flux  $\Phi$ , as expressed in Equation (1):

$$V = -N \frac{d\Phi}{dt} = -N \frac{dB A}{dt} \quad (1)$$

Magnetic flux  $\Phi$  is defined as the product of magnetic field strength  $B$  and the area  $A$  perpendicular to the magnetic field, i.e.,  $\Phi = B \cdot A$ . Therefore, if the magnetic field  $B$  remains constant, a reduction in the conductive cross-sectional area  $A$  – such as that caused by corrosion or fracture in the tendon – results in a corresponding decrease in the induced voltage  $V$ .



Based on this principle, a sensor has been developed to detect cross-sectional loss in prestressing strands located inside the ducts of external tendons. As illustrated in Figure 1, the EM sensor is installed to encircle the tendon duct, and an alternating current (AC) is applied to the 1<sup>st</sup> coil. As the sensor moves along the tendon, it generates a varying magnetic field that induces eddy currents within the steel strands. These eddy currents, in turn, generate a secondary magnetic field, which is detected by the receiving coil as an induced voltage.

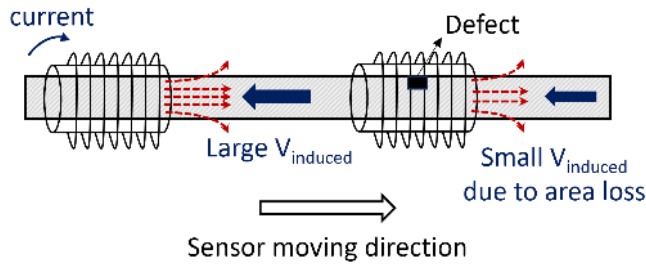


Figure 1. Principle of section loss detect

If there is a cross-sectional loss in the strands, the magnitude of the eddy currents – and thus the induced voltage – decreases compared to undamaged regions. By analyzing the variation in induced voltage, it is possible to identify and localize internal damage to the prestressing strands, even without direct access. This method detects damage based on the change in total magnetic flux, and is referred to as the Total Flux Change (TFC) approach.

## 2.2 Configuration and features of the TFC-based EM sensor

To enhance field applicability, the developed TFC-based EM sensor system was designed with an emphasis on lightweight components and low power consumption. The sensor itself adopts a detachable and portable configuration, improving installation efficiency and reducing operational burden in actual bridge environments.

Unlike conventional solenoid-type sensors that require time-consuming on-site winding of wires, the newly developed sensor consists of a separable frame that can be easily mounted and dismounted around the tendon within approximately two minutes. Wheels installed at the front and rear of the sensor enable smooth movement along the tendon surface during scanning.

The sensor consists of a 1<sup>st</sup> coil that generates an alternating magnetic field, and a 2<sup>nd</sup> coil located at the center of the sensor that detects the induced voltage via electromagnetic induction. To improve magnetic field concentration and signal sensitivity, eight magnetic cores are embedded within the sensor structure. In order to minimize overall weight, the sensor housing was constructed with a lightweight skeletal frame rather than a solid enclosure. The electromagnetic response of the detachable sensor was verified through COMSOL simulations, showing a distribution pattern comparable to that of conventional solenoid-type sensors.

For accurate detection of the small induced voltage in the 2<sup>nd</sup> coil, a flat ribbon type cable with a 15-pin D-sub connector was

used. This configuration enables the equivalent effect of winding a single wire 15 times, thereby increasing sensitivity. A portable audio amplifier (200 W) was adopted to generate the required alternating current at the desired frequency, avoiding the need for large, heavy power generators typically used in the field. The appearance of the developed EM sensor is shown in Figure 2.

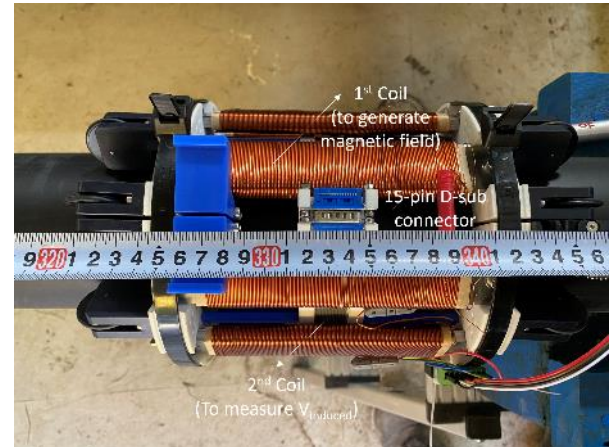


Figure 2. TFC-based EM sensor

The data acquisition (DAQ) system also emphasizes portability and reliability. A microcontroller unit (MCU) was employed to generate sinusoidal signals in the range of 10-40 Hz, which are then amplified by the audio amplifier and supplied to the 1<sup>st</sup> coil. The induced voltage from the 2<sup>nd</sup> coil is captured using a high-resolution analog-to-digital conversion board. The MCU wirelessly communicates with a laptop, allowing for real-time monitoring and data acquisition including 1<sup>st</sup> coil current, 2<sup>nd</sup> coil voltage, and distance measurements. The entire system is powered by commercial DeWalt rechargeable batteries, enhancing mobility and field usability. The DAQ system and battery pack for field operation of the sensor are shown in Figure 3.



Figure 3. DAQ system and battery of sensor

### 3 FIELD TEST RESULTS

#### 3.1 Overview of Test bridge

The Jeongneungcheon Overpass, completed in 1999, is located on one of the major expressways for vehicular traffic in Seoul, South Korea. The field tests for detecting cross-sectional loss in prestressing strands were conducted in 2<sup>nd</sup> section of the bridge. The section is a PSC box girder bridge constructed using a modified MSS (Movable Scaffolding System) method. In this approach, precast panels were assembled on both sides of the box girder to form a three-cell cross section. Both internal and external tendons were used in the prestressing system of this segment. An overview of the structural characteristics of the test section is provided in Table 1, and the appearance of the bridge is shown in Figure 4.

Table 1. Overview of Jeongneungcheon Overpass 2<sup>nd</sup> Section

Item	Description
Bridge name	Jeongneungcheon Overpass
Year	1999
Design load	DB-24 (43.2 ton)
Structural type (Superstructure)	PSC box girder & Steel box girder L=3,500 m
Length	(Steel box girder: 1,240 m, PSC box girder: 2,260 m)
Width	B=27.0 m
Number of lanes	Three lanes per direction
Bearing	Pot bearing
PSC construction method	MSS



Figure 4. Jeongneungcheon Overpass Bridge

#### 3.2 Target external tendons for NDT

The nondestructive testing for detecting cross-sectional loss was conducted on external tendons located between Pier 38 and Pier 39 of the bridge. Each span of the bridge includes twelve external tendons, which are installed within the box girder section. Six tendons are positioned on the left side and six on the right side of the PSC box girder, as shown in Figure 5.



Figure 5. PSC box girder of test bridge

Among the tendons on the left side, some tendons were selected for testing due to their accessibility for sensor installation. Each tendon consists of nineteen 15.2 mm diameter seven-wire strands enclosed in a polyethylene (PE) duct filled with grout. The diameter of the duct is 110 mm. An example of the external tendons installed inside the box girder is shown in Figure 6. The testing procedure using the developed EM sensor is illustrated in Figure 7.

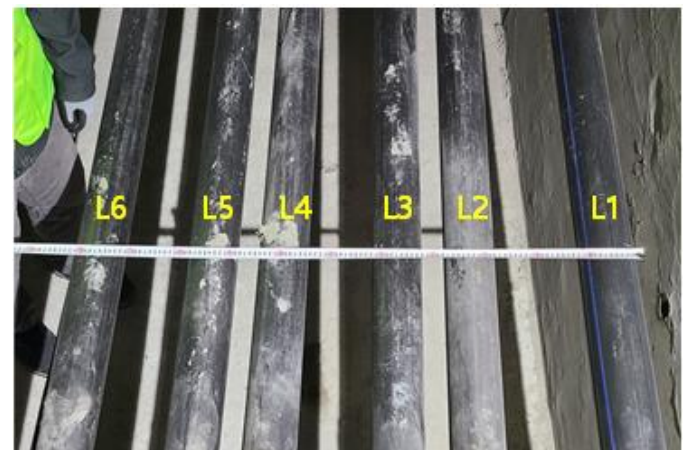


Figure 6. External tendons of test bridge





Figure 7. NDT process of TFC-based EM sensor

### 3.3 Test results

The NDT results for three external tendons of the Jeongneungcheon Overpass are shown in Figure 8, represented by the blue, green, and red solid lines. The plotted data correspond to the amplitude of the induced voltage measured by the sensor, after noise removal and mean value subtraction.

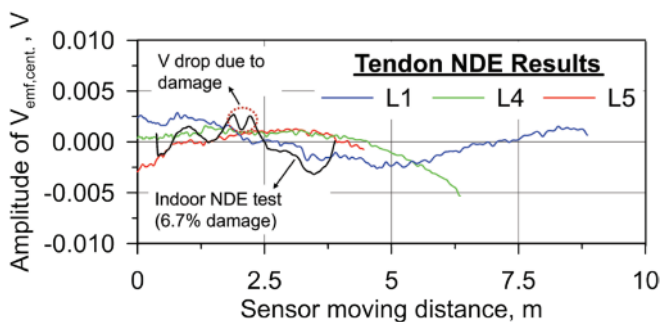


Figure 8. NDT results of TFC-based EM sensor

Among the tested tendons, L4 and L5 were replacement tendons installed after the external tendon rupture incident that

occurred in 2016. Therefore, these tendons are presumed to be free from significant strand damage. Although the induced voltage did not appear completely flat along the sensor travel distance—due to surface contamination, variations in the operator's walking speed, and electromagnetic interference from adjacent tendons—no distinct voltage drops were observed in these two cases.

In contrast, the response differed clearly from that observed in a controlled laboratory experiment conducted in 2023, where a tendon specimen with artificially introduced cross-sectional damage was tested. In the laboratory specimen with a 6.7% section loss (simulated by grinding the strand surface), a distinct decrease in the induced voltage amplitude was observed at the damaged location.

These results demonstrate that the EM sensor developed by KICT enables intuitive detection of cross-sectional loss in prestressing strands while maintaining sufficient workability for practical use in actual bridge environments.

## 4 CONCLUSIONS

This study presented the development and field application of a TFC-based EM sensor designed to detect cross-sectional loss in prestressing strands within external tendons of PSC bridges.

The sensor, developed based on Faraday's law of electromagnetic induction, demonstrated reliable performance in identifying potential damage zones by measuring changes in induced voltage. Field tests conducted on the Jeongneungcheon Overpass confirmed that the sensor could detect localized cross-sectional loss with clearly distinguishable signal behavior, even under the practical constraints of real bridge environments.

Compared to conventional solenoid-type sensors, the developed system significantly improved field applicability by introducing a lightweight, detachable design, wireless data acquisition, and low-power operation. These features enabled quick installation and stable measurement, proving the sensor's practicality for on-site inspections.

Future research will focus on further quantifying damage levels, validating the sensor performance under various damage conditions, and expanding its application to other bridge types and tendon layouts. Long-term monitoring and integration with digital maintenance platforms are also potential areas for future development. These findings highlight the potential of the TFC-based EM sensor as a practical and scalable solution for non-destructive inspection of PSC bridges.

## ACKNOWLEDGMENTS

This work was supported by the Korea Agency for Infrastructure Technology Advancement (KAIA) grant (grant No. RS-2022-00142566) funded by the Ministry of Land, Infrastructure and Transport.

## REFERENCES

[1] Korea Institute of Civil Engineering and Building Technology (KICT), Machine Learning Based Robotic NDT for Cable Section Loss of Marine Bridges, Final Report, KICT, Goyang, Korea, 2023.





[2] S. B. S. News, Jeongneungcheon Overpass fully closed...  
'Innovative' technology that lasts over 100 years turns out to be  
a bubble, SBS News, 2015. [Online]. Available:  
[https://news.sbs.co.kr/news/endPage.do?news\\_id=N10034295](https://news.sbs.co.kr/news/endPage.do?news_id=N1003429524)  
24.



# Session 31

## System-level SHM and Emerging Technologies

# Exploration of edge computing for monitoring a four-story building frame model

Qing-Chen Tang<sup>1</sup>, [ORCID](#), Emil Kool<sup>2</sup>, Daniel Colmenares<sup>3</sup>, Imane Bayane<sup>1</sup>, [ORCID](#), Raid Karoumi<sup>1</sup>, [ORCID](#)

<sup>1</sup>Department of Civil and Architectural Engineering, KTH Royal Institute of Technology, 100 44 Stockholm, Sweden

<sup>2</sup>IoTBridge AB, Danderyd, 182 33, Sweden

<sup>3</sup>Dewesoft AB, Importgatan 7, 422 46, Gothenburg

email: [qctang@kth.se](mailto:qctang@kth.se), [emil.kool@iotbridge.se](mailto:emil.kool@iotbridge.se), [daniel.colmenares@dewesoft.com](mailto:daniel.colmenares@dewesoft.com), [bayane@kth.se](mailto:bayane@kth.se), [raidk@kth.se](mailto:raidk@kth.se)

**ABSTRACT:** With the rapid development of sensing technologies in vibration-based monitoring systems, various kinds of devices are connected to exchange data with each other in virtue of cloud computing. However, challenges arise when transmitting and processing large volumes of data, particularly due to latency and bandwidth limitations. To address these issues, edge computing has emerged as a promising solution, enabling local data processing to reduce transmission delays and minimize data redundancy. In this paper, the possibility of edge computing on lightweight edge devices is explored including the KRYPTON® CPU data logger and the ESP32-S3 microcontroller. These two monitoring systems, one with accelerometers and the other with strain gauges, are deployed on a four-story building frame model under varying structural mass and damping conditions that affect dynamic properties. Each system autonomously collects and caches data (accelerations and strains) locally using embedded code, enabling reliable, low-latency edge processing. Experimental results demonstrate the systems' ability to detect changes in dynamic behavior, supporting applications in fatigue assessment and damage detection. The proposed approach is scalable to dense sensor networks for large-scale structural health monitoring, where edge computing significantly reduces reliance on cloud infrastructure.

**KEY WORDS:** Monitoring; System identification; Edge computing; Frame model; Structural dynamics.

## 1 INTRODUCTION

The primary goal of structural monitoring is to evaluate the condition of instrumented structures by extracting reliable information from measurement data [1], which can inform effective management and maintenance strategies. The success of this process depends mainly on the quality and reliability of the acquired data [2]. Civil engineering structures operate in complex and variable environments, often subject to demanding monitoring requirements. Consequently, the establishment of a reliable and robust sensor system is essential to ensure accurate and consistent data acquisition.

With the rapid development of sensing technologies in vibration-based monitoring systems, various kinds of devices are connected to exchange data with each other in virtue of cloud computing [3], which improves performance and efficiency in monitoring. For instance, accelerometers can be deployed to collect vibration data from concrete structures, which, compared to baseline data from undamaged structures via cloud-based platforms within the Internet of Things (IoT) framework, can enable the early detection of cracks [4]. However, problems may arise inevitably when processing and sending large amounts of data to the cloud center far from the site in a short period of time. As the structural responses are the crucial sources of data for detecting structural damage [5], sometimes data acquisition requires high-frequency sampling rates. If the bandwidth of the network is limited at the same time, it may cause network congestion and result in a slow network speed.

One promising solution is to offload the computing tasks by processing before sending them. In this manner, the data to be

processed is distributed to edge devices rather than cloud centers [6], [7], namely edge computing. Now edge computing is emerging to solve the problem of time delay and data redundancy in monitoring. For instance, the microcontroller unit (MCU) at each sensor node can serve as an edge device and perform data preprocessing locally [8]. Despite the potential of edge computing, it also faces a series of challenges in practice, including its application in monitoring and the related algorithms that can be run under limited computing resources [9], [10].

In this paper, explore the integration of edge computing into different lightweight edge devices, such as KRYPTON® CPU data logger and ESP32-S3 microcontroller. In each monitoring system, sensor nodes are distributed to collect the measurement data of a four-story building frame model considering different cases with variations of the structural mass and damping that can change structural dynamic properties. Through the vibration tests, different monitoring systems can collect the data of the frame model and operate independently for data caching with the programming codes embedded in the edge device, which makes it possible for edge computing with reliable data transmission and minimized data loss.

## 2 METHODOLOGY

This section presents the instrumented four-story frame structure, outlines the laboratory testing procedures and equipment, and details of the setup, implementation, and data processing methods.



### 2.1 Building frame model

The four-story frame model is composed of six wooden slabs ( $480 \times 240 \times 18 \text{ mm}^3$ ), two of them fixed together as the base (on the test setup) and the remaining as the four floor slabs, see Figure 1. Every two slabs are connected by steel columns (flexible bodies) at four corners to constrain the vertical displacement, and each column has a free length of 240 mm between two slabs with a cross-section area of  $1 \times 10 \text{ mm}^2$ . So, the four floors only undergo horizontal displacement, which can be simplified into a multiple-degree-of-freedom (MDOF) lumped mass system. The first two theoretical modal shapes are shown in Figure 1 and Figure 2, and the total weight of the frame model (including timber and steel) is 6.95 kg.

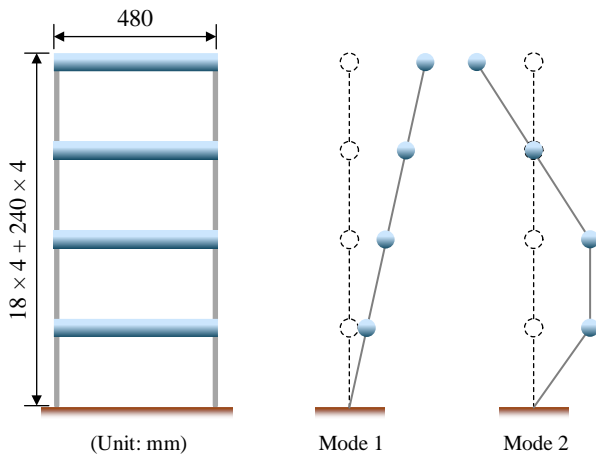


Figure 1. Illustration of the four-story frame model with the first two theoretical mode shapes

### 2.2 Testing cases

When performing the vibration test, the two following cases are considered:

- 1) The frame model only, as shown in Figure 1;
- 2) The frame model with a sloshing tank that contains 0.5 kg of pure water, placed on the second Floor as shown in Figure 2.

### 2.3 Testing setup and implementation

Two vibration tests were conducted in the laboratory. The first test features force-based excitation. The building frame model was fixed on the test-bed under sine sweep excitation and then single frequency excitation, both of which were provided by low-force LDS electrodynamic shaker, see Figure 2.

In this manner, the steel column connecting the foundation and the first floor of the frame will be subjected to the force with a constant amplitude, yet its frequency itself will change over time. At time  $t$ , the normalized response function of the linear sweep excitation is:

$$x(t) = \sin \left\{ 2\pi \left[ (f_2 - f_1) \left( \frac{t}{T} \right) + f_1 \right] \right\} \quad (1)$$

where  $T$  is the test duration;  $f_1$  is the start frequency;  $f_2$  is the end frequency. The nature of the frequency sweep is that the excitation signal input is composed of a single frequency at any given time.

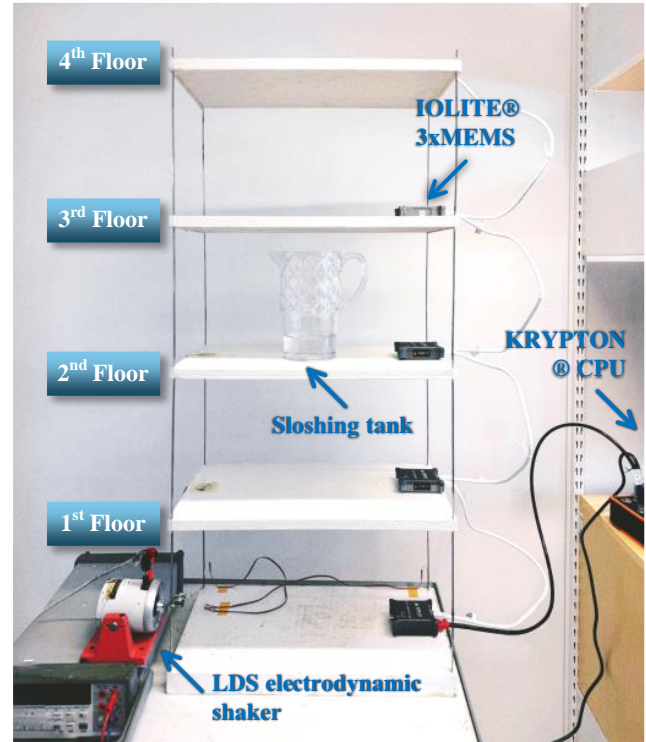


Figure 2. The four-story building frame model

The sweep can start from the lowest frequency, transition linearly to the highest frequency, and vice versa. In the function generator, the start frequency  $f_1$  was set as 0.1 Hz, the end frequency  $f_2$  as 10 Hz, with the test duration  $T$  of 180s. Due to the controllable variation of the excitation frequency, using frequency sweep excitation can preliminarily locate and identify the natural frequencies and mode shapes of the frame model.

After the sine sweep excitation, that was used to identify the frame's first four natural frequencies, the single frequency excitations were exerted, respectively, to get the damping ratios corresponding to each natural frequency of the frame model. Here, the shaker applied the force with a constant amplitude and constant excitation frequency.

The second test features controlled free vibrations, with the shaker removed. Using a ruler, the top floor was pushed sideways to a controlled position, see Figure 3, and then released. After the initial displacement, the frame model started to vibrate freely until the energy was completely dissipated.

Then, the whole process mentioned above was repeated considering the cases above in section 2.2 (with and without the sloshing tank).

### 2.4 Monitoring system and equipment

During the first testing, the low-noise accelerometers IOLITE® 3xMEMS (Figure 4) are arranged (with a total weight of 497 g) and fixed at the edge of each floor of the frame model using double-sided adhesive to reduce the signal shift and to ensure stable and reliable signals. Additionally, the  $x$ -axis direction of the sensor is parallel to that of the frame's horizontal displacement. Analog-to-digital conversion was done in each

accelerometer sensor, which eliminates the noise by analog cabling. Then, each accelerometer is linked to each other using the high-quality CAT6 cables through EtherCAT interface to form a daisy chain, limiting signal interference and data transmission error rates. Based on the IOLITE modular, DAQ device platform is embedded into each accelerometer distributed easily and synchronized down to 1  $\mu$ s device to device based on the distributed clocks. Then the acceleration signals produced are sent to the rugged IP67 micro-processor KRYPTON<sup>®</sup> CPU in the edge layer for processing the data on site. The data was collected at a sampling rate of 100 Hz, to avoid any problems with aliasing or signal distortion.

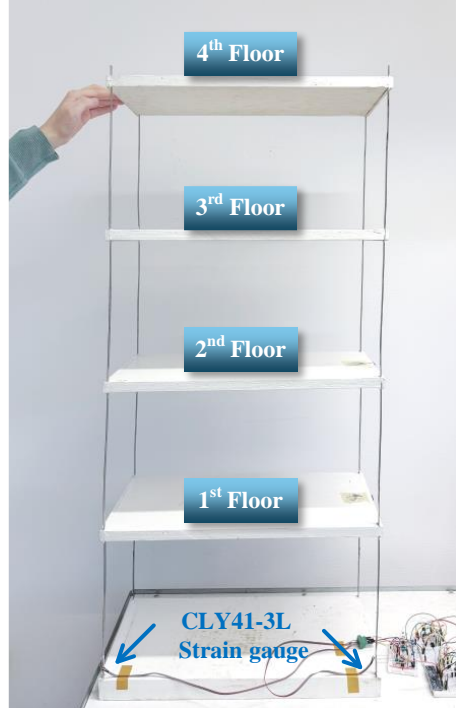


Figure 3. Controlled free vibration

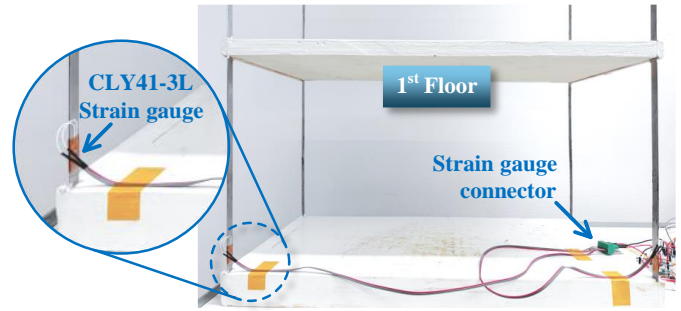


Figure 5. HBM CLY41-3L linear strain gauges

The strain-monitoring system adopts an edge computing architecture and consists of these two strain gauges, two external high-resolution analog-to-digital converters (ADCs), two instrumentation amplifiers, and most importantly an ESP32-S3 microcontroller (MCU) as the edge device, shown in Figure 6.

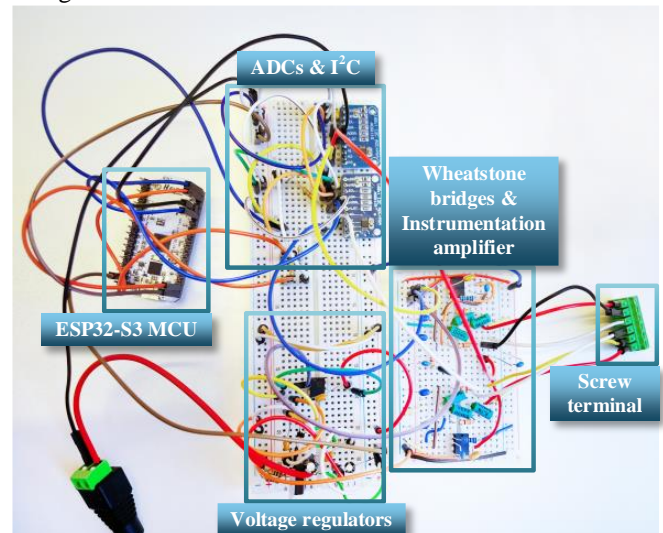


Figure 6 The experimental setup for the strain-monitoring system



Figure 4. IOLITE<sup>®</sup> 3xMEMS accelerometers (a) and KRYPTON<sup>®</sup> CPU data logger (b)

During the second testing, two HBM CLY41-3L linear strain gauges are glued on the smooth surface of the steel columns at the bottom, respectively, to measure strains of the steel columns under controlled free vibration, with the sampling rate of 128 Hz, as shown in Figure 5.

In the device layer, the strain gauges are configured in a Wheatstone quarter-bridge, powered by a low-dropout (LDO) voltage regulator to maintain a stable excitation voltage and suppress external interference. Then, the weak voltage variations from the bridge are amplified by a high common-mode rejection ratio instrumentation amplifier AD620, followed by a resistor-capacitor (RC) filter with a cutoff frequency of 3.4 kHz to effectively reduce high-frequency noise and enhance signal quality. To meet the requirements of real-time monitoring at the micro strain level ( $\mu$ m/m), the amplified signals are digitized by an external 16-bit resolution ADS1115, with a sampling rate of 128 Hz and a full-scale range of  $\pm 6.144$  V, where the RMS noise is 187.5  $\mu$ V and the peak-to-peak noise reaches 187.5  $\mu$ V. Finally, the digitalized signals are transmitted to the MCU via the I<sup>2</sup>C (Inter-Integrated Circuit) bus. A circuit schematic is presented in Figure 7 with design details of the electronic components.

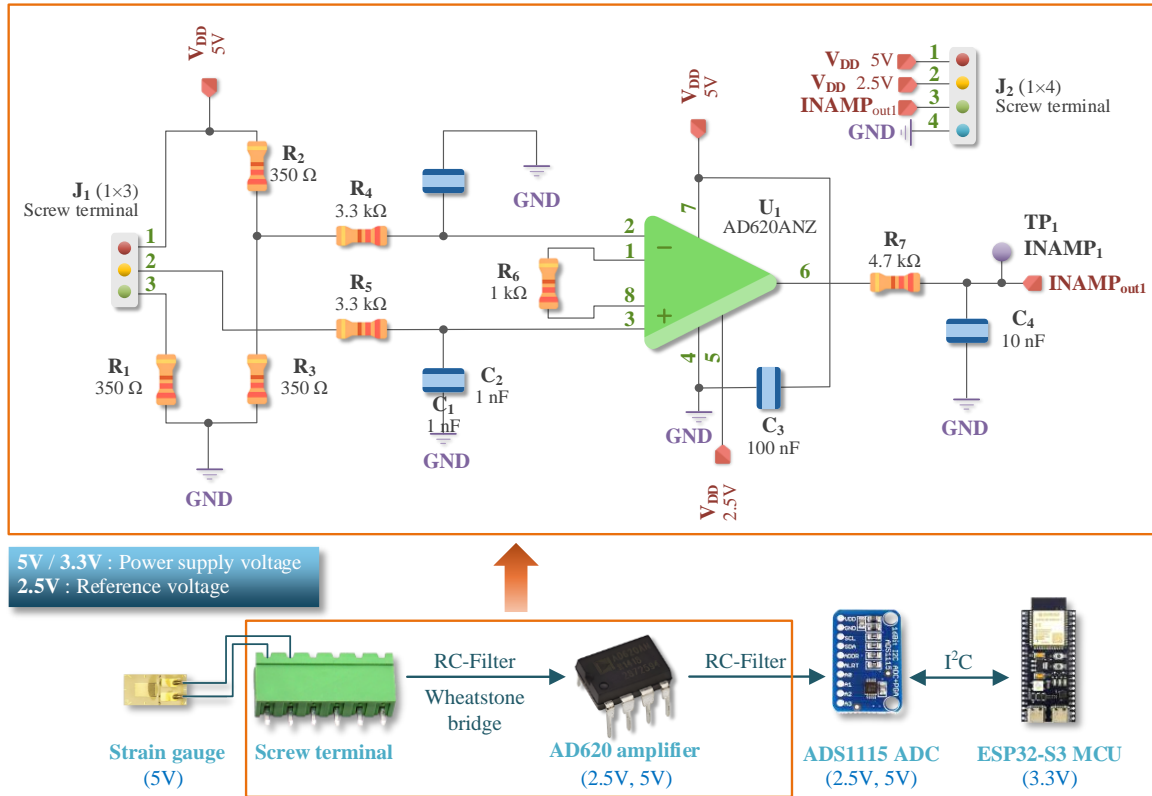


Figure 7 Circuit diagram with electronic components

It is noted that when extracting the amplified voltage difference in a Wheatstone quarter-bridge, the original bridge voltage must be reconstructed to obtain its accurate micro strain ( $\mu\epsilon$ ) value. Temperature compensation is not possible in this setup, causing normal and bending strains to be superimposed. The micro-strain  $\epsilon$  is calculated as:

$$\epsilon = \epsilon_n + \epsilon_b = \frac{4}{k} \cdot \frac{V_o}{V_s} - \epsilon_s \quad (2)$$

where  $\epsilon$  is the effective strain;  $\epsilon_n$  is the normal strain;  $\epsilon_b$  is the bending strain;  $\epsilon_s$  is the apparent strain;  $k$  is the factor corresponding to HBM CLY41-3L linear strain gauge;  $V_o$  is the voltage difference between the bridge legs;  $V_s$  is the excitation voltage.

In the edge layer, the lightweight ESP32-S3 MCU processes the data for the micro-strain. It serves as the edge computing core, equipped with a dual-core LX7 microprocessor. One core is dedicated to ADC sampling and data transmission, while the other performs real-time micro-strain ( $\mu\epsilon$ ) calculations, preventing data loss and task conflicts. Its support for hardware floating-point operations enables potential implementation of fatigue assessment methods at the edge, such as rain-flow counting. Synchronization between multiple strain gauges is achieved using the ESP32-S3's internal timer, which records a timestamp to align the measurement data in time when an ADC completes signal conversion. At the end, the micro-strains with recorded timestamps are transmitted to via a serial port a laptop where a Python script processes the incoming dataflow.

In the whole process, data acquisition, preprocessing, and transmission only happen locally (i.e. near the strain gauges), rather than relying on the remote cloud server. Particularly, edge computing offers low latency, real-time processing, and enhanced data privacy by reducing the need to transmit measured strain output signals to the cloud center. This preprocessing ensures that only the critical and useful data is transmitted to other systems, rather than raw, unprocessed signals, greatly reducing bandwidth requirements and costs.

## 2.5 Data processing

After the frequency sweep excitation, edge computing can be deployed on KRYPTON® CPU based on signals sampled over a period. Fast Fourier Transform (FFT) converts the discrete acceleration signals in time series to frequency domain to obtain the frame's vibration spectra, including amplitudes and phases.

Based on the amplitude peaks captured by FFT, the half power bandwidth method is used to calculate the modal damping ratio corresponding to each natural frequency. For a low damped structure ( $\zeta \ll 1$ ), the modal damping ratio is:

$$\zeta = (f_r - f_l)/2f_n \quad (3)$$

where  $f_n$  is the natural frequency corresponding to the resonance peak;  $f_l$  and  $f_r$  are the left and right frequencies at which the peak drops to half power of the resonance peak (-3 dB, or  $1/\sqrt{2}$  amplitude in the spectrum), respectively.



As for the free vibration, the damping ratio in a certain mode can be obtained by analyzing the amplitude decrement rate, i.e. Logarithmic Decrement:

$$\delta = \frac{1}{N} \ln[A(t)/A(t + nT)] \quad (4)$$

$$\zeta = \delta / \sqrt{4\pi^2 + \delta^2} \quad (5)$$

where  $A(t)$  and  $A(t+nT)$  are the amplitudes corresponding to time  $t$  and  $t+nT$ , respectively;  $T$  is the natural period;  $n$  is any integer number of successive, absolute peaks. Assume the structure is linearly elastic with small deformation, and there is a linear relationship between the strain and displacement in one dimension. Therefore, the amplitude of strains can be used in Equation (4).

Since vibration can occur throughout the whole frequency spectrum, filtering is required when using Equations (4) - (5) to keep only the one-order mode vibration.

According to the strain time series, the Rain-flow counting method is used for strain cycles. Then, the rain-flow histogram is obtained statistically for fatigue assessment in the future.

All the algorithms are programmed in Python language and run in the edge devices mentioned above.

### 3 TESTING RESULTS

This section presents the computing results of the building frame model, including its natural frequencies, damping ratios with strain cycle counting that is beneficial for structural damage detection and fatigue analysis in the future.

#### 3.1 Identification of structural dynamic properties

After finishing each vibration test, the output signals of the frame model with and without the sloshing tank are processed. As the floor acceleration at the foundation level has shown to be very small (relative to the other floors) it was neglected in this study. The accelerations from the second floor and the fourth floor with and without the sloshing tank on the second floor are shown in Figure 8.

From the time history acceleration of each floor, it is obvious that resonance occurs when the sweep frequency is near one of the frequencies of the frame model. Due to the proximity of the excitation to the first floor, its horizontal acceleration is more pronounced than that of the fourth floor.

Interestingly, when the sweep frequency reaches the frame model's natural frequency of the first mode (around 1 Hz), the sloshing tank placed on the second floor has very little effect in reducing the frame's model responses of each floor, because in the first mode, the second floor has small modal amplitude, see Figure 1. However, when the sweep frequency reaches the second mode (around 3 Hz), it exhibits a good performance in vibration reduction of each floor. The reason is that in the second mode, the displacements of the first, second and fourth floor are the largest, which makes the sloshing tank's damping effect to an ideal state except for the third floor (with zero displacement in the second mode). After the second mode, the sloshing tank does not reduce the structural responses so much.

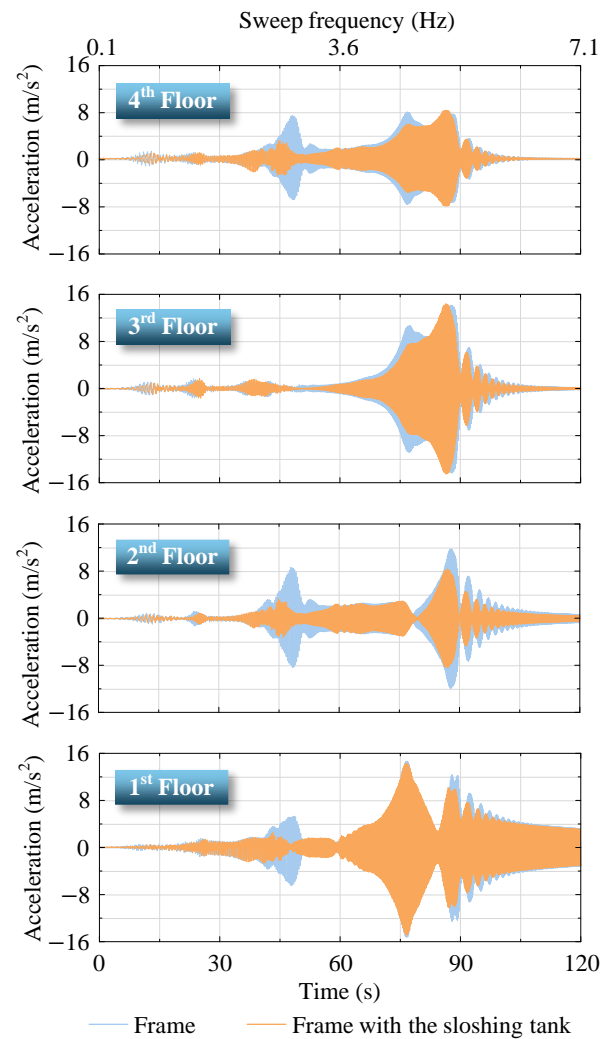
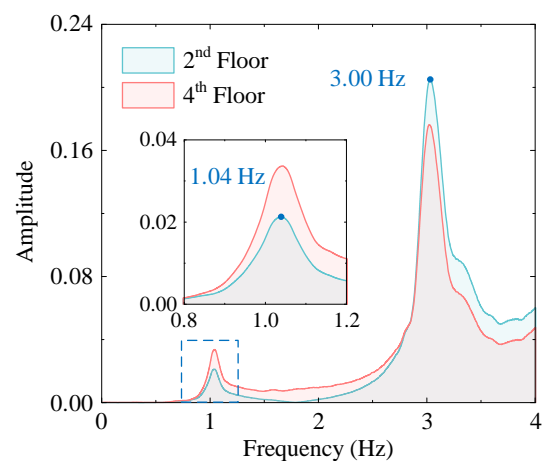
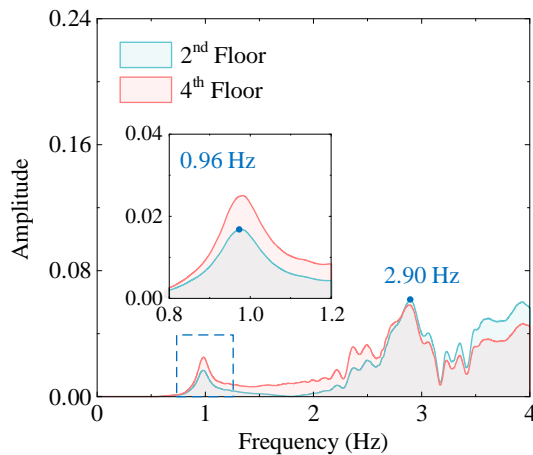


Figure 8. Acceleration time histories of the frame model with and without the sloshing tank on the second floor



(a) Without the sloshing tank



(b) With the sloshing tank on the second floor

Figure 9. Acceleration FFTs of the frame model in under frequency sweep excitation

According to the acceleration FFTs in Figure 9 (a), two peaks can be found, corresponding to the first two natural frequencies. From Figure 9 (b), the FFT shows again that the sloshing tank reduces more efficiently the vibration in the second mode. In addition, around the second mode, there are more smaller peaks than the scenario without the tank. Essentially, the tank annihilates the peak in the second mode – see Figure 9 (b), and separates it into several small peaks, which is similar to the mechanisms of a tuned mass damper. Because of extra weight and damping provided by the tank, the natural frequencies in each mode decrease a little bit.

However, the peak in the first mode is far less obvious than the peak in the second mode, see Figure 9 (a), which is related to the influence of the shaker position. From Figure 1, it is clearly shown that in the first mode, the maximum displacement happens on the top floor. During the first test, however, the shaker is fixed to apply the force in the middle of the steel column at the bottom, giving a small displacement in the first mode. Meanwhile, because of the frequency sweep excitation in a short duration during the testing, the frame model does not obtain sufficient energy from the shaker to establish a stable first-order modal response.

From Figure 10, dynamic strains of the frame model under controlled free vibration from strain gauge 1 are approximately sinusoidal throughout the entire frequency spectrum. Moreover, with the sloshing tank on the second floor, the frame model has a smaller oscillation.

Figure 11 presents the FFTs of strain gauge 1. As observed, the initial disturbance on the top floor has effectively excited the first mode. Also, the sloshing tank placed on the second floor reduces the structural responses in the second mode, not the first mode, which was also explained before.

Table 1 and Table 2 present the natural frequencies of the frame model with and without the sloshing tank, corresponding to the acceleration and strain FFTs, identified through the peak-picking algorithm within the range of [0, 4 Hz].

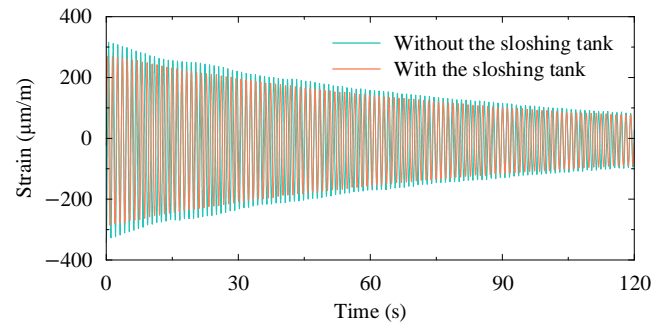


Figure 10. Dynamic strains of the frame model in time history from strain gauge 1

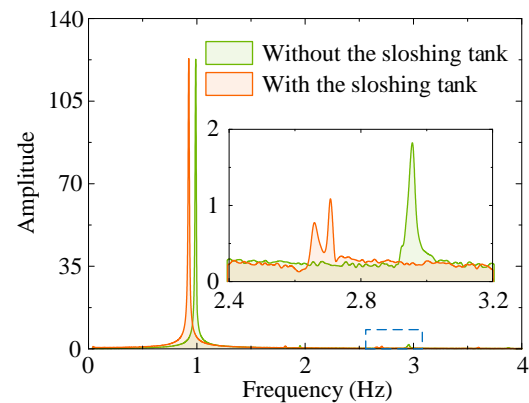


Figure 11. FFTs of strain gauge 1 (based on free vibration tests)

Table 1. Natural frequencies of the frame model without the sloshing tank

Mode	$f_n$ (Hz)		
	Sweep	Single	Free
1	1.04	1.03	0.99
2	3.00	2.99	2.96

Sweep: frequency sweep excitation; Single: single frequency excitation; Free: controlled free vibration.

Table 2. Natural frequencies of the frame model with the sloshing tank on the second floor

Mode	$f_n$ (Hz)		
	Sweep	Single	Free
1	0.96	0.95	0.92
2	2.90	2.87	2.77

Sweep: frequency sweep excitation; Single: single frequency excitation; Free: controlled free vibration.

The above results indicate that the natural frequencies in each mode of the frame model measured in different vibration tests are consistent (a maximum error of no more than 5%), within the allowable error range. In the controlled free vibration, the natural frequency measured is believed to be closer to the real one due to the absence/removal of the external vibration shaker.

During frequency sweep and single frequency excitations, factors such as excitation conditions, coupling effects, and phase lag have a significant impact on the results. The identification of the natural frequency of the frame model relies on resonance peaks, which are often close to the natural frequency of a structure; basically, when the structure system has damping or slight non-linearity, the acceleration resonance peak may be slightly shift. In addition, under vibration of an MDOF structure, interactions or coupling effects often exist between different modes, which may contribute to such "shift" of the observed resonance peaks even if the natural frequency itself has not changed. Theoretically, single frequency excitation has relatively smaller errors than the frequency sweep excitation due to more sufficient time for the structural system to follow the excitation in real-time. In contrast, during frequency sweep excitation, a certain natural frequency may have been "swept" over before the frame model fully establishes a steady-state response at that frequency, resulting in a response lag and a slightly higher observed natural frequency.

Table 3. Damping ratios of the frame model

Mode	$\zeta$ (%)	
	Single	Free
1	0.73 (0.78) <sup>a</sup>	0.75 (0.79) <sup>a</sup>
2	0.24 (0.34) <sup>a</sup>	0.27 (0.34) <sup>a</sup>

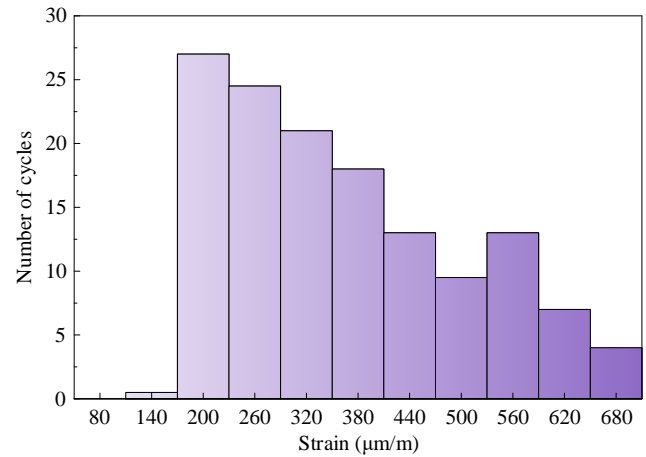
<sup>a</sup> Values in brackets are the cases with the sloshing tank.

Table 3 presents the damping ratios obtained under both single frequency excitation and free vibration. In fact, there are two peaks around 3 Hz in Figure 11. To avoid the overlapping of multiple modes, which are close to each other on the spectrum and result in inaccurate results. Thus, before the half-power bandwidth method, a bandpass filter with a bandwidth of 0.4 Hz was used to keep only the single mode vibration component when obtaining the damping ratio. As can be noted, the agreement is very good, indicating that the results from these two vibration tests are consistent, which verify reliability and correctness.

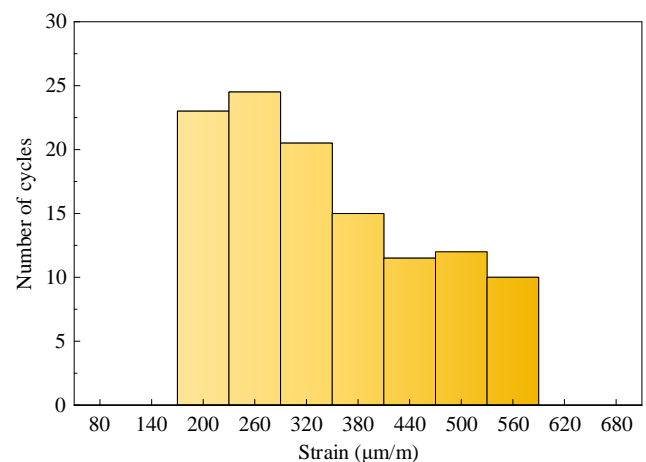
The damping ratio of the first mode is significantly higher than that of the second mode, indicating that the frame model experiences a faster energy dissipation because of a higher damping in the first mode. Additionally, the sloshing tank provides the higher damping among all modes, especially the second mode, with a more significant increase of 0.07-0.10%, indicating that the damper has a greater impact on the vibration mitigation in the second mode.

### 3.2 Strain cycle counting for fatigue assessment

From the dynamic strains obtained from strain gauge 1, the histograms for Rain-flow Counting are developed to give valuable information for future fatigue assessment.



(a) Without the sloshing tank



(b) With the sloshing tank on the second floor

Figure 12. Histograms of strain cycle counting from strain gauge 1

Figure 12 shows that most strain cycles concentrate between 200-320  $\mu\text{m/m}$ , making the greatest contribution to fatigue life of the frame model; The number of strain cycles decreases with the increase of the strain range with fewer cycles in the high strain range (500-600  $\mu\text{m/m}$ ).

An interesting observation is that with the sloshing tank, the number of cycles in the high strain region is reduced, indicating that the frame model is subjected to relatively mild strain fluctuations, and the sloshing tank can be an efficient method of vibration control.

## 4 CONCLUSIONS

In this study, the integration of edge computing into different lightweight edge devices is explored, including the KRYPTON® CPU data logger and the ESP32-S3 microcontroller.

In each monitoring system, sensor nodes are distributed to collect the measurement data (accelerations and strains) of a four-story building frame model considering two different cases with variations in the structural mass and damping. The experimental results demonstrate that these monitoring systems



can detect changes in structural dynamic properties under vibration, which provides a basis for future fatigue assessment and structural damage detection.

Finally, the proposed approach is scalable to dense sensor networks that can fuse information from many locations in a large-scale structure. Therefore, edge computing plays an important role in reducing data transmission to the cloud center and ultimately shaping a brighter future for structural health monitoring.

#### ACKNOWLEDGMENTS

This work is performed at the laboratory of the Department of Civil and Architectural Engineering, KTH Royal Institute of Technology, and is supported by *HORIZON-MSCA-2022-DN: BRIDGITISE* under Grant Agreement No. 101119554. The authors gratefully recognize these contributions. In addition, the authors would like to thank the companies DEWESoft and IoTBridge for providing the equipment and support during the vibration testing.

#### REFERENCES

- [1] H. V. Dang, Raza ,Mohsin, Nguyen ,Tung V., Bui-Tien ,T., and H. X. and Nguyen, "Deep learning-based detection of structural damage using time-series data," *Struct. Infrastruct. Eng.*, vol. 17, no. 11, pp. 1474–1493, Oct. 2021, doi: 10.1080/15732479.2020.1815225.
- [2] S. S. Saidin *et al.*, "Vibration-based approach for structural health monitoring of ultra-high-performance concrete bridge," *Case Stud. Constr. Mater.*, vol. 18, p. e01752, Jul. 2023, doi: 10.1016/j.cscm.2022.e01752.
- [3] Q. Meng and S. Zhu, "Anomaly detection for construction vibration signals using unsupervised deep learning and cloud computing," *Adv. Eng. Inform.*, vol. 55, p. 101907, Jan. 2023, doi: 10.1016/j.aei.2023.101907.
- [4] I. Abu-Mahfouz and A. Banerjee, "Crack detection and identification using vibration signals and fuzzy clustering," *Complex Adapt. Syst. Conf. Theme Eng. Cyber Phys. Syst. CAS Oct. 30 – Novemb. 1 2017 Chic. Ill. USA*, vol. 114, pp. 266–274, Jan. 2017, doi: 10.1016/j.procs.2017.09.038.
- [5] A. Tributsch and C. Adam, "An enhanced energy vibration-based approach for damage detection and localization," *Struct. Control Health Monit.*, vol. 25, no. 1, p. e2047, Jan. 2018, doi: 10.1002/stc.2047.
- [6] W. Shi, J. Cao, Q. Zhang, Y. Li, and L. Xu, "Edge computing: Vision and challenges," *IEEE Internet Things J.*, vol. 3, no. 5, pp. 637–646, Oct. 2016, doi: 10.1109/JIOT.2016.2579198.
- [7] S. Cui, T. Hoang, K. Mechtov, Y. Fu, and B. F. Spencer, "Adaptive edge intelligence for rapid structural condition assessment using a wireless smart sensor network," *Eng. Struct.*, vol. 326, p. 119520, Mar. 2025, doi: 10.1016/j.engstruct.2024.119520.
- [8] M. Abner, P. K.-Y. Wong, and J. C. P. Cheng, "Battery lifespan enhancement strategies for edge computing-enabled wireless bluetooth mesh sensor network for structural health monitoring," *Autom. Constr.*, vol. 140, p. 104355, Aug. 2022, doi: 10.1016/j.autcon.2022.104355.
- [9] Ryan Yount, Joud N. Satme, David P. Wamai, and Austin R. J. Downey, "Edge processing for frequency identification on drone-deployed structural health monitoring sensor nodes," presented at the Proc.SPIE, Jun. 2024, p. 130550L. doi: 10.1117/12.3013712.
- [10] Z. Zhou, X. Chen, E. Li, L. Zeng, K. Luo, and J. Zhang, "Edge intelligence: Paving the last mile of artificial intelligence with edge computing," *Proc. IEEE*, vol. 107, no. 8, pp. 1738–1762, Aug. 2019, doi: 10.1109/JPROC.2019.2918951.

# On the use of 6C seismic station for bending-to-shear and torsional building response assessment.

Yara Rossi<sup>1,2,3</sup>, ORCID (0000-0002-0067-0069), Philippe Guéguen<sup>1</sup>, ORCID (0000-0001-6362-0694), Felix Bernauer<sup>3</sup>, ORCID (0000-0002-9509-4905), Kate Huihsan Chen<sup>4</sup>, ORCID (0000-0002-5164-9681), Chen-Jen Lin<sup>5</sup>, ORCID (0000-0003-4374-4256), Chin-Shang Ku<sup>5</sup>, ORCID (0000-0002-1039-6833), Yaochieh Chen<sup>4</sup>, ORCID (0000-0001-6024-278X)

<sup>1</sup>Department of Geosciences, Université Grenoble Alpes, Rue de la Piscine 1381, 38610 Gieres, France

<sup>2</sup>Department of Earth Sciences, University of Oregon, 1275 E 13<sup>th</sup> Ave, Eugene, OR 97401, USA

<sup>3</sup>Department of Earth and Environmental Sciences, Ludwig Maximilians University of Munich, Theresienstrasse 41, 80333 München, Germany

<sup>4</sup>Department of Earth Sciences, National Taiwan Normal University, 162, Section 1, Helping E. Rd., Taipei City 106, Taiwan

<sup>5</sup>Institute of Earth Sciences, Academia Sinica, Taipei, 128, Section 2, Academia Rd., Nangang, Taipei 11529, Taiwan

email: yara.rossi@lmu.de, philippe.gueguen@univ-grenoble-alpes.fr, [Felix.Bernauer@lmu.de](mailto:Felix.Bernauer@lmu.de), [katepili@ntnu.edu.tw](mailto:katepili@ntnu.edu.tw), [youngman@earth.sinica.edu.tw](mailto:youngman@earth.sinica.edu.tw), [backnew@earth.sinica.edu.tw](mailto:backnew@earth.sinica.edu.tw), yaochieh77@gmail.com

**ABSTRACT:** To understand the behavior of healthy structures and the changes to their condition over time, it is imperative to perform experimental analysis of existing civil engineering structures. Development of novel sensors measuring rotations enable to directly measure important components of the system parameters, as they provide additional information on the structural response. Long-term monitoring of existing structures using 6C sensors – 3C translation and 3C rotation, enables a more in-depth analysis of the system parameters; frequency, modeshape and damping. Specifically, the translation-based characterization of the torsional mode can be enhanced through direct measurement of the torsional angle, center of torsion and more precise frequency extraction. Furthermore, the distinction between shear and bending can be analysed through the ratio of angle and deflection, instead of using proxies like frequency ratios or shear wave velocity. In this study, we analyse how using 6C datasets for structural characterization of high-rise buildings provide further information to understanding the system parameters and their variations over time. We find that the rotational components significantly contribute to the understanding of the vibration behavior and thereby propose to include 6C sensors to enhance the characterization of structures.

**KEY WORDS:** 6C dataset; structural characterization; shear; bending; rotation; translation; system property variation.

## 1 INTRODUCTION

Analyzing seismic data to observe the dynamic behavior of buildings is a well-established approach in structural monitoring. Traditionally, this has relied on accelerometers and seismometers to capture translational motion. Recently, sensors capable of detecting rotational motion have expanded these capabilities [1]. Combining rotational and translational data provides more details on the structures behavior. Collocating 3 components rotation and 3 components translation improves the frequency resolution for torsional modes, and enables the determination of 6C mode shapes at the roof level with minimal sensor footprint, as shown in [2].

A key analysis is to determine a baseline for a healthy structure, concerning the system properties—like resonance frequency, damping, mode shapes, and waveform-based signal statistics [3]. In the absence of damage, these features are expected to stay consistent over time. Unless environmental parameters such as temperature, wind, or precipitation change, then they can temporarily influence the system behavior [4], [5]. Torsional modes often respond differently to environmental variations compared to translational modes, as shown in [6].

The translational modes of structures can be approximated through a shear or Euler-Bernoulli beam [7]. However, real structures are a combination of both. The Timoshenko beam theory incorporates both bending and shear [8], and has been applied to real structures in [9], [10]. Multiple methods exist to assess the prevailing regime - shear or bending, including frequency ratios [8], interferometric determination of shear

velocity [8], and interstory drift analysis using sensor arrays [9]. Structural damage can alter stiffness, mass, or damping, which in turn modifies the curvature of the resonance mode shapes. Monitoring the variation of a mode shape between bending and shear thus provides critical insights to a structures health [3].

The torsional modes are influenced by the eccentricity of the structure - which exists when the center of mass and center of rigidity do not coincide and the center of torsion. Due to inherent asymmetries in the building design or construction, all buildings display some torsional motion, which is a key factor in seismic damage. Therefore, changes in torsional response are vital to track for structural health monitoring.

This work investigates how 6C measurements can enhance structural characterization and monitoring, specifically for shear-to-bending and torsional response.

## 2 SENSORS AND EXPERIMENT SET-UP

There are a handful of buildings that have been instrumented for continuous 6C monitoring such as the high-rise building TAIPEI101 in Taiwan [10]. Where two 6C stations are located on the 90<sup>th</sup> floor comprising of an Eentec R1 rotation sensor and a Kinemetrics accelerometer each. Eentec R1 rotation sensor has a sensibility of  $1.2 \cdot 10^{-7}$  rad/s which is frequency dependent and is sensitive to temperature [11]. Another common rotation sensor is the blueSeis-3A [12] with a sensitivity of  $2.5 \cdot 10^{-8}$  rad/s from DC to 50 Hz. The blueSeis-3A was used to monitor the high-rise building Prime Tower in Switzerland for 1.5 years [2]. Recently high-quality 6C inertial

measurement units have been assembled specifically for structural health monitoring. The sensor self-noise of the rotational sensor is at  $1.5 \cdot 10^{-6}$  rad/s, therefore depending on the vibration amplitude, not always low enough for ambient noise, but low enough for active experiments [13]. The optimal location for a rotation sensor on a building is generally at the top floor, where the amplitude is the largest and an approximate modeshape can be extracted. On bridges this location is still an open question due to unresolved boundary conditions and location of maximum amplitude for rotational motion.

### 3 METHODS

In this study, we analyze the ratio between the horizontal rotation angle and deflection as a proxy for the vibration regime of high-rise buildings. Additionally, we are investigating the ratio between torsion angle and the displacement to extract the center of torsion.

The amplitudes of rotation and translation for each mode can be estimated either through the simple power spectral density (PSD) peak picking method or a more sophisticated method such as the stochastic subspace identification. Either way it is imperative that the methods are applied to the rotation angle and displacement directly and not the classic rotation rate and acceleration timeseries. As the derived ratio needs to be in the units of rad/m. Additionally, the relative amplitudes between rotation and translation need to be kept and a normalization as is often applied for mode shapes would have to be applied to all 6 components in the same way.

#### 3.1 Ratio for shear-to-bending response

For the shear-to-bending response analysis the ratio between the rotation angle and deflection is calculated by simple division. For a symmetric quadratic building where the walls are oriented along the North-South axis the translational modes would either be in East or North direction. To analyse the East bending mode, the rotations around North are divided by the deflection in East. For the North bending mode, the rotations around the East are divided by the deflection in North.

#### 3.2 Ratio for center of torsion

For an analysis of the torsional mode concerning the center of torsion the ratio between the vertical rotation angle and the horizontal translation is calculated. The horizontal translation is highly dependent on the location of the 6C station on the floor. At the center of torsion almost no displacement will occur, while there will be more translation away of the center of torsion. So, in theory one can estimate the torsional ratio by dividing the torsional angle through either the North, East or total horizontal displacement. A change of this ratio will mean a change of the center of torsion.

#### 3.3 Variation of Ratio

It is expected that the ratio for both the shear-to-bending response as well as the center of torsion will vary due to environmental and operational changes. These are for example; temperature, humidity, air pressure, wind, rain and activation of a tuned mass damper. However, it is expected that an earthquake could influence the ratio similar to the modal frequencies, that often feel a drop and consecutive healing effect. Any permanent change of the ratio could hint at damage and would need to be investigated.

### 4 CONCLUSION

This study presents a new method based on the ratio between rotation angle and deflection. This ratio contains information on the mode shape, and thus the overall vibration regime. Here it is introduced to analyse 1) if a structure is in shear or bending, 2) where the center of torsion is for a structure and 3) why this ratio varies over time.

6C datasets enable the evaluation of vibration regimes in high-rise structures. However, the results depend strongly on accurate sensor placement, sensor quality, and the ability of sensors to remain unaffected by external influences aside from the measured motion.

### REFERENCES

- [1] C. J. Lin, W. G. Huang, H. P. Huang, B. S. Huang, C. S. Ku, and C. C. Liu, "Investigation of array-derived rotation in TAIPEI 101," *Journal of Seismology*, vol. 16, no. 4, pp. 721–731, 2012, doi: 10.1007/s10950-012-9306-7.
- [2] Y. Rossi, K. Tatsis, J. Clinton, E. Chatzi, and M. Rothacher, "A New Paradigm for Structural Characterization, including Rotational Measurements at a Single Site," *Bulletin of the Seismological Society of America*, Aug. 2023, doi: 10.1785/0120230026.
- [3] C. R. Farrar and K. Worden, *Structural Health Monitoring*. Wiley, 2012. doi: 10.1002/9781118443118.
- [4] J. F. Clinton, S. C. Bradford, T. H. Heaton, and J. Favela, "The observed wander of the natural frequencies in a structure," *Bulletin of the Seismological Society of America*, vol. 96, no. 1, pp. 237–257, 2006, doi: 10.1785/0120050052.
- [5] P. Guéguen, P. Johnson, and P. Roux, "Nonlinear dynamics induced in a structure by seismic and environmental loading," *The Journal of the Acoustical Society of America*, vol. 140, no. 1, pp. 582–590, Jul. 2016, doi: 10.1121/1.4958990.
- [6] Y. Chen *et al.*, "Dynamic Characteristics of TAIPEI 101 Skyscraper from Rotational and Translation Seismometers," *Bulletin of the Seismological Society of America*, vol. 113, no. 2, pp. 690–709, Apr. 2023, doi: 10.1785/0120220147.
- [7] C. Boutin and S. Hans, "Homogenisation of periodic discrete medium: Application to dynamics of framed structures," *Computers and Geotechnics*, vol. 30, no. 4, pp. 303–320, 2003, doi: 10.1016/S0266-352X(03)00005-3.
- [8] P. Guéguen, E. D. Mercierat, and F. Alarcon, "Parametric study on the interpretation of wave velocity obtained by seismic interferometry in beam-like buildings," *Bulletin of the Seismological Society of America*, vol. 109, no. 5, pp. 1829–1842, Oct. 2019, doi: 10.1785/0120190054.
- [9] J. Cai, G. Bu, C. Yang, Q. Chen, and Z. Zuo, "Calculation Methods for Inter-Story Drifts of Building Structures," *Advances in Structural Engineering*, vol. 17, no. 5, pp. 735–745, 2014.
- [10] K. G. Chen, J. H. Wang, B. S. Huang, C. C. Liu, and W. G. Huang, "Vibrations of the TAIPEI 101 skyscraper caused by the 2011 Tohoku earthquake, Japan," *Earth, Planets and Space*, vol. 64, no. 12, pp. 1277–1286, 2012, doi: 10.5047/eps.2012.04.004.
- [11] F. Bernauer, J. Wassermann, and H. Igel, "Rotational sensors-a comparison of different sensor types," *Journal of Seismology*, vol. 16, no. 4, pp. 595–602, 2012, doi: 10.1007/s10950-012-9286-7.
- [12] F. Bernauer *et al.*, "BlueSeis3A: Full Characterization of a 3C Broadband Rotational Seismometer," *Seismological Research Letters*, vol. 89, no. 2A, pp. 620–629, Mar. 2018, doi: 10.1785/0220170143.
- [13] L. Murray-Bergquist, F. Bernauer, and H. Igel, "Characterization of Six-Degree-of-Freedom Sensors for Building Health Monitoring," *Sensors*, vol. 21, no. 11, p. 3732, May 2021, doi: 10.3390/s21113732.



# Integration of Seismic Interferometry and System Identification Techniques for Real-Time Structural Health Monitoring: Automated Detection of Shear-Wave Velocity Changes Using Skyscraper Data for Validation

Erol Kalkan<sup>1</sup>, Mohammad AlHamaydah<sup>2</sup>, ORCID (0000-0002-5004-0778), Weiping Wen<sup>3</sup>

<sup>1</sup>QuakeLogic Inc., Roseville, CA, USA

<sup>2</sup>Department of Civil Engineering, American University of Sharjah, Sharjah, UAE

<sup>3</sup>Department of Civil Engineering, Harbin University, Harbin, China

email: erol@quakelogic.net, malhamaydeh@aus.edu, wenweiping@hit.edu.cn

**ABSTRACT:** This study presents an integrated approach that combines seismic interferometry and system identification techniques for real-time Structural Health Monitoring (SHM), enabling the automated detection of changes in shear-wave velocity profiles for damage assessment. The methodology is validated using data from a 62-story residential skyscraper in San Francisco, one of the tallest buildings in the Western U.S., equipped with 72 uniaxial accelerometers across 26 floors. The building incorporates advanced structural components, including buckling-restrained braces, outrigger columns, and a tuned liquid damper to mitigate seismic and wind-induced responses. Data from the 2014 M6.0 South Napa and 2018 M4.4 Berkeley earthquakes, as well as ambient vibration recordings, are analyzed to establish baseline dynamic properties, including modal parameters, shear-wave profiles, and wave attenuation. We monitor wave propagation velocities, normal mode frequencies, and intrinsic damping through deconvolution interferometry, enabling real-time identification of structural stiffness changes. Shear-wave travel-time curves from deconvolution show reduced velocities below the 28th floor, coinciding with buckling-restrained braces, while higher velocities are observed above. This integrated methodology offers a robust framework for automated damage detection and real-time structural health assessment, demonstrating the potential to enhance the resilience and safety of high-rise structures during seismic events.

**KEY WORDS:** Structural Health Monitoring (SHM); Seismic Interferometry; System Identification; Shear-Wave Velocity; Damage Detection; High-rise structures.

## 1 INTRODUCTION AND BACKGROUND

Structural Health Monitoring (SHM) plays a crucial role in maintaining the safety and resilience of critical infrastructure, particularly in regions prone to seismic activity. High-rise buildings in seismically active zones such as the San Francisco Bay Area must withstand frequent and potentially severe seismic events. San Francisco, situated above an intricate network of active faults, including the San Andreas Fault, faces considerable seismic hazards, with the U.S. Geological Survey (USGS) forecasting a high probability of significant earthquakes occurring within the next few decades [1].

This paper explores the application of an advanced integrated SHM methodology to One Rincon Hill South Tower, a landmark 62-story, 195-meter-tall residential skyscraper in San Francisco, California. Recognized as the tallest residential building in California, the tower is instrumented with 72 uniaxial accelerometers strategically distributed across 26 floors, facilitated through collaborative efforts between the USGS National Strong Motion Project and the California Geological Survey's Strong Motion Instrumentation Program. Unique design features, including buckling-restrained braces (BRBs), an outrigger column system, a tuned liquid damper (TLD), and a robust, twelve-foot-thick mat foundation, are incorporated to enhance its resistance against seismic and wind-induced forces.

The study aims to validate an innovative real-time SHM system integrating seismic interferometry and system identification methods. This integrated approach aims to automate the detection of structural anomalies, specifically through monitoring changes in shear-wave velocities and wave

attenuation characteristics. Validation is accomplished using data recorded during the 2014 M6.0 South Napa and 2018 M4.4 Berkeley earthquakes, alongside ambient vibration monitoring data.

Advancements in Structural Health Monitoring have increasingly focused on integrating sophisticated methods for more accurate and reliable damage detection. Modal analysis approaches, particularly Frequency Domain Decomposition (FDD), have become standard practice in determining fundamental structural properties such as natural frequencies, mode shapes, and damping ratios. These methods effectively identify changes indicative of structural deterioration or damage [2]-[3].

Seismic interferometry has emerged as an essential complementary approach within SHM, enabling the extraction of detailed structural parameters from seismic and ambient vibration data. The principle of seismic interferometry involves retrieving Green's functions between sensors, thereby providing insights into wave propagation velocities and intrinsic attenuation characteristics, independent of knowledge of the source excitation [4]-[5]. Among interferometric approaches, deconvolution interferometry is particularly beneficial in distinguishing between intrinsic structural attenuation and scattering attenuation, thereby significantly improving stiffness and damage detection accuracy within monitored structures [6]-[7].

Significant validation of deconvolution interferometry in SHM was conducted by Snieder and Safak [4], who accurately estimated structural wave velocities and intrinsic attenuation parameters in the Millikan Library, demonstrating notable

advantages over traditional interferometric methods. Additional validation performed by Kohler et al. [9] in the Factor Building reinforced these findings, indicating a robust potential for application in real-time SHM scenarios.

However, traditional interferometric and modal identification methods independently exhibit limitations, notably insufficient sensitivity to localized stiffness reductions, which are critical for early-stage damage detection. To address these challenges, recent research highlights the importance of integrating seismic interferometric techniques with sophisticated system identification methods, significantly improving the accuracy and reliability of real-time SHM systems [6],[8].

This study builds upon previous work by integrating seismic interferometry methods, specifically modal identification techniques, which are validated using extensive seismic datasets from an extensively instrumented skyscraper. This innovative integration significantly enhances SHM capabilities, particularly for high-rise structures subjected to dynamic seismic loads, enabling timely detection and accurate characterization of structural health, which is crucial for improving resilience and minimizing post-earthquake recovery periods.

## 2 METHODOLOGY

### 2.1 Seismic Instrumentation and Data Collection

The seismic instrumentation of the One Rincon Hill South Tower comprises a comprehensive network of 72 uniaxial accelerometers strategically distributed across 26 floors (Figures 1–4).



Figure 1. 195m skyscraper in San Francisco (photo is courtesy of Magnusson Klemencic Associates).

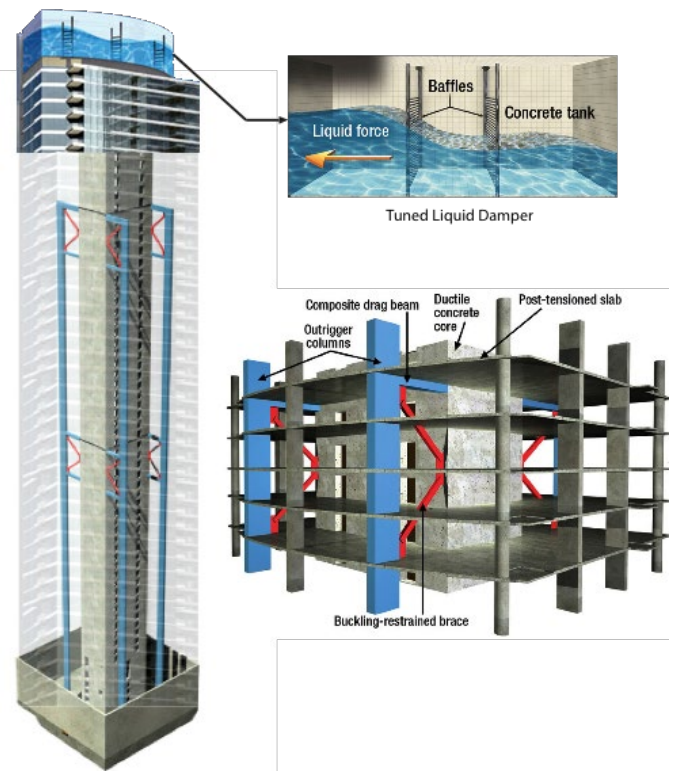


Figure 2. The primary seismic load-resisting system with concrete core and outriggers comprising buckling restrained braces. The water tank located at the roof level serves as a tuned liquid damper to mitigate wind forces (Figures modified from Magnusson Klemencic Associates).

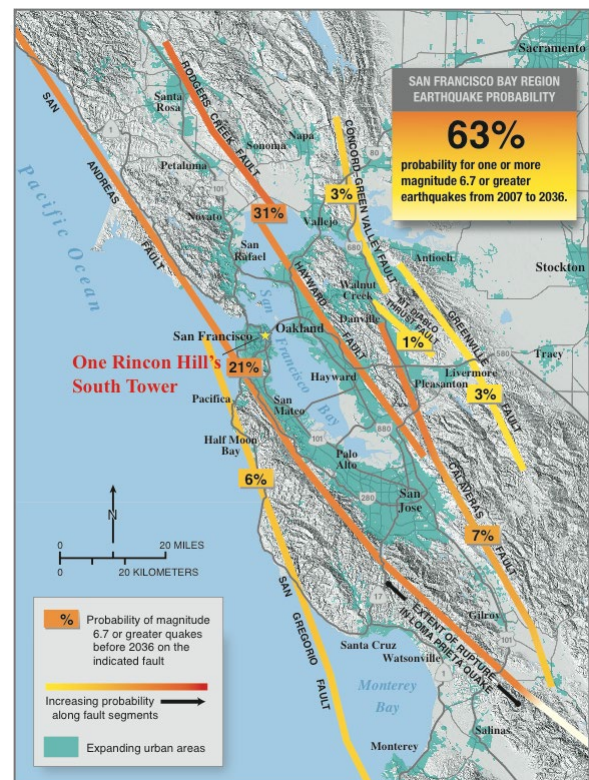


Figure 3. San Francisco Bay Area earthquake faults. The star sign indicates the location of the 195m skyscraper. (modified from <http://earthquake.usgs.gov/regional/nca/ucrf/>).



This dense array was meticulously designed and installed by the USGS's National Strong Motion Project in collaboration with the California Geological Survey's Strong Motion Instrumentation Program. Particular emphasis was placed on instrumenting floors equipped with critical structural elements, including buckling-restrained braces (BRBs) connecting the building to the outrigger systems at floors 26–32 and 52–55. Additional sensors placed at the base and roof levels facilitate the measurement of vertical accelerations, which are essential for quantifying the rocking motion induced by seismic excitation.

The recorded data include responses to two significant earthquakes: the 2014 M6.0 South Napa earthquake (epicentral distance of approximately 48.7 km) and the 2018 M4.4 Berkeley earthquake (epicentral distance of approximately 15.6 km). Ambient vibration measurements were also captured, providing a baseline for comparison of structural properties.

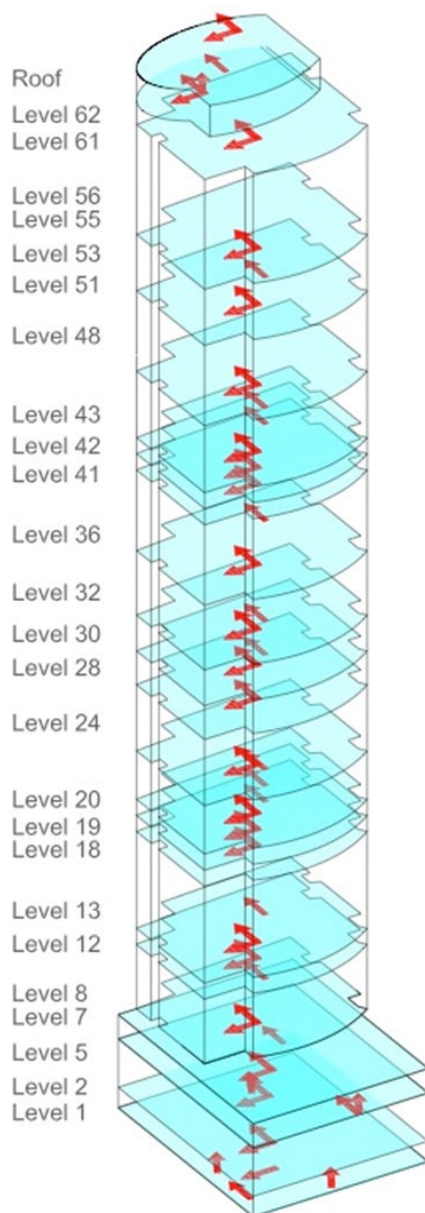


Figure 4. Sensor layout. Red arrows indicate the locations and the directional sensitivity of the accelerometers.

## 2.2 Seismic Interferometry and System Identification Framework

The methodology integrates seismic interferometry with system identification techniques for real-time structural health assessment. Seismic interferometry, particularly through the deconvolution approach, allows extraction of the structure's impulse response function (IRF) independent of external excitation sources. The governing equation for waveform deconvolution interferometry, adapted for building structures, can be expressed as in Eq. (1).

$$D(\omega, z) = \frac{U(\omega, z)}{U(\omega, H)} \quad (1)$$

where  $U(\omega, z)$  is the recorded seismic response at a specific height  $z$ , and  $U(\omega, H)$  represents the recorded response at the reference level  $H$ , typically the roof or base of the structure.

Eq. (1) may become ill-conditioned when the denominator approaches zero. To avoid this condition, the following regularized format is used as the estimator of deconvolution:

$$D(z, z_a, \omega) = [u(z, \omega)u^*(z_a, \omega)] / [|u(z_a, \omega)|^2 + \epsilon \langle |u(z_a, \omega)|^2 \rangle] \quad (2)$$

where superscript “\*” denotes the complex conjugate,  $\epsilon$  is the regularization parameter ( $\epsilon=0.01$  is used here, based on prior experience), and  $\langle |u(z_a, \omega)|^2 \rangle$  is the average power spectrum of  $u(z_a, \omega)$ .

System identification was executed using Frequency Domain Decomposition (FDD), an established modal analysis technique that effectively identifies modal parameters from ambient and seismic-induced vibrations. FDD facilitates modal parameter estimation by decomposing the spectral density matrices of the recorded accelerations into singular values, thus accurately identifying natural frequencies, mode shapes, and damping ratios of the structure [1]-[2].

The integrated approach involves calculating wave propagation velocities, normal mode frequencies, and intrinsic damping characteristics from the IRFs obtained via deconvolution interferometry. Shear-wave velocity profiles are computed explicitly by analyzing the propagation times of upgoing and downgoing shear waves through different building sections. Changes in these profiles effectively indicate stiffness alterations, potentially signifying structural damage or degradation [3],[5].

## 2.3 Analysis Procedures

Analysis began by establishing baseline modal parameters using ambient vibration data. Subsequently, earthquake data from the South Napa and Berkeley events were analyzed to quantify structural response under significant seismic loading conditions. This comparative assessment between baseline and event-specific modal parameters allowed for the precise detection and characterization of structural changes. Wave propagation velocities, intrinsic damping, and attenuation characteristics were estimated in real-time using advanced computational procedures integrating seismic interferometry and system identification.

Wavefield decomposition techniques were also utilized, providing causal (forward-time) and acausal (time-reversed) waveform comparisons. Discrepancies between these



waveforms facilitated precise estimation of intrinsic attenuation, as scattering attenuation remains invariant under time reversal, thus isolating intrinsic material damping characteristics effectively [3],[7].

The methodological rigor and integrated analytical procedures presented herein establish a robust framework for accurate real-time monitoring and damage detection capabilities in high-rise buildings, particularly under seismic excitations.

### 3 RESULTS AND DISCUSSION

#### 3.1 Baseline Dynamic Properties

Baseline modal properties of the One Rincon Hill South Tower were established using ambient vibration data and verified with earthquake-induced vibrations from the 2014 South Napa and 2018 Berkeley earthquakes. Modal analysis using Frequency Domain Decomposition (FDD) revealed the first five fundamental modes within the frequency range of up to 6 Hz. Identified modes included distinct bending and torsional behaviors. Specifically, the fundamental bending modes were clearly observable at frequencies below 1 Hz, consistent with expectations for a high-rise structure of this scale. Notably, ambient vibration data revealed subtle torsional modes, which were less prominent in the earthquake response data, indicating nonlinear behavior activated by seismic events.

#### 3.2 Shear-Wave Velocity Analysis

Utilizing deconvolution interferometry, distinct shear-wave velocity profiles were extracted, displaying apparent variations across the structural height of the building. Figures 5-6 and Table 1 illustrate these variations, which were particularly evident in areas around structural transitions, such as the presence of buckling-restrained braces and outrigger systems. Below the 28<sup>th</sup> floor, significantly reduced shear-wave velocities were consistently observed, correlating directly with the increased structural flexibility imparted by the BRBs. In contrast, increased velocities above this level underscored the effectiveness of outrigger columns and tuned liquid damper systems in enhancing structural rigidity. This spatial variation in wave velocity effectively delineates stiffness transitions, which are critical for accurate real-time monitoring and damage detection.

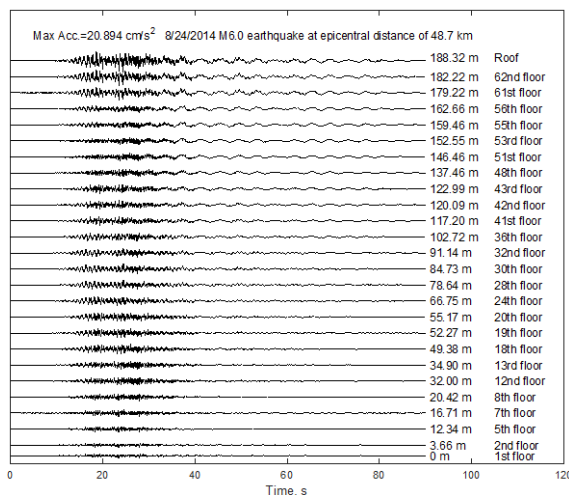


Figure 3. Recorded east-west waveforms from the 2017 M6.0 South Napa earthquake at an epicentral distance of 48.7 km.

Propagating waves from the first floor to the roof show amplification in the order of 4.2. The floor numbers and their corresponding height relative to the ground (1<sup>st</sup> floor) are depicted; the maximum roof acceleration is 20.894 cm/s<sup>2</sup>.

Table 1. Modified Shear-Wave Velocity Profiles.

Floor Range	Average Shear-Wave Velocity (m/s)
Below 28	210
28 to 52	350
Above 52	450

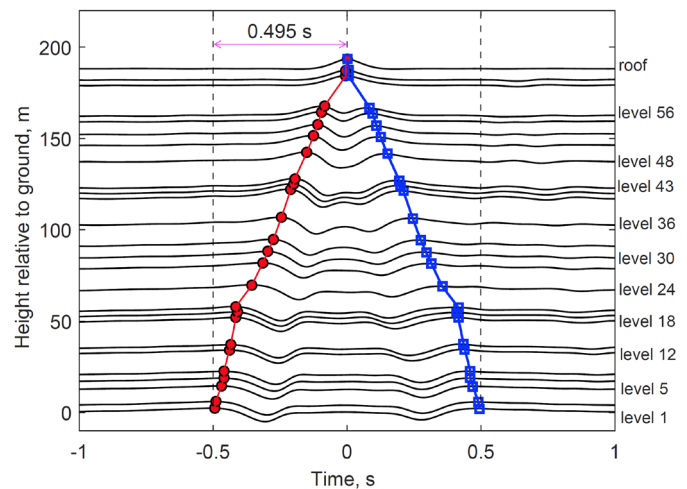


Figure 4. Deconvolved waveforms, calculated from the 2014 Napa earthquake east-west direction acceleration time series, are plotted as positive and negative amplitudes for each instrumented floor over time. The frequency range of the waveforms is 0–4 Hz.

#### 3.3 Intrinsic Damping and Attenuation Characteristics

The damping properties of the structure were quantitatively assessed using the impulse response functions (IRFs) derived from deconvolution interferometry. Results indicated intrinsic damping ratios of approximately 4.4% in the east-west direction and 3.7% in the north-south direction. These values align with expected damping ranges for high-rise buildings, reflecting effective energy dissipation during seismic excitation. Furthermore, wavefield decomposition analysis clearly distinguished between causal and acausal waveforms, allowing precise estimation of intrinsic attenuation. Variations in these characteristics across different building elevations indicated localized stiffness and damping alterations potentially associated with structural degradation or minor damage [3],[7].

These detailed results demonstrate the efficacy and reliability of the integrated SHM methodology proposed herein, providing a robust analytical framework capable of effectively detecting and localizing structural changes.

#### 3.4 Discussion

As demonstrated in this study, integrating seismic interferometry with advanced system identification techniques

significantly enhances real-time Structural Health Monitoring (SHM) capabilities, particularly in detecting subtle and localized changes in structural stiffness. The results demonstrate the clear advantages of this integrated methodology, particularly in terms of sensitivity and precision in detecting shear-wave velocity variations associated with structural anomalies.

The observed shear-wave velocity reductions below the 28th floor are particularly noteworthy, correlating directly with regions containing buckling-restrained braces (BRBs). These velocity reductions reflect structural flexibility intentionally designed to absorb and dissipate seismic energy. Conversely, higher shear-wave velocities identified above this zone demonstrate the significant rigidity provided by outrigger columns and tuned liquid dampers (TLD). Such explicit distinctions in velocity profiles serve as effective diagnostic markers, facilitating the precise localization of stiffness changes that potentially indicate structural deterioration or damage initiation.

The intrinsic damping characteristics obtained via deconvolution interferometry and wavefield decomposition provided precise estimates aligning closely with theoretical predictions and empirical data for high-rise structures. The ability to differentiate between intrinsic damping and scattering attenuation effects substantially improves over traditional SHM methodologies, which frequently fail to distinguish between these phenomena, thereby limiting adequate diagnostic accuracy.

However, some limitations of the current approach should be acknowledged. Specifically, assumptions of linear-elastic behavior under ambient vibrations may inadequately represent the structure's nonlinear response during significant seismic events. Enhancing the methodological framework to better account for nonlinear dynamics through advanced system identification approaches could substantially increase diagnostic robustness and reliability.

Moreover, practical considerations for real-world applications, such as computational demands, processing speed, and sensor robustness under extended environmental exposure, remain critical. Addressing these concerns through improved sensor technologies and optimized real-time computational algorithms is crucial for the practical implementation and widespread adoption of structural health management systems.

## 4 CONCLUSIONS AND FUTURE RESEARCH

### 4.1 Conclusions

This study comprehensively evaluated an integrated methodology combining seismic interferometry with system identification techniques, validated using extensive data from the instrumented One Rincon Hill South Tower. The methodology demonstrates robust capabilities for the automated and accurate real-time detection of structural stiffness variations through precise estimations of shear-wave velocities and intrinsic damping.

The major conclusions drawn from this research are:

- **Enhanced Damage Detection Sensitivity:** The integrated seismic interferometry and system identification approach significantly improves the detection and localization of

subtle stiffness reductions, which are essential for timely structural health assessments in high-rise buildings in seismic-prone regions.

- **Effective Characterization of Structural Components:** The methodology accurately delineated shear-wave velocity profiles corresponding explicitly to structural features, such as BRBs, outrigger columns, and tuned liquid dampers. This precise characterization offers actionable insights into structural integrity and performance under seismic conditions.
- **Improved Damping and Attenuation Estimations:** Intrinsic damping and attenuation properties were effectively isolated from scattering effects, significantly enhancing the reliability and diagnostic accuracy of structural condition assessments.
- **Identification of Linear versus Nonlinear Behaviors:** The study successfully differentiated structural responses induced by ambient conditions (linear-elastic) from those triggered by seismic events (nonlinear behaviors). Highlighting these differences underscores the necessity for continued methodological refinement in capturing comprehensive structural dynamics under seismic loads.

### 4.2 Future research

- Extending the developed integrated methodology to diverse structural types and construction materials broadens its applicability and effectiveness.
- Refining computational algorithms to ensure faster, more resource-efficient real-time structural analyses suitable for practical applications.
- Developing advanced nonlinear interferometric and system identification techniques capable of fully characterizing complex structural behaviors during significant seismic events.

Ultimately, the results and methodologies presented significantly advance the discipline of real-time structural health monitoring, promising substantial improvements in structural safety, resilience, and post-earthquake functionality. The presented method could make a significant contribution to many of the current structural engineering applications related to assessing structures under seismic effects, e.g., [10]–[44].

## ACKNOWLEDGMENTS

The authors thank the USGS National Strong Motion Project and the California Geological Survey for providing seismic instrumentation data. Special thanks to QuakeLogic Inc. and Harbin University for their continuous support of the authors. This research was partially financially supported by the American University of Sharjah (AUS) through the Faculty Research Grant program (FRG25-C-E33). The financial support is greatly appreciated. This paper represents the opinions of the authors and does not mean to represent the position or opinions of AUS.

## REFERENCES

- [1] U.S. Geological Survey. (2023). "Earthquake Probabilities in the San Francisco Bay Area." Retrieved from [https://earthquake.usgs.gov/hazards].

- [2] Peeters, B., De Roeck, G. (2001). One-year monitoring of the Z24-Bridge: Environmental effects versus damage events. *Earthquake Engineering & Structural Dynamics*, 30(2), 149-171.
- [3] Reynders, E., De Roeck, G., Pintelon, R. (2008). Uncertainty bounds on modal parameters obtained by stochastic subspace identification. *Mechanical Systems and Signal Processing*, 22(4), 948-969.
- [4] Snieder, R., Safak, E. (2006). Extracting the building response using seismic interferometry: Theory and application to the Millikan Library. *Bulletin of the Seismological Society of America*, 96(2), 586-598.
- [5] Wapenaar, K., Draganov, D., Snieder, R., Campman, X., Verdel, A. (2010). Tutorial on seismic interferometry: Basic principles and applications. *Geophysics*, 75(5), 75A195-75A209.
- [6] Vasconcelos, I., Snieder, R. (2008). Interferometry by deconvolution: Theory for acoustic waves and numerical examples. *Geophysics*, 73(3), S115-S128.
- [7] Halliday, D., Curtis, A. (2010). An interferometric theory of source-receiver scattering and imaging. *Geophysics*, 75(6), SA95-SA103.
- [8] Bakulin, A., Calvert, R. (2006). The virtual source method: Theory and case study. *Geophysics*, 71(4), S139-S150.
- [9] Kohler, M. D., Heaton, T. H., Bradford, S. C. (2007). Propagating Waves Recorded in the Steel, Moment-Frame Factor Building During Earthquakes. *Bulletin of the Seismological Society of America*, 97(4), 1334-1345.
- [10] M. AlHamaydeh, M. Elkafrawy, and S. Banu, "Seismic Performance and Cost Analysis of UHPC Tall Buildings in UAE with Ductile Coupled Shear Walls," *Materials (Basel)*, vol. 15, no. 8, pp. 2888--DOI, 2022.
- [11] M. AlHamaydeh, M. E. Elkafrawy, M. Kyaur, M. Elyas, and F. Uwais, "Cost Effectiveness of UHPC Ductile Coupled Shear Walls for High-Rise Buildings in UAE Subjected to Seismic Loading," in *2022 Advances in Science and Engineering Technology International Conferences (ASET)*, 2022, pp. 1-6.
- [12] M. AlHamaydeh and L. Elayyan, "Impact of diverse seismic hazard estimates on design and performance of Steel Plate Shear Walls buildings in Dubai, UAE," in *2017 7th International Conference on Modeling, Simulation, and Applied Optimization (ICMSAO)*, 2017, pp. 1-4.
- [13] M. AlHamaydeh, L. Elayyan, and M. Najib, "Impact of Eliminating Web Plate Buckling on the Design, Cost and Seismic Performance of Steel Plate Shear Walls," in *The 2015 World Congress on Advances in Structural Engineering and Mechanics (ASEM15)*, Incheon, Korea, 2015.
- [14] M. AlHamaydeh, S. Barakat, and O. Nassif, "Optimization of Quatropod Jacket Support Structures for Offshore Wind Turbines Subject to Seismic Loads Using Genetic Algorithms," in *The 5th International Conference on Computational Methods in Structural Dynamics and Earthquake Engineering (COMPDYN2015)*, Crete Island, Greece, 2015, pp. 3505-3513.
- [15] S. Barakat, M. AlHamaydeh, and O. Nassif, "Optimization of Seismic Isolation Systems with Viscous Fluid Dampers Using Genetic Algorithms," in *The 5th International Conference on Computational Methods in Structural Dynamics and Earthquake Engineering (COMPDYN2015)*, Crete Island, Greece, 2015, pp. 4086-4095.
- [16] M. AlHamaydeh and N. Aly, "Optimum Seismic Isolation System Design for Retrofitting and Upgrading Existing Concrete Bridges," in *The 2014 International Conference on Mechanics, Fluid Mechanics, Heat and Mass Transfer (MFHMT 2014)*, 2014, pp. 135-139.
- [17] M. Al Satari, "Estimation of Seismic Response Demands for R/C Framed Structures: An Insight Into The Nonlinear Seismic Behavior." *VDM Verlag, Saarbrücken, Germany*, 2008.
- [18] S. Hussain and M. Al Satari, "Design of a Seismic Isolation System with Supplemental Viscous Damping for a Near-Fault Essential Facility," in *The 14th World Conference on Earthquake Engineering*, 2008.
- [19] M. Al Satari and J. Anderson, "Nonlinearity Effects on the Seismic Behavior of RC Framed Structures," in *The 76th SEAOC Annual Convention*, 2007.
- [20] J. Anderson, V. Bertero, and M. Al Satari, "Inelastic Seismic Response of a Tilt-up Wall Building and Design Implications," in *The 74th SEAOC Annual Convention*, 2005.
- [21] M. H. Al Satari, "Estimation of Seismic Response Demands for RC Framed Structures," *University of Southern California*, 2005.
- [22] M. AlHamaydeh, M. E. Elkafrawy, N. G. Aswad, R. Talo, and S. Banu, "Evaluation of UHPC Tall Buildings in UAE with Ductile Coupled Shear Walls under Seismic Loading," in *2022 Advances in Science and Engineering Technology International Conferences (ASET)*, 2022, pp. 1-6.
- [23] S. Hussain and M. Al Satari, "Design of a Seismic Isolation System with Supplemental Viscous Damping for a Near-Fault Essential Services Facility," in *The 76th SEAOC Annual Convention*, 2007.
- [24] J. C. Anderson, V. V. Bertero, M. Kargahi, and M. Al Satari, "Seismic Performance of an Instrumented Tilt-up Wall Building." *Pacific Earthquake Engineering Research Center*, 2004.
- [25] A. H. ElSinawi, A. Jhemi, and M. AlHamaydeh, "Adaptive Seismic Isolation of Structures Using MR-Fluid Dampers," in *The 5th International Conference on Modeling, Simulation and Applied Optimization (ICMSAO'13)*, 2013.
- [26] M. AlHamaydeh, K. Galal, and S. Yehia, "Impact of Lateral Force-Resisting System and Design/Construction Practices on Seismic Performance and Cost of Tall Buildings in Dubai, UAE," *Earthq. Eng. Vib. J.*, vol. 12, no. 3, pp. 385-397, 2013.
- [27] M. AlHamaydeh, J. Abdalla, S. Abdalla, A. Al-Rahmani, and A. Mostafa, "Inelastic Seismic Demands For Reinforced Concrete Frames In Dubai," in *The 14th European Earthquake Engineering Conference (14EEEC)*, Aug. 30-Sept. 3, 2010.
- [28] S. Hussain, M. AlHamaydeh, and N. Aly, "Jakarta's First Seismic-Isolated Building - A 25 Story Tower," in *The 15th World Conference on Earthquake Engineering (15WCEE)*, September 24-28, 2012.
- [29] N. Aly, M. AlHamaydeh, and K. Galal, "Quantification of the Impact of Detailing on the Performance and Cost of RC Shear Wall Buildings in Regions with High Uncertainty in Seismicity Hazards," *J. Earthq. Eng.*, vol. 24, no. 3, pp. 421-446DOI, 2020.
- [30] M. AlHamaydeh, N. Aly, and K. Galal, "Effect of Diverse Seismic Hazard Estimates on Design and Performance of RC Shear Wall Buildings in Dubai, UAE," in *The 2015 World Congress on Advances in Structural Engineering and Mechanics (ASEM15)*, August 25-29, 2015.
- [31] M. AlHamaydeh, N. Aly, and K. Galal, "Impact of Seismicity on Performance and Cost of RC Shear Wall Buildings in Dubai, United Arab Emirates," *J. Perform. Constr. Facil.*, vol. 31, no. 5, 2017, doi: 10.1061/(ASCE)CF.1943-5509.0001079.
- [32] M. AlHamaydeh, S. Abdullah, A. Hamid, and A. Mustapha, "Seismic design factors for RC special moment resisting frames in Dubai, UAE," *Earthq. Eng. Vib.*, vol. 10, no. 4, pp. 495-506, 2011.
- [33] M. AlHamaydeh, G. Al-Shamsi, N. Aly, and T. Ali, "Seismic Risk Quantification and GIS-based Seismic Risk Maps for Dubai-UAE\Dataset," *Data Br.*, vol. 37, no. December, pp. 107565-107566, 2021.
- [34] M. AlHamaydeh, N. Aly, and K. Galal, "Seismic Response and Life-Cycle Cost of Reinforced Concrete Special Structural Wall Buildings in Dubai, UAE," *Struct. Concr.*, pp. 1-12, 2017, doi: 10.1002/suco.201600177.
- [35] M. AlHamaydeh and S. Hussain, "Innovative Design of a Seismically-Isolated Building with Supplemental Damping," in *The 14th European Earthquake Engineering Conference (14EEEC)*, Aug. 30-Sept. 3, 2010.
- [36] M. AlHamaydeh, M. E. Elkafrawy, F. M. Amin, A. M. Maky, and F. Mahmoudi, "Analysis and Design of UHPC Tall Buildings in UAE with Ductile Coupled Shear Walls Lateral Load Resisting System," in *2022 Advances in Science and Engineering Technology International Conferences (ASET)*, 2022, pp. 1-6, doi: 10.1109/ASET53988.2022.9735104.
- [37] M. AlHamaydeh, G. Al-Shamsi, N. Aly, and T. Ali, "Geographic Information System-Based Seismic Risk Assessment for Dubai, UAE: a Step towards Resilience and Preparedness," *Pract. Period. Struct. Des. Constr. ASCE*, vol. 27, no. 1, p. DOI-10, 2022.
- [38] M. AlHamaydeh, G. Al-Shamsi, N. Aly, and T. Ali, "Data for Seismic Risk Quantification and GIS-Based Seismic Risk Maps for Dubai-UAE," *Mendeley Data*, V5, <http://doi.org/10.17632/shpf7bdx7.5>, 2021.
- [39] M. AlHamaydeh and M. Siddiqi, "OpenSEES GUI for Elastomeric Seismic Isolation Systems," in *First Eurasian Conference on OpenSEES (OpenSEES Days Eurasia)*, Hong Kong, China, 2019.
- [40] M. Al Satari and S. Hussain, "Vibration-Based Wind Turbine Tower Foundation Design Utilizing Soil-Foundation-Structure Interaction," in *The 3rd International Conference on Modeling, Simulation and Applied Optimization (ICMSAO'09)*, 2009.
- [41] S. Hussain and M. Al Satari, "Vibration-Based Wind Tower Foundation Design," 2009.
- [42] M. AlHamaydeh and S. Hussain, "Optimized frequency-based foundation design for wind turbine towers utilizing soil-structure interaction," *J. Franklin Inst.*, vol. 348, no. 7, pp. 1470-1487, 2011.
- [43] M. AlHamaydeh, S. Barakat, and O. Nasif, "Optimization of Support Structures for Offshore Wind Turbines Using Genetic Algorithm with Domain-Trimming," *Math. Probl. Eng.*, vol. 2017, no. 5978375. DOI:10.1155/2017/5978375, pp. 1-14, 2017.
- [44] S. Hussain, P. Van Benschoten, M. Al Satari, and S. Lin, "Buckling Restrained Braced Frame (BRBF) Structures: Analysis, Design and Approvals Issues," in *The 75th SEAOC Annual Convention*, 2006.



# Experimental assessment of GNSS-smartphone performance in monitoring dynamic motion

Panos Psimoulis<sup>1</sup>, Chenyu Xue<sup>1</sup>, Jayamanne Oshadee Jayamanne<sup>1</sup>, Guangcai Li<sup>2, 3</sup>, Jianghui Geng<sup>2, 3</sup>

<sup>1</sup> Nottingham Geospatial Institute, University of Nottingham, United Kingdom

<sup>2</sup> Pride Lab, Wuhan University, Wuhan, China

<sup>3</sup> State Key Lab of Precision Geodesy, The Innovation Academy for Precision Measurement Science and Technology of the Chinese Academy of Sciences

email: [panagiotis.psimoulis@nottingham.ac.uk](mailto:panagiotis.psimoulis@nottingham.ac.uk), [chenyu.xue@nottingham.ac.uk](mailto:chenyu.xue@nottingham.ac.uk)

**ABSTRACT:** The recent advancements of GNSS technology have enabled multi-frequency and multi-GNSS observations even at high-rate measurements (up to 100Hz) with a few-mm to cm-level accuracy, broadening the potentials of GNSS application in monitoring dynamic motion of structures. Furthermore, recent studies have revealed the potential of low-cost consumer-grade GNSS receivers in deformation monitoring of civil engineering structures of even cm-level and indicated that the type of GNSS antenna is the main parameter affecting the quality of the GNSS data. In this study, we investigate the potential of dual-frequency smartphone-based GNSS measurements in monitoring dynamic motion of structures. The study is based on controlled experiments of static, slow and dynamic motion of various amplitude and motion frequency, where 1-Hz dual frequency GNSS smartphone measurements are assessed against more accurate geodetic measurements (GNSS and/or Robotic Total Station). The preliminary results show that the GNSS smartphone measurements may suffer from several cycle slips and strong multipath effects, due to the linear polarized GNSS antenna of the smartphone, but in several cases the GNSS smartphone measurements were able to express the dynamic motion. Also, in this study we examine the performance of the GNSS smartphone measurements in monitoring the dynamic response of Wilford Suspension bridge, under various patterns of dynamic loading.

**KEY WORDS:** GNSS-smartphone, deformation monitoring, dynamic motion, shake-table.

## 1 INTRODUCTION

Smartphones have been adopted in the last decades in many engineering applications. The broad use of smartphones in positioning and navigation applications has benefited from the development of dual-frequency GNSS receivers in some of the advanced smartphone models, enabling those smartphones of dual frequency carrier phase measurements. The first smartphone was Xiaomi Mi 8 (released in 2018) which supports dual frequency GPS/Galileo, single frequency BDS/GLONASS code pseudo-range and carrier phase measurements (Robustelli et al., 2019, Geng and Li, 2019). Nowadays, with the development of more advanced mobile phone chipsets, several smartphone manufacturers are releasing flagship phones supporting features such as L1/E1, L5/E5a dual frequency, multi-GNSS carrier phase measurements capability, etc. Thanks to GPSTest mobile app developed by Barbeau (2023), the capability of recent smartphones as of GNSS performance are crowdsourced and documented in GPSTest database (Barbeau, 2021).

Several studies were conducted focusing on the GNSS-performance of the first dual-frequency GNSS carrier phase Mi8. More specifically, Robustelli et al. (2019) used Xiaomi Mi8 in both single point positioning (SPP) and post-processing kinematic (PPK) applications, showing a RMS accuracy of around 5 m and 1-2 m for the SPP and PPK, respectively. On the other hand, Chen et al. (2019) employed Xiaomi Mi8 for real time precise point positioning and found that the RMS positioning error is 0.81 m and 1.65 m for horizontal and vertical respectively.

Since then, several other studies have been conducted assessing the performance of dual-frequency GNSS-

smartphones. Paziewski et al. (2021) assessed the GNSS observation quality of several smartphones, concluding that the smartphone GNSS data are noisier than the geodetic GNSS data, but still feasible to obtain a cm-level static solution. Li and Geng (2019) analysed GNSS measurement error characteristics from Nexus 9 tablets using both embedded and external antennas, revealing that the root mean squared (RMS) accuracy for the SPP is about 10-20 m, and cm-level precision can be achieved for static PPK solutions.

Hence, the first experiments reveal promising results about the quality of the smartphone-based GNSS measurements, indicating that they can achieve cm-level for relative PPK positioning (Pesyna et al., 2014; Wanning and Heßelbarth, 2020; Geng and Li, 2019; Dabov and Pietra, 2019). However, most of the experiments are based on static experiments and only one study is based on experiments of dynamic motion of smartphone experiments (Vazquez-Ontiveros, et al., 2024).

With the broader trend of applying low-cost GNSS receivers for monitoring applications (Xue et al., 2021; Xue et al., 2022; Xue and Psimoulis, 2023), there is great potential for mobile phones to be used for precise positioning services such as in SHM due to: 1) the relative low-cost with respect the geodetic GNSS receiver, 2) the raw smartphone GNSS measurements (code and carrier phase, etc.) which are accessible to the broader smartphone users community, 3) the potential of crowdsourcing data through the smartphones application, and 4) the availability of various sensors such as accelerometers, gyros, which can be combined with GNSS measurements in SHM applications (Lăpădat et al., 2021).

In general, it is expected that the code and carrier phase measurements of smartphones are of relatively lower quality

than those of geodetic receiver. However, it was shown that ambiguity resolution of L1 measurements, which is the prerequisite for achieving a precise solution of cm-level, can be achieved, as it was concluded from experimental study using a Huawei P30 smartphone (Wanninger and Heßelbarth, 2020).

Although there are a few studies regarding deformation monitoring with smartphones, most of them, only take advantage of its embedded accelerometer, their GNSS observation functionality is rarely assessed for its deformation monitoring applicability except for few conducted by Zeng et al., (2022) and Vazquez-Ontiveros et al. (2023). Vazquez-Ontiveros et al. (2023) found that an RMS error of 1.4 cm in the horizontal component could be achieved for kinematic circular trajectory with a rotating speed of 0.44 rad/s ( $\sim 0.07$  Hz) and an rotation radius (amplitude) of 19 cm and RMS errors of 0.7 cm, 1.2 cm, and 4.2 cm in the East, North, and Up components could be obtained with static experiment.

In this study, we present the preliminary results of controlled experiments, where smartphone GNSS measurements were conducted to monitor dynamic vertical and horizontal motion and evaluate the performance of the GNSS measurements. The preliminary results are promising, indicating the potential of smartphone GNSS measurements for dynamic motion monitoring.

## 2 METHODOLOGY

The study was based on two controlled experiments, aiming to simulate long-period/low-frequency (up to 0.2 Hz) cm-level or larger motion, meeting the main deflection characteristics (amplitude and frequency) of flexible structures (e.g., long bridges and tall buildings) under normal service conditions (Meng et al., 2018).

The first experiment involved a controlled vertical periodic motion (of up to 0.1 Hz) produced manually by a platform, following the methodology of the study (Peppas et al. 2018), and monitored by smartphone GNSS receiver and a robotic total station (RTS) measurement. The mm-level accuracy of RTS measurements served as the reference for evaluating the performance of the smartphone GNSS (Psimoulis et al., 2008).

The second experiment focused on controlled horizontal oscillations of up to 0.2 Hz, induced by a shake table. Multiple GNSS sensors, such as survey-grade, low-cost and smartphone-grade receivers, were attached to the shake table, along with several accelerometers, all subjected to the same excitations. The direct trajectory output of the shake table was used as a reference to assess the performance of different sensors. The analysis of the GNSS timeseries, using statistical and spectral techniques, was applied in both experiments to quantify measurement accuracy and identify their dominant frequencies.

## 3 CONTROLLED VERTICAL EXPERIMENT

The first experimental assessment aimed to evaluate the performance of GNSS-smartphone for monitoring low frequency cm-level vertical dynamic motion. We conducted an experiment on the open roof of Nottingham Geospatial Building (NGB), where periodic vertical oscillations were executed by using a heavy-duty tripod with a height-adjustable platform and manually controlled vertical movement. On the top of the tripod, a 360°-prism and metallic plate were mounted,

where the smartphone was securely placed. We manually introduced vertical periodic oscillations of about 0.05 Hz and 0.1 Hz by synchronising to a metronome, as described in Peppas et al., 2018, and the amplitude of 2 to 3 cm was controlled based on the graduation etched on the pole.

The setup of the vertical controlled experiment is shown in Figure 1, where the GNSS base station is consisted of Leica AS10 geodetic antenna and Leica GS10 geodetic receiver, recording in 1 Hz multi-GNSS observations (i.e. GPS, GLONASS, Galileo, BDS; Figure 1A). The Samsung S23 FE, equipped with the dual-frequency GNSS receiver, was set on top of a ground plate, to limit the multipath effect, recording 1Hz multi-GNSS observations, using the GnsLogger App, developed by Google (Google, 2024). The Samsung S23 FE could record L1/L5 GPS, B1i/B2a BDS, E1/E5a Galileo, and G1 GLONASS signals. Finally, the 360°-prism Leica prism was monitored by Leica TS30 RTS, which was recording at 10 Hz sampling-rate (Peppas et al., 2018, Peppas and Psimoulis, 2023).

We conducted six oscillations; (i) three oscillations of approximately 0.1 Hz frequency, and amplitude of  $\sim 2$  cm (A), and  $\sim 3$ cm (B) and (C); and (ii) three oscillations of approximately 0.05 Hz frequency and amplitude of  $\sim 1$  cm (D),  $\sim 2$  cm (E) and  $\sim 3$  cm (F).

The RTS ortho-height timeseries relative to the initial position (prior to the oscillation) were exported, expressing the vertical displacement of the oscillation. The smartphone GNSS data were logged in Receiver Independent Exchange Format (RINEX) 3.03 from the GnsLogger App. The GNSS data were post-processed using double-difference (DD) in kinematic mode in RTKLIB demo5 b34h (Everett, 2023) with mobile GNSS data as the rover and Leica GS10 data as the base. The multi-GNSS solutions were obtained using GPS, Galileo and BDS observations. The GLONASS observations were not used for the GNSS solution due to the GLONASS inter-frequency bias between the GNSS smartphone and the GNSS base station, which affects the ambiguity resolution of the GNSS measurements (Msaewe et al., 2017). The Up-component timeseries of the GNSS solution reflected vertical oscillation and was compared against the RTS vertical timeseries to evaluate the accuracy of the GNSS smartphone data.

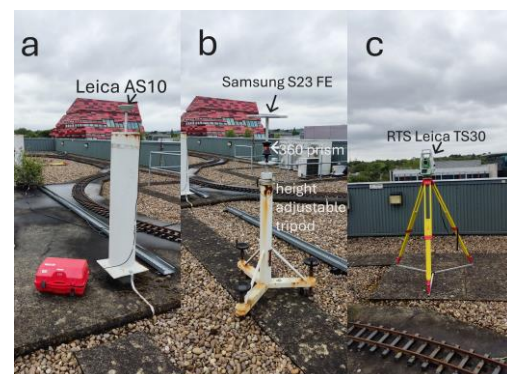


Figure 1. (left) The GNSS base station, (middle) the rover station with the prism and a metallic plate where the Samsung S23 FE has been mounted, and (left) the RTS recording the position of the prism.

Figure 2 shows the vertical component timeseries and Discrete Fourier Transform (DFT) spectra of the RTS and GNSS data for the oscillation case of  $\sim 0.05$  Hz frequency and  $\sim 3$  cm amplitude (case F) respectively. It is clearly observed the pattern of sinusoidal movement in the GNSS timeseries, with a slight downward drift with respect to the RTS timeseries, which can be the result of low-frequency noise due to multipath effect, to which is susceptible the linearly polarised smartphone antenna.

Likewise, Figure 3 are presented the Up-component timeseries and the respective spectra of GNSS and RTS data for case C (amplitude of  $\sim 3$  cm, frequency of  $\sim 0.1$  Hz). As in the experiments of 0.05 Hz, it is clearly observed the periodic pattern of the motion followed by both GNSS and RTS data, with the GNSS data characterized also by a low-frequency drift, most likely to multipath effect of the GNSS smartphone measurements.

To quantify the precision of the smartphone GNSS measurement in monitoring the oscillation amplitude, with respect to the RTS timeseries, we estimated the amplitude of the oscillations by using the peak values of each periodic cycle of GNSS and RTS timeseries and calculating the mean oscillation amplitude of each (GNSS and RTS) timeseries. Even though the low-frequency noise of the GNSS timeseries could lead to a drift of about 5-8 mm, the estimated oscillation amplitudes of GNSS smartphone data differ from that of the RTS timeseries by 3 cm and 5 cm for the cases F and C, respectively.

Table 1 shows mean amplitude of each experimental vertical motion as it was estimated from the RTS timeseries, the Root Mean Square (RMS) Error of the GNSS timeseries with respect to the amplitude of the RTS and the dominant frequency detected for each oscillation scenario derived from the spectral analysis of the RTS and the smartphone GNSS time-series. It is observed that the GNSS-smartphone precision in detecting the amplitude of the vertical oscillation ranges 2-5 mm. It should be noted though the impact of the low-frequency drift, which may not affect the estimation of the oscillation amplitude

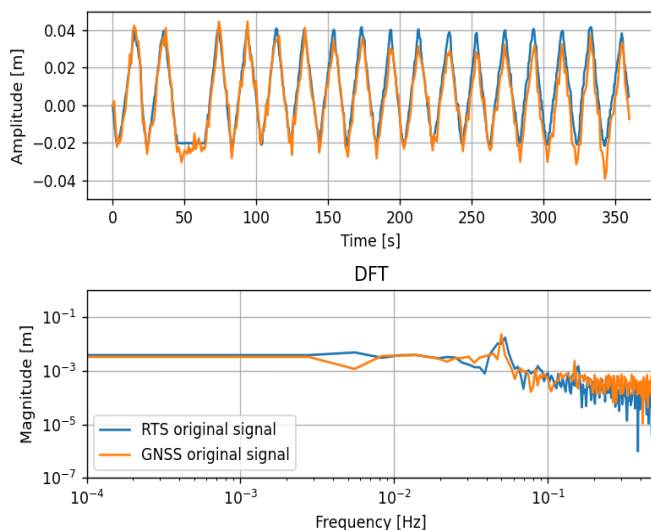


Figure 2. (top) RTS and GNSS-smartphone timeseries for case F oscillation case, and (bottom) the respective spectra

but it would affect the estimation of low-frequency semi-static displacement. As for the dominant frequency derivation, the maximum discrepancy between smartphone GNSS and RTS is around 0.007 Hz for 0.1 Hz detection, and 0.003 Hz for 0.05 Hz detection, equivalent to 6-7% bias in dominant frequency determination. It is also interesting to note that the spectra for RTS timeseries doesn't seem to have distinct peaks but rather shows an area of occurrence of multiple peaks as compared to the smartphone GNSS, indicating that it is more sensitive in differentiating different frequencies in the signal.

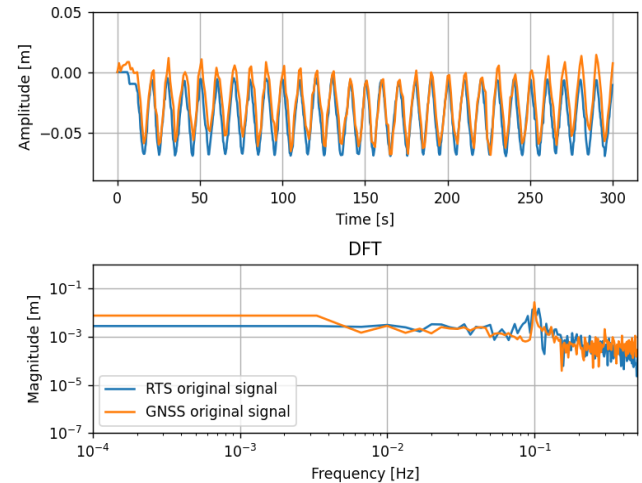


Figure 3. (top) RTS and GNSS-smartphone timeseries for the case C oscillation case, and (bottom) the respective DFT spectra

Table 1. Precision of the smartphone GNSS in monitoring the kinematic oscillatory displacement for scenarios A to F, and the corresponding dominant frequency from RTS and smartphone GNSS for each case

	RTS amplitude (mm)	RMS Error GNSS (mm)	Frequency (Hz)	
			RTS	GNSS
A	21	2.5	0.100	0.100
B	33	2.9	0.100	0.094
C	31	3.2	0.107	0.100
D	11	3.2	0.050	0.050
E	21	2.7	0.050	0.050
F	30	5.1	0.053	0.050

#### 4 CONTROLLED VERTICAL EXPERIMENT

The experiments of horizontal dynamic motion were based on a shake table and it was designed and conducted on the roof of Xinghu Experimental Building at Wuhan University in China. The roof is moderately open with few obstructions by surrounding buildings.

In Figure 5 is presented the experimental setup, where several mobile phones were placed on top of a shake table device, (i) with two smartphones placed outside using their internal GNSS



antenna (Huawei P40 and Samsung S23 FE), (ii) two mobile phones placed inside of two shielding boxes (Huawei P40 in the black box and Samsung S23 PE in the white box). The two shielding boxes and the geodetic receiver were both connected to the survey grade antenna via a signal splitter. Inside the two shielding boxes, there were two devices retransmitting the GNSS signal as received by the GNSS geodetic antenna to the smartphone. A patch antenna was also placed on the white shielding box connecting to a u-blox F9P module, and a survey-grade accelerometer was fixed on the side of the shake table.

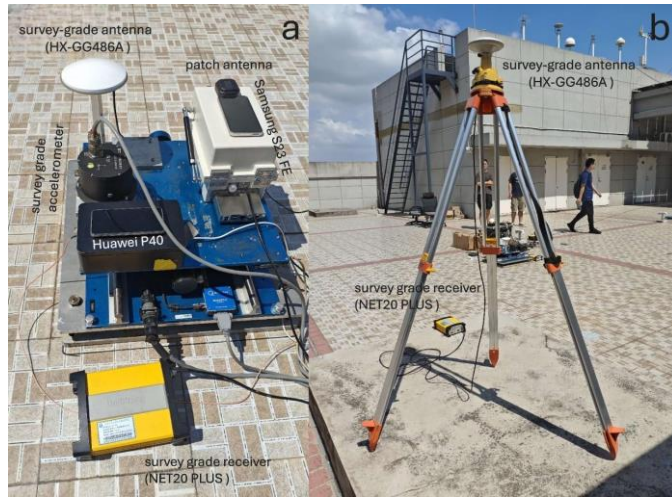


Figure 5. (left) The setup of the rover sensors (GNSS and accelerometer) on the shake table, and (right) the station consisted of survey-grade antenna and receiver

Both the geodetic rover and base station were measuring at a sampling rate of 10 Hz, recording GPS, Galileo, BDS, GLONASS and QZSS observations, while all four smartphones were configured so that the GPS (L1/L5), Galileo (E1/E5a), GLONASS (G1), QZSS (J1/J5), and BDS (B1i/B2a) GNSS raw data were recorded with application GeoDataLogger developed by PrideLab (2024) at a sampling frequency of 1Hz. Additionally, the u-blox receiver recorded GPS, Galileo, GLONASS), QZSS and BDS observations at 10Hz sampling rate.

The accelerometer data were also recorded in GeoDataLogger at the maximum capacity of the smartphone (e.g., around 125 Hz sampling frequency for Samsung and around 100Hz for the rest), while the survey grade accelerometer (TD) recorded at 100 Hz sampling frequency with GPS timestamp thanks to an external GNSS module.

The Quanser Shake Table II, controlled via a MATLAB script implemented in Simulink, was used to perform precise, programmed displacements. The shake table was rigidly bolted to the roof and carefully orientated in E-W direction. We performed in total 25 different motions with various amplitude and oscillating frequency oscillating in E/W direction, with amplitude ranging from 5mm, 10mm, 20mm, 40mm, and oscillation frequency ranging from 0.1 Hz, 0.2Hz, 0.5Hz, 1Hz, 1.5Hz, and 2Hz. Each oscillation lapsed around 2 minutes with at least 1 minute of static period in between consecutive oscillations. The shake table could output direct displacement

timeseries at a frequency of 100 Hz, which we employed as the reference data and the ground truth.

It is worth noting that from the experiment,

- i) Apart from the GNSS measurements and the geodetic accelerometer data, all other data was not initially synchronised to GNSS time, such as phone accelerometer measurement and shake table output timeseries.
- ii) The acceleration timeseries derived directly from the accelerometers output, with the oscillation axis being in East-West direction. The acceleration data of the smartphones were acquired depending on the orientation of each smartphone.
- iii) The smartphones can record 1Hz GNSS measurements, meaning that they can be used only for frequencies up to 0.5Hz, due to Nyquist theorem
- iv) The ublox measurement terminated halfway during the measurement, causing some data loss.

The GNSS data were post-processed using the open-source software RTKLIB demo5 b34k (Everett, 2024) in the kinematic mode, with the GNSS sensors on the shake table as rover and the geodetic receiver as base forming multiple baselines. The output from the RTKLIB is in E/N/U which is effectively the 3D projection of the baseline vector in the local E/N/U direction. All the GNSS post-processed solutions achieved ambiguity fix.

The synchronisation of the accelerometer and GNSS timeseries is based on finding and shifting the optimum lag when the cross correlation between the geodetic accelerometer and each accelerometer timeseries reached the maximum, indicating strong correlation. By adjusting the time for accelerometer timeseries, we aligned them to GNSS timestamps.

In this study, we focused only on oscillations with frequency motion up to 0.2 Hz, for which the 1 Hz smartphone GNSS data can be used to determine the oscillation frequency, as the Nyquist frequency is 0.5 Hz, based on the sampling rate of the GNSS smartphone data (i.e. 1Hz). The oscillation characteristics (amplitude and oscillation frequency) for the 9 sections from left to right are shown in Table 2. For higher frequencies, the 1-Hz GNSS smartphone data would need to be integrated with accelerometers data. Hence, we investigated only the performance of the 1-Hz GNSS data.

Table 2. Amplitude and frequency of the executed oscillations produced by the shake table.

Oscillation	Amplitude (mm)	Frequency (Hz)
1	5	0.1
2	10	0.1
3	20	0.1
4	40	0.1
5	5	0.2
6	10	0.2
7	20	0.2
8	40	0.2
9	40	0.2

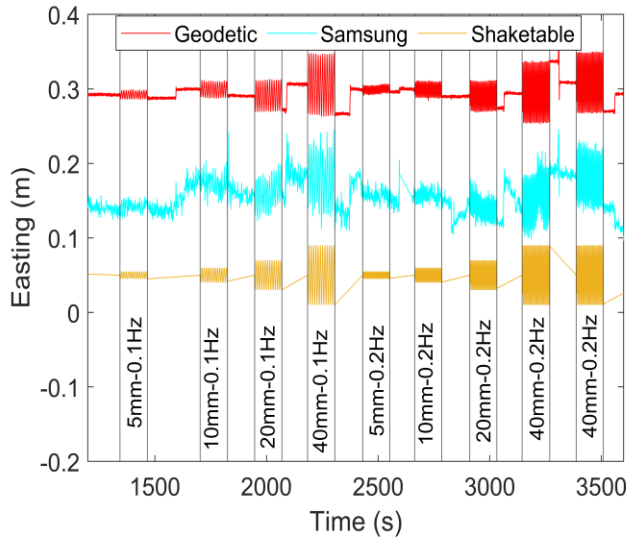


Figure 6. Original timeseries from different GNSS sensors. From top to bottom are 1) geodetic receiver/antenna, 2) Samsung S23 FE 3) output from shake table. The time-series are shifted to avoid overlap between them.

The RTKLIB setting for processing GNSS timeseries are utilising L1+L2/E5b+L5/E5a triple frequency option and GPS+Galileo+BDS multi-constellation configuration. Slightly different configuration settings were used for phones using internal antenna and the geodetic antenna due to the significant differences in the antenna since mobile phones antenna is more susceptible to multipath error, cycle slips.

In Figure 6, it is shown the timeseries of the geodetic GNSS receiver and the GNSS smartphone, as they have derived from the GNSS post-process, and the shake table timeseries (i.e. reference data). The start and end time for each oscillation is highlighted by two vertical lines segmenting the timeseries into 9 oscillation sections.

It can be shown in Figure 6 that the geodetic receivers with geodetic antenna time series doesn't seem to be affected by low frequency errors as much as the Samsung timeseries. Also, the noise level is significantly larger for Samsung as compared to geodetic receiver/antenna when the shake table was static. These indicate that the antenna grade is crucial for more precise results less affected by multipath. On the other hand, it is promising that the displacement/excitations could be detected from Samsung timeseries with a strong positive correlation with the geodetic GNSS and shake table timeseries, especially for 20- and 40-mm amplitude oscillations.

To enhance the GNSS timeseries, in terms of reducing the noise level, the GNSS timeseries was firstly filtered using high-pass Chebyshev filter with cutoff frequency of 0.05 Hz to mitigate the multipath bias and potential other source errors. Then, the residuals were calculated by the difference between the GNSS timeseries and the output from shake table.

In Table 3 is shown the true amplitude of each oscillation scenario, as it is derived from the shake table data (i.e. ground truth) and computed RMS error of the geodetic and the smartphone data in estimating the oscillation amplitude. It is observed that the RMSE of the geodetic data does not exceed 2 mm, with the maximum RMS error observed for the scenarios

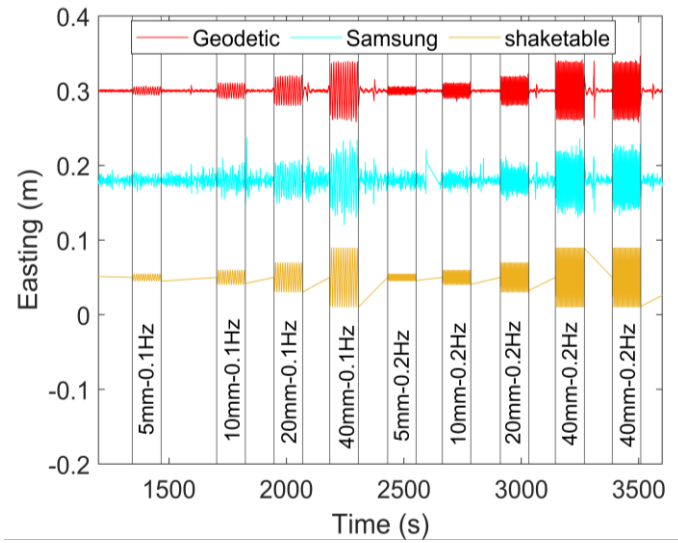


Figure 7. Similar to Figure 6, timeseries from different GNSS sensors but after high-pass filter

of large oscillation, i.e. 40mm. In all the other scenarios and for amplitude equal or smaller than 20mm, the RMS error is limited to less than 1 mm. Regarding the RMS error of the GNSS smartphone data in estimating the oscillation amplitude the RMS error is generally lower than 5 mm, as it is exceeding the threshold of 5 mm only for two scenarios of oscillations, i.e. 10 and 40mm for 0.1 Hz oscillation frequency. In general, the RMS error of the GNSS smartphone data is about two to four times larger than the geodetic solution. As expected, the overall performance of the GNSS smartphone data is lower, in terms of noise/errors, comparing it to the GNSS geodetic receiver, mainly due to the lower quality of the antenna, since the geodetic receiver/antenna are dedicated GNSS instruments, whereas the mobile phones has comparatively lower grade receiver and antenna. Also, it is observed that the GNSS smartphone has low performance in estimating the oscillation amplitude for the cases of 5 and 10 mm, as the achieved precision is of 3-6.5 mm level, while the results seem more promising for the cases of oscillation amplitude of 20 and 40 mm.

Table 3. Standard deviation of the residuals for different GNSS sensors with reference to Shake table timeseries

Oscillation Scenario	True amplitude (mm)	RMS Error (mm)	
	Shake Table	Geodetic	Smartphone
1 (0.1Hz)	5	0.8	4.0
2 (0.1Hz)	10	0.6	7.6
3 (0.1Hz)	20	0.7	4.3
4 (0.1Hz)	40	1.6	6.9
5 (0.2Hz)	5	0.8	3.6
6 (0.2Hz)	10	0.5	1.9
7 (0.2Hz)	20	0.7	2.3
8 (0.2Hz)	40	1.1	4.0
9 (0.2Hz)	40	1.5	2.5

In Figure 8 are presented the spectra of GNSS geodetic and GNSS smartphone timeseries of the experiment of 0.2 Hz and amplitude 20mm, as a representative spectral analysis of all the conducted experiments of oscillations. The spectrum of the GNSS smartphone data is limited to 0.5 Hz, as the sampling-rate was 1 Hz, whereas the GNSS geodetic timeseries is limited to 5 Hz, due to the respective 10 Hz sampling rate. It is clear that the oscillation frequency is accurately detected by both GNSS timeseries. The smartphone GNSS timeseries is characterized by higher noise level, especially for the frequency range higher than 0.2 Hz, as the frequency peaks correspond to higher amplitude, reflecting the more noisy data of GNSS smartphone with respect the GNSS geodetic data. For frequencies lower than 0.05 Hz, the noise has been limited due to the application of the high-pass filter.

In Table 4 are presented the dominant frequencies as they are estimated based on the spectral analysis of the GNSS geodetic data and the GNSS smartphone data and compared based on the frequencies of the oscillation as they derive from the shake

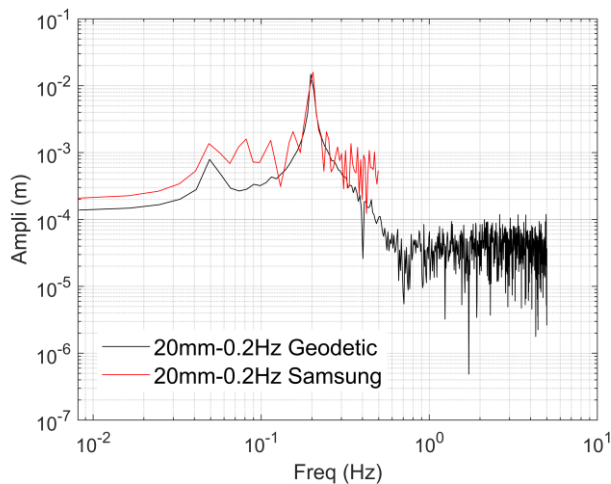


Figure 8. Spectra of GNSS geodetic and GNSS smartphone timeseries of the oscillation of 20mm amplitude ad 0.2 Hz frequency.

Table 4. Dominant frequency derived from each sensor, the percentages in brackets indicate the deviation in percentage from the reference dominant frequency derived from DFT of shake table timeseries.

	Frequency (Hz)		Shake table
	Geodetic	Samsung	
1	0.098 (2%)	0.098 (2%)	0.096
2	0.099 (2%)	0.098 (1%)	0.097
3	0.098 (2%)	0.098 (2%)	0.096
4	0.098 (2%)	0.098 (2%)	0.096
5	0.197 (-2%)	0.197 (-2%)	0.202
6	0.200 (-1%)	0.203 (0%)	0.203
7	0.197 (-3%)	0.203 (0%)	0.203
8	0.197 (-3%)	0.203 (0%)	0.203
9	0.202 (2%)	0.200 (1%)	0.199

table data (i.e. ground truth). It can be observed that frequencies estimated from the smartphone GNSS data deviate not more than 2-3% from the reference frequency derived from shake table output timeseries. Even though, for the oscillations of low amplitude (i.e. 5 and 10mm), the GNSS smartphone suffer from low-frequency noise resulting in ambiguous waveform, the dominant frequency for the oscillation could still be retrieved accurately. Similarly, we conducted DFT for the original timeseries. The frequency that can be detected from the original timeseries is shown in Table 4.

## 5 CASE STUDY: WILFORD BRIDGE MONITORING CAMPAIGN

To evaluate the feasibility of using smartphones for monitoring purposes, a preliminary monitoring campaign was carried out on Wilford Suspension bridge, a test site adopted for many experimental research projects of application of GNSS and surveying techniques in bridge SHM studies (Peppas et al., 2018, Psimoulis et al., 2016). We deployed several different grades of GNSS receivers ad Robotic Total Stations (RTS) on the bridge, to assess the performance of the various GNSS receivers, using the RTS as the ground truth (Psimoulis and Stiros, 2008). For this study we focused on the analysis of a geodetic grade GNSS station (GS04) consisted of Leica GS10 receiver ad AS10 antenna, and a smartphone Samsung S23. The GSS receiver were recording simultaneously the response of the bridge under the pedestrians' excitations, with the geodetic GSS receivers recording at 10 Hz sampling rate, while the smartphone was recording at 1 Hz sampling rate.

In Figure 9 are presented the vertical Up) GNSS timeseries of the geodetic and the smartphone, and it is obvious the higher noise level of the smartphone GNSS timeseries, indicating the larger GNSS receiver noise and the significant larger unpressed multipath effect (Peppas and Psimoulis, 2023).

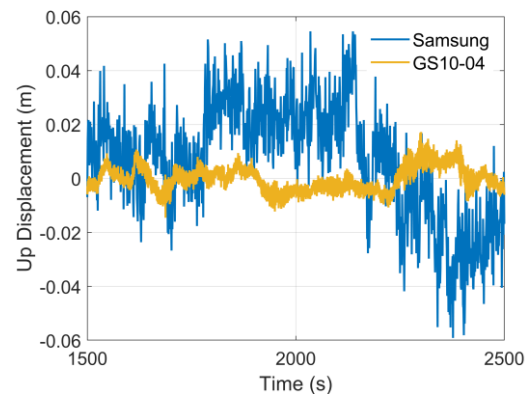


Figure 9. The GNSS timeseries from the geodetic grade GNSS station (GS04) and the smartphone Samsung S23 GNSS receiver. Both GNSS receivers are located at the midspan of the bridge.

To mitigate the low-frequency errors, a high pass filter with cut-off frequency of 0.05 Hz was applied. In Figure 10 are shown the filtered GNSS timeseries of the GS04 geodetic receiver and the smartphone, whereas several activities can be identified from the GS04 timeseries, whilst those response could not easily be identified in the Samsung timeseries,



probably due to i) the relatively high bridge modal frequency exceeding the Nyquist frequency of the GNSS smartphone recorded data and ii) the overall high noise level.

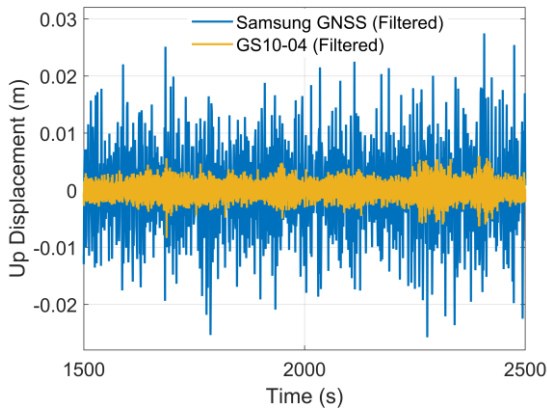


Figure 10. The same plot as Figure 9 presenting the highpass filtered GNSS timeseries of the geodetic and smartphone data.

To unveil the bridge displacements limited by the smartphone GNSS low sampling rate, a common approach is the integration of GNSS with accelerometer data. We adopted loosely coupled data integration using Kalman filter Rauch-Trung-Striebel smoothing algorithm. It could be seen in Figure 11 that the noise from the fused timeseries is greatly reduced from GNSS only solution. A few excitations are also identifiable in correlation with Leica geodetic timeseries and the acceleration timeseries.

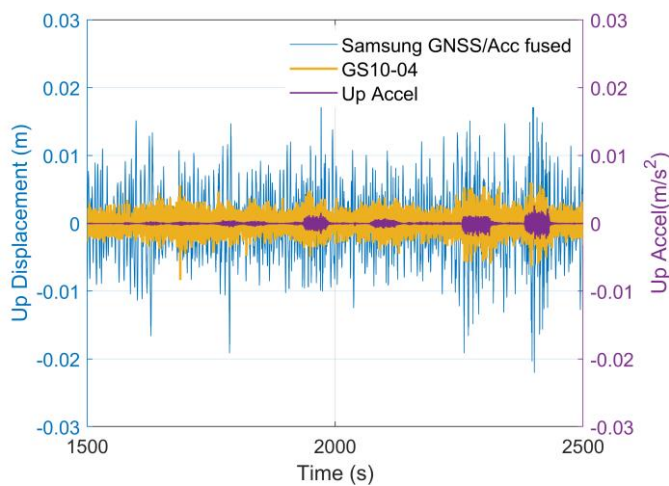


Figure 11 The highpass filtered timeseries of Leica geodetic GS04 solution, the smartphone solution after GNSS and acceleration data integration and the acceleration (after offset removal and scaling) timeseries

## 6 CONCLUSION

In this study, we analysed the performance of smartphones in monitoring vertical and horizontal oscillations with controlled oscillation setups, particularly for low frequency and low

amplitude displacement, with frequency less than 0.5 Hz, and amplitude less than 4 cm.

Based on the controlled experiments of horizontal and vertical motion recorded by smartphones with capacity of GNSS L1/L5, E1/E5a, dual frequency it is observed that it can detect the dynamic oscillation pattern in all cases. The dominant oscillation frequency was accurately detected in all cases meeting the same accuracy as that of geodetic GNSS data. Regarding the estimation of the oscillation amplitude, it is proved to be more noisy than the geodetic GNSS data, at is expected due to the susceptible to multipath effect of the linearly polarized GNSS antenna of the smartphones. The RMS error of estimating the oscillation amplitude ranges between 2 and 5 mm in most cases while the respective one for GNSS geodetic data was not more than 2 mm. More specifically, for oscillation amplitude less than 10mm, the estimation of the oscillation amplitude is more noisy, due to the relative high noise level of smartphone GNSS data, but for the estimation of the frequency it is proved very accurate. For oscillation amplitude larger than 10mm, the results of the GNSS smartphone data seemed to be more promising.

However, due to 1 Hz sampling rate from the mobile phone, the oscillation above 0.5 Hz could not be detected due to aliasing. Therefore, in the future research, we aim to investigate the sensor fusion between high frequency accelerometer measurement and GNSS measurement for detection of higher frequency displacement, which will allow further application of GNSS smartphone data in structural health monitoring (Xue et al., 2024).

## ACKNOWLEDGEMENTS

This work is funded by Royal Society International Exchange Collaboration grant with National Natural Science Foundation of China (IEC\NSFC\223184).

## REFERENCES

- Barbeau, S. (2021). Crowdsourcing GNSS features of Android devices. <https://bit.ly/gptest-device-database>
- Barbeau, S. (2023). GPSTest. [Mobile app] Google play store. Available at [https://play.google.com/store/apps/details?id=com.android.gptest&hl=en\\_GB](https://play.google.com/store/apps/details?id=com.android.gptest&hl=en_GB)
- Chen, B., Gao, C., Liu, Y., & Sun, P. (2019). Real-time precise point positioning with a Xiaomi MI 8 android smartphone. *Sensors*, 19(12), 2835.
- Dabove, P., & Di Pietra, V. (2019). Towards high accuracy GNSS real-time positioning with smartphones. *Advances in Space Research*, 63(1), 94-102.
- Everett, T. (2023). RTKLIB: demo5 b34h. Accessed December 05, 2024. <https://github.com/rtklibexplorer/RTKLIB/releases/>.
- Everett, T. (2024). RTKLIB: demo5 b34k. Accessed December 05, 2024. <https://github.com/rtklibexplorer/RTKLIB/releases/>.
- Geng, J., & Li, G. (2019). On the feasibility of resolving Android GNSS carrier-phase ambiguities. *Journal of Geodesy*, 93(12), 2621-2635.
- Google. (2024). GnsLogger App. [Mobile app] Google play store. Available at [https://play.google.com/store/apps/details?id=com.google.android.apps.location.gps.gnslogger&hl=en\\_GB](https://play.google.com/store/apps/details?id=com.google.android.apps.location.gps.gnslogger&hl=en_GB)

- Li, G., & Geng, J. (2019). Characteristics of raw multi-GNSS measurement error from Google Android smart devices. *GPS solutions*, 23(3), 90.
- Msaewe, H. A., Hancock, C. M., Psimoulis, P. A., Roberts, G. W., Bonenberg, L., & de Ligt, H. (2017). Investigating multi-GNSS performance in the UK and China based on a zero-baseline measurement approach. *Measurement*, 102, 186-199.
- Paziewski, J., Fortunato, M., Mazzoni, A., & Odolinski, R. (2021). An analysis of multi-GNSS observations tracked by recent Android smartphones and smartphone-only relative positioning results. *Measurement*, 175, 109162.
- Peppas, I., & Psimoulis, P. A. (2023). Detection of GNSS antenna oscillatory motion and multipath conditions via exploitation of multipath-induced SNR variations. *GPS Solutions*, 27(3), 117.
- Peppas, I., Psimoulis, P., & Meng, X. (2018). Using the signal-to-noise ratio of GPS records to detect motion of structures. *Structural control and health monitoring*, 25(2), e2080.
- Pesyna, K. M., Heath, R. W., & Humphreys, T. E. (2014, September). Centimeter positioning with a smartphone-quality GNSS antenna. In *Proceedings of the 27th International Technical Meeting of the Satellite Division of The Institute of Navigation (ION GNSS+ 2014)* (pp. 1568-1577).
- Psimoulis, P., Stiros, S. (2008). Experimental assessment of the accuracy of GPS and RTS for the determination of the parameters of oscillation of major structures. *Computer Aided Civil and Infrastructure Engineering*, 23(5), 389-403.
- Psimoulis, P., Pytharoulis, S., Karambalis, D., Stiros, S. (2008). Potential of Global Positioning System (GPS) to measure frequencies of oscillations of engineering structures. *Journal of Sound and Vibration*, 318(3), 606-623.
- Psimoulis, P., Peppas, I., Bonenberg, L.K., Ince, S., Meng, X. (2016). Combination of GPS and RTS measurements for the monitoring of semi-static and dynamic motion of pedestrian bridge, Proc. of 3<sup>rd</sup> Joint International Symposium on Deformation Monitoring, Vienna, Austria, Austria, 30 March - 1 April 2016. available [https://fig.net/resources/proceedings/2016/2016\\_03\\_jisdms\\_pdf/reviewed/JISDM\\_2016\\_submission\\_103.pdf](https://fig.net/resources/proceedings/2016/2016_03_jisdms_pdf/reviewed/JISDM_2016_submission_103.pdf)
- PrideLab. (2024). Smartphone multi-frequency GNSS and IMU data acquisition. available at <https://github.com/PrideLab/PRIDE-GeoDataLogger/tree/main>
- Robustelli, U., Baiocchi, V., & Pugliano, G. (2019). Assessment of dual frequency GNSS observations from a Xiaomi Mi 8 Android smartphone and positioning performance analysis. *Electronics*, 8(1), 91.
- Vazquez-Ontiveros, J. R., Martinez-Felix, C. A., Melgarejo-Morales, A., Retegui-Schietekatte, L., Vazquez-Becerra, G. E., & Gaxiola-Camacho, J. R. (2024). Assessing the quality of raw GNSS observations and 3D positioning performance using the Xiaomi Mi 8 dual-frequency smartphone in Northwest Mexico. *Earth Science Informatics*, 17(1), 21-35.
- Wanninger, L., & Heßelbarth, A. (2020). GNSS code and carrier phase observations of a Huawei P30 smartphone: Quality assessment and centimeter-accurate positioning. *GPS Solutions*, 24(2), 64.
- Xue, C., & Psimoulis, P. A. (2023). Monitoring the dynamic response of a pedestrian bridge by using low-cost GNSS receivers. *Engineering Structures*, 284, 115993.
- Xue, C., Psimoulis, P. A., & Meng, X. (2022). Feasibility analysis of the performance of low-cost GNSS receivers in monitoring dynamic motion. *Measurement*, 202, 111819.
- Xue, C., Psimoulis, P., Zhang, Q., & Meng, X. (2021). Analysis of the performance of closely spaced low-cost multi-GNSS receivers. *Applied Geomatics*, 13(3), 415-435.
- Xue, C., Psimoulis, P.A., Hancock, C., Ochieng, F.X., Yang, Y., Li, C., Bhatia, P., Li, Y., Tang, X., (2024), Analysis of the performance of GNSS receiver in monitoring the behaviour of the wind turbine nacelle, *Engineering Structures*, 317, 118633.

# Identification of Structural Dynamic Loads- From Physical Methods to Physics Informed Deep Learning Paradigm

Ying Lei<sup>1</sup>, Lijun Liu<sup>1</sup>, Fubo Zhang<sup>1</sup>

<sup>1</sup>Department of Civil Engineering, Xiamen University, Xiamen, 361005, China  
email: yleil@xmu.edu.cn, liulj214@xmu.edu.cn, fubozhang@stu.xmu.edu.cn

**ABSTRACT:** In this study, some progresses on the identification of structural dynamic loads are reported. First, a series of improved Kalman filter with unknown inputs developed by the authors for the identification of joint structural dynamic systems and dynamic loads are briefly reviewed. Then, some identification of structural dynamic loads using the physical guided deep learning paradigm are presented, including the identification of multi dynamic load positions and time histories using physics informed and enhanced Generative adversarial neural network (GAN) and Convolutional Long Short-Term Memory (ConvLSTM), respectively, the identification of full-field wind loads on buildings using physical informed recursive convolutional neural network (CNN), and the identification of stochastic fluctuating wind power spectrum on high-rise buildings using physical guided CNN with partial structural responses. The load type of the network during testing can be different from that during training. Through numerical simulation, it is proved that the proposed methods can learn the nonlinear mapping relationship between the structural responses and the external dynamic loads, and can reconstruct the load time histories well. The proposed methods are verified by numerical simulation and the results show that the deep learning methods can identify the unknown multi dynamic load positions and time histories, full-field wind loads on buildings and the stochastic fluctuating wind power spectrum on high-rise buildings.

**KEY WORDS:** Identification of structural dynamic loads; Physics informed deep learning; Physical methods.

## 1 INTRODUCTION

Identification of structural dynamic load is one of the core issues in the fields of structural health monitoring, vibration control and safety assessment. Its goal is to infer the dynamic loads acting on the structure (such as vehicle loads, wind loads, earthquake loads, etc.) from the response signals of the structure (such as displacement, acceleration, strain, etc.). With the development of technology, the methods in this field have gradually evolved from traditional methods that rely on physical models to data-driven deep learning methods. In this study, some progresses on the identification of structural dynamic loads are reported.

## 2 STRUCTURAL DYNAMIC LOAD IDENTIFICATION—PHYSICAL METHODS

### 2.1 Kalman filter with unknown input (KF-UI)

The Kalman Filter (KF) [1] is a recursive estimation method for structural states based on partial observations. As long as the estimated value of the state at the previous moment and the observation value of the current state are known, the optimal estimation value of the current state can be calculated. It is suitable for real-time online estimation of structural states and can consider the uncertainty of the model and the influence of observation noise. Therefore, it is widely used. However, when applying KF, the external inputs information of the structure needs to be known. In fact, the input information is often difficult to be fully observed. To overcome the limitations of the traditional KF, we proposed Kalman filter with unknown input (KF-UI) [2].

State equation

$$\mathbf{X}_{k+1} = \mathbf{A}_k \mathbf{X}_k + \mathbf{G}_k \mathbf{f}_k + \mathbf{w}_k \quad (1)$$

Observation equation

$$\mathbf{y}_k = \mathbf{C}_k \mathbf{X}_k + \mathbf{H}_k \mathbf{f}_k + \mathbf{v}_k \quad (2)$$

1) Time update for estimated states from  $k\Delta t$  to  $(k+1)\Delta t$ :

$$\tilde{\mathbf{x}}_{k+1/k} = \mathbf{A}_k \hat{\mathbf{x}}_{k/k} + \mathbf{G}_k \hat{\mathbf{f}}_{k/k} \quad (3)$$

The smallest variance estimator of state vector at  $(k+1)\Delta t$ :

$$\hat{\mathbf{x}}_{k+1/k+1} = \mathbf{K}_{k+1}^* \tilde{\mathbf{x}}_{k+1/k} + \mathbf{K}_{k+1} \mathbf{y}_{k+1} \quad (4)$$

$$\mathbf{K}_{k+1}^* \tilde{\mathbf{x}}_{k+1/k} = \tilde{\mathbf{x}}_{k+1/k} - \mathbf{K}_{k+1} (\mathbf{C}_{k+1} \tilde{\mathbf{x}}_{k+1/k} + \mathbf{H}_{k+1} \hat{\mathbf{f}}_{k+1}) \quad (5)$$

2) The final update equation of the smallest variance estimator of state vector at  $(k+1)\Delta t$ :

$$\hat{\mathbf{x}}_{k+1/k+1} = \tilde{\mathbf{x}}_{k+1/k} + \mathbf{K}_{k+1} (\mathbf{y}_{k+1} - \mathbf{C}_{k+1} \tilde{\mathbf{x}}_{k+1/k} - \mathbf{H}_{k+1} \hat{\mathbf{f}}_{k+1}) \quad (6)$$

The final update equation of error covariance matrix of the estimated state vector:

$$\begin{aligned} \tilde{\mathbf{P}}_{k+1/k}^x &= \tilde{\mathbf{e}}_{k+1/k}^x \tilde{\mathbf{e}}_{k+1/k}^{xT} \\ &= [\mathbf{A}_k \quad \mathbf{G}_k] \begin{bmatrix} \mathbf{P}_{k/k}^x & \mathbf{P}_{k/k}^{xf} \\ \mathbf{P}_{k/k}^{fx} & \mathbf{P}_{k/k}^f \end{bmatrix} \begin{bmatrix} \mathbf{A}_k^T & \mathbf{G}_k^T \end{bmatrix} + \mathbf{Q} \end{aligned} \quad (7)$$

3) The final update equation of unknown input at  $(k+1)\Delta t$ :

$$\begin{aligned} \mathbf{f}_{k+1} &= [\mathbf{H}_{k+1}^T \mathbf{R}^{-1} (\mathbf{I} - \mathbf{C}_{k+1} \mathbf{K}_{k+1}) \mathbf{H}_{k+1}]^{-1} \\ &\quad \mathbf{H}_{k+1}^T \mathbf{R}^{-1} (\mathbf{I} - \mathbf{C}_{k+1} \mathbf{K}_{k+1}) (\mathbf{y}_{k+1} - \mathbf{C}_{k+1} \tilde{\mathbf{x}}_{k+1/k}) \end{aligned} \quad (8)$$

To minimize the value of  $\mathbf{P}_{k+1/k+1}^x$ :

$$\mathbf{P}_{k+1/k+1}^x = \mathbf{e}_{k+1/k+1}^x \mathbf{e}_{k+1/k+1}^{xT} \quad (9)$$

$$\mathbf{K}_{k+1} = \tilde{\mathbf{P}}_{k+1/k}^x \mathbf{C}_{k+1}^T (\mathbf{R}_{k+1} + \mathbf{C}_{k+1} \tilde{\mathbf{P}}_{k+1/k}^x \mathbf{C}_{k+1}^T)^{-1} \quad (10)$$

Data fusion is applied to prevent the drifts in the identification caused by low-frequency noise.

$$\mathbf{y}_{k+1} = \mathbf{h}(\mathbf{Z}_{k+1}, \mathbf{f}_{k+1}, \mathbf{f}_{k+1}^u) + \mathbf{v}_{k+1} \quad (11)$$

### 2.2 Numerical simulation

Numerical simulation of the identification of unknown excitations for trusses verified the effectiveness of the method.



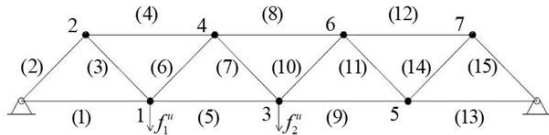


Figure 1. Truss structure

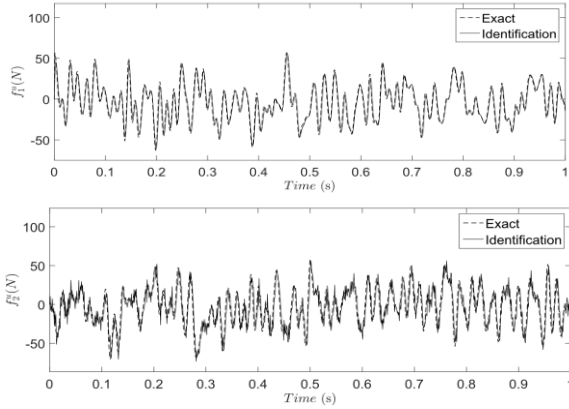


Figure 2. Identification results of unknown forces

### 2.3 A series of methods for Klamman Filter with Unknown Inputs

A series of methods for Klamman Filter with Unknown Inputs have been proposed by authors.

- 1) (Extended) Kalman filter under unknown input (KF-UI ; EKF-UI)
- 2) Kalman filter/Extended Kalman filter under unknown input without direct feedback (KF-UI-WDF; EKF-UI-WDF)
- 3) Unscented Kalman filter under unknown input(UKF-UI)
- 4) Unscented Kalman filter under unknown input (UKF-UI-WDF)
- 5) Particle filter under unknown input (PF-UI)
- 6) Unscented Kalman particle filter under unknown input (UKPF-UI)

## 3 STRUCTURAL DYNAMIC LOAD IDENTIFICATION—DEEP LEARNING METHODS

The data-driven method for dynamic load identification, which does not require a structural model, is more in line with the needs of actual engineering. Data-driven deep learning methods can establish functional mapping between network inputs (structural responses) and outputs (structural dynamic loads). Machine learning approaches with clear physical interpretability often demonstrate enhanced performance.

### 3.1 Physics-Guided Deep Learning for Multi Dynamic Load Identification

Existing methods require identical load distributions during training and testing, resulting in poor network generalizability and restricted applicability.

When a single load acts at  $j$ , the response at the structural measurement point  $i$ :

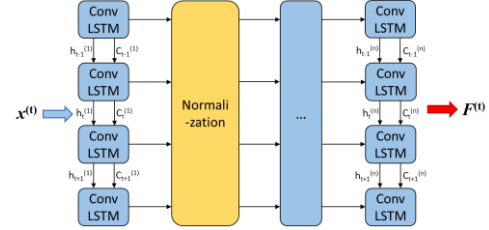
$$z_i^j(t) = \int_0^t h_i^j(t-\tau) f_j(\tau) d\tau \quad (12)$$

$$z_i^j = H_i^j f_j \quad (13)$$

Multiple loads  $f_n(n=1,2,\dots,n_f)$  acts on the structure, where  $n_f$  is the number of loads. The formula for the response of the  $i$ -th measurement point can be expressed as:

$$z_i = \sum_{j=1}^{n_f} H_i^j f_j \quad (14)$$

To solve the problem of identifying dynamic loads, it is necessary to find the inverse matrix of  $H$ . Since positive definite conditions need to be satisfied, it is essential to ensure that the observed number is greater than the number of unknown forces.



Numerical simulation of the identification of unknown excitations for outward-extending beams verified the effectiveness of the method.

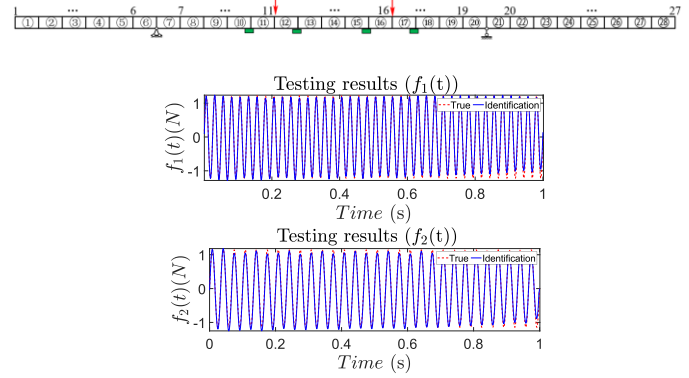


Figure 3. Identification results of unknown forces

### 3.2 Physics Guided Deep Learning for Wind Load Identification of Tall Buildings

It is more challenging to identify wind loads, because Wind load is a type of complex distributed dynamic load. Currently, methods for identifying wind loads mainly rely on theoretical inverse identification [3-4]. In this paper, a scheme for identifying full-field wind loads using a recursive convolutional neural network (CNN) inspired by physical mechanisms is proposed.

The wind load is discretized and sampled spatially. Based on spatial correlation to represent the wind profile. If the floor height is 3 meters. The correlation between the adjacent two floors is 0.954 and that between the three floors is 0.911. It can be assumed that the adjacent two floors are completely correlated. Therefore, spatial correlation can reduce the number of independent loads. The recursive form of the network, as well as the inspiration for its inputs and outputs, is inspired by the spatial correlation and the mapping relationship between wind loads and structural responses.

In this study, a 306-meter-high Australian office building is utilized, which is the 76-story Benchmark building established by IASC-ASCE [5]. In this case, the network is tested using

structural responses generated by the stationary Davenport spectrum, Harris spectrum and Kaimal spectrum.

To verify the accuracy of spatial identification results, wind load profiles at four time moments are shown in Figure 4. The time histories of wind loads at three heights are presented in Figure 5. The self-power spectrum of the wind load at the 60th floor and the cross-power spectrum between the 60th and 62nd floors are shown in Figure 6. The identification results of the power spectrum align well with the true values.

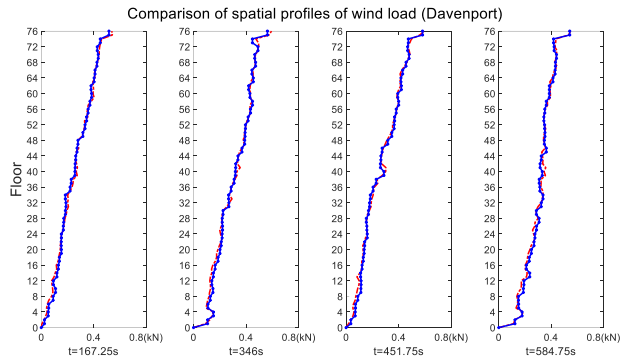


Figure 4. Identification of wind loads profiles (Davenport spectrum)

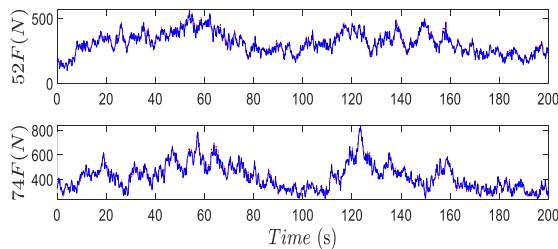
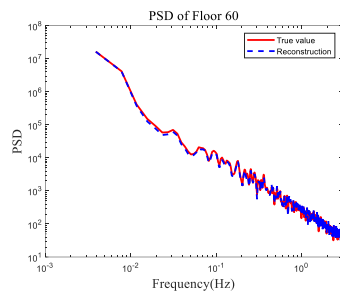
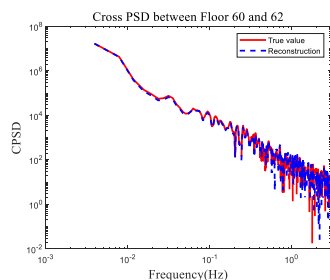


Figure 5. Identification of wind loading time histories (Davenport spectrum)



(a) PSD



(b) CPSD

Figure 6. Identification of the PSD and CPSD (Davenport spectrum)

## 4 CONCLUSIONS

In this study, some progresses on the identification of structural dynamic loads are reported. To overcome the limitations of the traditional KF, A series of methods for Klamman Filter with Unknown Inputs have been proposed by authors. The physical method is applicable to problems with clear models and simple scenarios. The deep learning method, on the other hand, breaks through the bottleneck of model dependence and is more suitable for complex scenarios in actual engineering. Machine learning approaches with clear physical interpretability often demonstrate enhanced performance. Physics-Guided deep learning for multi dynamic Load identification and for wind load identification of tall buildings are proposed respectively.

In the future, the integrated method of "physical model + data-driven" will become the mainstream. It will not only leverage the explanatory power of physical theories but also utilize the strong fitting ability of deep learning, promoting the development of dynamic load identification towards greater accuracy, robustness, and universality.

## REFERENCES

- [1] R.E. Kalman. A new approach to linear filtering and prediction problems, J. Basic Eng., 1960, 82(1), 35-45.
- [2] L.Liu, J. Zhu, Y. Su, Y. Lei. Improved Kalman filter with unknown inputs based on data fusion of partial acceleration and displacement measurements, Smart Structures and Systems, 2016,17(6), 903-915.
- [3] L. H. Zhi, P. Yu, Q. S. Li, B. Chen, andM. X. Fang, Identification of wind loads on super-tall buildings by Kalman filter, Comput. Struct. 2018, 208, 105.
- [4] O. W. Petersen, O. Oiseth, andE. Lourens, Wind load estimation and virtual sensing in long-span suspension bridges using physics-informed Gaussian process latent force models, Mech. Syst. Signal Proc. 2022,170, 22.
- [5] J. N. Yang, A. K. Agrawal, B. Samali, J. C. Wu, Spie, andSpie, A benchmark problem for response control of wind-excited tall buildings (Soc Experimental Mechanics Inc, Kissimmee, Fl, 2001).



# The SCSHM Benchmark Bridge: First Studies and Results



# Multi-purpose bridge strain data fusion for BWIM and structural monitoring

Tommaso Panigati<sup>1</sup>, 0009-0001-4077-8058, Maria Pina Limongelli<sup>1,2</sup>, 0000-0002-9353-5439

<sup>1</sup>Politecnico di Milano, Department of Architecture, Built environment and Construction engineering, Piazza Leonardo da Vinci 32, 20133 Milan, Italy

email: [tommaso.panigati@polimi.it](mailto:tommaso.panigati@polimi.it), [mariagiuseppina.limongelli@polimi.it](mailto:mariagiuseppina.limongelli@polimi.it).

## EXTENDED ABSTRACT

KEY WORDS: BWIM, Weight in motion, SHM, structural health monitoring

## 1 INTRODUCTION

This work presents some results obtained using bridge strain data relevant to the Society of Civil Structural Health Monitoring (SCSHM) bridge benchmark [1]. Data has been processed to obtain information on both bridge behavior and on the features of vehicles passing through the bridge. Namely, the processing of data from sensors located at different sections of the bridge enables to retrieve information relevant to a) the dynamic and static bridge characteristics and b) to the passing vehicle characteristics such as speed, weight, length and number of axles (see Figure 1). Furthermore, in this work it is shown how data fusion techniques permit to improve the quality of the estimation of relevant information extracted from multiple sensors, for both Bridge Weight-in-motion (BWIM) and structural monitoring in the SCSHM bridge benchmark.

## 2 METHODOLOGY

The proposed methodology, tested on the SCSHM benchmark, allows to extract data from multiple strain sensors positioned at different locations of the bridge. The use of multiple strain sensors enables the detection of time-related features, such as the velocity of the vehicle. Furthermore, each sensor enables the retrieval of diverse information. For instance, sensors closer to the road surface are more suitable for capturing the local

response to the passage of single axles, while sensors located on the beams capture the global bridge response in terms of deflection. If the bridge has several lanes, sensors located under each lane will be more sensitive to vehicles passing over that specific lane.

Each step of the methodology is here described. Concerning the bridge – related data, it is possible to use all the sensors to extract parameters that describe the dynamic behavior of the bridge, for example frequencies and modal shapes. This can be done either by processing the response of the during the passage of a vehicle, (for instance by taking an interval of 10 seconds centered on the strain peak during the transit), or by processing a longer signal obtained concatenating all the responses measured by the same sensor at a given location.

Vehicle-related information is also extracted from strain measurements. Vehicle velocity and direction are identified based on the time lag between the peak strains at two bridge cross sections. The gross vehicle weight is estimated using the area method, as presented in [2]. The length of each vehicle is calculated by dividing its speed by the duration of the strain history recorded at midspan. Since this strain history represents the measured influence line for strain at midspan in the time domain, it remains non-zero for a period longer than the actual time the vehicle spends crossing the midspan. To account for this discrepancy a calibrated fictitious length is subtracted from the initially estimated length.

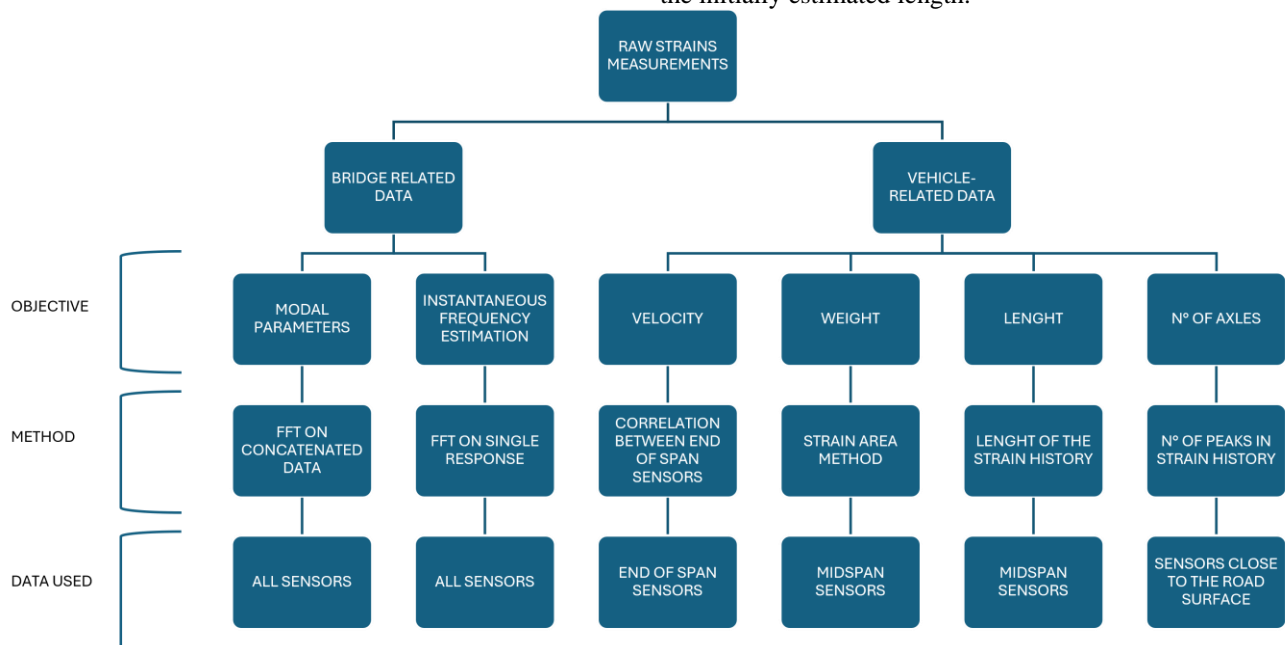


Figure 1. Flowchart of the proposed methodology.

The number of axles is calculated by counting the number of peaks in the strain histories for sensors close to the road surface, where each peak corresponds to consecutive axles (e.g. when two axles or three axles are very close to each other, as in the case of a semitrailer, only one peak is counted).

Finally, the joint analysis of data recorded by several sensors can provide enhanced information about the bridge condition and performance. For instance, the comparison of vehicle weight and number of axles may be useful for identifying overloaded vehicles. Furthermore, it is of interest to combine vehicle-related with bridge related data, for instance to investigate the dynamic response of the bridge in relation to different vehicle typologies and speed.

### 3 APPLICATION ON THE SCSHM BENCHMARK

The proposed methodology is applied to the study of the SCSHM bridge benchmark [1]. The investigated structure is a simply supported span, with a length of 22.71 m, carrying two lanes. The span is instrumented with 32 electric resistive strain gages to monitor strains and six thermocouples to monitor air/structure temperature under the deck. Strain gages are placed at several cross-sections (end of spans, midspan and  $\frac{3}{4}$  of the span) and at different locations within each section. The dataset contains data recorded during passages of more than 3000 vehicles, namely strains time histories from the 32 sensors, environmental temperature, and photos of the vehicles. The following results emerge from the analysis of data.

- The dynamic response is affected by the type and speed of the transiting vehicle and by temperature. The correlation between temperature and natural frequencies is shown in Figure 2 where results obtained from data relevant to the passage of more than 3000 vehicles are reported. Results highlight that an increase in temperature leads to a decrease in frequency. The decrease is more relevant where temperatures are below 0°C, due to the stiffening effect of ice, consistently with findings from other case studies [3].

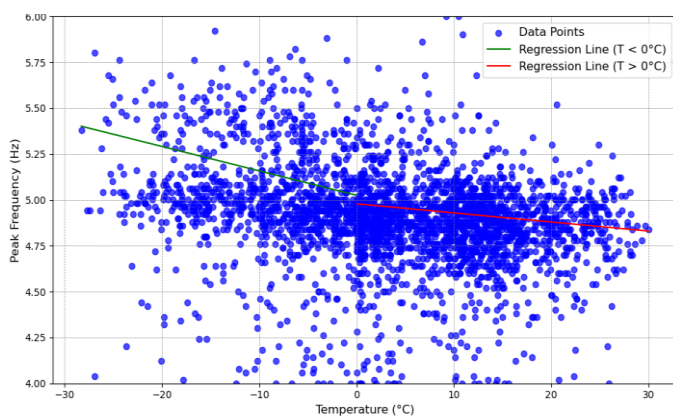


Figure 2. Scatter plot Temperature-Frequency for single vehicles passing through the bridge.

- The traffic composition in the two directions can be retrieved from the analysis of the velocity, direction and weight of each vehicle. Results suggest that the number of vehicles crossing the bridge in one direction is almost twice the number in the opposite

direction. Furthermore, the weight distribution is slightly different in the two directions.

- From the combined analysis of vehicle weights and the estimated number of axles (see Figure 3), it is possible to infer if the vehicle is loaded or not. The estimate might be improved by detecting each single axle instead of groups of axles.
- The integration of vehicle-related data into bridge-related data will contribute to improving the quality of the information. For instance, the vehicle weight can be better estimated by accounting for bridge stiffness correction due to environmental temperature than can be appraised from the relationship between frequencies and temperature.

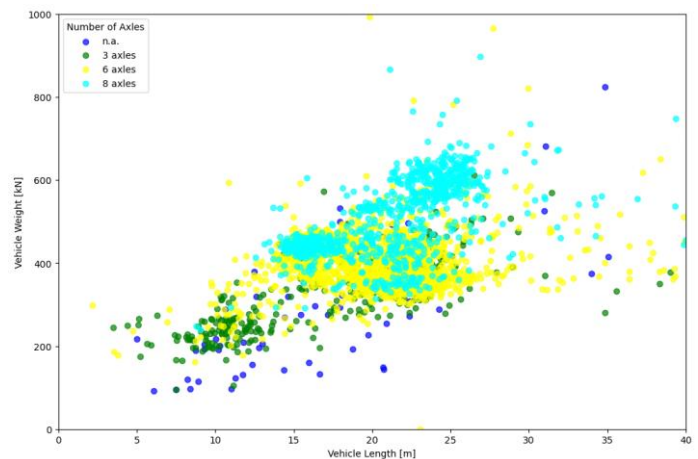


Figure 3. Scatter plot comparing vehicle length, vehicle weight and number of axles.

### ACKNOWLEDGMENTS

This work was supported by PRIN: PROGETTI DI RICERCA DI RILEVANTE INTERESSE NAZIONALE – Bando 2022, under grant number Prot. 2022P44KA8, provided by the Italian Ministry of Education, Universities and Research. This work was financed by European Union - Next Generation EU, Mission 4 Component 1 CUP D53D23003870006.

### REFERENCES

- [1] M. P. Limongelli *et al.*, “SCSHM benchmark study on bridge in-service structural monitoring,” *J Civ Struct Health Monit*, 2024, doi: 10.1007/s13349-024-00846-1.
- [2] K. Helmi, B. Bakht, and A. Mufti, “Accurate measurements of gross vehicle weight through bridge weigh-in-motion: a case study,” *J Civ Struct Health Monit*, vol. 4, no. 3, pp. 195–208, 2014, doi: 10.1007/s13349-014-0076-5.
- [3] B. Peeters and G. De Roeck, “One year monitoring of the Z24-bridge: Environmental influences versus damage events,” *Proceedings of the International Modal Analysis Conference - IMAC*, vol. 2, 2000.

# Vehicle speed estimation using convoluted reciprocity for bridge structural monitoring

Daniel Cantero<sup>1</sup>, [0000-0001-8947-8569]

<sup>1</sup>Structural Engineering, NTNU Norwegian University of Science and Technology, Trondheim, Norway  
email: daniel.cantero@ntnu.no

**ABSTRACT:** The estimation of vehicle speed is a critical first step in deriving vehicle weight from bridge responses. Various strategies have been developed to extract the speed of passing vehicles, primarily relying on sensors that capture signals with features related to the vehicle's axles. These signals are processed through diverse methods; however, existing strategies often fail to perform optimally across different structural configurations. To address these challenges, the convoluted reciprocity (CR) relationship was recently proposed, which was verified numerically and validated experimentally in a laboratory setting. In this document, the novel speed estimation strategy based on CR is applied to an operational bridge using signals from the SCSHM benchmark. The results confirm that CR provides a robust speed estimation method for cases when the signals lack individual axle features.

**KEY WORDS:** Speed; Vehicle; Bridge Monitoring; Convoluted Reciprocity; SCSHM.

## 1 INTRODUCTION

Instrumented bridges can be utilised for weighing vehicles as they pass over them, enabling the estimation of Gross Vehicle Weight (GVW) based on the integral of the recorded signal [1]. When integrated into Bridge Weigh-in-Motion (BWIM) systems, such instrumentation allows for the identification of individual axle loads and axle spacing. This technology has gained significant attention in recent years ([2], [3], [4], [5]) due to the valuable site-specific traffic data it provides, as well as its potential applications in structural health monitoring [6].

A crucial first step in any weighing solution based on bridge responses is determining the speed of the passing vehicle. This requires signals that provide reliable speed estimation. Standard approaches include FAD (Free of Axle Detectors) and NOR (Nothing on the Road) methods, which utilise specific signal features to estimate vehicle speed, axle count, and axle spacing [4]. Additionally, alternative methods have successfully employed acoustic signals generated by tyres passing over bridge expansion joints to determine vehicle speeds [7].

A recent study by the author [8] investigated various speed estimation strategies using strain sensors, demonstrating that existing methods perform well in most practical scenarios. However, a consistent theoretical framework for speed estimation was lacking. The standard approach relies on the cross-correlation of signals at different bridge locations, which is effective when distinct axle signatures are present but fails in certain cases, particularly for simply supported bridges. To address this limitation, [8] introduced the Convoluted Reciprocity (CR) relationship, developing a novel speed estimation method. This approach does not require signals to exhibit distinct axle features, making it more widely applicable. The Convoluted Reciprocity framework was theoretically derived, numerically verified, and experimentally validated in [8].

This document aims to present the limitations of the correlation-based method for speed estimation and to illustrate the effectiveness of the novel Convoluted Reciprocity (CR) approach. First, the shortcomings of the correlation method are visually demonstrated. Then, the CR concept is introduced and verified through numerical examples. Finally, the method is validated using real bridge measurements from the publicly available SCSHM dataset [9].

## 2 THE PROBLEM WITH CORRELATION

Arguably, the most common strategy for estimating the speed of a passing vehicle using bridge responses is based on correlating signals recorded at two separate locations along the bridge. The key idea is to determine the time lag that maximises the correlation between the signals, which indicates the time taken by the vehicle to travel between the sensor locations. Given the known sensor distance, the vehicle speed can then be directly estimated. This method assumes that the signals are shifted versions of each other and has been successfully applied in many cases. However, its effectiveness relies on the presence of distinct peaks corresponding to individual axles in the signals, which is not always guaranteed.

To illustrate this, synthetic bridge responses are used from a numerical simulation of a two-axle vehicle traversing a bridge, modelled using the open-source VBI-2D tool [10]. The vehicle's axles have equal weights and are spaced 5 m apart. The bridge has a span of 20 m, with strain measured at sensors located at  $\frac{1}{4}$  and  $\frac{3}{4}$  of the span, denoted as S25 and S75, respectively. The vehicle travels at a constant speed of 20 m/s (72 km/h). For verifying purposes, only the quasi-static response is simulated, excluding dynamic effects and noise.

For a bridge with fixed-fixed boundary conditions, the resulting signals are shown in Figure 1(a). The peaks corresponding to each axle are clearly distinguishable. Although the signals are not perfect shifted versions of each other, the correlation method performs accurately. By



computing the correlation and identifying the time lag that maximises it, the exact travel time between sensor locations is obtained, as illustrated in Figure 1(b). Consequently, the estimated speed in this case is precise.

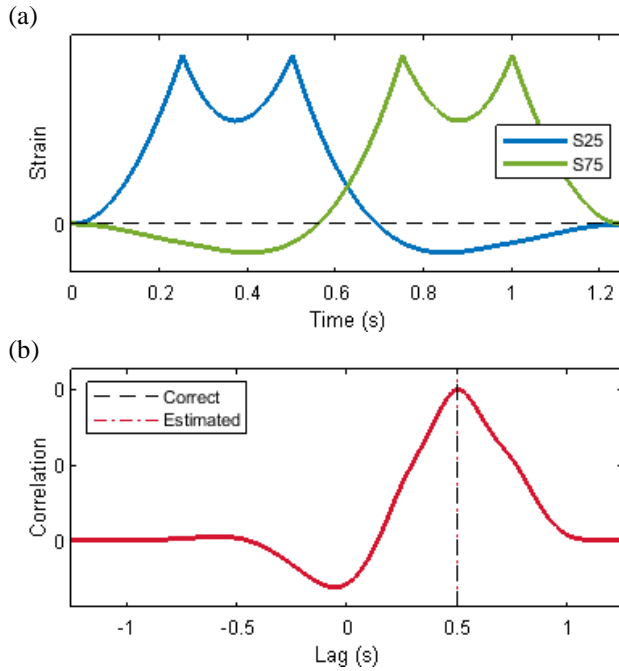


Figure 1. (a) Simulated fixed-fixed beam responses due to a 2-axle vehicle; (b) Cross-correlation of signals. Vertical lines indicate the time lag giving maximum correlation and the one that should have been obtained for correct speed estimation.

In contrast, for a simply supported bridge, the responses do not exhibit distinct peaks, leading to poor speed estimates using the correlation method. Figure 2(a) presents the simulated bridge responses for the same vehicle and bridge configuration but with simply supported boundary conditions. Applying the correlation method in this case (Figure 2(b)) results in a significantly inaccurate speed estimate. Specifically, the estimated speed is 47.62 m/s, corresponding to a 138% error.

Therefore, the correlation method is poorly suited for simply supported bridges due to the absence of distinct axle features. However, even in cases where clear axle features are present, such as fixed-fixed bridges, the method does not always guarantee perfect results. The speed estimation based on maximum correlation may still be imprecise, depending on the vehicle configuration and span length. This limitation is not new, and various correction strategies exist, but they are either specific to certain vehicle types or rely on signal processing techniques. A more detailed analysis can be found in [8]. Nevertheless, until now, no theoretically sound alternative had been established. This gap is addressed by the speed estimation method based on Convolved Reciprocity.

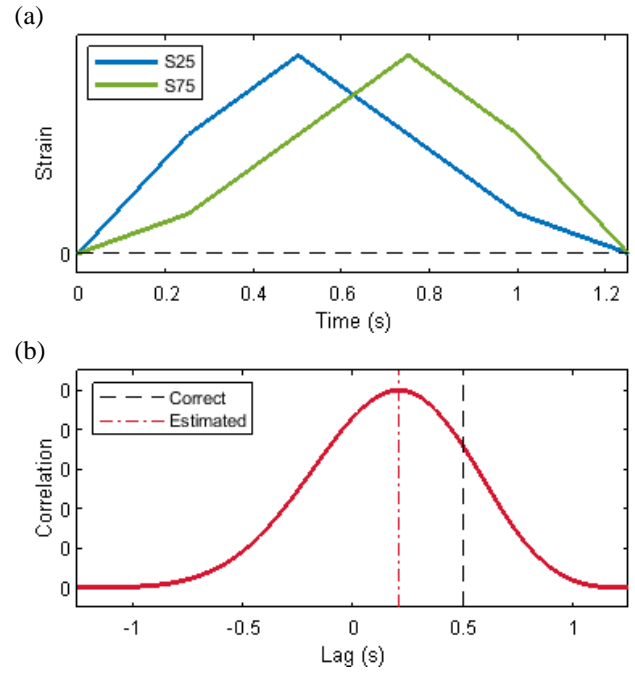


Figure 2. (a) Simulated simply supported beam responses due to a 2-axle vehicle; (b) Cross-correlation of signals. Vertical lines indicate the time lag giving maximum correlation and the one that should have been obtained for correct speed estimation.

### 3 CONVOLUTED RECIPROCITY

This section introduces the concept of Convolved Reciprocity and its application to speed estimation, originally presented in [8]. Here, a step-by-step example is provided to further explain and verify the method. The verification is performed using VBI-2D [10] under ideal conditions, considering perfect quasi-static signals without noise or dynamic disturbances. The analysis follows the same case as presented in Section 2, ensuring direct comparison with the correlation-based approach.

In [8], it was shown that a relationship exists between bridge responses at two different locations (A and B) for two different vehicle passages, say Vehicle 1 (V1) and Vehicle 2 (V2). This relationship is expressed in Eq. (1).

$$S_{A,V1}(t) \times S_{B,V2}(t) = S_{B,V1}(t) \times S_{A,V2}(t) \quad (1)$$

where  $S_{i,j}$  represents the measured load effect at location  $i$  due to the passage of vehicle  $j$ , and  $\times$  denotes the convolution operation. This relationship follows from the fact that any bridge response to a passing vehicle can be expressed as the convolution of the vehicle's forcing function with the corresponding influence line. By taking advantage of the commutative property of convolution, the expression is derived (see [8] for a detailed derivation). This result establishes a reciprocal relationship between signals recorded at different sensor locations and vehicle passages when convolved together, leading to the adopted term Convolved Reciprocity (CR). The expression can be further simplified to:

$$CR_{AB}(t) = CR_{BA}(t) \quad (2)$$

This relationship is rather powerful, as it connects any two load effects for any two vehicle passages. It holds under the

standard assumption that vehicles travel at a constant speed. Using this relationship, the speed of an unknown vehicle passage can be estimated if the response of a reference event is known. In practice, signals from a vehicle event with a known speed are stored as a reference, enabling the speed estimation of subsequent vehicle passages.

For example, Figure 3 presents the signals for a five-axle truck with axle spacing and load distribution as specified in [11], representing a typical European configuration for a fully loaded articulated five-axle truck. Since the vehicle speed is known for this reference event, the signals can be transformed into the spatial domain. This event serves as a calibration or reference event, providing a basis for speed estimation of other vehicle passages.

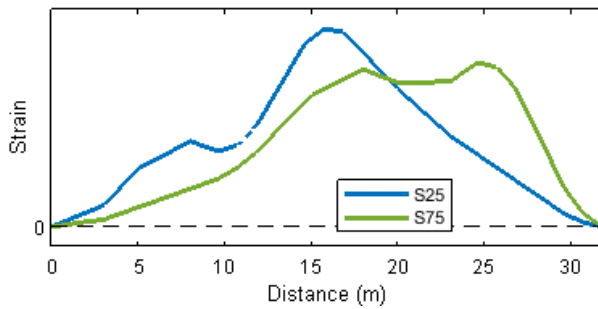


Figure 3. Simulated simply supported beam response due to a 5-axle truck.

Applying the Convolved Reciprocity (CR) relationship in the time domain, we estimate the speed of the unknown vehicle by iteratively testing different speed guesses and evaluating the CR relationship. For each guessed speed, the signals from Figure 3 are transformed accordingly into the time domain. By applying the relationship in Eq. (2), together with the signals in Figure 2(a), results are obtained for each speed guess. Figure 4 presents the left-hand side and right-hand side of Eq. (2) for different guessed speeds. The speed estimate that results in a match between both curves corresponds to the actual speed of the unknown vehicle event.

To systematically quantify the differences between both sides of Eq. (2), we evaluate the norm of their difference (see Eq. (3)). The study in [8] explored various norm choices and suggested that the 1-norm could be a suitable option. However, other p-norms may also yield good results. The best speed estimate can be determined by finding the speed that minimises the norm of the difference.

$$\|CR_{AB} - CR_{BA}\| = 0 \quad (3)$$

Figure 5 presents the norm of the difference between both sides of Eq. (2) for a range of guessed speeds. The minimum of this norm corresponds to the speed that best matches the actual speed of the unknown vehicle event. This example was conducted using ideal quasi-static responses, free from noise and disturbances. As a result, the speed estimation is exact, confirming the validity of the methodology. However, when applying this approach to real signals affected by noise and disturbances, the accuracy of the estimated speed may be impacted.

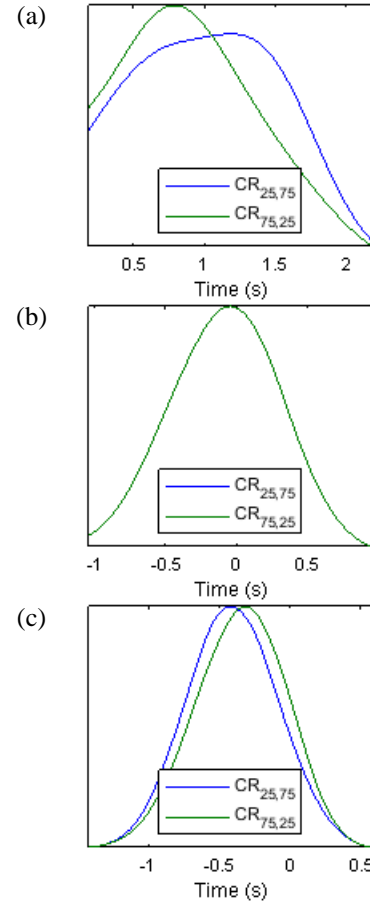


Figure 4. Detail of the CR for various speed guesses: (a) 10 m/s; (b) 20 m/s; (c) 30 m/s.

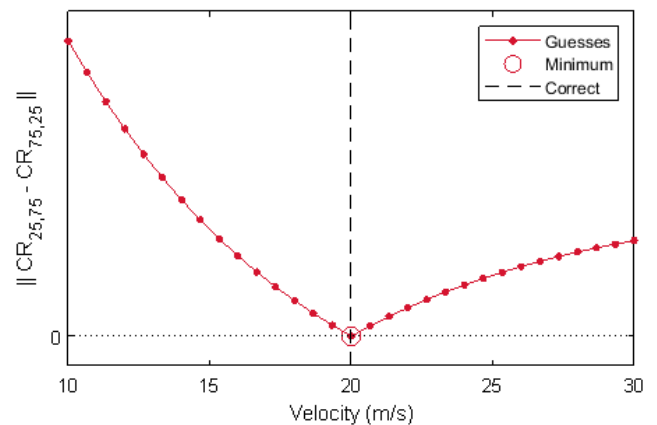


Figure 5. Norm values for a range of speed guesses.

#### 4 VALIDATION USING SCSHM

The CR method for speed estimation was verified in the previous section using ideal quasi-static bridge responses. This section focuses on validating the method under realistic conditions by applying it to data from a real bridge, where signals include noise and dynamic effects. The CR approach is tested using bridge responses from the SCSHM dataset [9], specifically for cases where the signals do not exhibit clear axle features.

#### 4.1 The SCSHM dataset

The dataset introduced in [9] corresponds to a nine-span bridge with a total length of 291 m, located in Manitoba, Canada. The bridge carries two lanes of traffic, one in each direction, and its superstructure consists of four lines of I-girders supporting a reinforced concrete (RC) deck. Of particular interest is Span 2, a simply supported span of 22.71 m, which is instrumented with strain gauges and thermocouples at various locations. The signals are sampled at 200 Hz, and only events exceeding a predefined strain threshold are recorded.

For this study, key sensors are those located at the ends of the span (Sections AA and EE), where strain gauges attached to the deck capture signals with clear individual axle features. These signals were used in [9] to accurately estimate vehicle speeds, and these estimates will be taken as the reference speeds in this work. Additionally, two other instrumented sections, FF (at approximately  $\frac{1}{4}$  span) and BB (at approximately  $\frac{1}{2}$  span), contain multiple strain gauges on each girder. Here, only the strain measured at the soffit will be considered. The dataset includes both strain measurements and vehicle photographs from several monitoring campaigns, totalling over 3,000 heavy vehicle crossing events. For further details on the instrumentation setup, refer to [9].

#### 4.2 Example for one event

As an example, this section estimates the speed of a vehicle passage using the signals from a reference event with a known speed. Specifically, the analysis focuses on vehicles travelling in the westbound lane, where strain gauges located on girder G2 are considered (channel 10 in section FF and channel 22 in section BB). The reference event corresponds to file 04/E00003 (event 3 in folder 04), with a recorded speed of 17.2 m/s (61.92 km/h) and a GVW of 433.3 kN. The signals used for the CR-based speed estimation are shown in Figure 6. For speed estimation, these signals are first transformed into the spatial domain using the known speed of the reference vehicle.

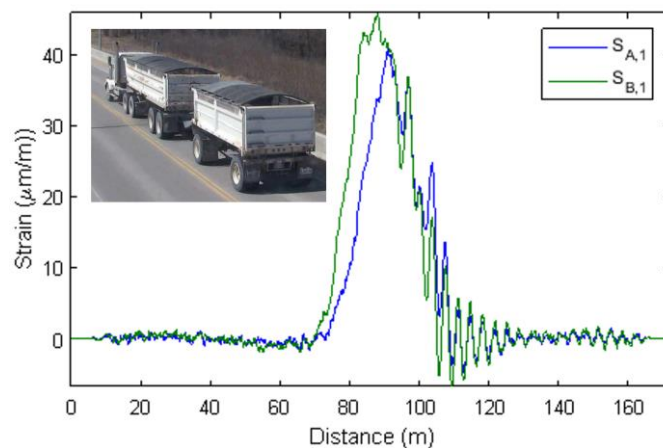


Figure 6. Signals of reference event (04/E00003).

The goal is to estimate the speed of an event with an unknown speed using the CR method. The event under analysis is 05/E00001, corresponding to a truck with a GVW of 319.9 kN. The signals for this event are shown in Figure 7. The dataset provides a recorded speed of 14.5 m/s (52.2 km/h), which will be used as the reference value for validation.

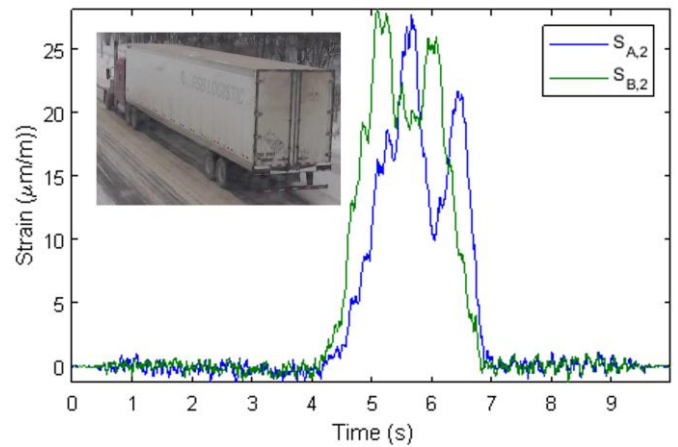


Figure 7. Signals of event to determine its speed (05/E00001).

Using the CR relationship, the estimated speed must satisfy Eq. (2). To apply this method, the speed of the reference vehicle is assumed, and the signal is transformed back into the time domain by assuming a different speed. As an example, this calculation is repeated for three different assumed speeds, and the results are plotted in Figure 8.

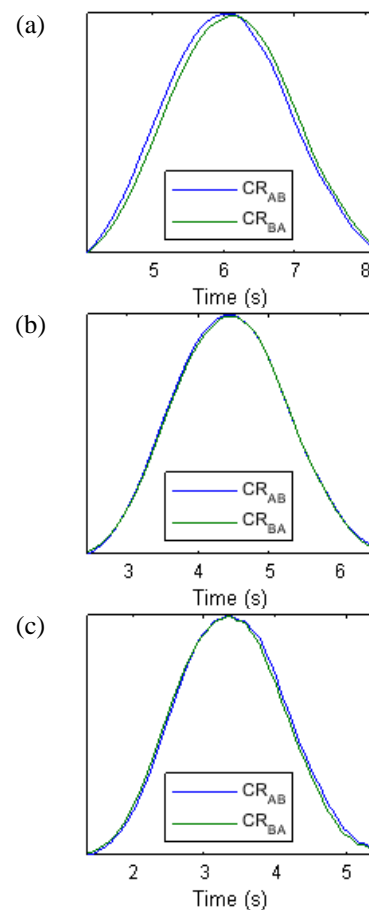


Figure 8. Detail of the CR for various speed guesses: (a) 40 km/h; (b) 50 km/h; (c) 60 km/h.

This process can be repeated for many more guesses. To evaluate the similarity between both CRs, the norm of the difference between both could be used. For this study, we adopted the 1-norm. Only a few guesses are shown below in



Figure 9 for visualization purposes. More guesses can be easily computed to refine the final speed estimation. The speed that gives the minimum norm is considered as the estimated speed of the event. Increasing the number of guesses, one obtains an estimated speed of 14.44 m/s (51.98 km/h), which for this case is almost a perfect match (-0.38% error).

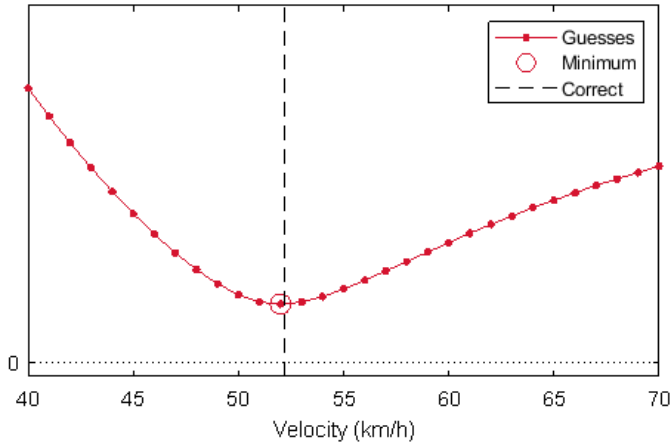


Figure 9. Norm values for a range of speed guesses.

#### 4.3 Database analysis

This section applies the CR method to estimate the speed of all the valid events available in folder 05 in the database. Note that only events with a single vehicle are considered. Also, events with missing pictures are removed. Therefore, a total of 2149 events are analysed below.

To apply the CR method to a real bridge, we need to use a reference event for each lane. Speed estimation for each lane is done separately. The bridge response is different for each lane, so we need to define one reference event for each lane. When processing, we can identify which lane the vehicle is traveling on simply from the maximum response values across different girders. Once this is detected, the CR method is applied for the corresponding reference vehicle.

Figure 10(a) shows all the speed estimation errors in terms of difference to those provided by the database. The same results can be visualized in a histogram in Figure 10(b). Overall, one can see that most of the speed estimates fall within the 5% band, which is reasonable for the goal of estimating the GVW of passing vehicles. However, there are some instances where much higher errors are observed.

The results below show that the histogram is not centred around zero value, indicating an underlying bias related to the selected reference vehicles. In this calculation, the reference events correspond to normal events traversing at normal operational speeds. In practice, it should be possible to calibrate the calculation by obtaining signals from a reference event with very slow speeds, one for each lane. We can make the reference vehicle passages occur at slow speeds, making these events almost perfectly quasi-static. The unknown events will have dynamics, introducing some error, which is the dispersion observed in the results. Furthermore, the separation between section FF and BB is rather small; results would improve with sensors placed further apart.

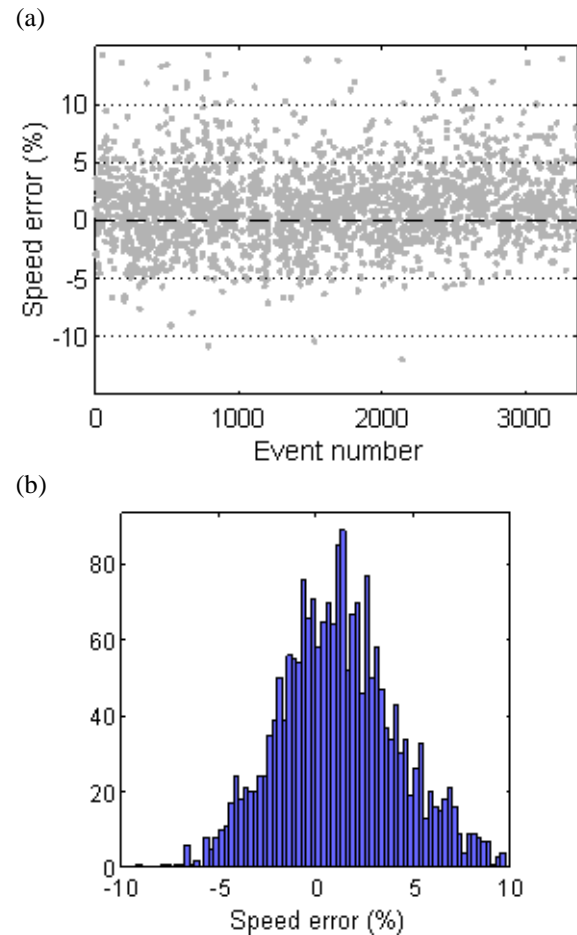


Figure 10. Single vehicle events speed estimation. (a) Estimation errors for each event; (b) Histogram of estimation errors.

Not shown here, but the possibility of improving the performance by signal processing the results was explored. Low-pass filtering and moving average filtering were explored to try to reduce the contributions of bridge dynamics and noise. However, the CR method seems to be rather robust, with only marginal reductions in errors observed. On one hand, this shows that the idea is robust and can be applied directly to unprocessed signals. On the other hand, this indicates that there is no easy way of improving the performance of the method simply by pre-processing the signals.

## 5 CONCLUSION

In general, when the goal is to estimate the speed of passing vehicles, signals with individual axle features should be used. In those cases, the standard correlation method provides satisfactory results. Nonetheless, this method is not theoretically sound nor valid for all bridge configurations.

This document has presented a methodology to estimate the speed of passing vehicles supported by the convoluted reciprocity relationship. First, an ideal numerical example is used to verify the concept. Then, the method is applied to the measured single vehicle events available in the SCSHM dataset. The reported speed estimation errors show some scatter, but most of them are within a 5% error band.

The methodology presented here enables the speed estimation for a wider range of possibilities. It is not strictly

necessary to have signals with clear individual axle features. Therefore, the methodology can use sensors that capture the global behaviour of the bridge. This opens the possibility of having vehicle weighting capabilities on existing monitoring systems, with other load effects, or installing them on bridges that do not have local responses that would show individual axle features. Sometimes bridges do not have locations with responses that have clear individual axle features, or the bridge has an existing installation with the original intention of SHM and no sensors with axle features. CR opens the possibility of estimating the speed also in those cases.

## REFERENCES

- [1] K. Helmi, B. Bakht, A. Mufti, Accurate measurements of gross vehicle weight through bridge weigh-in-motion: a case study, *Journal of Civil Structural Health Monitoring*, 4, 195–208, 2014.
- [2] M. Lydon, S.E. Taylor, D. Robinson, A. Mufti, E.J. O. Brien, Recent developments in bridge weigh in motion (B-WIM), *Journal of Civil Structural Health monitoring*, 6, 69-81 2016.
- [3] Y. Yu, C.S. Cai, L. Deng, State-of-the-art review on bridge weigh-in-motion technology, *Advances in Structural Engineering*, 19(9), 1514–1530, 2016.
- [4] A. Žnidarič, J. Kalin, M. Kreslin, Improved accuracy and robustness of bridge weigh-in-motion systems, *Structure and Infrastructure Engineering*, 14(4), 412–424, 2017.
- [5] B. Bakht, A. Mufti, *Bridges*. Springer International Publishing Switzerland 2015.
- [6] P. Debojyoti, R. Koushik, Application of bridge weigh-in-motion system in bridge health monitoring: A state-of-the-art review, *Structural Health Monitoring*, 22(6), 4194–4232, 2023.
- [7] B. Algohi, A. Mufti, D. Thomson, Detection of speed and axle configuration of moving vehicles using acoustic emission, *Journal of Civil Structural Health Monitoring*, 8, 353–362, 2018.
- [8] D. Cantero, C.W. Kim, Convolutional reciprocity and other methods for vehicle speed estimation in Bridge Weigh-in-Motion Systems, *ASCE Journal of Bridge Engineering*, 29(2), 04023114, 2024.
- [9] M.P. Limongelli, D. Thomson, S. Alampalli, A. Mufti, T. Schumacher, L. Martinelli, O. Lasri, H. Shenton, G. Chen, M. Noori, F. Raeisi, A. Silik, J. Dang, R. Hoensen, H. Li, N. Lu, Y.Q. Ni, I. Smith, Z. Wu, SCSHM benchmark study on bridge in-service structural monitoring, *Journal of Civil Structural Health Monitoring*, 15, 849–863, 2025.
- [10] D. Cantero, VBI-2D – Road vehicle-bridge interaction simulation tool and verification framework for Matlab, *SoftwareX*, 26, 101725, 2024.
- [11] D. Cantero, Z. Sarwar, A. Malekjafarian, R. Corbally, M.M. Alamdari, P. Cheema, J. Aggarwal, H.Y. Noh, J. Liu, Numerical benchmark for road bridge damage detection from passing vehicles responses applied to four data-driven methods, *Archives of Civil and Mechanical Engineering*, 24, 190, 2024.

# Physics-Informed Surrogate Modeling of the SCSHM Benchmark

Eray Temur<sup>1</sup> [0000-0002-7560-7101], Maria Pina Limongelli<sup>1</sup> [0000-0002-9353-5439]

<sup>1</sup>Politecnico di Milano, Department of Architecture, Built environment and Construction engineering, Piazza Leonardo da Vinci 32, 20133 Milan, Italy

email: eray.temur@polimi.it, mariagiuseppina.limongelli@polimi.it.

## EXTENDED ABSTRACT

**ABSTRACT:** This study presents a physics-informed surrogate modeling approach for the SCSHM Benchmark bridge using a dual-path LSTM Autoencoder architecture. By combining synthetic data from a finite element model and real strain measurements, the model effectively reconstructs structural responses under moving truck loads. Results show good agreement between predicted and measured strains. Limitations such as the absence of vehicle–structure interaction effects are discussed, with directions for future improvements.

**KEY WORDS:** Surrogate modeling, LSTM, SCSHM benchmark, structural health monitoring.

## 1 INTRODUCTION

This study presents preliminary results obtained using bridge strain data measured on the Society of Civil Structural Health Monitoring (SCSHM) bridge benchmark [1]. The benchmark dataset contains strain measurements and photos collected over nine months by strain gauges and a fixed camera during passages of heavy vehicles. A Finite Element (FE) model of the Benchmark is also made available together with the dataset. In this study, the FE model and the data have been utilized to build a surrogate model of the Benchmark structure.

Traditionally, FE models and detailed simulations have been employed to estimate the structural response with high-fidelity structural properties. While these models are accurate, they are computationally expensive. To address this challenge, surrogate models have emerged as an efficient alternative to approximate the structural response. Surrogate models in structural engineering have gained attention in applications such as response estimation, probabilistic assessment, and damage detection. Among data-driven methods, neural networks have demonstrated strength in capturing nonlinear mappings as well as learning from the data. Deep learning models have successfully predicted the response of the bridges subjected to dynamic train loads, demonstrating the potential of these models in emulating complex structural behavior [2]. Compared to traditional simulations, these models provide rapid and scalable analysis, which is particularly crucial for operational digital twins or near-real-time decision-making support systems.

In this context, Long Short-Term Memory (LSTM) networks have been an especially powerful tool to learn from time series data, thanks to their capabilities to capture long-term temporal dependencies in sequential data. LSTMs have been shown to work well in response prediction for bridge [3]. In addition to the capability to capture the long-term dependencies, LSTM Auto-Encoders (AE) learn an efficient representation of the input space by compressing and reconstructing data, enabling simultaneous learning and data compression. These fusion LSTM-AE models are ideal for surrogate modeling of bridge behavior under vehicle loading.

In this study, two parallel LSTM-AE architectures are combined and trained through strain simulated by the FE model and strain measured on the Benchmark. The architecture is

conditioned using specific physical conditions such as gross weight and velocity of the vehicles.

## 2 METHODOLOGY

The proposed methodology integrates physics-based finite element (FE) simulations with deep learning to accurately predict strain responses of a bridge under moving vehicle loads. A dual-path architecture is built, integrating two parallel LSTM-based Autoencoders (LSTM-AEs). The first is trained using strain responses obtained from a reduced-order FE model, and the second is trained on measured strain data. These parallel encoders are fused in a physics-informed manner to enable robust learning, even in the presence of sparse or noisy real-world measurements.

The reduced-order FE model of the bridge is created using the modal decomposition of mass and stiffness matrices derived from a high-fidelity FE model. Reduced matrices are then used in a state-space formulation to simulate the bridge's dynamic response under moving truck loads. The moving load is applied along the bridge using a defined vehicle path, velocity, and gross vehicle weight (GVW) estimated using the area method [4]. For unique combinations of GVW and velocity observed in the dataset, simulated time series are generated at specific sensor locations using the bending moment and structural geometry. These are then converted into macrostrain using the known strain gauge positions.

The proposed architecture consists of several key components: two parallel encoders, latent representations, conditions, and a decoder, as indicated in Figure 1. The first Encoder encodes the simulated strain signals into a latent representation. These synthetic signals are generated offline for each GVW-velocity pair, corresponding to the conditions observed in the real measurement dataset. The second Encoder encodes the measured strain data into a latent representation. The parameters GVW and vehicle velocity are used as inputs to the FE model and are inherently included in the real bridge measurements, since each truck has its own physical properties. They are also used as condition vectors, as they are fed into the decoder architecture. Finally, the decoder reconstructs the strain measurements using the combined latent representations from both the Encoders and the Condition Vector. The model is trained end-to-end to minimize the reconstruction error between the predicted and the actual measured strain time series.



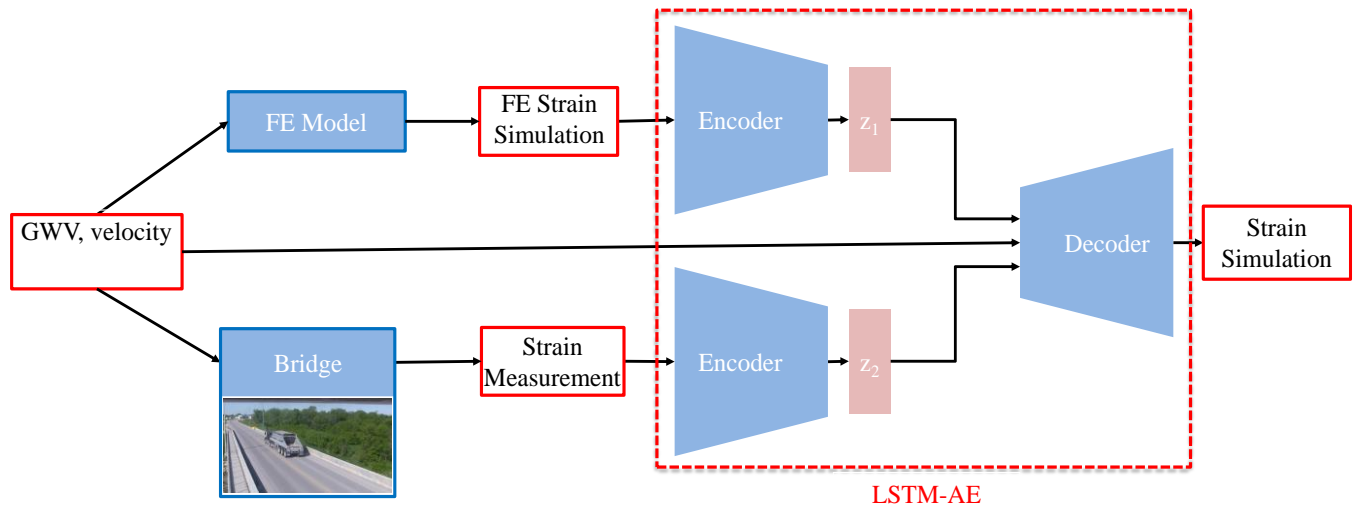


Figure 1. Flowchart of the proposed LSTM-AE architecture.

### 3 IMPLEMENTATION ON THE SCSHM BENCHMARK

The proposed methodology is implemented using strain data collected as part of the SCSHM bridge benchmark study [1]. The structure is a single-span, simply supported bridge with a length of 22.71 m, carrying two lanes. The selected bridge span is instrumented with 32 electric resistance strain gauges to monitor strains under the deck. Strain gages are placed at several cross-sections (end of spans, midspan, and  $\frac{3}{4}$  of the span) and different locations within each section. The dataset includes measurements recorded during controlled load tests as well as under normal traffic conditions. For this study, operational truck data is utilized due to its high volume and variability, which are essential for effectively training a deep learning-based architecture. To build the surrogate model, the structural responses measured by strain gauges located at the midspan section are selected. These midspan measurements are representative of the critical section where bending moments are typically maximal, making them well-suited for surrogate modeling.

Figure 2 and Figure 3 show the comparison between the predicted and measured strain time series at midspan gauges. They closely align both in shape and amplitude, showing that the model effectively learns the relationship between condition parameters and response evolution. Figure 2 illustrates the model's performance on the training set while Figure 3 on the testing set. The comparison highlights the ability of the LSTM to generalize to unseen data in the test set, where it maintains consistent accuracy even on condition pairs not explicitly encountered during training.

The proposed surrogate model integrating physics-informed simulations and measurement-based encoders via a dual LSTM Autoencoder architecture demonstrates good predictive performance in reconstructing bridge strain responses. Even though the model is trained using the full dual LSTM-AE architecture, only the trained latent representation and decoder, together with condition inputs, are used during prediction, providing a computationally efficient solution. Despite relying on a reduced portion of the architecture for prediction, which enhances computational efficiency, the model successfully

captures the dynamic characteristics of the structural response across varying vehicle loading scenarios.

However, it is worth noting that the current model does not account for the effect of the inertia of the moving vehicle, which may explain the absence of the fluctuations observed in the real measurement data. Neglecting this interaction can result in underestimation of transient strain fluctuations or increased scatter in the predicted responses. Therefore, this study should be considered as an initial attempt to build a surrogate model. The future work will focus on incorporating vehicle-bridge interaction into the simulation framework to enhance the fidelity.

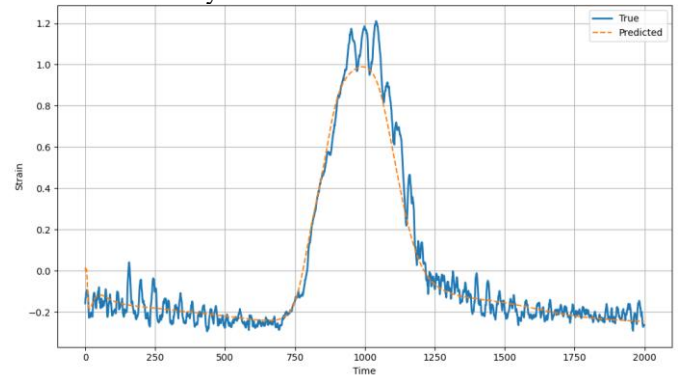


Figure 2. Strain prediction results for the training set.

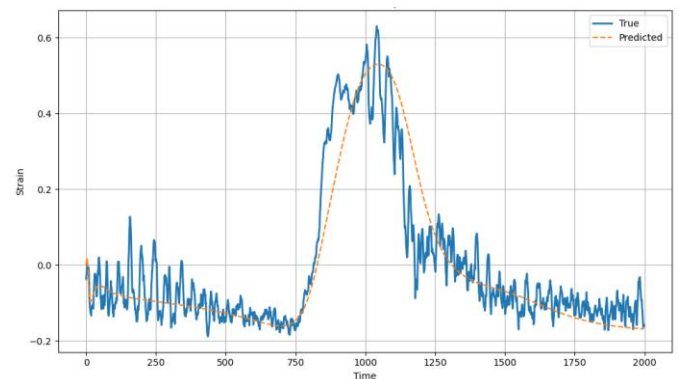


Figure 3. Strain prediction results for the validation set

## REFERENCES

- [1] M. P. Limongelli *et al.*, “SCSHM benchmark study on bridge in-service structural monitoring,” *Journal of Civil Structural Health Monitoring*, 2024, doi: 10.1007/s13349-024-00846-1.
- [2] A. Shajihan, K. Mechitov, G. Chowdhary, and B. F. Spencer Jr, “Physics-Informed Neural Network based Damage Identification for Truss Railroad Bridges,” Jan. 2025, *arXiv preprint arXiv:2502.00194*.
- [3] S. Tan, X. Ke, Z. Pang, and J. Mao, “Dynamic Response Prediction of Railway Bridges Considering Train Load Duration Using the Deep LSTM Network,” *Applied Sciences* 2024, Vol. 14, Page 9161, vol. 14, no. 20, p. 9161, Oct. 2024, doi: 10.3390/AP14209161.
- [4] K. Helmi, B. Bakht, and A. Mufti, “Accurate measurements of gross vehicle weight through bridge weigh-in-motion: a case study,” *Journal of Civil Structural Health Monitoring*, vol. 4, no. 3, pp. 195–208, 2014, doi: 10.1007/s13349-014-0076-5.

# Vibrational analysis of the benchmark data set

Douglas Thomson<sup>1</sup>

<sup>1</sup>Department of Electrical and Computer Engineering, University of Manitoba, Winnipeg, MB, R3T 5V6, Canada  
email: Douglas.Thomson@umanitoba.ca

**ABSTRACT:** Traffic induced vibration is a promising means of continuously monitoring structural behavior. The benchmark data set measures strain at points that will be subject to traffic induced vibration. However, magnitude and frequency spectrum of the induced vibration from an individual vehicle depends on many factors including the vehicle speed and axle weight distribution. Therefore, to obtain a spectrum that is representative the average vehicle induced vibration the vibration from many vehicles must be examined. In this work several methods for the analysis of the strain versus time data to extract traffic induced vibrational spectrums will be compared. Also, the number of vehicles that need to be analyzed to extract a repeatable vibrational spectrum will be examined. Typically, ~40-50 vehicles are needed to obtain a repeatable vibrational spectrum suitable to extract frequency peaks. This approach is used on the benchmark data set and changes in the vibration frequencies due to temperature induced structural changes can easily be observed. The temperature induced structural changes might be the basis training and testing data sets that could be used to evaluate the effectiveness of some damage detection algorithms.

**KEY WORDS:** SHMII-13; benchmark data, vibrational analysis, training data

## 1 INTRODUCTION

Structural vibrational analysis of bridges has been used for many purposes including structural assessment [1], damage detection [2], cable damping [2], damage detection in piers [3], girders [4], bearing restraint [5] and scour detection [6], [7], [8]. Vibrational analysis via moving test vehicles is also an exciting direction [9]. Vibrational analysis can be extracted from specialized instruments such as accelerometers and geophones, but can also be extracted from strain signals from strain gauges or strain sensors [10].

Some type of force must be applied to the structure in order to detect vibration of the structure. The excitation can be broadly classified as intentional or unintentional excitation. Intentional excitation can be in the form of hammers, dropped load, unbalance rotating shaft or known test vehicles. Unintentional excitation can be due to wind, water, ice impact or traffic. One advantage of unintentional sources is that they can excite the structure more or less constantly and allow for the continuous monitoring of the bridge. In this context, continuous means a time scale on the order of a fraction of a day. We can use the data from the benchmark data set to explore the sue of traffic induced vibration to extract vibrational information.

In this paper we examine the extraction of vibrational information from the benchmark data set. We examine alternative methods for the extraction of vibrational information from the strain versus time data in the benchmark data set. We examine the number of truck passages that are required to obtain a usable estimate of the vibrational frequencies of this bridge span. Suggestions for future vibrational analysis of this data set will also be given.

## 2 METHODS

### 2.1 Sampling strain versus time

The data being used is the individual truck sampled strain versus time data from the benchmark data set [11]. This publication contains the details of where the sensors were located and how the signals were sampled [11]. Briefly, the instrumentation was originally aimed to estimate the GVW of vehicles, investigate the transverse loading and to investigate the composite action in the structure. The span has two lanes and is 22 m long with 4 steel girders. An image of a truck passing over the girder is shown in Fig. 1.



Figure 1. Truck passing over the benchmark span.

The instrumentation included 32 electric resistive strain gages to monitor strains and six thermocouples to monitor air/structure temperature under the deck. The bridge was instrumented at six cross-sections.



The cross-section used in this work is the one located at midspan and has electrical resistance strain gauges (ESGs) were installed on the web of each girder to measure longitudinal strains at the top and bottom flanges, and at mid-height between the flanges. In this work only the strains near the bottom flange are used.

The data acquisition (DAQ) system features continuous strain sampling at 200 Hz, image collection for large events, data processing, and data transmission to a server. The strain data were filtered using a 7-point moving average window to remove electrical noise above 60 Hz.

The benchmark data set contains subsamples of the full data set. Each subsample was selected to contain the sampled strain versus time for a large truck. Each subsample contained 2000 sample points or about 10 seconds of sampled data. The data was selected such that the peak strain for the passing vehicle was in the center of the subsampled data.

An example of the sampled strain versus time is shown in Fig. 2A. In this plot the strains from each girder are offset by 20 microstrain per sensors so that the strain versus time behavior of each sensor can be easily observed. Before the passing of the vehicle there is no observable vibration. During and after the passage of the truck the vibration is clearly visible. After the truck leaves the span, during the period of free vibration without the weight of the truck, there are about 5 cycles per second [12]. This can be observed in the top strain versus time curve starting at about 6 seconds. Between 6 and 7 seconds there are about vibrational 5 cycles.

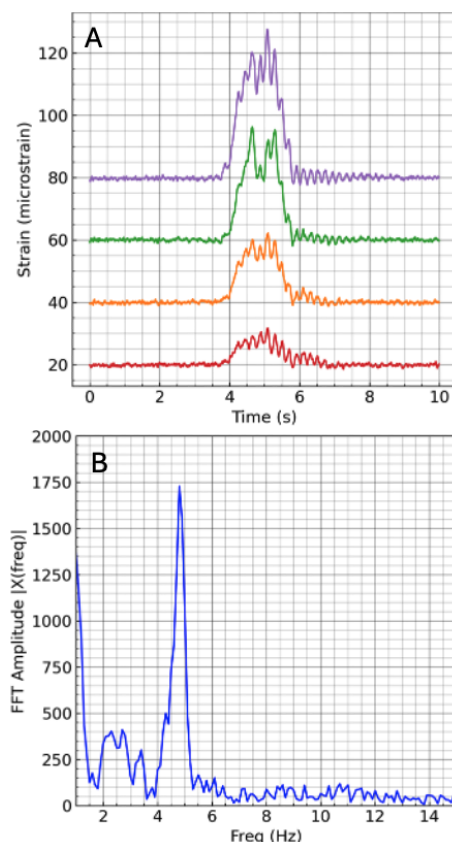


Figure 1. (A) Strains versus time for each of the 4 girders. (B) Spectrum of the strain. There is a vibrational peak at ~5Hz.

The strain versus time signals from the two outside girders were summed and then processed using an FFT from the Python numpy library. By using signals from the outside girders, vibration from trucks passing in both directions are captured. The outcome of the FFT analysis of Fig. 2A is shown in Fig. 2B. As expected, there is peak in the spectrum near 5 Hz. However, there is also considerable noise in the spectrum and the estimate of the peak position would have significant uncertainty. We will examine using averages of many such spectrums to improve the estimates of the vibrational frequency peaks. To do this N spectrums are averaged using a simple linear average. Using these initial estimates, a better estimate of the peak frequency was obtained by using a parabolic fit using two points lower and two points higher and the initial estimate. The peak of the parabola was then used as a refined estimate of the peak frequency. This means of estimating the peak position is computationally simple and produces a better estimate of the peak [13].

### 3 RESULTS AND DISCUSSION

There are several reasons why it may be necessary to use the average of vibrational spectrums from several trucks to obtain usable estimates of vibrational frequencies. When each truck passes it will preferentially induce vibration at certain frequencies. The frequencies that are preferentially excited will depend on factors like the velocity of the truck, the distance between axles, where the truck passes over the bridge and the vibrational properties of the truck.

An example of the variation in excited vibration is shown in Fig. 3(A) and 3(B). The two examples are passing at similar velocities with similar maximum strains. Both are traveling in the same direction. However, the induced vibration is not similar. In Fig. 3(A) during free vibration portion after the vehicle has left the span the vibration is largest on the side opposite the side on which the truck passed, in girder G4. After leaving the span the vibration on the girder nearest where the truck passed (G1), is much smaller and not observable. In contrast to this the in Fig. 3(B) the after the truck has passed and the girder is in the free vibration portion of the vibration the magnitude of vibration is roughly about the same in G1 and G4.

In Fig. 3(A) the vibration is torsional with one side moving and the other side nearly motionless. In Fig. 3(B) the vibration is more flexural with both sides moving up and down synchronously. The synchronous motion can be seen in Fig. 3(B) at 7 seconds where the strains in all the girders are at a maximum. In this example, for two similar trucks the mode of vibration is very different. It should be mentioned that these two examples were found within the first few trucks in the data set and did not require any extensive searching. Therefore, in general the vibration from a single truck may not excite all the modes of interest.

Using the benchmark data set, we can explore how many spectrums need to be considered by using stacked spectrum plots of the averaged spectrums. In these examples a simple linear average of spectrums is used. The numbers explored ranged from 40 to 200 spectrums. When less than 40 were used the number of misidentified vibrational peaks increased significantly. In Fig. 4(A) a stacked spectrum plot for an average of 200 spectrums is shown. In this plot each spectrum

is an average derived from 200 truck passages. Each peak is identified with a black plus sign. With 200 spectrums being averaged there are no misidentified peaks. For each spectrum there is a peak near 5 Hz and a second one from 10 to 12 Hz. The 10 to 12 Hz peak appears to be shifting from the averaged spectrum at the bottom to the averaged spectrum at the top.

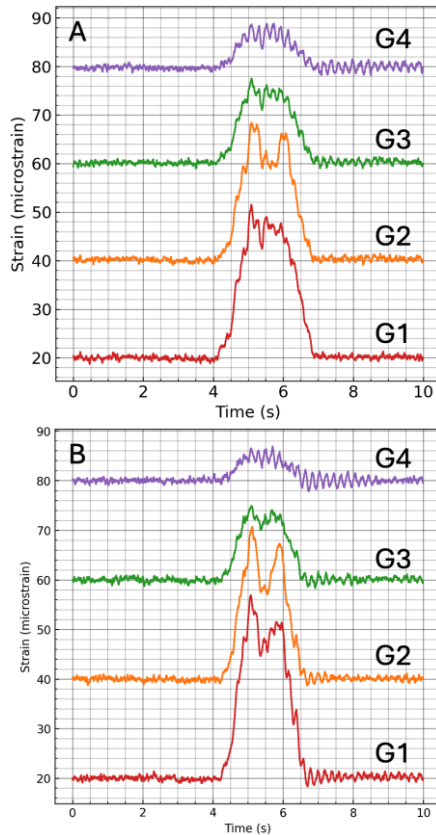


Figure 3. Strains versus time for the four girders. Fig. 3A is an example of asymmetric vibration. Fig. 3B is an example of symmetric vibration.

Each truck in the data set has a unique number from 0 to ~ 3300. As the truck number increases so does the date on which the data was acquired. Truck 0 was taken during a mid-winter cold period. By the time truck 3300 was taken it was mid-summer. The spectrums are arranged sequentially in number and therefore time. The bottom spectrum was from a colder period and the top one from a warmer period. The shift in frequencies is attributed to temperature effects. Therefore, the results of the peak frequency estimates have been plotted versus temperature.

In Fig. 4(B) 50 averages are used. The same two vibrational peaks are identified in most of the averaged spectrums. However, several misidentified peaks are also being identified due to the decreased signal to noise. Perhaps this could be improved with enhanced signal processing.

These same plots are done as colorized waterfall plots in Fig. 5 that help make the 10 to 12 Hz peak more easily observable. The change in the 10 to 12 Hz peak with the seasonal temperature changes is now clearly observable.

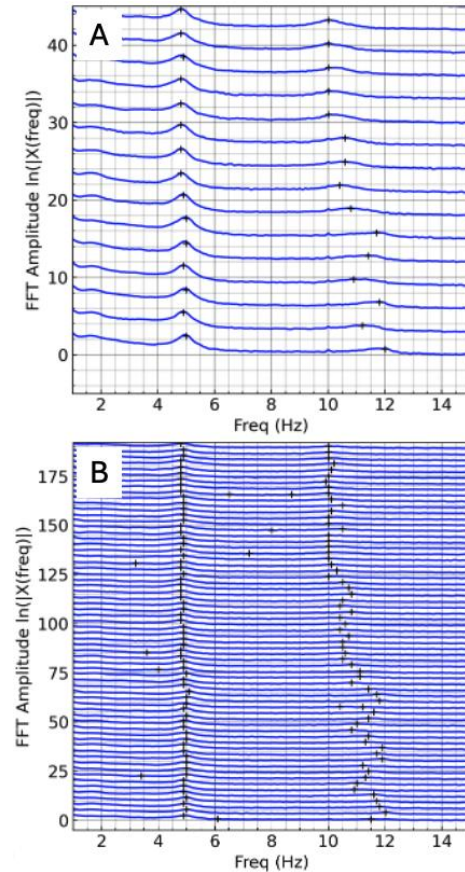


Figure 4. Waterfall vibration spectrum plots for averages of 200 trucks (A) and 50 trucks (B).

The correlation with temperature can be plotted more directly as each spectrum has also has an associated temperature. If we plot the average temperature of each average spectrum against the identified vibrational frequency the correlation is easily identified. In Fig. 6 this has been done for averages of 40, 50 and 200 averages. The peak frequencies are highly correlated with temperature. Although there may be other environmental effects coming into play over this season, temperature would appear to be the dominate influence. Principle component analysis could be used to quantify the effects of temperature versus the time of year. Also, as the number of averages drops below 40 the proportion of misidentified peaks increases rapidly.

Using motion sensors mounted on test vehicles to extract structural vibrational properties as the vehicle passes over the structure is an interesting approach for monitoring fleets of bridges [9]. For this field to advance large data sets of simulated and field observations are needed. Simulated data sets have been created [14]. It might also be possible to create field observation from the benchmark data set. The strain is directly related to displacement and therefore acceleration can also be calculated. Comparing cold and warm weather results would be a good test of damage detection using vehicle derived responses. Another potentially useful case would be if one wanted to simulate the use of a sensor trailer to measure the free vibration [15].

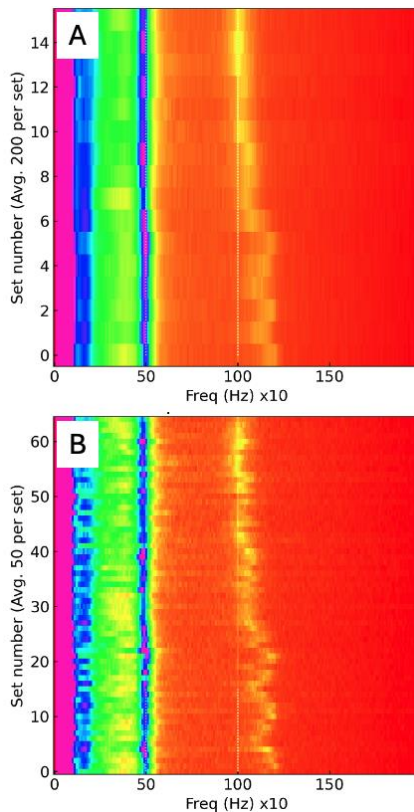


Figure 5. Waterfall vibration spectrum plots for averages of 200 trucks (A) and 50 trucks (B).

Whether or not a damage detection algorithm can detect damage using actual field derived data is often an open question. Only rarely do owners allow full scale structures to be damaged so that actual field responses before and after damage can be obtained [3]. However, temperature changes often lead to significant structural changes due to effects such as due to bearing restraint [5]. A first step towards testing damage detection algorithms could be the detection of temperature induced structural changes. Due to the temperature change over the observation period in the benchmark data set there are also significant easily observable structural changes. Evidence for this is the frequency change seen in Fig. 6B, for example. In order, for the frequency to change there must be some significant structural change. The temperature induced structural changes can also be easily observed in the girder distribution factors. Therefore, the data set could be divided into “good” and “damaged” data sets using temperature as a means of sorting. Here the “damaged” set would not correspond to actual structural damage but would have significant structural differences from the “good” data set. For example, trucks 2300 to 3300 could be chosen as the “good” data set and used to train an algorithm. Trucks could then be chosen to test a detection method. Trucks with larger temperature differences compared to the “good” set would have larger structural differences. This provides a means to quantitatively test detection algorithms. One could argue that these only tests detection of a particular type of structural change. However, this change does include changes in girder distribution factors, which are one of the common reasons bridge load ratings are reduced [16].

The benchmark data set also includes strains from multiple sections and it might also be possible to also extract vibrational mode shape information.

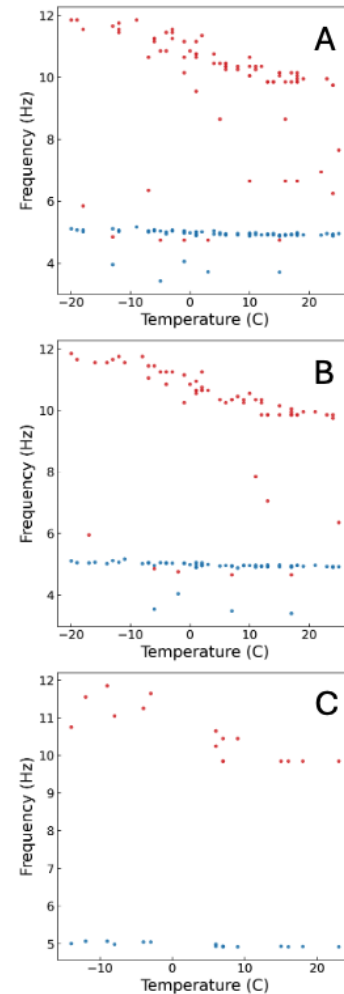


Figure 6. Plots of frequency peaks for averages of 40 trucks (A), 50 trucks (B) and 200 trucks (C).

#### 4 CONCLUSIONS

The sampled strain data from the benchmark data set can be used to extract vibrational frequency spectrums. The passages from several trucks need to be averaged to extract consistent vibrational peaks. Typically, 40 to 50 trucks are required. Temperature induced changes in the vibrational peaks can easily be observed. The temperature induced structural changes might be the basis training and testing data sets that could be used to evaluate the effectiveness of some damage detection algorithms.

#### ACKNOWLEDGMENTS

The Province of Manitoba for their financial and intellectual support of this work.

#### REFERENCES

- [1] Munzer Hassan and Olivier Burdet and Renaud Favre, “Interpretation of 200 Load Tests of Swiss Bridges,” pp. 319–326, 1993.
- [2] K. Y. Koo, J. M. W. Brownjohn, D. I. List, and R. Cole, “Structural health monitoring of the Tamar suspension bridge: TAMAR



- BRIDGE,” *Struct. Control Health Monit.*, vol. 20, no. 4, pp. 609–625, Apr. 2013, doi: 10.1002/stc.1481.
- [3] D. M. Siringoringo, Y. Fujino, and T. Nagayama, “Dynamic Characteristics of an Overpass Bridge in a Full-Scale Destructive Test,” *J. Eng. Mech.*, vol. 139, no. 6, pp. 691–701, Jun. 2013, doi: 10.1061/(ASCE)EM.1943-7889.0000280.
  - [4] J. R. Casas and J. J. Moughy, “Bridge Damage Detection Based on Vibration Data: Past and New Developments,” *Front. Built Environ.*, vol. 3, Feb. 2017, doi: 10.3389/fbuil.2017.00004.
  - [5] Y. Fu and J. T. DeWolf, “Monitoring and Analysis of a Bridge with Partially Restrained Bearings,” *J. Bridge Eng.*, vol. 6, no. 1, pp. 23–29, Feb. 2001, doi: 10.1061/(ASCE)1084-0702(2001)6:1(23).
  - [6] T. Bao, Z. L. Liu, and K. Bird, “Influence of soil characteristics on natural frequency-based bridge scour detection,” *Journal of Sound and Vibration*, vol. 446, pp. 195–210, Apr. 2019, doi: 10.1016/j.jsv.2019.01.040.
  - [7] C.-C. Chen, W.-H. Wu, F. Shih, and S.-W. Wang, “Scour evaluation for foundation of a cable-stayed bridge based on ambient vibration measurements of superstructure,” *NDT & E International*, vol. 66, pp. 16–27, Sep. 2014, doi: 10.1016/j.ndteint.2014.04.005.
  - [8] N. Boujia, F. Schmidt, C. Chevalier, D. Siegert, and D. Pham Van Bang, “Effect of Scour on the Natural Frequency Responses of Bridge Piers: Development of a Scour Depth Sensor,” *Infrastructures*, vol. 4, no. 2, p. 21, May 2019, doi: 10.3390/infrastructures4020021.
  - [9] Y. B. Yang and J. P. Yang, “State-of-the-Art Review on Modal Identification and Damage Detection of Bridges by Moving Test Vehicles,” *Int. J. Str. Stab. Dyn.*, vol. 18, no. 02, p. 1850025, Feb. 2018, doi: 10.1142/S0219455418500256.
  - [10] J. A. Laman and A. S. Nowak, “Load Distribution and Impact Factors for I-Girder Bridges,” *J. Bridge Eng.*, vol. 4, no. 4, pp. 289–290, Nov. 1999, doi: 10.1061/(ASCE)1084-0702(1999)4:4(289).
  - [11] M. P. Limongelli *et al.*, “SCSHM benchmark study on bridge in-service structural monitoring,” *J Civil Struct Health Monit.*, vol. 15, no. 3, pp. 849–863, Mar. 2025, doi: 10.1007/s13349-024-00846-1.
  - [12] D. Cantero, D. Hester, and J. Brownjohn, “Evolution of bridge frequencies and modes of vibration during truck passage,” *Engineering Structures*, vol. 152, pp. 452–464, Dec. 2017, doi: 10.1016/j.engstruct.2017.09.039.
  - [13] E. Rivera and D. J. Thomson, “Accurate strain measurements with fiber Bragg sensors and wavelength references,” *Smart Materials and Structures*, vol. 15, no. 2, pp. 325–330, 2006, doi: 10.1088/0964-1726/15/2/012.
  - [14] D. Cantero *et al.*, “Numerical benchmark for road bridge damage detection from passing vehicles responses applied to four data-driven methods,” *Arch. Civ. Mech. Eng.*, vol. 24, no. 3, p. 190, Jul. 2024, doi: 10.1007/s43452-024-01001-9.
  - [15] Y. Yang, H. Lu, X. Tan, H. K. Chai, R. Wang, and Y. Zhang, “Fundamental mode shape estimation and element stiffness evaluation of girder bridges by using passing tractor-trailers,” *Mechanical Systems and Signal Processing*, vol. 169, p. 108746, Apr. 2022, doi: 10.1016/j.ymssp.2021.108746.
  - [16] S. F. Breña, A. E. Jeffrey, and S. A. Civjan, “Evaluation of a Noncomposite Steel Girder Bridge through Live-Load Field Testing,” *J. Bridge Eng.*, vol. 18, no. 7, pp. 690–699, Jul. 2013, doi: 10.1061/(ASCE)BE.1943-5592.0000398.



# SHM of Tall and Historic Buildings

# Study of Semi-Rigid Joints Effect on Global Stiffness of Space Steel Structure Based on Monitoring Data

Cheng Yuan<sup>1</sup>, Wei Lu<sup>1</sup>, Jun Teng<sup>1</sup> and Weihua Hu<sup>1</sup>

<sup>1</sup>Harbin Institute of Technology, Shenzhen, 518071, China

email: Chengyuan@hit.stu.edu.cn, Lu.wei@hit.edu.cn, tengj@hit.edu.cn, huweihua@hit.edu.cn

**ABSTRACT:** In conventional structural design and analysis of space steel structures, joints are typically idealized as either perfectly hinged or fully rigid connections. However, actual joint behavior deviates significantly from these idealized assumptions, with joint stiffness exhibiting semi-rigid characteristics that critically affect global structural performance. This discrepancy between simplified joint models and real-world conditions leads to substantial errors in predicting structural stiffness through numerical simulations. This paper presents a novel methodology integrating structure health monitoring with refined finite element (FE) modeling to quantify the semi-rigid joints effect on global stiffness space steel structure. The joint stiffness parameters are inversely identified through stress and deformation monitoring data using Bayesian inference techniques; A multi-scale FE model incorporating semi-rigid joint behavior is developed through component-level validation; The stiffness evolution mechanism is rigorously validated against full-scale monitoring data from the Shenzhen Nanshan Science-Technology Innovation Center's space frame during its service period. Key findings demonstrate that joint flexibility reduces global stiffness by 18-22% compared to rigid-joint assumptions, with stiffness degradation rates showing strong correlation to stress redistribution patterns. The proposed joint-characterization framework provides a physics-based approach for tracking long-term stiffness evolution in space steel structures, offering significant improvements over conventional design methods in both accuracy and predictive capability.

**KEY WORDS:** Semi-Rigid Joints, Space Steel Structure Stiffness, Structure Health Monitoring.

## 1 INTRODUCTION

Structural connection joints are the critical components of space steel structures, which are subject to complex forces and are sensitive to defects. The mechanical properties and stress of the joints not only affect the safety of the joint itself but also have an influence on the stress distribution and deformation of the overall structure.

In China's "Code for Design of Steel Structures", it is stipulated that the truss and the space frame should be analyzed according to the hinge connection, while the single-layer space shell should be processed according to the rigid connection [[1]]. However, more and more engineering projects show that ideally hinged joints often have certain rigidity, while ideal rigid joints also have certain flexibility. The research work of Grogan [[2]] and Wheelar [[3]] show that neither completely rigid nor hinged joint exist in reality. The uncertainty of joint stiffness is mainly caused by the following factors. The structure discontinuity of the structure. The bolts are not tightened between the nodes and members connected by bolts, which leads to insufficient stiffness of the joints. The structure has defects. Due to geometric defects such as dislocation or slippage between components and nodes during installation, or physical defects such as cracks, the stiffness of joints decreases. The structure is deteriorating in its service life. The structure is affected by fatigue and corrosion, which leads to the deterioration of the joints.

The research on joint stiffness has received extensive attention in recent years. The "specification for structural steel structure" edited by AISC pointed out that the connection joints of steel structures should be divided into three situations, namely ideal

simple connection, fully restrained moment connections and partially restrained moment connections [[4]]. The Eurocode 3 also has a description similar to that in the AISC code, which divides the joints into three types: rigid, semi-rigid and hinged [[5]]. Although the Eurocode 3 and AISC code mention the general classification standards of three types of joints, there is no relevant description on how the stiffness of semi-rigid joints is determined, and how the attenuation of joint stiffness will affect the overall structure's stiffness.

The existing research mainly contains three methods for calculating the value of joint stiffness which are numerical simulation, laboratory specimen test and mathematical statistics. Liu [[6]] used Abaqus to model the pin joints to analyze their stiffness, and Cao [[7]] used Ansys to model the network frame joints to analyze their stiffness. The numerical simulation of joint stiffness is convenient, but the premise assumptions of material properties and connection methods used in finite element simulation may be different from the actual states of joints in reality. Liao [[8]] obtained the load-displacement curve of the joint by making a scaled model in the laboratory for loading, and then calculated the joint stiffness data. However, the scaled model cannot reflect the actual stress state of the full-scale structure. Frangopol [[9]] obtained the probability distribution curve of the deterioration degree of the connection joints of steel truss bridges by analyzing the test report data of a large number of bridges by means of mathematical statistics. However, there are certain regional differences in this method. The degree of corrosion and deterioration of steel structures under different climatic environments is significantly different. The probability



distribution cannot determine the change trend of joint stiffness of a specific structure.

In conclusion, there are premise assumptions for numerical simulation, differences between the scaled model and the full-scale structure for laboratory test, and regional differences in mathematical statistical analysis. In this paper, the field monitoring data of structural stress and displacement are obtained based on Nanshan Science and Technology Innovation Center monitoring project through stress sensors and prisms. The stiffness of the joints of steel truss are obtained by inversion of the monitoring data of stress and displacement by the deflection method. The updated joint stiffness is substituted into the finite element model. The influence of the joint stiffness on the overall stiffness of the structure is studied through the updated finite element model.

## 2 JOINT STIFFNESS CALCULATION

### 2.1 Joint Stiffness Calculation Method

The stiffness of the joints is calculated by the deflection method. The total beam deflection comprises two constituent parts: one part is the deflection caused by the ideal elastic deflection of the beam; the second part is the displacement of a point on the beam caused by the deformation of the joint, as shown in Fig. 1.

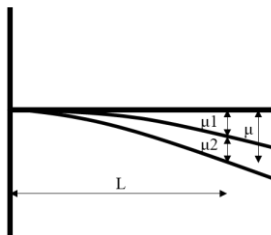


Figure 1. General view of deflection method

$\mu_1$  is the deflection of the ideal elastic deflection line of the beam at this point.  $\mu_2$  is the displacement at this point due to the deformation of the joint.  $\mu$  is the real deflection of the point, and  $L$  is the distance from the point to the joint.  $\mu$  can be calculated as:

$$\mu_1 + \mu_2 = \mu \quad (1)$$

The angle of downward deflection at the joint can be calculated as:

$$\theta_r = \frac{\mu}{L} = (\mu_1 + \mu_2)/L \quad (2)$$

In this project,  $\mu$  is obtained by prism observation in field monitoring, and  $\mu_1$  is obtained by linear elastic simulation with finite element software. The joint stiffness  $K_j$  can be calculated as:

$$K_j = M / \frac{(\mu - \mu_1)}{L} \quad (3)$$

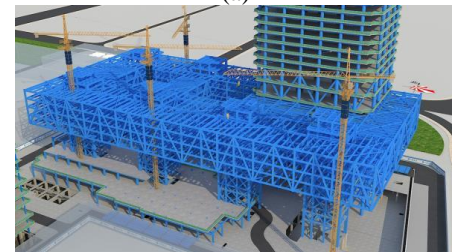
$M$  in formula (3) is the bending moment of the joint, which is obtained by finite element simulation.

### 2.2 Joint Stiffness calculation Results

Shenzhen Nanshan Science and Technology Innovation Center includes seven towers (A1-A7) and a huge podium surrounding the towers. The steel structure of the podium is located on the 7th to 11th floors, as shown in Fig. 2. The steel structure of the podium consists of a large span truss and a cantilevered truss structure.



(a)



(b)

Figure 2. Shenzhen Nanshan science and Technology Innovation Center. (a) completed structure rendering and (b) construction process

The typical joint of the large span steel truss of the podium of Nanshan Science and Technology Center is shown on Fig. 3. The joints and the members are connected by welding.



(a)



(b)



(c)

Figure 3. Typical joint (a) Joint model. (b) diagonal web is being welded to the bottom joint. (c) The installation of truss between A4-A5 is completed.

In this project, the vibrating wire stress sensor is used to monitor the stress of the structure. The prism and electronic total station are used to monitor the displacement of the structure. In this paper, the displacement monitoring data is used to calculate the real stiffness of the structure, and the stress monitoring data is used to verify the validity of the finite element model after updating the joint stiffness.

The stress sensors and prisms have been installed on the large-span trusses connecting the core tubes A1, A2, A4, and A5, and the stress and displacement of the structure at the current construction stage have been monitored. The positions of stress sensors and prisms are shown in Fig. 4.

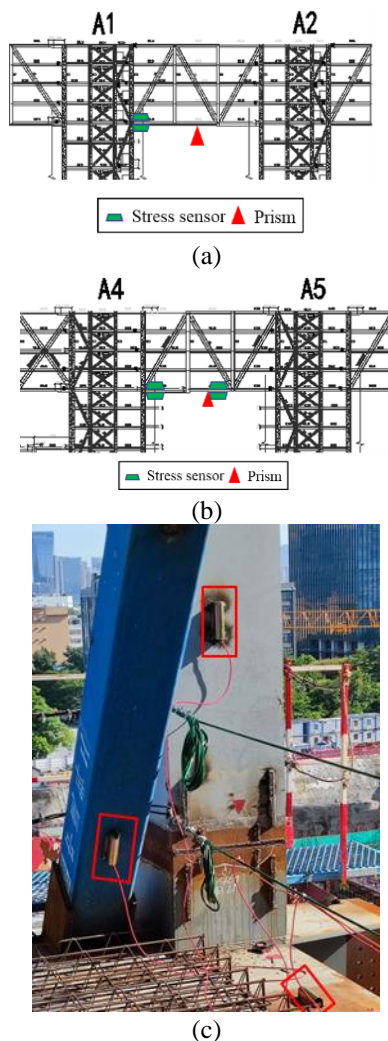


Figure 4. Stress sensors and Prisms on truss. (a) truss between A1-A2, (b) truss between A4-A5 and (c) sensor installation diagram (in red box)

The finite element analysis of the current phase of the structure was performed using Midas Gen, and the truss members were modeled as beam elements. The mid-span deflection of the lower chord and the bending moment at both ends of the lower chord of the large-span truss between A4 and A5 are calculated

only considering the self-weight load of the structure. The vertical displacement diagram and the stress diagram of the truss is shown in Fig. 5.

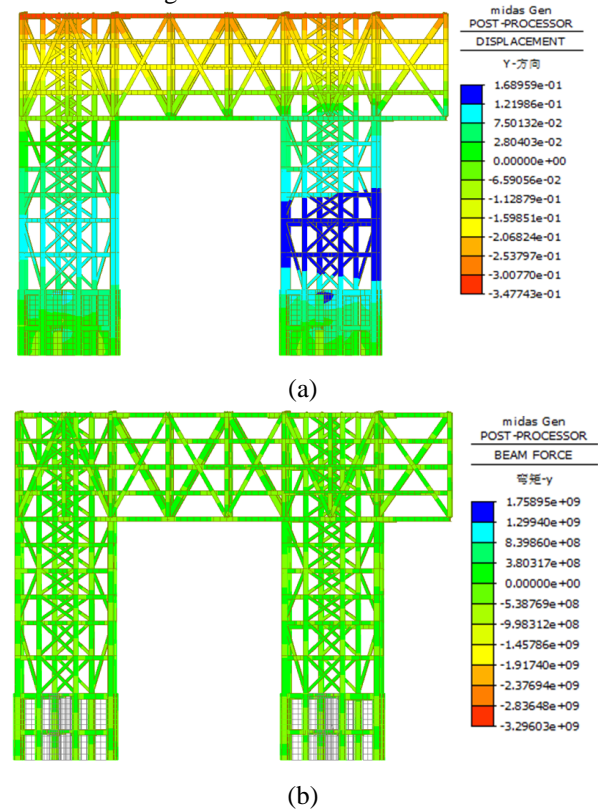


Figure 5. Finite element simulation. (a) vertical displacement diagram. (b) Stress diagram.

The deflection  $\mu_1$  produced by ideal elasticity at the mid-span of the large-span truss (the triangle mark in the figure) is extracted from Fig. 5. The bending moments  $M$  of joint L and R are extracted from Fig. 6 (b). and midspan deflection  $\mu$  of the truss between A4-A5 is 6 mm based on field monitoring data. The stiffness of joint L and R are calculated based on formula (3) and results are shown in Table 1.

Table 1. Joint stiffness results.

	Joint L	Joint R	Calculation method
$\mu$ (mm)		6	Monitoring data
$\mu_1$ (mm)		2.6	Finite element
$\theta_r$ (rad)	$3.96 \times 10^{-4}$	$3.96 \times 10^{-4}$	Formula (2)
$M$ (kN*m)	110.7	80.7	Finite element
$K_j$ (kN*m/rad)	$4.94 \times 10^5$	$3.60 \times 10^5$	Formula (3)

### 3 EFFECT ON GLOBAL STIFFNESS

#### 3.1 Updating of Joint Stiffness

According to the calculation results shown in Table 1, the previous rigid joint is updated with the stiffness  $4.94 \times 10^5$

kN\*m/rad,  $3.60 \times 10^5$  kN\*m/rad and  $4.27 \times 10^5$  kN\*m/rad (average of joint L and joint R).

The bottom joints of the web members of the trusses connecting A1-A2, A1-A4 and A4-A5 are updated with new stiffness. The joint locations for the updated stiffness are shown in Fig. 6. Twelve joints of the web members have undergone stiffness updates. The method of joint stiffness updating is to replace the original rigid joints in structural model with spring beams with springs at both ends.

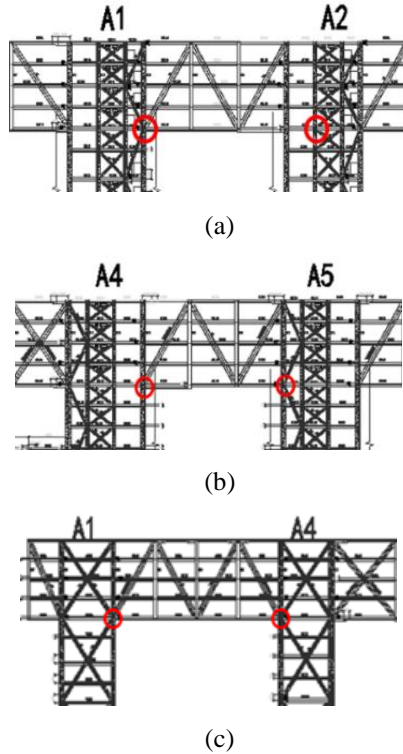


Figure 6. Positions of joints for stiffness updating. (a) truss A1-A2. (b) truss A4-A5. (c) truss A1-A4

### 3.2 Finite Element Model Verification

Five cases of joint stiffness cases are being simulated using finite element method which are rigid,  $4.94 \times 10^5$  kN\*m/rad,  $4.27 \times 10^5$  kN\*m/rad,  $3.60 \times 10^5$  kN\*m/rad and pinned. The load on the structure only considers the self-weight load. The remaining cases are simulated in the same way. The structural stress obtained from the finite element simulation is compared with the structural stress obtained from the field monitoring data to verify the model with updated joint stiffness.

The joint stress at the same position of the monitoring point is extracted from the structural stress diagram for comparison. The location of measuring points for structural monitoring is shown in Fig. 4. The comparison between the simulation results and the monitoring data is shown in Fig. 7.

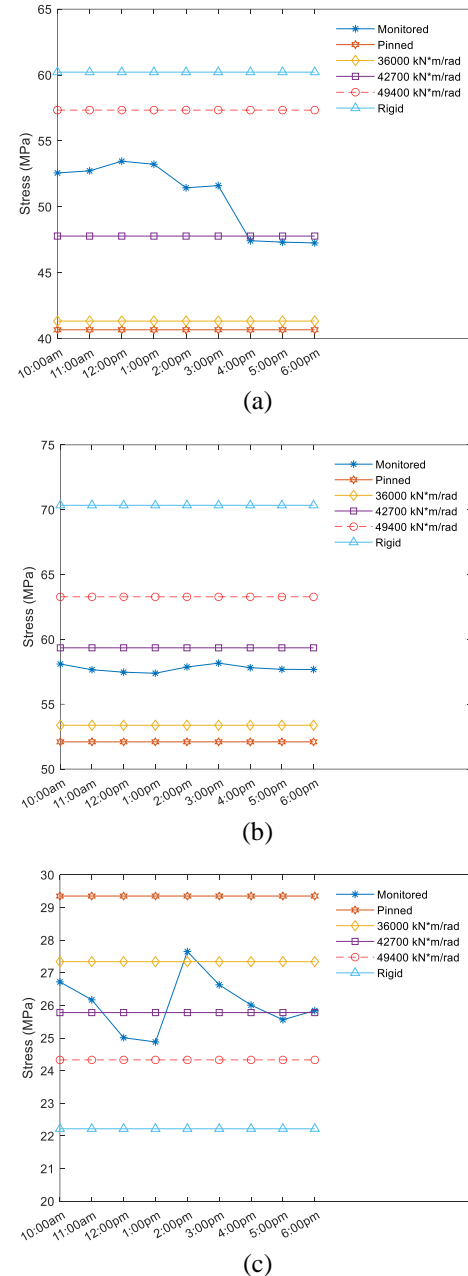


Figure 7. Comparison between the simulation results and the monitoring data. (a) stress at end of truss between A1-A2, (b) stress at end of truss between truss A4-A5 and (c) stress at midspan of truss A4-A5.

The following conclusions can be drawn from the comparison between monitoring data and simulated data in Fig. 7. The stress data simulated by the semi-rigid joint model are closer to the structural monitoring data. Among them, the model stress value after joint stiffness update with the average stiffness of joint L and joint is the closest to the monitoring data. This indicates that this stiffness is the closest approximation to the true stiffness of the bottom joint of the web member of the truss.

### 3.3 Effect of Joint Stiffness on Global Stiffness of Structure

According to the results in 3.2, it is considered that  $4.27 \times 10^5$  kN\*m/rad is the true stiffness of the bottom joint of the web member of the large-span truss. Apply different vertical



uniform loads to the structure and draw the load-deflection curves of the large-span trusses A4-A5. The load-deflection curves of the ideal rigid joint, semi-rigid joint and ideal hinged joint model are compared in Fig. 8.

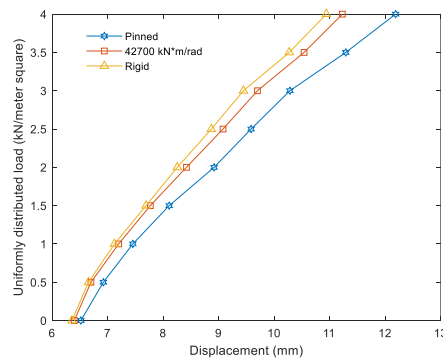


Figure 8. A4-A5 truss load-displacement curve.

It can be seen from Fig. 9. that the vertical stiffness of the ideal rigid joint model is the largest, followed by the semi-rigid joint model, and the vertical stiffness of the hinge joint model is the smallest. The truss load-deflection curves of the ideal rigid joint, semi-rigid joint and ideal hinged joint model are linearly fitted, and the slope of the load-deflection curve is the vertical stiffness of the A4-A5 large-span truss. The calculation results show that the vertical stiffness of the semi-rigid joint truss is 5.4% lower than the rigid joint model and 13.4% higher than the pinned joint model.

The mode shapes of the structure has been simulated to analysis the joint effect on global stiffness of the structure. The first-order mode is translation in the x-direction (parallel to the A1-A2 direction), the second-order mode is translation in the y-direction (parallel to the A1-A4 direction), and the third-order mode is translation in the x-direction. The mode shapes of the structure show in Figure 9. The frequency of the structure with different joint stiffness is shown in Table 2.

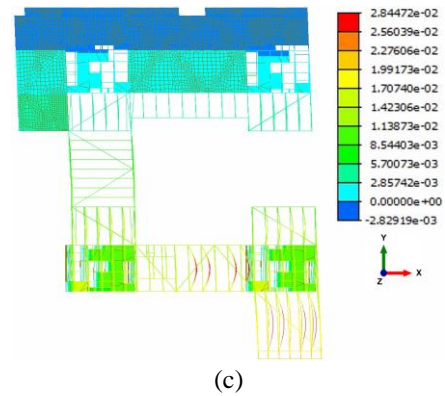
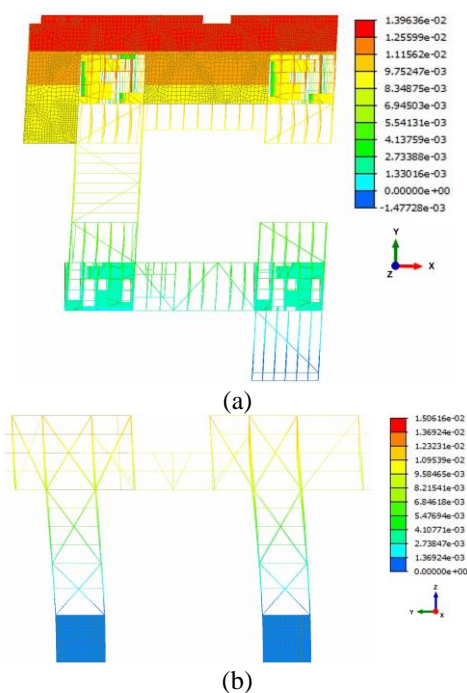


Figure 5. Mode shapes of the structure. (a) first order, (b) second order and (c) third order

Table 2. Frequency of the structure.

Mode order	Frequency (Hz)		
	Rigid joints	Semi-Rigid Joints	Pinned Joints
1	1.3369	1.2366	1.2256
2	1.4826	1.2823	1.2358
3	1.7203	1.3199	1.2286

The mode shape simulation result shows that natural frequency of the structure decreases as the joint stiffness reduces. Since frequency can reflect the stiffness of the structure, the result also tells that joint stiffness can strongly affect the global stiffness of the structure.

#### 4 CONCLUSION

The effect of joint stiffness on overall structure is studied in this paper. The influence of the stiffness characteristics of the joints at the end of the truss and the mid-span of the truss are different. For the joints at the end of the truss, the stress of the semi-rigid joint is larger than that of the hinged joint and smaller than that of the rigid joint; For the joints at the midspan of the truss, the stress of the semi-rigid joint is smaller than that of the hinged joint and greater than that of the rigid joint. The semi-rigid joint is most consistent with the field monitoring data. The load-deflection curve of the large-span truss is simulated, and the results show that the vertical stiffness of the truss of the semi-rigid joint model is 5.4% lower than that of the ideal rigid joint model and 13.4% higher than the hinged joint model. The conclusions of this paper can be references for other steel structure analysis.

#### ACKNOWLEDGMENTS

This work was supported by the National Natural Science Foundation of China [grant numbers 52122804, 51978214, 51878226], the National Major Scientific Research Instrument Development Program of China [grant number 51827811], and the Fundamental Research Funds for the Central Universities [grant number HIT.BRET.202101]. Xianwei Fang, Yizhan He, Hetia Shao and Jiayi Zheng assisted measuring the field monitoring data, which contributes a lot to this paper.

## REFERENCES

- [1] Design: Code for design of steel structures. National standard of the People's Republic of China GB\_50017-2003, 2003.
- [2] W. Grogan and J. Surtees, Experimental behavior of end plate connections reinforced with bolted backing angles. *Journal of Constructional Steel Research*, 50(1), 71-96, 1999.
- [3] A. T. Wheeler, M. J. Clarke and G. J. Hancock, Tests of bolted flange plate connections joining square and rectangular hollow sections. 40(1), 97-104, 1995.
- [4] Design AS.: Specification for structural steel buildings. AISC, December. 1999 Dec;27.
- [5] D. Beg, U. Kuhlmann, L. Danaine, B. Braun, Design of plated structures: Eurocode 3: Design of steel structures, part 1-5: Design of plated structures. John Wiley & Sons; 2012.
- [6] Y. X Liu, Structural construction response tracking method considering the stiffness of nodes. Master Thesis, 2022.
- [7] Z. G. Cao, L. Zheng, Z. Lin, Z. H. Li, Y. Sun, Influence of joint stiffness defects on stability of cylindrical cable-stiffened latticed shells. *Journal of Harbin institute of technology*. 54 (4), 118-123, 2022.
- [8] M. H. Liao, C. S. Guan, Finite element analysis on unloading construction of temporary support frame for curved steel structure roof. *The World of Building Materials* 39 (5), 55-57, 2018.
- [9] D. M. Frangopol, J. S. Kong, and E. S. Gharaibeh, Reliability-based life-cycle management of highway bridges. *Journal of Computing in Civil Engineering* 15(1), 27-34, 2001.

# Sustaining vertical giants: Autonomous monitoring solutions for the construction and lifecycle of tall buildings

Lidija Špiranec<sup>1</sup>

<sup>1</sup>Leica Geosystems AG, Heinrich-Wild-Strasse, 9435 Heerbrugg, Switzerland  
email: lidija.spiranec@leica-geosystems.com

**ABSTRACT:** As urban environments increasingly shift towards vertical development, the challenges associated with constructing and maintaining tall buildings have intensified. Real-time and dynamic monitoring systems play a vital role in addressing these issues by providing accurate positioning and deformation data. The integration of diverse monitoring technologies during and after the construction of high-rise buildings is crucial for ensuring structural integrity, safety, and efficiency.

By combining geodetic and geotechnical monitoring techniques, these systems offer comprehensive insights into building behaviour. The fusion of technologies like GNSS, IoT sensors, and remote sensing, alongside traditional survey methods, ensures precise data acquisition and analysis. This hybrid approach is essential for optimising construction and maintenance processes, reducing costs, and enhancing safety. Furthermore, the ability to process and analyse large volumes of monitoring data efficiently is critical for transforming raw data into actionable insights, aiding decision-makers in understanding the magnitude and direction of structural movements.

The successful implementation of these monitoring techniques on iconic high-rise buildings, such as the Burj Khalifa and One World Trade Center, highlights their importance in modern construction and post-construction maintenance. Ultimately, the intelligent use of integrated monitoring technologies supports sustainable and resilient urban development.

**KEY WORDS:** Autonomous; Deformation monitoring; Verticality; Positioning; High-rise; Tall buildings.

## 1 INTRODUCTION

In the rapidly evolving urban landscape, the shift towards constructing tall buildings presents unique challenges that demand innovative solutions. Ensuring the structural integrity and safety of these vertical giants requires advanced positioning and deformation monitoring technologies capable of delivering real-time and precise data on buildings' behaviour.

Environmental forces such as wind and temperature variations can lead to significant deformation during construction, therefore precise measurements are required to maintain vertical alignment and correct positioning. Traditional surveying methods, while effective at lower elevations, often reach their limits as buildings rise, necessitating the adoption of advanced active survey control systems.

In the lifecycle phase, the safety and integrity of tall buildings can again be at risk in case of nearby excavations or movements caused by natural events. In such cases, deformation monitoring is essential, to provide an understanding of structural behaviour.

In both phases of the building's timeline, deformation monitoring information is crucial for decision-makers.

## 2 CONSTRUCTION OF TALL BUILDINGS

### 2.1 Surveying challenges

Constructing tall buildings introduces a range of complex and unique surveying challenges primarily due to their height and slender profiles, which significantly alter the structure's rigidity compared to low-rise buildings. As the geometry shifts from a wide base to a narrow top, resistance to deformation decreases,

necessitating precise engineering surveying and monitoring systems to maintain vertical alignment and correct positioning. As depicted in Figure 1, environmental forces such as wind loads can cause deflection, varying with the stiffness of different elements and the location on the building. Temperature changes and sunlight can lead to uneven thermal expansion, causing the building to lean. Additionally, as construction progresses, the increasing mass leads to the compression of lower elements, potentially resulting in differential settlement and vertical alignment issues. This requires adjustments to the vertical datum to account for axial shortening and ensure the final height meets specifications.

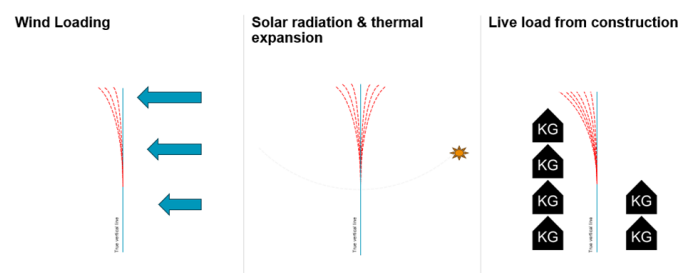


Figure 1 Environmental forces and live load impacting tall buildings [1]

Dimensional control is crucial for each floor's horizontal and vertical alignment, involving traditional survey methods like optical levelling, plumb line and total stations. These methods establish base gridlines at stable ground levels, with new references created as construction progresses. However, maintaining uninterrupted vertical lines of sight can be



challenging and costly, slowing down the construction progress and bringing risks to the structural stability of the high-rise building. For this reason, between 100m and 200m elevation from the ground level, the traditional and passive survey methods reach their limits and must be replaced with high-rise specific active survey control positioning methods.

## 2.2 Active survey control and deformation monitoring

The introduction of active survey control systems marks a significant advancement in the field of structural deformation monitoring and positioning systems for tall buildings. These systems leverage the power of interoperable connectivity between survey instrumentation and Internet of Things (IoT) sensors, providing real-time data that ensures accurate positioning. By automatically resolving positions to the necessary precision, active survey control systems reduce human error and enhance efficiency. These systems employ Global Navigation Satellite Systems (GNSS) and IoT sensors to continuously monitor and report positions, compensating for dynamic structural deformation. This capability establishes survey control points and a reference frame within specified tolerances, streamlining the engineering surveying process.

The solution provided by Leica Geosystems, Core Wall Control System (CWCS) shown in Figures 2 and 3, specifically developed and advanced for tall building construction over 15 years since the construction of Burj Khalifa [2], combines the following components:

- Leica iCON GNSS Smart Antennas placed on the uppermost floor to provide continuous, real-time positional data collocated with 360° prisms
- Robotic total stations, such as Leica TS16/60, measuring prisms and used for establishing and verification of the survey control using positional information provided by the monitoring software
- GeoCloud Drive service responsible for data transfer and synchronization of results between the field instrumentation and monitoring software
- WiSenMeshWAN® IoT inclinometers and distance meters deliver displacement information at various levels
- GeoMoS Monitor software for GNSS and IoT data processing and publishing positioning results consumed by total stations for stakeout

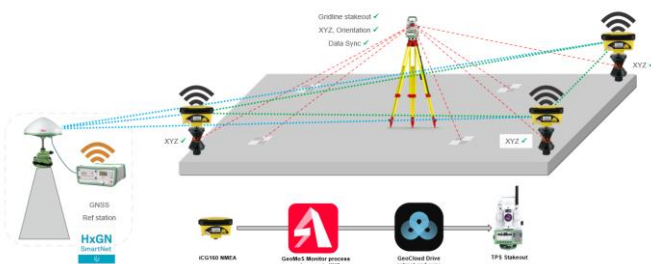


Figure 2 Leica Geosystems' CWCS solution [1]

The real-time information provided by these systems is used to determine live axial shortening values for structural compression. This is achieved through multiple vertically installed IoT distance sensors, while the rotation component from the sensors helps determine live structural tilt. Additionally, GNSS positioning data provides absolute XYZ locations at the upper working face of the building, creating a

comprehensive integrated solution. By combining these data sets with traditional monitoring of foundation deformation and environmental sensors, engineers gain a thorough understanding of where to place new elements at the upper workforce, ensuring that positional data is available and within tolerance when required.

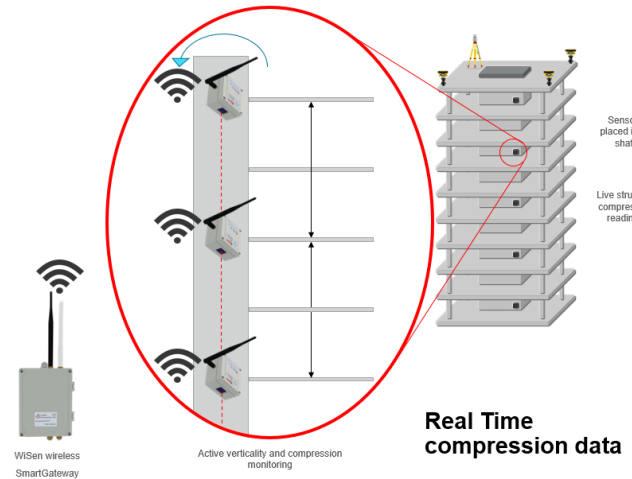


Figure 3 WiSenMeshWAN® solution for real-time compression readings [1]

Although the accuracy of live RTK GNSS positioning is around  $\pm 3\text{cm}$ , averaging the results over the period of at least one hour will significantly improve the accuracy. Figure 4 displays the combination of raw and averaged 6-hour RTK GNSS data, where raw data shows horizontal consistency within  $\pm 2\text{cm}$  over 24 hours, whereas averaged results filter out dynamic movements and reveal slow movements of the building influenced by cyclic environmental conditions, reaching the accuracy of  $\pm 5\text{mm}$ .

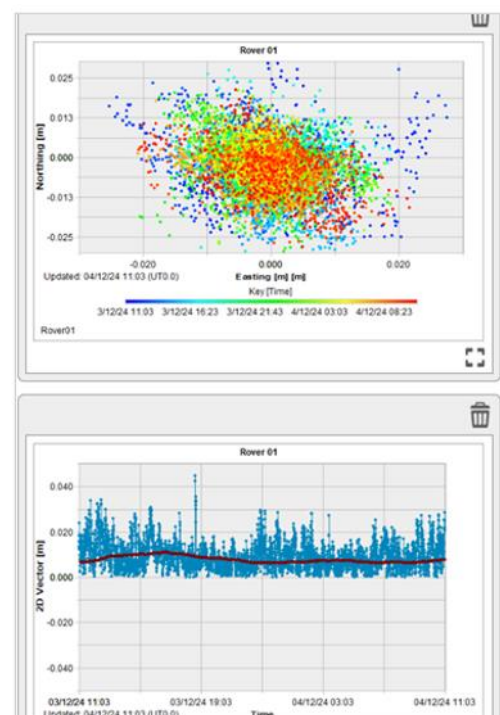


Figure 4 Raw and averaged RTK GNSS data over 6 hours

Real-time monitoring systems extend beyond construction, monitoring the building's lifespan and supporting future design models.

### 2.3 Real-life examples

Since the first implementation of the Core Wall Control System for the construction of Burj Khalifa, CWCS has been deployed and further developed in many iconic high-rise and super high-rise buildings worldwide. Some of the examples are:

- 432 Park Avenue in New York City [3] completed in 2015 and standing at 426m
- The Central Park Tower in New York City [4] – one of the tallest residential buildings with 472m, completed in 2020
- One World Trade Center in New York City – the tallest building in North America with 541m, completed in 2014
- Millenium Tower in Boston [5] – one of the tallest residential buildings in Boston with 208m of height, completed in 2016
- 22 Bishopsgate in London [6] – the second tallest building in the UK with 278m, completed in 2020
- The Shard in London [7] – the tallest building in the UK with 306m, completed in 2013

## 3 STRUCTURAL HEALTH MONITORING OF TALL BUILDINGS

Every building and structure changes over time due to various environmental and structural impacts and neglecting these changes can have serious consequences. Tall buildings are particularly impacted due to their unfavourable geometry. The most common causes of movements in urban environments include nearby construction, excavations, ageing of the structure, maintenance of the building, natural hazards and seismic activity.

### 3.1 Choosing the right technology

No single technology can fully capture the dynamic behaviour and the entire scope of high-rise and super high-rise buildings. Also, each technology has its advantages and limitations, which should be considered when designing the deformation monitoring system. Hence, a hybrid approach is essential [8].

In the case of geodetic monitoring, prism and GNSS measurements provide a complete 3D understanding of movements but are limited to a small number of single points depending on either a clear line of sight or an open sky. Automated 3D laser scanning in monitoring [9] on the other hand captures thousands of points per second, but can only deliver information about deformations perpendicular to the scanned surface. Geotechnical sensors, such as inclinometers and extensometers, provide point-specific data in a relative, non-georeferenced context. However, due to the IoT technology, they can be installed indoors and outdoors and create a self-forming dynamic radio mesh network which sends data to a gateway.

The fusion of geodetic and geotechnical data creates a more complete picture of building deformations. By cross-analysing data from different sources, engineers can validate findings and ensure the reliability of the monitoring system. This integration allows for early detection of potential issues, enabling proactive measures to maintain structural integrity.

### 3.2 Edge computing, automation and autonomy

The integration of edge computing, automation, and autonomy into monitoring solutions represents a significant advancement in the field [10]. These technologies enhance the efficiency and reliability of data acquisition and processing, enabling real-time insights into structural behaviour.

GeoMoS Edge is crucial in Leica Geosystems' monitoring systems because it addresses the significant challenge of data acquisition continuity during communication outages. Traditional monitoring systems rely heavily on stable communication between sensors and a central server, which can lead to data gaps and safety risks when communication is disrupted. GeoMoS Edge mitigates this issue by embedding a data acquisition component directly on a communication device, allowing the system to operate autonomously even during periods without connection to the GeoMoS monitoring software.

This autonomy ensures that measurements continue uninterrupted, eliminating data gaps that could otherwise pose safety threats. By replicating server functionality on edge devices such as Leica ComBox60, GeoMoS Edge can perform measurement cycles, assess data quality, and trigger repeated measurements if necessary. Once communication is restored, the collected data is seamlessly delivered to the central monitoring software.

## 4 CONCLUSION

The integration of deformation monitoring technologies in the construction and lifecycle management of tall buildings is the key for stability and health of the structure and the people in its vicinity. The combination of GNSS, IoT sensors, and traditional survey methods provides a comprehensive understanding of structural behaviour during its construction, allowing for precise positioning as the building grows. This hybrid approach, as demonstrated by Leica Geosystems' Core Wall Control System (CWCS), has proven effective in iconic buildings worldwide, starting from Burj Khalifa in the United Arab Emirates, over 22 Bishopsgate and The Shard in the United Kingdom, to The Central Park Tower, One World Trade Center and many others in the United States of America. By leveraging real-time data from geodetic and geotechnical sensors, engineers can monitor axial shortening, structural tilt, and environmental impacts with high accuracy, enabling proactive measures to address potential issues.

The continuous development of these technologies, including edge computing and automation, further enhances the reliability and efficiency of data acquisition and processing. Solutions like GeoMoS Edge ensure persistent monitoring even during communication outages, mitigating safety risks associated with data gaps. This autonomy allows for uninterrupted measurements and seamless data integration, supporting informed decision-making throughout a building's lifecycle.

Ultimately, the adoption of integrated monitoring solutions not only optimises construction and maintenance processes but also supports sustainable urban development. As cities continue to grow vertically, the demand for precise and reliable monitoring systems will increase, driving further innovation in the field. By embracing these technologies, stakeholders can ensure the safety, efficiency, and longevity of high-rise

buildings, contributing to resilient and sustainable urban environments.

## REFERENCES

- [1] L. Špiranec and S. Thurgood, Advanced Surveying Techniques for High-Rise Construction: Enhancing Precision and Sustainability, FIG Working Week 2025. Brisbane, Australia.
- [2] J. van Cranenbroeck, Controlling Vertical Towers. Reporter 63: The Global Magazine of Leica Geosystems, 29-31, 2010.
- [3] Leica Geosystems, [Innovative Vertical Alignment Systems Keeps 432 Park Ave Plumb](#), Case study, Website visited in 2025
- [4] Leica Geosystems, [Locating the floors of America's tallest residential building](#), Case study, Website visited in 2025
- [5] Leica Geosystems, [Keeping Boston's Millenium Tower on Target](#), Case study, Website visited in 2025
- [6] Leica Geosystems, [Precise positioning in London's sky](#), Case study, Website visited in 2025
- [7] Leica Geosystems, [The Shard: London's New Skyline](#), Case study, Website visited in 2025
- [8] L. Špiranec, Transforming big monitoring data into reliable information about movements. FIG e-Working Week 2023. Orlando, Florida, USA.
- [9] J. Wöllner, Automatisches Monitoring mit robusten Deformationsergebnissen aus automatisierter Scananalyse, 18. Internationaler Ingenieurvermessungskurs, Graz, 2017.
- [10] L. Špiranec and E. Niel, Innovative Edge Computing Technology for Autonomous Monitoring Systems. FIG e-Working Week 2021. Virtually in the Netherlands.



# Multi-scale digital twin for a high-rise structure combining ANN and monitoring data

Hetian Shao<sup>1</sup>, Wei Lu<sup>1</sup>, Wenchang Zheng<sup>1</sup>, Weihua Hu<sup>1</sup>, Jun Teng<sup>1</sup>, Eric M. Lui<sup>2</sup>

<sup>1</sup>School of Intelligent Civil and Ocean Engineering, Harbin Institute of Technology, 518055 Shenzhen, China

<sup>2</sup>Department of Civil & Environmental Engineering, Syracuse University, Syracuse, NY 13244-1240, USA

email: hetianshao@stu.hit.edu.cn, lu.wei@hit.edu.cn, 23s054026@stu.hit.edu.cn,

huweihua@hit.edu.cn, tengj@hit.edu.cn, emlui@syr.edu

**ABSTRACT:** The application of digital twin technology in high-rise buildings provides a comprehensive approach to maintaining construction safety, tracking project advancement, and evaluating service conditions. This paper proposes a novel multi-scale digital twin framework for high-rise structures. The macro-scale model is constructed using spring elements, taking into account the dynamic behavior of flexure-shear coupling in high-rise structures. The macro-scale digital twinning is achieved by updating the macro-scale model through the integration of modal monitoring data with Artificial Neural Networks (ANN). A multi-scale analysis method from the structural macro-level to components of the substructure is developed through information transfer at boundary nodes, achieving a balance between computational efficiency and the demand for accuracy of the local components. Integrated with multiple monitoring data sources, the proposed framework provides a technical pathway for multi-scale model updating, real-time response acquisition, and disaster risk assessment of high-rise structures.

**KEY WORDS:** High-rise building; Flexure-shear coupled behavior; Multi-scale analysis; Structural health monitoring; Artificial Neural Networks.

## 1 INTRODUCTION

Digital twins are increasingly recognized as pivotal innovations within the Architecture, Engineering, Construction, and Facility Management (AEC-FM) industry [1, 2]. As an advanced representation that bridges the digital and physical realms, digital twins enable researchers and practitioners to gain a more intuitive and in-depth understanding of the real-time state and operational principles of objects.

Incorporating mechanical information of the structure into the building's digital twin can provide an approach to maintaining construction safety, tracking project advancement, and evaluating service conditions. Typically, modal monitoring data of the building is used to correct the parameters of the structural design model [3, 4]. The advantage lies in the maturity and convenience of the monitoring methods, and the structural design model can be detailed to the component level, offering a high degree of adjustability. However, the computational efficiency of the design model is low, and model updating typically requires a large number of iterative calculations or reference samples.

The updating of macro-scale models is a very promising research direction, aimed at improving the efficiency of model updating while fully utilizing structural modal monitoring data [5, 6]. However, the coupling effects of bending and shear in high-rise structures as well as the complex inter-story force distribution can significantly affect the dynamic characteristics of macro-scale models. The mapping of macro-scale characteristics to model updating through modal monitoring data is also significantly influenced by the identification algorithms [7, 8]. Therefore, researching suitable macro-scale model carriers and model updating algorithms are the two main research directions in the identification of macro-scale models.

Macro-scale models can only represent the overall deformation of the structure and cannot delve into the load-

bearing status of local components. There are certain special components and critical load-bearing areas where there is a higher demand for monitoring and digital twin accuracy. To balance computational efficiency and simulation precision, a multi-scale structural model is an ideal research approach [9, 10]. Information transfer or coupling between different scales is key to implementing this technology. The multi-scale twin model that combines macro-scale models with component-scale substructure models is still an area that requires further research.

This paper proposes a multi-scale digital twin method that integrates both macro-scale and component-scale substructures. First, a macro-scale twin is realized through Artificial Neural Networks (ANN) and modal monitoring data, and then a substructure component-scale twin is achieved by constructing a floor boundary condition transmitter. Integrated with multiple monitoring data sources, the proposed framework provides a technical pathway for multi-scale model updating, real-time response acquisition, and disaster risk assessment of high-rise structures.

## 2 MACRO-SCALE MODEL UPDATING

### 2.1 Floor deformation characterization

Story response is often used to quantify the overall behavior of high-rise buildings. Therefore, the primary focus is on the displacements of the floor boundary nodes to represent the overall deformation situation of the high-rise buildings. Characterizing the displacements of the numerous boundary nodes on each floor is key to building a macro-scale model of high-rise structures.

In this paper, a high-rise frame core tube structure shown in Figure 1a is used as an example. The structure has 40 stories, each with a height of 4.0 meters. The columns and beams were

modeled using Euler-Bernoulli beam elements, and the core wall was modeled using shell elements. To simplify the complexity of constructing the macro-scale models, uniform member sizes and materials were adopted for all structural components. All columns were 800×800 mm<sup>2</sup> rectangular C40-RC columns and all beams were 500×1000 mm<sup>2</sup> rectangular C30-RC beams, except for the coupling beams in the core wall, which have a cross-section of 700×1400 mm<sup>2</sup>. The material properties are: C30 concrete ( $E = 3.0 \times 10^7$  kN/m<sup>2</sup>,  $\nu = 0.25$ ,  $\rho = 25$  kN/m<sup>3</sup>) and C40 concrete ( $E = 3.25 \times 10^7$  kN/m<sup>2</sup>, with  $\nu$  and  $\rho$  assumed identical to C30). The wall thickness of the core tube is 900 mm. This model also incorporates simplified simulations of infill walls, exterior curtain walls, and rigid panel zones, which, due to space limitations, are not discussed in detail in this paper. However, these structural details significantly increase the computational demands and time costs of the model. The multi-scale modeling approach proposed in this study is specifically designed to optimize this issue.

The structural analysis software OpenSees was used to model the structure (shown in Figure 1b) for batch extraction of the deformation of nodes. Modal analysis of the structure was performed (shown in Figure 2) under the assumption that deformations are restricted to the x-direction, with rigid constraints applied in the other two directions.

The deformation of the planes where the floor boundary nodes are located is illustrated in Figure 3. Due to the rigid floor assumption, the horizontal displacement is uniform at all points, while the vertical deformation and torsional deformation vary from point to point. Therefore, it is proposed to use two hypothetical planes to represent the overall situations of vertical displacement and torsional displacement, respectively. The vertical displacement of each node was fitted to a Hypothetical Vertical Displacement Plane (HVDP) using the least squares method. The bending deformation of the nodes in each slab was averaged to form a Hypothetical Bending Displacement Plane (HBDP). The angle of rotation of HBDP ( $\alpha_{HBDP_i}$  for the  $i^{th}$  floor) and HVDP ( $\beta_{HVDP_i}$  for the  $i^{th}$  floor) shown in Figure 3 represents their degree of displacement. For a given mode, the vertical and bending modal vectors of the boundary nodes of each story were fitted to an HVDP and HBDP, respectively. Examples of this fitting for the 1<sup>st</sup> floor of the 1<sup>st</sup> mode are given in Figure 4. Examples of the angles of the HBDPs and the HVDPs of the 1<sup>st</sup> and 2<sup>nd</sup> modes were calculated and shown in Figure 5.

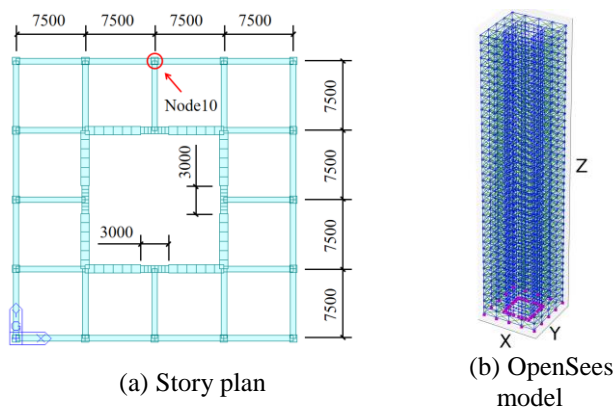


Figure 1. High-rise frame core tube structure.

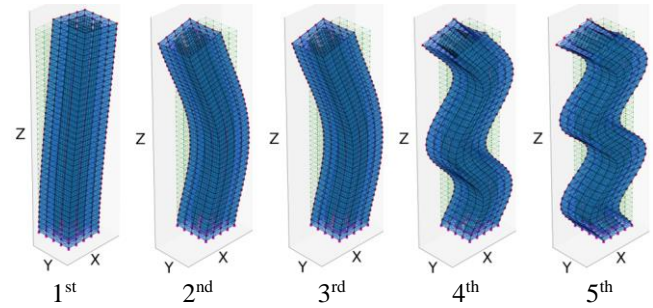


Figure 2. Mode shapes of the high-rise frame core tube structure.

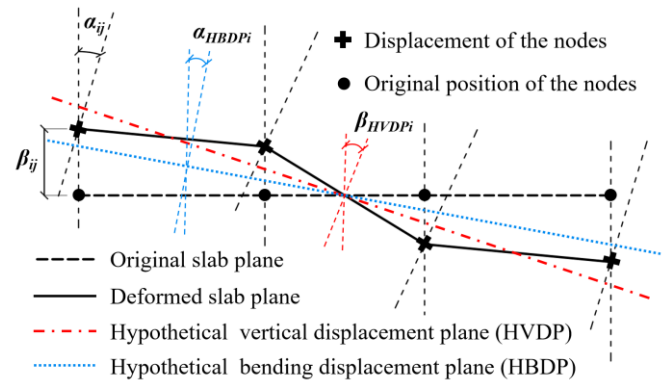
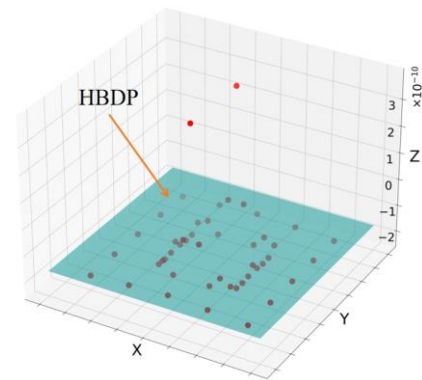
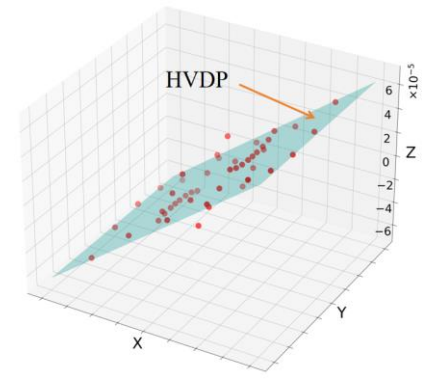


Figure 3. Displacements of the story nodes.



(a) HBDP



(b) HVDP

Figure 4. Hypothetical plane of the 1st mode of the 1st floor.

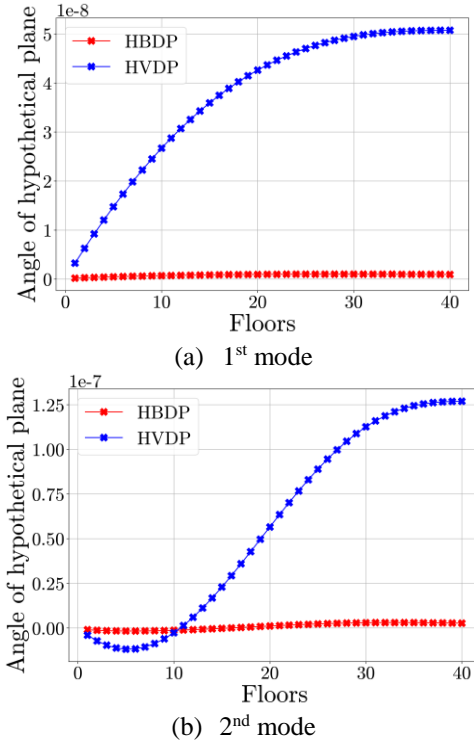


Figure 5. HBDP and HVDP

HBPV offers a way to isolate the displacement components induced by bending. The displacement  $\Delta_{Bi}$  induced by bending for the  $i^{\text{th}}$  floor can be approximated by the equation

$$\Delta_{Bi} = (\tan \varphi + \lambda \tan \omega) H_i \quad (1)$$

where  $\varphi$  is the angle of HBDP of the story below;  $\omega$  is the change in angle of HBDP of the story;  $H_i$  is the height of the story; and  $\lambda$  is a correction coefficient (set as 0.5 in the present study).

The displacement induced by shear  $\Delta_{Si}$  for the  $i^{\text{th}}$  floor can be calculated as

$$\Delta_{Si} = \Delta_{Ti} - \sum_{i=1}^N \Delta_{Bi} \quad (2)$$

where  $\Delta_{Ti}$  is the lateral displacement, and  $N$  is the total number of floors.

Two normalized difference parameters  $D_{VBi}$  and  $D_{BTi}$  are defined to represent the relationship of the boundary nodes.

$$D_{VBi} = \frac{N(\alpha_{HBDPi} - \beta_{HVDPi})}{\sum_{i=1}^N (|\alpha_{HBDPi}| + |\alpha_{HVDPi}|)} \quad (3)$$

$$D_{BTi} = \frac{N(\Delta_{Ti} - \Delta_{Bi})}{\sum_{i=1}^N (|\Delta_{Ti}| + |\Delta_{Bi}|)} \quad (4)$$

The introduction of these two hypothetical planes, along with the two normalized difference parameters, provides the theoretical foundation for the subsequent updating of the macro-scale model.

## 2.2 Model construction and recognition

To account for the coupling of bending and shear in high-rise structures, a macro-scale model framework was constructed using spring elements, as shown in Figure 6. Each floor is composed of four identical vertical members, two identical outside horizontal members, and one inside horizontal member. Spring elements that represent the axial, shear, and bending stiffnesses of each member are shown in Figure 7. The  $6 \times 6$  member stiffness matrix relating the axial, transverse, and rotational degrees-of-freedom for each node of the 2-node member with spring elements is given in Equation (5) and (6).

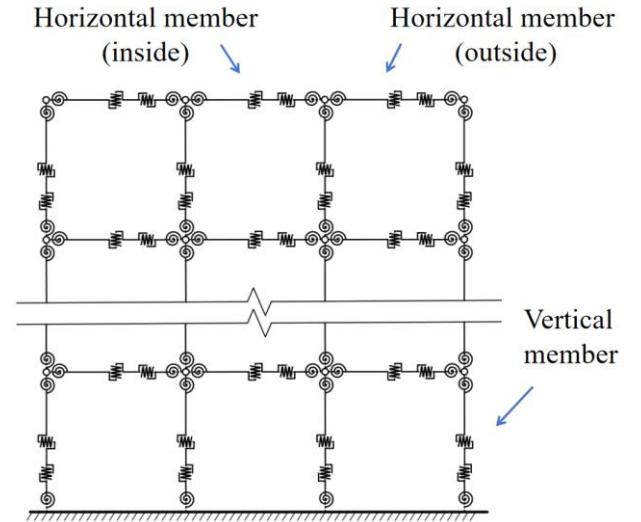


Figure 6. Macro-scale model of the high-rise structure.

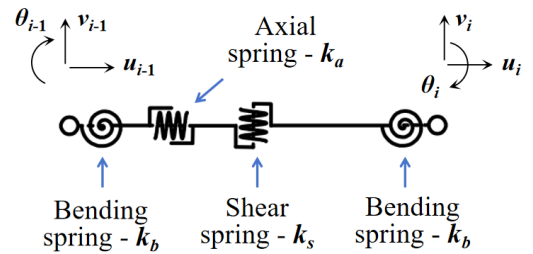


Figure 7. Member with springs

$$\frac{1}{\eta} \begin{pmatrix} k_a \eta & & & & & \text{sym.} \\ & 2k_b k_s & & & & \\ & k_b k_s l & k_b^2 + k_b k_s l^2 & & & \\ -k_a \eta & & & k_a \eta & & \\ & -2k_b k_s & -k_b k_s l & & 2k_b k_s & \\ & k_b k_s l & -k_b^2 & & -k_b k_s l & k_b^2 + k_b k_s l^2 \end{pmatrix} \quad (5)$$

$$\eta = 2k_b + k_s l^2 \quad (6)$$



The macro-scale model of the typical 40-story frame core tube structure is constructed using ANN and simulated modal monitoring data. As shown in Figure 8, natural frequencies, lateral mode vectors, angular mode vectors of the HBDP,  $D_{VB}$  and  $D_{BT}$  were selected as the features. The stiffness of the springs was the target to be recognized, i.e., a total of 7 stiffness coefficients ( $k_a$ ,  $k_b$ ,  $k_s$ ,  $k_{hb}$ ,  $k_{hs}$ ,  $k_{ihb}$  and  $k_{ihs}$ ).  $k_a$  is the axial stiffness,  $k_b$  and  $k_s$  are the bending and shear stiffness of the column,  $k_{hb}$  and  $k_{hs}$  are the bending and shear stiffness of the outside horizontal members, while  $k_{ihb}$  and  $k_{ihs}$  are the bending and shear stiffness of the inside horizontal members. The initial values of the stiffness parameters were roughly estimated through a small number of trial calculations, as shown in Table 1. 20000 samples were generated through Latin square sampling with the combination of different stiffness change ranges as shown in Table 2 and batch modal analysis. A type of ANN that is conducive to utilizing the spatial information between data, Convolutional Neural Networks (CNN) incorporating channel and spatial attention mechanisms (CBAM-CNN) [11] were used, and a (non-learnable) Fixed attention layer (FixAL) was selectively added to manually assign weights to different features [12]. The specific network architecture and hyperparameter settings of the ANN are shown in

Table 3 and Table 4, respectively.

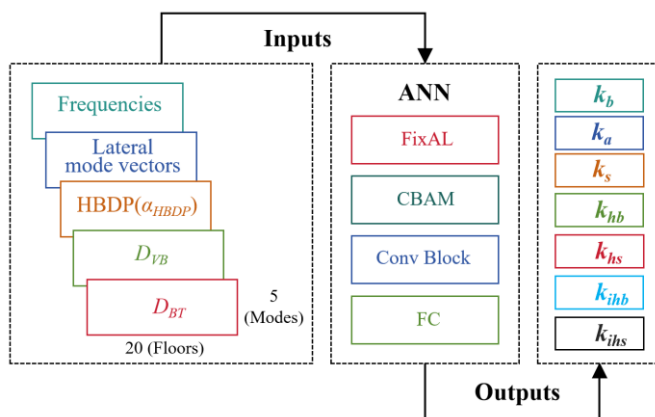


Figure 8. ANN model construction.

Table 1. Stiffness parameters

Stiffness	Initial	Recognized
$k_a$	$7.00 \times 10^7$	$6.92 \times 10^7$
$k_b$	$1.50 \times 10^{14}$	$1.58 \times 10^{14}$
$k_s$	$1.00 \times 10^{12}$	$9.87 \times 10^{11}$
$k_{hb}$	$8.00 \times 10^{13}$	$7.90 \times 10^{13}$
$k_{hs}$	$1.00 \times 10^{14}$	$9.87 \times 10^{13}$
$k_{ihb}$	$4.00 \times 10^{13}$	$3.94 \times 10^{13}$
$k_{ihs}$	$1.00 \times 10^{14}$	$9.88 \times 10^{13}$

The units of  $k_s$ ,  $k_a$ ,  $k_{hs}$ ,  $k_{ihs}$  are N/mm; and the units of  $k_b$ ,  $k_{hb}$ ,  $k_{ihb}$  are N-mm/rad

Table 2. Sample set stiffness variation ranges

Dataset	Variation ranges (%)	Size
1	(80-120)	10000
2	(90-110)	10000

Table 3. The main structure of the ANN

Layer	Type	Output size <sup>a</sup>
Input	Modal data	bs×1×5×5×40
FixAL <sup>b</sup>	Weight matrix-1	bs×1×5×5×40
	Weight matrix-2	bs×1×5×5×40
CB <sup>c</sup>	Conv3d	bs×16×5×5×40
	ReLU	-
	Max pooling	bs×16×2×2×20
CB	Conv3d	bs×32×2×2×20
	ReLU	-
	Max pooling	bs×32×2×2×10
CB	Conv3d	bs×64×2×2×10
	ReLU	-
CBAM <sup>d</sup>	Max pooling	bs×64×1×1×5
	Channel attention	bs×64×1×1×5
	Spatial attention	bs×64×1×1×5
DL <sup>e</sup>	-	-
FC <sup>f</sup>	Flatten	bs×320
	FC cells	bs×320
	ReLU	-
	FC cells	bs×1000
	ReLU	-
	FC cells	bs×256
Output	Stiffness parameters	bs×7

<sup>a</sup> bs = batch size; <sup>b</sup> FixAL = Fixed Attention Layer; <sup>c</sup> CB = Convolutional Block; <sup>d</sup> CBAM = Convolutional Block Attention Module; <sup>e</sup> DL = Dropout Layer; <sup>f</sup> FC = Fully Connected Layer

Table 4. Hyperparameter settings of the ANN

Parameters	Value
Number of epochs	50
Batch size	256
Learning rate	0.0001-0.00001
Kernel size of Conv3d	3×3×3
Weight decay	1.0e-3
(L2 regularization)	
Dropout rate	0.2

The learning curve is shown in Figure 9, and the recognized stiffness parameters with the developed ANN model are shown in Table 1. With the recognized stiffness parameters, the macro-scale model of the typical high-rise frame core tube building was constructed. The modal analysis of the macro-scale model was carried out as shown in Figure 10. Comparison of the dynamic characteristics of the macro-scale model and original full-order model is shown in Table 5, Figure 11, Figure 11 and Figure 12. It is evident that the recognized model provides a good fit for the macro-scale mechanical properties of the original full-order model.

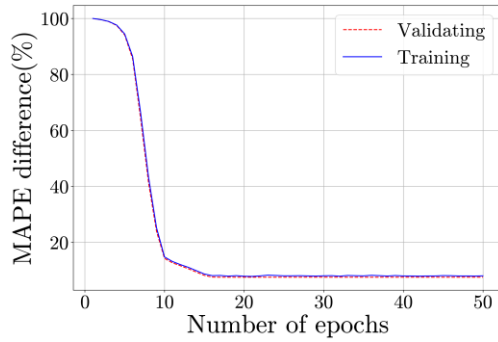


Figure 9. Maximum Absolute Percent Error (MAPE) difference.

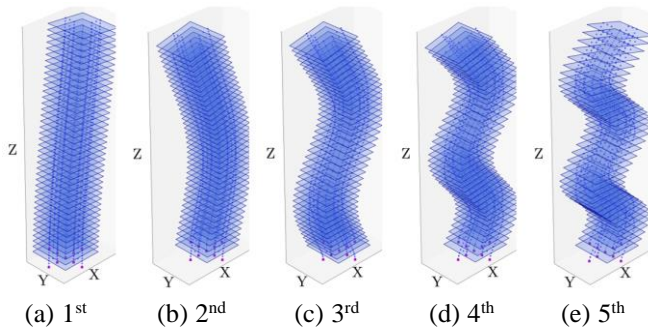


Figure 10. Mode shapes of the recognized macro-scale model.

Table 5. Comparison of the dynamic characteristics

Mode	Frequency (Hz)			MAC (%)	HBDP MAC (%)
	Original model	Recognized model	Difference (%)		
1	0.35	0.36	-2.15	1.000	0.9997
2	1.43	1.46	-2.15	0.9999	0.9978
3	3.00	2.97	1.02	0.9999	0.9986
4	4.67	4.67	0.11	0.9999	0.9986
5	6.54	6.55	-0.17	0.9996	0.9884

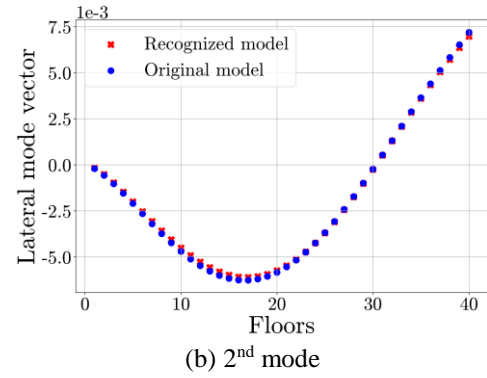
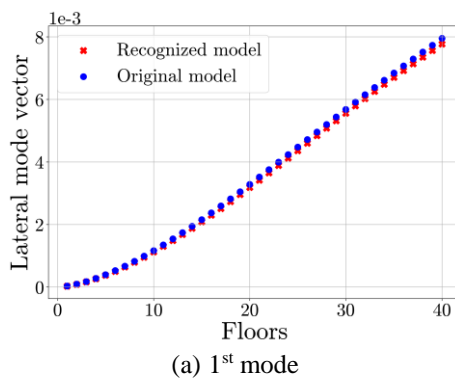


Figure 11. Lateral mode vectors of the models.

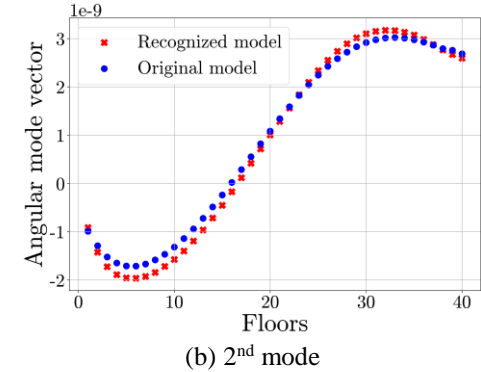
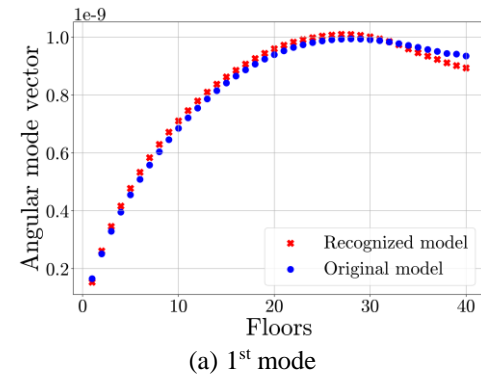
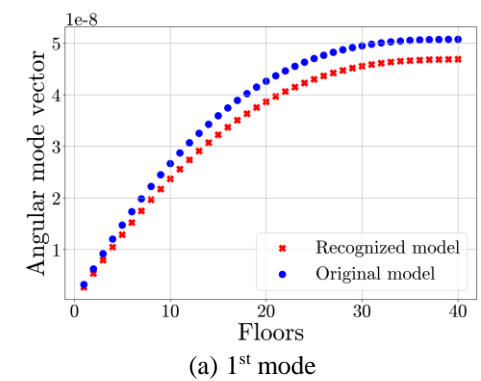


Figure 12. HBDP angles of the models.



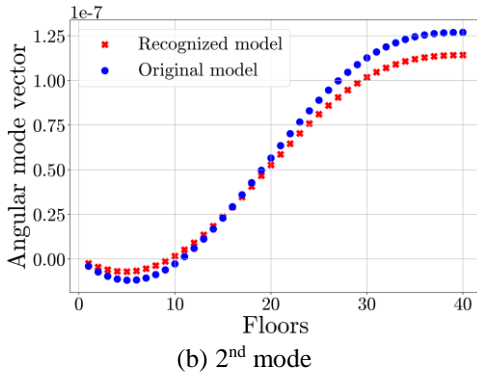


Figure 13. HVDP angles of the models.

### 3 MULTI-SCALE DIGITAL TWIN

#### 3.1 Multi-scale model

The macro-scale model proposed above can only analyze the structural response at the overall level of each floor. However, for certain special structural components or critical load-bearing areas, it is desirable to analyze the structural response of specific components.

Based on the proposed macro-scale model, this paper employs the transmission of boundary condition information to perform structural response calculations at the component level for substructures, thereby achieving multi-scale digital twins. The key to the method lies in constructing a boundary condition transmitter, as shown in Figure 14, which can expand and map the macro-scale deformation of a certain floor to the deformation of each boundary node on that floor. This paper constructs the boundary condition transmitter using the proposed HBDP, HVDP, and the proportional relationships of the modal vectors corresponding to each floor's boundary nodes under their first-order modes, as shown in Equations (7), and (8).

$$\Delta_{Bi} = \alpha_{HBDPi} M_{Bi} \quad (7)$$

$$\Delta_{Vi} = \beta_{HVDPi} M_{Vi} \quad (8)$$

where  $\Delta_{Bi}$  and  $\Delta_{Vi}$  are the bending and vertical displacements of the  $i^{\text{th}}$  node of the story in question, respectively;  $M_{bi}$  and  $M_{vi}$  are the displacements of the  $i^{\text{th}}$  node of the story in question per unit angle of  $\alpha_{HBDPi}$  and  $\beta_{HVDPi}$ , respectively.

The lateral displacement of each node is consistent with the lateral displacement of the macro-scale model. Using the displacements of the macro-scale model to map the displacements of the boundary nodes of the substructure model, the substructure's deformation can now be realized. The construction of the boundary condition transmitter can be refined according to the requirements, and can even further consider the coupling relationship between displacements of different degrees of freedom, which will be a subject of further research.

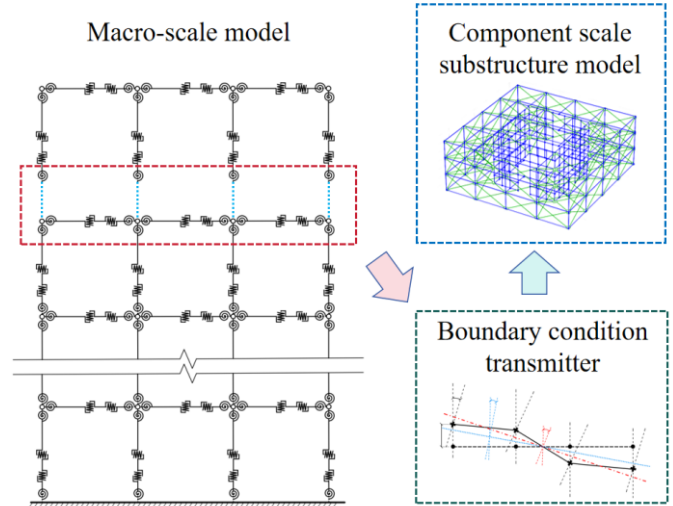


Figure 14. Deformation transfer from boundary nodes to the substructure.

#### 3.2 Substructural response

To verify the feasibility and accuracy of the proposed multi-scale model, the 20<sup>th</sup> and 21<sup>st</sup> floors of the high-rise frame core tube structure were selected as the objects of study. The mapping relationship  $M_{B19}$ ,  $M_{V19}$  and  $M_{B21}$ ,  $M_{V21}$  were established and the substructure model of the 20<sup>th</sup> and 21<sup>st</sup> floors was built. A static analysis was employed for an initial attempt (as shown in Figure 15a), specifically by applying a 1000 kN force in the horizontal direction on the topmost floor of the macro-scale model. The lateral deformations and HBDP and HVDP angles of the 19<sup>th</sup> and 21<sup>st</sup> floors were calculated. Subsequently, the displacements of the boundary nodes of the substructure were calculated using Equations (7) and (8) and applied to the substructure. The deformations of the substructure were further calculated and are depicted in Figure 16.

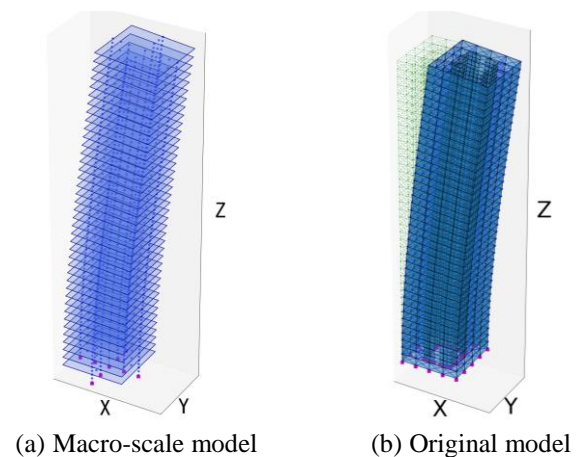


Figure 15. Deformation of the models.



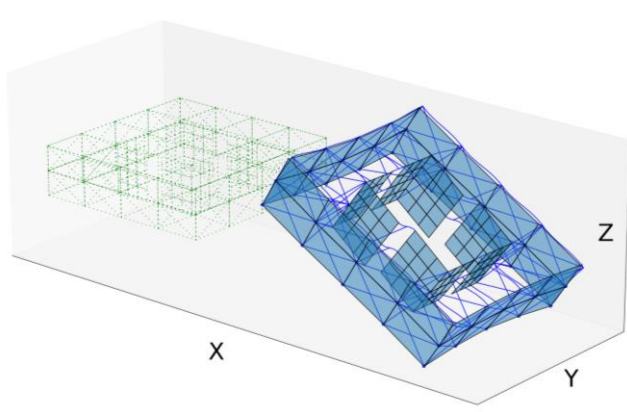


Figure 16. Deformation of the substructure (magnified).

For reference, a static analysis was performed on the original full-order model under the same loading condition. Meanwhile, the displacements of all nodes on the 20<sup>th</sup> floor for each degree of freedom were extracted from both the original full-order model and the substructure model for comparative study. Their absolute mean values and relative errors are shown in Table 6. The results show that the lateral displacement exhibits good agreement, while certain discrepancies exist in the vertical and torsional displacements. This is because the applied load distribution differs from the inertial force distribution during structural vibration.

Table 6. Comparison of the static deformation of the models

DOF	Absolute mean deformation		Error (%)
	Original model	Substructure model	
Lateral (mm)	4.40	4.54	3.26
Vertical (mm)	0.55	0.45	20.63
Torsional (rad)	9.03e-05	7.10e-05	21.40

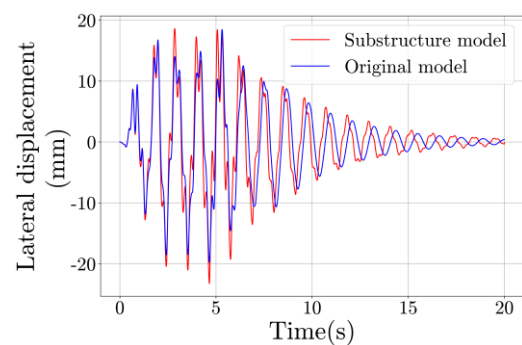
Incremental dynamic analyses were then conducted on both the original full-order model and the multi-scale model by applying the north-south component of the El Centro seismic wave with a total duration of 20 seconds. A Rayleigh damping ratio of 0.05 was assigned to the first five modes of the structures. Table 7 presents the absolute mean values and relative errors of time-history displacements for all degrees of freedom (DOF) at the 20<sup>th</sup>-floor nodes. Taking Node 10 on the 20<sup>th</sup> floor (shown in Figure 1) as an example, Figure 17 presents a comparison of time-history displacements for three degrees of freedom. As can be observed, the substructure model can effectively replicate the deformation characteristics of the full-order model. Some frequency shifts occur in the terminal vibration phase due to the minor omission of frequencies in the macro-scale model, as well as the accumulation over multiple cycles.

Notably, the multi-scale model's dynamic analysis required only 20 minutes of computational time (16 minutes for macro-scale model and 4 minutes for substructure model), significantly less than the full-scale model's 27 hours and 12 minutes under identical hardware configuration, achieving a

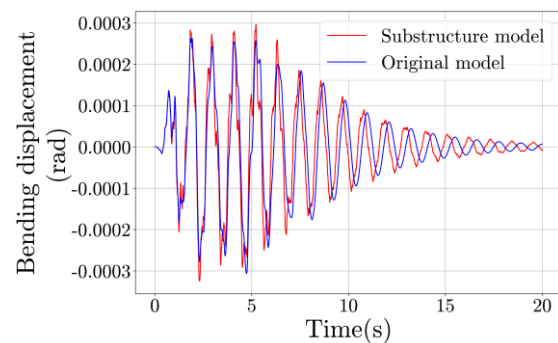
balance between computational efficiency and the demand for accuracy of the local components.

Table 7. Comparison of the dynamic deformation of the models

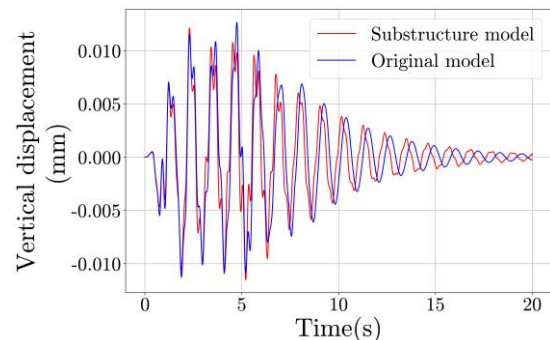
DOF	Absolute mean displacement		Error (%)
	Original model	Substructure model	
Lateral (mm)	4.23	4.43	4.58
Vertical (mm)	0.43	0.40	-7.23
Torsional (rad)	7.29e-05	7.27e-05	-0.36



(a) Lateral displacement



(b) Bending displacement



(c) Vertical displacement

Figure 17. Time-history displacements of Node 10 on the 20<sup>th</sup> floor

#### 4 CONCLUSION

This paper proposes a multi-scale digital twin method for high-rise structures. Taking a high-rise frame core tube structure as an example, a macro-scale model of the high-rise structure was constructed using a combination of spring elements, considering the coupling of bending and shear as well as the impact of the horizontal members on the structure. The macro-scale model was updated by combining Artificial Neural Networks (ANN) and modal monitoring data. Furthermore, an information transmitter was constructed using a linear mapping method to transfer the deformation from the macro-scale to the boundary nodes of the substructure at the story level, thereby enabling the calculation of deformations at the component scale of the substructure. The multi-scale digital twin method for high-rise buildings established in this study not only improves

the efficiency of model updating and computation, but also meets the need for high-precision computation of local components.

#### ACKNOWLEDGMENTS

This work was supported by the National Key Research and Development Program of China [grant numbers 2024YFC3810504], National Natural Science Foundation of China [grant numbers 52122804, 52438004, 52378296], and the Fundamental Research Project of Shenzhen Science and Technology Plan [grant number JCYJ20220531095013030].

#### REFERENCES

- [1] Hosamo HH, Imran A, Cardenas-Cartagena J, Svennevig PR, Svidt K, Nielsen HK. A review of the digital twin technology in the AEC-FM industry. *Adv Civ Eng* 2022;2022(1):2185170.
- [2] Park J, Lee JK, Son MJ, Yu C, Lee J, Kim S. Unlocking the potential of digital twins in construction: a systematic and quantitative review using text mining. *Buildings* 2024;14(3):702.
- [3] Ierimonti L, Venanzi I, Cavalagli N, Comodini F, Ubertini F. An innovative continuous Bayesian model updating method for base-isolated RC buildings using vibration monitoring data. *Mech Syst Signal Process* 2020;139:106600.
- [4] Nguyen A, Kodikara K ATL, Chan THT, Thambiratnam DP. Deterioration assessment of buildings using an improved hybrid model updating approach and long-term health monitoring data. *Struct Health Monit* 2019;18(1):5-19.
- [5] Lam HF, Hu J, Adeagbo MO. Bayesian model updating of a 20-story office building utilizing operational modal analysis results. *Adv Struct Eng* 2019;22(16):3385-3394.
- [6] Prabakaran K, Kumar A, Thakkar SK. Comparison of eigensensitivity and ANN based methods in model updating of an eight-story building. *Earthq Eng Vib* 2015;14:453-464.
- [7] Behmanesh I, Moaveni B, Lombaert G, Papadimitriou C. Hierarchical Bayesian model updating for structural identification. *Mech Syst Signal Process* 2015;64:360-376.
- [8] Akhlaghi MM, Bose S, Mohammadi ME, Moaveni B, Stavridis A, Wood RL. Post-earthquake damage identification of an RC school building in Nepal using ambient vibration and point cloud data. *Eng Struct* 2021;227:111413.
- [9] Wang FY, Xu YL, Qu W L. Mixed-dimensional finite element coupling for structural multi-scale simulation. *Finite Elem Anal Des* 2014;92:12-25.
- [10] Yue J, Qian J, Lei T, Lu L, Lu X. In situ lateral-loading test and micro-macro-scale simulation of an existing RC frame. *Soil Dyn Earthq Eng* 2013;45:35-44.
- [11] Woo S, Park J, Lee JY, Kweon IS. Cham: Convolutional block attention module, in: *Proceedings of the European conference on computer vision (ECCV)*.3-19;2018.
- [12] Zhang L, Cosmo L, Minello G, Torsello A, Rossi L. GraFix: A graph transformer with fixed attention based on the wl kernel, in: *International conference on pattern recognition*. Cham: Springer Nature Switzerland,15304:435-450;2024.

# Assessment method for torsional performance of high-rise buildings based on period ratio

Jiayi Zheng<sup>1</sup>, Wei Lu<sup>1\*</sup>, Weihua Hu<sup>1</sup>, Jun Teng<sup>1</sup>

<sup>1</sup>School of Intelligent Civil and Ocean Engineering, Harbin Institute of Technology (Shenzhen), Shenzhen, Guangdong, China  
email: 21b954012@stu.hit.edu.cn, lu.wei@hit.edu.cn, huweihua@hit.edu.cn, tengj@hit.edu.cn

**ABSTRACT:** The torsional performance of a structure significantly impacts the safety and service life of high-rise buildings. Due to deviations between real structures and design models, it is essential to evaluate the torsional performance of in-service high-rise buildings. This paper proposes a method for evaluating the torsional performance of in-service high-rise buildings based on the measured period ratio. By abstracting the high-rise building as an equivalent cantilever beam model with unidirectional eccentricity, the free vibration equation of the structure is derived, and the relationship between the period ratio, stiffness ratio, eccentricity, and radius of gyration is analyzed. The results indicate that changes in the period ratio can reflect the torsional performance of the structure. Based on the Latin Hypercube Sampling (LHS) and Kernel Density Estimation (KDE) methods, the probability density function and cumulative distribution function of the period ratio are established, and a four-level classification method for torsional performance is proposed. Application to a 40-story high-rise building validates the method. The research results provide a new theoretical basis and practical guidance for evaluating the torsional performance of in-service high-rise buildings.

**KEY WORDS:** Torsional performance assessment; Period ratio; High-rise buildings; Structural health monitoring.

## 1 INTRODUCTION

The torsional effect of high-rise buildings under external loads is a significant factor affecting their service performance. As building height increases, the dynamic response of structures to horizontal excitations such as wind loads and seismic actions becomes more complex, and the torsional effect significantly intensifies [1-7]. Torsional vibrations can lead to the redistribution of internal forces within the structure, exacerbate damage to local components, and even trigger overall instability. For instance, during the 1995 Kobe earthquake, several high-rise buildings experienced asymmetric damage due to torsional effects, further underscoring the importance of torsional control [8-9]. Therefore, the assessment and optimization of torsional performance have become central issues in the design and safety maintenance of high-rise buildings.

Accurately assessing the torsional performance of high-rise buildings is crucial for ensuring their service safety. Currently, domestic and international codes primarily evaluate the torsional performance of structures indirectly through parameters such as the period ratio. Article 3.4.3 of the Chinese code *Code for Seismic Design of Buildings* (GB 50011-2010) [10] explicitly stipulates that the period ratio (the ratio of torsional period to translational period) should not exceed 0.9 to avoid significant torsional irregularity; Article 4.3.5 of the Chinese code *Technical Specification for Concrete Structures of Tall Buildings* (JGJ 3-2010) [11] further specifies that strengthening measures are required when the period ratio exceeds 0.85. Similarly, the American ASCE 7-22 code also limits torsional effects through modal participation mass ratios [12]. However, these methods are largely based on theoretical models during the design phase and struggle to reflect the time-varying characteristics of torsional performance during service due to material degradation, load variations, and accidental eccentricities [13-14].

To bridge the gap between theoretical models and real structures, there is an urgent need to obtain actual dynamic

parameters of in-service buildings through Structural Health Monitoring (SHM) technology [15-17]. The period ratio, as a key indicator reflecting the torsional stiffness and mass distribution of a structure, can be dynamically updated through long-term monitoring data, thereby providing a more accurate assessment of the trends in torsional performance. However, there is currently a lack of research on the evaluation of in-service torsional performance based on measured period ratios.

This paper proposes a method for evaluating the torsional performance of in-service high-rise buildings based on measured period ratios, encompassing the following main aspects: Firstly, a theoretical relationship between the period ratio and the stiffness ratio, eccentricity, and radius of gyration is established using an equivalent cantilever beam model. Secondly, a probabilistic distribution of the period ratio is constructed using Latin Hypercube Sampling (LHS) and Kernel Density Estimation (KDE), and a four-level torsional performance classification standard is proposed. Finally, the engineering applicability of the method is validated using a 40-story reinforced concrete frame-shear wall structure as an example. The research results provide new theoretical foundations and practical guidance for the assessment of torsional performance in in-service high-rise buildings.

## 2 CLASSIFICATION METHOD FOR TORSIONAL PERFORMANCE LEVELS

### 2.1 Analysis of influencing factors of period ratio

To facilitate analytical derivation and computational modeling, a series of idealized assumptions are implemented in the structural characterization of the target high-rise building. Specifically, the structural system is postulated to exhibit unidirectional eccentricity along the Cartesian coordinate system - that is, a deliberate offset is introduced between the center of mass and the center of stiffness exclusively in the X direction, while maintaining perfect spatial coincidence of these two critical centers in the orthogonal Y direction. This intentional asymmetrical configuration is adopted to isolate and



investigate the torsional effects induced by eccentricity along a single principal axis, thereby simplifying the coupled lateral-torsional vibration analysis.

The entire high-rise building is abstracted as an equivalent cantilever beam element with prescribed geometric and material properties, as schematically illustrated in Figure 1. The rationale behind this modeling approach stems from multiple considerations: Firstly, the cantilever beam provides a mathematically tractable framework for solving equations of motion. Secondly, the unidirectional eccentricity assumption enables parametric investigation of torsion-translation coupling mechanisms without introducing unnecessary computational complexity from bidirectional interactions.

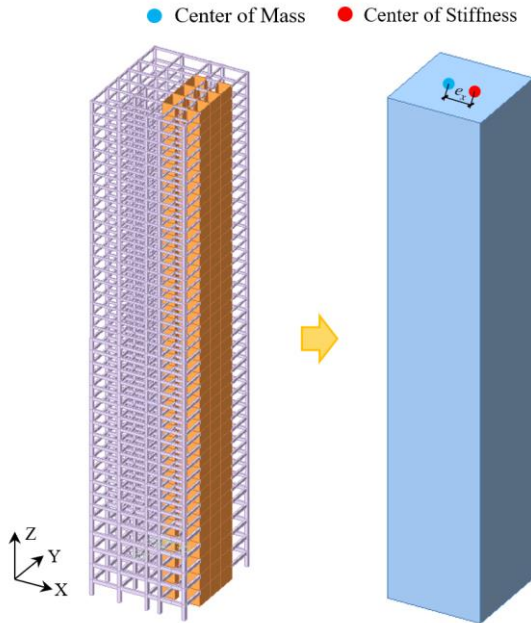


Figure 1. Schematic diagram of structural eccentricity.

The undamped free vibration motion equation of the structure is

$$\begin{bmatrix} M & \\ & J_c \end{bmatrix} \begin{bmatrix} \ddot{u}_y \\ \ddot{\theta} \end{bmatrix} + \begin{bmatrix} K_y & e_x K_y \\ e_x K_y & K_\theta \end{bmatrix} \begin{bmatrix} u_y \\ \theta \end{bmatrix} = \begin{bmatrix} 0 \\ 0 \end{bmatrix} \quad (1)$$

where  $M$  is the mass of the high-rise building;  $J_c$  is the mass moment of inertia about the center of mass,  $J_c = Mr^2$ , and  $r$  is the radius of gyration of the structure relative to the center of mass;  $u_y$  is the translational displacement in the Y direction;  $\theta$  is the torsion angle of the high-rise building;  $K_y$  is the translational stiffness in the Y direction,  $K_y = \sum_{i=1}^n K_{yi}$ , and  $K_{yi}$  is the horizontal lateral stiffness of the structural member in the Y direction;  $K_\theta$  is structural torsional stiffness,  $K_\theta = \sum_{i=1}^n K_{xi} x_i^2 + \sum_{i=1}^n K_{yi} y_i^2$ ,  $K_{xi}$  and  $K_{yi}$  are the horizontal lateral stiffness of the structural member in the X and Y directions respectively, and  $x_i$  and  $y_i$  are the distances from the component to the mass center, respectively;  $e_x$  is the eccentricity in the X direction.

Assume the response of the structure is

$$u_y(t) = A_y \sin(\omega t + \alpha) \quad (2)$$

$$\theta(t) = A_\theta \sin(\omega t + \alpha) \quad (3)$$

Substituting equations (2) - (3) into equation (1) and simplifying them, the circular frequency of the structure can be obtained. Assuming  $\omega_1 < \omega_2$ ,

$$\begin{cases} \omega_1 = \sqrt{\frac{(K_\theta + r^2 K_y) - \sqrt{(K_\theta - r^2 K_y)^2 + 4r^2 e_x^2 K_y^2}}{2Mr^2}} \\ \omega_2 = \sqrt{\frac{(K_\theta + r^2 K_y) + \sqrt{(K_\theta - r^2 K_y)^2 + 4r^2 e_x^2 K_y^2}}{2Mr^2}} \end{cases} \quad (4)$$

Defining stiffness ratio  $S_y = K_\theta / K_y$ , equation (4) is transformed into the following form:

$$\frac{T_2}{T_1} = \frac{\frac{2\pi}{\omega_2}}{\frac{2\pi}{\omega_1}} = \frac{\omega_1}{\omega_2} = \frac{\sqrt{(S_y + r^2) - \sqrt{(S_y - r^2)^2 + 4r^2 e_x^2}}}{\sqrt{(S_y + r^2) + \sqrt{(S_y - r^2)^2 + 4r^2 e_x^2}}} \quad (5)$$

From equation (5), it can be seen that the ratio of the second-order period to the first-order period  $\frac{T_2}{T_1}$  depends on  $S_y$ ,  $r$  and  $e_x$ .

For eccentric structures, each vibration mode of the structure is composed of the superposition of translational vibration mode and torsional vibration mode. Substitute equation (4) into equations (1) - (3) to solve the ratio of torsional amplitude to translational amplitude  $\frac{A_\theta}{A_y}$  in the vibration mode.

By substituting  $\omega_1$ ,

$$\frac{A_\theta}{A_y} = \frac{(\eta_y - r^2) - \sqrt{(\eta_y - r^2)^2 + 4r^2 e_x^2}}{2r^2 e_x} \quad (6)$$

By substituting  $\omega_2$ ,

$$\frac{A_\theta}{A_y} = \frac{(\eta_y - r^2) + \sqrt{(\eta_y - r^2)^2 + 4r^2 e_x^2}}{2r^2 e_x} \quad (7)$$

Equations (6) and (7) are the ratios of the amplitudes of the torsional direction to the translational direction in the first-order vibration mode and the second-order vibration mode, respectively.

For in-service high-rise buildings, the radius of gyration  $r$  remains constant; stiffness ratio  $S_y$  varies with the increase in service years; due to variations in live load distribution during the service life of the structure, as well as changes in stiffness of individual components over the same period, leading to shifts in the stiffness center, therefore the eccentricity  $e_x$  varies throughout the entire service life of the structure. The relationship between the torsional displacement ratio, stiffness ratio and eccentricity is shown in Figure 2.

As can be seen from Figure 2, the curve of the period ratio is divided into two parts: the rising section on the left side and the falling section on the right side. According to the calculations, for the rising section on the left side, the first-order vibration mode is torsion, and the second-order vibration mode is Y-direction translation. For the falling section on the right side, the first-order vibration mode is Y-direction translation, and the second-order vibration mode is torsion. Regarding the eccentricity, as the eccentricity increases, the ratio of the second-order period to the first-order period decreases.

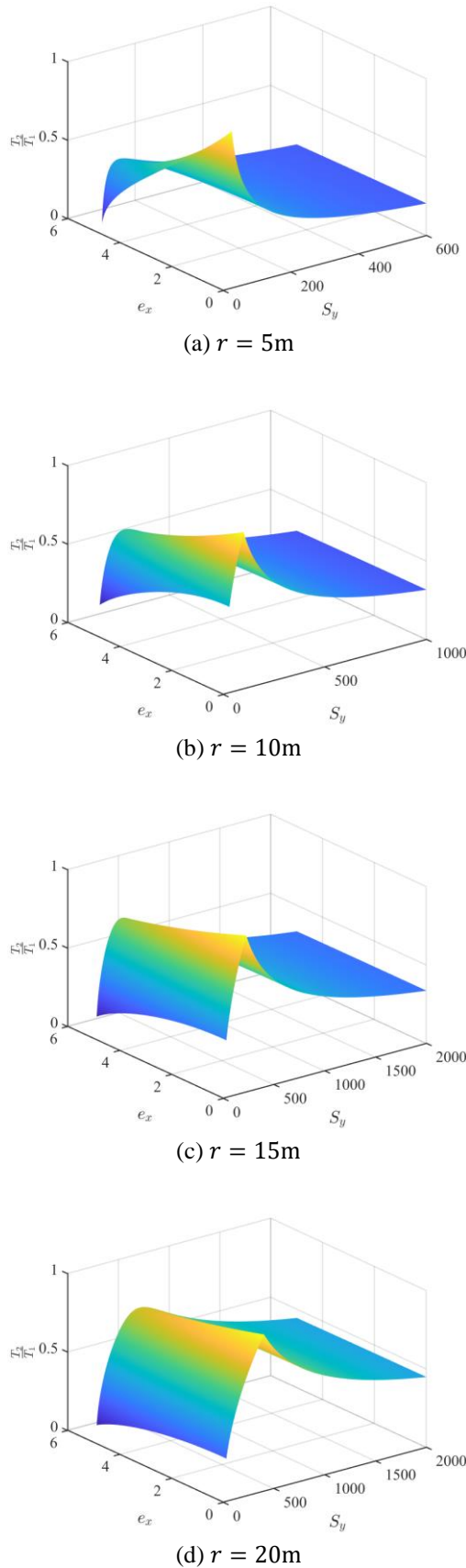


Figure 2. Period ratio curve.

## 2.2 Performance level classification method

As mentioned in Section 2.1, for in-service high-rise buildings, the radius of gyration  $r$  remains constant, while the eccentricity  $e_x$  and stiffness ratio  $S_y$  may vary. Regarding eccentricity, the Chinese code *Code for Seismic Design of Buildings* (GB 50011-2010) defines torsional irregularity in Clause 3.4.3 as follows: "Under the specified horizontal forces with accidental eccentricity, the ratio of the maximum value to the average value of the elastic horizontal displacement (or story drift) of the lateral force-resisting members at both ends of a story is greater than 1.2." Additionally, Clause 3.4.5 of the Chinese code *Technical Specification for Concrete Structures of Tall Buildings* (JGJ 3-2010) stipulates: "Under the specified horizontal seismic forces considering the influence of accidental eccentricity, the maximum horizontal displacement and story drift of the vertical members of a story should not exceed 1.2 times the average value of the story for Class A high-rise buildings, and should not exceed 1.5 times the average value of the story. For Class B high-rise buildings, mixed structures exceeding the height of Class A, and complex high-rise buildings referred to in Chapter 10 of this specification, the maximum horizontal displacement and story drift should not exceed 1.2 times the average value of the story, and should not exceed 1.4 times the average value of the story." Both code provisions mention the concept of "accidental eccentricity". Accidental eccentricity refers to the incomplete coincidence of the mass center and the stiffness center of a structure due to factors such as construction errors, material inhomogeneity, and uncertain load distribution, which results in additional torsional effects under external loads. To account for this uncertainty, seismic codes typically specify the introduction of an accidental eccentricity in calculations, generally taken as 5% of the structural plan dimensions. Therefore, it can be assumed that during the service life of the structure, the eccentricity follows a normal distribution, where the mean value of the eccentricity is the eccentricity of the design model. When the eccentricity is the mean value plus 5%, the distribution function of the eccentricity approaches 1 (here set to 0.999). This can be expressed in the following formula:

$$\mu_{e_x} = e_{xM} \quad (8)$$

where  $e_{xM}$  is the structural eccentricity obtained from the design model.

Assuming the distribution function of the eccentricity  $e_x$  is  $F_{e_x}$ , converting it to a standard normal distribution allows for the determination of the variance of the eccentricity  $e_x$ .

$$F_{e_x}(e_{xM} + a \cdot 5\%) \approx 0.999 \quad (9)$$

$$\sigma_{e_{xM}} = \frac{e_{xM} + a \cdot 5\% - e_{xM}}{3} = \frac{a \cdot 5\%}{3} = 0.01667a \quad (10)$$

$$\sigma_{e_x}^2 = 0.000278a^2 \quad (11)$$

where  $a$  is the length of the structure in the X direction.

Assuming the initial stiffness ratio of the structure is the same as that in the structural design model or digital twin model, the degradation function of the stiffness ratio follows an exponential function. That is, the variation of the stiffness ratio with service years, denoted as  $S_y(t)$ , is as follows:

$$S_y(t) = S_{yM} e^{-0.005t} \quad (12)$$

where  $S_{yM}$  is the structural stiffness ratio calculated by the structural design model or digital twin model;  $t$  is the service time in years.

Since  $t$  is a deterministic variable (assuming  $t$  ranges between 0 and 50),  $S_y$  is a deterministic function of  $t$ . Consequently, the distribution of  $S_y$  is contingent upon the distribution of  $t$ . Assuming that  $t$  follows a uniform distribution, the probability density function of  $S_y$  can be derived as follows:

$$f_{S_y}(S_y) = f(x) = \begin{cases} \frac{4}{S_y}, & S_{yM}e^{-0.005 \times 50} \leq S_y \leq S_{yM} \\ 0, & \text{others} \end{cases} \quad (13)$$

A Latin Hypercube Sampling (LHS) of  $e_x$  and  $S_y$  is performed, where  $e_x$  follows a normal distribution and  $S_y$  adheres to the distribution specified in equation 13. LHS is a statistical method for generating a near-random sample of parameter values from a multidimensional distribution. It is a form of stratified sampling that ensures that the entire range of each variable is represented in the sample. The method divides the distribution of each variable into intervals of equal probability and selects one sample from each interval. This approach guarantees that the samples are more evenly distributed across the range of possible values than in simple random sampling, leading to more precise and reliable results, especially in the context of computer simulations and sensitivity analyses. LHS is particularly useful when dealing with complex models that require significant computational resources, as it can reduce the number of simulations needed to achieve a given level of accuracy.

The period ratio of the sample is calculated according to equation (5), and the Probability Density Function (PDF)  $F$  of the period ratio is obtained by fitting using Kernel Density Estimation (KDE). KDE is a non-parametric statistical method used to estimate the probability density function of a random variable. Unlike parametric methods, KDE does not require any assumptions about the data distribution (e.g., normal distribution) and instead estimates the density function directly from the data itself. The core idea is to treat each data point as the center of a "kernel function" (e.g., Gaussian kernel, uniform kernel, etc.) and then sum all these kernel functions to form a smooth density curve.

After obtaining the probability density function of the period ratio  $\frac{T_2}{T_1}$ , it can be integrated to derive the distribution function of the period ratio  $\frac{T_2}{T_1}$ . Based on this distribution function, the torsional performance can be classified into four levels, as shown in Figure 3. Specifically,  $\frac{T_2}{T_1}|_1 = F^{-1}(0.20)$ ,  $\frac{T_2}{T_1}|_2 = F^{-1}(0.35)$ ,  $\frac{T_2}{T_1}|_3 = F^{-1}(0.50)$ ,  $\frac{T_2}{T_1}|_4 = F^{-1}(0.65)$ ,  $\frac{T_2}{T_1}|_5 = F^{-1}(0.80)$ ,  $\frac{T_2}{T_1}|_6 = F^{-1}(0.95)$ . The ordinate in Figure 3 represents the closeness coefficient, which is a concept within the Fuzzy Analytic Hierarchy Process (FAHP). FAHP is a decision analysis method that integrates fuzzy mathematics with the Analytic Hierarchy Process (AHP), designed to address issues of uncertainty and fuzziness. In FAHP, the closeness coefficient quantifies the proximity of alternatives to the ideal solution. The closeness coefficient indicates the

optimality of the alternatives, with values approaching 1 signifying more ideal solutions. This coefficient offers decision-makers a straightforward metric for ranking alternatives and is extensively applied in multi-criteria decision-making scenarios.

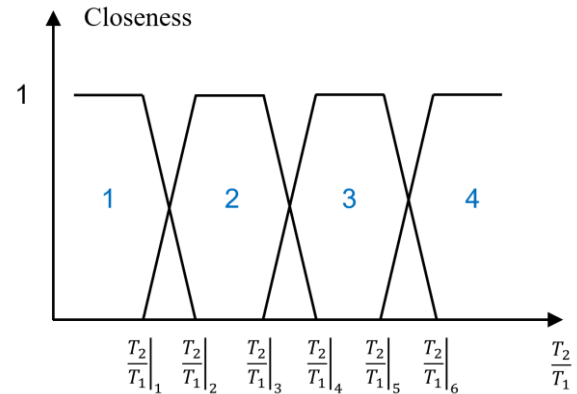


Figure 3. Membership function of torsional performance.

### 3 ENGINEERING APPLICATION

#### 3.1 Project overview

The high-rise building under investigation is a 40-story reinforced concrete frame-shear wall structure, with a total height of 150 meters. The lower section (1st to 5th floors) has a story height of 4.8 meters, while the upper section (6th to 40th floors) maintains a uniform height of 3.6 meters per story. In the longitudinal direction, the structure comprises five spans measuring 8.4 m, 5.7 m, 5.7 m, 5.7 m, and 8.4 m respectively, resulting in a total length of 33.9 meters. Transversely, the building features four spans with dimensions of 8.4 m, 8.4 m, 3.9 m, and 7.5 m, accumulating to a width of 28.2 meters. The structural design incorporates a floor dead load of 5.0 kN/m<sup>2</sup> and a live load of 2.0 kN/m<sup>2</sup>. Detailed specifications regarding component dimensions and material properties are provided in Table 1, while Figure 4 illustrates the structural layout of the high-rise building. A comprehensive three-dimensional finite element model was developed using midas Gen software, with the complete model visualization presented in Figure 5.

Table 1. Basic information of beams, columns, and shear walls.

Component type	Floor	Size	Material
Column	1-5	900mm×900mm	C60
	6-20	800mm×800mm	C60
	21-40	700mm×700mm	C60
Beam	1-5	500mm×1000mm	C60
	6-20	400mm×800mm	C60
	21-40	300mm×600mm	C60
Coupling Beam	1-5	500mm×1000mm	C60
	6-20	400mm×800mm	C60
	21-40	300mm×600mm	C60
Shear Wall	1-5	Thickness 500mm	C60
	6-20	Thickness 400mm	C60
	21-40	Thickness 300mm	C60



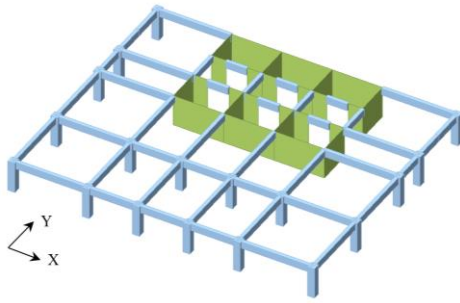


Figure 4. Layout plane of the high-rise building.

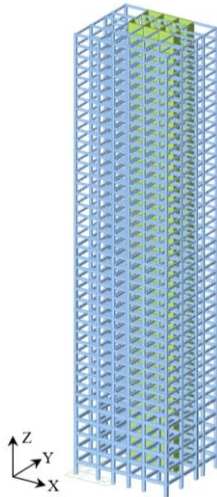


Figure 5. Three-dimensional finite element model.

It can be observed that the structure does not exhibit eccentricity in the X direction, but does have eccentricity in the Y direction. The modal analysis of the structure was conducted using midas Gen, and the results are presented in Table 2 and Figure 6. The first mode shape corresponds to translational motion in the Y direction with a period of 4.338 seconds. The second mode has a period of 3.424 seconds and is primarily characterized by translational motion in the X direction, with a component of torsional motion. The third mode shape is torsional, with a period of 2.321 seconds.

Table 2. Vibration period of the structure.

No.	Period(s)	Direction
1	4.338	Y
2	3.424	X
3	2.321	T

### 3.2 Torsional performance levels

This paper separately discusses the methodology for classifying the torsional performance levels of structural service based on the ratio of the third-order period to the second-order period  $\frac{T_3}{T_2}$ . Initially, the radius of gyration  $r$  of the structure is obtained based on the finite element model. For the high-rise building examined in this study,  $r = 13.50\text{m}$ .

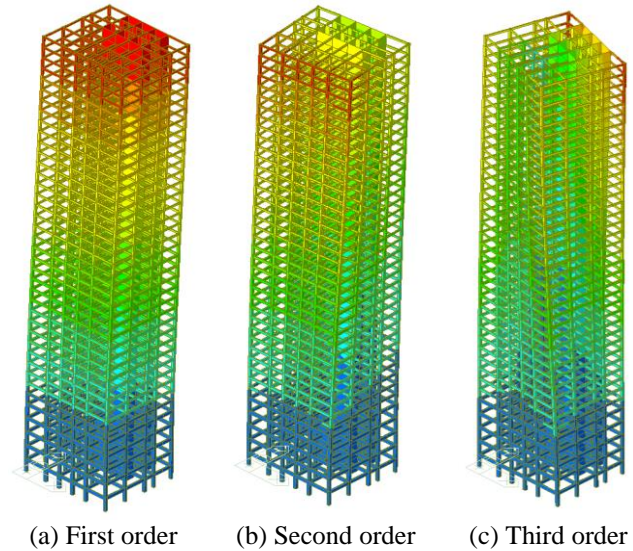
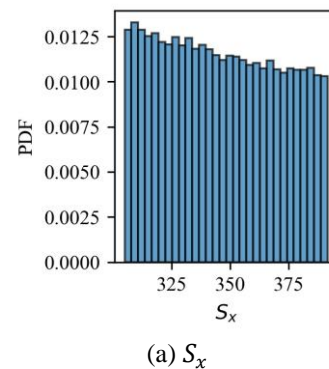
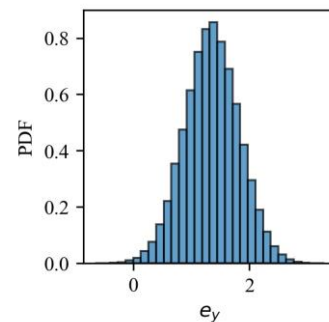


Figure 6. Structural vibration mode.

First, values of  $e_y$  and  $S_x$  are sampled using LHS, as illustrated in Figure 7 (a) and (b), respectively, with  $\mu_{e_y} = 1.35\text{m}$ ,  $\sigma_{e_y}^2 = 0.2211$ , and  $S_{xM} = 391.63$ . The  $\frac{T_3}{T_2}$  values for the samples are then calculated using equation (5), as shown in Figure 7 (c).


(a)  $S_x$ 

(b)  $e_y$

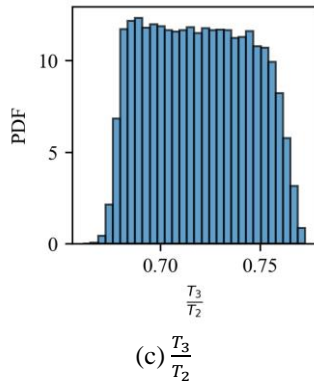


Figure 7. Latin Hypercube Sampling of parameters.

The KDE was applied to fit Figure 7 (c), resulting in the probability density distribution function of the period ratio, as illustrated in Figure 8. Subsequently, the cumulative distribution function of the period ratio was obtained by integrating the probability density function, which is depicted in Figure 9. The membership function of the in-service torsional performance of the structure is shown in Figure 10.

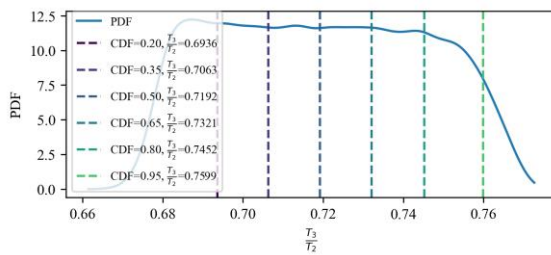
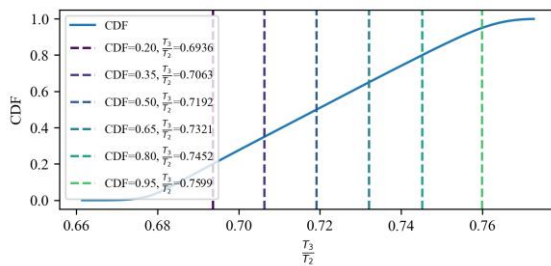
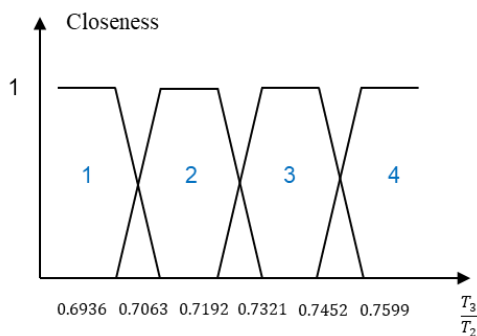

Figure 8. Probability density function of  $\frac{T_3}{T_2}$ .

Figure 9. Cumulative distribution function of  $\frac{T_3}{T_2}$ .


Figure 10. Membership function of torsional performance.

## 4 CONCLUSIONS

This paper proposes a method for evaluating the torsional performance of in-service high-rise buildings based on the measured period ratio, establishing a relationship between period ratio, stiffness ratio, eccentricity, and radius of gyration. Using Latin Hypercube Sampling and Kernel Density Estimation, a four-level classification method for torsional performance was developed and validated through a 40-story reinforced concrete frame-shear wall structure. The findings provide a new theoretical and practical approach for assessing torsional performance, bridging the gap between design models and real-world structural behavior.

## ACKNOWLEDGMENTS

This work was supported by the National Natural Science Foundation of China [grant numbers 52122804, 52438004, 52378296], the Fundamental Research Project of Shenzhen Science and Technology Plan [grant number JCYJ20220531095013030], and the Shenzhen Collaborative Innovation Project (grant number CJGJZD20220517142401002).

## REFERENCES

- [1] B. Ahmed, A. B. M. Palash, Analysis and design of high-rise reinforced concrete structures under torsional action, *Computational Engineering and Physical Modeling*, 2024, 7(3): 45-60.
- [2] Y. Hui, Y. Tamura, Q. Yang, Analysis of interference effects on torsional moment between two high-rise buildings based on pressure and flow field measurement, *Journal of Wind Engineering and Industrial Aerodynamics*, 2017, 164: 54-68.
- [3] A. Singh, D. P. N. Kontoni, S. Mandal, Wind-induced torsional loads and responses of tall buildings, *Research on Engineering Structures and Materials*, 2024, 10(3): 1281-1300.
- [4] S. Rahat Dahmardeh, M. Motamedi, A. Aziminejad, A study on the effects of torsional component of ground motions on seismic response of low- and mid-rise buildings, *The Structural Design of Tall and Special Buildings*, 2020, 29(4): e1699.
- [5] M. Kohiyama, H. Yokoyama, S. Maki, Torsional response of a bisymmetric structure induced by bending-torsion interaction in vertical members, *Japan Architectural Review*, 2022, 5(1): 3-19.
- [6] J. Hu, Z. Li, Z. Zhao, Full-scale measurements of translational and torsional dynamics characteristics of a high-rise building during Typhoon Sarika, *Materials*, 2022, 15(2): 493.
- [7] J. Hu, Z. Li, Z. Zhao, Field measurement on translational and torsional wind-induced response of a high-rise building during Typhoon Khanun, *Buildings*, 2022, 12(10): 1698.
- [8] H. Muguruma, M. Nishiyama, F. Watanabe, Lessons learned from the Kobe earthquake—A Japanese perspective, *Pci Journal*, 1995, 40(4): 28-42.
- [9] D. Mitchell, R. H. DeVall, K. Kobayashi, Damage to concrete structures due to the January 17, 1995, Hyogo-ken Nanbu (Kobe) earthquake, *Canadian Journal of Civil Engineering*, 1996, 23(3): 757-770.
- [10] Beijing: China Architecture & Building Press, Code for seismic design of buildings, GB 50011-2010.
- [11] Beijing: China Architecture & Building Press, Technical specification for concrete structures of tall building, JGJ 3-2010.
- [12] American Society of Civil Engineers, Minimum design loads and associated criteria for buildings and other structures (ASCE/SEI 7-22), 2022.
- [13] N. Mekaoui, T. Saito, Parametric study on accidental torsion in seismic design of buildings, *The 17th World Conference on Earthquake Engineering*, Sendai, Japan, September 13th to 18th, 2020.
- [14] G. K. Georgioussis, A. Mamou, On the significance of mass eccentricity on the elastic and inelastic torsional response of buildings, *The 17th World Conference on Earthquake Engineering*, Sendai, Japan, September 13th to 18th, 2020.



- [15] M. Mazzeo, D. De Domenico, G. Quaranta, Automatic modal identification of bridges based on free vibration response and variational mode decomposition technique, *Engineering Structures*, 2023, 280: 115665.
- [16] Y. Han, G. Wu, D. Feng, Structural modal identification using a portable laser-and-camera measurement system, *Measurement*, 2023, 214: 112768.
- [17] D. Tan, J. Li, H. Hao, Z. Nie, Target-free vision-based approach for modal identification of a simply-supported bridge, *Engineering Structures*, 2023, 279: 115586.





# Session 34

## Implementation and Digitalization in SHM

# Digitalization of existing measurement equipment as a valid basis for monitoring and structural behavior

Stefan Burtscher<sup>1</sup>, ORCID 0000-0002-5469-9596, Peter Huber<sup>1</sup>, ORCID 0009-0003-1935-4108, Morris Tutschku<sup>1</sup>, ORCID 0009-0007-0114-171X, Markus A. Schuch<sup>2</sup>, Florian Scharinger<sup>3</sup>, Matthias J. Rebhan<sup>4</sup>, ORCID 0000-0002-0638-6202

<sup>1</sup>Rocket NG GmbH, Stockerauerstraße 11-13/2, 2100 Korneuburg, Austria

email: stefan.burtscher@rocket-ng.at

<sup>2</sup>ÖBB Infrastruktur AG

<sup>3</sup>GDP ZT GmbH

<sup>4</sup>Institute of Soil Mechanics, Foundation Engineering and Computational Geotechnics, Faculty of Civil Engineering Sciences, Graz University of Technology, Rechbauerstraße 12, 8010 Graz, Austria

email: rebhan@tugraz.at

**ABSTRACT:** To determine damage and its effects, dense time series data is required, along with information from other sources like temperature changes that influence the main damage parameter and the structure itself. This allows the assessment of structural behavior, separating periodic and temperature-related effects from damage and ageing-related changes in load-bearing capacity. However, existing monitoring systems often lack proper documentation on measured values and their limits. Analog systems, suitable for early service life monitoring, provide readings at long intervals (years). Poor accessibility to remote measuring points further limits comprehensive time series data, including temperature correlations and other environmental correlations.

This article presents an approach that can be used to digitize different types of sensors and measuring devices in order to enable the autonomous and continuous generation of measurement data. The examples range from displacement transducers to force measuring devices, which were already installed in analogue form on existing civil engineering structures. The aim is to use digitalization to demonstrate a simple and cost-effective approach on using existing measurement technology as an initial basis for giving a statement about the behavior of the structure, its state of preservation and thus, in addition to supplementing the inspection process, also serve as a starting point for further monitoring.

**KEY WORDS:** SHM, monitoring, retrofitting, structural behavior, autonomous sensors, digitalization.

## 1 MONITORING AND STRUCTURAL BEHAVIOUR

### 1.1 Introduction

Bridges, tunnels, retaining walls, and similar structures are critical components of road and rail infrastructure. Over time, these structures inevitably age and deteriorate, necessitating regular maintenance and thorough safety assessments in form of inspections. As traffic volumes and loads continue to rise, maintenance intervals are shortened, and budget is limited such evaluations become even more essential.

Given the high costs of maintenance and the even greater expense of premature renewals, accurate assessment and prediction models are crucial (predictive maintenance). These models must be based on precise, objective, and physically accurate data that can be derived from inspections, sample testing, and monitoring.

Most infrastructure operators have their assets already digitalized and manage those via databases and graphical interfaces. This already digitalized data contains master data, drawings, information from the newly built structure and sometimes 3D-presentations of the structure. Periodic data on the state of preservation, such as inspection reports and laboratory analyses, are crucial for assessment. However, they are often not yet digitalized, preventing automated processing.

As part of the research project Candice, which was done for the Austrian Motorway Operator (ASFiNAG), a database with a graphical web interface has already been established to address this issue [1]. Additionally, forecasts for maintenance measures and a condition index have been calculated [2, 3]. Monitoring data was also incorporated into these calculations.

While data fusion was still largely manual, the approach demonstrated the effectiveness of combining monitoring data with condition data from other investigations.

This paper focuses on the transfer from a mostly manual reading of analogue measurement devices to an automated data transfer from the object under consideration to a data-platform, where an automatic storage is done and an individual display of relevant data to the user is possible. The digitalization especially with IoT devices allows for a constant flow of data, that offers several advantages for the assessment of structures:

- Direct measurement of physical values, ensuring accuracy vs. no subjective/false readings;
- Long-term data collection, capturing variations due to time of day, seasonal changes, temperature, humidity vs. usually 1 value per year or less at different seasons and environmental conditions influencing the measurement;
- Capture of rare or extreme events and influences of effects due to extreme weather conditions, earthquakes, sudden load impacts, settlements;
- Quantitative data providing objective insights for decision making rather than subjective evaluations based on a visual inspection of the structure;
- Elimination of human bias, ensuring reliability in assessments;
- Basic data set for extrapolation purposes related to the future behaviour of the structure;
- Real time integration with simulation and prediction models, enhancing cost planning, maintenance planning and resource management.

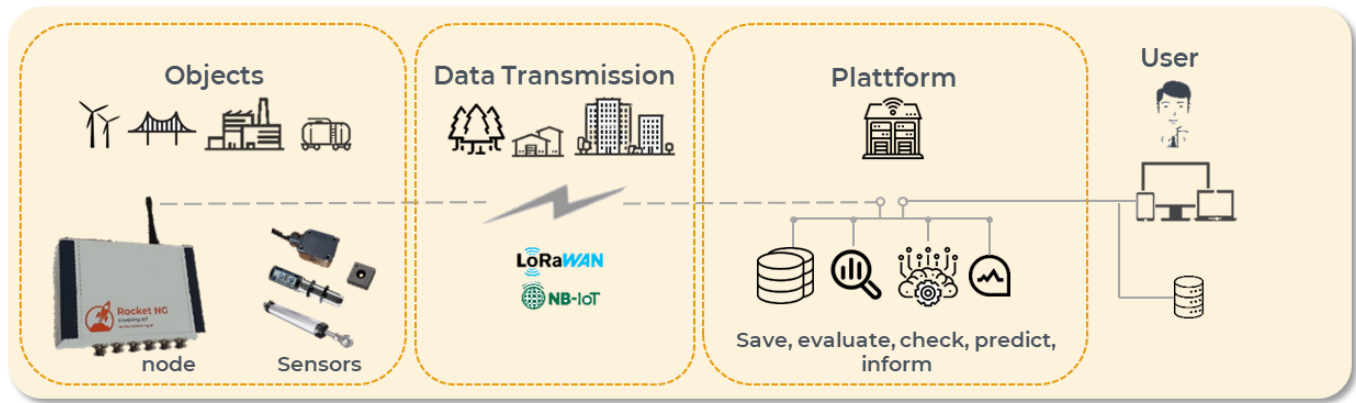


Figure 1: Interplay of the monitored assets (sensors and nodes), the data transmission, the platform, and the user.

In inspections the influence of temperature is frequently underestimated or too conservatively interpreted. In general, physical measures that are affected by environmental conditions are often difficult to assess, this holds for loads of pre-stressed anchors, inclinations, or displacements of components. As mentioned earlier accurate information is crucial to be used as a valid basis for decisions related to the maintenance, the safety assessment of the object and overall, the asset management combining both.

By leveraging monitoring, infrastructure managers can make informed decisions, optimize maintenance strategies, and extend their structures lifespan, making it a cost-effective solution. The description of the system used here clearly shows that digitalization and installing monitoring equipment are no longer hurdles.

### 1.2 IoT Type Monitoring

The IoT monitoring system presented and used in the following examples is an autonomous, innovative solution that enhances infrastructure monitoring for clients and contractors. It is in operation since many years across various applications and has already proven its reliability, robustness, and ease of use.

The system comprises of three main components as schematically shown in Figure 1:

1. On-site installation – sensors and IoT nodes placed on infrastructure assets are easily applicable even in areas without power access;
2. Data transmission network – nodes wirelessly transmit data to the platform for real-time assessment and can even be included into warning and alarm models;
3. Data platform – a secure database with evaluation models and web dashboards.

The design of the system for an autonomous operation, with battery-powered sensor nodes is capable of functioning for up to 15 years. Eliminating the need for fixed power sources significantly reduces installation complexity and associated disruptions, such as traffic closures. Data transmission is encrypted and automated, ensuring secure and reliable monitoring.

Key features and advantages of such an IoT system are:

- Plug & Forget: Fully automated system monitoring, with alerts for any issues;

- Edge Computing (AIoT): Onboard processing reduces data load and enables intelligent evaluation;
- Flexible Data Integration: External data sources can be fused for enhanced analysis;
- Instant Alerts: Critical conditions trigger automatic notifications via email, SMS, or warning and alarm systems;
- Real-Time Access: Mobile Apps and web-based dashboards provide instant insights - no additional software required;
- Data transmission is encrypted and automated, using the latest wireless technology.

The sensor node ( $16 \times 11 \times 7$  cm) is designed for harsh environmental conditions and ensures robust performance. It provides power to sensors, controls measurement cycles, stores data, and transmits information via low power WAN (1.5 km range in urban areas, 20+ km in open environments). The node supports multiple sensor connections (1, 2, or 6 channels), enabling flexible deployment across different assets.

The system requires no on-site configuration or specialized technical knowledge, significantly simplifying installation. Proper sensor mounting remains critical for ensuring measurement accuracy, though once installed, the network configuration and data transfer are entirely automated and need no interaction by the installation team. Furthermore, the system supports a wide range of sensor types, including:

- Displacement, strain, and force gauges;
- Pressure and temperature sensors (for air, solids, and liquids);
- Humidity sensors (ambient and material-based, including dew point calculations);
- Pluviometers and acoustic sensors for environmental monitoring;
- Corrosion monitoring and cathodic protection assessment;
- Water level measurement
- Water content and pore pressure determination in soils;
- Inclinations (for piers, retaining walls, mast, settlement of buildings and excavations ...).

Energy efficiency is a key design consideration, with preference given to low-power sensor alternatives to maximize battery life.



## 2 SELECTED APPLICATIONS

### 2.1 Reasons and benefits

As structures age, the parameters used to assess structural safety and durability worsen. This is particularly crucial for structures that approach their planned service life or which are in environments where environmental or load parameters change significantly over time. Examples here are the ground water conditions in geotechnical engineering or the impact due to winter maintenance such as de-icing agents. Due to the ageing infrastructure in Europe and most parts of the world digitalization of existing structures can be one tool to help address these issues with respect to longer lasting and safe infrastructure especially along road and railway networks.

By implementing dense monitoring systems, structures can be evaluated based on real-time, precise measurements rather than relying on conservative estimates dictated by standards. This approach can offer the possibility to extend the service life of structures by accurately measuring loads and issuing alerts before critical situations arise. The importance of such measurements increases as structures age, making digitalization even more crucial for older structures compared to newer ones.

However, most of the already installed measurement equipment is still analogue, nevertheless a wide range of these can be digitalized. In geotechnical engineering structures are often equipped with extensometers and inclinations for the determination of movements, load cells for the measurement of the currently applied anchor force and additionally, temperature and humidity measurements are available.

In the following some applications will be presented showing the potential of digitizing already existing measurement equipment and therefore offering an easy and cost-effective first insight into the behavior of a structure.

### 2.2 Digitalization of anchor load measurements

The retaining wall discussed here is shown in Figure 2 and is in service since the mid-1990s and some anchors are equipped with analog load measurement systems often applied in Austria.



Figure 2: View of the anchor wall.

In the course of an inspection, no serious defects or damages were found on the wall and the adjacent areas and a generally good state of preservation was attested. However, it was recognised that some of the anchor load measuring devices were only partially functional. Furthermore, a comprehensive time series regarding the anchor loads was not given.

For this reason, it was investigated how the existing hydraulic load cells could be reprocessed for analogue readings and how

digitalisation would be possible. The digitalization solely required an additional hydraulic connection and a smart node, which could easily be installed within one hour at the site.

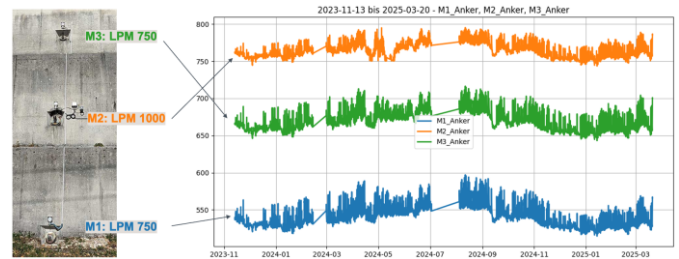


Figure 3: Time-series of anchor load measurements on three anchors along a cross-section.

Measurements show that the anchor loads are temperature-dependent, with significant variations throughout the year as shown in Figure 3. The observations further show that the higher capacity hydraulic load cell (indicated as LPM 1000) exhibits smaller force variations, than the two smaller (LPM 750) ones.

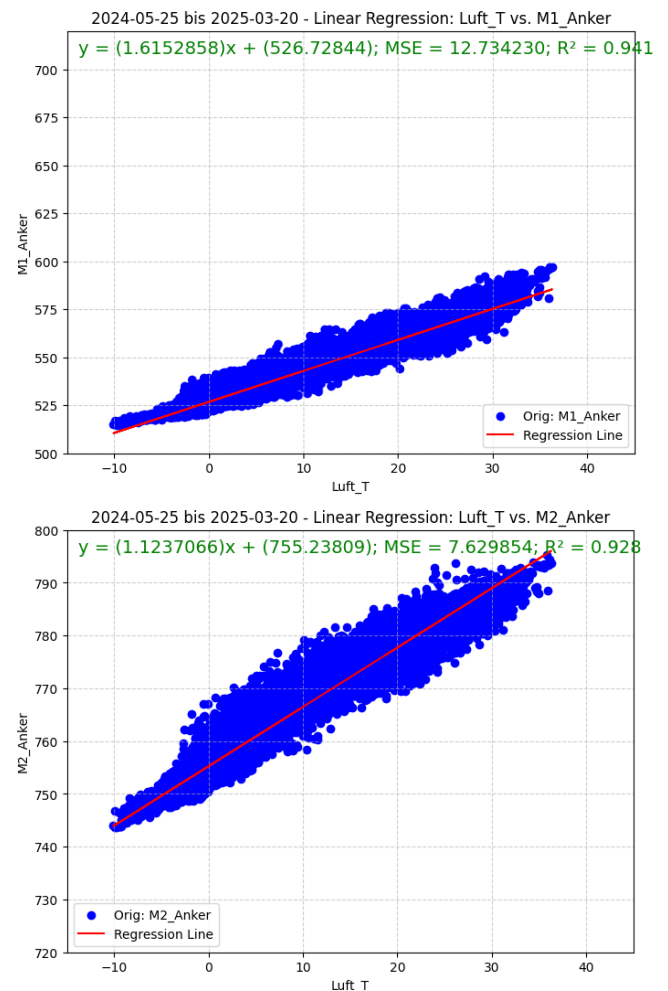


Figure 4: Correlation between anchor load (ordinate) and air-Temperature (abscissa) over a period of 1.5 years; top: M1 (LPM 750); bottom: M2 (LPM 1000).

Figure 4 illustrates the correlation between currently applied anchor load and air temperature for the two different LPM sizes, which were 750kN and 1000kN as given in the designation. It can be easily observed that there is an almost linear correlation between the anchor load measured and the air temperature. Thus, the change of the anchor load versus the air temperature can be calculated for:

1.55 kN/°C	LPM 750
1.10 kN/°C	LPM 1000

These values may be unique for the configuration found at this site and may not be applicable to other sites or structures. Nevertheless, those ranges of temperature related measurement results for anchor load plates are in alignment with the experience from anchor wall inspections as well as analogue readings of such measurement equipment.

### 2.3 Digitalization of extensometers

Figure 5 shows a detail of a extensometer of a retaining wall that is in service since decades. Based on observations during an inspection, it was recommended to shorten the measurement intervals, as the prevailing boundary conditions were now assessed to be more critical. In order to bridge the period until the structural reinforcement could be carried out, a suitable permanent monitoring system was implemented.

The extensometers were upgraded with nodes and sensors so that data was immediately available online and limits could be monitored 24/7. During the dense monitoring phase, a torrential rain event changed the environmental conditions even more. The new system was able to detect this immediately and action could be taken if necessary. Later, during the construction phase for the installation of new prestressed grouted anchors, valuable insights were also gained regarding the impact of anchor drilling on the system behavior of the structure.

Other applications include anchor force monitoring, bridge joints, pier tilting and deflection. Autonomy in the field is a must for economical implementation or upgrade of such monitoring.



Figure 5: Upgrade of existing extensometer for 24/7 and online measurement.

### 2.4 Static and dynamic crack width measurements

Crack monitoring was conducted on the center span of a three-span (45/70/45 m) cantilever bridge [4], where cracks were observed in the bottom plate and the webs of the hollow box. These cracks occurred in the transition zone, where the floor slab shifts from prestressed to non-prestressed, near the anchorages. Cracks in the floor slab are located within the prestressed zone, inclined at approximately 45° to the bridge axis, while those in the web follow a similar angle with continuous prestressing in this area.

Crack width monitoring, represented in green in Figure 6, covers five to six equally spaced cracks (~20 cm apart). The cracks run perpendicular to the measurement indications, with individual widths reaching up to 0.3 mm and a total width (sum of individual cracks) of up to 1.2 mm. Each group of cracks is monitored collectively, with the total crack width recorded. Warning thresholds were set for immediate detection of critical crack widths. Figure 7 illustrates crack width variations over a year. While significant, these variations remain within acceptable limits. Temperature measurements were incorporated to account for thermal deformations, as shown in Figure 7. The right-side diagram reveals that lower temperatures generally correlate with greater total crack widths, though the temperature effect is minimal. Detailed investigations revealed sudden spikes in crack width readings, suggesting abrupt crack openings. These spikes were detected in measurements taken at 15-minute intervals, indicating that dynamic loads were not fully captured by these static readings. To assess dynamic loads, the system was switched remotely to dynamic measurement mode, eliminating the need for on-site visits. In this mode, 10 measurements per second were taken and processed in the node (edge computing), evaluating maximum, minimum, and mean values over 5-minute intervals. On the platform, the dynamic range of crack width was calculated as the "Total Crack Width Range @ 5-minutes" (TCWR), representing the difference between maximum and minimum values within a 5-minute slot. Figure 8 shows the TCWR over a week, highlighting significant variations. During weekends, the TCWR remains low due to Austria's truck driving ban, with a notable increase at 22:00 on Sundays when the ban is lifted, peaking at 0.4 mm. Similar peaks occasionally occurred at 19:00 on weekdays. The highest TCWR (0.4 mm) was used to calculate the stress range in the reinforcement. Since mean stress is less influential for such steels, stress range remains the dominant fatigue parameter. The stress range calculation followed Eurocode 2 but incorporated refined parameters from literature [5]. Results indicated a dynamic stress range of ~90 N/mm<sup>2</sup>, well below critical limits. Combined with static calculations of mean stress, the findings confirm that reinforcement stresses are not critical.

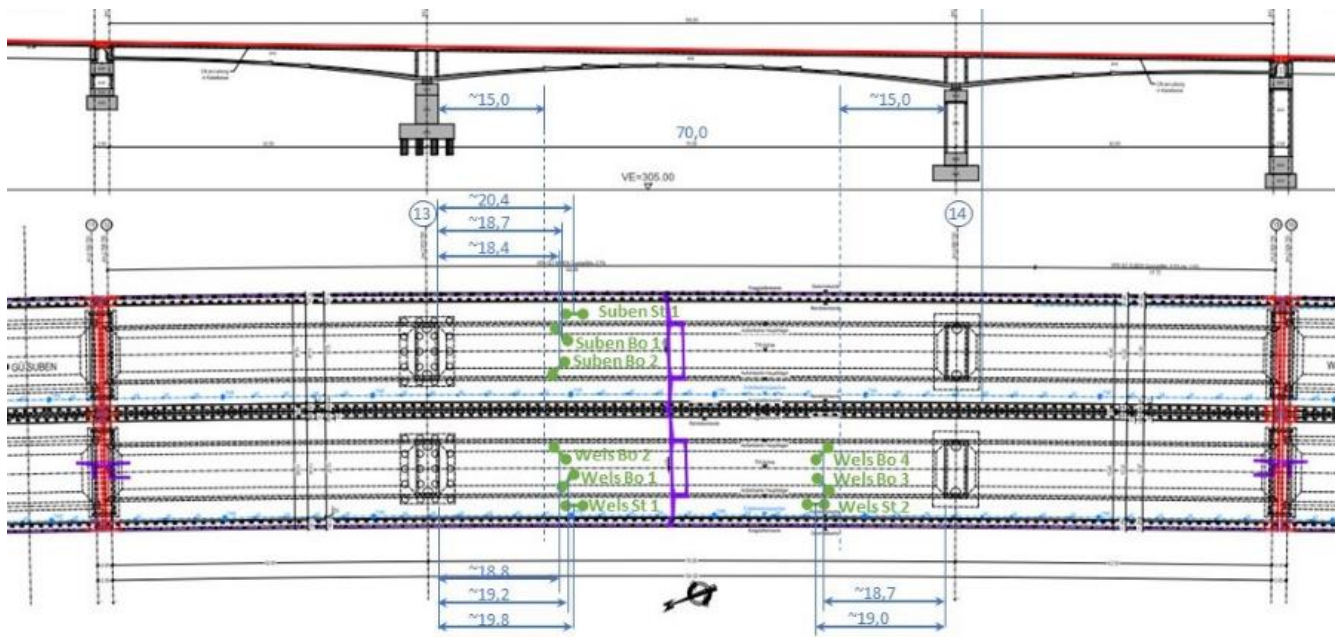


Figure 6: Overview of the three-span cantilever bridge. The monitoring of the total crack width is shown in green and the cracks run perpendicular to the measurements.

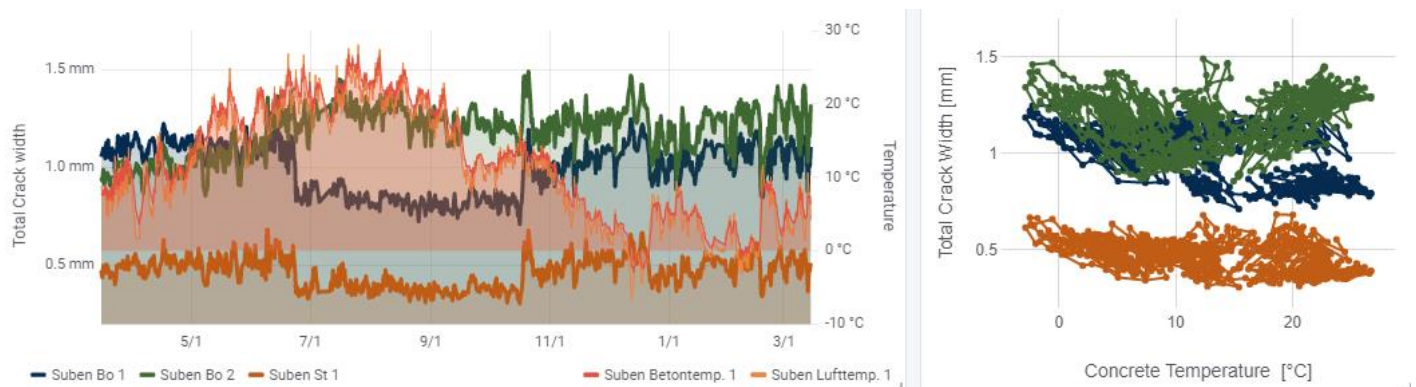


Figure 7: Variation of crack width for one year. Left diagram shows the values vs. time and the right diagram shows the values vs. concrete temperature.

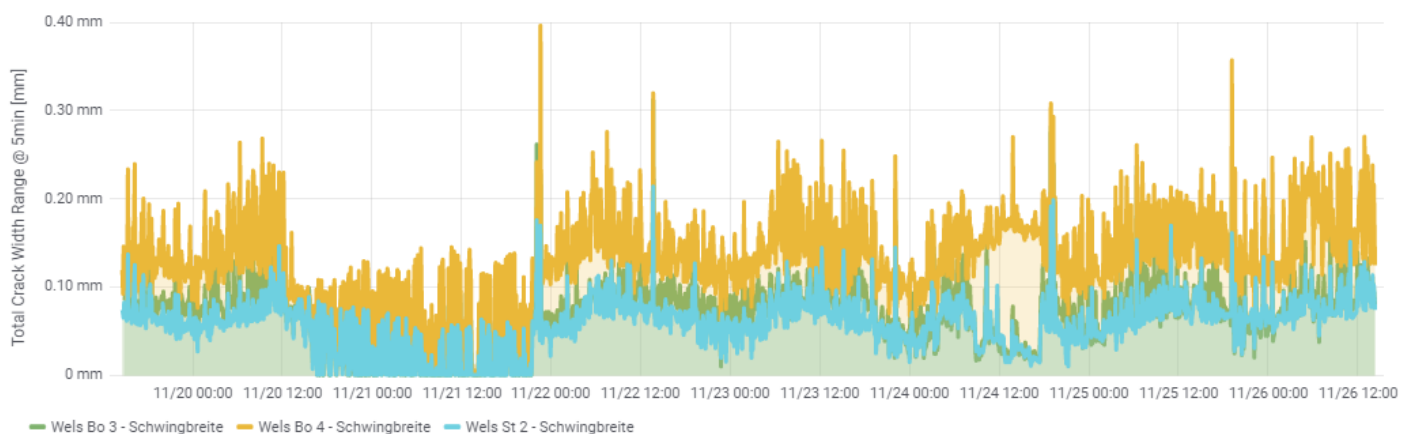


Figure 8: Max-Min-range of crack width for one week.



Energy consumption in dynamic measurement mode is higher due to continuous recording, processing, and data transmission at higher intervals. Battery life in this mode is estimated at ~1 months. However, after one week in dynamic mode, the system was switched back to 15-minute intervals for routine crack monitoring. The system has been operational for 4.5 years, with battery replacement expected in over six years.

The digitalization of the crack measurement was here an absolute game change because with manual readings it would have been enormously costly, the readings would not have been so dense, the temperature dependence would have been difficult to determine and dynamic measurements would not have been possible. through the digitalization of crack measurement, not only were costs saved by reducing on-site visits (and costs for lifting platforms), but the measurements also provided significantly more assessment options. This reduced the number of unknown effects and enabled a more detailed analysis, leading to a focused, durable, and cost-efficient rehabilitation.

### 3 DESIGN OF EXISTING STRUCTURES WITH AN INCREASED KNOWLEDGE LEVEL

There are currently only limited technical and legal guidelines on how to deal with existing infrastructure - especially with regard to existing damage or defects. Although there are already corresponding principles and concepts for this in maintenance and asset management, there is still a lack of corresponding guidelines and regulations, particularly in terms of recalculation and assessment.

Although the application of numerical models and the use of high-quality material laws can be used to define the bandwidths here, realistic modelling - especially of damage - is only possible to a limited extent. An example of this can be found in bridge construction. ÖNORM B 4008-2 [6] has laid the foundation for the recalculation of existing structures. Here, for example, the load models can be adjusted based on monitoring the traffic loads. This thus corresponds to a real load, which in turn can enable a more truthful design of the component loads and, above all, the deformations.

Furthermore, the integration of monitoring systems into this process could make a significant contribution. With regard to the difficulties of verifying the serviceability limits, the models can be adapted to a digital twin by comparing them with monitoring results. Based on such processes, damage patterns and their effects on the load-bearing behavior can also be taken into account more accurately.

### 4 CONCLUSIONS & SUMMARY

Using an IoT-based monitoring system provides a scalable, autonomous, and cost-effective approach to long-term infrastructure assessment. Its combination of wireless communication, edge computing, and real-time data processing enhances decision-making for maintenance and safety assessments. By eliminating complex on-site configurations and reducing energy consumption, such systems offer a robust and sustainable solution for modern infrastructure monitoring that does not require extensive training of workers on site.

The digitalization of existing structures is essential for extending the service life and ensuring safety, especially as

ageing and deteriorate prolong. Many structures, particularly in geotechnical and structural engineering, already have measurement systems in place, such as extensometers, inclinometers, and load cells. By upgrading these systems with modern sensors and online monitoring, real-time data can replace conservative assumptions, enabling more precise assessments. This helps detect critical changes early, preventing failures and reducing maintenance costs.

As infrastructure worldwide continues to age, digitalization becomes increasingly important to maintain structural integrity efficiently. Furthermore, with the progression of climate change-related effects such as the rise in mean temperature or the more frequent occurrence of torrential rainfall events, a more rapid increase in possible damage is to be expected, especially for civil infrastructure. Autonomous, cost-effective monitoring solutions can therefore offer a new possibility for monitoring, health inspection and structural assessment and can be seen as a valid basis for the asset management and the decision making related to it.

The presented applications demonstrate how existing measurement devices can be seamlessly integrated into digital systems, providing valuable insights for long-term structural health management.

### ACKNOWLEDGMENTS

We like to thank the Austrian Railways (ÖBB) and Austrian Motorways (ASFINAG) for their support in research projects that supported these results.

### REFERENCES

- [1] F. Binder, S.L. Burtscher, Verbesserte Bestimmung des Chlidgehaltes in Beton durch neues Messverfahren, p.88, in: 12. Symposium Experimentelle Untersuchungen von Baukonstruktionen. 1.06.2023, Dresden.
- [2] F. Binder, Schadensbeurteilungs- und Expertensystem für die Instandsetzung von korrodierenden Stahlbetonbauteilen, Ph.D-thesis at university of Applied Sciences, Vienna, 2021.
- [3] F. Binder, S.L. Burtscher, Concept to assess the performance on degrading concrete structures components, pages 129-134, Eurostruct 2023, Vienna.
- [4] S.L. Burtscher, P. Huber, F. Binder, H. Bauer Autonomous IoT for Condition Monitoring, Assessment and Predictive Maintenance - Advances and Examples, Eurostruct 2023, Vienna
- [5] Zilch K., Zehetmair G., Bemessung im konstruktiven Betonbau, Springer-Verlag GmbH, 2005.
- [6] ÖNORM B 4008-2, Bewertung der Tragfähigkeit bestehender Tragwerke - Teil 2: Brückenbau, Austrian Standards International, 120 pages, 2019.

# Increasing the value of bridge SHM data by leveraging network-level open data

Paul R.A. Fidler<sup>1</sup>, 0000-0003-4594-4323, Sam Cocking<sup>1</sup>, 0000-0003-2782-3464, Farhad Huseynov<sup>1</sup>, 0000-0002-5927-2444,  
Miguel Bravo Haro<sup>2</sup>, 0000-0003-0757-777X, Pedro Ubeda Luengo<sup>2</sup>, 0009-0000-4684-3511,  
Campbell R. Middleton<sup>1</sup>, 0000-0002-9672-0680, Jennifer M. Schooling<sup>3</sup>, 0000-0002-4777-0438

<sup>1</sup>University of Cambridge, Civil Engineering Building, 7a JJ Thomson Avenue, Cambridge CB3 0FA, United Kingdom

<sup>2</sup>City, University of London, Northampton Square, London EC1V 0HB, United Kingdom

<sup>3</sup>Anglia Ruskin University, East Road, Cambridge CB1 1PT, United Kingdom

email: praf1@cam.ac.uk, sc740@cam.ac.uk, fh392@cam.ac.uk, miguel.bravo-haro@city.ac.uk,  
pedro.ubeda-luengo@city.ac.uk, crm11@cam.ac.uk, jennifer.schooling@aru.ac.uk

**ABSTRACT:** Installing and maintaining structural health monitoring (SHM) systems on infrastructure assets can be expensive. These systems may produce large volumes of data that require processing and interpretation before the behaviour of the asset can be understood and assessed. However, in-depth understanding typically also requires knowledge of asset construction details and loading patterns. These data may be produced and stored using disparate systems, databases, and file types, creating additional challenges for data fusion and interoperability.

Additionally, there has been an increasing trend towards public bodies providing access to their data either reactively because of freedom of information requests, or proactively to encourage use by researchers or to allow others to provide innovative products or services using the data in ways not anticipated by those generating and providing them.

This paper presents potential strategies to leverage publicly available data from sources such as Network Rail Open Data Feeds, Rail Data Marketplace, OpenRail Data, OpenStreetMap and others, to contextualise and increase the value of SHM data. Data are considered from four instrumented railway bridges in the U.K., each of varying steel, concrete, and masonry construction. This paper presents scenarios by which these data might be used to gain network-level insights into other structures on the network and discusses the current difficulties in achieving this in practice.

**KEY WORDS:** Open data, Structural Health Monitoring, Data formats, Digital Twins.

## 1 INTRODUCTION

It is becoming increasingly common for structural health monitoring systems (SHM) to be deployed to monitor key transport infrastructure such as bridges. Interpretation of data generated by these systems is often challenging and may require additional information. For example, to understand the strains or deflection of a bridge deck it is also necessary to understand the applied loading, including loading from passing vehicles, or from environmental factors such as wind, or temperature. This requirement usually results in additional sensors being specified for the monitoring system.

For road bridges, detecting traffic can be done using lane occupancy sensors, cameras, or weigh-in-motion strips. As road traffic is usually completely unscheduled, there is no information known a priori about the traffic crossing the bridge. Interpreting these data can be challenging and it may be tempting to consider using machine learning (ML) techniques or computer vision to identify the type and position of vehicles. In some cases, such as in Bridge Weigh-In-Motion (B-WIM) systems where the primary purpose of the monitoring system is to weigh the road traffic [1], there may be sufficient sensor coverage to infer vehicle type directly from axle loads. However, in general vehicle identification may not be straightforward.

This need not however be the case for most railways. Railway operations, timetables, and signalling are increasingly digitised. The railway is a known environment, at least as far as those responsible for operating the railway are concerned. These data are already used to provide information to

passengers, e.g. through passenger information screens at stations. The data are also available to third-party developers of smartphone apps and websites. Leveraging data from railway timetables and signalling systems as an additional source of information for a bridge structural health monitoring system may mitigate the need for some sensors on the assets themselves.

### 1.1 Background

In 2015 researchers at the Centre for Smart Infrastructure and Construction (CSIC) at the University of Cambridge installed fibre-Bragg grating (FBG) strain and temperature gauges on two new railway bridges during construction: Bridges IB5 and UB11 in Staffordshire, UK.



Figure 1: Bridge IB5, Staffordshire, U.K.

Bridge IB5, shown in Figure 1, is of steel beam construction with an in situ concrete deck carrying two railway tracks [2],



while Bridge UB11, shown in Figure 2, is constructed from nine pre-tensioned concrete beams with an in situ concrete deck.

The initial goal of the project was to evaluate the potential benefits of installing instrumentation during construction and to create ‘self-sensing’ bridges as technology demonstrators for fibre-optic sensors and for Structural Health Monitoring in general. These were newly constructed bridges and so there was no concern regarding structural integrity, although the fibre-optic sensors were used to investigate creep and shrinkage of the concrete from pre-tensioning, through installation and after commissioning [3].



Figure 2. Bridge UB11, Staffordshire, U.K.

Initially the two Staffordshire bridges did not have permanently installed fibre-optic analysers or data loggers as there was no permanent power supply available on site. However, a power supply was provided in 2021, and permanent monitoring systems were installed, with IB5 upgraded with additional accelerometers, cameras and laser-based axle sensors [4]. These accelerometers and axle sensors were added to augment the existing FBG-based strain instrumentation to create a bridge weigh-in-motion (B-WIM) system [5].



Figure 3. Bridge HDB-19, London, U.K.

Subsequently, the centre also instrumented several other railway structures in the U.K. including Victorian and Edwardian masonry arch bridges, both of which were monitored due to potential concerns with the structures: Bridge HDB-19 in London – a three-span bridge instrumented with FBG strain and temperature sensors, and acoustic emission sensors; and CFM-5 in Yorkshire – a single span bridge instrumented with FBG strain sensors alongside conventional strain and displacement sensors and videogrammetry monitoring [6,7].



Figure 4. Bridge CFM-5, Yorkshire, U.K.

The monitoring systems on the two masonry arch bridges both used solar power. Despite using large deep-cycle batteries and multiple solar panels, these systems do not function 24 hours a day – the systems thus miss the structural response of the bridges for most train crossings.

### 1.2 Automated Train Identification

To interpret strain, deflection or accelerometer data measured during a crossing of a train over a bridge it is usually necessary to know information about the type of train, including axle loads and spacings. Trains of similar types are likely to produce similar responses, whereas trains of differing types may result in responses that are more difficult to compare.

Various techniques have been used to attempt train identification automatically. Alexakis *et al.* [8] limited their analyses of trains crossing the Marsh Lane viaduct, a masonry arch structure in Leeds, U.K., to only one type of train – the Class 185 three-car diesel multiple unit (DMU). Peak detection was used to identify train bogies and thereby determine which trains consisted of three carriages, while a comparison of readings from two adjacent arches was used to determine the train direction. The purpose of the monitoring was to evaluate whether the condition of the structure was deteriorating over time. Using a single train type allowed a comparison of the structural response from similar loading conditions on different dates. The trains identified as Class 185 trains represented approximately 50% of the traffic crossing the viaduct. Later analyses [9] identified other types of three-car train and Statistical Shape Analysis and a Support Vector Machine (SVM) was used to further classify these trains into Class 185, Class 155/158 and Class 170 respectively. The results were checked by visual observations of passing trains.

Cheng *et al.* [10] used gradient-based decision trees to identify and classify trains crossing Bridge CFM-5. A subset (4,900 out of 7,100) of train crossings identified using FBG strain data from July 2020 to October 2021 was labelled using timetable data obtained ‘by scraping publicly available records’. These labels were used to train a model using XGBoost [11] to classify trains based on features in the strain data such as number and spacing of peaks, amplitude and width of peaks etc. This model was then able to classify 930 further train crossing events over an 8-month period in 2023 achieving a classification accuracy of 97%.

To classify trains crossing Bridge IB5 where axles spacing and loading are provided via the B-WIM system, the authors used t-SNE (t-Distributed Stochastic Neighbour Embedding) – a statistical technique to group crossing trains into distinct



groups by reducing the dimensionality of input data. Input data include the number of axles, axle spacing, speed, axle loads etc. t-SNE is used to reduce these to just two dimensions which can then be plotted.

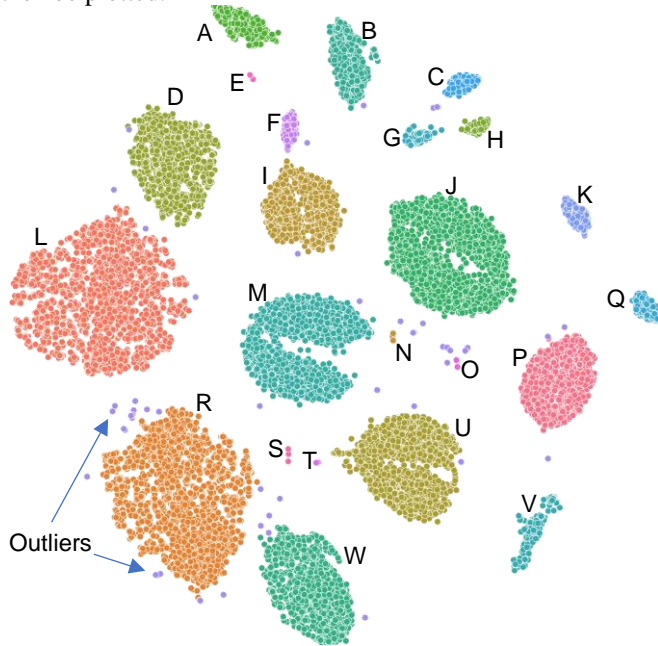


Figure 5. Groups of trains identified by t-SNE and DBSCAN unsupervised train classification

A clustering algorithm such as the Density-Based Algorithm for Discovering Clusters in Large Spatial Databases with Noise (DBSCAN) [13] is then used to distinguish separate groups of trains appearing as clusters within the plot.

Table 1. Labels assigned to groups shown in Figure 5 by manual inspection of video from on-bridge cameras

Label	Description	%
A	Class 390 9 car	2.28
B	Class 390 11 car	3.36
C	2 x Class 221 5 car (10 car total)	1.08
D	Class 350 175 tonne Direction 1	6.64
E	New Measurement Train	0.09
F	Class 220 4 car + Class 221 4 car (8 car total)	0.95
G	Class 221 4 car + Class 221 5 car (9 car total)	0.86
H	Class 221 5 car + Class 221 4 car (9 car total)	0.72
I	Class 220 4 car + Class 221 5 car (9 car total)	5.68
J	Class 221 5 car	11.27
K	Class 221 4 car	1.20
L	Class 350 165 tonne Direction 1	15.46
M	Class 220 4 car	9.85
N	Tamping Machine	0.18
O	Freight Locomotive	0.21
P	Class 221 5 car + Class 220 4 car (9 car total)	5.79
Q	Class 221 4 car + Class 220 4 car (8 car total)	1.14
R	Class 350 165 tonne Direction 2	14.41
S	Class 350 (axle detectors missed one axle)	0.13
T	2 x Class 350 (8 car total)	0.08
U	2 x Class 220 4 car (8 car total)	8.86
V	Freight Train	1.92
W	Class 350 175 tonne Direction 2	7.00
	Outliers	0.84

Figure 5 shows the plot resulting from 18,800 data points each representing a train. Only northbound trains are included due to limitations of the B-WIM system.

By referencing plots of the axle loads and inspecting video recordings from the cameras positioned on the bridge, labels may be manually assigned to these groups.

Some types of train such as the Class 220 Voyager and Class 221 Super Voyager look similar but may be distinguished using axle weights. Class 221 trains are heavier as they include tilting bogie mechanisms, absent on the Class 220. Similarly, Class 350 Desiro trains appear in four distinct groups on the plot. This is because there are two types within the class with differing total weights. This is likely because early Class 350 trains have dual-voltage capability and are able to use either the third rail system or overhead line equipment, while later Class 350s lack the third-rail pickup [14]. The axle loads are also asymmetric front to back relative to the direction of the train, which leads to two further groups.

Once labelled, the data can then be used as training data for ML techniques such as Random Forest [15] or XGBoost which can then be used to classify future trains.

Other methods that may be used for classifying trains on Bridge IB5 utilise computer vision (CV) and video from the on-site cameras directly. One such CV technique uses a vertical strip of pixels from each frame of a video of a passing train to produce a single 2D image where the x-axis represents time. Examples of such images are shown in Figure 6. A manually labelled set of these images is then used to train a model from a partially pretrained convolutional neural network (CNN) with Keras [16] as the deep learning framework. A dataset of 543 trains was randomly selected, of which 462 were used for image classification, split 85%/15% between training and testing images, respectively.



Figure 6. Examples of (a) Double 4-car Class 220/221, (b) 9-car Class 390, (c) 4-car Class 350, and (d) 5-car Class 221 trains approaching Bridge IB5. The still images are converted from moving video, with time along the x-axis

The results obtained are presented in Table 2 using a confusion matrix. These show classification accuracies of around 90% on average across all train classes. The CNN-based model achieved high classification accuracy despite the relatively small dataset of 543 samples, demonstrating the merit of the approach. However, it also highlights limitations which may not necessarily be solved by increasing the size of the training dataset.

Table 2. Confusion matrix of CNN-based train classification algorithm.

		Predicted				
		350	220/1 4-car	220/1 5-car	2×220/1 4-car	390
Actual	Train Class					
	350	96%	4%			
	220/1 4-car	6%	88%	6%		
	220/1 5-car		22%	78%		
	2×220/1 4-car				83%	17%
	390					100%

In particular, the model performs best when distinguishing visually distinct train types, but struggles with more subtle variations, such as between 4- and 5-car variants of Class 220/221 trains. These misclassifications suggest that incorporating additional features beyond image data, such as train speed or axle spacing, could significantly enhance model performance. Future work will explore hybrid models that combine visual and sensor-based inputs, as well as alternative machine learning techniques such as recurrent neural networks (RNNs) for temporal data or multimodal architectures that can process both image and numerical inputs simultaneously.

Computer vision techniques are however only applicable on SHM systems that incorporate cameras, such as the installation at Bridge IB5. It is also vulnerable to issues caused by poor lighting conditions such as at night or caused by inclement weather conditions leading to water or ice on the lens.

## 2 PUBLICALLY AVAILABLE RAIL DATA SOURCES

### 2.1 Network Rail

In the U.K. Network Rail is the organisation responsible for maintaining the track, signalling, most stations and operation of the railway in England, Scotland and Wales. It is not responsible for running train services, which are currently run by passenger and freight train operating companies (TOCs).

Network Rail provides access to some of its operational data including dynamic data on signalling, train movement data, and real-time performance measures, along with static data such as scheduling data and background data needed to interpret these datasets. Accessing the data requires registering an account on the Network Rail Open Data Platform [17] which is free of charge. The dynamic data are streamed via an ActiveMQ message queue connection, which requires a constant connection. Static data is available to download daily or monthly. These datasets have been used by mobile app developers to provide real-time information to passengers, such as the platform from which their train will depart, or whether their train is running late. The available datasets include:

- TD (Train describer): This is a real-time feed of train movements between signalling ‘berths’. The signalling ID

(or ‘headcode’) for each train is given, along with a ‘to’ and ‘from’ berth number representing a train movement. The signalling ID is only unique within a given signalling region at any one time. Berth numbers are not unique either. Timestamps are to the nearest second.

- TRUST (Train movement): This is another real-time feed of train movements between timing point locations (TIPLOCs), usually stations and junctions. Different message types describe train activation, movement, cancellation. Timestamps are provided to the nearest 30 seconds.
- SCHEDULE and VSTP: These provide details of services that are due to run. The schedule is updated once per day. Each service in the schedule can either be a one-off service, or be valid for a number of days, weeks or months. The VSTP dataset (Very Short-Term Plan) is a real-time feed of additional one-off services for ad-hoc movements not in the main schedule.

Documentation for the feeds is available on a wiki-style website [18] maintained by enthusiasts. Example source code of ActiveMQ clients able to fetch the data feeds is also available in multiple programming languages on GitHub [19].

Historical train movement data are not available from the Network Rail Open Data Feed. This limitation is not generally an issue for app developers but does limit what is available for interpreting past data from monitoring systems.

### 2.2 Rail Delivery Group

The Rail Delivery Group (formerly the Association of Train Operating Companies) in the U.K. provides additional feeds and APIs collectively known as DARWIN, which offer data for live departure and arrival screens, including estimated arrival and departure times for delayed trains. Also provided is the Historical Service Performance (HSP) API for historic performance data. HSP can be used to query details of past services, such as planned and actual arrival and departure times. However, as the DARWIN and HSP datasets are primarily used for passenger information they do not contain information about freight trains, and only list arrival and departure at stations, not showing the times when trains pass junctions.

### 2.3 Rail Data Marketplace

The Rail Delivery Group also runs the Rail Data Marketplace. This is a platform on which train operating companies, infrastructure providers, data aggregators, researchers, or rail enthusiasts may release datasets. Datasets include the Network Rail and Rail Delivery Group feeds described above, but also data on train operators’ carbon footprints, car park occupancy, train accessibility, fare information, occupancy and loading, complaints etc. Data providers may specify either an open or restricted licence for the data, and have the option of making data available publicly, or only to subscribers. The data may be made available free of charge or require payment.

### 2.4 OpenRail Data

The OpenRail Data website [24] combines data from the Network Rail SCHEDULE, VSTP and TRUST feeds to provide details of train movements, including cancellations, late/early running arrivals and some details of the type and class of train. Up to three years of historical data may be queried

using a variety of web-based forms, with results returned as an HTML page. The source code is available from a GitHub repository, and so it would be possible to run customised instances of this service, modified to produce output in alternative formats such as JSON or XML. However, this would not include historic data.

### 3 USING OPEN DATA FOR TRAIN IDENTIFICATION

The TD dataset gives timestamps for when trains on the network move between signalling berths. Berths are labelled with four-character identifiers, usually consisting of three or four digits. These do not indicate any human-readable place names, and there does not appear to be any available data linking berths with their geographic coordinates. It is however possible to look at all train movements that occur within a time window either side of a train crossing event as inferred from measurements by a monitoring system. This will result in many candidate berth numbers. Eventually however, after observing enough train crossings it is possible to narrow the berth numbers common to all crossings to find those berths that are likely to be located on either side of the bridge. Figure 7 illustrates one such possible method.

Using data from a typical day:

Create set U of all timestamped train movements from TD data  
Create a list X of timestamped bridge crossing events inferred from SHM data  
Create initially empty set C of candidate TD berth transitions  
Identify train movements in U that coincide (within a tolerance) of the first timestamped crossing event in X and add these movements (without timestamps) to set C  
For each further crossing event E in X:  
    Identify train movements in U that coincide (within a tolerance) with E and intersect these movements (without timestamps) with set C  
Output candidate TD berth transitions from set C

Figure 7. Possible algorithm to deduce TD berth transitions corresponding to train crossings identified by an SHM system

Alternatively, third-party websites such as OpenTrainTimes [23] provide topological track diagrams showing the real-time position of trains using TD data.

By using both TD and also TRUST data (which does include geographical human-readable locations) the creators of these sites have been able to infer the position of berths relative to stations and junctions. Although these track diagrams do not show bridge locations (except for intersection bridges where one railway track crosses another) by using these track diagrams it is nevertheless possible to narrow the search when attempting to identify TD berths located either side of a bridge.

Table 3 shows the berth transitions that most closely correspond in time to observed train crossings for the four instrumented bridges. For Bridges IB5 and UB11, these could be confirmed using the installed bridge monitoring system, while for Bridge HDB-19 these times were verified using

historical data as displayed on the OpenRail Data website [24] and comparing the actual arrival times of trains travelling between Enfield Chase station and Gordon Hill station, the two stations either side of the bridge which are not far apart. There are however points (or switches) north of HDB-19 allowing trains to cross the tracks to access the third platform at Gordon Hill station. Trains heading to or from the third platform have a slightly different berth number transition in the TD feed. For Bridge CFM-5 the crossing times of a few trains were observed and recorded in person during a site visit.

The TD data provides a very good correspondence with bridge crossings for Bridges IB5 and UB11. However, the only useful information provided by the feed besides the timestamp is the signalling ID, known as the headcode, of each train. This provides no train information such as the type of train or possible loading. This must be found either from the TRUST feed or via a third-party website such as OpenRail Data.

Since most of the data from the monitoring systems on these bridges dates from before the authors began logging the TD and TRUST feeds, the possibility of using historical data from OpenRail Data alone was investigated. For Bridges CFM-5 and HDB-19, this turns out to be relatively simple. For Bridge CFM-5 there are no intervening junctions between Church Fenton and Micklefield stations – so any train that reports at both locations consecutively must have crossed the bridge. The only complication is in calculating the most likely time of the crossing as the two stations are approximately 8 km apart, with the bridge located slightly closer to Church Fenton station.

Table 3. TD berth movements that correspond with observed bridge crossings

Crossing	Region	From Berth	To Berth
IB5 northbound	R3	4331	4333
IB5 southbound	R3	4334	4332
UB11 westbound	R3	5611	5615
HDB-19 northbound	Y8	865	869
	Y8	865	X872
HDB-19 southbound	Y8	870	864
	Y8	872	864
CFM-5 eastbound	Y2	709	711
CFM-5 westbound	Y2	714	708

Likewise in the case of Bridge HDB-19, any train reporting at both Enfield Chase and Gordon Hill stations will have crossed the bridge. However, it was noted that in the archived data several services are not shown stopping or passing Enfield Chase station at all. Trains do however all appear to report at Bowes Park station, slight further to the south, so both stations were used when searching for trains crossing the bridge.

For Bridges IB5 and UB11 however, the situation is slightly more complicated. Figure 8 shows the layout of the railway in the Norton Bridge area. Northbound trains travelling between Stafford and Madeley stations either use the West Coast Main Line through Norton Bridge Junction and under Bridge IB5, or they bypass Norton Bridge Junction entirely by crossing Bridge UB11. Northbound trains travelling between Stafford and Stone must cross Bridge IB5, but southbound trains from Stone to Stafford may travel either via Bridge IB5 or via Norton Bridge Junction.



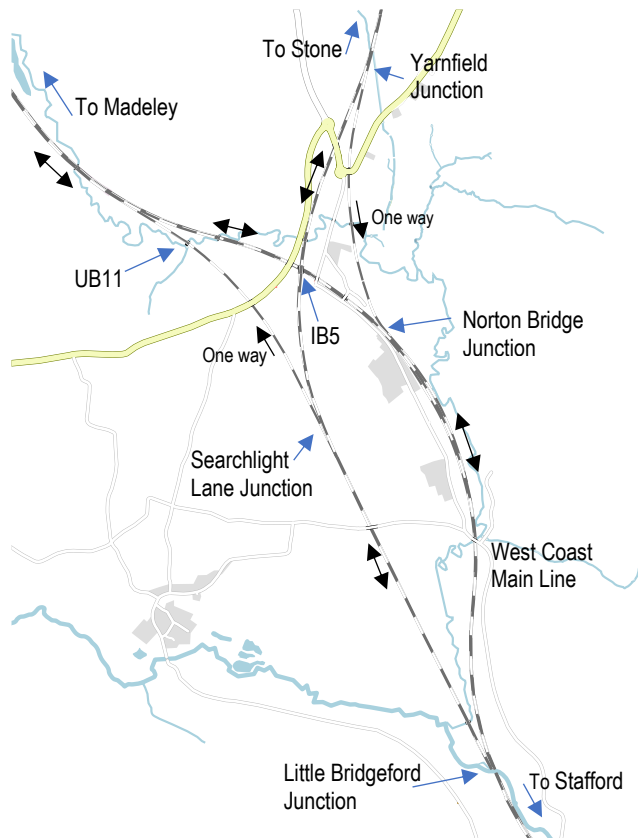


Figure 8. Map showing locations of Bridges IB5 and UB11, railway layout and junctions. (Map data © OpenStreetMap available under Open Database License)

Nevertheless, by inspecting details of several trains crossing the bridges, identifying their headcode ID from TD data, and then looking up details of each train on the OpenRail Data website, sets of rules were developed to identify trains crossing Bridge IB5 and UB11 using only historic data available from the OpenRail Data website.

### 3.1 Train and route information

Information available from the TRUST and Schedule feeds, or the historical data, includes data such as: The Train UID, the train operator code, signalling id (headcode), power, timing load, speed, catering code, seating class, train status etc. and the planned and actual arrival, departure and passing times at each timing point or station along the route.

Of these the power type, timing load and train status are the most useful for train identification. Power type refers to diesel, diesel multiple unit, electric, electric multiple unit or (for the New Measurement Train) 'HST'. Timing load is an overloaded field. It usually contains a number which if greater than 999 describes the declared load in tonnes. Otherwise, this number may indicate the declared load in tonnes, or the class of train – e.g. 350, 390 etc. There are some exceptions: a value of 506 indicates Class 350 upgraded to run at 110 mph (approx. 175 km/h) while a 'V' indicates a Class 220 or 221 train. The train status field indicates whether the train is a passenger or freight train. Any of the fields may be blank.

### 3.2 Comparison with Monitoring data

For the railway bridge monitoring systems that are operational 24/7, such as those on Bridges IB5 and UB11, there should be

SHM data for each train that crossed the bridges, and there should also be trains identified from TD, TRUST, or historic train movement data corresponding to each event. Where this is not the case, this indicates a possible fault with the monitoring system. For Bridge IB5 it is also possible to assess the coverage of the B-WIM system.

As can be seen from Table 1 the t-SNE+DBSCAN algorithm results in many different groupings for otherwise similar trains or combinations of similar trains. However, the train class information derived from the timing load field in archived data from OpenRail Data does not distinguish between Class 220 and 221 trains and lists these as a single class. Similarly, these data do not distinguish between 9 or 11-car Class 390 trains, or the different types of Class 350.

To allow for easier comparison between the loads classified using t-SNE+DBSCAN and traffic identification based on the archived data, similar load classifications from the t-SNE+DBSCAN results for crossings in July 2023 were added together. The results are shown in Table 4.

The classification of trains using groups found by the t-SNE+DBSCAN algorithm shows generally good agreement with the identifications derived directly from open data. The archived data deduced ten more train crossings than trains processed by the t-SNE+DBSCAN algorithm. This discrepancy is partly accounted for by double-crossing events where two trains cross the bridge in opposite directions within a few seconds of each other. The SHM system treats these double crossings as a single event prior to any processing by the B-WIM system.

Table 4. Comparison of B-WIM t-SNE load classifications and traffic identified from historic open data for trains crossing Bridge IB5 in July 2023

Description	B-WIM (t-SNE)		Archived data	
Class 220/221	650	50.94%	658	50.04%
Class 350	401	31.43%	421	32.02%
Class 390	154	12.07%	139	10.57%
Other passenger			7	0.53%
Freight	52	4.06%	60	4.56%
Tamping machine	2	0.16%		
NMT	1	0.08%	1	0.08%
Outliers	16	1.25%		
Total	1276	100.00%	1286	100.00%

Both methods are able to distinguish the New Measurement Train (NMT) from other trains. This train is a modified Class 43 High Speed Train, formerly used to carry passengers, but now instrumented with sensors to measure track alignment and gauge, and photograph defects while travelling at line speed. In the t-SNE+DBSCAN data it appears as its own (small) group labelled as 'E' in Figure 5. In the archived train movement data it is the only train with a train status of 'freight' but with a power type of 'HST' and a speed of 125 mph (approx. 200 km/h).

The B-WIM classifier identified two tamping machines. One of these on 7<sup>th</sup> July 2023 was mis-classified and was actually a 16-axle Class 350 passenger train, as verified by inspecting video of the crossing. However, only 10 axles were detected by the B-WIM system, which may have resulted in the train being incorrectly grouped. The second tamping machine on the

14<sup>th</sup> July as shown in Figure 9 was correctly identified from the B-WIM derived data. However, it was listed in the archived train movement data as a 715-tonne diesel freight train. The accompanying route information for the train showed that it originated at Whitacre Tamping Sidings, which would indicate that it was probably a tamping machine. The declared load of 715 tonnes is significantly larger than the load as shown on a placard on the side of the vehicle (99 tonnes) or the load as measured by the B-WIM system (102 tonnes).



Figure 9. Tamping vehicle heading after crossing Bridge IB5 on 14 July 2023

The archived train movement data are based on SCHEDULE and TRUST data. As previously discussed, these data alone are not able to distinguish between Class 220 and Class 221 trains.

Table 5. Comparison of trains deduced to have crossed Bridge HDB-19 and the FBG strain events recorded by the SHM system.

	TRUST data	FBG events	Proportion recorded
<b>Passenger</b>			
Class 387	35	2	5.7%
Class 700	11	0	0.0%
Class 717	1353	330	24.4%
Class 800/805	11	0	0.0%
Class 802	1	0	0.0%
Other electric	1	0	0.0%
<b>Sub total</b>	<b>1412</b>	<b>332</b>	<b>23.5%</b>
<b>Freight</b>			
400 tonnes	6	6	100.0%
600 tonnes	17	8	47.1%
715 tonnes	4	0	0.0%
800 tonnes	3	0	0.0%
1200 tonnes	19	2	10.5%
1235 tonnes	12	1	8.3%
1400 tonnes	9	7	77.8%
1600 tonnes	67	17	25.4%
Not declared	17	2	11.8%
<b>Sub total</b>	<b>154</b>	<b>43</b>	<b>27.9%</b>
<b>Other</b>			
NMT	2	1	50%
<b>Total</b>	<b>1567</b>	<b>369</b>	<b>23.5%</b>

However, other datasets available on the Rail Data Marketplace may solve this issue. CrossCountry Trains, which operates the Class 220 and 221 trains, makes the planned train formation of each train available. The data are available as daily CSV files and include serial numbers of the individual trainsets to be used for any given service. This is sufficient to determine the train class. Other train operating companies also make train formation data available.

For monitoring systems such as those used on Bridges HDB-19 and CFM-5 where power is supplied by solar panels and batteries, the monitoring system is likely to miss a significant fraction of train crossing events while the system is powered down. Using the data from TD or TRUST can provide an indication of which trains are missed, and whether the crossings that are recorded are likely to be indicative of the loads that typically cross the bridge.

FBG strain events from the SHM system on HDB-19 were compared with trains crossings from archived TRUST data for the period 1<sup>st</sup>–15<sup>th</sup> July 2023. When comparing timestamps between the SHM system and the archived TRUST data, it became apparent that the FBG data did not indicate whether the times had been recorded using UTC or daylight savings time. Since the trains mostly follow a repeating hourly timetable, most train crossings occurring at approximately the same times each hour. When the SHM system was initially installed there was no requirement for the system to synchronize with any external system or data. There was also nothing to prevent clock drift other than an intermittent Internet connection to time.microsoft.com using the NTP client available on Windows. However, after some investigation it appeared that the correlation between crossings and logged FBG events fit better with the archive TRUST data if it was assumed that the FBG timestamps were recorded using daylight savings time and not UTC. This illustrates the importance of looking ahead when specifying and commissioning SHM systems.

Table 5 shows the results of the comparison. It can be seen that approximately three quarters of the trains deduced to have crossed Bridge HDB-19 were not recorded by the FBG strain gauges. As the SHM system is solar powered, it only records data when the solar panels have charged the battery sufficiently for the system to operate, usually from mid-morning to mid-afternoon. Nevertheless, despite missing some classes of train completely, the system was able to record strain data during the crossings of a broadly representative sample of the total population of trains crossing Bridge HDB-19, including freight trains with the heaviest declared loads. However, if all that is required is a ‘standard’ train with which to compare data recorded on the structure from one day to the next to check whether the structural response is changing over time, then the Class 717 train would seem to be a good choice.

#### 4 NETWORK-LEVEL INSIGHTS

The Network Rail data feeds cover the movement of trains throughout England, Scotland and Wales. Once subscribed to the feed, data is available for all train movements on the network, not just in the locations originally of interest. One potential use case of these feeds would therefore be to derive bridge specific traffic models (if not necessarily load models) for every underline bridge, intersection bridge or viaduct on the network. For those bridges located up or down the track from a

bridge instrumented with a B-WIM system, it may even be possible to produce a bridge-specific load model, assuming the bridges have sufficient traffic in common. This however would require knowledge of the location of the bridges on the network, and ideally the locations of berth numbers either side of every bridge.

#### 4.1 Bridge Locations

Through a series of Freedom of Information (FoI) requests made by members of the public, Network Rail have released lists of structures on each line of the network. Data from these FoI requests are available in a curated form on the RailwayData website [21]. The bridges listed do not typically have either WGS84 coordinates, or UK Ordnance Survey (OS) grid reference, but instead are described using the number of miles and yards (or sometimes miles and chains) from some datum which is specific to each line.

Recently however, because of work done within Network Rail as part of its Bridge Strike Prevention Strategy, Network Rail has released a list [22] of low bridges at risk of being struck by road vehicles. As the intended use for the data is that they are incorporated into in-vehicle or smartphone-based GPS systems, this list includes bridge headroom data together with WGS84 and OS grid references coordinates in addition to the usual line/miles/yards location. It provides such coordinates for 5792 bridges, but as it only lists vulnerable bridges it is not a complete list of all underline or intersection bridges, or viaducts. The list includes Bridges CFM-5 and HDB-19, both rail-over-road bridges. It does not however list Bridges IB5 or UB11 as the first is an intersection bridge carrying the railway over another rail line, while the second carries the railway over a stream.

Another option is to use data from OpenStreetMap. OpenStreetMap is a collaborative volunteer organisation that is building a database of mapping data that is released under the permissive Open Database License. However, as a volunteer effort, there are no guarantees as to the accuracy of the data, or that they are consistently labelled in a way that makes it possible to query specific features, such as railways and bridges carrying railways.

As an open project, there are services that build upon OpenStreetMap to allow additional functionality such as searching for specific features within the data using simple queries. Overpass Turbo [26] is one such service. It includes a ‘wizard’ to compose queries from simple prompts.

A prompt such as:

```
"((bridge=yes or bridge=viaduct) and railway=rail) in England"
```

will result in a query that can be passed to the Overpass API with the matching features displayed on a map, as shown in Figure 10.

```
// fetch area "England" to search in
area(id:3608484939)->.searchArea;
// gather results
(
  nwr["bridge"="yes"]["railway"="rail"](area.searchArea);
  nwr["bridge"="viaduct"]["railway"="rail"](area.searchArea);
);
// print results
out geom;
```

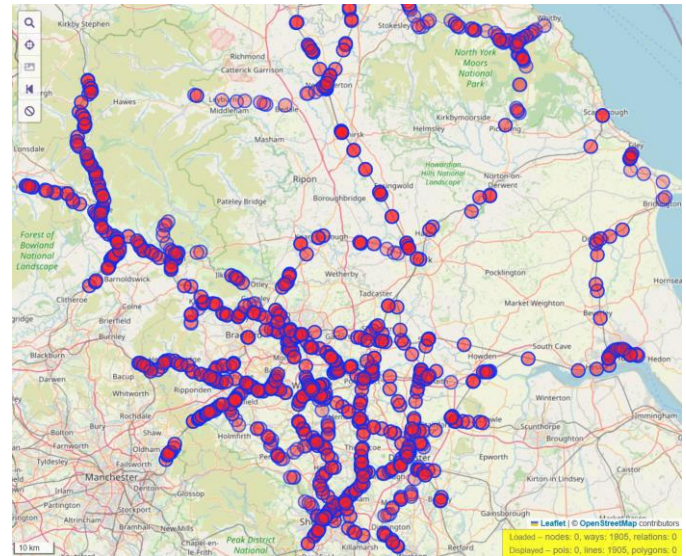


Figure 10. Result of running an Overpass API query to find locations of railway bridges and viaducts. (Map data © OpenStreetMap available under Open Database License)

#### 4.2 Signalling berth locations

There are various ways one could consider obtaining the locations of the signalling berths. One option would be to use the GPS position of trains on the network and compare this with the live TD feed. This would give the approximate location of each berth. These could then be compared with the GPS coordinates of the bridges, where known. These data are not provided in any currently available Network Rail open dataset, but third-party app developers of ‘Find My Train’-style apps may have GPS data generated by users of those apps as they travel by train. However, these data may not be open data. SignalBox.io have such a system but require users to sign up for an API key before accessing the data. Other companies such as Raildar, Tracksy.uk, Mistral-data and TrainPositions.com provide similar services under various subscription options.

Train operators in some other European countries do make real-time location data available. Irish Rail (Iarnród Éireann) provide this data via a simple URL, while in Finland train locations may be retrieved using a Real-Time General Transit Feed Specification (GTFS RT) feed or a via a web-based API.

Alternatively, as the location of each bridge is available from data in the FoI requests, albeit in line/mile/yards format, it may be more feasible to calculate TD berth positions in line/miles/yards format too. This could be done by looking at timestamps of TD berth transitions and comparing these with timestamps from TRUST data when trains report at locations with known positions, such as stations. Finding berths either side of a bridge could then be done simply by comparing berth miles and yards locations with bridge miles and yards locations.

## 5 RECOMMENDATIONS

- When planning to install a monitoring system, look for potentially useful open datasets early, whether related to traffic, weather, or anything else.
- Consider any secondary uses that the planned monitoring system may have that could be enabled with relatively small additions. (E.g. Added axle detectors to enable B-WIM that



then provides loading data for other bridges on the network.)

- Treat streaming datasets like sensor data. Data that is used for operational purposes may have little long-term value to the network operator, and these data are often ephemeral. To avoid these data becoming digital waste, log them from day one (or before). Do not assume that somebody else will preserve them.
- Log data first, process later. If datasets are difficult to interpret either because of the sheer volume of information or due to a lack of documentation, log them anyway. They can be processed later once the data are better understood.
- Ensure clocks on any monitoring systems are set accurately. If a permanent connection to the Internet is available this is usually achieved using Network Time Protocol (NTP) to keep clocks synchronised, otherwise, if outdoors, a simple GPS receiver can be used to provide accurate time. When comparing data from multiple sources it is vital that timestamps of data logged by monitoring systems and data from one or more external datasets may be compared. Agree on a time zone.
- Where data from monitoring systems is combined with as-designed and as-built data to form a digital twin, any additional data derived from open datasets should also be incorporated into the digital twin.

## 6 CONCLUSION

A wealth of data exists that can be used to better understand data generated by bridge monitoring systems on Britain's railways. However, the data are unlikely to be generated in exactly the format needed by a monitoring project. They are instead created (and deleted) according to the needs of the network and train operators.

Nevertheless, once a network-level data source has been identified and its potential benefits and limitations understood, it may have the potential to be used for train identification or bridge-specific load or traffic modelling for multiple monitoring projects. Identifying and logging potential data sources early mitigates issues relating to data retention. Data should be logged as early as possible in the project even if the ability to understand them and use them effectively comes later. Machine Learning and AI remain valuable tools with which to understand data generated from monitoring systems, but sometimes there are simpler ways, requiring less computational resources, to achieve the same goal.

## DATA AVAILABILITY

Data supporting this paper are available from the University of Cambridge Repository:  
<https://doi.org/10.17863/CAM.116750>.

## ACKNOWLEDGMENTS

The authors would like to thank Network Rail for making train movement and scheduling data available on their Open Data Feeds site, and for their continuing support of the Staffordshire Bridges and HDB-19 projects.

This work was made possible by the Centre for Smart Infrastructure and Construction (CSIC) and the Laing O'Rourke Centre for Construction Engineering Technology within the Department of Engineering at the University of

Cambridge. We would like to thank Prof. Changsu Shim (심창수) and the Chung-Ang University Industry Academic Cooperation Foundation, South Korea for funding from the 'Development of Digital Engineering Services for Roadside Structure Design, Manufacturing and Construction' project, and thank Chiho Jeon (전치호) and Jongbin Won (원종빈) for their assistance and support. The support of the EPSRC UKCRIC National Research Facility for Infrastructure Sensing experimental facilities (EP/P013848/1) is also much appreciated.

The authors would also like to thank Peter Hicks for maintaining the Rail OpenData Wiki, Phil Wieland for creating and running the OpenRail Data project and the developers of OpenTrainTimes Live Track diagrams website, and the many contributors to OpenStreetMap project.

For the purpose of open access, the authors have applied a creative commons attribution (CC BY) license to any author accepted manuscript version arising.

## REFERENCES

- [1] M. Lydon, S.E. Taylor, D. Robinson, A. Mufti and E.J.O. Brien. Recent developments in bridge weigh in motion (B-WIM). *Journal of Civil and Structural Health Monitoring* (2016) 6:69-81. 2016. DOI: 10.1007/s13349-015-0119-6
- [2] L.J. Butler W. Lin, J. Xu, N. Gibbons, M.Z.E.B. Elshafie and C.R. Middleton. Monitoring, modelling and assessment of a self-sensing railway bridge during construction. *Journal of Bridge Engineering*, ASCE, 23(10). 2018. DOI: 10.1061/(ASCE)BE.1943-5592.0001288
- [3] L.J. Butler, N. Gibbons, P. He, C.R. Middleton and M.Z.E.B. Elshafie. Evaluating the early-age behaviour of full-scale prestressed concrete beams using distributed and discrete fibre optic sensors. *Construction and Building Materials*. 126 (2016) pp. 894-912. 2016. DOI: 10.1016/j.conbuildmat.2016.09.086
- [4] P.R.A. Fidler, F. Huseynov, M. Bravo-Haro, V. Vilde, J.M. Schooling, C.R. Middleton, Augmenting an existing railway bridge monitoring system with additional sensors to create a bridge weigh-in-motion system and digital twin. Presented at SHMII-11: 11th International Conference on Structural Health Monitoring of Intelligent Infrastructure August 8-12, 2022, Montreal, QC, Canada. 2022.
- [5] F. Huseynov, P.R.A. Fidler, M. Bravo-Haro, V. Vilde, J.M. Schooling, C.R. Middleton. Setting up a real-time train load monitoring system in the UK using Bridge Weigh-In Motion technology - A case study. Presented at SHMII-11: 11th International Conference on Structural Health Monitoring of Intelligent Infrastructure August 8-12, 2022, Montreal, QC, Canada. 2022.
- [6] S. Cocking, D. Thompson, and M.J. DeJong. Comparative evaluation of monitoring technologies for a historic skewed masonry arch railway bridge. In: *Proceedings of ARCH 2019, the 9th International Conference on Arch Bridges*, Porto, Portugal, 2019. DOI: 10.1007/978-3-030-29227-0\_46
- [7] S. Cocking, H. Alexakis, and M.J. DeJong. Distributed dynamic fibre-optic strain monitoring of the behaviour of a skewed masonry arch railway bridge. *Journal of Civil Structural Health Monitoring*, 11(4), 989-1012, 2021. DOI: 10.1007/s13349-021-00493-w
- [8] H. Alexakis, A. Franza, S. Acikgoz, and M. DeJong. Structural health monitoring of a masonry viaduct with Fibre Bragg Grating sensors. In *IABSE Symposium, Guimaraes 2019: Towards a Resilient Built Environment Risk and Asset Management* - pp. 1560-1567. 2019. DOI: 10.17863/CAM.38693
- [9] H. Alexakis, F.D.H. Lau & M.J. DeJong. Fibre optic sensing of ageing railway infrastructure enhanced with statistical shape analysis. *Journal of Civil and Structural Health Monitoring* 11, 49-67 2021. DOI: 10.1007/s13349-020-00437-w
- [10] J. Cheng, A. Chen, M.J. DeJong, S. Cocking, Data-derived train classification and monitoring of masonry bridge, *Bridge Maintenance, Safety, Management, Digitalization and Sustainability*, p.3371-3379, CRC Press, 2024. DOI: 10.1201/9781003483755-399
- [11] T. Chen, T. and C. Guestrin.. XGBoost: A Scalable Tree Boosting System. In *Proceedings of the 22nd ACM SIGKDD International*

- Conference on Knowledge Discovery and Data Mining (pp. 785–794). New York, NY, USA: ACM. 2016. DOI: 10.1145/2939672.2939785
- [12] G. Hinton. Visualizing Data using t-SNE. *Journal of Machine Learning Research* 9. (2008) 2579-2605. 2008.
- [13] M. Ester, HP. Kriegel, J. Sander and X. Xu. A Density-Based Algorithm for Discovering Clusters in Large Spatial Databases with Noise. *Proceedings of the Second International Conference on Knowledge Discovery and Data Mining (KDD-96)*. AAAI Press. pp. 226–231. ISBN 1-57735-004-9. 1996.
- [14] British Rail Class 350. Wikimedia Foundation, Inc. Accessed 29-March-2025. [https://en.wikipedia.org/wiki/British\\_Rail\\_Class\\_350](https://en.wikipedia.org/wiki/British_Rail_Class_350)
- [15] T.K. Ho, Random decision forests. In *Proceedings of the 3rd International Conference on Document Analysis and Recognition (Vol. 1, pp. 278–282)*. IEEE. 1995.
- [16] F. Chollet et al. Keras: Deep Learning for Humans. <https://keras.io>. 2015.
- [17] Network Rail Open Data Platform. Network Rail. Accessed 12-March-2025. <https://publicdatafeeds.networkrail.co.uk>
- [18] Rail Open Data Wiki. Peter Hicks et al. Accessed 15-March-2025. <https://wiki.openraildata.com> <https://github.com/openraildata/ta.com>
- [19] Open Rail Data – GitHub. Peter Hicks et al. Accessed 15-March-2025. <https://github.com/openraildata>
- [20] Rail Data Marketplace. Rail Delivery Group. Limited. Accessed 07-March-2025. <https://raildata.org.uk/>
- [21] RailwayData | Bridges. [railwaydata.co.uk](https://railwaydata.co.uk). Accessed 15-March-2025. <https://railwaydata.co.uk/bridges>.
- [22] Network Rail Bridge Height Data. Network Rail. Accessed 11-March-2025. <https://www.networkrail.co.uk/wp-content/uploads/2024/11/Network-Rail-Bridge-Height-Data-1.xlsx>
- [23] OpenTrainTimes: Real-time Track Diagrams. OpenTrainTimes Ltd. Accessed 03-March-2025. <https://www.opentraintimes.com/maps>
- [24] OpenRail Real Time Railway Data. Charlwood House Systems. Accessed 07-March-2025. <https://www.charlwoodhouse.co.uk/rail/liverail>
- [25] GitHub - philwieland/openrail: Open Rail Data Processing. Accessed 07-March-2025. <https://github.com/philwieland/openrail/>
- [26] Overpass Turbo. Accessed 16-March-2025. <https://overpass-turbo.eu>

# ***A comprehensive workflow for digitizing and determining condition indicators for bridge and building construction***

Michael Olipitz<sup>1</sup>, Roland Jung<sup>2</sup>

<sup>1</sup>SDO ZT GmbH, Atelier Kunstmühle, Goritschach 19, 9184 St. Jakob i/R, Austria

<sup>2</sup>Departement of Smart Systems Technologies, Universität Klagenfurt, Lakeside B04, 9020 Klagenfurt, Austria  
email: office@olipitz.com, roland.jung@aau.at

**ABSTRACT:** This article describes a comprehensive workflow in several phases that integrates the latest information and communication technologies and enables significant improvements in the assessment of both our infrastructure structures, especially our bridge structures, and our building structures. For building construction, the workflow includes not only the PERIOD mode (= PM) for the normal situation, but also a so-called RESCUE mode (= RM), which provides significant support for emergency services in the event of natural disasters such as earthquakes. In all applications in infrastructure and building construction, a digital twin is created along the structural axis in Phase I and automatically converted into a BIM model (= BIM<sub>UAV</sub>). The resulting BIM<sub>UAV</sub> model forms the basis for documenting the general condition of the construction in Phase II, which is referred to as the level of maintenance (= LOM) and documented using component-specific damage catalogs. In both Phases I and II, autonomous multi-agent condition estimation for UAVs and innovative sensor technology (Lidar, GPS, UWB etc.) will be used, the application of which will be demonstrated on a specific bridge project. The anomalies represent performance indicators of the components or structure and are categorized according to component-specific damage catalogs, which also determine the respective degree of damage. The classification of anomalies into damage classes is automated using neural networks or AI. In the infrastructure sector, the algorithm in Phase III enables the asset management of bridge maintainers to conduct real-time condition analyses, service life predictions and estimates of the scope of upcoming refurbishment work using real monitoring data. In building construction, the archiving the LOM in the BIM model carried out in the PM in Phase II represents immense added value for the real estate. The rescue mode (RM) is specifically designed for emergency services and, based on simplified dynamic models in Phase III, enables rapid decision-making support for emergency services on site.

**KEY WORDS:** Monitoring for bridges and buildings, digital twins, BIM, drones, drone-sensor, condition assessment, level of maintenance, condition analysis, service life prediction and refurbishment.

## **1 GENERAL GUIDELINES**

Improvements in information and communication technology like digitizing and the commitment to climate compatibility are leading to disruptive changes to our existing strategies in planning, construction and maintenance concepts as well. [1] Building Information Modeling (BIM) and condition assessment using innovative sensors combined with innovative drone technology (UAV) have led to the disruptive improvements in structural inspection and thus the maintenance of our building constructions, both in the planning and construction process. The workflow described here for largely automated structural inspections in the future integrates the above-mentioned technological improvements for a comprehensive assessment of our existing buildings, both for bridge construction and building construction. This technology transfer in structural inspection helps us, above all, to utilize our existing resources more effectively and, above all, for longer, and in this kind is a significant contribution to climate compatibility in our construction world. The asset management of the bridge maintenance company, which focuses on the implementation and evaluation of structural inspections, is therefore the coordinated activity for the maintenance and therefore important for the national economic of every state.

Structural inspections for our existing buildings must be done regularly and are regulated by regulations, e.g., for buildings, by the ON-B1300 in [2] or by the state-specific building regulations in [3]. For our infrastructure structures, the type and scope of bridge inspections are regulated by the RVS guideline in [4]. The purpose of structural inspections of buildings and infrastructure is to document the level of maintenance (= LOM) of a structure throughout the service life and represents this data an important information with enormous national accounting. If natural disasters, such as earthquakes and explosions disaster as well, occur during a service life, the structural inspection is carried out in the so-called RESCUE mode (= RM). This allows on-site emergency services to receive a rapid, high-quality assessment of the stability of the supporting structure or parts of it. In the research project according to [5], the workflow 3D BUDI for the designated rescue mode was expanded and tested. The described workflow includes a continuous, digitally based structural inspection and, in Phase I, also enables the digitization of the existing building in the form of a BIM<sub>UAV</sub> model. Digitization is also an essential prerequisite for sustainable construction, as the acquired dataset enables targeted improvements for the refurbish concept. BIM (Building Information Modeling) has already established itself as a planning tool for new buildings, enabling a



supporting, so-called "digital twin" to map all information about a building, from planning through construction to operation. What is new, however, is that the temporal degradation processes of the performance indicators that occur during a building's very long service life can be archived in the digital twin, thus ensuring that the building's condition is always available in real time and enabling meaningful condition analyses to be carried out at any time. The digital twin, in combination with the informations of the level of maintenance (LOM), therefore offers the possibility of efficiently performing service and load-bearing conditions in condition analyses using recalculations. If unexpected natural events occur during a building's service life, a digital model becomes even more essential, as the research project in [5] was able to confirm. Digital building models enable rapid and efficient structural assessments based on simplified dynamic models, as can be seen in section 4.1.

Digital models or BIM models, which contain beside geometric and material information all informations about the level of maintenance (LOM) from the structure, have the quality to provide qualified statements about reliability, the probability of failure, and ultimately the service life prediction using probabilistic methods. This makes it possible for the first time in structural inspection to conduct an assessment of structures based exclusively on an objective basis, as opposed to the previously mostly subjective assessment.

The information of level of maintenance (LOM) of our existing buildings comes with the highest design-level for BIM model and leads to enormous resource and CO<sub>2</sub> savings. The informations only of geometry and material from digital model is therefore not insignificant for further refurbishment and replanning of the existing building. The BIM-modelling started in the design-phase with informations only of geometry and material (LOI = Level of information, LOG = Level of geometry) through the approval planning (LOC = level of concept) and ends, according to the current state of the art, after the construction of a building (LOD = level of development) in the as-built documentation (see also [6]).

For the BIM model, the documentation of the building's level of maintenance (LOM) thus achieves the highest level of maturity of a BIM model as well. The present workflow now makes it possible to automatically transfer the digital information on the level of maintenance into the digital twin (BIM model).

In bridge construction, the qualified review of a structure over time is carried out by Structural Health Monitoring (SHM) and is usually confronted with enormous amounts of data when evaluating the acquired data sets. Furthermore, the usual point cloud models created using the latest sensor technology do not routinely correspond to the standard of BIM model in all four BIM levels (LOI, LOG, LOC and LOD)

This workflow is implemented using drones are supported, which include autonomous multi-agent condition estimation according to [7] and can be controlled autonomously even in GPS-shielded areas. This drone technology is intended to make a significant contribution to the digitalization of our existing buildings in the future. In a first phase, the existing structures will be converted into a 3D BIM<sub>UAV</sub> in level LOG as autonomously as possible, and in a second phase, their condition will be documented and archived to scale over time

in the highest level of maintenance (LOM). A key component of the patent-pending workflow [8] is automated damage detection using neural networks, as has already been implemented, for example, for solid bridges in [9].

Ultimately, such improved BIM models including LOM, which have such a high maturity level, also enable detailed condition analyses and service life predictions via the structural assessment in the Phase III. Furthermore the intensity of the refurbish-work can be easily and precisely described.

The individual phases and tools of the workflow are briefly described below:

## 2 PHASE I: 3D BIM<sub>UAV</sub> MODEL OF THE EXISTING STRUCTURE

A digital twin of the existing building with real geometric and physical properties is created in the form of a BIM model using autonomously controlled UAV equipment (multi-agent condition estimation with UAV) with special sensors. The BIM model created from the real dimensions and properties serves as the basis for real global structural models (global factor method according to [10]) in both modes, the PERIOD mode (PM) and the RESCUE mode (RM).

The feasibility of phase I was demonstrated on a test bridge building during the research project [10]. Seven sensors were used: UWB, Lidar, digital-camera, GPS, barometer, magnetometer and IMU.

The drones were localized using UWB, GPS and IMU sensors. Figure 1 shows the test bridge with the drone swarm (Fig. 1b) and the UAV equipment in the operational area (Fig. 1a).

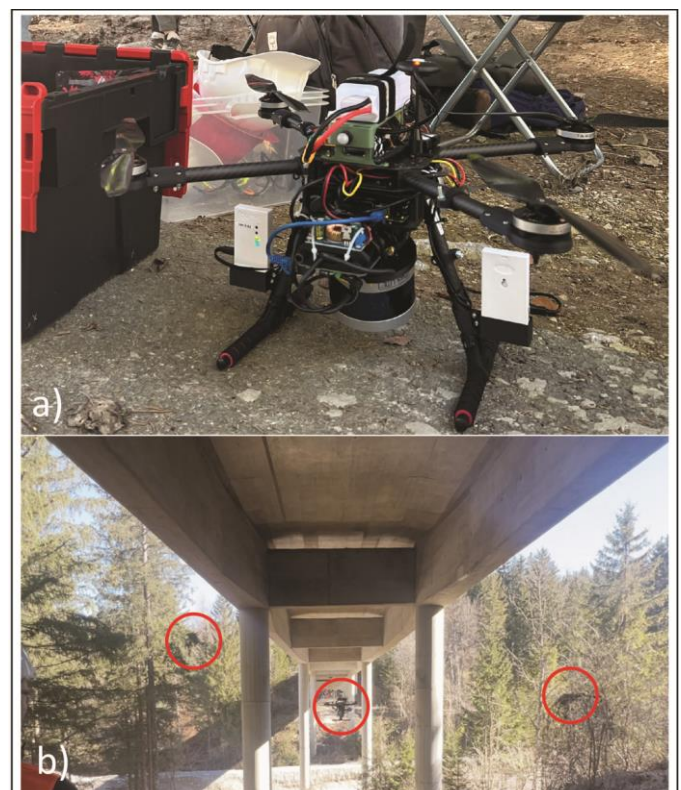


Figure 1. bridge-testing a) UAV with sensors, b) UAV swarm around the bridge in phase I

### 2.1 Phase I for bridge constructions

The workflow in [8] envisions the control of autonomous UAV swarms along the bridge axis, which create point cloud ring models using innovative sensors Lidar and cameras. Ring models have the advantage over full point cloud models that they generate significantly smaller amounts of data, which must be generated into a network model in a second step. Cross-sections are generated from the network model, with initial

tests (see Figure 1) already showing that very high levels of accuracy in cross-sectional geometry (precision  $10^{-3}$  [m]) can be achieved from the mesh-models. The cross-sections generated in the third step are then transferred to the BIM<sub>UAV</sub> model using commercial drawing software, e.g., Allplan software for bridge construction, in the fourth step. Figure 2 illustrates the four work steps.

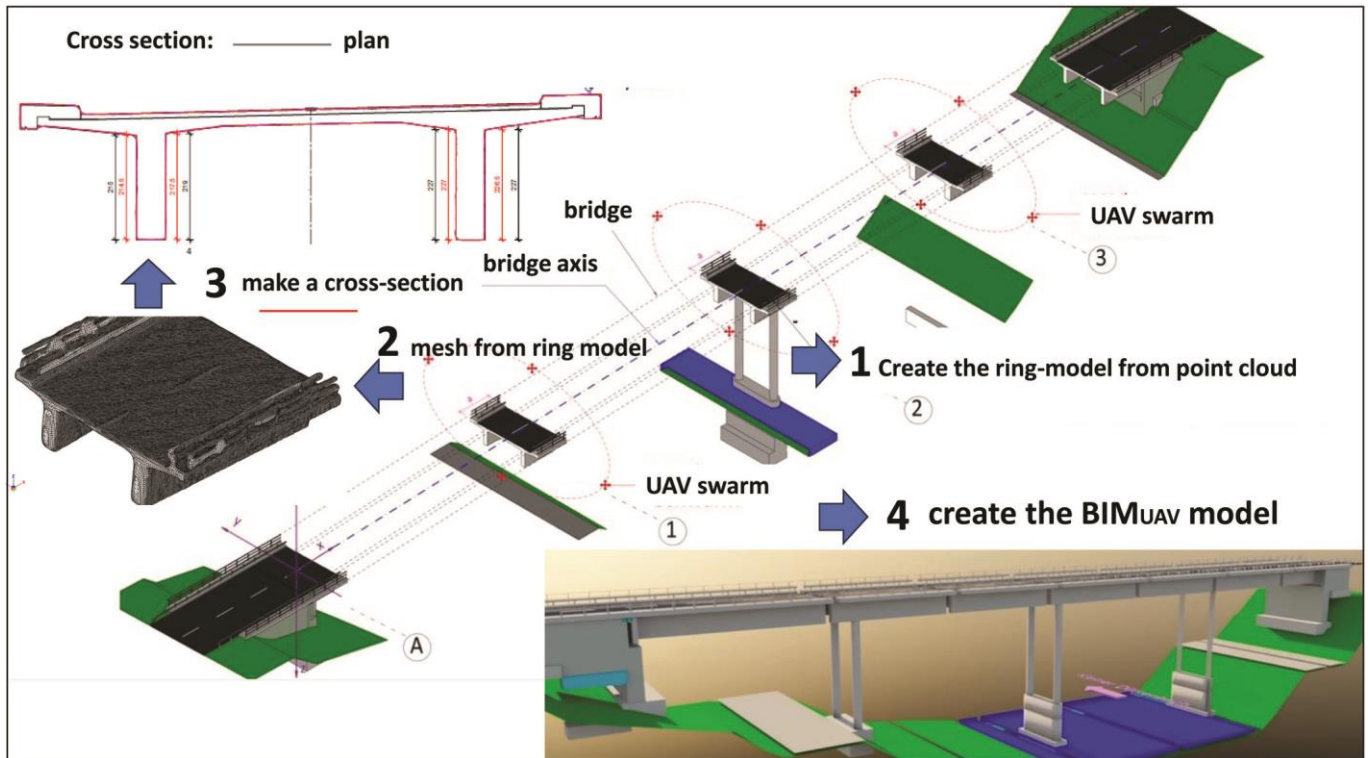


Figure 2. Four steps in phase I to create the BIM<sub>UAV</sub> model for bridges

### 2.2 Phase I for building construction

In building construction, the workflow provides for the control of autonomous drone swarms along the vertical building axis, with the UAVs inside the building communicating with the UAVs on the exterior facade. As in bridge construction, point cloud ring models are used to create the BIM<sub>UAV</sub> model. The

level-by-level linearized floor plan cross-sections (precision  $10^{-3}$  [m]) are transferred to the 3D BIM<sub>UAV</sub> model of a conventional software program such as software from Allplan or Revit using special excel sheet interpreters.

The BIM models created with the algorithm are referred to as 3D BIM<sub>UAV</sub> models.



## PHASE I: PERIOD & RESCUE MODE in building construction:

create the 3D-BIM<sub>UAV</sub> model for buildings along the structure axis

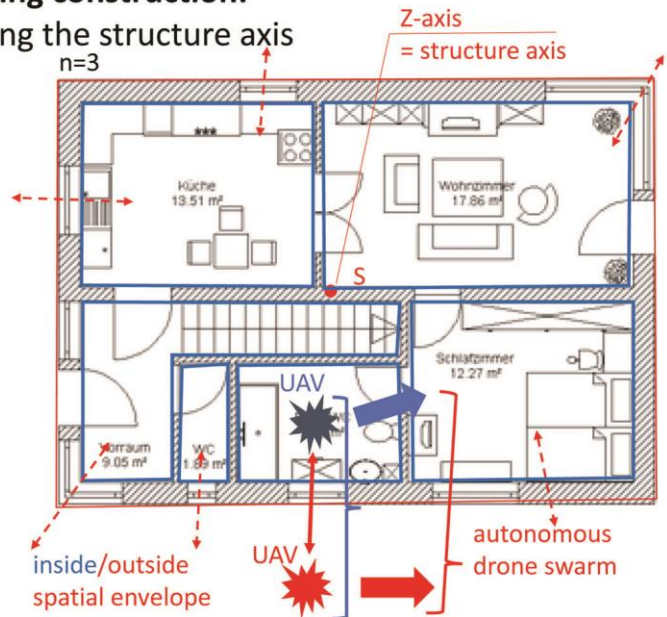
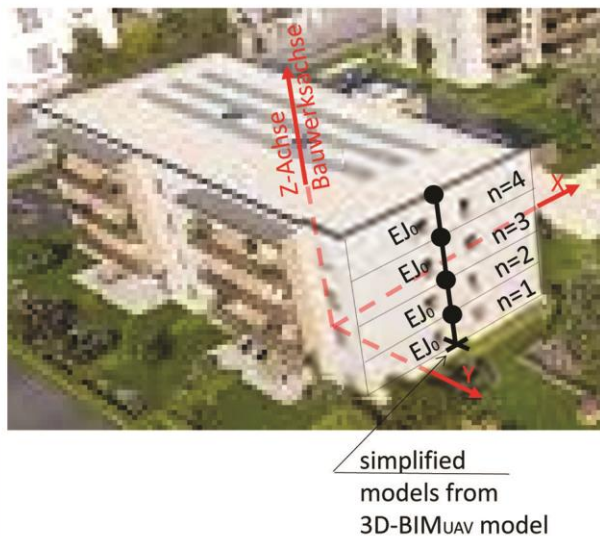


Figure 3. steps in phase I to create the BIM<sub>UAV</sub> model for building construction

### 3 DETERMINATION OF THE LEVEL OF MAINTENANCE IN PHASE II

For surveying the level of maintenance LOM the workflow using also autonomously controlled drones along a planned flight path, which can be created by the inspector in the BIM model. Damage classification like crack or spalling results the performance indicators by using AI and are summarized into a damage-catalog which based on special empirical values. The performance indicators classified by a damage-catalog are then graphically documented in the BIM model with simplified pictograms. But note that not every damage is also a performance indicator. This digitally records the level of maintenance of the construction and can be accessed at any time.

#### 3.1 performance indicators of bridge constructions

In bridge construction, the inspector designed in asset management determines the inspection plan, which performance indicators on the individual components are subject to routine monitoring and which kind of damages are to be identified during the inspection, thus process defining the flight path in phase II of the autonomously controlled UAVs. The point of interest in bridge construction represents the performance indicator (e.g., crack) on the main girder, as shown in Figure 4.

Automated damage detection using neural networks (AI), as in [9], classifies the performance indicator based on standardized damage catalogs separated by every modes – for Period mode (PM) and Rescue mode (RM) - and determines the degree of degradation of the performance indicator at the time of inspection.

Both the history and actual damages represented by performance indicator are recorded to scale on the surface of the BIM model for visual inspection.

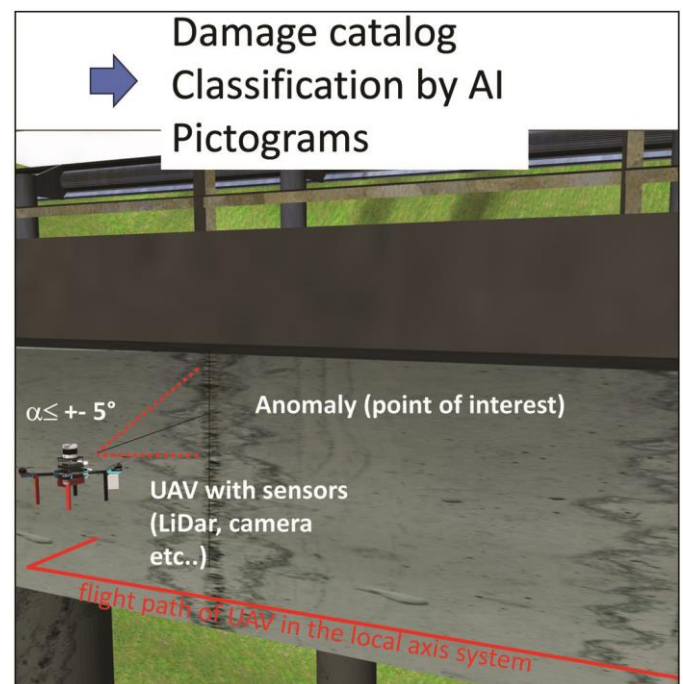


Figure 4. point of interest in phase II

#### 3.2 Classification of damage and damage-catalogs for building constructions

During periodic structural inspections (PERIOD mode) in building construction, the inspection plan is usually implemented using a swarm of drones processed instead of



individual drones. Individual drones are not sufficient to reach the point of interest inside the building. In building construction, the point of interest represents, for example, a component (e.g., wall panel, column, etc.) on each level. Images of this location are taken using innovative sensors, from which the material of the component can be determined and a damage classification can be carried out. With the help of the data set, automated damage classifications can also be carried out via neural networks and assigned to damage-catalogs. Separately defined damage-catalogs by material and component, such as those presented in [11] for the RESCUE mode (RM), enable an estimation of the stiffness reduction factors ( $EJ_{RB}$ ) according to the respective type of load (bending). In RESCUE mode, severe damage or destroyed floor sections are often present, requiring not only consideration of stiffness reduction at the component level for each floor, but also global statements at the building level. In RESCUE mode, therefore, statements about the load-bearing capacity of individual components or floor levels, as well as statements about the overall stability of the building, are necessary. A total failure of individual levels (the so-called soft-floor effect) is therefore also included in the structural assessment. One added value

provided by a complete 3D BIM model is undoubtedly the data archiving of the condition of the components or the entire building, which is done by recording the level of maintenance (LOM), certifies a highest level of maturity of the BIM model. The BIM model in PERIOD mode is enhanced with LOM to provide complete digital information on the condition of the individual components of the load-bearing structure, including their precise location, at the respective time of inspection. As already mentioned at the beginning, this enables a wide range of improvement options for the existing building with regard to renovation or refurbishment.

Figure 5 shows the damage classification sequence when a digital model of the existing structure is available in RESCUE mode.

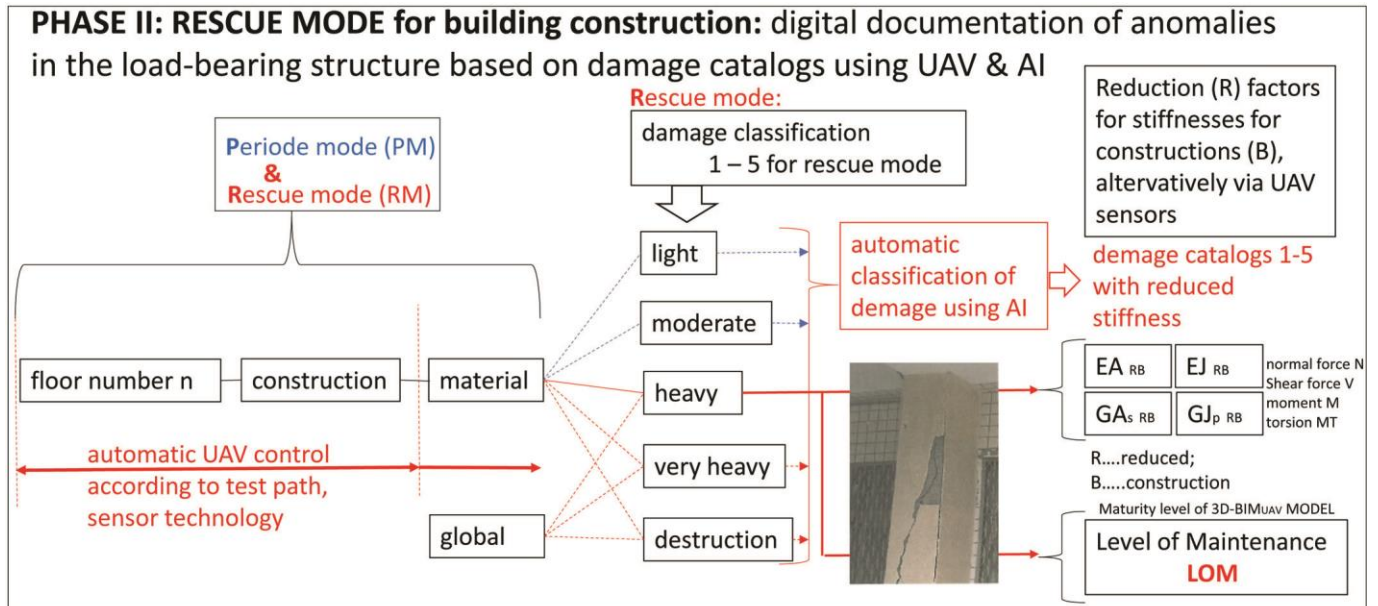


Figure 5. damage classification in phase II for the RESCUE mode (RM)

#### 4 MODEL-BASED STRUCTURAL ASSESSMENT IN PHASE III

The dataset derived from Phases I and II enables detailed condition analyses, remaining service life prediction and continuous updates of the cost of refurbishment.

Knowledge about the level of maintenance (LOM) of the key components of the existing structure over time and location, as well as their visual inspection in the BIM model, enables precise *condition analyses* regarding the causes of degradation and the future performance of the existing structure. Using the BIM model, different structural models can be generated for both modes, the period mode (PM) and rescue mode (RM), resulting in the following advantages:

Advantages of a perusal condition analysis in PM:

- Early detection of undesirable developments at the system level
- Early initiation of targeted improvements to extend the service life

Advantages of a perusal condition analysis in RM:

- Enable consolidated structural assessment for emergency services using simplified dynamic models

##### 4.1 Condition analysis in phase III

A perusal structural assessment of the effects of local structural damage on the structural condition of the structure under consideration can be performed using traditional static analyses from FE models or using modal parameters according to [12]. Modal parameters, especially in RESCUE mode, has the

advantage of providing a high-quality statement about changes to the structure due to damage. Furthermore, model updating can be enhanced with local dynamic test results, leading to highly meaningful results. In the simplified dynamic assessment, a simplified model is created from the 3D-BIM<sub>UAV</sub> model, in which the total of the story stiffnesses ( $EJ_o$ ) is reduced to a single beam. Material, structure, and construction methods are subsumed into a single member stiffness for this beam. The advantage is that, even within the same construction methods of buildings or bridge types, only marginal differences in the responses arise, thus resulting in significant simplifications compared to conventional static analyses, especially for rapid deployment in the event of a disaster in RESCUE mode.

A comparison of the change patterns of the natural frequencies and mode shapes between the reference model and the model update, which leads to reduced component stiffness due to the damage, enables a qualified statement on the failure probability  $p_f$  of the supporting structure in the event of a disaster. A corresponding demonstrator was successfully completed in [12] and is already fully operational.

Since complete data sets regarding the level of maintenance (LOM) of our existing buildings and consequently, a structural assessment of our buildings and infrastructure are currently largely lacking, it would be useful to close this knowledge gap in the future through further research on digital structural testing and structural assessment.

Figure 6 shows the process of the simplified story stiffness calculation for dynamic models in RESCUE mode.

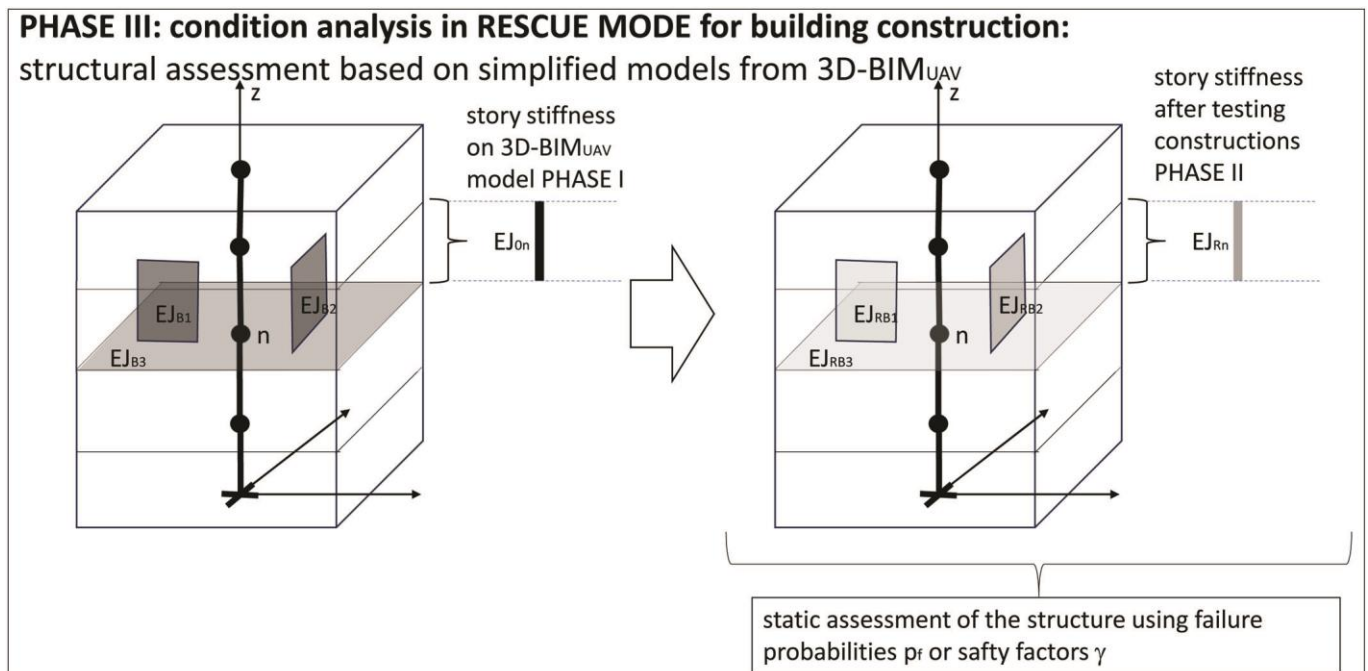


Figure 6. conditions analysis in phase III in RESCUE mode for building construction

#### 4.2 Determination of the service life prediction using probabilistic methods

The tool in 3D BUDI for determining the service life prediction of the structure uses the probabilistic assessment method based on performance indicators according to [10] to determine the reliability level  $\beta$  or the failure probability  $p_f$ . Through the time interval of regular monitoring established in the structural inspection, the performance indicators can be continuously updated with regard to the degree of degradation, and the corresponding safety index  $\beta$  value can thus always be determined and compared with the target reliability determined from the design. This results in qualitatively assessable statements about the service life prediction as well as statements about the maintenance and further intervention strategy.

### probabilistic method

$$\beta = -\theta^{-1}(p_f)$$

update of actual reliability  $\beta$  based  
on current knowledge and damage  
modeling

Figure 7. probabilistic method in phase III for service life prediction assessment

#### 4.3 Knowledge of the extent of rehabilitation in phase III

The quantitative determination of the level of maintenance from phase II across the entire structure enables the determination of the overall scope of a planned refurbishment at the time of inspection, both in building construction and bridge construction. These data sets enable the building owner to continuously update the costs of refurbishment for the respective structure that may be derived from the state of preservation. This provides the client with a qualitatively assessable basis for decision-making for upcoming initiatives on the building.

Figure 8 schematically illustrates the potential of a bridge with a continuously updated state of preservation in terms of type and extent for future initiatives by the maintainer.

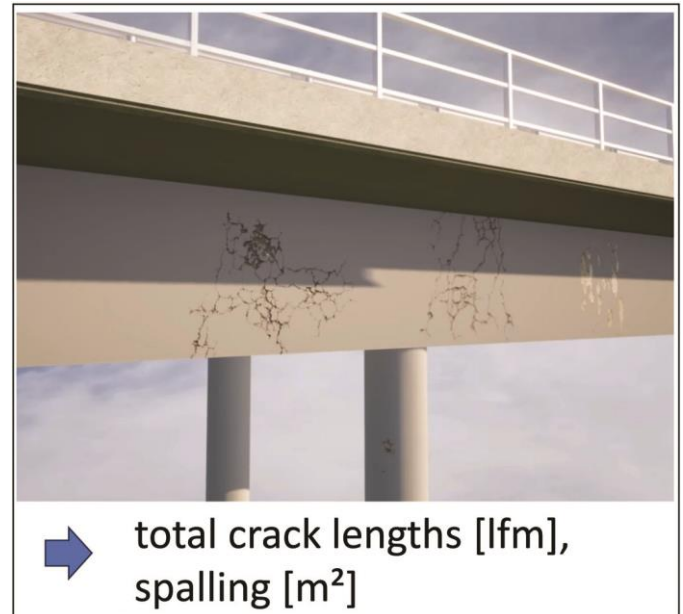


Figure 8. Automated determination of the rehabilitation scope from the LOM in phase III

In summary, it can be said that the present workflow 3D BUDI will enable clients to evaluate their existing buildings according to objective criteria and derive targeted arrangements from this. If we can preserve buildings longer through these measures, this will reduce our CO<sub>2</sub> emissions, which arise from the nationally and globally construction industry, and thus make a significant contribution to climate neutrality and thus to our society.

#### REFERENCES

- [1] Bergmeister, K.; Strauss, A.; Hoffmann, M. (2022): Digitale Zustandserfassung von Gebäuden, Infrastrukturbauwerken und Naturgefahren. Teil II Seite 535 -604. Beton Kalender: Nachhaltigkeit, Digitalisierung, Instandhaltung. Herausgegeben von Konrad Bergmeister, Frank Fingerloos und Jahn-Dietrich Wörner, Ernst & Sohn GmbH & Co KG.
- [2] Önorm B 1300 – Objektsicherheitsprüfung für Wohngebäude – Regelmäßige Prüfungen im Rahmen von Sichtkontrollen und zerstörungsfreien Begutachtungen.
- [3] Wiener Bauordnung § 129 Abs.5
- [4] RVS 13.03.11 Qualitätssicherung bauliche Erhaltung – Überwachung, Kontrolle und Prüfung von Kunstbauten
- [5] FFG Projekt Nr.:879684, Programm: KIRAS: UAV Rescue – UAV getragene Sensorik zur Unterstützung von Rettungsmissionen. Projektlaufzeit 01.01.2021 – 31.07.2023, 24 Monate.
- [6] Olipitz, M. (2023): Der optimierte Einsatz von Stahl in Bestandsstrukturen - am Beispiel der Videowall Stadion Salzburg. Zeitschrift: Stahlbau 92, Heft 5, Seite 287-297, Ernst & Sohn GmbH, Berlin. DOI:10.1002/stab.202300017
- [7] FFG Projekt Nr.:891124, Programm: Bridge: Robuste Multi-Agenten-Zustandsschätzung für Infrastruktur-Inspektionen in GPS-gestörten Gebieten. Projektlaufzeit 01.04.2022 – 30.04.2025, 36 Monate.
- [8] Einreichung zum Patent FFG Projekt Antragsnummer: 48527171.: 3D BUDI – 3D BIM UAV Defect Indicator. Einreichung am 21.12.2022
- [9] Flotzinger, J.; Braml, T. (2022): Automatisierte Klassifizierung von Schäden an Massivbrücken mittels Neuronaler Netze. Zeitschrift: Beton- und Stahlbetonbau 117, Heft 10, Seite 784-796, Ernst & Sohn GmbH, Berlin. DOI:10.1002/best.202200068
- [10] Strauss, A.; Bergmeister, K.; Seywald, C. (2023): Verlängerung der technischen Nutzungsdauer von Infrastrukturbauwerken auf Basis semiprobabilistischer Betrachtungen. Zeitschrift Beton- und Stahlbetonbau 118, Heft 8, Seite 575- 588, Ernst & Sohn GmbH, Berlin. DOI:10.1002/best.202300044.





- [11] Kohns, J.; Steniewicz, L.; Stark, A. (2022): Entwicklung von Schadenskatalogen für die visuelle Beurteilung von Gebäuden im Erdbebenfall. Zeitschrift: Bauingenieur BD 97 Nr.12. Seite 403-412. DOI: 10.37544/000 5-6650-2022-12-39
- [12] Kramer, T; Flesch, R (2020): Auswirkung lokaler Bauwerksschäden auf die modalen Parameter – Entwicklung eines Demonstrators. 2. Wiener Dynamik Tage 2020.

# Principles and Case Study of IMSGeo: Automatic Displacement Monitoring System for Construction Sites

Janina ZACZEK-PEPLINSKA<sup>1</sup>, 0000-0003-4875-4250, Maria Elżbieta KOWALSKA<sup>2</sup>, 0000-0002-4434-7829,  
Lech SALONI<sup>3</sup>, 0009-0009-0099-0159

<sup>1,2</sup> Faculty of Geodesy and Cartography, Warsaw University of Technology, Pl. Politechniki 1, 00-661 Warsaw, Poland,

<sup>3</sup> GEOalpin sp. z o.o., ul. Kolektorska 12, 01-692 Warsaw, Poland,

email: janina.peplinska@pw.edu.pl, maria.kowalska@pw.edu.pl, lech.saloni@geoalpin.pl

**ABSTRACT:** Displacement monitoring is a crucial aspect of the construction process, spanning all its stages. Surveying the changes occurring in the structure and its surroundings according to a suitable schedule is fundamental to ensuring work safety and mitigating investment risks. In this article, we highlight the distinctive features of the IMSGeo system, developed jointly by GEOalpin Ltd. and the Warsaw University of Technology (Department of Engineering Geodesy and Measuring Systems). The innovative solutions proposed in the system are characterized by the following integrated features: utilization of advanced adjustment algorithms within a cohesive system, adjustment of a multi-station network, analysis of reference system stability as an integral component of each measurement epoch, reflectless measurement of surfaces and structural elements of objects, presented as a unified 2D or 3D entity, capability to position measuring instruments (motorized/robotic total station) without the need for additional monitoring devices to ensure station stability, implementation of a fully mobile WEB platform for the presentation, interpretation, comprehensive analysis, and archiving of geodata, use of Internet cloud computing for data collection, analysis, presentation, and distribution of monitoring results, ensuring independence from local server infrastructure, user platform functionality designed based on survey research conducted among investors, contractors, inspectors, building supervision representatives, and property managers. The IMSGeo system does not require additional capital investments in infrastructure from investors or contractors and is highly available and scalable. The practical section of the article introduces the IMSGeo system's WEB platform and its implementation on a selected site in Warsaw, Poland.

**KEY WORDS:** structural health monitoring, geodetic displacement monitoring, geodetic services for investments, construction site safety, engineering geodesy.

## 1. INTRODUCTION

Systems for monitoring the condition of engineering structures have been developed for many years by both manufacturers and suppliers of geoinformation technologies [8],[13],[14], as well as scientific institutions [2],[3],[4]. There are many dedicated solutions known, the creation of which was inspired by specific needs. For example, the article of Wilde et al. [17] describes the assumptions of such a system in the context of monitoring the roof of the Forest Opera in Sopot. Other, similar solutions have been described in numerous publications [8], [16], [18], [19]. Historically, the period of the beginning and the middle of the 2000s in Poland was characterized by significant activity of geoinformation technology suppliers, especially in the context of implementing key projects of the dynamically developing national economy. Examples of the first and at the same time extremely successful implementations of integrated geomonitoring systems include implementations in the KGHM Polska Miedź SA company, the Bełchatów Brown Coal Mine [5], or during the construction (and the ongoing expansion) of the second line of the Warsaw Metro [7]. In highly industrialized countries of the world, the development of geodetic monitoring systems has been observed for several

decades. There are many examples of implementations and technological problems solved on these occasions. Many of them resulted in numerous publications of an interdisciplinary nature. It is worth mentioning here [1],[11], although the list of possible items to cite would certainly include thousands of scientific articles, technical reports, or chapters of monographic studies. There are also many textbooks published in many languages – mainly in English or German [10],[12]. Many similar studies can also be found on the domestic publishing market, for example [15]. Geomonitoring systems are also a dynamic, developing industry in the field of civil engineering. As a rule, however, these are closed systems, focused on the use of specific instruments and programs. In this area, there are practically no solutions with an open structure (so-called "open source"), and the possibilities offered by manufacturers - i.e. modules, functions, and procedures are usually ready-made geoinformatic products. These factors create a demand for flexible, mobile and fully scalable systems that can be adapted to real needs to the best extent possible. Observing current trends in the field of IT, one can notice the dominant role of mobile solutions (from "mobile technologies") developed to a large extent at the expense of sometimes ineffective desktop (stationary) solutions. The current, briefly presented state of

knowledge inspired the authors to conduct conceptual work aimed at:

- classifying available solutions in the field of geodetic monitoring and highlighting their characteristic features,
- indicating development opportunities in the context of designing new, universal solutions based on the existing state of knowledge and technology,
- proposing an innovative, unique solution that takes into account the contemporary needs of the construction industry and contemporary contractors of geodetic, geotechnical and construction-building works.

The presented topics are the subject of research by the Department of Engineering Geodesy and Measurement Systems, Faculty of Geodesy and Cartography of the Warsaw University of Technology, implementing a grant from the National Center for Research and Development in a consortium with the company GEOalpin Sp. z o.o. As part of this project, an intelligent deformation monitoring system with the acronym "IMSGeo" is being developed, the methodological assumptions and results of the work to date of which are presented later in the article.

## 2. SYSTEM ASSUMPTIONS

Robotic Total Station (RTS) is one of the spatial geomonitoring technology. It is based on using a total station (automated tachymeter) as a sensor collecting measurement points.

Could we treat the technology such as other geotechnical sensors as piezometers, inclinometers, pressure cells, etc? The main differences are:

- RTS is based on the "ancient" surveying trigonometric method,
- RTS use only a few active sensors (in many cases only one) Total station and a number of passive sensors prisms. Passive sensors don't work without an active sensor,
- RTS measurements are not collected strictly at the same time – usually we need a few minutes to collect back signal from all passive sensors – prism.

Over the last years we could observe the tendency to replace RTS with structural monitoring due to their higher accuracy.

RTS technology still has many advantages – for example: The installation of passive sensors (prisms) is quite easy. Usually the installation covers quite a big territory and is quite cheap – It does not need cabling or a wireless connection.

Some of them have not still implemented. RTS thanks to collected data in a spatial wide XYX reference system it gives the option of correlating data from others monitoring technologies together. Based on the adjustment with least squares methods we good extend the RTS needs keeping the highest accuracy for this technology.

Intelligent Monitoring System IMSGeo has come back to bases of adjustment theory and implemented it to automated monitoring and has opened this method for the challenge of integrating monitoring data in one high accuracy net reference.

Technological details, as well as differences in the functioning of geomonitoring systems offered on the market, concern both the type of recommended measurement instruments, the method of acquiring, processing and analyzing the acquired data, as well as the possibility of using the program for a given type of design tasks. Among all the

common features of the discussed solutions, the following criteria deserve special attention:

- the possibility of remote work with the system ("in the cloud") using mobile interfaces,
- the possibility of integrating automatic measurements of displacements performed with physical sensors (physical monitoring, also known as SHM - from "Structural Health Monitoring"),
- the possibility of handling automatic measurements with geodetic instruments (robot tachymeters, GNSS satellite receivers,
- the possibility of handling instruments from different manufacturers,
- the possibility of using reflectorless measurement technology (in the case of electronic tachymeters),
- the possibility of strict alignment of observations (using the least squares method).

## 3. METODOLOGY

For the purposes of the IMSGeo project, a dedicated research methodology was developed, which includes the following task blocks:

- development of procedures for automating the process of determining displacements along with the assessment of their significance based on geodetic measurements,
- functional assessment of the implementation of reflectorless monitoring measurements, within which both the implementation and conceptual aspects (selection of optimal grids of points of monitored structural elements) as well as computational aspects (surface approximation methods and point cloud alignment) are tested, as well as interpolation and visualization of the acquired data using various geostatistical algorithms,
- development of an optimal algorithm for aligning observations that allows for taking into account the non-permanent measuring station in the process of determining the displacements of controlled points, within which multi-variant simulations of the alignments of monitored control networks were performed, taking into account the stability or lack of stability of measuring stations,
- development of a "platform" for data exchange with access for the client using cloud computing, within which will be implemented newly developed procedures and algorithms using IT tools and a programming environment.

Test work on the operational efficiency of the system was carried out on a special test field in Łódź (the location of the consortium members' office – Warsaw University of Technology and Geoalpin Sp. z o.o.), while the functional assessment in indoor conditions (with the maximum reduction of the impact of systematic errors occurring outdoors) was carried out in the Main Hall of the Warsaw University of Technology (Figure 1).





Figure 1.

View of the test stand and the research team in the Main Hall of the Warsaw University of Technology (photo by Oskar Graszka).

According to the assumptions, the presentation of measurement results is realized in the form of a dedicated geoinformation platform (<https://imsgeo.geoalpin.pl/login>) (Figure 2), in a structured form (collected information is divided depending on measurement techniques and their location). The new, unique solution, unlike similar systems, does not require constant measurement control by a specialist and intelligently identifies both the displacement of reference points and the measurement station. In addition, the so-called "noises" caused by mechanical or meteorological disturbances are defined.

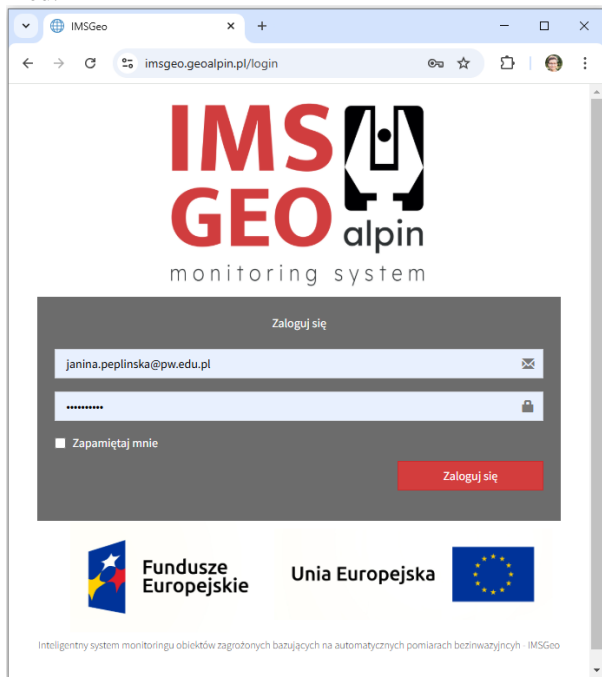


Figure 2. Website of the IMSGeo system.

Before starting to develop a functional analysis of the system and the database, a survey was conducted among experts representing various professional groups interested in implementing the monitoring system: architects, constructors, geotechnics, designers of bridges, roads and railways, hydrotechnics and others (Figure 3).

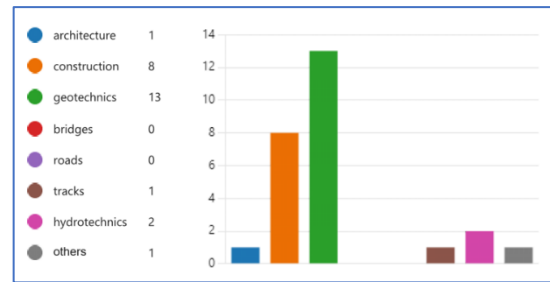


Figure 3.

Number of experts participating in the opinion survey on the desired functionality of the IMSGeo system.

Figures 4, 5, 6 present the survey results – answers given to selected closed-ended detailed questions. As can be seen, the greatest interest is in access to data via the Internet platform, and monitoring data are most often used to control the displacement of individual points of the facility, located in critical structural locations, and the data are needed for broadly understood analyses, in particular for the analysis of the risk of construction failure/disaster during the implementation of the investment and in the early phase of operation.

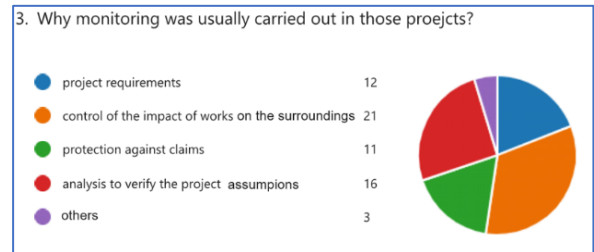


Figure 4. Summary of answers to the question 3: Why monitoring was usually carried out in those projects?

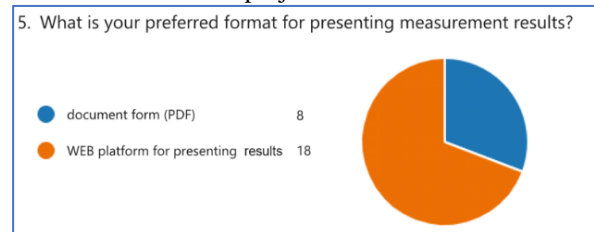


Figure 5. Summary of answers to the question 5: What is your preferred format for presenting measurement results?

Based on the collected opinions and their own experience, the team of authors created the IMSGeo platform, the main functionalities of which consist of the following modules: Map, Graphs, Results, Files and External Data (Figures 7, 8 and 9).

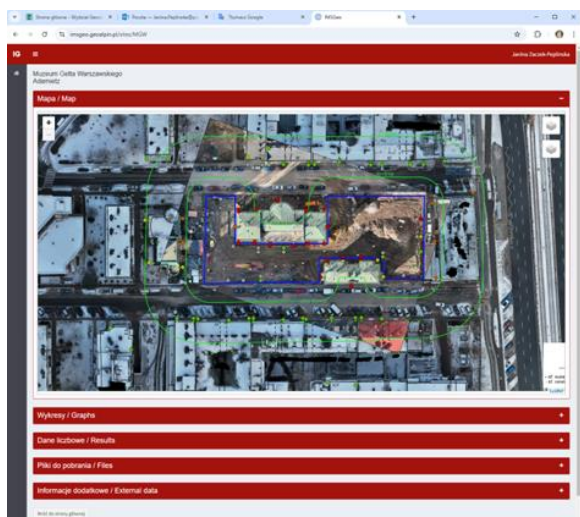


Figure 7. Main page of the IMSGeo system.

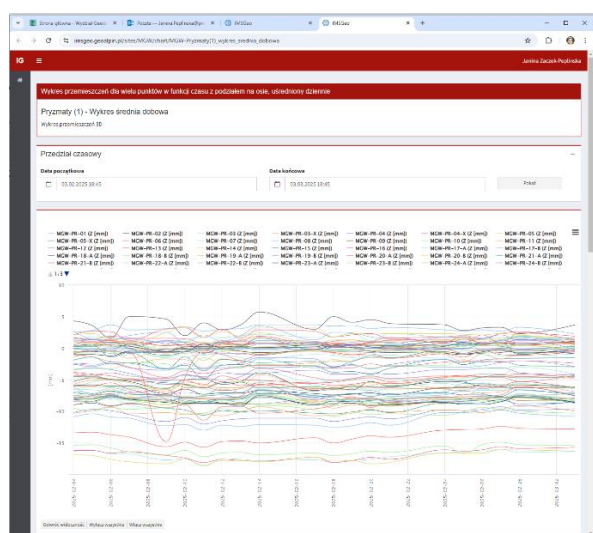


Figure 8. IMSGeo Graphs module: presentation of sample results.

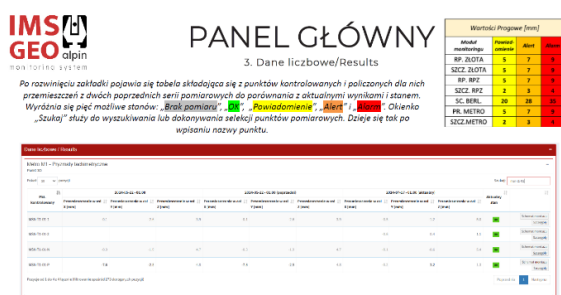


Figure 9. Results module of the IMSGeo system: presentation of the assessment of point displacements: color green means “OK”, color yellow means “Notifications”, color orange means “Alert”, color red means “Alarm”.

The IMSGeo geodetic monitoring system has already been implemented on construction sites in the center of Warsaw, and currently a team of surveyors and programmers is working on including inclinometric sensors (probes, horizontal and vertical chains, tilt meters) and hydrostatic

leveling techniques in the automatic system. New functionalities are being implemented in the "InteliGeo" project financed by the Polish Agency for Enterprise Development (PARP).

#### 4. CONCLUSIONS

Modern geodetic monitoring systems include both instrumental, teleinformatic and database solutions. Designing such solutions is a complex process that takes into account many elements from the borderline of various fields of knowledge. Therefore, before starting the study work, it is necessary to conduct an in-depth analysis of the current state of technology and define the areas that need to be developed. The authors of the article performed a functional assessment of most of the available commercial and dedicated solutions, characterized by different architectures or philosophies of operation. In relation to the conducted study work, a unique system concept was developed, which is currently being implemented in the form of a project financed by the Polish National Center for Research and Development. In detail, the project concerns the development of technology that allows for automatic performance of fast measurements without the participation of a surveyor, along with intelligent interpretation of results. This will allow for continuous examination of the condition of the object and ongoing assessment of the impact of various factors - e.g. construction works on neighboring buildings. Defined alarm situations (exceeding the permissible displacement ranges) will be automatically assessed, verified and reported. In terms of technical solutions, this approach constitutes a significant innovation in the field of building automatic monitoring systems for engineering objects.

#### ACKNOWLEDGEMENTS

The presented research is carried out within the framework of the NCBiR project entitled "Intelligent monitoring system for endangered objects based on automatic non-invasive measurements – IMSGeo" (a detailed description can be found on the dedicated websites at

<https://www.gik.pw.edu.pl/zgiisp/Badania-i-nauka/Projekt-POIR.01.01.01-00-0942-21-IMSGeo>

<https://geoalpin.pl/inteligentny-system-monitoringu-obiektow-zagrozonych-bazujacy-na-automatycznych-pomiarach-bezinywazyjnych-imsgeo>).

#### REFERENCES

- [1] M. Abdulkarem, K. Samsudin and F.Z. Rokhani, Wireless sensor network for structural health monitoring: A contemporary review of technologies, challenges, and future direction. Structural Health Monitoring, 2019, <https://doi.org/10.1177/1475921719854528>.
- [2] Automated System of Geodetic Monitoring, Lviv Polytechnic National University, Ukraine, <https://lpnu.ua/en/scientific-developments-directory/automated-system-geodetic-monitoring> [access: 17.02.2025].
- [3] GOCA - GNSS/LPS/LS-based online Control and Alarm System, Hochschule Karlsruhe – Technik und Wirtschaft, [http://goca.info/index\\_e.html](http://goca.info/index_e.html) [access: 15.02.2025].
- [4] R. Jäger and P. Spohn, GOCA - GNSS/LPS/LS Based Online Control and Alarm System Version 5.0, Hochschule Karlsruhe - Technik und Wirtschaft, Institute of Applied Research, Karlsruhe, 2017.

- [5] K. Karsznia, Z. Skalski and L. Czarnecki, System ciągłego monitoringu deformacji odkrywkowych wyrobisk górniczych a bezpieczeństwo prowadzenia robót górniczych, (en.: Continuous monitoring system of opencast mine deformations and the safety of mining operations) *Przegląd Górniczy* 10/2010, Nr 10 (1055), Tom 66(CVI), str. 167-17, 2010.
- [6] K. Karsznia and A. Tarnowska, Proposition of an integrated geodetic monitoring system in the areas at risk of landslides. *Challenges of Modern Technology, Town and Urban Planning, Architecture and Building Engineering*, str. 33-40, 2014.
- [7] J. Królikowski, Wyzwań od metra - Jak technologie geodezyjne pozwalają bezpiecznie dążyć II linię warszawskiego metra, strona internetowa (en.: Challenges from the metro - How geodetic technologies allow safe excavation of the second line of the Warsaw metro, website). *Archiwum Miesięcznika Geoinformacyjnego Geodeta*, <https://geoforum.pl/wydanie/1225/artykul/943/rozmawial-jerzy-krolkowski-wyzwan-od-metra-jak-technologie-geodezyjne-pozwalaja-bezpiecznie> [access: 18.04.2023].
- [8] Leica GeoMoS, Are you interested in movements? - technical brochure, Heerbrugg, Szwajcaria, 2015.
- [9] Leica Geosystems AG, Monitoring solutions – Assurance done right, technical brochure, Heerbrugg, Szwajcaria, 2018
- [10] M. Möser, G. Müller, H. Schlemmer, O. Heunecke, H. Kuhlmann, W. Welsch, A. Eichhorn and H. Neuner, *Auswertung geodätischer Überwachungsmessungen*. Wichmann-Verlag, ISBN 978-3-87907-467-9, 2013.
- [11] W. Odziemczyk, Analysis of deformations of the skylight construction at the main hall of The Warsaw University of Technology, *Reports on Geodesy and Geoinformatics*, vol. 97/2014; pp. 35-46, 2014, DOI:10.2478/rgg-2014-0010.
- [12] F. Sanso and A.J. Gil, *Geodetic Deformation Monitoring*. Springer-Verlag GmbH, ISBN: 3540385959
- [13] Soletanche Freyssinet, 2006, <https://www.soletanche-freyssinet.com/our-brands/sixense> [access: 13.02.2025].
- [14] Trimble Monitoring, <https://monitoring.trimble.com/products-and-solutions/trimble-4d-control> [access: 13.02.2025].
- [15] Wolski, B. (2008). *Monitoring metrologiczny obiektów geotechnicznych* (en.: Metrological monitoring of geotechnical objects). Wydaw. Politechniki Krakowskiej im. Tadeusza Kościuszki, Kraków.
- [16] M. Woźniak and W. Odziemczyk, Investigation of stability of precise geodetic instruments used in deformation monitoring. *Reports on Geodesy and Geoinformatics* vol. 104, pp. 79-90, 2017, doi: 10.1515/rgg-2017-0017.
- [17] K. Wilde, J. Chróścielewski, M. Miśkiewicz and M. Rucka, Diagnostics and monitoring of new textile roof of the Forest Opera in Sopot, *Proceedings of the XXVI Scientific Conference „Awarie budowlane”*, pp. 291-298, 2013.
- [18] T.H. Yi and H.N. Li, Methodology developments in sensor placement for health monitoring of civil infrastructures. *Int. J. Distrib. Sens. Netw.*, 8(8), pp. 612–726, 2012.
- [19] J. Zaczek-Peplinska, M. Pasik and P. Popielski, Geodetic monitoring of objects in the area of impact construction of tunnels and deep excavations – experiences and conclusions. *Acta Scientiarum Polonorum – Architectura*, 12 (2), pp. 17–31, 2013.